APPLIED NUCLEAR PHYSICS AT ACCELERATORS

EDITED BY: Marco Durante, Vincenzo Patera and Yolanda Prezado
PUBLISHED IN: Frontiers in Physics

frontiers Research Topics

ISSN 1664-8714
ISBN 978-2-88971-039-3
DOI 10.3389/978-2-88971-039-3

About Frontiers

Frontiers is more than just an open-access publisher of scholarly articles: it is a pioneering approach to the world of academia, radically improving the way scholarly research is managed. The grand vision of Frontiers is a world where all people have an equal opportunity to seek, share and generate knowledge. Frontiers provides immediate and permanent online open access to all its publications, but this alone is not enough to realize our grand goals.

Frontiers Journal Series

The Frontiers Journal Series is a multi-tier and interdisciplinary set of open-access, online journals, promising a paradigm shift from the current review, selection and dissemination processes in academic publishing. All Frontiers journals are driven by researchers for researchers; therefore, they constitute a service to the scholarly community. At the same time, the Frontiers Journal Series operates on a revolutionary invention, the tiered publishing system, initially addressing specific communities of scholars, and gradually climbing up to broader public understanding, thus serving the interests of the lay society, too.

Dedication to Quality

Each Frontiers article is a landmark of the highest quality, thanks to genuinely collaborative interactions between authors and review editors, who include some of the world's best academicians. Research must be certified by peers before entering a stream of knowledge that may eventually reach the public - and shape society; therefore, Frontiers only applies the most rigorous and unbiased reviews.
Frontiers revolutionizes research publishing by freely delivering the most outstanding research, evaluated with no bias from both the academic and social point of view. By applying the most advanced information technologies, Frontiers is catapulting scholarly publishing into a new generation.

What are Frontiers Research Topics?

Frontiers Research Topics are very popular trademarks of the Frontiers Journals Series: they are collections of at least ten articles, all centered on a particular subject. With their unique mix of varied contributions from Original Research to Review Articles, Frontiers Research Topics unify the most influential researchers, the latest key findings and historical advances in a hot research area! Find out more on how to host your own Frontiers Research Topic or contribute to one as an author by contacting the Frontiers Editorial Office: frontiersin.org/about/contact

APPLIED NUCLEAR PHYSICS AT ACCELERATORS

Topic Editors:
Marco Durante, GSI Helmholtz Center for Heavy Ion Research, Germany
Vincenzo Patera, Sapienza University of Rome, Italy
Yolanda Prezado, INSERM U1021 Signalisation normale et pathologique de l'embryon aux thérapies innovantes des cancers, France

Citation: Durante, M., Patera, V., Prezado, Y., eds. (2021). Applied Nuclear Physics at Accelerators. Lausanne: Frontiers Media SA. doi: 10.3389/978-2-88971-039-3

Table of Contents

frontiers in Physics

EDITORIAL
published: 19 May 2021
doi: 10.3389/fphy.2021.669271

Editorial: Applied Nuclear Physics at Accelerators

Vincenzo Patera[1], *Yolanda Prezado*[2] *and Marco Durante*[3,4]*

[1] Dipartimento di Scienze di Base e Applicate per l'Ingegneria, University "La Sapienza", Rome, Italy, [2] Institut Curie, Université PSL, CNRS UMR3347, Inserm U1021, Signalisation Radiobiologie et Cancer, Orsay, France, [3] Biophysics Department, GSI Helmholtzzentrum für Schwerionenforschung, Darmstadt, Germany, [4] Institute for Condensed Matter Physics, Technische Universität Darmstadt, Darmstadt, Germany

Keywords: biomedical research and development (R&D), high-energy ions, particle therapy, accelerators, space radiation protection

Editorial on the Research Topic

Applied Nuclear Physics at Accelerators

Nuclear physics has seen continuous application in many fields of science [1]. The fields span from energy to the environment, geophysics, materials research, astrophysics, and, of course, biology and medicine. Nuclear Physics plays a prominent role both in the diagnostics and therapy of different diseases [2].

Particle accelerators are fundamental tools in nuclear physics, and many applications are based on their technology. There are of course many kinds of accelerators that span a very wide range of energy and accelerate different types of particles. The number of particle accelerators in the world has increased rapidly in the past years, reaching a total number of about 40,000 excluding X-ray tubes and electron microscopes [3] (**Figure 1**). In spite of that, as shown in **Figure 1**, the number of large, high-energy accelerators in science has remained approximately constant in the twenty-first century. A possible motivation for this trend is the cost of such accelerators, which requires large national investments. It is not surprising that these large and expensive machines include intense applied physics programs [4] in order to provide direct benefits to society.

The largest nuclear physics accelerator under construction is the Facility for Antiprotons and Ion Research (FAIR) built by the GSI Helmholtz Center in Darmstadt (Germany) [5]. However, many other accelerators are under construction or in operation in Europe, Asia, South Africa, and America. Those new facilities are also either planning or upgrading the applied physics programs, mainly focused on biology and medicine.

The aim of the effective coordination of these efforts has led to the creation of the International Biophysics Collaboration, which goes beyond FAIR to involve many other accelerator facilities described in this special issue (Patera et al.). The biomedical applications depend on the intensity and energy available at accelerators. While many applications are possible with current machines, even more can become available at higher energies and intensities, such as those now achieved in the new machines.

The special issue had over 60 submissions, and with 56 accepted manuscripts it is one of the biggest in the *Frontiers in Physics* journal. This clearly shows the interest and relevance of the topic. Over half of the manuscripts are related to topics that can be already studied by means of the present accelerators, such as dosimetry (Bourgouin et al.; Kokurewicz et al.), imaging (Fiorina et al.; Magalhaes Martins et al.), radioisotope production (Niculae et al.), radiobiology (Fisher et al.; Schielke et al.), measurements of nuclear interaction cross-sections (Battistoni et al.; Norbury et al.), beam delivery (Bottura et al.; Dauvergne et al.), treatment planning (Gajewski Schiavi, et al.; Gajewski Garbacz, et al.), and modeling (Bellinzona et al.; Muraro et al.).

Edited and reviewed by:
Thomas Beyer,
Medical University of Vienna, Austria

***Correspondence:**
Marco Durante
M.Durante@gsi.de

Specialty section:
This article was submitted to Medical Physics and Imaging, a section of the journal Frontiers in Physics

Received: *18 February 2021*
Accepted: *12 March 2021*
Published: *19 May 2021*

Citation:
Patera V, Prezado Y and Durante M (2021) Editorial: Applied Nuclear Physics at Accelerators. Front. Phys. 9:669271. doi: 10.3389/fphy.2021.669271

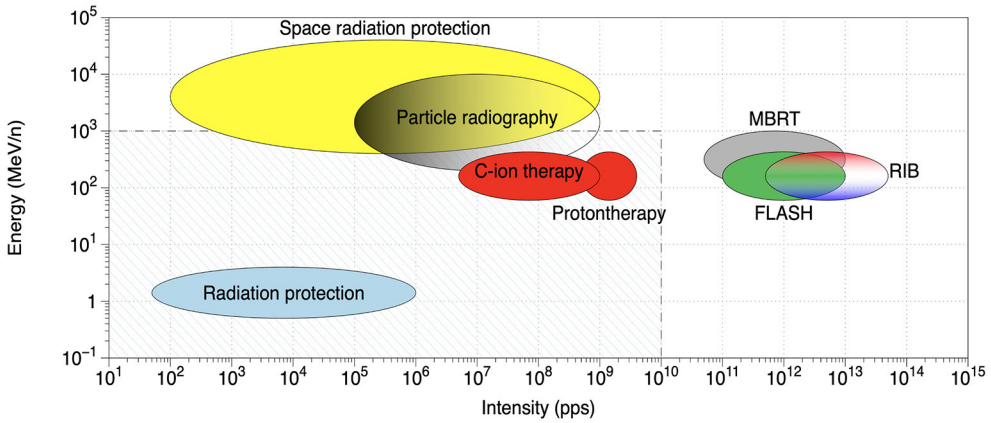

FIGURE 1 | Evolution of the number of accelerators worldwide in the past 50 years. The plot is based on data reported in [3] and is reproduced from [4] under Creative Commons license (CC BY-NC 3.0).

These papers give an overview of the activities ongoing at a particle accelerator in cancer therapy, basic radiation damage studies, and radiation protection. The remaining manuscripts deal with new topics that can be studied at new accelerators. A total of 10 papers focus on experiments that benefit from the higher intensity or from innovative delivery modalities of new accelerators, such as minibeam irradiation (Dal Bello et al.; Guardiola and Prezado), radioactive ion beams in therapy (Durante and Parodi), and ultra-high dose rate (FLASH) radiotherapy (Di Martino et al.; Vignati et al.). A sizeable part of the issue covers Research Topics that will benefit from the higher energy that can be achieved in new accelerators for space radiation research (Höeffgen et al.; Schuy et al.) or particle radiography (Alme et al.). This special issue has the goal to report the present landscape and the outlook of accelerator facilities, within and outside Europe, where the research into nuclear physics and biophysics applied to medicine and space is likely to have an important development in the next 10 years. With this in mind, seven papers now describe new facilities under construction (Amaldi et al.; Aymar et al.; Cirrone et al.; Patera et al.) and new concepts and ideas for accelerator experiments (Kim et al.). Last, but not least, this issue embeds also a paper related to the use of ionizing radiation in the quest for the COVID-19 vaccine (Durante et al.).

The variety of the topics in the issue and the great success of the initiative are very promising for the future application of accelerators to biology, medicine, and other sciences. The benefits of accelerators in society are already solid and evident, and they are likely to expand further in the near future.

AUTHOR CONTRIBUTIONS

All authors listed have made a substantial, direct and intellectual contribution to the work, and approved it for publication.

FUNDING

Part of the funding for the issue came from the ERC grant 883425 BARB.

ACKNOWLEDGMENTS

The editors take the chance to thank all the referees for their excellent work in finalizing this long issue.

REFERENCES

1. Hayes AC. Applications of nuclear physics. *Reports Prog Phys.* (2017) 80:026301. doi: 10.1088/1361-6633/80/2/026301
2. NuPECC. *Nuclear Physics for Medicine*. Strasbourg: European Science Foundation (2014). Available online at: www.nupecc.org
3. Chernyaev AP, Varzar SM. Particle accelerators in modern world. *Phys At Nucl.* (2014) 77:1203–15. doi: 10.1134/S1063778814100032
4. Durante M, Golubev A, Park W-Y, Trautmann C. Applied nuclear physics at the new high-energy particle accelerator facilities. *Phys Rep.* (2019) 800:1–37. doi: 10.1016/j.physrep.2019.01.004
5. Durante M, Indelicato P, Jonson B, Koch V, Langanke K, Meißner U-G, et al. All the fun of the FAIR: fundamental physics at the facility for antiproton and ion research. *Phys Scr.* (2019) 94:033001. doi: 10.1088/1402-4896/aaf93f

Conflict of Interest: The authors declare that the research was conducted in the absence of any commercial or financial relationships that could be construed as a potential conflict of interest.

frontiers in Physics

ORIGINAL RESEARCH
published: 26 May 2020
doi: 10.3389/fphy.2020.00169

A Single-Particle Trigger for Time-of-Flight Measurements in Prompt-Gamma Imaging

Paulo Magalhaes Martins[1,2]*, *Riccardo Dal Bello*[1,3], *Michael Seimetz*[4], *German Hermann*[5], *Thomas Kihm*[5] *and Joao Seco*[1,3]

[1] German Cancer Research Center – DKFZ, Heidelberg, Germany, [2] Instituto de Biofísica e Engenharia Biomédica, Faculdade de Ciências da Universidade de Lisboa, Lisbon, Portugal, [3] Department of Physics and Astronomy, University of Heidelberg, Heidelberg, Germany, [4] Instituto de Instrumentación para Imagen Molecular (I3M), CSIC-Universitat Politècnica de València, Valencia, Spain, [5] Max Planck Institute for Nuclear Physics, Heidelberg, Germany

Tracking of single particles accelerated by synchrotrons is a subject that crosses several physics fields. The high clinical intensities used in particle therapy that can exceed 10^9 p/s make this task very challenging. The tracking of the arrival time of single particles in the ion beam is fundamental for the verification of the particle range and dose delivered to the patient. We present a prototype made of scintillating fibers which has been used to provide time-of-flight (TOF) information for three beam species currently accelerated at the Heidelberg Ion-Beam Therapy Center (HIT). We have demonstrated a time-tracker for a prompt-gamma spectroscopy system that allows for a background TOF rejection with a sub-nanosecond time resolution.

Keywords: prompt-gamma, particle tracking, scintillating fibers, ion-beam therapy, synchrotrons

OPEN ACCESS

Edited by:
Vincenzo Patera, Sapienza University of Rome, Italy

Reviewed by:
Matteo Morrocchi, University of Pisa, Italy
Giuseppe Battistoni, National Institute for Nuclear Physics, Italy

***Correspondence:**
Paulo Magalhaes Martins
p.martins@dkfz.de

Specialty section:
This article was submitted to Medical Physics and Imaging, a section of the journal Frontiers in Physics

Received: *07 December 2019*
Accepted: *22 April 2020*
Published: *26 May 2020*

Citation:
Magalhaes Martins P, Dal Bello R, Seimetz M, Hermann G, Kihm T and Seco J (2020) A Single-Particle Trigger for Time-of-Flight Measurements in Prompt-Gamma Imaging. Front. Phys. 8:169. doi: 10.3389/fphy.2020.00169

1. INTRODUCTION

The correlation between the ion beam microstructure and the prompt-gamma ray production in synchrotron facilities has been investigated in the context of therapy monitoring by means of in-beam PET imaging [1, 2]. The prompt-gamma ray emissions during ion-beam therapy, at that time still considered mostly a source of background, eventually became a promising technique for range verification [3]. Several authors have meanwhile investigated the benefits of time-of-flight (TOF) measurements for background rejection in prompt gamma imaging (PGI) [4–9]. In cyclotron-based facilities, the use of the TOF information is rather straightforward as the arrival time of the proton bunches is highly correlated with the radio-frequency (RF) of the accelerator, being the bunch width in the order of 1–2 ns. However proton bunch drifts against the RF of the cyclotron have been observed [10]. In synchrotron facilities, a time-correlation of the prompt gamma radiation with the residual microstructure of the extracted beam is still observed [11], but the minimum bunch width is in the order of 10 ns. The information obtained thereof may be sufficient to track the inter- and intra-spill time between spills and bunches, respectively, to be used for in-beam PET. However, it is not sufficient for defining a useful TOF window for PGI. Provided the distance from the prompt-gamma detector to the target, typical TOF windows are usually within 1–3 ns [9, 12–14]. Many experiments in high-energy physics have achieved sub-ns TOF resolutions. Several types of detectors have been used in those experiments, such as plastic scintillator slabs [15], resistive plate chambers [16–18], and strip silicon detectors [19–21]. The plastic scintillator detectors have also been widely investigated for radiation dosimetry by Beddar et al. [22, 23], Beaulieu and Beddar [24] and Beddar and Beaulieu [25]. Many facilities use

plastic scintillator counters for beam monitoring. In the therapy with ion beams, plastic detector counters are usually placed after the beam extraction. However, this solution is just available during quality assurance, since particles hitting the detector will be scattered and will not reach the nozzle. Testa et al. [4] have proposed the use of an external beam monitor between the nozzle and the patient to determine the time correlation between the prompt gamma detection and the transverse position of the incident ions measured by the monitor. Several solutions for spatial tracking have meanwhile been presented either based on diamond detectors [26, 27], or based on plastic scintillating fibers [28, 29]. The aforementioned strip silicon detectors have presented promising results for beam characterization and monitoring in a clinical setting [30]. Several authors claimed the need for bunch monitors to create reliable range verification procedures in the clinical routine [10, 31–33]. In this work, we present a prototype of a trigger system capable of providing distinct time references for single particles accelerated at the Heidelberg Ion-Beam Therapy Center—HIT [34]. The information of the arrival time of those particles is correlated with the prompt-gamma arrival time measured in the $CeBr_3$ detectors to assess the system time resolution. The bunch width and peak interval for several beam species and energies are also shown thus demonstrating the need for such an external trigger. Finally, we evaluate the energy deposition for beam diagnostic purposes and provide results on the efficiency of tracking single particles.

The main requirements to our prototype of a trigger system are: triggering on single particles within an ion beam provided by a synchrotron; providing a sub-ns system time resolution; being able to cope with clinical intensities; being radiation hard; interacting as few as possible with the beam.

In this work, we will focus on the first three requirements. The last two requirements are partially satisfied by beam triggers based on scintillating fibers, which was demonstrated in previous studies [29, 35–38]. The radiation hardness remains as a major concern for the use of scintillating fibers under high intensities. Joram et al. consider that the moderate radiation hardness of plastic scintillators currently prevents their use in very harsh radiation environments [36]. The evaluation under clinical conditions is however beyond the scope of the current work.

2. MATERIALS AND METHODS

The HIT facility accelerates proton, helium, carbon, and oxygen ions from 48 to 515 MeV/u. Protons and carbon ions are routinely used in the clinical setting, while helium ions are currently being commissioned [39, 40], and oxygen ions still remain as a research beam species. In this work, we focus just on proton, helium, and carbon ion beams.

The intensities in clinical practice range from 2×10^6 to 8×10^7 p/s for carbon ions and from 8×10^7 to 3.2×10^9 p/s for protons in 10 intensity levels. The intensity is controlled via an intensity feedback system [41]. This system can however be switched off for achieving lower intensities. In that case, the beam can be bent via magnets up to 1° and the intensity at the nozzle can be lowered down to approximately 30–50 particles per second. The intensity can also be artificially changed by demanding a certain charge in the ionization chambers through the intensity feedback system. The latter is suitable to deliver intensities down to three orders of magnitude of the lowest clinical intensity (8×10^4 p/s for protons and 2×10^3 p/s for carbon ions).

For carbon beams, the beam size (the FWHM at the isocenter) ranges from 3.4 mm (E = 430.1 MeV/u) to 9.8 mm (88.8 MeV/u). For helium beams, the beam size ranges from 4.9 mm (E = 220.5 MeV/u) to 18.6 mm (50.6 MeV/u). For proton beams, the beam size ranges from 8.1 mm (E = 221.1 MeV/u) to 32.4 mm (48.1 MeV/u).

The HIT facility is equipped with two clinical horizontal rooms, a fully 360° gantry and an horizontal experimental room. All the experiments were performed in the experimental room, i.e., at the largest distance from the synchrotron extraction point.

2.1. Experimental Setup

The prompt gamma spectroscopy (PGS) system is composed of $CeBr_3$ detectors (ø $1.5'' \times 3''$) coupled to Hamamatsu R13089 photomultiplier tubes (PMTs) and plugged to a voltage divider. The anode output feeds our data acquisition system (DAQ) [42]. This is a module of a FlashCam FADC system, originally designed for cameras proposed for the Cherenkov Telescope array (CTA) [43].

Figure 1A shows a schematic drawing of our PGS system consisting of a primary prompt-gamma detector, a trigger for the incoming particles, and the electronics. The focus of the present study is the external trigger placed between the nozzle and the target and the TOF information on the incoming particles extracted thereof. **Figure 1C** shows a photo of the first setup with two $CeBr_3$ detectors facing each other at a distance of 15 cm from the beam axis. The target is composed by two flasks of water comprising a length of 6.4 cm of water and 0.45 cm of polystyrene. The distance from the target to the fibers active region was 27 cm.

Moreover, we performed experiments also with a second setup (**Figure 1D**). In this case, the target and the $CeBr_3$ were removed, while two EJ-200 scintillating tiles were introduced. The trigger and the scintillating plastics were placed along the beam axis to detect, in sequence, the beam particles delivered by the synchrotron and determine the intrinsic time resolution.

2.1.1. Trigger

We considered several options for our trigger. In a previous study, we used plastic scintillators and showed their ability to provide TOF information [44]. Such detectors are commonly used as start counters, but have a limited count rate of approximately 10^6 cps. We chose EJ-200 scintillating plastics with a squared area of 8×8 cm^2 and a respective thickness of 1 and 4 mm. Each of these was sealed with aluminum foil and black tape to make it light tight and coupled on one side with a silicone coupling component to a Hamamatsu PMT R13089.

For the prototype of an alternative trigger system presented in this study, we implemented a set of scintillating fibers with a square cross section of 500 μm. We designed dedicated supports to obtain a single layer of scintillating fibers (BCF–12 fast

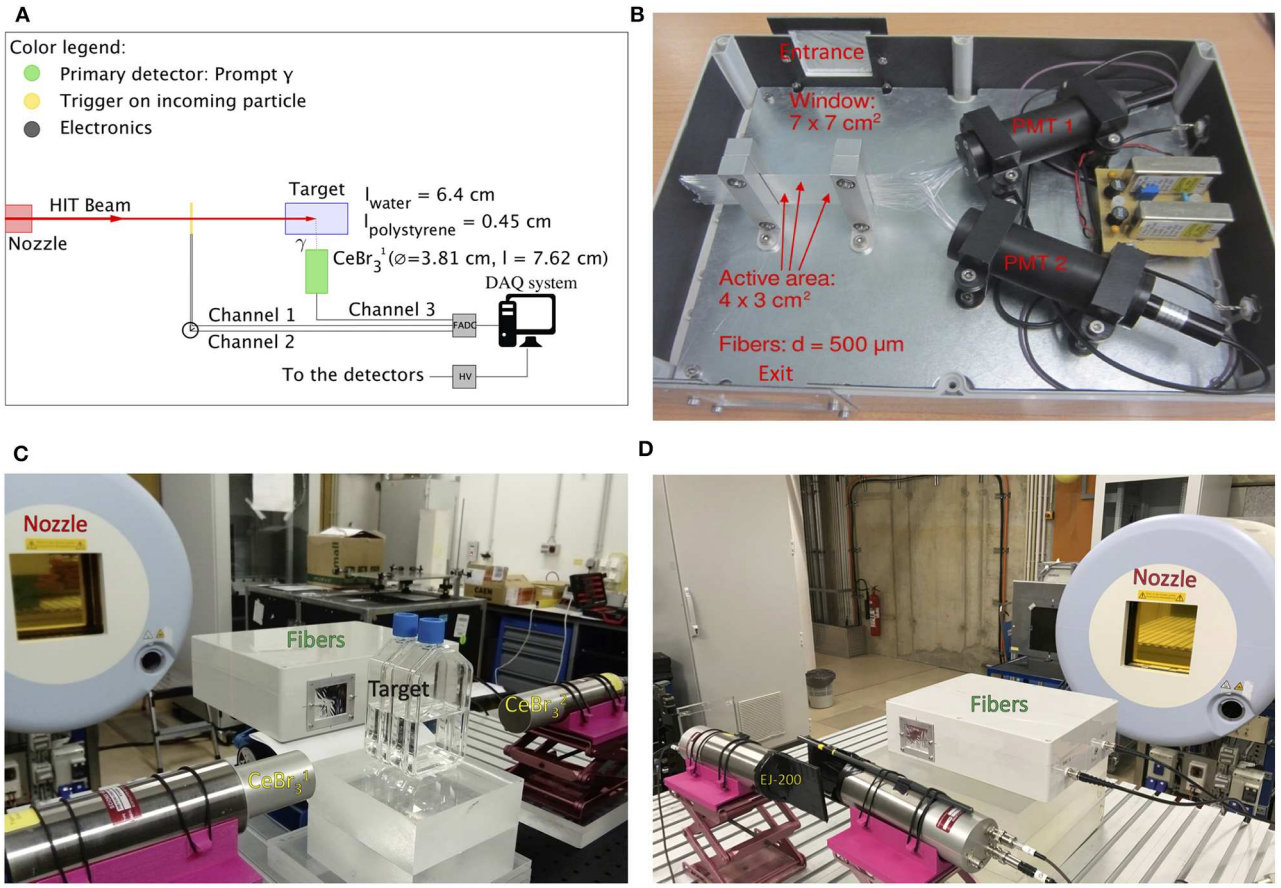

FIGURE 1 | (A) Schematic drawing of the first experimental setup comprising the PGS system and an external trigger detector between the nozzle and the target. **(B)** Photo of the prototype of a trigger system comprising scintillating fibers connected on one side to two independent PMTs in an alternating fashion. **(C)** Photo of the first experimental setup. **(D)** Photo of the second experimental setup with the scintillating fibers and the EJ-200 scintillating tiles placed, in sequence, along the beam axis.

scintillator fibers, decay time = 3.2 ns, Saint Gobain Crystals). The total active area was 4 × 3 cm^2. The fibers were connected on one side, in an alternating fashion, to two independent R647 PMTs with E849–35 socket assembly (Hamamatsu). The detector included an housing for light shielding equipped with an entrance and exit window for the beam (double aluminized mylar with a total thickness of 10 μm). High voltage supply modules are integrated in the prototype of a trigger system and powered by an external 12 V DC plug. The gain of the two channels has been pre-adjusted with a Sr–90 source. **Figure 1B** shows a photograph of the prototype of a trigger system without the top cover.

Each PMT provides an analog signal to the acquisition system. The signals are continuously digitized and stored in data files [42]. The post-processing is then performed offline. The information from the arrival time of the particles at the trigger is compared with the arrival time of these particles at the plastic scintillators to extract the intrinsic time resolution. In order to show the feasibility in a clinical scenario, we compare the arrival time of the irradiated particles at the trigger and the arrival time of the generated prompt-gamma at the $CeBr_3$ detectors which are placed perpendicular to the irradiated target. We then extract the system time resolution that has contributions from the time resolution of the fibers and the $CeBr_3$.

2.2. Data Acquisition, Processing, and Analysis

Our DAQ system has 24 channels, which are capable of acquiring at 250 MS/s with 12-bit precision. The samples are buffered in one FPGA and processed in a configurable way to derive a trigger decision. All electronics are read out via high 1 GB Ethernet network, using off-the-shelf switches and a standard commercial computer [42, 45].

The data is transferred from the DAQ to the PC through Gigabit Ethernet and stored event by event in binary data files. Those files were then converted to independent binary files containing the key information of each trace, i.e., the relative time assigned to the event, the dead time, and a standalone energy calculation. The data pulse processing and analysis were carried out offline in self-designed MATLAB routines.

It is possible to split an analog input signal onto four digitization channels which are phase shifted by 1 ns with respect to each other and therefore to effectively sample the signal at a

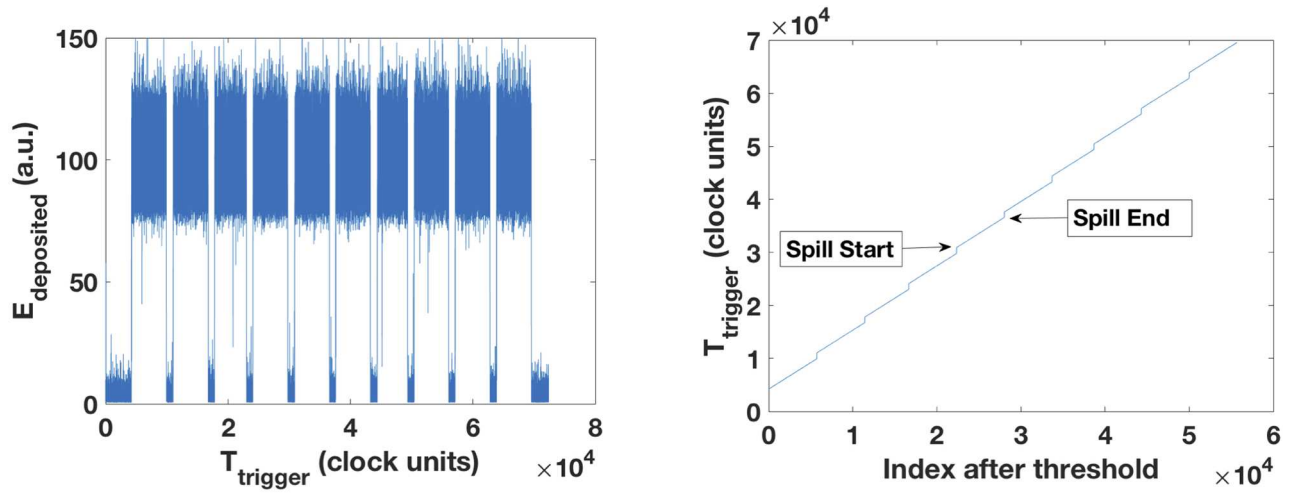

FIGURE 2 | (Left) Energy deposited in the trigger detector along the acquisition time. The relative acquisition is given by the internal clock of the FADC unit. **(Right)** After setting a threshold at 60 (a.u.), we obtain the index of the spill start and the spill end and the corresponding trigger time given by the FADC unit. The time difference between those times gives the time between spills.

rate of 1 GS/s. We used this clustering technique to acquire the data from the two PMT outputs of the scintillating fiber setup and the PMT outputs from both plastic detectors. In total, we used 16 channels (4 channels for each PMT). For the $CeBr_3$ detector, we opted for the larger sampling interval of $\delta t = 4$ ns. The signals in the $CeBr_3$ were only compared to the ones in the fibers. The maximum throughput of the DAQ system is approximately 200,000 events/s. The maximum stored data rate is 100 MByte/s.

In order to retrieve the arrival time and energy of the particles in every detector, we shaped the digital signal by convolving the input signal with an impulse response function. For fast evaluation and visualization purposes, we acquired traces comprising an adjustable time slice up to 15.6 μs and with a configurable offset relative to the time of the trigger. This acquisition mode displays the bunch structure within approximately 16 μs and permits a fast visualization of pile-up events. A **Supplementary Video** shows the single carbon particles arriving within the course of a single spill. These large traces were also used to determine the bunch width and peak interval for several beam species with different energies.

In order to determine the system time resolution and the intrinsic resolution of the fibers, we acquired traces of 240 ns with 1 GS/s sampling rate. The coincidences between the events in the scintillating fibers and the signals in the plastic or in the $CeBr_3$ detector were detected offline by analyzing the corresponding traces. A maximum of 3 peaks per trace and a minimum peak prominence on the processed data were considered. The time stamp was extracted from the half width at half height for each peak. Three Gaussian functions were analytically calculated with the values of the local peaks and widths and their maximum considered for calculating the energy deposition. All data were corrected for dead time.

2.3. Decomposition of the Cross-Talk Between Neighboring Fibers

During the manufacturing process, we deliberately avoided any cladding in order to avoid dead regions between the scintillating fibers. As a consequence, we observed a optical cross-talk between neighboring fibers, this effect being more evident for incident carbon ions due to their higher scintillation light yield. Every time we observe a single event from a carbon ion in an odd (even) fiber we observe a cross-talk event with smaller light yield in the even (odd) fiber. The larger signal can be taken into account and the smaller one discarded by evaluating the energy deposition in both odd and even fibers. After setting a threshold on the deposited energy and performing logical AND operations, we can decompose the events in three components: (a) the events that have an energy deposition in the odd or even fibers above that threshold and which generated an event in the neighboring fiber below that threshold; (b) events that generated a signal above the given threshold in both odd and even fibers; (c) events that generated a signal below the given threshold in both odd and even fibers. In the end, the relevant events from the first component (a) account for approximately 92% of the whole events and are the ones considered for further analysis.

2.4. Spill Structure

The spill macrostructure comprehends a period of approximately 5 s of irradiation followed by a pause of approximately 4 s. In order to determine the initial and final part of each spill, we use the reference clock of the FADC that runs at 250 MHz. This clock assigns a very precise relative time stamp to each event. To determine both the spill start and end, we calculated the first and second derivatives of the trigger time course (inversely proportional to the count rate) provided by the FADC clock. During the spill on, we have many triggered events close-by in time. Conversely, during spill off, very few events are detected. In the presence of a $CeBr_3$ detector, we used the time derivative of

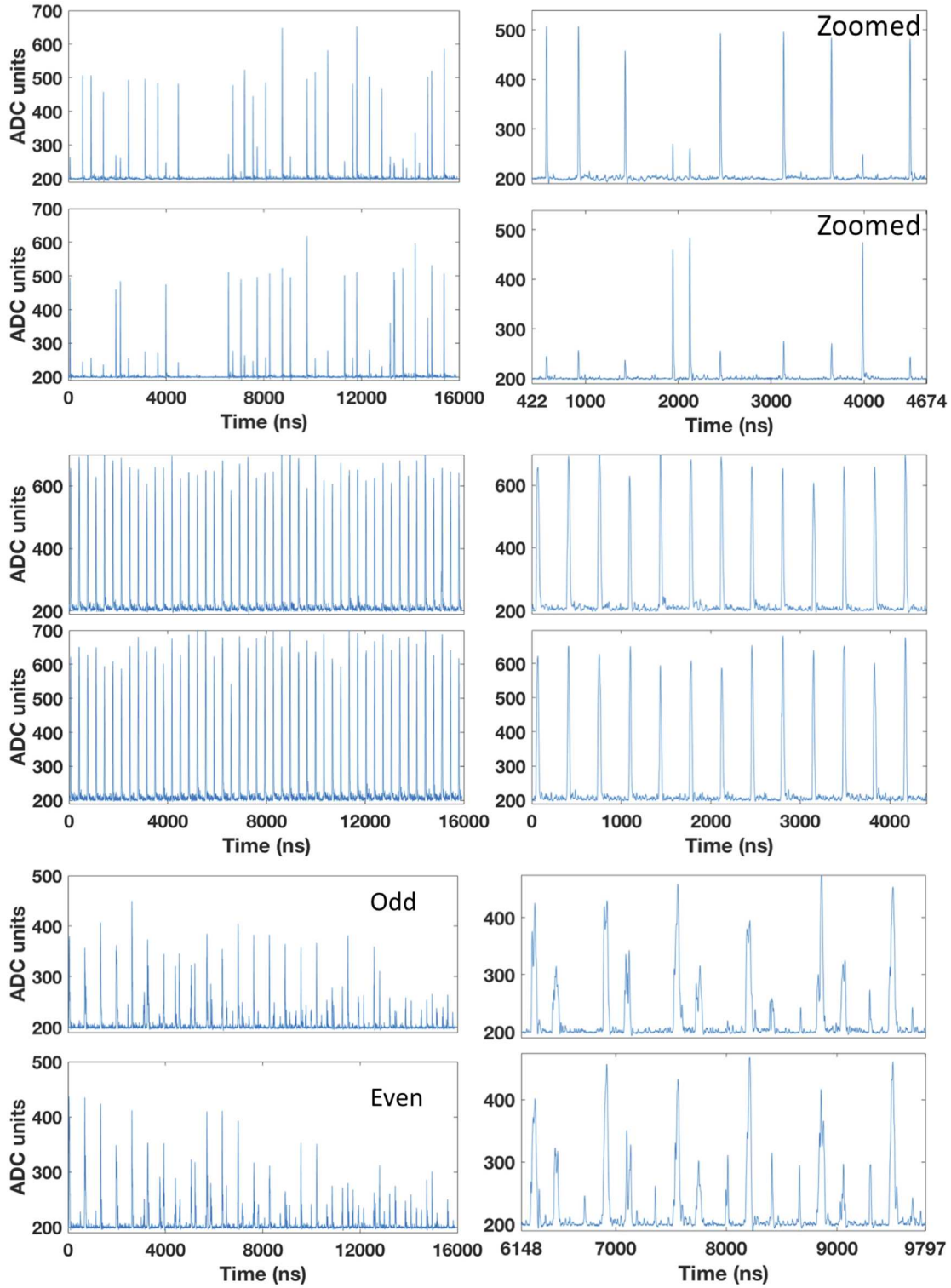

FIGURE 3 | Time microstructure for carbon **(top)**, helium **(middle)**, and proton **(bottom)** beams. The beam energies are 276, 146, and 145 MeV/u, respectively. The intensities are 2×10^6, 2×10^7, and 8×10^7 p/s, respectively. The trace duration is 16 μs and hits in both odd and even fibers are shown. The right plots correspond to a windowed region from the left plot. Cross-talk for carbon ions and multiple hits for protons are clearly visible.

the energy deposited in the $CeBr_3$ or the presence of overflows generated by scattered charged particles hitting directly the $CeBr_3$, as they immediately arise during spill on. During spill off, there is just the activation of the target with gamma-rays being emitted with an energy of 511 keV. Conversely, during spill on, the high energetic prompt-gammas immediately provide the information that the spill started. In the absence of a $CeBr_3$ detector, we used an external radioactive source to provide a continuous count rate that can be observed in **Figure 2** (left) even during spill off. This method is quite accurate within a few milliseconds. In the **Supplementary Video**, we can clearly see the start and the end of the carbon ion spill with 16 μs traces. **Figure 2** shows a straightforward method for determining the spill start and end by defining a threshold on the energy deposited in the trigger detector. During spill off, there are still activation related events acquired by the $CeBr_3$, but without any energy deposition in the fibers.

3. RESULTS

3.1. Single Particle Tracking

Figure 3 (left) shows the time microstructure of beams of protons, helium, and carbon. Displayed are the 16 μs traces acquired with both odd (top) and even (bottom) fibers. We observe a very regular time microstructure for the helium beams due to the very low energy. The beam travels from the injector to the nozzle with very few turns in the synchrotron. This results in a very small error in the bunch width (see **Table 1**).

Figure 3 (right) shows a zoom over a smaller time period, where the single particles are clearly distinguishable. For proton beams, we can even distinguish double and multiple hits within a bunch of particles. However, some multiple hits cannot be resolved for such intensity ($I_1 = 8 \times 10^7$ p/s). For higher clinical intensities, the protons are too close-by within the bunch to be distinguished with the current prototype of a trigger. For carbon ions, the cross-talk between odd and even fibers is clearly visible. Every hit in an odd or even fiber creates a simultaneous but smaller hit in the neighboring fiber. **Figure 4** shows an exemplary multiple hit with four events within 200 ns from a proton beam. These fours event would overlap and be discarded without the clustering technique.

Figure 5 shows a frame from the **Supplementary Video**. That video shows the arrival time of carbon ions within the course of a spill. The spill starts with a low particle rate within the first milliseconds and achieves the requested intensity afterwards. It eventually vanishes after approximately 4.85 s. The ramp-up time was already observed by Schoemers et al. [41].

3.2. Bunch Width and Peak Interval

Figure 6 shows a histogram of the arrival time of the helium and carbon ions over 10 spills for an energy of 180 and 276 MeV/u, respectively. The bunch widths refer to the average full width at half maximum (FWHM) obtained from all the peaks with the function *findpeaks*. For carbon ions, we observe a peak interval of 171.1 $\pm$ 2.6 ns and a minimum bunch width of 15.5 $\pm$ 1.6 ns. **Table 1** shows that as the energy of the helium ions increases, the bunch width gets larger. Due to the regular microstructure of the helium beams with lowest energy, we observe a very precise bunch width of 33.1 $\pm$ 0.5 ns. Also three components seem to arise and become more evident for higher energies. As expected, we observe that the peak interval between bunches decreases for an increasing energy of all beam species.

TABLE 1 | Bunch width and peak interval for proton, helium, and carbon beams for five energy steps ranging from 48.1 to 221.1 MeV/u, from 50.6 to 220.5 MeV/u, and from 88.8 to 430.1 MeV/u, respectively.

	Energy step	E1	E65	E135	E195	E255
	Energy (MeV)	48.1	105.4	145.5	180.5	221.1
^{1}H	Interval (ns)	352.2 ± 7.1	248.1 ± 4.1	217.1 ± 6.2	199.5 ± 3.6	185 ± 4.1
	Width (ns)	73.1 ± 10.4	48.5 ± 4.9	45.5 ± 4.2	44.2 ± 3	40.8 ± 3.8
	Energy (MeV/u)	50.8	106.6	146.3	180.3	220.5
^{4}He	Interval (ns)	347.7 ± 2	246.7 ± 4	216.4 ± 3.9	199.1 ± 5.2	185 ± 5.1
	Width (ns)	33.1 ± 0.5	38.5 ± 2.4	38.3 ± 2.4	39.5 ± 2.5	41.8 ± 2.5
	Energy (MeV/u)	88.8	197.6	276.1	346.4	430.1
^{12}C	Interval (ns)	–	192.7 ± 6.8	171.1 ± 2.6	159.1 ± 3.1	149.3 ± 3.5
	Width (ns)	–	26.9 ± 4.6	15.5 ± 1.6	16.8 ± 1.8	19.2 ± 2.1

The bunch widths refer to the average FWHM obtained from all the peaks.

3.3. Time Resolution

Figure 7 (left) shows the spectrum obtained from the time difference between the arrival of the prompt-gamma radiation generated by a thin target at the two $CeBr_3$ detectors and the carbon ions at the odd and even scintillating fibers. In **Figure 7** (right), we observe that the time difference between the $CeBr_3^1$ and the odd fibers shows a clear prompt component with a modeled Gaussian function in red. A delayed component from neutron and fragment induced prompt gamma is also observed. A faster component just before the prompt component may result from prompt-gamma induced by fragments produced in the nozzle and hitting directly the $CeBr_3$ detectors. This is in line with the results from Testa et al. [46] and Dal Bello et al. [47]. The prompt component demonstrates a system time resolution of approximately 0.85 ns FWHM.

Figure 8 shows the time spectrum obtained from the time difference between the arrival of the carbon ions at the plastic scintillator and at the scintillating fibers for five energy steps (E_1 = 88.8 MeV/u; E_{65} = 197.6 MeV/u, E_{130} = 276.1 MeV/u, E_{195} = 346.4 MeV/u, and E_{255} = 430.1 MeV/u). For this measurement the setup has been changed. For the previous measurements only the scintillating fibers were in the beam (in coincidence with the $CeBr_3$). Here the coincidences are made exclusively between the plastic scintillator and the odd scintillating fibers placed along the beam axis and spaced apart by 27.5 cm. The higher the energy the faster the particles and the lower the time elapsed between both detectors. A reproducible intrinsic time resolution of 0.7 ns FWHM was obtained for the five energy steps.

Figure 9 shows a slightly different time difference between the odd and the even scintillating fibers and the plastic detector. We observe a degradation of the time resolution for helium (1.56 ns FWHM) and proton (2.64 ns FWHM) beams attributable to an increased energy straggling (not shown).

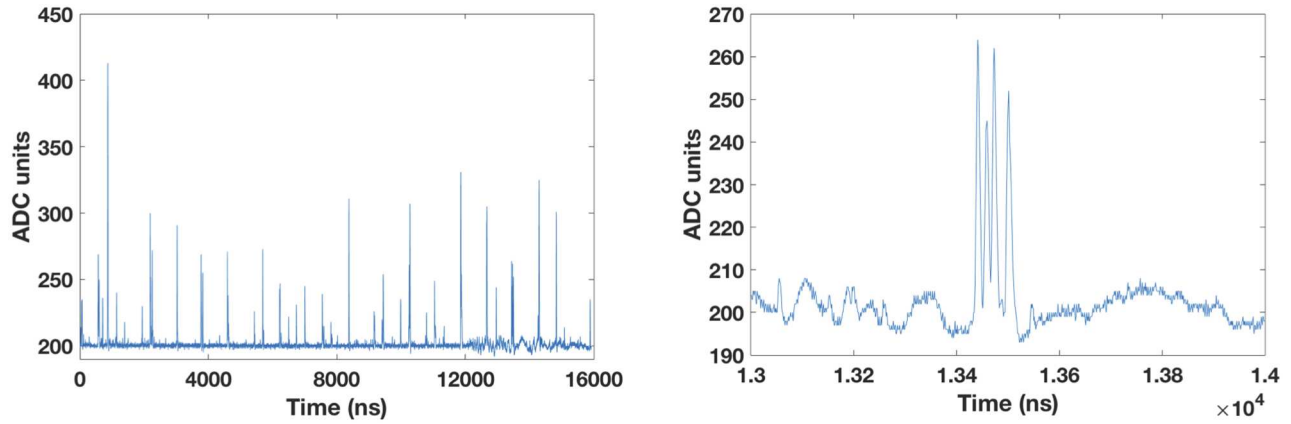

FIGURE 4 | (Left) A 16 μs trace from a proton beam with an intensity of 8×10^7 p/s. **(Right)** A zoom over the time interval from 13 to 14 μs shows a multiple hit with four events within 200 ns.

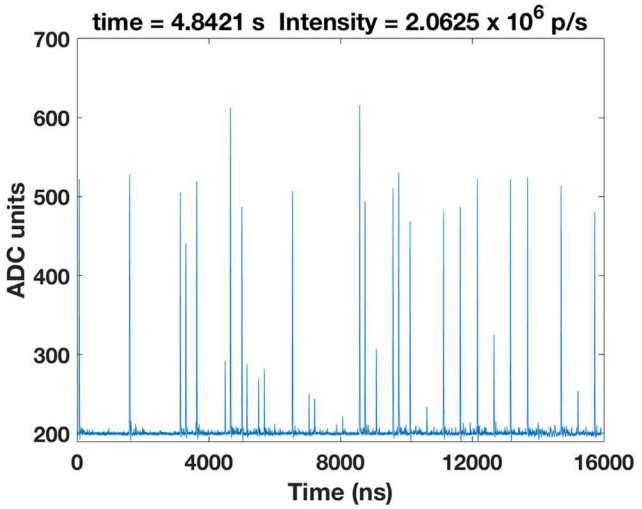

FIGURE 5 | Frame from an animation of the carbon ion spill course. Every frame in the **Supplementary Video** corresponds to a 16 μs trace. The spill lasts approximately 4.85 s. Only the initial and the last part of the spill are displayed. The nominal intensity is $I_1 = 2 \times 10^6$ p/s.

3.4. Energy Deposition

Figure 10 shows four spectra of the energy deposited by carbon and helium ions in both plastic scintillators and in the odd and even fibers. The carbon ion distributions present a Gaussian shape as expected from a Vavilov distribution in the Gaussian limit [48]. For lighter particles, the distributions resemble a Landau distribution as expected for such particles hitting a thin target. The proton beam distributions resemble the helium ions distributions (not shown).

Figure 11 presents the result from the decomposition of the four components associated to the interaction of the carbon ions with the odd and even fibers. As mentioned before, there is an evident cross-talk between odd and even fibers if irradiated by carbon ions. We can select from the events hitting the odd fibers, the ones that have a higher energy deposition in that fiber and a lower energy deposition in the neighboring fiber. Conversely, we can choose from the events hitting the even fibers, the ones that have a higher energy deposition in that fiber and a lower energy deposition in the neighboring fiber. We observe that 45.6% of the events deposit higher energy in the odd fibers and 46.2% in the even fibers, totalling 91.8% of the total events. The remaining 8% are described in section 2.3. In this analysis, the threshold was set at 200 (a.u.).

3.5. Efficiency

In order to evaluate the efficiency of the scintillating fibers, we lowered the beam intensity by two means: (a) bending the beam up to 1° via magnets; (b) collimating the beam with two PMMA blocks separated by a 1 mm spacer. For the determination of very low intensities, we bent the beam gradually and detected the scattered particles in the nozzle with the thicker plastic detector very close to the nozzle. We compared the count rate with the one obtained with the scintillating fibers. Since we clustered the channels from the fibers, the FADC throughput was limited to $\approx$ 28 kcps. For the first nominal intensity, we obtained a count rate in the plastic detector of $\approx$ 950 cps. We gradually bent the beam until we had a count rate of $\approx$ 30 cps. We acquired alternately the events from the plastic scintillator and the scintillating fibers.

In **Table 2**, we present the results from the acquisition of carbon ions with an intensity lowered from the nominal intensity $I_1 = 2 \times 10^6$ p/s down to 100 p/s. Both detectors match at run 6. We obtained a count rate in the scintillating fibers of $\approx$ 60.5 kcps, already corrected for a dead time of 53.6%, and a count rate of 29 cps in the plastic detector. The extrapolated count rate (ECR) is obtained from the count rate (CR) factor from the bunch monitor (BCM) measurements (CR Factor = 1 for nominal intensity I_1) multiplied by the measured CR in the scintillating fibers (SciFi) after dead time correction. We finally obtained an extrapolated count rate of 2.002×10^6 p/s which compares well with the nominal intensity of reference. Below those values (run 1–5), the plastic scintillator is not reliable due to large fluctuations in the count rate, while above those

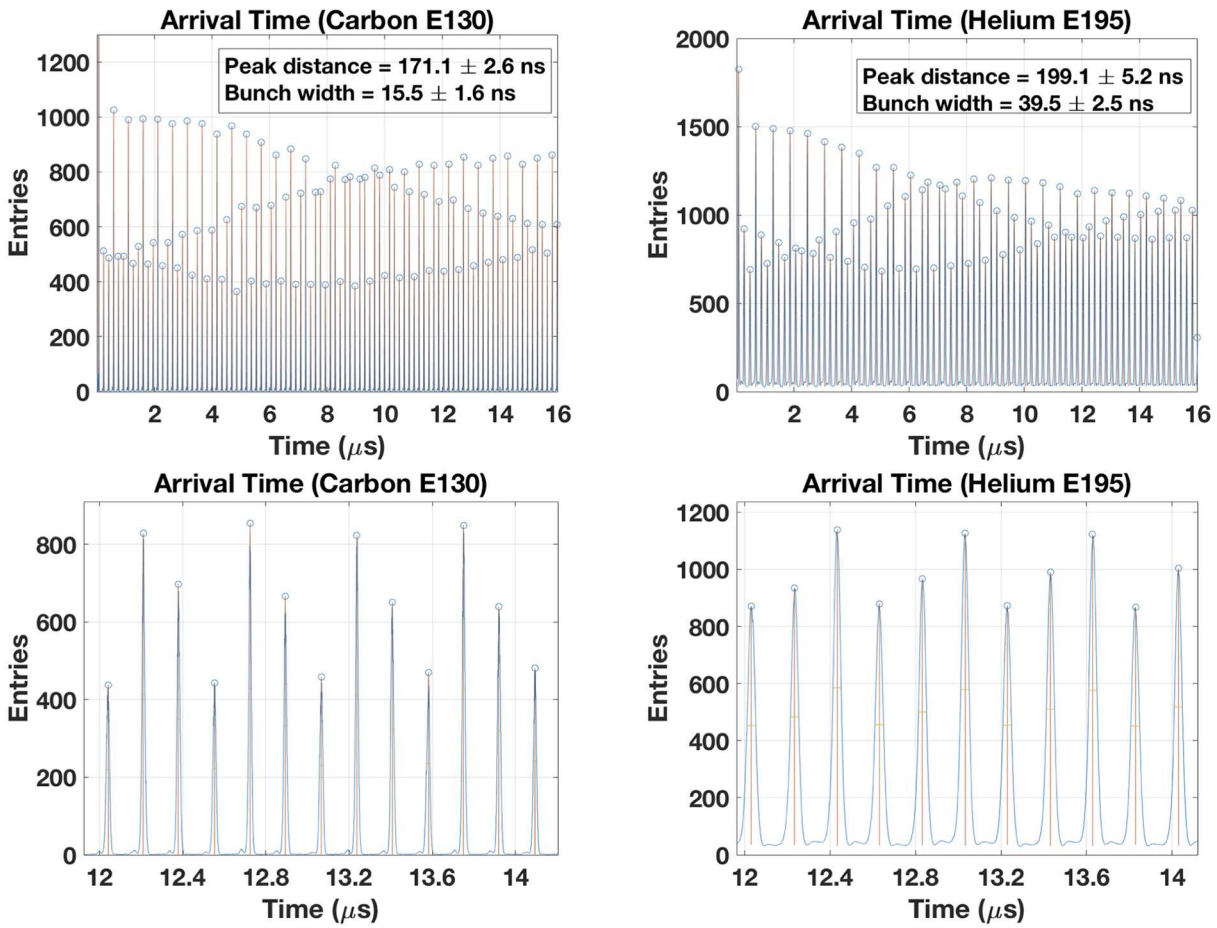

FIGURE 6 | Bunch width and peak interval of a carbon beam with 276 MeV/u **(left)** and a helium beam with 180 MeV/u **(right)**. A zoom over the region 12–14 μs shows the bunch width **(bottom)**.

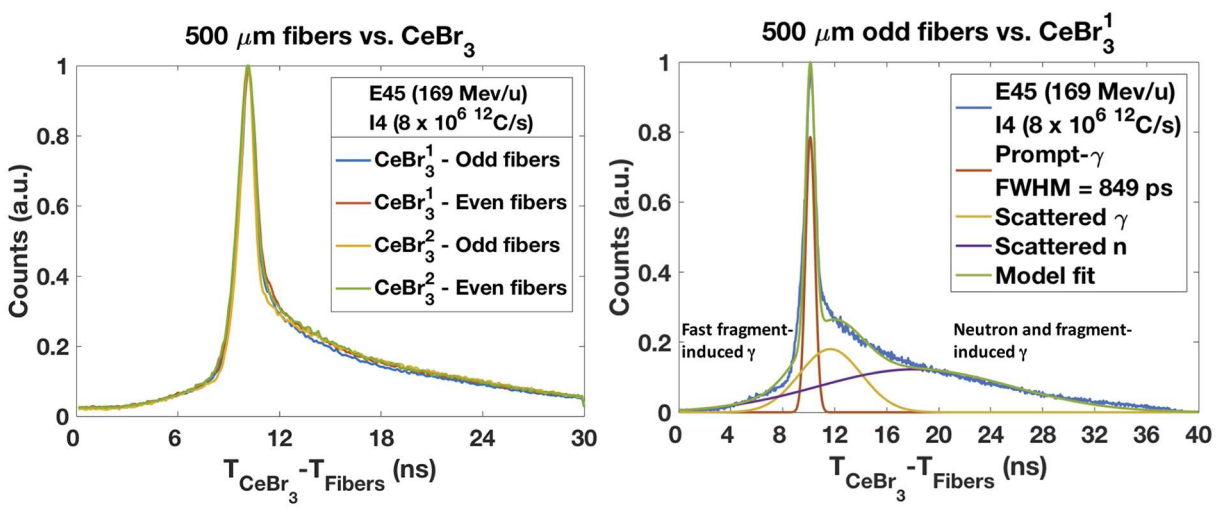

FIGURE 7 | Time resolution of the PGS system. **(Left)** The time difference between the arrival from prompt-gamma to the two $CeBr_3$ detectors and the arrival from carbon ions to the odd and even scintillating fibers. **(Right)** The time difference between the $CeBr_3^1$ and the odd fibers shows a prompt component (red) with 0.85 ns FWHM. A delayed component resulting from neutron and fragment induced γ-rays is observed and may be removed by TOF cuts. A fast component resulting from fragment induced γ-rays scattered in the nozzle is also visible.

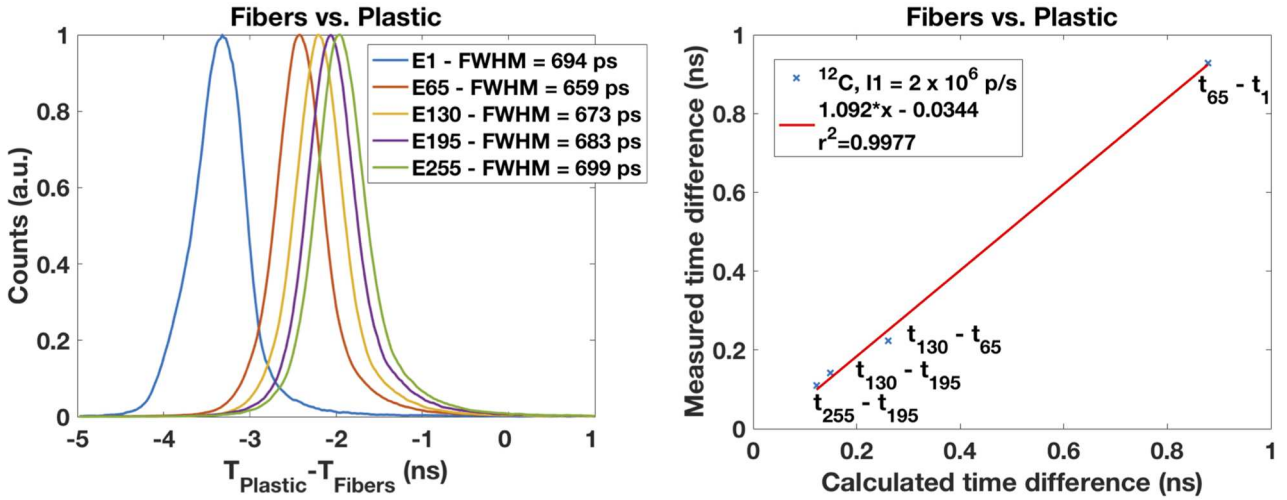

FIGURE 8 | (Left) Time resolution determined from the time between the arrival from carbon ions to the plastic detector and to the scintillating fibers. A reproducible value of 0.7 ns is observed for five energy steps covering the full energy range. The energy steps E_1, E_{65}, E_{130}, E_{195}, and E_{255} correspond to 88.8, 197.6, 276.1, 346,4, and 430.1 MeV/u, respectively. **(Right)** The higher the energy, the faster the particles and the smaller the time elapsed between detectors. If one takes the distance between the detectors of 27.5 cm, the change in $\delta t = t_{E''} - t_{E'}$ is consistent with the energy change.

values (run 7–11), the dead time starts playing an important role and the count rate in the scintillating fibers is not retrievable anymore. The trigger system has a non-paralyzable behavior and all events happening during the dead time are lost. The FADC is equipped with a dead time logic which monitors with time stamps the dead time of the system. The correction for the dead time is the one derived from the non-paralyzable case ($N \approx N_m/(1 - N_m\tau/T)$), where the actual number of events, N, are estimated by knowing the dead time, τ, during the given time interval, T.

In order to retrieve the relative efficiency of the scintillating fibers under the reference clinical intensities provided by the HIT accelerator [41], traces of 16 μs were acquired and the number of particles in each trace counted. We increased the intensity in order to evaluate the ability of two 0.5 mm fibers feeding alternate PMTs to cope with a collimated beam with a slit of 1 mm. For carbon ions, the beam size (FWHM at the isocenter) was 5.9 mm (E = 169.2 MeV/u). For protons, the beam size (FWHM at the isocenter) was 17.4 mm (E = 90.7 MeV/u). The beam intensity ranged from the intensity step 1 ($I_1 = 2 \times 10^6$ p/s for carbon ions and $I_1 = 8 \times 10^7$ p/s for protons) up to the intensity step 8 ($I_8 = 3 \times 10^7$ p/s for carbon ions and $I_8 = 1.2 \times 10^9$ p/s for protons). **Figure 12** shows the relative number of particles in each trace for the several intensity steps and the estimated intensity. We observe a linear behavior for carbon ions up to the intensity step 7 (2×10^7 p/s) both for odd and even fibers. For protons, there is an increasing underestimation of the true intensity as a result of the pile-up of multiple hits within bunches.

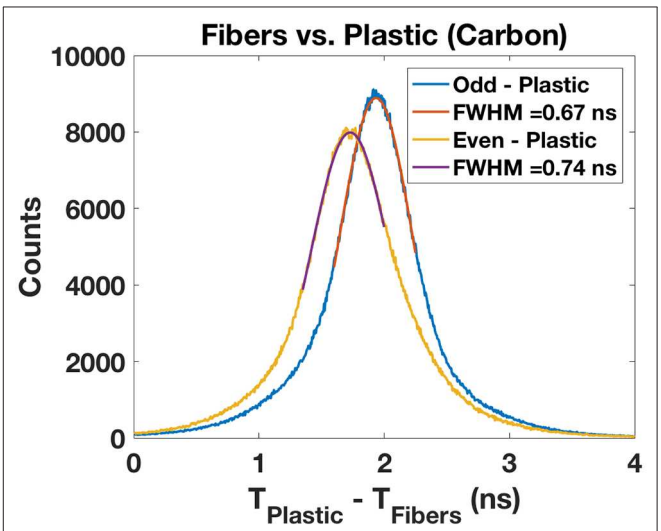

FIGURE 9 | Intrinsic time resolution for the odd and even scintillating fibers present within the alternating fashion. A reproducible value of 0.7 ns is obtained for both fiber bundles.

4. DISCUSSION

A small-scale prototype of a trigger system of a hadron beam time tracker for the measurement of the arrival time of single particles in an ion beam has been demonstrated. This prototype of a trigger system was able to track single particles within bunches of proton, helium, and carbon ions accelerated at the HIT facility provided the event pile-up and the dead time remained low. This is of utmost importance for PGI systems relying on the TOF information for range verification. For carbon ions, we demonstrated a time resolution for the prompt component of 0.85 ns FWHM. This allows for an efficient rejection of neutron and fragment induced prompt-gamma background. The results from the measurement of the carbon

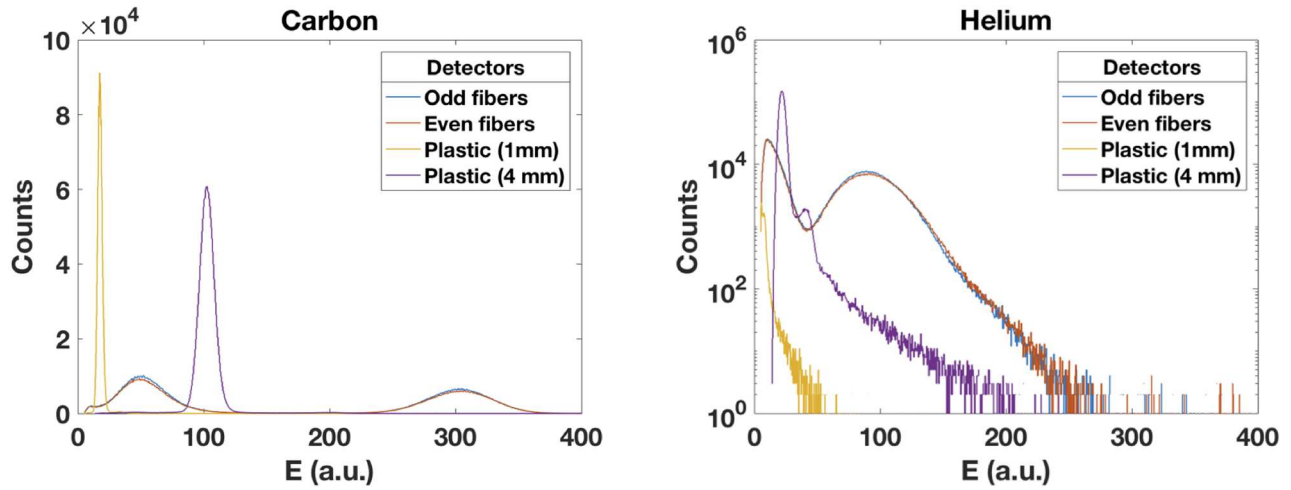

FIGURE 10 | Energy deposited by carbon **(left)** and helium **(right)** beams in the scintillating fibers and in the two plastic scintillators. An expected Gaussian shape for heavier particles is observed. The distributions from lighter particles resemble a Landau distribution as expected for a thin target.

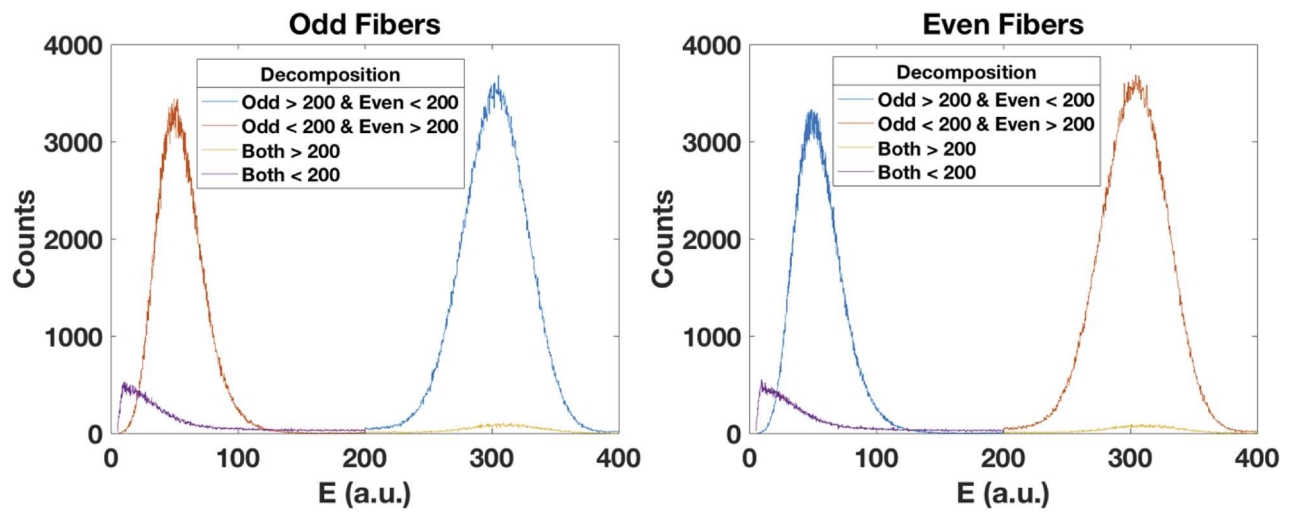

FIGURE 11 | The energy deposited by carbon ions in the scintillating fibers produces cross-talk in the corresponding neighboring fiber. For the odd fibers **(left)**, we can decompose the events by setting a threshold and performing logic operations. The blue curve corresponds to the relevant events. Conversely, for the even fibers **(right)**, the relevant events are represented in the red curve.

bunch width was in good agreement with previous results [11]. However, those results are clearly insufficient if compared with the proton bunch widths in cyclotron-based facilities where the protons are much less spread over the bunch and very well correlated with the cyclotron RF. Despite the absence of fiber cladding, we were able to decompose the cross-talk events between neighboring fibers by evaluating the energy deposited in the alternating fibers. This evaluation may be further used in beam diagnostics, e.g., in mixed beams [49, 50], where the carbon beams are used for treatment and the helium beams are used for imaging. Such prototype of a trigger system may also be used for cross-section measurements of carbon ions hitting a thin target. The carbon ions and the fragment (e.g., protons) component may be separated by measuring the energy deposition.

We plan to scale our prototype of a trigger system and build a 20×20 cm^2 detector to cover the full treatment area and work under active scanning beams. The current Saint-Gobain BCF-12 fibers have improved transmission for use in long lengths. Other fiber type, such as BCF-10 from Saint-Gobain or the SCSF-81 from Kuraray, have a shorter decay time (2.4 ns and 2.7 vs. 3.2 ns) and were optimized for diameters larger that 0.25 mm. The faster decay time and the fibers smaller cross-section could provide an improved solution for reducing the pile-up events. For such an area, we would need 400–800 scintillating fibers readout by independent detector elements. In order to cope with

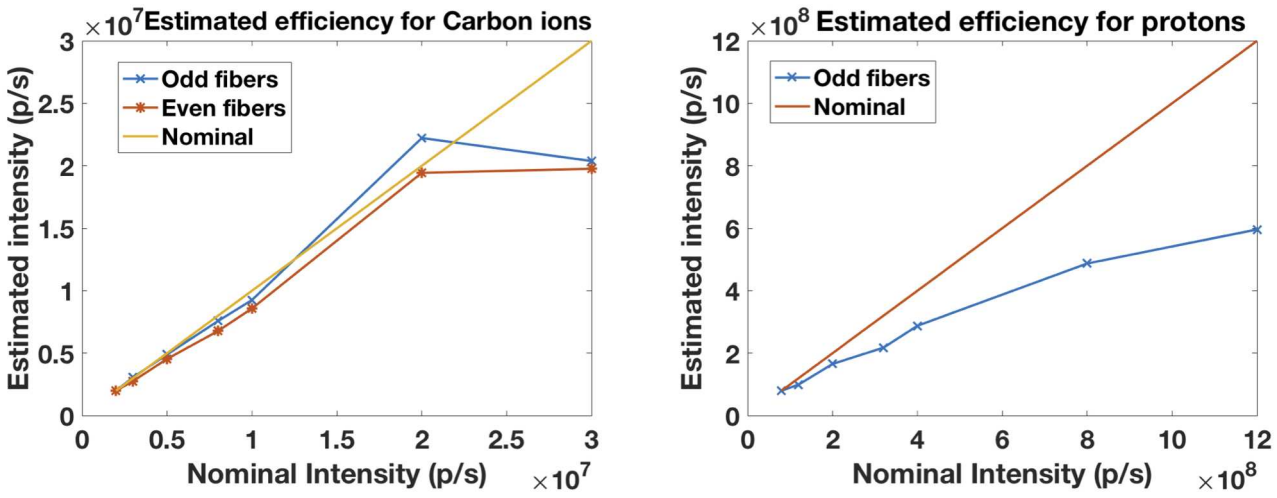

FIGURE 12 | Estimated relative efficiency for the detection of carbon ions **(left)** and protons **(right)** by the scintillating fibers for an intensity range of 2×10^6–3×10^7 p/s and 8×10^7–1.2×10^9 p/s, respectively. Results for odd and even fibers are shown for carbon ions as well as the ideal line.

TABLE 2 | Measured count rate (CR) in the plastic scintillator bunch monitor (BCM) and in the scintillating fibers (SciFi).

Run	1	2	3	4	5	6	7	8	9	10	11
BCM (cps)	–	–	–	–	–	29	122	238	356	465	950
CR Factor	–	–	–	–	–	33.3	7.77	3.99	2.67	2.05	1
SciFi (cps)	104	471	741	2.1 k	11.8 k	60 k	174 k	285 k	379 k	432 k	495 k
DT (%)	0	0	0	0	0	54	83	90	92	92	93
CCR (cps)	–	–	–	–	–	60 k	257 k	501k	749k	978k	2M
ECR (Mcps)	–	–	–	–	–	2.00	1.36	1.14	1.01	0.88	0.50

Dead time (DT) starts increasing at a CR of 28 kcps in the SciFi. The calculated count rate (CCR) is obtained from the nominal intensity of 2×10^6 p/s divided by the CR factor from the BCM measurements. The extrapolated count rate (ECR) is obtained from the CR factor from the BCM measurements multiplied by the measured CR in the SciFi after dead time correction.

the maximum intensities available at the HIT facility (3.2×10^9 p/s) and considering an average separation between bunches of approximately 150 ns, we would need to track 480 single particles per bunch. These particles may be spread over a small or a large area depending on the beam focus. If we consider a lateral spread of 3 cm (3σ), those 480 particles would be spread over 60 scintillating fibers with an average number of events per scintillating fiber and per bunch of ≈ 8. For carbon ion beams where intensities reach 5×10^7 ions/s and the lateral spread is smaller (≈ 1 cm), we would need 20 scintillating fibers to cope with approximately 8 particles per bunch and measure an average number of events per scintillating fiber and per bunch below 0.35. This is essentially an occupancy problem, and depends on the response time (analog bandwidth) of the system to single particles.

The interference of the prototype of a trigger system with the beam and its radiation hardness remained out of the scope of this paper. However, we plan to measure the water equivalent path length of the crossed material and the effect on beam degradation and test the scintillating fibers against radiation damage over routine clinical workflow conditions. Radiation damage is a major concern under clinical intensities. The several studies reported in the literature show the difficulty to draw a global and consistent picture [37, 51]. Scintillating fibers (SCSF-78M from Kuraray) have been tested up to doses of 60 kGy within the LHCb SciFi group [51]. Fluka simulations predict a maximum integrated ionizing dose to which the fibers are expected to be exposed of 35 kGy [52]. The specific condition for the scintillating fibers to be radiation hard, apart from transparency loss, include an unaffected scintillation light yield by an ionizing dose of up to 50 kGy. Moreover, the mechanical and geometrical properties of the scintillating fiber shall not change for an ionizing dose of up to 50 kGy. Most producers are generally unable to measure and guarantee those parameters [52]. The tests to scintillating fibers included the evaluation of the photon spectrum after propagation through the fibers, the attenuation length and the scintillation process. In the case of combining the fibers with silicon photomultipliers (SiPMs), further studies will also be needed as it is known that SiPMs are sensitive to radiation damage. An alternative to the scintillating fibers may be the large area polycrystalline diamond detectors which are know to be highly radiation hard and with an expected time resolution at the level of few tens of picoseconds and a spatial resolution at the level of 1 mm [26, 27]. They demand however complex dedicated integrated electronics with large number of channels.

In what concerns the data acquisition, we plan to acquire the data with multiple FADCs, therefore increasing the throughput of the system. The DAQ system can be extended to 2,304 channels featuring a maximum read out speed of 3.5 Gbytes/s. Each ADC card with 24 channels can deliver up to 100 MByte/s and all cards can be synchronized by an external clock and time distribution.

Finally, a clinical prototype of a trigger system comprising such scintillating fibers will provide a fundamental input to PGI

for the verification of the particle range and dose delivery to the patient.

DATA AVAILABILITY STATEMENT

The datasets generated for this study are available on reasonable request to the corresponding author.

AUTHOR CONTRIBUTIONS

PM designed and performed the experiments. RD attended and provided support during the experimental campaigns and he contributed to the design of the experiments and interpretation of the results. JS coordinated the project, acquired funding, and provided guidance during the design of the detector. MS, GH, and TK provided support with the detector and electronics used in the experimental setup. MS manufactured the trigger according to the design developed together with RD, PM, and JS. PM conducted the post-processing of the experimental data and he wrote the software to perform the quantitative analysis. All authors discussed content and researched data. They reported quantitative parameters that demonstrate the scintillating fiber trigger for time resolved detection of prompt gamma radiation.

FUNDING

PM was supported by a research fellowship for postdoctoral researchers from the Alexander von Humboldt Foundation, Bonn, Germany. RD was supported by the International Max Planck Research School for Quantum Dynamics in Physics, Chemistry and Biology, Heidelberg, Germany.

ACKNOWLEDGMENTS

The authors thank the staff of the Heidelberg Ion-Beam Therapy Center (HIT), Heidelberg, Germany, in particular Dr. Stephan Brons and Dipl.-Ing. (FH) Jochen Schreiner for the technical support. The authors also thank the radiation protection department of the DKFZ, in particular Dipl.-Ing. Mechthild Kämmer, for the support with calibration sources.

SUPPLEMENTARY MATERIAL

The Supplementary Material for this article can be found online at: https://www.frontiersin.org/articles/10.3389/fphy.2020.00169/full#supplementary-material

REFERENCES

1. Parodi K, Crespo P, Eickhoff H, Haberer T, Pawelke J, Schardt D, et al. Random coincidences during in-beam PET measurements at microbunched therapeutic ion beams. *Nucl Intrum Meth A*. (2005) **545**:446–58. doi: 10.1016/j.nima.2005.02.002
2. Crespo P, Barthel T, Frais-Kolbl H, Griesmayer E, Heidel K, Parodi K, et al. Suppression of random coincidences during in-beam PET measurements at ion beam radiotherapy facilities. *IEEE Trans Nucl Sci.* (2005) **52**:980–7. doi: 10.1109/TNS.2005.852637
3. Stichelbaut F, Jongen Y. Verification of the proton beams position in the patient by the detection of prompt gamma-rays emission. In: *39th Meeting of the Particle Therapy Co-Operative Group*. San Francisco, CA (2003). p. 16.
4. Testa E, Bajard M, Chevallier M, Dauvergne D, Le Foulher F, Freud N, et al. Monitoring the Bragg peak location of 73 MeVu carbon ions by means of prompt γ-ray measurements. *Appl Phys Lett.* (2008) **93**:093506. doi: 10.1063/1.2975841
5. Biegun AK, Seravalli E, Lopes PC, Rinaldi I, Pinto M, Oxley DC, et al. Time-of-flight neutron rejection to improve prompt gamma imaging for proton range verification: a simulation study. *Phys Med Biol.* (2012) **57**:6429–44. doi: 10.1088%2F0031-9155%2F57%2F20%2F6429
6. Smeets J, Roellinghoff F, Prieels D, Stichelbaut F, Benilov A, Busca P, et al. Prompt gamma imaging with a slit camera for real-time range control in proton therapy. *Phys Med Biol.* (2012) **57**:3371–405. doi: 10.1088%2F0031-9155%2F57%2F11%2F3371
7. Verburg JM, Riley K, Bortfeld T, Seco J. Energy- and time-resolved detection of prompt gamma-rays for proton range verification. *Phys Med Biol.* (2013) **58**:L37–49. doi: 10.1088%2F0031-9155%2F58%2F20%2Fl37
8. Golnik C, Hueso-González F, Müller A, Dendooven P, Enghardt W, Fiedler F, et al. Range assessment in particle therapy based on prompt γ-ray timing measurements. *Phys Med Biol.* (2014) **59**:5399–422. doi: 10.1088%2F0031-9155%2F59%2F18%2F5399
9. Lopes PC, Clementel E, Crespo P, Henrotin S, Huizenga J, Janssens G, et al. Time-resolved imaging of prompt-gamma rays for proton range verification using a knife-edge slit camera based on digital photon counters. *Phys Med Biol.* (2015) **60**:6063–85. doi: 10.1088%2F0031-9155%2F60%2F15%2F6063
10. Petzoldt J, Roemer KE, Enghardt W, Fiedler F, Golnik C, Hueso-González F, et al. Characterization of the microbunch time structure of proton pencil beams at a clinical treatment facility. *Phys Med Biol.* (2016) **61**:2432–56. doi: 10.1088%2F0031-9155%2F61%2F6%2F2432
11. Parodi K, Brons S, Forck P, Franczak B, Haberer T, Hoffmann TK, et al. Measurement of the carbon ion microstructure after KO extraction. In: *EXTERNAL-HIT-08* (2008). p. 381.
12. Verburg JM, Seco J. Proton range verification through prompt gamma-ray spectroscopy. *Phys Med Biol.* (2014) **59**:7089–106. doi: 10.1088%2F0031-9155%2F59%2F23%2F7089
13. Hueso-González F, Enghardt W, Fiedler F, Golnik C, Janssens G, Petzoldt J, et al. First test of the prompt gamma ray timing method with heterogeneous targets at a clinical proton therapy facility. *Phys Med Biol.* (2015) **60**:6247–72. doi: 10.1088%2F0031-9155%2F60%2F16%2F6247
14. Martins PM, Bello RD, Rinscheid A, Roemer K, Werner T, Enghardt W, et al. Prompt gamma spectroscopy for range control with $CeBr_3$. *CDBME.* (2017) **3**:113–7. doi: 10.1515/cdbme-2017-0023
15. Gil EC, Albarrán EM, Minucci E, Nüssle G, Padolski S, Petrov P, et al. The beam and detector of the NA62 experiment at CERN. *J Instrum.* (2017) **12**:P05025. doi: 10.1088%2F1748-0221%2F12%2F05%2Fp05025
16. Schüttauf A. Timing RPCs in FOPI. *Nucl Instrum Meth A.* (2004) **533**:65–8. doi: 10.1016/j.nima.2004.07.002
17. Alici A. Status and performance of the ALICE MRPC-based Time-Of-Flight detector. *J Instrum.* (2012) **7**:P10024. doi: 10.1088%2F1748-0221%2F7%2F10%2Fp10024
18. Blanco A, Fonte P, Garzon JA, Koenig W, Kornakov G, Lopes L. Performance of the HADES-TOF RPC wall in a Au + Au beam at 1.25 AGeV. *J Instrum.* (2013) **8**:P01004. doi: 10.1088%2F1748-0221%2F8%2F01%2Fp01004
19. Sadrozinski HFW, Ely S, Fadeyev V, Galloway Z, Ngo J, Parker C, et al. Ultra-fast silicon detectors. *Nucl Instrum Meth A.* (2013) **730**:226–31. doi: 10.1016/j.nima.2013.06.033
20. Cartiglia N, Staiano A, Sola V, Arcidiacono R, Cirio R, Cenna F, et al. Beam test results of a 16 ps timing system based on ultra-fast silicon detectors. *Nucl Instrum Meth A.* (2017) **850**:83–8. doi: 10.1016/j.nima.2017.01.021
21. Sadrozinski HFW, Seiden A, Cartiglia N. 4D tracking with ultra-fast silicon detectors. *Rep Prog Phys.* (2017) **81**:026101. doi: 10.1088%2F1361-6633%2Faa94d3

22. Beddar AS, Mackie TR, Attix FH. Water-equivalent plastic scintillation detectors for high-energy beam dosimetry: I. Physical characteristics and theoretical considerations. *Phys Med Biol.* (1992) **37**:1883–900. doi: 10.1088%2F0031-9155%2F37%2F10%2F006
23. Beddar AS, Mackie TR, Attix FH. Water-equivalent plastic scintillation detectors for high-energy beam dosimetry: II. Properties and measurements. *Phys Med Biol.* (1992) **37**:1901–13. doi: 10.1088%2F0031-9155%2F37%2F10%2F007
24. Beaulieu L, Beddar S. Review of plastic and liquid scintillation dosimetry for photon, electron, and proton therapy. *Phys Med Biol.* (2016) **61**:R305–43. doi: 10.1088%2F0031-9155%2F61%2F20%2Fr305
25. Beddar S, Beaulieu L. *Scintillation Dosimetry*. Boca Raton: CRC Press; Taylor & Francis Group (2016).
26. Gallin-Martel ML, Bes A, Boukhémiri A, Bosson G, Collot J, Dauvergne D, et al. Large area polycrystalline diamond detectors for online hadron therapy beam tagging applications. In: *2016 IEEE Nuclear Science Symposium, Medical Imaging Conference and Room-Temperature Semiconductor Detector Workshop (NSS/MIC/RTSD)* (Strasbourg), (2016). p. 1–5.
27. Marcatili S, Collot J, Curtoni S, Dauvergne D, Hostachy JY, Koumeir C, et al. Ultra-fast prompt gamma detection in single proton counting regime for range monitoring in particle therapy. *Phys Med Biol.* (2020). doi: 10.1088/1361-6560/ab7a6c
28. Kirn T. SciFi–A large scintillating fibre tracker for LHCb. *Nucl Instrum Meth A.* (2017) **845**:481–5. doi: 10.1016/j.nima.2016.06.057
29. Leverington BD, Dziewiecki M, Renner L, Runze R. A prototype scintillating fibre beam profile monitor for Ion Therapy beams. *J Instrum.* (2018) **13**:P05030. doi: 10.1088%2F1748-0221%2F13%2F05%2Fp05030
30. Vignati A, Monaco V, Attili A, Cartiglia N, Donetti M, Mazinani MF, et al. Innovative thin silicon detectors for monitoring of therapeutic proton beams: preliminary beam tests. *J Instrum.* (2017) **12**:C12056. doi: 10.1088%2F1748-0221%2F12%2F12%2Fc12056
31. Krimmer J, Dauvergne D, Létang JM, Testa E. Prompt-gamma monitoring in hadrontherapy: a review. *Nucl Intrum Meth A.* (2018) **878**:58–73. doi: 10.1016/j.nima.2017.07.063
32. Pausch G, Berthold J, Enghardt W, Römer K, Straessner A, Wagner A, et al. Detection systems for range monitoring in proton therapy: needs and challenges. *Nucl Instrum Meth A.* (2018) **954:**161227. doi: 10.1016/j.nima.2018.09.062
33. Hueso-González F, Bortfeld T. Compact method for proton range verification based on coaxial prompt Gamma-ray monitoring: a theoretical study. *IEEE Trans Radiat Plasma Med Sci.* (2020) **4:**170–83. doi: 10.1109/TRPMS.2019.2930362
34. Haberer T, Debus J, Eickhoff H, Jäkel O, Schulz-Ertner D, Weber U. The heidelberg ion therapy center. *Radiother Oncol.* (2004) **73**:S186–90. doi: 10.1016/S0167-8140(04)80046-X
35. Hara K, Hata K, Kim S, Mishina M, Sano M, Seiya Y, et al. Radiation hardness and mechanical durability of Kuraray optical fibers. *Nucl Instrum and Meth A.* (1998) **411**:31–40.
36. Joram C, Haefeli G, Leverington B. Scintillating fibre tracking at high luminosity colliders. *J Instrum.* (2015) **10**:C08005. doi: 10.1088%2F1748-0221%2F10%2F08%2Fc08005
37. Ekelhof RJ. *Studies for the LHCb SciFi Tracker - Development of Modules from Scintillating Fibres and Tests of their Radiation Hardness*. Technische Universitaet Dortmund (2016). Available online at: https://cds.cern.ch/record/2212494
38. Dauvergne D. Online control of particle therapy - CLaRyS collaboration. In: *Final MediNet Network Meeting*. Wiener Neustadt (2019). p. 18–25. Available online at: https://hal.archives-ouvertes.fr/hal-02350983
39. Tessonnier T, Mairani A, Chen W, Sala P, Cerutti F, Ferrari A, et al. Proton and helium ion radiotherapy for meningioma tumors: a Monte Carlo-based treatment planning comparison. *Radiat Oncol.* (2018) **13**:2. doi: 10.1186/s13014-017-0944-3
40. Mein S, Dokic I, Klein C, Tessonnier T, Böhlen TT, Magro G, et al. Biophysical modeling and experimental validation of relative biological effectiveness (RBE) for ^{4}He ion beam therapy. *Radiat Oncol.* (2019) **14**:123. doi: 10.1186/s13014-019-1295-z
41. Schoemers C, Feldmeier E, Naumann J, Panse R, Peters A, Haberer T. The intensity feedback system at Heidelberg Ion-Beam Therapy Centre. *Nucl Instrum Meth A.* (2015) **795**:92–9. doi: 10.1016/j.nima.2015.05.054
42. Werner F, Bauer C, Bernhard S, Capasso M, Diebold S, Eisenkolb F, et al. Performance verification of the FlashCam prototype camera for the Cherenkov Telescope Array. *Nucl Instrum Meth A.* (2017) **876**:31–4. doi: 10.1016/j.nima.2016.12.056
43. The CTA Consortium, Actis M, Agnetta G, Aharonian F, Akhperjanian A, Aleksić J, et al. Design concepts for the Cherenkov Telescope Array CTA: an advanced facility for ground-based high-energy gamma-ray astronomy. *Exp Astron.* (2011) **32**:193–316. doi: 10.1007/s10686-011-9247-0
44. Dal Bello R, Magalhaes Martins P, Graça J, Hermann G, Kihm T, Seco J. Results from the experimental evaluation of $CeBr_3$ scintillators for ^{4}He prompt gamma spectroscopy. *Med Phys.* (2019) **46**:3615–26. doi: 10.1002/mp.13594
45. Pühlhofer G, Bauer C, Bernhard S, Capasso M, Diebold S, Eisenkolb F, et al. FlashCam: a fully-digital camera for the medium-sized telescopes of the Cherenkov Telescope Array. In: *Proceedings of The 34th International Cosmic Ray Conference — PoS(ICRC2015)*. The Hague: Sissa Medialab (2016). p. 1–8. doi: 10.22323/1.236.1039
46. Testa M, Bajard M, Chevallier M, Dauvergne D, Freud N, Henriquet P, et al. Real-time monitoring of the Bragg-peak position in ion therapy by means of single photon detection. *Radiat Environ Biophys.* (2010) **49**:337–43. doi: 10.1007/s00411-010-0276-2
47. Dal Bello R, Martins PM, Brons S, Hermann G, Kihm T, Seimetz M, et al. Prompt gamma spectroscopy for absolute range verification of ¹²C ions at synchrotron based facilities. *Phys Med Biol.* (2020). doi: 10.1088/1361-6560/ab7973
48. Leo WR. 2. In: *Techniques for Nuclear and Particle Physics Experiments: A How-to Approach*. Berlin; Heidelberg: Springer Berlin Heidelberg (1994). p. 17–68. Available online at: https://doi.org/10.1007/978-3-642-57920-2_2
49. Graeff C, Weber U, Schuy C, Saito N, Volz L, Piersimoni P, et al. [OA027] Helium as a range probe in carbon ion therapy. *Phys Med.* (2018) **52**:11. doi: 10.1016/j.ejmp.2018.06.099
50. Mazzucconi D, Agosteo S, Ferrarini M, Fontana L, Lante V, Pullia M, et al. Mixed particle beam for simultaneous treatment and online range verification in carbon ion therapy: Proof-of-concept study. *Med Phys.* (2018) **45**:5234–43. doi: 10.1002/mp.13219
51. Blanc F. Scintillating Fiber Trackers: recent developments and applications. In: *14th ICATPP Conference on Astroparticle, Particle, Space Physics and Detectors for Physics Applications*. Como (2013). p. 20–4. Available online at: https://cds.cern.ch/record/1603129
52. Joram C, Uwer U, Leverington BD, Kirn T, Bachmann S, Ekelhof RJ, et al. *LHCb Scintillating Fibre Tracker Engineering Design Review Report: Fibres, Mats and Modules*. Geneva: CERN (2015). Available online at: https://cds.cern.ch/record/2004811

Conflict of Interest: The authors declare that the research was conducted in the absence of any commercial or financial relationships that could be construed as a potential conflict of interest.

frontiers in Physics

REVIEW
published: 12 August 2020
doi: 10.3389/fphy.2020.00234

Cancer Risk of Low Dose Ionizing Radiation

Yasser F. Ali[1,2], *Francis A. Cucinotta*[3], *Liu Ning-Ang*[1] *and Guangming Zhou*[1]*

[1] State Key Laboratory of Radiation Medicine and Protection, School of Radiation Medicine and Protection, Institute of Space Life Sciences, Medical College of Soochow University, Collaborative Innovation Center of Radiological Medicine of Jiangsu Higher Education Institutions, Suzhou, China, [2] Biophysics Lab, Physics Department, Faculty of Science, Al-Azhar University, Cairo, Egypt, [3] Department of Health Physics and Diagnostic Sciences, University of Nevada, Las Vegas, NV, United States

The radiation exposure of individuals has been on the rise due to an increased amount of radiation use, e.g., in medicine for diagnostic imaging and treatment procedures, industrial applications including military defense activities and nuclear power plants, and in academics for educational and scientific research. Space exploration missions and space tourism are additional areas of protracted low dose exposure situations with radiation types not present on the Earth. In contrast to high doses of ionizing radiation, cancer risk assessment of the more commonly encountered or protracted radiation exposure is still under debate and uncertainty making it fuzzy area. A major challenge lies in providing a scientific basis to estimate low dose radiation carcinogenesis risks. In this review we aim, through the collected epidemiological and experimental studies' data, to address the central questions in radiological protection; including quantification of the risks and uncertainties from low doses of ionizing radiation and what is a sound scientific consensus to advise on risk perception for low dose radiation exposure.

Keywords: low dose exposure, HBRL inhabitants, space exploration missions, nuclear industry workers, cancer risk

OPEN ACCESS

Edited by:
Vincenzo Patera, Sapienza University of Rome, Italy

Reviewed by:
Dimitris Emfietzoglou, University of Ioannina, Greece
Marco Durante, GSI Helmholtz Center for Heavy Ion Research, Germany

***Correspondence:**
Guangming Zhou
gmzhou@suda.edu.cn

Specialty section:
This article was submitted to Medical Physics and Imaging, a section of the journal Frontiers in Physics

Received: *03 February 2020*
Accepted: *28 May 2020*
Published: *12 August 2020*

Citation:
Ali YF, Cucinotta FA, Ning-Ang L and Zhou G (2020) Cancer Risk of Low Dose Ionizing Radiation. Front. Phys. 8:234. doi: 10.3389/fphy.2020.00234

INTRODUCTION

Health effects of exposure to ionizing radiation were identified shortly after the discovery of X-rays in 1895. Epilation was first probed then skin burns documented soon after [1]. With the invention of high voltage X-ray tubes and their implementation in medical clinics, injuries to tissues, known as tissue reactions, are a sequela of penetration of large amount of radiation into the body.

The carcinogenic effects of ionizing radiation are late effects that occur with a probability that depends on radiation dose. Cancer risk of low dose radiation has become an essential component of radiation protection and has attracted public and social concerns about safety in relation to variety of issues, such as medical imaging tests for the early detection of defeats, the future of nuclear power, environmental radiation exposure from terrestrial radon, nuclear weapons test fallout, radiological terrorism and human space exploration. For example, most radiological examinations produce doses in the range of 3–30 mSv. Obviously, high doses of ionizing radiation (>100 mSv) increases cancer risk [2], while at lower doses the situation is much less clear. Epidemiological studies suggest that the lowest dose value of ionizing radiation at which good evidence of increased cancer risks in human exists is ≈10–50 mSv for an acute exposure [3] and ≈50–100 mSv for prolonged exposure [4].

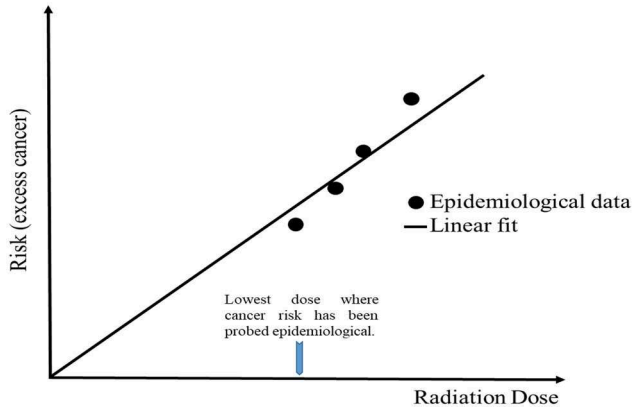

FIGURE 1 | LNT dose response model for radiation-induced stochastic health effects estimation. Its straight line extrapolated to zero assuming radiation has the potential to cause lesions at any dose value.

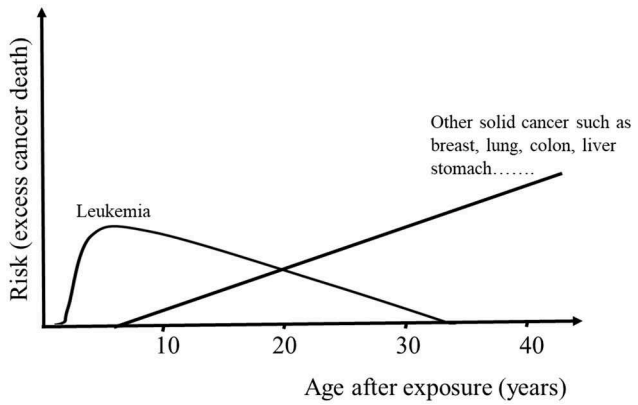

FIGURE 2 | Schematic overview of the documented findings regarding the late effect of the bomb-released radiation on cancer mortality throughout life. Leukemia risk shows a linear-quadratic response; increased in the early period after bombing then decreased, whereas other solid cancers followed a linear manner; continuing to increase as the cohort ages.

In order to quantify the risk of low dose radiation, large epidemiological studies are needed to get a useful degree of precision. For example, if excess cancer death cases have been recorded in sample size of 500 persons in response to 1,000 mSv dose exposure, then sample size of 50,000 would be needed for documenting the carcinogenic effect of 100 mSv, and ≈5 million for 10 mSv dose. In other words, the sample size should increase as the inverse square of the dose in order to maintain the statistical precision and power [5]. For several decades, the Linear non-threshold (LNT) model has been the standard risk assessment used by the radiation protection community to determine the health outcomes associated with low doses by means of extrapolation from the risk assessed at high doses [6], ICRP publications 99 and 103 [7, 8], UNSCEAR 2012 and 2017 reports [9, 10], and the BEIR VII report [11]. The LNT relationship is a practical way to fit limited epidemiology data. However, LNT is also often cast in terms of biophysical hypotheses, such as: (a) Damage induction is directly proportional to dose, from 1 mGy to 100 Gy; (b) mis-repair of DNA double-strand break (DSB) is thought to have a probability of inducing invasive neoplastic cell transformation, irrespective of DSB baseline rate and dose delivered to the cell. Intrinsic defense tools against carcinogenesis, such as DNA repair and programmed cell death, make the LNT model obsolete. It is regularly argued that the LNT model is overprotective and low-level radiation exposure may have health benefits as a set of data showed that these countermeasures are higher at low doses than at high doses and for fractionated or protracted irradiation than for acute irradiation [12]. By contrast, some biological effects of radiation, such as persistent transmissible genomic instability and bystander phenomena [13] could increase cancer risk above extrapolation [14]. The current risk estimation, depicted in **Figure 1**, is to extrapolate radiation-induced cancer risks from higher doses, where the risk is assessed epidemiologically, to lower doses.

Nuclear disaster causes additional negative effects on public perception concerning radiation risk, and results in overestimating health risks of radiation exposure even at extremely low levels of radiation (several mSv). Such public confusion in South Korea after the Fukushima accident resulted in temporary closures of schools, massive selling of radioprotective masks and refusal of Japanese farming products. All of these actions were adopted by public even in absence of strong evidence for radioactive contamination according to official announcements from the Korean government [15]. Radiation experts (biologists, epidemiologists, and physicists) should be able to reduce societal confusion about the health risk of low dose radiation exposure based on the experimental results and population-based observational data. Several low-dose exposure scenarios are identified.

NUCLEAR EMERGENCY AND WAR-TIME EXPOSURES

Japanese survivors of the atomic bombing in Hiroshima and Nagasaki are thought to be the most reliable source of information about long-term effects of radiation exposure on health because of the large size of the cohort of over 100,000 persons, consisting of both sexes and all ages, and a wide range of individually assessed doses. Radiation-associated excess rates of leukemia and solid cancers have schematically summarized in **Figure 2**.

Humanity has experienced these atomic bombs and other nuclear disasters, such as Chernobyl accident in 1986 and the latest devastating accident to date; Fukushima Daiichi NPP in 2011. Survivors of the nuclear bomb, who have not died from injuries produced by blast and heat from the bomb, have a radiation-related increased risk of cancer owing to late-onset effect of radiation, 60% of whom have doses of at least 5 mSv, and people exposed as children have a higher radiation-induced cancer risk than those exposed at older ages; the excess relative risk increased with dose for both utero and early childhood with

values of 1.0 and 1.7 per Sv, respectively [16, 17]. Additionally, the cancer risk declines with increasing age; for those exposed at age 30, the solid cancer risk is elevated by 47% per Sv above those at age 70 [18]. In addition to breast, ovary, bladder, lung, liver, nervous system and thyroid [19], radiation-associated increase in risk was reported for digestive and other respiratory systems [17, 18]. On the other hand, no increased risks for malignancies or other diseases have been observed in children who were conceived after parental exposure to bomb-released radiation [20] but continuing investigations is indispensable since the large number of additional cases provides a more stable database, needed for establishing limits and recommendations for radiation protection.

2020 marked the 34th anniversary since the Chernobyl nuclear power plant explosion in northern Ukraine. An adequate number of publications are dedicated to observing the consequences of the Chernobyl disaster that resulted in a massive release of radionuclides into the environment, affecting large nearby areas, Ukraine, Belarus and Russian Federation. Environmental exposure to ^{131}I carries an increased risk of thyroid cancer [21] and the risk is the greatest to those who were children at the time of exposure [22]. So, studies in clinical and pathological features of patients with post-Chernobyl papillary thyroid carcinoma have focused on children, who were 2 years old or less at the time of Chernobyl accident [23], as the most vulnerable group with the highest risk of developing cancer. Data came from Tronko et al. [24] demonstrating a strong association between ^{131}I and thyroid neoplasia risk including thyroid cancer and follicular adenoma (FA) for individuals who were $<$18 years old at the time of the accident with an excess odd ratio per Gy of 1.36 and 2.03, respectively. The excess risk is set to persist nearly three decades after exposure and underscore the importance of continued follow-up of this cohort to characterize long term patterns of ^{131}I risk. Finally, lens opacities were observed, particularly among interventional radiologists who may receive substantial lens doses. Evidence for genetic effects among exposed persons was inconsistent [22]. Finland and Sweden were among the countries most heavily affected by the radioactive fallout that spread out after the Chernobyl crisis. Many papers have appeared and claim to analyse the overall cancer incidence in relation to radiation dose from the Chernobyl accident in both the Finnish and Swedish populations [25–27]. Comprehensive cohort analysis did not show variation in the cancer incidence in relation to radiation exposure in any calendar period, or any subgroup by sex or age at the time of the accident. An analogous study failed to distinguish the effect of ^{137}Cs, released from Chernobyl accident, on cancer incidence in Sweden.

The United States carried out numerous nuclear weapon tests ($>$800 underground and $>$200 atmospheric atomic detonations) of the over 2,000 nuclear explosions that were conducted worldwide in the five decades from 1945 to 1996. A cohort of 115,329 American veterans has been assembled for the purpose of epidemiological research and compensation. Both red bone marrow and male breast doses have been estimated for approximately a 2,000-person subset of the veteran cohort to perform risk analyses for leukemia and male breast cancer mortality [28] but the results have not yet been published. Approximately two-thirds of participants received a total dose to red bone marrow of 5 mGy with little variability between test site or among military branches. Male breast doses were ∼20% higher than those of red bone marrow [29]. These dosimetry results indicate a need to continue close monitoring of this cohort for better understanding and prediction of disease risk following low dose exposures and to develop biologically-based dose response models [30].

OCCUPATIONAL EXPOSURE

Researchers have been trying to estimate the cancer risks of prolonged exposure to very low doses of ionizing radiation, which might be received from medical scans or from nuclear industry related work. Occupational doses from five different job categories are assessed and summarized in **Table 1**. Developed nuclear programs in USA, UK and France have employed hundred thousand of workers over the past years. The primary quantitative basis for radiation protection standard comes from epidemiological studies of survivors of atomic bombing of Hiroshima and Nagasaki in which people were exposed to varying doses of ionizing radiation. The National Radiological Protection Board (NRPB) defined "low dose" as values below 100 mGy for acute low dose exposures and below 5 mGy per hour for low dose rate. National Registry for Radiation Workers (NRRW-3) reported workers with individual accumulative dose value above 100 mGy, higher than the upper limit for "low dose" delivered acutely because no deviation in the dose-response from linearity has been reported, additionally total individual dose has accumulated over a prolonged time interval.

Risks associated with protracted low dose exposure are more relevant to health practitioners and nuclear-industry workers. Many of these workers have received low (an average of 11 mSv/y), above background doses of radiation which itself is about 2.3 mSv/y from sources, such as cosmic rays and radon [3], and their radiation doses have been monitored carefully overtime through the use of personal dosimeters.

The International Nuclear Workers study (INWORKS) was conducted in order to strengthen the scientific basis for protecting people from Low dose protracted or intermittent radiation exposure. This cohort includes workers from USA, UK and France who have received a precisely known dose and have been followed up to 60 years after exposure. The linear increase in the relative rate of cancer with a cumulative dose by 48% per Gy was summarized; of 66,632 known death by the end of fellow-up, 17,957 were due to solid cancer [32]. Strikingly, the cancer risk per unit of radiation dose among radiation workers was similar to the estimate that comes from studies of Japanese atomic bomb survivors [32]. Leuraud et al.'s [33] study confirmed that the risk of leukemia rose with prolonged low dose radiation exposure, although the rise was minuscule. This study provided very strong evidence of positive association between long term low dose radiation exposure and leukemogenesis; the excess relative risk of leukemia mortality excluding chronic lymphocytic leukemia was 2.96 per Gy. The International Commission on

Radiological Protection (ICRP) recommendations, which most radiation-protection authorities follow, call for the monitoring of individuals whose annual exposure exceed 6 mSv. They restrict exposure to 20 mSv annually over 5 years, with maximum of 50 mSv in any 1 year [34]. These low dose limits are adopted by ICRP to ascertain that risks and benefits of practices on ionizing radiation are balanced and to provide a border between tolerable and intolerable radiation doses.

SPACE EXPLORATION

On 1992, the Chinese government announced the manned space exploration program and approved the "3 steps" development strategy which planned to end by building a space station to conduct experiments on a large scale with long-term human participation. Between 1999 and 2002, Four preparatory unmanned spacecrafts, SZ-1 to SZ-4, have been successfully launched to test key equipment and technology in the spacecraft and assess the space environment risk on representative living systems, from the cellular level to the whole organism. Exploration activity has dramatically increased over the past 20 years. To date, 11 "Shenzhou" spacecrafts, Tiangong-1 aircraft, and Tiangong-2 Space Laboratory have been successfully launched. A large number of scientific experiments have been carried out smoothly, such as monitoring space radiation doses, assessing radiation health risks, and other exploratory studies which are considered to be a technical platform for the successful establishment of the Chinese Space Station (CSS) in 2022 [35]. There are many destinations for human space exploration, including the moon, low earth orbit (LEO), and Mars. Space radiation, isolation (Psychosocial problems) and microgravity are the main health problems associated with human exploratory missions in outer space [36–38]. Whole body doses of 1–2 mSv per day accumulate in interplanetary space and about 0.5–1 mSv per day on the planetary surface. Effective doses for 6-months space station missions are about 0.08 Sv and could exceed 1 Sv for a Mars mission [39–41]. Different national space agencies have issued specific recommendations for accumulative dose limits for LEO astronauts, such as ISS crew members in order to prevent unacceptable deterministic effects for red blood cells-forming organs, bone marrow, spleen and lymphatic tissue. CSA, ESA and RFSA adopt a single career dose limit of 1 Sv for all genders and ages while NASA and JAXA apply different exposure limitation, summarized in **Table 2**. The Chinese Space Agency set 0.15 and 0.2 Sv skin dose limits for 3- and 7-days missions and a relatively low limit for 30-days missions, 0.4 Sv compared to 1.5 Sv adopted by ESA and RFSA.

Space radiation comprises galactic cosmic rays (GCR), solar particle events (SPE), and trapped belt radiation. GCR originate from outside of the solar system and consist of 2% electrons and 98% baryons, which in turn are composed of 87% proton, 12% alpha-particle and 1% of heavy ions with high energy and charge [43]. The energy spectrum of GCR peaks near 1,000 MeV/u. Space flights in low earth orbit, such as missions on space shuttles, are protected by geomagnetic field and solid shielding of the Earth [44]. Thick shielding cannot be regarded as a solution for the issue of radiation in space; the very high energy of cosmic rays and the severe mass constraints in space flight represent a serious hindrance of effective shielding [45]. Radiation in space is substantially different from earth; high energy and charge particles (HZE) dominate the exposure in deep space, whereas γ-rays and low energy alpha-particles are the major contributors on Earth. This difference causes high uncertainty on the estimated radiation health risk [46–48]. Major uncertainties include radiation quality factors, dose-rate modifiers, the transfer of risk from one population to another and uncertainties related to radiation quality dependence of tumor lethality and non-targeted effects [46–48]. Only a few sources of HZE particles are currently available in the world for experimental studies. Ground-based research into space radiation is necessary to improve the understanding of biological effects of densely ionizing heavy ions, which in turn has a useful impact in predicting and reducing health risks for exposed individuals [49].

Chromosomal aberrations in peripheral blood lymphocytes is an important biomarker in predicting space radiation risk, as it provides simultaneous information on dose, and it has been measured extensively in astronauts during the past 10 years. The main contribution of biomarkers to manned space exploration is in reducing risk uncertainties that are estimated to be between 200 and 400% [50]. Upper 95% confidence intervals for cancer fatality could exceed 20% when non-targeted effects are included in risk estimates [51, 52]. Several reports have been published on chromosomal rearrangements in human cells induced by accelerated particles and other types of HZE [49, 53] and further contribute to carcinogenic risk in astronauts [43]. Some investigators have provided clear evidence for development and progression of intestinal tumors [54], hepatocellular carcinoma [55] and lung cancer [56] in response to HZE exposure.

The radiation environment in space is complex and contains mixture of charged particles with a range of energy. It was reported that a low dose of proton protects cells against chromosomal damage induced by subsequent exposure to doses from 1 GeV/u iron ions [57]. This phenomenon is well-known in radiation biology literature as an adaptive response that is classically defined as the ability of low dose radiation exposure to partially ameliorate the effect of subsequent exposure to high challenge doses of radiation. This adaptive response is temporary and does not last for a long time, maximizing within a few hours of exposure and decaying within 48 h. Upregulation of DNA repair, antioxidant status and the immune system are the main contributors for this property. Unirradiated (bystander) cells with which the proton-irradiated cells were co-cultured were also significantly protected from the DNA-damaging effects of the challenge dose. These results show that the protective adaptive responses can spread from cells targeted by low-LET space radiation to bystander cells in their vicinity [58]. However, it is not clear if it will hold up for the lower space doses and dose-rates compared to experimental doses.

Upon traveling to deep space (interplanetary travels), beside HZE particles, astronaut's bodies would also be hit by secondary radiation including neutrons and recoil nuclei produced by nuclear reactions in spacecraft walls. Hu et al. [59] compared

TABLE 1 | Occupational exposures for various job categories.

Workplace	Period	Monitored workers 10^3	Annual effective dose (mSv)
Uranium mining	2000–2002	12	1.9
Diagnostic radiology	2000–2002	6.670	0.5
Radiotherapy	2000–2002	264	0.5
Cyclotron			*WBD: 0.35–0.85 **WD: <7.95
Radiochemistry lab			*WBD: 0.60–1.80 **WD: <4.45

Data from UNSCEAR report [31].
**WBD, Whole body dose; **WD, wrist dose.*

TABLE 2 | The NASA and JAXA career effective dose limits for 1-year mission.

Agency	Personal traits				
	Gender	Age			
		30	40	50	60
NASA	M	0.78	0.88	1.00	1.17
	F	0.60	0.70	0.82	0.98
JAXA	M	0.60	1.00	1.20	1.20
	F	0.60	0.90	1.10	1.10

Limit values are estimated not to exceed a 3% Risk of Exposure Induced Death (REID) from fatal cancers at a 95% confidence level [42].
Dose limits are expressed in units of Sv.

TABLE 3 | Estimated annual effective doses to persons living in areas of high natural radiation background.

Regions of high environmental radiation	Annual effective dose
Ramsar, Iran	Range from 3.2 to 203 mSv
Kerala, India	Range from 1 to 45 mSv
Guarapari, Brazil	<7 mSv
Yangjiang, China	6.4 mSv

Values collected from Hendry et al. [64].

the biological effect of an iron beam with a shielded beam of the same average energy on cells in different cell cycle conditions. The conclusion that has been drawn from his study is that the biological effect of secondary particles should be examined for improved shielding design. Exposure of human and mice cells to simulated space radiation to measure the frequency of malignant transformation will aid in developing efficient countermeasures against space radiation-induced adverse effects. For example, Selenomethionine was shown to be a very promising countermeasure against HZE-induced cytotoxicity by enhancing DNA repair machinery in irradiated cells [60]. The oncogenic potential of cosmic rays is the main hindrance to interplanetary travel, ground-based research into space radiation plays a key role in reducing projected cancer risk uncertainty and development of physical (shielding) and biomedical (radioprotectors) countermeasures.

HIGH BACKGROUND RADIATION AREA

High natural radiation background areas (HBRA) have been of special interest as they provide opportunity for the study of biological effects of an environment that resembles the chronic exposure of future space colonists to doses of ionizing radiation of several orders of magnitude higher-than-normal levels [61]. Radionuclides, ^{232}Th, ^{235}U, ^{238}U, and radioisotope of Potassium (^{40}K), are the major sources of outdoor natural radiation. The knowledge of their distribution in soil, sand and rock plays an important role in protecting humans from serious health hazards.

Ramsar, Iran, due to the concentration of ^{226}Ra and its daughters which were brought to the earth's surface by hot springs, also Kerala, in India [62], and certain beaches in Brazil [63], due to radioactive mineral-rich sand, all are examples of regions with higher level of natural radiation (**Table 3**).

Guarapari region of Brazilian coast is a famous tourist attraction where thousands of people try to cure disease by lying on or cover themselves with black beach sand. Vasconcelos et al. [65] began to determine the reference level of this region using gamma spectrometry and compared their results with internationally accepted values. These authors observed that Areia preta beach in Guarapari has dose rate up to 87 μSv/h; the same dose rate that can be encountered in the 1 km vicinity of the Chernobyl power plant. Areia Preta may therefore has the highest background found in beaches in world, possibly due to activity concentration of ^{232}Th. It has been suggested to get rid of dark-yellow to brown monazite from noxiously radioactive spot to minimize risk of radiation injury and keep the black sand as attraction for tourism; the activity concentrations found in the mainly monazitic (dark yellow) sand fraction are up to 1000 times higher than the normal soil values. High natural radiation environment of Guarapari stimulate researchers to warn visitors from potential health risks at staying longer.

The southwest coastal line of the Kerala state in India is one of such regions known to have elevated levels of background radioactivity mainly due to monazite sand available with a high abundance of thorium. Inhalation, external exposure and ingestion are three main pathways of nature radiation exposure to human beings. It was reported that the inhalation dose varies from 0.1 to 3.53 mSv/y and the inhalation dose imported by indoor radon and its progeny is >50% of the total radiation dose [62]. Even if chromosomal aberrations were seen in the lymphocytes of exposed persons, the carcinogenicity has still not been established. A cohort study conducted in this region, the southwest coastal area of Kerala, during 2006–2009 to assess the role of high level natural radiation (≥0.1 mSv/y) on congenital mental radiation and cleft lip/palate has shown that the prevailing high natural radiation exposure does not increase the risk of these malfunction [66]. However, its widely known that stable translocation aberration is associated with human malignancies; certain types of leukemia are examples of this. Therefore, recent data are necessary to confirm whether high background induced unnatural aberrations activate oncogenes.

On the same hand, Yangjiang in Guangdong province, China, is categorized as a high background radiation area. It was

reported that the average annual effective dose to residents in HBRAs of Yangjiang was 6.2 mSv, about three times higher than that of the control area [67–69]. It was reported the annual dose received by the 0–7 age group was the highest among all age groups [70]. The individual cumulative dose to inhabitants living in houses built over 30 years ago was relatively low, compared with those living in houses built more recently [70]. However, this difference was not revealed in the control area. Yong-ling et al. [68] estimated that 88% of total amount of internal radiation dose to the residents in HBRA arose from the inhalation of ^{222}Rn, ^{220}Rn, and their products. An appropriate number of epidemiological studies were carried out to explore the cancer risk associated with low level radiation exposure [67, 70]. These studies did not find any statistically significant differences in all cancer mortality between control and high natural radiation area. Further, the relative cancer incidence risks of stomach, colon, liver, lung, bone, female breast and thyroid in Yangajiang were also not statistically different from the area with normal radiation levels. Thus, the typical level of natural radiation background in Yangjiang is insufficient to trigger a carcinogenesis risk increase in humans, and this conclusion may be partially owing to the enhanced immune function in the human body after long-term exposure in Yangjiang [69].

NUCLEAR MEDICINE AND RADIOTHERAPY

A double-edged sword is considered the best description for the status of ionizing radiation. It is harmful to health from its role as a carcinogen. However, it is beneficial for the use in both diagnostic and therapeutic medical application [71].

Radiotherapy is one of the most common and effective therapeutic modalities for the treatment of cancer. Usually 50% of all patients with localized malignant tumors are treated with radiation. Radiotherapy for cancer allows for the killing of the cancer cells but also presents a risk to the normal tissue surrounding the tumors and forming secondary malignant neoplasms at the same organ or at a distant part of the body. subsequent malignancies risk is the most significant late effect of radiation treatment experienced by cancer survivors [72]. Because of longer life expectancies, younger patients are certainly at greater risk [73, 74]. A large cohort study includes 5,798 Hodgkin's lymphoma patients treated with chemotherapy in Britain from 1963 to 2001—the majority of whom, 3,432, also received radiotherapy—has been conducted to assess secondary malignancy risks. Chemotherapy alone led to a raised risk of second cancer (RR, 2.0). However, this risk is lower and affects fewer anatomic sites than that of combined modalities (RR, 3.9) [74]. de Gonzalez et al. [75] performed a large-scale Surveillance, Epidemiology and End Results (SEER) analysis on cancer survivors who were treated with radiotherapy and documented a small increase in the risk of developing a second cancer. Other treated sites which have been investigated, including breast radiation treatment, again demonstrating the risk of second cancer development. The lungs and heart are likely to receive an amount of stray radiation during radiotherapy to breast cancers as they lie underneath the irradiated area. It has been reported that heart disease and lung cancer risks gradually increased after breast irradiation [76, 77]. Countermeasures are likely to be beneficial for cancer survivors after radiotherapy as they are capable of mitigating radiation-induced biological effects including damage of normal tissue surrounding tumors and radiation-induced secondary malignancies [78].

Many years ago, researchers proposed that accelerated proton and heavy ions could be used for localized cancer therapy based on their depth-dose distribution compared to photon radiation including X-ray and γ-rays [1]. Heavy ions are more effective than X-rays for killing cells as well as other endpoints, such as causing mutation [79]. Sethi et al. [80] published a retrospective review to see the incidence of second malignant neoplasms among retinoblastoma patients who received either photon (31 patients) or proton (55 patients) beams radiation. Cumulative incidence of second malignancies was significantly higher among the photon cohort (14% vs. 0; $p = 0.015$). Similarly, a retrospective study investigating the risk of secondary malignancies in prostate cancer patients found a lower risk with carbon ion radiotherapy (CIRT) compared to photon-based therapy [81], possibly due to the "Bragg peak" characteristic of particle therapy where low levels of energy are deposited outside of the target volume.

Radiation can induce apoptosis or trigger a DNA repair mechanism. In general, minor DNA damage is thought to temporarily halt the cell cycle to allow effective repair, while more severe damage can induce an apoptotic cell death program [82]. DNA is the quintessential target; the deleterious effects of radiation, mutation and carcinogenesis, are mainly due to irreparable damage to DNA. Wu et al. [83] provided evidence suggesting that extranuclear targets play a role in such damage. His data demonstrated that irradiation of cytoplasm produce gene mutation in nucleus through free radicals. His conclusion was that cytoplasmic traversal by ionizing radiation may be more dangerous than nuclear traversal, because the mutagenicity is accomplished by little or no killing of target cells. Radiation-induced carcinogenesis is a highly modifiable phenomenon by a non-carcinogenic process [84, 85]. The agents include the specific characteristics of the radiation, radiation type, dose rate, dose fractionation, dose distribution, etc., as well as many other contributing elements that are not specific to the radiation exposure, such as animal genetic characteristics, environment of the animal and animal age at exposure, as found from radiation-carcinogenesis studies in animals.

CONCLUSION

In this review, we provide discussion of the cancer risk that may arise following exposure to low dose ionizing radiation. Radiation-related cancer risk in the life span study (LSS) cohort of atomic bombs has been reported to continue raising throughout life. Significant dose response (ERR for all solid cancer) is observed even over 0–0.2 Gy dose range; supporting the hypothesis that there is no threshold below

which cancers are not induced. Identification of non-cancer disease risks, psychological consequences of nuclear disaster for instance is one of several important steps to accomplish a comprehensive exposure outcome study. Million Worker Study (MWS) includes many subjects, 12 times higher than Japanese bomb survivors, as well as covering the issues faced today concerning exposures delivered over years, such as medical, occupational and environmental exposure. This large number of cases along with accurate individual exposure information will reduce uncertainty in the calculation of excess relative risk per Gray (ERR/Gy) and thus provide more reliable assessment of the long term effects of radiation exposure.

During low Earth orbit, shuttle crew members experience 90-min light-dark cycles. In addition, light intensity aboard ISS, space radiation, gravity and magnetic field also greatly differ from those on the ground. Numerous ground-based studies into the biological threats of these environmental stressors are needed to predict and reduce health risks for exposed individuals. Benefits from lunar mission and deep-space human exploration to Mars must be balanced between cost and the safety of astronauts.

Data collected so far suggest that particle therapy leads to a lower risk of secondary malignancies than conventional X-ray techniques. Moreover, ion beam therapy characterized by a low therapeutic dose to healthy tissue and a neutron production even lower than from photon therapy. Therefore, it provides a promising tumor treatment choice.

AUTHOR CONTRIBUTIONS

GZ formed the work idea. YA literature collect and draft the article. FC and LN-A did the critical revision of the article. Eventually, FC, LN-A, and GZ gave their final approval of the version to be published. All authors contributed to the article and approved the submitted version.

FUNDING

This work was supported by the China National Natural Science Foundation awards (Nos. 11405235 and 81872622), National Key R&D Program of China (Nos. 2018YFC0115704, 2018YFC0115703, and 2018YFC0115705), China Postdoctoral Science Foundation (2018M632367), Jiangsu Postdoctoral Science Foundation (1701176B), and the Program of the Network-Type Joint Usage/Research Center for Radiation Disaster Medical Science.

REFERENCES

1. Hall EJ, Giaccia AJ. *Radiobiology for the Radiologist*. Philadelphia, PA: Lippincottt Williams & Wilkins (2012).
2. Imaoka T, Nishimura M, Iizuka D, Daino K, Takabatake T, Okamoto M, et al. Radiation-induced mammary carcinogenesis in rodent models: what's different from chemical carcinogenesis? *J Radiat Res.* (2009) **50**:281–93. doi: 10.1269/jrr.09027
3. Abbott A. Researchers pin down risks of low-dose radiation. *Nature.* (2015) **523**:17–8. doi: 10.1038/523017a
4. Tubiana M, Aurengo A, Averbeck D, Masse R. Recent reports on the effect of low doses of ionizing radiation and its dose–effect relationship. *Radiat Environ Biophys.* (2006) **44**:245–51. doi: 10.1007/s00411-006-0032-9
5. Brenner DJ, Doll R, Goodhead DT, Hall EJ, Land CE, Little JB, et al. Cancer risks attributable to low doses of ionizing radiation: assessing what we really know. *Proc Natl Acad Sci USA.* (2003) **100**:13761–6. doi: 10.1073/pnas.2235592100
6. Brenner DJ, Sachs RK. Brenner DJ. Estimating radiation-induced cancer risks at very low doses: rationale for using a linear no-threshold approach. *Radiat Environ Biophys.* (2006) **44**:253–6. doi: 10.1007/s00411-006-0029-4
7. ICRP. Low-dose extrapolation of radiation-related cancer risk. ICRP Publication 99. *Ann ICRP.* (2005) **35**:1–140. doi: 10.1016/j.icrp.2005.11.002
8. ICRP. The 2007 recommendations of the International Commission on Radiological Protection. ICRP Publication 103. *Ann ICRP.* (2007) **37**:1–332. doi: 10.1016/j.icrp.2007.10.003
9. UNSCEAR. *Sources, Effects Risks of Ionizing Radiation. Report to the General Assembly Scientific Annexes AB.* UNSCEAR 2012 Report. United Nations Scientific Committee on the Effects of Atomic Radiation. United Nations sales publication E.16.IX.1. New York, NY: United Nations (2015).
10. UNSCEAR. *Sources, Effects Risks of Ionizing Radiation. Report to the General Assembly Scientific Annexes AB.* UNSCEAR 2017 report. United Nations Scientific Committee on the Effects of Atomic Radiation. New York, NY: United Nations (2018).
11. National Research Council. *Health Risks from Exposure to Low Levels of Ionizing Radiation: BEIR VII Phase 2.* Washington, DC: The National Academies Press (2006).
12. Tubiana M, Feinendegen LE, Yang C, Kaminski JM. The linear no-threshold relationship is inconsistent with radiation biologic and experimental data. *Radiology.* (2009) **251**:13. doi: 10.1148/radiol.2511080671
13. Portess DI, Bauer G, Hill MA, O'Neill P. Low-dose irradiation of nontransformed cells stimulates the selective removal of precancerous cells via intercellular induction of apoptosis. *Cancer Res.* (2007) **67**:1246–53. doi: 10.1158/0008-5472.CAN-06-2985
14. Mullenders L, Atkinson M, Paretzke H, Sabatier L, Bouffler S. Assessing cancer risks of low-dose radiation. *Nat Rev Cancer.* (2009) **9**:596–604. doi: 10.1038/nrc2677
15. Seong KM, Kwon TW, Seo S, Lee D, Park S, Jin YW, et al. Perception of low dose radiation risks among radiation researchers in Korea. *PLoS ONE.* (2017) **12**:e0171777. doi: 10.1371/journal.pone.0171777
16. Preston DL, Cullings H, Suyama A, Funamoto S, Nishi N, Soda M, et al. Solid cancer incidence in atomic bomb survivors exposed in utero or as young children. *J Natl Cancer Inst.* (2008) **100**:428–36. doi: 10.1093/jnci/djn045
17. Preston DL, Shimizu Y, Pierce DA, Suyama A, Mabuchi K. Studies of mortality of atomic bomb survivors. Report 13: solid cancer and noncancer disease mortality: 1950–1997. *Radiat Res.* (2003) **160**:381–407. doi: 10.1667/RR3049
18. Kamiya K, Ozasa K, Akiba S, Niwa O, Kodama K, Takamura N, et al. Long-term effects of radiation exposure on health. *Lancet.* (2015) **386**:469–78. doi: 10.1016/S0140-6736(15)61167-9
19. Preston D, Ron E, Tokuoka S, Funamoto S, Nishi N, Soda M, et al. Solid cancer incidence in atomic bomb survivors: 1958–1998. *Radiat Res.* (2007) **168**:1–64. doi: 10.1667/RR0763.1
20. Ozasa K, Cullings HM, Ohishi W, Hida A, Grant EJ. Epidemiological studies of atomic bomb radiation at the Radiation Effects Research Foundation. *Int J Radiat Biol.* (2019) **95**:879–91. doi: 10.1080/09553002.2019.1569778
21. Yamashita S, Takamura N, Ohtsuru A, Suzuki S. Radiation exposure and thyroid cancer risk after the fukushima nuclear power plant accident in comparison with the chernobyl accident. *Radiat Prot Dosimetry.* (2016) **171**:41. doi: 10.1093/rpd/ncw189
22. Hatch M, Cardis E. Somatic health effects of Chernobyl: 30 years on. *Eur J Epidemiol.* (2017) **32**:1047–54. doi: 10.1007/s10654-017-0303-6
23. Fridman M, Lam AKY, Krasko O. Characteristics of young adults of Belarus with post-chernobyl papillary thyroid carcinoma: a long-term follow-up of patients with early exposure to radiation at the 30th

anniversary of the accident. *Clin Endocrinol.* (2016) **85**:971–8. doi: 10.1111/cen.13137
24. Tronko M, Brenner AV, Bogdanova T, Shpak V, Oliynyk V, Cahoon EK, et al. Thyroid neoplasia risk is increased nearly 30 years after the chernobyl accident. *Int J Cancer.* (2017) **141**:1585. doi: 10.1002/ijc.30857
25. Kurttio P, Seppä K, Pasanen K, Patama T, Auvinen A, Pukkala E, et al. Fallout from the chernobyl accident and overall cancer incidence in Finland. *Cancer Epidemiol.* (2013) **37**:585. doi: 10.1016/j.canep.2013.05.006
26. Alinaghizadeh H, Tondel M, Walinder R. Cancer incidence in northern Sweden before and after the Chernobyl nuclear power plant accident. *Radiat Environ Biophys.* (2014) **53**:495–504. doi: 10.1007/s00411-014-0545-6
27. Alinaghizadeh H, Wålinder R, Vingård E, Tondel M. Total cancer incidence in relation to137Cs fallout in the most contaminated counties in Sweden after the Chernobyl nuclear power plant accident: a register-based study. *BMJ Open.* (2016) **6**:e011924. doi: 10.1136/bmjopen-2016-011924
28. Till JE, Beck HL, Aanenson JW, Grogan HA, Mohler HJ, Mohler SS, et al. Military participants at US atmospheric nuclear weapons testing—methodology for estimating dose and uncertainty. *Radiat Res.* (2014) **181**:471–84. doi: 10.1667/RR13597.1
29. Beck HL, Till JE, Grogan HA, Aanenson JW, Mohler HJ, Mohler SS, et al. Red bone marrow and male breast doses for a cohort of atomic veterans. *Radiat Res.* (2017) **187**:221–8. doi: 10.1667/RR14458.1
30. Boice JD Jr, Ellis ED, Golden AP, Girardi DJ, Cohen SS, et al. The past informs the future: an overview of the million worker study and the Mallinckrodt chemical works cohort. *Health Phys.* (2018) **114**:381–5. doi: 10.1097/HP.0000000000000825
31. UNSCEAR. *Sources and Effects of Ionizing Radiation*. Volume I, Report to the General Assembly, With Scientific Annexes A and B–Sources. United Nations Scientific Committee on the Effects of Atomic Radiation (2010).
32. Richardson DB, Cardis E, Daniels RD, Gillies M, O'Hagan JA, Hamra GB, et al. Risk of cancer from occupational exposure to ionising radiation: retrospective cohort study of workers in France, the United Kingdom, and the United States (INWORKS). *BMJ.* (2015) **351**:h5359. doi: 10.1136/bmj.h5359
33. Leuraud K, Richardson DB, Cardis E, Daniels RD, Gillies M, O'hagan JA, et al. Ionising radiation and risk of death from leukaemia and lymphoma in radiation-monitored workers (INWORKS): an international cohort study. *Lancet Haematol.* (2015) **2**:e276–81. doi: 10.1016/S2352-3026(15)00094-0
34. Thorne M. ICRP publication 60: 1990 recommendations of the international commission on radiological protection. *Ann ICRP.* (1991) **21**:1–201. doi: 10.1016/0306-4549(92)90053-E
35. Pei W, Hu W, Chai Z, Zhou G. Current status of space radiobiological studies in China. *Life Sci Space Res.* (2019) **22**:1–7. doi: 10.1016/j.lssr.2019.05.001
36. Durante M, Cucinotta FA. Heavy ion carcinogenesis and human space exploration. *Nat Rev Cancer.* (2008) **8**:465. doi: 10.1038/nrc2391
37. Lei R, Zhou G, Hong MA, Zhuang F, Deng Y. Space life science of China in 2013. *Chin J Space Sci.* (2014) **34**:747–56. doi: 10.11728/cjss2014.05.747
38. Xu D, Zhao X, Li Y, Ji Y, Zhang J, Wang J, et al. The combined effects of X-ray radiation and hindlimb suspension on bone loss. *J Radiat Res.* (2014) **55**:720. doi: 10.1093/jrr/rru014
39. Cucinotta FA, Wu H, Shavers MR, George K. Radiation dosimetry and biophysical models of space radiation effects. *Gravit Space Biol.* (2003) **16**:11–8.
40. Cucinotta FA, Kim M-HY, Willingham V, George KA. Physical and biological organ dosimetry analysis for International Space Station Astronauts. *Radiat Res.* (2008) **170**:127–38. doi: 10.1667/RR1330.1
41. Kim M-HY, Cucinotta FA, Nounu HN, Zeitlin C, Hassler DM, Rafkin SCR, et al. Comparison of Martian surface ionizing radiation measurements from MSL-RAD with Badhwar-O'Neill 2011/HZETRN model calculations. *J Geophys Res Planets.* (2014) **119**:1311–21. doi: 10.1002/2013JE004549
42. McKenna-Lawlor S. Feasibility study of astronaut standardized career dose limits in LEO the outlook for BLEO. *Acta Astron.* (2014) **104**:565–73. doi: 10.1016/j.actaastro.2014.07.011
43. Zhou Z, Ware JH, Kennedy AR. Carbon and iron ion radiation-induced cytotoxicity and transformation *in vitro*. *Oncol Lett.* (2011) **2**:915–8. doi: 10.3892/ol.2011.342
44. Cucinotta FA, Durante M. Cancer risk from exposure to galactic cosmic rays: implications for space exploration by human beings. *Lancet Oncol.* (2006) **7**:431. doi: 10.1016/S1470-2045(06)70695-7
45. Durante M, Cucinotta FA. Physical basis of radiation protection in space travel. *Rev Mod Phys.* (2011) **83**:1245–81. doi: 10.1103/RevModPhys.83.1245
46. Cucinotta FA. A new approach to reduce uncertainties in space radiation cancer risk predictions. *PLoS ONE.* (2015) **10**:e0120717. doi: 10.1371/journal.pone.0120717
47. Cucinotta FA. Space radiation risks for astronauts on multiple International Space Station missions. *PLoS ONE.* (2014) **9**:e96099. doi: 10.1371/journal.pone.0096099
48. Cucinotta FA, To K, Cacao E. Predictions of space radiation fatality risk for exploration missions. *Life Sci Space Res.* (2017) **13**:1–11. doi: 10.1016/j.lssr.2017.01.005
49. George K, Durante M, Willingham V, Wu H, Yang TC, Cucinotta FA. Biological effectiveness of accelerated particles for the induction of chromosome damage measured in metaphase and interphase human lymphocytes. *Radiat Res.* (2003) **160**:425–35. doi: 10.1667/RR3064
50. Durante M. Biomarkers of space radiation risk. *Radiat Res.* (2005) **164**:467–73. doi: 10.1667/RR3359.1
51. Cucinotta FA, Cacao E. Non-targeted effects models predict significantly higher mars mission cancer risk than targeted effects models. *Sci Rep.* (2017) **7**:1832. doi: 10.1038/s41598-017-02087-3
52. Cucinotta FA, Cacao E, Kim MY, Saganti PB. Cancer and circulatory disease risks for a human mission to mars: private mission considerations. *Acta Astron.* (2018) **166**:529–36. doi: 10.1016/j.actaastro.2018.08.022
53. Hada M, Meador JA, Cucinotta FA, Gonda SR, Wu H. Chromosome aberrations induced by dual exposure of protons and iron ions. *Radiat Environ Biophys.* (2007) **46**:125–9. doi: 10.1007/s00411-006-0083-y
54. Trani D, Datta K, Doiron K, Kallakury B, Fornace AJ. Enhanced intestinal tumor multiplicity and grade *in vivo* after HZE exposure: mouse models for space radiation risk estimates. *Radiat Environ Biophys.* (2010) **49**:389–96. doi: 10.1007/s00411-010-0292-2
55. Weil MM, Ray FA, Genik PC, Yu Y, Mccarthy M, Fallgren CM, et al. Effects of ^{28}Si ions, ^{56}Fe ions, and protons on the induction of murine acute myeloid leukemia and hepatocellular carcinoma. *PLoS ONE.* (2014) **9**:e104819. doi: 10.1371/journal.pone.0104819
56. Ding LH, Park S, Xie Y, Girard L, Minna JD, Story MD. Elucidation of changes in molecular signalling leading to increased cellular transformation in oncogenically progressed human bronchial epithelial cells exposed to radiations of increasing LET. *Mutagenesis.* (2015) **30**:685–94. doi: 10.1093/mutage/gev028
57. Elmore E, Lao XY, Kapadia R, Swete M, Redpath JL. Neoplastic transformation in vitro by mixed beams of high-energy iron ions and protons. *Radiat Res.* (2011) **176**:291–302. doi: 10.1667/RR2646.1
58. Buonanno M, Toledo SMD, Howell RW, Azzam EI. Low-dose energetic protons induce adaptive and bystander effects that protect human cells against DNA damage caused by a subsequent exposure to energetic iron ions. *J Radiat Res.* (2015) **56**:502–8. doi: 10.1093/jrr/rrv005
59. Hu W, Pei H, Li H, Ding N, He J, Wang J, et al. Effects of shielding on the induction of 53BP1 foci and micronuclei after Fe ion exposures. *J Radiat Res.* (2013) **55**:10–6. doi: 10.1093/jrr/rrt078
60. Kennedy AR, Ware JH, Guan J, Donahue JJ, Biaglow JE, Zhou Z, et al. Selenomethionine protects against adverse biological effects induced by space radiation. *Free Radic Biol Med.* (2004) **36**:259–66. doi: 10.1016/j.freeradbiomed.2003.10.010
61. Durante M, Manti L. Human response to high-background radiation environments on earth and in space. *Adv Space Res.* (2008) **42**:999–1007. doi: 10.1016/j.asr.2007.02.014
62. Ben Byju S, Koya P, Sahoo B, Jojo P, Chougaonkar M, Mayya Y. Inhalation and external doses in coastal villages of high background radiation area in Kollam, India. *Radiat Protec Dosimetry.* (2012) **152**:**154**–8. doi: 10.1093/rpd/ncs213
63. Costa-de-Moura J, Wallfass CM, Bossew P. Health hazards of radioactive sands along the Coast of Espírito Santo/Brazil. *N. Jb. Geol. Paläont. Abh.* (2002) 225:127–36. doi: 10.1127/njgpa/225/2002/127
64. Hendry JH, Simon SL, Wojcik A, Sohrabi M, Burkart W, Cardis E, et al. Human exposure to high natural background radiation: what can it teach us about radiation risks? *J Radiol Prot.* (2009) **29**:A29–42. doi: 10.1088/0952-4746/29/2A/S03
65. Vasconcelos DC, Reis PAL, Pereira C, Oliveira AH, Santos TO, Rocha Z. Modelling natural radioactivity in sand beaches of Guarapari,

Espírito Santo State, Brazil. *World J Nucl Sci Technol.* (2013) **3**:65–71. doi: 10.4236/wjnst.2013.32011
66. Koya PK, Chougaonkar MP, Predeep P, Jojo PJ, Cheriyan VD, Mayya YS, et al. Effect of low and chronic radiation exposure: a case-control study of mental retardation and cleft lip/palate in the monazite-bearing coastal areas of southern Kerala. *Radiat Res.* (2012) **177**:109–16. doi: 10.1667/RR2699.1
67. Tao Z, Zha Y, Akiba S, Sun Q, Zou J, Li J, et al. Cancer mortality in the high background radiation areas of Yangjiang, China during the period between 1979 and 1995. *J Radiat Res.* (2000) **41**:31. doi: 10.1269/jrr.41.S31
68. Yuan YL, Morishima H, Shen H. The estimation of doses to the inhabitants arising from natural radiation source in the high background radiation area of Yangjiang, China. *Chin J Radiol Health*. (2004) **13**:1–7. Available online at: https://inis.iaea.org/search/search.aspx?orig_q=RN:36029092
69. Zou JM. Major results of the study on cancer mortality and its related factors among inhabitants in the high background radiation area (HBRA) of Yangjiang, Guangdong. *Chin Occup Med.* (2004) 3. Available online at: http://www.en.cnki.com.cn/Article_en/CJFDTOTAL-XYYX200403001.htm
70. Yuan Y, Shen H, Changsha, Zhao S. Recent advances of dosimetry investigation in the high background radiation area in Yangjiang,China. *Chin J Rodiat Mediat Protec.* (1995) **6**:77–100.
71. Christensen R, Alsner J, Brandt SF, Dagnaeshansen F, Kolvraa S, Serakinci N. Transformation of human mesenchymal stem cells in radiation carcinogenesis: long-term effect of ionizing radiation. *Regen Med.* (2008) **3**:849–61. doi: 10.2217/17460751.3.6.849
72. Newhauser WD, Durante M. Assessing the risk of second malignancies after modern radiotherapy. *Nat Rev Cancer.* (2011) **11**:438–48. doi: 10.1038/nrc3069
73. Jin F, Luo H-L, Zhou J, He Y-N, Liu X-F, Zhong M-S, et al. Cancer risk assessment in modern radiotherapy workflow with medical big data. *Cancer Manag Res.* (2018) **10**:1665–75. doi: 10.2147/CMAR.S164980
74. Swerdlow AJ, Higgins CD, Smith P, Cunningham D, Hancock BW, Horwich A, et al. Second cancer risk after chemotherapy for Hodgkin's lymphoma: a collaborative British cohort study. *J Clin Oncol.* (2011) **29**:4096–104. doi: 10.1200/JCO.2011.34.8268
75. de Gonzalez AB, Curtis RE, Kry SF, Gilbert E, Lamart S, Berg CD, et al. Proportion of second cancers attributable to radiotherapy treatment in adults: a cohort study in the US SEER cancer registries. *Lancet Oncol.* (2011) **12**:353–60. doi: 10.1016/S1470-2045(11)70061-4
76. Dracham CB, Shankar A, Madan R. Radiation induced secondary malignancies: a review article. *Radiat Oncol J.* (2018) **36**:85–94. doi: 10.3857/roj.2018.00290
77. Henson KE, McGale P, Taylor C, Darby SC. Radiation-related mortality from heart disease and lung cancer more than 20 years after radiotherapy for breast cancer. *Br J Cancer.* (2013) **108**:179–82. doi: 10.1038/bjc.2012.575
78. Ware J, ZhaozongZhou, Romero-Weaver A, Stevenwan X, Newberne P, Kennedy A. Effects of selenomethionine in irradiated human thyroid epithelial cells and tumorigenicity studies. *Nutr Cancer Int J.* (2011) **63**:1114–21. doi: 10.1080/01635581.2011.605981
79. Durante M, Loeffler JS. Charged particles in radiation oncology. *Nat Rev Clin Oncol.* (2010) **7**:37. doi: 10.1038/nrclinonc.2009.183
80. Sethi RV, Shih HA, Yeap BY, Mouw KW, Petersen R, Kim DY, et al. Second nonocular tumors among survivors of retinoblastoma treated with contemporary photon and proton radiotherapy. *Cancer.* (2014) **120**:126–33. doi: 10.1002/cncr.28387
81. Mohamad O, Tabuchi T, Nitta Y, Nomoto A, Sato A, Kasuya G, et al. Risk of subsequent primary cancers after carbon ion radiotherapy, photon radiotherapy, or surgery for localised prostate cancer: a propensity score-weighted, retrospective, cohort study. *Lancet Oncol.* (2019) **20**:674–85. doi: 10.1016/S1470-2045(18)30931-8
82. Baskar R. Emerging role of radiation induced bystander effects: cell communications and carcinogenesis. *Genome Integr.* (2010) 1:13. doi: 10.1186/2041-9414-1-13
83. Wu LJ, Randerspehrson G, Xu A, Waldren CA, Geard CR, Yu Z, et al. Targeted cytoplasmic irradiation with alpha particles induces mutations in mammalian cells. *Proc Natl Acad Sci USA.* (1999) **96**:4959–64. doi: 10.1073/pnas.96.9.4959
84. Kennedy AR. Factors that modify radiation-induced carcinogenesis. *Health Phys.* (2009) **97**:433–45. doi: 10.1097/HP.0b013e3181ac9262
85. Shuryak I, Ullrich RL, Sachs RK, Brenner DJ. The balance between initiation and promotion in radiation-induced murine carcinogenesis. *Radiat Res.* (2010) **174**:357–66. doi: 10.1667/RR2143.1

Conflict of Interest: The authors declare that the research was conducted in the absence of any commercial or financial relationships that could be construed as a potential conflict of interest.

frontiers in Physics

ORIGINAL RESEARCH
published: 14 August 2020
doi: 10.3389/fphy.2020.00272

Characterizing Radiation Effectiveness in Ion Beam Therapy Part I: Introduction and Biophysical Modeling of RBE Using the LEMIV

Michael Scholz[1], Thomas Friedrich[1], Giulio Magrin[2], Paolo Colautti[3], Aleksandra Ristić-Fira[4] and Ivan Petrović[4]*

[1] GSI Helmholtzzentrum für Schwerionenforschung, Darmstadt, Germany, [2] MedAustron Ion Therapy Center, Wiener Neustadt, Austria, [3] Laboratori Nazionali di Legnaro, INFN Istituto Nazionale di Fisica Nucleare, Legnaro, Italy, [4] Vinča Institute of Nuclear Sciences, University of Belgrade, Belgrade, Serbia

OPEN ACCESS

Edited by:
Yolanda Prezado, INSERM U1021 Signalisation normale et pathologique de l'embryon aux thérapies innovantes des cancers, France

Reviewed by:
Till Tobias Böhlen, Paul Scherrer Institut (PSI), Switzerland
Dimitris Emfietzoglou, University of Ioannina, Greece

***Correspondence:**
Michael Scholz
m.scholz@gsi.de

Specialty section:
This article was submitted to Medical Physics and Imaging, a section of the journal Frontiers in Physics

Received: 03 April 2020
Accepted: 18 June 2020
Published: 14 August 2020

Citation:
Scholz M, Friedrich T, Magrin G, Colautti P, Ristić-Fira A and Petrović I (2020) Characterizing Radiation Effectiveness in Ion Beam Therapy Part I: Introduction and Biophysical Modeling of RBE Using the LEMIV. Front. Phys. 8:272. doi: 10.3389/fphy.2020.00272

The specific advantages of ion beams for application in tumor therapy are attributed to their different macroscopic and microscopic energy deposition pattern as compared to conventional photon radiation. On the macroscopic scale, the inverted dose profile with a Bragg peak and small lateral scattering allow a better conformation of the dose to the tumor. On the microscopic scale, the localized energy deposition around the trajectory of the particles leads to an enhanced biological effectiveness, typically expressed in terms of the relative biological effectiveness (RBE). Experimental investigations reveal complex dependencies of RBE on many physical and biological parameters, as e.g., ion species, dose, position in the field and cell or tissue type. In order to complement the experimental work, different approaches are used for the characterization of the specific physical and biological properties of ion beams. In a set of two papers, which are linked by activities within a European HORIZON 2020 project about nuclear science and application (ENSAR2), we describe recent developments in two fields playing a key role in characterizing the increased biological effectiveness. These comprise the biophysical modeling of RBE and the microdosimetric measurements in complex radiation fields. This first paper gives a brief introduction into these fields and then focuses on aspects of biophysical modeling of RBE, specifically on semi-empirical approaches that are currently used in treatment planning for ion beam therapy. It summarizes the status and recent developments of the Local Effect Model (LEM) and its conceptual framework and shows examples of model validation using recent experimental data. The model is compared to other approaches, e.g., to the Microdosimetric-Kinetic Model (MKM), that builds the bridge to the experimental microdosimetric work.

Keywords: relative biological effectiveness (RBE), biophysical modeling, ion beam therapy, microdosimetry, heavy ion

INTRODUCTION

The main motivation for the application of ion beams in radiotherapy is their advantageous depth dose profile, allowing maximizing the dose to the tumor by simultaneously sparing the surrounding normal tissue as compared to conventional photon radiation [1–3]. Whereas, all ion species share this macroscopic property, in particular heavier ions like carbon ions show an additional advantage with respect to their biological effectiveness. They exhibit an increased biological effectiveness in particular toward lower energies, i.e., in the region where they come to rest when penetrating tissue (the so-called "Bragg peak") [4–6]. This increased effectiveness is expressed in terms of the relative biological effectiveness (RBE), which is defined by the doses required to achieve a given survival level with photons and ion beams, respectively, under otherwise identical conditions:

$$RBE = \left.\frac{D_{Photon}}{D_{Ion}}\right|_{Isoeffect}$$

A major determinant of the RBE is the linear energy transfer (LET) of the ions, characterizing the energy released to the material surrounding the ion trajectory per unit path length. The LET of monoenergetic beams is represented by a single value and increases with decreasing energy; this generally leads to a corresponding increase of RBE toward the Bragg peak region.

In case of irradiation fields formed by particles of different types and energies, LET is represented by a distribution. However, in order to simplify the representation, typically averaged LET values are considered. There are two frequently applied ways of calculating the average LET, the track average $\overline{LET_T}$ and the dose average $\overline{LET_D}$ [7], where the $\overline{LET_D}$ in general is more closely related to RBE than $\overline{LET_T}$ values.

Regarding the biologic effects of radiation, the induced cell killing is a frequently used endpoint to characterize RBE. If cell survival S(D) after irradiation with dose D is described in terms of the linear-quadratic model

$$S(D) = e^{-(\alpha D+\beta D^2)}$$

the changes of the parameters α and β after ion irradiation as compared to photon irradiation are typically characterized by [8]:

$$\boldsymbol{\alpha_{Ion} \geq \alpha_{Photon}}$$
$$\boldsymbol{\beta_{Ion} \leq \beta_{Photon}}$$

The changes primarily reflect the increase of the linear term α, i.e., the initial slope of the dose response curve. The impact on the quadratic term is less pronounced and subject to larger uncertainties. Overall, this results in more straightened dose response curves for high-LET radiation as compared to photon radiation.

For the dose prescription in ion beam therapy, the increased effectiveness needs to be adequately taken into account. However, although conceptually the definition of RBE is simple, it cannot be represented by a single fixed number in extended radiation fields, but actually depends in a complex way on several physical and biological parameters. Based on *in-vitro* studies, the fundamental RBE dependencies can be summarized as follows [8–11]:

1. RBE rises with LET up to a certain maximum and drops toward higher LET values.
2. The RBE(LET) curves are shifted toward higher LET values with increasing particle charge, i.e., for heavier particles.
3. RBE decreases with increasing dose and thus decreasing survival level.
4. RBE is higher for cells that are radioresistant against conventional photon radiation as compared to cells that are sensitive against photon radiation.

As a consequence of these relations, RBE values in typical treatment fields for ion beam therapy will vary with position in the target field and depend on the fractionation scheme used. Therefore, there is no single number for conversion of absorbed dose to RBE-weighted dose. To fully exploit the advantageous properties of ion beams, the systematic dependencies of the RBE have to be fully considered in treatment planning in ion beam therapy, allowing taking advantage of the vast experience made with conventional photon therapy.

Role of the Microscopic Energy Deposition Pattern

Careful analysis of the above-mentioned systematic dependencies of RBE clearly indicates that the increased effectiveness of ion beams is largely determined by their specific microscopic patterns of energy deposition: whereas photons deposit their energy by releasing secondary electrons almost randomly distributed within the irradiated volume, ions deposit their energy extremely localized and concentrated along the trajectory of the ion. Qualitatively, this localized higher energy density is expected to lead to more severe biological damages, e.g., clustered DNA damages, which finally result in a higher cell killing effect. The adequate characterization of the microscopic energy deposition patterns is thus a prerequisite for the detailed understanding of their biological effectiveness.

Although there is general agreement in the community about the relevance of the microscopic energy deposition pattern, it is less obvious at which spatial scales these patterns need to be characterized. For example, assuming the DNA within the cell nucleus to be a critical target for radiation damages points to the relevance of the nm scale [12–14]. In addition, analysis of the formation of radiation-induced chromosome aberrations suggests also the micrometer scale as particularly relevant [15]. Finally, early experimental data showed that the cell nucleus represents the gross sensitive target for most radiation effects [16], which points out the potential role of the 10 μm-scale. A recent combined experimental and modeling study further supports the importance of the 10 um-scale [17]. At the same time, this study revealed that the above mentioned three scales are not necessarily exclusive and that the relative importance of the different scales may strongly depend on the LET.

A wide range of experimental as well as theoretical approaches have been developed and discussed in order to address these aspects. Within a set of two papers, we discuss recent results obtained in two related fields: experimental microdosimetry and

biophysical modeling. In the following, we briefly introduce some key aspects of both fields and in the main part of this manuscript then focus on recent results obtained with a specific biophysical model – the Local Effect Model.

Experimental Microdosimetry

Experimental microdosimetry aims at the accurate characterization of the energy deposition pattern in micrometer dimensions and particularly also their fluctuations and distributions. Major developments of this field were implemented in the framework of neutron therapy, since neutrons – as ion beams – exhibit an increased effectiveness as compared to conventional photon radiation.

The microdosimetric approach assumes that the quality of the radiation action, namely the biological effect per unit of absorbed dose, merely depends on the energy deposition within micrometer-sized critical target sites within the cell nucleus, so called single-event imparted-energy ε_1. The ratio $\varepsilon_1/\bar{l}$, where $\bar{l}$ is the biological site mean-chord length of trajectories passing the site, is called lineal energy, y. Radiation fields as typical for ion beam therapy are characterized by a spectrum of y-values, and the distribution depends on the position in the radiation field. The biological effect is expected to be proportional to the dose delivered by each y-component of the spectrum, i.e., in general d(y) is indicative of the biological effect. RBE values can be obtained from the d(y)-spectrum by appropriate convolution with a weighting function r(y) that represents the increased effectiveness as a function of y [18]. A simplified exploitation of microdosimetric measurements is using the mean of the d(y) distribution, defined as: $\bar{y}_D = \int y \cdot d(y) \cdot dy$, or the mean corrected with a saturation function of y, which is called y* (ICRU 36).

Experimental measurements of microdosimetric spectra are frequently obtained using gas filled detectors, which actually have macroscopic sizes in the order of millimeter to centimeter. However, information on the micrometer scale is obtained by appropriate rescaling according to the different densities of gas and water. First microdosimeters were gas proportional counters made with tissue-equivalent plastic and filled with tissue-equivalent gas mixtures and were thus called TEPC (tissue-equivalent proportional-counter). TEPCs have a high detection efficiency, since they can detect also few ionization events thanks to the electron multiplication in the filling gas. However, they cannot operate in very high-intensity radiation fields, as their geometrical size is hardly < 1 mm. More recently, also solid-state detectors became available, made e.g., of silicon semiconductor material or of synthetic diamond. They are actually characterized by much smaller geometrical dimensions as compared to TEPCs; their geometrical size can be as small as 1 µm, making them fit to operate also in very intense radiation fields. However, this advantage has to be balanced with lower detection efficiency. The aspects of experimental microdosimetry will be developed more deeply in the second paper.

Biophysical Modeling

A thorough overview over the broad range of biophysical models addressing the aspects of high-LET radiation, covering extremely detailed so-called mechanistic models as well as semi-empirical and empirical approaches would be beyond the scope of this paper. We thus restrict here to some key aspects relevant for two models actually used in ion beam therapy at present, the Microdosimetric-Kinetic Model (MKM) [19, 20] and the Local Effect Model (LEM) [21–23].

The transition from the initial energy deposition to the final observable biological effect after a radiation insult includes numerous complex biological processes and pathways, from which many are still unknown or at least not yet accurately quantified, and any model thus can represent an approximation to reality only. One of the major challenges of modeling in the framework of treatment planning therefore is to find the right balance between accuracy and model complexity, i.e., number of different processes and mechanisms to be taken into account [24, 25].

Simplifications are made in both models typically with respect to two aspects:

1. Details of the stochastic distribution of energy deposition of ions around their trajectory on the level of individual secondary electrons are neglected.
2. The details of the complex biological processes, like e.g., the DNA damage signaling and repair pathways, and the corresponding uncertainties are "hidden" by making reference to the known photon dose response curve in a type of "black box" approach.

The models therefore do not aim at an *ab-initio* calculation/prediction of the biological effects of ion beams from first principles, but rather on a translation of what is known from photon radiation to the specific aspects of the microscopic energy deposition pattern of ion traversals through the cell nucleus.

The models mainly differ with respect to the level of detail on which the spatial distribution of energy deposition around the particle trajectory is taken into account. Whereas, e.g., the MKM is strongly linked to the facets of the experimental microdosimetry as described above and thus focuses on the energy deposition features on the micrometer scale, the LEM explicitly considers the impact of track structure on the nanometer, the micrometer and the 10-micrometer level [17].

Link Between Both Fields

The two aspects described above approach the problem of characterizing radiation quality from different directions and are, in a way, complementary. Microdosimetry focuses on the possibility to characterize experimentally the microcoscopic energy deposition in any complex radiation field, as it is typical for the superimposition of ion beams with different primary energies as required to form a spread-out Bragg-peak (SOBP). It is thus suitable to check radiation quality in typical patient plan like dose distributions and thus for quality assurance issues.

The modeling approach in contrast also makes use of some quantities and features of ion beam radiation, which cannot be directly measured in complex radiation fields. Instead, models make use of parametrizations, which are validated independently in specific experiments also under conditions which might even

be beyond typical patient treatment conditions, e.g., by using also heavier ions than carbon or a larger energy regime. An advantage of the modeling approach is that it facilitates taking into account aspects of microscopic energy deposition on any spatial level, and thus potentially allows a more accurate description of the underlying mechanisms leading to the increased RBE.

BIOPHYSICAL MODELING: GENERAL ASPECTS

In principle, protons as well as heavier ions exhibit an increased RBE toward the end of their range when penetrating tissue. However, the demand for RBE modeling for treatment planning in ion beam therapy is clearly more relevant in the case of heavier ions than for protons, since RBE values are substantially greater for heavy ions. Nevertheless, it is still under discussion whether a variable RBE instead of using a constant RBE = 1.1 could be beneficial in proton therapy [26–29]. Nonetheless, numerous simplified, empirical models have been proposed which are applicable solely to the case of protons, as they are based on certain simplified assumptions that are not valid for heavier ions [30].

At present, two different models are used in treatment planning for carbon-ion beam therapy: the Microdosimetric-Kinetic Model (MKM) is used in the Japanese facilities, whereas the Local Effect Model (LEM) is used in the European facilities. In both approaches, the characterization of the microscopic energy deposition pattern represents a major ingredient, although the details how this energy deposition pattern is translated into a biological response substantially differ. The characterization of the dose response curve after low-LET radiation represents the second pillar of these models. In the following, we briefly introduce the main concepts of these models. Although modeling results are presented in the results section only for the LEM, understanding the key aspects of the MKM is of relevance for the discussion and with respect to its link to the experimental microdosimetry approach presented in the second paper.

BASIC CONCEPTS OF MODELS

Local Effect Model

The LEM in its original version (LEM I; 21) is used for treatment planning in the European carbon ion facilities. For this first version of the model an accurate representation of the effects of carbon ions was the major focus, and the application to other ion species required corresponding adaptation of input parameters. More recently improved versions of the model have been developed, and the most recent version (LEM IV; [22, 23]) now allows the simultaneous consistent prediction of RBE over a wide range of particles with similar accuracy based on a single set of input parameters. The basic idea of the LEM is to predict effects of high-LET radiation based on the known effects of low-LET radiation in combination with the characterization of the inhomogeneous, localized energy deposition pattern of charged particles. The effect calculation within the LEM IV includes the following major steps:

1. Characterization of the microscopic spatial energy deposition pattern by means of an amorphous track structure approach. This reflects the mean energy deposition (so called local dose) as a function of the distance from the particle trajectory, largely given by $D(r) \sim 1/r^2$.
2. Determination of the spatial distribution of DSB of a single particle traversal through the cell nucleus derived from the amorphous track structure in combination with the known DSB yield of 30 DSB/Gy/nucleus after photon irradiation. Extremely high energy deposition in nanometer dimensions within the center of particle tracks can lead to correspondingly higher yields of DSB as compared to photon radiation by increased clustering of SSB leading to additional DSB.
3. Characterization of the clustering properties of DSB with respect to the giant loop substructure of the chromatin organization, containing typically 2 Mbp DNA and approximated by $\sim$0.5 μm sized subvolumes of the nucleus. Chromatin loops containing just a single DSB are called isolated DSB (iDSB), chromatin loops with 2 or more DSB are called clustered DSB (cDSB).
4. Determination of the trend to form clustered DSB, captured by the cluster index C, which is the ratio of cDSB to the total number of DSB,

$$C = \frac{N_{cDSB}}{N_{cDSB} + N_{iDSB}} \quad (1)$$

5. Determination of the photon dose leading to the same proportion of iDSB and cDSB, i.e., the same cluster index.
6. Calculation of the biological effect for this "iso-complexity" photon dose according to a (modified) LQ-approach.
7. Determination of the effect of ion irradiation from the effect of photons at the dose determined in the previous step by appropriate rescaling of the photon effect according to the total number of DSB induced by photon and ion irradiation, respectively.

LEM IV has been demonstrated to accurately represent experimental data *in-vitro* over a larger range of different ion species from protons to oxygen ions [22, 31–33]. Furthermore, besides *in-vitro* experiments also RBE for *in-vivo* experiments, e.g., the tolerance of the rat spinal cord, can be modeled with LEM IV [34, 35]. Interestingly, the concept of damage classification that has been developed for the LEM IV has been shown to be applicable also to other radiation qualities, and several key aspects like LQ-shape of survival curves, rejoining kinetics, dose rate effects and cell cycle effects are consistently modeled by this approach [36–38].

MKM

The MKM makes use of characterization of energy deposition in micrometer-sized volumes and of concepts implemented in the experimental microdosimetry branch. Its original version has been developed by Hawkins [19, 20], and subsequent further developments have been implemented in the framework of the Japanese heavy ion therapy projects [39, 40].

The key variable on which the MKM is based is the lineal energy y. However, predictions of the increased effectiveness

do not use the details of the corresponding microdosimetric spectrum, but rather it's dose weighted mean value $\overline{y_D}$. The basic assumption of the MKM is, that in a first approximation the shape of the y-distribution can be ignored as long as the value of $\overline{y_D}$ is identical for different distributions. The essential dependence reflecting the increased RBE in terms of the linear-quadratic parameters is then given by [41]:

$$\ln S(D) = \alpha_{Ion} D + \beta D^2 = \left(\alpha_0 + \frac{0.204 \cdot \beta \cdot y_D}{d^2}\right) D + \beta D^2 \qquad (2)$$

Here, α_{Ion} represents the linear term of the dose response curve after ion irradiation, α_0 the corresponding parameter for radiation qualities with LET→0 and d the diameter of the critical sensitive volume. The quantity β denotes the quadratic term of the dose response curves, which is identical to the value for photon radiation according to the MKM approach. Therefore, only the α-term is affected by high-LET radiation as compared to low-LET radiation. In a first approximation, α_0 can be identified with the α value obtained after photon reference radiation.

As Equation (2) describes a continuously increasing α with increasing $\overline{\mathbf{y}}_\mathbf{D}$, it is not compatible with the drop of RBE toward very high LET values which results from the overkill effect. However, a saturation correction has been introduced [40] in order to account for this effect. The correspondingly corrected dose mean lineal energy is denoted by y*, and replacing $\overline{\mathbf{y}}_\mathbf{D}$ by y* in Equation (2) then reflects the generally observed shape of RBE(LET) curves.

Equation (2) also allows the direct link to experimental microdosimetric measurements, from which $\overline{\mathbf{y}}_\mathbf{D}$ can be obtained [e.g., 38]. Simulated spectra can be used as well, using e.g., amorphous track structure approaches to derive $\overline{\mathbf{y}}_\mathbf{D}$ values for the use in conjunction with the MKM [42]. The MKM now serves as a replacement for the former experimentally based approach to characterize cellular RBE *in-vitro* within SOBPs in the Japanese treatment planning approach.

Other Models

Apart from the LEM and the MKM, other approaches are discussed for potential applications in ion beam therapy, as e.g., reported in [43–45]. However, a conceptual comparison of the models has revealed substantial differences e.g., with respect to the impact of overkill at very high LET and the change of the quadratic component with LET (see e.g., [46]). This underlines the need for a more detailed validation of the models by means of experimental data in order to assess the impact of these model differences on the accuracy of the model prediction.

RECENT RESULTS FOR LEM IV

In the following, we report about recent results obtained with the LEM IV with respect to a broad range of applications, comprising comparisons to experimental data *in-vitro* and *in-vivo*. In addition, we illustrate the impact of specific concepts underlying the LEM, highlighting the importance of different spatial scales to explain the systematic dependencies of RBE.

COMPARISON TO EXPERIMENTAL DATA AT INFN-LNS

Brief Description of Experimental Conditions and Simulation With TRiP98

Irradiations of cell samples were performed in Istituto Nazionale di Fisica Nucleare, Laboratori Nazionali del Sud (INFN – LNS), Catania, Italy, with 62 MeV/u carbon ions at the 0° beam line and with 62 MeV therapeutic protons at the CATANA (Centro di AdroTerapia e Applicazioni Nucleari Avanzate) facility for treatment of eye melanoma. Details of the experimental results and the corresponding reference experiments using photon radiation are given elsewhere [47, 48], and here we only briefly report the main experimental conditions relevant for this contribution.

Four different tumor cell lines (CRL5876, HTB140, HTB177, MCF7) have been used, covering a broad range of radiosensitivities. Proton irradiations were performed using a 62 MeV proton beam in the center of a 15 mm SOBP, located at 10–25 mm depth [47]. The corresponding $\overline{LET_D}$ was 4.7 keV/μm. Carbon ion irradiations were performed with a 62 MeV/u beam for both a monoenergetic beam as well as a small, about 2 mm wide SOBP, which however does not deliver a homogeneous dose [48]. Details of the corresponding dose distributions are reported in Romano et al. [49] (see also **Figure 1**). Irradiation of the cells with monoenergetic beams was performed at the proximal side of the Bragg peak, where ∼ 50% of the maximum relative dose are deposited (corresponding to 7.6 mm depth as marked in **Figure 1** (left) 1; LET: 198 keV/μm). Irradiation under a very narrow, 2 mm SOBP condition was performed at the position where about 98% of the maximum relative dose are reached (corresponding to 5.4 mm as marked in **Figure 1** (right); LET: 208 keV/μm). To obtain reliable statistics all irradiations with protons and carbon ions were performed in duplicate in three separate experiments, except those carried out with the monoenergetic carbon ions that were done in duplicate and repeated seven times. The increased repetition of irradiations with pristine carbon ions was necessary because of the delicate experimental conditions (positioning of cell samples) caused by a very narrow Bragg peak.

The corresponding depth-dose distributions were simulated using the TRiP98 treatment planning environment [50, 51] (**Figure 1**). Since this system had been developed for planning under the conditions relevant for the GSI pilot project, i.e., base data are only available for beam energies >80 MeV/u, some approximations had to be used in order to mimic the conditions reflecting the INFN-LNS experiments. First, the lower energies have been mimicked by artificially introducing some bolus material in the treatment planning system. This, however, is not expected to have a large impact on the predicted RBE values, as the contribution of fragments is still low even with the additional bolus material, and the primary C ions will dominate the effectiveness. Therefore, as long as the dose is simulated correctly, also predicted RBE values are close to those expected in the "real" situation. Second, dose and

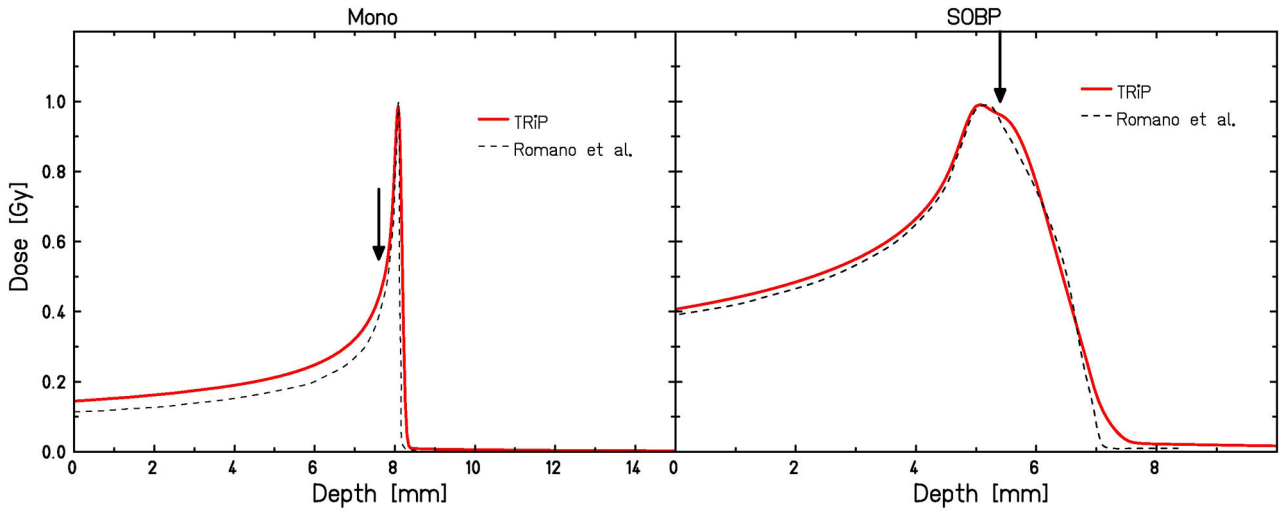

FIGURE 1 | Depth dose distributions for monoenergetic (left) and SOBP (right) carbon ion irradiation according to TRiP calculations used in this paper as compared to those reported by Romano et al. [49]. Irradiation positions are marked by arrows.

LET values are subject to uncertainties, which are particularly relevant in the case of monoenergetic carbon-ion irradiation conditions due to the pronounced dose and LET gradients at this position in depth. We thus performed the model calculations also for a variation of ± 0.1 mm around the planning position of 7.6 mm depth in order to get some feeling for the corresponding uncertainties of survival curve predictions. Practically, we simulated the error of ± 100 μm in cell samples positioning, based on the 50 μm step width of the mechanical device that was used for sample positioning. For the carbon ion "SOBP" conditions depth dose profiles were simulated using a 2 mm ripple filter [52], which results in a depth-dose profile in reasonable agreement with the profile reported by Romano et al. [49].

Comparison With LEM Predictions

The parameters listed in **Table 1** have been used as input for the LEM calculations [48]. For HTB140 cells, two different sets, a and b, have been used for comparison, since this cell line is characterized by an unusual, extreme radiation resistance, and thus very high doses are required to extract a reliable β-parameter. As experiments have been performed with γ-rays over different dose ranges, correspondingly different sets of LQ-parameters have been obtained and are used for the LEM calculations for that cell line.

Predicted survival curves for the different conditions are shown in **Figure 2** in comparison to the experimental data [48]. Surviving fractions are presented as mean values ± standard error of the mean of at least three (seven in the case of monoenergetic carbon ions) separate experiments. In general, standard error of the mean ranges from <5%, which is the case for smaller doses, to somewhat more than 15% for larger doses. This increase is the consequence of the fact that as the number of survived cell colonies falls (with the rise of dose) to 10^{-2} and further to 10^{-3} where there are only a few colonies that are counted, thus the statistics considerably deteriorates.

TABLE 1 | Photon input parameters for the LEM calculations shown in **Figure 2**.

Cell type	α (Gy^{-1})	β (Gy^{-2})	α/β (Gy)	D_t (Gy)
CRL5876	0.166 ± 0.059	0.042 ± 0.019	3.95	8.34
HTB140a [47]	0.036 ± 0.009	0.000 ± 0.000	inf	190
HTB140b [53]	0.0171 ± 0.0084	0.001 ± 0.0005	17.1	22.81
HTB177	0.120 ± 0.048	0.050 ± 0.016	2.4	6.64
MCF7	0.064 ± 0.176	0.057 ± 0.081	1.12	5.23

For protons, measured survival in general is lower than predicted by the LEM.

For the monoenergetic carbon ions, as expected the calculations are very sensitive to the exact depth position; for all cell lines, the curves assuming a depth shift of −0.1 mm as compared to the desired position agree reasonably well with the experimental data. Also, the curves for the SOBP conditions show good agreement with the experimental data, and as expected they are also much less sensitive to the exact position in depth.

HTB140 cells are characterized by two special features: an extremely low sensitivity and an almost linear photon dose response curve. Model calculations have therefore been performed with two different parameter sets HTB140a and HTB140b (see **Table 1**), assuming either purely linear photon dose response or a small β-term of 0.001 Gy^{-2} according to Petrovic et al. [53]. As this latter parameter set better reflects the photon dose response curve at higher doses, this dataset also is expected to result in more accurate LEM predictions for

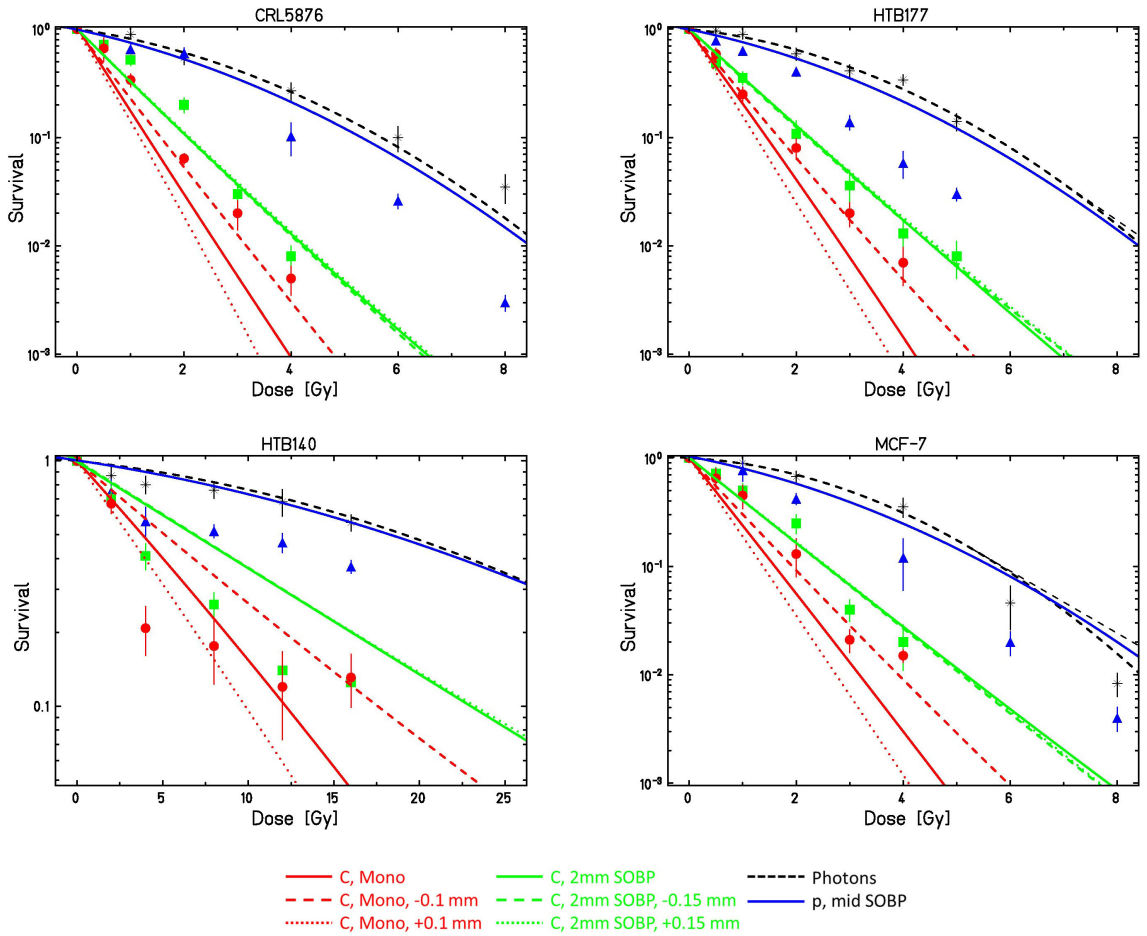

FIGURE 2 | Comparison of LEMIV model calculations (lines) with experimental cell survival data (symbols) obtained at the INFN-LNS beamlines with different cell lines and different radiation qualities. For details see text. Calculations for ± 0.1 and ± 0.15 mm refer to potential positioning inaccuracies as compared to the desired depth.

high-LET radiation; the corresponding comparison is shown in **Figure 2**. Although the detailed shape of the experimental dose response curves is not predicted by the LEM, at least the order of magnitude of the spread of sensitivities between photon and high LET radiation is correctly predicted.

Contribution of Different Spatial Scales: DSB-Clustering vs. Increased Yield

The direct comparison of LEM predictions for HTB140 cells based on the two different data sets is shown in **Figure 3**. For protons, no substantial difference is observed for the different input data sets. In contrast, for carbon ion irradiation, the curves significantly differ, but already for $\beta = 0$ a clearly increased RBE is predicted. This can be attributed to the increased DSB yield resulting from the extremely high local doses in the track center of the particle trajectories, i.e., it is a consequence of processes at the nm-scale. This increased yield is in line with predictions of other models like e.g., PARTRAC [54].

In that respect, the LEM substantially differs from the MKM which would predict RBE = 1 in the case of $\beta = 0$ according to Equation (2). If a small β is assumed, as in the parameter set HTB140b, according to the LEM the RBE is further increased, which then can be attributed to the higher lethality of clustered DSB as compared to isolated DSB. This higher lethality is a direct consequence of $\beta > 0$ according to the LEM concept, reflecting processes at the μm scale. In general, RBE is due to contributions from multiple coexisting scales.

Use of Focused Low-LET Proton Beams to Mimic High-LET

The role of the contribution on different spatial scales has been further demonstrated recently using a special irradiation technique based on focused low-LET proton beams [17]. The basic idea of the experimental concept is to mimic high-LET radiation by focusing low-LET radiation to a small spot of about micrometer dimension, which reflects both the size of important biological structures within the cell as well as typical extensions of the radial dose distribution of high LET light ions. The experiments demonstrated that for identical average macroscopic doses, focused low-LET protons show a substantially increased effectiveness as compared to conventional broad beam irradiation. In the framework of the LEM concept,

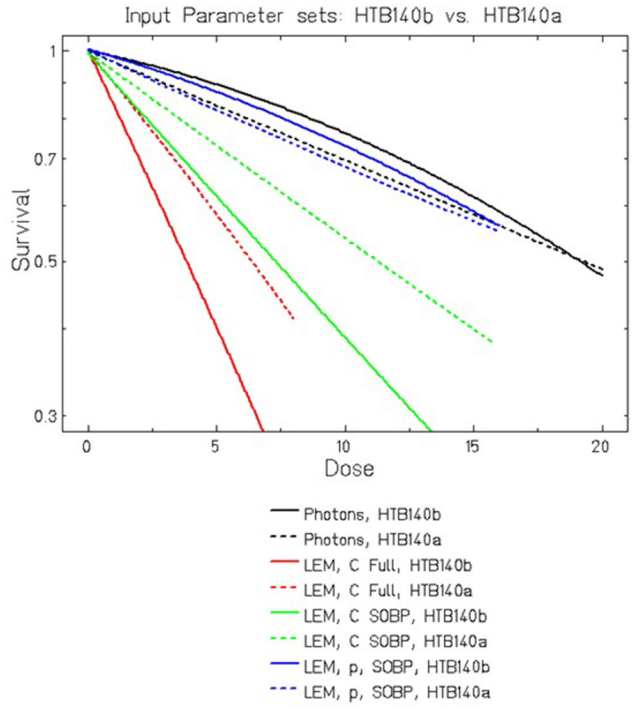

FIGURE 3 | Comparison of LEMIV model calculations for cell killing of HTB140 cells using two different input data sets (see **Table 1**). For carbon ions at high LET, even in the case of $\beta_{photon} = 0\ Gy^{-2}$ a substantially increased RBE is predicted, which is further enhanced if $\beta_{photon} > 0$ is assumed.

this is attributed to the clustering of DSB within giant loop chromatin compartments of about 0.5 μm size.

However, when comparing to e.g., carbon ions with the same energy deposition per spot, protons are still less effective. This difference arises from the extremely high local doses in the track centers of carbon ions, which lead to additional DSBs. Focusing low-LET protons to micrometer spots, however, is not sufficient to reach these high local doses – it would require to focus the protons on nm-sized spots, which is technically not feasible.

In **Figure 4** we show the LEM predictions of RBE for a hypothetic cell line characterized by typical L-Q parameters for the impact of spot size of low LET protons. The figure clearly shows the transition to elevated RBE levels as soon as the spot size is decreased below ∼1 μm. The figure also includes the information about the RBE that is expected for carbon ions for the same mean dose (arrow); the difference between the carbon ion and focused proton RBE values at small spot sizes is attributed to the increased DSB yield of C-ions as compared to protons, as explained above.

Validation *in-vivo*: Tolerance of the Rat Spinal Cord to Proton Irradiation

Model validation based on *in-vitro* data as shown e.g. in section Comparison to Experimental Data at INFN-LNS and in **Figure 2** is an important first step in testing a model that is considered for application in treatment planning for ion beam therapy. For the close link to the patient treatments, however, the validation by means of *in-vivo* experimental animal data is indispensable. First tests of the LEM in such preclinical experiments have been performed for carbon-ion irradiation of the skin of minipigs [55]. Larger systematic studies have then been performed based on the analysis of tolerance doses for the rat spinal cord [35, 56]. These studies also clearly demonstrated the better accuracy of the LEM IV as compared to the LEM I in particular in the critical high-dose/high-LET region. In the entrance channel at low LET, however, some systematic underestimation of the RBE by the LEM IV is observed. In order to clarify whether this is a general systematic effect at lower LET values or whether it is ion specific, comparison to data obtained with proton beams is an important pillar for the validation of the LEM.

Figure 5 shows a comparison of the LEM predictions with experimental data reported by Saager et al. for irradiation in typical therapy-like conditions, i.e., using a proton SOBP of 6 cm width located at 7–13 cm depth in water. RBE values were determined at different positions within the SOBP, corresponding to different LET values. LEM predictions are in reasonable agreement with the experimental data, demonstrating that, in general, the LEM IV allows RBE predictions also for lighter ions with correspondingly lower LET, and thus the systematic deviations found for carbon ions at low LET are specific for carbon ions and likely are a consequence of the high energy rather than the low LET itself.

Both experimental data and model predictions shown in **Figure 5** are in good agreement and support that also for protons at the distal edge of the SOBP elevated RBE values are observed, which are significantly above the RBE value of 1.1 that is currently assumed in treatment planning for proton therapy. Here, it has to be taken into account that the data were obtained for comparably high doses in 1 fraction (Fx) acute and 2Fx split-dose irradiations. Since the RBE is expected to further rise with decreasing doses, we have included in **Figure 5** also the LEM IV prediction of RBE for the typical 2 Gy/Fx dose that is frequently used in therapy. Substantially higher RBE values are expected for these lower doses. Experiments with higher fraction number and correspondingly lower doses are currently under way at the Heidelberg ion beam therapy facility HIT, and the results will represent an important data set to further validate the LEM for application to proton irradiation.

Accuracy of $\overline{LET_D}$ as Descriptor for RBE

Potentially increased RBE values in proton therapy which are above the standard value of 1.1 that is currently used in treatment planning [58] are under vivid debate now since many years [26–28]. A wide range of models has been developed for taking these increased RBE values into account. In contrast to models like the MKM and LEM these models for proton RBE are mostly empirical and parameterize the increase of RBE as a function of $\overline{LET_D}$. Rorvik et al. have compared 13 of these models, demonstrating that even when starting from identical conditions (i.e., assuming identical α_X/β_X-ratios for photon radiation) for all models there is a wide spread in the predicted RBE values. This might partially be because different

sets of experimental data are used to calibrate the models. One important aspect in that respect is the use of $\overline{LET_D}$ as a predictor of RBE. As we have recently shown, $\overline{LET_D}$ values are not necessarily a good predictor of RBE, and for conditions resulting in the same $\overline{LET_D}$ but based on different actual distributions the expected RBE values might also substantially differ [59]. In order to illustrate this, **Figure 6** shows RBE values along a typical SOBP as predicted with the LEM in conjunction with the TRiP98 treatment planning environment for protons and carbon ions in comparison to monoenergetic beams with identical $\overline{LET_D}$. For both particle types the SOBP values differ from those expected for the corresponding monoenergetic beam under track-segment conditions, although in opposite directions. Whereas, for protons higher RBE values are expected in the case of SOBP, for carbon ions these values are lower. This can be explained by the non-linearities of the RBE(LET) relationship under track-segment conditions [59]. The LET values relevant for mixed SOBP fields in the proton case cover the LET region to the left side of the RBE maximum, and thus the non-linear increase of RBE with LET leads to correspondingly higher weights of the high-LET contribution. In contrast, highest LET values in the carbon case are linked to the LET region to the right side of the RBE maximum, where RBE already drops as a result of overkill effects. Therefore, the highest LET components get an effectively lower weight in the energy/LET spectra representative for typical carbon-ion treatment fields, and $\overline{LET_D}$ in general cannot be considered as a unique predictor of RBE.

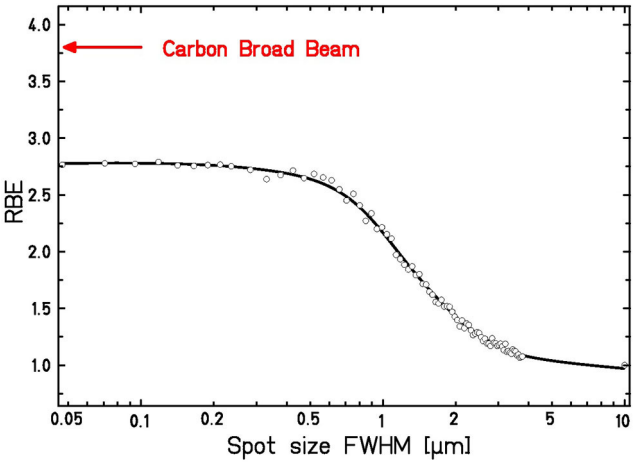

FIGURE 4 | Expected dependence of RBE for a hypothetic cell line on the spot size of focused high-energy, low-LET protons at a mean dose of 1.0 Gy. For comparison, the RBE for broad beam carbon ion irradiation is shown. Calculations are based on the LEM input parameters: $\alpha_{Photon} = 0.1\ Gy^{-1}$, $\beta_{Photon} = 0.05\ Gy^{-2}$, $D_t = 8$ Gy, $E_p = 19.95$ MeV, $LET_p = 2.67$ keV/µm, $E_C = 4.05$ MeV/u, $LET_C = 338$ keV/µm.

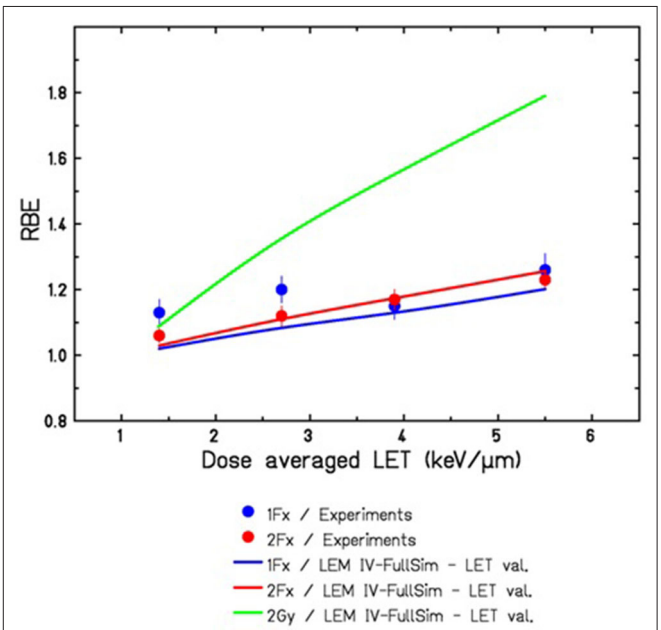

FIGURE 5 | Comparison of LEMIV based RBE predictions for tolerance doses of the rat spinal cord in a 60 mm proton SOBP ranging from 70 to 130 mm water-equivalent depths. Experimental data for 1Fx and 2Fx were taken from [57], corresponding to TD50 values ranging from 21.7 to 19.5 Gy for 1Fx and from 32.3 to 27.9 Gy for 2Fx irradiation. The full green line indicates the expected RBE for lower doses of 2 Gy/Fx, as it is typically used in the therapeutic situation.

DISCUSSION

In **Figure 2** we have demonstrated that the LEM is able to predict the general features of RBE for different cell lines and different radiation qualities. For monoenergetic carbon ions, the predictions significantly depend on the assumed depth position of the cell layer. Within the experimental uncertainties of positioning (estimated to be in the order of +/− 0.1 mm), however, the model predictions agree with the experimental data. Systematic underestimation of RBE has been observed for protons for doses > 2 Gy, whereas for doses ≤ 2 Gy the predicted effectiveness is still compatible with the experimental data. Previous comparisons of the LEM predictions for protons using a larger database have revealed mean deviations of <10% in the LET range up to 8–10 keV/µm [31], although individual experiments can show larger deviations similar to those seen in **Figure 2**.

Concerning the different cell lines, largest deviations between model prediction and experimental data are observed for the extremely radioresistant cell line HTB140. The experimental data indicate a trend to even negative bending of the dose response curves; this trend is not reflected by the LEM, although the order of magnitude of predicted RBE for the highest LET is compatible with the experimental data. One possible explanation for the somewhat unusual shape of the dose response curve could be the composition of subpopulations with substantially different radiosensitivities, as it occurs e.g., also for mixed oxic and hypoxic populations [60].

Concerning the general systematic dependencies, the results shown in **Figures 3**, **4** clearly demonstrate the impact of clustering effects on different spatial scales in the LEM; this aspect

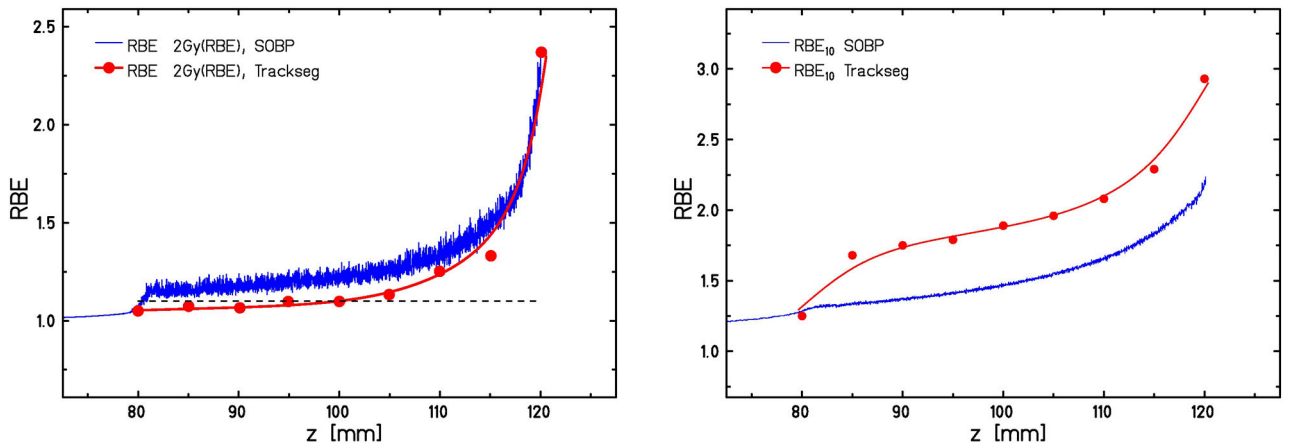

FIGURE 6 | Comparison of predicted RBE_{10} values for HTB177 cells along a 40 mm proton SOBP (left) and carbon SOBP (right) from 80 to 120 mm with RBE_{10} values expected for track segment conditions (i.e., monoenergetic beams) at the same dose mean LET. The dashed line in the left panel indicates the RBE of 1.1, which is currently used in treatment planning for proton therapy.

is particularly relevant for comparison with other models. Since apart from protons the LEM has been shown to also correctly reflect the systematic dependencies for focused carbon ions and lithium ions [17], which further supports the impact of clustering on different spatial scales. The corresponding contributions as a function of LET have been disentangled in more detail in Friedrich et al. [17].

The experiments using focused low-LET proton beams to mimic and explain high-LET effects represent an important pillar for benchmarking effect models and in particular for the validation of the LEM concept. However, although the LEM obviously correctly predicts the fundamental dependencies of RBE, its underlying concept is not necessarily the only possibility to explain the increased effectiveness. It would thus be of particular interest to compare also other models like the MKM or Repair-Misrepair-Fixation (RMF) model to the focused ion beam experiments and to analyze their predictive capacity for these conditions.

Apart from cell killing after acute ion beam radiation, the concept of damage clustering on the nm and μm level have been successfully applied also to other radiation types like high- and low-energy photon radiation [36, 61], to different conditions like e.g., cell cycle dependence of radiosensitivity [38] or the impact of dose rate [62] and to different end points like e.g., rejoining of DSB [37, 63]. As also in these cases in general good agreement between model predictions and experimental data has been found, this is taken as further support for the general concepts on which the LEM IV is based. The independent applicability to multiple endpoints and radiation phenomena within the same model framework using the same model parameters is a strong indication for the validity of the underlying mechanisms.

Modeling the effects of small focused beams might be in general also relevant for novel applications of so-called "spatially fractionated" irradiation like e.g., grid therapy. This therapy is characterized by extremely inhomogeneous lateral dose profiles, where peaks with very high doses are interlaced with valleys of almost zero dose. Both low-LET photon and proton irradiation as well as higher LET ion beam irradiation have been proposed in that respect [64–67]. Although this approach aims at reducing side effects in normal tissue by sparing the valley regions, the complementary higher effectiveness that is expected in the peak region will be relevant for a full characterization of this application. A general understanding of the impact on the biological effectiveness is thus of importance, but will presumably also require including geometrical properties of tissue repair processes that are not included in any RBE radiation effect model nor in any normal tissue complication model so far. This also requires correct modeling of *in-vivo* experimental systems that are frequently used to investigate the effectiveness of grid therapy [66]. An accurate prediction of biological effects *in-vivo* using standard broad beam irradiation is therefore a prerequisite for applications to more complex scenarios like grid therapy. Whereas, effects in the SOBP region of carbon ions are predicted by the LEM IV with reasonable accuracy, there is a trend to systematic underestimation of RBE in the entrance channel, i.e., at high energies [35]. Systematic comparison with larger data bases for *in-vitro* cell kill studies are currently ongoing in order to accurately quantify these deviations and to implement corresponding model improvements.

The correct representation of RBE also in the case of mixed fields, as they typically occur in the patient treatment situation, is of utmost importance in treatment planning. As shown in **Figure 6**, details of the energy/LET/particle spectrum can affect the RBE predicted by the LEM when compared to the corresponding mean values or single values representing track segment conditions. In that respect, it would be highly interesting to further investigate potential differences that would result from the corresponding microdosimetric concepts. For example, the approach using weighting functions makes use of the detailed y-spectrum,

whereas the MKM uses the corresponding dose-mean y-values. Since y essentially represents a 1-dimensional representation of track structure, similar to LET, one would expect here also similar differences as observed in the case of dose-mean LET. A direct comparison and analysis of potential differences between these two approaches could shed light on the impact of the shape of distributions from the microdosimetric perspective.

OUTLOOK

Comparing the two approaches used in the current and the accompanying paper, the major difference is that the modeling approach explicitly considers different spatial scales, whereas the microdosimetric approach focuses on aspects of the micrometer scale. It will thus be of major interest to further analyse the impact and relevance of the different scales for different irradiation scenarios. It would be particularly helpful to use the different approaches to develop hypothesis and specific scenarios that allow discriminating between the different aspects. In that respect, extension / translation of the microdosimetric concepts to the nanometer scale as described e.g., by Grosswendt [68], Selva et al. [69], and Mazzucconi et al. [70] are of further interest for a comparison with the LEM approach.

DATA AVAILABILITY STATEMENT

The raw data supporting the conclusions of this article will be made available by the authors, without undue reservation.

AUTHOR CONTRIBUTIONS

MS drafted the manuscript. MS and TF performed the LEM calculations. AR-F and IP supplied the experimental data obtained at the INFN-LNS facility and all relevant information for the model comparison. GM and PC contributed to the microdosimetry aspects. All authors contributed to improvements/corrections and approved the final version.

FUNDING

This work was supported by the European HORIZON 2020 ENSAR2 project, GRANT AGREEMENT NUMBER: 654002.

REFERENCES

1. Wilson RR. Radiological use of fast protons. *Radiology*. (1946) 47:487–91. doi: 10.1148/47.5.487
2. Schulz-Ertner D, Tsujii H. Particle radiation therapy using proton and heavier ion beams. *J Clin Oncol*. (2007) 25:953–64. doi: 10.1200/JCO.2006.09.7816
3. Schardt D, Elsässer T, Schulz-Ertner D. Heavy-ion tumor therapy: Physical and radiobiological benefits. *Rev Mod Phys*. (2010) 82:383–425. doi: 10.1103/RevModPhys.82.383
4. Blakely EA, Tobias CA, Yang TC, Smith KC, Lyman JT. Inactivation of human kidney cells by high-energy monoenergetic heavy-ion beams. *Radiat Res*. (1979) 80:122–60. doi: 10.2307/3575121
5. Tobias CA, Blakely EA, Alpen EL, Castro JR, Ainsworth EJ, Curtis SB, et al. Molecular and cellular radiobiology of heavy ions. *Int J Radiat Oncol Biol Phys*. (1982) 8:2109–20. doi: 10.1016/0360-3016(82)90554-5
6. Kraft G. Tumor therapy with heavy charged particles. *Prog Part Nucl Phys*. (2000) 45:S473–544. doi: 10.1016/S0146-6410(00)00112-5
7. ICRU Report No. 36: Microdosimetry. *J Int Commis Radiat Units Measure*. (1983) 19:1–120.
8. Friedrich T, Scholz U, Elsässer T, Durante M, Scholz M. Systematic analysis of RBE and related quantities using a database of cell survival experiments with ion beam irradiation. *J Radiat Res*. (2013) 54:494–514. doi: 10.1093/jrr/rrs114
9. Tobias CA, Blakely EA, Chang PY, Lommel L, Roots R. Response of sensitive human ataxia and resistant T-1 cell lines to accelerated heavy ions. *Br J Cancer Suppl*. (1984) 6:175–85. doi: 10.2172/7005318
10. Weyrather WK, Ritter S, Scholz M, Kraft G. RBE for carbon track-segment irradiation in cell lines of differing repair capacity. *Int J Radiat Biol*. (1999) 75:1357–64. doi: 10.1080/095530099139232
11. Furusawa Y, Fukutsu K, Aoki M, Itsukaichi H, Eguchi-Kasai K, Ohara H, et al. Inactivation of aerobic and hypoxic cells from three different cell lines by accelerated (3)He-, (12)C- and (20)Ne-ion beams. *Radiat Res*. (2000) 154:485–96. doi: 10.1667/0033-758720001540485:IOAAHC2.0.CO;2
12. Ward JF. Mechanisms of DNA repair and their potential modification for radiotherapy. *Int J Radiat Oncol Biol Phys*. (1986) 12:1027–32. doi: 10.1016/0360-30168690220-8
13. Nikjoo H, Uehara S, Wilson WE, Hoshi M, Goodhead DT. Track structure in radiation biology: theory and applications. *Int J Radiat Biol*. (1998) 73:355–64. doi: 10.1080/095530098142176
14. Goodhead DT. Initial events in the cellular effects of ionizing radiations: clustered damage in DNA. *Int J Radiat Biol*. (1994) 65:7–17. doi: 10.1080/09553009414550021
15. Neary GJ, Preston RJ, Savage JR. Chromosome aberrations and the theory of RBE. 3. Evidence from experiments with soft x-rays, and a consideration of the effects of hard x-rays. *Int J Radiat Biol Relat Stud Phys Chem Med*. (1967) 12:317–45. doi: 10.1080/09553006714550881
16. Munro TR. The relative radiosensitivity of the nucleus and cytoplasm of Chinese hamster fibroblasts. *Radiat Res*. (1970) 42:451–70. doi: 10.2307/3572962
17. Friedrich T, Ilicic K, Greubel C, Girst S, Reindl J, Sammer M, et al. DNA damage interactions on both nanometer and micrometer scale determine overall cellular damage. *Sci Rep*. (2018) 8:16063. doi: 10.1038/s41598-018-34323-9
18. Wambersie A, Hendry JH, Andreo P, DeLuca PM, Gahbauer R, Menzel H, et al. The RBE issues in ionbeam therapy: conclusions of a joint IAEA/ICRU working group regarding quantities and units. *Radiat Prot Dosimetry*. (2006) 122:463–70. doi: 10.1093/rpd/ncl447
19. Hawkins RB. A microdosimetric-kinetic model of cell death from exposure to ionizing radiation of any LET, with experimental and clinical applications. *Int J Radiat Biol*. (1996) 69:739–55. doi: 10.1080/09553009614548 1
20. Hawkins RB. A microdosimetric-kinetic model for the effect of non-poisson distribution of lethal lesions on the variation of RBE with LET. *Radiat Res*. (2003) 160:61–9. doi: 10.1667/RR3010
21. Scholz M, Kellerer AM, Kraft-Weyrather W, Kraft G. Computation of cell survival in heavy ion beams for therapy. The model and its approximation. *Radiat Environ Biophys*. (1997) 36:59–66. doi: 10.1007/s0041100 50055
22. Elsässer T, Weyrather WK, Friedrich T, Durante M, Iancu G, Krämer M, et al. Quantification of the relative biological effectiveness for ion beam radiotherapy: direct experimental comparison of proton and carbon ion beams and a novel approach for treatment planning. *Int J Radiat Oncol Biol Phys*. (2010) 78:1177–83. doi: 10.1016/j.ijrobp.2010.05.014
23. Friedrich T, Scholz U, Elsässer T, Durante M, Scholz M. Calculation of the biological effects of ion beams based on the microscopic spatial damage distribution pattern. *Int J Radiat Biol*. (2012) 88:103–7. doi: 10.3109/09553002.2011.611213

24. van der Schaaf A, Langendijk JA, Fiorino C, Rancati T. Embracing phenomenological approaches to normal tissue complication probability modeling: a question of method. *Int J Radiat Oncol Biol Phys*. (2015) 91:468–71. doi: 10.1016/j.ijrobp.2014.10.017
25. Olsen CH, Ottesen JT, Smith RC, Olufsen MS. Parameter subset selection techniques for problems in mathematical biology. *Biol Cybern*. (2019) 113:121–38. doi: 10.1007/s00422-018-0784-8
26. Paganetti H. Relative biological effectiveness (RBE) values for proton beam therapy. Variations as a function of biological endpoint, dose, and linear energy transfer. *Phys Med Biol*. (2014) 59:R419–72. doi: 10.1088/0031-9155/59/22/R419
27. Peeler CR, Mirkovic D, Titt U, Blanchard P, Gunther JR, Mahajan A, et al. Clinical evidence of variable proton biological effectiveness in pediatric patients treated for ependymoma. *Radiother Oncol*. (2016) 121:395–401. doi: 10.1016/j.radonc.2016.11.001
28. Jones B. Why RBE must be a variable and not a constant in proton therapy. *Br J Radiol*. (2016) 89:20160116. doi: 10.1259/bjr.20160116
29. Gensheimer MF, Yock TI, Liebsch NJ, Sharp GC, Paganetti H, Madan N, et al. *In vivo* proton beam range verification using spine MRI changes. *Int J Radiat Oncol Biol Phys*. (2010) 78:268–75. doi: 10.1016/j.ijrobp.2009.11.060
30. Rørvik E, Fjæra LF, Dahle TJ, Dale JE, Engeseth GM, Stokkevåg CH, et al. Exploration and application of phenomenological RBE models for proton therapy. *Phys Med Biol*. (2018) 63:185013. doi: 10.1088/1361-6560/aad9db
31. Grün R, Friedrich T, Krämer M, Scholz M. Systematics of relative biological effectiveness measurements for proton radiation along the spread out Bragg peak: experimental validation of the local effect model. *Phys Med Biol*. (2017) 62:890–908. doi: 10.1088/1361-6560/62/3/890
32. Krämer M, Scifoni E, Schuy C, Rovituso M, Tinganelli W, Maier A, et al. Helium ions for radiotherapy? Physical and biological verifications of a novel treatment modality. *Med Phys*. (2016) 43:1995. doi: 10.1118/1.4944593
33. Sokol O, Scifoni E, Tinganelli W, Kraft-Weyrather W, Wiedemann J, Maier A, et al. Oxygen beams for therapy: advanced biological treatment planning and experimental verification. *Phys Med Biol*. (2017) 62:7798–813. doi: 10.1088/1361-6560/aa88a0
34. Saager M, Glowa C, Peschke P, Brons S, Scholz M, Huber PE, et al. Carbon ion irradiation of the rat spinal cord: dependence of the relative biological effectiveness on linear energy transfer. *Int J Radiat Oncol Biol Phys*. (2014) 90:63–70. doi: 10.1016/j.ijrobp.2014.05.008
35. Saager M, Glowa C, Peschke P, Brons S, Grün R, Scholz M, et al. Fractionated carbon ion irradiations of the rat spinal cord: comparison of the relative biological effectiveness with predictions of the local effect model. *Radiat Oncol*. (2020) 15:6. doi: 10.1186/s13014-019-1439-1
36. Friedrich T, Durante M, Scholz M. Modeling cell survival after photon irradiation based on double-strand break clustering in megabase pair chromatin loops. *Radiat Res*. (2012) 178:385–94. doi: 10.1667/RR2964.1
37. Tommasino F, Friedrich T, Scholz U, Taucher-Scholz G, Durante M, Scholz M. A DNA double-strand break kinetic rejoining model based on the local effect model. *Radiat Res*. (2013) 180:524–38. doi: 10.1667/RR13389.1
38. Hufnagl A, Herr L, Friedrich T, Durante M, Taucher-Scholz G, Scholz M. The link between cell-cycle dependent radiosensitivity and repair pathways: a model based on the local, sister-chromatid conformation dependent switch between NHEJ and HR. *DNA Repair*. (2015) 27:28–39. doi: 10.1016/j.dnarep.2015.01.002
39. Kase Y, Kanai T, Matsumoto Y, Furusawa Y, Okamoto H, Asaba T, et al. Microdosimetric measurements and estimation of human cell survival for heavy-ion beams. *Radiat Res*. (2006) 166:629–38. doi: 10.1667/RR0536.1
40. Inaniwa T, Furukawa T, Kase Y, Matsufuji N, Toshito T, Matsumoto Y, et al. Treatment planning for a scanned carbon beam with a modified microdosimetric kinetic model. *Phys Med Biol*. (2010) 55:6721–37. doi: 10.1088/0031-9155/55/22/008
41. Hawkins RB. The relationship between the sensitivity of cells to high-energy photons and the RBE of particle radiation used in radiotherapy. *Radiat Res*. (2009) 17:761–76. doi: 10.1667/RR 1655.1
42. Kase Y, Kanai T, Matsufuji N, Furusawa Y, Elsässer T, Scholz M. Biophysical calculation of cell survival probabilities using amorphous track structure models for heavy-ion irradiation. *Phys Med Biol*. (2008) 53:37–59. doi: 10.1088/0031-9155/53/1/003
43. Waligórski MP, Hollmark M, Gudowska I, Lesia J. Cellular parameters and RBE-LET dependences for modelling heavy-ion radiotherapy. *Radiother Oncol*. (2004) 73(Suppl. 2):S173–5. doi: 10.1016/S0167-8140048 0043-4
44. Frese MC, Yu VK, Stewart RD, Carlson DJ. A mechanism-based approach to predict the relative biological effectiveness of protons and carbon ions in radiation therapy. *Int J Radiat Oncol Biol Phys*. (2012) 8:442–50. doi: 10.1016/j.ijrobp.2011.06.1983
45. Kamp F, Cabal G, Mairani A, Parodi K, Wilkens JJ, Carlson DJ. Fast biological modeling for voxel-based heavy ion treatment planning using the mechanistic repair-misrepair-fixation model and nuclear fragment spectra. *Int J Radiat Oncol Biol Phys*. (2015) 93:557–68. doi: 10.1016/j.ijrobp.2015.07.2264
46. Stewart RD, Carlson DJ, Butkus MP, Hawkins R, Friedrich T, Scholz M. A comparison of mechanism-inspired models for particle relative biological effectiveness (RBE). *Med Phys*. (2018) 45:e925–52. doi: 10.1002/mp.13207
47. Petrović I, Ristić-Fira A, Todorović D, Korićanac L, Valastro L, Cirrone P, et al. Response of a radioresistant human melanoma cell line along the proton spread-out Bragg peak. *Int J Radiat Biol*. (2010) 86:742–51. doi: 10.3109/09553002.2010.481322
48. Petrović I, Ristić-Fira A, Keta O, Petković V, Petringa G, Cirrone P, et al. A radiobiological study of carbon ions of different linear energy transfer in resistant human malignant cell lines. *Int J Radiat Biol. BioRxiv [Preprint]*. (2020).
49. Romano F, Cirrone GA, Cuttone G, Rosa FD, Mazzaglia SE, Petrovic I, et al. A monte carlo study for the calculation of the average linear energy transfer (LET) distributions for a clinical proton beam line and a radiobiological carbon ion beam line. *Phys Med Biol*. (2014) 59:2863–82. doi: 10.1088/0031-9155/59/12/2863
50. Krämer M, Scholz M. Treatment planning for heavy-ion radiotherapy: calculation and optimization of biologically effective dose. *Phys Med Biol*. (2000) 45:3319–30. doi: 10.1088/0031-9155/45/11/314
51. Krämer M, Scholz M. Rapid calculation of biological effects in ion radiotherapy. *Phys Med Biol*. (2006) 51:1959–70. doi: 10.1088/0031-9155/51/8/001
52. Weber U, Kraft G. Design and construction of a ripple filter for a smoothed depth dose distribution in conformal particle therapy. *Phys Med Biol*. (1999) 44:2765–75. doi: 10.1088/0031-9155/44/11/306
53. Petrović I, Ristić-Fira A, Todorović D, Valastro L, Cirrone P, Cuttone G. Radiobiological analysis of human melanoma cells on the 62 MeV CATANA proton beam. *Int J Radiat Biol*. (2006) 82:251–65. doi: 10.1080/09553000600669859
54. Friedland W, Dingfelder M, Kundrát P, Jacob P. Track structures, DNA targets and radiation effects in the biophysical monte carlo simulation code PARTRAC. *Mutat Res*. (2011) 711:28–40. doi: 10.1016/j.mrfmmm.2011.01.003
55. Zacharias T, Dörr W, Enghardt W, Haberer T, Krämer M, Kumpf R, et al. Acute response of pig skin to irradiation with 12C-ions or 200 kV X-rays. *Acta Oncol*. (1997) 36:637–42. doi: 10.3109/02841869709001328
56. Karger CP, Peschke P, Sanchez-Brandelik R, Scholz M, Debus J. Radiation tolerance of the rat spinal cord after 6 and 18 fractions of photons and carbon ions: experimental results and clinical implications. *Int J Radiat Oncol Biol Phys*. (2006) 66:1488–97. doi: 10.1016/j.ijrobp.2006.08.045
57. Saager M, Peschke P, Brons S, Debus J, Karger CP. Determination of the proton RBE in the rat spinal cord: Is there an increase towards the end of the spread-out Bragg peak? *Radiother Oncol*. (2018) 128:115–20. doi: 10.1016/j.radonc.2018.03.002
58. ICRU Report No. 78: *Prescribing, Recording, and Reporting Proton-Beam Therapy*. Bethesda, MD: International Commission on Radiation Units and Measurements Journal of the International Commission on Radiation Units and Measurements. (2007).
59. Grün R, Friedrich T, Traneus E, Scholz M. Is the dose-averaged LET a reliable predictor for the relative biological effectiveness? *Med Phys*. (2019) 46:1064–74. doi: 10.1002/mp.13347
60. Lindblom E, Dasu A, Lax I, Toma-Dasu I. Survival and tumour control probability in tumours with heterogeneous oxygenation: a comparison between the linear-quadratic and the universal survival curve models for high doses. *Acta Oncol*. (2014) 53:1035–40. doi: 10.3109/0284186X.2014. 925582

61. Friedrich T, Durante M, Scholz M. Modeling cell survival after irradiation with ultrasoft X rays using the giant loop binary lesion model. *Radiat Res*. (2014) 181:485–94. doi: 10.1667/RR13518.1
62. Herr L, Friedrich T, Durante M, Scholz M. A model of photon cell killing based on the spatio-temporal clustering of DNA damage in higher order chromatin structures. *PLoS ONE*. (2014) 9:e83923. doi: 10.1371/journal.pone.0083923
63. Tommasino F, Friedrich T, Scholz U, Taucher-Scholz G, Durante M, Scholz M. Application of the local effect model to predict DNA double-strand break rejoining after photon and high-LET irradiation. *Radiat Prot Dosimetry*. (2015) 166:66–70. doi: 10.1093/rpd/ncv164
64. Dilmanian FA, Eley JG, Krishnan S. Minibeam therapy with protons and light ions: physical feasibility and potential to reduce radiation side effects and to facilitate hypofractionation. *Int J Radiat Oncol Biol Phys*. (2015) 92:469–74. doi: 10.1016/j.ijrobp.2015.01.018
65. Prezado Y, Jouvion G, Guardiola C, Gonzalez W, Juchaux M, Bergs J, et al. Tumor control in RG2 glioma-bearing rats: a comparison between proton minibeam therapy and standard proton therapy. *Int J Radiat Oncol Biol Phys*. (2019) 104:266–71. doi: 10.1016/j.ijrobp.2019.01.080
66. Girst S, Greubel C, Reindl J, Siebenwirth C, Zlobinskaya O, Walsh DW, et al. Proton minibeam radiation therapy reduces side effects in an *in vivo* mouse ear model. *Int J Radiat Oncol Biol Phys*. (2016) 95:234–41. doi: 10.1016/j.ijrobp.2015.10.020
67. Billena C, Khan AJ. A current review of spatial fractionation: back to the future. *Int J Radiat Oncol Biol Phys*. (2019) 104:177–87. doi: 10.1016/j.ijrobp.2019.01.073
68. Grosswendt B. Nanodosimetry, from radiation physics to radiation biology. *Radiat Prot Dosimetry*. (2005) 115:1–9. doi: 10.1093/rpd/nci152
69. Selva A, De Nadal V, Cherubini R, Colautti P, Conte V. Towards the use of nanodosimetry to predict cell survival. *Radiat Prot Dosimetry*. (2019) 183:192–6. doi: 10.1093/rpd/ncy274
70. Mazzucconi D, Bortot D, Agosteo S, Pola A, Pasquato S, Fazzi A, et al. Microdosimetry at nanometric scale with an avalanche-confinement tepc: response against a helium ion beam. *Radiat Prot Dosimetry*. (2019) 183:177–81. doi: 10.1093/rpd/ncy230

Conflict of Interest: The authors declare that the research was conducted in the absence of any commercial or financial relationships that could be construed as a potential conflict of interest.

frontiers in Physics

REVIEW
published: 28 August 2020
doi: 10.3389/fphy.2020.00326

Radioactive Beams in Particle Therapy: Past, Present, and Future

Marco Durante[1,2]* *and Katia Parodi*[3]

[1] Biophysics Department, GSI Helmholtzzentrum für Schwerionenforschung, Darmstadt, Germany, [2] Institute of Condensed Matter Physics, Technische Universität Darmstadt, Darmstadt, Germany, [3] Department of Experimental Physics—Medical Physics, Ludwig-Maximilians-Universität München, Munich, Germany

Heavy ion therapy can deliver high doses with high precision. However, image guidance is needed to reduce range uncertainty. Radioactive ions are potentially ideal projectiles for radiotherapy because their decay can be used to visualize the beam. Positron-emitting ions that can be visualized with PET imaging were already studied for therapy application during the pilot therapy project at the Lawrence Berkeley Laboratory, and later within the EULIMA EU project, the GSI therapy trial in Germany, MEDICIS at CERN, and at HIMAC in Japan. The results show that radioactive ion beams provide a large improvement in image quality and signal-to-noise ratio compared to stable ions. The main hindrance toward a clinical use of radioactive ions is their challenging production and the low intensities of the beams. New research projects are ongoing in Europe and Japan to assess the advantages of radioactive ion beams for therapy, to develop new detectors, and to build sources of radioactive ions for medical synchrotrons.

Keywords: particle therapy, radioactive ion beams, carbon ions, oxygen ions, PET

OPEN ACCESS

Edited by:
Claudia Kuntner, Austrian Institute of Technology (AIT), Austria

Reviewed by:
Bruno Golosio, University of Cagliari, Italy
Timothy DeGrado, Mayo Clinic, United States

***Correspondence:**
Marco Durante
m.durante@gsi.de

Specialty section:
This article was submitted to Medical Physics and Imaging, a section of the journal Frontiers in Physics

Received: *25 April 2020*
Accepted: *14 July 2020*
Published: *28 August 2020*

Citation:
Durante M and Parodi K (2020) Radioactive Beams in Particle Therapy: Past, Present, and Future. Front. Phys. 8:326. doi: 10.3389/fphy.2020.00326

INTRODUCTION

Currently, ∼50% of cancer patients in Europe experience radiotherapy, generally by X-rays, as part of their treatment [1]. In recent years, photon radiotherapy has greatly improved its accuracy and safety thanks to image guidance (IGRT) [2]. However, charged particle therapy (CPT) with protons and light ions is rapidly growing all over the world, particularly in Europe [3]. In fact, thanks to the favorable depth-dose distribution, more normal tissue is spared with CPT compared to conventional radiotherapy with X-rays in virtually all sites, leading to high success/toxicity ratios [4]. Using ions heavier than protons, generally carbon ions, the physics advantages are added to the radiobiological properties, being stopping (high-LET) ions in the tumor region more effective than X-rays or protons for cell killing, while in the normal tissue, fast (low-LET) ions induce a toxicity comparable to sparsely ionizing radiation [5]. The experience at the National Institute of Radiological Sciences (NIRS) in Chiba (Japan) [6] and in the European centers [7] demonstrates that the radiobiological and physical rationale is actually translated in improved clinical results for several indications [8].

Yet, CPT remains controversial [9]. The first reason is the higher cost of the CPT facilities [10], especially the expensive heavy ion centers. Even if the cost is still much higher for particle therapy centers compared to linacs for X-rays, it is declining, mostly thanks to superconductive technologies now employed for the construction of the accelerators (cyclotrons, synchro-cyclotrons, or synchrotrons) [11, 12]. However, CPT is also limited in what should be the main advantage, i.e., the high precision made possible by the Bragg peak. CPT is indeed less robust than conventional radiotherapy because of considerable uncertainty on the particle range and poor image guidance [13]. While the lateral penumbra is shallower for protons than for X-rays, making the proton plans

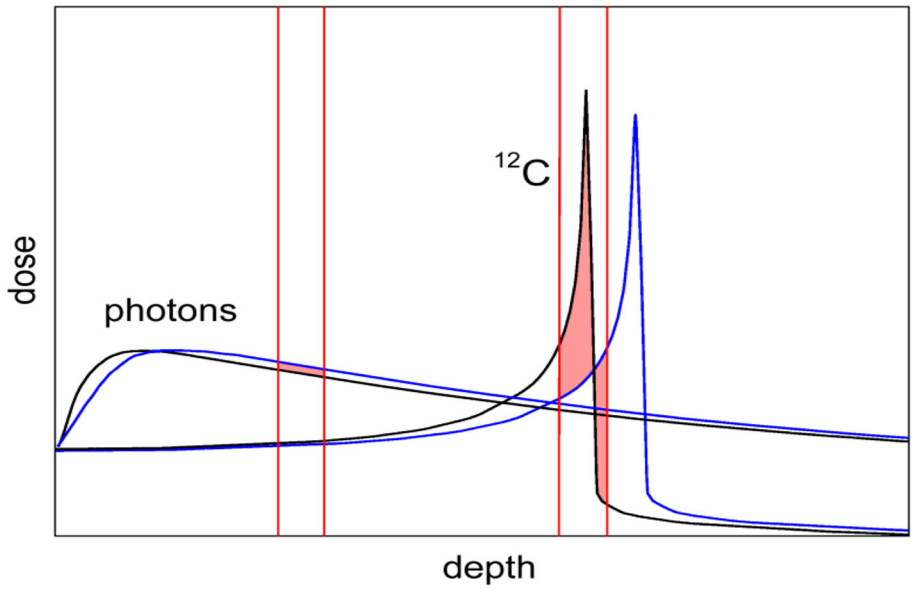

FIGURE 1 | Comparison of depth-dose distribution for heavy ions (^{12}C) and photons (X-rays). The Bragg peak gives the physical advantages of CPT. However, the figure shows that a small range shift caused, e.g., by a tissue inhomogeneity has a small impact on the X-ray curve, but in CPT it can significantly shift the Bragg peak from the target into a sensitive organ surrounding the tumor.

robust for misalignments in the direction orthogonal to the beam direction [14], for heavy ions, characterized by sharp dose gradients in all directions and very high doses in the distal ends, range uncertainty is the main physics limitation. Image guidance is essential for CPT, even more so than for X-rays, because a shift in the Bragg peak has a much larger impact on the dose than for photons (**Figure 1**). For moving targets this also occurs through the interplay effect, causing underdosage to part of the target [15]. In-room CT and cone-beam CT are emerging as the two image guidance methods of choice for CPT, but IGRT using X-rays is more accurate and robust [16] and is quickly improving thanks to the recent introduction of online magnetic resonance imaging (MRI) [17, 18]. Clinically, a substantial margin is added in CPT to the prescribed range in order to ensure tumor coverage, e.g., in proton therapy, this range margin is on the order of 3.5% of the prescribed range [19]. Wide margins jeopardize one of the main advantages of the Bragg peak: the steep dose gradients and the potential high accuracy and precision [20].

To tackle the range uncertainty problem, several methods for range verification have been developed. Imaging in radiology very often uses radioactive tracers, and it was indeed proposed already long ago [21] that radioactive ion beams (RIB) have the potential for simultaneous treatment and beam visualization, similar to theranostics with radioisotopes [22]. We will first describe the current methods for heavy ion beam visualization, and then the past experience is using RIB in cancer therapy. We will then argue that the current efforts for high-intensity accelerators can lead to a more effective use of RIB in therapy, pending experimental proof of the clinical advantages.

RANGE VERIFICATION IN PARTICLE THERAPY

Even if image guidance is less common in CPT compared to conventional radiotherapy, the physics of charged particles offers unique opportunities for *in vivo* range verification. In proton therapy, there is an increasing use of prompt γ-ray detectors that measure the emission of photons by nuclear reactions and their fast decay shortly before the Bragg peak [23]. The method has been tested also for high-energy C-ions in phantoms [24, 25]. Several other methods have been proposed, such as ionoacoustic measurements [26] or mixed beams [27]. For C-ions, it is also possible to measure secondary charged particles, such as protons emitted at large angles [28, 29]. A combination of different methods is under study for animal irradiators [30] and in clinical settings [31, 32]. Reviews of different methods for *in vivo* range verification can be found in Refs. [33–36].

The range verification method that has been tested most extensively in clinical practice is positron emission tomography (PET) [37]. PET is a well-known diagnostic imaging method, based on the detection of the two 511 keV photons emitted by annihilation of a positron with an electron in the media. Unlike conventional diagnostic imaging [38], currently PET in particle therapy exploits β^+-emitting isotopes produced by the particle beam in the patient's body by nuclear fragmentation [37]. In proton therapy, only target fragments can be used for imaging, while in heavy ion therapy, the projectile fragments provide a large part of the signal with better correlation to the dose. A list of typical radionuclides produced by target fragmentation in proton therapy or potential projectile fragments is provided in **Table 1**. The radioactive projectile fragments provide a peak in the activity

TABLE 1 | Positron-emitting isotopes that are found in proton therapy by target fragmentation and/or that have been considered as projectiles for RIB therapy.

Stable isotope	Positron-emitting isotopes	Half-life
^{12}C	^{11}C	20.33 min
	^{10}C	19.3 s
^{14}N	^{13}N	9.97 min
	^{12}N	11.0 ms
^{16}O	^{15}O	2.04 min
	^{14}O	1.17 min
^{19}F	^{18}F	1.83 h
	^{17}F	1.07 min
^{20}Ne	^{19}Ne	17.26 s
	^{18}Ne	1.66 s
^{31}P	^{30}P	2.50 min
	^{29}P	4.14 s

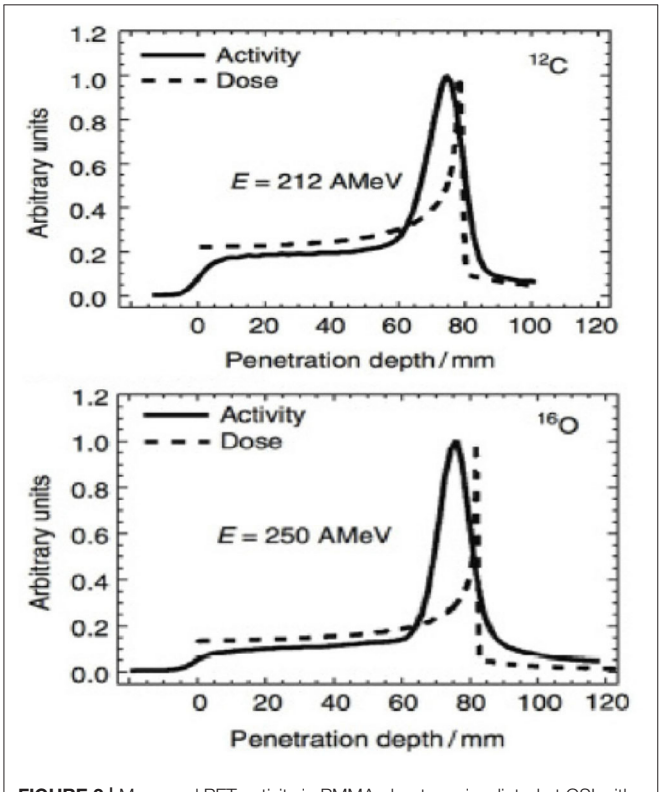

FIGURE 2 | Measured PET activity in PMMA phantoms irradiated at GSI with carbon or oxygen ions, showing the shift between activity and dose peak (measurements from Ref. [39]).

that is not observed in proton therapy (**Figure 2**) [40]. However, the activity peak invariably occurs upstream of the Bragg peak, because the light isotopes of the projectile have shorter range at the same velocity of the primary ion [13, 39]. Online PET was used for the first time clinically during the ^{12}C-ion pilot therapy project at GSI, Darmstadt, until 2008 [41], and a number of CPT centers are currently using PET for beam verification [32, 42–44], usually offline.

However, PET in C-ion therapy remains marginal and not really able to reduce range uncertainty as desired. The half-life of the most abundant induced radionuclides is too long for instantaneous feedback (**Table 1**), and the short-lived radionuclides are produced at a very low rate and exhibit a long positron range [45]. The measured activity is not directly correlated to the Bragg curve in phantoms (**Figure 2**), and the situation is worsened *in vivo* by the biological washout [43, 46]. An example comes from recent experiments on heavy-ion treatment of heart arrhythmia in a swine model, where online PET was used for range verification of a C-ion beam [47]. In **Figure 3**, we compare online to offline PET in a pig heart ventricular target irradiated with ^{12}C-ions. After 20 min, only the signal in the ribs is still visible in PET. The lack of a direct correlation with the dose (**Figure 2**) and the washout (**Figure 3**) makes resorting to Monte Carlo (MC) simulations [40] or other analytical calculations [48] currently unavoidable for data analysis. Furthermore, the activity is time-dependent according to the half-lives of the isotopes (**Table 1**) and the efficiency of the detector system in measuring the activity distribution. All these corrections currently limit the accuracy of PET-based range verification to about 2–5 mm [33, 42, 49].

RIB IN RADIOTHERAPY

The rationale for using RIB in therapy has looked in two directions. On one side, it was assumed that the radioactive decay can increase the dose in the target. This was similar to the rationale for using antiprotons [50] or pions [51] for therapy. Among radioactive isotopes, ^{9}C attracted attention because of its β-delayed decay in low-energy, densely ionizing particles [52]. However, despite some successful *in vitro* experiments [53], these approaches have been abandoned. The energy released by nuclear reaction in the target is indeed in the order of the nuclear shell energies, and such energy is always very small compared to the electromagnetic energy loss of the particle in the tumor. In fact, simulations show that the putative increase due to nuclear reactions in the target is negligible [54].

On the other hand, RIB can be used for image-guided particle therapy. In fact, the best way to increase the signal intensity in online PET would be the use of β^+ emitters for treatment. Using RIB, every primary ion will decay, essentially only at the end of the range, with the decay time always much longer than the travel time in the accelerator and in the patient's body. RIB would improve the count rate ∼10 × [55], reduce the shift between measured activity and dose (**Figure 2**), and mitigate the washout blur of the image (**Figure 3**) with short-lived isotopes and in-beam acquisition. Heavy ion therapy is nowadays only performed using carbon ions, because with heavier ions, the toxicity in normal tissues can be unacceptable. The Heidelberg Ion Therapy (HIT) center is currently planning to use oxygen ions for radioresistant tumors, and therefore looking at **Table 1**, one should consider isotopes of C, N, and O as potential projectiles in RIB therapy.

The idea of using RIB in therapy is certainly not new, as the potential advantage in terms of improved precision and accuracy

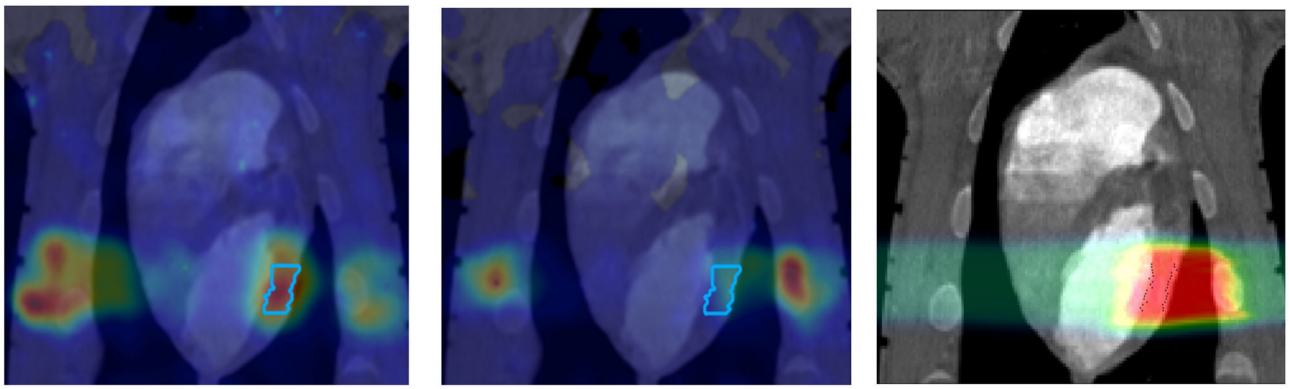

FIGURE 3 | PET images of a pig heart treated with ^{12}C-ions. The ventricular target is drawn in the treatment planning image overlaid to the CT **(Right)**. Online PET image **(Left)** was acquired during the treatment at GSI, while the offline (center) was registered 20 min after the treatment. PET imaging obtained with the online PET camera at GSI, courtesy of Helmholtzzentrum Dresden (HZDR); details in Ref. [47].

was clear since the beginning of CPT. Below, we will describe past efforts in this direction.

Lawrence Berkeley Laboratory

Cancer therapy using ions heavier than protons was first tested in the pilot project of the Lawrence Berkeley Laboratory (LBL) in USA led by Cornelius A. Tobias. The project started in 1975 and used He, C, Ne, Si, and Ar ions, treating 1,314 patients until the shutdown of the Bevalac accelerator in 1992 [56, 57]. The uncertainty in predicting the correct range of heavy ions from the CT images, produced by X-rays, was soon clear and the LBL physicists explored the possibility of using RIB for range verification [58]. The LBL studies focused on ^{19}Ne (**Table 1**) and built a modified PET detector (PEBA) consisting of two arrays of 64 BiGe scintillators in an 8 × 8 matrix arrangement, which are separated by a distance of ∼1 m (**Figure 4**). PEBA was already able to demonstrate an accuracy of ∼1 mm in range determination in phantoms [21].

Eulima

The European Light Ion Medical Accelerator (EULIMA) project was funded by EU within the 2nd Framework Program in 1989. The project was led by the cyclotron laboratory in Nice, which was already active in proton therapy for eye treatment [59]. The concerted action studied the feasibility of a hospital-based light ion ($2 \leq z \leq 10$) accelerator facility for the treatment of a large number of cancer patients in Europe. The project explored the idea of using a superconducting cyclotron, based on the experience in Nice, and carefully analyzed the option of irradiating the patients with radioactive isotopes of carbon, oxygen, or neon. Cyclotrons have the advantage of high intensity and simplicity of operation. However, superconducting cyclotrons for ions as heavy as carbon requires an intense R&D for magnetic field shaping and high voltage. Synchrotrons are instead flexible machines, energy can be rapidly changed, different ion species can be accelerated, and they are a well-established technology. For these reasons, the EULIMA feasibility study recommended using synchrotrons for heavy-ion therapy [60], and indeed all European ion beam centers are currently using synchrotrons. IBA, the leading company in cyclotrons for proton therapy, is still working on the idea of the superconducting cyclotron for carbon ions (C400) [61], in collaboration with GANIL at Caen (France), but the project is still ongoing.

GSI

The GSI Helmholtz Center for Heavy Ion Research in Darmstadt (Germany) treated the first patient in Europe with ions heavier than protons—carbon ions. The program was led by Gerhard Kraft and treated 440 patients with ^{12}C-ions between 1997 and 2008 [5, 62]. As noted in section Range Verification in Particle Therapy, the pilot project at GSI used for the first time PET online to verify the dose delivery (**Figure 5**). The group from Helmholtz Center Dresden that worked on the PET system also measured RIB, produced at the GSI fragment separator (FRS) [63]. They used ^{15}O, ^{17}F, and ^{19}Ne for testing the PET camera [64]. All patients in the pilot project were, however, treated with stable ^{12}C ions and PET images exploited mostly the ^{11}C projectile fragment produced by nuclear fragmentation. As shown in **Figure 3**, the same PET camera was recently used for irradiation of AV nodes and ventricles in swine hearts at GSI [47]. Radiotherapy for treatment of heart arrhythmia is considered a very promising non-invasive alternative to catheter ablation [65], and recent results with stereotactic radiosurgery for ventricular arrhythmia are very encouraging [66]. Charged particles are potentially much more effective for these kinds of treatment [67] because they require single high doses, and with X-rays, this can cause severe toxicity in the normal heart and other surrounding critical structures such as esophagus and lungs. However, the cardiac targets are small and rapidly moving, and therefore PET imaging plays a very important role for applications of heavy ions in non-cancer diseases. The first patient with ventricular arrhythmia has been treated with protons at CNAO (Pavia, Italy) in December 2019 [68].

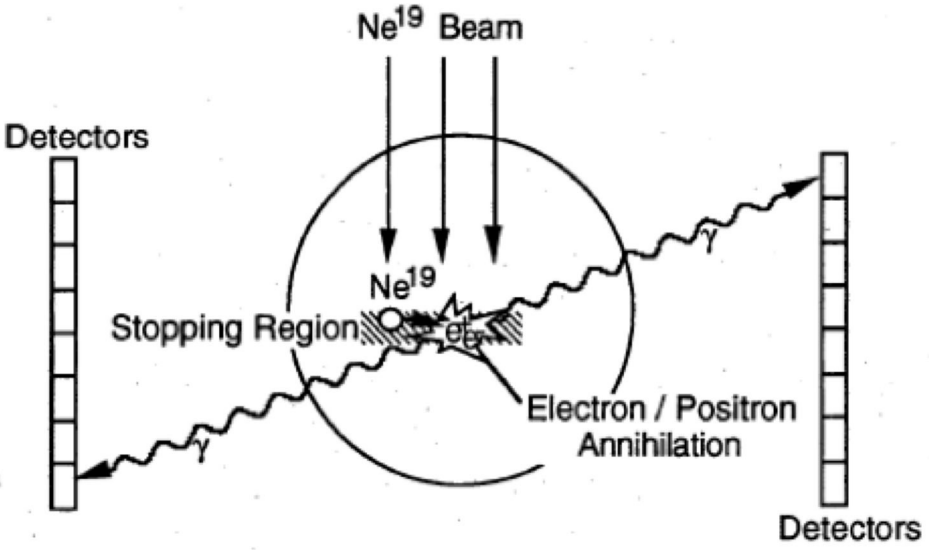

FIGURE 4 | PEBA detector developed at LBL for the visualization of ^{19}Ne ion range. Figure from Ref. [58].

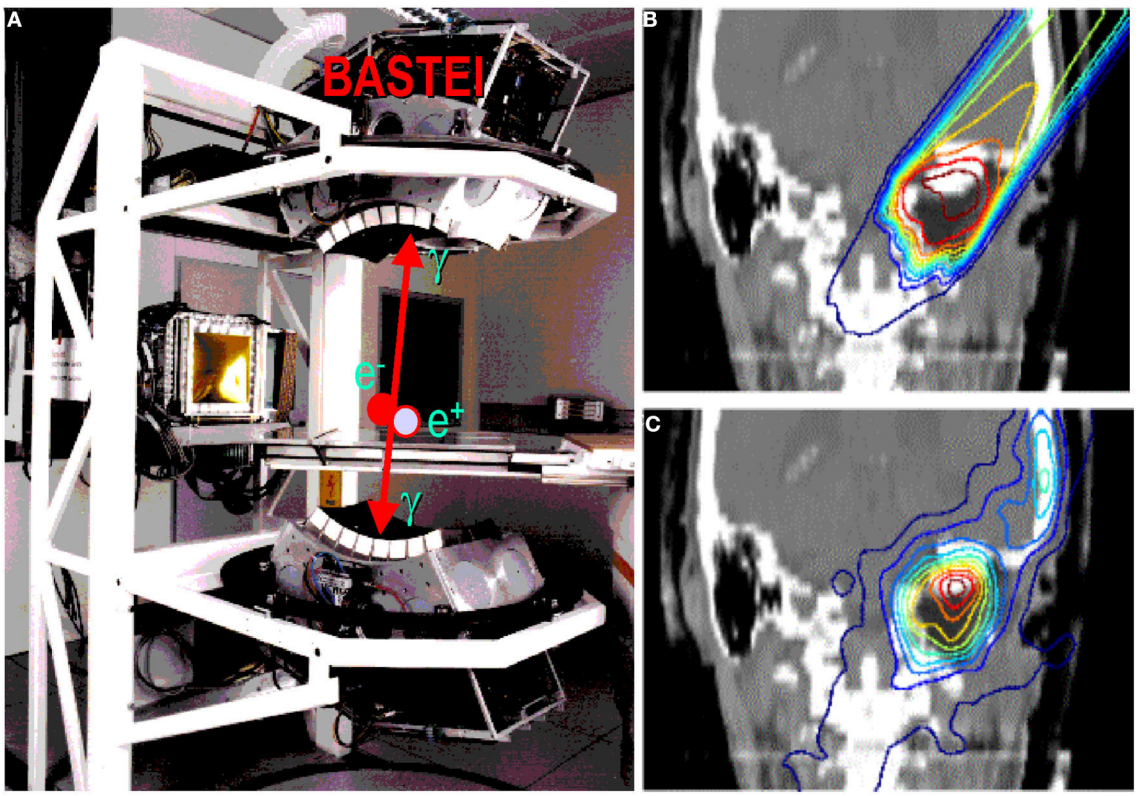

FIGURE 5 | (A) The PET camera (without housing) installed at the GSI treatment room (cave M) and used during the pilot project, as shown in the clinical case in **(B)** (prescribed dose according to treatment planning) and **(C)** (measured activity distribution, modified by the washout).

HIMAC

Certainly, the accelerator facility that has the longest history and success in RIB production and testing for cancer therapy is the HIMAC at NIRS in Chiba, Japan. Following the LBL pilot project, NIRS was the first center to treat patients with ions heavier than protons, specifically carbon ions.

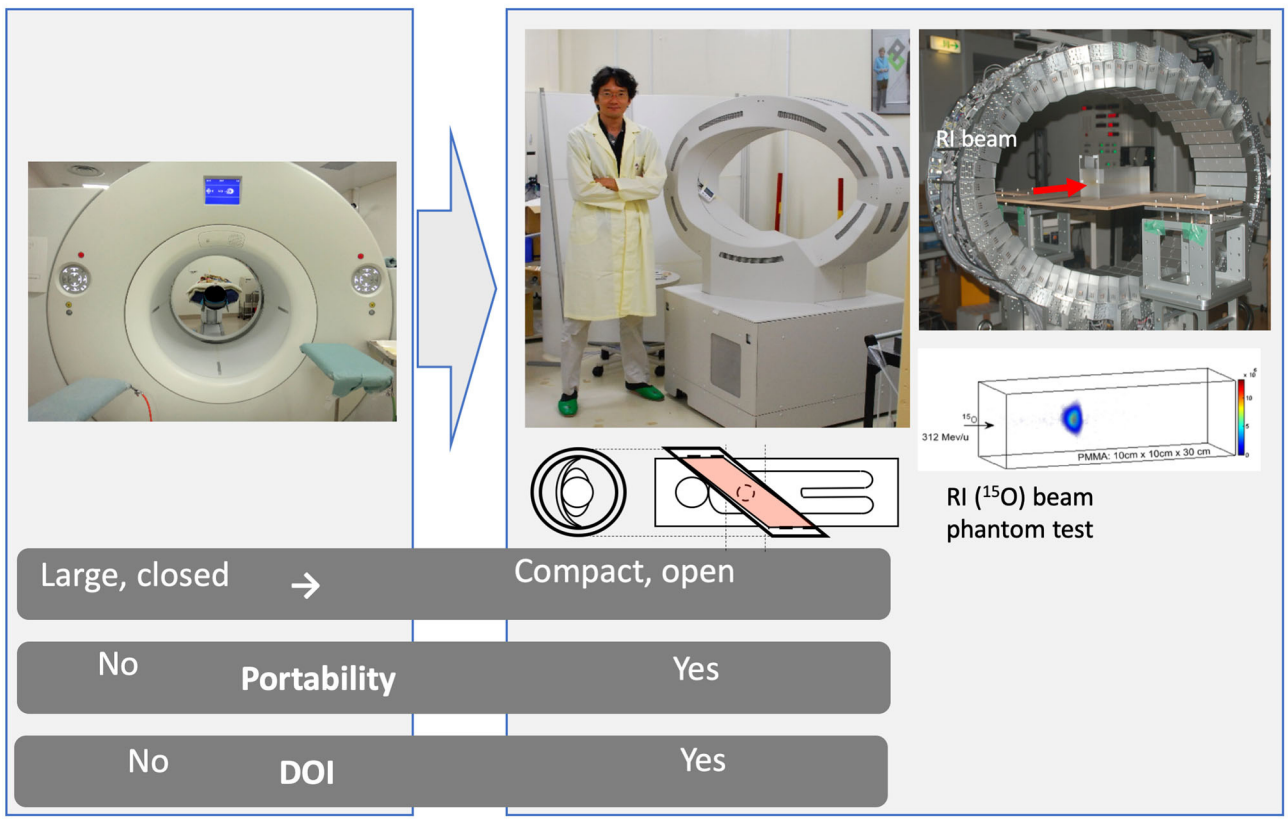

FIGURE 6 | The OpenPET imaging detector developed at NIRS in the Taiga Yamaya laboratory, along with images of a ^{15}O beam in a plastic target. Image from https://www.nirs.qst.go.jp/usr/medical-imaging/imaging-physics/index-en.html, reproduced with permission.

NIRS used the flexible and reliable HIMAC synchrotron for patient treatments and research [69], and most of the patients treated worldwide with C-ions were actually irradiated at HIMAC [6]. In over 20 years of clinical operation, NIRS has demonstrated excellent results in many tumor sites with acceptable toxicity, very often in hypofractionation [70]. NIRS has always invested in research and development in heavy ion therapy and has been studying RIB for therapy for 20 years [71]. Considering the low RIB intensity (see section RIB Production), NIRS physicists were trying to use the RIB beam at low intensity as a probe before application of the stable carbon therapeutic beam. The Yamaya laboratory at NIRS has developed a new concept of open-PET [72–74] (**Figure 6**) to visualize the beam and has applied the system to study the washout of radionuclides in animal targets [75, 76]. Optical beam imaging has also been recently used to visualize RIB at HIMAC [77]. The HIMAC studies demonstrate that RIB have similar radiobiological properties as stable isotopes of the same atomic number but produce far better quality images for range verification, with 5–11-fold improvements in the PET signal/noise ratio [78].

RIB PRODUCTION

The main hindrance to the full exploitation of RIB in cancer therapy is the low intensity. RIB are a very important modern topic in nuclear physics, as they allow to study the properties of nuclear matter far from the stability curve [79]. To produce RIB, two techniques are used at particle accelerators: Isotope-on-line (ISOL) and in-flight [80, 81] (**Figure 7**). ISOL is based on light-ion (usually ^{1}H or ^{2}H)-induced spallation or fission of thick targets (Ta or U). The radioactive fragments are extracted from the thick target through thermal diffusion at high temperature, effused to an ion source to become singly charged ions and finally accelerated toward a target. RIB production for therapy has so far used the in-flight technique, where RIB are obtained by fragmentation of the stable primary beam in thin targets (usually in C or Be). The reaction fragments, ejected in the forward direction with almost the same speed as that of the incident beam, are magnetically separated and then transferred to the experimental vault. The RIB (A, N-1) intensity is therefore determined by the fragmentation cross section of the primary beam (A, N). As shown in **Table 2**, the production cross section

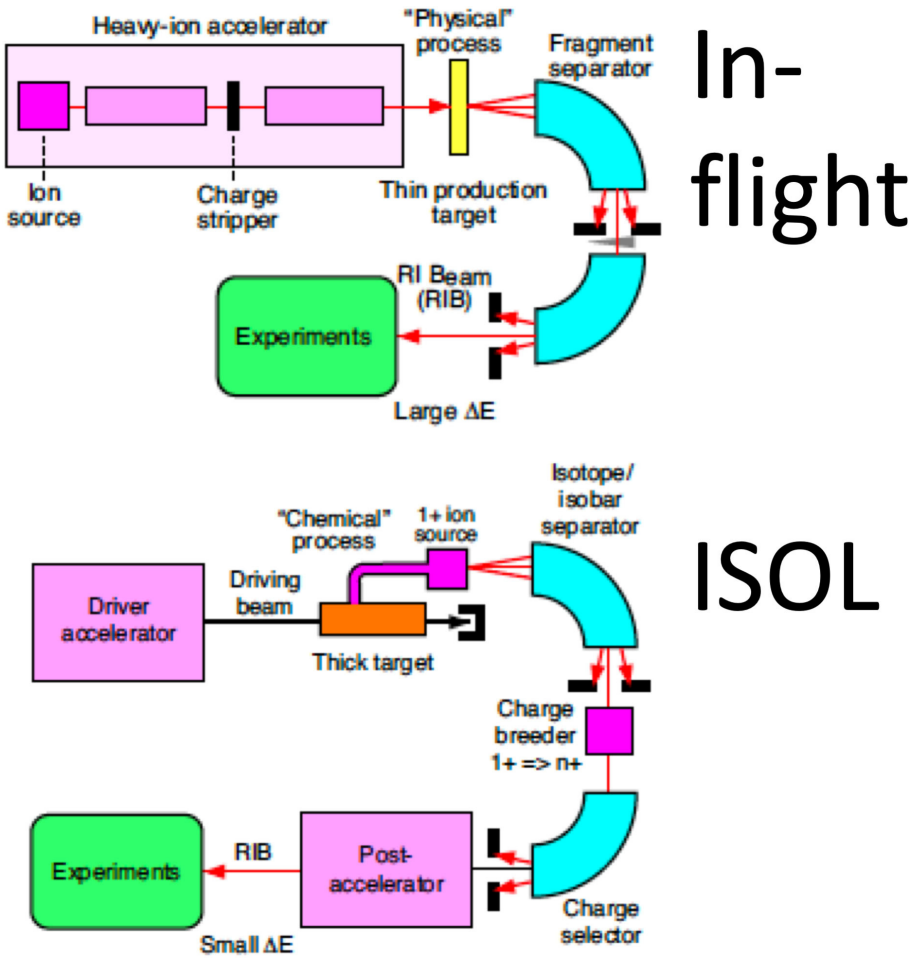

FIGURE 7 | Schematic drawing of the in-flight and ISOL methods for RIB production.

for light ions at high energy is ∼45 mb per one nucleon, and decreases an order of magnitude for every further nucleon. Beam intensity is consequently reduced to $< 10^{-2}$ for N-1 isotopes and 10^{-3} for N-2 isotopes. At HIMAC, beams of ^{11}C were produced with intensities ranging 10^5–10^6 pps [77, 82], still too low for a therapeutic C-ion treatment that requires 10^8–10^9 pps [5, 13].

An additional problem in the in-flight technique is the large momentum spread. This spread causes a shift between the Bragg peak and activity peak for RIB [83]. Even if this shift is smaller than the one observed using stable ions for treatment and projectile fragments for PET imaging (**Figure 2**), it increases with the momentum acceptance. Recent measurements at HIMAC shows that for ^{11}C, the shift is around 2 mm at 5% acceptance and is reduced to 0.1 mm at 0.5% momentum acceptance [84]. Momentum spreads can therefore translate in significant range spreads at the site of stopping (**Table 2**).

In-flight production of RIB would be impractical in current medical synchrotrons. Already at LBL, it was hypothesized to produce the RIB at low energy and then inject them in the high-energy medical accelerator [21]. The idea is to build a small cyclotron that can produce low-energy RIB with an ISOL system, and these ions are then injected in conventional synchrotrons. A source using low-energy electron beams for the production of ^{11}C has been designed and produced at HIMAC [85]. Within the MEDICIS-Promed project [86], CERN has proposed a charge breeding scheme based on an Electron Beam Ion Source for beam preparation of a radioactive ^{11}C beam [87]. The charge breeder is coupled to a medical synchrotron currently used for ^{12}C-ion therapy (such as MedAustron) to treat patients with ^{11}C using the same beam delivery devices of conventional heavy-ion therapy [88].

BARB

GSI-treated cancer patients with ^{12}C-ions accelerated at SIS, a 18 Tm synchrotron where the FRS has been used for many nuclear physics experiments [63]. SIS18 will be the injector of a new accelerator at 100 Tm, currently under construction for the Facility for Anti-protons and Ion Research (FAIR) [89] (**Figure 8**). A new FRS (super-FRS) will be built at SIS100 [90], to accommodate the ambitious physics program of the NuSTAR collaboration [91]. In addition to the nuclear

TABLE 2 | A MOCADI simulation of the RIB intensity at GSI FRS.

Primary beam	Intensity at SIS-18 (per cycle)	Secondary beams	Production cross-section (mb)	Intensity at FRS (pps)	Energy (MeV/n)	Range in water (cm)	Range straggling (cm)
^{12}C	8×10^{10}	^{10}C	4.8	2.3×10^{7}	334	17.2	0.4
		^{11}C	45.4	4.9×10^{8}	347	20.1	0.5
^{16}O	1×10^{11}	^{14}O	4.6	5.7×10^{7}	405	18.4	0.4
		^{15}O	45.6	9.1×10^{8}	416	20.6	0.4

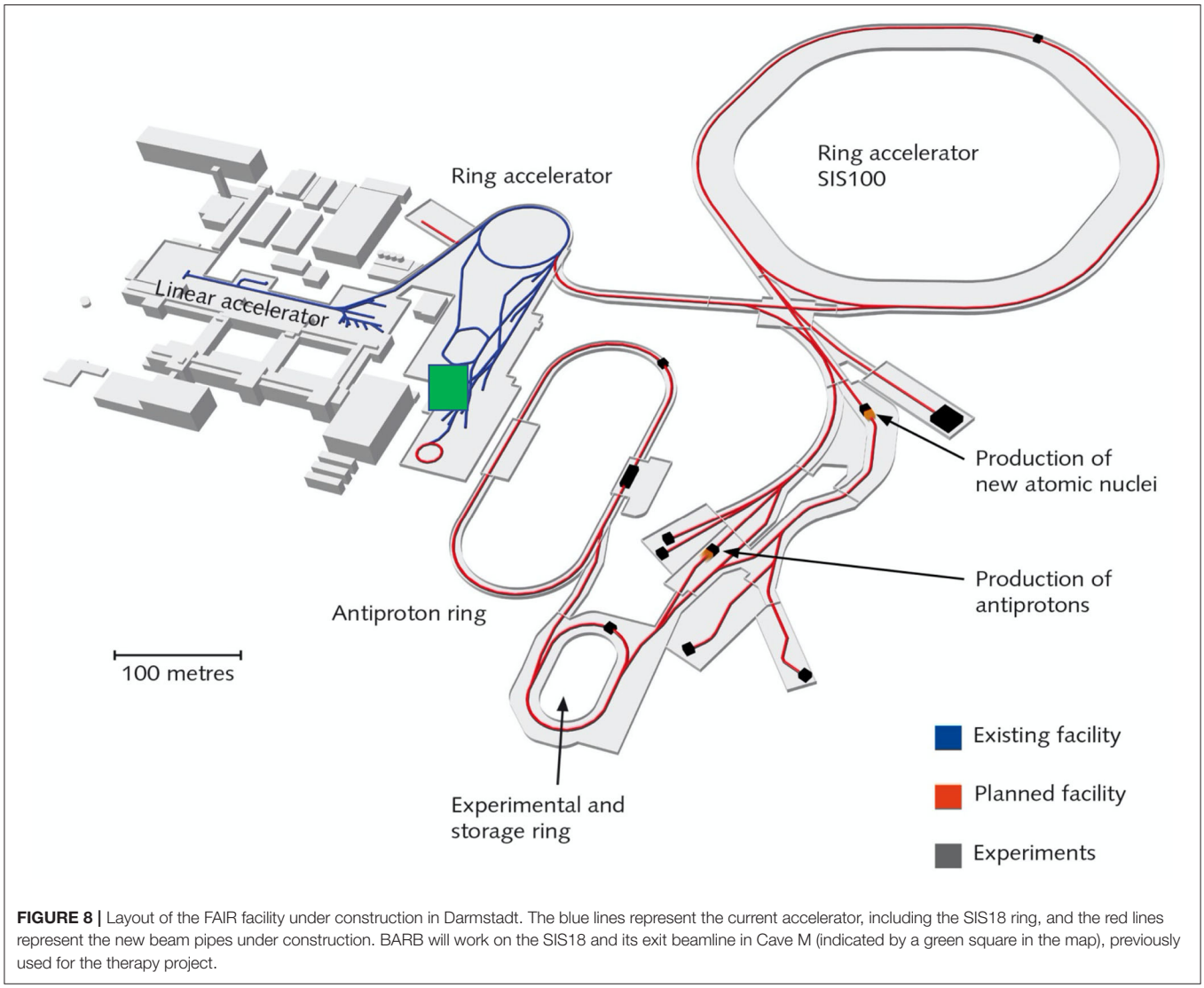

FIGURE 8 | Layout of the FAIR facility under construction in Darmstadt. The blue lines represent the current accelerator, including the SIS18 ring, and the red lines represent the new beam pipes under construction. BARB will work on the SIS18 and its exit beamline in Cave M (indicated by a green square in the map), previously used for the therapy project.

physics program, FAIR also includes a large applied physics program (APPA) in atomic physics, plasma physics, materials research, and biophysics [92]. The biophysics program at FAIR aims at exploiting the intensity and energy upgrades for therapy and space radiation protection research [93]. While SIS100 is under construction, the FAIR-phase-0 is already ongoing with the main goal of increasing the intensity by a factor of × 10,000 compared to the current values [94]. The intensity upgrade at SIS18 can be exploited to test RIB therapy in the same Cave M (**Figure 5**) where the pilot project was performed. The project Biomedical Applications of Radioactive ion Beams (BARB) (www.gsi.de/BARB) aims at testing ^{10,11}C and ^{14,15}O for simultaneous treatment and imaging at FAIR, with the goal of reaching sub-mm precision in range verification and to demonstrate the potential of RIB therapy in an animal model. BARB is funded by EU within the 2019

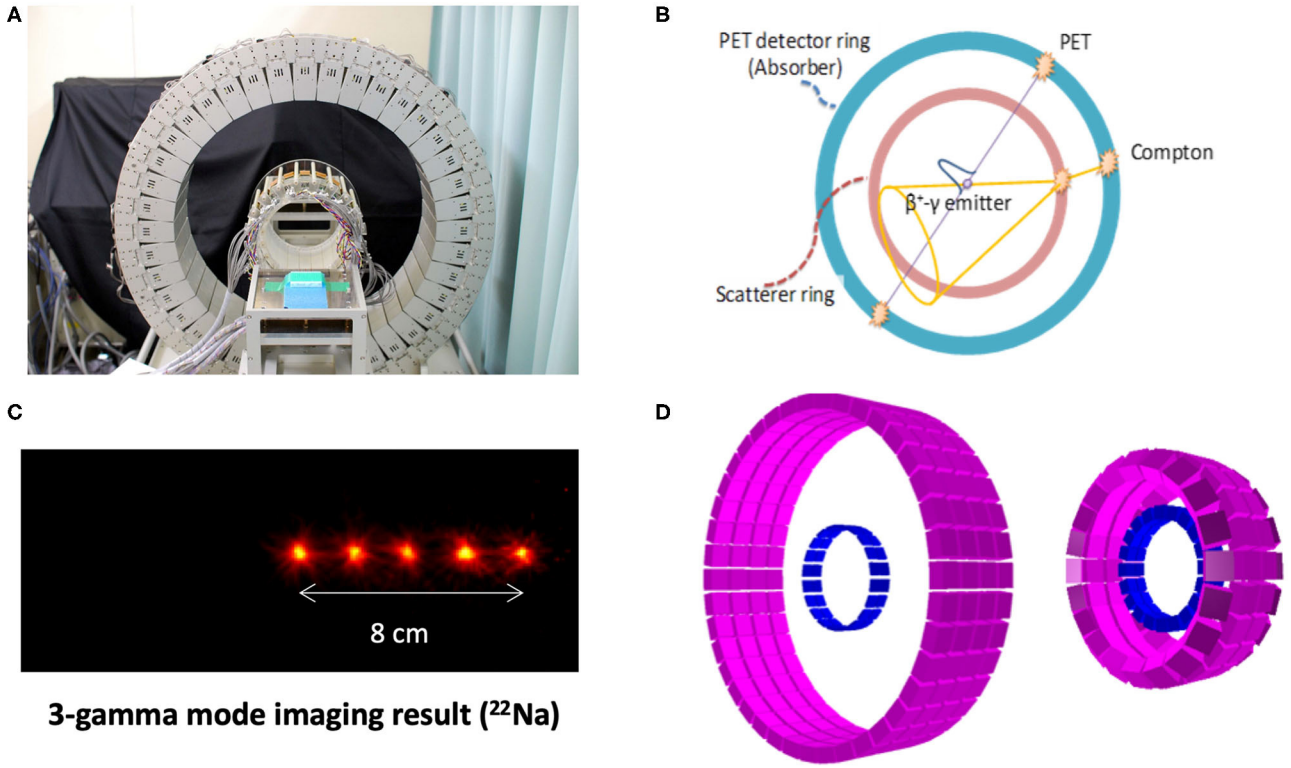

FIGURE 9 | WGI prototype at NIRS **(A)** for combined PET and Compton imaging **(B)**, along with its Compton imaging performance for the measurement of ^{22}Na sources, emitting a positron, and a 1,274 keV photon **(C)**. Corresponding simulation model **(D)** for optimization of the design [left: same design as **(A)**, right: modified design for improved Compton efficiency] (Source: NIRS and LMU).

ERC Advanced Grant call and is a 5-year project starting in late 2020.

FRS at FAIR

The radioactive ions of interest will be produced by fragmentation (one- or two-neutron removal, respectively) of relativistic primary beams (^{12}C, ^{16}O) in reaction targets (Be, C) placed at the entrance of the SIS18 FRS and separated in-flight [63]. As discussed in section RIB Production, the intensity of the RIB depends on the primary beam current, on the fragmentation cross-sections, and on the transport properties. **Table 2** gives the result of a Monte Carlo simulation with the GSI code MOCADI [95] using the intensities expected at SIS18 in FAIR-phase-0. The experimental activity in this task will focus on optimization of the accelerator parameters to reach the maximum intensities. The intensity in Cave M must be verified experimentally and critically depends on the size of the beam to be used for dosimetry and pre-clinical experiments in a mouse model. The MOCADI simulation indicates a range straggling $\sigma/R \sim 2.5\%$ for both light ions in the energy range of interest for therapy. The range straggling is a direct consequence of the momentum spread discussed in section RIB Production. Range straggling will therefore be carefully assessed during BARB in order to reach sub-millimeter precisions. It is also possible to apply methods to produce mono-energetic, pencil-like secondary beams for therapy, e.g., using the energy-focusing method that was developed at the FRS [96].

Hybrid Detector

The second innovative aspect of BARB is the use of a new γ-PET detector that will be designed and built at LMU. Cave M is equipped with an online PET (**Figure 5**), but even online PET can only register in-between the synchrotron beam spills, because the signal is obscured by the large prompt γ-ray signal during the irradiation [72, 97]. An improved detector should be able to exploit the prompt γ-ray emission [23] during beam extraction, in addition to the PET acquisition (and concomitant third-γ emission in case of ^{10}C and ^{14}O) in-between the synchrotron spills. BARB will build a hybrid detector concept aiming to exploit both the prompt γ-rays emitted in nuclear interactions during the beam-on time of the synchrotron pulsed delivery, and the delayed emission of the (γ-)β^+-emitting primary beam (superimposed to a minor contribution of positron emitting projectile and target fragments) in the beam pauses [37]. The new detector concept will be based on an advanced version of the γ-PET design originally proposed at LMU [98] and further developed in the framework of the International Open Laboratory and International Research Initiative between LMU and NIRS (**Figure 9**). The focus of these joint NIRS-LMU efforts has been on the imaging of nuclear medicine tracers that undergo

β^+-decay with simultaneous emission of a third prompt photon from the excited daughter nucleus, thus making it possible to achieve improved imaging performances by the intersection of the annihilation photons' line of response (LOR) and the third photon Compton cone [98]. A promising proof of concept of this so-called whole gamma imaging (WGI) [99] approach could be already demonstrated at NIRS in a mouse using ^{89}Zr, which has a β^+ and electron capture decay in ^{89m}Y with a half-life of 78 h. ^{89m}Y finally decays into the stable ^{89}Y by an emission of 909 keV γ-ray and a half-life of 15.7 s [100]. Hybrid PET, Compton, and Compton-PET imaging were obtained relying on the addition of a scatterer ring (94 mm diameter) made of GAGG scintillator crystals inside a full-size (660 mm diameter) PET scanner with depth-of-interaction Zr-doped GSO scintillator detectors already available at NIRS [101, 102]. While nuclear medicine tracer imaging is limited to single-γ energies up to $\sim$1 MeV, the energy of interest of prompt-γ typically lies in the 3–8 MeV interval and is a priori unknown. Hence, recent research at LMU has focused on design studies aiming to upgrade the NIRS detector in terms of enhanced efficiency of Compton imaging at these higher PG energies, without compromising the PET imaging performance. The desired improvements, initially focused on applications to proton therapy [103], could be achieved by increasing the thickness of the scattering layer and decreasing the relative distances between the scatterer and absorber rings (**Figure 9D**). In the framework of BARB, these efforts will be tailored to RIB and benefit from the reduced fluence of heavy ions compared to protons at the same treatment dose, resulting in relaxed signal processing rate requirements [104]. Moreover, higher resolution detectors tailored to small animal imaging will likely be employed, as currently under development in a joint effort between LMU and NIRS for a novel small animal in-beam PET scanner being realized for the SIRMIO ERC Consolidator Grant [30]. All these optimization design studies largely benefited from the collaboration between LMU and the University of Berkeley, USA (BACATEC; http://www.bacatec.de/) which aimed at developing a powerful simulation and image reconstruction framework, including a machine-learning algorithm for correct identification of the different types of event in the detectors [105]. Construction and detector testing for BARB will be performed in close collaboration between LMU and GSI groups.

CONCLUSIONS

For many years, RIB have been proposed as the ideal bullet for image-guided particle therapy. The main problem has been the production of RIB and the low beam intensity. Research in this field started already at LBL and is currently mostly driven by NIRS in Japan, with interesting results and design of innovative PET detectors. These problems can be overcome by future, high-intensity accelerators, or by injection of RIB in conventional synchrotrons. NIRS and CERN are studying RIB sources that can work with current medical synchrotrons. The practical advantage of RIB therapy compared to conventional stable-ion treatments remains, however, not demonstrated. This is the goal of the BARB project, currently ongoing at FAIR in collaboration with LMU in Germany. BARB will exploit the intensity upgrade in FAIR-phase-0 and a novel γ-PET detector for beam visualization. BARB, NIRS, and CERN results in the coming decade will clarify whether there is a role of RIB in cancer treatment.

AUTHOR CONTRIBUTIONS

Both authors collected the literature and wrote the paper.

FUNDING

This work was supported by ERC grant 883425 BARB.

ACKNOWLEDGMENTS

We thank Taiga Yamaya, Mohammad Safari, and Christian Graeff for providing some figures and for fruitful discussions. We are grateful to Christoph Scheidenberger for the MOCADI simulation in **Table 2**.

REFERENCES

1. Lievens Y, Borras JM, Grau C. Provision and use of radiotherapy in Europe. *Mol Oncol.* (2020) 14:1461–9. doi: 10.1002/1878-0261.12690
2. Jaffray DA. Image-guided radiotherapy: from current concept to future perspectives. *Nat Rev Clin Oncol.* (2012) 9:688–99. doi: 10.1038/nrclinonc.2012.194
3. Grau C, Durante M, Georg D, Langendijk JA, Weber DC. Particle therapy in Europe. *Mol Oncol.* (2020) 14:1492–9. doi: 10.1002/1878-0261.12677
4. Durante M, Orecchia R, Loeffler JS. Charged-particle therapy in cancer: clinical uses and future perspectives. *Nat Rev Clin Oncol.* (2017) 14:483–95. doi: 10.1038/nrclinonc.2017.30
5. Schardt D, Elsässer T, Schulz-Ertner D. Heavy-ion tumor therapy: physical and radiobiological benefits. *Rev Mod Phys.* (2010) 82:383–425. doi: 10.1103/RevModPhys.82.383
6. Tsujii H, Kamada T, Shirai T, Noda K, Tsuji H, Karasawa K, editors. *Carbon-Ion Radiotherapy*. Tokyo: Springer (2014). doi: 10.1007/978-4-431-54457-9
7. Rackwitz T, Debus J. Clinical applications of proton and carbon ion therapy. *Semin Oncol.* (2019) 46:226–32. doi: 10.1053/j.seminoncol.2019.07.005
8. Durante M, Debus J. Heavy charged particles: does improved precision and higher biological effectiveness translate to better outcome in patients? *Semin Radiat Oncol.* (2018) 28:160–7. doi: 10.1016/j.semradonc.2017.11.004
9. Bortfeld TR, Loeffler JS. Three ways to make proton therapy affordable. *Nature.* (2017) 549:451–3. doi: 10.1038/549451a
10. Verma V, Mishra MV, Mehta MP. A systematic review of the cost and cost-effectiveness studies of proton radiotherapy. *Cancer.* (2016) 122:1483–501. doi: 10.1002/cncr.29882
11. Farr JB, Flanz JB, Gerbershagen A, Moyers MF. New horizons in particle therapy systems. *Med Phys.* (2018) 45:e953–83. doi: 10.1002/mp.13193
12. Noda K, Furukawa T, Fujisawa T, Iwata Y, Kanai T, Kanazawa M, et al. New accelerator facility for carbon-ion cancer-therapy. *J Radiat Res.* (2007) 48:A43–54. doi: 10.1269/jrr.48.A43
13. Durante M, Paganetti H. Nuclear physics in particle therapy : a review. *Rep Prog Phys.* (2016) 79:096702. doi: 10.1088/0034-4885/79/9/096702
14. Lomax AJ. Myths and realities of range uncertainty. *Br J Radiol.* (2020) 93:20190582. doi: 10.1259/bjr.20190582
15. Bert C, Durante M. Motion in radiotherapy: particle therapy. *Phys Med Biol.* (2011) 56:R113–44. doi: 10.1088/0031-9155/56/16/R01

16. Pacelli R, Caroprese M, Palma G, Oliviero C, Clemente S, Cella L, et al. Technological evolution of radiation treatment: implications for clinical applications. *Semin Oncol.* (2019) 46:193–201. doi: 10.1053/j.seminoncol.2019.07.004
17. Bayouth JE, Low DA, Zaidi H. MRI-linac systems will replace conventional IGRT systems within 15 years. *Med Phys.* (2019) 46:3753–6. doi: 10.1002/mp.13657
18. Noble DJ, Burnet NG. The future of image-guided radiotherapy—is image everything? *Br J Radiol.* (2018) 91:20170894. doi: 10.1259/bjr.20170894
19. Paganetti H. Range uncertainties in proton therapy and the role of Monte Carlo simulations. *Phys Med Biol.* (2012) 57:R99–117. doi: 10.1088/0031-9155/57/11/R99
20. Durante M, Flanz J. Charged particle beams to cure cancer: Strengths and challenges. *Semin Oncol.* (2019) 46:219–25. doi: 10.1053/j.seminoncol.2019.07.007
21. Chu WT, Ludewigt BA, Renner TR. Instrumentation for treatment of cancer using proton and light ion beams. *Rev Sci Instrum.* (1993) 64:2055–122. doi: 10.1063/1.1143946
22. Cavaier RF, Haddad F, Sounalet T, Stora T, Zahi I. Terbium radionuclides for theranostics applications: a focus On MEDICIS-PROMED. *Phys Procedia.* (2017) 90:157–63. doi: 10.1016/j.phpro.2017.09.053
23. Krimmer J, Dauvergne D, Létang JM, Testa É. Prompt-gamma monitoring in hadrontherapy: a review. *Nucl Instruments Methods Phys Res Sect A.* (2018) 878:58–73. doi: 10.1016/j.nima.2017.07.063
24. Mattei I, Battistoni G, Bini F, Collamati F, De Lucia E, Durante M, et al. Prompt-γ production of 220 MeV/u 12C ions interacting with a PMMA target. *J Instrum.* (2015) 10:P10034. doi: 10.1088/1748-0221/10/10/P10034
25. Pinto M, Bajard M, Brons S, Chevallier M, Dauvergne D, Dedes G, et al. Absolute prompt-gamma yield measurements for ion beam therapy monitoring. *Phys Med Biol.* (2015) 60:565–94. doi: 10.1088/0031-9155/60/2/565
26. Lehrack S, Assmann W, Bertrand D, Henrotin S, Herault J, Heymans V, et al. Submillimeter ionoacoustic range determination for protons in water at a clinical synchrocyclotron. *Phys Med Biol.* (2017) 62:L20–30. doi: 10.1088/1361-6560/aa81f8
27. Mazzucconi D, Agosteo S, Ferrarini M, Fontana L, Lante V, Pullia M, et al. Mixed particle beam for simultaneous treatment and online range verification in carbon ion therapy: proof-of-concept study. *Med Phys.* (2018) 45:5234–43. doi: 10.1002/mp.13219
28. Piersanti L, Bellini F, Bini F, Collamati F, De Lucia E, Durante M, et al. Measurement of charged particle yields from PMMA irradiated by a 220 MeV/u 12C beam. *Phys Med Biol.* (2014) 59:1857–72. doi: 10.1088/0031-9155/59/7/1857
29. Félix-Bautista R, Gehrke T, Ghesquière-Diérickx L, Reimold M, Amato C, Turecek D, et al. Experimental verification of a non-invasive method to monitor the lateral pencil beam position in an anthropomorphic phantom for carbon-ion radiotherapy. *Phys Med Biol.* (2019) 64:175019. doi: 10.1088/1361-6560/ab2ca3
30. Parodi K, Assmann W, Belka C, Bortfeldt J, Clevert DA, Dedes G, et al. Towards a novel small animal proton irradiation platform: the SIRMIO project. *Acta Oncol.* (2019) 58:1470–5. doi: 10.1080/0284186X.2019.1630752
31. Traini G, Mattei I, Battistoni G, Bisogni MG, De Simoni M, Dong Y, et al. Review and performance of the dose profiler, a particle therapy treatments online monitor. *Phys Medica.* (2019) 65:84–93. doi: 10.1016/j.ejmp.2019.07.010
32. Ferrero V, Fiorina E, Morrocchi M, Pennazio F, Baroni G, Battistoni G, et al. Online proton therapy monitoring: clinical test of a Silicon-photodetector-based in-beam PET. *Sci Rep.* (2018) 8:4100. doi: 10.1038/s41598-018-22325-6
33. Knopf AC, Lomax A. *In vivo* proton range verification: a review. *Phys Med Biol.* (2013) 58:R131–60. doi: 10.1088/0031-9155/58/15/R131
34. Kraan AC. Range verification methods in particle therapy: underlying physics and monte carlo modeling. *Front Oncol.* (2015) 5:150. doi: 10.3389/fonc.2015.00150
35. Parodi K, Polf JC. *In vivo* range verification in particle therapy. *Med Phys.* (2018) 45:e1036–50. doi: 10.1002/mp.12960
36. Parodi K. Latest developments in *in-vivo* imaging for proton therapy. *Br J Radiol.* (2020) 93:20190787. doi: 10.1259/bjr.20190787
37. Parodi K. Vision 20/20: Positron emission tomography in radiation therapy planning, delivery, and monitoring. *Med Phys.* (2015) 42:7153–68. doi: 10.1118/1.4935869
38. Gambhir SS. Molecular imaging of cancer with positron emission tomography. *Nat Rev Cancer.* (2002) 2:683–93. doi: 10.1038/nrc882
39. Sommerer F, Cerutti F, Parodi K, Ferrari A, Enghardt W, Aiginger H. In-beam PET monitoring of mono-energetic 16 O and 12 C beams: experiments and FLUKA simulations for homogeneous targets. *Phys Med Biol.* (2009) 54:3979–96. doi: 10.1088/0031-9155/54/13/003
40. Kraan AC, Battistoni G, Belcari N, Camarlinghi N, Cirrone GAP, Cuttone G, et al. Proton range monitoring with in-beam PET: Monte Carlo activity predictions and comparison with cyclotron data. *Phys Medica.* (2014) 30:559–69. doi: 10.1016/j.ejmp.2014.04.003
41. Enghardt W, Parodi K, Crespo P, Fiedler F, Pawelke J, Pönisch F. Dose quantification from in-beam positron emission tomography. *Radiother Oncol.* (2004) 73:S96–8. doi: 10.1016/S0167-8140(04)80024-0
42. Handrack J, Tessonnier T, Chen W, Liebl J, Debus J, Bauer J, et al. Sensitivity of post treatment positron emission tomography/computed tomography to detect inter-fractional range variations in scanned ion beam therapy. *Acta Oncol.* (2017) 56:1451–8. doi: 10.1080/0284186X.2017.1348628
43. Bauer J, Unholtz D, Sommerer F, Kurz C, Haberer T, Herfarth K, et al. Implementation and initial clinical experience of offline PET/CT-based verification of scanned carbon ion treatment. *Radiother Oncol.* (2013) 107:218–26. doi: 10.1016/j.radonc.2013.02.018
44. Nishio T, Miyatake A, Ogino T, Nakagawa K, Saijo N, Esumi H. The development and clinical use of a beam ON-LINE PET system mounted on a rotating gantry port in proton therapy. *Int J Radiat Oncol.* (2010) 76:277–86. doi: 10.1016/j.ijrobp.2009.05.065
45. Buitenhuis HJT, Diblen F, Brzezinski KW, Brandenburg S, Dendooven P. Beam-on imaging of short-lived positron emitters during proton therapy. *Phys Med Biol.* (2017) 62:4654–72. doi: 10.1088/1361-6560/aa6b8c
46. Ammar C, Frey K, Bauer J, Melzig C, Chiblak S, Hildebrandt M, et al. Comparing the biological washout of β + -activity induced in mice brain after 12 C-ion and proton irradiation. *Phys Med Biol.* (2014) 59:7229–44. doi: 10.1088/0031-9155/59/23/7229
47. Lehmann HI, Graeff C, Simoniello P, Constantinescu A, Takami M, Lugenbiel P, et al. Feasibility study on cardiac arrhythmia ablation using high-energy heavy ion beams. *Sci Rep.* (2016) 6:38895. doi: 10.1038/srep38895
48. Pinto M, Kroeniger K, Bauer J, Nilsson R, Traneus E, Parodi K. A filtering approach for PET and PG predictions in a proton treatment planning system. *Phys Med Biol.* (2020) 65:095014. doi: 10.1088/1361-6560/ab8146
49. Nischwitz SP, Bauer J, Welzel T, Rief H, Jäkel O, Haberer T, et al. Clinical implementation and range evaluation of *in vivo* PET dosimetry for particle irradiation in patients with primary glioma. *Radiother Oncol.* (2015) 115:179–85. doi: 10.1016/j.radonc.2015.03.022
50. Bassler N, Alsner J, Beyer G, DeMarco JJ, Doser M, Hajdukovic D, et al. Antiproton radiotherapy. *Radiother Oncol.* (2008) 86:14–9. doi: 10.1016/j.radonc.2007.11.028
51. Bagshaw MA, Li GC, Pistenma DA, Fessenden P, Luxton G, Hoffmann WW. Introduction to the use of negative pi-mesons in radiation therapy: Rutherford 1964, revisited. *Int J Radiat Oncol.* (1977) 3:287–92. doi: 10.1016/0360-3016(77)90266-8
52. Li Q, Kanai T, Kitagawa A. The potential application of β-delayed particle decay beam 9 C in cancer therapy. *Phys Med Biol.* (2004) 49:1817–31. doi: 10.1088/0031-9155/49/9/016
53. Li Q, Furusawa Y, Kanazawa M, Kanai T, Kitagawa A, Aoki M, et al. Enhanced efficiency in cell killing at the penetration depths around the Bragg peak of a radioactive 9C-ion beam. *Int J Radiat Oncol.* (2005) 63:1237–44. doi: 10.1016/j.ijrobp.2005.08.006
54. Mancusi D, Sihver L, Niita K, Li Q, Sato T, Iwase H, et al. Calculation of energy-deposition distributions and microdosimetric estimation of the biological effect of a 9C beam. *Radiat Environ Biophys.* (2009) 48:135–43. doi: 10.1007/s00411-008-0206-8
55. Augusto RS, Bauer J, Bouhali O, Cuccagna C, Gianoli C, Kozłowska WS, et al. An overview of recent developments in FLUKA PET tools. *Phys Medica.* (2018) 54:189–99. doi: 10.1016/j.ejmp.2018.06.636

56. Castro JR. Results of heavy ion radiotherapy. *Radiat Environ Biophys.* (1995) 34:45–8. doi: 10.1007/BF01210545
57. Castro JR, Saunders WM, Tobias CA, Chen GTY, Curtis S, Lyman JT, et al. Treatment of cancer with heavy charged particles. *Int J Radiat Oncol Biol Phys.* (1982) 8:2191–8. doi: 10.1016/0360-3016(82)90569-7
58. Llacer J, Chatterjee A, Alpen EL, Saunders W, Andreae S, Jackson HC. Imaging by injection of accelerated radioactive particle beams. *IEEE Trans Med Imaging.* (1984) 3:80–90. doi: 10.1109/TMI.1984.4307660
59. Dendale R, Thariat J, Doyen J, Balosso J, Stefan D, Bolle S, et al. État des lieux de la protonthérapie en France en 2019. *Cancer/Radiothérapie.* (2019) 23:617–24. doi: 10.1016/j.canrad.2019.07.129
60. Mandrillon P, Farley FJM, Tang JY, Carli C, Cesari G, Fiétier N, et al. Feasibility studies of the EULIMA light ion medical accelerator. In: *3rd European Particle Accelerator Conference.* Berlin (1992). p. 179–191. Available online at: http://infoscience.epfl.ch/record/104653
61. Jongen Y, Abs M, Blondin A, Kleeven W, Zaremba S, Vandeplassche D, et al. Compact superconducting cyclotron C400 for hadron therapy. *Nucl Instruments Methods Phys Res Sect A.* (2010) 624:47–53. doi: 10.1016/j.nima.2010.09.028
62. Amaldi U, Kraft G. Radiotherapy with beams of carbon ions. *Reports Prog Phys.* (2005) 68:1861–82. doi: 10.1088/0034-4885/68/8/R04
63. Geissel H, Armbruster P, Behr KH, Brünle A, Burkard K, Chen M, et al. The GSI projectile fragment separator (FRS): a versatile magnetic system for relativistic heavy ions. *Nucl Instruments Methods Phys Res Sect B.* (1992) 70:286–97. doi: 10.1016/0168-583X(92)95944-M
64. Pawelke J, Byars L, Enghardt W, Fromm WD, Geissel H, Hasch BG, et al. The investigation of different cameras for in-beam PET imaging. *Phys Med Biol.* (1996) 41:279–96. doi: 10.1088/0031-9155/41/2/006
65. van der Ree MH, Blanck O, Limpens J, Lee CH, Balgobind BV, Dieleman EMT, et al. 'Cardiac Radioablation – a Systematic Review'. *Hear Rhythm.* (2020) 17:P1381–92. doi: 10.1016/j.hrthm.2020.03.013
66. Cuculich PS, Schill MR, Kashani R, Mutic S, Lang A, Cooper D, et al. Noninvasive cardiac radiation for ablation of ventricular tachycardia. *N Engl J Med.* (2017) 377:2325–36. doi: 10.1056/NEJMoa1613773
67. Bert C, Engenhart-Cabillic R, Durante M. Particle therapy for noncancer diseases. *Med Phys.* (2012) 39:1716–27. doi: 10.1118/1.3691903
68. Dusi V, Russo G, Forte GI, De Ferrari GM. Non-invasive ablation of cardiac arrhythmia. Is proton radiation therapy a step forward? *Int J Cardiol.* (2020) 316:64–6. doi: 10.1016/j.ijcard.2020.04.035
69. Murakami T, Tsujii H, Furusawa Y, Ando K, Kanai T, Yamada S, et al. Medical and other applications of high-energy heavy-ion beams from HIMAC. *J Nucl Mater.* (1997) 248:360–8. doi: 10.1016/S0022-3115(97)00135-9
70. Kamada T, Tsujii H, Blakely EA, Debus J, De Neve W, Durante M, et al. Carbon ion radiotherapy in Japan: an assessment of 20 years of clinical experience. *Lancet Oncol.* (2015) 16:e93–100. doi: 10.1016/S1470-2045(14)70412-7
71. Kanazawa M, Kitagawa A, Kouda S, Nishio T, Torikoshi M, Noda K, et al. Application of an RI-beam for cancer therapy: *In-vivo* verification of the ion-beam range by means of positron imaging. *Nucl Phys A.* (2002) 701:244–52. doi: 10.1016/S0375-9474(01)01592-5
72. Hirano Y, Yoshida E, Kinouchi S, Nishikido F, Inadma N, Murayama H, et al. Monte Carlo simulation of small OpenPET prototype with 11 C beam irradiation: effects of secondary particles on in-beam imaging. *Phys Med Biol.* (2014) 59:1623–40. doi: 10.1088/0031-9155/59/7/1623
73. Sakurai H, Itoh F, Hirano Y, Nitta M, Suzuki K, Kato D, et al. Positron annihilation spectroscopy of biological tissue in ^{11} C irradiation. *Phys Med Biol.* (2014) 59:7031–8. doi: 10.1088/0031-9155/59/22/7031
74. Mohammadi A, Yoshida E, Tashima H, Nishikido F, Inaniwa T, Kitagawa A, et al. Production of an 15 O beam using a stable oxygen ion beam for in-beam PET imaging. *Nucl Instruments Methods Phys Res Sect A.* (2017) 849:76–82. doi: 10.1016/j.nima.2016.12.028
75. Hirano Y, Takuwa H, Yoshida E, Nishikido F, Nakajima Y, Wakizaka H, et al. Washout rate in rat brain irradiated by a 11 C beam after acetazolamide loading using a small single-ring OpenPET prototype. *Phys Med Biol.* (2016) 61:1875–87. doi: 10.1088/0031-9155/61/5/1875
76. Toramatsu C, Yoshida E, Wakizaka H, Mohammadi A, Ikoma Y, Tashima H, et al. Washout effect in rabbit brain: in-beam PET measurements using 10 C, 11 C and 15 O ion beams. *Biomed Phys Eng Express.* (2018) 4:035001. doi: 10.1088/2057-1976/aaade7
77. Kang HG, Yamamoto S, Takyu S, Nishikido F, Mohammadi A, Horita R, et al. Optical imaging for the characterization of radioactive carbon and oxygen ion beams. *Phys Med Biol.* (2019) 64:115009. doi: 10.1088/1361-6560/ab1ccf
78. Chacon A, James B, Tran L, Guatelli S, Chartier L, Prokopvich D, et al. Experimental investigation of the characteristics of radioactive beams for heavy ion therapy. *Med Phys.* (2020) 47:3123–32. doi: 10.1002/mp.14177
79. Henning WF. Physics with energetic radioactive ion beams. *Nucl Instruments Methods Phys Res Sect B.* (1997) 126:1–6. doi: 10.1016/S0168-583X(97)00999-3
80. Raabe R. Making radioactive ion beams - Detecting reaction products. *Eur Phys J Plus.* (2016) 131:362. doi: 10.1140/epjp/i2016-16362-5
81. Blumenfeld Y, Nilsson T, Van Duppen P. Facilities and methods for radioactive ion beam production. *Phys Scr.* (2013) T152:014023. doi: 10.1088/0031-8949/2013/T152/014023
82. Iseki Y, Kanai T, Kanazawa M, Kitagawa A, Mizuno H, Tomitani T, et al. Range verification system using positron emitting beams for heavy-ion radiotherapy. *Phys Med Biol.* (2004) 49:3179–95. doi: 10.1088/0031-9155/49/14/012
83. Mohammadi A, Tashima H, Iwao Y, Takyu S, Akamatsu G, Nishikido F, et al. Range verification of radioactive ion beams of 11C and 15O using in-beam PET imaging. *Phys Med Biol.* (2019) 64:145014. doi: 10.1088/1361-6560/ab25ce
84. Mohammadi A, Tashima H, Iwao Y, Takyu S, Akamatsu G, Kang HG, et al. Influence of momentum acceptance on range monitoring of 11C and 15O ion beams using in-beam PET. *Phys Med Biol.* (2020) 65:125006. doi: 10.1088/1361-6560/ab8059
85. Katagiri K, Noda A, Nagatsu K, Nakao M, Hojo S, Muramatsu M, et al. A singly charged ion source for radioactive 11 C ion acceleration. *Rev Sci Instrum.* (2016) 87:02B509. doi: 10.1063/1.4935899
86. dos Santos Augusto R, Buehler L, Lawson Z, Marzari S, Stachura M, Stora T, et al. CERN-MEDICIS (Medical Isotopes Collected from ISOLDE): a new facility. *Appl Sci.* (2014) 4:265–81. doi: 10.3390/app4020265
87. Pitters J, Breitenfeldt M, Pahl H, Pikin A, Wenander F. Summary of charge breeding investigations for a future 11C treatment facility. *CERN Acceler Sci.* (2018).
88. Stora T, Wenander F, Pitters J, Cocolios T, Stagemann S, Augusto R, et al. Technical design report for a carbon-11 treatment facility. *MEDICIS Promed.* (2019). Available online at: https://indico.cern.ch/event/782482/contributions/3396488/attachments/1837112/3010836/TDR_11C_Treatment_Facility-Erice_v1--6.pdf
89. Durante M, Indelicato P, Jonson B, Koch V, Langanke K, Meißner UG, et al. All the fun of the FAIR: fundamental physics at the facility for antiproton and ion research. *Phys Scr.* (2019) 94:033001. doi: 10.1088/1402-4896/aaf93f
90. Winkler M, Geissel H, Weick H, Achenbach B, Behr KH, Boutin D, et al. The status of the super-FRS in-flight facility at FAIR. *Nucl Instruments Methods Phys Res Sect B.* (2008) 266:4183–7. doi: 10.1016/j.nimb.2008.05.073
91. Nilsson T. Radioactive ion beams at FAIR-NuSTAR. *Eur Phys J Spec Top.* (2008) 156:1–12. doi: 10.1140/epjst/e2008-00606-2
92. Stöhlker T, Bagnoud V, Blaum K, Blazevic A, Bräuning-Demian A, Durante M, et al. APPA at FAIR: from fundamental to applied research. *Nucl Instruments Methods Phys Res Sect B.* (2015) 365:680–5. doi: 10.1016/j.nimb.2015.07.077
93. Durante M, Golubev A, Park WY, Trautmann C. Applied nuclear physics at the new high-energy particle accelerator facilities. *Phys Rep.* (2019) 800:1–37. doi: 10.1016/j.physrep.2019.01.004
94. Bai M, Adonin A, Appel S, Bär R, Blell U, Bellachioma C, et al. Challenges of FAIR-phase-0. In: *9th International Particle Accelerator Conference.* Vancouver, BC: JACoW Publishing (2018). p. 2947–9.
95. Iwasa N, Weick H, Geissel H. New features of the Monte-Carlo code MOCADI. *Nucl Instruments Methods Phys Res Sect B.* (2011) 269:752–8. doi: 10.1016/j.nimb.2011.02.007
96. Scheidenberger C, Geissel H, Maier M, Münzenberg G, Portillo M, Savard G, et al. Energy and range focusing of in-flight separated exotic nuclei – A study for the energy-buncher stage of the low-energy branch of the Super-FRS. *Nucl Instruments Methods Phys Res Sect B.* (2003) 204:119–23. doi: 10.1016/S0168-583X(02)01898-0

97. Parodi K, Crespo P, Eickhoff H, Haberer T, Pawelke J, Schardt D, et al. Random coincidences during in-beam PET measurements at microbunched therapeutic ion beams. *Nucl Instruments Methods Phys Res Sect A.* (2005) 545:446–58. doi: 10.1016/j.nima.2005.02.002
98. Lang C, Habs D, Parodi K, Thirolf PG. Sub-millimeter nuclear medical imaging with high sensitivity in positron emission tomography using β + γ coincidences. *J Instrum.* (2014) 9:P01008. doi: 10.1088/1748-0221/9/01/P01008
99. Yamaya T, Yoshida E, Tashima H, Tsuji A, Nagatsu K, Yamaguchi M, et al. Whole gamma imaging (WGI) concept: simulation study of triple-gamma imaging. *J Nucl Med.* (2017) 58:152. doi: 10.1088/1361-6560/ab8e89
100. Deri MA, Zeglis BM, Francesconi LC, Lewis JS. PET imaging with 89Zr: from radiochemistry to the clinic. *Nucl Med Biol.* (2013) 40:3–14. doi: 10.1016/j.nucmedbio.2012.08.004
101. Tashima H, Yoshida E, Wakizaka H, Takahashi M, Nagatsu K, Tsuji A, et al. First 89Zr mouse demonstration of whole gamma imaging (WGI). *J Nucl Med Med.* (2019) 60:196.
102. Tashima H, Yoshida E, Okumura Y, Suga M, Kawachi N, Kamada K, et al. Whole gamma imaging: demonstration of the β+-γ coincidence. In: *117th Scientific Meeting of the Japan Society of Medical Physics*. Yokohama (2019).
103. Safari M, Zoglausser A, Lovatti G, Anangnostatou V, Nitta M, Tashima H, et al. Performance of a novel hybrid gamma-imaging technique toward future 3D reconstruction of proton beam range. In: *IEEE Medical Imaging Conference*. Manchester (2019).
104. Safari M, Dedes G, Thirolf P, Zoglauer A, Yamaya T, Durante M, et al. "Toward hybrid γ-PET imaging of radioactive ion beams at FAIR," In: *GSI Scientific Report*. Darmstadt (2019). p. 57.
105. Safari M, Zoglausser A, Lovatti G, Anangnostatou V, Nitta M, Tashima H, et al. Development of a novel simulation and image reconstruction toolkit for PET and PG. In: *European Association of Nuclear Meecine (EANM) Congress.* Barcellona (2019).

Conflict of Interest: The authors declare that the research was conducted in the absence of any commercial or financial relationships that could be construed as a potential conflict of interest.

frontiers in Physics

ORIGINAL RESEARCH
published: 31 August 2020
doi: 10.3389/fphy.2020.00337

Hybrid Active-Passive Space Radiation Simulation Concept for GSI and the Future FAIR Facility

Christoph Schuy[1], *Uli Weber*[1] *and Marco Durante*[1,2]*

[1] GSI Helmholzzentrum für Schwerionenforschung, Darmstadt, Germany, [2] Institut für Festkörperphysik, Technische Universität Darmstadt, Darmstadt, Germany

Space radiation is acknowledged as one of the main health risks for human exploration of the Solar system. Solar particle events (SPE) and the galactic cosmic radiation (GCR) can cause significant early and late morbidity, and damage mission critical microelectronics. Systematic studies of the interaction of energetic heavy ions with biological and electronic systems are typically performed at high-energy particle accelerators with a small subset of ions and energies in an independent and serialized way. This simplification can lead to inaccurate estimations of the harmful radiation effects of the full space radiation environment on man and machine. To mitigate these limitations, NASA has developed an irradiation system at the Brookhaven National Laboratory able to simulate the full GCR spectrum. ESA is also investing in ground-based space radiation studies in Europe, using the current and future facilities at GSI/FAIR in Darmstadt (Germany). We describe here an advanced hybrid active-passive space radiation simulation system to simulate GCR or SPE spectra. A predefined set of different monoenergetic ^{56}Fe beams will be fired on specially designed beam modulators consisting of filigree periodic structures. Their thickness, composition and geometry per used primary beam energy are optimized via 1D-transport calculations in such a way that the superposition of the produced radiation fields at the target position closely simulate the GCR in different scenarios. The highly complex modulators will be built using state-of-the-art manufacturing techniques like 3D-printing and precision casting. A Monte Carlo simulation of the spectrum produced in this setup is reported.

Keywords: galactic cosmic rays, solar particle events, space radiation protection, hybrid beam modulation, complex beam modulators

OPEN ACCESS

Edited by:
Udo Jochen Birk, University of Applied Sciences of the Grisons, Switzerland

Reviewed by:
David B. Stout, Independent Researcher, Culver City, United States
Daniele Margarone, Czech Academy of Sciences, Czechia

***Correspondence:**
Marco Durante
m.durante@gsi.de

Specialty section:
This article was submitted to Medical Physics and Imaging, a section of the journal Frontiers in Physics

Received: *27 May 2020*
Accepted: *20 July 2020*
Published: *31 August 2020*

Citation:
Schuy C, Weber U and Durante M (2020) Hybrid Active-Passive Space Radiation Simulation Concept for GSI and the Future FAIR Facility. Front. Phys. 8:337. doi: 10.3389/fphy.2020.00337

INTRODUCTION

The radiation environment in space is one of the major obstacles for future manned exploratory missions to the moon and beyond [1, 2]. Without earth's protective atmosphere and magnetosphere, integral structures, electronics and astronauts are bombarded by sporadic bursts of energetic light ions originating from the sun [3] and constantly by a background of highly energetic heavy charged particles originating from deep space [4]. To characterize the composition of the space radiation environment, several probes equipped with sophisticated radiation detectors measured dosimetric and physical quantities of interest in deep space while orbiting the Moon [5] or on the transit to Mars [6] and active detectors on board the international space station continuously measure in low

earth orbit [7]. In particular, measurements from the radiation assessment detector of the Mars science laboratory onboard the Curiosity rover could be used to assess the equivalent dose of an astronaut during a Mars mission [8] as well as particle yields and energy distributions [9] in realistic space weather conditions. However, directly linking this physical knowledge to its effects on e.g., complex biological systems is extremely challenging. Epidemiological data, often used to estimate radiation effects on earth, cannot easily be applied due to the vastly different types of radiation prevalent on earth and in space. Direct observations of biological effects based on astronauts are limited by their low number and not directly applicable to prolonged missions in deep space due to the different radiation environments found in low earth orbit and deep space. Therefore, ground-based high energy particle accelerator facilities are used since many years to study the mechanistic effects of high atomic number and energy particles on biological and electronical systems [10]. Typically, a selection of a few monoenergetic beams of different particle species are used in an independent and serialized way as a proxy to estimate the effects of the complex radiation field prevalent in space e.g., [11]. This approach, however, is completely neglecting possible synergistic effects of different particle species and energies impinging on the same target in close proximity in space and time. For example, it was shown that exposure to space relevant fluences of heavy ions can induce ion-species dependent short and long-term deficits in cognitive abilities and behavioral changes [12]. To understand this alarming prospect for manned space flight, a recent study [13] performed a fast sequential irradiation with 3 different ion species interacting with each target, verified detrimental effects and concluded that "based on what is seen with a single ion, it is hard to predict how combined exposures including any given ion might affect brain function."

Due to the limitations of the typical sequential approach to simulate all relevant physical, chemical and biological effects of the complex radiation field created by the GCR and SPEs [14] an advanced space radiation simulation concept was investigated and implemented at the NASA Space Radiation Laboratory (NSRL) [15–19]. To simulate SPEs the NSRL system employs a monoenergetic proton beam and a passive binary energy degrader to generate reference radiation fields modeled after two SPE events (1972 and 1989). In practice, this concept is similar to the generation of a spread-out Bragg peak in particle therapy. A cell sample is consecutively irradiated with a predefined fluence of proton beams of decreasing energy to reach a close approximation with a given proton energy and dose distribution. To simulate the GCR environment the NSRL system exploits recent upgrades to the BNL accelerators, enabling the acceleration of different ion species with multiple energies and a switching time of < 2 min, to sequentially approximate a complex mixed space radiation reference field. This reference field typically uses predefined fluences of five different heavy ion species (^{12}C, ^{16}O, ^{28}Si, ^{48}Ti, and ^{56}Fe) at several predefined energies each, and additional beams of hydrogen and helium ions in combination with a passive energy degrader. The NSRL beam selection strategy was mainly guided by the relative abundance of ions in the GCR, the energy spectra of protons and helium and the LET spectra of heavier charged particles. The superposition of all beams at the target creates a good approximation of the mixed radiation field prevalent at the blood forming organs behind 20 g/cm^2 aluminum shielding during solar minimum. A full simulated GCR exposure using the NSRL system with 500 mGy exposure requires around 75 min. To prepare the accelerator for this kind of irradiation, different ion sources need to be prepared for the injector and every ion and energy combination has to be guided thru the accelerator to reach the specific irradiation site. At GSI existing synchrotron, for example, setting up a new ion species and fine tune the accelerator takes several hours per ion. Each additional energy has to be checked and reoptimized by hand. Even though SIS-18 and FAIR [20, 21] are technically capable to follow the active approach as used at NSRL, the amount of setup time for all needed ion and energy combinations is not realistic for a multi-user experimental accelerator especially during the construction of FAIR with limited available beam time.

To mitigate the technical challenges of the NSRL concept two other simulation approaches exploiting nuclear fragmentation were proposed. A concept purely focusing on the reproduction of protons, neutrons and pions inside a spacecraft or habitat was studied *in-silico* for the high energy proton beams available at the Joint Institute for Nuclear Research in Dubna [22]. A 12 GeV proton beam interacts with several target stations and the superposition of all produced radiation fields at a specific target position yields a good representation of the proton, neutron and pion abundance and energy distributions found in a spacecraft. This concept fully neglects the deleterious effects of the heavy ion component and its increased biological effectiveness [23]. Another study proposed the use of a single monoenergetic beam of ^{56}Fe and a complex target [24]. The composition and geometry of the complex target was optimized *in-silico* to reproduce a realistic LET-spectra as found in space and first promising experimental test were performed at BNL [25]. However, the use of a single complex target highly limits the scalability of this approach in view of the extremely high energies available at FAIR.

To mitigate the aforementioned limitation, this work presents the current status of the development of a hybrid active-passive space radiation simulator optimized for GSI and the future FAIR facility. This GCR simulation concept exploits fast energy switching of a single heavy ion species (^{56}Fe) interacting with several energy dependent sets of complex, passive, periodic and multi material beam modulators and can be seen as a combination of the aforementioned active and passive simulation approaches.

MATERIALS AND METHODS

The hybrid active-passive simulation approach designed for GSI and the future FAIR facility employs a combination of geometrically complex, periodic, multi material, passive beam modulators and a number of actively varied energy steps of a single ion species (^{56}Fe for GCR or protons for SPE). The general workflow of the modulator design is based on the

optimization of complex 3D modulators for particle therapy [26] and extended to cover heavier ions, higher energies and especially multi material modulators.

Predefined LET-, yield- and energy spectra are subdivided in distinct primary ion energy steps and a set of complex periodic modulation geometries as well as optional additional material to increase scattering or the energy width of the primary beam are optimized by a fast-analytical pre-optimizer per chosen energy. Optimized geometries are semi-automatically converted in 3D computer aided design (CAD)-based geometries, multiplied and scaled to complex modulators and recalculated with Monte Carlo transport calculations. The recalculated modulators can be directly manufactured using a variety of rapid prototyping techniques and the production quality can be validated. Validated modulators are than benchmarked in-beam and characterized by a standard nuclear physics experimental setup and a tissue equivalent proportional counter (TEPC) assessing charge resolved energy distributions and LET spectra at the target position.

The necessary design and development steps are summarized in **Figure 1** and described in detail in the following sections.

Hybrid Active-Passive Simulation Concept

A monoenergetic particle field of an appropriate size (10^*10 cm^2 approximately) interacts with one or several complex modulators as shown in **Figure 2**. Each modulator set is optimized in such a way that it produces pre-defined homogeneous particle- and energy distributions for a given target area at a given target position. After a planned number of particles is delivered, another energy is requested from the accelerator and the modulator set is automatically exchanged. The superposition of all optimized particle and energy distributions deliver LET-, particle- and energy distributions at the target position that

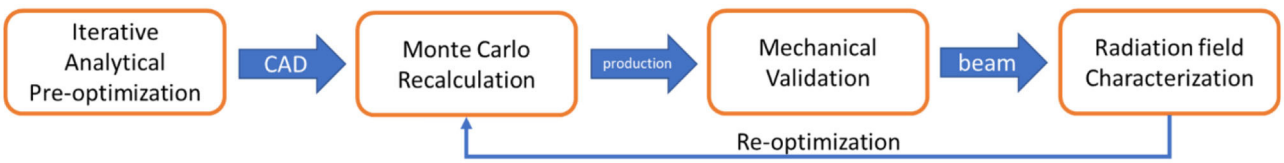

FIGURE 1 | Simplified schematic overview of the necessary development steps for hybrid active-passive space radiation simulation.

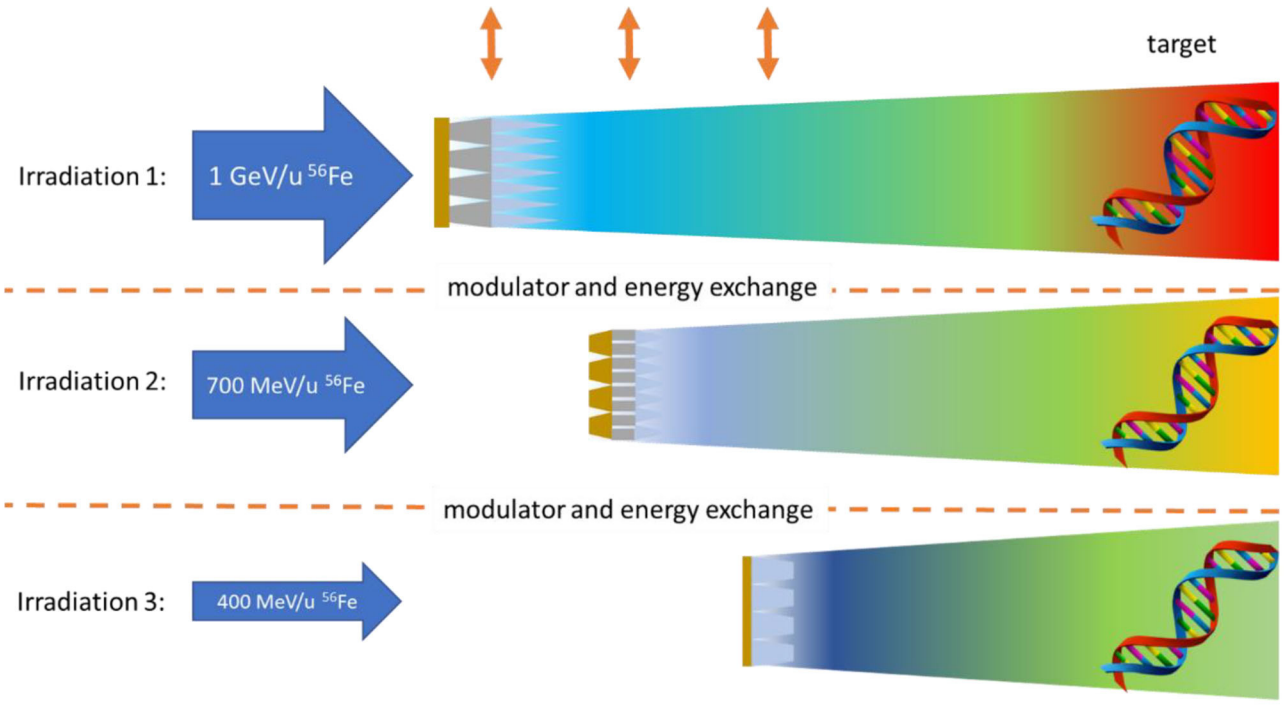

FIGURE 2 | Example of a target exposure using hybrid active-passive space radiation simulation. Different sets of complex modulators modulate a predetermined number of monoenergetic ^{56}Fe beams. After each successful irradiation, the beam energy as well as the corresponding complex modulators are automatically exchanged. The modulator geometry as well as their distance to the target area are optimized in such a way, that the superposition of all produced radiation fields approximates a homogeneous space-like radiation field of appropriate size at the target position.

approximate the radiation environment prevalent in different deep space mission scenarios or intense solar flares.

Analytical Pre-optimization

The pre-optimizer is currently under development and follows a constrained, multi-stage optimization approach. The implementation of the software is carried out in C++ for direct interfacing with the Monte Carlo toolkit Geant4 [27–29] and the data analysis framework ROOT [30].

Analytical beam transport is handled similar to GSIs in-house analytical treatment planning system TRiP98 [31, 32]. It uses a library of material-, energy-, and charge dependent pre-simulated datasets. This base data contains the kinetic energy spectra of particles after penetrating a defined thickness z of a target material M:

$$\mathbf{\Phi}_{\mathrm{M}}(\mathbf{E_0}, \mathbf{S_{i0}}; \mathbf{E}, \mathbf{S_i}; \mathbf{z}),$$

where E_0 is the beam energy, S_{i0} the ion species (e.g., Z = 26, A = 56) of the incident beam, and E is the free parameter of the spectra. The identifier S_i indicates the species of the particles that belongs to the spectrum. These can be either primary particles ($S_i = S_{i0}$) or any other relevant species produced by nuclear fragmentation. Each possible combination of different E_0, S_{i0}, S_i and z have to be pre-calculated for a given target material M to be analytically optimized. The data sets $\mathbf{\Phi}_{\mathrm{M}}$ are the basis for modeling the analytical beam transport and to perform an optimization of the thicknesses and shapes of the different modulators.

To analytically describe and optimize the radiation field produced by a complex modulation structure fully encompassed by a monoenergetic beam, the modulation structure is subdivided in N steps of different thickness z_j (**Figure 3**). The resulting radiation field behind each substructure depends on the energy (E_0) and particle species ($S_0 := A_0, Z_0$) of the penetrating beam as well as the material composition and thickness z_j. The radiation field in any depth can be calculated by the interpolation of the pre-simulated datasets Φ_{M}. The superposition $\Phi_{\mathrm{M,tot}} = \sum_{j=1..N} w_j \Phi_{\mathrm{M}}(...,z_j)$ of all substructures describes the full resulting radiation field after the modulator and a suitable air gap needed to homogenize the radiation field.

A radiation field with specific qualities $\Phi_{\mathrm{Wanted}}(S_i,E)$ can then be optimized by minimizing the function:

$$\chi^2 = \sum_{k,i} \left[\Phi_{\mathrm{wanted}}(S_i, E_k) - \sum_j \mathbf{w_j}\, \Phi_M(E_0, S_{i0} \ldots, S_i, E_k, z_j) \right]^2$$

via the weights w_j. The χ^2 must be summed over all relevant ion species i (primaries and fragments) and all bins k of their energy spectra. To optimize different quantities additional weighting factors can be introduced. The weight w_j directly corresponds to the shape of modulator.

Preliminary tests indicated that one modulation material is not sufficient to yield the desired spectra. Therefore, the propagation through two or three modulators with different materials is foreseen. This can be realized by using the same pre-optimization concept, but applying a convolution of multiple data sets Φ_{M1} and Φ_{M2} and two different modulator shapes w_{j1} and w_{j2}. The following formula describes the convoluted spectra after two successive modulators:

$$\Phi_{M1,M2}(E_k, S_i) = \sum_{l,n} \sum_{j1,j2} w_{j1} w_{j2} \Phi_{M2}(E_l, S_n; S_i, E_k; z_{j2}) \Phi_{M1}(E_0, S_{i0}; S_n, E_l; z_{j1})$$

To obtain a desired spectrum, the optimization can be performed similar to the χ^2-formula above, but both w_{j1} and w_{j2} are optimized simultaneously. The method can be extended to three or more modulators in an analogous way.

To minimize the amount of free optimization parameters, limit the accelerator setup time as well as the number of modulator sets, and guarantee modulator designs, which can be manufactured with available production techniques, a number of optimization constraints is applied during the optimization process including a maximum number of allowed energy steps and a material dependent minimum structure size.

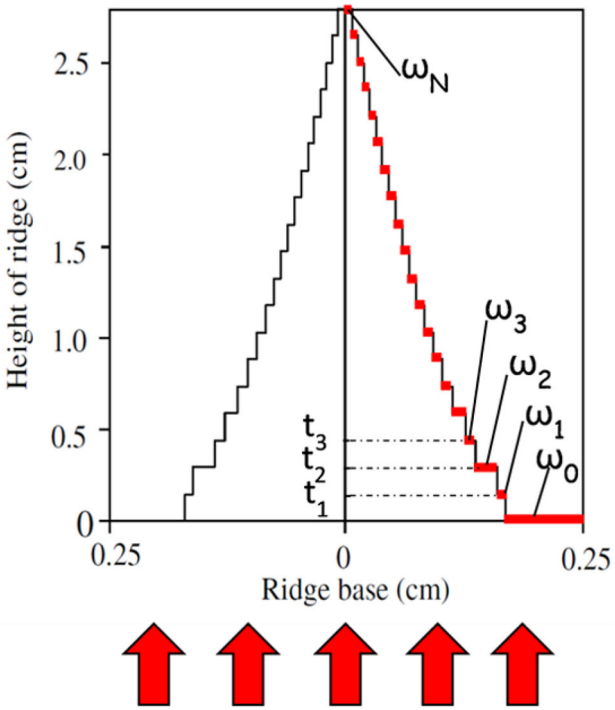

FIGURE 3 | Example of an iteratively optimized energy modulation structure with thickness steps t_N and accompanying weights ω_N. This concept can be realized for 3D printed structures e.g., pins instead of ridge leaves. Modified after [33].

Modulator Geometry

Pre-optimized modulation geometries are converted to 3D CAD-based geometries semi-automatically using FreeCAD v0.17 [34] and Python.

Optimized weights w_j are translated to constrained areas (SKETCHES) at specific heights. To later cover any given rectangular area, the basic constrained area type can be either quadratic or hexagonal and additional production specific offsets can be applied at this stage if necessary. All constrained areas are then converted to a solid object (LOFT). The created object is multiplied an appropriate number of times to reach the desired dimensions in x- and y direction and combined to the final modulator geometry (UNION). Afterwards additional structures like frames, mounting points as well as alignment structures can be added if necessary.

Monte Carlo Simulations

Monte Carlo transport calculations are used to create base data libraries for the pre-optimizer and to recalculate pre-optimized modulator designs.

The pre-optimizer relies on a library of pre-simulated base data to analytically optimize complex modulation structures. This library essentially contains information on all relevant nuclear interactions that any relevant heavy ion will undergo while interacting with a specific material M of thickness z as charge resolved kinetic energy spectra. These spectra can be obtained by simulating the appropriate ion, energy and material combination and scoring the resulting kinetic energy spectra of all created ions simultaneously at different material depths.

Final modulator geometries are exported as stereolithography files (STL) or as Polygon File Format (PLY) and can be directly used in Geant4 via CADMesh [35, 36]. Typically, the number of vertices as well as the file size of production quality modulator STLs is extremely high compared to standard Monte Carlo geometries. To facilitate the transport calculations lower resolution models are used during all simulations.

Manufacturing and Quality Control

Depending on the needed modulation material and geometry, several different state-of-the-art production techniques with distinct strength and weaknesses are available and need to be reviewed and tested for applicability in modulator fabrication. It is important to note, that no single production method works on different materials spanning the full density range from light polymers up to heavy metals.

Two promising methods for light, polymer-based materials are the additive manufacturing techniques polyjet and stereolithography (SLA), which have shown a good performance to accurately reproduce the filigree structures of complex 3D range modulators for particle therapy [26]. Medium-density materials, like aluminum and steel, can be manufactured in high quality by selective laser melting (SLM) or direct metal laser sintering (DMLS). For high density materials, such as gold or tungsten, precision casting and micro machining are promising production techniques.

Regardless of the chosen production modality, the precise reproduction of the small needle-like geometries or conical holes needed in complex modulator designs are highly challenging for all techniques. Therefore, mechanical quality control with suitable high-resolution measuring techniques like micro-CT or scanning electron microscopy is employed to verify the goodness of all produced modulators.

Experimental Validation

To benchmark the in-beam performance of the produced modulated radiation field and to guaranty the homogeneity of said field over the full target area, standard nuclear physics detectors will be used (**Figure 4**). The kinetic energy and particle yields will be measured using ΔE-E Telescopes and Time-of-Flight [37], whereas ΔE-Tissue Equivalent Proportional Counters (TEPC) will directly assess the resulting LET-distributions at different positions in the target area [38].

Beamline Implementation

The hybrid active-passive space radiation simulator described in this work will be implemented at the experimental site Cave A in GSI. Modulators will be attached to linear drives powered by pressurized air and remotely controlled via a valve terminal using an updated version of the existing Cave A raster scanning control software. This ensures that a modulator exchange can be performed during spill pause of GSIs SIS18 (typically < 2 s) and therefore facilitate the beamtime use. The software continuously monitors the beam intensity, controls the scanning magnets and provides an interface to the accelerator control system for requesting the beam or changing the primary particle energy. The current control system already supports the use of a fluence-controlled binary energy degrader and this functionality will be adapted for the use with the modulator exchange system. Additionally, Cave A allows for a maximum scattering distance between modulators and target area of up to 5 m to homogenize the produced radiation fields.

RESULTS

The technical feasibility of all steps described in section Material and Methods was verified and is presented below. CAD-based modulator design and quality control is exemplarily shown based on previous works on complex modulators for particle therapy, whereas modulator optimization, Monte Carlo recalculation and production was validated by designing and producing a 3D printed modulator reproducing the 1972 SPE [39] in steel. No benchmarking is shown for the experimental validation because the described experimental measurement methods and detection system were already used successfully multiple times before, whereas beamline integration is not yet possible at the current stage of the presented work.

2D Range Modulators for Particle Therapy

The development of complex range modulators for particle therapy faces similar challenges as described in this work and can therefore be directly used for benchmarking within the scope of this work. However, it is important to note that the requirements on dose reproduction of such medical filters and therefore on the production quality of the modulators is extremely high and might be excessive in the context of space radiation simulation.

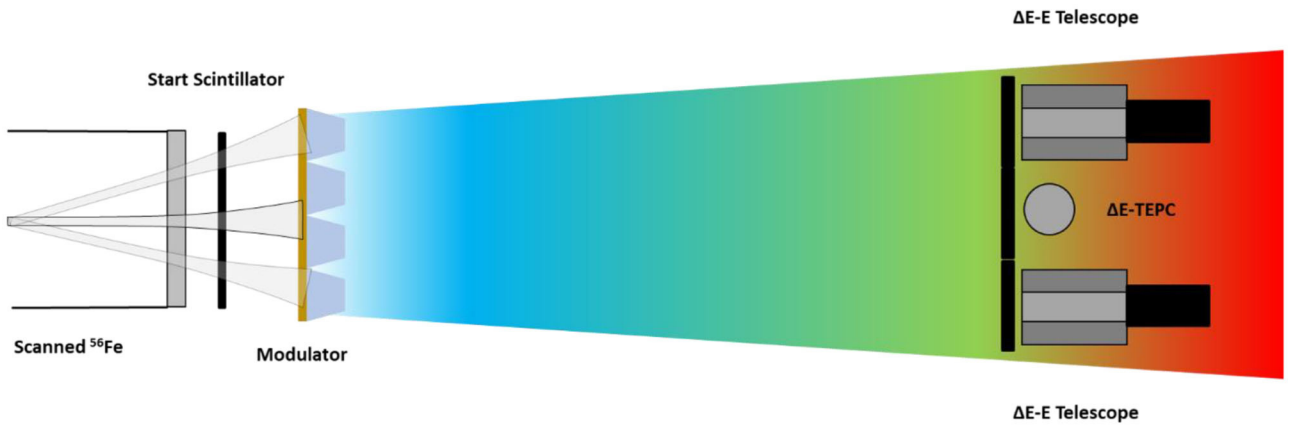

FIGURE 4 | Schematic of the experimental setup to assess modulator performance. The setup is capable of measuring all relevant physical values during a single modulator exposure simultaneously.

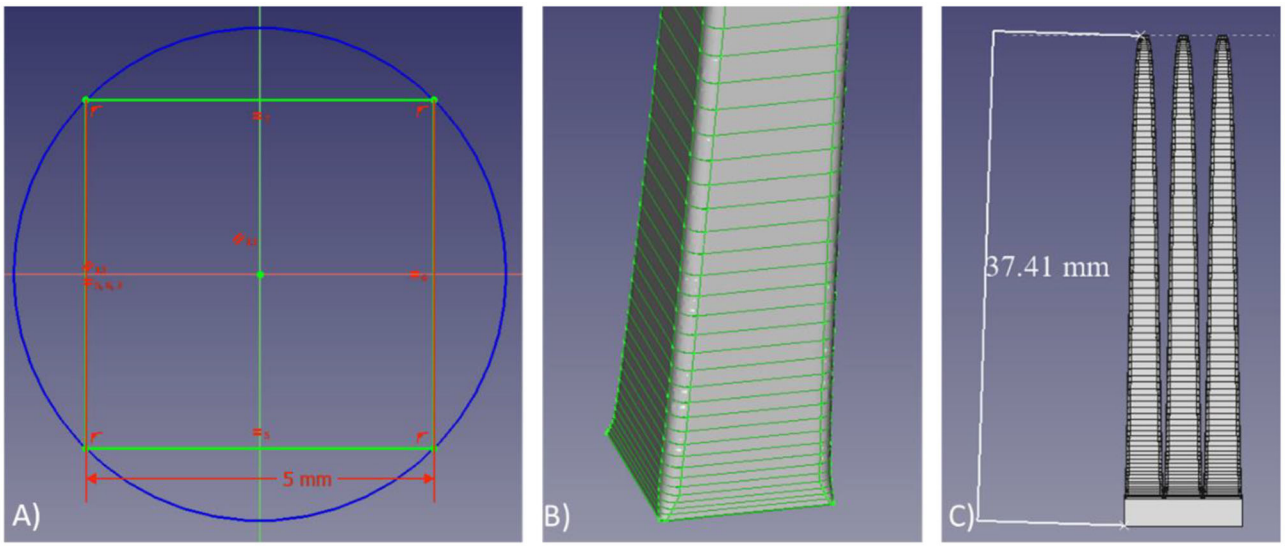

FIGURE 5 | Overview of the CAD-based modulator design: A set of weights ω is converted to one corresponding constrained 2D geometry per height **(A)**, lofted **(B)**, and multiplied **(C)**. The given scale is representative for complex modulators, but varies depending on exact use case.

The CAD-based design workflow of complex needle-like geometries is presented in **Figure 5**.

A set of weights ω_N at layer height N is converted to one corresponding 2D geometry per height defining an appropriate constrained area (**Figure 5A**). All resulting areas are lofted to create a solid geometry (**Figure 5B**). The solid geometry of a singular modulation structure can then be multiplied to obtain a full modulator (**Figure 5C**) or exported individually.

The importance of quality control of the produced modulation structures is exemplarily shown in **Figure 6**. The quality of a complex modulation structure printed by a Stratasys Objet 30 Pro was evaluated by a Werth TomoScope (**Figure 6A**). The small ridges at the base of the needle-like structures (**Figure 6B**) as well as their tips (**Figure 6C**) were identified as problematic areas. This specific Objet printer tends to fill small ridges or holes with unwanted material, whereas the tip of fine-detailed structures typically misses material. These production modality specific limitations are directly feed back to CAD-based modulator design and typically can be compensated.

Generation of a SPE Spectrum

A complex SPE modulator design, reproducing the 1972 SPE, was optimized using a similar but simplified approach as described in section Analytical Pre-optimization, implemented in MATLAB, and produced via 3D SLM printing in steel. The individual steps are showcased in **Figure 7**. Based on a given kinetic energy spectra a set of weights, representing a single modulation structure, was optimized (**Figure 7A**) and

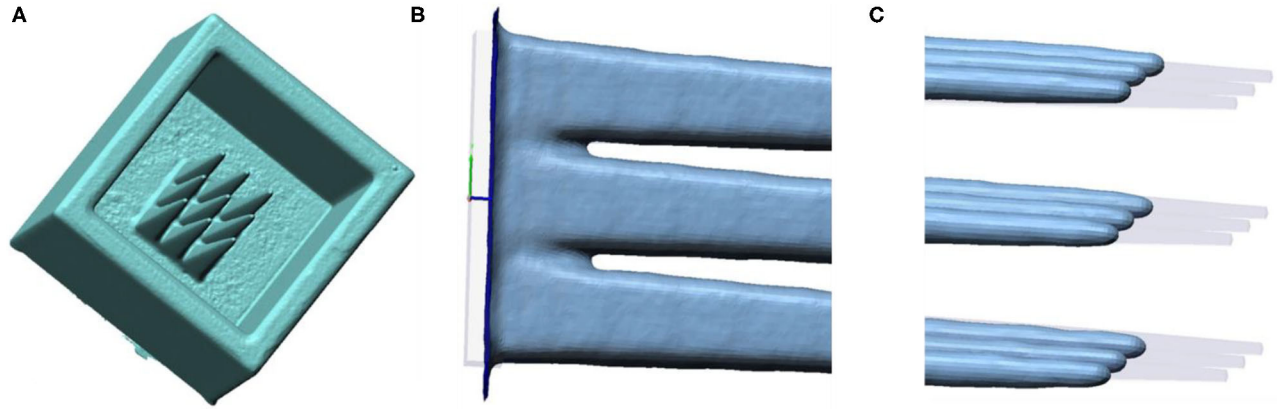

FIGURE 6 | Quality control of a complex 3D printed modulation structure **(A)**. The two problematic areas are the base **(B)** and the tip **(C)** and are presented in a zoomed in view. Small ridges in the base tend to receive too much material, whereas material tends to miss in the region of the tips. Picture courtesy of M. Weißer, Messtronik GmbH, Germany.

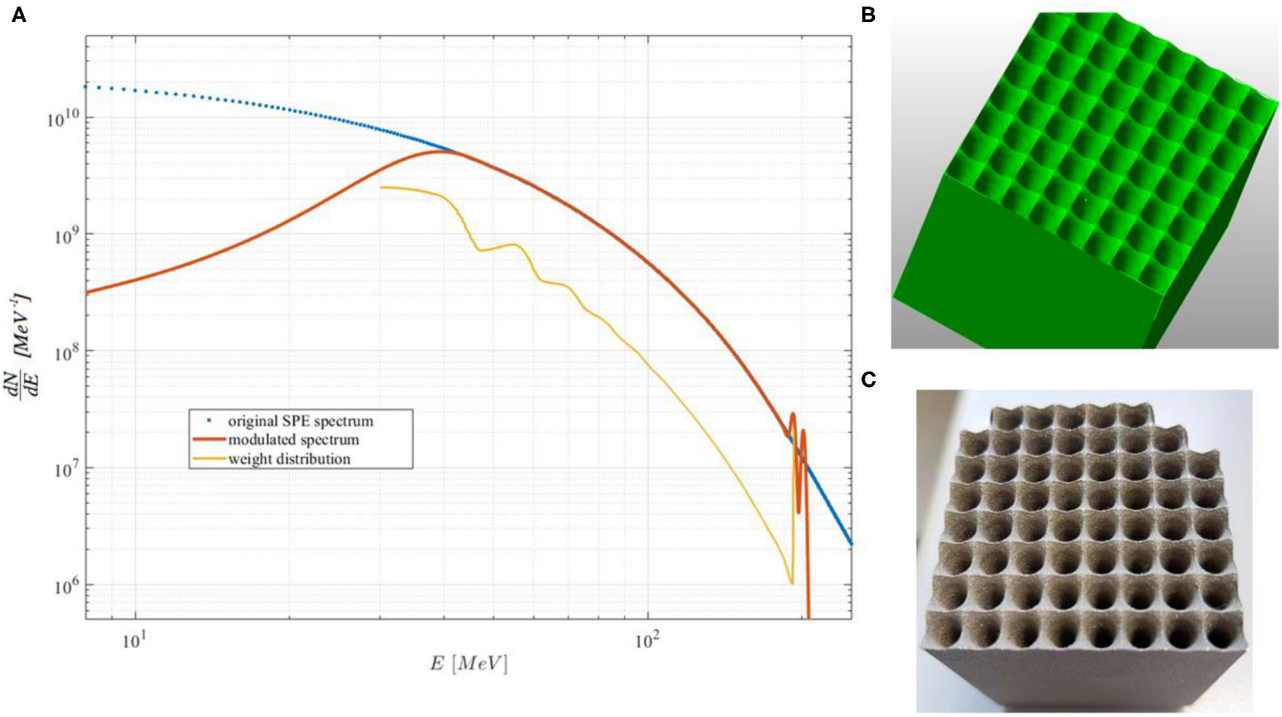

FIGURE 7 | Energy spectra and optimized weights for a modulator reproducing the 1972 SPE **(A)** were used to design **(B)** and produce **(C)** a complex SPE modulator.

converted to a full 3D modulator geometry (**Figure 7B**). After polygon reduction the resulting modulator STL still contained around 185k faces. This geometry was used as geometrical input for the Monte Carlo geometry as well as produced via SLM printing (**Figure 7C**). It is important to note that the current iteration of the optimized modulator only reproduces the SPE spectrum above 30 MeV. Nevertheless, this limitation is of no consequence for a realistic manned mission scenario due to the minimal shielding always offered by the astronauts space suit [40].

The optimized STL was imported to Geant4 via CADMesh, according to section Monte Carlo Simulations, and benchmarked with 220 MeV protons.

The simulation geometry is depicted in **Figure 8**. A monoenergetic 40 * 40 mm^2 220 MeV proton beam was generated at the edge of the air-filled world volume (left)

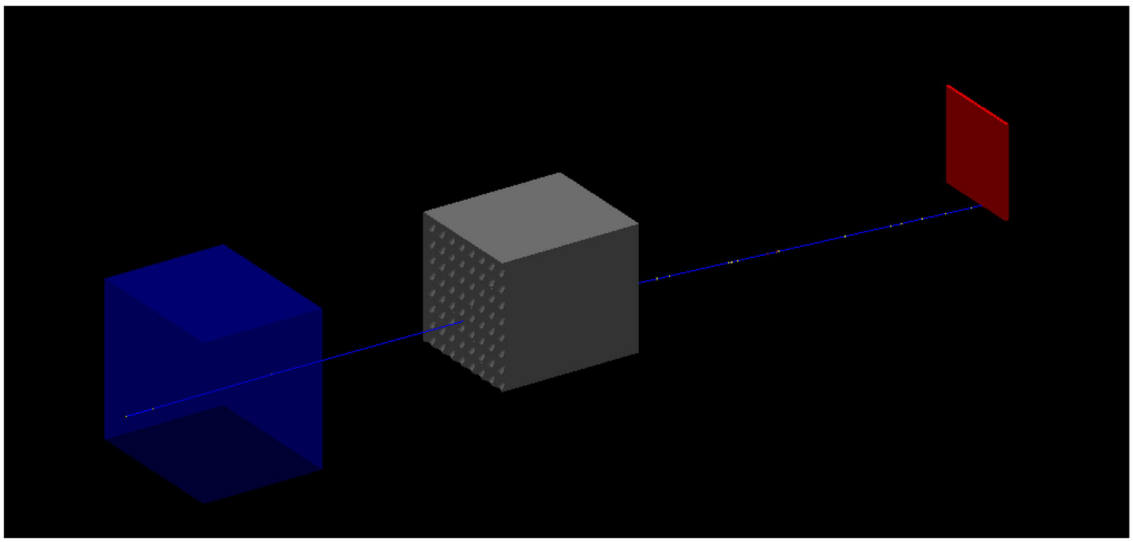

FIGURE 8 | Graphical representation of the Geant4 geometry as used in the presented simulation. The created particle traverses a block of water (blue) before interacting with the modulator (gray). Physical quantities are scored (red) after a suitable air gap. Distances are adjusted for easier visualization.

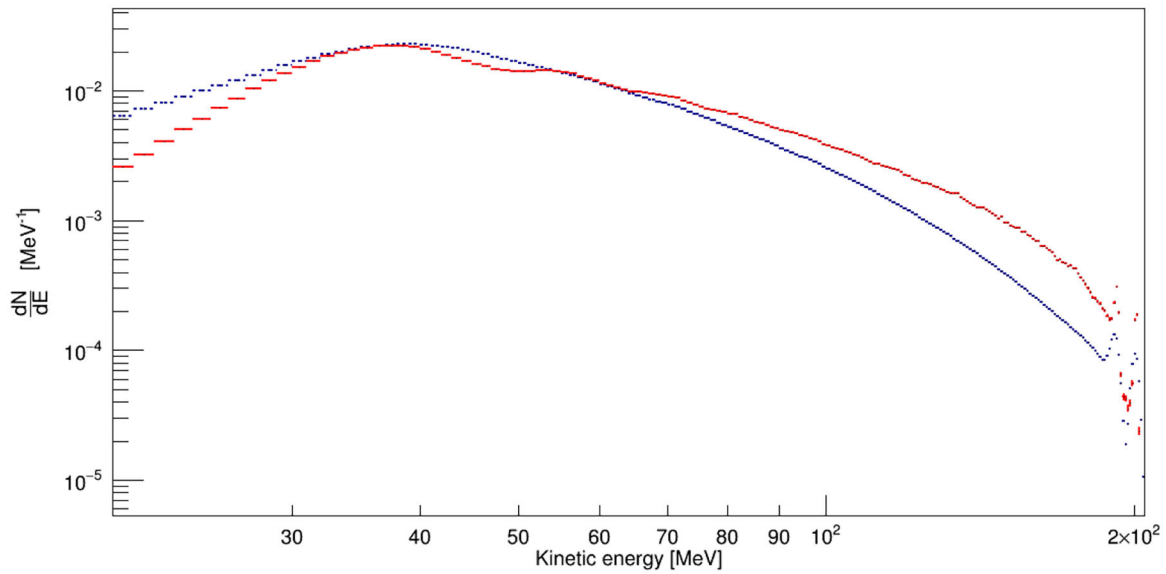

FIGURE 9 | Optimized (blue—dashed) and recalculated (red) normalized proton energy spectra of the 1972 SPE.

and traversing a 4 cm slab water target, also included in the modulator optimization, before impinging the steel modulator. Particles behind the modulator were scored after a suitable distance (20 cm) to blur out the modulation structures [41] in a 30 * 30 mm^2 centered air-filled sensitive detector volume (right) for particle charge, mass, kinetic energy as well as particle intersection point in x and y. The simulations were performed with Geant4 version 10.6 and the QGSP_BIC_EMY reference physics list. A comparison of the optimized proton energy spectra with the predictions of Geant4, both scaled to one, is shown in **Figure 9**. In general, the Monte Carlo prediction follows the optimized spectra reasonably well over the full energy range of interest. Especially the reproduction of the two overshoots in the high energy region shows the potential of the presented Monte Carlo approach. Deviations in the low and high energy region are mainly due to the not perfectly matching material composition between optimizer base data and Geant4 recalculation as well as the currently non-optimized handling of multiple scattering during the optimization. The structures in the simulated data starting at 40 MeV are most likely artifacts of a

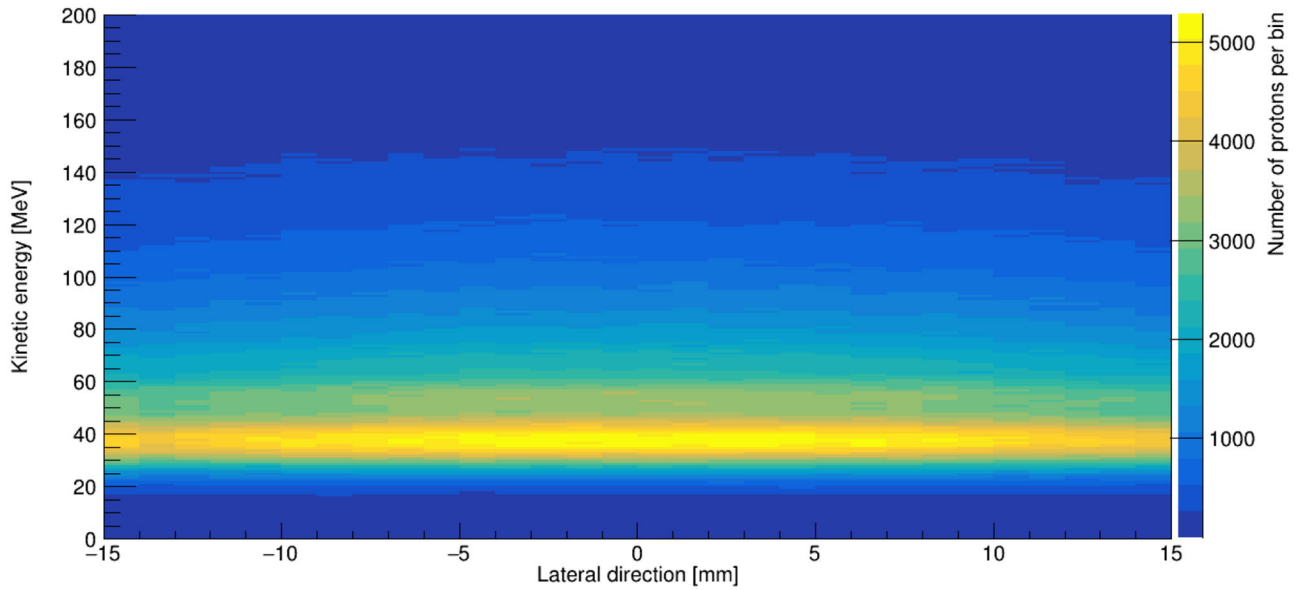

FIGURE 10 | Proton frequency per MeV and mm for 50 million primary protons and 20 cm distance between scorer and modulator.

too aggressive facet reduction of the modulator STL. As shown in **Figure 10**, the properties of the radiation field are homogenous within a reasonably large area mainly limited by the size of the modulator, the size of the primary particle field and the available distance between modulator and target area.

DISCUSSION

Compared to already implemented or proposed space radiation simulation concepts, the hybrid active-passive approach combines the flexibility of active systems, as used at NSRL, and the simplicity of the proposed passive systems. As the heaviest important constituent of the GCR, the use of Fe beams directly permits the creation of a mixed field including both, highly energetic Fe ions as well as all lighter elements through nuclear fragmentation, simultaneously.

Active energy variation permits a more precise shaping of the kinetic energies of especially lighter fragments without increasing the complexity of the accelerator setup or the irradiation time per sample too much, whereas the use of many delicate periodic modulation structures, instead of a single one, allows the creation of a large homogeneous field after a suitable scattering distance in air as needed for radiobiological experiments without compromising the reproduction quality of complex LET-distributions. Currently all elements needed for the implementation of such a system in GSIs Cave A, as presented in section Material and Methods, are under development. Nevertheless, important questions like suitable modulator materials, different production modalities and accompanying quality assurance techniques as well as reasonable GCR reference fields to be simulated are under investigation and will influence the final design and performance of the system.

Most likely, the amount of materials will be limited to plastics, aluminum and steel for complex modulator geometries as well as lead or gold foils to increase scattering or the energy width of the primary beam if needed. The rationale behind this material choice is to limit the amount of base data that needs to be simulated as well as the availability of mature production- and quality assurance methods suitable for the needed modulator dimensions. The large density differences of these three materials, furthermore, should give the pre-optimizer enough freedom to optimize a variety of realistic space radiation environments. A dedicated Monte Carlo study investigating the minimum number of different materials needed for this project is currently ongoing. Reliance on alternative implementation strategies, like the constant rotation of the complex modulators, similar to a modulator wheel as used in medical physics [42], to decrease the reliance on multiple scattering to homogenize the produced fields, seem not to be necessary, due to the comparatively large scattering distance available and the delicate and fine periodic structures of the proposed modulators. However, these alternative options might be investigated in the future especially for the application of the presented system to FAIR energies.

The choice and number of reference radiation fields to be simulated is under discussion and will be decided in the near future. One of the key aspects will be the comparability of data obtained with the NSRL system. Due to the reliance on nuclear fragmentation and the resulting continuous yield- and kinetic energy distributions produced by a hybrid system, the NSRL reference field might not be achievable with such a system. A dedicated *in-silico* study will be necessary to investigate the possible options and to find a suitable compromise.

Furthermore, the presented deviations of the optimized modulation function and the recalculated SPE modulator must

be investigated. The current version of the optimizer is not yet able to propagate the multiple scattering of the proton beam to arbitrary scattering distances and fully relies on the implicit scattering information provided by the geometry used during the simulation of the base data library. The software is currently updated to follow a similar scattering approach as TRiP98. Additionally, a new basic data library, purely based on Geant4, is currently created. The basic data library utilized in this work, shared part of its data with the development of complex range modulators for particle therapy, which relies on a different Monte Carlo transport code. Small deviations between the predictions of these transport codes will directly lead to a degradation of the modulator recalculation.

CONCLUSION

Within the scope of this work a hybrid active-passive space radiation simulation concept was introduced and the feasibility of the workflow was validated with the design and production of a complex modulator able to simulate the full proton energy spectra of the 1972 SPE with only a single primary proton beam energy. The experimental validation of the developed SPE modulator is foreseen in the near future. After successful validation, in theory all clinical particle therapy centers will be able to offer high quality SPE simulation for space radiation protection research employing such a modulator. Furthermore, due to its passive creation, the generated SPE reference radiation field will be highly comparable between different experimental sites. First in-beam tests using high energy ^{56}Fe beam and different optimized modulators for GCR simulation are foreseen to start in 2021 at Cave A.

DATA AVAILABILITY STATEMENT

All datasets generated for this study are included in the article/supplementary material.

AUTHOR CONTRIBUTIONS

CS wrote the majority of the paper, part of the used computational programs/scripts, and performed the Monte Carlo simulations used in this paper. UW wrote part of the used computational programs/scripts, performed the modulator optimization as well as proofread, and corrected the manuscript. MD proposed the development activity, wrote parts of the manuscript and proofread, and corrected the parts written by CS. The basic implementation strategy for the system as well as the general workflow was developed by all authors together during multiple discussions about the shortcomings of the currently used approach.

REFERENCES

1. Chancellor JC, Scott GBI, Sutton JP. Space radiation: the number one risk to astronaut health beyond low earth orbit. *Life*. (2014) **4**:491–510. doi: 10.3390/life4030491
2. Durante M. Space radiation protection: destination mars. *Life Sci Space Res*. (2014) **1**:2–9. doi: 10.1016/j.lssr.2014.01.002
3. Mewaldt RA, Cohen CMS, Labrador AW, Leske RA, Mason GM, Desai MI, et al. Proton, helium, and electron spectra during the large solar particle events of October-November 2003. *J Geophys Res Space Phys*. (2005) **110**:1–23. doi: 10.1029/2005JA011038
4. Simpson JA. Elemental and isotopic composition of the galactic cosmic rays. *Ann Rev Nucl Part Sci*. (1983) **33**:323–82. doi: 10.1146/annurev.ns.33.120183.001543
5. Mazur JE, Crain WR, Looper MD, Mabry DJ, Blake JB, Case AW, et al. New measurements of total ionizing dose in the lunar environment. *Space Weather*. (2011) 9:S07002. doi: 10.1029/2010SW000641
6. Zeitlin C, Hassler DM, Cucinotta FA, Ehresmann B, Wimmer-Schweingruber RF, Brinza DE, et al. Measurements of energetic particle radiation in transit to mars on the mars science laboratory. *Science*. (2013) **340**:1080–4. doi: 10.1126/science.1235989
7. Narici L, Berger T, Matthiä D, Reitz G. Radiation measurements performed with active detectors relevant for human space exploration. *Front Oncol*. (2015) **5**:273. doi: 10.3389/fonc.2015.00273
8. Guo J, Zeitlin C, Wimmer-Schweingruber RF, Hassler DM, Posner A, Heber B, et al. Variations of dose rate observed by MSL/RAD in transit to Mars. *Astron Astrophys*. (2015) **577**:A58. doi: 10.1051/0004-6361/201525680
9. Ehresmann B, Zeitlin C, Hassler DM, Wimmer-Schweingruber RF, Böhm E, Böttcher S, et al. Charged particle spectra obtained with the mars science laboratory radiation assessment detector (MSL/RAD) on the surface of mars. *J Geophys Res Planets*. (2014) **119**:468–79. doi: 10.1002/2013JE004547
10. Sihver L. Physics and biophysics experiments needed for improved risk assessment in space. *Acta Astronaut*. (2008) **63**:886–98. doi: 10.1016/j.actaastro.2008.04.013
11. Hughson RL, Helm A, Durante M. Heart in space: Effect of the extraterrestrial environment on the cardiovascular system. *Nat Rev Cardiol*. (2018) **15**:167–80. doi: 10.1038/nrcardio.2017.157
12. Parihar VK, Allen B, Tran KK, Macaraeg TG, Chu EM, Kwok SF, et al. What happens to your brain on the way to Mars. *Sci Adv*. (2015) **1**:e1400256. doi: 10.1126/sciadv.1400256
13. Raber J, Yamazaki J, Torres ERS, Kirchoff N, Stagaman K, Sharpton T, et al. Combined effects of three high-energy charged particle beams important for space flight on brain, behavioral and cognitive endpoints in B6D2F1 female and male mice. *Front Physiol*. (2019) **10**:179. doi: 10.3389/fphys.2019.00179
14. Chancellor JC, Blue RS, Cengel KA, Auñón-Chancellor SM, Rubins KH, Katzgraber HG, et al. Limitations in predicting the space radiation health risk for exploration astronauts. *NPJ Microgravity*. (2017) **8**:1–11. doi: 10.1038/s41526-018-0043-2
15. La Tessa C, Sivertz M, Chiang IH, Lowenstein D, Rusek A. Overview of the NASA space radiation laboratory. *Life Sci Sp Res*. (2016) **11**:18–23. doi: 10.1016/j.lssr.2016.10.002
16. Slaba TC, Blattnig SR, Norbury JW, Rusek A, LaTessa C, Walker SA. GCR Simulator Reference Field and a Spectral Approach for Laboratory Simulation. NASA/TP-2015-218698 (2015). Available online at: https://three.jsc.nasa.gov/articles/Slaba_gcrsim_HRP2015_THREE.pdf (accessed March 25, 2015).
17. Norbury JW, Schimmerling W, Slaba TC, Azzam EI, Francis F, Baiocco G, et al. Calactic cosmic ray simulation at the NASA space radiation laboratory. *Life Sci Space Res*. (2016) **8**:38–51. doi: 10.1016/j.lssr.2016.02.001
18. Kim MHY, Rusek A, Cucinotta FA. Issues for simulation of galactic cosmic ray exposures for radiobiological research at ground-based accelerators. *Front Oncol*. (2015) **5**:1–14. doi: 10.3389/fonc.2015.00122
19. Simonsen LC, Slaba TC, Guida P, Rusek A. NASA ' s first ground-based galactic cosmic ray simulator : enabling a new era in space radiobiology research. *PLoS Biol*. (2020) **18**:e3000669. doi: 10.1371/journal.pbio.3000669
20. Durante M, Indelicato P, Jonson B, Koch V, Langanke K, Meißner UG, et al. All the fun of the FAIR: fundamental physics at the facility for antiproton and ion research. *Phys Scr*. (2018) **94**:033001. doi: 10.1088/1402-4896/aaf93f
21. Stöhlker T, Bagnoud V, Blaum K, Blazevic A, Bräuning-Demian A, Durante M, et al. APPA at FAIR: from fundamental to applied research. *Nucl*

Instrum Methods Phys Res Sect B. (2015) **365**:680–5. doi: 10.1016/j.nimb.2015.07.077

22. Timoshenko GN, Krylov AR, Paraipan M, Gordeev IS. Particle accelerator-based simulation of the radiation environment on board spacecraft for manned interplanetary missions. *Radiat Meas*. (2017) **107**:27–32. doi: 10.1016/j.radmeas.2017.10.006
23. Durante M, Cucinotta FA. Physical basis of radiation protection in space travel. *Rev Mod Phys*. (2011) **83**:1245–81. doi: 10.1103/RevModPhys.83.1245
24. Chancellor JC, Guetersloh SB, Cengel KA, Ford JR, Katzgraber HG. Emulation of the space radiation environment for materials testing and radiobiological experiments. *arXiv Peprint* arXiv:1706.02727v1 (2017).
25. Chancellor JC, Guetersloh SB, Blue RS, Cengel KA, Ford JR, Katzgraber HG. Targeted nuclear spallation from moderator block design for a ground-based space radiation analog. *arXiv Peprint* arXiv:1706.02727v2 (2019).
26. Simeonov Y, Weber U, Penchev P, Ringbæk TP, Schuy C, Brons S, et al. 3D range-modulator for scanned particle therapy: development, Monte Carlo simulations and experimental evaluation. *Phys Med Biol*. (2017) **62**:7075–96. doi: 10.1088/1361-6560/aa81f4
27. Agostinelli S, Allison J, Amako K, Apostolakis J, Araujo H, Arce P, et al. Geant4—a simulation toolkit. *Nucl Instr Meth Phys Res A*. (2003) **506**:250–303. doi: 10.1016/S0168-9002(03)01368-8
28. Allison J, Amako K, Apostolakis J, Araujo H, Dubois PA, Asai M, et al. Geant4 developments and applications. *IEEE Trans Nucl Sci*. (2006) **53**:270–8. doi: 10.1109/TNS.2006.869826
29. Allison J, Amako K, Apostolakis J, Arce P, Asai M, Aso T, et al. Recent developments in Geant4. *Nucl Instr Meth Phys Res A*. (2016) **835**:186–225. doi: 10.1016/j.nima.2016.06.125
30. Brun R, Rademakers F. ROOT-an object oriented data analysis framework. *Nucl Instrum Methods Phys Res Sec A*. (1997) **389**:81–6. doi: 10.1016/S0168-9002(97)00048-X
31. Krämer M, Jäkel O, Haberer T, Kraft G, Schardt D, Weber U. Treatment planning for heavy-ion radiotherapy: physical beam model and dose optimization. *Phys Med Biol*. (2000) **45**:3299–317. doi: 10.1088/0031-9155/45/11/313
32. Kraemer M. Swift ions in radiotherapy – Treatment planning with TRiP98. *Nucl Instrum Methods Phys Res Sec B*. (2009) **267**:989–92. doi: 10.1016/j.nimb.2009.02.015
33. Akagi T, Higashi A, Tsugami H, Sakamoto H, Masuda Y, Hishikawa Y. Ridge filter design for proton therapy at Hyogo Ion Beam medical center. *Phys Med Biol*. (2003) **48**:N301–12. doi: 10.1088/0031-9155/48/22/N01
34. Riegel J, Mayer W, van Havre Y. *FreeCAD Version 0.17*. (2020). Available online at: http://www.freecadweb.org (accessed January 21, 2020).
35. Poole CM, Cornelius I, Trapp JV, Langton CM. A CAD interface for GEANT4. *Australas Phys Eng Sci Med*. (2012) **35**:329–34. doi: 10.1007/s13246-012-0159-8
36. Poole CM, Cornelius I, Trapp JV, Langton CM. Fast tessellated solid navigation in GEANT4. *IEEE Trans Nucl Sci*. (2012) **59**:1695–701. doi: 10.1109/TNS.2012.2197415
37. Gunzert-Marx K, Iwase H, Schardt D, Simon RS. Secondary beam fragments produced by 200 MeV/u 12 C ions in water and their dose contributions in carbon ion radiotherapy. *New J Phys*. (2008) **10**:075003. doi: 10.1088/1367-2630/10/7/075003
38. Martino G, Durante M, Schardt D. Microdosimetry measurements characterizing the radiation fields of 300 MeV/u 12C and 185 MeV/u 7Li pencil beams stopping in water. *Phys Med Biol*. (2010) **55**:3441–9. doi: 10.1088/0031-9155/55/12/011
39. Townsend LW, Wilson JW, Shinn JL, Curtis SB. Human exposure to large solar particle events in space. *Adv Sp Res*. (1992) **12**:339–48. doi: 10.1016/0273-1177(92)90126-I
40. Wilson J, Anderson B, Cucinotta F, Ware J, Zeitlin CJ. Spacesuit Radiation Shield Design Methods. *SAE Technical Paper 2006-01-2110* (2006). doi: 10.4271/2006-01-2110
41. Printz Ringbæk T, Simeonov Y, Witt M, Engenhart-Cabillic R, Kraft G, Zink K, et al. Modulation power of porous materials and usage as ripple filter in particle therapy. *Phys Med Biol*. (2017) **62**:2892–909. doi: 10.1088/1361-6560/aa5c28
42. Jia SB, Romano F, Cirrone GAP, Cuttone G, Hadizadeh MH, Mowlavi AA, et al. Designing a range modulator wheel to spread-out the Bragg peak for a passive proton therapy facility. *Nucl Instruments Methods Phys Res Sect A*. (2015) **806**:101–8. doi: 10.1016/j.nima.2015.10.006

Conflict of Interest: The authors declare that the research was conducted in the absence of any commercial or financial relationships that could be construed as a potential conflict of interest.

frontiers in Physics

ORIGINAL RESEARCH
published: 31 August 2020
doi: 10.3389/fphy.2020.00270

Ion Beam Stimulation Therapy With a Nanoradiator as a Site-Specific Prodrug

Jong-Ki Kim[1]*, *Seung-Jun Seo*[1] and *Jae-Geun Jeon*[2]

[1] Department of Biomedical Engineering and Radiology, School of Medicine, Daegu Catholic University, Daegu, South Korea, [2] Department of Periodontology, School of Dentistry, Kyungpook National University, Daegu, South Korea

In view of the fact that Bragg peak energy cannot be delivered individually to multiple scattered infiltrating tumors or diffuse lesions, the energy of the ion beam could instead be adjusted to traverse the entire body for the selective activation of nanoparticles (NPs) inside the target lesions with an ion fluence comparable to the Bragg peak. This Coulomb stimulation of NPs generates low-energy electrons (LEEs) and characteristic fluorescent X-rays (XFLs) from the NP surface; this effectively transforms inert NPs into nanoradiators, much like the conversion of a prodrug into a drug. In contrast, the relatively small plateau dose absorbed along the beam path ensures that there are minimal effects to normal tissue (NT). This simple but innovative approach enables unprecedented traversing ion beam stimulation therapy (TIBS) for infiltrating tumors or diffuse non-oncological lesions. The theoretical background and efficacy of TIBS has been demonstrated by several proof-of-concept studies with animal disease models and molecular-targeted high-Z NPs.

Keywords: ion transmission beam, Coulomb stimulation, high-Z nanoparticles, site-specific dose enhancement, therapeutic beacon, diffuse lesions, molecular targeting

OPEN ACCESS

Edited by:
Marco Durante,
GSI Helmholtz Center for Heavy Ion Research, Germany

Reviewed by:
Narayan Sahoo,
University of Texas MD Anderson Cancer Center, United States
Giacomo Cuttone,
Laboratori Nazionali del Sud (INFN), Italy
Yoshitaka Matsumoto,
University of Tsukuba, Japan

***Correspondence:**
Jong-Ki Kim
jkkim@cu.ac.kr

Specialty section:
This article was submitted to Medical Physics and Imaging, a section of the journal Frontiers in Physics

Received: *27 April 2020*
Accepted: *17 June 2020*
Published: *31 August 2020*

Citation:
Kim J-K, Seo S-J and Jeon J-G (2020) Ion Beam Stimulation Therapy With a Nanoradiator as a Site-Specific Prodrug. Front. Phys. 8:270. doi: 10.3389/fphy.2020.00270

INTRODUCTION

A proton or carbon ion beam dissipates energy at a specific depth by forming a Bragg peak during its passage through tissue depending on its energy; this concept has been used to deliver a therapeutic radiation dose to the target in conventional proton or carbon ion therapy. In contrast, traversing ion beam stimulation therapy (TIBS) is performed by a traversing ion beam, whose energy reaches beyond the depth at which a Bragg peak forms in the tissue, to activate high-Z nanoparticles (NPs) that can be either delivered to the pathological lesions by various targeting schemes or intrinsically integrated into the target by a pathological process. The ion fluence decreases gradually during this traversal due to nuclear reaction-mediated ion loss and abruptly reduces to zero at δ while being absorbed in medium with a liberating Bragg peak dose (BPD) [1, 2]. Consequently, the ion fluence passing through the NP-containing target is markedly larger than the number of ions absorbed in the surrounding NT, which can only reach the plateau dose (PD), as shown in **Figure 1**. Traversing ions selectively facilitate physical Coulomb interactions with high-Z NPs (Pt, Au, Gd, and Fe) in the target tissue, which is achieved by a relatively higher Z number and a higher ion-impact dose on NPs than on tissue elements. TIBS ionizes atoms via inelastic Coulomb scattering with atomic electrons in high-Z NPs, and as they pass, the NPs emit low-energy electrons (LEEs) and fluorescent X-rays (XFLs) via both Auger cascades [3, 4] and interatomic Coulomb decay (ICD) during the de-excitation process [5, 6], termed the Coulomb nanoradiator effect (CNR) [7].

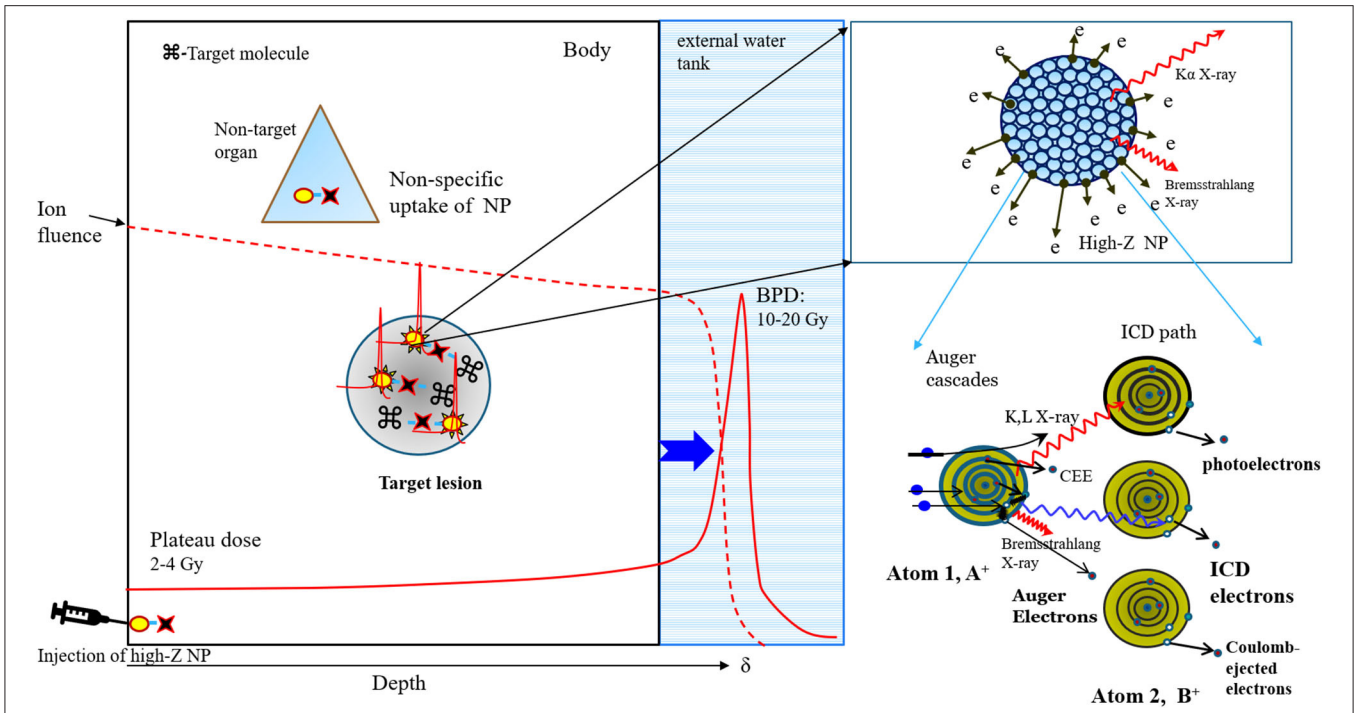

FIGURE 1 | Schematic diagram of low-energy electrons (LEEs) and characteristic X-ray fluorescence (XFL) emission from proton-stimulated high-Z nanoparticles in target tissue via Auger cascades and the interatomic Coulomb decay path (right panel). The proton fluence during the traversal of tissues (result of simulation, 2) containing target lesions with nanoparticles abruptly decays to zero at the Bragg peak position, resulting in the deposition of all energy, but the plateau dose is absorbed by the tissue along the beam path, resulting in the stimulation of nanoparticles with a dose comparable to BPD (left panel).

CNR-derived LEEs break up bonding of adjacent biomolecules in the target lesions directly [8, 9], resulting in damage to the lesions. Diffuse and multiple scattered lesions in various intractable cancers and non-oncological conditions, such as neoangiogenesis, atherosclerotic plaques with thrombosis, and neurodegenerative plaques, are excluded from the indications for radiotherapy or surgical treatment. Previously, bare iron-oxide nanoparticles were used for the treatment of either arterial thrombosis or brain glioma. Here, we designed new nanoparticles to target either LDL receptors for BBB crossing and glioma or scavenger receptors of macrophages and active thrombus in atheroma for better targeted delivery and site-specific activation by TIBS. In this work, we present the theoretical background for precise and effective therapeutic proton-TIBS with molecular-targeted high-Z NPs in animal disease models.

MATERIALS AND METHODS

Synthesis of Molecular-Targeted High-Z Nanoparticles

LDLR-targeting ApoB@AuNPs-Cy5 were synthesized by thiolating the ApoB peptide (3-mercaptopropionic acid-DWLKAFYDKVAEKLKEAFRLTRKRGLKLA-NH2: Anygen, Korea) and SH-PEG5000-Cy5.5 (Intechim, France) to 15 nm gold NPs (Nanoprobe, USA) using the same method described previously [10]. Scavenger receptor-A1 (SR-A1)-targeting PP1@AuNPs-Cy5 or VEGFR-targeting Flt1@AuNPs-Cy5 were also synthesized by thiolating the PP1 peptide (3-mercaptopropionic acid-LSLERFLRCWSDAPA-NH2) or the Flt1 peptide (3-mercaptopropionic acid-GGNQWFI-NH2) and SH-PEG5000-Cy5.5 to 15 nm AuNPs in the same way described above. Briefly, 1 mL stock solution of citrated AuNPs (0.5 mg/mL, 2.538 mM), SH-PEG-Cy5.5 (5 mg/mL, 1 mM) in distilled water, and either Flt1 or PP1 peptide (2.6 mg/mL, 2.863 mM) in dimethyl sulfoxide (DMSO) were prepared. In a typical synthesis of 10 μM Flt1@AuNP-Cy5.5 or PP1@AuNP-Cy5.5 nanocomplexes, 928.56 μL of distilled water was added to a bottle prior to mixing with 50 μL of SH-PEG-Cy5.5 and 17.5 μL of 100 μM each peptide for 5 min while stirring to produce a 1:1 molar ratio of SH-PEG-Cy5.5 to the peptide. Then, 3.94 μL of AuNP solution was added to the mixture of SHPEG-Cy5.5/Flt1 or PP1 peptide, resulting in a 5:1 molar ratio of thiol to gold at pH 7.4. Finally, the mixture of SH-PEG-Cy5.5/Flt1 or PP1/AuNPs was stirred at room temperature for 2 h to allow for the complete formation of gold nanocomplexes. To purify the complex, reactants were centrifuged at 16,000 rpm for 10 min. After decanting the supernatant, the pellet was resuspended in 0.5 or 1 mL of phosphate-buffered saline (PBS).

Thrombus-targeting Fuc@Fe3O4 NPs were synthesized by conjugating aminated fucoidan to citrated iron oxide NPs (ION) using EDC/NHS chemistry. Aminated fucoidan was prepared by reacting epichlorohydrin-treated fucoidan with 30% ammonia

water at 40°C for 90 min [11]. Briefly, we prepared 10 ml of ION solution by adding 4 ml citrated ION solution (40 mg) to 6 ml MES buffer (pH 6). A total of 1–10 mg of aminated fucoidan was dissolved in 1 ml PBS buffer. We then added 0.4 mg EDC to the ION solution and stirred for 15 min after adding 1.1 mg sulfo-NHS to ION solution and adjusting pH to 7.0 using sodium bicarbonate (0.7 ml). Then 1 ml of aminated fucoidan was mixed with ION solution containing EDC/NHS and stirred for 2 h. Fucoidan-conjugated ION was condensed with strong magnet to separate unreacted components which was decanted finally after washing PBS several times. The formation of peptide bonding was confirmed by FT-IR spectroscopy.

Animal Models

The procedures used for the laboratory animals were approved by the Institutional Animal Care and Use Committee of Catholic University Hospital of Daegu (approval numbers, DCIAFCR 151007-7-Y and 181029-22Y).

F98 Rat Glioma Model

A total of 2×10^5 F98 glioma cells were implanted in the frontal lobe of Fischer 333 rats by stereotactic surgery as described previously [12]. Briefly, after immobilizing the rats in a rodent stereotactic frame, an incision was made in the skin, and a burr hole was made in the skull. One million tumor cells were injected at a rate of 1–2 microliters/minute using a microsyringe (Hamilton, Reno, NV, US) mounted on a stereotactic frame (Kopf Instruments, Tujunga, CA, US) at coordinates of 1 mm lateral and 1 mm posterior to the bregma and 1.5 mm below the dura. Tumor growth was evaluated with 4.7 T MRI 5 days after implanting the cells. In this study, a total of six rats were divided into two experimental groups for two irradiation doses (10 and 5 Gy) and three rats were left untreated to act as a proton alone control.

Ligated-Artery Mouse Atheroma Model

A partial ligation of the left coronary artery (LCA) was carried out in C57BL/6 mice ($n = 6$) as previously described [13]. Briefly, three of four caudal branches of the LCA (left external carotid, internal carotid, and occipital artery) were ligated with 6–0 silk sutures, while the superior thyroid artery was left intact. C57Bl/6 mice were continuously fed a high-fat diet post-ligation. After 4 weeks, the mice were monitored by blood flow measurement and surgery to identify atheromatous plaque in the affected vessel. Three mice were treated with TIBS, and the other three were untreated as control.

Proton-TIBS

Proton irradiation was performed at KOMAC TR102 (Kyungju, South Korea). Intraperitoneal injections of 100 mg/kg ketamine and 20 mg/kg xylazine cocktail were administered under anesthesia. A pristine proton transmission beam, with the Bragg-peak behind the body (PS), was irradiated at 24 h after injection of NP, based on results of previous measurement of maximum uptake in tumor [7] or thrombus [14].

The rat or mouse was positioned in an upright position by tying a thread around a tooth in a sample mounter. Then the proton beam traversed through the head of the rat or the neck of the mouse from anterior to posterior. Rats that had grown tumors and mice that had developed obstructed arteries with atheroma were irradiated using a designed collimator and blocks to avoid unnecessary exposure to radiation. The irradiation energy was 100 MeV, which is sufficiently high to traverse the head of the rat or the neck of the mouse, and the single entrance dose was either 10 or 4 Gy, as measured by a TM30013 Farmer chamber (PTW), at the frontal surface of the sample.

Histologic and Imaging Analysis

The flow patency of the ligated atheroma mouse model was evaluated using a Doppler flow meter 7 days after treatment, and the mice were then euthanized. The treated vessels were removed and then subjected to fixation and staining for histologic analysis. The areas of the remaining thrombus from three different cross-sectional planes (middle, proximal, and distal; thickness of 20 μm) in the dissected vessels were measured using default image analysis software with an optical microscope (Axiophot, Zeiss, Germany).

Glioma model rats were killed 7 days after treatment by an overdose injection of sodium pentobarbital. The brains were removed, fixed in 10% formaldehyde, paraffin embedded, and sectioned through the area of irradiation. The 5-μm-thick sections were stained with hematoxylin and eosin, and the tumor was examined microscopically. Fluorescence imaging of extracted brain hemispheres was performed 24 h after IV injection of ApoB@AuNPs-Cy5 in F98 rat glioma models using an *in vivo* fluorescence imaging system (FOBI, NeoScience Co. Ltd, Korea).

Human retinal microvascular endothelial cells (HRMECs) treated with Flt1@AuNPs-Cy5 were embedded in two-chamber slides (SPL, Korea) using a mounting medium (Dako, Denmark) and examined using an optical microscope or a fluorescence confocal microscope (Nikon confocal microscope A1, Japan).

RESULTS AND DISCUSSION

Theoretical Background of TIBS

Therapeutic Beacon of High-Z NPs With CNR

Prior to becoming nanoradiators under TIBS, NPs retain inert prodrug status without cytotoxic effects due to appropriate coating [7, 15, 16]. Therefore, even if non-specific uptake by non-target organs or tissues occurs, the NPs do not exert harmful effects as long as the ion beam is not irradiated incidentally on the area of non-specific NP absorption. Since the locations of lesions associated with cancer or other diseases are normally identified by clinical imaging studies prior to therapy, ion beams can be irradiated specifically to target lesions, generating virtual drugs from high-Z NPs with CNR effects while avoiding the exposure of non-targets. This advantage may resolve the major bottleneck in nanomedicine by avoiding side effects from non-specific uptake of nanoforms of drugs by unwanted organs or tissues, which occurs often after administration, particularly via intravenous injection. Non-specific delivery of NPs is unavoidable and occurs irrespective of conjugating the NPs to targeting marker molecules in the circulatory system [17].

One way to overcome this problem is to design cleavable molecular links between nano-formulated drugs and inhibitor molecules that are cleaved by tissue-specific enzymes overexpressed in the target lesion [18]. Cleavage of the linking molecule by the enzyme liberates the inhibitor and produces the drug effect of the nanodrug. However, this method is limited due to the lack of such lesion/tissue-specific cleaving enzymes. In contrast, TIBS can activate the drug effect from any high-Z NPs delivered to the target site, irrespective of the biochemical status of the lesion.

Comparison of Traversing Ion Beams With X-Ray Photons

Depth-dose distribution

Both ion beams and X-ray photons can activate high-Z NPs but have different interaction mechanisms and depth-dose distributions when passing through the tissue. Conventional broad-band X-rays with an energy of MeV yield much larger entrance doses than traversing pristine ion beams; thus, X-ray irradiation should be spatially and temporally fractionated to activate NPs safely by photoelectric absorption. Monochromatic X-ray photons such as 50 or 68–82 KeV photons that excite either Gd or Au NPs show a depth-dose distribution comparable to that of traversing pristine ion beams, but intense beams are only currently available in synchrotron radiation facilities. Traversing pristine ion beams only deposit PDs while passing through the body via multiple Coulomb scattering (MCS), so the majority of the ion fluence is transmitted to and interacts with high-Z NPs by Coulomb scattering, as depicted in **Figure 1**. Importantly, this property of the traversing ion beam enables selective activation of the high-Z NP prodrug while preserving the surrounding NT, and emerging TIBS is feasible for various diseases that were formerly not indicated for radiotherapy or surgical intervention.

Interaction with high-Z NPs

When an ion beam impacts NPs, it first ionizes compositional atoms of the NPs by inelastic Coulomb scattering, and it then yields CNR effects on both ionized and neutral atoms during the deactivation process. Ionization may occur simultaneously at multiple electronic levels, yielding CNR in multiple levels of a given impact atom and surrounding neutral atoms. X-ray photons ionize the NP atoms mainly through photoelectric absorption, which produces similar nanoradiator effects during deactivation. Monochromatic X-rays induce a nanoradiator effect in resonance on the K-line electrons, while broad-band X-rays potentially induce multiple energy levels through additional Compton scattering but are subject to attenuation and elevated entrance doses. Consistently, a simulation study demonstrated that a monochromatic Au K-line X-ray was more effective in inducing stronger dose enhancement than a MeV X-ray under a given irradiation dose [19].

Under an entrance dose of 10 Gy and the same dose of Gd-oxide NPs, the relative nanoradiator dose from irradiation with a 45 MeV proton stimulation was compared to that from a 50 KeV synchrotron X-ray photon. The proton-derived enhancement was 1.58 times larger than the X-ray-derived enhancement [20].

We tried to compare the therapeutic efficacy of Au-nanoradiators in proton stimulation therapy in a Balb/c tumor model with that of Au-nanoradiators in broad-band X-ray irradiation using gold NPs of the same size for a similar tumor size. Complete tumor regression was achieved either by X-ray-derived photoelectric nanoradiators with tumor uptake of 3.2 mg Au/g tissue or by proton-stimulated nanoradiators with 58–79 μg Au/g tissue in tumors [7, 21]. This suggests that the proton-TIBS is more efficient for producing the same therapeutic effect with a relatively smaller tissue density of AuNPs. Taken together, these results show that producing the nanoradiator effect by Coulomb scattering on multiple inner valence levels or on multiple electrons in the inner shell of an NP atomic cluster from high-energy proton-TIBS has received relatively higher rates of induction compared with X-ray photoelectric nanoradiators based on the resonance of energy matched to a valence level.

In addition, iron oxide NPs can be effectively activated to produce CNR effects by high-energy protons or carbon ion beams, but neither monochromatic 7 keV X-rays (corresponding to Fe-K lines) nor MeV X-rays [19, 22] could produce nanoradiator doses effectively due to either rapid attenuation in deep tissue or inefficient photoelectric absorption and production of Auger and ICD-type electrons from Fe atomic clusters, respectively. However, combining 7 keV X-ray and iron oxide NPs is an effective tool in treating superficial lesions, such as a recurrence of breast cancer on the chest wall or cutaneous lymphomas [23]. Therefore, compared with X-ray photons, TIBS may exploit NPs with a relatively wider range of Z-values to generate nanoradiator doses. Dose-enhancement from the proton-mediated CNR effect was previously reported [24].

Comparison of Traversing Ion Beams With Neutron Beams in BNCT

There was no direct quantitative comparison study between TIBS and BNCT using the same animal model. Neutron beams have a similar depth-dose distribution, including escalation of the entrance dose, with the broad band X-ray photon. Boron compounds in the target can capture neutron beams as X-rays are photoelectrically absorbed in high-Z NPs to enable them to emit electrons. Therefore, the depth-dose is different to that of the ion transmission beam with the Bragg-peak behind the body in which transmission ion fluence is comparable to Bragg-peak and may bring about fundamentally different efficiency and mechanism in interaction with receiving NP to generate dose enhancement. To compare therapeutic efficacy between TIBS and BNCT, it is necessary to prepare the same size of an NP sample in the same disease model under the same irradiation dose. This study will be performed in collaboration with a Japanese group in the near future.

In general, an ion beam is efficient and convenient at delivering to the target due to the charged particles being

comparable with neutron particles. Moreover, preparation for molecular targeting of high-Z NP in TIBS is relatively well-established compared with targeting a boron compound in BNCT. However, a specific molecular probe is required for each disease in TIBS. TIBS is just emerging and is subject to repeated study from other groups for further evaluation.

Prospective Medical Application of TIBS With a Targeted High-Z Prodrug

In a clinical setting, ion beam energy is preferred, as it ensures accurate transmission to the target within the body. As proton energy modulates electron emission from NP [24], optimized energy is preferable to maximize dose enhancement at the target.

Because ion beam stimulation selectively activates NPs while saving NT, it is possible to treat multiple pathologic lesions that are mixed with or disseminated into NT, such as infiltrative tumors, multiple cancer metastases, brain cancer in sensitive regions, vulnerable plaque or thrombosis in atherosclerotic blood vessels, neoangiogenesis-derived retinal diseases, and amyloid plaques in neurodegenerative diseases. All these pathologic hallmarks have previously been beyond the indications for conventional radiotherapy, including proton treatment, or surgical intervention. We demonstrated the feasibility of TIBS in animal models of these diseases with successful treatment in prior studies [7, 12, 14, 25] and with the proposed targeted NPs in the present study, as shown in **Figures 2–4**. In a tumor model [7, 12], we have shown that complete regression of small-sized tumors can be achieved by only proton-TIBS with a 5–10 Gy entrance dose under a given IV injection of iron oxide or gold NPs (100–300 mg/kg) without using BPD. Multiple small nodule-like lesions scattered in NT often have been encountered in various invasive cancers or in recurrences in adjacent critical function organs.

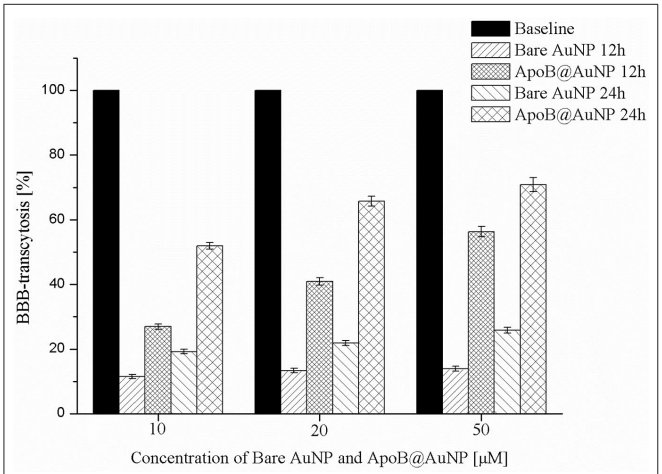

FIGURE 2 | The results of TEER test of ApoB@AuNP. BBB crossing was increased in NP in a dose-dependent manner and enhanced more than two times compared with bare gold nanoparticles, suggesting LDLR-based transcytosis.

In a carotid arterial thrombus mouse model [14], we delivered 100 mg/BW iron oxide NPs via intravenous thrombus-derived obstruction in the affected carotid artery prior to single TIBS with a 2–4 Gy entrance dose.

Flow recovery was observed only in CNR-treated mice, with >50% removal of the thrombus, without damaging the vascular endothelium. A 2.5-fold greater reduction in thrombus-enabled flow recovery was observed in the CNR group than in the proton-only control groups ($p < 0.01$, 14). In a transgenic AD mouse model [25], we submitted the results of the study to a separate journal for publication. Taken together, the results of the proof-of-concept studies suggest the feasibility of TIBS for overcoming the challenges of treating infiltrative brain tumors, ruptured vulnerable plaques with thrombosis, or diabetic macular edema (DME)-associated retinal vein occlusion (RVO).

In an F98 infiltrative glioma rat model, we administered blood-brain barrier (BBB)-permeable and glioma-targeting LDLR-receptor-binding ApoB@AuNPs-Cy5 intravenously 24 h prior to proton-TIBS. The result of the TEER test demonstrated an enhanced efficiency in BBB crossing of APoB@AuNP compared with bare AuNP as shown in **Figure 2**. Red fluorescence of cyanine indicated delivery of NPs to both the

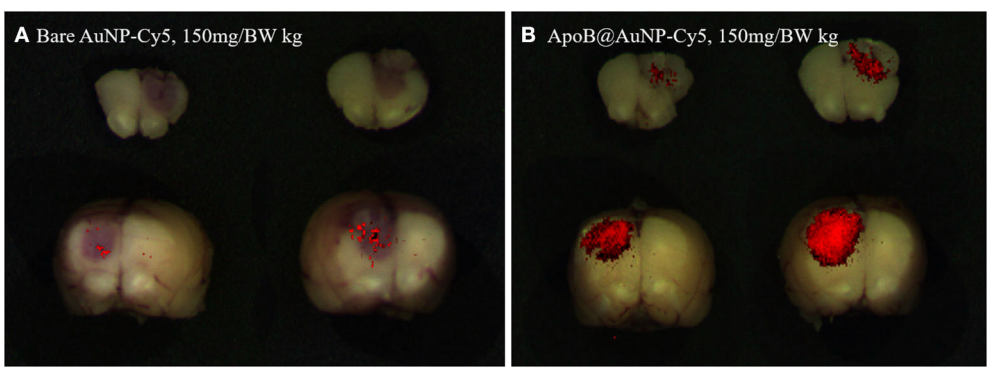

FIGURE 3 | Fluorescence imaging of AuNP-Cy5 **(A)** and ApoB@AuNP-Cy5 **(B)** that were taken up in glioma target at 24 h after IV injection of 150 mg/BW kg in glioma model. Much larger targeted-NP was taken up in the glioma mass compared with bare NP.

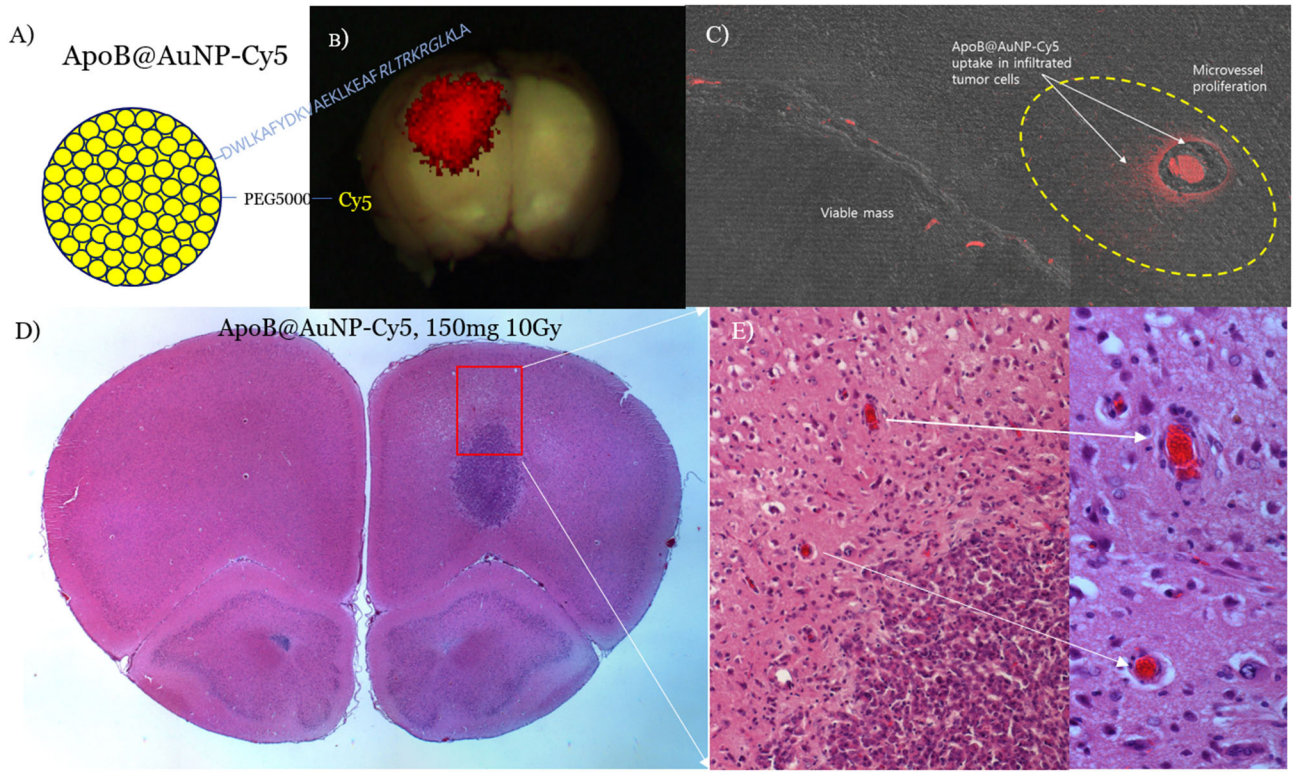

FIGURE 4 | ApoB@AuNPs-Cy5 were synthesized by conjugating a thiolated ApoB peptide and quenching-free SH-PEG5000-Cy5.5 to 10 nm AuNPs **(A)**. Red fluorescence of LDLR-targeting ApoB@AuNPs-Cy5 showed crossing of the BBB and preferential uptake in the main mass (BBB-disrupted, 24 h after iv) **(B)** and infiltrative microvessel proliferation (MVP) in the BBB-intact control (3 days after iv) **(C)** in the F98 glioma rat model. Single 10 Gy proton-TIBS demonstrated a reduction in MVP and removal of infiltrated cancer cells along the microvessel **(D,E)**.

main mass and infiltrative microvessel proliferation (MVP), as shown in **Figures 3**, **4B,C**, suggesting BBB crossing. Fluorescence imaging of molecular targeted ApoB@AuNPs-Cy5 demonstrated an uptake 11 times larger in the glioma target compared with non-targeted bare gold NP as shown in **Figure 2**. All rats presented appropriate MVP surrounding the glioma tumor mass. MVP was controlled in a dose-dependent manner; two were completely responsive (CR), and one had partial regression (PR) in 10 Gy-treated rats, in 5 Gy-treated rats, one was CR and two were PR. Proton-TIBS with an entrance dose of 10 Gy yielded an absence of cancer cells along the microvascular endothelium in **Figures 4D,E**. MVP was distributed in the surrounding NT where the BBB was intact in contrast to areas where the BBB was ruptured in the main tumor mass. Therefore, this result suggested that ApoB@AuNPs-Cy5 crossed the BBB since overexpression of LDLR was observed in both BBB and glioma cells.

Due to the fact that activated macrophages are taken up in vulnerable plaques of atherosclerotic blood vessels, scavenger receptor (SR-A1)-binding PP1-conjugated gold NPs (PP1@AuNPs) (**Figure 5A**) can be taken up by the plaque in a ligated-artery atheroma mouse model (**Figure 5B**). We achieved flow recovery from atheromatous obstruction of blood vessels in all three mice by reducing the plaque with 4-Gy proton-TIBS, as demonstrated in **Figures 4C,D**. Recently, we found thrombolytic fucoidan that activated plasma tPA by binding with the tPA-inhibitor PAI-1, which induced thrombolysis in a thrombosis animal model [26]. We propose thrombus-targeting fucoidan-conjugated iron oxide NPs (TB-fuco@Fe3O4), as shown in **Figure 6A**, to treat DME with RVO or VEGFR-binding Flt1@AuNPs [10] to treat neoangiogenesis-derived age-related macular degeneration (AMD), or diabetic macular retinopathy, as shown in **Figure 5**. Because fucoidan is also known to bind selectively to P-selectin overexpressed in active thrombi [27], TB-fuco@Fe3O4 can be potentially targeted to sites of thrombosis in RVO prior to TIBS, which may induce flow recovery by a combined nanoradiator dose and thrombolytic fucoidan. We tested this hypothesis by TIBS after administration of TB-fuco@Fe3O4 in the same artery ligation atheroma model, where atheroma can often be accompanied by a thrombus, as shown in **Figure 6B**. Proton-TIBS with 4 Gy achieved flow recovery by reducing both the thrombus and atheroma without damaging the normal architecture of the blood vessels, as shown in **Figure 6C**. We also developed VEGFR-binding Flt1@AuNPs-Cy5 that showed VEGFR binding and transcytosis in HRMECs, as shown in **Figures 6D–F**. Fluorescence imaging showed binding of Flt1@AuNPs-Cy5 to VEGFR in the membrane (**Figure 6E**) and subsequent transcytosis (**Figure 6F**). These NPs were proposed to treat AMD or DMR through the ocular DDS system, as reported previously [28], for the treatment

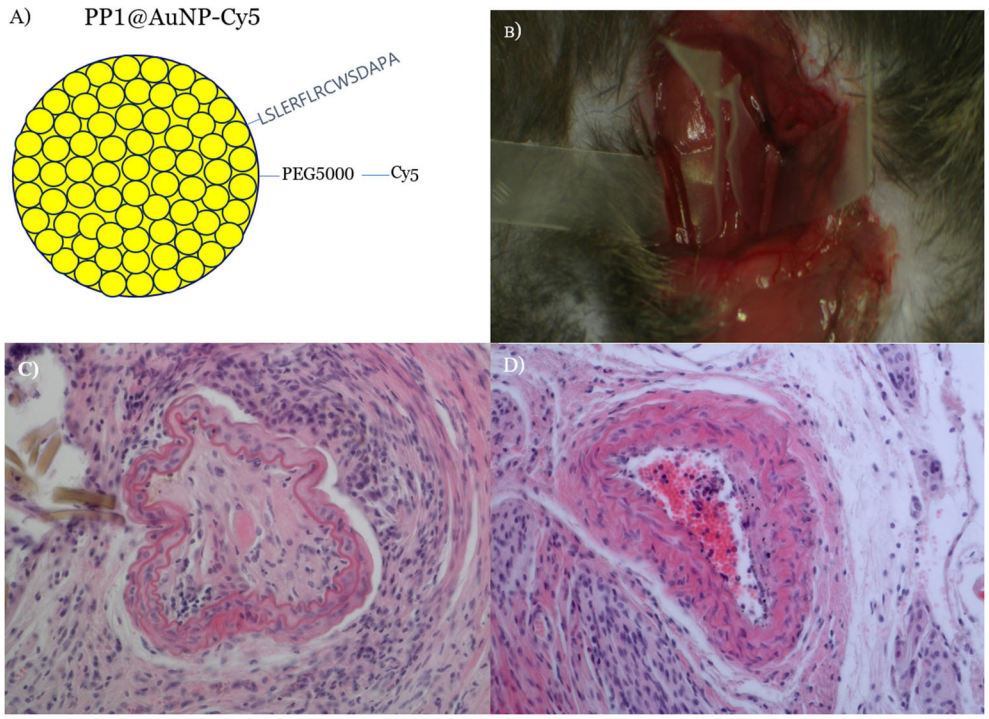

FIGURE 5 | SR-A1-binding PP1@AuNPs were prepared **(A)** and delivered via IV in a carotid artery-ligated atheromatous mouse model **(B)**. Proton-TIBS (4 Gy) induced flow recovery by reducing plaque and preserving the normal structure of blood vessels **(D)** compared with the untreated obstruction control **(C)**. The patency of the blood vessel was checked by a Doppler flow probe [21] and red blood cells were shown due to recovered blood flow in the central part of the treated blood vessel.

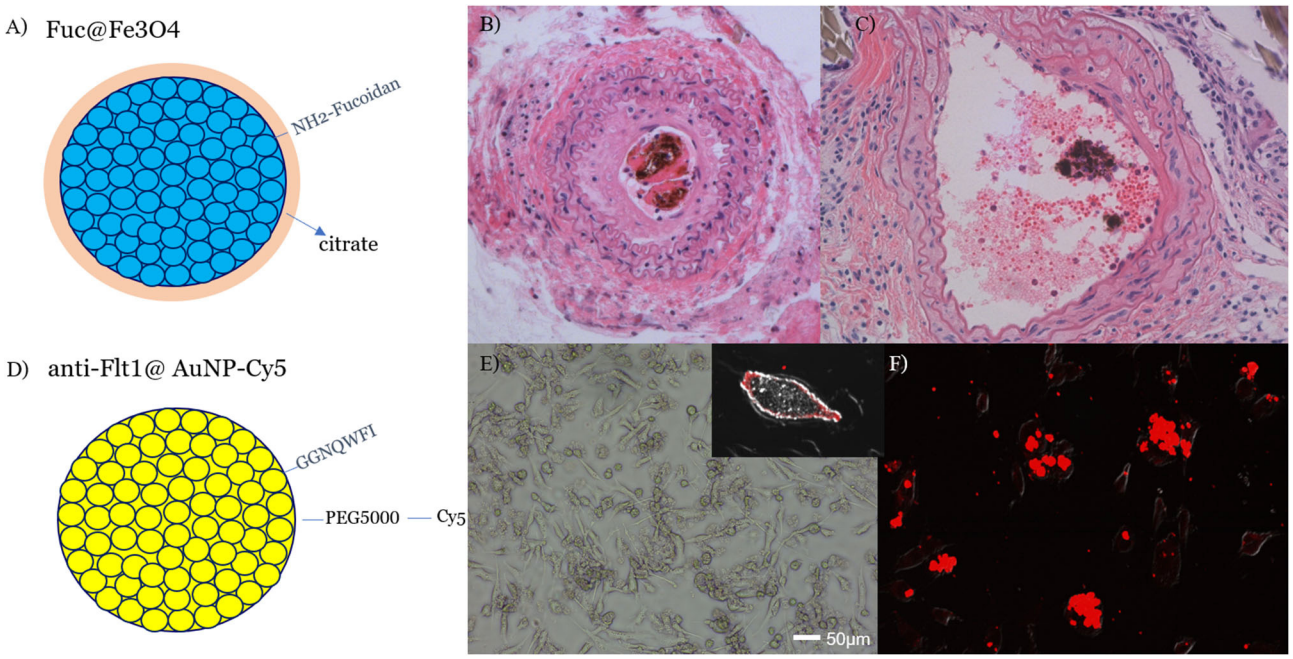

FIGURE 6 | A thrombolytic aminated fucoidan, targeting active thrombi, was conjugated to citrated iron oxide NPs **(A)** and delivered to a carotid artery-ligated and lipid-fed atheromatous mouse model with accompanied thrombosis **(B)**. Next, 4 Gy proton TIBS showed flow recovery and partial removal of both the central thrombus and atheroma **(C)**. Dark materials in **(B,C)** were clusters of iron oxide NP that were taken up in thrombus. Central red blood cells in **(C)** indicated flow-recovery after treatment that was checked by a Doppler flow probe. VEGFR1(Flt1)-binding Flt1@AuNPs-Cy5 were prepared **(D)** and showed receptor binding in the membrane **(E)** and transcytosis in HRMECs **(F)** [21]. TIBS using either Fuc@Fe3O4 or Flt1@AuNPs will be applied to DME/RVO or AMD retinal disease models, respectively.

of abnormal angiogenesis and endothelial cells together using TIBS [10].

Furthermore, TIBS can be easily implemented with high-dose radiotherapy, such as FLASH or microbeam radiotherapy (MRT), which are known to have NT-preserving effects. This combination may greatly enhance therapeutic precision in addition to selective activation of targeted high-Z nanoparticles by TIBS. Overall, TIBS may provide new precision medicine through the development of targeted high-Z NPs; precision is achieved by nano-to-microscale transport of the CNR, with accompanying ROS generation and selective activation of NPs at the target site.

For further development of treatment planning, we aim to develop methodology to calculate the electron emissions from combined Auger cascades and an ICD path from high-Z nanoparticles under TIBS. This may be put into the treatment planning of TIBS in a clinical setting.

DATA AVAILABILITY STATEMENT

The raw data supporting the conclusions of this article will be made available by the authors, without undue reservation.

ETHICS STATEMENT

The animal study was reviewed and approved by Institutional Animal Care and Use Committee of Catholic University Hospital of Daegu.

AUTHOR CONTRIBUTIONS

J-KK designed all the experiments and wrote the manuscript. S-JS carried out the experiments on carotid artery-ligated atheroma model with synthesizing molecular targeting gold nanoparticles. J-GJ carried out the experiment on infiltrative glioma model. All authors contributed to the article and approved the submitted version.

FUNDING

This work was partly supported by the Rare Isotope Science Project of the Institute for Basic Science funded by the Ministry of Science and ICT and NRF of Korea (2013M7A1A1075764).

REFERENCES

1. Newhauser WD, Zhang R. The physics of proton therapy. *Phys Med Biol.* (2015) **60**:R155. doi: 10.1088/0031-9155/60/8/R155
2. Ulmer W, Matsinos E. Theoretical methods for the calculation of Bragg curves and 3D distributions of proton beams. *Eur Phys J Spec Top.* (2011) **190**:1–81. doi: 10.1140/epjst/e2010-01335-7
3. Wälzlein C, Scifoni E, Krämer M, Durante M. Simulations of dose enhancement for heavy atom nanoparticles irradiated by protons. *Phys Med Biol.* (2014) **59**:1441–58. doi: 10.1088/0031-9155/59/6/1441
4. Kim KH, Kim HT, Kim JH, Seo SJ, Chung DS, Kim JK. Investigation of tumor cell cytoxicity from particle induced x-ray emission from 45 MeV proton beam irradiated ferrite nanoparticle. *Int J PIXE.* (2009) **19**:143–55. doi: 10.1142/S0129083509001837
5. Kim HK, Titze J, Schöffler M, Trinter F, Waitz M, Voigtsberger J, et al. Enhanced production of low energy electrons by alpha particle impact. *Proc Natl Acad Sci USA.* (2011) **108**:11821. doi: 10.1073/pnas.1104382108
6. Kim HK, Gassert H, Schoffler MS, Titze JN, Waitz M, Voigtsberger J, et al. Ion-impact-induced interatomic Coulombic decay in neon and argon dimers. *Physical Rev A.* (2013) **88**:042707. doi: 10.1103/PhysRevA.88.042707
7. Kim JK, Seo SJ, Kim HT, Kim KH, Chung MH, Kim KR, et al. Enhanced proton treatment in mouse tumors through proton irradiated nanoradiator effects on metallic nanoparticles. *Phys Med Biol.* (2012) **57**:8309. doi: 10.1088/0031-9155/57/24/8309
8. Barrios R, Skurski P, Simons J. Mechanism for damage to DNA by low-energy electrons. *J Phys Chem B.* (2002) **106**:7991–4. doi: 10.1021/jp013861i
9. Alizadeh E, Orlando TM, Sanche L. Biomolecular damage induced by ionizing radiation: the direct and indirect effects of low-energy electrons on DNA. *Annu Rev Phys Chem.* (2015) **66**:379–98. doi: 10.1146/annurev-physchem-040513-103605
10. Seo SJ, Lee SH, Kim KH, Kim JK. Anti-Flt1 peptide and cyanine-conjugated gold nanoparticles for the concurrent antiangiogenic and endothelial cell proton treatment. *J Biomed Mater Res B Part B.* (2019) **107**:1272–83. doi: 10.1002/jbm.b.34220
11. Soeda S, Ohmagari Y, Shimeno H, Nagamatsu A. Preparation of aminated fucoidan and its evaluation as an antithrombotic and antilipemic agent. *Biol Pharm Bull.* (1994) **17**:784–8. doi: 10.1248/bpb.17.784
12. Seo SJ, Jeon JK, Jeong EJ, Chang WS, Choi GH, Kim JK. Enhancement of tumor regression by coulomb nanoradiator effect in proton treatment of iron-oxide nanoparticle-loaded orthotopic rat glioma model: implication of novel particle induced radiation therapy. *J Cancer Ther.* (2013) **4**:25–32. doi: 10.4236/jct.2013.411A004
13. Nam D, Ni CW, Rezvan A, Suo J, Budzyn K, Llanos A, et al. Partial carotid ligation is a model of acutely induced disturbed flow, leading to rapid endothelial dysfunction and atherosclerosis. *Am J Physiol Heart Circ Physiol.* (2009) **297**:H1535–43. doi: 10.1152/ajpheart.00510.2009
14. Jeon JK, Han SM, Min SK, Seo SJ, Ihm K, Chang WS, et al. Coulomb nanoradiator-mediated, site-specific thrombolytic proton treatment with a traversing pristine Bragg peak. *Sci Rep.* (2016) **6**:37848. doi: 10.1038/srep37848
15. Arami H, Khandhar A, Liggitt D, Krishnan KM. *In vivo* delivery, pharmacokinetics, biodistribution and toxicity of iron oxide nanoparticles. *Chem Soc Rev.* (2015) **44**:8576. doi: 10.1039/C5CS00541H
16. Carnovale C, Bryant G, Shukla R, Bansal V. Gold nanoparticle biodistribution and toxicity: role of biological corona in relation with nanoparticle characteristics. In: Rai M, Shegokar R, editors. *Metal Nanoparticles in Pharma.* Cham: Springer (2017). pp. 419–36.
17. Almeida JP, Chen AL, Foster A, Drezek R. *In vivo* biodistribution of nanoparticles. *Nanomedicine.* (2011) **6**:815–35. doi: 10.2217/nnm.11.79
18. Mutlu H, Geiselhart CM, Barner-Kowollik C. Untapped potential for debonding on demand: the wonderful world of azo-compounds. *Mater Horiz.* (2018) **5**:162–83. doi: 10.1039/C7MH00920H
19. Montenegro M, Nahar SN, Pradhan AK, Huang K, Yu, Y. Monte Carlo simulations and atomic calculations for auger processes in biomedical nanotheranostics. *J Phys Chem A.* (2009) **113**:12364–9. doi: 10.1021/jp905323y
20. Seo SJ, Kim TJ, Hyodo K, Zaboronok A, You H, Peach K, et al. Enhanced generation of reactive oxygen species by the nanoradiator effect from core-inner shell photo-excitation or proton impact on nanoparticle atomic clusters. *Radiat Environ Biophys.* (2015) **54**:423–31. doi: 10.1007/s00411-015-0612-7
21. Hainfeld JF, Slatkin DN, Smilowitz HM. The use of gold nanoparticles to enhance radiotherapy in mice. *Phys Med Biol.* (2004) **49**:N309–15. doi: 10.1088/0031-9155/49/18/N03
22. Jafari S, Cheki M, Tavakoli MB, Zarrabi A, Ghazikhanlu Sani K, Afzalipour R. Investigation of combination effect between 6 MV X-ray radiation and polyglycerol coated superparamagnetic iron oxide nanoparticles on U87-MG cancer cells. *J Biomed Phys Eng.* (2020) **10**:15–24. doi: 10.31661/jbpe.v0i0.929

23. Choi GH, Seo SJ, Kim KH, Kim HT, Park SH, Lim JH, et al. Photon activated therapy (PAT) using monochromatic Synchrotron x-rays and iron oxide nanoparticles in a mouse tumor model: feasibility study of PAT for the treatment of superficial malignancy. *Radiat Oncol.* (2012) **7**:184. doi: 10.1186/1748-717X-7-184
24. Seo SJ, Jeon JK, Han SM, Kim JK. Reactive oxygen species-based measurement of the dependence of the Coulomb nanoradiator effect on proton energy and atomic Z value. *Int J Radiat Biol.* (2017) **93**:1239. doi: 10.1080/09553002.2017.1361556
25. Kim JK, Jeon JG, Chang WS, Choi YS. Proton stimulation targeting Aβ plaque-associated magnetite reduces both iron redox toxicity and the plaque burden and improves cognitive function in an Alzheimer's disease mouse model (2020).
26. Choi YS, Min SK, Usoltseva R, Silchenko A, Zvyagintseva T, Ermakova S, et al. Thrombolytic fucoidans inhibit the tPA-PAI1 complex, indicating activation of plasma tissue-type plasminogen activator is a mechanism of fucoidan-mediated thrombolysis in a mouse thrombosis model. *Thromb Res.* (2018) **161**:22–5. doi: 10.1016/j.thromres.2017.11.015
27. Rouzet F, Bachelet-Violette L, Alsac JM, Suzuki M, Meulemans A, Louedec L, et al. Radiolabeled fucoidan as a p-selectin targeting agent for *in vivo* imaging of platelet-rich thrombus and endothelial activation. *J Nucl Med.* (2011) **52**:1433–40. doi: 10.2967/jnumed.110.085852
28. Wang C, Seo SJ, Kim JS, Lee SH, Jeon JK, Kim JW, et al. Intravitreal implantable magnetic micropump for on-demand VEGFR targeted drug delivery. *J Control Rel.* (2018) **283**:105–12. doi: 10.1016/j.jconrel.2018.05.030

Conflict of Interest: The authors declare that the research was conducted in the absence of any commercial or financial relationships that could be construed as a potential conflict of interest.

frontiers in Physics

ORIGINAL RESEARCH
published: 11 September 2020
doi: 10.3389/fphy.2020.00374

Transforming an IORT Linac Into a FLASH Research Machine: Procedure and Dosimetric Characterization

Giuseppe Felici[1], Patrizio Barca[2], Salvatore Barone[1], Eleonora Bortoli[2], Rita Borgheresi[2], Silvia De Stefano[1], Massimo Di Francesco[1], Luigi Grasso[1], Stefania Linsalata[2], Daniela Marfisi[2], Matteo Pacitti[1] and Fabio Di Martino[2]**

[1] R&D Department, Sordina IORT Technologies, Aprilia, Italy, [2] U.O. Fisica Sanitaria, Azienda Universitaria Ospedaliera Pisana, Pisa, Italy

Since Favaudon's paper of 2014, there has been an increasing interest in FLASH radiotherapy. The FLASH modality could represent a breakthrough in radiation oncology; nevertheless, it brings new scientific and technological challenges. Currently, one of the main limits the scientific community has to cope with is the lack of a common technological platform to experiment with. Considering this framework, the possibility of readapting existing linac platforms to produce a FLASH beam is particularly attractive and different attempts have been already made. The purpose of this article is to illustrate how it is possible to transform a dedicated Intra Operative Radio Therapy (IORT) mobile linac into a FLASH research machine. Compared to the modification required by a standard medical linac, such transformation is easier, does not affect the machine settings and can be rapidly performed by the final user. NOVAC 7 is an IORT linac which can reach a maximum dose-per-pulse up to 13 cGy/pulse (average dose rate 39 Gy/min); such dose rate can be significantly increased by modifying the collimation system.
Four different Source Surface Distance (SSD) can be obtained:

- Clinical reference configuration;
- Upper applicator only (SSD 50 cm);
- Monitor chambers housing only (SSD 7 cm);
- Dismounted monitor chambers (SSD 1.6 cm).

The fourth configuration allows reaching values of dose-per-pulse up to around 18 Gy/pulse and dose rates up to around 500 Gy/s, at a Pulse Repetition Frequency (PRF) of 30 Hz. The other three configurations can be obtained without using any tool and without changing NOVAC settings, until reaching a FLASH dose rate in the third configuration. For FLASH configurations, relative and absolute dosimetric characterization of the beam were performed using radiochromic films EBT3. NOVAC7 transformed in FLASH mode can be used both for dosimetric testing and characterization of detectors and for radiobiological studies on cells and organoids, offering a wide range of dose-per-pulse, from 3 cGy/pulse up to 18 Gy/pulse; dose rates correspondingly change from 3 cGy/s up to 540 Gy/s.

Keywords: FLASH, high dose-per-pulse, electron beam, Novac, IORT

OPEN ACCESS

Edited by:
Vincenzo Patera, Sapienza University of Rome, Italy

Reviewed by:
Till Tobias Böhlen, Centre Hospitalier Universitaire Vaudois (CHUV), Switzerland
Lorenzo Nicola Mazzoni, Careggi University Hospital, Italy

****Correspondence:***
Giuseppe Felici
giuseppe.felici@sordina.com
Fabio Di Martino
f.dimartino@ao-pisa.toscana.it

Specialty section:
This article was submitted to Medical Physics and Imaging, a section of the journal Frontiers in Physics

Received: *04 June 2020*
Accepted: *31 July 2020*
Published: *11 September 2020*

Citation:
Felici G, Barca P, Barone S, Bortoli E, Borgheresi R, De Stefano S, Di Francesco M, Grasso L, Linsalata S, Marfisi D, Pacitti M and Di Martino F (2020) Transforming an IORT Linac Into a FLASH Research Machine: Procedure and Dosimetric Characterization. Front. Phys. 8:374. doi: 10.3389/fphy.2020.00374

INTRODUCTION

The FLASH effect in radiotherapy is a radiobiological effect characterized by a loss of radiobiological effectiveness (RBE) on healthy tissue and an unaltered therapeutic efficacy on tumor tissue; this effect is obtained by delivering the entire therapeutic dose in a very short time, <100 ms with a dose rate above 40 Gy/s [1, 2]. The experimental evidences of the FLASH effect were obtained *in vivo*, using 4–6 MeV energy electron beams, and the robustness of these results are validated by the fact that they were reproduced in various animal models (mice, rat, zebrafish, pig, cats), in various organs (lung, skin, gut, brain) and by various radiobiology researchers [1–8]. These evidences aroused considerable interest in the radiotherapy community, due to the possible clinical implications [9, 10].

However, for a possible clinical use of the FLASH effect, several issues must be addressed and understood. The radiobiological mechanism underlying the FLASH effect is still unknown: oxygen consumption has been proposed as a possible solution but other works highlighted how this mechanism, probably, cannot be considered the only one [11–15].

Additionally, the dependence of the FLASH effect on some parameters characterizing the radiation beam are not fully known: only the dependences on the average dose-rate and on the duration of the entire irradiation have been clearly observed so far. The role of dose-per-pulse, instantaneous dose-per-pulse (i.e., dose-per-pulse divided by pulse duration), pulse duration and frequency still remain to be entirely understood [1–3, 9].

Finally, the dosimetric problems related to the response of the on-line dosimeters to these dose-per-pulse values (saturation problems) are important and completely new to scientific community; this aspect causes difficulties in monitoring the stability of the beam output and in the accuracy of the dosimetric measurements. Even though many issues related to FLASH remain to be understood, such effect was observed only for average dose rates above 40 Gy/s. In the following, "FLASH dose rate" or "FLASH beam" will indicate beams with average dose rate above such threshold.

Because of this scenario, it would be important to increase the number of centers where a technology capable of delivering FLASH beam is available and where researchers can study the FLASH mechanisms. Up to now, all experimental data have been obtained either by using re-adapted standard medical linac [16] or using industrial machines [17–19].

This work shows how an accelerator dedicated to IORT (Novac7, SIT, Aprilia, Italy) can be set up to obtain different dose-per-pulse regimes and, consequently, dose-rates; in particular, two of these configurations allow to obtain FLASH beams. Such configurations were characterized by means of Gafchromic EBT3 films [20]. EBT3 were chosen because of their excellent spatial resolution, dose-rate (dose-per-pulse) independence [21–24] and energy independence for photon and electron beams above hundreds of keV [21, 25].

Radiochromic films [20] provide absolute measurements of absorbed dose to water after conversion of the film response by means of an accurate calibration procedure to be determined for any specific radiochromic film dosimetry system, which consists in the combination of the film model and the densitometer, usually a flat-bed scanner, together.

Few studies investigated the dose-rate and dose-per-pulse dependence of radiochromic films [21, 22, 24]; however they all agree in reporting small or negligible dependence in their response with respect to both variables. At the dose-rate values of conventional clinical linacs, with a dose-per-pulse up to 1×10^{-3} Gy/pulse, Borca et al. [21] reported, for EBT3 radiochromic film, a dose-rate dependence in the range of 0.1–0.6 Gy/min within 1% for 6 and 15 MV photon beams. Jaccard et al. [22] reported, for conventional linac electron beams of 4, 8, and 12 MeV and EBT3, negligible variation in the range of 0.6–4.4 Gy/min.

Karsch et al. [23] reported, for a 20 MeV electron beam (5 ps pulse width) from the superconductive linear accelerator ELBE, a EBT radiochromic film dependence with respect to the dose-per-pulse of 2% up to about 2×10^{-2} Gy/pulse and within 5% up to about 7.5×10^{-2} Gy/pulse.

Jaccard et al. [22] also investigated the usability of Gafchromic EBT3 as reference dosimeters for an Oriatron eRT6 electron linac and concluded that EBT3 films are dose-per-pulse independent between about 4×10^{-3} Gy/pulse and 18 Gy/pulse.

Dosimetric and geometric properties of the beams obtained in the two FLASH NOVAC configurations have been evaluated in terms of dose to the build-up, dose at different depths and transversal dose profiles. These results can be useful to all NOVAC7 users, to design radiobiological experiments and/or study the response of the various dosimeters to FLASH dose-rate values. It is interesting to remind that, before the FLASH promises attracted the attention of scientific community, IORT linacs represented a challenge both from the dosimetric [26–31] and radiobiological point of view [32].

MATERIALS AND METHODS

Radiochromic Films Calibration

For calibration purposes, Gafchromic EBT3 film samples of 5×5 cm^2 were irradiated using a Varian Clinac DHX-S (Varian Medical Systems, Palo Alto, CA), with a 6 MeV electron beam. The electron beam was previously calibrated in water, following the IAEA TRS 398 protocol guidelines [33] using a Roos reference chamber [34] at SSD = 100 cm and an applicator of 20×20 cm^2. The films were irradiated in the same set-up except for the material, a Plastic Water® phantom, at the equivalent z_{ref} depth in Plastic Water®, calculated as suggested by the IAEA TRS 398 protocol [33]. In order to obtain a calibration curve, the films were exposed, as described before, in a dose range from 2 to 20 Gy, with steps of 2 Gy. The post irradiation readings were made after 48 h. A black cardboard template was fitted into the scanner to ensure the reproducibility of the film positioning on the central location of the scan surface. The films were scanned after a 15 min warm-up time of the flatbed scanner and 3 empty scans to stabilize it. Films were acquired in transmission mode with all the image enhancement filters turned off, with a resolution of 127 dpi and at 48-bit RGB (Red, Green, Blue, 16 bits per channel). All of them were scanned

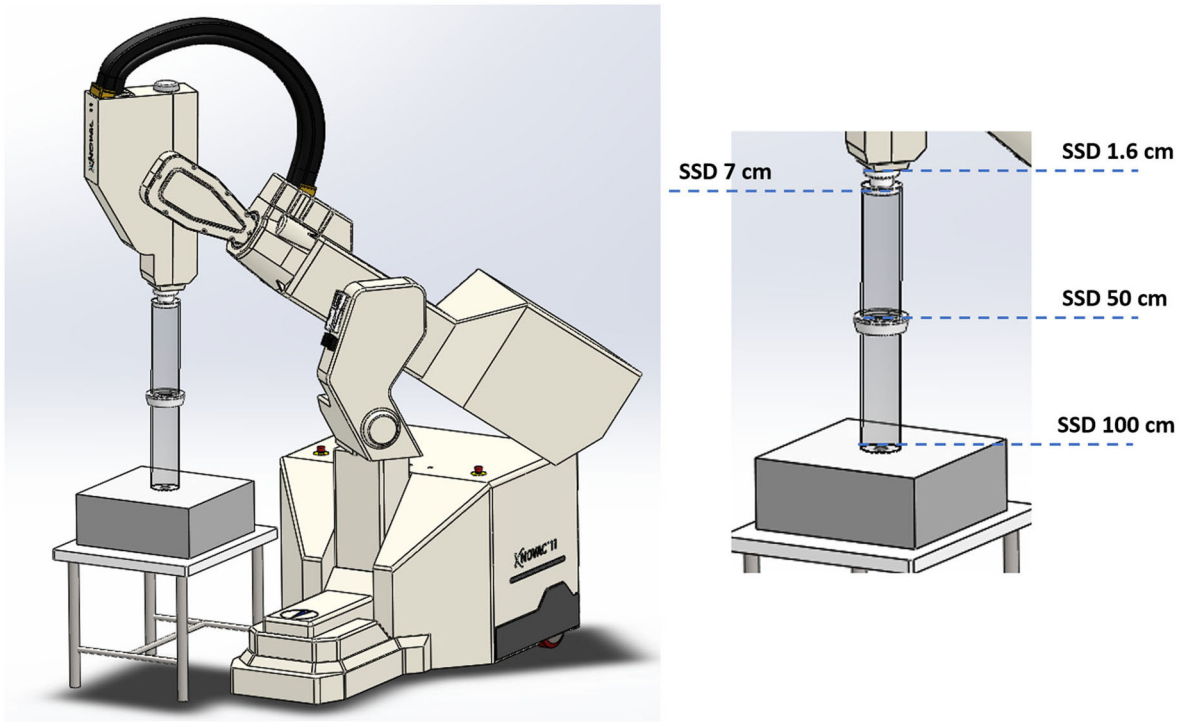

FIGURE 1 | Four collimation configurations obtained acting on Novac7 collimation system architecture.

in portrait orientation, i.e., the side of the 5 × 5 cm^2 film sample corresponding to the long edge of the original film was positioned along the scanning direction. The images were saved in TIFF format.

A 2D Wiener filter was applied to both pre- and post-irradiation images, as suggested in [35]. The aforementioned protocol was used to obtain for each film sample the average net optical density $\overline{netOD}$, which is the difference between the irradiated and unirradiated optical density, over five 6 × 6 mm^2 ROI (Region of Interest) positioned around the center of the radiation field. For each film sample the absorbed dose to water, D, measured with the ionization chamber, was plotted vs. the corresponding average $\overline{netOD}$ for the Red channel. The calibration curve was determined by fitting the experimental data through the following equation:

$$D = a \cdot \overline{netOD} + b \cdot \overline{netOD}^{n} \quad (1)$$

where *a*, *b,* and *n* are the fitting parameters. All the analysis was performed using home-made scripts in MATLAB R2018a environment (MathWorks, Natick, MA, USA). The dose curves fitting procedure was performed in two steps, following the method described in [35], which suggested to fix the parameter *n* after the first procedure to reduce the fitting uncertainty. Hence, once fixed *n,* a second fitting procedure was carried out, obtaining new values for the parameters *a* and *b* with their corresponding uncertainties.

NOVAC7

FLASH irradiations were performed using the IORT NOVAC7 (SIT, Aprilia, Italy) accelerator [36].

NOVAC7 provides four nominal electron energies (3, 5, 7, and 9 MeV) and the electron beam collimation system is purely passive; NOVAC7 does not use any scattering foil for beam broadening. The collimation system consists of polymethylmethacrylate (PMMA) cylindrical applicators that can be directly attached to the radiant head. The applicator is made of two parts: an upper part called applicator holder or upper applicator—directly mounted to the radiant head- and the terminal part called terminal applicator, which is connected to the upper applicator by means of a ring nut. The PMMA wall of the applicator is 5 mm thick, the internal diameter ranges from 4 to 10 cm and the very end of the terminal can be flat or beveled. The length of the applicators determines the SSD, which is 100 cm for the reference applicator with a diameter of 10 and 80 cm for the others. Thanks to this relatively simple architecture, it is possible to obtain several collimation configurations (**Figure 1**). Every configuration lead to a different SSD and, consequently, to a different resulting dose-per-pulse. The measurements were performed using the nominal energy of 7 MeV, which is the most used in the clinical practice and the closest to the electron energies for which the experimental FLASH effects were highlighted.

It is well worth underlying that, in general, the average dose-rate DR generated by a pulsed electron beam is directly

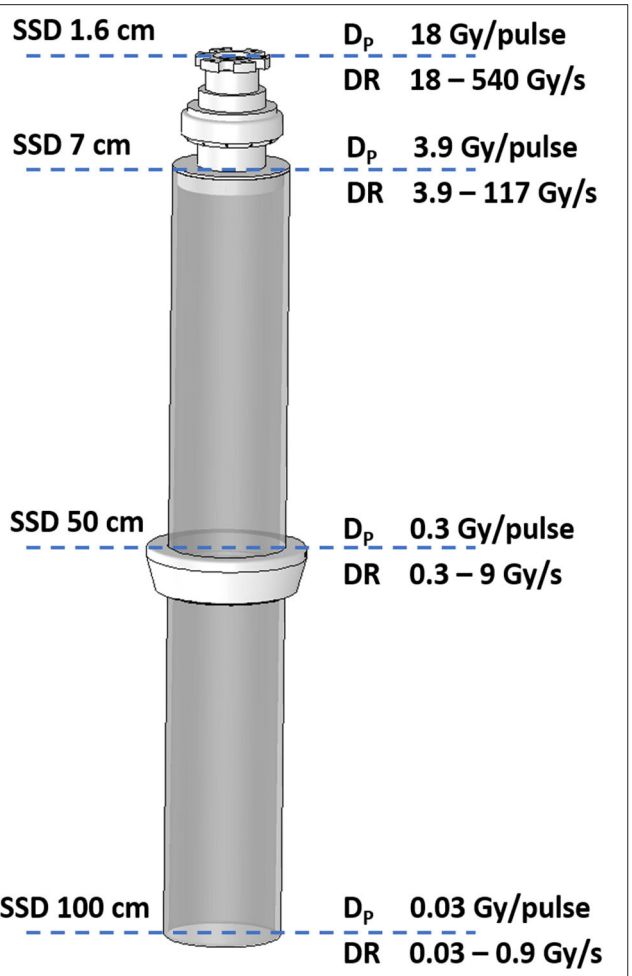

FIGURE 2 | Detail of collimator with the indications of the four SSD and the corresponding possible maximum achievable dose-per-pulse (D_p) and dose rate (DR) for the 7 MeV e-beam.

proportional to the dose-per-pulse D_p

$$DR = PRF \cdot D_p \tag{2}$$

where PRF is the pulse repetition frequency. The instantaneous dose rate IDR (or dose rate within pulse) is obtained dividing the dose-per-pulse D_p by the pulse length Δt. For the NOVAC Δt is about 2.5 μs, its IDR can be easily calculated as

$$IDR \cong 4 \cdot 10^5 D_p \tag{3}$$

Due to the relatively low PRF (5 Hz in Clinical mode, up to 30 Hz in Service mode), dose rate is not extremely high; nevertheless, the dose-per-pulse can reach very high values.

Measurements

The different setups were obtained as follows:

(1) Clinical reference configuration: (SSD 100 cm);
(2) Upper applicator connected to the monitor chambers housing (SSD 50 cm);
(3) Monitor chambers housing only (SSD 7 cm);
(4) Dismounted monitor chambers (SSD 1.6 cm).

NOVAC 7 monitor chambers behavior remains unaffected in configurations 1, 2, and 3 (short term stability better than 0.5%); in the fourth configuration instead, NOVAC can be operated only setting the number of pulses to be delivered. In **Figure 2** such configurations, together with the possible maximum achievable dose-rates, are detailed. For all four configurations, the maximum dose-per-pulse value on the central axis of the beam in equivalent water phantom was measured, while for the last two configurations, being the only ones reaching FLASH values (called FLASH1 and FLASH2, corresponding to SSD of 7 and 1.6 cm, respectively), depth-dose measurements and dose profiles were also performed. The experimental setup used to characterize the beam in these two operating modes is shown in **Figure 3**. In order to characterize the beam in terms of dose-per-pulse and depth-dose curve, the radiochromic films were inserted perpendicularly to the electron-beam axis between Plastic Water® slabs at different depths for the first (1) and second (2) FLASH regimen, as reported in **Table 1**. Then, the accelerator head was put in contact with the first slab (see **Figure 3**, on the right).

Given the short distance between the first Plastic Water® layer and the beam exit window, it was possible to center the films manually with great accuracy. Moreover, the instantaneous darkening after the irradiation provided the possibility of an immediate check of the correct positioning.

The dimensions of films (5 × 5 cm^2) were suitable to include all the useful beam considering its broadening in depth. All the irradiations were performed using the nominal energy 7 MeV and delivering, for each point of measure, a total dose between 10 and 20 Gy. The total number of pulses delivered was changed according to the specific set-up, ranging from 400 pulses in clinical configuration down to just one pulse in FLASH 2 mode.

The radiochromic films irradiated with FLASH beams were read after 48 h through the same reading procedure adopted for their calibration.

To determine the amount of dose delivered in each image pixel of the films, the $netOD_i$ for the i-th pixel was calculated [according to Equation (1)], then it was converted in dose using the calibration curve. Thus, the distribution of dose in the transverse plane was obtained at each depth for each FLASH condition.

A series of dose profiles were extracted from the above-mentioned dose maps for each measurement depth. The central region of each map was considered and the dose values of eight consecutive horizontal/vertical lines were averaged pixel by pixel to obtain the final dose profiles along the horizontal/vertical direction (thereinafter *x* and *y*).

To provide an estimation of the beam size, the Full Width at Half Maximum (FWHM) of the curves was used. All the profiles were fitted with a Gaussian function (Gaussian fits were performed by using Matlab R2018a fit tools), as shown in **Figures 6**, **7**.

FIGURE 3 | Schematic view of the experimental set-up. On the left, the set-up with the accelerator head. On the right, the configuration during the irradiation (notice the proximity between beam window exit and the Plastic Water® slabs).

TABLE 1 | Film positions at different depth for the two FLASH configurations.

FLASH beam 1 depths [mm]	0	6	10	15	20	25	30	
FLASH beam 2 depths [mm]	0	6	11	13	15	17	22	32

The beam profiles were exploited to choose the ROI size for dose calculation as a compromise between two conflicting requirements: a larger ROI size allows to reduce the statistical error, while a smaller ROI increases the dose distribution uniformity. To preserve such advantages by minimizing the above-mentioned trade-off, ROI sizes variable with depth were adopted. In particular, ROI size was chosen in order to guarantee dose values fluctuation lower than 2% inside. The average dose delivered inside these ROIs is used to calculate the corresponding dose-per-pulse value.

Depth-dose curve was obtained from the depth-dose distribution and the depth corresponding to the 50% of the maximum absorbed dose, R_{50}, was evaluated.

RESULTS

Dose-Response Curves for EBT3 Calibration

The dose values plotted as function of the netOD are shown in **Figure 4**, together with the fitting curve calculated with the parametrization given in Equation (1). The corresponding fitting parameters are a = 14.07 ± 0.04 Gy, b = 52 ± 2 Gy, and $n = 3.45$.

FLASH Beams Characterization

Figure 5 shows the relative dose distributions measured in the two operating modes: FLASH beam 1 on the left and FLASH beam 2 on the right. The dose distribution measured on the film is not uniform in the radial direction.

The profiles measured at each depth are presented in **Figure 6** (FLASH beam 1) and in **Figure 7** (FLASH beam 2). As confirmed by R^2 values reported in the figures, the profiles are well-approximated by a Gaussian curve except for the FLASH beam 2 profiles close to phantom surface ($R^2 < 0.99$).

The beam profiles along the x and y axes are reported in **Figures 6**, **7** as function of the depths. The beam becomes significantly narrower when removing the monitor chamber, providing the smallest FWHM (**Figure 7**). Furthermore, the beam size increases with increasing depth in both irradiation modes, although the dependency from the measurement depth is not the same for the two cases (**Figure 8**).

The different width of the beam in the two configurations is due to both the different distance and the presence/absence of the two monitor chambers. A NOVAC7 monitor chamber basically consists of two aluminum electrodes, each 0.02 mm thick behaving as a thin scattering element [28].

The depth-dose distributions measured in the Plastic Water® phantom are shown in **Figure 9** for the two FLASH regimens. The maximum dose-per-pulse values and their relative errors obtained from **Figure 9** are presented in **Table 2**. The highest dose-per-pulse value is reached without monitor chamber (FLASH beam 2). In **Table 2**, the R_{50} calculated from the dose deposition curves are presented.

The uncertainty associated to dose measurements is 3% at SSD 100 cm, where the dose is measured by means of ionization chamber [26–28, 31] and 5% for all other points, where EBT3 are used. EBT3 tends to underestimate dose deposition when beam energy is below few tenths of keV [25]; therefore a higher uncertainty affects surface dose measurements. However, due to the very limited range of such electrons, this effect can be

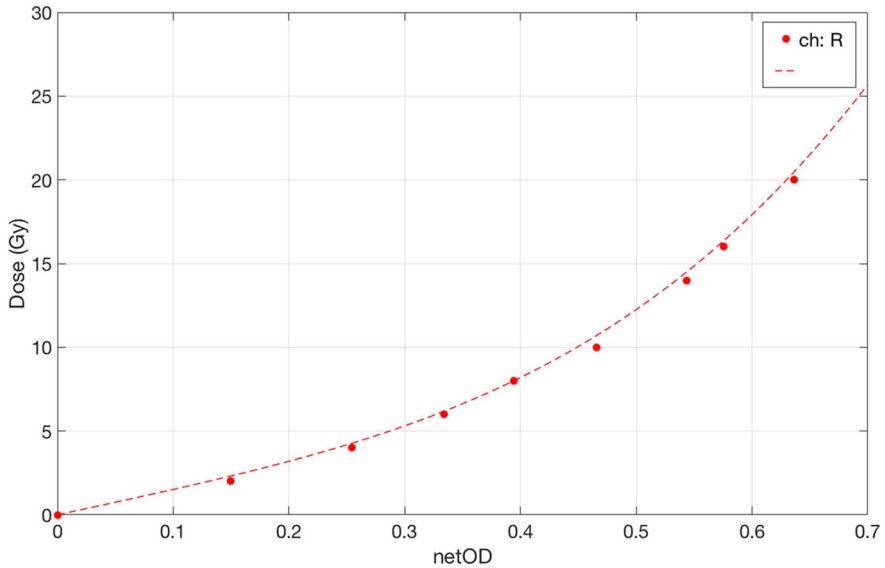

FIGURE 4 | Dose-response curve of EBT3 under conventional dose-rate irradiation with 6 MeV electrons in the range 0–20 Gy. The fit curve is plotted as dotted line.

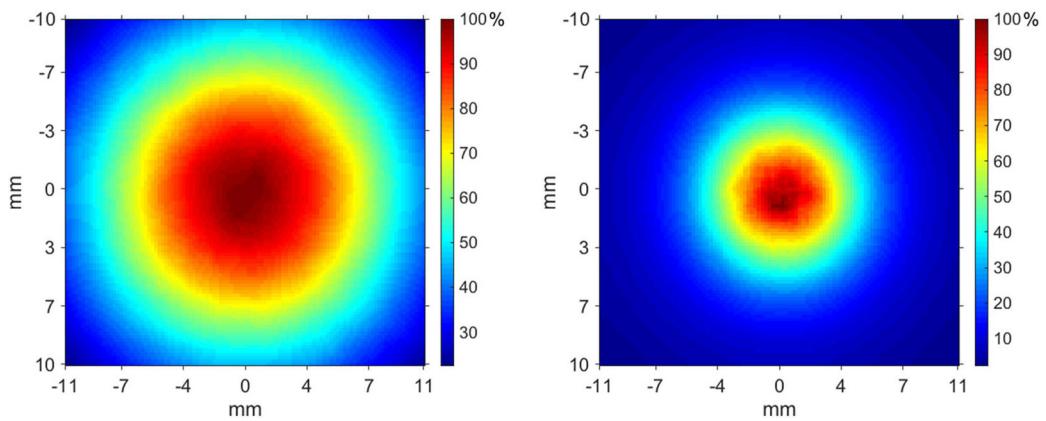

FIGURE 5 | Transverse dose distribution measured at 6 mm in Plastic Water® slabs—FLASH beam 1 (left), FLASH beam 2 (right).

considered negligible beyond 2–3 mm, and, consequently, it does not affect build-up measurements reported in **Table 2**.

DISCUSSION AND CONCLUSION

Currently, the two centers that published most of the FLASH results, Marie Curie Institute in Paris and University of Lausanne, adopted Kinetron and Oriatron, respectively, linacs originally designed for industrial use [1–3, 5, 7–9, 17–19].

Another possible solution is described in [16], where a procedure for modifying a standard clinical linac in order to get a FLASH beam is illustrated.

Several research groups are working to build a dedicated FLASH machine; not only electron based machines [37] are considered, but also linacs for X-ray [38] or proton accelerators [39]. The concept of PHASER [38] is particularly interesting, but its feasibility remains extremely challenging both from the clinical and the technological point of view. Clinical difficulties related to "FLASH IMRT" are discussed in [40]; furthermore, the generation of a X-ray beam capable of reaching FLASH dose rate requires at least four times the electron current needed for linac working in electron mode [refer to NIST data [41] for Bremsstrahlung efficiency]. On the other hand, the effective implementation of FLASH with proton is feasible, even though it also poses several technological issues. However, the maximum dose rates achievable are significantly lower respect to electron based linacs, and many issues, in particular those related to real time beam monitoring, remain unsolved (Jolly et al. unpublished).

In this context, the possibility of expanding the number of researchers who can experiment with a FLASH beam may represent a crucial element for speeding up and validating the understanding of all phenomena involved.

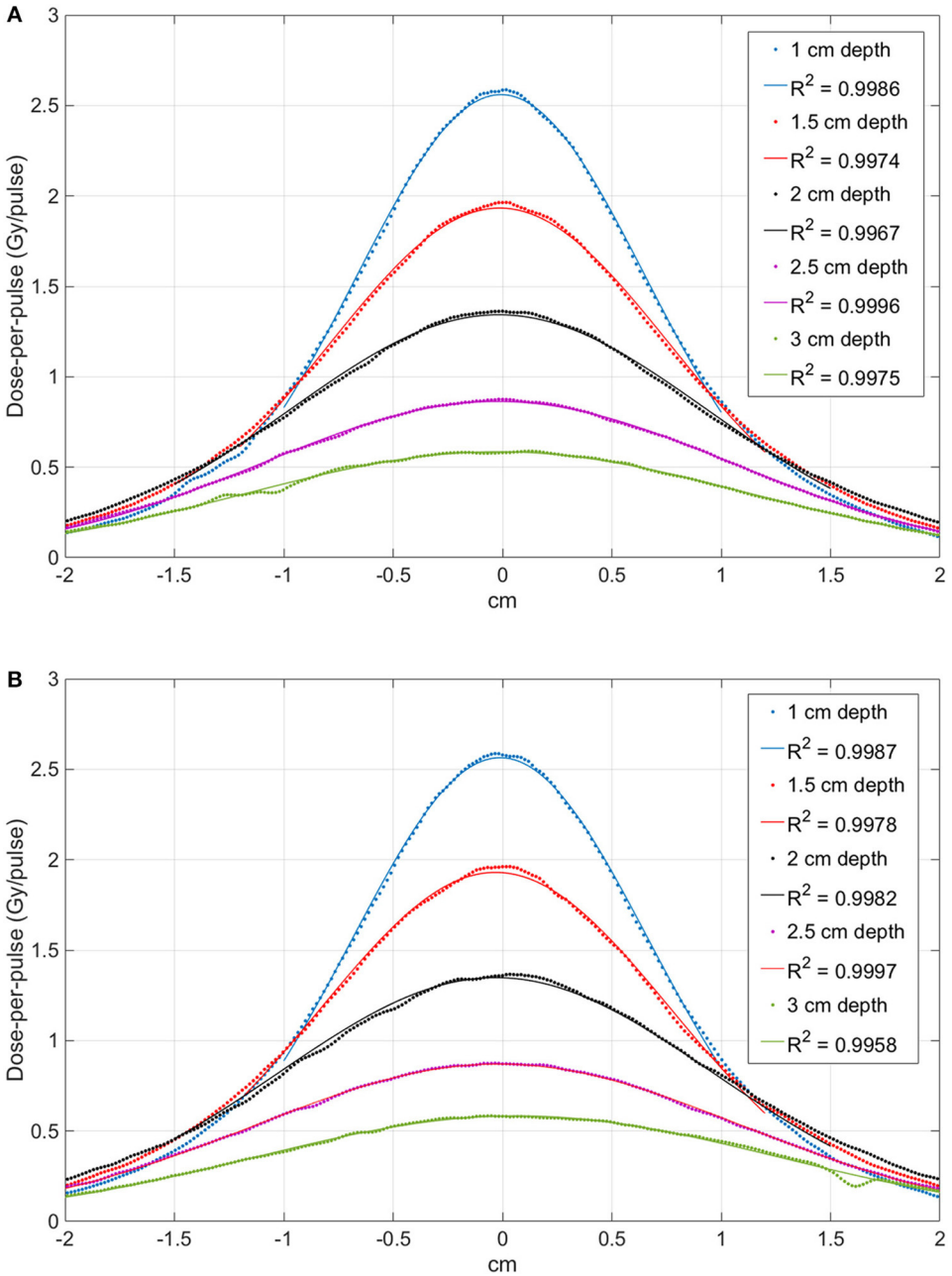

FIGURE 6 | Comparison between the profiles obtained at different depth with the FLASH beam 1. Image **(A)** shows the X-profiles while image **(B)** shows the Y-profiles. The superimposed continuous lines show the fit with a Gaussian function; R^2 values are reported for each curve.

This work described a procedure for transforming NOVAC, an IORT linac, into a FLASH machine: two out of four configurations identified reach the FLASH region (dose rate >40 Gy/s).

The geometric and dosimetric characterization of the beams was obtained through the use of Gafchromic EBT3 radiochromic films; EBT3 films were chosen because of their excellent spatial resolution, energy independence above hundreds of keV [25] and dose-per-pulse independence [21, 22, 24]. Good levels of accuracy in measuring absolute dose could also be reached provided that a rigorous protocol is established [35].

The difference between the depth deposition curves in the different configurations, as shown in **Figure 9**, can be explained by the different electron spectra. The beam exiting the accelerating waveguide has a small but significant low energy tail [28]; such spectral component is entirely absorbed and filtered along the beam optic. In fact, the low energy components have a high spatial divergence and are either absorbed or scattered

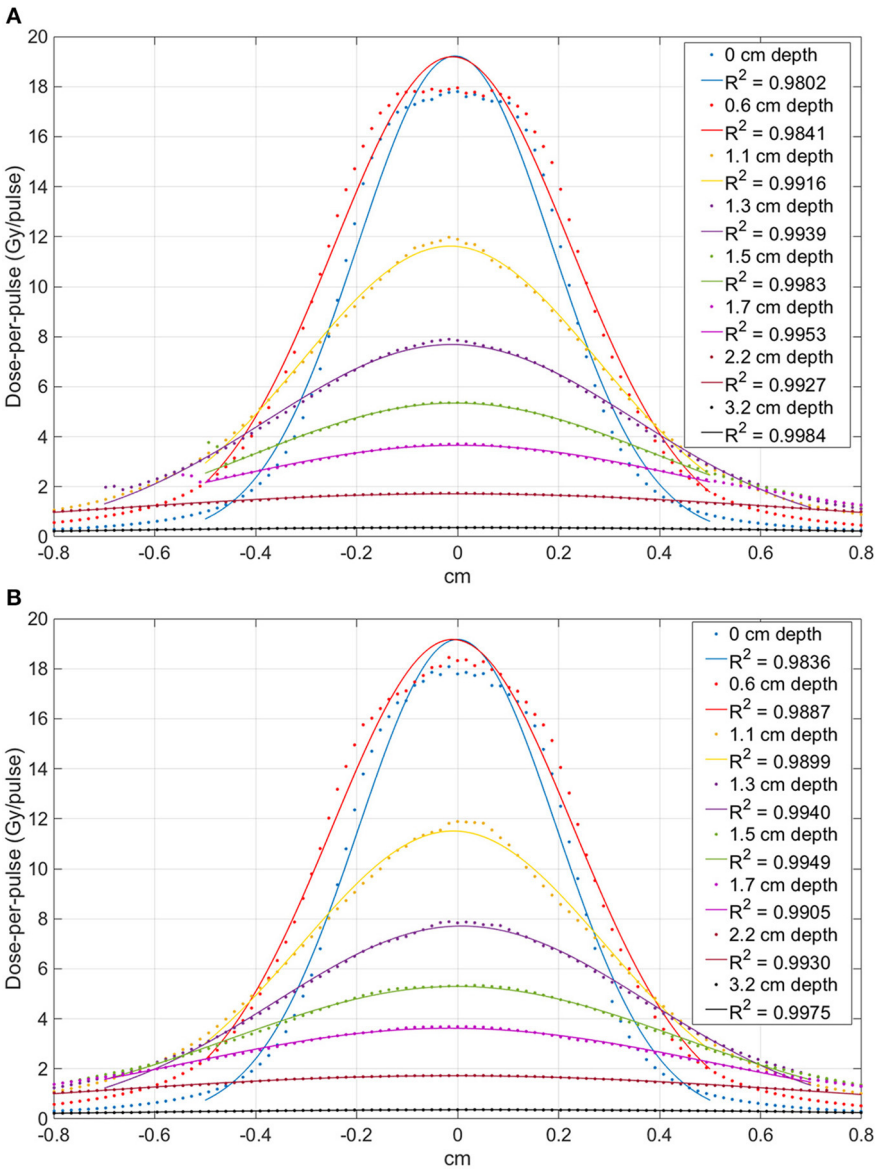

FIGURE 7 | Comparison between the profiles obtained at different depth with the FLASH beam 2. Image **(A)** shows the X-profiles while image **(B)** shows the Y-profiles. The superimposed continuous lines show the fit with a Gaussian function; R^2 values are reported for each curve.

away. Nevertheless, when measuring the beam at SSD 1.6 cm such component is still present. At SSD 7 cm (after the two monitor chambers) a significant fraction of such low energy electrons has been already absorbed or scattered away and the functional shape of the curve changes accordingly, with an increase of the parameter R_{50}. The advantage of this approach respect to the methods discussed by Lempart et al. [16] consists in its reproducibility and simplicity (no tool is needed and the modification is entirely and easily reversible). Fields sizes achievable are smaller (0.5 vs. 4 cm FWHM) but dose-per-pulse is higher (18 vs. 5 Gy/pulse).

The solution of transforming NOVAC7 IORT linac into a FLASH research machine is straightforward and gives to its users the possibility of investigating mainly the detectors response to the new challenging dose-per-pulse region; any detector with transverse dimensions compatible with the beams produced can be tested (for example, all the dosimetry diodes and small plane parallel chamber such as PTW Adv. Markus).

This aspect is extremely important because passive dosimeters like TLDs, alanine pellets, Fricke gels could be considered suitable with respect to dose-per-pulse (dose-rate) independence also at FLASH regimen, but they all lack of spatial resolution and they do not provide on-line dosimetric information, while most of the active read out dosimeters are apparently affected by significant saturation problems [37].

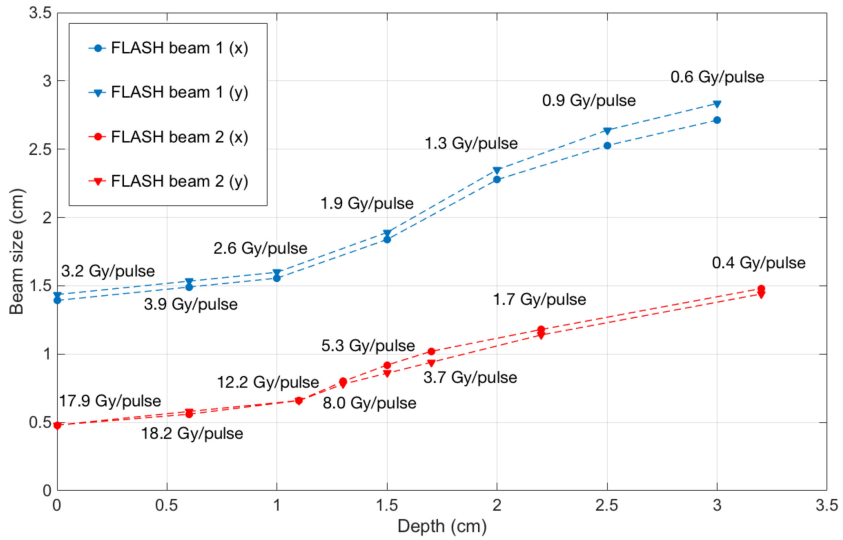

FIGURE 8 | Beam FWHM measured at different depths inside solid water with FLASH beam 1 (blue) and FLASH beam 2 (red), with the corresponding dose-per-pulse.

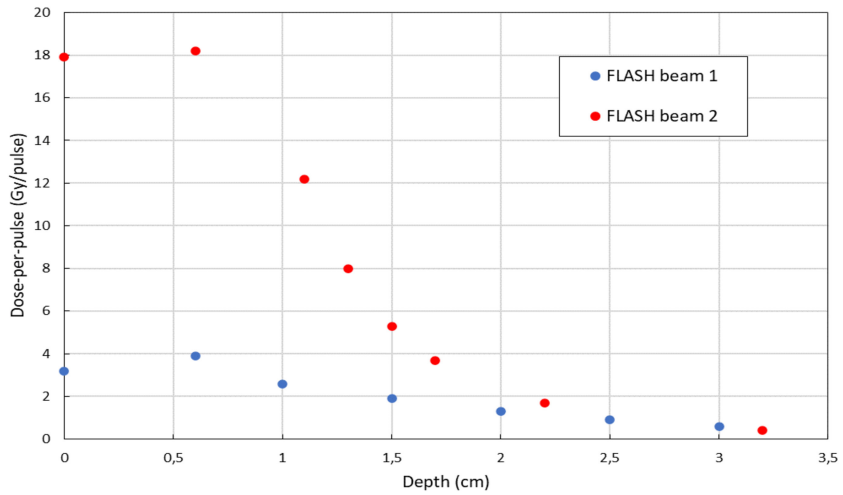

FIGURE 9 | Depth-dose distribution of electrons measured in a plastic phantom with EBT3 in FLASH beam 1 mode (blue) and FLASH beam 2 mode (red).

TABLE 2 | Maximum dose-per-pulse values and R_{50} obtained for the two irradiation modalities.

	Maximum dose-per-pulse [Gy/pulse]	R_{50} [cm]
CLINICAL BEAM—SSD 100 cm	0.030 ± 0.001	2.6 ± 0.1
SSD 50 cm	0.300 ± 0.015	2.6 ± 0.1
FLASH beam 1—SSD 7 cm	3.9 ± 0.2	1.7 ± 0.1
FLASH beam 2—SSD 1.6 cm	18.2 ± 0.9	1.2 ± 0.1

All the active detector commonly used in radiation therapy dosimetry have a signal collection time shorter than pulses repetition time (from 2 to 10 ms for a typical PRF of a conventional linac ranging from 400 to 100 Hz); consequently, the saturation effect is influenced exclusively by the dose-per-pulse. Even in clinical configuration, NOVAC7 accelerator for IORT, with dose-per-pulse ranging from 3 to 13 cGy/pulse, represents a critical situation in the use of ionization chambers and several solutions have been already proposed to overcome this drawback [26–31].

Nevertheless, due to the small dimensions of the fields where FLASH dose rates are achievable, the only biological experiments that can be performed with NOVAC are cells plate or organoids [42] irradiation.

The possibility of transforming NOVAC into a FLASH device may lead to an increase in the number of researchers who can work with a FLASH beam, investigating and resolving the numerous dosimetric issues in order to set up rigorous radiobiological experiments and clinical trials.

DATA AVAILABILITY STATEMENT

The raw data supporting the conclusions of this article will be made available by the authors, without undue reservation.

AUTHOR CONTRIBUTIONS

GF and FD designed the study. FD, GF, and SL have written the paper. Measurements and data analysis have been performed by all the authors.

FUNDING

Sordina IORT Technologies S.p.A. has paid open access publication fees.

ACKNOWLEDGMENTS

The authors thank Ilaria Breglia for the English revision of the paper.

REFERENCES

1. Favaudon V, Caplier L, Monceau V, Pouzoulet F, Sayarath M, Fouillade C, et al. Ultrahigh dose-rate FLASH irradiation increases the differential response between normal and tumor tissue in mice. *Sci Transl Med.* (2014) **6**:245ra93. doi: 10.1126/scitranslmed.3008973
2. Fouillade C, Favaudon V, Vozenin M-C, Romeo P-H, Bourhis J, Verrelle P, et al. Les promesses du haut débit de dose en radiothérapie. *Bull Cancer.* (2017) **104**:380–4. doi: 10.1016/j.bulcan.2017.01.012
3. Montay-Gruel P, Petersson K, Jaccard M, Boivin G, Germond J-F, Petit B, et al. Irradiation in a flash: unique sparing of memory in mice after whole brain irradiation with dose rates above 100 Gy/s. *Radiother Oncol.* (2017) **124**:365–9. doi: 10.1016/j.radonc.2017.05.003
4. Bourhis J, Montay-Gruel P, Gonçalves Jorge P, Bailat C, Petit B, Ollivier J, et al. Clinical translation of FLASH radiotherapy: why and how? *Radiother Oncol.* (2019) **139**:11–7. doi: 10.1016/j.radonc.2019.04.008
5. Bourhis J, Sozzi WJ, Jorge PG, Gaide O, Bailat C, Duclos F, et al. Treatment of a first patient with FLASH-radiotherapy. *Radiother Oncol.* (2019) **139**:18–22. doi: 10.1016/j.radonc.2019.06.019
6. Buonanno M, Grilj V, Brenner DJ. Biological effects in normal cells exposed to FLASH dose rate protons. *Radiother Oncol.* (2019) **139**:51–5. doi: 10.1016/j.radonc.2019.02.009
7. Simmons DA, Lartey FM, Schüler E, Rafat M, King G, Kim A, et al. Reduced cognitive deficits after FLASH irradiation of whole mouse brain are associated with less hippocampal dendritic spine loss and neuroinflammation. *Radiother Oncol.* (2019) **139**:4–10. doi: 10.1016/j.radonc.2019.06.006
8. Montay-Gruel P, Acharya MM, Petersson K, Alikhani L, Yakkala C, Allen BD, et al. Long-term neurocognitive benefits of FLASH radiotherapy driven by reduced reactive oxygen species. *Proc Natl Acad Sci USA.* (2019) **116**:10943–51. doi: 10.1073/pnas.1901777116
9. Vozenin M-C, Baumann M, Coppes RP, Bourhis J. FLASH radiotherapy international workshop. *Radiother Oncol.* (2019) **139**:1–3. doi: 10.1016/j.radonc.2019.07.020
10. Freeman T. FLASH radiotherapy: from preclinical promise to the first human treatment. *Physics World*. (2019). Available online at: https://physicsworld.com/a/flash-radiotherapy-from-preclinical-promise-to-the-first-human-treatment/
11. Durante M, Brauer-Krisch E, Hill M. Faster and safer? FLASH ultra-high dose rate in radiotherapy. *BJR.* (2017) 91. doi: 10.1259/bjr.20170628
12. Spitz DR, Buettner GR, Petronek MS, St-Aubin JJ, Flynn RT, Waldron TJ, et al. An integrated physico-chemical approach for explaining the differential impact of FLASH versus conventional dose rate irradiation on cancer and normal tissue responses. *Radiother Oncol.* (2019) **139**:23–7. doi: 10.1016/j.radonc.2019.03.028
13. Pratx G, Kapp DS. A computational model of radiolytic oxygen depletion during FLASH irradiation and its effect on the oxygen enhancement ratio. *Phys Med Biol.* (2019) **64**:185005. doi: 10.1088/1361-6560/ab3769
14. Spitz DR, Buettner GR, Limoli CL. Response to letter regarding "An integrated physico-chemical approach for explaining the differential impact of FLASH versus conventional dose rate irradiation on cancer and normal tissue responses." *Radiother Oncol.* (2019) **139**:64–5. doi: 10.1016/j.radonc.2019.07.009
15. Petersson K, Adrian G, Butterworth K, McMahon SJ. A quantitative analysis of the role of oxygen tension in FLASH radiation therapy. *Int J Radiat Oncol Biol Phys.* (2020) **107**:539–47. doi: 10.1016/j.ijrobp.2020.02.634
16. Lempart M, Blad B, Adrian G, Bäck S, Knöös T, Ceberg C, et al. Modifying a clinical linear accelerator for delivery of ultra-high dose rate irradiation. *Radiother Oncol.* (2019) **139**:40–5. doi: 10.1016/j.radonc.2019.01.031
17. Lansonneur P, Favaudon V, Heinrich S, Fouillade C, Verrelle P, De Marzi L. Simulation and experimental validation of a prototype electron beam linear accelerator for preclinical studies. *Phys Med.* (2019) **60**:50–7. doi: 10.1016/j.ejmp.2019.03.016
18. Jaccard M, Durán MT, Petersson K, Germond J-F, Liger P, Vozenin M-C, et al. High dose-per-pulse electron beam dosimetry: commissioning of the Oriatron eRT6 prototype linear accelerator for preclinical use. *Med Phys.* (2018) **45**:863–74. doi: 10.1002/mp.12713
19. Jorge PG, Jaccard M, Petersson K, Gondré M, Durán MT, Desorgher L, et al. Dosimetric and preparation procedures for irradiating biological models with pulsed electron beam at ultra-high dose-rate. *Radiother Oncol.* (2019) **139**:34–9. doi: 10.1016/j.radonc.2019.05.004
20. *Gafchromic^{TM} Radiotherapy Films Chemistry: Radiochromic Film*. Available online at: https://www.ashland.com/industries/medical/medical-radiation-dosimetry/gafchromic-radiotherapy-films#
21. Borca VC, Pasquino M, Russo G, Grosso P, Cante D, Sciacero P, et al. Dosimetric characterization and use of GAFCHROMIC EBT3 film for IMRT dose verification. *J Appl Clin Med Phys.* (2013) **14**:158–71. doi: 10.1120/jacmp.v14i2.4111
22. Jaccard M, Petersson K, Buchillier T, Germond J-F, Durán MT, Vozenin M-C, et al. High dose-per-pulse electron beam dosimetry: usability and dose-rate independence of EBT3 Gafchromic films. *Med Phys.* (2017) **44**:725–35. doi: 10.1002/mp.12066
23. Karsch L, Beyreuther E, Burris-Mog T, Kraft S, Richter C, Zeil K, et al. Dose rate dependence for different dosimeters and detectors: TLD, OSL, EBT films, and diamond detectors: dose rate dependence for different dosimeters an detectors. *Med Phys.* (2012) **39**:2447–55. doi: 10.1118/1.3700400
24. Cirrone GAP, Petringa G, Cagni BM, Cuttone G, Fustaino GF, Guarrera M, et al. Use of radiochromic films for the absolute dose evaluation in high dose-rate proton beams. *J Inst.* (2020) **15**:C04029. doi: 10.1088/1748-0221/15/04/C04029
25. Eduardo Villarreal-Barajas J, Khan RFH. Energy response of EBT3 radiochromic films: implications for dosimetry in kilovoltage range. *J Appl Clin Med Phys.* (2014) **15**:331–8. doi: 10.1120/jacmp.v15i1.4439
26. Di Martino F, Giannelli M, Traino AC, Lazzeri M. Ion recombination correction for very high dose-per-pulse high-energy electron beams: ksat evaluation for very high dose-per-pulse electron-beams. *Med Phys.* (2005) **32**:2204–10. doi: 10.1118/1.1940167
27. Laitano RF, Guerra AS, Pimpinella M, Caporali C, Petrucci A. Charge collection efficiency in ionization chambers exposed to electron beams with high dose per pulse. *Phys Med Biol.* (2006) **51**:6419–36. doi: 10.1088/0031-9155/51/24/009
28. Righi S, Karaj E, Felici G, Di Martino F. Dosimetric characteristics of electron beams produced by two mobile accelerators, Novac7 and Liac, for intraoperative radiation therapy through Monte Carlo simulation. *J Appl Clin Med Phys.* (2013) **14**:6–18. doi: 10.1120/jacmp.v14i1.3678
29. Karaj E, Righi S, Di Martino F. Absolute dose measurements by means of a small cylindrical ionization chamber for very high dose per pulse high energy

electron beams: small cylindrical chamber used in IORT dosimetry. *Med Phys.* (2007) **34**:952–8. doi: 10.1118/1.2436979
30. Pimpinella M, Andreoli S, De Angelis C, Della Monaca S, D'Arienzo M, Menegotti L. Output factor measurement in high dose-per-pulse IORT electron beams. *Phys Med.* (2019) **61**:94–102. doi: 10.1016/j.ejmp.2019.04.021
31. Scalchi P, Ciccotelli A, Felici G, Petrucci A, Massafra R, Piazzi V, et al. Use of parallel-plate ionization chambers in reference dosimetry of NOVAC and LIAC ® mobile electron linear accelerators for intraoperative radiotherapy: a multi-center survey. *Med Phys.* (2017) **44**:321–32. doi: 10.1002/mp.12020
32. Scampoli P, Carpentieri C, Giannelli M, Magaddino V, Manti L, Moriello C, et al. Radiobiological characterization of the very high dose rate and dose per pulse electron beams produced by an IORT (intra operative radiation therapy) dedicated linac. *Transl Cancer Res.* (2017) **6**:S761–8. doi: 10.21037/tcr.2017.05.21
33. International Atomic Energy Agency. *Absorbed Dose Determination in External Beam Radiotherapy: An International Code of Practice for Dsimetry Based on Standards of Absorbed Dose to Water*. Vienna: International Atomic Energy Agency (2001).
34. *Roos® Electron Chamber*. Available online at: https://www.ptwdosimetry.com/en/products/roos-electron-chamber/
35. Devic S, Tomic N, Lewis D. Reference radiochromic film dosimetry: review of technical aspects. *Phys Med.* (2016) **32**:541–56. doi: 10.1016/j.ejmp.2016.02.008
36. *NOVAC 11: Mobile IOeRT Accelerator*. Available online at: https://www.soiort.com/products/novac/
37. Di Martino F, Barca P, Barone S, Bortoli E, Borgheresi R, De Stefano S, et al. FLASH radiotherapy with electrons: issues related to the production, monitoring and dosimetric characterization of the beam. *Front Phys.* (2020).
38. Maxim PG, Tantawi SG, Loo BW. PHASER: a platform for clinical translation of FLASH cancer radiotherapy. *Radiother Oncol.* (2019) **139**:28–33. doi: 10.1016/j.radonc.2019.05.005
39. Magliari A. *FLASH Radiotherapy: A Look at Ultra-High Dose Rate Research and Treatment Plans*. (2019). Available online at: https://pubs.medicaldosimetry.org/pub/30D748A9-9A0A-F92E-82B9-723FCF2832BA
40. Maxim PG, Keall P, Cai J. FLASH radiotherapy: newsflash or flash in the pan? *Med Phys.* (2019) **46**:4287–90. doi: 10.1002/mp.13685
41. *Stopping Power and Range Tables for Electrons*. Available online at: https://physics.nist.gov/cgi-bin/Star/e_table.pl
42. Kirsch DG, Diehn M, Kesarwala AH, Maity A, Morgan MA, Schwarz JK, et al. The Future of Radiobiology. *J Natl Cancer Inst.* (2018) **110**:329–40. doi: 10.1093/jnci/djx231

Conflict of Interest: SB, SD, MD, GF, LG, and MP are SIT employees; GF is a SIT shareholder. Nonetheless, they confirm that this does not affect the design and preparation of the paper neither the analysis nor the interpretation of data.

The remaining authors declare that the research was conducted in the absence of any commercial or financial relationships that could be construed as a potential conflict of interest.

frontiers in Physics

ORIGINAL RESEARCH
published: 14 September 2020
doi: 10.3389/fphy.2020.00375

Beam Monitors for Tomorrow: The Challenges of Electron and Photon FLASH RT

Anna Vignati[1,2]*, *Simona Giordanengo*[2], *Federico Fausti*[2,3], *Oscar A. Martì Villarreal*[1,2], *Felix Mas Milian*[1,4], *Giovanni Mazza*[2], *Zahra Shakarami*[1,2], *Roberto Cirio*[1,2], *Vincenzo Monaco*[1,2] and *Roberto Sacchi*[1,2]

[1] Physics Department, Università degli Studi di Torino, Turin, Italy, [2] INFN—National Institute for Nuclear Physics, Turin Division, Turin, Italy, [3] DE.TEC.TOR. Devices & Technologies Torino S.r.l., Turin, Italy, [4] Department of Exact and Technological Sciences (DCET), Universidade Estadual de Santa Cruz, Ilhéus, Brazil

The emergent FLASH RadioTherapy (RT) uses ultrahigh dose-rate irradiation (up to 10^7 Gy/s instantaneous dose-rate in each μs pulse) to deliver a single high dose of irradiation in a very short time (<200 ms). Pre-clinical studies at ultrahigh dose-rates recently showed an increased ratio between tumoricidal effect and normal tissue toxicity (therapeutic index), compared to conventional RT at standard Gy/min dose-rates. If confirmed by biological *in vivo* validations, this could represent a breakthrough in cancer treatment. However, the reliability and the accuracy of experimental studies are nowadays limited by the lack of detectors able to measure online the beam fluence at FLASH dose-rates. The behavior of standard beam monitors (gas-filled ionization chambers) is compromised by the volume recombination caused by the amount of charges created per unit volume and unit time, due to the large dose-rate. Moreover, due to the lack of proper monitoring devices and to the uncertainties of its future applications, very few facilities are able to deliver at present FLASH irradiations. In this contribution, we report about the physical and technological challenges of monitoring high and ultra-high dose-rates with electrons and photon beams, starting from the pre-clinical and clinical constraints for new devices. Based on the extensive experience in silicon detectors for monitoring applications in RT with external beams, the work then investigates silicon sensors as a possible option to tackle such extreme requirements and a rugged thin and large (e.g., 10 × 10 cm^2) flat detector (silicon-based sensor + readout electronics) is therefore outlined. This study aims at presenting the FLASH-RT dosimetry problem and analyzing the possibilities for a silicon sensor to be employed as sensing device for several FLASH scenarios, including some ideas on the readout part. However, more detailed simulations and studies are demanded to delineate more precisely the technical choices to be undertaken in order to tackle the clinical accuracy required on the beam fluence, typically a few %, during photon and electron high and ultra-high irradiations, the required minimal perturbation of the beam and the high level of radiation resistance.

Keywords: FLASH RT, electron beams, photon beams, beam monitors, silicon detector

OPEN ACCESS

Edited by:
Vincenzo Patera, Sapienza University of Rome, Italy

Reviewed by:
Michela Marafini, Centro Fermi - Museo storico della fisica e Centro studi e ricerche Enrico Fermi, Italy
Leonello Servoli, Istituto Nazionale di Fisica Nucleare di Perugia, Italy

***Correspondence:**
Anna Vignati
anna.vignati@unito.it

Specialty section:
This article was submitted to Radiation Detectors and Imaging, a section of the journal Frontiers in Physics

Received: *01 July 2020*
Accepted: *03 August 2020*
Published: *14 September 2020*

Citation:
Vignati A, Giordanengo S, Fausti F, Martì Villarreal OA, Mas Milian F, Mazza G, Shakarami Z, Cirio R, Monaco V and Sacchi R (2020) Beam Monitors for Tomorrow: The Challenges of Electron and Photon FLASH RT. Front. Phys. 8:375. doi: 10.3389/fphy.2020.00375

INTRODUCTION

A typical Radiotherapy (RT) treatment delivers a total dose of 20–80 Gy to the target in tens of fractions (generally, 2 Gy per fraction) to fulfill the dose constraints due to normal tissue complications. The irradiation duration depends on the accelerators: present kV and MV sources provide dose-rates ranging from 0.5 to 10 Gy/min.

In parallel, the emergent and highly promising FLASH RT is proposing a completely different dose fractionation, which consists in the delivery of a single irradiation at ultrahigh instantaneous dose-rates (up to 10^7 Gy/s in each μs pulse) in a very short time (<200 ms) [1, 2].

This technique has recently drawn great attention because of the reduced toxicity at the normal tissue level observed in pre-clinical studies on cells and animals, compared to conventional RT at standard dose-rates [3]. Moreover, at the time of writing, the first patient, affected by a highly resistant skin lymphoma, was treated with FLASH modality, with an impressive early result [4]. If confirmed by ongoing research and biological *in vivo* validations, this could represent a breakthrough in cancer treatment.

However, biological validations *in vivo* are mandatory to bring the needed global consensus on FLASH, but the reliability and the accuracy of experimental studies are nowadays limited by the lack of traceable active detectors. Standard beam monitors (gas-filled ionization chambers), in fact, cannot be used for ultrahigh dose-rates, because of the high rate of charge recombination. Additionally, ionization chambers need several tens of μs (30–300 μs for 0.5–5 mm air gap) to collect the ions [5] and are too slow to control a FLASH beam, which delivers tens of Gy in a few μs.

Due to the lack of proper monitoring devices, and the uncertainties of its future applications, very few facilities are able to deliver, at present, ultrahigh dose-rate irradiation, and these mostly provide electron and proton beams [3].

On the other side, a number of advanced devices, mainly based on silicon diodes, have been developed to reliably measure the complex delivered dose-map achievable with modern RT techniques [6]. Starting from the results obtained with these devices, this work aims at studying and defining the characteristics of a rugged, thin and large silicon detector able to monitor the dose during photon and electron FLASH irradiations.

In the following, we report the physical characteristics of FLASH beams, the principles of the online dose delivery, and the requirements for a new beam monitor. The work then describes the results obtained by simulating the behavior of a new silicon detector on ultrahigh dose-rates irradiations and the related open issues.

MATERIALS AND METHODS

In the same way as conventional RT, the FLASH treatment outcome will strongly rely on the dose delivery accuracy, at both the particle accelerator level and the beam shaping and monitoring system, including the detectors for the online measurements of the main beam parameters.

In this section, we present the physical characteristics of FLASH beams, which impose new challenges for the next generation of detectors mandatory to guarantee the patient safety and treatment accuracy with FLASH irradiations. The main features of the existing beam monitors are rapidly reviewed before describing the characteristics of the new silicon detector, assumed as a viable option to tackle the challenging of monitoring FLASH beams.

FLASH Beam Characteristics

Dose Rates

X-rays and electrons used in conventional RT are produced by linear accelerators (LINAC) in which radiofrequency (RF) waves periodically accelerate the electrons providing pulsed radiation output.

The pulse duration is controlled by the pulse modulator and ranges from 2 to 6 μs, while the pulse repetition frequency (PRF) is usually adjustable in discrete values, typically from 50 to 1,000 Hz, by the PRF generator [7, 8]. This means that the existing accelerators show duty cycles from 0.01 to 0.6%.

The beam delivery time structure is crucial for FLASH treatments because the requirement of a specific mean dose-rate, typically >40 Gy/s, entails a much higher pulsed dose-rate during the duty cycle of the accelerator. For example, considering a LINAC with pulse duration of 6 μs and PRF of 1,000 Hz, or 1 ms period (see the blue example in **Figure 1**), a FLASH mean dose-rate of 100 Gy/s can be delivered in 6 μs pulses with instantaneous dose-rates of 16 kG/s. At the other extreme, with a pulse duration of 2 μs and PRF of 50 Hz, the same average dose-rate requires an instantaneous dose-rate 60 times larger. The FLASH instantaneous dose-rates reported in literature range from 10^3 Gy/s up to 10^6 Gy/s for photons and even higher (10^7 Gy/s) for electrons [1, 9].

Beam Monitors in Conventional Radiotherapy

The beam monitor consists of a set of transmission ionization chambers, covering the whole cross sectional area of the radiation beam, which are designed to monitor the delivered dose and dose-rate, as well as additional operating parameters such as beam flatness and symmetry [10]. During irradiation, the charge collected in each chamber is quantified in terms of Monitor Units (MU), calibrated to correspond to 1 cGy dose in standard reference conditions. Once the pre-set number of MUs has been reached in the primary ionization chamber, the irradiation is terminated. At present, a secondary chamber is required for redundancy: if the primary chamber fails, underestimating the dose, the second one is used to terminate the treatment. To avoid sensitivity changes resulting from fluctuations in temperature and pressure, these chambers may be sealed or vented and are properly calibrated according to the measured gas temperature and pressure. They are thin and use low atomic number materials for their entry and exit windows, to be as transparent as possible to the beam. In addition to being part of all the beam delivery systems in all clinical RT facilities, gas-filled ionization chambers

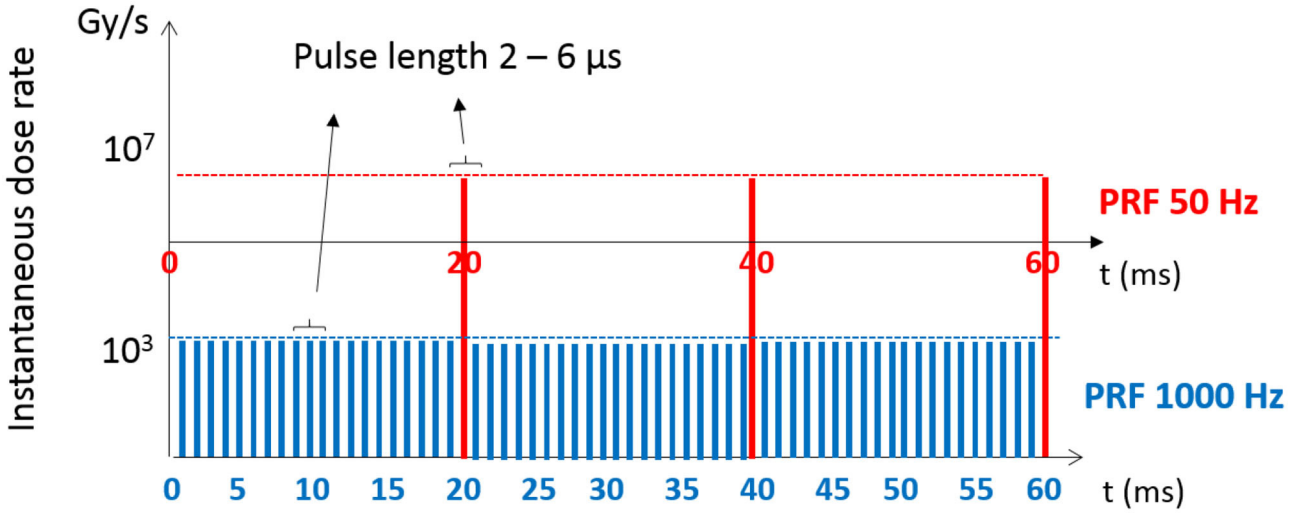

FIGURE 1 | Flash instantaneous dose-rate for an average dose-rate of 100 Gy/s delivered by a LINAC working at two different PRF: 50 and 1,000 Hz.

are also used for commissioning of RT LINAC [11] and for Quality Assurance (QA). Because of their limited complexity and simple mechanical construction, they offer several advantages such as robustness, ease of operation, and show no indication of performance degradation due to aging effects, even after several years of irradiation.

FLASH irradiations cause a radical change in the beam characteristics, in the delivery time structure and, above all, in the average and instantaneous dose-rate (see section FLASH Beam Characteristics), which points-out the limits of ionization chambers. Although correction factors have been shown to be effective up to 2 kGy/s [12], nevertheless ionization chambers cannot be used for ultrahigh dose-rates, because of the high rate of recombination. The latter depends on the amount of charges created per unit volume and unit time, i.e. on the dose-rate, which is the quantity to be measured. Although specific models have been recently developed to characterize the saturation and compute the absolute dose, this saturation effect may vary depending on the beam characteristics and irradiation setup, which makes the establishment of the correction factors inaccurate and time-consuming [13]. Additionally, ionization chambers need several tens of µs (30–300 µs for 0.5–5 mm air gap) to collect the charges and are too slow to monitor a FLASH beam, which delivers tens of Gy in a few µs.

This scenario clearly draws the need of new monitoring devices, essential to perform thorough pre-clinical studies on the biological mechanisms underpinning the effectiveness of FLASH therapy, and we here explore silicon detectors as a viable option, among alternative technologies that can be considered.

Silicon Detector

Silicon devices have been early proposed for dosimetry in RT [14], because of the well-developed manufacturing technology, their high sensitivity (tens of thousand times larger than ionization chambers with same active volume) and excellent spatial resolution, and find nowadays application ranging from QA procedures to *in vivo* dosimetry. Indeed, in the last decades, modern RT techniques started challenging the role of ionization chambers. Tomotherapy, Cyberknife, Intensity Modulated Radiotherapy (IMRT), and Volumetric Modulated Arc Therapy (VMAT) produce radiation closely shaped on the target tumor volume. This is performed by complex radiation fields, characterized by high dose gradients and strong variations in space and time of both dose-rate and beam energy spectrum. Ionization chambers are not recommended for measurements in high dose gradients, as they greatly suffer from both low sensitivity and low spatial resolution. Thus, in recent years, a number of advanced devices, mainly based on silicon diodes, have been developed to reliably measure the delivered dose-map, meeting the requirements of conformal radiation monitoring for clinical RT [6].

On the contrary, thin planar silicon devices have never been used so far as on-line monitoring systems on therapeutic beam lines, as gas-filled ionization chambers currently represent the state-of-the-art for beam monitoring during RT treatments. For beam monitoring of both electrons and photons at ultrahigh dose-rate irradiations the choice of the proper silicon technology (hybrid or monolithic), the design and development of the proper geometry for the silicon sensor in terms of surface and thickness of the single element (pixel/strip) and segmentation (number of elements in the detector) are still to be defined.

The major parameters to be considered in the design regard the instantaneous dose-rates that range from 10^3 Gy/s up to 10^7 Gy/s, the final detector size and the distance at which the detector will be positioned with respect to the source. The needed sensitive area is at minimum 10×10 cm^2 to allow the replacement of the monitor chambers currently used by LINACs, but should be made larger if a larger distance is needed. Indeed, the detector position into the nozzle leads to very different fluence rates, increasing by two orders of magnitude, when the detector is

TABLE 1 | Summary of the main characteristics of two possible read-out architectures.

Read-out architecture	Charge Sensitive Amplifier (CSA)	Recycling integrator
Max charge per pulse	240 pC	400 pC
Limitations	Maximum capacity of feedback capacitor	Maximum subtraction frequency
Possible strategies to overcome limitations	Slope of the signal ramp measurement (TDC or ADC)	Charge quantum adaptation to irradiations

moved from one meter distance from the source to the closest point to the source itself. This implies very different requirements from both silicon detector and electronics point of views, to maintain the same charge collection efficiency, and therefore the same accuracy in the dose-rate measurements.

In this work, the typical FLASH dose-rates were used to simulate the fluence rate of electrons and photons on the silicon sensor surface and the rate of charge generated in a detector element as a function of its sensitive area, sensor thickness and of the particle energy. A substantial number of unknown factors, as for example the onset of plasma conditions within the silicon, which could lead to short-circuit, or the dose-rate dependence represent a big issue. Therefore, the study of the recombination effect, saturation, and sensor linearity with dose-rate, along with possible strategies to correct for those effects and to identify the limits of such corrections, is a fundamental step, which still need to be considered. To tackle the new challenges, detailed simulations and modeling of the detector behavior in such a large flux environment must be done and benchmarked against, for example, passive dosimetry.

Front-End Readout

Given the ultrahigh dose-rates expected in FLASH irradiations, a large segmentation of the sensor is required to limit the current to readout from each channel. Thin pixelated sensors, covering the cross sectional area of the beam, readout by a fully custom front-end ASIC bump bonded to the sensor offer the possibility of combining flux measurement and spatial information in a unique compact detector. The front-end ASIC should be designed to readout the charge in the sensor channel dealing with the high peak pulsed current of FLASH beams, avoiding the amplifier saturation and without dead-time during the beam pulses. Two different approaches are described in the following and their main features are summarized in **Table 1**.

The natural choice for the front-end is the use of a Charge Sensitive Amplifier (CSA), which integrates the input charge on a feedback capacitor C_f, followed by a shaper and an Analog to Digital Converter (ADC) that digitizes the voltage amplitude at the end of each beam pulse. Assuming a modern Complementary Metal-Oxide Semiconductor (CMOS) technology, the capacity density cannot exceed $\sim$100 fF/μm^2 leading to a maximum C_f ranging between 10 and 100 pF, depending on the area available over the pixel surface. Using the typical bias voltage of 1.2 V, a maximum charge between 12 and 120 pC (corresponding to a maximum current of 6 and 60 μA for a pulse of 2 μs duration) could be measured in each pulse before saturation of the amplifier. These limits could be increased at most by a factor 2 by using a larger bias voltage for the analog part of the channel (e.g., 2.5 V), while biasing the digital part with a lower voltage.

Different strategies can be implemented to overcome these limits, at the price of increasing the complexity of the front-end design.

Figure 2 shows the block diagram of a modified version of the circuit described above where the slope of the initial ramp of the signal is also measured. In case of saturation of the CSA, the total charge can be recovered from the measured slope using a calibration curve determined experimentally. The slope can be determined by measuring the time taken by the signal to increase from a lower voltage V_{th1} to a higher voltage V_{th2}, using a Time to Digital Converter (TDC) where the start and stop signals are provided by the lower (V_{th1}) and upper (V_{th2}) thresholds of a double threshold discriminator, as shown in the lower branch of **Figure 2**. Alternatively, an ADC can be used to measure the output voltage after a fixed time delay from the start signal provided by a single threshold discriminator. The overall electronics readout uncertainty should be kept at the level of per mill.

A different method, based on a CSA and an active feedback, can be used to limit the amplifier saturation while keeping a dead-time-free front-end readout. This method, based on the recycling integrator architecture, has been applied successfully in several versions of TERA ASICs developed by our group in the last years for particle therapy applications [15]. Referring to **Figure 3**, when the output of the CSA crosses the discriminator threshold (V_{th-} for negative and V_{th+} for positive input currents), a pulse, generated by the Pulse Generator block, is sent to the C_{sub} capacitor. Two opposite charges, given by the product $C_{sub} \cdot (V_{pulse+} - V_{pulse-})$ are generated across the capacitor which, with proper synchronization of the two switches shown in the figure, can be used to subtract a constant negative or positive charge quantum, depending on the polarity of the input current, from the charge integrated by the amplifier. With a steady input current, this feedback mechanism prevents data loss caused by the front-end saturation without introducing any deadtime. However, the subtraction mechanism is driven by an external clock and can operate up to a maximum input current, where the maximum subtraction frequency is reached. The number of subtracted charge quanta, stored in a counter, provide a digitized measurement of the input charge. A fast access to the counter may also provide the possibility of monitoring the charge during the pulse, if desired.

Assuming a maximum subtraction frequency of 100 MHz, a charge quantum of 1 pC, and in the worst scenario of pulses of 2 μs duration, a maximum of 200 pC of charge can be subtracted. This extends by the same amount the charge that can integrated before saturation, as calculated above. With the appropriate choice of the feedback capacitor, charges up to 400 pC per

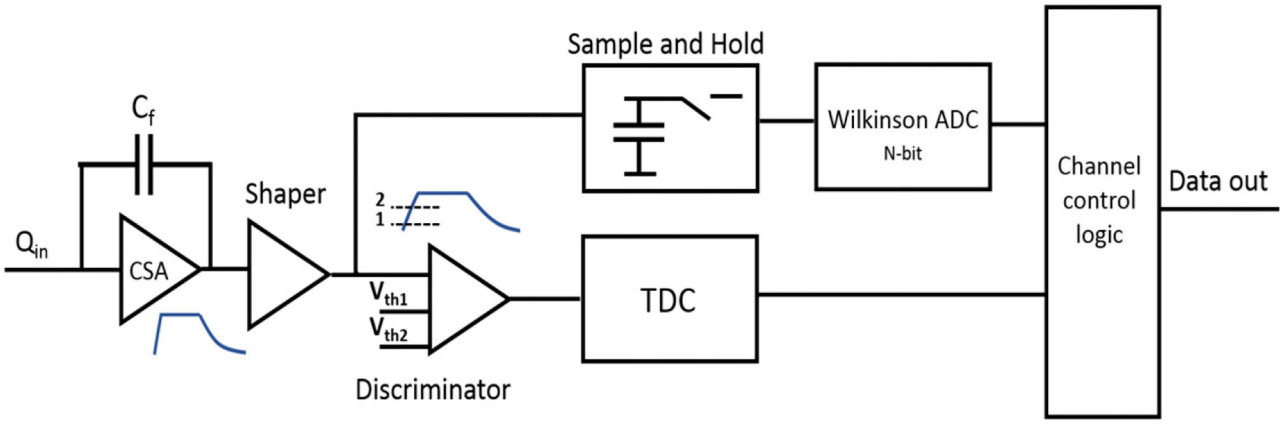

FIGURE 2 | Block diagram of a circuit where an ADC is used to digitize the voltage amplitude at the output of the Charge Sensitive Amplifier (CSA) feedback capacitance, after the entire pulse duration time. The initial slope of the signal is also measured using a TDC and a double threshold discriminator.

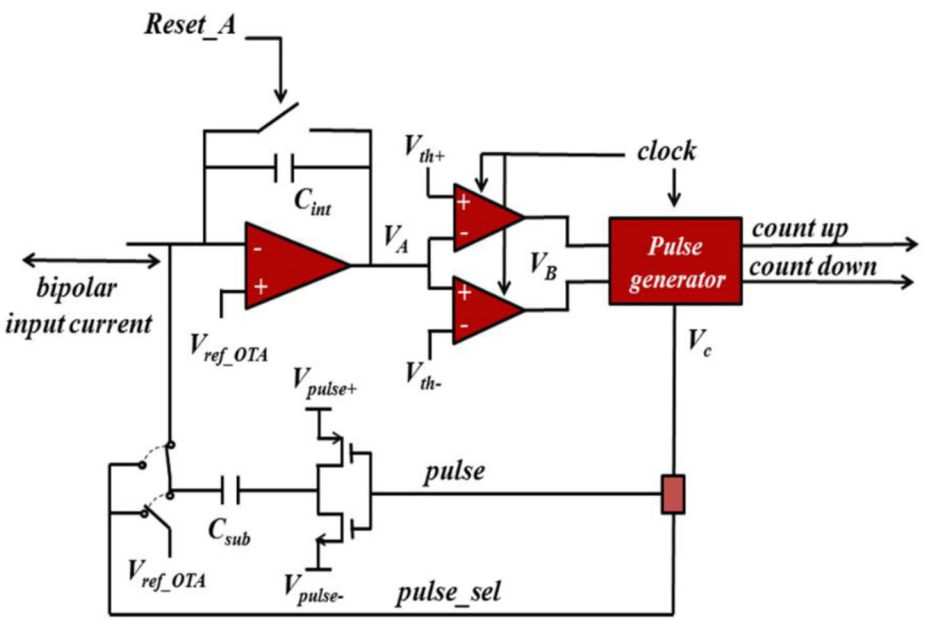

FIGURE 3 | Example of recycling integrator functional blocks diagram.

pulse could be measured (i.e., up to 200 μA of current during the pulse).

The choice of the charge quantum determines the charge sensitivity of the front-end and hence the sensitivity to the delivered dose. An average number of subtractions per pulse larger than 100 is needed to achieve a 1% sensitivity in each pulse. Considering the worst scenario of a PRF of 50 Hz this would correspond to a sensitivity of 0.02% for the total treatment. Smaller values of the charge quantum would bring the system closer to saturation whereas larger values would degrade the sensitivity to the dose measurement of each single pulse. The readout should allow for varying the charge quantum in a broad range to adapt to all possible irradiation conditions. This could be achieved both by implementing few parallel capacitors that can be independently added *via* digital configuration lines to obtain the total capacitance C_{sub} and by varying the V_{pulse} voltages.

The accuracy of the subtraction mechanism is determined by the accuracy of the voltage difference ($V_{pulse+} - V_{pulse-}$) and of the capacity C_{sub}; although the former can be made very accurate by using external voltage sources, accuracies of ∼10% with channel-by-channel variations up to few % are to be expected for the capacity [16]. An accurate calibration of the charge quantum for each channel using an external current source is therefore mandatory to compensate for this effect.

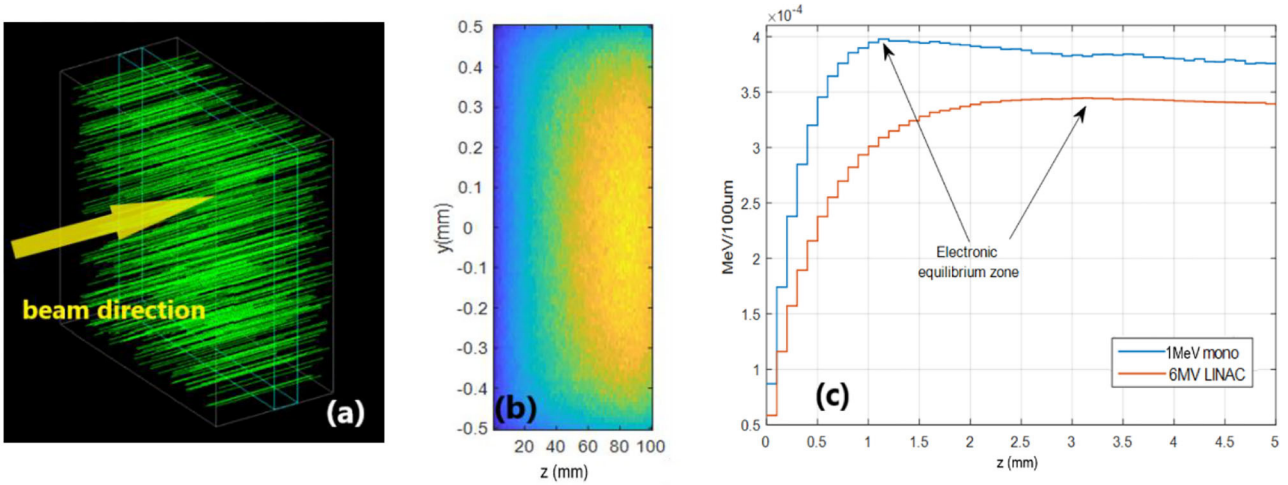

FIGURE 4 | (a) View of the geometry used for the Monte Carlo simulation. **(b)** Projection in the *yz* plane of the energy deposited by the 1 MeV photon beam in the sensor. **(c)** Average deposited energy per photon in 100 μm slices as a function of the depth *z* in the silicon. Results are shown both for monoenergetic 1 MeV photons and for a photon beam with the energy spectrum of a 6 MV LINAC. The arrows point to the depth where the electronic equilibrium is reached.

RESULTS

Rate of Charge Production From Photons and Electrons in Silicon

The rate of charge Q generated in a silicon sensor element at the FLASH ultrahigh dose-rate strongly depends on its active area, on the sensor thickness, on the particle energy and on the dose-rate. It can be derived by the following equation:

$$\frac{Q}{\Delta t} = \frac{e \cdot \bar{\varepsilon}}{W} \cdot S \cdot \phi, \tag{1}$$

where $\phi = N/S \cdot \Delta t$ is the rate of electrons/photons hitting the sensor per unit surface (fluence rate), S is the active area of the pixel, $\bar{\varepsilon}$ is the average energy released per particle, $W = 3.6\ eV$ is the average energy required to create an electron-hole pair in silicon and $e = 1.6 \times 10^{-19}\ C$.

To estimate the average energy released per particle $\bar{\varepsilon}$, Monte Carlo simulations using the Geant4 code with the standard electromagnetic interaction physics package, option three[1], were performed. Three cases were considered: a monoenergetic photon beam of 1 MeV energy, a photon beam with the energy spectrum of a 6 MV LINAC and a beam of 6 MeV electrons, representative of the electron beam energies used to treat skin and superficial disease [7, 17]. The detector pixel was modeled as silicon box of 1 mm^2 surface in the *xy* plane, and 100 μm in *z*, which is a typical silicon wafer thickness, and 10^9 beam particles were distributed uniformly in the *xy* plane and directed along *z*, perpendicularly to the sensor surface, as shown in **Figure 4a**. The silicon pixel volume was divided into 10^6 voxels of $10 \times 10 \times 1\ \mu m^3$ to record the tridimensional distribution of the energy released by impinging photons, electrons and secondary particles, and the resulting energy was normalized by the total number of particles used in the simulation.

Figure 4b shows a projection in the *yz* plane of the energy deposited by the 1 MeV energy photon beam. The distribution is non-uniform because, given the small thickness of the silicon plane, electrons set in motion by Compton scattered photons lead to an increase of energy deposited with depth, the well-known build-up effect. The build-up occurs within a few millimeters from the surface until electronic equilibrium is reached, as shown in **Figure 4c** where the simulation was repeated using a thicker silicon absorber to show the effect. It can be observed that the energy deposited in the first 100 μm amounts to <20% of the energy deposited when electronic equilibrium is reached.

Figure 5a shows the average energy deposited in the sensor per photon in 1 μm slices along *z*, showing the steady increase due to the build-up up to 90 μm, followed by a small decrease due to the lack of the contribution of backscattered particles close to the detector backplane. The corresponding cumulative distribution shown in **Figure 5b** represents the average energy released per particle ($\bar{\varepsilon}$) as a function of the detector thickness crossed by the beam. For a 100 μm thick sensor, it amounts to $\bar{\varepsilon} = 57eV/phot$ for a monoenergetic 1 MeV beam and $\bar{\varepsilon} = 42eV/phot$ for the 6 MV LINAC beam. However, using the smaller thickness of 20 μm, this quantity can be reduced by more than a factor 10 ($4.6eV/phot$ and $3.5eV/phot$, respectively).

The study was repeated for a 6 MeV electron beam, showing a more uniform energy deposition about three orders of magnitude larger than for photons, $\sim 0.4keV/\mu m$ per particle, leading to $\bar{\varepsilon} = 40keV/elec$ for a 100 μm thick sensor.

Although considering the dependence of the energy loss distribution from the thickness of the silicon sensor [18], we decided to assume a constant energy deposition per unit length of $0.4keV/\mu m$. Thus, we accepted an error of a factor 2 in the worst case, acknowledging that the present work aims at providing an

[1] Available online at: geant4.web.cern.ch

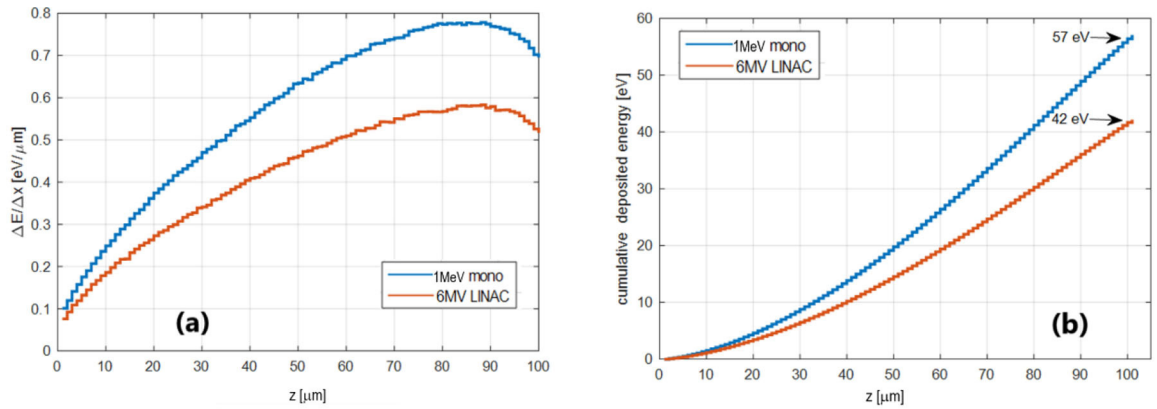

FIGURE 5 | (a) Average energy deposited per photon in 1 μm slices along *z*. **(b)** Cumulative deposited energy per photon as a function of the traversed thickness. In each subfigure, the two curves refer to a monoenergetic 1 MeV beam and to a 6 MV LINAC beam.

approximated evaluation of the orders of magnitude involved in the FLASH irradiations scenarios.

In order to relate the fluence rate of photons passing through the sensor (ϕ in Equation 1) to the dose-rate $\Delta D/\Delta t$, a rough estimation can be obtained from the photon intensity attenuation law

$$I = I_o \cdot e^{-\mu x}, \tag{2}$$

where I_o is the incident intensity, I the transmitted intensity, μ the linear attenuation coefficient and x the absorber thickness. The intensity variation $\Delta I = I_0 - I$ thus represents the deposited energy ΔE per unit of time and surface in thickness x. For a small thickness one obtains

$$\Delta I = \frac{\Delta E}{S \cdot \Delta t} = I_o \cdot \mu x = E_o \phi \cdot \mu x, \tag{3}$$

where $\phi = N/S \cdot \Delta t$ is the fluence rate of photons of energy E_o. The dose-rate, i.e., the deposited energy ΔE per unit of mass and time in thickness x, can be expressed using Equation 3 as

$$\frac{\Delta D}{\Delta t} = \frac{\Delta E}{m \cdot \Delta t} = \frac{1}{x \cdot \rho} \frac{\Delta E}{S \cdot \Delta t} = E_o \, (\mu/\rho) \cdot \phi, \tag{4}$$

leading to the following relation between particle fluence rate and dose-rate:

$$\phi = \frac{1}{E_o \cdot (\mu/\rho) \cdot} \cdot \frac{\Delta D}{\Delta t}. \tag{5}$$

As an example, for a photon beam with $E_o = 1$ MeV, delivering a dose-rate of 1 Gy/s, and using $\frac{\mu}{\rho}(1\,MeV)_{water} \approx 5 \times 10^{-2}\ cm^2/g$, the fluence rate would be $\phi \sim 10^{11}\ \frac{photons}{cm^2 \cdot s}$.

However, in the medical practice, the dose is defined using a standard procedure because the conversion from dose to particle beam fluence depends on the field parameters and on the procedure used to measure the dose. Indeed, in the standard protocols, the dose is measured at the depth of the dose maximum in a water phantom (with a surface at the isocenter of the machine, i.e., usually at 100 cm from the source) along the axis of a square 10×10 cm^2 uniform irradiation field [7, 8].

A Monte Carlo simulation using the Geant4 code was performed to estimate the reference dose. Parallel beams of photons with 1 MeV energy, photons with 6 MV LINAC energy spectrum and electrons of 6 MeV were used as sources to deliver a 10×10 cm^2 uniform field of dose in a $40 \times 40 \times 40$ cm^3 water phantom. The phantom was divided into 64,000 voxels of 1 cm^3 volume where the average dose was determined as the energy released in the voxel divided by the voxel mass.

In **Figure 6**, the upper plots show the dose distribution map in the central *yz* plane obtained with the three simulated beams, whereas the lower plots show the dose as a function of the phantom depth along the central axis of the irradiated field. Following the standard procedure, the dose $D_{\max}$ is the dose measured at the maximum along the central axis of the irradiation field (lower plot in **Figure 6**). For each of the three simulations, the number N_{sim} of particles used is also reported. From these results, the particle fluence rate ϕ for a given dose-rate $\Delta D/\Delta t$ can be expressed as follows

$$\phi = \frac{\Delta D}{\Delta t} \cdot \frac{N_{sim}}{A \cdot D_{\max}}, \tag{6}$$

where $A = 10 \times 10$ cm^2 represents the field size.

Considering for example a dose-rate of 1 Gy/s, Equation 6 yields the following fluence rates

$$1.98 \times 10^{11} \frac{photons}{cm^2 \cdot s}, \quad 1.24 \times 10^{11} \frac{photons}{cm^2 \cdot s} \quad \text{and} \quad 2.43 \times 10^{9} \frac{electrons}{cm^2 \cdot s}$$

for the 1 MeV photon beam, for photon beam of a 6 MV LINAC, and for the 6 MeV electron beam, respectively. The fluence rates for photons are found to be in agreement with the rough calculation based on Equation 5.

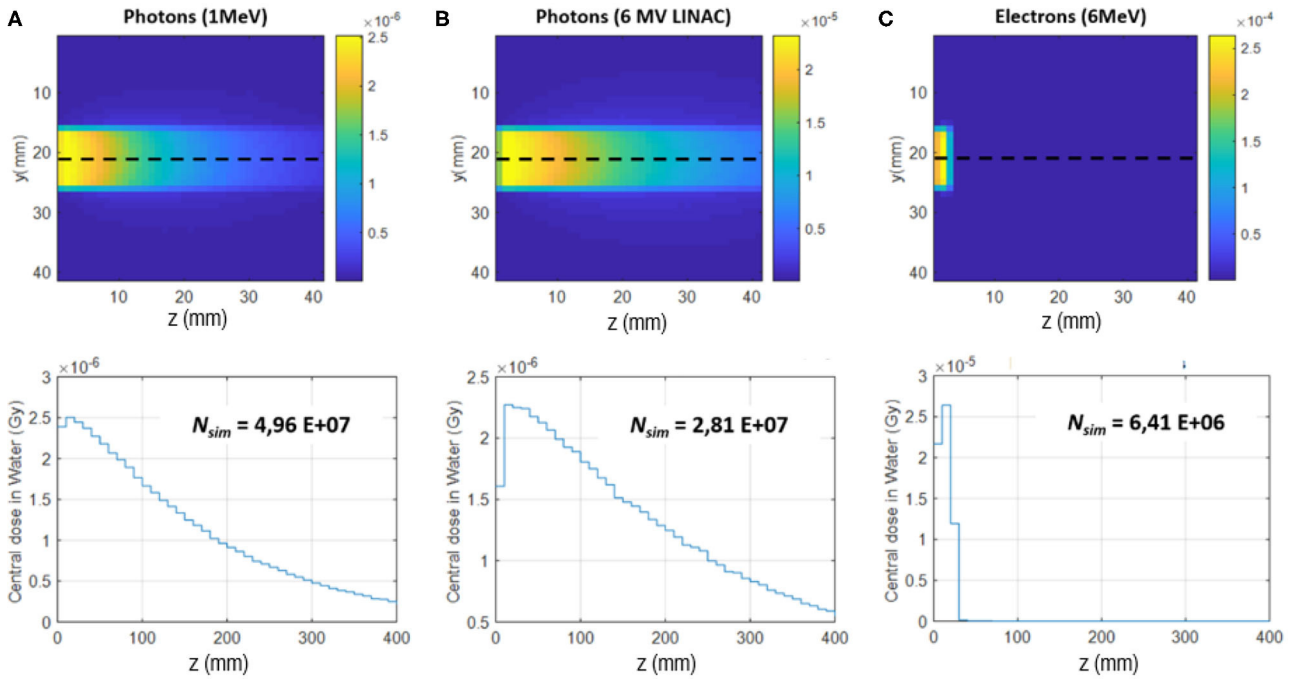

FIGURE 6 | Upper plots: simulated dose distribution maps expressed in Gy, averaged in 1 cm^3 voxels, in the central *yz* plane. Lower plots: dose distributions along the central axis (i.e., along the dotted lines of the upper plots). The results correspond to a 10 × 10 cm^2 uniform field in a 40 × 40 × 40 cm^3 water phantom irradiated with **(A)** 1 MeV monoenergetic photons, **(B)** photons from 6 MV LINAC, and **(C)** 6 MeV electrons. The number of particles N_{sim} used in the simulation is reported.

From these values, weighted with the actual dose-rate, and using Equation 1, the rate of charge production in the silicon can be derived for different beams, dose-rates, sensor area, and thickness.

Table 2 reports the expected rate of charge production in the silicon bulk of the sensor element, together with the total charge produced in a pulse of 5 μs duration, for different scenarios: large (1 mm^2) and small (50 × 50 μm^2) pixel sizes, normal (100 μm) and very thin (20 μm) sensors, lower and upper limit of the FLASH instantaneous dose-rates as reported in the literature.

DISCUSSION

FLASH irradiations require the development of new systems for monitoring the beam fluence at the ultrahigh dose-rates. The detectors will have to be compliant with the requirements of the pre-clinics and clinics environments to develop a full system, 100% reliable, able to work within the existing accelerator facilities.

The potentials and limits of silicon detectors, well-known in conventional RT for relative dose verification, are studied in these extremely challenging conditions. According to the preliminary studies reported in this work, the design of a silicon sensor and its readout-electronics requires a remarkable technological effort to allow reading out the charge produced in FLASH beam pulses.

As shown in **Table 2**, the active thickness of the sensors will need to be reduced down to a few tens of microns. Indeed, it is found that, for photon beams, a reduction of the thickness from 100 to 20 μm lowers the energy released by over a factor 10. In order to limit the charge build-up effect into the sensor, the active area should be exposed to the beam with the minimum of dead material in front of it. Processing technologies which combine back-side reading with thinning procedures *via* wet etching [19] can be exploited to achieve this goal. Thin sensors have the additional benefit, given the small charge collection time, of reducing the charge recombination probability in the silicon, leading to a better performance, especially at large fluences [20]. Reducing the pixel area allows cutting down the charge produced in each sensor element, but increases the number of readout channels and reduces the area available for the circuit front-end implementation. On the other hand, the readout of an increasing number of pixels would require the implementation of data reduction strategies to avoid transmitting unnecessary information.

In order to find the best compromise and optimize the detector design, each of the above-mentioned aspects must be properly considered, and other effects need to be taken into account with accurate simulations, such as the contribution to the energy deposited in the sensor of backscattered particles.

The data reported in **Table 2** also tell that the outlined silicon sensor + readout electronics strategy could plausibly deal with the entire FLASH dose-rate range for photons, but only with the lower limit of the dose-rate range for electrons. Indeed, the enormous flux of incoming electrons would probably generate a plasma condition within the silicon, which could

TABLE 2 | Rate of charge production and total charge produced in a pulse of 5 μs (in parenthesis) in the detector element for different beams, dose-rates, pixel area, and sensor thickness.

Beam	Dose rate (Gy/s)	Rate of charge produced (μC/s) (pC of charge produced in 5 μs pulses)			
		Sensor thickness 100 μm		Sensor thickness 20 μm	
		Pixel area		Pixel area	
		1×1 mm^2	50×50 μm^2	1×1 mm^2	50×50 μm^2
Monoenergetic 1 MeV photons	10^3	5.0	$1.3 \cdot 10^{-2}$	$4.0 \cdot 10^{-1}$	$1.0 \cdot 10^{-3}$
		(25)	(0.063)	(2.0)	(0.0051)
	10^6	$5.0 \cdot 10^3$	$1.3 \cdot 10^1$	$4.0 \cdot 10^2$	1.0
		(25,000)	(63)	(2,000)	(5.1)
6 MV LINAC photons	10^3	2.3	$5.8 \cdot 10^{-3}$	$1.9 \cdot 10^{-1}$	$4.8 \cdot 10^{-4}$
		(12)	(0.029)	(0.96)	(0.0024)
	10^6	$2.3 \cdot 10^3$	5.8	$1.9 \cdot 10^2$	$4.8 \cdot 10^1$
		(12,000)	(29)	(960)	(2.4)
6 MeV electrons	10^3	$4.3 \cdot 10^1$	$1.1 \cdot 10^{-1}$	8.6	$2.2 \cdot 10^{-2}$
		(220)	(0.54)	(43)	(0.11)
	10^7	$4.3 \cdot 10^5$	$1.1 \cdot 10^3$	$8.6 \cdot 10^4$	$2.2 \cdot 10^2$
		(2,200,000)	(5,400)	(430,000)	(1,100)

lead to short-circuit. It is worth noticing that we might have overestimated of a factor 2, at worst, the energy deposited per μm of sensor in the case of electrons, since it has been demonstrated that this is dependent on the sensor thickness considered (either 20 or 100 μm in our study) [18]. However, this error doesn't change the general conclusions about electron FLASH irradiations. Interestingly, although nearly all the pre-clinical FLASH studies available so far have been performed using single dose irradiations, first evidence was recently showed about the isoefficacy of hypo-fractionated FLASH regimen. This suggests the possibility to use FLASH RT as a "boost" at the beginning of the treatment with instantaneous dose-rate $<10^6$ (photons) and 10^7 (electrons) Gy/s, being followed by high precision conventional RT [21]. Moreover, the advent of FLASH therapy with electron beams will probably precede the one with photons, as the production of ultrahigh dose rates photon beams has more complications [21]. Therefore, it is worth investigating a new reliable silicon-based detector, starting from tackling unknown but expected conditions like plasma creation within the silicon and saturation.

CONCLUSIONS

In this work, we report about the physical and technological challenges of monitoring high and ultra-high dose-rates with electrons and photon beams, starting from the pre-clinical and clinical constraints for new devices. To this aim, based on the extensive experience in silicon detectors for monitoring applications in RT with external beams, the technological efforts needed to develop a silicon-based device and its readout electronics are delineated. Our preliminary studies found out that this technology could allow monitoring photon beams in their entire FLASH dose-rate range, but could deal only with the lower limit of the dose-rate range for electrons. However, this limitation does not deny that a silicon sensor could be a viable option for monitoring FLASH RT, at least up to the achievable dose-rate scenarios, starting from deepening the knowledge about expected phenomena, such as plasma creation within the silicon.

DATA AVAILABILITY STATEMENT

The raw data supporting the conclusions of this article will be made available by the authors, without undue reservation.

AUTHOR CONTRIBUTIONS

AV, SG, and FM devised the work with the supervision from RC, VM, and RS. AV, SG, and OM investigated the silicon part, while FF and GM focused on the electronics readout part of the work. FM and ZS performed simulations and calculations. All authors discussed the results, contributed to the writing of the manuscript, and approved the submitted version.

REFERENCES

1. Favaudon V, Caplier L, Monceau V, Pouzoulet F, Sayarath M, Fouillade C, et al. Ultrahigh dose-rate FLASH irradiation increases the differential response between normal and tumor tissue in mice. *Sci Transl Med.* (2014) **6**:1–10. doi: 10.1126/scitranslmed.3008973
2. Fiorino C, Guckemberger M, Schwarz M, van der Heide UA, Heijmen B. Technology-driven research for radiotherapy innovation. *Mol Oncol.* (2020) **14**:1500–13. doi: 10.1002/1878-0261.12659

3. Vozenin M-C, Baumann M, Coppes RP, Bourhis J. FLASH radiotherapy international workshop. *Radiother Oncol.* (2019) **139**:4–6. doi: 10.1016/j.radonc.2019.07.020
4. Bourhis J, Sozzi WJ, Jorge PG, Gaide O, Bailat C, Duclos F, et al. Treatment of a first patient with FLASH-radiotherapy. *Radiother Oncol.* (2019) **139**:18–22. doi: 10.1016/j.radonc.2019.06.019
5. Giordanengo S, Palmans H. Dose detectors, sensors, and their applications. *Med Phys*. (2018) **45**:e1051–72. doi: 10.1002/mp.13089
6. Bruzzi M. Nuclear instruments and methods in physics research a novel silicon devices for radiation therapy monitoring. *Novel Silicon Devices Rad Therapy Monitor*. (2016) **809**:105–12. doi: 10.1016/j.nima.2015.10.072
7. Mayles P, Nahum A, Rosenwald JC. *Handbook of Radiotherapy Physics: Theory and Practice*. Boca Raton, FL: Taylor & Francis Group, CRC Press (2007). p. 1–1453. doi: 10.1201/9781420012026
8. International Atomic Energy Agency. *Absorbed Dose Determination in External Beam Radiotherapy*. Technical Reports Series No. 398, IAEA, Vienna (2001).
9. Vozenin MC, Hendry JH, Limoli CL. Biological benefits of ultra-high dose rate FLASH radiotherapy: sleeping beauty awoken. *Clin Oncol.* (2019) **31**:407–15. doi: 10.1016/j.clon.2019.04.001
10. Greene D, Williams P. *Linear Accelerators for Radiation Therapy*. Boca Raton, FL: CRC Press (2017). doi: 10.1201/9780429246562
11. Jaccard M, Durán MT, Petersson K, Germond JF, Liger P, Vozenin MC, et al. High dose-per-pulse electron beam dosimetry: commissioning of the Oriatron eRT6 prototype linear accelerator for preclinical use: commissioning. *Med Phys.* (2018) **45**:863–74. doi: 10.1002/mp.12713
12. Kry S, Popple R, Molineu A, Followill D. SU-E-T-375: ion recombination correction factors (Pion) for varian truebeam high dose rate therapy beams. *Med Phys.* (2012) **39**:3790. doi: 10.1118/1.4735462
13. Jorge PG, Jaccard M, Petersson K, Gondré M, Durán MT, Desorgher L, et al. Dosimetric and preparation procedures for irradiating biological models with pulsed electron beam at ultra-high dose-rate. *Radiother Oncol.* (2019) **139**:34–9. doi: 10.1016/j.radonc.2019.05.004
14. Jones AR. The application of some direct current properties of silicon junction detectors to γ-ray dosimetry. *Phys Med Biol.* (1963) **8**:451–9. doi: 10.1088/0031-9155/8/4/307
15. Fausti F, Mazza G, Attili A, Mazinani MF, Giordanengo S, Lavagno M, et al. Design and characterization of a 64 channels ASIC front-end electronics for high-flux particle beam detectors. *Nucl Instr Method Phys Res Sect A Accel Spectrometers Detect Assoc Equip.* (2017) **867**:25. doi: 10.1016/j.nima.2017.04.025
16. La Rosa A, Mazza G, Donetti M, Marchetto F, Luetto L, Attili A, et al. Design and test of a 64-channel charge measurement ASIC developed in CMOS 0.35 μm technology. *Nucl Instr Method Phys Res Sect A Accel Spectrometers Detect Assoc Equip*. (2007) **583**:461–8. doi: 10.1016/j.nima.2007.09.024
17. Hogstrom KR, Almond PR. Review of electron beam therapy physics. *Phys Med Biol.* (2006) **51**:R25. doi: 10.1088/0031-9155/51/13/R25
18. Meroli S, Passeri D, Servoli L. Energy loss measurement for charged particles in very thin silicon layers. *J Instrum.* (2011) **6**:P06013. doi: 10.1088/1748-0221/6/06/P06013
19. Richter RH, Andricek L, Fischer P, Heinzinger K, Lechner P, Lutz G, et al. Design and technology of DEPFET pixel sensors for linear collider applications. *Nucl Instr Method Phys Res Sec A*. (2003) **511**:250–6. doi: 10.1016/S0168-9002(03)01802-3
20. Petasecca M, Moscatelli F, Pignatel GU. Analysis and simulation of charge collection efficiency in silicon thin detectors. *Nucl Instr Method Phys Res Sect A*. (2005) **546**:291–5. doi: 10.1016/j.nima.2005.03.051
21. Bourhis J, Montay-Gruel P, Gonçalves Jorge P, Bailat C, Petit B, Ollivier J, et al. Clinical translation of FLASH radiotherapy: why and how? *Radiother Oncol.* (2019) **139**:11–7. doi: 10.1016/j.radonc.2019.04.008

Conflict of Interest: The authors declare that the research was conducted in the absence of any commercial or financial relationships that could be construed as a potential conflict of interest.

frontiers in Physics

REVIEW
published: 18 September 2020
doi: 10.3389/fphy.2020.00318

Investigating the Effects of Cosmic Rays on Space Electronics

Stefan K. Höeffgen, Stefan Metzger and Michael Steffens*

Business Unit Nuclear Effects in Electronics and Optics, Fraunhofer Institute for Technological Trend Analysis INT, Euskirchen, Germany

The radiation environment in space has severe adverse effects on electronic systems. To evaluate radiation sensitivity, electronics are tested on earth with different types of irradiation sources. Cosmic rays (CR) are the most difficult to simulate on earth, because CR can have energies up to 10^{20} eV, with a flux maximum of around 1 GeV/n. However, only particles with energies up to several GeV/nucleon are relevant for radiation effect testing of space electronics due to the negligible fluxes beyond. Traditionally single-event effects of these particles were simulated with heavy ions having energies of only a few MeV/n because for "large" devices only the energy loss, often referred to as linear energy transfer (LET), had to be matched. Heavy ions of such high energies can produce secondary particles through nuclear interactions which can induce additional ionization that leads to adverse effects. The need to investigate these effects has grown since electronic devices now incorporate heavier elements (e.g., Cu, W) close to sensitive elements which can have significantly larger nuclear cross sections than in the 1 to 10 MeV/n energy regime. At the moment there is a large trend in the space community to increasingly use commercial off-the-shelf (COTS) electronic devices. One of the reasons is that many challenging space applications can only be met with COTS devices because there are simply no space-qualified devices [often referred to as High Reliability (HiRel)] available with the necessary performance. Another trend in the evolution of Si-based microelectronic integrated circuits is to create 3-dimensional (3D) structures. There are already commercially available 3D NAND-Flash devices [i.e., a type of non-volatile computer memory that uses floating-gate transistors that resembles a NAND (NOT-AND) gate] with several tens of active layers stacked on top of each other. These structures cannot be tested with low energy ions, due to the large depths of the sensitive volumes alone. For radiation tests ion beams are needed that provide constant LET over the whole stack (> 128 layers). In addition, e.g., in systems in a package, one finds several dies stacked on top of each in a single package. To investigate the aforementioned device types, the beam has to be able to penetrate through all the dies.

Keywords: single-event effect, space electronics, radiation effects, satellite systems, heavy ion accelerators, cosmic rays (CR)

OPEN ACCESS

Edited by:
Vincenzo Patera, Sapienza University of Rome, Italy

Reviewed by:
John Norbury, National Aeronautics and Space Administration (NASA), United States
Dimitris Emfietzoglou, University of Ioannina, Greece

****Correspondence:***
Stefan Metzger
stefan.metzger@int.fraunhofer.de

Specialty section:
This article was submitted to Medical Physics and Imaging, a section of the journal Frontiers in Physics

Received: *31 May 2020*
Accepted: *10 July 2020*
Published: *18 September 2020*

Citation:
Höeffgen SK, Metzger S and Steffens M (2020) Investigating the Effects of Cosmic Rays on Space Electronics. Front. Phys. 8:318. doi: 10.3389/fphy.2020.00318

INTRODUCTION

The radiation environment in space has severe adverse effects on humans, electronics, and materials. The most challenging part of the environment for our understanding of the effects is related to highly charged, highly energetic (HZE) heavy ions. As with cosmic rays (CRs), these ions can have energies of up to 1,020 eV with a maximum flux at around 1 GeV/n [1].

Only very few facilities in the world are capable of reaching high enough energies to realistically simulate CRs. The only facility in Europe is the GSI Helmholtzzentrum für Schwerionenforschung (GSI) in Darmstadt, Germany, with its heavy ion synchrotron SIS-18, which can reach energies of 1.5 GeV/n. The new heavy ion synchrotron SIS-100 of the Facility for Antiproton and Ion Research (FAIR) will extend this energy beyond 10 GeV/n. With both accelerators a very large part of the CR spectrum will be covered, opening unprecedented research possibilities. The available ion species at FAIR covers antiprotons (for selected experiments) and the whole periodic table from $Z = 1$ (hydrogen) to $Z = 92$ (uranium) [2].

Possible space radiation research is foreseen at the BIOMAT cave, operated by the APPA collaboration (Atomic, Plasma Physics, and Applications) [3].

This review looks at the possibilities FAIR offers for research on the effects of galactic cosmic rays on space electronics typically used onboard satellites or future manned space missions. In this review, we conduct an analysis of the open issues in space radiation effects on electronics that would require high energy heavy ions. Finally, some recommendations for a space radiation research program are given.

OPEN ISSUES CONCERNING THE EFFECTS OF GALACTIC COSMIC RAYS IN ELECTRONIC DEVICES

Open issues concerning electronics involving relativistic heavy ions are 2-fold. Firstly there are possible effects in the material that are different for ions of the same LET for higher energy than for lower energy [e.g., single-event effects (SEE) due to nuclear reactions]. Then there are new technologies that simply cannot be tested with low energy ions due to the limited range of the ions.

Dependence of the SEE Cross Sections on Ion Energy

Introduction

The radiation environment in space has severe adverse effects on electronic systems. To evaluate radiation sensitivity, electronics are tested on earth with various irradiation sources. Cosmic rays (CR) are the most difficult to simulate on earth. CR can have energies up to 1,020 eV, with a flux maximum at around 1 GeV/n [1]. For reasons of cost effectiveness and availability, the qualification tests on earth are done at accelerators with much lower energies, usually in the 10 MeV/n range, e.g., at the Heavy Ion Facility (HIF) of the Université catholique de Louvain, Belgium[1], or the RADiation Effects Facility (RADEF) of the University of Jyväskylä, Finland[2].

The lack of accelerators capable of providing relativistic ions has raised concerns about the fidelity of accelerator-based tests for simulating the response of parts to the real high energy ion environment found in space [4]. Early tests compared the single-event upset (SEU) cross section for ions with a few MeV/n and a hundred or more MeV/n with the same surface LET. They showed either no difference [5–7], or a lower cross section for the high energy ions in the threshold region, where direct ionization is sufficient to induce a SEE [8–10]. This lower cross section was explained by the heavy ion track structure [10]. Ions with higher energy will produce secondary electrons, which have themselves higher energy and can therefore travel farther away from the ion track. Thus, the track radius gets larger for ions with higher energy. This means they deposit less charge in the core area and are potentially less effective than the low energy ions.

More recently, another concern regarding high energy heavy ions has been raised, namely, that of nuclear interactions of high energy ions and the semiconductor materials of which the integrated circuits (IC) are made [11]. Here is an example of the results of a measurement campaign concentrating on high fluence measurements below threshold [12]. A 256 kbit static random-access memory (SRAM) was split into 16 blocks with different feedback resistors to produce different threshold LETs. **Figure 1** shows the results for block 3 with a threshold for direct ionization-induced SEUs of about 10 MeVcm²/mg. Low-energy heavy ion irradiations were performed using the tandem Van de Graaff at Brookhaven National Laboratory (BNL) with 11 different ions from C to Au, while high energy heavy ion irradiations were performed at the Texas A&M University (TAMU) heavy ion cyclotron with 5 different ions from Ne to Xe at different energies to result in different LETs. Here even the low-energy ions (10 MeV/n, BNL) produced a low cross section tail of SEUs down to an LET of 1.5 MeVcm²/mg, while the high energy ions (40 MeV/n, TAMU) produce a tail with an order of magnitude larger cross section in the region between 3 and 10 MeVcm²/mg of LET. Calculations have shown that the ion beams at both accelerators have enough energy to exceed the Coulomb barrier and produce Si recoil particles with a maximum LET of about 14 MeVcm²/mg [13]. To further test the assumption of nuclear reactions, a data point was taken with a very low energy (1 MeV/n) carbon beam. Although the beam was able to penetrate several microns deep into the sensitive region, it was not able to exceed the Coulomb barrier and produce recoils [13]. No SEUs have been measured for this data point.

Previous Measurements at GSI

To further investigate the possible influence of high energy heavy ions on electronics testing and to get an answer to the question marks in **Figure 2**, the European Space Agency (ESA) started a project using high energy beams at GSI [14, 15]. The comparisons

[1] Available online at: https://uclouvain.be/en/research-institutes/irmp/crc/applications-technologiques.html (accesses July 07, 2020).

[2] Available online at: https://www.jyu.fi/science/en/physics/research/infrastructures/accelerator-laboratory/radiation-effects-facility (accessed July 07, 2020).

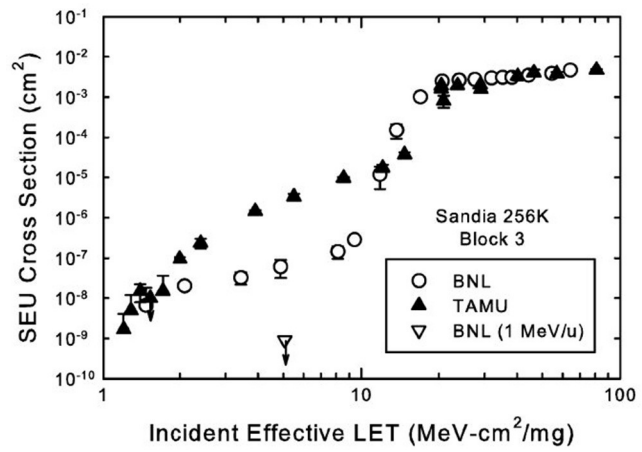

FIGURE 1 | Measured SEU cross section for block 3 of the Sandia 256 kbit SRAM taken with low energy (BNL) and high energy (TAMU) heavy ions [12]. Reproduced with permission from IEEE.

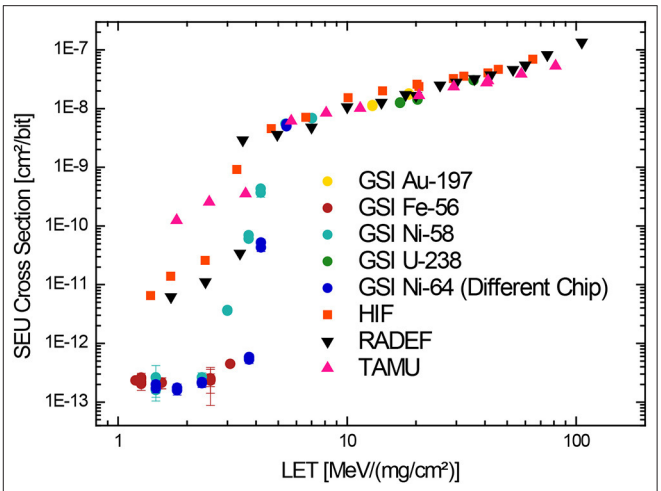

FIGURE 3 | Overview of results measured at GSI, TAMU, and RADEF [14].

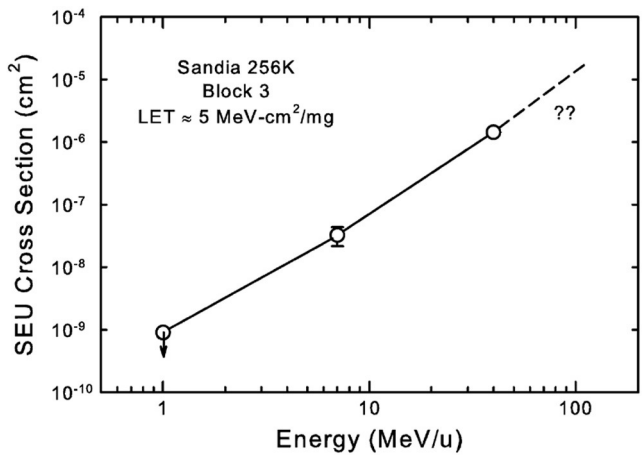

FIGURE 2 | Measured SEU cross section for block 3 of the Sandia 256 kbit SRAM taken with heavy ions having an LET of 5 (MeV cm²/mg) as a function of energy [12]. Reproduced with permission from IEEE.

were done with the ESA SEU Monitor, which was irradiated at GSI with Fe-56, Ni-58, Ni-64, Au-197, and U-238 ions. The irradiations were done in air and the lid of the chip package was removed.

Figure 3 gives an overview of the results of the irradiations at GSI [14] as well as data taken at RADEF with 6 ions of their standard 9.3 MeV/n cocktail beam [16] and ions of 15 and 25 MeV/n at TAMU [17]. Above the ionization threshold of ca. 4 MeVcm²/mg, there is very good agreement between the GSI (Au-197 and U-238), the TAMU, and the RADEF data. There is no energy effect for ions with similar LET in the range between 10 (RADEF) and 1,000 MeV/n.

A more interesting area is below the threshold region. To emphasize this region, we used a logarithmic x-axis. All data points are based on measured events. So even at 10 MeV/n (RADEF), ions below the ionization threshold are able to produce SEUs. The cross section rises further by over an order of magnitude by increasing the energy of the ions to 25 MeV/n (TAMU). The ions used at GSI were Fe-56, Ni-58, and Ni-64 with energies between 150 and 1,500 MeV/n in the sub-threshold region. The cross section is about two orders of magnitude lower than at 10 MeV/n.

Figure 4 shows the energy dependence for the two different LETs 1.8 and 2.4 MeVcm²/mg. There is an initial increase of the SEU cross section for low energies that was noticed previously in [12]. However, a noticeable decrease of the cross section over nearly 3 orders of magnitude was measured at higher energies of a few hundreds of MeV/n. The authors of [12] did not have access to high energy data and hence they questioned how far this increase would go. At least for the SEU Monitor our data show that the cross section will go down to higher energies. The open question remained as to what the worst-case testing energy for a specific type of chip would be.

There is also a discrepancy within the high energy data for the GSI measurements in the ionizing threshold area (see **Figure 5**). The Fe-56 and Ni-58 data were taken by Fraunhofer INT using the same SEU Monitor while the Ni-64 data were taken by V. Ferlet-Cavrois (ESA) using a different SEU Monitor. The Ni-64 data seem to have a steeper threshold curve which is also shifted to higher LETs. This is quite surprising because both measurements use the same element albeit different isotopes. The dosimetry at GSI is usually very precise and there is a very good agreement of all data above and below threshold. This fact rules out dosimetry as a possible systematic effect. This leaves chip to chip variations as a possible systematic effect causing the differences between the Ni-58 and Ni-64 data. There is however also a discrepancy between the Ni-58 and the Fe-56 data around an LET of 3 MeVcm²/mg. These two measurements were done using the same chip. This suggests that the effect is due to physical mechanisms not yet fully understood.

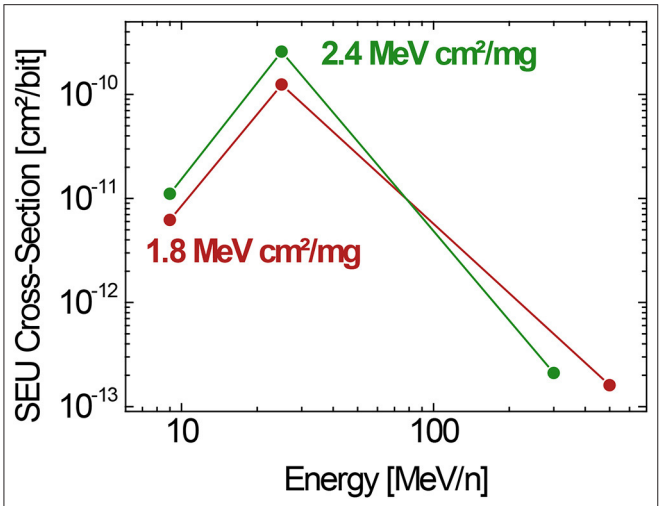

FIGURE 4 | Comparison of energy dependence at specific LET from [14].

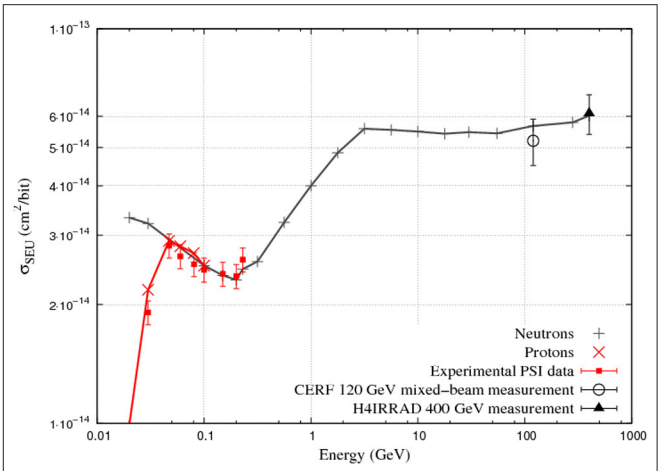

FIGURE 6 | Simulated proton and neutron SEU cross section of the ESA SEU Monitor compared to experimental proton measurements at PSI [19].

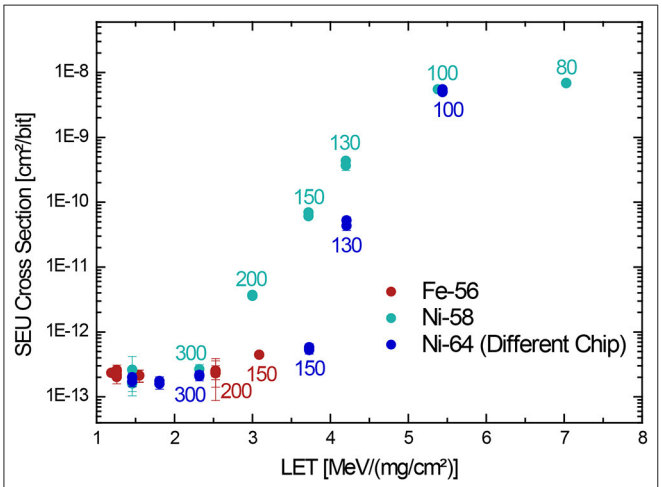

FIGURE 5 | Overview of results measured at GSI, TAMU, and RADEF [14]. The numbers at the data points are the ion energy in MeV/n.

Simulations of the ESA SEU Monitor and New Measurements

As part of their "Radiation to Electronics" (R2E) program, the European Organization for Nuclear Research (CERN) in Geneva, Switzerland investigated energy effects on the SEE cross section of electronics. These investigations also included, in collaboration with ESA, studies on the ESA SEU Monitor [18–21].

They first started with Monte-Carlo simulations, using **FLU**ktuierende **KA**skade (FLUKA) [21], of the interactions of protons and neutrons (and pions) with the ESA SEU Monitor (see **Figure 6**) [18–20]. They compared their results of the simulations to the measured cross section at PSI. They found a significant rise of the cross section in the energy range of the protons between 0.3 and 2 GeV. The devices were, as is commonly done in proton irradiations, simulated and irradiated without removing their lid. That means a 420 μm thick layer of Kovar with a gold and nickel plating covered the ESA SEU Monitor.

Although high energy hadrons are the main concern to electronics in the LHC environment, there were also FLUKA simulations done regarding the influence of high energy heavy ions on the ESA SEU Monitor [21]. The simulations were compared to the measurements previously done at RADEF, HIF, TAMU, and GSI [14], shown in section Previous Measurements at GSI, as well as to new measurements done at the Center for Advanced Radiation Technology (KVI) in Groningen, The Netherlands. **Figure 7** give an overview of the experimental data including the new KVI measurements. On the left, the results are shown as a function of LET and on the right as a function of ion energy.

The representation on the right of **Figure 7** is especially insightful since the LET of the primary ion is not a relevant quantity for effects based on nuclear reactions, as is the case in sub-threshold SEE. This goes one step further than **Figure 4**, which still compared the energy dependence of the cross sections only for ions having the same LET.

Figure 7 also shows some very peculiar behavior. While the C-13 and N-15 measurements done at HIF and RADEF at 10 MeV/n are fully compatible, the cross sections of the C-12 and Ne-20, both measured at KVI, show a distinctly opposite behavior. The C-12 cross sections decrease with energy and nicely fit the gap between the 10 MeV/n data and the high energy data taken at GSI. The Ne-22 cross section on the other hand increased with energy. The cross section is also fully compatible with the Ne-22 cross section previously measured at TAMU and with energy of 25 MeV/n.

Figure 8 shows the comparison of Monte Carlo simulations with the previous experimental data. The deposited energy in the sensitive volume is provided by the Monte Carlo (MC) Code [either FLUKA or CRÈME MC [22, 23]] and the probability of having an SEU is calibrated to the measured cross section above the threshold.

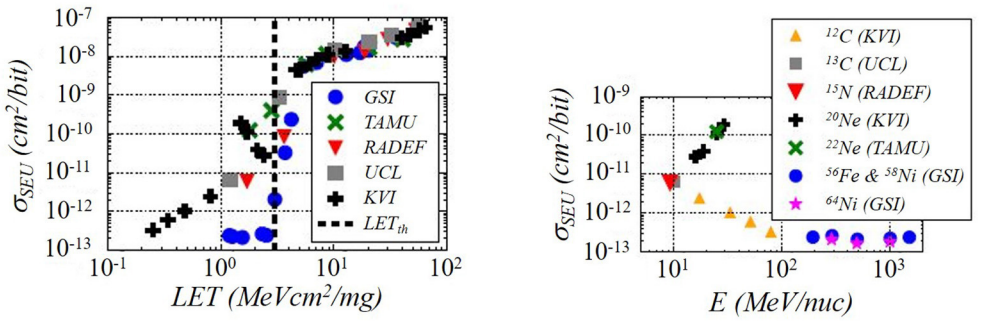

FIGURE 7 | Summary of heavy ion irradiations of the ESA SEU Monitor as a function of LET (left) and energy (right) [21]. Reproduced with permission from IEEE.

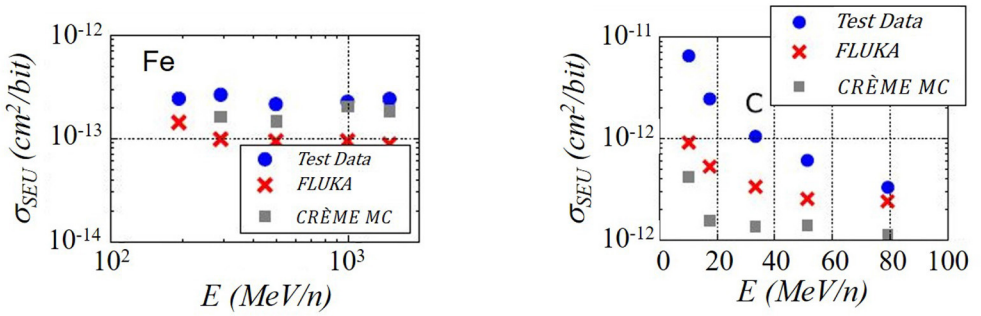

FIGURE 8 | Comparison of FLUKA simulations of heavy ion irradiations of the ESA SEU Monitor with experimental data [21]. Reproduced with permission from IEEE.

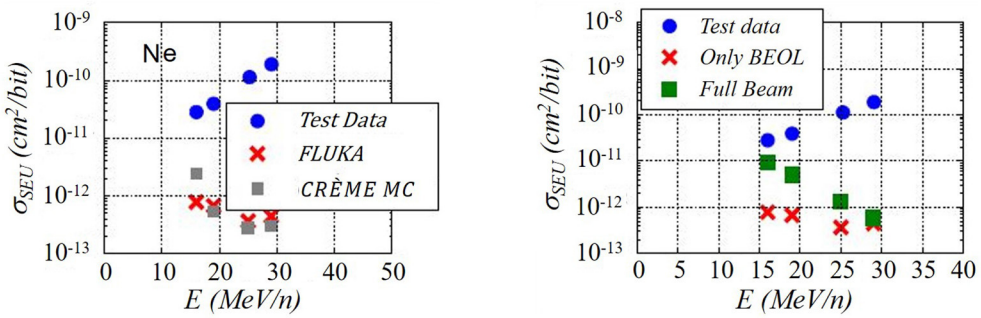

FIGURE 9 | FLUKA simulations of heavy ion irradiations of the ESA SEU Monitor at TAMU (left) and comparison of the cross sections of ions with LET of 1.8 MeV-cm²/mg (right) [21]. BEOL, back end of line. Reproduced with permission from IEEE.

For the high energy data on the left of **Figure 8**, the simulations are within reasonable agreement with the iron measurements done at the GSI. The carbon measurements on the right of **Figure 8** show the correct trend, while noticeably underestimating the data. The discrepancies are less for higher energies. It is interesting to notice that the FLUKA simulations are closer to the data for carbon while the CRÈME simulations are closer to the data for iron. In particular this stresses the need to use FAIR to improve the simulation codes for the interaction and transport of particles and nuclei in matter in the corresponding energy range.

Figure 9 shows on the left the FLUKA and CRÈME simulations in comparison to the neon data taken at KVI. Here the simulations underestimate the data up to a factor of 400. Also, the unusual trend of an increasing cross section found in the data cannot be reproduced by simulation. The data from KVI are, as already mentioned, in agreement with measurements at TAMU. In addition, pulse height measurements with a pin diode showed no contamination by other ion species or energies. Also, there is published data, where simulations underestimate the data for 40 MeV/n argon ions by the same margin [24]. The authors of [21] discuss several possible reasons:

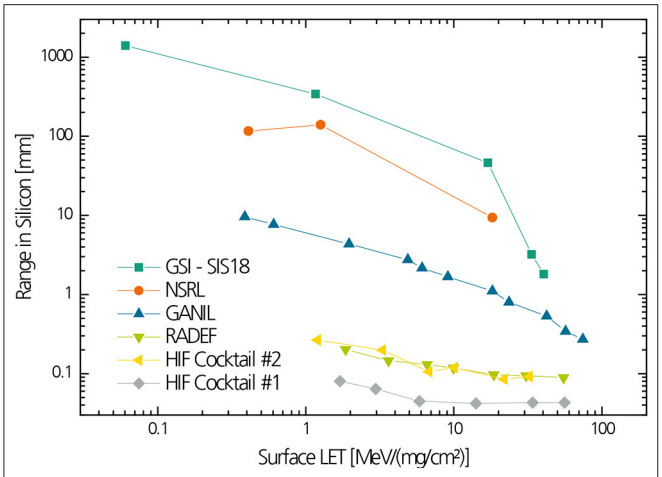

FIGURE 10 | Range in silicon vs. effective LET for several European heavy ion accelerators. Also included is the NASA Space Radiation Laboratory (NSRL) at the Brookhaven National Laboratory.

Firstly there could be a material effect. There is no indication that the SRAMs of the ESA SEU Monitor contain tungsten or other heavy elements that have a significant fission cross section [18]. The inclusion of a 50 nm tungsten slab directly above the sensitive volume showed that there are only effects for LET thresholds above 20 MeVcm^2/mg, which is much higher than the ∼3 MeVcm^2/mg of the ESA SEU Monitor.

Secondly, there could be beam size effects. Size effects refer to energy deposition inside the sensitive volume that comes from the space between the edges of the sensitive volume and the edge of the beam. The simulations were done with a beam size of 40 × 40 μm^2. An increase of the beam size to 200 × 200 μm^2 showed no difference.

Thirdly, there could also be an effect of the beam elements. To account for this the exit window, air, and degraders have been included in the simulation for Ne. The results are shown in **Figure 9** on the right as green squares. As can be seen, the inclusion shifts the points somewhat in the right direction but cannot reproduce the increase in the cross section with energy.

Finally, the simulation code could insufficiently describe the nuclear reactions involved. This was reported for similar simulations with GEANT4 [24]. The authors of [24] reported a serious underestimation of the inelastic fragment production energy for the then available models used in GEANT4. The nuclear models of FLUKA on the other hand are used and have been benchmarked for use in medical physics, where a high precision in fragment production energies is important [25]. This stresses again the need to use FAIR to improve the simulation codes as mentioned before.

Open Issues Concerning Energy Effects

There is a very recent publication by the CERN and ESA showing new cross sections for more modern SRAMs containing tungsten in the energy range of several 10s of MeV/n at KVI [26]. These measurements focus on SEL measurements, which have a higher LET threshold and are therefore more sensitive to the effects of nuclear reactions. The result is a consistent decrease of the sub-LET threshold cross section with energy. The cross sections can also be reproduced more or less satisfactorily with integral rectangular parallelepiped (IRPP) Monte Carlo simulations. The increase of the cross section with energy for the ESA SEU Monitor can still be seen for Ne-20, but not for C-12 and O-16. This increase remains an unsolved challenge.

The authors of [26] also extend their simulations to energies in the GeV/n regime and do rate calculations for a CR environment. They calculate even for their most sensitive component, an SRAM containing tungsten with an LET threshold of 15 MeVcm^2/mg, only a sub-LET threshold of below 10%. In addition, they claim the rate to be dominated by protons (85%), mainly due to their much higher fluxes. They admit however that for devices with even higher LET thresholds (e.g., above the iron knee at ∼30 MeVcm^2/mg) for which the high-Z fragments with larger LET could dominate the overall SEE rate. The same goes for packages that introduce a large amount of high-Z material near the sensitive volume [e.g., gold packages discussed in [27]].

Although these predictions are a relief for the space community regarding the hardness assurance, they are mainly based on simulations. A campaign with high energy protons, as well as ions, is needed to verify these predictions.

So far, all investigations of energy effects have concentrated on Si devices (some containing tungsten near the sensitive volume). So far, no results of investigations have been published with SiC or GaN devices, which are increasingly used in power electronics and high frequency devices.

Experimental Needs for High Energy Ions

Beside the need of high energy accelerators for investigating the contribution of secondary particles to SEE, this kind of accelerator has important experimental advantages compared to a low energy one.

Heavy ions with energies of only a few MeV/n have ranges in silicon of only about 100 μm (see **Figure 10**). Therefore, all irradiations must be performed inside a vacuum tube at the routinely used low energy accelerators. This needs for example a lot of feedthroughs and different electrical connectors. But for the operation of high-speed electronic devices (in the range of hundreds of Mbit/s or above) like in modern double data rate (DDR) 3 or 4 synchronous dynamic random-access memory (SDRAM) the distance between test instrumentation and device under test (DUT) is limited to a few centimeters (typically < 10 cm). This is difficult to guarantee at standard installations. For the testing of high-power devices, an efficient cooling system must be provided, particularly when the irradiation should be performed at different temperatures. And when the DUTs are changed it takes a quarter of an hour to proceed with the test because the chamber must be evacuated again.

Another problem of using low energy ions is that the LET varies dramatically inside the DUT and so the energy loss inside the sensitive volume is not the same as at the surface of the device. Therefore, one has to know exactly how the device is assembled to calculate the correct LET value. The problem becomes even worse if one tries to tilt the chip in order to increase the LET

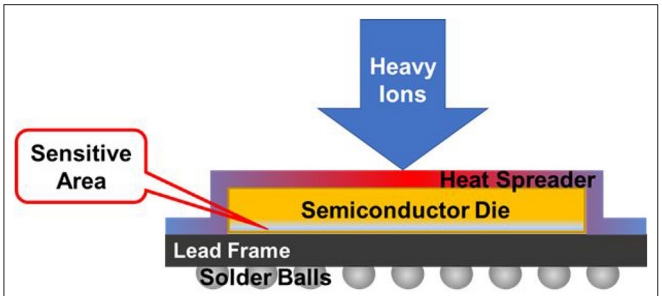

FIGURE 11 | Package of a modern SOC device.

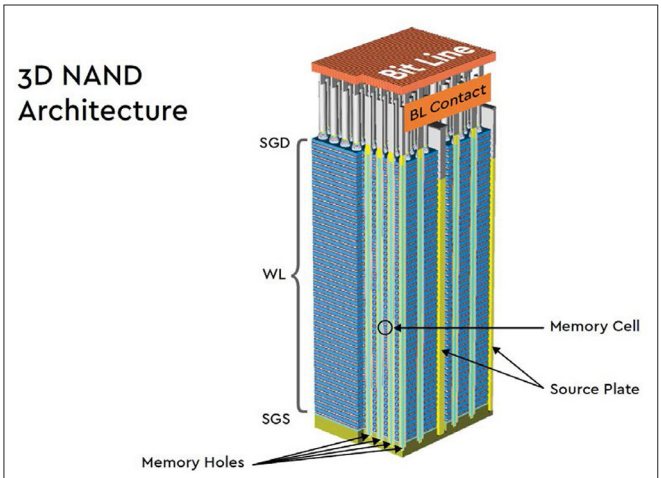

FIGURE 12 | Sketch of a modern 3D NAND FLASH structure architecture from Western Digital [32].

or has to irradiate the devices from the backside [28]. In most of the cases of irradiating modern devices with low energy heavy ions the experimenter has to open the chip or to thin it down to a few tens of μm because the range of ions in the semiconductor material is typically less than a few hundred μm (at maximum). So even at normal incidence the ions would not reach the sensitive volume because of their short range. Thinning became more difficult with the advent of new chip packages, e.g., ball grid arrays (BGA), and the increasing number of layers and metallization. Thickness non-uniformity can be rather large and make it necessary to calculate the correct LET for each specific point of the device [28].

Irradiations are usually limited to tilt angles of 60–70°, because otherwise there is too much matter between the beam and the sensitive area. But it can be shown that half of the CR flux hits the device at angles larger than 60° [29]. Here the device might be very sensitive to multiple bit upsets (MBU) along the ion track, which can reduce or even negate the effectiveness of error correction codes.

While a lot of the discussed issues make testing at low energy accelerators more and more challenging, recent technologies can make it impossible (see **Figure 11**) because the penetration depth of these ions is too small by far. A recent study of a state-of-the-art system on a chip (SOC) devices by NASA showed that thermal problems after opening and removing the heat spreader will limit the use of low energy accelerators [30].

These devices are commonly in a flip chip package with a heat spreader covering one side providing the necessary contact with the heat sink (see **Figure 11**). This heat spreader forms a layer of copper (300 μm for the Freescale P2020 as an example) on top of the chip, impenetrable for ions from low energy accelerators [31]. Removing the heat spreader completely might damage the device. In [31] it is recommended that the heat spreader is only removed over small areas of the die at a time, while attaching a modified heat sink to the remaining portion. It is foreseeable that this approach can use smaller and smaller areas and will fail in the future.

The current trend in the evolution of Si-based microelectronic integrated circuits is to create 3-dimensional structures. There are already commercially available 3D NAND-Flash devices with several tens of active layers stacked on top of each other (see **Figure 12**). These structures will be impossible to test with low energy ions, due to the large depths of the sensitive volumes alone. For testing ions are needed that provide constant LET over the whole stack [128 layers as of June 2019 [33], continuously growing]. Because of their commercial availability, 3D NAND-Flash devices could serve as representative components to develop general Radiation Hardness Assurance methods for 3D technologies including new failure mechanisms.

It might be commercially more interesting to test whole boards, systems, or even small satellites, than to qualify every part separately. Because of the high range of the beam, it would be feasible to make a campaign, where a large number of devices are tested simultaneously by stacking several boards. Extending the previous point, whole systems or even small satellites could be tested at FAIR with the 10 GeV/n beam to, e.g., test the effectiveness of mitigation techniques on system level.

SUMMARY AND RECOMMENDED RESEARCH

So far there has only been one campaign to compare the effects of heavy ions of several MeV/n to 1 GeV/n. The device, the ESA SEU monitor, was of older design but very thoroughly characterized at different accelerator facilities. There were some unexpected results that could not be completely answered with simulations of the device. Based on this, a preliminary research program for energy effects on modern Si-based microelectronics should include:

- An extension of the measurements with the SEU monitor up to 10 GeV/n. Although the SEU monitor is of older design, its character as a reference device, that was tested at nearly all relevant accelerators for radiation effects in Europe and that was intensively simulated, makes it a must for any research on energy effects.
- A measurement program similar to the SEU monitor with devices having a higher SEU thresholds (hardened) as well as SEL measurements. SEL is an effect with an intrinsic high threshold (the SEU monitor is SEL free). The devices should contain at least tungsten, possibly also other new materials

recently used in novel IC designs. A first step would be comparisons of 10–30 MeV/n, e.g., at RADEF and KVI with 100–1,000 MeV/n at SIS-18 in cave A/M. These could later be extended to energies up to 10 GeV/n at SIS-100 and the BIOMAT cave. This program should help to answer the very relevant question of the magnitude of the energy effects under realistic CR conditions and whether it will be necessary to use very high energy heavy ions for qualification in the future.

Other materials are also already used in other areas than digital microelectronics. Wide band gap materials such as SiC and GaN are increasingly applied in power and high-frequency devices. These materials have a wider band gap and higher density then Si-based devices. It is therefore interesting to investigate the possible influences of the ion energy on these devices regarding the track structure.

A contribution of nuclear reactions to effects in devices can also originate from the packaging. Since the sudden occurrence of unexpected destructive events is a major hardness assurance concern, the influence of the micro environment created by the interaction of the packaging and high energy ions should be further investigated.

Other than the effect of the energy regarding interactions of the ions provided by FAIR, the very high penetration depth of these ions has experimental advantages that could be exploited in the following studies:

- There is a strong interest for using state-of-the-art microprocessors or even system on a chip (SoC) devices in space. These devices have high requirements on cooling. Without a heat spreader made out of copper of several hundreds of μm thickness, the device will be damaged during operation because of excessive heat and by no means can be tested with low energy accelerators. A series of interesting COTS devices could be qualified to choose those that can be used in a space environment. The SIS-18 energies will probably suffice for these tests.
- The current trend in the evolution of Si-based microelectronic integrated circuits is to create 3-dimensional structures. There are already commercially available 3D NAND-Flash devices with several tens of active layers stacked on top of each other. These structures will be impossible to test with low energy ions, due to the large depths of the sensitive volumes alone. For testing, ions are needed that provide constant LET over the whole stack (e.g., 128). Because of their commercial availability, 3D NAND-Flash devices could serve as representative components to develop general Radiation Hardness Assurance methods for 3D technologies including new failure mechanisms.
- It might be commercially more interesting to test whole boards or systems than to qualify every part separately. Because of the high penetrations of the beam it would be feasible to make a campaign where a large number of devices are tested simultaneously by stacking several boards in a row. A first study would be a proof of concept of how many devices could be tested in one campaign.
- Extending the previous point, whole systems or even small satellites could be tested at FAIR with the 10 GeV/n beam to, e.g., test the effectiveness of mitigation techniques on a system level.

AUTHOR CONTRIBUTIONS

SH, SM, and MS contributed to the design and implementation of the research, to the analysis of the results, and to the writing of the manuscript. All authors contributed to the article and approved the submitted version.

FUNDING

Part of the work was funded by ESA under Contract No. 4000110709/14/NL/MV.

REFERENCES

1. Stassinopoulos EG, Raymond JP. The space radiation environment for electronics. *Proc IEEE*. (1988) 76:1423–42. doi: 10.1109/5.90113
2. FAIR. *Baseline Technical Report*, Vol. 1. Darmstadt: FAIR (2006).
3. FAIR. *Baseline Technical Report*, Vol. 5. Darmstadt: FAIR (2006).
4. Stapor WJ, McDonald PT, Knudson AR, Campbell AB, Glagola BG. Charge collection in silicon for ions of different energy but same linear energy transfer (LET). *IEEE Trans Nucl Sci*. (1988) 35:1585–90. doi: 10.1109/23.25502
5. Ecoffet R, Duzellier S, Falguère D, Guibert L, Inguimbert C. Low LET cross-section measurements using high energy carbon beam. *IEEE Trans Nucl Sci*. (1997) 4:2230–6. doi: 10.1109/23.659040
6. Koga R, Crain SH, Crain WR, Crawford KB, Hansel SJ. Comparative SEU sensitivies to relativistic heavy ions. *IEEE Trans Nucl Sci*. (1998) 45:2475–82. doi: 10.1109/23.736488
7. Dodd PE, Musseau O, Shaneyfelt MR, Sexton FW, D'hose C, Hash GL, et al. Impact of ion energy on single-event upset. *IEEE Trans Nucl Sci*. (1998) 45:2483–91. doi: 10.1109/23.736489
8. Criswell TL, Measel PR, Wahlin KL. Single event upset testing with relativistic heavy ions. *IEEE Trans Nucl Sci*. (1984) 31:1559–62. doi: 10.1109/TNS.1984.4333548
9. Duzellier S,Falguère D, Moulière L, Ecoffet R, Buisson J. SEE results using high energy ions. *IEEE Trans Nucl Sci*. (1995) 42:1797–802. doi: 10.1109/23.488781
10. Musseau O, Gardic F, Roche P, Corbière T, Reed RA, Buchner S, et al. Analysis of multiple bit upsets (MBU) in a CMOS SRAM. *IEEE Trans Nucl Sci*. (1996) 43:2879–88. doi: 10.1109/23.556881
11. Warren KM, Weller RA, Mendenhall MH, Reed RA, Ball DR, Howe CL, et al. The contribution of nuclear reactions to heavy ion single event upset cross section measurements in a high-density SEU hardened SRAM. *IEEE Trans Nucl Sci*. (2005) 52:2125–31. doi: 10.1109/TNS.2005.860677
12. Dodd PE, Schwank JR, Shaneyfelt MR, Felix JA, Ferlet-Cavrois V, Paillet P, et al. Impact of heavy ion energy and nuclear interactions on single–event upset and latchup in integrated circuits. *IEEE Trans Nucl Sci*. (2007) 54:2303–11. doi: 10.1109/TNS.2007.909844
13. Reed RA, Weller RA, Schrimpf RD, Mendenhall MH, Warren KM, Massengill LW. Implications of nuclear reactions for single event effects test methods and analysis. *IEEE Trans Nucl Sci*. (2006) 53:3356–62. doi: 10.1109/TNS.2006.885950
14. Hoeffgen SK, Metzger S, Alpat B, Menichelli M, Desorgher L. *Investigation and Analysis of Very High Energy Accelerators for Radiation Simulation*. ESA-ESTEC ITT/1-5897/08/NL/JK Final Report. Noordwijk (2011).

15. Hoeffgen SK, Durante M, Ferlet-Cavrois V, Harboe-Sørensen R, Lennartz W, Kündgen T, et al. Investigations of single event effects with heavy ions of energies up to 1.5 GeV/n. *IEEE Trans Nucl Sci.* (2012) 59:1161–6. doi: 10.1109/TNS.2012.2201502
16. Harboe-Sorenson R, Guerre FX, Roseng A. Design, testing and calibration of a reference seu monitor system. In: *RADECS 2005, Proceedings of the 8th European Conference on Radiation and Its Effects on Components and Systems*. Agde (2005). p. B3-1–7. doi: 10.1109/RADECS.2005.4365561
17. Harboe-Sørensen R, Harboe-Sørensen R, Poivey C, Fleurinck N, Puimege K, Zadeh A, et al. The technology demonstration module on-board PROBA-II. *IEEE Trans Nucl Sci.* (2011) 58:1001–7. doi: 10.1109/TNS.2010.2095468
18. García Alía R, Biskup B, Brugger M, Calviani M, Poivey C, Roed K, et al. SEU measurements and simulations in a mixed field environment. *IEEE Trans Nucl Sci.* (2013) 60:2469–76. doi: 10.1109/TNS.2013.2249096
19. Hoeffgen SK, Metzger S, Brings R, Felden O, Gebel R, Maier R, et al. Past, present and future activities for radiation effects testing at JULIC/COSY. In: *Cyclotrons 2013, Proceedings of the 20th International Conference on Cyclotrons and their Applications*. Vancouver, BC (2013). p. 88–90.
20. García Alía R, Brugger M, Danezeca S, Ferlet-Cavrois V, Poivey C, Roed K, et al. SEE measurements and simulations using monoenergetic GeV-energy hadron beams. *IEEE Trans Nucl Sci.* (2013) 60:4142–9. doi: 10.1109/TNS.2013.2279690
21. García Alía R, Bahamonde C, Brandenburg S, Brugger M, Daly E, Ferlet-Cavrois V, et al. Sub-LET threshold SEE cross section dependency with ion energy. *IEEE Trans Nucl Sci.* (2015) 62:1558–78. doi: 10.1109/TNS.2015.2483021
22. Tylka AJ, Adams JH Jr, Boberg PR, Brownstein B, Dietrich WF, Flueckiger EO, et al. CREME96: a revision of the cosmic ray effects on microelectronics code. *IEEE Trans Nucl Sci.* (1997) 44:2150–60. doi: 10.1109/23.659030
23. Weller RA, Mendenhall MH, Reed RA, Schrimpf RD, Warren KM, Sierawski BD, et al. Monte carlo simulation of single event effects. *IEEE Trans Nucl Sci.* (2010) 57:1726–46. doi: 10.1109/TNS.2010.2044807
24. Reed RA, Weller RA, Mendenhall MH, Lauenstein JM, Warren KM, Pellish JA, et al. Impact of ion energy and species on single event effects analysis. *IEEE Trans Nucl Sci.* (2007) 54:2312–21. doi: 10.1109/TNS.2007.909901
25. Ferrari A, Sala PR, Fasso A, Ranft J. *FLUKA, A Multi-Particle Transport Code* Geneva: CERN (2005). doi: 10.2172/877507
26. García Alía R, Brugger M, Ferlet-Cavrois V, Brandenburg S, Calcutt J, Cerutti F, et al. Proton dominance of Sub-LET threshold GCR SEE rate. *IEEE Trans Nucl Sci.* (2017) 64:388–97. doi: 10.1109/TNS.2016.2628363
27. Turflinger TL, Clymer DA, Mason LW, Stone S, George JS, Savage M, et al. RHA implications of proton on gold-plated package structures in SEE evaluations. *IEEE Trans Nucl Sci.* (2015) 62:2468–75. doi: 10.1109/TNS.2015.2496288
28. Harboe-Sorenson R, Guerre FX, Lewis G. Heavy-Ion SEE test concept and results for DDR-II memories. *IEEE Trans Nucl Sci.* (2006) 54:2125–30. doi: 10.1109/TNS.2007.909747
29. Pellish JA, Xapsos MA, LaBel KA, Marshall PW, Heidel DF, Rodbell KP, et al. Heavy ion testing at the galactic cosmic ray energy peak. In: *RADECS 2009, Proceedings of the 10th European Conference on Radiation and Its Effects on Components and Systems*. Bruges (2009). p. 559–62.
30. Guertin SM. *SOC SEE Qualification Guideline,* 4th edn. NEPP Electronic Technology Workshop. Greenbelt (2013).
31. Guertin SM. *FY11 End of Year Report NEPP SOC Devices*. Pasadena: JPL Publ. (2012).
32. Klein A, Harlin S. *Western Digital and the 3D NAND Revolution – Understanding 3D NAND Technology and its Future Challenges*. Western Digital Technology Brief (2017).
33. Anton S. *SK Hynix Starts Production of 128-Layer 4D NAND, 176-Layer Being Developed*. (2019). Available online at: https://www.anandtech.com/show/14589/sk-hynix-128-layer-4d-nand (accessed July 07, 2020).

Conflict of Interest: The authors declare that the research was conducted in the absence of any commercial or financial relationships that could be construed as a potential conflict of interest.

frontiers in Physics

ORIGINAL RESEARCH
published: 29 September 2020
doi: 10.3389/fphy.2020.567738

LhARA: The Laser-hybrid Accelerator for Radiobiological Applications

Galen Aymar[1], Tobias Becker[2], Stewart Boogert[3], Marco Borghesi[4], Robert Bingham[1,5], Ceri Brenner[1], Philip N. Burrows[6], Oliver C. Ettlinger[7], Titus Dascalu[8], Stephen Gibson[3], Timothy Greenshaw[9], Sylvia Gruber[10], Dorothy Gujral[11], Claire Hardiman[11], Jonathan Hughes[9], W. G. Jones[8,12], Karen Kirkby[13], Ajit Kurup[8], Jean-Baptiste Lagrange[1], Kenneth Long[1,8], Wayne Luk[8], John Matheson[1], Paul McKenna[5,14], Ruth McLauchlan[11], Zulfikar Najmudin[7], Hin T. Lau[8], Jason L. Parsons[15,16], Jaroslaw Pasternak[1,8], Juergen Pozimski[1,8], Kevin Prise[17], Monika Puchalska[18], Peter Ratoff[14,19], Giuseppe Schettino[20,21], William Shields[3], Susan Smith[22], John Thomason[1], Stephen Towe[23], Peter Weightman[8], Colin Whyte[5] and Rachel Xiao[24]*

[1] STFC Rutherford Appleton Laboratory, Didcot, United Kingdom, [2] Maxeler Technologies Limited, London, United Kingdom, [3] John Adams Institute for Accelerator Science, Royal Holloway, University of London, Egham, United Kingdom, [4] Centre for Plasma Physics, Department of Physics, Queens University Belfast, Belfast, United Kingdom, [5] Department of Physics, SUPA, University of Strathclyde, Glasgow, United Kingdom, [6] John Adams Institute for Accelerator Science, University of Oxford, Oxford, United Kingdom, [7] John Adams Institute for Accelerator Science, Imperial College London, London, United Kingdom, [8] Department of Physics, Imperial College London, London, United Kingdom, [9] Department of Physics, University of Liverpool, Liverpool, United Kingdom, [10] Christian Doppler Laboratory for Medical Radiation Research for Radiation Oncology, Medical University of Vienna, Vienna, Austria, [11] Imperial College Healthcare NHS Trust, The Bays, St Mary's Hospital, London, United Kingdom, [12] Imperial Patient and Public Involvement Group, Imperial College London, London, United Kingdom, [13] Division of Cancer Sciences, School of Medical Sciences, University of Manchester, Manchester, United Kingdom, [14] Daresbury Laboratory, Cockcroft Institute, Sci-Tech Daresbury, Liverpool, United Kingdom, [15] Institute of Translational Medicine, Department of Molecular and Clinical Cancer Medicine, University of Liverpool, Liverpool, United Kingdom, [16] The Clatterbridge Cancer Centre, Liverpool, United Kingdom, [17] Centre for Cancer Research Cell Biology, School of Medicine, Dentistry and Biomedical Sciences, Queens University Belfast, Belfast, United Kingdom, [18] Atominstitut, Technische Universität Wien, Vienna, Austria, [19] Physics Department, Lancaster University, Lancaster, United Kingdom, [20] National Physical Laboratory, London, United Kingdom, [21] University of Surrey, London, United Kingdom, [22] STFC Daresbury Laboratory, Liverpool, United Kingdom, [23] Leo Cancer Care, London, United Kingdom, [24] Corerain Technologies, Shenzhen, China

OPEN ACCESS

Edited by:
Vincenzo Patera,
Sapienza University of Rome, Italy

Reviewed by:
Lorenzo Manti,
University of Naples Federico II, Italy
Giuseppe A. Pablo Cirrone,
Laboratori Nazionali del Sud (INFN), Italy

***Correspondence:**
Ajit Kurup
a.kurup@imperial.ac.uk

Specialty section:
This article was submitted to Medical Physics and Imaging, a section of the journal Frontiers in Physics

Received: 30 May 2020
Accepted: 28 August 2020
Published: 29 September 2020

Citation:
Aymar G, Becker T, Boogert S, Borghesi M, Bingham R, Brenner C, Burrows PN, Ettlinger OC, Dascalu T, Gibson S, Greenshaw T, Gruber S, Gujral D, Hardiman C, Hughes J, Jones WG, Kirkby K, Kurup A, Lagrange J-B, Long K, Luk W, Matheson J, McKenna P, McLauchlan R, Najmudin Z, Lau HT, Parsons JL, Pasternak J, Pozimski J, Prise K, Puchalska M, Ratoff P, Schettino G, Shields W, Smith S, Thomason J, Towe S, Weightman P, Whyte C and Xiao R (2020) LhARA: The Laser-hybrid Accelerator for Radiobiological Applications. Front. Phys. 8:567738. doi: 10.3389/fphy.2020.567738

The "Laser-hybrid Accelerator for Radiobiological Applications," LhARA, is conceived as a novel, flexible facility dedicated to the study of radiobiology. The technologies demonstrated in LhARA, which have wide application, will be developed to allow particle-beam therapy to be delivered in a new regimen, combining a variety of ion species in a single treatment fraction and exploiting ultra-high dose rates. LhARA will be a hybrid accelerator system in which laser interactions drive the creation of a large flux of protons or light ions that are captured using a plasma (Gabor) lens and formed into a beam. The laser-driven source allows protons and ions to be captured at energies significantly above those that pertain in conventional facilities, thus evading the current space-charge limit on the instantaneous dose rate that can be delivered. The laser-hybrid approach, therefore, will allow the radiobiology that determines the response of tissue to ionizing radiation to be studied with protons and light ions using a wide variety of time structures, spectral distributions, and spatial configurations at instantaneous dose rates up to and significantly beyond the ultra-high dose-rate "FLASH" regime. It is proposed that LhARA be developed in two stages. In the first stage, a programme of *in vitro* radiobiology will be served with proton beams with energies between 10 and 15 MeV. In stage two, the beam will be accelerated using a fixed-field

alternating-gradient accelerator (FFA). This will allow experiments to be carried out *in vitro* and *in vivo* with proton beam energies of up to 127 MeV. In addition, ion beams with energies up to 33.4 MeV per nucleon will be available for *in vitro* and *in vivo* experiments. This paper presents the conceptual design for LhARA and the R&D programme by which the LhARA consortium seeks to establish the facility.

Keywords: radiobiology, novel acceleration, proton beam therapy (PBT), ion beam therapy, laser-driven acceleration, plasma lens, fixed-field alternating-gradient acceleration

LAY SUMMARY

It is well-established that radiation therapy (RT) is an effective treatment for many types of cancer. Most treatments are delivered by machines that accelerate electrons which are then used to produce a beam of high-energy photons (X-rays) which are directed at a tumor to kill cancer cells. However, healthy tissue anywhere in the path of the photon beam is also irradiated and so can be damaged. Modern X-ray therapy is able to reduce this damage by using several beams at different angles. Recent years have seen the use of a new type of machine in which protons are accelerated to produce proton beams (rather than photon beams) which are directed at a tumor. These proton beams can be arranged to deposit almost all of their energy in a small volume within a tumor so they cause little damage to healthy tissue; a major advantage over photon beams. But proton machines are large and expensive, so there is a need for the development of proton machines that are smaller, cheaper and more flexible in how they can be used. The LhARA project is aimed at the development of such proton machines using a new approach based on high power lasers. Such new machines could also make it easier to deliver the dose in very short high-intensity pulses and as a group of micro-beams—exciting recent research has shown that this brings improved effectiveness in killing cancer cells while sparing healthy tissue. The technology to be proved in LhARA should enable a course of RT to be delivered in days rather than weeks. Scientifically, there is a need to understand better the basic processes by which radiation interacts with biological matter to kill cancer cells—the investigation of these processes involves physics as well as biology. Thus the most important aim of LhARA is to pursue this radiobiological research in new regimens and from this to develop better treatments. LhARA will also pursue technological research into laser-hybrid accelerators.

1. INTRODUCTION

Cancer is the second most common cause of death globally [1]. In 2018, 18.1 million new cancer cases were diagnosed, 9.6 million people died of cancer-related disease, and 43.8 million people were living with cancer [2, 3]. It is estimated that 26.9 million life-years could be saved in low- and middle-income countries if radiotherapy capacity could be scaled up [4]. Novel techniques incorporated in facilities that are at once robust, automated, efficient, and cost-effective are required to deliver the required scale-up in provision.

Radiation therapy a cornerstone of cancer treatment, is used in over 50% of cancer patients [5]. The most frequently used types of RT employ photon or electron beams with MeV-scale energies. Proton and ion beams offer substantial advantages over X-rays because the bulk of the beam energy is deposited in the Bragg peak. This allows dose to be conformed to the tumor while sparing healthy tissue and organs at risk. The benefits of proton and ion-beam therapy (PBT) are widely recognized. PBT today is routinely delivered in fractions of ~ 2 Gy per day over several weeks; each fraction being delivered at a rate of $\lesssim 5$ Gy/min deposited uniformly over the target treatment volume. There is evidence of therapeutic benefit when dose is delivered at ultra-high rate, $\gtrsim 40$ Gy/s, in "FLASH" RT [6–10] or when multiple micro-beams with diameter <1 mm distributed over a grid with inter-beam spacing $\sim$ 3 mm are used [11–16]. However, the radiobiological mechanisms by which the therapeutic benefit is generated using these approaches are not entirely understood.

LhARA, the Laser-hybrid Accelerator for Radiobiological Applications, is conceived as the new, highly flexible, source of radiation that is required to explore the mechanisms by which the biological response to ionizing radiation is determined by the physical characteristics of the beam. A high-power pulsed laser will be used to drive the creation of a large flux of protons or ions which are captured and formed into a beam by strong-focusing plasma lenses. The plasma (Gabor) lenses provide the same focusing strength as high-field solenoids at a fraction of the cost. Rapid acceleration will be performed using a fixed-field alternating-gradient accelerator (FFA), thereby preserving the unique flexibility in the time, energy, and spatial structure of the beam afforded by the laser-driven source.

The LhARA facility may be developed in two stages. In the first stage, the laser-driven beam, captured and transported using plasma lenses and bending magnets, will serve a programme of *in vitro* radiobiology with proton beams of energy of up to 15 MeV. In stage two, the beam will be accelerated using an FFA. This will allow experiments to be carried out *in vitro* and *in vivo* with proton-beam energies of up to 127 MeV. Ion beams (including C^{6+}) with energies up to 33.4 MeV per nucleon will also be available.

The laser pulse that initiates the production of protons or ions at LhARA may be triggered at a repetition rate of up to 10 Hz. The time structure of the beam may therefore be varied to interrupt the chemical and biological pathways that determine the biological response to ionizing radiation using 10 ns to 40 ns long proton or ion bunches repeated at intervals as small as 100 ms. The technologies chosen to capture, transport, and

accelerate the beam in LhARA ensure that this unique capability is preserved. The LhARA beam may be used to deliver an almost uniform dose distribution over a circular area with a maximum diameter of between 1 and 3 cm. Alternatively, the beam can be focused to a spot with diameter of $\sim$ 1 mm.

The technologies that will be developed in LhARA have the potential to make PBT available to the many. The laser-hybrid approach will allow radiobiological studies and eventually radiotherapy to be carried out in completely new regimens, delivering a variety of ion species in a broad range of time structures, spectral distributions, and spatial configurations at instantaneous dose rates up to and potentially significantly beyond the current ultra-high dose-rate "FLASH" regime.

The "pre Conceptual Design Report" (pre-CDR) for LhARA [17] lays the foundations for the development of full conceptual and technical designs for the facility. The pre-CDR also contains a description of the R&D that is required to demonstrate the feasibility of critical LhARA components and systems. This paper presents a summary of the contents of the pre-CDR and lays out the vision of the LhARA consortium.

2. MOTIVATION

RT delivered using protons and ions, PBT, has the potential to overcome some of the fundamental limitations of X-rays in cancer treatment through the targeted delivery of the radiation dose [18]. The Particle Therapy Co-Operative Group (PTCOG) currently lists 90 proton therapy facilities and 12 carbon ion therapy facilities worldwide, located predominantly in high-income countries [19]. Low- and middle-income countries (LMIC) are relatively poorly served, indeed nearly 70% of cancer patients globally do not have access to RT [5].

2.1. The Case for a Systematic Study of the Radiobiology of Proton and Ion Beams

The efficacy of proton and ion beams is characterized by their relative biological effectiveness (RBE) in comparison to a reference photon beam. The treatment-planning software that is in use in the clinic today assumes an RBE value for protons of 1.1 [20], meaning that, compared to X-rays, a lower dose of protons is needed to produce the same therapeutic effect. However, the rapid rise in the linear energy transfer (LET) at the Bragg peak leads to significant uncertainties in the RBE. Furthermore, it is known that RBE depends strongly on many factors, including particle energy, dose, dose rate, the degree of hypoxia, and tissue type [21]. Indeed, RBE values from 1.1 to over 3 have been derived from *in vitro* clonogenic-survival assay data following proton irradiation of cultured cell lines derived from different tumors [21–23]. RBE values of $\sim$ 3 are accepted for high-LET carbon-ion irradiation, although higher values have been reported [24]. RBE uncertainties for carbon and other ion species are at least as large as they are for protons. These uncertainties can lead to an incorrect estimation of the dose required to treat a particular tumor. Overestimation can lead to the damage of healthy tissue, while an underestimate can lead to the tumor not being treated sufficiently for it to be eradicated.

The radiotherapeutic effect is caused largely by irreparable damage to the cell's DNA. The spectrum of DNA damage induced within tumor cells changes in response to differences in RBE. Larger RBE values, corresponding to higher LET, can increase the frequency and complexity of DNA damage, in particular causing DNA double-strand breaks (DSB) and complex DNA damage (CDD), where multiple DNA lesions are induced in close proximity [25, 26]. These DNA lesions are a major contributor to radiation-induced cell death as they represent a significant barrier to the cellular DNA-repair machinery [25]. However, a number of other biological factors contribute to varying RBE in specific tumors, including the intrinsic radio-sensitivity of the tissue, the level of oxygenation (hypoxia), the growth and re-population characteristics, and the associated tumor micro-environment. Consequently, there is still significant uncertainty in the precise radiobiological mechanisms that arise and how these mechanisms determine the impact of PBT. Detailed systematic studies of the biophysical effects of the interaction of protons and ions, under different physical conditions, with different tissue types will provide important information on RBE variation and could enable enhanced patient treatment-planning algorithms to be devised. In addition, studies examining the impact of combination therapies with PBT (e.g., targeting the DNA damage response, hypoxia signaling mechanisms and also the tumor micro-environment) are currently sparse; performing these studies will therefore provide input vital to the development of future personalized patient-therapy strategies using PBT.

2.2. The Case for Novel Beams for Radiobiology

Extending the range of beam characteristics used in PBT delivery may have significant therapeutic benefits. Delivery of RT at high dose rates has led to noticeably reduced lung fibrosis in mice, reduced skin toxicity in mini-pigs, and reduced side-effects in cats with nasal squamous-cell carcinoma, effects currently thought to be mediated via local oxygen depletion [10, 27]. In fact, the first patient with $CD30^+$ T-cell cutaneous lymphoma has been safely treated with electrons delivered at FLASH dose rates [28]. In addition, therapeutic benefit has been demonstrated with the use of multiple micro-beams [12]. However, there is still significant uncertainty regarding the thresholds and the radiobiological mechanisms underlying these effects. Extensive further study both *in vitro* and in appropriate *in vivo* models is required.

The LhARA facility will provide access to proton and stable ion beams, provide a wide variety of temporal, spatial, and spectral fractionation schemes, and deliver reliable and reproducible biological data with fewer constraints than at current clinical centers. LhARA will allow direct radiobiological comparisons of the effects of different charged particles at different energies and dose rates and enable unique mechanistic studies (e.g., examination of the oxygen depletion hypothesis for FLASH). In addition, LhARA will enable exhaustive evaluations of RBE using more complex end-points (e.g., angiogenesis and inflammation) in addition to routine survival measurements. The ability to evaluate charged particles in conjunction with other

therapies (immunotherapy and chemotherapy) and to perform *in vivo* experiments with the appropriate animal models is of great importance given the current lack of evidence in these areas. LhARA therefore has the potential to provide the radiobiological data required to improve clinical practice.

The simulations of LhARA presented in this document have been used to estimate the dose delivered as a function of energy for protons and carbon ions. These simulations, described in sections 3.3 and 3.4, show instantaneous particle rates of the order of 10^9 particles per shot can be achieved, corresponding to average dose rates of up to $\gtrsim$120 Gy/s for protons and $\gtrsim$700 Gy/s for carbon ions. These estimates are based on the baseline specifications for LhARA.

2.3. Laser-Hybrid Beams for Radiobiology and Clinical Application

High-power lasers have previously been proposed as an alternative to conventional proton and carbon-ion facilities for radiotherapy [29–32]. Laser-driven sources have also been proposed as the basis for electron, proton and ion-beams for radiobiology [33–40]. While a number of cell irradiation experiments have been conducted with laser-accelerated ions [37, 38, 41, 42], these have been limited in scope to a single-shot configuration. More recent projects (e.g., A-SAIL [43], ELI [44], and SCAPA [45]) will also investigate radiobiological effects using laser-driven ion beams. These studies will also address various technological issues [42, 46–49].

A beam line to provide ion-driven beams for multi-disciplinary applications, ELIMAIA (ELI Multidisciplinary Applications of laser-Ion Acceleration) is being brought into operation at the Extreme Light Infrastructure (ELI) [50, 51]. This beam line will include the "ELI MEDical and multidisciplinary applications" (ELIMED) beam line which will allow radiobiological investigations to be carried out [46, 50, 52–55]. LhARA is distinguished from this facility in that the energy at which the beam will be captured has been chosen to maximize the shot-to-shot stability of the particle flux.

Protons and ions at conventional facilities are captured at energies of several tens of keV. At such low energies, the mutual repulsion of the particles, the "space-charge effect," limits the maximum instantaneous dose rate. The laser-driven source allows protons and ions to be captured at significantly higher energies, thus evading the current space-charge limit. Rapid acceleration will be performed using a fixed-field alternating-gradient accelerator (FFA), thereby preserving the unique flexibility in the time, energy, and spatial structure of the beam afforded by the laser-driven source. Modern lasers are capable of delivering a Joule of energy in pulses that are tens of femtoseconds in length at repetition rates of $\gtrsim$10 Hz. Laser-driven ion sources create beams that are highly divergent, have a large energy spread, and an intensity that can vary by up to 25% pulse-to-pulse [56]. These issues are addressed in the LhARA conceptual design through the use of Gabor lenses to provide strong focusing and to allow energy selection. In addition, sophisticated instrumentation will be used in a fast feedback-and-control system to ensure that the dose delivered is both accurate and reproducible. This approach will allow multiple ion species, from proton to carbon, to be produced from a single laser by varying the target foil and particle-capture optics.

LhARA will prove the principle of the novel technologies required for the development of future therapy facilities. The legacy of the LhARA programme will therefore be: a unique facility dedicated to the development of a deep understanding of the radiobiology of proton and ion beams; and the demonstration in operation of technologies that will allow PBT to be delivered in completely new regimens.

3. THE LhARA FACILITY

The LhARA facility, shown schematically in **Figure 1**, has been designed to serve two end stations for *in vitro* radiobiology and one end station for *in vivo* studies. The principle components of Stage 1 of the LhARA accelerator are: the laser-driven proton and ion source; the matching and energy selection section; beam delivery to the low-energy *in vitro* end station; and the low-energy abort line. Stage 2 is formed by the injection line for the fixed-field alternating-gradient accelerator (FFA); the FFA; the extraction line; the high-energy abort line; beam delivery to the high-energy *in vitro* end station; and the transfer line to the *in vivo* end station. Proton beams with energies of between 10 and 15 MeV will be delivered directly from the laser-driven source to the low-energy *in vitro* end station via a transfer line. The high-energy *in vitro* end station and the *in vivo* end station will be served by proton beams with energy between 15 and 127 MeV and by ion beams, including C^{6+} with energies up to 33.4 MeV/u. The design parameters for the various components of LhARA are given in **Tables 1**, **2**. The design of the LhARA facility is described in the sections that follow.

3.1. Laser-Driven Proton and Ion Source

A novel solution for proton and ion acceleration is to use a compact, flexible laser-driven source coupled to a state-of-the-art beam-transport line. This allows an accelerating gradient of $\gtrsim$10 GV/m to be exploited at the laser-driven source. We propose to operate in the laser-driven sheath-acceleration regime [57–60] for ion generation. An intense, short laser pulse will be focused onto a target. The intense electric field generated on the front surface of the target accelerates the surface electrons, driving them into the material. Electrons which gain sufficient energy traverse the target, ionising the material as they go. A strong space-charge electric field, the "sheath," is created as the accelerated electrons exit the rear surface of the target. This field in turn accelerates protons and ions present as contaminants on the surface. The sheath-acceleration scheme has been shown to produce ion energies >40 MeV/u at the highest laser intensities [56]. The maximum proton energy (E_p) scales with laser intensity (I) as, $E_p \propto I^{\frac{1}{2}}$. The laser required to deliver a significant proton flux at 15 MeV is commercially available.

The distribution of proton and ion energies observed in laser-driven beams exhibits a sharp cut-off at the maximum energy and, historically, the flux of laser-accelerated ion beams has varied significantly shot-to-shot. To reduce these variations, the

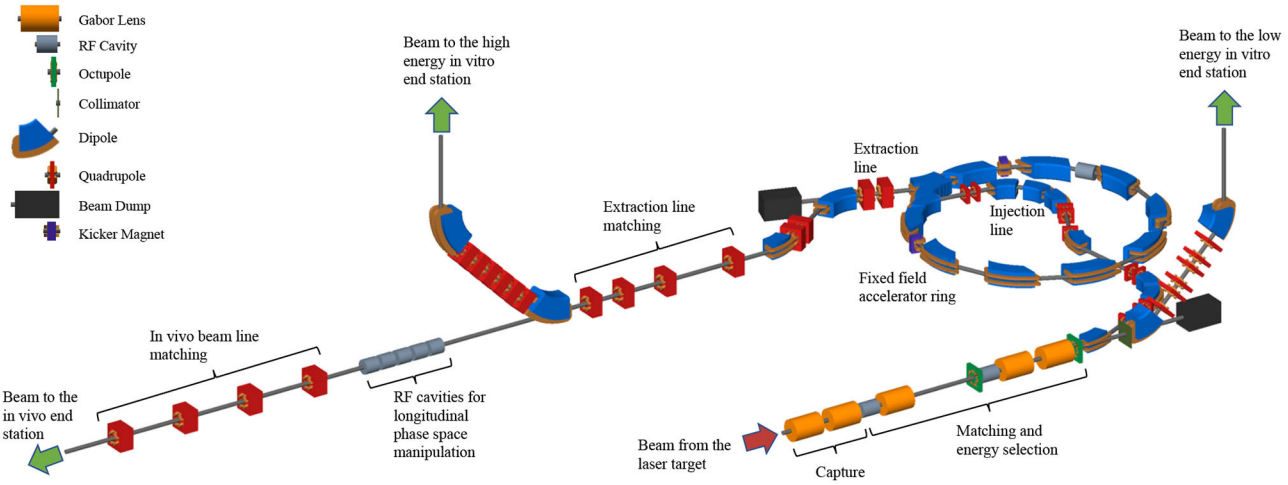

FIGURE 1 | Schematic diagram of the LhARA beam lines. The particle flux from the laser-driven source is shown by the red arrow. The "Capture" section is followed by the "Matching and energy selection" sections, the beam is directed either into the 90° bend that takes it to the low-energy *in vitro* end station, toward the FFA injection line, or to the low-energy beam dump. Post-acceleration is performed using the FFA, on extraction from which the beam is directed either to the high-energy *in vitro* end station, the *in vivo* end station, or the high-energy beam dump. Gabor lenses are shown as orange cylinders, RF cavities as gray cylinders, octupole magnets as green discs, collimators as dark-green bars, dipole magnets are shown in blue, quadrupole magnets are shown in red, beam dumps (black rectangles) and kicker magnets are also shown.

choice has been made to select particles from the plateau of the two-temperature energy spectrum of the laser-accelerated ion beam [61, 62]. This should enhance ion-beam stability and allow reproducible measurements to be carried out at ultra-high dose rates using a small number of fractions. To create the flux required in the plateau region, it is proposed that a 100 TW laser system is used. A number of commercial lasers are available that are capable of delivering $>$ 2.5 J in pulses of duration $<$ 25 fs, at 10 Hz with contrast better than $10^{10}:1$. Shot-to-shot stability of $<$ 1% is promised, an important feature for stable ion-beam production.

3.1.1. Target

Key to the operation of this configuration is a system that refreshes the target material at high repetition-rate in a reproducible manner. A number of schemes have been proposed for such studies, including high-pressure gases [63–65], cryogenic hydrogen ribbons [66–68], liquid sheets [69], and tape drives [70]. For LhARA, a tape drive based on the system developed at Imperial College London is proposed [56]. This system is capable of reliable operation at target thicknesses down to 5 μm, using aluminium or steel foils, and down to 18 μm using plastic tapes. Such tape-drive targets can be operated at high charge (up to 100 pC at 15 ± 1 MeV, i.e., $> 10^9$ protons per shot) and can deliver high-quality proton and ion fluxes at repetition rates of up to 10 Hz or greater.

The careful control of the tension of the tape in a tape-drive target is critical for reproducible operation. The tape must be stretched enough to flatten the surface, but not enough to cause plastic deformations. Surface flatness is important for a number of reasons. Rippling of the front surface modifies the laser absorption dramatically; uncharacterised rippling can make shot-to-shot variations significant and unpredictable [70]. Similarly, rear surface perturbations can modify the sheath field, resulting in spatial non-uniformities of the proton beam or suppression of the achievable peak energies. Tape drives with torsion control and monitoring to maintain a high-quality tape surface have been designed and operated in experiments at Imperial College London. The development of these targets continues with a view to the production of new, thinner tapes for improved ion generation and the creation of ion species other than protons and carbon. This is an active area of R&D that will continue with the development of LhARA.

3.2. Proton and Ion Capture

The use of an electron cloud as a focusing element for charged-particle beams was first proposed by Gabor [71]. The electron cloud is confined within the lens using a long cylindrical anode placed within a uniform solenoid field (see **Figure 2**). Such a configuration is commonly known as a "Penning trap" and has found wide application in many fields [72]. Variations on the Penning trap where axial apertures in the cathodes are introduced, such as the Penning-Malmberg trap [73, 74] are attractive for beam-based applications due to the excellent access provided to the plasma column.

The focal length of a Gabor lens of length l is given in terms of the electron number density by [76]:

$$\frac{1}{f} = \frac{e^2 n_e}{4\epsilon_0 U} l; \tag{1}$$

where e is the magnitude of the electric charge of the electron, n_e is the number density of the electrons confined within the lens,

TABLE 1 | Design parameters of the components of the LhARA facility.

Parameter	Value or range	Unit
Laser driven proton and ion source		
Laser power	100	TW
Laser energy	2.5	J
Laser pulse length	25	fs
Laser rep. rate	10	Hz
Required maximum proton energy	15	MeV
Proton and ion capture		
Beam divergence to be captured	50	mrad
Gabor lens effective length	0.857	m
Gabor lens length (end-flange to end-flange)	1.157	m
Gabor lens cathode radius	0.0365	m
Gabor lens maximum voltage	65	kV
Number of Gabor lenses	2	
Alternative technology: solenoid length	1.157	m
Alternative technology: solenoid max field strength	1.3	T
Stage 1 beam transport: matching and energy selection, beam delivery to low-energy end station		
Number of Gabor lenses	3	
Number of re–bunching cavities	2	
Number of collimators for energy selection	1	
Arc bending angle	90	Degrees
Number of bending magnets	2	
Number of quadrupoles in the arc	6	
Alternative technology: solenoid length	1.157	m
Alternative technology: solenoid max field strength (to serve the injection line to the Stage 2)	0.8 (1.4)	T

The parameter table is provided in a number of sections. This section contains parameters for the Laser-driven proton and ion source, the Proton and ion capture section, and the Stage 1 beam transport section.

TABLE 2 | Design parameters of the components of the LhARA facility.

Parameter	Value or range	Unit
Stage 2 beam transport: FFA, transfer line, beam delivery to high-energy end stations		
Number of bending magnets in the injection line	7	
Number of quadrupoles in the injection line	10	
FFA: Machine type	single spiral scaling FFA	
FFA: Extraction energy	15–127	MeV
FFA: Number of cells	10	
FFA: Orbit R_{min}	2.92	m
FFA: Orbit R_{max}	3.48	m
FFA: Orbit excursion	0.56	m
FFA: External R	4	m
FFA: Number of RF cavities	2	
FFA: RF frequency	1.46–6.48	MHz
FFA: harmonic number	1, 2 or 4	
FFA: RF voltage (for 2 cavities)	4	kV
FFA: spiral angle	48.7	Degrees
FFA: Max B field	1.4	T
FFA: k	5.33	
FFA: Magnet packing factor	0.34	
FFA: Magnet opening angle	12.24	degrees
FFA: Magnet gap	0.047	m
FFA: Ring tune (x,y)	(2.83,1.22)	
FFA: γ_T	2.516	
FFA: Number of kickers	2	
FFA: Number of septa	2	
Number of bending magnets in the extraction line	2	
Number of quadrupoles in the extraction line	8	
Vertical arc bending angle	90	Degrees
Number of bending magnets in the vertical arc	2	
Number of quadrupoles in the vertical arc	6	
Number of cavities for longitudinal phase space manipulation	5	
Number of quadrupoles in the *in vivo* beam line	4	
***In vitro* biological end stations**		
Maximum input beam diameter	1–3	cm
Beam energy spread (full width)	Low-energy end station: ≤ 4	%
	High-energy end station: ≤ 1	%
Input beam uniformity	< 5	%
Scintillating fiber layer thickness	0.25	mm
Air gap length	5	mm
Cell culture plate thickness	1.3	mm
Cell layer thickness	0.03	mm
Number of end stations	2	
***In vivo* biological end station**		
Maximum input beam diameter	1–3	cm

(Continued)

ϵ_0 the permittivity of free space, and U the kinetic energy of the particle beam. The desired focusing strength determines n_e which in turn allows the anode voltage and magnetic-field strength to be calculated [75, 76]. The focal lengths required to capture the proton and ion beams at LhARA have been chosen such that the necessary electron number densities lie well within the range achieved in published experiments.

For a given focal length, the magnetic field strength required in the Gabor lens is smaller than that of a solenoid that would give equivalent focusing. In the non-relativistic approximation, the relationship between the magnetic field strength in the Gabor lens, B_{GBL}, and the equivalent solenoid, B_{sol}, is given by [76]:

$$B_{\mathrm{GBL}} = B_{\mathrm{sol}} \sqrt{Z \frac{m_e}{m_p}}\,; \tag{2}$$

where Z is the charge state of the ions. In the case of a proton beam, the reduction factor is 43. This means the cost of the solenoid for a Gabor lens can be significantly lower than the cost of a solenoid of equivalent focusing strength.

TABLE 2 | Continued

Parameter	Value or range	Unit
Beam energy spread (full width)	≤ 1	%
Input beam uniformity	< 5	%
Beam options	Spot-scanning, passive scattering, micro-beam	

The parameter table is provided in a number of sections. This section contains parameters for the Stage 2 beam transport and the in vitro *and* in vivo *end stations.*

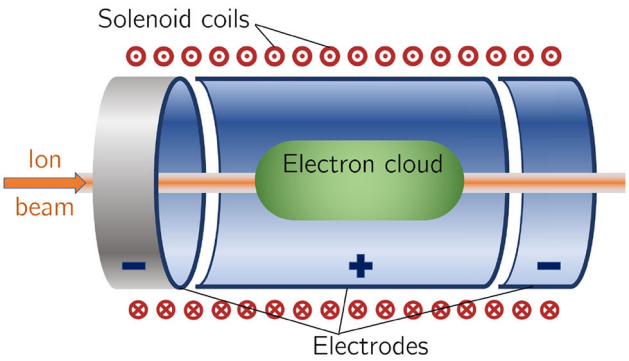

FIGURE 2 | Schematic diagram of a Penning-Malmberg trap of the type proposed for use in the Gabor lenses to be used in LhARA. The solenoid coils, and the direction of current flow, are indicated by the red circles (the central dots indicate current emerging from the picture, crosses current entering it). The confining electrostatic potential is provided using a central cylindrical anode and two cylindrical negative end electrodes. The ion beam enters on-axis from the left and the electron cloud is indicated by the green shaded area.

Instability of the electron cloud is a concern in the experimental operation of a Gabor lens; azimuthal beam disruption due to the diocotron instability has been observed and described theoretically [77]. Theory indicates that the diocotron instability is most problematic under well-defined geometric conditions. The reliable operation of a Gabor lens in a regime free from this instability has yet to be demonstrated. Gabor lenses promise very strong focusing, simple construction, and low magnetic field, all attractive features for LhARA. However, these attractive features come at the cost of relatively high voltage operation ($\gtrsim 50$ kV) and possible vulnerability to instability.

With reliable operation of Gabor lenses as yet unproven, we plan a two-part experimental and theoretical programme of research to investigate their suitability. Initial work will include: the theoretical study of lens stability using a full 3D particle-in-cell code, such as VSIM [78]; and the development of electron-density diagnostics based on interferometric measurement of the resulting refractive-index change. A test Gabor lens will be constructed to allow validation of both the simulation results and a new diagnostic tool using an alpha emitter as a proxy for the LhARA beam. In addition, the initial investigation will include the design of an injection system to fill the lens with the required electron cloud. Should it prove impossible to produce a suitable Gabor lens, it will be necessary to use high-field solenoids to produce the equivalent focusing effect.

3.3. Beam Transport and Delivery to the Low-Energy *in vitro* End Station

The beam transport line to the low-energy *in vitro* end station must produce a uniform dose distribution at the cell layer. Beam losses must be minimized for radiation safety and to maximize the dose that can be delivered in a single shot. The transport line has been designed to minimize regions in which the beam is brought to a focus to reduce the impact of space-charge forces on the beam phase-space. An optical solution was initially developed using Beamoptics [79] and MADX [80]. Accurate estimation of the performance of the beam line requires the inclusion of space-charge forces and particle-matter interactions. Performance estimation was therefore performed using Monte Carlo particle-tracking from the ion source to the end station. BDSIM [81], which is based on the GEANT4 toolkit, was used for the simulation of energy deposition arising from beam interactions with the material in the accelerator and the end station. GPT [82] was used for evaluating the full 3D impact of space-charge effects.

An idealized Gaussian beam was generated with a spot size of 4 μm FWHM, an angular divergence of 50 mrad, 35 fs FWHM bunch length, and an energy spread of 1×10^{-6} MeV. The maximum estimated bunch charge is 1×10^{9} protons. The presence of a substantial electron flux produced from the laser target compensates the high proton charge density in the vicinity of the ion-production point. To approximate the partial space-charge compensation in this region, it was assumed that co-propagating electrons would fully compensate the space-charge forces over the first 5 cm of beam propagation. Beyond this, the proton beam was assumed to have separated from the co-propagating electrons sufficiently for space-charge to become a significant effect and cause emittance growth. Therefore, a further 5 cm drift was simulated including space-charge forces. At a distance of 10 cm from the ion source, the beam is at the exit of the laser-target vessel. The kinematic distributions of ions in the beam were stored at this point and passed to the relevant BDSIM and GPT simulations of the downstream beam line.

The Stage 1 beam line, shown schematically in **Figure 3**, is composed of five sections: beam capture; matching and energy selection; beam shaping; vertical arc matching; and an abort line. The capture section uses two Gabor lenses to minimize the transverse momentum of particles in the beam. Beyond the capture section, an RF cavity permits control of the bunch length and manipulation of the longitudinal phase-space. A third Gabor lens then focuses the bunch to a small spot size after which a second RF cavity is located to provide further longitudinal phase-space manipulation. Two further Gabor lenses ensure the beam is again parallel before it enters the vertical 90° arc. All Gabor lenses have an inner radius of 3.65 cm and an effective length of 0.857 m. All lenses operate at a cathode voltage of <65 kV.

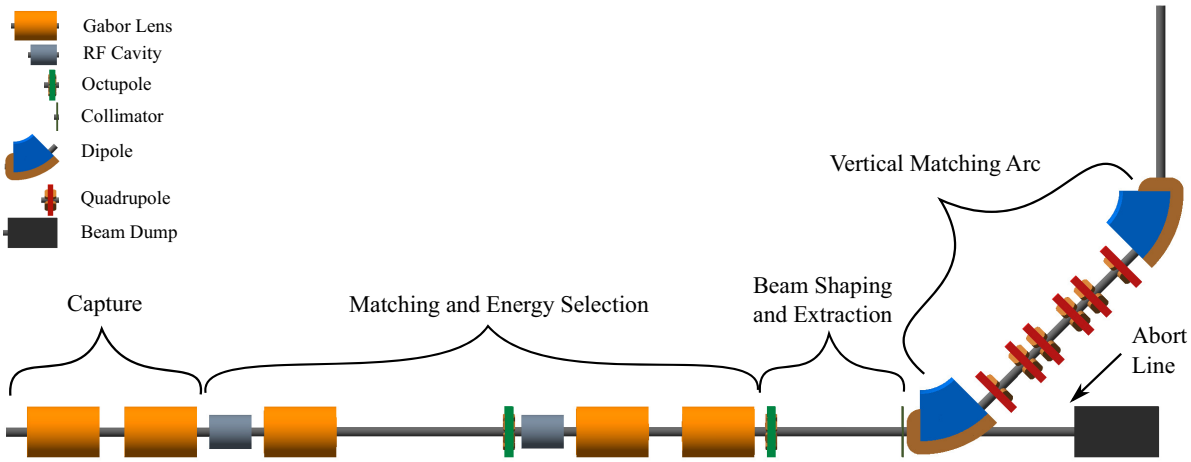

FIGURE 3 | Beam transport for Stage 1 of LhARA visualized in BDSIM, showing five machine sections. The capture section is composed of two Gabor lenses (orange cylinders). The matching and energy selection section includes three Gabor lenses, two RF cavities (gray cylinders) and an octupole magnet (green disc). The beam shaping and extraction section includes a second octupole and a collimator (vertical dark-green bar). The vertical matching arc directs the beam into the low-energy *in vitro* end station and is composed of two 45° dipoles (blue and brown) and six quadrupoles (red). The total length of this beam line is 17.3 m.

The parallel beam that emerges from the final Gabor lens, provides significant flexibility for the inclusion of beam shaping and extraction systems. Beam uniformity will be achieved using octupole magnets to provide third-order focusing to perturb the first-order focusing of the Gabor lenses. Such schemes have been demonstrated in magnetic lattices in a number of facilities [83–85]. A suitable position for the first octupole was identified to be after the final Gabor lens where the beam is large; its effect on the beam is expected to be significant. Octupoles were only modeled in BDSIM as GPT does not have a standard component with an octupolar field. The typical rectangular transverse distribution resulting from octupolar focusing requires collimation to match the circular aperture through which the beam enters the end station. A collimator is therefore positioned at the start of the vertical arc. Further simulations are required to determine the optimum position of the second octupole and to evaluate the performance of the octopoles. The switching dipole which directs the beam to the injection line of the FFA in Stage 2 will be located between the second octupole and the collimator, requiring the octupole to be ramped down for Stage 2 operation.

The vertical arc uses transparent optics in an achromat matching section to ensure that the first-order transfer map through the arc is equivalent to the identity transformation and that any dispersive effects are canceled. A 2 m drift tube is added after the arc to penetrate the concrete shielding of the end station floor and to bring the beam to bench height. The abort line consists of a drift space followed by a beam dump. Ramping down the first vertical dipole causes the beam to enter the dump and prevents particle transportation to the end station.

The underlying physics of plasma-lens operation cannot be simulated in BDSIM or GPT. It can, however, be approximated using solenoid magnets of equivalent strength. RF cavity fields were not simulated.

To produce the results shown here, 10,000 particles were simulated, corresponding to the estimated maximum bunch charge of 1×10^9 protons. **Figure 4** shows excellent agreement between horizontal and vertical transverse beam sizes in BDSIM and MADX, verifying the beam line's performance in the absence of space-charge effects. Reasonable agreement between BDSIM and GPT is also seen when space-charge forces are included in GPT. Emittance growth is observed prior to the first solenoid, affecting the optical parameters throughout the machine. However, the resulting beam dimensions at the cell layer of 1.38 cm horizontally and 1.47 cm vertically are not significantly different from those in BDSIM. If needed, further adjustments of the Gabor lens and arc-quadrupole strengths may compensate for any space-charge effects. The transmission efficiency of the beam line is ∼100%.

The small bunch dimensions in both transverse planes at the focus after the third Gabor lens, where the energy selection collimator will be placed, could be of concern if the effect of space-charge has been underestimated. Similar bunch dimensions are achieved in the vertical arc. Here, however, quadrupolar focusing is confined to a single plane to mitigate possible further emittance growth.

To investigate beam uniformity, BDSIM simulations with and without octupoles and collimation for beam shaping were conducted. Each octopole was assumed to have a magnetic length of 0.1 m and pole-tip radius of 5 cm. The strength parameter, k_3, of each octupole was arbitrarily set to 6,000. A 2 cm thick iron collimator with a 40 mm diameter aperture was positioned 1.5 m downstream of the octupole. **Figure 5** shows the beam phase-space and particle distributions at the Stage 1 end station for the transverse and longitudinal axes with and without beam shaping. Without octupoles, the spatial profile is Gaussian, as expected. Inclusion of the octupoles and collimation system improves beam

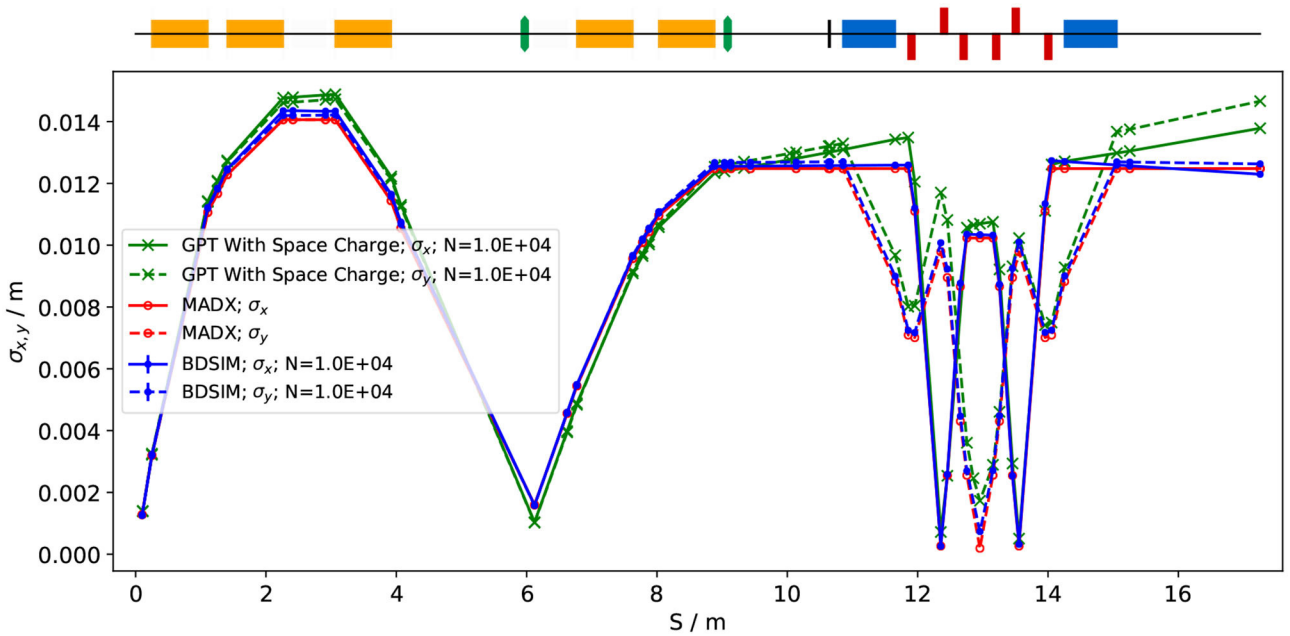

FIGURE 4 | Horizontal (solid lines) and vertical (dashed lines) beam sizes through the *in vitro* beam transport, simulated including space-charge effects in GPT (green), and without space-charge in MADX (red) and BDSIM (blue).

uniformity. The total beam width is 3.58 cm horizontally and 3.46 cm vertically, which is sufficient to irradiate one well in a six-well cell-culture plate. Further optimization is required to improve uniformity whilst optimizing beam-line transmission, which is ∼70% for the results presented in **Figure 5**.

An aberration can be seen in both transverse planes with and without beam shaping. This effect originates upstream of the octupoles in the solenoids used to approximate the Gabor lenses, and persists to the end station. The aberration is a concern, but is likely to change when the solenoids are replaced by full electromagnetic simulation of the Gabor lenses, at which point it will be further investigated.

The non-Gaussian energy distribution without beam shaping is a result of space-charge forces at the ion source; the distribution persists to the end station as no components which affect the longitudinal phase space were simulated. The Gaussian distribution seen with beam shaping reflects the effects of the collimation.

The proposed design is capable of delivering beams of the desired size to the *in vitro* end station. Space-charge effects affect the beam-transport performance but it is believed that these can be mitigated with minor adjustments to the Gabor lenses in the capture section. Initial studies indicate that a uniform beam can be delivered with further optimization of the octupoles and collimator.

3.3.1. Alternative Design

To mitigate potential emittance growth from space-charge forces, an alternative beam line design was developed in which the final two Gabor lenses in the matching and energy selection section are replaced by four quadrupoles, limiting any bunch focusing to one plane at a time. The resulting machine is reduced in length to 15.4 m. Without space-charge effects, a beam width of 2.5 mm at the end station can be achieved. With space-charge, emittance growth prior to the first solenoid is once again observed leading to an increased beam size at the entrance of the first quadrupole, resulting in a spatially asymmetric and divergent beam at the end station. It is believed that the space-charge effects can be compensated by applying the same Gabor lens optimization as in the baseline design and adjusting the quadrupole settings to deliver beam parameters similar to those achieved in the absence of space charge. The alternative design provides a solution that is more resilient to space-charge effects than the baseline, however, only the lower bound on the desired beam size has been achieved so far. For this design, further optimization is required not only to improve optical performance but also to optimize octupole settings and to determine whether a beam with the desired uniformity can be delivered to the end station.

3.4. Post-acceleration and Beam Delivery to the *in vitro* and *in vivo* End Stations

A fixed-field alternating-gradient accelerator (FFA), based on the spiral scaling principle [86–89], will be used to accelerate the beam in LhARA Stage 2 to obtain energies greater than the 15 MeV protons and 4 MeV/u carbon (C^{6+}) ions delivered by the laser-driven source. FFAs have many advantages for both medical and radiobiological applications, such as: the capability to deliver high and variable dose; rapid cycling with repetition rates ranging from 10 to 100 Hz or beyond; and the ability to deliver various beam energies without the use of energy degraders. An FFA is relatively compact due to the use of combined function magnets, which lowers the overall cost compared to conventional

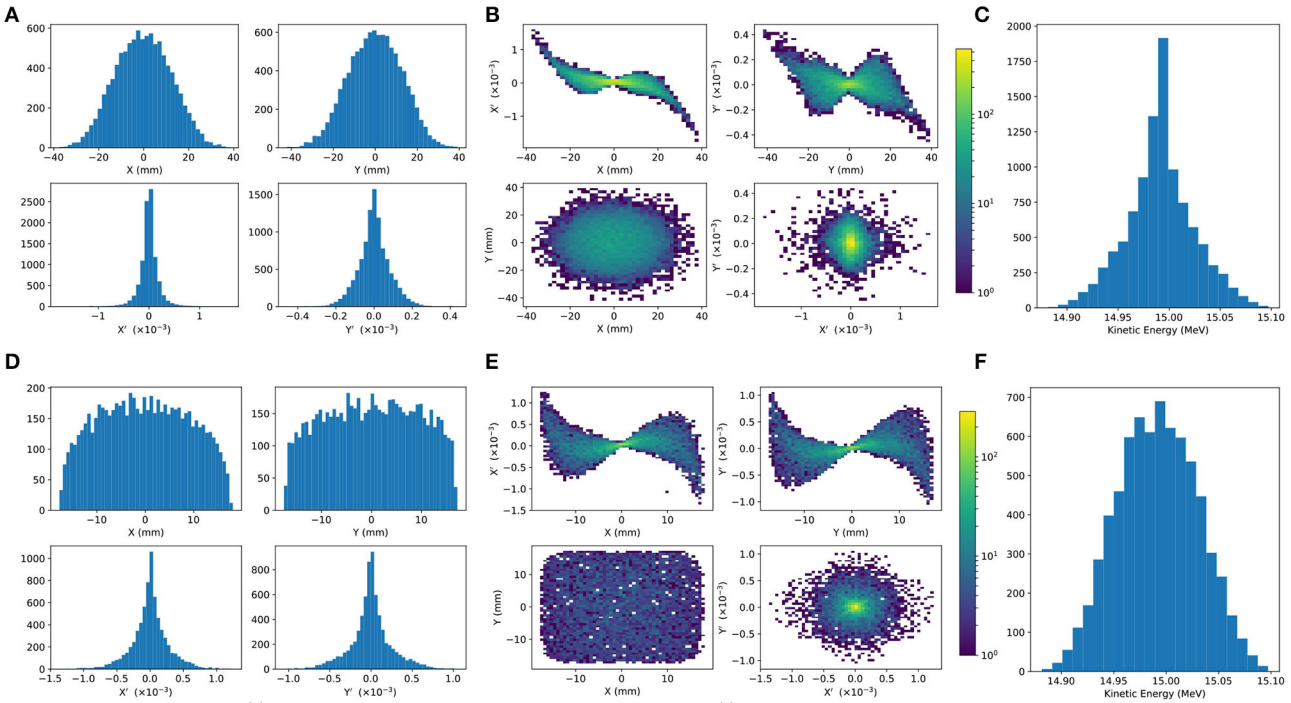

FIGURE 5 | Beam phase space distributions at the end-station in the transverse plane, (X, Y); X′ and Y′ give the slope relative to the Z axis. The transverse phase space is shown in **(A,B)** for simulations without octupolar focusing and collimation, with the kinetic energy distribution shown in **(C)**. The same phase space distributions simulated with the effect of octupoles and collimation are in figures **(D–F)**.

accelerators capable of delivering beams at a variety of energies such as synchrotrons. Extraction can be both simple and efficient and it is possible for multiple extraction ports to be provided. Furthermore, FFAs can accelerate multiple ion species, which is very important for radiobiological experiments and typically very difficult to achieve with cyclotrons.

A typical FFA is able to increase the beam momentum by a factor of three, though a greater factor may be achieved. For LhARA, this translates to a maximum proton-beam energy of 127 MeV from an injected beam of 15 MeV. For carbon ions (C^{6+}) with the same rigidity, a maximum energy of ∼33.4 MeV/u can be produced.

The energy at injection into the FFA determines the beam energy at extraction. The injection energy will be changed by varying the focusing strengths in the Stage 1 beam line from the capture section through to the extraction line and the FFA ring. Appropriate adjustments to the frequency and phase of the RF in the FFA ring will also be made. This will allow the required energy slice from the broad spectrum produced at the laser-driven source to be captured and transported to the FFA. The FFA will then accelerate the beam, acting as a 3-fold momentum multiplier. This scheme simplifies the injection and extraction systems since their geometry and location can be kept constant.

A second, "high-energy," *in vitro* end station will be served by proton beams with a kinetic energy in the range 15–127 MeV and carbon-ion beams with energies up to 33.4 MeV/u. The extraction line from the FFA leads to a 90° vertical arc to send the beam to the high-energy *in vitro* end station. If the first dipole of the arc is not energized, the beam will be sent to the *in vivo* end station. The extraction line of the FFA includes a switching dipole that will send the beam to the high-energy-beam dump if it is not energized. The detailed design of the high-energy abort line,

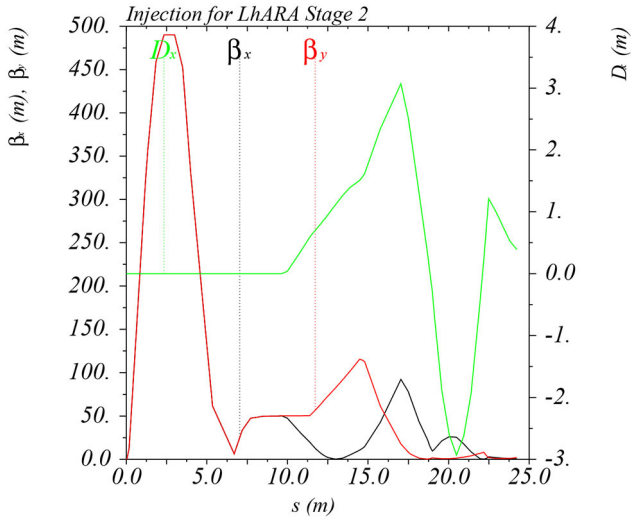

FIGURE 6 | Twiss β_x and β_y functions and dispersion in the beam line consisting of the modified Stage 1 lattice and the transfer line allowing injection of the beam into the FFA ring. The distance *s* runs from the laser target to the exit of the injection septum.

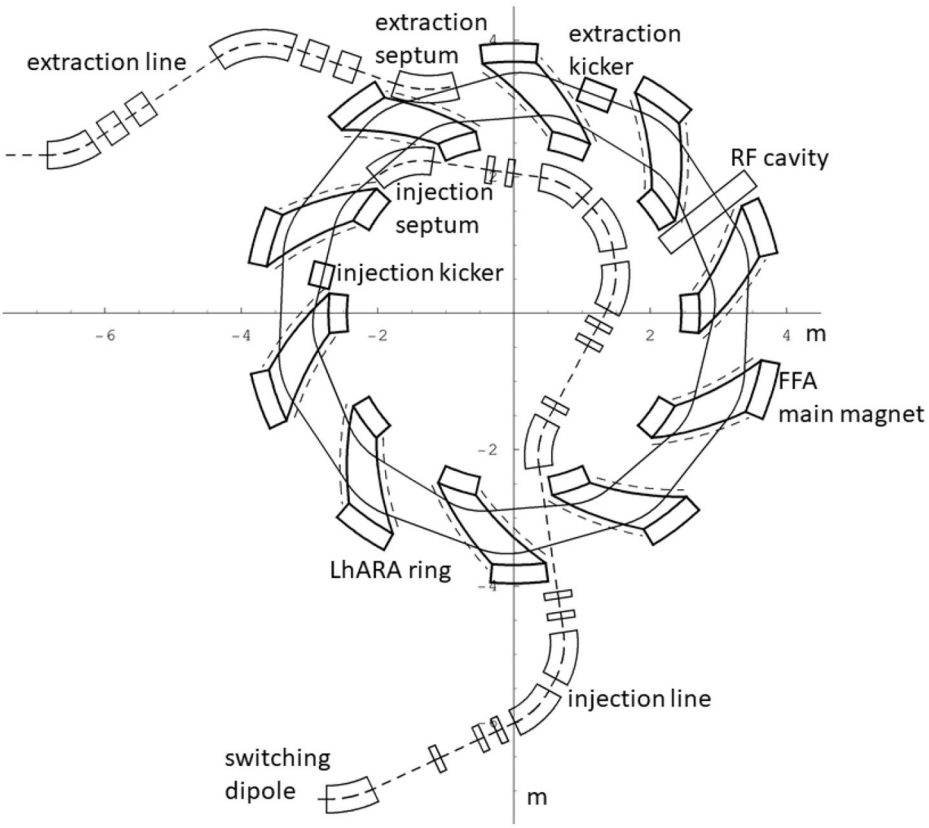

FIGURE 7 | The layout of the injection line from the switching dipole to the injection septum together with the FFA ring, some of its subsystems and the first part of the extraction line.

taking into account the requirement that stray radiation does not enter the end stations, will be performed as part of the LhARA R&D programme.

3.4.1. Injection Line

In order to inject the beam into the FFA, the settings of the Stage 1 beam line need to be adjusted to reduce the Twiss β function. The required Stage 1 optical parameters are shown in **Figure 6**. The beam is diverted by a switching dipole into the injection line which transports the beam to the injection septum magnet. The injection line matches the Twiss β functions in both transverse planes and the dispersion of the beam to the values dictated by the periodic conditions in the FFA cell (**Figure 6**). The presence of dispersion in the injection line allows a collimator to be installed for momentum selection before injection. The beam is injected from the inside of the ring, which requires that the injection line crosses one of the straight sections between the FFA magnets (see **Figure 7**).

3.4.2. FFA Ring

The magnetic field, B_y, in the median plane of a scaling spiral FFA is given by [86–88]:

$$B_y = B_0 \left[\frac{R}{R_0}\right]^k F\left(\theta - \ln\left[\frac{R}{R_0}\right]\tan\zeta\right); \qquad (3)$$

where B_0 is the magnetic field at radius R_0, k is the field index, ζ corresponds to the spiral angle and F is the "flutter function." This field law defines a zero-chromaticity condition, which means the working point of the machine is independent of energy (up to field errors and alignment imperfections). This avoids the need to cross any resonances, which would reduce the beam quality and could lead to beam loss.

Table 2 gives the main design parameters of the FFA ring. The ring consists of ten symmetric cells, each containing a single combined-function spiral magnet. The choice of the number of cells is a compromise between the size of the orbit excursion, which dictates the radial extent of the magnet, and the length of the straight sections required to accommodate the injection and extraction systems.

The betatron functions and dispersion in one lattice cell at injection are shown in **Figure 8A**. The tune diagram, showing the position of the working point of the machine in relation to the main resonance lines, is shown in **Figure 8B**. Tracking studies were performed using a step-wise tracking code in which the magnetic field is integrated using a Runge-Kutta algorithm [90]. The magnetic field in the median plane was obtained using the ideal scaling law (Equation 3). Enge functions were used to give the fringe fields. The field out of the median plane was obtained using Maxwell's equations and a 6th-order Taylor expansion

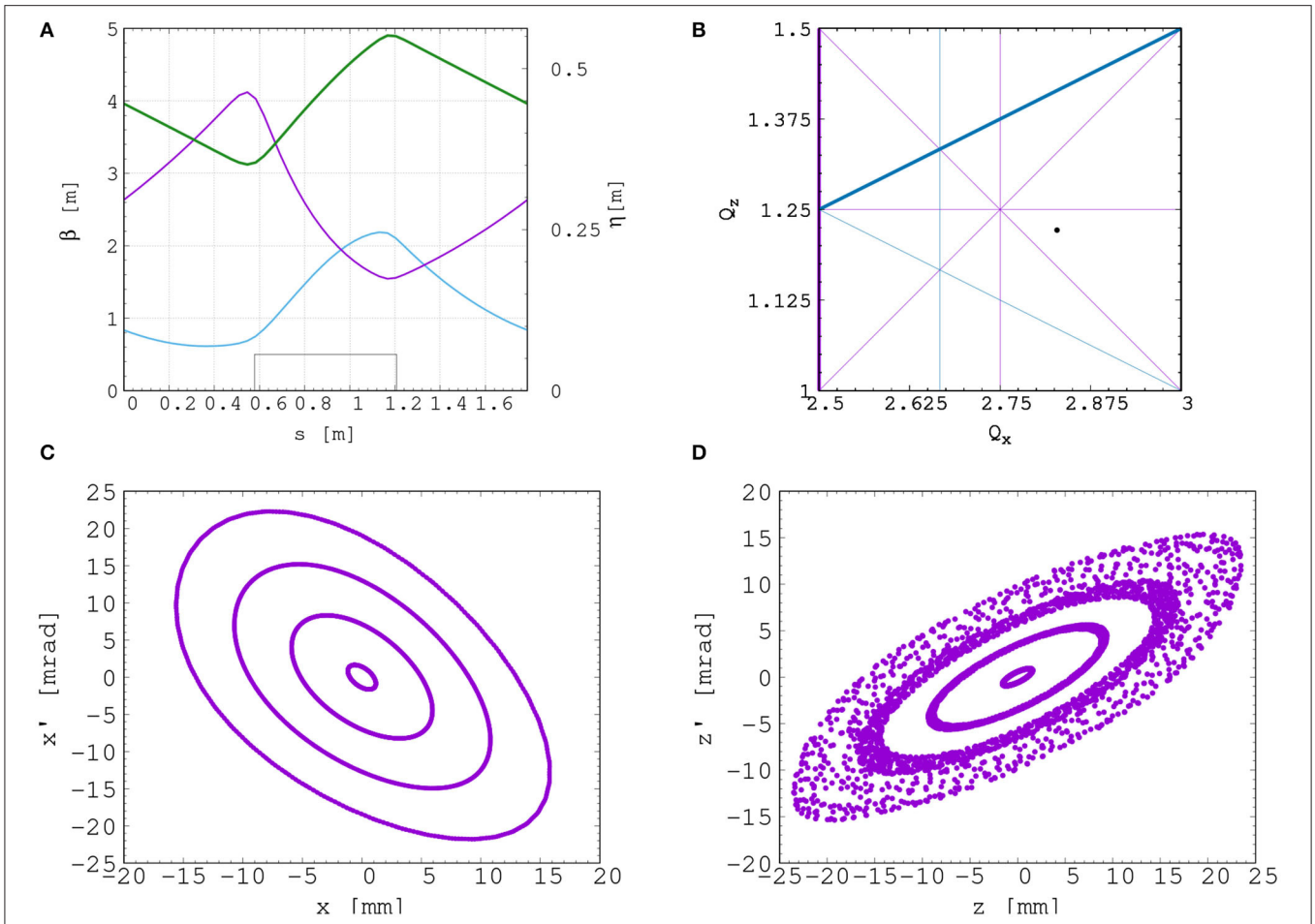

FIGURE 8 | Beam optics and tracking in the FFA. Twiss β_h (blue), β_v (purple) functions, and dispersion (green) in one lattice cell of the FFA ring **(A)**. The working point of the FFA ring at (2.83, 1.22) on the tune diagram **(B)**. The results of the horizontal **(C)** and vertical **(D)** dynamical acceptance study in the FFA ring, where a 1 mm offset is assumed in the vertical and horizontal planes, respectively.

of the field. The dynamic acceptance for 100 turns, shown for the horizontal and vertical planes in **Figures 8C,D**, respectively, is significantly larger than the beam emittance. This statement holds even for the pessimistic scenario in which the emittance is assumed to be ten times larger than nominal. These results confirm that a good machine working point has been chosen.

A full aperture, fast injection of the beam will be performed using a magnetic septum, installed on the inside of the ring, followed by a kicker magnet situated in a consecutive lattice cell, as shown in **Figure 7**. The specifications of the injection system are dictated by the parameters of the beam at injection, which are summarized for the nominal proton beam in **Table 3**. The beam at injection has a relatively small emittance and short bunch length, which limits the intensity accepted by the ring due to the space-charge effect. An intensity of $\sim 10^9$ protons will be accepted by the ring assuming the nominal beam parameters. Space-charge effects will be severe immediately after injection, but will quickly be reduced due to the debunching of the beam. Fast extraction of the beam over the full aperture will be performed using a kicker magnet followed by a magnetic septum installed in a consecutive lattice cell close to the extraction orbit.

TABLE 3 | Summary of the main parameters for the proton beam at the injection to the FFA ring.

Parameter	Unit	Value
Beam energy	MeV	15
Total relative energy spread	%	±2
Nominal physical RMS emittance (both planes)	π m rad	4.1×10^{-7}
Incoherent space charge tune shift		−0.8
Bunching factor		0.023
Total bunch length	ns	8.1
Bunch intensity		10^9

These parameters correspond to the nominal (maximum) acceleration mode of operation.

Acceleration of the beam to 127 MeV will be done using an RF system operating at harmonic number $h = 1$ with an RF frequency range from 2.89 to 6.48 MHz. The RF voltage required

for 10 Hz operation is 0.5 kV. However, at this relatively low voltage the energy acceptance at injection is ±0.7%. Operating with a voltage of 4 kV increases the energy acceptance to ±2%. This voltage can be achieved with one cavity [91]. Here, two cavities are proposed to provide greater operational stability. Normal conducting spiral-scaling FFA magnets, similar to the ones needed for LhARA, have been successfully constructed [89, 92] using either distributed, individually-powered coils on a flat pole piece or using a conventional gap-shaping technique. For the LhARA FFA, we propose a variation of the coil-dominated design recently proposed at the Rutherford Appleton Laboratory in R&D studies for the upgrade of the ISIS neutron and muon source. In this case, the nominal scaling field is achieved using a distribution of single-powered windings on a flat pole piece. The parameter k can then be tuned using up to three additional independently-powered windings. The extent of the fringe field across the radius of the magnet must be carefully controlled using a "field clamp" to achieve zero chromaticity. An active clamp, in which additional windings are placed around one end of the magnet, may be used to control the flutter function and thereby vary independently the vertical tune of the FFA ring. The FFA is required to deliver beams over a range of energy; each energy requiring a particular setting for the ring magnets. Therefore, a laminated magnet design may be required to reduce the time needed to change the field. The magnet gap of 4.7 cm given in **Table 2** is estimated assuming a flat-pole design for the magnet.

3.4.3. Extraction Line

Substantial margins in the beam parameters were assumed in the design of the extraction line from the FFA due to uncertainties in the beam distributions originating from the Stage 1 beam transport, the FFA injection line, and potential distortions introduced by the presence of space-charge effects during acceleration in the ring. The beam emittance was therefore allowed to be as large as a factor of 10 greater than the nominal value, which was derived by assuming that the normalized emittance is conserved from the source, through the Stage 1 beam line, and in the FFA ring. In the nominal case, the physical emittance of the beam is affected by adiabatic damping only. Substantial flexibility in the optics of the extraction line is required, as the extraction line must accommodate a wide spectrum of beam conditions to serve the *in vitro* and *in vivo* end-stations.

Detailed studies were carried out for proton beams with kinetic energies of 40 and 127 MeV. **Table 4** gives the Twiss β values for different beam sizes for the 40 and 127 MeV proton-beam energies assuming a Gaussian beam distribution. The optics and geometric acceptance of the system is approximately the same for the 40 and 127 MeV beams, justifying the working hypothesis that beam emittance is approximately the same for both beam energies. This assumption will be revised as soon as space-charge simulations for the entire system are available.

The first two dipoles and four quadrupoles of the extraction line bend the beam coming from the extraction septum of the FFA such that it is parallel to the low-energy beam line while ensuring that dispersion is closed. Closing the dispersion is critical, as off-momentum particles will follow trajectories different to those followed by particles with the design momentum and therefore impact the size and shape of the beam downstream. The second part of the extraction line consists of four quadrupoles which transport the beam either to the first dipole of the vertical arc that serves the high-energy *in vitro* end station or to the *in vivo* end station if this dipole is not energized. These quadrupoles provide the flexibility required to produce the different beam sizes for the *in vitro* end station, as specified in **Table 4**.

TABLE 4 | Beam emittance values and target β values for different beam sizes for 40 and 127 MeV beams.

	40 MeV protons (nominal)	127 MeV protons (nominal)	127 MeV protons (pessimistic)
RMS emittance (ϵ_x, ϵ_y) [π mm mrad]	0.137	0.137	1.37
β [m] for a 1 mm spot size	0.46	0.46	0.039
β [m] for a 10 mm spot size	46	46	4.5
β [m] for a 30 mm spot size	410	410	40

The beam size is taken to be four times the sigma of the transverse beam distribution.

3.4.4. High-Energy *in vitro* Beam Line

The high-energy *in vitro* beam line transports the beam from the extraction line to the high-energy *in vitro* end station. The 90° vertical bend is a scaled version of the low-energy vertical arc, following the same design principles, and also consists of two bending dipole magnets and six quadrupole magnets. To accommodate the higher beam energies, the lengths of the magnets were scaled in order to ensure that peak magnetic fields were below the saturation limits of normal conducting magnets. The bending dipole magnet lengths were increased to 1.2 m each and the quadrupole lengths were tripled to 0.3 m. The overall length of the arc then becomes 6 m, compared to 4.6 m for the low energy *in vitro* arc. This difference in arc length means the high-energy *in vitro* arc finishes about 0.9 m higher than the low-energy one. This difference can easily be accommodated by adjusting the final drift lengths.

The quadrupole strengths for the scaled high-energy *in vitro* arc were obtained using MADX calculations, tracking simulations using BDSIM show good agreement with these (see **Figure 9**). The input beam distribution used in BDSIM was assumed to be Gaussian with Twiss $\beta = 46$, which gives a beam size of about 10 mm. Small deviations from the BDSIM results were observed in GPT simulations due to space-charge effects.

3.4.5. *In vivo* Beam Line

To facilitate efficient small-animal handling, the end station dedicated to *in vivo* experiments will be positioned adjacent to the principle road access to the facility. If the first dipole of the high-energy *in vitro* arc is not energized, the beam is sent to the *in vivo* end station. From the end of the extraction line, 7.7 m of drift is necessary to clear the first bending dipole of

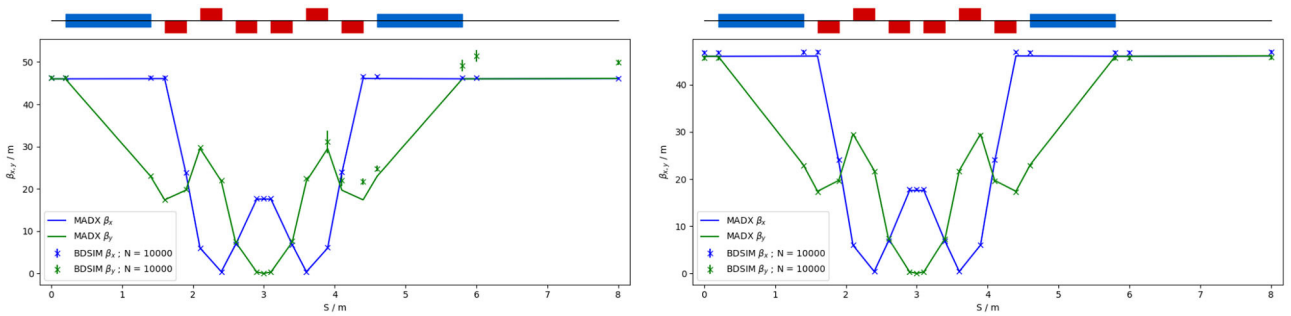

FIGURE 9 | Comparison of MADX and BDSIM simulation of 40 MeV (left) and a nominal 127 MeV (right) proton beam passing through the high energy *in vitro* arc simulated with 10^4 particles (in BDSIM).

the *in vitro* arc, to provide space for the five RF cavities needed for longitudinal phase-space manipulation and to allow space for diagnostic devices. Following this drift is a further 6.6 m of beam line that includes four quadrupoles, each of length 0.4 m, which are used to perform the final focusing adjustments of the beam delivered to the *in vivo* end station. A final 1.5 m drift length is reserved for scanning magnets so spot scanning can be performed and to allow for penetration of the shielding of the *in vivo* end station. In total, the *in vivo* beam line is 15.6 m in length.

The flexible design can match the various $\beta_{x,y}$ values given in **Table 4**, but not the smallest target value of $\beta_{x,y} = 0.039$ m for the pessimistic scenario, which is very challenging. To verify that the optics design can provide the required beam sizes, simulations were performed with BDSIM using an input Gaussian beam generated with the Twiss β values given in **Table 4**. **Figure 10** shows the results for a 40 MeV proton beam and a nominal emittance 127 MeV proton beam matched in order to obtain beam sizes of 1, 10, and 30 mm.

3.5. Instrumentation

Commercial off-the-shelf (COTS) instrumentation will be used for Stages 1 and 2 of LhARA wherever possible. However, the characteristics of the beam (e.g., very high charge-per-bunch, low-to-moderate energy) will require that some custom solutions be developed. The authors are developing two concepts, termed SciWire and SmartPhantom, for the low- and high-energy *in vitro* end stations, respectively. These detectors can also be used for beam diagnostics and may find application at other facilities. Instrumentation for the detection of secondary particles arising from the interaction of the beam with tissue is not discussed here but is an important area that will be studied in the future.

3.5.1. SciWire

For the Stage 1 beam, the maximum proton energy is 15 MeV. Shot-to-shot characterization of the beam is essential and requires the use of a very thin detector with a fast response. The SciWire [93] is being developed to provide energy and intensity profile measurements for low-energy ion beams. A single SciWire plane consists of two layers of 250 μm square-section scintillating fibers, with the fiber directions in the two layers orthogonal to each other. A series of back-to-back planes provides a homogeneous volume of scintillator. If there are enough planes to stop the beam, the depth of penetration will allow the beam energy to be inferred. This is a destructive measurement so would only be performed when experiments are not running. A single plane, however, can be used for 2D beam-profile measurements while the beam is being delivered for experiments. Light from the SciWire fibers may be detected using a CMOS camera or photodiodes. If the instrumentation is sufficiently fast, the SciWire can be used to derive feedback signals for beam tuning.

3.5.2. SmartPhantom

To study the dose profile of Stage 2 beams in real time, the SmartPhantom [94] is being developed. This is a water-filled phantom, instrumented with planes of scintillating fibers, used to infer the dose distribution with distance. The detection elements of the SmartPhantom are 250 μm diameter, round scintillating fibers. Each fiber station consists of two planes of fibers, in which the fiber directions are orthogonal. Five fiber stations are arranged in the phantom in front of the cell-culture flask. The fibers may be coupled to photodiodes, or a CMOS camera. Simulations in GEANT4 are being used to develop analysis techniques to determine the position of the Bragg peak shot-by-shot. The beam profile and dose delivered can then be calculated in real time.

3.5.3. Beam Line Instrumentation

The requirement for instrumentation begins with the Ti:Sapphire laser. The laser focal spot will be characterized using a camera-based system and high-speed wavefront measurements [95] from COTS vendors.

For the Stage 1 beam line, beam position monitors (BPMs) will be needed for beam steering. Because of the low beam energy, non-intercepting BPMs using capacitive pickup buttons will be used. Custom pickups will be needed to match the beam pipe geometry, but COTS electronics are available. The beam current will be monitored near the end of each beam line, using integrating current toroids (ICT), backed up with the option of insertable multi-layer Faraday cups (MLFC) to give absolute beam current and energy measurements. Beam profiles could be measured by secondary emission monitor (SEM) grids on both

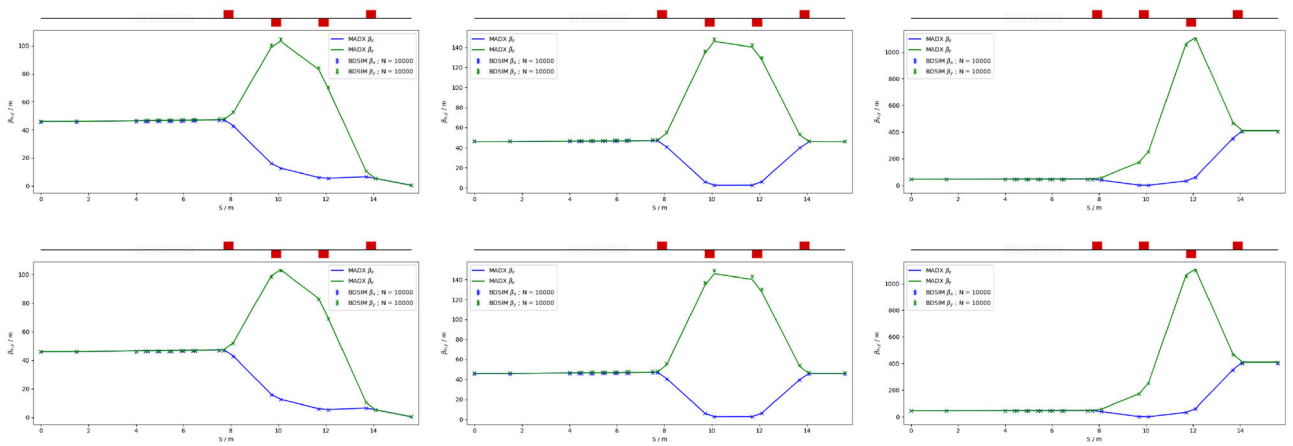

FIGURE 10 | MADX and BDSIM simulations of the *in vivo* beam line for a 40 MeV proton beam (top row) and a nominal 127 MeV proton beam (bottom row) with quadrupoles matched to obtain $\beta_{x,y} = 0.46$ m **(left)**, $\beta_{x,y} = 46$ m **(middle)**, and $\beta_{x,y} = 410$ m **(right)** at the end of the beam line for 10^4 particles.

Stage 1 and Stage 2 beam lines. For Stage 1, these monitors will be mounted on pneumatic actuators to avoid scattering. Each end station could be equipped with insertable "pepper-pot" emittance monitors and a transverse deflection cavity with fluorescent screen could be provided for bunch shape measurements.

The BPMs on the FFA will require pickup designs suitable for the unusual, wide and shallow vacuum vessel. The FFA at the KURNS facility in Kyoto has a similar layout [96] and uses a kicker and capacitive pickup to perform tune measurements in each transverse direction. A minimum of one BPM every second cell will be used in the FFA so that the beam orbit can be measured. BPMs will also be required close to the injection and extraction septa. The BPM system may be able to use COTS electronics, but the pickups will be based on the KURNS design of multiple electrodes arranged across the vacuum vessel width.

The data acquisition system needs to be able to store calibration data and apply corrections in real time. It is necessary to be able to find the beam center from a profile, even when the profile may be non-Gaussian and possibly asymmetric. Field programmable gate arrays (FPGAs) can be used to perform fast fitting and pattern recognition of beam profiles. The instrumentation will be integrated with the accelerator control system and will provide fast feedback and adjustment of the beam parameters in real time.

3.6. Biological End Stations

In order to deliver a successful radiobiological research programme, high-end and fully equipped *in vitro* and *in vivo* end-stations will be housed within the LhARA facility. The two *in vitro* end-stations (high and low energy) will contain vertically-delivered beam lines which will be used for the irradiation of 2D monolayer and 3D-cell systems (spheroids and patient-derived organoids) in culture. The beam line within the end-stations will be housed in sealed units that will be directly sourced with appropriate gases (carbon dioxide and nitrogen), allowing the cells within culture plates to be incubated for a short time in stable conditions prior to and during irradiation. This will also enable the chamber to act, where necessary, as a hypoxia unit (e.g. 0.1–5% oxygen concentration). Furthermore, these sealed units will contain robotics to enable the numerous cell culture plates housed within to be placed into and taken out of the beam.

The *in vitro* end-stations will be located within a research laboratory equipped with state-of-the-art facilities. The laboratory will include all the necessary equipment for bench-top science, sample processing and analysis (e.g., refrigerated centrifuges and light/fluorescent microscopes), along with the equipment required for contaminant-free cell culture (e.g., humidified CO_2 cell culture incubators, Class II biological safety cabinets), and for the storage of biological samples and specimens (e.g., −20 and −80°C freezers and fridges). The laboratory will also house an X-ray irradiator (allowing direct RBE comparisons between conventional photon irradiation, and the proton and carbon ions delivered by the accelerator), a hypoxia chamber (for long-term hypoxia studies), a robotic workstation (for handling and processing of large sample numbers, aiding high-throughput screening experiments), and an ultra-pure-water delivery system. These facilities will enable a myriad of biological end-points to be investigated in both normal- and tumor-cell models not only from routine clonogenic survival and growth assays, but also from significantly more complex end-points (e.g., inflammation, angiogenesis, senescence, and autophagy).

The *in vivo* end-station will be served with relatively high-energy proton and carbon ions capable of penetrating deeper into tissues allowing the irradiation of whole animals. The ability to perform *in vivo* pre-clinical studies is vital for the future effective translation of the research into human cancer patients where optimum treatment strategies and the reduction of side-effects are crucial. The *in vivo* end-station will allow the irradiation of a number of small-animal models (e.g., xenograft mouse and rat models) which can further promote an examination of particular ions on the appropriate biological end-points (e.g., tumor growth and normal tissue responses). The end-station will contain a small-animal handling area which will allow for the anaesthetization of animals prior to irradiation.

To enable the irradiation of small target volumes with a high level of precision and accuracy, an image guidance system (e.g., computed tomography) will be available. The animals will subsequently be placed in temperature-controlled holder tubes enabling the correct positioning of the relevant irradiation area in front of the beam line. The beam size is sufficient to give flexibility in the different irradiation conditions, in particular through passive scattering, pencil-beam scanning, and micro-beam irradiation, to be investigated at both conventional and FLASH dose rates. It is envisaged that the animals will be taken off-site post-irradiation to a nearby animal-holding facility for a follow-up period where biological measurements will be conducted.

3.7. Infrastructure and Integration

The LhARA facility will encompass two floors of roughly 42 m in length and 18 m in width. The ground floor will contain the laser, accelerator, and *in vivo* end station while the first floor will house the laboratory area and the two *in vitro* end stations. The entire facility will require radiation protection in the form of concrete shielding. There will be three principal areas: a radiation controlled-access area, a laser controlled-access area, and a laboratory limited-access area.

For a facility such as LhARA, laser, radiation and biological safety are primary concerns. It is envisaged that LhARA will be built at a national laboratory or equivalent research institute which has an established safety-management system and culture in place.

The infrastructure and integration of the LhARA facility will require R&D in four key areas: risk analysis (project risks), risk assessments (safety risks), radiation simulations, and controls development. The risk analysis will cover all aspects of the facility, such as funding and resource availability, not just technical risks. A safety-risk assessment will be performed to describe and control all potential safety risks in the facility. The safety-risk assessment will, to a reasonable degree, identify all pieces of equipment that require safety mitigations and identify control measures that must be put in place. Coupled closely with the safety-risk assessment, radiation simulations will be developed to characterize the radiation hazards in and around the LhARA facility. The last area to require R&D will be the control systems. It is expected that the facility will use the Experimental Physics and Industrial Control System [97], which can be further developed at this stage.

4. PERFORMANCE

The dose distributions delivered to the end stations were evaluated using BDSIM. **Figure 11** shows the energy lost by the beam as it enters the low-energy *in vitro* end station. The beam passes through the vacuum window, a layer of scintillating fiber, and a 5 mm air gap. The beam then enters the cell-sample container, assumed to be polystyrene, which supports a 30 μm thick layer of cells, modeled using the GEANT4 material "G4_SKIN_ICRP" [98]. The transverse momentum of protons in the beam was assumed to follow a Gaussian distribution, with a lateral spread small enough for the beam to be fully contained within the required spot size of 3 cm. **Figure 11** shows that a proton beam with 10 MeV kinetic energy does not reach the cell layer. The Bragg peak of a 12 MeV proton beam is located close to the cell layer, while a 15 MeV beam, the maximum energy specified for delivery to the low-energy *in vitro* end station, has a Bragg peak located beyond the cell layer. LhARA's ability to deliver various beam energies will allow the investigation of the radiobiological effects of irradiation using different parts of the Bragg peak, effectively varying the LET across the sample. RF cavities are placed in both the stage 1 and the stage 2 beam lines to allow the manipulation of the energy of the bunch as a function of time. This facility will allow the study of the impact of a "spread-out Bragg peak" (SOBP).

The maximum dose that can be delivered was evaluated for a variety of beam energies. In order for the dose to be reported in units of Gray it is necessary to define the volume within which the energy deposition is to be integrated. Therefore, the dose was estimated from simulations by calculating the energy deposited in a volume of water corresponding in size to the sensitive volume of a PTW 23343 Markus ion chamber [99] placed at the position of the Bragg peak in each case. This choice allows the doses and dose-rates reported here to be compared to those of operating facilities. The cylindrical sensitive volume of the ion chamber has a radius of 2.65 mm and a depth of 2 mm, giving a volume of about 4.4×10^{-8} m^3. The total energy deposited within the chamber was recorded and converted into dose in units of Gray.

For the low-energy *in vitro* end station, the minimum spot size has a diameter of 10 mm, which is larger than the area of the chamber. A single shot of 10^9 protons at 12 MeV with this spot size deposits 3.1×10^{-4} J in the chamber volume, corresponding to a dose of 7.1 Gy. For this simulation, the thickness of the sample container was reduced so that the Bragg peak could be positioned within the chamber volume. For the bunch length of 7.0 ns, the maximum instantaneous dose rate is 1.0×10^9 Gy/s and the average dose rate is 71 Gy/s, assuming a repetition rate of 10 Hz. A single shot of 10^9 protons at 15 MeV deposits 5.6×10^{-4} J in the chamber volume, corresponding to a dose of 12.8 Gy. This gives an instantaneous dose rate of 1.8×10^9 Gy/s and an average dose rate of 128 Gy/s assuming the same bunch length and repetition rate as for the 12 MeV case.

For the high-energy *in vitro* end station, a similar design to the low-energy end station was used, but the air gap was increased from 5 mm to 5 cm and a water phantom was placed at the end of the air gap instead of a cell culture plate. The water phantom used in the simulation was based upon the PTC T41023 water phantom [100]. In addition, the smaller minimum design beam size of 1 mm was used. A single shot of 10^9 protons at 127 MeV deposits 6.9×10^{-4} J in the chamber at the pristine Bragg peak depth, corresponding to a dose of 15.6 Gy, an instantaneous dose rate of 3.8×10^8 Gy/s and an average dose rate of 156 Gy/s. The end-station design assumed for a 33.4 MeV/u carbon beam was the same as that used for the low-energy *in vitro* end station due to the limited range in water of the carbon beam. The intensity of the beam is assumed to be a factor of 12 less than that for protons in order to preserve the same strength of the space-charge effect at injection into the FFA with the same beam parameters because the incoherent space charge tune shift is proportional to q^2/A and

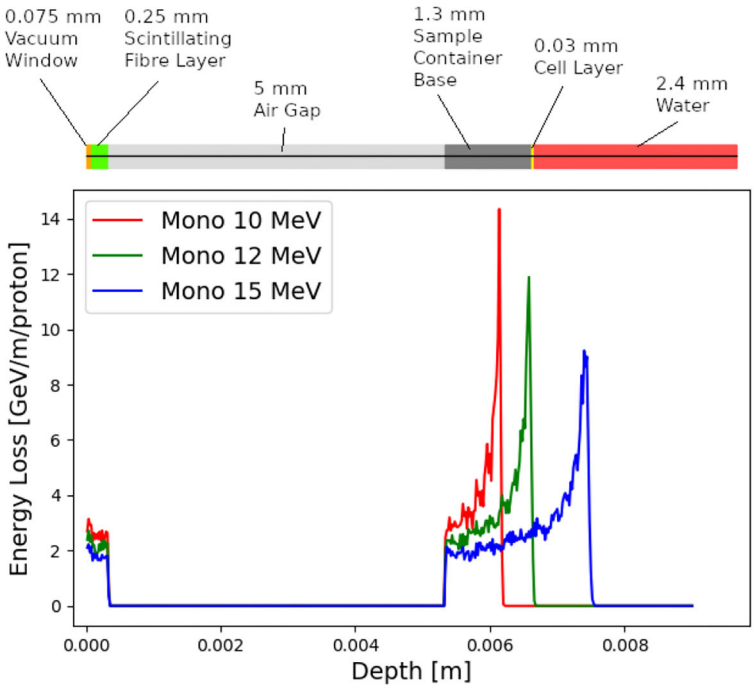

FIGURE 11 | Energy loss as a function of depth in the low-energy *in vitro* end station for three mono-energetic proton energies: 10, 12, and 15 MeV. Each beam was simulated using 10^4 particles at the start of the end station. The material through which the beam passes is indicated above the figure. The vacuum window is plotted at a depth value of 0 m. The beam deposits energy in the vacuum window and the layer of scintillating fiber before passing through an air gap and entering the sample container.

inversely proportional to $\beta^2\gamma^3$, where q is the particle charge, A its mass number, and β and γ its relativistic parameters. A single pulse of 8.3×10^7 ions deposits 3.2×10^{-3} J at the depth of the pristine Bragg peak, leading to an instantaneous dose rate of 9.7×10^8 Gy/s and a maximum average dose rate of 730 Gy/s.

The expected maximum dose rates are summarized in **Table 5**. The instantaneous dose rates depend on the bunch length which differs depending on the energies. For the low-energy *in vitro* line, a 7 ns bunch length is assumed for all energies. For the higher energies, a 127 MeV proton beam is delivered with a bunch length of 41.5 ns, and a bunch length of 75.2 ns for a 33.4 MeV/u carbon beam. The same repetition rate of 10 Hz was used for all energies. The minimum beam size at the start of the end station for the 12 and 15 MeV proton-beam simulations was 1 cm. A 1 mm beam size was used for the 127 MeV proton beam and 33.4 MeV/u carbon-ion beam simulations.

5. CONCLUSIONS

The initial conceptual design of LhARA, the Laser-hybrid Accelerator for Radiobiological Applications, has been described and its performance evaluated in simulations that take into account the key features of the facility. LhARA uses a laser-driven source to create a large flux of protons or light ions which are captured and formed into a beam by strong-focusing plasma lenses, thus evading prevalent space-charge limits on the instantaneous dose rate that can be delivered. Acceleration, performed using a fixed-field alternating-gradient accelerator, preserves the unique flexibility in the time, spectral, and spatial structure of the beam afforded by the laser-driven source. The ability to trigger the laser pulse that initiates the production of protons or ions at LhARA will allow the time structure of the beam to be varied to interrupt the chemical and biological pathways that determine the biological response to ionizing radiation. The almost parallel beam that LhARA will deliver can be varied to illuminate a circular area with a maximum diameter of between 1 and 3 cm with an almost uniform dose, or focused to a spot with diameter of $\sim$ 1 mm. These features will allow radiobiological studies to be carried out in completely new regimens, delivering a variety of ion species in a broad range of time structures and spatial configurations at instantaneous dose rates up to and potentially significantly beyond the current ultra-high dose-rate "FLASH" regime.

The enhanced understanding these studies will provide, may in turn result in new approaches to radiotherapy, decreasing the radio-toxicity for normal tissue while maintaining or enhancing the tumor-control probability. Further, by developing a triggerable system that incorporates dose-deposition imaging in a fast feedback-and-control system, in the long term LhARA has the potential to remove the requirement for a large gantry for proton and ion therapy, laying the foundations for "best in class" treatments to be made available to the many by reducing the footprint of future particle-beam therapy systems.

TABLE 5 | Summary of expected maximum dose per pulse and dose rates that LhARA can deliver for minimum beam sizes.

	12 MeV protons	15 MeV protons	127 MeV protons	33.4 MeV/u carbon
Dose per pulse	7.1 Gy	12.8 Gy	15.6 Gy	73.0 Gy
Instantaneous dose rate	1.0×10^9 Gy/s	1.8×10^9 Gy/s	3.8×10^8 Gy/s	9.7×10^8 Gy/s
Average dose rate	71 Gy/s	128 Gy/s	156 Gy/s	730 Gy/s

These estimates are based on Monte Carlo simulations using a bunch length of 7 ns for 12 and 15 MeV proton beams, 41.5 ns for the 127 MeV proton beam and 75.2 ns for the 33.4 MeV/u carbon beam. The average dose rate is based on the 10 Hz repetition rate of the laser source.

The radiobiology programme in combination with the demonstration in operation of the laser-hybrid technique means that the LhARA programme has the potential to drive a step-change in the clinical practice of proton- and ion-beam therapy.

DATA AVAILABILITY STATEMENT

The raw data supporting the conclusions of this article will be made available by the authors without undue reservation.

AUTHOR CONTRIBUTIONS

GA: integration engineering. TB: led Maxeler contributions. SB: led JAI team at RHUL. MB: laser-acceleration. RB: plasma-dynamics calculations. CB: led the STFC Central Laser Facility contributions. PB: led the JAI Oxford contributions. OE: particle distributions at the target. TD: beam dynamics calculations. SGi: simulation of the particle transport. TG: University of Liverpool lead author. SGr: ion-beam radiobiology. DG: advised on clinical applications. CH: led the medical-physics team at Charing Cross Hospital. JH: *in-vitro* and *in-vivo* end-station design. WJ: provided the Lay Summary. KK: advised on the end-stations. AK: project manager. J-BL: FFA design. KL: project leader. WL: real-time and offline processing. JM: led specification of instrumentation. PM: led Stratchclyde contributions. RM: advised on imaging and instrumentation. ZN: led the laser-driven source team. HL: transfer-line design. JLP: led the radiobiology work package. JPa: led the accelerator-system design. JPo: provided the initial concept. KP: advised on the radiobiology programme. MP: contributed to the end-station diagnostics. PR: led the Cockcroft Institute's contributions. GS: advised on dosimetry. WS: simulated LhARA Stage 1. SS: led the Daresbury Laboratory contributions. JT: led the ISIS engineering effort. ST: advised on technology development. PW: novel diagnostic-systems. CW: plasma-lens project lead. RX: advised on the data-handling aspects. All authors contributed to the article and approved the submitted version.

FUNDING

The work described here was made possible by a grant from the Science and Technology Facilities Council (ST/T002638/1, ST/P002021/1). Additional support was provided by the STFC Rutherford Appleton and Daresbury Laboratories and members of the LhARA consortium.

ACKNOWLEDGMENTS

We gratefully acknowledge all sources of support. A pre-publication review of the pre-CDR for LhARA was carried out by P. Bolton (LMU, Munich), M. Lamont (CERN), Y. Prezado (Institut Curie), and F. Romano (INFN-LNS and the National Physical Laboratory). We were grateful to the review panel for their support and detailed feedback on the draft pre-CDR.

REFERENCES

1. The World Health Organisation. *Cancer* (2020). Available online at: https://www.who.int/news-room/fact-sheets/detail/cancer
2. Bray F, Ferlay J, Soerjomataram I, Siegel RL, Torre LA, Jemal A. Global cancer statistics 2018: GLOBOCAN estimates of incidence and mortality worldwide for 36 cancers in 185 countries. *CA Cancer J Clin*. (2018) **68**:394–424. doi: 10.3322/caac.21492
3. Fitzmaurice C, Akinyemiju TF, Al Lami FH, Alam T, Alizadeh-Navaei R, Allen C, et al. Global, regional, and national cancer incidence, mortality, years of life lost, years lived with disability, and disability-adjusted life-years for 29 cancer groups, 1990 to 2016. *JAMA Oncol*. (2018) **4**:1553. doi: 10.1200/JCO.2018.36.15_suppl.1568
4. Atun R, Jaffray DA, Barton MB, Bray F, Baumann M, Vikram B, et al. Expanding global access to radiotherapy. *Lancet Oncol*. (2015) **16**:1153–86. doi: 10.1016/S1470-2045(15)00222-3
5. Datta NR, Rogers S, Bodis S. Challenges and opportunities to realize "The 2030 Agenda for Sustainable Development" by the United Nations: implications for radiation therapy infrastructure in low- and middle-income countries. *Int J Radiat Oncol Biol Phys*. (2019) **105**:918–33. doi: 10.1016/j.ijrobp.2019.04.033
6. Berry RJ. Effects of radiation dose-rate: from protracted, continuous irradiation to ultra-high dose-rates from pulsed accelerators. *Br Med Bull*. (1973) **29**:44–7. doi: 10.1093/oxfordjournals.bmb.a070955
7. Favaudon V, Caplier L, Monceau V, Pouzoulet F, Sayarath M, Fouillade C, et al. Ultrahigh dose-rate FLASH irradiation increases the differential response between normal and tumor tissue in mice. *Sci Transl Med*. (2014) **6**:245ra93. doi: 10.1126/scitranslmed.3008973
8. Durante M, BrÃďuer-Krisch E, Hill M. Faster and safer? FLASH ultra-high dose rate in radiotherapy. *Br J Radiol*. (2018) **91**:20170628. doi: 10.1259/bjr.20170628
9. Vozenin MC, Hendry JH, Limoli CL. Biological benefits of ultra-high dose rate FLASH radiotherapy: sleeping beauty awoken. *Clin Oncol*. (2019) **31**:407–15. doi: 10.1016/j.clon.2019.04.001
10. Wilson JD, Hammond EM, Higgins GS, Petersson K. Ultra-high dose rate (FLASH) radiotherapy: silver bullet or fool's gold? *Front Oncol*. (2020) **9**:1563. doi: 10.3389/fonc.2019.01563

11. Prezado Y, Fois G. Proton-minibeam radiation therapy: a proof of concept. *Med Phys*. (2013) **40**:031712. doi: 10.1118/1.4791648
12. Prezado Y, Jouvion G, Hardy D, Patriarca A, Nauraye C, Bergs J, et al. Proton minibeam radiation therapy spares normal rat brain: long-term clinical, radiological and histopathological analysis. *Sci Rep*. (2017) **7**:14403. doi: 10.1038/s41598-017-14786-y
13. Prezado Y, Dos Santos M, Gonzalez W, Jouvion G, Guardiola C, Heinrich S, et al. Transfer of minibeam radiation therapy into a cost-effective equipment for radiobiological studies: a proof of concept. *Sci Rep*. (2017) **7**:17295. doi: 10.1038/s41598-017-17543-3
14. Prezado Y, Jouvion G, Patriarca A, Nauraye C, Guardiola C, Juchaux M, et al. Proton minibeam radiation therapy widens the therapeutic index for high-grade gliomas. *Sci Rep*. (2018) **8**:16479. doi: 10.1038/s41598-018-34796-8
15. González W, Prezado Y. Spatial fractionation of the dose in heavy ions therapy: an optimization study. *Med Phys*. (2018) **45**:2620–7. doi: 10.1002/mp.12902
16. Martínez-Rovira I, GonzÃąlez W, Brons S, Prezado Y. Carbon and oxygen minibeam radiation therapy: an experimental dosimetric evaluation. *Med Phys*. (2017) **44**:4223–9. doi: 10.1002/mp.12383
17. The LhARA Consortium. *The Laser-hybrid Accelerator for Radiobiological Applications*. CCAP-TN-01 (2020). Available online at: https://ccap.hep.ph.ic.ac.uk/trac/raw-attachment/wiki/Communication/Notes/CCAP-TN-01.pdf
18. Loeffler JS, Durante M. Charged particle therapyâĂŤoptimization, challenges and future directions. *Nat Rev Clin Oncol*. (2013) **10**:411–24. doi: 10.1038/nrclinonc.2013.79
19. PTCOG. Particle Therapy Co-Operative Group (2020).
20. Paganetti H, van Luijk P. Biological considerations when comparing proton therapy with photon therapy. *Semin Radiat Oncol*. Philadelphia, PA: W. B. Saunders (2013) **23**:77–87. doi: 10.1016/j.semradonc.2012.11.002
21. Paganetti H. Relative biological effectiveness (RBE) values for proton beam therapy. Variations as a function of biological endpoint, dose, and linear energy transfer. *Phys Med Biol*. (2014) **59**:R419. doi: 10.1088/0031-9155/59/22/R419
22. Chaudhary P, Marshall TI, Perozziello FM, Manti L, Currell FJ, Hanton F, et al. Relative biological effectiveness variation along monoenergetic and modulated Bragg peaks of a 62-MeV therapeutic proton beam: a preclinical assessment. *Int J Radiat Oncol Biol Phys*. (2014) **90**:27–35. doi: 10.1016/j.ijrobp.2014.05.010
23. Wilkens JJ, Oelfke U. A phenomenological model for the relative biological effectiveness in therapeutic proton beams. *Phys Med Biol*. (2004) **49**:2811–25. doi: 10.1088/0031-9155/49/13/004
24. Karger CP, Peschke P. RBE and related modeling in carbon-ion therapy. *Phys Med Biol*. (2017) **63**:01TR02. doi: 10.1088/1361-6560/aa9102
25. Vitti ET, Parsons JL. The radiobiological effects of proton beam therapy: impact on DNA damage and repair. *Cancers*. (2019) **11**:946. doi: 10.3390/cancers11070946
26. Carter RJ, Nickson CM, Thompson JM, Kacperek A, Hill MA, Parsons JL. Complex DNA damage induced by high linear energy transfer alpha-particles and protons triggers a specific cellular DNA damage response. *Int J Radiat Oncol Biol Phys*. (2018) **100**:776–84. doi: 10.1016/j.ijrobp.2017.11.012
27. Wilson J, Hammond EM, Higgins GS, Petersson K. Corrigendum: ultra-high dose rate (FLASH) radiotherapy: silver bullet or fool's gold? *Front Oncol*. (2020) **10**:210. doi: 10.3389/fonc.2020.00210
28. Bourhis J, Sozzi WJ, Jorge PG, Gaide O, Bailat C, Duclos F, et al. Treatment of a first patient with FLASH-radiotherapy. *Radiother Oncol*. (2019) **139**:18–22. doi: 10.1016/j.radonc.2019.06.019
29. Bulanov SV, Esirkepov TZ, Khoroshkov VS, Kuznetsov AV, Pegoraro F. Oncological hadrontherapy with laser ion accelerators. *Phys Lett A*. (2002) **299**:240–7. doi: 10.1016/S0375-9601(02)00521-2
30. Fourkal E, Li JS, Ding M, Tajima T, Ma CM. Particle selection for laser-accelerated proton therapy feasibility study. *Med Phys*. (2003) **30**:1660–70. doi: 10.1118/1.1586268
31. Malka V, Fritzler S, Lefebvre E, d'HumiÃĺres E, Ferrand R, Grillon G, et al. Practicability of proton therapy using compact laser systems. *Med Phys*. (2004) **31**:1587–92. doi: 10.1118/1.1747751
32. Ledingham KWD, McKenna P, Singhal RP. Applications for nuclear phenomena generated by ultra-intense lasers. *Science*. (2003) 300:1107–111.
33. Kraft SD, Richter C, Zeil K, Baumann M, Beyreuther E, Bock S, et al. Dose-dependent biological damage of tumour cells by laser-accelerated proton beams. *New J Phys*. (2010) **12**:85003. doi: 10.1088/1367-2630/12/8/085003
34. Fiorini F, Kirby D, Borghesi M, Doria D, Jeynes JC, Kakolee KF, et al. Dosimetry and spectral analysis of a radiobiological experiment using laser-driven proton beams. *Phys Med Biol*. (2011) **56**:6969–82. doi: 10.1088/0031-9155/56/21/013
35. Yogo A, Maeda T, Hori T, Sakaki H, Ogura K, Nishiuchi M, et al. Measurement of relative biological effectiveness of protons in human cancer cells using a laser-driven quasimonoenergetic proton beamline. *Appl Phys Lett*. (2011) **98**:053701. doi: 10.1063/1.3551623
36. Bin J, Allinger K, Assmann W, Dollinger G, Drexler GA, Friedl AA, et al. A laser-driven nanosecond proton source for radiobiological studies. *Appl Phys Lett*. (2012) **101**:243701. doi: 10.1063/1.4769372
37. Doria D, Kakolee KF, Kar S, Litt SK, Fiorini F, Ahmed H, et al. Biological effectiveness on live cells of laser driven protons at dose rates exceeding 10^9 Gy/s. *AIP Adv*. (2012) **2**:011209. doi: 10.1063/1.3699063
38. Zeil K, Baumann M, Beyreuther E, Burris-Mog T, Cowan TE, Enghardt W, et al. Dose-controlled irradiation of cancer cells with laser-accelerated proton pulses. *Appl Phys B*. (2013) **110**:437–44. doi: 10.1007/s00340-012-5275-3
39. Masood U, Bussmann M, Cowan TE, Enghardt W, Karsch L, Kroll F, et al. A compact solution for ion beam therapy with laser accelerated protons. *Appl Phys B*. (2014) **117**:41–52. doi: 10.1007/s00340-014-5796-z
40. Zlobinskaya O, Siebenwirth C, Greubel C, Hable V, Hertenberger R, Humble N, et al. The effects of ultra-high dose rate proton irradiation on growth delay in the treatment of human tumor xenografts in nude mice. *Radiat Res*. (2014) **181**:177–83. doi: 10.1667/RR13464.1
41. Pommarel L, Vauzour B, Mégnin-Chanet F, Bayart E, Delmas O, Goudjil F, et al. Spectral and spatial shaping of a laser-produced ion beam for radiation-biology experiments. *Phys Rev Acceler Beams*. (2017) **20**:1–10. doi: 10.1103/PhysRevAccelBeams.20.032801
42. Manti L, Perozziello FM, Borghesi M, Candiano G, Chaudhary P, Cirrone GAP, et al. The radiobiology of laser-driven particle beams: focus on sub-lethal responses of normal human cells. *J Instrum*. (2017) **12**:C03084. doi: 10.1088/1748-0221/12/03/C03084
43. A-SAIL Project. *A-SAIL Project*. (2020). Available online at: https://www.qub.ac.uk/research-centres/A-SAILProject/
44. Cirrone GAP, Margarone D, Maggiore M, Anzalone A, Borghesi M, Jia SB, et al. ELIMED: a new hadron therapy concept based on laser driven ion beams. In: Esarey E, Schroeder CB, Leemans WP, Ledingham KWD, Jaroszynski DA, editors. *Laser Acceleration of Electrons, Protons, and Ions II; and Medical Applications of Laser-Generated Beams of Particles II; and Harnessing Relativistic Plasma Waves III*, Vol. **8779**. Prague: International Society for Optics and Photonics. SPIE (2013). p. 216–25.
45. Wiggins SM, Boyd M, Brunetti E, Butler NMH, Feehan JS, Gray RJ, et al. Application programmes at the Scottish Centre for the application of plasma-based accelerators (SCAPA). In: Jaroszynski DA, Hur M, editors. *Relativistic Plasma Waves and Particle Beams as Coherent and Incoherent Radiation Sources III*, Vol. **11036**. International Society for Optics and Photonics. SPIE (2019). p. 93–103.
46. Romano F, Schillaci F, Cirrone GAP, Cuttone G, Scuderi V, Allegra L, et al. The ELIMED transport and dosimetry beamline for laser-driven ion beams. *Nucl Instr Methods Phys Res A*. (2016) **829**:153–8. doi: 10.1016/j.nima.2016.01.064
47. Masood U, Cowan TE, Enghardt W, Hofmann KM, Karsch L, Kroll F, et al. A light-weight compact proton gantry design with a novel dose delivery system for broad-energetic laser-accelerated beams. *Phys Med Biol*. (2017) **62**:5531–55. doi: 10.1088/1361-6560/aa7124
48. Chaudhary P, Gwynne D, Doria D, Romagnani L, Maiorino C, Padda H, et al. Effectiveness of laser accelerated ultra high dose rate protons in DNA DSB damage induction under hypoxic conditions. In: *44th EPS Conference on Plasma Physics, EPS 2017*, Vol. **44F**. Belfast: European Physical Society (EPS) (2017). p. P1.217.
49. Margarone D, Cirrone GAP, Cuttone G, Amico A, AndÃš L, Borghesi M, et al. ELIMAIA: a laser-driven ion accelerator for multidisciplinary applications. *Quant Beam Sci*. (2018) **2**:8. doi: 10.3390/qubs2020008
50. Cirrone GAP, Catalano R, Cuttone G, Margarone D, Schillaci F, Petringa G. Generation control and application of flash radiation beam from laser-matter

interaction: the ELIMAIA-ELIMED beamline. *Nuovo Cim C*. (2020) **43**:15. doi: 10.1393/ncc/i2020-20015-6
51. Schillaci F, Andò L, Cirrone G, Cuttone G, Maggiore M, Margarone D, et al. Advanced beam transport solutions for ELIMAIA: a user oriented laser-driven ion beamlines. In: *10th International Particle Accelerator Conference*. Melbourne, VIC (2019). p. TUPTS005.
52. Cirrone G, Allegra L, Amato A, Amico A, Candiano G, Caruso A, et al. Status, plans and potential applications of the ELIMED beam line at ELI-beamlines. In: *7th International Particle Accelerator Conference*. Busan (2016). p. WEXB01.
53. Milluzzo G, Scuderi V, Amico AG, Borghesi M, Cirrone GAP, Cuttone G, et al. Laser-accelerated ion beam diagnostics with TOF detectors for the ELIMED beam line. *JINST*. (2017) **12**:C02025. doi: 10.1088/1748-0221/12/02/C02025
54. Pipek J, Romano F, Milluzzo G, Cirrone GAP, Cuttone G, Amico AG, et al. Monte Carlo simulation of the ELIMED beamline using Geant4. *JINST*. (2017) **12**:C03027. doi: 10.1088/1748-0221/12/03/C03027
55. Milluzzo G, Pipek J, Amico AG, Cirrone GAP, Cuttone G, Korn G, et al. Geant4 simulation of the ELIMED transport and dosimetry beam line for high-energy laser-driven ion beam multidisciplinary applications. *Nucl Instrum Meth A*. (2018) **909**:298–302. doi: 10.1016/j.nima.2018.02.066
56. Dover NP, Nishiuchi M, Sakaki H, Kondo K, Lowe HF, Alkhimova MA, et al. Demonstration of repetitive energetic proton generation by ultra-intense laser interaction with a tape target. *High Energy Density Phys*. (2020) **37**:100847. doi: 10.1016/j.hedp.2020.100847
57. Clark EL, Krushelnick K, Davies JR, Zepf M, Tatarakis M, Beg FN, et al. Measurements of energetic proton transport through magnetized plasma from intense laser interactions with solids. *Phys Rev Lett.* (2000) **84**:670–3. doi: 10.1103/PhysRevLett.84.670
58. Snavely RA, Key MH, Hatchett SP, Cowan TE, Roth M, Phillips TW, et al. Intense high-energy proton beams from petawatt-laser irradiation of solids. *Phys Rev Lett.* (2000) **85**:2945–8. doi: 10.1103/PhysRevLett.85.2945
59. Daido H, Nishiuchi M, Pirozhkov AS. Review of laser-driven ion sources and their applications. *Rep Prog Phys*. (2012) **75**:56401. doi: 10.1088/0034-4885/75/5/056401
60. Roth M, Schollmeier M. Ion acceleration-target normal sheath acceleration. *CAS-CERN Accelerator School: Plasma Wake Acceleration 2014, Proceedings*. (2014) 1, 231–270. doi: 10.5170/CERN-2016-001.231
61. Clark EL, Krushelnick K, Zepf M, Beg FN, Tatarakis M, Machacek A, et al. Energetic heavy-ion and proton generation from ultraintense laser-plasma interactions with solids. *Phys Rev Lett.* (2000) **85**:1654–7. doi: 10.1103/PhysRevLett.85.1654
62. Passoni M, Bertagna L, Zani A. Target normal sheath acceleration: theory, comparison with experiments and future perspectives. *New J Phys.* (2010) **12**:045012. doi: 10.1088/1367-2630/12/4/045012
63. Willingale L, Nagel SR, Thomas AGR, Bellei C, Clarke RJ, Dangor AE, et al. Characterization of high-intensity laser propagation in the relativistic transparent regime through measurements of energetic proton beams. *Phys Rev Lett.* (2009) 102:125002. doi: 10.1103/1007
64. Bin J, Ma W, Wang H, Streeter M, Kreuzer C, Kiefer D, et al. Ion acceleration using relativistic pulse shaping in near-critical-density plasmas. *Phys Rev Lett.* (2015) **115**:064801. doi: 10.1103/PhysRevLett.115.064801
65. Chen SN, Vranic M, Gangolf T, Boella E, Antici P, Bailly-Grandvaux M, et al. Collimated protons accelerated from an overdense gas jet irradiated by a 1 m wavelength high-intensity short-pulse laser. *Sci Rep.* (2017) **7**:13505. doi: 10.1038/s41598-017-12910-6
66. Margarone D, Velyhan A, Dostal J, Ullschmied J, Perin JP, Chatain D, et al. Proton acceleration driven by a nanosecond laser from a cryogenic thin solid-hydrogen ribbon. *Phys Rev X*. (2016) **6**:041030. doi: 10.1103/PhysRevX.6.041030
67. Gauthier M, Curry CB, Göde S, Brack FE, Kim JB, MacDonald MJ, et al. High repetition rate, multi-mev proton source from cryogenic hydrogen jets. *Appl Phys Lett.* (2017) **111**:114102. doi: 10.1063/1.4990487
68. Obst L, Göde S, Rehwald M, Brack FE, Branco J, Bock S, et al. Efficient laser-driven proton acceleration from cylindrical and planar cryogenic hydrogen jets. *Sci Rep.* (2017) **7**:10248. doi: 10.1038/s41598-017-10589-3
69. Morrison JT, Feister S, Frische KD, Austin DR, Ngirmang GK, Murphy NR, et al. MeV proton acceleration at kHz repetition rate from ultra-intense laser liquid interaction. *New J Phys.* (2018) **20**:22001. doi: 10.1088/1367-2630/aaa8d1
70. Noaman-ul Haq M, Ahmed H, Sokollik T, Yu L, Liu Z, Yuan X, et al. Statistical analysis of laser driven protons using a high-repetition-rate tape drive target system. *Phys Rev Accel Beams*. (2017) **20**:041301. doi: 10.1103/PhysRevAccelBeams.20.041301
71. Gabor D. A space-charge lens for the focusing of ion beams. *Nature*. (1947) **160**:89–90. doi: 10.1038/160089b0
72. Thompson RC. Penning traps. In: *Trapped Charged Particles*. Advanced Textbooks in Physics. World Scientific (Europe) (2015). p. 1–33. doi: 10.1142/9781786340139_0001
73. deGrassie JS, Malmberg JH. Waves and transport in the pure electron plasma. *Phys Fluids*. (1980) **23**:63–81. doi: 10.1063/1.862864
74. Malmberg JH, Driscoll CF, Beck B, Eggleston DL, Fajans J, Fine K, et al. Experiments with pure electron plasmas. *AIP Conf Proc*. (1988) **175**:28–74. doi: 10.1063/1.37613
75. Reiser M. Comparison of Gabor lens, gas focusing, and electrostatic quadrupole focusing for low-energy ion beams. In: *Proceedings of the 1989 IEEE Particle Accelerator Conference. Accelerator Science and Technology*, Vol. **3**. Chicago, IL (1989). p. 1744–7.
76. Pozimski J, Aslaninejad M. Gabor lenses for capture and energy selection of laser driven ion beams in cancer treatment. *Laser Part Beams*. (2013) **31**:723–33. doi: 10.1017/S0263034613000761
77. Meusel O, Droba M, Glaeser B, Schulte K. Experimental studies of stable confined electron clouds using Gabor lenses. *Conf Proc C*. (2013) **1206051**:157–60. doi: 10.5170/CERN-2013-002.157
78. *VSim for Plasma* (2020). Available online at: https://www.txcorp.com/vsim
79. Autin B, Carli C, D'Amico T, Gröbner O, Martini M, Wildner E. *Beam Optics: A Program for Analytical Beam Optics*. European Organization for Nuclear Research (CERN). CERN-98-06 (1998). Available online at: http://inis.iaea.org/search/search.aspx?orig_q=RN:30052986
80. Grote H, Schmidt F. MAD-X: an upgrade from MAD8. *Conf Proc C*. (2003) **030512**:3497. doi: 10.1109/PAC.2003.1289960
81. Nevay LJ, Boogert ST, Snuverink J, Abramov A, Deacon LC, Garcia-Morales H, et al. BDSIM: an accelerator tracking code with particle-matter interactions. *Comput Phys Commun*. (2020) **252**:107200. doi: 10.1016/j.cpc.2020.107200
82. De Loos MJ, Van der Geer SB. *General Particle Tracer: A New 3D Code for Accelerator and Beamline Design* (1996). Available online at: https://cds.cern.ch/record/860825
83. Tsoupas N, Lankshear R, Snead CL, Ward TE, Zucker M, Enge HA. Uniform beam distributions using octupoles. In: *Proceedings of PAC 1991*. San Francisco, CA (1991). p. 1695–7.
84. Urakabe E, Fujita Y, Hiramoto K, Inoue M, Iwashita Y, Kanazawa M, et al. Beam-profile control using an octupole magnet. *Jpn J Appl Phys*. (1999) **38**:6145–9. doi: 10.1143/JJAP.38.6145
85. Amin T, Barlow R, Ghithan S, Royb G, Schuhb S. Formation of a uniform ion beam using octupole magnets for BioLEIR facility at CERN. *JINST*. (2018) **13**:P04016. doi: 10.1088/1748-0221/13/04/P04016
86. Krest D, Laslett L, Jones LW, Symon K, Terwilliger K. *Fixed Field Alternating Gradient Particle Accelerators*. Madison, WI: Midwestern Universities Research Association (MURA). MURA-109, MURA-DWK-KRS-LJL-LWJ-KMT-3 (1956).
87. Symon KR, Kerst DW, Jones LW, Laslett LJ, Terwilliger KM. Fixed-field alternating-gradient particle accelerators. *Phys Rev*. (1956) **103**:1837–59. doi: 10.1103/PhysRev.103.1837
88. Fourrier J, Martinache F, Meot F, Pasternak J. Spiral FFAG lattice design tools. Application to 6-D tracking in a proton-therapy class lattice. *Nucl Instrum Meth A*. (2008) **589**:133–42. doi: 10.1016/j.nima.2008.01.082
89. Tanigaki M, Mori Y, Inoue M, Mishima K, Shiroya S, Ishi Y, et al. Present status of the ffag accelerators in kurri for ADS study. In: *EPAC 2006–Contributions to the Proceedings*. Edinburgh (2006).
90. Lagrange JB, Appleby RB, Garland JM, Pasternak J, Tygier S. Racetrack FFAG muon decay ring for nuSTORM with triplet focusing. *JINST*. (2018) **13**:P09013. doi: 10.1088/1748-0221/13/09/P09013

91. Yonemura Y, Arima H, Ikeda N, Ishibashi K, Maehata K, Noro T, et al. Status of center for accelerator and beam applied science of Kyushu University. In: *EPAC 2008–Contributions to the Proceedings*. Genoa (2008).
92. Planche T, Fourrier J, Lancelot JL, Meot F, Neuveglise D, Pasternak J. Design of a prototype gap shaping spiral dipole for a variable energy protontherapy FFAG. *Nucl Instrum Meth A*. (2009) **604**:435–42. doi: 10.1016/j.nima.2009.02.026
93. Kurup A. Diagnostics for LhARA. In: *Low Energy Ion Beam Diagnostics Workshop*. London: Imperial College (2019).
94. Barber G. *Outline Design and Cost Estimate for the Smartphantom*. CCAP-TN-INST-01, The Centre for the Clinical Application of Particles, Imperial College London. (2018). Available online at: https://ccap.hep.ph.ic.ac.uk/trac/raw-attachment/wiki/Communication/Notes/SmartPhantom.pdf (accessed September 21, 2020).
95. Wang H. Wavefront measurement techniques used in high power lasers. *High Power Laser Sci Eng*. (2014) **2**:e25. doi: 10.1017/hpl.2014.28
96. Uesugi T. *Betatron Tune Measurement*. Osaka: FFA School. (2018).
97. The EPICS Collaboration. *The Experimental Physics and Industrial Control System* (2020). Available online at: https://epics-controls.org
98. NIST. *NIST Standard Reference Database 124*. Gaithersburg, MD: National Institute of Standards and Technology (2017).
99. *Ionizing Radiation Detectors*. Freiburg: PTW-Freiburg Physikalisch-Technische Werkstatten Dr. Pychlau GmbH (2020). Available online at: https://www.ptwdosimetry.com/fileadmin/user_upload/DETECTORS_Cat_en_16522900_12/blaetterkatalog/blaetterkatalog/pdf/complete.pdf (accessed September 21, 2020).
100. *User Manual Water Phantom*. Freiburg: PTW-Freiburg Physikalisch-Technische Werkstatten Dr. Pychlau GmbH (2009).

Conflict of Interest: TB was employed by Maxeler Technologies and RX was employed by the company Corerain Technologies.

The remaining authors declare that the research was conducted in the absence of any commercial or financial relationships that could be construed as a potential conflict of interest.

frontiers in Physics

ORIGINAL RESEARCH
published: 29 September 2020
doi: 10.3389/fphy.2020.568145

Beam Monitor Calibration for Radiobiological Experiments With Scanned High Energy Heavy Ion Beams at FAIR

Francesca Luoni[1,2], Uli Weber[1], Daria Boscolo[1], Marco Durante[1,2], Claire-Anne Reidel[1,3], Christoph Schuy[1], Klemens Zink[4,5] and Felix Horst[1,4]*

[1] Biophysics Department, GSI Helmholtzzentrum für Schwerionenforschung GmbH, Darmstadt, Germany, [2] Festkörperphysik Department, Technical University of Darmstadt, Darmstadt, Germany, [3] Université de Strasbourg, CNRS, IPHC UMR 7871, Strasbourg, France, [4] Institute of Medical Physics and Radiation Protection, Technische Hochschule Mittelhessen (THM) University of Applied Sciences, Giessen, Germany, [5] Marburger Ionenstrahl-Therapiezentrum (MIT), Albrecht-Kossel-Strasse, Marburg, Germany

OPEN ACCESS

Edited by:
Wouter van Elmpt,
Maastricht University, Netherlands

Reviewed by:
Hugo Palmans,
National Physical Laboratory,
United Kingdom;
MedAustron Ion Therapy
Center, Austria
Stefaan Vynckier,
Catholic University of Louvain,
Belgium

***Correspondence:**
Uli Weber
u.weber@gsi.de

Specialty section:
This article was submitted to
Medical Physics and Imaging,
a section of the journal
Frontiers in Physics

Received: 31 May 2020
Accepted: 17 August 2020
Published: 29 September 2020

Citation:
Luoni F, Weber U, Boscolo D,
Durante M, Reidel C-A, Schuy C,
Zink K and Horst F (2020) Beam
Monitor Calibration for Radiobiological
Experiments With Scanned High
Energy Heavy Ion Beams at FAIR.
Front. Phys. 8:568145.
doi: 10.3389/fphy.2020.568145

Precise and reliable monitoring of the particle rate is of great importance at accelerator facilities worldwide. In this article we describe the standard beam monitor calibration currently employed at the multi-purpose experimental sites Cave A and Cave M at GSI, where intense highly energetic ion beams are routinely used for a wide variety of experiments. An absolute dose-to-water measurement is performed with an air-filled ionization chamber and transferred into a calibration per primary particle. This is necessary for the raster scanning system used to enable the irradiation of extended fields, required for biophysical experiments in the research fields of particle therapy or space radiation protection. The main focus of this work is to understand through Monte Carlo simulations whether the currently used dosimetry procedure is valid for all the ion species and energies that are provided at GSI Cave A and Cave M by the SIS18 synchrotron and that will be provided by the SIS100 at FAIR. With this aim the detailed geometry of the PTW 30013 Farmer ionization chamber currently used at GSI was implemented in the transport code FLUKA and the beam quality correction factor k_Q for different energies and ion species was calculated. Further details about the robustness of the calibration are investigated as well, e.g., appropriate irradiation depth of biological samples. Evidence is presented that for ions above 1 GeV/u the k_Q factor decreases due to the density effect, which modifies the water-to-air stopping power ratio at relativistic energies. These findings are of particular importance for future biophysics experiments with ion beams from the SIS100 in the framework of the FAIR project. For energies in the regime of several GeV/u the constant *kQ* value as used in common practice should be replaced with the energy-dependent correction factor provided in this work.

Keywords: heavy ion dosimetry, beam monitor calibration, raster scanning, beam quality correction factor, k_Q, radiobiological irradiations, farmer ionization chamber

1. INTRODUCTION

The majority of radiation biophysics experiments require a beam application systems that can apply a defined and reliable absorbed dose. This is valid both for nuclear physics experiments and irradiations of biological samples. The accuracy of the dosimetry and of the absolute calibration of the beam application system directly translates into that of the experiment.

Radiobiological experiments typically aim on studying and understanding dose-response relationships for different radiation qualities and for various biological endpoints. At GSI, irradiations of biological samples in the research fields of particle therapy or space radiation protection are performed with high-energy heavy ions from the SIS18 synchrotron in Caves A and M, which are equipped with a magnetic scanning system that can deflect ion beams in horizontal and vertical directions. This so-called intensity modulated raster scanning method was developed at GSI as part of the carbon ion therapy pilot project [1]. When homogenous dose distributions are irradiated, the absorbed dose depends on the distance of the scan spots and the number of particles applied per spot. A large area parallel plate ionization chamber is typically used to monitor the beam intensity during the irradiation and to trigger the scanning control system for steering the beam to the next spot when the required particle number is reached. Optionally, especially when performing experiments related to radiotherapy, a position sensitive detector such as a multi wire proportional chamber is used to control the lateral beam position [2].

The beam monitor ionization chamber must be calibrated in terms of the number of primary particles. Adapted from ion-beam therapy, this calibration is typically performed indirectly via an absorbed dose-to-water measurement with an air-filled ionization chamber under defined reference conditions (field size, measurement depth). The calibration in terms of the absorbed dose can be transferred into a calibration in terms of primary particle via the primary fluence obtained by a radiation transport calculation [3, 4].

This beam monitor calibration method is very robust but bares some potential for systematic errors. The reason is that the procedure was developed for carbon ions in the energy range used in radiotherapy, i.e., 70 to 430 MeV/u, while radiobiological experiments performed in Cave A also make use of much heavier ions (typically up to ^{56}Fe) and much higher energies, i.e., up to 1 GeV/u. Therefore, it is necessary to quantify the uncertainty that can result from this variation of the measurement conditions. Systematic errors in dose delivery can also occur if the samples are irradiated at a depth different from the reference depth used for the beam monitor calibration. Even a small difference between the two points can actually make a difference because the entrance channel of the depth dose distributions for heavy ions are not flat.

The aims of the present work are to quantify the accuracy of the beam monitor calibration currently performed at GSI and to investigate with Monte Carlo simulations if the method can be adapted to future radiobiological experiments at the FAIR facility, which will provide heavy ion beams with energies up to 10 GeV/u [5].

2. METHODS AND MATERIALS

2.1. Raster Scanning System in GSI Caves A and M

In GSI Caves A and M a raster scanning system is used to irradiate samples with a defined fluence or dose, which can be delivered homogenously to a well-defined arbitrary area. The raster scanning system is used for both irradiation of biological samples and physics experiments, e.g., nuclear physics measurements or detector tests. The heavy ion pencil beams used for irradiations have an approximately Gaussian lateral profile with a FWHM (full-width-half-maximum) that typically ranges from about 4 to about 12 mm, depending on the ion species, their kinetic energy, the beam exit window and the magnet setting used. When samples are irradiated with the raster scanning system, the area is divided into a raster of scan spots having a typical distance of a few millimeters. When a homogenous field is irradiated, the scan spot distance must be smaller than the $\sigma = \mathrm{FWHM}/(2\sqrt{2\ln 2}) \simeq \mathrm{FWHM}/2.355$ of the pencil beam to ensure that the Gaussian beam spots can add up to a homogeneous distribution. Once the irradiation is completed, the dose is homogeneous in the center of the irradiated area and falls off with a Gaussian-like profile at the edges. The homogeneous dose at the center of the field results from a homogeneous fluence Φ which can be calculated from Equation (1)

$$\Phi = \frac{N}{d_{scan}^2} \tag{1}$$

where N is the number of particles per scan spot and d_{scan} is the scan spot distance. The scanning area has to be much larger than the width of the scan spot. It is recommended to keep the scan area 10-20 times larger than the beam FWHM, in order to avoid the outer halo-contributions of the pencil beam spot getting lost in the superposition of the beam spots [6]. For a free-in-air irradiation, assuming a monoenergetic ion beam and neglecting δ electron effects, the absorbed dose to water D_w (the typical dosimetric quantity in radiotherapy and radiobiology) can be estimated according to Equation (2)

$$D_w = \Phi \cdot \frac{S}{\rho_w} = \frac{N}{d_{scan}^2} \cdot \frac{S}{\rho_w} \tag{2}$$

where ρ_w is the density of water and S is the stopping power (energy loss per path length) of water for the ion used for the irradiation. If the irradiation is not done free-in-air, S must be calculated for the particle spectrum at the irradiation depth. However, this is not straightforward due to the complexity of the nuclear fragmentation reactions generating the mixed radiation field.

Since the beam is delivered in spills and the beam intensity is subject to statistical fluctuations coming from the slow extraction of the synchrotron, the delivery time for the required particle number N can vary from spot to spot. The number of ions delivered to the sample is monitored continuously and as soon as the number of ions required for one spot is reached, the beam is moved to the next spot by the scanning magnets. A

large area parallel plate ionization chamber positioned in front of the beam exit window is typically used as beam monitor. Depending on the intensity, also a plastic scintillator for low particle rates or a secondary electron monitor (SEETRAM) for high rates can be used. The ionization chamber output signal is transferred into a current-to-frequency converter (IFC), which is an amplifier converting the current output from the parallel plate ionization chamber into digital pulses. One pulse corresponds to a certain charge quantum (e.g., 1 pC) depending on the set sensitivity range. The pulses are continuously generated, so that the output frequency is proportional to the current output from the ionization chamber, which is in turn proportional to the particle rate of the incoming beam. The IFC output is connected to the scanner control unit, which counts the number of pulses and moves the beam from spot to spot when the number of pulses corresponding to the number of particles per spot N is reached. The measurement chain is shown in **Figure 1**.

The system needs to be calibrated in terms of number of IFC pulses per number of ions transmitted through the monitor ionization chamber.

2.2. Beam Monitor Calibration

The monitor calibration factor has to be determined experimentally for every ion species at different energies and should be checked daily before the irradiations. Checking the monitor calibration is an important quality assurance task in particle therapy facilities [7, 8]. In principle the beam monitor can be calibrated with different methods [9]. Since the calibration is done in terms of the primary particle number, it could be performed by cross calibration with a particle counter or on basis of a charge or fluence measurement. The first method has the problem that the working intensity ranges of particle counters like plastic scintillators and the monitor ionization chamber are very different, while it is preferable to perform the calibration with the intensity actually used for irradiation of the samples. An instrument that is well-suited to measure the integral charge in an ion beam pulse is the Faraday cup. Some proton therapy centers use Faraday cups as the dosimetric standard for absolute calibration of the beam monitors [9–12]. A Faraday cup does not provide a dose information but directly the primary particle number if the beam is pure. However, Faraday cup measurements are rather sensitive to delta electrons, either scattered inside the collection volume from outside or vice versa. Those perturbations can be prevented e.g., by guard rings and magnetic fields [12] but for high energy beams they get more pronounced due to the increasing delta electron energies. Furthermore, for heavy ion beams there are some additional practical limitations concerning the use of Faraday cups, in particular due to the long range of secondary fragments created in nuclear reactions that would require very thick copper volumes to collect the entire charge carried by the beam. A calibration of the beam monitor can also be performed on basis of a fluence measurement using nuclear track etching detectors like CR39 [13] or fluorescent nuclear track detectors [14]. Before starting up the carbon ion therapy project at GSI, most radiobiological irradiations at Caves A and M were actually based on CR39. The monitor calibration for irradiations with low energy heavy ions at the GSI UNILAC is still being performed

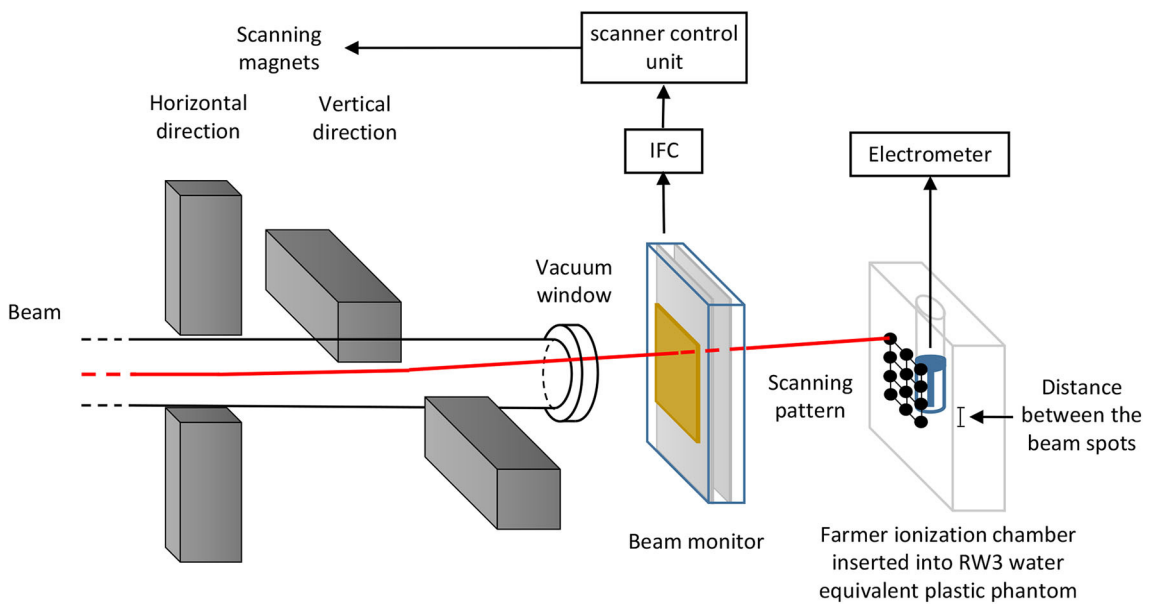

FIGURE 1 | Schematic of the setup used in GSI cave A for the calibration of the beam monitor in terms of primary particles via an absolute dose measurement with a Farmer type ionization chamber in a water equivalent plastic phantom. Vertical and horizontal scanning magnets controlled by the scanner control unit deflect a pencil beam to scan over the irradiated sample. The scanner control unit gets an input signal from a current-to-frequency converter (IFC) coupled to the beam monitor, which in GSI Caves A and M is typically a large area parallel plate ionization chamber. The beam monitor measures the number of particles applied per spot, which is used to control the raster scanning system. The schematic is not to scale.

like this. However, for high energy heavy ion beams the CR39 etching technique has turned out to be not accurate enough. The main problems lie in the less pronounced tracks at high energy and in the track overlapping at high fluences.

The particle fluence is directly related to the absorbed dose (see Equation 2), therefore an absolute dose measurement can serve as an alternative method to calibrate the beam monitor in terms of primary particle number. Ionization chambers are stable to operate and give more reliable and reproducible measurement results than e.g., nuclear track detectors, especially at high particle beam rates ($> 10^8$ ions/s). Therefore, when the carbon therapy project at GSI was started, absolute dosimetry in terms of absorbed dose to water using thimble ionization chambers was established as the standard for ion beam therapy irradiations of patients and biological samples with high energy heavy ions [3, 4].

The IAEA TRS-398 code of practice gives basic recommendations on how to perform absolute dosimetry in terms of absorbed dose to water with air-filled ionization chambers for all kinds of radiotherapy beams [15]. Especially for protons, there have been a lot of recent investigations to further improve the proposed techniques and to establish a common standard [12, 16]. The method developed for carbon therapy at GSI (also applied almost identically at the clinical ion-beam therapy centers in Heidelberg and Marburg) makes use of a Farmer-type ionization chamber (PTW Farmer 30013) positioned at a low depth in a water-equivalent plastic (RW3) phantom [3, 4]. The signal of the Farmer chamber is read out with a high precision electrometer. At GSI Caves A and M a UNIDOS E universal dosimeter is used. The Farmer chamber is inserted into a 2 cm thick phantom made of water equivalent plastic (RW3) [3, 4]. The effective water equivalent measurement depth of the Farmer chamber in the phantom is 4.8 mm, to which the beam exit window, monitor chamber and air gap (typically about 2 mm of water equivalent depth) must be added. This depth is large enough to ensure δ electron equilibrium (the depth dose profile shows a build-up effect due to δ electrons in the first millimeters) but also low enough to approximate the beam as pure (with increasing depth more and more primary ions fragment into lighter ions). For the calibration measurements, the reference chamber is irradiated by a large scanned field (at least 5×5 cm^2) which should preferably be re-scanned multiple times to achieve a homogeneous dose distribution. The absorbed dose to water at the reference depth per primary fluence has to be known to calibrate the beam monitor in terms of primary particle number (see Equation 2). The most precise way to obtain this relation is the calculation with a suitable radiation transport code (e.g., Monte Carlo codes like Geant4 [17] or FLUKA [18–20]), considering all materials in the beam line (vacuum exit window, beam monitors, air gaps, RW3 phantom).

Notably, systematic discrepancies, in the order of a few percent, between fluence measurements and absorbed dose to water measurements based on air-filled ionization chambers, have been reported [12–14]. Those deviations have not been fully explained yet. However, in GSI Caves A and M they rely on the usage of ionization chambers as it is the standard method in particle therapy, which is the main background of the research activities performed. In addition, recent water calorimetry experiments have shown good agreement with the ionization chamber concept [21, 22].

2.3. Dose Measurement and Correction Factors

The Farmer ionization chamber is a commonly used ionization chamber type for absolute dose measurements in radiotherapy. The one used in Caves A and M is a PTW TM30013 Farmer chamber, which consists of a vented cylindrical-shaped air volume (nominal volume 0.6 cm^3) with a central electrode and is surrounded by a graphite electrode within a waterproof plastic housing. Further details about the Farmer chamber can be found in [15]. The ionization chamber is read out with a PTW UNIDOS E universal electrometer.

The following basic dosimetric equation describes how to determine the absorbed dose to water using an air-filled ionization chamber:

$$D_w(z_{ref}) = M_{corr} \cdot N_{D,w} \cdot k_Q \tag{3}$$

$N_{D,w}$ is the calibration factor in terms of absorbed dose to water provided by the manufacturer (converting the measured charge to absorbed dose to water), determined with ^{60}Co photons at a water depth of 5 cm. $N_{D,w}$ is tracable to the secondary standard ^{60}Co source of the PTW dosimetry company. k_Q is the beam quality correction factor, which takes into account the different responses of the ionization chamber to the operational beam quality Q (e.g., heavy ions) and to the calibration quality Q_0 (^{60}Co photons). z_{ref} is the reference depth in water used for the beam monitor calibration. If a cylindrical ionization chamber is used for the dose measurement, not the reference point of the ionization chamber (central electrode) but the effective point of measurement has to be positioned at the reference depth. For proton and heavy ion dosimetry with cylindrical ionization chambers the effective point of measurement is located $0.75 \cdot r$ upstream of the reference point where r is the inner radius of the chamber [15]. Taking the effective point of measurement into account is of particular importance for the beam monitor calibration if the depth dose profile has a gradient at the measurement depth. M_{corr} is the electrometer charge reading from the ionization chamber corrected for changes in air density, incomplete saturation and polarity effects. Details on those corrections are found in the existing dosimetry protocols (e.g., TRS-398 [15] or DIN-6801-1 [23]).

2.4. Dosimetry in GSI Caves A and M

In GSI Caves A and M on a daily basis, before the absolute dose measurement, the k_{TP} correction factor accounting for changes in air density is determined. It takes into account differences in temperature and pressure between the air filling conditions in the cave and those during the calibration of the ionization chamber. k_{TP} is determined according to the TRS-398 dosimetry potocol [15].

An irradiation plan for a certain dose is prepared assuming a theoretical calibration factor f_e, which is then corrected according to the difference between the planned dose and the dose read out

TABLE 1 | Examples of recommended *W*-values for protons and heavy ions in the gas mixtures typically filling the ionization chambers used at GSI Caves A and M.

Gas	Particle	*W* / eV/ion pair	Uncertainty / %	Source
Air	^{1}H	34.44	0.4%	[25]
	^{12}C	34.71	1.5%	[25]
Ar	^{1}H	27	4%	[26]
	^{4}He	26.31	0.7%	[26]
CO_2	^{1}H	34.5	4%	[26]
	^{4}He	34.21	0.7%	[26]
Ar(80%)CO_2(20%)	^{1}H	28.3	3%	
	^{4}He	27.7	0.6%	

The W-values for protons and ^{12}C ions in air are from ICRU Report 90 [25]. The W-values for and low energy protons and alpha particles in argon and carbon dioxide were taken from ICRU Report 31 [26]. The W-values for the argon and carbon dioxide gas mixture were calculated (see text).

with the electrometer. This is how the beam monitor calibration is performed at GSI Caves A and M.

In the absence of calculations performed with a suitable radiation transport code, an estimation of the monitor calibration factor f_e (beam particles per monitor pulse) can be obtained by:

$$f_e = \frac{F}{\frac{E}{W} \cdot e} \tag{4}$$

F is the conversion factor of the current-to-frequency converter (charge per pulse from the IFC, e.g., 1 pF/pulse. E is the average energy deposited by a single beam particle in the active volume of the parallel plate ionization chamber [24], which can be estimated multiplying the linear energy transfer of the particle in the gas filling of the chamber by the thickness of the active volume of the chamber. The W-value is the mean energy required to form an ion pair in the detector gas [15], and e is the elementary charge. Examples of W-values given in the literature [25, 26] can be found in **Table 1**. In general, the W-value is specific for different detector gases and depends on the radiation quality, i.e., radiation type and energy. However, empirical observations show that for protons and heavy ions the W-value is rather independent of the ion type and energy at the high energies treated in this work [3, 27]. The values given for the gas mixture 80% argon and 20% carbon dioxide (volume percentages), which is the typical detector gas mixture used in the GSI beam monitor chambers, were obtained through the formula $1/W_{\mathrm{mix}} = \sum_i (C_i/W_i)$ [28], where C_i are the mass concentrations of the gas components in the mixture.

Once the monitor calibration factor f_e is determined, the free-in-air absorbed dose to water D_w can be related to the primary fluence through the following approximation:

$$D_w = f_e \cdot \frac{n}{d_{scan}^2} \cdot \frac{S}{\rho_w} \tag{5}$$

n being the number of accumulated IFC pulses per beam spot before switching to the next spot.

2.5. Beam Quality Correction Factor k_Q

The k_Q correction factor is specific for the ionization chamber model and depends on the beam quality. In the TRS-398 dosimetry protocol [15] a table of recommended (theoretical) heavy ion k_Q values for different ionization chamber types is given, however, it is not distinguished between different heavy ions due to the lack of data at the time of publication. For the PTW Farmer 30013 ionization chamber, a $k_Q = 1.032$ is recommended. This is the value used for the monitor calibration that is performed before all radiobiological experiments at GSI Caves A and M. Since the k_Q values given in TRS-398 are stated valid only for ions between ^{4}He and ^{40}Ar at energies between 100 and 450 MeV/u, but GSI also delivers heavier ions (e.g., ^{56}Fe) with higher energies (up to 1 GeV/u), the validity of the k_Q value requires further attention. Especially in view of the future FAIR facility where energies of up to 10 GeV/u will be available for radiobiological experiments, it is necessary to further investigate the assumption of an energy and ion independent k_Q. In the TRS-398 protocol k_Q is derived by Equation (6)

$$k_Q = \frac{(S_{w,air})_Q}{(S_{w,air})_{Q_0}} \cdot \frac{p_Q}{p_{Q_0}} \cdot \frac{(W_{air})_Q}{(W_{air})_{Q_0}} \tag{6}$$

where $S_{w,air}$ denotes the water-to-air stopping power ratio at the operational beam quality Q and at the calibration beam quality Q_0 (^{60}Co photons). W_{air} is the mean energy required to form an ion pair in air and p is the perturbation factor of the ionization chamber that accounts for its deviation from being an ideal Bragg-Gray detector [15]. For protons and heavy ions, TRS-398 assumes the detector perturbation to be negligible ($p_Q = 1$).

Today advanced computational methods, in particular powerful Monte Carlo codes, are available to study the response of ionization chambers in different radiation fields [29–32]. The calculation of k_Q factors by means of Monte Carlo simulation can be also described by Equation (7) [33, 34]:

$$k_Q = \frac{(D_w/\bar{D}_{air})_Q}{(D_w/\bar{D}_{air})_{Q_0}} \cdot \frac{(W_{air})_Q}{(W_{air})_{Q_0}} \tag{7}$$

where D_w is the absorbed dose scored in a small water voxel at the effective point of measurement of the ionization chamber and $\bar{D}_{air}$ is the absorbed dose scored in the active air volume of the ionization chamber (modeled in full geometrical detail). The ratio of the W_{air} values is the same as in Equation (6) and must be obtained from experiments or from literature (in this work the values from the recent ICRU 90 publication [25] were used, see also **Table 1**).

Recently, a high precision measurement of the k_Q value of the PTW 30013 Farmer chamber for 383 MeV/u ^{12}C ions by means of water calorimetry has been performed at HIT, Heidelberg [21]. It is in good agreement with the TRS-398 recommended value.

2.6. Monte Carlo Simulations

Monte Carlo simulations using the FLUKA code (version 2011.2x.5) were performed to obtain $D_w/\bar{D}_{air}$ ratios to calculate

k_Q correction factors according to Equation (7). Simulations were carried out for different ion species (^{1}H, ^{4}He, ^{12}C, ^{40}Ar, ^{56}Fe) at different energies (350 MeV/u, 1 GeV/u, 4 GeV/u, 10 GeV/u) for a field size of 5 × 5 cm^2. The geometry of the PTW 30013 Farmer chamber was modeled according to blueprints from the manufacturer (geometry with delta electron tracks shown in **Figure 2**) and it was positioned with the effective point of measurement at a water depth of 7 mm, a typical measurement depth at GSI Cave A (4.8 mm phantom depth plus about 2 mm vacuum window, monitor chamber and air gap). The mean dose in the active volume $\bar{D}_{air}$ was scored in the air volume inside the chamber. The absorbed dose to water at the reference point D_w was obtained in a separate simulation where a small scoring voxel (0.2 cm^3) made of water was positioned at the measurement depth.

In FLUKA, charged particles can be transported down to 1 keV and their energy loss is treated with a condensed history approach. Single Coulomb scattering events are condensed in a multiple scattering algorithm. Hadron–nucleus collisions are treated via the PEANUT model while nucleus-nucleus collisions are treated via the BME for kinetic energies below 125 MeV/u and via the RQMD model for higher energies.

The transport settings were chosen to be the same as reported by Baumann et al. [33] because they were optimized specifically for ionization chamber calculations with heavy charged particles. All simulations were performed with full electromagnetic transport (photon and electron transport down to 1 keV) and with the physics models set to the highest precision level (e.g., full Rayleigh and Coulomb scatter corrections, heavy fragment evaporation and coalescence). Recently, a Fano cavity test performed by Lourenco et al. [35] showed that the FLUKA code passes the test within 0.15% if the step size in the multiple Coulomb scattering algorithm is set small enough compared to the dimensions of the cavity of interest. Therefore, in order to maximize the transport precision for the simulations of the energy deposition in the small cavities, the multiple Coulomb scattering was suppressed in these regions by adding the MULSOPT card to the FLUKA input file. Using this card, the minimum step length for multiple Coulomb scattering was increased by a factor of 10000 and single scattering was activated.

The material definitions of air, graphite and water were defined according to the ICRU 90 recommendations [25] (details reported by Baumann et al. [33]). For the other materials (e.g., PMMA, aluminum), the standard FLUKA definitions were used.

The most recent W_{air} values for heavy ions and ^{60}Co photons from the ICRU 90 report [25] (34.71 eV ± 1.5% for heavy ions and 33.97 eV ± 0.35% for ^{60}Co photons) were used instead of the values given in TRS-398 [15]. The PTW 30013 Farmer chamber $D_w/\bar{D}_{air}$ ratio for ^{60}Co photons was taken from [34] as 1.112 ± 0.1%.

For an independent calculation of k_Q according to the original definition using Equation (6), the energy-dependent water-to-air stopping power ratios $(S_{w,air})_Q$ were extracted from FLUKA for the different ions by using the DELTARAY card. The heavy ion perturbation factors were assumed to be negligible ($p_Q = 1$ as recommended in TRS-398 [15]). The product of the stopping power ratio and the perturbation factor $(S_{w,air})_{Q_0} \cdot p_{Q_0} = 1.112$ for ^{60}Co photons were also taken from TRS-398 [15]. The W_{air} values used for the calculations were the same as stated above (taken from the ICRU 90 report [25]).

Simulations of the laterally integrated depth dose profiles for ^{1}H, ^{12}C, and ^{56}Fe ions in water at two different energies were performed with the aim of evaluating the error in the dose delivery due to an eventual difference between the reference depth of the beam monitor calibration (4.8 mm) and the actual depth of the irradiated samples. These simulations were performed in a water phantom (50 × 50 cm^2) and the elements of the beamline were simplified as 1 mm water slab followed by 1 m of air.

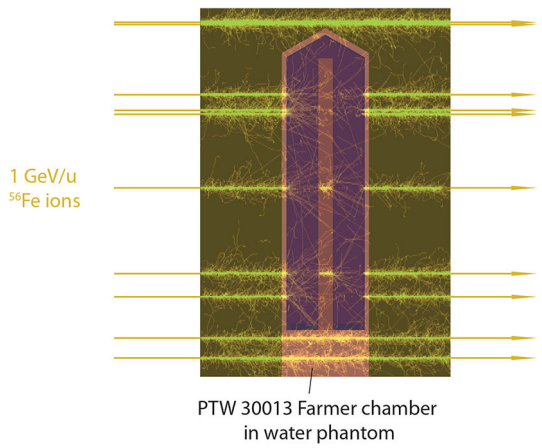

FIGURE 2 | FLUKA simulation of the irradiation of a PTW 30013 Farmer ionization chamber in a water phantom with 1 GeV/u ^{56}Fe ions. The tracks of the δ electrons produced by interaction of the primary ions with the phantom material are shown.

3. RESULTS AND DISCUSSION

3.1. Energy and Ion Dependence of the Water-to-Air Stopping Power Ratio

The FLUKA code allows an extraction of stopping power tables. From the tables for water and air, the water-to-air stopping power ratio $S_{w,air}$ as a function of energy for different ions was obtained. The results are shown in **Figure 3** and are in accordance with recent data reported by other authors [36].

It can be observed that the water-to-air stopping power ratio is independent of the ion species for energies above 100 MeV/u, which justifies the assumption of a k_Q value independent of the ion species if ion type specific detector perturbations and variations of the W_{air} value are neglected. The $(W_{air})_Q$ term of Equation (6) is indeed assumed to be ion independent within a 1.5% uncertainty [25]. Concerning the p_Q term, ion specific variations in the level of permille or even percent can be expected, however, there are no reliable experimental data on heavy ion perturbation factors and their calculation would require very realistic and well benchmarked transport codes. New precision measurements of all dosimetric key data for heavy ions, especially

the W_{air} value, would be useful to decrease the overall uncertainty of the k_Q value.

From **Figure 3** it can also be observed that above 1 GeV/u, when the ions get highly relativistic, the stopping power ratio is not constant anymore, but drops down steeply. This decrease is due to the density effect, which causes a reduction of the stopping power of water for high-energy ions while it does not affect the stopping power of air as its density is about 1,000 times lower than the density of water. Therefore, air-filled ionization chambers show an over-response to high energetic ions if applied for absorbed dose to water measurements. This has to be taken into account within the beam quality correction. This effect is well-known for dosimetry in high energy photon therapy [37], but it is a novelty in the scope of ion beam dosimetry for the unique high energy heavy ion beams that will be available at FAIR. The assumption of an energy-independent k_Q value seems therefore reasonable in the kinetic energy range 100 MeV/u to 1 GeV/u, which are the energies provided by the current GSI SIS18 accelerator, while for ions with greater energies, which will be available with the future SIS100 synchrotron at FAIR, an energy-specific k_Q value should be used instead.

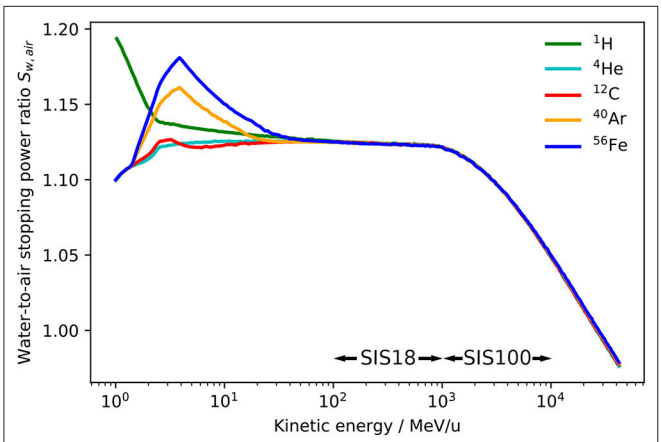

FIGURE 3 | Unrestricted water-to-air stopping power ratio $S_{w,air}$ as a function of energy for ^{1}H, ^{4}He, ^{12}C, ^{40}Ar, and ^{56}Fe ions extracted from the FLUKA Monte Carlo code. The energy ranges provided by the heavy ion accelerators SIS18 and SIS100 are indicated.

3.2. Energy and Ion Dependence of the PTW 30013 Farmer Chamber Beam Quality Correction Factor k_Q

$D_w/\bar{D}_{air}$ ratios for ^{1}H, ^{4}He, ^{12}C, ^{40}Ar, and ^{56}Fe ions were obtained with FLUKA radiation transport simulations through a geometrical model of the PTW Farmer chamber and a water geometry with a small scoring voxel at the effective measurement position of the chamber. From these dose ratios, beam quality correction factors k_Q were obtained for the ions listed above over a wide span of energies using Equation (7). The results are reported in **Table 2**.

In **Figure 4** they are compared with the constant value $k_Q = 1.032$, which is recommended for heavy ions by the TRS-398 protocol [15] and currently used for the beam monitor calibration at GSI Cave A and M. Additionally, they are compared with an energy-dependent calculation based on the formalism from TRS-398 (Equation 6) using as input for the term $(S_{w,air})_Q$ the energy-dependent water-to-air stopping power

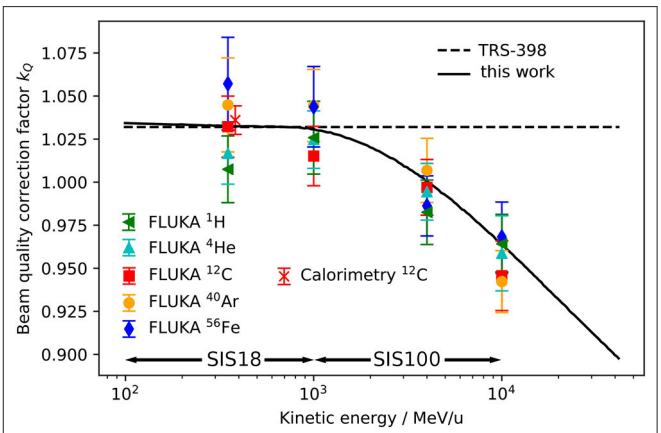

FIGURE 4 | Beam quality correction factor k_Q for the PTW 30013 Farmer ionization chamber positioned with the effective point of measurement at a water depth of 7 mm for ^{1}H, ^{4}He, ^{12}C, ^{40}Ar, and ^{56}Fe calculated using $(D_w/\bar{D}_{air})_Q$ from FLUKA simulations as inputs for Equation (7) (symbols) are compared with the constant heavy ion k_Q recommended in the TRS-398 dosimetry protocol [15] (dashed line) and an energy-dependent calculation using the water-to-air stopping power ratio for protons extracted from the FLUKA code in Equation (6) (solid line). For comparison a ^{12}C k_Q value measured by means of water calorimetry [21] is shown. The energy ranges provided by the heavy ion accelerators SIS18 and SIS100 are indicated.

TABLE 2 | Beam quality correction factors k_Q for the PTW 30013 Farmer ionization chamber positioned with the effective point of measurement at a water depth of 7 mm for ^{1}H, ^{4}He, ^{12}C, ^{40}Ar, and ^{56}Fe calculated with the FLUKA code for kinetic energies of 350 MeV/u, 1 GeV/u, 4 GeV/u, and 10 GeV/u.

Energy	^{1}H		^{4}He		^{12}C		^{40}Ar		^{56}Fe	
GeV/u	k_Q	σ	k_Q	σ	k_Q	σ	k_Q	σ	k_Q	σ
0.35	1.007	0.019	1.017	0.018	1.032	0.018	1.045	0.027	1.057	0.027
1	1.026	0.021	1.025	0.017	1.015	0.017	1.044	0.021	1.044	0.023
4	0.982	0.019	0.994	0.016	0.997	0.016	1.007	0.019	0.986	0.017
10	0.964	0.017	0.959	0.022	0.946	0.020	0.942	0.018	0.968	0.020

The σ column reports the uncertainty related to the k_Q values (1σ).

ratios from FLUKA (**Figure 3**). Also the k_Q value measured for 383 MeV/u ^{12}C by means of calorimetry [21] is reported.

The error bars of the FLUKA data points contain the statistical uncertainty of the Monte Carlo simulation and the systematic uncertainties of the other input parameters of Equation (7). The uncertainties are discussed in detail in section 3.4. It can be seen that the k_Q value for 350 MeV/u ^{12}C ions calculated with FLUKA and the value measured by Osinga-Blaettermann [21] at the ^{12}C ion therapy facility HIT in Heidelberg by means of water calorimetry, are in good agreement. This is a confirmation of the validity of the FLUKA simulations performed within this study. By comparing the FLUKA simulation results with the constant k_Q value given in the TRS-398 protocol (dashed line) it can be observed that the value recommended in the protocol is perfectly suited for ^{12}C ions at therapeutic energies. However, it also shows that a constant k_Q should only be used for energies lower than 1 GeV/u. The k_Q calculated using the energy-dependent water-to-air stopping power ratio for protons from FLUKA (above 100 MeV/u it is practically independent of the ion species) as input for Equation (6) (solid line) reflects well the trend of the single k_Q values obtained by detailed ionization chamber simulation. At energies between 100 MeV/u and 1 GeV/u it is practically identical to the constant value (dashed line). The same drop as in **Figure 3** due to the density effect above 1 GeV/u can be observed. The agreement of the single data points and the solid line is within 2.5%. The deviations of the data points from the solid line and the differences between the various ion species can be ascribed to the perturbation factors p_Q (see Equation 6), which are neglected in the simplified calculation (assumption: $p_Q = 1$) but considered by the full Monte Carlo calculation.

Figures 3, **4** indicate that the assumption of an energy-independent k_Q value is reasonable for energies below 1 GeV/u, which is the energy range currently used at GSI Cave A, but not appropriate for higher energies, which will be available at FAIR. Indeed, not taking into account the energy dependence of the correction factor k_Q would lead to a systematic error in absolute dosimetry of up to 7.5% at energies of 10 GeV/u. This error would directly translate into the absolute calibration of the dose application system and needs to be avoided. The variation of the k_Q factor for different ion species due to different detector perturbations is in the order of 2.5%, which is in the same order as the systematic uncertainty of the calculated k_Q values. Those different detector perturbations for different ions might be negligible in view of the accuracy needed for radiobiological experiments.

TRS-398 recommends to use the residual range as beam quality specifier for proton beams, while for heavy ions no unique specifier is given. **Figure 4** shows that the (residual) energy per nucleon could be used as a reasonable index of the beam quality for dose measurements in the entrance channel of high energy heavy ion beams. Therefore, for practical use we recommend to apply the energy-dependent k_Q value calculated according to the TRS-398 formalism (solid line in **Figure 4**) for absolute dosimetry and beam monitor calibration in future radiobiological experiments at FAIR.

3.3. Heavy Ion Depth Dose Profiles: Robustness of the Dose Delivery

The depth dose profile at low depth is determined by the interplay of four different effects: (1) in the first millimeters of the target, there is a steep dose build-up until a δ electron equilibrium is reached [38, 39]. Its extension depends on the maximum δ electron energy and therefore on the velocity of the primary ions. (2) The energy loss of the primary ions in the target leads to an increase of their energy loss with depth and therefore to an increase of the dose. On the other hand, fragmentation reactions can (3) decrease or (4) increase the mean energy loss. The decrease is due to removal of primary ions and the increase to the build-up of secondary fragments, which is partly overlaid by the δ electron build-up. How these effects superimpose is not trivial and depends on many factors. **Figure 5** shows calculated depth dose profiles in water for ^{1}H, ^{12}C, and ^{56}Fe ions at different energies. As the measurement of the absolute dose is performed with the Farmer chamber at a water depth of 4.8 mm, this is the only depth where the absolute dose is accurately determined. For this reason the dose is normalized to a water depth of 4.8 mm

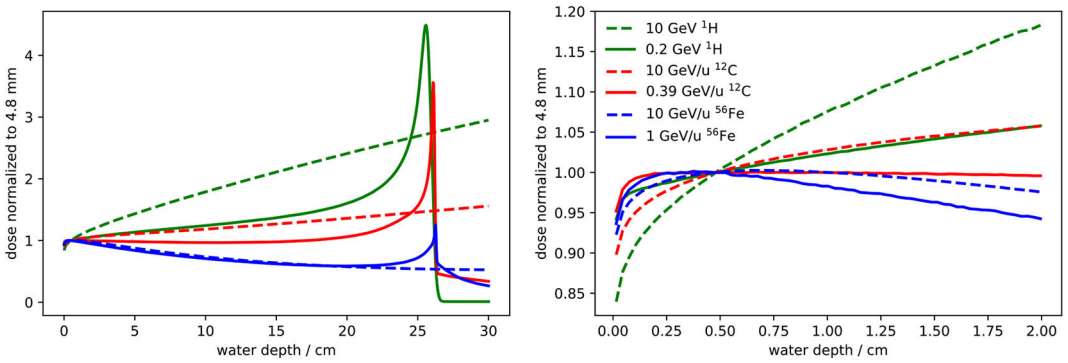

FIGURE 5 | Depth dose profiles for ^{1}H, ^{12}C, and ^{56}Fe ions at two different energies obtained with FLUKA simulations: one energy corresponds to a penetration depth of about 25 cm in water and the other is the maximum energy provided by SIS100 (10 GeV/u). The dose is normalized to a water depth of 4.8 mm, which is the reference depth for the beam monitor calibration. It is the only depth where the absolute dose is accurately determined. In the left panel the profiles up to a water depth of 30 cm are reported, while in the right panel the depth dose profiles are shown with a zoom into the entrance channel.

with the aim of studying the robustness of the dose delivery if the actual depth of the irradiated samples deviates from the reference depth.

Figure 5 shows that the entrance channel of the depth dose profile is not a plateau for most heavy ion beams. Therefore irradiations of radiobiological samples should preferably be performed at the reference depth. If the sample is irradiated at a different depth, the dose might vary significantly, even if the shift is only a few millimeters. For this reason, the relative dose profile should be calculated using a reliable radiation transport code that considers all relevant physical effects. From the calculated depth dose profile normalized to the reference depth (like the profiles shown in **Figure 5**) and from the nominal dose measured by the beam monitor, the dose at the actual irradiation depth can be obtained.

3.4. Uncertainty Analysis

Table 3 breaks down the uncertainty of calculated k_Q values obtained by means of Monte Carlo simulations according to Equation (7) (uncertainties in **Table 2** and **Figure 4**) in its components. All stated uncertainties describe 1σ of the confidence interval.

The type A uncertainty of Monte Carlo simulations due to the limited number of particle histories can be calculated as the standard deviation of the output from individual simulation runs using different random number seeds. They are considerably larger for the heavy ion simulations than for the ^{60}Co photons because photon simulations are more efficient in terms of calculation time.

The type B uncertainty of Monte Carlo calculated $(D_w/\bar{D}_{air})_{^{60}Co}$ ratios (due to uncertainties in the radiation physics and transport models, geometry, etc.) were estimated to be 0.5% based on an intercode comparison by Baumann et al. [33] and a benchmark experiment by Renner et al. [40]. The corresponding type B uncertainty of the $(D_w/\bar{D}_{air})_{heavy\ ion}$ ratios from FLUKA simulations is more difficult to estimate but certainly larger than the uncertainty for ^{60}Co photons. The water-to-air stopping power ratios in FLUKA (shown in **Figure 3**) can be considered realistic, however, inaccuracies in the physics models (in particular those describing nuclear reactions) or simplifications in the detector geometry model can lead to uncertainties in the predictions of detector perturbations.

The type B uncertainty of the $(D_w/\bar{D}_{air})_{heavy\ ion}$ ratio was estimated to be about $1-2\%$ and probably depends on the ion species and energy since the FLUKA code is for some ions better benchmarked than for others. Especially for ^{12}C ions in the therapeutic energy range its transport and physics models are well-developed [41] which reflects in the good agreement of the Monte Carlo result and the water calorimetry measurement (see **Figure 4**).

Since the W_{air} values are required as input in Equation (7) also their uncertainties have to be considered for calculated k_Q values. While the uncertainty of the ^{60}Co literature value $(W_{air})_{^{60}Co} = 33.97 \pm 0.35\%$ is rather low, the corresponding $(W_{air})_{heavy\ ion} = 34.71 \pm 1.5\%$ value has a considerably larger uncertainty. A reduction of this uncertainty by new measurements would increase the accuracy of calculations in heavy ion dosimetry. Even if the stated uncertainty is lower, the $(W_{air})_{proton} = 34.44 \pm 0.4\%$ value shown in **Table 1** was not used for the k_Q calculations, because it was optimized specifically for protons in the therapeutic energy range ($50-250$ MeV/u) while the proton simulations in this work were done for 350 MeV and above.

Aside from the k_Q value, also other factors contribute to the overall uncertainty of an absolute dose measurement and beam monitor calibration in terms of primary particle number. In **Table 4** estimated uncertainties of the input quantities of Equation (3) and the conversion into primary fluence are listed.

The uncertainty of the calibration factor $N_{D,w}$ determined with ^{60}Co photons can differ slightly between individual chamber models and is typically listed in the calibration sheet (0.55% for the PTW 30013 Farmer used at GSI). The estimated typical value of 0.5% is in accordance with a recent dosimetry intercomparison between different proton therapy centers where an agreement on that scale was described [42]. The uncertainty of $N_{D,w}$ could in principle be further reduced by calibration at a primary standard dosimetry laboratory instead of using a secondary standard ^{60}Co source which is the common procedure for instance at the company PTW. However, as pointed out in TRS-398 [15] the overall improvement is only marginal while the effort would increase strongly.

For ^{12}C ions a precise calorimetric measurement of k_Q with an uncertainty $<$ 1% is available, while for other ions such experimental k_Q values are missing. Therefore, Monte Carlo calculated k_Q values for different ions with uncertainties around $2-3\%$ are provided in this work for the energy range that will be available for radiobiological experiments at the FAIR facility.

TABLE 3 | Contributions to the uncertainty of heavy ion k_Q values obtained by Monte Carlo simulations.

Quantity	Uncertainty	
	Type A	Type B
$(D_w/\bar{D}_{air})_{^{60}Co}$	0.1%	0.5%
	Type A	Type B
$(D_w/\bar{D}_{air})_{heavy\ ion}$	$1-2\%$	$1-2\%$
$(W_{air})_{^{60}Co}$	0.35%	
$(W_{air})_{heavy\ ion}$	1.5%	

TABLE 4 | Uncertainties of beam monitor calibration in terms of primary particle number.

Quantity	Uncertainty
$N_{D,w}$	0.5%
Measured k_Q	1%
Monte Carlo k_Q	3%
$D_w(z_{ref})/\Phi$	$1-5\%$
Total	$1.5-5.9\%$

Another important quantity for the calibration of the beam monitor in terms of primary particle numbers is the absorbed dose to water at the reference depth per primary fluence $D_w(z_{ref})/\Phi$ which is typically obtained by Monte Carlo simulation. Its uncertainty can be considered to be low for well-characterized particles like protons or ^{12}C ions at therapeutic energies (in the order of 1% [43]) but is estimated up to 5% for more exotic ions and energies. As for the $(D_w/\bar{D}_{air})_{heavy\ ion}$ ratios, the main uncertainty in the Monte Carlo simulation are the nuclear reaction models. An inaccurate modeling of the attenuation or build-up effects (see **Figure 5**) leads to uncertainties in the absorbed dose to water at the reference depth. For radiobiological irradiations where the quantity of interest is typically absorbed dose, the uncertainty of $D_w(z_{ref})/\Phi$ is of minor importance. However, in some experiments an accurate determination of the primary particle number is required. An example are recent attempts to measure absolute nuclear reaction cross sections by means of activation where the determination of the primary particle number represented a major source of uncertainty [44, 45].

In summary the estimated uncertainties, considering that they are independent, add up to values between 1.5% (lower values) and 5.9% (upper values) for the absolute monitor calibration in terms of primary particle number. The lower uncertainty can be reached for the well-characterized protons and ^{12}C ions in the therapeutic energy range while for other ion species the calibration will be less accurate. Improvements in accuracy can be reached by further development and benchmarking of Monte Carlo transport models against experimental data, but also by new measurements of dosimetric key data like heavy ion W_{air} values or direct measurement of k_Q values by means of water calorimetry.

4. CONCLUSIONS

The absolute dosimetry and beam monitor calibration procedure as currently applied at GSI Cave A and M were explained in detail and an uncertainty analysis was performed. The accuracy of the beam quality correction factor k_Q to be applied for the PTW 30013 Farmer ionization chamber was studied in detail as it is a main contributor to the overall accuracy of the calibration procedure and subsequent dose delivery. The Monte Carlo study performed within the present work showed that the assumption of k_Q being ion independent is valid within an uncertainty of 2.5%, while the assumption of k_Q being energy independent is valid only up to energies of 1 GeV/u. Therefore, the constant value $k_Q = 1.032$ recommended for the PTW 30013 chamber and heavy ions by the TRS-398 protocol [15] and currently used for the beam monitor calibration at GSI Caves A and M, is suitable for the experiments currently performed. However, for experiments at FAIR, in which the energy of the accelerated ions will reach up to 10 GeV/u, the constant k_Q value should be replaced with the energy-dependent correction factor provided in this work. The reason for the need of an energy-dependent beam quality correction factor has been identified as the density effect on the water-to-air stopping power ratio.

In addition, it is recommended to irradiate biological samples at the reference depth of 4.8 mm. If a sample has a lower depth by itself, for instance cell flasks with a typical wall thickness of 1 mm, it is recommended to introduce a bolus preferably consisting of water-equivalent material (e.g., PMMA or RW3).

DATA AVAILABILITY STATEMENT

The original contributions presented in the study are included in the article/supplementary material, further inquiries can be directed to the corresponding author/s.

AUTHOR CONTRIBUTIONS

FL and FH compiled the manuscript with support and input from UW, DB, CS, C-AR, KZ, and MD. FH performed the Monte Carlo simulations and made the considerations for k_Q with support from KZ. FL performs daily monitor calibration and dosimetry at GSI Cave A supported by UW, DB, C-AR, and CS. UW and MD guided and assigned the work. All authors contributed to the article and approved the submitted version.

FUNDING

This work was partially supported by EU Horizon2020 grant 73,0983 (INSPIRE). The measurements were performed in Caves A and M in the frame of FAIR Phase-0 supported by the GSI Helmholtzzentrum für Schwerionenforschung in Darmstadt (Germany).

REFERENCES

1. Haberer T, Becher W, Schardt D, Kraft G. Magnetic scanning system for heavy ion therapy. *Nucl Instrum Methods Phys Res A*. (1993) **330**:296–305. doi: 10.1016/0168-9002(93)91335-K
2. Badura E, Brand H, Essel HG, Haberer T. Control system for cancer therapy with a heavy ion beam at GSI. *IEEE Trans Nucl Sci*. (2000) **47**:170–3. doi: 10.1109/23.846141
3. Hartmann GH, Jäkel O, Heeg P, Karger CP, Krießbach A. Determination of water absorbed dose in a carbon ion beam using thimble ionization chambers. *Phys Med Biol*. (1999) **44**:1193–206. doi: 10.1088/0031-9155/44/5/008
4. Jäkel O, Hartmann GH, Karger CP, Heeg P, Vatnitsky S. A calibration procedure for beam monitors in a scanned beam of heavy charged particles. *Med Phys*. (2004) **31**:1009–13. doi: 10.1118/1.1689011
5. Durante M, Golubev A, Park WY, Trautmann C. Applied nuclear physics at the new high-energy particle accelerator facilities. *Phys Rep*. (2019) **800**:1–37. doi: 10.1016/j.physrep.2019.01.004
6. Bellinzona VE, Ciocca M, Embriaco A, Fontana A, Mairani A, Mori M, et al. On the parametrization of lateral dose profiles in proton radiation therapy. *Phys Med*. (2015) **31**:484–92. doi: 10.1016/j.ejmp.2015.05.004
7. Moyers MF, Toth TL, Sadagopan R, Chvetsov AV, Unkelbach J, Mohan R, et al. Task Group Report No. 202 - Physical uncertainties in the planning and delivery of light ion beam treatments. *Med Phys*. (2020) **202**:1–107. doi: 10.37206/200

8. Arjomandy M, Taylor P, Ainsley C, Safai S, Sahoo N, Pankuch M, et al. Task Group Report No. 224 - comprehensive proton therapy machine quality assurance. *Med Phys*. (2019) **46**:e678–705. doi: 10.1002/mp.13622
9. Karger CP, Jäkel O, Palmans H, Kanai T. Dosimetry for ion beam radiotherapy. *Phys Med Biol*. (2010) **55**:R193–234. doi: 10.1088/0031-9155/55/21/R01
10. Grusell E, Isacsson U, Montelius A, Medin J. Faraday cup dosimetry in a proton therapy beam without collimation. *Phys Med Biol*. (1995) **40**:1831–40. doi: 10.1088/0031-9155/40/11/005
11. Pedroni E, Scheib S, Böhringer T, Coray A, Grossmann M, S L, et al. Experimental characterization and physical modelling of the dose distribution of scanned proton pencil beams. *Phys Med Biol*. (2005) **50**:541–61. doi: 10.1088/0031-9155/50/3/011
12. Gomà C, Lorentini S, Meer D, Safai S. Proton beam monitor chamber calibration. *Phys Med Biol*. (2014) **59**:4961–71. doi: 10.1088/0031-9155/59/17/4961
13. Fukumura A, Hiraoka T, Omata K, Takeshita M, Kawachi K, Kanai T, et al. Carbon beam dosimetry intercomparison at HIMAC. *Phys Med Biol*. (1998) **43**:3459–63.
14. Osinga JM, Brons S, Bartz JA, Akselrod MS, Jäkel O, Greilich S. Absorbed dose in ion beams: comparison of ionisation- and fluence-based measurements. *Radiat Protect Dosimetr*. (2014) **161**:387–92. doi: 10.1093/rpd/ncu004
15. Andreo P. *Absorbed Dose Determination in External Beam Radiotherapy: An International Code of Practice for Dosimetry based on Standards of Absorbed Dose to Water*. IAEA TRS 398 (2006).
16. Palmans H, Vatnitsky SM. Beam monitor calibration in scanned light-ion beams. *Med Phys*. (2016) **43**:5835–47. doi: 10.1118/1.4963808
17. Agostinelli S, Allison J, Amako K, Apostolakis J, Araujo H, Arce P, et al. Geant4 - a simulation toolkit. *Nucl Instrum Methods Phys Res Sect A Accelerat Spectrom Detect Assoc Equip*. (2003) **506**:250–303. doi: 10.1016/S0168-9002(03)01368-8
18. Ferrari A, Sala PR, Fassò A, Ranft J. *FLUKA: A Multi-Particle Transport Code*. CERN-2005-10, INFN/TC_05/11, SLAC-R-773 (2005).
19. Böhlen TT, Cerutti F, Chin MPW, Fassò A, Ferrari A, Ortega PG, et al. The FLUKA code: developments and challenges for high energy and medical application. *Nucl Data Sheets*. (2014) **120**:211–4. doi: 10.1016/j.nds.2014.07.049
20. Battistoni G, Bauer J, Boehlen TT, Cerutti F, Chin MPW, Dos Santos Augusto R, et al. The FLUKA code: an accurate simulation tool for particle therapy. *Front Oncol*. (2016) **11**:116. doi: 10.3389/fonc.2016.00116
21. Osinga-Blättermann JM, Brons S, Greilich S, Jäkel O, Krauss A. Direct determination of k Q for Farmer-type ionization chambers in a clinical scanned carbon ion beam using water calorimetry. *Phys Med Biol*. (2017) **62**:2033–54. doi: 10.1088/1361-6560/aa5bac
22. Renaud J, Palmans H, Sarfehnia A, Seuntjens J. Absorbed dose calorimetry. *Phys Med Biol*. (2020) **65**:05TR02. doi: 10.1088/1361-6560/ab4f29
23. Normenausschuss Radiologie. *Procedures of Dosimetry With Probe-type Detectors for Proton and Ion Radiation - Part 1: Ionization Chambers*. DIN 6801-1:2019-09 (2019).
24. Kraft G, Weber U. Tumor therapy with ion beams. In: Grupen C, Buvat I, editors. *Handbook of Particle Detection and Imaging*. Heidelberg: Springer. (2012). p. 1179–205.
25. International Commission on Radiation Units and Measurements. ICRU Report 90: key data for ionizing-radiation dosimetry: measurement standards and applications. *J ICRU*. (2016) **14**:1–110. doi: 10.1093/jicru/ndw034
26. International Commission on Radiation Units and Measurements. ICRU Report 31: Average energy required to produce an ion pair. *J ICRU*. (1979) **25**:os16.
27. Knoll GF. *Radiation Detection and Measurement*, New York, NY; Chichester; Weinheim; Brisbane; Toronto; Singapore: John Wiley & Sons, Inc. (2000).
28. Paul H, Berger MJ. *Atomic and Molecular Data for Radiotherapy and Radiation Research*. IAEA-TECDOC–799. (1995).
29. Wulff J, Heverhagen JT, Zink K. Monte-Carlo-based perturbation and beam quality correction factors for thimble ionization chambers in high-energy photon beams. *Phys Med Biol*. (2008) **53**:2823–36. doi: 10.1088/0031-9155/53/11/005
30. Wulff J, Heverhagen JT, Zink K, Kawrakow I. Investigation of systematic uncertainties in Monte Carlo- calculated beam quality correction factors. *Phys Med Biol*. (2010) **55**:4481–93. doi: 10.1088/0031-9155/55/16/S04
31. Gomà C, Andreo P, Sempau J. Monte Carlo calculation of beam quality correction factors in proton beams using detailed simulation of ionization chambers. *Phys Med Biol*. (2016) **61**:2389–406. doi: 10.1088/0031-9155/61/6/2389
32. Gomà C, Sterpin E. Monte Carlo calculation of beam quality correction factors in proton beams using PENH. *Phys Med Biol*. (2019) **64**:185009. doi: 10.1088/1361-6560/ab3b94
33. Baumann KS, Horst F, Zink K, Gomà C. Comparison of penh, fluka, and Geant4/topas for absorbed dose calculations in air cavities representing ionization chambers in high-energy photon and proton beams. *Med Phys*. (2019) **46**:4639–53. doi: 10.1002/mp.13737
34. Baumann KS, Kaupa S, Bach C, Engenhart-Cabillic R, Zink K. Monte Carlo calculation of beam quality correction factors in proton beams using TOPAS/GEANT4. *Phys Med Biol*. (2020) **65**:055015. doi: 10.1088/1361-6560/ab6e53
35. Lourenço A, Bouchard H, Galer S, Royle G, Palmans H. The influence of nuclear interactions on ionization chamber perturbation factors in proton beams: FLUKA simulations supported by a Fano test. *Med Phys*. (2019) **46**:885–91. doi: 10.1002/mp.13281
36. Burigo LN, Greilich S. Impact of new ICRU 90 key data on stopping-power ratios and beam quality correction factors for carbon ion beams. *Phys Med Biol*. (2019) **64**:195005. doi: 10.1088/1361-6560/ab376e
37. Czarnecki D, Poppe B, Zink K. Impact of new ICRU Report 90 recommendations on calculated correction factors for reference dosimety. *Phys Med Biol*. (2018) **63**:155015. doi: 10.1088/1361-6560/aad148
38. Pfuhl T, Horst F, Schuy C, Weber U. Dose build-up effects induced by delta electrons and target fragments in proton Bragg curves—measurements and simulations. *Phys Med Biol*. (2018) **63**:175002. doi: 10.1088/1361-6560/aad8fc
39. Kern A, Bäumer C, Kröninger K, Mertens L, Timmermann B, Walbersloh J, et al. Determination of surface dose in pencil beam scanning proton therapy. *Med Phys*. (2020) **47**:2277–2288. doi: 10.1002/mp.14086
40. Renner F, Wulff J, Kapsch RP, Zink K. Uncertainties in Monte Carlo-based absorbed dose calculations for an experimental benchmark. *Phys Med Biol*. (2015) **60**:7637–53. doi: 10.1088/0031-9155/60/19/7637
41. Böhlen TT, Cerutti F, Dosanjh M, Ferrari A, Gudowska I, Mairani A, et al. Benchmarking nuclear models of FLUKA and GEANT4 for carbon ion therapy. *Phys Med Biol*. (2010) **55**:5833–47. doi: 10.1088/0031-9155/55/19/014
42. Bäumer C, Ackermann B, Hillbrand M, Kaiser FJ, Koska B, Latzel H, et al. Dosimetry intercomparison of four proton therapy institutions in Germany employing spot scanning. *Z Med Physik*. (2017) **27**:80–5. doi: 10.1016/j.zemedi.2016.06.007
43. Parodi K, Mairani A, Brons S, Hasch BG, Sommerer F, Naumann J, et al. Monte Carlo simulations to support start-up and treatment planning of scanned proton and carbon ion therapy at a synchrotron-based facility. *Phys Med Biol*. (2012) **57**:3759–84. doi: 10.1088/0031-9155/57/12/3759
44. Horst F, Adi W, Aricò G, Brinkmann KT, Durante M, Reidel CA, et al. Measurement of PET isotope production cross sections for protons and carbon ions on carbon and oxygen targets for applications in particle therapy range verification. *Phys Med Biol*. (2019) **64**:205012. doi: 10.1088/1361-6560/ab4511
45. Bäumer C, Bäcker CM, Gerhardt M, Grusell E, Koska B, Kröninger K, et al. Measurement of absolute activation cross sections from carbon and aluminum for proton therapy. *Nucl Instrum Methods Phys Res Sect B Beam Interact Mater Atoms*. (2019) **440**:75–81. doi: 10.1016/j.nimb.2018.11.020

Conflict of Interest: The authors declare that the research was conducted in the absence of any commercial or financial relationships that could be construed as a potential conflict of interest.

frontiers in Physics

REVIEW
published: 30 September 2020
doi: 10.3389/fphy.2020.568027

Solving the Issue of Ionizing Radiation Induced Neurotoxicity by Using Novel Cell Models and State of the Art Accelerator Facilities

Celine Schielke[1], *Carola Hartel*[1], *Marco Durante*[1,2], *Sylvia Ritter*[1] *and Insa S. Schroeder*[1]*

[1] *Biophysics Department, GSI Helmholtzzentrum für Schwerionenforschung, Darmstadt, Germany,* [2] *Institut für Festkörperphysik, Technische Universität Darmstadt, Darmstadt, Germany*

Cognitive dysfunction induced by ionizing radiation remains a major concern in radiation therapy as well as in space mission projects. Both fields require sophisticated approaches to improve protection of the brain and its neuronal circuits. Radiation therapy related research focusses on advanced techniques imposing maximal effect on the tumor while minimizing toxicity to the surrounding tissue. Research for example has led to the revival of spatially fractionated radiation therapy (SFRT) and the advent of FLASH radiotherapy. To investigate the influence of the space radiation environment on brain cells, low dose, high LET radiation in addition to simulated microgravity have to be studied. Both research areas, however, call for cutting-edge cellular systems that faithfully resemble the architecture of the human brain, its development and its regeneration to understand the mechanisms of radiation-induced neurotoxicity and their prevention. In this review, we discuss the proposed mechanisms of neurotoxicity such as the loss of complexity within the neuronal networks, vascular changes, or neuroinflammation. We compare the current *in vivo* and *in vitro* studies of neurotoxicity including animal models, animal and human neural stem cells, and neurosphere models. Particularly, we will address the new and promising technique of generating human brain organoids and their potential use in radiation biology.

Keywords: ionizing radiation, brain, neurotoxicity, X-rays, heavy ions, radiotherapy, space research, brain organoids

OPEN ACCESS

Edited by:
Udo Jochen Birk, University of Applied Sciences Graubünden, Switzerland

Reviewed by:
Lembit Sihver, Vienna University of Technology, Austria
Christa Baumstark-Khan, Helmholtz Association of German Research Centers (HZ), Germany
Barbara Julia Obryk, Polish Academy of Sciences, Poland

***Correspondence:**
Insa S. Schroeder
i.schroeder@gsi.de

Specialty section:
This article was submitted to Medical Physics and Imaging, a section of the journal Frontiers in Physics

Received: *01 June 2020*
Accepted: *24 August 2020*
Published: *30 September 2020*

Citation:
Schielke C, Hartel C, Durante M, Ritter S and Schroeder IS (2020) Solving the Issue of Ionizing Radiation Induced Neurotoxicity by Using Novel Cell Models and State of the Art Accelerator Facilities. Front. Phys. 8:568027. doi: 10.3389/fphy.2020.568027

INTRODUCTION

Humans are unavoidably exposed to ionizing radiation (IR) from environmental and artificial sources [1]. The severity of radiation effects on the human organism depends on the dose and quality of radiation. High-LET (linear energy transfer) charged particles like carbon (^{12}C) ions lead, due to densely ionization events, to more severe damage compared to sparsely ionizing low-LET radiation, e.g., X- and γ-rays [2]. Regarding radiation impacts, the human brain is divided into different sub-structures at risk [3], but the effects of IR on the brain are still poorly understood. Thus, additional research is required in the fields of radiation therapy and space research for adapted risk assessment and for the development of adequate shielding methods [4, 5]. Cell [6] and animal models [7] provided first insights into the mechanisms underlying radiation-induced neurotoxicity such as impaired connectivity and neuronal function that govern

cognitive capabilities. However, these models lack the unique and complex architecture of the human brain, e.g., expanded neuronal cell diversity of millions of neurons organized in distinct functional regions, allowing higher cognitive abilities in humans [8]. So-called cerebral brain organoids exhibit several key features of the *in vivo* brain architecture and cell complexity and thus offer a more realistic microenvironment to investigate the impact of different noxae on the human brain [9]. This innovative model may improve our understanding of the mechanisms of radiation-induced late effects and enable the development of adequate countermeasures. Furthermore, brain organoids could be helpful to test the impact of novel irradiation modalities like SFRT and FLASH therapy before they are applied to the clinics.

NEUROTOXIC EFFECTS OF IONIZING RADIATION ON THE HUMAN BRAIN

The present knowledge of IR effects on the human brain is based primarily on data from epidemiological studies, particularly on Japanese atomic bomb survivors, as well as on cancer patients treated with radiotherapy. However, the affected persons were exposed at different ages and to different radiation qualities that influenced the varying outcomes of the radiation impacts [10, 11].

Epidemiological studies of prenatally exposed atomic-bomb survivors of Hiroshima and Nagasaki demonstrate that IR has, dependent on the dose and developmental stage, adverse effects on the developing brain. These manifest themselves in reduced head volumes in ∼42 % of the children irradiated *in utero* with doses from 0.5 to 0.99 Gy at gestational weeks 8–15 [12]. Additionally, exposure to 0.5–0.99 Gy negatively affected the neurocognition, shown in a decline in school performances in 38 % [13] and a reduction of 21–29 points in intelligence quotient (IQ)-tests per 1 Gy absorbed dose for individuals irradiated at gestational weeks 8–15 [14]. These studies demonstrate the harmful effects of IR on the developing brain, particularly at critical stages of neocortical development, such as gestational weeks 8–15. Furthermore, a cohort study of children that underwent conventional photon-radiotherapy with doses of 0.01–2.8 Gy during infancy (<18 months) due to cutaneous hemangioma, displayed cognitive impairments at the age of 18/19 years. These effects were noticeable as a decrease in high school attendance at doses greater than 0.1 Gy as well as a dose-response relation for cognitive performance measured by cognitive tests aimed at learning ability, and logical reasoning [15]. IR-induced long-term effects also have been reported for pediatric and adult patients with primary or metastatic brain tumors receiving 4–65 Gy cranial photon-radiotherapy [11]. Adverse effects become apparent ≥6 month after treatment and manifest themselves in progressive impairments, which are comparable with Alzheimer's disease, such as deficits in memory, executive function, sustained attention, processing speed and learning, leading to a reduction of the patient's quality of life [11, 16, 17]. The extend of the radiation damage depends on age at irradiation, total dose, fractionation, and field size and the combination with other noxae, e.g., chemotherapeutics [11, 17]. Children are more strongly affected than adults due to the higher radio-sensitivities of the developing brain and a longer lifespan. It was shown that children that received 20–55 Gy of craniospinal photon radiotherapy due to central nervous system (CNS) malignancies at the age of ≤3 years displayed intellectual disability ($\emptyset = -1.34$ IQ-points per year) compared to non-irradiated children ($\emptyset = +0.91$ IQ-points per year) [18]. This phenomenon was observable after the completion of therapy and during the follow-up time of ∼7.5 years. Also, photon irradiation of adult patients with primary, supratentorial brain tumors verifiably led to radiation-induced cognitive deficits, measured by worse results in experimental memory tests after fractionated radiotherapy with a total dose to the tumor of about 46–63 Gy [19]. Altogether, these studies confirm conventional treatment related impairments at any age of patients. Even though photon-based radiotherapy has been continually improved and still remains the standard modality for the treatment of brain tumors, particle-based radiotherapy that mostly relies on protons and carbon ions and enables a more efficient treatment of brain cancer patients, came into focus [20]. In contrast to photons, particle irradiation exhibits an advantageous dose distribution due to a unique absorption profile in the tissue with lower entrance doses and well-defined depth range with maximum dose deposition and increasing relative biological effectiveness (RBE) at the end of their range, called Bragg Peak. This depth-dose profile enables precise irradiation of deep-seated tumors while sparing the surrounding healthy tissue [21]. The use of protons and heavy ions to treat cancer was invented by researchers of the Lawrence Berkeley Laboratory, CA, USA in 1958 (Berkeley "synchrocyclotron") [22]. However, it was first implemented clinically in Japan, in 1994, using the Heavy Ion Medical Accelerator in Chiba (HIMAC) [23]. In Europe, a patient pilot study (1997–2008) with ^{12}C-ions at the Heavy Ion Synchrotron (SIS18) at GSI Helmholtz Center for Heavy Ion Research, Darmstadt (Germany), showed a promising outcome of tumor control and minimal toxicity for irradiation of skull base chordomas and chondrosarcomas [21, 24]. It led to the transfer of particle radiotherapy from physics laboratories to the Heidelberg Ion-Beam Therapy (HIT) Center that was opened in 2009. Due to a decreased neurotoxicity and increased success rate of particle therapy, the number of facilities and thus the number of patients treated with protons and ^{12}C-ions steadily increased in recent years[1]. Meanwhile, 104 particle therapy facilities are in clinical operation worldwide[2]. For protons, reduced neurotoxic effect compared to photons was demonstrated by the studies of Kahalley et al. [25, 26]. Pediatric patients treated for brain tumors with protons showed less neuropsychological impairments in terms of intelligence, perceptual reasoning, processing speed, and working memory than those treated with X-rays [25, 26]. However, considering that continuously improved diagnostics and radiation treatments lead to an increased number of patients with longer lifespan and thus a higher risk for developing treatment-related late effects, the need for adequate model systems and suitable irradiation modalities arises.

[1]https://www.ptcog.ch/index.php/ptcog-patient-statistics
[2]https://www.ptcog.ch/index.php/facilities-in-operation

Cognitive deficits are also a major concern in long-term space mission beyond the shielding of the Earth's magnetosphere as reviewed by Cucinotta et al. [27]. Radiation-induced neurotoxicity is of particular interest, because the radiation environment in space differs significantly from the terrestrial. Terrestrial radiation exposure result mainly from radon-emitted, low energy alpha particles, and sparsely ionizing radiations, i.e., X-, β-, or γ-rays, while in deep space high-energy protons, helium, and heavier ions predominate. Therefore, space radiation induced biological damages can differ from those experienced on Earth. Moreover, effects of other spaceflight relevant factors, such as microgravity or disturbed circadian rhythm, may synergistically impair brain function. During long-term space missions the estimated total body equivalent dose for astronauts amounts to 1–2 mSv per day [28]. Potential CNS risks are reduced motor functions, neurocognitive deficits, probability of the occurrence of Alzheimer's disease and premature aging [27]. As an example, a NASA study on identical twins indicates the potentially harmful effects of galactic cosmic radiation on the human brain. The space-twin, that participated in a one-year mission, demonstrated a post-flight decline in cognitive performance and speed, which persisted during the whole observation time of 6 months, compared to the twin that stayed on Earth [29]. These risks may compromise astronauts' behavior under emergency conditions in deep space and justify the need of improved shielding methods. As the space radiation field and its effects are rather complex, it is difficult to predict the consequences for astronauts. Innovative accelerator facilities such as those available at FAIR/GSI can be used to simulate this mixed radiation field allowing a deeper insight into the CNS risk associated with cosmic radiation as well as the development of improved shielding methods. In summary, studying the effects of IR on the human brain is highly relevant, not only in context of risk assessment in radiotherapy, but also in terms of space research with a focus on shielding technologies.

Conventional Model Systems Used to Investigate IR-Induced Neurotoxic Effects

Because the molecular and cellular mechanisms underlying IR-induced neurocognitive deficits are still largely unknown, *in vitro* or *in vivo* models of the brain's neurophysiology were developed to address this topic.

One of the earliest neuronal cell types are so-called neural stem cells (NSCs). These multipotent, dividing stem cells exist in the developing, embryonic brain as well as in the adult brain of mammalian organisms and represent the early precursors of the CNS-generating neurons and glia cells (astrocytes and oligodendrocytes) [30]. In rodents, two special niches of high-density cell division have been identified: the subventricular zone (SVZ) lining the lateral forebrain ventricles and the subgranular layer of the dentate gyrus (DG) in the hippocampus. In both sites of the rodent brain lifelong neurogenesis, i.e., differentiation of self-renewing NSCs into neurons and glia, takes place. These newly born neurons and glia cells then mature and migrate into the cortical, neuronal circuits to participate in cognitive functions like learning and memory [31, 32]. Whether and how adult human neurogenesis takes part, is highly debated and a challenging research topic [33, 34]. *De novo* formation of human neurons has been analyzed using doublecortin (DCX) or PSA-NCAM as markers for intermediate progenitor cells and early immature neurons (often dubbed "neuroblasts"). However, the source of these cells may not be embryonic-like NSCs but rather astrocytic cells [35]. Thus, human NSCs derived from embryonic/pluripotent stem cells may not reflect adult neurogenesis and its radiosensitivity, yet, they exhibit features of cancer stem cells [36] and therefore still contribute significantly to the radiation biology field. Consequently, mammalian NSCs were isolated from fetal or adult brain or differentiated from pluripotent stem cells, cultured as two-dimensional (2D) monolayers and used as *in vitro* models for radiation effects on neurogenesis [37]. Likewise, the more mature neurons can be isolated from human brain or can be differentiated *in vitro* from human NSCs. By applying various differentiation and growth factors, neurons of distinct subtypes including GABAergic, dopaminergic, and motor neurons were already generated and successfully used for studying neuronal functionality, synaptic plasticity, and injury [38]. However, these 2D-cell cultures do not consider the three-dimensionality of brain tissue. As a more realistic model system, neurospheres (NS), i.e., three-dimensional (3D) aggregates of several neural and neuronal progenitor types, derived from NSCs in suspension, were established. Within the NS, neural cells are able to self-renew, generate various neuronal and glial subtypes at different stages of maturation [39] and display neuronal function in the form of spontaneously generated action potentials [40]. An organ-like microenvironment with some degree of structural or organizational integrity can be achieved, as shown by Merz et al. [41], by culturing rodent and human tissue slices of about 300 μm at an air-liquid interface. These slices even display the tissues' natural 3D-architecture up to 6 months. Finally, animal models, especially rodents, are used to investigate the radiation effects on the brain. The advantages of using animals as model organisms include, besides physiological similarity to humans, the entire vascularization and the complex biochemical and biomechanical microenvironment of the whole mammalian brain [7, 42].

IR-Induced Neurotoxic Effects

As seen from **Table 1**, several studies focused on the potential effects of sparsely IR on hippocampal neurogenesis. The observed radiation effects include a dose-dependent loss of NSCs [43, 44, 46, 47], a decreased proliferation rate of surviving NSCs [41, 43, 46–48, 53], impairments in the differentiation capability into neuronal and glial cells [44] and morphological changes in dendritic structure and neurite length [45, 50] leading to changes in synaptic transmission and therefore to a disturbed neuronal plasticity. Interestingly, these effects already occur at doses of about 1–2 Gy. This is of particular interest, because fractionated radiotherapy is usually performed with 1–3 Gy per fraction [68]. As seen from studies by Isono et al. [47], Morini et al. [48], and Yokota et al. [46], the effects on the NSCs were enhanced when irradiation was performed with particles, e.g., ^{12}C-ions. These results verify the high radiation-sensitivity of non-differentiated neural stem and progenitor

TABLE 1 | Data collection of *in vitro* and *in vivo* studies on the effects of IR.

Model	Irradiation	Effects	References
Mouse NSCs	γ-rays 2 Gy *in utero* at E14.5 days of $p21^{-/-}$ and wt* mice	• Marked difference in the radiation response between lateral ganglionic eminences (LGE) and dorsal telencephalon • Particularly high apoptosis rate in SVZ cells of the LGE • Induction of G2/M and intra-S checkpoints within irradiated LGE, but no effect on the p21-dependent G1/S • Restoration of the pool of proliferating radial glia cells and massive cell death of intermediate progenitor cells 24 h post-IR	[43]
Human NSCs	γ-rays 1, 2, 5 Gy	• Reduced differentiation potential even for 2 and 5 Gy • 1- 5 Gy: reduced cell numbers by more than three-fold • G2/M arrest after 5 Gy • Rapid induction of apoptosis after 5 Gy • Dose-dependent increase in oxidative stress	[44]
Human NSCs	γ-rays chronic exposure for 72 h with a total dose of 0.031, 0.124, 0.496 Gy	• Cell area and neurite length decrease in MAP2+ neural cells • Increased number of γ-H2AX nuclear foci • Altered gene expression profile at 72 h	[45]
Human NSCs	γ-rays (0.2 keV/μm) 0.5, 1, 2, 4, 8 Gy ^{12}C (108 keV/μm) 0.5, 1, 2, 4, 8 Gy	• Dose-dependent growth inhibition • Dose-dependent increased apoptosis • ^{12}C-ions more effective than γ-rays	[46]
Human NSCs	X-rays (150-kVp, ∼1 Gy/min) 2–10 Gy ^{12}C (290 MeV/u, SOBP*, average LET 50 keV/μm) 2 - 10 Gy	• Decreased growth rate • IR induced dose-dependent apoptosis in both cases (∼90%), rarely necrosis • ^{12}C-ions more effective than X-rays	[47]
Human NSCs	X-rays 2 - 20 Gy ^{12}C (SOBP, 246-312 MeV/u, LET 86.6–97.8 keV/μm) 5 - 20 Gy	• ≥10 Gy: Reduction in viability up to 56% 48 h post-IR, stronger effect 7 days post-IR • 48h post-IR: no strong statistically significant effect • 7 days post-IR: reduction in viability up to 62 %	[48]
Mouse NS	^{56}Fe (600 MeV/u, fluence: 500–30,000 pa/cm^2) 0–8 Gy	• Dose-dependent reduced cell survival • Neurosphere cultures contain populations of cells with different sensitivities to irradiation • Exposure to IR lead to dose-dependent rise in oxidative stress	[49]
Neurons from E18 rat hippocampi after 21 days in culture	γ-rays 10 Gy	• Initial increase in spines and excitatory synapses followed by decrease in spine/synapse density with altered spine dynamics • changes in synaptic structural plasticity	[50]
Archival and autopsy human hippocampal tissue	13.2–36 Gy total body IR or craniospinal with/without boost to the posterior fossa	• 10- to 100-fold (child) reduction of hippocampal neurogenesis (decreased generation of early DCX^+ neurons) • radiation-induced inflammation (two-fold more activated microglia)	[51]
Mouse hippocampal slices	X-rays 7, 30 Gy	• Decreased cell number • Morphological changes • Increase in migration velocity of microglia	[52]
Human brain tumor slices	X-rays 1, 2, 4, 40 Gy ^{12}C (9.8 MeV/u on target, LET 170 MeV/u) 0.13–21.7 Gy	• 40 Gy blocked the normal proliferation • Dose- dependent DNA damage (double-strand breaks)	[41]
Human brain tumor slices	X-rays 4 Gy ^{12}C (50-mm-width SOBP, LET range: 50–70 keV/μm) 4 Gy	• ∼ 50% inhibition of proliferation after 24 h • Increase in cell death • ∼ 40% inhibition of proliferation after 24 h, massive DNA-damage • Increase in cell death after 2 Gy	[53]
Rhesus macaques	γ-rays 6.75–8.05 Gy whole body	• IR led to worse long-term results in visual discrimination tests suggesting relative deficiency in cognitive flexibility	[54]

(Continued)

TABLE 1 | Continued

Model	Irradiation	Effects	References
Mouse	X-rays 10 Gy bilateral hippocampus/cortex	• Hippocampal-dependent spatial learning and memory impairments in the Barnes maze • Reduction of hippocampal neurogenesis (reductions in proliferation and DCX^+ neurons in the SGZ)	[55]
Rat	X-rays 2, 10 Gy brain	• Dose-dependent inhibition of neural precursor cell proliferation in the hippocampus • Depletion of neural progenitor cells exposed to 10 Gy • 97% reduction in newborn neurons • No adverse effect on astrocytes or oligodendrocytes • Neuroinflammation (increase activated microglia)	[56]
Mouse	X-rays 2, 5, 10 Gy brain	• Dose-dependent increased apoptosis • Proliferating cells in SGZ reduced by 93–96% • Dose-dependent decrease of immature neurons up to 40–60 % • No effect on astrocytes or oligodendrocytes • Neuroinflammation (increase activated microglia)	[57]
Rat	X-rays 6 Gy whole brain IR	• Long-term suppression of neurogenesis in olfactory bulb and dentate gyrus • No long-term reduction of progenitor cells in SVZ, but marked decrease in dentate gyrus • Only acute, but not persistent activation of microglia	[58]
Rat	X-rays 25 Gy brain	• Suppression of SVZ proliferation in neuroblasts and interneurons, recovery in the olfactory bulb • Limited proliferation of oligodendrocyte precursors (O-A2) followed by demyelination • Restoration of endothelium • White matter necrosis • Early loss of young oligodendrocyte progenitors and delayed loss of more mature oligodendrocytes lineage cells in human tissue	[59]
Rat	X-rays 8, 10, 13 Gy brain ^{56}Fe (1 GeV/u) 0.2, 0.4, 0.6 Gy	• >10 Gy: Hippocampal spatial memory impairment evaluated by Barnes maze • ≥ 0.2 Gy Hippocampal spatial memory impairment (Barnes maze test)	[60]
Rat	^{56}Fe (1 GeV/u) 1.5 Gy whole body IR	• Impaired spatial learning and memory tested in Morris water maze	[61]
Rat	^{56}Fe (1 GeV/u) 1.5 Gy brain	• Increase in reference memory errors negatively correlated with proteins expression that play roles in cognition (PRKA, synaptophysin, DCF of the striatum and synaptophysin of the frontal cortex)	[62]
Mouse	^{56}Fe (600 MeV/u, LET 175.2 keV/μm at the target surface) 0.5–4 Gy brain	• Dose-related decrease in hippocampal neurogenesis • Neuroinflammation (increase in numbers of newly born activated microglia)	[63]
Rat	^{56}Fe (1 GeV/u) 0.02 Gy brain	• Significant impairments in learning and memory tested by the attentional set-shifting test	[64]
Mouse	^{56}Fe (600 MeV/u) 0.1, 0.2, 0.5 Gy whole body IR	• Cognitive impairment in novel object recognition tested in Morris water maze • Cognitive effects not induced by oxidative damage	[65]
Mouse	Protons (1GeV/u) 0–0.2 Gy whole body IR	• ≥ 0.1 Gy decreased hippocampal cell proliferation • ≥ 0.5 Gy decreased neurogenesis • No astrocyte or microglia activation	[66]
Mouse	Protons (250 MeV/u) 0.1, 1 Gy whole body IR	• Dose-dependent reductions in dendritic complexity (~33 %) and spine density (50–75 %) along hippocampal neurons • Dose-responsive reductions in neurons' synaptophysin expression	[67]

The table shows the dose range applied in the respective study. Endpoints may have been obtained using smaller dose ranges or single doses; energies and doses are indicated when provided by the authors.

**wt, wildtype; SOBP, Spread-Out Bragg Peak; ^{12}C, carbon; ^{56}Fe, iron; pa, particles.*

cells and correlate with the radiation-sensitive stage of early embryonic neurogenesis. Despite differences in neurogenesis between humans and rodents, as discussed above, there are some similarities in the radiation response, e.g., activation of microglia [51, 52, 56, 58]. Astrocyte and endothelium mediated secondary vascular abnormalities and the subsequent disruption of the blood brain barrier cause this activation of microglia, the phagocytic cells of the CNS. This induces chronic neuroinflammation via the release of pro-inflammatory cytokines, which also leads to degenerative changes in the white matter [51, 56, 57, 69]. *In vitro* and *in vivo* studies have shown that IR can further lead to an increase of oxidative stress producing DNA-damage and causes apoptotic cell death in neuronal, glial, and endothelial cell types in NSCs and NS [44, 49] as well as in rats [59]. In rodents, the radiation-induced loss of glial oligodendrocyte progenitor cells followed by demyelination of neurons ends up with white matter necrosis [59], which is also seen in humans [70]. These impacts on mammalian brains may contribute to impairments in behavior and to memory deficits as assessed by the Barnes maze [55, 60] and visual discrimination tests [54] and may also mirror cognitive defects seen in humans.

Studies analyzing the effects of space-relevant ^{56}Fe-ions on rodents (see **Table 1**) have shown that doses < 1 Gy impair neurogenesis as well as neuronal function [62, 63] and can cause cognitive deficits. The irradiated animals exhibit persistent hippocampal and cortical based performance decrements in memory and behavioral tests [60, 61, 64, 65]. Comparative studies demonstrated that even exposure to 0.2 Gy ^{56}Fe (1 GeV/u) resulted in cognitive impairments whereas X-ray exposure did not result in memory deficits until doses > 10 Gy indicating a high effectiveness of Fe (estimated RBE ~ 50) [60]. Additionally, mice that were exposed to protons with doses as low as 0.1–0.5 Gy also showed a decreased hippocampal cell proliferation and deficits in neurogenesis and synaptic plasticity [66]. These findings demonstrate the stronger effect of particle irradiation compared to photons and strengthen concerns about potential cognitive changes after space mission. However, the animal studies have been performed predominantly with ^{56}Fe-ions and therefore do neither represent the full complexity of the space radiation environment, nor the continuous irradiation over several weeks and months in space.

In summary, these findings demonstrate the complex and dynamic effects of radiation on multiple cell types of the brain, including NSCs, oligodendrocytes, astrocytes, microglia, and neurons as well as vascular endothelial cells (**Figure 1**). Furthermore, comparative studies demonstrated the greater effectiveness of space relevant ^{56}Fe-ions on CNS cells in comparison to photons. These radiation mediated impacts may contribute to diverse brain damages and neurodegenerative diseases, even though the detailed mechanisms of cognitive impairments remain largely unknown.

Limitations of Conventional Model Systems

The model systems listed above, particularly the *in vitro* ones, have disadvantages. Despite the progress that has been made in understanding the hallmarks of brain development and neurogenesis as well as in investigating the neurotoxicity of IR using of 2D-cell cultures, these cell systems display distinct differences in morphology, metabolism, and differentiation compared to the *in vivo* situation [6]. Specifically, the NSC monolayer system only allows investigating IR effects on the very early and primitive neurogenesis as discussed above. Therefore, they neither address processes in the adult brain nor are they capable of reflecting the complex cell-layering and diversity seen in the human brain's architecture. The same applies to neurons cultivated *in vitro* as monolayers. In contrast, 3D-neurospheres contain cells at multiple stages of differentiation but lack cell-organization and hierarchical complexity found in the human brain *in vivo* [71]. A more relevant model is presented by human brain slice cultures from postmortem tissue or resected tissue from operations [72]. *In vitro*, their morphology and physiological characteristics can be partly preserved for up to 50 days [73]. However, there are striking differences between postmortem and resected slices in the processing of slices and transfer to the *in vitro* conditions, neuronal survival has to be sustained by elaborate culture conditions and finally procurement of human brain slices is challenging and impedes larger studies. In radiation biology, rodent studies are frequently used allowing first insights into the molecular mechanisms underlying cognitive dysfunction. However, apart from the ethical discussions on the use of animals in research, mice, and humans display species-specific differences, that speak against the use of animals as a model [42]. In addition to obvious differences in brain size and architecture due to the folding of the human brain, particularly the existence of neural stem cells, called outer radial glia, residing in the outer subventricular zone, and a greater diversity in neuronal cell types [74–76] sets the human brain apart from other mammalian ones. Notably, even between homologous human and mouse cell types, single-nucleus RNA-sequencing analyses verified significant differences in gene expression [8]. All these main features of the human brain allow for higher cognitive functions, but also justify the need for a more adapted and adequate brain model to investigate the molecular and functional effects of radiation in various brain regions and cell types. Some of the disadvantages of the discussed models can be overcome by human brain organoids that will be discussed in the following chapter.

ORGANOIDS AS NOVEL *IN VITRO* TOOL FOR THE HUMAN BRAIN

In recent years, so-called brain or cerebral organoids, differentiated from human embryonic stem cells (hESCs) or patient-relevant induced pluripotent stem cells (iPSCs), came into focus as a novel *in vitro* tool in regenerative medicine/disease modeling [77], whereas the potential for radiation biology is not yet exploited. Organoids are 3D spontaneously self-organized, organ-like structures that are able to develop into various interdependent brain regions containing different organ-specific cell types arranged in distinct layers (**Figure 2**). In contrast to rodent models, these organoids exhibit several key features of

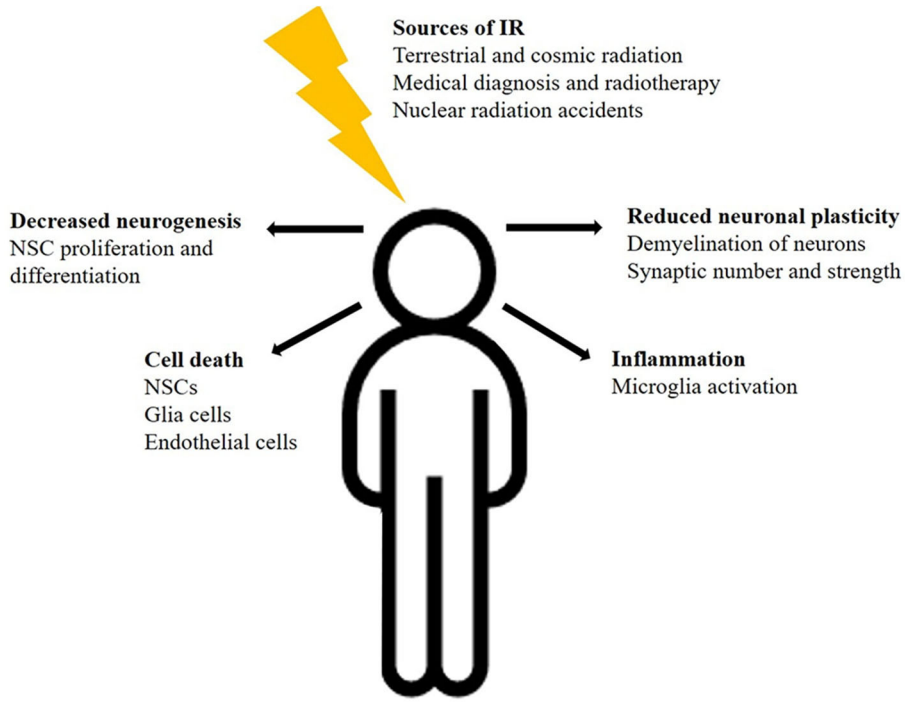

FIGURE 1 | Schematic illustration of IR-sources and possible radiation effects on the human brain.

the human *in vivo* brain organogenesis like an independent progenitor layer with the unique neural stem cells called outer radial glia. In addition, it has already been reported that animal models failed to recapitulate the symptoms of human neurological diseases, such as micro- and macrocephaly while human organoids have this ability. Therefore, they provide a novel predictive preclinical tool to investigate the detailed molecular mechanisms underlying congenital, cognitive diseases and the effects of potential neuro-therapeutics in functional human tissues [78]. Brain organoids thus provide the opportunity to model unique features of early human brain development, as well as human neurogenesis and neuro-regeneration [9, 79], and may allow a better understanding of the mechanisms underlying ionizing radiation-induced cognitive impairments and disease.

Mimicking *in vivo* patterning by supplementing external patterning factors, organoids of diverse functional brain regions, including organoids of the ventral forebrain [80, 81], midbrain [82, 83], hypothalamus [84], cerebellum [85], and pituitary [86] were generated in suspension. Culture conditions were improved by using spinning reactors and orbital shakers at moderate throw and speed, which provide enhanced nutrient and oxygen supply and culture time without causing adverse shear stress. Such sustained suspension culture leads to an enhanced differentiation process of neurons compared to those derived in 2D-monolayers and the formation of active neuronal networks [84, 87–89]. In addition, different region-specific spheroids, such as cortical spheroids of the dorsal and ventral forebrain, can be fused to generate so-called "assembloids" (**Figure 3**). Consequently, migration of interneurons and the interactions between different brain regions or different cell types can be tracked [90–93]. Other studies demonstrated the incorporation of microglia as the brains innate immune cells into the organoid-model [94, 95]. This allows investigating the effects of combined therapies, e.g., radio- and immunotherapy, on the human CNS. Another approach is the generation of brain tumors in normal organoids as a realistic microenvironment [96] that will permit a better understanding of tumor and normal tissue interaction in response to IR. Yet, radiobiological studies using brain organoids have not been published. However, brain organoids were recently implemented in ground-based experiments investigating the effects of microgravity on neural progenitor cell fate [97]. They showed an altered gene expression of rostral-caudal and cortical markers that may influence brain structure and physiology, indicating the usability of brain organoids in space radiation research to identify the mechanisms affecting brain function and, e.g., in the development of new shielding methods to protect the brain's neuronal circuits. In our own studies, we were able to reproducibly show radiation impacts such as apoptosis and necrosis changing the structure and composition of cerebral organoids (unpublished data).

But even if organoids currently are viewed as state-of-the-art *in vitro* models of the human brain, there are still challenges to be overcome. Because of the lack of endothelial cells and thus vascularization, organoids will develop a necrotic core and terminal maturation and differentiation is limited. Therefore, Giandomenico et al. [98] chose an alternative approach for an improved oxygen supply cultivating organoid slices at an air-liquid interface. These organoid slices demonstrated an increased

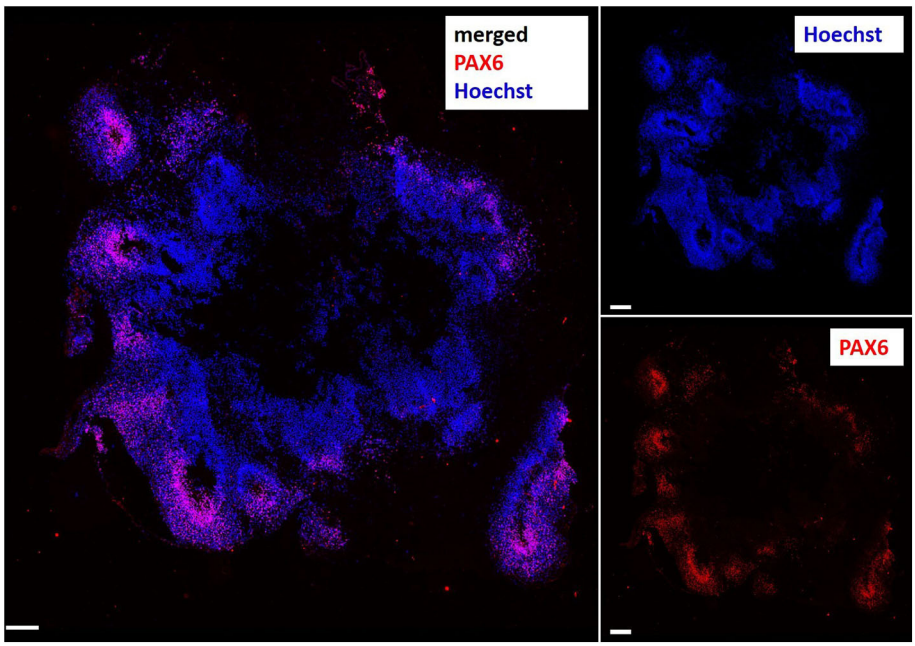

FIGURE 2 | Immunocytochemical staining of a cerebral organoid slice showing human brain-like hierarchical organization with the radial glia marker PAX6 (Paired box 6, red) in the inner ventricular layer of the brain lobes. Nuclei stained with Hoechst 33342 (blue). Scale bar: 200 μm.

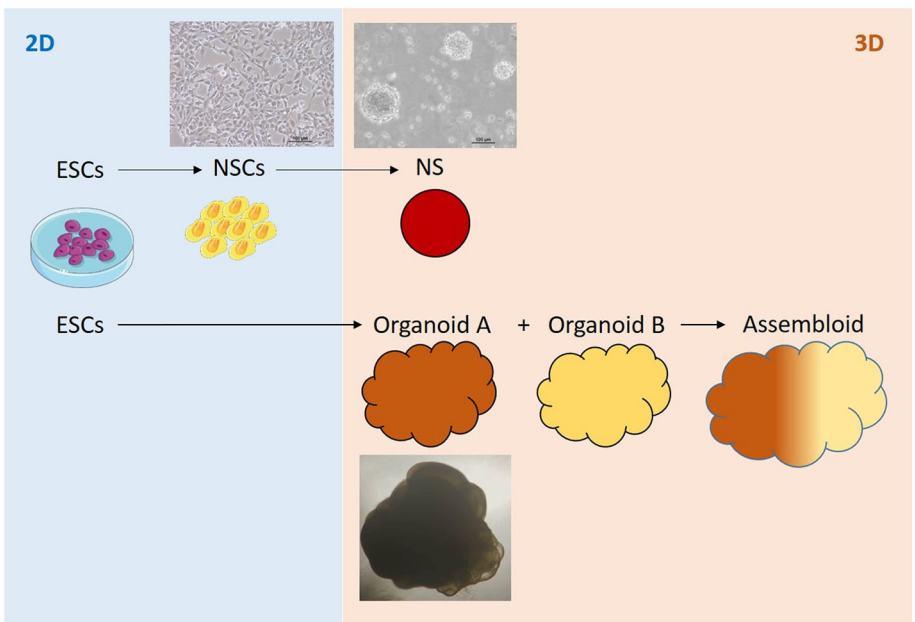

FIGURE 3 | Pluripotent, embryonic stem cell (ESCs) -based 2D-, 3D cell- and organoid systems as *in vitro* tools for studying the effects of ionizing radiation on the human brain.

survival rate and an extensive axon outgrowth reminiscent of nerve tracts. Another issue is the lack or scarcity of glial cell populations. A new differentiation approach uses more complex differentiation factors to generate mature oligodendrocytes in brain organoids [99]. Nevertheless, the batch variations and thus heterogeneity of the generated organoids still poses a problem for statistically significant and expressive results, although there are new methods for generating more homogeneous organoids by using microfilaments as floating scaffolds [100]. Despite these improvements, it is technically very challenging to

obtain homogeneous batches and the organoids show statistical variabilities also seen in animal experiments; therefore, more sophisticated bioengineering techniques are presently explored. One approach is the use of 3D bio printing technologies to produce consistent scaffolds as a basis of organoid formation. A further challenge is the adaptation of standardized analytical protocols such as immunochemical staining procedures to 3D-brain organoids. In the same line, single-cell mRNA sequencing [88] techniques have been proven more meaningful than standard polymerase chain reactions (PCR). Despite these challenges, brain organoids represent a versatile model system allowing a variety of studies that will improve the understanding of radiation impacts on the human brain at any stage of development and regeneration.

IMPROVING PARTICLE THERAPY AND RADIATION RISK ASSESSMENT USING BRAIN ORGANOIDS AT STATE OF THE ART ACCELERATOR FACILITIES

New accelerators such as the Facility for Antiproton and Ion Research (FAIR) in Darmstadt, Germany, that is to be completed in 2025, can produce heavy ion beams up to around 10 GeV/n as compared to 1 GeV/n with the current setting (reviewed in [101]). This is particularly relevant for ground-based studies of possible galactic cosmic radiation (GCR) effects, as part of the particle flux in the GCR exceeds 1 GeV/n [102]. However, very few studies to date have addressed high-energy ranges $>$ 1 GeV/n. Meaningful risk assessment specifically of interplanetary missions therefore will rely on those state of the art accelerator facilities and brain organoids can serve as a high throughput biological risk model. While astronauts are subject to chronic irradiation, accelerator-based experiments normally use acute exposure due to beamtime constraints, even though long-term experiments are technically feasible. High beam intensities, delivered by facilities like FAIR, are also of interest for the use of ultra-high dose rate (FLASH) radiotherapy with protons or potentially heavy ions such as carbon. This experimental radiation modality can reduce neurotoxic effects in the healthy tissue by increasing the dose rate to $\geq$40 Gy/s. Even though the detailed mechanisms underlying the greater radioresistance are still unknown, acute oxygen depletion within the irradiated tissue or chromatin remodeling is discussed as possible cause for the increased effectiveness [103]. Here again, organoids serve as ideal models due to their innate oxygen gradient within their various layers from the hypoxic core to the normoxic outer layer of the cortical plate. An initial study of a first patient with subcutaneous T-cell lymphoma confirmed the benefits of FLASH radiation by demonstrating a complete response of the tumor and minimal normal tissue toxicities [104]. However, the remaining studies focus mainly on animal models, e.g. Montay-Gruel et al. [205] demonstrated that spatial memory of mice is preserved after 10 Gy FLASH-whole-brain irradiation with mean dose rates above 100 Gy/s, whereas 10 Gy whole-brain irradiation at a conventional dose rate (0.1 Gy/s) impairs spatial memory [105]. Due to the limited number of suitable accelerator facilities providing the necessary technology to perform FLASH irradiations [106] and the lack of suitable human biological models, studies regarding FLASH radiotherapy are rare and translation to the clinics remains a challenge. High throughput, organoid based studies could shed light on the molecular mechanisms of the observed effects, particularly the contribution of hypoxia, and overcome these challenges.

Of particular interest in radiation therapy is also the use of ions other than protons and carbon. Helium ions for instance are discussed to be more suitable than protons due to an improved RBE in the Bragg-Peak region and an improved oxygen enhancement ratio [107] and therefore may be especially beneficial for pediatric patients [108] in terms of long-term side effects particularly to the brain. Research accelerator facilities offer the possibility to test these rarely used ions and mixed ion modalities (proton, helium, oxygen, carbon) on their neurotoxic behavior and to ensure risk-free implementation into the clinics.

Another approach to improve radiotherapy outcome is the so-called spatially fractionated radiotherapy (SFRT), the inhomogeneous irradiation with a stack or grid of small radiation beams. Depending on the beam spot size, these are known as spatially fractionated mini- or microbeam SFRT. Photon SFRT with a spot size in the mm range was first introduced more than a century ago to reduce skin necrosis and is used clinically (in combination with conventional radiotherapy) for many years [109]. In contrast, microbeam SFRT is still in a pre-clinical stage. In animal models, extremely high doses of hundreds of Gy delivered by microbeam photon SFRT were tolerated well e.g., by rat brain [110] and spinal cord [111], raising hopes that spatially fractionated radiotherapy allows dose escalation and thus improved tumor control without severe normal tissue complications. Compared to photon SFRT, SFRT with protons, and potentially heavier accelerated ions, combines the advantages of SFRT and particle therapy (reviewed in [112]) and is well tolerated by brain tissue in a rat animal model [113]. Recent clinical proof-of-concept studies and constant technical improvements enable the transition of proton SFRT to clinical application [114–116]. Photon SFRT and especially proton or heavy ion SFRT have great therapeutic potential, allowing tumor dose escalation with good normal tissue tolerance. However, the biological mechanisms behind SFRT are not fully understood. In this rapidly developing field, human brain organoids, combining the advantages of a human brain architecture and a reliable *in vitro* system, can be a useful tool both in the exploration of new SFRT techniques as well as in the discovery of the biological mechanisms underlying SFRT.

CONCLUSION

Despite remaining challenges, brain organoids present the most realistic human *in vitro* brain model so far and have enormous potential to pave the way for new research findings in the field of radiation research. These model systems will allow meaningful research and improvements in the fields of cancer therapy (acute high dose exposure) and space radiation (chronic low dose exposure) protection while partly replacing

and streamlining time-consuming and ethically controversial animal studies. Furthermore, in contrast to the clinical facilities, new research facilities such as FAIR offer the implementation of varying and more complex experimental designs due to more flexible changes in irradiation conditions. Combining both, state of the art biological models and state of the art accelerators will enable us to address issues in radiation biology in an unprecedented fashion.

AUTHOR CONTRIBUTIONS

CS: data acquisition and manuscript writing. CH, SR, and IS: data acquisition, manuscript writing, and review. MD: manuscript review. All authors contributed to the article and approved the submitted version.

FUNDING

This work was funded by the Bundesministerium für Bildung und Forschung (BMBF) within the Brain Radiation Assay project (02NUK049A).

ACKNOWLEDGMENTS

The authors thank all the members of the working group for their valuable comments, helpful critiques, and discussions.

REFERENCES

1. United Nations Scientific Committee on the Effects of Atomic Radiation. *Sources and Effects of Ionizing Radiation*. 1st ed. New York, NY: United Nations; 2010
2. Krämer M, Kraft G. Track structure and DNA damage. *Adv Space Res*. (1994) **14**:151–9. doi: 10.1016/0273-1177(94)90465-0
3. Scoccianti S, Detti B, Gadda D, Greto D, Furfaro I, Meacci F, et al. Organs at risk in the brain and their dose-constraints in adults and in children: a radiation oncologist's guide for delineation in everyday practice. *Radiother Oncol*. (2015) **114**:230–8. doi: 10.1016/j.radonc.2015.01.016
4. Soussain C, Ricard D, Fike JR, Mazeron J-J, Psimaras D, Delattre J-Y. CNS complications of radiotherapy and chemotherapy. *Lancet*. (2009) **374**:1639–51. doi: 10.1016/S0140-6736(09)61299-X
5. Durante M, Cucinotta FA. Physical basis of radiation protection in space travel. Rev. Mod. *Phys*. (2011) **83**:1245–81. doi: 10.1103/RevModPhys.83.1245
6. Duval K, Grover H, Han L-H, Mou Y, Pegoraro AF, Fredberg J, Chen Z. Modeling physiological events in 2D vs. 3D cell culture. *Physiology (Bethesda)*. (2017) **32**:266–77. doi: 10.1152/physiol.00036.2016
7. Verhaegen F, Granton P, Tryggestad E. Small animal radiotherapy research platforms. *Phys Med Biol*. (2011) **56**:R55–83. doi: 10.1088/0031-9155/56/12/R01
8. Hodge RD, Bakken TE, Miller JA, Smith KA, Barkan ER, Graybuck LT, et al. Conserved cell types with divergent features in human versus mouse cortex. *Nature*. (2019) **573**:61–8. doi: 10.1038/s41586-019-1506-7
9. Lancaster MA, Renner M, Martin C-A, Wenzel D, Bicknell LS, Hurles ME, et al. Cerebral organoids model human brain development and microcephaly. *Nature*. (2013) **501**:373–9. doi: 10.1038/nature12517
10. Hladik D, Tapio S. Effects of ionizing radiation on the mammalian brain. *Mutat Res*. (2016) **770**:219–30. doi: 10.1016/j.mrrev.2016.08.003
11. Crossen JR, Garwood D, Glatstein E, Neuwelt EA. Neurobehavioral sequelae of cranial irradiation in adults: a review of radiation-induced encephalopathy. *J Clin Oncol*. (1994) **12**:627–42. doi: 10.1200/JCO.1994.12.3.627
12. Otake M, Schull WJ. Radiation-related small head sizes among prenatally exposed A-bomb survivors. *Int J Radiat Biol*. (1993) **63**:255–70. doi: 10.1080/09553009314550341
13. Yoshimaru H, Otake M, Fujikoshi Y, Schull WJ. Effect on school performance of prenatal exposure to the Hiroshima atomic bomb. *Nihon Eiseigaku Zasshi*. (1991) **46**:747–54. doi: 10.1265/jjh.46.747
14. Schull WJ, Otake M, Yoshimaru H. *Effect on Intelligence Test Score of Prenatal Exposure to Ionizing Radiation in Hiroshima and Nagasaki*. Hiroshima: Radiation Effects Research Foundation (1988).
15. Hall P, Adami H-O, Trichopoulos D, Pedersen NL, Lagiou P, Ekbom A, et al. Effect of low doses of ionising radiation in infancy on cognitive function in adulthood: Swedish population based cohort study. *BMJ*. (2004) **328**:19. doi: 10.1136/bmj.328.7430.19
16. Meyers CA, Brown PD. Role and relevance of neurocognitive assessment in clinical trials of patients with CNS tumors. *J Clin Oncol*. (2006) **24**:1305–9. doi: 10.1200/JCO.2005.04.6086
17. Roddy E, Mueller S. Late effects of treatment of pediatric central nervous system tumors. *J Child Neurol*. (2016) **31**:237–54. doi: 10.1177/0883073815587944
18. Fouladi M, Gilger E, Kocak M, Wallace D, Buchanan G, Reeves C, et al. Intellectual and functional outcome of children 3 years old or younger who have CNS malignancies. *J Clin Oncol*. (2005) **23**:7152–60. doi: 10.1200/JCO.2005.01.214
19. Armstrong CL, Shera DM, Lustig RA, Phillips PC. Phase measurement of cognitive impairment specific to radiotherapy. *Int J Radiat Oncol Biol Phys*. (2012) **83**:e319–24. doi: 10.1016/j.ijrobp.2011.12.083
20. Durante M, Loeffler JS. Charged particles in radiation oncology. *Nat Rev Clin Oncol*. (2010) **7**:37–43. doi: 10.1038/nrclinonc.2009.183
21. Kraft G. Tumor therapy with heavy charged particles. *Prog Particle Nucl Phys*. (2000) **45**:S473–544. doi: 10.1016/S0146-6410(00)00112-5
22. Lawrence JH, Tobias CA, Born JL, Mccombs RK, Roberts JE, Anger HO, et al. Pituitary irradiation with high-energy proton beams: a preliminary report. *Cancer Res*. (1958) **18**:121–34
23. Kitagawa A, Fujita T, Muramatsu M, Biri S, Drentje AG. Review on heavy ion radiotherapy facilities and related ion sources (invited). *Rev Sci Instrum*. (2010) **81**:02B909. doi: 10.1063/1.3268510
24. Schulz-Ertner D, Nikoghosyan A, Thilmann C, Haberer T, Jäkel O, Karger C, et al. Results of carbon ion radiotherapy in 152 patients. *Int J Radiat Oncol Biol Phys*. (2004) **58**:631–40. doi: 10.1016/j.ijrobp.2003.09.041
25. Kahalley LS, Peterson R, Ris MD, Janzen L, Okcu MF, Grosshans DR, et al. Superior intellectual outcomes after proton radiotherapy compared with photon radiotherapy for pediatric medulloblastoma. *J Clin Oncol*. (2020) **38**:454–61. doi: 10.1200/JCO.19.01706
26. Kahalley LS, Ris MD, Grosshans DR, Okcu MF, Paulino AC, Chintagumpala M, et al. Comparing intelligence quotient change after treatment with proton versus photon radiation therapy for pediatric brain tumors. *J Clin Oncol*. (2016) **34**:1043–9. doi: 10.1200/JCO.2015.62.1383
27. Cucinotta FA, Alp M, Sulzman FM, Wang M. Space radiation risks to the central nervous system. *Life Sci Space Res*. (2014) **2**:54–69. doi: 10.1016/j.lssr.2014.06.003
28. Cucinotta FA, Durante M. Cancer risk from exposure to galactic cosmic rays: implications for space exploration by human beings. *Lancet Oncol*. (2006) **7**:431–5. doi: 10.1016/S1470-2045(06)70695-7
29. Garrett-Bakelman FE, Darshi M, Green SJ, Gur RC, Lin L, Macias BR, et al. The NASA Twins Study: A multidimensional analysis of a year-long human spaceflight. *Science*. (2019) **364**:eaau8650. doi: 10.1126/science.aau8650
30. Götz M, Nakafuku M, Petrik D. Neurogenesis in the developing and adult brain-similarities and key differences. *Cold Spring Harb Perspect Biol*. (2016) **8**:a018853. doi: 10.1101/cshperspect.a018853
31. Doetsch F, Caillé I, Lim DA, García-Verdugo JM, Alvarez-Buylla A. Subventricular zone astrocytes are neural stem cells in the adult mammalian brain. *Cell*. (1999) **97**:703–16. doi: 10.1016/S0092-8674(00)80783-7

32. Palmer TD, Takahashi J, Gage FH. The adult rat hippocampus contains primordial neural stem cells. *Mol Cell Neurosci*. (1997) **8**:389–404. doi: 10.1006/mcne.1996.0595
33. Bergmann O, Spalding KL, Frisén J. Adult neurogenesis in humans. *Cold Spring Harb Perspect Biol*. (2015) **7**:a018994. doi: 10.1101/cshperspect.a018994
34. Kempermann G, Gage FH, Aigner L, Song H, Curtis MA, Thuret S, et al. Human adult neurogenesis: evidence and remaining questions. *Cell Stem Cell*. (2018) **23**:25–30. doi: 10.1016/j.stem.2018.04.004
35. Magnusson JP, Frisén J. Stars from the darkest night: unlocking the neurogenic potential of astrocytes in different brain regions. *Development*. (2016) **143**:1075–86. doi: 10.1242/dev.133975
36. Reinhard J, Brösicke N, Theocharidis U, Faissner A. The extracellular matrix niche microenvironment of neural and cancer stem cells in the brain. *Int J Biochem Cell Biol*. (2016) **81**:174–83. doi: 10.1016/j.biocel.2016.05.002
37. Gage FH. Mammalian neural stem cells. *Science*. (2000) **287**:1433–8. doi: 10.1126/science.287.5457.1433
38. Yan Y, Shin S, Jha BS, Liu Q, Sheng J, Li F, et al. Efficient and rapid derivation of primitive neural stem cells and generation of brain subtype neurons from human pluripotent stem cells. *Stem Cells Transl Med*. (2013) **2**:862–70. doi: 10.5966/sctm.2013-0080
39. Monni E, Congiu T, Massa D, Nat R, Diana A. Human neurospheres: from stained sections to three-dimensional assembly. *Transl Neurosci*. (2011) **2**:43–8. doi: 10.2478/s13380-011-0007-4
40. Mayer M, Arrizabalaga O, Lieb F, Ciba M, Ritter S, Thielemann C. Electrophysiological investigation of human embryonic stem cell derived neurospheres using a novel spike detection algorithm. *Biosens Bioelectron*. (2018) **100**:462–8. doi: 10.1016/j.bios.2017.09.034
41. Merz F, Müller M, Taucher-Scholz G, Rödel F, Stöcker H, Schopow K, et al. Tissue slice cultures from humans or rodents: a new tool to evaluate biological effects of heavy ions. *Radiat Environ Biophys*. (2010) **49**:457–62. doi: 10.1007/s00411-010-0293-1
42. Perlman RL. Mouse models of human disease: An evolutionary perspective. *Evol Med Public Health*. (2016) **2016**:170–6. doi: 10.1093/emph/eow014
43. Etienne O, Roque T, Haton C, Boussin FD. Variation of radiation-sensitivity of neural stem and progenitor cell populations within the developing mouse brain. *Int J Radiat Biol*. (2012) **88**:694–702. doi: 10.3109/09553002.2012.710927
44. Acharya MM, Lan ML, Kan VH, Patel NH, Giedzinski E, Tseng BP, Limoli CL. Consequences of ionizing radiation-induced damage in human neural stem cells. *Free Radic Biol Med*. (2010) **49**:1846–55. doi: 10.1016/j.freeradbiomed.2010.08.021
45. Katsura M, Cyou-Nakamine H, Zen Q, Zen Y, Nansai H, Amagasa S, et al. Effects of chronic low-dose radiation on human neural progenitor cells. *Sci Rep*. (2016) **6**:20027. doi: 10.1038/srep20027
46. Yokota Y, Wada Y, Funayama T. Distinct modes of death in human neural stem and glioblastoma cells irradiated with carbon-ion radiation and gamma-rays. *Int J Radiat Biol*. (2020) **96**:172–8. doi: 10.1080/09553002.2020.1683639
47. Isono M, Yoshida Y, Takahashi A, Oike T, Shibata A, Kubota Y, et al. Carbon-ion beams effectively induce growth inhibition and apoptosis in human neural stem cells compared with glioblastoma A172 cells. *J Radiat Res*. (2015) **56**:856–61. doi: 10.1093/jrr/rrv033
48. Morini J, Babini G, Barbieri S, Baiocco G, Ciocca M, Ivaldi GB, et al. A comparison between X-ray and carbon ion irradiation in human neural stem cells. *Radiat Prot Dosimetry*. (2019) **183**:102–6. doi: 10.1093/rpd/ncy231
49. Tseng BP, Giedzinski E, Izadi A, Suarez T, Lan ML, Tran KK, et al. Functional consequences of radiation-induced oxidative stress in cultured neural stem cells and the brain exposed to charged particle irradiation. *Antioxid Redox Signal*. (2014) **20**:1410–22. doi: 10.1089/ars.2012.5134
50. Duman JG, Dinh J, Zhou W, Cham H, Mavratsas VC, Paveškovic M, et al. Memantine prevents acute radiation-induced toxicities at hippocampal excitatory synapses. *Neuro Oncol*. (2018) **20**:655–65. doi: 10.1093/neuonc/nox203
51. Monje ML, Vogel H, Masek M, Ligon KL, Fisher PG, Palmer TD. Impaired human hippocampal neurogenesis after treatment for central nervous system malignancies. *Ann Neurol*. (2007) **62**:515–20. doi: 10.1002/ana.21214
52. Menzel F, Kaiser N, Haehnel S, Rapp F, Patties I, Schöneberg N, et al. Impact of X-irradiation on microglia. *Glia*. (2018) **66**:15–33. doi: 10.1002/glia.23239
53. Merz F, Gaunitz F, Dehghani F, Renner C, Meixensberger J, Gutenberg A, et al. Organotypic slice cultures of human glioblastoma reveal different susceptibilities to treatments. *Neuro Oncol*. (2013) **15**:670–81. doi: 10.1093/neuonc/not003
54. Hanbury DB, Peiffer AM, Dugan G, Andrews RN, Cline JM. Long-term cognitive functioning in single-dose total-body gamma-irradiated rhesus monkeys (Macaca mulatta). *Radiat Res*. (2016) **186**:447–54. doi: 10.1667/RR14430.1
55. Raber J, Rola R, LeFevour A, Morhardt D, Curley J, Mizumatsu S, et al. Radiation-induced cognitive impairments are associated with changes in indicators of hippocampal neurogenesis. *Radiat Res*. (2004) **162**:39–47. doi: 10.1667/RR3206
56. Monje ML, Mizumatsu S, Fike JR, Palmer TD. Irradiation induces neural precursor-cell dysfunction. *Nat Med*. (2002) **8**:955–62. doi: 10.1038/nm749
57. Mizumatsu S, Monje ML, Morhardt DR, Rola R, Palmer TD, Fike JR. Extreme sensitivity of adult neurogenesis to low doses of X-irradiation. *Cancer Res*. (2003) **63**:4021–7.
58. Hellström NAK, Björk-Eriksson T, Blomgren K, Kuhn HG. Differential recovery of neural stem cells in the subventricular zone and dentate gyrus after ionizing radiation. *Stem Cells*. (2009) **27**:634–41. doi: 10.1634/stemcells.2008-0732
59. Panagiotakos G, Alshamy G, Chan B, Abrams R, Greenberg E, Saxena A, et al. Long-term impact of radiation on the stem cell and oligodendrocyte precursors in the brain. *PLoS ONE*. (2007) **2**:e588. doi: 10.1371/journal.pone.0000588
60. Britten RA, Davis LK, Johnson AM, Keeney S, Siegel A, Sanford LD, et al. Low (20 cGy) doses of 1 GeV/u (56)Fe—particle radiation lead to a persistent reduction in the spatial learning ability of rats. *Radiat Res*. (2012) **177**:146–51. doi: 10.1667/rr2637.1
61. Shukitt-Hale B, Casadesus G, McEwen JJ, Rabin BM, Joseph JA. Spatial learning and memory deficits induced by exposure to iron-56-particle radiation. *Radiat Res*. (2000) **154**:28–33. doi: 10.1667/0033-7587(2000)154[0028:slamdi]2.0.co;2
62. Denisova NA, Shukitt-Hale B, Rabin BM, Joseph JA. Brain signaling and behavioral responses induced by exposure to 56 Fe-particle radiation. *Radiat Res*. (2002) **158**:725–34. doi: 10.1667/0033-7587(2002)158[0725:BSABRI]2.0.CO;2
63. Rola R, Fishman K, Baure J, Rosi S, Lamborn KR, Obenaus A, et al. Hippocampal neurogenesis and neuroinflammation after cranial irradiation with (56)Fe particles. *Radiat Res*. (2008) **169**:626–32. doi: 10.1667/RR1263.1
64. Lonart G, Parris B, Johnson AM, Miles S, Sanford LD, Singletary SJ, Britten RA. Executive function in rats is impaired by low (20 cGy) doses of 1 GeV/u (56)Fe particles. *Radiat Res*. (2012) **178**:289–94. doi: 10.1667/RR2862.1
65. Haley GE, Yeiser L, Olsen RHJ, Davis MJ, Johnson LA, Raber J. Early effects of whole-body (56)Fe irradiation on hippocampal function in C57BL/6J mice. *Radiat Res*. (2013) **179**:590–6. doi: 10.1667/RR2946.1
66. Sweet TB, Panda N, Hein AM, Das SL, Hurley SD, Olschowka JA, et al. Central nervous system effects of whole-body proton irradiation. *Radiat Res*. (2014) **182**:18–34. doi: 10.1667/RR13699.1
67. Parihar VK, Pasha J, Tran KK, Craver BM, Acharya MM, Limoli CL. Persistent changes in neuronal structure and synaptic plasticity caused by proton irradiation. *Brain Struct Funct*. (2015) **220**:1161–71. doi: 10.1007/s00429-014-0709-9
68. Seegenschmiedt MH, Micke O, Muecke R. Radiotherapy for non-malignant disorders: state of the art and update of the evidence-based practice guidelines. *Br J Radiol*. (2015) **88**:20150080. doi: 10.1259/bjr.20150080
69. Reinhold HS, Calvo W, Hopewell JW, van den Berg AP. Development of blood vessel-related radiation damage in the fimbria of the central nervous system. *Int J Radiat Oncol Biol Phys*. (1990) **18**:37–42. doi: 10.1016/0360-3016(90)90264-K
70. Valk PE, Dillon WP. Radiation injury of the brain. *Am J Neuroradiol*. (1991) **12**:45
71. Jensen JB, Parmar M. Strengths and limitations of the neurosphere culture system. *Mol Neurobiol*. (2006) **34**:153–62. doi: 10.1385/MN:34:3:153
72. Qi X-R, Verwer RWH, Bao A-M, Balesar RA, Luchetti S, Zhou J-N, Swaab DF. Human brain slice culture: a useful tool to study brain

disorders and potential therapeutic compounds. *Neurosci Bull*. (2019) **35**:244–52. doi: 10.1007/s12264-018-0328-1
73. Verwer RWH, Hermens WTJMC, Dijkhuizen P, ter Brake O, Baker RE, Salehi A, et al. Cells in human postmortem brain tissue slices remain alive for several weeks in culture. *FASEB J*. (2002) **16**:54–60. doi: 10.1096/fj.01-0504com
74. Lui JH, Hansen DV, Kriegstein AR. Development and evolution of the human neocortex. *Cell*. (2011) **146**:18–36. doi: 10.1016/j.cell.2011.06.030
75. Fish JL, Dehay C, Kennedy H, Huttner WB. Making bigger brains-the evolution of neural-progenitor-cell division. *J Cell Sci*. (2008) **121**:2783–93. doi: 10.1242/jcs.023465
76. Wang X, Tsai J-W, LaMonica B, Kriegstein AR. A new subtype of progenitor cell in the mouse embryonic neocortex. *Nat Neurosci*. (2011) **14**:555–61. doi: 10.1038/nn.2807
77. Di Lullo E, Kriegstein AR. The use of brain organoids to investigate neural development and disease. *Nat Rev Neurosci*. (2017) **18**:573–84. doi: 10.1038/nrn.2017.107
78. Wang H. Modeling Neurological Diseases With Human Brain Organoids. *Front Synaptic Neurosci*. (2018) **10**:15. doi: 10.3389/fnsyn.2018.00015
79. Lancaster MA, Knoblich JA. Generation of cerebral organoids from human pluripotent stem cells. *Nat Protoc*. (2014) **9**:2329–40. doi: 10.1038/nprot.2014.158
80. Sakaguchi H, Kadoshima T, Soen M, Narii N, Ishida Y, Ohgushi M, et al. Generation of functional hippocampal neurons from self-organizing human embryonic stem cell-derived dorsomedial telencephalic tissue. *Nat Commun*. (2015) **6**:8896. doi: 10.1038/ncomms9896
81. Kadoshima T, Sakaguchi H, Nakano T, Soen M, Ando S, Eiraku M, Sasai Y. Self-organization of axial polarity, inside-out layer pattern, and species-specific progenitor dynamics in human ES cell-derived neocortex. *Proc Natl Acad Sci USA*. (2013) **110**:20284–9. doi: 10.1073/pnas.1315710110
82. Jo J, Xiao Y, Sun AX, Cukuroglu E, Tran H-D, Göke J, et al. Midbrain-like organoids from human pluripotent stem cells contain functional dopaminergic and neuromelanin-producing neurons. *Cell Stem Cell*. (2016) **19**:248–57. doi: 10.1016/j.stem.2016.07.005
83. Monzel AS, Smits LM, Hemmer K, Hachi S, Moreno EL, van Wuellen T, et al. Derivation of human midbrain-specific organoids from neuroepithelial stem cells. *Stem Cell Reports*. (2017) **8**:1144–54. doi: 10.1016/j.stemcr.2017.03.010
84. Qian X, Nguyen HN, Song MM, Hadiono C, Ogden SC, Hammack C, et al. Brain-region-specific organoids using mini-bioreactors for modeling ZIKV exposure. *Cell*. (2016) **165**:1238–54. doi: 10.1016/j.cell.2016.04.032
85. Muguruma K, Nishiyama A, Kawakami H, Hashimoto K, Sasai Y. Self-organization of polarized cerebellar tissue in 3D culture of human pluripotent stem cells. *Cell Rep*. (2015) **10**:537–50. doi: 10.1016/j.celrep.2014.12.051
86. Suga H, Kadoshima T, Minaguchi M, Ohgushi M, Soen M, Nakano T, et al. Self-formation of functional adenohypophysis in three-dimensional culture. *Nature*. (2011) **480**:57–62. doi: 10.1038/nature10637
87. Paşca AM, Sloan SA, Clarke LE, Tian Y, Makinson CD, Huber N, et al. Functional cortical neurons and astrocytes from human pluripotent stem cells in 3D culture. *Nat Methods*. (2015) **12**:671–8. doi: 10.1038/nmeth.3415
88. Quadrato G, Nguyen T, Macosko EZ, Sherwood JL, Min Yang S, Berger DR, et al. Cell diversity and network dynamics in photosensitive human brain organoids. *Nature*. (2017) **545**:48–53. doi: 10.1038/nature22047
89. Sakaguchi H, Ozaki Y, Ashida T, Matsubara T, Oishi N, Kihara S, Takahashi J. Self-organized synchronous calcium transients in a cultured human neural network derived from cerebral organoids. *Stem Cell Rep*. (2019) **13**:458–73. doi: 10.1016/j.stemcr.2019.05.029
90. Bagley JA, Reumann D, Bian S, Lévi-Strauss J, Knoblich JA. Fused cerebral organoids model interactions between brain regions. *Nat Methods*. (2017) **14**:743–51. doi: 10.1038/nmeth.4304
91. Birey F, Andersen J, Makinson CD, Islam S, Wei W, Huber N, et al. Assembly of functionally integrated human forebrain spheroids. *Nature*. (2017) **545**:54–9. doi: 10.1038/nature22330
92. Song L, Yuan X, Jones Z, Griffin K, Zhou Y, Ma T, Li Y. Assembly of human stem cell-derived cortical spheroids and vascular spheroids to model 3-D brain-like tissues. *Sci Rep*. (2019) **9**:5977. doi: 10.1038/s41598-019-42439-9
93. Xiang Y, Tanaka Y, Patterson B, Kang Y-J, Govindaiah G, Roselaar N, et al. Fusion of regionally specified hPSC-derived organoids models human brain development and interneuron migration. *Cell Stem Cell*. (2017) **21**:383–98.e7. doi: 10.1016/j.stem.2017.07.007
94. Lin Y-T, Seo J, Gao F, Feldman HM, Wen H-L, Penney J, et al. APOE4 Causes widespread molecular and cellular alterations associated with Alzheimer's disease phenotypes in human iPSC-derived brain cell types. *Neuron*. (2018) **98**:1141–54.e7. doi: 10.1016/j.neuron.2018.05.008
95. Ormel PR, Vieira de Sá R, van Bodegraven EJ, Karst H, Harschnitz O, Sneeboer MAM, et al. Microglia innately develop within cerebral organoids. *Nat Commun*. (2018) **9**:4167. doi: 10.1038/s41467-018-06684-2
96. Bian S, Repic M, Guo Z, Kavirayani A, Burkard T, Bagley JA, et al. Genetically engineered cerebral organoids model brain tumor formation. *Nat Methods*. (2018) **15**:631–9. doi: 10.1038/s41592-018-0070-7
97. Mattei C, Alshawaf A, D'Abaco G, Nayagam B, Dottori M. Generation of neural organoids from human embryonic stem cells using the rotary cell culture system: effects of microgravity on neural progenitor cell fate. *Stem Cells Dev*. (2018) **27**:848–57. doi: 10.1089/scd.2018.0012
98. Giandomenico SL, Mierau SB, Gibbons GM, Wenger LMD, Masullo L, Sit T, et al. Cerebral organoids at the air-liquid interface generate diverse nerve tracts with functional output. *Nat Neurosci*. (2019) **22**:669–79. doi: 10.1038/s41593-019-0350-2
99. Marton RM, Miura Y, Sloan SA, Li Q, Revah O, Levy RJ, et al. Differentiation and maturation of oligodendrocytes in human three-dimensional neural cultures. *Nat Neurosci*. (2019) **22**:484–91. doi: 10.1038/s41593-018-0316-9
100. Lancaster MA, Corsini NS, Wolfinger S, Gustafson EH, Phillips AW, Burkard TR, et al. Guided self-organization and cortical plate formation in human brain organoids. *Nat Biotechnol*. (2017) **35**:659–66. doi: 10.1038/nbt.3906
101. Durante M, Golubev A, Park W-Y, Trautmann C. Applied nuclear physics at the new high-energy particle accelerator facilities. *Phys Rep*. (2019) **800**:1–37. doi: 10.1016/j.physrep.2019.01.004
102. NCRP. *Information Needed to Make Radiation Protection Recommendations for Space Missions Beyond Low-Earth Orbit: Recommendations of the National Council on Radiation Protection and Measurements*. Bethesda, MD: National Council on Radiation Protection and Measurements (2006).
103. Durante M, Bräuer-Krisch E, Hill M. Faster and safer? FLASH ultra-high dose rate in radiotherapy. *Br J Radiol*. (2018) **91**:20170628. doi: 10.1259/bjr.20170628
104. Bourhis J, Sozzi WJ, Jorge PG, Gaide O, Bailat C, Duclos F, et al. Treatment of a first patient with FLASH-radiotherapy. *Radiother Oncol*. (2019) **139**:18–22. doi: 10.1016/j.radonc.2019.06.019
105. Montay-Gruel P, Petersson K, Jaccard M, Boivin G, Germond J-F, Petit B, et al. Irradiation in a flash: Unique sparing of memory in mice after whole brain irradiation with dose rates above 100Gy/s. *Radiother Oncol*. (2017) **124**:365–9. doi: 10.1016/j.radonc.2017.05.003
106. Wilson JD, Hammond EM, Higgins GS, Petersson K. Ultra-high dose rate (FLASH) radiotherapy: silver bullet or fool's gold? *Front Oncol*. (2019) **9**:1563. doi: 10.3389/fonc.2019.01563
107. Tessonnier T, Mairani A, Chen W, Sala P, Cerutti F, Ferrari A, et al. Proton and helium ion radiotherapy for meningioma tumors: a Monte Carlo-based treatment planning comparison. *Radiat Oncol*. (2018) **13**:2. doi: 10.1186/s13014-017-0944-3
108. Knäusl B, Fuchs H, Dieckmann K, Georg D. Can particle beam therapy be improved using helium ions? A planning study focusing on pediatric patients. *Acta Oncol*. (2016) **55**:751–9. doi: 10.3109/0284186X.2015.1125016
109. Mohiuddin M, Fujita M, Regine WF, Megooni AS, Ibbott GS, Ahmed MM. High-dose spatially-fractionated radiation (GRID): a new paradigm in the management of advanced cancers. *Int J Radiat Oncol Biol Phys*. (1999) **45**:721–7. doi: 10.1016/S0360-3016(99)00170-4
110. Slatkin DN, Spanne P, Dilmanian FA, Gebbers JO, Laissue JA. Subacute neuropathological effects of microplanar beams of x-rays from a synchrotron wiggler. *Proc Natl Acad Sci USA*. (1995) **92**:8783–7. doi: 10.1073/pnas.92.19.8783
111. Dilmanian FA, Zhong Z, Bacarian T, Benveniste H, Romanelli P, Wang R, et al. Interlaced x-ray microplanar beams: a radiosurgery approach with clinical potential. *Proc Natl Acad Sci USA*. (2006) **103**:9709–14. doi: 10.1073/pnas.0603567103

112. Meyer J, Eley J, Schmid TE, Combs SE, Dendale R, Prezado Y. Spatially fractionated proton minibeams. *Br J Radiol*. (2019) **92**:20180466. doi: 10.1259/bjr.20180466
113. Prezado Y, Jouvion G, Hardy D, Patriarca A, Nauraye C, Bergs J, et al. Proton minibeam radiation therapy spares normal rat brain: long-term clinical, radiological and histopathological analysis. *Sci Rep*. (2017) **7**:14403. doi: 10.1038/s41598-017-14786-y
114. Henry T, Ureba A, Valdman A, Siegbahn A. Proton grid therapy. *Technol Cancer Res Treat*. (2017) **16**:749–57. doi: 10.1177/1533034616681670
115. Lansonneur P, Mammar H, Nauraye C, Patriarca A, Hierso E, Dendale R, et al. First proton minibeam radiation therapy treatment plan evaluation. *Sci Rep*. (2020) **10**:7025. doi: 10.1038/s41598-020-63975-9
116. Schneider T, Marzi L de, Patriarca A, Prezado Y. Advancing proton minibeam radiation therapy: magnetically focussed proton minibeams at a clinical centre. *Sci Rep*. (2020) **10**:1384. doi: 10.1038/s41598-020-58052-0

Conflict of Interest: The authors declare that the research was conducted in the absence of any commercial or financial relationships that could be construed as a potential conflict of interest.

frontiers in Physics

ORIGINAL RESEARCH
published: 30 September 2020
doi: 10.3389/fphy.2020.568124

Immunological Changes During Space Travel: A Ground-Based Evaluation of the Impact of Neutron Dose Rate on Plasma Cytokine Levels in Human Whole Blood Cultures

Randall Fisher[1], Bjorn Baselet[2], Randy Vermeesen[2], Marjan Moreels[2], Sarah Baatout[2], Farzana Rahiman[3], Xanthene Miles[1], Shankari Nair[1], Peter du Plessis[1], Monique Engelbrecht[1,4], Roya J. Ndimba[1], Julie Bolcaen[1], Jaime Nieto-Camero[1], Evan de Kock[1] and Charlot Vandevoorde[1]*

[1] Radiation Biophysics Division, iThemba LABS (Laboratory for Accelerator Based Sciences), Nuclear Medicine Department, National Research Foundation, Cape Town, South Africa, [2] Radiobiology Unit, Institute for Environment, Health and Safety, Belgian Nuclear Research Center, SCK CEN (Studiecentrum voor Kernenergie Centre d'Étude de l'énergie Nucléaire), Mol, Belgium, [3] BioSkin Lab, Department of Medical Biosciences, Faculty of Natural Sciences, University of the Western Cape, Cape Town, South Africa, [4] Department of Medical Biosciences, Faculty of Natural Sciences, University of the Western Cape, Cape Town, South Africa

OPEN ACCESS

Edited by:
Marco Durante, Gesellschaft für Schwerionenforschung (GSI) Helmholtz Center for Heavy Ion Research, Germany

Reviewed by:
Alexander Helm, Gesellschaft für Schwerionenforschung (GSI) Helmholtz Center for Heavy Ion Research, Germany
Dörthe Schaue, UCLA David Geffen School of Medicine, United States
Lynnette H. Cary, Uniformed Services University of the Health Sciences, United States

***Correspondence:**
Randall Fisher
rfisher@tlabs.ac.za

Specialty section:
This article was submitted to Medical Physics and Imaging, a section of the journal Frontiers in Physics

Received: 31 May 2020
Accepted: 13 August 2020
Published: 30 September 2020

Citation:
Fisher R, Baselet B, Vermeesen R, Moreels M, Baatout S, Rahiman F, Miles X, Nair S, du Plessis P, Engelbrecht M, Ndimba RJ, Bolcaen J, Nieto-Camero J, de Kock E and Vandevoorde C (2020) Immunological Changes During Space Travel: A Ground-Based Evaluation of the Impact of Neutron Dose Rate on Plasma Cytokine Levels in Human Whole Blood Cultures. Front. Phys. 8:568124. doi: 10.3389/fphy.2020.568124

A better understanding of the combined impact of different space stressors on human health is urgently warranted, considering the upcoming long-duration missions beyond lower Earth orbit. Therefore, a growing number of particle accelerator facilities implement ground-based set-ups to study the effect of simulated space radiation with simulated psychological or physical stressors. The immune system is highly sensitive to these types of stressors and limited information is currently available on the impact of the complex space radiation environment on the astronauts' immune function. This pilot study presents a first step in the implementation of a ground-based set-up with neutron irradiation, which is considered to be an important secondary component in space radiation fields. The effect of dose rate on immune alterations was studied using the *in vitro* cytokine release assay. Whole blood samples ($n = 8$) were exposed to 0.125 or 1 Gy of neutron irradiation (fluence-weighted average energy: 29.8 MeV) at a lower dose rate (LDR) of 0.015 Gy/min and a higher dose rate (HDR) of 0.400 Gy/min. Immediately post-irradiation, blood samples were stimulated with lipopolysaccharide (LPS), heat-killed *Listeria monocytogenes* (HKLM) or lectin pokeweed mitogen (PWM), and incubated for 24 h. Cell-mediated immunity was examined by analysing interleukin-2 (IL-2), interferon-gamma (IFN-γ), tumour necrosis factor-alpha (TNF-α), and interleukin-10 (IL-10) plasma levels. Stimulants significantly increased all cytokine levels except IL-2, where only PWM induced a significant increase. In general, no statistically significant changes were observed in IL-2, IFN-γ, and TNF-α concentrations at different neutron doses and dose rates when compared to their stimulated, sham-irradiated controls. After PWM-stimulation, IL-10 levels were significantly increased at 0.125 Gy HDR and 1 Gy LDR. In a pooled

analysis, the HDR significantly increased IL-2 titres (under PWM-stimulation) and IFN-γ titres (with all stimulants), but significantly decreased TNF-α secretion in unstimulated cultures. Due to the limited sample number, no strong conclusions could be made in this pilot study on the effect of neutron radiation as a single stressor on cytokine secretion in response to different stimuli. However, some interesting trends and dose rate effects were observed, which pave the way for future investigations on the synergistic effects of multiple space stressors on immune cell function.

Keywords: radiation in space, immune system, space radiobiology, terrestrial analog, cytokine release assay *in vitro*, dose rate effect, astronaut health, neutron radiation

INTRODUCTION

Space travel comprises a unique and complex stress model composed of both physical (cosmic radiation and microgravity) and psychological stress factors, known to induce a large variety of systemic physiological effects that are proven to be detrimental to astronaut's health [1–3]. Of the observed outcomes, a dysfunctional immune system remains a major concern for future manned exploration beyond lower Earth orbit (LEO) or to Mars [4]. Recent studies confirm that immunological changes are an in-flight phenomenon, observed throughout short-duration Space Shuttle missions or a long-duration stay on the International Space Station (ISS) [5–8]. During interplanetary missions, crewmembers will spend an unprecedented amount of time in space, where the synergy of the elevated radiation exposure coupled with persisting immune alterations could potentially increase the cancer incidence, jeopardising astronaut's health and mission success [7, 9–12]. For this reason, the potential impact of space radiation on the dysregulation of normal immune function will be the focus of this pilot study [13, 14].

The innate and adaptive immunity form the pillars of the human immune system and work on both the humoral and cell-mediated level. Humoral immunity has been less extensively studied in astronauts leading to rather inconsistent results [15, 16], while the impairment of cell-mediated immunity has been confirmed during and after spaceflights [4]. NASA's analysis of cell-mediated immunity in the Twin Study, revealed that 50 of the 62 studied cytokines were differentially abundant pre-, in-, and post-flight, between the spaceflight and ground-based subject [8]. Cytokines are produced by virtually all innate and adaptive immune cells, but especially by T-helper (Th) lymphocytes. The measurement of plasma cytokine concentrations in the mitogen-stimulated blood of astronauts has been used to monitor immune function and specific alterations in lymphocyte subpopulations [17]. A cells inability to produce specific cytokines is indicative of a potentially significant immune alteration that could reduce immune defences during spaceflight [18]. Important for effective cell-mediated immunity are the pro-inflammatory interleukin-2 (IL-2), interferon gamma (IFN-γ), and tumour necrosis factor alpha (TNF-α) cytokines, and the anti-inflammatory cytokine interleukin-10 (IL-10). However, these cytokines are not easily classed since they could be capable of inducing both pro-and-anti-inflammatory effects [19].

Mechanisms that produce immune system dysregulation during spaceflight have not been clearly identified, mainly due to the high costs of spaceflight experiments, the scarcity of missions and experimental variations between flights [20]. Terrestrial spaceflight analogues are a more accessible alternative to study spaceflight-related health effects, their causative factors and to test potential countermeasures [21]. For example, several ground-based studies could clearly demonstrate the dramatic impact of microgravity on the immune system [21–28]. However, during space travel, radiation and psychological stress factors (e.g., isolation, sleep deprivation, and heavy workload) may have a significant synergistic or antagonistic effect on human immunity [29, 30]. Here, terrestrial analogues offer not only financial and repeatability advantages but also the opportunity to determine the relative contribution of the individual space stressors to the observed health effect by simulating them both individually and in combination.

Space radiation has been recognized as a major health risk for astronauts as current estimates suggest a round-trip to Mars would result in >0.6 Sv or 60% of an astronaut's career dose [31, 32]. However, uncertainties on the existing biological data limit the risk assessments for manned, deep space mission [33]. To improve the current radiation risk estimation models, a growing number of particle accelerator facilities configure ground-based analogues for biology experiments [34, 35]. The iThemba Laboratory for Accelerator Based Sciences (LABS) is such a particle accelerator facility in South Africa, with a rather unique, well-characterized quasi-monoenergetic neutron beam line, covering an energy range from 30 up to 200 MeV for metrology purposes, with great potential for space radiobiology studies [36]. The space radiation environment is a complex mixture of particles of galactic (galactic cosmic rays or GCR) and solar (solar particle events or SPEs) origin, as well as their secondaries (such as neutrons), that are produced by interactions with the spacecraft materials and astronaut's bodies. Secondary neutrons may cover a complete energy range from thermal neutrons (0.5–1 MeV) up to several GeV and are considered to be highly carcinogenic and far more effective to induce biological damage than low linear energy transfer (LET) radiation [37–40]. Unique patterns of DNA damage, gene expression, repair proteins mobilization, cytokine activation, and cellular microenvironment remodelling are observed following exposure to high-LET radiation.

Particle accelerators are the only facilities where the health risks of high energy neutrons (>20 MeV) can be studied [41]. Therefore, limited information is currently available on the impact of higher energy neutron irradiation on human health, which has been identified as a particular concern for civil aviation [42–44]. During long-term manned missions, both the magnitude and duration of space radiation exposure will increase, subjecting the flight crew to chronic, low doses and low dose rates of secondary neutrons, for which there is limited biological data pertaining to the immune impact. Recently, there has been a growing interest to study the interaction between high-LET radiation and human immunity, to explore the combined use of particle therapy and immunotherapy in cancer treatments [45, 46]. However, the exposure conditions in space and particle therapy are quite different. During particle therapy, an acute, high and localized radiation dose will be delivered to the tumour. In contrast, the space radiation environment is characterised by a chronic, low dose and dose rate of high-LET particles that impact the astronauts whole body and could adversely affect their immune system [10].

New insights and radiobiology data on high-LET radiation effects at low dose rates will improve current risk projections for space exploration and hopefully aid in the development and evaluation of possible countermeasures [47]. With this goal, the "Optimization and validation of a unique ground-based *in vitro* model to study space health effects" (INVEST) project was launched, which aims to implement a ground-based *in vitro* model to study space health effects at iThemba LABS, with a specific emphasis on neutrons at low doses and low dose rates. The focus of this first pilot study was to optimize the *in vitro* cytokine-release assay in collaboration with the project partner SCK CEN, to investigate the impact of low dose rate neutrons on cell-mediated immunity. For this pilot experiment, the clinical fast neutron therapy beam line was used to irradiate whole blood samples of healthy adult volunteers, at a lower dose rate (LDR) or a higher (or normal clinical) dose rate (HDR).

Recall antigens and mitogens were used in this study to assess the impact of neutron irradiation on the cytokine production capacity of activated lymphocytes. A previous study observed no increase in any adaptive immunity cytokines in astronauts 6 months aboard the ISS, suggesting that the astronauts were simply free from infectious diseases while in flight [48]. A potential alternative explanation for this observation is the diminished T lymphocyte function and reduced activation in astronauts due to the spaceflight, which will hinder their cytokine response [49]. Here, the lymphocytes were intentionally stimulated *ex vivo* to mimic a challenged immune scenario, to monitor the disruptive effect of neutron dose and dose rate on the cytokine release profile. This method has been extensively used to study immune system dysregulation in several *ex vivo* studies related to short and long duration spaceflights and in terrestrial analogues [13, 29, 50, 51].

MATERIALS AND METHODS

Sample Collection

Ethical approval was obtained from the South African Human Sciences Research Council (protocol number REC 3/23/10/19) in accordance with the 1975 Declaration of Helsinki, as revised in 2000. Participants were recruited via an institution-wide email addressed to iThemba LABS employees, in Cape Town, South Africa. Written, informed consent was obtained from non-smoking, non-medicating, male volunteers with no diagnosed history of chronic illness ($n = 8$; age range: 22–63 years). Due to the known variability in cytokine response between individual subjects and the small sample size of this pilot study, the study was restricted to male adult volunteers to limit the potential influence of gender on the circulating cytokines levels in baseline samples [52]. Peripheral blood samples were collected into heparin-treated vacutainers (Becton Dickinson Company, New Jersey, USA) and stored at room temperature before irradiation.

In vitro Irradiation

Whole blood samples were retained at room temperature for ∼24 h before being exposed to a clinical fast neutron beam generated by bombarding 66 MeV protons on a Beryllium target ($p + 9\text{Be} \rightarrow n + 9\text{B}$-1.85 MeV, plus several breakup reactions) [53] in sterile 2.0 mL cryogenic vials (NEST Biotechnology Co., Ltd., Wuxi, China). A hydrogenous filter reduced the contribution of thermal and epithermal neutrons. This results in a neutron spectrum with a fluence-weighted average energy of ∼29.8 MeV for the 290 mm × 290 mm field that was used for the irradiations [53]. The source-to-phantom surface distance was 1,500 mm and irradiations were carried out at a gantry angle of 270°, resulting in a horizontal beam directed on the water tank containing the blood samples at 37°C. Two radiation doses of 0.125 or 1 Gy were administered at two different dose rates: a lower dose rate (LDR) of 0.015 Gy/min and a higher dose rate (HDR) of 0.400 Gy/min. Sham-irradiated samples were retained in the control room, receiving only ambient radiation. The output factor (1.097 Gy/Monitor Unit) was measured with an Exradin T2 thimble ionization chamber placed at the same position as the blood samples (at a depth of 52 mm in the water tank). The wall of this chamber is made from A-150 tissue-equivalent (TE) plastic and the 0.53 cm^3 active chamber volume was filled with a propane-based TE gas. Calibrations were performed according to the neutron dosimetry protocol of the ICRU Report 45 [54].

Whole Blood Immune Cell Stimulation

The *in vitro* cytokine release assay is a modified version of the methods described by Feuerecker et al. [51] and Van Walleghem et al. [22]. Post-exposure, irradiated whole blood was distributed equally amongst culture tubes and diluted 1 to 1 in 750 µl Roswell Park Memorial Institute (RPMI) medium (Gibco, Massachusetts, USA), supplemented with 10% foetal calf serum (Lonza, Basel, Switzerland), 1% penicillin and streptomycin (Lonza), with-or-without an immune cell stimulant, in sterile 2.0 ml cryovials. Pokeweed mitogen (PWM) (Sigma-Aldrich, Missouri, USA), heat-killed *Listeria monocytogenes* (HKLM) (InvivoGen, Toulouse, France), or lipopolysaccharide (LPS) (Sigma-Aldrich) were used as immune stimulants at final concentrations of 0.5, 5, and 5 µg/ml, respectively, as previously optimized [21]. Unstimulated samples were included to provide a baseline control condition for every stimulated sample and to confirm that the stimulation achieved the desired effect.

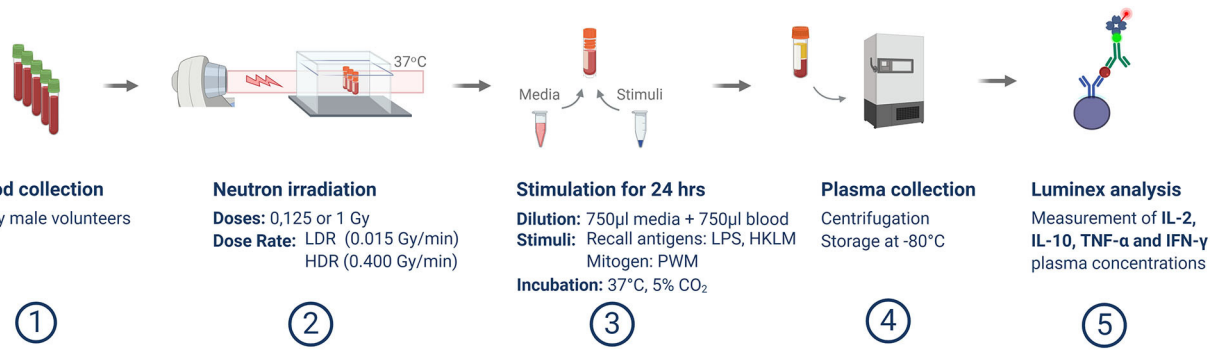

FIGURE 1 | Overview of experimental methodology. This schematic template illustrates the study process from blood sample collection, irradiation and stimulation, up to Luminex analysis.

Post-irradiation and stimulation (or sham-irradiation and no stimulation, in the case of controls), whole blood cultures were maintained at 37°C for 24 h and the plasma was separated by 1,500 g centrifugation for 15 min before the supernatant was transferred to cryovials and stored at −80°C. The complete experiment is outlined in **Figure 1**.

Luminex Measurement of Cytokine Concentrations

For this pilot study, four key cell-mediated immunity cytokines, IFN-γ, IL-10, IL-2, and TNF-α were quantified down to their respective assay limits of 0.4, 1.6, 1.8, and 1.2 pg/ml. The R&D systems (Minnesota, USA) Luminex assay was conducted exactly to the manufacturer's instructions as described elsewhere [29] with two exceptions: only four cytokines were analysed here and the Luminex assays were performed on a MAGPIX® system (Luminex Corp., Texas, USA). A further 1 to 1 dilution of the plasma in assay diluent was performed to render analyte concentrations within the assay's linear range.

Data Analysis

Statistics

Statistical analysis was conducted using IBM SPSS Statistics 19 (New York, USA) while figures were plotted using GraphPad Prism version 8.0 (California, USA). Cytokine data was presented as grouped subject data with means and standard error of the mean (SEM). In cases where the cytokine concentration could not be confidently extrapolated from the standard curve, the MAGPIX® system reported an "out of range" value. In these instances, the assay's minimum detection limit value was substituted for the "out of range" samples to enable statistical analysis. To ensure normal distribution, data was $\log_{10}$-transformed and verified by a Shapiro Wilk test (data not shown). A repeated measures one-way ANOVA was used to identify significant relationships between the unstimulated and stimulated, irradiated and sham-irradiated samples as well as the relationships between HDR and LDR irradiated samples. An overall dose effect was determined using repeated measures one-way ANOVA analysis on the pooled data of all irradiated samples (0, 0.125, or 1 Gy total dose) for each cytokine-stimulant pair. This elucidates the effect of a specific dose on cytokine secretion compared to the sham-irradiated control, disregarding the dose rate. Similarly, the dose rate effect was determined using the same analysis on the pooled dose rate results within each cytokine-stimulant pair, regardless of the administered radiation dose. Relationships were deemed significant when $P < 0.05$.

Effect Size Calculations

Due to the small sample size of this study and the resulting low power to test statistical significance, effect size (ES) values were calculated to determine the size by which the experimental group varies from the control groups, expressed as the number of standard deviations. A negative ES value specifies that the experimental group mean is "x" amount of standard deviations below the control mean, while a positive value indicates the contrary. The ES assists in describing trends and relationships between groups and is defined by the formula:

$$\mathrm{ES} = \frac{(\textit{experimental mean} - \textit{control mean})}{\textit{control standard deviation}}$$

In the present study, the ES was calculated to identify the effect of various neutron doses in reference to the sham-irradiated control. However, in order to determine the effect of neutron dose rate, the lower, 0.015 Gy/min dose rate was compared to the standard higher, 0.400 Gy/min dose rate, so the HDR group is used as the "control" in the formula above.

RESULTS

Validation of the Cytokine Release Assay

Cytokines are soluble molecules which play a key role in innate and adaptive immune responses. To validate the *in vitro* cytokine release assay used for this pilot study, cytokine titres in the unstimulated (baseline) samples were compared to the stimulated samples. With a few exceptions, only minimal detectable cytokine concentrations were observed at baseline for all donors and the majority of the basal IL-2 and IFN-γ cytokine levels were even below the detection limit for most donors (**Figure 2**). Based on previous studies, it was expected that the different stimuli would up-regulate plasma cytokine

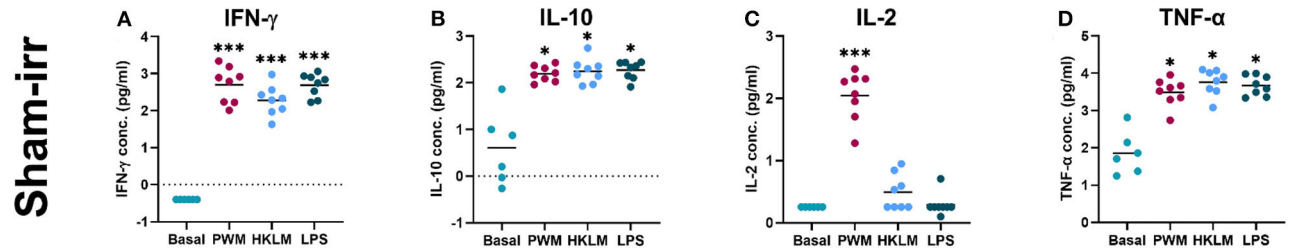

FIGURE 2 | Cytokine release assay validation—recall antigen and mitogen stimulation of whole blood samples. The graphs display the increase in $\log_{10}$-transformed, cytokine titres between the unstimulated (Basal) and the recall antigen- or mitogen-stimulated (PWM, HKLM, or LPS) samples. The dots represent the measurements of the individual participants and the horizontal lines denote means. The asterisks indicate various levels of significant difference (***$P < 0.001$ and *$P < 0.05$). **(A)** All three stimuli significantly increased IFN-γ secretion. **(B)** All three stimuli result in a significant increase of IL-10 secretion compared to the basal level. **(C)** Only PWM significantly increased IL-2 titres. **(D)** All three stimuli resulted in a significant increase in TNF-α levels.

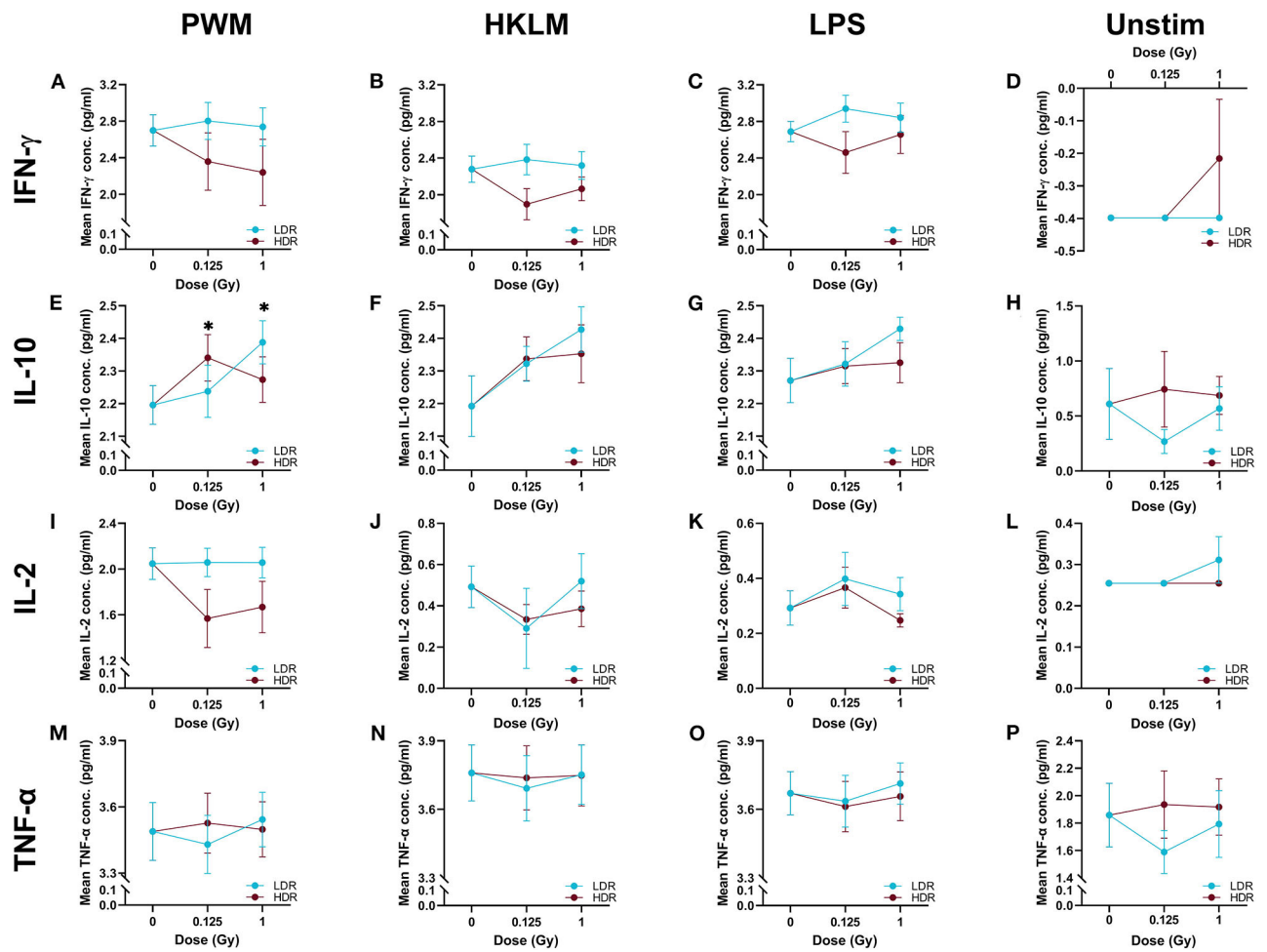

FIGURE 3 | The $\log_{10}$-transformed mean cytokine concentrations. The above figures display the mean IFN-γ, IL-10, IL-2, and TNF-α titres in the stimulated ($n = 8$) and unstimulated ($n = 6$), irradiated and sham-irradiated groups, with error bars indicating the SEM. When stimulated with PWM, 0.125 Gy neutrons given at the higher dose rate and 1 Gy given at the lower dose rate, significantly increase IL-10 secretion (*$P < 0.05$) when compared to the sham-irradiated control (Graph **E**). Graphs **(A)** to **(D)** and **(F)** to **(P)** display no significant relationships.

levels in whole blood cultures [55]. This was indeed observed for three of the four measured cytokines (IFN-γ, IL-10, and TNF-α), irrespective of the stimulant used for lymphocyte activation (**Figure 2**). IL-2 concentrations deviated from this trend. For some of the donors, the measured values were still below the assay detection limit of 1.8 pg/ml after 24 h of stimulation and out of the normal physiological range for healthy adults (9.4–15.9 pg/ml) [56]. Minor, non-significant increases in

IL-2 concentration were observed after 24-h stimulation with HKLM or LPS for 50 and 25% of the donors, respectively. PWM-stimulation on the contrary, induced a significant IL-2 increase for all donors compared to the basal levels ($P < 0.001$; **Figure 2C**).

Impact of Neutron Dose and Dose Rate on Cytokine Release

In most cases, neutron irradiation had no statistically significant impact on cytokine secretion in stimulated and unstimulated whole blood cultures, as depicted by the comparison of group means in **Figure 3**. Under PWM-stimulation however, exceptions to the norm were observed when the measured IL-10 concentration in the sham-irradiated cultures was compared to the concentration in either the 1 Gy LDR-treated group, or the 0.125 Gy HDR-treated group ($P < 0.05$; **Figure 3E**). The lack of statistical significance under the other stimulant or neutron treatment conditions might be attributable to the low participant numbers, resulting in a lack of statistical power to test the hypothesis. Nonetheless, some interesting but non-significant trends were observed, that allude to response patterns.

To independently monitor the effect of individual neutron doses and dose rates on cell-mediated immunity parameters, cytokine concentrations from various groups were pooled by disregarding either the dose rate (for dose comparisons) or the dose (for dose rate comparisons), within each stimulant and cytokine group. **Table 1** presents the observations from these pooled comparisons. Again, a significant increase was observed in IL-10 secretion in PWM-stimulated samples compared to the stimulated control group concentration, for both the low and higher neutron dose of 0.125 ($P < 0.05$) and 1 Gy ($P < 0.01$). Moreover, the pooled comparison between the LDR and HDR highlights significantly suppressed IFN-γ secretion after HDR exposure in all stimulated cultures ($P < 0.01$) and a significantly suppressed IL-2 secretion in PWM-stimulated cultures ($P < 0.05$; **Table 1**). A "native" response to HDR neutron treatment was observed by a significant increase in TNF-α in unstimulated cultures ($P < 0.01$; **Table 1**).

TABLE 1 | Summary of significant observations from pooled dose and dose rate comparison.

Dose comparison				
Cytokine	**Stimulant**	**Agent**	**Effect on titre vs. Ctrl**	***P*-Value**
IL-10	PWM	0.125Gy total dose	Increase	<0.05
IL-10	PWM	1Gy total dose	Increase	<0.01
Rate comparison				
Cytokine	**Stimulant**	**Agent**	**Effect on titre vs. LDR**	***P*-Value**
IFN-γ	PWM, HKLM or LPS	HDR	Decrease	<0.01
IL-2	PWM	HDR	Decrease	<0.05
TNF-α	None	HDR	Increase	<0.01

The term "Agent" refers to the factor identified as having the significant impact on the measured plasma cytokine titre. The "Effect on titre" present the trend in relation to the sham-irradiated control (in the case of dose comparison) and in relation to the alternative dose rate (in the dose rate comparison). The dose rate comparisons presented here indicate that, IFN-γ and IL-2 secretion in stimulated cultures were significantly lower in HDR-treated cultures, when compared to LDR-treated cultures.

Effect Size

Effect size (ES) calculations were an eloquent solution to highlight trends between normally distributed groups, in light of the limited sample size and the large intra-participant cytokine response variation (**Table 2**). To see the influence of the neutron radiation dose and dose rate on *in vitro* cytokine secretion, the data analysis strategy detailed in the Effect Size Calculations section, was employed.

Dose Effect Size

"Dose ES" calculations revealed a downregulation of IL-2 secretion compared to the unirradiated samples for most stimuli conditions, except for LPS, after both the 0.125 and 1 Gy dose, delivered at the HDR. This effect was most pronounced for PWM-stimulated cultures and it is advisable to only focus on the PWM results since IL-2 levels in LPS and HKLM stimulated cultures were below the detection limit in most cases (**Figure 2**).

There was a general increase in IL-10 concentration in all irradiated conditions compared to the unirradiated samples, regardless of the stimulant used. However, the LDR minimally suppressed IL-10 secretion in the unchallenged immune system at 0.125 Gy (**Figure 3H**).

Considering the IFN-γ ES data, the HDR seemed to have a more pronounced impact on the cytokine secretion levels at both 0.125 and 1 Gy, regardless of the stimulant employed (**Table 2**). The LDR-treated samples typically showed higher, slight increases in IFN-γ plasma levels at 0.125 and 1 Gy. Unfortunately, no ES could be identified for unstimulated (basal) samples since IFN-γ baseline values were below the detectable limit of the assay. Neutron treatment had minimal impact on the TNF-α concentrations except in the unstimulated groups where the 0.125 Gy LDR marginally reduced TNF-α secretion in comparison to the same HDR dose point.

Dose Rate Effect

While **Tables 1**, **2** mainly focus on the statistical significance of the observed effects and the size of the shifts in cytokine levels between the LDR and HDR, it is advisable to consult (**Figure 3**) which illustrates the potential decrease or increase of the observed trend. The "Dose rate ES" analysis indicates consistently higher IL-2 and IL-10 levels at the 1 Gy neutron dose in the LDR treatment arm compared to HDR arm for all stimuli. For IL-2, the combination of the LDR-0.125 Gy and PWM-stimulation resulted in higher cytokine levels compared to the HDR-0.125 Gy condition, while the opposite effect on IL-10 levels. The most reliable IL-2 conclusions can be drawn on the PWM stimulation, which suggest a dose rate effect, whereas the effects on IL-10 levels seem to be dose-specific

TABLE 2 | Effect size.

		Dose ES				Dose rate ES	
		LDR vs. 0 Gy		HDR vs. 0 Gy		LDR vs. HDR	
	Dose	0.125 Gy	1 Gy	0.125 Gy	1 Gy	0.125 Gy	1 Gy
IL-2	Basal	Undef	Undef	Undef	Undef	Undef	Undef
	PWM	0.029	0.027	−1.218	−0.964	0.667	0.613
	HKLM	−0.707	0.095	−0.554	−0.376	−0.214	0.503
	LPS	0.600	0.287	0.420	−0.255	0.151	1.410
IL-10	Basal	−0.432	−0.052	0.169	0.098	−0.541	−0.280
	PWM	0.250	1.144	0.861	0.463	−0.511	0.578
	HKLM	0.281	0.683	0.339	0.397	−0.080	0.296
	LPS	0.263	0.820	0.228	0.282	0.045	0.594
IFN-γ	Basal	Undef	Undef	Undef	Undef	Undef	Undef
	PWM	0.211	0.077	−0.701	−0.945	0.501	0.486
	HKLM	0.259	0.097	−0.945	−0.530	1.014	0.698
	LPS	0.800	0.487	−0.730	−0.101	0.743	0.315
TNF-α	Basal	−0.472	−0.114	0.136	0.104	−0.575	−0.248
	PWM	−0.158	0.147	0.103	0.025	−0.252	0.127
	HKLM	−0.193	−0.022	−0.062	−0.031	−0.115	0.009
	LPS	−0.131	0.159	−0.218	−0.051	0.075	0.186

*Effect sizes (ES) were calculated based on the log10-transformed cytokine concentrations the basal (n = 6) or stimulated (n = 8) samples exposed to neutron doses of 0, 0.125, and 1 Gy at either LDR 0.015 Gy/min or HDR 0.400 Gy/min dose rate. The "Dose ES" column illustrates the number of standard deviations by which the irradiated group mean deviates from the sham-irradiated group mean. The "Dose rate ES" column compares the effect of the LDR on cytokine secretion, using the HDR as the control group across two doses, 0.125 and 1 Gy. Red-shaded cells indicate an increase, while blue-shaded cells indicate the converse. The intensity of the cell's colour represents the magnitude of the effect, while the red-shaded cells indicate higher levels and blue-shaded cells the converse. "Undef" denotes instances where the standard deviation in the control group was zero, because basal cytokine levels were below the assay detection limit. This lack of standard deviation prevented effect size calculations. It is important to remember that the dose rate ES values reflect the number of standard deviations by which the LDR-group mean differs from the HDR-group mean. For example, the dose rate ES calculation for the IL-2 concentration in PWM-stimulated cultures indicates that, at the 1 Gy dose points (top right corner), the LDR cultures had higher IL-2 concentration than its HDR counterpart. This is also indicated by the red shade of this cell. Although, this does not indicate the relationship relative to the control population (that can be seen in **Figure 3**). In this respect, the Dose rate ES table is better understood when read in conjunction with **Figure 3**.*

with no conclusive dose rate effect. ES calculations confirmed the pooled statistical analysis of IFN-γ measurements as there was a clear trend in dose rate effect (**Table 2**), where the HDR exposures gave rise to a decrease in IFN-γ secretion for the three different stimuli at both neutron doses (**Figures 3A–C**) when compared to the LDR treatment group and the unirradiated control samples. Considering TNF-α dose rate ES data, the LDR seems to reduce cytokine secretion in the unchallenged immune system but the dose rate had marginal impact on the cytokine levels in stimulated cultures.

DISCUSSION

Although it is well-known that dysregulation of the immune function occurs and persists during spaceflight, the exact nature of the immunological changes and their specific cause has not yet been fully elucidated. Therefore, the present study used the *in vitro* cytokine release assay to monitor alterations in the plasma levels of pro- (IFN-γ, IL-2, and TNF-α) and anti-inflammatory (IL-10) cytokines induced by low (0.125 Gy) or high (1 Gy) neutron doses administered at two different dose rates (0.400 or 0.015 Gy/min). The cytokine response of the immune cells was measured after 24 h of stimulation with mitogens or recall antigens. To the best of our knowledge, this is the first study measuring the effect of neutron irradiation and potential dose rate effects on the cytokine release capacity of immune cells, to address the knowledge gap on chronic exposure to neutrons in light of the anticipated interplanetary travel and exploration of the Martian surface [57–59]. In general, this pilot study did not reveal statistically significant changes in cytokine release after neutron irradiation. However, some first trends after neutron exposure were observed depending on the cytokine and the stimuli used.

During the *in vitro* cytokine release assay, whole blood samples were supplemented with recall antigens or mitogens (PWM, HKLM, and LPS). The addition of the stimuli resulted in an expected upregulation of plasma cytokine levels (**Figure 2**) in line with previous observations, confirming the efficacy of the assay [55]. Basal IL-2 and IFN-γ concentrations were below the assay detection limit, indicating that the study population was indeed healthy and there was no sign of infection [56]. In a previous study, IL-2 secretion was only increased for 50% of the subjects after exposure to LPS [22]. We observed an increase for only 25% of the donors after LPS stimulation. Moreover,

the only statistically significant increase in IL-2 concentration was observed after PWM stimulation. IL-2 acts by priming CD8+ T cells to eliminate virus-infected cells. The low IL-2 secretion following stimulation with HKLM and LPS are possibly due to these mitogens mimicking a bacterial, rather than a viral challenge.

At the unstimulated baseline, TNF-α concentrations were within the expected normal physiological range with one participant showing a titre roughly 50% higher than the other study participants. Studies conducted to investigate cytokine levels in healthy subjects have established differing "normal" baseline cytokine profiles based on the characteristics of their study populations and the method of cytokine measurement [19, 60]. Based on the great variation in baseline cytokine levels amongst donors and the limited availability of comparative study data, it was decided that none of the donors could be excluded from the statistical analysis in this study based on a literature comparison alone. In addition, a large intra-individual variation was also observed in the exposed samples which is reflected by the relatively broad error bars in **Figure 3**. While no conclusive results could be obtained in the present study, it might be valuable to investigate cytokines responses at individual level after irradiation exposure in future studies.

Evidence suggests that IL-2 stimulation during the primary immune response is critical for secretion of CD8+ T lymphocytes to combat viral infections [61]. During an infection, a co-ordinated action by pro-inflammatory cytokines must guarantee the clearing of the invading pathogen. Once this is achieved, they are downregulated by anti-inflammatory cytokines such as IL-10, before tissue damage or pathology occurs. A timely and dynamic balance exists between pro- and anti-inflammatory cytokines to ensure an infection is resolved [62]. In this study, only the effects of neutron irradiation on the PWM-induced IL-2 secretion can be taken in consideration, since all the other stimulation conditions produced IL-2 concentrations that were below the assay detection limit (**Figure 2**). A non-statistically significant trend was observed for the dose rate in the PWM-stimulated group, where the HDR suppressed IL-2 secretion compared to LDR exposure for both 0.125 and 1 Gy (**Figure 3I**). In a challenged immune system, a potential neutron-induced IL-2 suppression could give rise to reduced primary and secondary antigen-specific CD8+ expansion and an inefficient immune response [63].

IL-10 is described as a pleiotropic cytokine, since it acts in both innate and adaptive immunity as an anti-inflammatory molecule [64] and is involved in the prevention and limitation of immune reactions [65]. A significant increase was observed in IL-10 secretion under PWM-stimulation and neutron treatment at LDR 1 Gy and HDR 0.125 Gy (**Figure 3E**). IL-10 was the only anti-inflammatory cytokine included in this study and the only cytokine that showed a consistent, but not statistically significant upregulation after neutron irradiation and stimulation (**Table 2**—left side). These results indicate that neutron irradiation could induce anti-inflammatory activity, independent of the dose rate.

Previous research conducted on rats flown on the US Space Shuttle revealed that the animals had suppressed IFN-γ levels which could be associated with a heightened risk to viral infections [66]. IFN-γ plays an essential role in the innate and adaptive immune response against pathogens and tumour development but unregulated IFN-γ secretion can cause pathological inflammatory conditions [67]. The grouped dose rate analysis highlighted an inverse relationship between IFN-γ levels and dose rate, suggesting that the LDR may facilitate a competent immune response to viral challenge, while the HDR resulted in a non-statistically significant downregulation after stimulation. This trend, which can be observed in **Figures 3A–C**, and was confirmed by the effect size calculations that showed a suppression of the IFN-γ secretion after HDR irradiation in response to stimulation (**Table 2**—left side).

TNF-α is an important factor for T lymphocyte signalling and activation to induce an appropriate response from initiation to pathogen elimination and has a well-defined role in the defence against several bacterial pathogens [68, 69]. In this study, TNF-α is the only cytokine for which no real trends could be observed in the stimulated, irradiated whole blood cultures. However, the upregulation of IL-10 secretion might have antagonised the TNF-α levels in the stimulated cultures. An interesting yet not statistically significant response was observed in the unstimulated group, where LDR neutrons downregulated the TNF-α secretion after 0.125 Gy compared to the HDR (**Figure 3P**). This suggests that, even before mitogen stimulation, a dose rate-dependent response is visible and LDR neutron radiation might induce a suppressed ability to mount an effective immune response.

Significant reductions in mitogen-stimulated production of different cytokines was observed in peripheral blood mononuclear cells isolated from whole blood samples, that were collected during long-duration spaceflight [7]. The inability of the dysregulated immune system to respond and clear infections or pre-cancerous cells is concerning in light of the confined living condition and radiation-rich environment that astronauts will inhabit during interplanetary trips. While most of the observed immune alterations up to now have been linked and attributed to microgravity conditions in ground-based set-up, some components of the immune system are among the most radiosensitive tissues in the body. Unfortunately, results on the effect of cosmic radiation on the immune system remain limited [10, 20]. Most evidence for the effects of space radiation exposures in humans has been derived from epidemiological studies on the atomic-bomb survivors, radiotherapy patients, and occupationally exposed workers. While these studies provide valuable insights, our knowledge on the true risks from low dose rate exposure to high-LET radiation relevant to space is limited and remains one of the main challenges to predict space radiation health risks for exploration astronauts [70]. Currently, NASA's most advanced GCR simulators provides some insight into the effect of GCR on biological systems [70]. A recent study by Moreno-Villanueva and colleagues examined the combined and individual effects of γ-radiation (radiation source undefined), simulated microgravity and physiological stress on isolated, unstimulated, peripheral blood mononuclear cells [29]. They concluded that radiation significantly influenced cytokine secretion but only under simulated microgravity conditions.

In addition, pre-exposure to simulated psychological stress mitigated the effects of microgravity. These important findings suggest possible synergistic effects that may offer some level of protective compensation during spaceflight. Since no additional space stressors were used in the current pilot study, this could also be one of the reasons why almost no significant effects on cytokine secretion could be observed with neutron irradiation alone.

When astronauts go beyond LEO, they are exposed to high doses of space radiation, consisting of protons and heavy charged nuclei, as well as secondary neutrons of a wide spectrum of energies produced by interaction of the charge particles with the human body, spacecraft and other material surroundings [71]. Most existing studies on neutron radiation focus on their carcinogenic risks and are primarily based on experiments with exposures to neutron energies below 20 MeV, while simulation and dosimetry studies illustrate that neutron energies in space environment go up to much higher energies [58]. In addition, measurements on the Martian surface show that neutrons will be a significant contributor to measured absorbed dose and it is estimated that they contribute ∼15% toward the intravehicular dose to astronauts [57, 58, 72]. Though the immune impact of neutron irradiation is poorly studied, a gene expression study by Broustas et al. illustrated a clear suppression of immune cell function after 1 Gy neutron irradiation and downregulation of genes that were related to the immune system response and B and T cell physiology [73].

This pilot study has several limitations, where the small study population presented one of the main constraints to draw statistically significant conclusions. However, it is a first illustration of the size of variation, which can form the basis for appropriate sample sizes calculation and to test the feasibility of future experiments [74, 75]. The LDR in the current study is still much higher than the expected intravehicular dose rate during cosmic travel, which is estimated be 0.3–0.6 mGy per day or 2.08×10^{-4} to 4.17×10^{-4} mGy/min [58]. The measured dose rate for the Martian neutron spectrum ranges from 8 to 740 MeV was 0.014 ± 0.004 mGy/day [57, 59]. We were unfortunately limited to a dose rate of 0.015 Gy/min due to the detection limits of the electronics of the clinical neutron therapy beam line that was used in this study. However, this 25-time reduction in dose rate compared to the HDR of 0.400 Gy/min, was considered to be sufficient for this proof-of-principle study. Moreover, we were able to demonstrate a neutron dose rate effect on DNA double strand break induction as early as 30 min after irradiation with the same irradiation set-up [50]. It should also be noted that an absorbed neutron dose of 1 Gy as used in this pilot study is not trivial and is possibly much higher than the expected absorbed neutron doses for astronauts on a Mars mission. However, since this was a pilot study, it was decided to include a low (0.125 Gy) and high (1 Gy) neutron dose in order to evaluate the effect of the dose in this first step of the project. Neutron exposures of this magnitude are expected to induce apoptosis in a substantial proportion of the lymphocyte population and the lack of viability or apoptosis data can be seen as a limitation in this study.

Despite the limited number of study participants, the results demonstrate some first trends in certain cytokine secretions after irradiation with fast neutrons, where dose rate only seems to have an impact on the IFN-γ and IL-2 secretion after specific stimulation. However, the majority of these observations were not statistically significant. Another important limitation of this pilot study is the use of whole blood samples and not highly purified subpopulations. Therefore, this method does not provide the ability to identify the specific population of cells responsible for the observed increase or decrease in cytokine secretion. The use of whole blood may also be advantageous because it can display differences in cytokine secretion due to complex cell–cell interactions and the plasma, thereby better reflecting the *in vivo* environment. Notwithstanding these limitations and with great caution taken to not generalise the effects from a finite sample population, we can conclude that there is future scope for these types of experiments.

An important objective for future experiments is to take the additional layers of spaceflight complexity into consideration by mimicking the synergistic effect of multiple space stressors in a ground-based experiment, as outlined by Moreno-Villanueva et al. [29]. In addition, the future goal should also include *in vivo* experiments with neutrons and other high-LET radiation qualities relevant to the space radiation environment, with special emphasis for spaceflight-relevant low dose rates. Moreover, future studies should include cell viability and cell cycle assessments in order to take into consideration the starting concentration of cells in each sample, which can have a significant effect on the cytokine measurements. Unfortunately, lower dose rates remain technically challenging to administer to biological samples and beam time limitations at accelerator facilities might hinder the administration of the ultra-low dose rates observed in space. In spite of these limitations, the INVEST collaboration endeavours to further ground-based space research in Africa and to examine the individual and combined effects of spaceflight stressors (radiation, physiological stress, and microgravity) on the human immune system. Given the intended future of human spaceflight and the rapid expansion of the capabilities for human missions to the moon and Mars, there is a pressing need to improve the understanding of the space radiation risk, predict likely clinical outcomes of interplanetary radiation exposure, and develop appropriate and effective mitigation strategies for future missions [70]. The current study on low dose and dose rate neutron irradiation presents a first small step toward the giant leap still needed to achieve this goal.

DATA AVAILABILITY STATEMENT

The raw data supporting the conclusions of this article will be made available by the authors, without undue reservation.

ETHICS STATEMENT

The studies involving human participants were reviewed and approved by the South African Human Sciences Research

Council (HSRC) Research Ethic Committee in affiliation with the South African National Health Research Ethics Council of the SA National Department of Health (NHREC No. 290808-015) and also has US OHRP Federal-wide Assurance (FWA) accreditation (FWA 00006347, IRB No. 00003962). The patients/participants provided their written informed consent to participate in this study.

AUTHOR CONTRIBUTIONS

CV, MM, and BB conceptualised and designed the experiments. JN-C, EK, XM, SN, PP, ME, RN, JB, CV, and RF performed the irradiation experiments, dosimetry, and laboratory work. BB and RV provided training to RF in the *in vitro* cytokine release assay. CV, BB, RV, and RF analysed the data and FR performed the statistical analysis. CV, FR, and RF wrote the paper. CV, MM, and SB were the grant holders of the INVEST project. CV was the principal investigator in South Africa and secured funding for the experiments. All authors contributed to and approved the final version of the article.

FUNDING

Funding for the collaborative networking between South Africa and Belgium for this study was made available by the joint SA-NRF and Belgian Federal Science Policy Office (BELSPO) funding program under grant reference number BELS180425324336. Research consumables and beam time costs were funded by NRF iThemba LABS institutional grant. EU Horizon 2020 - EURopeAn MEDical application and Radiation prOteCtion Concept: strategic research agenda aNd ROadmap interLinking to heaLth and digitization aspects (EURAMED Rocc-n-roll) research funding, with grant agreement number 899995 of SB.

ACKNOWLEDGMENTS

The authors would like to thank the study participants for their gracious blood donations, as well as Sister Yvette Macdonald, for blood sample collection. We must thank the National Research Foundation of South Africa for funding this collaboration and the Physics Advisory Committee of iThemba LABS for beam time approval.

REFERENCES

1. Cogoli A. The effect of space flight on human cellular immunity. *Environ Med.* (1993) **37**:107–16.
2. Taylor GR, Dardano JR. Human cellular immune responsiveness following space flight. *Aviat Space Environ Med.* (1983) 54(12 Pt 2):S55–9.
3. Hawkins W, Zieglschmid J. *Clinical Aspects of Crew Health.* Biomedical Results of Apollo (1975).
4. Frippiat JP, Crucian BE, de Quervain DJ, Grimm D, Montano N, Praun S, et al. Towards human exploration of space: the THESEUS review series on immunology research priorities. *NPJ Microgr.* (2016) **2**:16040. doi: 10.1038/npjmgrav.2016.40
5. Nagasawa H, Huo L, Little JB. Increased bystander mutagenic effect in DNA double-strand break repair-deficient mammalian cells. *Int J Radiat Biol.* (2003) **79**:35–41. doi: 10.1080/713864984
6. Taylor GR, Neale LS, Dardano JR. Immunological analyses of US space shuttle crewmembers. *Aviat Space Environ Med.* (1986) 57:213–7.
7. Crucian B, Stowe RP, Mehta S, Quiriarte H, Pierson D, Sams C. Alterations in adaptive immunity persist during long-duration spaceflight. *NPJ Microgr.* (2015) **1**:15013. doi: 10.1038/npjmgrav.2015.13
8. Garrett-Bakelman FE, Darshi M, Green SJ, Gur RC, Lin L, Macias BR, et al. The NASA twins study: a multidimensional analysis of a year-long human spaceflight. *Science.* (2019) **364**:eaau8650. doi: 10.1126/science.aau8650
9. Crucian BE, Choukèr A, Simpson RJ, Mehta S, Marshall G, Smith SM, et al. Immune system dysregulation during spaceflight: potential countermeasures for deep space exploration missions. *Front Immunol.* (2018) **9**:1437. doi: 10.3389/fimmu.2018.01437
10. Fernandez-Gonzalo R, Baatout S, Moreels M. Impact of particle irradiation on the immune system: from the clinic to mars. *Front Immunol.* (2017) **8**:177. doi: 10.3389/fimmu.2017.00177
11. Fernandes JV, Cobucci RN, Jatoba CA, Fernandes TA, de Azevedo JW, de Araujo JM. The role of the mediators of inflammation in cancer development. *Pathol Oncol Res.* (2015) **21**:527–34. doi: 10.1007/s12253-015-9913-z
12. Grivennikov SI, Greten FR, Karin M. Immunity, inflammation, and cancer. *Cell.* (2010) **140**:883–99. doi: 10.1016/j.cell.2010.01.025
13. Gueguinou N, Huin-Schohn C, Bascove M, Bueb JL, Tschirhart E, Legrand-Frossi C, et al. Could spaceflight-associated immune system weakening preclude the expansion of human presence beyond earth's orbit? *J Leukoc Biol.* (2009) **86**:1027–38. doi: 10.1189/jlb.0309167
14. Akiyama T, Horie K, Hinoi E, Hiraiwa M, Kato A, Maekawa Y, et al. How does spaceflight affect the acquired immune system? *NPJ Microgr.* (2020) **6**:14. doi: 10.1038/s41526-020-0104-1
15. Rykova MP, Antropova EN, Larina IM, Morukov BV. Humoral and cellular immunity in cosmonauts after the ISS missions. *Acta Astronaut.* (2008) **63**:697–705. doi: 10.1016/j.actaastro.2008.03.016
16. Konstantinova IV, Rykova MP, Lesnyak AT, Antropova EA. Immune changes during long-duration missions. *J Leukoc Biol.* (1993) **54**:189–201. doi: 10.1002/jlb.54.3.189
17. Crucian BE, Cubbage ML, Sams CF. Altered cytokine production by specific human peripheral blood cell subsets immediately following space flight. *J Interferon Cytokine Res.* (2000) **20**:547–56. doi: 10.1089/10799900050044741
18. Sonnenfeld G. Effect of space flight on cytokine production. *Acta Astronaut.* (1994) **33**:143–7. doi: 10.1016/0094-5765(94)90119-8
19. Monastero RN, Pentyala S. Cytokines as biomarkers and their respective clinical cutoff levels. *Int J Inflam.* (2017) **2017**:4309485. doi: 10.1155/2017/4309485
20. Moreels M, de Saint-Georges L, Vanhavere F, Baatout S. Stress and radiation responsiveness. In: Choukèr A, editor. *Stress Challenges and Immunity in Space: From Mechanisms to Monitoring and Preventive Strategies.* Cham: Springer Nature Switzerland AG (2011). p. 239. doi: 10.1007/978-3-642-22272-6_17
21. Crucian B, Simpson RJ, Mehta S, Stowe R, Chouker A, Hwang S-A, et al. Terrestrial stress analogs for spaceflight associated immune system dysregulation. *Brain Behav Immun.* (2014) **39**:23–32. doi: 10.1016/j.bbi.2014.01.011
22. Van Walleghem M, Tabury K, Fernandez-Gonzalo R, Janssen A, Buchheim J-I, Choukèr A, et al. Gravity-related immunological changes in human whole blood cultured under simulated microgravity using an *in vitro* cytokine release assay. *J Interferon Cytokine Res.* (2017) **37**:531–40. doi: 10.1089/jir.2017.0065
23. Morey-Holton E, Globus R, Kaplansky A, Durnova G. The hindlimb unloading rat model: literature overview, technique update and comparison with space flight data. *Adv Space Biol Med.* (2005) **10**:7–40. doi: 10.1016/S1569-2574(05)10002-1
24. Hoff P, Belavý DL, Huscher D, Lang A, Hahne M, Kuhlmey A-K, et al. Effects of 60-day bed rest with and without exercise on cellular and

humoral immunological parameters. *Cell Mol Immunol.* (2015) **12**:483–92. doi: 10.1038/cmi.2014.106
25. Shearer WT, Ochs HD, Lee B-N, Cohen EN, Reuben JM, Cheng I, et al. Immune responses in adult female volunteers during the bed-rest model of spaceflight: antibodies and cytokines. *J Allergy Clin Immunol.* (2009) **123**:900–5. doi: 10.1016/j.jaci.2008.12.016
26. Sonnenfeld G. The immune system in space and microgravity. *Med Sci Sports Exerc.* (2002) **34**:2021–7. doi: 10.1097/00005768-200212000-00024
27. Sonnenfeld G, Butel JS, Shearer WT. Effects of the space flight environment on the immune system. *Rev Environ Health.* (2003) **18**:1–17. doi: 10.1515/REVEH.2003.18.1.1
28. Cogoli A, Bechler B, Cogoli-Greuter M, Criswell SB, Joller H, Joller P, et al. Mitogenic signal transduction in tlymphocytes in microgravity. *J Leukoc Biol.* (1993) **53**:569–75. doi: 10.1002/jlb.53.5.569
29. Moreno-Villanueva M, Feiveson AH, Krieger S, Kay Brinda A, von Scheven G, Bürkle A, et al. Synergistic effects of weightlessness, isoproterenol, and radiation on DNA damage response and cytokine production in immune cells. *Int J Mol Sci.* (2018) **19**:3689. doi: 10.3390/ijms19113689
30. Yatagai F, Honma M, Dohmae N, Ishioka N. Biological effects of space environmental factors: a possible interaction between space radiation and microgravity. *Life Sci Space Res.* (2019) **20**:113–23. doi: 10.1016/j.lssr.2018.10.004
31. Zeitlin C, Hassler D, Cucinotta F, Ehresmann B, Wimmer-Schweingruber R, Brinza D, et al. Measurements of energetic particle radiation in transit to Mars on the Mars science laboratory. *Science.* (2013) **340**:1080–4. doi: 10.1126/science.1235989
32. Cucinotta FA, Chappell LJ. Updates to astronaut radiation limits: radiation risks for never-smokers. *Rad Res.* (2011) **176**:102–14. doi: 10.1667/RR2540.1
33. Chancellor JC, Scott GB, Sutton JP. Space radiation: the number one risk to astronaut health beyond low earth orbit. *Life.* (2014) **4**:491–510. doi: 10.3390/life4030491
34. Walsh L, Schneider U, Fogtman A, Kausch C, McKenna-Lawlor S, Narici L, et al. Research plans in Europe for radiation health hazard assessment in exploratory space missions. *Life Sci Space Res.* (2019) **21**:73–82. doi: 10.1016/j.lssr.2019.04.002
35. Durante M, Golubev A, Park W-Y, Trautmann C. Applied nuclear physics at the new high-energy particle accelerator facilities. *Phys Rep.* (2019) **800**:1–37. doi: 10.1016/j.physrep.2019.01.004
36. Mosconi M, Musonza E, Buffler A, Nolte R, Röttger S, Smit F. Characterisation of the high-energy neutron beam at iThemba LABS. *Radiat Measure.* (2010) **45**:1342–5. doi: 10.1016/j.radmeas.2010.06.044
37. Broerse J. Biological effects of neutrons. In: Thomas RH, Perez-Mendez V, editors. *Advances in Radiation Protection and Dosimetry in Medicine*. Boston, MA: Springer Science & Business Media (1980). p. 415–29.
38. Goodhead DT. Neutrons are forever! historical perspectives. *Int J Radiat Biol.* (2019) **95**:957–84. doi: 10.1080/09553002.2019.1569782
39. Casadei D. Neutron astronomy. *arXiv Preprint arXiv:170102788.* (2017).
40. Armstrong T, Colborn B. Predictions of secondary neutrons and their importance to radiation effects inside the International Space Station. *Radiat Measure.* (2001) **33**:229–34. doi: 10.1016/S1350-4487(00)00152-9
41. Nelson GA. Fundamental space radiobiology. *Gravit Space Res.* (2007) 16:29–36.
42. Heilbronn LH, Borak TB, Townsend LW, Tsai P-E, Burnham CA, McBeth RA. Neutron yields and effective doses produced by Galactic Cosmic Ray interactions in shielded environments in space. *Life Sci Space Res.* (2015) **7**:90–9. doi: 10.1016/j.lssr.2015.10.005
43. Goldhagen P, Clem J, Wilson J. The energy spectrum of cosmic-ray induced neutrons measured on an airplane over a wide range of altitude and latitude. *Radiat Protect Dosim.* (2004) **110**:387–92. doi: 10.1093/rpd/nch216
44. O'sullivan D. Exposure to galactic cosmic radiation and solar energetic particles. *Radiat Protect Dosim.* (2007). **125**:407–11. doi: 10.1093/rpd/ncm317
45. Helm A, Ebner DK, Tinganelli W, Simoniello P, Bisio A, Marchesano V, et al. Combining heavy-ion therapy with immunotherapy: an update on recent developments. *Int J Part Ther.* (2018) **5**:84–93. doi: 10.14338/IJPT-18-00024.1
46. Ebner DK, Tinganelli W, Helm A, Bisio A, Yamada S, Kamada T, et al. The immunoregulatory potential of particle radiation in cancer therapy. *Front Immunol.* (2017) **8**:99. doi: 10.3389/fimmu.2017.00099
47. Takahashi A, Ikeda H, Yoshida Y. Role of high-linear energy transfer radiobiology in space radiation exposure risks. *Int J Part Ther.* (2018) **5**:151–9. doi: 10.14338/IJPT-18-00013.1
48. Crucian BE, Zwart SR, Mehta S, Uchakin P, Quiriarte HD, Pierson D, et al. Plasma cytokine concentrations indicate that in vivo hormonal regulation of immunity is altered during long-duration spaceflight. *J Interferon Cytokine* Res. (2014) **34**:778–86. doi: 10.1089/jir.2013.0129
49. Crucian BE, Stowe RP, Pierson DL, Sams CF. Immune system dysregulation following short-vs long-duration spaceflight. *Aviat Space Environ Med.* (2008) **79**:835–43. doi: 10.3357/ASEM.2276.2008
50. Nair S, Engelbrecht M, Miles X, Ndimba R, Fisher R, du Plessis P, et al. The impact of dose rate on DNA double-strand break formation and repair in human lymphocytes exposed to fast neutron irradiation. *Int J Mol Sci.* (2019) **20**:5350. doi: 10.3390/ijms20215350
51. Feuerecker M, Mayer W, Kaufmann I, Gruber M, Muckenthaler F, Yi B, et al. A corticoid-sensitive cytokine release assay for monitoring stress-mediated immune modulation. *Clini Exp Immunol.* (2013) **172**:290–9. doi: 10.1111/cei.12049
52. Koelman L, Pivovarova-Ramich O, Pfeiffer AF, Grune T, Aleksandrova K. Cytokines for evaluation of chronic inflammatory status in ageing research: reliability and phenotypic characterisation. *Immun Ageing.* (2019) **16**:11. doi: 10.1186/s12979-019-0151-1
53. Jones D, Symons J, Fulcher T, Brooks F, Nchodu M, Allie M, et al. Neutron fluence and kerma spectra of ap (66)/Be (40) clinical source. *Med Phys.* (1992) **19**:1285–91. doi: 10.1118/1.596922
54. Mijnheer BJ, Goodman LJ, Hall EJ, Menzel HG, Parnell CJ, Rassow J, et al. Report 45. *J Int Commission Radiat Units Measure.* (2016) **os23**:NP. doi: 10.1093/jicru/os23.2.Report45
55. Duffy D, Rouilly V, Libri V, Hasan M, Beitz B, David M, et al. Functional analysis via standardized whole-blood stimulation systems defines the boundaries of a healthy immune response to complex stimuli. *Immunity.* (2014) **40**:436–50. doi: 10.1016/j.immuni.2014.03.002
56. Kleiner G, Marcuzzi A, Zanin V, Monasta L, Zauli G. Cytokine levels in the serum of healthy subjects. *Mediat Inflamm.* (2013) **2013**:434010. doi: 10.1155/2013/434010
57. Köhler J, Ehresmann B, Zeitlin C, Wimmer-Schweingruber R, Hassler D, Reitz G, et al. Measurements of the neutron spectrum in transit to Mars on the Mars Science laboratory. *Life Sci Space Res.* (2015) **5**:6–12. doi: 10.1016/j.lssr.2015.03.001
58. Norbury JW, Schimmerling W, Slaba TC, Azzam EI, Badavi FF, Baiocco G, et al. Galactic cosmic ray simulation at the NASA Space Radiation Laboratory. *Life Sci Space Res.* (2016) **8**:38–51. doi: 10.1016/j.lssr.2016.02.001
59. Guo J, Zeitlin C, Wimmer-Schweingruber R, Hassler DM, Köhler J, Ehresmann B, et al. Measurements of the neutral particle spectra on Mars by MSL/RAD from 2015-11-15 to 2016-01-15. *Life Sci Space Res.* (2017) **14**:12–7. doi: 10.1016/j.lssr.2017.06.001
60. Farber DL. Biochemical signaling pathways for memory T cell recall. *Semin Immunol.* (2009) **21**:84–91. doi: 10.1016/j.smim.2009.02.003
61. Sa Q, Woodward J, Suzuki Y. IL-2 produced by CD8+ immune T cells can augment their IFN-γ production independently from their proliferation in the secondary response to an intracellular pathogen. *J Immunol.* (2013) **190**:2199–207. doi: 10.4049/jimmunol.1202256
62. Cicchese JM, Evans S, Hult C, Joslyn LR, Wessler T, Millar JA, et al. Dynamic balance of pro-and anti-inflammatory signals controls disease and limits pathology. *Immunol Rev.* (2018) **285**:147–67. doi: 10.1111/imr.12671
63. Boyman O, Sprent J. The role of interleukin-2 during homeostasis and activation of the immune system. *Nat Rev Immunol.* (2012) **12**:180–90. doi: 10.1038/nri3156
64. Fiorentino DF, Bond MW, Mosmann T. Two types of mouse T helper cell. IV. Th2 clones secrete a factor that inhibits cytokine production by Th1 clones. *J Exp Med.* (1989) **170**:2081–95. doi: 10.1084/jem.170.6.2081
65. Moore KW, de Waal Malefyt R, Coffman RL, O'Garra A. Interleukin-10 and the interleukin-10 receptor. *Ann Rev Immunol.* (2001) **19**:683–765. doi: 10.1146/annurev.immunol.19.1.683

66. Berry WD, Murphy JD, Smith BA, Taylor GR, Sonnenfeld G. Effect of microgravity modeling on interferon and interleukin responses in the rat. *J Interferon Res.* (1991) **11**:243–9. doi: 10.1089/jir.1991.11.243
67. Alspach E, Lussier DM, Schreiber RD. Interferon γ and its important roles in promoting and inhibiting spontaneous and therapeutic cancer immunity. *Cold Spring Harbor Perspect Biol.* (2019) **11**:a028480. doi: 10.1101/cshperspect.a028480
68. Ye L-L, Wei X-S, Zhang M, Niu Y-R, Zhou Q. The significance of tumor necrosis factor receptor type II in CD8+ regulatory T cells and CD8+ effector T cells. *Front Immunol.* (2018) **9**:583. doi: 10.3389/fimmu.2018.00583
69. Thakur A, Mikkelsen H, Jungersen G. Intracellular pathogens: host immunity and microbial persistence strategies. *J Immunol Res.* (2019) **2019**:1356540. doi: 10.1155/2019/1356540
70. Chancellor JC, Blue RS, Cengel KA, Aunon-Chancellor SM, Rubins KH, Katzgraber HG, et al. Limitations in predicting the space radiation health risk for exploration astronauts. *NPJ Microgr.* (2018) **4**:8. doi: 10.1038/s41526-018-0043-2
71. Cucinotta FA, Durante M. Cancer risk from exposure to galactic cosmic rays: implications for space exploration by human beings. *Lancet Oncol.* (2006) **7**:431–5. doi: 10.1016/S1470-2045(06)70695-7
72. Wilson JW, Townsend LW. A benchmark for galactic cosmic-ray transport codes. *Radiat Res.* (1988) **114**:201–6. doi: 10.2307/3577217
73. Broustas CG, Xu Y, Harken AD, Garty G, Amundson SA. Comparison of gene expression response to neutron and x-ray irradiation using mouse blood. *BMC Genomics.* (2017) **18**:2. doi: 10.1186/s12864-016-3436-1
74. In J. Introduction of a pilot study. *Korean J Anesthesiol.* (2017) **70**:601. doi: 10.4097/kjae.2017.70.6.601
75. Van Teijlingen E, Hundley V. The importance of pilot studies. *Nurs Stand.* (2002) **16**:33. doi: 10.7748/ns2002.06.16.40.33.c3214

Conflict of Interest: The authors declare that the research was conducted in the absence of any commercial or financial relationships that could be construed as a potential conflict of interest.

frontiers in Physics

REVIEW
published: 06 October 2020
doi: 10.3389/fphy.2020.565055

Mapping the Future of Particle Radiobiology in Europe: The INSPIRE Project

Nicholas T. Henthorn[1,2†], Olga Sokol[3†], Marco Durante[3,4], Ludovic De Marzi[5], Frederic Pouzoulet[6], Justyna Miszczyk[7], Pawel Olko[7], Sytze Brandenburg[8,9], Marc Jan van Goethem[8,9], Lara Barazzuol[9,10], Makbule Tambas[9], Johannes A. Langendijk[9], Marie Davídková[11], Vladimír Vondráček[12], Elisabeth Bodenstein[13], Joerg Pawelke[13,14], Antony J. Lomax[15,16], Damien C. Weber[15,17,18], Alexandru Dasu[19,20], Bo Stenerlöw[20], Per R. Poulsen[21], Brita S. Sørensen[21], Cai Grau[21], Mateusz K. Sitarz[21], Anne-Catherine Heuskin[22], Stephane Lucas[22], John W. Warmenhoven[1,2], Michael J. Merchant[1,2], Ran I. Mackay[1,23] and Karen J. Kirkby[1,2]*

[1] Division of Cancer Sciences, Faculty of Biology, Medicine and Health, School of Medical Sciences, The University of Manchester, Manchester, United Kingdom, [2] Manchester Academic Health Science Centre, The Christie NHS Foundation Trust, Manchester, United Kingdom, [3] Department of Biophysics, GSI Helmholtzzentrum für Schwerionenforschung, Darmstadt, Germany, [4] Department of Condensed Matter Physics, Technische Universität Darmstadt, Darmstadt, Germany, [5] Radiation Oncology Department, Institut Curie, PSL Research University, Paris, France, [6] Translational Research Department, Experimental Radiotherapy Platform, Institut Curie, PSL Research University, Orsay, France, [7] Department of Experimental Physics of Complex Systems, Institute of Nuclear Physics Polish Academy of Sciences, Krakow, Poland, [8] KVI-Center for Advanced Radiation Technology, University of Groningen, Groningen, Netherlands, [9] Department of Radiation Oncology, University Medical Center Groningen, University of Groningen, Groningen, Netherlands, [10] Section of Molecular Cell Biology, Department of Biomedical Sciences of Cell and Systems, University Medical Center Groningen, University of Groningen, Groningen, Netherlands, [11] Department of Radiation Dosimetry, Nuclear Physics Institute of the CAS, Prague, Czechia, [12] Proton Therapy Center Czech, Prague, Czechia, [13] OncoRay – National Center for Radiation Research in Oncology, Faculty of Medicine and University Hospital Carl Gustav Carus, Helmholtz-Zentrum Dresden – Rossendorf, Technische Universität Dresden, Dresden, Germany, [14] Helmholtz-Zentrum Dresden – Rossendorf, Institute of Radiooncology - OncoRay, Dresden, Germany, [15] Centre for Proton Therapy, Paul Scherrer Institute, Villigen, Switzerland, [16] Department of Physics, ETH, Zurich, Switzerland, [17] Department of Radiation Oncology, University of Zurich, Zurich, Switzerland, [18] Department of Radiation Oncology, University of Bern, Bern, Switzerland, [19] The Skandion Clinic, Uppsala, Sweden, [20] Department of Immunology, Genetics and Pathology, Uppsala University, Uppsala, Sweden, [21] Danish Center for Particle Therapy, Aarhus University Hospital, Aarhus, Denmark, [22] LARN-Laboratory, Namur Research Institute for Life Sciences (NARILIS), University of Namur, Namur, Belgium, [23] Christie Medical Physics and Engineering, The Christie NHS Foundation Trust, Manchester, United Kingdom*

Particle therapy is a growing cancer treatment modality worldwide. However, there still remains a number of unanswered questions considering differences in the biological response between particles and photons. These questions, and probing of biological mechanisms in general, necessitate experimental investigation. The "Infrastructure in Proton International Research" (INSPIRE) project was created to provide an infrastructure for European research, unify research efforts on the topic of proton and ion therapy across Europe, and to facilitate the sharing of information and resources. This work highlights the radiobiological capabilities of the INSPIRE partners, providing details of physics (available particle types and energies), biology (sample preparation and post-irradiation analysis), and researcher access (the process of applying for beam time). The collection of information reported here is designed to provide researchers both in Europe and worldwide with the tools required to select the optimal center for their research needs. We also highlight areas of redundancy in capabilities and suggest areas for future investment.

Keywords: proton therapy, radiotherapy, radiobiology, beamline, irradiation

OPEN ACCESS

Edited by:
Federico Giove, Centro Fermi - Museo storico della fisica e Centro studi e ricerche Enrico Fermi, Italy

Reviewed by:
Michela Marafini, Centro Fermi - Museo storico della fisica e Centro studi e ricerche Enrico Fermi, Italy
Giuseppe A. Pablo Cirrone, Laboratori Nazionali del Sud (INFN), Italy

***Correspondence:**
Marco Durante
m.durante@gsi.de

† These authors have contributed equally to this work

Specialty section:
This article was submitted to Medical Physics and Imaging, a section of the journal Frontiers in Physics

Received: *23 May 2020*
Accepted: *02 September 2020*
Published: *06 October 2020*

Citation:
Henthorn NT, Sokol O, Durante M, De Marzi L, Pouzoulet F, Miszczyk J, Olko P, Brandenburg S, van Goethem MJ, Barazzuol L, Tambas M, Langendijk JA, Davídková M, Vondráček V, Bodenstein E, Pawelke J, Lomax AJ, Weber DC, Dasu A, Stenerlöw B, Poulsen PR, Sørensen BS, Grau C, Sitarz MK, Heuskin A-C, Lucas S, Warmenhoven JW, Merchant MJ, Mackay RI and Kirkby KJ (2020) Mapping the Future of Particle Radiobiology in Europe: The INSPIRE Project. Front. Phys. 8:565055. doi: 10.3389/fphy.2020.565055

INTRODUCTION

There is a growing investment in proton and heavy ion therapy worldwide, with 89 proton centers and 12 carbon centers currently in clinical operation [according to the Particle Therapy Co-Operation Group (PTCOG)] [1]. Of these worldwide facilities, 31 proton centers (∼35%) and four carbon centers (∼33%) are located in Europe [2]. Despite the increasing adoption of particle therapy there remains a number of unanswered questions about this relatively new treatment modality [3]. These questions range widely in scope and include physical (e.g., range uncertainties or organ motion), biological (e.g., uncertainties in relative biological effectiveness and lack of clinically relevant *in vivo* data), and societal aspects (e.g., cost-effectiveness and radiotherapy demand) [4]. Many clinical centers offer beam time for research activities to address some of these questions [5]. However, access and utilization of this beam time can be difficult due to a lack of supply and/or funding. Rectifying this situation requires targeted efforts from both researchers and funders alike.

The European project "Infrastructure in Proton International Research" (INSPIRE) was created to allow researchers across Europe access to "state-of-the-art" research capabilities in centers for proton therapy. In addition, multi-ion research centers (research facility of UMCG, Groningen, the Netherlands; GSI, Darmstadt, Germany) augment the particle research portfolio. INSPIRE aims to integrate research activities in protons (and heavy ions) across Europe through eight objectives:

1) Developing new infrastructure by bringing together clinical, academic, and industrial research activities.
2) Enabling access to research infrastructure for researchers in both the public and private sector.
3) Providing training for the next generation of researchers in the field.
4) Facilitating knowledge exchange to promote best research practices throughout Europe.
5) Developing joint research activities (JRAs) that will improve the facilities available within the infrastructure.
6) Developing JRAs in fields where technological challenges exist to improve European competitiveness.
7) Developing an innovation pipeline to translate research into clinical practice and industrial products.
8) To conduct research within the principles of responsible research and innovation.

The project is comprised of 17 European partners, 11 of which offer beam time through transnational access (TNA) (**Table 1**); a complete list of the INSPIRE partners can be found at https://protonsinspire.eu/. Further to the partners discussed in this work, the University of Namur (Belgium) is also an INSPIRE partner taking part in radiobiological research, but with their nearby partner center under development does not offer TNA through INSPIRE. However, once operational their resources will be available outside of the current INSPIRE project. Most of these partners are either clinical centers or have very close connections to clinical centers (**Figure 1**), for example the radiobiological capabilities of CHRISTIE and UNIMAN are shared. A close clinical link is essential to aid the design of the research at inception and to ensure its relevance and future translation to the clinic.

TABLE 1 | The INSPIRE partners offering equipment and support for radiobiological experiments through transnational access.

Center	Abbreviation	Location	Website
Aarhus University	AU	Aarhus, Denmark	https://www.en.auh.dk/departments/the-danish-centre-for-particle-therapy/
The Christie NHS foundation trust	CHRISTIE	Manchester, UK	https://www.christie.nhs.uk
GSI Helmholtz center for heavy Ion research	GSI	Darmstadt, Germany	https://www.gsi.de/work/forschung/biophysik.htm
The Henryk Niewodniczański institute of nuclear physics polish academy of sciences	IFJ PAN	Kraków, Poland	https://inspire.ifj.edu.pl/en/index.php/dostep-do-infrastruktury-badawczej/
Curie institute	Institut curie	Paris, France	https://institut-curie.org/page/research-and-development-proton-therapy-center
Nuclear physics institute of the Czech academy of sciences	NPI-CAS	Prague, Czech Republic	http://www.ujf.cas.cz/en/
Paul Scherrer institute	PSI	Zurich, Switzerland	https://www.psi.ch/en
Skandion clinic	Skandion	Uppsala, Sweden	https://skandionkliniken.se/
Technical University of Dresden	TUD	Dresden, Germany	https://www.oncoray.de/research/offer-for-users/
University medical center Groningen	UMCG	Groningen, Netherlands	**Clinical facility:** https://www.umcgradiotherapie.nl/en/umc-groningen-department-of-radiation-oncology **Research facility:** https://www.rug.nl/kvi-cart/research/facilities/agor/
University of Manchester	UNIMAN	Manchester, UK	https://www.bmh.manchester.ac.uk/research/domains/cancer/proton/

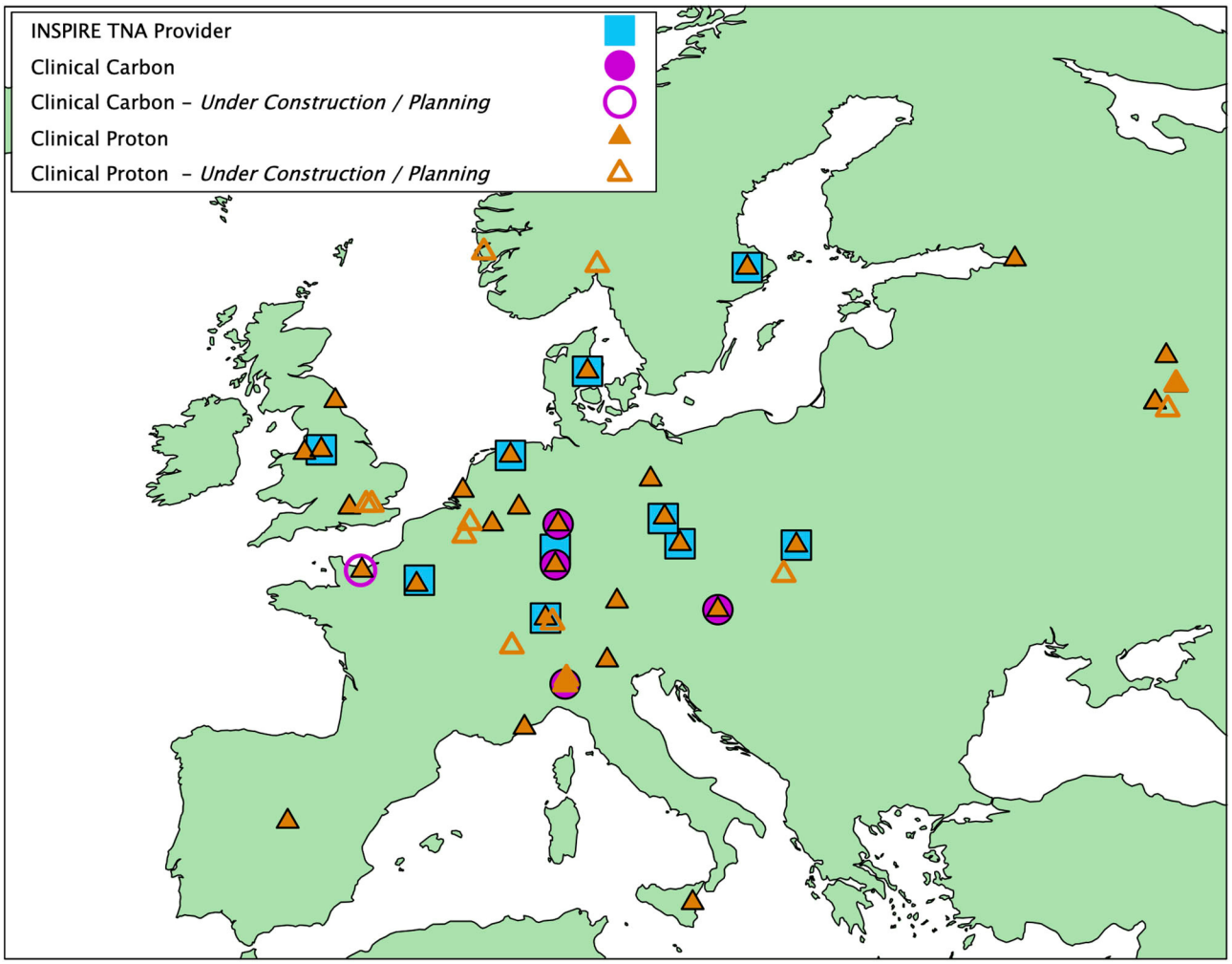

FIGURE 1 | European clinical proton therapy centers (closed triangle, 26 centers), carbon therapy centers (closed circle, 4 centers), and INSPIRE partners offering radiobiological TNA (closed squares, 11 centers—there is some overlap between centers). Open symbols show centers currently in the planning stage or under construction. Information is from the PTCOG website [1].

Further to the information hosted by each institute's website, and the information presented in this work, the following references give more information and available setups for Institut Curie [6–8], TUD [9–16], IFJ PAN [17], UMCG [18–24], and GSI [25–31].

Through INSPIRE we are able to investigate important research questions together and benefit from cross-validation. An immediate example is the variability in data for proton relative biological effectiveness (RBE) that has been seen in the literature over the years [32–35]. A coordinated effort amongst the INSPIRE partners is allowing this variability to be investigated both computationally and experimentally, and the results made available to researchers across Europe through INSPIRE's experimental and modeling JRA. This systematic and coordinated approach will highlight factors leading to variation and propose mitigation strategies for future studies. These mitigation strategies will help to develop best practices for proton radiobiology research and build upon previous work on the topic [36]. Alongside coordinated research INSPIRE also seeks to improve the infrastructure available to European researchers through its TNA. Many research centers have invested significantly to develop their research, constructing accelerators, beamlines, and purchasing experimental equipment. INSPIRE also continually upgrades its research capabilities by taking research developed through JRA and making it available to the wider research community via TNA. This means that INSPIRE is able to offer the very latest technology and capabilities.

TNA provides researchers an opportunity to access beam time and funding for experiments at INSPIRE partners. The beam time is offered to all researchers and is not limited to INSPIRE partners. Furthermore, whilst the beam time is largely accessible for European researchers, up to 30% of the hours are available to researchers outside the EU. The application process

is managed through the INSPIRE website (https://protonsinspire.eu). Prior to submitting the application through the online form, the researchers are advised to contact the representative of the relevant partner site to discuss the technical details of their proposed experiment. Before being transferred to an independent international user selection panel (USP), the refined application, submitted via the online form, is first assessed to ensure that the requested TNA site has the capacity and infrastructure to perform the experiment. Afterwards, the application is evaluated by at least two members of the USP for its technical and scientific excellence, as well as future potential and impact. Priority is given to users who have not had access to the TNA before. The INSPIRE website contains details about each center, links to websites, and contact information for general enquiries aimed to aid the potential researcher.

The information provided in this paper acts as a corollary to the INSPIRE website, where up-to-date information is maintained. Here, we provide details of the TNA radiobiology capabilities of each INSPIRE partner. Similar information, at least in terms of the physics capabilities, has previously been presented by the European Particle Therapy Network [37] and can be used alongside this work. Planning of a radiobiological experiment requires the knowledge of not only the beamline for the sample irradiation, but also of the available equipment and capabilities of the biological laboratories on site. The latter are essential for the sample preparation and post-processing. In this work, we aim to provide comprehensive information on the facilities available across INSPIRE. We specify details of the "physics," including location, beamlines, particle types, energies, and field sizes. We specify details of the "logistics," including details of sample types, positioning, and automation. We specify details of the "biology," including the available equipment for sample preparation and post-irradiation processing. Finally, we discuss future perspectives for ongoing development and further investment. The details provided here act as a resource for the potential researcher to select the optimal center for their experimental needs. However, it should be noted that there is often flexibility in many of the aspects we report. As such the information we provide should be used as a guide and more specific details can be obtained through communication with a specific partner or through INSPIRE's help desk. It is apparent that the capabilities, at least in terms of "physics," between many partners are similar. This level of redundancy is desirable, enabling repetition to ensure scientific rigor, however, establishing these centers requires a large investment and

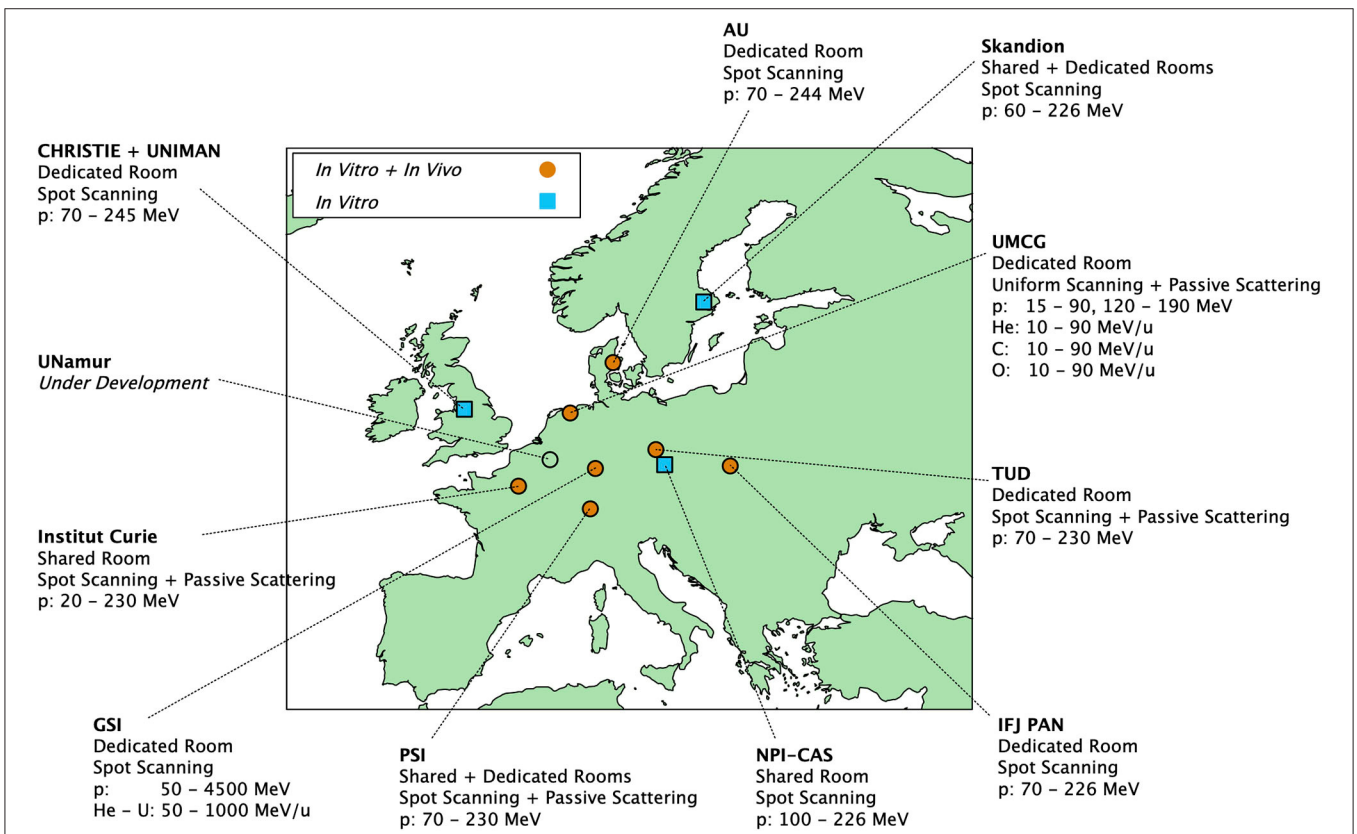

FIGURE 2 | INSPIRE partners offering radiobiological investigation with particles. The quoted energies are as extracted from the beamlines, lower energies are available with beam degraders. Centers offering both *in vitro* and *in vivo* experiments are marked with orange circles, while those offering only *in vitro* experiments are shown as blue squares. Protons, Helium, Carbon, and Oxygen ions are available at the research facility of UMCG. Protons and ions up to Uranium ions are available at GSI.

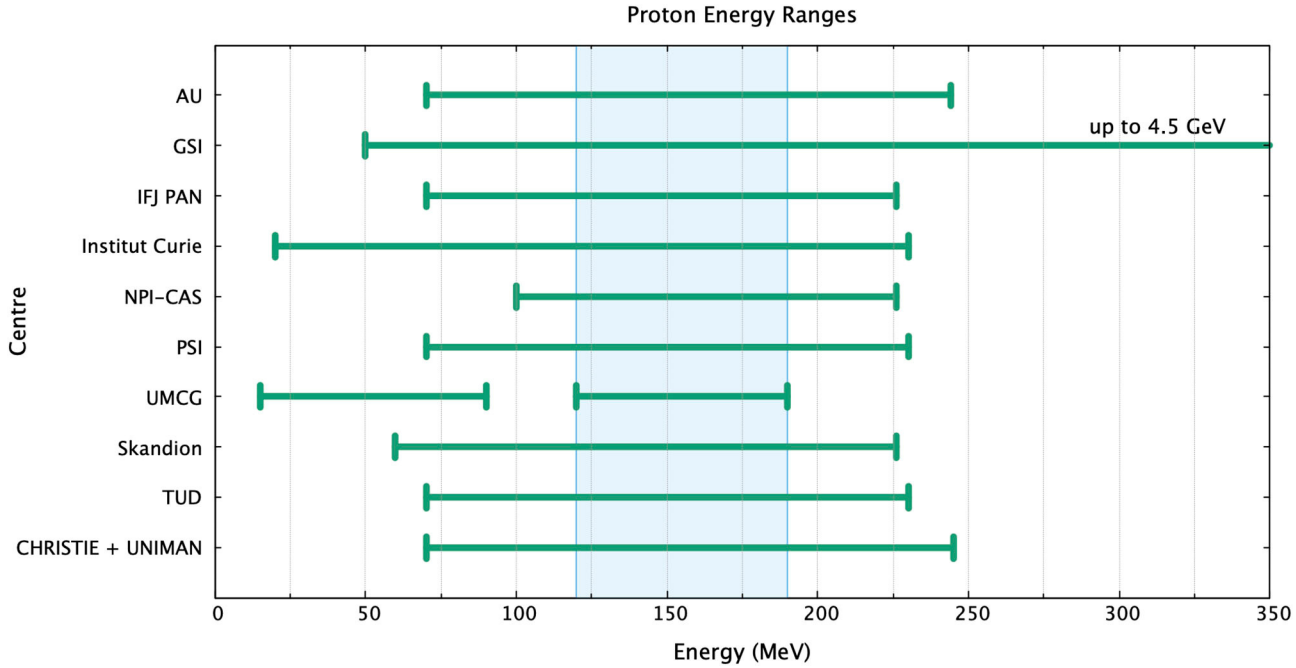

FIGURE 3 | Proton energies available at INSPIRE partners as extracted from the accelerator. The highest proton energy is available at GSI (up to 4.5 GeV). The lowest energies are available at the UMCG research facility (15 MeV) and Institut Curie (20 MeV). The overlapping region (shaded area) is between 120 and 190 MeV. Energies can be further degraded in front of the sample.

through INSPIRE they are able to work effectively together to ensure optimum utilization.

PHYSICS – LOCATION, BEAMLINES, PARTICLES, ENERGIES, AND FIELDS

A researcher often faces large heterogeneity when performing experiments between centers, with differences in protocol, setup, irradiation, and sample processing. Despite this there are a number of overlaps in beam properties and possible experiments between centers. **Figure 2** shows a summary of capabilities for the INSPIRE TNA partners.

TNA providers mainly cover central and northern Europe, with a similar distribution to clinical centers (**Figure 1**). Geographic positioning of centers is an important factor to minimize both travel expenses and logistics. A new initiative with the South East European International Institute for Sustainable Technologies (SEEIST) [38, 39] aims to enable researchers from the south east of Europe to access INSPIRE's capabilities while they are developing their own facilities.

All of the TNA providers can supply protons, with two centers, GSI and the research facility of UMCG, additionally offering other ion types of clinical interest, such as carbon, helium, or oxygen. As can be seen from **Figure 3**, in general, the energies available from the accelerator are similar between providers. The most overlapping energy region is between 120 and 190 MeV—experiments at this energy can be done at all of the partner centers. The highest possible energies can be achieved at GSI, reaching up to 1 GeV/u for heavy ions and 4.5 GeV/u for protons, with relevance to proton radiography [40] experiments, while most of the other institutes are limited to a maximum of 230–240 MeV/u. The lowest possible proton energies are offered at the research facility of UMCG (15 MeV) and Institut Curie (20 MeV). Energies can be further degraded before the sample to investigate increased proton linear energy transfer, with a relevance for end of range effects. Access to even lower energies can be obtained through the EU project RADIATE [41].

Eight TNA providers have a dedicated research room. This can be useful for studies that require longer irradiations and/or longer follow-up, it also gives more freedom to experiments that require a complex or non-standard sample setup. However, the cost of such studies should always be considered. Whilst the sample may be able to remain in the room post-irradiation this will often inactivate the room using valuable resources. A shared room has the downside of limited usage, due to clinical commitments, although it has the added benefit of rigorous quality assurance to a clinical standard. However, it should be noted that all partners undertake measures to ensure dosimetry and quality of beam delivery in their research rooms.

Figure 4 shows examples of beamlines for the CHRISTIE + UNIMAN, Skandion, the research facility of UMCG, TUD, GSI, and Institut Curie partners.

There is a range of maximum available scanned field sizes across the INSPIRE partners, shown in **Figure 5**. Six partners, PSI, Skandion, NPI-CAS, IFJ PAN, AU, and Institut Curie, offer the same field size (30×40 cm^2). TUD and CHRISTIE + UNIMAN offer the same field size but in the landscape

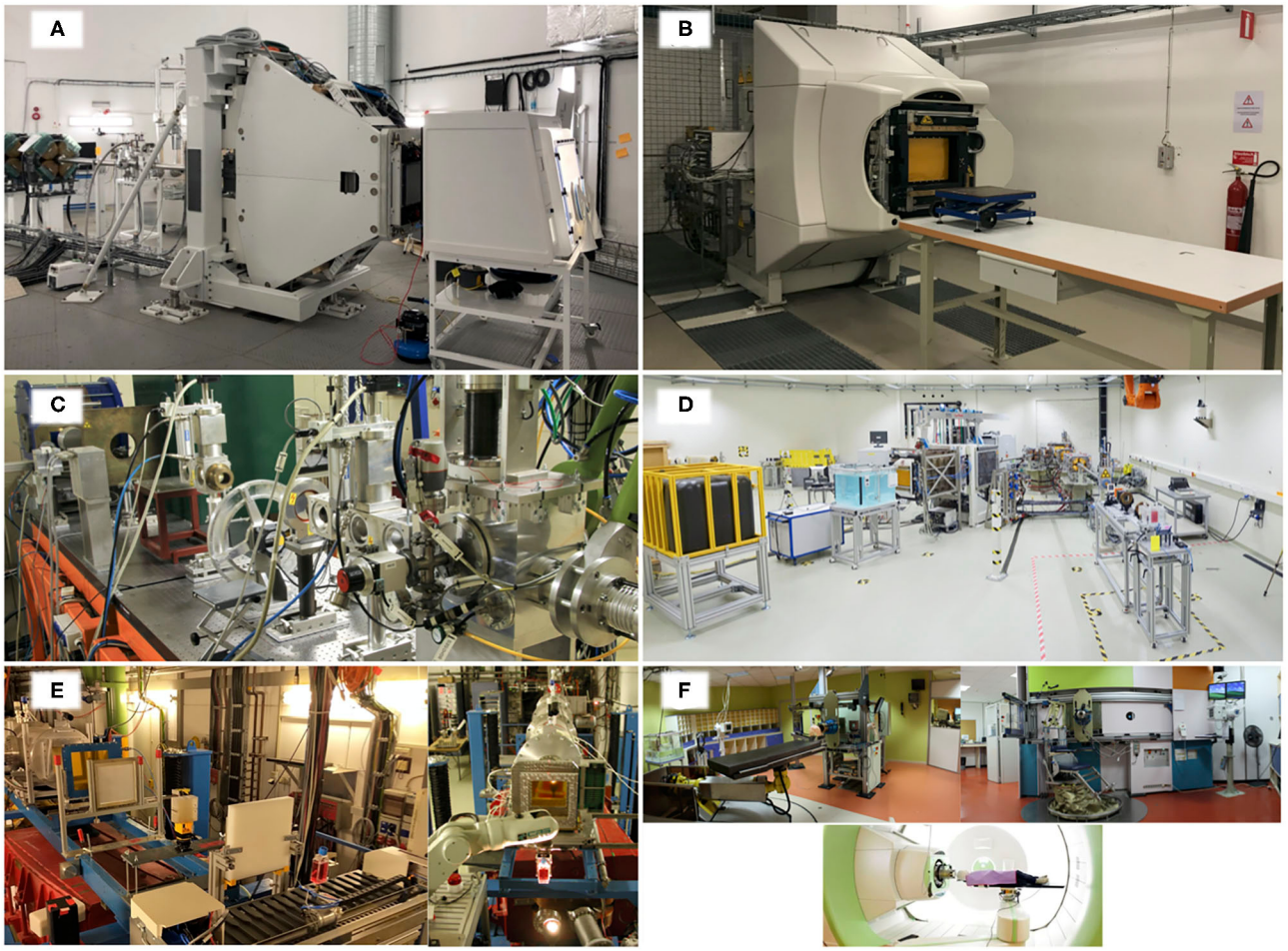

FIGURE 4 | Beamline setup for **(A)** UNIMAN + CHRISTIE, **(B)** Skandion, **(C)** the research facility of UMCG, **(D)** TUD, **(E)** GSI, and **(F)** Institut Curie. UNIMAN has a beamline leading to a Varian scanning nozzle, samples are placed in front of the nozzle (pictured is a hypoxia cabinet). Skandion has a beamline leading to an IBA scanning nozzle, samples are placed on an adjustable table in front of the nozzle. The research facility of UMCG has a flexible beamline setup using optical benches; picture shows a study on the effect of magnetic fields in combination to proton irradiation [23]. TUD has two beamlines in the dedicated experimental room, one with a pencil beam scanning nozzle (left) and one static beamline (right). In the picture, setups with water tank and beam dump at the scanning beamline and passive double scattering setup for radiobiological experiments at the static beamline are shown. GSI shows the beamline setup for "Cave A," equipped with the robotic system for sample exchange. Institut Curie shows three irradiation rooms; "Room Y1" —horizontal beam up to 201 MeV (left), "Room Y2" —horizontal beam up to 76 MeV (right), and "IBA Room" —gantry up to 230 MeV (bottom).

orientation (40×30 cm^2). All partners offer a field size large enough to irradiate most *in vitro* sample types, such as tissue culture flasks or microplates. The field size may become a limitation for larger non-standard samples, or simultaneous irradiation of multiple samples. Though in some cases the field size may be increased by introducing scatterers.

Choice of reference radiation is an important aspect in general for radiobiology. The biological effects of protons are often quoted relative to the more familiar photon case, most notably the relative biological effectiveness for cell kill. A variety of reference photon qualities are used between the INSPIRE partners. Several partners have the possibility to choose between clinical LINACs and kilovoltage X-ray machines (CHRISTIE + UNIMAN, TUD, NPI-CAS, Institut Curie, UMCG), whilst the capabilities of others are more limited. The difference in reference radiation may lead to slight differences in relative effect measurements, making inter-center comparisons more complicated. However, it should be noted that this is a problem for radiobiology in general and is not limited to INSPIRE partners [42].

LOGISTICS – SAMPLES, POSITIONING, AND AUTOMATION

The mode of sample irradiation is an important consideration, including sample orientation and possibility of automated handling. Monolayers of cells, grown in a flask or microplate, should not be free from media for a long duration of time to avoid drying. As such, several centers, particularly with horizontal

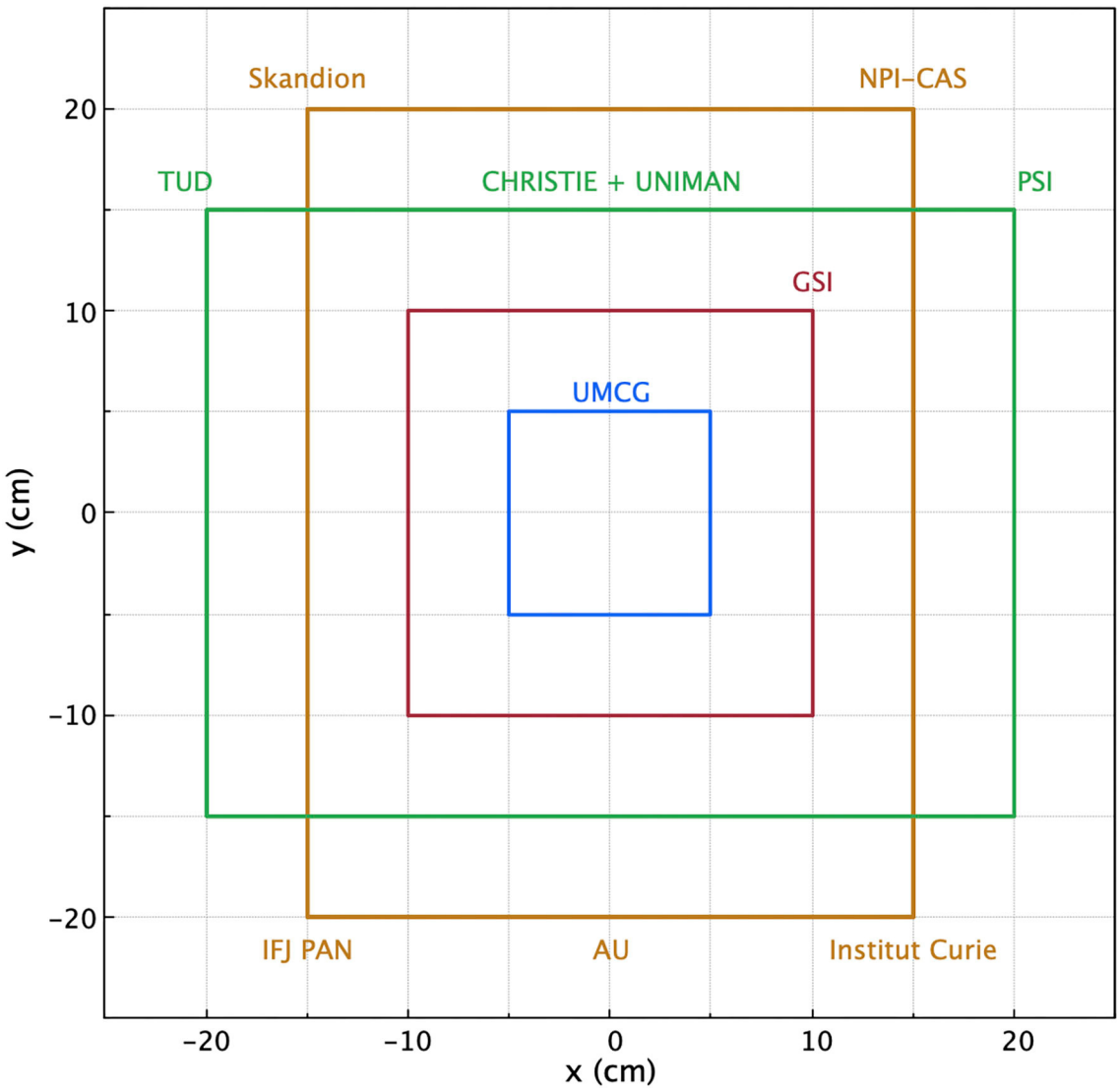

FIGURE 5 | Maximum available scanned field sizes of the INSPIRE partners, ranging from 10 × 10 cm^2 to 30 × 40 cm^2. Larger field sizes may be available by introducing scatterers.

beamlines, employ automated sample handling. Here, the sample can remain in a horizontal orientation and is lifted up only when presented to the beam for irradiation. Automated sample handling also has the added benefits of improving repeatability and minimizing access to the irradiation room, increasing sample throughput. Four centers employ automated sample handling. All the centers have the capability of a horizontal beamline, though four can additionally offer a vertical beam direction, and six offer more irradiating angles by using gantries. The sample type that can be irradiated is a limitation defined by the system. Most centers have flexibility here, with all capable of irradiating at least flasks and well-plates. The sample type capability may go beyond this (as long as it can be fixed in front of the beam and meet the safety regulations of the experimental room) and should be further discussed with the partner institute. **Table 2** shows a summary of these details.

Figure 6 shows examples of sample presentation to the beam at Christie + UNIMAN, the research facility of UMCG, Institut Curie, GSI, and AU. The system at CHRISTIE + UNIMAN (**Figure 6A**) employs a 6-axis robot mounted inside a hypoxia end station. The space limitations of the hypoxia cabinet mean that at most a mix of up to 36 samples can be housed at a time. The fingers of the robot are designed for T75 flasks or 96-well-plates, limiting the sample type. However, other samples can be used so long as they have the same footprint as a 96-well-plate or through use of customized sample holders, alternatively a large range of samples can be used without the robot. Similar to the CHRISTIE + UNIMAN system, the GSI system (**Figure 6D**) holds samples in the horizontal position lifting them to the beam for irradiation. This change in orientation minimizes the time that cells are free from media, ensuring a good cellular environment and avoiding

sample drying. Alternatively, samples can be prepared so that the culture vessel is full of cell media, which is the case for the research facility of UMCG (**Figure 6B**) and Institut Curie (**Figure 6C**).

BIOLOGY – SAMPLE PREPARATION AND PROCESSING

Alongside the physics capabilities, the biological equipment available at a center will often define the type and complexity of experiments that are possible. This impacts both the pre-irradiation sample preparation and post-irradiation analysis. For some experiments it is not possible to prepare samples prior to transport to the irradiating center. Similarly, it is not always possible to fix samples following irradiation ready for transport to the home institute. **Table 3** gives details of the *in vitro* biological equipment available at INSPIRE partners. In most cases the equipment detailed in **Table 3** is shared between the INSPIRE partner and other groups at the same institute. Therefore, these details should be used as a guide for maximum available equipment. Similarly, extra resources may be available at a partner's sister institute. Researchers requiring the use of any of this equipment should discuss their needs with the relevant partner.

Common amongst all centers is the availability of flow hoods and incubators, with TUD offering the largest capacity for sample preparation and storage. At the moment, only one center, UNIMAN, has a hypoxia station for irradiation of samples under variable oxygen tension. This offers the capability for studying the oxygen enhancement ratio and probing new fields such as the FLASH effect under strictly controlled conditions. The hypoxia station at UNIMAN is positioned directly at the beam nozzle, which prevents O_2 fluctuations in the sample while it is being transported from the laboratory to the irradiation facility. Additionally, the irradiation in hypoxic conditions is possible at AU and GSI, where the samples can be gassed inside specially designed containers prior the transportation to the experimental room. The availability of more sophisticated post-irradiation analysis, such as flow cytometry, FACS, mass spectrometry, PCR, and sequencing is varied amongst the partners. Similarly, the advanced microscopy available amongst the partners is varied, though the majority have fluorescent and confocal microscopes available.

While all the INSPIRE TNA partners mentioned in this work offer the environment for *in vitro* studies, the *in vivo* capabilities are slightly more limited, as seen in **Figure 2**. Despite the data from cell experiments being a valuable preliminary tool for studying the effects of proton beams, all of the physiological processes and their complex interplay cannot be reproduced *in vitro*, and thus the clinical treatments must first be simulated using animal models before moving onto human trials. **Table 4** shows the *in vivo* capabilities of the INSPIRE TNA providers.

In vivo experiments bring the added complexity of ethical review. INSPIRE has a well-established ethics platform for both its TNA and JRA, which is overseen by an ethics panel comprised of international experts in the field. The partners must also follow both the official regulations of their country/state as well as those of the TNA provider. Moreover, these regulations might vary from one state to another within the same country (for example, in Germany). Ethics applications in EU generally require a FELASA (Federation of European Laboratory Animal Science Associations) certification for participating scientists that cover the duration of the relevant research. In addition to that, country-specific licenses might be required. In the latter case, exceptions can be made when the guest scientists are only irradiating the animals without leaving them at the TNA facility. The application for the ethical approval is normally done well in advance, as the review procedure can last up to several months. All of the paperwork relating to ethical approval is retained by the partner and made available to the EU upon request. In addition, for some experiments the EU requires copies of the ethical permissions prior to any experiment taking place.

TABLE 2 | Beamline and radiobiological sample details of the INSPIRE partners.

Center	Beam direction (H/V)	Gantry	Automated sample exchange	Sample type			
				Flask	Petri dish	Well-plate	Other vessels
AU	H	x	x	✓	x	✓	✓
GSI	H	x	✓	✓	x	✓	✓
IFJ PAN	H	✓	x	✓	✓	✓	✓
Institut Curie	H + V	✓	✓	✓	✓	✓	x
NPI-CAS	H + V	✓	x	✓	✓	✓	x
PSI	H + V	✓	x	✓	✓	✓	✓
UMCG	H	x	✓	✓	✓	✓	✓
Skandion	H + V	✓	x	✓	✓	✓	✓
TUD	H	x	x	✓	✓	✓	✓
CHRISTIE + UNIMAN	H	✓	✓	✓	x	✓	✓

All centers can offer a horizontal beamline, with the four able to irradiate samples from above or at user-defined angles using a gantry. There is flexibility in sample types, but the majority of centers have the ability to irradiate flasks and well-plates.

FUTURE PERSPECTIVES

As has been shown, the resources available within the INSPIRE network are state-of-the-art. Further to this a number of new centers are under development and will soon be accessible to the research community. For example, the Proteus ONE IBA center at Charleroi (Belgium) will offer both *in vitro* and *in vivo* capabilities complete with a basic *in vitro* lab and animal facility on site, with researcher access offered through partnership with Namur. Belgium is also developing a center at Leuven, which will also offer *in vitro* and *in vivo* research capabilities. Furthermore, the European

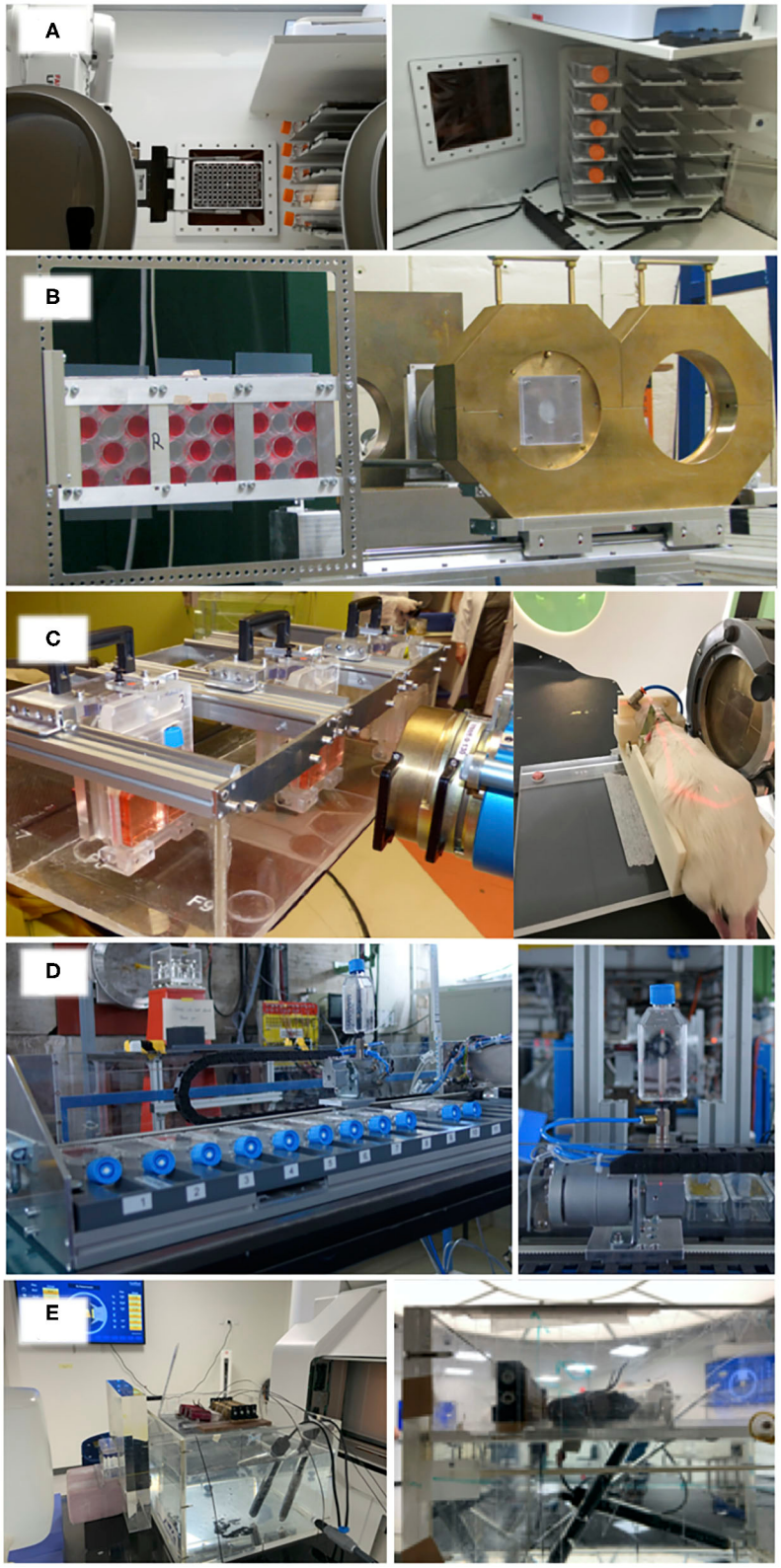

FIGURE 6 | Setup for sample irradiation at **(A)** CHRISTIE + UNIMAN, **(B)** UMCG research facility, **(C)** Institut Curie, **(D)** GSI, and **(E)** AU. The CHRISTIE + UNIMAN system is a 6-axis robotic arm mounted in a hypoxia cabinet, allowing irradiation at different oxygen tensions from 0.1 to 20%. The robot picks samples from a "hotel" and holds them in front of a beam window within the cabinet, before either replacing the sample to the hotel or moving to an automated fixation system (left). The hotel

(Continued)

FIGURE 6 | can house up to 36 samples, a mix of T75 flasks or 96-well-plates (right). The system of the UMCG research facility shows the sequential irradiation of three 12-well-plates. Wells are filled with cell media and sealed with parafilm. The Institut Curie system shows sequential irradiation of six *in vitro* samples (left), and immobilized *in vivo* irradiation (right). The GSI system allows for sequential irradiation of 16 tissue culture flasks. The flasks remain in the horizontal position whilst not being irradiated (left), preventing the cell layer inside from drying. The robotic system lifts the sample and presents it to the beam (right), replacing it when irradiation is complete. The AU system shows an *in vivo* setup for mouse leg irradiation.

TABLE 3 | *In vitro* biological analysis equipment available at the INSPIRE partners.

Center	# of laminar flow cabinets	# of incubators	Hypoxia irradiation station	Chemical hood	Flow cytometry	FACS	Biological mass spectrometry	PCR	Sequencing	Fluorescent microscope	Confocal microscope	Super resolution microscope
AU	1	1	x	x	x	x	x	✓	x	x	✓	x
GSI	2	4	x	✓	✓	✓	x	✓	x	✓	✓	x
IFJ PAN	2	1	x	✓	x	x	x	✓	x	✓	✓	x
Institut curie	1	1	x	✓	✓	✓	✓	✓	✓	✓	✓	✓
NPI-CAS	2	3	x	✓	x	x	x	✓	✓	✓	x	x
PSI*	0	1	x	x	x	x	x	x	x	x	x	x
UMCG	2	2	x	✓	✓	✓	✓	✓	✓	✓	✓	x
Skandion	4	4	x	✓	✓	✓	✓	✓	✓	✓	✓	✓
TUD	6	12	x	✓	✓	x	x	✓	x	✓	✓	x
CHRISTIE + UNIMAN	5	5	✓	✓	✓	✓	✓	✓	✓	✓	✓	✓

** Biological equipment at PSI is available at a partner institute and will need to be discussed.*

TABLE 4 | *In vivo* capabilities available at the INSPIRE partners.

Center	Animals	Capacity (max. No. of animals)	Max. days before irradiation	Onsite immobilization	Onsite anesthesia	Models used	Imaging	Histology
AU	Rats, mice	80 rats, 200 mice	7	x	x	Normal tissue and a range of tumor models (syngenic and xenografts)	x	x
GSI	Rats, mice	80	7	x	x	x	x	✓
IFJ PAN	Rats, mice, hamsters	100	7	✓	✓	x	MRI	x
Institut Curie	Rats, mice	100 rats, 40 mice	A few months	✓	✓	Normal tissue and a range of tumor models (syngenic and xenografts), orthotopic grafts, specific tissue toxicity assays	CT, X-ray, OCT, Bioluminescence	✓
PSI*	Mice, Zebrafish	–	–	✓	✓	–	–	–
UMCG	Rats, mice, zebrafish	132 rats, 264 mice	7	✓	✓	Normal tissue and a range of tumor models	✓	✓
TUD	Rats, mice, zebrafish	100	7	✓	✓	Zebrafish embryo strain wild type AB; NMRI nu/nu Nude, C57Bl/6JRj and C3H/HeNRj	CT, X-ray, MRI, Proton radiography, Bioluminescence, PET, Ultrasound	✓

** In vivo irradiation at PSI has previously been done, but capacities and equipment need to be discussed.*

project SEEIST [38, 43] will develop capabilities in South-eastern Europe, filling in some geographical gaps shown in **Figure 1**. As well as developing a new heavy ion center the SEEIST project will have access to resources provided by INSPIRE.

There is a growing European interest into studying the effectiveness of heavy ions, with four operational carbon centers and two new centers under construction. A 2019 meeting of UK clinicians, scientists, engineers, and stakeholders began the process of considering future UK development of heavy ion

therapy. There are also ongoing investigations into the clinical utilization of other particle types. For example, Helium has been seen as an intermediate between protons and carbon [44–46]. Other studies investigate the possibilities of combining multiple beams within one treatment plan to ensure a more uniform RBE distribution [47], or better treatment of hypoxic tumors [48]. The INSPIRE network is well-placed for the associated radiobiological investigations here, in particular with the partner institutes GSI and UMCG.

There has been a worldwide renewed interest in radiotherapy delivery techniques and improved normal tissue sparing. For example, spatially fractionated proton therapy [49–52] and ultra-high dose rate (FLASH) [53–56]. In these cases, the radiobiological mechanism driving the effect remains elusive. In particular, the differences between photon and particle therapy requires further investigation. Alongside this, the combination of particle therapy with immunotherapy [57, 58] is an exciting treatment that requires mechanistic understanding. Again, the INSPIRE network provides resources for investigation here, particularly through *in vivo* work, with results being directly useful for clinical adoption.

In vivo radiobiological research is a crucial step along the path to clinical implementation. Seven of the 11 partners discussed in this work are currently performing *in vivo* research (AU, GSI, IFJ PAN, Institut Curie, PSI, TUD, UMCG). Further to this, CHRISTIE + UNIMAN are beginning development of a second beamline for *in vivo* work. Skandion are also in the early stages of planning future *in vivo* work. This added capacity, and the currently available capacity, is sure to aid in the clinical efficacy of proton therapy.

The connection between research activities and clinically relevant questions must be made stronger. There are close links between many INSPIRE partners and clinical centers, which aids in this connection. However, it is important that the clinical community become more involved with research at inception. With a limited amount of finances this will ensure prioritization of the most pertinent research and advance clinical translation, all for the benefit of the patient.

CONCLUSION

In this work we have given details about the radiobiological capabilities of partners involved in the INSPIRE project, including how the resources can be accessed. It is clear that whilst there are a number of differences between the partners there are also a number of similarities. This allows for investigations into the cause of variance in published radiobiological data, such as the planned joint experiment of the INSPIRE partners. However, establishing these research centers requires significant investment and, as can be seen, many of the capabilities are already in place. More effort must be made to develop and utilize the resources currently available to us. Efforts are being made to further increase *in vivo* capabilities, whilst *in vitro* research is invaluable for identifying and probing mechanisms, *in vivo* research is crucial for clinical adoption. Also required here is a closer relationship with clinical partners, ensuring a good direction for future research. With a renewed interest in radiotherapy delivery techniques, and the unknown biological mechanisms, now is certainly and exciting time for particle radiobiology. Mechanisms that the INSPIRE network is well-placed to address.

AUTHOR CONTRIBUTIONS

MDu designed the structure of the manuscript. NH and OS wrote the manuscript with input from the other authors. OS and MDu provided information for GSI. LD and FP provided information for Institut Curie. JM and PO provided information for IFJ PAN. SB, MG, LB, MT, and JL provided information for UMCG. MDa and VV provided information for NPI-CAS. EB and JP provided information for TUD. AL and DCW provided information for PSI. AD and BS provided information for Skandion. PP, BSS, CG, and MS provided information for AU. A-CH and SL provided information for Namur. NH, JW, MM, RM, and KK provided information for UNIMAN and CHRISTIE. MDu leads the radiobiology work package of the INSPIRE project. KK leads the INSPIRE project. All authors reviewed and agreed the manuscript.

FUNDING

This work was funded by the European Union's Horizon 2020 research and innovation programme under grant agreement no 730983 (INSPIRE).

REFERENCES

1. PTCOG. *Particle Therapy Facilities in Operation*. (2020). Available online at: https://www.ptcog.ch/ (accessed May 11, 2020)
2. Grau C, Durante M, Georg D, Langendijk JA, Weber DC. Particle therapy in Europe. *Mol Oncol*. (2020) 14:1492–9. doi: 10.1002/1878-0261.12677
3. Durante M, Orecchia R, Loeffler JS. Charged-particle therapy in cancer: clinical uses and future perspectives. *Nat Rev Clin Oncol*. (2017) **14**:483–95. doi: 10.1038/nrclinonc.2017.30
4. Bortfeld TR, Loeffler JS. Three ways to make proton therapy affordable. *Nature*. (2017) **549**:451–3. doi: 10.1038/549451a
5. Durante M. Proton beam therapy in Europe: more centres need more research. *Br J Cancer*. (2018) **120**:777–8. doi: 10.1038/s41416-018-0329-x
6. Patriarca A, Fouillade C, Auger M, Martin F, Pouzoulet F, Nauraye C, et al. experimental set-up for flash proton irradiation of small animals using a clinical system. *Int J Radiat Oncol*. (2018) **102**:619–26. doi: 10.1016/j.ijrobp.2018.06.403
7. Calugaru V, Nauraye C, Noël G, Giocanti N, Favaudon V, Mégnin-Chanet F. Radiobiological characterization of two therapeutic proton beams with different initial energy spectra used at the institut curie proton therapy center in orsay. *Int J Radiat Oncol Biol Phys*. (2011) **81**:1136–43. doi: 10.1016/j.ijrobp.2010.09.003
8. Calugaru V, Nauraye C, Cordelières FP, Biard D, De Marzi L, Hall J, et al. Involvement of the artemis protein in the relative biological efficiency observed with the 76-mev proton beam used at the institut curie proton

therapy center in orsay. *Int J Radiat Oncol Biol Phys.* (2014) **90**:36–43. doi: 10.1016/j.ijrobp.2014.05.018
9. Beyreuther E, Baumann M, Enghardt W, Helmbrecht S, Karsch L, Krause M, et al. Research facility for radiobiological studies at the university proton therapy dresden. *Int J Part Ther.* (2018) **5**:172–82. doi: 10.14338/IJPT-18-00008.1
10. Müller J, Schürer M, Neubert C, Tillner F, Beyreuther E, Suckert T. Multi-modality bedding platform for combined imaging and irradiation of mice. *Biomed Phys Eng Express.* (2020) 6:037003.
11. Suckert T, Müller J, Beyreuther E, Azadegan B, Brüggemann A, Bütof R, et al. High-precision image-guided proton irradiation of mouse brain sub-volumes. *Radiother Oncol.* (2020) **146**:205–12. doi: 10.1016/j.radonc.2020.02.023
12. Szabó ER, Brand M, Hans S, Hideghéty K, Karsch L, Lessmann E, et al. Radiobiological effects and proton RBE determined by wildtype zebrafish embryos. *PLoS ONE.* (2018) **13**:e0206879. doi: 10.1371/journal.pone.0206879
13. Beyreuther E, Brand M, Hans S, Hideghéty K, Karsch L, Leßmann E, et al. Feasibility of proton FLASH effect tested by zebrafish embryo irradiation. *Radiother Oncol.* (2019) **139**:46–50. doi: 10.1016/j.radonc.2019.06.024
14. Müller J, Neubert C, von Neubeck C, Baumann M, Krause M, Enghardt W, et al. Proton radiography for inline treatment planning and positioning verification of small animals. *Acta Oncol.* (2017) **56**:1399–405. doi: 10.1080/0284186X.2017.1352102
15. Kormoll T, Duplicy A, Enghardt W, Helmbrecht S, Hueso Gonzalez F. 106: A beam control system for an experimental beam line operated parallel to a therapeutic beam line. *Radiother Oncol.* (2014) **110**:S52–3. doi: 10.1016/S0167-8140(15)34127-X
16. Helmbrecht S, Baumann M, Enghardt W, Fiedler F, Krause M, Lühr A. Design and implementation of a robust and cost-effective double-scattering system at a horizontal proton beamline. *J Instrum.* (2016) **11**:T11001. doi: 10.1088/1748-0221/11/11/T11001
17. Bogdali-Suślik AM, Rawojć K, Miszczyk J, Panek A, Wozniak M, Szewczyk K, et al. Influence of therapeutic proton beam on glioblastoma multiforme proliferation index — A preliminary study. *Acta Phys Pol A.* (2020) **137**:64–9. doi: 10.12693/APhysPolA.137.64
18. Brandenburg S, Ostendorf R, Hofstee M, Kiewiet H, Beijers H. The irradiation facility at the AGOR cyclotron. *Nucl Instruments Methods Phys Res Sect B Beam Interact Mater Atoms.* (2007) **261**:82–5. doi: 10.1016/j.nimb.2007.04.304
19. van Goethem M-J, Niemantsverdriet M, Brandenburg S, Langendijk JA, Coppes RP, van Luijk P. Development of a facility for high-precision irradiation of cells with carbon ions. *Med Phys.* (2011) **38**:256–63. doi: 10.1118/1.3528164
20. Nagle PW, Hosper NA, Ploeg EM, van Goethem M-J, Brandenburg S, Langendijk JA, et al. The *in vitro* response of tissue stem cells to irradiation with different linear energy transfers. *Int J Radiat Oncol Biol Phys.* (2016) **95**:103–11. doi: 10.1016/j.ijrobp.2016.02.020
21. Bijl HP, van Luijk P, Coppes RP, Schippers JM, Konings AWT, van der Kogel AJ. Influence of adjacent low-dose fields on tolerance to high doses of protons in rat cervical spinal cord. *Int J Radiat Oncol Biol Phys.* (2006) **64**:1204–10. doi: 10.1016/j.ijrobp.2005.06.046
22. van Luijk P, Novakova-Jiresova A, Faber H, Schippers JM, Kampinga HH, Meertens H, et al. Radiation damage to the heart enhances early radiation-induced lung function loss. *Cancer Res.* (2005) **65**:6509–11. doi: 10.1158/0008-5472.CAN-05-0786
23. Nagle PW, van Goethem M-J, Kempers M, Kiewit H, Knopf A, Langendijk JA, et al. *In vitro* biological response of cancer and normal tissue cells to proton irradiation not affected by an added magnetic field. *Radiother Oncol.* (2019) **137**:125–9. doi: 10.1016/j.radonc.2019.04.028
24. van Luijk P, Pringle S, Deasy JO, Moiseenko V V, Faber H, Hovan A, et al. Sparing the region of the salivary gland containing stem cells preserves saliva production after radiotherapy for head and neck cancer. *Sci Transl Med.* (2015) **7**:305ra147. doi: 10.1126/scitranslmed.aac4441
25. Merk B, Voss KO, Müller I, Fischer BE, Jakob B, Taucher-Scholz G, et al. Photobleaching setup for the biological end-station of the darmstadt heavy-ion microprobe. *Nucl Instruments Methods Phys Res Sect B Beam Interact Mater Atoms.* (2013) **306**:81–4. doi: 10.1016/j.nimb.2012.11.043
26. Abdollahi E, Taucher-Scholz G, Durante M, Jakob B. Upgrading the GSI beamline microscope with a confocal fluorescence lifetime scanner to monitor charged particle induced chromatin decondensation in living cells. *Nucl Instruments Methods Phys Res Sect B Beam Interact Mater Atoms.* (2015) **365**:626–30. doi: 10.1016/j.nimb.2015.07.005
27. Sokol O, Scifoni E, Tinganelli W, Kraft-Weyrather W, Wiedemann J, Maier A, et al. Oxygen beams for therapy: advanced biological treatment planning and experimental verification. *Phys Med Biol.* (2017) **62**:7798–813. doi: 10.1088/1361-6560/aa88a0
28. Graeff C, Lüchtenborg R, Eley JG, Durante M, Bert C. A 4D-optimization concept for scanned ion beam therapy. *Radiother Oncol.* (2013) **109**:419–24. doi: 10.1016/j.radonc.2013.09.018
29. Schuy C, Tessa C La, Horst F, Rovituso M, Durante M, Giraudo M, et al. Experimental assessment of lithium hydride's space radiation shielding performance and monte carlo benchmarking. *Radiat Res.* (2018) **191**:154. doi: 10.1667/RR15123.1
30. Pleskac R, Abou-Haidar Z, Agodi C, Alvarez MAG, Aumann T, Battistoni G, et al. The FIRST experiment at GSI. *Nucl Instruments Methods Phys Res Sect A Accel Spectrometers Detect Assoc Equip.* (2012) **678**:130–38. doi: 10.1016/j.nima.2012.02.020
31. Bert C, Gemmel A, Saito N, Chaudhri N, Schardt D, Durante M, et al. Dosimetric precision of an ion beam tracking system. *Radiat Oncol.* (2010) **5**:61. doi: 10.1186/1748-717X-5-61
32. Paganetti H. Relative biological effectiveness (RBE) values for proton beam therapy. Variations as a function of biological endpoint, dose, and linear energy transfer. *Phys Med Biol.* (2014) **59**:R419–72. doi: 10.1088/0031-9155/59/22/R419
33. Friedrich T, Scholz U, Elsässer T, Durante M, Scholz M. Systematic analysis of RBE and related quantities using a database of cell survival experiments with ion beam irradiation. *J Radiat Res.* (2013) **54**:494–514. doi: 10.1093/jrr/rrs114
34. Tommasino F, Durante M. Proton radiobiology. *Cancers.* (2015) **7**:353–81. doi: 10.3390/cancers7010353
35. Carabe A, Moteabbed M, Depauw N, Schuemann J, Paganetti H. Range uncertainty in proton therapy due to variable biological effectiveness. *Phys Med Biol.* (2012) **57**:1159–72. doi: 10.1088/0031-9155/57/5/1159
36. Durante M, Paganetti H, Pompos A, Kry SF, Wu X, Grosshans DR. Report of a national cancer institute special panel: characterization of the physical parameters of particle beams for biological research. *Med Phys.* (2018) **46**:e37–52. doi: 10.1002/mp.13324
37. Dosanjh M, Jones B, Pawelke J, Pruschy M, Sørensen BS. Overview of research and therapy facilities for radiobiological experimental work in particle therapy. report from the European particle therapy network radiobiology group. *Radiother Oncol.* (2018) **128**:14–8. doi: 10.1016/j.radonc.2018.03.008
38. Damjanovic S. SEEIIST: South East European International Institute for Sustainable Technologies. *Europhys News.* (2019) **50**:31–2. doi: 10.1051/epn/2019404
39. Amaldi U, et al. South East European International Institute for Sustainable Technologies (SEEIIST). *Front Phys.* (2020).
40. Prall M, Durante M, Berger T, Przybyla B, Graeff C, Lang PM, et al. High-energy proton imaging for biomedical applications. *Sci Rep.* (2016) **6**:27651. doi: 10.1038/srep27651
41. RADIATE. Research And Development with Ion Beams – Advancing Technology in Europe.
42. Paganetti H, Blakely E, Carabe-Fernandez A, Carlson DJ, Das IJ, Dong L, et al. Report of the AAPM TG-256 on the relative biological effectiveness of proton beams in radiation therapy. *Med Phys.* (2019) **46**:e53–78. doi: 10.1002/mp.13390
43. SEEIST. The South East European International Institute for Sustainable Technologies.
44. Tessonnier T, Mairani A, Brons S, Sala P, Cerutti F, Ferrari A, et al. Helium ions at the heidelberg ion beam therapy center: comparisons between fluka monte carlo code predictions and dosimetric measurements. *Phys Med Biol.* (2017) **62**:6784–803. doi: 10.1088/1361-6560/aa7b12
45. Knäusl B, Fuchs H, Dieckmann K, Georg D. Can particle beam therapy be improved using helium ions? – A planning study focusing on pediatric patients. *Acta Oncol.* (2016) **55**:751–9. doi: 10.3109/0284186X.2015.1125016
46. Krämer M, Scifoni E, Schuy C, Rovituso M, Tinganelli W, Maier A, et al. Helium ions for radiotherapy? Physical and biological verifications of a novel treatment modality. *Med Phys.* (2016) **43**:1995–2004. doi: 10.1118/1.4944593

47. Kopp B, Mein S, Dokic I, Harrabi S, Böhlen TT, Haberer T, et al. Development and validation of single field multi-ion particle therapy treatments. *Int J Radiat Oncol Biol Phys.* (2020) **106**:194–205. doi: 10.1016/j.ijrobp.2019.10.008
48. Sokol O, Krämer M, Hild S, Durante M, Scifoni E. Kill painting of hypoxic tumors with multiple ion beams. *Phys Med Biol.* (2019) **64**:045008. doi: 10.1088/1361-6560/aafe40
49. Prezado Y, Jouvion G, Patriarca A, Nauraye C, Guardiola C, Juchaux M, et al. Proton minibeam radiation therapy widens the therapeutic index for high-grade gliomas. *Sci Rep.* (2018) **8**:16479. doi: 10.1038/s41598-018-34796-8
50. Henry T, Ödén J. Interlaced proton grid therapy – Linear energy transfer and relative biological effectiveness distributions. *Phys Medica.* (2018) **56**:81–9. doi: 10.1016/j.ejmp.2018.10.025
51. González W, Prezado Y. Spatial fractionation of the dose in heavy ions therapy: An optimization study. *Med Phys.* (2018) **45**:2620–27. doi: 10.1002/mp.12902
52. Prezado Y, Jouvion G, Hardy D, Patriarca A, Nauraye C, Bergs J, et al. Proton minibeam radiation therapy spares normal rat brain: long-term clinical, radiological and histopathological analysis. *Sci Rep.* (2017) **7**:1–7. doi: 10.1038/s41598-017-14786-y
53. Vozenin M-C, De Fornel P, Petersson K, Favaudon V, Jaccard M, Germond J-F, et al. The advantage of flash radiotherapy confirmed in mini-pig and cat-cancer patients. *Clin Cancer Res.* (2018) **25**:35–42. doi: 10.1158/1078-0432.CCR-17-3375
54. Durante M, Brauer-Krisch E, Hill M. Faster and safer? FLASH ultra-high dose rate in radiotherapy. *Br J Radiol.* (2017) **91**:20170628. doi: 10.1259/bjr.20170628
55. Favaudon V, Caplier L, Monceau V, Pouzoulet F, Sayarath M, Fouillade C, et al. Ultrahigh dose-rate FLASH irradiation increases the differential response between normal and tumor tissue in mice. *Sci Transl Med.* (2014) **6**:245ra93. doi: 10.1126/scitranslmed.3008973
56. Harrington KJ. Ultrahigh dose-rate radiotherapy: next steps for FLASH-RT. *Clin Cancer Res.* (2019) **25**:3–5. doi: 10.1158/1078-0432.CCR-18-1796
57. Durante M, Brenner DJ, Formenti SC. Does heavy ion therapy work through the immune system? *Int J Radiat Oncol Biol Phys.* (2016) **96**:934–6. doi: 10.1016/j.ijrobp.2016.08.037
58. Durante M, Formenti S. Harnessing radiation to improve immunotherapy: better with particles? *Br J Radiol.* (2020) **93**:20190224. doi: 10.1259/bjr.20190224

Conflict of Interest: The authors declare that the research was conducted in the absence of any commercial or financial relationships that could be construed as a potential conflict of interest.

frontiers in Physics

ORIGINAL RESEARCH
published: 06 October 2020
doi: 10.3389/fphy.2020.565422

Real-Time PET Imaging for Range Verification of Helium Radiotherapy

Ikechi Ozoemelam[1], Emiel van der Graaf[1], Marc-Jan van Goethem[1], Maciej Kapusta[2], Nan Zhang[2], Sytze Brandenburg[1] and Peter Dendooven[1]*

[1] KVI-Center for Advanced Radiation Technology, University of Groningen, Groningen, Netherlands, [2] Siemens Medical Solutions USA, Inc., Knoxville, TN, United States

Real-time range verification of particle beams is important for optimal exploitation of the tissue-sparing advantages of particle therapy. Positron Emission Tomography (PET) of the beam-induced positron emitters such as ^{15}O ($T_{1/2} = 122$ s) and ^{11}C ($T_{1/2} = 1223$ s) has been used for monitoring of therapy in both clinical and preclinical studies. However, the half-lives of these nuclides preclude prompt feedback, i.e., on a sub-second timescale, on dose delivery. The *in vivo* verification technique relying on the in-beam PET imaging of very short-lived positron emitters such as ^{12}N ($T_{1/2} = 11$ ms), recently proposed and investigated in feasibility experiments with a proton beam, provides millimeter precision in range measurement a few tens of milliseconds after the start of an irradiation. With the increasing interest in helium therapy, it becomes relevant to study the feasibility of prompt feedback using PET also for helium beams. A recent study has demonstrated the production of very short-lived nuclides ($T_{1/2} = 10$ ms attributed to ^{12}N and/or ^{13}O) during irradiation of water and graphite with helium ions. This work is aimed at investigating the range verification potential of imaging these very short-lived nuclides. PMMA targets were irradiated with a 90 AMeV ^4He pencil beam consisting of a series of pulses of 10 ms beam-on and 90 ms beam-off. Two modules of a modified Siemens Biograph mCT PET scanner (21×21 cm^2), installed 25 cm apart, were used to image the beam-induced PET activity during the beam-off periods. For the irradiation of PMMA, we identify the very short-lived activity earlier observed to be ^{12}N ($T_{1/2} = 11.0$ ms). The range precision determined from the ^{12}N activity profile that is measured after just one beam pulse was found to be 9.0 and 4.1 mm (1σ) with 1.3×10^7 ^4He ions per pulse and 6.6×10^7 ^4He ions per pulse, respectively. When considering 4.0×10^7 ^4He ions, which is about the intensity of the most intense distal layer spot in a helium therapy plan, a range verification precision in PMMA of 5.7 mm (1σ) can be realized. The range precision scales approximately with the inverse square root of the number of ^4He ions, i.e., the relative statistical accuracy of the number of coincidence events. Thus, when summing data over about 10 distal layer spots, this study shows good prospects for obtaining 1.8 mm (1σ) precision in range verification, within 50 ms after the start of a helium irradiation by in-beam PET imaging (scanner 29% solid angle) of ^{12}N.

Keywords: helium ion therapy, range uncertainties, N-12 production, imaging, dose delivery verification

OPEN ACCESS

Edited by:
Marco Durante, GSI Helmholtz Center for Heavy Ion Research, Germany

Reviewed by:
Maria Giuseppina Bisogni, University of Pisa, Italy
Denis Dauvergne, Center National de la Recherche Scientifique (CNRS), France

****Correspondence:***
Ikechi Ozoemelam
ikechisamuel@gmail.com

Specialty section:
This article was submitted to Medical Physics and Imaging, a section of the journal Frontiers in Physics

Received: *25 May 2020*
Accepted: *28 August 2020*
Published: *06 October 2020*

Citation:
Ozoemelam I, van der Graaf E, van Goethem M-J, Kapusta M, Zhang N, Brandenburg S and Dendooven P (2020) Real-Time PET Imaging for Range Verification of Helium Radiotherapy. Front. Phys. 8:565422. doi: 10.3389/fphy.2020.565422

INTRODUCTION

Charged particles (in particular protons and carbon ions) are increasingly used for radiotherapy of cancers. The main rationale for their use, compared to irradiation with photons, is their favorable dose distribution: a reduced integral dose and an energy-dependent depth for the dose maximum (so called Bragg peak). Such dose distributions fulfill the therapeutic goal of having a sufficient dose in the tumor while minimizing the dose to co-irradiated healthy tissues. While protons and carbon ions remain the main charged particles used in cancer therapy, a renewed interest in therapy with helium ions has developed in recent years [1–5], with implementation planned for centers such as the Heidelberg Ion Beam Therapy Center (HIT) [6–8]. In pioneering clinical trials at the Lawrence Berkeley Laboratory, around 2,000 patients were treated with helium ions [9–11]. The rising interest in helium ions is driven by their advantages over protons and carbon ions: a smaller lateral penumbra compared to protons (see e.g., [4, 12]); and factors related to their lesser fragmentation [13] and potentially cheaper implementation cost relative to carbon ions.

In spite of the theoretical benefits attributed to the precise dose deposition of charged particles, the practical realization is hampered by the enhanced sensitivity of particle beams to differences between the data and models on which treatment plans are based and the actual situation during patient irradiation. These deviations originate, among others, from range uncertainties due to factors such as inaccuracies in the patient model (CT imaging and conversion to stopping power required for dose calculation), patient motion, setup errors and anatomical changes [14, 15]. Consequently, mitigation strategies including the use of larger safety margins [15, 16], robust optimization ([17–21], and review [22]) and sub-optimal beam directions [23] are adopted to provide robustness against these effects. Such strategies ensure tumor coverage at the expense of a larger dose to healthy tissue/organs at risk (OAR), and thus sub-optimally exploit the inherent dosimetric benefit of charged particle therapy. Motivated by the need to fully exploit these benefits, dual energy CT ([24, 25] and review by [26]) and proton imaging [27–29], which provide better information on the relative stopping power and thus lead to less range uncertainties, are being investigated. In addition to these imaging techniques, *in vivo* range verification techniques have been introduced and are being investigated as quality assurance tools for monitoring of the accuracy of dose delivery (see e.g., reviews [23, 30, 31]). A treatment protocol employing such a technique could enable the use of smaller range margins during treatment planning and/or the use of more optimal beam directions, i.e., also stopping the beam in close vicinity of OARs, effectively reducing the volume of irradiated healthy tissue. This contributes to minimizing the probability of complications, which increases the quality of life and reduces follow-up health care costs.

Given the absence in particle therapy of primary radiation exiting the patient body, *in vivo* verification techniques rely on the detection of secondary emissions resulting from particle interactions in the body: annihilation photons ([32–36] among others; review papers [37–39]), prompt gamma rays ([40–48] among others and review [49]), other secondary particles [50–52], and iono-acoustic waves [53–57].

Positron Emission Tomography (PET) imaging is the pioneering technique for *in vivo* range verification [32]. The technique relies on the imaging of the photons originating from the annihilation of positrons emitted in the radioactive decay of beam-induced radionuclides. An advantage of the PET technique is that it is based on a well-established nuclear medicine imaging technology and thus requires less effort in translation to routine clinical use. Three main strategies have been proposed for clinical implementation: "In-beam" imaging during the irradiation with a scanner integrated into the beam delivery nozzle [36, 58, 59]; "in-room" imaging after completion of the irradiation with a PET scanner installed in the treatment room and starting within about 2 min after the irradiation [35, 60, 61]; and offline imaging after completion of the irradiation with a PET scanner installed outside the treatment room and starting more than 5 min after irradiation [62–65]. The delayed data acquisition with respect to the irradiation, in the in-room and offline implementations, presents an advantage for the PET *in vivo* verification technique. For these implementations, the PET signal is essentially free of background signal interference from other beam-induced signals (neutrons, prompt photons and other secondary particles). Handling such interference is possible with the in-beam PET implementation. Its realization depends on the width and period of the beam pulses; coincidence window and time resolution of the scanner and may require pile-up rejection. A simulation study evaluating the performance of these strategies in terms of achievable count statistics (not including very-short lived positron emitters), image quality, cost of integration and impact on the treatment workflow is presented in [66]. Although, according to [66], the in-beam strategy gives the best performance, it faces a foremost challenge of a high integration cost. Consequently, the authors recommend the in-room strategy as a compromise between the high cost of integration of in-beam PET and the loss of count statistics as well as workflow impediments associated with the offline strategy.

The retrieval of prompt feedback (i.e., on a sub-second timescale) on dose delivery by individual irradiation spots requires the collection of sufficient counting statistics within a short period. The in-beam PET implementation, previously investigated at synchrocyclotrons, are incapable of providing such statistics due to the imaging of positron emitting nuclides with half-lives between 2 and 20 min during the irradiation pauses. For example, Pennazio et al. [59] reach a 1–2 mm range precision 190 s after the start of the irradiation. Thus, the absence of prompt feedback precludes the intra-fraction initiation of corrective actions to improve the dose delivery accuracy. We have shown that in addition to these longer-lived nuclides, very short-lived nuclides such as ^{12}N ($T_{1/2} = 11$ ms) are copiously produced during proton irradiation of carbon-rich tissues [67, 68]. Based on this finding, Buitenhuis et al. [69] and Ozoemelam et al. [70] performed experiments on the potential of imaging ^{12}N for range verification. A drawback of ^{12}N imaging is the positron range blurring, due to the high positron endpoint energy of 16.4 MeV, which will impact the retrieval of range information. Despite the large ^{12}N positron range, millimeter

precision range measurements can be performed when imaging the ^{12}N produced by 5×10^8 protons on both graphite and PMMA targets [69, 70].

As treatment with helium ions regains new interest, the optimal use of this ion would also benefit from an *in-vivo* verification technique. In contrast to protons and other therapeutic ions, there is a paucity of studies on PET monitoring of helium beam therapy. Early investigations [32] show that positron emitting isotopes [^{15}O ($T_{1/2} = 2.05$ min) and ^{11}C ($T_{1/2} = 20.3$ min)] are produced on carbon-rich materials and soft tissues, and could potentially indicate the range of helium beams, provided that technical limitations of the prevalent imaging hardware could be resolved. The limitations experienced at that time include the unavailability of on-line detection systems which allow the detection of short-lived nuclides and reduce biological washout of the nuclides; signal deterioration by background radiation; poor detector spatial resolution and sensitivity. Several decades after this investigation, most of these limitations have received significant attention and detection systems for on-line monitoring with improved detector resolution and sensitivity [35, 36, 59, 69–73] and methods for suppressing background radiation [69, 74] have been developed. More recent investigations into the feasibility of in-beam PET for therapeutic ^{3}He beams [75] and off-line PET with ^{4}He beams [76] provide a quantitative estimation of the production rates of the relevant radionuclides mentioned in Ref. [32], and highlight significant reduction in measured activity levels, especially in oxygen-rich materials, when changing from an in-beam detection to off-line strategies. As the imaging of the longer-lived nuclides, presented in these studies, does not provide prompt feedback on beam-delivery, alternative approaches based on the detection of prompt gamma photons have been investigated [77, 78].

The production of a very short-lived activity with a half-life of about 10 ms, attributed to ^{12}N and/or ^{13}O, was observed during irradiation of both carbon-rich and oxygen-rich targets with helium ions [79]. This activity could potentially be used to obtain prompt feedback on dose delivery. In this paper, we investigate the near-real time range verification capabilities, especially the precision, in helium beam radiotherapy by PET imaging of this very short-lived activity.

MATERIALS AND METHODS

Irradiation Setup

The experiment was performed at the AGOR cyclotron of the KVI-Center for Advanced Radiation Technology (KVI-CART), University of Groningen. **Figure 1** shows the experimental setup. A beam of 90 AMeV ^{4}He ions was used to irradiate PMMA

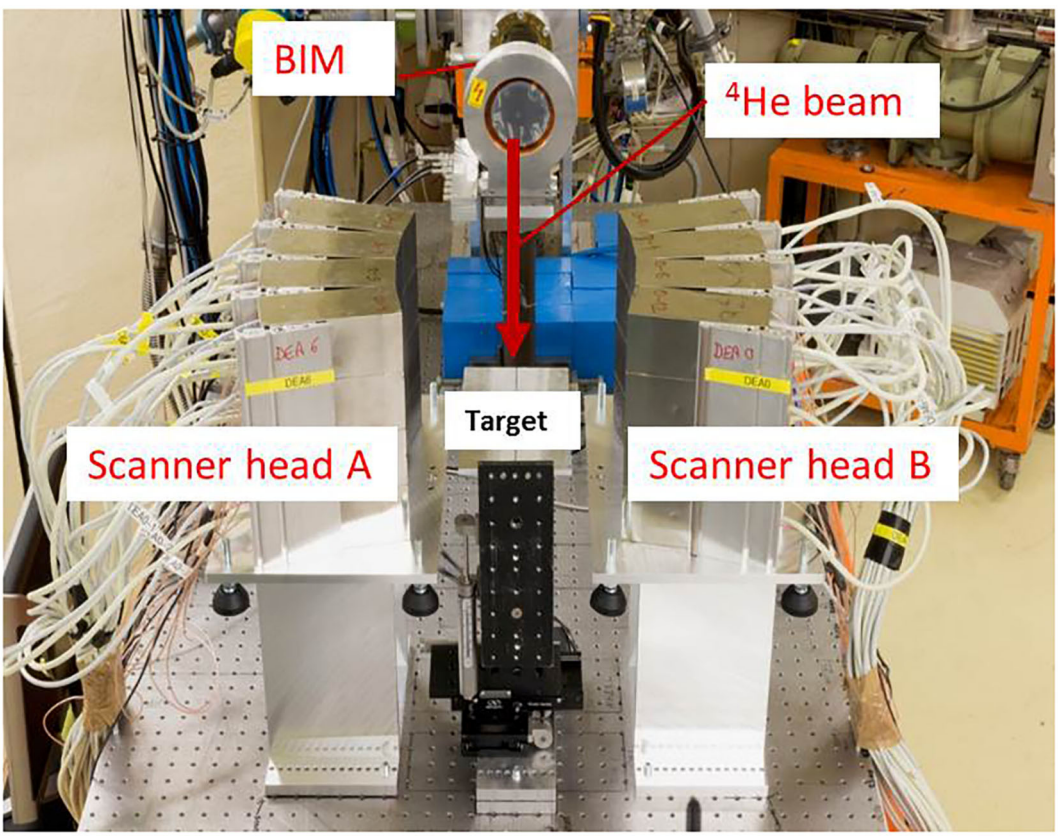

FIGURE 1 | Setup for imaging beam-induced positron activity. The ^{4}He beam direction is indicated by the red arrow. The beam bombards PMMA targets installed in-between two modules of a Siemens Biograph mCT PET Scanner, Scanner head A, and B. The beam intensity monitor (BIM) is indicated.

targets (see section Target and PET Scanner Setup). The beam was delivered through a horizontal beam line to the experimental area. The intensity of the beam was monitored with an air ionization chamber [beam intensity monitor (BIM)] placed after the exit window of the beam line. A paddle-shaped (100 × 100 mm^2 area and 1 cm thick) NE102A plastic scintillation detector, capable of counting each ^{4}He ion at low beam intensity, was used to calibrate the BIM in terms of beam intensity. The width of the beam at the target position was 6.5 mm FWHM in both vertical and horizontal direction, as measured using a harp-type (wire grid) beam profiler. To allow imaging of the short-lived PET nuclides without interference from the prompt radiation associated with the beam pulses, the ^{4}He beam was delivered in pulses consisting of 10 ms beam on and 90 ms beam off. The beam pulsing was realized with an electrostatic beam chopper in the injection line of the cyclotron. The chopper was controlled by a pulse generator that was also used to switch the detectors on and off. Two beam intensities were used: 1.3×10^7 and 6.6×10^7 ^{4}He ions per 10 ms pulse. After switching the beam on, the full beam intensity is reached within about 0.5 ms. Switching off the beam is slower: the intensity drops to 3% of its value after 3.0 ms. The targets were irradiated for 600 cycles (60 s) with data acquired during the beam pauses and an additional 70 s, while still pulsing the detectors, after the end of the irradiation. The data from the first second of irradiation are used to determine the range precision using the very short-lived activity (see section Range Verification Using 12N). The longer irradiation time enables to compare the number of counts from the very short-lived and the longer-lived activities (see section Time Spectrum of Activity).

Target and PET Scanner Setup

The dimensions of the PMMA targets (width × height × length) were 120 × 120 × 100 mm^3. The targets were installed with their short side parallel to the beam direction. As the ion range in PMMA calculated using SRIM [80] is 55 mm, the target thickness was sufficient to completely stop the ion beam and the positrons emitted by ^{12}N/^{13}O. **Table 1** shows the threshold for production of ^{12}N/^{13}O and other short-lived positron emitters during irradiation of carbon and oxygen with ^{4}He. Only the reaction channels with the lowest threshold energy are shown. The lowest threshold energy, for the production of ^{18}Ne on ^{16}O, of 29.7 MeV represents a helium range in water of 0.7 mm. The other reactions have threshold energies from 50.6 to 75.4 MeV, corresponding to a helium range in water from 1.9 to 3.9 mm. Thus, the distal edge of the activity profile is located few mm proximal to the ion range. Compared to protons, the proximal shift of the activity distal edge relative to the range is smaller because of the higher stopping power of helium.

The target was mounted such that the center of the field of view (FoV) of the scanner corresponded to a depth of 55 mm in the target. The central axes of the target and the scanner FoV were aligned with the beam direction. The distance between the centers of the two scanner modules was 252 mm. To investigate the range verification performance, PET data was acquired for the following target configurations: nominal and insertion of 1.9 ± 0.1, 3.0 ± 0.1, 4.9 ± 0.1, and 9.4 ± 0.3 mm PMMA range shifters at the proximal surface of the targets.

TABLE 1 | Reaction threshold energies for the production of very short-lived positron emitters produced by ^{4}He on carbon and oxygen (from https://www.nndc.bnl.gov/qcalc/index.jsp).

Nuclide	Target ^{12}C		Target ^{16}O	
	Reaction channel	Threshold (MeV)	Reaction channel	Threshold (MeV)
^{12}N	triton n	50.6	alpha triton p	56.4
^{13}O	3n	59.9	alpha 3n	65.1
^{9}C	alpha 3n	70.8	2alpha 3n	75.4
^{8}B	alpha triton n	61.2	2alpha triton n	66.4
^{18}Ne	(not possible)	–	2n	29.7

Only the reaction channels with the lowest threshold energy are given.

PET System

The PET system used in this experiment is 1/6 of a Siemens Biograph mCT clinical scanner with custom-modified detectors. Two detector panels were installed opposite each other for PET imaging of the beam-induced positron activity. Each panel has an area 210 × 210 mm^2 and is composed of a 4 × 4 array of block detectors. A block detector comprises a 13 × 13 array of 4 × 4 × 20 mm^3 LSO scintillation crystals read out by 4 photomultiplier tubes (PMTs). The energy signals are transmitted through Ethernet cables (CAT 6A twisted pair cables with RJ-45 jacks) to two Detector Electronics Assemblies (DEA) which encode position, energy and time of arrival of the photons. A coincidence unit receives the processed signals from the DEA, determines valid coincidence events and transmits the data to a data acquisition computer. A coincidence time window of 4 ns and an energy discrimination window of 435–650 keV were used. The panels were installed such that they curve around the vertical axis with a radius of curvature of 42 cm (see **Figure 1**).

Custom modifications were implemented to ensure good detector performance under the high radiation levels present during the helium beam irradiation. As each block detector is exposed to a γ-ray flux of around 10^8 s^{-1}, estimated from [81], during the beam-on periods, which exceeds the capacity of the PMTs, the PMT voltage dividers were modified such that the detectors can be effectively switched off during the beam-on periods. The detector pulsing is controlled by a TTL signal that is synchronized with the beam pulsing. After the detector is switched on, a period of 300 μs is required for the detector to become operational, while a shorter time of 130 μs is required to switch the PMT off. Despite the short time required to switch the PMT on, a longer delay of the start of the data acquisition after switching off the beam was used. An optimum delay of 3 ms was experimentally determined and applied as a compromise between exposure of the detector to prompt radiation resulting from the tail of the beam-on pulse and early detection of the beam-induced PET counts. Although the PMT becomes operational within 300 μs, a temporarily lowering of the PMT gain with a recovery time of about 25 ms was observed. This effect was investigated and quantified with ^{68}Ge radioactive sources in a coincidence setup with 2 block detectors as well as with data from part of the post-irradiation period (50–70 s after end of irradiation) using the complete scanner. In this period, the PET activity is due to the

decay of long-lived positron emitters, thus the time spectrum should have a constant activity within the 90 ms detector-on period. The time spectrum of coincidence events from both these investigations is shown in **Figure 2**. A period of about 5 ms is required to attain 90% of the maximum count rate in the 435–650 keV pulse height window used. We compared the detector recovery for irradiation with the two beam intensities applied in this study. No significant difference was observed for the intensity range used here. It cannot be excluded that an intensity dependence exists over a larger intensity range. The time spectra have been corrected with a time dependent normalization factor as shown in **Figure 2** to take the PMT gain recovery into account. Applying this correction on the data collected 30–50 s after the completion of the 60 s irradiation results in a constant count rate in the detector-on period, correctly reflecting the constant PET activity.

Image Reconstruction

The images of the beam-induced activity were reconstructed using the algorithm introduced in Ref. [69] and further described in Ref [70]. The reconstruction algorithm creates a 2D histogram of the intersection of the Lines of Response (LoR) with the plane coinciding with the helium pencil beam (i.e., the beam central axis). The Depth of Interaction (DoI) in the detector was set to a depth of 8 mm. Although more sophisticated algorithms such as the 3D maximum-likelihood expectation-maximization [82] provide a more accurate depiction of the activity distribution, these require high count statistics and a significant processing time. As the imaging of the short-lived nuclides is aimed at near real-time feedback using the relatively small short-lived positron activity and also given the accurate knowledge of the position of the pencil beam, the image reconstruction algorithm used here is considered sufficient for this purpose. A reconstruction grid over an area of 208 × 208 with 8 × 8 mm^2 pixel was used.

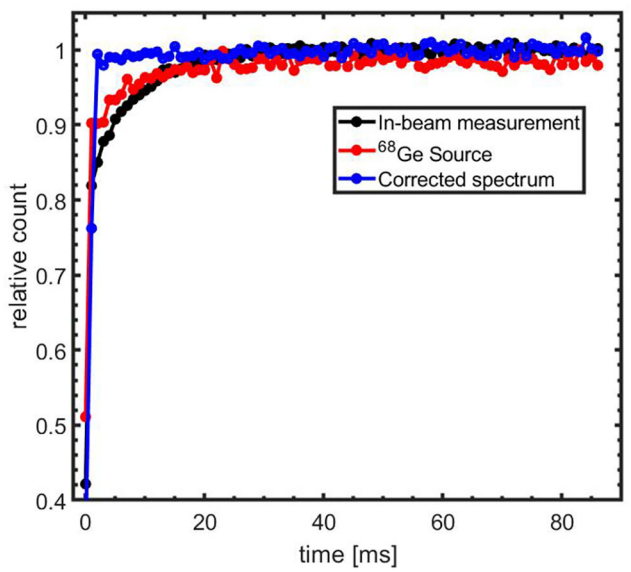

FIGURE 2 | Time spectrum of coincidence events after switching-on the PMTs. Spectrum for acquisition using radioactive lab sources (red) and 50–70 s post-irradiation measurement (black). The blue line represents a corrected spectrum of the 30–50 s post-irradiation data using the 50–70 s post-irradiation data as a normalization factor.

The LoR is determined from the IDs of the two coincident crystals. This information and the time tags of the coincidence events were recorded in a list-mode data file by the PET system. Time tags were inserted into the data stream at 1 ms intervals. The inclusion of the time tags was necessary to ensure proper identification of the short-lived nuclide activity contribution (See section Reconstruction of the Short-Lived Positron Emitter Contribution). The time tag values were inserted relative to the beginning of data acquisition. The beam pulsing was synchronized with the detector switching, but could not be synchronized with the start of the PET data acquisition. Irradiation was started shortly after the start of the data acquisition of the scanner. Due to the asynchronous start of data acquisition and irradiation, the exact start of the irradiation with respect to the time tags was determined through an analysis of the variations in the event rate. The data acquisition generally starts with a low pre-irradiation count rate followed by a marked increase in the coincidence rate due to beam-induced activity. As targets with no measurable initial activity were used in all measurement runs, the clear gradient in the count rate, seen in the acquired data, was used to identify the first beam-off period which served as reference for the subsequent pulses, which were identified by adding 100 ms time tag intervals.

The recovery of the coincidence rate (section PET System) was taken into account during the image reconstruction by weighting each LoR by a factor equal to the inverse of the coincidence recovery factor associated with the time bin of the LoR. Further to this correction, the 2D images were corrected for the non-uniform sensitivity of the PET system determined through measurements with calibrated ^{68}Ge line sources crossing the center of the scanner FoV. The absolute sensitivity of the scanner, measured with a calibrated ^{68}Ge point source (activity accuracy 0.6% 1σ) in the center of the FoV, was 2.2%.

Reconstruction of the Short-Lived Positron Emitter Contribution

The beam-induced positron emitters are indistinguishable on the basis of the 511 keV annihilation photons. To reconstruct the distribution of the short-lived nuclides, a weighted subtraction of images reconstructed for two different time windows in the beam-off period was performed. The first image, also referred to as the early image, was reconstructed using events from the time period 1–59 ms and contains contributions from both ^{12}N and longer-lived nuclides. The second image, referred to as the late image, was reconstructed using events from the period 60–86 ms and contains only counts from longer-lived nuclides. A weighting factor of 2.19, corresponding to the ratio of the duration of the early to late time windows, was used to scale the late image before the image subtraction step.

Detection of Range Shifts

To determine the shift in the range of the ^{4}He ions due to changes in target configuration, 1D activity profiles, with bin

width of 8 mm, along the direction of the ion beam were obtained from the 2D images reconstructed using the method described in section Reconstruction of the Short-Lived Positron Emitter Contribution. The 1D activity profile is a projection of the 2D image on the horizontal axis. The algorithm for detection of the range shift follows that used in Ref. [83] where the points in a given profile are shifted in the x-direction and compared to a reference profile to obtain the shift which minimizes the summed absolute difference between the two profiles. In this work, the activity profiles were normalized to their respective maximum and linearly interpolated in 0.08 mm bin widths and shifted in 0.08 mm steps relative to a reference profile. For each shift δ the root mean square difference between the profiles was calculated as

$$g(\delta) = \sqrt{\frac{\sum_{i=1}^{T}\left[A_{ref}(i) - A_{shift}(i-\delta)\right]^2}{T}} \quad (1)$$

where i is the index of the reference (A_{ref}) and range-shifted (A_{shift}) activity profiles; T is the number of bins in the profile. Indices in the activity profiles, starting from 500 bins (i.e., 40 mm) from the downstream edge of the FoV (depth bin = 0) to the 80% activity level on the proximal slope of the activity peak, were included in the comparison. The proximal slope represents the edge of the target where the beam enters the target. **Figure 3** shows the Region of Interest (RoI) used for profile comparison. Because of potentially non-overlapping ROIs, the bin offset between the proximal edges of the ROIs, δ_o, was determined. For a proximal shift of the profile as depicted in **Figure 3**, δ_o bins with zero counts were appended to the left side of the profile with a corresponding number of bins removed from the right side of the profile. For a distal shift, the appendage and clipping of bins was performed on the range-shifted profile. The range shift in mm was found as

$$A_{ref} - A_{shift} = \left[\delta_o + \text{argmin}_\delta(g(\delta))\right] * 0.08 \quad (2)$$

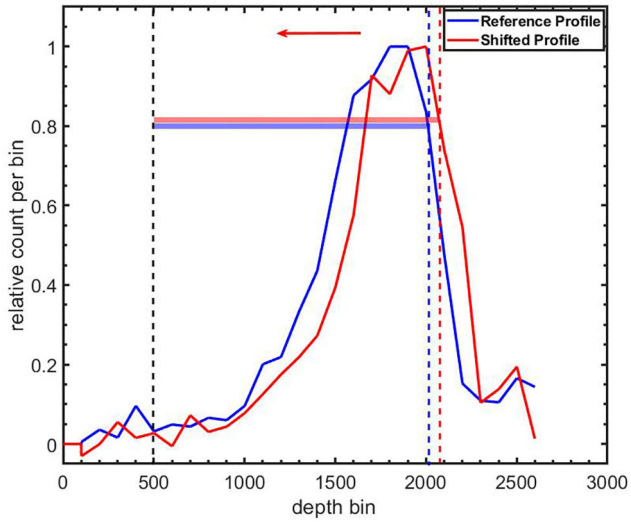

FIGURE 3 | Definition of regions of interest (RoIs) for comparing a shifted ^{12}N profile (Red line) to a reference ^{12}N profile (blue line). The corresponding colored horizontal bars indicate the extent of the RoIs. The lower level of both RoIs are the same and correspond to 500 bins (bin width = 0.08 mm) from the downstream edge of the field-of-view (depth bin = 0). The beam direction is indicated by the leftward arrow.

RESULTS

Time Spectrum of Activity

Figure 4 (left) shows the time spectrum of the beam-off periods of the first five pulses summed over ten irradiations with 6.6×10^7 ^{4}He ions per pulse. Each irradiation was performed with a fresh target. The decay of a short-lived contribution on top of a longer-lived contribution is clearly seen. A fit of the first pulse, as shown in **Figure 4** (right), gives a contribution with a half-life of 11.1 ± 0.3 ms. This fit value is consistent with ^{12}N and thus resolves the ^{12}N/^{13}O ambiguity in our previous study [79]. In the subsequent text we will therefore refer to the very short lived contribution as being due to ^{12}N. **Figure 5** shows the evolution of the longer-lived activity contributions within the first 10 s of a single irradiation. Shown are the total counts from long-lived contributions in the time window 1–59 ms, as well as the ratio of the long-to-total counts. At the start of the irradiation, 71% of the total count is due to ^{12}N. However, this fraction reduces to only 9% by 10 s into the irradiation due to a build-up of relatively fast decaying longer-lived nuclides. To identify and retrieve the fractions of these nuclides, the spectrum was fitted with a three-component exponential growth-in function:

$$F(t) = F_1\left(1 - exp^{-\lambda_1 t}\right) + F_2\left(1 - exp^{-\lambda_2 t}\right) + F_3\left(1 - exp^{-\lambda_3 t}\right) + Ct \quad (3)$$

with F_1, F_2, F_3, and C representing the contributions of three components and a constant. The decay constants of the components are represented by λ_1, λ_2 and λ_3. The combination of components consisting of ^{9}C ($T_{1/2}$ = 127 ms), ^{8}B ($T_{1/2}$ = 770 ms), ^{18}Ne ($T_{1/2}$ = 1.7 s), and a constant due to contributions of longer-lived nuclides [^{10}C ($T_{1/2}$ = 19.3 s), (^{17}F ($T_{1/2}$ = 64.8 s), ^{14}O ($T_{1/2}$ = 70.6 s), ^{15}O ($T_{1/2}$ = 122 s),^{13}N ($T_{1/2}$ = 598 s),^{11}C ($T_{1/2}$ = 1223 s), and ^{18}F ($T_{1/2}$ = 6586 s)], as expected from the measurements presented in ref. [79], was found to give the best fit to data.

Imaging of ^{12}N

The reconstructed images after corrections for the detector coincidence recovery and scanner sensitivity, as described in section Image Reconstruction, are displayed in **Figure 6**. The images were reconstructed from events arising from the first pulse (left column) and the sum of the first 10 pulses (right column) during the irradiation of PMMA with pencil beams of 1.3×10^7 ^{4}He ions per pulse. The ^{12}N images were reconstructed with ∼200 and 2,000 counts (without corrections for scanner uniformity and detector recovery) due to the decay of ^{12}N, respectively. A higher variance in pixel values and also pixels with negative values are seen in

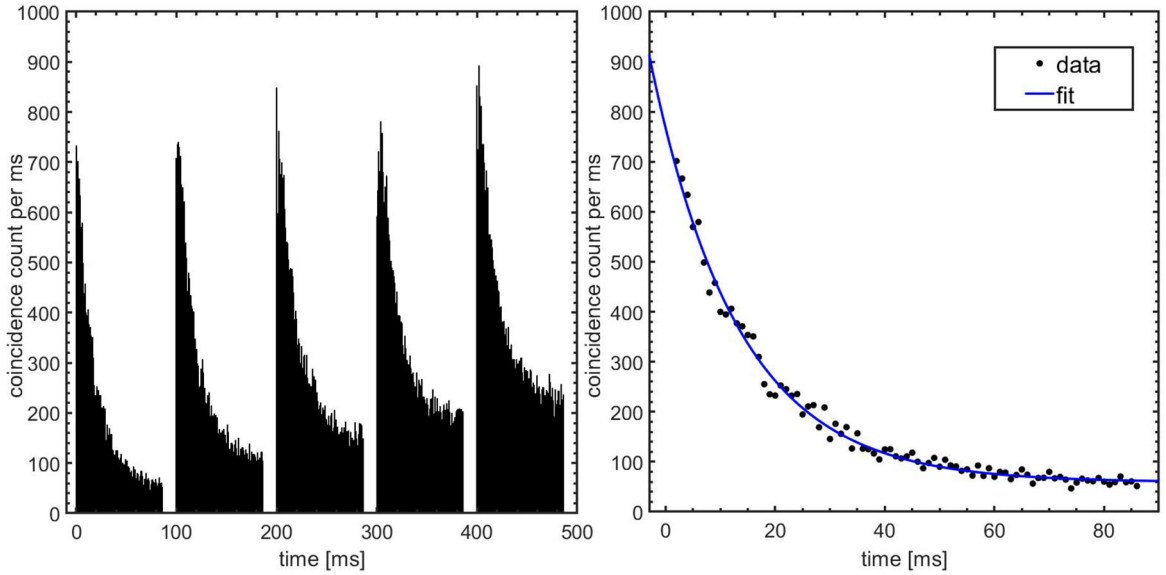

FIGURE 4 | Time spectrum of beam-induced activity. Left: Coincidence counts vs. time for the first five beam periods. The data shown are summed over 10 irradiations with 6.6 × 10^7 ^{4}He ions per pulse. The beam-on periods during which the detectors are switched off are easily recognized. Right: Fit of the corrected data after the first irradiation pulse with a single decay contribution and a constant. The fit considers data in the interval 2–86 ms.

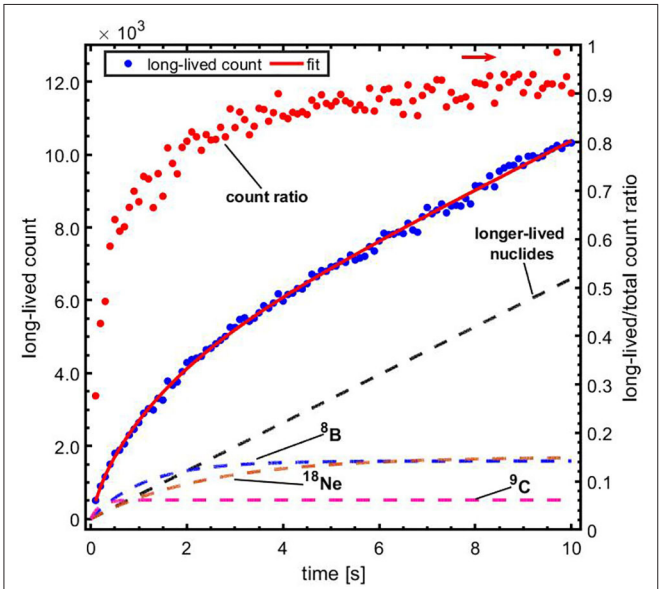

FIGURE 5 | The contribution of long-lived nuclides vs. time, during the first 10 s of the irradiation. Blue data, left vertical axis: total counts from long-lived contributions in the time window 1–59 ms of each beam-off period, with a fit to the data using Equation (3); red data, right vertical axis (indicated by the rightward arrow): ratio of the long-lived to total counts. The respective contributions of the indicated nuclides and the longer-lived nuclides are represented with the dashed lines.

the ^{12}N images due to the weighted subtraction of the late image from the early image. **Figure 7** shows 1-dimensional profiles perpendicular to the beam of an image reconstructed following irradiation with 6.6 × 10^9 ^{4}He ions (sum of the first 10 pulses of 10 datasets obtained from irradiations with 6.6 × 10^7 ^{4}He ions per pulse). The broader lateral width of the ^{12}N profile is caused by the much larger ^{12}N positron range.

Range Verification Using ^{12}N

The range verification performance of imaging ^{12}N was assessed through irradiation of PMMA targets in various configurations. The pixel values of 2D images were summed along the vertical axis into 1D activity profiles. To minimize the effect of the rather quick build-up of the long-lived nuclides as an irradiation progresses (see **Figures 4**, **5**) which increases the statistical uncertainty in the ^{12}N profiles, only data obtained from the first second of an irradiation, containing 10 ^{4}He ion pulses, were evaluated. In the first second of irradiation, the fractional contribution of the long-lived nuclides to the total count is smallest and varies between 29% in the first pulse to 68% in the 10th pulse (mean value = 0.58 ± 0.14). Nevertheless, the count variation is averaged out in the analysis that follows and we thus consider the ^{12}N profiles from the 10 pulses in the first second as nominally identical.

The range shift relative to a nominal (reference) target configuration was determined by comparing the 1-dimensional range-shifted profile of the modified target configuration with the reference profile. The best matching shift was retrieved as described in section Detection of Range Shifts. The reference profile was obtained from the average of 2 independently measured profiles and corresponds to a statistics of 1.32 × 10^9 ^{4}He ions. The independently measured profiles were obtained as follows

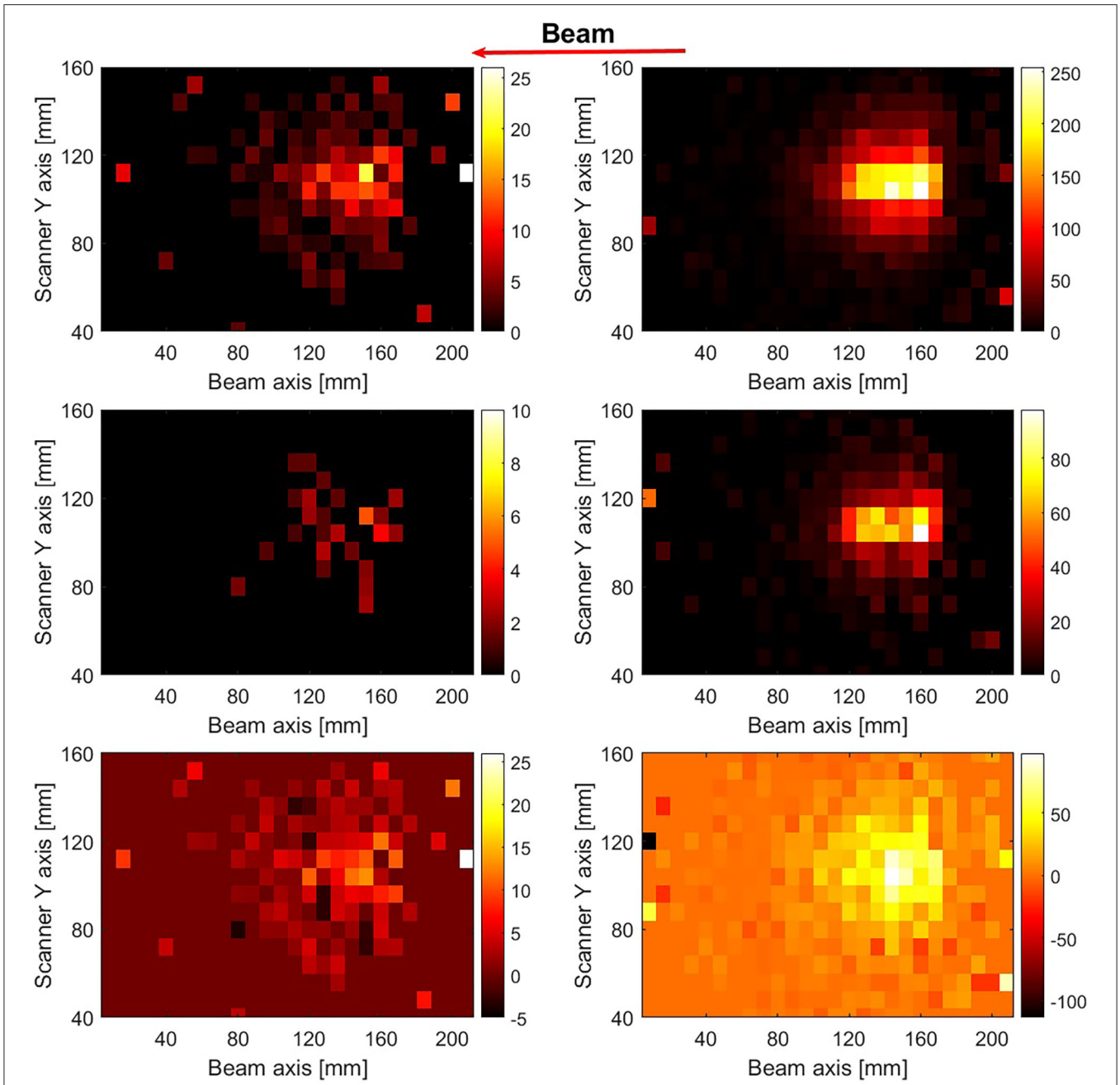

FIGURE 6 | 1-dimensional profiles of the beam-induced activity. Profiles along the scanner axis perpendicular to the beam are shown for the late (red) and ^{12}N (blue) images. The lines are included to guide the eyes.

a. The count data of 100 pulses were randomly sampled with replacement (the randomly sampled data can be re-used) from the first second (10 pulses) of irradiation with 6.60×10^7 ^{4}He ions per pulse, giving a data set equivalent to the sum of 10 pulses or 6.60×10^8 ^{4}He ions.
b. The sampled count data were summed and reconstructed into 1-dimensional profiles.

The range shifts for the range-shifted target configurations when irradiating the targets with the experimentally applied ^{4}He beam intensities (1.34×10^7 and 6.60×10^7 ^{4}He ions per pulse) were determined as the mean of the shifts of the 10 profiles reconstructed from the first second of irradiation. The uncertainties associated with the measured range shifts were determined from the standard deviation of the shifts.

As clinical applications may involve irradiations using beam intensities other than 1.34×10^7 and 6.60×10^7 ^{4} He ions per pulse, a bootstrap sampling technique [84] was used to generate quasi-independent samples. Sampling from the first 10 pulses of an irradiation was performed to combine counts from

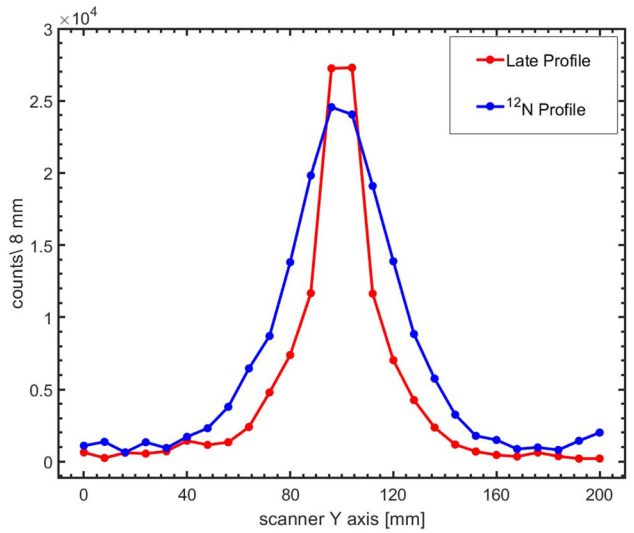

FIGURE 7 | 2D reconstructed PET images of the first pulse (left column) and the sum of the first 10 pulses (right column) for irradiation of PMMA with 1.3 × 10^7 ^{4}He ions per pulse. The beam direction is indicated by the leftward arrow. The images in the top and middle row were reconstructed using events occurring between beam-off time 1–59 ms (early image) and 60–86 ms (late image), respectively. The images were corrected for the scanner sensitivity and the coincidence recovery. The bottom row shows the ^{12}N image after the scaled subtraction of the late images from the early images.

multiples pulses, thus providing ^{12}N counts consistent with an irradiation with a higher number of ^{4}He ions per pulse. Samples having statistics corresponding to irradiations with (2.68, 6.71, 10.7, and 13.4) × 10^7 ^{4}He ions were generated by summing the counts from two, five, eight and ten pulses of 1.34 × 10^7 ^{4}He ions randomly sampled with replacement from the first second of the irradiation. The same sampling was performed for irradiations with 6.60 × 10^7 ^{4}He ions per pulse to obtain statistics corresponding to irradiations with (1.32, 3.3, 5.28, and 6.60) × 10^8 ^{4}He ions. To get good quality estimators (the mean and standard deviation) while approaching statistical independence, 500 bootstrapped samples were generated. After the bootstrapped sampling, the 1-dimensional profiles for each of these samples were constructed and the range shift determined using the procedure described in section Detection of Range Shifts.

In **Figure 8**, the ^{12}N profiles are shown for the nominal target configuration and with PMMA range shifters of 1.9 ± 0.1, 4.9 ± 0.1, and 9.4 ± 0.3 mm directly upstream of the target. The ^{12}N profiles displayed were obtained for statistics corresponding to an irradiation with 6.6 × 10^8 ^{4}He ions (realized by bootstrap sampling with replacement from 10 pulses of irradiation with 6.6 × 10^7 ^{4}He ions per pulse, as described above). Four out of the 500 bootstrapped sample profiles are shown alongside the reference profile for each case. As seen in **Figure 8**, the introduction of range shifters upstream of the target moves the profiles upstream with respect to the reference profile.

The distribution of the range shifts obtained from the bootstrapped samples is shown in **Figure 9** for two values of the number of ^{4}He ions per pulse. The mean value of the shifts of the sampled profiles is taken as the measured range shift due to the change in the target configuration. The measured range shifts for different configurations are summarized in **Table 2**. The precision of the measured range shifts was determined as the standard deviation of the range shifts from the 500 bootstrapped samples. The weighted mean deviations from the pre-set shifts are also given in **Table 2**. The weighted mean deviations indicate that the pre-set shifts are reproduced within the error bars for the respective number of ions.

The precision in the range shift measurement using ^{12}N profiles as function of the number of ^{4}He ions is shown in **Figure 10**. The data points represent the mean precision of the different configurations. The data points were then fitted with a power law function of the form: $BN^{-0.5}$, where N is the number of ^{4}He ions, the exponent 0.5 representing the effect of counting statistics. The fit parameter is: B = (363.2 ± 9.3) × 10^2. The higher precision as the number of ^{4}He ions increases is clearly seen and conforms quite well to the fitting function. It shows that non-statistical contributions, for e.g., scanner spatial resolution, to the precision are very small. Using this fitting model and parameters, we estimate that the precision on the measured range shifts when irradiating PMMA with 4.0 × 10^7 (a single distal layer spot), 1.2 × 10^8 (3 distal layer spots), and 4.0 × 10^8 (10 distal layer spots) ^{4}He ions is 5.7 mm (1σ), 3.3 mm (1σ), and 1.8 mm(1σ), respectively.

DISCUSSION

Although PET-based range verification can be implemented through the imaging of longer-lived positron emitters such as ^{15}O ($T_{1/2}$ = 122 s) and ^{11}C ($T_{1/2}$ = 1218 s) during irradiations with ^{3}He ions [75] and ^{4}He ions [32, 76], the realization of a fast feedback on the ion range is hampered by the half-lives of the positron emitters which necessitate rather long data acquisition periods. We present, in this current study, the performance of a PET-based near real time range verification technique for helium beam radiotherapy which relies on the imaging of the short-lived positron emitter ^{12}N with half-life of 11 ms.

A PET scanner consisting of two modified PMT-based detector modules from a Siemens Biograph mCT PET scanner was used to monitor the beam-induced activity following irradiation with ^{4}He ions. As mentioned in section PET System, the PMTs were switched off during the beam-on as a protective measure against the high radiation flux during the beam-on periods. Despite the fast recovery of the PMT signal of about 300 μs, it was observed that recovery of the coincidence count rate took 20–30 ms. Further investigations into the origin of this effect showed it to be due to a time-dependent gain shift of the PMTs. This recovery has been accounted for in the data analysis through the time-dependent efficiency correction factor. For future applications, a PMT gain shift correction could be implemented in either hardware or software, leading to 30% more coincidence counts and thus about 15% better precision in range measurement as the precision is largely determined by the counting statistics.

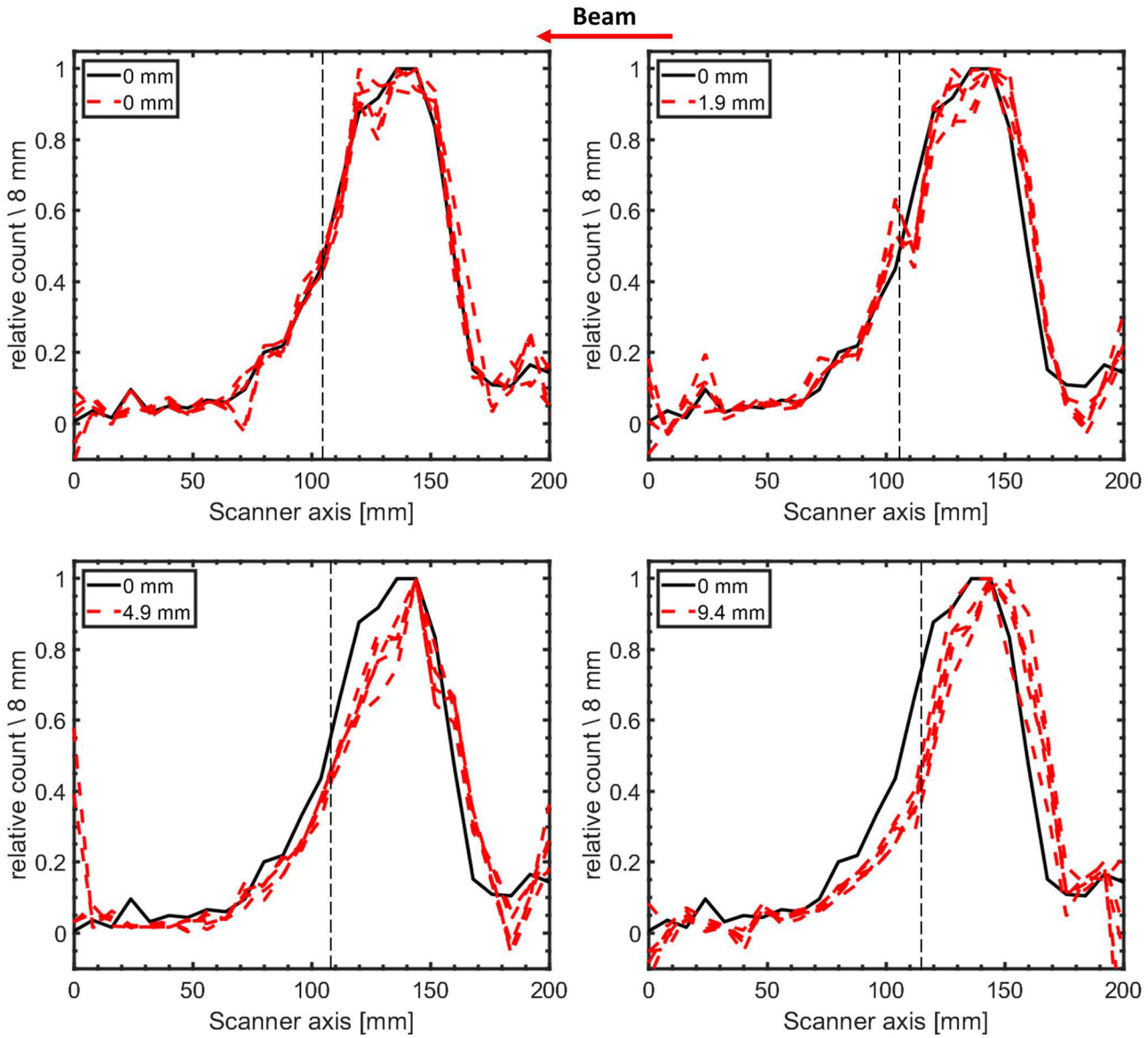

FIGURE 8 | 1-dimensional ^{12}N activity profiles (4 bootstrapped samples) of modified target configurations (red dashed lines) contrasted with the reference profile obtained in the nominal configuration (black line). The expected range shift for all four profiles is indicated by the label values. The helium ion range is indicated by the dashed vertical black lines. The activity profiles for the modified targets were reconstructed from the counts following an irradiation with 6.6×10^8 ^{4}He ions (10 pulses of irradiations with 6.6×10^7 ^{4}He ions per pulse sampled with replacement from the first second of irradiation). The profiles have been normalized to their respective maximum activity. The beam direction is indicated by the arrow.

Analysis of the time spectrum of the coincidence events (**Figure 4**) shows that a very short-lived contribution with half-life of 11.1 ± 0.3 ms is produced, confirming our previous study [79]. Whereas, our previous study makes no specific claims as to which combination of the short-lived nuclides ^{12}N ($T_{1/2} = 11.000 \pm 0.016$ ms) and ^{13}O ($T_{1/2} = 8.58 \pm 0.05$ ms) is produced, the half-life of the activity contribution seen here strongly suggests that almost exclusively ^{12}N is produced on PMMA.

The images of the activity contributions were reconstructed using the intersection of the LoR with the vertical plane containing the beam central axis. A weighted subtraction of two images, reconstructed using data acquired early and late into the beam-off period, was adopted to disentangle the ^{12}N contribution from the longer-lived ones. This approach, however, impacts the uncertainties in the ^{12}N distribution and the precision of the range measurement. A potentially more robust approach, that would be worth further study, for retrieval of the short-lived contribution could involve a half-life analysis of the pixel values of dynamic images acquired during the beam-off period as implemented for dual-isotope imaging in standard PET

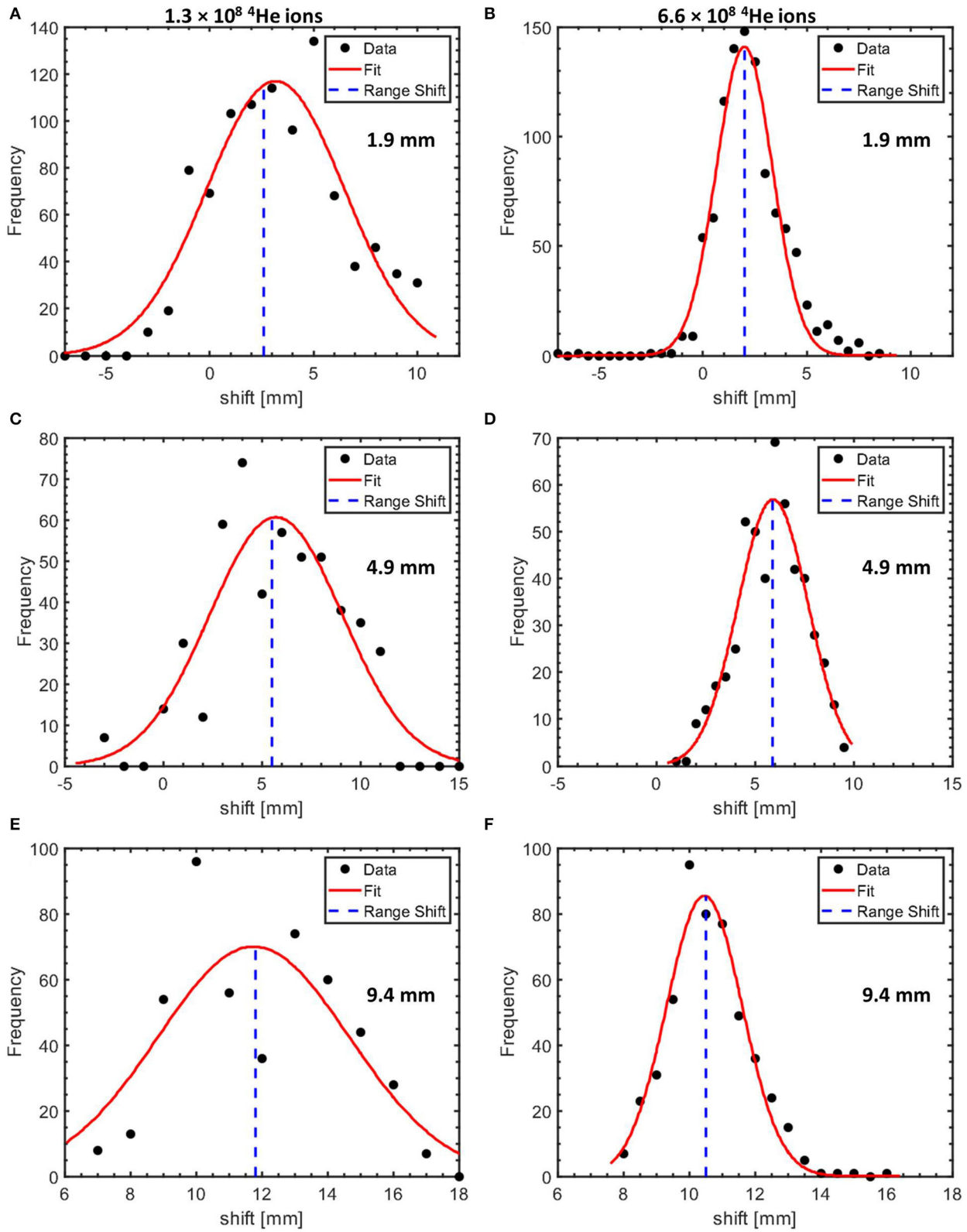

FIGURE 9 | Histograms of the measured range shifts for target configurations with 1.9 mm **(A,B)**, 4.9 mm **(C,D)**, and 9.4 mm **(E,F)** PMMA affixed to the PMMA target proximal surface. The shifts obtained using datasets equivalent to an irradiation of a PMMA target with 1.3×10^8 and 6.6×10^8 ^{4}He ions are shown in the left and the right column, respectively. The histograms are fitted with a Gaussian with the mean values indicated by the blue dotted line.

TABLE 2 | Precision of range verification for various configurations of PMMA targets and number of ^{4}He ions.

No. of ^{4}He ions	Pre-set range shift [mm]					Weighted mean deviation pre-set—measured shift [mm]
	0.0	1.9	3.0	4.9	9.4	
	Measured shift [mm]					
2.7×10^7	4.6 ± 9.3	3.3 ± 6.5	4.7 ± 5.6	4.2 ± 5.1	11.6 ± 6.9	-1.2 ± 6.3
6.7×10^7	3.9 ± 7.6	4.7 ± 3.4	3.3 ± 2.5	3.1 ± 6.0	12.7 ± 3.7	$-1.5. \pm 3.7$
1.3×10^8	0.1 ± 2.2	2.6 ± 3.6	1.9 ± 2.6	5.5 ± 3.2	11.8 ± 2.9	-0.4 ± 2.8
6.6×10^8	0.3 ± 1.4	2.0 ± 1.4	1.1 ± 1.4	5.9 ± 1.8	10.5 ± 1.1	-0.2 ± 1.4

The measured shifts are relative to the nominal (0 mm pre-set range shift) configuration. The uncertainty in the shifts is obtained from the standard deviation of the range shifts of 500 bootstrapped samples from the 10 measured profiles within the first second of the irradiation. The weighting for the mean deviation is the respective uncertainty on the measured shift. The uncertainty on the weighted mean deviation was multiplied by square root of 5 to be compatible with the respective number of helium ions.

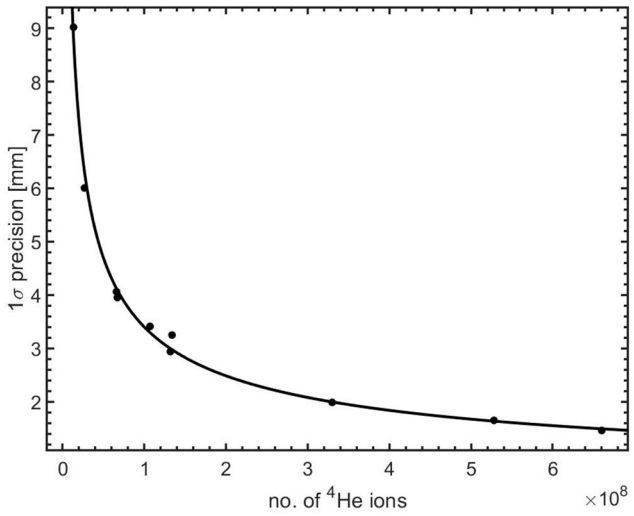

FIGURE 10 | Precision in range shift measurement as a function of the number of ^{4}He ions irradiating a PMMA target. The solid line is a power law ($BN^{-0.5}$) fit to the data.

imaging [85]. Such analysis can also be performed on the 1D profiles. A suitable model would comprise two components: a single exponential term for the ^{12}N contribution and a constant for longer lived contributions. A foremost challenge, however, foreseen in this approach is its susceptibility to the low counting statistics observed during irradiation.

With the image subtraction technique used in this work, we measured the shifts in the activity profiles relative to a reference profile for range shifters of different thickness. The observed mean deviations from the ground truth are consistent with the precision for the respective number of ^{4}He ions per pulse. The precision, as a function of the number of ^{4}He ions per pulse, for measuring range shifts was evaluated by calculating the standard deviation of the measured shifts for several profiles using bootstrap sampling. It is clear from **Figure 10** that increasing the number of helium ions per pulse results, as expected, in a better precision of the range shift measurement. The precision of the range measurement should be ideally better than 2 mm in order for it to be clinically relevant [86, 87]. For the delivery of a dose of 1 Gy during irradiations with protons, the most intense distal layer spot contains about 2×10^8 protons [43]. Given the 4 times higher stopping power of ^{4}He ions, the delivery of the same dose would require a conservative estimate of 4×10^7 ^{4}He ions in the highest weight distal layer spot. As such, the corresponding precision of 5.7 mm (1σ) for a single spot in this layer is poorer than the desired value of 2 mm. One approach to reach better statistics is to group neighboring spots together. By aggregating 10 distal layer spots, all containing a total of 4×10^8 ^{4}He ions, we calculate that the precision of range shift measurement using ^{12}N, in an optimized irradiation condition, is 1.8 mm (1σ). For a precision of 2 mm to be clinically useful, the range accuracy (difference between measured dose range and dose range in the treatment plan) needs to be smaller than the precision.

The experimental results presented in this work apply to a scanner with a solid angle coverage of 29% and a pulsed irradiation with a beam pulse duration of 10 ms and a 3 ms delay between irradiation and data acquisition. We envision that in future clinical deployment, the range verification precision could be further improved by increasing the solid angle coverage of the scanner, reducing the pulse duration and minimizing the delay before data acquisition starts as much as possible. **Table 3** shows the realizable precision for various scanner geometries, scanner panel separation distances and beam delivery and data acquisition time structures. The values given in **Table 3** have been estimated using the inverse dependence of the precision on $\sqrt{R}$, where R represents the ratio of the ^{12}N counts for the extrapolated system and the one used here. The ratio of the ^{12}N counts seen by two different scanner geometries depends mainly on the solid angle coverage of the system provided that other factors are the same. These factors include the amount of beam-induced activity, intrinsic detector efficiency, the amount of attenuation in the target and the 511 keV net peak fraction. The values in **Table 3** are thus valid for a 12-cm thick PMMA target (equivalent to 15 cm of water). Additional factors in precision of 1.15, 1.13, and 1.10 account for the additional count rate for (1) an optimal system with no PMT gain shift, (2) a reduction of the pulse duration from 10 to 3 ms and (3) elimination of the 3 ms delay before the start of the data acquisition, respectively.

TABLE 3 | Estimation of the precision for helium ion range measurement using various scanner geometries and time structures of beam delivery and data acquisition.

Panel separation distance (cm)	Scanner panel size (cm)	Solid angle (%)	Relative count	Precision (1σ) (mm)							
				10^7 ^{4}He ions per spot		4.0×10^7 ^{4}He ions per spot		1.2×10^8 ^{4}He ions per spot		4.0×10^8 ^{4}He ions per spot	
				$T_{on} = 10$ ms $T_d = 3$ ms	$T_{on} = 3$ ms $T_d = 0$ ms	$T_{on} = 10$ ms $T_d = 3$ ms	$T_{on} = 3$ ms $T_d = 0$ ms	$T_{on} = 10$ ms $T_d = 3$ ms	$T_{on} = 3$ ms $T_d = 0$ ms	$T_{on} = 10$ ms $T_d = 3$ ms	$T_{on} = 3$ ms $T_d = 0$ ms
25	21 × 21	29	1.0	11.5	8.1	5.7	4.1	3.3	2.3	1.8	1.3
	42 × 21	57	2.0	8.1	5.7	4.1	2.9	2.3	1.7	1.3	0.9
30	21 × 21	22	0.8	13.0	9.2	6.5	4.6	3.8	2.7	2.1	1.5
	42 × 21	45	1.6	9.2	6.5	4.6	3.3	2.7	1.9	1.5	1.0
	53 × 21	56	1.9	8.2	5.8	4.1	2.9	2.4	1.7	1.3	0.9
50	21 × 21	10	0.3	19.6	13.9	9.8	6.9	5.7	4.0	3.1	2.2
	42 × 21	20	0.7	13.9	9.8	6.9	4.9	4.0	2.8	2.2	1.6
	63 × 21	29	1.0	11.3	8.0	5.7	4.0	3.3	2.3	1.8	1.3

Attenuation effects of a 12 cm thick PMMA object have been included in the estimates. T_{on} is the beam-on period and T_d is the time delay between the beam-off and detector-on.

As seen in **Table 3**, for the highest weighted distal layer spot, a gain in precision by a factor of 2 is expected when imaging with a scanner having 56% solid angle coverage, optimized irradiation pulse duration and prompt data acquisition. Using such a scanner with an aggregation of 10 highly weighted distal layer spots, a precision of 0.9 mm (1σ) can be realized.

For *in vivo* verification purposes, the measured ^{12}N activity range needs to be connected to the dose range, the clinically relevant quantity. The minimum distance between the edges of a positron emitter activity and the dose is the range of a helium beam with an energy equal to the threshold energy of the nuclear reaction leading to the positron emitter. The thresholds for the very short-lived positron emitters observed in this work (see **Figure 5**) are given in **Table 2**. Only the reaction channels with the lowest threshold energy are given. The lowest threshold energy, for the production of ^{18}Ne on ^{16}O, of 29.7 MeV represents a helium range in water of 0.7 mm. The other reactions have threshold energies from 50.6 to 75.4 MeV, corresponding to a helium range in water from 1.9 to 3.9 mm. The thresholds for production of ^{12}N on ^{12}C and ^{16}O correspond to a helium range of 1.9–2.3 mm in water. When implementing ^{12}N imaging in clinical practice, the distance between the activity and beam ranges will need to be determined with an accuracy and precision that is better than the ^{12}N activity range uncertainty such that the overall beam range uncertainty is dominated by the experimental uncertainty in the ^{12}N activity range. The uncertainty in the distance between the ^{12}N activity range and beam range depends on the shape and the definition of the location of the distal edge of both the ^{12}N activity and the dose profile. This requires that the shape of the reaction cross section at low energy is known. The shape of the dose distal edge, determined by the initial beam energy spread and the amount of energy straggling, follows from the treatment planning system (TPS) and will be as accurate as the dose calculation of the TPS. The way to implement this in clinical practice is to incorporate the energy dependence of the cross section with sufficient detail into the TPS and that way determine the relationship between the ^{12}N activity range (which is measured) and the dose range (which is the clinically relevant quantity). To this end, the production cross sections of the relevant very short-lived positron emitters need to be determined in future work.

Clinical implementation of range verification based on ^{12}N imaging will require a modification of the standard pencil beam delivery scheme in which beam spots are delivered as fast as possible in order to minimize the overall duration of the irradiation. ^{12}N imaging of individual spots as we present in this work needs a beam pause of about 50 ms between spots. Having such pauses throughout a full irradiation would extend the duration too much. However, such a pause only makes sense for spots (or accumulation of some neighboring spots) that have sufficient intensity to give sufficiently accurate range information. This limits the introduction of beam pauses between spots to at most the few most distal layers. The extension of an irradiation can be further limited by introducing beam pauses only between distal layer spots located in carefully selected critical regions. This strategy of using so-called probe beams has in recent years been proposed by several authors [88–90]. It is expected that information from these spots can be used to assess the accuracy of the remaining spots in the treatment plan. The delivery scheme may thus be planned such that the beam is first delivered to these critical regions with sufficient beam-off time to measure the ^{12}N decay. Depending on the outcome of this initial range verification, a decision can then be reached on the continuation of beam delivery or the implementation of corrective actions.

Imaging making use of the PET events from both the short and long-lived activities will enhance the count statistics and the range measurement precision. However, as an irradiation progresses, the events from the long-lived activities created during previously irradiated spots, layers and treatment fields, make real-time feedback impossible. Real-time feedback including the longer-lived activities shown in **Figure 5**, when using the image reconstruction method adopted in this study, works only in the very beginning of an irradiation. The 2D image reconstruction method is unable to discriminate positron annihilation events that originate from different lateral positions along the direction between the scanner panels. One way to

disentangle these is event selection using a Time-of-Flight (ToF) system with a Coincidence Resolving Time (CRT) of at least 130 ps (given the 20 mm RMS ^{12}N positron range) and verifying the spots or group of spots separated laterally by this distance. The use of PET scanners with significantly better CRT than the 550 ps of our present scanner is being considered to investigate the utility of ToF in the reconstruction.

CONCLUSION

The proof-of-principle of real-time range verification using short-lived positron emitters has been demonstrated for helium beam radiotherapy by irradiating PMMA targets. We showed that monitoring an irradiation on the basis of ^{12}N activity imaging, at clinical beam intensity, is feasible and that near real-time feedback can be retrieved within 50 ms (i.e., 5 half-lives of ^{12}N) into an irradiation. The attainable precision of range measurements was found to be promising for future clinical application. The range measurement precision with the most intense distal pencil beam spot of 4×10^7 ions, using a scanner with a sensitivity of 2.2% at the center of the FoV and solid angle coverage of 29%, is 5.7 mm (1σ). By aggregating counts from 10 distal layer spots, further improvement by a factor of 3.2 [1.8 mm (1σ)] can be achieved. Aggregated imaging of 10 distal layer spots with a scanner of 56% solid angle coverage and beam spot durations much shorter than 10 ms will lead to a precision gain by a factor of 6.3 [0.9 mm (1σ)]. The increase of long-lived positron emitter activity as an irradiation progresses decreases the precision of real-time feedback via ^{12}N imaging. In future studies, methods to reduce the effect of the long-lived nuclides will be explored. Furthermore, given the characteristic timescales of the fast component of biological washout in tissues occurring within several tens of seconds after production [91], the very short-lived nuclides utilized in this work are not susceptible to the washout effect.

DATA AVAILABILITY STATEMENT

The raw data supporting the conclusions of this article will be made available by the authors under reasonable request.

AUTHOR CONTRIBUTIONS

PD, IO, and SB: conceptual design of the experiments. MK and NZ: design and production of the detector modifications and support in scanner operations. IO, PD, EG, and M-JG: experiments. IO, PD, SB, EG, MK, NZ, and M-JG: critical revision of manuscripts. All authors contributed to the article and approved the submitted version.

FUNDING

The PET scanner used in this work was made available under a collaboration agreement between the University of Groningen and Siemens Healthcare Nederland B.V.

ACKNOWLEDGMENTS

The authors would like to thank the following people for their contributions: F. Olivari and T. Rodriguez for their assistance during the experiments. P. Lemmens and S. Piersma for the design and production of the TTL switching box for PMT control. H. Kiewiet for assistance in installing the experimental setup at the irradiation hall and beam intensity calibrations. The operators of the AGOR cyclotron for stable beam operations.

REFERENCES

1. Kempe J, Gudowska I, Brahme A. Depth absorbed dose and LET distributions of therapeutic ^{1}H, ^{4}He, ^{7}Li, and ^{12}C beams. *Med Phys.* (2006) 34:183–92. doi: 10.1118/1.2400621
2. Grün R, Friedrich T, Krämer M, Zink K, Durante M, Engenhart-Cabillic R, et al. Assessment of potential advantages of relevant ions for particle therapy: a model based study. *Med Phys.* (2015) 42:1037–47. doi: 10.1118/1.4905374
3. Tommasino F, Scifoni E, Durante M. New ions for therapy. *Int J Particle Ther.* (2015) 2:428–38. doi: 10.14338/IJPT-15-00027.1
4. Durante M, Paganetti H. Nuclear physics in particle therapy: a review. *Rep Prog Phys.* (2016) 79:096702. doi: 10.1088/0034-4885/79/9/096702
5. Knäusl B, Fuchs H, Dieckmann K, Georg D. Can particle beam therapy be improved using helium ions? – a planning study focusing on pediatric patients. *Acta Oncol.* (2016) 55:751–9. doi: 10.3109/0284186X.2015.1125016
6. Krämer M, Scifoni E, Schuy C, Rovituso M, Tinganelli W, Maier A, et al. Helium ions for radiotherapy? Physical and biological verifications of a novel treatment modality. *Med Phys.* (2016) 43:1995–2004. doi: 10.1118/1.4944593
7. Mairani A, Dokic I, Magro G, Tessonnier T, Kamp F, Carlson DJ, et al. Biologically optimized helium ion plans: calculation approach and its *in vitro* validation. *Phys Med Biol.* (2016) 61:4283–99. doi: 10.1088/0031-9155/61/11/4283
8. Tessonnier T, Mairani A, Chen W, Sala P, Cerutti F, Ferrari A, et al. Proton and helium ion radiotherapy for meningioma tumors: a Monte Carlo-based treatment planning comparison. *Radiat Oncol.* (2018) 13:2. doi: 10.1186/s13014-017-0944-3
9. Jermann M. Particle Therapy Patient Statistics (per end of 2018). *Ptcog.ch.* (2018). Available online at: https://ptcog.ch/images/patientstatistics/Patientstatistics-updateDec2018.pdf (accessed Febraury 25, 2020).
10. Saunders W, Castro JR, Chen GTY, Collier JM, Zink SR, Pitluck S, et al. Helium-ion radiation therapy at the lawrence berkeley laboratory: recent results of a northern california oncology group clinical trial. *Radiat Res.* (1985) 104:S227–34. doi: 10.2307/3576652
11. Castro JR, Char DH, Petti PL, Daftari IK, Quivey JM, Singh RP, et al. 15 years experience with helium ion radiotherapy for uveal melanoma. *Int J Radiat Oncol Biol Phys.* (1997) 39:989–96. doi: 10.1016/S0360-3016(97)00494-X
12. Tessonnier T, Mairani A, Brons S, Haberer T, Debus J, Parodi K. Experimental dosimetric comparison of ^{1}H, ^{4}He, ^{12}C and ^{16}O scanned ion beams. *Phys Med Biol.* (2017) 62:3958–82. doi: 10.1088/1361-6560/aa6516
13. Rovituso M, Schuy C, Weber U, Brons S, Cortés-Giraldo M, La Tessa C, et al. Fragmentation of 120 and 200 MeV u^{-1} ^{4}He ions in water and PMMA targets. *Phys Med Biol.* (2017) 62:1310–26. doi: 10.1088/1361-6560/aa5302
14. Lomax AJ. Intensity modulated proton therapy and its sensitivity to treatment uncertainties 1: the potential effects of calculational uncertainties. *Phys Med Biol.* (2008) 53:1027–42. doi: 10.1088/0031-9155/53/4/014
15. Paganetti H. Range uncertainties in proton therapy and the role of monte carlo simulations. *Phys Med Biol.* (2012) 57:R99–117. doi: 10.1088/0031-9155/57/11/R99

16. Albertini F, Hug EB, Lomax AJ. Is it necessary to plan with safety margins for actively scanned proton therapy? *Phys Med Biol.* (2011) 56:4399–13. doi: 10.1088/0031-9155/56/14/011
17. Unkelbach J, Bortfeld T, Martin BC, Soukup M. Reducing the sensitivity of IMPT treatment plans to setup errors and range uncertainties via probabilistic treatment planning. *Med Phys.* (2009) 36:149–63. doi: 10.1118/1.3021139
18. Unkelbach J, Chan TCY, Bortfeld T. Accounting for range uncertainties in the optimization of intensity modulated proton therapy. *Phys Med Biol.* (2007) 52:2755–73. doi: 10.1088/0031-9155/52/10/009
19. Pflugfelder D, Wilkens J, Oelfke U. Worst case optimization: a method to account for uncertainties in the optimization of intensity modulated proton therapy. *Phys Med Biol.* (2008) 53:1689–700. doi: 10.1088/0031-9155/53/6/013
20. Fredriksson A, Forsgren A, Hårdemark B. Minimax optimization for handling range and setup uncertainties in proton therapy. *Med Phys.* (2011) 38:1672–84. doi: 10.1118/1.3556559
21. Unkelbach J, Paganetti H. Robust proton treatment planning: physical and biological optimization. *Semin Radiat Oncol.* (2018) 28:88–96. doi: 10.1016/j.semradonc.2017.11.005
22. Unkelbach J, Alber M, Bangert M, Bokrantz R, Chan TCY, Deasy JO, et al. Robust radiotherapy planning. *Phys Med Biol.* (2018) 63:22TR02. doi: 10.1088/1361-6560/aae659
23. Knopf A, Lomax A. *In vivo* proton range verification: a review. *Phys Med Biol.* (2013) 58:R131–60. doi: 10.1088/0031-9155/58/15/R131
24. Hünemohr N, Krauss B, Dinkel J, Gillmann C, Ackermann B, Jäkel O, et al. Ion range estimation by using dual energy computed tomography. *Zeitschrift Medizinische Physik.* (2013) 23:300–13. doi: 10.1016/j.zemedi.2013.03.001
25. Bär E, Lalonde A, Royle G, Lu HM, Bouchard H. The potential of dual-energy CT to reduce proton beam range uncertainties. *Med Phys.* (2017) 44:2332–44. doi: 10.1002/mp.12215
26. van Elmpt W, Landry G, Das M, Verhaegen F. Dual energy CT in radiotherapy: current applications and future outlook. *Radiother Oncol.* (2016) 119:137–44. doi: 10.1016/j.radonc.2016.02.026
27. Huesman RH, Rosenfeld AH, Solmitz FT. *Comparison of Heavy Charged Particles and X-Rays for Axial Tomograpic Scanning.* Davis, CA: California Univ Davis; Dept of Engineering (1975). doi: 10.2172/4146950
28. Esposito M, Waltham C, Taylor JT, Manger S, Phoenix B, Price T, et al. PRaVDA: the first solid-state system for proton computed tomography. *Phys Med.* (2018) 55:149–54. doi: 10.1016/j.ejmp.2018.10.020
29. Volz L, Piersimoni P, Bashkirov VA, Brons S, Collins-Fekete CA, Johnson RP, et al. The impact of secondary fragments on the image quality of helium ion imaging. *Phys Med Biol.* (2018) 63:195016. doi: 10.1088/1361-6560/aadf25
30. Parodi K, Polf J. *In vivo range verification in particle therapy. Med Phys.* (2018) 45:e1036–50. doi: 10.1002/mp.12960
31. Parodi K. *In vivo* dose verificatio. In: Paganetti H, editor. *Proton Therapy PhysicsBoca.* Raton, FL: CRC Press (2011). p. 489–524. doi: 10.1201/b11448-17
32. Maccabee HD, Madhvanath U, Raju MR. Tissue activation studies with alpha-particle beams. *Phys Med Biol.* (1969) 14:213–24. doi: 10.1088/0031-9155/14/2/304
33. Bennett GW, Goldberg AC, Levine GS, Guthy J, Balsamo J, Archambeau JO. Beam localization via 15O activation in proton-radiation therapy. *Nucl Inst Methods.* (1975) 125:333–8. doi: 10.1016/0029-554X(75)90246-3
34. Paans AMJ, Schippers JM. Proton therapy in combination with PET as monitor: a feasibility study. *IEEE Trans Nucl Sci.* (1993) 40:1041–4. doi: 10.1109/23.256709
35. Nishio T, Miyatake A, Ogino T, Nakagawa K, Saijo N, Esumi H. The development and clinical use of a beam ON-LINE PET system mounted on a rotating gantry port in proton therapy. *Int J Radiat Oncol Biol Phys.* (2010) 76:277–86. doi: 10.1016/j.ijrobp.2009.05.065
36. Enghardt W, Crespo P, Fiedler F, Hinz R, Parodi K, Pawelke J, et al. Charged hadron tumour therapy monitoring by means of PET. *Nucl Inst Methods Phys Res Sect A.* (2004) 525:284–88. doi: 10.1016/j.nima.2004.03.128
37. Studenski MT, Xiao Y. Proton therapy dosimetry using positron emission tomography. *World J Radiol.* (2010) 2:135. doi: 10.4329/wjr.v2.i4.135
38. Fiedler F, Kunath D, Priegnitz M, Enghardt W. Online irradiation control by means of PET. In: Linz U, editor. *Ion Beam Therapy.* Berlin: Springer (2012). p. 527. doi: 10.1007/978-3-642-21414-1_31
39. Zhu X, El Fakhri G. Proton therapy verification with PET imaging. *Theranostics.* (2013) 3:731–40. doi: 10.7150/thno.5162
40. Min CH, Kim CH, Youn MY, Kim JW. Prompt gamma measurements for locating the dose falloff region in the proton therapy. *Appl Phys Lett.* (2006) 89:183517. doi: 10.1063/1.2378561
41. Polf JC, Peterson S, Ciangaru G, Gillin M, Beddar S. Prompt gamma-ray emission from biological tissues during proton irradiation: a preliminary study. *Phys Med Biol.* (2009) 54:731–43. doi: 10.1088/0031-9155/54/3/017
42. Testa E, Bajard M, Chevallier M, Dauvergne D, Le Foulher F, Freud N, et al. Monitoring the Bragg peak location of 73 MeV/u carbon ions by means of prompt γ-ray measurements. *Appl Phys Lett.* (2008) 93:093506. doi: 10.1063/1.2975841
43. Smeets J, Roellinghoff F, Prieels D, Stichelbaut F, Benilov A, Busca P, et al. Prompt gamma imaging with a slit camera for real-time range control in proton therapy. *Phys Med Biol.* (2012) 57:3371–405. doi: 10.1088/0031-9155/57/11/3371
44. Golnik C, Hueso-González F, Müller A, Dendooven P, Enghardt W, Fiedler F, et al. Range assessment in particle therapy based on prompt γ -ray timing measurements. *Phys Med Biol.* (2014) 59:5399–422. doi: 10.1088/0031-9155/59/18/5399
45. Perali I, Celani A, Bombelli L, Fiorini C, Camera F, Clementel E, et al. Prompt gamma imaging of proton pencil beams at clinical dose rate. *Phys Med Biol.* (2014) 59:5849–71. doi: 10.1088/0031-9155/59/19/5849
46. Hueso-González F, Fiedler F, Golnik C, Kormoll T, Pausch G, Petzoldt J, et al. Compton camera and prompt gamma ray timing: two methods for *in vivo* range assessment in proton therapy. *Front Oncol.* (2016) 6:80. doi: 10.3389/fonc.2016.00080
47. Xie Y, Bentefour EH, Janssens G, Smeets J, Vander Stappen F, Hotoiu L, et al. Prompt gamma imaging for *in-vivo* range verification of pencil beam scanning proton therapy *Int J Radiat Oncol Biol Phys.* (2017) 99:210–8. doi: 10.1016/j.ijrobp.2017.04.027
48. Hueso-González F, Rabe M, Ruggieri TA, Bortfeld T, Verburg JM. A full-scale clinical prototype for proton range verification using prompt gamma-ray spectroscopy. *Phys Med Biol.* (2018) 63:185019. doi: 10.1088/1361-6560/aad513
49. Krimmer J, Dauvergne D, Létang JM, Testa É. Prompt-gamma monitoring in hadrontherapy: a review. *Nuclear Inst Methods Phys Res Sect A.* (2018) 878:58–73. doi: 10.1016/j.nima.2017.07.063
50. Rucinski A, Battistoni G, Collamati F, De Lucia E, Faccini R, Fralliccardi PM, et al. Secondary radiation measurements for particle therapy applications: charged particles produced by ^{4}He and ^{12}C ion beams in a PMMA target at large angle. *Phys Med Biol.* (2018) 63:055018. doi: 10.1088/1361-6560/aaa36a
51. Henriquet P, Testa E, Chevallier M, Dauvergne D, Dedes G, Freud N, et al. Interaction vertex imaging (IVI) for carbon ion therapy monitoring: a feasibility study. *Phys Med Biol.* (2012) 57:4655–69. doi: 10.1088/0031-9155/57/14/4655
52. Gwosch K, Hartmann B, Jakubek J, Granja C, Soukup P, Jäkel O, et al. Non-invasive monitoring of therapeutic carbon ion beams in a homogeneous phantom by tracking of secondary ions. *Phys Med Biol.* (2013) 58:3755–73. doi: 10.1088/0031-9155/58/11/3755
53. Hayakawa Y, Tada J, Arai N, Hosono K, Sato M, Wagai T, et al. Acoustic pulse generated in a patient during treatment by pulsed proton radiation beam. *Radiat Oncol Invest.* (1995) 3:42–45. doi: 10.1002/roi.2970030107
54. Patch SK, Santiago-Gonzalez D, Mustapha B. Thermoacoustic range verification in the presence of acoustic heterogeneity and soundspeed errors –Robustness relative to ultrasound image of underlying anatomy. *Med Phys.* (2019) 46:318–27. doi: 10.1002/mp.13256
55. Kellnberger S, Assmann W, Lehrack S, Reinhardt S, Thirolf P, Queirós D, et al. Ionoacoustic tomography of the proton Bragg peak in combination with ultrasound and optoacoustic imaging. *Sci Rep.* (2016) 6:29305. doi: 10.1038/srep29305
56. Lehrack S, Assmann W, Bertrand D, Henrotin S, Herault J, Heymans V, et al. Submillimeter ionoacoustic range determination for protons in water at a clinical synchrocyclotron. *Phys Med Biol.* (2017) 62:L20–30. doi: 10.1088/1361-6560/aa81f8
57. Jones KC, Nie W, Chu JCH, Turian JV, Kassaee A, Sehgal M, et al. Acoustic-based proton range verification in heterogeneous tissue: simulation studies. *Phys Med Biol.* (2018) 63:025018. doi: 10.1088/1361-6560/aa9d16

58. Parodi K, Ponisch F, Enghardt W. Experimental study on the feasibility of in-beam PET for accurate monitoring of proton therapy. *IEEE Trans Nucl Sci.* (2005) 52:778–86. doi: 10.1109/TNS.2005.850950
59. Pennazio F, Battistoni G, Bisogni MG, Camarlinghi N, Ferrari A, Ferrero V, et al. Carbon ions beam therapy monitoring with the INSIDE in-beam PET. *Phys Med Biol.* (2018) 63:145018. doi: 10.1088/1361-6560/aacab8
60. Min CH, Zhu X, Winey BA, Grogg K, Testa M, El Fakhri G, et al. Clinical application of in-room positron emission tomography for *in vivo* treatment monitoring in proton radiation therapy. *Int J Radiat Oncol Biol Phys.* (2013) 86:183–9. doi: 10.1016/j.ijrobp.2012.12.010
61. Min CH, Zhu X, Grogg K, El Fakhri G, Winey B, Paganetti H. A recommendation on how to analyze in-room PET for *in vivo* proton range verification using a distal PET surface method. *Technol Cancer Res Treat.* (2015) 14:320–5. doi: 10.1177/1533034614547457
62. Parodi K, Paganetti H, Shih HA, Michaud S, Loeffler JS, DeLaney TF, et al. Patient study of *in vivo* verification of beam delivery and range, using positron emission tomography and computed tomography imaging after proton therapy. *Int J Radiat Oncol Biol Phys.* (2007) 68:920–34. doi: 10.1016/j.ijrobp.2007.01.063
63. Nishio T, Miyatake A, Inoue K, Gomi-Miyagishi T, Kohno R, Kameoka S, et al. Experimental verification of proton beam monitoring in a human body by use of activity image of positron-emitting nuclei generated by nuclear fragmentation reaction. *Radiol Phys Technol.* (2008) 1:44–54. doi: 10.1007/s12194-007-0008-8
64. Knopf AC, Parodi K, Paganetti H, Bortfeld T, Daartz J, Engelsman M, et al. Accuracy of proton beam range verification using post-treatment positron emission tomography/computed tomography as function of treatment site. *Int J Radiat Oncol Biol Phys.* (2011) 79:297–304. doi: 10.1016/j.ijrobp.2010.02.017
65. Nischwitz SP, Bauer J, Welzel T, Rief H, Jäkel O, Haberer T, et al. Clinical implementation and range evaluation of *in vivo* PET dosimetry for particle irradiation in patients with primary glioma. *Radiother Oncol.* (2015) 115:179–85. doi: 10.1016/j.radonc.2015.03.022
66. Shakirin G, Braess H, Fiedler F, Kunath D, Laube K, Parodi K, et al. Implementation and workflow for PET monitoring of therapeutic ion irradiation: a comparison of in-beam, in-room, and off-line techniques. *Phys Med Biol.* (2011) 56:1281–98. doi: 10.1088/0031-9155/56/5/004
67. Dendooven P, Buitenhuis HJT, Diblen F, Heeres PN, Biegun AK, Fiedler F, et al. Short-lived positron emitters in beam-on PET imaging during proton therapy. *Phys Med Biol.* (2015) 60:8923–47. doi: 10.1088/0031-9155/60/23/8923
68. Dendooven P, Buitenhuis HJT, Diblen F, Heeres PN, Biegun AK, Fiedler F, et al. Corrigendum: short-lived positron emitters in beam-on PET imaging during proton therapy (2015 Phys. Med. Biol. 60 8923). *Phys Med Biol.* (2019) 64:129501. doi: 10.1088/1361-6560/ab23d7
69. Buitenhuis HJT, Diblen F, Brzezinski KW, Brandenburg, S, Dendooven P. Beam-on imaging of short-lived positron emitters during proton therapy. *Phys Med Biol.* (2017) 62:4654–72. doi: 10.1088/1361-6560/aa6b8c
70. Ozoemelam I, van der Graaf E, van Goethem M-J, Kapusta M, Zhang N, Brandenburg S, et al. Feasibility of quasi-prompt PET-based range verification in proton therapy. *Phys Med Biol.* (2020). doi: 10.1088/1361-6560/aba504. [Epub ahead of print].
71. Kraan AC, Battistoni G, Belcari N, Camarlinghi N, Ciocca M, Ferrari A, et al. Online monitoring for proton therapy: a real-time procedure using a planar PET system. *Nucl Instrum Methods Phys Res Sect A.* (2015) 786:120–6. doi: 10.1016/j.nima.2015.03.059
72. Tashima H, Yoshida E, Inadama N, Nishikido F, Nakajima Y, Wakizaka H, et al. Development of a small single-ring OpenPET prototype with a novel transformable architecture. *Phys Med Biol.* (2016) 61:1795–809. doi: 10.1088/0031-9155/61/4/1795
73. Yoshida E, Tashima H, Shinaji T, Shimizu K, Wakizaka H, Mohammadi A, et al. Development of a whole-body dual ring OpenPET for in-beam PET. *IEEE Trans Radiat Plasma Med Sci.* (2017) 1:293–300. doi: 10.1109/TRPMS.2017.2703823
74. Crespo P, Barthel T, Frais-Kolbl H, Griesmayer E, Heidel K, Parodi K, et al. Suppression of random coincidences during in-beam PET measurements at ion beam radiotherapy facilities. *IEEE Trans Nucl Sci.* (2005) 52:980–7. doi: 10.1109/TNS.2005.852637
75. Fiedler F, Crespo P, Parodi K, Sellesk M, Enghardt W. The feasibility of in-beam PET for therapeutic beams of ^{3}He. *IEEE Trans Nucl Sci.* (2006) 53:2252–9. doi: 10.1109/TNS.2006.877854
76. Bauer J, Tessonnier T, Debus J, Parodi K. Offline imaging of positron emitters induced by therapeutic helium, carbon and oxygen ion beams with a full-ring PET/CT scanner: experiments in reference targets. *Phys Med Biol.* (2019) 64:225016. doi: 10.1088/1361-6560/ab48b4
77. Mattei I, Bini F, Collamati F, Lucia ED, Fralliccardi PM, Iarocci E, et al. Secondary radiation measurements for particle therapy applications: prompt photons produced by 4 He, 12 C and 16 O ion beams in a PMMA target. *Phys Med Biol.* (2017) 62:1438. doi: 10.1088/1361-6560/62/4/1438
78. Dal Bello R, Magalhaes Martins P, Graça J, Hermann G, Kihm T, Seco J. Results from the experimental evaluation of CeBr scintillators for He prompt gamma spectroscopy. *Med Phys.* (2019) 46:3615–26. doi: 10.1002/mp.13594
79. Ozoemelam I, van der Graaf E, Brandenburg S, Dendooven P. The production of positron emitters with millisecond half-life during helium beam radiotherapy. *Phys Med Biol.* (2019) 64:235012. doi: 10.1088/1361-6560/ab51c3
80. ZieglerJ, Ziegler M, Biersack J. SRIM—the stopping and range of ions in matter. *Nucl Instrum Methods Phys Res B.* (2010) 268:1818–23. doi: 10.1016/j.nimb.2010.02.091
81. Hueso-González F, Biegun AK, Dendooven P, Enghardt W, Fiedler F, Golnik C, et al. Comparison of LSO and BGO block detectors for prompt gamma imaging in ion beam therapy. *J Inst.* (2015) 10:P09015. doi: 10.1088/1748-0221/10/09/P09015
82. Shepp LA, Vardi Y. Maximum likelihood reconstruction for emission tomography. *IEEE Trans Med Imaging.* (1982) 1:113–22. doi: 10.1109/TMI.1982.4307558
83. Knopf A, Parodi K, Paganetti H, Cascio E, Bonab A, Bortfeld T. Quantitative assessment of the physical potential of proton beam range verification with PET/CT. *Phys Med Biol.* (2008) 53:4137–51. doi: 10.1088/0031-9155/53/15/009
84. Efron B. Bootstrap methods: another look at the jackknife. *Ann Stat.* (1979) 7:1–26. doi: 10.1214/aos/1176344552
85. Huang SC, Carson RE, Hoffman EJ, Kuhl DE, Phelps ME. An investigation of a double-tracer technique for positron computerized tomography. *J Nucl Med.* (1982) 23:816–22.
86. Parodi K. On- and off-line monitoring of ion beam treatment. *Nucl Instrum Methods Phys Res Sect A.* (2016) 809:113–9. doi: 10.1016/j.nima.2015.06.056
87. Pausch G, Berthold J, Enghardt W, Römer K, Straessner A, Wagner A, et al. Detection systems for range monitoring in proton therapy: needs and challenges. *Nucl Instrum Methods Phys Res Sect A.* (2020) 954:161227. doi: 10.1016/j.nima.2018.09.062
88. Chen M, Zhong Y, Shao Y, Jiang S, Lu W. Mid-range probing—towards range-guided particle therapy. *Phys Med Biol.* (2018) 63:13NT01. doi: 10.1088/1361-6560/aaca1b
89. Mumot M, Algranati C, Hartmann M, Schippers JM, Hug E, Lomax AJ. Proton range verification using a range probe: definition of concept and initial analysis. *Phys Med Biol.* (2010) 55:4771–82. doi: 10.1088/0031-9155/55/16/010
90. Hammi A, Koenig S, Weber DC, Poppe B, Lomax AJ. Patient positioning verification for proton therapy using proton radiography. *Phys Med Biol.* (2018) 63:245009. doi: 10.1088/1361-6560/aadf79
91. Mizuno H, Tomitani T, Kanazawa M, Kitagawa A, Pawelke J, Iseki Y, et al. Washout measurement of radioisotope implanted by radioactive beams in the rabbit. *Phys Med Biol.* (2003) 48:2269–81. doi: 10.1088/0031-9155/48/15/302

Conflict of Interest: MK and NZ were employed by the company Siemens Medical Solutions. The authors declare that this study received funding from Siemens Medical Solutions. The funder had the following involvement with the study: the PET scanner with custom-modified detectors was provided and comments on the manuscript were given.

frontiers in Physics

ORIGINAL RESEARCH
published: 06 October 2020
doi: 10.3389/fphy.2020.575906

Investigation of Biophysical Migration Parameters for Normal Tissue and Metastatic Cancer Cells After Radiotherapy Treatment

Valeria Panzetta[1,2]*, *Giuseppe La Verde*[3,4], *Mariagabriella Pugliese*[3,5], *Cecilia Arrichiello*[6], *Paolo Muto*[6], *Marco La Commara*[3,4], *Vittoria D'Avino*[3], *Paolo A. Netti*[1,2] and *Sabato Fusco*[1,2]*

[1] Centro di Ricerca Interdipartimentale sui Biomateriali, Università degli Studi di Napoli Federico II, Naples, Italy, [2] Center for Advanced Biomaterial for Health Care, Istituto Italiano di Tecnologia, Naples, Italy, [3] Istituto Nazionale di Fisica Nucleare (INFN), Sezione di Naples, Naples, Italy, [4] Dipartimento di Farmacia, Università degli Studi di Napoli Federico II, Naples, Italy, [5] Dipartimento di Fisica "Ettore Pancini", Università degli Studi di Napoli Federico II, Naples, Italy, [6] Radiotherapy Unit, Istituto Nazionale Tumori-Istituti di Ricovero e Cura a Carattere Scientifico (IRCCS)-Fondazione "G. Pascale", Naples, Italy

OPEN ACCESS

Edited by:
Vincenzo Patera,
Sapienza University of Rome, Italy

Reviewed by:
Andrea Attili,
National Institute of Nuclear Physics of Rome, Italy
Alexander Helm,
GSI Helmholtz Centre for Heavy Ion Research, Germany

***Correspondence:**
Valeria Panzetta
valeria.panzetta@unina.it
Sabato Fusco
sabfusco@unina.it

Specialty section:
This article was submitted to Medical Physics and Imaging, a section of the journal Frontiers in Physics

Received: 24 June 2020
Accepted: 24 August 2020
Published: 06 October 2020

Citation:
Panzetta V, La Verde G, Pugliese M, Arrichiello C, Muto P, La Commara M, D'Avino V, Netti PA and Fusco S (2020) Investigation of Biophysical Migration Parameters for Normal Tissue and Metastatic Cancer Cells After Radiotherapy Treatment. Front. Phys. 8:575906. doi: 10.3389/fphy.2020.575906

A large body of literature has demonstrated that the mechanical properties of microenvironment have a key role in regulating cancer cell adhesion, motility, and invasion. In this work, we have introduced two additional parameters, named cell trajectory extension and area traveled by cell, to describe the tendency of normal tissue and metastatic cancer cells to move in a directional way when they interact with physio-pathological substrates, characterized by stiffnesses of 1–13 kPa, before and after treatment with 2 doses of X-rays (2 and 10 Gy). We interpreted these data by evaluating also the impact of substrate stiffness on 2 morphological parameters which indicate not only the state of cell adhesion, but also cell polarization, prerequisite to directional movement, and the formation of protrusions over cell perimeters. We believe that a so wide analysis can give an efficient and easily readable overview of effects of radiation therapy on cell-ECM crosstalk when used as therapeutic agent.

Keywords: breast cancer, mechanobiology, cell motility analysis, extracellular matrix stiffness, radiotherapy

INTRODUCTION

Cells have continuous interactions with surrounding environments and the relative mechanical dynamics are today recognized as powerful conditioning factors for cells' behavior [1–5]. The healthy functioning of many human tissues, indeed, originates from the correct interactions between cell cytoskeleton and extracellular matrix (ECM). When altered by genetic or environmental factors, they have a determinant contribution in many diseases' occurrence and progression [6–11]. In case of tumors, where the ECM may represent up to half of the entire mass, higher level fibrillar constituents (collagen, fibronectin, etc.) and specific molecular expression profiles are found. Such modification in architecture and composition gives rise to a negative loop that induces a compromised feedback between cells and the surroundings matrix. The composition and mechanical identity of ECM, for instance, can regulate the cell epithelial-mesenchymal transition (EMT), a metastases precursor process in which cells acquire a more stem-like character. To promote migration, in fact, cancer cells have to activate differentiating genes, and degrade cell-cell junction by the downregulation of the associated proteins and the upregulation of those

appointed to adhere and/or lyse the matrix [12–16]. It has been reported that in breast tumors the stiffness can induce the nuclear translocation of transcription factors as YAP or TWIST1, both related to the EMT process [17–20], thus suggesting a very close relationship between ECM mechanical properties and tumor metastatic potential. One of the most consolidated therapeutic strategy adopted this day to contrast tumor progression is the radiotherapy (RT). Although its direct and well-established cytotoxic effect on cancer cells by DNA damage, different reports in literature suggested that in some cases hypoxia, typical of different tumors, can reduce the efficacy of RT, influencing the outcome of treatment of tumor, and leading to high recurrence and increased distant metastases [21]. On the other hand, there is a large evidence that the dose heterogeneity across normal tissue (dose gradient) and the modification of normal tissue tolerance to dose when irradiated volume changes (volume effects) have an important impact on the problem concerning second cancer risks [22, 23]. The dose-volume question is principally related to conventional and 3D conformal radiation therapy, whereas modern techniques and, in particular, intensity modulated radiation therapy (IMRT) seems to reduce the risks of second cancer risks [24]. Several mechanisms that promote this counterproductive effect have been identified, including vascular damage, EMT, and cytokine production [25]. The clinical significance of these findings is still largely unknown and new cell biophysical parameters have to be identified in order to assess how RT treatments can promote increased cell migration [26, 27] and enhanced growth of distant metastases [25, 28] as well as reduction of cell migration [29, 30] and inhibition of distant tumor growth, also known as the abscopal effect [31]. Along this path, we proposed here a continuation of our previous work [29] by the introduction of new biophysical parameters that can be used by different researcher interested into basic and clinical translation of mechanobiology investigation. In particular, in this study we focused our attention on breast cancer, a consolidated model used to understand cancer progression and metastasis and generally treated with RT from stages I to III to reduce the risk of recurrence after surgery. In details, we have investigated the behavior of a normal epithelial cell line (MCF10A) and a highly aggressive and invasive adenocarcinoma cell line (MDA-MB-231) through a migration experimental campaign on polyacrylamide (PAAm) substrates mimicking pathophysiological stiffness (1–13 kPa). Study was conducted in control conditions and 72 h after the exposure to two different doses of X-rays, 2 and 10 Gy, which represent the daily dose in radiotherapy treatment and the single maximum dose for the treatment of metastasis. In order to obtain a more detailed comparison of the cells' responses to RT to ECM stiffness simulating pathophysiological microenvironments, two biophysical parameters and the mean square displacement (MSD) of the cells were derived from the analysis of the trajectory. The single and combined evaluation of these parameters, together with the analysis of cell morphological features, gives more insights into the effects of RT on cell-ECM crosstalk when used as therapeutic agent.

MATERIALS AND METHODS

Substrate Preparation and Functionalization

PAAm substrates with two different mechanical properties were produced by using two solutions of acrylamide and methylene-bis-acrylamide (4% acrylamide/0.15% methylene-bis-acrylamide and 10% acrylamide/0.1% methylene-bis-acrylamide corresponding to 1.3 and 13 kPa, respectively) and then functionalized with bovine collagen type I. More detailed information can be found in [32].

Cell Culture and Irradiation

MCF10A cells were grown in Lonza mammary epithelium-based medium (MEBM), supplemented with bovine pituitary extract (BPE), human epidermal growth factor (hEGF) (0.1%), insulin (0.1%), hydrocortisone (0.1%), gentamicin–amphotericin (GA-1000; 0.1%).

MDA-MB-231 cells were grown in Lonza Dulbecco's modified Eagle medium (DMEM/F-12) supplemented with 10% fetal bovine serum (FBS, Gibco, Eggenstein, Germany), 1% L-glutamine (Sigma, St. Louis, MO, USA), and 1% penicillin–streptomycin (Sigma, St. Louis, MO, USA).

24 h after cell culture, MCF10A and MDA-MB-231 cells were exposed to two different doses of X-rays, 2 and 10 Gy, with a dose rate equal to 5 Gy/min, using a 6MeV energy beam, at the National Cancer Institute "PASCALE" of Naples. Additional information can be found in [29].

Migration Parameters

MCF10A and MDA-MB-231 cells were cultured on PAAm substrates at a final density of 1,000 cells/cm^2, to guarantee a sparse-cell condition also 72 h after irradiation (time of analysis), necessary to avoid the formation of cell-cell contacts that could override the effect of substrate stiffness. Cell migration experiment were performed as previously reported [29]. Briefly, images of cells were acquired every 10 min for a total duration of 24 h. Single cell trajectories were determined using ImageJ and Manual Tracking plugin (http://rsweb.nih.gov/ij/). Their orientation was calculated by using the ellipse-fitting function in ImageJ and, then, cell trajectories were rigidly rotated around the starting point P(x(0), y(0)) by using the rotation matrix as represented in **Figure 1**. After the coordinate transformation, we obtained the new coordinates $x'(t)$ and $y'(t)$ at every time t and the principal direction of the rotated trajectory results to be aligned to y'-axis. Once rotated, the net displacements traveled along x'- and y'-directions were calculated as follows

$$\Delta x' = x'_{\max} - x'_{\min} \quad (1)$$

$$\Delta y' = y'_{\max} - y'_{\min} \quad (2)$$

where $x'/y'_{\max}$ and $x'/y'_{\min}$ are the maximum ad the minimum values of the rotated coordinates x' and y'.

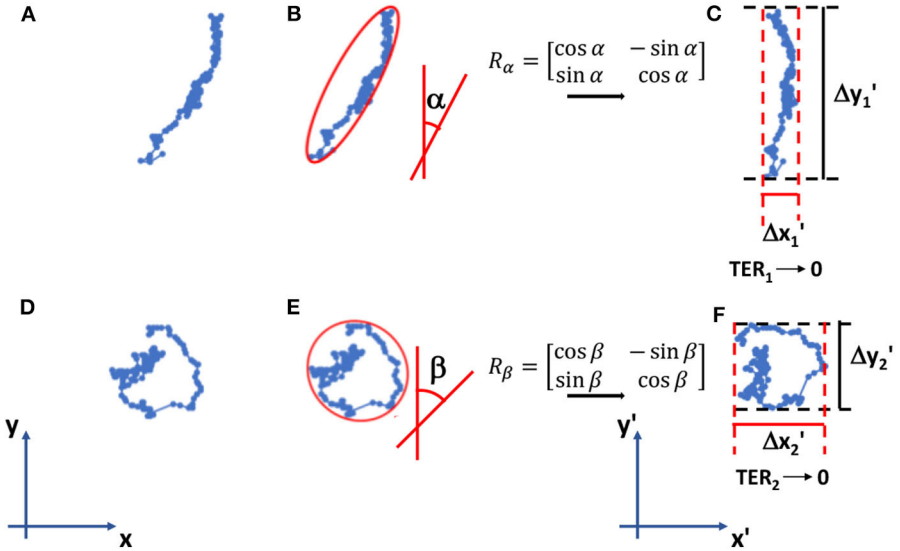

FIGURE 1 | Examples of cell trajectories **(A–D)** in the reference system. Their orientations α and β are calculated using the fitting-ellipse function in Image J **(B–E)** and then the rotation matrices R_α and R_β rotate the trajectories in the new reference system x′-y′ **(C–F)**. Here, we calculate TER parameter as indicated in formulas (1)–(3). TER_1 approaches to 0 (elongated trajectory), whereas TER_2 is close to 1 (round/random trajectory).

The trajectory extension ratio (TER) and the area traveled (AT) were calculated with the following expressions

$$TER = \frac{\Delta x'}{\Delta y'} \quad (3)$$

$$AT = \frac{\pi\ \Delta x' \Delta y'}{4} \quad (4)$$

MSD on x′- and y′- directions (MSD_x and MSD_y) were calculated, starting from rotated trajectories, using the following formula:

$$MSD_x(\tau) = \left\langle \left[x'(t-\tau) - x'(t)\right]^2 \right\rangle \quad (5)$$

$$MSD_y(\tau) = \left\langle \left[y'(t-\tau) - y'(t)\right]^2 \right\rangle \quad (6)$$

where x′ (t) and y′(t) are the rotated coordinates of cell at time t, τ is the lag time and <> indicated the temporal mean.

Cell Morphological Parameters

MCF10A and MDA-MB-231 cells were cultured on PAAm substrates at a final density of 1,000 cells/cm^2. Cells were fixed and stained for the evaluation of morphological parameters in control condition and 72 h after irradiation. Actin cytoskeleton and nuclei were stained with Alexa 488 phalloidin and Hoechst 33342, respectively. More detailed information on staining protocol can be found in [29]. Images of stained cells were acquired with Olympus IX81 inverted microscope equipped with a 10× objective. Images were imported into ImageJ software (NIH, Bethesda, MD, USA) for quantification of cell morphological parameters. We used nuclei to locate isolated cells. Individual cells, identified by visualization of single nuclei, were outlined and changes in cell shape in control and irradiated conditions were quantified by two morphological parameters, the shape factor (SF) and circularity index (CI), defined as follows:

$$SF = \frac{4\pi A}{P^2} \quad (7)$$

$$CI = \frac{axis_{minor}}{axis_{major}} \quad (8)$$

where A and P are the area and the perimeter of cells calculated by using the "Measure" command in ImageJ, whereas $axis_{major}$ and $axis_{minor}$ are the major and the minor axis of the best-fitting ellipse determined by using the ellipse-fitting function in ImageJ.

Statistical Analysis

Statistical comparisons were performed with a Student's unpaired test. *P*-values of <0.05 denote statistically significant differences.

RESULTS

Migration Parameters

Time-lapse video analysis was performed to compare the motility of mammary epithelial and adenocarcinoma cells on polyacrylamide substrates with different stiffness's, 1.3 and 13 kPa, in response to irradiation with 2 doses of X-rays (2 and 10 Gy). In order to describe the ability of cells to move and their tendency to do it in a directional way, we introduced two additional parameters defined in Materials and Methods section: TER and AT by the cells. In particular, to individuate the principal direction of displacement, the trajectories were rotated by the orientation angle calculated using the fitting-ellipse function in ImageJ (**Figures 1B–E**) and, then, TER was calculated as indicated in formula 3. Analyzing the definition, TER can vary

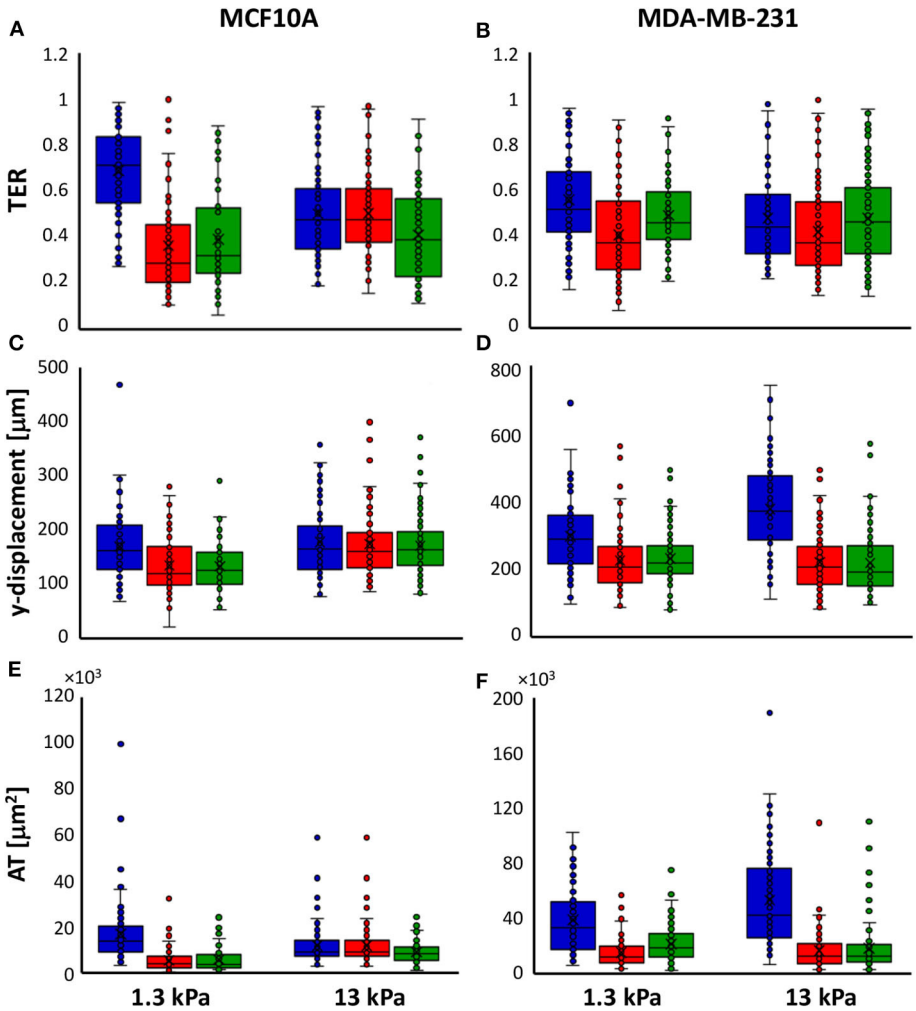

FIGURE 2 | Box plots (mean, median, interquartile range, and outliers) of TER **(A,B)**, y-displacement **(C,D)** and AT **(E,F)** parameters of MCF10A **(A–E)** and MDA-MB-231 cells **(B–F)** in control condition (blue) and 72 h after irradiation with doses of 2 Gy (red) and 10 Gy (green). $n > 58$ for MCF10A cells, $n > 82$ for MDA-MB-231 cells.

between 0 and 1 and is inversely related to the directionality of cells: values close to 1 indicate random trajectories, whereas when TER approaches to 0 the trajectories are approximated with a straight line (**Figure 1**). It is also important to highlight that in our analysis, we did not consider the values of orientation angles, because our substrates are homogeneous and no chemical or topographic pattern is present on them; consequently, the orientation angles are homogeneously distributed (data not shown). TER of both normal and cancer cell lines was strongly affected by substrate stiffness. In particular, TER of MCF10A cells decreased of 27% (**Figure 2A**), whereas that of MDA-MB-231 cells of 14% when substrate stiffness increased, indicating that the directionality of cell trajectories was greater on stiffer substrates mimicking pathological environment (**Figure 2B**). By a deep analysis of these data, it is possible to observe that, even though the stiffness affected the directionality of both cell lines, this effect was more relevant for normal cells than for tumor ones: on soft substrate, TER of MDA-MB-231 cells is 19 and 5% lower than that of MCF10A cells, respectively, on soft and stiff substrates, but the difference is significant only on 1.3 kPa polyacrylamide (t-test, $P = 1.5 \times 10^{-5}$, **Figures 2A,B**). Results demonstrated that the stiffness of the microenvironment by itself could enhance cell directionality, but at the same time the tumor metastatic phenotype confers on cells properties that are critical for invasion. Besides TER, we analyzed also two other parameters, the displacement along the principal direction y′ and AT. MCF10A cells moved along y′ in a not dependent way from substrate stiffness (**Figure 2C**, **Table 1**), whereas their AT decreased of 28% in a significant way (**Figure 2E**, **Table 1**) when they adhere on stiff substrate. On the contrary, both displacement along y′ and AT of MDA-MB-231 exhibited a significant increase of 27 and 38% when cells are cultured on stiff substrate rather than on soft one (**Figures 2D–F**, **Table 1**). After the evaluation of cell response to substrate stiffness in control

TABLE 1 | Statistical analysis for trajectories data.

		Control	2 Gy		10 Gy	
		13 kPa	1.3 kPa	13 kPa	1.3 kPa	13 kPa
Control	1.3 kPa	***, ** NS, ### ¶¶, ¶¶	***, *** ###, ### ¶¶¶, ¶¶¶	***,*** NS, ### ¶¶, ¶¶	***,* ###, ### ¶¶¶, ¶¶¶	***,** NS,### ¶¶¶,¶¶¶
	13 kPa		***, * ###, ### ¶¶¶, ¶¶¶	NS, * NS, ### NS, ¶¶¶	**, NS ###, ### ¶¶¶, ¶¶¶	**, NS NS, ### ¶¶, ¶¶
2 Gy	1.3 kPa			***, NS ###, NS ¶¶,¶¶¶	NS, *** NS, NS NS, NS	NS, * ###, NS ¶¶¶, ¶¶¶
	13 kPa				**, ** ###, NS ¶¶¶, ¶¶¶	**,* NS, NS ¶¶¶, ¶¶
10 Gy	1.3 kPa					NS, NS ###, NS ¶¶¶, ¶¶¶

Asterisks (*) refer to TER of MCF10A (left) and MDA-MB-231 cells (right), hash signs (#) to y-displacement and pilcrow signs (¶) to AT$^{***,\#\#\#,\P\P\P}P < 0.001$, $^{**,\P\P}P < 0.01$, $^{*,\P}P < 0.05$, *NS, not significant.*

condition, we investigated the effects of two different doses of X-rays, 2 and 10 Gy, on the migration parameters. Seventy-two hours after irradiation, MCF10A cells cultured on soft substrate responded to irradiation by reducing all the parameters in a very significant way in an independent manner from the delivered dose: TER decreased of 47%, the principal displacement of 21% and AT of 68% when cells were irradiated with the lower dose of 2 Gy; whereas TER, the principal displacement and AT decreased of 43%, 22 and 66% in the case of the dose of 10 Gy (**Figures 2A–E**, **Table 1**). On stiff substrate, the dose of 2 Gy had no effects, whereas cells responded to the higher dose of X-rays by reducing their migration parameters also in this case, even though in a less pronounced way compared to cells adhering on 1.3 kPa polyacrylamide (TER, the principal displacement and AT reduced of 15, 10, and 30%, respectively) (**Figures 2A–E**, **Table 1**). Metastatic cancer cells resulted to be more sensitive to irradiation, in particular on stiff substrate. Only TER was more significantly reduced when cells adhered on soft substrate: it decreased of 27 and 12% after irradiation with doses of 2 and 10 Gy, respectively, reaching values close or lower than that of control cells on stiff substrate (**Figure 2B**, **Table 1**). However, the reduction of TER, that is associated to a greater directionality during migration, was also accompanied by a significant decrease of the principal displacement (26 and 20% after irradiation with 2 and 10 Gy, respectively) and AT (61 and 45% after irradiation with 2 and 10 Gy, respectively) (**Figures 2D–F**, **Table 1**). On stiff substrate, TER reduced only when cells were irradiation with the lower dose (reduction of 12%), whereas the principal displacement diminished by 42 and 46% and AT by 69 and 66% after irradiation with 2 and 10 Gy, respectively (**Figures 2B–F**, **Table 1**).

In order to interpret our data in relation with previous results concerning cell velocity and reported in [29], we performed also a correlation analysis between TER and velocity data. In the case of normal tissue cells, TER and velocity resulted to be not or negatively correlated in control condition (correlations are equal to −0.11 and close to 0 on soft and stiff substrates, respectively), whereas we observed a weak positive correlation for cells irradiated with the dose of 2 Gy (0.11 on soft substrate and 0.15 on the stiff one) and a moderate positive correlation after irradiation with the dose of 10 Gy (0.26 on soft substrate and 0.24 on the stiff one). TER and velocity of metastatic cancer cells exhibited low or absent correlation on soft substrate (0.09 in control condition and ∼0 after irradiation with both doses), indicating that their directional behavior is weakly affected by the velocity (as also indicated by the high values of persistence time evaluated in [29] in all conditions and also when their velocities are reduced in a drastic way. When metastatic cells were cultured on stiff substrates, the correlation increases passing by 0.05 in control condition to 0.19 and 0.17 after irradiation with 2 and 10 Gy, exhibiting a behavior similar to that of normal tissue cells.

Mean Square Displacements

In our analysis, we decomposed the MSD in the two components calculated along directions x and y after rotation, MSD_x and MSD_y, and reported them in a log-log plot ($\log(MSD_{x/y})$ on the y-axis and log(Lag Time) on the x-axis (**Figure 3**). The slope α of these plots is a suitable indicator for cell directionality: log-log curve with slope $\alpha = 1$ indicates a random migration, whereas we describe as subdiffusive cell motion characterized from $\alpha < 1$ and superdiffusive a MSD with $1 < \alpha < 2$ ($\alpha = 2$ for cells that move along a straight line); $\log(MSD_{x/y})$ curve showing a slope close to zero indicates a random caged migration.

In control condition, MCF10A cells on soft substrate exhibited MSD with similar amplitude along the two directions (the MSD_x/MSD_y ratio was comprised between 0.8 and 1 at all lag times) and slopes very close to 1 ($\alpha = 0.945$, $R^2 = 0.9804$ and $\alpha = 1.002$, $R^2 = 0.986$ on 1.3 and 13 kPa, respectively), indicating that there was not a preferential direction during migration, in agreement with TER data (**Figure 3**). When cells were cultured in control condition on stiff substrate, the log-log plot of x-component of MSD was not well-fitted with a linear equation ($\alpha = 0.4529$, $R^2 = 0.6576$), because cell migration showed two different regimes: in the first 4 h $\log(MSD_x)$ exhibited a slope close to 1 ($\alpha = 0.9902$, $R^2 = 0.9737$), whereas in the rest of investigated time the curve flattened and the slope approached zero, indicating a caged migration (**Figure 3**). On the contrary, the log-log plot of y-component of MSD exhibited a slope close to 1.2 ($\alpha = 1.1752$, $R^2 = 0.9737$) and its amplitude increased up to 1,400% compared to MSD_x, meaning that cells move preferentially along y-axis as also indicated by TER parameter (**Figure 2**). Metastatic cells denoted a behavior, in terms of MSD, more similar to normal tissue cells on stiff substrate. In fact, independently of substrate stiffness, their MSD_x showed a subdiffusive behavior with slopes equal to 0.7314 ($R^2 = 0.8562$) and 0.794 ($R^2 = 0.8645$) on 1.3 and 13 kPa substrates, respectively. However, also in these cases it is possible to observe two different regimes: in the first 4 h both log-log plots slopes were close to 1.2 ($\alpha = 1.2282$, $R^2 = 0.9992$ and $\alpha = 1.1578$, $R^2 = 0.9975$ on 1.3 and 13 kPa, respectively), whereas

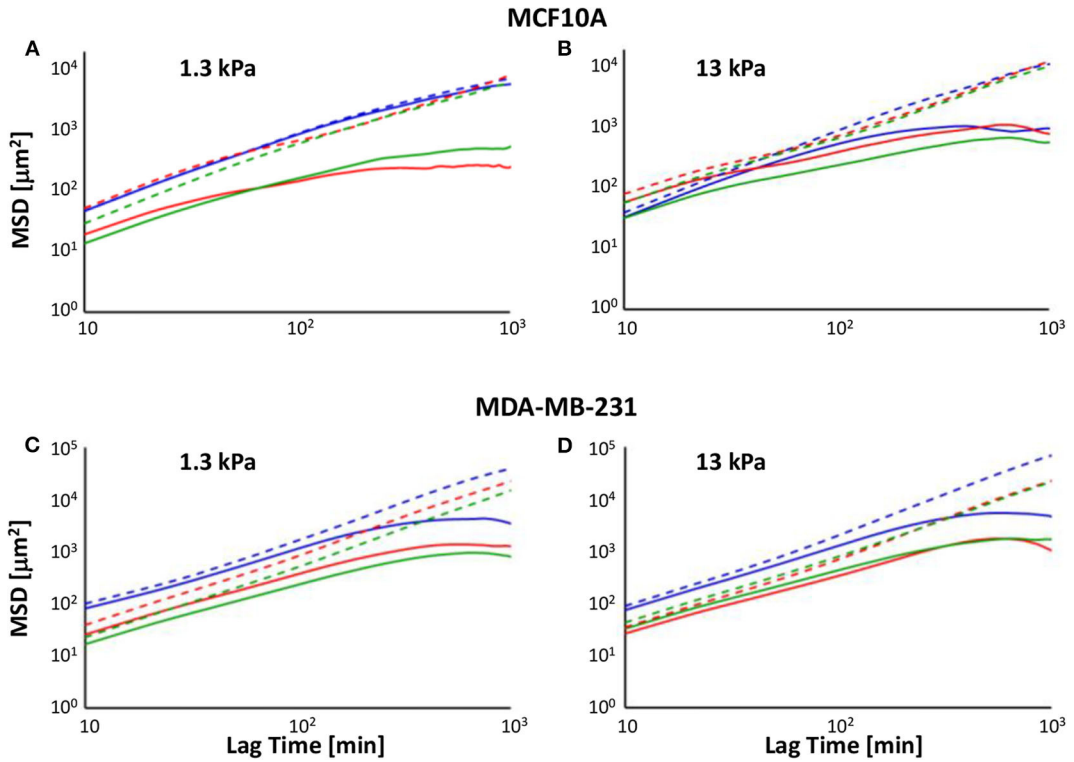

FIGURE 3 | Log-log plot of MSDs along x′- (solid line) and y′- (dotted lines) directions of MCF10A **(A,B)** and MDA-MB-231 cells' **(C,D)** trajectories on soft **(A–C)** and stiff **(B–D)** PAAm substrates, in control condition (blue) and 72 h after irradiation with doses of 2 Gy (red) and 10 Gy (green).

they approached to zero successively, indicating again a caged migration (**Figure 3**). The log-log plot of y-component of MSD exhibited slopes higher than 1 ($\alpha = 1.3864$, $R^2 = 0.998$ and $\alpha = 1.526$, $R^2 = 0.990$ on 1.3 and 13 kPa, respectively) and their amplitudes increased up to 1,400 and 2,100% compared to MSD_x on 1.3 and 13 kPa substrates. These findings support the results obtained in terms of TER: MDA-MB-231 cells were characterized by a more directional movement compared to MCF10A and this characteristic was particularly relevant on stiff substrate (**Figure 3D**), as also indicated by higher persistence time evaluated in our previous work [29]. Seventy-two hours after irradiation, the significant reduction of TER of normal tissue cells was accompanied by a change of mode of migration, as evidenced by the analysis of MSD. On soft substrate, the slope of MSDx was sensitively lower than 1 for both doses ($\alpha = 0.3737$, $R^2 = 0.7826$ and $\alpha = 0.6392$, $R^2 = 0.9155$ for cells irradiated with 2 and 10 Gy, respectively), but as in control condition on stiff substrate, it is possible to individuate two different regimes: cells irradiated with lower dose exhibited $\log(MSD_x)$ with a slope equal to 0.7039 ($R^2 = 0.9726$) until 4 h, whereas this value decreased to 0 successively (caged migration); cells irradiated with 10 Gy showed a pure diffusive motion until 4 h ($\alpha = 0.9479$, $R^2 = 0.9926$) and then a subdiffusive migration ($\alpha = 0.2799$, $R^2 = 0.9143$). On the other side, $\log(MSD_y)$ exhibited a slope slightly higher than 1 ($\alpha = 1.0501$, $R^2 = 0.9883$ and $\alpha = 1.069$, $R^2 = 0.994$ for cells irradiated with 2 and 10 Gy, respectively) and MSD_y amplitude enhanced to values 100 and 14 higher than those of MSD_x of cells irradiated with 2 and 10 Gy. This finding indicates that irradiation had a more important effect on cells exposed to 2 Gy, as also attested by the lower values of TER, but also that, in any case, normal tissue cells continued to preserve their less motile and directional motion on soft substrate (**Figures 2**, **3**). MCF10A cells cultured on stiff substrate exhibited a subdiffusive migration on x-direction after irradiation, in fact the slopes of log-log plots resulted to be sensitively lower than 1 and equal to 0.492 ($R^2 = 0.8205$) and 0.5273 ($R^2 = 0.8274$) after that doses of 2 and 10 Gy had been administered. However, also in these cases the slopes of the curves changed after the first 4 h, passing from ∼0.8 ($\alpha = 0.7538$, $R^2 = 0.9948$ and $\alpha = 1.069$, $R^2 = 0.994$ for cells irradiated with 2 and 10 Gy, respectively) to 0 (**Figure 3**). On the y-direction the mode of migration was not importantly affected by the irradiation, in fact the slopes remained close to 1.2, but the maximum value of MSD_y/MSD_x ratio increased slightly after irradiation with the low dose and in a more relevant way when cells were treated with the high dose (the ratio passed from 14 in control condition to 18 and 24 after irradiation with 2 and 10 Gy). The behavior of MDA-MB-231 cells was not affected in a strong way by irradiation. In particular, the slope of $\log(MSD_x)$ was lower than 1 ($\alpha = 0.724$, $R^2 = 0.8701$ and $\alpha = 0.7545$, $R^2 = 0.8946$ for cells cultured on soft substrate and irradiated with 2 and 10 Gy, respectively, $\alpha = 0.779$, $R^2 = 0.827$ and $\alpha = 0.7579$, $R^2 = 0.9157$ for cells cultured on stiff substrate and irradiated with

2 and 10 Gy, respectively), even though the dynamics motion continued to be slightly superdiffusive until 4 h ($\alpha = 1.1097$, $R^2 = 0.9981$ and $\alpha = 1.09151$, $R^2 = 0.9986$ for cells cultured on soft substrate and irradiated with 2 and 10 Gy, $\alpha = 1.1279$, $R^2 = 0.9995$ and $\alpha = 1.073$, $R^2 = 0.9984$ for cells cultured on soft substrate and irradiated with 2 and 10 Gy, respectively) and entrapped at succeeding lag times. The slope of log(MSDy) increased slightly compared to control condition passing from 1.3864 to 1.4297 ($R^2 = 0.9991$) and 1.4499 ($R^2 = 0.9996$), whereas the maximum value of MSD_y/MSD_x ratio increased from 14 to 26 and 32 after irradiation with 2 and 10 Gy, when cells were attached to soft polyacrylamide. On stiff substrate, the slope of log(MSDy) slightly decreased passing from 1.526 in control condition to 1.491 ($R^2 = 0.9984$) and 1.4093 ($R^2 = 0.9988$) and the maximum value of MSD_y/MSD_x ratio increased from 21 to 28 and 23 after irradiation with 2 and 10 Gy.

Morphological Parameters

It is extensively known that mode of cell migration is strictly correlated to cell adhesion and morphology and, for this reason, we used two additional morphological parameters, SF and CI (see Materials and Methods section), to describe the role of substrate stiffness and the effects of irradiation on these parameters. Both parameters can change between 0 and 1, where the upper bound connotes a perfect circular cell, whereas the lower bound indicates, in the case of SF, a cell with very pronounced border roughness (from a mathematical point of view we can say that the cell is characterized by a high fractal dimension), and, in the case of CI, a cell that can be approximated with a straight line. Normal cells exhibited low values of SF not dependent on substrate stiffness (0.23 and 0.22 on 1.3 and 13 kPa substrates, respectively), whereas their CI enhanced by 19% when cells are cultured on stiff substrate, indicating a more flattened and round shape (**Figures 5A–C**, **Table 2**). On the contrary, metastatic cancer cells exhibited a significantly lower SF on stiff polyacrylamide (0.28 and 0.22 on 1.3 and 13 kPa substrates, respectively) and a CI close to that of MCF10A on soft substrate and not dependent on substrate stiffness (0.46 and 0.49 on 1.3 and 13 kPa substrates, respectively) (**Figures 5B–D**, **Table 2**). 72 h after irradiation with 2 and 10 Gy, normal cells on soft substrate reduced their SF of 18 and 14%, whereas on stiff substrate SF increased by 16% when cells were irradiated with a dose of 2 Gy and decreased by 21% when the dose administered was equal to 10 Gy (**Figure 5A**, **Table 2**). The effects on CI were more relevant: MCF10A cells decreased their CI of 53 and 43% on soft substrate and of 42 and 36% on stiff substrate (**Figure 5C**, **Table 2**). The effects of X-rays on MDA-MB-231 were not significant, except for two cases: on soft substrate SF of cells irradiated with a dose of 2 Gy increased by 12%, whereas on stiff substrate SF of cells irradiated with a dose of 10 Gy increased by 36% (**Figures 5B–D**, **Table 2**). Furthermore, we analyzed in which way irradiation affected the degree to which individual morphological data deviate from the average deviation of data points from the mean by calculate the percent deviation PD ($PD = \left[\frac{SD}{\mu}\right]\%$, where SD is the standard of the mean and μ is the mean value of the data. In the following, we refer to PD of SF and PD of CI as PD_{SF} and PD_{CI}. We observed that in normal tissue cells, both PD_{SF} and PD_{CI} increased after irradiation: on soft substrate, PD_{SF} enhanced passing from 39% in control condition to 46 and 48% after irradiation with 2 and 10 Gy, respectively. PD_{CI} on soft substrate was not affected by irradiation with low dose, whereas increased from 43% in control condition to 69% when the dose of 10 Gy was administered. On stiff substrate, both doses significantly increased PD_{CI}, which passed from 37% in control condition to 61 and 57% after irradiation with 2 and 10 Gy, respectively. The effects of irradiation on PD_{SF} and PD_{CI} of MDA-MB-231 were less important, but not absent: on soft substrate PD_{SF} in control condition is equal to 44% and increased up to 46 and 48% after irradiation with 2 and 10 Gy, whereas on stiff substrate it passed from 35 to 44% and 46% after the administration of the two doses if X-ray, 2 and 10 Gy. Analyzing the PD_{CI} of metastatic cancer cells, we observed that it changed slightly after irradiation, reducing from 43% in control condition to 41% when the cells were on soft substrate and irradiated with dose of 2 Gy and increasing up to 49% when the dose administered was higher (10 Gy). PD_{CI} related to MDA-MB-231 cells increased from 37 to 40% and 42% after irradiation with 2 and 10 Gy, respectively.

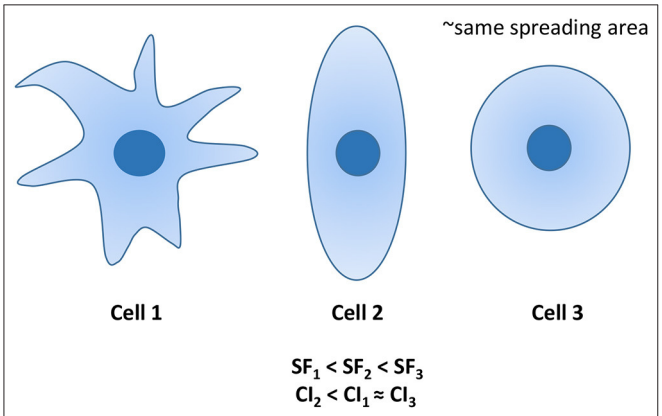

FIGURE 4 | Examples of 3 cells with similar spreading areas, but different morphologies. Cell 1 is characterized by the lowest SF, whereas its CI is similar to that of the circular cell 3. Differently, cell 2 exhibits the lowest CI, whereas its SF is intermediated CI_1 and CI_3.

DISCUSSION

Despite the overall breast cancer rate declined of 40% from 1990 to 2017, breast cancer continued to be the most common cancer diagnosed and the principal cause of cancer death among women worldwide [33, 34]. Moreover, the incidence rate of metastatic disease increased until 2011 and practically all deaths from breast cancer result from the spread of breast cancer cells to other vital organs, such as lung, liver or brain, through the process of metastasis [33, 35, 36]. In order to reduce the risk of breast cancer recurrence and to alleviate the symptoms of metastasis, most of breast cancer is treated with radiation therapy [33]. Basing

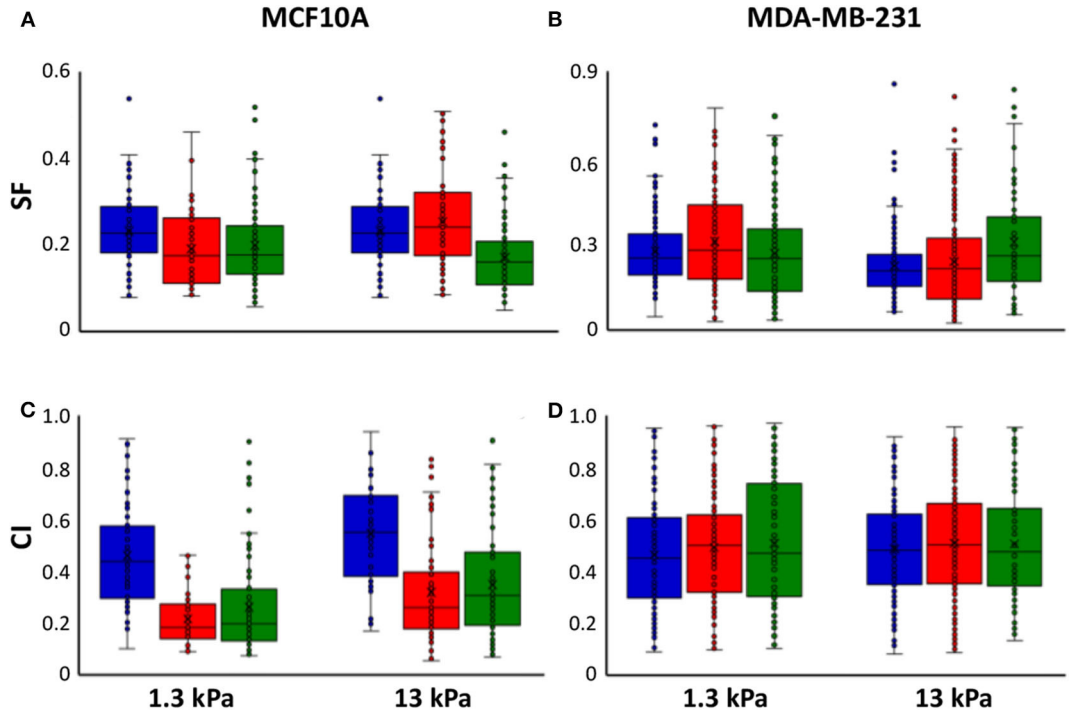

FIGURE 5 | Box plots (mean, median, interquartile range and outliers) of SF **(A,B)** and CI **(C,D)** MCF10A **(A–C)** and MDA-MB-231 cells **(B–D)** in control condition (blue) and 72 h after irradiation with doses of 2 Gy (red) and 10 Gy (green). $n > 50$ for MCF10A cells, $n > 75$ for MDA-MB-231 cells.

TABLE 2 | Statistical analysis for morphological data.

		Control	2 Gy		10 Gy	
		13 kPa	1.3 kPa	13 kPa	1.3 kPa	13 kPa
Control	1.3 kPa	NS, # ***, NS	*, ### *, NS	NS, ### **, #	*, ### NS, NS	***, ## NS, NS
	13 kPa		NS, ### ***, NS	*, ### NS, NS	NS, ### *, NS	**, ### ***, NS
2 Gy	1.3 kPa			***, ### ***, NS	NS, # *, NS	NS, ### NS, NS
	13 kPa				**, NS NS, NS	***, NS NS, NS
10 Gy	1.3 kPa					*, ## **, NS

Asterisks (*) refer to SF of MCF10A (left) and MDA-MB-231 cells (right), hash signs (#) to CI$^{***,###}P < 0.001$, $^{**,##}P < 0.01$, $^{*,\#}P < 0.05$, NS, not significant.

on these considerations, it becomes necessary to understand the mechanisms that underline the process of metastasis, taking into account also the contribution of the microenvironment in which cells naturally live, and to examine the effect of radiation therapy on the motile and metastatic capacity of cells.

The velocity represents the most used parameter to describe a key cellular function as the migration. Nevertheless, it could be not completely adequate to illustrate the effective proclivity of metastatic cells to move far away from the origin site toward lymph nodes and distant tissues to form secondary tumors. In our previous work [29], we used the velocity and the persistence time to indicate the effects of irradiation on the migratory behavior of mammary epithelial and adenocarcinoma cells cultured on polyacrylamide substrates of different mechanical stiffness. Here, we introduced two different parameters to further investigate the mode of cell migration: TER and AT by the cells. TER is strictly related to the directionality of the cell and it approaches to 1 when the trajectory is contained into a perfect circle (the displacements along the two orthogonal directions are exactly the same) and to 0 when the trajectory is approximated with a straight line (**Figure 1**). AT gives indication on the area effectively explored by the cells in a certain time of analysis (24 h here). Taken together with the velocity, these parameters can offer a more comprehensive view of the characteristics of migration of normal tissue and metastatic cancer cells on substrates mimicking different *in vivo* conditions (normal and tumor-like environment) and after therapeutic treatments such as radiotherapy.

The analysis of both normal tissue and metastatic cancer cell lines revealed that the extension ratio of the trajectory was strongly affected by the stiffness of the substrates. In particular, in control condition TER significantly decreased by increasing the stiffness of the substrate for both MCF10A and MDA-MB-231 cells (**Figures 2A,B**), whereas the migration velocity found in our previous work [29] decreased in normal tissue and increased in metastatic cancer cell lines as effect of ECM stiffening, respectively. On one hand, the opposite finding in terms of

velocity in MCF10A and MDA-MB-231 cells can be explained by considering that the migration is regulated by the dynamics of focal adhesions [37, 38], that is substantially dependent on the pathophysiological state of cells. In particular, focal adhesion kinase (FAK) has a central role in the dynamic regulation of focal adhesions and cells overexpressing FAK, such as MDA-MB-231 cells, displayed impaired focal adhesions and enhanced cell migration [39–42]. On the other hand, results suggest that the stiffness regulates in a similar way TER and that the stiffening of the tumor ECM increases the directionality of cell trajectory independently from cell type and, consequently, cell velocity. This result also gives more insights about previous findings on persistence time [29] and supports previous observation demonstrating that stiff substrates promote directional migration [43]. In particular, it has been demonstrated that substrate stiffness regulates RhoA/ROCK1/p-MLC and RhoA/ROCK2/p-cofilin pathways, strongly implicated in the progression and metastasis of many cancers included breast cancer, through the activation of integrin β1 and FAK [44–46]. MCF10A cells resulted to have a persistence time very close to 0 min independently of substrate stiffness and a TER that decrease sensitively moving from soft to stiff substrate. While an almost null persistence time could be interpreted as a random motion in terms of cell trajectory, the TER decrease clearly indicates that motion has a predominant direction, if the whole trajectory is considered along the entire time range of observation. Seventy-two hours after irradiation, MCF10A cells cultured on soft substrate decreased strongly their TER without dependence on administered dose, whereas only the dose of 10 Gy affected the extension rate of cells cultured on stiff substrate (**Figure 2A**). We think that in MCF10A cells the lengthening of the trajectories, evidenced by TER reduction (**Figure 2A**, **Table 1**), was correlated to the decrease of cell velocity previously reported [29], as also evidenced by the increase of correlation between TER and velocity data. The effects of irradiation were less pronounced in MDA-MB-231 cells cultured on soft substrates (**Figure 2B**, **Table 1**), because their trajectories in control condition exhibited a more elongated and directional shape compared to normal tissue cells (**Figure 2A**, **Table 1**). However, similarly to MCF10A cells, also metastatic cells reduced the extension ratio of their trajectories, even though in a more sensitive way after the administration of the lower dose (**Figures 2A,B**, **Table 1**). On stiff substrates, only the low dose increased significantly the extension of the trajectories, but both doses, as previously observed, reduced in a drastic way the mean cell velocity (**Figures 2A,B**, **Table 1**). The reduction of the extension ratio was also in this case accompanied by a lowered cell velocity and, for this reason, an analysis of both displacements along the principal direction of the migration and area traveled by the cells was performed. MCF10A cells showed a displacement in the principal direction not affected by ECM stiffness, whereas the area traveled in 24 h was significantly lower on stiff substrate, as consequence of the reduced velocity but a more directional movement which reduced the extension ratio (**Figures 2A–E**, **Table 1**). On the contrary, metastatic cells exhibited displacement in the principal direction and migration area increasing with substrate stiffness (**Figures 2D–F**, **Table 1**), in agreement with the mean velocity and the extension of trajectories. These findings indicate that, even though the ECM stiffness has a regulatory effect on the directionality of cell migration, normal tissue cells on stiff substrate move less than their diseased counterpart. This observation supports the indication that both oncogene-expressing cells and supra-physiological ECM stiffness are necessary to favor the tumor onset [7, 47]. Seventy-two hours after the irradiation, both normal tissue and metastatic cancer cells on soft substrate reduced significantly the displacement along the principal direction and the migration area, meaning that, even though their directionality increased, as also indicated by TER values, the net displacement along the principal direction decreased together with the velocity. Interestingly, this effect on the migration area was not dependent on the dose administered in the case of healthy cells, whereas it was more relevant for metastatic cells irradiated with the lower dose (**Figures 2C,D**, **Table 1**). In this work, we did not explore the mechanism that underlie the behavior of normal tissue and metastatic cancer cells discussed here. Nevertheless, there are some experimental evidences that ionizing radiations could have an important impact on the expression of some proteins, such as integrins, paxillin, FAK, involved in the formation of focal adhesions, that are determinant in both adhesion and migration [48, 49]. Then, changes in pattern involving these proteins are likely to affect both of these processes. In this regard, it has been observed that X-rays can induce over-expression of paxillin [49–51] and promote phosphorylation of FAK and p130cas [49, 52, 53]. The increased expression of paxillin, that is the downstream target of FAK phosphorylation, could be responsible for an increased adhesion of cells after irradiation and consequently for decreased motility, as previously observed in both normal and cancer cells [50, 51, 54]. However, FAK and p130CAS phosphorylation plays a key role in directional migration [55] and the activation of FAK and p130CAS indicated by the increased phosphorylation could explain the increased directionality observed here. Obviously, further research is needed to substantiate these suggestions: the definition of these parameters, that are easy to interpret and do not require high expertise in biophysics (differently from MSD), together with the identification of the molecular mechanisms guiding cell behavior in response to irradiation by means of more complex and tissue-like culture conditions (not only mechanical properties, but also intratumoral solid stresses, dimensionality-−2D vs. 3D vs. 2.5D curved surfaces, and topographical signals) might generate a basic knowledge with powerful translational significance.

In order to verify the validity of the parameters here introduced, particularly those related to TER, we analyzed the movement of both cells lines in terms of MSD. In fact, in the context of cell migration, the MSD is a good parameter able to carry out information about diffusion coefficient and directionality of a migration trajectory [29, 56]. Our finding suggest that metastatic cancer cells move faster and more persistently compared to normal tissue cells on soft substrate, whereas stiff ECM seems to bolster ballistic motion along rotated y-direction of both cell lines, in agreement with experimental evidences previously reported [57–60]. The analysis of MSD components showed that irradiation had important effects on

the migratory behavior of normal tissue cells, that exhibited more directional migration along y-direction when cultured on soft substrate. On the contrary, our findings denote that irradiation did not affect the tendency of metastatic cells to move directionally, as also evidenced by persistence time and TER values (**Figure 2**) [29], but slowed down in a very forceful way cell velocity, AT values and the displacement along rotated y-direction (**Figure 2**).

It is particularly relevant to consider that cell motility can be explained by evaluating not only the amount of adhesion in terms of spreading area (for example normal tissue cells become less motile by increasing their adhesion to the substrate), but also in terms of cell shaping: cell cytoskeleton is responsible for cell shape and, consequently, for various types of cell movement [61, 62]. In our previous paper we already analyzed the ability of MCF10A and MDA-MB-231 cells to mechanosense the microenvironment by measuring their spreading area before and after irradiation [29]. In fact, several works demonstrated that when the stiffness and, then, the resistance provided by the substrate increases, cells can generate acto-myosin forces to assemble integrin clusters, a prerequisite to form large and mature focal adhesions which, in turn, regulate spreading area and cytoskeleton assembly [2, 32, 56, 63–65]. In addition to adhesion area, substrate stiffness can affect also other morphological parameters and the intimate connection between cell and microenvironment is often discusses also in terms of cell shaping [66–69]. That being said, a deeper analysis of influence of substrate stiffness and irradiation on cell morphology has been performed by introducing two parameters to describe cell shape: SF and CI (see Materials and Methods section and both ranging from 0 to 1 (**Figure 4**). SF is related to cell perimeter, assuming max value of 1 for circular cells and approaching 0 when cells have rugged and irregular boundaries. CI quantifies how rounded a cell is and it is equal to 1 for circular cells and approaches to 0 in case of elongated cells. SF helps to emphasize the presence of membrane protrusions (filopodia, lamellipodia, blebs) that are important for adhesion, migration and mechanosensing [70]. MCF10A cells showed a low SF (∼0.2), that decreases with substrate stiffness but in a not significant way, whereas their SF resulted to be higher on soft substrate, where cells exhibited a more flattened shape (**Figure 5**). On the contrary, MDA-MB-231 cells exhibited a SF that decreased significantly with substrate stiffness and higher than that of normal tissue cells on soft substrate. Furthermore, normal tissue and metastatic cancer cells displayed similar CI on stiff substrate (**Figure 5**, **Table 2**). The effects of irradiation on MCF10A and MDA-MB-231 cells were very different and sometimes opposite. In particular, normal tissue cells cultured on both soft and stiff substrates reduced significantly their CI and SF independently on dose received; the only exception was represented by cells on stiff substrate and irradiated with lower dose that increased their SF (**Figure 5**, **Table 2**). We suppose that the reduction of CI, indicating a more elongated cell shape, is responsible for the reduction of TER contributing to the increased directionality of MCF10A cells (**Figures 2**, **3**) [71]. In fact, morphological polarization can induce asymmetrical redistribution of forces (lower traction forces at cell rear) and consequently the initiation of a directional migration [72]. Nevertheless, the reduction of SF could be also considered associated to an increased adhesion of normal tissue cells, that consequently exhibit lower migration velocity [29] and reduced AT (**Figure 2**). On the contrary, the irradiation had not relevant effects on CI and SF of metastatic cells on both soft and stiff substrates. The only exceptions were represented by cells cultured on soft substrate and irradiated with lower dose and cells cultured on stiff substrate and irradiated with higher dose that increased their SF (cells appeared more flattened and to have more regular boundaries). This is in agreement with MSD data, which denote not significant effects of irradiation on the dynamics of migration. On the contrary, the reduced migration of MDA-MB-231 cells can be explained by the enhanced adhesion, higher spreading area and more stretched nuclei [29], all conditions that would suggest a more assembled cell cytoskeleton.

As already discussed, to unravel the mechanisms that regulate cell behavior after irradiation, it will be needed to study the molecular pathways involving adhesion molecules, first of all integrins, FAK and paxillin, which can have important impacts on both adhesion and invasion. In fact, whereas integrin clustering is the fundamental to guarantee a proper adhesion, paxillin has an important role in the regulation of cell adhesion and motility and is a key participant in physiological and pathological context (immune response, epithelial morphogenesis, oxidative stress—which can be consequent to X-ray irradiation, cancer development, and metastasis) and FAK regulates the dynamics of focal adhesion and, consequently, cell migration. It has been already demonstrated that irradiation could promote integrin expression, improve cell adhesion and inhibit invasion capability of glioblastoma cells [48]. Conversely, Rieken et al. observed that increased expression of integrins promoted motile behavior of the same tumor cells [73]. Furthermore, as previously reported, irradiation impacts also on the expression of paxillin and activation of both paxillin and FAK [50, 51, 54, 55] and this could explain the change of mode of migration we observed in our work.

CONCLUSIONS

In summary, we proposed two additional parameters, TER and AT, to describe cell migration of normal tissue and metastatic cancer cells before and after irradiation when they interact with physiological (1.3 kPa) and supra-physiological (13 kPa) ECM. In particular, we found that irradiation induced a sensitive reduction of TER values in MCF10A cells, indicating that trajectories are more elongated and directionally oriented compared to control condition. On the contrary, TER of MDA-MB-231 cells' trajectories did not change in a relevant way, indicating that the mode of migration of metastatic cancer cells, characterized by directionality and high persistence time [reported in [29]] also in control condition, was not significantly affected by RT. However, irradiation induced also

a significant decreased of the area explored by cells during their movement (AT). Basing on the results found in terms of morphological parameters and on previous literature here discussed, we supposed that the variations observed in cell motility after irradiation could be ascribed to a different regulation of molecular pathways involving adhesion molecules (integrins, paxillin, FAK), that play a leading role in adhesion and migration. This being said, further investigations will be needed to substantiate these suggestions: the definition of these parameters, that are easy to interpret and do not require high expertise in biophysics (differently from MSD), together with the identification of the molecular mechanisms guiding cell behavior in response to irradiation by means of more complex and tissue-like culture conditions (not only mechanical properties, but also intratumoral solid stresses, dimensionality−−2D vs. 3D vs. 2.5D curved surfaces, and topographical signals) might generate a basic knowledge with powerful translational significance.

DATA AVAILABILITY STATEMENT

The raw data supporting the conclusions of this article will be made available by the authors, without undue reservation.

AUTHOR CONTRIBUTIONS

VP and SF conceived of the presented work and wrote the original draft. VP and GL carried out the experiments. VP performed data analysis. CA defined and performed radiation treatment plans. All authors discussed the results and contributed to the final version of the manuscript. All authors contributed to the article and approved the submitted version.

FUNDING

This work was supported by Modeling and Verification for Ion beam Treatment planning (MoVe-IT) project, INFN CSN5 Call.

REFERENCES

1. Wells RG. The role of matrix stiffness in regulating cell behavior. *Hepatology.* (2008) **47**:1394–400. doi: 10.1002/hep.22193
2. Fusco S, Panzetta V, Embrione V, Netti PA. Crosstalk between focal adhesions and material mechanical properties governs cell mechanics and functions. *Acta Biomater.* (2015) **23**:63–71. doi: 10.1016/j.actbio.2015.05.008
3. Dufort CC, Paszek MJ, Weaver VM. Balancing forces: architectural control of mechanotransduction. *Nat Rev Mol Cell Biol.* (2011) **12**:308–19. doi: 10.1038/nrm3112
4. Discher DE, Janmey P, Wang Y. Tissue cells feel and respond to the stiffness of their substrate. *Science.* (2005) **310**:1139–43. doi: 10.1126/science.1116995
5. Guimarães CF, Gasperini L, Marques AP, Reis RL. The stiffness of living tissues and its implications for tissue engineering. *Nat Rev Mater.* (2020) **5**:351–70. doi: 10.1038/s41578-019-0169-1
6. Panzetta V, Musella I, Rapa I, Volante M, Netti PA, Fusco S. Mechanical phenotyping of cells and extracellular matrix as grade and stage markers of lung tumor tissues. *Acta Biomater.* (2017) **57**:334–41. doi: 10.1016/j.actbio.2017.05.002
7. Panciera T, Citron A, Di Biagio D, Battilana G, Gandin A, Giutti S, et al. Reprogramming normal cells into tumour precursors requires ECM stiffness and oncogene-mediated changes of cell mechanical properties. *Nat Mater.* (2020) **19**:797–806. doi: 10.1038/s41563-020-0615-x
8. Panciera T, Azzolin L, Cordenonsi M, Piccolo S. Mechanobiology of YAP and TAZ in physiology and disease. *Nat Rev Mol Cell Biol.* (2017) **18**:758–70. doi: 10.1038/nrm.2017.87
9. Walker C, Mojares E, del Río Hernández A. Role of extracellular matrix in development and cancer progression. *Int J Mol Sci.* (2018) **19**:3028. doi: 10.3390/ijms19103028
10. He X, Lee B, Jiang Y. Cell-ECM interactions in tumor invasion. In: Rejniak K. editor. *Systems Biology of Tumor Microenvironment*. Cham: Springer (2016). p. 73–91.
11. Mohan V, Das A, Sagi I. Emerging roles of ECM remodeling processes in cancer. *Semin Cancer Biol.* (2020) **62**:192–200. doi: 10.1016/j.semcancer.2019.09.004
12. Aguilar-Cuenca R, Juanes-García A, Vicente-Manzanares M. Myosin II in mechanotransduction: master and commander of cell migration, morphogenesis, and cancer. *Cell Mol Life Sci.* (2014) **71**:479–92. doi: 10.1007/s00018-013-1439-5
13. Hood JD, Cheresh DA. Role of integrins in cell invasion and migration. *Nat Rev Cancer.* (2002) **2**:91–100. doi: 10.1038/nrc727
14. Müller T, Bain G, Wang X, Papkoff J. Regulation of epithelial cell migration and tumor formation by β-catenin signaling. *Exp Cell Res.* (2002) **280**:119–33. doi: 10.1006/excr.2002.5630
15. Dongre A, Weinberg RA. New insights into the mechanisms of epithelial–mesenchymal transition and implications for cancer. *Nat Rev Mol Cell Biol.* (2019) **20**:69–84. doi: 10.1038/s41580-018-0080-4
16. Deryugina EI, Quigley JP. Matrix metalloproteinases and tumor metastasis. *Cancer Metastasis Rev.* (2006) **25**:9–34. doi: 10.1007/s10555-006-7886-9
17. Warren JSA, Xiao Y, Lamar JM. YAP/TAZ activation as a target for treating metastatic cancer. *Cancers.* (2018) **10**:115. doi: 10.3390/cancers10040115
18. Hsiang-his HH, Kuo CC, Lin BX, Huang YH, Lin CW. Elevation of YAP promotes the epithelial-mesenchymal transition and tumor aggressiveness in colorectal cancer. *Exp Cell Res.* (2017) **350**:218–25. doi: 10.1016/j.yexcr.2016.11.024
19. Cheng GZ, Chan J, Wang Q, Zhang Q, Sun CD, W LH. Twist transcriptionally up-regulates AKT2 in breast cancer cells leading to increased migration, invasion, and resistance to paclitaxel. *Cancer Res.* (2007) **67**:1979–87. doi: 10.1158/0008-5472.CAN-06-1479
20. Yang Z, Zhang X, Gang H, Li X, Li Z, Wang T, et al. Up-regulation of gastric cancer cell invasion by Twist is accompanied by N-cadherin and fibronectin expression. *Biochem Biophys. Res. Commun.* (2007) **358**:925–30. doi: 10.1016/j.bbrc.2007.05.023
21. Weichselbaum RR, Dahlberg W, Beckett M, Karrison T, Miller D, Clark J. et al. Radiation-resistant and repair-proficient human tumor cells may be associated with radiotherapy failure in head- and neck-cancer patients. *Proc Natl Acad Sci.* (1986) 83:2684–2688. doi: 10.1073/pnas.83.8.2684
22. Schaapveld M, Aleman BMP, van Eggermond AM, Janus CPM, Krol ADG, van der Maazen RWM, et al. Second cancer risk up to 40 years after treatment for Hodgkin's lymphoma. *N Engl J Med.* (2015) **373**:2499–511. doi: 10.1056/NEJMoa1505949
23. Grantzau T, Overgaard J. Risk of second non-breast cancer after radiotherapy for breast cancer: a systematic review and meta-analysis of 762,468 patients. *Radiother Oncol.* (2015) **114**:56–65. doi: 10.1016/j.radonc.2014.10.004
24. Journy NM, Morton LM, Kleinerman RA, Bekelman JE, Berrington de Gonzalez A. Second primary cancers after intensity-modulated vs 3-dimensional conformal radiation therapy for prostate cancer. *JAMA Oncol.* (2016) **2**:1368–70. doi: 10.1001/jamaoncol.2016.1368
25. Vilalta M, Rafat M, Graves EE. Effects of radiation on metastasis and tumor cell migration. *Cell Mol Life Sci.* (2016) **73**:2999–3007. doi: 10.1007/s00018-016-2210-5
26. Imaizumi H, Nishihara A, Minami K, Koisumi M, Matsuura N, Hieda M. X-ray-enhanced cancer cell migration requires the linker of nucleoskeleton and cytoskeleton complex. *Cancer Sci.* (2018) **109**:1158–65. doi: 10.1111/cas.13545

27. Jung JW, Hwang SY, Hwang JS, Oh ES, Park S, Han IO Ionising radiation induces changes associated with epithelial-mesenchymal transdifferentiation increased cell motility of A549 lung epithelial cells. *Eur J Cancer.* (2007) **43**:1214–24. doi: 10.1016/j.ejca.2007.01.034
28. De Bacco F, Luraghi P, Medico E, Reato G, Girolami F, Perera T, et al. Induction of MET by ionizing radiation and its role in radioresistance and invasive growth of cancer. *J Natl Cancer Inst.* (2011) **103**:645–61. doi: 10.1093/jnci/djr093
29. Panzetta V, La Verde G, Pugliese M, Artiola V, Arricchiello C, Muto P, et al. Adhesion and migration response to radiation therapy of mammary epithelial and adenocarcinoma cells interacting with different stiffness substrates. *Cancers.* (2020) **12**:1170. doi: 10.3390/cancers12051170
30. Hohmann T, Grabiec U, Vogel C, Ghabdan C, Ensminger S, Bache M, et al. The impact of non-lethal single-dose radiation on tumor invasion and cytoskeletal properties. *Int J Mol Sci.* (2017) **18**:2001. doi: 10.3390/ijms18092001
31. Siva S, MacManus MP, Martin RF, Martina OA. Abscopal effects of radiation therapy: a clinical review for the radiobiologist. *Cancer Lett.* (2015) **35**:82–90. doi: 10.1016/j.canlet.2013.09.018
32. Panzetta V, Guarnieri D, Paciello A, Della Sala F, Muscetti O, Raiola L, et al. ECM mechano-sensing regulates cytoskeleton assembly and receptor-mediated endocytosis of nanoparticles. *ACS Biomater Sci Eng.* (2017) **3**:1586–94. doi: 10.1021/acsbiomaterials.7b00018
33. DeSantis CE, Ma J, Gaudet MM, Newman LA, Miller KDM, Goding Sauer A, et al. Breast cancer statistics, 2019. *CA Cancer J Clin.* (2019) **69**:438–51. doi: 10.3322/caac.21583
34. Siegel RL, Miller KD, Jemal A. Cancer statistics, 2019. *CA Cancer J Clin.* (2019) **69**:7–34. doi: 10.3322/caac.21551
35. Redig AJ, McAllister SS. Breast cancer as a systemic disease: a view of metastasis. *J Intern Med.* (2013) **274**:113–26. doi: 10.1111/joim.12084
36. Lawson DA, Bhakta N, Kessenbrock K, Prummel KD, Yu Y, Takai K et al. Single-cell analysis reveals a stem-cell program in human metastatic breast cancer cells. *Nature.* (2015) **526**:131–5. doi: 10.1038/nature15260
37. Fusco S, Panzetta V, Netti PA. Mechanosensing of substrate stiffness regulates focal adhesions dynamics in cell. *Meccanica.* (2017) **52**:3389–98. doi: 10.1007/s11012-017-0676-3
38. Carragher NO, Frame MC. Focal adhesion and actin dynamics: a place where kinases and proteases meet to promote invasion. *Trends Cell Biol.* (2004) **14**:241–9. doi: 10.1016/j.tcb.2004.03.011
39. Schlaepfer DD, Mitra SK. Multiple connections link FAK to cell motility and invasion. *Curr Opin Genet Dev.* (2004) **14**:92–101. doi: 10.1016/j.gde.2003.12.002
40. Luo M, Guan JL. Focal adhesion kinase: a prominent determinant in breast cancer initiation, progression and metastasis. *Cancer Lett.* (2010) **289**:127–39. doi: 10.1016/j.canlet.2009.07.005
41. Wu GS, Aong YL, Yin ZQ, Guo JJ, Wang SP, Zhao WW, et al. Ganoderiol A-enriched extract suppresses migration and adhesion of MDA-MB-231 cells by inhibiting FAK-SRC-paxillin cascade pathway. *PLoS ONE.* (2013) **8**:e76620. doi: 10.1371/journal.pone.0076620
42. McLean GW Avizienyte E, Frame MC. Focal adhesion kinase as a potential target in oncology. *Expert Opin Pharmacother.* (2003) **4**:227–34. doi: 10.1517/14656566.4.2.227
43. Peng Y, Chen Z, Chen Y, Li S, Jiang Y, Yang H. ROCK isoforms differentially modulate cancer cell motility by mechanosensing the substrate stiffness. *Acta Biomater.* (2019) **88**:86–101. doi: 10.1016/j.actbio.2019.02.015
44. Kamai T, Tsujii T, Arai K, Takagi K, Asami H, Ito Y, et al. Significant association of Rho/ROCK pathway with invasion and metastasis of bladder cancer. *Clin Cancer Res.* (2003) **9**:2632−41. Available online at: https://clincancerres.aacrjournals.org/content/9/7/2632
45. Wong CC, Wong CM, Tung EK, Man K, Ng IO. Rho-kinase 2 is frequently overexpressed in hepatocellular carcinoma and involved in tumor invasion. *Hepatology.* (2009) **49**:1583–94. doi: 10.1002/hep.22836
46. Lane J, Martin TA, Watkins G, Mansel RE, Jiang WG. The expression and prognostic value of ROCK I and ROCK II and their role in human breast cancer. *Int J Oncol.* (2008) 33:585–93. doi: 10.3892/ijo_00000044
47. Seewaldt V. ECM stiffness paves the way for tumor cells. *Nat Med.* (2014) **20**:332–3. doi: 10.1038/nm.3523
48. Cordes N, Hansmeier B, Beinke C, Meineke D, Van Beuningen D. Irradiation differentially affects substratum-dependent survival, adhesion, and invasion of glioblastoma cell lines. *Br J Cancer.* (2003) **89**:2122–32. doi: 10.1038/sj.bjc.6601429
49. Beinke C, Van Beuningen D, Cordes N. Ionizing radiation modules of the expression and tyrosine phosphorylation of the focal adhesion-associated proteins focal adhesion kinase (FAK) and its substrates p130cas and paxillin in A549 human lung carcinoma cells *in vitro*. *Int J Radiat Biol.* (2003) **79**:721–31. doi: 10.1080/09553000310001610231
50. Panzetta V, De Menna M, Bucci D, Giovannini V, Quarto M, Fusco S, et al. X-ray irradiation affects morphology, proliferation and migration rate of healthy and cancer cells. *J Mech Med Biol.* (2015) **15**:1540022. doi: 10.1142/S0219519415400229
51. Panzetta V, Musella I, Pugliese M, Piccolo C, Pasqua G, Netti PA, et al. Effects of high energy X-rays on cell morphology and functions 2017. In: *IEEE 5th Portuguese Meeting on Bioengineering (ENBENG).* Coimbra: IEEE (2017).
52. Wick W, Wick A, Schulz JB, Dichgans J, Rodemann HP, Weller M. Prevention of irradiation-induced glioma cell invasion by temozolomide involves caspase 3 activity and cleavage of focal adhesion kinase. *Cancer Res.* (2002) **62**:1915–9. Available online at: https://cancerres.aacrjournals.org/content/62/6/1915.long
53. Eke I, Cordes N. Radiobiology goes 3D: how ECM and cell morphology impact on cell survival after irradiation. *Radiother Oncol.* (2011) **99**:271–8. doi: 10.1016/j.radonc.2011.06.007
54. Salgia R, Li JL, Ewaniuk DS, Wang YB, Sattler M, Chen WC, et al. Expression of the focal adhesion protein paxillin in lung cancer and its relation to cell motility. *Oncogene.* (1999) **18**:67–77. doi: 10.1038/sj.onc.1202273
55. Yu JA, Deakin NO, Turner CE. Paxillin-kinase-linker tyrosine phosphorylation regulates directional cell migration. *Mol Biol Cell.* (2009) **20**:4706–19. doi: 10.1091/mbc.e09-07-0548
56. Gorelik R, Gautreau A. Quantitative and unbiased analysis of directional persistence in cell migration. *Nat Protoc.* (2014) **9**:1931. doi: 10.1038/nprot.2014.131
57. Stroka KM, Aranda-Espinoza H. Neutrophils display biphasic relationship between migration and substrate stiffness. *Cell Motil Cytoskeleton.* (2009) **66**:328–41. doi: 10.1002/cm.20363
58. Schlüter DK, Ramis-Conde I, Chaplain MAJ. Computational modeling of single-cell migration: the leading role of extracellular matrix fibers. *Biophys J.* (2012) **103**:1141–51. doi: 10.1016/j.bpj.2012.07.048
59. Levental KR, Yu H, Kass L, Lakins JN, Egeblad M, et al. Matrix crosslinking forces tumor progression by enhancing integrin signaling. *Cell.* (2009) **139**:891–906. doi: 10.1016/j.cell.2009.10.027
60. Acerbi I Cassereau L, Dean I, Shi Q, Au A, Park C, et al. Human breast cancer invasion and aggression correlates with ECM stiffening and immune cell infiltration. *Integr Biol.* (2015) **7**:1120–34. doi: 10.1039/c5ib00040h
61. Pollard TD Cooper JA. Actin, a central player in cell shape and movement. *Science.* (2009) **326**:1208–12. doi: 10.1126/science.1175862
62. Mogilner A, Keren K. The shape of motile cells. *Curr Biol.* (2009) **19**:R762–71. doi: 10.1016/j.cub.2009.06.053
63. Engler A, Bacakova L, Newman C, Hategan A, Griffin M, Discher D. Substrate compliance versus ligand density in cell on gel responses. *Biophys J.* (2004) **86**:617–28. doi: 10.1016/S0006-3495(04)74140-5
64. Reinhart-King CA, Dembo M, Hammer DA. The dynamics and mechanics of endothelial cell spreading. *Biophys J.* (2005) **89**:676–89. doi: 10.1529/biophysj.104.054320
65. Califano JP, Reinhart-King CA. A balance of substrate mechanics and matrix chemistry regulates endothelial cell network assembly. *Cell Mol Bioeng.* (2008) **1**:122. doi: 10.1007/s12195-008-0022-x
66. Califano JP, Reinhart-King CA. Substrate stiffness and cell area predict cellular traction stresses in single cells and cells in contact. *Cell Mol Bioeng.* (2010) **3**:68–75. doi: 10.1007/s12195-010-0102-6
67. Yeung T, Georges PC, Flanagan LA, Marg B, Ortiz M, Funaki M, et al. Effects of substrate stiffness on cell morphology, cytoskeletal structure, and adhesion. *Cell Motil. Cytoskeleton.* (2005) **60**:24–34. doi: 10.1002/cm.20041

68. Chiang MY, Yangben Y, Lin NJ, Zhong JL, Yang L. Relationships among cell morphology, intrinsic cell stiffness and cell–substrate interactions. *Biomaterials*. (2013) **34**:9754–62. doi: 10.1016/j.biomaterials.2013.09.014
69. Panzetta V, Fusco S, Netti PA. Cell mechanosensing is regulated by substrate strain energy rather than stiffness. *Proc Natl Acad Sci USA*. (2019) **116**:22004–13. doi: 10.1073/pnas.1904660116
70. Krause M, Gautreau A. Steering cell migration: Lamellipodium dynamics and the regulation of directional persistence. *Nat Rev Mol Cell Biol*. (2014) **15**:577–90. doi: 10.1038/nrm3861
71. Petrie RJ, Doyle AD, Yamada KM. Random versus directionally persistent cell migration. *Nat Rev Mol Cell Biol*. (2009) **10**:538–49. doi: 10.1038/nrm2729
72. Hennig K, Wang I, Moreau P, Valon L, DeBeco S, Coppey M, et al. Stick-slip dynamics of cell adhesion triggers spontaneous symmetry breaking and directional migration of mesenchymal cells on one-dimensional lines. *Sci Adv*. (2020) **6**:eaau5670. doi: 10.1126/sciadv.aau5670
73. Rieken S, Habermehl D, Wuerth L, Brons S, Mohr A, Lindel K, et al. Carbon ion irradiation inhibits glioma cell migration through downregulation of integrin expression. *Int J Radiat*. (2012) **83**:394–9. doi: 10.1016/j.ijrobp.2011.06.2004

Conflict of Interest: The authors declare that the research was conducted in the absence of any commercial or financial relationships that could be construed as a potential conflict of interest.

frontiers in Physics

BRIEF RESEARCH REPORT
published: 07 October 2020
doi: 10.3389/fphy.2020.567215

On the Role of Single Particle Irradiation and Fast Timing for Efficient Online-Control in Particle Therapy

Denis Dauvergne[1], Oreste Allegrini[2], Cairo Caplan[3], Xiushan Chen[2], Sébastien Curtoni[1], Ane Etxebeste[2,4], Marie-Laure Gallin-Martel[1], Maxime Jacquet[1], Jean Michel Létang[4], Jayde Livingstone[1,2], Sara Marcatili[1], Christian Morel[3], Étienne Testa[2] and Yannick Zoccarato[2]*

[1] Université Grenoble Alpes, CNRS/IN2P3, Grenoble INP, LPSC-UMR 5821, Grenoble, France, [2] Université de Lyon, Université Lyon 1, CNRS/IN2P3, Institut de Physique des Deux Infinis de Lyon, UMR 5822, Villeurbanne, France, [3] Aix-Marseille Univ, CNRS/IN2P3, CPPM, Marseille, France, [4] Université de Lyon, CREATIS, CNRS, UMR 5220, INSERM U1044, INSA-Lyon, Université Lyon 1, Centre Léon Bérard, Villeurbanne, France

OPEN ACCESS

Edited by:
Vincenzo Patera,
Sapienza University of Rome, Italy

Reviewed by:
Simona Giordanengo,
National Institute of Nuclear Physics of Turin, Italy
Francesco Pennazio,
National Institute of Nuclear Physics of Turin, Italy

***Correspondence:**
Denis Dauvergne
denis.dauvergne@lpsc.in2p3.fr

Specialty section:
This article was submitted to Medical Physics and Imaging, a section of the journal Frontiers in Physics

Received: 29 May 2020
Accepted: 31 August 2020
Published: 07 October 2020

Citation:
Dauvergne D, Allegrini O, Caplan C, Chen X, Curtoni S, Etxebeste A, Gallin-Martel M-L, Jacquet M, Létang JM, Livingstone J, Marcatili S, Morel C, Testa É and Zoccarato Y (2020) On the Role of Single Particle Irradiation and Fast Timing for Efficient Online-Control in Particle Therapy. Front. Phys. 8:567215. doi: 10.3389/fphy.2020.567215

Within the frame of the CLaRyS collaboration, we discuss the assets of using a reduced-intensity *in vivo* treatment control phase during one or a few beam spots at the beginning of a particle therapy session. By doing so we can improve considerably the conditions for secondary radiation detection and particle radiography. This also makes Time-of-Flight (ToF) resolutions of 100 ps rms feasible for both the transmitted particles and secondary radiations, by means of a single-projectile counting mode using a beam-tagging monitor with time and position registration. This opens up new perspectives for prompt-gamma timing and Compton imaging for range verification. ToF-based proton computed tomography (CT) and ToF-assisted secondary proton vertex imaging in carbon therapy are also discussed, although for the latter, no evidence of any benefit at small observation angles is anticipated. The reduction of the beam intensity during one or a few spots on the various accelerators for particle therapy should not significantly reduce the patient workflow.

Keywords: particle therapy, range verification, prompt-gamma, proton radiography, proton interaction vertex imaging, time-of-flight, fast timing

INTRODUCTION

In vivo range verification in particle therapy remains an important challenge to improve the treatment quality. Indeed, uncertainties in the treatment planning, anatomical evolution between planning imaging and actual treatment fraction, patient positioning and moving, may cause deviations between planned dose and actual delivered dose. Thus, the beneficial impact of the ballistic precision is reduced by the necessity of additional security margins, and by limiting irradiation fields to those avoiding directions where organs at risk are located immediately behind the ion range [1, 2]. Several techniques are being intensively developed, either based on secondary radiation [Positron Emission Tomography (PET), Prompt-gamma (PG), ionoacoustic waves, bremsstrahlung], or on the improvement of planning imaging to get more accurate range prediction [2–8]. However, the implementation of *in vivo* range verification devices faces several

issues. Among them, one needs to collect and treat sufficiently accurate data during the smallest possible fraction of the patient irradiation (ideally a single pencil beam spot), and get the relevant information in the shortest possible time, in order to continue with the treatment if safe conditions are met, or to minimize the consequences of a deviation. In addition, the device should comply with the environment of the treatment room, and the range verification procedure should not reduce the patient flow beyond the acceptable.

In the present paper, we propose to address these two issues of a real-time verification compatible with the clinical workflow, with the device that has been developed within the CLaRyS collaboration. We discuss on the opportunity offered by a reduced beam intensity for PG and ion imaging. More specifically, we focus on the assets of reducing the clinical beam intensity for a short period (one or a few beam spots in pencil beam scanning mode), in such a way that each single incident particle is identifiable, like in list-mode ion-CT, where all relevant information like upstream/downstream positions and directions, energy, is recorded for each projectile. First, this will relax important constraints on particle detection rates during beam delivery at clinical intensities [9, 10]. Second, fast Time-of-Flight (ToF) at the level of 100 ps rms may be used to improve existing modalities such as prompt-gamma Compton imaging, prompt-gamma timing, proton radiography, and secondary proton imaging. Third, we briefly discuss a few technical aspects of implementing a beam intensity reduction, which should not reduce significantly the patient flow.

PROMPT-GAMMA RANGE VERIFICATION

Prompt-gamma (PG) detection offers the unique opportunity for range verification in real time with a few-millimeter precision at a single proton pencil-beam spot scale [4]. Indeed, high-energy gamma rays (1–10 MeV range) are emitted within a very short time (mostly less than a picosecond) after inelastic collisions between primary protons and target nuclei, and may escape the patient body without further interaction. Although part of the PGs are also induced by secondary particles (e.g., neutrons), the PG emission profile is then correlated to the proton range. Several PG-based techniques are proposed to control the treatments. Prompt-gamma imaging (PGI) requires the directional detection of gamma rays, using either mechanical or electronic collimation (e.g., with Compton cameras). Range verification requires at least 1D imaging along the beam direction. Prompt-Gamma Peak Integral (PGPI) considers the integrated yields issued from the patient, with time-of-flight (ToF) selection [11]; it is connected to the energy deposited in the patient, and may provide 3D information about the beam path by using several detectors. Prompt-Gamma Timing (PGT) provides the ToF distribution that is correlated with the proton range [12]. Prompt-Gamma Spectroscopy (PGS) combines partial collimation to select part of the range in the field of view, and PG spectral information with good resolution, in order to extract information on chemical composition and range, from energy- and (A,Z)-nuclear-dependence of individual gamma emission-line probabilities [13]. ToF is necessary in PGS to enhance signal-to-background ratio.

For ions heavier than protons, PG detection is less performing since smaller amounts of projectiles are used to deliver the same physical and biological doses, and thus, treatment verification should be considered for larger amounts of incident particles than single spots.

All the PG-based detection methods face the issue of acquiring sufficient statistics within a short time, at high instantaneous count rate. Basically, in clinical conditions, a typical proton beam spot represents 10^7 particles that are delivered at an average intensity of 10^{10} protons/s at cyclotrons and synchro-cyclotrons dedicated to protons, i.e., within about 1 ms. This amount of protons per spot may vary by plus/minus one order of magnitude typically: it is higher for some distal spots [14], or when particular care is taken during the planning stage to boost spots dedicated to verification [15], and it is much smaller for proximal spots. For a 10 cm proton range in tissue equivalent matter, about 3% of the projectiles will generate primary PG by nuclear collisions [4]. A single detector with 3×10^{-3} absolute detection efficiency (e.g., a 100% intrinsic efficiency scintillator of 7.5 cm diameter located at 30 cm) would then detect 10^3 PG during 1 ms, at an instantaneous count rate of 10^6/s achieved with a proton beam flux of 10^{10} protons/s. Moreover, this count rate may be doubled if one accounts for other radiation species impinging the detector (secondary gamma rays, neutrons, etc.). On the one hand, this represents a challenge, as pointed out by Pausch et al. [9], since detectors need to cope with a counting rate varying from about 0 (beam pauses between spots) to more than 10^6 Hz during 1 ms almost without transient regimes. On the other hand, such a statistics of 10^3 counts would hold for fields of view covering the whole proton range (in the case of methods such as PGPI and PGT). If the detection system is aimed at imaging the PG fall-off close to the Bragg peak, then the statistics in the restricted area of interest is reduced accordingly. The precision of the fall-off retrieval is proportional to the contrast-to-noise ratio [16], and thus to $\frac{1}{\sqrt{N_{PG}}}$, where N_{PG} is the number of detected PG in the region of interest. Passive collimation reduces the flux of incoming PG on a detector, yielding to low detection efficiency, without substantial reduction of the neutron background if ToF is not implemented. Thus, large detection volumes with segmented readout are necessary, like for the knife-edge-slit camera developed by IBA and Politecnico-Milano [17] that has been used in clinics. This shifts the issue of count rate per detector to a large acquisition-flow handling. Compton imaging may yield to higher detection efficiency than collimated devices. However, at clinical beam intensity, the coincidence rate between the two detection stages is dominated by fortuitous coincidence events induced by quasi-simultaneous projectiles [10, 18, 19]. A significant reduction of the incident flux is needed in order to minimize this background source [10], at the level of one incident proton within the duration of the time-coincidence window, unless efficient filtering strategies are used, which has not been demonstrated so far.

Going further, the reduction of the incident beam intensity to a level where individual projectile identification is possible,

presents not only the asset of better PG detection conditions but also the opportunity for high-resolution ToF. Basically, 1–2 ns ToF resolution makes it possible to select PG issued from a patient, and to discriminate them from massive particles like neutrons at sufficiently large distances, at the scale of a proton bunch delivered by a cyclotron (of the order of 1 ns). This is the strategy used for the PGPI technique and in the development of PGT at Oncoray. However, in the latter case, this bunch length is the main limitation of the accuracy of PGT [20, 21] at clinical beam intensities. The reduction of the ToF resolution down to 100 ps rms would translate to a PG vertex position determination of 1–2 cm rms resolution (observation at 90°), proportional to the proton velocity: indeed, 1 cm rms holds for $\beta = v/c = 0.3$, i.e., 3 cm from the end of the proton range. Note that this resolution depends on the observation angle: it is smaller at backward angles, for which proton-to-vertex and photon-to-detector transit times are adding, both increasing monotonically with the vertex depth. Such resolution is typically the same as the point spread response of a multi-collimated camera [17, 22] or a Compton camera [23], without any collimation.

Prompt Gamma Timing

Recently, Marcatili et al. published first results on PGT with about 100 ps rms ToF resolution, using fast monolithic scintillators and a diamond-detector beam trigger [24]. They estimated the achievable probability with 95% confidence level to detect a 3-mm thickness variation of an air cavity in a PMMA phantom with 10^8 incident protons and a single detector having a detection efficiency of 1.5×10^{-3}. In order to illustrate the asset of such 100 ps time-resolution in single proton counting mode, **Figure 1** compares the results derived from PGT with 162 MeV proton beams at clinical intensities (in bunch-counting mode with $>10^2$ protons/bunch, where the ToF is measured between a detected PG relative to the accelerator HF signal) from Werner et al. [21] and those obtained in Marcatili et al. [24] with 68 MeV protons in single incident particle regime (i.e., the ToF is measured relative to the arrival of the single proton that induced the PG). In the first case, a 2-cm air cavity is inserted in a PMMA phantom at 9 cm depth. In the latter case, a 2.5 cm thick air gap is inserted at 1 cm depth. In the bunch-counting mode, the effect of the air cavity results in a shift of the mean value and a broadening of the PGT spectrum, as observed from the difference between both the colored curves. However, the width of the time distribution is dominated by the pulse duration (∼3 ns FWHM). In contrast, the shape of the distribution in single proton counting mode reflects mainly the flight time of a proton inside the target (of the order of 1 ns), and the air insert is clearly observed as a separation of two components in the PGT distribution in the target. In addition, the authors of ref. [21] mentioned that the large statistical fluctuations observed were caused by the limited statistics available for a single beam spot. Single counting mode makes it possible to improve the statistics by reducing dead-time and improving the detection solid angle with closer detectors. This is also illustrated in **Figure 1**, where both spectra were acquired with similar numbers of incident protons (of the order of one large beam spot).

Compton Prompt-Gamma Imaging

In the frame of the CLaRyS collaboration project, a large area Compton camera has been designed [23], the sizes and detection geometry of which are reported in **Figure 2A**. Compton reconstructible events consist in a single Compton scattering in the first stage (7 planes of $9 \times 9 \times 0.2$ cm^3 position-sensitive silicon detectors) followed by total or partial absorption of scattered photons in a $38 \times 38 \times 3$ cm^3 pixellated-BGO scintillator absorber. A beam hodoscope is used to measure the beam-transverse position and time of arrival. Therefore, the Compton cone, whose axis is the line joining the interaction vertices in the scatterer and absorber stages, and whose angle is determined by the energy deposited in both the stages in the case of full absorption, intersects the beam trajectory in two points. Actually, the two solutions are not points, but correspond to extended zones, which size depends on (i) the beam extension in the transverse plane due to beam size and lateral scattering, (ii) the CC spatial resolution [10]. The latter depends on the spatial and energy resolutions of both the scatter and absorber detectors, and on the Doppler broadening corresponding to the electron Compton profiles of the scattering material (the heavier material, the larger angular broadening of the cone [25]). The expected spatial resolution of the Compton camera for a point source, polychromatic PG energy spectrum is 8.3 mm FWHM [23].

Among the two intersection points (or volumes), one is the correct vertex, provided full absorption occurred in the absorber. The second one will contribute to background if not rejected by basic considerations (e.g., when located outside the target). Using this line-cone intersection method, no time-consuming reconstruction algorithm is required if one could identify the right point among the two intersection points. **Figure 2B** represents, for the particular geometry shown in **Figure 2A**, the simulated distribution of distances separating the two solution-points [26]. The camera axis is centered at 10 cm proton penetration depth, and the distance between the beam and the scatter detector is 20 cm. The average value of the distribution is 14.7 cm, i.e., of the same order of magnitude as the proton range (∼14.8 cm at 160 MeV [27]). Their corresponding transient time in the PMMA phantom is 1.3 ns. This distance is much larger than the extension of the line-cone intersection volumes due to spatial resolution. Thus, it is expected that a detector time resolution of a few hundreds of ps will make it possible to identify the right solution. These expectations are confirmed in a forthcoming paper by our collaboration, showing that the precision of the PG fall-off retrieval reaches the one obtained with a state-of-art iterative reconstruction algorithm, when ToF selection is used at 200 ps rms resolution or less.

ION RADIOGRAPHY

The basic idea of ion radiography is to measure the relative stopping power of the traversed material, and thus the Water Equivalent Thickness (WET), by means of the energy loss of transmitted ions, either by calorimetry, or by the residual range in a reference material [28]. This energy loss is tightly connected to the electronic density, which makes ion radiography

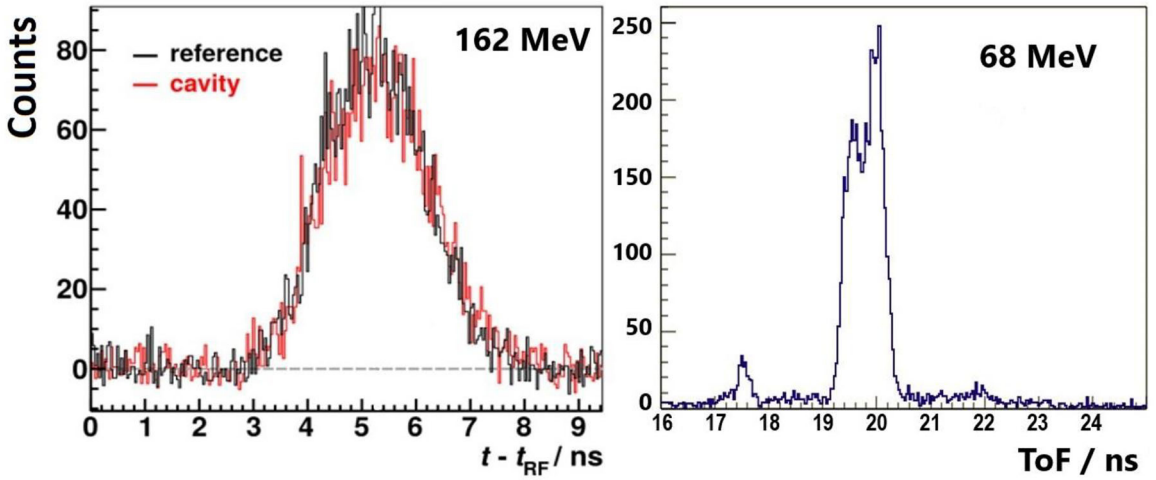

FIGURE 1 | Experimental prompt-gamma timing spectra obtained with proton beams in PMMA targets; **(Left)** at clinical intensity, with synchronization to the cyclotron RF signal (pulse by pulse basis for a single beam spot of 3.8×10^8 protons, data from [21] with authors permission, with and without a 2 cm air cavity at 9 cm depth); **(Right)** ion-per-ion basis at 68 MeV, using a diamond beam trigger at low intensity, a 2.5 cm thick air insert is located at 1 cm from the target entrance. The number of protons used to generate the second histogram is similar ($\sim 3 \times 10^8$) [24].

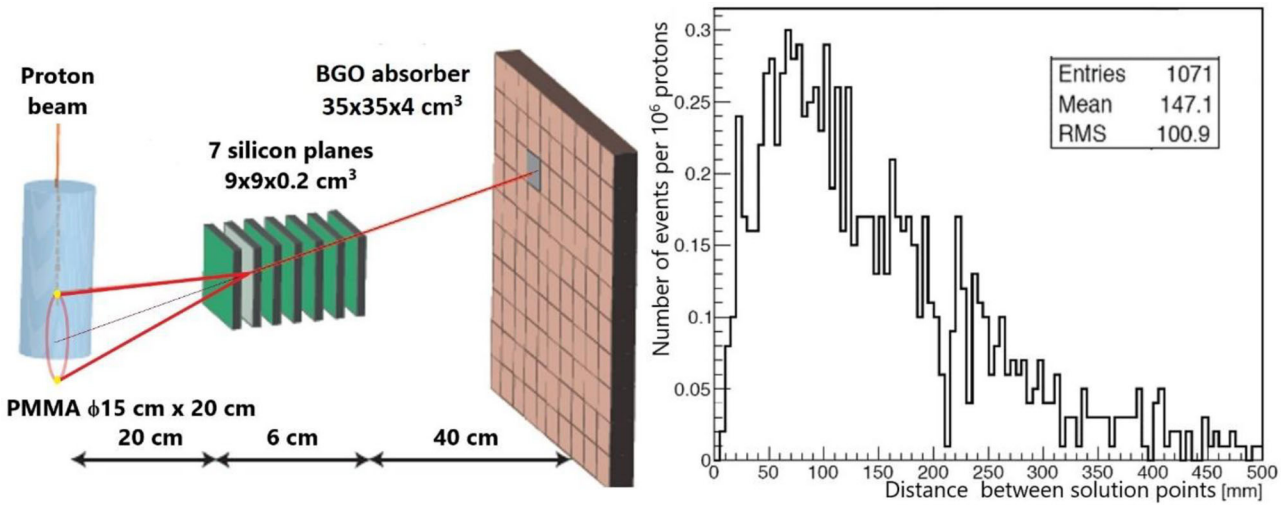

FIGURE 2 | (Left) scheme of the CLaRyS Compton camera used for range verification in simulations for 160 MeV protons. The two yellow points represent two line-cone intersection points. **(Right)** using this geometry, distribution of distances between the two line-cone intersection points deduced from Compton kinematics in the case of an interaction in each stage of the camera (data from [26]).

relevant for particle treatment planning, without uncertainty in the conversion factor between X-ray absorption and electronic density (Hounsfield units). Thus, ion tomography may improve the precision of planning imaging, currently performed with X-ray CT, if an overall advantage is obtained by combining the following criteria: (i) minimize the induced dose, (ii) minimize the exposition time at the particle treatment place, (iii) optimize spatial resolution, and (iv) optimize accuracy on WET. For the latter criterion, the necessary precision on the energy loss measurement is below 1% [28], which requires appropriate calorimetry or residual range determination. The spatial resolution is conditioned by particle tracking, but is inherently limited by multiple scattering inside the patient. Two strategies may be followed: either spot-by-spot or single particle tracking [29, 30]. The integration mode with spot by spot tracking presents the advantage of a simplified tracking device, but the disadvantage of poorer spatial resolution, caused by the initial spot size, and the consequent indetermination of the path in the case of mixed-fields, i.e., when various integrated electronic densities are met within the same spot,

due to varying structures in the transverse plane. Gianoli et al. compared the two methods in proton radiography, using the Most Likely Path (MLP) reconstruction algorithms. They have shown that the additional blurring caused by the spot size can be at least partially compensated at the cost of a higher statistics, hence a higher dose, relative to single proton tracking [29]. For carbon ion radiography, with reduced scattering relative to protons, Meyer et al. have shown that with the integration mode, performance approaching those of the list mode could be obtained [31]. However, the list mode remains the gold standard for proton or ion radiography for optimizing the spatial resolution, at the expense of a beam intensity compatible with single particle detection.

In the list mode option, the information on the energy loss inside the patient could be obtained from ToF, provided large enough distances between the patient and the downstream detector are used. Indeed, measuring small variations of the transient time inside the patient is out of reach, since this time is of the order of 1–2 ns: 1% resolution in the energy loss would translate into a 5–10 ps time resolution. However, a ToF detector may measure variations of the residual velocity. For particles exiting the patient at typically 1/3 of the speed of light, 1% of kinetic energy variation corresponds to 100 ps flight time variation over 2 m. Thus, it appears feasible to design a proton-CT device based on fast trackers, optimized for low residual energies. The asset of such a device is a simplified detector for spatial and time measurement relative to separate tracking and calorimetry detectors. Recently, Worstell et al. [32] published a first progress report on the development of a ToF-based proton radiography device: fast position sensitive detectors (large area micro-channel plates) are used to track particles with a time resolution that is expected to be smaller than 100 ps.

SECONDARY PROTON IMAGING

This technique consists in the detection of secondary light charged particles (proton and its isotopes deuteron and tritium) under irradiation with heavier ions (helium or heavier ions) [33–36]. Such particles are created with a high probability during quasi-elastic and inelastic collisions. **Figure 3** shows a simulated energy distribution of protons at emission in a thin PMMA target by incident carbon ions at three different energies [37]. The energy spectrum is quite broad, but only high energy secondary protons have a chance in practice to escape from the patient body (100 MeV protons have a range of 75 mm in water [27]). For the high-energy part of the distributions, one may observe a maximum at velocities that are close to the carbon projectile velocity. However, the velocity distribution above that threshold is still very large. Thus, protons that are detected outside a patient are more likely emitted from the entrance than close to the end of range. In addition, protons emitted from the entrance region will reach the exit before those emitted in depth, due to the combined effect of higher slowing-down of carbon ions before the vertex, and the higher average proton velocity during their path to exit. Simulations have shown that, in the case of 200 MeV/u carbon ions incident on a head phantom, the correlation between ToF and vertex position is not sufficient to improve significantly the vertex localization obtained by tracking at low observation angle (10°), when considering ToF information. This is due to the broad proton energy distribution as shown in **Figure 3**, but also to the fact that carbon ions and secondary protons do not have sufficiently different velocities at the emission point. Moreover, like for PG, observation at small forward angles is not a favorable case for ToF discrimination because the total path length of primary plus secondary particle is the same whatever the vertex position. Observation at larger angles, like in the INSIDE design (60°) [38, 39], or even at 90° [40], could be more favorable, because path lengths—and therefore ToF–are increasing with depth. However, one has to keep in mind that emission yields per solid angle unit drop down dramatically when the angle increases [37], which raises statistics issues for a small number of spots. This remains an open question.

NEED FOR A BEAM TAGGING SYSTEM

Without using a beam monitor, the temporal resolution of the synchronization between the accelerator HF and the detection of prompt secondary particles at the patient place is limited to the bunch duration at the exit of the accelerator, convolved with the time dispersion due to the longitudinal momentum spread during beam transport. This is independent of the beam intensity. The bunch duration depends on the accelerator type: it is typically about 1 ns for a cyclotron, 8 ns for a synchro-cyclotron, and 20–50 ns for a synchrotron [4]. Moreover, the passive degradation of the energy between two different beam spots induces a time phase shift relative to the accelerator HF for an isochronous accelerator. This makes a time calibration necessary for each energy change. Therefore, a beam tagging system can be used advantageously to detect the time of arrival of ions on the patient, provided it is able to cope with high counting rates, either in clinical-intensity bunch modes, or in single particle counting regime. For bunch detection, secondary particle detectors can be used [20, 41], whereas scintillator-based hodoscopes are generally proposed for single particle counting, with timing resolutions of several hundred picoseconds [39, 42]. Thin ultra-fast silicon detectors (UFSD) have been explored for such purpose [43]. Using another technology, we have shown that a temporal resolution close to 100 ps rms is expected by means of diamond detectors, on condition that large areas are available with detector-grade crystals [24, 44]. Relatively large polycrystalline diamonds are available and provide such a time resolution for highly ionizing particles such as carbon ions. However, high energy protons may require high-quality single-crystals to reach both the detection efficiency and the good time resolution. A diamond beam-hodoscope is under construction by our collaboration. Such a beam tagging system has necessarily a finite thickness and will be located upstream from the patient. The impact on range shift (about 2 mm WET) needs to be accounted for in the treatment planning system, and the impact on secondary radiation additional dose corresponds to the same 2 mm WET. The distance between hodoscope and patient should be kept as small as possible to minimize the impact of multiple

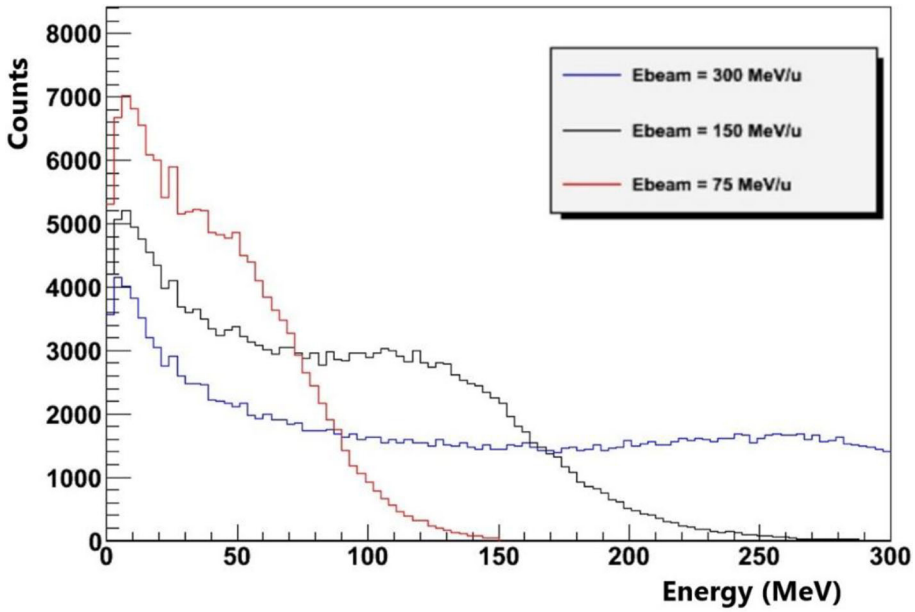

FIGURE 3 | Geant4 simulation of the energy distribution of secondary protons at emission inside a thin PMMA target by carbon ions at three different energies. Nuclear reactions are modeled with the QMD model (data from [33]).

scattering, with the constraint of being compatible with the patient positioning system.

BEAM INTENSITY REDUCTION

Reduction Factors and Possible Irradiation Delay

The beam intensity reduction should satisfy two criteria: first, the beam tagging system should handle all the incident particles and provide time stamp with the requested resolution. This requires typically 10 ns between two consecutive signals in a single readout channel. This can be achieved by means of detector segmentation anyway (for instance, 0.25 mm^2 pixel size is requested for a flux of 4×10^{10} proton/cm^2/s). Second, non-ambiguous assignment of the secondary particle detection to the primary projectile should be obtained. Depending on the observation distance and ToF resolution, this condition will constrain a second trigger probability on the hodoscope to a negligible value within a period of 1 to 5 ns.

At clinical proton beam intensities, the average beam intensity is about 2 nA during an irradiation spot, i.e. 1.2×10^{10} proton/s over 1–10 ms. At least 1 ms is required to shift between two adjacent spots (magnetic scanning), and more to change the energy (insertion of degrader device, or change of synchrotron energy). For carbon ions, the intensity is typically 10^7-10^8 ions/s at European synchrotron systems, up to 3×10^8 ions/s at SAGA-HIMAT [45–47]. About 10^5 ions are needed for a single spot, with the same duration as for protons.

All accelerated beams have a pulsed structure at the nanosecond time scale (which we refer to as nanopulse structure below), which may be superimposed to the microsecond, or even second–scale pulse structure on synchro-cyclotrons and synchrotrons. For a 100 MHz cyclotron with around 1 ns pulse duration, the above condition corresponds to a probability of having one particle per pulse to be one order of magnitude larger than the probability to have more than one particle per pulse [$p(1) > 10 \times p(N>1)$]. Assuming a Poisson distribution, this leads to a maximum average number of particles per pulse of 0.2. Relative to proton therapy intensities, this is a reduction by a factor of 1/1,000. For a proton synchro-cyclotron like IBA-S2C2, around 8 ns nanopulses are extracted with a period of 16 ns and 2 protons could be considered within the same nanopulse: indeed this should lead to identifiable events in most cases with a segmented detector. Thus, the average number of protons per pulse could be slightly higher than 0.2 (about 0.5). The reduction factor compared to clinical intensity is then a factor 1/10,000. As for synchrotrons, they have longer nanopulse durations (20–50 ns) which depend on the ion species. Correspondingly, the average number of particles per pulse should be about 2–5. This represents almost no reduction relative to clinical intensity in the case of carbon therapy (at 10^7 ions/s), and a factor smaller than 1/100 for proton therapy.

A reduction of the beam intensity during one or a few pencil-beam spots will extend the duration of the spot delivery, but not the time needed to change the spot position or energy. Thus, an intensity reduction by 1/1,000 will extend the spot duration by 0.5 s for a 10^7-proton-spot relative to a 2 nA-nominal intensity cyclotron. For a proton synchro-cyclotron, the extension is larger (5 s per spot). For a synchro-cyclotron delivering protons at 0.1 nA nominal intensity, the extension is also 1 s per spot. For carbon therapy, the extension of spot duration will be at the level of milliseconds, if any.

Monitoring the dose delivered at low intensity with a system compatible with high-intensity dose monitoring may represent an issue. Current monitoring devices are based on ionization chambers, like the IC2/3 that have been developed for proton therapy with IBA-cyclotrons [48, 49]. The sensitivity of this detector technology is of the order of several hundreds of protons per monitor unit and the signal/noise ratio with low beam intensity could be an issue. Therefore, the effect of large dark current on the control of the beam fluence and position and other noise source like radiophonic noise would need to be evaluated. Nevertheless, as the total charge to be integrated during a beam spot is unchanged when intensity varies, we expect that the electronic noise will not be a problem for beam fluence control at low particle rate. Additionally, such ionization chambers may work at pA currents for proton beams and have been calibrated for a wide range of dose rate (0.5–8 Gy/min) [49].

Technical Implementation of Beam Intensity Reduction

The easiest way to proceed to a beam reduction without changing any other characteristics (energy, time structure and emittance) is the insertion of a kind of pepper pot device [50] at the accelerator injection. The reduction factor is known and reproducible since it depends only on the geometry of the inserted filter. Insertion/extraction is fast, and no activation is generated, since particles have an energy of a few tens of keV at this stage. However, some compact injection geometries cannot make possible the insertion of such a device. Thus, a possibility would consist in stacking the accelerated beam at fixed frequency with the same number of particles as in normal operation, and use a slow extraction mode of the whole spill with an appropriate field. This procedure is possible with a synchrotron or a synchro-cyclotron [Mandrillon, personal communication]. In this case, no additional injection should be necessary, since a single spill contains enough particles for a single beam spot. Both strategies have the advantage of using all accelerated particles, which does not induce additional activation.

DISCUSSION AND CONCLUSION

We propose to implement a reduced-intensity, *in vivo* and real-time treatment control phase at the beginning of a particle therapy session. By achieving a single projectile counting mode with a beam tagging monitor, with time and position registration, one can improve considerably the conditions for secondary radiation detection and particle radiography. The first consequence is a reduction of the detection rate during beam delivery, which may considerably improve the quality of the data acquisition: reduction of dead-time, improvement of signal-to-background ratio, reduction/suppression of transient regimes. Moreover, the beam hodoscope provides directly the time of arrival of ions at the patient position, without calibration at each energy change.

More specifically, ToF resolutions of 100 ps rms can be achieved. This has a strong impact on PG imaging, since an information of 100 ps ToF directly translates into a position information of about 1 cm close to the PG fall-off. This opens up new perspectives for PG timing and Compton imaging. ToF proton-CT has been proposed and is being investigated by other groups. A potential benefit of ToF for secondary proton imaging in carbon therapy needs further investigations at large observation angles.

Besides this, other techniques like in-beam PET or ionoacoustic ultra-sound imaging would rather benefit from intense bunches with low duty cycle: maximization of the radiation source during a short time, and long time for signal collection (acoustic wave propagation and detection) and statistic accumulation (e.g., short-lived beta+ emission with few ms lifetime). Therefore, beam intensity reduction is not favorable for such techniques.

The reduction of the beam intensity during one or a few spots on the various accelerators for particle therapy should induce delays of the irradiation of the order of seconds at maximum, and therefore will not significantly reduce the patient workflow.

DATA AVAILABILITY STATEMENT

The raw data supporting the conclusions of this article will be made available by the authors, without undue reservation.

AUTHOR CONTRIBUTIONS

All authors belong to the CLaRyS collaboration. They have contributed to the instrumental, experimental, or simulation work that has led to the contents of this article. They meet at least one of the four authorship criteria following International Committee of Medical Journal Editors (ICMJE) recommendations. DD is the main writer of the text. All authors have contributed to the amendments of the text. They gave their consent on the final version.

FUNDING

The authors acknowledge the support from ITMO-Cancer (CLaRyS-UFT project) and LAbEx PRIMES (ANR-11-LABX-0063).

ACKNOWLEDGMENTS

This work is carried out in the frame of Labex PRIMES (ANR-11-LABX-0063) and within the framework of the EU Horizon 2020 project RIA-ENSAR2/MediNet (654 002). The authors would like to thank J.-M. Fontbonne for helpful discussion about ionization chamber operation vs. beam intensity and Pierre Mandrillon about the intensity reduction at synchro-cyclotrons.

REFERENCES

1. Paganetti H. Range uncertainties in proton therapy and the role of Monte Carlo simulations. *Phys Med Biol.* (2012) **57**:R99–117. doi: 10.1088/0031-9155/57/11/R99
2. Knopf AC, Lomax A. *in vivo* proton range verification: a review. *Phys Med Biol.* (2013) **58**:R131–60. doi: 10.1088/0031-9155/58/15/R131
3. Kraan AC. Range verification methods in particle therapy: underlying physics and monte carlo modeling. *Front Oncol.* (2015) **5**:150. doi: 10.3389/fonc.2015.00150
4. Krimmer J, Dauvergne D, Létang JM, Testa É. Prompt-gamma monitoring in hadrontherapy: a review. *Nucl Instum Methods Phys Res Section A.* (2018) **878**:58–73. doi: 10.1016/j.nima.2017.07.063
5. Parodi K, Polf JC. *in vivo* range verification in particle therapy. *Med Phys.* (2018) **45**:e1036–50. doi: 10.1002/mp.12960
6. Parodi K. Latest developments in *in-vivo* imaging for proton therapy. *BJR.* (2019) **93**:20190787. doi: 10.1259/bjr.20190787
7. Xie Y, Bentefour H, Janssens G, Smeets J, Stappen FV, Hotoiu L, et al. Prompt gamma imaging for *in vivo* range verification of pencil beam scanning proton therapy. *Int J Radiat Oncol Biol Phys.* (2017) **4**:27. doi: 10.1016/j.ijrobp.2017.04.027
8. Ferrero V, Fiorina E, Morrocchi M, Pennazio F, Baroni G, Battistoni G, et al. Online proton therapy monitoring: clinical test of a Silicon-photodetector-based in-beam PET. *Sci Rep.* (2018) **8**:4100. doi: 10.1038/s41598-018-22325-6
9. Pausch G, Berthold J, Enghardt W, Römer K, Straessner A, Wagner A, et al. Detection systems for range monitoring in proton therapy: needs and challenges. *Nucl Instum Methods Phys Res Section A.* (2020) **954**:161227. doi: 10.1016/j.nima.2018.09.062
10. Fontana M, Ley JL, Dauvergne D, Freud N, Krimmer J, Létang JM, et al. Monitoring ion beam therapy with a compton camera: simulation studies of the clinical feasibility. *IEEE Trans Radiat Plasma Med Sci.* (2020) **4**:218–32. doi: 10.1109/TRPMS.2019.2933985
11. Krimmer J, Angellier G, Balleyguier L, Dauvergne D, Freud N, Herault J, et al. A cost-effective monitoring technique in particle therapy via uncollimated prompt gamma peak integration. *Appl Phys Lett.* (2017) 110:154102. doi: 10.1063/1.4980103
12. Golnik C, Hueso-González F, Müller A, Dendooven P, Enghardt W, Fiedler F, et al. Range assessment in particle therapy based on prompt γ-ray timing measurements. *Phys Med Biol.* (2014) **59**:5399–422. doi: 10.1088/0031-9155/59/18/5399
13. Joost M Verburg JS. Proton range verification through prompt gamma-ray spectroscopy. *Phys Med Biol.* (2014) **59**:7089–106. doi: 10.1088/0031-9155/59/23/7089
14. Grevillot L, Bertrand D, Dessy F, Freud N, Sarrut D. A monte carlo pencil beam scanning model for proton treatment plan simulation using GATE/GEANT4. *Phys Med Biol.* (2011) **56**:5203–19. doi: 10.1088/0031-9155/56/16/008
15. Tian L, Landry G, Dedes G, Kamp F, Pinto M, Niepel K, et al. Toward a new treatment planning approach accounting for *in vivo* proton range verification. *Phys Med Biol.* (2018) **63**:215025. doi: 10.1088/1361-6560/aae749
16. Roellinghoff F, Benilov A, Dauvergne D, Dedes G, Freud N, Janssens G, et al. Real-time proton beam range monitoring by means of prompt-gamma detection with a collimated camera. *Phys Med Biol.* (2014) **59**:1327–38. doi: 10.1088/0031-9155/59/5/1327
17. Perali I, Celani A, Bombelli L, Fiorini C, Camera F, Clementel E, et al. Prompt gamma imaging of proton pencil beams at clinical dose rate. *Phys Med Biol.* (2014) **59**:5849–71. doi: 10.1088/0031-9155/59/19/5849
18. Ortega PG, Torres-Espallardo I, Böhlen TT, Cerutti F, Chin MPW, Ferrari A, et al. Noise evaluation of prompt-gamma technique for proton-therapy range verification using a Compton Camera. In: *2013 IEEE Nuclear Science Symposium and Medical Imaging Conference* (Seoul). (2013). p. 1–7. Available online at: https://ieeexplore.ieee.org/document/6829310
19. Rohling H, Priegnitz M, Schoene S, Schumann A, Enghardt W, Hueso-González F, et al. Requirements for a compton camera for *in vivo* range verification of proton therapy. *Phys Med Biol.* (2017) **62**:2795–811. doi: 10.1088/1361-6560/aa6068
20. Petzoldt J, Roemer KE, Enghardt W, Fiedler F, Golnik C, Hueso-González F, et al. Characterization of the microbunch time structure of proton pencil beams at a clinical treatment facility. *Phys Med Biol.* (2016) **61**:2432–56. doi: 10.1088/0031-9155/61/6/2432
21. Werner T, Berthold J, Hueso-González F, Koegler T, Petzoldt J, Roemer K, et al. Processing of prompt gamma-ray timing data for proton range measurements at a clinical beam delivery. *Phys Med Biol.* (2019) **64**:105023. doi: 10.1088/1361-6560/ab176d
22. Pinto M, Dauvergne D, Freud N, Krimmer J, Letang JM, Ray C, et al. Design optimisation of a TOF-based collimated camera prototype for online hadrontherapy monitoring. *Phys Med Biol.* (2014) **59**:7653–74. doi: 10.1088/0031-9155/59/24/7653
23. Roellinghoff F, Richard MH, Chevallier M, Constanzo J, Dauvergne D, Freud N, et al. Design of a Compton camera for 3D prompt-[gamma] imaging during ion beam therapy. *Nucl Instr Methods Phys Res Section A.* (2011) **648**:S20–2. doi: 10.1016/j.nima.2011.01.069
24. Marcatili S, Collot J, Curtoni S, Dauvergne D, Hostachy JY, Koumeir C, et al. Ultra-fast prompt gamma detection in single proton counting regime for range monitoring in particle therapy. *Phys Med Biol.* (2020). [Epub ahead of print].
25. Fontana M, Dauvergne D, Létang JM, Ley JL, Testa É. Compton camera study for high efficiency SPECT and benchmark with anger system. *Phys Med Biol.* (2017) **62**:8794–812. doi: 10.1088/1361-6560/aa926a
26. Ley JL. *Mise en Oeuvre d'un Démonstrateur de Caméra Compton Pour L'imagerie en Médecine Nucléaire et Pour le Contrôle en Temps Réel de L'hadronthérapie à L'aide des Rayonnements Gamma Prompts* (Thesis). Univ. Lyon 1 (2015). Available online at: http://www.theses.fr/2015LYO10334 (accessed May 11, 2017).
27. Ziegler JF, Ziegler MD, Biersack JP. SRIM – the stopping and range of ions in matter (2010). *Nucl Instrum Methods B.* (2010) **268**:1818–23. doi: 10.1016/j.nimb.2010.02.091
28. Johnson RP. Review of medical radiography and tomography with proton beams. *Rep Prog Phys.* (2017) 81:016701. doi: 10.1088/1361-6633/aa8b1d
29. Gianoli C, Meyer S, Magallanes L, Paganelli C, Baroni G, Parodi K. Analytical simulator of proton radiography and tomography for different detector configurations. *Phys Med Eur J Med Phys.* (2019) **59**:92–9. doi: 10.1016/j.ejmp.2019.03.002
30. Krah N, Khellaf F, Létang JM, Rit S, Rinaldi I. A comprehensive theoretical comparison of proton imaging set-ups in terms of spatial resolution. *Phys Med Biol.* (2018) **63**:135013. doi: 10.1088/1361-6560/aaca1f
31. Meyer S, Gianoli C, Magallanes L, Kopp B, Tessonnier T, Landry G, et al. comparative monte carlo study on the performance of integration- and list-mode detector configurations for carbon ion computed tomography. *Phys Med Biol.* (2017) **62**:1096–112. doi: 10.1088/1361-6560/aa5602
32. Worstell WA, Adams BW, Aviles M, Bond J, Cascio E, Cremer T, et al. First results developing time-of-flight proton radiography for proton therapy applications. In: *Medical Imaging 2019: Physics of Medical Imaging* (International Society for Optics and Photonics). p. 109480G.
33. Amaldi U, Hajdas W, Iliescu S, Malakhov N, Samarati J, Sauli F, et al. Advanced quality assurance for CNAO. *Nucl Instr Methods Phys Res Section A.* (2010) **617**:248–9. doi: 10.1016/j.nima.2009.06.087
34. Henriquet P, Testa E, Chevallier M, Dauvergne D, Dedes G, Freud N, et al. Interaction vertex imaging (IVI) for carbon ion therapy monitoring: a feasibility study. *Phys Med Biol.* (2012) **57**:4655–69. doi: 10.1088/0031-9155/57/14/4655
35. Gwosch K, Hartmann B, Jakubek J, Granja C, Soukup P, Jäkel O, et al. Non-invasive monitoring of therapeutic carbon ion beams in a homogeneous phantom by tracking of secondary ions. *Phys Med Biol.* (2013) **58**:3755–73. doi: 10.1088/0031-9155/58/11/3755
36. Piersanti L, Bellini F, Bini F, Collamati F, Lucia ED, Durante M, et al. Measurement of charged particle yields from PMMA irradiated by a 220 MeV/u 12C beam. *Phys Med Biol.* (2014) **59**:1857. doi: 10.1088/0031-9155/59/7/1857
37. Reithinger V. *Assurance Qualité des Traitements par Hadronthérapie Carbone Par Imagerie de Particules Promptes Chargées.* (Thesis). Univ. Lyon 1 (2015). Available online at: https://tel.archives-ouvertes.fr/tel-01441452/document (accessed May 11, 2017).
38. Marafini M, Attili A, Battistoni G, Belcari N, Bisogni MG, Camarlinghi N, et al. The INSIDE project: innovative solutions for in-beam

dosimetry in hadrontherapy. *Acta Physica Polonica A.* (2015) **127**:1465–7. doi: 10.12693/APhysPolA.127.1465

39. Traini G, Mattei I, Battistoni G, Bisogni MG, De Simoni M, Dong Y, et al. Review and performance of the dose profiler, a particle therapy treatments online monitor. *Physica Medica.* (2019) **65**:84–93. doi: 10.1016/j.ejmp.2019.07.010
40. Battistoni G, Collamati F, De Lucia E, Faccini R, Marafini M, Mattei I, et al. Design of a tracking device for on-line dose monitoring in hadrontherapy. *Nucl Instr Methods Phys Res Section A.* (2017) **845**:679–83. doi: 10.1016/j.nima.2016.05.095
41. Magalhaes Martins P, Dal Bello R, Seimetz M, Hermann G, Kihm T, Seco J. A single-particle trigger for time-of-flight measurements in prompt-gamma imaging. *Front Phys.* (2020) **8**:169. doi: 10.3389/fphy.2020.00169
42. Krimmer J, Chevallier M, Constanzo J, Dauvergne D, Rydt MD, Dedes G, et al. Collimated prompt gamma TOF measurements with multi-slit multi-detector configurations. *J Instru.* (2015) **10**:P01011. doi: 10.1088/1748-0221/10/01/P01011
43. Vignati A, Monaco V, Attili A, Cartiglia N, Donetti M, Mazinani MF, et al. Innovative thin silicon detectors for monitoring of therapeutic proton beams: preliminary beam tests. *J Inst.* (2017) **12**:C12056. doi: 10.1088/1748-0221/12/12/C12056
44. Gallin-Martel M-L, Abbassi L, Bes A, Bosson G, Collot J, Crozes T, et al. A large area diamond-based beam tagging hodoscope for ion therapy monitoring. *EPJ Web Conf.* (2018) **170**:09005. doi: 10.1051/epjconf/201817009005
45. Kanazawa M, Endo M, Himukai T, Kitamura M, Mizota M, Nakagawara A, et al. Scanning Irradiation System at SAGA-HIMAT. In: *Proceedings of IPAC2017* (Copenhagen, Denmark), 4698–700. Available at: https://accelconf.web.cern.ch/IPAC2017/papers/thpva101.pdf
46. Colautti P, Conte V, Selva A, Chiriotti S, Pola A, Bortot D, et al. Microdosimetric study at the cnao active-scanning carbon-ion beam. *Radiat Prot Dosimetry.* (2018) **180**:157–61. doi: 10.1093/rpd/ncx217
47. Krantz C, Cee R, Faber F, Feldmeier E, Fischer T, Galonska M, et al. Slow extraction techniques at the marburg ion-beam therapy centre. In: *Proceedings of the 9th International Particle Accelerator Confernce.* Vancouver, BC (2018).
48. Patera V, Sarti A. Recent advances in detector technologies for particle therapy beam monitoring and dosimetry. In: *IEEE Transactions on Radiation and Plasma Medical Sciences.* (2020) **4**:133–46. doi: 10.1109/TRPMS.2019.2951848
49. Courtois C, Boissonnat G, Brusasco C, Colin J, Cussol D, Fontbonne JM, et al. Characterization and performances of a monitoring ionization chamber dedicated to IBA-universal irradiation head for pencil beam scanning. *Nucl Instr Methods Phys Res Section A.* (2014) **736**:112–7. doi: 10.1016/j.nima.2013.10.014
50. Laune B, Malard M, Anne R, Boy L, Bibet D, Guillot J, et al. *Diagnostic System Dedicated to the Radioactive Ion Beams at the SPIRAL Facility.* (2020). IOP Publishing, 163–166. Available at: http://hal.in2p3.fr/in2p3-00007813 (accessed July 16, 2020).

Conflict of Interest: The authors declare that the research was conducted in the absence of any commercial or financial relationships that could be construed as a potential conflict of interest.

frontiers in Physics

REVIEW
published: 07 October 2020
doi: 10.3389/fphy.2020.00362

Understanding the Effects of Deep Space Radiation on Nervous System: The Role of Genetically Tractable Experimental Models

Giada Onorato[1,2,3,4], *Elia Di Schiavi*[1]* and *Ferdinando Di Cunto*[2,3]*

[1] Institute of Biosciences and Bioresources (IBBR), Consiglio Nazionale delle Ricerche (CNR), Naples, Italy, [2] Department of Neuroscience "Rita Levi Montalcini", University of Torino, Turin, Italy, [3] Neuroscience Institute "Cavalieri Ottolenghi", Orbassano, Italy, [4] Dipartimento di Scienze e Tecnologie Ambientali, Biologiche e Farmaceutiche dell'Università della Campania "Luigi Vanvitelli", Caserta, Italy

Space agencies are working to establish a permanent human presence on the moon and to reach Mars within the next few decades. In these missions, astronaut crew members will be exposed to moderate doses of the highly energetic particles that compose galactic cosmic rays (GCR). GCR consist of alpha particles, protons, and high atomic number ions, stripped of their electrons (HZE), which are relatively rare, but are also highly ionizing. HZE are particularly damaging to biological tissues, because they can penetrate to much deeper layers of shielding materials than gamma rays and x-rays and produce within tissues long ionization tracks, with strongly clustered damage to information molecules. The consequences of such damage to central nervous system health is a major concern. A strong development of new knowledge and models, which may help to predict the risk of individual astronauts, is an absolute requirement in this field. Genetically tractable animal models offer unique opportunities to directly investigate the genetic and molecular events that may affect the biological response to GCR and related radiation.

Keywords: space medicine, radiation, HZE, animal models, *C. elegans*, neurodegeneration, genetic predisposition

OPEN ACCESS

Edited by:
Yolanda Prezado, INSERM U1021 Signalisation normale et pathologique de l'embryon aux thérapies innovantes des cancers, France

Reviewed by:
Eliedonna Cacao, University of Nevada, Las Vegas, United States
Catherine M. Davis, Johns Hopkins Medicine, United States

***Correspondence:**
Elia Di Schiavi
elia.dischiavi@ibbr.cnr.it
Ferdinando Di Cunto
ferdinando.dicunto@unito.it

Specialty section:
This article was submitted to Medical Physics and Imaging, a section of the journal Frontiers in Physics

Received: *27 May 2020*
Accepted: *28 July 2020*
Published: *07 October 2020*

Citation:
Onorato G, Di Schiavi E and Di Cunto F (2020) Understanding the Effects of Deep Space Radiation on Nervous System: The Role of Genetically Tractable Experimental Models. Front. Phys. 8:362. doi: 10.3389/fphy.2020.00362

INTRODUCTION

Compared to the terrestrial surface, space represents a hostile environment, characterized by the combination of microgravity, and a peculiar radiative environment, which could lead to severe health issues for astronaut crews engaged in long-term missions. Among these factors, exposure to radiation dominated by particle shots and GCR of extremely high energy is of special concern [1, 2]. Efficient shielding of such radiation is very difficult, considering the mass constraints which spaceships need to respect. Therefore, it has been noted that "lack of knowledge about the biological effects of, and responses to, space radiation is the single most important factor limiting the prediction of radiation risk associated with human space exploration" [3, 4]. The observations from the ExoMars Trace Gas Orbiter indicate that a 6-month mission to Mars would imply a radiation dose equal to 60% of the limit which is commonly recommended for the full career of an astronaut [5]. Without major technological leaps in shielding strategies [6], intrinsic or induced biological resilience to space radiation chronic exposure will probably be among the crucial factors to decide about risk acceptability. Individual sensitivity to acute or chronic exposure to radiation is dependent on genetic background [7]. Following recent developments in sequencing technologies, determination of individual genomes and acquisition of multi-omic

information on individuals' biological samples has become a relatively low-cost routine. In theory, these resources could allow for the screening of many crew candidates, to identify those possessing particularly sensitive or resistant biological backgrounds. However, our knowledge of the genetic and biological traits associated with sensitivity to space radiation is still very limited [7]. NASA has underscored four risks that may imply important health concerns for astronauts: acute radiation syndrome, carcinogenesis, degenerative tissue alterations, and central nervous system (CNS) loss of performance [3]. Among them, the latter is particularly difficult to understand and predict. Nevertheless, recent reports have started to shed some light on this issue [8, 9].

In this review, we will briefly summarize the peculiar features of space radiation and the problems posed by its simulation. We will then highlight established and more recent studies on the impact of ionizing radiations and/or space conditions on CNS structure and function, in humans and experimental models. In particular, we will try to summarize the experiments that, in our opinion, are more informative with regard to functional CNS changes that may derive from the exposure of mammalian brain to mission-relevant doses of HZE particles. For a deeper perspective on these topics, the reader is referred to more extensive surveys [10–12]. Afterwards, we will review the studies on genetic factors affecting the general sensitivity to radiation. Finally, we will highlight the experimental models that could provide fundamental insight about genetic and biological factors influencing the response of mature neural networks to space radiation, with particular regard to *C. elegans*.

SPACE AND SPACE-RELEVANT RADIATION

The 2006 report by the National Council on Radiation Protection and Measurements (NCRP), concerning space missions beyond low-earth orbit (LEO) [13], underscored that "current space radiation guidelines pertain only to missions in LEO and are not considered relevant for missions beyond LEO. The acceptable levels of risk for space exploration beyond LEO have not been defined at this time and need to be dealt with before sending manned missions to colonize the moon or to deep space, such as a mission to Mars" [13]. Space environment beyond LEO is characterized by a flux of ionizing radiation mostly composed of protons and heavier nuclei stripped of their orbital electrons, but also include a minority (2%) of electrons and positrons. Manned missions beyond LEO will face the challenge of radiation from three different sources: solar particle events (SPE), galactic cosmic radiation (GCR) and intra-vehicular secondary radiation.

SPE occur when protons emitted by the Sun become accelerated, close to the Sun or in interplanetary space. SPE frequency is correlated with sunspot activity and their occurrences oscillate in phase with the solar cycle. SPE can produce large quantities of protons with energies >30 MeV, at fluences in excess of 109 protons/cm^2 [8]. On missions outside of LEO, SPE dose inside a spaceship can be as high as 100 mGy/h, but can reach peaks of 500 mGy/h during extravehicular activity [14]. Due to the high flux and relatively low energy, SPE radiation is absorbed by the most superficial tissues. Skin lesions, hematological, and immunological dysfunctions are therefore the main consequences. For the same reason, shielding is an effective counter-measure. Therefore, although they may certainly contribute to cancer risk and tissues degeneration, SPE are not expected to cause major direct alterations of CNS function.

GCR is composed of nuclei accelerated to relativistic speeds, originating from outside our solar system (**Figure 1**). Electrons and positrons are of minor concern, because they are stopped by modest shielding. GCR nuclei span a wide range of energy and linear energy transfer (LET). The major components consist of hydrogen (87%), and helium (12%) nuclei, with the remaining 1–2% of particles are comprised from $Z = 3$ (Li) to $Z = 28$ (Ni) [15]. High-Z and energy particles (HZE), such as iron ($Z = 26$), are particularly challenging, because every particle can cause damage to cellular DNA which is difficult to repair [16] and no reasonable thickness of shielding material can safely stop them [6]. GCR particle energy allows them to penetrate very deeply into biological tissues, as well as other organic and inorganic materials. In particular, HZE nuclei are an outstanding threat to body cells, which may strongly contribute to the cumulative equivalent dose absorbed by astronauts beyond LEO. Shielding is only partially effective to reduce the doses experienced inside a spacecraft [2, 6], but increasing shields' thickness leads to the production of high levels of secondary radiation, which can be absorbed even more easily by biological tissues [17]. HZE nuclei may strongly contribute to the carcinogenic risk to which crew members are exposed. Indeed, even at relatively low energy, iron ions are shown to be potent inducers of ovarian tumors formation in rodents [18]. Due to their high penetration power, GCR can efficiently reach CNS cells and pose a major risk to CNS function. However, the effects of chronic exposure to this kind of radiation on nervous system function and CNS cells' survival, as well as the factors that may protect from such damage, are still not well-understood.

The interaction of energetic protons and HZE nuclei with spacecraft structures can produce an additional intravehicular radiation hazard. Secondary radiation includes beta particles, x-rays, gamma rays, neutrons, protons, alpha particles, and heavy-charged particles, mostly produced in nuclear fission reactions. Secondary radiation has lower particle energy, but can be even more disruptive to tissues than incident radiation particles, delivering a significant fraction of the total dose absorbed during missions. Although the capability of such radiation to deeply penetrate into biological tissues is lower than incident GCR, it can be sufficiently high enough to deliver a significant dose to CNS cells.

On this basis, it should be evident that crew members of missions aimed at the moon, asteroids or Mars will be exposed to a very complex radiation environment, which can significantly change qualitatively and quantitatively in space and time. Predicting the equivalent dose associated to the different conditions is an extremely difficult task [4]. Among the major challenges, it is very problematic to understand the consequences of chronic exposure to low doses of extremely energetic GCR,

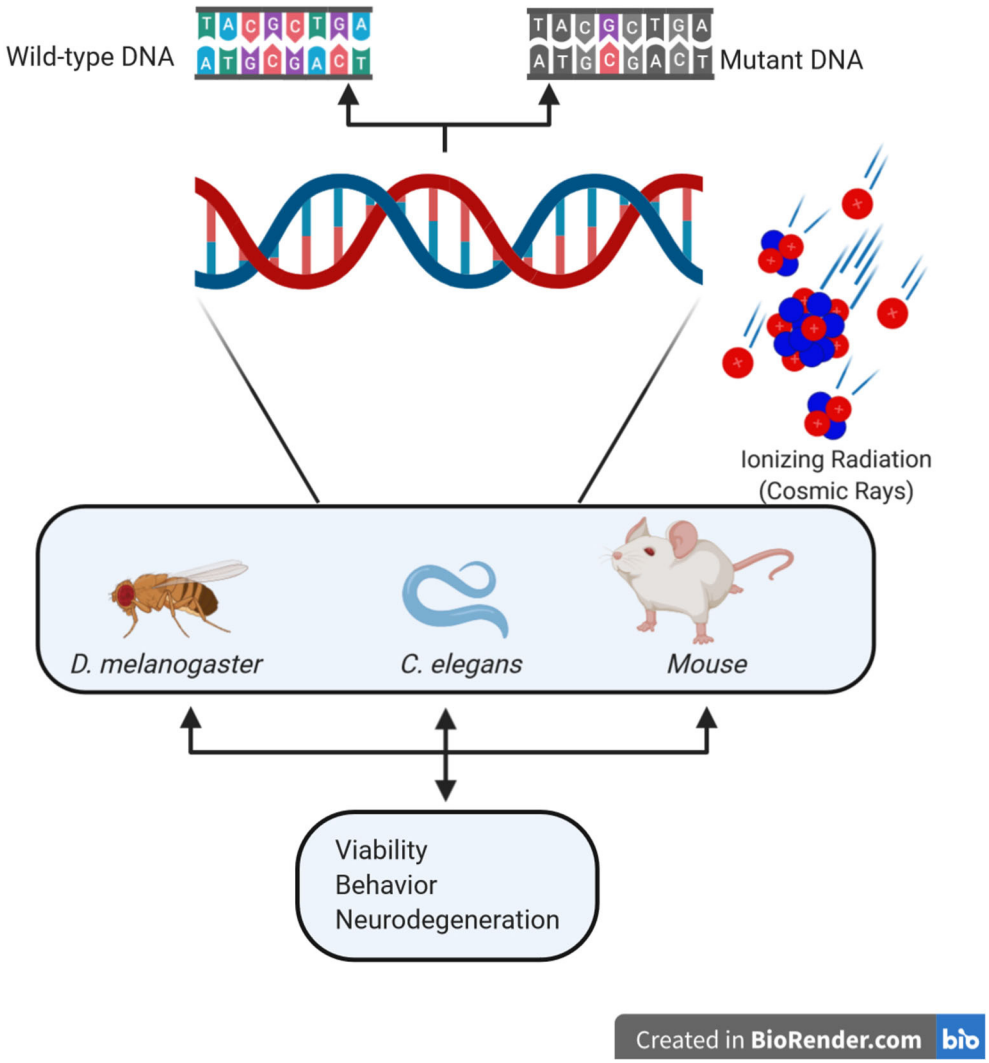

FIGURE 1 | Schematic representation of the main components of space radiation and of the principal model organisms used to study their effects on differentiated neural tissues.

combined with the secondary radiation. High LET radiation is very damaging to informational biomolecules, especially DNA. Different gene expression programs and different sets of protein phosphorylation events are produced when cells and tissues are exposed to low vs. high doses of conventional radiations [1]. So far, the strongest direct evidence about genotoxicity of GCR in humans is the cytogenetic comparison of cells obtained from Gemini vs. Apollo astronauts, showing a doubling in chromosome breaks [19]. Many studies of high-LET radiation effects have been so far performed on animal models, especially rodents. However, these studies suffer major limitations [4]. They have been limited to a maximal particle energy of 1 GeV/n, thus excluding particles possessing the highest energy, which are estimated to contribute to approximately half of the dose [4]. Moreover, they were conducted using mono-energetic beams and acute, single-ion exposures, instead of complex energy spectra with diverse ion composition [4]. GCR simulation facilities, such as the NASA Space Radiation Laboratory (NSRL) in the US and the Facility for Antiproton Research (FAIR) in Europe are constantly improving on this limitation, by increasing particles energy and developing protocols for sequential exposure to different ion beams. However, sequential beam exposures appear to be not completely adequate in mimicking simultaneous exposure to a wide spectrum of particles and energies, since it has been shown that the order of delivered particles can significantly modify the biological effects [20]. Moreover, the dose-rate administered through accelerators will probably remain higher than low fluency radiation occurring during real missions [21, 22].

Non-linearity of biological effects of GCR could also depend on adaptation mechanisms. After missions in ISS, astronauts' lymphocytes showed complex chromosomal rearrangements,

involving more than three chromosomes [23], which decreased but did not reach control levels even after many years. Nevertheless, controls performed after a second mission did not show a proportional increase of chromosomal aberrations, suggesting that an adaptive response may take place [23]. On this basis, it is evident that direct measurement of the biological effectiveness of space radiation, using adequate living experimental models, should be considered an inevitable milestone of space exploration.

EFFECTS OF SPACE-RELEVANT RADIATION ON MAMMALIAN CNS

In theory, human exploration of space may imply acute and late radiation risks to the CNS [8, 24]. Acute CNS risks include functional changes that may compromise astronauts' performance during the mission, such as altered cognition and mood, as well as abnormal motor coordination. Acute effects could derive from exposure to SPE, that can reach 0.5 Gy in the case of concomitant extra-vehicular activity (EVA) or permanent spaces not properly shielded [25, 26]. However, the energies of SPE are usually limited to the 10–100 MeV range, allowing efficient shielding and implying that most energy is delivered to superficial tissues, especially skin. In addition, it must be considered that doses of IR up to 2 Gy are currently used in brain radiotherapy, with limited immediate side effects. The concern about CNS functions is much more related to the cumulative medium-term and long-term alterations, produced by prolonged exposure to a low-fluency ($<$ 20 mGy/h) of protons, HZE nuclei and neutrons, deriving from SPE flares, GCR, and their combinations in time. Neural alterations induced by space flight may impact on learning and memory, motor function, orientation, bio-rhythms regulation, and neuro-psychological changes, such as emotional control and risk evaluation [8, 27]. The latest possible effects are neurodegenerative disorders, such as Alzheimer's and Parkinson's diseases (AD and PD, respectively).

Direct evidence of CNS effects produced by moderate radiation doses of ($\leq$ 2 Gy) derive from studies performed on atomic bombs survivors and Chernobyl accident victims, who showed memory and cognitive impairments, as well as psychiatric disorders and altered electroencephalographic (EEG) patterns [28, 29]. These studies are limited by uncertain dosimetry, short exposure times, and radiation type. Additional evidence has been obtained from radiotherapy patients, who often show chronic fatigue, depression, and other behavioral changes [30, 31]. However, administered doses are too high and inhomogeneous to be fully relevant for the space environment. This is particularly true for the few "opportunistic" studies conducted on patients treated with protons and other charged particle beams for different types of intracranial tumors [32–34] and cerebrovascular disorders [35, 36]. Interestingly, many of these studies have shown that cognitive impairment is not evident in the first year but becomes detectable during long-term follow-up. Importantly, brain MRI (magnetic resonance imaging) surveys of 11 astronauts, involved in long LEO missions, clearly showed that long-term microgravity can contribute to brain changes caused by radiation exposure [37].

Data from non-human primates, irradiated with relatively high doses in different experiments, mostly confirmed the detrimental effects of radiation on the execution of different behavioral tasks [8, 38]. Similar conclusions have been obtained with pilot tests performed at much lower doses, which produced changes in food preferences and degradation in test performance [39]. However, a provocative study performed with doses on the order of 1 Gy suggests that chronic exposure to space-related conditions can enhance some behavioral traits. A group of rhesus monkey males were subjected to 20 to 40 exposures of fast neutrons and gamma rays, achieving cumulative doses of up to 600 cGy [40, 41]. During the first six months of follow-up no alterations were observed. However, behavioral tests performed after 9–10 months were indicative of decreased distractibility in the irradiated animals, with increased performance in attention tests, which persisted at 14, 36, and 78 months.

Analyses of rodent models have provided the most extensive evidence about the potential neurocognitive complications caused by GCR (**Table 1**), which could affect skills critical for missions, as well as long-term neuro-psychological health [8, 10, 24]. Low doses (5-20 cGy) of 1 MeV/n ^{56}Fe particles lead to severe deficits of mean spatial memory performance in rats, three months after exposure [42–44]. Similar effects where obtained by irradiating rats with low doses of ^{48}Ti [65], supporting the notion that LET-dependency of neurocognitive impairment may be relatively independent of cell killing. RBE of HZE particles on memory alteration was extremely high, if considering that x-ray exposure can alter memory in rats only at doses as high as 10 Gy [66]. Since performance in the attentional set-shifting test was also compromised [44], these experiments indicate that mission-relevant exposure to HZE particles may decrease function in the hippocampus and many other different brain regions, including the prefrontal and cingulate cortex as well as the basal forebrain. Similar effects were obtained in mice, exposed to 5–30 cGy 600 of MeV/n ^{48}Ti and ^{16}O [47]. Even though ^{48}Ti was more effective on disrupting recognition memory, significant long-lasting alterations in novelty and temporal discrimination tests were induced even by the lowest dose of ^{16}O [47]. Moreover, reduced fear extinction and increased anxiety were detected [47]. Another crucial insight of studies in mice is that the effects of GCR could be strongly influenced by sex and gender. Adult male mice, exposed to simulated GCR (single doses, as high as 50 cGy), showed long term effects like anxiety-related phenotypes, reduced social interaction, and impaired memory [48]. In contrast, female mice of the same age were largely protected from these phenotypes [48].

Interestingly, the studies performed in rodents showed a high inter-individual variability in HZE-induced neurobehavioral deficits. In particular, in the low-range dosage, deficits were particularly pronounced in a subgroup of poor-learner animals [43]. This result strongly suggests the involvement of individual genetic factors, although the specific involved loci were not investigated.

The great sensitivity of CNS to HZE particles is related not only to radiation-induced neuronal cell death, but may derive

TABLE 1 | Summary table of the principal genes affecting response to space-relevant radiation in the principal experimental models, including the altered behavior and functionality with the indicated radiation exposure.

Model organism	Genetic background	Radiation source	Effect
Mouse/Rat	Wild-type	5-20cGy of 1MeV/n ^{56}Fe	↓↑ Spatial memory [42–44]
			Anxiety [45]
			Depression-like behavior [46]
		5-30cGy of 600MeV/n ^{48}Ti or ^{16}O	Alteration of functions in hippocampus, cingulate cortex, and basal forebrain [47]
			Disruption of recognition memory [47]
		GCR-like radiations	Alteration of synapses and spine morphology in behaviorally-relevant areas [12, 47]
			Microglia activation and synapse loss in males [48]
			Anxiety phenotypes in males [48]
			Reduced social interactions in males [48]
			Impaired memory in males [48]
	ATM heterozygosity	1GeV ^{56}Fe	↑↑ Unrepaired DNA DSB [49]
			Neurological sensitivity [50, 51]
	Transgenically expressed *APP23* (AD model)	1-4 Gy of 600MeV/n ^{56}Fe	Electrophysiological alterations in males [52]
	Transgenically expressed *ApoE3* (AD model)	2 Gy ^{56}Fe	Impairment in spatial memory [53]
	Transgenically expressed *APP/PSEN1* (AD model)	0.1-1 Gy of 150MeV protons	↑ Amyloid Aβ deposition [54]
D. melanogaster	Wild-type	GCR-like radiations	Alteration of immune response [55]
			Deregulation of the expression of genes involved in metabolism and lifespan regulation [56]
			Extension of lifespan [56]
		Low-dose-γ radiation	Behavioral alterations [57]
C. elegans	Wild-type	GCR-like radiations	↑ Deletion mutations [58, 59]
			Deregulation of neuromuscular and neuronal genes [58, 59]
			Extension of lifespan due to the upregulation of *daf-16* [60]
			↑↑ DNA DSB and deletion mutations [61]
			Apoptosis and cell-cycle arrest in germ cells [61]
			Alteration of fertility and embryos' development [62]
			Behavioral alterations [63, 64]
	Transgenically expressed PolyQ in muscle cells (Huntington model)		↓ Accumulated aggregates [60]

from the alteration of different aspects of neuronal function [42]. Irradiation reduced dendritic complexity and spine density and altered the morphology of dendritic spine in behaviorally-relevant areas [12, 47]. HZE particles were also capable of disrupting synaptic integrity and inducing neuroinflammation, which persisted for more than 6 months after exposure [47]. Microglia activation is mechanistically important in determining the long-term synaptic and memory deficits, because these phenotypes can be prevented by transiently depleting microglia cells, through the administration of a CSFR-1 inhibitor 7 days after irradiation [67, 68]. Even these phenotypes appear to be sex-dependent, since microglia activation and synapse loss were observed only in males, after exposure to GCR-like radiation [48]. Irradiation produced many different neurophysiological alterations, which have been well-measured in the perirhinal cortex, including changes in both intrinsic and extrinsic neuronal properties [69]. Studies in rodents also showed that the effects of irradiation on CNS transcriptional activity and epigenetic state can be potentiated by simulated microgravity [70].

GENETIC MODIFIERS OF SPACE RADIATION IMPACT ON CNS

The studies discussed above provide strong evidence that the deep space radiation environment may influence the function and plasticity of neural networks controlling human behavior, within mission time and beyond. An even more challenging problem is to establish whether specific genetic variants or variant combinations would make individuals particularly sensitive or resilient to these hostile conditions. The identification of relatively radiosensitive sub-populations within human communities has important implications for space medicine, because it would be unethical to expose radiosensitive individuals

to conditions that may produce a severe clinical response. Moreover, the existence of a significantly radiosensitive subpopulation would pose a big challenge to epidemiological studies addressing dose-response relationships, because it would hamper the conceptual assumptions necessary for linear extrapolations from high to low doses [71].

A large body of knowledge is available about genetic factors that may influence human sensitivity to radiations. Not surprisingly, most of the strongest genetic players are involved in some of the pathways that cope with DNA damage. A better understood factor is the status of the ATM gene. The encoded protein belongs to the PI3-kinase family and responds to DNA damage, especially double strand breaks (DSB), by phosphorylating a plethora of proteins playing critical roles in DNA repair, as well as in the control of the cell division cycle [72]. The inactivation of both ATM copies is responsible for the ataxia-telangiectasia (AT) syndrome, which is characterized by extreme radio-sensitivity, cancer predisposition, and cerebellar neurodegeneration. A more relevant question for space medicine is whether individuals heterozygous for ATM mutations, who represent at least 1% of the US population [73], are more radiosensitive than normal people. Studies performed on small groups of patients, showing severe late consequences of radiotherapy, revealed a disproportionate frequency of ATM heterozygous mutations and also suggested that other genetic factors are involved [71, 74]. The possibility that ATM heterozygosity is an important susceptibility factor to HZE effects was confirmed by studies on cultured human cells [75] and on haplo-insufficient mice [50, 51]. Importantly, the latter studies showed increased neurological sensitivity of ATM heterozygous mice to relatively low doses of 1GeV ^{56}Fe particles. Besides ATM, a number of other rare recessive disorders are characterized by increased radio-sensitivity [76]. These include Fanconi anemia, Nijmegen breakage syndrome (caused by mutation in NBS1 gene), MRE11 deficiency, and other more rare disorders [76, 77]. All these conditions share a deficiency in coping with the radiation-induced DSB, because of reduced DSB sensing, impaired homologous recombination (HR), or defective non-homologous end-joining (NHEJ). While these diseases are not expected to be present in crew member candidates, it is conceivable that heterozygous inactivation of the same genes could increase the risk of abnormal radiation sensitivity in apparently normal subjects. Besides ATM, modestly increased sensitivity to x-ray has been demonstrated in NBS1 heterozygous mutant cells [78]. It is not known whether HZE particles could unmask an even higher sensitivity in these conditions. The potential consequences on CNS of heterozygous mutations in crucial DSB repair genes are even more obscure. Increased neurodegeneration occurring in homozygous patients is suspected to derive from the accumulation of unrepaired DNA DSB [49]. Indeed, defective DNA repair has also been observed in neurodegenerative disorders associated with aging, which include Alzheimer's disease (AD), Parkinson's disease (PD), amyotrophic lateral sclerosis (ALS) [79–82], and epilepsy [83]. Although most studies linking DNA damage to neurodegeneration are correlative [49], recent evidence obtained on a mouse model of AD-like neurodegeneration indicates that DSBs accumulate before the onset of neurodegeneration [84], suggesting a causal link.

Genetic susceptibility factors to neurodegenerative disorders may also synergistically interact with space-relevant radiation. Irradiation of APP/PSEN1 transgenic mice with 0.1–1.0 Gy of 150 MeV protons increased amyloid Aβ deposition, but did not worsen the functional and biochemical alterations that characterize this AD model [54].

In contrast, APP23 transgenic male mice, irradiated with 1–4 Gy of 600 MeV/n ^{56}Fe, showed accelerated electrophysiological alterations in the hippocampus [52]. Even at much lower doses (10 or 50 cGy) of 1 GeV/n ^{56}Fe ions showed genotype-specific changes in neuropathology and behavior of AD-like transgenic mice [85]. Interestingly, even in this case the phenotype showed complex differences between males and females [85]. Transgenic mice expressing the E3 variant of ApoE were more sensitive to impairment in spatial memory induced by 2 Gy ^{56}Fe irradiation, as compared to mice expressing E2 or E4 variants [53].

Even less information is available about genetic conditions that may increase radio-resistance, especially in the CNS. To this regard, the best understood pathway is the one activated by the p53 tumor suppressor TP53. However, although partial TP53 loss of function may help cells to better survive, it would also increase the risk of cancer [86].

Altogether, these studies strongly support the notion that specific genetic factors may influence the effect of the space radiation environment. However, they also underscore the difficulties that the analysis of genomic data must face, in order to predict the risks of a specific subject. These limits are primarily due to our primitive understanding of the interaction between HZE radiation and genetic susceptibility factors. A second important problem is the likely polygenic nature of the genetic susceptibility, requiring the elaboration of sophisticated polygenic risk scores. It is unlikely that the latter could be developed using standard genome wide association studies, when considering the extremely small subjects' number that direct epidemiologic studies can reasonably include. A possible way around this problem could be offered by astronaut-specific induced pluripotent stem cells (iPSC). Thanks to the present development of stem cell technologies, iPSC can be differentiated in most of the relevant cell types, including CNS cells. The direct determination of radio-sensitivity of astronaut-specific cells could provide accurate predictive biomarkers, regardless of the underlying genetic background [87]. Moreover, innovative polygenic risk scores could be derived by better dissecting the biological details of the interaction between HZE radiation and genetically tractable animal models, which are relatively easy to study in space-like and actual deep space conditions.

ROLE OF GENETICALLY TRACTABLE MODELS IN THE STUDY OF BIOLOGICAL EFFECTS OF SPACE RADIATION

The use of relatively simple and fully tractable experimental models is pivotal to investigate the impact of deep space

conditions on different aspects of multicellular organisms' biology, including genome stability, behavior, and neuronal survival. In this respect, a simpler vertebrate alternative is offered by small fish models, such as Zebrafish and Medaka [88, 89]. However, the most flexible alternative to mammalian models for studying the impact of space environment on adult neural cells is offered by the invertebrates *Drosophila melanogaster* and *Caenorhabditis elegans* (**Figure 1** and **Table 1**). Indeed, they have a very small size (3 and 1 mm long, respectively), a very short life cycle (2 and 0.5 weeks, respectively), and life span (90 and 21 days, respectively), as well as a simple anatomy including a nervous system; their entire genome, physiological, and behavioral characteristics are well-understood [90]. Thanks to the availability of thousands of genetically modified strains, it is possible to assess the functional relevance of specific genetic alterations and to test sophisticated genetic hypotheses. Practically, these models can allow for the screening of many gene candidates, to identify those conferring particularly sensitive or resistant biological backgrounds. Being invertebrates, they both raise fewer concerns for experimentation, as compared to vertebrates. However, considering their good genomic and cell biology phylogenetic conservation, they have been and will be fundamental for understanding the molecular mechanisms and physiological processes which characterize more complex organisms, such as humans. Multiple times the Nobel prize has been awarded to researchers working with these two models, thus acknowledging their fundamental contribution to understanding details of the molecular processes underlying many human diseases. In addition, they have been shown to be highly versatile models in studies covering different topics highly relevant to space biology and medicine, which include the genetics and molecular biology of aging, development, muscle physiology, and radiation response.

D. melanogaster has been used in space missions since 2015, during the Fruit Fly Lab-01 (FFL-01), which provided housing for fruit flies under conditions of microgravity and simulated Earth gravity. Experiments revealed that ionizing space radiations can alter innate immune responses [55]. Chronic low-dose-γ radiation led to behavioral alteration in *D. melanogaster*, inducing impaired climbing activity and exploratory movement [57]. Low-dose radiation affects the expression of genes involved in *D. melanogaster* metabolism and lifespan regulation, causing a surprising extension [56]. However, it is still largely unknown how this effect may occur.

Caenorhabditis elegans is a nematode with a defined number of cells (959 somatic cells in the adult), among which 302 are neurons. It has proven to be a useful model organism for investigating molecular and cellular aspects of neuron development and neurodegeneration in numerous human diseases, including PD and other neurodegenerative conditions [91, 92]. Moreover, the degeneration of specific neuronal populations, can be easily analyzed in living animals [93], thanks to their transparency and the expression of fluorescent proteins. The choice of *C. elegans* is specifically justified by the following elements: a high resistance to extreme conditions (also thanks to a cuticle); the possibility of hibernation (i.e., as dauer larvae, a resistant larval stage) and of freezing; the self-fertilizing hermaphroditism that avoid the need for crossings; a large progeny (300 eggs per each animal); and the possibility to culture them in microfluidic devices [94].

Caenorhabditis elegans has traveled 12 times in space and experiments have been performed in the Space Shuttle and on the ISS. Therefore, much information has been obtained, which will not be discussed here [95]; in relation with the focus of the present review, *C. elegans* explored space for the first time on STS-42, allowing researchers to demonstrate no alteration in males mating behavior during spaceflight [96]. In the STS-76 mission, a high number of mutations were shown as the direct effect of space radiation and not microgravity. In particular, high-LET charged particles caused deletion mutations [58, 59]. ICE-First (International *C. elegans* Experiment-I) was the fifth spaceflight for the nematode, and the first on-board the ISS [97]. Results from the space flight experiment provided information on how radiation and microgravity influences worm development throughout the life cycle and worm muscle physiology, as well as which are the changes in gene expression [97]. Interestingly, relevant spaceflight-induced changes in expression of neuromuscular and neuronal genes have been specifically determined [58, 59]. Moreover, genes involving lifespan extension, such as *daf-16*, are upregulated after spaceflight, suggesting that space-flight might increase nematodes' survival [60]. These effects seem related to the alteration of neuronal and endocrine signaling involved in "longevity-promoting" processes, similar to those activated by dietary-restriction signaling [60].

A model for Huntington's and related neurodegenerative disorders, transgenically expressing polyQ in muscle cells, accumulates aggregates with aging. This accumulation was suppressed in *C. elegans* after spaceflight and gene expression analysis showed that aging in *C. elegans* may be slowed through neuronal and endocrine adaptation to space-related stressors [60].

Contrary to the abundant information on genome stability and muscle physiology after spaceflights, less is known of the neuron response, despite *C. elegans* being selected as an elective model for neurobiology studies [98, 99]. More information has been obtained on Earth, by studying the effects of radiation on the nematode. Ionizing radiation induces several changes in terms of biological and physiological processes [61]. As in mammalian cells, they can induce DNA DSB and deletions, leading to apoptosis and cell-cycle arrest. This occurs especially in the germ cells in which, after irradiation, apoptosis and cell-cycle arrests significantly increase [61]. Adult nematodes tolerate both acute and chronic high-dose irradiation with minor consequences, apart from a reduction of fertility, thus allowing for studying the effects on adult animals. Parental exposure leads to DNA damage in embryos, but the progeny maintains high reproductive capacity, despite a reduction of somatic growth [62]. Interestingly, the cell death pathway activated by ionizing radiation in germ cells is different from the pathway involved in physiological apoptosis [62]. Recently, transcriptome sequencing revealed a series of novel ionizing radiation-response genes [100]. Moreover, radiosensitive (e.g., *rad-1* and *rad-2*) and radioresistant (e.g., *cdc-25.3*) mutants have been identified [101,

102]. Ionizing irradiations also have effects on learning behavior and the locomotory rate. In particular, radiation affects salt chemotaxis learning behavior, which is an associative learning paradigm [63, 64]. This phenotype resembles the taste aversion observed in the group of male rhesus monkeys described above [40, 41], or in rodents [45]. Moreover, the altered learning produced by radiation was inhibited in the *gpc-1* mutant, lacking one gamma subunit of the heterotrimeric G-protein. The effects of radiations on the locomotor behavior have also been studied. The ionizing radiations induced a reduction of the locomotor rate, mediated by a pathway different from the dopaminergic pathway in place for bacterial mechano-sensing [63].

All these results explain how *C. elegans* offers potential for the design of an innovative biological dosimeter. The frequency and types of mutations generated and maintained in *C. elegans* have been deeply assessed [103, 104]. An interesting step forward will be to use *C. elegans* as an accumulating dosimeter for neuronal defects. The possibility of phenotyping neural cells at high resolution, in combination with the genetic tractability of *C. elegans* could make the nervous system of this small organism an excellent model to assess the consequences of chronic exposure to relatively low doses of space-relevant radiations, although it will be necessary to adapt the dose to its short lifespan and high radio-resistance. Using standard and genetically modified strains and dynamic microscopy, the phenotyping could be done over multiple/daily treatments during life. The following quantities can be measured and correlated with the radiation dose: movement, chemotaxis, and expression of fluorescent markers to monitor neurons morphology. Moreover, thanks to its short life-cycle, the phenotyping could be done in *C. elegans* over multiple generations in space, as NASA has called for. The combination with sequencing technologies, which have recently been implemented on board the ISS, will allow analyses of space-induced genetic and epigenetic changes, in strict correlation to phenotypic changes, during missions on the ISS and beyond [105]. The peculiar features of *C. elegans*, including the possibility of maintaining it in hibernation and growing within microfluidic devices, would make it ideally suited as an innovative bio-dosimeter for deep space missions, including those conducted through micro-satellite platforms. In summary, the resources, features, and knowledge offered by genetically tractable animal models, in particular *C. elegans*, make them excellent resources for studying the direct effects of cosmic radiation on neuron survival and function, in simulation experiments and, even more importantly, in real spaceflight missions.

AUTHOR CONTRIBUTIONS

FD conceived and wrote the manuscript. ED conceived and wrote the manuscript. GO surveyed literature and contributed to writing and editing. All authors contributed to the article and approved the submitted version.

FUNDING

The financial support to FD by Fondazione CRT is gratefully acknowledged. Research in the FD lab was also funded by the Associazione Italiana per la Ricerca sul Cancro (AIRC–grant IG 23341).

ACKNOWLEDGMENTS

The authors apologize for any unintentional omissions of references to previous work.

REFERENCES

1. Chancellor JC, Scott GBI, Sutton JP. Space radiation: the number one risk to astronaut health beyond low earth orbit. *Life.* (2014) **4**:491–510. doi: 10.3390/life4030491
2. Durante M. Space radiation protection: destination mars. *Life Sci Space Res.* (2014) **1**:2–9. doi: 10.1016/j.lssr.2014.01.002
3. Council NR. *Managing Space Radiation Risk in the New Era of Space Exploration*. (2008). Available online at: https://www.nap.edu/catalog/12045/managing-space-radiation-risk-in-the-new-era-of-space-exploration (accessed September 21, 2020)
4. Chancellor JC, Blue RS, Cengel KA, Auñón-Chancellor SM, Rubins KH, Katzgraber HG, et al. *Limitations in predicting the space radiation health risk for exploration astronauts*. *NPJ Microgravity*. (2018) **4**:8. doi: 10.1038/s41526-018-0043-2
5. de Vera JP, Alawi M, Backhaus T, Baqué M, Billi D, Böttger U, et al. Limits of life and the habitability of mars: the ESA space experiment BIOMEX on the ISS. *Astrobiology*. (2019) **19**:145–57. doi: 10.1089/ast.2018.1897
6. Wilson JW, Cucinotta FA, Kim MH, Schimmerling W. Optimized shielding for space radiation protection. *Phys Med.* (2001) **17** (Suppl. 1):67–71.
7. Rajaraman P, Hauptmann M, Bouffler S, Wojcik A. Human individual radiation sensitivity and prospects for prediction. *Ann ICRP*. (2018) **47**:126–41. doi: 10.1177/0146645318764091
8. Nelson GA, Simonsen LC, Huff JL. NASA evidence report: Risk of acute and late central nervous system effects from radiation exposure (2016). Available online at: https://humanresearchroadmap.nasa.gov/Evidence/reports/CNS.pdf (accessed September 8, 2016).
9. Cucinotta FA, Cacao E. Risks of cognitive detriments after low dose heavy ion proton exposures. *Int J Radiat Biol.* (2019) **95**:985–98. doi: 10.1080/09553002.2019.1623427
10. Kiffer F, Boerma M, Allen A. Behavioral effects of space radiation: A comprehensive review of animal studies. *Life Sci Space Res.* (2019) **21**:1–21. doi: 10.1016/j.lssr.2019.02.004
11. Carr H, Alexander TC, Groves T, Kiffer F, Wang J, Price E, et al. Early effects of 16O radiation on neuronal morphology and cognition in a murine model. *Life Sci Space Res.* (2018) **17**:63–73. doi: 10.1016/j.lssr.2018.03.001
12. Cekanaviciute E, Rosi S, Costes SV. Central nervous system responses to simulated galactic cosmic rays. *Int J Mol Sci.* (2018) **19**:1–14. doi: 10.3390/ijms19113669
13. Townsend LW, Chairman, Badhwar GD, Braby LA, Blakely EA, Cucinotta FA, et al. Report No. 153 – Information Needed to Make Radiation Protection Recommendations for Space Missions Beyond Low-Earth Orbit (2006). *NCRP Bethesda, MD*. Available Online at: https://ncrponline.org/shop/reports/report-no-153-information-needed-to-make-radiation-protection-recommendations-for-space-missions-beyond-low-earth-orbit-2006/
14. Carnell L. "Evidence Report: Risk of Acute Radiation Syndromes Due to Solar Particle Events" (2016), (available at https://ntrs.nasa.gov/search.jsp?R=20160003870).

15. Badhwar GD, O'Neill PM. Long-term modulation of galactic cosmic radiation and its model for space exploration. *Adv Space Res.* (1994) **14**:749–57. doi: 10.1016/0273-1177(94)90537-1
16. Tucker JD, Marples B, Ramsey MJ, Lutze-Mann LH. Persistence of chromosome aberrations in mice acutely exposed to 56Fe+26 ions. *Radiat Res.* (2004) **161**:648–55. doi: 10.1667/RR3177
17. Slaba TC, Bahadori AA, Reddell BD, Singleterry RC, Clowdsley MS, Blattnig SR. Optimal shielding thickness for galactic cosmic ray environments. *Life Sci Space Res.* (2017) **12:**1–15. doi: 10.1016/j.lssr.2016.12.003
18. Mishra B, Lawson GW, Ripperdan R, Ortiz L, Luderer U. Charged-iron-particles found in galactic cosmic rays are potent inducers of epithelial ovarian tumors. *Radiat Res.* (2018) **190**:142–50. doi: 10.1667/RR15028.1
19. Maalouf M, Durante M, Foray N. Biological effects of space radiation on human cells: history, advances outcomes. *J Radiat Res.* (2011) **52**:126–46. doi: 10.1269/jrr.10128
20. Elmore E, Lao X-Y, Kapadia R, Swete M, Redpath JL. Neoplastic transformation in vitro by mixed beams of high-energy iron ions and protons. *Radiat Res.* (2011) **176**:291–302. doi: 10.1667/RR2646.1
21. Norbury JW, Schimmerling W, Slaba TC, Azzam EI, Badavi FF, Baiocco G, et al. Galactic cosmic ray simulation at the NASA Space Radiation Laboratory. *Life Sci Space Res.* (2016) **8**:38–51. doi: 10.1016/j.lssr.2016.02.001
22. Slaba TC, Blattnig SR, Norbury JW, Rusek A, Tessa CL, Walker SA. *GCR Simulator Reference Field and a Spectral Approach for Laboratory Simulation, NASA Technical Publication*. Langley, VA: NASA (2015).
23. Cucinotta FA, M.-Kim HY, Willingham V, George KA. Physical and biological organ dosimetry analysis for international space station astronauts. *Radiat Res.* (2008) **170**:127–38. doi: 10.1667/RR1330.1
24. Parihar VK, Allen B, Tran KK, Macaraeg TG, Chu EM, Kwok SF, et al. What happens to your brain on the way to Mars. *Sci Adv.* (2015) **1**:e1400256. doi: 10.1126/sciadv.1400256
25. Parsons JL, Townsend LW. Interplanetary crew dose rates for the August 1972 solar particle event. *Radiat Res.* (2000) **153**:729–33. doi: 10.1667/0033-7587(2000)153[0729:ICDRFT]2.0.CO;2
26. M.-Kim HY, Cucinotta FA, Wilson JW. A temporal forecast of radiation environments for future space exploration missions. *Radiat Environ Biophys.* (2007) **46**:95–100. doi: 10.1007/s00411-006-0080-1
27. Strangman GE, Sipes W, Beven G. Human cognitive performance in spaceflight and analogue environments. *Aviat Space Environ Med.* (2014) **85**:1033–48. doi: 10.3357/ASEM.3961.2014
28. Bromet EJ, Havenaar JM, Guey LT. A 25 year retrospective review of the psychological consequences of the Chernobyl accident. *Clin Oncol.* (2011) **23**:297–305. doi: 10.1016/j.clon.2011.01.501
29. Yamada M, Kasagi F, Mimori Y, Miyachi T, Ohshita T, Sasaki H, et al. Incidence of dementia among atomic-bomb survivors–Radiation Effects Research Foundation Adult Health Study. *J Neurol Sci.* (2009) **281**:11–4. doi: 10.1016/j.jns.2009.03.003
30. Greene-Schloesser D, Robbins ME. Radiation-induced cognitive impairment–from bench to bedside. *Neuro-oncology.* (2012) **14**(Suppl. 4):iv37–44. doi: 10.1093/neuonc/nos196
31. Greene-Schloesser D, Robbins ME, Peiffer AM, Shaw EG, Wheeler KT, Chan MD. Radiation-induced brain injury: a review. *Front Oncol.* (2012) **2**:73. doi: 10.3389/fonc.2012.00073
32. Mohamed Ali, Mathis T, Bensadoun R-J, Thariat J. Radiation induced optic neuropathy: Does treatment modality influence the risk? *Bull Cancer.* (2019) **106**:1160–76. doi: 10.1016/j.bulcan.2019.09.008
33. Tabrizi S, Yeap BY, Sherman JC, Nachtigall LB, Colvin MK, Dworkin M, et al. Long-term outcomes and late adverse effects of a prospective study on proton radiotherapy for patients with low-grade glioma. *Radiother Oncol.* (2019) **137**:95–101. doi: 10.1016/j.radonc.2019.04.027
34. Lesueur P, Calugaru V, Nauraye C, Stefan D, Cao K, Emery E, et al. Proton therapy for treatment of intracranial benign tumors in adults: a systematic review. *Cancer Treat Rev.* (2019) **72**:56–64. doi: 10.1016/j.ctrv.2018.11.004
35. Fabrikant JI, Levy RP, Steinberg GK, Phillips MH, Frankel KA, Lyman JT, et al. Charged-particle radiosurgery for intracranial vascular malformations. *Neurosurg Clin N Am.* (1992) **3**:99–139. doi: 10.1016/S1042-3680(18)30685-5
36. Steinberg GK, Fabrikant JI, Marks MP, Levy RP, Frankel KA, Phillips MH, et al. Stereotactic helium ion Bragg peak radiosurgery for intracranial arteriovenous malformations. Detailed clinical and neuroradiologic outcome. *Stereotact Funct Neurosurg.* (1991) **57**:36–49. doi: 10.1159/000099554
37. Lev MH. The long-term effects of spaceflight on human brain physiology. *Radiology.* (2020) **295**:649–50. doi: 10.1148/radiol.2020201164
38. Sinclair WK. Radiation protection issues in galactic cosmic ray risk assessment. *Adv Space Res.* (1994) **14**:879–84. doi: 10.1016/0273-1177(94)90553-3
39. Taylor HL, Smith JC, Hatfield CA. Immediate Behavioral Detection of X-Rays by the Rhesus Monkey" (Florida State Univ Tallahassee, 1967). Available online at https://apps.dtic.mil/seo/citations/AD0660580
40. Brown W, McDowell A, Haley T, Snider R. *Human Research Program Space Radiation Program Element. Response of the Nervous System to Ionizing Radiation*. New York,NY: Academic Press, (1962). p. 729–46.
41. Melville GS, Brown WL, McDowell AA, Pickering JE, Harrison GW, Leffingwell TP, et al. Some effects of mixed ionizing radiations on Rhesus primates exposed under laboratory conditions. *SAM-TR-66-48. Tech Rep SAM-TR.* (1966) 1–27.
42. Britten RA, Davis LK, Johnson AM, Keeney S, Siegel A, Sanford LD, et al. Low (20 cGy) doses of 1 GeV/u (56)Fe–particle radiation lead to a persistent reduction in the spatial learning ability of rats. *Radiat Res.* (2012) **177**:146–51. doi: 10.1667/RR2637.1
43. Wyrobek AJ, Britten RA. Individual variations in dose response for spatial memory learning among outbred wistar rats exposed from 5 to 20 cGy of (56) Fe particles. *Environ Mol Mutagen.* (2016) **57**:331–40. doi: 10.1002/em.22018
44. Lonart G, Parris B, Johnson AM, Miles S, Sanford LD, Singletary SJ, et al. Executive function in rats is impaired by low (20 cGy) doses of 1 GeV/u (56)Fe particles. *Radiat Res.* (2012) **178**:289–94 doi: 10.1667/RR2862.1
45. Rabin BM, Hunt WA, Joseph JA. An assessment of the behavioral toxicity of high-energy iron particles compared to other qualities of radiation. *Radiat Res.* (1989) **119**:113–22. doi: 10.2307/3577371
46. Son Y, Yang M, Kim JS, Kim J, Kim SH, Kim JC, et al. Hippocampal dysfunction during the chronic phase following a single exposure to cranial irradiation. *Exp Neurol.* (2014) **254**:134–44. doi: 10.1016/j.expneurol.2014.01.018
47. Parihar VK, Allen BD, Caressi C, Kwok S, Chu E, Tran KK, et al. Cosmic radiation exposure and persistent cognitive dysfunction. *Sci Rep.* (2016) **6**:34774. doi: 10.1038/srep34774
48. Krukowski K, Grue K, Frias ES, Pietrykowski J, Jones T, Nelson G, et al. Female mice are protected from space radiation-induced maladaptive responses. *Brain Behav Immun.* (2018) **74**:106–20. doi: 10.1016/j.bbi.2018.08.008
49. Madabhushi R, Pan L, Tsai L-H. DNA damage and its links to neurodegeneration. *Neuron.* (2014) **83**:266–82. doi: 10.1016/j.neuron.2014.06.034
50. Yamamoto ML, Hafer K, Reliene R, Fleming S, Kelly O, Hacke K, et al. Effects of 1 GeV/nucleon (56)Fe particles on longevity, carcinogenesis and neuromotor ability in atm-deficient mice. *Radiat Res.* (2010) **175**:231–9. doi: 10.1667/RR2312.1
51. Worgul BV, Smilenov L, Brenner DJ, Vazquez M, Hall EJ. Mice heterozygous for the ATM gene are more sensitive to both X-ray and heavy ion exposure than are wildtypes. *Adv Space Res.* (2005) **35**:254–9. doi: 10.1016/j.asr.2005.01.030
52. Vlkolinsky R, Titova E, Krucker T, Chi BB, Staufenbiel M, Nelson GA, et al. Exposure to 56Fe-particle radiation accelerates electrophysiological alterations in the hippocampus of APP23 transgenic mice. *Radiat Res.* (2010) **173**:342–52. doi: 10.1667/RR1825.1
53. Yeiser LA, Villasana LE, Raber J. ApoE isoform modulates effects of cranial ^{56}Fe irradiation on spatial learning and memory in the water maze. *Behav Brain Res.* (2013) **237**:207–14. doi: 10.1016/j.bbr.2012.09.029
54. Rudobeck E, Bellone JA, Szücs A, Bonnick K, Mehrotra-Carter S, Badaut J, et al. Low-dose proton radiation effects in a transgenic mouse model of Alzheimer's disease - Implications for space travel. *PLoS ONE.* (2017) **12**:e0186168. doi: 10.1371/journal.pone.0186168

55. Gilbert R, Torres M, Clemens R, Hateley S, Hosamani R, Wade W, et al. Spaceflight and simulated microgravity conditions increase virulence of Serratia marcescens in the Drosophila melanogaster infection model. *NPJ Microgravity.* (2020) **6**:4. doi: 10.1038/s41526-019-0091-2
56. Ma L, Ma J, Xu K. Effect of spaceflight on the circadian rhythm, lifespan and gene expression of Drosophila melanogaster. *PLoS ONE.* (2015) **10**:e0121600. doi: 10.1371/journal.pone.0121600
57. Kim CS, Seong KM, Lee BS, Lee IK, Yang KH, Kim J-Y, et al. Chronic low-dose γ-irradiation of *Drosophila melanogaster* larvae induces gene expression changes and enhances locomotive behavior. *J Radiat Res.* (2015) 56:475–84. doi: 10.1093/jrr/rru128
58. Hartman PS, Hlavacek A, Wilde H, Lewicki D, Schubert W, Kern RG, et al. A comparison of mutations induced by accelerated iron particles versus those induced by low earth orbit space radiation in the FEM-3 gene of Caenorhabditis elegans. *Mutat Res.* (2001) **474**:47–55. doi: 10.1016/S0027-5107(00)00154-8
59. Gao Y, Xu D, Zhao L, Sun Y. The DNA damage response of C. elegans affected by gravity sensing and radiosensitivity during the Shenzhou-8 spaceflight. *Mutat. Res.* (2017) **795**:15–26. doi: 10.1016/j.mrfmmm.2017.01.001
60. Honda Y, Higashibata A, Matsunaga Y, Yonezawa Y, Kawano T, Higashitani A, et al. Genes down-regulated in spaceflight are involved in the control of longevity in Caenorhabditis elegans. *Sci Rep.* (2012) **2**:487. doi: 10.1038/srep00487
61. Sakashita T, Takanami T, Yanase S, Hamada N, Suzuki M, Kimura T, et al. Radiation biology of caenorhabditis elegans: germ cell response, aging and behavior. *J Radiat Res.* (2010) **51**:107–21. doi: 10.1269/jrr.09100
62. Maremonti E, Eide DM, Oughton DH, Salbu B, Grammes F, Kassaye YA, et al. Gamma radiation induces life stage-dependent reprotoxicity in Caenorhabditis elegans via impairment of spermatogenesis. *Sci Total Environ.* (2019) **695**:133835. doi: 10.1016/j.scitotenv.2019.133835
63. Sakashita T, Hamada N, Ikeda DD, Suzuki M, Yanase S, Ishii N, et al. Locomotion-learning behavior relationship in Caenorhabditis elegans following gamma-ray irradiation. *J Radiat Res.* (2008) **49**:285–91. doi: 10.1269/jrr.07102
64. Sakashita T, Hamada N, Ikeda DD, Yanase S, Suzuki M, Ishii N, et al. Modulatory effect of ionizing radiation on food-NaCl associative learning: the role of gamma subunit of G protein in Caenorhabditis elegans. *FASEB.* (2008) **22**:713–20. doi: 10.1096/fj.07-9259com
65. Britten RA, Jewell JS, Duncan VD, Davis LK, Hadley MM, Wyrobek AJ. Spatial memory performance of socially mature wistar rats is impaired after exposure to low (5 cGy) doses of 1 GeV/n 48Ti particles. *Radiat Res.* (2017) **187**:60–5. doi: 10.1667/RR14550.1
66. Yang L, Yang J, Li G, Li Y, Wu R, Cheng J, et al. Pathophysiological responses in rat and mouse models of radiation-induced brain injury. *Mol Neurobiol.* (2017) **54**:1022–32. doi: 10.1007/s12035-015-9628-x
67. Krukowski K, Feng X, Paladini MS, Chou A, Sacramento K, Grue K, et al. Temporary microglia-depletion after cosmic radiation modifies phagocytic activity and prevents cognitive deficits. *Sci Rep.* (2018) **8**:7857. doi: 10.1038/s41598-018-28390-1
68. Rosi S. The final frontier: Transient microglia reduction after cosmic radiation exposure mitigates cognitive impairments and modulates phagocytic activity. *Brain Circ.* (2018) **4**:109–13. doi: 10.4103/bc.bc_24_18
69. Tseng BP, Giedzinski E, Izadi A, Suarez T, Lan ML, Tran KK, et al. Functional consequences of radiation-induced oxidative stress in cultured neural stem cells and the brain exposed to charged particle irradiation. *Antioxid Redox Signal.* (2014) **20**:1410–22. doi: 10.1089/ars.2012.5134
70. Overbey EG, Paul AM, da Silveira WA, Tahimic CGT, Reinsch SS, Szewczyk N, et al. Mice exposed to combined chronic low-dose irradiation and modeled microgravity develop long-term neurological sequelae. *Int J Mol Sci.* (2019) **20**:4094. doi: 10.3390/ijms20174094
71. Hall EJ, Brenner DJ, Worgul B, Smilenov L. Genetic susceptibility to radiation. *Adv Space Res.* (2005) **35**:249–53. doi: 10.1016/j.asr.2004.12.032
72. Mavrou A, Tsangaris GT, Roma E, Kolialexi A. The ATM gene and ataxia telangiectasia. *Anticancer Res.* (2008) **28**:401–5.
73. Swift M, Reitnauer PJ, Morrell D, Chase CL. Breast other cancers in families with ataxia-telangiectasia. *N Engl J Med.* (1987) **316**:1289–94. doi: 10.1056/NEJM198705213162101
74. Hall EJ, Schiff PB, Hanks GE, Brenner DJ, Russo J, Chen J, et al. A preliminary report: frequency of A-T heterozygotes among prostate cancer patients with severe late responses to radiation therapy. *Cancer J Sci Am.* (1998) **4**:385–9.
75. Peng Y, Nagasawa H, Warner C, Bedford JS. Genetic susceptibility: radiation effects relevant to space travel. *Health Phys.* (2012) **103**:607–20. doi: 10.1097/HP.0b013e31826945b9
76. Lindsay KJ, Coates PJ, Lorimore SA, Wright EG. The genetic basis of tissue responses to ionizing radiation. *Br J Radiol.* (2007) **80**:S2–6. doi: 10.1259/bjr/60507340
77. Gatti RA. The inherited basis of human radiosensitivity. *Acta Oncol.* (2001) **40**:702–11. doi: 10.1080/02841860152619115
78. Neubauer S, Arutyunyan R, Stumm M, Dörk T, Bendix R, Bremer M, et al. Radiosensitivity of ataxia telangiectasia and Nijmegen breakage syndrome homozygotes and heterozygotes as determined by three-color FISH chromosome painting. *Radiat Res.* (2002) **157**:312–21. doi: 10.1667/0033-7587(2002)157[0312:ROATAN]2.0.CO;2
79. Jacobsen E, Beach T, Shen Y, Li R, Chang Y. Deficiency of the Mre11 DNA repair complex in Alzheimer's disease brains. *Brain Res Mol Brain Res.* (2004) **128**:1–7. doi: 10.1016/j.molbrainres.2004.05.023
80. Shackelford DA. DNA end joining activity is reduced in Alzheimer's disease. *Neurobiol. Aging.* (2006) **27**:596–605. doi: 10.1016/j.neurobiolaging.2005.03.009
81. Bender A, Krishnan KJ, Morris CM, Taylor GA, Reeve AK, Perry RH, et al. High levels of mitochondrial DNA deletions in substantia nigra neurons in aging and Parkinson disease. *Nat Genet.* (2006) **38**:515–7. doi: 10.1038/ng1769
82. Kraytsberg Y, Kudryavtseva E, McKee AC, Geula C, Kowall NW, Khrapko K. Mitochondrial DNA deletions are abundant and cause functional impairment in aged human substantia nigra neurons. *Nat Genet.* (2006) **38**:518–20. doi: 10.1038/ng1778
83. Burla R, La Torre M, Zanetti G, Bastianelli A, Merigliano C, Del Giudice S, et al. Saggio, p53-Sensitive Epileptic Behavior and Inflammation in Ft1 Hypomorphic Mice. *Front Genet.* (2018) **9**:581. doi: 10.3389/fgene.2018.00581
84. Kim D, Frank CL, Dobbin MM, Tsunemoto RK, Tu W, Peng PL, et al. Deregulation of HDAC1 by p25/Cdk5 in neurotoxicity. *Neuron.* (2008) **60**:803–17. doi: 10.1016/j.neuron.2008.10.015
85. Liu B, Hinshaw RG, Le KX, Park M-A, Wang S, Belanger AP, et al. Space-like 56Fe irradiation manifests mild, early sex-specific behavioral and neuropathological changes in wildtype and Alzheimer's-like transgenic mice. *Sci Rep.* (2019) **9**:12118. doi: 10.1038/s41598-019-48615-1
86. Mirzayans R, Andrais B, Scott A, Wang YW, Murray D. Ionizing radiation-induced responses in human cells with differing TP53 status. *Int J Mol Sci.* (2013) **14**:22409–35. doi: 10.3390/ijms141122409
87. Wnorowski A, Sharma A, Chen H, Wu H, Shao N-Y, Sayed N, et al. Effects of Spaceflight on Human Induced Pluripotent Stem Cell-Derived Cardiomyocyte Structure and Function. *Stem Cell Reports.* (2019) **13**:960–9. doi: 10.1016/j.stemcr.2019.10.006
88. Maruyama K, Iwanami N, Maruyama-Hayakawa T, Doi K, Wang B. A small fish model for quantitative analysis of radiation effects using visualized thymus responses in GFP transgenic medaka. *Int J Radiat Biol.* (2019) **95:**1144–9. doi: 10.1080/09553002.2019.1589019
89. Yasuda T, Kamahori M, Nagata K, Watanabe-Asaka T, Suzuki M, Funayama T, et al. Abscopal activation of microglia in embryonic fish brain following targeted irradiation with heavy-ion microbeam. *Int J Mol Sci.* (2017) **18**:1428. doi: 10.3390/ijms18071428
90. Di Schiavi E, Andrenacci D. Invertebrate models of kallmann syndrome: molecular pathogenesis and new disease genes. *Curr Genomics.* (2013) **14**:2–10. doi: 10.2174/138920213804999174
91. Martinelli S, Cordeddu V, Galosi S, Lanzo A, Palma E, Pannone L, et al. Co-occurring WARS2 and CHRNA6 mutations in a child with a severe form of infantile parkinsonism. *Parkinsonism Relat Disord.* (2020) **72**:75–9. doi: 10.1016/j.parkreldis.2020.02.003

92. Rizzo F, Nizzardo M, Vashisht S, Molteni E, Melzi V, Taiana M, et al. Key role of SMN/SYNCRIP and RNA-Motif 7 in spinal muscular atrophy: RNA-Seq and motif analysis of human motor neurons. *Brain.* (2019) **142**:276–94. doi: 10.1093/brain/awy330
93. Gallotta I, Mazzarella N, Donato A, Esposito A, Chaplin JC, Castro S, et al. Neuron-specific knock-down of SMN1 causes neuron degeneration and death through an apoptotic mechanism. *Hum Mol Genet.* (2016) **25**:2564–77. doi: 10.1093/hmg/ddw119
94. de Carlos Cáceres, Porto DA, Gallotta I, Santonicola P, Rodríguez-Cordero J, Di Schiavi E, et al. elegans neurodegeneration mutants enabled by microfluidics and image analysis algorithms. *Integr Biol.* (2018) **10**:539–48. doi: 10.1039/C8IB00091C
95. Ishioka N, Higashibata A. *Space Experiments Using C. elegans as a Model Organism*. *Handbook of Space Pharmaceuticals*. Pathak Y, M. Araújo dos Santos, Zea L, Eds. Cham: Springer International Publishing. (2019). p. 1–32
96. Nelson GA, Schubert WW, Kazarians GA. Richards GF, development and chromosome mechanics in nematodes: results from IML-1. *Adv Space Res.* (1994) **14**:209–14. doi: 10.1016/0273-1177(94)90405-7
97. Szewczyk NJ, Tillman J, Conley CA, Granger L, Segalat L, Higashitani A, et al. Description of International Caenorhabditis elegans Experiment first flight (ICE-FIRST). *Adv Space Res.* (2008) **42**:1072–9. doi: 10.1016/j.asr.2008.03.017
98. Brenner S. The genetics of Caenorhabditis elegans. *Genetics.* (1974) **77**:71–94.
99. Ankeny RA. The natural history of Caenorhabditis elegans research. *Nat Rev Genet.* (2001) **2**:474–9. doi: 10.1038/35076538
100. Xu Y, Chen L, Liu M, Lu Y, Yue Y, Liu Y, et al. High-throughput transcriptome sequencing reveals extremely high doses of ionizing radiation-response genes in Caenorhabditis elegans. *Toxicol Res.* (2019) **8**:754–66. doi: 10.1039/c9tx00101h
101. Hartman PS. Epistatic interactions of radiation-sensitive (rad) mutants of Caenorhabditis elegans. *Genetics.* (1985) **109**:81–93.
102. Weidhaas JB, Eisenmann DM, Holub JM, Nallur SV. A Caenorhabditis elegans tissue model of radiation-induced reproductive cell death. *Proc Natl Acad Sci USA.* (2006) **103**:9946–51. doi: 10.1073/pnas.0603791103
103. Zhao Y, Johnsen R, Baillie D, Rose A. Worms in space? A model biological dosimeter. *Gravit Space Biol Bull.* (2005) **18**:11–16.
104. Zhao Y, Lai K, Cheung I, Youds J, Tarailo M, Tarailo S, et al. A mutational analysis of Caenorhabditis elegans in space. *Mutat Res.* (2006) **601**:19–29. doi: 10.1016/j.mrfmmm.2006.05.001
105. Montague TG, Almansoori A, Gleason EJ, Copeland DS, Foley K, Kraves S, et al. Gene expression studies using a miniaturized thermal cycler system on board the International Space Station. *PLoS ONE.* (2018) **13**:e0205852. doi: 10.1371/journal.pone.0205852

Conflict of Interest: The authors declare that the research was conducted in the absence of any commercial or financial relationships that could be construed as a potential conflict of interest.

frontiers in Physics

ORIGINAL RESEARCH
published: 07 October 2020
doi: 10.3389/fphy.2020.00299

High-Energy Charged Particles for Spatially Fractionated Radiation Therapy

Consuelo Guardiola[1,2] *and Yolanda Prezado*[3]*

[1] Universite Paris-Saclay, CNRS/IN2P3, IJCLab, Orsay, France, [2] Universite de Paris, IJCLab, Orsay, France, [3] Institut Curie, PSL Research University, University Paris Saclay, Inserm U 1021-CNRS UMR 3347, Orsay, France

Spatially fractionated radiotherapy (SFRT) offers a gain in normal tissue sparing with respect to standard seamless irradiations. The benefits of SFRT may be further enhanced by replacing the commonly used photon beams by charged particles. Along this line, proton SFRT has already shown a significant widening of the therapeutic window for radioresistant tumors in preclinical studies. The goal of this work was to investigate whether the use of superior energies as compared to the clinical ones, as well as heavy ions could lead to a further improvement of SFRT. New facilities such as FAIR, RAON, or some others associated with the International Biophysics collaboration will be able to provide very intense high-energy ion beams, enabling the experimental evaluation of the Monte Carlo simulations reported in this work. Our results indicate that proton SFRT could benefit from the use of higher beam energies (ĩ GeV). Concerning heavy ions, such as carbon or neon, the main advantage would be the possible theragnostic use. Biological experiments are needed to validate these results, and they will be the subject of future experimental proposals at those new facilities.

Keywords: spatially fractionated radiotherapy, heavy ions, Monte Carlo simulations, new accelerators, charged particle therapy

OPEN ACCESS

Edited by:
Zhen Cheng,
Stanford University, United States

Reviewed by:
Jose M. Perez,
Centro de Investigaciones Energéticas, Medioambientales y Tecnológicas, Spain
Till Tobias Böhlen,
Centre Hospitalier Universitaire Vaudois (CHUV), Switzerland

***Correspondence:**
Yolanda Prezado
yolanda.prezado@curie.fr

Specialty section:
This article was submitted to Medical Physics and Imaging, a section of the journal Frontiers in Physics

Received: *01 May 2020*
Accepted: *30 June 2020*
Published: *07 October 2020*

Citation:
Guardiola C and Prezado Y (2020) High-Energy Charged Particles for Spatially Fractionated Radiation Therapy. Front. Phys. 8:299. doi: 10.3389/fphy.2020.00299

1. INTRODUCTION

Spatial fractionation of the dose, such as in minibeam radiation therapy (MBRT), has already proven its capacity to spare normal tissues [1–4]. Spatially fractionated radiotherapy (SFRT) has been mainly explored using photons, such as in LINAC-based Grid therapy [2] or synchrotron micro and minibeam radiation therapies [1, 3–6].

However, SFRT may be further improved by partnering its benefits with the advantages of charged particles for therapy [7, 8]. Recently, proton minibeam radiation therapy (clinical beams) has demonstrated a net gain in normal tissue sparing [9–12]. An equivalent or superior tumor control than with standard seamless irradiations was observed after pMBRT [12, 13]. This holds even in cases where highly heterogeneous dose distributions were delivered.

In contrast to the flat dose profiles in conventional radiotherapy, the profiles in SFRT follow a pattern of areas of high dose (peaks) followed by areas of low dose (valley). The ratio between peak and valley doses, the so-called peak-to-valley-dose ratio (PVDR), is considered to be an important dosimetric parameter in SFRT, as it plays an important role in the biological response. Different

studies suggest that high PVDR with low valleys favor tissue sparing, while low PVDR with high valleys increase tumor control [14].

Dosimetry evaluations in heavy ions MBRT have shown favorable dose distributions for normal tissue sparing [8, 15]. Indeed very high peak-to-valley dose ratios and minimal contribution of high linear energy transfer (LET) nuclear fragments to the valley regions, which are believed to be responsible for normal tissue sparing [14], were obtained. Additionally, the possible gain in normal tissue sparing of MBRT might allow a renewed use of very heavy ions (Ne, Ar, and Si) for the treatment of hypoxic tumors [15], which remains one of the main challenges in radiation therapy. Heavy ions, such as Neon, were used in the past, demonstrating a high capacity for hypoxic cell tumor killing [16, 17]. However, their use was discontinued due to important side effects [17]. The first biological experiments performed using Ne MBRT at HIMAC (NIRS-QST) seem to validate our hypothesis, namely, a gain in normal tissue sparing thanks to the combination of Ne ions with MBRT [18].

The advent of new accelerators, able to provide very intense high energy (up to 10 GeV/A) ions beams, opens up for new possibilities for the exploration of charged particles MBRT. This is the case of facilities such as FAIR (Facility for Antiproton and Ion Research, www.gsi.de), Rare Isotope Science Project (RAON, https://www.ibs.re.kr), or some others associated with the recently created International Biophysics collaboration (IBC). In particular, the use of high-energy beams (around 1 GeV/A) would reduce multiple coulomb scattering (MCS), which could lead to higher PVDR in normal tissues than with clinical-relevant energies. The resulting narrow penumbras could make the beams to act as "remote scalpels" for radiosurgery applications [7, 19]. This could find important applications in the treatment of non-cancer diseases, such as arteriovenous malformations or some types of epilepsy [20]. In addition, the reduction of MSC would allow the use of narrower beams, while keeping a good ratio between dose deposited in the trajectory of the primary beam and scattered dose. Moreover, high-energy beams may enable a theragnostics use, as the exiting beam could be employed for imaging purposes. The high beam intensity of those new facilities might allow to combine SFRT and FLASH therapy [21]. Very high dose rates will also open new possibilities in SFRT: moving targets (such as lung) could safely start to be considered without the risk of jeopardizing the spatial fractionation of the widows.

Indeed, the use of relativistic protons was already proposed for plateau (non-Bragg peak) stereotactic radiosurgery in the late 70s [22]. More than a thousand of patients have been treated at PNPI synchrocyclotron with 1GeV for image-guided stereotactic radiosurgery (IGSpRS) [23].

The aim of this dosimetry study was to assess whether the combination of high energy charged particles beams and MBRT could offer an advantage in SFRT. A very first evaluation of the use of high energy (1 GeV) protons for SFRT was reported by Prezado et al. [7]. This new investigation aims at completing that first study and extend it toward heavy ions, with the goal of evaluating the interest of this new approach.

2. MATERIALS AND METHODS

Monte Carlo simulations were performed to evaluate the dose distributions of high energy protons, ^{12}C and ^{20}Ne minibeam radiation therapy.

2.1. Monte Carlo Simulations

The GEANT4 (GEANT4.10.3)-based GATE (release 8.0) toolkit was employed. One of the recommended physics list for hadrontherapy by the GATE collaboration was employed [24]. The so-called QGSP_BIC_HP builder and standard option 3 were used to describe the hadronic and electromagnetic interactions, respectively. A range cut of 20 μm was considered for protons, electrons, positrons, and gammas. Values of 75 and 85.7 eV were used for the ionization potentials in water and air, respectively [24, 25].

The beams impinged into either (i) a cubic-shaped water phantom (20 x 20 x 500 cm) or (ii) computed tomography (CT) DICOM images of anonymized human patients, both embedded in air. The method described in [26] was followed to convert Hounsfield Units (HU), i.e., voxel values, into materials, for dose calculations.

Particle sources were modeled by means of *General Particle Source* (GPS), which considers a Gaussian shape for the energy spectrum. Three irradiation configurations were created: broad beam, single minibeam, and minibeam arrays. Different beam energies of 400, 700, and 1,000 MeV/u were used (maximum range of 3.25 m water equivalent for the highest proton energy). Energy spreads of 0.1% MeV of total energy were simulated in all cases. A realistic beam divergence of 3 mrad was assumed.

The dimensions of the beam source were 2 x 2 cm in the case of broad beam irradiations and 50 μm, 600 μm, and 1 mm x 2 cm in the case of MBRT. The narrowest beam width is the one used in Microbeam Radiation Therapy [1]. Beam widths of 600 μm are the most commonly used in MBRT studies. We decided to evaluate thicker beams as well, those around 1 mm, as they still provide a significant normal tissue sparing [12]. The sources were placed at 7 cm far away from the phantom. The minibeam arrays consisted of five minibeams with a center-to-center distances (ctc) of 1,200 μm (commonly used in MBRT) and 3,500 μm, which has been shown to minimize the contribution of heavy nuclear fragments to the valleys [8].

Doses were recorded by using the GATE dose-actor. They were tallied in bins of one tenth of the minibeam widths in each case, 2 mm, and 1 mm in the lateral, vertical, and beam directions, respectively. Depth dose profiles (PDD) and peak-to-valley dose ratios (PVDR) were assessed over the tally bin size along the beam transversal axis by taking the doses in the central peak and its adjacent valley. The statistical uncertainty in dose in each voxel was calculated as reported in [27].

The total number of primary particles simulated was 10^8, leading to a global uncertainty of less than 1%.

3. RESULTS

This section reports on the calculated dose distributions of both broad beam and MBRT irradiation with high energy proton,

carbon, and neon beams. Dose are recorded along the tallies of the central axis.

3.1. Broad-Beam Dose Distributions

Figure 1 upper-left shows the depth dose curves in water for 2 x 2 cm large proton beams with energies going from 400 MeV to 1 GeV. In contrast to the dose deposition in depth with clinically relevant energies, there is a continuous decrease in the dose deposited in depth up to the Bragg peak [28]. The ratio between the dose deposited at the entrance and at the Bragg Peaks increases with the beam energy. **Figure 1** upper-right to lower-right depicts the proportion of secondary particles as a function of depth for the three energies (400, 700, and 1,000 MeV) considered. The trend is the same for all the three energies: secondary nuclear products and electrons amount for roughly 10% of the total dose, being higher the contribution of the first ones. Gamma rays contribution is several orders of magnitude lower than other ones.

Figure 2 shows the contribution of both primary and secondary particles to the total dose in the case of 700 and 1,000 MeV/u of Carbon and Neons beams. The dose deposited by the secondary nuclear products increases with the atomic number of the ion at shallow depths and can overpass the dose contribution of the primary ions for the higher energies (1,000 MeV/u).

3.2. Minibeam Radiation Therapy

Figure 3 upper-row shows the depth dose curves of one single 1,000 MeV proton minibeam (50 μm, 600 μm, and 1mm-wide beam). On the right side, the depth dose curves zoomed in the range from 0 to 160 mm (approximative lateral length of a human head [29]) are depicted. In the case of 50 μm-wide beams, the important lateral scattering results in a rapid fall off of the deposited dose after a few centimeters. Consequently, those narrow beams were deemed not to be suitable for charged particle SFRT. The curves are almost flat for the thicker beam widths evaluated (600 μm and 1 mm) up to 7 cm in depth. From that depth on, the depth dose curve decreases rapidly in the case of 600 μm-wide beam, helping to reduce the dose deposited upstream. This could be an interesting feature for the treatment of brain tumors. Central and lowest rows depict the

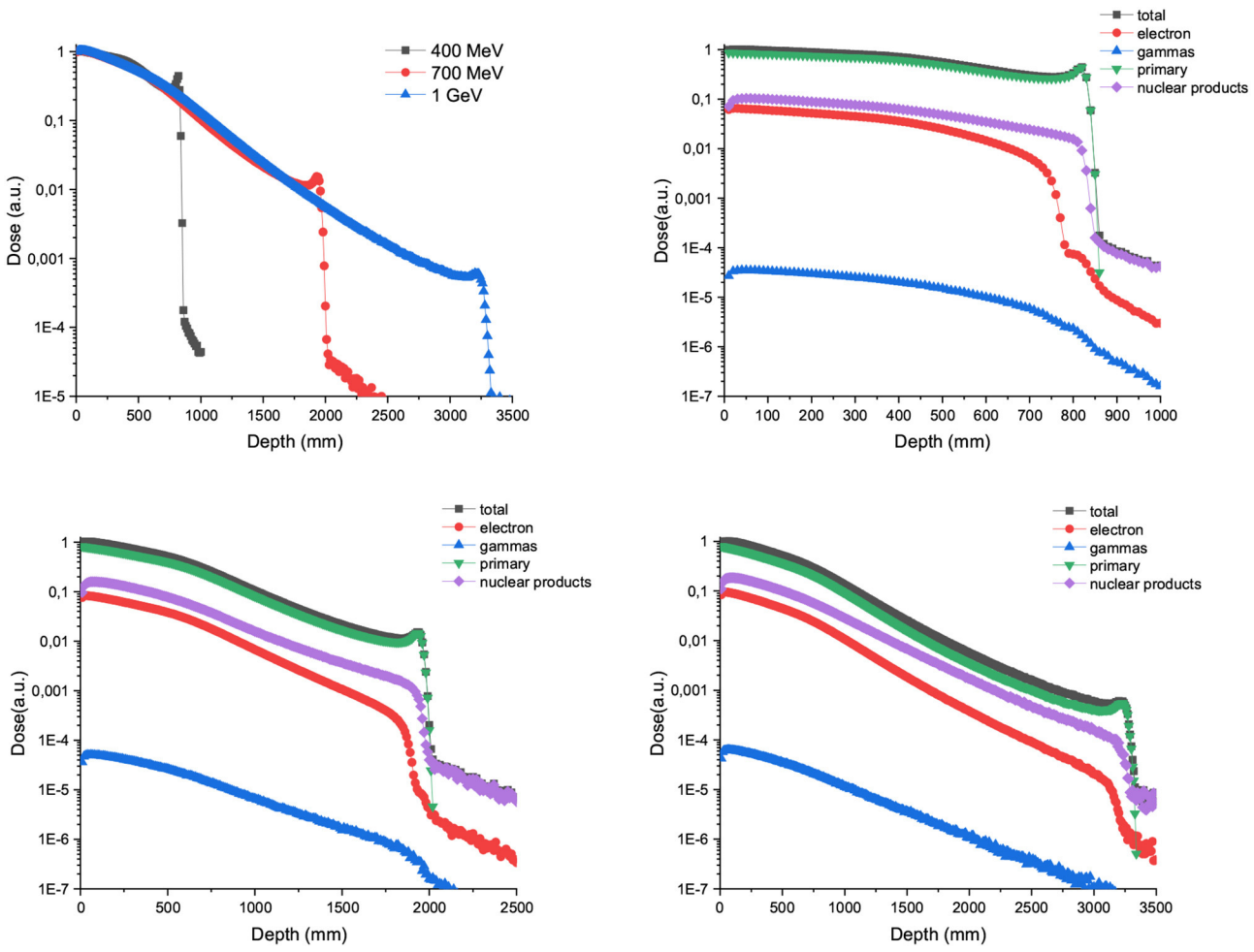

FIGURE 1 | Left panel in the upper row: Depth dose curves resulting from broad-beam irradiations with 400, 700, and 1,000 MeV proton beams. The plots in the upper row right column and the lower row show the contribution of the secondary particles to the total dose for the three energies evaluated.

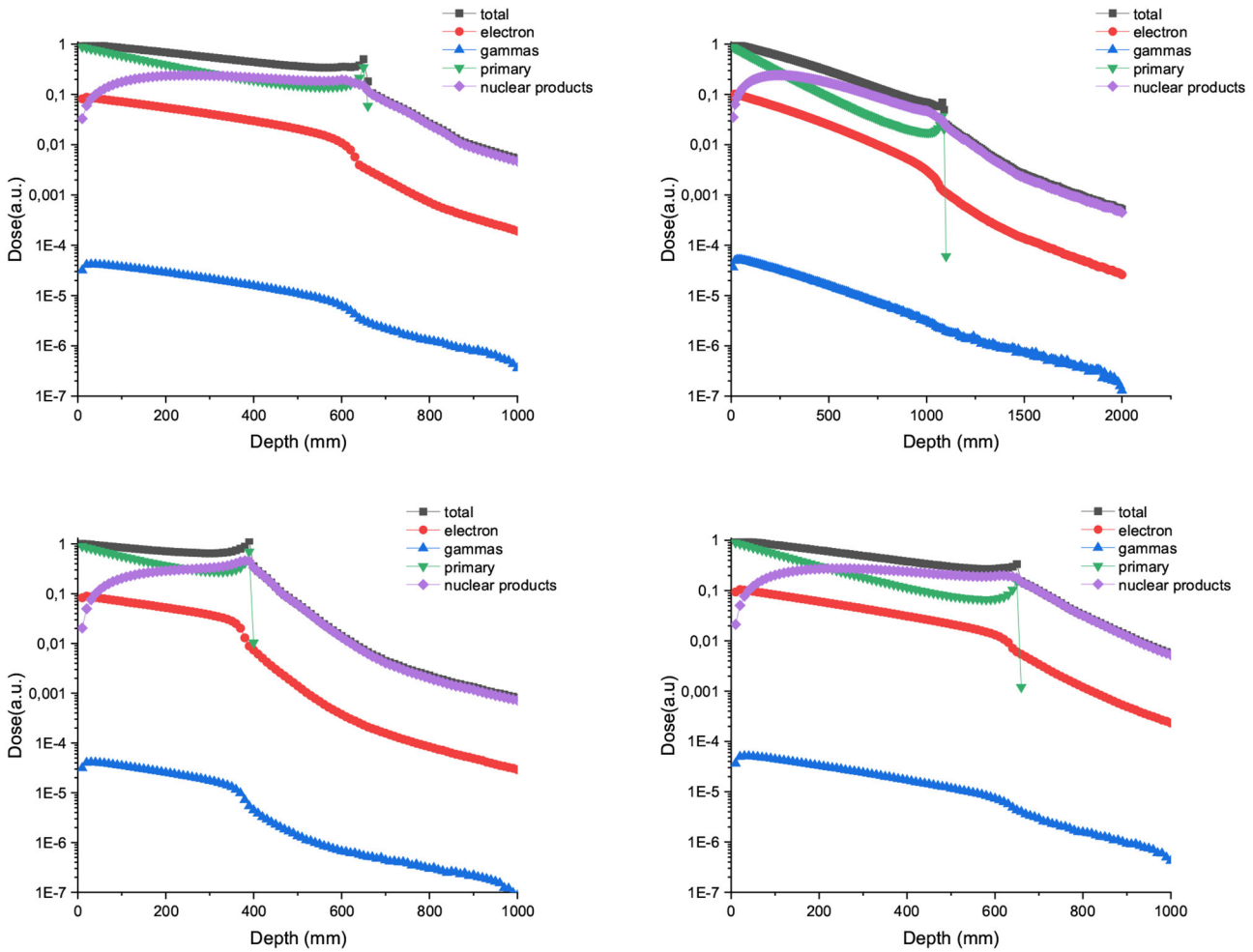

FIGURE 2 | Relative dose deposition of primary and secondary particles to the total dose as a function of depth when a water tank is irradiated with 700 (left) and 1,000 MeV/u (right) carbon (up) and neon ions (bottom) broad beams.

depth dose curves for 700 and 1,000 MeV/u C and Ne ions, respectively. No important difference was observed for any of the configurations in the first 16 cm depth. In contrast, a more rapid fall off in the dose as a function of depth is observed for C and Ne in comparison with protons. This is a result of a more important attenuation in depth due to a higher rate of nuclear fragmentation [30].

Figure 4 shows the depth dose curves for the central beam of arrays of proton minibeams of different energies, widths and ctc. The three rows corresponds to the three energies evaluated: 400 MeV (uppermost row), 700 MeV (central row), and 1,000 MeV (lowest row). The dose deposition along the total beam range and the first 16 cm depth are shown in the left and right columns, respectively. The curves are flatter with respect to the case of one unique minibeam. The larger the width and ctc of the array, the deeper the distance before the dose deposition starts decreasing rapidly. **Figure 5** shows the contribution of the secondary products to the valley doses. The main contribution in the first 20 cm are nuclear products, particularly the secondary protons for all the beam energies evaluated.

Figure 6 shows the PVDR values for the proton minibeams for the same aforementioned configurations. The highest PVDR are achieved with 600 μm-wide beams and ctc of 3,500 μm (middle), being around five times higher than the PVDR for a ctc of 1,200 μm (down). For this later case, a homogenization is reached at around 10 cm depth. Intermediate values are obtained in the case of one array of beams 1 mm wide. PVDR values are higher than the ones used previously in preclinical studies [11–13], and which had shown a net gain in normal tissue tolerances. Therefore, an even higher sparing of normal tissue might be expected. The PVDR values are similar or even lower than the values that could be obtained with magnetically focused 100 MeV proton beams [31]. The lower the beam energy is, the higher the PVDR in the first centimeters. The reason is that at these high beam energies, the stopping power follows an inverse relation with the beam energy (www.nist.gov). Consequently, the dose deposition by the

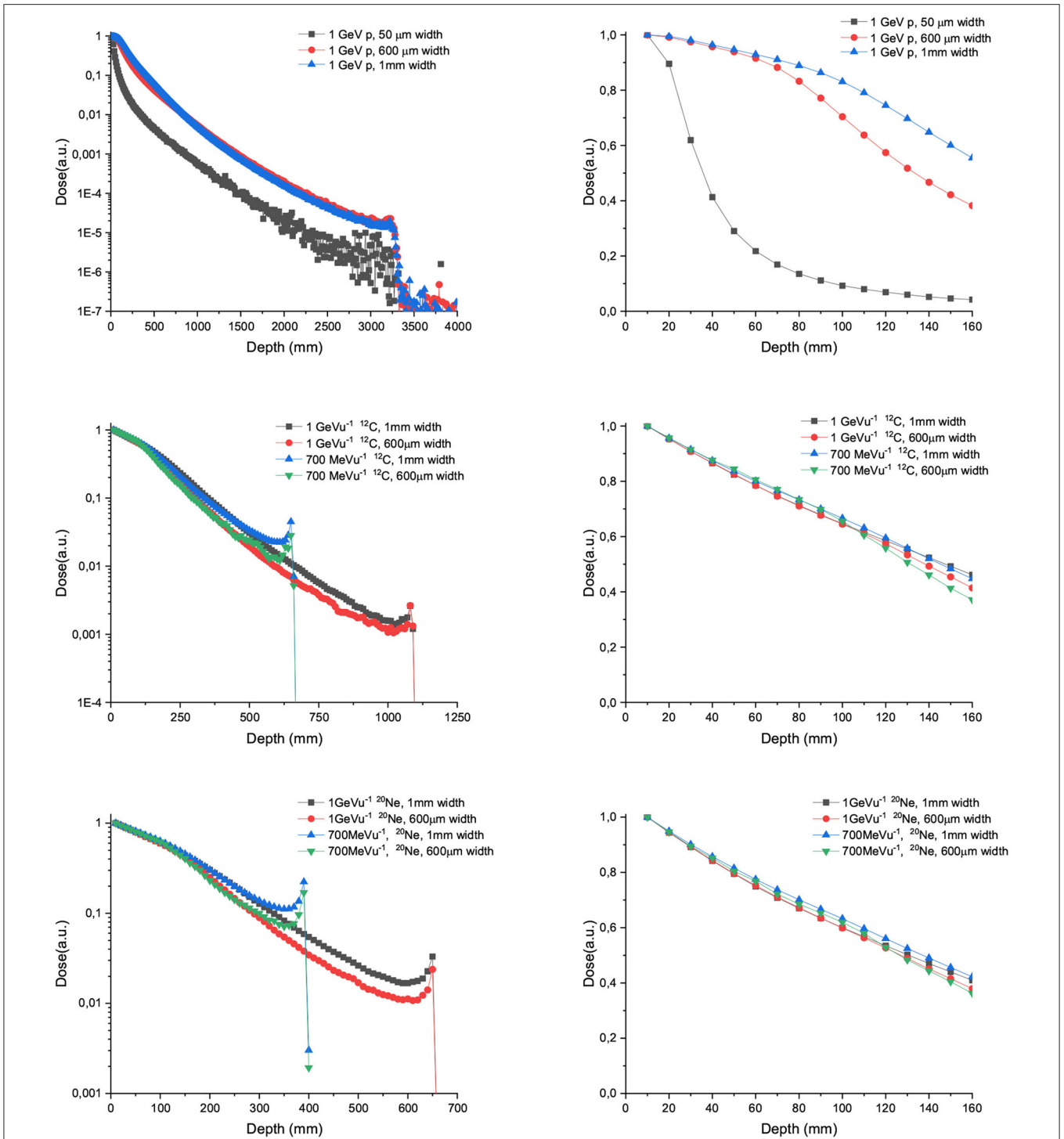

FIGURE 3 | Depth dose curves for 50 μm, 600 μm, and 1 mm-wide 1,000/u GeV protons (upper row), carbon (central row), and Neon (lower row) beams in water tank. The left column shows the full range, while the right one depicts only the first 16 cm.

primary beam follows an inverse relationship with the beam energy. In addition, the secondary products are more forward directed depositing their energy at deeper depths. This results in smaller peak doses at shallower depths for the highest energies. Since the valley doses are very small, the PVDR is dominated by the peaks at this range of beam energies.

Figure 7 depicts the depth dose curves for the central minibeam in the case of C and Ne ions of 700 and 1,000 MeV/u.

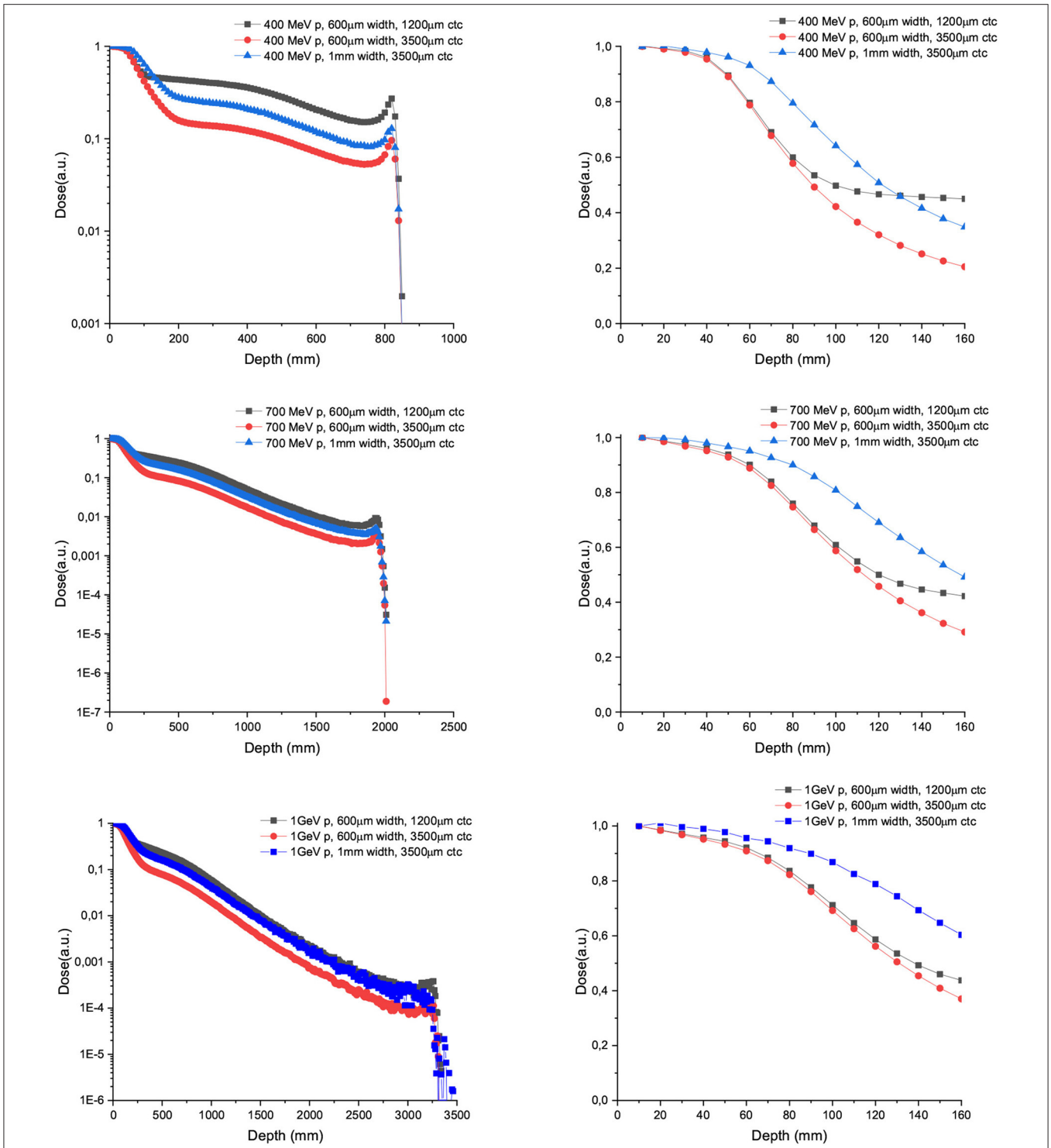

FIGURE 4 | Depth dose curves for the central minibeam of arrays of 600 μm and 1 mm-wide protons of 400 (upper row), 700 (central row), and 1,000 MeV (lower row) minibeams in water tank. Two ctcs are compared. The left column shows the full range, while the right one depicts only the first 16 cm.

The beam width and ctc considered were 600 and 3,500 μm. **Figure 8** shows the contribution of nuclear products, electrons and gammas to the valley doses for 700 MeV carbon and neon 600 μm-wide beams. Nuclear products are the dominant ones at almost all depths, which is in contrast to trends observed at lower beam energies [15].

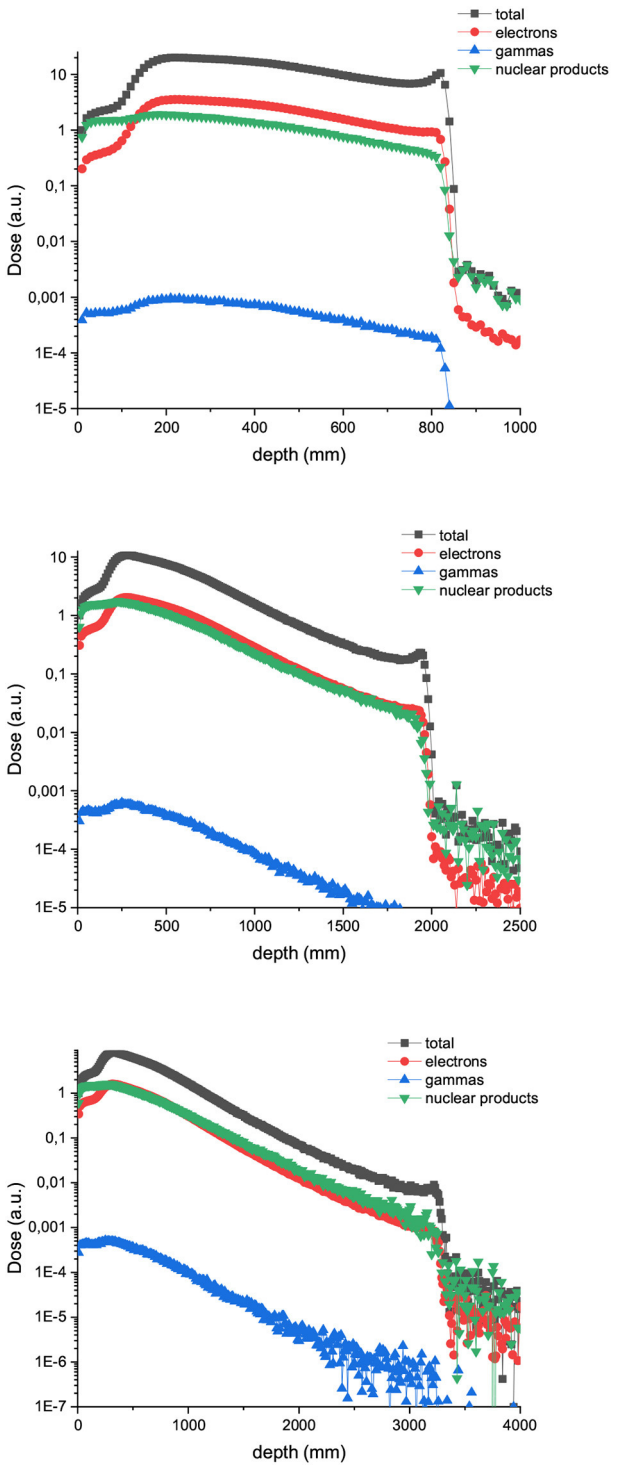

FIGURE 5 | Composition of the valley doses in the case of 400 (up), 700 (middle), and 1,000 MeV (down) proton minibeams.

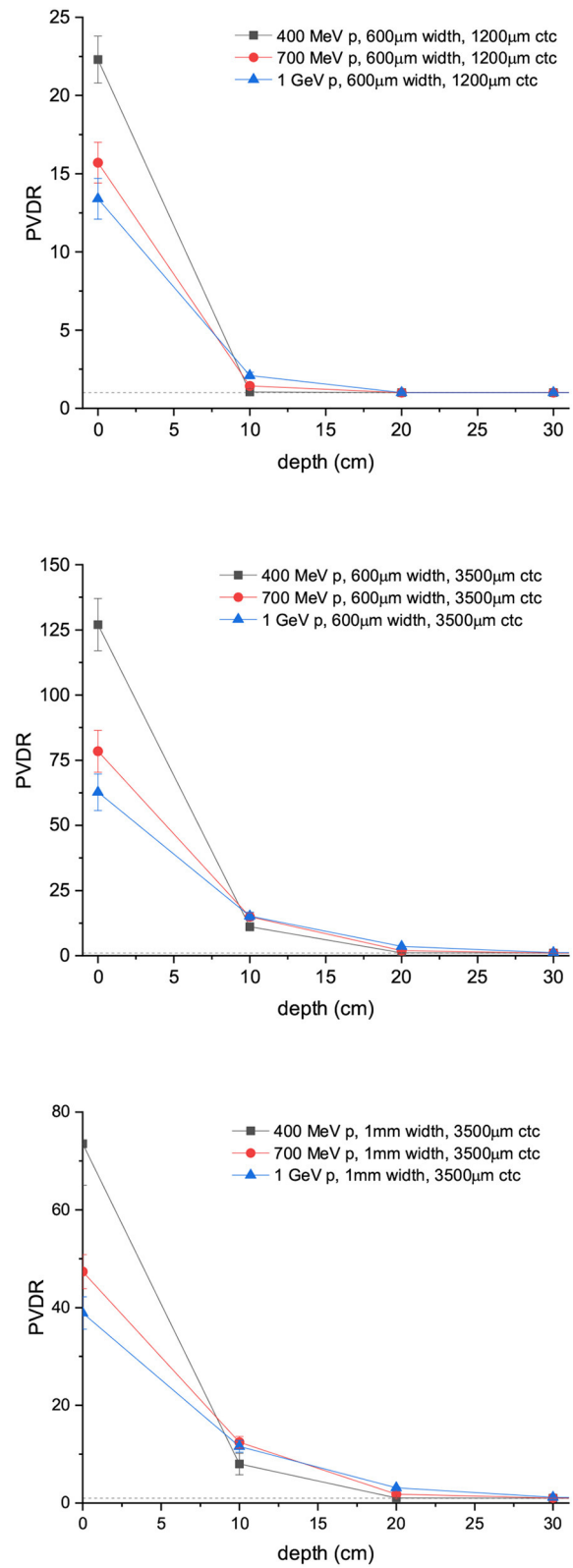

FIGURE 6 | PVDR values for arrays of protons minibeams are shown: 600 μm-wide beams and 1,200 μm ctc (up); 600 μm-wide beams and 3,500 μm ctc (middle); 1 mm-wide beams and 3,500 μm ctc (down).

PVDR values for Carbon and Ne MBRT are a factor 2 or higher than in the case of protons, with Ne ions offering the highest PVDR at the entrance (See **Figure 9**). **Figure 10** showing how the peak and valley doses vary as a function of the ion

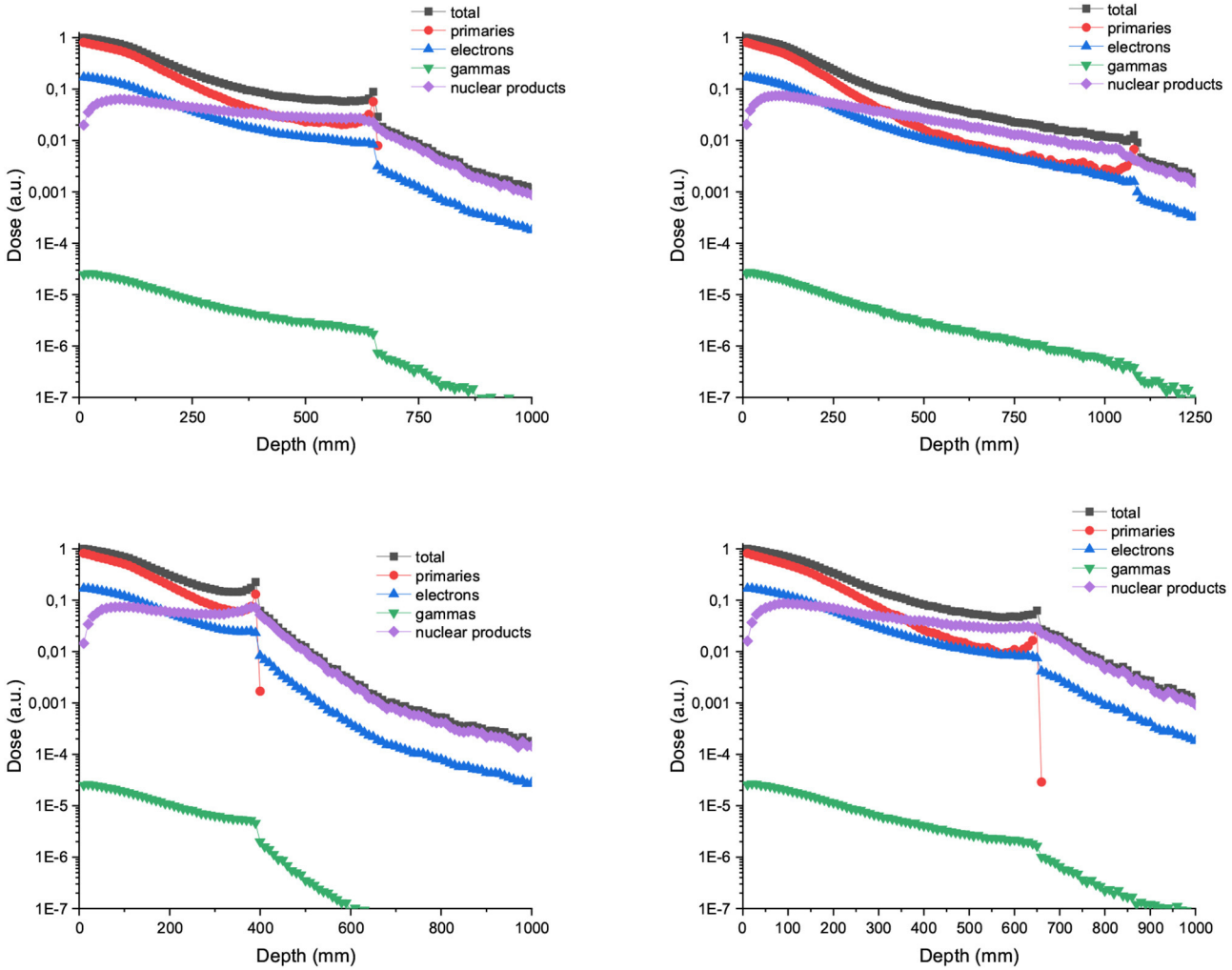

FIGURE 7 | (Up) PDD curve for 700 (left) and 1,000 MeV/u (right) Carbon minibeams of 600 μm witdth and 3,500 μm ctc. **(Bottom)** PDD curve for 700 (left) and 1,000 MeV/u (right) Neon minibeams of 600 μm witdth and 3,500 μm ctc.

and beam energy (same number of primary particle simulates) illustrates why the PVDR decreases with beam energy in the first centimeters.

Finally, to illustrate a possible patient's scenario, we have evaluated the dose distribution in an anonymized human head anatomy. We have simulated an irradiation with 1,000 MeV/u proton MBRT. The beam width and ctc were 600 and 3,500 μm, respectively (See **Figure 11**). The depth dose curve shows that the dose deposition in the peak regions is almost constant in depth. The spatial fractionation can be maintained at all depths.

4. DISCUSSION

Radiotherapy, despite being in the forefront of cancer treatments, continues to be limited by the tolerances of normal tissues. Different strategies based on distinct dose delivery methods, such as SFRT or FLASH therapy [32], offer promise to overcome that limitation. This would allow widening the therapeutic window for radioresistant tumors or pediatric cancers.

SFRT has been mainly explored with photons, both with medical LINACs [2] and at large synchrotrons [3]. The implementation at LINACs with MV photons suffers from important lateral scattering resulting in high valley doses, and a low flux, which results in the need of using large (around 1 cm^2) beam sizes. On the other hand the beamtime at large synchrotrons is limited, and the penetration depth of the low-energy synchrotron x-rays provided is short. Charged particle SFRT has been proposed as a promising alternative [7] to fully profit from the advantages of the spatial fractionation of the dose. Among the main advantages, one can cite the possibility of achieving a homogenous dose coverage of the target with one unique array or the fact of having a negligible (or inexistent) dose deposition after the Bragg Peak. Biological experiments with clinically relevant energies have already shown the gain in normal tissue sparing provided by charged particles SFRT [10, 11, 18].

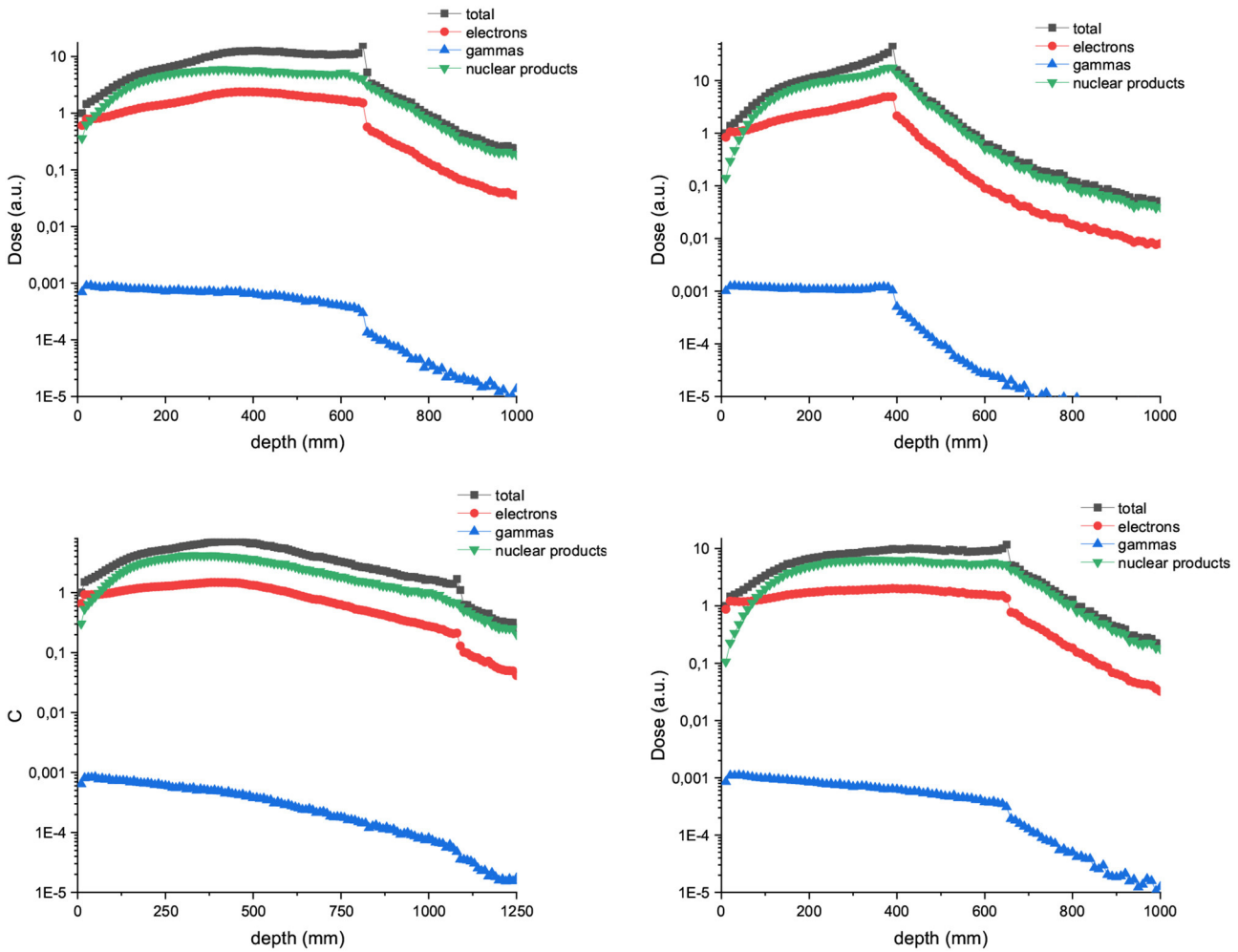

FIGURE 8 | Composition of the valley doses in the case of arrays of 600 μm witdth and 3,500 μm ctc carbon (left) and neon (right). The beam energy is 700 MeV/u in the upper row and 1,000 MeV/u in the lower row.

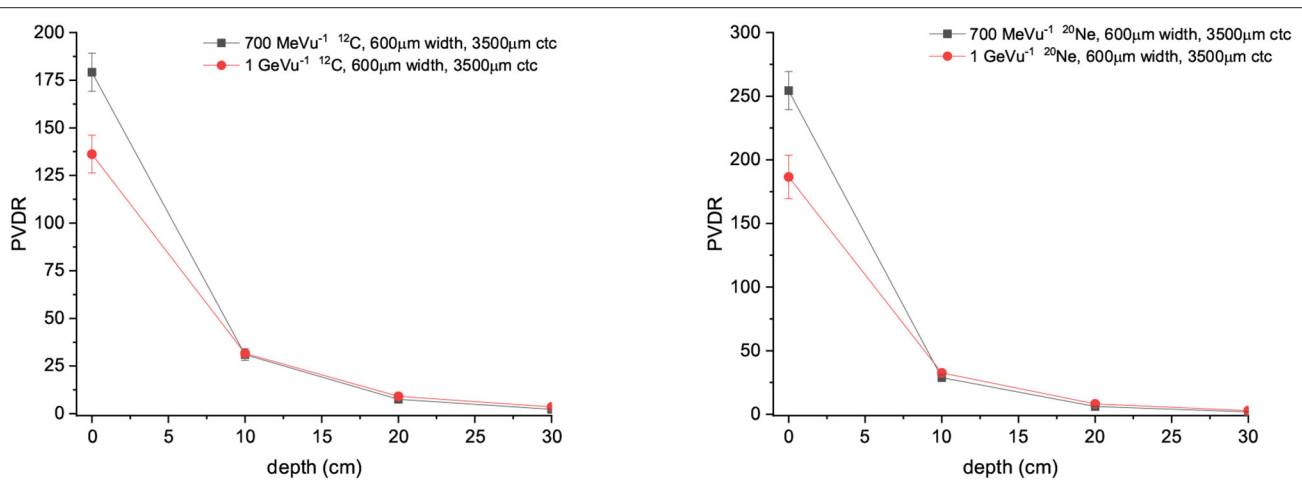

FIGURE 9 | (Left) PVDR values for Carbons minibeams of 600 μm witdth and 3,500 μm ctc. **(Right)** PVDR for Neons minibeams of 600 μm witdth and 3,500 μm ctc.

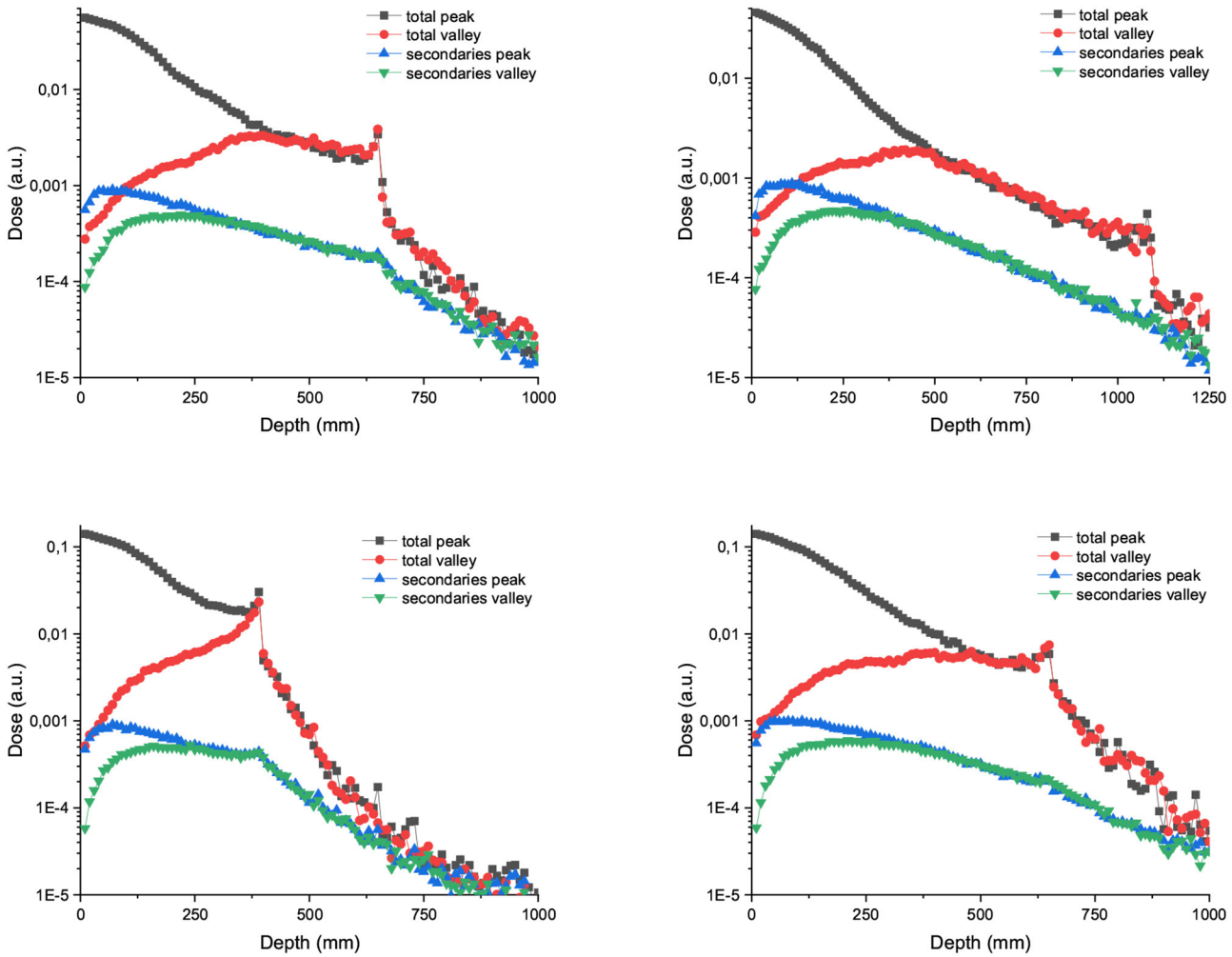

FIGURE 10 | Left: Peak and valley doses in depth and distribution of secondaries for arrays of 600 μm width and 3,500 μm carbon (up) and neon (down) minibeams. The beam energies are 700 MeV/u in the left column and 1,000 MeV/u in the right column.

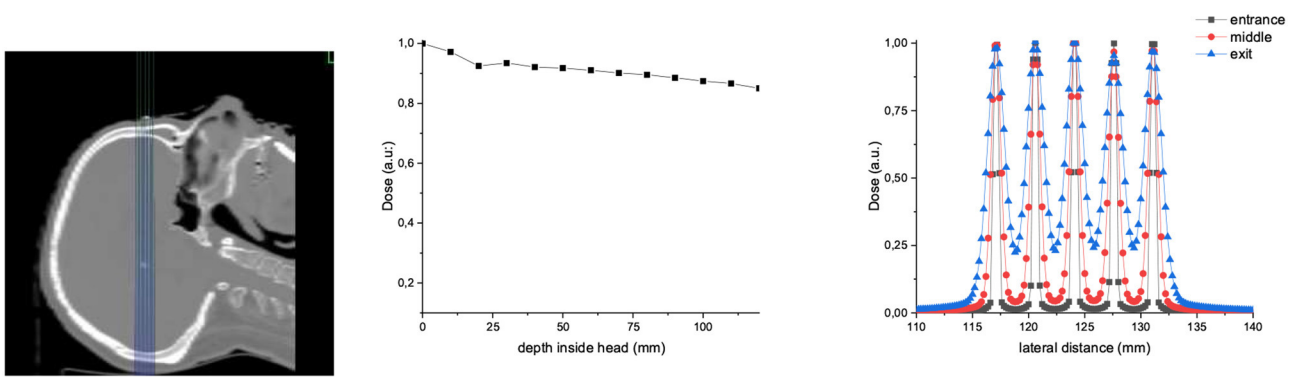

FIGURE 11 | Dose distributions in an anonymized human patient irradiated with 1,000 MeV/u proton MBRT (600 μm width and 3,500 μm ctc). Two-dimensional dose distributions, PDD, and lateral dose profiles at different depths are shown on the left, middle, and right, respectively.

New accelerators, such as FAIR or Raon, will offer intense and high-energy beams (up to 10 Gev/u). The aim of this work was to investigate whether a further improvement in SFRT can be obtained by using those new beams. The rational was the possible benefit of the reduction of MSC for high energies. In addition, the use of higher beam energies (around 1 GeV/u)

might enable theragnostic applications as the same beam can be used for treatment and online imaging. The ultrahigh dose rates that will be available would allow partnering FLASH and charged particle SFRT. This might allow using MBRT for moving targets like lung, today restricted due to possible blurring of the minibeam patterns due to respiratory motion.

Concerning protons, our study shows that energies slightly higher than the ones used in clinical practice (400 MeV) for protons offer very interesting features: an almost flat peak dose deposition in depth in the first centimeters and a rapid falloff after 7 cm depth for beams 1 mm wide (**Figure 4**). This could be of interest for a theragnostic treatment of brain tumors. Indeed a higher tumor-to-entrance ratio than with clinical energies could be obtained. Thanks to the rapid falloff after the first centimeters, the dose deposited in the contralateral hemisphere will be relatively low, and the existing beam could be used for image guidance. It should also be highlighted that energies up to 400 MeV could already be produced in some ion beam therapy centers. This energy leads to the highest PVDR values at shallow depths out of the three energies evaluated. Beam widths of 600μm combined with 700 or 1,000 MeV follow the same pattern just described. In all cases, an homogenization can be obtained at around 10 cm of depth with a ctc of 1,200 μm. For larger ctc distances, crossfiring, or interlacing several arrays could be used as a strategy to increase the valley dose in the tumor. One of the advantages of increasing the energy in proton minibeams is that the depth dose curve of each minibeam is flat in the first centimeters in comparison with that obtained with 100–200 MeV protons minibeams. This would result in a more favorable tumor to entrance dose ratio.

Higher PVDR are obtained with Carbon and Neon than with protons at all depths. The higher capacity of those ions to activate the immune system might compensate for those larger PVDR in the tumor with respect to protons. The PVDR are not significantly higher than the ones obtained in previous works with clinical relevant energies [15]. The secondary nuclear products represent a larger contribution to the valley doses than at currently clinically relevant energies [15].

Consequently, to increase the beam energy in proton SFRT seems to provide some advantages from dosimetric point of view, while in the case of heavier ions, such as carbon, no clear advantage could be extracted from this dosimetry evaluation other than a theragnostic use.

Indeed, 600 μm proton minibeams of 400 MeV lead to similar PVDR than C ions of 1 GeV/u in the phantom entrance (127 vs. 136 respectively), while a more homogeneous dose distribution could be obtained in the target. The valley doses will be less impacted by high-LET nuclear fragments contributions. Therefore, a further optimization in SFRT could be achieved by using high energy submillimetric proton beams. Biological experiments are needed to validate these results and they will be the subject of future experimental proposals at those new facilities.

DATA AVAILABILITY STATEMENT

The raw data supporting the conclusions of this article will be made available by the authors, without undue reservation.

AUTHOR CONTRIBUTIONS

CG performed the Monte Carlo simulations and data analysis. YP conceived the project. CG and YP wrote the manuscript. All authors contributed to the article and approved the submitted version.

ACKNOWLEDGMENTS

Calculation time was granted at MareNostrum Barcelona Supercomputing Center from the Partnership for Advanced Computing in Europe [PRACE Project Access Call 19th (proposal number 2019204903)] and the Centre de Calcul de lIN2P3 (CCIN2P3).

REFERENCES

1. Slatkin DN, Spanne P, Dilmanian FA, Gebbers JO, Laissue JA. Subacute neuropathological effects of microplanar beams of x-rays from a synchrotron wiggler. *Proc Natl Acad Sci USA*. (1995) **92**:8783–7. doi: 10.1073/pnas.92.19.8783
2. Mohiuddin M, Fujita M, Regine WF, Megooni AS, Ibbott GS, Ahmed MM. High-dose spatially-fractionated radiation (GRID): a new paradigm in the management of advanced cancers. *Int J Radiat Oncol Biol Phys*. (1999) **45**:721–7. doi: 10.1016/S0360-3016(99)00170-4
3. Dilmanian FA, Zhong Z, Bacarian T, Benveniste H, Romanelli P, Wang R, et al. Interlaced x-ray microplanar beams: a radiosurgery approach with clinical potential. *Proc Natl Acad Sci USA*. (2006) **103**:9709–14. doi: 10.1073/pnas.0603567103
4. Prezado Y, Deman P, Varlet P, Jouvion G, Gil S, Le Clec'H C, et al. Tolerance to dose escalation in minibeam radiation therapy applied to normal rat brain: long-term clinical, radiological and histopathological analysis. *Radiat Res*. (2015) **184**:314–21. doi: 10.1667/RR14018.1
5. Bouchet A, Serduc R, Laissue JA, Djonov V. Effects of microbeam radiation therapy on normal and tumoral blood vessels. *Phys Med*. (2015) **31**:634–41. doi: 10.1016/j.ejmp.2015.04.014
6. Deman P, Vautrin M, Edouard M, Stupar V, Bobyk L, Farion R, et al. Monochromatic minibeams radiotherapy: from healthy tissue-sparing effect studies toward first experimental glioma bearing rats therapy. *Int J Radiat Oncol Biol Phys*. (2012) **82**:693–700. doi: 10.1016/j.ijrobp.2011.09.013
7. Prezado Y, Fois GR. Proton-minibeam radiation therapy: a proof of concept. *Med Phys*. (2013) **40**:031712. doi: 10.1118/1.4791648
8. Gonzalez W, Prezado Y. Spatial fractionation of the dose in heavy ions therapy: an optimization study. *Med Phys*. (2018) **45**:2620–7. doi: 10.1002/mp.12902
9. Zlobinskaya O, Girst S, Greubel C, Hable V, Siebenwirth C, Walsh DW, et al. Reduced side effects by proton microchannel radiotherapy: study in a human skin model. *Radiat Environ Biophys*. (2013) **52**:123–33. doi: 10.1007/s00411-012-0450-9
10. Girst S, Greubel C, Reindl J, Siebenwirth C, Zlobinskaya O, Walsh DWM, et al. Proton minibeam radiation therapy reduces side effects in an *in vivo* mouse ear model. *Int J Radiat Oncol Biol Phys*. (2016) **95**:234–41. doi: 10.1016/j.ijrobp.2015.10.020
11. Prezado Y, Jouvion G, Hardy D, Patriarca A, Nauraye C, Bergs J, et al. Proton minibeam radiation therapy spares normal rat brain: long-term clinical, radiological and histopathological analysis. *Sci Rep*. (2017) **7**:14403. doi: 10.1038/s41598-017-14786-y

12. Prezado Y, Jouvion G, Patriarca A, Nauraye C, Guardiola C, Juchaux M, et al. Proton minibeam radiation therapy widens the therapeutic index for high-grade gliomas. *Sci Rep*. (2018) **8**:16479. doi: 10.1038/s41598-018-34796-8
13. Prezado Y, Jouvion G, Guardiola C, Gonzalez W, Juchaux M, Bergs J, et al. Tumor control in RG2 glioma-bearing rats: a comparison between proton minibeam therapy and standard proton therapy. *Int J Radiat Oncol Biol Phys*. (2019) **104**:266–71. doi: 10.1016/j.ijrobp.2019.01.080
14. Dilmanian FA, Button TM, Le Duc G. Response of rat intracranial 9L gliosarcoma to microbeam radiation therapy. *Neuro Oncol*. (2002) **4**:26–38. doi: 10.1215/15228517-4-1-26
15. Peucelle C, Mart?nez-Rovira I, Prezado Y. Spatial fractionation of the dose using neon and heavier ions: a Monte Carlo study. *Med Phys*. (2015) **42**:5928–36. doi: 10.1118/1.4930960
16. Linstadt DE, Castro JR, Phillips TL. Neon ion radiotherapy: results of the phase I/II clinical trial. *Int J Radiat Oncol Biol Phys*. (1991) **20**:761–9. doi: 10.1016/0360-3016(91)90020-5
17. Castro JR, Linstadt DE, Bahary JP, Petti PL, Daftari I, Collier JM, et al. Experience in charged particle irradiation of tumors of the skull base: 1977-1992. *Int J Radiat Oncol Biol Phys*. (1994) **29**:647–55. doi: 10.1016/0360-3016(94)90550-9
18. Prezado Y, Bergs J. Ne-MBRT - a worldwide first implementation of spatial fractionation for very heavy ions. In: *PTCOG58*. (2019).
19. Bert C, Engenhart-Cabillic R, Durante M. Particle therapy for noncancer diseases. *Med Phys*. (2012) **39**:1716–27. doi: 10.1118/1.3691903
20. Larsson B, Leksell L, Rexed B, Sourander P, Mair W, Andersson B. The high-energy proton beam as a neurosurgical tool. *Nature*. (1958) **182**:1222–3. doi: 10.1038/1821222a0
21. Favaudon V, Caplier L, Monceau V, Pouzoulet F, Sayarath M, Fouillade C, et al. Ultrahigh dose-rate FLASH irradiation increases the differential response between normal and tumor tissue in mice. *Sci Transl Med*. (2014) **6**:245ra93. doi: 10.1126/scitranslmed.3008973
22. Tobias CA. Pretherapeutic investigations with accelerated heavy ions. *Radiology*. (1973) **108**:145–58.
23. Abrosimov NK, Gavrikov YA, Ivanov ea E M. 1000 MeV proton therapy facility at Petersburg Nuclear Physics Institute Synchrocyclotron. *J Phys*. (2006) **41**:424–32. doi: 10.1088/1742-6596/41/1/047
24. Grevillot L, Frisson T, Zahra N, Bertrand D, Stichelbaut F, Freud N, et al. Optimization of GEANT4 settings for proton pencil beam scanning simulations using GATE. *NIM B*. (2010) **268**:3295–305. doi: 10.1016/j.nimb.2010.07.011
25. Seravalli E, Robert C, Bauer J, Stichelbaut F, Kurz C, Smeets J, et al. Monte Carlo calculations of positron emitter yields in proton radiotherapy. *Phys Med Biol*. (2012) **57**:1659–73. doi: 10.1088/0031-9155/57/6/1659
26. Schneider U, Pedroni E, Lomax A. The calibration of CT Hounsfield units for radiotherapy treatment planning. *Phys Biol Med*. (1996) **41**:111–24. doi: 10.1088/0031-9155/41/1/009
27. Chetty IJ, Rosu M, Kessler ML, Fraass BA, Ten Haken RK, Kong FM, et al. Reporting and analyzing statistical uncertainties in Monte Carlo-based treatment planning. *Int J Radiat Oncol Biol Phys*. (2006) **65**:1249–59. doi: 10.1016/j.ijrobp.2006.03.039
28. Yu Q. Energy deposition calculated by PHITS code in Pb spallation target. *NIM B*. (2016) **367**:8–13. doi: 10.1016/j.nimb.2015.11.014
29. Harling OK, Roberts KA, Moulin DJ, Rogus DR. Head phantoms for neutron boron capture therapy. *Med Phys*. (1995) **22**:579–83. doi: 10.1118/1.597545
30. Rovituso M, La Tessa C. Nuclear interactions of new ions in cancer therapy: impact on dosimetry. *Transl Cancer Res*. (2017) **6**:S914–33. doi: 10.21037/tcr.2017.06.46
31. Schneider T, De Marzi L, Patriarca A, Prezado Y. Advancing proton minibeam radiation therapy: magnetically focussed proton minibeams at a clinical centre. *Sci Rep*. (2020) **10**:1384. doi: 10.1038/s41598-020-58052-0
32. Mazal A, Prezado Y, Ares C, de Marzi L, Patriarca A, Miralbell R, et al. FLASH and minibeams in radiation therapy: the effect of microstructures on time and space and their potential application to protontherapy. *Br J Radiol*. (2020) **93**:20190807. doi: 10.1259/bjr.20190807

Conflict of Interest: The authors declare that the research was conducted in the absence of any commercial or financial relationships that could be construed as a potential conflict of interest.

frontiers in Physics

REVIEW
published: 16 October 2020
doi: 10.3389/fphy.2020.00380

Biomedical Research Programs at Present and Future High-Energy Particle Accelerators

Vincenzo Patera[1], Yolanda Prezado[2], Faical Azaiez[3], Giuseppe Battistoni[4], Diego Bettoni[5], Sytze Brandenburg[6†], Aleksandr Bugay[7], Giacomo Cuttone[8], Denis Dauvergne[9], Gilles de France[10], Christian Graeff[11], Thomas Haberer[12], Taku Inaniwa[13], Sebastien Incerti[14], Elena Nasonova[7], Alahari Navin[10], Marco Pullia[15], Sandro Rossi[15], Charlot Vandevoorde[3] and Marco Durante[11,16]*

[1] Dipartimento di Scienze di Base e Applicate per l'Ingegneria, University "La Sapienza", Rome, Italy, [2] Institut Curie, University Paris Saclay, Orsay, France, [3] iThemba LABS, NRF, Cape Town, South Africa, [4] TIFPA, INFN, Trento, Italy, [5] LNL, INFN, Legnaro, Italy, [6] KVI-CART, University of Groningen, Groningen, Netherlands, [7] JINR, Dubna, Russia, [8] LNS, INFN, Catania, Italy, [9] Université Grenoble-Alpes, CNRS/IN2P3, UMR5821, LPSC, GDR MI2B, LabEx PRIMES, Grenoble, France, [10] GANIL, Caen, France, [11] Biophysics Department, GSI Helmholtzzentrum für Schwerionenforschung, Darmstadt, Germany, [12] HIT, University of Heidelberg, Heidelberg, Germany, [13] NIRS, QST, Chiba, Japan, [14] Université de Bordeaux, CNRS/IN2P3, UMR5797, Centre d'Études Nucléaires de Bordeaux Gradignan, Gradignan, France, [15] CNAO, Pavia, Italy, [16] Institut für Festkörperphysik, Technische Universität Darmstadt, Darmstadt, Germany

Biomedical applications at high-energy particle accelerators have always been an important section of the applied nuclear physics research. Several new facilities are now under constructions or undergoing major upgrades. While the main goal of these facilities is often basic research in nuclear physics, they acknowledge the importance of including biomedical research programs and of interacting with other medical accelerator facilities providing patient treatments. To harmonize the programs, avoid duplications, and foster collaboration and synergism, the International Biophysics Collaboration is providing a platform to several accelerator centers with interest in biomedical research. In this paper, we summarize the programs of various facilities in the running, upgrade, or construction phase.

Keywords: accelerators, particle therapy, space radiation protection, high-energy ions, biomedical research

OPEN ACCESS

Edited by:
Zhen Cheng,
Stanford University, United States

Reviewed by:
Lucio Rossi,
European Organization for Nuclear Research (CERN), Switzerland
Silvia Capuani,
National Research Council (CNR), Italy

****Correspondence:***
Marco Durante
m.durante@gsi.de

†Present address:
Sytze Brandenburg
Department of Radiation Oncology, University Medical Center Groningen, University of Groningen, Groningen, Netherlands

Specialty section:
This article was submitted to Medical Physics and Imaging, a section of the journal Frontiers in Physics

Received: *25 May 2020*
Accepted: *05 August 2020*
Published: *16 October 2020*

Citation:
Patera V, Prezado Y, Azaiez F, Battistoni G, Bettoni D, Brandenburg S, Bugay A, Cuttone G, Dauvergne D, de France G, Graeff C, Haberer T, Inaniwa T, Incerti S, Nasonova E, Navin A, Pullia M, Rossi S, Vandevoorde C and Durante M (2020) Biomedical Research Programs at Present and Future High-Energy Particle Accelerators. Front. Phys. 8:380. doi: 10.3389/fphy.2020.00380

INTRODUCTION

Particle accelerators have provided an extensive contribution to research beyond particle and nuclear physics. Astrophysics, atomic physics, plasma physics, materials research, environmental science, archaeometry, homeland security, space radiation research, biology, and medicine largely use and benefit from particle accelerators [1]. Biomedical applications are particularly important, for their impact on societal health [2]. One of the main medical applications of accelerators is certainly the production of radioisotopes to be used for imaging, therapy, or both (theranostics) [3–5]. Accelerators also spawned charged-particle therapy, a technique for cancer treatments that exploits the Bragg peak of charged particles and can reduce toxicity and improve local control compared to conventional X-ray radiotherapy [6]. Fast neutrons have been used in the past for cancer therapy but then dismissed because of inacceptable toxicities [7]. Epithermal and thermal neutrons can, however, effectively kill tumors loaded with ^{10}B, the so-called boron-neutron capture therapy (BNCT) [8, 9]. BNCT has been hampered by the necessity of using nuclear reactors

for treatment but is now revived by the perspective of using dedicated proton accelerators [10]. Cyclotrons and synchrotrons for charged-particle therapy are blooming worldwide [11–13], and many of these centers have intense preclinical research programs [14]. Research in space radiation protection also needs accelerators to simulate the cosmic radiation that astronauts find in the space environment [15–19]. In fact, most of our knowledge on radiation risk in space comes from experiments at particle accelerators [20, 21].

Many new large-scale accelerators are under construction worldwide, with the primary goal of basic research in nuclear physics, generally exploring the region far from stability [22]. Most of the accelerators centers have ambitious biomedical research programs that are innovative and potentially can lead to breakthrough discoveries thanks to the characteristics of the new facilities, generally with higher intensity and energy than current accelerators have [23]. **Figure 1** shows some of the opportunities that can exploit the characteristics of new accelerators or the upgrade of existing facilities. High energy is obviously important for space radiation research, because cosmic rays have energies up to TeV [24, 25] but can also be useful for particle radiography [26], an important technique to reduce range uncertainty in particle therapy. High intensity can potentially be a major breakthrough in particle therapy: ultrafast treatments are convenient for patient welfare and for clinical workflow and can mitigate the problem of moving targets [27]. Recent results with electron beams suggest that dose rates exceeding 40 Gy/s reduce toxicity in the normal tissue while maintaining tumor local control (FLASH radiotherapy) [28, 29]. High intensity is also useful for spatially fractionated radiotherapy using protons [30] or heavier ions [31], a method that largely reduces normal tissue toxicity in animal models [32–34]. Finally, radioactive ion beams (RIB), one of the main nuclear physics topics that justify the construction of new nuclear physics facilities [35], are potentially an extraordinary tool for therapy as they allow the online visualization of beams during irradiation [36].

While all these research programs are exciting, it is important to avoid duplications, exploit synergism, and foster collaborations and strong links between clinical accelerators and nuclear physics accelerators planning applied biomedical research. For these reasons, many facilities have joined the International Biophysics Collaboration [37] that had a first meeting in Darmstadt in May 2019 [38]. Here, we present the biomedical research programs of several accelerator facilities that have joined the Biophysics Collaboration.

BIOMEDICAL RESEARCH PROGRAMS AT PARTICLE ACCELERATORS

Fair

The Facility for Antiprotons and Ion Research (FAIR) is currently under construction in Darmstadt [39]. As shown in **Figure 2**, the current SIS18 synchrotron (18 Tm) at GSI will become the injector of the new SIS100 (100 Tm) ring. All ions from H to U can be accelerated up to around 10 GeV/n. FAIR will also reach intensities up to $\times$10,000 higher than those currently available at GSI, and this intensity upgrade is already ongoing at SIS18 in the framework of the so-called FAIR-phase-0 [40]. While the official opening of the SIS100 is slated for 2017, research is currently ongoing within the FAIR-phase-0. Research activity at FAIR is structured into four pillars: NuSTAR, CBM, PANDA, and APPA. APPA deals with applied research (biophysics and materials research) and atomic and plasma physics [41]. FAIR is a user facility, and research is proposed by collaborations. The Biophysics Collaboration is indeed based at FAIR[1] but, unlike other collaborations, includes other accelerator facilities, and aims at a distributed research program.

The biophysics research program at FAIR imposes on the exceptional experience of the Biophysics Department in both heavy-ion therapy and space radiation research [Kraft et al. submitted]. In fact, GSI was the first center in Europe to treat patients with accelerated ^{12}C ions [42] and is currently the reference center of ESA for the ground-based research program [16] called IBER[2]. With the end of the therapy in 2007, GSI activity focused on heavy-ion basic research, with applications to therapy and space radiation protection. Research at FAIR will therefore continue in these directions, according to the new opportunities that the SIS100 energies and the upgraded intensities offer (**Figure 1**). The new research programs include the construction of a galactic cosmic ray simulator [43], high-energy particle radiography [44], FLASH irradiations with heavy ions [45], and testing of carbon and oxygen radioactive isotopes for therapy and simultaneous imaging by PET [36], a program that has been supported by a recent ERC Advanced Grant (BARB)[3]. The Biophysics Department will benefit from FAIR with a new experimental vault, the APPA cave (**Figure 3**), where especially high-energy space radiation protection experiments will be performed.

NICA

The Nuclotron-based Ion Collider fAcility (NICA) is a new accelerator facility designed at the Joint Institute for Nuclear Research (JINR, Dubna, Russia) to study properties of dense baryonic matter [46, 47]. The NICA facility (**Figure 4**) includes the injection complex, a new superconducting booster synchrotron, the existing modernized superconducting heavy-ion synchrotron "Nuclotron," a new collider with two superconducting storage rings and with two interaction points [one for heavy-ion studies with the multipurpose detector (MPD) and another for polarized beams for the spin physics detector (SPD) experiment], an electron cooling system, new beam transfer channels, and the experimental zone for extracted beams with a Baryonic Matter at Nuclotron (BM@N) detector. The main goal of the project is the study of hot and dense strongly interacting matter in heavy-ion (up to Au) collisions. A study of spin physics with extracted and colliding beams of polarized deuterons and protons is also planned. Gold ions will be accelerated up to a kinetic energy of 4.5 GeV/u; the polarized

[1] www.gsi.de/bio-coll
[2] www.gsi.de/IBER
[3] www.gsi.de/BARB

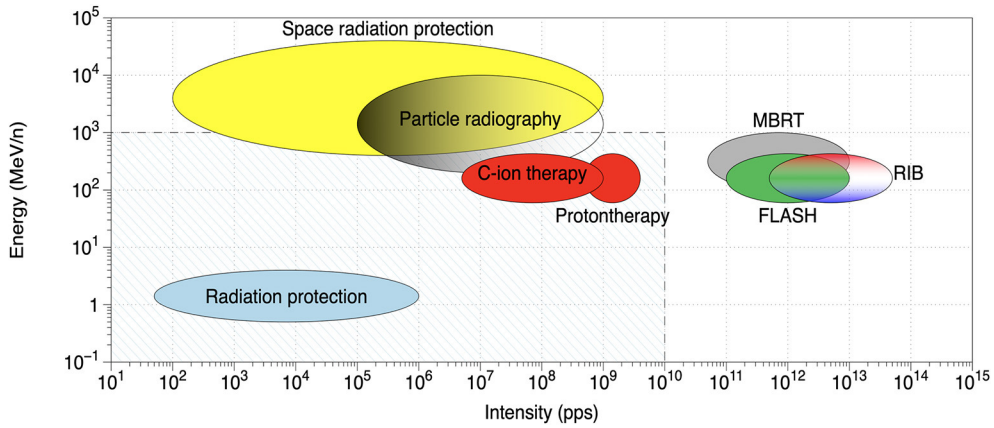

FIGURE 1 | Radiation research at accelerators. The shaded region includes values of energy and intensities covered by the present accelerators. MBRT, minibeam radiotherapy; RIB, radioactive ion beams; FLASH, high-dose-rate radiotherapy.

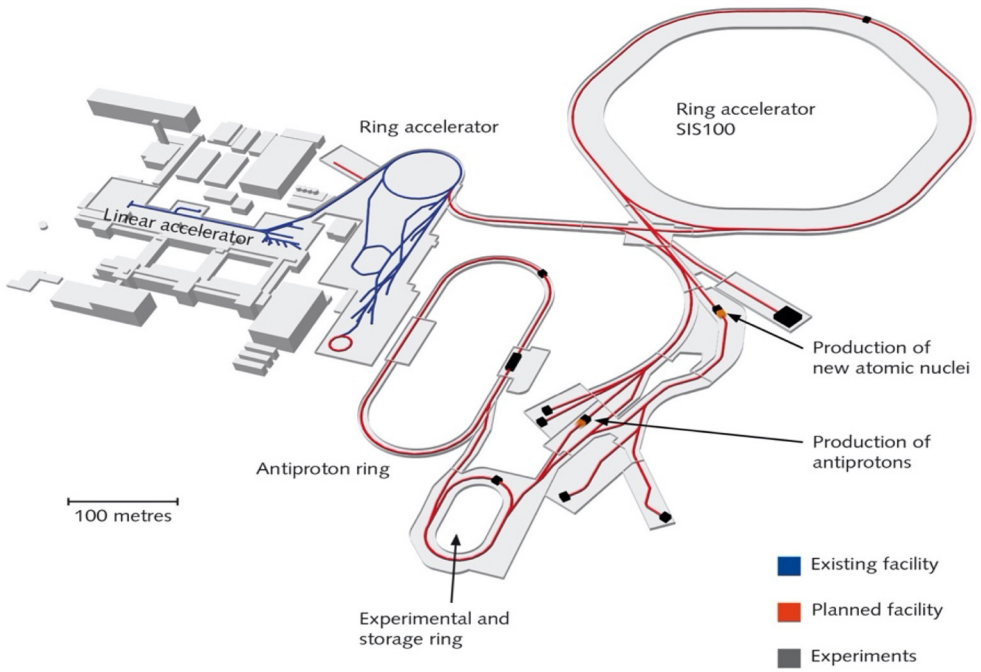

FIGURE 2 | Layout of the FAIR facility under construction in Darmstadt (Germany).

protons, up to 12.6 GeV. Two modes of operation are foreseen: collider mode and extracted beams. The proposed program allows one to search for possible signs of phase transitions and critical phenomena as well as to shed light on the problem of the nucleon spin structure. For applied physics research, three new experimental areas are planned. Topics of interest are radiobiology and particle therapy, cosmic ray simulation, radiation hardness of electronic devices, novel technologies in materials science, and nuclear energetics. Ion beams with an energy of 250–800 MeV/u extracted from Nuclotron will be used for these experiments. The commissioning of beamlines and experimental stations for applied research as a part of basic NICA configuration is expected in 2022.

The biomedical research program carried out by the Laboratory of Radiation Biology (LRB) at the NICA complex will be focused on studying heavy-ion action at the molecular, cellular, tissue, and organism levels of biological organization. Primary attention will be paid to research on experimental animals' central nervous system (CNS) disorders because the CNS must be considered a critical system when evaluating the

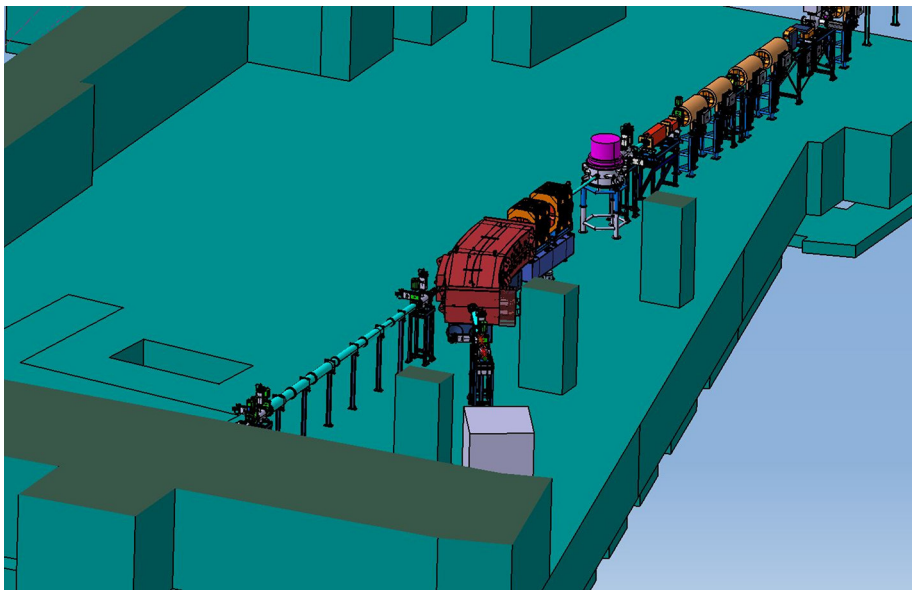

FIGURE 3 | Beamline for BIOMAT applications in the APPA cave at FAIR.

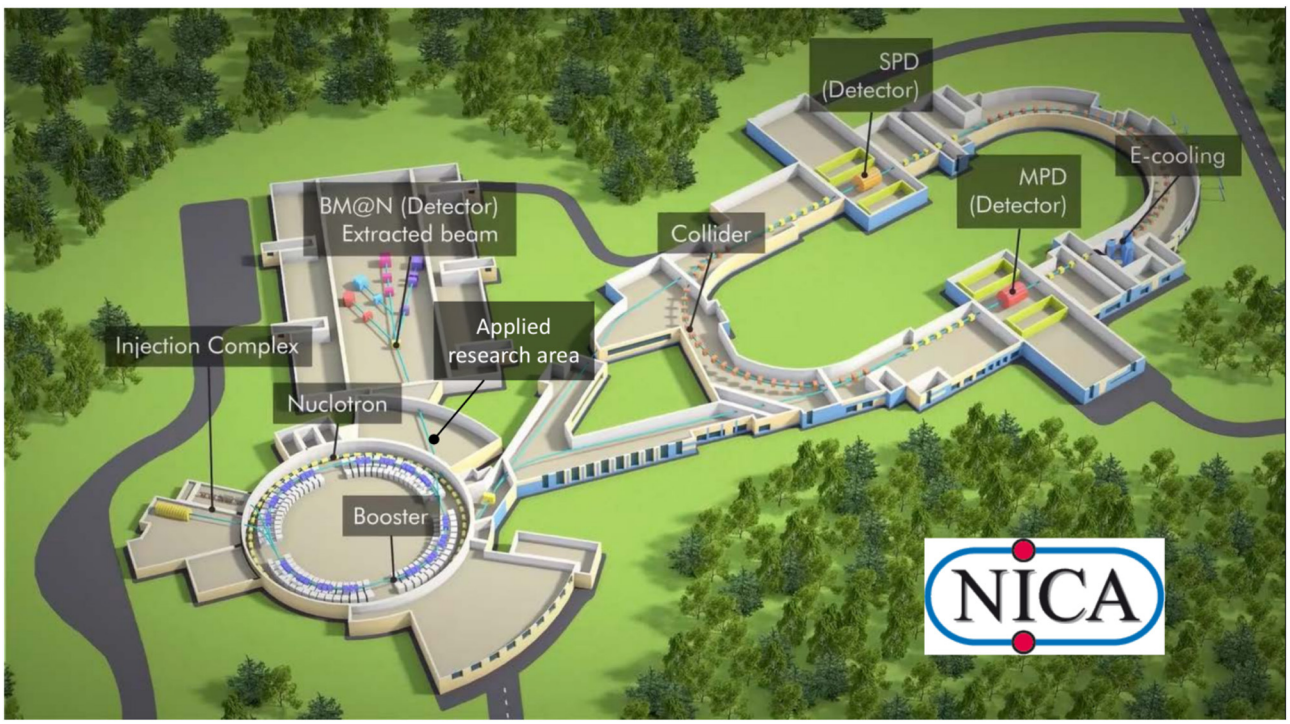

FIGURE 4 | Layout of the NICA facility under construction in Dubna (Russia).

radiation exposure risk for the interplanetary mission crews and considering the possible side effects of the radiotherapy of brain tumors. The main advantage of LRB and NICA is an excellent opportunity to perform large-scale *in vivo* animal exposures in collaboration with leading Russian experts in this field, who have all the necessary licenses. The research on rodents includes behavioral studies, pathomorphological studies of irradiated brain structures with the aim of modern immunohistochemical methods and morphometry, cytogenetics, and neurochemical and electrophysiological studies. Worldwide unique experiments

on primates for the estimation of radiation risks of CNS disorders and carcinogenesis are in progress at the LRB. The LRB also develops a hierarchy of mathematical models to simulate radiation-induced pathologies at different organization levels and time scales. In addition to the traditional Monte Carlo technique, the LRB's approach involves computational methods from different knowledge areas (molecular dynamics and simulation of brain neural networks). The radiation research program at NICA can contribute to a better reproduction of the space environment. The LRB has proposed a novel Nuclotron-based technique of modeling radiation fields with continuous particle energy spectra generated by galactic cosmic rays inside spacecraft in deep space.

A huge amount of experimental work has to be done at accelerators worldwide to understand how heavy charged particles may disturb the CNS performance after cancer therapy or during space flights. Certainly, there is a strong need for broad international collaboration in this field.

iThemba Labs

With more than 30 years of operation of the separated sector cyclotron, the iThemba Laboratory for Accelerator Based Sciences (LABS) is the largest facility for accelerator-based sciences in the southern hemisphere. It is one of the research infrastructure platforms of the National Research Foundation (NRF) in South Africa, with the main goals of supporting research of strategic importance, training the future research workforce, and providing access to unique infrastructure for national and international users.

The facility has a long history and expertise in radiation biophysics research, which went hand in hand with the start of the particle therapy program in 1988 with a 66 MeV p + Be isocentric neutron therapy system and a fixed 200 MeV proton therapy facility [48]. In the first decades, the research program was dominated by clinical research and the development and optimization of particle therapy treatment modalities. Today, the new Radiation Biophysics Division is driving a multidisciplinary research program that converges the existing expertise in the field of radiation biology and medical physics, to investigate the relationship between radiation quality and biological effects. Researchers can make use of the well-characterized 200 MeV proton beamline, as well as the neutron beamlines available at iThemba LABS. The latter includes a rather unique quasi mono-energetic neutron metrology beamline, with beam energies ranging from 30 to 200 MeV, using (p, n) reactions on thin Li and Be targets [49]. Currently, very little information is available on the biological effects of high-energy neutrons (>20 MeV) that are most pertinent to applications in civil aviation, future manned space missions, and particle therapy. Therefore, the well-characterized neutron fields at iThemba LABS will be of growing importance in the coming years, to fill this gap in an attempt to decrease the existing uncertainties on neutron weighting factors and the relative biological effectiveness at higher neutron energies.

Next to research projects with external particle beams, there is a growing interest in radioisotope research. This is attributable to the launch of the South African Isotope Facility (SAIF) at iThemba LABS in 2019, which includes the acquisition of IBA's Cyclone® 70 cyclotron (**Figure 5**) [50, 51]. The advent of the new 70 MeV cyclotron at iThemba LABS will not only increase South Africa's radioisotope production capacity but will also boost research into new solutions for nuclear medicine applications. This will be achieved through the optimization of isotope production processes, research in radiochemistry, radiolabeling, and preclinical radiobiological studies on newly developed radiopharmaceuticals. In the coming years, a strong focus will go to the development of new theranostic radiopharmaceuticals and the production of astatine-211, a promising isotope for targeted α-particle therapy [52].

On the one hand, the research program of the Radiation Biophysics Division at iThemba LABS can be summarized in cancer detection and therapy projects, with a main focus on radioisotopes and particle therapy. This comprises studies on systemic effects and the tumor microenvironment, such hypoxia and tumor angiogenesis. On the other hand, there is a set of research projects linked to radiation protection, which includes biological dosimetry projects and the implementation and validation of the first ground-based setup for space radiobiology research in Africa. For all projects, microdosimetry and Monte Carlo simulations remain vital tools, in order to assess the microscopic patterns of energy deposition by radiation, which ultimately govern the observed biological effects [53]. Lastly, the location of iThemba LABS provides the advantage to conduct projects that are unique to Africa, including studies on potential inter-ethnic differences in radiation sensitivity and the cancer resistance of large long-living mammals, such as African elephants [54].

The SAIF project at iThemba LABS, as outlined in **Figure 5**, is designed in two phases. Phase 1 consists of a radioisotope facility with four production targets and the initial phase (phase 0) of the Low Energy Radioactive Ion Beam (LERIB) facility. Here, the high-intensity proton beam from the SSC (up to 250 μA) will be used as a driver for the Isotope Separation On-Line (ISOL) production of radioactive isotopes of special interest in, for example, the study of neutron-rich nuclei involved in the r-process. Phase 2 will comprise the building of a new driver for the production of RIB, based on a high-intensity electron beam and the photo-fission method for the production of neutron-rich exotic isotopes which will be used as higher-intensity low-energy RIB but also accelerated high-intensity RIB using the SSC as a post-accelerator.

HIMAC

In the National Institute of Radiological Sciences (NIRS), carbon ion radiotherapy has been conducted since 1994 using the Heavy-Ion Medical Accelerator in Chiba (HIMAC). During the past 25 years, this radiotherapy has been applied to various tumors, and the optimum dose-fractionation protocols have been developed for these tumors through dose-escalation clinical trials [55–58]. To date, more than 12,000 patients have been treated with the HIMAC. Besides the clinical studies, various physical studies have been conducted to develop new treatment methods and devices such as respiratory gating [59], layer stacking [60], 3D pencil beam scanning [61], and a superconducting

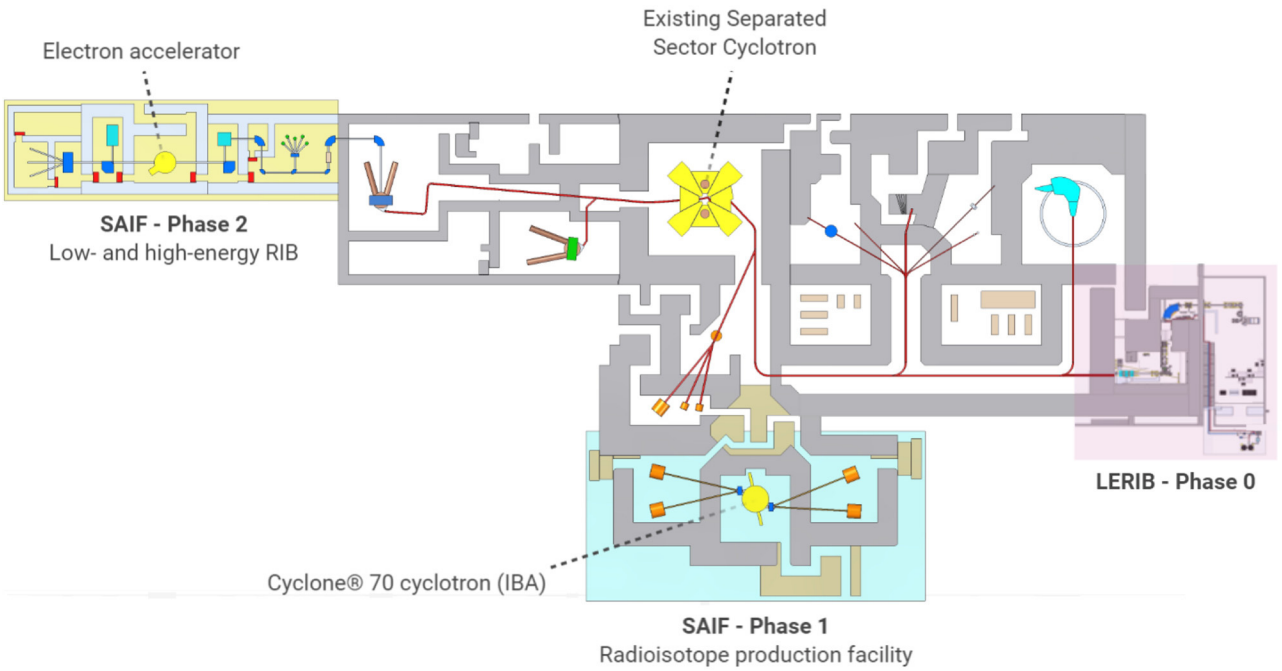

FIGURE 5 | Layout of the main facility at iThemba LABS and its future developments. SAIF phase 1 includes phase 0 of the LERIB facility (shaded in pink) and the new 70 MeV cyclotron with its target stations (shaded in blue). The second phase of the project includes the installation of a Rhodotron in the area shaded in yellow for the production of radioactive ion beams (RIB).

rotating gantry [62]. For further development of charged-particle therapy, the NIRS initiated a new research project referred to as "Quantum Scalpel." The Quantum Scalpel consists mainly of two research topics. The first topic is downsizing and cost reduction of the treatment facility. By combining high-power laser and superconducting magnet technologies, the facility size will be reduced to ∼1/6 that of the HIMAC, i.e., 20 × 10 m^2. The second topic is maximizing the clinical effects and minimizing the treatment period. For this, researchers in the Department of Accelerator and Medical Physics are developing a hypo-fractionated multi-ion radiotherapy (HFMIT) in which several ion species are delivered in one treatment session to optimize the dose and linear energy transfer (LET) distributions simultaneously [63]. Clinical trials of the HFMIT will start in 2022 following a series of commissioning tests. In other projects, emerging technologies such as immunotherapy, magneto-particle therapy [64], and FLASH radiotherapy [29] have been found to show enhanced novel effects with charged-particle beams. Investigations at the NIRS continue on all of these technologies.

GANIL and MI2B

The largest facility for nuclear physics in France located in Caen is jointly run by CEA and CNRS. GANIL as well as its major upgrade SPIRAL2 (**Figure 6**) is engaged in research with ion beams with the main focus of the laboratory being fundamental nuclear physics. This is supplemented by strong programs in accelerator-based atomic physics, condensed matter, radiobiology, and industrial applications. The intensity and variety of beams delivered by the cyclotrons and the superconducting linear accelerator and the associated state-of-the-art scientific instruments make GANIL-SPIRAL2 a unique and outstanding multidisciplinary facility [65]. GANIL-SPIRAL2 is the only facility in the world today which provides high-intensity stable beams, beams of short-lived nuclei (RIB) produced both by the ISOL technique and by the in-flight separation technique and intermediate energy neutron beams [66]. The large heavy-ion accelerator complex of five cyclotrons delivers stable beams (carbon to uranium) from energies around 1–95 MeV per unit mass with current up to 10 μA. Fragmentation beams range from light to medium mass nuclei. The reaccelerated beams produced using SPIRAL1 beams range from 1.2 to 25 MeV/A for around 35 isotopes today. A new ion source has been commissioned, so more new RIB for different elements are available, and more will be available[4] in the near future. The new superconducting LINAC will provide the most intense beams from protons to Ni up to 14.5 MeV per unit mass. Continuous and quasi-mono-energetic beams of neutrons will be available. The flux at NFS will be up to 2 orders of magnitude higher than those of other existing time-of-flight facilities for a part spectrum in the 1–40 MeV range. The latter will open new and unique avenues.

Materials science research at GANIL is studied using a large range of energies and beams along with versatile

[4]https://www.ganil-spiral2.eu/scientists/ganil-spiral-2-facilities/available-beams/

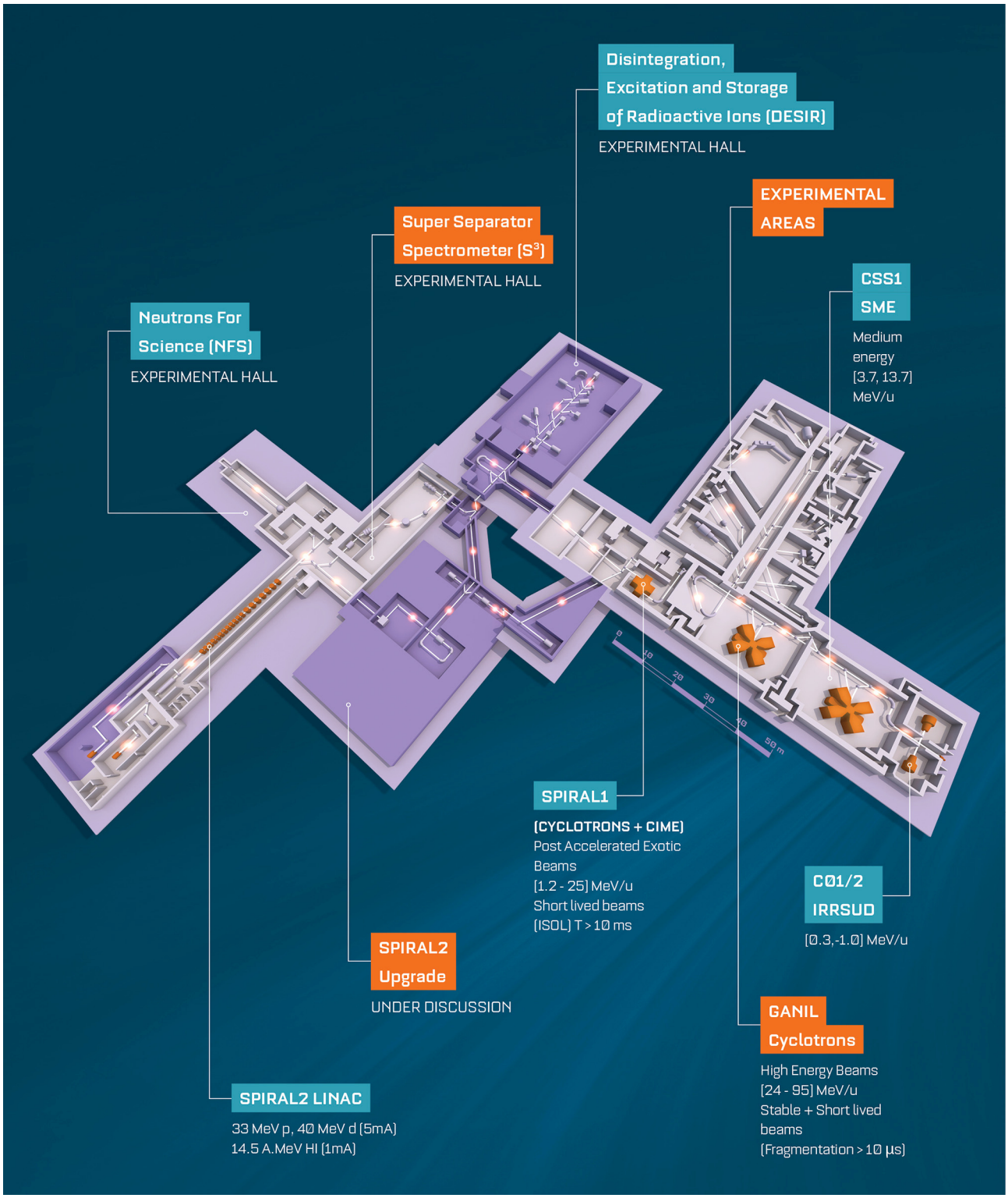

FIGURE 6 | Layout of the GANIL-SPIRAL2 facility in Caen (France).

tools. High-energy ions provide quality beams for studies on nanostructuration of selective membranes and sensor developments based on topical 2D materials (graphene, MoS2, etc.). Exploiting time/depth-resolved characterizations to their limit, the sensitivity of functional inorganic materials to dense electronic excitations is studied. Advanced experimental setups

also provide *in situ* analysis for organic polymers (CESIR or CASIMIR) or astro-ices (IGLIAS) as simulators for alpha radiation, cosmic rays, or solar winds.

The relevant biomedical activities span a variety of topics. Measurements of double differential cross section for charged particles with 95 MeV/A C beams on targets of various elements that are relevant to hadron therapy were performed. Irradiation and hardening of electronic components for space are performed using heavy and energetic ions. The studies include single-event effect (SEE) to improve the architectures and define testing standards used in space. Dedicated equipment for irradiation of polymeric films allow industrial production with various ion track densities and ultimately very fine and uniform filters. The LARIA center at GANIL studies various aspects related to the study and understanding of the biological effects related to direct and indirect (bystander) impacts by carbon beams in cancer treatment. The topics range from understanding differential cellular responses of radioresistant tumors to conventional radiotherapy and hadrontherapy to exploring the fundamental mechanisms of communication between irradiated and normal cells, etc. The facilities for these activities include cell culture room, two sterile hoods, four CO_2 incubators, a microscope, water baths, centrifuges, etc. All the above activities are run at the cyclotrons. Light-ion beams from the LINAC, like alpha and ^{6,7}Li beam on Pb and Bi targets, will be used to perform R&D on the production of innovative radioelements for nuclear medicine and in particular alpha emitters. This will consist in cross-section measurements to determine the optimum energies maximizing the cross section for the nuclei of interest (e.g., the promising ^{211}At) [67] while minimizing those for nearby contaminants (^{210}At and ^{209,210}Po in the case of ^{211}At); to develop high-power target stations to sustain the very high beam current from the new LINAC; and to find new and promising production routes. The NFS facility can be used for irradiation of cells, for characterization of detectors, and also for the study of the single-event defects.

In France, several irradiation facilities for biomedical applications are being coordinated by CNRS within the so-called "*Groupement de Recherche* MI2B."[5] MI2B animates a national network of clinical-based and academic research-based irradiation facilities called ResPlanDir, dedicated to dosimetry, instrumentation, and radiobiology, by supporting harmonization of practices. Among the various irradiation modalities, one should mention the availability of a complete panel of proton and light-ion irradiation platforms: AIFIRA at CENBG-Bordeaux[6] proposes up to 3.5 MeV proton or alpha particle microbeams (size of typically 1.5 μm FWHM in air) equipped with an online microscope. This makes possible the selective irradiation of single-layered cells. CYRCé at IPHC-Strasbourg[7] is a combined platform for radioisotope production working for academic research, with a newly functional proton irradiation platform with energy ranging from keV to 24 MeV[8] for cell or small-animal irradiation (possibility to tune a spread-out Bragg peak up to 6 mm), a biological laboratory with small animals, and preclinical imaging (PET and SPECT). The ARRONAX facility[9] is a combined research and innovative radioisotope production facility, delivering protons (35 and 70 MeV), deuterons (15 and 35 MeV), and alpha particles (70 MeV). A dedicated experimental irradiation room (**Figure 7**) has been equipped for physics and materials science experiments and cell irradiation by means of a vertical beamline.

INFN and CNAO

The National Institute for Nuclear Physics (INFN) in Italy has several accelerator facilities with biomedical applications, including Laboratori Nazionali del Sud (LNS) in Catania [68], the first center in Italy to treat patients with proton therapy for eye tumors, and the Trento Institute for Fundamental Physics and Applications (TIFPA), where an experimental vault [69] with two beamlines delivering protons with energies up to 230 MeV is available in the local proton therapy center, where two other rooms are equipped with isocentric gantries for treating patients.

The INFN National Laboratories of Legnaro (LNL) are devoted to the study of fundamental nuclear physics and astrophysics together with the development of technologies relevant to these disciplines. Ever since its foundation, LNL has carried out a significant applied physics research, developing very relevant programs in the biomedical field with the existing LNL accelerators as well as the future SPES facility. Applications of ion beams in multidisciplinary physics are a long-standing tradition of LNL. These activities are carried out mainly at the AN2000[10] and CN[11] Van de Graaff accelerators and partly at the Tandem[12]. The CN (1–6 MV) and AN2000 (0.2–2.2 MV) provide a total of 12 beamlines and deliver around 2,700 h/year of beamtime (^{1}H, ^{2}H, ^{3}He, ^{4}He, ^{14}N, and ^{15}N). The main activities at the AN and the CN in the field of interdisciplinary physics are radiobiology [70, 71], dosimetry, materials microanalysis with IBA methods, study of novel neutron detectors based on innovative materials, single-ion irradiation for quantum technologies, and HpGe, Si, and diamond detector characterization.

LNL has a very long and strong tradition in the field of microdosimetry and nanodosimetry [72, Colautti et al. submitted]. In particular, Legnaro is one of the leading laboratories for the construction of miniaturized tissue equivalent proportional counters. Legnaro is in contact with various radiotherapy centers for the supply of these detectors or the microdosimetric characterization of therapeutic beams (Detector/MedAustron, SCK, JINR). These detectors can be used for quality assurance of treatment planning systems which include linear energy transfer calculations. In the field of nanodosimetry, STARTRACK is one of three detectors in the world for measuring the stochastics of radiation interaction at

[5]https://www.mi2b.fr/
[6]http://www.cenbg.in2p3.fr/-AIFIRA-Home-?lang=en
[7]http://www.iphc.cnrs.fr/-Cyclotron-CYRCE-.html
[8]http://www.iphc.cnrs.fr/-PRECy-.html
[9]https://www.arronax-nantes.fr/
[10]http://www.lnl.infn.it/index.php/en/accelerators-3/an-2000
[11]http://www.lnl.infn.it/index.php/en/accelerators-3/cn
[12]http://www.lnl.infn.it/index.php/en/accelerators-3/tandem-xtu

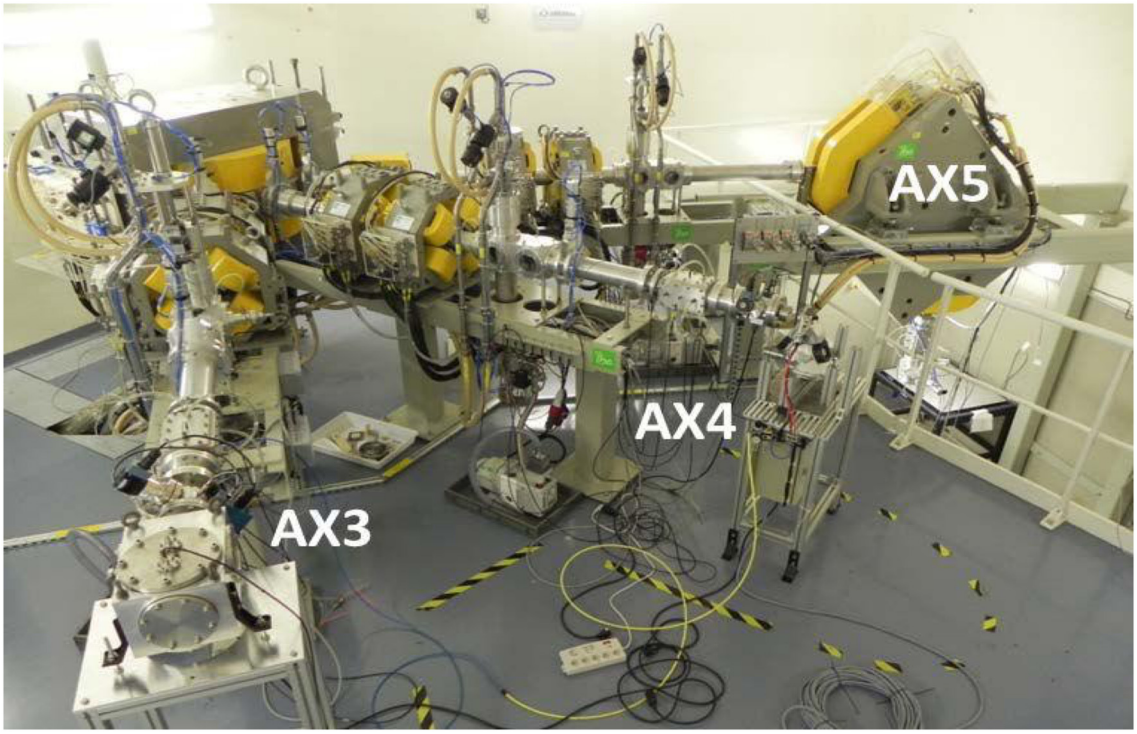

FIGURE 7 | Experimental cave at ARRONAX (Nantes, France). AX5 is a vertical irradiation beamline.

the DNA level [73]. It is installed and running at Tandem. A portable version is under construction.

Selective Production of Exotic Species (SPES)[13] is a second-generation ISOL facility on which the short- and long-term strategies of the laboratory are centered [74]. It is an interdisciplinary project, ranging over nuclear physics, nuclear medicine, and materials science. SPES will provide a RIB facility for the study of neutron-rich unstable nuclei of interest to nuclear and astronuclear physics research [75]. At the same time, it will host a laboratory for research and production of radioisotopes to be applied in nuclear medicine. SPES is based on a dual-exit high-current cyclotron, with proton beam energy ranging between 35 and 70 MeV and a maximum beam intensity of 0.75 mA, used as a proton driver to supply an ISOL system with a UCx Direct Target able to sustain a power of 10 kW and produce neutron-rich ions at intensities 1 order of magnitude higher than existing facilities. The second exit will be used for applied physics: radioisotope production for medicine and neutrons for materials study. Quasi-mono-energetic neutrons at energies ranging 30–70 MeV will be produced using a 10 mA proton beam at an expected intensity around $5{\cdot}10^5$ $n{\cdot}cm^{-2}{\cdot}s^{-1}$ at 3 m from the Li production target. The layout of the facility is shown in **Figure 8**. The proton beam from the cyclotron can be sent to two ISOL target caves (ISOL1 and ISOL2), three caves for radioisotopes production (RIFAC) and developments (RILAB), and an area for neutron production and materials study. SPES was designed to pursue also the aim of studying the production of innovative radionuclides for medicine (LARAMED) starting from the assumption that new radioisotopes may show unprecedented biological properties. Nonstandard radionuclide production is a fundamental opportunity for nuclear medicine in order to identify new radiopharmaceutical classes for diagnostic and therapeutic applications. RILAB will be dedicated to research in the field of radioisotopes (cross-section measurements, high-power target tests, etc.), whereas RIFAC will be devoted to the production of novel radioisotopes (^{64}Cu, ^{67}Cu, ^{82}Sr, ^{68}Ge, etc.). In June 2018, the INFN board of directors has approved the contracts for the supply of beam and the lease of laboratory space to BEST Theratronics for the commercial production of radioisotopes, initially using the ISOL2 cave. Also, in the field of nuclear medicine, the ISOLPHARM project will exploit the ISOL technique to produce a large variety of carrier-free radioisotopes with high radionuclidic purity (INFN international patent). The layout of SPES was designed in such a way as to operate two targets at the same time, distributing the beam according to a schedule that minimizes the radiation problems. It should be considered that the activation of materials at a beam power of 20–30 kW does not allow operating the same target for a long time. Considering a shift of 2 weeks with 2 days for beam preparation, 12 days of beam on target, and seven shifts for maintenance, we can offer about 5,000 h/year of beam dedicated to the ISOL targets and 5,000 for applications.

INFN has also collaborated on the construction of the experimental vault for dedicated biomedical research in the

[13]https://web.infn.it/spes/index.php/home/spe

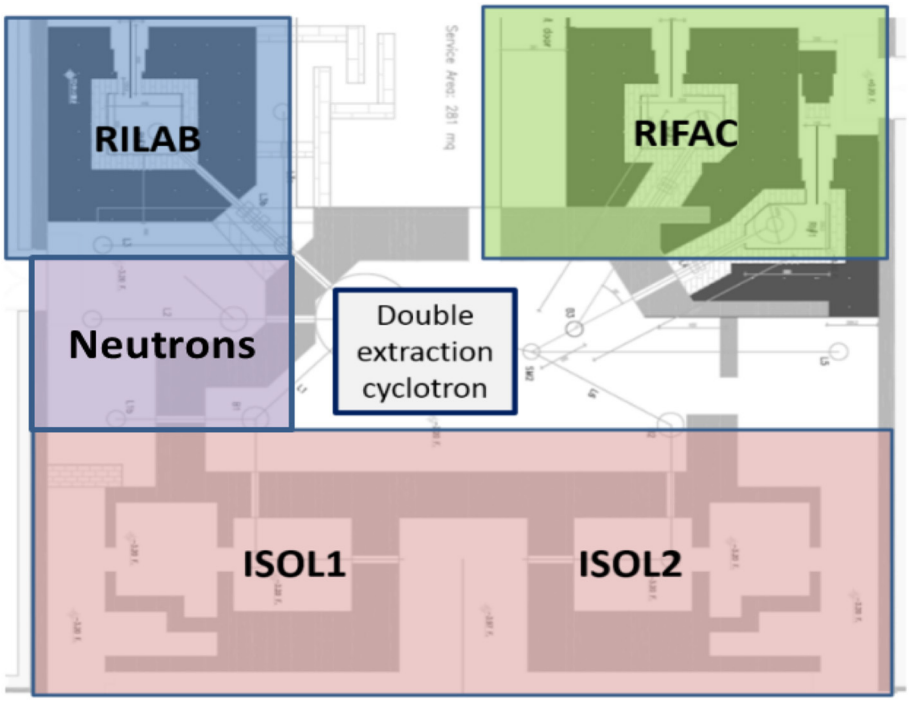

FIGURE 8 | Layout of the SPES facility under construction in Legnaro (Italy).

National Center for Oncological Hadrontherapy (CNAO) in Pavia. CNAO [76, 77] is one of the four centers in Europe in which hadrontherapy is administered with both protons and carbon ions. The main accelerator is a 25-m-diameter synchrotron designed to accelerate ions injected at 7 MeV/u up to the maximum energy corresponding to the magnetic rigidity of 6.35 Tm. For C^{6+} ions, this corresponds to 400 MeV/u; in the case of protons, the maximum available energy of 250 MeV corresponds to a magnetic rigidity of 2.43 Tm, well below the technically achievable maximum. For other ions that will be produced with a dedicated third source presently under construction, the maximum rigidity would still be 6.35 Tm, and the corresponding particle range would be determined by their charge and mass.

CNAO has a 2-fold institutional purpose including both therapy and research, and it also provides great opportunities to perform various research activities related to radiation biophysics, radiobiology, space research, and detector development. For researchers, a dedicated experimental irradiation room is available in time slots not impacting patients' treatment but specifically devoted to research purposes (i.e., some night shifts and weekends, typically) and, if applicable, in a parasitic modality during daily treatments, for the experiments in which the duration is not important and the measurement itself can be "paused" for an indefinite time. The beam distribution in the CNAO experimental room is based on the same active system in use in the treatment rooms. According to the needs of the experiment to be performed, the experimental beamline can be arranged in four different configurations depending on the space required downstream the target or the dimensions of the scanning field (**Figure 9**). The beam intensities available range from the clinical ones ($<10^{10}$ protons per spill and $< 4{\cdot}10^{8}$ carbon ions per spill) down to a few particles per second.

CNAO offers the opportunity to external researchers to use its beams to perform basic and preclinical studies and to take advantage of a cell culture laboratory for sample preparation and processing. Thanks to a strong collaboration with the University of Pavia, in CNAO, it is also possible to carry out *in vivo* irradiations with small rodents, taking advantage of the nearby animal house facility, after technical evaluation and approval by the local ethical committee. Typical activities carried on at CNAO are development and test of beam monitors and of dosimeters, the development of the dose delivery system to improve the scanning technique (e.g., 4D treatments), the verification of dose delivered to the target, and of course radiobiology. The main topics for the present radiobiological research in CNAO comprise tissue, cell, and molecular experimental activities aiming to investigate the mechanisms of response after particle irradiation. In particular, one of the interests is modulation of the malignant behavior of surviving tumor cells by reducing or promoting their invasiveness or migration. Cellular and molecular mechanisms of radioresistance after irradiation with carbon ions, immune stimulatory effects of radiation, and immunosuppressive properties of high-LET radiations and abscopal effect are also subjects being studied at CNAO. One hot topic for CNAO radiobiological research is the evaluation of existing and/or new radiosensitizing agents with high-LET radiations. Physical amplification of LET by nuclear interaction, e.g., of protons on boron nuclei is also being studied.

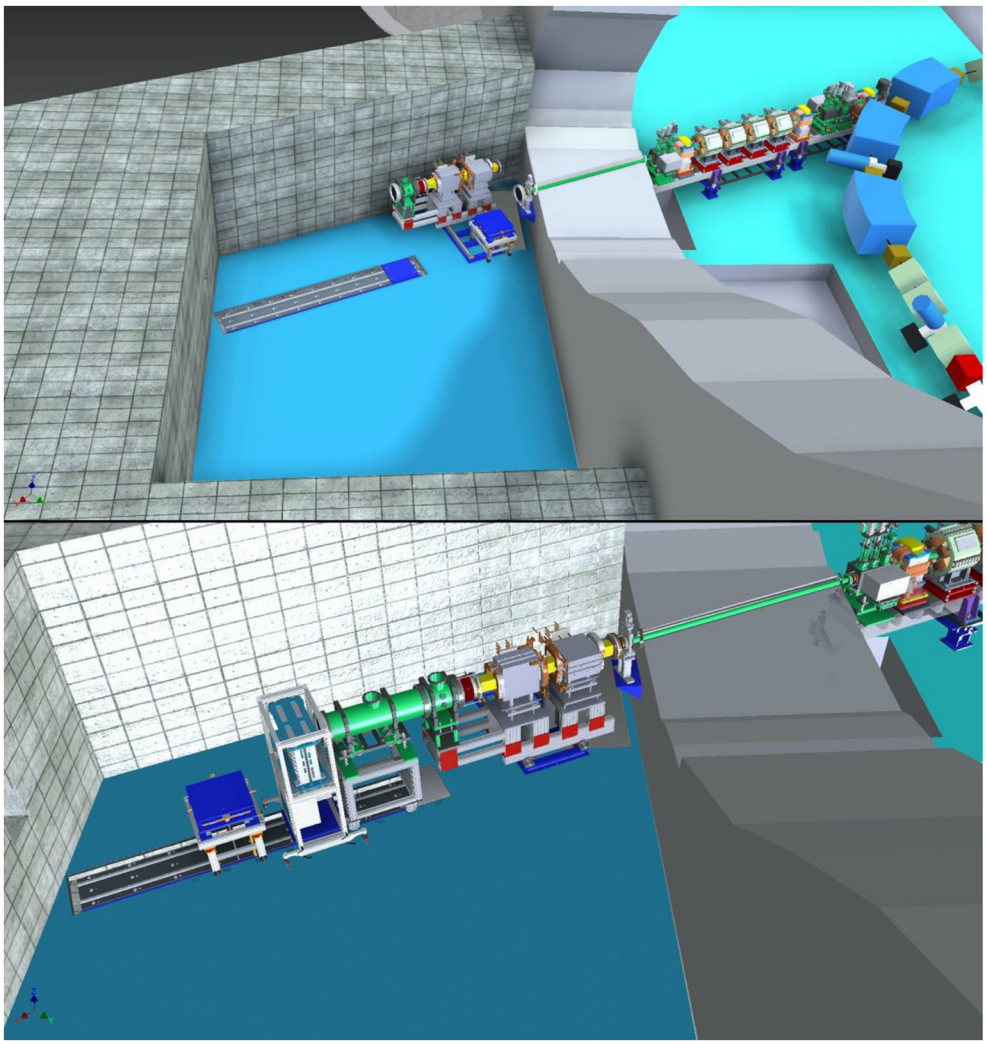

FIGURE 9 | The experimental room at CNAO can be arranged in different configurations according to the experiment requirements.

This subject might become even more interesting since CNAO is willing to build a new boron neutron capture therapy (BNCT) facility in the next future. At CNAO, the introduction of an accelerator-based BNCT system is indeed presently under consideration. This activity will be performed, strengthening collaborations with INFN, University of Pavia, and other institutions, since the introduction of BNCT requires a properly structured multidisciplinary research phase with distributed skills (medical doctors, radiobiologists, medical physicists, chemists, etc.). Furthermore, the BNCT needs the development of biomedical imaging techniques for the mapping of the biodistribution of compounds enriched in ^{10}B and for the selection of the ideal time interval of irradiation with thermal neutrons [78, 79].

HIT

The Heidelberg Ion-Beam Therapy Center (HIT) at the Hospital of the University of Heidelberg (UKHD) is the first dedicated and hospital-based particle therapy center in Europe offering clinical scanned proton and carbon ion beams [80]. The treatment with helium ions is planned to start in late 2021, and oxygen beams are offered for preclinical research. Dose delivery is based on the intensity-controlled raster scanning method. The maximum field size is 200 × 200 mm^2. The first worldwide rotating carbon ion gantry could be realized at HIT. Today, about 40% of patient treatments are executed at this unique device that combines robotic patient positioning, raster scanning dose delivery, and video-based patient tracking.

HIT has started routine patient treatment at a horizontally fixed beamline in November 2009. The carbon ion gantry is in clinical use since October 2012. In total, about 6,200 patients have been treated at HIT. It is an extension to the already available oncological methods at the Heidelberg University Hospital and indirectly complements the existing radiotherapy department hosting seven electron accelerators including tomotherapy and

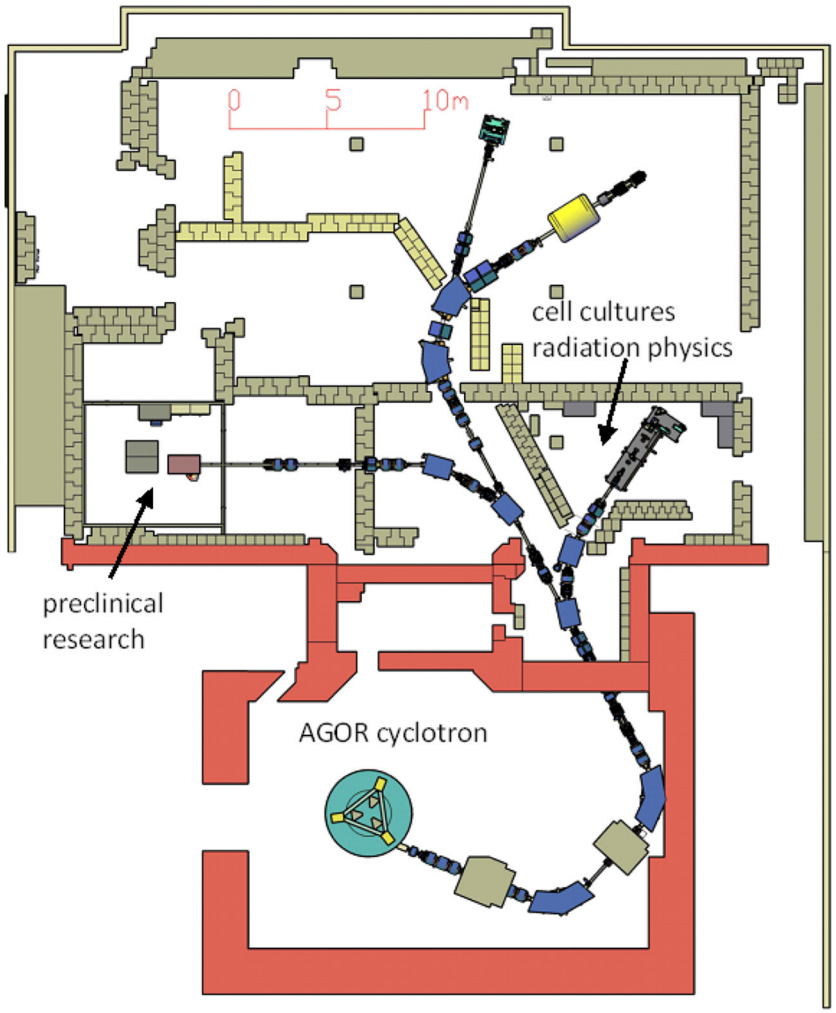

FIGURE 10 | Floor plan of the AGOR accelerator facility with the new infrastructure for image-guided preclinical research.

a gamma knife. In addition to patient care, a broad research program in the area of radiation oncology and accelerator physics, medical physics, and biophysics [81–83], annually using about 1,000 h of beamtime, is pursued at HIT. Large-scale clinical studies in the field of ion beam therapy as well as methodological studies are conducted here [84].

HIT operates an irradiation facility for preclinical research that delivers four ion species: protons and helium, carbon, and oxygen ions. HIT's accelerator system provides energies up to 430 MeV/u for helium, carbon, and oxygen ions and up to 480 MeV for protons. For all ions, energy libraries are established that allow for millimeter-range steps within the therapeutic window (Bragg peak depth between 2 and 32 cm in water). For protons and helium ions, higher ranges/energies can be offered for research purposes. Within the center, laboratories for medical physics and experiment preparation as well as a dedicated rodent housing are located directly at the research cave. Laboratories for radiobiology are hosted in the attached building for conventional radiation therapy.

KVI-CART

The core of the accelerator facility at the KVI-Center for Advanced Radiation Technology (KVI-CART), University of Groningen (UG), the Netherlands, is the superconducting cyclotron AGOR [85], built in collaboration with the Institut de Physique Nucléaire (Orsay, France) and operational in Groningen since 1996. It accelerates ion beams of all elements to a variable energy. Initially designed for research in nuclear physics and fundamental interactions, the focus of the research at the facility has, in relation with the establishment of a clinical proton therapy clinic at the University Medical Center Groningen (UMCG), in recent years shifted toward the radiation physics and biology of particle therapy.

Access to the facility is governed by the guidelines set out in the European Charter for Access to Research Infrastructures[14,15].

[14]https://ec.europa.eu/research/infrastructures/pdf/2016_charterforaccessto-ris.pdf#view=fit&pagemode=none
[15]https://www.rug.nl/kvi-cart/research/facilities/agor/

TABLE 1 | A comparison of the accelerator facilities in the Biophysics Collaboration.

Name	Status	Location	Accelerator	Ions	Maximum energy
FAIR	Under construction (starts 2025)	Darmstadt, Germany	Synchrotron (100 Tm)	H to U	~10 GeV/n
GSI	In operation in FAIR-phase-0	Darmstadt, Germany	Synchrotron (18 Tm)	H to U	~1 GeV/n
NICA	Under construction	Dubna, Russia	Synchrotron	Up to Au	Up to 4.5 GeV/n for Au, up to 800 MeV/n for biomedical applications
iThemba	In operation; under upgrade	Cape Town, South Africa	Cyclotron	H	200 MeV. A 70 MeV cyclotron will be used for isotopes
HIMAC	In operation	Chiba, Japan	Synchrotron	He to Fe	~400 MeV/n for C-ions
GANIL	In operation	Caen, France	Cyclotrons	H to U	95 MeV/n
MI2B	In operation	France	Network of different small accelerators	H, He	~70 MeV
SPES	Under construction at LNL-INFN	Legnaro, Italy	Cyclotron	H	70 MeV
LNS-INFN	In operation; under upgrade	Catania, Italy	Cyclotron	H to Au	80 MeV/n (H to Ne), 50 MeV/n (Au)
CNAO	In operation	Pavia, Italy	Synchrotron	H and C	250 MeV (H), 400 MeV/n (C)
HIT	In operation	Heidelberg, Germany	Synchrotron	H, He, C, and O	480 MeV (H), 430 MeV (He to O)
KVI-CART	In operation	Groningen, The Netherlands	Cyclotron	H to Pb	190 MeV (H), 90 MeV/n (He to O), 75 MeV/n (Ne)

Highlighted in yellow are the facilities with clinical operation.

Since 1998, research on normal tissue damage in radiotherapy is performed in collaboration with the Radiation Oncology and Cell Biology departments of the UMCG. The experiments use mainly proton and carbon beams and have two main focal points: *in vivo* studies of non-local effects in (partial) irradiations of organs such as parotid [86], heart–lung system [87, 88], and neural tissues [89] and *in vitro* studies of various aspects of the radiation response of stem cells [90, 91].

For this research, a versatile, modular beamline [92] has been built that is also used for experiments in medical radiation physics and for radiation hardness testing with both protons and various heavy ions. The on-site laboratory facilities for the radiation biology research comprise an animal accommodation for wild-type rodents and two laboratories equipped with CO_2 incubators and flow cabinets. In the coming years, the capabilities and capacity for radiation biology research will be substantially expanded. Currently, an additional beamline specifically for *in vivo* studies, equipped with 3D X-ray and bioluminescence imaging and 2D proton radiography at the irradiation position and funded by the Dutch cancer society KWF, is under development. In **Figure 10**, the floor plan of the accelerator facility, showing both the existing beamline for biomedical experiments and the new beamline, is displayed. With this new infrastructure, among others, more detailed studies of the spatial differentiation of the radiation response of normal and tumor tissues, interaction between particle irradiation, and systemic therapy, and biological effectiveness will be performed. At this new beamline, small animal irradiations will be performed with proton and helium beam as well as X-rays using different irradiation modalities. Besides the shoot-through method [89] employing 150–190 MeV protons, spread-out Bragg peak irradiations using primary beam energies up to 90 MeV/amu (range in water at 60 mm for both protons and helium) can also be performed. Both passive scattering and pencil beam scanning will be available, and the irradiations can be CW or pulsed with variable pulse duration ($\geq$ 10 μs) and a frequency of up to 2 kHz. The design calculations for the beamline indicate that pencil beams with 0.5 mm FWHM are feasible. Based on preliminary experiments, local dose rates up to at least 1,000 Gy/s should be achievable for both proton and helium irradiations in pencil beam scanning.

In conjunction with this new infrastructure, additional animal accommodations with associated laboratories will be built to provide optimal research conditions. The capacity of the laboratories for *in vitro* research will also be expanded. A setup for live-cell confocal microscopy immediately after irradiation is under development in collaboration with Amsterdam UMC.

To facilitate the use of the new infrastructure by external users, we will, in collaboration with the central animal research facility of UG and UMCG, offer a "one stop shop" service. Based on the detailed experiment design developed in collaboration with the users, we will arrange the required Dutch authorizations, procure the required animals, perform the irradiations, and, when desired by the user, perform the post-irradiation follow-up experiments. The data will be provided to the users through a research data management platform controlled by the users.

The current radiation physics research by both internal and external users focuses on near-real-time *in vivo* range verification in particle therapy [93, 94] and various aspects of dosimetry, including characterization of the LET distribution of particle beams [95] and tissue relative stopping powers [96].

CONCLUSIONS

Biomedical research programs at particle accelerators cover a vast range of topics such as particle therapy, radioisotope

production for medicine, and radioprotection in space. Along with accelerator facilities with long tradition, there are several new accelerators now under construction that can enrich the nuclear physics weaponry for biological and medical research (**Table 1**). Collaboration is a key point to exploit the translational potential of these researches and maximize the benefit for patients. Only a strong network of different centers can exploit synergies, avoid duplications, and raise the quality and the impact of biomedical research at accelerators. To this aim, the successful model of the large high-energy physics experiment could be also adopted in the applied nuclear physics community. The International Biophysics Collaboration [37] has the ambition and the potentiality to provide such a network to foster collaborations, exchange of hardware, design of innovative research programs, and support for funding applications. Such a large collaboration will help research at accelerators to maintain its extraordinary role as a nuclear physics tool for biology and medicine.

AUTHOR CONTRIBUTIONS

Authors from the different laboratories wrote different sections of the manuscript. MD produced the first draft that was then discussed and modified by all authors.

FUNDING

This work was partly supported by EU Horizon 2020 grant 73,0983 (INSPIRE), EU ERC AdG 883435 (BARB), and SIRIC 2018–2022: INCa-DGOS-Inserm_12554.

REFERENCES

1. Hayes AC. Applications of nuclear physics. *Reports Prog Phys.* (2017) **80**:026301. doi: 10.1088/1361-6633/80/2/026301
2. NuPECC. *Nuclear Physics for Medicine*. Strasbourg: European Science Foundation (2014). Available online at: www.nupecc.org
3. IAEA. *Cyclotron Produced Radionuclides: Physical Characteristics and Production Methods*. Vienna: IAEA Technical Report Serie (2009).
4. Cavaier RF, Haddad F, Sounalet T, Stora T, Zahi I. Terbium radionuclides for theranostics applications: a focus on MEDICIS-PROMED. *Phys Procedia.* (2017) **90**:157–63. doi: 10.1016/j.phpro.2017.09.053
5. Qaim SM. Cyclotron Production of Medical Radionuclides. In: Vértes A, Nagy S, Klencsár Z, Lovas RG, Rösch F, editors. *Handbook of Nuclear Chemistry*. Boston, MA: Springer US (1903–1933). doi: 10.1007/978-1-4419-0720-2_39
6. Durante M, Loeffler JS. Charged particles in radiation oncology. *Nat Rev Clin Oncol.* (2010) **7**:37–43. doi: 10.1038/nrclinonc.2009.183
7. Specht HM, Neff T, Reuschel W, Wagner FM, Kampfer S, Wilkens JJ, et al. Paving the road for modern particle therapy – what can we learn from the experience gained with fast neutron therapy in Munich? *Front Oncol.* (2015) **5**:262. doi: 10.3389/fonc.2015.00262
8. Nedunchezhian K. Boron neutron capture therapy - a literature review. *J Clin Diagnostic Res.* (2016) **10**:ZE01–4. doi: 10.7860/JCDR/2016/19890.9024
9. Barth RF, Zhang Z, Liu T. A realistic appraisal of boron neutron capture therapy as a cancer treatment modality. *Cancer Commun.* (2018) **38**:36. doi: 10.1186/s40880-018-0280-5
10. Kiyanagi Y, Sakurai Y, Kumada H, Tanaka H. Status of accelerator-based BNCT projects worldwide. *AIP Conf Proc.* (2019) **2160**:050012. doi: 10.1063/1.5127704
11. PTCOG. *Particle Therapy Facilities in Operation*. (2020) Available online at: https://www.ptcog.ch/ (accessed May 11, 2020).
12. Grau C, Durante M, Georg D, Langendijk JA, Weber DC. Particle therapy in Europe. *Mol Oncol.* (2020) **14**:1492–9. doi: 10.1002/1878-0261.12677
13. Jermann M. Particle therapy statistics in 2014. *Int J Part Ther.* (2015) **2**:50–4. doi: 10.14338/IJPT-15-00013
14. Durante M. Proton beam therapy in Europe: more centres need more research. *Br J Cancer.* (2019) **120**:777–8. doi: 10.1038/s41416-018-0329-x
15. La Tessa C, Sivertz M, Chiang IH, Lowenstein D, Rusek A. Overview of the NASA space radiation laboratory. *Life Sci Space Res.* (2016) **11**:18–23. doi: 10.1016/j.lssr.2016.10.002
16. Walsh L, Schneider U, Fogtman A, Kausch C, McKenna-Lawlor S, Narici L, et al. Research plans in Europe for radiation health hazard assessment in exploratory space missions. *Life Sci Space Res.* (2019) **21**:73–82. doi: 10.1016/j.lssr.2019.04.002
17. Simonsen LC, Slaba TC, Guida P, Rusek A. NASA's first ground-based galactic cosmic ray simulator: enabling a new era in space radiobiology research. *PLOS Biol.* (2020) **18**:e3000669. doi: 10.1371/journal.pbio.3000669
18. Durante M. Space radiation protection: destination Mars. *Life Sci Space Res.* (2014) **1**:2–9. doi: 10.1016/j.lssr.2014.01.002
19. Thomason JWG. The ISIS spallation neutron and muon source—The first thirty-three years. *Nucl Instrum Methods Phys Res Sect A Accel Spectrom Detect Assoc Equip.* (2019) **917**:61–7. doi: 10.1016/j.nima.2018.11.129
20. Durante M, Kronenberg A. Ground-based research with heavy ions for space radiation protection. *Adv Space Res.* (2005) **35**:180–4. doi: 10.1016/j.asr.2004.12.034
21. Durante M, Cucinotta FA. Heavy ion carcinogenesis and human space exploration. *Nat Rev Cancer.* (2008) **8**:465–72. doi: 10.1038/nrc2391
22. Bracco A. The NuPECC long range plan 2017: perspectives in nuclear physics. *Nucl Phys News.* (2017) **27**:3–4. doi: 10.1080/10619127.2017.1352311
23. Durante M, Golubev A, Park WY, Trautmann C. Applied nuclear physics at the new high-energy particle accelerator facilities. *Phys Rep.* (2019) **800**:1–37. doi: 10.1016/j.physrep.2019.01.004
24. Durante M, Cucinotta FA. Physical basis of radiation protection in space travel. *Rev Mod Phys.* (2011) **83**:1245–81. doi: 10.1103/RevModPhys.83.1245
25. Cronin J. Cosmic rays: the most energetic particles in the universe. *Rev Mod Phys.* (1999) **71**:S165–72. doi: 10.1103/RevModPhys.71.S165
26. Johnson RP. Review of medical radiography and tomography with proton beams. *Reports Prog Phys.* (2018) **81**:016701. doi: 10.1088/1361-6633/aa8b1d
27. Bert C, Durante M. Motion in radiotherapy: particle therapy. *Phys Med Biol.* (2011) **56**:R113–44. doi: 10.1088/0031-9155/56/16/R01
28. Vozenin MC, De Fornel P, Petersson K, Favaudon V, Jaccard M, Germond JF, et al. The advantage of FLASH radiotherapy confirmed in mini-pig and cat-cancer patients. *Clin Cancer Res.* (2019) **25**:35–42. doi: 10.1158/1078-0432.CCR-17-3375
29. Harrington KJ. Ultrahigh dose-rate radiotherapy: next steps for FLASH-RT. *Clin Cancer Res.* (2019) **25**:3–5. doi: 10.1158/1078-0432.CCR-18-1796
30. Prezado Y, Jouvion G, Patriarca A, Nauraye C, Guardiola C, Juchaux M, et al. Proton minibeam radiation therapy widens the therapeutic index for high-grade gliomas. *Sci Rep.* (2018) **8**:16479. doi: 10.1038/s41598-018-34796-8
31. González W, Prezado Y. Spatial fractionation of the dose in heavy ions therapy: an optimization study. *Med Phys.* (2018) **45**:2620–7. doi: 10.1002/mp.12902
32. Schültke E, Balosso J, Breslin T, Cavaletti G, Djonov V, Esteve F, et al. Microbeam radiation therapy — grid therapy and beyond: a clinical perspective. *Br J Radiol.* (2017) **90**:20170073. doi: 10.1259/bjr.20170073
33. Grotzer MA, Schültke E, Bräuer-Krisch E, Laissue JA. Microbeam radiation therapy: clinical perspectives. *Phys Med.* (2015) **31**:564–7. doi: 10.1016/j.ejmp.2015.02.011
34. Dilmanian FA, Zhong Z, Bacarian T, Benveniste H, Romanelli P, Wang R, et al. Interlaced x-ray microplanar beams: a radiosurgery approach with clinical potential. *Proc Natl Acad Sci USA.* (2006) **103**:9709–14. doi: 10.1073/pnas.0603567103

35. Henning WF. Physics with energetic radioactive ion beams. *Nucl Instrum Methods Phys Res Sect B Beam Interact Mater Atoms.* (1997) **126**:1–6. doi: 10.1016/S0168-583X(97)00999-3
36. Durante M, Parodi K. Radioactive beams in particle therapy: past, present, and future. *Front Phys.* (2020) 8:326. doi: 10.3389/fphy.2020.00326
37. Durante M, Prezado Y, Patera V. The biophysics collaboration for research at FAIR and other new accelerator facilities. *Europhys News.* (2019) **50**:27–30. doi: 10.1051/epn/2019403
38. Durante M, Pleskac R, Graeff C. The biophysics collaboration: biomedical research at new accelerators. *GSI Sci Rep.* (2019) 1–2.
39. Durante M, Indelicato P, Jonson B, Koch V, Langanke K, Meißner UG, et al. All the fun of the FAIR: fundamental physics at the facility for antiproton and ion research. *Phys Scr.* (2019) **94**:033001. doi: 10.1088/1402-4896/aaf93f
40. Bai M, Adonin A, Appel S, Bär R, Bellachioma MC, Blell U, et al. Challenges of FAIR-phase-0. In: *9th International Particle Accelerator Conference*. Vancouver, BC: JACoW Publishing (2018). p. 2947–9.
41. Stöhlker T, Bagnoud V, Blaum K, Blazevic A, Bräuning-Demian A, Durante M, et al. APPA at FAIR: from fundamental to applied research. *Nucl Instruments Methods Phys Res Sect B Beam Interact Mater Atoms.* (2015) **365**:680–5. doi: 10.1016/j.nimb.2015.07.077
42. Kraft G. Tumor therapy with heavy charged particles. *Prog Part Nucl Phys.* (2000) **45**:473–544. doi: 10.1016/S0146-6410(00)00112-5
43. Schuy C, Weber U, Durante M. Hybrid active-passive space radiation simulation for concept GSI and the future FAIR facility. *Front Phys.* (2020). doi: 10.3389/fphy.2020.00337
44. Prall M, Durante M, Berger T, Przybyla B, Graeff C, Lang PM, et al. High-energy proton imaging for biomedical applications. *Sci Rep.* (2016) **6**:27651. doi: 10.1038/srep27651
45. Simeonov Y, Durante M, Engenhart-Cabillic R, Parodi K, Schuy C, Tinganelli W, et al. FLASH irradition by tumor conformal beam application with 3D modulators and biological verification. In: Durante M, Pleskac R, Graeff C, editors. *GSI Scientific Report*. (2019). p. 53. doi: 10.15120/GSI-2019-00596
46. Kekelidze V, Kovalenko A, Lednicky R, Matveev V, Meshkov I, Sorin A, et al. Status of the NICA project at JINR. *Nucl Part Phys Proc.* (2016) **273–5**:170–4. doi: 10.1016/j.nuclphysbps.2015.09.021
47. Kekelidze V, Lednicky R, Matveev V, Meshkov I, Sorin A, Trubnikov G. NICA project at JINR. *Phys Part Nucl Lett.* (2012) **9**:313–6. doi: 10.1134/S1547477112040164
48. Jones DTL, Yudelev M, Hendrikse WLJ. Physical characteristics of the South African high energy neutron therapy facility. *Radiat Prot Dosimetry.* (1988) **23**:365–8. doi: 10.1093/rpd/23.1-4.365
49. Mosconi M, Musonza E, Buffler A, Nolte R, Röttger S, Smit FD. Characterisation of the high-energy neutron beam at iThemba LABS. *Radiat Meas.* (2010) **45**:1342–5. doi: 10.1016/j.radmeas.2010.06.044
50. Barnard H, Conradie J, Beukes P, Nemulodi F, Mira J, Naidoo C, et al. The South African isotope facility. In: *9th International Particle Accelerator Conference - IPAC2018*. Vancouver, BC: JACoW Publishing (2018). p. 1240–3.
51. Conradie JL, Anthony LS, Azaiez F, Baard S, Bark RA, Barnard AH, et al. Progress with a new radioisotope production facility and construction of radioactive beam facility at ithemba LABS. In: *International Conference on Cyclotrons and their Applications*. Cape Town: JACoW Publishing (2019). p. 17–20. doi: 10.18429/JACoW-Cyclotrons2019-MOB02
52. Lindegren S, Albertsson P, Bäck T, Jensen H, Palm S, Aneheim E. Realizing clinical trials with Astatine-211: the chemistry infrastructure. *Cancer Biother Radiopharm.* (2020) 35:S24. doi: 10.1016/j.jmir.2019.03.076
53. Debrot E, Tran L, Chartier L, Bolst D, Guatelli S, Vandevoorde C, et al. SOI microdosimetry and modified MKM for evaluation of relative biological effectiveness for a passive proton therapy radiation field. *Phys Med Biol.* (2018) **63**:235007. doi: 10.1088/1361-6560/aaec2f
54. Abegglen LM, Caulin AF, Chan A, Lee K, Robinson R, Campbell MS, et al. Potential mechanisms for cancer resistance in elephants and comparative cellular response to DNA damage in humans. *JAMA.* (2015) **314**:1850–60. doi: 10.1001/jama.2015.13134
55. Tsujii H, Kamada T, Shirai T, Al E. In:Tsujii H, Kamada T, Shirai T, Noda K, Tsuji H, Karasawa K, editors. *Carbon-Ion Radiotherapy*. Tokyo: Springer Japan (2014). doi: 10.1007/978-4-431-54457-9
56. Kamada T, Tsujii H, Blakely EA, Debus J, De Neve W, Durante M, et al. Carbon ion radiotherapy in Japan: an assessment of 20 years of clinical experience. *Lancet Oncol.* (2015) **16**:e93–100. doi: 10.1016/S1470-2045(14)70412-7
57. Tsujii H, Kamada T, Baba M, Tsuji H, Kato H, Kato S, et al. Clinical advantages of carbon-ion radiotherapy. *New J Phys.* (2008) **10**:1–16. doi: 10.1088/1367-2630/10/7/075009
58. Okada T, Kamada T, Tsuji H, Mizoe J, Baba M, Kato S, et al. Carbon ion radiotherapy: clinical experiences at national institute of radiological science (NIRS). *J Radiat Res.* (2010) **51**:355–64. doi: 10.1269/jrr.10016
59. Minohara S, Kanai T, Endo M, Noda K, Kanazawa M. Respiratory gated irradiation system for heavy-ion radiotherapy. *Int J Radiat Oncol.* (2000) **47**:1097–103. doi: 10.1016/S0360-3016(00)00524-1
60. Kanai T, Kanematsu N, Minohara S, Komori M, Torikoshi M, Asakura H, et al. Commissioning of a conformal irradiation system for heavy-ion radiotherapy using a layer-stacking method. *Med Phys.* (2006) **33**:2989–97. doi: 10.1118/1.2219771
61. Furukawa T, Hara Y, Mizushima K, Saotome N, Tansho R, Saraya Y, et al. Development of NIRS pencil beam scanning system for carbon ion radiotherapy. *Nucl Instrum Methods Phys Res Sect B Beam Interact Mater Atoms.* (2017) **406**:361–7. doi: 10.1016/j.nimb.2016.10.029
62. Iwata Y, Noda K, Shirai T, Murakami T, Furukawa T, Mori S, et al. Design of a superconducting rotating gantry for heavy-ion therapy. *Phys Rev Spec Top Accel Beams.* (2012) **15**:044701. doi: 10.1103/PhysRevSTAB.15.044701
63. Inaniwa T, Kanematsu N, Noda K, Kamada T. Treatment planning of intensity modulated composite particle therapy with dose and linear energy transfer optimization. *Phys Med Biol.* (2017) **62**:5180–97. doi: 10.1088/1361-6560/aa68d7
64. Inaniwa T, Suzuki M, Sato S, Noda A, Iwata Y, Kanematsu N, et al. Enhancement of biological effectiveness of carbon-ion beams by applying a longitudinal magnetic field. *Int J Radiat Biol.* (2019) **95**:720–4. doi: 10.1080/09553002.2019.1569774
65. Gales S. GANIL-SPIRAL2: a new era. *World Sci.* (2012). doi: 10.1142/9789814417952_0001
66. Gales S. SPIRAL2 at GANIL: a world leading ISOL facility at the dawn of the next decade. *Prog Part Nucl Phys.* (2007) **59**:22–31. doi: 10.1016/j.ppnp.2006.12.021
67. Parker C, Lewington V, Shore N, Kratochwil C, Levy M, Lindén O, et al. Targeted Alpha Therapy, an Emerging Class of Cancer Agents. *JAMA Oncol.* (2018) **4**:1765–72. doi: 10.1001/jamaoncol.2018.4044
68. Cirrone GAP, Cuttone G, Raffaele L, Salamone V, Avitabile T, Privitera G, et al. Clinical and research activities at the CATANA facility of INFN-LNS: from the conventional hadrontherapy to the laser-driven approach. *Front Oncol.* (2017) **7**:223. doi: 10.3389/fonc.2017.00223
69. Tommasino F, Rovituso M, Fabiano S, Piffer S, Manea C, Lorentini S, et al. Proton beam characterization in the experimental room of the trento proton therapy facility. *Nucl Instrum Methods Phys Res Sect A Accel Spectrom Detect Assoc Equip.* (2017) **869**:15–20. doi: 10.1016/j.nima.2017.06.017
70. Belli M, Bettega D, Calzolari P, Cera F, Cherubini R, Dalla Vecchia M, et al. Inactivation of human normal and tumour cells irradiated with low energy protons. *Int J Radiat Biol.* (2000) **76**:831–9. doi: 10.1080/095530000500 28995
71. Belli M, Bettega D, Calzolari P, Cherubini R, Cuttone G, Durante M, et al. Effectiveness of monoenergetic and spread-out bragg peak carbon-ions for inactivation of various normal and tumour human cell lines. *J Radiat Res.* (2008) **49**:597–607. doi: 10.1269/jrr.08052
72. Mazzucconi D, Bortot D, Rodriguez PM, Pola A, Fazzi A, Colautti P, et al. A wall-less tissue equivalent proportional counter as connecting bridge from microdosimetry to nanodosimetry. *Radiat Phys Chem.* (2020) **171**:108729. doi: 10.1016/j.radphyschem.2020.108729
73. Bantsar A, Colautti P, Conte V, Hilgers G, Pietrzak M, Pszona S, et al. State of the art of instrumentation in experimental nanodosimetry. *Radiat Prot Dosimetry.* (2018) **180**:177–81. doi: 10.1093/rpd/n cx263
74. de Angelis G, Fiorentini G. The Legnaro national laboratories and the SPES facility: nuclear structure and reactions today and tomorrow. *Phys Scr.* (2016) **91**:113001. doi: 10.1088/0031-8949/91/11/113001

75. de Angelis G. The SPES radioactive ion beam facility at the Legnaro National Laboratories and the EDM search. *J Phys Conf Ser.* (2018) 1056:012014. doi: 10.1088/1742-6596/1056/1/012014
76. Rossi S. The status of CNAO. *Eur Phys J Plus.* (2011) **126**:1–39. doi: 10.1140/epjp/i2011-11078-8
77. Rossi S. The national centre for oncological hadrontherapy (CNAO): status and perspectives. *Phys Medica.* (2015) **31**:333–51. doi: 10.1016/j.ejmp.2015.03.001
78. Altieri S, Bortolussi S, Bruschi P, Chiari P, Fossati F, Stella S, et al. Neutron autoradiography imaging of selective boron uptake in human metastatic tumours. *Appl Radiat Isot.* (2008) **66**:1850–5. doi: 10.1016/j.apradiso.2008.05.007
79. Wittig A, Michel J, Moss RL, Stecher-Rasmussen F, Arlinghaus HF, Bendel P, et al. Boron analysis and boron imaging in biological materials for Boron neutron capture therapy (BNCT). *Crit Rev Oncol Hematol.* (2008) **68**:66–90. doi: 10.1016/j.critrevonc.2008.03.004
80. Haberer T, Debus J, Eickhoff H, Jäkel O, Schulz-Ertner D, Weber U. The heidelberg ion therapy center. *Radiother Oncol.* (2004) **73**:S186–90. doi: 10.1016/S0167-8140(04)80046-X
81. Dokic I, Mairani A, Niklas M, Zimmermann F, Chaudhri N, Krunic D, et al. Next generation multi-scale biophysical characterization of high precision cancer particle radiotherapy using clinical proton, helium-, carbon- and oxygen ion beams. *Oncotarget.* (2016) **7**:56676–89. doi: 10.18632/oncotarget.10996
82. Mairani A, Dokic I, Magro G, Tessonnier T, Bauer J, Böhlen TT, et al. A phenomenological relative biological effectiveness approach for proton therapy based on an improved description of the mixed radiation field. *Phys Med Biol.* (2017) **62**:1378–95. doi: 10.1088/1361-6560/aa51f7
83. Schoemers C, Feldmeier E, Naumann J, Panse R, Peters A, Haberer T. The intensity feedback system at Heidelberg ion-beam therapy centre. *Nucl Instruments Methods Phys Res Sect A Accel Spectrom Detect Assoc Equip.* (2015) **795**:92–9. doi: 10.1016/j.nima.2015.05.054
84. Combs SE, Jäkel O, Haberer T, Debus J. Particle therapy at the Heidelberg ion therapy center (HIT) – Integrated research-driven university-hospital-based radiation oncology service in Heidelberg, Germany. *Radiother Oncol.* (2010) **95**:41–4. doi: 10.1016/j.radonc.2010.02.016
85. Schreuder HW. AGOR: initial beam tests, transport and commissioning. In: Cornell JC, editor. *Proceedings, 14th International Conference on Cyclotrons and their Applications.* Cape Town: World Scientific Publishing (1996). p. 6–11
86. van Luijk P, Pringle S, Deasy JO, Moiseenko VV, Faber H, Hovan A, et al. Sparing the region of the salivary gland containing stem cells preserves saliva production after radiotherapy for head and neck cancer. *Sci Transl Med.* (2015) **7**:305ra147. doi: 10.1126/scitranslmed.aac4441
87. Ghobadi G, van der Veen S, Bartelds B, de Boer RA, Dickinson MG, de Jong JR, et al. Physiological interaction of heart and lung in thoracic irradiation. *Int J Radiat Oncol.* (2012) **84**:e639–46. doi: 10.1016/j.ijrobp.2012.07.2362
88. van der Veen SJ, Ghobadi G, de Boer RA, Faber H, Cannon MV, Nagle PW, et al. ACE inhibition attenuates radiation-induced cardiopulmonary damage. *Radiother Oncol.* (2015) **114**:96–103. doi: 10.1016/j.radonc.2014.11.017
89. van Luijk P, Bijl HP, Coppes RP, van der Kogel AJ, Konings AWT, Pikkemaat JA, et al. Techniques for precision irradiation of the lateral half of the rat cervical spinal cord using 150 MeV protons. *Phys Med Biol.* (2001) **46**:2857–71. doi: 10.1088/0031-9155/46/11/307
90. Nagle PW, van Goethem MJ, Kempers M, Kiewit H, Knopf A, Langendijk JA, et al. *In vitro* biological response of cancer and normal tissue cells to proton irradiation not affected by an added magnetic field. *Radiother Oncol.* (2019) **137**:125–9. doi: 10.1016/j.radonc.2019.04.028
91. Nagle PW, Hosper NA, Barazzuol L, Jellema AL, Baanstra M, van Goethem MJ, et al. Lack of DNA damage response at low radiation doses in adult stem cells contributes to organ dysfunction. *Clin Cancer Res.* (2018) **24**:6583–93. doi: 10.1158/1078-0432.CCR-18-0533
92. Brandenburg S, Ostendorf R, Hofstee M, Kiewiet H, Beijers H. The irradiation facility at the AGOR cyclotron. *Nucl Instruments Methods Phys Res Sect B Beam Interact Mater Atoms.* (2007) **261**:82–5. doi: 10.1016/j.nimb.2007.04.304
93. Golnik C, Hueso-González F, Müller A, Dendooven P, Enghardt W, Fiedler F, et al. Range assessment in particle therapy based on prompt γ -ray timing measurements. *Phys Med Biol.* (2014) **59**:5399–422. doi: 10.1088/0031-9155/59/18/5399
94. Buitenhuis HJT, Diblen F, Brzezinski KW, Brandenburg S, Dendooven P. Beam-on imaging of short-lived positron emitters during proton therapy. *Phys Med Biol.* (2017) **62**:4654–72. doi: 10.1088/1361-6560/aa6b8c
95. Wagenaar D, Tran LT, Meijers A, Marmitt GG, Souris K, Bolst D, et al. Validation of linear energy transfer computed in a Monte Carlo dose engine of a commercial treatment planning system. *Phys Med Biol.* (2020) **65**:025006. doi: 10.1088/1361-6560/ab5e97
96. van Abbema JK, van Goethem MJ, Mulder J, Biegun AK, Greuter MJW, van der Schaaf A, et al. High accuracy proton relative stopping power measurement. *Nucl Instruments Methods Phys Res Sect B Beam Interact Mater Atoms.* (2018) **436**:99–106. doi: 10.1016/j.nimb.2018.09.015

Conflict of Interest: The authors declare that the research was conducted in the absence of any commercial or financial relationships that could be construed as a potential conflict of interest.

frontiers in Physics

REVIEW
published: 20 October 2020
doi: 10.3389/fphy.2020.565861

Virus Irradiation and COVID-19 Disease

Marco Durante[1,2]*, *Kai Schulze*[3], *Sebastien Incerti*[4], *Ziad Francis*[5], *Sara Zein*[4] and *Carlos Alberto Guzmán*[3]

[1] Biophysics Department, GSI Helmholtzzentrum für Schwerionenforschung, Darmstadt, Germany, [2] Institute of Condensed Matter Physics, Technische Universität Darmstadt, Darmstadt, Germany, [3] Department of Vaccinology and Applied Microbiology, Helmholtz Zentrum für Infektionsforschung (HZI), Braunschweig, Germany, [4] CNRS/IN2P3, UMR5797, Center d'Études Nucléaires de Bordeaux Gradignan, Université de Bordeaux, Bordeaux, France, [5] Faculty of Sciences, U.R. Mathématiques et Modélisation, Saint Joseph University, Beirut, Lebanon

Virus irradiation has been performed for many decades for basic research studies, sterilization, and vaccine development. The COVID-19 outbreak is currently causing an enormous effort worldwide for finding a vaccine against coronavirus. High doses of γ-rays can be used for the development of vaccines that exploit inactivated virus. This technique has been gradually replaced by more practical methods, in particular the use of chemicals, but irradiation remains a simple and effective method used in some cases. The technique employed for inactivating a virus has an impact on its ability to induce an adaptive immune response able to confer effective protection. We propose here that accelerated heavy ions can be used to inactivate SARS-CoV-2 viruses with small damage to the spike proteins of the envelope and can then provide an intact virion for vaccine development.

Keywords: COVID-19, SARS-CoV-2, virus, gamma rays, heavy ions

OPEN ACCESS

Edited by:
Zhen Cheng,
Stanford University, United States

Reviewed by:
David B. Stout,
Independent Researcher, Culver City, United States
Hui Shi,
Stanford Bio-X, Stanford University, United States

***Correspondence:**
Marco Durante
m.durante@gsi.de

Specialty section:
This article was submitted to Medical Physics and Imaging, a section of the journal Frontiers in Physics

Received: *26 May 2020*
Accepted: *24 August 2020*
Published: *20 October 2020*

Citation:
Durante M, Schulze K, Incerti S, Francis Z, Zein S and Guzmán CA (2020) Virus Irradiation and COVID-19 Disease. Front. Phys. 8:565861. doi: 10.3389/fphy.2020.565861

INTRODUCTION

The coronavirus disease in 2019 (COVID-19), caused by the severe acute respiratory syndrome coronavirus 2 (SARS-CoV-2) [1], is an unprecedented health emergency in this century. The World Health Organization declared COVID-19 a pandemic in March 2020. From the start of the pandemic to August 2020, over 22 million cases have been reported worldwide, resulting in over 780,000 casualties. Lacking effective antiviral drugs, the rush to develop an effective vaccine is enormous [2, 3], with over 100 vaccines in pre-clinical evaluation and 10 already in clinical trials [4].

There are several techniques in use to find the most effective vaccine against SARS-CoV-2, including innovative RNA vaccines, viral vector-, or protein-based vaccines [5]. However, the conventional method of using weakened or inactivated viruses is still avidly pursued and has produced some of the most promising vaccines under test [6, 7].

Techniques for virus inactivation are both chemical and physical, the latter including heat, UV, and ionizing radiation (usually γ-rays). The method used for inactivation is important, because the damage to the epitopes will reduce the efficacy of the vaccine. Several studies have measured the impact of different chemical and physical methods on the efficacy of the inactivated virus [8–10]. Chemicals, such as formaldehyde, hydrogen peroxide, binary ethylenimine derivatives, or β-propiolactone, are very practical but can damage the envelope protein and leave toxic residuals. Gamma radiation is therefore still considered a very safe and effective method [11] as shown in many recent reports [12–16].

VIRUS RADIOBIOLOGY

Inactivation of virus by radiation has been studied for over a century [17–19]. Virus radiosensitivity is lower when the irradiation is performed in growth medium compared to water and strongly depends on the size of the virion envelope [20, 21]. Viruses are lacking enzymes and are therefore unable to repair any damage in their nucleic acids. These simple targets are therefore the perfect objects to test the target theory of radiation action, introduced by Lea [22]. According to the target theory, the hit probability P for N targets to be hit n times by radiation follows the Poisson distribution:

$$P = \left[1 - e^{-vD} \sum_{k=0}^{n-1} \frac{(vD)^k}{k!}\right]^N$$

where v is the target volume and D the radiation dose. In the simple case of $N = n = 1$, the equation is reduced to the simple single-hit–single-target model:

$$S = e^{-vD} = e^{-\sigma F}$$

where $F = D{\cdot}LET$ is the fluence (in particles/cm^2), LET the radiation linear energy transfer (in MeV·cm^2/g, often expressed in keV/μm in water), and $\sigma = v/LET$ is the inactivation cross-section (in cm^2). The target theory cannot describe cellular repair effect but is perfectly able to describe the inactivation of the viruses. The survival curves are in fact always linear (in logarithmic scale), and assuming a given energy for the inactivation event, the volume v can be calculated from the slope. Using charged particles, the inactivation cross-section can provide the area of the sensible target, under the assumption that every traversal is lethal [23, 24]. **Figure 1** shows typical survival curves of viruses, whereas in **Figure 2**, we report the inactivation cross-section as a function of LET. The inactivation of the virus is caused by the damage to the nucleic acid, either RNA or DNA. A single-strand break (for single-stranded virus) or a double-strand break is generally sufficient to make the product of the viral nucleic acid not viable. An additional source of inactivation is the damage to the capsid, that can lead to release of the DNA (or RNA) from the viral envelope (**Figure 3**). Even at high doses, however, this mechanism is less important than direct damage to the DNA [25].

For high-energy heavy ions, part of the inactivation can derive from the high-energy electrons emitted along the tracks (δ-rays—see **Figure 4**). Virus targets were instrumental for the elaboration of the first amorphous track structure models of radiation by Robert Katz [26], where the radial dose is assumed to decrease as r^{-2} by increasing the distance r from the primary ion track. In the single-hit–single-target model, the inactivation cross-section for heavy ions can be written as a product of the geometrical cross-section times the inactivation probability (1 – S), dependent on the distance r from the track:

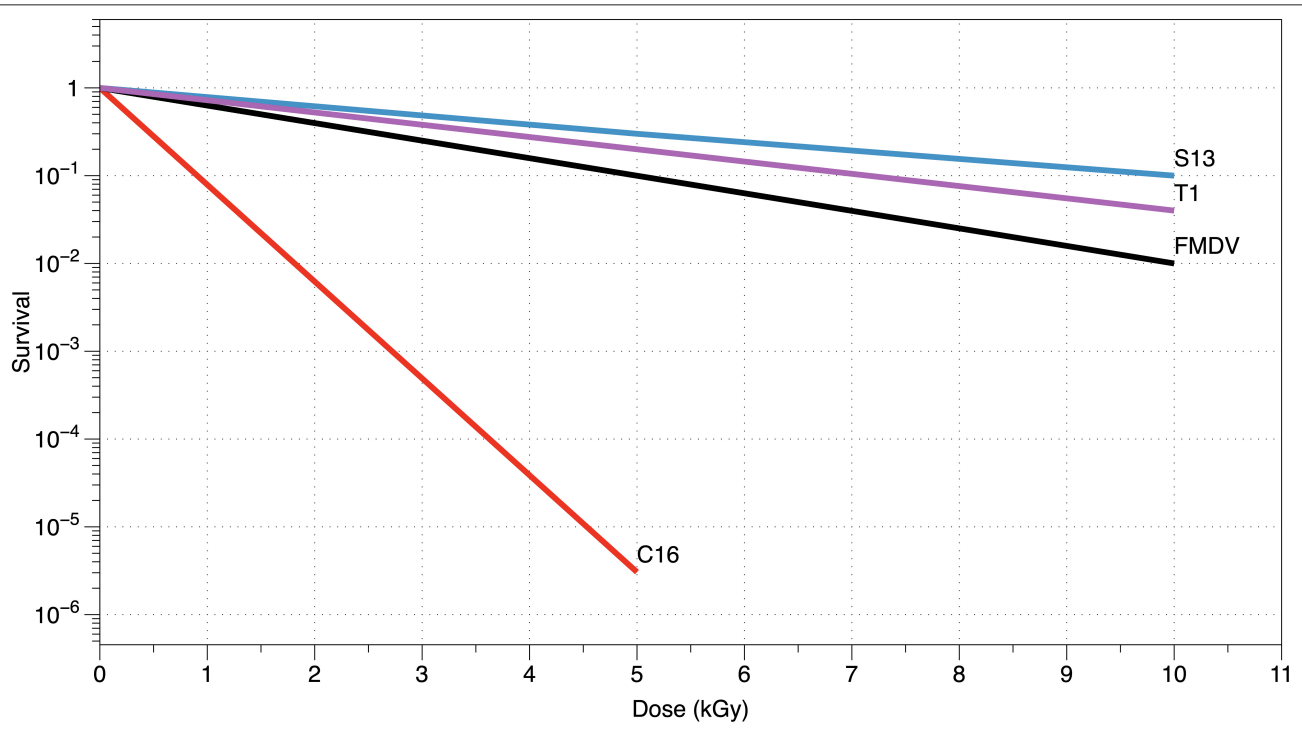

FIGURE 1 | Virus radiosensitivity. Survival of different viruses to X- or γ-rays is plotted vs. the dose (in kGy) for different viruses. C16 bacteriophage [19] is larger (50–70 nm) compared to the S13 [18] and T1 [23] bacteriophages and to the foot-and-mouth-disease picornavirus (FMDV) [21].

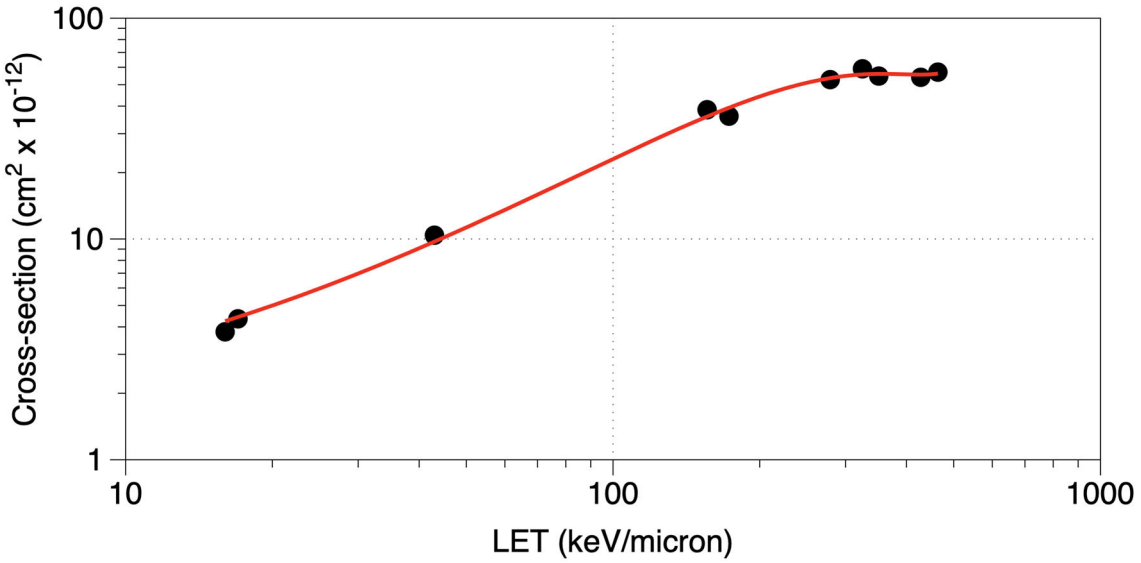

FIGURE 2 | Inactivation efficiency increases with LET. Inactivation cross-section of the bacteriophage T1 plotted vs. the particle LET (in keV/μm in water) following exposure to different heavy ions (He, C, O, F, Ne, and A). Data points combined from references [23, 24]; the line is a guide for the eye.

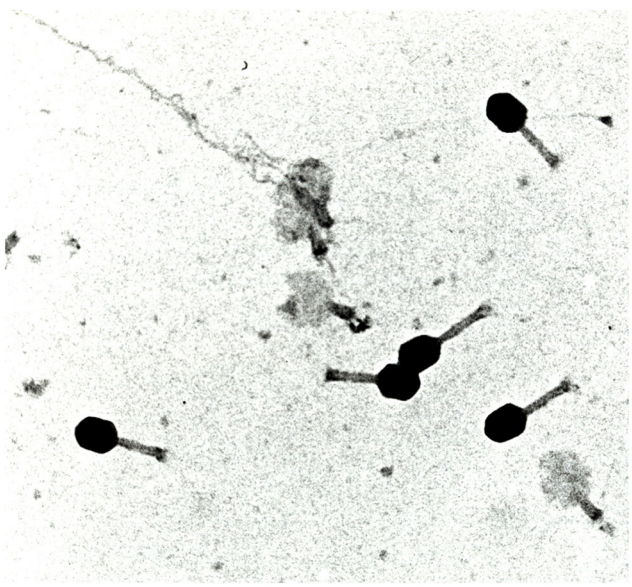

FIGURE 3 | Images of radiation-induced damage in virus. The photo shows the bacteriophage T4 irradiated with protons (details in Ref. [25]). Black heads retain the DNA, and white heads have lost the molecule, which is seen flowing out of the envelope in some viruses. Electron microscope photograph from the Tandem accelerator of the University Federico II, Naples, Italy, courtesy of Prof. Gianfranco Grossi.

$$\sigma = 2\pi \int_0^R \left(1 - e^{-\frac{D(r)}{D_0}}\right) r dr$$

where $D(r)$ is the radial dose, D_0 is the mean lethal dose (derived from experiments with γ- or X-rays), and R is the maximum track radius (i.e., the range of the δ-rays with maximum energy). The calculation of σ requires several parameters to estimate the radial dose $D(r)$ and the mean inactivation dose D_0 from γ-ray experiments. The results of the Katz' model for dry enzymes and viruses are in good agreement with experimental data [27].

Based on the Katz theory, Liu et al. [28] derived a simple analytical expression for the inactivation cross-sections of viruses:

$$\sigma = A r_0^2 \left(ln \frac{R^2}{r_0^2} + B\right)$$

where $r_0^2 = C\frac{z^2}{\beta^2 D_0^2}$ is the distance from the track corresponding to the γ-ray mean dose level D_0, z is the ion effective charge, β is the ion velocity, R is the maximum track radius, C is a constant depending on the absorbing medium, and A and B are two free parameters. Using $A = 3.88$ and $B = 0.753$, the authors fitted very well the published results [28], showing that ion radiosensitivity of viruses can be accurately predicted from the γ-ray radiosensitivity.

A modified version of the amorphous track structure is still used today in treatment planning for heavy ion therapy in cancer patients [29].

RADIATION AND VACCINES

Beyond the basic radiobiology applications, irradiation of viruses was, since the beginning, used for vaccine development [30]. Despite the fact that the use of chemicals often requires extensive and time-consuming downstream processing in order to detoxify them, it has gradually overcome γ-ray sterilization, as it can easily be applied under good manufacturing practice (GMP) conditions. For instance, influenza viruses of the seasonal flu split

or subunit vaccines are inactivated using chemical agents, such as formaldehyde [14]. However, the efficacy of these vaccines usually reaches only 60–70%, and even less in the elderly (∼20–30%) [31]. This might be also in part explained by a negative impact of the chemicals on viral surface antigenic structures that are the targets of the human immune system for the elicitation of a protective response. In this regard, γ-irradiated influenza vaccines seem to be more effective not only at stimulating strong antigen-specific antibody production but also at priming cross-reactive cytotoxic T cells, thereby protecting mice against a heterologous influenza virus [32]. Similar results have been observed using gamma radiation for the development of vaccine prototypes against HIV [33], Ebola [12], rotavirus [16], and polio [34].

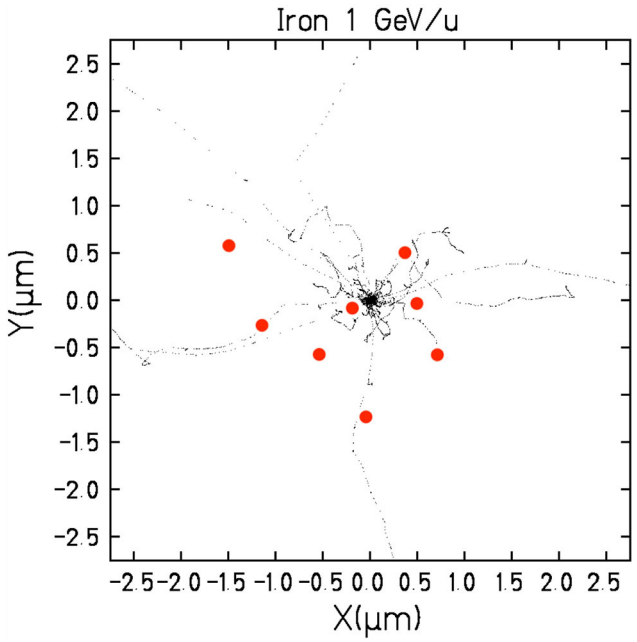

FIGURE 4 | Track structure and virus. Simulation with the TRAX Monte Carlo code of a 1 GeV/n ^{56}Fe-ions in water. Each black dot represents an ionization event. The track is seen exiting from the plane in bird's eye view. Axes are spatial coordinates in μm from the track center. The red spheres give the approximate size of the coronavirus.

However, high doses of γ-rays also cause damage to the surface molecules. Radioprotectors can be used to limit this damage [34, 35], but they can also protect the nucleic acids, and therefore the net advantage is dubious. Even if there is not a clear evidence that γ-rays provide a better-quality inactivated virus than chemical methods, there is an increasing demand of these radiation sources to produce inactivated virus with reduced damage to surface antigenic proteins and no requirements to remove chemical compounds after inactivation [36].

CHARGED PARTICLES FOR VACCINE DEVELOPMENT

A new strategy to reduce the epitope damage while maintaining lesions to the nucleic acids can be the use of a different radiation quality. Electrons produced with linacs are commonly used for sterilization of materials [37]. High-energy electrons were soon used for virus inactivation as replacement of ^{60}Co γ-ray sources [38] and until recently for food sterilization [39]. More recently, low-energy electrons have been explored because they present limited radioprotection problems and can be used in GMP laboratories. A beam of 200-keV electrons maintains the antigenic properties in several inactivated virus [40]. A Monte Carlo simulation of SARS-CoV-2 virus has shown that best results in terms of reduced damage to the spike proteins would be obtained with 2-keV electrons [41]. However, the main drawback of low-energy electrons is their limited range (in water,

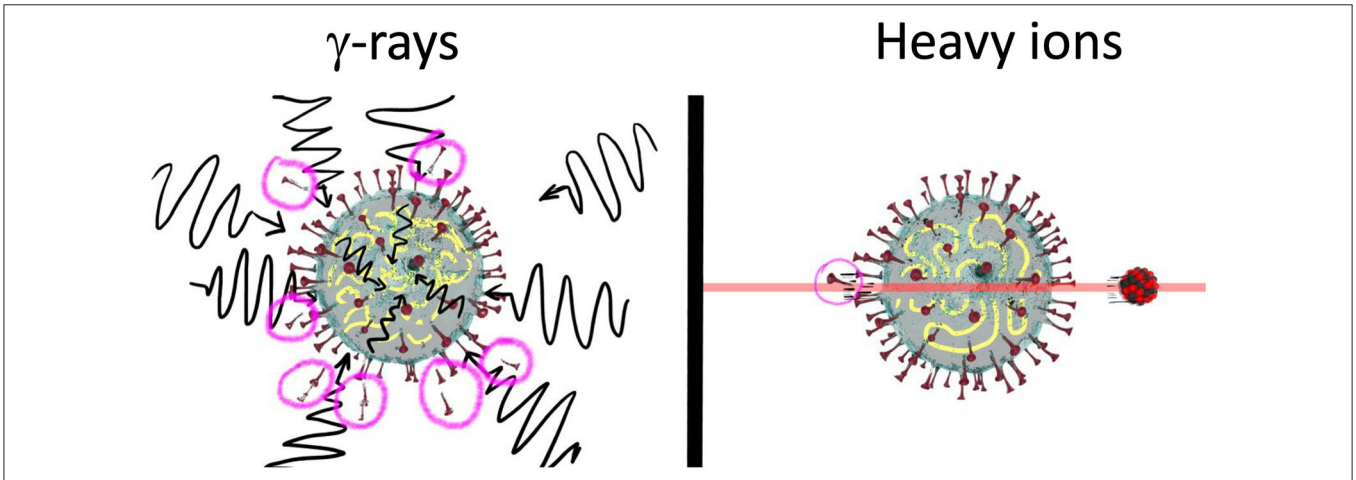

FIGURE 5 | High- and low-LET radiation for virus inactivation. Schematic representation of the action of sparsely and densely ionizing radiation on SARS-CoV-2. High doses of γ-rays can inactivate the virus, but will damage many membrane proteins, whereas single (or few) heavy ion traversals will produce limited membrane damage while maintaining a high inactivation probability. Sparing of membrane epitopes is essential to elicit the immune response toward vaccine generation.

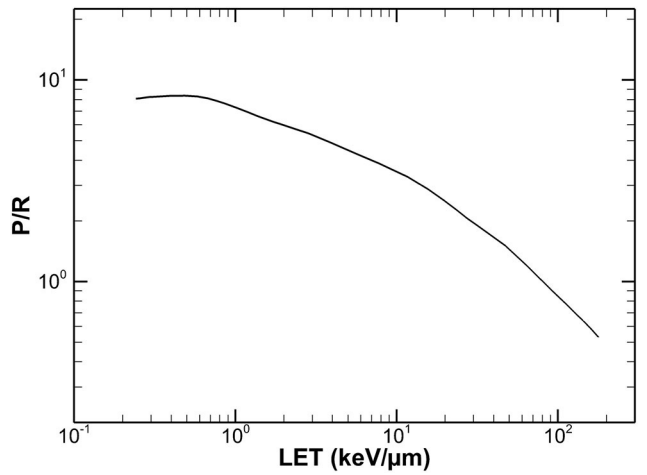

FIGURE 6 | Simulated ratio of damages to membrane and nucleic acids. Geant4-DNA simulation of the ratio of the damages to spike proteins and RNA (P/R ratio) for radiation of different LET (in keV/μm in water). The curve provides only the trend as a function of the LET alone, the actual points showing the complex dependence from the velocity and charge can be found in reference [42].

∼0.45 mm at 200 keV and ∼0.2 μm at 2 keV), which makes it impossible to process large volumes of pathogen suspensions as necessary for vaccine manufacturing.

High-energy heavy ions (**Figure 4**) have instead long penetration distances and reduced attenuation compared to γ-rays and electrons. Compared to sparsely ionizing radiation, they can inactivate the virus with very limited damage to membrane epitopes, because a single high-LET ion can severely damage the nucleic acid but will touch the virus envelope only in the point of entrance and exit (**Figure 5**). The effectiveness in inactivation per unit dose is lower for particles compared to γ-rays, but the effectiveness per particle traversal increases with LET (**Figure 2**). For this very reason, we have recently performed a Monte Carlo calculation to evaluate the possible use of heavy ions for the production of SARS-CoV-2 vaccine [42]. The Geant4-DNA extension [43–46] of the Geant4 Monte-Carlo toolkit [47–49] was used to simulate ionizing particle tracks and energy deposition inside the SARS-CoV-2 model. We focused on the ratio of the damage to the spike proteins (SARS-CoV-2 epitope) [50] and strand breaks in the ∼30-kbp single-stranded viral RNA. We will call this protein/RNA damage ratio P/R. **Figure 6** gives the trend of the P/R ratio as a function of LET. Even if P/R depends not only on LET but also on the track structure [42], the trend in **Figure 6** shows the expected advantage of using heavy ions, with a reduction of P/R of about an order of magnitude. Heavy ions such as Fe 1 GeV/n (**Figure 4**) have ranges of over 25 cm in water-equivalent materials, thus allowing irradiation of plastic boxes containing several cryovials with frozen virus, as often done in γ-irradiation inactivation [51]. High-energy heavy ions require of course large accelerators, but many of them are currently in operation or under construction and have intense programs in applied sciences, especially biomedical research [52].

CONCLUSIONS

Ionizing radiation has been used for decades to inactivate viruses. Early studies have contributed to our understanding of radiation action in living organisms. Inactivated viruses are still an important tool for vaccine development, and ionizing radiation has been used for years to this goal. One of the main problems of inactivated viruses is the damage to epitopes, which might reduce their ability to elicit an effective protective immune response post-vaccination. We have shown that densely ionizing heavy ions are potentially ideal to inactivate the virus with minimal damage to the envelope proteins and may therefore represent a new powerful tool for the development of vaccines against SARS-CoV-2 and other viruses.

AUTHOR CONTRIBUTIONS

MD proposed the idea. KS and CG contributed to the section on vaccine production and virus. SI, ZF, and SZ contributed to the section on physics and simulation and in particular produced the results in **Figure 6**. All authors contributed to the article and approved the submitted version.

FUNDING

This work was partly supported by EU Horizon 2020 grant 730983 (INSPIRE).

ACKNOWLEDGMENTS

We thank Daria Boscolo for the TRAX simulation image in **Figure 4** and Serena Durante for the cartoon in **Figure 5**.

REFERENCES

1. Wu F, Zhao S, Yu B, Chen YM, Wang W, Song ZG, et al. A new coronavirus associated with human respiratory disease in China. *Nature.* (2020) 579:265–9. doi: 10.1038/s41586-020-2008-3
2. Amanat F, Krammer F. SARS-CoV-2 vaccines: status report. *Immunity.* (2020) 52:583–9. doi: 10.1016/j.immuni.2020.03.007
3. Kaur SP, Gupta V. COVID-19 vaccine: a comprehensive status report. *Virus Res.* (2020) 288:198114. doi: 10.1016/j.virusres.2020.198114
4. WHO. *Draft Landscape of COVID 19 Candidate Vaccines.* Available online at: https://www.who.int/who-documents-detail/draft-landscape-of-covid-19-candidate-vaccines (accessed May 12, 2020).
5. Callaway E. The race for coronavirus vaccines: a graphical guide. *Nature.* (2020) 580:576–7. doi: 10.1038/d41586-020-01221-y
6. Gao Q, Bao L, Mao H, Wang L, Xu K, Yang M, et al. Development of an inactivated vaccine candidate for SARS-CoV-2. *Science.* (2020) 369:77–81. doi: 10.1126/science.abc1932

7. Wang H, Zhang Y, Huang B, Deng W, Quan Y, Wang W, et al. Development of an inactivated vaccine candidate, BBIBP-CorV, with potent protection against SARS-CoV-2. *Cell.* (2020) 182:713–21.e9. doi: 10.1016/j.cell.2020.06.008
8. Astill J, Alkie T, Yitbarek A, Taha-Abdelaziz K, Bavananthasivam J, Nagy É, et al. Examination of the effects of virus inactivation methods on the induction of antibody- and cell-mediated immune responses against whole inactivated H9N2 avian influenza virus vaccines in chickens. *Vaccine.* (2018) 36:3908–16. doi: 10.1016/j.vaccine.2018.05.093
9. Furuya Y, Regner M, Lobigs M, Koskinen A, Mullbacher A, Alsharifi M. Effect of inactivation method on the cross-protective immunity induced by whole "killed" influenza A viruses and commercial vaccine preparations. *J Gen Virol.* (2010) 91:1450–60. doi: 10.1099/vir.0.018168-0
10. Sabbaghi A, Miri SM, Keshavarz M, Zargar M, Ghaemi A. Inactivation methods for whole influenza vaccine production. *Rev Med Virol.* (2019) 29:e2074. doi: 10.1002/rmv.2074
11. Furuya Y. Return of inactivated whole-virus vaccine for superior efficacy. *Immunol Cell Biol.* (2012) 90:571–8. doi: 10.1038/icb.2011.70
12. Marzi A, Halfmann P, Hill-Batorski L, Feldmann F, Shupert WL, Neumann G, et al. An Ebola whole-virus vaccine is protective in nonhuman primates. *Science.* (2015) 348:439–42. doi: 10.1126/science.aaa4919
13. Arama C, Troye-Blomberg M. The path of malaria vaccine development: challenges and perspectives. *J Intern Med.* (2014) 275:456–66. doi: 10.1111/joim.12223
14. Pica N, Palese P. Toward a universal influenza virus vaccine: prospects and challenges. *Annu Rev Med.* (2013) 64:189–202. doi: 10.1146/annurev-med-120611-145115
15. Motamedi-Sedeh F, Soleimanjahi H, Jalilian AR, Mahravani H, Shafaee K, Sotoodeh M, et al. Development of protective immunity against inactivated Iranian isolate of foot-and-mouth disease virus type O/IRN/2007 using gamma ray-irradiated vaccine on BALB/c mice and Guinea pigs. *Intervirology.* (2015) 58:190–6. doi: 10.1159/000433538
16. Shahrudin S, Chen C, David SC, Singleton EV, Davies J, Kirkwood CD, et al. Gamma-irradiated rotavirus: a possible whole virus inactivated vaccine. *PLoS ONE.* (2018) 13:e0198182. doi: 10.1371/journal.pone.0198182
17. Bachofer CS. Direct Effect of X-rays on bacterial viruses, modified by physical state, in relation to the target theory. *Science.* (1953) 117:280–2. doi: 10.1126/science.117.3037.280
18. Pollard E. The action of ionizing radiation on viruses. *Adv Virus Res.* (1954) 2:109–51. doi: 10.1016/S0065-3527(08)60531-X
19. Wollman E, Holweck F, Luria S. Effect of radiations on bacteriophage C16. *Nature.* (1940) 145:935–6. doi: 10.1038/145935b0
20. Sullivan R, Fassolitis AC, Larkin EP, Read RB, Peeler JT. Inactivation of thirty viruses by gamma radiation. *Appl Microbiol.* (1971) 22:61–65. doi: 10.1128/AEM.22.1.61-65.1971
21. Smolko EE, Lombardo JH. Virus inactivation studies using ion beams, electron and gamma irradiation. *Nucl Instrum Methods Phys Res B.* (2005) 236:249–53. doi: 10.1016/j.nimb.2005.04.055
22. Lea DE. *Action of Radiations on Living Cells*. New York, NY: Cambridge University Press (1947).
23. Schambra PE, Hutchinson F. The action of fast heavy ions on biological material: II. Effects on T1 and ϕX-174 bacteriophage and double-strand and single-strand DNA. *Radiat Res.* (1964) 23:514–26. doi: 10.2307/3571746
24. Fluke DJ, Brustad T, Birge AC. Inactivation of Dry T-1 bacteriophage by helium ions, carbon ions, and oxygen ions: comparison of effect for tracks of various ion density. *Radiat Res.* (1960) 13:788–808. doi: 10.2307/3570854
25. Gialanella G, Grossi GF, Macchiato MF, Napolitano M, Speranza PR. Contributions of various types of damage to inactivation of T4 bacteriophage by protons. *Radiat Res.* (1983) 96:462–75. doi: 10.2307/3576113
26. Butts JJ, Katz R. Theory of RBE for heavy ion bombardment of dry enzymes and viruses. *Radiat Res.* (1967) 30:855–71. doi: 10.2307/3572151
27. Chunxiang Z, Dunn DE, Katz R. Radial distribution of dose and cross-sections for the inactivation of dry enzymes and viruses. *Radiat Prot Dosimetry.* (1985) 13:215–8. doi: 10.1093/rpd/13.1-4.215
28. Liu X, Mianfeng Li, Yu KN. Inactivation cross section of ions for dry enzymes and viruses. *Phys Med Biol.* (1994) 39:1757–61. doi: 10.1088/0031-9155/39/10/016
29. Friedrich T, Scholz U, Elsässer T, Durante M, Scholz M. Calculation of the biological effects of ion beams based on the microscopic spatial damage distribution pattern. *Int J Radiat Biol.* (2012) 88:103–7. doi: 10.3109/09553002.2011.611213
30. Pollard E. Inactivation of viruses for vaccine purposes using ionizing radiation and heat. *Yale J Biol Med.* (1957) 29:436–43.
31. Simpson CR, Lone NI, Kavanagh K, Ritchie LD, Robertson C, Sheikh A, McMenamin J. Trivalent inactivated seasonal influenza vaccine effectiveness for the prevention of laboratory-confirmed influenza in a Scottish population 2000 to 2009. *Eurosurveillance.* (2015) 20:21043. doi: 10.2807/1560-7917.ES2015.20.8.21043
32. Alsharifi M, Müllbacher A. The γ-irradiated influenza vaccine and the prospect of producing safe vaccines in general. *Immunol Cell Biol.* (2010) 88:103–4. doi: 10.1038/icb.2009.81
33. Kang CY, Gao Y. Killed whole-HIV vaccine; employing a well established strategy for antiviral vaccines. *AIDS Res Ther.* (2017) 14:47. doi: 10.1186/s12981-017-0176-5
34. Tobin GJ, Tobin JK, Gaidamakova EK, Wiggins TJ, Bushnell RV, Lee WM, et al. A novel gamma radiation-inactivated sabin-based polio vaccine. *PLoS ONE.* (2020) 15:e0228006. doi: 10.1371/journal.pone.0228006
35. Gaidamakova EK, Myles IA, McDaniel DP, Fowler CJ, Valdez PA, Naik S, et al. Preserving immunogenicity of lethally irradiated viral and bacterial vaccine epitopes using a radio- protective $Mn2^{+}$-peptide complex from deinococcus. *Cell Host Microbe.* (2012) 12:117–24. doi: 10.1016/j.chom.2012.05.011
36. Seo HS. Application of radiation technology in vaccines development. *Clin Exp Vaccine Res.* (2015) 4:145–58. doi: 10.7774/cevr.2015.4.2.145
37. Lancker M, Bastiaansen L. Electron-beam sterilization. Trends and developments. *Med Device Technol.* (2000) 11:18–21.
38. Traub FB, Friedemann U, Brasch A, Huber W, Kaplan H. High intensity electrons as a tool for preparation of vaccines. *J Immunol.* (1951) 67:379–84.
39. Mark Plavsic RWN. Efficacy of electron beam for viral inactivation. *J Microb Biochem Technol.* (2015) 7:173–76. doi: 10.4172/1948-5948.1000200
40. Fertey J, Bayer L, Grunwald T, Pohl A, Beckmann J, Gotzmann G, et al. Pathogens inactivated by low-energy-electron irradiation maintain antigenic properties and induce protective immune responses. *Viruses.* (2016) 8:319. doi: 10.3390/v8110319
41. Feng G, Liu L, Cui W, Wang F. Electron beam irradiation on novel coronavirus (COVID-19): A Monte–Carlo simulation. *Chin Phys B.* (2020) 29:048703. doi: 10.1088/1674-1056/ab7dac
42. Francis Z, Incerti S, Zein SA, Lampe N, Guzman CA, Durante M. *Monte Carlo Simulation of SARS-CoV-2 Radiation-Induced Inactivation for Vaccine Development.* (2020). Available online at: http://arxiv.org/abs/2005.06201 (accessed August 10, 2020).
43. Incerti S, Ivanchenko A, Karamitros M, Mantero A, Moretto P, Tran HN, et al. Comparison of GEANT4 very low energy cross section models with experimental data in water. *Med Phys.* (2010) 37:4692–708. doi: 10.1118/1.3476457
44. Incerti S, Kyriakou I, Bernal MA, Bordage MC, Francis Z, Guatelli S, et al. Geant4-DNA example applications for track structure simulations in liquid water: a report from the Geant4-DNA Project. *Med Phys.* (2018) 45:e722–39. doi: 10.1002/mp.13048
45. Incerti S, Baldacchino G, Bernal M, Capra R, Champion C, Francis Z, et al. The GEANT4-DNA project. *Int J Model Simul Sci Comput.* (2010) 01:157–78. doi: 10.1142/S1793962310000122
46. Bernal MA, Bordage MC, Brown JMC, Davídková M, Delage E, El Bitar Z, et al. Track structure modeling in liquid water: a review of the Geant4-DNA very low energy extension of the Geant4 Monte Carlo simulation toolkit. *Phys Medica Eur J Med Phys.* (2015) 31:861–74. doi: 10.1016/j.ejmp.2015.10.087
47. Agostinelli S, Allison J, Amako K, Apostolakis J, Araujo H, Arce P, et al. Geant4—a simulation toolkit. *Nucl Instrum Methods Phys Res A.* (2003) 506:250–303. doi: 10.1016/S0168-9002(03)01368-8
48. Allison J, Amako K, Apostolakis J, Araujo H, Dubois PA, Asai M, et al. Geant4 developments and applications. *IEEE Trans Nucl Sci.* (2006) 53:270–8. doi: 10.1109/TNS.2006.869826
49. Allison J, Amako K, Apostolakis J, Arce P, Asai M, Aso T, et al. Recent developments in Geant4. *Nucl Instrum Methods Phys Res A.* (2016) 835:186–225. doi: 10.1016/j.nima.2016.06.125

50. Walls AC, Park YJ, Tortorici MA, Wall A, McGuire AT, Veesler D. Structure, function, and antigenicity of the SARS-CoV-2 spike glycoprotein. *Cell.* (2020) 181:281–92.e6. doi: 10.1016/j.cell.2020.02.058
51. David SC, Lau J, Singleton EV, Babb R, Davies J, Hirst TR, et al. The effect of gamma-irradiation conditions on the immunogenicity of whole-inactivated Influenza A virus vaccine. *Vaccine.* (2017) 35:1071–9. doi: 10.1016/j.vaccine.2016.12.044
52. Durante M, Golubev A, Park WY, Trautmann C. Applied nuclear physics at the new high-energy particle accelerator facilities. *Phys Rep.* (2019) 800:1–37. doi: 10.1016/j.physrep.2019.01.004

Conflict of Interest: The authors declare that the research was conducted in the absence of any commercial or financial relationships that could be construed as a potential conflict of interest.

frontiers in Physics

ORIGINAL RESEARCH
published: 22 October 2020
doi: 10.3389/fphy.2020.568243

A High-Granularity Digital Tracking Calorimeter Optimized for Proton CT

Johan Alme[1], Gergely Gábor Barnaföldi[2], Rene Barthel[3], Vyacheslav Borshchov[4], Tea Bodova[1], Anthony van den Brink[3], Stephan Brons[5], Mamdouh Chaar[1], Viljar Eikeland[1], Grigory Feofilov[6], Georgi Genov[1], Silje Grimstad[7], Ola Grøttvik[1], Håvard Helstrup[7], Alf Herland[7], Annar Eivindplass Hilde[7], Sergey Igolkin[6], Ralf Keidel[8], Chinorat Kobdaj[9], Naomi van der Kolk[3], Oleksandr Listratenko[4], Qasim Waheed Malik[10], Shruti Mehendale[1], Ilker Meric[7], Simon Voigt Nesbø[7], Odd Harald Odland[1,11], Gábor Papp[12], Thomas Peitzmann[3], Helge Egil Seime Pettersen[11], Pierluigi Piersimoni[1], Maksym Protsenko[4], Attiq Ur Rehman[1], Matthias Richter[10], Dieter Röhrich[1], Andreas Tefre Samnøy[1], Joao Seco[13,14], Lena Setterdahl[1], Hesam Shafiee[1,7†], Øistein Jelmert Skjolddal[7], Emilie Solheim[1], Arnon Songmoolnak[1,9], Ákos Sudár[2,15], Jarle Rambo Sølie[7], Ganesh Tambave[1], Ihor Tymchuk[4], Kjetil Ullaland[1], Håkon Andreas Underdal[7], Monika Varga-Köfaragó[2], Lennart Volz[13,14], Boris Wagner[1], Fredrik Mekki Widerøe[1], RenZheng Xiao[1,16], Shiming Yang[1], Hiroki Yokoyama[3]*

[1]Department of Physics and Technology, University of Bergen, Bergen, Norway, [2]Wigner Research Centre for Physics, Budapest, Hungary, [3]Institute for Subatomic Physics, Utrecht University/Nikhef, Utrecht, Netherlands, [4]Research and Production Enterprise "LTU", Kharkiv, Ukraine, [5]Heidelberg Ion-Beam Therapy Center (HIT), Heidelberg University Hospital, Heidelberg, Germany, [6]Saint Petersburg State University, St. Petersburg, Russia, [7]Department of Computer Science, Electrical Engineering and Mathematical Sciences, Western Norway University of Applied Sciences, Bergen, Norway, [8]Center for Technology and Transfer, (ZTT), University of Applied Sciences Worms, Worms, Germany, [9]School of Physics, Suranaree University of Technology, Nakhon Ratchasima, Thailand, [10]Department of Physics, University of Oslo, Oslo, Norway, [11]Department of Oncology and Medical Physics, Haukeland University Hospital, Bergen, Norway, [12]Institute for Physics, Eötvös Loránd University, Budapest, Hungary, [13]Department of Biomedical Physics in Radiation Oncology, German Cancer Research Center, Heidelberg, Germany, [14]Department of Physics and Astronomy, Heidelberg University, Heidelberg, Germany, [15]Budapest University of Technology and Economics, Budapest, Hungary, [16]College of Mechanical and Power Engineering, China Three Gorges University, Yichang, China

A typical proton CT (pCT) detector comprises a tracking system, used to measure the proton position before and after the imaged object, and an energy/range detector to measure the residual proton range after crossing the object. The Bergen pCT collaboration was established to design and build a prototype pCT scanner with a high granularity digital tracking calorimeter used as both tracking and energy/range detector. In this work the conceptual design and the layout of the mechanical and electronics implementation, along with Monte Carlo simulations of the new pCT system are reported. The digital tracking calorimeter is a multilayer structure with a lateral aperture of 27 cm × 16.6 cm, made of 41 detector/absorber sandwich layers (calorimeter), with aluminum (3.5 mm) used both as absorber and carrier, and two additional layers used as tracking system (rear trackers) positioned downstream of the imaged object; no tracking upstream the object is included. The rear tracker's structure only differs from the calorimeter layers for the carrier made of ~200 μm carbon fleece and carbon paper (carbon-epoxy sandwich), to minimize scattering. Each sensitive layer consists of 108 ALICE pixel detector (ALPIDE) chip sensors (developed for ALICE, CERN) bonded on a polyimide flex and subsequently bonded to a larger flexible printed circuit board. Beam tests tailored to the pCT operation have been performed using high-energetic (50–220 MeV/u) proton and ion beams at the

OPEN ACCESS

Edited by:
Vincenzo Patera,
Sapienza University of Rome, Italy

Reviewed by:
Chiara Gianoli,
Ludwig Maximilian University of Munich, Germany
Carlo Civinini,
INFN, Italy

***Correspondence:**
Pierluigi Piersimoni
pierluigi.piersimoni@uib.no;
pierluigi.piersimoni@gmail.com

†Present address:
TechnipFMC—FMC Technologies Measurement Solutions Inc., Norway

Specialty section:
This article was submitted to Medical Physics and Imaging, a section of the journal Frontiers in Physics

Received: 31 May 2020
Accepted: 16 September 2020
Published: 22 October 2020

Citation:
Alme J, Barnaföldi GG, Barthel R, Borshchov V, Bodova T, van den Brink A, Brons S, Chaar M, Eikeland V, Feofilov G, Genov G, Grimstad S, Grøttvik O, Helstrup H, Herland A, Hilde AE, Igolkin S, Keidel R, Kobdaj C, van der Kolk N, Listratenko O, Malik QW, Mehendale S, Meric I, Nesbø SV, Odland OH, Papp G, Peitzmann T, Seime Pettersen HE, Piersimoni P, Protsenko M, Rehman AU, Richter M, Röhrich D, Samnøy AT, Seco J, Setterdahl L, Shafiee H, Skjolddal ØJ, Solheim E, Songmoolnak A, Sudár Á, Sølie JR, Tambave G, Tymchuk I, Ullaland K, Underdal HA, Varga-Köfaragó M, Volz L, Wagner B, Widerøe FM, Xiao R, Yang S and Yokoyama H (2020) A High-Granularity Digital Tracking Calorimeter Optimized for Proton CT. Front. Phys. 8:568243. doi: 10.3389/fphy.2020.568243

Heidelberg Ion-Beam Therapy Center (HIT) in Germany. These tests proved the ALPIDE response independent of occupancy and proportional to the particle energy deposition, making the distinction of different ion tracks possible. The read-out electronics is able to handle enough data to acquire a single 2D image in few seconds making the system fast enough to be used in a clinical environment. For the reconstructed images in the modeled Monte Carlo simulation, the water equivalent path length error is lower than 2 mm, and the relative stopping power accuracy is better than 0.4%. Thanks to its ability to detect different types of radiation and its specific design, the pCT scanner can be employed for additional online applications during the treatment, such as *in-situ* proton range verification.

Keywords: proton CT, ALICE pixel detector (ALPIDE), Monte Carlo, hadrontherapy, Complementary Metal Oxide Semiconductor (CMOS)

INTRODUCTION

Particle therapy, especially with proton beams, has been used and become widely accepted in the last 20 years. The number of dedicated facilities around the world is increasing year by year on a worldwide scale. The most appealing advantage of this technique derives from the physical properties of charged particles crossing matter, which experience a continuous slow down across their path, until they stop and release a large fraction of their initial energy at the end of their range, where the Bragg peak originates. As foreseen by Wilson in 1946 [1] this property allows, in principle, to focus the energy deposition at a certain depth in the human body (e.g., the tumor), sparing nearby tissue and having very low or no exit dose. However, due to the stochastic nature of the particle energy loss, precise calculation of proton range is inevitably uncertain even for simple geometries and materials. For this reason, range uncertainty has become a crucial and still debated topic in proton therapy. On the other hand, even though the precise position of the Bragg peak may be blurred by uncertainty, the considerable clinical benefits of proton therapy is undoubted [2]. To correctly predict the beam range in such a complex geometry as a human body can be, an accurate model of the relative stopping power (RSP, that is, the stopping power of a certain material relative to that of water) of each different material crossed by the particles before reaching the target tumor is needed. Currently, X-ray CT scans are used to image the patient and measure the photon attenuation expressed in Hounsfield unit (HU). Using calibration procedures, HUs for each material are converted to RSP for treatment planning [3]. Together with morphological changes, anatomical deformation due to internal motion, the conversion from HU to RSP is one of the main sources of uncertainty in the range determination, causing errors up to 3.5%, corresponding to up to 4 mm of possible misplacement of the Bragg peak at 10 cm water equivalent range in the patient [4, 5]. Proton CT (pCT) has been acknowledged as having a high potential in reducing uncertainties in proton therapy treatment planning. The strength of pCT is the direct reconstruction of a 3D map of RSP values in the target. The first pCT system idea dates back to 1963, when Cormack proposed protons as probe for CT scans [6]. The concept of modern pCT scanners is based on the tracking of each single proton history, measuring the direction and position before and after the imaged object and registering the residual energy or range after the object is crossed. Therefore, a typical pCT system must include thin tracking detectors and an energy/range detector. Due to multiple Coulomb scattering the proton track across the target is not a straight line, affecting the spatial resolution of proton imaging. To address this issue, several trajectory estimation methods [7–9] are employed to reconstruct each single proton trajectory using the most likely path (MLP) formalism. Processing the measured particle information by mean of sophisticated image reconstruction algorithms [10–14], a pCT scanner is able to directly yield a 3D map of the RSP values inside the object. Many pCT systems have been proposed and developed in the past 20 years [15, 16] achieving promising results for RSP accuracy and spatial resolution with both Monte Carlo (MC) simulated and experimental setups [17–20]. Lately, the RSP accuracy of pCT was proven to be well below 1% and performs better than modern techniques such as dual energy CT scans [21, 22]. Additionally, pCT has shown reduced noise level and lower dose deposition on the patient with respect to conventional X-ray CT [23, 24]. In recent years, along with protons, heavier ions (mostly helium or carbon) have been considered for imaging given their smaller deviation due to multiple Coulomb scattering. The expected effect of an improved spatial resolution was observed, once the ion fragmentation was taken into account [25–31].

The Bergen pCT collaboration was established at the University of Bergen (Norway) among many institutions across the world[1] with the purpose to design and build a

[1]The members of the Bergen pCT collaboration are: University of Bergen, Norway; Helse Bergen, Norway; Western Norway University of Applied Science, Bergen, Norway; Wigner Research Center for Physics, Budapest, Hungary; DKFZ, Heidelberg, Germany; Saint Petersburg State University, Saint Petersburg, Russia, Germany; Utrecht University, Netherlands; RPE LTU, Kharkiv, Ukraine; Suranaree University of Technology, Nakhon Ratchasima, Thailand; China Three Gorges University, Yichang, China; University of Applied Sciences Worms, Germany; University of Oslo, Norway; Eötvös Loránd University, Budapest, Hungary.

prototype pCT scanner. The aim of the project is to overcome most of the critical limitations of the currently existing prototypes. The most distinctive feature of the prototype design is the employment of a digital tracking calorimeter (DTC), that is, a layer-by-layer pixel detector based on pixelated silicon sensors. Previously, a calorimeter with such features was built and successfully tested with particle beams showing very good performances, despite a number of imperfections, most notably a large fraction of dead or otherwise unusable pixels [32, 33]. Through the participation in the ALICE collaboration at CERN, the Bergen pCT group was able to benchmark the prototype DTC for proof-of-concept for pCT purposes. The idea behind was to use a single technology for both tracking and residual energy measurement in order to simplify the system assembly and to guarantee stable operation in a clinical environment. Using experimental data and MC simulation, proton tracks across the sensor layers were analyzed. A charge diffusion model was applied to estimate the energy deposition by using the size of the charge diffused area and a model fit of the Bragg curve was employed to estimate the residual range, achieving a range resolution of 4% for each proton track. The readout system was able to handle an effective proton frequency of 1 MHz by using 500 concurrent proton tracks in each readout frame uniformly distributed throughout the 16 cm^2 aperture of the detector [34, 35].

In this work an evolution of the described prototype is presented: a novel DTC specifically designed and optimized for pCT, used as both tracking and energy/range detector. This work is then a comprehensive overview of all the multidisciplinary studies necessary to develop the project, which consists in assembling thousands of small silicon detectors together, to form a full scale pCT scanner.

To build such a complex and advanced device, investigations are necessary in order to find solutions to the challenging mechanical and electronic requirements for the successful function of the system. Moreover, the speed of the readout and data processing has to be kept high enough to have a clinically useable instrument. Other aspects to consider are the radiation damage of the instruments, the image reconstruction accuracy, the sensor response when irradiated with a medical beam, just to give some examples. In the following sections, the laborious research work carried out by the Bergen pCT group is described in detail. Nevertheless, to get to the final design, the DTC development was supported by previous studies from the Bergen pCT collaboration.

The new pCT system needs to fulfill the mandatory innovative requirements to handle pencil beams with therapeutic characteristics: high particle rate and localized dose depositions. Therefore, the readout speed has to be fast enough to handle many tracks at the same time and achieve an accurate determination of the ranges of individual protons. The Bergen pCT group has designed both the mechanical and the electronics setup described in detail in the following sections. MC simulations were used to evaluate the potential imaging accuracy of the novel system and the possible damage caused by radiation to the electronic components. Beam tests tailored to the pCT operation with protons and heavier ions have been performed in order to study the cluster size vs. energy deposition in the epitaxial layer of the sensors and to evaluate the maximum rate (particles per 10 μs/frame) the chip can handle.

MATERIALS AND METHODS

Design of the Digital Tracking Calorimeter

The segmented DTC has been designed as a multilayer structure made of several detector/absorber sandwich layers, which will function both as tracking system and range/energy detector. The detector will track the traversing particles and assign an energy difference or water equivalent path length (WEPL) to the each single crossing proton and this information will be used in image and CT reconstruction as explained in previous publications [34, 36].

Most pCT scanners currently available utilize a tracking system consisting of two layers of tracking detectors upstream (front tracker) and two more layers downstream (rear tracker) of the object to be imaged. However, in the Bergen pCT scanner, the front tracker has not been included and the information about the impinging proton position and direction will be inferred from the beam optics response of the monitoring system. A system that does not include a front tracker set (denoted *single-sided*, as opposite to the usual pCT scanners with both front and rear tracker planes called *double-sided*) presents some advantages for the design and assembly stages, reducing set-up complexity, final cost, and physical impact on the treatment room. From the operational point of view, a single-sided system would be able to allow a higher particle rate, since the pairing of particle hits measured on the rear tracker with the measurements on the front tracker could be avoided. For a more detailed discussion of this topic please refer to the work of Sølie et al. [37].

Although tracking system and energy/range detector form a unique assembly (the DTC), in the next sections they will be described as separate structures and will be referred to as *rear trackers* and *calorimeter*, respectively, in order to better specify the different characteristics.

The ALICE Pixel Detector Chip

The basic sensor chosen is the ALICE pixel detector (ALPIDE), a monolithic active pixel sensor, initially developed for the upgrade of the inner tracking system of the ALICE experiment at the LHC (CERN) [38]. The ALPIDE is manufactured using the commercial 180 nm Complementary Metal Oxide Semiconductor (CMOS) Imaging Sensor process by Tower Semiconductor. A cross sectional view of the ALPIDE pixel is shown in **Figure 1A**, where the collection diode and the CMOS components are visible. The chip is fabricated on a substrate with a high-resistivity (~kΩ cm), 25 μm thick epitaxial layer. The high resistivity helps to increase the depletion volume of the *pn* junction formed by the collection *n*-well and the *p*-type active volume. The depletion volume can further be increased by applying reverse substrate bias voltage of up to −6 V. The increase in the size of the depletion volume helps in drifting charge to collection diode while reducing charge diffusion. The *n*-wells of CMOS transistors are embedded in additional deep

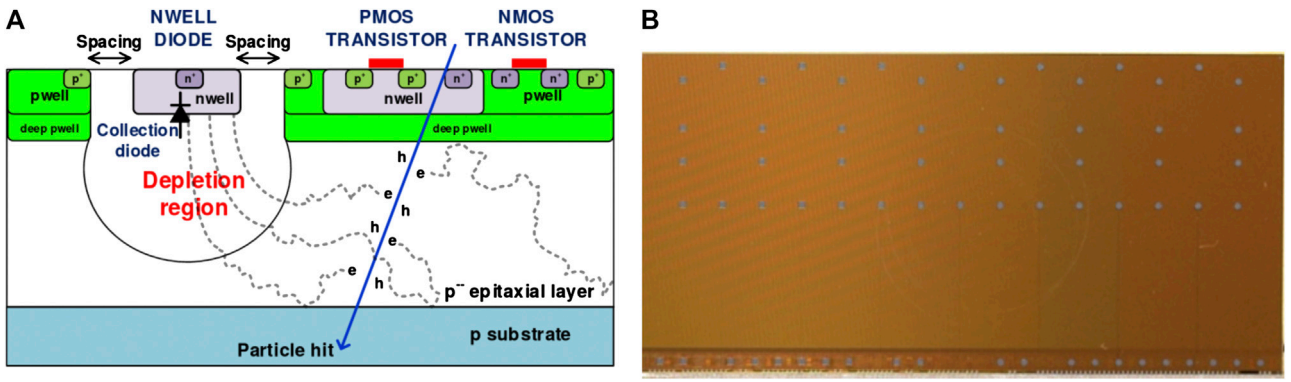

FIGURE 1 | (A) Cross sectional view of ALICE pixel detector (ALPIDE) pixel showing the collection diode and the CMOS components. The image was published as Figure 1 in Ref. 68, Creative Commons Attribution 3.0 License CC BY 3.0. **(B)** Photograph of the ALPIDE. Interface pads used for bonding to the printed circuit board are visible (gray squares).

p-wells so that all the charge will be collected only at the *n*-well diode. A photograph of a manufactured ALPIDE sensor chip glued to the flexible flat cable is shown in **Figure 1B**.

The chip measures 30 mm × 15 mm and contains a matrix of 1,024 × 512 pixels with in-pixel amplification, shaping, discrimination and multi-event buffering. The pixel size is about 29 μm × 29 μm, which makes the ALPIDE a highly granular sensor capable of simultaneous tracking of multiple particles. The readout of the pixel matrix is hit driven, meaning that the matrix is inactive if there are no hits. The data compression is achieved by implementing a zero-suppression method where data samples of a value smaller than the detection threshold are suppressed. The threshold is applied globally to all the ALPIDE pixels. The S-Curve scan is used to determine the charge threshold and temporal noise of the ALPIDE front-end circuit [39]. The data compression scheme provides efficient detection of particles at high rate. For minimum ionizing charged particles a resolution for the track position measurement of 5 μm, a detection efficiency of 99.99%, and background probability less than 10^{-5} event/pixel were achieved with ALPIDE [40]. The above-mentioned features make the ALPIDE chip an ideal candidate for the DTC.

Current Design of the Proton CT System

Recommended Specifications for the Digital Tracking Calorimeter

The detailed design optimization studies done with MC simulated data by Pettersen et al. [34] focused on different absorber materials and the thickness of the absorber layers. Considering the expectation of the prototype, practical restrictions and MC simulated data, some recommendations were followed, as described below.

(1) The DTC should have an aperture of 27 cm × 15 cm, to be able to image at least a pediatric head in a single scan.
(2) In the longitudinal direction, the DTC should be comprised of alternate layers of ALPIDE sensors and aluminum absorber layers. Given that the fraction of correctly reconstructed tracks and absorber thickness are inversely proportional, the thickness of the absorber should be kept as low as possible, strictly below 4 mm. In this fashion, 41 layers (each made of ALPIDE chips and a support of 3.5 mm-thick aluminum) are required to fully encompass the range of a 230 MeV proton beam and will form the calorimeter. Each layer corresponds to 7.5 mm water equivalent thickness.
(3) Two more layers will be used as rear trackers. Therefore, they should contain as little material as possible, apart from the sensitive volume of the ALPIDE, in order to reduce the positioning errors due to scattering. This could be achieved by thinning down the support on which the ALPIDEs will be mounted and not including the absorber layer between them.

The Digital Tracking Calorimeter Prototype

A schematic representation of the DTC is shown in **Figure 2**. The incoming particles will first face the tracking layers, which will have minimum material, as explained above. In **Figure 2**, the support on which the tracker layer will be mounted is not shown, to reveal the arrangement of the sensors in the DTC layers. More explanation can be found in the next section. The sensor layers are stacked in such a way that the transition card (TC) corresponding to alternate layers comes on the opposite side of the main stack, in order to make room for the readout electronics. To fully contain the range of 230 MeV proton beam, 41 aluminum absorber layers will be used, excluding the rear trackers. According to the recommendations made after the design optimization studies, the area of the sensitive part of each layer is designed to be 27 cm × 16.6 cm. Details about distribution of the ALPIDE in these layers is explained in the following sections.

The Digital Tracking Calorimeter Layers

Each sensitive layer, whether used as a tracker or in the calorimeter, has the same building blocks and design. **Figure 3A** shows the basic structure of half a layer. Each

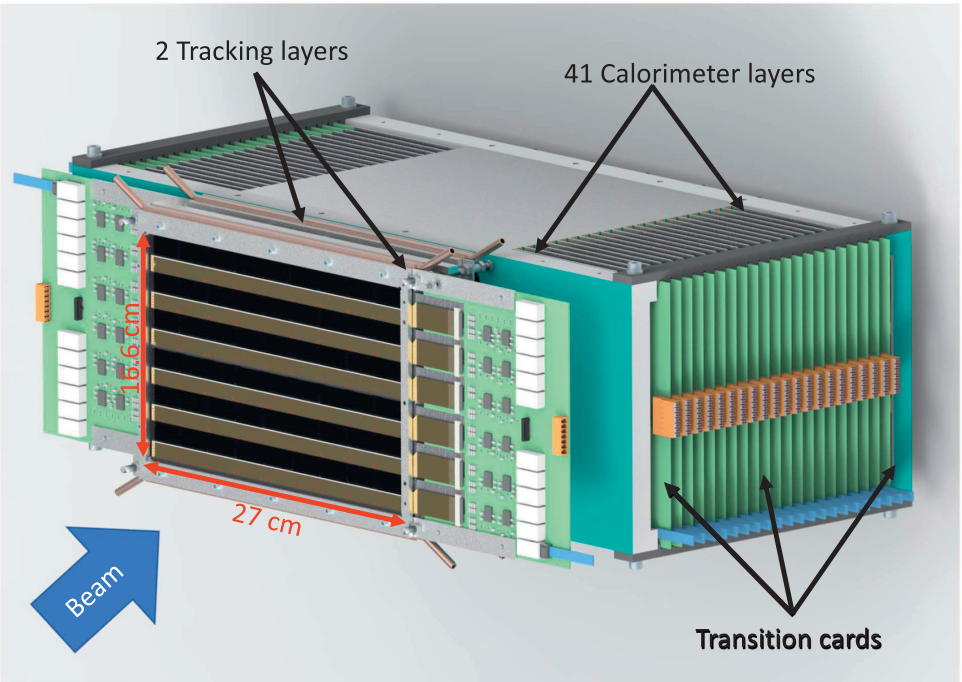

FIGURE 2 | The general structure of the Bergen pCT system. To reveal the arrangement of the sensors in the layer, the support where the ALICE pixel detector (ALPIDE) sensors will be mounted in the rear trackers is not shown.

ALPIDE chip is mounted on a flex cable, and a collection of nine ALPIDEs mounted on flex cable is called a *string*. Three such strings are then glued to an aluminum carrier (Al 99.5, that is a commercial alloy with aluminum content >99% and a heat conductivity of 220 W/mK, close to that of pure aluminum) of dimension 100 mm × 290 mm × 1 mm called a slab. There are two types of slabs: a top slab (T-slab) and a bottom slab (B-slab). Together they make a half layer, as shown in **Figure 3A**. Although the area of the two aluminum carriers, supporting a top and a bottom slab, is more than the recommended sensitive area of 27 cm × 15 cm, it is not entirely populated by ALPIDE chips, since nearly half of the area is non-sensitive flex cables. Thus, the construction of one layer is achieved by constructing another half layer, with alternated positions of ALPIDEs as compared to the previous half layer. The two halves of the layer are then stacked with the ALPIDEs facing each other and with an air-gap of 2 mm (ensured by an aluminum spacer) between the aluminum carrier boards, as depicted in the side-view schematic of the layer structure in **Figure 3B**.

Calorimeter Layers

In the calorimeter, the thickness of the absorber layer is chosen to be 3.5 mm. To construct a T- or a B-slab three strings made of 100 μm thick ALPIDE chips will be mounted on a 1 mm thick aluminum carrier board of dimension 100 mm × 290 mm × 1 mm, as described above. To make sure that the two half layers are vertically aligned, they will be screwed to one face of an aluminum absorber plate (Al 99.5) of dimension 200 mm × 290 mm × 1.5 mm. To assemble a layer, T- and B-slabs are placed on the absorber (chip face up), with both spacers positioned on top of the slabs. After placing a second set of slabs (with chips face down) the whole assembly is fixed by screws. The alignment is done with temporal dowel pins inside the fixing holes. The alternate layers will be rotated around the direction of the beam, to make room for the corresponding readout electronics part. These layers stacked along the beam direction form the calorimeter (**Figure 2**). Units and spacers will be assembled with the help of long screws passing through the aligned holes as shown in the side view of the layer structure in **Figure 3B**. The entire assembly is then supported by an aluminum frame and other support structures. With reference to the side view of the layer structure shown in **Figure 3B**, in the direction of the proton beam, one full calorimeter layer is composed of: the aluminum carriers (1 mm thick), half layer of sensors not facing the proton beam directly, an air gap of 2 mm (ensured by 2 mm thick aluminum spacers), half layer of sensors facing the proton beam, the aluminum carriers on which the sensors are mounted (1 mm thick), and the aluminum absorber plate (1.5 mm thick). In total the calorimeter will comprise 41 of such layers.

Tracking Layers

In order to minimize the non-sensor material in the tracking layers, 50 μm thick ALPIDE chips will be mounted on ~0.2 mm thick carbon-epoxy sandwich sheets of area 200 mm × 290 mm. These sheets are made of three layers of carbon paper and two layers of carbon fleece and have similar thermal conductivity as that of an aluminum plate of same dimensions. More information

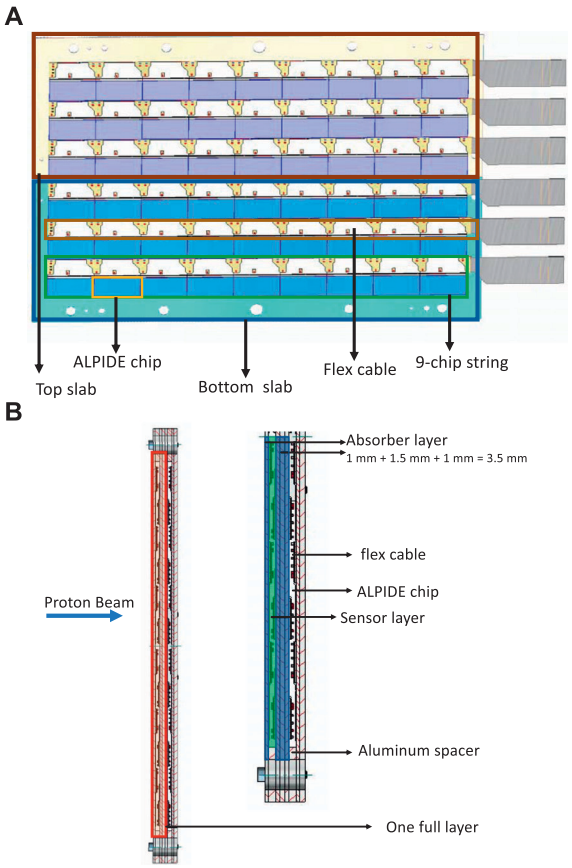

FIGURE 3 | (A) Half a layer consisting a top slab (T-Slab) and a bottom slab (B-slab). Each of the slabs is built by gluing three strings of ALICE pixel detector (ALPIDE) sensors glued to an aluminum carrier. **(B)** Schematic side view of two layers in the calorimeter (left), and half layer with details (right).

about this material can be found in Refs. 41 and 42. The arrangement of the ALPIDE chips in a half layer will be the same as shown in **Figure 3A**, except that a single carbon-epoxy slab supported by an aluminum frame will carry the chips. This makes the half layer more stable and easier to handle with respect to the layers in the calorimeter made of two half slabs. Two half layers, with chips facing each other, are then clamped together with 2 mm thick aluminum spacers sandwiched between them at the top and bottom. Analogous to the calorimeter layer, in the direction of the proton beam, one full tracker layer is composed of: a carbon-epoxy sandwich sheet (0.2 mm thick) with half layer of sensors not facing the proton beam directly, an air gap of 2 mm, a half layer of sensors facing the proton beam, and a carbon-epoxy sandwich sheet. The half layer of sensors is 0.2 mm thick. The second layer will be constructed exactly in the same way and placed at a distance 50 mm in accordance with literature [43].

Cooling of the Digital Tracking Calorimeter

For the most common operating conditions of a pCT scan, the power consumption by each chip is estimated to be 202 mW, corresponding to ~900 W for the full DTC. This estimation is based on the work of Šuljić et al. [44]. Other parts of the detector such as TCs and readout electronics also require cooling. The cooling mechanisms of each separate part of the detector, according to the requirement for each component, is described below.

Calorimeter Layers

The temperature distribution in the calorimeter layers was investigated based on the simplified geometry shown in **Figure 4**. The half layers are well isolated from each other by air gaps. The thermal resistances of chips, cables, glue, absorbers, and carrier plates perpendicular to the layers are negligible, thus a two-dimensional temperature distribution was considered. To study the steady state temperature distribution, load and geometry were assumed to be homogeneous across the string, so the temperature of a point just depends on its longitudinal coordinate. The heat transfer was studied in the absorber and carrier plates only. The detailed calculations can be found in Ref. 45. The liquid cooling system will likely use water as a coolant and each layer temperature will be monitored by temperature sensors.

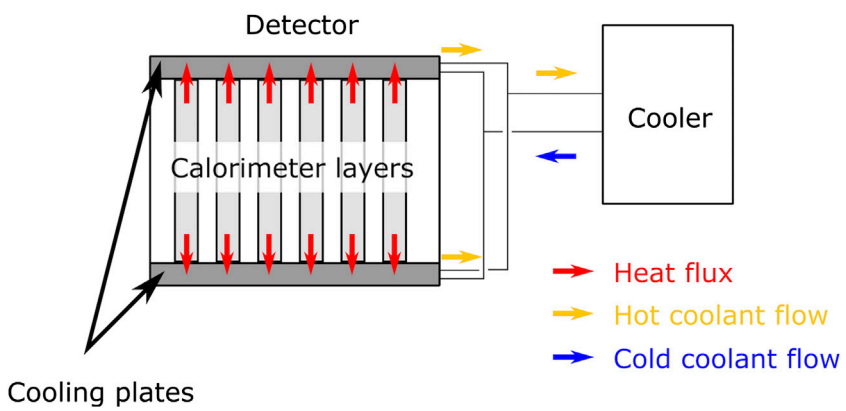

FIGURE 4 | Cooling concept of the calorimeter layers: two aluminum cold plates, each of dimension 20 mm × 290 mm × 280 mm, will be placed above and below the calorimeter layers as a part of a closed loop liquid-cooling system.

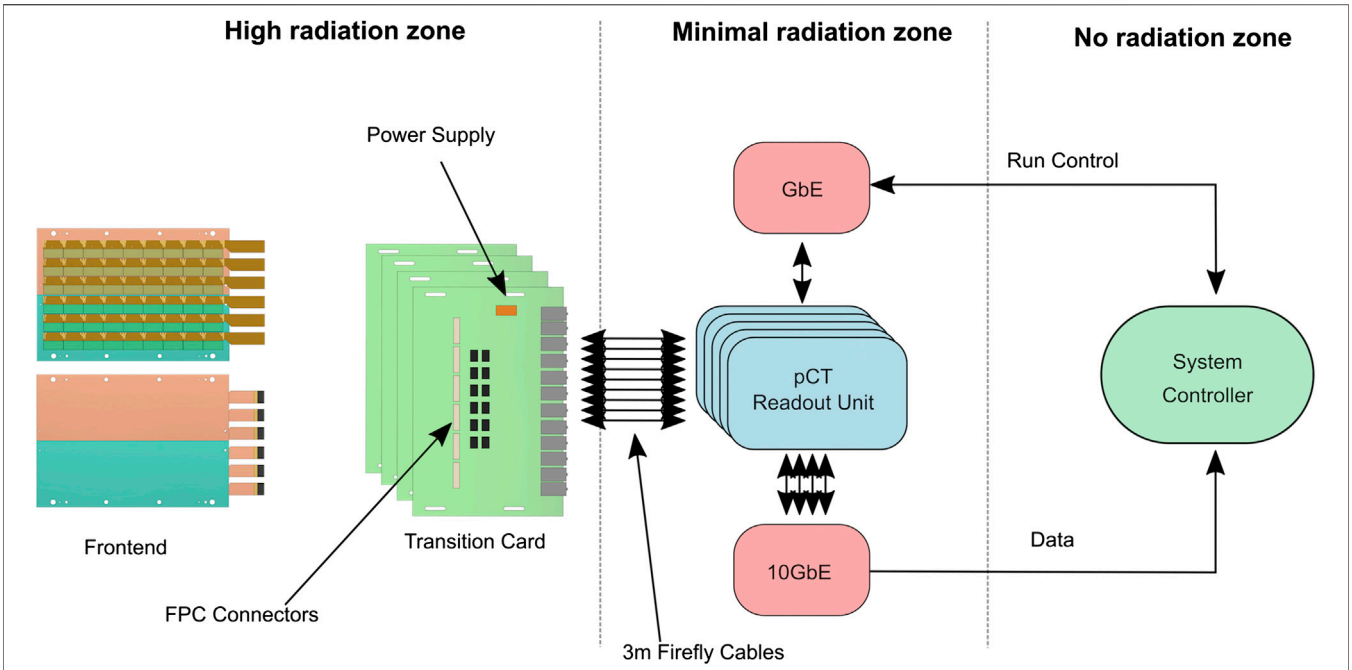

FIGURE 5 | The pCT system electronics architecture.

Tracker Layers

In the tracker layers, the chips will be mounted on very thin carbon-epoxy sandwich sheets with similar heat draining capacity as that of an aluminum sheet of the same dimension, which may pose challenges for cooling. Hence, a combination of air and liquid cooling will be used to cool these layers. As depicted in **Figure 2**, the aluminum support frames around the carbon-epoxy sandwich sheets are fitted with water cooling on the top and bottom edges. In addition, an airflow around the carbon-epoxy sandwich sheets will be used to cool the chips. Parts of the air-cooling system are not shown in **Figure 2**.

Transition Cards

The TCs will be monitored by a temperature sensor mounted on each one of them, and they will be cooled by forced air.

The Digital Tracking Calorimeter Electronics

Conceptual Design

The pCT data acquisition (DAQ) and run-control system consists of three distinct parts: 1) the frontend electronics, 2) the TC, and 3) the pCT readout unit (pRU). In **Figure 5** a schematic of the Bergen pCT system electronics architecture is shown.

The DAQ and run-control system were designed to satisfy the requirements described below.

(1) Radiation must not damage nor critically interfere with the operation of the detector. As shown in **Figure 5**, the first two components are placed in a high-radiation area, while the pRUs are placed in an area with much less ionization fluence, at least 2 m from the detector center. This reduces the particle fluence and relaxes the requirements for radiation mitigation techniques employed on the pRU. MC simulations (described in *Simulated Radiation Damage*) of the radiation environment with a beam intensity of 10^7 s^{-1} shows that for all the FPGAs of the system, one can expect a single event upset (SEU) every 2,933 s. This is within an acceptable rate and can be handled with simple off-the-shelf mitigation techniques.

(2) The system is capable to interface 108 × 43 pixel sensors with both slow control and high-speed data capture. Careful considerations were taken into account both on the frontend electronics design, the TC, and the pRU to minimize noise and errors.

(3) Clock and trigger signals must be deterministically distributed to all the sensor chips.

(4) The system must be able to handle the data stream generated by a 5 μs frame time and a proton beam intensity of at least 10^7 s^{-1}. The 5 μs frame time represents a lowest limit which should never be reached in a real case scenario. System C-simulations [46] with these numbers gave a data rate of roughly 1.4 Gbit/s for each layer [47], as shown in **Figure 6**. The simulation of data rates for the first layer of detector was performed with a 230 MeV proton scanning beam and an intensity of 10^7 s^{-1}. The pRU firmware is designed to deal with up to seven times these data rates.

The system is based on a trigger-less readout architecture, i.e., no external nor any high-level trigger system is implemented. However, a continuous sequence of pulses from the readout electronics is used to initiate data frames on the sensors. All

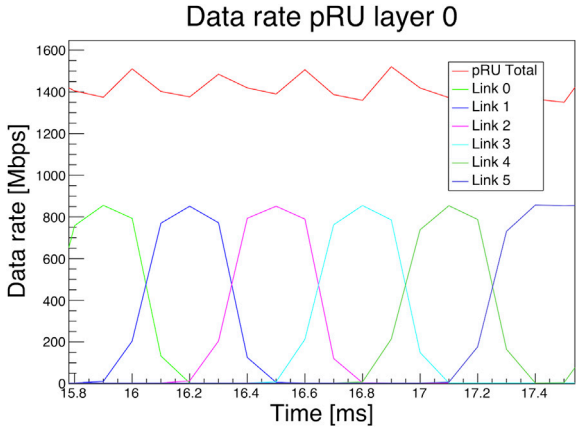

FIGURE 6 | Monte Carlo simulation of data rates for the first layer of the detector with a 230 MeV proton scanning beam and an intensity of 10^7 s^{-1}. The beam scans over the detector plane in 65 ms. The plot was published as Figure 1 in Ref. 47, Creative Commons Attribution-Non Commercial-No Derivatives 4.0 International License (CC BY-NC-ND 4.0).

pixels firing within the time frame are stored in a snapshot of data. The frame duration is set to be shorter than the pulse interval, typically slightly less than 10 μs. The gap between each frame is at minimal 25 ns, but it can be optimized in the future to avoid a lot of so-called double hits (that is a particle's signal detected within two separate frames). The frame frequency, frame duration, and gap are customizable, but always constant for a given run. When the final time between each 2D projection is known, this time is used to create trains of continuous pulses, i.e., several sequences of pulses, with longer pause between each sequence.

Frontend Electronics

Each detector layer is electrically identical and is composed of 108 ALPIDE chip sensors. Nine chips are mounted together on a string where clock and slow control signals are shared. The chips are configured in high-speed data mode, and each chip has its own 1.2 Gbit/s low-voltage differential signaling (LVDS) data link. No signal multiplexing is possible because of the periodically high data rates. As described in The DTC Layers, a full layer is constructed by having two half-layers facing each other. This causes an air gap of about 2 mm inside a layer, providing room for critical decoupling capacitors. The ALPIDEs are bonded to thin, flexible printed circuits (FPCs) of aluminum and polyimide called chip cables or flex. Single-point Tape-Automated Bonding is chosen instead of traditional wire-bonding to increase reliability [48]. The chip cables are bonded with the same method to longer FPCs in the size of the string, providing the electrical connection outside of the detector area. Using chip cables for connecting the ALPIDEs to multilayered longer FPCs allows to perform ALPIDE functional testing after Single-point Tape-Automated Bonding and exclude mounting defective chips in the strings. Such an approach allows the increase of reliability and production yield at assembling string and DTC as a whole. Several iterations of chip cables and string FPCs have been produced and tested. In the final version (**Figure 7A**), the chip cables are bonded to the 88 μm pads on the side of the ALPIDE chips. Testing the prototype of the string (**Figure 7B**) has shown that this method provides the best results in terms of jitter and noise on the high-speed links.

TC is used as an intermediate medium between the frontend electronics and the readout electronics for each layer. These cards also deliver stable power to the sensors. Six FPC connectors are mounted on each side of the printed circuit board providing both power and signaling connectivity to the sensors. As the TC is placed in a high-radiation area, only pre-tested radiation tolerant components are used for power regulation. Twelve Samtec FireFly connectors are used to transmit data from the TC, and control and clock signals from the readout electronics.

Readout Electronics

The pRU is under development but is clearly defined based on testing with the Xilinx VCU118 Evaluation Kit. The pRU is based on a Xilinx Kintex Ultrascale FPGA. The FPGA's native I/O primitives provide high enough bandwidth to handle the 108 data links without employing multi-gigabit transceiver pins reducing the need for a larger and more expensive FPGA [47]. **Figure 8** shows the functional block diagram of the pRU. The FireFly connectors are connected to the High-

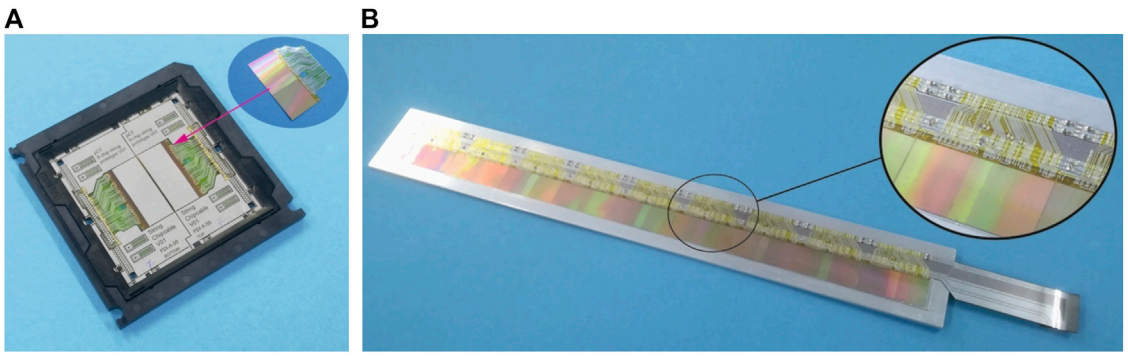

FIGURE 7 | (A) The chip cable embedded on a plastic frame with two ALICE pixel detectors (ALPIDE) mounted on it. **(B)** A pCT string containing nine ALPIDE chips.

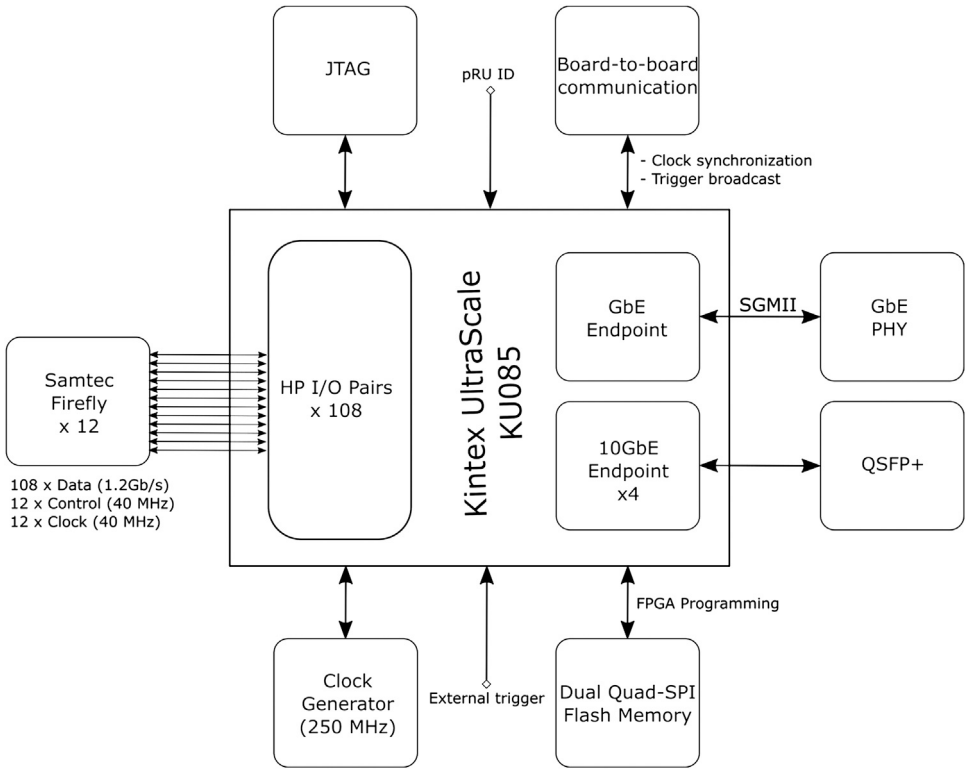

FIGURE 8 | Block diagram of the pCT readout unit board.

Performance (HP) I/O banks of the FPGA. A single I/O bank handles 24 LVDS pairs, so a total of 4.5 I/O banks are used for this purpose, less than 50% of the total available pins. Simple Gigabit Ethernet for run control is provided using IPBus protocol [49], and up to four separate 10 Gbit Ethernet links are provided to handle the data offload. A custom protocol is implemented to obtain a safe high-speed data transmission over user datagram protocol (UDP). The pRUs are placed together in a crate that supplies power and allows for board-to-board communication and synchronization.

Data Processing and Track Reconstruction

Readout Performances

During the prototype phase, the focus for the readout software is to provide small and scalable tools. An upper limit of the expected data rate is used to estimate the size of the system. The short acquisition time of approximately 1 s allows to store all data on host machines and run most of the raw data processing without intermediate or permanent storage. The pRU is supporting up to four independent 10 Gbit links for the data offload, giving a maximum amount of data of 5–10 GB per layer for a 1–2 s acquisition window. This is an upper limit; the actual data rate depends on beam conditions and the position of the layer in the setup. As illustrated in **Figure 6**, the data rate for the first layer with a realistic beam intensity will be much lower than the upper estimate. The total amount of data for an acquisition window of 1 s will be approximately 10 GB. The readout software is designed as a collection of smaller applications communicating via message queues and shared memory. These software components run independently and in parallel and can be distributed as multiple instances on several host machines. Following this variable approach, the readout system can be scaled according to the needs. The main part of the readout software is a client application connecting to servers running on the pRU hardware. Data between pRU and the client(s) are transferred using UDP network protocol. A dedicated transport format on top of UDP, the pCT Data Transport Protocol (pDTP), has been defined to ensure a reliable communication between clients and servers. Accordingly, the client application is named pDTPClient. The pDTPClient stores data in shared memory regions of the host machines and announces them to the subsequent processors. Preliminary measurements for the raw transport between pRU and host machine have been presented in Grøttvik et al. [47]. For further processing, reconstruction, and storage of data, the pRU data is handled by a parser/decoder application which unpacks and sorts ALPIDE chip data as prerequisite for further processing and monitoring of the data. For the prototype phase the collection of individual applications will be used together with scripts and command line interface.

The readout speed of the DTC can be easily adapted to the beam facility where it is operated. It can handle either spill-operated or quasi-continuous beams at synchrotron or cyclotron facilities, respectively. In any case, the estimated dataset size for a 2D

projection is limited to 400–800 GB transmitted over 1–2 s. The regular dataset size is expected to be below 400 GB over 2 s, so, as first estimate, 200 Gbit/s uplink and 20 GB/s disk write speed should be sufficient. Until first realistic full experimental runs are taking place, it is not clear how much bandwidth and latency is needed. Therefore, the system is laid out for scalability on each level. Each readout card has a Quad Small Form-factor Pluggable (QSFP+) connector that is capable of outputting 40 Gbit/s. It will be connected by 5 m copper cables ending in four 10 Gbit/s connectors on a regular 48-port ethernet switch. These switches usually have several fast uplink ports. The switch will be connected by at least two 100 Gbit/s uplinks to the DAQ computer(s). The data will be transferred first into RAM that acts as a burst buffer before writing to disk. A modern single non-volatile memory Express solid state disk, that is connected via peripheral component interconnect Express 4, can have a write performance of up to 6.5 GB/s, so a redundant array of independent disks of those solid state disks should achieve the necessary write speed of 20 GB/s. The data will be moved to a large capacity storage to free the fast redundant array of independent disks for the next measurements. Each readout card should take care of several detector layers, the exact number can be adjusted to the hit density of different layers. Current Ethernet switches can provide up to 400 Gbit/s per socket, although not with copper cables, so the few uplink cables might be optical. This will be also beneficial for a more flexible positioning of the computers. It is also possible to add more switches, if the internal bandwidth is not sufficient. Additional network interface cards with hardware offload capacity can be added. Since the data has a timestamp, the output stream can be segmented and saved on several DAQ computers to avoid bottlenecks and to be combined in a later step.

Track Reconstruction in the Digital Tracking Calorimeter

Thanks to the segmented structure of the DTC, it is possible to track proton histories crossing the several layers. In an experimental run, a high multiplicity of proton tracks will be recorded in each readout cycle in order to increase the proton rate above the electronics frame acquisition rate of ~10 μs^{-1}. The resulting data output will consist of pixel-clusters centered around each of the 50–100 proton tracks contained in a single readout. An extrapolating track-following algorithm will trace the estimated path of each proton, starting from the clusters in the distal layers of the detector [50]. A track is considered correctly reconstructed when it contains both the endpoints of the true track. Using a track scoring and track splitting model described in previous publications [36, 51], between 75 and 95% of the tracks can be correctly reconstructed, depending on object thickness, multiplicity and pencil beam size. The remaining are predominantly pairwise confused close tracks, mainly in the Gaussian core of the pencil beam, due to multiple and high angle scattering. Their effect on the reconstructed images has not been quantified but is expected to be minor due to the 3σ filters applied during image reconstruction. The *dE/dz* curve of each track can be then calculated from the sizes of the clusters along the track and a Bragg-Kleeman depth dose curve will be used for precise range fitting, for rejection of nuclear events, and for particle identification in the case of ion imaging, leading to a sub-millimeter systematic range resolution for object sizes ranging between 0 and 300 mm WEPL [36].

Expected Digital Tracking Calorimeter Performances: Experimental and Simulated Investigations

Experimental Setups

The ALPIDE chips were tested by the Bergen pCT collaboration to evaluate the response to different sources of radiation. Using an ^{241}Am source the cluster evolution within the epitaxial layer could be studied. A cluster is defined as the collection of neighboring pixels that fires within the same time frame. When a particle traverses the epitaxial layer of the ALPIDE it deposits charge, which can be collected by the individual collection diodes of the pixels. A pixel records a hit and stores it in one of the three in-pixel memory banks, if the signal from the analog front-end surpasses the threshold limit. The evolution of a cluster could be observed by using a sufficiently fast data frame rate.

To identify clusters in the readout frames, an algorithm was used that isolates one frame and loops through the pixel matrix (1,024 × 512) until it finds a hit. It then proceeds to find the nearest neighbor. If this is adjacent to the selected pixel the cluster size increases. If the nearest neighbor is not adjacent or there are no more hits in the selected frame, the cluster size is stored, and the size of the next cluster is calculated.

The cluster size distribution of low and high occupancy environments was studied to verify that the charge collection process in the analog front-end of the ALPIDE is independent of occupancy. Ideally, a low occupancy run consists in setting a particle rate low enough to have single clusters per frame, compared to high occupancy when many clusters in the same frame are collected. This is not always possible with a real beam at medical facilities, so the low occupancy was studied with a particle rate as low as possible (15 kHz) and the high occupancy with a 10 times higher rate (145 kHz).

The experimental data presented in this work were acquired at the Heidelberg Ion Therapy (HIT) facility, Heidelberg, Germany in two different experiments in July and December 2018. Proton, helium, and carbon ions were used to irradiate the ALPIDE chips. For the experiment of July 2018, a telescope detector composed of three different ALPIDEs was assembled and installed at the HIT facility. For the helium beam five different energies were tested: 220.5, 200.38, 150.11, 100.19, and 50.57 MeV/u, corresponding to a FWHM at the isocenter of 10.1, 10.2, 11.1, 12.9, and 20.6 mm, respectively. For the proton beam three energies were tested: 221.06, 200.11, and 48.12 MeV, corresponding to 12.6, 12.8, and 32.7 mm FWHM at the isocenter, respectively. The extraction time for the beam was 12 s. The data frame rate was set at 100 kHz, with a frame duration of 9.750 μs. The intensity of the beam was approximately 100 kHz. For the experiment of December 2018, in addition to proton and helium ions, also carbon ion beams were used for irradiation. The ALPIDE chips were glued to a flex cable similar to the one that will be used for the final prototype. The energies used were 48.12 MeV for protons, 50.50 MeV/u for helium, and 88.83 MeV/u for carbon. Additionally, plastic degraders [made of polymethyl methacrylate (PMMA)] were

used in order to have different sections of the Bragg curve (from plateau to peak) on the ALPIDE chip, so that the different response of the chips could be studied. The beam intensity and extraction time were the same as for the July experiment. The back bias was set to 0 V for both the experiments.

Simulated Imaging with the Digital Tracking Calorimeter

Simulation Setup

The MC framework GATE version 8.2 [52, 53] with Geant4 version 10.5.1 [54, 55] was used to build an accurate representation (described below) of the DTC sandwich structure in terms of slabs that account for the full material budget of the DTC. This model was used to simulate and reconstruct proton radiographs (pRad) and full pCT scans with different phantoms, as explained below. The physics builder list QBBC_EMZ was activated for the simulations, as recommended by the GATE Radiation Therapy and Dosimetry working group. The simulation world was filled with air with default step limits and production cuts. The step length inside the DTC was limited by the small slab thicknesses and production thresholds for γ, $e^{\pm}$ and protons were set to approximately half the slab thickness in the respective geometries inside the DTC. The mean ionization potential of water was set to 78 eV. The beam characteristics at the beam window position placed 500 mm before the isocenter are reproduced from **Table 1** in the work by Sølie et al. [37]. A total of 5,000 protons per beam spot was kept consistent across all simulations to ensure sufficient statistics and approximate the expected protons intensity of 10^7 protons per second in a realistic scenario.

Modeling of the Digital Tracking Calorimeter

The MC implemented DTC is a model of the system described in the previous sections. The MC model used in this work had exactly the same materials and material budget as the planned detector, except that all the detector components were approximated as slabs with different thicknesses to eliminate the intended overlapping structures and subsequent calibration. These components included support plates functioning as carriers and energy absorbers (carbon-epoxy sheets for the trackers, aluminum for the calorimeter), epoxy glue, ALPIDE and accompanying flex cables. The flex cables were simulated as three Al/polyimide foiled dielectric components (chip-cable, top, and bottom) and a Kapton spacer. No casings or structural supports surrounding the outside of the detector were included in the simulations since these have no impact on the proton interactions, tracking, and final energy reconstruction. The simulation reproduced the same structures of 43 ALPIDE/carrier sandwich layers described above. The layers in the calorimeter were simulated as the assembly of 3.5 mm thick aluminum plates spaced 2 mm apart, two slabs of silicon representing the ALPIDE, flex cables, and glue. This structure was repeated a total of 41 times, amounting to a length of 225.5 mm. As for the real DTC, the rear trackers differ from the calorimeter layers for the carriers made of carbon-epoxy sheets instead of aluminum, and a thinner ALPIDE chip. The total volume of the simulated DTC was 270.0 mm ×165.0 mm × 225.5 mm. In **Figure 9** a representation of the MC modeled detector with details of the slab thicknesses and materials is shown.

The distance between the first plane of the tracker pair to the phantom edge was set to 150 mm and the distance between tracking planes in each set was 50 mm based on the results from Bopp et al. [43] and Krah et al. [56].

Simulated Proton Radiographs and Proton CT

To give an estimate of the performance of the final DTC prototype, reconstructed images from GATE simulations are presented. The simulation considers a detailed model of the final tracking layers of the DTC as described in the previous section. The accuracy and precision of the reconstructed WEPL information achieved with the DTC was modeled following the detailed investigation on the systematic and stochastic uncertainty presented in the work of Pettersen et al. [36], repeating the analysis for the final 3.5 mm aluminum absorbers chosen for the DTC. The modeling was performed as a two-step process. First, the residual energy of the protons was determined from an ideal energy scorer placed right before the first tracking layer and converted to WEPL by integrating the inverse stopping power in water from initial to residual energy. The necessary stopping power table was obtained from the Geant4 code underlying the GATE simulations directly, by calculating the stopping power in water at steps of 0.01 MeV using the GetTotalDEDX function of the G4EmCalculator class. Second, to model the detector response in simulations, for each proton, the WEPL obtained from the MC simulation, calculated from the difference between the initial and outgoing energy, is shifted by the systematic uncertainty inherent to the detector response. Then, this WEPL is blurred-out by sampling from a Gaussian distribution with standard deviation given by the range straggling in the detector. These detector responses are characterized by the work done by Pettersen et al. [36] and applied to the MC model of the detector presented above. This is henceforth called the *modeled* setup.

For the sake of comparison, an ideal pCT system (no material budget in the trackers and exact energy measurement of incoming and outgoing energy) was simulated to be compared to the modeled DTC. A realistic proton therapy beam line was modeled utilizing the GATE pencil beam scanning [57]. The pencil beam lateral FWHM was set to 7 mm, with an angular divergence of 2.5 mrad and emittance of 3.0 mrad mm. An equal number of particles was used in each pencil beam spot, and the lateral distance between spots was set to 7 mm. The distance between source and isocenter was 500 mm.

Simulated Phantoms

Two different phantom geometries were implemented as described below.

- To assess the achievable RSP accuracy of the system the Catphan® (The Phantom Laboratory, Salem, NY, United States) CTP404 module (henceforth called *CTP404 phantom*) was used. The phantom is made of an epoxy

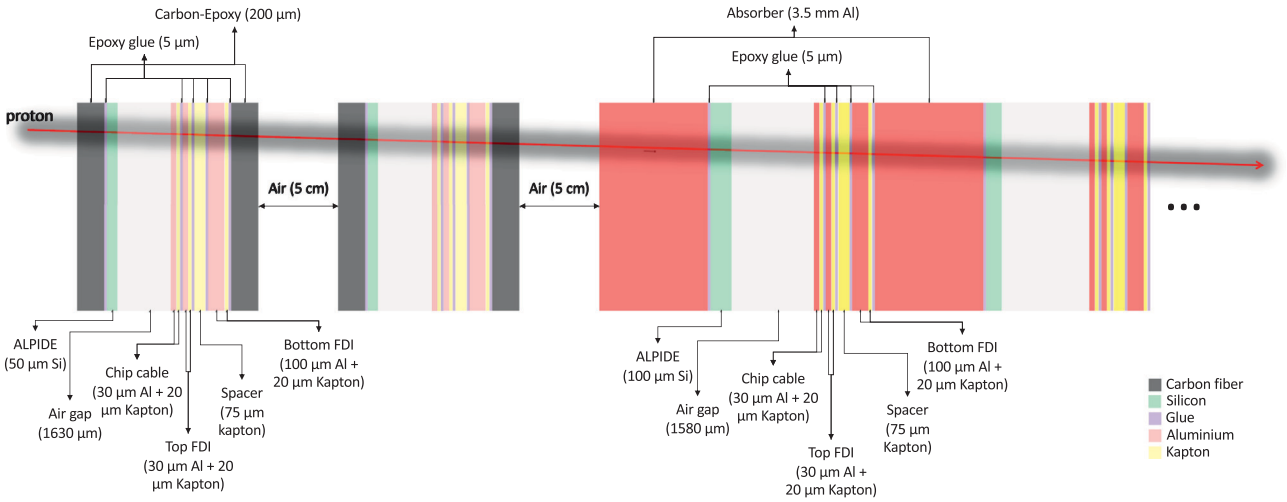

FIGURE 9 | Detector geometry consisting of slabs approximating the final material budget of the digital tracking calorimeter as implemented in the GATE simulation.

cylinder of 40 mm height, and 150 mm diameter, and contains eight cylindrical cavities of 12.2 mm diameter, six of which are filled with different plastic inserts, and 2 with air. For material and compositions please refer to Table I in Piersimoni et al. [30]. RSP values for each material were calculated from MC simulations and are: 1.363 (Delrin), 1.179 (PMMA), 1.048 (Polystyrene), 1.003 (LDPE), 0.886 (PMP), 1.833 (Teflon), and 1.143 (Epoxy).

- For a clinically relevant case, a digitized pediatric head phantom based on the CIRS model HN715 (Norfolk, VA, United States) was simulated. The head is a high resolution (0.1875 mm × 0.1875 mm × 1.25 mm) voxelized geometry implemented by Giacometti et al. [18]. The phantom comprises different human tissue materials ranging from brain to tooth enamel. A detailed tissue composition can be found in Sølie et al. [37].

The phantoms were placed such that their rotational center coincided with the isocenter of the pencil beam scanning system. The distance between the phantom edge and the first tracking layer of the DTC was 150 mm.

Image Acquisition

Full pCT scans of both phantoms were acquired in a step-and-shoot technique from 360 projections separated by 1° angular steps. This reflects the future application of the prototype, as the necessity to rely on a scanned beam for list-mode particle imaging (tracking each single particle crossing the object) without front trackers makes a continuous scan acquisition infeasible. Each projection contained 3.5×10^6 protons at initial energy of 230 MeV. A total of 1.3×10^8 protons entered the reconstruction volume of the CTP404 phantom module, and 7.9×10^8 protons entered the reconstruction volume of the head phantom. In addition, a proton radiograph was acquired of the head phantom, for which 10^7 primary protons at 230 MeV initial energy were used.

Image Reconstruction

Before image reconstruction a 2.5σ-filter on the proton angles was applied to filter out the large angle scattering not described by the scattering theory underlying the MLP [8]. Similarly, during the reconstruction, a 3σ-filter is applied to the WEPL distribution in order to remove unusually large energy losses and nuclear interactions [24]. Since the modeled WEPL does not consider the additional nuclear interactions that protons may undergo in the DTC, a 3σ-WEPL filter is sufficient to ensure high quality images [58]. For the final prototype, additional data filters will act on the track reconstruction, measured cluster sizes and the Bragg-peak fitting performed [64].

To minimize the error in the proton path estimation associated to the absence of the front tracker, the extended MLP formalism developed by Krah et al. [56] was employed, with some modifications adopted to speed up the reconstruction time, as explained below. This formalism enables MLP estimation in a single-sided setup utilizing the known parameters from the pencil beam scanning system (spot positions, lateral and angular uncertainty, as well as lateral/angular covariance). The necessary beam parameters were obtained at the same distance to the phantom as would be the innermost front tracker plane in a double-sided system.

Radiographic images were produced using the maximum likelihood image reconstruction method developed by Collins-Fekete et al. [59]. For pCT reconstructions the diagonally-relaxed orthogonal row projection iterative reconstruction algorithm with total variation superiorization was used [12]. An analytical Feldkamp-David-Kress CT reconstruction based on rear tracker binning produced the starting point for the iterative algebraic reconstruction. For computational efficiency, only the entrance and exit position/direction of each proton were calculated from the extended MLP formalism, while the extended MLP using a MLP-cubic spline path (CSP) [60] hybrid was approximated. For this hybrid, first the optimized entrance and exit position/direction vectors are calculated from the extended MLP,

then these optimized position/direction vectors are used as input to a CSP estimate. The CSP estimate results faster than the MLP as a consequence of fewer floating-point operations to be performed at each depth. Although this approximates the performance of the full extended MLP formalism, it retains the runtime benefit of the CSP algorithm. The slice thickness was set to 1.25 mm for both the phantoms, and 455 × 455 pixels per slice (0.35 mm pixel size) and 240 × 240 pixels per slice (0.75 mm pixel size) were set for the reconstruction of the CTP404 and pediatric head phantom, respectively. The data were divided into 40 optimization blocks per iteration and the algorithm was stopped after eight iterations. The reconstruction parameters were kept the same as in previous studies [18, 19, 30, 31] investigating the same phantoms with different detector designs, such that a direct comparison between different pCT systems is possible. Optimization of the parameter settings for the single-sided design was out of the scope of this work.

Simulated Radiation Damage

To perform a pCT scan, DTC and readout electronics need to be placed directly in the path of the proton beam exiting a patient. In a potential clinical setting, the DTC will also likely be fixed onto a rotating gantry and be present during proton therapy. A relatively large amount of radiation is therefore expected to hit radiation sensitive readout electronics. Inside a proton therapy treatment room where energetic hadrons are present, SEUs are expected to be the main radiation damage effect as the SRAM based FPGAs used in the pRU are particularly prone to experiencing them. SEUs are induced by single particle hits that are energetic enough to cause a change in the data state of a memory cell in the FPGA (a bit flip) and it is one of the main concerns for the pRU [61]. Other damaging effects affecting the potential lifetime of electronics include the total ionizing dose (TID) and non-ionizing energy loss (NIEL). The FLUKA MC code [62, 63] offers explicit scoring of relevant particles, called "hadrons with energy greater than 20 MeV" (HADGT20M) affecting the rate of SEU, and "fluence of Silicon 1 MeV-neutron equivalent" particles scaling with NIEL. The HADGT20M and Silicon 1 MeV-neutron equivalent fluence inside and surrounding the DTC was investigated using FLUKA version 2011-3.0 in combination with Flair version 3.0-10.

A general pCT setting consisting of 230 MeV scanned proton beams passing through a cylindrical water phantom (height 20 cm and radius 8 cm), and a separate proton therapy setting forming a 5 cm wide spread out Bragg peak (proton energies 77–116 MeV) covering a 5 cm × 5 cm × 5 cm target volume in the center of the cylindrical water phantom were tested. In these FLUKA studies, the maximum dose deposited on the ALPIDEs composing the DTC, and in six separate FPGA objects located at increasing lateral distance (10, 50, 100, 200, 300, and 400 cm) away from the DTC was evaluated.

The radiation environment formed by the two relevant particle fluences, and the deposited dose were normalized to an assumed intensity of 10^7 protons per second for pCT, and 3.11×10^8 protons per second in proton therapy. The proton intensity in proton therapy was based on an average treatment fraction delivering a physical dose of 2 Gy inside the target volume in 100 s.

The FPGA health in terms of number of SEU can be approximated by:

$$N_{SEU} = \sigma_{SEU} \times \Phi_{HEH} \times N_B, \quad (1)$$

where σ_{SEU} is the SEU cross section of the FPGA, Φ_{HEH} is the fluence of >20 MeV hadrons, and N_B is the amount of configuration memory [61].

RESULTS

ALPIDE Response

The ALPIDE chips were intensively tested to verify their response to different radiation field as described above. Exposing the ALPIDE chip to an ^{241}Am source, the evolution of the cluster shape could be observed using a 1 MHz data frame period with a frame duration of 750 ns. The signal produced by the ^{241}Am source has a time over threshold 4–6 μs, so for each pulse (every 1 μs), a data frame window matched up with the signal from the analog frontend and the hit was read out. This allowed to have the same cluster in several consequent frames. In **Figure 10A** an example of a typical cluster registered on a readout frame is reported.

In **Figure 10B** the cluster size distributions for proton, helium, and carbon ion beams at the minimum available energies at HIT (48.12 MeV, 50.57 MeV/u, and 88.83 MeV/u, respectively) are shown. As expected, the cluster size is bigger for higher linear energy transfer (LET) radiation (i.e., carbon). A second peak for small size cluster is visible for ions (more prominent for carbon) which can be attributed to nuclear fragments produced along the beam line or on the metal layer on top of the ALPIDE chip. In **Figure 10C** a hit-map on the single ALPIDE chip in a high occupancy environment for a 50.57 MeV/u helium beam is reported.

For the low (15 kHz particle rate) and high (145 kHz) occupancy runs, an average of 55.91 and 934.6 pixels firing per frame (corresponding to 0.01 and 0.17% of the total number of pixels in the ALPIDE) was readout by the ALPIDE, respectively. As shown in **Figure 10D**, the distributions are similar in shape for both high and low occupancy environments, confirming that the ALPIDE response is independent of occupancy.

In **Figure 11A** a plot of the cluster size as a function of the energy deposited on the epitaxial layer of the ALPIDE is shown. The energy deposited for different energies and particles was evaluated through the MC simulation of the 25 μm thick silicon epitaxial layer of the ALPIDE chip. The experimental data were taken from both the experiments at HIT. The points reported in the plot represent the mean of the Gaussian fit of the cluster distributions and the error bars are given by the standard deviations of such Gaussians. The relation shown in **Figure 11A**, together with a Bragg-Kleeman depth dose curve will be used to reconstruct tracks inside the DTC, allowing for precise range fitting, for rejection of nuclear events and for particle identification in the case of ion imaging, as explained above. In **Figure 11B** the fraction of correctly reconstructed

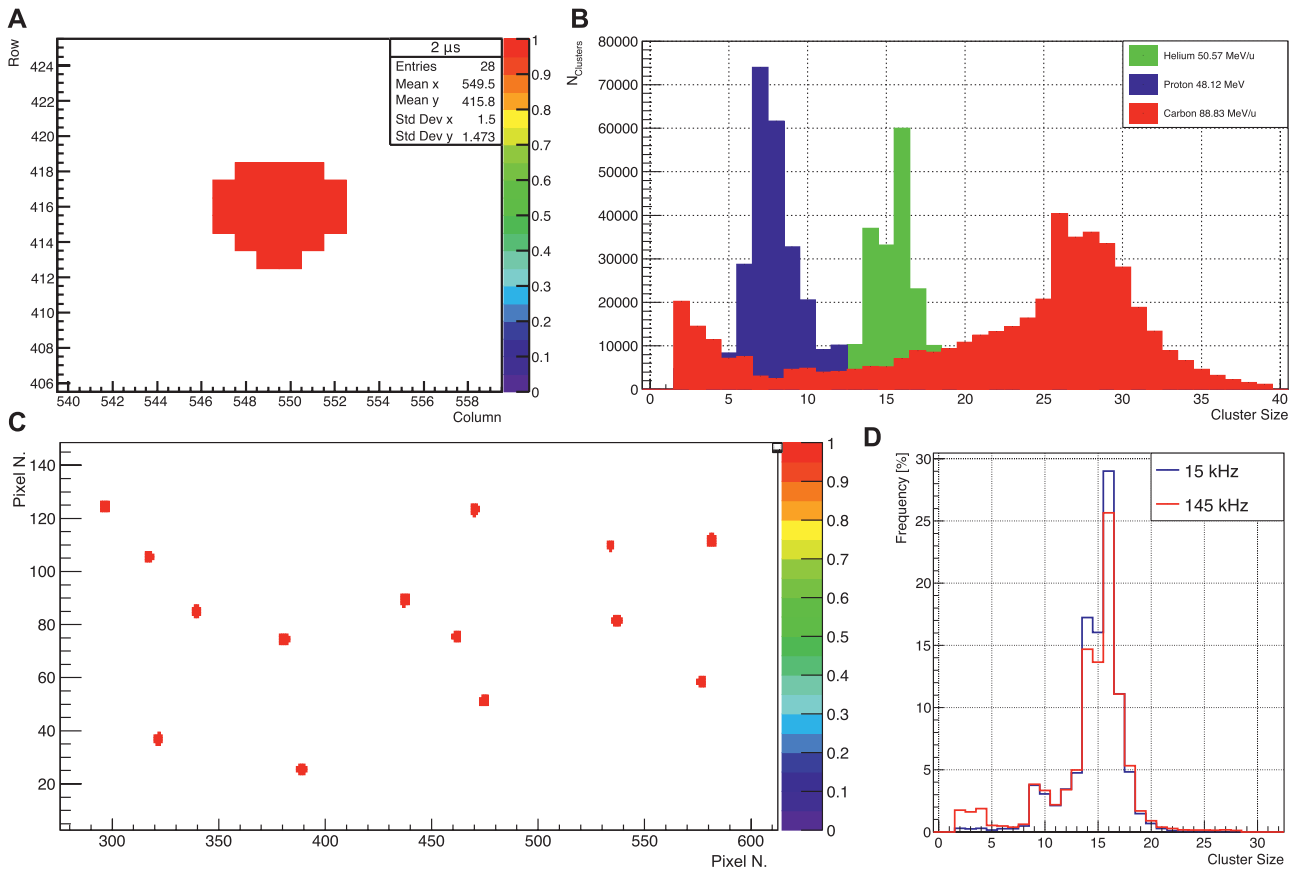

FIGURE 10 | (A) Example of a cluster detected by the ALICE pixel detector (ALPIDE) chip from an ^{241}Am source after 2 µs. Frame period 1 MHz, Frame Duration 750 ns. **(B)** Proton, helium, and carbon ion cluster distributions at the minimum energies available at HIT. **(C)** ALPIDE Hit map in a high occupancy environment. **(D)** Cluster distribution in a single ALPIDE chip in both high (15 kHz) and low (145 kHz) occupancy environments.

tracks using proton and helium primaries crossing two simulated cubic water phantoms with 5 and 16 cm size is shown. The study was performed on charge diffused MC data. For helium ions, less affected by scattering while crossing the object under study, a higher number of tracks correctly reconstructed was obtained for both phantoms [64]. The track reconstruction process currently

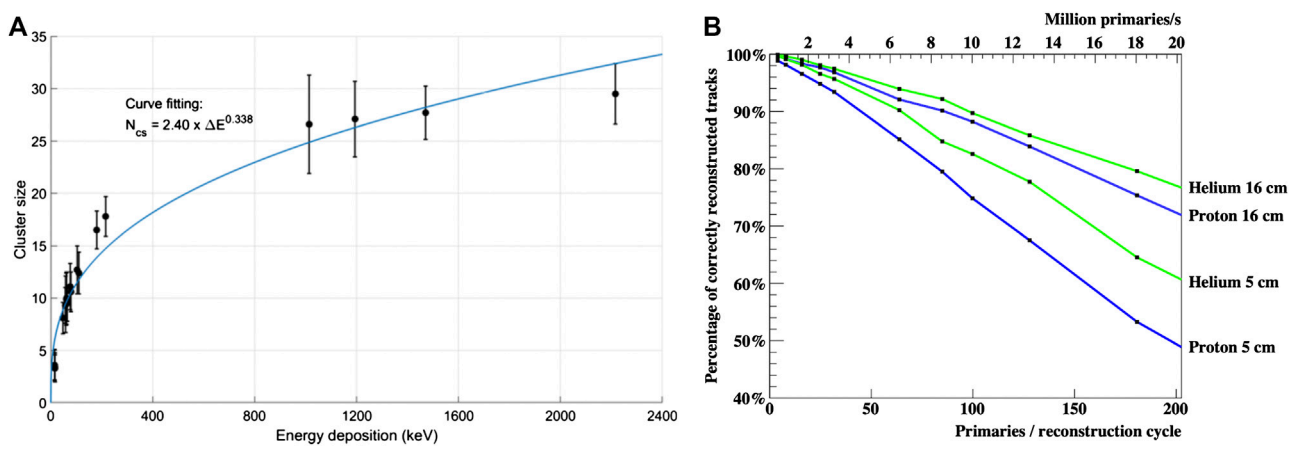

FIGURE 11 | (A) A plot of the cluster size as a function of the energy deposition in the epitaxial layer of the ALICE pixel detector (ALPIDE) chip. The energy deposition was evaluated through MC simulation, the cluster sizes are experimental point taken during the two experiments at the HIT facility. **(B)** Percentage of correctly reconstructed tracks for proton and helium primaries for two simulated water phantoms. The number of primaries per reconstruction cycle is the number of primaries in a Gaussian pencil beam with an FWHM of 7 mm. Two different imaged objects are shown with thickness of 5 and 16 cm.

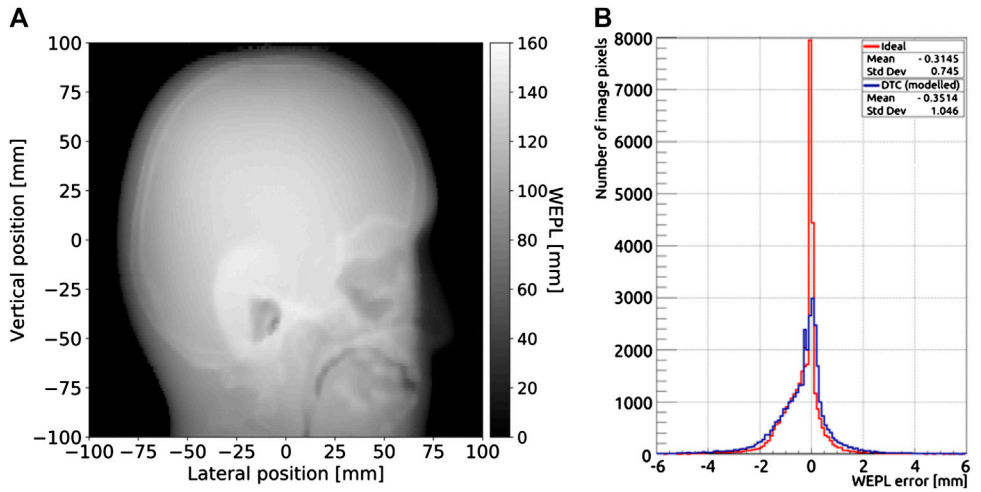

FIGURE 12 | (A) Reconstruction of a pRad of the head phantom acquired in the modeled setup. **(B)** Comparison of the distributions of the water equivalent thickness error in pRads of the head phantom for the ideal and modeled setups.

requires approximately 1.5 ms per primary track using a single Intel® Xeon® GOLD 6136 CPU @ 3 GHz. Thus, a pRad containing four million primaries could be acquired at ~0.5 s, with a reconstruction time of 2 min on the 48 available cores. However, the track reconstruction algorithm is suitable for GPU vectorization and this would further reduce the execution time.

Reconstructed Images from Simulation

In **Figure 12A** a pRad of the head phantom in the modeled DTC setup is shown. In **Figure 12B** a comparison of the distributions of the WEPL errors in pRad reconstruction for the ideal and the modeled setup is shown. The error distribution results wider for the modeled setup than for the ideal setup, 0.745 mm standard deviation of the ideal compared to the modeled 1.045 mm. For the modeled setup, a higher error is observed in the facial structures consisting of high gradient regions.

The CTP404 phantom reconstructed with a simulated full pCT scan is shown in **Figure 13A** using the DTC modeled setup. In **Figure 13B** a comparison of the average RSP percent errors (calculated as the difference between the reconstructed value and the reference value, divided by the reference value) for each material in the CTP404 phantom (excluding air) for the ideal and the modeled setups is shown. The mean RSP values were measured in a small area (shown in **Figure 13A** by the small colored circles) in the center of each insert and averaged over 10 reconstructed slices. The error bars represent the relative standard deviation of each RSP distribution. For both the setups the RSP error for each material is below 0.5%. Although in most cases (except for PMMA and Delrin) the

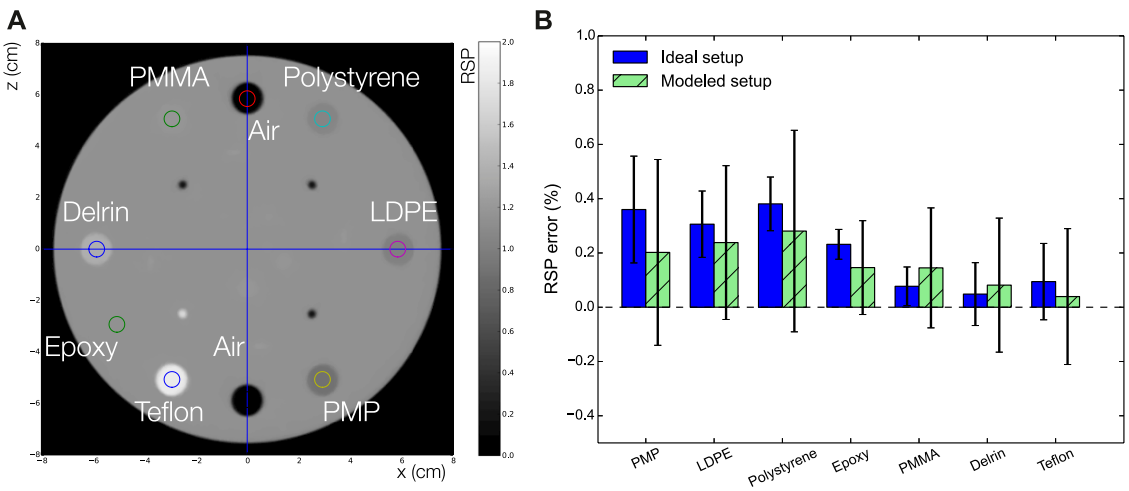

FIGURE 13 | (A) A The simulated CTP404 phantom reconstructed with a full pCT scan for the modeled setup. **(B)** Comparison of the percentage relative errors for each insert material in the CTP404 phantom for the ideal and modeled setups.

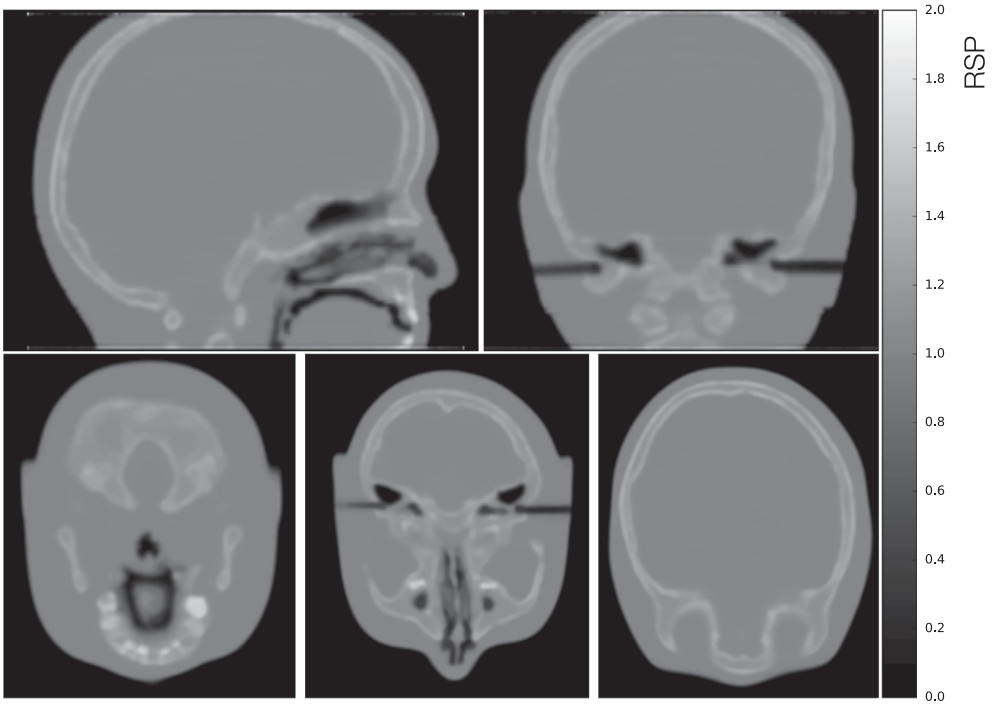

FIGURE 14 | From top left to bottom left clockwise: Sagittal, coronal, and three axial views of a full pCT reconstruction of the simulated head phantom in the modeled setup.

RSP error is smaller for the modeled setup than the ideal, the error bars for the modeled setup are sometimes two times as big as the errors, indicating a high level of noise for the modeled setup. The average error for all the materials in the CTP404 phantom is 0.214 and 0.162% for the ideal and the modeled setups, respectively. In **Figure 14** different views of the head phantom reconstructed for the modeled setup are shown. The images result clean with no artifacts and all the salient structures in the head (brain, bones, teeth, and air cavities) are well distinguishable. The reconstruction time for these images was 4,383.17 s (about 1.5 h) using an Intel® Xeon® E5-2697 v2 CPU @ 2.70GHz with 48 cores, and an NVIDIA® GeForce GTX 650 GPU.

Radiation Damage

Based on the observed fluence and dose deposited inside FPGA objects and inside the DTC, the expected SEU rate and time until FPGA and ALPIDE reach their respective TID and NIEL limits are collected in **Table 1**. According to **Eq. 1**, a single SEU event for the full system every 2,933 s is expected at a distance of 200 cm, considering σ_{SEU} equal to 1.89×10^{-15} cm^2/bit for the employed FPGAs [65] with a configuration memory of 512 Mbit.

TABLE 1 | Expected FPGA and ALPIDE health and lifetime from being exposed in both pCT and proton therapy.

Distance from DTC (cm)		pCT	Proton therapy
1 SEU		Time (s)	Time (s)
10		20.4	8.0
50		197.2	66.2
100		689.7	224.7
200		2,932.6	1,022.5
300		6,410.3	2,415.5
400		11,286.7	4,329.0
Dose (TID-limit)		**Lifetime (s)**	**Lifetime (s)**
10		1.40×10^{10}	1.14×10^{10}
50		1.23×10^{11}	7.66×10^{10}
100		6.02×10^{11}	2.89×10^{11}
200		4.12×10^{12}	1.14×10^{12}
300		6.45×10^{12}	2.35×10^{12}
400		1.43×10^{13}	3.91×10^{12}
Peak values in the ALPIDE	Dose (TID)	2.89×10^8 s	2.88×10^8 s
	NIEL limit	1.94×10^8 s	1.69×10^8 s

ALPIDE, ALICE pixel detector; DTC, digital tracking calorimeter; pCT, proton CT. All the 43 FPGAs are considered as a single system and the time it takes for a single SEU to occur is estimated (1 SEU). A conservative TID limit of 100 Gy for the FPGA is used. The ALPIDE design limits are 27,000 Gy and 1.7×10^{13} MeV n_{eq} cm^{-2} for TID and NIEL limits, respectively, as given in Mager et al. [38]. A safety factor of 10 is included in all calculations and estimations.

DISCUSSION

The work presented is a report of the design and development of the Bergen pCT scanner. The most distinguishable characteristic of the detector is the high granularity DTC which functions both as tracking system and energy/range detector, allowing a high multiplicity of incoming particle tracks to be reconstructed simultaneously. Starting from the basic ALPIDE chip, the final

prototype scanner will have a size (27 cm × 16.6 cm) big enough to image at least a human head in a single DAQ run. To achieve the necessary area, the ALPIDE chips will be bounded side by side in strings of nine mounted in flex cable which will be in turn glued on an aluminum carrier. The system comprises 43 degrader/sensor sandwiches (2 used for the rear trackers, 41 for the calorimeter) forming a single assembly, the DTC. Thanks to the technology employed, the tracker system and the calorimeter will employ the same basic sensor, the ALPIDE chip, allowing a simplification of the readout.

As described in *The Digital Tracking Calorimeter Electronics*, the electronic system is based on a trigger-less readout architecture and designed to continuously capture data with minimal integration time over a short period of time. With these features, a capture rate of 10 μs with a gap of roughly 250 ns for only few seconds will provide enough data for a single 2D-image. Therefore, a readout sequence will be started from the control room, and a single readout unit will act as a master and initiate the continuous pulse sequence from the other readout units. The dimension of a head radiograph is approximately 18 cm × 18 cm, and about 100 primaries/mm^2 after filtering are necessary for the reconstruction. Considering object and detector attenuation, track reconstruction and the whole image generation process, an effective survival rate of at least 40% can be expected for protons. This would mean that ~6 M primaries for an image are needed and since 100 primaries per readout cycle can be comfortably reconstructed, with a frame time of 10 μs this corresponds to 10 M primary particles/s, that is about half a second per radiograph. For a full pCT scan, assuming 100 primaries/mm^3 (according to Johnson et al. [66]) for a head volume of 2.26 × 10^6 mm^3, 560 M histories would be needed. This corresponds to ~60 s for a full CT acquisition and it means that the system is fast enough to be used in a clinical environment, capable to handle the high-rate medical beams used in treatment centers. The final system will be able to handle a beam frequency comparable to or better than the pCT systems currently available can manage [15], depending on the scanning modality and the beam spot size.

To allow future system upgrades, the electronics, integrated with the mechanical design, was designed with scalability in mind. Each layer of the detector requires identical units of electronics. Adding more layers to the detector will only require duplication of existing hardware and firmware. For this reason, all communication to the control room is done via Ethernet protocols, allowing simple connections of switches to add more layers. The optimized choice of chip cables and string FPCs for the system will allow a good handling of jitter and noise on the high-speed links. Regarding the readout software, a few host machines will be enough to run the applications needed to unpack and sort ALPIDE chip data and serve the full data readout. The applications can be controlled by a SCADA, a decision about the concrete Run Control system will be taken based on the experience with the prototype system. Upcoming DAQ systems, like ALICE O2, are being developed with distributed workflows in mind and can process the extreme high bandwidths requirements of upcoming LHC experiments. The same system could be also beneficial to improve the speed of data handling during a pCT scan.

Based on the TID and NIEL radiation hardness of the ALPIDE (**Table 1**) the DTC will not reach its TID limit until after 289 Ms (9.2 years) and NIEL limit after 194 Ms (6.2 years) of constant exposure to radiation from pCT. The full system with all the FPGA components at a lateral distance of 200 cm from the DTC is expected to experience a single SEU only every 2,933 s. The DTC is therefore expected to be sufficiently radiation tolerant to survive and stay healthy in the radiation environment inside a treatment room for several years without losing operational efficiency.

The preliminary experiments conducted on the single ALPIDE chip have shown the capability of the ALPIDE to handle high rate beam spills. As shown in **Figure 10D**, the chip will respond equally in both a high or low occupancy environments, giving the same averaged cluster size for particles with the same initial energy. The ALPIDE sensor response was therefore proved to be independent of occupancy. The ALPIDE was also successfully tested for higher LET beams (helium and carbon ions) showing a clear difference in response for different charged particles, even when the initial energy per nucleon was similar (**Figure 10B**). The bias voltage was set to 0 V for the experiments reported in this work. However, the use of non-zero bias could reduce the size of the clusters, enhancing the resolution of the hit position measurements. For this reason, the ALPIDE chips composing the tracker layers will be operated in bias mode. With the data collected at the HIT facility for different ion species at various energies spread all over the energy range available, it was possible to extrapolate a curve of the dependency of the cluster size on the energy deposited on the ALPIDE epitaxial layer. Thanks to the tracking algorithm and the different cluster size distributions generated from each different ion species the DTC will function as a continuous tracking device able to collect a topology of different interactions, such as hadronic processes or Coulomb scattering, which will present very different trajectory path and cluster distributions all over the 43 layers of the DTC. This will allow, prior to the reconstruction process, to discriminate different particles at different energies, meaning that it will possible to distinguish a primary (useful for the reconstruction) from a secondary (to be discarded). First investigations about distinguishing secondary particles from primary helium ions in the DTC can be found in Pettersen et al. [64].

For the modeled MC simulation, pRad, and pCT reconstructions showed encouraging results for WEPL and RSP accuracy. The modeled setup gave results comparable to the ideal setup for both pRad and pCT, reflecting the expected performances of the DTC. The mean RSP error for the reconstructed material in the CTP404 phantom was better than 0.2% for the modeled setup.

However, the mean accuracy was better than that for the ideal system. The reason could depend on the sampling from a Gaussian distribution of the WEPL blurring, which provides more flexibility to the optimization in the modeled setup rather than the ideal one. Nevertheless, the mean RSP accuracy per insert for modeled and

ideal setup agree with each other within their uncertainty. In addition, there is a large variance in the per-voxel RSP accuracy (represented by the large error bars in **Figure 13B**) present for the modeled case, as expected from the increased WEPL noise.

The pCT of the head phantom yielded clear artifact-free images, enabling the distinction of different anatomical features. However, it has to be noted that the modeled setup here presents somewhat of an ideal case scenario for the DTC performance: the accuracy of the track reconstruction in the DTC is subject to the impinging particle fluence. An increased particle fluence leads to an increased confusion of tracks, which for heterogeneous objects may influence the systematic and stochastic WEPL uncertainty. Future efforts will optimize the number of correctly reconstructed tracks in the DTC, potentially utilizing machine learning methods. Nevertheless, the overall performance of the DTC can be expected to fulfill the goal of achieving an RSP accuracy of better than 1%. The spatial resolution achievable with a single sided pCT setup was not object of the present work, but it was investigated in a previous publication [37]. A reduced performance was observed compared to that of an imaging system comprising also front tracking detectors, as expected. However, the obtained spatial resolution might be sufficient for treatment planning, where usually relatively large voxel sizes are used (typically 1 mm × 1 mm × 2 mm) so that the low sampling frequency provided by these voxels relaxes the requirement on spatial resolution. Krah et al. [56] have calculated a value of 0.3 line-pair/mm as lower limit spatial resolution needed for treatment planning. The demand on spatial resolution is therefore not very strict. A full comparison in terms of spatial resolution, noise and RSP accuracy of the DTC pCT image reconstructions to the performance of other existing pCT prototype systems will be the subject of further investigations.

At the time of writing, the device is under construction, the ALPIDE mass production has started and the first ALPIDE strings are being bonded and will be ready to be tested soon. After the testing the assembly phase will follow and the first full setup will be ready to be installed in medical facilities, presumably in 2 years. Once ready, thanks to its ability to detect and distinguish different types of radiation and its specific design, the pCT scanner can be employed not solely for proton imaging but also for additional online applications during the treatment allowing motion tracking during respiration, complementing other X-ray or surfaced based methods [67]. Given the lack of the front tracker, the detector could be positioned downstream of the patient during the treatment with a carbon-helium mixed beam, where carbon ions would be used for treatment and helium ions would be used for verification [67]. Furthermore, placing the detector beside the treated patient at an opportune angle, secondary radiation (e.g., charged nuclear fragments, neutron) originating from the Bragg peak area could be tracked for *in situ* range verification.

DATA AVAILABILITY STATEMENT

The raw data supporting the conclusions of this article will be made available by the authors, without undue reservation.

AUTHOR CONTRIBUTIONS

DR supervised the full project, PP structured and organized the whole manuscript. SM, AB, FW, GB, and ÀS worked on the mechanical design of the DTC and contribute to the writing of relative sections. OG, MR, TB, AH, ØJ, VE, KU, and HH developed the electronics and readout software and contributed to the writing of the concerning sections. VB, IT, MP, and OL were responsible for the developing, designing and creating of the chip cables, the multi-layered flexes, and the string prototypes. HP developed the tracking algorithm and wrote the related section and. HP and JRS built and run the MC simulations used for the imaging reconstruction. JRS studied the effect of radiation on the electronics and wrote the relative section. LV, JS, and SB made possible and arranged the experiments at the HIT facility. LV, OG, VE, QM, MK, ÁS, GT, JRS, and PP collaborated directly to the experiments at HIT and at the elaboration of the collected data. VE and ATS created the plots shown in the experimental results. PP and LV produced the reconstructed pCT images. The remaining co-authors contributed to the conception and the developing of the project participated in the review process of the manuscript.

FUNDING

This work is supported by the Research Council of Norway (Norges forskningsråd), grant number 250858; the Trond Mohn Foundation, grant number BFS2017TMT07; and the Hungarian National Research, Development and Innovation Office (NRDIO) OTKA K120660 and 2019-2.1.6-859NEMZ_KI-2019-00011 grants.

ACKNOWLEDGMENTS

The authors would like to thank the HIT facility for providing beam time, and the HIT accelerator engineers for helping with the beam delivery and the Thailand Center of Excellence in Physics and Development and Promotion of Science and Technology Talents Project (DPST) for supporting the Suranaree University of Technology (Nakhon Ratchasima, Thailand) on the pCT project.

REFERENCES

1. Wilson RR. Radiological use of fast protons. *Radiology* (1946) **47**(5):487–91. doi:10.1148/47.5.487
2. Lomax AJ. Myths and realities of range uncertainty. *Br J Radiol* (2020) **93**(1107): 20190582. doi:10.1259/bjr.20190582
3. Schneider U, Pedroni E, Lomax A. The calibration of CT Hounsfield units for radiotherapy treatment planning. *Phys Med Biol* (1996) **41**(1):111–24. doi:10.1088/0031-9155/41/1/009
4. Paganetti H. Range uncertainties in proton therapy and the role of Monte Carlo simulations. *Phys Med Biol* (2012) **57**(11):R99–117. doi:10.1088/0031-9155/57/11/r99
5. Yang M, Zhu XR, Park PC, Titt U, Mohan R, Virshup G, et al. Comprehensive analysis of proton range uncertainties related to patient stopping-power-ratio

estimation using the stoichiometric calibration. *Phys Med Biol* (2012) **57**(13): 4095–115. doi:10.1088/0031-9155/57/13/4095
6. Cormack AM. Representation of a function by its line integrals, with some radiological applications. *J Appl Phys* (1963) **34**(9):2722–7. doi:10.1063/1.1729798
7. Collins-Fekete CA, Volz L, Portillo SK, Beaulieu L, Seco J. A theoretical framework to predict the most likely ion path in particle imaging. *Phys Med Biol* (2017) **62**(5):1777–90. doi:10.1088/1361-6560/aa58ce
8. Schulte RW, Penfold SN, Tafas JT, Schubert KE. A maximum likelihood proton path formalism for application in proton computed tomography. *Med Phys* (2008) **35**(11):4849–56. doi:10.1118/1.2986139
9. Williams DC. The most likely path of an energetic charged particle through a uniform medium. *Phys Med Biol* (2004) **49**(13):2899–911. doi:10.1088/0031-9155/49/13/010
10. Hansen DC, Seco J, Sørensen TS, Petersen JBB, Wildberger JE, Verhaegen F, et al. A simulation study on proton computed tomography (CT) stopping power accuracy using dual energy CT scans as benchmark. *Acta Oncol* (2015) **54**(9):1638–42. doi:10.3109/0284186x.2015.1061212
11. Penfold SN, Rosenfeld AB, Schulte RW, Schubert KE. A more accurate reconstruction system matrix for quantitative proton computed tomography. *Med Phys* (2009) **36**(10):4511–8. doi:10.1118/1.3218759
12. Penfold SN, Schulte RW, Censor Y, Rosenfeld AB. Total variation superiorization schemes in proton computed tomography image reconstruction. *Med Phys* (2010) **37**(11):5887–95. doi:10.1118/1.3504603
13. Poludniowski G, Allinson NM, Evans PM. Proton computed tomography reconstruction using a backprojection-then-filtering approach. *Phys Med Biol* (2014) **59**(24):7905–18. doi:10.1088/0031-9155/59/24/7905
14. Rit S, Dedes G, Freud N, Sarrut D, Létang JM. Filtered backprojection proton CT reconstruction along most likely paths. *Med Phys* (2013) **40**(3):031103. doi:10.1118/1.4789589
15. Johnson RP. Review of medical radiography and tomography with proton beams. *Rep Prog Phys* (2018) **81**(1):016701. doi:10.1088/1361-6633/aa8b1d
16. Poludniowski G, Allinson NM, Evans PM. Proton radiography and tomography with application to proton therapy. *Br J Radiol* (2015) **88**(1053):20150134. doi:10.1259/bjr.20150134
17. Esposito M, Waltham C, Taylor JT, Manger S, Phoenix B, Price T, et al. PRaVDA: the first solid-state system for proton computed tomography. *Phys Med* (2018) **55**:149–54. doi:10.1016/j.ejmp.2018.10.020
18. Giacometti V, Bashkirov VA, Piersimoni P, Guatelli S, Plautz TE, Sadrozinski HF, et al. Software platform for simulation of a prototype proton CT scanner. *Med Phys* (2017) **44**(3):1002–16. doi:10.1002/mp.12107
19. Piersimoni P, Ramos-Mendez J, Geoghegan T, Bashkirov VA, Schulte RW, Faddegon BA. The effect of beam purity and scanner complexity on proton CT accuracy. *Med Phys* (2017) **44**(1):284–98. doi:10.1002/mp.12013
20. Plautz TE, Bashkirov V, Giacometti V, Hurley RF, Johnson RP, Piersimoni P, et al. An evaluation of spatial resolution of a prototype proton CT scanner. *Med Phys* (2016) **43**(12):6291–300. doi:10.1118/1.4966028
21. Dedes G, Dickmann J, Niepel K, Wesp P, Johnson RP, Pankuch M, et al. Experimental comparison of proton CT and dual energy x-ray CT for relative stopping power estimation in proton therapy. *Phys Med Biol* (2019) **64**(16): 165002. doi:10.1088/1361-6560/ab2b72
22. Yang M, Virshup G, Clayton J, Zhu XR, Mohan R, Dong L. Theoretical variance analysis of single- and dual-energy computed tomography methods for calculating proton stopping power ratios of biological tissues. *Phys Med Biol* (2010) **55**(5):1343–62. doi:10.1088/0031-9155/55/5/006
23. Depauw N, Seco J. Sensitivity study of proton radiography and comparison with kV and MV x-ray imaging using GEANT4 Monte Carlo simulations. *Phys Med Biol* (2011) **56**(8):2407–21. doi:10.1088/0031-9155/56/8/006
24. Schulte RW, Bashkirov V, Loss Klock MC, Li T, Wroe AJ, Evseev I, et al. Density resolution of proton computed tomography. *Med Phys* (2005) **32**(4): 1035–46. doi:10.1118/1.1884906
25. Collins-Fekete C-A, Volz L, Portillo SKN, Beaulieu L, Seco J. A theoretical framework to predict the most likely ion path in particle imaging. *Phys Med Biol* (2017) **62**(5):1777–90. doi:10.1088/1361-6560/aa58ce
26. Gehrke T, Gallas R, Jäkel O, Martišíková M. Proof of principle of helium-beam radiography using silicon pixel detectors for energy deposition measurement, identification, and tracking of single ions. *Med Phys* (2018) **45**(2):817–29. doi:10.1002/mp.12723
27. Hansen DC, Bassler N, Sørensen TS, Seco J. The image quality of ion computed tomography at clinical imaging dose levels. *Med Phys* (2014) **41**(11):111908. doi:10.1118/1.4897614
28. Magallanes L, Meyer S, Gianoli C, Kopp B, Voss B, Jakel O, et al. Upgrading an integrating carbon-ion transmission imaging system with active scanning beam delivery toward low dose ion imaging. *IEEE Trans Radiat Plasma Med Sci* (2020) **4**(2):262–8. doi:10.1109/trpms.2019.2948584
29. Martišíková M, Gehrke T, Berke S, Aricò G, Jäkel O. Helium ion beam imaging for image guided ion radiotherapy. *Radiat Oncol* (2018) **13**(1):109. doi:10.1186/s13014-018-1046-6
30. Piersimoni P, Faddegon BA, Mendez JR, Schulte RW, Volz L, Seco J. Helium CT: Monte Carlo simulation results for an ideal source and detector with comparison to proton CT. *Med Phys* (2018) **45**(7):3264–74. doi:10.1002/mp.12942
31. Volz L, Piersimoni P, Bashkirov VA, Brons S, Collins-Fekete C-A, Johnson RP, et al. The impact of secondary fragments on the image quality of helium ion imaging. *Phys Med Biol* (2018) **63**(19):195016. doi:10.1088/1361-6560/aadf25
32. De Haas AP, Nooren G, Peitzmann T, Reicher M, Rocco E, Röhrich D, et al. The FoCal prototype-an extremely fine-grained electromagnetic calorimeter using CMOS pixel sensors. *J Inst Met* (2018) **13**(01):P01014. doi:10.1088/1748-0221/13/01/p01014
33. Rocco E. Highly granular digital electromagnetic calorimeter with MAPS. *Nucl Part Phys Proc* (2016) **273–275**:1090–5. doi:10.1016/j.nuclphysbps.2015.09.171
34. Pettersen HES. *A digital tracking calorimeter for proton computed tomography*. [PhD thesis]. Bergen (Norway): University of Bergen (2018)
35. Pettersen HES, Alme J, Biegun A, Van Den Brink A, Chaar M, Fehlker D, et al. Proton tracking in a high-granularity digital tracking calorimeter for proton CT purposes. *Nucl Instrum Methods Phys Res A* (2017) **860**:51–61. doi:10.1016/j.nima.2017.02.007
36. Pettersen HES, Alme J, Barnaföldi GG, Barthel R, Van Den Brink A, Chaar M, et al. Design optimization of a pixel-based range telescope for proton computed tomography. *Phys Med* (2019) **63**:87–97. doi:10.1016/j.ejmp.2019.05.026
37. Sølie JR, Volz L, Pettersen HES, Piersimoni P, Odland OH, Roehrich D, et al. Image quality of list-mode proton imaging without front trackers. *Phys Med Biol* (2020) **65**(13):135012. doi:10.1088/1361-6560/ab8ddb
38. Mager M. ALPIDE, the monolithic active pixel sensor for the ALICE ITS upgrade. *Nucl Instrum Methods Phys Res B* (2016) **824**:434–8. doi:10.1016/j.nima.2015.09.057
39. Yang P, Aglieri G, Cavicchioli C, Chalmet PL, Chanlek N, Collu A, et al. Low-power priority address-encoder and reset-decoder data-driven readout for monolithic active pixel sensors for tracker system. *Nucl Instrum Methods Phys Res B* (2015) **785**:61–9. doi:10.1016/j.nima.2015.02.063
40. Aglieri Rinella G. The ALPIDE pixel sensor chip for the upgrade of the ALICE inner tracking system. *Nucl Instrum Methods Phys Res B* (2017) **845**:583–7. doi:10.1016/j.nima.2016.05.016
41. Poonsawat W, Kobdaj C, Sitta M, Yan Y. Stave module design and development of the new ALICE inner tracking system. *J Instrum* (2019) **14**(05):P05003. doi:10.1088/1748-0221/14/05/p05003
42. Zherebchevsky VI, Altsybeev IG, Feofilov GA, Francescon A, Gargiulo C, Igolkin SN, et al. Experimental investigation of new ultra-lightweight support and cooling structures for the new inner tracking system of the ALICE detector. *J Instrum* (2018) **13**(08):T08003. doi:10.1088/1748-0221/13/08/t08003
43. Bopp C, Rescigno R, Rousseau M, Brasse D. The impact of tracking system properties on the most likely path estimation in proton CT. *Phys Med Biol* (2014) **59**(23):N197–210. doi:10.1088/0031-9155/59/23/n197
44. Šuljić M. ALPIDE: the monolithic active pixel sensor for the ALICE ITS upgrade. *J Instrum* (2016) **11**:C11025. doi:10.1088/1748-0221/11/11/c11025
45. Sudár Á. *Measurement of the temperature distribution inside a calorimeter*. [BSc thesis]. Budapest (Hungary): Budapest University of Technology and Economics (2020)
46. IEEE standard systemC(R) language reference manual. In: IEEE Std 1666-2005; 2006 Mar 31; IEEE. p. 1–423. doi:10.1109/IEEESTD.2006.99475

47. Grøttvik O, Alme J, Barthel R, Bodova T, Borshchov V, Van den Brink A, et al. Development of readout electronics for a digital tracking calorimeter. In: Topical workshop on electronics for particle physics; 2020 Mar (2019) p. 370. doi:10.22323/1.370.0090
48. Borshchov VM, Listratenko OM, Protsenko MA, Tymchuk IT, Fomin OO. Innovative microelectronic technologies for high-energy physics experiments. *Met Funct Mater* (2017) **23**(4):143–53. doi:10.15407/fm24.01.143
49. Larrea CG, Harder K, Newbold D, Sankey D, Rose A, Thea A, et al. IPbus: a flexible Ethernet-based control system for xTCA hardware. *J Instrum* (2015) **10**(02):C02019. doi:10.1088/1748-0221/10/02/c02019
50. Strandlie A, Frühwirth R. Track and vertex reconstruction: from classical to adaptive methods. *Rev Mod Phys* (2010) **82**(2):1419–58. doi:10.1103/revmodphys.82.1419
51. Pettersen HES, Meric I, Odland OH, Shafiee H, Sølie JR, Röhrich D. Proton tracking algorithm in a pixel-based range telescope for proton computed tomography. In: CTD2018 EPJ web of conferences; 2018 Mar 20–22; Seattle, WA (Forthcoming 2018) Available from: https://arxiv.org/abs/2006.09751 (Accessed June 2020).
52. Jan S, Benoit D, Becheva E, Carlier T, Cassol F, Descourt P, et al. GATE V6: a major enhancement of the GATE simulation platform enabling modelling of CT and radiotherapy. *Phys Med Biol* (2011) **56**(4):881–901. doi:10.1088/0031-9155/56/4/001
53. Jan S, Santin G, Strul D, Staelens S, Assié K, Autret D, et al. GATE: a simulation toolkit for PET and SPECT. *Phys Med Biol* (2004) **49**(19):4543–61. doi:10.1088/0031-9155/49/19/007
54. Agostinelli S, Allison J, Amako K, Apostolakis J, Araujo H, Arce P, et al. Geant4—a simulation toolkit. *Nucl Instrum Methods Phys Res A* (2003) **506**(3):250–303. doi:10.1016/s0168-9002(03)01368-8
55. Allison J, Amako K, Apostolakis J, Araujo H, Arce Dubois P, Asai M, et al. Geant4 developments and applications. *IEEE Trans Nucl Sci* (2006) **53**(1):270–8. doi:10.1109/tns.2006.869826
56. Krah N, Khellaf F, Letang JM, Rit S, Rinaldi I. A comprehensive theoretical comparison of proton imaging set-ups in terms of spatial resolution. *Phys Med Biol* (2018) **63**(13):135013. doi:10.1088/1361-6560/aaca1f
57. Grevillot L, Bertrand D, Dessy F, Freud N, Sarrut D. GATE as a GEANT4-based Monte Carlo platform for the evaluation of proton pencil beam scanning treatment plans. *Phys Med Biol* (2012) **57**(13):4223–44. doi:10.1088/0031-9155/57/13/4223
58. Volz L, Piersimoni P, Johnson RP, Bashkirov VA, Schulte RW, Seco J. Improving single-event proton CT by removing nuclear interaction events within the energy/range detector. *Phys Med Biol* (2019) **64**(15):15NT01. doi:10.1088/1361-6560/ab2671
59. Collins-Fekete CA, Brousmiche S, Portillo SK, Beaulieu L, Seco J. A maximum likelihood method for high resolution proton radiography/proton CT. *Phys Med Biol* (2016) **61**(23):8232–48. doi:10.1088/0031-9155/61/23/8232
60. Collins-Fekete C-A, Doolan P, Dias MF, Beaulieu L, Seco J. Developing a phenomenological model of the proton trajectory within a heterogeneous medium required for proton imaging. *Phys Med Biol* (2015) **60**(13):5071–82. doi:10.1088/0031-9155/60/13/5071
61. Røed K. *Single event upsets in SRAM FPGA based readout electronics for the time projection chamber in the ALICE experiment*. [Doctoral thesis]. Bergen (Norway): University of Bergen (2009)
62. Böhlen TT, Cerutti F, Chin MPW, Fassò A, Ferrari A, Ortega PG, et al. The FLUKA code: developments and challenges for high energy and medical applications. *Nucl Data Sheets* (2014) **120**:211–4. doi:10.1016/j.nds.2014.07.049
63. Ferrari A, Sala PR, Fasso A, Ranft J. *FLUKA: a multi-particle transport code*. Report No.: INFN-TC-05-11. Geneva, Switzerland: CERN (2005)
64. Pettersen HES, Volz L, Sølie JR, Alme J, Barnaföldi GG, Barthel R, et al. *Helium radiography with a digital tracking calorimeter—a Monte Carlo study for secondary track rejection*. Manuscript submitted to Physics in Medicine and Biology (2020)
65. Hiemstra DM, Kirischian V, Brelski J. Single event upset characterization of the Kintex UltraScale field programmable gate array using proton irradiation. In: IEEE radiation effects data workshop (REDW); 2016 June 11–15; Portland, United States (2016) p. 1–5.
66. Johnson RP, Bashkirov V, Dewitt L, Giacometti V, Hurley RF, Piersimoni P, et al. A fast experimental scanner for proton CT: technical performance and first experience with phantom scans. *IEEE Trans Nucl Sci* (2016) **63**(1):52–60. doi:10.1109/tns.2015.2491918
67. Spadea MF, Baroni G, Gierga DP, Turcotte JC, Chen GTY, Sharp GC. Evaluation and commissioning of a surface based system for respiratory sensing in 4D CT. *J Appl Clin Med Phys* (2011) **12**(1):162–169.
68. Kim D, Rinella GA, Cavicchioli C, Chanlek N, Collu A, Degerli Y, et al. Front end optimization for the monolithic active pixel sensor of the ALICE inner tracking system upgrade. *J Inst Met* (2016) **11**(02):C02042. doi:10.1088/1748-0221/11/02/c02042

Conflict of Interest: The authors declare that the research was conducted in the absence of any commercial or financial relationships that could be construed as a potential conflict of interest.

The reviewer CG declared a past co-authorship with one of the authors SB to the handling editor.

frontiers in Physics

ORIGINAL RESEARCH
published: 22 October 2020
doi: 10.3389/fphy.2020.564836

Proposal of a Chemical Mechanism for Mini-Beam and Micro-Beam Efficacy

Riccardo Dal Bello[1,2,3†], *Tobias Becher*[1,2†], *Martina C. Fuss*[4], *Michael Krämer*[4] and *Joao Seco*[1,2*]

[1] Division of Biomedical Physics in Radiation Oncology, German Cancer Research Center (DKFZ), Heidelberg, Germany, [2] Department of Physics and Astronomy, Heidelberg University, Heidelberg, Germany, [3] Department of Radiation Oncology, University Hospital Zurich, University of Zurich, Zurich, Switzerland, [4] Biophysics Department, GSI Helmholtzzentrum für Schwerionenforschung, Darmstadt, Germany

OPEN ACCESS

Edited by:
Yolanda Prezado,
INSERM U1021 Signalisation normale et pathologique de l'embryon aux thérapies innovantes des cancers, France

Reviewed by:
Morgane Dos Santos,
Institut de Radioprotection et de Sûreté Nucléaire, France
Till Tobias Böhlen,
Center Hospitalier Universitaire Vaudois (CHUV), Switzerland
Rachel Delorme,
UMR5821 Laboratoire De Physique Subatomique Et Cosmologie (LPSC), France

***Correspondence:**
Joao Seco
j.seco@dkfz-heidelberg.de

[†] These authors have contributed equally to this work

Specialty section:
This article was submitted to Medical Physics and Imaging, a section of the journal Frontiers in Physics

Received: 22 May 2020
Accepted: 11 September 2020
Published: 22 October 2020

Citation:
Dal Bello R, Becher T, Fuss MC, Krämer M and Seco J (2020) Proposal of a Chemical Mechanism for Mini-Beam and Micro-Beam Efficacy. Front. Phys. 8:564836. doi: 10.3389/fphy.2020.564836

This simulation study proposes a chemical mechanism to define a surrogate to the tumor control during micro- and mini-beam radiation therapy (MBRT). The main focus is proton-MBRT (pMBRT) and the methods developed are applied also to photon-MBRT (MRT). In both cases, the classical interpretation of physical dose cannot be used to explain the observed biological effect and a change of paradigm may be required. MBRT was reported to provide tumor control with reduced side effects when compared to standard dose delivery. The underlying mechanisms leading to a differential response of the normal tissue and the tumor are still unknown. In this work, we propose a chemical mechanism to describe the efficacy of MBRT. The model was developed starting from the observation that pMBRT led to long term survival without significant side effects of rats implanted with a high-grade glioma. We distribution of a generic radiation-induced molecule or radical could be a surrogate to describe the biological effect. The specific mechanisms leading to cell damage were outside the scope of this work. The molecules and radicals were selected according to a set of properties: (i) they should be stable to allow diffusion achieving coverage of the dose-valleys, (ii) they should reach a steady state in production versus removal, (iii) they should be a product of water radiolysis, and (iv) they should have oxidizing capacity. A convolution model was developed to assess the property (i) keeping the analysis as general as possible. The tumor coverage was defined widening the interpretation of the ICRU-62 recommendations. The properties (ii) and (iii) were investigated with the TRAX-CHEM software. The property (iv) was used to exclude not relevant chemical species. The results show that hydrogen peroxide fulfills all the requirements. Moreover, the modeling of its temporal and spatial distributions demonstrate that a uniform coverage of the target by this reactive oxygen specie (ROS) can be achieved during the beam-on time. The model was compared and proven to be compatible with three independent photon micro-beam and proton mini-beam animal experiments. We conclude that hydrogen peroxide is a good candidate to describe the mini-beam and micro-beam efficacy. Further experiments are proposed to experimentally benchmark the model and to correlate the hydrogen peroxide concentration to the tumor control probability.

Keywords: mini-beam, micro-beam, TRAX, MBRT, proton therapy, proton mini-beam, hydrogen peroxide, spatially fractionated radiation therapy

1. INTRODUCTION

Technological developments play an important role in the improvement of cancer therapy. Radiation-therapy is, in particular, a rapidly evolving field and it is used as a form of treatment for as many as half of the cancer patients [1]. The refinement of the treatment techniques improved patient care and led to an increase in the survival rate. Long term survivors are the ones who potentially benefit the most from the developments aiming to reduce the side effects of radiation-therapy. The most commonly chosen approach to affect the lesions without inducing side effects is improving the conformality of the dose delivery. A prominent example is the increasing usage of advanced photon delivery techniques such as volumetric modulated arc therapy [2]. Further reduction to the dose delivered to normal tissue may be obtained with beams of charged particles. While electron beams can be employed for superficial tumors, high energy proton, and ion beams allow to escalate the dose to deep located target volumes while reducing the burden to the normal tissue due to their physical and biological characteristics [3]. Further improvements will be investigated at the new generation facilities [4]. In general, the approaches adopted in clinical practice aim to achieve tumor control by delivering a uniform dose to the target volume. In pre-clinical studies several other options have been investigated, which not always base their rationale on uniform dose distributions and conformality. A prominent case is the micro- and mini-beam radiation therapy (MBRT), where a spatial pattern of high-dose beamlets alternates with low-dose valleys. This has been investigated in animal experiments with photon beams (MRT) at synchrotron facilities [5] and recently at dedicated light sources [6]. Also recently, proton beams were deployed as well (pMBRT) [7]. The investigation of MBRT requires a change of paradigm. The reduction of the side effects to the organs at risk are not achieved by reducing their integral dose, but thanks to a differential response of normal and tumor tissue to the radiation delivered with a well-defined spatial fractionation. Two recent studies investigated the tumor response to MRT for mice implanted with squamous carcinoma [6] and to pMBRT for rats implanted with high-grade glioma [8]. In the former, the tumor growth delay was compared between a tumor-bearing control group, mice treated with broad-beam and with micro-beams. Two different dose levels were investigated. In the latter, a long term follow-up was performed to monitor the side effects and tumor response for normal and tumor-bearing animals. The rats were either part of the control group or were treated with mini-beams at one dose level. The animal experiments reported that pMBRT preserved the tumor control. The interpretation of such result is the aim of the current study. Moreover, a previous MRT study performed at a synchrotron facility was also taken into account [9]. In this case, Regnard et al. found that the probability to ablate the implanted intracerebral 9L gliosarcoma increased by a factor more than 7 when decreasing the spacing of micro-beams from 200 to 100 μm. Differences in normal tissue toxicity were also observed, but will not be further investigated in the current study, which will focus on the MBRT efficacy in tumor tissue. All the previous studies included histological analysis.

MBRT has been investigated at two different spatial scales. In both cases, the setup utilizes arrays of parallel thin radiation planes separated by short distances. In first approximation, along the transverse profile, the radiation can be modeled by a series of equidistant rectangular peaks separated by valleys without direct delivery of the beam. We aimed to keep the study as simple as possible in order to avoid biases in the results due to the choice of free parameters. The profiles can be characterized by their center-to-center distance *c-t-c*, i.e., the spacing between the areas with direct radiation, and the full width half maximum of the radiation peaks *FWHM*. In the case of mini-beams, the *c-t-c* can be as wide as few millimeters and the *FWHM* up to the millimeter scale [8]. To achieve such beam profiles, dedicated mechanical collimators are typically designed [10]. The presence of a collimator leads on one hand to a reduction of the dose rate with respect to a broad beam irradiation and on the other hand to scattering of the primary radiation. The former is taken into account in the current study by analyzing the total irradiation time, which if long enough may allow the propagation of radiolysis products in the valleys. The latter leads to the presence of a non-zero dose in the valleys, which is then characterized by the peak to valley dose ratio *PVDR*. High values are achievable with novel techniques such as magnetic focusing for ion beams [11]. The physical dose delivered in the valleys is therefore small compared to the average dose delivered in the tumor, which leads to a significant part of the tumor volume to be under-dosed. Nonetheless, several animal experiments report delayed tumor growth [6], improved survival fraction [12], and tumor control with cases of tumor eradication [8]. Such effects cannot be explained by the low physical dose delivered to the valleys. Alternative interpretations including cell-signaling cascades have been proposed for the normal tissue sparing [13]. Recently, the correlation between tissue damage and the level of reactive oxygen species (ROS) has been proposed [14]. The related radiolysis products can be nowadays accurately modeled by dedicated simulation codes, such as TRAX-CHEM [15]. This work aims to fill the gap in the interpretation of the tumor control observed in MBRT, combining the previously mentioned results to investigate a chemical mechanism for mini-beam and micro-beam efficacy.

This study consists in three subsequent phases. First, we investigate the spatial distributions of the physical dose and the radiolysis products during MBRT. Then, we analyze and model the spatial and temporal evolution of the molecules and radicals produced by the radiation beam. Finally, the model is used to interpret previous MBRT animal experiments.

2. MATERIALS AND METHODS

The spatial distribution of ROS was investigated to develop a model interpreting the MBRT efficacy. The current work was based on simulations and it provides a more in-depth analysis of previously published MBRT animal studies. No animal experiments were conducted within the current study.

The model was developed starting from the observation that pMBRT led to long term survival without significant side effects of rats implanted with a high-grade glioma [8]. It was then applied to MRT used to irradiate mice with squamous carcinoma [6] and rats with intracerebral 9L gliosarcoma [9]. We selected the three previously cited studies since they provided all the parameters required to compare the simulations to the experimental data. Namely, the complete dosimetric description of the irradiation, the total irradiation time, and the observation of a biological effect. We investigated whether the distribution of a radiation-induced molecule or a radical could be a surrogate to describe the biological effect. The specific mechanisms leading to cell damage were outside the scope of this work. Four properties were defined, to restrict the investigation solely to relevant radiation-induced molecules or radicals. The conditions were:

(i) it should be stable to allow diffusion during beam-on, achieving coverage of the dose-valleys
(ii) it should reach a steady state in production versus removal within few microseconds of beam-on
(iii) it should be a product of water radiolysis
(iv) it should have oxidizing capacity to allow damage of proteins, lipids and DNA.

The choice of the conditions was motivated by the following properties. (i) The relevant distance of diffusion is the one that the molecules and radicals can reach during beam-on. In absence of radiation, the reactive chemical species are rapidly removed by antioxidants [16]. (ii) The steady state is required since the time scale of the biological effects is much longer compared to the one of the physics phenomena that trigger the process. Fast processes that do not reach the steady state, while contributing indirectly to the steady state of other processes, are not expected to be directly correlated to a biological effect. The radiation-induced molecules or radicals that reach the steady state are chosen as a potential surrogate for the biological effect. (iii) The surrogate for the biological effect of MBRT should be directly or indirectly generated by ionizing radiation. Therefore, other processes leading to water dissociation were excluded. (iv) The reactivity of the molecule or radical is required in order to induce a chemical or biological effect.

The study was divided in three subsequent phases. First, the property (i) was assessed keeping the analysis as general as possible. We investigated the diffusion of molecules and radicals from their production in the peaks to the valleys. No constraints were imposed at this stage. The details are presented in section 2.1. The second phase investigated the properties (ii) and (iii) with the software TRAX-CHEM [17]. The simulations were based on the properties of the proton mini-beams reported by [8]. The spatial distributions of twelve different molecules and radicals were tracked over several orders of magnitude of their time evolution. The details are provided in section 2.2. Finally, in the third phase, we compared the characteristic diffusion times of the molecules and radicals with the irradiation times adopted in the previous mini-beam [8] and micro-beam [6] animal studies. The methodology of the comparison is presented in section 2.3.

2.1. Generalization of the Dose Coverage Concept

2.1.1. From Physical Dose to *gRM* Concentration

This study investigates the secondary water products produced by radiation, known as radiolysis. We define *gRM* as the generic Radical or Molecule produced during radiolysis, and that diffuses through the cells after being produced. The international recommendation of ICRU established that the dose values in the PTV should be confined within 95 to 107% of the prescribed dose [18]. This classical concept of physical dose coverage of the target volume is not respected in MBRT, due to the presence of low-dose valleys (**Figure 1**). We hypothesize that a coverage within 95 and 107% is not provided directly by the physical dose, but by a secondary product of the interaction between ionizing radiation and water target. As a matter of fact, the values assumed by the physical dose will not enter directly our model, which will focus on the distribution of the secondary products. The *gRM* is created at the interaction point between the ionizing radiation and the target and it can be any of the radicals and molecules listed in **Table 1**. Its concentration at the moment of creation is assumed to be directly proportional to the physical dose. Starting from a point-like physical dose distribution and assuming the condition (i) to be respected, at a given time point, the *gRM* will have a given spatial distribution. Keeping the analysis as general as possible, we model such distribution with a Gaussian function. In a one dimensional representation, the *gRM* distribution is parameterized by its amplitude A_k, standard deviation σ_k and mean μ_k. While $\mu_k = 0$ for the symmetry properties of the problem, the other parameters evolve in time according to the specific properties of each radical or molecule: $A_k := A_k(t)$ and $\sigma_k := \sigma_k(t)$. Given a physical dose distribution $D(x)$, the relative concentration of *gRM* can be calculated with a convolution:

$$\rho_{gRM}(x) = k \cdot D(x) \circledast \frac{1}{2\pi\sigma_k} e^{-\frac{x^2}{2\sigma_k^2}} \tag{1}$$

where k is a normalization factor. In other words, the distribution $D(x)$ is converted into $\rho_{gRM}(x)$ through a kernel of width σ_k. Likewise, the prescribed physical dose can be converted into a mean concentration of *gRM*. It is promptly seen that for a classical uniform $D(x)$ respecting the ICRU recommendation, also $\rho_{gRM}(x)$ is within the 95 to 107% limits. On the other hand, for MBRT, such condition is not respected by $D(x)$ but it may be respected by $\rho_{gRM}(x)$ depending on the value assumed by σ_k.

2.1.2. Calculation of σ_k in Previous pMBRT Studies

Prezado et al. reported that the pMBRT used in their experiments were characterized by a width of 1.1 mm at 1 cm depth, *PVDR* of approximately 6.25 and *c-t-c* = 3.2 mm [8]. We calculated the value of σ_k required for $\rho_{gRM}(x)$ to be within the 95 to 107% limits for this experiment. The physical dose distribution was reproduced with a series of identical Gaussian functions. A more direct approach adopting rectangular functions was also investigated (**Figure 1**). The Equation (1) was applied to the physical dose distribution and the uniformity of *gRM* was recorded at varying σ_k. The smallest σ_k producing a $\rho_{gRM}(x)$ distribution respecting the ICRU recommendation was recorded

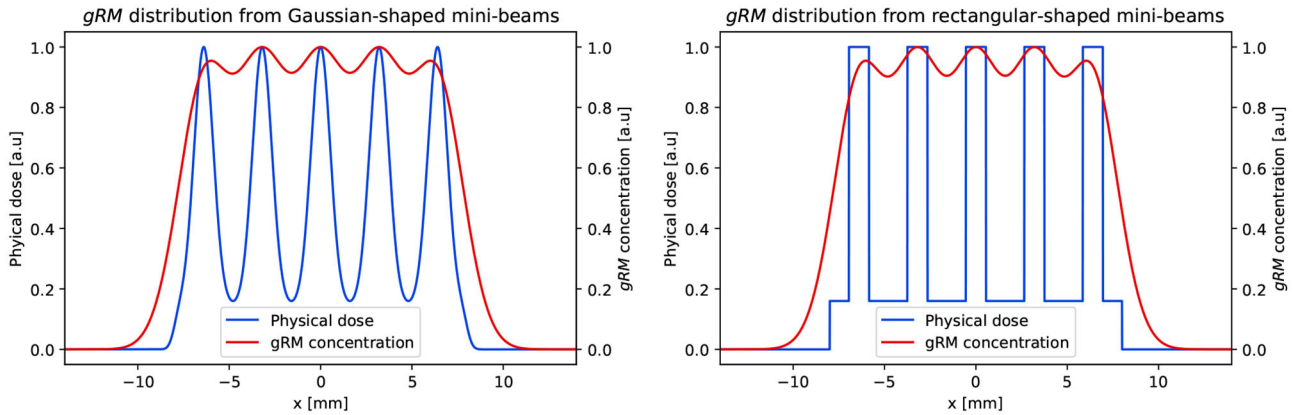

FIGURE 1 | One dimensional representation of the conversion from the physical dose deposited by pMBRT to the spatial distribution of a generic molecule or radical (*gRM*). Two scenario are compared: **(left)** Gaussian shaped and **(right)** rectangular shaped mini-beams. In both cases, the following parameters were adopted: *c-t-c* = 3200 μm, *FWHM* = 1100 μm, *PVDR* = 6.25, and σ_k = 1250 μm. The data matches the values in [8], which reported the dosimetric data at a depth of 1 cm.

as $\hat{\sigma}_k$. We compared the $\hat{\sigma}_k$ values obtained with Gaussian-shaped and rectangular-shaped mini-beams. An exemplary conversion of $D(x)$ into $\rho_{gRM}(x)$ for the two cases is presented in **Figure 1**. The same approach was then applied to MRT experiments. The value of $\hat{\sigma}_k$ was calculated for the micro-beam experiment reported by [6]. Here, the dosimetric parameters were: width = 50 μm and *c-t-c* = 350 μm. The *PVDR* was not explicitly reported, but the authors say that it was much higher than 48. We adopted *PVDR* = 50 in our simulations. It should be noted that higher values would have negligible influence on the results of the gRM distribution, as its value at high *PVDR* is dominated by the peak dose. Finally, we calculated $\hat{\sigma}_k$ for the two irradiation conditions reported by [9]. In the first case, a *c-t-c* = 200 μm was used and the *PVDR* was 42.3 at 5 mm. In the second one, a *c-t-c* = 100 μm was used and the *PVDR* was 14.2 at 5 mm. All the experiments were performed with beams of width = 25 μm generated with a dedicated collimator at the European Synchrotron Radiation Facility (ESRF) [19]. We will reference the experiments with the same nomenclature used by Regnard et al., i.e., series 200*[1] for the first and series 100RL for the second

2.2. Simulation of the Radiolysis Products

2.2.1. The TRAX-CHEM Software

The evolution of proton tracks in water through the physical, pre-chemical, and chemical stage was simulated using the TRAX [20] code and its recent extension TRAX-CHEM [17]. Implementation of track chemistry in water [17], the addition of dissolved oxygen [21], and the respective reaction channels have been previously described in detail. In brief, physical particle interactions are simulated with an event-by-event Monte Carlo approach. Ionization and electronic excitation events lead to molecular dissociations whose coordinates and ionization or excitation state are passed over to the prechemical stage together with thermalized secondary electrons. There, molecular dissociation and thermalization of the fragments are simulated and conclude after ∼ 1 ps. These radiolytic species are then tracked as they diffuse and react with each other according to well-known rate constants, and the products of reactions amongst themselves or with water or dissolved molecular oxygen are continuously included into the pool of active chemical species, whereas the consumed reactants are removed. The type of radical and coordinates of all active species are recorded at specified intermediate time points. The spatial dissolution of the track structure into a microscopically homogeneous distribution is normally reached at ∼ 1 μs together with chemical equilibrium. Photon beams were not simulated in the current study. We defined the temporal evolution of the distribution of the molecules based on proton simulations only. This is justified by the fact that the primary radical yields as well as the diffusion process of the molecular species in water are insensitive to radiation quality at low linear energy transfer.

2.2.2. Temporal Evolution of A_k and σ_k

For radiolysis simulation with TRAX-CHEM, conditions were set as follows. The source was an infinitesimally thin proton beam of kinetic energy E_k = 92 MeV, i.e., equivalent to the mean energy at 1 cm depth in water of the beams used in the experiments reported by [8]. It was placed immediately in front of the target volume where interactions can take place. The target was a water cylinder of 3 μm height and 10 μm radius with an oxygenation value of 6%, resembling physiological conditions at body temperature. Secondary particles (electrons) were followed explicitly through all interaction events until 7 eV, i.e., below the threshold for electronic excitations. At that point, the residual kinetic energy was converted into one final displacement in a random direction according to [22]. We tracked over time the distribution of twelve radiolysis products in order to identify a potential *gRM* fulfilling the requirement (ii). **Table 1** summarizes the molecules and radicals tracked. The simulations were sampled at multiple time points from 10^{-12}

[1]The group 200* includes the series 200LR1, 200LR2, 200RL

to 10^{-5} s. An example of the production and diffusion of $OH^{\bullet}$, H_2O_2, and other species is reported in **Figure 2**. We first analyzed the temporal evolution of $A_k(t)$ for all the molecules and radicals and then $\sigma_k(t)$ for the ones respecting the condition (ii).

The total number of molecules or radicals for each of the species listed in **Table 1** was recorded at multiple time points. In this analysis, the number of events was integrated over the whole target. The species were separated in two categories, depending on their behavior at the latest simulation time point. In the first category, we included the species that did not reach a steady state and were still increasing or decreasing in their total amount. In the second category, we included only the species that reached the steady state, i.e., $\partial A_k/\partial t \simeq 0$. The first were excluded from further analysis as the condition (ii) was not respected.

We analyzed the radial positions of the species in the second category. This was done taking into account the absolute distance from the beam axis and collecting the data in histograms. The chosen landmark of the distribution was P_{68}, i.e., the 68th percentile. Its value evolved with time. We defined $\sigma_k(t) := P_{68}(t)$ and their values were collected at the previously defined time points of the simulation. The temporal evolution of $\sigma_k(t)$ was fitted with a power law for $t > t_1$, where t_1 was the first time point of the simulation where $A_k(t)$ reached a steady-state. The functional form was chosen in accordance to the data presented in section 3.2. The parameterization was $\sigma_k(t) = a \cdot (t/t_0)^b$. We fixed the parameter $t_0 = 1$ s, which defines the unit for the time.

TABLE 1 | Breakdown of the molecules, radicals, and ions followed in the TRAX-CHEM simulations.

$^{\bullet}OH$	H_3O^+	$^{\bullet}H$	H_2O
e^-	H_2	H_2O_2	OH^-
O_2	$^{\bullet}HO_2$	$^{\bullet}O_2^-$	HO_2^-

2.3. Tumor Coverage by *gRM* in Previous MBRT Animal Experiments

Keeping the analysis as general as possible, we assume that a given *gRM* fulfills the conditions (i)–(iv) and that it can be identified by the methods presented in sections 2.1, 2.2. For such *gRM*, it can be defined a characteristic time $\hat{t}$ at which also the generalized definition of tumor coverage by ICRU is fulfilled. This can be promptly calculated by inverting the parameterization, i.e.,

$$\hat{t} = t_0 \cdot a^{-\frac{1}{b}} \cdot \left(\hat{\sigma}_k\right)^{\frac{1}{b}}. \tag{2}$$

This characteristic time can be correlated with the beam-on in the animal experiments, being the latter the only significant time scale for the radiochemical processes. We postulate that (2) corresponds to the minimum beam-on time required for a MBRT irradiation to achieve tumor coverage by *gRM*. This assumption is justified by the phenomena happening at longer and shorter time scales. For beam-on times longer than $\hat{t}$, the steady state of *gRM* has already been reached and therefore the postulate applies. For beam-on times shorter than $\hat{t}$, the steady state of *gRM* may not always be reached through simple diffusion at a later time point. Metabolic processes remove molecules and radicals from the target and therefore modify the *gRM* distribution. Therefore, we directly compared the time scale of $\hat{t}$ with the beam-on time. Given t_{exp}, the beam-on time in a MBRT experiment, the *gRM* can be a potential surrogate to describe the biological effect if the condition $t_{\text{exp}} \geq \hat{t}$ is met. Therefore, we analyzed previous MBRT animal experiments where tumor control was reported and we compared their t_{exp} with our calculation of $\hat{\sigma}_k$ and $\hat{t}$.

The pMBRT experiment by Prezado et al. was conducted with collimated proton beams [8]. They reported that the irradiation was performed with a dose rate of $\dot{D} = 2\,\text{Gy} \cdot \text{min}^{-1}$ at 1 cm depth. This depth was also the reference point used to report the mini-beam width. The peak dose was $D = 70$ Gy, which converts into an irradiation time of $\hat{t} = 35\,\text{min} = 2100$ s. This value was used for our analysis.

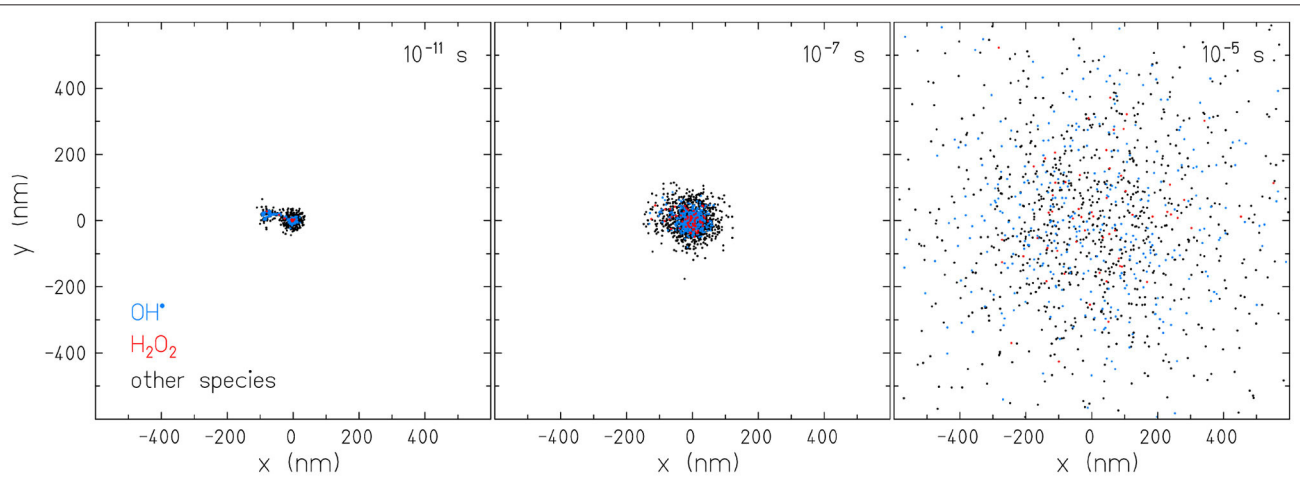

FIGURE 2 | Two dimensional representation of the temporal diffusion of molecules and radicals simulated with the software TRAX-CHEM. The events displayed are produced by a proton beam with kinetic energy $E_k = 92$ MeV in water.

The MRT experiment by Dombrowsky et al. was conducted with photon beams at the Munich compact light source (MuCLS) [6]. The authors reported explicitly the irradiation time, which varied depending on the experimental setup. The integral dose rate for MRT was up to 0.6 Gy · min^{-1}. Fluctuations of the instantaneous values of $\dot{D}$ lead to total irradiation times of (5.6 ± 0.8) min for the delivery of $D = 3$ Gy. For the purpose of our model, the shortest irradiation time showing a biological effect is the relevant one. Therefore, we calculated the minimum t_{exp} that could be achieved with $\dot{D} = 0.6$ Gy · min^{-1}, i.e., $t_{exp} = 300$ s. This value was used for our analysis.

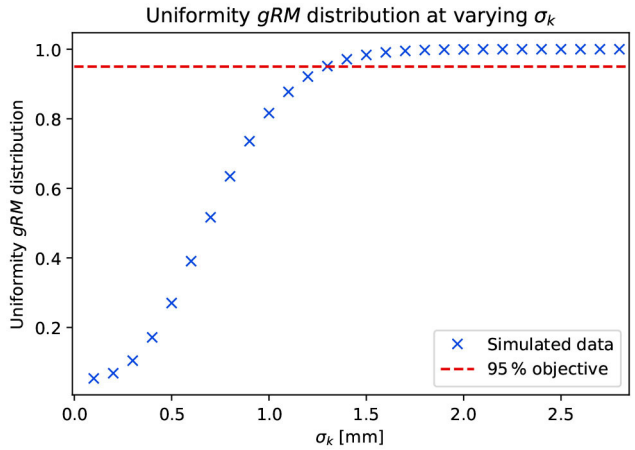

FIGURE 3 | Dependence of the uniformity of the ROS spatial distribution with respect to the value of σ_k adopted in the convolution of the physical dose distribution. The parameterization of the physical dose distribution is analog to what is presented in **Figure 1**.

The MRT experiment by Regnard et al. was conducted with synchrotron radiation at the beamline dedicated to biomedical research of the ESRF [19]. Compared to the previously described experiments, MRT at synchrtoron facilities can achieve significantly higher dose rates and therefore shorter irradiation times. The authors reported that the effective beam-on time was adjusted as a function of the ring current. The duration of the irradiation was approximately 1 s, value which we used for our analysis.

It should be noted that the depth at which the MBRT are investigated is a free parameter. The depths were fixed in the previous experimental studies in relation to the tumor location. The model presented in the current study takes in account the dose distribution in the tumor, independently from its depth in the animal. Therefore, the model is applicable at any arbitrary depth, as long as the dose distribution is available.

3. RESULTS

3.1. Calculation of σ_k in Previous MBRT Studies

The requirement of 95 to 107% coverage was respected as soon as *gRM* reached a lateral distribution with uniformity >0.95. **Figure 3** shows the evolution of the *gRM* uniformity with respect to the value assumed by σ_k. A steep increase is observed for approximately 0.5 mm $< \sigma_k <$ 1.5 mm. Outside this range, the shape of the *gRM* distribution is dominated by the *c-t-c* value ($\sigma_k <$ 0.5 mm) or by the convolution kernel ($\sigma_k >$ 1.5 mm). The $\hat{\sigma}_k$ lies within the previously mentioned range. Therefore, its value depends simultaneously on the distribution of the physical dose and on the diffusion properties of *gRM*. Deviations smaller than 3% were observed when comparing $\hat{\sigma}_k$ calculated from Gaussian-shaped mini-beams and rectangular-shaped mini-beams. The latter was used in the rest of the study.

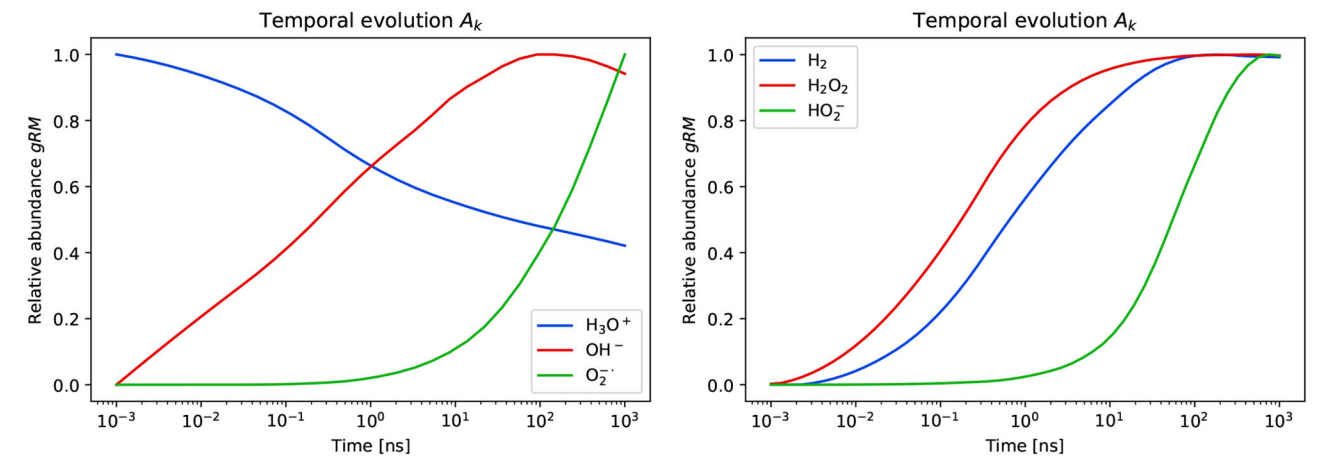

FIGURE 4 | Temporal evolution of the amount of molecules and radicals produced in the TRAX-CHEM simulations. The abundance of *gRM* are normalized by the maximum values reached within the time range of the simulations. A sub-set of six among the twelve simulated species are shown. These are further sub-divided in the first **(left)** and second **(right)** category depending on the behavior at the latest simulation time point.

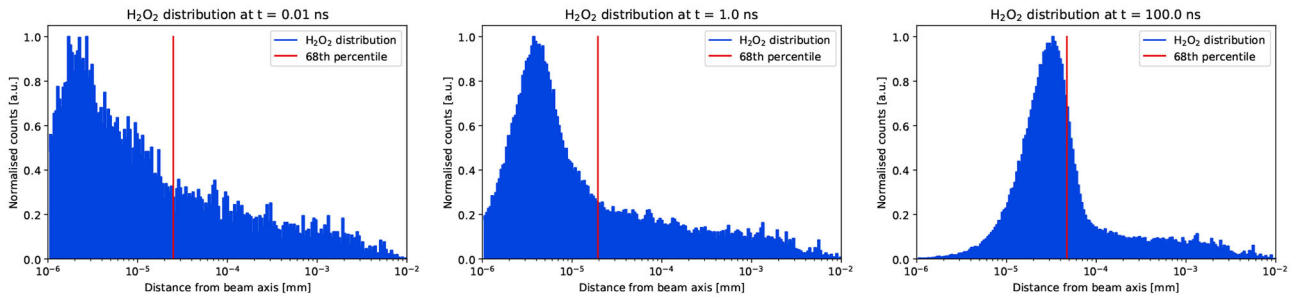

FIGURE 5 | Instantaneous spatial distributions of the hydrogen peroxide sampled at three time points. The blue histograms show the data extracted from the TRAX-CHEM simulations and the red vertical lines show the position of P_{68}. The counts are normalized to the maximum at every time point.

The values obtained for $\hat{\sigma}_k$ were

$$\hat{\sigma}_k = \begin{cases} 1293\,\mu\text{m} & \text{for Prezado et al. [8]} \\ 149\,\mu\text{m} & \text{for Dombrowsky et al. [6]} \\ 83\,\mu\text{m} & \text{for 200* in Regnard et al. [9]} \\ 41\,\mu\text{m} & \text{for 100LR in Regnard et al. [9]} \end{cases} \tag{3}$$

The calculation of the values (3) did not assume any a priori information regarding the generation and diffusion properties of the chemical species. We observe that the values required by $\hat{\sigma}_k$ are approximately half the *c-t-c* distance.

3.2. Temporal Evolution of A_k and σ_k

The dependency of A_k on the time point of the TRAX-CHEM simulation is presented in **Figure 4**. The two categories of chemical species are reported in two separate plots. Only a sub-set of the species in the first category is shown for conciseness. The ones excluded from the plots are not relevant for the following steps of the current study. The steady state was reached by the following:

$$H_2O_2 \quad , \quad H_2 \quad , \quad HO_2^- \tag{4}$$

while the remaining species listed in **Table 1** did not respect $\partial A_k/\partial t \simeq 0$. All three in (4) respected the condition (iii). Among them, only H_2O_2 respected the condition (iv), which is a reactive oxygen species (ROS) and can be expected to be associated with cellular damage [14]. Therefore, the further analysis is restricted to hydrogen peroxide. For this ROS, the condition $\partial A_k/\partial t \simeq 0$ is respected. In particular, for $t > 50$ ns we observed deviations of $A_k(t)$ smaller than 0.25% from its mean value. Therefore, we set $t_1 = 50$ ns.

The time-dependent histograms representing the spatial distribution of the hydrogen peroxide radicals are shown in **Figure 5**. The values of P_{68} are calculated and reported in the plot. At positions close to the beam axis, the number of H_2O_2 decreases with increasing time due to the diffusion. A minimum is observed in **Figure 5** for $t = 100$ ns due to the logarithmic representation of the distance from the beam axis and the ordinate scale. This takes into account the total number of molecules at a given radial distance from the beam axis and does not normalize by the volume over which such molecules are distributed. The same data, plotted with a normalization by the volume is provided in the **Supplementary Material** of the article. The values P_{68} were then used to parameterize $\sigma_k(t)$.

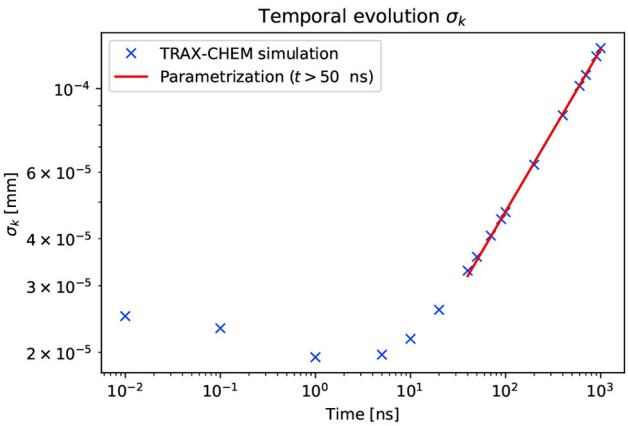

FIGURE 6 | Temporal evolution of the lateral displacement from the beam axis of H_2O_2. The crosses show the data points extracted from the TRAX-CHEM simulations. The red line is the parameterization of the data points for $t > t_1$, where $t_1 = 50$ ns according to the temporal evolution of A_k.

The evolution of $\sigma_k(t)$ and the power law fit for $t > t_1$ are shown in **Figure 6**. This was parameterized with the variables in SI units. The fit parameters were:

$$\begin{cases} a = (4.8 \pm 0.2) \cdot 10^{-5}\ \text{m} \\ b = (4.3 \pm 0.3) \cdot 10^{-1} \\ t_0 = 1\ \text{s} \end{cases} \tag{5}$$

The parameterization (5) was used to extrapolate $\sigma_k(t)$ for times greater than the last simulation time point.

3.3. Tumor Coverage by H_2O_2 in Previous MBRT Animal Experiments

The minimum widths of the Gaussian kernels to ensure coverage of the target by H_2O_2 were reported in Equation (3). Inserting the values (5) into (2), we obtained the following minimum

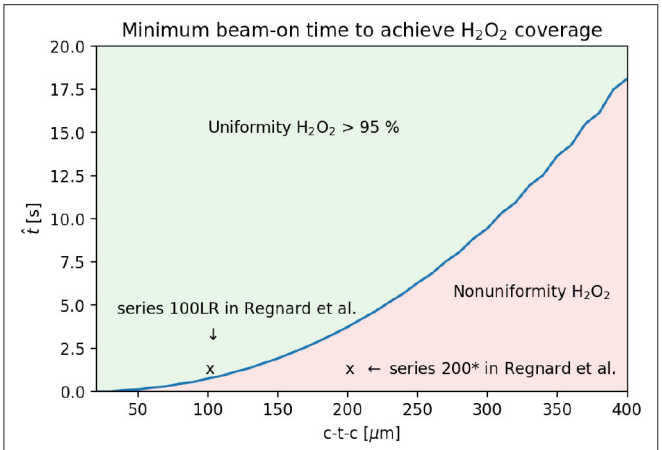

FIGURE 7 | Prediction of the minimum beam-on time required to achieve uniform H_2O_2 coverage for syncrotron experiments with $PVDR = 71$ and beam width 25 μm. The prediction is compared with previous experimental data [9].

irradiation times that would ensure the required diffusion of hydrogen peroxide in the previous MBRT animal experiments:

$$\hat{t} = \begin{cases} 2120 \pm 240 \text{ s} & \text{for Prezado et al. [8]} \\ 13.9 \pm 1.5 \text{ s} & \text{for Dombrowsky et al. [6]} \\ 3.5 \pm 0.4 \text{ s} & \text{for 200* in Regnard et al. [9]} \\ 0.70 \pm 0.08 \text{ s} & \text{for 100LR in Regnard et al. [9]} \end{cases} \quad (6)$$

while the experimental irradiation times were

$$t_{\text{exp}} = \begin{cases} 2100 \text{ s} & \text{for Prezado et al. [8]} \\ 300 \text{ s} & \text{for Dombrowsky et al. [6]} \\ 1 \text{ s} & \text{for Regnard et al. [9]} \end{cases} \quad (7)$$

In three out of the four experiments analyzed, it was valid that $t_{\text{exp}} \geq \hat{t}$. In such cases, according to the model presented, the H_2O_2 provided a coverage between 95 and 107% of its mean concentration. As a matter of fact these experiments were associated with high probabilities of tumor ablation or growth delay. For the series 200* in Regnard et al., the uniform coverage of H_2O_2 was not reached during beam-on, since $t_{\text{exp}} < \hat{t}$. This should be attributed to the high dose rate achievable at a synchrotron and an increased *c-t-c* spacing. The group 200* registered 2 ablated tumors in 32 irradiated rats. The series 100RL produced 5 tumor ablations out of 11 rats.

We further investigated the differences between the series 200* and 100RL. The worst case scenario to achieve H_2O_2 coverage was taken into account, i.e., the maximum $PVDR = 71$ reported at the skin entrance by [9]. We calculated for varying *c-t-c* what would be the minimum $\hat{t}$ predicted by our model. The result and the comparison with the experimental data is presented in **Figure 7**. The series 100LR belongs to the region with uniform H_2O_2 distribution, while the series 200* is attributed to the one where such uniformity is not achieved.

4. DISCUSSION

This simulation study identified the distribution of hydrogen peroxide as the candidate to interpret the mini-beam and micro-beam efficacy. This molecule is a product of water radiolysis, it is stable and it rapidly reaches the steady state in production versus removal. Moreover, the H_2O_2 has a strong oxidizing capacity leading to damage of proteins, lipids, and DNA. Such known properties are now combined with the observation that the distribution of hydrogen peroxide had become uniform in previous MBRT animal experiments where tumor control was achieved. The plausibility of our hypothesis that a radical or molecule can be used as surrogate to describe the biological effect induced by MBRT is therefore confirmed and hydrogen peroxide was identified as the chemical candidate. This is further supported by the different tumor ablation probability reported by Regnard et al. between the group 200* and 100LR. In the former, the uniform H_2O_2 coverage was not reached during beam-on and the fraction of animals with tumor ablation was seven-fold smaller compared to the 100LR series, in which H_2O_2 diffused uniformly over the target.

The presented model aimed to identify a candidate for the biological efficacy of MBRT in tumors. The investigation of the differential effect between the former and normal tissue was outside the scope of the current study. Nonetheless, the identification of the hydrogen peroxide as the surrogate to mini-beam and micro-beam efficacy can be used as a starting point for such analysis. We discuss two phenomena, one physical and one biological, which act in favor of a differential effect between tumor and normal tissue. The first, related to the physics of MBRT, applies especially to pMBRT. We hypothesized that the tumor control is obtained because a homogeneous distribution of hydrogen peroxide covers the target volume. Such coverage is obtained due to a well-tuned combination of proton mini-beam size and center-to-center spacing, which combined with H_2O_2 diffusion during beam-on, covers uniformly the tumor. On the other hand, for pMBRT, the *PVDR* is high at the normal tissue in the entry channel and it degrades with depth until reaching the target [11]. Therefore, while an homogeneous H_2O_2 distribution is reached at the tumor, this is not always the case for the normal tissue. In such case, dose volume effects may apply also to the hydrogen peroxide distribution and therefore lead to a higher tolerance of pMBRT in the normal tissue. This applies especially to pMBRT experiments tuning the beam energy to deliver the Bragg peak at the tumor location. The second, related to ROS biology, applies also to MRT. Cancer cell have significantly higher intracellular ROS levels relative to normal healthy cells [23]. For this reason we believe that normal cells have a higher tolerance to ROS relative to cancer cells, making them more resistant to oxidative stress induced by MBRT through H_2O_2. Despite these two phenomena, the differential effect in normal and tumor tissue is a key aspect of MBRT and will require further investigation. The following discussion will focus on the biological efficacy of MBRT in tumors.

This work was a simulation study aiming to provide further interpretation of previous animal experiments. Few simplification and assumptions were made. We did not aim to

reproduce the physical dose distribution irradiated to the animals in the previous studies with the highest accuracy achievable. This was out of the scope of the current work and it is instead the objective of studies dedicated to the beam design [11] or treatment plans evaluation [24]. On the other hand, these simplifications should not affect the results. The chosen approach consisted in defining the physical dose distribution based on the parameters *c-t-c*, *FWHM*, and *PVDR* reported by the authors. The simplest model based on rectangular-shaped $D(x)$ was compared to a more realistic $D(x)$ made of multiple Gaussian peaks (**Figure 1**). The deviation in the estimation of $\hat{\sigma}_k$ with the two models was limited to the percent level. Therefore, it can be assumed that a further refinement of the $D(x)$ from the multiple Gaussian peaks to a more complex simulation reproducing with high fidelity the previous MBRT experiments would not contribute significantly to the accuracy of the results presented in this work. Therefore, the use of rectangular-shaped $D(x)$ distributions is justified. The little susceptibility of $\hat{\sigma}_k$ to small deviations of $D(x)$ could be interpreted in the light of the data presented in **Figure 3**. The ICRU objective of 95% uniformity is reached at the upper end of the steep part of the curve, i.e., toward the part where the curve tends asymptotically to 100% uniformity. Among the parameters in (1), this part of the curve is mostly dependent on σ_k. Therefore, the spatial and temporal diffusion properties of the hydrogen peroxide provide a greater contribution compared to small deviations in the distribution of the physical dose. The ICRU objective of 95% was assumed without error in this study. However, this recommendation is the result of a long history of clinical experience in many different conditions and therefore should not be assumed as valid a priori for every application. Since the 95% of the dose is a minimum objective, it means that lower values may still provide the desired biological endpoint. For what concerns our study, lower uniformity values are correlated to shorter irradiation times required to achieve the desired *gRM* distribution. Therefore, even in presence of a lower objective such as 90%, the values presented in (6) would still support the applicability of our model when compared to (7). The maximum dose objective of 107% does not enter directly in our model. Finally it should be reminded that MBRT introduces a change of paradigm. Therefore there is no evidence yet that the parameters defined in the ICRU are strictly required to observe tumor control. This study investigated whether a generalization of such recommendation, which would still be valid and applicable in the conventional therapy, could be adopted in MBRT experiments. The current chemical-stage analysis comes as a complement to previous studies analyzing the biological effects of spatially fractionated dose distributions. While not all the biological phenomena, such as the higher tolerance of normal tissue, could be described through our proposed model; we showed how the spatial distribution of H_2O_2 is a potential highly relevant parameter and should be further investigated. The correct interpretation of such microscopic mechanisms of action is required in order for spatially fractionated radiation to advance toward a potential future clinical implementation [25].

One further assumption in the study was the extrapolation of the parameterization $\sigma_k(t)$ to larger time scales compared to the ones simulated with TRAX-CHEM. In particular, the simulations ran until 10^{-5} s while the interpretation of the previous animal experiments required times up to the order of 10^2 s for micro-beams and 10^3 s for mini-beams. This extrapolation is supported by three facts. First, the distribution of H_2O_2 is parameterized solely by $A_k(t)$ and $\sigma_k(t)$ in the current study. The TRAX-CHEM simulations were run until it was verified that $\partial A_k/\partial t \simeq 0$ was respected and $\sigma_k(t)$ was the only varying quantity. Deviations of $A_k(t)$ smaller than 0.25% were observed from t_1 until the latest simulation point, i.e., over 3 orders of magnitude in time. Further simulations beyond this time point would require additional computational burden without a significant increase of the results accuracy. Second, the physical properties of hydrogen peroxide are close to the ones of water [26]. For example, its dipole moment is only 22% larger than the one of H_2O, it is uncharged and protonated at physiological pH. Therefore, the diffusion in the extracellular space of hydrogen peroxide is not expected to be dumped and it can reach extended spatial distances. Moreover, hydrogen peroxide is commonly treated as a molecule that freely crosses membranes, with only some exceptions [26]. Such property, combined with the condition (iv), supports the choice of H_2O_2 as a surrogate for radiation damage to the cells. Third, this extrapolation was based on the property (i), which is the long term stability of the hydrogen peroxide. This was simulated by TRAX-CHEM in water. Shorter times can be expected in a cellular environment, where the hydrogen peroxide is removed by specific enzymes [27]. Nonetheless, the stability of H_2O_2 concentration over several minutes up to the hour is observed also in cell cultures [28]. The stability of the concentration investigated in the current work is limited to the beam-on time. Therefore, the extrapolation of the data presented in **Figure 6** to larger time points is justified. Future work may include investigations with more realistic phantoms for the simulations and a comparison to biological data. Moreover, the absolute concentration of H_2O_2 should also be the subject of investigation of future more advanced simulations taking into account the surrounding biological environment. A comparison of the ROS levels in the experiments and the simulation simulation predictions can then be performed. In the current study we adopted a simple geometry in order to investigate the basic phenomena related to out hypothesis. Finally, the comparison between different simulation codes such as TOPAS-nBio [29], [30], and PARTRAC [31] may also be of interest in future stages of the project.

The work presented supports the potential explanation of the MBRT anti-tumor efficacy though the distribution of H_2O_2. The current study does not demonstrate the correlation between the hydrogen peroxide concentration and the tumor control. Further experimental studies will be necessary to assess such correlation. If this is confirmed, the concentration of this ROS can be used as a marker for the MBRT effect. Ideally, the level of hydrogen peroxide will have to be measured by dedicated experiments. The predictions obtained with the simulations should be confirmed with a direct measurement of the absolute H_2O_2 concentration in real-time during beam-on with dedicated reagents, e.g., Amplex^{TM} Red [32]. This would allow not only to experimentally benchmark the kernel used for the conversion from physical

dose to ROS concentration, but also to assess the absolute value of $\rho_{gRM}(x)$ in the experimental setup. The level of H_2O_2 after the diffusion process should then be correlated to the tumor control parameters in animal experiments. Damaging reactions caused by ROS are known to induce cell death by oxidative stress. Previous studies show that even at concentrations below the required threshold, single ROS activated protein can lead to cell death [33]. Moreover, H_2O_2 is involved in developmental control by triggering apoptosis and cell proliferation [34]. Finally, an additional model describing the differential response of normal tissue and tumor would be required to interpret the absence of brain damage observed in the proton mini-beam experiments [8]. The investigation of additional models, the specific mechanisms involved and the correlation between the hydrogen peroxide concentration and the tumor control are left for future studies. According to the results presented in this work, we limit the discussion in presenting H_2O_2 as the candidate to interpret the mini-beam and micro-beam efficacy.

5. CONCLUSION

A simulation study to investigate a potential surrogate to describe the efficacy of mini-beam and micro-beam radiation therapy was presented. The hydrogen peroxide fulfilled the required conditions; namely, it is a product of water radiolysis, it is stable, it reaches rapidly the steady state in production versus removal and it has oxidizing capacity to allow damage of proteins, lipids, or DNA. It was demonstrated that the H_2O_2 produced in the dose-peaks diffuses to the dose-valleys during beam-on leading to a homogeneous ROS distribution over the target. This distribution respected the reinterpretation of the ICRU recommendation for target coverage, while this was not respected by the physical dose. The model was tested on three previous independent photon micro-beam and proton mini-beam animal experiments. When the predicted minimum irradiation time matched the experimental data, the biological effect was maximum. A reduced tumor ablation probability was observed in one experiment in which the H_2O_2 did not cover uniformly the target. We can conclude that the hydrogen peroxide is a good candidate to describe the mini-beam and micro-beam efficacy.

DATA AVAILABILITY STATEMENT

The raw data supporting the conclusions of this article will be made available by the authors, without undue reservation.

AUTHOR CONTRIBUTIONS

JS proposed the concept of H_2O_2 as a surrogate and designed the objectives and structure of the study. RD planned the investigation strategy and conducted the study. TB defined the input parameters, ran the simulations, and exported the data to generate the plots included in the manuscript. MF and MK provided access to the TRAX-CHEM simulation code and tuned it to the objectives of the current study. All the authors contributed to the interpretation of the results. All authors read and approved the final manuscript.

ACKNOWLEDGMENTS

RD was supported by the International Max Planck Research School for Quantum Dynamics in Physics, Chemistry and Biology, Heidelberg, Germany. The authors thank the three reviewers for the constructive feedback during the review process.

SUPPLEMENTARY MATERIAL

The Supplementary Material for this article can be found online at: https://www.frontiersin.org/articles/10.3389/fphy.2020.564836/full#supplementary-material

REFERENCES

1. Citrin DE. Recent developments in radiotherapy. *New Engl J Med*. (2017) **377**:1065–75. doi: 10.1056/NEJMra1608986
2. Teoh M, Clark CH, Wood K, Whitaker S, Nisbet A. Volumetric modulated arc therapy: a review of current literature and clinical use in practice. *Br J Radiol*. (2011) **84**:967–96. doi: 10.1259/bjr/22373346
3. Durante M, Orecchia R, Loeffler JS. Charged-particle therapy in cancer: clinical uses and future perspectives. *Nat Rev Clin Oncol*. (2017) **14**:483–95. doi: 10.1038/nrclinonc.2017.30
4. Durante M, Golubev A, Park WY, Trautmann C. Applied nuclear physics at the new high-energy particle accelerator facilities. *Phys Rep*. (2019) **800**:1–37. doi: 10.1016/j.physrep.2019.01.004
5. Bräuer-Krisch E, Serduc R, Siegbahn EA, Le Duc G, Prezado Y, Bravin A, et al. Effects of pulsed, spatially fractionated, microscopic synchrotron X-ray beams on normal and tumoral brain tissue. *Mutat Res*. (2010) **704**:160–6. doi: 10.1016/j.mrrev.2009.12.003
6. Dombrowsky AC, Burger K, Porth AK, Stein M, Dierolf M, Günther B, et al. A proof of principle experiment for microbeam radiation therapy at the Munich compact light source. *Radiat Environ Biophys*. (2019) **59**:111–20. doi: 10.1007/s00411-019-00816-y
7. Prezado Y, Jouvion G, Guardiola C, Gonzalez W, Juchaux M, Bergs J, et al. Tumor control in RG2 glioma-bearing rats: a comparison between proton minibeam therapy and standard proton therapy. *Int J Radiat Oncol Biol Phys*. (2019) **104**:266–71. doi: 10.1016/j.ijrobp.2019.01.080
8. Prezado Y, Jouvion G, Patriarca A, Nauraye C, Guardiola C, Juchaux M, et al. Proton minibeam radiation therapy widens the therapeutic index for high-grade gliomas. *Sci Rep*. (2018) **12**:16479. doi: 10.1038/s41598-018-34796-8
9. Regnard P, Duc GL, Bräuer-Krisch E, Troprés I, Siegbahn EA, Kusak A, et al. Irradiation of intracerebral 9L gliosarcoma by a single array of microplanar x-ray beams from a synchrotron: balance between curing and sparing. *Phys Med Biol*. (2008) **53**:861–78. doi: 10.1088/0031-9155/53/4/003
10. Guardiola C, Peucelle C, Prezado Y. Optimization of the mechanical collimation for minibeam generation in proton minibeam radiation therapy. *Med Phys*. (2017) **44**:1470–8. doi: 10.1002/mp.12131
11. Schneider T, De Marzi L, Patriarca A, Prezado Y. Advancing proton minibeam radiation therapy: magnetically focussed proton minibeams at a clinical centre. *Sci Rep*. (2020) **10**:1–10. doi: 10.1038/s41598-020-58052-0
12. Dilmanian FA. Response of rat intracranial 9L gliosarcoma to microbeam radiation therapy. *Neuro-Oncology*. (2002) **4**:26–38. doi: 10.1215/15228517-4-1-26

13. Dilmanian FA, Qu Y, Feinendegen LE, Pe na LA, Bacarian T, Henn FA, et al. Tissue-sparing effect of x-ray microplanar beams particularly in the CNS: is a bystander effect involved? *Exp Hematol*. (2007) **35**(4 Suppl.):69–77. doi: 10.1016/j.exphem.2007.01.014
14. Montay-Gruel P, Acharya MM, Petersson K, Alikhani L, Yakkala C, Allen BD, et al. Long-term neurocognitive benefits of FLASH radiotherapy driven by reduced reactive oxygen species. *Proc Natl Acad Sci USA*. (2019) **166**:10943–51. doi: 10.1073/pnas.1901777116
15. Krämer M, Durante M. Ion beam transport calculations and treatment plans in particle therapy. *Eur Phys J D*. (2010) **60**:195–202. doi: 10.1140/epjd/e2010-00077-8
16. Sies H, Berndt C, Jones DP. Oxidative stress. *Annu Rev Biochem*. (2017) **86**:715–48. doi: 10.1146/annurev-biochem-061516-045037
17. Boscolo D, Krämer M, Durante M, Fuss MC, Scifoni E. TRAX-CHEM: a pre-chemical and chemical stage extension of the particle track structure code TRAX in water targets. *Chem Phys Lett*. (2018) **698**:11–8. doi: 10.1016/j.cplett.2018.02.051
18. Landberg T, Chavaudra J, Dobbs J, Gerard JP, Hanks G, Horiot JC, et al. Report 62. *J Int Commiss Radiat Units Measure*. (1999) **32**:NP. doi: 10.1093/jicru/os32.1.Report62
19. Elleaume H, Charvet AM, Berkvens P, Berruyer G, Brochard T, Dabin Y, et al. Instrumentation of the ESRF medical imaging facility. *Nuclear Instrum Methods Phys Res*. (1999) **428**:513–527. doi: 10.1016/S0168-9002(99)00167-9
20. Krämer M, Kraft G. Calculations of heavy-ion track structure. *Radiat Environ Biophys*. (1994) **33**:91–109. doi: 10.1007/BF01219334
21. Boscolo D, Krämer M, Fuss MC, Durante M, Scifoni E. Impact of target oxygenation on the chemical track evolution of ion and electron radiation. *Int J Mol Sci*. (2020) **21**:424. doi: 10.3390/ijms21020424
22. Zaider M, Vracko MG, Fung AYC, Fry JL. Electron transport in condensed water. *Proc Eleventh Sympos Microdosim*. (1994) **52**:139. doi: 10.1093/rpd/52.1-4.139
23. Perillo B, Di Donato M, Pezone A, Di Zazzo E, Giovannelli P, Galasso G, et al. ROS in cancer therapy: the bright side of the moon. *Exp Mol Med*. (2020) **52**:192–203. doi: 10.1038/s12276-020-0384-2
24. Lansonneur P, Mammar H, Nauraye C, Patriarca A, Hierso E, Dendale R, et al. First proton minibeam radiation therapy treatment plan evaluation. *Sci Rep*. (2020) **10**:7025. doi: 10.1038/s41598-020-63975-9
25. Coleman CN, Ahmed MM. Implementation of new biology-based radiation therapy technology: when is it ready so "perfect makes practice?" *Int J Radiat Oncol Biol Phys*. (2019) **105**:934–7. doi: 10.1016/j.ijrobp.2019.08.013
26. Bienert GP, Schjoerring JK, Jahn TP. Membrane transport of hydrogen peroxide. *Biochim Biophys Acta*. (2006) **1758**:994–1003. doi: 10.1016/j.bbamem.2006.02.015
27. Ng CF, Schafer FQ, Buettner GR, Rodgers VGJ. The rate of cellular hydrogen peroxide removal shows dependency on GSH: mathematical insight into *in vivo* H2O2 and GPx concentrations. *Free Radic Res*. (2007) **41**:1201–11. doi: 10.1080/10715760701625075
28. Kern M, Fridrich D, Reichert J, Skrbek S, Nussher A, Hofem S, et al. Limited stability in cell culture medium and hydrogen peroxide formation affect the growth inhibitory properties of delphinidin and its degradation product gallic acid. *Mol Nutr Food Res*. (2007) **51**:1163–72. doi: 10.1002/mnfr.200700004
29. Schuemann J, McNamara AL, Ramos-Méndez J, Perl J, Held KD, Paganetti H, et al. TOPAS-nBio: an extension to the TOPAS simulation toolkit for cellular and sub-cellular radiobiology. *Radiat Res*. (2018) **191**:125. doi: 10.1667/RR15226.1
30. Incerti S, Douglass M, Penfold S, Guatelli S, Bezak E. Review of Geant4-DNA applications for micro and nanoscale simulations. *Phys Med*. (2016) **32**:1187–200. doi: 10.1016/j.ejmp.2016.09.007
31. Friedland W, Dingfelder M, Kundrát P, Jacob P. Track structures, DNA targets and radiation effects in the biophysical Monte Carlo simulation code PARTRAC. *Mutat Res*. (2011) **711**:28–40. doi: 10.1016/j.mrfmmm.2011.01.003
32. Victorelli S, Passos JF. Reactive oxygen species detection in senescent cells. In: *Methods in Molecular Biology*. Vol. 1896. New York, NY: Humana Press Inc. (2019). p. 21–9. doi: 10.1007/978-1-4939-8931-7_3
33. Wagner D, Przybyla D, Op Den Camp R, Kim C, Landgraf F, Keun PL, et al. The genetic basis of singlet oxygen-induced stress response of *Arabidopsis thaliana*. *Science*. (2004) **306**:1183–5. doi: 10.1126/science.1103178
34. Hachiya M, Akashi M. Catalase regulates cell growth in HL60 human promyelocytic cells: evidence for growth regulation by H2O2. *Radiat Res*. (2005) **163**:271–82. doi: 10.1667/RR3306

Conflict of Interest: The authors declare that the research was conducted in the absence of any commercial or financial relationships that could be construed as a potential conflict of interest.

frontiers in Physics

REVIEW
published: 28 October 2020
doi: 10.3389/fphy.2020.550458

Characterizing Radiation Effectiveness in Ion-Beam Therapy Part II: Microdosimetric Detectors

Paolo Colautti[1], *Giulio Magrin*[2]*, *Hugo Palmans*[2,3], *Miguel A. Cortés-Giraldo*[4] and *Valeria Conte*[1]

[1] Istituto Nazionale di Fisica Nucleare (INFN), Laboratori Nazionali di Legnaro, Legnaro, Italy, [2] MedAustron Ion Therapy Center, Wiener Neustadt, Austria, [3] National Physical Laboratory, Teddington, United Kingdom, [4] Department of Atomic, Molecular and Nuclear Physics, Universidad de Sevilla, Sevilla, Spain

The specific advantages of ion beams for application in tumor therapy are attributed to their different macroscopic and microscopic energy deposition pattern as compared to conventional photon radiation. On the macroscopic scale, the dose profile with a Bragg peak at the highest depths and small lateral scattering allow a better conformation of the dose to the tumor. On the microscopic scale, the localized energy deposition around the trajectory of the particles leads to an enhanced biological effectiveness, typically expressed in terms of clinically significant relative biological effectiveness (RBE). Experimental investigations reveal complex dependencies of RBE on many physical and biological parameters, as e.g. ion species, dose, position in the field, and cell or tissue type. In order to complement the experimental work, different approaches are used for the characterization of the specific physical and biological properties of ion beams. In a set of two papers, which are linked by activities within a European HORIZON 2020 project about nuclear science and application (ENSAR2), we describe recent developments in two fields playing a key role in characterizing the increased biological effectiveness. These comprise the biophysical modeling of RBE and the microdosimetric measurements in complex radiation fields. This second paper focuses on microdosimeters and on the importance of providing the instrumental measurement of the spectra of the imparted energy. The relevance of microdosimetric quantities, complementary to the absorbed dose is emphasized. This parts provides an overview of the microdosimetric concepts and the recent experimental developments in the field of microdosimetry applied to ion beam therapy. Finally, a non-exhaustive, dedicated section in included to emphasize the relevance of Monte Carlo simulations as tool for the design of the microdosimetric detectors and for the interpretation of the experimental results. For the two distinctive clinical beams of protons and carbon ions, the lineal-energy parameters are correlated to the clinical concept of Linear Energy Transfer (LET) and RBE. The possibilities of applying experimental microdosimetry in ion-beam therapy are discussed considering the consolidated irradiation characteristics as well as the most recent developments.

Keywords: microdosimetry, ion-beam therapy, hadrontherapy, protontherapy, linear energy transfer (LET), relative biological effectiveness (RBE), monte–carlo simulation

OPEN ACCESS

Edited by:
Yolanda Prezado, INSERM U1021 Signalisation normale et pathologique de l'embryon aux thérapies innovantes des cancers, France

Reviewed by:
Andreas Berg, Medical University of Vienna, Austria
Anatoly Rosenfeld, University of Wollongong, Australia

***Correspondence:**
Giulio Magrin
giulio.magrin@medaustron.at

Specialty section:
This article was submitted to Medical Physics and Imaging, a section of the journal Frontiers in Physics

Received: *09 April 2020*
Accepted: *11 September 2020*
Published: *28 October 2020*

Citation:
Colautti P, Magrin G, Palmans H, Cortés-Giraldo MA and Conte V (2020) Characterizing Radiation Effectiveness in Ion-Beam Therapy Part II: Microdosimetric Detectors. Front. Phys. 8:550458. doi: 10.3389/fphy.2020.550458

INTRODUCTION

This work is the second of two parts focusing on characterizing radiation effectiveness in ion-beam therapy. The first part, on biophysical modeling of relative biological effectiveness (RBE), is published by Scholz et al. [1]. It is cited in this work as "Part I." Part I includes a general introduction on the concepts and the rationale of ion-beam therapy as well as the essential equations that describe the biophysical and physical quantities for the characterization of radiation effectiveness.

When high-energy photons are used in the clinic to treat tumors, there is a unique relationship between the absorbed dose, which is proportional to the photon fluence, and the relative number of surviving cells. When light ions are used, this unique relationship does not hold anymore: the number of surviving cells at distinct points in the patient's body can be different even if the absorbed dose in those points is the same. Equal physical doses of different radiation types do not always result in the same amount of biological damage. This fact suggests that the radiation capability of damaging living cells depends not only on the mean value of energy imparted but also on the microscopic probability distribution of energy imparted at the subcellular level. When deciding on a dose prescription for a new ion beam, the radiation oncologist has to take into account the varying effectiveness of radiation within various regions (depths) in the irradiated tissue [2]. A scaling factor known as the ***RBE*** is used to evaluate the biological effective dose. The ***RBE*** is defined as the ratio of a dose of photons to a dose of any other particle to obtain the same radiobiological effect. The ***RBE*** varies, among other factors, with the radiation quality (type and velocity of the ion), with the biological end point, with dose, and with dose rate [3]. However, it has been found that ***RBE*** depends, to a first approximation, on the linear energy transfer (***LET***), the average amount of energy that an ionizing particle transfers by purely "electronic" interactions (ionization or excitation) to the material traversed per unit distance. It is worth noticing that ***LET*** is a non-stochastic quantity, being an average, and it is strictly defined at a point of energy transfer. However, irradiation targets always have a finite volume, rather than being a dimensionless point, and the interaction of ionizing particles with this target volume is always a stochastic process. In this work, LET is considered as "unrestricted," which means that it accounts for the total kinetic energies of the electrons released in the collision of the charged particle. The correlation between LET and RBE is widely discussed in Part I. Microdosimetry is that part of radiation physics that deals with the stochastic analysis of the energy imparted by an ionizing particle to a sample of finite size [4]. An illustration of the stochastic nature of the energy imparted is provided in the next paragraph and in **Figure 1**. When the sample has the material composition and the size of a living cell or of one of its substructures, microdosimetry describes the primary radiation effect on the biological structure corresponding to that size, i.e., the living cell. Operative physical quantities are defined, which can be measured with special nuclear detectors called microdosimeters; International Commission on Radiation Units and Measurements (ICRU) Report 36 on Microdosimetry [4] and "Microdosimetry: Experimental Methods and Applications" [6] are general references for the detailed description of the quantities and comprehensive formalisms.

In the following, a summary is given of the state of the art of studies aimed to investigate the use the microdosimeters as LET and RBE monitors in therapeutic proton and carbon ion beams.

THE PHYSICAL BASE OF THE RADIATION ACTION ON HUMAN CELLS

In **Figure 2**, RBE_{10} data are plotted against ***LET*** values of protons and carbon ions [7]. In order to produce these radiobiological data, monolayers of human cells were irradiated with mono-energetic protons and carbon ions, the ***LET*** value of which was calculated. Different ***LET*** values were obtained by changing the ion energy. Radiobiological measurements usually have a precision of about 10% when performed by the same research group. However, data in **Figure 2** show higher ***RBE*** fluctuations, since they originate from different experimental scenarios. In addition, while substantial uncertainties on ***RBE*** are widely acknowledged, there may be uncertainties as high as 15% in the consistency of the calculation of ***LET*** [8]. Without a significant reduction of the uncertainties, it is difficult to assess whether or not the RBE is a unique function of ***LET***, independent of particle type. **Figure 2** shows clearly that, to a first approximation and within uncertainties, the ***RBE*** can be described as a function of ***LET***: it increases with the ***LET*** value up to about 150 keV/μm, then it decreases likely because of damage saturation at high ***LET*** values. However, some experimental data are not consistent with the unique dependence of ***RBE*** on ***LET*** [9], pushing the researcher to deeper study of the physical basis of the biological action of radiation. As discussed in detail in Part I in the section "Accuracy of LET_D as Descriptor for RBE," there is indeed a general awareness that the biological effect depends, rather than on ***LET***, on the density of energy imparted by a single particle to a biological structure, which is of fundamental importance for the cell surviving. The size of the relevant biological volume V might be as large as the cell itself (∼10 μm of thickness) or smaller as a chromosome (about 1 μm of thickness) or as small as the DNA strand (2 nm of thickness). The *energy imparted* is called ε. The energy imparted by a single particle is indicated using the subscript 1 (ε_1). Its linear density is called lineal energy and defined as:

$$y = \frac{\varepsilon_1}{\bar{l}} \tag{1}$$

where $\bar{l}$ is the biological site's mean-path length of primary tracks. The value of $\bar{l}$ is assessed, *via* calculations or simulations, considering the distribution of the actual paths of the particles in the sensitive volume, which depend on the track directions and the shape of the site. In equation (1), the *path length* (the term follows the nomenclature suggested by Bolst et al. [10]) substitutes the *chord length* used in the definition of lineal energy given in the ICRU Report 36 [4] and ICRU Report 85 [11]. In the original definition, $\bar{l}$ is specified for μ-randomness as described by Kellerer [12] and is independent on the beam direction. As an example, the mean chord length of a sphere

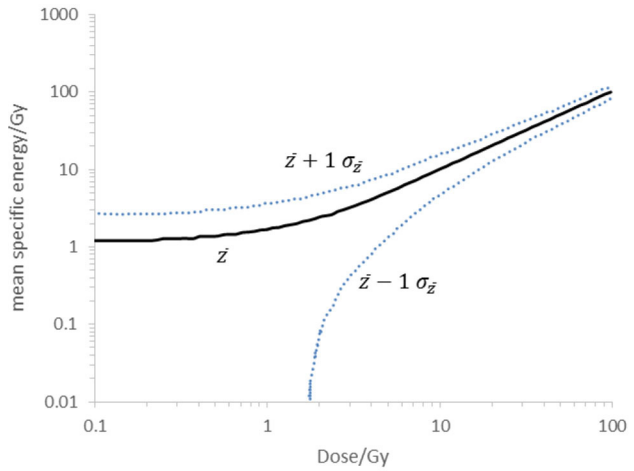

FIGURE 1 | Multi-event mean specific energy in a critical cylindrical volume of 1 μm in diameter (volume without 0 events) at a given dose, *D*. Calculation for a 60 MeV modulated proton beam at the Bragg peak with $y_F = 7$ keV·μm^{-1} and $y_D = 7$ keV·μm^{-1} (solid line). The dotted lines indicate the borders of the specific energy within 1 SD of the mean value in the actual energy distribution. Calculation was performed following the method described by Booz [5].

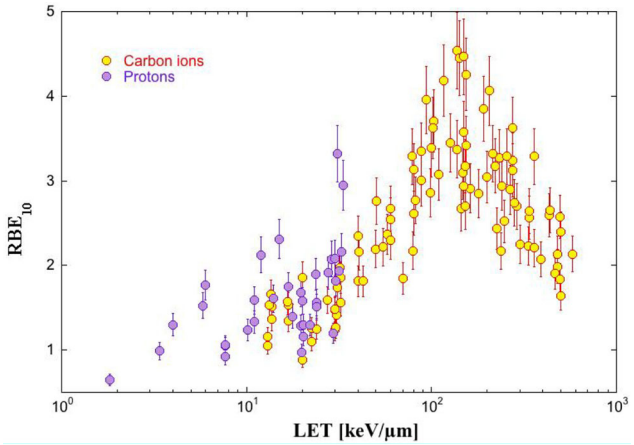

FIGURE 2 | Relative biological effectiveness (***RBE***) for asynchronous radioresistant human cell (different cell lines) after irradiation with protons and carbon ions is plotted against the particle linear energy transfer (***LET***) in tissue. The $\boldsymbol{RBE}_{10}$ means that the ***RBE*** values have been taken at 10% of cell surviving fraction. Data from Friedrich et al. [7].

corresponds to 4/3 of its radius. The choice made for equation (1) of substituting the mean path length to the mean chord length is done since this quantity is more representative of the local density of energy imparted.

The unusual term "lineal energy" was adopted to remember the specific physical nature of y, which is, differently from ***LET***, a stochastic quantity. In fact, $\boldsymbol{\varepsilon_1}$ is a stochastic quantity too, since its value changes every time new particles interact with the cell, even if the particle type and initial energy are the same. This results from the non-deterministic nature of the atomic and nuclear processes. Therefore, repeated measurements of y give rise to a spectrum of values indicated by the probability density function $f(y)$. The average obtained from $f(y)$ is called *frequency mean* of y, and it is written as $\bar{y}_F$:

$$\bar{y}_F = \int y \cdot f(y) dy \tag{2}$$

In microdosimetry, the specific energy z is defined as follows:

$$\mathbf{z} = \frac{\varepsilon}{m} \tag{3}$$

where m is the mass of V. **Figure 1** illustrates the stochastic nature of the energy imparted in a site size of 1 μm for a proton beam at the Bragg peak. The specific energy spectrum might exhibit a very broad width related to a site of about 1 μm size. As an example, the mean specific energy and the lines characterizing ±1 SD of the spectrum at different dose levels are indicated in **Figure 1**. In this example, for the dose of 2 Gy, the specific energies in the micrometric site range between the values of 0.7 and 4.7 Gy, within 1 SD to the mean value.

The specific energy of a single event is written $\boldsymbol{z_1}$ and is proportional to y:

$$\mathbf{z_1} = \mathbf{y}\frac{\bar{l}}{\mathbf{m}} \tag{4}$$

Repeated measurements of $\boldsymbol{z_1}$ give rise to a spectrum of values, the average of which is called *frequency mean* of $\boldsymbol{z_1}$ and is denoted $\bar{\mathbf{z}}_{\mathbf{1F}}$.

The microdosimetric spectrum represented by $f(y)$ indicates the probability to have, in V, an event with lineal energy y or specific energy $\boldsymbol{z_1}$. The y or $\boldsymbol{z_1}$ spectra display the stochastic behavior of these quantities, as well as the heterogeneity of the types and energies of the particles crossing the detector. Note that the microdosimetric spectrum of a particle depends on the size and shape of V, as well as on the radiation field anisotropy. Therefore, the same mono-energetic ion beam may give rise to different microdosimetric spectra in volumes of different sizes. Effects of a specific path length distribution on the measured microdosimetric spectrum can be studied through Monte Carlo simulations and mathematical models [13].

MICRODOSIMETRIC DETECTORS

Microdosimetric detectors can be based on gas counters or on solid-state counters (SSD). The first microdosimeters were gas proportional counters made with tissue-equivalent plastic and filled with tissue-equivalent gas mixtures. Because of that, they were called tissue-equivalent proportional counters (TEPCs). Miniaturized TEPCs (mini-TEPCs) with sensitive volumes of <1 mm have been manufactured in order to be operable in high-intensity therapeutic ion beams [14] (**Figure 3**). The simulated site size is determined by adjusting the gas density, so that the same amount of energy is imparted to the gas cavity as for the simulated volume of biological tissue. The energy imparted to a spherical cavity with a diameter of 1 mm and filled at about half

of atmospheric pressure is equivalent to the energy imparted to a 1-μm sphere of tissue, the density of which is 1 g/cm^3. Therefore, it is customary to say that the sensitive volume of the mini-TEPC simulates 1 μm of tissue. However, mini-TEPCs can simulate different site sizes by changing the gas pressure. Mini-TEPCs operate in the range from about 0.3 to 2 μm.

The silicon telescope is a detector used in nuclear physics to detect every single ion emerging from a nuclear reaction. The telescope idea has been exploited to manufacture a microdosimeter, where the 2-μm ΔE stage is the sensitive volume and the E stage is used to determine charge and energy of the ions. A scaling factor can be applied to convert $\boldsymbol{\varepsilon_1}$ in silicon to $\boldsymbol{\varepsilon_1}$ in tissue [13] (**Figure 3**). The non-tissue-equivalence of silicon is dealt with by using, as scaling factor for the energy imparted, the ratio of the electronic stopping power in tissue and in silicon. Furthermore, a shape equivalence correction is applied to compare spectra obtained with detector sensitive volumes of different shapes. Other silicon counters have been developed and are nowadays on the market with the name of MicroPlus Bridge [15] (**Figure 4**). These detectors, unlike silicon telescopes, are formed by a single thin layer and provide different settings as matrixes of detectors with different cross sections and thicknesses [16]. The so-called "Mushroom" version features a 50 × 50 matrix of cylindrical sensitive volumes with thicknesses that range between 2 and 10 μm and diameter of 18 μm [17]. Microdosimeters based on Schottky diode and made of synthetic diamond of thickness varying from 0.3 to 10 μm have been manufactured as well [18] (**Figure 4**).

TEPCs have high detection efficiency, since they can detect also few ionization events—thanks to the electron multiplication in the filling gas. However, the electrodes are biased at several hundreds of volts, they need accurate gas pressure control and energy calibration, and they have limited capabilities in high-intensity radiation fields because the geometrical cross-sectional area of the sensitive volume can hardly be reduced below 1 mm^2. Solid-state microdosimeters have lower detection efficiency because they rely on the collection of the free charges generated in the sensitive volume not taking advantage of internal charge amplification. On the other side, they are biased at low voltage and the thickness of the sensitive volume can be as small as 1 μm, making them suitable for operation even in very intense radiation fields. Moreover, pixelated arrays of detectors can be constructed, allowing the simultaneous two-dimensional mapping of the radiation field.

It is worth underlining that microdosimetry measures the probability distribution of the energy deposit $\boldsymbol{\varepsilon_1}$, which obviously depends on the radiation field properties but also on the composition, size, and shape of the sensitive volume. Therefore, detectors that differ in material composition, size, and shape might be measuring different microdosimetric distributions, according to their specific response function.

All the microdosimeters described above estimate the energy imparted by measuring the free charges produced in the medium and then converting the number of those measured charges to energy imparted through the multiplication by the W-value, the mean energy expended to form an ion pair. W-value for different particles is not constant. It increases for higher Z-ions, resulting in additional uncertainty.

An interesting conceptual design has been proposed for a microcalorimeter that measures directly the energy imparted rather than the ionization [19]. The realization of such a detector is however a great challenge. In particular, the definition of the thermal behavior of this detector is complex. The goal is to determine the radiation-induced temperature increase in a tissue-equivalent absorber while the temperature measurement is performed on the superconductor, which is in thermal contact with the absorber. Fathi et al. [20] discussed this topic proposing a correction of the microdosimetric spectra from microcalorimeters. Another major challenge for the realization of microdosimeters based on microcalorimetry is the difficulty in translating a cryogenic detection to a clinical environment.

Other prototypes of microdosimeters have been studied and developed to be used in ion-beam therapy including TEPCs [21], solid state detectors [22, 23], gas electron multiplier (GEM) detectors [24], and films [25].

ASSESSING VARIATIONS OF LINEAR ENERGY TRANSFER IN PROTON DATA

As is discussed in the section "Basic Concepts of Models" of Part I, in proton therapy, a constant $\boldsymbol{RBE} = 1.1$ is assumed along the entire spread-out Bragg peak (SOBP). However, radiobiological data show that the proton ***RBE*** at the end of the range is more than twice the ***RBE*** value at the entrance [26] and thus the choice of a constant value is questionable. This finding is consistent with the radiobiological data of **Figure 2** if we consider that the proton ***LET*** value at the end of a proton track in tissue is about 85 keV/μm.

The current practice of proton therapy planning with a constant ***RBE*** of 1.1 is thus questionable. As a first step, several treatment planning systems (TPS) are already offering the possibility to take the ***LET*** variation along the penetration depth into account. In view of the implementation of ***LET***-based treatment planning systems, it is necessary to develop tools and methods for the quality assurance of ***LET*** determination and calculation. Microdosimetry could offer valuable tools for that purpose [27].

The frequency mean lineal energy has the same physical dimensions as ***LET***, but not necessarily the same value. In fact, the ***LET*** is defined at a point for a mono-energetic ion beam [28]; therefore, its value does not depend on $\boldsymbol{V}$. Conversely, $\bar{\boldsymbol{y}}_{\mathbf{F}}$ does not include the energy transported outside the volume $\boldsymbol{V}$ by fast electrons or secondary ions (it averages only the $\boldsymbol{\varepsilon_1}$ events occurring inside $\boldsymbol{V}$). Moreover, $\bar{\boldsymbol{y}}_{\mathbf{F}}$ automatically averages the $\boldsymbol{y}$ values due to ions of different energies and of different types. This last feature makes microdosimeters suitable to measure the mean lineal energy density in a mixed radiation field like that one of therapeutic ion beams. Therefore, as far as $\bar{\boldsymbol{y}}_{\mathbf{F}}$ can substitute the ***LET***, the mean $\boldsymbol{RBE_{10}}$ values of **Figure 2** can be represented as a function of the frequency mean lineal energy. A similar figure can be obtained for ***RBE,*** which are therapeutically significant

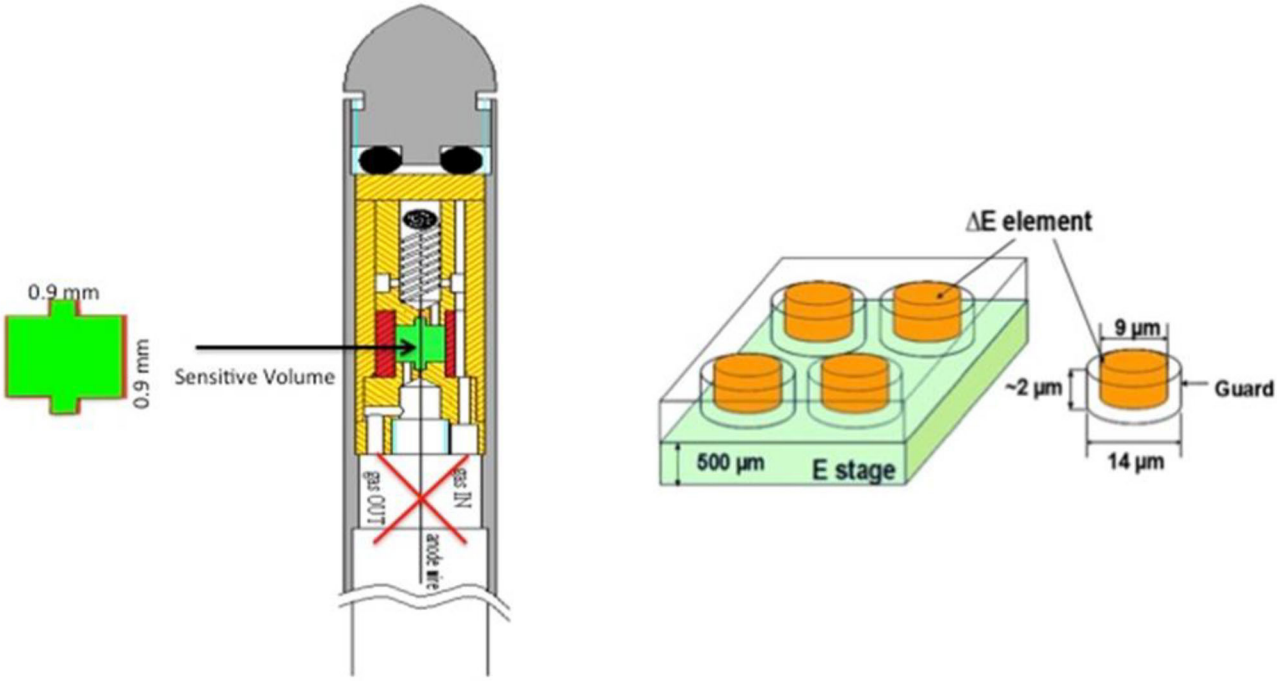

FIGURE 3 | (Left): Cross section of the mini-tissue-equivalent proportional counter (TEPC); the green area is the detector sensitive volume; the red cross points out the possibility to work both in gas flow modality and in sealed modality [14]. **(Right)**: Sketch of the pixelated silicon telescope with four (out of many) sensitive elements [13].

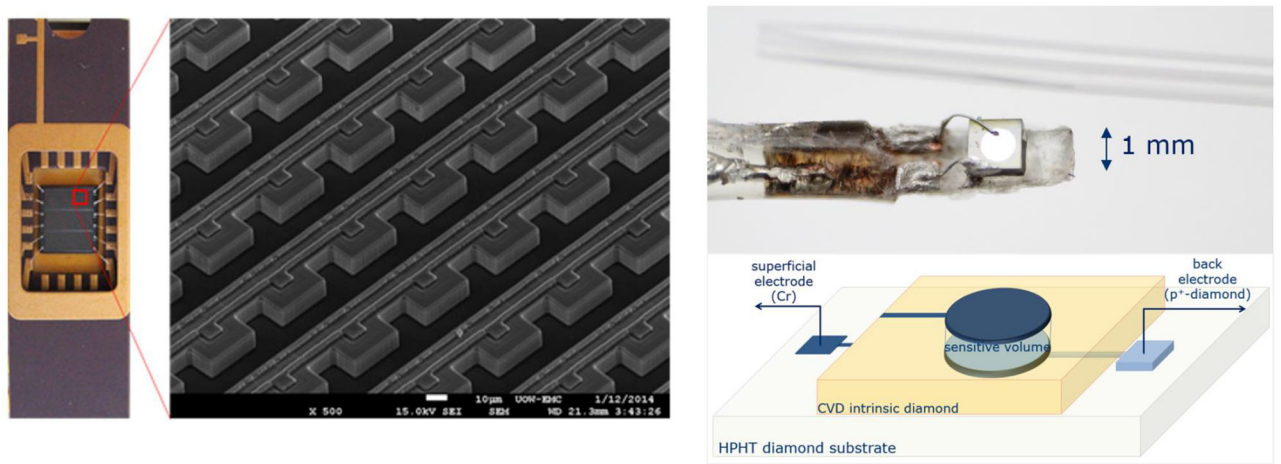

FIGURE 4 | (Left): MicroPlus Bridge probe and electron-microscope scanning showing an array of sensitive volumes of the bridge microdosimeter. **(Right)**: Diamond microdosimeter and its schematic representation showing the external circular electrode defining the sensitive volume.

and can be used by clinicians to adapt the absorbed dose data in therapeutic plans. This process would result in a decrease of the absorbed dose at distal depths.

The dose distribution $d(y)$ is calculates as:

$$\mathbf{d}(\mathbf{y}) = \frac{\mathbf{y} \cdot \mathbf{f}(\mathbf{y})}{\bar{\mathbf{y}}_{\mathbf{F}}} \tag{5}$$

In mixed radiation fields, the dose weighted distribution is frequently preferred to $f(y)$ because dose weighted quantities, e.g., the dose-averaged LET ($\overline{LET}_D$), better correlate to the radiobiological effectiveness. The mean value of y weighted by $d(y)$ is called the dose mean lineal energy:waker

$$\bar{\mathbf{y}}_{\mathbf{D}} = \int y \cdot d(y) dy \tag{6}$$

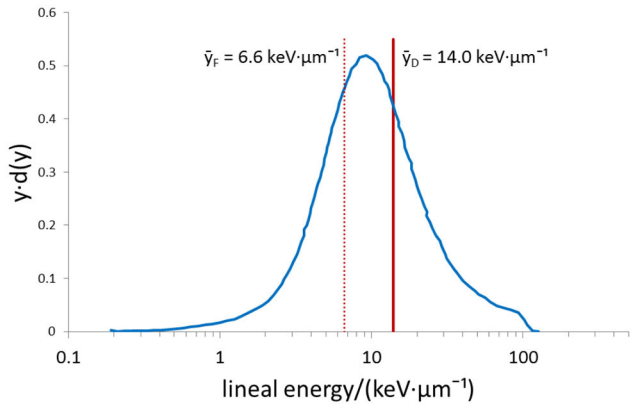

FIGURE 5 | Typical microdosimetric spectrum collected using a tissue-equivalent proportional counter (TEPC) in a proton beam. The two vertical lines represent the mean values $\bar{y}_F$ and $\bar{y}_D$ estimated from the spectrum.

(See also in Part I the section "Role of the Microscopic Energy Deposition Pattern"). A typical microdosimetric spectrum of a proton beam collected with TEPC and the corresponding mean values are presented in **Figure 5**. Also this quantity has the same physical dimensions of ***LET***, its meaning being the mean ***y*** value of events that contribute to the absorbed dose. The correspondence between measured $\bar{y}_D$ values and calculated $\overline{LET}_D$ values must be studied and characterized. Afterward, microdosimetric characterization in terms of $\bar{y}_D$ can be used for the quality assurance of ***LET***-based treatment plans [27].

Data of **Figure 6** (taken from Conte [29]), show two sets of $\bar{y}_D$ values (taken with the mini-TEPC in two separate shifts of measurements) compared with $\overline{LET}_D$ values simulated with Geant4 Monte Carlo code with energy imparted in the same tissue equivalent sensitive volume size 1.0 µm as in used TEPC. They suggest that microdosimeters could be accurate ***LET*** monitors, given that the difference between the two sets of values is <5% [32].

THE MICRODOSIMETER AS RELATIVE BIOLOGICAL EFFECTIVENESS MONITOR

Another possibility is to use the peculiarity of the radiobiological microdosimetric model to directly monitor the ***RBE***.

The microdosimetric model assumes that, as far as biological effects of radiation are concerned, the radiation quality (physical) can be adequately characterized by the probability distribution of lineal energy in a sensitive site representative of the biological target that is supposed to be critical for the biological observable. The ***y*** distribution measured by a microdosimeter is considered equal to the ***y*** distribution in the biological site if the detector sensitive volume is tissue-equivalent and its size, calculated at a density of 1 g·cm^{-3}, is the same as that of the critical biological site. The model is sketched in **Figure 7** where the analogy between the measured ***y*** events and ***y*** events experienced by chromosomes is presented. The microdosimetric spectrum represents in fact all the possible y values occurring in the cell chromosome at the passage of one ionizing particle.

Since the mean effect (for a given radiation field, cellular target, and biological end point) of an ion impinging on a living cell is expected to be always the same, while $\bar{y}_F$, and $\bar{y}_D$ depend on ***V***, it is legitimate to ask oneself whether the value of ***V*** has a radiobiological meaning (e.g., if the size of ***V*** can be really interpreted as the size of the "critical" living cell structure, like the heart of a human being). If the critical site really existed, the microdosimetric spectrum in that volume ***V*** would likely be stronger correlated to radiobiological data than microdosimetric spectra in volumes of different sizes. As discussed in Part I in the section "Role of the Microscopic Energy Deposition Pattern," an important aspect that needs to be considered is that multiple volume sizes are relevant with respect to different biological pathways to cell damage and thus that a multiscale characterization is needed for a full description of the relation between the physical energy deposition and the biological effect [33].

THE MICRODOSIMETER TO MONITOR RELATIVE BIOLOGICAL EFFECTIVENESS, PROTON DATA

The $\bar{y}_D$ value cannot directly mimic the ***RBE*** for the simple reason that its value increases always with the ion ***LET*** value. Instead, the ***RBE*** value reaches a maximum and then it decreases (**Figure 2**), since after the destruction of the biological target, a further increase of linear energy-deposition density (which corresponds also to an increase of the proton dose) cannot contribute to any additional effects.

A possibility to simulate the "saturation effect" that appears in **Figure 2** is to "weigh" the ***d(y)*** spectrum with a biological response function ***r(y)***, which represents the expected biological effect due to the dose component with lineal energy ***y***. The ***RBE*** microdosimetric assessment, which is called RBE_{micros}, would therefore be:

$$\mathrm{RBE}_{micros} = \int_{y_{min}}^{y_{max}} r(y) \cdot d(y) \cdot dy \qquad (7)$$

A successful ***r(y)*** function was extracted from the experimental comparison of ***TEPC*** microdosimetric spectra in 2-µm tissue-equivalent sites in photon, proton, and fast neutron beams and the ***RBE*** for crypt cell regeneration after 8 Gy of dose on living rats exposed to the same beams [34–36]. The determination of the biological effectiveness on mouse crypt cells for the characterization of clinical proton beam has been widely discussed and applied [26, 37–43]; With such a response function, the RBE_{micros} values of the Nice therapeutic proton beam are able to monitor the specific ***RBE*** value with good accuracy [44].

In **Figure 8**, the plot representing the dependence of RBE_{10} on ***LET*** (from **Figure 2**) is superimposed on the plot of RBE_{micros}

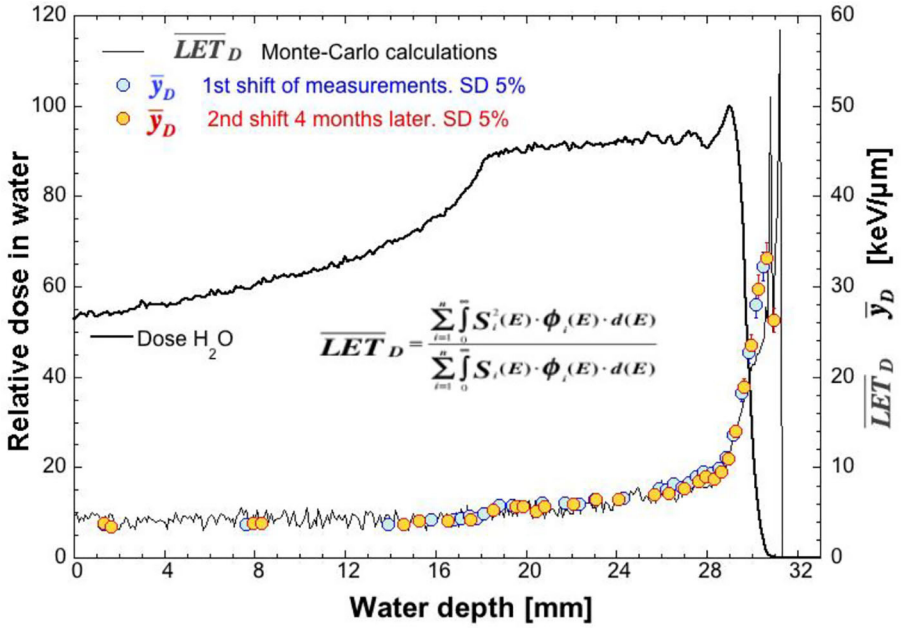

FIGURE 6 | $\bar{y}_D$ values [measured with the mini-tissue-equivalent proportional counter (TEPC)] and dose-averaged linear energy transfer ($\overline{LET}_D$) values (calculated with the Geant4 Monte Carlo code) at different water depths in the CATANA therapeutic proton facility (taken from ICRU [29]). The large statistical fluctuations of the Monte Carlo calculation at the highest depths are due to the limited number of particles reaching those depths. In the insert, the formula used to calculate $\overline{LET}_D$ is shown.

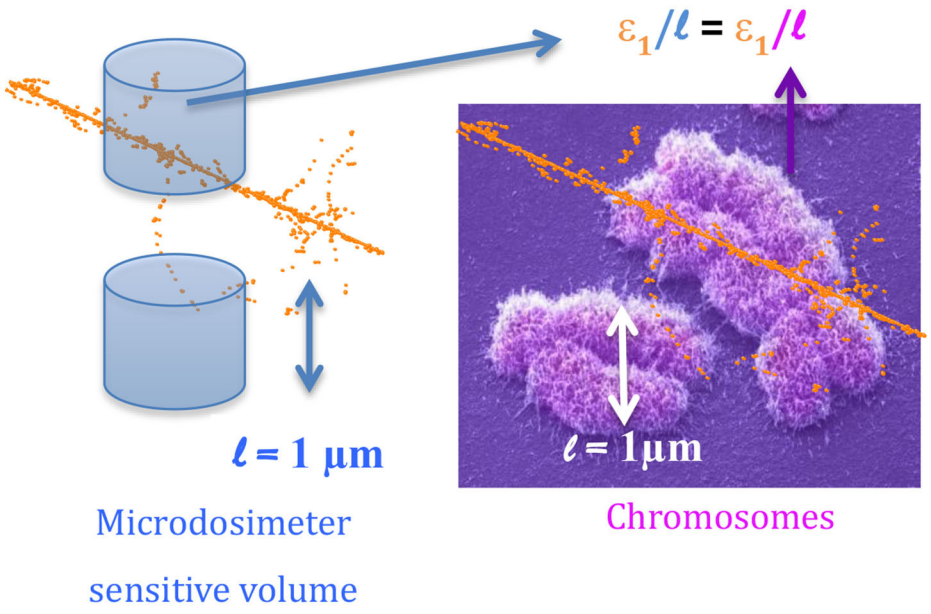

FIGURE 7 | Sketch of the microdosimetric model. The blue cylinder represents the sensitive volume V of the microdosimeter featuring a diameter of about 1 µm, the same size of the chromosome (right side of the figure). The orange dots are points where the charged particle imparts the energy (ionization or excitation events). The energy imparted to two chromosomes by the same single particle track is different (right side of the figure). Similarly, the energy imparted to the detector by the same particle can be different.

data vs. the microdosimetric mean $\bar{y}_D$ values measured at the CATANA therapeutic proton beam. Microdosimetric values follow rather well the linear best fit of radiobiological data (red line). These findings suggest that microdosimetric spectra in a volume V of about 1 µm of tissue-equivalent thickness can be used to simulate the dependence of RBE on LET

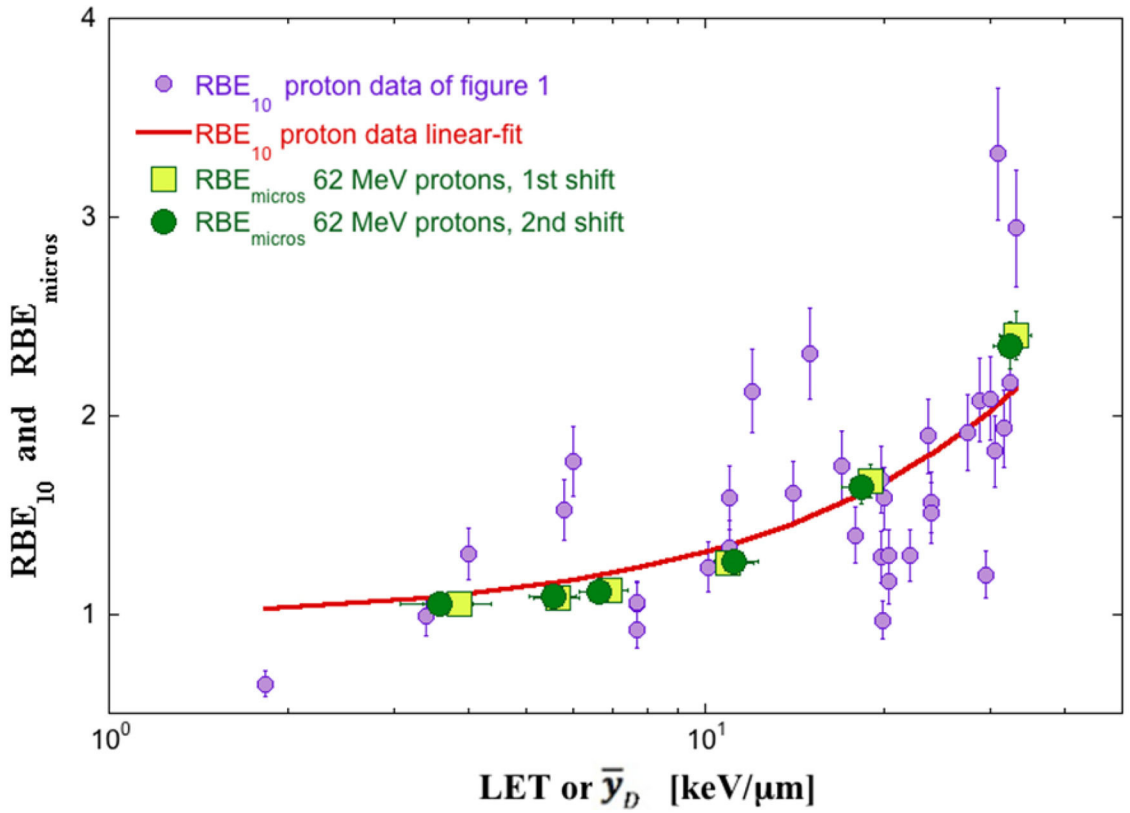

FIGURE 8 | The relative biological effectiveness microdosimetric assessment (**RBE_{micros}**) (squares and circles) vs. measured **$\bar{y}_D$** [mini-tissue-equivalent proportional counter (TEPC) measurements in 1-µm site at the 62 MeV proton beam of CATANA] and **RBE_{10}** (violet circles) vs. calculated linear energy transfer (**LET)** values. The red line is the linear best fit of **RBE_{10}** data. Squares and circles point out two different shifts of measurements 4 months apart. Data from ICRU [29].

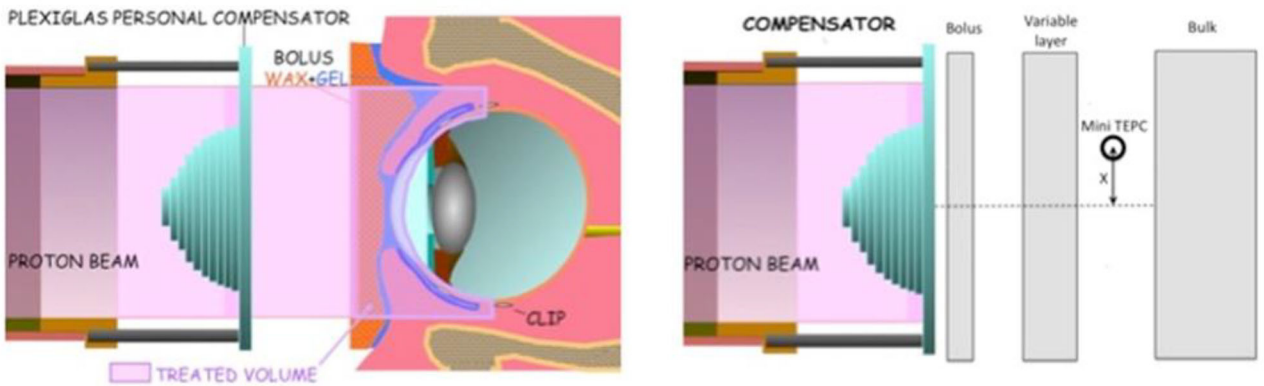

FIGURE 9 | (Left): Sketch of the irradiation setup of the conjunctival melanoma treatment. The compensator is a polymethyl methacrylate (PMMA) phantom, which is designed to shape the spread-out Bragg peak (SOBP) as the conjunctive. **(Right)**: Sketch of the irradiation setup used for microdosimetric measurements, where the gray rectangles are PMMA layers, which substitute bolus and patient eye. The mini-tissue-equivalent proportional counter (TEPC) distance from the beam axis (X) has 0.1 mm of precision. Data from De Nardo et al. [30].

for crypt cell regeneration in living rats with an accuracy of about 5%. New weighting functions $r(y)$ can be unfolded for other specific biological endpoints and using microdosimetric spectra collected with other detector types to provide, through equation (7), specific insights on the ***RBE*** of the tumor and healthy tissue.

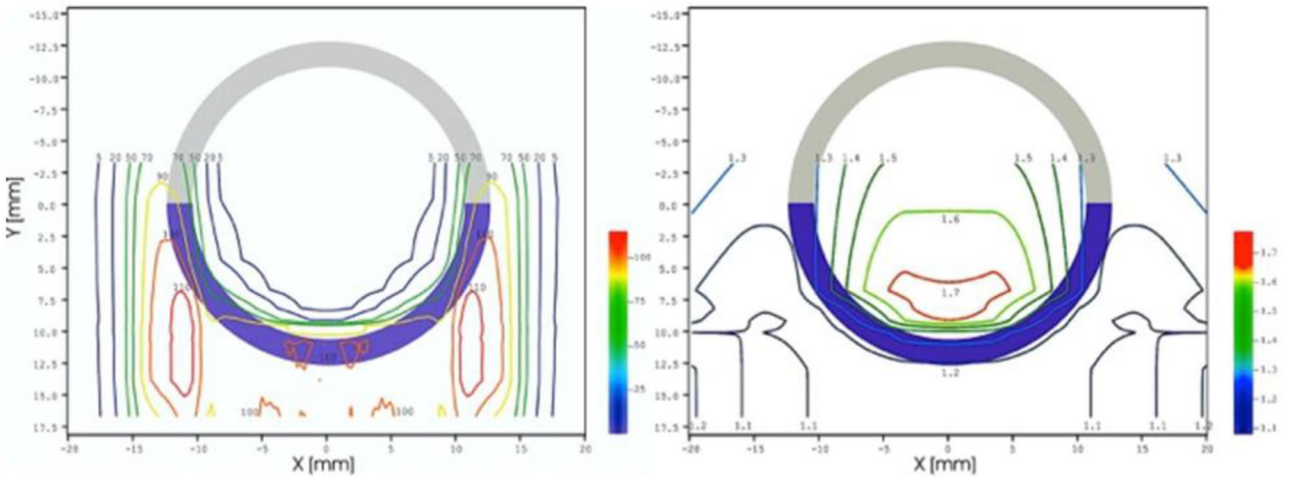

FIGURE 10 | (Left): ***Iso-dose*** curves of conjunctival melanoma treatment plan sketched in **Figure 9**. **(Right)**: ***Iso-relative biological effectiveness microdosimetric assessment*** (***RBE$_{micros}$***) curves obtained from microdosimetric measurements. Data from De Nardo et al. [30].

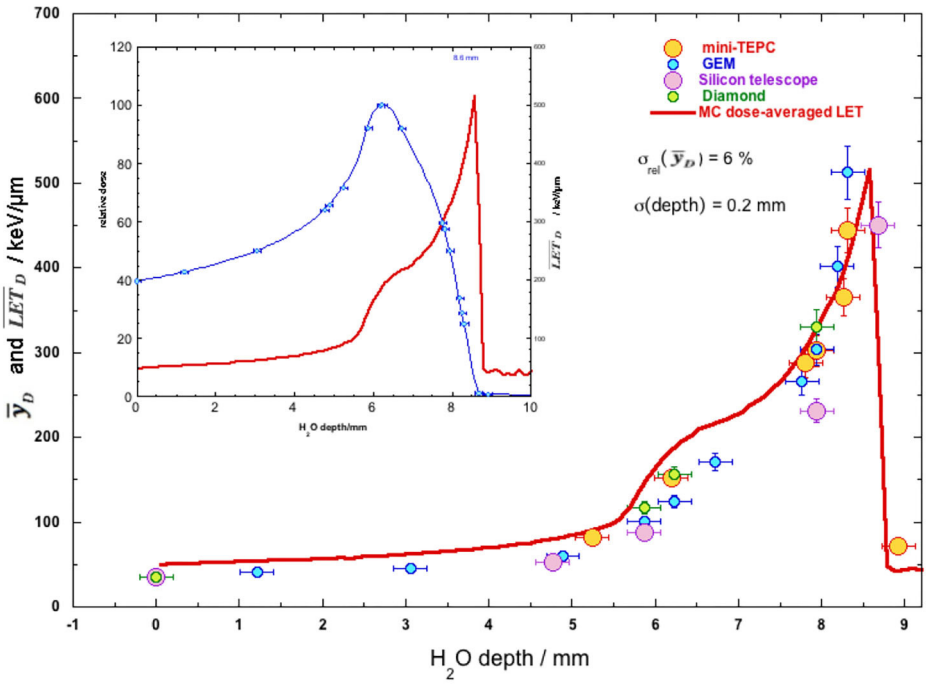

FIGURE 11 | Measured $\bar{y}_D$ and calculated dose-averaged linear energy transfer ($\overline{LET_D}$) values in water of ^{12}C ion beam of 62 MeV/u at different water depths. The $\bar{y}_D$ values of the four different detectors have been plotted with different colors. In the insert, the relative dose (blue thin line) and the $\overline{LET_D}$ depth profile (red thick line) with the detector positions are presented. Data from Colautti et al. [8].

HOW TO USE RELATIVE BIOLOGICAL EFFECTIVENESS MICRODOSIMETRIC ASSESSMENT VALUES IN A THERAPEUTIC PLAN: AN EXAMPLE

The conjunctival melanoma is a rare tumor (3% of all ocular melanomas), which is difficult to treat with success by using conventional radiotherapy. At the Center Antoine Lacassagne in Nice (France), the 65 MeV proton beam provided by the MEDICYC cyclotron is used to treat the conjunctival melanoma. However, the complexity of the irradiation (see left side of **Figure 9**), which uses a hemispherical polymethyl methacrylate (PMMA) plastic, compensator, raises questions about the

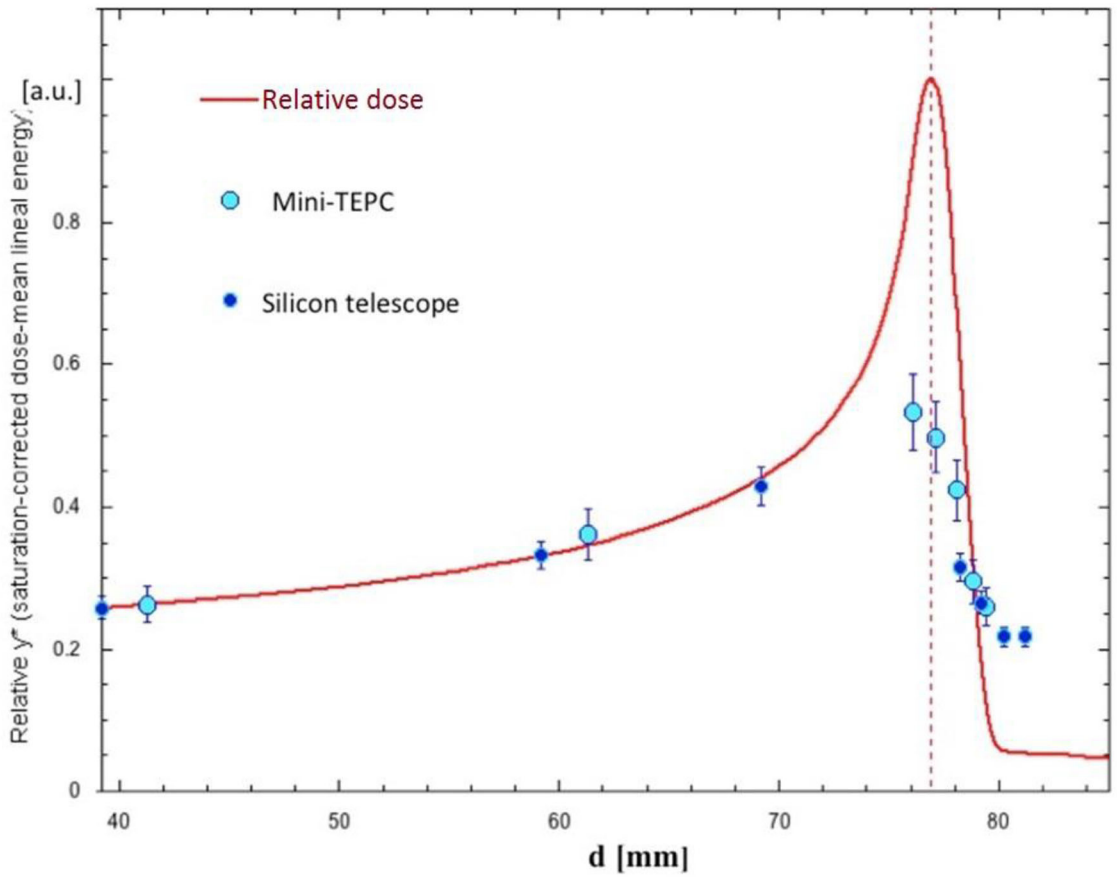

FIGURE 12 | *y** (saturation-corrected dose mean lineal energy with saturation value of $y_0 = 124$ keV/μm, see text) measured with the mini-tissue-equivalent proportional counter (TEPC) and the silicon telescope detector at the Italian National Center for Oncological Hadrontherapy (CNAO). The active beam of 189.5 MeV/u uniformly scanned a slice of 30 × 30 mm^2. The y* values have been scaled to the relative dose value at the beam entrance. Data from Colautti et al. [8].

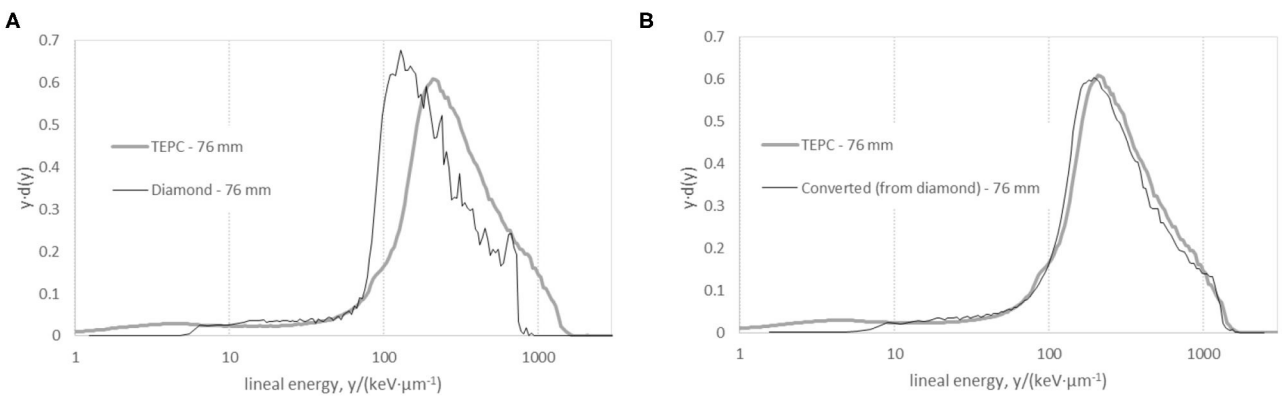

FIGURE 13 | Microdosimetric spectra of Italian National Center for Oncological Hadrontherapy (CNAO) 195 MeV/u carbon ion clinical beam at a water-equivalent depth of 76 mm. **(A)** Spectra collected with the cylindrical propane-based mini-tissue-equivalent proportional counter (TEPC) (gray thick line) and with the diamond microdosimeter (black thin line). **(B)** The diamond spectrum was recalculated to represent the response of the cylindrical propane-based mini-TEPC. TEPC data from Colautti et al. [8] and diamond data from Magrin et al. [31].

variability of radiation quality across the conjunctiva. To answer these questions, a microdosimetric approach was used.

The patient irradiation setup was simulated with a PMMA phantom, the compensator being the same as the one used for treatment (see right side of **Figure 9**). Microdosimetric spectra

were measured with a mini-TEPC placed at different lateral distances from the proton beam axis.

In the left side of **Figure 10**, the iso-dose curves of the traditional treatment plan are plotted, while in the right side of the figure, the iso-$\boldsymbol{RBE_{micros}}$ curves are plotted. The iso-$\boldsymbol{RBE_{micros}}$ curves are obtained using the $\boldsymbol{RBE_{micros}}$ values calculated from equation (7) at the different positions.

Microdosimetric data show that $\boldsymbol{RBE_{micros}}$ is almost invariant with value between 1.2 and 1.3 throughout all of the conjunctiva. In this experimental example, microdosimetric measurements confirmed the goodness of the treatment plan. The results of **Figure 10** show how to implement an "upgraded" treatment plan, which includes $\boldsymbol{RBE_{micros}}$ data.

MICRODOSIMETRIC MONITORING OF THERAPEUTIC CARBON ION BEAMS

Figure 2 shows clearly that carbon ions reach a biological effectiveness higher than protons at the end of the track, where the ***LET*** values are in the range 100–200 keV/μm. The increase of ***RBE*** at the end of the carbon ion range is one main factor that justifies the high cost and complexity of the particle accelerators that are necessary to accelerate the ions up to the energy necessary to treat deep-seated tumors (∼5 GeV). Therefore, in carbon ion therapy, the ***RBE*** variation with depth in the irradiated tissue must be taken into account when optimizing a treatment plan (in order to maximize the tumor control probability and minimize the normal tissue complications probability). Considering the complexity of the radiation field produced by carbon ions inside the patient body, the microdososimetric characterization is a useful experimental tool. Complementary to models that describe the radiation biological action, microdosimeters can be used to monitor ***LET***, $\boldsymbol{RBE_{10}}$. More generally, microdosimeters might serve as an instrumental support to improve the comparison among different radiation centers concerning therapeutic gain.

The Microdosimeter to Monitor Linear Energy Transfer, Carbon Ion Data

In the section Assessing Variations of Linear Energy Transfer in Proton Data, the advantages and the disadvantages of some current microdosimeters have been presented, the main drawback of solid-state detectors being the relatively high detection threshold, which makes them less suited to monitor low ***LET*** radiation and in general the ***LET*** in therapeutic proton beams (**Figure 6**). The discriminator level of the solid-state detectors depends on the thickness of the sensitive volume. The silicon and diamond detectors described in the section Microdosimetric Detectors with physical thickness of ∼2 μm have a discrimination level just below 10 keV·μm^{-1} [13, 18]. When the thickness is increased to 10 μm, the discrimination level decreases to about 2 keV·μm^{-1} for diamond detectors and 0.2 keV·μm^{-1} for the MicroPlus/Mushroom detectors [15]. The low sensitivity limits are less severe with carbon ions, since microdosimetric spectra shift toward higher values and show low contributions from small y-values.

In order to test the capability of different detectors to monitor the $\overline{\boldsymbol{LET_D}}$ of carbon ion beams, four different microdosimeters (the mini-TEPC, the silicon telescope, the diamond microdosimeter described in the section The Microdosimeter as Relative Biological Effectiveness Monitor, and a multi-element gas counter with GEM technology [45]) have been exposed to the same carbon ion beam of 62 MeV/u [8]. In **Figure 11**, the $\bar{\mathbf{y}}_\mathbf{D}$ values measured at different depths in a water-equivalent phantom are plotted together with the $\overline{\boldsymbol{LET_D}}$ values calculated with the Geant4 Monte Carlo code (see the inserted algorithm in **Figure 6**). The figure shows that, in spite of the detectors' differences, the $\bar{\mathbf{y}}_\mathbf{D}$ values are very similar, the relative standard deviation of the mean of all the data being 15%. Part of this variance is certainly due to the detector position uncertainty. Therefore, all the microdosimeters are able to monitor the calculated $\overline{\boldsymbol{LET_D}}$ as $\overline{\boldsymbol{LET_D}} = k \cdot \bar{\mathbf{y}}_\mathbf{D}$, where the proportionality factor k depends on the beam anisotropy as well as on the detector's angular response. For instance, k assumes the values of 1, and 1.08, for a unidirectional beam with the direction normal to the face of a slab detector and to the axis of a cylindrical detector, respectively. For spherical detectors, k is always 1.125, for isotropic as well as unidirectional beams. It should be studied for each therapeutic facility before using any microdosimeter as $\overline{\boldsymbol{LET_D}}$ monitor.

A similar comparison was performed with the 195 MeV/u active carbon ion beam of the Italian National Center for Oncological Hadrontherapy (CNAO) in Pavia, Italy, by using the mini-TEPC and the diamond microdosimeter [31]. Also in this case, the $\mathbf{y_D}$ value differences are within 15% with a standard deviation of 6%, being mainly attributable to the detector position uncertainty in a radiation field, the microdosimetric quality of which changes rapidly with depth.

The Microdosimeter to Monitor Relative Biological Effectiveness, Carbon Ion Data

As far as $\bar{\mathbf{y}}_\mathbf{D}$ is able to properly monitor $\overline{\boldsymbol{LET_D}}$, proportionality with the $\boldsymbol{RBE_{10}}$ cannot be assumed because of the saturation effect that results in the reduction of RBE at very high LET in **Figure 2**. The microdosimetric spectrum should be properly weighted, but the weighting function used for proton therapy discussed in the section The Microdosimeter to Monitor Relative Biological Effectiveness, Proton Data does not seem to work with carbon ions [46]. These differences arise from the distinct characteristics of the track structures of protons and carbon ions, also in the case of identical $\overline{\boldsymbol{LET_D}}$. The section "Use of Focused Low-LET Proton Beams to Mimic High-LET" of Part I provides additional details. For carbon ion irradiation, the saturation effect can be introduced with the so-called "saturation-corrected dose mean lineal energy" or $\boldsymbol{y^*}$.

$$y* = \frac{y_0^2 \cdot \int [1 - e^{-\left(\frac{y}{y_0}\right)^2}] \cdot f(y) dy}{\int y \cdot f(y) dy} \tag{8}$$

where the free parameter $\boldsymbol{y_0}$ is the y-value at which the biological effect saturates [4].

The ^{12}C therapeutic active beam of CNAO was used to derive y^* based on y measured with the mini-TEPC and the silicon telescope microdosimeter. **Figure 12** shows the very similar results obtained with the two detectors at different depths in a water phantom. As expected, the y^* value increases with the depth up to a maximum value and then it decreases mimicking the saturation effect of **Figure 2**.

The y^* value has been inserted in the microdosimetric kinetic model (MKM) (see Part I) to assess RBE_{10} of human salivary gland cells at the Heavy Ion Medical Accelerator in Chiba (HIMAC) therapeutic facility with a 290 MeV/u carbon ion beam. Measurements performed with a large TEPC (12.7 mm of diameter) are able to monitor the clinic biological dose with good accuracy [47]. The measurements have been repeated with the MicroPlus Bridge detector giving the same results, but in the distal edge where the large geometrical size of the TEPC could have compromised the position accuracy [48].

PROSPECTIVE OF MICRODOSIMETRY IN THE CLINICS

In carbon ion therapy, the passive beam spread modality used in the initial years to conform the radiation to the tumor targets has been gradually replaced by scanned beams [49]. The daily fraction is delivered to the patient from different portals and, for each portal, the pencil beam is scanned in three dimensions to thousands of different spot positions to cover the tumor target. Scanned carbon ion beams created new constraints and needs for experimental microdosimetry. Non-uniform distributions of the dose are feasible, and this is a feature used in the so-called "intensity modulated" therapy with ion beams. Thanks to the additional degrees of freedom, for each portal, the conformation of the irradiation can be adapted, optimizing the radiation quality across the target. Examples of these modalities are the "*LET*-painting" [50, 51] and the "Kill-painting" [52]. In these techniques, the radiation is delivered not only to preserve the dosimetric and the biological constraints but also to optimize the distribution of *LET* in the first case and to maintain uniform cell killing in volumes with heterogeneous radiosensitivity in the second case.

The complex radiation fields in these modalities show, inevitably, large *LET* gradients. In this scenario, the spectra collected with the microdosimeters in water phantoms can be used as radiation quality specifiers. The spatial density of the measurements can be increased where the LET gradient is higher or in the sub-volumes corresponding to critical, radiosensitive locations.

For carbon ion therapy beams, there are numerous microdosimetric data collected with a variety of detectors, gaseous and solid (a non-exhaustive selection is provided in the references [31, 46, 47, 53–55]). However, as discussed in the *Introduction*, the shape and material of the microdosimeters affect the experimental outcomes. To guarantee a univocal assessment of the radiation quality, the characteristics of the microdosimeters should be fixed. In particular, the "standards" for volume size, shape, aspect ratio, and the material to be used as reference for the microdosimetric spectra should be defined and become the reference for all the different detectors.

An example of spectral conversion is shown in **Figure 13** and refers to data collected at 195 MeV/u carbon ion clinical beam of CNAO. It compares the spectrum collected with a propane-filled mini-TEPC [55] and the spectrum collected with a diamond microdosimeter and converted based on the shape and the material of the mini-TEPC [31]. The spectra conversion is the result of two successive conversion steps [56]. The first transforms the experimental spectrum collected with slab diamond detector to the spectrum that would be collected by a propane-filled slab detector using a function of the stopping powers of the two materials. The second conversion transforms the spectrum of the slab propane-filled detector to the spectrum that, for the same material, would be collected by a cylindrical detector, based on the path length distributions of the two shapes.

The experimental spectrum for the diamond detector is shifted toward lower lineal energies compared to the experimental spectrum collected with the propane-filled mini-TEPC (**Figure 13A**). This is due to two conditions. First, for the same particle energy, the energy imparted per unit of length and unit of mass is lower in diamond than in propane. Second, the maximum path length of a cylindrical detector is 27% higher than its mean path length (for irradiation normal to the cylinder axis) while, for a slab detector, maximum and mean path lengths coincide. This results in extending the spectrum of the cylindrical detectors toward higher lineal energy values.

Overall, after the conversion, the two spectra show a good agreement. The effect of the low sensitivity in solid-state detectors, discussed in the section Assessing Variations of Linear Energy Transfer in Proton Data, is visible in the diamond spectrum at lineal energies below 9 keV·μm^{-1}. A metrological approach needs to be established where univocal methodologies for the detector calibration and formalism for the representation of the spectra are implemented and shared among the users. This should include the uncertainty budget assessment of microdosimetric measurement performed with different tools and methods. The role played by Monte Carlo simulations in this process is discussed in the section Monte Carlo Codes in Microdosimetry.

It is worth mentioning here the work of Hagiwara et al. [57], indicating the potential value of microdosimetric data for the clinical outcome of ion beam therapy. In this clinical-based investigation, the outcomes of local control and overall survival in pancreatic tumors are assessed with retrospective studies and examined in relation to the dose mean *LET*. $\overline{LET}_D$ values are computed within the tumor volume and compared to the clinical outcome defined as lack of local control of tumor. The results show that the lowest value of $\overline{LET}_D$ within the tumor volume is a prognostic factor related to local failure. In all case studies, the 18-month local control was maintained at 100% when the minimum $\overline{LET}_D$ was maintained above 44 keV·μm^{-1}. In the plans where $\overline{LET}_D$ declines below 44 keV·μm^{-1}, the local control dropped to 34%. This is the example of a new paradigm in which the *LET* is explicitly taken into consideration for the outcome of the treatment, without the intermediate role of the RBE. As discussed in the section Microdosimetric Monitoring of

Therapeutic Carbon Ion Beams, microdosimetric spectra provide an estimate of ***LET*** in terms of track and dose mean values. However, the heterogeneity of the particle energies and species in different points of the target is not completely represented by single parameters, such as the averaged ***LET***. Computations based on microdosimetric spectra, collected experimentally in complex phantoms, may provide a representation of the ***LET*** distributions. However, limited data are available yet for proving the accuracy of these derived ***LET*** distributions for complex phantoms and tissue structure.

The relevance of the measurement uncertainty of microdosimetric spectra and ***LET*** distributions with reference to the uncertainties of the biological outcome and clinical factors is still unclear. Furthermore, the environment surrounding the tumor may play an important factor. Investigating this should be part of the metrological approach suggested above. Note that the uncertainties on microdosimetric quantities, although smaller, may not be negligible compared to the biological uncertainties, contrary to the uncertainty of macroscopically measured absorbed dose to water. The spread of experimental data that relate biological to physical quantities may be determined not only by the substantial uncertainties of the biological data but also by the physical quantities at a microscopic scale. Monte Carlo simulations are a well-suited tool to aid establishing this uncertainty propagation chain.

MONTE CARLO CODES IN MICRODOSIMETRY

Radiation transport Monte Carlo codes have become frequent tools in microdosimetry research from both a theoretical and an experimental approach. In the last years, general-purpose Monte Carlo codes, such as FLUKA [58], Geant4 [59–61], and PHITS [62], have been used to verify the experimental outcomes, in which case it is key to include an appropriate modeling of the detector response [63, 64].

With properly validated interaction models, Monte Carlo simulations give a reliable benchmark to experimental data obtained with either TEPC or solid-state microdosimeters (see the sections The Microdosimeter as Relative Biological Effectiveness Monitor and The Microdosimeter to Monitor Linear Energy Transfer, Carbon Ion Data) [29, 65–67]. As indicated in the section The Physical Base of the Radiation Action on Human Cells, it is possible to evaluate the influence of specific path length distributions on the measured microdosimetric spectra by means of Monte Carlo simulation. The mixed radiation field properties can be evaluated by Monte Carlo simulations, and thus the contribution of each secondary ion can be quantified and be used as a reference to interpret the experimental microdosimetric spectra [68, 69]. These determinations can also help to evaluate correction factors to convert microdosimetric quantities measured in solid-state microdosimeters to equivalent ones in tissue (see the section Prospective of Microdosimetry in the Clinics) [10]. Also, as indicated in the section Assessing Variations of Linear Energy Transfer in Proton Data, Monte Carlo simulations constitute a powerful tool for the design phase of new concepts of microdosimetry detectors, as sensitivity analysis can be carried out with numerical simulations, saving costs [70]. Microdosimetry calculations have been used as a benchmark to define a method suitable for scoring $\overline{LET}_D$ in voxelized geometries [71].

To become a reliable tool, it is very important to ensure that the code has been properly validated for the simulation of the relevant types of interactions taking place within a microdosimeter. Indeed, measurements carried out with microdosimeters of different types have been used to assess the accuracy of these codes at microscale measurements, not only for track structure but also for fragmentation of ion beams, by means of experimental microdosimetry distributions [72] or radial dose profiles [73, 74].

It is worth to mention that all general-purpose codes cited above use a condensed history approach to model the electronic interactions of charged particles with matter. This approach allows an increase of computational efficiency by grouping a certain number of electronic collisions within a single simulation step; in addition, secondary electrons set in motion below a given threshold are not explicitly tracked, so that its energy is considered to have been deposited at the volume where the ionization occurred. For instance, the minimum threshold that can be set in FLUKA is 1 keV, whereas for some physics lists of the Geant4 toolkit, it can be as low as 100 eV. Thus, it is expected that the accuracy of calculations using the condensed history methods may not be optimal for submicrometric sensitive volumes, especially if electron transport plays a significant role. Actually, it has been found that FLUKA can reproduce satisfactorily lineal energy distributions obtained with a TEPC down to an equivalent size of 25 nm for carbon ion tracks, but not for proton tracks due to the typically longer range of secondary electrons in proton tracks at therapeutic energies [75, 76]. More accurate calculations can be achieved with track structure Monte Carlo codes, in which single electronic collisions are one by one simulated and all secondary electrons are produced (and thus less efficient in terms of computing time). Nevertheless, this improved spatial accuracy can be jeopardized by the uncertainties on individual interaction cross sections.

An example of pure track structure code for ion tracks in liquid water is PARTRAC [77]. In this sense, the Geant4 toolkit incorporates the extension Geant4-DNA, which includes interaction models and cross sections for electrons in liquid water down to 9 eV, protons and alphas down to 100 eV, and ions down to 0.5 MeV/u, as well as diffusion of radicals in liquid water [78–81]. Also, Geant4 incorporates a track structure extension for silicon material, Geant4-MicroElec, modeling electrons down to 16 eV and protons and ions down to 50 keV/u [82].

Monte Carlo codes can be used to generate libraries of microdosimetric quantities to be incorporated into treatment planning systems for radiobiology optimizations. In this sense, recent works [83, 84] suggest that modeling mean values and standard deviations of microdosimetric quantities is sufficient in

order to produce a comprehensive data set for proton therapy treatment planning systems.

Further, TOPAS framework [85], which wraps the Geant4 toolkit, has recently incorporated an extension providing users with the possibility of calculating microdosimetry spectra [86].

CONCLUSIONS

In ion therapy, beam quality assurance cannot be reduced to the correctness of the delivered absorbed dose alone. That is the case because the biological/clinical effect depends also on the ***RBE*** of the mixed radiation field, which in turn varies with depth. The lineal energy (y) spectrum measured with a microdosimeter is an adequate methodological approach to monitor the stochastic distributions of the energy deposited at the microscopic level, and the mean values of these distributions correlate strongly with the calculated $\overline{LET}_D$. Based on the measured y–distribution *via* application of a biological weighting function, or based on measured saturation-corrected dose mean lineal energy values y^* *via* the modified MKM, the RBE_{10} of proton and carbon ion therapeutic beams can be estimated. These estimations are in good agreement with radiobiological data. However, the optimal exploitation of microdosimeters in clinic is still under experimental investigation. Experimental microdosimetry offers valuable tools for the quality assurance of ***LET***-based treatment plans, for the validation of Monte Carlo simulations, for the intercomparison of different therapeutic centers, and more in general to improve the understanding of underlying physical characteristics of the radiation interaction that correlate with different biological effectiveness.

AUTHOR CONTRIBUTIONS

PC drafted the manuscript, the Introduction, and the Conclusion. PC and VC contributed to the description of the microdosimetric detectors, their use in proton and carbon-ion beams to assess LET and RBE (sections from Assessing Variations of Linear Energy Transfer in Proton Data, The Microdosimeter as Relative Biological Effectiveness Monitor, The Microdosimeter to Monitor Relative Biological Effectiveness, Proton Data, How to Use Relative Biological Effectiveness Microdosimetric Assessment Values in a Therapeutic Plan: An Example, and Microdosimetric Monitoring of Therapeutic Carbon Ion Beams). HP and GM contributed to the prospective in carbon-ion therapy (section Prospective of Microdosimetry in the Clinics). MC-G contributed to the MC aspects (section Monte Carlo Codes in Microdosimetry). All authors contributed to improvements, corrections, and approval of the final version.

FUNDING

This work is part of the project ENSAR2 that has received funding from the European Union's Horizon 2020 research and innovation programme under grant agreement No 654002.

REFERENCES

1. Scholz M, Friedrich T, Magrin G, Colautti P, Petrovic I, Ristić-Fira A. Characterizing radiation effectiveness in ion beam therapy Part I: introduction and biophysical modelling of RBE, Using the LEMIV. *Front Phys.* (2020) **8:**272. doi: 10.3389/fphy.2020.00272
2. Relative Biological Effectiveness in Ion Beam Therapy. IAEA Technical Reports Series No. 461. English.
3. ICRU. *Fundamental Quantities and Units for Ionizing Radiation*, International Commission on Radiation Units and Measurements, ICRU Report 60. Bethesda, MD, (1998).
4. ICRU. *Microdosimetry, International Commission on Radiation Units and Measurements,* ICRU Report 36. Bethesda, MD, (1983).
5. Booz J. Mapping of fast neutron radiation quality. In: Burger G, Ebert HG, editors. *Proceedings of the Third Symposium on Neutron Dosimetry in Biology and Medicine*, Report No. EUR 5848, Luxembourg: Commission of the European Communities (1978).
6. Lindborg L, Waker A. *Microdosimetry: Experimental Methods and Applications.* Boca Raton, FL: CRC Press Taylor & Francis Group (2017) doi: 10.1201/9781315373737
7. Friedrich T, Scholz U, Elsässer T, Durante M, Scholz M. Systematic analysis of RBE and related quantities using a database of cell survival experiments with ion beam irradiation. *J Radiat Res.* (2013) **54-3:**494–514. doi: 10.1093/jrr/rrs114
8. Colautti P, Conte V, Selva A, Chiriotti S, Pola A, Bortot D, et al. Miniaturized microdosimeters as LET monitors: first comparison of calculated and experimental data performed at the 62 MeV/u ^{12}C beam of INFN-LNS with four different detectors. *Phys Med.* (2018) **52:**113–21. doi: 10.1016/j.ejmp.2018.07.004
9. Belli M, Cherubini R, Finotto S, Moschihi G, Sapora O, Tabocchini MA. RBE-LET relationship for the survival of V79 cells irradiated with low energy protons. *Int J Radiat Biol.* (1989) **55:**93–104. doi: 10.1080/09553008914550101
10. Bolst D, Guatelli S, Tran LT, Chartier L, Lerch MLF, Matsufuji N, et al. Correction factors to convert microdosimetry measurements in silicon to tissue in 12C ion therapy. *Phys Med Biol.* (2017) **62:**2055–69. doi: 10.1088/1361-6560/aa5de5
11. ICRU. Fundamental quantities and units for ionizing radiation, International Commission on Radiation Units and Measurements, ICRU report 85. *J ICRU.* (2011) **11:**1–31. doi: 10.1093/jicru_ndr011
12. Kellerer AM. Chord-length distributions and related quantities for spheroids. *Radial Res.* (1984) **98:**425–37. doi: 10.2307/3576477
13. Agosteo S, Colautti P, Fanton I, Fazzi A, Introini MV, Moro D, et al. Study of a solid state microdosemeter based on a monolithic silicon telescope: irradiations with low-energy neutrons and direct comparison with a cylindrical TEPC. *Radiat Prot Dosimetry.* (2011) **143:**432–5. doi: 10.1093/rpd/ncq481
14. De Nardo L, Cesari V, Donà G, Magrin G, Colautti P, Conte V, Tornielli G. Mini-TEPCs for radiation therapy. *Radiat Prot Dosimetry.* (2004) **108:**345–52 doi: 10.1093/rpd/nch023
15. Rosenfeld AB. Novel detectors for silicon based microdosimetry, their concepts and applications. NIM A. 809, 156–70, 2016. Advanced in Detectors and Application for Medicine. Fabio Sauli, Alberto Del Guerra, Alessandro Olivo and Peter Thirolf Editor. doi: 10.1016/j.nima.2015.08.059
16. Prieto-Pena J, Gómez F, Fleta C, Guardiola C, Pellegrini G, Donetti M, et al. Microdosimetric spectra measurements on a clinical carbon beam at nominal therapeutic fluence rate with silicon cylindrical microdosimeters. *IEEE Trans. Nuclear Sci.* (2019) **66–7:**1840–7. doi: 10.1109/TNS.2019.2921453
17. Tran LT, Chartier L, Prokopovich DA, Bolst D, Povoli M, ummanwar A, et al. Thin silicon microdosimeter utilizing 3D MEMS technology: charge collection study and its application in mixed radiation fields. *IEEE Trans Nuclear Sci.* (2018) **65:**467–472. doi: 10.1109/TNS.2017.2768062

18. Verona C, Magrin G, Solevi P, Bandorf M, Marinelli M, Stock M, et al. Toward the use of single crystal diamond based detector for ion-beam therapy microdosimetry. *Radiat Meas.* (2018) **110:**25–31. doi: 10.1016/j.radmeas.2018.02.001
19. Galer S, Hao L, Gallop J, Palmans H, Kirkby KJ, Nisbet A. Design concept for a novel SQUID-based microdosimeter. *Radiat Prot Dos.* (2011) **143:**427–31. doi: 10.1093/rpd/ncq475
20. Fathi K, Galer S, Kirkby KJ, Palmans H, Nisbet A. Coupling monte carlo simulations with thermal analysis for correcting microdosimetric spectra from a novel micro-calorimeter. *Rad Phys Chem.* (2017) **140:**406–11. doi: 10.1016/j.radphyschem.2017.02.055
21. Mazzucconi D, Bortot D, Agosteo S, Pola A, Pasquato S, Fazzi A, et al. Microdosimetry at nanometric scale with an avalanche-confinement tepc: response against a helium ion beam. *Rad Protect Dosimetry*. (2019) **183:**177–81. doi: 10.1093/rpd/ncy230
22. Bradley PD, Rosenfeld AB, Zaider M. Solid state microdosimetry. *Nuclear Instr Methods Phys Res Sec B*. (2001) **184:**135–57. doi: 10.1016/S0168-583X(01)00715-7
23. Tran LT, Chartier L, Bolst D, Pogossov A, Guatelli S, Petasecca M, et al. Characterization of proton pencil beam scanning and passive beam using a high spatial resolution solid-state microdosimeter. *Med Phys.* (2017) **44:**6085–95. doi: 10.1002/mp.12563
24. Farahmand M, Bos AJ, De Nardo L, van Eijk CW. First microdosimetric measurements with a TEPC based on a GEM. *Rad Protect Dosimetry*. (2004) **110:**839-43. doi: 10.1093/rpd/nch144
25. Shin J, Cho S, Park S, Lee S, Kwak J, Kim S, et al. SU-E-T-234: LET measurement using nuclear emulsion and monte carlo simulation for proton beam. *Med Phys.* (2012) **39:**3757. doi: 10.1118/1.4735297
26. Paganetti H. Relative biological effectiveness (RBE) values for proton beam therapy. Variations as a function of biological endpoint, dose, and linear energy transfer. *Phys Med Biol.* (2014) **59:**R419–72. doi: 10.1088/0031-9155/59/22/R419
27. Wagenaar D, Tran LT, Meijers A, Marmitt GG, Souris K, Bolst D, et al. Validation of linear energy transfer computed in a monte carlo dose engine of a commercial treatment planning system. *Phys Med Biol.* (2020) **65:**025006. doi: 10.1088/1361-6560/ab5e97
28. ICRU. *Linear Energy Transfer, International Commission on Radiation Units and Measurements*, ICRU Report 16, Washington, DC, (1970).
29. Conte V, Bianchi A, Selva A, Petringa G, Cirrone GAP, Parisi A, et al. Microdosimetry at CATANA 62 MeV proton beam with a sealed miniaturized TEPC. *Phys Med.* (2019) **64:**114–22. doi: 10.1016/j.ejmp.2019.06.011
30. De Nardo L, Colautti P, Hérault J, Conte V, Moro D. Microdosimetric characterisation of a therapeutic proton beam used for conjunctival melanoma treatments. *Radiat Meas.* (2010) **45:**1387–90. doi: 10.1016/j.radmeas.2010.05.034
31. Magrin G, Verona C, Ciocca M, Marinelli M, Mastella E, Stock M, et al. Microdosimetric characterization of clinical carbon-ion beams using synthetic diamond detectors and spectral conversion methods. *Med Phys.* (2020) **47:**713–21. doi: 10.1002/mp.13926
32. Petringa G, Pandola L, Agosteo S, Catalano R, Colautti P, Conte V, et al. Monte Carlo implementation of new algorithms for the averaged-dose and -track linear energy transfer evaluation in 62 MeV clinical proton beams. *Phys Med Biol.* (2020). doi: 10.1088/1361-6560/abaeb9
33. Palmans H, Rabus H, Belchior AL, Bug MU, Galer S, Giesen U, et al. Future development of biologically relevant dosimetry. *Br J Radiol*. (2015) **87:**20140392. doi: 10.1259/bjr.20140392
34. Pihet P, Menzel HG, Schmidt R, Beauduin M, Wambersie A. Biological weighting function for rbe specification of neutron therapy beams. Intercomparison of 9 European centres. *Radiat Prot Dosim.* (1990) **31:**1-4. doi: 10.1093/oxfordjournals.rpd.a080709
35. Loncol T, Cosgrove V, Denis JM, Gueulette J, Mazal A, Menzel HG, et al. Radiobiological effectiveness of radiation beams with broad LET spectra: microdosimetric analysis using biological weighting functions. *Radiat Prot Dosim.* (1994) **52:**347–52. doi: 10.1093/rpd/52.1-4.347
36. Tung CJ. Microdosimetric relative biological effectiveness of therapeutic proton beams. *Biomed J.* (2015) **38:**399–407. doi: 10.4103/2319-4170.167072
37. Gueulette J, Bohm L, Slabbert JP, De Coster BM, Rutherfoord GS, Ruifrok A, et al. Proton relative biological effectiveness (RBE) for survival in mice after thoracic irradiation with fractional doses. *Int J Radiat Oncol Biol Phys.* (2000) **47:**1051–8. doi: 10.1016/S0360-3016(00)00535-6
38. Gueulette J, Slabbert JP, Böhm L, De Coster BM, Rosier JF, Octave-Prignot M, et al. Proton RBE for early intestinal tolerance in mice after fractionated irradiation. *Radiother Oncol.* (2001) **61:**177–84. doi: 10.1016/S0167-8140(01)00446-7
39. Gueulette J, Blattmann H, Pedroni E, Coray A, De Coster BM, Mahy P, et al. Relative biologic effectiveness determination in mouse intestine for scanning proton beam at Paul Scherrer Institute, Switzerland. Influence of motion. *Int J Radiat Oncol Biol Phys*. (2005) **62:**838–45. doi: 10.1016/j.ijrobp.2005.03.048
40. Gueulette J, Boehm L, De Coster B-M, Vynckier S, Octave-Prignot M, Schreuder AN, et al. RBE variation as a function of depth in the 200 MeV proton beam produced at the national accelerator centre in faure (South Africa). *Radiother Oncol.* (1997) **42:**303–9 doi: 10.1016/S0167-8140(97)01919-1
41. Gueulette J, Gregoire V, Octave-Prignot M, Wambersie A. Measurements of radiobiological effectiveness in the 85 MeV proton beam produced at the cyclotron CYCLONE of Louvain-la-Neuve. *Belgium Radiat Res.* (1996) **145:**70–4. doi: 10.2307/3579197
42. Uzawa A, Ando K, Furusawa Y, Kagiya G, Fuji H, Hata M, et al. Biological intercomparison using gut crypt survivals for proton and Carbon-ion beams. *J Radiat Res.* (2007) **48:**A75–80. doi: 10.1269/jrr.48.A75
43. Mason KA, Gillin MT, Mohan R, Cox JD. Preclinical biologic assessment of proton beam relative biologic effectiveness at proton therapy center Houston. *Int J Radiat Oncol Biol Phys*. (2007) **68:**968–70. doi: 10.1016/j.ijrobp.2007.03.051
44. De Nardo L, Cesari V, Iborra N, Conte V, Colautti P, Herault J, et al. Microdosimetric assessment of nice therapeutic proton beam biological quality. *Phys Med*. (2004) **20:**71–77. doi: 10.1093/rpd/ncq483
45. De Nardo L, Dal Corso F, Pegoraro M. Microdosimetric measurements in gamma and neutron fields with a tissue-equivalent proportional counter based on a gas electron multiplier. *Rad Prot Dosim*. (2017) **175:**260–66. doi: 10.1093/rpd/ncw294
46. Gerlach R, Roos H, Kellerer AM. Heavy Ion RBE and microdosimetric spectra. *Radiat Prot Dosim.* (2002) **99:**413–8. doi: 10.1093/oxfordjournals.rpd.a006821
47. Kase Y, Kanai T, Sakama M, Tameshige Y, Himukai T, Nose H, et al. Microdosimetric approach to NIRS-defined biological dose measurement for carbon-ion treatment beam. *J Radiat Res.* (2011) **52:**59–68. doi: 10.1269/jrr.10062
48. Tran LT, Chartier L, Prokopovich DA, Reinhard MI, Petasecca M, Guatelli S, et al. 3D-mesa "bridge" silicon microdosimeter: charge collection study and application to RBE studies in 12C radiation therapy. *IEEE Trans Nuclear Sci.* (2015) **148:**44–51. doi: 10.1109/TNS.2015.2391102
49. PTCOG, *Particle Therapy Co-Operative Group Website.* Available online at: https://www.ptcog.ch/index.php/facilities-in-operation (accessed April 6, 2020).
50. Bassler N, Jäkel O, Søndergaard CS, Petersen JB. Dose- and LET-painting with particle therapy. *Acta Oncol.* (2010) **49:**1170–6. doi: 10.3109/0284186X.2010.510640
51. Bassler N, Toftegaard J, Lühr A, Sørensen BS, Scifoni E, Krämer M, et al. LET-painting increases tumour control probability in hypoxic tumours. *Acta Oncol*. (2014) **53:**25–32. doi: 10.3109/0284186X.2013.832835
52. Tinganelli W, Durante M, Hirayama R, Krämer M, Maier A, Kraft-Weyrather W, et al. Kill-painting of hypoxic tumours in charged particle therapy. *Sci Rep*. (2015) **5:**17016. doi: 10.1038/srep17016
53. Martino G, Durante M, Schardt D. Microdosimetry measurements characterizing the radiation fields of 300 MeV/u 12C and 185 MeV/u 7Li pencil beams stopping in water. *Phys Med Biol*. (2010) **55:**3441–9. doi: 10.1088/0031-9155/55/12/011
54. Alrowaili ZA, Lerch MLF, Petasecca M, Carolan MG, Metcalfe PE, Rosenfeld AB. Beam perturbation characteristics of a 2D transmission silicon diode array, magic plate. *J Appl Clin Med Phys.* (2016) **17:**85–98. doi: 10.1120/jacmp.v17i2.5932
55. Conte V, Colautti P, Chiriotti S, Moro D, Ciocca M, Mairani A. Mini-TEPC microdosimetric study of carbon ion therapeutic beams at CNAO. *EPJ Web Conf*. (2017) **153:**01012. doi: 10.1051/epjconf/201715301012
56. Magrin G. A method to convert spectra from slab microdosimeters in therapeutic ion-beams to the spectra referring to microdosimeters

of different shapes and material. *Phys Med Biol*. (2018) **63:**215021. doi: 10.1088/1361-6560/aae655
57. Hagiwara Y, Bhattacharyya T, Matsufuji N, Isozaki Y, Takiyama H, Nemoto K, et al. Influence of dose-averaged linear energy transfer on tumour control after carbon-ion radiation therapy for pancreatic cancer. *Clin Transl Radiat Oncol*. (2020) **21:**19–24. doi: 10.1016/j.ctro.2019.11.002
58. Battistoni G, Bauer J, Boehlen TT, Cerutti F, Chin MPW, Dos Santos Augusto R, et al. The fluka code: an accurate simulation tool for particle therapy. *Front Oncol*. (2016) **6:**116. doi: 10.3389/fonc.2016.00116
59. Agostinelli S, Allison J, Amako K, Apostolakis J, Araujo H, Arce P, et al. Geant4—a simulation toolkit. *Nucl Instruments Methods Phys Res Sect A*. (2003) **506:**250–303. doi: 10.1016/S0168-9002(03)01368-8
60. Allison J, Amako K, Apostolakis J, Araujo H, Arce Dubois P, Asai M, et al. Geant4 developments and applications. *IEEE Trans Nucl Sci*. (2006) **53:**270–8. doi: 10.1109/TNS.2006.869826
61. Allison J, Amako K, Apostolakis J, Arce P, Asai M, Aso T, et al. Recent developments in Geant4. *Nucl Instr Methods Phys Res Sect A*. (2016) **835:**186–225. doi: 10.1016/j.nima.2016.06.125
62. Sato T, Iwamoto Y, Hashimoto S, Ogawa T, Furuta T, Abe S, et al. Features of Particle and Heavy Ion Transport code System (PHITS) version 3.02. *J Nucl Sci Technol*. (2018) **55:**684–90. doi: 10.1080/00223131.2017.1419890
63. Guardiola C, Quirion D, Pellegrini G, Fleta C, Esteban S, Cortés-Giraldo MA, et al. Silicon-based three-dimensional microstructures for radiation dosimetry in hadrontherapy. *Appl Phys Lett*. (2015) **107:**023505. doi: 10.1063/1.4926962
64. Galer S, Shipley DR, Palmans H, Kirkby KJ, Nisbet A. Monte Carlo simulation of a TEPC for microdosimetry of carbon ions. *Rad Phys Chem*. (2017) **140:**412–8. doi: 10.1016/j.radphyschem.2017.02.028
65. Livingstone J, Prokopovich DA, Tran LT, Guatelli S, Petasecca M, Lerch MLF, et al. Charge collection in n-SOI planar microdosimeters. *IEEE Trans Nucl Sci*. (2013) **60:**4289–96. doi: 10.1109/TNS.2013.2283307
66. Gómez F, Fleta C, Esteban S, Quirion D, Pellegrini G, Lozano M, et al. Measurement of carbon ion microdosimetric distributions with ultrathin 3D silicon diodes. *Phys Med Biol*. (2016) **61:**4036–47. doi: 10.1088/0031-9155/61/11/4036
67. Bianchi A, Selva A, Colautti P, Bortot D, Mazzucconi D, Pola A, et al. Microdosimetry with a sealed mini-TEPC and a silicon telescope at a clinical proton SOBP of CATANA. *Radiat Phys Chem*. (2020) **171:**108730. doi: 10.1016/j.radphyschem.2020.108730
68. Burigo L, Pshenichnov I, Mishustin I, Bleicher M. Microdosimetry spectra and RBE of 1H, 4He, 7Li and 12C nuclei in water studied with Geant4. *Nucl Instr Methods Phys Res Sect B*. (2014) **320:**89–99. doi: 10.1016/j.nimb.2013.10.018
69. Agosteo S, Introini MV, Pola A, Sagia E. Response of a silicon telescope microdosimeter to 400 AMeV carbon ions. *Radiat Meas*. (2014) **71:**524–8. doi: 10.1016/j.radmeas.2014.05.023
70. Anjomani Z, Hanu AR, Prestwich WV, Byun SH. Monte Carlo design study for thick gas electron multiplier-based multi-element microdosimetric detector. *Nucl Instr Methods Phys Res Sect A*. (2014) **757:**67–74. doi: 10.1016/j.nima.2014.04.063
71. Cortés-Giraldo MA, Carabe A. A critical study of different Monte Carlo scoring methods of dose average linear-energy-transfer maps calculated in voxelized geometries irradiated with clinical proton beams. *Phys Med Biol*. (2015) **60:**2645–69. doi: 10.1088/0031-9155/60/7/2645
72. Bolst D, Guatelli S, Tran LT, Chartier L, Davis J, Biasi G, et al. Validation of Geant4 for silicon microdosimetry in heavy ion therapy. *Phys Med Biol*. (2020) **65:**045014. doi: 10.1088/1361-6560/ab586a
73. Incerti S, Psaltaki M, Gillet P, Barberet P, Bardiès M, Bernal MA, et al. Simulating radial dose of ion tracks in liquid water simulated with Geant4-DNA: a comparative study. *Nucl Instruments Methods Phys Res Sect B*. (2014) **333:**92–8. doi: 10.1016/j.nimb.2014.04.025
74. Tsuda S, Sato T, Ogawa T. Measurement of the stochastic radial dose distribution for a 30-MeV proton beam using a wall-less tissue-equivalent proportional counter. *Radiat Prot Dosimetry*. (2015) **168:**190–6. doi: 10.1093/rpd/ncv285
75. Mazzucconi D, Bortot D, Pola A, Agosteo S, Pasquato S, Fazzi A, et al. Monte Carlo simulation of a new TEPC for microdosimetry at nanometric level: response against a carbon ion beam. *Radiat Meas*. (2018) **113:**7–13. doi: 10.1016/j.radmeas.2018.03.006
76. Mazzucconi D, Bortot D, Pola A, Fazzi A, Colautti P, Conte V, et al. Nano-microdosimetric investigation at the therapeutic proton irradiation line of CATANA. *Radiat Meas*. (2019) **123:**26–33. doi: 10.1016/j.radmeas.2019.02.012
77. Friedland W, Kundrát P, Becker J, Eidemüller M. Biophysical simulation tool partrac: modelling proton beams at therapy-relevant energies. *Radiat Prot Dosimetry*. (2019) **186:**172–5. doi: 10.1093/rpd/ncz197
78. Incerti S, Kyriakou I, Bernal MA, Bordage MC, Francis Z, Guatelli S, et al. Geant4-DNA example applications for track structure simulations in liquid water: a report from the Geant4-DNA Project. *Med Phys*. (2018) **45:**e722–39. doi: 10.1002/mp.13048
79. Bernal MA, Bordage MC, Brown JMC, Davídková M, Delage E, El-Bitar Z, et al. Track structure modeling in liquid water: a review of the Geant4-DNA very low energy extension of the Geant4 Monte Carlo simulation toolkit. *Phys Med*. (2015) **31:**861–74. doi: 10.1016/j.ejmp.2015.10.087
80. Incerti S, Ivanchenko A, Karamitros M, Mantero A, Moretto P, Tran HN, et al. Comparison of GEANT4 very low energy cross section models with experimental data in water. *Med Phys*. (2010) **37:**4692–708. doi: 10.1118/1.3476457
81. Li J, Li C, Qiu R, Yan C, Xie W, Wu Z, et al. DNA strand breaks induced by electrons simulated with Nanodosimetry Monte Carlo Simulation Code: NASIC. *Radiat Prot Dosimetry*. (2015) **166:**38–43. doi: 10.1093/rpd/ncv171
82. Raine M, Gaillardin M, Paillet P. Geant4 physics processes for silicon microdosimetry simulation: improvements and extension of the energy-range validity up to 10 GeV/nucleon. *Nucl Instruments Methods Phys Res Sect B Beam Interact with Mater Atoms*. (2014) **325:**97–100. doi: 10.1016/j.nimb.2014.01.014
83. Bertolet A, Baratto-Roldán A, Cortés-Giraldo MA, Carabe-Fernandez A. Segment-averaged LET concept and analytical calculation from microdosimetric quantities in proton radiation therapy. *Med Phys*. (2019) **46:**4204–14. doi: 10.1002/mp.13673
84. Bertolet A, Cortés-Giraldo MA, Carabe-Fernandez A. On the concepts of dose-mean lineal energy, unrestricted and restricted dose-averaged LET in proton therapy. *Phys Med Biol*. (2020) **65:**075011. doi: 10.1088/1361-6560/ab730a
85. Perl J, Shin J, Schümann J, Faddegon B, Paganetti H. TOPAS: an innovative proton Monte Carlo platform for research and clinical applications. *Med Phys*. (2012) **39:**6818–37. doi: 10.1118/1.4758060
86. Zhu H, Chen Y, Sung W, McNamara AL, Tran LT, Burigo LN, et al. The microdosimetric extension in TOPAS: development and comparison with published data. *Phys Med Biol*. (2019) **64:**145004. doi: 10.1088/1361-6560/ab23a3

Conflict of Interest: The authors declare that the research was conducted in the absence of any commercial or financial relationships that could be construed as a potential conflict of interest.

frontiers in Physics

ORIGINAL RESEARCH
published: 28 October 2020
doi: 10.3389/fphy.2020.00346

A Simple Approach for Experimental Characterization and Validation of Proton Pencil Beam Profiles

*Paulina Stasica[1,2], Jakub Baran[1], Carlos Granja[3], Nils Krah[4,5], Grzegorz Korcyl[6], Cristina Oancea[3], Monika Pawlik-Niedźwiecka[1,6], Szymon Niedźwiecki[6], Marzena Rydygier[7], Angelo Schiavi[8], Antoni Rucinski[1] and Jan Gajewski[1]**

[1] Proton Radiotherapy Group (NZ62), Institute of Nuclear Physics Polish Academy of Sciences, Kraków, Poland, [2] Faculty of Physics and Applied Computer Science, AGH University of Science and Technology, Kraków, Poland, [3] ADVACAM, Prague, Czechia, [4] University of Lyon, CNRS, CREATIS UMR 5220, Lyon, France, [5] University of Lyon, CNRS, IP2I UMR 5822, Lyon, France, [6] Faculty of Physics, Astronomy and Applied Computer Science, Jagiellonian University, Kraków, Poland, [7] Cyclotron Center Bronowice, Institute of Nuclear Physics Polish Academy of Sciences, Kraków, Poland, [8] Department of Basic and Applied Sciences for Engineering, Sapienza University of Rome, Rome, Italy

A precise characterization of therapeutic proton pencil beams is essential for the commissioning of any treatment planning system (TPS). The dose profile characterization includes measurement of the beam lateral dose profile in the beam core and far from the beam core, in the so called low-dose envelope, and requires a sophisticated detection system with a few orders of magnitude dynamic range. We propose the use of a single-quantum-sensitive MINIPIX TIMEPIX detector, along with an in-house-designed holder to perform measurements of the pencil beam dose profile in air and in water. We validated the manufacturer calibration of the MINIPIX TIMEPIX detector in proton beams of various energies and compared the deposited energy spectra to Monte Carlo (MC) simulations. The precision of the lateral dose profile measurements has been systematically validated against Krakow proton facility commissioning data and dose profile simulations performed with MC codes Gate/Geant4 and Fred. We obtained an excellent agreement between MINIPIX TIMEPIX measurements and simulations demonstrating the feasibility of the system for a simple characterization and validation of proton pencil beams. The proposed approach can be implemented at any proton therapy facility to acquire experimental data needed to commission and validate analytical and MC-based TPS.

Keywords: proton therapy, dose, semiconductor pixel detector, Timepix detector, Monte Carlo simulation

OPEN ACCESS

Edited by:
Yolanda Prezado, INSERM U1021 Signalisation normale et pathologique de l'embryon aux thérapies innovantes des cancers, France

Reviewed by:
Jeff Buchsbaum, National Institutes of Health (NIH), United States
Marie Vidal, Centre Antoine Lacassagne, France

***Correspondence:**
Jan Gajewski
jan.gajewski@ifj.edu.pl

Specialty section:
This article was submitted to Medical Physics and Imaging, a section of the journal Frontiers in Physics

Received: *30 May 2020*
Accepted: *22 June 2020*
Published: *28 October 2020*

Citation:
Stasica P, Baran J, Granja C, Krah N, Korcyl G, Oancea C, Pawlik-Niedźwiecka M, Niedźwiecki S, Rydygier M, Schiavi A, Rucinski A and Gajewski J (2020) A Simple Approach for Experimental Characterization and Validation of Proton Pencil Beam Profiles. Front. Phys. 8:346. doi: 10.3389/fphy.2020.00346

1. INTRODUCTION

The dosimetric advantage of proton beams in radiotherapy is due to their depth-dose distribution (Bragg curve), which allows us to minimize the dose deposited in healthy tissues and to maximize it in the tumor region [1, 2]. After many years of research and development, a growing interest in proton radiotherapy is observed. According to data provided by the Particle Therapy Co-Operative Group (https://www.ptcog.ch/, 2020), there are 91 proton (or proton and carbon ion) radiotherapy facilities in operation, 33 under construction, and 27 in the planning stage all around the world. Upon startup of each new proton facility, for the purpose of launching a treatment planning system (TPS), a commissioning of the proton pencil beam is required. The beam commissioning, which includes, e.g., an experimental characterization of lateral and longitudinal beam profiles, is a demanding and time-consuming experimental procedure. In this paper, we propose a new

approach for characterization of lateral beam profiles in air and in water to simplify the procedure of beam data library acquisition and TPS commissioning.

The procedure of dosimetric commissioning and validation of single pencil beams was established and applied by several ion beam therapy facilities [3–5]. It is usually performed within commercially available active and/or passive dosimetry systems. However, the existing solutions do not offer dynamic range, and the possibility to perform measurements in water with single quantum sensitivity has not been reported as feasible when using only one device. Passive dosimetry (TLD, photochromic films) might have wider dynamic range, but the dose is integrated. Such detectors often require technologically complicated and time-consuming post-processing, and the response is often dependent on the LET. Scintillator-based detectors, such as Lynx, show a dynamic range of two orders of magnitude and cannot be easily used in water due to its large size. Active dosimetry with ionization chambers requires a complex correction procedure for temperature, pressure, recombination effect, etc. Moreover, none of these methods are single-quantum sensitive.

The state-of-the-art experimental approach for proton beam commissioning is to measure lateral dose profiles in air with a scintillating screen and CCD camera [6–10]. This method allows us only to measure the major component of the lateral beam dose profile characterized by a Gaussian distribution. In fact, primary particles scatter on the passive components of a beam delivery system, such as gantry nozzle equipment and range shifters/compensators, building up an additional dose envelope of the lateral beam profiles [6], which is recognized as a nuclear halo. The nuclear halo is often approximated in TPS by a double Gaussian model of proton pencil beam. The accurate characterization of pencil beam lateral dose profiles is particularly important for facilities using very small beam sizes as the uncertainty of the nuclear halo modeling is propagated over a greater number of beams [6, 11]. Also, the effect is pronounced for small, shallowly located targets that are irradiated with a limited number of beams because the uncertainties are not averaged [11]. Still, the measurements of the dose envelope are often neglected because characterization of pencil beam nuclear halo requires dedicated detector technology with sufficient sensitivity and accuracy.

In order to compensate for the uncertainties in the beam modeling caused by the dose envelope, some of the proton centers investigate and develop new detection techniques for characterization of the lateral beam profile far from the beam core. For instance, in the Krakow proton facility, passive dosimetry [12, 13] or single particle sensitive methods like scCVD diamond detectors [14] have been investigated. Refer to the following publications and their references for review of beam halo measurement approaches [15, 16] and more generally proton beam commissioning protocols [17–20].

Within the commissioning stage, a validation of the beam model implementation in TPS is required, and it is typically performed by means of experimental measurements in water. The dose in complex radiation fields consisting of several pencil beams is usually measured, and, if necessary, field size factors are applied to correct for experimental and computational uncertainties of the pencil beam modeling [21]. The introduction of Monte Carlo (MC) tools in the clinical routine offers computational accuracy, allowing for consideration of the nuclear halo in patient treatment plan simulations. However, the experimental validation of single pencil beam dose profiles in water, including the nuclear halo, is even more demanding than in air because it requires operation of the detector in water. There is still a necessity to provide more accurate, fast, and easy-to-use experimental methods for characterization of the low-dose envelope of proton pencil beams.

Here, we propose an alternative to the existing solutions, to be applied for measurements in air and in water with higher resolution, single particle sensitivity, and improved detector dynamic range. Our approach allows for experimental characterization and validation of lateral and longitudinal dose profiles of a proton beam halo up to 150 mm off the beam core. For this purpose, we used MiniPix Timepix semiconductor pixel detector, an in-house-developed detector holder, and water phantom. The proposed experimental setup can be used for commissioning and validation measurements both in air and in water. We measured pencil beam profiles and compared the results to the facility commissioning data, TPS calculations, and Monte Carlo (MC) simulations, demonstrating the feasibility of the approach.

2. MATERIALS AND METHODS

2.1. Proton Radiotherapy Facility

The Krakow proton beam facility has been in clinical operation since October 2016, offering protons for radiation therapy treatment as well as for physics and radiobiology experiments. The Krakow facility offers stable beam intensities ranging from 1 to 300 nA and scanning pencil beam within an energy range from 70 to 226 MeV, which corresponds to range in water from 4.2 to 31.8 cm. The microstructure of the proton beam produced by C-235 IBA cyclotron in Krakow consists of 0.79 ns micropulses generated with the frequency 106 MHz, which is common to all beam intensity settings. The lateral beam size (1σ) ranges depending on the proton beam energy and application of a range modulator (range shifter - RS) from about 3 to 15 mm. The RS made of 4.2 cm thick PMMA material, mounted at the gantry nozzle, is used to modulate proton range.

In Krakow, Eclipse TPS version 13.6 (Varian Medical Systems, Palo Alto, CA, US), commissioned against experimental data, is used for treatment planning. The TPS in this version is equipped only with an analytical pencil beam algorithm [22]. Longitudinal dose profile measurements were performed in water using a Bragg Peak Chamber (PTW, Freiburg, Germany). Lateral dose profiles in air were measured using Lynx scintillating screen (IBA Dosimetry, Schwarzenbruck, Germany) and thermoluminescence detectors (TLDs) in the primary Gaussian and the dose envelope regions, respectively. Eclipse TPS was used to compute 3D pencil beam dose profiles in water. In addition to the clinical TPS, the dose profiles were simulated using a secondary dose computation tool, Fred MC code [23] that was commissioned and validated for quality assurance purposes in Krakow [Gajewski et al. accepted]. The

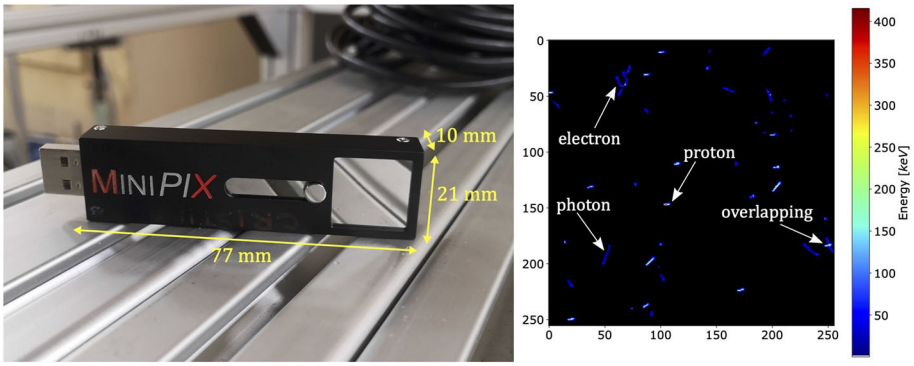

FIGURE 1 | The MINIPIX TIMEPIX detector equipped with a TIMEPIX ASIC and 300 μm thick silicon sensor **(left)** and an example frame obtained from the measurements **(right)**. Clusters are produced by different particles in mixed radiation field of proton pencil beam in water. Low-LET narrow, curly tracks are typical for electrons, high-LET wide, straight tracks for energetic heavy charged particles such as protons, and low-LET straight tracks are characteristic for photons. In the right side of the frame, an example of overlapping clusters is shown.

proton beam model used by the clinical TPS and FRED have been adopted for GATE/Geant4 simulations performed in this work.

2.2. MINIPIX TIMEPIX Detector and Data Acquisition Software

In this study, we propose using the technology of pixel semiconductor detectors, TIMEPIX from ADVACAM (https://advacam.com), for characterization of therapeutic proton pencil beams and validation of TPS and MC simulations. TIMEPIX is a commercial version of MEDIPIX detector developed at CERN and is widely used for radiation research, e.g., in proton and ion beam therapy [24–29], in brachytherapy [27, 30], in radiation dosimetry [31–34], in particle accelerator environments [35], or for space radiation characterization on board of the International Space Station [36–38]. The single particle sensitivity of the device finds applications in particle therapy as well as for very small field dosimetry needed for investigations on *in-vitro* and animal model systems [39].

Due to the single-quantum sensitivity and particle tracking capability, TIMEPIX technology enables particle-by-particle dosimetry of proton pencil beams in wide dynamic range. It is achievable thanks to hybrid semiconductor pixel architecture and highly integrated signal electronics (amplifier, amplitude discriminators, and digital counter). TIMEPIX processes signal from single-quantum events on-board using a megahertz frequency clock and multi-channel analyzer with 11.8k channels per pixel enabling measurement of the number of events, the energy, or the time of interaction. These features offer a wide dynamic range of the MINIPIX TIMEPIX in term of quantum sensitivity and noiseless particle type identification (neutrons, X rays, light, and heavy charged particles) as well as measurements of particle flux (from single particles up to 10^6 in event by event spectrometry tracking mode and 10^8 in integrated counting mode), linear energy transfer (0.1–500 keV/μm *in silicon*), or directional tracking in a wide field of view (2π solid angle) [40].

In this work, a compact MINIPIX TIMEPIX detector was used (**Figure 1**, left). The entire MINIPIX TIMEPIX has dimensions of 77 × 21 × 10 mm, and its total weight is 25 g. The sensitive volume of the semiconductor silicon sensor (14.08 × 14.08 × 0.3 mm) consists of a 2D array of 256 × 256 pixels, and each has dimensions of 55 × 55 μm. The ionizing particle penetrating the sensitive volume of the MINIPIX TIMEPIX produces electric charge, which is collected by adjacent electrode pixels forming a cluster. The charge collected by each pixel is converted by an analog-to-digital (ADC) converter into a signal. As long as the ADC output is not saturated and its response is linear to the collected charge, we can assume that the measured energy deposited by two or more particles in the same time and position (overlapping) is equal to a sum of the single energy depositions (non-overlapping). The signal read-out is performed in each pixel individually in a single frame acquisition time of typical length of about 1–100 ms. The MINIPIX TIMEPIX frame read-out dead-time is 22 ms. Data acquisition electronics is fully integrated, connected to the computer via USB port and does not require a dedicated cooling system. The temperature effect on energy deposition measurement is negligible [41]. For more details on the TIMEPIX detector technology, refer to [40, 42, 43] and references.

The MINIPIX TIMEPIX detector is equipped with a data acquisition and real-time visualization software, PIXET PRO, which also provides data processing tools for cluster morphology analysis. **Figure 1** (right) shows an example of data frame acquired in Krakow. The morphology of each cluster is characterized by the following: the position of the cluster center of mass, the total energy deposited, the cluster length, and the angle at which the particle enters the detector. The cluster analysis enables identification of impinging particle type [43]. The analysis of multiple clusters enables particle-by-particle experimental characterization of the mixed radiation fields consisting of primary and secondary protons, secondary electrons, photons, etc. Depending on the primary particle fluence, the single frame acquisition time needs to be adjusted for each measurement individually in order to minimize the overlapping of the clusters. The cluster overlapping effect occurs

when different particles at short time intervals produce clusters, which are so close to each other that they overlap and are recognized by PIXET PRO software as a single cluster of larger energy deposition. The shortest single frame acquisition time (1 ms) determines the maximal primary particle fluence, which can be used for measurement. In case of measurements performed in the beam core, the lowest clinically available beam current (1 nA) was too high to avoid the detector saturation. Therefore, the unregulated accelerator dark current was used for measurements in the beam core and the stable beam current of 1 nA off the beam core.

2.3. Dose Calculation Engines

In this work, the dose distributions were calculated using the clinical TPS used in the Krakow proton facility (cf. section 2.1) as well as two MC toolkits: GATE/Geant4 (version 8.2), interfaced to Geant4 (version 10.4.p2) [44] and FRED MC (version 3.0.18) [23]. GATE/Geant4 is a full MC simulation engine transporting all the primary and secondary particles contributing to the dose deposition. FRED is a fast, GPU-accelerated MC tool transporting primary and secondary protons, deuterons, and tritons, whereas the energy from gammas and delta-electrons is deposited at their production point. Because the GPU parallelization and physics are trimmed down to the processes relevant for proton dose calculations, the computation time is reduced up to a factor 100 with respect to GATE/Geant4 computations running on CPU [45].

2.4. Calibration Measurements

The MINIPIX TIMEPIX detector is calibrated by the manufacturer aiming at a uniform response of each individual pixel to energy depositions from X-rays source [46]. In principal, primary and/or secondary particles can enter the detector surface at any angle, which specially occurs measuring mixed radiation field produced by a proton beam in water. In this work, we performed a validation of the detector response to proton beams impinging the detector surface at different angles. We compared the energy deposition spectra obtained experimentally to MC simulations. Moreover, the measurements allowed to determine optimal detector angle with respect to the beam core used in further acquisitions.

2.4.1. Experimental Setup and Data Acquisition

The MINIPIX TIMEPIX was exposed to proton pencil beams of nominal energies E70, E100, E150, and E200, corresponding to proton mean energies and energy spreads (standard deviation) at the detector position of 70.5 (0.6) MeV, 100.1 (0.8) MeV, 149.9 (1) MeV, and 199.6 (1) MeV, respectively. For each nominal energy, the detector was positioned at the isocentre in air (in the beam core) at β angles ranging from 27° to 83°. We defined β as the angle between the normal to the silicon sensor surface and the proton beam axis (cf. **Figure 2**). The accelerator dark current was used allowing to keep the particle fluence low enough to avoid saturation of the detector and to minimize the cluster overlapping.

2.4.2. Monte Carlo Simulations

We performed MC simulations of the calibration setup in GATE/Geant4 toolkit. The MINIPIX TIMEPIX detector active volume was simulated as a $14.08 \times 14.08 \times 0.3\,\mathrm{mm}^3$ cube made out of silicon ($\rho = 2.33\,\mathrm{g/cm}^3$, $\mathrm{I_{pot}} = 173\,\mathrm{eV}$ [47]). The detector was positioned at the isocentre at β angles, mimicking the experimental conditions. For simulations of proton pencil beams, the MC implementation of the clinical beam model based on Krakow proton facility commissioning measurements was used. We used the QGSP_BIC_HP_EMZ physics list, which contains the high precision (HP) model for low-energy neutrons and the most precise electromagnetic physics (EMZ) [48]. We used production cuts in the active volume of $10\,\mu$m for protons, electrons, and gammas. For each individual calibration simulation the total number of 10^6 primary particles were simulated. Using a phase space actor in GATE/Geant4 we scored the type, energy, angle, and position of the incidence of each primary particle crossing the detector surface. The history of the interactions and energy depositions of primary and secondary particles of unique identification number (UID) was scored using a GATE/Geant4 sensitive volume.

2.4.3. Data Analysis

The results scored by the phase space actor and the GATE/Geant4 sensitive volume were merged based on the primary particle UID. The total energy deposited in the detector by a single primary proton was calculated as a sum of all energy depositions from the primary and secondary particles scored inside the GATE/Geant4 sensitive volume.

For each primary proton energy and detector angular position (β), the energy deposition distributions obtained from the MINIPIX TIMEPIX measurements were compared to the GATE/Geant4 simulations. Due to a simplified geometry implemented in the MC simulations, i.e., omitting the detector case and the PMMA holder, in simulations, all the primary particles entered the detector at nearly the same angle β (cf. **Figure 2**). In fact, in the experimental conditions, the particles can enter the detector at different angles because they scatter on the MINIPIX TIMEPIX case and on the holder. For this reason, to compare the results of measurements and simulations, we filtered out from the experimental data particles, entering the detector at an angle different than $\pm 3°$. The β angle was obtained from the cluster morphology by calculating its track in the silicon sensor. In addition we compared the mean deposited energy measured by the MINIPIX TIMEPIX detector and simulated in GATE/Geant4 to the deposited energy calculated based on PSTAR data of proton stopping power *in silicon* [47].

2.5. Dose Profile Characterization

The experimental setup was used for two types of dose profile measurements. We performed lateral dose profile measurements in air to demonstrate the capability of the MINIPIX TIMEPIX detector to be used for commissioning and characterization of proton therapeutic pencil beams. Next, we performed lateral and longitudinal dose profile measurements in water to validate the pencil beam propagation performed by TPS and MC simulations.

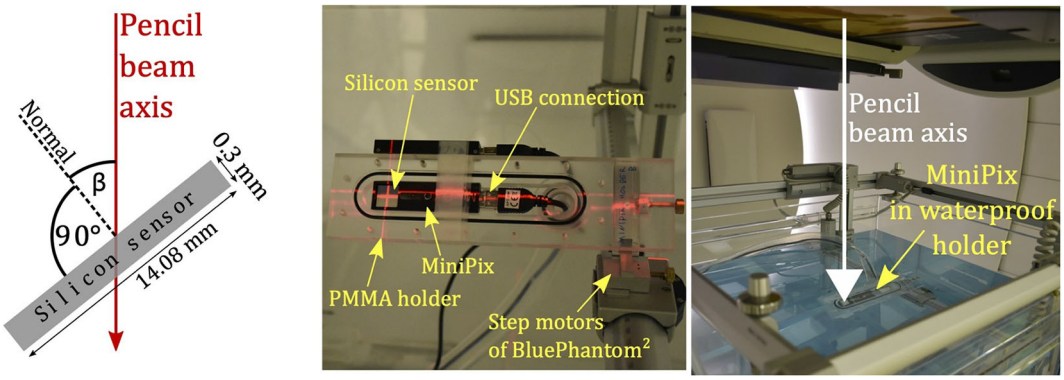

FIGURE 2 | Schematic illustration of MINIPIX TIMEPIX detector silicon sensor and the definition of β angle between the normal to the silicon sensor surface and proton pencil beam axis **(left)**, MINIPIX TIMEPIX placed in the PMMA holder positioned in water phantom without the waterproof cover **(middle)**, and immersed in the water phantom filled with water for profile measurements **(right)**.

2.5.1. Experimental Setup, Beam Conditions, and Data Acquisition

The MINIPIX TIMEPIX detector was positioned in a dedicated, waterproof, in-house-designed PMMA holder mounted inside the water phantom (BluePhantom^2 by IBA). We enclose the technical sketch of the PMMA holder in **Supplementary Materials**. The detector sensitive volume was positioned at isocentre using water phantom step motors and laser patient positioning system. Based on the step motor movement and laser positioning system accuracy, we estimate the setup positioning uncertainty as 1 mm. The MINIPIX TIMEPIX was positioned at an angle $\beta = 45^\circ$. See the middle panel of **Figure 2** for the detector placed in the phantom (in air) without the waterproof cover and the right panel of **Figure 2** for the detector placed in water.

The lateral proton pencil beam profiles in air and in water were acquired for proton beams at nominal energies E100, E150, and E200 with and without range shifter. All the measurements were performed using the lowest possible accelerator beam current of 1 nA to keep the beam current stable between measurements. The shortest acquisition time frame duration used by Timepix was 1 ms. Therefore, the time architecture of the beam is negligible for the measurements performed in the integration mode. For the 1 nA beam current, we did not perform measurements with the detector placed in the beam core (0–20 mm away from the isocentre), as, at such a current, the primary proton yield leads to detector saturation for a single acquisition frame. For dose profile measurements, the time frame duration was set by the software operator based on a real-time visual assessment of the data in the PIXET PRO software. Before starting the data acquisition, while the beam was on, the most optimal time frame duration was selected allowing acquisition of the maximal possible number of clusters in one frame and avoiding cluster overlapping effect. The total acquisition time of each measurement in single point of radiation field depends on particle fluence, and it was from 20 to 40 s and thus resulted in the order of 10^4–10^6 registered single particle events (clusters). In total, we performed 26 proton pencil beam lateral and longitudinal dose profile measurements.

For measurements in air, MINIPIX TIMEPIX was positioned at the gantry room isocentre, and lateral profiles were acquired at the distance from 30 to 180 mm away from the isocentre. Following the measurements in air, BluePhantom^2 was filled with water. See **Figure 3** for simulated 2D dose distributions of proton pencil beams in water with and without range shifter for three investigated nominal proton beam energies. Note that each detector position along the axis of measurement data acquired with a 2D MINIPIX TIMEPIX detector is integrated to one measurement point corresponding to center of mass of the detector surface. This is because the analysis of the acquired data has shown that the particle fluence and energy deposition gradient within the 14×14 mm^2 detector frame do not vary for measurement points from 45 to 150 mm away from the beam core. The dose distributions are overlapped with lines indicating which lateral and longitudinal dose profiles were measured. We measured lateral dose profiles at three depths, at 1/2 and 3/4 of the proton beam range, and as in the Bragg peak position. For 150 MeV proton beam, the longitudinal profiles were measured at the distance of 25, 37, 49, and 61 mm away from the isocentre.

2.5.2. Monte Carlo Simulations

The dose distributions in water for the nominal energies used in the experiment with and without the RS were calculated using clinical TPS (analytical dose computation algorithm) as well as simulated in GATE/Geant4 and FRED MC engines. In GATE/Geant4, we used the QGSP_BIC_HP_EMZ physics list with 1 mm production cut for gammas, electrons, and positrons and 10 μm for protons. In both MC engines, a high statistics of 10^9 primaries were simulated in order to obtain the beam dose envelope in water up to 150 mm far from the beam core. The dose was scored in water in $2 \times 2 \times 2$ mm^3 voxels.

2.6. Data Analysis

The data pre-processing was performed using PIXET PRO track processing tool, which provided a list of clusters and their parameters for each measurement performed at the given point of radiation field. For analysis of the dose profiles we extracted from PIXET PRO, we noted the following: (i) the

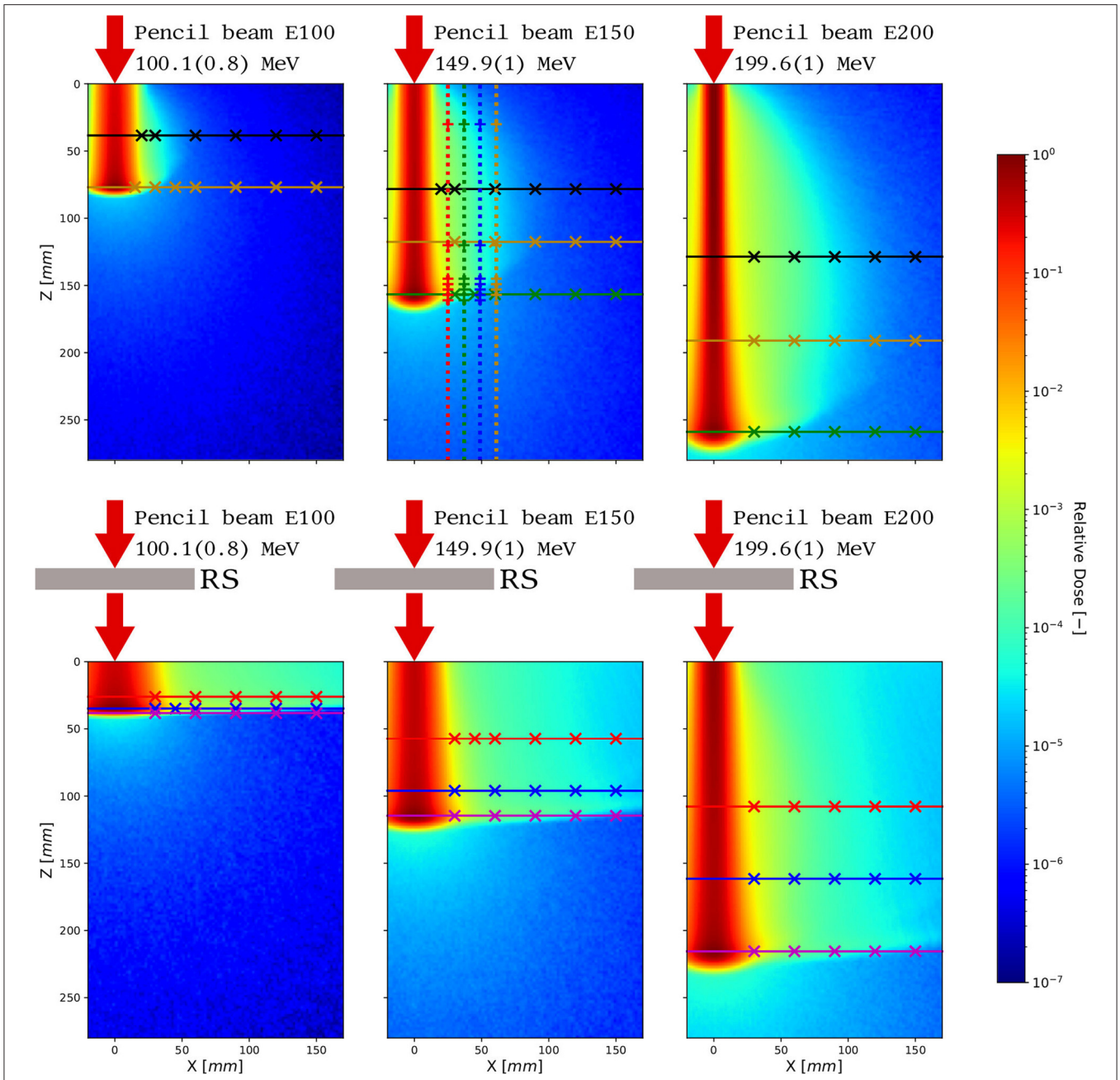

FIGURE 3 | 2D dose profiles obtained from MC simulation of proton beams at three nominal energies with (bottom) and without (top) the RS. The lateral and longitudinal dose profiles measured with MINIPIX TIMEPIX are shown, and the measurement points are marked with crosses. The color convention used to illustrate measured dose profiles is the same as the one used in the figures in the results sections 3.3 and 3.4.

total energy deposition in each cluster, (ii) the cluster position in the detector sensor, (iii) the total number of frames, and (iv) the frame duration time for each measurement point. For each measurement point, we calculated the relative dose rate D:

$$D = \frac{1}{t_{acq} \cdot n} \cdot \frac{\sum_i E_i}{m} \text{ [Gy/s]}, \quad (1)$$

where E_i is the total energy deposited by a particle in a cluster, m is the mass of the detector silicon sensor, t_{acq} is the frame acquisition time (constant within one measurement point), and n is the total number of frames acquired in one measurement point.

The visualization and comparison of the lateral dose profiles obtained experimentally in air and in water to simulations were performed as follows. The maximum value of the lateral beam dose profile simulated in GATE/Geant4, FRED, and TPS were

normalized. The dose experimental profiles were adjusted to the corresponding simulated profiles using least mean square algorithm. This was the optimal method to visualize and compare the experimental and simulation results because the dose rate at the profile maximum varies depending on primary beam energy and measurement depth. The value of relative dose rate obtained experimentally was not modified between the measurement points within a single profile.

Next, we compared lateral and longitudinal dose profiles measured with MiniPix Timepix in water with the simulations of 3D dose profiles performed with clinical TPS, fast MC code Fred, and full MC code Gate/Geant4. A median filter with kernel size of 5 was used for lateral Gate/Geant4 profiles at the distance larger than 50 mm from the beam core to compensate for the statistical fluctuations of MC simulation.

For the purpose of visualization of the longitudinal dose profile measurement in water, the maximum value of the 3D dose distribution simulated in Gate/Geant4, Fred, and TPS was normalized to 1. The longitudinal profiles simulated at the distance from beam core are plotted according to the normalization, and the MiniPix Timepix measurement results were adjusted to the simulations using the same least mean square algorithm.

3. RESULTS

3.1. Calibration Measurements

Figure 4 (left panel) shows an example of energy deposition spectra for detector angle $\beta = 57^\circ$ (cf. **Figure 2** left panel) and nominal proton energy E150. The spectrum obtained experimentally (raw data) exhibits considerable amount of clusters with low-energy depositions (below 0.4 MeV) and particles incoming at significantly smaller angles than β. These clusters are produced mostly by photons originating from the gantry nozzle equipment (plane-parallel and multiwire ionization chambers), which are not explicitly simulated in the Gate/Geant4. The main energy deposition peak, with the maximum of about 0.5 MeV, is produced by the protons entering the detector at angle $57 \pm 3^\circ$. The peaks to the right, with the maximum of about 1 MeV and 1.6 MeV, result from the overlapping effect, where respectively two or three primary protons overlap creating a single clusters with the doubled or tripled energy deposition. The overlapped clusters exhibit larger incident angles than the primaries in the main energy deposition peak. The overlapping effect is not taken into account in Gate/Geant4 simulations. In order to compare the spectra obtained experimentally with the MC simulations, all the particles incoming at angles different than $57 \pm 3^\circ$ were filtered out. As a result of the filtration, the energy depositions from particles produced at the gantry nozzle equipment, as well as from overlapping clusters are removed from the energy deposition spectrum. **Figure 4** (left panel) shows the spectra obtained experimentally before and after filtering, spectra obtained from simulations, and the measured angle of the incoming particles as a function of deposited energy.

Figure 4 (middle panel) shows energy deposition spectra for nominal energy E150 and various β angles after angle filtering $\beta \pm 3^\circ$. The maximum value and width of the energy deposition spectra increase with the detector angle. This is because the average track length, thus the total energy deposited by a single particle crossing the detector active volume, increases with the detector angle with respect to the beam direction. The main energy deposition peak shapes, and positions are comparable with the simulations. The mean deposited energy obtained from MiniPix Timepix measurements (after filtering), simulated in Gate/Geant4 MC and calculated based on PSTAR stopping power data are presented in **Figure 4** (right panel). The mean deposited energy simulated in Gate/Geant4 is consistent within 100 keV with the value expected from the PSTAR database in the entire range of the investigated detector angles and energies. The discrepancy between the mean energy deposition measured with MiniPix Timepix and the expected value from the PSTAR database, for detector angle β less than 73°, ranges from 1 to 60 keV. For angles greater than 73° it is higher, up to 550 keV. This might be an effect of registering particles scattered on the MiniPix Timepix case made of aluminum, which produce long clusters of large energy depositions. Therefore, for the beam profile measurements in water and in air, the detector angle of 45° was chosen.

3.2. Beam Spot Profiles in Air

Figure 5 shows proton pencil beam lateral profiles measured for nominal energies E100, E150, and E200 in air, at the isocentre, without and with the RS. The profile shapes measured with MiniPix Timepix correspond well to TPS beam model data obtained during the facility commissioning. The high sensitivity of MiniPix Timepix allowed to perform measurements in significant distance from the beam core (from 30 mm up to 180 mm) in relative dose range of three orders of magnitude. This allowed to measure the buildup of the nuclear halo.

3.3. Lateral Profiles in Water

Figure 6 shows MiniPix Timepix results in water performed with and without the RS for three nominal beam energies E100, E150, and E200. The measurement results of (i) the first Gaussian term obtained with the Lynx scintillating screen and (ii) the low-dose envelope (nuclear halo) obtained with MiniPix Timepix are compared with Gate/Geant4 and Fred MC simulations.

We observed an excellent agreement between the shape of the profiles obtained experimentally with Lynx and MiniPix Timepix and simulated with full MC code Gate/Geant4 up to 150 mm far from the beam core. The shapes of the lateral dose profiles were also accurately reproduced at different depths in water and behind the RS. In Fred simulations, the shapes of the lateral dose profiles in comparison to MiniPix Timepix measurements were well-mimicked up to four orders of magnitude. The disagreement for more distant measurement points is due to the fact the Fred code does not transport secondary gammas and electrons. Note, that in terms of performance, tracking rate achieved with GPU-accelerated MC code Fred was up to $3.6 \cdot 10^6$ primary/s on a single GPU card, compared to $1.1 \cdot 10^3$ primary/s with Gate/Geant4 running on CPU cluster.

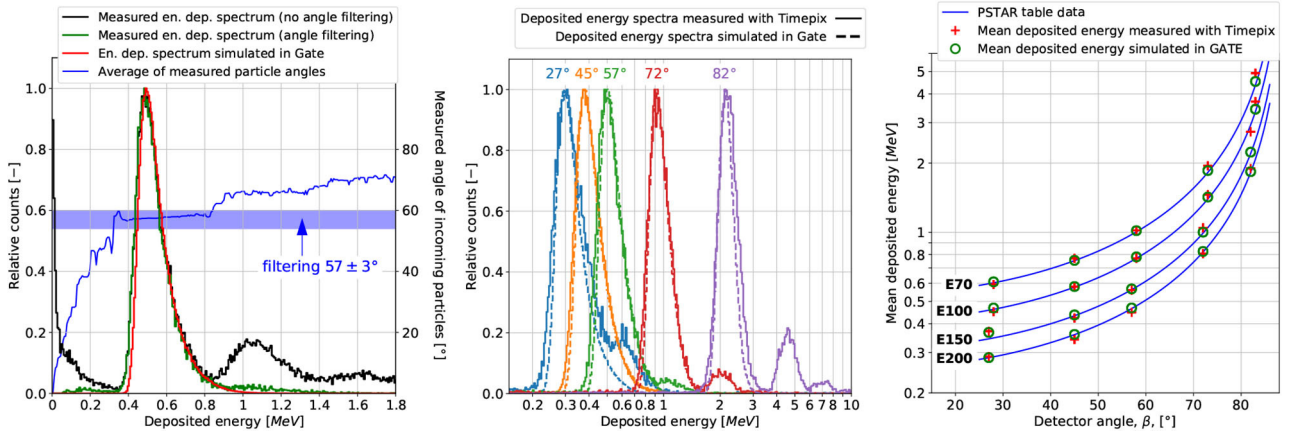

FIGURE 4 | Example of energy deposition spectrum for proton beam at the nominal energy E150 measured with MINIPIX TIMEPIX positioned at angle $\beta = 57°$ before and after filtering for the particles incidence angle ($\pm 3°$) as well as the one obtained from GATE/Geant4 MC simulation **(left)**. Energy deposition spectra after applying the cluster filtering procedure for nominal energy E150 and various β detector angles **(middle)**. Mean energy deposited in MINIPIX TIMEPIX was exposed to nominal proton energies E70, E100, E150, and E200 when positioned at various angles. The measurement results are compared to MC simulations and data calculated based on PSTAR stopping power tables **(right)**.

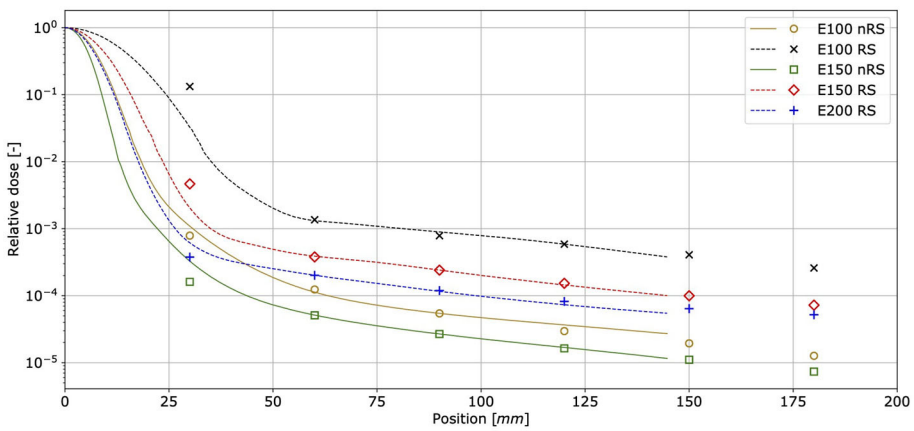

FIGURE 5 | Lateral pencil beam dose profiles measured at the gantry room isocentre in air for primary proton beams at three nominal energies. Points correspond to MINIPIX TIMEPIX measurement results, whereas solid and dashed lines are the data obtained from TPS beam model without RS (nRS) and with RS, respectively.

3.4. Longitudinal Profiles in Water

Figure 7 presents proton pencil beam longitudinal dose profiles in water for beam nominal energy E150. The beam range measured with MINIPIX TIMEPIX is in agreement with the GATE/Geant4 simulations, even at the distance of 61 mm from the beam core, whereas TPS does not predict any dose at this distance.

4. DISCUSSION

In the frame of this work we performed a validation of the detector calibration for protons. The comparison of the calibration measurements and MC simulations demonstrate that the MINIPIX TIMEPIX accurately measures energy deposited by proton beams. The comparison of the mean energy deposition in the detector to MC simulation results and PSTAR data indicates that positioning of the detector at 45° with respect to the beam axis is the most optimal for the measurements. The calibration measurements provide information on the energy deposited by particles producing separate or overlapping clusters (c.f. **Figure 4**, middle panel). The total energy deposited by several particles forming separate clusters and an overlap of clusters is nearly the same. Therefore, we assume that cluster overlapping does not influence the total dose measured in a single frame, as long as the signal in a pixel is within the dynamic range from 4 keV/pixel up to 2 MeV/pixel [49]. Here, we performed only the validation of the calibration for protons in energy range from 70 to 200 MeV, whereas in the mixed radiation field in water, a wider energy spectrum of particles can be registered by the detector. The response of the MINIPIX TIMEPIX detector to other radiation types was studied elsewhere [Granja et al., under review].

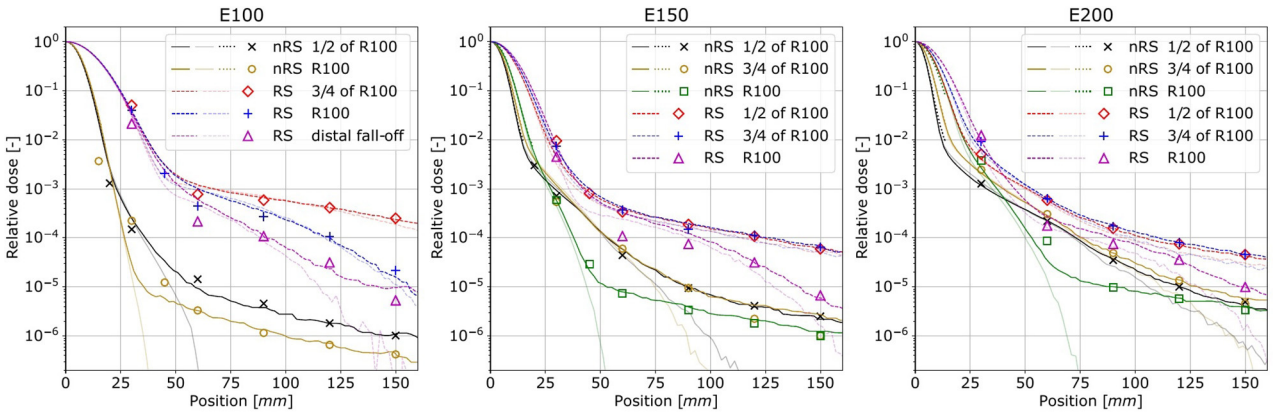

FIGURE 6 | Lateral beam dose profiles measured in water at different depths for three beam nominal energies. Points correspond to MINIPIX TIMEPIX measurement results, dotted lines are results of measured with LYNX detector, whereas solid and dashed lines are the GATE/Geant4 data without (nRS) and with RS, respectively. Corresponding transparent lines presents FRED simulations result.

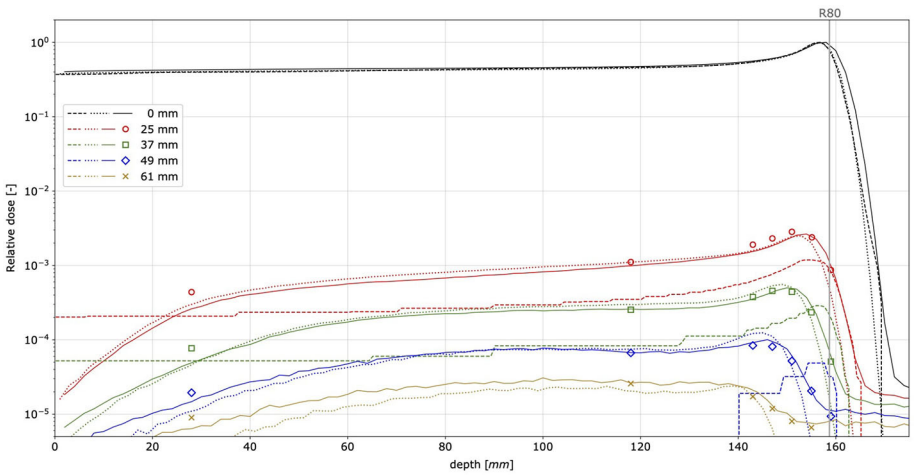

FIGURE 7 | Longitudinal pencil beam dose profiles measured in water for proton beam nominal energy E150. Points correspond to MINIPIX TIMEPIX measurement results, whereas for solid, dotted, and dashed lines, they correspond to GATE/Geant4, FRED, and TPS simulations, respectively. The mean proton range of 158.7 mm is marked by a vertical line (R80).

The measurements of the lateral and longitudinal pencil beam dose profiles performed with the MINIPIX TIMEPIX detector in air and in water show its capability to measure the dose with the dynamic range of up to four orders of magnitude. The measurements of the beam lateral profiles in air correspond well to the TPS beam model data obtained during the facility commissioning. The beam lateral and longitudinal profiles measured in water are in an excellent agreement with GATE/Geant4 simulations. We presented the relative difference between measurements and simulations normalized to the dose value in the beam core. For the lateral beam profiles in air, the relative difference is below 0.004% for the beam halo measurement points at 45–150 mm away from the beam core and 10% for the measurements at 30 mm away from the beam core. In case of lateral beam profiles in water the difference between the measurement and simulation is below 0.1% of the dose in the beam core. The difference increases up to 1.3% for the measurement points at 30 mm off the beam core. Higher discrepancy between measurements and simulations close to the beam core results from high dose gradients in this region. This leads to significantly different particle fluence measured in different locations of the detector sensitive area measuring close to the beam core. For longitudinal beam profiles in water the relative difference between the measurement and simulation is less than 0.12%. Because of the limited time resolution of the MINIPIX TIMEPIX detector, it was not possible to perform measurements in the beam core, where the fluence of particles was high, causing detector saturation. A new generation of the TIMEPIX detectors, the MINIPIX TIMEPIX 3 (ADVACAM), offers time resolution better than the MINIPIX TIMEPIX used in this work. MINIPIX TIMEPIX 3 will allow for measurements in the beam core and in therapeutic fields, where the particle

fluence is high. This will be particularly important for patient treatment plan verification when several beams of various energies contribute to in-point distributions of LET spectrum. In order to minimize the fraction of particles scattered on the aluminum detector case, an alternative, e.g., PMMA case, should be considered.

Since MiniPix Timepix provides information about a single particle energy deposition and its track length, it is possible to calculate the linear energy transfer (LET) value of each particle penetrating the detector sensor. Future work will focus on an experimental characterization of the energy deposition and the LET spectra in mixed radiation fields produced by therapeutic proton beams in water. The results will be used for validation of MC codes and TPS, aiming at improved physical and biological modeling in proton radiotherapy.

DATA AVAILABILITY STATEMENT

The raw data supporting the conclusions of this article will be made available by the authors, without undue reservation.

AUTHOR CONTRIBUTIONS

PS, AR, JG, CG, GK, CO, MP-N, SN, and MR performed the experiments. PS and JG made the experiment data analysis and prepared figures. CG and CO provided expertise in MiniPix Timepix data analysis. JG performed the MC simulations, analyzed the data, and prepared the figures. MP-N and JB provided expertise in Gate/Geant4 MC simulations and data analysis. AS developed and made substantial improvements in Fred source code required to enable presented studies. PS, AR, and JG drafted the manuscript. NK extensively reviewed the manuscript. AR and JG designed the project. AR acquired funding. All authors contributed to the article and approved the submitted version.

FUNDING

This project was carried out within the Reintegration programme of the Foundation for Polish Science co-financed by the EU under the European Regional Development Fund—grant no. POIR.04.04.00-00-2475/16-00.

ACKNOWLEDGMENTS

We acknowledge Aleksander Krempa from Krakow proton therapy center for IT support during implementation of this project. This research was supported in part by computing resources of ACC Cyfronet AGH. We acknowledge the support of NVIDIA Corporation with the donation of the GPU used for Fred MC simulations.

SUPPLEMENTARY MATERIAL

The Supplementary Material for this article can be found online at: https://www.frontiersin.org/articles/10.3389/fphy.2020.00346/full#supplementary-material

Supplementary Data Sheet 1 | PMMA holder technical sketch.

Supplementary Data Sheet 2 | PMMA holder technical sketch.

Supplementary Data Sheet 3 | PMMA holder technical sketch.

Supplementary Data Sheet 4 | PMMA holder technical sketch.

Supplementary Data Sheet 5 | PMMA holder technical sketch.

REFERENCES

1. Durante M, Orecchia R, Loeffler JS. Charged-particle therapy in cancer: clinical uses and future perspectives. *Nat Rev Clin Oncol*. (2017) **14**:483. doi: 10.1038/nrclinonc.2017.30
2. Durante M. Proton beam therapy in Europe: more centres need more research. *Brit J Cancer*. (2018) **120**:777–8. doi: 10.1038/s41416-018-0329-x
3. Grevillot L, Bertrand D, Dessy F, Freud N, Sarrut D. A Monte Carlo pencil beam scanning model for proton treatment plan simulation using GATE/GEANT4. *Phys Med Biol*. (2011) **56**:5203. doi: 10.1088/0031-9155/56/16/008
4. Testa M, Schümann J, Lu HM, Shin J, Faddegon B, Perl J, et al. Experimental validation of the TOPAS Monte Carlo system for passive scattering proton therapy. *Med Phys*. (2013) **40**:121719. doi: 10.1118/1.4828781
5. Fracchiolla F, Lorentini S, Widesott L, Schwarz M. Characterization and validation of a Monte Carlo code for independent dose calculation in proton therapy treatments with pencil beam scanning. *Phys Med Biol*. (2015) **60**:8601–19. doi: 10.1088/0031-9155/60/21/8601
6. Harms J, Chang CW, Zhang R, Lin L. Nuclear halo measurements for accurate prediction of field size factor in a Varian ProBeam proton PBS system. *J Appl Clin Med Phys*. (2020) **21**:197–204. doi: 10.1002/acm2.12783
7. Saini J, Cao N, Bowen SR, Herrera M, Nicewonger D, Wong T, et al. Clinical commissioning of a pencil beam scanning treatment planning system for proton therapy. *Int J Part Therapy*. (2016) **3**:51–60. doi: 10.14338/IJPT-16-0000.1
8. Pidikiti R, Patel BC, Maynard MR, Dugas JP, Syh J, Sahoo N, et al. Commissioning of the world's first compact pencil-beam scanning proton therapy system. *J Appl Clin Med Phys*. (2018) **19**:94–105. doi: 10.1002/acm2.12225
9. Boon SN, van Luijk P, Böhringer T, Coray A, Lomax A, Pedroni E, et al. Performance of a fluorescent screen and CCD camera as a two-dimensional dosimetry system for dynamic treatment techniques. *Med Phys*. (2000) **27**:2198–208. doi: 10.1118/1.1289372
10. Russo S, Mirandola A, Molinelli S, Mastella E, Vai A, Magro G, et al. Characterization of a commercial scintillation detector for 2-D dosimetry in scanned proton and carbon ion beams. *Phys Med Eur J Med Phys*. (2017) **34**:48–54. doi: 10.1016/j.ejmp.2017.01.011
11. Zhu XR, Poenisch F, Lii M, Sawakuchi GO, Titt U, Bues M, et al. Commissioning dose computation models for spot scanning proton beams in water for a commercially available treatment planning system. *Med Phys*. (2013) **40**:041723. doi: 10.1118/1.4798229
12. Gajewski J, Klosowski M, Olko P. Two-dimensional thermoluminescence dosimetry system for proton beam quality assurance. *Radiat Meas*. (2016) **90**:224–7. doi: 10.1016/j.radmeas.2015.12.019
13. Sądel M, Bilski P, Sankowsk a M, Gajewski J, Swakoń J, Horwacik T, et al. Two-dimensional radiation dosimetry based on LiMgPO4 powder embedded into silicone elastomer matrix. *Radiat Meas*. (2020) **133**:106255. doi: 10.1016/j.radmeas.2020.106255
14. Rydygier M, Jastrzab M, Krzempek D, Nowak T, Grzanka L, Bednarczyk P, et al. Radiotherapy proton beam profilometry with scCVD diamond detector in single particle mode. *Radiat. Protect. Dosimetry*. (2018) **180**:282–5. doi: 10.1093/rpd/ncx305
15. Lin L, Ainsley CG, Mertens T, De Wilde O, Talla PT, McDonough JE. A novel technique for measuring the low-dose envelope of pencil-beam scanning spot profiles. *Phys. Med. Biol*. (2013) **58**:N171–80. doi: 10.1088/0031-9155/58/12/N171
16. Grevillot L, Stock M, Palmans H, Osorio Moreno J, Letellier V, Dreindl R, et al. Implementation of dosimetry equipment and phantoms at the

MedAustron light ion beam therapy facility. *Med Phys*. (2018) **45**:352–69. doi: 10.1002/mp.12653
17. Karger CP, Jäkel O, Palmans H, Kanai T. Dosimetry for ion beam radiotherapy. *Phys Med Biol*. (2010) **55**:21. doi: 10.1088/0031-9155/55/21/R01
18. Chang CW, Huang S, Harms J, Zhou J, Zhang R, Dhabaan A, et al. A standardized commissioning framework of Monte Carlo dose calculation algorithms for proton pencil beam scanning treatment planning systems. *Med Phys*. (2020) **47**:1545–57. doi: 10.1002/mp.14021
19. Giordanengo S, Manganaro L, Vignati A. Review of technologies and procedures of clinical dosimetry for scanned ion beam radiotherapy. *Phys Med*. (2017) **43**:79–99. doi: 10.1016/j.ejmp.2017.10.013
20. Giordanengo S, Palmans H. Dose detectors, sensors, and their applications. *Med Phys*. (2018) **45**:e1051–72. doi: 10.1002/mp.13089
21. Schwaab J, Brons S, Fieres J, Parodi K. Experimental characterization of lateral profiles of scanned proton and carbon ion pencil beams for improved beam models in ion therapy treatment planning. *Phys Med Biol*. (2011) **56**:7813–27. doi: 10.1088/0031-9155/56/24/009
22. Soukup M, Fippel M, Alber M. A pencil beam algorithm for intensity modulated proton therapy derived from Monte Carlo simulations. *Phys Med Biol*. (2005) **50**:5089–104. doi: 10.1088/0031-9155/50/21/010
23. Schiavi A, Senzacqua M, Pioli S, Mairani A, Magro G, Molinelli S, et al. Fred: a GPU-accelerated fast-Monte Carlo code for rapid treatment plan recalculation in ion beam therapy. *Phys Med Biol*. (2017) **62**:7482–504. doi: 10.1088/1361-6560/aa8134
24. Bisogni MG, Cirrone GAP, Cuttone G, Del Guerra A, Lojacono P, Piliero MA, et al. Medipix2 as a tool for proton beam characterization. *Nuclear Instrum Methods Phys Res A*. (2009) **607**:48–50. doi: 10.1016/j.nima.2009.03.115
25. Jakubek J, Granja C, Jakel O, Martisikova M, Pospicil S. Detection and track visualization of primary and secondary radiation in hadron therapy beams with the pixel detector Timepix. In: *IEEE Nuclear Science Symposium Conference Record*. Knoxville: IEEE. (2010). p. 1967–9. doi: 10.1109/NSSMIC.2010.5874118
26. Gallas RR, Arico G, Burigo LN, Gehrke T, Jakubek J, Granja C, et al. A novel method for assessment of fragmentation and beam-material interactions in helium ion radiotherapy with a miniaturized setup. *Phys Med*. (2017) **42**:116–26. doi: 10.1016/j.ejmp.2017.09.126
27. Rosenfeld A, Alnaghy S, Petasecca M, Cutajar D, Lerch M, Pospisil S, et al. Medipix detectors in radiation therapy for advanced quality-assurance. *Radiat Measurements*. (2020) **130**:106211. doi: 10.1016/j.radmeas.2019.106211
28. Martiíková M, Jakubek J, Granja C, Hartmann B, Oplka L, Pospíil S, et al. Measurement of secondary radiation during ion beam therapy with the pixel detector Timepix. *J Instrument*. (2011) **6**:C11014. doi: 10.1088/1748-0221/6/11/C11014
29. Opalka L, Granja C, Hartmann B, Jakubek J, Jaekel O, Martisikova M, et al. Linear energy transfer and track pattern recognition of secondary radiation generated in hadron therapy beam in a PMMA target. *J Instrument*. (2013) **8**:C02047. doi: 10.1088/1748-0221/8/02/C02047
30. Loo K, Petasecca M, Safavi M, Lerch M, Han Z, Jakubek J, et al. BrachyView: a novel in-body imaging system for prostate brachytherapy. In: *IEEE Nuclear Science Symposium Conference Record*. Valencia: IEEE. (2011). p.279–81. doi: 10.1109/NSSMIC.2011.6154497
31. Rosenfeld AB. Electronic dosimetry in radiation therapy. *Radiat Meas*. (2006) **41**(Suppl. 1):134–53. doi: 10.1016/j.radmeas.2007.01.005
32. Reza S, Wong WS, Fröjdh E, Norlin B, Fröjdh C, Thungström G, et al. Smart dosimetry by pattern recognition using a single photon counting detector system in time over threshold mode. *J Instrument*. (2012) **7**:C01027. doi: 10.1088/1748-0221/7/01/C01027
33. Rubovič P, Bergmann B, Ekendahl D, Hulka J, Judas L, Kohout Z, et al. Timepix detector as a tool for X-ray and gamma dosimetry. *Radiat Meas*. (2017) **107**:39–42. doi: 10.1016/j.radmeas.2017.10.012
34. Michel T, Bohnel M, Durst J, Sievers P, Anton G. Low energy dosimetry with photon counting pixel detectors such as medipix. *IEEE Trans Nuclear Sci*. (2009) **56**:417–23. doi: 10.1109/TNS.2009.2015229
35. George SP, Severino CT, Fröjdh E, Murtas F, Silari M. Measurement of an accelerator based mixed field with a Timepix detector. *J Instrument*. (2015) **10**:P03005. doi: 10.1088/1748-0221/10/03/P03005
36. Kroupa M, Bahadori A, Campbell-Ricketts T, Empl A, Hoang SM, Idarraga-Munoz J, et al. A semiconductor radiation imaging pixel detector for space radiation dosimetry. *Life Sci Space Res*. (2015) **6**:69–78. doi: 10.1016/j.lssr.2015.06.006
37. Stoffle N, Pinsky L, Kroupa M, Hoang S, Idarraga J, Amberboy C, et al. Timepix-based radiation environment monitor measurements aboard the International Space Station. *Nuclear Instrum Methods Phys Res A*. (2015) **782**:143–8. doi: 10.1016/j.nima.2015.02.016
38. Turecek D, Pinsky L, Jakubek J, Vykydal Z, Stoffle N, Pospisil S. Small dosimeter based on Timepix device for international space station. *J Instrument*. (2011) **6**:C12037. doi: 10.1088/1748-0221/6/12/C12037
39. Dudak J, Zemlicka J, Krejci F, Polansky S, Jakubek J, Mrzilkova J, et al. X-ray micro-CT scanner for small animal imaging based on Timepix detector technology. *Nuclear Instrum Methods Phys Res A*. (2015) **773**:81–6. doi: 10.1016/j.nima.2014.10.076
40. Granja C, Kudela K, Jakubek J, Krist P, Chvatil D, Stursa J, et al. Directional detection of charged particles and cosmic rays with the miniaturized radiation camera MiniPIX Timepix. *Nuclear Instrum Methods Phys Res A*. (2018) **911**:142–52. doi: 10.1016/j.nima.2018.09.140
41. Turecek D, Jakubek J. Dependence on temperature and pixel threshold of the calibration for the Timepix detector and its correction method. *J Instrument*. (2013) **8**:C01010. doi: 10.1088/1748-0221/8/01/C01010
42. Ballabriga R, Campbell M, Llopart X. Asic developments for radiation imaging applications: the medipix and timepix family. *Nuclear Instrum Methods Phys Res A*. (2018) **878**:10–23. doi: 10.1016/j.nima.2017.07.029
43. Granja C, Jakubek J, Polansky S, Zach V, Krist P, Chvatil D, et al. Resolving power of pixel detector Timepix for wide-range electron, proton and ion detection. *Nuclear Instrum Methods Phys. Res A*. (2018) **908**:60–71. doi: 10.1016/j.nima.2018.08.014
44. Sarrut D, Bardiés M, Boussion N, Freud N, Jan S, Létang J, et al. A review of the use and potential of the GATE Monte Carlo simulation code for radiation therapy and dosimetry applications. *Med Phys*. (2014) **41**:64301. doi: 10.1118/1.4871617
45. Rucinski A, Gajewski J, Olko P, Rinaldi I, Patera V, Schiavi A. GPU-accelerated Monte Carlo code for fast dose recalculation in proton beam therapy. *Acta Phys Polonica B Proc Suppl*. (2017) **2017**:1–6. doi: 10.5506/APhysPolB.48.1625
46. Jakubek J. Precise energy calibration of pixel detector working in time-over-threshold mode. *Nuclear Instrum Methods Phys Res A*. (2011) **633**:262–66. doi: 10.1016/j.nima.2010.06.183
47. Berger MJ, Coursey JS, Zucker MA, Chang J. *Stopping-Power & Range Tables for Electrons, Protons, and Helium Ions*. (2017). Available online at: https://www.nist.gov/pml/stopping-power-range-tables-electrons-protons-and-helium-ions
48. Resch AF, Elia A, Fuchs H, Carlino A, Palmans H, Stock M, et al. Evaluation of electromagnetic and nuclear scattering models in GATE/Geant4 for proton therapy. *Med Phys*. (2019) **46**:2444–56. doi: 10.1002/mp.13472
49. Granja C, Jakubek J, Martisikova M, Kodaira S, Polansky S, Krist P, et al. Dynamic range and resolving power of the Timepix detector to heavy charged particles. *J Instrument*. (2018) **13**:C11003. doi: 10.1088/1748-0221/13/11/C11003

Conflict of Interest: CG and CO are employed by ADVACAM, Prague, Czechia.

The remaining authors declare that the research was conducted in the absence of any commercial or financial relationships that could be construed as a potential conflict of interest.

frontiers in Physics

ORIGINAL RESEARCH
published: 29 October 2020
doi: 10.3389/fphy.2020.00365

Characterization of the Secondary Neutron Field Produced in a Thick Aluminum Shield by 1 GeV/u ^{56}Fe Ions Using TLD-Based Ambient Dosimeters

Daria Boscolo[1], Daniela Scognamiglio[1,2], Felix Horst[1,3], Uli Weber[1], Christoph Schuy[1], Marco Durante[1,4], Chiara La Tessa[5], Ekaterina Kozlova[1], Alexey Sokolov[1], Irina Dinescu[6], Torsten Radon[1], Désirée Radeck[7] and Miroslav Zbořil[7]*

[1] Biophysics Department, GSI Helmholtzzentrum für Schwerionenforschung GmbH, Darmstadt, Germany, [2] Department of Physics, University of Naples Federico II, Naples, Italy, [3] Institute of Medical Physics and Radiation Protection, Technische Hochschule Mittelhessen, Giessen, Germany, [4] Institute of Solid State Physics, Technical University Darmstadt, Darmstadt, Germany, [5] University of Trento and Trento Institute for Fundamental Physics and Applications (TIFPA), Istituto nazionanale di fisica nucleare (INFN), Povo, Italy, [6] Horia Hulubei National Institute for Research and Development in Physics and Nuclear Engineering and Faculty of Applied Physics, University Politehnica of Bucharest, Bucharest, Romania, [7] Physikalisch-Technische Bundesanstalt, Braunschweig, Germany

OPEN ACCESS

Edited by:
Paul Sellin, University of Surrey, United Kingdom

Reviewed by:
Hector Rene Vega-Carrillo, Autonomous University of Zacatecas, Mexico
Zhonglu Wang, Penn State Milton S. Hershey Medical Center, United States

***Correspondence:**
Felix Horst
f.horst@gsi.de

Specialty section:
This article was submitted to Radiation Detectors and Imaging, a section of the journal Frontiers in Physics

Received: *22 June 2020*
Accepted: *28 July 2020*
Published: *29 October 2020*

Citation:
Boscolo D, Scognamiglio D, Horst F, Weber U, Schuy C, Durante M, La Tessa C, Kozlova E, Sokolov A, Dinescu I, Radon T, Radeck D and Zbořil M (2020) Characterization of the Secondary Neutron Field Produced in a Thick Aluminum Shield by 1 GeV/u ^{56}Fe Ions Using TLD-Based Ambient Dosimeters. Front. Phys. 8:365. doi: 10.3389/fphy.2020.00365

The neutron ambient dose equivalent induced by galactic cosmic-ray-like (1 GeV/u ^{56}Fe) radiation stopped in a thick aluminum shield was measured at different angles with a GSI neutron ball, the standard TLD (thermoluminescent dosimeters)-based neutron dosimeter for area monitoring at the GSI facility. In order to measure reliably at large angles, a modified version of the GSI ball, including a set of three more sensitive TLD600H/700H cards, instead of one standard TLD600/700 card was used. The modified GSI balls were calibrated in neutron reference fields of ^{241}Am-Be(α,n) available at the Physikalisch-Technische Bundesanstalt (PTB). The neutron ambient dose equivalent was measured at five different angles (15, 40, 90, 115, and 130 degrees) with respect to the beam direction and compared to the calculated detector response and neutron ambient dose equivalent results from FLUKA simulations. The dosimeter readings were corrected for signal contributions coming from secondary charged particles. An agreement within 15% was found between the measured and calculated GSI ball response and an agreement within 30% was found between experiments and calculated neutron dose equivalents.

Keywords: space radiation shielding, neutron production, ion fragmentation, TLD, neutron detectors, Monte Carlo

1. INTRODUCTION

Long-term manned space missions to Mars and the construction of a permanent Moon base with a large crew both represent two of the most challenging new frontiers of human space flight exploration. However, the effects of space radiation on the health of astronauts is one of the most serious limiting factors to the realization of such explorations [1–3]. In order to predict the biological effects of radiation exposure and develop possible mitigation strategies, space agencies are developing complex risk models [4, 5]. However, the predictability of these models is strongly

limited by the large uncertainties of the basic physical and radiobiological models and the limited amount of experimental data for the reaction and production cross-sections of particles from galactical cosmic radiation (GCR) [6].

When studying shielding approaches for planetary habitats, the exploitation of *in-situ* materials to build very thick shielding represents one of the most realistic strategies with which to maximize shielding efficiency while limiting costs. In this context, the lack of experimental data on neutron and light ion production after thick shielding material by highly energetic ion radiation represents one of these significant knowledge gaps. Recent studies demonstrated that, behind thick shielding ($\geq$ 20 g/cm^2), up to 80–90% of the total dose equivalent to various body organs comes from light secondary fragments and neutrons [7–9]. In particular, secondary neutrons—abundantly produced through all phases of a nuclear fragmentation process—represent a severe threat for the astronauts' health due to their high penetration length and their increased biological effectiveness.

Motivated by these gaps in data, a series of experimental studies for secondary particle production in thick targets for space radiation protection applications have been performed at the HIMAC accelerator in Japan by NASA-associated research groups from the USA; more recent studies have been performed at NSRL at Brookhaven National Laboratory [10–12]. However, despite the significant experimental effort invested in these campaigns, measurement gaps are still reported [13].

Radiation transport codes represent a powerful and very important tool for radiation protection in space. However, the uncertainties regarding the nuclear physics models and the lack of necessary experimental data needed to improve these models lead to large differences among the major particle transport codes used for space radiation application [14]. Recent studies demonstrated that different Monte Carlo (MC) codes could reproduce the measured neutron dose distributions behind shielding materials irradiated with protons only with an accuracy of a factor of two [15].

In this context, an accelerator-based experimental campaign within the framework of the ESA-IBER program is currently taking place in Cave A of GSI (Helmholtzzentrum für Schwerionenforschung, Darmstadt) by a collaboration with the PTB (Physikalisch-Technische Bundesanstalt, Braunschweig), TIFPA (Trento Institute of Fundamental Physics and Application, Trento), the Radiation protection department of GSI, and the Biophysics department of GSI. This project aims at a full characterization of the neutron and light fragment field generated by galactic cosmic ray-like radiation (1 GeV/u ^{56}Fe ions) fully stopping in a thick aluminum target. The measurement method consists of a multi-detector system including four complementary detectors and measurement techniques. In particular, the secondary neutron yield and the neutron ambient dose equivalent at different angles will be measured with the active PTB Bonner sphere spectrometer (BSS) NEMUS and the TLD-based GSI neutron ball dosimeters, respectively. The double differential yield of the secondary fragments will be measured with ToF (Time of flight) and energy loss measurements via ΔE-E telescopes while the TEPC (tissue equivalent proportional counter) will allow a microdosimetric characterization in terms of lineal energy spectra.

In this work, the results obtained from GSI neutron balls within the first experimental run are presented. These dosimeters, consisting of a moderator sphere equipped with thermoluminescence dosimeters (TLDs) sensitive to thermal neutrons, have been used to measure the angular distribution of the neutron ambient dose equivalent around a thick target at different angular positions. For this experimental campaign, a modified version of the GSI ball, including a set of three sensitive TLD600H/700H cards, was used. In order to achieve the maximum accuracy, the full detector setup was calibrated in the PTB ^{241}Am-Be(α,n) neutron reference field. After describing the calibration procedure, and the experimental setup, the measured neutron ambient dose equivalent distribution is presented. A dedicated study is carried out to quantify the signal contributions coming from secondary protons interacting with the GSI balls. Consequently, the dosimeter readings are corrected for this over-response due to secondary protons. The experimental results are finally compared with Monte Carlo simulations showing a good agreement between the measured and calculated neutron dose equivalent distribution.

2. MATERIALS AND METHODS

2.1. GSI Ball: A TLD-Based Neutron Dosimeter

GSI balls are the standard neutron dosimeters used at the GSI (Helmholtzzentrum für Schwerionenforschung in Darmstadt) accelerator site for environmental monitoring all over the facility [16–18]. The detectors consist of a 32 cm diameter polyethylene sphere (density 0.954 g/cm^3) with a 1 cm thick lead layer inside. At the sphere center, a TLD card of the Harshaw type is used as the radiation-sensitive element. The polyethylene moderates up to 10 MeV neutrons down to thermal energies so that they can be detected by the TLDs. For more energetic neutrons, for which the polyethylene moderator becomes insufficient, a lead layer converts the high-energy neutrons into detectable evaporation neutrons by spallation reactions. The geometrical design of the GSI ball dosimeter was optimized through Monte Carlo transport codes (FLUKA and MCNPX) [19, 20] to reproduce the ambient dose equivalent, $H^*(10)$, (as given in the ICRP74 [21]) in a neutron energy range spanning from thermal up to GeVs. The calculated response was validated with mono-energetic neutron beams up to 19 MeV and quasi-mono-energetic neutrons of 500 and 800 MeV [22, 23]. In **Figure 1**, the response function of the new GSI ball dosimeters is depicted together with the response function of the standard model of GSI ball (with one card) and with the energy-dependent dose equivalent curve from [24, 25]. Within this project, five GSI balls were used to measure the neutron-ambient dose equivalent at different angles; among these, three were a new prototype able to hold up to three TLD cards, thus providing improved measurement statistics. A schematic representation of a GSI ball from a different projection and of the sensitive element consisting of a

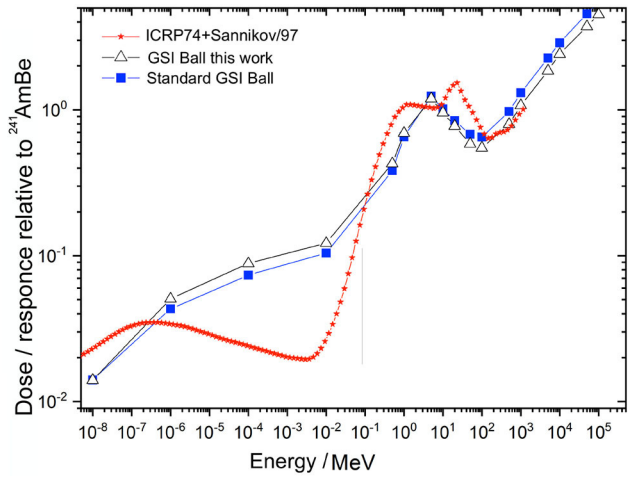

FIGURE 1 | Calculated neutron fluence response of the standard GSI ball (scatter-line with solid blue squares) and the new GSI ball holding three TLD cards (scatter-line with black open triangles) and the fluence-to-dose conversion function for ambient dose equivalent $H^*(10)$ [24, 25] (red stars).

cylindrical insert holding the three TLD600H/TLD700H cards is shown in **Figure 2**.

The TLD cards contain two pairs of different TLD chips based on LiF: two TLD600 and two TLD700. The two TLD600 chips, enriched in ^{6}Li, can detect photons, charged particles and thermal neutrons (through the ^{6}Li(n,α)^{3}H reaction), while the two TLD700 chips, where the ^{6}Li fraction has been depleted, respond identically to the TLD600 to gamma radiation and charged particles but are not as sensitive to thermal neutrons. This allows a separation of the neutron TL signal in a mixed radiation field by subtraction of the TLD700 signal from the one measured by the TLD600 [26–28]. The readout procedure of the TLD600H/700H crystals is described in the **Supplementary Material**. In this work, to measure accurately at positions where the neutron yield is very low (large angles and backwards positions), the standard TLD600/700 cards were replaced by more sensitive TLD600H/700H cards [29], which are able to provide reliable readings from doses of two μGy instead of 20 μGy [30]. The higher sensitivity (TL light output per absorbed dose) is achieved by different doping of the LiF material (doped with Mg, Cu and P instead of Mg and Ti). However, the different composition does not only affect the sensitivity but also the dose-response function and saturation behavior and consequently also the relative TL efficiency for densely ionizing radiation. Even though the TLD600H/700H material is expected to be 10–30 times more sensitive to photons than the standard TLD600/700 chips [31], for neutron dosimetry, this higher sensitivity is reduced (for the chips used in this work) to only a factor of 7 when considering also the difference of the relative TL efficiency to thermal neutrons. This quantity is about a factor of 3 lower for the TLD600H material compared to TLD600. This can be explained by the higher sensitivity at low doses since to the Mg, Cu, and P doping goes along with a lower saturation level. The factor of 3 observed in this work is in accordance with the prediction by microscopic models [32].

2.1.1. Dosimeter Calibration

All TLD600H/700H cards used during this project have been calibrated, in terms of dose per TL signal, with gamma radiation from a ^{137}Cs source available at GSI with a nominal activity of 364 MBq. Response factors to gamma radiation, R_γ, obtained for all crystals (four per card) are shown separately for TLD600H and TLD700H in the **Supplementary Material**. Averaging all irradiated crystals, it can be observed that both TLD types show the same R_γ: an average response of 0.59 nC μGy^{-1} (with a maximum of 0.69 nC μGy^{-1} and a minimum of 0.45 nC μGy^{-1}) for TLD600H and 0.57 nC μGy^{-1} (with a maximum of 0.66 nC μGy^{-1} and a minimum of 0.49 nC μGy^{-1}) for TLD700H. A large response variability between the crystals is observed and has to be taken into account when performing precision measurements, thus exhibiting the need for individual crystal calibration.

After determining the response of every single crystal to gamma radiation, all the GSI balls used during the experiments were calibrated in terms of the neutron ambient dose equivalent using the neutron field generated by a ^{241}Am-Be(α,n) source available at GSI with a nominal activity of 370 GBq. A detailed description of the neutron calibration procedure performed can be found in [20]. To exclude any uncertainties coming from the dosimeter setup, the calibration was performed with the exact same combination of cards and moderators used during the experiment. An additional calibration for a single GSI ball holding three cards was performed with the reference ^{241}Am-Be(α,n) source at PTB. On this occasion, corrections for the scattered neutrons contributions have been made by means of the shadow cones technique [33, 34]. A difference of 20% was found between the average neutron response, R_n, measured at GSI and the ones measured at PTB, probably coming from the missing correction for the scattered neutron contribution at GSI. Neutron calibration results with the ^{241}Am-Be(α,n) are reported in the **Supplementary Material**.

2.2. Experimental Setup

Two sets of five neutron dosimeters were irradiated in the secondary radiation field generated by the nuclear interaction of a 1 GeV/u ^{56}Fe beam fully stopped in a cylindrical aluminum target 20 cm in diameter with a height of 20 cm in GSI's Cave A. The primary radiation and the target selection was chosen to be relevant for space shielding applications: the 1 GeV/u ^{56}Fe beam is often used as reference radiation for studying GCR, and aluminum constitutes one of the main construction material for spacecrafts and is typically used as reference material. The neutron ambient dose equivalent was measured at 5 different angles with respect to the beam axis at (15, 40, 90, 115, and 130 degrees). Two independent repetitions of the experiment have been performed in order to guarantee the measurement reproducibility. Each measurement set was composed by three new GSI ball prototypes (holding three TLD600H/TLD700H cards) and two standard GSI ball dosimeter (holding one TLD card) respectively at angles of 15, 40, and 130 degrees and at 90 and 115 degrees. A schematic representation of the experimental

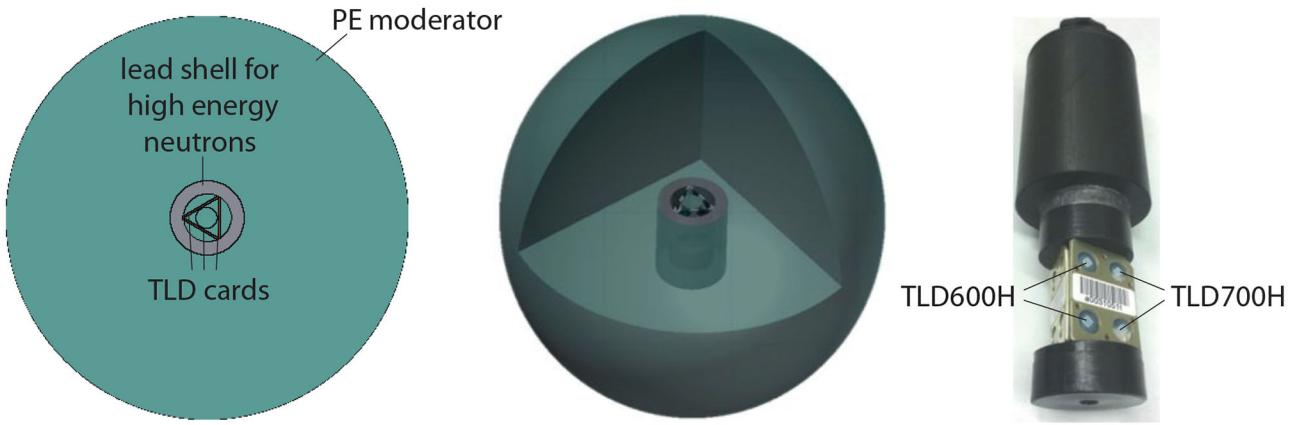

FIGURE 2 | GSI ball layout with PE moderator, lead layer, and the cylindrical insert holding three TLD cards.

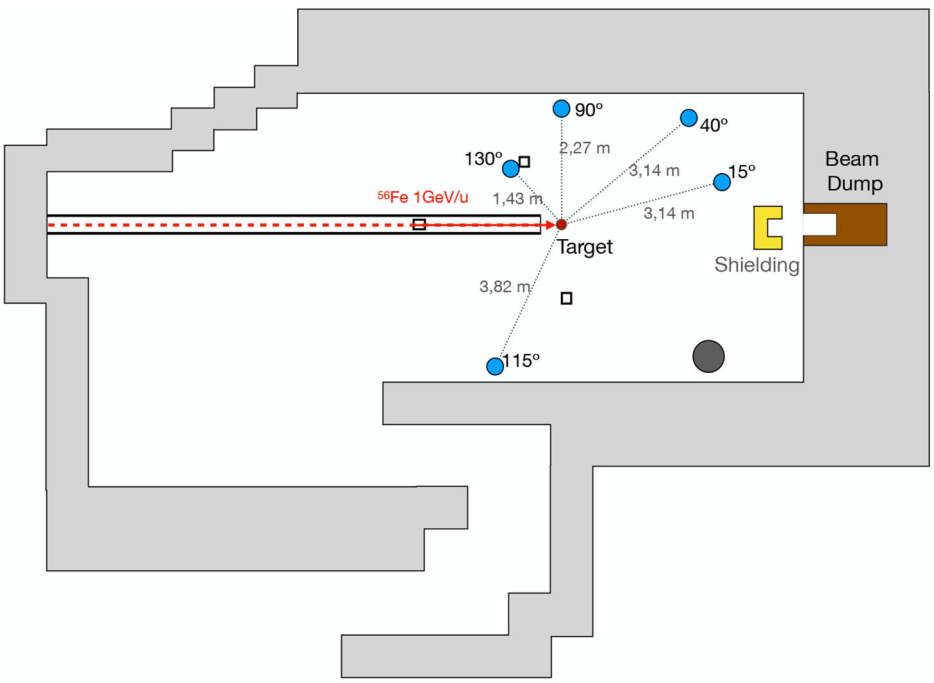

FIGURE 3 | Schematic representation of the experimental cave with its concrete walls and experimental setup and horizontal projection.

setup and of the experimental room is shown in **Figure 3**. The primary beam, a pencil beam (with a FWHM of about 1.2 cm), was constantly monitored during the irradiation with a parallel plate ionization chamber [35] while the beam position and focus was verified with Radiochromic films and a light screen. The beam monitor ionization chamber was calibrated in terms of primary particles by a dose measurement as described in detail in [36]. In order to reduce the contribution of back-scattered neutrons and of neutrons produced in the backwards direction—through the interaction of secondary radiation with the material present in the experimental room and with the walls—dedicated PE shielding was placed in front of the beam dump and under the target position. The optimization of the shielding installation was performed with FLUKA simulations which allowed to define the most critical areas in the experimental room and establish reasonable measures to limit the background signal coming from the cave.

2.3. Cave Geometry and FLUKA Simulations

The FLUKA Monte Carlo particle transport code (version 2011.2x.5) [37, 38], used with the rQMD-2.4 model [39] and

in combination with the graphical user interface flair [40], has been used for the planning of the experiment and for the interpretation of the results. The whole setup, including the full Cave geometry, represented in **Figure 3** has been implemented in the simulation geometry and used to analyze the expected neutron and secondary particle field at the detector position and in the experimental area. All simulations have been performed with physics and transport parameters, including evaporation, coalescence, electromagnetic dissociation, and activation of the low-energy neutron optimized transport function. To compare with experimental values, the secondary neutron spectra have been scored in the detector volume, and the dosimeter response was then calculated by folding the simulated spectra with the energy-dependent response function of the GSI balls [41]. Additionally, the ambient dose equivalent calculated from ICRP74 [21] has been also scored in the volumes covered by the dosimeters.

Two-dimensional neutron ambient dose equivalent maps have been calculated in order to establish possible shielding approaches reducing the contribution of scattered neutrons at the measurement positions as much as possible. A 2D simulation of the dose equivalent distribution in the cave during the experiment is shown in **Figure 4** at the height of the beamline.

2.3.1. Secondary Proton Correction

As described in section 2.1, the subtraction of the TLD700H signal from the TLD600H signal allows the removal of contributions from particles other than neutrons. However, with this technique, enhancements of the TLD600H signal caused by tertiary neutrons produced within the GSI ball, for instance by secondary charged fragments, cannot be distinguished from real neutron dose. At small angles, close to the incident beam direction, projectile fragments with high energies are present and might lead to a significant contribution especially for the 15° measurements. In particular, dose readings are expected to be perturbed by energetic protons that are able to reach the lead layer in the center of the GSI ball and produce spallation neutrons. The neutron ambient dose equivalents measured in the ^{56}Fe ion experiments described in this work were, thus, corrected for the contributions of secondary protons. The secondary proton spectra at the measurement positions were obtained from the FLUKA simulations of the experiment, see **Figure 5A**. However, as planned in the original IBER 17 project, secondary particle spectra were measured with ToF and energy loss measurements via ΔE-E telescopes. Those spectra were then used as the source in another FLUKA simulation where the GSI ball geometry is irradiated with protons, which is similar to the simulations performed to obtain the neutron response function of the dosimeter [41]. After normalizing the simulation results to the calibration field (^{241}Am-Be neutrons) and subtracting the TLD600H signal contributions induced directly by the incident protons (these doses are also measured by the TLD700H chips), the neutron dose readings obtained during the measurements can be corrected for the influence of secondary protons.

Projectile fragments heavier than protons (e.g. deuterons, tritons, or helium) were neglected in the correction of the dose readings since the perturbation due to those fragments can be considered as a second-order effect. Their fluences at the measurement positions were also scored

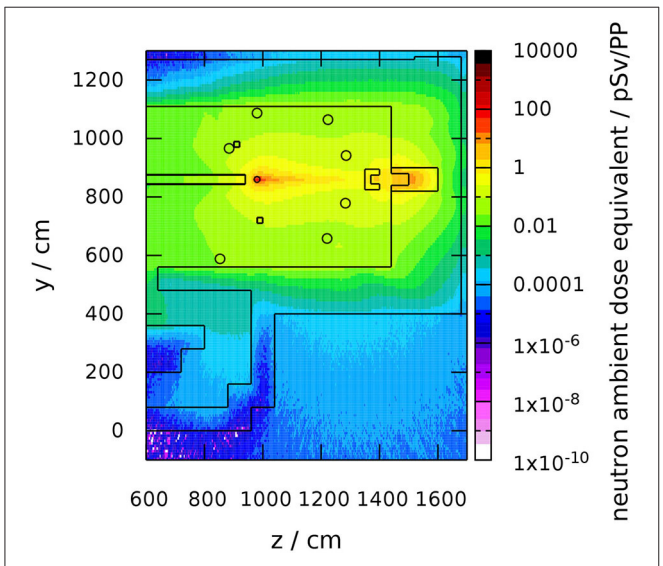

FIGURE 4 | Simulated neutron ambient dose equivalent distribution, normalized per primary particle, in the experimental room during the IBER 17 experiment.

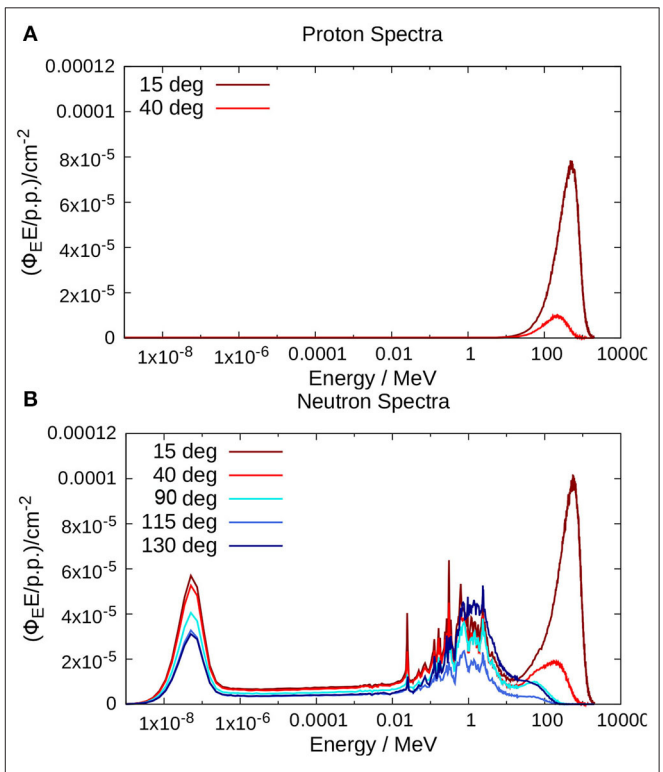

FIGURE 5 | (A) Calculated secondary proton spectrum at the 15 and 40 degree position. **(B)** Calculated neutron spectrum (fluence per unit lethargy) at the different dosimeter positions.

in the FLUKA simulation of the experiment but they were more than one order of magnitude smaller than the proton fluences.

3. RESULTS AND DISCUSSION

Results for the neutron ambient dose equivalent measured by the TLDs at the different positions normalized per primary particle are reported in **Table 1** together with the distances between the detector and the target center. For the two smallest angles, the contribution to the measured neutron dose equivalent coming from neutrons produced by the interaction of secondary protons with the moderator, and in particular with the lead layer included in the GSI ball, has been calculated with FLUKA simulations, and its effect on the measured values is also reported in **Table 1**. The simulated proton spectra in the detector volumes are shown in **Figure 5A** while **Figure 6** depicts 2D fluence maps of secondary protons and tertiary neutrons in the GSI ball. Despite the strong directionality of the secondary proton field, it can be observed that the generated neutron field at the TLD card position is rather isotropic, thus justifying the use of an average correction on the reading of the three cards inside the detector. An effect of up to about 30% was found for the 15-degree position while a much lower contribution, of approximately 5%, is obtained at 40 degrees. A 30% uncertainty was estimated for the applied secondary proton corrections. Lower contributions are expected at larger angles justifying the application of the correction only at the two most forwarded angles. For kinematic reasons, indeed, the higher energy proton projectile fragments are produced in forward direction and are also visible from the simulated secondary proton spectra in **Figure 5A**. Experimental results have been compared to FLUKA predictions of the neutron ambient dose equivalent at the different measuring positions. A comparison of the calculated neutron ambient dose equivalent, $H^*(10)$ with the experimental measurements—with and without the neutron contribution coming from the secondary proton field—is shown in **Figure 7**. Even though the data analysis and simulation have been performed for the exact detector positions, for better visualization and interpretation, the data presented in **Figure 7** have been re-normalized to a 1 m distance

TABLE 1 | The neutron ambient dose equivalent per primary particle (p.p.) measured at the different dosimeter positions (reported distances are calculated from the center of the target center to the center of the dosimeters) are reported together with the measurement values corrected by the contribution of neutrons produced by the interaction of the secondary proton field with the dosimeter moderator (correction applied only to the two smallest angles).

Detector position/deg	Distance from the target center / m	Neutron ambient dose equivalent / μSv/p.p.	Neutron ambient dose equivalent (with proton correction) / μSv/p.p.
15	3.14	$1.5 \cdot 10^{-7} \pm 7\%$	$1.1 \cdot 10^{-7} \pm 20\%$
40	3.14	$5.4 \cdot 10^{-8} \pm 6\%$	$5.1 \cdot 10^{-8} \pm 8\%$
90	2.27	$3.9 \cdot 10^{-8} \pm 7\%$	$3.9 \cdot 10^{-8} \pm 7\%$
115	3.82	$1.0 \cdot 10^{-8} \pm 16\%$	$1.0 \cdot 10^{-8} \pm 16\%$
130	1.43	$4.6 \cdot 10^{-8} \pm 9\%$	$4.6 \cdot 10^{-8} \pm 9\%$

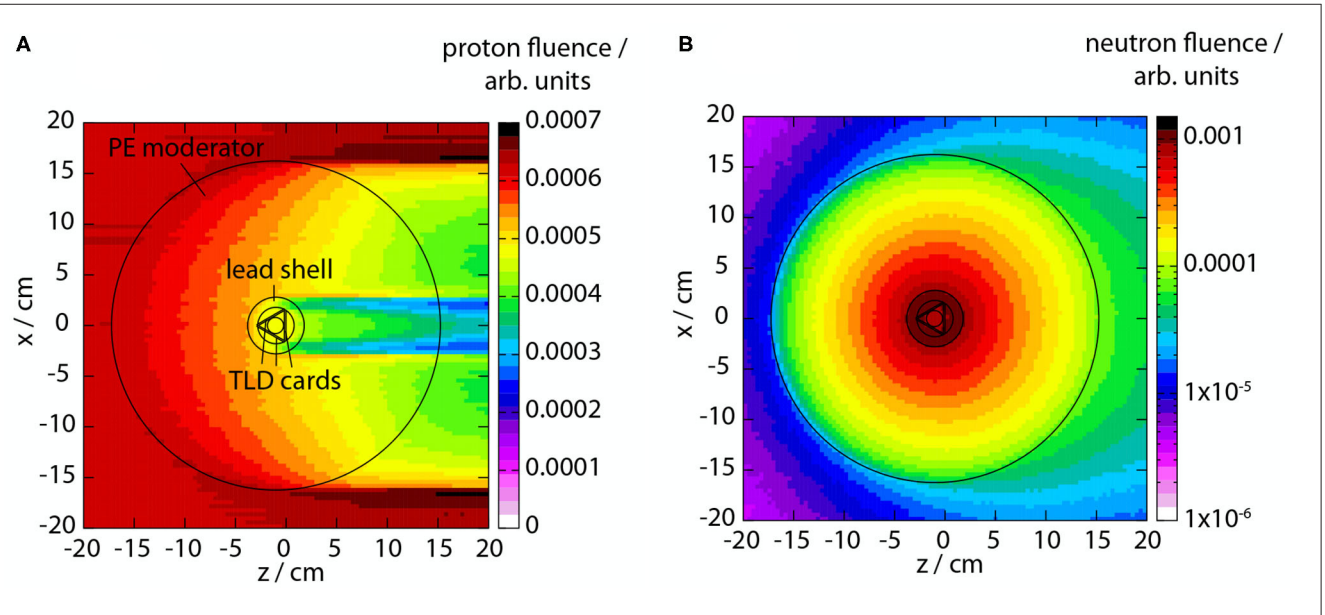

FIGURE 6 | (A) Secondary proton field impinging on the dosimeter and **(B)** simulated neutron field generated by the proton interaction with the dosimeter moderator.

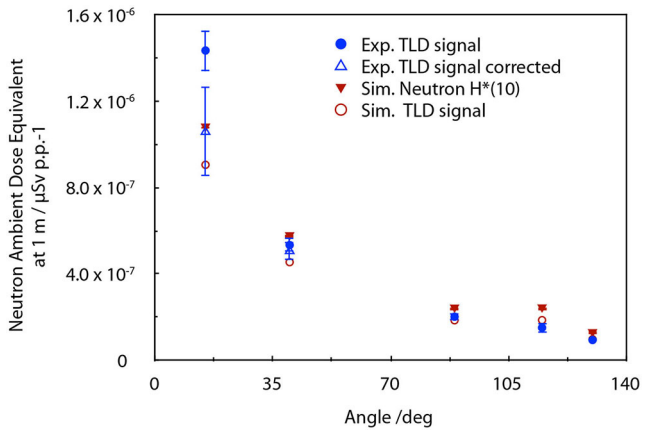

FIGURE 7 | Measured neutron ambient dose equivalent per primary particle at different angles normalized to a distance of 1 m from the target center (see text). Experimental values are presented with (blue open triangles) and without (blue solid circles) secondary proton corrections and compared with the predicted dosimeter response (open red circles) and the predicted neutron ambient dose $H^*(10)$ (solid red triangles). Uncertainties bars are partially hidden by the symbols.

from the target center by applying the inverse square law. This normalization is only an approximation because it assumes idealized conditions with a point source and a constant neutron energy distribution at each angle scaling only with the distance from the target. However, it is useful to get an idea of the angular distribution of the neutron ambient dose equivalent because the distances between target and detectors were not equal for all measurement positions. For the experimental data, the uncertainty reported is the maximum between the statistical error on the detector reading and the standard deviation between the readings of the three cards held in a GSI ball. For the most forward angle, the calculated ambient dose equivalent is around 30% lower with respect to the measured value. However, after applying the correction for the secondary proton contribution this difference reduces significantly to a 2% difference. For large angles (40 to 130 degrees), the simulated neutron ambient dose equivalent results are always larger than the experimental values, showing an agreement within 25%. A larger deviation of about 40% is observed for the 115-degree angle. This significant difference is mainly due to larger uncertainties on the detector position introduced by the complexity of the Cave geometry and by the fact that this detector, different from the others, was not exactly at the beam height. These uncertainties can affect both the experimental results and the simulated contribution of scattered neutron from the walls and equipment present in the cave at the time of the experiment. Even though the detector readings are a good estimate for the neutron ambient dose equivalent, the expected detector response at the different measurement position has also been calculated by folding the simulated neutron spectra with the GSI ball response function. The simulated neutron spectra (fluence per unit lethargy) at the different dosimeter positions are shown in **Figure 5B**. For the small angles (forward direction with respect to the beam), the spectra are dominated by a pronounced peak at about 560 MeV followed by two other smaller peaks: one at 1 MeV (evaporation neutrons) and one in the thermal neutron region. At larger angles, the high-energy peak becomes less important and disappears in the backward direction. This is because the higher-energy neutron projectile fragments show a pronounced forward direction due to the reaction kinematics while the evaporation neutrons are rather isotropic and the thermalized neutrons fill the cave homogeneously. The greater number of events reported in the 130 degree spectrum of this specific dosimeter was because it was positioned significantly closer to the target compared to the other detectors (only 1.43 m), see **Table 1** and **Figure 3**. The simulated detector responses, re-normalized to a 1 m distance from the target center, are also reported in **Figure 7**. At the larger angles, except for a deviation of 20% at 115 degrees, the measurements agree with the calculated detector response within 10%. However, at the 15 degree angle, an agreement of only 15% between the experimental data (including secondary fragment corrections) and the expected TLD response can be observed. Several factors might contribute to this deviation, including the contribution of additional neutrons generated by other secondary fragments here neglected and small inaccuracies in the geometry or material description in the FLUKA calculations (in a region where the neutron dose contribution has a large gradient).

For all investigated detector positions, the calculated $H^*(10)$ results always turned out to be larger than the measured and calculated GSI Ball responses. This can be explained because, in the neutron energy range between 0.1 and 500 MeV, the GSI ball response function underestimates the neutron ambient dose equivalent, see **Figure 1**.

4. CONCLUSION AND OUTLOOK

The work presented here is part of a larger experimental campaign aiming at the establishment of a multi-detector setup for the characterization of the neutron and light fragment field generated by galactic cosmic-ray-like radiation in thick shielding material. The mixed radiation field, generated by 1 GeV/u ^{56}Fe ions fully stopped in a thick aluminum target, has been characterized in terms of neutron ambient dose equivalent with GSI ball neutron dosimeters, the standard neutron dosimeter for area monitoring at the GSI accelerator facility. The neutron ambient dose has been measured at five different positions, and FLUKA calculations were carried out to predict the GSI ball response and the neutron ambient dose equivalent at the detector positions. Corrections at the more forward positions have been applied in order to exclude the contribution of tertiary (and higher-order) neutrons produced by the interaction of secondary protons with the detector moderator. The good agreement between the measured and calculated values—within a well-defined irradiation condition and using a standard reference ion beam and target material—demonstrated the validity of the approach and open up the possibility of investigating more complex irradiation scenarios. Different and less studied radiation qualities and more complex shielding materials could indeed be tested in future experiments with the presented

approach. Moreover, secondary fragment spectra measured with different experimental setups can be used for more accurate secondary proton and light fragment correction, as planned in future experiments. The capability of the GSI balls to give a good estimation of the neutron ambient dose equivalent over a range of neutron energies ranging from thermal to several GeVs makes these detectors particularly interesting for space radiation protection application. They allow us to get directly biologically relevant quantities also in complex radiation fields and for space relevant energies. They provide interesting data for benchmarking and validation of radiation transport codes and risk models. Additionally, thanks to the large range of energy covered, the possibility of measuring at very high intensities (being a passive detector it does not suffer from dead time effects) make this detector very suitable for ground based accelerator studies, especially for upcoming facilities like FAIR (Facility for Antiproton and Ion Research, Darmstadt, Germany) where ion beams of intensities up to 10^{11} particles/s (and protons up to 5×10^{12} particles/s) and energies up to 10 GeV/u (29 GeV for protons) will be reached.

DATA AVAILABILITY STATEMENT

The raw data supporting the conclusions of this article will be made available by the authors, without undue reservation.

AUTHOR CONTRIBUTIONS

DB wrote the manuscript with support from FH. CS, MZ, EK, DR, CL, UW, MD, DB, and FH conceived and planned the experiments. DS, EK, DB, FH, CS, AS, ID, and MZ carried out the experiments. DS, EK, and DR, carried out the detector calibrations. DB and EK analyzed the data. DB and FH planned and carried out the simulations. TR and UW provided support and material for the experiment. All authors provided critical feedback and helped shape the manuscript.

FUNDING

This work was supported by European Space Agency (ESA)-IBER 17 project. The results are based on the experiment IBER-010, which was performed in Cave A at the GSI Helmholtzzentrum fuer Schwerionenforschung, Darmstadt (Germany) in the frame of FAIR Phase-0.

SUPPLEMENTARY MATERIAL

The Supplementary Material for this article can be found online at: https://www.frontiersin.org/articles/10.3389/fphy.2020.00365/full#supplementary-material

REFERENCES

1. Durante M, Cucinotta FA. Physical basis of radiation protection in space travel. *Rev Mod Phys*. (2011) **83**:1245–81. doi: 10.1103/RevModPhys.83.1245
2. Cucinotta FA, Kim MHY, Chappell LJ. Report No.: NASA/TP-2011-216155. Space radiation cancer risk projections and uncertainties-2010 (2011).
3. Durante M. Space radiation protection: destination Mars. *Life Sci Space Res*. (2014) **1**:2–9. doi: 10.1016/j.lssr.2014.01.002
4. Norbury JW, Slaba TC, Aghara S, Badavi FF, Blattnig SR, Clowdsley MS, et al. Advances in space radiation physics and transport at NASA. Life Sci Space Res. (2019) 22:98–124. doi: 10.1016/j.lssr.2019.07.003
5. Walsh L, Schneider U, Fogtman A, Kausch C, McKenna-Lawlor S, Narici L, et al. Research plans in Europe for radiation health hazard assessment in exploratory space missions. *Life Sci Space Res*. (2019) **21**:73–82. doi: 10.1016/j.lssr.2019.04.002
6. Norbury JW, Slaba TC. Space radiation accelerator experiments-the role of neutrons and light ions. *Life Sci Space Res*. (2014) **3**:90–4. doi: 10.1016/j.lssr.2014.09.006
7. Walker SA, Townsend LW, Norbury JW. Heavy ion contributions to organ dose equivalent for the 1977 galactic cosmic ray spectrum. *Adv Space Res*. (2013) **51**:1792–9. doi: 10.1016/j.asr.2012.12.011
8. Slaba TC, Blattnig SR, Norbury JW, Rusek A, La Tessa C. Reference field specification and preliminary beam selection strategy for accelerator-based GCR simulation. *Life Sci Space Res*. (2016) **8**:52–67. doi: 10.1016/j.lssr.2016.01.001
9. Slaba TC, Bahadori AA, Reddell BD, Singleterry RC, Clowdsley MS, Blattnig SR. Optimal shielding thickness for galactic cosmic ray environments. *Life Sci Space Res*. (2017) **12**:1–15. doi: 10.1016/j.lssr.2016.12.003
10. Nakamura T, Heilbronn L. *Handbook on Secondary Particle Production and Transport by High-Energy Heavy Ions*. World Scientific (2006). doi: 10.1142/5973
11. Nakamura T, Heilbronn L. *Handbook on Secondary Particle Production and Transport by High-Energy Heavy Ions:(with CD-ROM)*. World Scientific (2006).
12. Castellanos, LA, McGirl NA, Srikrishna AP, Heilbronn L, La Tessa C, Rusek A, et al. "Thick-target yields of secondary ions and neutrons for validation of radiation transport codes," in *2017 IEEE Aerospace Conference* (Big Sky, MT), 1–10. doi: 10.1109/AERO.2017.7943575
13. Norbury JW, Miller J. Review of nuclear physics experimental data for space radiation. *Health Phys*. (2012) **103**:640–2. doi: 10.1097/HP.0b013e318261fb7f
14. Norbury JW, Slaba TC, Sobolevsky N, Reddell B. Comparing HZETRN, SHIELD, FLUKA and GEANT transport codes. *Life Sci Space Res*. (2017) **14**:64–73. doi: 10.1016/j.lssr.2017.04.001
15. Schuy C, Tessa CL, Horst F, Rovituso M, Durante M, Giraudo M, et al. Experimental assessment of lithium hydride's space radiation shielding performance and Monte Carlo benchmarking. *Radiat Res*. (2019) **191**:154–61. doi: 10.1667/RR15123.1
16. Rollet S, Agosteo S, Fehrenbacher G, Hranitzky C, Radon T, Wind M. Intercomparison of radiation protection devices in a high-energy stray neutron field, Part I: Monte Carlo simulations. *Radiat Meas*. (2009) **44**:649–59. doi: 10.1016/j.radmeas.2009.03.029
17. Wiegel B, Agosteo S, Bedogni R, Caresana M, Esposito A, Fehrenbacher G, et al. Intercomparison of radiation protection devices in a high-energy stray neutron field, Part II: Bonner sphere spectrometry. *Radiat Meas*. (2009) **44**:660–72. doi: 10.1016/j.radmeas.2009.03.026
18. Silari M, Agosteo S, Beck P, Bedogni R, Cale E, Caresana M, et al. Intercomparison of radiation protection devices in a high-energy stray neutron field. Part III: Instrument response. *Radiat Meas*. (2009) **44**:673–91. doi: 10.1016/j.radmeas.2009.05.005
19. Fehrenbacher G, Gutermuth F, Kozlova E, Radon T, Schuetz R. Neutron dose measurements with the GSI ball at high-energy accelerators. *Radiat Protect Dosimet*. (2007) **125**:209–12. doi: 10.1093/rpd/ncl127

20. Gutermuth F, Radon T, Fehrenbacher G, Festag J. The response of various neutron dose meters considering the application at a high energy particle accelerator. *Kerntechnik*. (1987). **68**:172–9.
21. ICRP. *Conversion Coefficients for Use in Radiological Protection Against External Radiation*. ICRP Publication 74 Ann ICRP (1996). doi: 10.1016/S0146-6453(96)90003-2
22. Fehrenbacher G, Kozlova E, Gutermuth F, Radon T, Schütz R, Nolte R, et al. Measurement of the fluence response of the GSI neutron ball dosemeter in the energy range from thermal to 19 MeV. *Radiat Protect Dosimet*. (2007) **126**:546–8. doi: 10.1093/rpd/ncm110
23. Fehrenbacher G, Gutermuth F, Kozlova E, Radon T, Aumann T, Beceiro S, et al. Measurement of the fluence response of the GSI neutron ball in high-energy neutron fields produced by 500 AMeV and 800 AMeV deuterons. *Radiat Protect Dosimet*. (2007) **126**:497–500. doi: 10.1093/rpd/ncm100
24. Sannikov A, Savitskaya E. Ambient dose equivalent conversion factors for high energy neutrons based on the ICRP 60 recommendations. *Radiat Protect Dosimet*. (1997) **70**:383–6. doi: 10.1093/oxfordjournals.rpd.a031982
25. Pelliccioni M. Overview of fluence-to-effective dose and fluence-to-ambient dose equivalent conversion coefficients for high energy radiation calculated using the FLUKA code. *Radiat Protect Dosimet*. (2000) **88**:279–97. doi: 10.1093/oxfordjournals.rpd.a033046
26. Lee J, Pradhan A, Kim J, Kim B, Yim K. Response of 6LiF: Mg, Cu, Si and 7LiF: Mg, Cu, Si TLD pairs to the neutrons and photon mixtures. *J Nuclear Sci Technol*. (2008) **45**:233–6. doi: 10.1080/00223131.2008.10875830
27. Vega-Carrillo HR. TLD pairs, as thermal neutron detectors in neutron multisphere spectrometry. *Radiat Meas*. (2002) **35**:251–4. doi: 10.1016/S1350-4487(01)00291-8
28. Vega-Carrillo HR, Guzman-Garcia KA, Gallego E, Lorente A. Passive neutron area monitor with pairs of TLDs as neutron detector. *Radiat Meas*. (2014) **69**:30–4. doi: 10.1016/j.radmeas.2014.08.006
29. *Thermo Scientific Harshaw TLD Materials and Dosimeters*. Technical report. BRRMSI-TLD-0616 (2016). Available online at: https://assets.thermofisher.com/TFS-Assets/LSG/Catalogs/Dosimetry-Materials-Brochure.pdf
30. Kozlova E, Sokolov A, Pyshkina M, Radon T. *Testing of New Sensitive TLD Cards*. GSI Scientific Report (2016).
31. RadPro Product Brochure. *RadPro International GmbH*. (2020). Available online at: https://www.radpro-int.com
32. Horowitz Y, Olko P. The effects of ionisation density on the thermoluminescence response (efficiency) of LiF:Mg,Ti and LiF:Mg,Cu,P. *Radiat Protect Dosimet*. (2004) **109**:331–48. doi: 10.1093/rpd/nch310
33. Eisenhauer C. Two-component analytical model to calculate room-return correction for calibration of neutron instruments. *Radiat Protect Dosimet*. (1992) **42**:267–77.
34. Vega-Carrillo HR, Manzanares-Acu na E, I niguez MP, Gallego E, Lorente A. Study of room-return neutrons. *Radiat Meas*. (2007) **42**:413–9. doi: 10.1016/j.radmeas.2007.01.036
35. Kraft G, Weber U. Tumor therapy with ion beams. In: *Handbook of Particle Detection and Imaging*. Berlin; Heidelberg: Springer-Verlag (2012). p. 1179. doi: 10.1007/978-3-642-13271-1_47
36. Luoni F, Weber U, Boscolo D, Reidel CA, Zink K, Horst F. Beam monitor calibration for radiobiological experiments with scanned high energy heavy ion beams for FAIR. Front Phys. (2020) **8**:568145. doi: 10.3389/fphy.2020.568145
37. Battistoni G, Boehlen T, Cerutti F, Chin PW, Esposito LS, Fassó A, et al. Overview of the FLUKA code. *Ann Nuclear Ener*. (2015) **82**:10–8. doi: 10.1016/j.anucene.2014.11.007
38. Fasso A, Ferrari A, Ranft J, Sala PR. Report No.: CERN-2005-010, SLAC-R-773, INFN-TC-05-11. *FLUKA: A Multi-Particle Transport Code*. CERN Yellow Reports: Monographs (2005). doi: 10.2172/877507
39. Sorge H, Stöcker H, Greiner W. Poincaré invariant Hamiltonian dynamics: modelling multi-hadronic interactions in a phase space approach. *Ann Phys*. (1989) **192**:266–306. doi: 10.1016/0003-4916(89)90136-X
40. Vlachoudis V. FLAIR: a powerful but user friendly graphical interface for FLUKA. In: *Proc. Int. Conf. on Mathematics, Computational Methods & Reactor Physics (M&C 2009)*. Saratoga Springs, NY (2009).
41. Horst F, Fehrenbacher G, Zink K. On the neutron radiation field and air activation around a medical electron linac. *Radiat Protect Dosimet*. (2017) **174**:147–58. doi: 10.1093/rpd/ncw120

Conflict of Interest: The authors declare that the research was conducted in the absence of any commercial or financial relationships that could be construed as a potential conflict of interest.

frontiers in Physics

BRIEF RESEARCH REPORT
published: 30 October 2020
doi: 10.3389/fphy.2020.576284

Can We Assess Early DNA Damage at the Molecular Scale by Radiation Track Structure Simulations? A Tetranucleosome Scenario in Geant4-DNA

Lorenzo Petrolli[1,2], *Francesco Tommasino*[1,2], *Emanuele Scifoni*[2]* and *Gianluca Lattanzi*[1,2]*

[1] Department of Physics, University of Trento, Trento, Italy, [2] Trento Institute for Fundamental Physics and Applications, Istituto Nazionale di Fisica Nucleare, Trento, Italy

Advanced track structure codes excel as state-of-the-art tools to low-scale dosimetric models: the rational evolution for a cell-like scenario is detailed within a microsecond of an ion collision, that is the standard timescale for critical DNA modifications. The *in vitro* DNA double-strand breaks (DSB) yield is matched indirectly by nanodosimetric track structure assessments; however, the score to specific DSB *motifs* (i.e., the yield associated to each DSB distance between DNA cuts) is mostly overlooked. In this work, we extend the PDB4DNA example of the Geant4-DNA toolkit, to briefly assess the hit and DSB scores over a nucleosome tetramer framework (Protein Data Bank entry: 1zbb). We describe a critical scenario that biases the statistical significance for an event-by-event track structure assessment at the nanometric scale, based on a Shannon's entropy estimate of the volumetric hit score; finally, we draw a tentative correlation between the mean DSB quality and a proton track, and conclude that short-distanced DSBs by direct effect are favored within a Bragg peak-relevant energy range.

Keywords: tetranucleosome, PDB4DNA, DNA double strand breaks, Geant4-DNA, track structure, chromatin, Monte Carlo simulations, ion beam irradiation

OPEN ACCESS

Edited by:
Marco Durante,
GSI Helmholtz Center for Heavy Ion Research, Germany

Reviewed by:
Ziad Francis,
Saint Joseph University, Lebanon
Fabrizio Cleri,
Université de Lille, France

***Correspondence:**
Emanuele Scifoni
emanuele.scifoni@tifpa.infn.it
Gianluca Lattanzi
gianluca.lattanzi@unitn.it

Specialty section:
This article was submitted to Medical Physics and Imaging, a section of the journal Frontiers in Physics

Received: *25 June 2020*
Accepted: *29 September 2020*
Published: *30 October 2020*

Citation:
Petrolli L, Tommasino F, Scifoni E and Lattanzi G (2020) Can We Assess Early DNA Damage at the Molecular Scale by Radiation Track Structure Simulations? A Tetranucleosome Scenario in Geant4-DNA. Front. Phys. 8:576284. doi: 10.3389/fphy.2020.576284

INTRODUCTION

Mechanistic estimates of cell radiosensitivity benefit from the sharply detailed information on the local density of radiation-induced, DNA-lethal events in cell nuclei, down to a nanometric scale [1, 2].

The description of a rational frame for the overall outcome associated to a specific radiation quality (which leads to the early cell reaction) involves several research fields. Particularly, this is critical to ion beam irradiation, which is associated with a highly complex energy deposition cascade. The event-by-event reconstruction of the cell-like scenario, however, forces a choice in scale and time; indeed, advanced Monte Carlo radiation track structure toolkits depict the microsecond timescale of radiolytic radical diffusion and reactivity [3–6], while molecular dynamics (MD) may achieve a few microseconds of non-reactive, all-atom DNA dynamics [7, 8]. Beside actual technical limitations, however, there is a multitude of choices as to which chromatin scenarios are worth the simulation effort, to what extent, and what to look for.

As nuclear DNA suffers all carriers of molecular toxicity, cells enable substrate-selective recovery mechanisms [9]; each mechanism is associated to one activation factor, that senses a defined DNA aberration class (i.e., base excisions, DNA strands crosslinks, strand breaks, etc.)—still, we lack a rational scenario to describe the subsequent scale of mechanistic evolution for the DNA lesion [10]. All aforementioned DNA modification examples relate, in fact, to a wide variety of biochemical scenarios; it was remarked that the early dynamics for a short double-stranded DNA chain, as it suffers a double-strand break (DSB) event—that is, the close cuts in the covalent DNA backbone over the two strands—is defined markedly by the distance between strand cuts [11]. Furthermore, broken DNA chains are resilient to thermal fluctuations in the nucleosome, where the core histone tails hold the DNA ends, within a few microseconds [12].

Track structure toolkits benefit from coarse criteria that qualify as a DSB any closely associated, local energy deposition event over the DNA backbone (either beyond or within an arbitrary dose threshold) to a certain likelihood [6, 13, 14]. We assume, however, that different DSB motifs are distinctly harmful, and short-distanced DSBs alone would unfold nucleosomal DNA within a few microseconds of an ion collision, while it seems unlikely that a DSB frame distanced by 10 bases would crack by thermal fluctuations. The mechanistic assessment of DSB distances meets a biochemical intuition; in fact, the explicit scenario that unfolds after a DSB event, and the kinetic implications distinct DSBs have on cell activation factors, are not fully known. Furthermore, while track structure mechanistic assessments are meant to focus the overall radiation field effect on a local scale, to indirectly match absolute strand break outcomes, the score to specific DSB distances is mostly overlooked.

We hereby show the results of a brief assessment for a proton track structure within a Bragg peak-related energy range, at a nanometric scale. As a fit environment, we exploited and extended the basic PDB4DNA example classes [15] of the Geant4-DNA toolkit [16–19], to keep track of the hit and DSB distance scores (by early direct effect), over a nanometric water simulation frame. The natural framework to such analysis are the atomic crystal coordinates of a nucleosome tetramer [20] (hereafter *tetranucleosome*, Protein Data Bank entry 1ZBB [21]). Nucleosomes define the elemental units of chromatin in the eukaryotic cell [22, 23], where a 147 bp double-stranded DNA helix wraps a core histone octamer over 1.67 turns [24]; furthermore, nucleosomes are threaded as "beads" into 30-nm-wide chromatin fibers [25], thus the tetrameric framework involves linear, *linker* DNA chains and *wrapped* core DNA, and fairly depicts a chromatin-like scenario.

Initially, our first aim was to track the likelihood of each nucleotide over the nucleosome tetramer framework to be involved by a DSB event. However, our assessment revealed a critical scenario, where the hit collection over the tetranucleosome DNA backbone is statistically biased by a "truncated" track structure artifact; we thus involve a statistical estimator based on Shannon's entropy to assess the level of bias for a collection of hit events, within the nanometric volume. As the hit artifact is trivially fixed by an expansion of the water box, we finally draw a tentative correlation between the mean DSB quality and a proton track, and conclude that short-distanced DSBs by direct effect are favored within a Bragg peak-related energy range.

MATERIALS AND METHODS

The PDB4DNA example of the Geant4-DNA toolkit includes a set of C++ libraries that let users create nanometric simulation volumes, tailored over the atomic coordinates of DNA biomolecular structures (available within the RCSB Protein Data Bank, RRID:SCR_012820 [26]). Protein Data Bank (PDB) files collect exhaustive information of a biomolecule's framework as, for instance, a detailed list of atom coordinates in a readable ASCII format; DNA nucleotides are further classified and labeled by a serial index that codifies their location over the DNA chain (1–694 for the overall nucleosome tetramer framework referred to in this work).

The 1ZBB PDB entry describes the elemental symmetrical unit for the nucleosome tetramer (i.e., a dinucleosome). This was further transformed via a dedicated PDB file editor (VMD, RRID:SCR_001820 [27]) and added with its complementary element, to achieve a full tetrameric framework (694 bp) that was associated to the PDB4DNA example; the edited PDB file records were fixed to comply with the PDBlib reader format criteria (these are detailed in [15]).

We will hereafter refer to the tetranucleosome-tailored water box extracted by PDB4DNA ($13.0 \times 15.2 \times 25.4$ nm) as the *reference volume*; all framework-related information, that is, the DNA atomic coordinates and nucleotides' center of mass, is implicitly extracted and cached within the Geant4 environment. Such default reference volume (a G4Box instance) is made of G4_WATER (a NIST database material) and lies within a void environment of "Galactic," vacuum material.

The basic PDB4DNA analysis tools keep track of the overall energy deposition, single- and DSB scores within the water box. We extended the default classes and involved a further set of ROOT [28] histograms to keep track of[1] (i) the energy deposition events (*hits*) score over the reference volume coordinates; (ii) the hits and DNA strand breaks score over the DNA backbone; (iii) the DNA DSBs *distance* score, as the absolute distance between individual strand breaks over complementary DNA strands, within a 10 bp threshold. A DNA strand break is scored as an overall 8.22-eV dose deposition (lower threshold) to a nucleotide backbone moiety, that is, the ribose-phosphate residue. Several criteria that yield reliable estimates of DNA strand breaks by early direct effect are detailed in the literature [29]; however, we remark that our analysis, in this concern, is merely qualitative.

The overall dataset was collected within the Geant4 (version 10.02-P03) toolkit environment [30–32]; "raw" data were analyzed via ROOT scripts as detailed in the "Results" section. Each of several runs covered 10^7 tracks and diverse volume

[1] Data are collected at runtime, on a track basis, and analyzed offline.

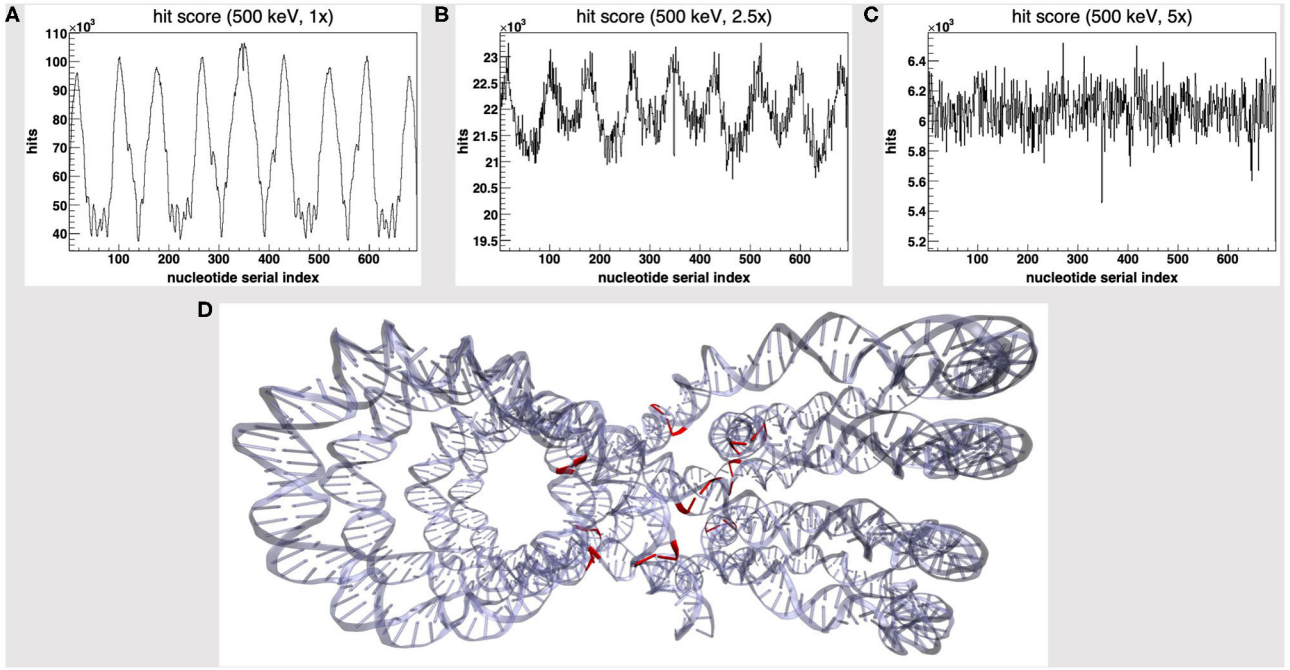

FIGURE 1 | Hit score over the nucleotides serial index, for a set of 500 keV-protons PDB4DNA runs at a **(A)** 1-fold, **(B)** 2.5-fold, and **(C)** 5-fold linear expansion of the reference volume sizes; the spiked behavior shown by the hit counter in **(A)** vanishes off as the water box is expanded. **(D)** The nucleotide cluster at the core of the tetranucleosome framework (in red) involves the hit counter spikes in **(A)**.

choices; however, the default G4EmDNAPhysics list constructor[2] to low-energy electron cross-sections[3] was set. The default PDB4DNA layout involves an isotropic, outer spherical source, that is defined over the vertex coordinates of the reference volume; thus, particles (500 keV to 5 MeV protons, in this work) are randomly shot by the edges toward the water box. The source is bound to the active box, therefore it stretches as the water volume is expanded (*vide infra*). Such scenario let us factor varied, random nucleosome layouts in the overall assessment, that is representative of a chromatin fiber scenario.

RESULTS

Hit Score Analysis Within a Nanometric-Sized Volume: The Hit Artifact

We started by the default PDB4DNA extension layout, where particles (500 keV protons) randomly strike the reference volume by a perfectly isotropic, spherical source. **Figure 1A** shows how the hit counter (the score to each energy deposition event over the DNA backbone) is explicitly non-homogenous, as well as the strand break and DSB counters (not shown here). We expected an explicit dependence for the hit score on local DNA morphology, hence the likelihood for a nucleotide to be involved by a DSB event would vary between the linker and core DNA chains; however, no such correlation seems to arise, as the hit spikes in **Figure 1A** involve nucleotides over *linker* and *wrapped* DNA likewise. Remarkably, such spikes describe a cluster of DNA nucleotides over the "core" of the tetranucleosome framework (highlighted in red in **Figure 1D**), which we show to be an artifact (*vide infra*); indeed, the hit counter to all energy deposition events within the reference volume (**Figure 2A**) shows that the central core is oversampled effectively over the z-axis (as defined in the nucleosome tetramer PDB atom coordinates file). The same holds true for the x-and y-axes (not shown here).

We will hereafter refer to such effect as a *hit artifact*. As particles leak off the water box (to a vacuum environment), their tracks are cut off. Hence, no further collisions/events are detailed by the reference volume outer shell, and we lack track information at the system boundary, where there is a local unbalance. As a consequence, a minor dose fraction is deposited over outlying DNA nucleotides, and the dosimetric information we draw out of the tetranucleosome framework is an effective oversample of the reference volume central core (that is incidentally taken up by linker DNA chains), while we overlook the outlying nucleosome compartments. Such hit artifact remarks how we likely misestimate the early effect of an ion traversal over a small DNA framework, as we lack either boundary conditions or track information at its outer solvation shell.

To avoid the hit artifact, we expanded the water box further off the default size of the reference volume, i.e., we symmetrically applied a multiplicative *linear expansion factor* to each box size (1–5-fold). **Figures 1A–C** show the hit counter spikes effectively

[2]It involves low-energy electromagnetic interactions by electrons (excitation, ionization, vibrational excitation, attachment, elastic scattering) and light ions (excitation, ionization, charge increase/decrease).

[3]To a quantitative assessment, the G4EmDNAPhysics_option4 and G4EmDNAPhysics_option6 list constructors shall be favored—see Incerti et al. [19].

vanish off the DNA backbone, as well as the DNA strand break counter (not shown here), where the water volume is expanded; hence, such trivial symmetrical expansion ensures all nucleotides are sampled evenly over the tetranucleosome framework. So, while we expect the hit artifact to apply to all nanometric systems likewise, a substantially thick "solvation shell" makes sure the track is detailed over the reference volume (and the DNA backbone), which now lies within a wider water box. This raises a further issue, that is, to achieve a convenient tradeoff in track structure details and the least effort, i.e., to establish where the water box is overexpanded.

Shannon's Entropy as a Bias Estimator to Achieve a Convenient Expansion Tradeoff

We will hereafter refer to the *volume hit score* (VHS) as the overall score of energy deposition events within the reference volume frame, while the *DNA hit score* (DHS) is the subset of all VHS events that fall over the DNA backbone; such scorers effectively estimate the overall amount of information we collect (and lose) over the reference volume frame, while the water box is expanded.

The VHS increases with the volume expansion, as shown in **Figure 3A**; this is expected, as a thick solvation shell ensures an increase in the overall information we collect over the reference (and its outer) volume, as shown explicitly in **Figures 2A–C**. However, **Figure 3B** shows that the DHS coincidently decreases, thus we scored fewer hits over the DNA backbone, while the hit counter had increased within the reference volume.

The latter outcome looks counterintuitive; however, nucleotides effectively take up a minor fraction of a nucleosome volume. By the PDB4DNA default scenario (1-fold expansion factor), we overstrike the tetranucleosome "crowded" core,

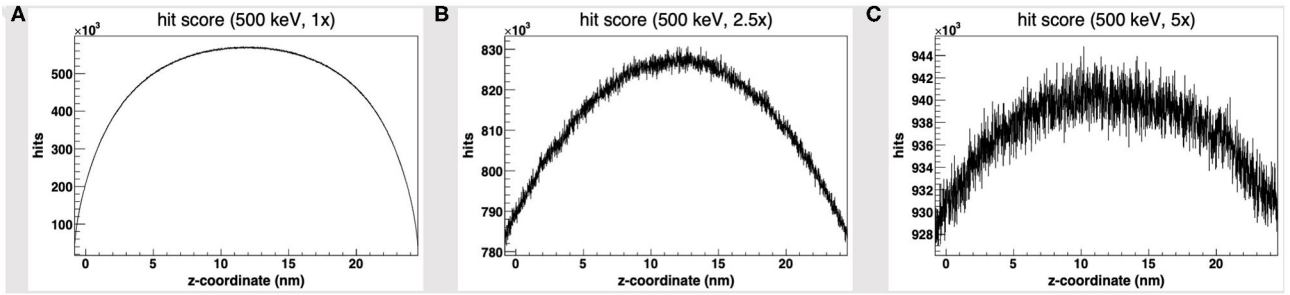

FIGURE 2 | Hit score over the z-axis [as defined in the nucleosome tetramer Protein Data Bank (PDB) atom coordinates file] to all dose deposition events within the reference volume frame, for a set of 500 keV-protons PDB4DNA runs at a **(A)** 1-fold, **(B)** 2.5-fold, and **(C)** 5-fold linear expansion of the reference volume sizes; the reference volume is oversampled at its core, whereas the disparity to the outlying compartments is explicit to smaller systems (hit artifact).

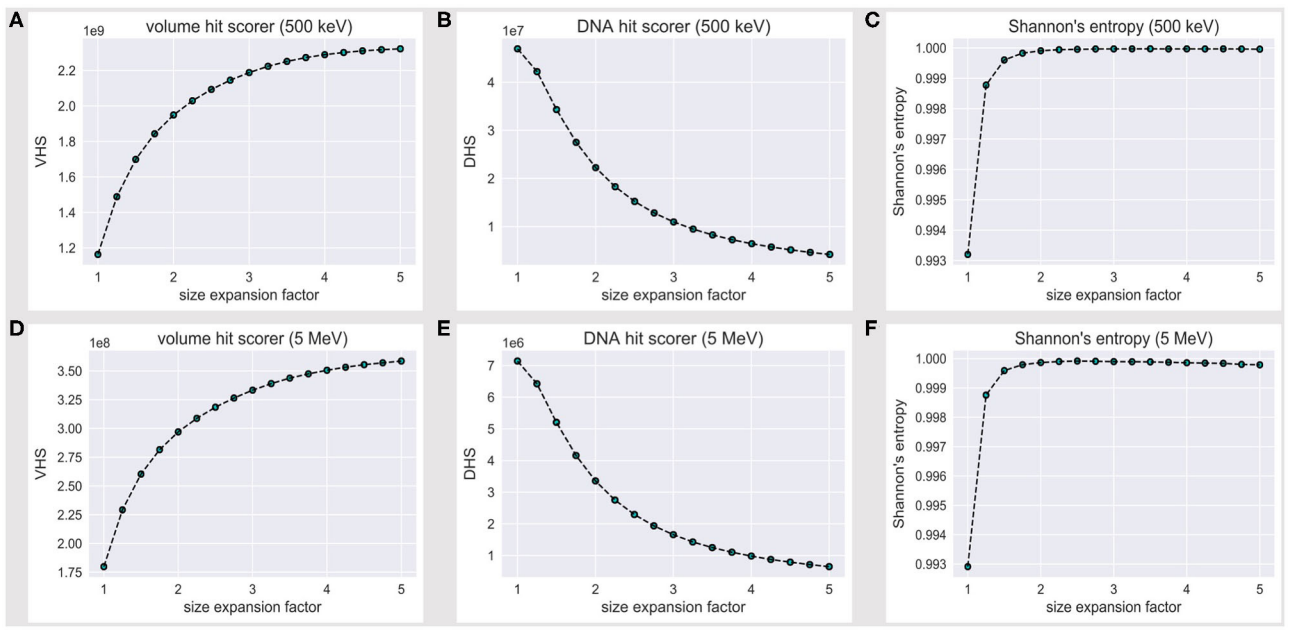

FIGURE 3 | Volume hit score (VHS) at **(A)** 500 keV and **(D)** 5 MeV; DNA hit score (DHS) at **(B)** 500 keV and **(E)** 5 MeV; the VHS increase with the expansion of the water box is associated with a decrease in the DHS. The level of flatness for the DNA hit counter is established via a normalized Shannon's entropy formula (Eq. 1) at **(C)** 500 keV and **(F)** 5 MeV; no significant increase in *S* is achieved beyond a 2.5-fold linear expansion of the reference volume sizes.

where tracks are extremely effective; they turn less effective over the DNA backbone, however, as we shoot over a wider water system (lower DHS). This likely reflects an uneven nucleotide framework, where a major hit fraction strikes an outlying volume associated to a low nucleotide concentration.

To establish and quantify the level of flatness for the DNA hit counter (and estimate a VHS–DHS tradeoff), we referred to a normalized Shannon's entropy formula, defined as:

$$S = -\frac{1}{\log N}\sum_{i=1}^{N} p_i \log p_i \quad (1)$$

where the index i runs over the $N = 694$ nucleotide pairs, and p_i is defined as the hit score over the i-th nucleotide pair, divided by the overall DNA hit score; therefore, S varies between 0 (maximally biased distribution) and 1 (unbiased distribution).

Figure 3C shows that Shannon's entropy increases steeply with the linear expansion factor; however, no significant increase in S is achieved beyond a 2.5-fold expansion of the default reference volume sizes, which we therefore established as a minimum threshold to achieve an unbiased sample of the tetranucleosome DNA backbone.

Such a threshold is, however, strictly bound to the 500 keV scenario. We thus extended the assessment to a 5-MeV particle case; **Figures 3D,E** show the volume and DNA hit score to behave exactly alike at 500 keV and 5 MeV, within an order of magnitude decrease for all values in the latter case, as expected by an effective difference in LET, i.e., with fewer energy deposition events overall. Remarkably, the 500-keV steep increase in Shannon's entropy (**Figure 3C**) is matched at 5 MeV (**Figure 3F**)—likewise, S is maximum at a 2.5-fold linear expansion factor of the default reference volume sizes. We therefore established a 2.5 expansion factor to be a minimum threshold to achieve an unbiased and statistically significant sample of the tetranucleosome framework, within the 500 keV−5 MeV energy range.

The Distance Mean Score

In view of the latter outcome, we extended our assessment of the 500-keV to 5-MeV energy range scenario at fixed 2.5-fold volume expansion and involved a further estimator we will hereafter refer to as double strand break distance mean score (DMS).

It is widely shared that the definition of the DNA double strand break is based over a threshold distance criterion between individual strand breaks over complementary DNA strands [33]. Such criterion is rational to a microdosimetry level of theory; each DSB *motif* (that is associated to a strand breaks distance), however, implies a local unique chemical aberration and mechanical behavior, where the (virtual) timescales for a broken DNA framework to crack by thermal fluctuations vary in each DSB scenario [11]. We thus added a ROOT histogram that kept track of each DSB distance.

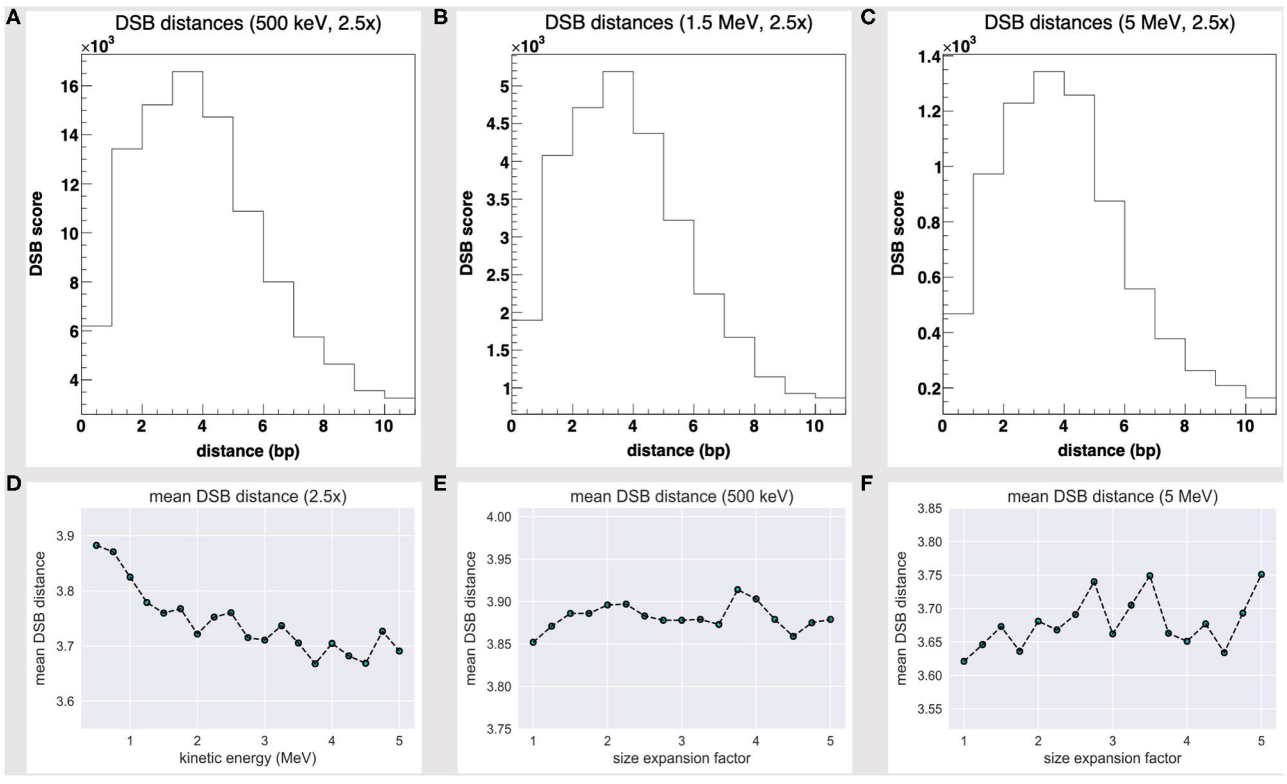

FIGURE 4 | DSB distance scores at fixed 2.5-fold linear size expansion, at **(A)** 500 keV, **(B)** 1.5 MeV, and **(C)** 5 MeV; all share a Poisson fit and are biased towards short-distanced DSBs. The DSB distance mean score at a fixed 2.5-fold size expansion **(D)** shows a slight decrease with the particle energy and fluctuates as the water box is expanded at **(E)** 500 keV and **(F)** 5 MeV.

The DSB distance scores at 500 keV, 1.5 MeV, and 5 MeV seemingly share a Poisson fit, as shown by **Figures 4A–C**, and are biased towards short-distanced DSBs; **Figure 4D** further shows how the DSB DMS decreases slightly with the particle energy, within the 500 keV to 5 MeV range. While we lack a yet significant dataset (that extends over a wider energy range), we would speculate the existence of an effective correlation between a particle track structure and a "mean DSB event" quality, over a unique DNA framework. Rather remarkably, short-distanced DSB events by direct effect (one- to five-nucleotide distance) would thus look favored by a proton source within a Bragg peak-related energy range.

We further realized that the DSB DMS value slightly fluctuates as the volume is expanded—**Figures 4E,F** show the DMS within a 1- to 5-fold linear size expansion, at 0.5 and 5 MeV. As we overexpand the water box sizes beyond a 2.5-fold factor (that is, the threshold where we achieve a substantially thick solvation shell and moderate the DHS loss), we shall collect no further track structure information and collaterally oversample the water volume far off the tetranucleosome framework; thus, we expect the DSB DMS to converge eventually.

DISCUSSION

We detailed a brief assessment of the early, direct DNA lesions associated to the energy deposition track by a proton beam isotropic source over a Bragg peak-related energy range. We extended the default PDB4DNA (a Geant4-DNA example) C++ classes and involved a set of ROOT histograms to keep track of the hit and DNA strand break scores over a nanometric-sized water box, tailored over the atomic coordinates of a nucleosome tetramer (Protein Data Bank entry: 1ZBB).

By the default PDB4DNA extension layout, we achieved a non-homogeneous, spiked hit score over the nucleosome tetramer DNA backbone, which describes a nucleotides cluster over the reference volume central core and where the outlying nucleosome compartments are undersampled; this leads to a local unbalance in the hit counts. We thus symmetrically expanded each of the reference volume box sizes up to 5-fold and allowed a thick solvation shell about the nucleosome tetramer, where an ion track is not broken off; we eventually established (via a normalized Shannon's entropy formula) that a 2.5 linear size expansion threshold achieves an unbiased sample of the nucleosome tetramer DNA backbone, within a 500 keV to 5 MeV energy range.

Clinical treatments (10^8-10^9 ions/cm^2 fluence) strike cell nuclei by a few hundred projectiles; *in silico* track structure assessments of a nucleosome (that is a frame size smaller by a factor 10^8 than a cell nucleus) shall thus infer mean dosimetric information at the nanometric level, which we achieved by an exhaustive and unbiased collection of events over the DNA backbone. A bias estimation by a Shannon's entropy algorithm is, however, strictly framework dependent: in fact, we shall expect it to be not as effective where DNA is highly symmetrical over the volume.

In conclusion, we remarked that a DSB coarse nanodosimetric description based over a distance threshold (i.e., that is inclusive of all double strand break *motifs*, within an arbitrary distance) is weak by molecular dynamics (MD) criteria, where we are not allowed chemical ambivalence. To such aim, we noticed that the DSB distance scores share a Poisson fit and are biased towards short-distanced DSBs (one- to five-nucleotide distance), within a 500 keV to 5 MeV proton energy range. As a further biophysical estimator, the DSB DMS slightly fluctuates as the volume is expanded and decreases with the particle energy. While we lack a yet significant dataset and a careful assessment of DSB criteria, we speculated a correlation between a particle quality and energy and a "mean break event" assumption (by direct effect), whereby particles are associated with a DSB distance likelihood based over a track structure description. We acknowledge, however, that a further, updated analysis, where indirect effects are taken into account will be needed.

As done initially in Landuzzi et al. [11] and Cleri et al. [12], MD shall be exploited to further assess the early evolution of chromatin-like DNA frameworks, despite within limited timescales, as a clear scenario of early DNA lesions is collected. To create a cross framework, where to meet a nanodosimetric and biochemical intuition, further structural feedback shall be collected, whereas, to date, we lack atomistic datasets to irradiated, chromatin-like frameworks. An isolated attempt that unifies DNA lesions by ion irradiation and classic MD was carried out in the context of a multiscale approach [34], although explicitly focused on the channels of shockwave induction by local heat spikes in high-LET regimes. As exhaustive datasets on the local features of clustered DNA lesions by different radiation sources will become accessible, multiscale approaches shall become straightforward; however, such issues are yet a matter for further debate.

DATA AVAILABILITY STATEMENT

The raw data supporting the conclusions of this article will be made available by the authors, without undue reservation.

AUTHOR CONTRIBUTIONS

LP carried out the numerical simulations and analysis and wrote the draft. All authors conceived the current ideas, discussed the assessment, reviewed, and contributed to the draft.

FUNDING

This work was partially supported by the INFN CSN5 Call MoVe IT.

ACKNOWLEDGMENTS

The authors wish to thank Drs. Yann Perrot, Emmanuel Delage, and Sebastien Incerti for useful intellectual discussions.

REFERENCES

1. Friedrich T, Scholz U, Elsässer T, Durante M, Scholz M. Calculation of the biological effects of ion beams based on the microscopic spatial damage distribution pattern. *Int J Radiat Biol*. (2012) **88**:103–7. doi: 10.3109/09553002.2011.611213
2. Hawkins RB. A microdosimetric-kinetic model for the effect of non-poisson distribution of lethal lesions on the variation of RBE with LET. *Radiat Res*. (2003) **160**:6169. doi: 10.1667/rr3010
3. Karamitros M, Luan S, Bernal MA, Allison J, Baldacchino G, Davidkova M, et al. Diffusion-controlled reactions modeling in Geant4-DNA. *J Comput Phys*. (2014) **274**:841–82. doi: 10.1016/j.jcp.2014.06.011
4. Boscolo D, Krämer M, Durante M, Fuss MC, Scifoni E. TRAX-CHEM: A pre-chemical and chemical stage extension of the particle track structure code TRAX in water targets. *Chem Phys Lett*. (2018) **698**:11–8. doi: 10.1016/j.cplett.2018.02.051
5. Ramos-Méndez J, Perl J, Schuemann J, McNamara A, Paganetti H, Faddegon B. Monte Carlo simulation of chemistry following radiolysis with TOPAS-nBio. *Phys Med Biol*. (2018) **63**:105014. doi: 10.1088/1361-6560/aac04c
6. Friedland W, Dingfelder M, Kundrát P, Jacob P. Track structures, DNA targets and radiation effects in the biophysical Monte Carlo simulation code PARTRAC. *Mutat Res*. (2011) **711**:28–40. doi: 10.1016/j.mrfmmm.2011.01.003
7. Dans PD, Walther J, Gómez H, Orozco M. Multiscale simulation of DNA. *Curr Opin Struct Biol*. (2016) **37**:29–45. doi: 10.1016/j.sbi.2015.11.011
8. Shaytan AK, Armeev GA, Goncearenco A, Zhurkin VB, Landsman D, Panchenko AR. Coupling between histone conformations and DNA geometry in nucleosomes on a microsecond timescale: atomistic insights into nucleosome functions. *J Mol Biol*. (2016) **428**:221–37. doi: 10.1016/j.jmb.2015.12.004
9. Jackson SP, Bartek J. The DNA-damage response in human biology and disease. *Nature*. (2009) **461**:1071–8. doi: 10.1038/nature08467
10. McMahon SJ, Prise KM. Mechanistic modelling of radiation responses. *Cancers*. (2019) **11**:e205. doi: 10.3390/cancers11020205
11. Landuzzi F, Palla PL, Cleri F. Stability of radiation-damaged DNA after multiple strand breaks. *Phys Chem Chem Phys*. (2017) **19**:14641–51. doi: 10.1039/c7cp02266b
12. Cleri F, Landuzzi F, Blossey R. Mechanical evolution of DNA double-strand breaks in the nucleosome. *PLoS Comput Biol*. (2018) **14**:e1006224. doi: 10.1371/journal.pcbi.1006224
13. Nikjoo H, O'Neill P, Goodhead DT, Terrissol M. Computational modelling of low-energy electron-induced DNA damage by early physical and chemical events. *Int J Radiat Biol*. (1997) **71**:467–83. doi: 10.1080/095530097143798
14. Lampe N, Karamitros M, Breton V, Brown JMC, Kyriakou I, Sakata D, et al. Mechanistic DNA damage simulations in Geant4-DNA part 1: a parameter study in a simplified geometry. *Phys Medi*. (2018) **48**:135–45. doi: 10.1016/j.ejmp.2018.02.011
15. Delage E, Pham QT, Karamitros M, Payno H, Stepan V, Incerti S, et al. PDB4DNA: implementation of DNA geometry from the protein data bank (PDB) description for Geant4-DNA Monte-Carlo simulations. *Comput Phys Commun*. (2015) **192**:282–8. doi: 10.1016/j.cpc.2015.02.026
16. Incerti S, Baldacchino G, Bernal M, Capra R, Champion C, Francis Z, et al. The Geant4-DNA project. *Int J Model Simul Sci Comput*. (2010) **1**:157–78. doi: 10.1142/S1793962310000122
17. Incerti S, Ivanchenko A, Karamitros M, Mantero A, Moretto P, Tran HN, et al. Comparison of GEANT4 very low energy cross section models with experimental data in water. *Med Phys*. (2010) **37**:4692–708. doi: 10.1118/1.3476457
18. Bernal MA, Bordage MC, Brown JMC, Davídková M, Delage E, El Bitar Z, et al. Track structure modeling in liquid water: a review of the Geant4-DNA very low energy extension of the Geant4 Monte Carlo simulation toolkit. *Phys Med*. (2015) **31**:861–74. doi: 10.1016/j.ejmp.2015.10.087
19. Incerti S, Kyriakou I, Bernal MA, Bordage MC, Francis Z, Guatelli S, et al. Geant4-DNA Example applications for track structure simulations in liquid water: a report from the Geant4-DNA project. *Med Phys*. (2018) **45**:e722–39. doi: 10.1002/mp.13048
20. Schalch T, Duda S, Sargent DF, Richmond TJ. X-ray structure of a tetranucleosome and its implications for the chromatin fibre. *Nature*. (2005) **436**:138–41. doi: 10.1038/nature03686
21. Schalch T, Duda S, Sargent DF, Richmond TJ. Structure of the 4_601_167 Tetranucleosome, RCSB Protein Data Bank ID "1ZBB" (2005). doi: 10.2210/pdb1zbb/pdb
22. Olins AL, Olins DE. Spheroid chromatin units (ν bodies). *Science*. (1974) **183**:330–2. doi: 10.1126/science.183.4122.330
23. Kornberg RD, Lorch Y. Twenty-five years of the nucleosome, fundamental particle of the eukaryote chromosome. *Cell*. (1999) **98**:285–94. doi: 10.1016/s0092-8674(00)81958-3
24. Davey CA, Sargent DF, Luger K, Maeder AW, Richmond TJ. Solvent mediated interactions in the structure of the nucleosome core particle at 1.9 Å resolution. *J Mol Biol*. (2002) **319**:1097–113. doi: 10.1016/S0022-2836(02)00386-8
25. Boulé JB, Mozziconacci J, Lavelle C. The polymorphisms of the chromatin fiber. *J Physi Condensed Matter*. (2014) **27**:033101. doi: 10.1088/0953-8984/27/3/033101
26. Berman HM, Westbrook J, Feng Z, Gilliland G, Bhat TN, Weissig H, et al. The protein data bank. *Nucleic Acids Res*. (2000) **28**:235–42. doi: 10.1093/nar/28.1.235
27. Humphrey W, Dalke A, Schulten K. VMD: visual molecular dynamics. *J Mol Graphics*. (1996) **14**:33–8. doi: 10.1016/0263-7855(96)00018-5
28. Brun R, Rademakers F. ROOT - an object oriented data analysis framework. *Nucl Instrum Methods Phys Res A*. (1997) **389**:81–6. doi: 10.1016/S0168-9002(97)00048-X
29. Schuemann J, McNamara AL, Warmenhoven JW, Henthorn NT, Kirkby KJ, Merchant MJ, et al. A new standard DNA damage (SDD) data format. *Radiat Res*. (2019) **191**:76–92. doi: 10.1667/RR15209.1
30. Agostinelli S, Allison J, Amako K, Apostolakis J, Araujo H, Arce Dubois P, et al. Geant4 - a simulation toolkit. *Nucl Instrum Methods Phys Res A*. (2003) **506**:250–303. doi: 10.1016/S0168-9002(03)01368-8
31. Allison J, Amako K, Apostolakis J, Araujo H, Arce Dubois P, Asai M, et al. Geant4 developments and applications. *IEEE Trans Nucl Sci*. (2006) **53**:270–8. doi: 10.1109/TNS.2006.869826
32. Allison J, Amako K, Apostolakis J, Arce Dubois P, Asai M, Aso T, et al. Recent developments in Geant4. *Nucl Instrum Methods Phys Res A*. (2016) **835**:186–225. doi: 10.1016/j.nima.2016.06.125
33. Elsässer T, Scholz M. Cluster effects within the local effect model. *Radiat Res*. (2007) **167**:319–29. doi: 10.1667/RR0467.1
34. de Vera P, Surdutovich E, Mason NJ, Currell FJ, Solov'yov AV. Simulation of the ion-induced shock waves effects on the transport of chemically reactive species in ion tracks. *Eur Phys J D*. (2018) **72**:147. doi: 10.1140/epjd/e2018-90167-x

Conflict of Interest: The authors declare that the research was conducted in the absence of any commercial or financial relationships that could be construed as a potential conflict of interest.

frontiers in Physics

ORIGINAL RESEARCH
published: 30 October 2020
doi: 10.3389/fphy.2020.567340

Calorimeter for Real-Time Dosimetry of Pulsed Ultra-High Dose Rate Electron Beams

Alexandra Bourgouin[1,2,3]*, *Andreas Schüller*[3], *Thomas Hackel*[3], *Rafael Kranzer*[4,5], *Daniela Poppinga*[5], *Ralf-Peter Kapsch*[3] and *Malcolm McEwen*[1]

[1] Ionizing Radiation Standards, National Research Council of Canada, Ottawa, ON, Canada, [2] Department of Physics, Carleton University, Ottawa, ON, Canada, [3] Physikalisch-Technische Bundesanstalt (PTB), Braunschweig, Germany, [4] Medical Campus Pius Hospital, University Clinic for Medical Radiation Physics, Carl von Ossietzky University Oldenburg, Oldenburg, Germany, [5] Physikalisch-Technische Werkstätten-Freibug, Freiburg, Germany

An aluminum calorimeter was investigated as a possible real-time dosimeter for electron beams with an ultra-high dose per pulse (DPP), as used in FLASH radiation therapy (a few Gy/pulse). Ionization chambers, the most widely used active dosimeter type in conventional external beam radiation therapy, suffer from large ion recombination losses at these conditions. Passive dosimeters, such as alanine, are independent of dose rate but do not provide real-time read-out. In this work it is shown that the response of alanine is independent of the DPP in the investigated ultra-high DPP range (up to 2.3 Gy/pulse). Alanine dose measurements were then used to determine the ion recombination correction for an Advanced Markus plane-parallel ionization chamber at ultra-high DPP. Ion collection losses larger than 50% were observed. Therefore, ionization chambers are not considered suitable for accurate dosimetry in FLASH radiation therapy. As an alternative, in a second (independent) experiment an aluminum open-to-atmosphere calorimeter, operated in the quasi-adiabatic mode was investigated at ultra-high DPP electron radiation. The beam pulse charge, and thus the DPP, was varied to evaluate the linearity of the calorimeter response in the DPP range between 0.3 and 1.8 Gy/pulse. On average, the standard deviation of the calorimeter response was 0.1%. The response was proportional to the DPP in the investigated range. The average deviation of the linear fit of the calorimeter dose as a function of the beam pulse charge was <0.5%. This preliminary investigation suggests that a simplified calorimeter design is suitable as a dosimeter with real-time read-out for clinical FLASH radiation therapy beams.

Keywords: FLASH, dosimetry, ultra-high dose per pulse, calorimeter, alanine, ionization chamber, ion recombination

OPEN ACCESS

Edited by:
Yolanda Prezado, INSERM U1021 Signalisation Normale et Pathologique de L'embryon Aux Thérapies Innovantes des Cancers, France

Reviewed by:
Hugo Palmans, National Physical Laboratory, United Kingdom; MedAustron Ion Therapy Center, Austria
Kristoffer Petersson, University of Oxford, United Kingdom

***Correspondence:**
Alexandra Bourgouin
alexandra.bourgouin@ptb.de

Specialty section:
This article was submitted to Medical Physics and Imaging, a section of the journal Frontiers in Physics

Received: *29 May 2020*
Accepted: *17 August 2020*
Published: *30 October 2020*

Citation:
Bourgouin A, Schüller A, Hackel T, Kranzer R, Poppinga D, Kapsch R-P and McEwen M (2020) Calorimeter for Real-Time Dosimetry of Pulsed Ultra-High Dose Rate Electron Beams. Front. Phys. 8:567340. doi: 10.3389/fphy.2020.567340

INTRODUCTION

FLASH radiation therapy is a promising new cancer therapy modality in the early stages of development. The total prescribed radiation dose is delivered with an ultra-high dose rate in less than a second instead of one or more delivery fractions with a few minutes duration at conventional dose rates. A number of studies support the hypothesis that this novel treatment modality could significantly reduce the adverse side effects of radiation therapy on the healthy tissue exposed to

radiation for equal dose delivery [1–6], this is the so-called FLASH effect. For details see a review by Wilson et al. [6] and the references therein. As the adverse side effects are reduced, the prescribed dose could be increased resulting in improved tumor control [5].

Most of the pre-clinical studies investigating the FLASH effect have been done so far with electron radiation fields generated by dedicated linear accelerators [7, 8] or modified clinical linear accelerators [9, 10] using radiation pulses of an ultra-high dose per pulse (DPP). The FLASH effect has also been observed with photon radiation from a synchrotron light source [2]. A compact apparatus for implementing FLASH photon radiation is currently under development [11]. Most recently, a clinical apparatus able to deliver FLASH proton radiation therapy was used to carry out the first clear proton FLASH radiation therapy which mediated normal tissue radioprotection [12]. In 2019, the successful treatment of the first human patient with FLASH radiation therapy was reported [4]. The patient received radiation with electrons in one fraction of 90 ms with 10 pulses of 1.5 Gy/pulse, corresponding to a mean dose rate of ∼167 Gy/s.

To date, FLASH radiation therapy research has focused on finding pragmatic solutions that allow for the use of ultra-high dose rate beams in the research setting, but there has been limited focus on reference dosimetry under such conditions. There are limited data on the functionality of existing standard dosimeters when they are used to measure beams for FLASH irradiation [7, 8, 13, 14]. It is important to establish if these dosimeters are appropriate when used for ultra-high dose rate application [3]. Without a clear understanding of the fundamental dosimetry issues, there is potential for significant dosimetric errors, as was seen with the development of small-field photon beam dosimetry [15]. If an error is made in dosimetry, then the difference in tissue response between conventional and ultra-high dose rate irradiation at a seemingly equal total dose may be due to this error and not due to the FLASH effect. It is a crucial point in particular because the intra-pulse dose rate, the mean dose rate, and the irradiation time of conventional and FLASH radiation therapy differs by orders of magnitude (for electrons, e.g., 10^2 vs. 10^6 Gy/s, 0.05 Gy/s vs. $>$ 40 Gy/s, or 4 min vs. $<$ 100 ms, respectively).

Researchers have used passive, integrating dosimeters such as radiochromic films, thermoluminescent dosimeters (TLDs), and alanine dosimeters for the dosimetry of FLASH radiation therapy beams [16–18]. Passive dosimeters, however, have the disadvantage that they cannot be read out in real time - determining an accurate dose with these methods can take hours or even days. Even with a recently developed method optimized for fast measurements, it still takes ∼8 min to read out a dose from an alanine sample [18]. As this is a new delivery regime, there has been little testing of these passive detectors at ultra-high DPP values, and one therefore cannot rule out non-linear behavior. Alanine is known to be independent of dose rate [19–21], which has been used for radiation processing dosimetry at mean dose rates of several kGy/min for decades [20]. However, this dosimeter requires specialized read-out using EPR spectrometry, and therefore tends to be limited to a small number of laboratories worldwide.

Ionization chambers are the gold standard for reference dosimetry in external beam radiation therapy: they are precise, stable, well-understood, relatively easy to use, and they provide a real-time read-out. The disadvantage of using ionization chambers is that the obtained reading, which is measured in terms of the charge collected in the sensitive volume of the chamber, requires the use of corrections and a conversion factor to determine the equivalent absorbed dose to water D_w, the required quantity in radiation therapy. One of the correction factors specifically of concern for dosimetry for FLASH radiation therapy is ion recombination which is, in the case of a pulsed beam, dependent on the amount of charge created in the sensitive volume per pulse. Thus, the ion recombination correction factor k_S increases with increasing DPP [22]. In the DPP range for standard clinical linear accelerators (0.1–3 mGy per pulse), the ion recombination correction is in the order of a few tenths of a percent (up to a maximum of around 3%) [22].

The clinical use of high DPP electron beams generated by mobile linear accelerators dedicated for intraoperative radiation therapy (IORT) has increased, which has resulted in extensive work to investigate the ion recombination effects of ionization chambers in high DPP beams with 20 - 120 mGy/pulse [23–27]. This is ∼10–40 times larger than for conventional radiation therapy accelerators. Ion recombination correction factors k_S for these beams can be in the range of 1.15–2.34 [23], i.e., ion collection losses of 13–57%. This is far beyond the recommendations of international dosimetry protocols [28–30] for the accurate application of ionization chambers for reference dosimetry.

Furthermore, at high DPP, the effect of free electrons produced in the chamber's cavity, which can be directly collected by the anode without forming negative ions, contribute to the ion collection efficiency [24, 31]. Laitano et al. [24] pointed out that the determination of the correction factor for ion recombination based on the Jaffe plots, which is traditionally recommended in the dosimetry protocols, leads to considerably inaccurate values (up to 40%). This is even true of approaches taking into account that free electrons are associated with large uncertainty (2% instead of 0.2%).

However, the ultra-high DPP range used for FLASH radiotherapy with hundreds of mGy/pulse up to some Gy/pulse [3, 4, 13] is even one or two orders of magnitude larger than the high DPP range of IORT devices. Ionization chambers can show ion collection losses of 50–90% in ultra-high DPP beams [13, 32]. The measurement uncertainty would therefore be dominated by the uncertainty of the k_S factor and thus an accurate determination of the dose with slight uncertainty comparable to those reached at conventional radiation therapy is not possible in this way. Therefore, ionization chambers used for dosimetry in conventional radiation therapy are not considered suitable for accurate dosimetry in FLASH radiotherapy.

One detector type with real-time read-out that has not been considered for dosimetry for clinical FLASH radiation therapy beams so far, primarily because it is not found in clinical research settings, is the absorbed dose calorimeter. Only very recently McManus et al. [32] used a graphite calorimeter as a dose reference for the determination of the collection efficiency of a

Roos ionization chamber in ultra-high pulse dose rate electron beams up to 5 Gy/pulse. A calorimeter has the potential to realize absorbed dose D in terms of its definition (the quotient of the energy absorbed, E, and the volume of matter with mass, m, in which it is absorbed). The calorimetry dose equation is given by

$$D = \Delta T \cdot c \cdot k_{\mathrm{ht}} \cdot k_{\mathrm{p}} \cdot k_{\mathrm{dd}} \cdot k_{\mathrm{HD}}, \quad (1)$$

where, ΔT is the radiation-induced temperature rise, c is the specific heat capacity of the absorbing material, k_{ht} is the heat loss correction factor, and k_{p} and k_{dd} are correction factors for the radiation field perturbation from the heterogeneous composition of the calorimeter and beam non-uniformity, respectively (volume averaging of the absorber component of the calorimeter). k_{HD} is a correction factor that takes account of any radiochemical interactions, which would break the proportionality between the energy absorbed and the temperature rise. As shown in Equation 1, there is no parameter directly dependent on the dose rate or DPP and, therefore, a calorimeter should respond linearly with dose over a wide range of DPP values, including the range used for FLASH radiation therapy. The heat loss correction factor can introduce a dependence on the DPP value, but for this to be the case, the time constant for heat loss must be of the order of the irradiation time. However, calorimeter thermal time constants are in the range 30–600 s, at least an order of magnitude greater than the anticipated irradiation time for FLASH. A calorimeter is inherently a real-time dosimeter, otherwise it is not possible to determine the radiation-induced temperature rise. The temperature rise can be determined immediately and automatically; it does not require either a calibration or any post-irradiation processing.

In this work, the performance of an aluminum calorimeter was investigated in high-energy, ultra-high DPP electron beams. For comparison, a plane-parallel ionization chamber and an alanine dosimetry system were also investigated in another independent experiment.

MATERIALS AND METHODS

Accelerator

The experiments were carried out at the Metrological Electron Accelerator Facility (MELAF) [33] of the German National Metrology Institute, PTB. The facility provides a research linear accelerator (commissioned in 2012) for research in dosimetry for radiation therapy which features increased intensity for ultra-high DPP and considerably larger energy ranges (0.5–50 MeV) than conventional medical accelerators (typically 4 to 22 MeV). The accelerator provides a pulsed beam with about 2.5 μs pulse width. All irradiations reported in this work were carried out with 5 Hz pulse repetition frequency.

The research electron accelerator works on the same principle as medical accelerators but is equipped with beam line instrumentations for a precise characterization of the beam parameters. For the accurate determination of the energy, a magnetic spectrometer is used. As a non-destructive beam current monitor an Integrating Current Transformer (ICT) from Bergoz (in-flange version, windings ratio 50:1) is integrated in the beamline. The beam pulse charge can be typically varied in a range from 1 to 150 nC. The precision for the measurement of the charge of a single beam pulse is +/- 0.015 nC ($k = 1$) [34], i.e., for pulses > 10 nC that were mainly used in this work, the contribution to the uncertainty of the measured pulse charge is < 0.15%. The profile of a typical beam in the beam line has a Gaussian shape with a FWHM of about 4 mm [34]. At the end of the beam line the electrons pass through a vacuum window consisting of a 0.1 mm thick Cu foil which scatters the beam. The diameter of this beam exit window is much larger (diameter > 3 cm) than the width of the beam, thus all electrons detected by the ICT contribute to the radiation field.

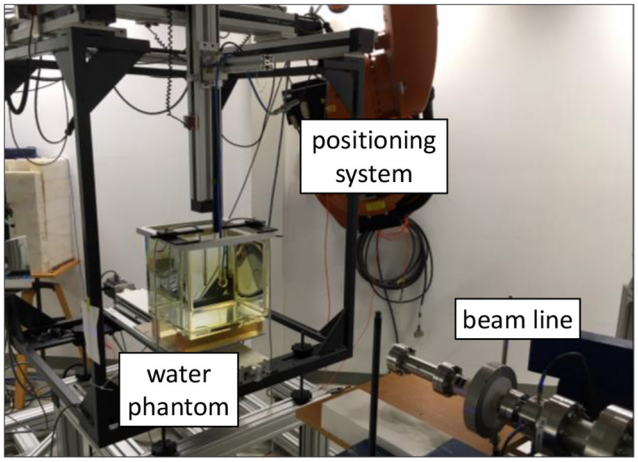

FIGURE 1 | Water phantom in front of the beamline of PTB's research linear accelerator. Inside the water phantom is an ionization chamber mounted on a 3D positioning system.

Ionization Chamber

The ion collection efficiency of a plane-parallel Advanced Markus ionization chamber (PTW, type 34045, s/n: 1279) in an ultra-high DPP beam of up to 2.5 Gy/pulse was investigated. The chamber was placed in a 30 × 30 × 30 cm water phantom with 2 cm thick poly-methyl methacrylate (PMMA) walls and a 0.3 cm thick PMMA entrance window, positioned 70 cm in front of the beam exit window (see **Figure 1**). The chamber was mounted on a precise motorized 3D positioning system which allowed for controlled longitudinal movement of the ionization chamber along the central beam axis for depth dose measurements and controlled lateral movement to determine a cross-sectional dose distribution of the radiation field.

A 24 MeV electron beam was used. The chosen energy is not important for the comparison of the dosimeters. However, with higher energies higher DPP values can be achieved. In addition, the depth dose curve has a flatter slope with larger penetration depth, so the measurement position is less critical.

For the read-out of the ionization chamber, an analog electrometer (Keithley 616) was used in the current mode. The reading, M, of the electrometer returned via an output voltage

was recorded by means of a 16-bit analog-to-digital converter and analyzed by in-house-developed software. A calibrated current source (Keithley 6430) was used to calibrate the electrometer with its read-out system. The Advanced Markus chamber was calibrated at PTB's ^{60}Co reference field in terms of absorbed dose to water traceable to the PTB's primary standard water calorimeter [35]. The conversion of the ionization chamber signal to absorbed dose to water followed the German protocol DIN 6800-2 [30]:

$$D_{\mathrm{w}} = N'_{\mathrm{Co60,\,Dw}} \cdot (M - M_0) \cdot k_{\mathrm{E}} \cdot k_{\mathrm{S}} \cdot k_{\mathrm{pol}} \cdot k_{\mathrm{TP}}, \qquad (2)$$

where $N'_{\mathrm{Co60,\,Dw}}$ is the calibration factor of the detector with respect to ^{60}Co radiation, M is the reading of the dosimeter corrected for the reading without irradiation M_0, k_E is the quality correction factor accounting for the difference in the detector's response between ^{60}Co radiation and high-energy electron radiation, and k_S is the correction factor for ion recombination. The factors k_{pol} and k_{TP} take into account the polarity effect and effects associated with the ambient conditions, respectively.

The radiation quality correction factor k_E can be determined with lowest uncertainty at the reference depth z_{ref}. Thus, the chamber was positioned there. The reference depth depends on the radiation quality index R_{50} which was determined according to DIN 6800-2 [30] from the measured depth dose distribution. For the current setup end energy, z_{ref} was found to be 5.5 cm. Air pressure and temperature as well as the polarity effect were measured for k_{TP} and k_{pol}. The response of the chamber without taking into account any ion recombination correction factor $D_{\mathrm{w}}/k_{\mathrm{S}}$ was determined applying Equation 2 without k_{S}. The DPP reference value was determined from the charge per beam pulse measured by means of the ICT, calibrated using alanine dosimeters positioned at the same position (z_{ref}) as the chamber.

Alanine Dosimetry System

Reference dose measurements were performed using cylindrical alanine pellets with a diameter of 5 mm and a height of 3 mm. The alanine pellets were irradiated to an approximate dose of 14 Gy at different charge per beam pulse values. The charge of each beam pulse was recorded by means of the ICT. For the highest used pulse charge (∼120 nC) only 6 pulses were irradiated, for the lowest (∼2 nC) 463 pulses were irradiated.

For each different charge per pulse setting, a stack of eight alanine pellets were irradiated simultaneously in a PMMA tube positioned in the water phantom at z_{ref} instead of the ionization chamber (see **Figure 1**) with the rotational axis of the stack perpendicular to the beam central axis. The dose response of alanine is known to depend on the temperature during irradiation (0.19%/°C) [36]. Thus, enough time (∼10 min) was allowed for the alanine pellets to achieve temperature equilibrium in the water phantom. The temperature T of the water phantom was close to the reference temperature $T_0 = 293.15$ K. It was measured during irradiation using a Pt100 platinum resistance temperature sensor.

Ionizing radiation produces stable free radicals in alanine, which can be detected via electron spin resonance (ESR). The irradiated alanine pellets were read out using a Bruker EMX 1327 electron spin resonance (ESR) spectrometer at PTB. The alanine/ESR dosimetry system was calibrated at the ^{60}Co reference of the PTB. Thus, the alanine dose measurement is traceable to PTB's primary standard water calorimeter [35]. Uncertainties of 0.4–0.6% ($k = 1$) were reached for ^{60}Co radiation in the range of 5–25 Gy [36]. The methodology at PTB's alanine/ESR dosimetry system is standardized and extensively tested. Further details of the methodology can be found elsewhere [36–38]. A correction factor $k_{\mathrm{T}} = 1 - c_{\mathrm{T}} \cdot (T - T_0)$ for the temperature during the irradiation was applied, where the temperature coefficient $c_{\mathrm{T}} = (1.9 \pm 0.2)\ 10^{-3}$ K. The relative uncertainty of k_{T} is 0.04%. A beam quality correction factor $k_{\mathrm{E}}^{\mathrm{Alanine}} = 1.012$ (the equivalent of k_{E} for an ionization chamber) was applied for the used 24 MeV electron beam [38]. This factor does not depend on energy in the range of 6–22 MeV and is thus assumed to be valid for 24 MeV as well [39]. The relative uncertainty of $k_{\mathrm{E}}^{\mathrm{Alanine}}$ is 1%. The absorbed dose to water determined from the alanine measurements was then used to cross-calibrate the ICT in terms of a dose per beam pulse charge in order to have a reference at the investigation of the ionization chambers response.

Calorimeter

The majority of primary standard absorbed dose calorimeters have been optimized for operation at standard therapy dose rates, to measure a dose of around 2–4 Gy delivered over a period of 1–2 min. The radiation-induced temperature for such a delivered dose is of the order of mK and therefore complex calorimeter systems have been developed. The most common absorbing mediums are water and graphite and for either medium, thermal isolation (and hence long thermal time constants) is very desirable to minimize the corrections required for conductive heat loss. For a review of absorbed dose calorimetry see Renaud et al. [40].

FLASH delivery is very different from the irradiation conditions that these calorimetric standards have been designed for, and this means that a more flexible design is required, not tailored to a specific beam output (calorimeters should be applicable to electron, proton, and photon beams with ultra-high dose rates). Also, the ultra-high DPP (and hence high total dose delivered in a short time) means that thermal isolation is not such a constraint and a simpler design can be employed.

Calorimeters have been used for high dose rate measurements for the dosimetry of radiation processing beams [41] but there has been little investigation of few-pulse irradiations to date.

The calorimeter used in this investigation is an open-to-atmosphere aluminum calorimeter, whose design can be traced back to a graphite calorimeter developed at the NPL for industrial processing dose measurement [42]. In contrast to the more common graphite calorimeters used in a number of primary standards laboratories, the specific calorimeter employed here uses aluminum as an absorber material, which was chosen because a number of previous investigations had indicated that the granular nature of bulk graphite leads to inhomogeneities and impurities that can be difficult to quantify. Aluminum, in contrast, is obtainable in a very pure, highly homogenous form.

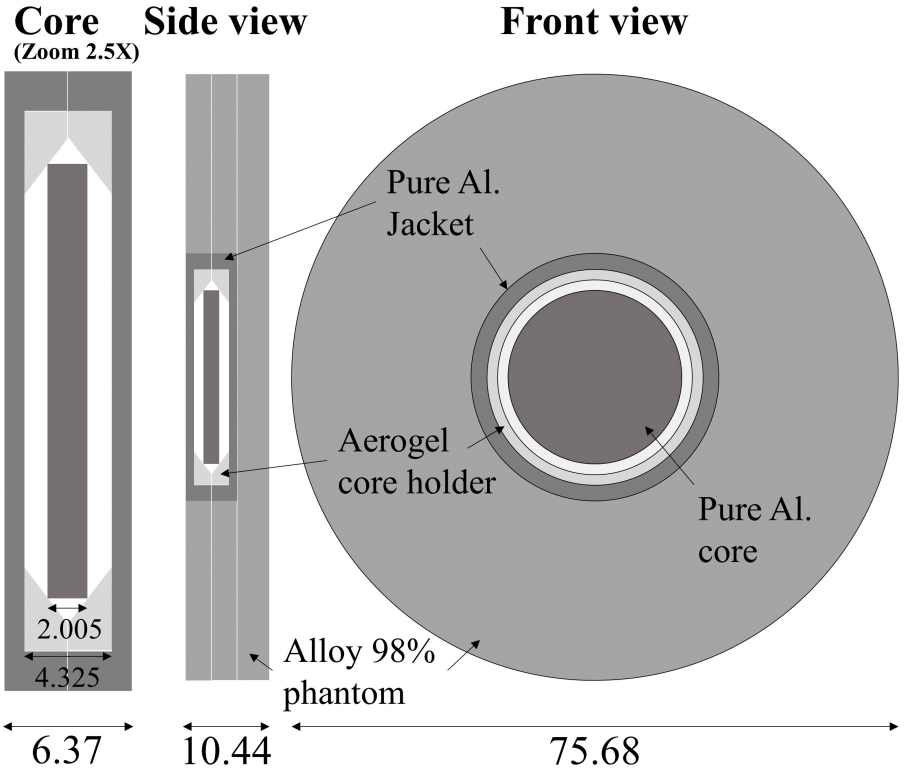

FIGURE 2 | Schematic of calorimeter (without insulating material). The thermistors are not shown.

The calorimeter design is shown in **Figure 2**. The main features of the calorimeter are: a core of 21.7 mm diameter and 2.01 mm thickness of 99.999% aluminum; thermal isolation provided by a 1 mm air gap on all sides; the absorber is kept in position by a space constructed of a silica-based aerogel (Airloy®X103M, Aerogel Technologies, LLC), which is only in contact with the absorber at the edges of the aluminum disc. A pair of thermistors in series, combined with an AC bridge, are used to determine the radiation-induced temperature rise [43], for details see Bourgouin et al. [44] which used the same measurement system with an earlier calorimeter design. The outer parts of the calorimeter are constructed of 6061 aluminum alloy for ease of machining and reduced cost, only the core and the jacket are pure aluminum. The entire aluminum assembly is enclosed in expanded polystyrene foam (density 0.028 g/cm^3) to provide thermal isolation from the environment.

Equation 1 also shows that the absorbed dose determined by a calorimeter is dependent on the medium used to absorb the energy and therefore a correction is required to convert it from the absorbed dose to the calorimeter medium to the equivalent absorbed dose to water value. This correction is independent of DPP and is usually calculated using Monte Carlo techniques (see e.g., [45]). In this initial investigation an approximated conversion factor from aluminum to water was used for presentation purposes, determined by averaging the mass restricted collisional stopping power ratio over the calculated energy spectrum yielding the relation $D_{\mathrm{w}} = 1.23\, D_{\mathrm{Al}}$.

The specific heat capacity c in Equation 1 is independent of the dose rate and is assumed to be constant during the measurement as the temperature rise is of the order of a few mK. Both radiation field perturbation and beam non-uniformity correction factors are calculated here using Monte Carlo radiation transport techniques. These correction factors are dependent on the radiation beam energy and field size/shape. The heat loss correction factor is calculated here using finite element methods (FEM) using an energy map derived from a 2-D or 3-D dose distribution obtained from a Monte Carlo simulation. The heat loss correction factor is dependent on the radiation time [44] but independent of the dose rate. It was assumed that aluminum exhibits no heat defect (i.e., any radiochemical reactions have no significant impact on the radiation-induced temperature rise).

The calorimeter was positioned at a distance of 0.9 m from the beam exit window of the accelerator (**Figure 3**). The pencil electron beam was broadened by a double scattering foil system consisting of the copper foil of the vacuum exit window and a 1 mm thick disk of aluminum positioned 3.5 cm away on the beam central axis. A 10 × 10 cm standard clinical electron applicator from an Elekta Precise linear accelerator was used in order to generate a square radiation field with an approximately parabolic radial profile within the center portion. The radiation field was shaped to be similar to that from a previous experiment with this calorimeter [44], so that the existing simulations for field perturbation and beam non-uniformity correction factors were suitable.

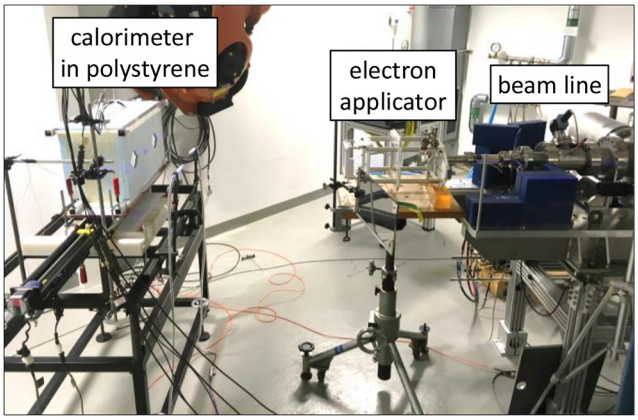

FIGURE 3 | Calorimeter in front of the beamline of PTB's research linear accelerator. The calorimeter is on the left, enclosed in blue polystyrene, the end of the beam line is on the right.

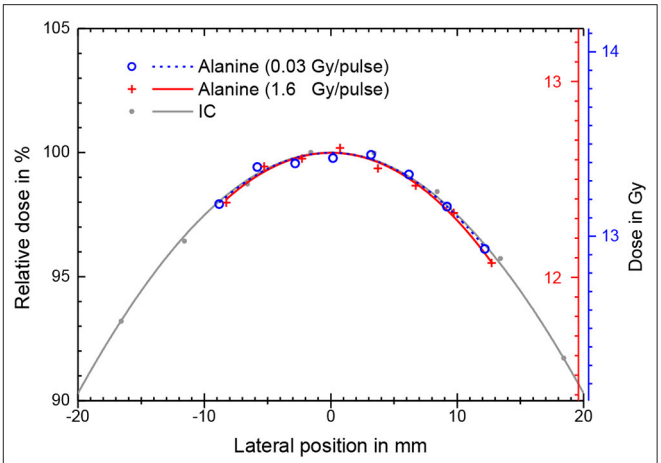

FIGURE 4 | Absolute absorbed dose (right y-axis) as measured by stacks of eight alanine pellets for different beam pulse charges and thus different DPP. The corresponding lines are best fits of a 2nd order polynomial function. Also shown is a relative ionization measurement (only left y-axis) with the ionization chamber at low DPP in the same water depth with a Gaussian fit.

The electron energy used for the investigation of the response of the calorimeter was 50 MeV. The choice of energy is somewhat arbitrary for the investigation where the focus is varying the DPP, but a very high energy provides a flatter depth-dose curve and therefore a more uniform temperature environment for the calorimeter core. For the measurements in the ultra-high DPP range 10 beam pulses were delivered within 2 s to the calorimeter while the charge of each beam pulse was measured simultaneously with the ICT. The pulse charge, and thus the DPP, was varied between 5 and 45 nC per pulse (0.3–1.8 Gy per pulse). The measurement was repeated five times for each pulse charge setting.

RESULTS

Dose Per Beam Pulse Charge From Alanine Measurements

The radiation field from the research accelerator is not flat, as is typical for a clinical linear accelerator, and without any electron dual scattering foil systems [46, 47] for electron beam flattening (as used in the second experiment with the calorimeter) the radiation field shows a Gaussian shape (**Figure 4**). There is good agreement between the relative lateral ionization measurement with the Advanced Markus ionization chamber and the alanine measurements at different DPP. Both detectors average over a comparable range of the dose gradient (alanine 3 mm, ionization chamber 5 mm). For the determination of the absolute dose at the central beam axis (the position of the ionization chamber during the k_S determination) a 2nd order polynomial function was fitted to the alanine datapoints and the maximum at lateral position 0 was taken.

Figure 5 shows the dose per beam pulse (gray squares) determined this way as a function of the charge per beam pulse measured simultaneously by means of the ICT. The linear fit of the alanine data is used as the calibration function for the determination of the actual DPP at the position of the sensitive volume of the Advanced Markus ionization chamber from the measured beam pulse charge.

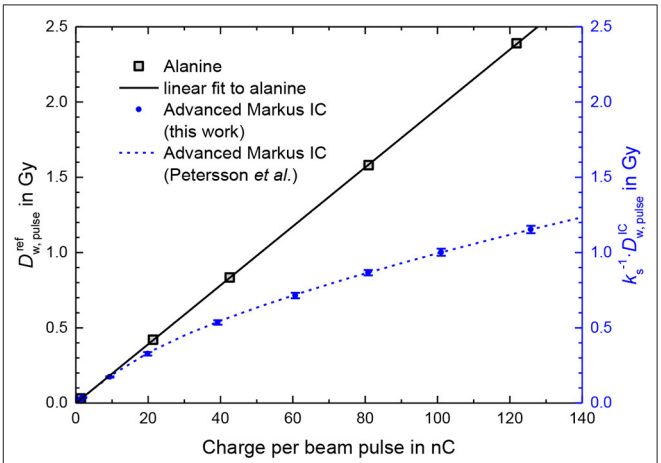

FIGURE 5 | Dose per pulse $D^{ref}_{w,pulse}$ determined by means of PTB's alanine dosimetry system (gray squares) as a function of the measured charge per beam pulse. Also shown are measurements with an Advanced Markus ionization chamber at a 300 V operating voltage without taking into account any ion recombination correction factor k_S at the same position and conditions as the alanine (blue dots). The dashed line represents the fit function to measurements by Petersson et al. [13].

Ion Recombination Correction for the Advanced Markus Chamber

The blue dots in **Figure 5** show the dose per beam pulse measured with the Advanced Markus ionization chamber at a 300 V operating voltage without taking into account any ion recombination correction factor $D^{IC}_{w,pulse}/k_S$ as a function of the charge per beam pulse. The deviation from the dose per pulse

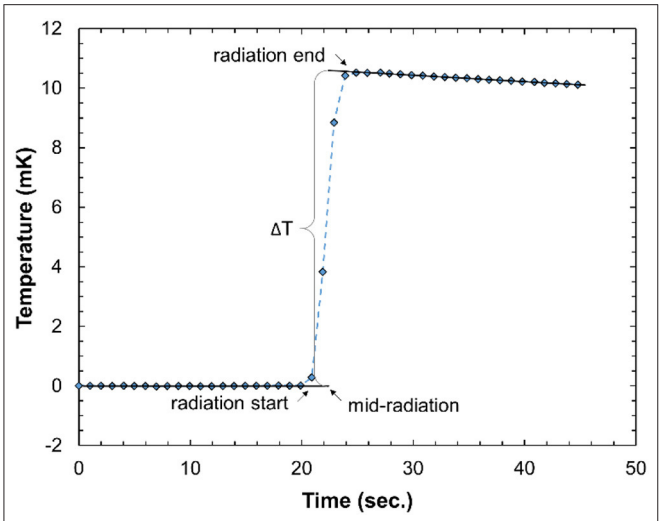

FIGURE 6 | Typical calorimeter temperature-time trace from 10 radiation pulses of about 1 Gy/pulse. The data acquisition rate is 1 Hz.

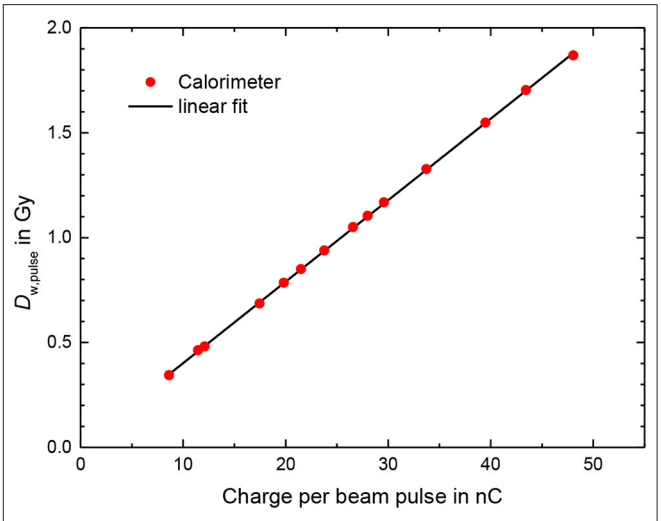

FIGURE 7 | Dose per pulse from calorimeter measurements $D^{calo}_{w,pulse}$ according to Equation 1 using an conversion factor from dose to aluminum in dose to water of 1.23 as a function of the charge per beam pulse measured by the ICT. Line: linear fit.

reference $D^{ref}_{w,pulse}$ measured by means of the ICT calibrated with alanine increases with the increasing charge per pulse/increasing dose per pulse. The blue dashed line represents the fit function given in Ref. [13] by Petersson et al. for experimentally determined k_S values for the Advanced Markus chamber at 300 V from, among others, comparison with radiochromic film measurements. This function is $k_S = (1 + (D^{ref}_{w,pulse}/300)^{2.5})^{0.144}$, where $D^{ref}_{w,pulse}$ is expressed in mGy.

At 1.5 Gy/pulse (as applied for the first treatment of a human with FLASH radiotherapy) the ion recombination correction amounts to 79%. The measurement uncertainty is therefore dominated by the uncertainty of the k_S factor and thus an uncertainty of the dose measurement comparable to those reached at conventional radiation therapy (< 2%), seems not possible with this ionization chamber type.

Calorimeter Measurements

A typical calorimeter temperature-trace recorded in this work is shown in **Figure 6**. The radiation-induced temperature rise, ΔT, is obtained by linearly extrapolating the pre- and post-irradiation traces to the center of the irradiation time as illustrated. The difference in the gradient of the pre- and post-irradiation traces is due to the relatively poor thermal isolation of the calorimeter, but this does not have a large effect on the accuracy of the results since the irradiation time is relative short compared to the heat transfer time constant. The good signal-to-noise ratio indicates that the calorimeter is sensitive enough to also measure a single pulse at ultra-high DPP. For a series of irradiations, the standard deviation of the temperature rise, normalized to the delivered beam charge, was typically 0.1%, comparable with primary standard calorimeters in electron beams (e.g., [48]).

There are variations in the post-irradiation gradient. These are random with respect to the DPP and therefore likely due to external environmental factors. The heat loss is significantly larger than for a water calorimeter, primarily due to the high thermal conductivity of the aluminum and the simple thermal isolation of the calorimeter core. However, the time constant for the heat loss is an order of magnitude larger than the irradiation time and therefore the calorimeter can be considered to be operating in a quasi-adiabatic mode. The heat loss correction, k_{ht}, is therefore small (< 0.5%) and does not impact the overall uncertainty in the calorimeter dose determination.

The results for the calorimeter measurements (**Figure 7**), for measurements carried out on two different days, show that there is good repeatability between the two sets of measurements and that there is a linear relationship between the calorimeter dose and beam pulse.

The deviation of the calorimeter response from the linear fit function shown in **Figure 7** was generally smaller than 0.5% (**Figure 8**). The bars in **Figure 8** for the calorimeter represent only type A standard uncertainty for a sequence of 5 measurements in close succession with the same conditions and are therefore a measure of the short-term repeatability, not the actual uncertainty. The mean charge of the 10 delivered pulses are measured with absolute uncertainty of +/-0.005 nC, thus for the used pulse charges of more than 10 nC the uncertainty contribution is smaller than 0.05%. The uncertainty of the charge measurement is therefore probably not the main reason for the fluctuation of the values.

The deviations of the alanine dose measurements from the ICT calibration function shown in **Figure 5**, used as reference for the experiment with the ionization chamber, reveals a good linearity as well (squares in **Figure 8**). The corresponding bars in **Figure 8** represent the statistical uncertainty contributions ($k = 1$) due to the variation in the homogeneity and mass as well as in the measured ESR signal of the alanine test pellets resulting in a relative uncertainty of 0.2% of the total dose measured with

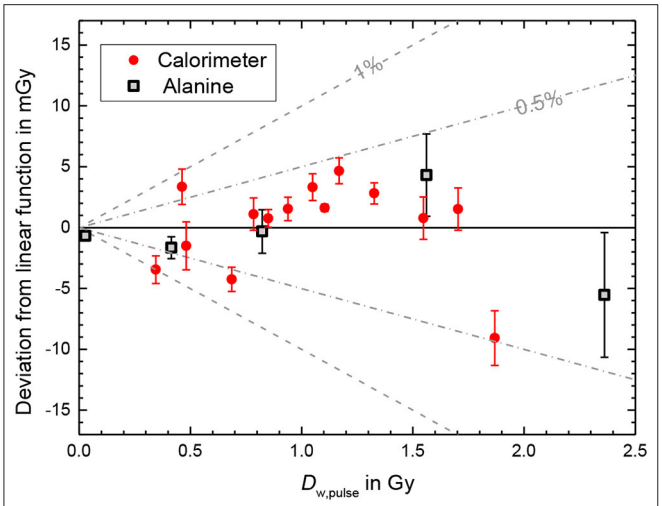

FIGURE 8 | Deviation of the calorimeter response from the linear fit function shown in **Figure 7** as a function of the dose per pulse. The bars represent only type A standard uncertainty for a sequence of 5 measurements and do not represent the actual uncertainty. Also shown is the deviations of the alanine dose measurements from the ICT calibration function show in **Figure 5**. The bars represent the statistical uncertainty contributions ($k = 1$, see text).

eight pellets. The absolute uncertainties for the delivered total doses (about 14 Gy) are ∼30 mGy. The absolute uncertainty of the DPP increases with the DPP, since at low DPP about 500 beam pulses are needed to deliver 14 Gy while at the highest DPP only 6 pulses were irradiated to reach the same dose level. In the studied DPP range the deviation from the linear behavior is smaller than 0.5%. Good linearity was expected since the ICT signal was found to be linear with the pulse charge [34], the dose is proportional to the number of irradiated electrons and alanine is known to be independent of dose rate [19]. The data in **Figure 8** indicate that the linearity of the calorimeter is comparable with the alanine dosimetry system.

DISCUSSION

There is very good agreement between the ion recombination correction k_S of the Advanced Markus chamber determined by Petersson et al. [13] and in this work (**Figure 5**). However, Petersson et al. had examined three different specimens of an Advanced Markus chamber and observed a noticeable spread in the k_S values between the specimens (e.g., up to 3.2% deviation from the mean value at 2.5 Gy/pulse). Therefore, the remarkably good agreement of the specimen examined here with the mean value of the three specimens examined by Petersson et al. does not allow for a conclusion about the universality of the k_S function for all specimens of this chamber type.

The initial measurements with the calorimeter described above suggest that such a calorimeter could be a suitable real-time detector for the accurate dosimetry of ultra-high DPP beams. The simple aluminum calorimeter used provides sufficient precision for clinical radiation dosimetry measurements and approaches that of primary standard electron beam calorimeters [48, 49]. The simplicity of the calorimeter design means that it could potentially be used in a clinical setting to directly determine the absorbed dose to water. However, for such an application there are three additional requirements, the first being the determination of the conversion factor from aluminum to water. This has been done for graphite using Monte Carlo radiation transport simulations (e.g., [44]) and therefore should be straightforward for this similar design. An achievable overall standard uncertainty in the determination of absorbed dose to water using this calorimeter design is 0.5%. The second requirement is that the thermal isolation is sufficient for a clinical setting. The irradiation area at PTB's research linear accelerator is carefully temperature controlled, to provide a stable background against which the radiation-induced temperature rise can be measured, but this might not be the case for a radiation therapy linac bunker. It may be that some form of additional temperature control will be required and then a design such as that developed by McEwen and Duane [50] could be used. The third requirement is a full validation of the calorimeter as an absorbed dose standard. This would include long-term stability testing, confirmation of the absence of an accumulated-dose dependence, measurements in a range of electron beams, and a comparison with existing dosimetry standards.

The very short irradiation times of FLASH radiotherapy, which makes this calorimeter design very suitable, also means that other operating modes of ionizing radiation calorimeters cannot be used. For example, the isothermal mode extensively used by the Laboratoire National Henri Becquerel (LNHB) [51] uses electrical heating to maintain a constant (elevated) temperature of the calorimeter and adjusts the electrical power dissipation to compensate for the energy deposited by the radiation beam. It has been shown that this mode can provide lower Type A uncertainties ($< 0.1\%$) but the time constant of the isothermal control systems is not fast enough to work within such short irradiation times.

The aluminum calorimeter used here can be optimized further. The current geometry is suitable for standard large fields (10×10 cm) but a smaller core or cylindrical, rather than plane-parallel geometry, may be better. A design such as that developed by Renaud et al. [52] would be worth investigating as this could be used in small IMRT fields (3×3 cm or smaller) for both photon and electron beams. Aluminum may not be suitable for all beam modalities (e.g., kV x-rays, protons, heavy ions) but even in these situations, the linearity of the calorimeter is unaffected, and it could therefore still be useful as a transfer detector for another dosimeter. In addition to geometric modifications, there is the potential to simplify the data acquisition system, given the high signal-to-noise obtained for these high DPP values. Replacing the multi-component AC-bridge read-out with a high-accuracy digital multimeter should still yield a suitable signal and offer a more routine operation in a clinical setting. As shown in **Figure 8**, one can argue that the calorimeter out-performs alanine, in terms of precision, linearity, and immediacy and therefore an optimized calorimeter design could be the default detector for clinical FLASH beams, rather than being used to validate other detector systems.

CONCLUSION

Three detector systems were investigated for the accurate dosimetry of electron beams with ultra-high DPP. Measurements were carried out in high-energy electron beams of a research linear accelerator, in a DPP range of at least 0.3–1.8 Gy/per pulse, i.e., around 1.5 Gy/pulse as applied for the treatment with FLASH radiotherapy. Passive alanine dosimeters were shown to have a linear response with the DPP up to at least 2.4 Gy/pulse, but there is no real-time read-out. The alanine system was used, however, as reference to determine the ion recombination correction for an Advanced Markus plane-parallel ionization chamber, studied as a possible real-time dose monitor at ultra-high DPP. The correction was found to be 79% at 1.5 Gy/pulse, consistent with previously reported results using radiochromic film as a reference. Therefore, ionization chambers used for dosimetry in conventional radiation therapy are not considered suitable for accurate dosimetry in FLASH radiation therapy. Finally, an aluminum open-to-atmosphere calorimeter, operating in the quasi-adiabatic mode, was investigated as an alternative real-time dosimeter for FLASH radiotherapy. The precision of the calorimeter was estimated to be $< 0.2\%$ and the response of the calorimeter was found to be proportional to the dose per pulse in the investigated range of 0.3 to 1.8 Gy/pulse with an average deviation from the linear fit compared to the pulse charge being $< 0.5\%$. This linearity was consistent with that determined for alanine, confirming the suitability of a simplified calorimeter design that could be used for real-time dosimetry of clinical FLASH therapy radiation beams.

DATA AVAILABILITY STATEMENT

The raw data supporting the conclusions of this article will be made available by the authors, without undue reservation.

AUTHOR CONTRIBUTIONS

AB co-developed the calorimeter, performed, and evaluated the calorimeter measurements. AS carried out the irradiation of the calorimeter, the alanine probes, and the ionization chamber. TH performed and evaluated the alanine measurements. RK and DP performed and evaluated the measurements with the ionization chamber. MM and R-PK developed the research plan and oversaw the research. All authors contributed to the article and approved the submitted version.

FUNDING

This project has received funding from the EMPIR program co-financed by the Participating States and from the European Union's Horizon 2020 research and innovation program.

ACKNOWLEDGMENTS

We thank Christoph Makowski for the operation of the electron accelerator. The assistance of Markus Meier in the preparation of the experiments is gratefully acknowledged.

REFERENCES

1. Favaudon V, Caplier L, Monceau V, Pouzoulet F, Sayarath M, Fouillade C, et al. Ultrahigh dose-rate FLASH irradiation increases the differential response between normal and tumor tissue in mice. *Sci Trans Med.* (2014) **6**:245. doi: 10.1126/scitranslmed.3008973
2. Montay-Gruel P, Bouchet A, Jaccard M, Patin D, Serduc R, Aim W, et al. X-rays can trigger the FLASH effect: Ultra-high dose-rate synchrotron light source prevents normal brain injury after whole brain irradiation in mice. *Radiother Oncol.* (2018) **129**:582–8. doi: 10.1016/j.radonc.2018.08.016
3. Montay-Gruel P, Acharya MM, Petersson K, Alikhani L, Yakkala C, Allen BD, et al. Long-term neurocognitive benefits of FLASH radiotherapy driven by reduced reactive oxygen species. *Proc Natl Acad Sci USA.* (2019) **166**:10943–51. doi: 10.1073/pnas.1901777116
4. Bourhis J, Sozzi WJ, Jorge PG, Gaide O, Bailat C, Duclos F, et al. Treatment of a first patient with FLASH-radiotherapy. *Radiother Oncol.* (2019) **139**:18–22. doi: 10.1016/j.radonc.2019.06.019
5. Bourhis J, Montay-Gruel P, Gonçalves Jorge P, Bailat C, Petit B, Ollivier J, et al. Clinical translation of FLASH radiotherapy: Why and how? *In Radiother Oncol.* (2019) **139**:11–7. doi: 10.1016/j.radonc.2019.04.008
6. Wilson JD, Hammond EM, Higgins GS, Petersson K. Ultra-High Dose Rate (FLASH) radiotherapy: silver bullet or fool's gold? *Front Oncol.* (2020) **9**:1563. doi: 10.3389/fonc.2019.01563
7. Jaccard M, Durán MT, Petersson K, Germond JF, Liger P, et al. High dose-per-pulse electron beam dosimetry: commissioning of the Oriatron eRT6 prototype linear accelerator for preclinical use. *Med Phys.* (2018) **45**:863–74. doi: 10.1002/mp.12713
8. Favaudon V, Lentz JM, Heinrich S, Patriarca A, de Marzi L, Fouillade C, et al. Time-resolved dosimetry of pulsed electron beams in very high dose-rate, FLASH irradiation for radiotherapy preclinical studies. *Nucl Instrum Methods Phys Res B.* (2019) **944**:162537. doi: 10.1016/j.nima.2019.162537
9. Schüler E, Trovati S, King G, Lartey F, Rafat M, Villegas M, et al. Experimental platform for ultra-high dose rate FLASH irradiation of small animals using a clinical linear Accelerator. *Int J Rad Oncol Biol Phys.* (2017) **97**:195–203. doi: 10.1016/j.ijrobp.2016.09.018
10. Lempart M, Blad B, Adrian G, Bäck S, Knöös T, Ceberg C, et al. Modifying a clinical linear accelerator for delivery of ultra-high dose rate irradiation. *Radiother Oncol.* (2019) **139**:40–5. doi: 10.1016/j.radonc.2019.01.031
11. Maxim PG, Tantawi SG, Loo BW. PHASER: a platform for clinical translation of FLASH cancer radiotherapy. *Radiother Oncol.* (2019) **139**:28–33. doi: 10.1016/j.radonc.2019.05.005
12. Diffenderfer ES, Verginadis II, Kim MM, Shoniyozov K, Velalopoulou A, Goia D, et al. Design, implementation, and *in vivo* validation of a novel proton FLASH radiation therapy system. *Int J Rad Oncol Biol Phys.* (2020) **106**:440–8. doi: 10.1016/j.ijrobp.2019.10.049
13. Petersson K, Jaccard M, Germond, J.-F., Buchillier T, Bochud F, et al. High dose-per-pulse electron beam dosimetry - a model to correct for the ion recombination in the Advanced Markus ionization chamber. *Med Phys.* (2017) **44**:1157–67. doi: 10.1002/mp.12111
14. Lansonneur P, Favaudon V, Heinrich S, Fouillade C, Verrelle P, De Marzi L. Simulation and experimental validation of a prototype electron beam linear accelerator for preclinical studies. *Phys Med.* (2019) **60**:50–7. doi: 10.1016/j.ejmp.2019.03.016
15. Palmans H, Andreo P, Huq MS, Seuntjens J, Christaki KE, Meghzifene A. Dosimetry of small static fields used in external photon beam radiotherapy: Summary of TRS-483, the IAEA–AAPM international Code of Practice for reference and relative dose determination. *Med Phys.* (2018) **45**:e1123–45. doi: 10.1002/mp.13208
16. Jaccard M, Petersson K, Buchillier T, Germond, JF, Durán MT, et al. High dose-per-pulse electron beam dosimetry: Usability and dose-rate independence of EBT3 Gafchromic films. *Med Phys.* (2017) **44**:725–35. doi: 10.1002/mp.12066

17. Jorge PG, Jaccard M, Petersson K, Gondré M, Durán MT, Desorgher L, et al. Dosimetric and preparation procedures for irradiating biological models with pulsed electron beam at ultra-high dose-rate. *Radiother Oncol.* (2019) **139**:34–9. doi: 10.1016/j.radonc.2019.05.004
18. Gondré M, Jorge PG, Vozenin, M.-C., Bourhis J, Bochud F, et al. Optimization of alanine measurements for fast and accurate dosimetry in FLASH radiation therapy. *Rad Res.* (2020). doi: 10.1667/rr15568.1
19. ISO (2004). *International Organization for Standardization. Practice for Use of the Alanine-EPR Dosimetry System. ISO/ASTM Standard 51607*. (Geneva: ISO). Available online at: https://www.iso.org/standard/39026.html
20. Regulla DF, Deffner U. A system of transfer dosimetry in radiation processing. *Radiat Phys Chem*. (1983) **22**:305–9. doi: 10.1016/0146-5724(83)90034-1
21. Kudoh H, Celina M, Kaye RJ, Gillen KT, Clough RL. Response of alanine dosimeters at very high dose rate. *Appl Radiat Isot*. (1997) **48**:497–9. doi: 10.1016/S0969-8043(96)00281-3
22. Bruggmoser G, Saum R, Schmachtenberg A, Schmid F, Schüle E. Determination of the recombination correction factor kS for some specific plane-parallel and cylindrical ionization chambers in pulsed photon and electron beams. *Phys Med Biol*. (2007) **52**:35–50. doi: 10.1088/0031-9155/52/2/N01
23. Di Martino F, Giannelli M, Traino AC, Lazzeri M. Ion recombination correction for very high dose-per-pulse high-energy electron beams. *Med Phys.* (2005) **32**:2204–10. doi: 10.1118/1.1940167
24. Laitano RF, Guerra AS, Pimpinella M, Caporali C, Petrucci A. Charge collection efficiency in ionization chambers exposed to electron beams with high dose per pulse. *Phys Med Biol.* (2006) **51**:6419–36. doi: 10.1088/0031-9155/51/24/009
25. Scalchi P, Ciccotelli A, Felici G, Petrucci A, Massafra R, Piazzi V, et al. Use of parallel-plate ionization chambers in reference dosimetry of NOVAC and LIAC ® mobile electron linear accelerators for intraoperative radiotherapy: a multi-center survey. *Med Phys.* (2017) **44**:321–32. doi: 10.1002/mp.12020
26. Pimpinella M, Andreoli S, De Angelis C, Della Monaca S, D'Arienzo M, Menegotti L. Output factor measurement in high dose-per-pulse IORT electron beams. *Phys Med*. (2019) **61**:94–102. doi: 10.1016/j.ejmp.2019.04.021
27. D'Arienzo M, Andreoli S, Pimpinella M. Evaluation of the uncertainty associated with the ion recombination correction in high dose-per-pulse electron beam dosimetry: an MC approach. *Phys Med Biol*. (2020) **65**:09NT01. doi: 10.1088/1361-6560/ab79c2
28. Almond PR, Biggs PJ, Coursey BM, Hanson WF, Huq MS, Nath R, et al. AAPM's TG-51 protocol for clinical reference dosimetry of high-energy photon and electron beams. *Med Phys.* (1999) **26**:1847–70.
29. International Atomic Energy Agency. *Absorbed Dose Determination in External Beam Radiotherapy: An International Code of Practice for Dosimetry Based on standards of Absorbed Dose to Water. Tech Rep TRS-398.* Vienna: IAEA (2000).
30. DIN 6800-2:2008-03. Procedures of dosimetry with probe type detectors for photon and electron radiation - Part 2: Ionization chamber dosimetry of high energy photon and electron radiation. *Acta Radiol Oncol.* (1980) **19**:55–79. doi: 10.31030/1409685
31. Boag JW, Hochhäuser E, Balk OA. The effect of free-electron collection on the recombination correction to ionization measurements of pulsed radiation. *Phys Med Biol*. (1996) **41**:885–97. doi: 10.1088/0031-9155/41/5/005
32. McManus M, Romano F, Lee ND, Farabolini W, Gilardi A, Royle G, et al. The challenge of ionisation chamber dosimetry in ultra-short pulsed high dose-rate very high energy electron beams. *Sci Rep.* (2020) **10**:9089. doi: 10.1038/s41598-020-65819-y
33. Schüller A, Pojtinger S, Meier M, Makowski C, Kapsch RP. The metrological electron accelerator facility (MELAF) for research in dosimetry for radiotherapy. In: *IFMBE Proceedings*. Vol. 68.589–93 Springer Verlag (2019). doi: 10.1007/978-981-10-9023-3_109
34. Schüller A, Illemann J, Renner F, Makowski C, Kapsch RP. Traceable charge measurement of the pulses of a 27 MeV electron beam from a linear accelerator. *J Instrum.* (2017) **12**:P03003. doi: 10.1088/1748-0221/12/03/P03003
35. Krauss A. The PTB water calorimeter for the absolute determination of absorbed dose to water in 60Co radiation. *Metrologia.* (2006) **43**:259–72. doi: 10.1088/0026-1394/43/3/008
36. Anton M. Uncertainties in alanine/ESR dosimetry at the physikalisch-technische bundesanstalt. *Phys Med Biol.* (2006) **51**:5419–40. doi: 10.1088/0031-9155/51/21/003
37. Anton M, Kapsch RP, Krauss A, Von Voigts-Rhetz P, Zink K, McEwen M. Difference in the relative response of the alanine dosimeter to megavoltage x-ray and electron beams. *Phys Med Biol.* (2013) **58**:3259–82. doi: 10.1088/0031-9155/58/10/3259
38. Vörös S, Anton M, Boillat B. Relative response of alanine dosemeters for high-energy electrons determined using a fricke primary standard. *Phys Med Biol.* (2012) **57**:1413–32. doi: 10.1088/0031-9155/57/5/1413
39. McEwen M, Miller A, Pazos I, Sharpe P. Determination of a consensus scaling factor to convert a Co-60-based alanine dose reading to yield the dose delivered in a high energy electron beam. *Radiat Phys Chem.* (2020) **171**:108673. doi: 10.1016/j.radphyschem.2019.108673
40. Renaud J, Palmans H, Sarfehnia A, Seuntjens J. Absorbed dose calorimetry. *Phys Med Biol.* (2020) **65**:05TR02. doi: 10.1088/1361-6560/ab4f29
41. Miller A, Kovas A. Application of calorimeters for routine and reference dosimetry at 4-10 MeV industrial electron accelerators. *Int J Radiat Appl Instrumentation.* (1990) **35**:774–8. doi: 10.1016/1359-0197(90)90314-8
42. Burns D T, McEwen M, Williams A J. An NPL absorbed dose calibration service for electron beam radiotherapy. In: SP Flitton, editor. *Proc. Int. Symp. on Measurement Assurance in Dosimetry.* Vienna: IAEA (1994). p. 61.
43. Ross CK, Seuntjens J, Klassen N, Shortt K. The NRC sealed water calorimeter: correction factors and performance. In: *Proceedings of the Workshop on Recent Advances in Calorimetric Absorbed Dose Standards*. Teddington: National Physical Laboratory (2000).
44. Bourgouin A, Cojocaru C, Ross C, McEwen M. Determination of Wair in high-energy electron beams using graphite detectors. *Med Phys.* (2019) **46**:5195–208. doi: 10.1002/mp.13772
45. Nutbrown RF, Duane S, Shipley DR, Thomas RAS. Evaluation of factors to convert absorbed dose calibrations from graphite to water for the NPL high-energy photon calibration service. *Phys Med Biol.* (2002) **47**:441–54. doi: 10.1088/0031-9155/47/3/306
46. Grusell E, Montelius A, Brahme A, Rikner G, Russell K. A general solution to charged particle beam flattening using an optimized dual-scattering-foil technique, with application to proton therapy beams. *Phys Med Biol.* (1994) **39**:2201–16. doi: 10.1088/0031-9155/39/12/005
47. Carver RL, Hogstrom KR, Price MJ, LeBlanc JD, Pitcher GM. Real-time simulator for designing electron dual scattering foil systems. *J Appl Clin Med Phys.* (2014) **15**:323–42. doi: 10.1120/jacmp.v15i6.4849
48. Krauss A, Kapsch RP. Direct determination of k Q factors for cylindrical and plane-parallel ionization chambers in high-energy electron beams from 6 MeV to 20 MeV. *Phys Med Biol.* (2018) **63**:035041. doi: 10.1088/1361-6560/aaa71e
49. McEwen MR, DuSautoy AR, Williams AJ. The calibration of therapy level electron beam ionization chambers in terms of absorbed dose to water. *Phys Med Biol.* (1998) **43**:2503–19.
50. McEwen MR, Duane S. A portable calorimeter for measuring absorbed dose in the radiotherapy clinic. *Phys Med Biol.* (2000) **45**:3675–91. doi: 10.1088/0031-9155/45/12/312
51. Daures J, Ostrowsky A. New constant-temperature operating mode for graphite calorimeter at LNE-LNHB. *Phys Med Biol.* (2005) **50**:4035–52. doi: 10.1088/0031-9155/50/17/008
52. Renaud J, Sarfehnia A, Bancheri J, Seuntjens J. Aerrow: a probe-format graphite calorimeter for absolute dosimetry of high-energy photon beams in the clinical environment. *Med Phys.* (2018) **45**:414–28. doi: 10.1002/mp.12669

Conflict of Interest: RK and DP are employees of PTW Freiburg.

The remaining authors declare that the research was conducted in the absence of any commercial or financial relationships that could be construed as a potential conflict of interest.

frontiers in Physics

ORIGINAL RESEARCH
published: 02 November 2020
doi: 10.3389/fphy.2020.570697

FLASH Radiotherapy With Electrons: Issues Related to the Production, Monitoring, and Dosimetric Characterization of the Beam

Fabio Di Martino[1], Patrizio Barca[1], Salvatore Barone[2], Eleonora Bortoli[1], Rita Borgheresi[1], Silvia De Stefano[2], Massimo Di Francesco[2], Luigi Faillace[3], Lucia Giuliano[3], Luigi Grasso[2], Stefania Linsalata[1], Daniela Marfisi[1], Mauro Migliorati[3], Matteo Pacitti[2], Luigi Palumbo[3] and Giuseppe Felici[2]**

[1] U.O. Fisica Sanitaria, Azienda Universitaria Ospedaliera Pisana, Pisa, Italy, [2] Sordina IORT Technologies, R&D Department, Aprilia, Italy, [3] Sapienza University of Rome, Rome, Italy

OPEN ACCESS

Edited by:
Vincenzo Patera,
Sapienza University of Rome, Italy

Reviewed by:
Alessio Sarti,
Sapienza University of Rome, Italy
Tiziana Rancati,
Istituto Nazionale dei Tumori (IRCCS), Italy

***Correspondence:**
Fabio Di Martino
f.dimartino@ao-pisa.toscana.it
Giuseppe Felici
giuseppe.felici@sordina.com

Specialty section:
This article was submitted to Medical Physics and Imaging, a section of the journal Frontiers in Physics

Received: 08 June 2020
Accepted: 22 September 2020
Published: 02 November 2020

Citation:
Di Martino F, Barca P, Barone S, Bortoli E, Borgheresi R, De Stefano S, Di Francesco M, Faillace L, Giuliano L, Grasso L, Linsalata S, Marfisi D, Migliorati M, Pacitti M, Palumbo L and Felici G (2020) FLASH Radiotherapy With Electrons: Issues Related to the Production, Monitoring, and Dosimetric Characterization of the Beam. Front. Phys. 8:570697. doi: 10.3389/fphy.2020.570697

Various *in vivo* experimental works carried out on different animals and organs have shown that it is possible to reduce the damage caused to healthy tissue still preserving the therapeutic efficacy on the tumor tissue, by drastically reducing the total time of dose delivery (<200 ms). This effect, called the FLASH effect, immediately attracted considerable attention within the radiotherapy community, due to the possibility of widening the therapeutic window and treating effectively tumors which appear radioresistant to conventional techniques. Despite the experimental evidence, the radiobiological mechanisms underlying the FLASH effect and the beam parameters contributing to its optimization are not yet known in details. In order to fully understand the FLASH effect, it might be worthy to investigate some alternatives which can further improve the tools adopted so far, in terms of both linac technology and dosimetric systems. This work investigates the problems and solutions concerning the realization of an electron accelerator dedicated to FLASH therapy and optimized for *in vivo* experiments. Moreover, the work discusses the saturation problems of the most common radiotherapy dosimeters when used in the very high dose-per-pulse FLASH conditions and provides some preliminary experimental data on their behavior.

Keywords: radiotherapy, FLASH effect, FLASH electron linac, beam monitoring system, saturation problems

INTRODUCTION

FLASH Radiotherapy (FLASH-RT) is a radiotherapy technique which consists of administering the entire radiation at dose-rate orders of magnitude higher than conventional ones [1].

Various *in vivo* preclinical experiments carried out on different animals and organs have shown a reduction of the side effects on healthy tissues still preserving the therapeutic efficacy on the tumor tissue, by using electron beams of 4–6 MeV at a dose rate higher than 40 Gy/s, for a total irradiation duration of <200 ms. The robustness of the FLASH effect is validated by the fact that it has been reproduced in various animal models (mice, rats, zebrafish, pigs, and cats), various organs (lung, skin, gut, and brain), and various radiobiology research works [2–8].

These results attracted considerable attention within the radiotherapy community for their potential clinical applications: in fact, the possibility of being able to increase the administered

dose to the target without increasing the damage to the neighboring tissues would allow to effectively treat tumors, otherwise radioresistant to conventional radiotherapy techniques (CONV-RT) [9, 10].

Nevertheless, there are still many questions to be addressed, before using the FLASH effect in the clinical practice. The radiobiological mechanism underlying the FLASH effect is still unknown [11]; oxygen consumption has been proposed as a possible explanation [12–14] but other works underlined the limits of this explanation attempt and the need of further investigations [11, 13].

There are also different aspects still to be clarified regarding the dependence of the FLASH effect on various beam parameters and the irradiated tissue. The dependence on the LET of the radiation used is still an unknown factor; the majority of the experiments were performed with electron beams (energy 4–6 MeV). There are significant difficulties in obtaining beams with sufficient intensity to reach the FLASH effect with X-ray [15], protons [16], and heavy ions; nevertheless, several attempts were done. The interested reader can find an exhaustive review of the state of the art in a paper recently published by Esplen et al. [17].

Only the dependence on the average dose rate and on the duration of the entire irradiation has been clearly observed so far. The roles of dose-per-pulse, instantaneous dose per pulse (dose per pulse divided by pulse duration), and pulse duration and frequency still remain to be understood.

This is essentially due to the fact that the accelerators used up to now for *in vivo* FLASH experiments are electron accelerators designed for industrial use [18–20] or modified medical accelerators, where diffuser filters and monitor chambers have been mechanically dismounted and removed from the beam path [21]. Therefore, such accelerators are not able to perform beam parameters real-time monitoring as well as provide an accurate and reproducible output.

The linacs used did not have the possibility to modify the beam geometry in order to obtain homogeneous dose profiles on fields of different sizes and geometries. For this reason, such electron beam did not allow neither performing accurate irradiation of well-defined volumes nor studying the dependencies of the effect on the volume of the irradiated tissue from a quantitative point of view.

Moreover, the dosimetry is complicated by the saturation problems typical of all clinical dosimeters which provide online information to these dose-per-pulse values. In all the experimental works published so far [18–21], the dosimetry was performed using independent dose-rate dosimeters, in most cases radiochromic films. Radiochromic films do not have the same accuracy of other detectors (for example ionization chambers), they do not provide online dosimetric information, and they are not able to control any changes in the output during the experiment.

All these aspects, together with the objective difficulties of obtaining quantitative radiobiological data from *in vivo* experiments, have contributed, so far, to not definitively and quantitatively understand the dependencies of the FLASH effect on the various parameters that characterize the beam used and the tissue irradiated.

The main issues covered hereafter are as follows:

- The problems concerning the realization of an accelerator dedicated to the production of FLASH electron beams, in order to both optimize the experimental characterization phase and, as a perspective, provide suggestions for the future clinical applications.
- The issues concerning the saturation of the current available dosimeters.

Regarding the linac, this work is focused on problems and solutions concerning:

1. The production and acceleration of a fluence capable of reaching the level needed to achieve the FLASH effect on large/clinical volumes.
2. Reduction of the radiation leakage produced by the radiant head/gantry, as defined in NCRP151 [22].
3. Possibility to vary the dimensions and geometric shape of the beam.
4. Online fluence monitoring system, which should be compliant with IEC 60601-2-1 requirements [23].
5. Possibility of delivering in FLASH/non-FLASH mode without changing the irradiation setup.

The discussion on the new linac proposal, ElectronFlash, is presented in section 2, "A dedicated research linac proposal."

The problems concerning the dosimetric characterization of a FLASH electron beam due to the saturation of the dosimeters commonly used in the clinical practice are also addressed.

In particular, the behavior of three classes of dosimeters has been analyzed:

1. Ionization chambers (PTW Advanced Markus).
2. Semiconductors (diamond and diode).
3. Scintillators.

The ionization chambers already showed significant recombination problems at dose-per-pulse values typical of IORT beams [24–27], which are about 2 orders of magnitude lower than FLASH ones. In that case, the use of the ionization chambers had been made possible by quantifying k_{sat}–a corrective factor to account for the loss of charge collected due to recombination—by means of a formula deriving from the Boag [28] theory. This formula takes into account the fraction of free electrons (p), which is the fraction of electrons that are not captured by the polarized oxygen molecules present in the chamber air cavity.

In order to quantify accurately k_{sat}, and, consequently, be able to use the ionization chamber as a dosimeter for FLASH beams, the theory of recombination should be rewritten for FLASH dose-per-pulse values (dose per pulse around 1 Gy/p or higher), taking into account the shielding effects of moving charges (please refer to **Appendix**, Section 1—Ionization Chambers).

The saturation problems of semiconductor and scintillation dosimeters for FLASH dose-per-pulse values have not been investigated yet. Semiconductor detectors are characterized by a negligible time of electron–hole displacement; each pair of electron holes, if invested by the radiation, is capable of providing a signal but cannot be reused. This aspect suggests a negligible

saturation (energy absorbed by the dosimeter but not revealed by its detection system) until all the electron–hole pairs available within the material have been used. Beyond such value, the saturation suddenly reaches 100%: this is the cutoff dose-per-pulse value, beyond which all the energy absorbed inside the detector is not revealed and the value read by the dosimeter no longer grows. Therefore, the saturation is expected to be negligible up to a cutoff value and, once this threshold is trespassed, it is no longer correctable. If FLASH dose-per-pulse values are beyond such cutoff, these dosimeters cannot be used in this context.

The scintillators instead have reusable, hence non-exhaustible scintillation centers; however, the system has a deadtime given by both the crystal scintillation time and the electronics. This implies that a saturation increasing at increasing dose-per-pulse values may arise at lower dose-rate values; however, the threshold value for which saturation is no longer correctable is probably higher. A method for the correction of the saturation can be implemented (please refer to **Appendix**, Section 2—Scintillators).

In this paper, some preliminary experimental data collected irradiating various dosimeters in FLASH modality will be shown.

In particular, the saturation of two semiconductor dosimeters (PTW T60017 Dosimetry Diode and PTW T60019 microDiamond) and a scintillation dosimeter (DoseWire^{TM} Series 10) was assessed experimentally at different dose-per-pulse values.

Since ElectronFlash was not yet operational in 2019, all the measurements were performed with an IORT dedicated electron linear accelerator NOVAC11, in a nonclinical configuration.

A DEDICATED RESEARCH LINAC PROPOSAL

A common clinical specification for the minimum FLASH dose rate has not been identified yet; the minimum amount of e-beam current is not known either. Furthermore, the optimal beam optic for delivering FLASH RT in electron mode is still under investigation. Therefore, the exact number of electrons to be accelerated has not been identified yet. In the following, the peak current of 100 mA for the accelerated e-beam is chosen as a reasonable, even preliminary, guess (at least with an optimized beam collimation system). Moreover, literature [2] suggests that the whole dose should be delivered in $<$200 ms. Such beam current features pose new and additional challenges both for beam monitoring system (inside the linac) and for linac commissioning, which are briefly discussed and analyzed in the following sections. The solution proposed in this work is the design of a new research linac.

System Architecture

In order to consolidate the promising radiobiological results given by the FLASH effect, a specifically designed linac is necessary. This idea led Institut Curie (https://institut-curie.org/), who pioneered the research in this field [1, 2, 18], to look for a dedicated linac: the system ElectronFlash (in the following identified as EF) has been designed according to this request. The system is a research linac operating in electron mode only, with energies 5 and 7 MeV, and a dose rate ranging from 0.01 to 4,000 Gy/s and higher. Pulse duration can be set according to the user need in a wide range.

EF can be installed in a common radiotherapy bunker; the first unit will be installed at Orsay Research Center of Institut Curie in summer 2020.

The system drawing is shown in **Figure 1** and the system block diagram is shown in **Figure 2.**

The accelerating wave guide has been designed by adopting the radial focusing technique: the e-beam radial dynamics is guided by the electric field of the cavities and not by an external solenoid. This approach, though challenging from the manufacturing point of view, not only allows a better control with virtually no X-ray leakage, but also the design of a lighter and more compact system.

The accelerating waveguide concept is based on the experience gained by SIT staff in the design of IORT-dedicated linacs [29].

Beam dynamics simulations have been performed by La Sapienza SBAI Department (https://www.sbai.uniroma1.it/) in order to optimize the tank for high current beam. The guide is shown in **Figure 3** together with some outputs of beam dynamics simulation performed with PARMELA code (https://laacg.lanl.gov/laacg/services/serv_codes.phtml). It is shown that no scattering happens between e-beam and the radiofrequency (RF in the following) cavities: e-beam radial dimensions are always smaller than the diameter hole (8 mm) of the RF cavities beam channel, as shown in **Figure 3**.

A different approach has been implemented for e-beam collimation compared to the standard medical linac. Instead of using thick scattering foil, the beam is defocused by two quadrupoles into the desired field. Such approach provides several advantages for a linac operating in FLASH mode:

- Fluence transmission into the target is optimized, as long as the only element the e-beam scatters with is the thin titanium window that seals the vacuum tube.
- Due to the absence of thick scattering elements leakage radiation is minimized.
- Large/clinical fields are achievable by properly setting the quadrupoles current.

It is remarkable that such beam optic system implies that the ratio of the doses for two different fields F1 and F2 is given by:

$$\frac{D_{F1}}{D_{F2}} \cong \frac{S_{F2}}{S_{F1}}$$

where D_{F1} and D_{F2} are the delivered doses and S_{F1} and S_{F2} are the surfaces of the two fields.

Beam Energy Monitoring

In order to comply with the standard IEC 60601-2-1 [23], beam monitoring in the FLASH region requires not only a real time measurement of the beam current (which is proportional to the absorbed dose) but also a real-time check of the average energy of the beam.

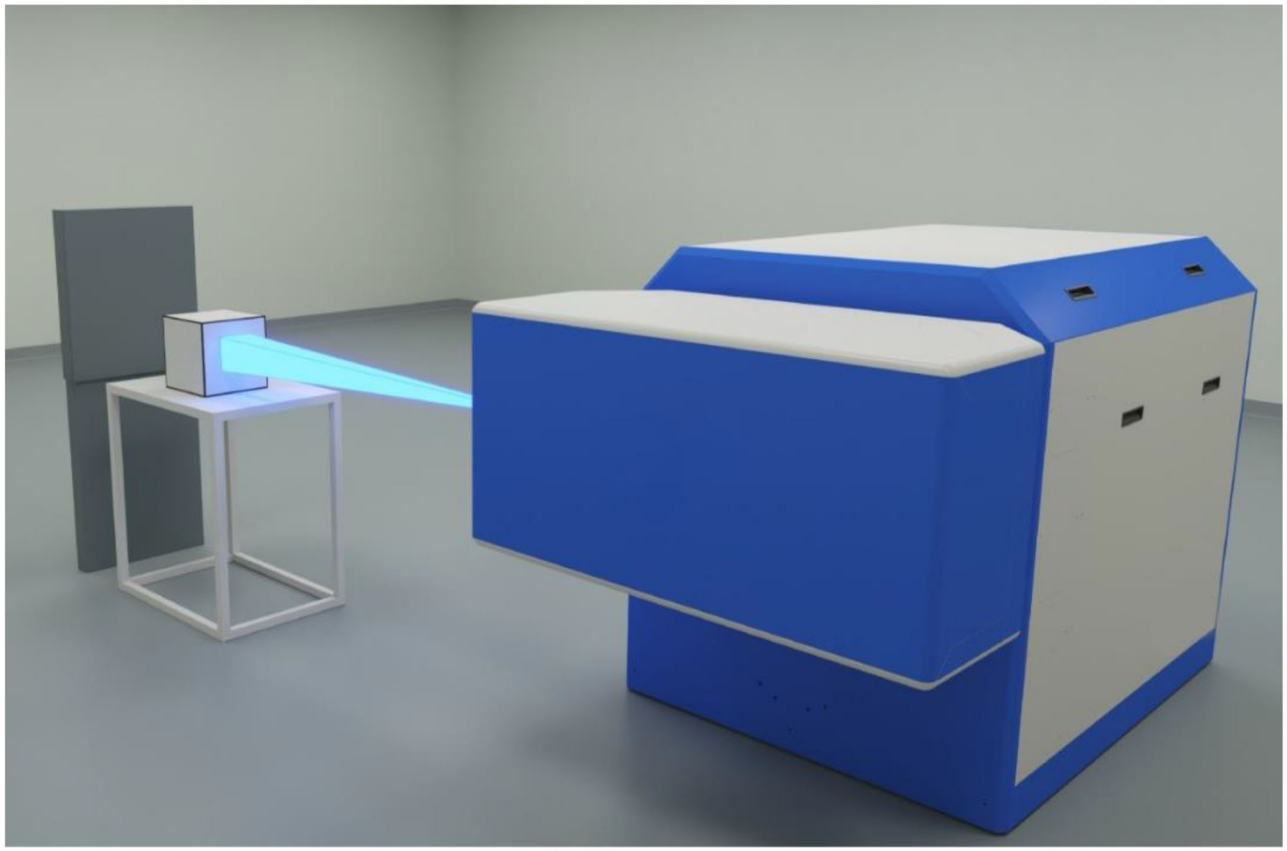

FIGURE 1 | ElectronFlash.

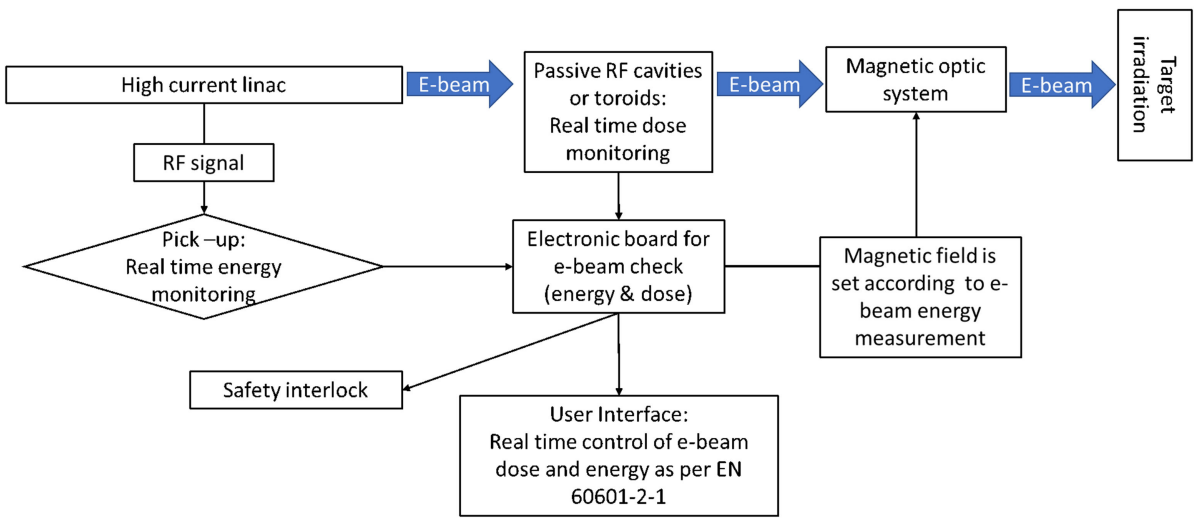

FIGURE 2 | ElectronFlash block diagram.

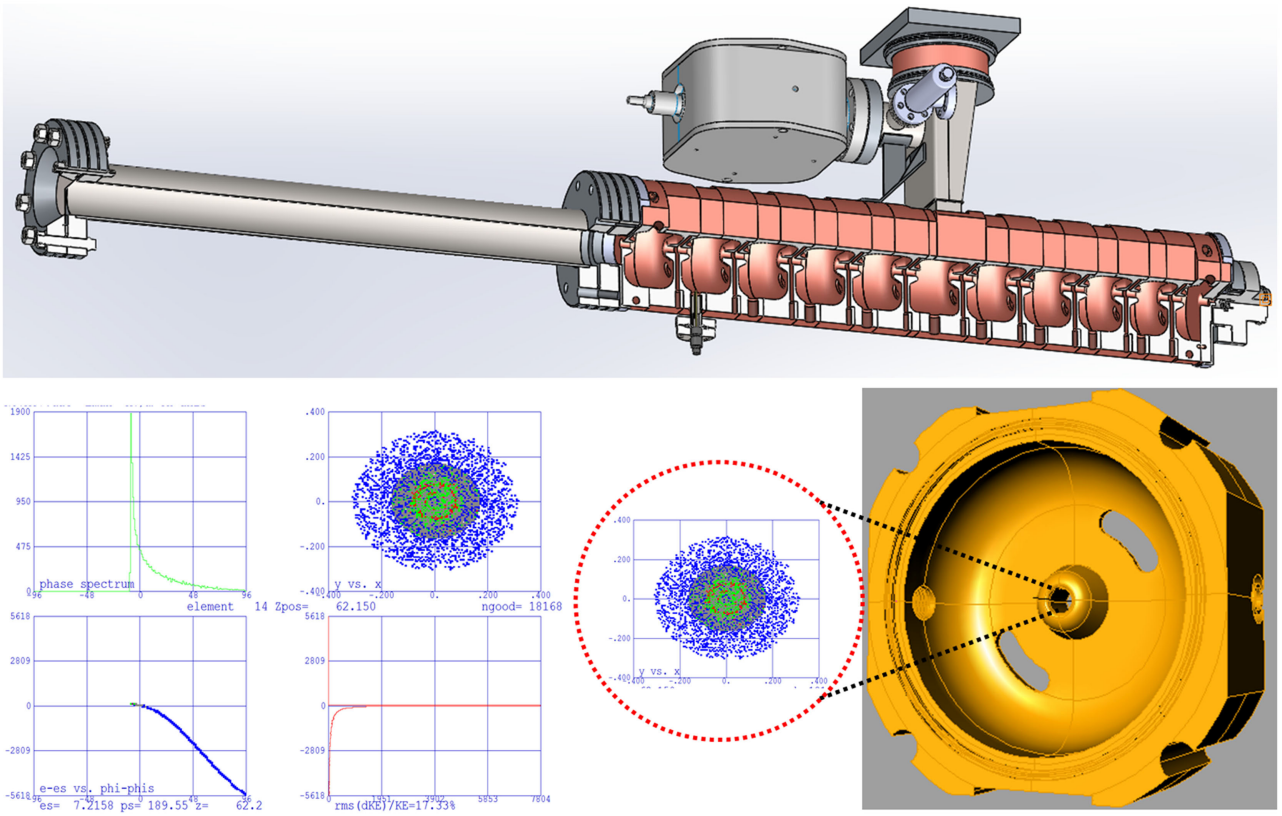

FIGURE 3 | Accelerating tank and beam dynamics simulation.

The standard IEC 60601-2-1, in the paragraph 201.10.1.2.101.5 ("Selection and Display of Energy") requires that:

"IRRADIATION shall be TERMINATED if the mean ENERGY, Ei, of the ELECTRONS striking:

[. . .]

- the ELECTRON RADIATION window deviates by more than ±20% or ± 2 MeV, whichever is the lesser during ELECTRON IRRADIATION, from the value of mean ENERGY that would occur under normal operating conditions for the selected energy and mode of operation."

In a radiofrequency powered linac, the power generated by the RF source can be written as:

$$W_{TOT} = W_{LINAC} + W_{e-beam}$$

where W_{LINAC} is the power absorbed by the accelerating waveguide and W_{e-beam} is the power absorbed by the beam itself. If the power absorbed by the e-beam becomes comparable with the power absorbed by the accelerating tank, e-beam current variation influences the beam energy.

Assuming a monochromatic spectrum,

$$W_{e-beam}\ [W] \cong I_{e-beam}[A] \cdot E_{e-beam}\ [eV]$$

the precise calculus of the power absorbed by the accelerating waveguide, W_{LINAC}, can be performed as described in [30]; for an accelerating waveguide operating in the S band, designed for 10 MeV, W_{LINAC} is around 2 MW.

The percentage energy variation of the electron beam can be roughly estimated as (refer to [30] for a detailed calculus).

$$\frac{\Delta E}{E} \cong \sqrt{\frac{\Delta W_{e-beam}}{W_{TOT}}}$$

In the abovementioned hypotheses, a beam current variation slightly >10% induces an energy variation >20%. It is therefore clear that a specific system for checking energy constancy is mandatory. Such system should operate independently with respect to the dose monitoring system.

The solution proposed is illustrated in **Figure 4**: e-beam energy can be real time monitored, pulse by pulse, by means of a signal taken by a pick-up positioned inside a RF cavity. The operation principle is briefly described; further details can be found in [30]. The total energy gain ΔK_{TOT} in the accelerating waveguide is:

$$\Delta K_{TOT} = N_{ACC} \cdot \Delta K$$

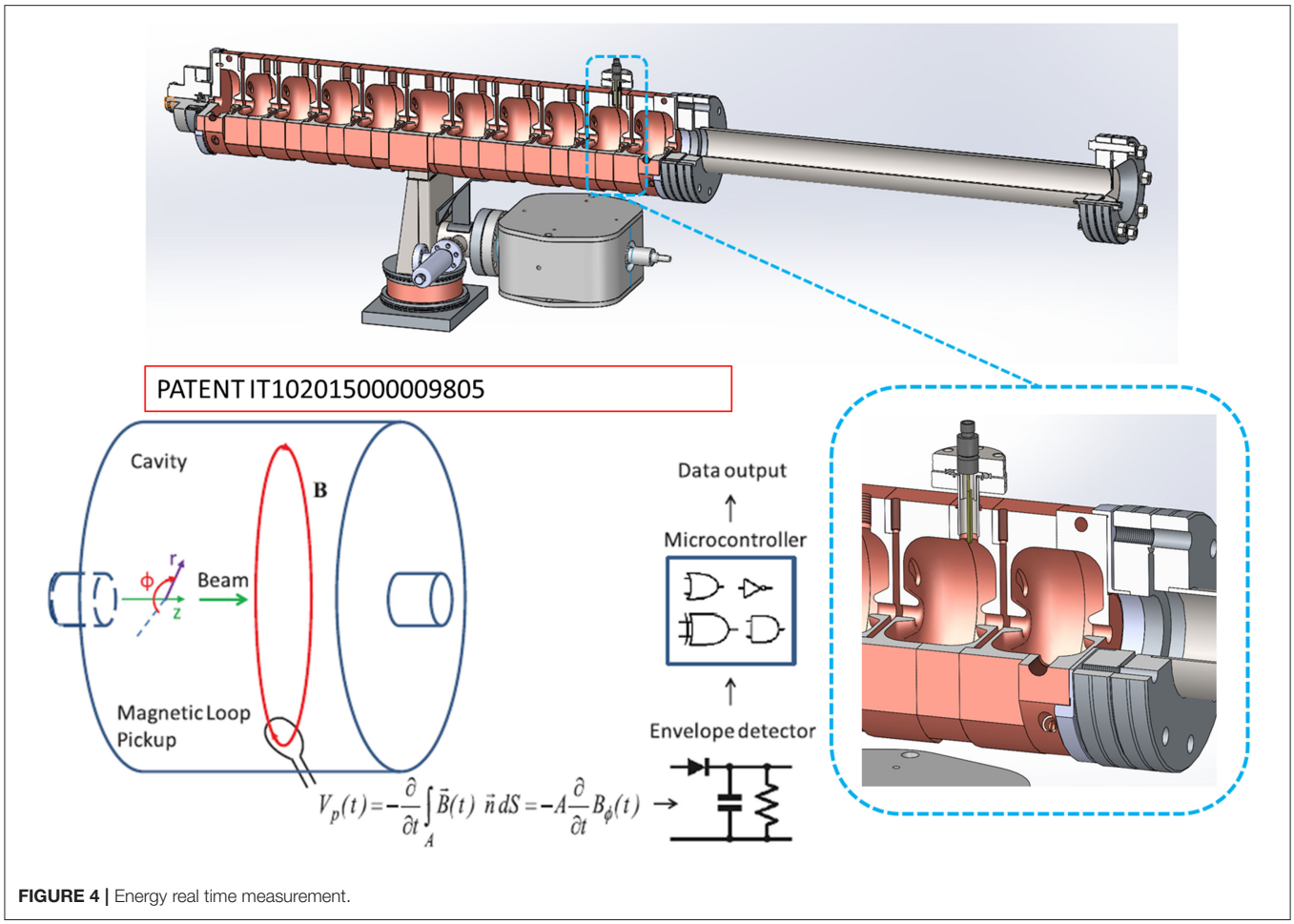

FIGURE 4 | Energy real time measurement.

where N_{ACC} is the number of the accelerating cavities and ΔK is the energy gain per single cavity.

In general, $\Delta K \propto E_0$ where E_0 is the spatial average of the longitudinal electrical field along the cavity (at a fixed time, when e-beam is in phase with the field). Inside each cavity, the electric field has a fixed ratio respect to the magnetic field B. Therefore, the measurement of such field provides a real time, nondestructive measurement of the electric field E_0 and, therefore, of overall energy of the accelerated e-beam [31]. The time derivative of the magnetic flux generated by B is measured through the pick-up shown in **Figure 4** so that,

$$\Delta K \propto \int \frac{\partial}{\partial t}\overrightarrow{B(t)}$$

the speed of such system is determined by the electronic board maximum speed, as long as signal detection itself is luminal. Such technique provides an online and easy system for checking energy constancy, with a precision better than 5%.

Output Monitoring: Beyond Monitor Chambers

Ionization chamber technology appears probably not adequate both for beam monitoring and dose measurements. There are, at least, two issues:

- Assuming the electrical field inside the ionization chamber not being affected by the one generated by the ionization, the current models [32] cannot describe properly the ionization chamber behavior;
- Response time of the chamber itself.

The dose monitor system must guarantee that the correct dose is delivered within the required tolerance levels. Furthermore, the dose monitor system should respond quickly enough to shut off the beam when the dose set is reached. The drift time of the electrons within an ionization chamber operating in FLASH regime is probably too slow to reach this goal; hence, new dose monitoring techniques will be required. A solution for overcoming all the issues related to ionization chamber operation in the FLASH region represents a change of paradigm. Fluence can be detected by means of in vacuum electrical measurements. Such techniques, widely adopted in high-energy physics, are still not common in medical linacs but represent indeed the most promising perspective.

The system EF has been designed in order to produce both FLASH and conventional dose rates. Therefore, a dual-dose monitoring system has been implemented (**Figure 5**) to allow an adequate fluence reading within a

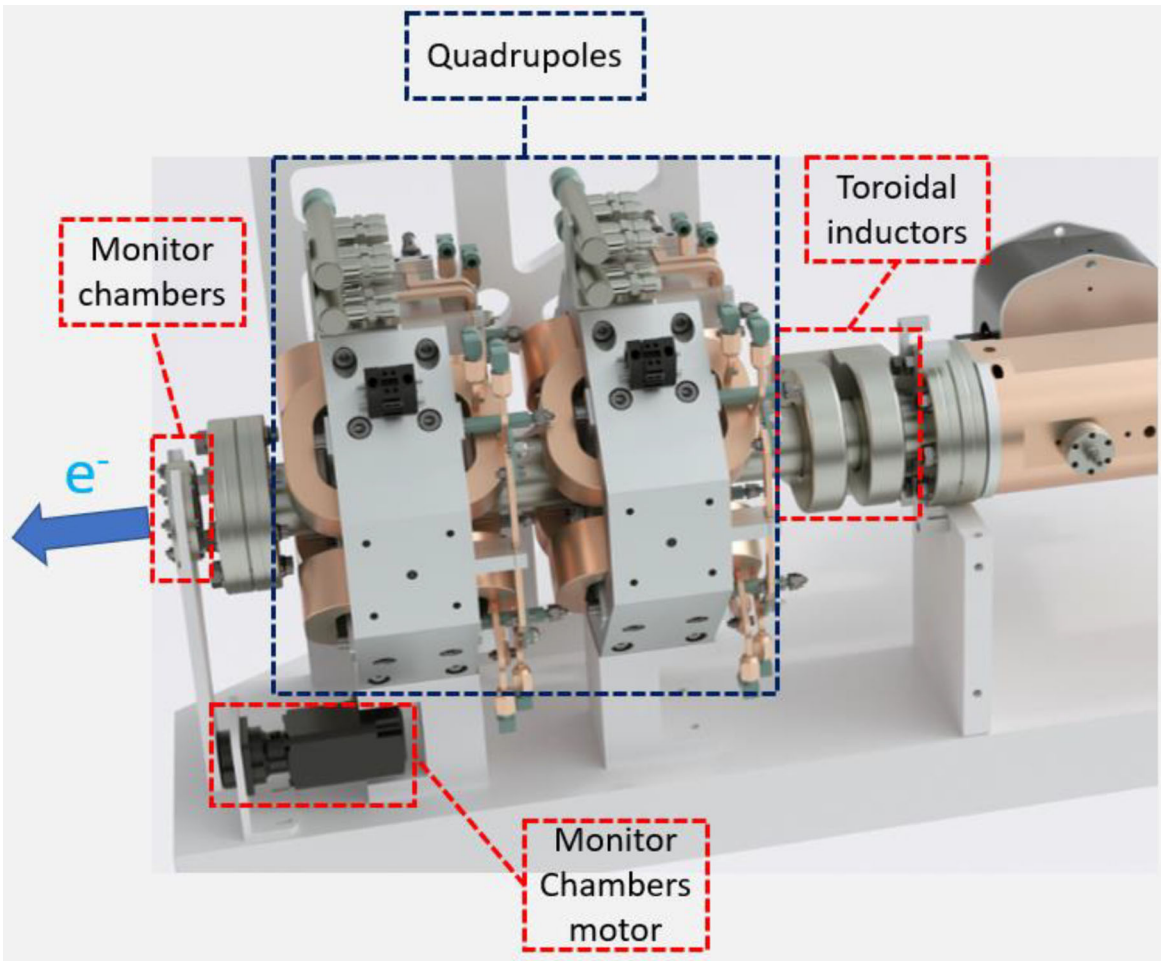

FIGURE 5 | e-beam monitoring system.

very broad range (0.01 cGy/p−40 Gy/p) for FLASH and conventional modality.

In FLASH modality, e-beam output is monitored by means of two toroidal inductors and monitor chambers are positioned outside the beam line; in conventional modality, the monitor chambers are inserted along the beam line, as illustrated in **Figure 5**. Because of their sensitivity of 10 V/A, the toroidal inductors provide a fast and robust signal up to few milliamperes of beam current. The dual hardware allows to get a very good signal to noise ratio in every operational mode.

A possible alternative to toroidal inductors is represented by a passive resonant cavity, as proposed by Leggieri et al. [33]: the beam, while crossing the cavity, induces a resonant electromagnetic field that can be detected through a pick-up. The voltage at pick-up terminations is representative of the real time beam current and is elaborated, by a microcontroller system, for the output monitoring.

The passive resonant cavity reading, for a given beam current, can be varied by changing parameters such as its internal shape and material [34]; however, an optimized monitor system capable of appropriately monitoring a beam in a wide range (1–100 mA for ElectronFlash) would necessarily require at least two different cavities, each optimized for a specific range. Furthermore, this solution requires the a fine tuning of each cavity and its thermostating at the same linac temperature. On the other hand, the dual monitoring system implemented in ElectronFlash adopts two different technologies (monitor chambers and toroidal inductors), achieving in principle the same overall accuracy. Monitoring system performances will be experimentally verified and validated after ElectronFlash installation.

SATURATION PROBLEMS OF ONLINE DOSIMETERS USED IN THE CLINICAL PRACTICE

The dose-rate DR generated by a pulsed electron beam is directly proportional to the dose-per-pulse D_p

$$DR = PRF \cdot D_p$$

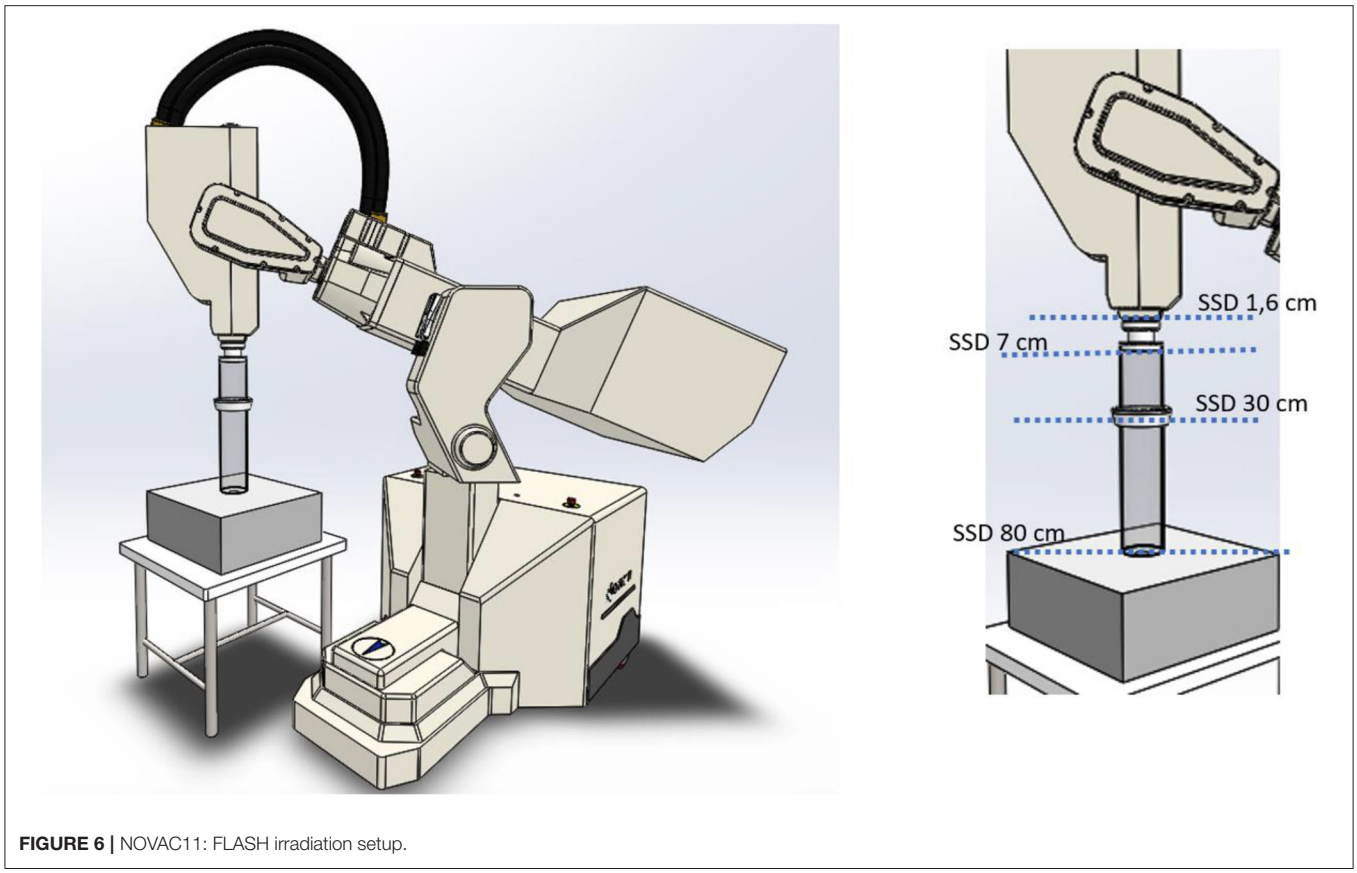

FIGURE 6 | NOVAC11: FLASH irradiation setup.

where PRF is the pulse repetition frequency.

At PRF smaller than 100 Hz, all the dosimeters analyzed have a shorter signal collection time with respect to the repetition time of the pulses ($\geq$ 10 ms), and, consequently, the saturation is influenced only by the dose-per-pulse (duration of the pulse is around 2.5 μs).

Considering a standard frequency of 30 Hz, in order to reach FLASH dose-rate values (> 40 Gy/s) it is necessary to produce dose-per-pulse higher than 1 Gy/p. This value is at least one or two orders of magnitude greater than the dose-per-pulse produced respectively by IORT and conventional linacs, for which the most common online dosimeters were designed, produced, and tested.

Materials and Methods

Absolute dose in a PMMA phantom was measured with a 10-MeV electron beam produced by a NOVAC11 mobile accelerator. The dose-per-pulse has been increased by a minimum of 5 cGy/p in reference conditions up to 40 Gy/p by modifying the collimation system as described in detail in section Experimental Setup. In order to investigate dosimeter saturation problems in FLASH dose-per-pulse conditions, different types of detectors were irradiated at increasing dose-per-pulse up to FLASH values (40 Gy/p), using as reference the measurements performed with independent dose-rate radiochromic films dosimeters.

Experimental Setup

Currently, IORT dedicated linacs are characterized by a significantly high dose-per-pulse [26, 27], typically around 5 cGy/p, with a pulse repetition frequency ranging from 1 to 30 Hz: dose rates higher than conventional ones are achievable. This feature, together with the very simple beam collimation system, makes the system itself particularly attracting for a preliminary study of the dosimeters behavior in FLASH mode.

In order to produce an electron beam with dose-rate values proper of a FLASH beam (>1 Gy/p), a preexisting dedicated IORT electron linear accelerator has been considered, the NOVAC11.

NOVAC11 provides 4 nominal electron energies (4, 6, 8, 10 MeV) and the electron beam collimation system is purely passive: NOVAC11 does not use any scattering foil for beam broadening that is obtained by means of a hard-docking collimation system. Such collimation system consists of two separated polymethylmethacrylate (PMMA) cylindrical applicators that can be directly attached to the radiant head. The applicator is made of two parts: an upper part called applicator holder or upper applicator—directly mounted to the radiant head—and the terminal part called terminal applicator, which is connected to the upper one by means of a ring nut. The PMMA applicators have 5 mm wall thickness, internal diameter ranging from 3 to 10 cm, and a flat or beveled end. The length of the applicators

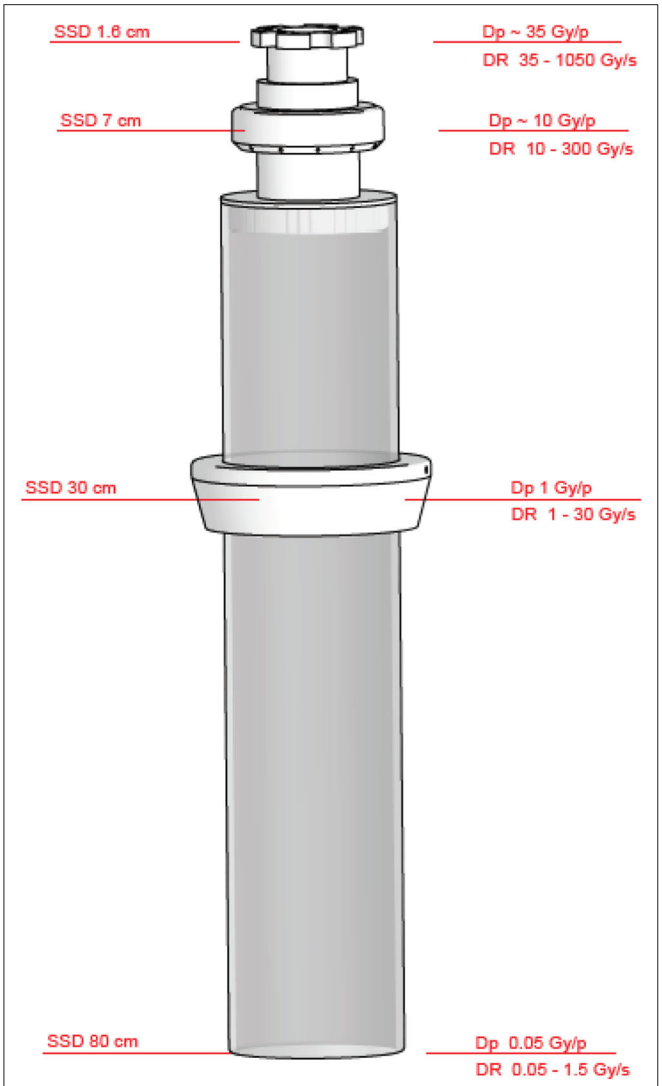

FIGURE 7 | Beam collimation and achievable SSDs, maximum dose rates, and dose per pulse achievable with NOVAC11 (applicator Ø10 cm).

determines the Source Surface Distance (SSD), which is 80 cm for the reference applicator with a diameter of 10 cm. Thanks to this relatively simple architecture, it is possible to obtain several collimation configurations (**Figure 6**). Every configuration leads to a different SSD and, consequently, to a different resulting dose-per-pulse.

The different setups are obtained as follows:

- Clinical reference configuration: upper and terminal applicator connected to the chambers housing (SSD 80 cm).
- Upper applicator connected to the monitor chambers housing (SSD 30 cm).
- Only monitor chambers housing (SSD 7 cm).
- Dismounted monitor chambers (SSD 1.6 cm).

In **Figure 7**, such configurations, together with the possible maximum achievable dose-rates, are detailed.

A more detailed description on how Novac can be converted into a FLASH research machine, and its dosimetric characterization is available in [28].

Dosimetric Equipment and Measurements

Even though NOVAC11 is not able to produce a FLASH beam suitable for radiobiological experiments, it is however possible, by changing the SSD, to reach a very high dose-per-pulse beam inside a small spot homogenous enough for the irradiation of small dosimeters like those considered in the present study. Due to the unsuitability of the dosimeters commonly used in the clinical practice—as they show saturation problems approaching to FLASH dose-rates—reference dosimetry was performed using radiochromic films. Radiochromic films are dose-rate independent, hence they allow an extensive dosimetric characterization of the e-beam. The GAFCHROMIC EBT-XD [35] calibration curve has been obtained by irradiating the films with increasing dose values in the range from 0 to 150 Gy, by positioning the films in a PMMA solid phantom at R_{100} depth. The calibration fitting function, according to the optimized protocol for calibration and dosimetry [36] distributed by Ashland, is represented by the rational function:

$$f(x) = A + B/(x - C)$$

where A, B, and C are parameters of the function, and $f(x)$ and x are, respectively, the absorbed dose in cGy and the color value in 16 bpch [36], as read by the RGB scanner Epson 1680 Pro. Cross-calibration between optical densities and absolute dose-response has been performed by means of an ionization chamber in a conventional dose-rate range.

The detectors to be tested have been chosen among the commercially available ones adequate for measuring the beam produced by IORT linacs. IORT linac is the highest dose-per-pulse machine among the currently available medical linacs (3–13 cGy/p against 0.07–0.3 cGy/p). Radiochromic films (GAFCHROMIC EBT-XD) irradiated within a PMMA phantom have been considered as reference.

The online dosimetric systems tested were:

- PTW TW34045 Advanced Markus® Electron Chamber [37].
- PTW TM60017 Dosimetry Diode E [38].
- PTW TW60019 microDiamond [39].
- DoseVue DoseWire™ Series 100 scintillating fiber [40].

DoseWire is an inorganic scintillator detector consisting of a hemispherical 0.1 cc active volume of europium-doped yttrium oxide. The emission light is in the range 600–650 nm. If the dosimeter is used in its standard counter mode, the minimum time between two consecutive events, in order that the system is able to discriminate them, is of the order of 20 ns.

Results

Calibration curve calculated by the dedicated software FilmQA Pro is shown in **Figure 8**.

The focus of the present work is the saturation phenomena of the dosimetric systems tested. As previously discussed, saturation phenomena are primarily caused by the value of the dose-per-pulse D_p. At a value of 1 cGy/p, either the dosimeters cannot show

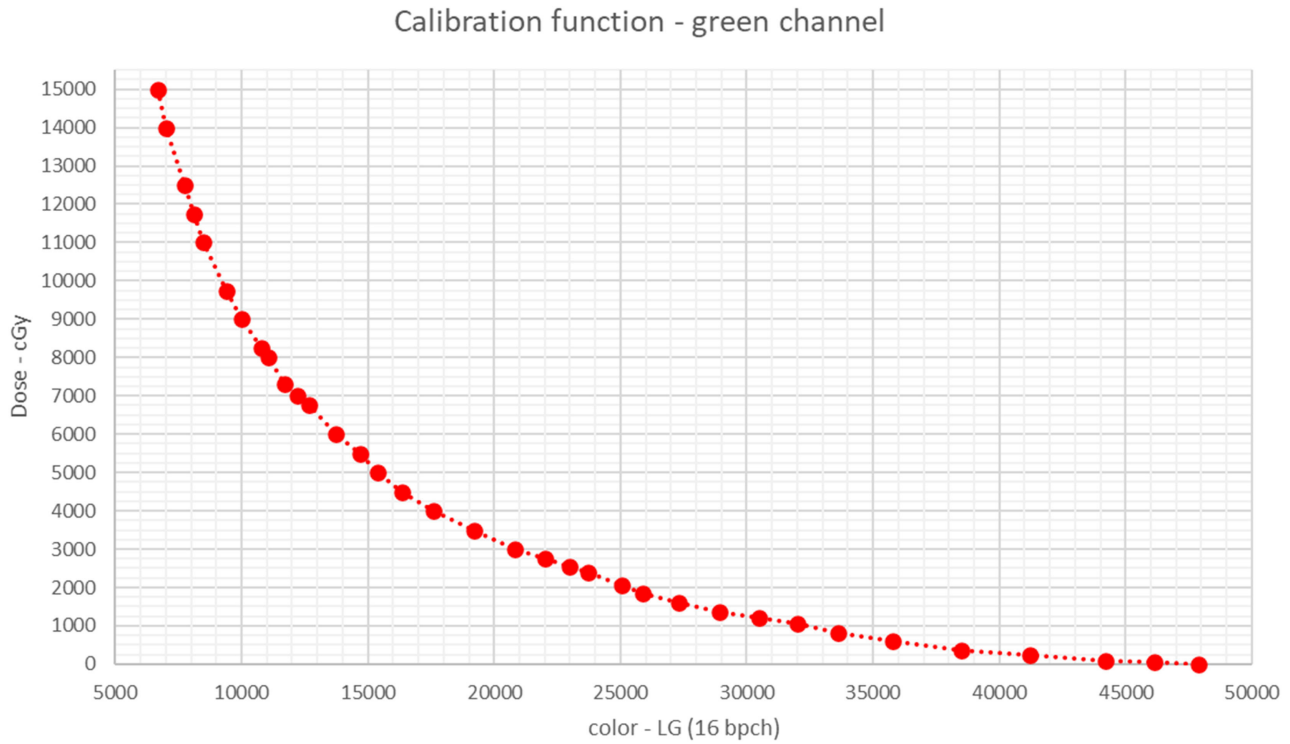

FIGURE 8 | Calibration fitting function in the green channel, as calculated by FilmQA Pro.

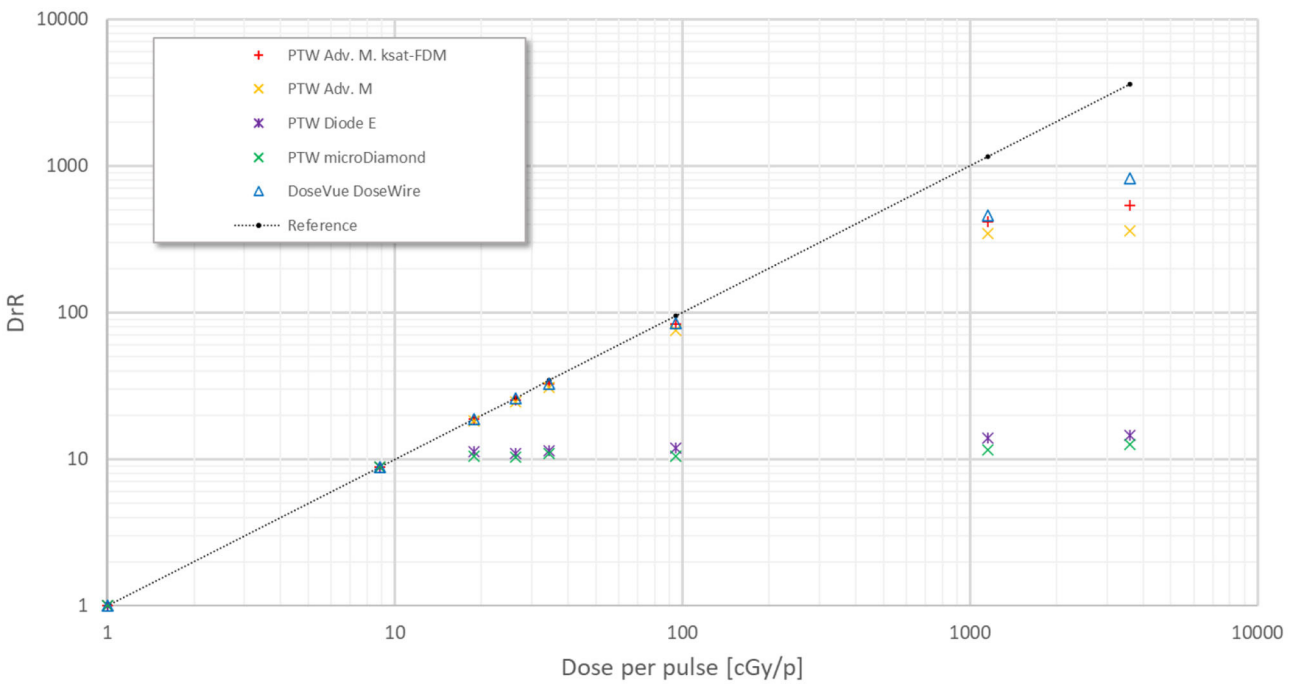

FIGURE 9 | DrR vs. dose per pulse.

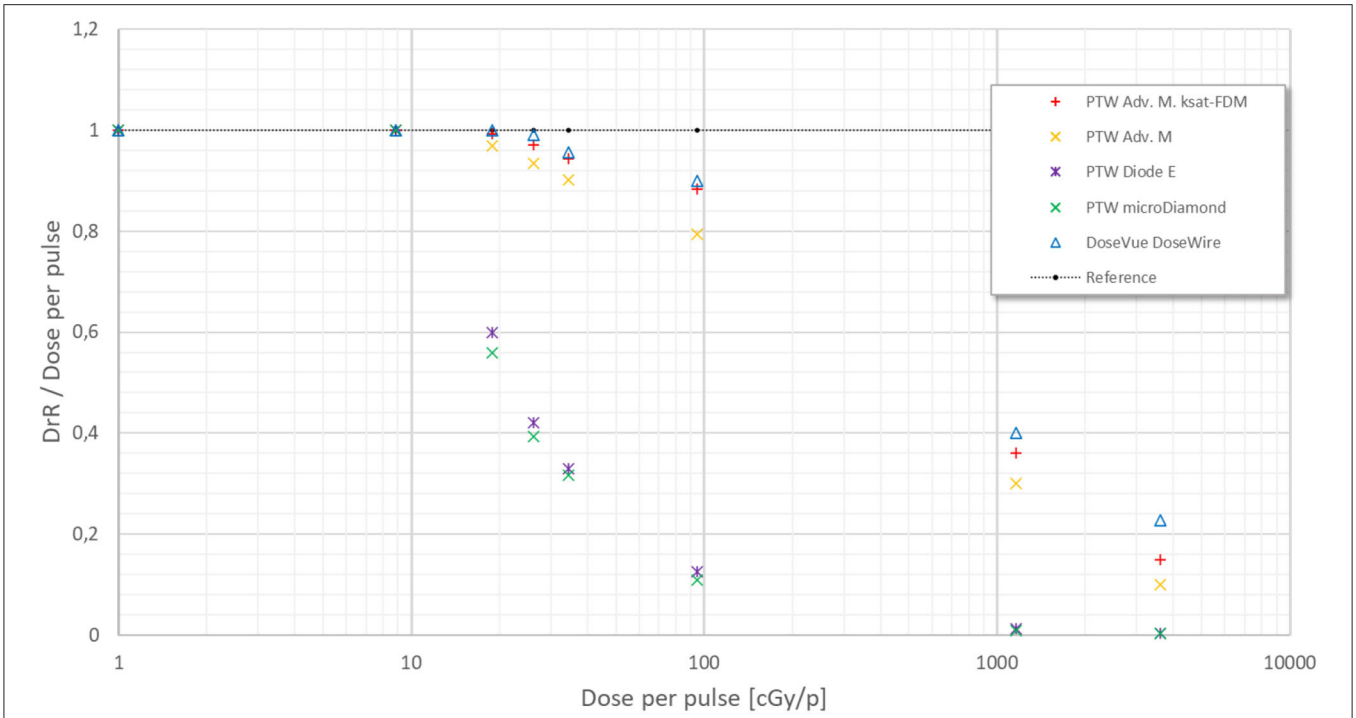

FIGURE 10 | DrR/dose-per-pulse vs. dose-per-pulse.

saturation phenomena (scintillator, diode, and microdiamond [26]) or their saturation can be correctly calculated (ionization chambers [24, 25, 27]). Then, we have considered the ratio between the reading of each dosimeter at varying the dose-per-pulse and its reading at $D_p = 1$ cGy/p; such ratio is called DrR (dosimeter reading ratio) in **Figure 9**.

DrR is defined as

$$DrR = \frac{R}{R|_{D_p\,=\,1\ cGy/p}} = \frac{R}{R_{REF}}$$

DrR combined standard uncertainty can be estimated as $\sigma_{DrR} = \sqrt{\left(\frac{\sigma_R}{R}\right)^2 + \left(\frac{\sigma_{R_{REF}}}{R_{REF}}\right)^2}$. The quantity $\frac{\sigma}{R}$ is evaluated as the standard deviation over five consecutive measurements and results always around or <0.7%; therefore, the combined standard uncertainty is smaller than 1% and it is not shown in the graphs of **Figures 9**, **10**.

The graphs are displayed in a double log plot in order to facilitate their visualization. Such approach offers an immediate and qualitative picture of dosimeters behavior in a very wide range. Ideally, for a dosimeter not affected by any saturation phenomena, DrR is a line with angular coefficient equal to 1, as for radiochromic films (reference black line in **Figure 9**).

In **Figure 10**, the ratio between DrR and the dose-per-pulse as measured by radiochromic films is reported.

The measurements performed offer a clear, even though preliminary, picture of the inadequacy of the current dosimetric equipment when operating in the FLASH region.

PTW Diode E and microDiamond semiconductors show a nonreversible saturation beyond a threshold around 15 cGy/p. DoseVue DoseWire™ Series 100 scintillators show a negligible saturation up to 1 Gy/p, it increases significantly up to at least 11 Gy/p and it reaches a cutoff value between 11 and 36 Gy/p.

PTW Advanced Markus® Ionization chamber saturation cannot be adequately described according to the methods reported in literature for values above 30 cGy/p: the Laitano et al. [25] model does not provide any solution while the Di Martino model [24] greatly underestimates the recombination effect, as shown in **Figure 10**. Such experimental results are consistent with the data reported by McManus et al. [41], even they adopt a Very High Energy Electrons (VHEE) system and the maximum dose per pulse is 5.26 Gy/p.

DISCUSSION AND CONCLUSION

The recent experimental evidence of the FLASH effect obtained *in vivo* has generated great interest within the radiotherapy community due to its potential and important clinical implications.

Before the radiobiological mechanisms underlying this effect could be fully understood, several technological and scientific challenges must be faced.

Such challenges affect the irradiator as well as the measuring devices.

This work presents the design of an electron linac dedicated to ultra-high dose rate experiments, ElectronFlash [42].

The specific problems and requirements generated by the acceleration and monitoring of a Flash electron beam are discussed, and some possible solutions are presented. The first EF unit will be installed in Institut Curie during summer 2020; a complete characterization of its performances will be presented in a future manuscript.

While electron linacs may be the simplest implementation for a Flash irradiator, they may represent the most complex challenge for dosimetry. Radiofrequency (RF)-powered electron linacs produce a heavily pulsed beam, with a dose per pulse up to 40 Gy/p or higher, with a pulse repetition frequency (PRF) up to 400 Hz.

On the other hand, proton and carbon ion accelerators produce a continuous or almost continuous beam; even when reaching the ultra-high dose rate region, their dosimetric characterization can be performed adopting the common dosimetric protocols, provided that saturation is determined with a different approach (the recombination theory for proton and light ions has been presented and discussed in [43]).

Thus, while Flash proton beams may be successfully measured within the framework of the current protocols [44], even with some adjustment in the determination of recombination factor [43], Flash electron beams may require a complete change of paradigm. The experimental results with ionization chambers, which confirm the data presented by McManus et al. [41], show the inadequacy of the current approaches [24, 25, 44] in determining the chamber saturation.

The analysis performed in **Appendix**, Section 1—Ionization Chambers shows that, for electron beams around 1 Gy/p or higher, the electric field generated by ionized charges exceeds the one generated by the polarization applied and, therefore, cannot be neglected. This may lead to the need of introducing a different, more complex model, capable of describing properly the chamber ionization behavior in the ultra-high dose rate region.

This may lead to the need of introducing a different and more complex model capable of describing properly the chamber ionization behavior in the ultra-high dose rate region.

Other dosimeters were studied: semiconductor diodes and scintillators.

The tested semiconductor dosimeters have a total saturation at a precise dose-per-pulse value (cutoff value) around 15 cGy/p that is significantly lower than the FLASH dose-per-pulse values. Hence, semiconductor dosimeters currently available on the market cannot be used.

The tested scintillator shows a dose-per-pulse response as expected, with the saturation increasing with the dose-per-pulse, reaching a cutoff value between 11 and 36 Gy/p, where saturation is no longer correctable.

The scintillator was used in its standard mode (counter mode); nevertheless, the analysis performed in **Appendix**, Section 2—Scintillators suggests that a better behavior could be reached if the system works in integrator mode, introducing a correction for the deadtime.

Additional studies are required for assessing this result properly.

The present work offers some possible solutions in the design of an electron Flash linac and raises many questions about its dosimetric characterization which remain to be answered.

A new linac concept has been described, a system capable of accelerating and monitoring the fluence needed for reaching the Flash beam dose rates studied so far [1, 2, 4, 5] and even beyond; the specific solutions implemented were discussed and its performances will be described in a future work after its installation in Institut Curie.

However, the Flash electron beam dosimetric characterization still poses unsolved challenges, for online dosimeters, both concerning relative and absolute dosimetry.

In particular, the current description of ionization chambers behavior in the Flash region for electron beams is not adequate. When dose-per-pulse is around or above 1 Gy/p, the shielding effect of the electric field generated by the ionized charges, during their movement toward the two opposite electrodes, is no longer negligible. Therefore, the current recombination models [24, 25, 44], which totally neglect such effect, do not properly describe saturation phenomena in FLASH dose-per-pulse regime. New theoretical models must be developed and experimentally validated before ionization chambers could be used for FLASH beam dosimetry.

In conclusion, it is possible to state that there is a lot of research to be done before the dosimetric characterization of Flash electron beams will be fully understood.

DATA AVAILABILITY STATEMENT

The raw data supporting the conclusions of this article will be made available by the authors, without undue reservation.

AUTHOR CONTRIBUTIONS

FM and GF designed the study. FM, LGr, and GF wrote the manuscript. LF, LGi, MM, and LP performed the simulations shown in **Figure 3**. All authors discussed the manuscript and performed the experimental job. All authors contributed to the article and approved the submitted version.

FUNDING

Sordina IORT Technology has provided funds for open access fees.

ACKNOWLEDGMENTS

The authors thank Ilaria Breglia for the English revision of the paper and Emiliano D'Agostino, DoseVue founder, for his helpful scientific comments and discussion.

SUPPLEMENTARY MATERIAL

The Supplementary Material for this article can be found online at: https://www.frontiersin.org/articles/10.3389/fphy.2020.570697/full#supplementary-material

REFERENCES

1. Fouillade C, Favaudon V, Vozenin M-C, Romeo P-H, Bourhis J, Verrelle P, et al. Les promesses du haut débit de dose en radiothérapie. *Bull Cancer (Paris).* (2017) 104:380–4. doi: 10.1016/j.bulcan.2017.01.012
2. Favaudon V, Caplier L, Monceau V, Pouzoulet F, Sayarath M, Fouillade C, et al. Ultrahigh dose-rate FLASH irradiation increases the differential response between normal and tumor tissue in mice. *Sci Transl Med.* (2014) 6:245ra93–ra93. doi: 10.1126/scitranslmed.3008973
3. Montay-Gruel P, Petersson K, Jaccard M, Boivin G, Germond J-F, Petit B, et al. Irradiation in a flash: Unique sparing of memory in mice after whole brain irradiation with dose rates above 100 Gy/s. *Radiother Oncol.* (2017) 124:365–9. doi: 10.1016/j.radonc.2017.05.003
4. Bourhis J, Montay-Gruel P, Gonçalves Jorge P, Bailat C, Petit B, Ollivier J, et al. Clinical translation of FLASH radiotherapy: why and how? *Radiother Oncol.* (2019) 139:11–7. doi: 10.1016/j.radonc.2019.04.008
5. Bourhis J, Sozzi WJ, Jorge PG, Gaide O, Bailat C, Duclos F, et al. Treatment of a first patient with FLASH-radiotherapy. *Radiother Oncol.* (2019) 139:18–22. doi: 10.1016/j.radonc.2019.06.019
6. Buonanno M, Grilj V, Brenner DJ. Biological effects in normal cells exposed to FLASH dose rate protons. *Radiother Oncol.* (2019) 139:51–5. doi: 10.1016/j.radonc.2019.02.009
7. Simmons DA, Lartey FM, Schüler E, Rafat M, King G, Kim A, et al. Reduced cognitive deficits after FLASH irradiation of whole mouse brain are associated with less hippocampal dendritic spine loss and neuroinflammation. *Radiother Oncol.* (2019) 139:4–10. doi: 10.1016/j.radonc.2019.06.006
8. Montay-Gruel P, Acharya MM, Petersson K, Alikhani L, Yakkala C, Allen BD, et al. Long-term neurocognitive benefits of FLASH radiotherapy driven by reduced reactive oxygen species. *Proc Natl Acad Sci U S A.* (2019) 116:10943–51. doi: 10.1073/pnas.1901777116
9. Vozenin M-C, Baumann M, Coppes RP, Bourhis J. FLASH radiotherapy International Workshop. *Radiother Oncol.* (2019) 139:1–3. doi: 10.1016/j.radonc.2019.07.020
10. Freeman T. *FLASH Radiotherapy: From Preclinical Promise to the First Human Treatment.* Phys World (2019). Available online at: https://physicsworld.com/a/flash-radiotherapy-from-preclinical-promise-to-the-first-human-treatment/
11. Durante M, Brauer-Krisch E, Hill M. Faster and safer? FLASH ultra-high dose rate in radiotherapy. *Br J Radiol.* (2018) 91:20170628. doi: 10.1259/bjr.20170628
12. Spitz DR, Buettner GR, Petronek MS, St-Aubin JJ, Flynn RT, Waldron TJ, et al. An integrated physico-chemical approach for explaining the differential impact of FLASH versus conventional dose rate irradiation on cancer and normal tissue responses. *Radiother Oncol.* (2019) 139:23–7. doi: 10.1016/j.radonc.2019.03.028
13. Pratx G, Kapp DS. A computational model of radiolytic oxygen depletion during FLASH irradiation and its effect on the oxygen enhancement ratio. *Phys Med Biol.* (2019) 64:185005. doi: 10.1088/1361-6560/ab3769
14. Spitz DR, Buettner GR, Limoli CL. Response to letter regarding "An integrated physico-chemical approach for explaining the differential impact of FLASH versus conventional dose rate irradiation on cancer and normal tissue responses." *Radiother Oncol.* (2019) 139:64–5. doi: 10.1016/j.radonc.2019.07.009
15. Maxim PG, Keall P, Cai J. FLASH radiotherapy: newsflash or flash in the pan? *Med Phys.* (2019) 46:4287–90. doi: 10.1002/mp.13685
16. Jolly S, Owen H, Schippers M, Welsch C. Technical challenges for FLASH proton therapy. *Phys Med.* (2020) 78:71–82. doi: 10.1016/j.ejmp.2020.08.005
17. Esplen NM, Mendonca MS, Bazalova-Carter M. Physics and biology of ultrahigh dose-rate (FLASH) radiotherapy: a topical review. *Phys Med Biol.* (2020). doi: 10.1088/1361-6560/abaa28. [Epub ahead of print].
18. Lansonneur P, Favaudon V, Heinrich S, Fouillade C, Verrelle P, De Marzi L. Simulation and experimental validation of a prototype electron beam linear accelerator for preclinical studies. *Phys Med.* (2019) 60:50–7. doi: 10.1016/j.ejmp.2019.03.016
19. Jaccard M, Durán MT, Petersson K, Germond J-F, Liger P, Vozenin M-C, et al. High dose-per-pulse electron beam dosimetry: commissioning of the Oriatron eRT6 prototype linear accelerator for preclinical use. *Med Phys.* (2018) 45:863–74. doi: 10.1002/mp.12713
20. Jorge PG, Jaccard M, Petersson K, Gondré M, Durán MT, Desorgher L, et al. Dosimetric and preparation procedures for irradiating biological models with pulsed electron beam at ultra-high dose-rate. *Radiother Oncol.* (2019) 139:34–9. doi: 10.1016/j.radonc.2019.05.004
21. Lempart M, Blad B, Adrian G, Bäck S, Knöös T, Ceberg C, et al. Modifying a clinical linear accelerator for delivery of ultra-high dose rate irradiation. *Radiother Oncol.* (2019) 139:40–5. doi: 10.1016/j.radonc.2019.031
22. National Council on Radiation Protection and Measurements. *Structural Shielding Design and Evaluation for Megavoltage X- and Gamma-Ray Radiotherapy Facilities: Recommendations of the National Council on Radiation Protection and Measurements*. Bethesda, MD: National Council on Radiation Protection and Measurements (2005).
23. Medical Electrical Equipment - Part 2-1: Particular Requirements for the Basic Safety and Essential Performance of Electron Accelerators in the Range 1 MeV to 50 MeV.
24. Di Martino F, Giannelli M, Traino AC, Lazzeri M. Ion recombination correction for very high dose-per-pulse high-energy electron beams: ksat evaluation for very high dose-per-pulse electron-beams. *Med Phys.* (2005) 32:2204–10. doi: 10.1118/1.1940167
25. Laitano RF, Guerra AS, Pimpinella M, Caporali C, Petrucci A. Charge collection efficiency in ionization chambers exposed to electron beams with high dose per pulse. *Phys Med Biol.* (2006) 51:6419–36. doi: 10.1088/0031-9155/51/24/009
26. Pimpinella M, Andreoli S, De Angelis C, Della Monaca S, D'Arienzo M, Menegotti L. Output factor measurement in high dose-per-pulse IORT electron beams. *Phys Med.* (2019) 61:94–102. doi: 10.1016/j.ejmp.2019.04.021
27. Scalchi P, Ciccotelli A, Felici G, Petrucci A, Massafra R, Piazzi V, et al. Use of parallel-plate ionization chambers in reference dosimetry of NOVAC and LIAC ® mobile electron linear accelerators for intraoperative radiotherapy: a multi-center survey. *Med Phys.* (2017) 44:321–32. doi: 10.1002/mp.12020
28. Felici G, Barca P, Barone S, Bortoli E, Borgheresi R, De Stefano S, et al. Transforming an IORT Linac Into a FLASH Research Machine: procedure and dosimetric characterization. *Front Phys.* (2020) 8:374. doi: 10.3389/fphy.2020.00374
29. Felici G, DiFrancesco M, De Stefano S, Grasso L. 349. IORT dedicated linac radiation protection: a novel approach. *Phys Med.* (2018) 56:271–2. doi: 10.1016/j.ejmp.2018.04.357
30. Wangler TP. *RF Linear Accelerators*. 1st edn. Weinheim: Wiley (2008).
31. Dispositivo di Misura dell'energia del Fascio di Particelle in Uscita da Acceleratori IORT. Italian Patent IT102015000009805
32. Khan FM, Gibbons JP. *Khan's the Physics of Radiation Therapy*. Philadelphia, PA: Lippincott Williams & Wilkins/Wolters Kluwer (2014).
33. Leggieri A, Passi D, di Paolo F, Ciccotelli A, De Stefano S, Marangoni F, et al. Real-time beam monitor for charged particle medical accelerators. *IEEE Trans Nucl Sci.* (2016) 63:869–77. doi: 10.1109/TNS.2015.2504403
34. Stevens P, Van Hoof F, Messens E, Holvoet M, Verellen D. IORT & stray radiation: comparison of 2 commercial linacs. in: *Electronic Poster: Physics Track: Radiation Protection, Secondary Tumour Induction and Low Dose (Incl. Imaging)* (2019) 133(Suppl 1):S909S910. doi: 10.1016/S0167-8140(19)32111-5
35. Gafchromic™ radiotherapy films Chemistry: Radiochromic Film. Available online at: https://www.ashland.com/industries/medical/medical-radiation-dosimetry/gafchromic-radiotherapy-films#
36. Lewis D, Micke A, Yu X, Chan MF. An efficient protocol for radiochromic film dosimetry combining calibration and measurement in a single scan: efficient protocol for radiochromic film dosimetry. *Med Phys.* (2012) 39:6339–50. doi: 10.1118/1.4754797
37. Advanced Markus® Electron Chamber. Available online at: https://www.ptwdosimetry.com/en/products/advanced-markus-electron-chamber/
38. Dosimetry Diode E Type 60017. Available online at: https://www.rpdinc.com/ptw-dosimetry-diode-981.html

39. microDiamond. Available online at: https://www.ptwdosimetry.com/en/products/microdiamond/
40. DoseVue DoseWire™ Series 100. Available online at: https://www.dosevue.com/index.php/product-line
41. McManus M, Romano F, Lee ND, Farabolini W, Gilardi A, Royle G, et al. The challenge of ionisation chamber dosimetry in ultra-short pulsed high dose-rate Very High Energy Electron beams. *Sci Rep*. (2020) 10:9089. doi: 10.1038/s41598-020-65819-y
42. Dispositivo Per Il Trattamento Radioterapico Di Malati Oncologici. Italian Patent Application N. 102019000016760 19.09.2019
43. Rossomme S, Delor A, Lorentini S, Vidal M, Brons S, Jäkel O, et al. Three-voltage linear method to determine ion recombination in proton and light-ion beams. *Phys Med Biol*. (2020) 65:045015. doi: 10.1088/1361-6560/ab3779
44. International Atomic Energy Agency ed. *Absorbed Dose Determination in External Beam Radiotherapy: An International Code of Practice for Dosimetry Based on Standards of absoorbed doose to watoer*. Vienna: International Atomic Energy Agency (2001).

Conflict of Interest: SB, SD, MD, GF, LGr, and MP are SIT employees; GF is a SIT shareholder. Nonetheless, they confirm that this does not affect the design and preparation of the paper neither the analysis nor the interpretation of data.

The remaining authors declare that the research was conducted in the absence of any commercial or financial relationships that could be construed as a potential conflict of interest.

The handling editor declared a past supervisory role with one of the authors MP.

frontiers in Physics

CORRECTION
published: 27 January 2021
doi: 10.3389/fphy.2020.630534

Corrigendum: FLASH Radiotherapy With Electrons: Issues Related to the Production, Monitoring, and Dosimetric Characterization of the Beam

Fabio Di Martino[1], Patrizio Barca[1], Salvatore Barone[2], Eleonora Bortoli[1], Rita Borgheresi[1], Silvia De Stefano[2], Massimo Di Francesco[2], Luigi Faillace[3], Lucia Giuliano[3], Luigi Grasso[2], Stefania Linsalata[1], Daniela Marfisi[1], Mauro Migliorati[3], Matteo Pacitti[2], Luigi Palumbo[3] and Giuseppe Felici[2]**

[1]U.O. Fisica Sanitaria, Azienda Universitaria Ospedaliera Pisana, Pisa, Italy, [2]Sordina IORT Technologies, R&D Department, Aprilia, Italy, [3]Sapienza University of Rome, Rome, Italy

Keywords: radiotherapy, FLASH effect, FLASH electron linac, beam monitoring system, saturation problems

A Corrigendum on

FLASH Radiotherapy With Electrons: Issues Related to the Production, Monitoring, and Dosimetric Characterization of the Beam

by *Fabio, D. M., Patrizio, B., Salvatore, B., Eleonora, B., Rita, B., Silvia, D. S., Massimo, D. F., Luigi, G., Stefania, L., Daniela, M., Matteo, P., and Giuseppe, F. (2020). Front. Phys. 8:481. doi: 10.3389/fphy.2020.570697*

In the original article, the following authors were missing: Luigi Faillace, Lucia Giuliano, Mauro Migliorati, Luigi Palumbo. The corrected **Author Contributions** statement appears below.

Affiliation 3, 'Sapienza University of Rome, Rome, Italy', is also added for authors LF, LG, MM, and LP.

The authors apologize for these errors and state that this does not change the scientific conclusions of the article in any way. The original article has been updated.

AUTHOR CONTRIBUTIONS

FM and GF designed the study. FM, LGr, and GF wrote the manuscript. LF, LGi, MM, and LP performed the RF and beam dynamics simulations for the accelerating waveguide. All authors discussed the manuscript and performed the experimental job. All authors contributed to the article and approved the submitted version.

Conflict of Interest: SB, SD, MD, GF, LGr, and MP are SIT employees; GF is a SIT shareholder. LF, LGi, MM, and LP work was partially financed by a SIT research contract. Nonetheless, they confirm that this does not affect the design and preparation of the paper neither the analysis nor the interpretation of data.

The remaining authors declare that the research was conducted in the absence of any commercial or financial relationships that could be construed as a potential conflict of interest.

OPEN ACCESS

Approved by:
Frontiers Editorial Office, Frontiers Media SA, Switzerland

***Correspondence:**
Fabio Di Martino
f.dimartino@ao-pisa.toscana.it
Giuseppe Felici
giuseppe.felici@sordina.com

Specialty section:
This article was submitted to Medical Physics and Imaging, a section of the journal Frontiers in Physics

Received: *17 November 2020*
Accepted: *10 December 2020*
Published: *27 January 2021*

Citation:
Di Martino F, Barca P, Barone S, Bortoli E, Borgheresi R, De Stefano S, Di Francesco M, Faillace L, Giuliano L, Grasso L, Linsalata S, Marfisi D, Migliorati M, Pacitti M, Palumbo L and Felici G (2021) Corrigendum: FLASH Radiotherapy With Electrons: Issues Related to the Production, Monitoring, and Dosimetric Characterization of the Beam. Front. Phys. 8:630534. doi: 10.3389/fphy.2020.630534

frontiers in Physics

ORIGINAL RESEARCH
published: 09 November 2020
doi: 10.3389/fphy.2020.578662

Single Molecule Localization Microscopy Analyses of DNA-Repair Foci and Clusters Detected Along Particle Damage Tracks

Michael Hausmann[1], Charlotte Neitzel[1], Elizaveta Bobkova[1], David Nagel[1], Andreas Hofmann[2], Tatyana Chramko[3], Elena Smirnova[3], Olga Kopečná[4], Eva Pagáčová[4], Alla Boreyko[3], Evgeny Krasavin[3], Iva Falkova[4], Dieter W. Heermann[2], Götz Pilarczyk[1], Georg Hildenbrand[1], Felix Bestvater[5] and Martin Falk[4]**

[1]Kirchhoff-Institute for Physics, Heidelberg University, Heidelberg, Germany, [2]Institute for Theoretical Physics, Heidelberg University, Heidelberg, Germany, [3]Joint Institute for Nuclear Research, Dubna, Russia, [4]Czech Academy of Sciences, Institute of Biophysics, Brno, Czech Republic, [5]German Cancer Research Center (DKFZ), Heidelberg, Germany

OPEN ACCESS

Edited by:
Yolanda Prezado,
INSERM U1021 Signalisation Normale et Pathologique de L'embryon aux ThÃ©rapies Innovantes des Cancers, France

Reviewed by:
Charlot Vandevoorde,
iThemba Laboratory, South Africa
Judith Reindl,
Munich University of the Federal Armed Forces, Germany

***Correspondence:**
Michael Hausmann
hausmann@kip.uni-heidelberg.de
Martin Falk
falk@ibp.cz

Specialty section:
This article was submitted to Medical Physics and Imaging, a section of the journal Frontiers in Physics

Received: 30 June 2020
Accepted: 22 September 2020
Published: 09 November 2020

Citation:
Hausmann M, Neitzel C, Bobkova E, Nagel D, Hofmann A, Chramko T, Smirnova E, Kopečná O, Pagáčová E, Boreyko A, Krasavin E, Falkova I, Heermann DW, Pilarczyk G, Hildenbrand G, Bestvater F and Falk M (2020) Single Molecule Localization Microscopy Analyses of DNA-Repair Foci and Clusters Detected Along Particle Damage Tracks. Front. Phys. 8:578662. doi: 10.3389/fphy.2020.578662

High-LET (Linear Energy Transfer) particle irradiation as being provided from heavy ion accelerator facilities has an increasing impact on bio-medical research and cancer treatment. Nevertheless, there are a lot of open questions concerning the understanding of damaging mechanisms and repair processes within the light of radio-sensitivity and thus, individualized medical applications. The three-dimensional architecture of genomes on the meso- and nano-scale acts in combination with epigenetic gene activation as an important player of gene regulation and fundamental biological processes such as DNA damage response and repair. So far only little is known about the impact of high-LET particles on the chromatin architecture along the passing track when they are "lumbering" through the cell nucleus. How does a cell nucleus manage such complex damages and re-organize the chromatin toward functionally intact units? Is there a radio-sensitivity related difference in this reaction? Here, we present some approaches to investigate spatial and topological parameters of chromatin to glimpse some aspects related to these questions. Two cell lines, a radio-resistant glioblastoma and a radio-sensitive fibroblast cell line, were used and irradiated by ^{15}N-ions in 90° and 10° radiation beam geometry. Nano-probing of particle induced damage sites along particle tracks, and the recruited DNA repair proteins (as presented here for 53BP1 and Rad51) in combination with super-resolution Single Molecule Localization Microscopy (SMLM) are powerful methods for geometric and topological analyses to study particle related mechanisms of chromatin conformation and repair complexes in single cells. We used variable tools for such investigations based on image free high precision SMLM, nano-scaled molecule distribution analyses, appropriate metrics following Ripley's distance frequencies and cluster formation analyses, as well as topological quantifications employing persistence homology. The data reveal a cell type specific nano-architecture of DNA damage foci along particle tracks and their dynamic molecular re-arrangements during repair. Comparing the topology of repair foci by persistence homology suggests similarities of repair cluster formation along given particle tracks. Our studies contribute to

the molecular understanding of cellular radiation response at sub-light microscopic chromatin levels; thereby showing how chromatin architecture around complex damage sites and repair foci nano-architecture may contribute to ongoing repair processing. The methodological approach presented here may give a basis for improved biological dosimetry or radiotherapies in the future.

Keywords: heavy ion irradiation, single molecule localization microscopy, Ripley distance frequency analysis, topological analysis, persistent homologies, ionizing radiation-induced foci, DNA double strand breaks

INTRODUCTION

All over the Universe, matter is subjected to extreme conditions as for instance high temperatures, pressures, and densities. Stellar collisions and explosions prepare ultra-fast heavy ions interacting with any material crossing their ways. With mankind´s quest to discover space and our planetary system not only by vehicles but also by manned space missions, an understanding of interactions of these heavy ions with biological and especially cellular systems has become an urgent demand to science [1]. Modern nuclear accelerators enable researchers to create radiation conditions of space in the earth-based laboratory. Particle beams of various elements at different intensities and qualities can be generated and applied on cells, tissues, organs or organisms. While protective systems to control or even to avoid accidental exposure of humans on space missions are under development [2, 3], targeted applications as for instance the powerful treatment tool against aggressive tumors especially brain tumors, have been established worldwide in medicine [4, 5].

Up to now research has delivered a huge amount of knowledge and findings of biological, epigenetic response to low-LET (Linear Energy Transfer) photon and high-LET particle irradiation; thereby a lot of questions concerning damaging profiles and repair response remain unanswered [6–10]. Scientific results improving the understanding of mechanisms behind damaging and repair are demanded in order to optimize space mission planning or to individualize radiation treatment [11]. Therefore not only defined radiation experiments in accelerator facilities are required but also novel tools to elucidate components of epigenetic control and their impact on radiation response.

Radiation induced DNA damages are depending on the dose, dose rate, LET, radiation type, cell radio-sensitivity, DNA repair capacity, etc. In contrast to low-LET photon irradiation which induces DNA damages in a coarse gain pattern, high-LET particles (e.g., protons, α-particles, heavy ions) pass the chromatin in linear tracks [12] along which a complex damaging process happens, which locally may lead to an overload of single (SSB) and double strand breaks (DSB) [13–15]. The most severe damages being created are complex double-stranded breaks (DSBs) of the DNA molecule [16]. These complex lesions consist of several SSBs and DSBs generated in close mutual proximity in combination with other types of DNA damages [17] and highly challenge all repair mechanisms being available for cellular survival [18–20]. Multiple complex DSBs often remain unrepaired which leads to cell death, the treatment effect envisaged in successful radiation cancer therapy.

On the other hand, escaping cell death, the complexity of lesions increases the risks of dysfunctional cells with mutations and chromosome aberrations, a serious problem, which medical radiation treatment schemes always have to avoid [21–23]. In contrast to cell death being required for heavy ion radiation therapy, radiation protection in the field of long-term space missions planned [2] should save the cells in their best functional conditions. These extremely opposite demands show the urgent need for further investigations in order to better understand the mechanisms of DNA damaging and repair.

In general, the genome is responding to DSBs by specific phosphorylation of histone H2AX in a 2 Mbp region surrounding the chromatin damage site, which can be visualized in form of so-called γH2AX foci [24, 25] against which specific antibodies are available. Inside these foci, the cell starts to repair the damage by recruiting and releasing a complex network of proteins along given repair pathways. The main repair pathways are the canonic non-homologous end-joining (c-NHEJ), the homologous recombination (HR) and the less precisely classified alternative (or backup) pathways, such as Ku-independent non-homologous end-joining (a-NHEJ), single-strand annealing (SSA) or microhomology-mediated end-joining (MMEJ) [26–30].

All these repair pathways are functioning differently and recruit different series and amounts of repair proteins to the initially induced γH2AX damage foci. The main differences in the chosen pathways are the speed and quality of repair. HR is very precise in maintaining the base sequence of the damaged region exactly; thereby it is slow since an appropriate DNA sequence template has to be arranged, the damaged sites have to be resected correctly, and nucleotide by nucleotide has to be reconstructed. In contrast to HR, c-NHEJ is fast but tolerates the loss of some nucleotides in the new strand after trimming and "sticking" the broken ends together. a-NHEJ and other alternative pathways only seem to play a significant role after multiple damaging by high dose exposure. Due to a lack of availability of enough repair proteins, broken ends are repaired under omitting some typical c-NHEJ proteins with the consequence of being slow and more error prone. Repair errors also occur due to illegitimate recombination between short homologous sequences or repeats.

At a first glimpse, it appears that a cell decides individually or even randomly which repair pathway is used at a given damage site. However, a more detailed view on repair processes reveals that repair pathway selection is depending on several conditions like the phase of the cell cycle, the chromatin structure and compaction at the site of damage, the complexity and multiplicity of DSBs, the general radiation sensitivity of the cell type, and potentially several other factors [19, 31–42]. All these factors

contributing to repair pathway choice at a given damage site in a given cell type require a complex epigenetic controlling system [9, 10] that may interact according to so far not fully understood rules.

Beyond the "classical" epigenetic systems following so far known epigenetic protein pathways, another level of epigenetic function and control appears to be relevant for further consideration especially in case of complex damaging processes. This epigenetic system, not pushed into the focus of investigations, yet, is the chromatin architecture. Chromatin architecture is known to be functionally organized [43, 44] on the micro-, meso- and nano-scale, and its relaxation and precisely regulated re-arrangements were observed at damage sites [6, 45]; reviewed in Ref. 8 [9, 10]. On the sub-micro scale, local chromatin architecture changes after DNA-damage induction and along repair processes. In the context of chromatin architecture, two perspectives have to be considered: a) the broken chromatin strands with their chemically different ends, environment of H2AX phosphorylation and variable mobility [6]; [8], and b) the spatial organization of repair protein during formation and release of repair complexes (visible as repair foci). Understanding how spatial arrangements of chromatin and recruited proteins impact DNA repair, requires a precise analysis of geometry and topology of single molecules of γH2AX as well as of by repair proteins forming foci, e.g., MRE11, 53BP1, RAD51, etc. Counting of these foci, generally known as Ionizing Radiation-Induced Foci (IRIFs), by means of light microscopy has become a well established measure for intra-cellular dosimetry [14, 46, 47]. Until recently, the investigations of nano-architecture of chromatin and repair complexes had to rely on electron microscopy [48–50], which, however, suffers from serious limitations and disadvantages. A breakthrough in the field was brought about by the development of super-resolution light microscopy techniques [51, 52], based on specific labeling of the target molecules that allowed to overcome Abbes' diffraction limit [15, 45, 53–56].

For low-LET radiation, the numbers of DSBs and labeled γH2AX foci are directly correlated, although it is still under debate whether and how many DSBs are joined together within one IRIF. For high-LET radiation, it has become obvious that foci are enlarged and their number is considerably below the predicted number of DSBs [14, 57, 58]. This phenomenon can be explained by overlapping and aggregation of several foci in a not well defined way. The internal architecture and complexity of repair foci after high-LET particle traversing, however, have not been systematically and thus satisfyingly investigated. The spatial structure, organization, and topology of IRIF thus remain to be intensively discussed. Open questions such as the arrangement of elementary or functional foci sub-units call for further research on the nature and typical parameters (shape, size, quantitative composition, etc.) of these still mysterious structures and their relationship to particular repair pathways.

Investigations using super-resolution light microscopy or electron microscopy revealed sub-structures like clusters within γH2AX or repair protein (e.g., 53BP1, MRE11, Rad51, pATM etc.) foci. These cluster can be observed independently of nature or the LET of radiation [49, 54, 56, 59–65]. For low-LET irradiation, the number of repair-focus sub-units (clusters) seems to better correlate with the number of DSBs and damage complexity than the number of IRIFs detected at the microscale [54]. In addition, after low-LET irradiation, γH2AX cluster sub-units were found to show high topological similarity provided they were closely associated to heterochromatin [66].

For high-LET irradiation, beyond the analyses of γH2AX foci and sub-units [15, 16], it has become obvious that the architecture and topology of the clusters of the follow-up recruited repair proteins is important with respect to the question of spatial organization of molecules as epigenetic control systems. 53BP1 foci were analyzed in more detail [15, 55, 56] after high-LET radiation exposure. 53BP1 is involved in NHEJ and acts as a stabilizing factor during HR [67]. 53BP1 binds to methylated regions of histones where it interacts with other repair proteins, for instance to promote NHEJ. During such interactions, 53BP1 could be displaced from the primary damaged sites [68, 69] opening them for instance for access of BRCA1 or CtIP.

SMLM [70, 71] has been successfully applied to study DNA repair and cluster formation of γH2AX molecules under low-LET radiation condition [53, 54, 72] and during long-term cell culture under folate deficiency [73]. Foci and sub-focus clusters of repair proteins were also investigated after particle irradiation [15, 55, 56].

SMLM of fluorescently tagged 53BP1 molecules was performed and clusters of these tags were determined as sub-units of repair foci, so that the formation and relaxation of these clusters could be studied during the repair period [15, 55].

In the article presented here, we continue in the analysis of 53BP1 clustering after ^{15}N particle irradiation with the focus on cluster size and environment during repair. In addition, we will show that persistent homologies of clusters as being calculated by topological methods of mathematics show different degrees of similarities in cell lines of high and low radio-sensitivity. These tools exemplarily presented here may be used to classify foci with respect of their follow-up repair mechanisms. Nitrogen ions were used as they are relevant for both space research and radiotherapy. They are present in galactic and solar cosmic radiation [74] and are extensively produced when cosmic radiation interacts with the atmosphere [75]. Interestingly, Pioneer 10 spacecraft have revealed increased (up to the factor of 20) amounts of N (and O) ions relative to their abundance in galactic or solar cosmic rays, pointing to specific sources of this component of cosmic radiation in the Universe [76]. N-ions are also generated during hadron radiation therapy and may significantly contribute to the patients' absorbed dose [77]. Nitrogen ion beams have been also studied as promising particles for radiotherapy [78].

MATERIALS AND METHODS

Cell Culture and Specimen Preparation

Cell culturing and specimen preparation has been described in detail elsewhere [14, 15, 55]. In brief: Primary neonatal human dermal fibroblasts (NHDF) and human U87 glioblastoma cells

TABLE 1 | Radiation values of the experiments.

Irradiation angle	Dose [Gy]	Energy [MeV/n]	LET [keV/μm]	Fluence [10^6/cm] per 1 Gy	Expected Mean Number of Particles/Nucleus
10°	1.3	13.1	181.4	3.40	2.1
90°	4.0	13.0	182.9	3.41	25.4

were cultured in Dulbecco's modified Eagle medium (DMEM) supplemented with 10% fetal calf serum (FCS) and a 1% gentamicin-glutamine solution (all reagents from Sigma-Aldrich). For the ion-radiation experiments, the cells were maintained in T 25 cell flasks at 37 °C in a humidified atmosphere with 5% CO_2. 16 – 18 h before irradiation, cells were seeded on glass coverslips fixed on bottoms of Petri dishes and cultivated until 80% confluence. The cells were irradiated at room temperature. After irradiation the samples were further cultivated and individual slides in duplicates were fixed with 4% formaldehyde/PBS (phosphate-buffered saline) at indicated periods of times post-irradiation (PI), ranging from 5 min PI to 24 h PI (5, 15 min (10° only), 30, 45 min (10° only), 1, 2, 4, 8, 24 h). This approach ensured that cells of the same condition (proliferation phase, cell cycle distribution, and physiological status) were analyzed at all post irradiation time point. For fluorescence labeling, the cells were washed twice in 1x PBS, permeabilized in 0.2% Triton X-100 at RT, washed again three times in 1× PBS, and incubated in 2% bovine serum albumin (BSA) for 60 min at RT. Primarily rabbit anti-53BP1 (ab21083, Abcam) antibodies or rabbit anti-Rad51 (ab63801, Abcam) antibodies, respectively, were added to the cells and the cells were rinsed with 0.2% Triton X-100 and washed three times with 1× PBS for 5 min at RT. The secondary antibodies, AlexaFluor 594-conjugated goat anti-rabbit (Johnson Laboratories) (53BP1), or Alexa Fluor 568-conjugated donkey anti-rabbit (ThermoFisher Scientific) (Rad51), respectively, were applied to the cells for 30 min and again the cells were washed three times in 1× PBS for 5 min and counterstained with DAPI. After washing the slides three times in 1× PBS for 5 min each, the cover slips were air dried, and the cells were embedded in ProLong Gold® (ThermoFisher Scientific) for SMLM. Prolong Gold was left to polymerize for 24 h in the dark at RT before the slides were sealed with nail polish and stored.

Specimen Irradiation

As described in detail elsewhere [14] ^{15}N ions were accelerated using a U 400M isochronous cyclotron in the Flerov Laboratory of Nuclear Reaction at the Joint Institute for Nuclear Research (JINR, Dubna) [79]. The radiation conditions applied are summarized in **Table 1**.

In the experiments, cells were exposed to an average of about 2 and 25 particles per nucleus for 10° and 90° irradiation, respectively. This corresponds to the doses of 1.3 Gy (10° irradiation) and 4.0 Gy (90° irradiation). The values were calculated as described in Ref. 80; for the average nuclear area of 186 μm^2. The non-homogeneity within the irradiation field of 14 mm in diameter was less than 5%, as monitored using five identical flow-type ionization chambers; the central chamber served as the monitor of the radiation dose [79]. The energy and corresponding LET values of ions at the plane of the cell monolayer were calculated using LISE++ software [81].

The cells were irradiated on glass coverslips at Petri dish bottoms tangentially or perpendicularly. The side of the coverslips covered with cells was oriented toward the ion beam so that the cells were hit by the particles before the beam entered the culture medium in the Petri dish. During irradiation, the cells were kept in a thermostable box, ensuring a constant temperature of 37 °C and prevention from infection during the whole procedure. After irradiation, the cells were immediately placed back into the incubator until fixation. For microscopic analyses, the cell nuclei were fixed at numerous periods of time after irradiation (5 min–24 h PI), as explained in detail in paragraph *Cell Culture and Specimen Preparation*.

Single Molecule Localization Microscopy

A detailed description of the SMLM instrument has been published elsewhere [53, 54, 64, 82]. In brief: The microscope has an oil-objective (100×/NA 1.46) and four lasers 405 nm/491 nm, respectively. Measurements were done with the 561 nm wavelength laser. An in-built electron multiplier (EM-gain) enhances signals detected by the EmCCD camera (80 nm/px). The microscope was installed on a Smart-Table compensating for vibrations, and provided with a water-cooling system to keep constant temperature and to minimize drifts. Lasers were controlled using the "Omicron Control Center" program and image acquisition was carried out using "Live Acquisition v. 2.6.0.14" software. For thermal stabilization, first measurements with the microscope were performed 1 h after booting.

A protocol for automatized localization image acquisition was used. In brief, an initial excitation switched most fluorophores into a reversibly bleached state; then 2,000 single image frames were taken at maximum laser power with an exposure time of 100 ms per image frame. Wide-field images were always taken before localization image acquisition. For each time point during the repair period, a minimum of 23 cells was imaged. The image data stacks were stored as *.tif stacks and subjected to further computational analysis as described below.

Data Evaluation and Image Processing

The local positions of the detected dye molecules of the antibodies were obtained from registration of molecular blinking events according to an algorithm described elsewhere [82], which is based on subtraction of the brightness values of two successive frames. This method enables the differentiation of the blinking events from the background. A so-called "Orte-Matrix" was produced, which contained information about the signal

TABLE 2 | Cluster parameters of the experiment.

cluster values	53BP1				Rad51	
Cell line	NHDF	U87	NHDF	U87	NHDF	U87
Irradiation angle	*10°*	*10°*	*90°*	*90°*	*10°*	*10°*
Radius [nm]	200	200	200	200	200	200
Min Number of points	65	65	84	55	60	60

amplitude, the lateral x- and y-coordinates, the standard deviations in the *x*- and *y*-direction, position errors, etc. This "Orte-Matrix" was the starting data set for all further evaluation procedures and for the construction of artificial images of the cell nuclei.

Mathematical procedures and algorithms were applied on these raw coordinate data of the detected labeling points instead on processed images. The data analysis program is modularly built up and was programmed in Python (https://www.python.org) (Gote, Neitzel et al., manuscript in preparation). Several algorithms developed are based on Ripley's point-to-point distance frequency measure structure information [84] or use DBSCAN [85]) in order to obtain information whether the fluorophores were localized in clusters. The point-to-point distances were measured by distances from each given central point to its peripheral ones. Without regarding absolute position information, the graphical display of absolute and relative distance frequencies makes it possible to discriminate between specimen structure signals and background signals. The envelope function of the distance frequency histogram is correlating to functional arrangements of points [53].

A homogeneous point-to-point distance distribution leads to a linear increase in the distance frequency histogram. The slope of the straight line is scaled with the number of detected points. If the points appear in clusters, smaller distances are more frequent resulting in a peak. The width of the peak gives the maximum distance between two points in the cluster and thus the cluster diameter. The area under the peak is a measure relative to the point density in a cluster. The shape of the peak gives a measure of the homogeneity of the distribution of points in the cluster. If clusters are embedded in a pointillist background, the result consists of three parts: a) a homogeneous distribution (linear increase); b) a cluster distribution (peak) and c) a cross term or additional peak, which contains the distances between the points of two neighboring clusters.

According to the DBSCAN algorithm [85], clusters are compact regions of increased local density of points. The amount of all points inside a given radius around a point must have a minimum value to define a cluster. If any points inside such a cluster also meet the cluster definition they are attributed to the same cluster. The cluster size is the maximum area in which all points meet the cluster criteria. Inside clusters various characteristics can be examined and compared to the point distributions outside the clusters.

The following cluster parameters describing the minimum number of points within a given radius were interactively determined (**Table 2**).

Novel analytical methods for 53BP1 cluster characterization were applied using procedures of persistence homology [66]. This method, using established calculations and mathematical operations, allows two point distributions, here the point distributions of 53BP1 clusters of two irradiation schemes, to be compared to each other in a cell-independent manner, thereby giving a mathematical measure of their similarity [86].

The major principle of this analysis for persistent topologies is to record properties of point patterns, which are invariant under certain deformations of the object. Mathematically these deformations correspond to continuous transformations of the topological space defined by the structures. For 53BP1 clusters, the attention was focused on two properties: a) the number of "components", which are independent from each other in such sense that connections between points only exist within the respective components; b) the number of "holes" of the structures inside the components. In algebraic topology, these properties are called the Betti numbers for zero- and one-dimensional simplicial complexes. They are the topological invariants that distinguish between different topological spaces.

SMLM data sets of repair foci are clustered point-sets for which components and holes can be defined [66]. In the following, this procedure is briefly described: A geometric relationship among cluster points is obtained by growing spheres of radius α around each point. Whenever two of these spheres mutually embed each-other's center, these centers are connected by a line. The connected points belong to the same component. With increasing radii of the spheres, more and more points are connected to previously disjoint components. Thus, the number of components is decreasing with increasing of the radius α. At the end of the procedure, a single component is remaining. For the definition of holes, the simplest polygon, the triangle, is appropriate. Whenever a component of three connecting lines of points forms a triangle, the area of the triangle is considered as a hole. With reducing the number of disjunct components, the number of holes is increasing and decreasing again.

The amounts of components and holes are depending on the value of α. For the formation of each component and each hole, a bar of a barcode pattern starts. The end of the respective bar is fixed at the disappearance of components and holes with increasing α [87]. The mathematical transfer of the spatially organized pattern of labeling points into barcodes contains information about components and holes in a compact and illustrative way. The sets of barcodes for each 53BP1 cluster were compared with each other and their similarity was calculated. The procedure used for quantification of the barcodes similarity is based on the Jaccard index [88]. A detailed description and illustration is presented in Refs. 66 and 86. The result of this normalized similarity measure is a value between 0 and 1, where a value of 0 means no overlap of two bars and 1 the identity of two bars. The similarity of barcodes of different dimensions is defined as the average of the individual similarity values of the bars of a cluster. Such topological comparisons are independent of the scale and the perspective on the clusters so that it is possible to compare variably large foci randomly orientated to the microscopic detection system.

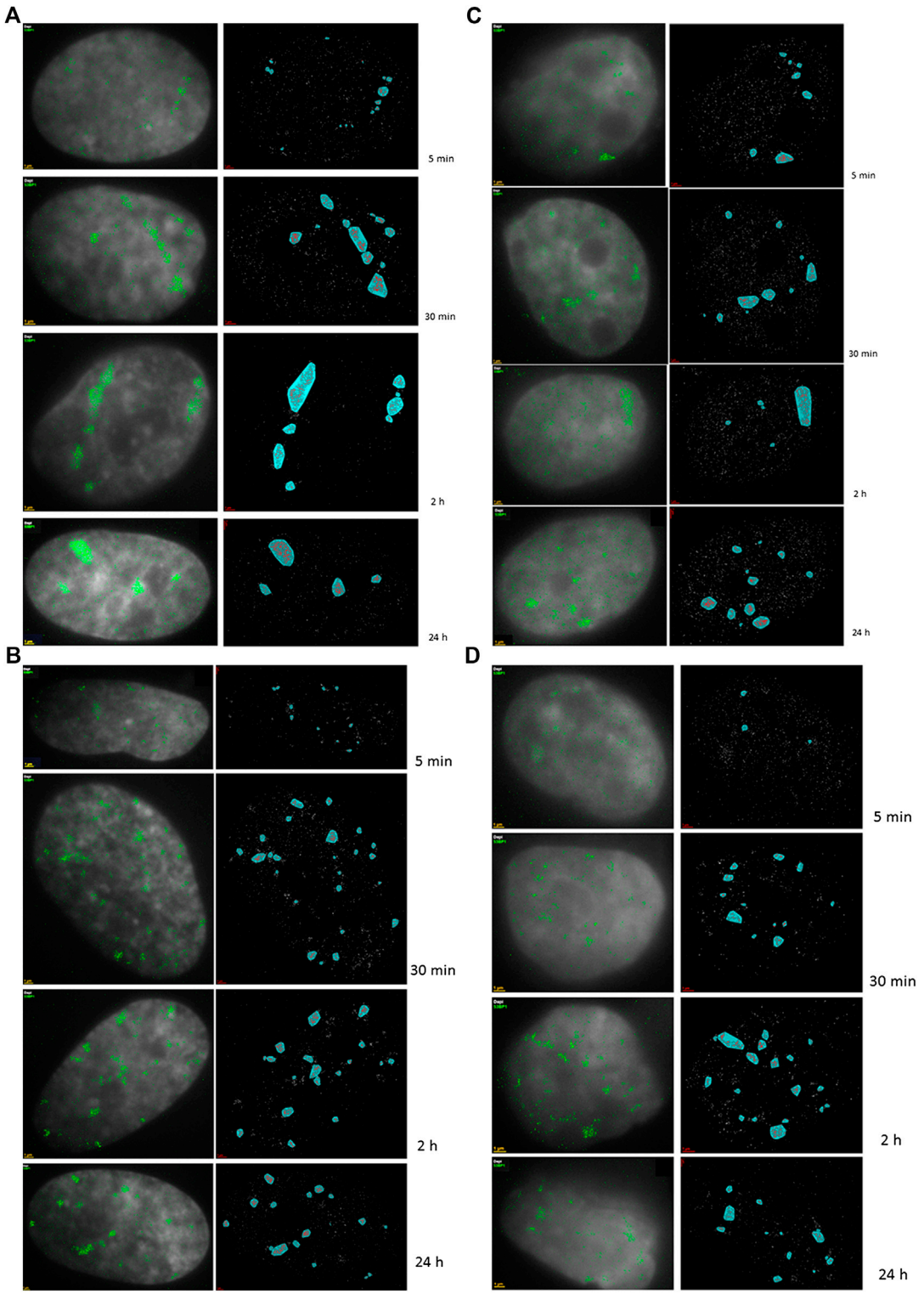

FIGURE 1 | 2D density SMLM images of 53BP1 repair proteins. Typical examples are shown for fluorescently-labelled 53BP1 proteins in NHDF cells **(A,B)** and U87 cells **(C,D)** after 1.3 Gy tangential ^{15}N-irradiation **(A,C)** (10° angle between the ion beam and the cell layer) and 4 Gy perpendicular ^{15}N-irradiation **(B,D)** (90° angle between the ion beam and the cell layer). The time values indicate the period PI when the samples were taken as aliquots of the same irradiated culture and fixed. For comparison, examples of non-irradiated control cells are presented. The left columns are merged images of SMLM data and wide-field images. In the right columns the SMLM image data and cluster areas are shown. The scale bars equal to 1 μm.

RESULTS

The Neonatal Human Dermal Fibroblast (NHDF) line was studied as model of normal (non-transformed) cells with relatively higher radio-sensitivity while U87 glioblastoma cells were selected for their high radio-resistance [55] and aggressive cancer phenotype. In addition, forming the skin, NHDF fibroblasts are always irradiated by external radiation sources. Glioblastoma (U87 cells) then represents a tumor treated by radiation but with poor results only due to its high radio-resistance. Both cell types were exposed to high-LET ^{15}N ions in two different geometries (i.e., under the angle of 10°and 90° as described in *Materials and Methods*) and IRIF formed by γH2AX and selected repair proteins (53BP1 and Rad51) were studied with SMLM in different periods of time post-irradiation (PI), ranging from 5 min PI to 24 h PI. Within the first minutes after irradiation, 53BP1 proteins were recruited to the damaged sites, visualized as γH2AX foci. 53BP1 foci provide information of the early recruitment of proteins for repair. In the previous studies [15, 55], we have shown that DSB repair proceeds much slower in cells exposed to (high-LET) ^{15}N ions than in cells irradiated with low-LET γ-rays. Also, it emerged obvious that 53BP1 repair foci differ in their parameters for NHDF and U87 cells. Here, the 53BP1 data sets already investigated by SMLM [55] were further analyzed for structural clustering and topological similarity. In addition, data sets of the same cell types and radiation conditions were prepared also for Rad51 protein, which is, unlike 53BP1, selectively involved in DSB repair via homologous recombination. The first data of Rad51 labeling and spatial organization of Rad51 foci were elucidated and compared to results obtained for 53BP1 repair protein participating both in NHEJ and HR. Focus formation and clustering, persistent homologies, and structural changes during the post-irradiation (PI) period of repair were analyzed at several repair relevant time points (5, 15 min (10° only), 30, 45 min (10° only), 1, 2, 4, 8, 24 h).

In contrast to U87 cells, NHDF fibroblasts quickly recruited the majority of the 53BP1 proteins (~60%) to the damaged chromatin sites along the particle tracks so that clusters have already been visible and well developed at 5 min PI, though their number progressively increased within the first 30 min PI. In both cell types, the cluster numbers were maintained until 8 h and then started to decrease; thereby a considerable proportion of clusters persisted even after 24 h PI (**Figure 1**).

U87 cells contained 53BP1 clusters also prior to irradiation (control samples) which was not observed in NDHF cells. In U87 cells, the formation of 53BP1 clusters in tracks was delayed up to 30 min PI and the relative number of recruited 53BP1 proteins was always less than 40% of the protein pool available. These results thus confirmed our previous observations [55]. In **Figure 1**, illustrative examples of SMLM images of 53BP1 foci/clusters are shown for the two cell lines, the two radiation schemes, and different periods PI. The left images show wide-field images of DAPI-stained nuclei with inserted point signals of individual 53BP1 molecules acquired with SMLM. The right columns then provide the corresponding SMLM images of the 53BP1 foci after cluster area determination. For the 10° irradiation angle, the specimens of both cell lines showed characteristic tracks highlighted by dense arrangements of labeling tags. At later periods PI, the tracks partly dissolved and separated protein cluster units became visible dispersed, over the cell nuclei. In contrast to the 10° irradiation experiments, the 90° irradiation experiments showed more clusters irregularly dispersed over the cell nucleus. Since the dose was higher in these experiments, all these clusters may represent a separate particle track perpendicular to the image plain.

The following investigations are reasoned by the hypothesis that repair proteins form characteristic, similarly sized clusters at the damaged chromatin sites. These proteins are recruited to and released from clusters during the repair period; thereby their spatial topology can be expected to show high similarity provided the chromatin environment around the damage sites is also similar and the same repair mechanism has been activated. The correct topological arrangement is assumed to be required for the downstream repair steps so that the follow-up repair protein molecules could correctly access the damaged chromatin sites. The results presented here support these ideas and show by which mathematical operations the biophysical verification of the hypothesis could be approached.

To further investigate the dynamics and cluster formation of tagged 53BP1 molecules, Ripley distance analysis was applied that is based on relative frequency histograms of pairwise point distances. The distance frequency histograms were compared for all repair time points of each cell type and each radiation condition. In **Figure 2**, the results are presented. The controls of both cell lines showed a peak at smaller distances, which indicates these small distances occur very frequently, i.e., the labeled proteins are often arranged in such closely adjacent conformations (=cluster conformations). These clusters are embedded in a random distribution of points which can be concluded from the linearly increasing frequency of larger distances. Note that the histograms show the relative frequency of distances but do not give information about the absolute number of distances or clusters.

Shortly after irradiation, the formation of clusters increases in NHDF cells but not in U87 cells. Subsequently, from 1 h PI, the absolute cluster frequency was decreasing in NHDF cells. For longer periods PI (2–24 h), some clusters remained while the rest of protein labeling points followed a strong random distribution (**Figures 2A,B**). This behavior was found for both, the 10° and 90° irradiation schemes, though it was less pronounced for 90° (compare **Figure 2A** vs. **2B**).

The cluster and labeling point dynamics appeared to be different in U87 cell nuclei (**Figures 2C,D**). Significant clusters were found also in the non-irradiated controls, embedded within a random labeling point pattern. For the 10° irradiation scheme, the amount of labeling points was increasing and larger clusters were formed after 5 min PI (**Figure 2C**). From 15 min PI until the end of the period of investigation (24 h), the clusters kept their size and remained. Some minor fluctuations within some randomly dispersed labeling points were observed. For the 90° irradiation scheme, the control showed the same behavior as for the 10° irradiation scheme, separate clusters within an

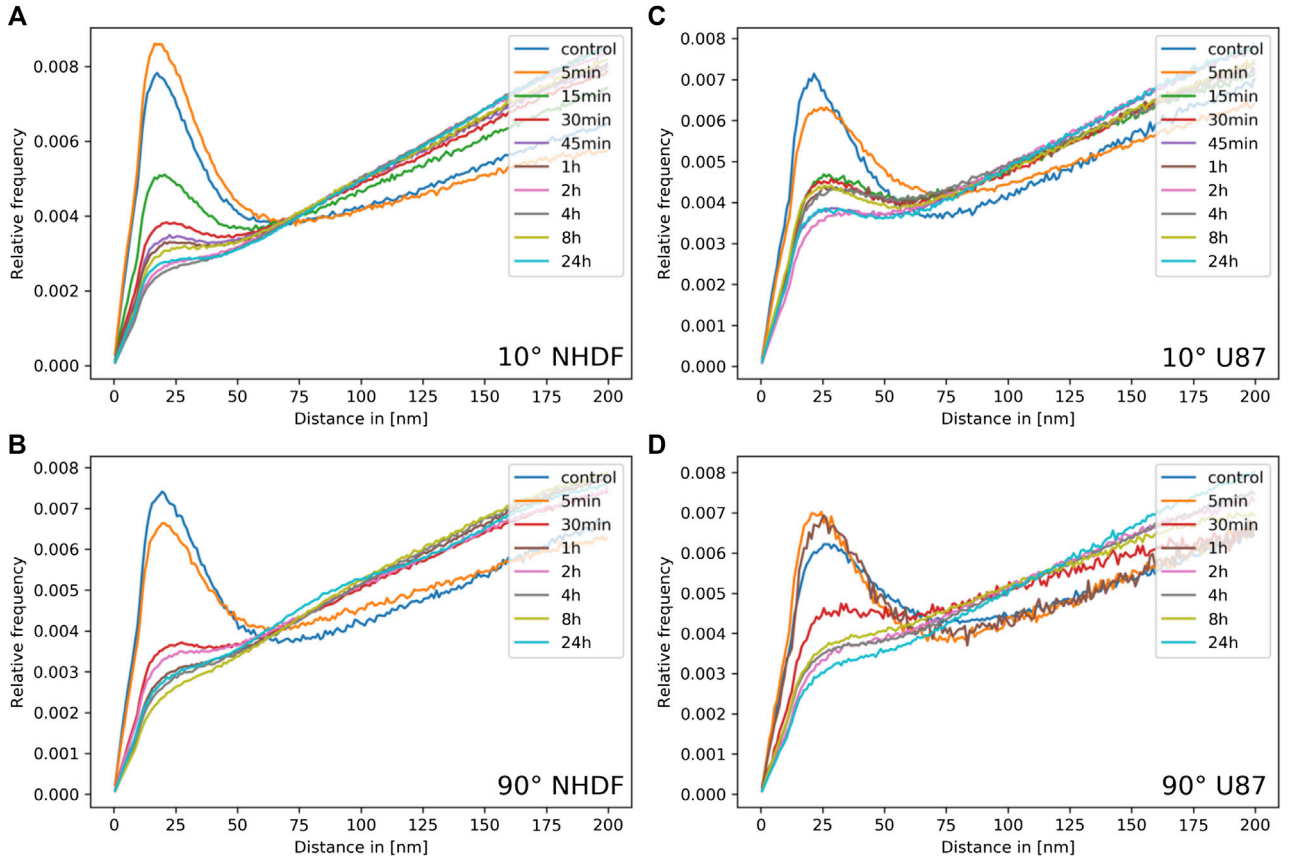

FIGURE 2 | Ripley distance frequency analysis. The relative frequencies of pairwise distances are presented for the aliquots of the irradiated cell samples at different time points PI (color label of curves); **(A)** NHDF and **(C)** U87cells irradiated under 10° irradiation angle; **(B)** NHDF and **(D)** U87cells irradiated under 90° irradiation angle.

TABLE 3 | Overview of the number of clusters included into the analyses of persistent homologies.

	NHDF, 10°	NHDF, 90°	U87, 10°	U87, 90°
Number of clusters evaluated	198	297	146	219

environment of randomly dispersed labeling points. However, after irradiation with the high dose (4 Gy), the situation was different as fluctuations in cluster formation and size appeared until 2 h PI (**Figure 2D**). Between 2 and 24 h PI, a low clustering frequency within a strong random distribution of labeling points could be seen.

These measurements, in conclusion, indicate that 53BP1 clusters are quickly formed after irradiation. With the progress of the early repair period (ending at about 30 min or 1 h PI) one part of the clusters becomes dispersed while the other part persists within a growing amount of randomly distributed proteins. These persistent clusters remained in cell nuclei until the end of the investigation period (24 h PI).

In the next step, we decided to analyze "remaining" 53BP1 clusters at 2 h PI in terms of the persistent homology and determined the degree of their mutual topological similarity. Based on the pointillist information obtained by SMLM, we used this new analytical method for 53BP1 cluster characterization after high-LET ^{15}N ion irradiation for the first time. A cell independent, pairwise comparison of point distributions (here the point distributions of two 53BP1 clusters) with each other was elaborated for a selected ensample of clusters. For the evaluation, the following total numbers of clusters were considered (**Table 3**):

The resulting barcodes of 0 (components) and 1 (holes) dimensions were compared in both directions and a mathematical measure of their similarity was calculated and visualized in heatmap descriptions (**Figure 3**). For both cell types the similarity measure as being determined by the Jaccard index was very high for the components (>0.9) independent of the irradiation scheme (**Figures 3A,B, a**). This indicates that the complex, ion-induced damages are marked with a specific repair cluster setup. On the other hand the similarity measure for the holes was below 0.5 for both cell types and radiations schemes (**Figures 3A,B, b**). Interestingly the similarity of holes was on average higher for NHDF (**Figure 3A, b**) than for U87 cells (**Figure 3B, b**).

The similarity values obtained by averaging of components and holes values for each 53BP1 cluster are presented in **Figures 3A,B, c**. When the clusters of the 10° irradiations scheme were

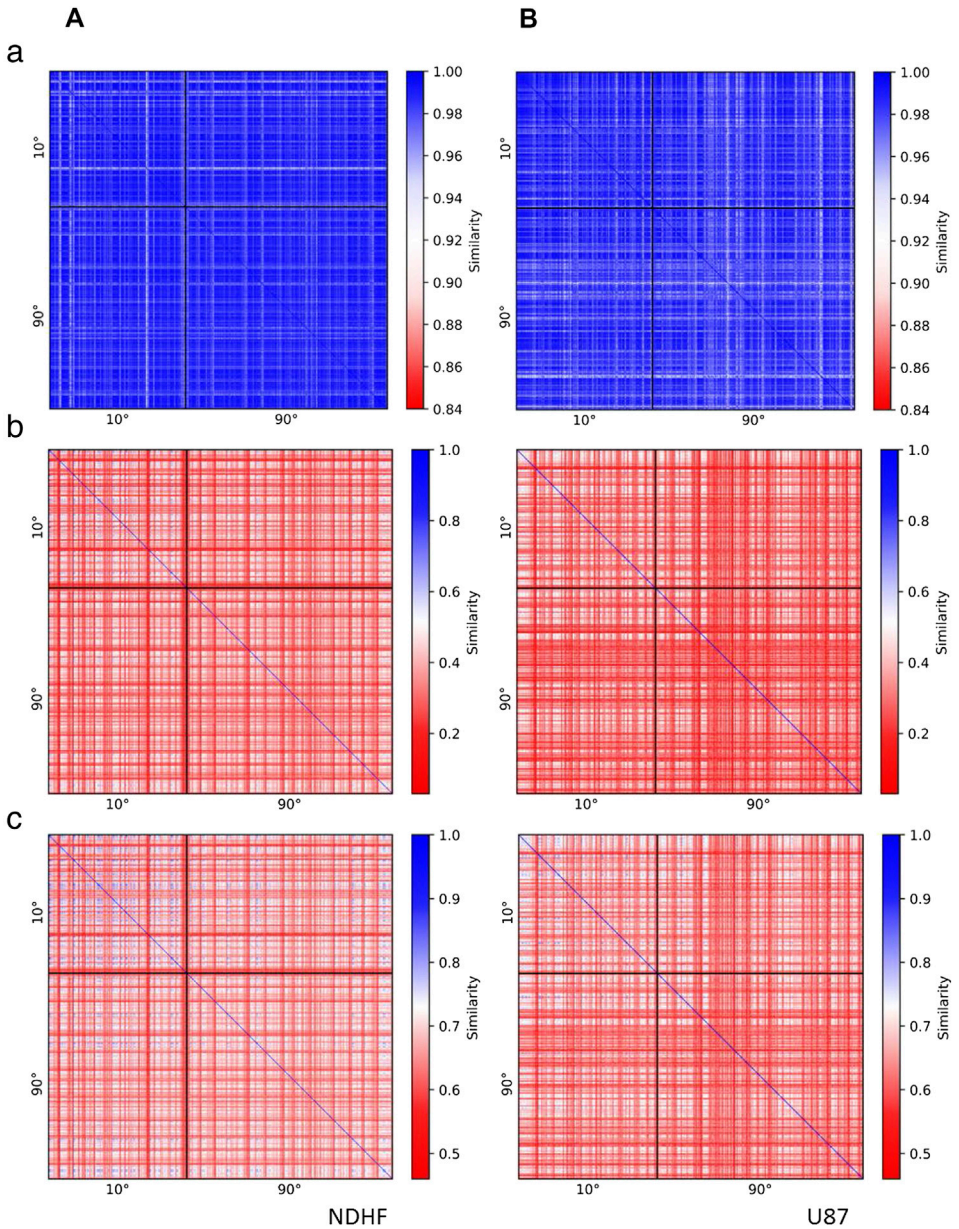

FIGURE 3 | Heatmaps indicating the similarity of 53BP1 clusters in **(A)** NHDF cells and **(B)** U87 cells irradiated under an irradiation angle of 10° or 90° and fixed 2 h PI. The heatmaps show **(a)** the similarity of the barcodes of dimension 0 (components), **(b)** the similarity of the barcodes of dimension 1 (holes), **(c)** the average similarity of the barcodes of dimension 0 and 1. The comparison of clusters in cells irradiated with 10° (90°) is shown in the upper left (lower right) corner of the heatmaps. In the upper right (lower left) corner clusters in cells irradiated with 10° (90°) are compared to clusters in cells irradiated with 90° (10°). Clusters occurring in the same cell are located next to each other in the heatmap. Blue color indicates that the compared clusters have similar topological characteristics, whereas red color indicates differing cluster characteristics.

compared, the Jaccard indices laid between 0.55 and 0.82 for both cell types. The frequency distribution was broad without a peak for NHDF cells whereas U87 showed a clear peak at 0.64 (**Figure 4**). Comparing the clusters of the 90° irradiation scheme, the peak was at 0.63 for U87 cells. This value was also obtained for the comparison of the 10° with the 90° irradiation scheme. For these two comparisons (90° vs. 90°, 10° vs. 90°), NHDF cells showed a bimodal peak distribution with one peak at 0.67 and another peak at 0.72 (**Figure 4**). In general it can be concluded that the more radio-sensitive NHDF cells revealed a higher topological similarity in 53BP1 clustering than the more radio-resistant U87 cells.

53BP1 is known to be preferentially involved in NHEJ but it could also act as a stabilizing factor during HR. So in a very first approach we wanted to see whether under harsh damaging conditions occurring during high-LET ion irradiation, HR is

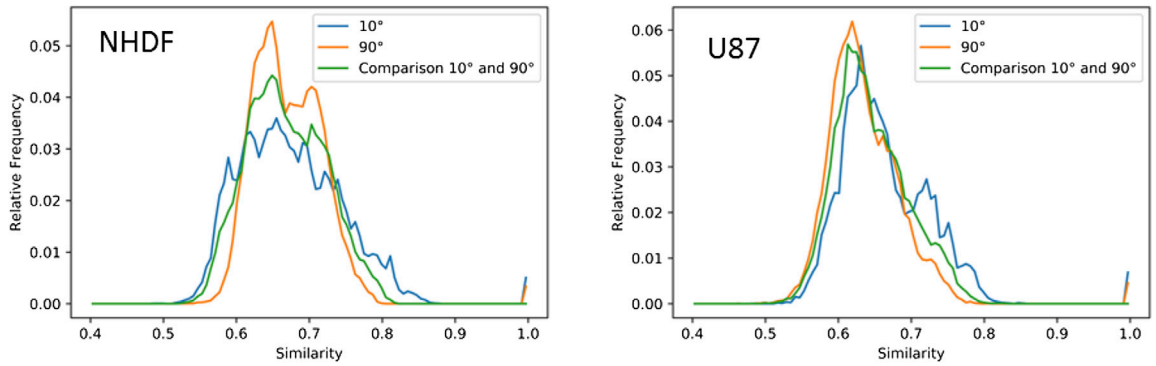

FIGURE 4 | Normalized histograms of the frequencies of similarity values of barcodes (Jaccard indices) of 53BP1 clusters in NHDF and U87 cells irradiated under 10° or 90° irradiation angle and fixed 2 h PI. The distributions of the average similarity of dimension 0 and 1 barcodes of 53BP1 clusters in NHDF (compare **Figure 3A,c**) and U87 (Compare **Figure 3B,c**) cells are shown. The similarity distributions of clusters in cells irradiated under an angle of 10° (values from the upper left part of the heatmaps) are shown in blue, the similarity distributions of clusters in cells irradiated under 90° (values of the lower right part of the heatmaps) are shown in orange, and the similarity distributions obtained when comparing clusters in cells irradiated with 10° to clusters in cells irradiated with 90° (values of the upper right part of the heatmap) are depicted in green.

used for DNA damage repair. Therefore we labeled γH2AX and Rad51 simultaneously in cell nuclei of the two cell lines under the 10° irradiation scheme. In **Figure 5A**, a typical example is shown. It was obvious that also HR was employed as a repair pathway for broken chromatin in the track. In these cases, the Rad51 signals were always completely embedded in a γH2AX environment. However, the frequency of Rad51 clusters was very different for the cells analyzed. For both cell types, nearly no Rad51 cluster was found in the control. An increase of Rad51 clusters emerged between 1 and 8 h PI for NHDF and between 2 and 8 h PI for U87. The number of Rad51 clusters at 24 h PI was again on the level of the non-irradiated control specimen (**Figure 5B**).

DISCUSSION

High-LET particle radiation has a Janus-faced nature. On one side it is highly dangerous and risky, as for instance during space mission. Even single particles could have a significant damaging effect on individual cells, with an unpredictable outcome for astronauts on space missions. On the other hand, high-LET particles can inactivate cells deeply inside the patients' bodies, making them an ideal tool for radiation treatment, especially of brain tumors or tumors embedded in very sensitive (and potentially vital) tissues. Therefore radio-protection as well as radio-therapy require a better understanding of the processes which the cells employ to repair complex damage events along the particle track.

Heavy ion accelerator facilities offer defined high-LET radiation conditions as for instance in terms of the particle type, dose, irradiation angle etc. Hence, particle accelerators allow precise and defined experiments on given cell models, which are a prerequisite for sophisticated systematic analyses of DNA damaging and repair upon specific irradiation conditions. Research opportunities offered by these facilities have therefore rocketed bio-medical research.

High-LET particles lumbering through the chromatin of a cell nucleus induce a very complex damage pattern highlighted by γH2AX foci and other foci of recruited repair proteins. So far it is neither known how many damaged sites associate and are eventually repaired within one focus (visible at the microscale), nor whether the foci have an internal nano-structure composed of smaller sub-units (clusters), representing a single damage each, which are potentially functionally organized. A correct repair of the associated broken DNA ends indicates that the relevant repair units may be smaller clusters, for some reason aggregated in foci. Otherwise, multiple damage concentrated within one repair focus, would promote miss-repair in a much higher extent than it is observed. Hence, it cannot be excluded that the hypotheses of "repair factories", postulated but not confirmed to explain DSB repair and formation of chromosomal aberrations at the microscale (reviewed in Ref. 8), will be revitalized at the nanoscale. Therefore, it is of high interest to better understand the spatial organization of repair foci and consequently the repair mechanism resulting from defined spatial arrangements of repair protein clusters. This has motivated us to perform sophisticated microscopy studies of repair protein foci along particle damage tracks by means of super-resolution SMLM. Systematic investigations have been started using the radiation facility at JINR Institute (Dubna, Russia) by applying different doses of various high-LET particle radiation types at different doses and under different irradiation angles to well established cell systems of different radio-sensitivity. In Ref. 55; we analyzed the abundance and recruitment dynamics of 53BP1 repair protein, which indicated significant differences in IRIF nano-architecture between radiosensitive normal fibroblasts (NHDF) and cancerous, highly radioresistant U87 cells. Here, we have continued these studies with a special focus on cluster formation and topological cluster similarity. Ripley distance frequency analysis in combination with calculations of similarity values after evaluation of persistent homology provided novel insights

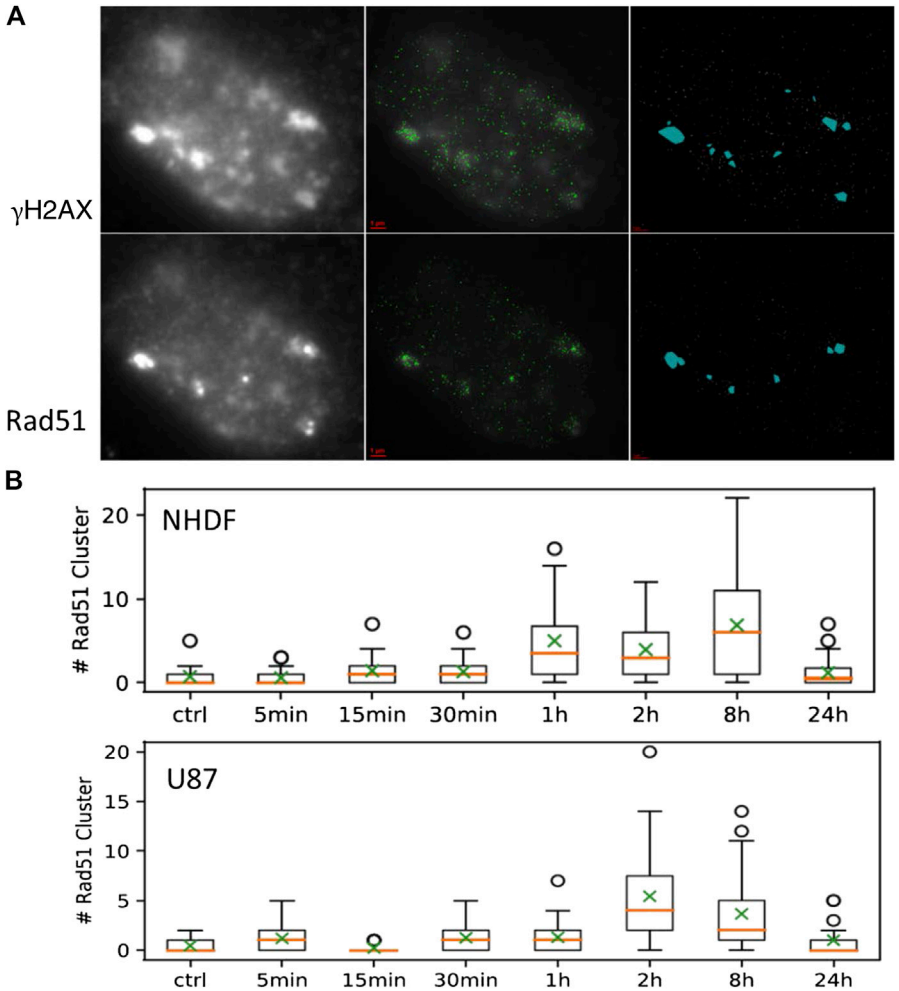

FIGURE 5 | (A) Example of an NHDF cell nucleus taken from the sample 1 h PI (irradiation angle 10°). Left: wide-field overview images taken in the color plain of γH2AX (upper row) and Rad51 (lower row); middle: SMLM image of the protein loci merged with the wide-field image; right: identified clusters as detected by the DBSCAN algorithm. **(B)** Box plots for the numbers of Rad51 clusters for NHDF and U87 cells determined in aliquots at different time points PI.

into the nano-architecture of repair foci that form at damaged sites in different cell types.

For normal NHDF fibroblasts, our data on 53BP1 molecules within IRIF revealed cluster formation and relaxation that was comparable for the two different radiations schemes and doses applied. In contrast, U87 cells showed a more variable cluster formation with fluctuations during the repair time. Moreover, independently of dose and irradiation angle the topology of the clusters was highly similar for NHDF cells in comparison to U87 cells. The high topological similarity of 53BP1 clusters in NHDF may indicate that, for both applied irradiation schemes, the 53BP1 clusters forming along the ion-induced chromatin damage have a specific, thus potentially functional setup. One reason for the existence of this setup may be the presence of several complex damage sites within the clusters instead of one single DSB. Further, with 53BP1 being located in the perichromatin and interchromatin [61], the specific arrangement of 53BP1 may be caused by the chromatin structure. Similar to our findings, the presence of resembling substructures of 53BP1 foci has also been observed by Reindl et al., who found that 53BP1 foci are subdivided into nano-foci of a constant size, thence no difference was observable in the setup of the nano-foci after low-LET proton and high-LET carbon ion irradiation [63, 89].

In addition, the comparison of the two cell lines (NHDF and U87) indicated that the loss of radio-sensitivity may be associated with a reduction of topological similarity of 53BP1 clusters. One possible explanation for this may be that, due to defects in DNA damage repair, U87 cells fail to build up clusters in a standard structured manner. In that case, the increased radio-resistance may originate from a "radiation adaptation" leading to cell survival with an unrepaired genome instead of more efficient repair [53]. As cancer cells often have modifications in their chromatin structure, another option would be that the characteristics in the repair cluster setup of U87 cells and their increased radio-resistance may be associated with chromatin re-

arrangements characteristic for carcinogenesis in general or specifically for this cell type. Nevertheless, a combination of several phenomena seems to be the most probable explanation. In Ref. 55; we observed that the more complex 53BP1 clusters disappeared much faster from U87 cells compared to NHDF fibroblasts though the overall repair kinetics of both cell types was more similar. This could mean that while some repair pathways are defective, the others are augmented.

Here, we wanted to introduce novel technical and mathematical approaches. The results of 53BP1 SMLM analysis revealed the potential of these proposed approaches. Future investigations will therefore be directed not only to further analyses of the clustering and topological similarity of 53BP1 at other time points PI but also to systematic investigations on γH2AX foci that directly indicate the reaction of chromatin to (low-LET vs. high-LET) radiation damage.

In general, the structure of the chromatin and the arrangement of proteins involved in repair may influence repair process and even the pathway choice by determining the accessibility of the damage site for follow-up proteins [55, 66, 90]. It has been proposed that 53BP1 is excluded from the center of the repair region and relocated to the outer part, if the DSB repair is directed to HR. This reposition opens space for loading of particular HR proteins, such as Rad51 [63, 67, 69, 91]. Hence, the structure of 53BP1 clusters may have a direct impact on the pathway selection. This correlation remains to be studied in future. As the first attempt to investigate the relationship between a specific topology of 53BP1 clusters, chromatin architecture at the damage sites, and initiation of HR, we have checked whether the HR marker, Rad51, is recruited to the damage track. In order not to find a Rad51 cluster or focus just by chance somewhere in the nucleus, we irradiated the cells in a sharp (10°) angle, which allowed us to visualize particle tracks trough the nucleus (using γH2AX as the damage marker) in the x-y plane of the microscope with much better resolution compared to 90° irradiation [14]. Indeed, during later repair times we found a considerable increase of Rad51 clusters that colocalized with γH2AX, indicating an increase in HR activity. This may be surprising since the harsh complex damage generated by high-LET particles could be expected to be a very challenging target for HR. On the other hand there seems to be special chromatin conditions that favor HR repair at high-LET damage sites. So far this data on the repair pathway selection at specific DSB sites are preliminary but indicate the need of further investigations in order to better understand how chromatin architecture affects chromatin functionality in relation to DNA damage repair. As presented here, powerful mathematical procedures applicable to SMLM data of repair processes are available that will shed new light into the shadow of complex damage events along particle tracks. As well, modern particle accelerators offer systematic evaluation of damage events induced by different types of precisely defined high-LET particle radiation.

DATA AVAILABILITY STATEMENT

All datasets presented in this study are included in the article.

AUTHOR CONTRIBUTIONS

Conceptualization, MH and MF; methodology, MH, MF, and AH; software, CN and AH; validation, CN, EB, DN, IF; formal analysis, CN, EB, DN, XX; investigation, CN, EB, DN, TC, ES, OK, EP; resources, AB, EK, FB, MH; data curation, CN, EB; writing—original draft preparation, MH; writing—review and editing, MF, CN; visualization, CH.; Supervision, MH, GP, GH, EK, DH, MF; project administration, MH, MF; funding acquisition, MH, MF. All authors have read and agreed to the published version of the manuscript.

FUNDING

The work was supported by the Czech Science Foundation (projects GACR 20-04109J and GACR 19-09212S to MF, by the Deutsche Forschungsgemeinschaft (DFG) grant (H1601/16-1) to MH, by the Heidelberg University Mobility Grant for International Research Cooperation within the excellence initiative II of the Deutsche Forschungsgemeinschaft (DFG) to MH, and by the German-Czech exchange project grant of the Deutsche Akademischer Auslandsdienst (DAAD-19-03) to M.H. and M.F. The cooperation with JINR Dubna was supported by the grants from the MEYS CR to MF (The Projects of the Czech Plenipotentiary and the 3-Plus-3 Project).

ACKNOWLEDGMENTS

The authors thank Harry Scherthan, Bundeswehr Institute for Radiobiology, Munich, for his help in urgent cases of material delivery and for many fruitful discussions.

REFERENCES

1. Chancellor J, Scott G, Sutton J. Space Radiation: the number one risk to astronaut health beyond low earth orbit. *Life* (2014) **4**:491–510. doi:10.3390/life4030491
2. Kennedy AR. Biological effects of space radiation and development of effective countermeasures. *Life Sci Space Res* (2014) **1**:10–43. doi:10.1016/j.lssr.2014.02.004
3. Walsh L, Schneider U, Fogtman A, Kausch C, McKenna-Lawlor S, Narici L, et al. Research plans in Europe for radiation health hazard assessment in exploratory space missions. *Life Sci Space Res* (2019) **21**:73–82. doi:10.1016/j.lssr.2019.04.002
4. Durante M, Orecchia R, Loeffler JS. Charged-particle therapy in cancer: clinical uses and future perspectives. *Nat Rev Clin Oncol* (2017) **14**:483–95. doi:10.1038/nrclinonc.2017.30
5. Rackwitz T, Debus J. Clinical applications of proton and carbon ion therapy. *Semin Oncol* (2019) **46**:226–32. doi:10.1053/j.seminoncol.2019.07.005
6. Falk M, Lukasova E, Gabrielova B, Ondrej V, Kozubek S. Chromatin dynamics during DSB repair. *Biochim Biophys Acta* (2007) **1773**:1534–45. doi:10.1016/j.bbamcr.2007.07.002
7. Falk M, Lukášová E, Kozubek S. Chromatin structure influences the sensitivity of DNA to γ-radiation. *Biochim Biophys Acta* (2008) **1783**:2398–414. doi:10.1016/j.bbamcr.2008.07.010

8. Falk M, Lukasova E, Kozubek S. Higher-order chromatin structure in DSB induction, repair and misrepair. *Mutat Res* (2010 Apr-Jun) **704** (1-3):88–100. doi:10.1016/j.mrrev.2010.01.013.
9. Falk M, Hausmann M, Lukášová E, Biswas A, Hildenbrand G, Davídková M, et al. Determining omics spatiotemporal dimensions using exciting new nanoscopy techniques to assess complex cell responses to DNA damage: part A-radiomics. *Crit Rev Eukaryot Gene Expr* (2014) **24**:205–23. doi:10.1615/critreveukaryotgeneexpr.2014010313
10. Falk M, Hausmann M, Lukášová E, Biswas A, Hildenbrand G, Davídková M, et al. Determining omics spatiotemporal dimensions using exciting new nanoscopy techniques to assess complex cell responses to DNA damage: part B-structuromics. *Crit Rev Eukaryot Gene Expr* (2014) **24**:225–47. doi:10.1615/critreveukaryotgeneexpr.v24.i3.40
11. Chancellor JC, Auñon-Chancellor SM, Charles J. Medical Implications of Space Radiation Exposure Due to Low-Altitude Polar Orbits. *Aerosp Med Hum Perf* (2018) **89**:3–8. doi:10.3357/amhp.4956.2018
12. Bilski P, Marczewska B, Gieszczyk W, Kłosowski M, Naruszewicz M, Sankowska M, Kodaira S. Fluorescent imaging of heavy charged particle tracks with LiF single crystals. *J Lumin* (2019) **213**:82–7. doi:10.1016/j.jlumin.2019.05.007
13. Jacob B, Taucher-Scholz G. Interaction of heavy ions with nuclear chromatin: spatiotemporal investigations of biological responses in a cellular environment. *Nucl Instrum Methods Phys Res B* (2006) **245**:292–7. doi:10.1016/j.nimb.2005.11.117
14. Jezkova L, Zadneprianetc M, Kulikova E, Smirnova E, Bulanova T, Depes D, et al. Particles with similar LET values generate DNA breaks of different complexity and reparability: a high-resolution microscopy analysis of γH2AX/53BP1 foci. *Nanoscale* (2018) **10**:1162–79. doi:10.1039/c7nr06829h
15. Depes D, Lee J-H, Bobkova E, Jezkova L, Falkova I, Bestvater F, et al. Single molecule localization microscopy as a promising tool for γH2AX/53BP1 foci exploration. *Eur Phys J D* (2018) **72**:158. doi:10.1140/epjd/e2018-90148-1
16. Nikitaki Z, Nikolov V, Mavragani IV, Mladenov E, Mangelis A, et al. Measurement of complex DNA damage induction and repair in human cellular systems after exposure to ionizing radiations of varying linear energy transfer (LET). *Free Radic Res* (2016) **50**:64–78. doi:10.1080/10715762.2016.1232484
17. Schipler A, Iliakis G. DNA double-strand-break complexity levels and their possible contributions to the probability for error-prone processing and repair pathway choice. *Nucleic Acids Res* (2013) **41**:7589–605. doi:10.1093/nar/gkt556
18. Mladenov E, Magin S, Soni A, Iliakis G. DNA double-strand-break repair in higher eukaryotes and its role in genomic instability and cancer: cell cycle and proliferation-dependent regulation. *Semin Canc Biol* (2016) **37–38**:51–64. doi:10.1016/j.semcancer.2016.03.003
19. Ceccaldi R, Rondinelli B, D'Andrea AD. Repair pathway choices and consequences at the double-strand break. *Trends Cell Biol* (2016) **26**:52–64. doi:10.1016/j.tcb.2015.07.009
20. Dueva R, Iliakis G. Alternative pathways of non-homologous end joining (NHEJ) in genomic instability and cancer. *Transl Cancer Res* (2013) **2**:163–77. doi:10.3978/j.issn.2218-676X.2013.05.02
21. Mladenov E, Magin S, Soni A, Iliakis G. DNA double-strand break repair as determinant of cellular radiosensitivity to killing and target in radiation therapy. *Front Oncol* (2013) **3**:113. doi:10.3389/fonc.2013.00113
22. Bhattacharjee S, Nandi S. Synthetic lethality in DNA repair network: a novel avenue in targeted cancer therapy and combination therapeutics. *IUBMB Life* (2017) **69**:929–37. doi:10.1002/iub.1696
23. Jeggo PA, Löbrich M. How cancer cells hijack DNA double-strand break repair pathways to gain genomic instability. *Biochem J* (2015) **471**:1–11. doi:10.1042/bj20150582
24. Rogakou EP, Pilch DR, Orr AH, Ivanova VS, Bonner WM. DNA Double-stranded Breaks Induce Histone H2AX Phosphorylation on Serine 139. *J Biol Chem* (1998) **273**:5858–68. doi:10.1074/jbc.273.10.5858
25. Kinner A, Wu W, Staudt C, Iliakis G. Gamma-H2AX in recognition and signaling of DNA double-strand breaks in the context of chromatin. *Nucleic Acids Res* (2008) **36**:5678–94. doi:10.1093/nar/gkn550
26. Chang HHY, Pannunzio NR, Adachi N, Lieber MR. Non-homologous DNA end joining and alternative pathways to double-strand break repair. *Nat Rev Mol Cell Biol* (2017) **18**:495–506. doi:10.1038/nrm.2017.48
27. Iliakis G, Murmann T, Soni A. Alternative end-joining repair pathways are the ultimate backup for abrogated classical non-homologous end-joining and homologous recombination repair: implications for the formation of chromosome translocations. *Mutat Res Genet Toxicol Environ Mutagen* (2015) **793**:166–75. doi:10.1016/j.mrgentox.2015.07.001
28. Jasin M, Rothstein R. Repair of strand breaks by homologous recombination. *Cold Spring Harb Perspect Biol* (2013) **5**:a012740. doi:10.1101/cshperspect.a012740
29. Shibata A, Jeggo PA. Canonical DNA non-homologous end-joining; capacity versus fidelity. *Br J Radiol* (2020) **23**:20190966. doi:10.1259/bjr.20190966
30. Löbrich M, Jeggo P. A process of resection-dependent nonhomologous end joining involving the Goddess Artemis. *Trends Biochem Sci* (2017) **42**:690–701. doi:10.1016/j.tibs.2017.06.011
31. Rothkamm K, Krüger I, Thompson LH, Löbrich M. Pathways of DNA double-strand break repair during the mammalian cell cycle. *Mol Cell Biol* (2003) **23**:5706–15. doi:10.1128/mcb.23.16.5706-5715.2003
32. Shrivastav M, De Haro LP, Nickoloff JA. Regulation of DNA double-strand break repair pathway choice. *Cell Res* (2008) **18**: 134–47. doi:10.1038/cr.2007.111
33. Goodarzi AA, Noon AT, Jeggo PA. The impact of heterochromatin on DSB repair. *Biochem Soc Trans* (2009) **37**:569–76. doi:10.1042/bst0370569
34. Goodarzi AA, Jeggo P, Lobrich M. The influence of heterochromatin on DNA double strand break repair: getting the strong, silent type to relax. *DNA Repair* (2010) **9**:1273–82. doi:10.1016/j.dnarep.2010.09.013
35. Brandsma I, Gent DC. Pathway choice in DNA double strand break repair: observations of a balancing act. *Genome Integr* (2012) **3**:9. doi:10.1186/2041-9414-3-9
36. Aparicio T, Baer R, Gautier J. DNA double-strand break repair pathway choice and cancer. *DNA Repair* (2014) **19**:169–75. doi:10.1016/j.dnarep.2014.03.014
37. Kakarougkas A, Jeggo PA. DNA DSB repair pathway choice: an orchestrated handover mechanism. *Br J Radiol* (2014) **87**:20130685. doi:10.1259/bjr.20130685
38. Clouaire T, Legube G. DNA double strand break repair pathway choice: a chromatin based decision? *Nucleus* (2015) **6**:107–13. doi:10.1080/19491034.2015.1010946
39. Maier P, Hartmann L, Wenz F, Herskind C. Cellular pathways in response to ionizing radiation and their targetability for tumor radiosensitization. *Int J Mol Sci* (2016) **17**:102. doi:10.3390/ijms17010102
40. Li J, Xu X. DNA double-strand break repair: a tale of pathway choices. *Acta Biochim Biophys Sin* (2016) **48**:641–6. doi:10.1093/abbs/gmw045
41. Majidinia M, Yousefi B. DNA repair and damage pathways in breast cancer development and therapy. *DNA Repair* (2017) **54**:22–9. doi:10.1016/j.dnarep.2017.03.009
42. Janssen A, Colmenares SU, Lee T, Karpen GH. Timely double-strand break repair and pathway choice in pericentromeric heterochromatin depend on the histone demethylase dKDM4A. *Genes Dev* (2019) **33**:103–15. doi:10.1101/gad.317537.118
43. Cremer T, Cremer M, Hübner B, Strickfaden H, Smeets D, Popken J, et al. The 4D nucleome: evidence for a dynamic nuclear landscape based on co-aligned active and inactive nuclear compartments. *FEBS Lett* (2015) **589**:2931–43. doi:10.1016/j.febslet.2015.05.037
44. Cremer T, Cremer M, Hübner B, Silahtaroglu A, Hendzel M, Lanctôt CH, et al. The interchromatin compartment participates in the structural and functional organization of the cell nucleus. *BioEssays* (2020) **42**:1900132. doi:10.1002/bies.201900132
45. Strickfaden Y, Máté G, Müller P, Hillebrandt S, Krufczik M, Bach MR, et al. Radiation induced chromatin conformation changes analysed by fluorescent localization microscopy, statistical physics, and graph theory. *PLoS One* (2015) **10**:e0128555. doi:10.1371/journal.pone.0128555
46. Kaufmann K, Barnard S, Moquet J, Ellender M, Rana Z, Burdak-Rothkamm S. DNA damage foci: meaning and significance. *Environ Mol Mutagen* (2015) **56**:491–504. doi:10.1002/em.21944
47. Schumann S, Eberlein U, Muller J, Scherthan H, Lassmann M. Correlation of the absorbed dose to the blood and DNA damage in leukocytes after internal *ex-vivo* irradiation of blood samples with Ra-224. *Eur J Nucl Med Mol I* (2018) **8**:77. doi:10.1186/s13550-018-0422-4.
48. Rübe CE, Lorat Y, Schuler N, Schanz S, Wennemuth G, Rübe C. DNA repair in the context of chromatin: new molecular insights by the nanoscale detection of

DNA repair complexes using transmission electron microscopy. *DNA Repair* (2011) **10**:427–37. doi:10.1016/j.dnarep.2011.01.012
49. Lorat Y, Brunner CU, Schanz S, Jakob B, Taucher-Scholz G, Rübe CE. Nanoscale analysis of clustered DNA damage after high-LET irradiation by quantitative electron microscopy-the heavy burden to repair. *DNA Repair* (2015) **28**:93–106. doi:10.1016/j.dnarep.2015.01.007
50. Timm S, Lorat Y, Jakob B, Taucher-Scholz G, Rübe CE. Clustered DNA damage concentrated in particle trajectories causes persistent large-scale rearrangements in chromatin architecture. *Radiother Oncol* (2018) **129**: 600–10. doi:10.1016/j.radonc.2018.07.003
51. Cremer C, Masters BR. Resolution enhancement techniques in microscopy. *Eur Phys J H* (2013) **38**:281–344. doi:10.1140/epjh/e2012-20060-1
52. Cremer C, Birk U. Perspectives in super-resolved fluorescence microscopy: what comes next? *Front Phys* (2016) **4**:11. doi:10.3389/fphy.2016.00011
53. Hausmann M, Ilić N, Pilarczyk G, Lee J-H, Logeswaran A, Borroni AM, et al. Challenges for super-resolution localization microscopy and biomolecular fluorescent nano-probing in cancer research. *Int J Mol Sci* (2017) **18**:2066. doi:10.3390/ijms18102066
54. Krufczik M, Wagner E, Lee J-H, Schrock G, Schaufler W, Krufczik M, et al. Super-resolution localization microscopy of radiation-induced histone H2AX-phosphorylation in relation to H3K9-trimethylation in HeLa cells. *Nanoscale* (2018) **10**:4320–31. doi:10.1039/c7nr08145f
55. Bobkova E, Depes D, Lee J-H, Jezkova L, Falkova I, Pagacova E, et al. Recruitment of 53BP1 proteins for DNA repair and persistence of repair clusters differ for cell types as detected by single molecule localization microscopy. *Int J Mol Sci* (2018) **19**:3713. doi:10.3390/ijms19123713
56. Scherthan H, Lee J-H, Maus E, Schumann S, Muhtadi R, Chojowski R, et al. Nanostructure of clustered DNA damage in leukocytes after in-solution irradiation with the alpha emitter Ra-223. *Cancers* (2019) **11**:1877. doi:10.3390/cancers11121877
57. Costes SV, Boissière A, Ravani S, Romano R, Parvin B, Barcellos-Hoff MH. Imaging features that discriminate between foci induced by high- and low-LET radiation in human fibroblasts. *Radiat Res* (2006) **165**:505–15. doi:10.1667/rr3538.1
58. Hauptner A, Friedland W, Dietzel S, Drexler GA, Greubel C, Hable V, et al. Spatial distribution of DNA double-strand breaks from ion tracks. *Ion beam science: solved and unsolved problems*. Copenhagen, Denmark: Royal Danish Academy of Sciences and Letters (2006) p. 59–85.
59. Hable V, Drexler GA, Brüning T, Burgdorf C, Greubel C, Derer A, et al. Recruitment kinetics of DNA repair proteins Mdc1 and Rad52 but not 53BP1 depend on damage complexity. *PLoS One* (2012) **7**:e41943. doi:10.1371/journal.pone.0041943
60. Lorat Y, Timm S, Jacob B, Taucher-Scholz G, Rübe CE. Clustered double-strand breaks in heterochromatin perturb DNA repair after high linear energy transfer irradiation. *Radiother Oncol* (2016) **121**:427–37. doi:10.1016/j.radonc.2016.08.028
61. Perez RL, Best G, Nicolay NH, Greubel C, Rossberger S, Reindl J, et al. Superresolution light microscopy shows nanostructure of carbon ion radiation-induced DNA double-strand break repair foci. *FASEB J* (2016) **30**:2767–76. doi:10.1096/fj.201500106r
62. Natale F, Rapp A, Yu W, Maiser A, Harz H, Schall A, et al. Identification of the elementary structural units of the DNA damage response. *Nat Commun* (2018) **8**:15760. doi:10.1038/ncomms15760
63. Reindl JS, Girst S, Walsh DWM, Geubel C, Schwarz B, Siebenwirth C, et al. Chromatin organization revealed by nanostructure of irradiation inducedγH2AX, 53BP1 and Rad51 foci. *Sci Rep* (2017) **7**:40616. doi:10.1038/srep40616.
64. Eryilmaz M, Schmitt E, Krufczik M, Theda F, Lee J-H, Cremer CF, et al. Localization microscopy analyses of MRE11 clusters in 3D-conserved cell nuclei of different cell lines. *Cancers* (2018) **10**:25. doi:10.3390/cancers10010025
65. Bestvater D, Memmel S, Doose S, Neubauer J, Zimmermann H, Flentje M, et al. Nanostructure of DNA repair foci revealed by superresolution microscopy. *FASEB J* (2018) **12**:fj201701435. doi:10.1096%2Ffj.201701435
66. Hofmann A, Krufczik M, Heermann D, Hausmann M. Using persistent homology as a new approach for super-resolution localization microscopy data analysis and classification of γH2AX foci/clusters. *Int J Mol Sci* (2018) **19**: 2263. doi:10.3390/ijms19082263
67. Kakarougkas A, Ismail A, Klement K, Goodarzi AA, Conrad S, Freire R, et al. Opposing roles for 53BP1 during homologous recombination. *Nucleic Acids Res* (2013) **41**:9719–31. doi:10.1093/nar/gkt729
68. Chapman JR, Taylor MRG, Boulton SJ. Playing the end game: DNA double-strand break repair pathway choice. *Mol Cell* (2012) **47**:497–510. doi:10.1016/j.molcel.2012.07.029
69. Reindl J, Drexler GA, Girst S, Greubel C, Siebenwirth C, Drexler SE, et al. Nanoscopic exclusion between Rad51 and 53BP1 after ion irradiation in human HeLa cells. *Phys Biol* (2015) **12**:066005. doi:10.1088/1478-3975/12/6/066005
70. Lemmer P, Gunkel M, Baddeley D, Kaufmann R, Urich A, Weiland YJ, et al. SPDM: light microscopy with single-molecule resolution at the nanoscale. *Appl Phys B* (2008) **93**:1–12. doi:10.1007/s00340-008-3152-x
71. Reymann P, Gunkel M, Weiland Y, Müller P, Baddeley D, Kaufmann RA, et al. Using conventional fluorescent markers for far-field fluorescence localization nanoscopy allows resolution in the 10-nm range. *J Microsc* (2009) **235**:163–71. doi:10.1111/j.1365-2818.2009.03196.x
72. Eberle JP, Rapp A, Krufczik M, Eryilmaz M, Gunkel M, et al. Super-resolution microscopy techniques and their potential for applications in radiation biophysics. In: H Erfle, editor *Super-resolution microscopy–methods and protocols. Methods in Molecular Biology*. **Vol. 1663**. New York, NY: Humana Press (2017) p. 1–13.
73. Bach M, Savini C, Krufczik M, Cremer C, Rösl F, Hausmann M. Super-resolution localization microscopy of γ-H2AX and heterochromatin after folate deficiency. *Int J Mol Sci* (2017) **18**:1726. doi:10.3390/ijms18081726
74. Aguilar M, Cavasonza A, Alpat B, Ambrosi G, Arruda L, Attig N, et al. AMS Collaboration. Precision measurement of cosmic-ray nitrogen and its primary and secondary components with the alpha magnetic spectrometer on the International Space Station. *Phys Rev Lett* (2018) **121**:051103. doi:10.1103%2FPhysRevLett.121.051103
75. Mathew KJ, Murty SVS. Cosmic ray produced nitrogen in extra terrestrial matter. *J Earth Syst Sci* (1993) **102**:415–37. doi:10.1007%2FBF02841731
76. McDonald FB, Teegarden BJ, Trainor JH, Webber WR. The anomalous abundance of cosmic-ray nitrogen and oxygen nuclei at low energies. *Astrophys J* (1974) **187**:L105. doi:10.1086/181407
77. Ying C, Bolst D, Rosenfeld A, Guatelli S. Characterization of the mixed radiation field produced by carbon and oxygen ion beams of therapeutic energy: a Monte Carlo simulation study. *J Med Phys* (2019) **44**:263–9. doi:10.4103/jmp.jmp_40_19
78. Tran LT, Bolst D, Guatelli S, Pogossov A, Petasecca M, Lerch MLF, et al. The relative biological effectiveness for carbon, nitrogen, and oxygen ion beams using passive and scanning techniques evaluated with fully 3D silicon microdosimeters. *Med Phys* (2018) **45**:2299–308. doi:10.1002/mp.12874
79. Bezbakh AA, Zager VB, Kaminski G, Krylov AI, Krylov VA, Teterev YG, et al. Upgrading the genome facility for radiobiological experiments with heavy-ion beams. *Phys Part Nucl Lett* (2013) **10**:175–8. doi:10.1134%2FS1547477113020039
80. Jakob B, Scholz M, Taucher-Scholz G. Biological imaging of heavy charged-particle tracks. *Radiat Res* (2003) **159**:676–84. doi:10.1667/0033-7587(2003)159[0676:biohct]2.0.co;2
81. Tarasov OB, Bazin D. LISE++: exotic beam production with fragment separators and their design. *Nucl Instrum Methods Phys Res B* (2016) **376**: 185–7. doi:10.1016%2Fj.nimb.2016.03.021
82. Krufczik M, Sievers A, Hausmann A, Lee J-H, Hildenbrand G, Schaufler W, et al. Combining low temperature fluorescence DNA-hybridization, immunostaining, and super-resolution localization microscopy for nano-structure analysis of ALU elements and their influence on chromatin structure. *Int J Mol Sci* (2017) **18**: 1005. doi:10.3390/ijms18051005
83. Stuhlmüller M, Schwarz-Finsterle J, Fey E, Lux J, Bach M, Cremer CK, et al. *In situ* optical sequencing and structure analysis of a trinucleotide repeat genome region by localization microscopy after specific COMBO-FISH nano-probing. *Nanoscale* (2015) **7**:17938–46. doi:10.1039/c5nr04141d
84. Hinderhofer BD. Modelling Spatial Patterns. *J R Stat Soc B* (1977) **39**:172–92. doi:10.1111/j.2517-6161.1977.tb01615.x
85. Ester M, Kriegel HP, Sander G, Xu X. A density-based algorithm for discovering clusters a density-based algorithm for discovering clusters in large spatial databases with noise. In: Proceedings of the second international conference on knowledge discovery and data mining; 4–8 August 1996; Portland, OR; p. 226–31. Available from: https://www.aaai.org/Papers/KDD/1996/KDD96-037.pdf

86. Máté G, Hofmann A, Wenzel N, Heermann DW. A topological similarity measure for proteins. *Biochim Biophys Acta* (2014) **1838**:1180–90. doi:10.1016/j.bbamem.2013.08.019
87. Ghrist R. Barcodes: the persistent topology of data. *Bull Am Math Soc* (2007) **45** (01):61–76. doi:10.1090/s0273-0979-07-01191-3
88. Jaccard P. Etude comparative de la distribution florale dans une portion des Alpes et des Jura. *Bull Soc Vaud Sci Nat* (1901) **37**:547–79. doi:10.5169%2Fseals-266450
89. Schwarz B, Friedl AA, Girst S, Dollinger G, Reindl J. Nanoscopic analysis of 53BP1, BRCA1 and Rad51 reveals new insights in temporal progression of DNA-repair and pathway choice. *Mutat Res* (2019) **816–818**:111675. doi:10.1016/j.mrfmmm.2019.111675
90. Kumar R, Horikoshi N, Singh M, Gupta A, Misra HS, Albuquerque K, et al. Chromatin modifications and the DNA damage response to ionizing radiation. *Front Oncol* (2012) **2**:214. doi:10.3389/fonc.2012.00214
91. Hunt JR, Sossick AJ, Boulton SJ, Jackson SP. BRCA1-associated exclusion of 53BP1 from DNA damage sites underlies temporal control of DNA repair. *J Cell Sci* (2012) **125**:3529–34. doi:10.1242/jcs.105353

Conflict of Interest: The authors declare that the research was conducted in the absence of any commercial or financial relationships that could be construed as a potential conflict of interest.

frontiers in Physics

ORIGINAL RESEARCH
published: 12 November 2020
doi: 10.3389/fphy.2020.567864

Monte Carlo Modeling of DNA Lesions and Chromosomal Aberrations Induced by Mixed Beams of Alpha Particles and X-Rays

Beata Brzozowska[1]*, *Adrianna Tartas*[1] and *Andrzej Wojcik*[2,3]

[1]Biomedical Physics Division, Faculty of Physics, Institute of Experimental Physics, University of Warsaw, Warsaw, Poland, [2]Department of Molecular Biosciences, The Wenner-Gren Institute, Stockholm University, Stockholm, Sweden, [3]Institute of Biology, Jan Kochanowski University, Kielce, Poland

Prediction of health risks associated with exposure to mixed beams of high- and low-linear energy transfer ionizing radiation is based on the assumption that the biological effect caused by mixed radiation equals the sum of effects resulting from the action of individual beam components. Experimental studies have demonstrated that the cellular effects in cells exposed to mixed radiations are higher than that calculated based on the assumption of additivity. The present work contains a comparative analysis of published results on chromosomal aberrations in human peripheral blood lymphocytes exposed to mixed beams of alpha particles and X-rays with computer simulations using the PARTRAC program based on Monte Carlo methods. PARTRAC was used to calculate the levels of DNA single-strand breaks (SSB) and double-strand breaks (DSB—both complex and simple) and the level of chromosomal aberrations. SSB and DSB yields were found to be additive. A synergistic effect was obtained at the level of chromosomal aberrations, being in good agreement with the experimental results. This result demonstrates that the synergistic action of mixed beams results from processing of SSB and DSB and not from their initial frequencies. The level of synergy was dependent on the composition of the mixed beam, with highest level at 50:50 ratio of alpha particles and X-rays.

Keywords: ionizing radiation, linear energy transfer, Monte Carlo modeling, mixed beams, chromosomal aberrations, DNA damage

OPEN ACCESS

Edited by:
Yolanda Prezado, INSERM U1021 Signalisation normale et pathologique de l'embryon aux thérapies innovantes des cancers, France

Reviewed by:
Carmen Villagrasa, Institut de Radioprotection et de Sûreté Nucléaire, France
Alexandros G. Georgakilas, National Technical University of Athens, Greece

***Correspondence:**
Beata Brzozowska
beata.brzozowska@fuw.edu.pl

Specialty section:
This article was submitted to Medical Physics and Imaging, a section of the journal Frontiers in Physics

Received: *30 May 2020*
Accepted: *05 October 2020*
Published: *12 November 2020*

Citation:
Brzozowska B, Tartas A and Wojcik A (2020) Monte Carlo Modeling of DNA Lesions and Chromosomal Aberrations Induced by Mixed Beams of Alpha Particles and X-Rays. Front. Phys. 8:567864. doi: 10.3389/fphy.2020.567864

INTRODUCTION

Correct processing of DNA damage is crucial for maintaining the genomic stability of cells. Among the most important sources of DNA damage in humans is ionizing radiation, both of natural and man-made origin [1, 2]. Radiation is a potent inducer of DNA double-strand breaks (DSB), many of which are complex in nature and pose serious problem in the DNA repair machinery [3, 4]. Per unit radiation dose, the level of complex DSB increases with ionization density, which is described as the linear energy transfer (LET) [5, 6].

Biological effects of radiations characterized by various LETs have been analyzed in numerous studies. The majority of studies focused on analyzing effects induced by radiation of a single quality. However, environmental, occupational, and medical exposures are often mixed, showing simultaneous action of radiations with different LETs. Examples include gamma radiation plus alpha particles in high natural background radiation areas [1], gamma radiation and neutrons plus

charged particles during aircraft or space flight operation [7], and gamma radiation and neutrons plus protons during some forms of radiotherapy [8, 9].

The interesting question behind mixed beam exposure is whether the radiations interact, resulting in effects that are higher than that expected based on an additive action of the single beam components. Using a dedicated mixed beam exposure facility [10], we could demonstrate in several studies that this is indeed the case [11–16].

Two radiation types may interact via various mechanisms leading to a synergistic effect. First, it is possible that the action of both radiation types in a target volume will lead to an increased density of ionization events and an increase in LET. Such effect could lead to an augmented level of single-strand breaks (SSB) and DSB and higher DNA damage complexity. Second, it is possible that exposure to one type of radiation transforms the DNA damage response machinery in such a degree that the additional damage induced by the other radiation type will not be signaled and/or repaired properly [13]. Results published so far suggest that mixed beam exposure overwhelms the DNA repair machinery [14, 15]. Up to this time, we have not been able to study the question whether mixed beam exposure leads to higher than expected yield of SSB and DSB, resulting in higher DSB complexity.

The distribution of hits inside a nucleus can be calculated with great precision by Monte Carlo (MC) simulation methods [6, 17, 18]. Methods are used to precisely calculate the number of hits within a certain volume in a certain time and per a certain dose. The track structure analyses rely on an "event-by-event" description of the physical and chemical processes following irradiation. Each type of interaction for an ingoing particle is described by the deposited energy and the position where the interaction takes place. This information allows studying spatial correlations of lesions within the DNA molecule and between different chromosomes within a cell nucleus. The PARTRAC codes [19] combine track structure calculations with a multilevel cellular DNA model; moreover, cellular repair processes and the formation of chromosomal aberrations (CA) can also be simulated [20].

The aim of the present study was to simulate, using PARTRAC codes, the formation of SSB, DSB, and CA in human peripheral blood lymphocytes exposed to mixed beams as described in the study by Staaf et al. [10, 11]. The computed chromosomal aberration frequencies were compared with the published experimental results [12].

MATERIALS AND METHODS

Experimental Data

Experimental data were generated using the mixed beam exposure facility MAX [10] available at the Stockholm University that allows exposure of cells to two different types of ionizing radiation: alpha particles and X-rays. The source of alpha particles was Am-241 with a energy of 5.49 MeV, yielding a dose rate of 0.21 Gy/min. The source of X-rays was an X-ray tube operating at 190 kV and 4 mA, yielding a dose rate of 0.07 Gy/min. The X-ray energy spectrum had a single peak at 80 keV and is described in the study by Brehwens et al. [21].

Staaf et al. [12] analyzed translocations and complex aberrations in human peripheral blood lymphocytes (from a single male donor) exposed to mixed beams. A complex aberration was defined as an exchange resulting from at least three primary breaks in two or more chromosomes [22]. Chromosomal aberrations were analyzed in chromosomes 2, 8, and 14 using fluorescence *in situ* hybridization for combined doses of 0.20, 0.40, and 0.80 Gy X-rays (X); 0.13, 0.27, and 0.54 Gy alpha particles (α); and 0.20X + 0.07α, 0.40X + 0.13α, and 0.40X + 0.27α Gy mixed beams. A linear-quadratic, dose–response curve for complex aberrations was observed after X-rays, and a linear dose–response curve was observed after alpha particles. Higher than expected from additivity frequencies of complex aberrations were observed at chromosomal aberration levels of 1.3 and 1.6 aberrations per cell. The uncertainties were not included in the publication, so they were calculated based on Poisson distribution and used for comparison with MC simulations. To expand the dose range, the fitted dose–response curves for experimental data were used.

Staaf et al. [12] presented aberration frequencies scored in chromosomes 2, 8, and 14. For comparing the observed frequencies with those generated by MC simulations, whole-genome frequencies of aberrations were calculated as described by Lucas et al. [23], assuming that the fraction of the male human whole-genome DNA represented by chromosomes 2, 8, and 14 is 0.0803, 0.0488, and 0.0338, respectively [24]. The envelopes of additivity [25] were constructed based on dose–response curves for CA induced by X-rays and alpha radiation.

The edges of the envelopes of additivity correspond to two isobolograms created for heteroadditive and isoadditive forms of interaction between these two types of radiation. Isoaddition is calculated based on assumption that two agents have the same mechanism of action, so that the combined effect is superadditive. Heteroaddition is calculated based on assumption that when the two agents have different mechanism of action, the combined effect is additive. The mixed beam data inside the envelope of the additivity mean the additive mixed beam effect, if they are outside, that the effect is either synergistic (to the left) or antagonistic (to the right).

MC Simulations

PARTRAC codes were used to model the frequencies of SSB, DSB, and CA. MC simulations were performed for the three types of ionizing radiations used by Staaf et al. [12]. Simulations were carried out for 1,000 cell nuclei of cells with a spherical shape and a diameter of 10 μm, being an approximation of published data [26]. It was assumed that each cell nucleus contains a total genomic length of 6.6 Gbp. Details of the model of chromatin structure inside the nucleus are described in the study by Friedland et al. [19].

Photon irradiation was simulated with PARTRAC by implementation of the spectrum of X-rays generated by a 190 kVp machine. Photons were generated randomly from the surface of the cytoplasm, and the simulations were performed until the dose values are achieved. The doses delivered to a cell

nucleus were calculated based on energy deposition of X-rays passing through the cell nucleus. The energy limit for photon and electron scattering was 20 and 10 eV, respectively. The simulated dose range (0.2–2.43 Gy) for X-ray irradiation was wider than that used in the experiment. In case of alpha particle exposure, the simulated dose range started from 0.3 Gy, which is more than the dose of 0.13 Gy obtained experimentally, but it contains higher values till 2.33 Gy. Alpha particles with the energy spectra of Am-241 were generated based on Poisson distribution, and the dose was determined as division of the deposited energy by the mass of the target. The increased dose ranges for both types of radiation resulted in wide dose range of 0.44–4.76 Gy for mixed beam simulations. The physical and chemical interactions were generated separately for X-rays and alpha particles, and the combined information about track structures was used to calculate the DSB and SSB induced by mixed beams.

PARTRAC allows studying complex DNA damage and repair processes at each elementary stage: starting from the physical interaction with the DNA, through the indirect interactions coming from the water radiolysis products (chemical module), until the response at the level of chromosomal aberrations due to misrepair of DNA damage. Details of the physical, chemical, and biological modules that were used to model the level of chromosomal aberrations are described elsewhere [19, 27]. The parameters of the CA model were taken from Friedland et al. [28] but disregarding the special DNA structure of the hybrid cell type in that study. The DSB was considered when two DNA breaks were separated by no more than 10 bp. The DSB cluster was defined by two or more DSB occurred within a genomic distance of 25 bp.

The CA induction model starts from radiation-induced DNA damage assessed by overlapping radiation track structures with the DNA molecule as described above. The repair of DNA DSB via nonhomologous end joining is considered. The use of nonhomologous end joining and not of homologous recombination repair is considered because the simulations were carried out for unstimulated peripheral blood lymphocytes that are in the G_0 phase of the cell cycle. Additionally, to the initial spatial distribution and complexity, the simulation includes diffusive motion, enzymatic processing, synapsis, and ligation of individual DSB ends. Improper joining of DNA fragments results in different chromosome aberration types simulated with the PARTRAC repair module by tracking the chromosome origin of the ligated fragments and the positions of centromeres. The motion of DNA ends is modeled considering chromatin mobility within time scales of a few hours. For a model validation, the number of dicentrics per cell was calculated with PARTRAC and compared with published results [27, 28].

RESULTS

The physical interactions of X-rays and alpha particles with the DNA molecule and the chemical reactions were simulated to calculate the DNA damage and its location in the nucleus using the appropriate modules of PARTRAC. High-energy helium nuclei ionize densely along their tracks when they pass the cell nucleus, giving rise to highly clustered and complex DNA lesions. High-energy photons and the energetic electrons liberated via photoelectric and Compton effect interact sparsely with electrons of atoms and can travel long distances inside a cell nucleus before they interact. Examples of simulated ionization events for X-rays and alpha particles are shown in **Figure 1** (the simulations of early DNA damage take also into account excitation of the water medium, but they are not shown in the figure).

Verification of the Simulation Model Using Single-Strand Breaks and Double-Strand Breaks

In PARTRAC, DNA molecule structure includes the double helix, nucleosomes, chromatin fibers, chromatin fiber loops, chromatin domains, and chromosomes, which are represented by more than 6 billion DNA base pairs. The geometrical information about the interactions with the DNA can be translated into genomic distances given as numbers of base pairs from the end of the hit chromosomes and thus used to define the DNA damage size and position. The configuration of the damage can be retrieved as the number and position of individual SSB and DSB. The linear dependence of the dose of X-rays and alpha particles and the amount of SSB and DSB formation after physical and chemical stages are shown in **Figure 2**. For 1 Gy of X-rays (1,299 ± 40) SSB and (56 ± 7) DSB were induced per nucleus. According to theoretical predictions, 1 Gy of X-rays causes about 1000 SSB [29] and 50 DSB [30] per nucleus. Experimental data indicate that radiation causes about 923 SSB [31], and the ratio between SSB and DSB is equal to 25 [32]. Taking into account the uncertainties of performed simulations, it can be assumed that the simulated mean values of SSB and DSB are in line with experimental data and calculations performed with independent MC tools. The total SSB (110 ± 10) and DSB (21 ± 4) yields per 1 Gy and 1 Gbp calculated for alpha irradiation emitted from Am-241 source are comparable to simulated values (72 and 16, respectively) with Geant4-DNA published in the study by de la Fuente Rosales et al. [33].

Additionally, the SSB and DSB numbers were simulated for a simultaneous exposure of cells to alpha particles and X-rays. Because the linear function given by the equation $y = Ax + B$ was fitted to all performed simulations (presented in **Table 1**), the expected numbers of SSB and DSB calculations based on additivity assumption could be generated. Both sets of results are shown in **Figure 3**. The simulated SSB and DSB induced by mixed beams are in agreement with calculated sums of SSB and DSB of alpha particles and X-rays simulated independently.

The equality of linear regression coefficients was tested with the Student's *t*-test. The aim was to verify that the two Pearson's linear correlation coefficients in tested samples are equal. The determined p value was 0.007 for SSB and 0.03 for DSB, indicating that the correlation coefficients do not differ.

The difference between low- and high-LET radiation interactions within cells is described by spatial distributions of ionization acts inside a nucleus. As shown in **Figure 4**, DSB clusters appear more often for densely ionizing alpha particles as compared with X-ray irradiation. However, PARTRAC calculations

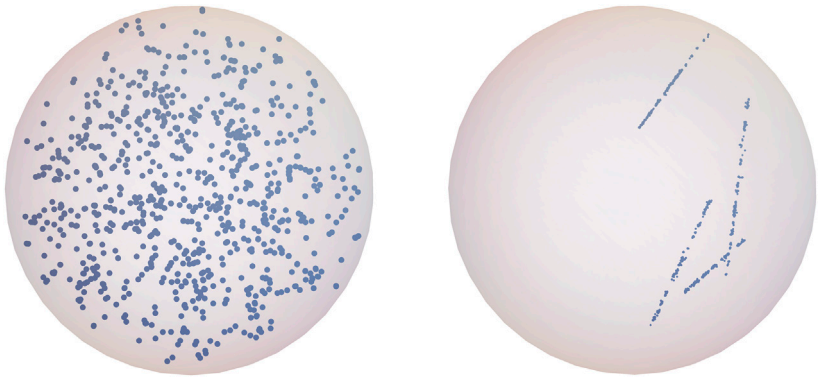

FIGURE 1 | The simulated spatial ionization distribution within an exemplary lymphocyte nucleus after X-ray (left panel) and alpha irradiation (right panel) with the dose equal 1 Gy.

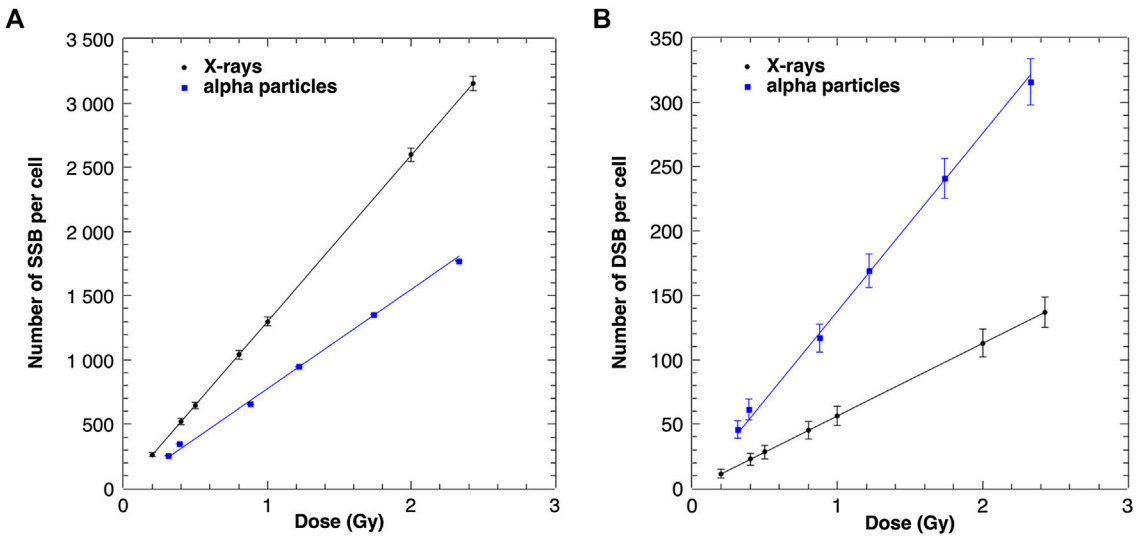

FIGURE 2 | Modeled numbers of SSB **(A)** and DSB **(B)** induced in a cell nucleus after X-ray and alpha particle irradiation as a function of the absorbed dose. The uncertainties are given as standard deviations.

TABLE 1 | Dose–response fitting parameters for simulated SSB and DSB induced by X-rays, alpha particles, and mixed beams.

	X-rays	Alpha particles	Mixed beams	Sum of X and α
SSB				
A	1,300 ± 20	774 ± 10	1,030 ± 20	1,020 ± 30
B	2 ± 20	0.0 ± 0.4	4 ± 30	10 ± 40
R^2	0.9999	0.9953	0.9983	0.9984
DSB				
A	56 ± 4	138 ± 5	96 ± 6	96 ± 8
B	0 ± 3	0.0 ± 0.4	−2 ± 9	−2 ± 10
R^2	0.9999	0.9982	0.9987	0.9989

The last column represents parameters calculated as a sum of parameters for alpha particles (50%) and X-rays (50%). R^2 *describes goodness of fit.*

for mixed beams containing 50% of alpha particles and 50% of X-rays gives the total number of DSB clusters as the sum of DSB clusters induced by alpha particles and X-rays independently.

Cellular Response in the Form of Chromosomal Aberrations

The calculated total numbers of CA formation in spherical cells (human peripheral blood lymphocytes) were compared with experimental data [12] collected previously in our laboratory for cells exposed to X-rays, alpha particles, and mixed beams. The results are shown in **Figures 5** and **6**. The uncertainties of data points scored during the experiment were calculated as square roots of variations based on Poisson distribution.

Although the calculated numbers of CA per cell for X-ray irradiation are described by linear quadratic function: $CA = (0.08 \pm 0.05) - (0.3 \pm 0.2)D + (1.3 \pm 0.1)D^2$, the dose response for alpha exposure is given by the formulae: $CA = (-0.3 \pm 0.2) + (4.3 \pm 0.2)D$.

Comparison of CA dose responses of cells irradiated with X-rays shows different trends obtained with experimental data and MC simulations. The experimental data were described by

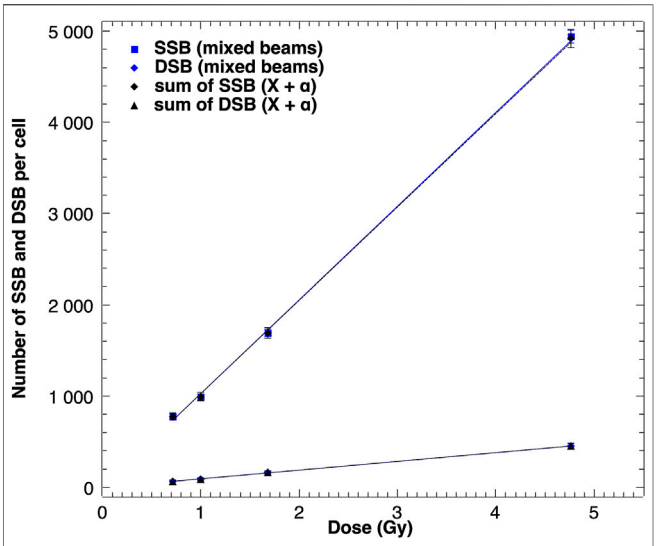

FIGURE 3 | Modeled numbers of SSB and DSB induced in a cell nucleus by mixed beams of alpha particles and X-rays and sums of SSB and DSB induced by both radiation types given independently. Error bars indicate standard deviations.

linear function in contrast to PARTRAC calculations, showing linear quadratic relationship. However, CA was scored experimentally only up to 0.8 Gy, where the quadratic element has smaller impact than the linear one. The scaling factor equal to 3.3 for simulations of CA induced by X-rays was introduced. The number of CA induced by alpha irradiation modeled with PARTRAC is higher than that induced by the experimental data ($CA_{\mathrm{exp}} = (0.0002 \pm 0.0001) + (3.90 \pm 0.01)D$) and needed to be divided by a factor 2. According to Student's t-test, both linear functions are in agreement ($p < 0.05$).

Number of chromosomal aberrations induced by mixed beam radiation and modeled with PARTRAC was comparable to the experimental data, and no scaling factor was needed. The simulated dose response is described by the linear function: $CA = -(0.01 \pm 0.01) + (5.2 \pm 0.3)D$ and differs from linear quadratic function describing experimental data. However, simulated data points are in agreement with the experimental data because the experimental uncertainties are large with respect to error bars of simulations.

Synergism or Additivity

Analogous to the approach taken by Staaf et al. [12], envelopes of additivity were prepared and compared with simulations of mixed beams consisting of equal contributions of both radiation qualities. In the experimental study [12], exposure to alpha particles and X-rays always started simultaneously, with X-ray irradiation source remaining on for a few minutes after the alpha exposure was stopped. There is no dose-rate model implemented in the PARTRAC codes, so simulations of X-ray and alpha particle irradiation were performed separately and combined for mixed beam calculations. It is assumed that cells need 48 h to repair the damage before they reach the first posttreatment mitosis. The results are shown in **Figure 7**.

Data points showing simulated numbers of CA induced by mixed beam radiation are located outside of the left envelope borders, indicating an interaction of alpha particles and X-rays leading to CA frequencies higher than predicted based on assuming additivity.

The same procedures were performed for two different composition of mixed beams: containing 80% X rays (and remaining 20% of alpha particles) and 80% alpha particles (and 20% of X rays). The results are shown in **Figure 8**.

The data points representing mixed beam-induced CA were again outside the left envelope borders, indicating synergism. However, a stronger synergistic effect was observed following

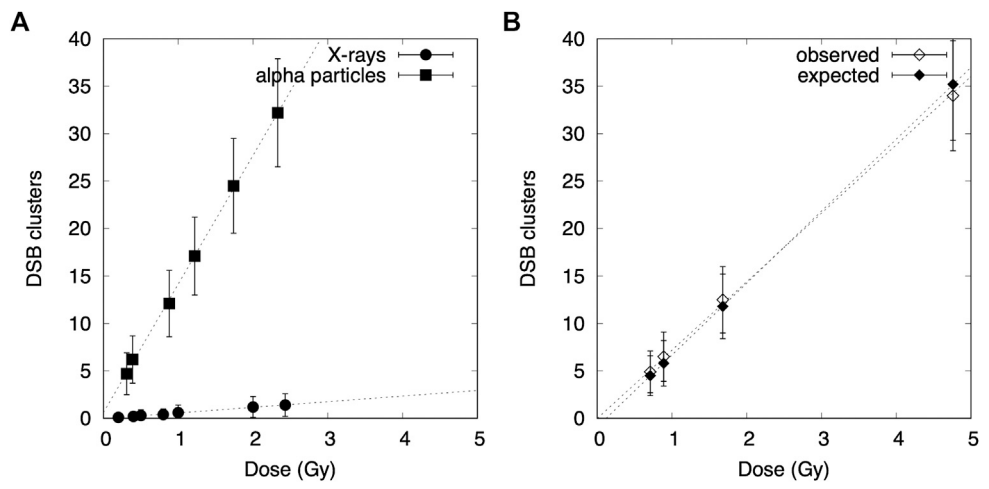

FIGURE 4 | Dose–response curves for simulated DSB clusters in lymphocytes exposed to X-rays, alpha particles, and mixed beams: **(A)** comparison between alpha particles and X-rays, **(B)** calculated values for a mixed beam simulation compared with expected values if additivity is preserved.

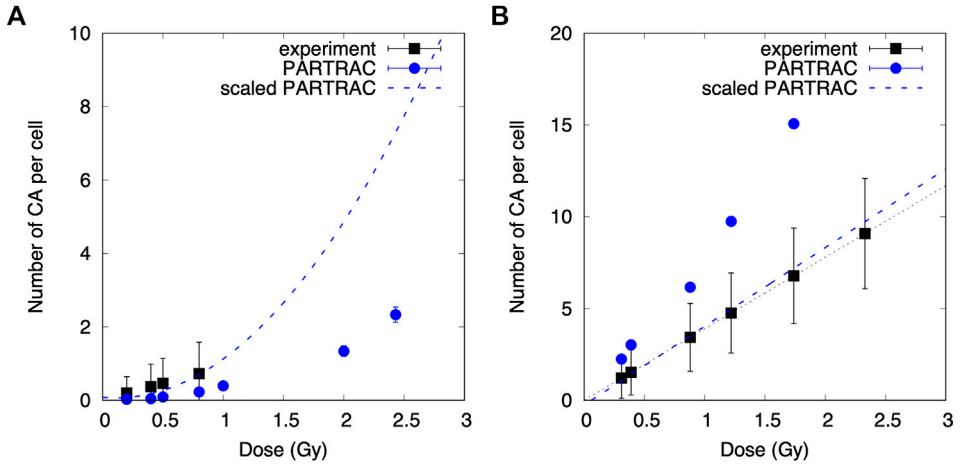

FIGURE 5 | Comparison of modeled and experimental results. Linear quadratic and linear relationships between the number of chromosomal aberrations (CA) scored for a cell induced by X-rays **(A)** and alpha particles **(B)** and the dose for experimental data and MC simulations. The blue dashed lines represent PARTRAC calculations including scaling factors.

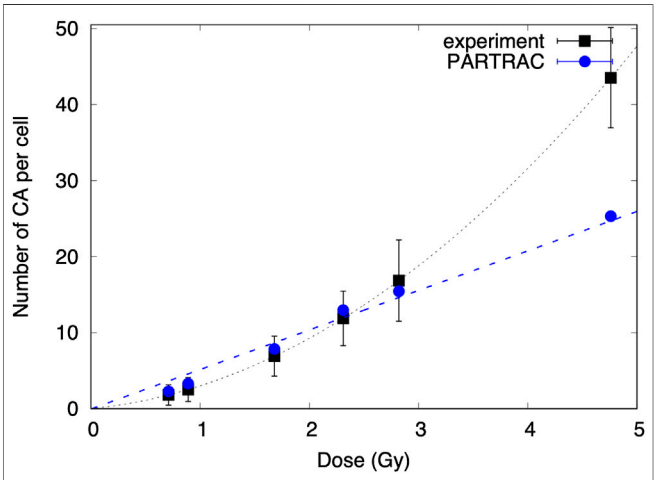

FIGURE 6 | The number of chromosomal aberrations scored for a cell induced by mixed beams as a function of the dose for experimental data and MC simulations.

exposure of cells to 20% alpha particles and 80% X-rays as compared to 80% alpha particles and 20% X-rays.

DISCUSSION

The characteristics of the physical features of the interaction of ionizing radiations with living matter and accompanying chemical reactions are a major determinant of their final biological consequences. The complexity of DNA damage increases with ionization density, poses serious problems for the DNA repair machinery, and increases the probability of misrepair. A combined action of alpha particles and X-rays results in an interaction of lesions leading to increased damage complexity and impaired damage repair. An interaction of the two types of radiations leads to an increase in biological effectiveness of mixed beam, beyond the level expected from additivity dependent on contribution of beam component with high LET.

There are differences between PARTRAC calculations and experimental number of chromosomal aberrations induced by radiation from X-ray tube and Am-241. Discrepancy in the number of dicentrics was previously observed and discussed for alpha and photon irradiation [27]. The scaling factors obtained from these adaptations were implemented in PARTRAC codes and used to model CA within this analysis. Nevertheless, the cellular response varies depending on the cell system, giving different number and different type of chromosomal aberrations (including dicentrics). CA overestimation by a factor of 2 in the alpha irradiation simulations may result from those aberrations that are not experimentally detectable. Underestimation of the number of CA induced by X-rays may come from the scaling factor introduced from dicentric analysis.

Synergistic effect in CA induction is observed for PARTRAC calculations, which were adapted using the experimental data collected at the Stockholm University. There are no signs of synergism observed after the physicochemical phase of interaction between ionizing radiation and cells. Spatial distributions of ionizations acts within a nucleus lead to spatial distributions of DNA damage, which can be classified as DSB or SSB of DNA. Alpha radiation, which densely ionizes the cell, gives more DSB, whereas X-rays damage DNA sparsely creating more SSB. The number of DSB and SSB from alpha and X-ray radiations given together is just a sum of DSB and SSB coming from single exposures. Complexity of the DNA damage is described not by absolute values of induced DNA breaks, but it depends on their relative position in a small volume of nuclear matter. Mixed beams produce clusters including DNA strand breaks, which are more difficult to be repaired. The complexity of

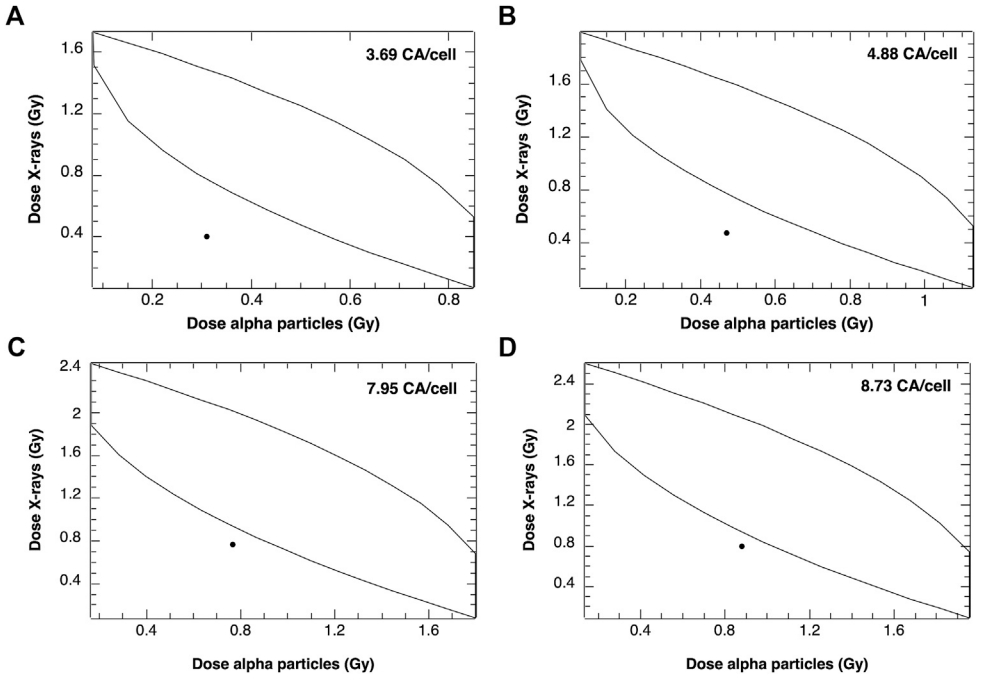

FIGURE 7 | Envelopes of additivity calculated for 4 selected frequencies of chromosomal aberrations (CA), from mixed beams composed of 50:50 alpha particles and X-rays: A: 3.69 CA/cell, B: 4.88 CA/cell, C: 7.95 CA/cell and D: 8.73 CA/cell. The mixed beam doses were 0.71 Gy **(A)**, 0.94 Gy **(B)**, 1.53 Gy **(C)**, and 1.68 Gy **(D)**.

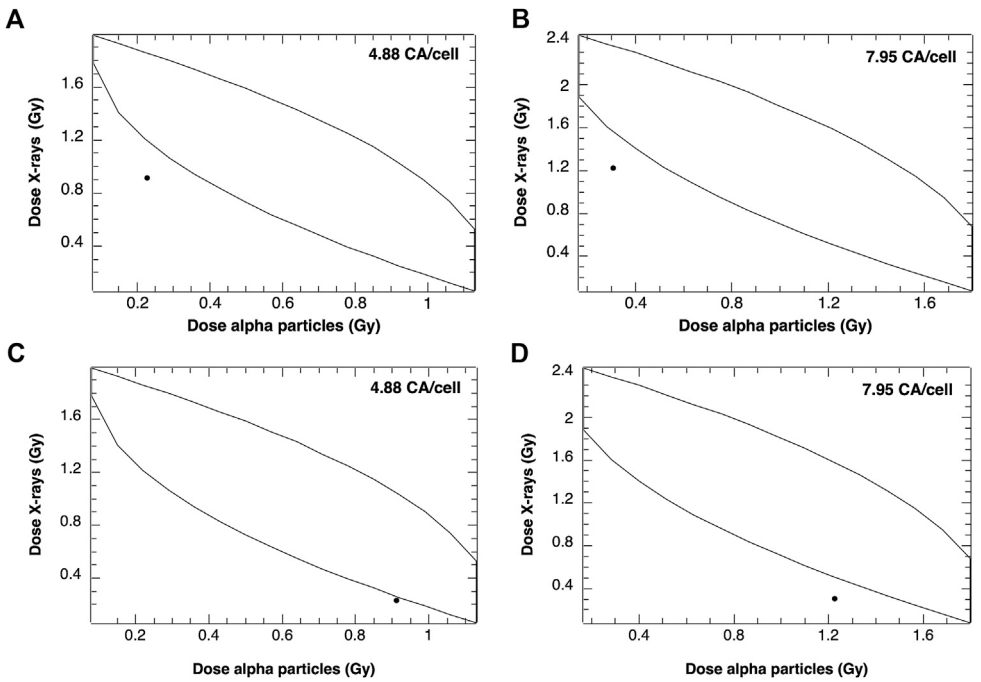

FIGURE 8 | Envelopes of additivity calculated for 2 selected frequencies of CA for mixed beams composed of 20% alpha particles and 80% X-rays **(A), (B)** and 80% alpha particles and 20% X-rays **(C), (D)**. The mixed beam doses for 4.88 CA/cell and 7.95 CA/cell were 0.94 and 1.53 Gy, respectively.

DNA damage and focus induction for mixed beams consisting of different LET radiations was also modeled with PARTRAC codes [34].

The deviations from additive approach appeared in the last interaction phase, which is the biological response of the irradiated cells. Based on the calculated envelopes of additivity, the synergistic effect of CA induction using MC simulations was confirmed. MC modeling allowed us to perform different compositions of mixed beams to study the impact of high-LET radiation contribution. When the cells were irradiated with mixed beams containing 50% of both types of radiations or X-rays with small addition of alpha particles (20%), the stronger synergistic effect was seen for a given CA number per cell. Using mixed beams with large contribution of high-LET radiation, the effect becomes less significant.

The synergistic effect results from joining of broken DNA ends due to DSB from alpha particle irradiation with those from photon irradiation. In X-ray irradiated cells, the broken DNA ends are spread over the whole cell nucleus. They rarely undergo misrejoining with DNA ends from other chromosomes as long as the dose is relatively low. Alpha particle tracks typically cross the territories of a few chromosomes so that DNA ends from adjacent chromosome territories may misrejoin and form CA. The linear increase with dose or the number of alpha tracks per nucleus shows that the intertrack contribution (joining of DSB ends from different alpha particle tracks) is small under the conditions studied here. However, the presence of DSB ends in many chromosomes due to X-ray irradiation under mixed beam condition is supposed to considerably enhance the misrejoining probability for alpha particle–induced DNA ends aligned along the particle tracks.

In a recent study, Pantelias et al. [35] demonstrated that exposure to high-LET radiation induces chromosome shattering, which may give rise to chromothripsis. The scale of chromosomal rearrangements leading to chromothripsis is in excess of 1,000 bp, corresponding to a distance of 50–100 nm. The PARTRAC code does not consider such large-scale chromosomal rearrangements. On the other hand, despite applying the technique of chemically induced premature chromosome condensation, chromothripsis was not observed by Staaf et al. [12], suggesting that human peripheral blood lymphocytes with such extensive damage do not reach the G2 phase of the cell cycle or the mitosis, possibly by undergoing interphase death. In this respect, the results obtained by MC simulation with the PARTRAC codes are compatible with the reference experimental results.

CONCLUSIONS

Mathematical modeling, like PARTRAC codes, allows testing the mechanisms of cellular response to ionizing radiation, which are proposed based on experimental data. It can be done for different experimental scenarios taking into account different cell lines, radiation qualities, and experimental setups. The only price of doing it is computing power, which is not an issue nowadays. Using temporal and spatial evolution of particle track structure, the DNA damage in form of DSB and SSB induced by radiations with low- and high-LET was simulated. It was used to investigate morphological changes of chromosomes in cells after simultaneous exposure to alpha particles and X-rays. Although the PARTRAC simulation code allows the calculations of early DNA damage and has been validated based on numerous irradiation scenarios, the biophysical model of chromosomal aberration induction is still fragile. Modeling the DNA repair mechanism is very sophisticated, and it should always takes into account the reproducibility of the experimental data. The synergism observed in series of experiments performed at the Stockholm University was confirmed using adapted Monte Carlo simulations of chromosomal aberrations.

The action of mixed beams is interesting from the perspective of how cells cope with different forms of DNA damage. This is an important question in the area of genome stability, which is relevant both for basic cell research and for a deeper understanding of processes leading to radiation-induced transformation of cells. It is relevant for the assessment of cancer risk due to exposure to mixed beams as encountered during modern external beam radiotherapy with high-energy photons or with protons.

DATA AVAILABILITY STATEMENT

The raw data supporting the conclusions of this article will be made available by the authors, without undue reservation.

AUTHOR CONTRIBUTIONS

BW: conceptualization, methodology, writing of original draft preparation; AT: data curation and writing of original draft preparation; AW: conceptualization, writing, reviewing, and editing.

FUNDING

BW was supported in part by a grant from NCN, Poland (2016/23/D/ST7/03544). AT was supported by the Polish Funds for Science. AW is supported by grants from the Swedish Radiation Safety Authority (SSM).

ACKNOWLEDGMENTS

The authors thank Werner Friedland for providing the PARTRAC codes, valuable discussions, and helpful comments.

REFERENCES

1. Hendry JH, Simon SL, Wojcik A, Sohrabi M, Burkart W, Cardis E, et al. Human exposure to high natural background radiation: what can it teach us about radiation risks? *J Radiol Prot* (2009) 29(2A):A29–42. doi:10.1088/0952-4746/29/2a/s03
2. Sodickson A, Baeyens PF, Andriole KP, Prevedello LM, Nawfel RD, Hanson R, et al. Recurrent CT, cumulative radiation exposure, and associated radiation-induced cancer risks from CT of adults. *Radiology* (2009) 251(1):175–84. doi:10.1148/radiol.2511081296
3. Lomax ME, Folkes LK, O'Neill P. Biological consequences of radiation-induced DNA damage: relevance to radiotherapy. *Clin Oncol* (2013) 25(10):578–85. doi:10.1016/j.clon.2013.06.007
4. Mavragani IV, Nikitaki Z, Souli MP, Aziz A, Nowsheen S, Aziz K, et al. Complex DNA damage: a route to radiation-induced genomic instability and carcinogenesis. *Cancers* (2017) 9(7):91. doi:10.3390/cancers9070091
5. Goodhead DT. Energy deposition stochastics and track structure: what about the target? *Radiat Protect Dosim* (2006) 122:3–15. doi:10.1093/rpd/ncl498
6. Nikjoo H, O'Neill P, Wilson WE, Goodhead DT. Computational approach for determining the spectrum of DNA damage induced by ionizing radiation. *Radiat Res* (2001) 156:577–83. doi:10.1667/0033-7587(2001)156[0577:cafdts]2.0.co;2
7. Durante M, Cucinotta FA. Heavy ion carcinogenesis and human space exploration. *Nat Rev Cancer* (2008) 8:465–72. doi:10.1038/nrc2391
8. Takam R, Bezak E, Marcu LG, Yeoh E. Out-of-field neutron and leakage photon exposures and the associated risk of second cancers in high-energy photon radiotherapy: current status. *Radiat Res* (2011) 176:508–20. doi:10.1667/rr2606.1
9. Yonai S, Furukawa T, Inaniwa T. Measurement of neutron ambient dose equivalent in carbon-ion radiotherapy with an active scanned delivery system. *Radiat Protect Dosim* (2014) 161 (1–4):433–6. doi:10.1093/rpd/nct251
10. Staaf E, Brehwens K, Haghdoost S, Pachnerova-Brabcova K, Czub J, Braziewicz J, et al. Characterization of a setup for mixed beams exposure of cells to 241Am alpha particles and X-rays. *Radiat Protect Dosim* (2012) 151:570–9. doi:10.1093/rpd/ncs024
11. Staaf E, Brehwens K, Haghdoost S, Nievaart S, Pachnerova-Brabcova K, Czub J, et al. Micronuclei in human peripheral blood lymphocytes exposed to mixed beams of X-rays and alpha particles. *Radiat Environ Biophys* (2012) 51:283–93. doi:10.1007/s00411-012-0417-x
12. Staaf E, Deperas-Kaminska M, Brehwens K, Haghdoost S, Czub J, Wojcik A. Complex aberrations in lymphocytes exposed to mixed beams of 241Am alpha particles and X-rays. *Mutat Res* (2013) 756:95–100. doi:10.1016/j.mrgentox.2013.05.001
13. Sollazzo A, Brzozowska B, Cheng L, Lundholm L, Haghdoost S, Scherthan H, et al. Alpha particles and X-rays interact in inducing DNA damage in U2OS cells. *Radiat Res* (2017) 188:400–11. doi:10.1667/rr14803.1
14. Sollazzo A, Brzozowska B, Cheng L, Lundholm L, Scherthan H, Wojcik, A. Live dynamics of 53BP1 Foci following simultaneous induction of clustered and dispersed DNA damage in U2OS cells. *Int J Mol Sci* (2018) 19:519. doi:10.3390/ijms19020519
15. Cheng L, Brzozowska B, Sollazzo A, Lundholm L, Lisowska L, Haghdoost S, et al. Simultaneous induction of dispersed and clustered DNA lesions compromises DNA damage response in human peripheral blood lymphocytes. *PLoS One* (2018) 13(10):e0204068. doi:10.1371/journal.pone.0204068
16. Cheng L, Brzozowska-Wardecka B, Lisowska H, Wojcik A, Lundholm L. Impact of ATM and DNA-PK inhibition on gene expression and individual response of human lymphocytes to mixed beams of alpha particles and X-rays. *Cancers* (2019) 11(12):2013. doi:10.3390/cancers11122013
17. Friedland W, Kundrat P. "Modeling of radiation effects in cells and tissues." In: A Brahme, editor. *Comprehensive biomedical physics* Vol. 9. Amsterdam, Netherlands: Elsevier (2014) p. 105–42.
18. Nikjoo H, Girard P. A model of the cell nucleus for DNA damage calculations. *Int J Radiat Biol* (2012) 88:87–97. doi:10.3109/09553002.2011.640860
19. Friedland W, Dingfelder M, Kundrat P, Jacob P. Track structures, DNA targets and radiation effects in the biophysical Monte Carlo simulation code PARTRAC. *Mutat Res* (2011) 711:28–40. doi:10.1016/j.mrfmmm.2011.01.003
20. Friedland W, Kundrat P. Track structure based modelling of chromosome aberrations after photon and alpha-particle irradiation. *Mutat Res* (2013) 756:213–23. doi:10.1016/j.mrgentox.2013.06.013
21. Brehwens K, Bajinskis A, Staaf E, Haghdoost S, Cederwall B, Wojcik A. A new device to expose cells to changing dose rates of ionising radiation. *Radiat Protect Dosim* (2012) 148(3):366–71. doi:10.1093/rpd/ncr092
22. Savage JRK, Simpson PJ. FISH "painting" patterns resulting from complex exchanges. *Mutat Res* (1994) 312:51–60. doi:10.1016/0165-1161(94)90008-6
23. Lucas JN, Poggensee M, Straume T. Translocations between two specific human chromosomes detected by three-color "chromosome painting". *Cytogenet Cell Genet* (1993) 62:11–2. doi:10.1159/000133434
24. Deperas-Kaminska M, Zaytseva EM, Deperas-Standylo J, Mitsyn GV, Molokanov AG, Timoshenko GN, et al. Inter-chromosomal variation in aberration frequencies in human lymphocytes exposed to charged particles of LET between 0.5 and 55 keV/μm. *Int J Radiat Biol* (2010) 86:975–85. doi:10.3109/09553002.2010.496028
25. Steel GG, Peckham MJ. Exploitable mechanisms in combined radiotherapy–chemotherapy: the concept of additivity. *Int J Radiat Oncol Biol Phys* (1979) 5:85–91. doi:10.1016/0360-3016(79)90044-0
26. Sharma S, Cabana R, Shariatmadar S, Krishan A. Cellular volume and marker expression in human peripheral blood apheresis stem cells. *Cytometry* (2008) 73A:160–7. doi:10.1002/cyto.a.20524
27. Friedland W, Kundrat P. Chromosome aberration model combining radiation tracks, chromatin structure, DSB repair and chromatin mobility, *Radiat Protect Dosim* (2015) 166(1–4):71–4. doi:10.1093/rpd/ncv174
28. Friedland W, Kundrát P, Schmitt E, Becker J, Ilicic K, Greubel C, et al. Modeling studies on dicentrics induction after sub-micrometer focused ion beam grid irradiation. *Radiat Protect Dosim* (2019) 183(1–2):40–4. doi:10.1093/rpd/ncy266
29. Hill MA, O'Neill P, McKenna WG. Comments on potential health effects of MRI induced DNA lesions: quality is more important to consider than quantity. *Eur Heart J Cardiovasc Imaging* (2016) 17(11):1230–8. doi:10.1093/ehjci/jew163
30. Newman HC, Prise KM, Folkard M, Michael BD. DNA double-strand break distributions in X-ray and a-particle irradiated V79 cells: evidence for non-random breakage, *Int J Radiat Biol* (1997) 71(4):347–63. doi:10.1080/095530097143978
31. Milian FM, Gouveia AN, Gual MR, Echeimberg JO, Arruda-Neto JDT, Garcia F, et al. In vitro effects of gamma radiation from 60Co and 137Cs on plasmid DNA. *J Biol Phys* (2007) 33(2):155–60. doi:10.1007/s10867-007-9050-3
32. Fulford J, Nikjoo H, Goodhead DT, O'Neill P. Yields of SSB and DSB induced in DNA by AlK ultrasoft X-rays and a-particles: comparison of experimental and simulated yields, *Int J Radiat Biol* (2001) 77(10):1053–66. doi:10.1080/09553000110069308
33. de la Fuente Rosales L, Incerti S, Francis Z, Bernal MA. Accounting for radiation-induced indirect damage on DNA with the Geant 4-DNA code. *Phys Med* (2018) 51:108–16. doi:10.1016/j.ejmp.2018.06.006
34. Brzozowska B, Galecki M, Tartas A, Friedland W, Wojcik A. *Modeling of radiation-induced foci features in cell exposed to alpha and X-ray radiation using particle track structures* manuscript in preparation.
35. Pantelias A, Zafiropoulos D, Cherubini R, Sarchiapone L, De Nadal V, Pantelias GE, et al. Interphase cytogenetic analysis of G0 lymphocytes exposed to α-particles, C-ions, and protons reveals their enhanced effectiveness for localized chromosome shattering—a critical risk for chromothripsis. *Cancers* (2020) 12:2336. doi:10.3390/cancers12092336

Conflict of Interest: The authors declare that the research was conducted in the absence of any commercial or financial relationships that could be construed as a potential conflict of interest.

frontiers in Physics

ORIGINAL RESEARCH
published: 13 November 2020
doi: 10.3389/fphy.2020.568302

Dosimetry for New Radiation Therapy Approaches Using High Energy Electron Accelerators

Karolina Kokurewicz[1], Andreas Schüller[2], Enrico Brunetti[1], Anna Subiel[3], Rafael Kranzer[4,5], Thomas Hackel[2], Markus Meier[2], Ralf-Peter Kapsch[2] and Dino A. Jaroszynski[1]**

[1]Department of Physics, SUPA and University of Strathclyde, Glasgow, United Kingdom, [2]Physikalisch-Technische Bundesanstalt (PTB), Dosimetry for Radiation Therapy and Diagnostic Radiology, Braunschweig, Germany, [3]National Physical Laboratory, Medical Radiation Science, Teddington, United Kingdom, [4]Physikalisch-Technische Werkstätten (PTW), R&D, Freiburg, Germany, [5]University Clinic for Medical Radiation Physics, Medical Campus Pius Hospital, Carl von Ossietzky University Oldenburg, Oldenburg, Germany

We have performed dosimetry studies using electron beams with energies up to 50 MeV, which exceed current clinical energy ranges and approaches the bottom end of the very high energy electron range. 50 MeV electron beams can reach deep-seated tumors. In contrast to photon beams, electron beams can be generated with ultra-high dose rates by linear accelerators, which could enable FLASH radiotherapy of deep-seated tumors. The response of radiochromic film and alanine is compared with dose measurements using an ionisation chamber. Energy dependence is not observed within the measurement uncertainty in the investigated energy range from 15 to 50 MeV.

Keywords: radiochromic films, dosimetry, very high energy electrons, very high energy electron radiotherapy, dose-rate independent detectors, alanine dosimetry, ionisation chamber, ion recombination correction

OPEN ACCESS

Edited by:
Yolanda Prezado, INSERM U1021 Signalisation normale et pathologique de l'embryon aux thérapies innovantes des cancers, France

Reviewed by:
Till Tobias Böhlen, Centre Hospitalier Universitaire Vaudois (CHUV), Switzerland
Fabio Di Martino, Pisana University Hospital, Italy

****Correspondence:***
Enrico Brunetti
enrico.brunetti@strath.ac.uk
Dino A. Jaroszynski
d.a.jaroszynski@strath.ac.uk

Specialty section:
This article was submitted to Medical Physics and Imaging, a section of the journal Frontiers in Physics

Received: *31 May 2020*
Accepted: *28 September 2020*
Published: *13 November 2020*

Citation:
Kokurewicz K, Schüller A, Brunetti E, Subiel A, Kranzer R, Hackel T, Meier M, Kapsch R-P and Jaroszynski DA (2020) Dosimetry for New Radiation Therapy Approaches Using High Energy Electron Accelerators. Front. Phys. 8:568302. doi: 10.3389/fphy.2020.568302

INTRODUCTION

Radiotherapy (RT) is a cost-effective method of treating cancer, which alone or in combination with other cancer treatments contributes toward approximately 50% of cancer survivals [1–3]. To improve treatment outcomes and reduce adverse side effects, new treatment modalities should maximize tumor control, while minimizing damage to surrounding healthy tissues. FLASH radiotherapy is a promising treatment modality [4–8], which relies on delivery of therapeutic doses in less than a second (e.g., 90 ms [7]) at ultra-high dose rates (>40 Gy/s [4]), which are orders of magnitude higher than currently used in conventional radiotherapy. The extremely short duration of delivery of radiation leads to a reduction in normal tissue toxicity, while maintaining effective tumor control (FLASH effect) [4, 6, 9–11].

Most FLASH RT studies have been conducted using electron beams from dedicated linear accelerators with energies of 4–6 MeV [12, 13], or modified clinical linear accelerators with energies up to 20 MeV [14, 15]. Although modified clinical linear accelerators can deliver electron beams with ultra-high dose rates, the limited penetration depth of the clinical energy range (4–22 MeV) remains an obstacle in FLASH RT clinical trials. The percentage depth dose (PDD) profile for 15 MeV electrons, shown in **Figure 1** as blue curve, indicates that clinical electron beams cannot reach tumors deeper than 10 cm. This limits FLASH RT with electrons to preclinical studies using small animals such as mice or cats [3, 9, 11] as well as human patients with superficial tumors [7] and indications for intraoperative radiotherapy (IORT) [10].

Beams of electrons with energies exceeding the clinical energy range overcome the depth limitation. Electrons with 100–250 MeV are known as very high energy electrons (VHEEs) [17,

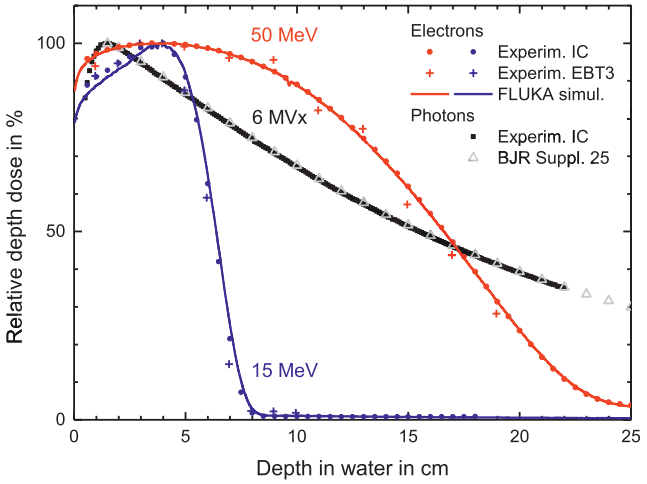

FIGURE 1 | PDD profile in water for 15 MeV (blue) and 50 MeV (red) unflattened electron beams measured in this work using an ionisation chamber (dots) and EBT3 radiochromic film (crosses), and simulations using FLUKA (solid curves), in addition to PDD profile of a 6 MV, 10 cm × 10 cm photon field, measured with PTB's clinical accelerator (black dots) and reference data set from BJR Supplement 25 [16] (triangles).

18]. They have sharp penumbra and are insensitive to tissue inhomogeneity. In contrast to photon or proton beams, they enable better dose conformity for some tumors located in close proximity to tissue with varying densities, which also spares surrounding normal tissue [18–20]. The dosimetric benefits of VHEEs over photons have been investigated by Bazalova-Carter et al. [18] using a treatment planning system, where they compared VHEE treatment with clinical 6 and 15 MV state-of-the-art volumetric modulated arc therapy (VMAT) [21] photon plans. They reported that 100 MeV electron beams resulted in significant sparing of organs at risk (OAR), compared with conventional photon RT.

The majority of current radiotherapy treatments are administered using photon radiation produced by clinical linear accelerators. 6 MV photons, the most commonly used, deposit their maximum dose typically over a depth of 1–2 cm followed by an exponential decrease (see **Figure 1** black dots), resulting in lower relative dose deposition in the depth of a deep-seated tumor (10–15 cm). However, the application of VMAT, where the radiation dose is delivered continuously as the gantry of the treatment machine rotates around the patient, enables dose to be concentrated also in a deep-seated tumor while minimizing it in the surrounding normal tissue and OAR.

The FLASH effect has been also observed with photon radiation (from a synchrotron light source) [10], but currently there is no method for generating ultra-high dose rate photon beams by means of a linear accelerator for FLASH RT of deep-seated tumors. However, 50 MeV electrons, as used in our study, can reach deep-seated tumors situated at depths of 10–15 cm (red curve in **Figure 1**). In contrast to photons, they can be generated with ultra-high dose rates by linear accelerators. This can enable FLASH RT also for deep-seated tumors.

Laser-driven accelerators are a promising solution for future RT machines as they are capable of producing electron bunches with energies from clinical to VHEE range suitable for depositing dose at ultra-high rates [22–25]. Research is underway to develop laser-driven accelerators for RT applications at facilities such as the Scottish Center for the Application of Plasma-based Accelerators (SCAPA), located at the University of Strathclyde in the United Kingdom. A vertical beam line utilising sub-picosecond electron bunches from a laser-driven accelerator with energies up to 150 MeV at the SCAPA facility is dedicated to *in vitro* and *in vivo* VHEE studies [26].

Accurate and reliable dosimeters are required to translate VHEE RT into the clinical stage, and also for application of sub-picosecond electron bunches from laser-driven accelerators used in pulsed radiolysis, laboratory astrophysics and warm dense matter studies. Ionisation chambers (ICs), are common detectors used in reference dosimetry for conventional external beam radiation therapy. However, they suffer from significant ion recombination effects when exposed to VHEE beams which deposit the dose at ultra-high rates and/or ultra-high dose per pulse (DPP) [27, 28]. Currently there are no dosimetry protocols available, either for FLASH RT or VHEE, nor recommendations for reliable dosimeters and validated methods for these novel modalities. At present no primary standard exists that can be used as a reference for determining the deviations of dosimeters under such conditions.

The work presented here aims to study the energy dependence of two passive, dose-rate independent detectors, EBT3 radiochromic film [29] and alanine [30], for application in electron fields of up to 50 MeV. The response of the dosimeters is compared with absolute dose measurements performed using an ionisation chamber. The DPP is reduced to a level where the ion recombination effect of the ionisation chamber type used is sufficiently small and models for quantifying the ion recombination correction are available. For this purpose, the distance to the source was increased while reducing the charge per beam pulse. An investigation of the deviations due to the ion recombination effects at ultra-high DPP as present in FLASH RT [31] and VHEE accelerators [27] is not the focus of this work.

MATERIALS AND METHODS

Accelerator

The experiments have been carried out at the Metrological Electron Accelerator Facility (MELAF) [32] at the German national metrology institute Physikalisch-Technische Bundesanstalt (PTB). The facility provides a research linear accelerator (commissioned in 2012) for investigating dosimetry for radiotherapy at ultra-high pulse dose rates (the FLASH RT regime), and over a large energy range of 0.5–50 MeV. This is considerably larger than for conventional medical accelerators, which typically operate between 4 and 22 MeV. Furthermore, in contrast to commercial medical accelerators, all electron beam parameters of the PTB research accelerator are adjustable and can

be measured with a high degree of accuracy. Therefore, it is possible to study radiation effects as a function of their fundamental physical quantities such as energy and fluence.

The research accelerator delivers pulsed electron beams with a fixed macropulse duration of about 2.5 μs and a 3 GHz micropulse fine structure. The term *beam pulse* here in the following refers to a macropulse. The accelerator provides controllable mean dose rates via variable pulse charge (about 1–150 nC per beam pulse) and adjustable pulse repetition frequency (1–100 Hz). All measurements presented here are conducted at a repetition frequency of 5 Hz. An Integrating Current Transformer (ICT), provided by Bergoz Instrumentation (in-flange version, windings ratio 50:1), is included in the beamline to non-destructively measure the charge of each electron pulse with a precision of ±0.03 nC [33]. The minimum charge per pulse used in this work is 2 nC and at least 100 pulses are measured to determine the charge with a precision better than 0.15%.

The kinetic energy of the electrons can be varied continuously, in contrast to medical accelerators where only a few fixed beam energies can be selected. The nominal energies are varied from 15 to 50 MeV with an increment of 5 MeV. The beam energy is measured with a magnetic spectrometer shortly before the dosimeters are irradiated. An example of an energy measurement is shown in **Figure 2**. The beams are quasi mono-energetic with full-width at half-maximum (FWHM) energy spread of less than 0.2 MeV. The measured actual energies are 15.8, 19.7, 25.6, 31.1, 36.0, 41.3, 46.1, and 49.0 MeV.

The transverse beam profile and divergence are measured using three 2d wire scanners placed at different positions along the beam line. All beams have Gaussian transverse cross-sections with a FWHM of about 3 mm and divergence of less than 0.1°. **Figure 3** shows a typical measured beam profile.

At the end of the beam line the electrons pass through a 0.1 mm thick Cu vacuum window which scatters the beam. The diameter of this window was much larger (>3 cm) than the beam width, thus all electrons detected by the ICT contributed to the radiation field. This results in an unflattened electron radiation field with a Gaussian shape. The beam width increases with decreasing energy and increasing distance from the exit window. **Figure 4** shows the 2-dimensional lateral relative dose distribution of a 40 MeV electron field recorded with an IC matrix (PTW OCTAVIUS Detector 1500) positioned 1 m after the exit window in air. A 1-dimensional cross section through the central beam axis has Gaussian shape ($R^2 > 0.9995$).

Setup

A $30 \times 30 \times 30$ cm^3 water phantom with 2 cm thick poly-methyl methacrylate (PMMA) walls is placed with its 0.3 cm thick PMMA entrance window in a distance of 200 cm from the beam exit window along the central beam axis. The beam FWHM at the entrance window of the phantom is greater than 8 cm for all beam energies. Custom-made PMMA holders are used to position the EBT3 films, the alanine pellets and the IC inside the water phantom. A 3-dimensional precision motorized positioning system allows i) to place the dosimeters at a certain depth along the central beam axis, ii) to perform controlled longitudinal movement of the IC along the central beam axis for depth dose measurements, and iii) to perform controlled lateral movements to determine the cross-sectional dose distribution of the radiation field. **Figure 5** shows a photograph of the water phantom with the positioning systems in front of the beam line.

The dosimeters are irradiated successively at the same position to ensure they receive equal dose and are irradiated with identical dose gradient within the radiation field. The beam pulse charge measured by the ICT is used as reference for successive irradiation of the different dosimeters, because the charge is proportional to the dose. Two ICs (Wellhöfer IC10) are mounted in the water phantom at the depth of the respective dosimeter under investigation, about 10 cm left and right from the central beam axis. They are used as radiation monitors to verify the ICT signal. The ratio of the signals from both radiation monitor ICs is used to verify that the maximum of the radiation field does not change its position over time. **Figure 6** shows the typical response of one of the radiation monitor chambers in the water phantom as function of the signal from the ICT beam current monitor during an irradiation. The typical pulse-to-pulse charge fluctuations (<3%) are proportional to the dose response from the radiation monitor.

Dosimeters

Ionisation chamber

A parallel-plate Advanced Markus IC (PTW 34045, s/n:1279) is used to determine the absorbed dose to water D_w. The signal from the IC is read out using an analogue electrometer (Keithley 616) in current mode. The reading, M, of the analogue electrometer is recorded using a 16-bit analogue-to-digital-converter and analysed using custom software. A calibrated current source (Keithley 6430) is used to calibrate the electrometer with its own read-out system. The Advanced Markus chamber is calibrated using PTB's Co-60 reference field in terms of absorbed dose to water, which is traceable to the PTB's primary standard water calorimeter [34].

For absolute dose measurements the signal of the Advanced Markus chamber is converted to absorbed dose to water, D_w, following the German protocol DIN 6800-2 recommendations [35] for dosimetry in conventional radiotherapy:

$$\boldsymbol{D_w = N'_{Co_{60},\ D_w} \cdot (M - M_0) \cdot k_E \cdot k_S \cdot k_P \cdot k_{T,p}}, \qquad (1)$$

where $N'_{Co_{60},\ D_w}$ is the calibration factor of the chamber with respect to Co-60 radiation, M is the reading of the dosimeter corrected for the reading without irradiation M_0, k_E is the quality correction factor accounting for the difference in detector's response between Co-60 radiation and high-energy electron radiation, and k_S is the correction factor for ion recombination. The factors k_P and $k_{T,p}$ take into account the effects of polarity and the ambient conditions, respectively. The reference conditions, procedures and the approximation formulas in the DIN 6800-2 [35] are consistent with those in IAEA's Code of Practice (CoP) TRS398 [36, 37].

The radiation quality correction factor k_E in **Eq. 1** is the product of a chamber design dependent constant k''_E and a

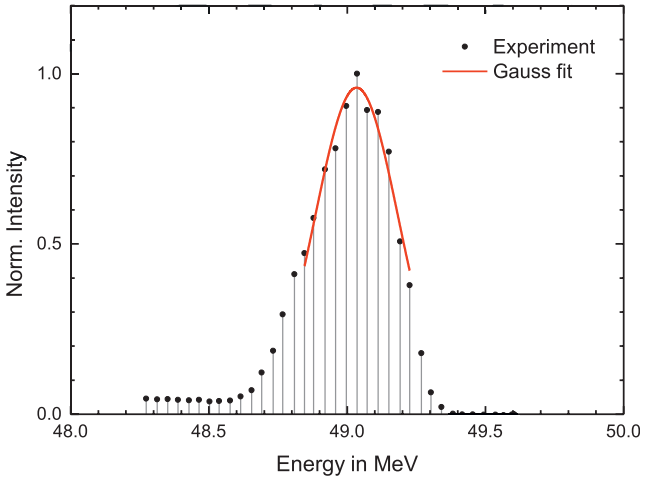

FIGURE 2 | Example of an energy measurement using the magnetic spectrometer. A Gauss function is fitted to the upper part to half maximum to determine the peak position and width.

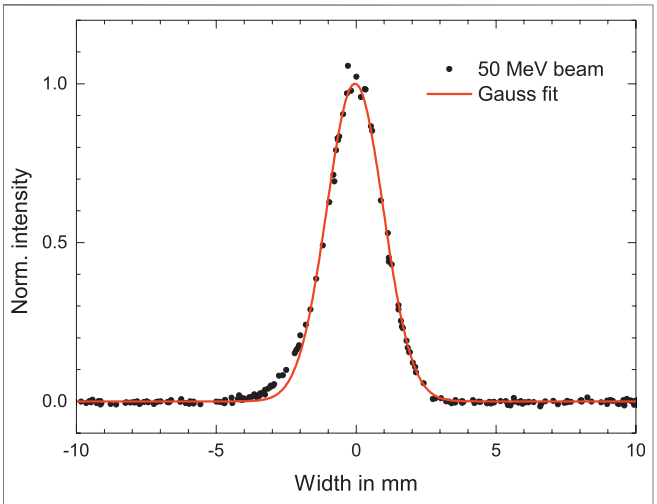

FIGURE 3 | Vertical beam profile obtained for 50 MeV nominal energy with a wire scanner.

chamber independent function k'_E, which is essentially the energy dependent stopping power ratio. According to DIN 6800-2 [35] k''_E for the Advance Markus chamber is equal to 0.985. At the reference depth, z_{ref}, the value k'_E is calculated using the following equation:

$$k'_E = 1.106 - 0.1312 \cdot (R_{50})^{0.214}, \quad (2)$$

where the half-value depth, i.e., the depth at which the absorbed dose is dropped to 50% of its maximum value, R_{50}, of the energy dependent depth dose distribution is given in cm. **Equation 2** is valid only for the measurements at the reference depth, z_{ref}, which is determined by:

$$z_{ref} = 0.6 \cdot R_{50} - 0.1, \quad (3)$$

where R_{50} and z_{ref} are expressed in cm. R_{50} must be determined experimentally for each energy from the half-value depth of the ionisation current depth curve $R_{50,Ion}$, i.e., the half-value depth of the chamber signal as a function of the depth in water, by

$$R_{50} = 1.029 \cdot R_{50,\,Ion} - 0.06\,\mathbf{cm} \quad \text{for} \quad R_{50,\,Ion} \leq 10\,\mathbf{cm}, \quad (4)$$

$$R_{50} = 1.059 \cdot R_{50,\,Ion} - 0.37\,\mathbf{cm} \quad \text{for} \quad R_{50,\,Ion} > 10\,\mathbf{cm}. \quad (5)$$

The ion recombination correction factor, k_S, in **Eq. 1** depends on the DPP and the applied chamber voltage U. In this work k_S is determined using two methods. The method recommended in DIN 6800-2 [35] is to obtain k_s from Jaffé plots. This is described and investigated for many types of ionisation chambers in DPP ranging from 0.15 to 42 mGy/pulse [35, 38]. For a Jaffé plot U is gradually changed during irradiation while the associated IC reading $M(U)$ is recorded and then $1/M(U)$ is plotted versus $1/U$. If the obtained Jaffé plot is linear, then the ionisation chamber reading at infinite chamber voltage can be determined by linear extrapolation to $1/U = 0$. If the Jaffé plot is normalized to the reading at chambers operating voltage the y-intercept of the linear fit is equal to k_S. In this work, the voltage of the chamber, irradiated at z_{ref}, is changed gradually from chamber's operating voltage 300–20 V for different DPP values in the range of 10–40 mGy/pulse in order to determine k_s from Jaffé plots.

The high DPP range (20–120 mGy/pulse) delivered by linear accelerators in IORT is comparable to the DPP range used in this work. Extensive studies have been carried out on ion recombination effects of ICs for high DPP beams [39–42]. A method of determining k_S for high DPP ranges without using a dose reference has been introduced by Laitano et al. [39]. This approach takes into account free electrons produced in the chamber, which are collected by the anode without being attached to oxygen molecules, described by three different models proposed by Boag et al. [43]. This approach has been applied by Pimpinella et al. [42] with the assumption that the third Boag's model provides the best description. The approach of Laitano et al. [39] with the third Boag's model is used in this work as second method for k_s determination. The free-electron fraction p is calculated according to Laitano et al. [39] for the Advanced Markus chamber to yield $p = 0.6855$. Then numerical calculations using formula A.3 in the appendix of Ref. 39 are carried out.

The polarity effect of the Advanced Markus chamber has been investigated for clinical electron beams by Pearce et al. [44] who observed a large polarity correction effect for lower energy clinical beams (≈4 MeV). However, with increase in energy the correction due to polarity diminished, which for 9 MeV is 0.48%. In this work $k_p = 1$ is assumed and an uncertainty of 0.5% is assigned. The correction factor $k_{T,P}$ has been calculated from pressure and temperature measured during IC exposures and found to be between −0.3 and +0.6 %.

To determine the dose at a depth other than z_{ref} an additional correction factor $k_{NR,\,E}$ must be included in **Eq. 2**. The PDD in **Figure 1** results from the signal of the Advance Markus chamber

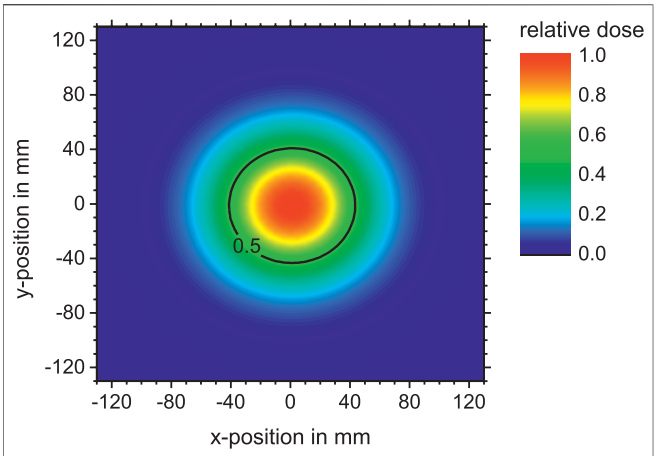

FIGURE 4 | 2-dimensional dose distribution of 40 MeV electron beam in air captured with an ionisation chamber matrix (PTW OCTAVIUS 1500) 1 m from the exit window.

FIGURE 5 | Photograph of the setup. Water phantom inside the frame of the 3D positioning system in front of the accelerator beam line.

after the conversion to a dose by taking into account $k_{NR,\ E}$ according to DIN 6800-2 [35].

Alanine

The alanine pellets are produced with diameter of 5 and 3 mm height. The pellets are arranged in stacks of 8 pellets to form a cylinder. The alanine stacks are positioned within a PMMA tube at z_{ref} with the longer dimension perpendicular to the beam central axis. Their response is temperature dependent (0.18%/°C) [45]. To account for this dependence, and to ensure that the pellets are at thermal equilibrium with their environment, the temperature of the water is recorded, and irradiation not commenced until the pellets have been immersed for about 10 min. At each energy an alanine stack is irradiated with a nominal dose of 15 Gy while the charge of the electron beam pulses was simultaneously measured. Uncertainties of 0.4–0.6% (k = 1) are reached at Co-60 radiation for irradiations in the range of 5–25 Gy [46]. For the conversion of the alanine's response to electron radiation an additional radiation quality correction factor k_E^{ala} has to be applied. This factor is known with an uncertainty of 1 % for electron energies up to 22 MeV [47]. A detailed description of PTB's alanine dosimetry system and readout of the irradiated pellets can be found elsewhere [46–49].

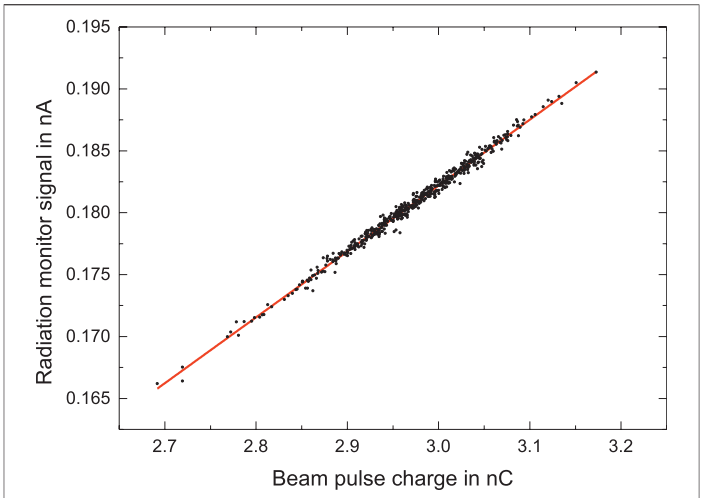

FIGURE 6 | Typical response of the radiation monitor chamber in the water phantom as function of the beam pulse charge measured with the ICT.

GafChromic™ EBT3 films

GafChromic™ EBT3 films (www.gafchromic.com) from lot #06141702 (chemical composition provided in **Supplementary Table S1**) are used to measure the dose absorbed to water. The films are placed at z_{ref} and exposed to 6 dose levels between 5 and 20 Gy for all electron energies, while keeping all other beam settings fixed. The doses are delivered by varying the number of beam pulses in the range of 140–1600. The pulse charge is recorded with the ICT.

Stacks of equispaced films in a dedicated holder, as shown in **Figure 7**, are used to measure PDD profiles for all energies. All films in the stack together are 0.28 cm thick. The water equivalent thickness of the whole stack is about 0.3 cm. The measured PDD profiles are compared with those obtained with the IC and Monte Carlo (MC) simulations.

All films are scanned one week after irradiation to avoid differences in film self-development after exposure [50]. A multichannel flatbed EPSON Expression 10000XL Pro scanner is used to record the digital image of each film. All films are scanned in the same orientation to avoid variations in optical properties due to scanning orientation [51]. Images are measured in transmission using the RGB-positive mode at a depth of 16 bits per color channel with a spatial resolution of 127 dpi, which corresponds to a pixel size of 0.2 mm × 0.2 mm. Images are saved in TIFF format and analysed using a python script, following the protocol described by Devic et al. [50]. A single unexposed piece

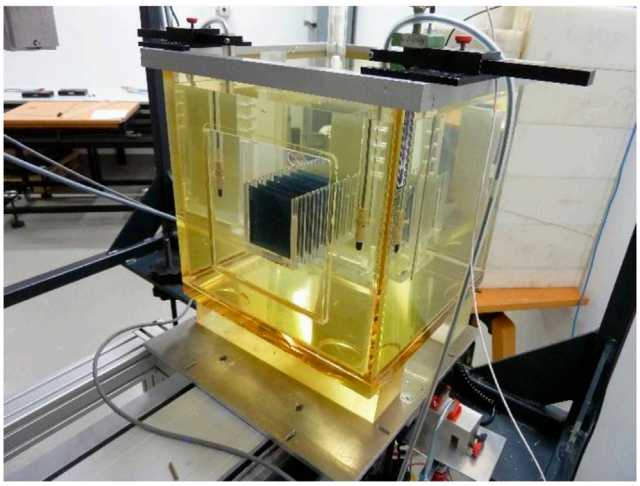

FIGURE 7 | Stack of equispaced EBT3 films in a dedicated holder after exposure to electron beam.

of film, which is kept together with the exposed films, is used as a control. A Wiener filter is applied to the irradiated and control film images.

A region of interest (ROI) of 25 × 25 pixels (5 × 5 mm^2) is selected from the central area of the film, which is comparable with the cross-section of the sensitive volume of the Advanced Markus chamber (5 mm in diameter). The average pixel value (PV) within the ROI is used to calculate the net optical density (netOD), which is the change in optical density before and after irradiation, given by $netOD = \log_{10}(PV_{before}/PV_{after})$. Absolute response is determined using the green color channel, which is preferable for doses up to 40 Gy [52, 53].

Calibration of the EBT3 film has been performed at NPL with 12 MeV electron beams and a dose rate of 600 cGy/min using a clinical linear accelerator (Elekta Synergy). To avoid variations due to different lot numbers, film from the same batch is used for both the measurements at PTB and calibration at NPL. The irradiation is performed in a 30 × 30 × 30 cm^3 solid-water phantom at 5 different dose levels between 1 and 20 Gy under reference conditions (source-to-surface distance of 100 cm and 20 × 20 cm^2 field size) at z_{ref} = 2.8 cm. The dose delivered to each film have been established based on the output measurements at reference conditions using a Roos IC (PTW 34001), which has been traceably calibrated in terms of D_w to NPL's primary standard graphite calorimeter [54]. The dose is determined from the netOD values and the dose-response calibration curve is fitted using the following analytical function:

$$D = a \cdot netOD + b \cdot netOD^n, \quad (6)$$

where *a, b* and *n* are fit parameters.

Monte Carlo Simulation

Simulations have been carried out using the FLUKA MC code (FLUKA2011 Version 2x.7) [55, 56] with 10^7 particles and 10 cycles. The physics settings are described in the FLUKA manual under the physics package PRECISIOn. The photonuclear reactions are activated by the card PHOTONUC. The threshold for transport and production of δ-particles and photons (ECUT, PCUT) is set to 10 keV.

In the model, a monoenergetic parallel beam with a Gaussian cross-section (3 mm FWHM) is scattered by the 0.1 mm thick Cu foil of the vacuum exit window at the end of the beam line. The incident electron beam parameters are measured (see section *Accelerator*). The electrons propagate in air from the source (exit window) to the phantom.

The dose distribution in water is simulated by a 30 × 30 × 30 cm^3 water cube defined with a FLUKA USRBIN mesh that has a resolution of 0.065 cm. The on-axis dose is calculated within a 0.5 × 0.5 × 30 cm^3 rectangular volume around the central beam axis.

RESULTS AND DISCUSSION

EBT3 Film Calibration

The red crosses in **Figure 8** shows the reference dose applied to the EBT3 films at NPL as a function of the resulting netOD value obtained from the respective film. The data points are fitted to the analytical function given in **Eq. 6** (red curve).

The radiation quality correction factor k_E^{ala} to correct alanine's response for electron radiation is known up to 22 MeV [47]. The alanine dose measurements for 15 and 20 MeV can therefore be traced to the PTB's primary standard. They can, in turn, be used to calibrate EBT3 film irradiated under the same conditions. For comparison, the doses determined using alanine for 15 and 20 MeV are plotted as function of the corresponding netOD values in **Figure 8** as open circles and squares, respectively. The resulting dose-response calibration curve from a fit to **Eq. 6** is also shown. It is similar to the NPL's calibration curve. In the studied dose range of 5–20 Gy the resulting dose difference between NPL and PTB calibration can vary from −1% up to 4%. The dose values determined with EBT3 in this work are based on the NPL calibration function.

Ion Recombination Correction for the Advanced Markus Ionisation Chamber

The mean dose rates used in this investigation vary between 3 and 12 Gy/min, which is within the range of conventional radiotherapy. However, the DPP, ranging from 10 mGy to 40 mGy per pulse, is significantly higher than for a medical accelerator (0.1–3 mGy per pulse) and comparable with that used in IORT, where non-negligible ion recombination effects have been reported [39, 40, 42, 57, 58]. Two approaches for evaluation of a k_S factors i) the Jaffé plots and ii) the method described by Laitano et al. [39] (described in section *Ionisation Chamber*) were applied and compared against each other.

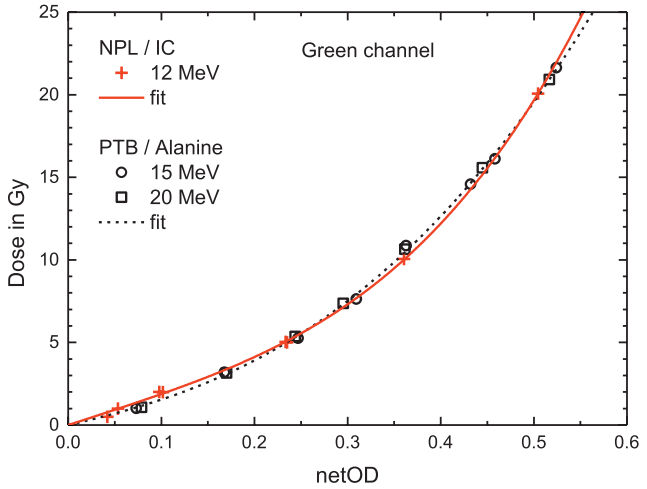

FIGURE 8 | Reference dose applied to the EBT3 films at NPL plotted against the resulting netOD values from the green channel (red crosses). Also shown are the doses applied to the EBT3 films at PTB, measured with alanine, at 15 and 20 MeV, respectively (open circles and squares, respectively). The solid and dashed lines represent fits using **Eq. 6**.

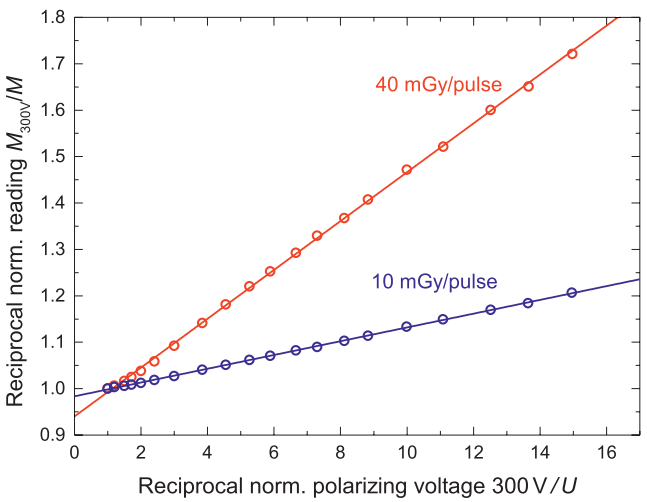

FIGURE 9 | Jaffé plots: reciprocal readings 1/*M* of the Advance Markus chamber as function of the reciprocal chamber voltages 1/*U*, normalized to the reading at 300 V for 10 mGy/pulse (blue circles) and 40 mGy/pulse (red circles), respectively. Solid lines represent linear fits to the data points.

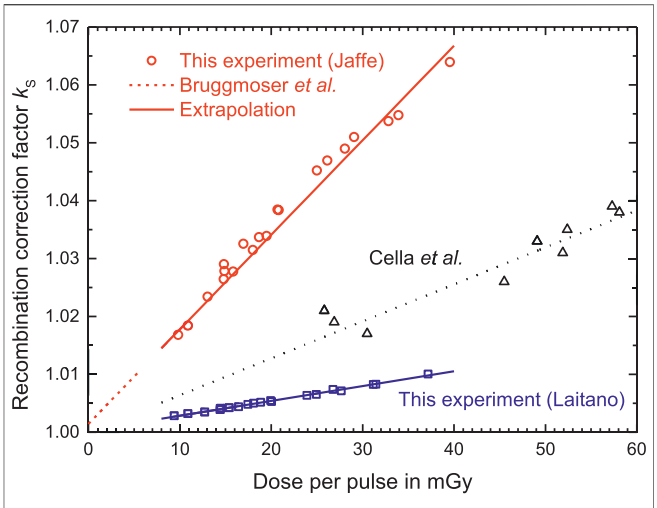

FIGURE 10 | k_S factor as a function of dose per pulse determined for the Advanced Markus chamber at 300 V operating voltage using Jaffé plots (open circles) and approach from Laitano et al. [39] (open squares). For comparison, the k_S function from Bruggmoser et al. [38], recommend in the DIN 6800-2 protocol, is shown in the range where determined experimentally (dashed red line) and extrapolated to the high DPP range used in the current experiment (solid red line). Also shown are the results from an experimental determination by Cella et al. [40] using a Fricke dosimeter as reference. Lines: linear fits.

Figure 9 shows Jaffé plots for the lower and upper edge of the studied DPP range. The *y*-intercept ($1/k_s$) of the linear fits is 0.98 and 0.94, respectively, yielding k_S of 1.02 and 1.06. These ion recombination correction factors are significantly higher than in conventional RT (typically <1.01).

The open circles in **Figure 10** represents k_S factors determined using the Jaffé plots approach. The dashed red line represents the k_s function given by Bruggmoser et al. [38] $k_S = 1 + (0.43 + 0.49 \cdot D_{w,\mathrm{pulse}})/U$, where $D_{w,\ \mathrm{pulse}}$ is the DPP expressed in mGy and U is the chamber voltage expressed in V, for $U = 300$ V in the experimentally determined DPP range up to 5.5 mGy/pulse. This function is recommended for the Advanced Markus chamber in the DIN 6800-2 [35] protocol. The red solid line is the extrapolation to the high DPP investigated here. There's no indication of any inaccuracy in determination of ion recombination factor by Jaffé plots because the plots shown in **Figure 9** are well represented by linear fits. Moreover, the extrapolation of Bruggmosers function is also in good agreement with the determined k_s values (**Figure 10**). However, Laitano et al. [39] pointed out that the observed linearity in Jaffé plots may motivate one to perform a zero linear extrapolation to find the factor k_s even in conditions of high DPP and that this can lead to considerably inaccurate determination of k_s (up to 40%). The blue squares in **Figure 10** represent the results obtained employing Laitano's approach using the same data as for the Jaffé plots. The function, that represents best fit to the series of data points $k_S = 0.00026\,\mathrm{mGy}^{-1} \cdot D_W + 1.0003$. After comparing both methods, it was found that the k_s factors determined by Jaffé plots yield 1.5–5% higher values in the used DPP range.

For comparison, the results from an experimental determination of k_s from Cella et al. [40] are also shown in **Figure 10**. These were determined by comparing the dose determined with an Advanced Markus chamber without taking into account any recombination effects against a reference dose determined with Fricke dosimeters, i.e., no theoretical assumptions were needed. In the relevant DDP range these values are about 0.3–1.5% larger than the results from this work using Laitano's approach.

Comparison of Different Methods for Relative Dose Measurements

Figure 1 shows relative depth dose curves measured with the IC and EBT3 films for 15 and 50 MeV electron beams produced by the PTB research accelerator using the experimental setup described in *Setup*. The measurements have been compared with Monte Carlo calculations carried out using FLUKA, which incorporates an accurate physics model of electron interactions with matter within the investigated energy range. The ion chamber measurements for the 50 MeV beam are in excellent agreement with the MC simulations. However, some discrepancy exists between measured and calculated data for the 15 MeV beam at 1–3 cm. The PDD measured at discrete positions with EBT3 films is significantly more scattered compared to the IC measurement due to substantial uncertainties associated with this detector, which can easily reach 5% [52]. They vary between +3 and −9% with respect to the PDD measured with the IC.

The radiation field at the depth of the detectors is not homogenous, in particular at higher energies. Therefore, the relative dose distributions in lateral directions are recorded for each energy at two different depths to determine the exact position of the beam central axis at dose maximum. **Figure 11** shows lateral dose distributions for the two extremes of the electron energy range used in this study and thus the narrowest and broadest radiation field used at PTB.

The variations in dose within the sensitive volume of the Advanced Markus Chamber (±2.5 mm from the beam axis, marked in **Figure 11**) is less than 0.5%, even for the narrowest radiation field (50 MeV). This indicates that on the beam axis the deviation due to non-uniform radiation fields is negligible. The data points from the stack of 8 alanine pellets (green crosses) are consistent with the IC results. The data points from the radiochromic film (open diamonds) scatters more than IC and alanine data but represent well the lateral profile.

Figure 12 shows R_{50} measured as function of electron energy. The relative depth dose profiles have been measured and calculated for all beam energies. The agreement between the FLUKA simulations and IC measurements, shown in Figures 1 and 12, indicate that the dosimetry procedures recommended by DIN6800-2 for homogeneous fields are also applicable to unflattened radiation fields, as investigated in this work.

R_{50} depends on the energy and the field size. For comparison, the R_{50} values established in this study are plotted in **Figure 12** together with the R_{50} values determined for 20 × 20 cm^2 and 4 × 4 cm^2 fields. The R_{50} of the used unflattened Gaussian shaped field is in between the R_{50} values of the small and the large flat fields. With increasing energy, the width of the radiation field becomes smaller and thus R_{50} tends to the extrapolated line for the smaller field.

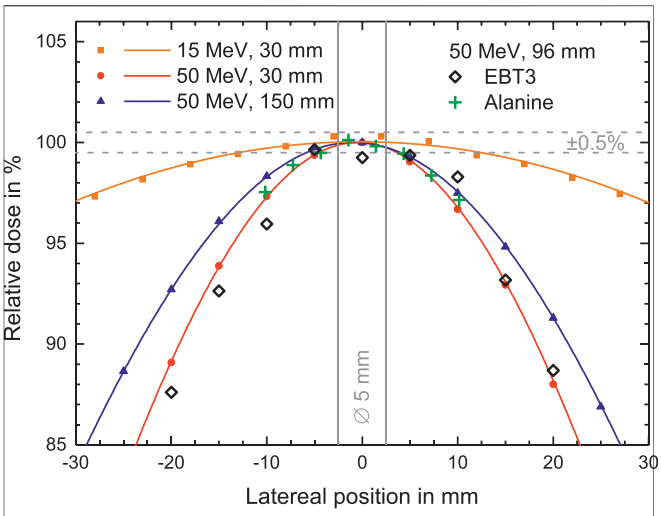

FIGURE 11 | The lateral dose profiles for 15 and 50 MeV at 30 mm depth in water as well as for 50 MeV at 150 mm depth measured with the ionisation chamber (solid symbols). Also shown are the results of EBT3 films in 5 mm steps (open diamonds), and the stack of 8 alanine pellets (green crosses) for 50 MeV at 96 mm depth. Solid lines represent Gaussian fits to the data points. The vertical bar indicates the position and size of the sensitive volume of the Advanced Markus chamber (5 mm).

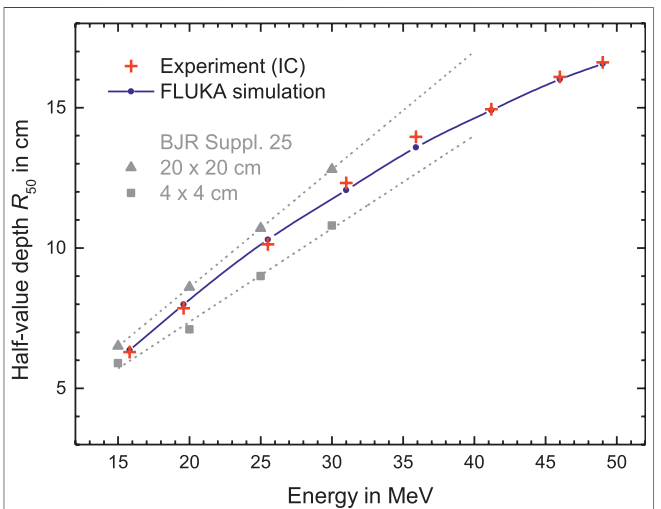

FIGURE 12 | R_{50} plotted as function of the energy, measured with the IC (red crosses) and calculated using FLUKA (blue dots) for the inhomogeneous field. The reference data from BJR Supplement 25 [16] for homogeneous radiation fields with 20 × 20 cm^2 (triangles) and 4 × 4 cm^2 (squares) field sizes are included for comparison. Dashed lines represent linear extrapolations to higher energies.

Comparison of Different Methods for Absolute Dose Measurements

None of the three dose measurement methods can serve as a reference because one cannot rule out effects due to non-standard radiation fields. Therefore, the three dosimetry methods can only be compared against each other. **Figure 13** shows the dose at z_{ref} per unit charge measured by the ICT, for the three different dosimeters as a function of electron beam energy. The dose rises with increase in energy. The slope increases because the width of the radiation field decreases with increasing energy and thus a larger fraction of the beam electrons deposits energy close to the central beam axis. A least square fit of a 2nd order polynomial function is fitted to all data points of the three dosimeters to

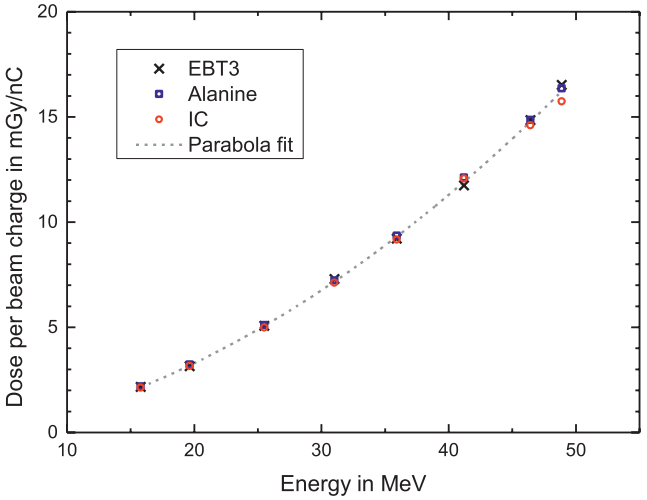

FIGURE 13 | Dose per unit charge measured with EBT3 film (crosses), alanine (squares), and ionisation chamber (circles) at the reference depth. Dashed curve represents 2nd order polynomial fit to all data points.

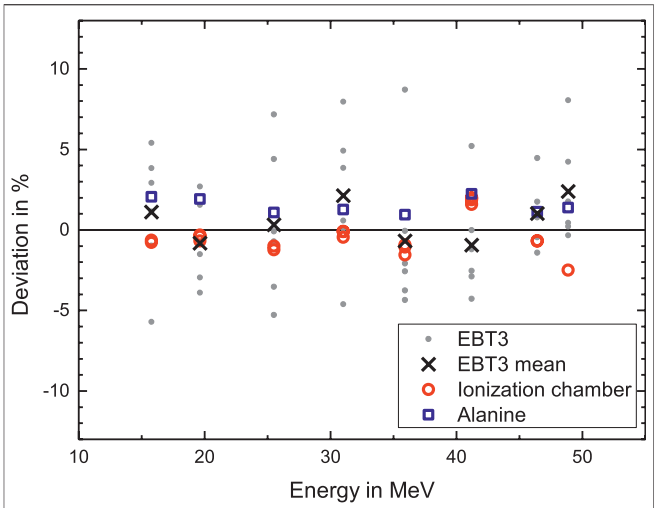

FIGURE 14 | Deviation of the dose response for EBT3 films (green channel), alanine and IC, from the fit curve shown in **Figure 13**.

evaluate deviations of each point from the common trend. **Figure 14** shows the percentage deviation (for the three types of detectors) from the fit function.

The response of EBT3 films has been averaged over 6 measurements (gray dots) carried out for doses in the range 5–20 Gy. The data points for single films are scattered within several percent (max. 9%) around the common mean value for all dosimeters (Zero line in **Figure 14**). The deviation (σ = 3.7%) is not correlated with the delivered dose or beam energy. The mean values of the 6 measurements (crosses) agree with the mean of the alanine and IC results to within 3%. No energy dependence is observed within the uncertainty.

The dose at the central beam axis from the dose measurements with the stack of 8 alanine pellets is obtained as the maximum of a Gaussian fit to the 8 doses captured along the lateral beam profile (see green crosses in **Figure 11**). The blue squares in **Figure 14** represent the percentage deviation of the alanine dosimeter measurements from the common trend. The relative uncertainty was estimated to 1.1% (k = 1). The main contribution is the uncertainty in the radiation quality correction factor k_E^{ala} (1%) [47]. No beam quality dependence is observed within investigated energy range. This indicates that the assumption that k_E^{ala} is constant, as it is at lower energies [47], is adequate. A systematic shift of 1.9% on average can be observed, with respect to the results from the IC evaluated using k_s from Laitano's approach (open circles in **Figure 14**). This may indicate that this k_s is too small. If the fit function to the results of Cella et al. [40] (dotted line in **Figure 10**) is used, then the mean deviation is about 0.9%. The relative uncertainty of the IC measurements is estimated to be 1.5%. Therefore, the average shift is within the uncertainties. However, the variation in the difference between IC and alanine results (0.4% at 40 MeV, 3.8% at 50 MeV) cannot explained by the considered uncertainty contributions: the uncertainty of alanine without the contribution of the constant k_E^{ala} is only 0.4% and the approximations that introduce an uncertainty when converting the IC signal into a dose are smooth functions of energy. Approaches taking into account the free electrons at determination of k_s are associated with large uncertainty [39] but IC measurements with different DPP are consistent with each other (multiple data points for IC at each energy in **Figure 14**). Due to the relatively large scattering of the difference between alanine and IC measurement it is not possible to make a conclusion about whether Laitano's approach is correct. Further investigations with lower measurement uncertainty are planned to reveal the cause of the systematic difference between IC and alanine dose determination and its variation.

Neither the DIN 6800-2 [35] nor the TRS398 [36] protocol provide recommendations for high DPP beams, or mention limits due to effects of the free electron fraction in determining k_s. Petersson et al. [31] reported up to 75% ion collection losses due to recombination effects for ultra-high DPP beams in FLASH RT (hundreds of mGy/pulse to few Gy/pulse). The data presented in the published literature [39, 42, 57, 58] and in this work indicates that there is a strong need to develop a clear dosimetry guidance to support accurate dosimetry of high and ultra-high DPP beams.

CONCLUSION

Three different dosimetry methods, including EBT3 radiochromic film, ionisation chamber, and alanine, have been investigated for electron beams with energies exceeding the clinical range up to 50 MeV in support of future studies of VHEE radiotherapy, and FLASH radiotherapy with VHEE beams.

All three methods provide similar results for relative dosimetry (depth dose curve, lateral dose profile). However, results from the EBT3 film has a variance of several percent, when compared with IC and alanine measurements. The half-value depth of measured percentage depth dose profiles of the unflattened radiation fields agrees well with MC simulations. This indicates that the dosimetry procedures for homogeneous fields are also applicable to unflattened radiation fields.

The ion recombination correction factor for the Advanced Markus IC is determined with an approach which considers free electrons. Comparing this approach with the results from Jaffé plots it is found that the latter yields 1.5–5% higher values for the high dose-per-pulse range.

The absolute dose measurements of the three methods have been compared against each other. For all beam energies single EBT3 film measurements show relatively high percentage deviations (up to 9%) over the dose range independent of the delivered dose. However, the mean values of 6 measurements agree well with the mean of the dose values from IC and alanine (mean deviation 1.2%, maximum deviation 3%). No energy dependence is observed within the uncertainty in the investigated energy range up to 50 MeV.

DATA AVAILABILITY STATEMENT

All datasets presented in this study are included in the article/**Supplementary Material**.Data associated with research published in this paper is available at https://doi.org/10.15129/ef9926f7-6177-4650-9768-91ac42fdf0ee.

AUTHOR CONTRIBUTIONS

KK, ASc, EB, MM, and TH performed the measurements at PTB. ASc evaluated the IC measurements. RK calculated the correction for ion recombination. TH prepared and evaluated the alanine samples. KK read doses from the radiochromic films. The calibration of films with clinical linear accelerator at NPL was carried out by KK and ASu. KK and EB carried out the FLUKA simulations and analysis. DJ conceived the project and provided overall leadership. R-PK oversaw the research at PTB. All authors contributed to the analysis and interpretation of the results in addition to writing the manuscript.

FUNDING

This project has received funding from the EMPIR program co-financed by the Participating States, from the European Union's Horizon 2020 research and innovation program. This work was funded by EPSRC (grant no. EP/J018171/1, EP/J500094/1 and EP/N028694/1) and the EC's LASERLAB-EUROPE (grant nos. 654148 and 871124).

ACKNOWLEDGMENTS

We would like to thank to Christoph Makowski for the maintenance and operation of the electron accelerator.

SUPPLEMENTARY MATERIAL

The Supplementary Material for this article can be found online at: https://www.frontiersin.org/articles/10.3389/fphy.2020.568302/full#supplementary-material

REFERENCES

1. Rosenblatt E, Zubizarreta E. *Radiotherapy in cancer care: facing the global challenge*. Vienna: International Atomic Energy Agency (2017). https://www-pub.iaea.org/MTCD/Publications/PDF/P1638_web.pdf.
2. Delaney G, Jacob S, Featherstone C, Barton M. The role of radiotherapy in cancer treatment. *Cancer.* (2005). 104:1129–37. doi:10.1002/cncr.21324
3. Slotman BJ, Leer JWH. Infrastructure of radiotherapy in The Netherlands: evaluation of prognoses and introduction of a new model for determining the needs. *Radiother Oncol.* (2003). 66:345–9. doi:10.1016/s0167-8140(03)00025-2
4. Favaudon V, Caplier L, Monceau V, Pouzoulet F, Sayarath M, Fouillade C, et al. Ultrahigh dose-rate flash irradiation increases the differential response between normal and tumor tissue in mice. *Sci Transl Med.* (2014). 6:245–93. doi:10.1126/scitranslmed.3008973
5. Durante M, Bräuer-Krisch E, Hill M. Faster and safer? FLASH ultra-high dose rate in radiotherapy. *Br J Radiol.* (2018). 91:20170628. doi:10.1259/bjr.20170628
6. Vozenin M.-C, Hendry JH, Limoli CL. Biological benefits of ultra-high dose rate FLASH radiotherapy: sleeping beauty awoken. *Clin Oncol.* (2019). 31:407–15. doi:10.1016/j.clon.2019.04.001
7. Bourhis J, Sozzi WJ, Jorge PG, Gaide O, Bailat C, Duclos F, et al. Treatment of a first patient with flash-radiotherapy. *Radiother Oncol.* (2019). 139:18–22. doi:10.1016/j.radonc.2019.06.019
8. Bourhis J, Montay-Gruel P, Gonçalves Jorge P, Bailat C, Petit B, Ollivier J, et al. Clinical translation of FLASH radiotherapy: why and how? *Radiother Oncol.* (2019). 139:11–7. doi:10.1016/j.radonc.2019.04.008
9. Montay-Gruel P, Petersson K, Jaccard M, Boivin G, Germond J.-F, Petit B, et al. Irradiation in a flash: unique sparing of memory in mice after whole brain irradiation with dose rates above 100 Gy/s, *Radiother Oncol.* (2017). 124:365–9. doi:10.1016/j.radonc.2017.05.003
10. Montay-Gruel P, Bouchet A, Jaccard M, Patin D, Serduc R, Aim W, et al. X-rays can trigger the FLASH effect: ultra-high dose-rate synchrotron light source prevents normal brain injury after whole brain irradiation in mice. *Radiother Oncol.* (2018). 129:582–8. doi:10.1016/j.radonc.2018.08.016
11. Vozenin M.-C, De Fornel P, Petersson K, Favaudon V, Jaccard M, Germond J.-F, et al. The advantage of flash radiotherapy confirmed in mini-pig and cat-cancer patients. *Clin Cancer Res.* (2019). 25:35. doi:10.1158/1078-0432.ccr-17-3375
12. Jaccard M, Durán MT, Petersson K, Germond J.-F, Liger P, Vozenin M.-C, et al. High dose-per-pulse electron beam dosimetry: commissioning of the oriatron ert6 prototype linear accelerator for preclinical use. *Med Phys.* (2018). 45:863–74. doi:10.1002/mp.12713
13. Favaudon V, Lentz J.-M, Heinrich S, Patriarca A, de Marzi L, Fouillade C, et al. Time-resolved dosimetry of pulsed electron beams in very high dose-rate, FLASH irradiation for radiotherapy preclinical studies. *Nucl Instrum Methods Phys Res Sect A Accel Spectrom Detect Assoc Equip.* (2019). 944:162537. doi:10.1016/j.nima.2019.162537
14. Schüler E, Stefania T, Gregory K, Frederick L, Marjan R, Manuel V, et al. Experimental platform for ultra-high dose rate FLASH irradiation of small animals using a clinical linear accelerator. *Int J Radiat Oncol Biol Phys.* (2017). 97:195–203. doi:10.1016/j.ijrobp.2016.09.018
15. Lempart M, Blad B, Adrian G, Bäck S, Knöös T, Ceberg C, et al. Modifying a clinical linear accelerator for delivery of ultra-high dose rate irradiation. *Radiother Oncol.* (2019). 139:40–5. doi:10.1016/j.radonc.2019.01.031
16. The British Journal of Radiology Supplement 25. *Central axis depth dose data for use in radiotherapy.* London, UK: British Institute of Radiology (1996). ISBN 0905749383.
17. DesRosiers C, Moskvin V, Bielajew AF, Papiez L. 150–250 MeV electron beams in radiation therapy. *Phys Med Biol.* (2000). 45:1781–805. doi:10.1088/0031-9155/45/7/306

18. Bazalova-Carter M, Qu B, Palma B, Hårdemark B, Hynning E, Jensen C, et al. Treatment planning for radiotherapy with very high-energy electron beams and comparison of VHEE and VMAT plans. *Med Phys.* (2015). 42:2615–25, doi:10.1118/1.4918923
19. Palma B, Bazalova-Carter M, Hårdemark B, Hynning E, Qu B, Loo BW, et al. Assessment of the quality of very high-energy electron radiotherapy planning. *Radiother Oncol.* (2016). 119:154. doi:10.1016/j.radonc.2016.01.017
20. Schüler B, Eriksson K, Hynning E, Hancock SL, Hiniker SM, Bazalova-Carter M, et al. Very high-energy electron (VHEE) beams in radiation therapy; treatment plan comparison between VHEE, VMAT, and PPBS. *Med Phys.* (2017). 44:2544–55. doi:10.1002/mp.12233
21. Teoh M, Clark CH, Wood K, Whitaker S, Nisbet A. Volumetric modulated arc therapy: a review of current literature and clinical use in practice. *Brit J Radiol.* (2011). 84:967–996. doi:10.1002/mp.12233
22. Giulietti A. *Laser-driven particle acceleration towards radiobiology and medicine, biological and medical physics, biomedical engineering.* Berlin: Springer (2016).
23. Mangles SPD, Murphy CD, Najmudin Z, Thomas AGR, Collier JL, Dangor AE, et al. Monoenergetic beams of relativistic electrons from intense laser-plasma interactions. *Nature.* (2004). 431:535–8. doi:10.1038/nature02939
24. Kokurewicz K, Brunetti E, Welsh GH, Wiggins SM, Boyd M, Sorensen A, et al. Focused very high-energy electron beams as a novel radiotherapy modality for producing high-dose volumetric elements. *Sci Rep.* (2019). 9:10837. doi:10.1038/s41598-019-46630-w
25. Malka V, Faure J, Gauduel YA. Ultra-short electron beams based spatio-temporal radiation biology and radiotherapy. *Mutat Res Rev Mutat Res.* (2010). 704:142–51. doi:10.1016/j.mrrev.2010.01.006
26. Wiggins SM, Marie B, Enrico B, Nick MHB, James SF, Ross JG, et al. Application programmes at the Scottish Centre for the application of plasma-based accelerators (SCAPA). *Proc SPIE.* (2019). 11036:110360T. doi:10.1117/12.2520717
27. McManus M, Romano F, Lee ND, Farabolini W, Gilardi A, Royle G, et al. The challenge of ionisation chamber dosimetry in ultra-short pulsed high dose-rate Very High Energy Electron beams. *Sci Rep.* (2020). 10:9089. doi:10.1038/s41598-020-65819-y
28. Subiel A, Moskvin V, Welsh GH, Cipiccia S, Reboredo D, DesRosiers C, et al. Challenges of dosimetry of ultra-short pulsed very high energy electron beams. *Phys Med.* (2017). 42:327–31. doi:10.1016/j.ejmp.2017.04.029
29. Jaccard M, Petersson K, Buchillier T, Germond J.-F, Durán MT, Vozenin M.-C, et al. High dose-per-pulse electron beam dosimetry: usability and dose-rate independence of EBT3 Gafchromic films. *Med Phys.* (2017). 44:725–35. doi:10.1002/mp.12066
30. Kudoh H, Celina M, Kaye RJ, Gillen KT, Clough RL. Response of alanine dosimeters at very high dose rate. *Appl Radiat Isot.* (1997). 48:497–9. doi:10.1016/s0969-8043(96)00281-3
31. Petersson K, Jaccard M, Germond J.-F, Buchillier T, Bochud F, Bourhis J, et al. High dose-per-pulse electron beam dosimetry—a model to correct for the ion recombination in the Advanced Markus ionization chamber. *Med Phys.* (2017). 44:1157–67. doi:10.1002/mp.12111
32. Schüller A, Pojtinger S, Meier M, Makowski C, Kapsch R-P. The metrological electron accelerator facility (MELAF) for research in dosimetry for radiotherapy, *IFMBE Proc.* (2018). 68:589–93. doi:10.1007/978-981-10-9023-3_109
33. Schüller A, Illemann J, Renner F, Makowski C, Kapsch R-P. Traceable charge measurement of the pulses of a 27 MeV electron beam from a linear accelerator, *J Inst Met.* (2017). 12:P03003. doi:10.1088/1748-0221/12/03/p03003
34. Krauss A. The PTB water calorimeter for the absolute determination of absorbed dose to water in60Co radiation. *Metrologia.* (2006). 43:259–72. doi:10.1088/0026-1394/43/3/008
35. DIN 6800-2:2008-03. *Procedures of dosimetry with probe type detectors for photon and electron radiation—Part 2: ionization chamber dosimetry of high energy photon and electron radiation*. Berlin, Germany: Beuth Verlag 10.31030/1409685
36. International Atomic Energy Agency. Absorbed dose determination in external beam radiotherapy (2001). Technical Rep. Series No. 398. Vienna: IAEA.
37. Hartmann GH. Absorbed dose determination for high energy photon and electron beams at a PRIMUS linear accelerator using the documents DIN 6800-2 and TRS-398. *Z Med Phys.* (2003). 13:241–50. doi:10.1078/0939-3889-00183
38. Bruggmoser G, Saum R, Schmachtenberg A, Schmid F, Schüle E. Determination of the recombination correction factorkSfor some specific plane-parallel and cylindrical ionization chambers in pulsed photon and electron beams. *Phys Med Biol.* (2007). 52, N35–N50. doi:10.1088/0031-9155/52/2/N01
39. Laitano RF, Guerra AS, Pimpinella M, Caporali C, Petrucci A. Charge collection efficiency in ionization chambers exposed to electron beams with high dose per pulse, *Phys Med Biol.* (2006). 51:6419. doi:10.1088/0031-9155/51/24/009
40. Cella L, Liuzzi R, Salvatore M. The Italian affair: the employment of parallel-plate ionization chambers for dose measurements in high dose-per-pulse IORT electron beams. *Med Phys.* (2010). 37:2918–24. doi:10.1118/1.3432601
41. Besheli MG, Ioannis S, Klemens Z, Budach W. Determination of the ion recombination correction factor for intraoperative electron beams. *Z Med Phys.* (2016). 26:35–44.
42. Pimpinella M, Andreoli S, De Angelis C, Della Monaca S, D'Arienzo M, Menegotti L. Output factor measurement in high dose-per-pulse IORT electron beams. *Phys Med.* (2019). 61:94–102. doi:10.1016/j.ejmp.2019.04.021
43. Boag JW, Hochhäuser E, Balk OA. The effect of free-electron collection on the recombination correction to ionization measurements of pulsed radiation. *Phys Med Biol.* (1996). 41:885–97. doi:10.1088/0031-9155/41/5/005
44. Pearce J, Thomas R, DuSautoy A. The characterization of the Advanced Markus ionization chamber for use in reference electron dosimetry in the UK. *Phys Med Biol.* (2006). 51:473–83. doi:10.1088/0031-9155/51/3/001
45. Puhl JM, Desrosiers MF. Advancements in accuracy of the alanine dosimetry system. Part 2. The influence of the irradiation temperature. *Radiat Phys Chem.* (2000). 57:1–9. doi:10.1016/s0969-806x(99)00339-4
46. Anton M. Uncertainties in alanine/ESR dosimetry at the physikalisch-technische Bundesanstalt. *Phys Med Biol.* (2006). 51:5419–40. doi:10.1088/0031-9155/51/21/003
47. Vörös S, Anton M, Boillat B. Relative response of alanine dosemeters for high-energy electrons determined using a Fricke primary standard. *Phys Med Biol.* (2012). 57:1413–32. doi:10.1088/0031-9155/57/5/1413
48. Anton M, Allisy-Roberts PJ, Kessler C, Burns DT. A blind test of the alanine dosimetry secondary standard of the PTB conducted by the BIPM. *Metrologia.* (2014). 51:06001. doi:10.1088/0026-1394/51/1a/06001
49. Anton M, Kapsch R-P, Krauss A, von Voigts-Rhetz P, Zink K, McEwen M. Difference in the relative response of the alanine dosimeter to megavoltage x-ray and electron beams. *Phys Med Biol.* 58:3259–3282. doi:10.1088/0031-9155/58/10/3259
50. Devic S, Tomic N, Lewis D Reference radiochromic film dosimetry: Review of technical aspects. (2016). *Phys Med.* 32:541–56. doi:10.1016/j.ejmp.2016.02.008
51. Poppinga D, Schoenfeld AA, Doerner KJ, Blanck O, Harder D, Poppe B. A new correction method serving to eliminate the parabola effect of flatbed scanners used in radiochromic film dosimetry. *Med Phys.* (2014). 41:021707. doi:10.1118/1.4861098.
52. Marroquin EYL, Herrera González JA, Camacho López MA, Barajas JEV, García-Garduño OA. Evaluation of the uncertainty in an EBT3 film dosimetry system utilizing net optical density. *J Appl Clin Med Phys.* (2014). 17(5):466. doi:10.1120/jacmp.v17i5.6262
53. Borca VC, Pasquino M, Russo G, Grosso P, Cante D, Sciacero P, et al. Dosimetric characterization and use of GAFCHROMIC EBT3 film for IMRT dose verification. *J Appl Clin Med Phys.* (2013). 14:158–71. doi:10.1120/jacmp.v14i2.4111
54. McEwen MR. The calibration of therapy level electron beam ionization chambers in terms of absorbed dose to water. *Phys Med Biol.* (2006). 43:9. doi:10.6028/nist.sp.250-40
55. Andersen V, Ballarini F, Battistoni G, Cerutti F, Empl A, Fassó A, et al. The application of FLUKA to dosimetry and radiation therapy. *Radiat Protect Dosim.* (2005). 116:113–7. doi:10.1093/rpd/nci040

56. Battistoni G, Boehlen T, Cerutti F, Chin PW, Esposito LS, Fassò A, et al. Overview of the FLUKA code. *Ann Nucl Energy.* (2015). 82:10–8. doi:10.1016/j.anucene.2014.11.007
57. Di Martino F, Giannelli M, Traino AC, Lazzeri M. Ion recombination correction for very high dose-per-pulse high-energy electron beams. *Med Phys.* (2005). 32:2204–10. doi:10.1118/1.1940167
58. Scalchi P, Ciccotelli A, Felici G, Petrucci A, Massafra R, Piazzi V, et al. Use of parallel-plate ionization chambers in reference dosimetry of NOVAC and LIACmobile electron linear accelerators for intraoperative radiotherapy: a multi-center survey. *Med Phys.* (2017). 44:321–32. doi:10.1002/mp.12020

Conflict of Interest: RK is employed by Physikalisch-Technische Werkstätten (PTW)

The remaining authors declare that the research was conducted in the absence of any commercial or financial relationships that could be construed as a potential conflict of interest.

frontiers in Physics

ORIGINAL RESEARCH
published: 13 November 2020
doi: 10.3389/fphy.2020.564907

ELIMED-ELIMAIA: The First Open User Irradiation Beamline for Laser-Plasma-Accelerated Ion Beams

Giuseppe A. P. Cirrone[1], Giada Petringa[1], Roberto Catalano[1], Francesco Schillaci[2], Luciano Allegra[1], Antonino Amato[1], Renato Avolio[1], Michele Costa[1], Giacomo Cuttone[1], Antonin Fajstavr[2], Giuseppe Gallo[1], Lorenzo Giuffrida[2], Mariacristina Guarrera[1], Georg Korn[2], Giuseppina Larosa[1], Renata Leanza[1], Enzo Lo Vecchio[1], Gustavo Messina[1], Giuliana Milluzzo[1,3], Veronika Olsovcova[2], Salvatore Pulvirenti[1], Jan Pipek[1], Francesco Romano[1], Daniele Rizzo[1], Antonio D. Russo[1], S. Salamone[1], Valentina Scuderi[1], Andriy Velyhan[2], Salvatore Vinciguerra[1], Martina Zakova[2,4], Emilio Zappalà[1] and Daniele Margarone[2,3]*

[1] Laboratori Nazionali del Sud Istituto Nazionale di Fisica Nucleare (INFN-LNS), Catania, Italy , [2] ELI-Beamlines, Institute of Physics (FZU), Czech Academy of Sciences, Prague, Czechia, [3] Centre for Plasma Physics, Queen's University of Belfast, Belfast, United Kingdom, [4] FNSPE, Czech Technical University in Prague, Prague, Czechia

OPEN ACCESS

Edited by:
Vincenzo Patera,
Sapienza University of Rome, Italy

Reviewed by:
Kenneth Long,
Imperial College London,
United Kingdom
Mehmet Burcin Unlu,
Boğaziçi University, Turkey

***Correspondence:**
Giuseppe A. P. Cirrone
pablo.cirrone@lns.infn.it

Specialty section:
This article was submitted to Medical Physics and Imaging, a section of the journal Frontiers in Physics

Received: 22 May 2020
Accepted: 02 September 2020
Published: 13 November 2020

Citation:
Cirrone GAP, Petringa G, Catalano R, Schillaci F, Allegra L, Amato A, Avolio R, Costa M, Cuttone G, Fajstavr A, Gallo G, Giuffrida L, Guarrera M, Korn G, Larosa G, Leanza R, Lo Vecchio E, Messina G, Milluzzo G, Olsovcova V, Pulvirenti S, Pipek J, Romano F, Rizzo D, Russo AD, Salamone S, Scuderi V, Velyhan A, Vinciguerra S, Zakova M, Zappalà E and Margarone D (2020) ELIMED-ELIMAIA: The First Open User Irradiation Beamline for Laser-Plasma-Accelerated Ion Beams. Front. Phys. 8:564907. doi: 10.3389/fphy.2020.564907

The main effort of the laser-driven ion acceleration community is aimed at improving particle beam features (in terms of final maximum energy, particle charge, and beam divergence) and to demonstrate reliable approaches for use for multidisciplinary applications. An ion acceleration target area based on unique laser capabilities is available at ELI-Beamlines (Extreme Light Infrastructure) in the Czech Republic; it is called ELIMAIA (ELI Multidisciplinary Applications of laser-Ion Acceleration) and aims to provide stable and characterized beams of particles accelerated by high-power lasers to offer them to the user community for interdisciplinary studies. The ELIMAIA section dedicated to ion focusing, selection, characterization, and irradiation is named ELIMED (ELI MEDical and multidisciplinary applications). Thanks to ELIMED, very high-dose-rate (around Gy/min) controlled proton and ion beams, with energy levels ranging from 5 to 250 MeV, will be transported to an in-air section dedicated to absolute and relative dosimetry of the laser-generated ions. A transmission dual-gap air ionization chamber will allow an on-line, non-destructive characterization of the ion dose at the user sample irradiation point. The uncertainty in the final dose released onto the sample is expected to be well below 5%. An ELIMED radiobiology pilot experiment is scheduled for 2021, during which *in-vitro* cell irradiations will be carried out with well-controlled proton beams. In this work, the status of the ELIMED/ELIMAIA beamline will be described along with a complete definition of the main dosimetric systems and of their calibrations carried out at conventional accelerators.

Keywords: protontherapy, dosimetry, Monte Carlo, laser-driven, ELIMED, laser-driven ions

1. INTRODUCTION

Ion acceleration driven by pulsed laser-plasma sources is a rapidly emerging field of Physics resulting from recent high-power laser technology achievements in terms of ultra-high intensities ($> 10^21$ W/cm^2) reached on target. This has allowed us to explore extreme regimes of laser-matter interaction. Ultra-high electric and magnetic fields are generated in the laser-target interaction, and plasma electrons (known as hot electrons) are accelerated to relativistic energies in a very compact approach (um-scale). Typically, such a plasma electron heating mechanism leads to the acceleration of high-energy ion beams from a thin solid target (um-thick foil) based on a sheath field, which is created on the target's rear surface. Charge separation and proton/ion acceleration occurs for a very short time, and ions and electrons ultimately co-propagate in vacuum. Recent experiments have recorded proton energies around 100 MeV [1]. However, laser-driven ion beams are still not ready for societal applications, which require advanced beam parameters in terms of divergence, energy spread, homogeneity, and stability. Newly developed laser technologies based on diode-pumped lasers, such as various systems recently installed at ELI-Beamlines [2], will enable users to explore new laser-plasma acceleration schemes of interest for multidisciplinary applications. However, for such novel high peak power (1–10 PW), high repetition rate (up to 10 Hz) laser systems will have to demonstrate that the key challenge to progressing laser-driven ion sources from the realms of scientific curiosity to applications of benefit for the economy and society, i.e., high rep-rated capability and stability both of the laser and the particle sources, is successfully solved.

Hadrontherapy is a radiation therapy technique used for cancer treatment known for its high ballistic precision and radiobiological effectiveness, which is peculiar for hadrons with respect to electrons and gamma-rays [3, 4]. The idea of using hadrons for cancer treatment was first proposed in 1946 by the physicist Robert Wilson. The first patients were treated in the 1950s in nuclear physics research facilities by means of non-dedicated accelerators. Initially, the clinical applications were limited to few parts of the body, as accelerators were not powerful enough to allow protons to penetrate deep in the tissues. In the late 1970s, improvements in accelerator technology, coupled with advances in medical imaging and computing, made proton therapy a viable option for routine medical applications. However, only in the beginning of the 1990s were proton facilities established in clinical settings, the first of these being in Loma Linda, USA. Currently, about 30 proton centers are either in operation or in construction worldwide. Although protons are used in several hospitals, the next step in radiation therapy is the use of carbon and other ions. These have some clear advantages even over protons in providing both local control of very aggressive tumors and a lower acute or late toxicity, thus enhancing the quality of life during and after cancer treatment. Since the birth of hadrontherapy, more than 120,000 patients have been treated globally with hadrons, including 20,000 with carbon ions. In Europe, the interest in hadrontherapy has grown rapidly, and the first dual ion (carbon and protons) clinical facility in Heidelberg, Germany, started treating patients in 2009. Three more of such facilities are now in operation treating patients: CNAO in Pavia, MIT in Marburg, and MedAustron in Wiener Neustadt. Globally, there is a huge momentum within particle therapy, especially concerning treatment with protons. By 2020, it was expected there would be almost 100 centers around the world with over 30 in Europe. Even if within expansion, the number of hadrontherapy centers worldwide is still limited mainly due to the associated large costs for implementation and operation; this stems not only from the need of sophisticate acceleration systems (particularly for heavier ions) but also for the complexity of ion beam delivery systems (known as "gantries"), radiation protection (shielding), and facility management. One of the main objectives of the scientific community working in the field of laser-plasma ion acceleration is to demonstrate stable, flexible and compact (cost-effective) acceleration schemes for potential societal applications [5]. Moreover, a laser-plasma source offers the possibility of simultaneous delivery of particle (ions and electrons) and photon (X/gamma rays) beams, thus enabling hybrid approaches of interest to cancer therapy [6].

2. ELIMED: THE ION BEAM TRANSPORT AND DOSIMETRIC SECTION OF THE ELIMAIA BEAMLINE

The objective of the laser-driven ion target area ELIMAIA (ELI Multidisciplinary Applications of laser-Ion Acceleration) at ELI-Beamlines (Extreme Light Infrastructure) is to provide beams of particles accelerated by petawatt-class lasers suitable for multidisciplinary applications. Ion beams produced and accelerated in laser-matter interaction processes show high intensities, several ion charge states, broad energy spectra, and energy-dependent angular distributions. As a consequence, a beamline for laser-accelerated ions must be able to define and control particle energy and angular distribution. The ELIMAIA beamline consists of two principal subsystems: the Ion Accelerator section and the ELI MEDical applications (ELIMED) section. ELIMED, in turn, consists of three main parts: ion collection and focusing, ion energy selection, and in-air transport [7, 8]. The goal of the collection and focusing section is to collimate the ion beam and to reduce its initial high divergence. The focusing element is composed of a set of permanent magnet quadrupoles (PMQs). Quadrupoles are necessary to obtain a focusing effect on both transversal planes as well as for suitable matching with the acceptance of the following selection system. The energy selector system (ESS) consists of four tunable resistive dipoles arranged with alternating fields and whose magnetic characteristics can be varied depending on the energy and ion species to be selected. A rectangular aperture, locate after the second dipole, allows us to control the beam energy spread. The transported ion and proton beams are monitored along the beamline with several diagnostics based on solid-state detectors. In particular, diamond and silicon carbide (SiC) are extensively used along the beamline in a time-of-flight configuration (TOF) [9, 10]. The possibility to perform accurate shot-to-shot measurements of the dose released to user samples

is a key feature guaranteed by the ELIMED diagnostic systems. In particular, ELIMED's absolute dosimetry system has been created to be independent from dose-rate and to allow on-line dosimetric evaluation with an error rate below 5%. The ELIMED dosimetry system is based on three main devices: a Secondary Electron Monitoring (SEM), a Multi-Gaps Ionization Chamber (MGIC), and a Faraday Cup (FC) for absolute dosimetry. Passive detectors, such as CR39 and radiochromic films (RCF), are also used to benchmark active ion diagnostic and dosimetry devices.

2.1. Beam Transport Elements

Figure 1 shows a photo of the ELIMAIA beamline. The Ion Accelerator section is visible in the photo only as a large laser-target interaction vacuum chamber (top-left), and laser/plasma optical and diagnostic devices for the two available PW-class lasers are not visible. Since the basic features of laser-driven ions are adverse to efficient beam manipulation (large divergence and energy spread), the use of several beam transport stages is mandatory. The ELIMED ion beam transport section is entirely shown in **Figure 1** (blue and orange color). It consists of three main sub-systems. The Ion Collection section, located in a dedicated vacuum chamber close to the laser-target interaction point, is used to capture ions within a certain energy range, inject them into the energy selection system, and also provide a rough energy selection capability. This section consists of a set of five PMQs with high magnetic field gradient of 50 T/m [11, 12] (1.8 T over a 36 mm magnetic bore) placed on a displacement system to adjust the beam optical elements for different ion energies based on the energy selection system (ESS) configuration. Ions with a given energy spread are focused into a position where the energy selection occurs (radial plane) and their angular aperture is reduced angular aperture in the transverse plane, which is as required for an optimal matching between the acceptance and the transmission efficiency of the ESS. This device consists of a double dispersive mode magnetic chicane, made of four C-shaped electromagnetic dipoles with laminated core and a selection slit set in the middle plane [13], to cut the undesired energy components of incoming ions. The ELIMED ESS can select protons with 300 MeV maximum energy and heavier ions with 60 MeV per nucleon. The chicane is based on a fixed reference trajectory with variable magnetic field (0.063–1.22 T) to cover a large expected ion energy range. The energy spread of the selected ion beam has a linear dependence on the slit aperture (10 mm aperture corresponds to a spread of 10% FWHM). After the chicane, the ion beam is delivered to a final beam shaping section, which consists of two resistive quadrupoles (gradients up to 10 T/m over a 50 mm bore) and two correction elements for a fine focusing and alignment of the ion beam onto the user sample. The use of a laminated core for the electromagnets guarantees a fast change in the magnetic field, reducing the hysteresis effect. The whole ELIMED beamline, but the collection section, can thus be used as an active energy modulator. The possibility to carry out high resolution on-axis ion spectrometry has recently been investigated and is being implemented as an upgrade of the ESS, which will be used as a combined device: a selection chicane (as described) or a Thomson Parabola spectrometer using the first dipole and a set of electrodes placed inside the selector chamber. A feasibility study proposed in [14] shows the main feature of the upgraded chicane and the diagnostic performances in the case of its use as a Thomson Parabola spectrometer. It basically consists of the first dipole in the chicane used as a magnetic deflector plus two electrostatic deflectors to be installed in the vacuum chamber. In this way, the spectrometer will have a sector with a wide dynamic range and wide charge separation but relatively low energy resolution of about 10.

2.2. Monte Carlo Simulations

The whole ELIMED beamline for laser-driven ion beam transport and characterization (including detectors for ion diagnostics and dosimetry) can be modeled by numerical simulations using the Geant4 Monte Carlo toolkit [15–17].

The ELIMED beamline simulation [18–20] is a powerful and reliable tool with which to predict the dosimetric parameters as well as the biological effects of high-dose-rate, pulsed ion beams on the human body. The ELIMED simulation software is divided into three different parts following the three main beamline sections as described in section 2.1: a part related to ion beam collection and diagnostics, one related to ion beam selection and transport, and finally a section related to ion beam dosimetry and samples irradiation [7]. A sketch of the ELIMED beamline as simulated by the Geant4 application is reported in **Figure 2**. Accurate magnetic field maps, obtained with the COMSOL and OPERA software for each quadrupole, are included in the application for a realistic simulation of the focusing effect by an accurate implementation of the high field gradients. A grid of the magnetic field maps for each single dipole of the ESS is also included in the ESS simulation.

2.3. Dosimetric System

The dosimetric system has been realized to meet the specific requirements of radiobiological experiments that cannot accept uncertainties above 5% in the absorbed dose measured at each shot. The definition of a protocol (including the detectors to be used, methods, and procedures) for absolute and relative dosimetry is, in fact, mandatory for the future clinical use of laser-driven proton beams in order to obtain absolute dose measurements with an accuracy and a precision comparable to what is typically required in clinical applications. The system must be suitable for operation with pulsed, high-intensity beams also in the presence of a strong electromagnetic noise associated with the interaction of ultra-high intensity lasers with a plasma target. All the detectors involved must be capable of measuring bunches of particles that are very short in time (1–10 ns) and very intense (typically 10^8 particle per bunch at the sample/detector). In order to accomplish this task, fast, low-noise, and variable-gains charge amplifiers were designed and realized at INFN-LNS and installed at ELI-Beamlines. The developed amplifier will allow to measure the total charge in each dosimetric system device at a repetition rate of 1 Hz, simultaneously minimizing the error.

This system includes three main devices: a secondary emission monitor, a multi-gap in-transmission ionization chamber for relative dose measurements, and a Faraday cup, which is designed to carry out absolute dosimetry. A sample irradiation system with

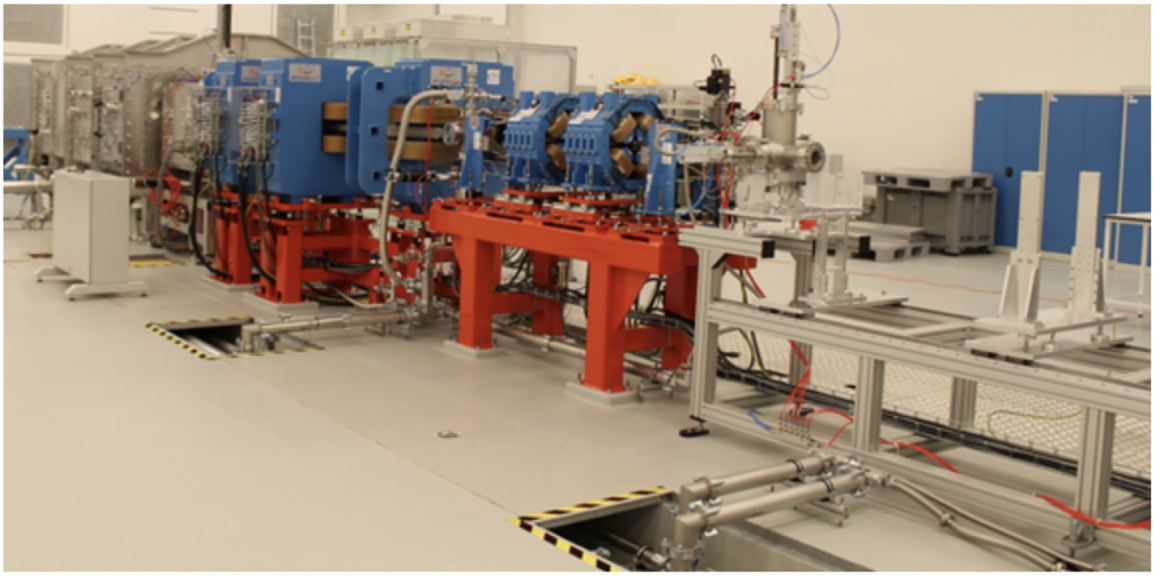

FIGURE 1 | ELIMED ion beam line connected to the Interaction chamber (first chamber from the left), where the laser-acceleration occurs and where the collection systems sits. It follows the ESS and the beam shaping section. After this last section, the beam is delivered in the in-air dosimetry station.

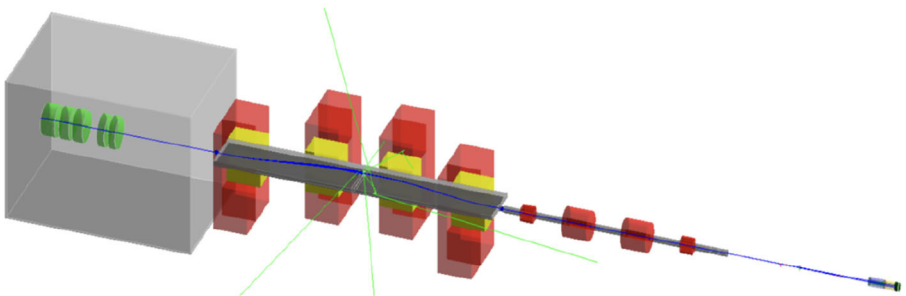

FIGURE 2 | Visualization of the complete beamline model.

sub-mm precision, dedicated to user samples (e.g., biological cells), is located at the end of the in-air section. **Figure 3** shows a general outlook of the ELIMED beamline dosimetric section. The SEM detector, positioned in-vacuum just before the in-air section, is made of a thin (15 μm thick) tantalum foil. It is electrically insulated from the rest of the beamline by a polymethylmethacrylate (PMMA) frame. An actuator allows to move the SEM detector in/out the beamline axis. The SEM operating principle is based on the measurement of secondary electron emission (SEE) generated when multi-MeV charged particles pass through the tantalum foil. The detected signal is correlated to the incident beam current and can provide online information directly connected to the released dose at a given point if properly cross-calibrated against a reference dosimeter. The MGIC, developed by DE.TEC.TOR. S.r.l., Italy, is an innovative device realized for real-time dose monitoring delivered shot-to-shot. It consists of two consecutive ionization chambers, with a different inter-electrode gap of 5 and 10 mm, independently supplied with a voltage ranging from −1,000 to +1,000 V as well as −2,000 to +2,000 V, respectively. The presence of the second gap allows us, exploiting the different collection efficiency among the two chambers, to correct for any ion recombination effect caused by the expected extremely high dose rate (MGy-GGy per second). In order to overcome saturation effects typical of conventional dosimeters when used with laser-driven ions, an innovative FC has been designed and realized for absolute dosimetry. The FC was designed on the basis of previous works [21, 22], and the introduction of new geometrical solutions, aiming to optimize the charge collection efficiency and reduce uncertainties, related to the charge collection, which was explored by [23]. An additional electrode with a special beveled shape-coaxial and internal to the standard one in which a bias can be applied in the range between −2,000 and +2,000V, has been introduced. The final resulting electric field inside the FC is the combination of two field coming from the two coaxial electrodes. This special configuration of the electrodes produces

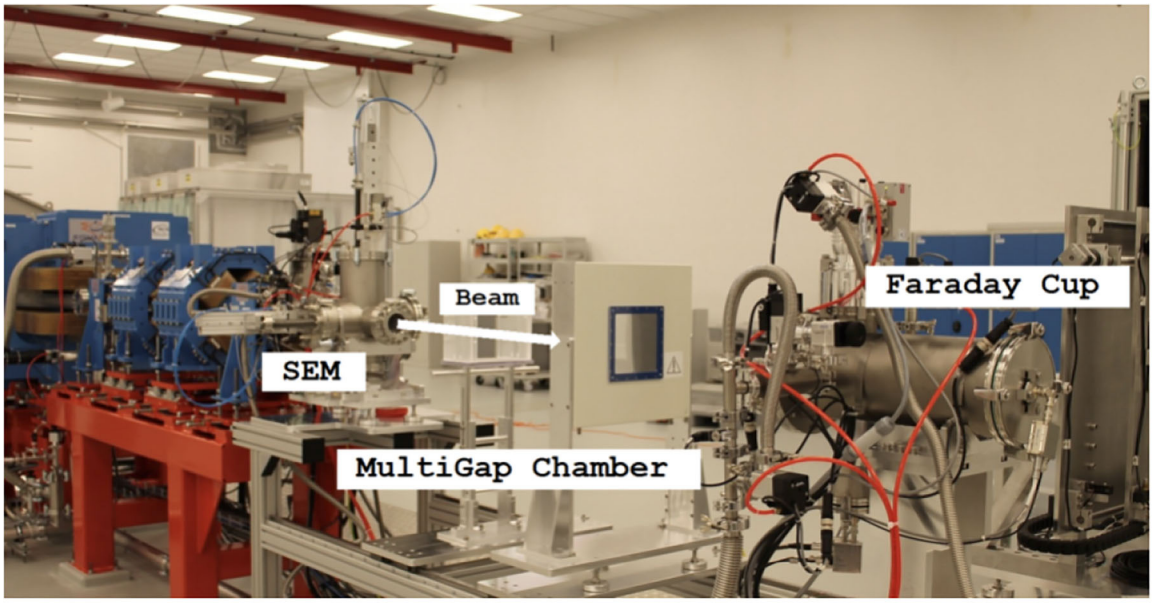

FIGURE 3 | Dosimetric section of ELIMED beamline: SEM and MG ionization chambers compose the relative dosimetry section, and FC is the element devoted to the absolute dosimetry.

an asymmetric electric field able to minimize the negative effects of the secondary electrons generated by the interaction of protons with the thin entrance window and the cup material itself. The beam energy spectra and the surface of its spot on the FC are necessary for the dose evaluation and will be measured using stacks of radiochromic films. They can be used both as a single detector, to precisely measure the transversal dose distributions profiles, or in stack configuration, in order to obtain information on the energy of the accelerated protons through an iterative procedure based on deconvolution methods (see section 2.4). The use of RCF films, if properly calibrated, also allows for an accurate measurement of the released dose distributions at the irradiation point with a spatial resolution less than 200 μm [24]. Solid state nuclear track detectors (CR-39 type) will also be used, representing a useful tool for charged particle fluences and spectroscopic analysis by measuring the track diameter arising from incident particles and extracting the corresponding energy from a suitable calibration curve [25].

2.3.1. FC Preliminary Characterization With a 35 MeV Conventional Proton Beam

The FC was firstly characterized with conventional (not pulsed and with intensities of the order of 400 pA) proton beams in terms of accuracy in absolute dose estimation during an experimental campaign carried out at the Zero Degree beamline of the INFN-LNS laboratory (Catania, Italy) [26]. The detector was positioned at the beamline isocenter and irradiated with a 35 MeV proton beam. The proton beam field was circular with a diameter of 15 mm. Size and homogeneity of the beam spot (in terms of space distribution) were measured for each experimental session using radiochromic film detectors (EBT3 type). The dose delivered was monitored online by an in-transmission ionization chamber previously calibrated with a Markus chamber (mod. 3002). A fixed dose of 5.13 ± 0.15 Gy was delivered for each measurement. The FC efficiency

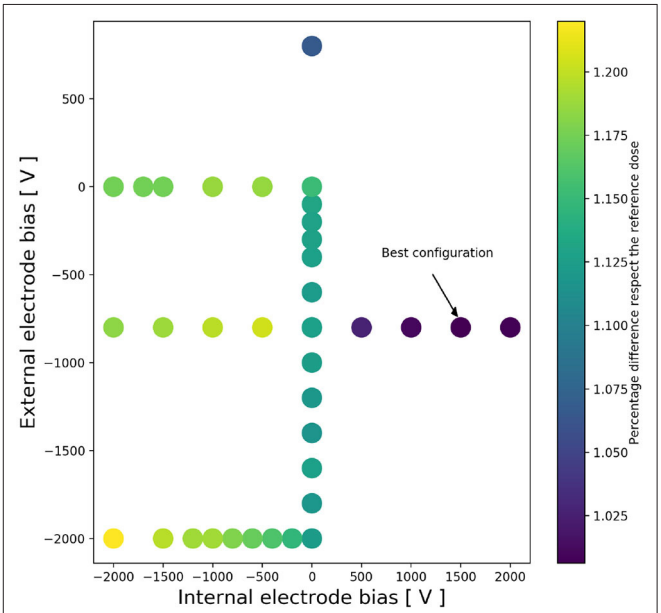

FIGURE 4 | Two dimensional scatter plot indicating the percentage difference between the dose measured by the Faraday Cup and the released dose. The discrepancy level is represented by a different color. The best configuration, obtained by applying the voltage of +1,500 to −800 V to the internal and external electrode, respectively, is indicated in the figure with a black arrow.

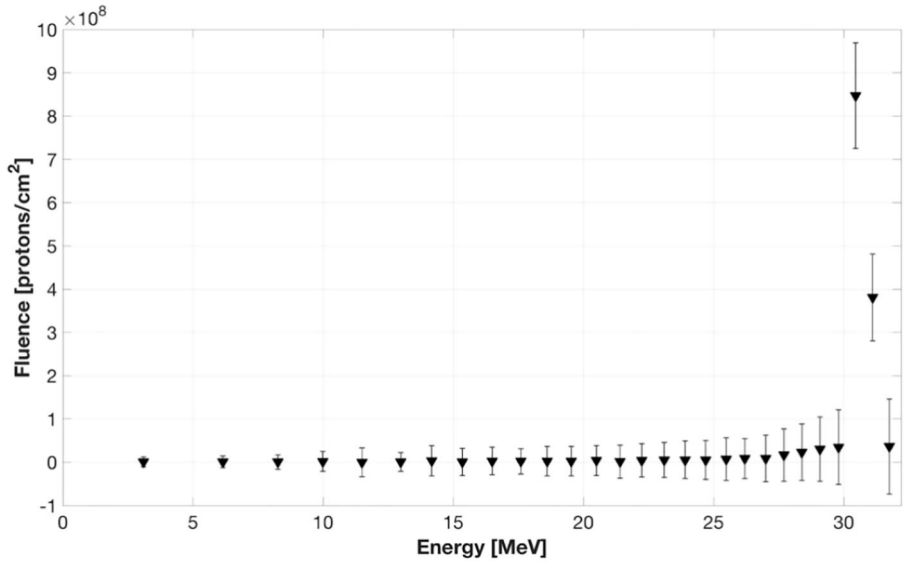

FIGURE 5 | Incident proton energy spectra obtained irradiating a stack of RCFs with 35 MeV monoenergetic beam of CATANA experimental room of LNS-INFN.

was evaluated by varying the voltage of the two electrodes. The working configuration corresponds to the maximum charge collection efficiency coupled with the minimum uncertainty due to the contribution of secondary electrons generated in the interaction between the beam and the detector itself [21]. The two-dimensional scatter plot of **Figure 4** reports the percentage difference (expressed as a color gradient) between the dose measured by the FC and the dose released for each couple of applied voltage. The optimal configuration for which we register the minimal discrepancy corresponds to an electric field generated when −800 and +1,500 V are applied (circle indicated with the arrow) to the external and internal electrodes, respectively. In this case, the percentage discrepancy between the dose measured with the FC and the absolute dose monitored with the ionization chamber is 0.7%. Discrepancies up to 18% are observed for the other configurations.

2.4. Spectroscopy and Dosimetry With Radiochromic Films

Radiochromic film is a dosimetric detection medium with high dynamic range and independent response from the incident dose rate. In general, RCF detectors contain one or more active layers of microcrystalline monometric dispersion buried in a plastic substrate [27, 28]. When an ionizing radiation hits it, the active material undergoes polymerization and changes its color with a degree of color conversion that, in a first approximation, is proportional to the absorbed dose. This makes possible the correlation (or calibration) between the absorbed dose and film darkening, which can be evaluated in terms of Optical Density (OD) [29]. The OD is the quantity able to quantify the intensity reduction of light transmitted through the film after the exposure. The correctness and precision in the OD calibration process represents the basis of an accurate measurement with an RCF. The OD value is obtained using a commercial scanner. RCFs arranged in a stack configuration can be used to detect the typical large divergence and continuous energy spectrum of laser-driven ion beams. The thickness of RCF is of the order of a hundred micrometers and can easily be crossed by protons of few MeVs. The stack consists of alternating layers of RCFs. Each layer allows detecting protons with different energies thus the entire spectrum of the incident proton beam can be reconstructed. In the framework of the ELIMED project, an analytical procedure able to reconstruct the incident energy spectra in a RCF stack was developed and validated [30]. The algorithm considers the dose read in the last irradiated layer of the stack and subtracts it from all previous layers applying specific weight coefficients for each layer. The whole process can be summarized the following:

$$D^k_{prim} = D^k_{tot} - \sum_{i=k+1}^{N} D^k_{prim} \frac{w_{ki}}{w_{ii}}, \tag{1}$$

where D^k_{prim} represent the dose matrix related to the primary protons on the k-th layer of the stack; N is the number of layers in a stack, D^k_{tot} is the dose matrix of the k-th layer taking into account all the traversing protons, and the ratio $\frac{w_{ki}}{w_{ii}}$ represents the fraction of energy loss in the k-th layer of the stack of primary protons able to reach the i-th layer (i>k), which was acquired adopting the SRIM simulation programme [31]. The D^k_{prim} is then converted in particle fluence Φ^k_{prim} through:

$$\Phi^k_{prim} = \frac{\sum_{l,m} D^k_{prim,lm}}{A D^k_{proton}}, \tag{2}$$

where A is the area of the selected ROI constituted by LxM pixels (l=1,..., L, m=1,..., M), and D^k_{proton} is the dose delivered by a single primary proton, and is calculated by SRIM. In order to verify the analysis approach above described, we tested the

whole procedure irradiating the films with protons accelerated by the Superconducting Cyclotron available at Laboratori Nazionali del Sud-INFN (Catania, I). We positioned a stack of 31 RCF (EBT3 type) with the first film positioned at the isocenter of the CATANA experimental room; the stack was then irradiated with a monoenergetic beam of 35 MeV in energy. In **Figure 5**, the incident proton energy spectra derived with the described approach is shown.

3. USER APPLICATIONS AT THE ELIMED FACILITY

The most recent studies performed with laser-driven particle bunches aim to compare the characteristics of such novel beams with the ones available at conventional accelerators. This is a key requirement to establish and validate irradiation procedures in analogy with the ones already existing when user samples are irradiated with conventional sources. The ELIMED beamline, indeed, was designed and realized with the long-term goal of exploring medical applications and to obtain extremely high shot-to-shot reproducibility, high precision in the delivered dose, quasi-monoenergetic beam spectra at the biological sample, and reproducibility of the transported beams. These specific characteristics can be certainly exploited for various multidisciplinary applications other than the medical ones; one example is the broad (Boltzman-like) energy spectrum of laser accelerated ions [32]. Most radiation occurring in space has an exponential or power-law energy distribution that cannot easily be reproduced with conventional accelerators. Radiation exposure is regarded as one of the main problems in long-term manned space missions. In this framework, it can be worthwhile to investigate the effects of beams with broad energy distributions on biological samples as well as on electronic devices and materials, and this can be easily carried out at the user sample irradiation station of ELIMED. Laser-accelerated proton beams transported and selected at ELIMED could be also used as an innovative diagnostic technique in the field of Cultural Heritage. Adopting these beams could have considerable advantages over conventional PIXE (proton-induced X-ray emission), PIGE (proton-induced gamma-ray emission), and DPAA [33] (Depth Proton Activation Analysis) spectroscopy. Protons accelerated by laser-matter interaction have the advantage of allowing complete chemical analysis on a larger volume of the artworks and deeper and more precise "layer by layer" analysis [34]. Moreover, the future perspective to develop extremely feasible and portable PIXE systems based on laser-matter interaction can be studied and consolidated. Finally, a laser-driven ion acceleration user beamline could open the possibility to use plasma and ions generated in the high-power laser interaction for production of medical isotopes by innovative production schemes [35]. Lasers could provide many advanced features with respect to methods based on conventional accelerators, where target activation represents a strong limitation. Presently, two different isotope-based imaging techniques are used in medical clinics: SPECT (Single Photon Emission Computed Tomography) and PET (Positron Emission Tomography). Both are mainly based on 18F, 11C, 15O, and 13N decay produced by the interaction of protons with solid targets. ELIMED could be the first worldwide facility able to produce radioisotopes for imaging techniques as well as clinical proton beams with the same accelerator machine based on laser-target interaction [36]. The ELIMAIA beamline will additionally offer the possibility to explore innovative schemes of interaction between well-controlled and characterized ion beams (thanks to the ELIMED section) and high-density plasmas for pump-probe investigations of warm dense matter [37], fast ignition approach to inertial confinement fusion [38], and estimation of ion-stopping power in plasma [39].

DATA AVAILABILITY STATEMENT

The raw data supporting the conclusions of this article will be made available by the authors, without undue reservation.

AUTHOR CONTRIBUTIONS

GAPC and DM are the inventors of the ELIMAIA/ELIMED beamlines. DM is in charge of the laser beam transport and focusing, laser-target interaction, ion acceleration and diagnostics at the source, while GAPC is in charge of the ion beam transportation and selection, of the design of the in-air irradiation section of the beamline and of the dosimetry and diagnostic systems. GP, RC, GC, RL, AV, VS, and GMi were involved in the development and tests of the dosimetric systems. FS was the main designer of the electromagnetic transport elements. AR supported him in many aspects. GMi, FR, MZ, and JP were involved in the Monte Carlo and PIC simulations. LA, AA, RA, MC, AF, GG, LG, EL, GMe, SP, DR, SS, SV, and EZ performed the beamline installation at the ELI-Beamlines premise. GC and GK supervise the entire activity. All authors contributed to the article and approved the submitted version.

FUNDING

This work has been supported by the project ELI—Extreme Light Infrastructure—phase 2 (CZ.02.1.01/0.0/0.0/15-008/0000162) from European Regional Development Fund, by the Ministry of Education, Youth and Sports of the Czech Republic (Project No. LQ1606) and by the project Advanced Research Using High Intensity Laser Produced Photons and Particles (CZ.02.1.01/0.0/0.0/16-019/0000789). This work has also been financially supported by the ELIMED INFN project.

REFERENCES

1. Higginson A, Gray RJ, King M, Dance RJ, Williamson SDR, Butler NMH, et al. Near-100 MeV protons via a laser-driven transparency-enhanced hybrid acceleration scheme. *Nat Commun*. (2018) 9:724. doi: 10.1038/s41467-018-03063-9
2. Hein J, Silva LO, Korn G, Gizzi LA, et al. Outline of the ELI-Beamlines facility. In: *Diode-Pumped High Energy and High Power Lasers; ELI: Ultrarelativistic Laser-Matter Interactions and Petawatt Photonics; and HiPER: the European Pathway to Laser Energy.* Prague (2011). 808010-1–808010-10.
3. Orecchia R, Zurlo A, Loasses A, Krengli M, Tosi G, Zurrida S, et al. Particle beam therapy (hadrontherapy): basis for interest and clinical

experience. *Eur J Cancer*. (2008) 34:459–68. doi: 10.1016/S0959-8049(97)10044-2
4. Official page of the Particle Therapy Cooperative Group. An organisation for those interested in proton, light ion and heavy charged particle radiotherapy. Available online at: http://www.ptcog.ch//
5. Romano F, Schillaci F, Cirrone GAP, Cuttone G, Scuderi V, Allegra L, et al. The ELIMED transport and dosimetry beamline for laser-driven ion beams. *Nuclear Instrum Methods Phys Res A*. (2016) 829:153–8. doi: 10.1016/j.nima.2016.01.064
6. DeLaney TF, Liebsch NJ, Pedlow FX, Adams J, Dean S, Yeap BY, et al. Phase II study of high-dose photon/proton radiotherapy in the management of spine sarcomas. *Int J Radiat Oncol Biol Phys*. (2009) 74:732–9. doi: 10.1016/j.ijrobp.2008.08.058
7. Margarone D, Cirrone GAP, Cuttone G, Amico AG. ELIMAIA: a laser-driven ion accelerator for multidisciplinary applications. *Quant Beam Sci*. (2018) 8:2. doi: 10.3390/qubs2020008
8. Cirrone GAP, Romano F, Scuderi V, Amato A, Candiano G, Cuttone G, et al. Transport and dosimetric solutions for the elimed laser-driven beam line. *Nuclear Instrum Methods Phys Res A*. (2015) 796:99–103. doi: 10.1016/j.nima.2015.02.019
9. Milluzzo G, Scuderi V, Amico AG, Borghesi M, Cirrone GAP, Cuttone G, et al. Laser-accelerated ion beam diagnostics with TOF detectors for the ELIMED beam line. *J Instrum*. (2017) 12:C02025. doi: 10.1088/1748-0221/12/02/C02025
10. Scuderi V, Milluzzo G, Doria D, Alejo A, Amico A, Booth N, et al. Time of Flight based diagnostics for high energy laser driven ion beams. *J Instrum*. (2017) 12:C03086. doi: 10.1088/1748-0221/12/03/C03086
11. Schillaci F, Cirrone GAP, Cuttone G, Romano F, Scuderi V, Allegra L, et al. Status of the ELIMED Beamline at the ELIMAIA facility. *J Instrum*. (2016) 11:C12052. doi: 10.1088/1748-0221/11/12/c12052
12. Schillaci F, Cirrone GAP, Cuttonea G, Maggiorec M, Andoa L, Amatoa A, et al. Design of the ELIMAIA ion collection system. *J Instrum*. (2014) 10:T12001. doi: 10.1088/1748-0221/10/12/t12001
13. Schillaci F, Maggiore M, Andó L, Cirrone GAP, Cuttone G, Romano F, et al. Design of a large acceptance, high efficiency energy selection system for the ELIMAIA beam-line. *J Instrum*. (2016) 11:P08022. doi: 10.1088/1748-0221/11/08/P08022
14. Schillaci F, Nevrkla M, Maggiore M, Goncalves L, Cirrone PGA, Velyhan A, et al. Design of a high energy Thomson Parabola ion spectrometer for the ELIMAIA beamline. *J Instrum*. (2019) 14:T06004. doi: 10.1088/1748-0221/14/06/T06004
15. Agostinelli S, Allison J, Amako K, Apostolakis J, Araujo H, Arce P, et al. Geant4 - A simulation toolkit. *Nuclear Instrum Methods Phys Res A*. (2003) 506:250–303. doi: 10.1016/S0168-9002(03)01368-8
16. Alliso J, Amako K, Apostolakis J, Araujo H, Arce P, Asai M, et al. Geant4 developments and applications. *IEEE Trans Nuclear Sci*. (2006) 53:270–8. doi: 10.1109/TNS.2006.869826
17. Allison J, Amako K, Apostolakis J, Arce P, Asai M, Aso T, et al. Recent developments in Geant4. *Nuclear Instrum Methods A*. (2016) 835:186–225. doi: 10.1016/j.nima.2016.06.125
18. Milluzzo G, Pipek J, Amico AG, Cirrone GAP, Cuttone G, Korn G, et al. Transversal dose distribution optimization for laser-accelerated proton beam medical applications by means of Geant4. *Phys Med*. (2018) 54:166–72. doi: 10.1016/j.ejmp.2018.07.008
19. Milluzzo G, Pipek J, Amico AG, Cirrone GAP, Cuttone G, Korn G, et al. Geant4 simulation of the ELIMED transport and dosimetry beam line for highenergy laser-driven ion beam multidisciplinary applications. *Nuclear Instrum Methods Phys Res A*. (2018) 909:298–302. doi: 10.1016/j.nima.2018.02.066
20. Milluzzo G, Pipek J, Amico AG, Cirrone GAP, Cuttone G, Korn G, et al. Monte Carlo simulation of the ELIMED beamline using Geant4. *J Instrum*. (2017) 12:C03027. doi: 10.1088/1748-0221/12/03/C03027
21. Cambria R. Proton beam dosimetry: a comparison between the Faraday cup and an ionization chamber. *Phys Med Biol*. (1997) 42:1185–96. doi: 10.1088/0031-9155/42/6/014
22. Cuttone G, Raffaele L, Barone-Tonghi L, Rovelli A, Sabini MG, Egger E, et al. First Dosimetry Intercomparison Results for the CATANA project. *Phys Med*. (1999) 15:121–130.
23. Thomas DJ, Hodges GS, Seely DG, Moroz NA, Kvale TJ. Performance enhancement study of an electrostatic Faraday cup detector. *Nuclear Instrum Methods Phys Res Sec A*. (2005) 536:11–21. doi: 10.1016/j.nima.2004.07.211
24. Cirrone GAP, Petringa G, Cagni BM, Cuttonea G, Fustaino GF, Guarreraa M, et al. Use of radiochromic films for the absolute dose evaluation in high dose-rate proton beams. *J Instrum*. (2020) 15:C04029. doi: 10.1088/1748-0221/15/04/C04029
25. Jeong TW, Singh PK, Scullion C, Ahmed H, Hadjisolomou P, Jeon C, et al. CR-39 track detector for multi-MeV ion spectroscopy. *Sci Rep*. (2017) 7:2152. doi: 10.1038/s41598-017-02331-w
26. Cuttone G, Cirrone GAP, Di Franco G, La Monaca V, Lo Nigro S, Ott J, et al. CATANA protontherapy facility: the state of art of clinical and dosimetric experience. *Eur Phys J Plus*. (2011) 126:65. doi: 10.1140/epjp/i2011-11065-1
27. Xu XH, Liao Q, Wu JM, Geng YX, Li DY, Zhu JG, et al. Detection and analysis of laser driven proton beams by calibrated gafchromic HD-V2 and MD-V3 radiochromic films. *Rev Sci Instrum*. (2019) 90:033306. doi: 10.1063/1.5049499
28. Devic S. Radiochromic film dosimetry: past, present, and future. *Phys Med*. (2011) 27:122–34. doi: 10.1016/j.ejmp.2010.10.001
29. Karsch L, Beyreuther E, Burris-Mog T, Kraft S, Richter C, Zeil K, et al. Dose rate dependence for different dosimeters and detectors: TLD, OSL, EBT films and diamond detectors. *Med Phys*. (2012) 39:2447–55. doi: 10.1118/1.3700400
30. Karsch L, Margarone D, Candiano G, Kim IJ, Jeong TM, Psikal J, et al. Radiochromic film diagnostics for laser-driven ion beams. In: *Research Using Extreme Light: Entering New Frontiers with Petawatt-Class Lasers II*. Prague (2012).
31. SRIM. *The Stopping and Range of Ions in Matter; SRIM2019*. Available online at: http://www.srim.org
32. Bolton P, Parodi K, Schreiber J. *Applications of Laser-Driven Particle Acceleration*. Boca Raton; New York, NY: CRC Press (2018). doi: 10.1201/9780429445101
33. Pappalardo G, Esposito A, Cirrone GA, Cuttone G, Garraffo S, Pappalardo L, et al. Effects of the behaviour of the proton-induced isotopes production on the analysis of ancient alloys. *Nuclear Instrum Methods Phys Res Sec B*. (2008) 266:2286–91. doi: 10.1016/j.nimb.2008.03.074
34. Barberio CM, Veltri S, Sciscio M, Antici P. Laser-accelerated proton beams as diagnostics for cultural heritage. *Sci Rep*. (2017) 7:40415. doi: 10.1038/srep40415
35. Cucoanesa AS, Balabanskia DL, Canova F, Cuong P, Negoita F, Puicea F, et al. On the potential of laser driven isotope generation at ELI-NP for positron emission tomography. In: *Medical Applications of Laser-Generated Beams of Particles IV: Review of Progress and Strategies for the Future*. Prague (2017). doi: 10.1117/12.2273769
36. Amato E, Italiano A, Margarone D, Pagano B, Baldari S, Korn G. Future laser-accelerated proton beams at ELI-Beamlines as potential source of positron emitters for PET. *J Instrum*. (2016) 11:C04007. doi: 10.1088/1748-0221/11/04/C04007
37. Patel PK, Mackinnon AJ, Key MH, Cowan TE, Foord ME, Allen M, et al. Isochoric heating of solid-density matter with an ultrafast proton beam. *Phys Rev Lett*. (2003) 91:125004. doi: 10.1103/PhysRevLett.91.125004
38. Roth M, Cowan TE, Key MH, Hatchett SP, Brown C, Fountain W, et al. Fast ignition by intense laser-accelerated proton beams. *Phys Rev Lett*. (2001) 86:436–9. doi: 10.1103/PhysRevLett.86.436
39. Cayzac W, Frank A, Roth M. Experimental discrimination of ion stopping models near the Bragg peak in highly ionized matter. *Nat. Commun*. (2017) 8:15693. doi: 10.1038/ncomms15693

Conflict of Interest: The authors declare that the research was conducted in the absence of any commercial or financial relationships that could be construed as a potential conflict of interest.

frontiers in Physics

ORIGINAL RESEARCH
published: 16 November 2020
doi: 10.3389/fphy.2020.579081

Ionizing Radiation Effects on Hs 578Bst Microtubules

L. Bruni[1], *M. Manghi*[1,2], *E. Gioscio*[1,3], *V. Caorsi*[4], *F. M. Rizzi*[2] *and S. Croci*[1,2]*

[1]*Museo Storico della Fisica e Centro Studi e Ricerche Enrico Fermi, Rome, Italy,* [2]*Dipartimento di Medicina e Chirurgia, Università di Parma, Parma, Italy,* [3]*Fondazione IRCCS Istituto Nazionale dei Tumori di Milano, Milan, Italy,* [4]*Abbelight, Paris, France*

Microtubules are one of the three components of the cell cytoskeleton. They are hollow wires, with a diameter of about 25 nm, formed by 13 laterally associated protofilaments composed by dimers of α and β-tubulin. Microtubules are dynamic structures which undergo constant modifications by shrinking and elongating in a phenomenon called treadmilling. Microtubules intervene in various fundamental aspects of the biology of a cell. They contribute to determine the shape of a cell, play a role in the cell movement, and in the intracellular transport of organelles during motion and mitotic chromosome segregation. Despite the relevance of the processes mediated by microtubules most studies on the effects of ionizing radiations focus their attention on the damages delivered to DNA. In this paper we attempt to assess the effects borne by IRs to the microtubules network as a biological target. In this study we irradiated Hs 578Bst cells (a no-cancer, no-immortalized, human breast epithelial cell line) with an 8 Gy single dose of either X-rays or protons. After the irradiated cells fixation, the microtubules were imaged by means of stochastic optical reconstruction microscopy to characterize the network disruption. In our results, Microtubules fibers integrity appears to not have been significantly affected at the administered dose of protons and X-rays, nonetheless we observed differences in the MT network distribution and fiber curvatures.

Keywords: microtubules, protons, Hs 578Bst cell line, ionizing radiations, super resolution microscopy

OPEN ACCESS

Edited by:
Marco Durante,
GSI Helmholtz Center for Heavy Ion Research, Germany

Reviewed by:
Valeria Panzetta,
University of Naples Federico II, Italy
Francesco Tommasino,
University of Trento, Italy

***Correspondence:**
S. Croci
simonetta.croci@unipr.it

Specialty section:
This article was submitted to Medical Physics and Imaging, a section of the journal Frontiers in Physics

Received: *01 July 2020*
Accepted: *17 September 2020*
Published: *16 November 2020*

Citation:
Bruni L, Manghi M, Gioscio E, Caorsi V, Rizzi FM and Croci S (2020) Ionizing Radiation Effects on Hs 578Bst Microtubules. Front. Phys. 8:579081. doi: 10.3389/fphy.2020.579081

INTRODUCTION

Microtubules (MT) are one of the three components of the eukaryotic cell cytoskeleton. MTs are modular structures composed of protofilaments which are sequences of heterodimers made by pairs of α- and β-tubulin monomers ($\alpha\beta$-tubulin) that align in a head-to-tail fashion [1]. Filaments of $\alpha\beta$-tubulin laterally associate eventually closing up to form a hollow wire-like structure made of 13 protofilaments. MTs are dynamic structures which undergo constant elongation and shrinkage through polymerization and depolymerization in a phenomenon called treadmilling. The homeostasis of the MT lattice, alternatively defined "dynamic instability," is thus controlled by the balance between the processes of adding and removing $\alpha\beta$-tubulin heterodimers which determines the phases of growth and shortening of the tubules. The phase when the balance of the process tips in favor of a rapid depolymerization is called "catastrophe," whereas the opposite phase, where protofilaments recover, is called "rescue" [2, 3]. Since protofilaments are oriented sequences of polar $\alpha\beta$-tubulin heterodimers their concatenation results in the construction of protofilaments with polar ends that exhibit different behavior with respect to the processes of polymerization and depolymerization, the first taking place prevalently at the "plus end" of the filament where β-tubulin is exposed.

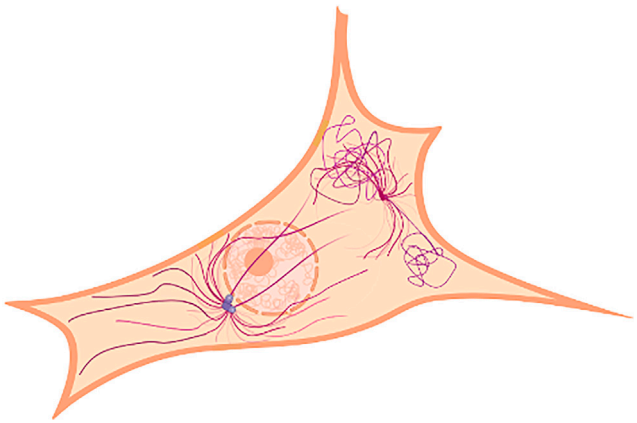

FIGURE 1 | Schematic representation of a centrosomal microtubule-organizing center tied to the nucleus and the microtubule organization proximal to the edge of a cell.

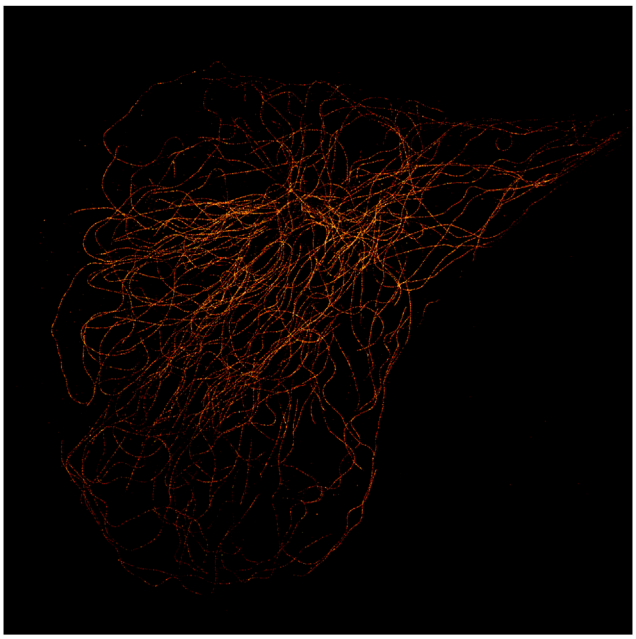

FIGURE 2 | MT STORM image of a control cell (Hs 578Bst cell line). α-Tubulin probed with mouse anti-human primary antibody and goat anti-mouse AlexaFluor 555 as the secondary antibody.

The hydrolysis of GTP bound to the E-site of β-tubulin into GDP is the key process that drives the MT conformational changes, leading the entire web toward rearrangements and generating mechanical strain on the microtubules [4, 5].

MTs stretch out from cellular structures called microtubule-organizing centers (MTOC) and extend toward the boundary of the cell. Centrosome-based MTOCs (cMTOC) were thought to be the most relevant centers organizing MTs until a recent paper [6] showed that in several animal cells they are neither the only nor the most relevant MTOCs, since they account for less than 10% of the overall MTs web. In these cells other cytoplasmatic sites, such as the Golgi bodies and other sites located in proximity of the cell boundary, were found to originate and organize MT bundles. This new fact sheds light on the MT network role and importance and is spurring new studies on the topic. **Figure 1** depicts an example of MTs organization, distribution, and density as it could be structured in a fibroblast. Even though MTOCs can be everywhere throughout the cell cytoplasm, the MT density in fibroblasts is unevenly distributed and generally higher in regions far from the cell boundaries. **Figure 2** shows the MT network of a cell taken from the control set of our experiment reconstructed by means of STORM imaging.

Treadmilling causes the MT web to transform and rearrange generating mechanical strain [5]. The dynamic instability between the phases of growth and shrinkage induces MTs to constantly bend and buckle that often results in MT lattice breaking, a type of event that, at a sufficiently high occurrence rate, affects many cellular activities, such as migration, motility, and chromosome segregation [7]. The MTs elastic properties are the physical factors that determine the way MT fibers respond to mechanical strain and stimuli. These properties ultimately are determined by the molecular structure of the filaments and it has been shown that any disruption that may interfere with the polymerization also alters the basic elastic characteristics of an MT (e.g., the Young modulus) thus changing its mechanical properties [8, 9]. MTs are involved in an extensive range of cellular processes such as intracellular transport, chromosome separation during mitosis, cell polarity, and morphogenesis tuning. MTs make up structural elements that control cilia and flagella. Since MTs are fundamental constituents of other cytoskeletal structures, such as the mitotic spindle involved in the cellular proliferation, they became a biological target for the treatment of cancer.

IRs are largely used for treating oncological pathologies because rapidly proliferating cancer cells are more sensitive than normal cells in relation to DNA damages. Nonetheless therapeutic protocols make use of different types of radiations, namely photons and protons, each one having different RBE [10–12].

RBE is measured from the dose response curve using an endpoint, namely the survival fraction, as a reference. The survival curve is usually fitted with a linear-quadratic mathematical model which is still today the most important tool in preclinical and clinical radiobiology. The interpretation of linear-quadratic model parameters could be strictly linked to DNA damages such as base damages or strand break [13]. However many could be considered as primary endpoints such as double strand breaks, chromosome aberrations, mutations, foci formation, and micronuclei formation which also fit the linear-quadratic relationship leading to the same RBE relationship as for cell survival [14].

It is a general assumption that, similarly to genomic DNA, macromolecules that play vital roles in the cell physiology are affected by IRs but less is known about the IR specific

effectiveness in damaging such structures. It can be argued that specific radiation types can have differential disruption efficacies that could lead to differential probabilities of cellular death [15, 16].

For example tumor cells irradiated with protons show a higher apoptotic rate than those irradiated with photons. Some studies suggest that proton irradiation might significantly impair the primary cancer cells step-up to the metastasis formation and in addition low-energy protons could comparatively be more effective than photons in inhibiting the metastatic cells migration [17]. For this reason when examining radiation effects on cellular growth the specific damages delivered to cytoskeletal structures ought to be taken into account.

It is well established that there are effects that are not related to the direct delivery of energy to the DNA of cells affected by radiation. These effects include signaling pathways that are not dependent on DNA damage, bystander responses, adaptive responses, low dose hypersensitivity, genomic instability, and the inverse dose-rate effect [18].

The aim of the present paper is to carry out a preliminary study of cytoskeletal microtubules as biological targets of IRs such as protons and X-rays. We irradiated with an 8 Gy single dose of either X-rays or protons since in unpublished data collected with atomic force microscopy we observed that significant cytoskeletal remodeling took place at about 8 Gy.

In the case of breast cancer the therapeutic approach includes the irradiation of non-cancer tissue bordered by the neoplastic resected masses. For this reason in the presented study we used the Hs 578Bst cell that comes from the normal breast tissue peripheral to an infiltrating ductal carcinoma and is the nearest cellular model to the breast epithelial tissue used in a conventional cell biology laboratory. We irradiated cells taken from the Hs 578Bst cell line and attempted an assessment of the induced modifications by comparing the MT networks density, distribution, and curvature using stochastic optical reconstruction microscopy (STORM).

MATERIALS AND METHODS

Cell Culture

Cells of the human breast cancer Hs 578Bst cell line were purchased from American Type Culture Collection (ATCC) in partnership with LGS standard. Hs 578Bst cells were cultivated on Hybrid Care Medium (ATCC), provided with 10% of fetal bovine serum (Invitrogen). Cells were incubated at 37°C in a humidified atmosphere at 5% CO_2. The cell culture dilution was carried out as soon as 90–100% of the cell dish bottom was covered, and the cell medium was refreshed every 48–72 h.

Sample Preparation and Irradiation

Before cell seeding and irradiation, the coverglasses (Marienfeld), 20 mm^2 wide and 1.5 mm thick, were sealed on the bottom of the cell dishes, in order to avoid them floating through the medium. The bottom was previously washed with PBS (Lonza) 1X, suitable for cell culture. The dishes were left open under the cabinet flow for about 30′ to dry them and to secure the coverglass sealing. After, the sealing cells were seeded homogeneously on the coverglass, at the concentration of 4,000 cells/ml. Cells were irradiated 24 h after this procedure was completed.

Proton Irradiation of Hs 578Bst Cell

Since the experimental set up of the proton irradiation facility required the dishes to be placed upright, they were completely filled with medium in order to keep the cells submerged. To prevent medium leaking, dishes were wrapped with parafilm®. Cells were irradiated at the Proton Therapy Center (Trento—Italy) with a 150 MeV proton beam and a dose rate of 1.2 Gy/min. The total dose delivered was 8 Gy without fractioning, a dose that corresponds to the center of the spread-out Bragg peak. The combination of a tantalum foil and a collimation system (made of PVC) ensured a homogeneous dose delivery into an area of 6 cm^2, significantly larger than the cell dish size [19]. After the irradiation, each sample was placed into an incubator suitable for cell culturing, waiting for the induced radioactivity to decay.

Hs 578Bst Cell Line X-Ray Irradiation

X-ray irradiation was done using an Xstrahl cabinet irradiator at the Trento Institute for Fundamental Physics and Applications facility. Single exposure 8 Gy doses were delivered at an applied voltage of 195 kVp. The cell dishes were placed on a rotating plate within the irradiator cabinet, so as to uniformly deliver the dose to the overall cell cultures.

Nanoscopy Imaging

Sample Preparation

After the sample irradiation procedure, cell medium was removed and samples were washed with PHEM 1.5X. After prefixation/denaturation with a mix of glutaraldehyde (Sigma) and triton (Sigma), cells were fixed with paraformaldehyde (Sigma) and glutaraldehyde (Sigma) for 10′ and then washed three times with PBS 1X (Sigma). After blocking with BSA (Invitrogen), cells were incubated with anti α-tubulin (Sigma) for 1 h at 37°C. The antibody was diluted in PBS with BSA at 1%. Following the primary hybridization, the samples were washed with PBS 1X, to get rid of antibody excess and incubated with secondary antibody [Alexafluo 555—(Sigma)] diluted in PBS 1X supplemented by BSA 1%. The reaction took 1 h at 37°C. Then the samples were washed with PBS 1X from the excess of the antibody mix solution and fixated with formaldehyde (Sigma) and again washed with PBS 1X. After the aldehyde reactions were blocked with NH4Cl, the samples were stocked at 4°C within sterile PBS 1X waiting for super resolution microscopy measurements.

Imaging

Samples were mounted with the SMART Kit buffer (Abbelight, Paris, France). The 3D STORM images were acquired using a SAFe360 module (Abbelight) coupled to an inverted bright-field Olympus IX71 microscope, equipped with a ×100 oil-immersion objective with a high numerical aperture (1.49 NA). This quad-view system (dual-cam sCMOS cameras, Orcaflash v4, Hamamatsu) provided 3D nanoscopy information with high isotropic localization precision (15 nm × 15 nm × 15 nm).

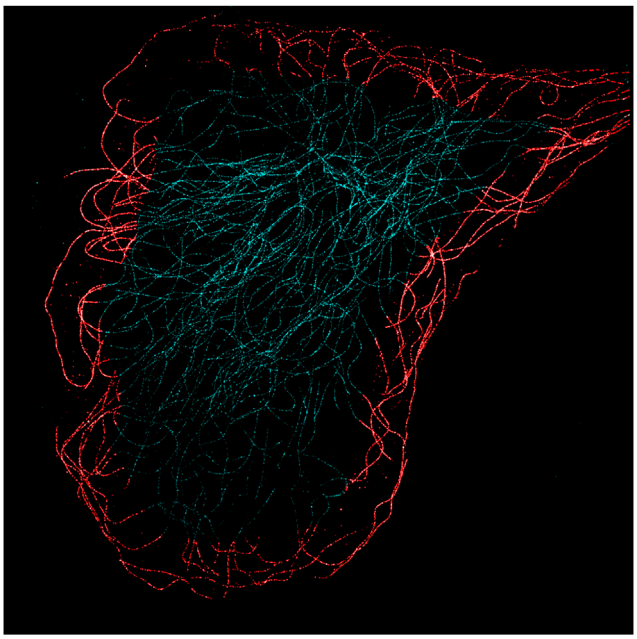

FIGURE 3 | MT STORM image of a control cell (Hs 578Bst cell line). The 4 μm annular band marked in red is the region selected to evaluate the MT occupancy and curvature.

Axial information was obtained by a technique named DAISY [20], coupling super-critical angle fluorescence (SAF) and strong astigmatism of the point spread function. Twenty-thousand frames at 50 ms were acquired to collect the single-molecule detections and reconstruct a nanoscopy image. The resulting coordinate tables and images were processed and analyzed using the SAFe NEO software (Abbelight).

Statistical and Data Analysis

STORM images were analyzed using the ImageJ software [21] to calculate the MT area occupancy. Control and irradiated groups were compared with one-way ANOVA and a Tukey statistical test. Filament reconstruction and MT curvature were calculated with the MATLAB® based SIFNE software [22]. Statistics and graphing were performed in MATLAB. For each population the Kolmogorov–Smirnov statistical test was performed on a subpopulation of 300 randomly extracted values.

RESULTS

The contribution of secondary radiation generated by the interaction between the proton beam and the experimental setup (Petri dish and culture medium) was estimated with a Monte Carlo Fluka simulation [14, 15] whose details are outside the scope of this paper. The simulation results showed this contribution to be negligible with respect to the dose delivered by the primary beam (secondary dose contribution <1%).

A comparison of the MT network structural organization between control and irradiated cells showed no observable MT ruptures. We estimated for each cell both the total and peripheral occupancy ratio of the MT network. The total occupancy ratio was calculated dividing the total MT network extension, measured as the number of MT-identified pixels, by the total area of the cell. The total area of the cell was estimated by counting the number of pixels contained in a polygonal region drawn as to accurately delimit the external boundary of the cell. The peripheral occupancy ratio was calculated dividing the MT network extension contained in an annular region along the cell boundary by the total MT network extension. The annular band of a cell was delimited on the outer edge by the polygon that contains the entire cell and, on the inner edge, by the same polygon rescaled by a factor suitable to have a ~4 μm width. **Figure 3** shows an example of such annular bands. The generally lower density of MTs near the cell boundaries and the smaller cellular thickness in such regions reduce the probability of MT overlapping and buckling thus enabling a more accurate identification and analysis of the fibers with SIFNE. **Table 1** summarizes the computed total and peripheral occupancy ratios.

The different occupancies are also evident in the 3D color visualization (supplemented material). The control cell shows a higher (**Supplementary Figure S1**) (green) region clearly located near the nucleus, a cell zone where the centrosomal microtubule-organizing center (cMTOC) is placed. Usually in proliferating (i.e., cancer cells) and not in differentiated cells the cMTOC is found in a similar cell site [17]. The MT network of control cells seems to originate from a specific point near the nucleus. On the contrary, in the irradiated samples it is not possible to recognize such organization and a different distribution is also demonstrated by a color map indicating different altitudes. Control and irradiated groups were compared with a one-way ANOVA test that showed no statistical difference in the total occupancy ratios ($p = 0.12$) but revealed a significant difference in the peripheral occupancy ratio when comparing the control and the irradiated groups ($p = 0.02$). The outcome of the former test was confirmed by a Tukey test which indicated significant differences between the control and proton irradiated groups ($p = 0.02$) as well as between the control and X-ray irradiated groups ($p = 0.03$). The same test rejected a difference between the two irradiated groups ($p = 0.88$). The second characteristic investigated was the MTs curvature. The molecular aspects of MT functions have been intensively studied, but how the global MT networks collectively contribute to the physical and biochemical attributes of cells has not been fully understood [8, 23]. Nonetheless, the potential importance of the latter is supported by emerging examples in which the physical properties of MTs directly participate in cellular physiology in a highly regulated manner [6, 24].

The analysis of microtubule bending, especially *in vivo*, may serve as a useful tool for measuring the net mechanical stress in different regions of the cell. In addition, microtubule buckling

TABLE 1 | Computed total and peripheral occupancy ratios.

(%)	Control	Protons	X-ray
Total occupancy ratio	21 ± 9	25 ± 12	7 ± 4
Peripheral occupancy ratio	54 ± 9	98 ± 20	92 ± 8

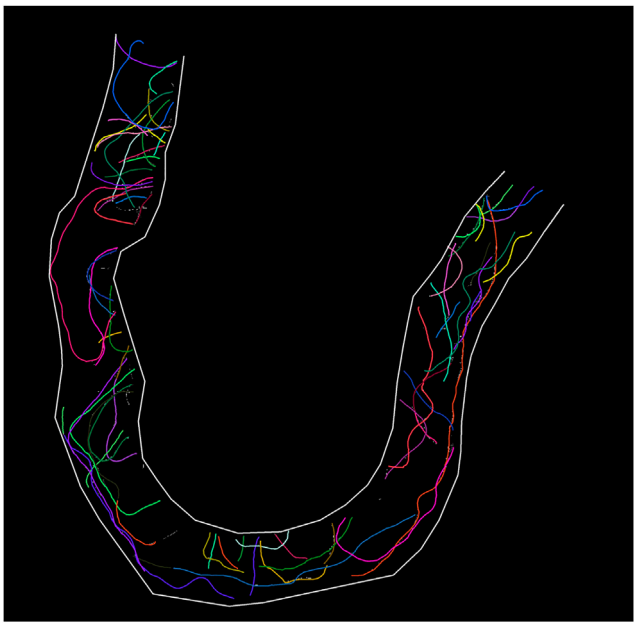

FIGURE 4 | Microtubule reconstructed filaments occupying the 4 μm band identified as the leading edge of the cell. MTs were reconstructed with the SIFNE software, using the cell shown in **Figure 3**.

near the cell edge suggests mechanical compression [25]. To analyze MT curvatures we used SIFNE software, to both reconstruct the MTs and calculate the curvature values of each selected filament [22].

We selected a sector of the annular band that encompassed the leading edge of the cell, where the curvatures of the MTs were more evident. In **Figure 4**, an example of the SIFNE-reconstructed MTs is displayed for the selected sector of a control cell. In migrating cells, the MT structure is polarized toward the direction where the cells are moving. In fibroblasts and endothelial cells, the centrosome and most MTs are oriented toward the leading edge [26]. Also epithelial cells have MTs oriented in such a way that plus ends are stretched toward the leading edge, where the MTs growth prevalently takes place [9, 27, 28].

We extracted from the SIFNE internal data structures the whole collection of single pixelwise (pw) curvature data in order to proceed with the computation of the mean values. Since the curvature average values were calculated out of the whole set of individual reconstructed MT pixels contained in the selected sector we disregarded the fact that filaments had in general been clipped by the selection of the region of interest. For each cell and for all reconstructed filaments the pw curvature values were computed [22]. In **Figure 5A** shows the distributions of the pixelwise curvature values of the control and of the X-ray irradiated cells while in **Figure 5B** the same distributions are shown for the control and proton irradiated cells. The pw curvature mean and standard deviation (SD) of each group are shown in **Table 2**.

TABLE 2 | Pixelwise curvature mean and standard deviation (SD) of each group.

Control (rad/mm)	Protons (rad/mm)	X-ray (rad/mm)
0.33 ± 0.48	0.35 ± 0.60	0.34 ± 0.49

These values in **Table 2** are in complete agreement with literature [29].

A pairwise comparison of the control group with the two irradiated groups based on the Kolmogorov-Smirnov test did not reveal statistical difference (p = 0.76 for the control/protons

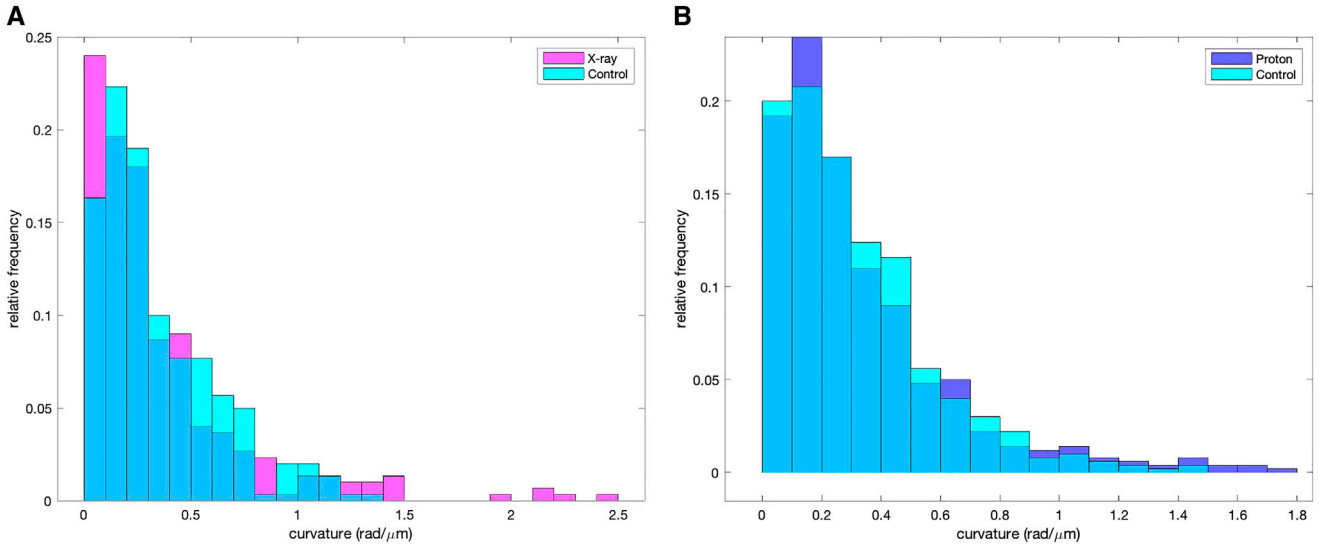

FIGURE 5 | Pixelwise curvature distribution of the reconstructed MTs of the control and the proton-irradiated samples **(A)**. Relative pixelwise curvature distributions of the reconstructed MTs of the control and X-ray irradiated samples **(B)**.

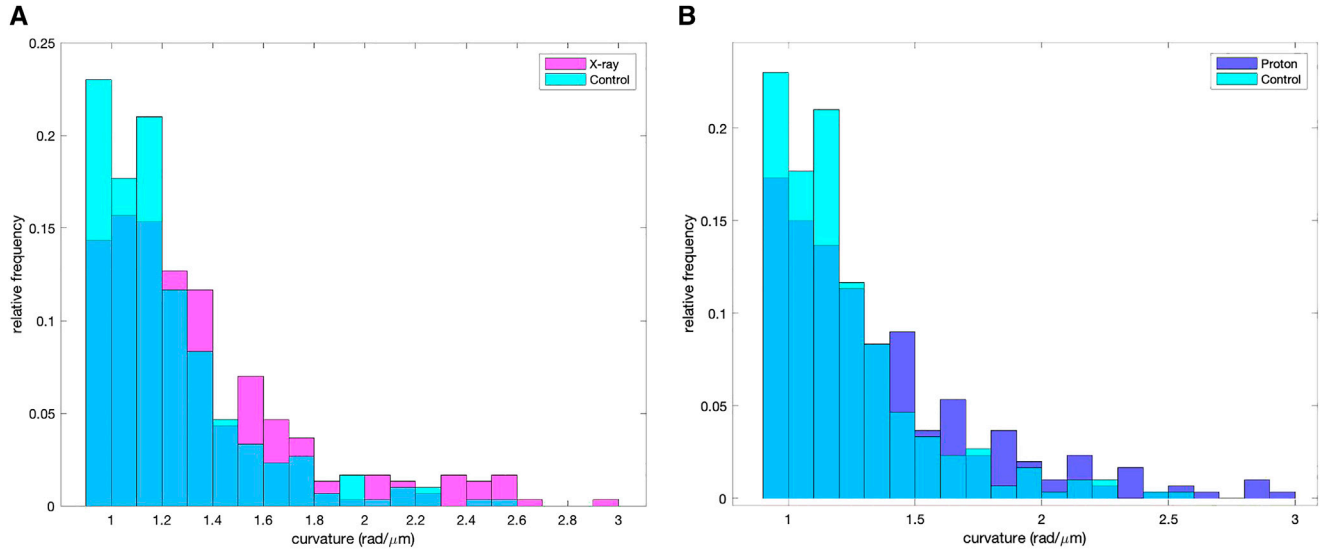

FIGURE 6 | Pixelwise curvature distribution of the reconstructed MTs for pixelwise curvature values >0.92 rad/μm. **(A)** Control and proton-irradiated samples, **(B)** control and X-ray irradiated samples.

comparison, $p = 0.23$ for control/X-ray comparison). We explain the lack of significant difference between the groups with the fact that the curvature distributions are highly concentrated at low values, as the median values of the curvatures were 0.27 rad/μm for the control group and ~0.25 rad/μm for both the irradiated groups. We then focused our attention on the high curvature values in the tail of the distributions limiting our analysis to values higher than 0.92 rad/μm (which delimits the 5% highest values in the control group). Some studies made quantitative analysis of the conditions that led to MT breaking [29] and showed an overall average curvature value of 0.39 rad/μm whereas MTs that eventually broke had a much higher average curvature of 1.5 rad/μm. Various processes contribute to bringing an MT into the curvature range that might lead to rupture, all of them affecting the molecular structure of the MT and reducing the tubule Young modulus. The modulation of the MT mechanical properties exerted by the association to external proteins is a possible mechanism that might account for the breaking of MTs in cells under compression and the interaction with kinesins could be the cause of molecular alterations that reduce the Young modulus [7]. We therefore restricted our analysis to the highest curvature value range to seek information about the fibers that might have undergone some process that degraded their pristine mechanical features.

The MT curvature distribution comparisons are shown in **Figure 6A** (control and X-ray irradiated groups) and in **Figure 6B** (control and proton irradiated groups). The Kolmogorov–Smirnov test on the high curvature distribution values shows a clear difference between control and proton-irradiated populations ($p = 6 \times 10^{-5}$) as well as between control and X-ray irradiated groups ($p = 7 \times 10^{-5}$). The same statistical test could not differentiate between protons and X-ray irradiated distributions ($p = 0.89$). Such high curvature distributions had a median value of 1.13 rad/μm for the control, 1.24 rad/μm for the proton-irradiated, and 1.23 rad/μm for the X-ray irradiated group.

DISCUSSION AND CONCLUSION

It is easy to notice that in the control cells the MTs do not evenly fill all the cell districts. The MT network seems to be more dense is some regions and, likewise, the percentage of MT-occupied areas varies when different cells are compared. Prior to cell fixation, if the cells were migrating toward a particular coverslip district, the MTs lattice and its web structure were constantly under modification and rearrangement. The observed variability is also due to the fact that we chose different cell morphologies to create a wider picture of the control cell MT distribution. Our analysis of the MT area occupancy revealed two findings correlated to the MTs distribution inside the cells. The first is connected to the MT density: the control and the proton-irradiated groups have the same MT area occupancy ratio, while cells irradiated with X-rays, show lower MT density values. Nevertheless the ANOVA test did not reveal any difference between the groups and, if any difference existed, a larger number of samples would have been needed in order to improve the statistical power of the test.

The second aspect is linked to the MTs distribution between control and irradiated groups. The Tukey test for the peripheral occupancy ratio indicated a significant difference between control and irradiated groups and no difference between the irradiated groups. The control indicates that the MTs are more concentrated into the central part of the cell while the irradiated groups exhibit a substantially constant density throughout. Proton and X-ray irradiations might have damaged, either directly or indirectly, the cMTOC pushing the cells toward a reorganization of the cMTOC sites. Cell cycle progression and cellular differentiation are associated

with a significant loss of centrosomal activities as well as its MTOC properties. As a consequence the reorganization of microtubules into non-centrosomal arrays is mandatory for cell life [30, 31]. A change in MT distributions, in particular in the case of proton-irradiated samples where the MT density did not change, could be a sign of MT severing or reorganization.

Concerning the MT curvature results and considering only curvatures higher than 0.92 rad/μm, we observe a significant difference between control and irradiated groups, with a significantly higher pw curvature median value. Because the curvature is strictly connected to the external mechanical stress and to the Young's modulus, these differences need to be investigated in detail in order to better understand the reasons why they occur. Higher compression could be a cause in the case of proton-irradiated cells, where the MTs density in that region is higher with respect to the control group. However this does not explain X-ray data, where the density is lower. Higher curvature could be a sign of change of the Young's modulus due to a modification of the intrinsic MT proprieties or an alteration in the MT surroundings, for example because of the presence of proteins binding to the MT molecular structure [32]. At this point, there could be many a speculation about the biological explanations for these findings also because many questions are still open [33].

In conclusion, results show that MTs respond in a similar way in the case of proton and X-ray irradiation, both in terms of MT peripheral occupancy and in terms of the change of MT curvature. Nevertheless, a larger number of cells is needed to create clearer statistical insight into MT total occupancy after X-ray or proton irradiations. Because of the MT dimensions, that are comparable with DNA, and given the self-repairing and self-healing capabilities of MTs, MTs could be a promising biological target for IRs. Unlike DNA, which is located in the nucleus of the cell, the MT network is distributed throughout the cell therefore it can be an indicator of possible damages that may occur alongside the cell edge as well as in the area near the nucleus.

DATA AVAILABILITY STATEMENT

The raw data supporting the conclusions of this article will be made available by the authors, without undue reservation.

AUTHOR CONTRIBUTIONS

LB, MM, FR, EG, VC, and SC. SC and LB conceived the presented work; LB carried out the experiments; SC performed data analysis; FR attended the brainstorming about the biological implications; EO performed the Fluka simulations; VC performed STORM measurements together with SC and LB; MM discussed the results giving contribute to data analysis and to the final version of the manuscript.

FUNDING

Museo Storico della Fisica e Centro Studi e Ricerche Enrico Fermi, Rome, Italy supported this research with a grant. The publication costs of the manuscript have been supported by the Italian Ministry for Education University and Research, PRIN 2017, Grant # 2017T8CMCY.

ACKNOWLEDGMENTS

We would like to warmly thank Prof Vincenzo Patera (Università degli Studi di Roma, La Sapienza) and Dr Michela Marafini (Università degli Studi di Roma—La Sapienza and Museo Storico della Fisica e Centro Studi e Ricerche Enrico Fermi) for the Fluka simulations. We would like to thank Prof Francesco Tommasino, Dr. Emanuele Scifoni, and Dr. Enrico Verroi for supporting us over the course of X-ray and protons irradiations at TIFPA—Trento Institute for Fundamental Physic and Applications and Proton Therapy Center—Trento. We would like to thank Prof. Giuseppe Pedrazzi (University of Parma) for their contribution to the statistical analysis.

SUPPLEMENTARY MATERIAL

The Supplementary Material for this article can be found online at: https://www.frontiersin.org/articles/10.3389/fphy.2020.579081/full#supplementary-material

REFERENCES

1. Ohi R, Zanic M. Ahead of the curve: new insights into microtubule dynamics, *F1000Res* (2016) 5:314. doi:10.12688/f1000research.7439.1
2. Manka SW, Moores CA. Microtubule structure by cryo-EM: snapshots of dynamic instability. *Essays Biochem* (2018) 62:737–51. doi:10.1042/EBC20180031.
3. Van Steenbergen V, Boesmans W, Li Z, de Coene Y, Vints K, Baatsen P, et al. Molecular understanding of label-free second harmonic imaging of microtubules. *Nat Commun* (2019) 10:3530. doi:10.1038/s41467-019-11463-8.
4. Alushin GM, Lander GC, Kellogg EH, Zhang R, Baker D, Nogales E. High-resolution microtubule structures reveal the structural transitions in αβ-tubulin upon GTP hydrolysis. *Cell* (2014) 157:1117–29. doi:10.1016/j.cell.2014.03.053.
5. Schaedel L, John K, Gaillard J, Nachury MV, Blanchoin L, Théry M. Microtubules self-repair in response to mechanical stress. *Nat Mater* (2015) 14:1156–63. doi:10.1038/nmat4396.
6. Karsenti E, Nédélec F, Surrey T. Modelling microtubule patterns. *Nat Cell Biol* (2006) 8:1204–11. doi:10.1038/ncb1498.
7. Kabir AMR, Sada K, Kakugo A. Breaking of buckled microtubules is mediated by kinesins. *Biochem Biophys Res Commun* (2020) 524:249–54. doi:10.1016/j.bbrc.2020.01.082.
8. Vorobjev IA, Svitkina TM, Borisy GG. Cytoplasmic assembly of microtubules in cultured cells. *J Cell Sci* (1997) 110(Pt 21):2635–45.
9. Waterman-Storer CM, Salmon ED. Actomyosin-based retrograde flow of microtubules in the Lamella of migrating epithelial cells influences microtubule dynamic instability and turnover and is associated with microtubule breakage and treadmilling. *J Cell Biol* (1997) 139:417–34. doi:10.1083/jcb.139.2.417.
10. Zhang X, Lin SH, Fang B, Gillin M, Mohan R, Chang JY. Therapy-resistant cancer stem cells have differing sensitivity to photon versus proton beam radiation. *J Thorac Oncol* (2013) 8:1484–91. doi:10.1097/JTO.0b013e3182a5fdcb.
11. Durante M. New challenges in high-energy particle radiobiology. *Br J Radiol* (2014) 87:20130626. doi:10.1259/bjr.20130626.

12. Tommasino F, Durante M. Proton radiobiology. *Cancers* (2015) 7:353–81. doi:10.3390/cancers7010353.
13. McMahon SJ. The linear quadratic model: usage, interpretation and challenges. *Phys Med Biol* (2018) 64:01TR01. doi:10.1088/1361-6560/aaf26a.
14. Paganetti H. Relative biological effectiveness (RBE) values for proton beam therapy. Variations as a function of biological endpoint, dose, and linear energy transfer. *Phys Med Biol* (2014) 59:R419–72. doi:10.1088/0031-9155/59/22/R419.
15. Reisz JA, Bansal N, Qian J, Zhao W, Furdui CM. Effects of ionizing radiation on biological molecules-mechanisms of damage and emerging methods of detection. *Antioxidants Redox Signal* (2014) 21:260–92. doi:10.1089/ars.2013.5489.
16. Niemantsverdriet M, van Goethem M-J, Bron R, Hogewerf W, Brandenburg S, Langendijk JA, et al. High and low LET radiation differentially induce normal tissue damage signals. *Int J Radiat Oncol Biol Phys* (2012) 83:1291–7. doi:10.1016/j.ijrobp.2011.09.057.
17. Jasińska-Konior K, Pochylczuk K, Czajka E, Michalik M, Romanowska-Dixon B, Swakoń J, et al. Proton beam irradiation inhibits the migration of melanoma cells. *PLoS ONE* (2017) 12:e0186002. doi:10.1371/journal.pone.0186002.
18. Prise KM, Schettino G, Folkard M, Held KD. New insights on cell death from radiation exposure. *Lancet Oncol* (2005) 6:520–8. doi:10.1016/S1470-2045(05)70246-1.
19. Tommasino F, Rovituso M, Bortoli E, La Tessa C, Petringa G, Lorentini S, et al. A new facility for proton radiobiology at the Trento proton therapy centre: design and implementation. *Phys Med* (2019) 58:99–106. doi:10.1016/j.ejmp.2019.02.001.
20. Cabriel C, Bourg N, Jouchet P, Dupuis G, Leterrier C, Baron A, et al. Combining 3D single molecule localization strategies for reproducible bioimaging. *Nat Commun* (2019) 10:1980. doi:10.1038/s41467-019-09901-8.
21. Rasband WS. *ImageJ*. Available at: https://imagej.nih.gov/ij/ (2019) 1997–2018.
22. Zhang Z, Nishimura Y, Kanchanawong P. Extracting microtubule networks from superresolution single-molecule localization microscopy data. *MBoC* (2017) 28:333–45. doi:10.1091/mbc.e16-06-0421.
23. Vasileva E, Citi S. The role of microtubules in the regulation of epithelial junctions. *Tissue Barriers* (2018) 6:1539596. doi:10.1080/21688370.2018.1539596.
24. Ando D, Korabel N, Huang KC, Gopinathan A. Cytoskeletal network morphology regulates intracellular transport dynamics. *Biophys J* (2015) 109:1574–82. doi:10.1016/j.bpj.2015.08.034.
25. Bouchet BP, Akhmanova A. Microtubules in 3D cell motility. *J Cell Sci* (2017) 130:39–50. doi:10.1242/jcs.189431.
26. Wittmann T, Waterman-Storer CM. Cell motility: can Rho GTPases and microtubules point the way?. *J Cell Sci* (2001) 114:3795–803.
27. Wadsworth P. Regional regulation of microtubule dynamics in polarized, motile cells. *Cell Motil Cytoskeleton* (1999) 42:48–59. doi:10.1002/(SICI)1097-0169(1999)42:1<48::AID-CM5>3.0.CO;2-8
28. Ballestrem C, Wehrle-Haller B, Hinz B, Imhof BA. Actin-dependent lamellipodia formation and microtubule-dependent tail retraction control-directed cell migration. *MBoC* (2000) 11:2999–3012. doi:10.1091/mbc.11.9.2999.
29. Odde DJ, Ma L, Briggs AH, DeMarco A, Kirschner MW. Microtubule bending and breaking in living fibroblast cells. *J Cell Sci* (1999) 112(Pt 19):3283–8.
30. Muroyama A, Lechler T. Microtubule organization, dynamics and functions in differentiated cells. *Development* (2017) 144:3012–21. doi:10.1242/dev.153171.
31. Wu J, Akhmanova A. Microtubule-organizing centers. *Annu Rev Cell Dev Biol* (2017) 33:51–75. doi:10.1146/annurev-cellbio-100616-060615.
32. VanBuren V, Cassimeris L, Odde DJ. Mechanochemical model of microtubule structure and self-assembly kinetics. *Biophys J* (2005) 89:2911–26. doi:10.1529/biophysj.105.060913.
33. Bailey M, Conway L, Gramlich MW, Hawkins TL, Ross JL. Modern methods to interrogate microtubule dynamics. *Integr. Biol* (2013) 5:1324. doi:10.1039/c3ib40124c.

Conflict of Interest: The authors declare that the research was conducted in the absence of any commercial or financial relationships that could be construed as a potential conflict of interest.

frontiers in Physics

ORIGINAL RESEARCH
published: 18 November 2020
doi: 10.3389/fphy.2020.568176

Calculation of the Beam-Modulation Effect of the Lung in Carbon Ion and Proton Therapy With Deterministic Pencil Beam Algorithms

*Toke Printz Ringbæk[1,2], Alina Santiago[1,2,3], Leszek Grzanka[4], Kilian Baumann[1,5], Veronika Flatten[1,5], Rita Engenhart-Cabillic[1,3], Niels Bassler[6,7,8], Klemens Zink[3,5] and Uli Weber[9]**

[1]Department of Radiotherapy and Radiation Oncology, Philipps-University, Marburg, Germany, [2]Department of Radiotherapy, University Hospital Essen, Essen, Germany, [3]Department of Radiotherapy and Radiation Oncology, University Medical Center, Gießen and Marburg, Giessen, Germany, [4]Institute of Nuclear Physics, Polish Academy of Sciences, Krakow, Poland, [5]University of Applied Science, Gießen-Friedberg, Giessen, Germany, [6]Department of Physics, Medical Radiation Physics, Stockholm University, Stockholm, Sweden, [7]Department of Oncology and Pathology, Medical Radiation Physics, Karolinska Institute, Stockholm, Sweden, [8]Department of Experimental Clinical Oncology, Aarhus University Hospital, Aarhus, Denmark, [9]GSI Helmholtzzentrum für Schwerionenforschung, Darmstadt, Germany

OPEN ACCESS

Edited by:
Yolanda Prezado,
INSERM U1021 Signalisation normale et pathologique de l'embryon aux thérapies innovantes des cancers, France

Reviewed by:
Kevin Souris,
Catholic University of Louvain, Belgium
Urszula Jelen,
Ingham Institute of Applied Medical Research, Australia

***Correspondence:**
Uli Weber
U.Weber@gsi.de

Specialty section:
This article was submitted to Medical Physics and Imaging, a section of the journal Frontiers in Physics

Received: 31 May 2020
Accepted: 14 October 2020
Published: 18 November 2020

Citation:
Ringbæk TP, Santiago A, Grzanka L, Baumann K, Flatten V, Engenhart-Cabillic R, Bassler N, Zink K and Weber U (2020) Calculation of the Beam-Modulation Effect of the Lung in Carbon Ion and Proton Therapy With Deterministic Pencil Beam Algorithms. Front. Phys. 8:568176. doi: 10.3389/fphy.2020.568176

Ion beams passing through lung tissue show more pronounced energy straggling than expected for solid materials of the same thickness. Energy straggling in active scanning particle therapy can enlarge the pencil beam Bragg peaks in-depth as well as displace them, deteriorating the dose coverage of a target within the lung. While this is not yet considered in any known treatment planning system, we implement a mathematical model to be used for treatment planning, using TRiP98, which relies on a deterministic pencil beam algorithm. Through a randomization process based on a continuous Poisson probability distribution, the HU values of lung voxels are replaced with a modified value in successive iterations. The beam-modulation effect of the lung can thus be taken into account in treatment planning by recalculating the dose n times for n randomized CTs using the raster scan file of a plan that was optimized on the nonmodulated CT. The evaluation follows by averaging the resulting n dose distributions and comparing to the corresponding nonmodulated dose distribution, attending at dosimetric indices and dose-volume histograms. In this work, the functionality of these routines was tested for proton and carbon ion plans for two selected lung cancer patient cases with deep-seated tumors, showing that, with existing standard tools, it is possible to calculate the beam-modulation effect of the lung in TRiP98 in a transparent way. Variable model parameters, such as modulation power, voxel size and density voxel selection range, were evaluated. Furthermore, a systematic study for spherical geometries in a lung tissue CT cube is presented to investigate general trends.

Keywords: ion beam therapy, particle therapy, proton therapy, lung cancer, treatment planning, pencil beam scanning

1. INTRODUCTION

With the dose deposited locally in the energy-dependent narrow Bragg peak (BP) after which little-to-no-dose is given, particle therapy offers potentially more conformal treatments, as compared to photon irradiation, with improved normal tissue sparing. In particular with the pencil beam scanning method, where the lateral beam displacement is done by magnets and the range of each BP is changed by modulating the beam energy, a more conformal dose delivery, with fewer field directions, can be achieved compared to photons [1, 2].

Due to the porous nature of the lung, ion beams passing through a lung (or lung substitute material) show a more pronounced energy straggling than for solid materials [3, 4]. A substantial broadening of the BP shape has been found when irradiating lung tissue [5, 6]. So far, current treatment planning systems (TPS) assume no additional BP broadening due to tissue heterogeneities. Ordinary planning CT images cannot capture this beam-modulation effect of the lung since the CT voxel size spatially undersamples the microscopic lung alveoli. However, the beam-modulation effect of the lung could be of clinical relevance for lung tumor treatments, which motivates this study. If this broadening effect is not taken into consideration, it can potentially lead to an undesired inhomogeneity in the dose distribution, underdosage of the planning target volume (PTV) and overdosage of the healthy surrounding normal tissue, especially in the distal region close to the PTV [3, 7].

Through the use of a 3D printed binary voxel model (the voxels in the geometry are either composed by air or by the printing plastic material) the BP degradation of lung irradiation for protons has been shown to cause for initial beam energies of 140 and 200 MeV an increase of up to 60% for the 80–20% distal beam fall-off as compared to the unperturbed reference curve [5]. Using a similar binary voxel model, a mathematical method for estimating the broadening effect of a porous material has been developed [4, 6, 8]. The degree of this broadening depends on the average size of the microscopic structures as well as on the material density and thickness. For materials with a fine ($< 500\ \mu m$) and homogeneous microscopic structure, the BP enlargement has been shown to be well-described by a modulation of the unperturbed reference Bragg curve for water with a normal distribution and its sigma as a parameter for the strength of the modulation effect.

Treatment planning studies investigating the effects on the dose uncertainties in treatment plans of lung cancer patients are limited to a few published works. Flatten et al. [9] investigated the effects of the BP degradation in proton beams by using CT phantoms with spherical targets of variable sizes placed at different depths in the lung. The lung modulation has been implemented in the TOPAS Monte Carlo tool [6] using sets of modulated DICOM images. It was shown that the underdosage of the target volume, due to the BP degradation, increases with an increasing depth of the tumor in lung and a decreasing tumor volume. In a further study by the same group [10] the effects were investigated on proton treatment plans of lung cancer patients. It was found that the maximum underdosage of the target volume due to the BP degradation was in the order of 5% while the average underdosage was roughly 2%. In another study [11] the effects on clinical treatment plans in proton beams were investigated using an analytical approach: Instead of using sets of modulated DICOM images and Monte Carlo tools, the pristine proton BPs were convolved using the MatRad toolkit [12] with several superimposed normal distributions of sigma values defined by certain modulation power values of the lung tissue. The underdosage of the target volumes was comparable to the results from Baumann [6]. However, to the best of our knowledge, there are no studies investigating the modulation effects for treatment planning with carbon ion beams. For carbon ion beams a more pronounced modulation effect is expected, because of the much sharper carbon BPs compared to protons. The lack of a carbon ion TPS for carbon ion beams that can calculate the lung modulation effect was a main motivation for this work.

To take the lung modulation effect into account directly, the CT resolution is crucial [5]. The resolution of a clinical CT image used for treatment planning is typically around 1 mm but the biological porous structure of the lung leading to the modulation is in the μm range. To work with CTs with μm resolution, assuming such images can be obtained, would lead to an impractically large data array and time increase in the handling of the DICOM data. The method presented in this work bypasses this problem.

The aim of the present work is to show that, with existing deterministic pencil beam dose calculation algorithms like the one in TRIP98 [13–15], it is possible to calculate the beam-modulation effect of the lung tissue. Here the term, "deterministic" applies to dose calculation algorithms with analytical functions that describe a 3D pencil beam dose distribution and deliver reproducible results without random seeds. TRiP98 is a treatment planning system that was developed for research and patient treatment at the Helmholtzzentrum für Schwerionenforschung, Darmstadt, Germany (GSI). It was used to treat 440 patients during the GSI pilot project. The basic algorithms and the pencil beam model of TRIP98 were implemented into the carbon ion planning module of the Siemens Syngo PT TPS [16] that is currently used at the ion beam facilities in Heidelberg (HIT), Marburg (MIT), Shanghai (SPHIC) and Pavia (CNAO). Although we are using a deterministic pencil beam dose calculation, the results of the procedure cannot be considered entirely deterministic because the sampling of the HU values is done with random functions.

The beam-modulation effect calculation is done by implementing a mathematical model based on a continuous Poisson probability distribution within the open-source PyTRiP tool [17]. Through a randomization process, the HU value of each selected lung voxel is changed into a modified value. The lung beam-modulation effect on patient treatment plans can then be estimated by recalculating the dose n times for n randomized CTs, using raster scan files for plans optimized on nonmodulated CTs and afterward averaging the n dose distributions. Thus the result can be compared to the corresponding nonmodulated dose distribution. Using spherical PTV geometries and two selected patient cases, we evaluated a number of different model and planning parameters to show their respective relevance in terms of PTV coverage deterioration as a result of the lung modulation effect for carbon ion as well as for proton plans.

2. MATERIALS AND METHODS

2.1. Treatment Planning System TRiP98 and Python Package PyTRiP98

All treatment plans were calculated using the ion TPS TRiP98 [13–15].

In former studies [18, 19], facility-specific baseline data, including depth-dose distributions and lateral profiles, were generated with SHIELD-HIT12A [20] for both carbon ions and protons.

PyTRiP [17, 21] is an open-source python package for, among other purposes, facilitating the work with TRiP98 and with TRiP native files. PyTRiP can import, export, convert and modify such files and execute TRiP98 locally or remotely. PyTRiP enables scripting large parameter studies of treatment plans and more advanced and automatized (programmable) manipulation than what a commercial TPS usually allows. PyTRiP handles the CT and planning contour files, as well as dose cubes from calculated plans and permits extensive manipulation on these objects, making it possible to randomize n CTs, recompute a plan on each of them and average all the calculated dose cubes.

The presented concept follows Baumann et al. [6] but is done in a fully automated and integrated environment and works for a standard pencil beam algorithm.

2.2. Mathematical Implementation of CT Randomization

For each investigated planning case, first a treatment plan on the unmodified planning CT is calculated, producing a raster scan file for each case. Afterward, a dose recalculation, using these raster scan files, is done n times following the mathematical method described below. This is based on the "binary voxel model" for porous targets, where the target is divided into high and low density voxels, which each traversing particle will hit with probabilities of p and (1-p), respectively, [4, 6]. The probability for hitting k voxels with high density is thus given by a binomial distribution, which, for a large number of voxels, can be approximated by a normal distribution. While this normal distribution can be subsequently used to modulate the individual PBs, here we will modify the CT voxels of a certain volume of interest (VOI), in this case the ipsilateral lung $\mathrm{VOI_{lung}}$.

First the tissue density in each voxel of the CT image is calculated using the standard HU conversion table of TRiP98. Then, the voxels of $\mathrm{VOI_{lung}}$ (within a user-defined density range ρ_{range} from ρ_{min} to ρ_{max}) are selected and defined as the voxels to be modulated. The modulation power $\mathrm{P_{mod}}$ as defined prior is a good estimation for the strength of the lung modulation effect [4, 6, 8–10] and given as a second user-defined input parameter:

$$P_{mod} = \frac{\sigma^2}{t} \tag{1}$$

with σ being the Gaussian sigma from the normal distribution and t the mean water-equivalent path length. The larger the value of P_{mod}, the broader the BP and the wider its distal fall-off.

Both parameters ρ_{range} and P_{mod} are discussed in more detail below and are investigated within this work.

The water-equivalent voxel length $t = \rho_{\mathrm{H_2O}} \cdot d$ is then calculated for each individual voxel, where d is the voxel size and $\rho_{\mathrm{H_2O}}$ is the water-equivalent density of the given voxel. For the case that the beam is parallel to one of the three CT axes, d is simply assigned as either d_x, d_y, or d_z, being the voxel length in the x-, y- and z-directions, respectively. If the beam direction is oblique, then the intersection lengths through each voxel can differ much from each other. We found that for our model, d can be well described by:

$$d = \left[\left(\frac{n_x}{d_x}\right)^{\frac{3}{2}} + \left(\frac{n_y}{d_y}\right)^{\frac{3}{2}} + \left(\frac{n_z}{d_z}\right)^{\frac{3}{2}}\right]^{-\frac{2}{3}} \tag{2}$$

where $n = (n_x, n_y, n_z)$ is the normalized direction vector parallel to the beam. This formula approximates the mean-quadratic length divided by the mean length of the intersection pieces, (averaged over many shifted beams and voxels) and was tested with a simple ray-tracing program.

In each of the n runs the following procedure is performed for all selected lung voxels. The water-equivalent path length through the voxel is randomized corresponding to P_{mod}. The first approach would be a sampling by a Gaussian distribution with a width $\sigma = (P_{\mathrm{mod}} \cdot d \cdot \rho_{H_2O})^{1/2}$ around the water equivalent density $\rho_{\mathrm{H_2O}}$ of the individual voxel. However, such a Gaussian density distribution, for voxel sizes in the millimeter range, has a relevant contribution in the negative range (for details, see Ref. 6), which must be corrected by an adapted distribution with a singular weight at $\rho_{\mathrm{H_2O}} = 0$. This is in accordance to the above mentioned binary voxel model and the corresponding Poisson distribution $P(n)$, which describes the discrete probability distribution for hitting n non-void voxels when traversing a row of the binary voxels. However, since a discrete Poisson distribution cannot be applied here, a continuous Poisson distribution for the water-equivalent thickness t' was chosen instead:

$$P\left(t'; t, P_{mod}\right) = A_0\delta(x) + \frac{1-A_0}{\delta}\exp\left(\frac{\log(\lambda)t'}{\delta} - \lambda - \ln\Gamma\left(\frac{t'}{\delta}+1\right)\right)$$

$$\delta = \delta(t, P_{mod}); \lambda = \lambda(t, P_{mod}); A_0 = A_0(t, P_{mod}) \tag{3}$$

The delta-Dirac function $\delta(x)$ adds the aforesaid singular weight for $t' = 0$ (**Figure 1**). The gamma function replaces the factorial function normally occurring in a non-continuous Poisson distribution for non-integers in order to generalize the formula into the continuous Poisson distribution. The distribution parameters, δ, λ and A_0, depend on the nonmodulated values t and the modulation power P_{mod}. The dependencies were calculated for 30 different values for P_{mod}, from 0.1 to 0.8 mm, and for 40 different t values, from 0.1 to 2.0, and interpolation between the matrix elements in these pre-calculated matrices were used to obtain other values. The mathematical principle behind these calculations are given in the subsection below.

For the density sampling of the individual voxels with an initial density ρ_{H_2O} and (mean) size d the following density distribution is then applied:

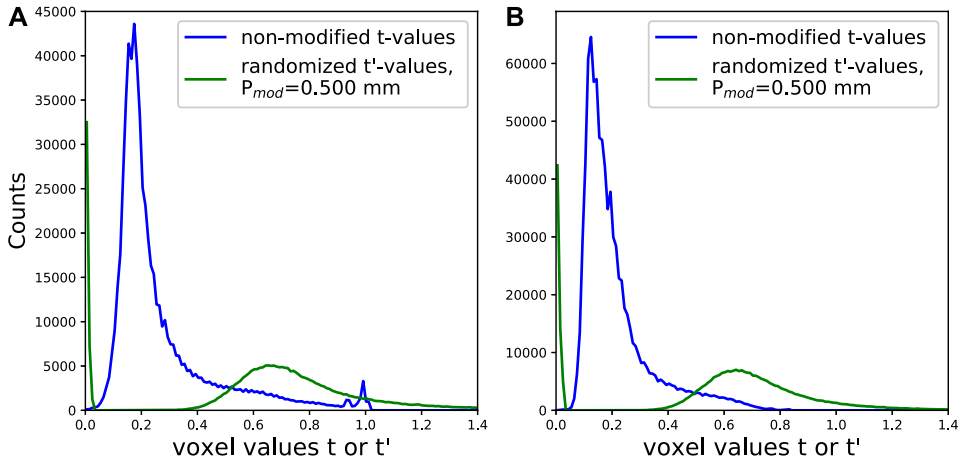

FIGURE 1 | Histogram of the WEPL voxel values in the beam direction of the original CT (*t* values in blue) and after application of the randomization voxel modulation routine (*t′* values in green) for **(A)** patient P1, and **(B)** P2, with respectively large and small PTV sizes (for details, see patient selection subsection). The bins at $t' = 0$ for the modulated functions are divided by 10 not to dilute the plot. VOI_{lung} was equal to all voxels in the ipsilateral lung, meaning no ρ_{range} parameter value was used.

$$\tilde{P}(\rho'_{H_2O}) = P(t' = d \cdot \rho_{H_2O}; \delta, \lambda, A_{0)} \tag{4}$$

At the end HU(ρ') for all selected voxels are found using the previously loaded lookup-table and a final randomized (henceforth called "modified") CT, usable in TRiP98 for dose computation, is obtained. By recalculating the dose n times on n different modified CTs and averaging these n dose cubes, one obtains a dose distribution that takes the beam-modulation effect of the lung into account. This can then be compared to the original plan dose distribution.

In comparison to the previous work [6], where $P(t')$ was individually optimized as a discrete function for each density value and each P_{mod}, the method presented here is much faster and can be easily reproduced with the provided tables [22]. By simultaneously calculating on 24 CPUs, for $n = 100$, the whole recalculation procedure lasted 15–20 min when using the TRiP dose calculation algorithm "all-point" and 50–100 min when using the more complex "multiple scattering" algorithm [23].

2.2.1. Calculation of the Poisson Distribution Parameters

The mathematical principle for the calculation of the tables of the Poisson distribution $P(t')$ parameters $\delta(t, P_{\mathrm{mod}})$, $\lambda(t, P_{\mathrm{mod}})$ and $A_0(t, P_{\mathrm{mod}})$ is that these parameters were adapted such that when folding $P(t')$ N times by itself, the resulting distribution best fits the Gaussian distribution for the total path length $N \cdot t$ and P_{mod}:

$$\underbrace{P(t';\delta,\lambda,A_0) * \mathrm{P}(t';\delta,\lambda,A_0) * \ \ldots\ * \mathrm{P}(t';\delta,\lambda,A_0)}_{\mathrm{N\ times}} = C\exp\left(\frac{-(t'-Nt)^2}{2\sigma^2}\right) \tag{5}$$

N is chosen as a value large enough (typically 10), that the contribution of the negative part of the Gaussian distribution (right term in **Eq. 5**) becomes negligible. The idea behind this concept is that $P(t')$ substitutes the Gaussian distribution, avoiding non-physical negative contributions for the density distribution in the single voxels. The tables for $\delta(t, P_{\mathrm{mod}})$, $\lambda(t, P_{\mathrm{mod}})$ and $A_0(t, P_{\mathrm{mod}})$ and the scripts for their calculation can be downloaded from Mendeley [22].

2.2.2. Benchmark With an Analytical Convolution

Our PyTRiP routine was tested against our well-established analytical convolution method [6] (which has been confirmed experimentally [4, 8]) for 130 and 230 MeV/u carbon ion beams. For this test we used $n = 60$, $P_{\mathrm{mod}} = 0.500$ mm and ρ_{range} from 0.1 to 0.5 g/cm^3 to calculate the modified doses. A lung tissue cube with constant HU of −741 HU [24] and a length of 15 cm in the beam direction was placed within a water phantom, starting at 3 cm water phantom depth z. For each depth value z of the modulated curve the pristine depth-dose curve (in water equivalent scale) was individually convoluted by a Gaussian filter, with a σ-value given as $(t \cdot P_{\mathrm{mod}})^{1/2}$, where t is the water equivalent thickness of the lung tissue in the beam path up to the depth z.

The comparisons of the Bragg curves can bee seen in **Figure 2**. The agreement between the analytical curves and the curves from our PyTRiP routine is clearly seen.

2.2.3. Lung Voxel Selection Range

When selecting the VOI_{lung} voxels to be randomized, instead of using all voxels in the lung, we implemented a voxel selection by a user-defined density range ρ_{range}. By using all lung voxels, one would end up modulating a case-specific variable number of non-porous voxels such as massive vessels.

We adopted values of ρ_{range} from 0.1 to 0.5 g/cm^3 using experimental data from an inflatable pig lung set-up [4, 6, 8]

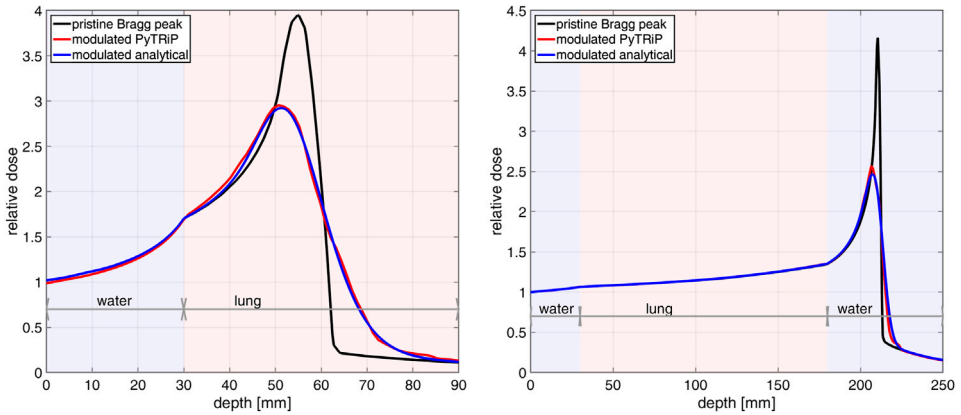

FIGURE 2 | Modulation effect of the lung tissue for a 130 MeV/u **(left)** and a 230 MeV/u **(right)** carbon ion beam. The curves compare the analytically modulated Bragg curves (blue) vs. the Bragg curves modulated by PyTRiP (red) for a 15 cm lung cube starting at 3 cm inside a water phantom.

and visually analyzing the CT slices of our two patient cases and the density values of different structures observed within the lung. It is assumed that voxels within this range are lung voxels as well as any edge voxel that consists half of air and half of tissue. Both of these can lead to a modulation effect. In addition to this preselected range, we evaluated the effect on the patient plans when varying ρ_{range}.

2.3. Study of Spherical Planning Geometries

For a systematic analysis of the modulation effect as a function of the isocenter depth d_{ic} (placed at the PTV center) and the target size, plans for simulated spherical geometries were calculated for carbon ions. The spheres, composed of water, were placed within a cubic CT phantom, containing only voxels with a constant single Hounsfield unit value of −741, representing the lung environment [24].

First, a sphere of a constant 17 mm radius was placed at variable d_{ic} values of 40, 70, 100, 125, 150, 175, 200, 225, 250, and 260 mm. Second, spheres with variable radii, from 8 to 15 mm in steps of 1 mm, from 17 to 25 mm in steps of 2 mm, and of 28 mm, were placed at a constant d_{ic} = 100 mm.

For the sphere planning study, n = 100 and P_{mod} = 0.400 mm were used and all lung voxels were taken into account for the modulation. All plans were single field plans with the beam parallel to the z-axis. A 2 × 2 mm^2 lateral grid, a 3 mm depth step size and a lateral contour extension of 0.7·FWHM$_{\text{iso}}$ were used. All plans where optimized for the physical dose with the "ap"-algorithm. At d_{ic} = 40 mm, a 4 mm bolus was required.

2.4. Patient Selection and Planning

Two lung cancer patient cases, henceforth called P1 and P2, with different PTV volumes V_{PTV} and locations were selected. They were originally treated with photons at the university hospital in Marburg. For P1 the PTV is deep-seated and located close to the spine, whereas the PTV for P2 is centrally located. For both cases, the tumors are not close to the thorax wall, as some distance in the lung is required for the degradation effect. The PTVs were sufficiently small as to not drastically decrease the lung volume to be modulated. The isocenter slice of both patient geometries, P1 and P2, is given in **Figure 3**, showing for each patient case the PTV position and an exemplary dose distribution calculated on the non-modulated CTs.

Multiple plans for each of the two patients were created for protons as well as for carbon ions, focusing on the latter. For each nonmodulated case (planned on the nonmodulated CTs), planning parameters such as raster scan grid size, energy step size and optimization margins yielding the best PTV coverage with respect to dose conformity and target homogeneity were found by iterations. For the nonmodulated plans the planning objective was to deliver at least 95% of the prescribed dose to 98% of the PTV [25]. All plans were 1- or 2-field plans and optimized for physical (absorbed) dose. For the carbon ion cases, a 3 mm thick ripple filter was applied to broaden the BP, as is routine in the clinic [26].

Coplanar fields were used for the study. In order to have data with beams traversing different distances through the lung tissue s_{lung}, variable field angles were chosen. For the carbon ions, a horizontal field direction at 0° as well as −45°, +45° and +90° to horizontal were selected. For carbon ions dual-field plans with 0° and +45° field angles and with 0° and +90° field angles were

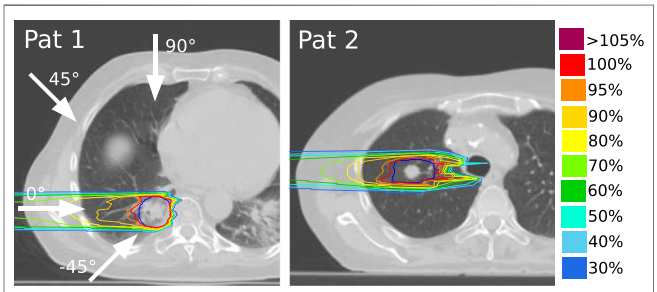

FIGURE 3 | Patient geometries and nonmodulated carbon ion dose distributions for a horizontal beam for P1 **(left)** and P2 **(right)**. Shown here are the isocenter transversal slices. The arrows indicate the four different field angles used in this work. The PTV contours are shown in dark blue.

TABLE 1 | PTV volumes V_{PTV} and estimated travel distances through the lung to the isocenter s_{lung} for both patient cases.

Patient	V_{PTV} (cm^3)	s_{lung}, 0° (mm)	s_{lung}, +45° (mm)	s_{lung}, −45° (mm)	s_{lung}, +90° (mm)
P1	41.9	74 ± 5	107 ± 5	62 ± 4	128 ± 5
P2	11.6	53 ± 4	58 ± 4	61 ± 4	65 ± 4

calculated as well. For protons 0°, −45°, and +45° to horizontal was used for P1 and 0° for P2. The 0° and +45° options match the fixed beamlines at the Marburger Ionenstrahl–Therapiezentrum and Shanghai Proton and Heavy Ion Center. Some of these field directions might not be clinically relevant, since sensitive structures and long distances through the lung are typically avoided, but were included here for investigative purposes. **Table 1** shows the s_{lung} for the investigated field angles and the V_{PTV} values. The s_{lung} values were estimated as the distance starting from the surface of the lung to the isocenter, placed in the middle of the PTV, along the central path of the beam. The V_{PTV} values were given by TRiP.

For protons, the "multiple scattering" algorithm was used for optimization and dose calculation, which considers the broadening of the beam as a function of patient depth [15]. For the carbon ion plans the much faster "all-points" algorithm, which is considering only all neighboring raster beam spots that may contribute to a given voxel [15], was used as this is normally sufficient for carbon ion plans [27]. Although comparisons between carbon ion plans with the two algorithms showed a slight difference in the plans (data not shown), the relative coverage difference between a modulated and nonmodulated dose distribution when comparing the algorithms was, even in the worst case, less than 0.5 percentual point (pp).

In addition to the main study, we calculated for the patient case P1 a range of carbon ion plans with lateral contour extensions from 0.6·$FWHM_{iso}$ to 1.2·$FWHM_{iso}$ in steps of 0.1, and for each of these with beam spot spacing of 2 and 3 mm and depth steps of 2 and 3 mm. A coplanar horizontal field was used for all plans. Dose distributions, calculated on the original CT, were compared to modulated doses with P_{mod} = 0.400 mm and ρ_{range} = 0.1–0.5 g/cm^3. The goal was to estimate the influence of the planning parameters on the relative difference in PTV coverage between the nonmodulated and modulated dose distributions.

2.4.1. Evaluation of the Parameters of the Lung Modulation Model

For the patient cases, the model parameters n, d, P_{mod} and ρ_{range} were evaluated.

The parameter n was evaluated for values of 24, 48, 72, 100, 120, 150, 200, and 400. For P_{mod}, we chose 0.300, 0.400, 0.500, and 0.600 mm, as our former works show that realistic values of P_{mod} lie below 0.600 mm. For the treatment planning cases with oblique fields for P1, plans with three different values of mean voxel length d were calculated: One following **Eq. 2** yielding d = 0.8439 mm, one using the unchanged length of the voxel $d = d_x$ = 0.9473 mm, and the last value was obtained using the maximum diagonal length through the voxel calculated with trigonometry as $d = \sqrt{2}\, d_x$ = 1.339 mm. The parameter ρ_{range} was evaluated by changing the maximum and minimum density value. We evaluated plans with ρ_{range} of 0.2–0.4, 0.2–0.5, 0.1–0.3, 0.1–0.4, 0.1–0.5, 0.0–0.5, 0.0–0.8, and 0.1–0.8 g/cm^3 and additionally ran calculations modulating all lung voxels.

After the parameter study was done, selected values of these parameters were then used throughout the paper: n = 100, ρ_{range} = 0.1–0.5 g/cm^3, P_{mod} = 0.400 mm and d corresponding to **Eq. 2**.

2.4.2. Plan Evaluation

PTV coverage, dose homogeneity and planning conformity were used for dosimetric plan evaluations. In each patient case, the doses to lung, spinal cord, trachea and heart were compared between nonmodulated and modulated dose distributions. $V_{95\%}$, being the volume receiving at least 95% of the prescribed dose, was used for evaluating the PTV coverage. The homogeneity index (HI) and the conformity index (CI) were defined as:

$$HI = \frac{D_{2\%} - D_{98\%}}{D_{prescribed}} \tag{6}$$

$$CI = \frac{V_{95\%pi}}{V_{PTV}} \tag{7}$$

where $V_{95\%pi}$ is the volume within the patient receiving 95% of the prescribed dose.

3. RESULTS

In general, the coverage and dose homogeneity of the PTVs were found to be worse for the modulated doses compared to the dose distributions calculated on the original CTs. This leads to a PTV dose overestimation by the TPS. The change in dose homogeneity was mainly due to a change in the minimum dose $D_{98\%}$. As expected, the relative difference between the modulated and nonmodulated dose distributions increases for larger values of P_{mod}.

From n =72 to 400 the dose distribution for the modified plans only changes with maximum 0.1 pp in $V_{95\%}$ and $D_{98\%}$, while $D_{2\%}$ remains constant. We adopted the value n = 100 throughout the rest of the work.

3.1. Spherical Geometries

Figure 4 summarizes the results for modulated and nonmodulated dose distributions calculated for the spherical targets with 17 mm radius in a lung tissue CT cube. In **Figures 4A**,**B**), the DVHs for the nonmodulated and modulated dose distributions are shown for 6 different d_{ic} values. In **Figure 4C**, $V_{95\%}$ as a function of d_{ic} is plotted for both the nonmodulated and modulated dose distributions and the differences between the corresponding pairs of values of the PTV coverage are shown in **Figure 4D**. **Figure 4D** shows a clear linear dependency of the relative difference in coverage as a function of d_{ic}.

In **Figure 5A**, the $V_{95\%}$ values for plans with d_{ic} = 100 mm and variable PTV radii are shown. The relative difference in

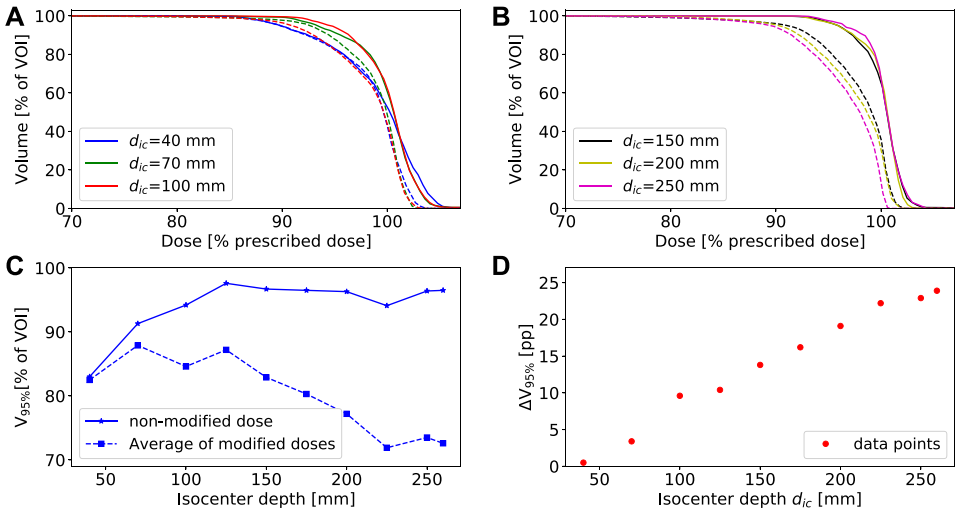

FIGURE 4 | A),(B) show selected DVHs for a spherical PTV with a 17 mm radius at 6 different isocenter depths d_{ic} for carbon ion plans on the non-modified CT (full lines) and for the same cases but for 100 summed dose cubes on 100 modified CTs with P_{mod} = 0.400 mm (dashed lines). **(C)** The PTV $V_{95\%}$ for all non-modulated and modulated cases for 17 mm PTV radius and variable d_{ic}. **(D)** The relative difference in PTV $V_{95\%}$, i.e., the difference of the two curves represented in subfigure **(C)**.

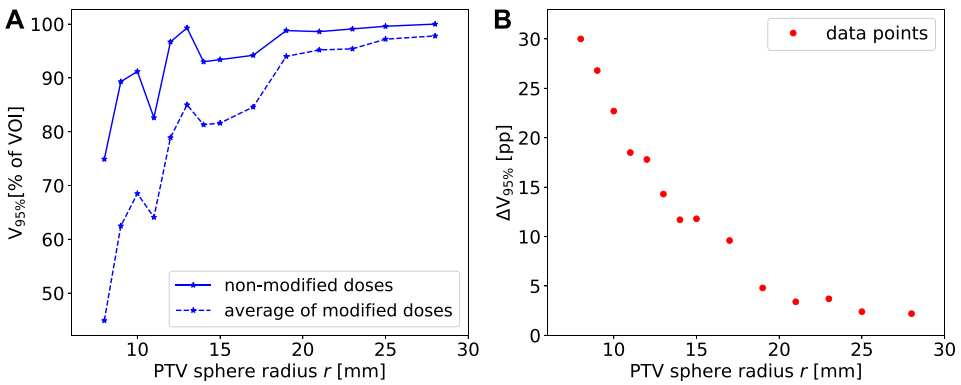

FIGURE 5 | (A) The PTV $V_{95\%}$ for the non-modulated and modulated cases for spherical PTVs with variable radii at d_{ic} = 100 mm with P_{mod} = 0.400 mm. All plans are for carbon ions. **(B)** The relative difference in PTV $V_{95\%}$, i.e., the difference of the two curves represented in **(A)**.

$V_{95\%}$ between the nonmodulated and modulated dose distributions is given in **Figure 5B**. In general the larger the PTV volume the better the coverage for both the nonmodulated and modulated dose distributions with an approximated exponential decrease of the relative coverage difference with PTV radius.

In both cases of **Figures 4C**, **5A**, some outliers can be seen in the individual $V_{95\%}$-curves. Importantly, they occur for both the nonmodulated and modulated case, leaving their relative difference consistent. This is to be expected as the "modulated plans" are dose recomputations of the nonmodulated ones. Similar curve shapes were seen when using other coverage indices, as for example $V_{90\%}$, $V_{80\%}$ or the mean dose (data not shown). One deviation from the smooth tendency that can be easily explained is the very superficial case at d_{ic} = 40 mm. Here, there is very little lung tissue in front of the PTV, resulting in a marginal difference between the nonmodulated and modulated dose distributions. Additionally, due to the low beam energies required at such low depth, a 4 mm bolus was applied, which might lead to an inferior coverage independently of the lung modulation effect.

3.2. Patient Plans

Dosimetric indexes $V_{95\%}$, $D_{98\%}$, $D_{2\%}$ and dose homogeneity HI of the carbon ion patient plans are presented in **Table 2** (for P1) and **Table 3** (for P2) for the nonmodulated cases and for the recalculated modulated dose distributions. The planning cases for P2 for ± 45° field angles have been omitted due to not fulfilling the planning objectives. In **Table 2**, dosimetric indices are additionally given for the three different values of

TABLE 2 | Dosimetric indices for carbon ion treatment plans for P1 with ρ_{range} of 0.1–0.5 g/cm^3 and different planning parameters.

Field angles	P_{mod} (mm)	$V_{95\%}$ (%)	$D_{98\%}$ (%)	$D_{2\%}$ (%)	HI
0°	Non-mod	98.7	96.9	102.8	0.059
0°	0.300	95.6	90.7	101.7	0.110
0°	0.400	94.2	88.9	101.6	0.127
0°	0.500	92.9	86.9	101.6	0.147
0°	0.600	91.1	84.7	101.5	0.168
+45°	Non-mod	99.0	96.9	102.9	0.060
+45°	0.300	95.0	91.3	101.8	0.105
+45°	0.400	93.2	89.1	101.7	0.126
+45°	0.500	91.1	86.9	101.7	0.148
+45°	0.600	88.5	84.0	101.7	0.177
+45°, $d = d_x$	0.300	95.6	91.8	101.8	0.100
+45°, $d = d_x$	0.400	94.0	90.3	101.8	0.115
+45°, $d = d_x$	0.500	92.4	88.8	101.7	0.129
+45°, $d = d_x$	0.600	90.6	86.5	101.7	0.152
+45°, $d = \sqrt{2}\, d_x$	0.300	96.1	92.3	101.9	0.096
+45°, $d = \sqrt{2}\, d_x$	0.400	94.7	90.8	101.9	0.111
+45°, $d = \sqrt{2}\, d_x$	0.500	93.3	89.5	101.8	0.123
+45°, $d = \sqrt{2}\, d_x$	0.600	91.7	87.6	101.8	0.142
−45°	Non-mod	99.4	98.4	102.0	0.036
−45°	0.300	98.6	96.3	101.6	0.053
−45°	0.400	98.3	95.6	101.6	0.060
−45°	0.500	97.7	94.7	101.5	0.068
−45°	0.600	97.4	94.1	101.5	0.074
−45°, $d = d_x$	0.300	98.7	96.6	101.6	0.050
−45°, $d = d_x$	0.400	98.4	95.8	101.6	0.058
−45°, $d = d_x$	0.500	98.1	95.2	101.6	0.064
−45°, $d = d_x$	0.600	97.7	94.7	101.6	0.069
−45°, $d = \sqrt{2}\, d_x$	0.300	98.8	96.7	101.6	0.049
−45°, $d = \sqrt{2}\, d_x$	0.400	98.5	96.0	101.6	0.056
−45°, $d = \sqrt{2}\, d_x$	0.500	98.3	95.6	101.6	0.060
−45°, $d = \sqrt{2}\, d_x$	0.600	97.8	94.8	101.6	0.068
+90°	Non-mod	99.1	96.8	102.4	0.056
+90°	0.300	98.1	95.6	102.1	0.065
+90°	0.400	97.6	94.7	102.1	0.074
+90°	0.500	97.0	93.8	102.1	0.083
+90°	0.600	96.2	93.0	102.0	0.090
0° and +45°	Non-mod	99.3	97.0	101.6	0.046
0° and +45°	0.300	98.2	95.3	101.4	0.061
0° and +45°	0.400	97.7	94.6	101.3	0.067
0° and +45°	0.500	97.2	94.1	101.3	0.072
0° and +45°	0.600	96.3	92.8	101.3	0.085
0° and +90°	Non-mod	99.4	97.5	102.2	0.047
0° and +90°	0.300	98.4	96.0	101.7	0.057
0° and +90°	0.400	97.9	95.2	101.7	0.065
0° and +90°	0.500	97.4	94.4	101.7	0.073
0° and +90°	0.600	96.8	93.7	101.6	0.079

Were d *is not stated, it was calculated following* ***Eq. 2****. For the cases of the modulated dose distributions,* n = *100.*

TABLE 3 | Dosimetric indices for carbon ion treatment plans for P2 with ρ_{range} of 0.1–0.5 g/cm^3 and different planning parameters.

Field angles	P_{mod} (mm)	$V_{95\%}$ (%)	$D_{98\%}$ (%)	$D_{2\%}$ (%)	HI
0°	Non-mod	98.4	95.6	103.1	0.075
0°	0.300	97.5	94.4	101.6	0.072
0°	0.400	96.8	93.6	101.4	0.077
0°	0.500	96.2	92.9	101.2	0.083
0°	0.600	95.0	91.4	101.1	0.097
+90°	Non-mod	97.4	93.2	103.0	0.098
+90°	0.300	96.2	91.5	101.3	0.098
+90°	0.400	95.4	90.4	101.1	0.107
+90°	0.500	93.4	86.6	101.1	0.145
+90°	0.600	91.2	85.0	101.0	0.161
0° and +45°	Non-mod	99.3	97.0	102.5	0.055
0° and +45°	0.300	97.1	93.4	100.9	0.075
0° and +45°	0.400	95.3	92.1	100.8	0.087
0° and +45°	0.500	93.0	89.8	100.6	0.108
0° and +45°	0.600	90.9	88.8	100.6	0.118

The value of d *was calculated following* ***Eq. 2****. For the cases of the modulated dose distributions,* n = *100.*

As can be seen comparing **Tables 2–4** and by comparing **Figures 6**, **7**, the relative differences between nonmodulated and modulated dose distributions are larger for carbon ions than for protons, which can be attributed to the generally sharper carbon ion BPs. Actually, for all cases of the modulated proton plans for P1, the drop in $V_{95\%}$ never compromised the planning objective of giving at least 95% prescribed dose to 98% of the PTV volume. Our conclusion is that the lung modulation effect is not very severe for proton treatment planning. This is in agreement with other findings [10, 11]. We focus on the carbon ions plans for further analysis due to the larger modulation effect observed for this particle type relative to protons.

TABLE 4 | Dosimetric indices for proton treatment plans for P1 and P2 with ρ_{range} of 0.1–0.5 g/cm^3 and different planning parameters for each for the two patients.

Planning case	P_{mod} (mm)	$V_{95\%}$ (%)	$D_{98\%}$ (%)	$D_{2\%}$ (%)	HI
P1, 0°	Non-mod	99.6	99.0	101.5	0.025
P1, 0°	0.300	99.3	98.7	101.1	0.032
P1, 0°	0.400	99.0	97.5	101.1	0.036
P1, 0°	0.500	98.8	96.8	101.0	0.041
P1, 0°	0.600	98.5	96.1	101.0	0.049
P1, +45°	Non-mod	99.5	97.4	102.6	0.052
P1, +45°	0.300	99.0	96.8	101.8	0.050
P1, +45°	0.400	98.7	96.2	101.7	0.055
P1, +45°	0.500	98.3	95.7	101.7	0.059
P1, +45°	0.600	98.0	95.0	101.7	0.067
P1, −45°	Non-mod	99.5	97.8	102.4	0.046
P1, −45°	0.300	99.4	97.7	102.1	0.044
P1, −45°	0.400	99.2	97.4	102.1	0.047
P1, −45°	0.500	99.1	97.2	102.1	0.049
P1, −45°	0.600	99.1	97.1	102.1	0.050
P2, 0°	Non-mod	99.3	97.6	102.3	0.047
P2, 0°	0.300	98.1	95.2	101.7	0.065
P2, 0°	0.400	97.7	94.3	101.7	0.073
P2, 0°	0.500	97.0	93.0	101.5	0.086

For the modulated doses, n = *100.*

d used for the oblique beam cases. Dosimetric indexes for the proton patient plans are given in **Table 4** for both patient cases.

DVHs for PTV, trachea and lung in the nonmodulated and modulated dose distributions in selected one-beam plans for P1 (horizontal and oblique beams) and P2 (horizontal beam) are shown for carbon ions and protons in **Figures 6**, **7**, respectively. No difference was found in the DVHs with and without lung modulation for the organs not displayed in these graphs. Zoomed plots for the DVHs of the PTV help to see the relative differences between nonmodulated and modulated dose distributions.

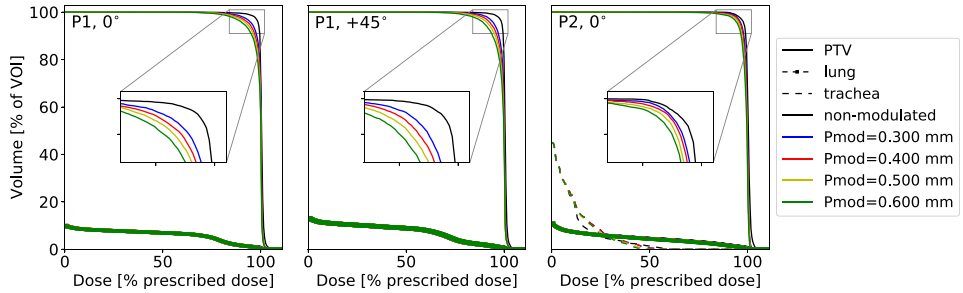

FIGURE 6 | DVHs of relevant VOIs for ^{12}C plans on the non-modified CTs compared to plans on n = 100 plans summed for n = 100 modified CTs with different P_{mod} values. Three treatment planning cases are shown with P1 planned with a horizontal field as well as with one 45° to horizontal and with patient case P2 with a horizontal field. Plans were optimized and calculated for physical dose with a 2 × 2 mm^2 raster scan size and a 3 mm depth step size.

Of all the displayed DVHs, only those corresponding to the trachea for the case P2 exhibit a slightly changed maximum dose when considering the lung modulation effect ($D_{2\%}$ changes from 45.5% of the prescribed dose for the non-modulated plan to 38.9% for the case of P_{mod} = 0.600 mm). In the low dose region, the DVH for the trachea is slightly larger for the modified doses compared to the nonmodulated one. For example $V_{20\%}$ = 7.3% of the prescribed dose for the nonmodulated dose compared to 10.4% of the prescribed dose for the dose distribution calculated with P_{mod} = 0.600 mm. None of these findings bear however a clinical relevance.

The dose to the lung displays minimal changes between modulated and nonmodulated dose distributions. Due to the generally smaller beam spot sizes of carbon ion beams, the ipsilateral lung could be better spared using carbon ions with approximately half the integral dose given to the lung compared to the proton plans. As an example, for P1, the $V_{5\%}$ with a horizontal proton beam is 18.8% of the prescription dose compared to 8.9% delivered with carbon ions.

Due to the tumor location of the selected patients, far from critical organs (the spinal cord for example), we will focus on assessment of the changes in target coverage as presented in **Tables 2–4**.

In **Figure 8** is shown the relative difference between the $V_{95\%}$ of the nonmodulated doses and the modulated doses calculated for the values of P_{mod} = 0.300 mm (blue plots) and P_{mod} = 0.600 mm (green plots) as a function of the distance traversed through the lung s_{lung}. The general trend of the sphere study, that a larger relative difference is seen for smaller PTV sizes, is present. However, that the relative difference is larger for a larger value of s_{lung} is only partially confirmed. For P1, when comparing the single field plans at 0° and +45°, the relative differences between the nonmodulated and modulated dose distributions are larger for the +45° case. This is expected since at this angle the beam traverses a larger amount of lung tissue. However, the beam at 0° yields a larger relative difference than for −45° by a large margin, even for the lowest P_{mod} value, although s_{lung} is slightly lower for the −45° setup. For the largest s_{lung} value at +90°, a much smaller relative difference between nonmodulated and modulated doses are observed than for the 0° and −45° angles.

In the clinic, single field plans would rarely be used. Therefore, we also included selected few dual-field plans in the study. The dual-field plans are providing better and more conform target coverage, also for the nonmodulated doses and it can be seen that the drop in target coverage caused by the beam-modulation effect is slightly smaller for the dual-field plans relative to the nonmodulated ones.

3.2.1. The Effect of the Voxel Length *d*

As expected, and as can additionally be seen in **Table 2**, the relative difference between the plans with different values of d are significantly larger for the +45° cases where the particles traverse

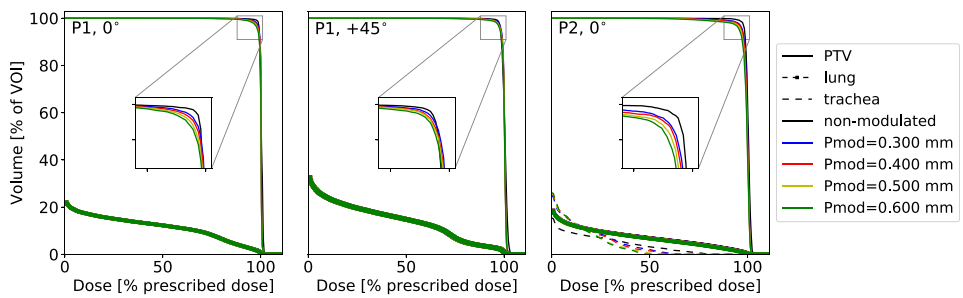

FIGURE 7 | DVHs of selected VOIs for proton plans on the non-modified CTs compared to plans on n = 100 summed modified CTs with different P_{mod} values. Three treatment planning cases are shown for P1 planned with a horizontal field as well as with one oblique field at +45° as well as for P2 with a horizontal field. Plans were optimized and calculated for physical dose with a 3 × 3 mm^2 raster scan size and a depth step size of 3 mm P1 and 2 mm for P2.

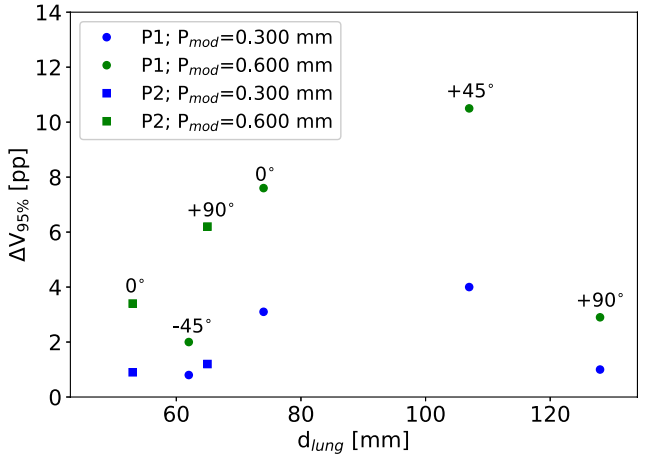

FIGURE 8 | The difference in target coverage between the non-modulated doses and the doses calculated with P_{mod} = 0.300 mm (blue plots) and P_{mod} = 0.600 mm (green plots) as a function of the amount of lung traversed by the particle beam (see **Table 1**). Circles mark data for P1, squares mark data for P2. For the P_{mod} = 0.600 mm plots the matching field angles are shown. All plans are for carbon ions.

roughly twice the amount of lung tissue compared to the −45° cases. Also, it can be seen that the larger the value of P_{mod}, the more critical a variation in d becomes. However, even for +45° the largest decrease in $V_{95\%}$ seen between d = 0.8439 mm and d = 1.339 mm is 2.9 pp. For −45°, the largest decrease is only 0.4 pp.

3.2.2. Selecting Modulation Lung Voxels

Dosimetric indexes for plans with P_{mod} = 0.400 mm and variable ρ_{range} values are listed in **Table 5** for carbon ion plans and **Table 6** for proton plans. Values for the nonmodulated cases are given for comparison.

The same trends for $V_{95\%}$ and HI as for ρ_{range} = 0.1–0.5 g/cm^3 are seen. For protons, the dependency of the ρ_{range} parameter on the plans is generally much lower when compared to carbon ions, as the relative differences between modulated and nonmodulated dose distributions are generally lower for protons. In the case of the largest variation for the protons plans, there is a decrease in $V_{95\%}$ of 1.4 pp when using the narrowest ρ_{range} of 0.2–0.4 g/cm^3 compared to using all the voxels in the ipsilateral lung. There HI has an increase of approximately 43%. In comparison, for the carbon ions, the extreme case of P1 shows a decrease in $V_{95\%}$ of 4.2 pp when comparing ρ_{range} = 0.2–0.4 g/cm^3 with using all the voxels and an 58% HI increase. The less severe case of P2 shows for the same comparison a coverage drop of only 1.8 pp and a small HI increase of 16%.

Both of the extreme cases, ρ_{range} = 0.2–0.4 g/cm^3 or no fixed ρ_{range}, are unrealistic choices. For P2, the $V_{95\%}$ values of the experimentally estimated ρ_{range} = 0.1–0.5 g/cm^3 lie in between the values of these two extremes for both protons and carbon ions. For protons, this is also the case for P1. For carbon ions for P1, the difference in $V_{95\%}$ from ρ_{range} = 0.2–0.4 g/cm^3 to ρ_{range} = 0.1–0.5 g/cm^3 is 1.7 pp, while for ρ_{range} = 0.1–0.5 g/cm^3 compared to the case with no ρ_{range} limit is 2.5 pp.

3.2.3. Effect of Changes on the Planning Parameter Settings

Figure 9 shows a boxplot with outliers for coplanar horizontal field plans for P1 with variable planning parameters (see the materials and methods section). Nonmodulated and modulated doses, calculated with P_{mod} = 0.400 mm, are shown separately. All plans that in the nonmodulated cases had $V_{95\%}$ below 98.0% or a

TABLE 5 | Dosimetric indices for carbon ion plans for patients P1 and P2 and P_{mod} = 0.400 mm for variable values of ρ_{range}.

Planning case	ρ_{range} (g/cm^3)	$V_{95\%}$ (%)	$D_{98\%}$ (%)	$D_{2\%}$ (%)	HI
P1	Non-mod	98.7	96.9	102.8	0.059
P1	0.2–0.4	95.9	91.6	101.6	0.100
P1	0.2–0.5	94.9	89.8	101.7	0.119
P1	0.1–0.3	96.5	92.2	101.8	0.095
P1	0.1–0.4	95.3	90.0	101.7	0.117
P1	0.1–0.5	94.2	88.9	101.6	0.127
P1	0.0–0.5	94.1	88.7	101.7	0.130
P1	0.1–0.8	92.2	86.3	101.6	0.153
P1	0.0–0.8	92.1	86.0	101.5	0.155
P1	All voxels	91.7	85.8	101.6	0.158
P2	Non-mod	98.4	95.6	103.1	0.075
P2	0.2–0.4	97.8	94.7	102.0	0.073
P2	0.2–0.5	97.7	94.6	102.1	0.075
P2	0.1–0.3	97.6	94.7	101.6	0.069
P2	0.1–0.4	97.1	94.1	101.5	0.074
P2	0.1–0.5	96.8	93.6	101.4	0.077
P2	0.0–0.5	97.1	93.9	101.4	0.075
P2	0.1–0.8	96.4	93.2	101.3	0.081
P2	0.0–0.8	96.4	92.9	101.3	0.084
P2	All voxels	96.0	92.5	101.2	0.087

All plans are calculated with horizonzal fields, e.g., with the +0° option with planning parameters given in the material and methods section.

TABLE 6 | Dosimetric indices for proton plans for patients P1 and P2 and P_{mod} = 0.400 mm for variable values of ρ_{range}.

Planning case	ρ_{range} (g/cm^3)	$V_{95\%}$ (%)	$D_{98\%}$ (%)	$D_{2\%}$ (%)	HI
P1	Non-mod	99.6	99.0	101.3	0.023
P1	0.2–0.4	99.2	97.8	101.0	0.032
P1	0.2–0.5	99.2	97.7	101.1	0.034
P1	0.1–0.4	99.2	97.7	101.0	0.033
P1	0.1–0.3	99.4	98.3	101.0	0.027
P1	0.1–0.5	99.1	97.5	101.1	0.036
P1	0.0–0.5	99.0	97.4	101.1	0.037
P1	0.1–0.8	98.8	96.8	101.1	0.043
P1	0.0–0.8	98.8	96.7	101.1	0.044
P1	All voxels	98.7	96.5	101.2	0.047
P2	Non-mod	99.3	97.6	102.3	0.047
P2	0.2–0.4	98.5	96.3	101.7	0.054
P2	0.2–0.5	98.4	96.0	101.6	0.056
P2	0.1–0.3	98.9	94.8	101.5	0.067
P2	0.1–0.4	98.0	95.0	101.6	0.066
P2	0.1–0.5	97.8	94.4	101.7	0.072
P2	0.0–0.5	97.8	94.4	101.6	0.071
P2	0.1–0.8	97.3	93.4	101.6	0.082
P2	0.0–0.8	97.3	93.7	101.6	0.080
P2	All voxels	97.1	93.2	101.5	0.083

All plans are calculated with horizonzal fields, e.g. with the +0° option with planning parameters given in the material and methods section.

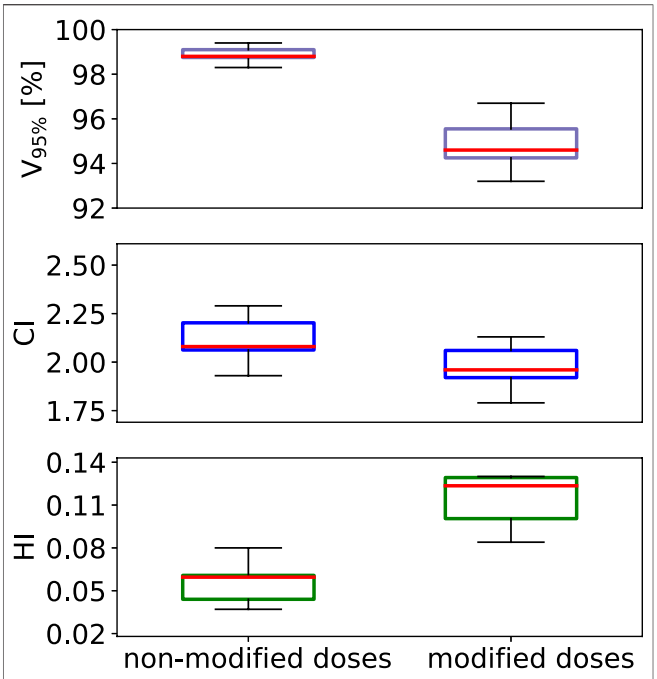

FIGURE 9 | A standard boxplot (median, 1. and 3. quartiles and whiskers including the outliers) for $V_{95\%}$, HI and CI data sets obtained for patient case P1 using a horizontal beam for non-modulated as well as modulated dose distributions for carbon ions. A set of variable planning parameters was used as given in the materials and method section.

CI above 2.5 were omitted from this study, as they did not fulfill the planning objectives.

It is seen how $V_{95\%}$, for the modulated dose distributions, varies more from a change in planning parameters. We observed that the better the nonmodulated plan was, in terms of PTV coverage and dose homogeneity, the smaller the relative difference between the nonmodulated and the modulated dose distribution.

For a small number of plans with specific parameter settings, the dose distribution was even improved by the lung modulation, in terms of PTV coverage and homogeneity. It was seen that, in some cases, it is possible to first calculate an inferior plan for the nonmodulated case, which due to the broader and slightly displaced BPs caused by the lung-modulation effect can result in a plan fulfilling the planning objectives for the modulated case. As an example, we show in **Figure 10** DVHs for a plan calculated on patient case P2, for a non-modified case (solid lines) compared to the sum of doses calculated on 100 modified CTs (dashed lines). A horizontal field was used, with beam spot spacing of 3 mm, energy step 3 mm, and lateral contour extension $1.2{\cdot}\mathrm{FWHM}_{\mathrm{iso}}$ with values of $P_{\mathrm{mod}} = 0.400$ mm and $\rho_{\mathrm{range}} = 0.1$–$0.5$ g/cm^3 for the calculation of the modulation effect. $V_{95\%} = 97.7\%$ and HI = 0.102 were found for the nonmodulated doses and $V_{95\%} = 97.0\%$ and HI = 0.061 were found for modulated doses, respectively. Although the values of the PTV coverage were similar for these two cases and slightly lower still for the modulated case, the HI value was reduced by one third after the modulation, as the much steeper fall-off for that DVH curve in **Figure 10** also illustrates.

4. DISCUSSION

The beam-modulation effect caused by the porous material of the lung results in a lower PTV coverage and dose homogeneity. This effect is clearly more pronounced for carbon ions than for protons, as the sharper the initial BP the stronger the modulation effect. The modulation effect is generally negligible in proton treatments, as compared to the other dose delivery and treatment uncertainties related to protons, which confirms the work of Baumann et al. [10]. Among such uncertainties are particle range uncertainties, patient setup errors, inter-fractional anatomy changes (e.g., weight loss, tumor shrinkage, etc.) and intra-fractional tumor motion. Additionally, TPS algorithms often have problems handling the air cavities and sharp density gradients present in the lung.

Using spherical geometries, we show that when 1) increasing the distance the beam travels through the lung tissue and/or when 2) reducing the PTV size, the effect of the beam-modulation increases. Both tendencies have been shown previously only for protons [9]. The latter effect fits the general knowledge that a good PTV coverage is more difficult to obtain for smaller PTVs when using broader BPs. For the non-modulated plans, the PTV coverage increases with an increasing depth, while for the modulated cases, the larger the depth of the target in the lung the larger the beam-modulation effect. This altogether yields the increasing relative difference with depth between the non-modulated and modulated dose distributions.

These trends were only partially confirmed for the patient cases. The systematic study on spherical target geometries represents a simplified scenario, while for patient cases there are many degrees of freedom and many further parameters in

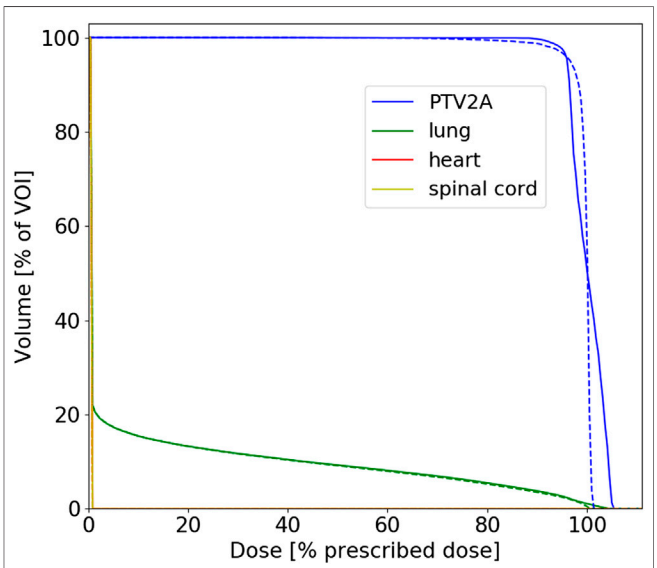

FIGURE 10 | DVHs for proton plans calculated on patient case P2 for non-modified (solid lines) vs. sum of 100 modified CTs (dashed lines). The corresponding planning parameters and dosimetric indexes are given in the text.

consideration, such as case-dependent planning parameters and much more complex patient geometries. The angle from which the beam comes might lead to a large change in the relative difference between modulated and nonmodulated dose distributions. Our conclusions are based on our limited number of planning cases, but in this work, a wider general test of the lung modulation model as well as the systematic study with spheres were prioritized.

The largest uncertainties in our model (and as an extension in any similar routine dealing with the lung modulation) lie in the parameters P_{mod} and ρ_{range}. As P_{mod} has been investigated in other works, we focused on ρ_{range}, which has not been studied before. A too large ρ_{range} would mean that non-porous biological lung structures, such as massive vessels, are falsely taken into account as porous voxels and the calculated modulation effect would be slightly larger than the actual modulation. On the other hand, by choosing a too small ρ_{range} the modulation effect of the lung would be underestimated, which in particular for heavier ions can be important (as the effect is more pronounced for heavier ions as indicated in this work). We found that the upper limit might be more critical than the lower limit, since a too low upper limit would filter out too much porous lung material from the calculation. As long as the lower limit is kept within a reasonable value, which can easily be determined from CT voxel histograms, this value only marginally influences the modulation results. One should do at least a manual filtering of voxels containing visible big vessels and/or similar biological structures, which should not be modified.

Another, less important, parameter in the model is the voxel length d. For beam angles running parallel to the CT axis d is trivially the voxel length in that direction whereas, for any other angles, it must be calculated. The effect on the lung modulation of the value of d was found to be not so dramatic and only important when the distance through the lung traveled by the particles is large. We recommend using the tested formula, given in this work as **Eq. 2**.

The specifically chosen example shown in **Figure 10** might indicate that, in some rare planning cases, an inferior dose coverage of the PTV can actually be improved by the lung modulation effect, although, in the large majority of cases, not taking the lung modulation effect into consideration in treatment planning is a net disadvantage for the patients.

The mathematical model described in this work could, in theory, be built into other TPSs too. We note, although, that the "future" of implementing the lung modulation into a TPS lies within MC codes when these will be coupled to treatment planning in a more general way. MC codes allow for on-the-fly modulation of the voxels during the actual treatment planning process and not by recomputing the dose on many different modulated CTs, followed by summing up the dose distribution to estimate the modulation effect. However, even with MC available, for the case that a deterministic TPS mode would still be opted for—for instance to calculate biologically effective dose with the Linear Effect Model (LEM) [14, 28]—the concept presented in this work is an appropriate option for recalculation of treatment plans and for assessment of the lung modulation effect. For carbon ion therapy, the authors estimate that TPS with deterministic pencil algorithms are assumed to remain still in clinical use in the next years. Additionally, deterministic TPS programs, like TRiP98 and matRad [11], will play an important role for educational purposes.

5. CONCLUSION

With existing standard tools, it is possible in a transparent and reproducible way, to implement and calculate the beam-modulation effect of the lung in a known TPS for particles. Our evaluation of two selected lung cancer patients is in line with previous results. For protons, the lung modulation effect is found to be negligible compared to other dose delivery uncertainties related to particle therapy treatments of the lung. For carbon ions, the effect is significantly more pronounced and cannot be ignored. The decrease in both PTV coverage and dose homogeneneity, caused by the modulation effect, could lead to underdosage within the PTV and to overdosage in the healthy normal tissue surrounding the PTV. Planning parameters and beam angles also have an impact on the relative difference between nonmodulated dose distributions and those taking the beam-modulation effect into account, caused by the porous nature of lung tissue.

DATA AVAILABILITY STATEMENT

The original contributions presented in the study are included in the article, further inquiries can be directed to the corresponding author.

ETHICS STATEMENT

Ethical review and approval was not required for the study on human participants in accordance with the local legislation and institutional requirements. Written informed consent from the participants was not required to participate in this study in accordance with the national legislation and the institutional requirements.

AUTHOR CONTRIBUTIONS

UW devised the project, the main conceptual ideas and project outline. TR, AS, KZ, and UW further developed the project with AS and KZ supervising the work and providing financial support. TR, LG, and NB developed the software tools for the manuscript, based on a mathematical model developed by UW. TR performed the computations, the data gathering and the data analysis. TR and AS created the images and graphs. KB, VF, and RE provided the patient data. TR wrote the manuscript with input from all authors.

FUNDING

The authors TR and AS acknowledge the financial support of the German fund for research "Deutsche Forschungsgemeinschaft" (DFG), case number SA 3085/1-1, Granted to AS. The study was also performed in the frame of FAIR Phase-0 supported by the GSI Helmholtzzentrum für Schwerionenforschung in Darmstadt (Germany).

ACKNOWLEDGMENTS

The authors acknowledge the access to TRiP98, provided by M. Krämer and the GSI, and the cluster time at the PLGRID infrastructure in Krakow under Grant Number ccbmc7. The authors Ringbæk and Santiago acknowledge the support of M. Stuschke and S. Qamhiyeh from the Radiotherapy Department at Essen University Hospital. We thank Michelle Lis (GSI) for the linguistic improvement of the manuscript.

REFERENCES

1. Haberer T, Becher W, Schardt D, Kraft G. Magnetic scanning system for heavy ion therapy. *Nucl Instrum Methods Phys Res Sect A Accel Spectrom Detect Assoc Equip* (1993) 330:296. doi:10.1016/0168-9002(93)91335-k
2. Lomax AJ, Bortfeld T, Goitein G, Debus J, Dykstra C, Tercier P-A, et al. Treatment planning inter-comparison of proton and intensity modulated photon radiotherapy. *Radiother Oncol* (1999) 51:257–71. doi:10.1016/s0167-8140(99)00036-5
3. Coucke GO, Titt U, Mirkovic D, Mohan R. Density heterogeneities and the influence of multiple Coulomb and nuclear scatterings on the Bragg peak distal edge of proton therapy beams. *Phys Med Biol* (2008) 53:4605–19. doi:10.1088/0031-9155/53/17/010
4. Ringbæk TP, Simeonov Y, Witt M, Cabillic-Engenhart R, Kraft G, Zink K, et al. Modulation power of porous materials and usage as ripple filter in particle therapy. *Phys Med Biol* (2017) 62:2892–909. doi:10.1088/1361-6560/aa5c28
5. Titt U, Sell M, Unkelbach J, Bangert M, Mirkovic D, Oelfke U, et al. Degradation of proton depth dose distributions attributable to microstructures in lung-equivalent material. *Med Phys* (2015) 42:6425–32. doi:10.1118/1.4932625
6. Mohan K-S, Witt M, Weber U, Engenhart-Cabillic R, Zink K. An efficient method to predict and include Bragg curve degradation due to lung-equivalent materials in Monte Carlo codes by applying a density modulation. *Phys Med Biol* (2017) 62:3997–4016. doi:10.1088/1361-6560/aa641f.
7. Espana M, Paganetti H. Uncertainties in planned dose due to the limited voxel size of the planning ct when treating lung tumors with proton therapy. *Phys Med Biol* (2011) 56:3472–56. doi:10.1088/0031-9155/56/13/007.
8. Witt M, Weber U, Simeonov Y, Zink K. SU-E-T-671: range-modulation effects of carbon ion beams in lung tissue. *Med Phys* (2015) 42:3491. doi:10.1118/1.4925034.
9. Flatten V, Baumann K, Weber U, Engenhart-Cabillic R, Zink K. Quantification of the dependencies of the Bragg peak degradation due to lung tissue in proton therapy on a ct-based lung tumor phantom. *Phys Med Biol* (2019) 64:155005. doi:10.1088/1361-6560/ab2611
10. Baumann K, Flatten V, Weber U, Lautenschläger S, Eberle F, Zink K, et al. Effects of the Bragg peak degradation due to lung tissue in proton therapy of lung cancer patients. *Radiat Oncol* (2019) 14:155005. doi:10.1186/s13014-019-1375-0.
11. Winter J, Ellerbrock M, Jäkel O, Greilich S, Bangert M. Analytical modeling of depth-dose degradation in heterogeneous lung tissue for intensity-modulated proton therapy planning. *Phys Imaging Radiat Oncol* (2020) 14:32–8. doi:10.1016/j.phro.2020.05.001.
12. Wieser H-P, Cisternas E, Wahl N, Ulrich S, Stadler A, Mescher H, et al. Development of the open-source dose calculation and optimization toolkit matrad. *Med Phys* (2017) 44:2556–68. doi:10.1002/mp.12251.
13. Müller M, Jäkel O, Haberer T, Kraft G, Schardt D, Weber U. Treatment planning for heavy-ion radiotherapy: physical beam model and dose optimization. *Phys Med Biol* (2000) 45:3299–317. doi:10.1088/0031-9155/45/11/313.
14. Krämer M, Scholz M. Treatment planning for heavy-ion radiotherapy: calculation and optimization of biologically effective dose. *Phys Med Biol* (2000) 45:3319–30. doi:10.1088/0031-9155/45/11/314.
15. Krämer M, Durante M. Ion beam transport calculations and treatment plans in particle therapy. *Eur Phys J D* (2010) 60:195–202. doi:10.1140/epjd/e2010-00077-8.
16. Dreher C, Habermehl D, Ecker S, Brons S, El-Shafie R, Jäkel O, et al. Optimization of carbon ion and proton treatment plans using the raster-scanning technique for patients with unresectable pancreatic cancer. *Radiother Oncol* (2015) 10:850–860. doi:10.1186/s13014-015-0538-x.
17. Toftegaard J, Petersen JP, Bassler N. PyTRiP—a toolbox and gui for the proton/ion therapy planning system trip. *J Phys: Conf Ser* (2014) 489:012045. doi:10.1088/1742-6596/489/1/012045.
18. Ringbæk TP, Weber U, Santiago A, Iancu G, Wittig A, Grzanka L, et al. Validation of new 2d ripple filters in proton treatments of spherical geometries and non-small cell lung carcinoma cases. *Phys Med Biol* (2018) 62:245020. doi:10.1088/1361-6560/aaede9
19. Ringbæk TP, Weber U, Santiago A, Simeonov Y, Fritz P, Krämer M, et al. Dosimetric comparisons of carbon ion treatment plans for 1d and 2d ripple filters with variable thicknesses. *Phys Med Biol* (2016) 61:4327. doi:10.1088/0031-9155/61/11/4327
20. Bassler N, Hansen DC, Lühr A, Thomsen B, Petersen JP, Sobolevsky N. SHIELD-HIT12A—a Monte Carlo particle transport program for ion therapy research. *J Phys Conf* (2014) 489:012004. doi:10.1088/1742-6596/489/1/012004
21. [Dataset] doi:10.5281/zenodo.4008066.Zenodo.org (2019)
22. [Dataset] doi:10.17632/6jh3m9xtjx.1. Mendeley link (2019)
23. [Dataset]*MK. Trip98 online manual*. Available from: http://bio.gsi.de/DOCS/trip98.html (2009)
24. Schneider W, Bortfeld T, Schlegel W. Correlation between CT numbers and tissue parameters needed for Monte Carlo simulations of clinical dose distributions. *Phys Med Biol* (2000) 45:459–78. doi:10.1088/0031-9155/45/2/314.
25. Journal of the ICRU prescribing, recording and reporting proton-beam therapy (2007) Technical Report, Bethesda, MA: International Comission on Radiation Units and Measurements. Vol 7 No 2 (2007). Report 78.
26. Schlegel U, Kraft G. Design and construction of a ripple filter for a smoothed depth dose distribution in conformal particle therapy. *Phys Med Biol* (1999) 44:2765–75. doi:10.1088/0031-9155/44/11/306.
27. Gemmel A, Hasch B, Ellerbrock M, Weyrather WK, Krämer M. Biological dose optimization with multiple ion fields. *Phys Med Biol* (2008) 53:6991–7012. doi:10.1088/0031-9155/53/23/022.
28. Scholz M, Kellerer AM, Kraft-Weyrather W, Kraft G. Computation of cell survival in heavy ion beams for therapy. *Radiat Environ Biophys* (1997) 36:59–66. doi:10.1007/s004110050055.

Conflict of Interest: The authors declare that the research was conducted in the absence of any commercial or financial relationships that could be considered as a potential conflict of interest.

frontiers in Physics

ORIGINAL RESEARCH
published: 19 November 2020
doi: 10.3389/fphy.2020.567990

The MONDO Tracker: Characterisation and Study of Secondary Ultrafast Neutrons Production in Carbon Ion Radiotherapy

Marco Toppi[1,2], Giuseppe Battistoni[3], Alessandro Bochetti[4,5,6], Patrizia De Maria[7], Micol De Simoni[4,6], Yunsheng Dong[3,8], Marta Fischetti[1,6], Gaia Franciosini[4,6], Leonardo Gasparini[9], Marco Magi[1,6], Enrico Manuzzato[9], Ilaria Mattei[3], Riccardo Mirabelli[4,5,6], Silvia Muraro[3], Luca Parmesan[9], Vincenzo Patera[1,5,6], Matteo Perenzoni[9], Alessio Sarti[1,5,6], Angelo Schiavi[1,6], Adalberto Sciubba[1,5,6], Giacomo Traini[5,6], Serena Marta Valle[3] and Michela Marafini[5,6]*

[1]Dipartimento di Scienze di Base e Applicate per l'Ingegneria, "Sapienza" Università di Roma, Rome, Italy, [2]Istituto Nazionale di Fisica Nucleare, Laboratori Nazionali di Frascati, Frascati, Italy, [3]Istituto Nazionale di Fisica Nucleare, Sezione di Milano, Milan, Italy, [4]Dipartimento di Fisica, "Sapienza" Università di Roma, Rome, Italy, [5]Museo Storico della Fisica e Centro Studi e Ricerche Enrico Fermi, Rome, Italy, [6]Istituto Nazionale di Fisica Nucleare, Sezione di Roma, Rome, Italy, [7]Scuola di Specializzazione in Fisica Medica, "Sapienza" Università di Roma, Rome, Italy, [8]Dipartimento di Fisica, Università degli Studi di Milano, Milan, Italy, [9]Integrated Radiation and Image Sensors (IRIS), Fondazione Bruno Kessler, Trento, Italy

OPEN ACCESS

Edited by:
Laurent Ottaviani, Aix-Marseille Université, France

Reviewed by:
Peter R. Hobson, Queen Mary University of London, United Kingdom
David Christian, Fermilab (DOE), United States

***Correspondence:**
Riccardo Mirabelli
riccardo.mirabelli@roma1.infn.it

Specialty section:
This article was submitted to Radiation Detectors and Imaging, a section of the journal Frontiers in Physics

Received: *23 June 2020*
Accepted: *16 October 2020*
Published: *19 November 2020*

Citation:
Toppi M, Battistoni G, Bochetti A, De Maria P, De Simoni M, Dong Y, Fischetti M, Franciosini G, Gasparini L, Magi M, Manuzzato E, Mattei I, Mirabelli R, Muraro S, Parmesan L, Patera V, Perenzoni M, Sarti A, Schiavi A, Sciubba A, Traini G, Valle SM and Marafini M (2020) The MONDO Tracker: Characterisation and Study of Secondary Ultrafast Neutrons Production in Carbon Ion Radiotherapy. Front. Phys. 8:567990. doi: 10.3389/fphy.2020.567990

Secondary neutrons produced in particle therapy (PT) treatments are responsible for the delivery of a large fraction of the out-of-target dose as they feebly interact with the patient body. To properly account for their contribution to the total dose delivered to the patient, a high precision experimental characterisation of their production energy and angular distributions is eagerly needed. The experimental challenge posed by the detection and tracking of such neutrons will be addressed by the MONDO tracker: a compact scintillating fiber detector exploiting single and double elastic scattering interactions allowing for a complete neutron four-momentum reconstruction. To achieve a high detection efficiency while matching the fiber (squared, 250 μm side) high granularity, a single photon sensitive readout has been developed using the CMOS-based SPAD technology. The readout sensor, with pixels of $125 \times 250\ \mu m^2$ size, will be organised in tiles covering the full detector surface and will implement an autotrigger strategy to identify the events of interest. The expected detector performance in the context of neutron component characterisation in PT treatments delivered using carbon ions has been evaluated using a Monte Carlo simulation accounting for the detector response and the neutrons production spectra.

Keywords: neutron tracking, particle therapy, carbon ions radiotherapy, secondary radiation monitoring, SPAD technology

1 INTRODUCTION

Particle therapy (PT) is a modern technique of solid tumor treatment that exploits the energy deposit of charged light ion beams, highly localised in the target region defined as "Bragg-Peak," to preserve the healthy tissues. The interaction of therapeutic beams with the patient, besides releasing the dose necessary to induce the tumor cells apoptosis, produces secondary particles (neutral and charged radiation and beam fragments) whose contribution to the total dose is generally negligible. However,

secondary neutrons can deposit an absolute nonnegligible energy in and out of field even far away from the target volume (voxel) as they are weakly interacting with the patient's body [1 2]. Their contribution has hence to be taken into account with the highest possible precision when performing the treatment plan optimisation and evaluating the dose absorbed by the organs at risk. To this aim, a high precision experimental characterisation of the secondary neutron spectra and fluxes is eagerly needed.

So far, the experimental attempts have been focused on measuring the total neutron production yields and energies, regardless of their production points summing up all the contributions coming from different production processes. To separate the secondary neutrons, produced directly from the beam interactions with the patient, from the ternary neutral component generated in the iterative interactions of fragmentation products with the treatment room and the patient itself, a tracking detector would hence be needed. Tracking the primary neutrons produced by the PT beam interactions with the patient tissues, which have energies of hundreds of MeV, is extremely challenging from the experimental point of view.

The MONDO tracker [3, 4] was designed, as a primary goal, to provide such capability for these ultrafast neutrons and to this aim exploits the detection single (SES) and double (DES) (consecutive) elastic scattering interactions. The detector is made out of a compact matrix of thin plastic scintillating fibers, assembled in orthogonally oriented layers, and has a total size of $16 \times 16 \times 20\,\mathrm{cm}^3$.

The tracker layout has been optimised to ensure a detection efficiency of the order of 10^{-1} and 10^{-3} for SES and DES events, respectively. The details on the fiber choice (squared fibers with 250 μm side), the implemented layout, and the related readout performed using the SPAD technology have been already presented elsewhere [5]. The final tracker will be realised with the same technique previously described by means of a constant step motorized system able to weave a single plane of fibers. Fibers of the same layers are then glued together, dropping a small quantity of glue in fiber interspace. Between each plane, a 5 μm aluminized Mylar foil will be placed in order to prevent the intralayer crosstalk.

The readout sensor will be able to cover the full detector area, providing the necessary spatial resolution (matching the fiber granularity) and detection efficiency. An autotrigger algorithm will be implemented using a two-level strategy (at pixel and chip level), allowing a significant combinatorial background reduction, while keeping a very high efficiency for signal events [6].

The strategy to evaluate the tracker's expected performance when detecting monoenergetic neutrons originating from a point-like source has already been discussed in detail elsewhere [7]. In this contribution, we present the evaluation of the expected performance using a detailed MC simulation of the neutrons production during a carbon ion PT treatment. The MC simulation was implemented using an accurate description of the detector geometry and accounted also for the trigger strategy.

The pixel size has been chosen in order to oversample the fiber; however, a fiber-pixel coupling is not expected to be possible, as the size of the fibers can range with a tolerance of about 6%. Calibration would be performed before operating the final detector. In order to take into account the nonperfect match between pixel and fibers, a fiber/pixel misalignment of 1 μm in both directions has been introduced in the simulation.

At present time, the Mylar foils and the glue are not included in the MC simulation.

The simulation was used as the basis for the background rejection algorithm development and to evaluate the performance of the fragment energy measurement strategies (for both partially and fully contained tracks). In this work, the elastic scattering event selection was performed exploiting MC truth information: protons emitted from single and double elastic scattering are selected using an *elastic* flag that identified the events. The secondary neutron spectra expected from a carbon ion beam impinging on a PMMA target have been used to evaluate the detector neutron tracking performance in a PT case scenario.

In the following, we present the simulation details, and we report the expected detector performance, in terms of both back-pointing resolution and efficiency.

2 MATERIALS AND METHODS

To evaluate the expected performance of the MONDO neutron tracker in a clinical environment, an MC simulation has been used. In the following, we describe the procedure used to evaluate the detector performance and the details about the simulation configuration.

The MC simulation studies discussed in this manuscript, used to evaluate the expected performance of the MONDO tracker in the context of PT applications, are based on the FLUKA code (FLUKA 2011.2c) [8, 9]. In particular, the study presented hereafter aimed at the evaluation of the detector backtracking efficiency and energy resolution.

The back-pointing performance is crucial in order to discriminate the scattered neutrons coming from the target and the ones produced by subsequent interactions with the treatment room environment. The latter contribution is an unavoidable background when using traditional, nontracking, neutron detectors. In this case, only the overall neutron production can be measured. Instead, by using a tracking detector like MONDO, it is possible to measure the neutron flux disentangling the different components. The precision achievable on the neutron production point plays a crucial role in this task. For this reason, an MC simulation has been set up to evaluate the MONDO potential in detecting the emission point of the neutrons produced by PT hadron beams (e.g., p or ^{12}C). The neutron production induced by a hadron beam is represented schematically in **Figure 1**. MONDO is a compact, movable detector and can be placed in different positions and at different angles with respect to the neutron production point. In this way, it is possible to reconstruct neutron production fluxes as a function of the emission angles. Moreover, the irreducible background of ternary neutrons produced from secondary interactions with patients and with the treatment room can be identified and rejected, thanks to the tracking capability of

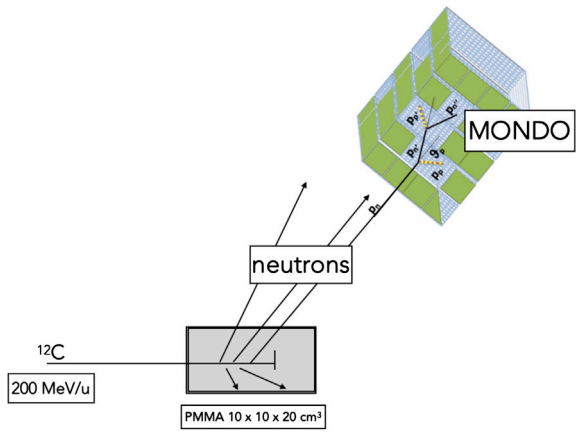

FIGURE 1 | Schematic representation of the detection of a DES event in MONDO for a neutron produced in a target by a particle therapy beam. The beam (p or ^{12}C) interacts with the target (e.g., patient tissues or material placed on the beamline) producing neutrons detectable in MONDO. The neutron emission point can be measured once the neutron four-momentum reconstruction is performed and the relative position of the detector and the target is known.

the detector. The distance between detector and neutrons production source (e.g., the fraction of solid angle) will be adapted to the specific treatment room and chosen beam rate. Assuming that the tracker is used to study the neutron production induced by PT beams, different strategies in the data analysis can be pursued depending on the experimental conditions. It is possible to exploit the reconstruction of single elastic scattering events (SES), assuming that the production point is known when studying the beam interactions with a thin target. Whenever the production point is not known (as in the case of PT applications), it is however possible to perform the full reconstruction of double elastic scattering events (DES) and measure the neutron four-momentum disentangling the primary and secondary radiation components. In **Figure 1**, a schematic representation of a DES event reconstruction is shown, showing the principle behind the neutron emission point measurement.

A detailed description of the detection strategy of how SES and DES can be used to measure the neutron characteristic is discussed elsewhere [4, 10]. In the following, the two-step approach adopted in the simulation to specifically reproduce the conditions expected in the PT environment is discussed.

Firstly, the expected neutron spectra, produced in PT treatments, have been obtained by means of a dedicated MC simulation. The energy of the neutrons produced by the interactions of ^{12}C ions of 200 MeV/u energy with a PMMA phantom (volume: 10 × 10 × 20 cm^3) has been obtained. The primary ions were shot at the center of the entrance phantom face (x and y planes), along the z-axis.

The second step has been the study of the interaction of such neutrons with the detector in a simplified setup: neutrons with the proper energy spectra (obtained in the previous step) have been generated, assuming a point-like source placed 20 cm away from the detector. The neutrons were shot along the z-axis in the detector center, while the entrance face of MONDO lies in the x and y planes.

The MONDO tracker layout used for the simulation has been optimised for the reconstruction of neutrons produced in PT applications [4]. The simulated detector has 800 layers of 16 cm × 16 cm × 250 μm fibers made of plastic scintillating material, x-y oriented, for a total size of 16 × 16 × 20 cm^3.

The response of the MONDO detector has been carefully included in the simulation to evaluate the resolution on the neutron energy and direction reconstruction, for both SES and DES events. The interactions of all the particles with the fiber matrix have been recorded by FLUKA and the details in the conversion of the collected light, at the fiber output, and the number of pixels that had an over threshold signal have been obtained.

The SPAD-based readout, described in Ref. 5, has been implemented in the simulation allowing us to test the reconstruction algorithms starting from the information provided in terms of pixels that have a signal over the threshold when a particle interacts with the corresponding fiber. The readout response has been simulated in an external dedicated code that uses as input the energy release in the fibers and processes this information following the measured performances [6]. When a scintillating fiber is crossed by a particle, it releases a dE fraction of its energy. Pixels associated with fibers are generated matching the fiber coordinates with the pixel one. Since fibers and pixels have different dimensions (and the mismatch between fiber matrix and sensor tiles is simulated with the introduction of a difference of 1 μm in both pixel dimensions), each generated pixel can be associated with two or more contiguous fibers. The dE released in the fiber has been converted in terms of photoelectrons detected by a single pixel. The energy release dE is first converted into scintillating photons considering the fiber light yield and the trapping efficiency. Conversion from scintillating photons to detected photoelectrons has obtained considering the pixel Fill Factor (FF 30%), the photon detection probability (PDP 33%), and the maximum number of SPADs in one pixel (30 SPAD). Fill Factor has been introduced considering that the active area is limited to the high part of the pixel; thus, only photons produced in correspondence with the area covered by SPADs can be considered in the conversion. To obtain the number of activated SPAD in a single pixel, all the photons produced from the fibers overlying the active area of the considered pixel have been considered. Since a SPAD can convert only one photon in photoelectron for each event, the formula

$$N^{n}_{SPAD} = PDP \times \frac{SPAD - N^{n-1}_{SPAD}}{SPAD} + N^{n-1}_{SPAD} \quad (1)$$

must be applied to all the considered photons impinging on the considered pixel. N^{n}_{SPAD} represents the number of occupied SPADs when the $n-$th photon is impinging on pixel and $SPAD$ is the number of total SPADs in one pixel.

The noise of the detector (dark current) has been included in the simulation of the detector but in this study, this

contribution has not been taken into account and only the physical interactions of the particles with the detector have been considered. A more detailed experimental characterisation of the sensor is needed in order to implement reasonable values and obtain a realistic tracking evaluation.

The detector performance has been studied using different energy spectra as input: either monochromatic or following the expected energy dependence in case of a PT application scenario. The obtained results are shown in the following section.

3 RESULTS

3.1 Monochromatic Beams

The kinetic energy of the recoil protons produced via elastic scattering interaction is calculated via range measurements in the MONDO baseline approach. Therefore, full containment of the proton tracks in the detector is required. To study the impact on the efficiency achievable in the neutron tracking, monoenergetic neutron beams in the range between 30 and 300 MeV have been studied. Neutrons undergoing both SES and DES were reconstructed applying the full containment constraint to the scattered protons and the obtained results were presented in Ref. 11. The expected DES (SES) interactions range from 10^{-3} (10^{-1}) to 10^{-4} (10^{-2}) as a function of the neutron energy. The proton containment in the MONDO detector, due to the need for computing kinetic energy via range, impacts strongly for neutrons above 100 MeV and in particular for DES events where the detection probability drops exponentially after 100 MeV.

For this reason, a different and complementary strategy has been developed in order to recover some of the events that were not totally contained inside the detector. In order to compute the proton kinetic energy, the deposited energy in each fiber and the timing of the scintillation photons have been studied. The proton dE/dx has been studied as a function of the track length and particle depth with respect to its production point along its direction. Monoenergetic neutrons have been used also to evaluate the achievable detector energy resolution. For all the reconstructed neutrons, the difference between the production and detected energy has been studied and the RMS of the resulting distribution, normalized to incoming neutron energy, has been used to compute the relative energy resolution.

For all the events with proton crossing at least 10 fibers, the length of the particle tracks inside the detector has been reconstructed for both contained and noncontained protons and the value of the energy loss in the single fibers provided from the FLUKA simulation has been collected for the first 40% of the total number of fibers composing the track. The choice of 40% allows us to consider only the initial flat part of the energy release distribution as a function of the particle path, excluding the Bragg-Peak area. The β value associated with the computed mean energy loss has been evaluated from the Bethe-Bloch equation. The initial proton kinetic energy

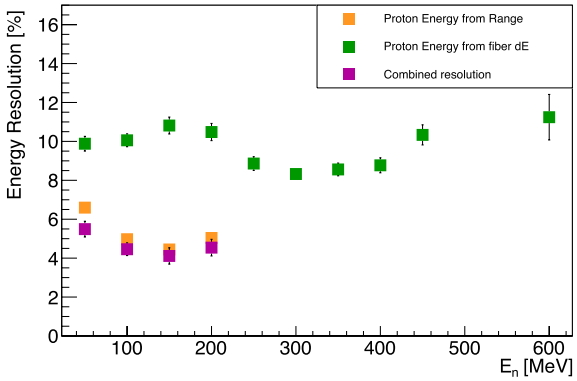

FIGURE 2 | Energy resolution for DES events as a function of the incoming neutron kinetic energy. Orange squares represent the energy resolution obtained via energy-range measurements while the green squares show resolution obtained from the dE/dx measurement. Violet squares represent the resolution obtained from the combination of the two methods.

that will be used from the reconstruction of the incoming neutron energy and direction can be computed from the obtained β.

The results are shown in **Figure 2** both for the neutron four-momentum reconstruction performed using the range (fully contained events, shown in orange) and for the energy loss inside the fibers for partially contained events (shown in green). While for neutron incoming energies below 200 MeV, the dominant contribution to the resolution is clearly the one that comes from the range measurements, while above 200 MeV, the full containment requirement is not fulfilled by most of the tracks, and hence the energy loss method is the only viable one.

While the energy resolution achievable with the range method is more performing (3% vs. 6%), the kinetic energy measurement via the energy loss detection inside the fibers allows reconstructing events above 200 MeV, providing a neutron full four-momentum measurement.

The monoenergetic beams have been used to study the back-pointing resolution as a function of the incoming neutron energy. The event reconstruction proceeds as detailed in Ref. 10: DES events are flagged and selected by means of MC truth information, the events are processed, and the production point is obtained, backtracking the reconstructed neutron in the plane that contains the point-like source. The distribution in the x and y planes for neutrons with incoming energy of 100 MeV is shown in the left picture of **Figure 3**.

The projections along the x and y directions can be obtained and a Gaussian fit can be performed in order to extract the single neutron reconstruction emission point resolution. The results for the projections in the x direction are shown in **Figure 3** (right, full markers) as a function of the neutron energies. In order to evaluate the intrinsic resolution on the neutron production point related to the uncertainty on the production angles and energy loss in the fibers, the back-pointing has been computed exploiting the MC truth kinetic

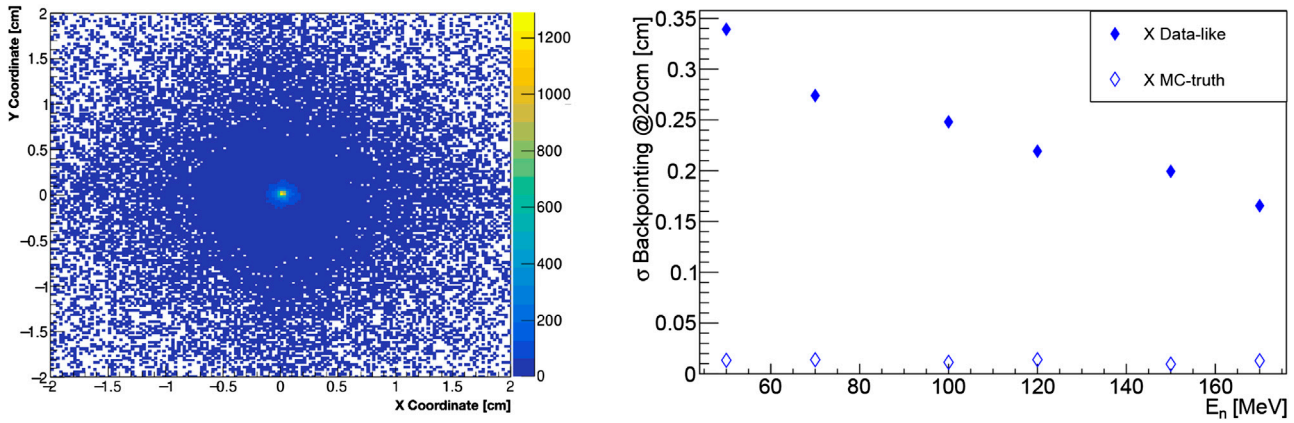

FIGURE 3 | (Left) Two-dimensional reconstructed emission point at 20 cm from MONDO detector. The distribution is symmetric for both *x* and *y* planes. **(Right)** Back-pointing resolution for the X-projection as a function of the neutron kinetic energy. Emission point at 20 cm from MONDO detector is assumed. The resolutions obtained from MC truth proton energy and direction are also shown. The error bars correspond to the statistical contribution in the back-pointing resolution measurement.

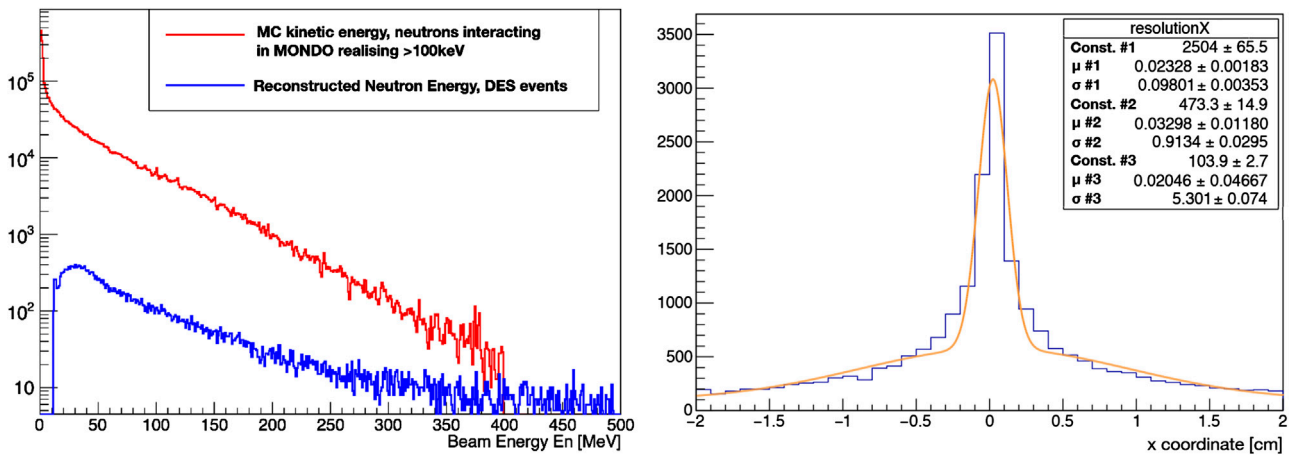

FIGURE 4 | (Left) Comparison between the simulated neutron spectrum generated from a 200 MeV ^{12}C ion beam on a PMMA target and the spectrum reconstructed by MONDO. **(Right)** Profile of the reconstructed emission point at 20 cm from MONDO detector. The distribution is symmetric for both *x* and *y* planes. Only the *x* plane is shown.

energy of the protons; thus, the empty markers show the resolution obtained in backtracking the neutron on its production plane. As can be seen, such contribution is nearly negligible and confirms the observation that the dominant contribution to the neutron tracking resolution in DES events is related to the error in reconstructing the protons angle and energy. The achievable resolution is below ~ 3.5 mm in the full explored energy range (above 70 MeV) and improves with the neutron energy as the proton multiple scattering decreases allowing a more precise reconstruction of the protons' direction and hence of the scattering angles. It has to be stressed that this back-pointing resolution fulfills the MONDO requirement of separating the ternary neutron component, coming from the treatment room, from the secondary one produced in the patient.

3.2 PT-Like Beams

The energy spectra of the neutrons produced in the interactions of carbon ions of 200 MeV/*u* with a PMMA target have been used to generate neutrons in a PT-like scenario, as represented in **Figure 1**. In **Figure 4** (left), the spectra of the neutron generated in the PMMA impinging on the MONDO detector depositing at least 100 keV in one fiber are shown in red. The blue spectra show the reconstructed energy of the neutrons interacting in MONDO via DES. As well as in the previous study, the MC truth has been exploited to select the DES events; thus, no inelastic contamination is included here.

For all the reconstructed events, a production point distribution in the plane containing the point-like source has been obtained. In **Figure 4** (right), the profile along the *x*-axis of the reconstructed point is shown. A similar symmetric behavior

in the x and y projections is observed as in the case of monoenergetic beams. A fit with a function implementing three Gaussian components is performed in order to account for the different contributions to the tracking resolution and the impact of a tail at large values: an overall resolution of ~ 3 mm is obtained as the weighted average of the three measured σ values.

4 DISCUSSION

The potential of the MONDO tracker in characterising the neutrons produced in a PT treatment with carbon ions has been explored using neutrons from a point-like source placed 20 cm from the detector face, according to the energy spectrum of neutrons produced in PT conditions (from FLUKA simulation). For this initial study, the neutrons have been produced with only a specific angle of impact in the center of the detector (zero neutron angles). Future developments foresee the study of achievable detection efficiency and resolution with more realistic scenarios in which neutrons have a widespread spatial emission and direction distributions.

While the geometry and readout structure have been implemented in the MC simulation, the detector electronic noise and the fiber crosstalk have not yet been introduced in the analysis of the MC-data events, as an experimental and complete characterisation of the readout sensor coupled with the scintillating fibers is still ongoing.

A preliminary event reconstruction software for which the full simulation chain is accounted, starting from the particles' interactions with the MONDO fibers up to the signal collection (readout response in terms of pixels with signals over threshold), has been implemented and DES events have been reconstructed and used to evaluate the detector performance.

Results have been obtained for monoenergetic beams and for neutrons generated with the energy spectrum expected in PT applications. In that condition, an energy resolution of $\sim 3-6\%$ has been evaluated for DES events, while the expected back-pointing resolution is below 3.5 mm (for a neutron source placed 20 cm from the detector surface).

The preliminary results presented hereafter fully support the capability of MONDO to monitor the neutrons produced in PT treatments with the required precision needed to disentangle the secondary and ternary neutron components, thus the direct production of beam interactions with the patient tissues from the neutrons produced by interactions with the surrounding environment.

DATA AVAILABILITY STATEMENT

The raw data supporting the conclusions of this article will be made available by the authors, without undue reservation.

AUTHOR CONTRIBUTIONS

All the authors contributed to the MONDO detector conception and development. MT contributed to the prototype test and readout characterisation. GB developed the MC code of the detector and participated in the prototype test beams. AB and GT contributed to the prototype readout characterisation and to the mechanical assembly of prototypes. MD, PD and YD contributed to the prototype test beams and to the MC development. MF and GF contributed to the readout characterisation and MC development. RM contributed to the prototype test characterisation, to the readout conception and test, to the MC development, and to the mechanical definition of the assembly strategy. MaM contributed to the mechanical definition and assembly procedure definition of the detector and its prototype. IM, SM, and AnS developed the MC framework for the carbon on target simulation. AdS, AlS, and VP developed the MC code of the detector, contributed to the readout conception, and participated in the test and characterisation of the detector prototypes and in the mechanical definition of the assembly strategy. LG, EM, and LP developed the innovative readout sensor SBAM. MiM supervised, coordinated, and contributed to the full system development and implementation, to the detector characterisation, and to the MC framework development.

REFERENCES

1. Gunzert-Marx K, Schardt D, Simon RS. Fast neutrons produced by nuclear fragmentation in treatment irradiations with 12C beam. *Radiat Protect Dosim* (2004) 110:595–600. doi:10.1093/rpd/nch138.
2. Hultqvist M, Gudowska I. Secondary absorbed doses from light ion irradiation in anthropomorphic phantoms representing an adult male and a 10 year old child. *Phys Med Biol* (2010) 55:6633–53. doi:10.1088/0031-9155/55/22/004
3. Schardt M, Patera V, Pinci D, Sarti A, Sciubba A, Spiriti E. Mondo: A neutron tracker for particle therapy secondary emission fluxes measurements. *Nucl Instrum Methods Phys Res Sect A Accel Spectrom Detect Assoc Equip* (2016) 824: 210–211. doi:10.1016/j.nima.2015.10.109.
4. Marafini M, Gasparini L, Mirabelli R, Pinci D, Patera V, Sciubba A, et al. MONDO: a neutron tracker for particle therapy secondary emission characterisation. *Phys Med Biol* (2017) 62:3299–312. doi:10.1088/1361-6560/aa623a.
5. Mirabelli R, Gasparini L, Magi M, Marafini M, Pinci D, Sarti A, et al. The mondo detector prototype development and test: steps toward an spad-cmos-based integrated readout (SBAM sensor). *IEEE Trans Nucl Sci* (2018) 65:744–51. doi:10.1109/TNS.2017.2785768.
6. Manuzzato E, Gioscio E, Mattei I, Mirabelli R, Patera V, Sarti A, et al. A 16 × 8 Digital-SiPM array with distributed trigger generator for low SNR particle tracking. *IEEE Solid-State Circuits Lett* (2019) 2:75–8. doi:10.1109/LSSC.2019.2934598.
7. Valle S, Battistoni G, Patera V, Pinci D, Sarti A, Sciubba A, et al. The mondo project: A secondary neutron tracker detector for particle therapy. *Nucl Instrum Methods Phys Res Sect A: Accel Spectrom Detect Ass Equip* (2017) 845:556–9. doi:10.1016/j.nima.2016.05.001.
8. Ferrari A, Sala PR, Fasso A, Ranft J. FLUKA: a multi-particle transport code (Program version 2005) (2005) p. 405. CERN-2005-010, SLAC-R-773, INFN-TC-05-11 (2005).
9. Battistoni G, Bauer J, Boehlen T. T, Cerutti F, Chin M. P. W, Dos Santos Augusto R, et al. The fluka code: An accurate simulation tool for particle therapy. *Front Oncol* (2016) 6:116. doi:10.3389/fonc.2016.00116.
10. Giacometti V, Battistoni G, De Simoni M, Dong Y, Fischetti M, Gioscio E, et al. Characterisation of the mondo detector response to neutrons by means of a fluka Monte Carlo simulation. *Radiat Meas* (2018) 119:144–149. doi:10.1016/j.radmeas.2018.10.006.

11. Gioscio E, Battistoni G, Bochetti A, De Simoni M, Dong Y, Fischetti M, et al. Development of a novel neutron tracker for the characterisation of secondary neutrons emitted in particle therapy. *Nucl Instrum Methods Phys Res Sect A Accel Spectrom Detect Assoc Equip* (2020) 958:162862. doi:10.1016/j.nima.2019.162862.

Conflict of Interest: The authors declare that the research was conducted in the absence of any commercial or financial relationships that could be construed as a potential conflict of interest.

frontiers in Physics

ORIGINAL RESEARCH
published: 19 November 2020
doi: 10.3389/fphy.2020.567732

Estimating the Relative Biological Effectiveness of Auger Electron Emitter ^{123}I in Human Lymphocytes

Hein Fourie[1†], Shankari Nair[2†], Xanthene Miles[2], Daniel Rossouw[2], Philip Beukes[3], Richard T. Newman[1], Jan Rijn Zeevaart[4], Charlot Vandevoorde[2] and Jacobus Slabbert[2]*

[1]Department of Physics, Stellenbosch University, Stellenbosch, Cape Town, South Africa, [2]Nuclear Medicine Department, NRF iThemba LABS, Cape Town, South Africa, [3]Department of Radiation Safety Health Environment and Quality, iThemba LABS, Cape Town, South Africa, [4]Department of Radiochemistry, South African Nuclear Energy Corporation, Pretoria, South Africa

OPEN ACCESS

Edited by:
Yolanda Prezado, INSERM U1021 Signalisation normale et pathologique de l'embryon aux thérapies innovantes des cancers, France

Reviewed by:
Dimitris Emfietzoglou, University of Ioannina, Greece
Jean-Pierre Pouget, Institut National de la Santé et de la Recherche Médicale (INSERM), France

***Correspondence:**
Shankari Nair
snair@tlabs.ac.za

†These authors have contributed equally to this work.

Specialty section:
This article was submitted to Medical Physics and Imaging, a section of the journal Frontiers in Physics

Received: *30 May 2020*
Accepted: *14 October 2020*
Published: *19 November 2020*

Citation:
Fourie H, Nair S, Miles X, Rossouw D, Beukes P, Newman RT, Zeevaart JR, Vandevoorde C and Slabbert J (2020) Estimating the Relative Biological Effectiveness of Auger Electron Emitter ^{123}I in Human Lymphocytes. Front. Phys. 8:567732. doi: 10.3389/fphy.2020.567732

Auger electron emitters are considered to be a promising strategy for targeted radionuclide therapy of metastatic diseases, given their high linear energy transfer (LET) and short range in tissue which could potentially limit normal tissue toxicity. Particularly Auger electron emitters that can be targeted into the DNA of tumor cells have been considered as an attractive cancer therapy in the past decade. In this study, the efficiency of the Auger electron emitter ^{123}I (half-life 13.2 h) to induce chromosomal damage was investigated by using the cytokinesis-block micronucleus assay. A stannylated deoxyuridine was synthesized and radiolabeled with ^{123}I, resulting in ^{123}IUdR that carried the Auger electron emitter across the nuclear membrane and allowed its incorporation into newly synthesized DNA. The DNA damage caused by the ^{123}I Auger cascade was estimated by evaluating the induced micronuclei frequencies in human peripheral blood lymphocytes obtained from three different donors. The isolated lymphocytes were stimulated with phytohemagglutinin (1 mg/ml) for 48 h before pulse labeling with ^{123}IUdR and the S-phase fraction was determined using flow cytometry. Geant4 Monte Carlo calculations were performed to determine the absorbed dose in cells by the Auger emitter. The relative biological effectiveness (RBE) was calculated by comparing the dose response curves for ^{123}IUdR with the reference dose response curves, obtained with ^{60}Co γ-ray irradiation in this study, for lymphocytes of the same donors. This resulted in a range of individual RBE values from 3 up to 10, depending on the donor and the radiation dose. In addition, dose limiting RBE values (RBE_{Max}) were calculated for each donor and ranged from 5 to 11, dependent on the inherent radiosensitivity of the donors. This study provides valuable information on the RBE of Auger electron emitter ^{123}I, which is identified as a promising theranostic radionuclide for future targeted radionuclide therapy.

Keywords: iododeoxyuridine, auger electron, ^{123}I, micronucleus assay, relative biological effectiveness, GEANT4 Monte Carlo simulations

INTRODUCTION

The Auger effect refers to the emission of a cascade of low energy electrons, including Auger, Coster-Kronig (CK), and super-CK electrons (collectively called Auger electrons) as a result of radioactive decay by electron capture or internal conversion. Both processes result in the creation of inner shell electron vacancies that are filled by electron transitions from shells of higher energy, resulting in the release of energy either as characteristic x-rays or as low-energy Auger electrons [1, 2]. The Auger effect was first discovered in independent work by Lize Meitner and Pierre Auger in the 1920's [3–5]. Many radionuclides that are commonly used in nuclear medicine follow this decay process, including ^{123}I, ^{125}I, ^{67}Ga, ^{99}mTc, ^{111}In, ^{201}Tl and others as described in Ref. 6. However, it took many years since the discovery of Auger electrons before radiobiologists observed the extreme cytotoxic effect of Auger electron emitters, particularly when they are incorporated into the nucleus of cells [7, 8]. This prompted the interest to use Auger electron emitters as a promising radionuclide therapy for the treatment of various types of cancer [6, 9]. Radionuclide therapy, as an alternative to external beam radiotherapy or brachytherapy, almost exclusively uses energetic electrons from particle emitting isotopes. It takes advantage of their limited range in tissue in order to deliver relatively high doses to tumors whilst sparing surrounding healthy tissue. The most commonly used β-particle emitters have a tissue penetration range in the order of up to 1–10 mm, depending on the energy, characterized by a low linear energy transfer (LET) of approximately 0.2 keV/μm [10]. Consequently, high radionuclide concentrations are required in the targeted tissue to make them effective. The β-particle emitters also induce a cross-fire effect, which results in the irradiation of not only the target cell but additional neighboring cells in their range. This might be beneficial to homogenize the radiation dose in large solid tumors, but it is rather disadvantageous for the treatment of a small cluster of tumor cells and it might also result in greater hematological toxicity [10–12]. In recent years, α-particle emitters have regained interest and popularity, based on new, optimized production processes and the availability of various targeting vectors, such as monoclonal antibodies [13, 14]. Their range in tissues is about 50–100 μm depending on the α-particle energy. Since they deposit most of their energy at the end of their track in a very small volume with a high relative biological effectiveness (RBE), cancer cells can be significantly damaged while causing minimal toxicity to surrounding healthy cells. Recent clinical studies have given encouraging results for targeted alpha-particle therapy (TAT) in the treatment of metastatic, castration-resistant prostate cancer and the number of promising radiopharmaceuticals for clinical TAT is growing rapidly [15, 16]. However, while it has been a long-standing research goal, the majority of the Auger electron emitter therapy studies still remain preclinical [10]. Both α-particle and Auger electron emitters are considered as high LET radiation qualities; with an LET of 80–100 keV/μm for α-particle emitters and an LET of 4–26 keV/μm for Auger electron emitters [15]. As a result, the path length of Auger electrons is much shorter compared to α-particles, typically <0.5 μm [16]. Another important difference is the lack of a cross-fire effect for Auger electron emitters. For α-particle emitters on the contrary, recent studies did observe a significant therapeutic effect on large tumors, pointing in the direction of a cross-fire effect [17, 18]. In the situation of DNA-associated decay, the RBE of Auger electrons is very similar to α-particles. The main challenge for Auger emitter therapy remains the requirement to target the radioisotope into individual tumor cells and more specifically, into the nucleus of those cell. On the other hand, this makes Auger emitters even more appealing, since they have a lower toxicity when they decay outside the cell nucleus (e.g., cytoplasm or outside cells), in contrast to α- and β-particle emitters [8, 19]. However, a growing body of evidence suggests that internalization in the cell nucleus is not obligatory for Auger electron emitters to induce cell killing, although the cytotoxic effect is less prominent than in the case of nuclear DNA targeting [20, 21].

Since nuclear localization seems to be of critical importance for the efficacy of Auger emitter therapy, several labeling methods and experimental approaches have been tested in the past decades in order to target Auger emitter to the nucleus of cancer cells [6]. More recent radiolabeling efforts are focused on monoclonal antibodies or peptides that recognize cell surface receptors displayed on cancer cells [22]. However, most of the pioneering work has come from using radiolabeled iododeoxyuridine, in particular with ^{125}I- or ^{123}I-5-iodo-2-deoxyuridine (IUdR) [16]. These thymidine analogues are directly incorporated into cellular DNA during the synthesis-phase (S-phase) of the cell cycle and provide one of the most reliable methods for the experimental measurement of the radiobiological effects of these nanometer range Auger emitters [10]. The dependence on the synthesis phase of the cell cycle for the incorporation poses a restriction to *in vivo* applications, but it is still very useful for *in vitro* proof of principle studies.

While ^{125}I is one of the more commonly used radioisotopes to study *in vivo* and *in vitro* Auger electron induced DNA damage, ^{123}I was chosen for this study. Despite the fact that it only releases about 14% of its decay energy in the form of Auger electrons, its relatively short half-life of 13.2 h makes it possible to deposit biologically detectable quantities of radiation energy over a short period of time. It makes this radioisotope also a good candidate for therapy, since this half-life would adapt well for peptide or oligonucleotide labeling and the biodistribution could be followed by scintigraphy based on the 159 keV γ-radiation [10]. The relatively long half-life of ^{125}I (59.4 days) would require exposing the cells to the isotope for weeks to accumulate enough disintegrations that result in detectable levels of biological damage. Using such long lived isotopes requires cryogenic freezing of *in vitro* cell samples in a mixture containing dimethyl sulfoxide (DMSO). The latter is a free radical scavenger with radio-protective properties and previous studies have shown a significant reduction in biological effects of DNA-bound Auger emitters in the presence of DMSO, pointing to the importance of indirect effects [23]. Therefore, it was decided to use ^{123}I in this study, so the cell samples could be

exposed to the radionuclide under normal physiological conditions.

The short range of the Auger electrons coincides with the 2 nm diameter of the DNA helix, since the typical high LET Auger emitter cascade will deposit its highest energy in a range of 1–2 nm [24]. Therefore, it is generally accepted that one decay of ^{125}I and ^{123}I associated with the DNA, will result in one DNA double-strand break (DSB). In addition, Auger electron emitters also damage the cells indirectly via the radiolysis of water and the production of free radicals, such as reactive oxygen species (ROS). More recently, several studies have investigated the non-targeted effect of Auger-electron emitters, known as bystander effects, on more distant cells [25–27]. Previous studies which made use of ^{125}I- and ^{123}I-iododeoxyuridine (IUdR) measured RBE values of 8 and 7 respectively in Chinese hamster V79 lung fibroblasts [24, 28]. It has been demonstrated by several authors that Auger electron emitters will cause complex and multiple DSB to the DNA via direct interaction or through the ROS production [29, 30], which can result in cell death if unrepaired or chromosomal aberrations in the case of misrepair [31–33]. The induction of complex DNA damage that challenges the cells' repair capacity, is generally accepted to be the underlying mechanism of the high genotoxic potential of Auger emitters. However, a recent study by Schmitz et al. highlighted that only a limited number of studies are available on chromosomal aberrations induced by Auger emitters [32]. In their study, the authors illustrated a strong genotoxic effect on ^{125}IUdR, even at a low dose of 0.2 Gy, by analyzing chromosomal aberrations and apoptosis in human peripheral blood lymphocytes for the first time [32]. To the best of our knowledge, similar *in vitro* data on ^{123}IUdR is not available yet, however Hindorf et al. did establish the feasibility of treating B-cell lymphoma with internalized ^{123}I or ^{125}I using Monte Carlo dosimetry calculations [34, 35]. In the current study, the micronucleus assay was used since it is considered to be one of the most reliable methods to determine chromosome damage as it enables the measurement of both chromosome loss and chromosome breakage. Micronuclei (MNi) are small extranuclear bodies resulting from chromosome breaks. The cytokinesis-block micronucleus (CBMN) assay is the preferred method to measure MNi in genetic toxicology testing, since it restricts the scoring to once-divided binucleated (BN) cells. This BN appearance is obtained by adding cytochalasin-B (Cyto-B) to the cell cultures, which inhibits the completion of cytokinesis. Restricting the scoring of MNi to these BN cells prevents confounding factors due to suboptimal or altered cell division kinetics [36]. Over the years, the CBMN assay has proven to be a very reliable, thoroughly validated and standardized technique in the field of radiation biology to evaluate *in vivo* radiation exposure of occupational, medical and accidentally exposed individuals and to assess individual *in vitro* radiosensitivity or cancer susceptibility [37].

Dosimetry calculations are needed in order make a good interpretation of the radiobiological effects caused by an internally distributed radionuclide and to allow comparison with the effects observed with an external beam source. Early attempts to determine the absorbed dose used semi-analytical methods according to the MIRD schema [38, 39]. Monte Carlo methods have been used to overcome the limitations of analytical methods in describing the transport of low energy charged particles at the cellular level [40–42]. Direct comparisons of radionuclide microdosimetry are complicated since different radionuclide emission spectra, particle interaction cross section tables, low-energy physics models, simulation geometry and other approximations are employed by the different Monte Carlo codes. In this work, we employ the open-source and well-documented Geant4-DNA Monte Carlo toolkit which has been widely used for nano- and microdosimetric applications [43], and previously described in [44]. The ^{123}I-iododeoxyuridine (^{123}IUdR) was synthesized to carry ^{123}I across the cell membrane and be incorporated into synthesizing DNA. Human lymphocytes were used in this study, which reside predominantly in the G0 phase, the DNA pre-synthetic stage of the cell cycle. Therefore, lymphocytes were stimulated to undergo *in vitro* mitoses using phytohemagglutinin (PHA) in order to push the cells into the S-phase and allow maximum incorporation of ^{123}IUdR. As previously mentioned, chromosomal damage was evaluated with the CBMN assay and RBE values were calculated at several levels of biological effect as well as RBE_{Max} by comparison with ^{60}Co γ-ray irradiations.

MATERIALS AND METHODS

Synthesis of ^{123}I-Iododeoxyuridine

All reagents were received from commercial sources (Sigma-Aldrich, Merck South Africa) and were used without further purification. All reactions were performed under a nitrogen atmosphere; unless otherwise stated. ^{123}IUdR synthesis was performed using a modified protocol from that of Uddin et al. [45]. Hexabutylditin (200 μL) was added to a solution of 5-iodo-2′-deoxyuridine (50.0 mg) and tetrakis (triphenylphosphine) palladium (0) ($Pd(PPh_3)_4$) (7.00 mg) in anhydrous dioxane (3 ml) and heated at 100°C for 18 h. The reaction progress was monitored by thin layer chromatography (TLC) using aluminum backed silica-gel 60 F-254 plates (Merck, South Africa) and was observed using both ultraviolet and fluorescent light. Following completion, the reaction mixture was cooled to room temperature, concentrated under vacuum and subjected to flash chromatography using Kieselgel 60 silica gel (Sigma, South Africa), hexane and ethyl acetate to afford 5-(tributylstannyl)-2′-deoxyuridine (48.2 mg, 67%) as a yellow oil.

Synthesis of ^{123}IUdR, 2

5-(Tributylstannyl)-2′-deoxyuridine (0.50 mg) and $Na^{123}I$ (8 μL, ^{123}I produced *via* the ^{127}I (p, 5n) ^{123}Xe cyclotron reaction and recovered as no-carrier-added $Na^{123}I$ in 0.01 M NaOH solution) were reacted at room temperature in the presence of *N*-chlorosuccinimide (1.00 mg) in a (1:2) DMSO: phosphate-buffered saline (PBS) solution for 20 min. The reaction was then quenched by the addition of an aqueous solution of sodium thiosulfate (0.5 mg) in deionized water (0.5 ml). The quenched mixture was further diluted with deionized water (2 ml) and loaded on a pre-conditioned (3 ml methanol; 2 ml

deionized water) reversed phase C18 mini-cartridge (500 mg C18, 3 cc, Sep-Pak, Waters, United States). Elution was carried out with the eluent composed of 5% ethanol in 95% deionized water with a flow rate of 1 ml/min, at $\lambda = 254$ nm and produced a peak at $t_r = 17.1$ min on a high-performance liquid chromatography (HPLC) C18 column (250 mm × 4.6 mm, 5 μm) (Phenomenex Luna, United States). The radiochemical content of the labeled product was determined using a CsI (Tl) radioactivity detector (Carroll and Ramsey Model 105S-1). The radioactivity content of ^{123}IUdR constituted approximately 52.9 MBq (or 1.43 mCi), was further diluted to 2.00 ml of 5% ethanol in water. The collected fraction of ^{123}IUdR was diluted in Roswell Park Memorial Institute (RPMI) medium (Gibco, ThermoFisher, South Africa), supplemented with 10% fetal calf serum (Lonza, South Africa) and 1% penicillin and streptomycin (Lonza, South Africa) to a final activity concentration of 26.5 MBq/mL.

Blood Sample Collection and Experimental Conditions

The ethics approval for the study was obtained from the Human Research Ethics Committee at Stellenbosch University (reference number: S12/04/091). Blood samples were collected by venipuncture from three male adult volunteers (25–50 years), from whom informed consent was obtained prior to the experiments. Blood samples were collected in lithium-heparin collection tubes and peripheral blood mononuclear cells (PBMCs) were isolated from whole blood using density gradient cell separation medium (Histopaque-1077, Merck). The PBMCs were counted and suspensions of approximately 1×10^6 cells/1.00 ml were pipetted into a 15 ml round bottom tube. Samples were divided for irradiations with ^{60}Co γ-rays and the labeling with ^{123}IUdR. Each sample set included a sham-irradiated control sample. For all radiation exposure conditions, lymphocytes were stimulated to divide in culture using phytohemagglutinin (PHA, 1 mg/ml) and kept at 37°C in a humidified 5% CO_2 incubator for 48 h.

Thereafter, the cell suspensions from each donor were exposed to graded doses of ^{123}IUdR (0, 0.19, 0.37, 0.56, 0.74, 0.93, 1.9, and 3.7 MBq) diluted in culture medium at 37°C. After a 1 h pulse labeling, samples were washed (two times) with cold PBS to remove excess ^{123}IUdR that was not incorporated into the cell. The radioactivity levels were then measured in a 3-inch well type NaI (Tl) scintillation detector (CANBERRA model 802 series) that was coupled to a multi-channel analyzer (Silena). The Silena EMCA 2000 software was used to collect the characteristic γ-ray emissions of ^{123}I at 159 keV. The readings were corrected for detector efficiency, photo-peak abundance, and decay. After readings were completed, the culture tubes were left at room temperature for 24 h in order to accumulate radiation damage. After these 24 h, the cell pellet was resuspended in fresh complete RMPI medium containing PHA (1mg/ml, Sigma Aldrich, South Africa) and cytochalasin B (6mg/ml, Sigma Aldrich, South Africa) at 37°C in a humidified 5% CO2 incubator for 24 h.

For the cultures irradiated with ^{60}Co γ-rays, the isolated, stimulated lymphocytes were exposed to graded doses of 0, 0.5, 1, 2, and 4 Gy. Cell suspensions were placed between a 5 mm thick sheet of Perspex (build-up) and 50 mm backscatter material with a dose rate of 0.49 Gy/min for a 300 mm × 300 mm field size at 750 mm Source to Surface Distance (SSD). Thereafter, cytochalasin B (6mg/ml, Sigma Aldrich, South Africa) was added and cultures were incubated for a further 24 h.

Cytokinesis Block Micronucleus Assay

After exposure to either ^{60}Co γ-rays or ^{123}IUdR, the cell cultures were harvested at total culture time of 72 h. This involved washing the pelleted sample with a cold hypotonic KCl solution (0.075 M). Samples were then washed using methanol: acetic acid: ringer fixative solution (10:1:11) and stored at 4°C overnight. Samples were then washed with methanol: acetic acid (10:1) solution. Thereafter, concentrated cell suspensions were dropped on clean microscope slides and stained with acridine orange. For each sample, approximately 500 binucleated lymphocytes were manually scored using a fluorescent microscope (Zeiss, Axio Imager A1) at 20× magnification. At least 3 slides were analyzed per exposure condition and the average number of micronuclei per 500 BN cells was calculated for each condition.

S-phase Fraction Determination

The ^{123}IUdR incorporation in the DNA of the lymphocytes depends on the fraction of cells that goes through the S-phase of the cell cycle. Therefore, flow cytometry was used in this study to determine the number of cells which were in S-phase at the time they were labeled with ^{123}IUdR. Two lymphocyte cultures (one stimulated by PHA and one non-stimulated) from each donor were used for this purpose. A bromodeoxyuridine (BrdU) kit (BD Pharmingen, Germany) was used to detect active DNA synthesis, through antibody-based staining of BrdU, together with total DNA content based 7-AAD staining. BrdU is a synthetic nucleoside and well-known thymidine analogue, which can be incorporated into newly synthesized DNA of replicating cells during S-phase. This staining technique makes it possible to clearly separate cells in G1 from early S-phase, or late S-phase from G2/M [46]. The non-stimulated culture was used to determine the background counts which should be subtracted from the stimulated culture. Briefly, cells were stimulated with PHA as described previously, pulse labeled with BrdU for 1 h and analyzed after 48 h in culture. The cultures were fixed and permeabilized using the BD Cytofix/Cytoperm buffer and incubated with DNase for 1 h at 37°C. Thereafter, the samples were washed with the BD Perm/Wash buffer and incubated with the anti-BrdU antibody for 20 min at room temperature in the dark. The samples were washed again and total DNA was stained using 20 uL 7-AAD, resuspended in about 1 ml of the provided staining buffer and events acquired using the BD Accuri C6 Flow cytometer ((BD, Becton Dickinson and Company, San Jose, United States).

Determination of the Absorbed Dose (MBq to Gy)

The Geant4 Monte Carlo toolkit was used to calculate the dose delivered to the cells by the incorporation of ^{123}I into the cellular DNA as previously described in [44]. The dosimetric calculations for these *in vitro* experiments with ^{123}IUdR involved converting the energy imparted by the incorporated activity A_0 in a mass M of cells into an absorbed dose value D. The absorbed dose is defined as the mean energy imparted $\bar{E}$ by ionizing radiation to matter of mass m in a finite volume V by $D = \bar{E}/m$.

The mass of a spherical shape, $m = \rho V = 4/3\pi r^3$, can be obtained using the density and the volume, or the radius if it is known.

The dependence of the dose absorbed on the size and geometry of the cell is clear from the definition of absorbed dose. For this reason, experimental measurements of the diameters of isolated and stimulated lymphocytes were made using light microscopy and a calibrated imaging system. The total number of intra-nuclear decays during the 24 h period could be derived by integration of the experimentally obtained average incorporated radioactivity [47]. ^{123}I has a half-life τ of 13.2 h (the decay constant $\lambda = Ln\ (2)/t$. The activity at a time t is given by:

$$A(t) = A_0 e^{-\lambda t} = A_0 e^{-\ln(2)t/\tau} \quad (1)$$

The number of disintegrations after a time Δt would then be given by:

$$N(\Delta t) = \int_0^{\Delta t} A(t)dt = \frac{A_0 \tau}{\ln(2)}\left[1 - e^{-\ln(2)\Delta t/\tau}\right] \quad (2)$$

As described by Makrigiorgos et al., the cumulated radiation dose to the cells may be calculated by using the total number of decays, the average $\overline{E}$ energy deposited in the cell per decay, and the cellular dimensions [28]. Sefl et al. concluded that under relevant clinical conditions, the uptake rate of the radiopharmaceutical is an important additional factor that needs to be considered in radiobiological models of cell survival in targeted radionuclide therapy [48]. In our study, the incorporated activity A_0 was measured experimentally in the cell pellet using a 3-inch well type NaI-scintillation detector. To improve the radionuclide uptake, the ^{123}IUdR was introduced to the lymphocytes 48 h after stimulation, when a large percentage of the cells would be in S-phase. To further prevent additional radionuclide uptake, the residual activity was washed out and cold medium was used to prevent further division. Therefore, the uptake rate as defined by Sefl et al. was not taken into consideration in the dose calculations that were performed as part of this study. Following from equation [2] the absorbed dose in the mass M of cells is determined by:

$$D\,[Gy] = \frac{N(\Delta t) \cdot \overline{E} \cdot 1.6 \times 10^{-19}}{M} \quad (3)$$

The average energy $\bar{E}$ deposited in a cell per decay was obtained from Monte Carlo simulations using the Geant4-DNA toolkit and described in Fourie et al. [44]. The Geant4-DNA extension of the Geant4 Monte Carlo toolkit simulates electron tracks and their energy deposition, collision-by-collision, down to the excitation threshold of liquid water (7.5 eV); opposed to other MC codes like MCNP or EGS which are limited down to 1 keV. In the study by Fourie et al., spheres of unit density water were used to represent a cell and its nucleus in suspension. The G4EmDNAPhysics physics list and Livermore models were used to describe all particle interactions during the simulation. The G4RadioActiveDecayPhysics class along with the built in ENSDF emission data from Brookhaven National Laboratory was used to simulate the radioactive decay of ^{123}I and resultant x-ray and electron emissions. Readers are referred to [49] for more details.

The mass M in which the cumulative energy is deposited is obtained from the mass of total number of cells seeded per culture, corrected by the S-phase fraction. Sefl et al. investigated the effect of cell geometry on S-values (energy deposited per unit activity) using the Geant4 Monte Carlo toolkit with the Geant4-DNA low-energy extension [50]. For the ^{125}I radionuclide they found the S-values of the commonly used spherical geometry corresponded within 5% to ellipsoid geometries when the radionuclide was distributed within the cell. For the most oblong ellipsoid, the dose to the nucleus was 22% less compared to the spherical geometry when the radionuclide was distributed in the cytoplasm. Similarly to Fourie et al. [44], they found the dose to the nucleus was a factor of 10 less when the radionuclide was distributed outside of the nucleus. The S-phase fraction attempts to approximate the number of cells in the sample which incorporated the ^{123}I into the nucleus.

Relative Biological Effectiveness

The resulting radiation-induced chromosomal damage is expressed as the number of MNi per 500 BN cells. This value was then plotted against the absorbed dose and a dose-response curve was fitted to the data points. For low-LET radiation (e.g., ^{60}Co γ-rays) the curve usually had the linear-quadratic form, which can be described as $y = c + \alpha D + \beta D^2$. Here, y represents the number of micronuclei (per 500 BN cells) induced by a dose D. The background MNi frequency of each donor c (obtained from the control sample which was not exposed to radiation) is subtracted from each data point before the line fitting is done, resulting in $y = \alpha D + \beta D^2$. For high-LET radiation, the α-term becomes large and eventually the β-term becomes biologically less relevant and also statistically "masked" such that the dose response is approximated by a linear equation.

The RBE is expressed as the ratio of the absorbed doses of a low-LET reference radiation quality (e.g., 250 kV X-rays or ^{60}Co γ-rays) to a test radiation quality which produce the same level of biological effect (i.e., in this specific study: the doses $D_{Co\text{-}60}$ and $D_{I\text{-}123}$ which produce y MN). The dose producing the effect y can be determined by solving for D in the fitted dose-response curves.

$$RBE = \frac{D_{Co-60}}{D_{I-123}} = \frac{D_{\text{linear-quadratic}}}{D_{\text{linear}}} = \frac{-\alpha_{Co-60} + \sqrt{\alpha_{Co-60}{}^2 + 4\beta y}}{2\beta} \div \frac{y}{\alpha_{I-123}} \quad (4)$$

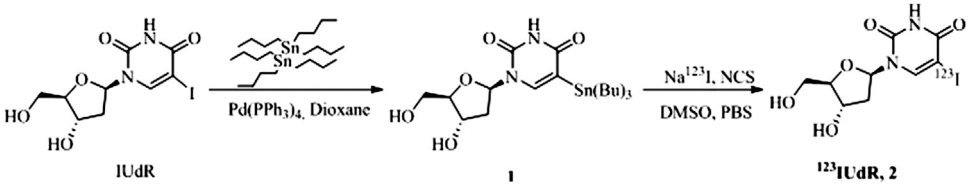

FIGURE 1 | Synthesis and labeling scheme of ^{123}I-iododeoxyuridine, 2.

The RBE value is dependent on the spatial distribution of the energy imparted, the density of ionizations per path length of ionizing particles and the reference radiation. The IAEA TRS 405 and the ICRP-ICRU RBE Committee defined two representative RBE values: the maximum value of relative biological effect (RBE_{Max}) and the minimum relative biological effect (RBE_{Min}) [51, 52]. RBE_{min} is the RBE at very high doses; whilst RBE_{Max}, also known as the dose limiting RBE, is the RBE at near zero dose and can be represented by the ratio of the initial slopes (α–values) of the dose-effect curves for the studied radiation and the reference radiation:

$$RBE_{Max} = \frac{\alpha_{I-123}}{\alpha_{Co-60}} \quad (5)$$

Statistical Analysis

Data presented includes the mean number of MN ± standard deviation where applicable and radioactivity levels of independent experiments on different days. Statistical analysis and curve fitting were performed using GraphPad Prism Software Version 5.00 for Windows. Results were considered to be statistically significant at $p < 0.05$.

RESULTS

Radiolabeling of ^{123}I-Iododeoxyuridine

The radiolabeling of IUdR (**Figure 1**) was achieved by first producing a tin intermediate by heating 5-iodo-2′-deoxyuridine with hexabutylditin and tetrakis (triphenylphosphine) palladium (0) ($Pd(PPh_3)_4$) in anhydrous dioxane for 18 h [45]. The tin intermediate was produced via the palladium-catalyzed metal-halogen exchange reaction, whereby the palladium (0) catalyst is oxidatively added to the carbon-iodine bond, followed by transmetallation of one of the tin groups to the palladium center with removal of bromotributyltin [53]. The reaction progress was monitored by thin layer chromatography (TLC) and once the reaction was completed, the reaction mixture was subjected to column chromatography using ethyl acetate and hexane as mobile phase to isolate **1** as a yellow oil in 67% yield. The structure was confirmed using high performance liquid chromatography (HPLC) and ^{1}H NMR (proton nuclear magnetic resonance) spectroscopy. Then, ^{123}IUdR, **2**, was successfully synthesized by adding $Na^{123}I$ to a solution of **1** and *N*-chlorosuccinimide in DMSO and PBS for 20 min at room temperature. The reaction was stopped by the addition an aqueous solution of sodium metabisulfite to quench any iodine in the reaction mixture. Thereafter, purification was done by reverse phase HPLC using a solution of 5% ethanol in deionized water to obtain **2** with approximately 52 MBq (or 1.4 mCi) radioactivity.

Incorporation of ^{123}I-Iododeoxyuridine

The ^{123}IUdR incorporation into DNA of isolated lymphocytes is dependent on the fraction of cells that goes through the synthesis phase of the cell cycle. Cell cycle analysis was performed with flow cytometry to determine the percentage of cells that were in S-phase during pulse-labelling with ^{123}IUdR. Two lymphocyte cultures of approximately 1 × 106 cells each (one stimulated by PHA and one non-stimulated) were used from each donor to determine the S-phase fractions. The non-stimulated culture served as the background count which was subtracted from the stimulated culture. After subtraction, the fraction of lymphocytes which incorporated BrdU was found to be approximately 22% for donor 1, 22% for donor 2, 13% for donor 3. The residual radioactivity that was measured after the different wash steps is presented in **Figure 2** for donor 3 after 1 h pulse-labelling with ^{123}IUdR. This clearly illustrates that stimulated lymphocytes could incorporate ^{123}IUdR more effectively than their non-stimulated counterparts. Comparing the slopes of the fitted trend-lines, the average uptake of ^{123}IUdR at different activity levels increased by a factor of 2 due to the addition of PHA.

^{123}I-Iododeoxyuridine Dose Response Curve

The lymphocyte samples were exposed to concentrated solutions containing ^{123}IUdR, washed with cold PBS and residual radioactivity levels were measured in a well type sodium iodide scintillation detector. These measured activities were converted to absorbed dose (Gy) as described in a previous publication using equation [3, 44]. The International Atomic Energy Agency reports that peripheral lymphocytes 48 h after stimulation have a cell volume of about 500 μm^3. Using a calibrated image analysis system, an average cell diameter for our isolated and stimulated lymphocytes was found to be 9.8 ± 1.7 μm (~486 μm^3). Therefore, in the absorbed dose calculations, a cellular diameter of 10 μm and a nuclear diameter of 8 μm were assumed. The resulting absorbed dose and associated induced MNi per 500 BN cells are presented in **Table 1** for the three donors.

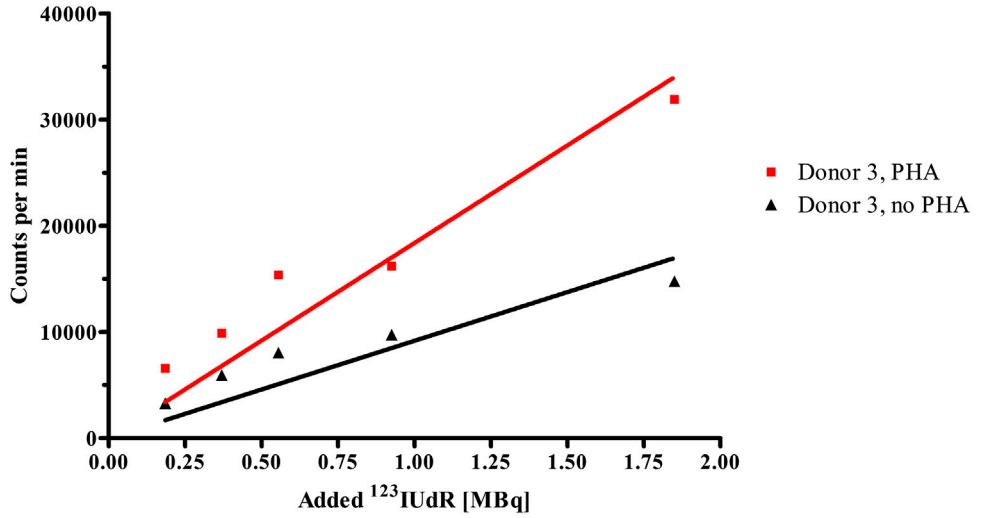

FIGURE 2 | Radioactivity levels incorporated by stimulated (PHA) and non-stimulated (no PHA) lymphocyte cultures of Donor 3 after the 1 h pulse-labelling with 123IUdR activities.

The ^{123}IUdR activity levels resulted in a higher absorbed dose for donor 3, compared to donors 1 and 2, while the S-phase fraction of donor 3 was only 13%. The higher absorbed dose value might be attributable to the fact that a different synthesis batch was used for donor 3, while donor 1 and 2 came from the same batch. Therefore, it is suspected that the new batch had a higher labeling efficiency, thereby leading to an increase in uptake for donor 3 per added activity.

A linear relationship between micronuclei frequency and ^{123}I activity (converted to absorbed dose values) could be established, as shown in **Figure 3**. The background counts are subtracted from the individual dose points, hence the linear fit intercepts the origin. The lowest activity level of 0.19 MBq ^{123}IUdR did not induce a significant increase in MNi compared to the background MNi frequency of each donor ($p = 0.24$), but a significant increase was observed from 0.37 MBq ^{123}IUdR onwards ($p < 0.05$). The MNi frequencies induced by the higher dose points (>1 Gy) deviate significantly from a linear response. This under-response could be a characteristic of cell death or mitotic delay due to the high biological effectiveness of Auger electrons. Therefore, these higher dose points were not taken into account for the linear fit presented in **Figure 3**. In addition, the 1.85 MBq of ^{123}IUdR activity induced a very high level of MNi for donor 2 (207 MNi/500 BN cells). This point was considered as an outlier and not included in the fitting.

Dose Response Curve Donor After ^{60}Co Dose Response Curve

In order to determine the biological effectiveness of the ^{123}I Auger electrons, lymphocytes from the same donors were exposed to a reference radiation quality, ^{60}Co γ-rays, with graded doses ranging from 0.5 up to 4 Gy. The observed number of MNi per 500 BN cells for each donor were plotted against the dose, which resulted in the characteristic linear-quadratic dose-response curves for low-LET radiation for each donor, as shown in **Figure 4**. Again, the induced MNi frequencies were plotted, where the background counts from the sham-irradiated controls were subtracted for each dose point. **Table 2** shows the α- and β-values obtained from the linear-quadratic curves as

TABLE 1 | The mean absorbed dose (Gy) and mean micronuclei (per 500 BN cells) induced following exposure to different levels of ^{123}IUdR activity.

^{123}IUdR added (MBq)	Donor 1		Donor 2		Donor 3	
	Gy	MN	Gy	MN	Gy	MN
0	0	43 ± 7	0	36 ± 7	0	82 ± 16
0.19	0.16 ± 0.02	44 ± 10	0.05 ± 0.01	45 ± 13	0.18 ± 0.02	107 ± 28
0.37	0.10 ± 0.02	69 ± 9	0.14 ± 0.02	72 ± 17	0.26 ± 0.02	138 ± 18
0.56	–	–	–	–	0.55 ± 0.05	156 ± 2
0.74	0.17 ± 0.02	84 ± 10	0.13 ± 0.02	79 ± 16	–	–
0.93	–	–	–	–	0.92 ± 0.08	210 ± 28
1.85	0.57 ± 0.05	116 ± 17	0.27 ± 0.05	207 ± 27	1.41 ± 0.13	190 ± 23
3.70	1.85 ± 0.16	137 ± 27	1.56 ± 0.14	154 ± 22	–	–

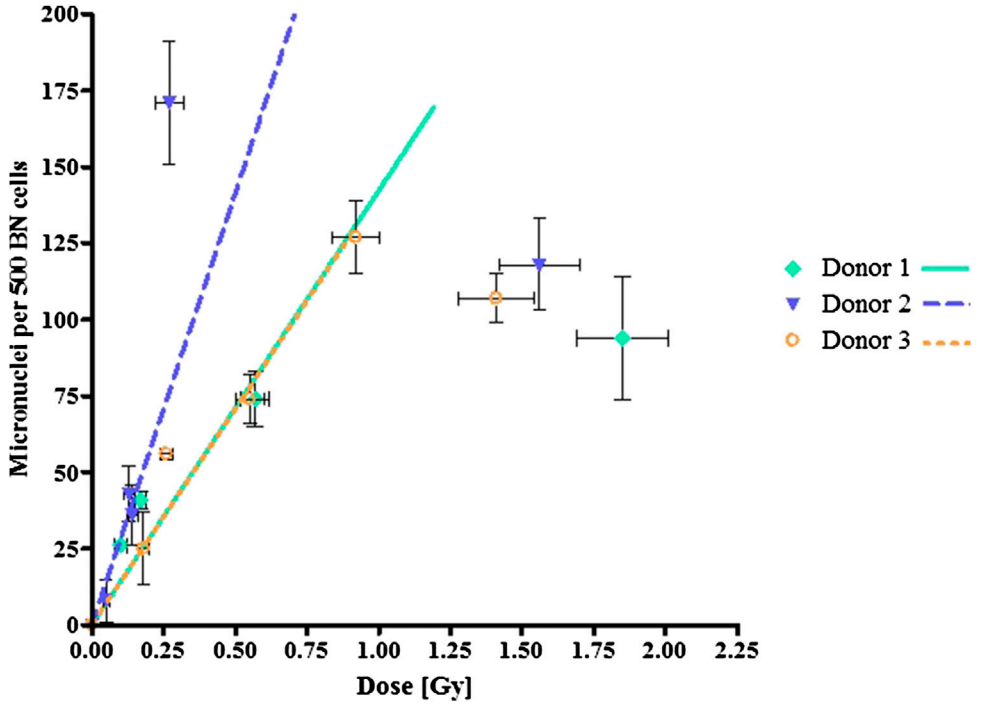

FIGURE 3 | Dose-response curves following exposure to 123IUdR activities presenting micronuclei formation as a function of absorbed radiation dose (Gy). The error bars are the standard deviations of the mean micronuclei frequency/500 BN cells for each dose point.

described in **Eqs 4** and **5**. The α-values for the Auger emitter are significantly greater than that of the reference radiation, indicating that the lymphocytes are more radiosensitive to the Auger electron emitter thereby causing more biological damage than the ^{60}Co reference radiation quality.

The Relative Biological Effectiveness

Using the fitted curves obtained from the ^{123}I and ^{60}Co experiments with the same donors, the RBE was calculated using equations [4] for each ^{123}I dose point reported in **Table 1** (which induces a specific number of MNi, i.e. the biological effect). In this way, a range of RBE values was obtained for each donor, depending on the dose under investigation. This calculated RBE range is given in **Table 3** and visually presented in **Figure 5**. The dose-limiting RBE (RBE_{Max}) was obtained from the α-values of the fitted dose-response curves as outlined in equation [5] and is also listed in **Table 3**.

As shown in **Figure 5** the RBE plateaus for each donor, reaching RBE_{Min} values between 3 and 5, suggesting that above a certain dose level, the relative effectiveness of the Auger electrons to induce a certain response remains constant. Much larger RBE values were observed at the radiation doses below 0.1 Gy, particularly for donor 1 and 2 (see **Figure 5**). This observation is in line with the general rule that RBE values increase with decreasing dose. Based on our findings, it seems that the variation in the RBE values for the different donors is much more pronounced at low doses. This could be indicative of donor specific cellular response at low doses. In addition, a rather large variation was observed in RBE_{Max} values, where the dose limiting RBE for donor 3 was almost half the value of donor 1 and 2.

DISCUSSION

Owing to the ability of Auger electron emitters to deposit their energy in an extremely small volume, typically in the range of cubic nanometers, Auger electron emitters are now increasingly considered for therapeutic purposes [54]. There are few satisfying vectors available for specifically targeting the nuclear DNA of cancer cells; historically antibodies or peptides are used to target cancer cell membranes but, following internalization in the cells using these vectors, the transport from the cytoplasm to the nucleus is one of the key stages in the delivery of Auger emitter therapy as recently described by Rosenkranz et al. [55]. The number of pre-clinical studies with Auger electron emitters is growing, which is illustrated in two very recent publication with the ^{123}I-Meitner-Auger PARP1 inhibitor (^{123}I-MAPi) and a small-molecule Auger electron emitter targeting the prostate-specific membrane antigen (PSMA) [56, 57]. ^{123}I-MAPi the first Auger-based theranostic PARP inhibitor able to directly deliver its lethal damage in the DNA of glioblastoma cells [56]. The isotope ^{123}I is an ideal candidate for targeted radionuclide therapy, due to its Auger decay and the opportunity to simultaneously image the tumor with SPECT imaging based

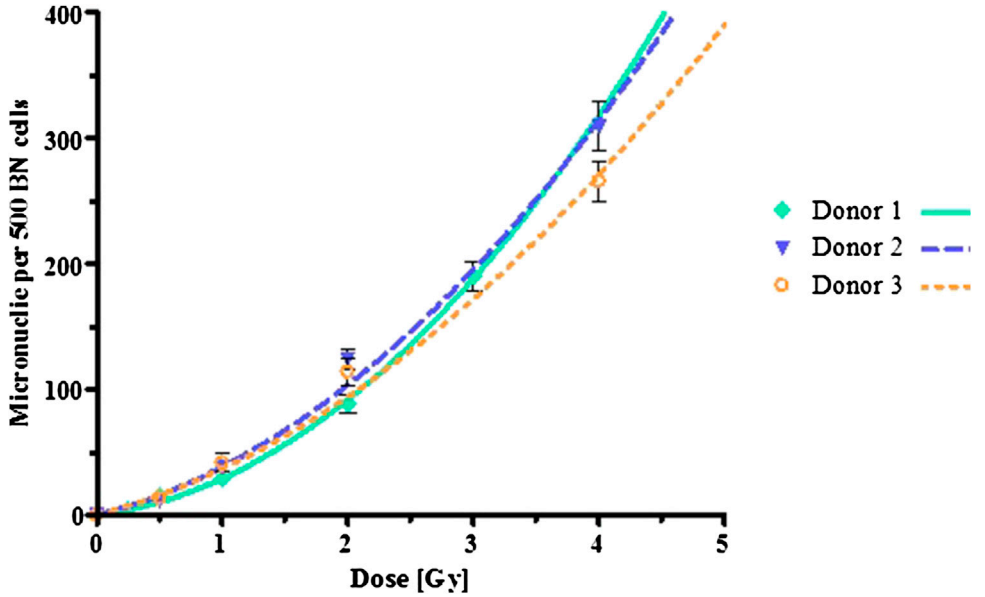

FIGURE 4 | Dose-response curves following exposure to ^{60}Co γ-rays radiation. The error bars are the standard deviations of the mean micronuclei formation per dose point.

on its characteristic 159 keV γ-ray, which provides the option to calculate dosimetry and treatment efficacy. However, ^{123}I is less often studied compared to its ^{125}I counterpart for radiobiology investigations and therefore, information on the RBE of the Auger emitter ^{123}I remains limited. This study aimed to add to the evidence of the high-LET characteristics of this radionuclide, by using ^{123}IUdR incorporated in the DNA of lymphocytes of healthy adult volunteers in order to get a better understanding of the induced chromosomal damage and respective RBE values. When comparing the dose response curves obtained with ^{60}Co γ-rays and ^{123}IUdR Auger electrons, RBE values ranging from 3 to 10 were observed, depending on the radiation dose and the donor.

The CBMN assay was used to estimate the radiation damage in this study, instead of the dicentric and chromatid aberration assays that were previously used by other research group to investigate the biological effects of Auger emitting isotopes [32, 58–60]. As outlined in a study of Slabbert *et al.* on inter-donor variations in radiosensitivity to high- and low-LET radiation, the CBMN assay is a useful endpoint for RBE studies that involve high-LET radiation qualities [61]. The radiation-induced MNi stem from acentric chromosome fragments that are directly associated with dicentric formations [62]. In addition, the fact that lymphocytes present a synchronous population of resting G0 cells at the start of the experiments, with a uniform radiosensitivity, is an advantage compared to cell lines which are distributed in different phases of the cell cycle. The work of Slabbert *et al.* used the same CBMN method on lymphocytes of four different donors to illustrate that variations in the RBE_{Max} of high-LET radiation, namely fast p (66)/Be neutrons (29 MeV), differ due to a different inherent radiosensitivity to low-LET radiation [61]. Therefore, dose-response curves of ^{60}Co γ-rays, generally accepted as the reference radiation quality for RBE calculations, of the same donors were included in this study. From the sets of lymphocyte data of the three donors, a slight inter-donor variability in the dose-responses to ^{60}Co γ-rays was noted, being indicative for the inherent radiosensitivity, which was also observed by Vral et al. [63]. A linear relationship between micronuclei frequency and ^{123}I activity could be established as shown in **Figure 3** for all donors. In general, even low doses of approximately 0.15 Gy of ^{123}I already induced a significant increase in chromosomal damage. Furthermore, it was observed that the higher dose points deviated significantly from linearity. This stunted response might be attributable to a critical amount of lethal damage or a G2/M cell cycle arrest at the higher damage,

TABLE 2 | Slopes of the fitted curves for ^{123}IUdR and ^{60}Co γ-ray exposures. The α- and β-values correspond to the linear-quadratic curve fitting.

—	Donor 1		Donor 2		Donor 3	
	α [Gy^{-1}]	β [Gy^{-2}]	α [Gy^{-1}]	β [Gy^{-2}]	α [Gy^{-1}]	β [Gy^{-2}]
^{123}I	142.3 ± 21.3	–	282.8 ± 27.7	–	141.9 ± 8.7	–
^{60}Co	12.3 ± 3.2	16.8 ± 1.2	25.0 ± 9.7	13.4 ± 2.7	26.4 ± 9.5	10.4 ± 2.7

TABLE 3 | The RBE ranges and RBE_{Max} values for ^{123}I as test radiation and ^{60}Co as reference radiation.

Donor	RBE range	RBE_{Max}
1	3 ± 1 to 9 ± 2	11 ± 3
2	5 ± 3 to 10 ± 4	11 ± 4
3	3 ± 3 to 4 ± 3	5 ± 2

which limits the number of viable or BN cells expressing MNi for scoring. However, this plateau was not observed in the linear fit of Schmitz *et al.* for chromosomal aberrations after exposure to ^{125}IUdR [32]. In the current study, the higher dose points were not taken into account for the linear fit. The observed plateau in our study indicates that the type of DNA damage caused by ^{123}IUdR is structurally more complex and therefore comparable with clustered high LET-type damage, which challenges the DNA damage repair machinery of the cells [29]. Another explanation for the observed plateau effect might be attributable to bystander effects, which are estimated to contribute approximately 30% to the total cell killing effect of Auger electron emitters [27]. In this study, the uptake at the higher radioactivity level might have been inferior, meaning that the observed plateau is coming from the bystander effect which might be less dose dependent compared to the direct cell killing effect. While there is no reason to assume that the uptake at 3.7 MBq did not increase compared to 1.85 MBq in our study, further investigations on the contribution of direct and bystander effects to the MN results could be interesting.

As previously mentioned, the attempts to use Auger emitters as cancer therapy have been hindered by the limited range of the emitted radiation and the difficulty of reliably deliver the electron close enough to the DNA target [64, 65]. The short range of Auger emitters makes them advantageous for disseminated cells and metastasis, but for larger solid tumors, a larger number of Auger electron emitting radionuclides might be needed to obtain the same level of cytotoxic effects as cross-firing β-emitters. This was previously illustrated in a study where tumor bearing rats were exposed to ^{111}In-octreotide peptide receptor radionuclide therapy, where a complete response was observed in rats with a small (<1 cm^3) tumors, but only partial regression was observed in rats with larger lesions [66]. The short range of most Auger electron emitters requires a very close proximity to the DNA. Therefore, it was decided to use a carrier molecule in this study that allows to build the radionuclide directly into the DNA, namely 5-iododeoxyuridine. However, the lack of a satisfying vector to specifically target nuclear DNA of cancer cells remains a limitation since IUdR would also target healthy cells in S-phase. In addition, radiolabeled deoxyribonucleotides are known to have a rapid washout and the limitation to only target cells in the S-phase. However, it is well known that the percentage of cells in S-phase is higher in tumors compared to normal tissue [67]. In this *in vitro* study, lymphocytes were stimulated with PHA, since human lymphocytes reside predominantly in the G0 phase. In order to determine the fraction of cells that was in S-phase during the pulse labeling this cell proliferation was compared to non-stimulated lymphocytes of the same donor. As shown in **Figure 2**, incorporated ^{123}I radioactivity increased linearly with the added total activity and stimulated lymphocytes are able to incorporate approximately double the ^{123}IUdR amount than their non-stimulated counterparts. This trend was also noted by Kassis et al. in their studies using ^{125}IUdR [68]. A difference in S-phase fraction was observed between the different donors in this study. This variability is not unusual, since it is generally accepted that the time when PHA-stimulated lymphocytes enter their first S-phase can range from 24 h up to 100 h. Sörén et al. calculated that the total number of lymphocytes that entered S-phase during a 6 days culture period with PHA was approximately 40% of the initial population [69].

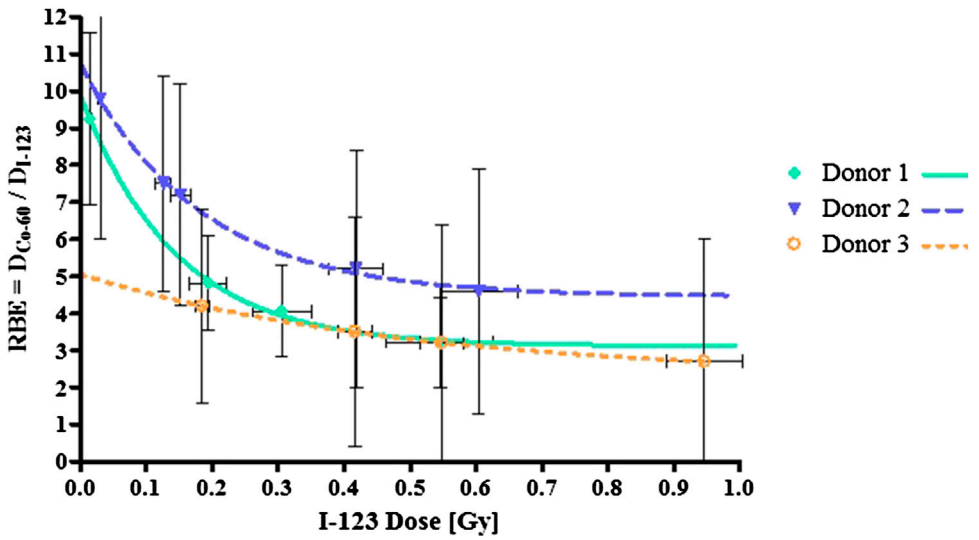

FIGURE 5 | RBE values based on the data points in the linear region of the ^{123}I dose-response curves for each donor. The error bars are the standard deviations of the mean RBE per dose point.

Previous cell killing experiments illustrated that DNA-incorporated ^{125}I is as effective as 5 MeV alpha-particles, which could be useful for the treatment of radioresistant tumors [19]. However, RBE values differ significantly between different studies. As previously mentioned, RBE values on ^{123}IUdR are limited, however some studies using ^{125}IUdR found RBE values that are within the range of RBE values observed in this study. Roa et al. reported RBE values of 7.9 ± 2.4 for ^{125}IUdR for spermatogonial cells [70]. The RBE relative to X-rays was estimated to be 7.3 by Kassis et al. in the ^{125}IUdR in the radiotherapy of brain tumors in rats [71]. While a study by Yasui *et al.* gives a RBE of 3.1 for ^{125}IUdR based on cell survival in Chinese hamster ovary cell line transfected with human estrogen receptor [72]. The difference in RBE values can be attributable to the fact that RBE is an empirical value which depends on several parameters such as radiation dose, biological effect and cells type, to only name a few. Another important consideration which is receiving growing attention recently, is the dose rate effect in targeted radionuclide therapy [73]. While the absorbed dose rate in conventional external beam radiotherapy is approximately 60 Gy/h, the irradiation in targeted radionuclide therapy is usually protracted from hours to days at a low dose rate of <1 Gy/h. This could be considered as a limitation in the current study, where the dose rates for the ^{123}IUdR exposures were very low (0.02 Gy/min at the activity level of 3.7 MBq) compared to the dose rate of the reference ^{60}Co γ-rays radiation quality (0.49 Gy/min) that was used to calculate the RBE. This limitation also applies to the previously mentioned studies where RBE values were calculated for Auger electron emitters. While it has long been considered that the dose rate dependence of high-LET radiation qualities is negligible, there is a growing body of evidence that suggest the contrary [73–76]. In addition, several studies describe an inverse dose rate effect, where increased cytotoxic effects per Gy are observed at low dose rates compared to high dose rates, while others studies contradict these findings [77–80]. Future studies are needed to confirm these observations and investigate the underlying mechanisms. Furthermore, the RBE values might also depend on the exposure conditions and the type of Auger emitter that was used. Direct comparison of various Auger electron emitting radionuclides is complicated due to the diverse electron emission spectra of these isotopes [67]. As already mentioned in the introduction, it was decided to use ^{123}I in this study instead of the more frequently used other Auger electron emitters, such as ^{125}I, in order to avoid the need to freeze the samples to accumulate disintegrations in the presence of anti-freeze agent DMSO. Since it is known that both the presence of DMSO and the irradiation of cells in frozen state has a radioprotective effect on cellular damage, it was decided that these conditions were best avoided for the assessment of the RBE of Auger electron emitters. This might also be important to have a clear idea of the impact of the two main damaging effects associated with Auger decay as described by Adelstein et al. [54]. Including a direct effect at the immediate decay site and an indirect effect many bases away from the decay site, which is due to radiolysis and the subsequent production of ROS. ^{123}I might also be more interesting for clinical applications than ^{125}I, due to its potential to function as a theranostic radionuclide. In addition, the physical half-life of radionuclides used in targeted radionuclide therapy should preferably be in the same order of magnitude as biological half-lives. It is therefore assumed that the most suitable physical half-life ranges from a few hours up to some days when a targeted approach is considered for disseminated cells [67].

The energy deposited in the cell is required to calculate the absorbed dose from the radioactive decay of ^{123}I. It has been shown that this depends highly on the subcellular localization of the Auger electron emitter [28, 44]. The nucleus of the target cell, its cytoplasm, and the extracellular region can be considered as source regions. In the study done by Fourie *et al.*, using Geant4 simulations, it was found that the energy deposited in the target nucleus per ^{123}I decay in the nucleus equals 4.1 keV/decay and the energy deposited in the nucleus per decay in the cytoplasm equals 0.5 keV/decay [44]. That is, the overall contribution from the cytoplasm source region to the energy deposited in the cell nucleus per decay is ~10% of the total. Furthermore, the contributions from decays external to the cell stemming from photons and the few high-energy conversion electrons amounts to a nuclear deposition of 0.024 keV/decay, less than 0.5% of the total energy deposited in the nucleus. Correspondingly, Makrigiorgos et al. concluded in their studies that cytoplasmic (7%) and external (<0.5%) dose contributions to the nucleus were negligible and that the cell survival mainly depends on the nuclear dose from ^{123}I decays in the cell nucleus [28]. However, Humm et al. stated that considerable *in vitro* experimental evidence exists to suggest that the absorbed dose to the nucleus alone is insufficient to predict the biological effects of Auger electron emitters concentrated in the cell nucleus [2]. Therefore, the microdosimetry calculations should include the energy deposition in all regions of the cell, especially when in use in comparison studies in radiobiological experiments. Using a calibrated microscopic image analysis system, the average cell diameter for our isolated and stimulated lymphocytes in suspension was found to be 9.8 ± 1.7 μm (~486 μm^3). The IAEA reports that peripheral lymphocytes 48 h after stimulation have a cell volume of about 500 μm^3 [81]. In our dosimetric calculations, a cellular diameter of 10 μm and a nuclear diameter of 8 μm were assumed. These mathematical assumptions were also used by Kassis *et al.* and Bousis et al. [24, 42, 47, 82]. The average energy deposited within the entire cell with the above geometry was calculated to be 4.5 keV per ^{123}I decay when distributed uniformly in the nucleus and this energy value was used to determine the absorbed dose values listed in **Table 1** [44].

There is a growing body of evidence that other sensitive sites besides the DNA, such as the cell membrane and mitochondria, could be critical targets in Auger emitter therapy. This would mean that nuclear uptake is not strictly required for Auger electron emitters in order exhibit their cytotoxic effect. The group of Pouget et al. could illustrate tumor growth delay with ^{125}I labeled non-internalizing antibodies [21, 27]. Furthermore, a different research group used an ^{111}In labeled non-internalizing

peptide F3, which induced a marked drop in colony survival and a delay in tumor growth [83]. However, the mechanisms by which membrane-associated Auger electron emitters can cause cytotoxicity has not yet been elucidated and should be the focus of future research efforts. In addition, recent studies also described radiation-induced bystander effects (RIBE) from Auger electron emitters, which might induce cytotoxicity in neighboring cells that have not been directly irradiated themselves [6]. These bystander effects might overcome the limitation that only a limited number of tumor cells get damaged by the Auger electrons directly because it is impossible to target every single cell in a tumor. These recent observations illustrate that nuclear localization might not be an absolute requirement and could open up the scope to label ^{123}I in the future with small molecules or peptides to develop novel targeted theranostic applications.

The current investigation found a linear increase in MNi induction with increasing ^{123}IUdR activity. This linear dose-response for ^{123}IUdR exposures is indicative of the high-LET nature of Auger electron emitters, which is also reflected in the high RBE that goes up to values of 10 for some of the donors. To our knowledge, no other study has evaluated chromosomal damage in human lymphocytes induced by DNA incorporated ^{123}I. Previous studies have reported a reduction in the variation of inter-donor radiosensitivity in lymphocytes for other forms of high-LET radiation like fast neutrons and α-particles when compared to low-LET radiation, however this could not be confirmed in this study. The current study provides useful information on the RBE of the Auger electron emitter ^{123}I, which might play a growing role as theranostic radionuclide in the near future.

DATA AVAILABILITY STATEMENT

The raw data supporting the conclusions of this article will be made available by the authors, without undue reservation.

ETHICS STATEMENT

The experiments were approved by the REC ethical clearance (reference number: S12/04/091) obtained from Stellenbosch University.

AUTHOR CONTRIBUTIONS

HF, SN. and JS. conceived and designed the experiments; XM performed lymphocyte isolations; SN, XM and HF. performed the radiobiology experiments under the guidance of PB; SN and DR performed the radiosynthesis and analysis, HF, SN, and CV analyzed the data; HF, SN and CV wrote the paper. RN, JS and JRZ are the grant holders in South Africa and secured funding for the experiments. All authors contributed to and approved the final version of the article, including the authorship list. The authors declare no conflict of interest.

ACKNOWLEDGMENTS

The authors would like to thank the Nuclear Technologies in Medicine and the Biosciences Initiative (NTeMBI), for their funding. NTeMBI is a national technology platform developed and managed by the South African Nuclear Energy Corporation (Necsa) and funded by the South African Department of Science and Innovation. The financial assistance of the National Research Foundation (NRF) toward this research is hereby acknowledged. Opinions expressed and conclusions arrived at, are those of the authors and are not necessarily to be attributed to the NRF. Additionally, this work was supported by a University Development Cooperation "VLIR Own Initiative Program" between Belgium and South Africa. The content of this manuscript has been published as part of the thesis of Hein Fourie [60].

REFERENCES

1. Howell RW. Auger processes in the 21st century. *Int J Radiat Biol* (2008) 84(12): 959–75. doi:10.1080/09553000802395527.
2. Humm JL, Howell RW, Rao DV. Dosimetry of auger-electron-emitting radionuclides: report no. 3 of AAPM nuclear medicine task group No. 6. *Med Phys* (1994) 21(12):1901–15. doi:10.1118/1.597227.
3. Auger P. The Auger effect. *Surf Sci* (1975) 48(1):1–8. doi:10.1016/0039-6028(75)90306-4.
4. Auger P. Sur les rayons β secondaires produits dans un gaz par des rayons X. *C R Acad Sci* (1923) 177:169–71.
5. Meitner L. Über die Entstehung der ?-Strahl-Spektren radioaktiver Substanzen. *Z Phys* (1922) 9(1):131–44. doi:10.1007/bf01326962.
6. Ku A, Facca VJ, Cai Z, Reilly RM. Auger electrons for cancer therapy–a review. *EJNMMI Radiopharmacy Chem* (2019) 4(1):27. doi:10.1186/s41181-019-0075-2.
7. Hofer KG, Hughes WL. Radiotoxicity of intranuclear tritium, 125 iodine and 131 iodine. *Radiat Res* (1971) 47(1):94–101. doi:10.2307/3573291.
8. Hofer KG, Harris CR, Smith JM. Radiotoxicity of Intracellular67Ga,125I and3H. *Int J Radiat Biol Relat Stud Phys Chem Med* (1975) 28(3):225–41. doi:10.1080/09553007514550991.
9. Martin RF, Feinendegen LE. The quest to exploit the Auger effect in cancer radiotherapy - a reflective review. *Int J Radiat Biol* (2016) 92(11):617–32. doi:10.3109/09553002.2015.1136854.
10. Buchegger F, Perillo-Adamer F, Dupertuis YM, Bischof Delaloye A. Auger radiation targeted into DNA: a therapy perspective. *Eur J Nucl Med Mol Imag* (2006) 33(11):1352–63. doi:10.1007/s00259-006-0187-2.
11. Salem R, Lewandowski RJ, Atassi B, Gordon SC, Gates VL, Barakat O, et al. Treatment of unresectable hepatocellular carcinoma with use of 90Y microspheres (TheraSphere): safety, tumor response, and survival. *J Vasc Intervent Radiol* (2005) 16(12):1627–39. doi:10.1097/01.rvi.0000184594.01661.81.
12. Vallabhajosula S, Goldsmith SJ, Hamacher KA, Kostakoglu L, Konishi S, Milowski MI, et al. Prediction of myelotoxicity based on bone marrow radiation-absorbed dose: radioimmunotherapy studies using 90Y- and 177Lu-labeled J591 antibodies specific for prostate-specific membrane antigen. *J Nucl Med* (2005) 46(5):850–8.
13. Kozempel J, Mokhodoeva O, Vlk M. Progress in targeted alpha-particle therapy. What we learned about recoils release from in vivo generators. *Molecules* (2018) 23(3):581. doi:10.3390/molecules23030581.
14. Tafreshi NK, Doligalski ML, Tichacek CJ, Pandya DN, Budzevich MM, El-Haddad G, et al. Development of targeted alpha particle therapy for solid tumors. *Molecules* (2019) 24(23):4314. doi:10.3390/molecules24234314.

15. Kassis AI. Molecular and cellular radiobiological effects of Auger emitting radionuclides. *Radiat Protect Dosim* (2011) 143(2–4):241–7. doi:10.1093/rpd/ncq385.
16. Kassis AI, Adelstein SJ. Radiobiologic principles in radionuclide therapy. *J Nucl Med* (2005) 46 (Suppl. 1):4s–12s.
17. Haberkorn U, Giesel F, Morgenstern A, Kratochwil C. The future of radioligand therapy: α, β, or both? *J Nucl Med* (2017) 58(7):1017–8. doi:10.2967/jnumed.117.190124.
18. Poty S, Francesconi LC, McDevitt MR, Morris MJ, Lewis JS. α-Emitters for radiotherapy: from basic Radiochemistry to clinical studies-Part 1. *J Nucl Med* (2018) 59(6):878–84. doi:10.2967/jnumed.116.186338.
19. Rao D, Howell R, Narra V, Govelitz G, Sastry KR. *In-vivo* radiotoxicity of DNA-incorporated 125I compared with that of densely ionising alpha-particles. *Lancet* (1989) 334(8664):650–3. doi:10.1016/s0140-6736(89)90896-9.
20. Paillas S, Ladjohounlou R, Lozza C, Pichard A, Boudousq V, Jarlier M, et al. Localized irradiation of cell membrane by auger electrons is cytotoxic through oxidative stress-mediated nontargeted effects. *Antioxidants Redox Signal* (2016) 25(8):467–84. doi:10.1089/ars.2015.6309.
21. Pouget J-P, Santoro L, Raymond L, Chouin N, Bardiès M, Bascoul-Mollevi C, et al. Cell membrane is a more sensitive target than cytoplasm to dense ionization produced by auger electrons. *Radiat Res* (2008) 170(2):192–200. doi:10.1667/rr1359.1.
22. Chastel A, Worm DJ, Alves ID, Vimont D, Petrel M, Fernandez S, et al. Design, synthesis, and biological evaluation of a multifunctional neuropeptide-Y conjugate for selective nuclear delivery of radiolanthanides. *EJNMMI Res* (2020) 10(1):16. doi:10.1186/s13550-020-0612-8.
23. Goddu SM, Narra VR, Harapanhalli RS, Howell RW, Rao DV. Radioprotection by dmso against the biological effects of incorporated radionuclides *in Vivo*: comparison with other radioprotectors and evidence for indirect action of auger electrons. *Acta Oncol* (1996) 35(7):901–7. doi:10.3109/02841869609104044.
24. Kassis AI, Fayad F, Kinsey BM, Sastry KSR, Taube RA, Adelstein SJ. Radiotoxicity of 125 I in mammalian cells. *Radiat Res* (1987) 111(2):305–18. doi:10.2307/3576987.
25. Mothersill C, Rusin A, Fernandez-Palomo C, Seymour C. History of bystander effects research 1905-present; what is in a name? *Int J Radiat Biol* (2018) 94(8):696–707. doi:10.1080/09553002.2017.1398436.
26. Boyd M, Ross SC, Dorrens J, Fullerton NE, Tan KW, Zalutsky MR, et al. Radiation-induced biologic bystander effect elicited *in vitro* by targeted radiopharmaceuticals labeled with alpha-, beta-, and auger electron-emitting radionuclides. *J Nucl Med* (2006) 47(6):1007–15.
27. Paillas S, Ladjohounlou R, Lozza C, Pichard A, Boudousq V, Jarlier M, et al. Localized irradiation of cell membrane by auger electrons is cytotoxic through oxidative stress-mediated nontargeted effects. *Antioxidants Redox Signal* (2016) 25(8):467–84. doi:10.1089/ars.2015.6309.
28. Makrigiorgos GM, Kassis AI, Baranowska-Kortylewicz J, McElvany KD, Welch MJ, Sastry KSR, et al. Radiotoxicity of 5-[123 I]iodo-2'-deoxyuridine in V79 cells: a comparison with 5-[125 I]iodo-2'-deoxyuridine. *Radiat Res* (1989) 118(3):532–44. doi:10.2307/3577411.
29. Sedelnikova OA, Rogakou EP, Panyutin IG, Bonner WM. Quantitative detection of (125)IdU-induced DNA double-strand breaks with gamma-H2AX antibody. *Radiat Res* (2002) 158(4):486–92. doi:10.1667/0033-7587(2002)158[0486:qdoiid]2.0.co;2.
30. Piron B, Paillas S, Boudousq V, Pelegrin A, Bascoul-Mollevi C, Chouin N, et al. DNA damage-centered signaling pathways are effectively activated during low dose-rate Auger radioimmunotherapy. *Nucl Med Biol* (2014) 41(Suppl. 1):e75–83. doi:10.1016/j.nucmedbio.2014.01.012
31. Woo DV, Li D, Mattis JA, Steplewski Z. Selective chromosomal damage and cytotoxicity of 125I-labeled monoclonal antibody 17-1a in human cancer cells. *Cancer Res* (1989) 49(11):2952–8.
32. Schmitz S, Oskamp D, Pomplun E, Kriehuber R. Chromosome aberrations induced by the Auger electron emitter 125I. *Mutat Res Genet Toxicol Environ Mutagen* (2015) 793:64–70. doi:10.1016/j.mrgentox.2015.08.007.
33. Schwartz JL, Mustafi R, Hughes A, DeSombre ER. DNA and chromosome breaks induced by iodine- 123-labeled estrogen in Chinese hamster ovary cells. *Radiat Res* (1996) 146(2):151–8. doi:10.2307/3579587.
34. Hindorf C, Emfietzoglou D, Lindén O, Kostarelos K, Strand S-E. Internal microdosimetry for single cells in radioimmunotherapy of B-cell lymphoma. *Canc Biother Rad* (2005) 20(2):224–30. doi:10.1089/cbr.2005.20.224.
35. Hindorf C, Emfietzoglou D, Lindén O, Bousis C, Fotopoulos A, Kostarelos K, et al. Single-cell dosimetry for radioimmunotherapy of B-cell lymphoma patients with special reference to leukemic spread. *Canc Biother Rad* (2007) 22(3):357–66. doi:10.1089/cbr.2007.347.
36. Fenech M. Cytokinesis-block micronucleus cytome assay. *Nat Protoc* (2007) 2(5):1084–104. doi:10.1038/nprot.2007.77.
37. Vral A, Fenech M, Thierens H. The micronucleus assay as a biological dosimeter of *in vivo* ionising radiation exposure. *Mutagenesis* (2011) 26:11–7. doi:10.1093/mutage/geq078.
38. Howell RW, Rao DV, Sastry KSR. Macroscopic dosimetry for radioimmunotherapy: nonuniform activity distributions in solid tumors. *Med Phys* (1989) 16:66–74. doi:10.1118/1.596404.
39. Goddu SM, Howell RW, Rao DV. Cellular dosimetry: absorbed fractions for monoenergetic electron and alpha particle sources and S-values for radionuclides uniformly distributed in different cell compartments. *J Nucl Med* (1994) 35:303–16.
40. Nikjoo N, Emfietzoglou D, Charlton DE. The Auger effect in physical and biological research. *Int J Radiat Biol* (2008) 84(12):1001–26. doi:10.1080/09553000802460172.
41. Bousis C, Emfietzoglou D, Nikjoo H. Calculations of absorbed fractions in small water spheres for low-energy monoenergetic electrons and the Auger-emitting radionuclides123I and125I. *Int J Radiat Biol* (2012) 88(12):916–21. doi:10.3109/09553002.2012.666003.
42. Bousis C, Emfietzoglou D, Hadjidoukas P, Nikjoo H. Monte Carlo single-cell dosimetry of Auger-electron emitting radionuclides. *Phys Med Biol* (2010) 55(9):2555–72. doi:10.1088/0031-9155/55/9/009.
43. Incerti S, Douglass M, Penfold S, Guatelli S, Bezak E. Review of Geant4-DNA applications for micro and nanoscale simulations. *Phys Med* (2016) 32:1187–200. doi:10.1016/j.ejmp.2016.09.007.
44. Fourie H, Newman RT, Slabbert JP. Microdosimetry of the Auger electron emitting123I radionuclide using Geant4-DNA simulations. *Phys Med Biol* (2015) 60(8):3333–46. doi:10.1088/0031-9155/60/8/3333.
45. Uddin MJ, Crews BC, Blobaum AL, Kingsley PJ, Ghebreselasie K, Saleh SS, et al. Synthesis and evaluation of [123I]-indomethacin derivatives as COX-2 targeted imaging agents. *J Label Compd Radiopharm* (2009) 52(9):387–93. doi:10.1002/jlcr.1615.
46. Cecchini MJ, Amiri M, Dick FA. Analysis of cell cycle position in mammalian cells. *J Vis Exp* (2012) (59):3491. doi:10.3791/3491.
47. Kassis AI, Makrigiorgos GM, Adelstein SJ. Implications of radiobiological and dosimetric studies of DNA-incorporated 123I: the use of the auger effect as a biological probe at the nanometre level. *Radiat Protect Dosim* (1990) 31(1–4):333–8. doi:10.1093/rpd/31.1-4.333.
48. Šefl M, Kyriakou I, Emfietzoglou D. Technical Note: impact of cell repopulation and radionuclide uptake phase on cell survival. *Med Phys* (2016) 43(6):2715–20. doi:10.1118/1.4948504
49. Fourie H, Newman RT, Slabbert JP. Microdosimetry of the Auger electron emitting123I radionuclide using Geant4-DNA simulations. *Phys Med Biol* (2015) 60:3333–46. doi:10.1088/0031-9155/60/8/3333.
50. Šefl M, Incerti S, Papamichael G, Emfietzoglou D. Calculation of cellular S-values using Geant4-DNA: the effect of cell geometry. *Appl Radiat Isot* (2015) 104:113–23. doi:10.1016/j.apradiso.2015.06.027.
51. Dale RG, Jones B. The assessment of RBE effects using the concept of biologically effective dose. *Int J Radiat Oncol Biol Phys* (1999) 43(3):639–45. doi:10.1016/s0360-3016(98)00364-2.
52. Carabe-Fernandez A, Dale RG, Jones B. The incorporation of the concept of minimum RBE (RbEmin) into the linear-quadratic model and the potential for improved radiobiological analysis of high-LET treatments. *Int J Radiat Biol* (2007) 83(1):27–39. doi:10.1080/09553000601087176.
53. Clayden J, Greeves N, Warren S, Wothers P. *Organic chemistry*. New York, NY: Oxford University Press (2001) 1133 p.
54. Adelstein SJ, Kassis AI, Bodei L, Mariani G. Radiotoxicity of iodine-125 and other auger-electron-emitting radionuclides: background to therapy. *Canc Biother Rad* (2003) 18(3):301–16. doi:10.1089/108497803322285062.

55. Rosenkranz AA, Slastnikova TA, Durymanov MO, Georgiev GP, Sobolev AS. Exploiting active nuclear import for efficient delivery of Auger electron emitters into the cell nucleus. *Int J Radiat Biol* (2020). 1–11. doi:10.1080/09553002.2020.1815889.
56. Pirovano G, Jannetti SA, Carter LM, Sadique A, Kossatz S, Guru N, et al. Targeted brain tumor radiotherapy using an auger emitter. *Clin Cancer Res* (2020) 26(12):2871–81. doi:10.1158/1078-0432.CCR-19-2440
57. Shen CJ, Minn I, Hobbs RF, Chen Y, Josefsson A, Brummet M, et al. Auger radiopharmaceutical therapy targeting prostate-specific membrane antigen in a micrometastatic model of prostate cancer. *Theranostics* (2020) 10(7):2888–96. doi:10.7150/thno.38882.
58. McLean JR, Blakey DH, Douglas GR, Bayley J. The Auger electron dosimetry of indium-111 in mammalian cells *in vitro*. *Radiat Res* (1989) 119(2):205–18. doi:10.2307/3577614.
59. Sundellbergman S, Bergman R, Johanson K. Chromosome damage induced by decay of 3H and 125I incorporated into DNA of Chinese hamster cells. *Mutat Res Fund Mol Mech Mutagen* (1985) 149(2):257–63. doi:10.1016/0027-5107(85)90032-6.
60. Bingham D, Bonner PT, Cox R, Edwards AA, Gardin I, Haines JW, et al. Comparison of cytogenetic damage in cultured cells from cobalt-60 gamma-radiation and the Auger emitter zinc-65. *Int J Radiat Biol* (2000) 76(9):1223–31. doi:10.1080/09553000050134456.
61. Slabbert JP, August L, Vral A, Symons J. The relative biological effectiveness of a high energy neutron beam for micronuclei induction in T-lymphocytes of different individuals. *Radiat Meas* (2010) 45(10):1455–7. doi:10.1016/j.radmeas.2010.06.060.
62. Norppa H, Falck GC. What do human micronuclei contain? *Mutagenesis* (2003) 18(3):221–33. doi:10.1093/mutage/18.3.221.
63. Vral A, Verhaegen F, Thierens H, De Ridder L. Micronuclei induced by fast neutrons Versus60Co γ-rays in human peripheral blood lymphocytes. *Int J Radiat Biol* (1994) 65(3):321–8. doi:10.1080/09553009414550381.
64. Bavelaar BM, Lee BQ, Gill MR, Falzone N, Vallis KA. Subcellular targeting of theranostic radionuclides. *Front Pharmacol* (2018) 9:996. doi:10.3389/fphar.2018.00996.
65. Kassis AI. Cancer therapy with Auger electrons: are we almost there? *J Nucl Med* (2003) 44(9):1479–81.
66. Capello A, Krenning E, Bernard B, Reubi J-C, Breeman W, de Jong M. 111In-labelled somatostatin analogues in a rat tumour model: somatostatin receptor status and effects of peptide receptor radionuclide therapy. *Eur J Nucl Med Mol Imag* (2005) 32(11):1288–95. doi:10.1007/s00259-005-1877-x.
67. Cornelissen B, A Vallis K. Targeting the nucleus: an overview of Auger-electron radionuclide therapy. *Cddt* (2010) 7(4):263–79. doi:10.2174/157016310793360657.
68. Kassis AI, Sastry KSR, Adelstein SJ. Kinetics of uptake, retention, and radiotoxicity of 125 IUdR in mammalian cells: implications of localized energy deposition by auger processes. *Radiat Res* (1987) 109(1):78–89. doi:10.2307/3576869.
69. Sörén L. Variability of the time at which PHA-stimulated lymphocytes initiate DNA synthesis. *Exp Cell Res* (1973) 78(1):201–8. doi:10.1016/0014-4827(73)90055-4.
70. Rao DV, Narra VR, Howell RW, Lanka VK, Sastry KSR. Induction of sperm head abnormalities by incorporated radionuclides: dependence on subcellular distribution, type of radiation, dose rate, and presence of radioprotectors. *Radiat Res* (1991) 125(1):89–97. doi:10.2307/3577986.
71. Kassis AI, Wen PY, Van den Abbeele AD, Baranowska-Kortylewicz J, Makrigiorgos GM, Metz KR, et al. 5–[125I]iodo-2'-deoxyuridine in the radiotherapy of brain tumors in rats. *J Nucl Med* (1998) 39(7):1148–54.
72. Yasui LS, Hughes A, DeSombre ER. Production of clustered DNA damage by125I decay. *Acta Oncol* (2000) 39(6):739–40. doi:10.1080/028418600750063811.
73. Pouget J-P, Lozza C, Deshayes E, Boudousq V, Navarro-Teulon I. Introduction to radiobiology of targeted radionuclide therapy. *Front Med* (2015) 2:12. doi:10.3389/fmed.2015.00012.
74. Stevens DL, Bradley S, Goodhead DT, Hill MA. The influence of dose rate on the induction of chromosome aberrations and gene mutation after exposure of plateau phase V79–4 cells with high-LET alpha particles. *Radiat Res* (2014) 182(3):331–7. doi:10.1667/rr13746.1.
75. Nair S, Engelbrecht M, Miles X, Ndimba R, Fisher R, du Plessis P, et al. The impact of dose rate on DNA double-strand break formation and repair in human lymphocytes exposed to fast neutron irradiation. *Int J Mol Sci* (2019) 20(21):5350. doi:10.3390/ijms20215350.
76. Sgouros G, Knox SJ, Joiner MC, Morgan WF, Kassis AI. MIRD continuing education: bystander and low dose-rate effects: are these relevant to radionuclide therapy? *J Nucl Med* (2007) 48(10):1683–91. doi:10.2967/jnumed.105.028183.
77. Matsuya Y, McMahon SJ, Tsutsumi K, Sasaki K, Okuyama G, Yoshii Y, et al. Investigation of dose-rate effects and cell-cycle distribution under protracted exposure to ionizing radiation for various dose-rates. *Sci Rep* (2018) 8(1):8287. doi:10.1038/s41598-018-26556-5.
78. Barnard SGR, McCarron R, Moquet J, Quinlan R, Ainsbury E. Inverse dose-rate effect of ionising radiation on residual 53BP1 foci in the eye lens. *Sci Rep* (2019) 9(1):10418. doi:10.1038/s41598-019-46893-3.
79. Mitchell JB, Bedford JS, Bailey SM. Dose-rate effects in mammalian cells in culture: III. Comparison of cell killing and cell proliferation during continuous irradiation for six different cell lines. *Radiat Res* (1979) 79(3):537–51. doi:10.2307/3575179.
80. Gholami YH, Willowson KP, Forwood NJ, Harvie R, Hardcastle N, Bromley R, et al. Comparison of radiobiological parameters for (90)Y radionuclide therapy (RNT) and external beam radiotherapy (EBRT) *in vitro*. *EJNMMI phys* (2018) 5(1):18. doi:10.1186/s40658-018-0217-8.
81. IAEA-EPR. *Cytogenetic dosimetry: application in preparedness for and response to radiation emergencies*. Vienna, Austria 2011.
82. Emfietzoglou D, Bousis C, Hindorf C, Fotopoulos A, Pathak A, Kostarelos K. A Monte Carlo study of energy deposition at the sub-cellular level for application to targeted radionuclide therapy with low–energy electron emitters. *Nucl Instrum Methods Phys Res Sect B Atoms* (2007) 256(1):547–53. doi:10.1016/j.nimb.2006.12.055.
83. Drecoll E, Gaertner FC, Miederer M, Blechert B, Vallon M, Müller JM, et al. Treatment of peritoneal carcinomatosis by targeted delivery of the radio-labeled tumor homing peptide bi-DTPA-[F3]2 into the nucleus of tumor cells. *PloS One* (2009) 4(5):e5715. doi:10.1371/journal.pone.0005715.

Conflict of Interest: Author Prof. JRZ is employed by The South African Nuclear Energy Corporation.

The remaining authors declare that the research was conducted in the absence of any commercial or financial relationships that could be construed as a potential conflict of interest.

frontiers in Physics

REVIEW
published: 25 November 2020
doi: 10.3389/fphy.2020.567800

Challenges in Monte Carlo Simulations as Clinical and Research Tool in Particle Therapy: A Review

S. Muraro[1], *G. Battistoni*[1] *and A.C. Kraan*[2]*

[1]INFN, Sezione di Milano, Milano, Italy, [2]INFN, Sezione di Pisa, Pisa, Italy

The use and interest in Monte Carlo (MC) techniques in the field of medical physics have been rapidly increasing in the past years. This is the case especially in particle therapy, where accurate simulations of different physics processes in complex patient geometries are crucial for a successful patient treatment and for many related research and development activities. Thanks to the detailed implementation of physics processes in any type of material, to the capability of tracking particles in 3D, and to the possibility of including the most important radiobiological effects, MC simulations have become an essential calculation tool not only for dose calculations but also for many other purposes, like the design and commissioning of novel clinical facilities, shielding and radiation protection, the commissioning of treatment planning systems, and prediction and interpretation of data for range monitoring strategies. MC simulations are starting to be more frequently used in clinical practice, especially in the form of specialized codes oriented to dose calculations that can be performed in short time. The use of general purpose MC codes is instead more devoted to research. Despite the increased use of MC simulations for patient treatments, the existing literature suggests that there are still a number of challenges to be faced in order to increase the accuracy of MC calculations for patient treatments. The goal of this review is to discuss some of these remaining challenges. Undoubtedly, it is a work for which a multidisciplinary approach is required. Here, we try to identify some of the aspects where the community involved in applied nuclear physics, radiation biophysics, and computing development can contribute to find solutions. We have selected four specific challenges: i) the development of models in MC to describe nuclear physics interactions, ii) modeling of radiobiological processes in MC simulations, iii) developments of MC-based treatment planning tools, and iv) developments of fast MC codes. For each of them, we describe the underlying problems, present selected examples of proposed solutions, and try to give recommendations for future research.

Keywords: Monte Carlo, particle therapy, computing, radiobiology, treatment planning, nuclear interactions, range monitoring

OPEN ACCESS

Edited by:
Marco Durante,
GSI Helmholtz Center for Heavy Ion Research, Germany

Reviewed by:
Harald Paganetti,
Massachusetts General Hospital, Harvard Medical School, United States
Xun Jia,
University of Texas Southwestern Medical Center, United States

***Correspondence:**
A.C. Kraan
aafke.kraan@pi.infn.it

Specialty section:
This article was submitted to Medical Physics and Imaging, a section of the journal Frontiers in Physics

Received: *30 May 2020*
Accepted: *12 August 2020*
Published: *25 November 2020*

Citation:
Muraro S, Battistoni G and Kraan AC (2020) Challenges in Monte Carlo Simulations as Clinical and Research Tool in Particle Therapy: A Review. Front. Phys. 8:567800. doi: 10.3389/fphy.2020.567800

1 INTRODUCTION

The use of Monte Carlo (MC) techniques and their interest in the field of medical physics have been rapidly increasing in the past years. This is the case especially in particle therapy, where high accuracy in dose calculations, patient geometry, beam model, and all aspects in the physics of interactions are crucial elements for a successful planning of patient treatment and its verification. Thanks to the possibility to track particles in 3D in a fully detailed geometry and to take into account all relevant physics processes on their way, MC simulations have become an essential calculation tool.

Applications in particle therapy where MC simulations have proven to be a very useful tool are several. For instance, they are crucial in the design and commissioning of novel clinical facilities, allowing for shielding calculations and full treatment head simulations. MC simulations are also a valuable tool for the commissioning of treatment planning systems (TPS), where they can provide accurate look-up tables describing 3D dose distributions of particle beams, that include electromagnetic and nuclear interactions of the primary particles and all secondaries produced. Furthermore, MC simulations allow to accurately include various radiobiological effects in dose calculations, thanks to the possibility of coupling to dedicated models. These properties make MC simulations suitable for dose calculations of complex patient cases. Especially if highly heterogeneous tissues are involved, MC methods are generally considered to be more accurate than analytical calculation methods [1–3]. Finally, thanks to the capability of performing detailed simulations of nuclear interactions, MC are also fundamental for the development of in-beam treatment monitoring strategies through positron-emission tomography, the detection of prompt photons, or other fragments from nuclear de-excitation.

A vast amount of works concerning MC simulations in particle therapy have been published in the past decades. Several reviews are also available, including, for instance, general works about MC techniques in particle therapy [4–7], MC simulations for range monitoring [8], the role of MC simulations in radiobiological modeling of treatment outcomes [9], and MC simulations in GPU dose calculations [10]. The high demand for accurate calculation tools and the general consensus that MC simulations can provide the requested accuracy for complex dose calculations have led to a more widespread use of these tools in daily clinical practice, especially in proton therapy, where commercial treatment planning systems have started to offer MC calculation tools. In most cases, these are specifically developed and optimized codes. However, the use of general purpose and fully detailed MC codes is still limited. Among the reasons are the complexity of the usage of the codes, the excessive computation times, the need to improve nuclear interaction models, the lack of data for tuning these models, and the complexity to combine radiobiology and physics into a single calculation tool.

In this review, we discuss some of the ongoing developments and challenges that remain to be faced in order to improve the accuracy of MC simulations and to facilitate their use in clinics and in research. Undoubtedly, a multidisciplinary approach is required to overcome many of the remaining challenges. It is beyond the scope of this review to include all the available literature and topics that regard MC simulations in particle therapy. Here, we try to identify some of the aspects where the community involved in applied nuclear physics, radiation biophysics, and computing development can contribute to find solutions. We have selected four specific challenges for this review:

1. The development of models in MC to describe nuclear physics interactions, including data to benchmark MC codes.
2. The development of MC simulations including calculations of RBE, LET, and microdosimetry.
3. The development of MC-based treatment planning
4. The development of fast MC codes.

Below, we take an in-depth look at these issues, and describe the problematics, the ongoing developments, and the future directions, trying to emphasize the role of applied nuclear physics in overcoming these challenges. A complete review of all ongoing works about the above topics is beyond the scope of this work. Therefore, the selection of works that were chosen to be highlighted in this article should be considered as non-exhaustive.

2 DEVELOPMENT OF NUCLEAR INTERACTION MODELS IN MC CODES

Charged hadrons of energies relevant in particle therapy (up to a few hundred MeV/nucleon) interact in tissue by electromagnetic and nuclear interactions [11]. Concerning the former, inelastic collisions with atomic electrons, resulting in ionization and atomic excitation, cause the particle to continuously lose energy along its path. Energy losses can be well described by the Bethe-Bloch formalism, predicting an increasing energy loss with decreasing particle energy. This is the main process governing the shape of the Bragg peak for charged particle beams in material. Also, discrete inelastic energy losses can occur in the form of delta-rays. Moreover, charged particles undergo numerous elastic Coulomb scatterings from the nuclei themselves (multiple Coulomb scattering, MCS), causing lateral broadening of the incoming particle beam. Modeling electromagnetic interactions is highly complicated in MC codes, but usually considered sufficiently accurate. On the contrary, hadronic physics models are still not considered completely satisfactory [12].

In this section, we try to point out the most important difficulties and challenges in nuclear physics model building, quoting the features of some of the most widely used MC codes used for particle therapy. Then, we shall summarize the possible impact of nuclear interaction modeling in dose calculation and in the evaluation of additional quantities useful for particle therapy. In particular, we shall focus the discussion on secondary particle production for range monitoring purposes. Finally, we shall present a summary of existing experimental data which are useful for tuning and benchmarking calculation models.

2.1 Main Problematics in the Development of Nuclear Interaction Models

There are many aspects of hadronic interactions that are relevant for correctly describing interactions of protons or heavier ions in the energy range relevant to particle therapy. Among them, we point out nuclear reaction cross section, elastic cross section, secondary particles, and fragment production, considering at the same time multiplicity, angle, and energy distributions. Secondary nucleons, particles, and fragments produced in nuclear reactions can considerably affect the spatial pattern of energy deposition and must be carefully taken into account. In particular, for the case of ion projectiles, nuclear fragmentation reactions are responsible for the deterioration of the physical selectivity in the longitudinal and transverse dimension, especially around the Bragg peak region. The amount of fragments produced generally increases with the mass and charge of the primary particle.

The commonly used general purpose modern MC codes make use of phenomenological models. Although a common approach is to fit existing data to predict certain quantities, in our opinion, they should be built upon reliable physical bases to have full predictive capability. In practice, this means that these models have to be built according to a "microscopic" approach, that is, starting from the fundamental properties of the nucleus and of its constituents. All relevant conservation laws have to be fulfilled, and correlations within each single interaction must be preserved. The treatment of nuclear environment and all phases following the primary fast interaction (pre-equilibrium, evaporation, fission, and de-excitation) is to be taken into account.

Models of this kind have necessarily a number of parameters that must be tuned by means of experimental data at single interaction level. In order to achieve a reliable level of predictive power, the number of these parameters should be kept minimal and their dependence on projectiles, targets, and energies should be predetermined without adapting them to the specific situation. On the one hand, this approach allows in principle to achieve a high degree of reliability. On the other hand, this might result in complex algorithms which can be demanding in terms of computing power with respect to simpler solutions, such as the parametric interpolation (or extrapolation) of existing data. It must also be pointed out that is not always possible, within a given model, to achieve the same level of accuracy at all energies or in the whole accessible phase space. Furthermore, in the therapeutic energy range, it is not always possible to rely upon a single model. Great care has to be taken in order to ensure the proper continuity in the transition from one model to another. Different MC codes have found different solutions to the above problems. In the following, we shall summarize the nuclear models adopted for a few of the most relevant MC codes presently used in particle therapy.

2.2 Approaches and Proposed Solutions to Model Nuclear Interactions

2.2.1 GEANT4

GEANT4 is used by a large number of experiments and projects in a variety of application domains, including medical physics and radiation protection. In the case of GEANT4 [13–15], the user has the possibility of selecting different models by specifying the so-called physics list. Reference physics lists are available in Ref. 16. In the context of particle therapy, an often recommended choice is the one called QGSP_BIC_EMY, which includes, beyond a Quark Gluon String model for the multi-GeV energy range, a Binary Cascade model. The GEANT4 Binary Cascade is a hybrid between a classical intranuclear cascade and a quantum molecular dynamic model [17–19] for the simulation of inelastic scattering of hadrons and light ions of intermediate energies. It is considered valid down to 200 MeV. New developments are under investigation to improve models for energies below this value, an example of which was published recently [20]. However, this study also highlighted the need for many more improvements in nuclear interaction modeling and calculation speed.

There are user-friendly interfaces to GEANT4 which are used by different groups working in particle therapy. For instance, the TOPAS (TOol for PArticle Simulation) toolkit [21, 22] wraps and extends the GEANT4 Simulation Toolkit to facilitate the use of MC simulations in radiotherapy environments. It allows the user to configure pre-built components (nozzles, patient geometry, dosimetry, and imaging components) to simulate a wide variety of treatments with no required knowledge of any programming language. Another example is GATE (GEANT4 Application for Tomographic Emission) [23]. It has been developed by the OpenGate collaboration and encapsulates the GEANT4 libraries, providing a toolkit mostly oriented to nuclear medicine by easily including detailed geometry of many imaging devices. It has been tested in the context of particle therapy, especially for range monitoring applications [24–26].

In order to respond to the need of benchmarking the code against reference data, the GEANT4 community has recently developed a testing system, denominated G4-Med [27], which is specifically oriented to medical physics. Among the different options, it offers the possibility of benchmarking both electromagnetic and hadronic physics processes and models available in the pre-built, physics lists. A whole chapter is dedicated to the topic of hadronic models in the specific context of particle therapy. Total cross section of hadron–nucleus and nucleus-–nucleus collisions have been compared to the data publicly available in the EXFOR database. Different subjects have been considered: yields, charge changing, and double differential cross sections. Tests concerning comparisons with Bragg peaks have been also reported. A detailed discussion on the quality of these benchmarks can be found in the report.

In addition to this recent work, in the context of proton therapy, we point out the work of Hall et al. [28], where GEANT4 results were compared to accurate measurement of longitudinal absolute dose profiles for 177 MeV protons at different radial distances from the beam axis, up to a radius of 10 cm. The test is sensitive to the dose envelope originating from nuclear interactions. Excellent agreement is reported over five orders of magnitude in the dose scale.

2.2.2 FLUKA

In the case of FLUKA [29, 30], the number of available physics models is limited. The code automatically selects the appropriate model for each interaction according to the energy of projectile.

The nuclear environment, down to a few MeV, is provided by the interaction model called PEANUT (Pre-Equilibrium Approach to NUclear Thermalization) [31–33]. Interactions proceed along the steps of a generalized intranuclear cascade, followed by pre-equilibrium particle emission and by an equilibrium phase. For residual having A < 16, a Fermi breakup model is implemented [34]. In the emission of nucleons, a coalescence model is considered. The excitation energy still remaining after nuclear evaporation is dissipated by emission of γ rays. Competition of gamma ray emission with particle evaporation is considered. In the case of nucleus–nucleus collisions, for incident energies below ~ 130 MeV/u, FLUKA makes use of the BME (Boltzmann master equation) model [35], which simulates the thermalization of a composite nucleus created in the complete or incomplete fusion of two ions. For increasing energy, FLUKA relies on the RQMD (Relativistic Quantum Molecular Dynamic) model [17, 36], which can also be run in intranuclear cascade mode.

2.2.3 PHITS

A QMD approach has been chosen also in the PHITS (Particle and Heavy Ion Transport code System) code [37, 38] for the treatment of hadron–nucleus and nucleus–nucleus collisions. Here, the JQMD (JAERI Quantum Molecular Dynamics) code is used [18]. JQMD is combined with the JAM (Jet AA Microscopic Transport Model) code [39], which implements a hadronic cascade approach, capable of dealing with hadron–hadron collisions up to center-of-mass energy $\sqrt{s}$ ~ 100 GeV. At the end of the dynamical stage of the interaction, excited residual nuclei are treated by the GEM (Generalized Evaporation Model) model [40] to generate light particle evaporation and fission processes. Benchmarks of PHITS are reported in Ref. 41.

2.2.4 MCNP

MCNP (Monte Carlo NParticle), now in the version MCNP6 [42], developed at Los Alamos National Laboratories, is one of the most important general purpose three-dimensional MC codes. It is well known in nuclear physics and used for studies including criticality, shielding, and detector response, but also dosimetry and many other applications, such as medical ones. As far as hadron–nucleus and nucleus–nucleus interactions are concerned, also MCNP makes use of different models depending on energy. For incident energy below 1 GeV, of relevance for particle therapy, interactions are mostly treated by means of the INC (intranuclear cascade) approach. The MCNP6 default option for reactions induced by d, t, ^{3}He, ^{4}4He is the ISABEL INC generator, described in Ref. 43, and can be used also for nucleons and heavy ions with E < 1 GeV. It can optionally include pre-equilibrium reactions described by the MPM (multistage pre-equilibrium model) [44]. Evaporation reactions are treated with EVAP [45], while for fission, RAL [46] or HETFIS [47, 48] can be chosen. A newer and improved model is CEM03.03 [49–51] which has its own treatment of pre-equilibrium, evaporation, and fission reactions. It considers also coalescence of nucleons into complex particles up to ^{4}He and Fermi breakup of excited or unstable nuclei with mass numbers up to A = 12. Another recent alternative for the INC approach is INCL [52] for nucleons, d, t, ^{3}He, and ^{4}He at energies up to several GeV. It does not consider pre-equilibrium and makes use of the abration–ablation model implemented in the ABLA code [53, 54], developed at GSI, to describe evaporation and fission.

2.2.5 SHIELD-HIT

SHIELD-HIT, in its last version SHIELD-HIT12A [55, 56], is a MC particle transport program optimized for proton and ion particle therapy. Nuclear reactions are treated within the MSDM (multistage dynamical model) generator [57]. It is composed of a fast cascade stage of nuclear reaction, which, according to projectile energy, is treated by the DCM (Dubna Cascade Model) [58] or by the QGSM (Quark-Gluon String Model) [59, 60]. At the end of the cascade stage, nucleons which are close to each other in phase space can coalesce to form a complex particle. Pre-compound emission of nuclei is handled by a cascade-exciton model [61]. Subsequent equilibrium de-excitation is handled by Fermi breakup, according to the implementation described in Ref. 62. Then, evaporation/fission competition and multi-fragmentation of highly excited nuclei follow.

2.3 Impact of Nuclear Reaction Models on Dose Calculations

Nuclear interactions cause the attenuation of primary ions and build up of secondary ions, aspects that are crucial for accurate dose delivery and dosimetry [12]. Inelastic interactions are responsible for beam attenuation of the primary beam with penetration depth, and elastic interactions contribute to beam broadening. In the case of carbon ions, it was estimated with MC simulations that up to about 40% of the dose in the region between the entrance channel and the Bragg peak is delivered by fragments [63]. Thus, wrongly modeled cross sections would clearly lead to discrepancies in longitudinal and lateral dose distributions between measurements and MC simulations. A vast amount of works exist, mostly in the context of proton and carbon therapy, showing excellent agreements between MC codes and dosimetric measurements, both in terms of lateral and longitudinal dose (Bragg peak measurements). An example of a measured Bragg peak together with a GEANT4 MC simulation is shown in **Figure 1**. Results with analogous quality of agreement have been obtained also for other codes, including FLUKA comparisons with HIT [1], CNAO [64], and GSI [65].

From these nice agreements in dose distributions, one may conclude that we have reached a satisfactory level of accuracy of the description of nuclear reactions in MC codes for physical dose calculations. However, this is only partially true, and several important improvements in the context of dose calculations remain to be done:

- For particles other than protons and carbon ions, the agreement in physical dose between MC codes and measurements is still not fully satisfactory. For instance, some significant discrepancies were found between simulations and data of spread-out Bragg peaks of Helium atoms in water [67, 68]. These differences were

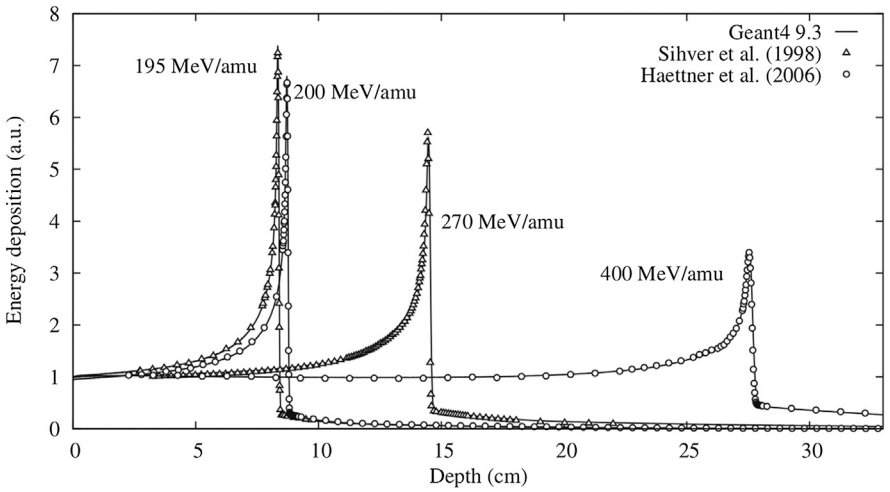

FIGURE 1 | From Lechner et al. [66]: an example of an excellent agreement between data and GEANT4 MC simulations in predicting the depth–dose profile of carbon ion beams.

attributed to an underestimation of dose contributions from secondary particles produced at large angles.

- Nuclear interactions strongly affect biological dose [12]. Secondary fragments produced during nuclear interactions lead to an altered spatial dose distribution, because different fragments have different ranges and angular distributions. Some of these fragments may hardly contribute to the physical dose, but they can lead to a modification of the LET spectra, which results in a difference of RBE for the same delivered dose. Thus, even when longitudinal and lateral physical dose measurements show excellent agreements with a MC code, this does not automatically imply that the biological dose in the patient is correctly calculated. In **Section 4**, we discuss the importance of biological aspects in more detail.
- Other aspects different from nuclear interactions can affect the prediction of dose distribution. For instance, in proton therapy, δ-ray electron build-up effects are important in the dose build-up region [69], and should be correctly accounted for in physical and biological dose calculations.

Summarizing, physical dose is indeed an important measure to validate the description of nuclear reaction models in MC codes, and newly developed models should always be validated with dose measurements. However, evaluating physical dose alone is not enough, as will become clear in the next paragraph.

2.4 Impact on the Calculation of Secondary Particle Production

Although dose calculation is the primary role of MC application in particle therapy, there are other aspects in which this kind of tool turns out to be essential. These are related to the capability of providing a reliable prediction of secondary particles produced in nuclear interactions. We have mentioned above that nuclear reactions influence the spectrum of fragments and how this can be crucial for the correct evaluation of both physical and biological doses. Moreover, although of scarce numerical relevance for dosimetry, production of secondary particles is relevant for various other issues, including the implementation of range monitoring techniques, neutron production, shielding, treatment facility design, or full treatment head simulations. In the following, we discuss the issues that we consider most complex: range monitoring and neutron production.

2.4.1 Calculation of Secondary Products for Range Monitoring Purposes

The nuclear processes that can yield secondary radiation suited for range monitoring application are three: the production of β^+ emitting nuclei, the de-excitation of nuclei by means of prompt photon emission, and the fragmentation of ion projectiles into fast hadrons capable of escaping out of the patient. In all cases, a MC prediction of the measured distributions is essential for their effective use for range monitoring purposes. Here, we summarize the main issues which are of interest for these processes as far as MC codes are concerned.

- Production of β^+ emitting nuclides. Nuclear β^+ decays produce positrons that annihilate with electrons, resulting in an almost back-to-back 511 keV photon pair that can be detected. The most likely β^+ emitting isotopes that can be formed are ^{10}C, ^{11}C, ^{15}O, and ^{13}N. Much research has been dedicated to range monitoring with PET, summarized, for instance, in various reviews [8, 70–72]. The capability of MC codes to provide a reliable prediction of the production of these isotopes is strongly correlated to the quality that the physics models achieve in managing the fragmentation process in general, and all the other stages occurring in the nuclei following the fast interaction. An alternative approach to full modeling, whenever validated experimental measurement of production cross sections

exist (as, for instance, those available in EXFOR database), is to fit them and interface them to the simulated track length distribution. In range monitoring, both approaches are being used. The general situation is that the most important general purpose codes are able to predict the production of the most abundant nuclides (like ^{11}C or ^{15}O) with a sufficient quality. The main challenge remains in the capability of predicting nuclides with short lifetimes, where also the available experimental measurements are scarce. Data that can be used to improve the accuracy of MC models for the production of short-lived isotopes for range monitoring are discussed in Section 2.5. All stages concerning transport of positrons and their decay can be considered more standard and manageable without particular difficulty.

- Prompt gamma from nuclear de-excitation. Prompt gamma imaging methods are based on the detection of prompt photons that are emitted in the de-excitation phase of a nuclear interaction. The distribution of prompt gammas is correlated with the beam range. A recent review is written by Krimmer et. al. [73]. In the past years, MC developers started to pay particular attention to correctly predicting prompt gamma distributions. Also, in this case, the complexity of non-elastic nuclear reactions makes it difficult to accurately reproduce the level and shape of prompt γ emission. Of course the quality in the prediction of residual nuclei and of their excitation, as for the case of β^+ emitters, is important. Whenever possible, photon energies and branching ratios should be sampled according to existing databases of known nuclear levels and transitions. For example, they can be derived from data provided by the most recent release of the RIPL [74] data provided by IAEA. However, not only the level energies, but also spin and parity have an influence on photon emission. Furthermore, the shape of emission lines is subject to Doppler broadened due to nuclear recoil, and this also deserves attention in the development of the interaction model.
- Production of fast charged hadrons. The principle of range monitoring in ion therapy by means of hadrons escaping the patient (mainly protons) was proposed about a decade ago [75] and since then investigated by different research groups, see Section 2.5. Fast hadron production is clearly part of nuclear fragmentation, and therefore we are again dealing with the physics models which are relevant to dose calculations. However, as discussed in Ref. 76, the most accurate result in the measurement of a proton emission distribution correlated with a longitudinal dose profile, is achieved by detecting particles emitted at large angles with respect to the beam direction. This involves a limited region of the available phase space and it is not trivial for available calculation models to reproduce with the same quality both fragmentation at small angles (the most important as far as dose is concerned) and the emission at large angles. As discussed later, there is a lack of experimental data useful for model tuning and benchmarking, and available data are limited in angle and primary energy [77, 78]. Double differential cross sections are eagerly needed. More available data will be discussed in Section 2.5.

2.4.2 Calculation of Neutron Production and Interaction

MC codes allow to evaluate neutron production during a particle therapy treatment. The simulation of neutrons with energy exceeding ~ 10 MeV is provided by the same models discussed so far for charged particles. The situation is different for lower energies, since neutron cross sections have a complex structure. They cannot be calculated and usually one has to rely upon evaluated nuclear data files. Different libraries are accessible (ENDF/B, JEFF, JENDL, CENDL, ROSFOND, and BROND) [79, 80] and are periodically updated. By means of dedicated software codes, it is possible to obtain cross sections to be used within MC codes.

Simulations have been used to evaluate the risk of secondary cancer due to neutron exposure, especially in the comparison between passive and active scanning (see for instance [81–85]). At present, there is some consensus that risks deriving from neutrons are negligible with respect to those associated to the primary beam, at least as far proton therapy is concerned. The contribution of neutrons to dose is therefore normally neglected in treatment planning. However, there remain other cases in which the calculation of neutron interactions is important:

- for prompt γ detection for range monitoring purposes, the evaluation of background deriving from neutron interactions is relevant.
- The long-term effects of neutron production should be done with MC models that include radiobiological models [83, 84].
- In Boron neutron capture therapy (BNCT) [86, 87], which is based on the direct use of neutrons. It is one of the cases in which treatment planning and dosimetry are strongly based on MC. One of the main reference codes for BNCT is MCNP [42, 88], which was used for treatment planning [89]. More recently also PHITS [37, 38] has entered in use for this purpose [90]. A comparison of results obtained with GEANT4 for different physics list, and with FLUKA, is reported in Ref. 91. MC simulations are also widely used in BNCT to design new beams for the specific application [92, 93].

For reliable neutron production models, benchmarking nuclear interaction models with neutron data are important. Fortunately, a large amount of neutron production data at an enormous energy range is already available from reactor experiments and radiation protection in space, as we will see in Section 2.5. Finally, even though neutrons might not seem very interesting in the context of charged particle therapy, we point out that neutron data are very powerful to constrain nuclear interaction models.

2.5 Data for Benchmarking and Tuning Nuclear Physics Codes

To determine the effects of secondary particles and to exploit them in range monitoring, MC models can be used to predict the yields and characteristics of the secondary particles. The accuracy

TABLE 1 | Cross section measurements on thin targets for tissue-like targets in the energy range up to 400 MeV/u.

Incident beam	Energy [MeV/u]	Target	Measurement	References
^{4}He	70–220	H, C, O, and Si	Charge and mass changing cross sections	Horst et al. [98, 99]
^{4}He, C	135, 290, and 400	C, Li	Double differential cross section measurements of neutron production	Handbook [97], chapter 3
^{12}C, ^{20}Ne	83, 200, 250, and 300	C, Al, Ca, Fe, Zn, Y, and Ag	Total cross sections	Kox et al. [100, 101]
^{12}C	30 to 400	Be, C, and Al	Total reaction cross section as function of projectile energy	Takechi et al. [102]
^{12}C	200 to 400	Water and polycarbonate	Total and partial charge changing cross sections for production of fragments up to $Z = 4$ at various energies	Toshito et al. [103]
^{12}C	62	C	Double differential cross sections and angular distributions of secondary charged fragments up to 25°	De Napoli et al. [104]
^{12}C	95	C, CH_2, Al, Al_2O_3, and Ti	Double differential cross sections for secondary charged fragment production ranging from protons to carbon isotopes	Dudouet et al. [77]
^{12}C	50	C, CH_2, Al, Al_2O_3, Ti, and PMMA	Double differential cross section for secondary charged fragment production ranging from protons to carbon isotopes	Divay et al. [78]
^{12}C	115, 153, 221, 281, and 353	C, plastic scintillator, and PMMA	Energy differential cross section at 60° and 90° of fragments with $Z = 1$	Mattei et al. [105]

of the predictions ultimately relies on the ability to correctly model the relevant production cross sections. In our opinion, experimentally measured cross sections are the most valuable data that are needed to tune the models in the relevant range of ion species, energies, and target mass. In particular, single and double differential cross sections are the most interesting measurements.

A collection of measured cross sections in the energy range from 100 MeV/u up to 10 GeV/u can be found in reviews by Norbury [94], Sihver [95], and Bauhoff [96], focusing mostly on radiation protection in space. Moreover, the handbook by Heilbronn and Nakamura [97] contains lots of data for neutron production, mostly from design studies of heavy ion accelerator facilities and radiation protection in space. In the context of radiotherapy, much effort has been done in the last decades to improve the accuracy of MC codes in the energy range up to 400 MeV/u for tissue-like targets. However, although a large amount of valuable data are available for the purpose of benchmarking and tuning calculation models, at present, there still remain significant gaps. In the following, we summarize some of the most relevant measurements that have to be considered. We divide them into three categories: i) measurements of cross sections on thin targets, ii) measurements performed on thick targets, and iii) measurements specifically oriented for range monitoring purposes.

2.5.1 Measurements of Cross Sections on Thin Targets

These measurement concern total cross sections, partial cross sections, and single and double differential cross sections of specific processes. While total cross sections are valuable to predict primary beam attenuation, partial cross sections, and single and double differential cross sections are important to predict yields, angles, and energies of secondary particles. The usage of thin targets is most appropriate for tuning MC models, because the energy of the beam does not decrease, and the model parameters can be isolated from transport issues. A non-exhaustive selection of cross section measurements that have frequently been used for tuning nuclear models in MC simulations in the particle therapy energy range is reported in **Table 1**.

The majority of the cross section measurements in **Table 1** are for carbon projectiles; however, the growing amount of interest in particle therapy with other projectiles has led to recent new initiatives. For instance, valuable new cross section measurements for ^{4}He [98, 99] are displayed in **Figure 2**. This figure illustrates a general problem with many cross sections: there are differences between data sets, and for analytical or MC model parameterizations, it is ambiguous with which measurements the tuning should be done. New data are thus useful to resolve ambiguities between data sets.

As reported in 2010 by Böhlen [63], a tuning of the hadronic models in FLUKA and GEANT4 was based on some of the measurements in **Table 1**, revealing several shortcomings in both codes, in particular at lower energies. Further developments in the improvement of the nuclear models in GEANT4 were reported afterward [104, 106, 107], and new efforts are currently in progress [20]. PHITS, FLUKA, and MCNP6 were recently benchmarked with experimental data for neutron production cross sections [108].

Concerning protons, the work by Braunn et. al. [109], aimed at benchmarking the TALYS nuclear reaction code, contains a large number of references of total proton–nucleus cross section measurements as a function of energy in the range up to 250 MeV with tissue-like targets.

Despite the progress made over the years, **Table 1** shows that double differential cross section measurements for charged fragment production are still scarce, while such measurements are the most essential for tuning nuclear reaction models. Measurements that are specifically aimed at improving the knowledge for particle therapy are planned in 2021 by the FOOT collaboration [110]. The ultimate goal of this experiment is to provide measurements of energy differential cross sections for the production of charged fragments with an accuracy of 5–10%. This would provide reference data sets for

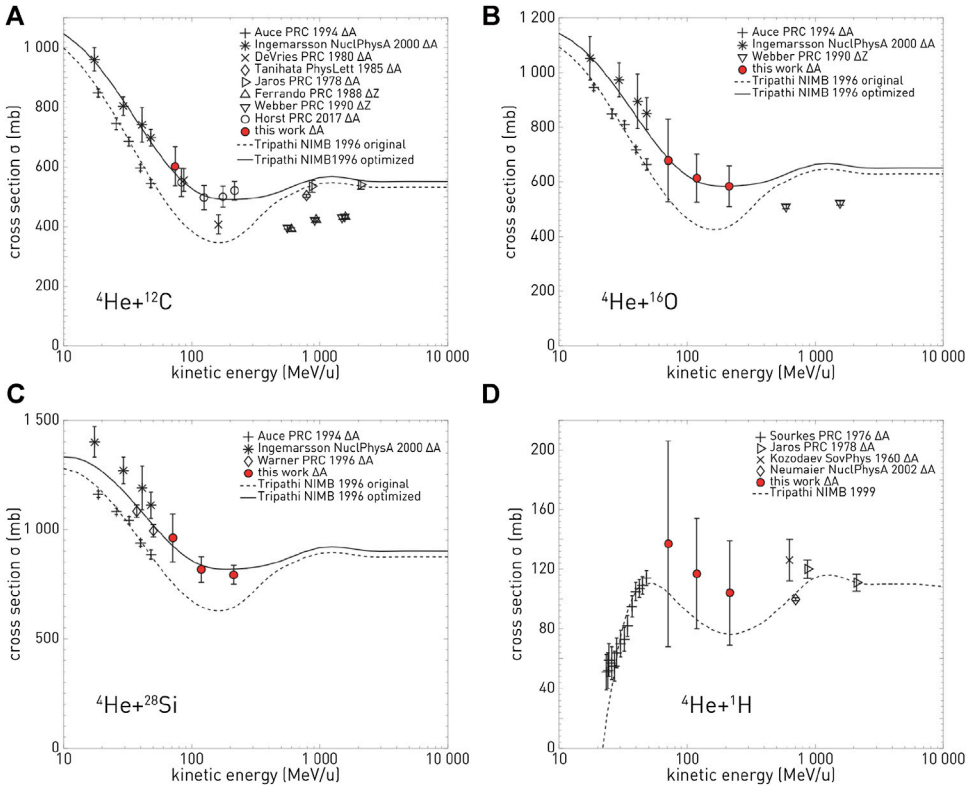

FIGURE 2 | Cross section measurements from Horst et al. [99]: in red, the new measured mass-changing cross sections for ^{4}He ions on C **(top left)**, O **(top right)**, Si **(bottom left)**, and H **(bottom right)** targets, compared with different data from the literature and with two parameterizations of the measurements.

model benchmarking with a high level of accuracy. However, for processes or phase space regions where there is a complete lack of data, even less accurate measurement would be valuable.

2.5.2 Measurements on Thick Targets

These measurements include cross sections, primary beam attenuation studies, Faraday cup measurements, fragmentation yields, and emission angles. Rather than being directly useful for model tuning, these measurements allow us to assess the overall accuracy of MC codes, that is, transport, nuclear, and electromagnetic interactions together. A vast amount of measurements on thick targets have been done in the last decades; however, only a handful are useful for MC benchmarking. First, they should include a clear description of the experimental setup. Second, the physical quantities should be reported in absolute units. In **Table 2**, a selection of valuable measurements is presented. Of these measurements, the cross section measurements by Schall [111], Heattner [112, 113], and Golvschenko [114, 115] are most suitable for benchmarking MC codes at particle therapy energies, and these data were used for benchmarking FLUKA [63], GEANT4 [63], PHITS [116], and SHIELD-HIT [55, 56]. Examples of studies aimed at studying emission angles and fragment yields were performed for PHITS [117], FLUKA [118], and GEANT4 [119], allowing for additional improvements in these codes. A recent experimental work of Aricò et al. [120] points out that there are differences in secondary fragment production between water and PMMA targets. Furthermore, simulations were performed using FLUKA, and some differences were found between experimental measurements and calculations. All these differences should be taken into account when dosimetric measurements are performed using PMMA instead of water phantoms.

A different approach is represented by charge measurements performed by means of a multilayer Faraday Cup. For example, in the work of Rinaldi et al. [121], a FLUKA simulation of protons at 160 MeV was compared to existing experimental data. This is an integral test which allows to estimate the accuracy of MC models in reproducing the overall range of nuclear secondaries produced in target fragmentation. However, as remarked by the authors, it cannot provide any specific check of a particular reaction channel. Besides FLUKA, also other MC codes have been previously compared to the same kind of measurements. For instance, SHIELD-HIT is considered in Henkner et al. [122], MCNPX in Mascia et al. [123], and GEANT4 in Zacharatou et al. [124] and in Hall et al. [28].

2.5.3 Measurements That Were Performed in the Context of Range Monitoring

These measurements are those that specifically concern the production of secondaries which can be exploited for range monitoring, a topic where the reliability of nuclear models in

TABLE 2 | A non-exhaustive selection of measurements on thick targets relevant to particle therapy: projectile, energy, target material, measurement, literature with MC-data comparisons, and reference with first author.

Incident beam	Energy [MeV/u]	Target	Measurement	References
^{4}He	120 and 200	Water and PMMA	Attenuation of primary beam and build-up of secondary charged fragments in depths	Rovituso et al. [125]
^{4}He	220	Water and PMMA	Attenuation of primary beam, and build-up of secondary hydrogen ions due to fragmentation	Aricò et al. [118]
^{4}He	102, 125, and 145	PMMA	Flux of fragments behind Bragg peak at 5 angles between 0 and 30° from beam-line	Marafini et al. [126]
^{12}C	110 to 250	C, paraffin, and water	Total charge changing cross section and partial cross sections for B and Be fragment production	Golovschenko et al. [114]
^{11}B, ^{12}C, ^{14}N, ^{16}O, ^{26}F, ^{20}Ne	200 to 670	Water, carbon, lucite, polyethylene, and aluminum	Total and partial charge changing cross sections through primary beam attenuation measurements, buildup of nuclear fragments	Schall et al. [111]
^{4}He, ^{12}C	100 to 400	C	Double differential cross section measurements for neutron production	Handbook [97], chapter 2
^{12}C, ^{16}O	57, 93, and 95	Graphite, Plexiglas, and polyethylene	Fragment emission angle distributions	Sihver et al. [127]
^{12}C	56	Thick muscle and cortical bone	Production yields of produced fragments and energy spectra of most abundant fragments ($Z \leq 5$ isotopes) at 0°	De Napoli et al. [119]
^{12}C	150, 290, 400, and 490	PMMA	Fluence and LET of various fragments	Matsufuji et al. [128]
^{12}C	200	Thick water	Detect all fragments and present energy spectra at various angles (0°, 5°, 10°, 20°, and 30°) with respect to the beam axis for charged fragments ($Z \leq 2$ isotopes) and neutrons	Gunzert-Marx et al. [117]
^{12}C	200, 400	Thick water	Energy and angular distributions of fragment isotopes from $Z = 1$ to $Z = 5$ at 6 depths before and behind Bragg peak, build-up curves of secondary fragments, and attenuation of primary carbon beams	Haettner et al. [112, 113]
^{12}C	213, 226, and 250	Thick PMMA	Show back-projection of distributions on the beam-axis of secondary charged particle tracks detected at 30° from the beam-axis, as well as lateral projections (HIT)	Gwosch et al. [129]
^{12}C	290	Thick water	Investigate spatial fragment distribution: Primary beam angular distributions and projectile fragments ($Z \leq 5$) angular distributions. Also multiplicity distributions.	Matsufuji et al. [130]
^{12}C, ^{14}N, ^{16}O	200, 270, and 300	Thick water	Z distributions of beam fragments, total and charge-changing cross sections, Bragg peak measurements	Schardt et al. [131]
^{12}C	430	Water and PMMA	Primary beam attenuation Attenuation and yield of different fragments	Aricò et al. [120]

TABLE 3 | Summary of measurements in the context of range monitoring studies.

Incident beam	Energy [MeV/u]	Target	Technique	Measurement	Refs.
P	160	PMMA	Prompt γ	Energy spectra and yields at 90°	Smeets et al. [143]
P	230	Water	Prompt γ	Energy spectra and yields at 90°	Verburg et al. [151, 152]
P	48	4 samples with varying amount of O, C, H	Prompt γ	Energy spectra and yields at 90°	Polf et al. [153]
^{12}C	73, 95, and 305	PMMA and water	Prompt γ	Time-of-flight and energy spectra at 90°	Testa et al. [154–156]
^{12}C	220	Polymethyl methacrylate	Prompt γ	Energy spectra and yields at 90°	Vanstalle et al. [157]
^{12}C	95 and 310	PMMA and water	Prompt γ	Energy spectra and yields at 90°	Pinto et al. [144]
^{12}C	80	PMMA	Prompt γ	Energy spectra and yields at 90°	Agodi et al. [158]
^{4}He, ^{12}C, ^{16}O	100 to 300	PMMA	Prompt γ	Yields at 60°, 90°, and 120°	Mattei et al. [159]
^{12}C	80	PMMA	Fast charged hadrons	Proton yields at 60° and 90°	Agodi et al. [160]
^{12}C	220	PMMA	Fast charged hadrons	Fragments with Z = 1 at 90°	Piersanti et al. [76], Mattei et al. [161]
^{4}He, ^{12}C	120–220	PMMA	Fast charged hadrons	Secondary protons at 90°	Rucinski et al. [162]
^{16}O	—	PMMA	Fast charged hadrons	Yields of fragments with Z = 1 as function of energy and production position at 60° and 90°	Rucinski et al. [163]
^{12}C	400	Composite target	Fast charged hadrons	Secondary fragments for angles 34° to 81°	Alexandrov et al. [164, 165]
p, ^{12}C	40–220(p), 65–430(C)	Graphite and beryllium oxide	β+	Cross section measurements of ^{10}C, ^{11}C, and ^{15}O	Horst et al. [136]
p, ^{12}C	110, 140, 175 (p), 212, 260, and 343 (C)	PMMA	β^{+}	Absolute activity distributions and total production cross sections of ^{10}C, ^{11}C, and ^{15}O	Pshenichnov et al. [166]
P	55	Water, carbon, phosphorus, nd calcium	β+	Number of short lived β+ emitters	Dendooven et al. [139]
P	10 to 70	Polyethylene and water	β^{+}	Cross sections of 4 specific reaction channels for production of ^{11}C, ^{15}O, ^{13}N	Akagi et al. [167]
P	10 to 70	Polyethylene	β^{+}	Cross sections of specific reaction channels for production of ^{11}C and ^{10}C	Matsushita et al. [133]

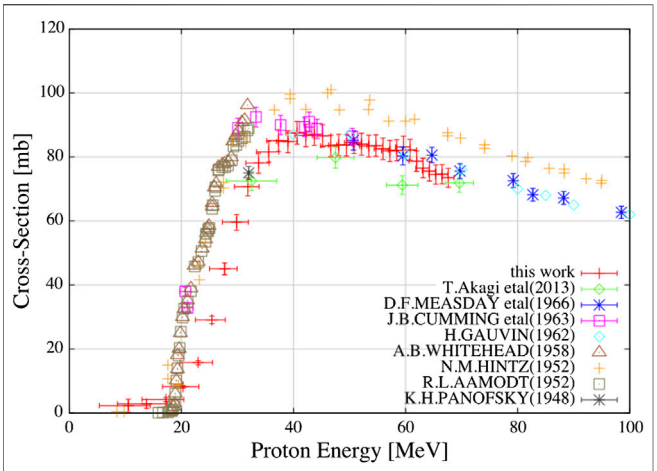

FIGURE 3 | Cross section measurements for ^{11}C from different groups in the past 70 years, with new recent measurements included. Reproduced with permission from Matsushita et al. [133] Discrepancies between various measurements are visible.

MC is of particular relevance. These secondaries include β^+ emitting nuclei, prompt gammas, and energetic secondary charged fragments. We summarize a selection of these measurements in **Table 3**. Again the list is non-exhaustive, and we selected only those measurements that were reported in absolute physics quantities on homogeneous targets, since we consider these as the most suitable for the benchmarking of MC models.

As far as β^+ emitting nuclei are concerned, a large amount of measurements is available for offline, in-room, and online monitoring. Most of them are measurements of the detection of the activity spatial distribution. However, the data which are particularly useful for MC model tuning are cross section measurements. Actually there are not yet enough cross section data available. Existing data have large uncertainties, and to achieve a range accuracy below 1 mm, more accurate cross section measurements are needed [132]. The case for which more data are available is that of ^{11}C production in p-^{12}C collisions. **Figure 3**, taken from the work of Matsushita et al. [133], illustrates a situation which points out that considerable systematic differences exist between different data sets. Clearly, the uncertainty of the predictions of MC models can be, at best, of the same order as the experimental uncertainty. FLUKA was compared with these cross section data, starting from the work of Sommerer [134], and the quality of results, as summarized in Figure 7 of the article of Battistoni et al. [135], can be considered satisfactory. The comparison with data for ^{11}C and ^{15}O production is shown. These are the two most relevant radionuclides in case of PET monitoring in proton therapy, but other isotopes can be important, especially in in-beam PET. Less data are available in case of ^{10}C production. Recently, new cross section data for ^{10}C, ^{11}C, and O^{15}, very useful for future benchmark studies, were published by different groups [133, 136], where the work of Horst et al [136] concerns also data relative to C–C and C–O collisions. Since recently, the use of PET monitoring technique is under consideration also in the case of ion therapy [137]. The prediction capability for short-lived β^+ emitters remains subject to uncertainties. A recent comparison [138] between GEANT4 for short-lived β^+ emitting nuclei with data [139] clearly demonstrated the need for improvement.

Regarding prompt gammas, soon after the first proposal to use prompt gamma detection for particle therapy [140], it was realized that existing MC models were not reliable, see, for instance [141]. This has led to many new developments, among which the Envision project [142], in the context of European FP7 program, dedicated to imaging in ion therapy, which also stimulated new efforts for the improvement of existing codes and the development of new ones. For instance, valuable measurements in the framework of Envision were reported by Smeets et al. [143] and Pinto et al. [144], as well as several studies aimed at improving the accuracy of MC codes like MCNPX [143], GEANT4 [145], and TOPAS [146]. The study by Dedes et al. [145] revealed that prompt gamma yields were strongly overestimated by GEANT4 [145]. Improvements in GEANT4 were reported in 2016 [147], and good results for the FLUKA code concerning the prediction of both yields and energies of prompt gammas are obtained [135].

Finally, charged fast hadrons were considered more recently for range monitoring purposes [148–150] in the context of ion therapy. **Table 3** summarizes various measurements that are useful for MC benchmarking. From the point of view of fundamental cross sections of interest in this case, also data reported in **Table 1** are very useful. However, the approach aiming at achieving more spatial precision [149] requires the use of fragments emitted at large angles (mostly protons). Simulating such processes is challenging, because only a few of the total number of charged hadron secondaries produced are emitted at large angles. In fact, the standard available biasing techniques (importance biasing and biasing of inelastic cross section) do not apply in this context, especially when a comparison with experimental data on the basis of event-by-event reconstruction is required. It would be possible to develop dedicated variance reduction techniques for this purpose. In addition there is lack of data at large production angles to benchmark production models. A recent attempt to perform this kind of measurements for ^{12}C interactions on different elements is reported in Ref. 105.

2.6 Future Directions in Model Development

In the last decade, many important developments of interest for particle therapy concerned the use of MC. So far, the attention has been mainly focused on the treatments with proton and ^{12}C beams. Therefore, also the efforts in the development of nuclear models were necessarily concentrated on the interactions of these projectiles. More recently, the attention is focusing on ^{4}He interactions, since this appears to be most probable application of new ion beams for therapy [168]. The case of ^{16}O projectiles is also a next study case. Consequently, future work to improve MC models should be oriented in the same direction.

It turns out that adopted hadronic models are in general adequate for physical dose calculations. However, it is clear

that none of the models considered in the above-discussed MC codes, or others, is capable, alone, to provide reliable predictions in all clinical and research applications. Due to their intrinsic phenomenological nature, experimental data are needed to drive model development and to allow their benchmark. In this respect, our claim is that the most valuable data for this purpose are single and double differential cross sections, measured on thin target experiments. Unfortunately, in the whole range of interest for particle therapy, there is still a significant lack of measurements, mainly concerning nucleus–nucleus interactions. In the next years, new data are expected from the FOOT experiment [110]. Of course, also indirect approaches and measurements on thick targets, often involving multiple interactions and different energies, are very important for model validation.

Finally, we would like to point out that a judgment of the level of accuracy of certain model may strongly depend on the scope of use. The capability of correctly reproducing in detail the cross sections may not be necessary in all cases. For instance, a model can be accurate in reproducing the physical dose but not enough for range verification techniques. In any case, MC models require a continuous work of upgrade and development. This concerns both the improvement of physics modeling and the optimization of their algorithmic implementation. Actually, the complexity of the description of interactions can result in elevated consumption of computing time. As we shall discuss also in the next sections, this aspect remains one of the major limitations in the use of general purpose MC codes in clinical practice.

3 MONTE CARLO AND RADIOBIOLOGICAL MODELING

3.1 Rationale

The capability of performing a reliable calculation of physical dose is a necessary condition for an MC to be used in particle therapy. However, this is not sufficient, and the evaluation of effective biological dose is eventually required. This is a fundamental aspect which is particularly important in ion therapy. In fact, one of the most important reasons for the use of carbon or heavier ions in particle therapy is their increased relative biological effectiveness (RBE) in the Bragg peak region. A primary ion beam will give rise to a mixed radiation field with particles and nuclear fragments of different charge, energy, and LET. Each of them will have a different biological impact, even for the same imparted physical dose in the same kind of tissue. This is related to the different ionization density which the different particles will produce on length scales comparable to the size of DNA structure and cell nuclei. Many complex biological aspects are involved that may give rise to significant uncertainties in effective biological dose calculations. Thus, the study of radiobiological effects cannot be limited just to the physics of the interactions of radiation with matter, but should include the modeling of biological factors. Below, we discuss strategies that have recently been developed to take into account some biological effects in MC dose calculations in clinical and research context.

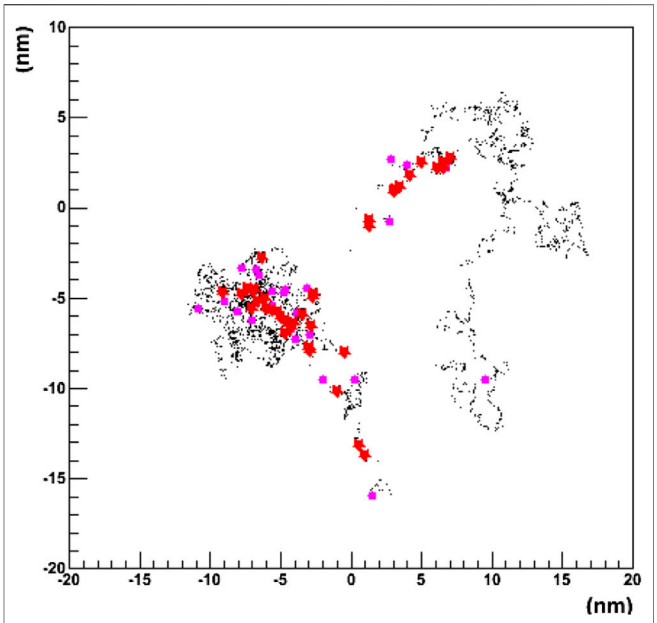

FIGURE 4 | Projected 2D pattern generated by a single 1 keV electron in liquid water using the GEANT4-DNA physics processes. The primary particle originates at the (0,0) position. Different colors represent different physics processes [172].

3.2 The Track Structure Approach

This review mainly concerns MC codes adopting the condensed history approach, while radiobiological calculations are most properly performed by means of track structure codes. These are codes designed to track the passage of electrons and ions simulating each individual basic interaction and recording positions and energy depositions of all produced particles. Besides the description of physical processes, radiochemistry models must be implemented in these codes to take into account the many body processes relevant for radiobiological purposes. Track structure codes are in general able to perform calculations on microscopic (nanometric) volume scales in liquid water, making their application in simulations of actual treatments highly unpractical from the point of view of computing power. However, they remain fundamental, together with mathematical models of the cell structure, for the investigation of all basic mechanisms related to biological effects of radiation. Among the examples of codes belonging to this class, we can quote PARTRAC [169], able to perform calculations on microscopic scales in liquid water, and TRAX [170, 171], which can deal with different materials. Results obtainable by these codes can in principle be coupled with the radiation field simulation achievable with general purpose MC codes.

A recent approach aiming to merge the track structure approach into the framework of a general purpose MC code is the GEANT4-DNA project [172]. It was started in the context of the studies for radiation protection in space missions. The code currently includes the interactions of light particles (electrons)

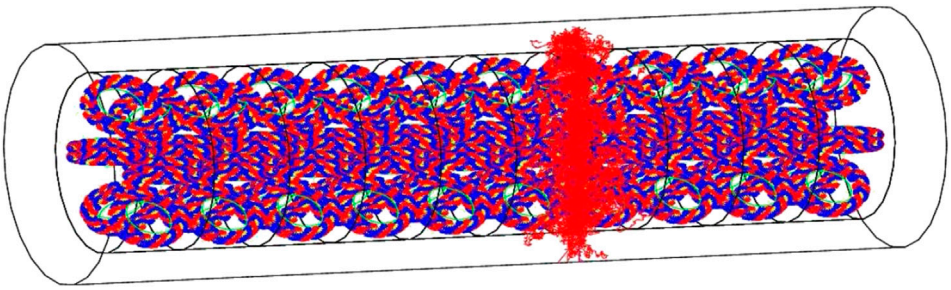

FIGURE 5 | Visualization of a whole chromatin fiber irradiated by a single 500 keV He^{+} particle, emitted perpendicularly to the main revolution axis of the fiber. Individual bases are modeled as sectors of cylindrical shells, with an inner radius of 0.5 nm and an outer radius of 1.185 nm. They have a thickness of 0.33 nm. The positions of 100 pairs of bases are parameterized into a DNA helix loop. [172].

and ions including hydrogen and helium isotopes down to the eV scale in liquid water. An example of the tracking capabilities of the code is shown in **Figure 4**, where the 2D pattern generated in liquid water by a single 1 keV electron is shown.

Thanks to the geometrical modeling capabilities of GEANT4, it allows to implement the geometry of biological targets at sub-micrometric scales. In particular, it can use either a voxelized or an atomistic approach. The latter allows to model targets at nanometric scales, such as the DNA molecule, using the combination of standard mathematical volumes, as shown in **Figure 5**. A chemistry model can be coupled to simulate indirect effects of radiation due to the generation of molecular radical species.

Another attempt is being made in the context of the TOPAS [21, 22] project, where an extension was developed called TOPAS-nBio [22, 173], which is aimed at the modeling of detailed biological effects at the nanometer scale, facilitating and extending the use of GEANT4-DNA models for subcellular geometries, physics, and chemistry processes.

3.3 Coupling of General Purpose MC Codes With Radiobiological Models

A common approach to evaluate the RBE-weighted dose (D_{RBE}) in a MC simulation is to obtain the RBE by exploiting the survival probability S of cells as function of physical dose D as predicted by the linear quadratic dependence, inspired by the dual radiation model of [174] formulated as

$$S = e^{-\alpha D - \beta D^2}. \qquad [1]$$

Here, α and β are parameters, which depend on several variables including those of biological nature, such as the tissue type, and of physical nature, like particle type, energy, dose, and LET. The RBE factor, for a given survival level S, is then given by

$$RBE = 2\beta_i \left[-\alpha_X + \sqrt{\alpha_X^2 - 4\beta_X \ln S} \right] \Big/ 2\beta_X \left[-\alpha_i + \sqrt{\alpha_i^2 - 4\beta_i \ln S} \right], \qquad [2]$$

where α_X and β_X are the coefficients for photons, while α_i and β_i are the coefficients for the ions of interest (at a given LET).

When general purpose condensed history MC codes are considered, the most common approach is to rely on a precomputed database of the coefficients α and β. They can be estimated by numerical radiobiological models, such as the local effect model (LEM) [175–178] or the microdosimetric kinetic model (MKM) [179–185]. Alternatively, they can be obtained from experimental data or from track structure simulations. One of the first examples of this approach within a MC can be found in the work of Kase et al. [186], using GEANT4 in the context of ion therapy activity at NIRS. In the case of FLUKA [135], a general interface is available to the user in order to provide a database in terms of α and β for different tissue types and for the different components of the radiation field as a function of energy per nucleon. As implemented also in other codes, in order to compute the biological effect, FLUKA performs the calculation of dose-weighted averages $\overline{\alpha}_j$ and $\overline{\beta}_j$:

$$\overline{\alpha}_j = \frac{\sum_i \Delta d_{i,j} \cdot \alpha_{i,j}}{\sum_i \Delta d_{i,j}} \quad \text{and} \quad \sqrt{\overline{\beta}_j} = \frac{\sum_i \Delta d_{i,j} \cdot \sqrt{\beta_{i,j}}}{\sum_i \Delta d_{i,j}}, \qquad [3]$$

where $\Delta d_{i,j}$ is the dose from the ith charged particle (composing the mixed radiation field) with associated $\alpha_{i,j}$ and $\beta_{i,j}$ in voxel j and i runs over all particles depositing dose in voxel j. Eventually, RBE and RBE-weighted dose values can be determined for each voxel of the irradiated target knowing the absorbed dose and the dose-weighted averages $\overline{\alpha}_j$ and $\overline{\beta}_j$

As an example, we report in **Figure 6** $\overline{\alpha}$ and $\overline{\beta}$ (left panel) and the absorbed dose and D_{RBE} (right panel) for a carbon ion biologically optimized spread-out Bragg peak, as available at CNAO. The SOBP was calculated for a homogeneous dose distribution of 3 Gy-RBE in a cubic shaped target of side 6 cm centered at 9 cm depth in water. The FLUKA weighting was achieved for a cell line having $(\alpha/\beta)_X = 2$ Gy, as obtained from photon irradiation measurements.

Another example where this approach was applied is a newly developed radiobiological model denominated BIANCA [187, 188], implemented in the form of MC simulation as well, which takes into account the development of complex DNA lesions, chromosomic aberrations, and their capability of inducing clonogenic cell death. In Ref. 188, the coupling of BIANCA with the FLUKA MC is reported. This work shows a comparison of survival data of CHO cells after an irradiation

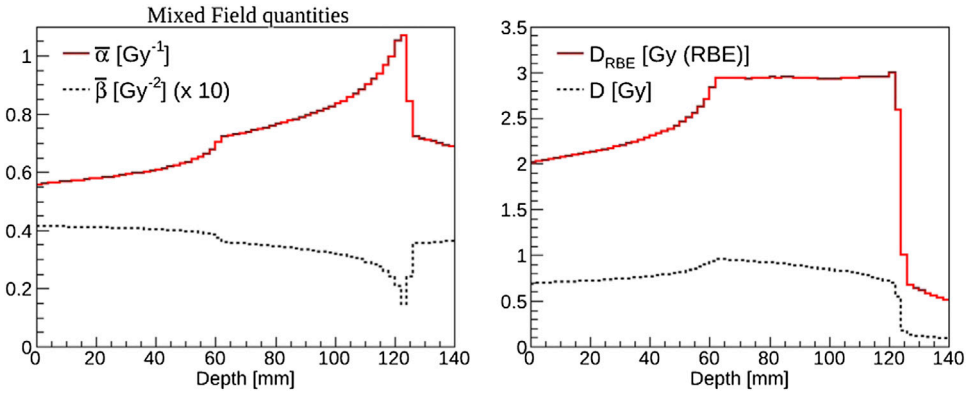

FIGURE 6 | Example of biological weighting of dose performed with FLUKA [135] in the case of a carbon ion spread-out Bragg peak for a cube-shaped target of side 6 cm centered at 9 cm in water. Left panel: $\overline{\alpha}$ (solid line) and $\overline{\beta}$ (dashed line) calculated as a function of depth in water. The β results have been rescaled by a factor of ten for display purposes. Right panel: absorbed dose (dashed line) and D_{RBE} (solid line) values calculated as a function of depth in water.

mimicking a clinically relevant scenario using carbon ions and protons. An interesting result of this work is reported in **Figure 7**.

Different RBE models can produce different results, and this can result in different dose prescriptions. This aspect has been studied in detail for carbon ion therapy at CNAO with the help of MC calculation. The starting point is that it was considered to take as reference the clinical protocols assessed in the past in the NIRS Japanese center. At NIRS the MKM radiobiological model was used, while, for several years, the treatment planning system of CNAO, as in the rest of Europe, was based on the LEM-I model. Since 2012, Fossati et al. [190] showed that for the same D_{RBE}, significant variations of the physical dose D in the target volume, up to 15–20%, were found when comparing the two approaches. In order to minimize target physical dose variations, and possible consequent risks of undercoverage of target, prescription dose conversion factors, as suggested in Ref. 190 in a study with water phantoms, were validated for a series of patient cases by Molinelli et al. [191] by means of simulations performed with the FLUKA MC, where the alpha, beta radiobiological parameters from LEM-I were used according to the procedure described in this section. Further studies using MC simulations are reported in the work Magro et al. [192]. A Matlab-based tool was developed to generate a biological database, that is, a set of input tables of some model-specific parameters for a variety of particles, based on the MKM mode. This database was benchmarked with published ICRU energy loss tables. Then, using this database together with the information about the mixed-radiation field (particle type, energy, *etc*), FLUKA can calculate the RBE-weighted dose of the mixed-radiation field in each voxel. To clinically benchmark the coupling of FLUKA with the NIRS approach, a few real patient treatments were simulated, corresponding to different prescripted dose levels. The simulation results (physical dose, effective dose, and RBE) were compared to the results obtained by means of the TPS adopted at NIRS. Some discrepancies were found, but the general level of agreement was considered satisfactory. A similar investigation has been more recently performed for ^{4}He ions, as reported in the work of Mein et al. [193] using both MC and an analytical calculation platform.

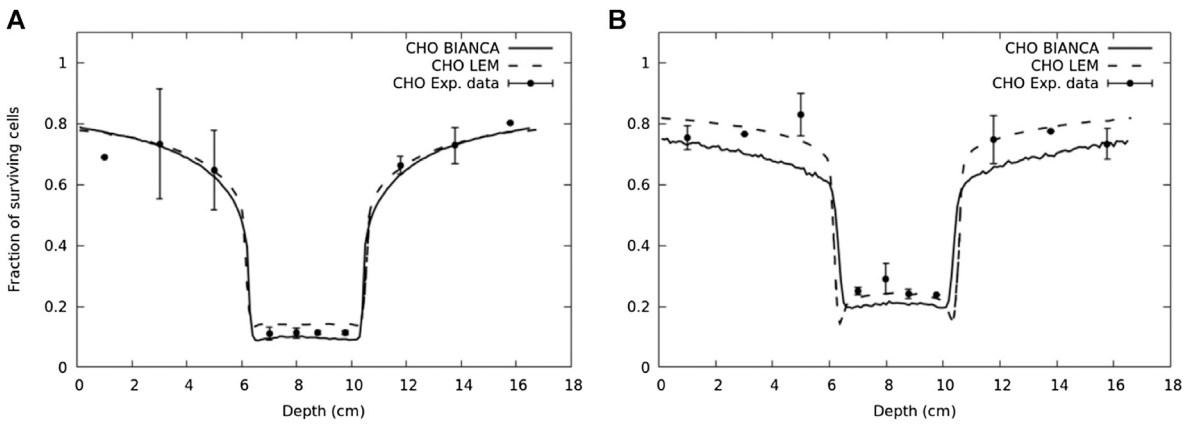

FIGURE 7 | Surviving fraction for CHO cells in a typical two-port irradiation with carbon ions (panel **(A)**) and protons (panel **(B)**) [188]. The solid lines represent the predictions performed by BIANCA interfaced to FLUKA, the points are experimental data taken from Ref. 189, and the dashed lines represent the prediction performed by LEM model [189].

3.4 Semi-Analytical Approaches

The dose average linear energy transfer (LET_D) is frequently used as physical quantity to describe the biological effectiveness of the mixed radiation field. LET_D is the dose-weighted mean value of the particle LET distribution at depth z in the radiation field consisting of dose contribution D_i from all particle species i and is defined as

$$LET_D(z) = \frac{\Sigma_i \int LET_i(E) D_i(E,z) dE}{\Sigma_i \int D_i(E,z) dE} = \frac{\Sigma_i \int LET_i^2(E) \phi_i(E,z) dE}{\Sigma_i \int LET_i(E) \phi_i(E,z) dE}. \quad [4]$$

The quantities $LET_i(E)$ and $\phi_i(E,z)$ can be evaluated by means of MC codes so that LET_D can be calculated by means of **Eq. 4**. This can be exploited to evaluate RBE in the case of proton therapy, where it is possible to make use of phenomenological models which predict proton RBE as a function of LET, dose, and the (α, β) tissue-specific parameters for photons. The most common models of this type, derived from the analysis of proton RBE experimental data, are those of Wedenberg [194], Wilkens [195], McNamara [196], and Carabe [197].

Dependence of RBE on LET can be fitted in different ways. For example, in the Wedenberg model [194], RBE is given by

$$RBE\left(LET, D, (\alpha/\beta)_X\right) = \frac{1}{2D}\left(\frac{\alpha}{\beta}\right)_X + \frac{1}{D}\sqrt{\frac{1}{4}\left(\frac{\alpha}{\beta}\right)_X^2 + \left(qLET + \left(\frac{\alpha}{\beta}\right)_X\right)D + D^2} \quad [5]$$

where q is a parameter obtained by experimental data, different for each cell line.

Instead, the RBE expressions of McNamara [196] is given by

$$RBE\left(LET, D, (\alpha/\beta)_X\right) = \frac{1}{2D}\left(\sqrt{\left(\frac{\alpha}{\beta}\right)_X^2 + 4D\left(\frac{\alpha}{\beta}\right)_X\left(p_0 + \frac{p_1}{(\alpha/\beta)_X}LET\right) + 4D^2\left(p_2 + p_3\sqrt{\left(\frac{\alpha}{\beta}\right)_X}LET\right)^2} - \left(\frac{\alpha}{\beta}\right)_X\right) \quad [6]$$

where $p_0 = 0.999064$, $p_1 = 0.35605$ Gy keV^{-1} μm, $p_2 = 1.1012$, and $p_3 = 0.0038703$ Gy$^{-0.5}$ keV μm.

These kind of approaches can be useful in proton therapy to take into account variations in RBE, as alternative to the common assumption in clinical treatments of a constant RBE value of 1.1. In principle, it is possible to introduce these parameterizations also in ion therapy; however, it is usually preferred to make use of more sophisticated phenomenological or mechanistic models.

3.5 Future Directions and Developments

Considering the present state of the art, the possibility of making use of track structure simulation within a MC calculation of particle therapy treatments seems to be confined, for the moment, to research activities. In fact, the exceptionally high computing time which is required by such an approach can discourage to adopt this solution for a systematic study of clinical cases, and treatment planning in particular, even when accelerating techniques or large clusters are employed. It can be considered sometimes for retrospective analyses of clinical data. In general, the use of an interface to pre-calculated tables from external radiobiological models will remain the most practical solution for MC simulations.

Future developments, useful for biologically oriented treatment planning, need to consider not only RBE but also other important radiobiological quantities. One of the most important parameters is the oxygen enhancement ratio (OER) and its dependence on physical variables. This parameter is particularly interesting in view of the use of high-LET radiation for the treatment of hypoxic tumors, as discussed, for instance, in the works of Scifoni and Sokol et al. [198–200].

The development of new generation treatment planning is also considering the radiobiological effect of target fragmentation in proton therapy. As proposed in Ref. 201, this phenomenon may contribute to an increase of RBE especially in the entrance channel, and neglecting this contribution can bring to an underestimation of damage to the healthy tissues. The investigation of this particular aspect, usually not considered so far, requires both experimental activity and MC simulations. This is also a theme where the importance of modeling nuclear interactions, as discussed in **Section 2**, is emerging [202, 203].

Other topics in which MC simulation can be important in the context of radiobiology is the comprehension of possible mechanisms leading to the enhancement of radiobiological effectiveness. An attempt in this direction is the recent suggestion concerning the additions of specific radioisotopes (like ^{11}B or ^{19}F) to exploit nuclear reactions triggered by protons on these nuclei. These reactions can generate short-range high-LET alpha particles inside the tumors, thereby allowing a highly localized DNA-damaging action [204]. Another interesting challenge is coming from the possible extension of the FLASH Radiotherapy approach [205, 206] to particle therapy, that is, the delivery of very high dose rates ($\geq$ 100 Gy/s). It has been suggested that such high dose rates can enhance differential effects between normal tissue behavior with respect to the tumor. From the point of view of MC codes, no changes are expected for the physics of interactions of radiation in matter, while specific radiobiological models are still under investigation and development.

4 DEVELOPMENT OF MC-BASED TREATMENT PLANNING

4.1 Introduction

Over the past years, the superior accuracy of MC calculations with respect to analytical calculations has been confirmed in many studies. This is thanks to the more accurate implementation of physical (and possibly radiobiological) processes, the fact that

the material composition is included in calculations, and the precise tracking algorithms. At present, MC dose calculations are therefore successfully used for various purposes in treatment planning and related research. Although the applications of MC in treatment planning are mostly in forward dose calculations (to compute the dose distribution in a tissue given a treatment plan), new developments are ongoing to include them in inverse dose calculations (to find a treatment plan whose execution will achieve a desired dose distribution).

In the next paragraphs, we shall first summarize some considerations on the role of MC in the present use of MC in treatment planning systems. Then, we shall present an example of developments in MC-based treatment planning systems, and we finish with some consideration about the underlying problematics and developments.

4.2 Present Usage of MC in Treatment Planning

MC simulations play an important role in the development and commissioning of treatment planning systems. Different treatment planning systems exist for particle therapy. A discussion of these tools goes beyond the purpose of the present review, but a few general issues can be mentioned. For dose delivery with spot spanning, commercial treatment planning systems are usually based on fast analytic dose engines using pencil beam algorithms. Such algorithms are often developed with the help of MC dose calculations, since it is not possible to rely completely upon analytic expressions or available tabulations. Many treatment planning systems require that the user provides specific measurements and MC simulations of pencil beams in water as a part of the TPS commissioning process for a given facility.

Moreover, MC simulations are currently often used for verifying the treatment plans of commercial treatment planning systems for complex patient dose calculations. Such verifications are often desired in situations which are characterized by large density heterogeneities (see, e.g., [1–3]), at least for a limited number of patient cases. The TPS prescription is used as input to the MC, which performs a forward dose calculation, that can be compared with the analytical result.

The clinical interest in high-accuracy MC tools is demonstrated by the fact that vendors of commercial treatment planning systems have since recently started to provide the user with MC-based dose calculation kernels for proton therapy, albeit only for forward calculations:

- The RayStation ® [207] TPS provides the user the possibility to perform forward MC dose calculations for protons, based on a condensed history MC for primary and secondary protons, while heavier secondaries are considered only using a continuous slowing down approximation [208]. This MC dose engine has been validated also in clinical context [209]. Here, the authors demonstrated the superior accuracy of the MC dose engine with respect to the analytical algorithm in specific situations: in the presence of range shifters, large air gaps, or when beam directions are tangential to the patient surface. This may also depend on patient anatomy [2, 3]. RayStation also includes a tool allowing for an easy comparison between the MC and the analytical result, so discrepancies can be easily identified.
- The Eclipse treatment planning system provides users a MC dose algorithm for proton therapy, AcurosPT [210]. Here, computational run time is minimized by simplifying and eliminating less significant physics processes. The algorithm was benchmarked with TOPAS.

4.3 Recent New Developments in MC-Based TPS

There are several promising new developments in the usage of MC calculations in treatment planning. For instance, in the context of ion therapy, new developments are ongoing in the TRiP98 (treatment planning for particles) [211, 212] tool. This TPS was created as analytical dose calculation and optimization tool and used clinically for carbon ion radiotherapy at GSI until 2008, taking advantage from the development of the LEM radiobiological model carried on at GSI [175–178, 213, 214]. In the clinical applications of TRiP98, the LEM-I version was adopted. It also served as prototype for the clinical TPS Syngo® RT Planning Software [215]. The original TRiP98 used a 1-dimensional deterministic transport algorithm, and the broadening of the ion beam as a function of depth was accounted for by means of a double Gaussian function. In order to overcome this kind of limitations, a fast MC algorithm was developed within TRiP98, as reported in the article of Iancu et al. [216]. This dose kernel could potentially also be used for plan optimization.

Also, in the development of ion treatment planning at HIMAC, MC has played a role. As reported in a dedicated textbook [217], GEANT4 was used to build the prediction of ion species and their kinetic energies of the therapeutic carbon-ion beam and to predict the dose mean-specific energy (z^*) which is necessary for their microdosimetric radiobiological model.

A recent example of MC dose calculation tool for both proton and heavy ion therapy is the work of Russo et al. [218, 219]. It describes a TPS computing kernel for different ion types, called PlanKIT (Planning Kernel for Ion Therapy), developed within a collaboration between IBA and INFN, currently only used for research. This TPS is based on the use of a "Beamlet Superposition (BS) model." The concept, similar to what is adopted in other projects, is that an ion beam can be thought of as composed of subunits, here called Beamlet, that are obtained splitting the beam phase space in smaller phase spaces. The total irradiation result is obtained by summing the interactions of the different beamlets, computed with FLUKA MC simulations. In this way, it is possible to produce universal Look-Up tables of physical and radiobiological quantities, like dose, track-averaged, and dose-averaged LET and, by coupling to the MKM radiobiological model, α and β coefficients to derive RBE according to the linear quadratic model. The main advantages deriving from this approach were two: i) the possibility to simulate the irradiation with different ions species and ii) the

evaluation of several physical and radiobiological quantities at the same time. At present, only forward calculations can be performed with PlanKIT.

All above mentioned examples, with exception of the TriP98 research, are examples where MC is used as forward dose calculation tool. Considering the recognized quality of results in dose calculation which can be obtained by means of simulation, it is natural to consider also the possibility of coupling MC to an optimization code for inverse dose calculations, so that MC accuracy would be assured for all stages in treatment planning, from development to clinical use. This would have a few important advantages:

- It would allow to include the most accurate description of physics, geometry, beam models, and materials during all stages of treatment planning, including plan optimization, that is, the calculation process to obtain all beam weights by optimizing the dose in terms of target coverage and OAR dose.
- It would allow to consider the actual composition of tissues. In fact, TPS calculations are usually performed just considering a water equivalent path length environment. For electromagnetic processes, this is generally not a problem, but for processes involving nuclear interactions, it may lead to errors, especially in calculations for high density regions in the patient (bone and implants), or in modeling treatment heads and beam shape devices.
- It would be possible to simultaneously predict dose and secondary particle production, useful for treatment verification techniques.

One of the first attempts to proceed in this direction has been reported in the work of Mairani et al. [220], which describes the development of a MC treatment planning (MCTP tool) for proton therapy based on the FLUKA code. The workflow of this solution is illustrated in **Figure 8**.

The procedure requires as input a set of pre-optimized pencil beams $P^1(N^1)$. Here, N^1 is the initial pre-optimized guess for the fluences that is obtained with a commercial TPS or fast MC, starting from all the possible beams P_0 available in a given therapy facility in terms of energy values and positions. Then, the MC-optimized solution, $P_2(N_2)$, is obtained iteratively by an optimizer algorithm which runs over a MC calculated dose kernel, that is, 2-dimensional matrix of $d_{i,j}$ values (dose in voxel j of patient geometry deposited by pencil beam i). Hereby, an RBE-weighed dose kernel is achieved by either using a fixed RBE value of 1.1 or using pre-computed tables of radiobiological coefficients, as described in **Section 3**. An optimizer code, taking as input the MC dose kernel, produces the treatment plan by minimizing a cost function which takes into account the prescribed dose to the planned target volume (PTV) and a set of dose limits for organs at risk (OAR).

This approach has been initially validated at CNAO by comparing the results to those achieved by the standard TPS adopted in the facility. **Figure 9** reports the results of one of those comparisons.

The project was soon extended to ion therapy, as described in the work by Böhlen et al. [221]. Since then, it has been used mainly for research purposes. For instance, we can quote two examples: i) the investigation of the robustness of ion beam therapy treatment plans with respect to uncertainties in biological treatment [222] and ii) the study and validation of treatments with different ion species, including ^{4}He and ^{16}O (also protons and C), by comparing results with dosimetric measurements, as performed at the Heidelberg Ion Therapy Center [223].

4.4 Developments and Perspectives

As mentioned in the conclusions of **Section 3**, work is ongoing in view of a new generation of TPS considering new features, as other radiobiological parameters and target fragmentation, and the possible use of new ions other than ^{12}C. In all these cases, the use of MC will undoubtedly remain important both for development and check. A new case study where simulation can play a fundamental role (provided that the coupling with radiobiological modeling is properly implemented) is the optimization calculations for multiple ion treatments, as described by Sokol et al. [200]. Here, the combination of ^{4}He and ^{16}O beams has been considered as advantageous to achieve the "kill painting" approach [198, 224]. The first studies have been performed by means of the multi-ion biological optimization (MIBO) version of TRiP98 where specific algorithms to consider OER were added.

The MC approach discussed in Section 4.3 to treatment planning is surely of great interest and is potentially an innovative breakthrough. A few issues are still hampering the application in clinical practice. The most obvious difficulty is the large computing power that is required by full MC calculations, several hours for a multi-field proton therapy treatment plan [220]. From a clinical point of view, treatment planning with full MC can become attractive only if the required time is comparable to that employed using the standard approach, even if the quality of physics can be superior. Of course it is possible to reduce computation time by running parallel independent histories on a cluster of CPUs. However, the use of a very large cluster is not straightforward for all therapy centers. Instead, a more promising road is the development of fast MC techniques. This will be reviewed in **Section 5**. As we shall see, new attempts to develop MC treatment planning environments are under way [225, 226].

Finally, higher computation speed is not the unique requirement. In order to facilitate the use of MC in treatment planning in a clinical environment, it is important to develop the necessary software interfaces for the integration with TPS and image processing.

5 DEVELOPMENT OF FAST MC CODES

As mentioned previously, a major issue hindering widespread clinical implementation of MC simulations is computational efficiency. The complexity in the implementation of physics models and transport algorithms is very demanding in terms of computing power. Considering that a normal MC simulation

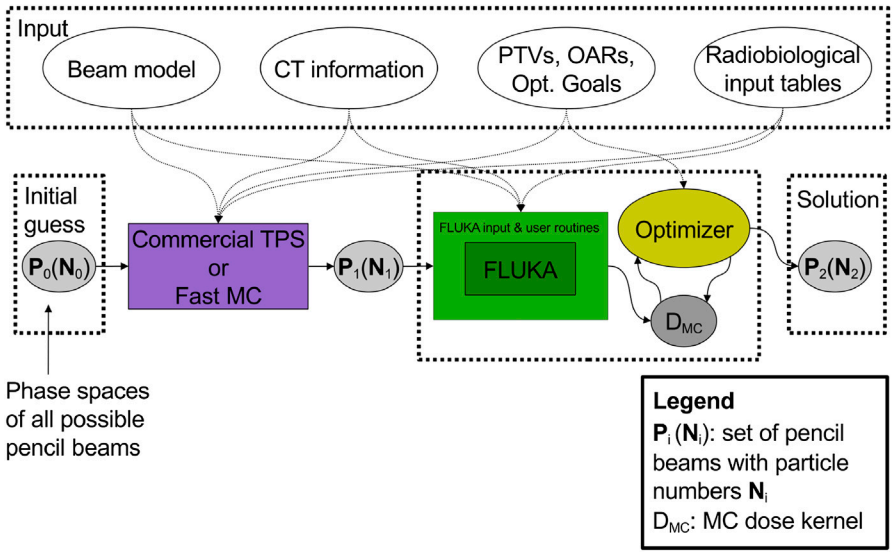

FIGURE 8 | Workflow of the multi-step procedure for dose calculation and optimization of the work of Mairani et al. [220].

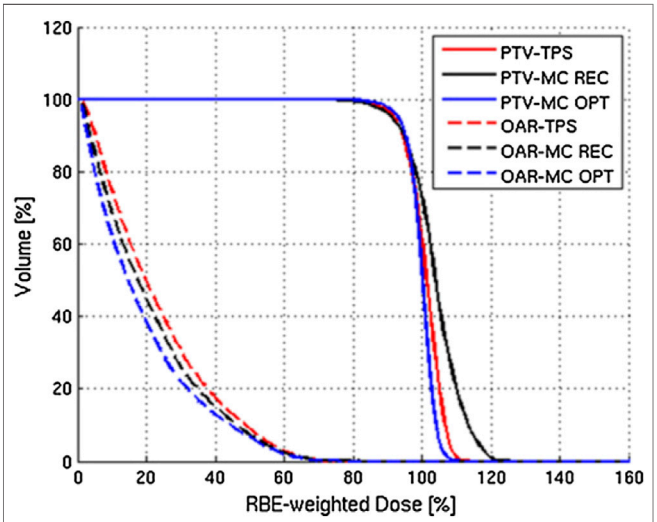

FIGURE 9 | Example of results of the MC TPS tool of Mairani et al. [220]: DVHs for PTV and OAR calculated for a three-field patient case (chordoma in the head–neck district). The standard TPS results (labeled TPS) are compared with the MC-recalculated (labeled MC REC) and MCTP (labeled MC OPT) ones.

of a treatment often requires transporting a large number of particles, usually large computer clusters have to be used. For this reason, in the last years, the interest for the development of fast simulation techniques has grown considerably. These attempts make either use of new technologies in computing hardware, or they adopt dedicated algorithmic solutions. Since it is often sufficient to have a code fully dedicated to dose calculation, a significant contribution to the speedup is also obtained by simplifying the structure of the code with respect to a general purpose MC, focusing only on the relevant processes. In this Section, we highlight a few examples of fast MC code development.

5.1 Current Methods to Speed up Monte Carlo Simulations

5.1.1 Usage of Graphics Processing Units (GPU)

The progress in the use of graphics processing units (GPU) allowed a new effective direction in the search for higher computation speed. This approach, pushed by computed graphics, has allowed for the development of techniques for general purpose computing exploiting the high degree of parallel operation which characterize these hardware units. This has brought to the approach denominated "General Purpose computing with Graphics Processing Units" (GPGPU). MC is one of those computing cases which can profit from the high degree of parallelism allowed by this technology, since events may be processed in many different cores at the same time. A comprehensive review about advantages and challenges about GPU proton dose calculations (analytical and MC) was written by Jia et al. [10].

The GPGPU architectures have evolved in time, and since about 2007 commercial solutions are available with full possibility of programming. Probably, the most diffused and interesting hardware units are those produced by NVIDIA® through the CUDA® (Compute Unified Device Architecture) platform [227]. CUDA® is a development environment which allows the writing of applications by means of the extension of diffused programming languages, like C/C++, overcoming the difficulties of assembly languages. CUDA® compilers for other languages are also commercially available. Programs exploiting the GPGPU architecture can be also written using the OpenCL (Open Computing Language) software libraries. MC algorithms

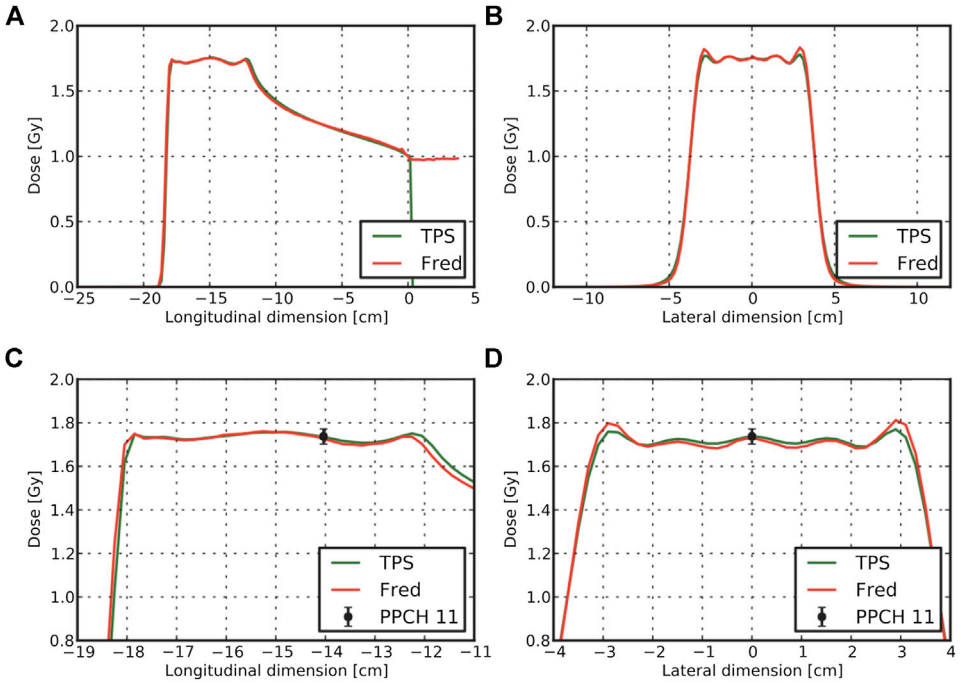

FIGURE 10 | Results for the comparison of FRED results with TPS adopted at CNAO for a SOBP cube at 15 cm depth in water resulting from a treatment plan with protons. TPS and FRED dose lineouts through the cube center are shown in panels **(A)** and **(B)**. Enlarged version of the profiles together with the measured dose level for a pinpoint ionization chamber is visible in panels **(C)** and **(D)** [225].

must in general be rewritten in order to efficiently exploit GPU features, taking also into account possible limitations and bottlenecks, as those coming from the interactions between CPU and GPU memories. Limits such as the size of global and shared memory, maximum number of threads per block, and number of stream multiprocessors are GPU dependent. In the case of MC simulations, there exist some limitations to the effective number of parallel threads in a GPU. The large number of cores (typically thousands) cannot, in practice, be totally exploited at all times. The random structure in MC algorithms generates the so-called thread divergence, which limits the actual number of cores which effectively run in parallel. However, the achievable gain factor remains in any case significant.

A recent example of a MC simulation framework exploiting the GPU approach for pencil beam dose calculations is the FRED (Fast paRticle thErapy Dose evaluator) [225] code, developed in the context of treatment planning for proton therapy. Using effective models for particle-medium electromagnetic and nuclear interactions, it allows for tracking and scoring of energy deposition of primary and secondary particles, also in a voxel geometry imported from CT scans. Single pencil-beam dose simulations have been validated. A merit of this framework is that, since the beginning of its development, it already contained all the optimization tools for full treatment plan MC-based calculations. Moreover, not only the use of the water path length approximation is possible, but also simulating realistic materials. The tracing kernel can achieve an event processing rate of 10 million primary/s on a single GPU card. This performance allows to recalculate a treatment plan at 1% of the total particles in a few minutes.

As an example of the quality achievable with this tool, in **Figure 10**, we show the dose comparison between measurements, FRED, and the commercial TPS used at CNAO, for a spread-out Bragg Peak (SOBP) corresponding to a uniform dose irradiation in a 6-cm sided cube volume at 15 cm of depth in water. Panels (a) and (c) show the longitudinal dose profiles, while panels (b) and (d) show the transversal profiles.

Preclinical application of FRED is presently being studied in Kracow, also in conjunction with the development of plastic-scintillator-based PET detectors for particle therapy delivery monitoring [228]. Further development of FRED for carbon ion treatments is in progress.

Moving to an example in a more clinical context, complete 4-D patient dose calculations in proton therapy including respiratory motion can be ran on GPUs, as reported in Ref. [229]. The GPU calculations include the distribution of the treatment plan according to breathing phase, calculations, and dose accumulation from the various breathing phases. Proton transport simulations were done according to the track-repeating algorithm (described below). Simplified approaches for electromagnetic and nuclear physics processes were used. Validation of the GPU dose calculations was done against GEANT4/TOPAS in terms of secondary particle yields, energy and angular distributions, and for treatment plans [230]. The calculations are fast enough to have allowed for the development of a GPU-based TPS [231].

A GPU-based proton MC tool (GPUMCD) has been developed by Maneval et al. [232]. They introduced a rigorous formalism for energy loss calculation at the typical proton energies used in therapy. The purpose was to accelerate the MC dose calculations by allowing larger steps while preserving accuracy. A lookup table linking the fractional energy loss per step length, ϵ, to the equivalent restricted stopping power L_{eq} was created. The mean energy loss for any step length was simply defined as the product of the step length with L_{eq}. The proton CSDA (continuous slowing-down approximation) was modeled with the L_{eq} formalism and added to GPUMCD. GEANT4 had been used as reference for the validation. This formalism was found to lead to an intrinsic efficiency gain factor ranging between 30–630, increasing with the prescribed accuracy of simulations. It can be considered a promising variance reduction technique for computing proton dose distributions. Combined with GPU acceleration, the total acceleration provided by the L_{eq} formalism with respect to CPU-based GEANT4 simulations was found to be the order of 10^5.

Still in proton therapy, a calculation package for proton dose calculations, gPMC (GPU Proton Monte Carlo), was developed [233]. This framework aims at improving speed without applying simplified approaches. Protons are transported according to a class II condensed history scheme and continuous slowing down. Production of delta-electrons is considered, but their kinetic energy is deposited locally. Regarding nuclear interactions, the empirical strategy developed in Ref. 234 is adopted (described in more detail below). Only proton–proton elastic reactions, proton–oxygen elastic reactions, and inelastic interactions were included. The framework was validated using TOPAS/GEANT4 and performing the gamma passing rate analysis. It can be noted that the authors of this work explicitly mention some technical problems, typically encountered in the interaction between GPUs and CPU, and their solution. Since then, developers of GPU-based MC codes have progressively learned how to manage and overcome these difficulties.

For carbon therapy, recently a framework called goCMC (GPU OpenCL Carbon Monte Carlo) was developed, simulating particle transport in voxelized geometry [235]. The package operates using the OpenCL framework. Electromagnetic processes are modeled by the standard class II condensed history scheme with a continuous slowing down approach. Regarding nuclear interactions, only 4 (inelastic) reactions are included, and secondary particle production is simulated using pre-computed tables, containing particle yields, energy, and scattering angle probabilities. The disadvantage of this method is that energy and momentum conservation is not assured event-by-event, as in full MC simulations. The method was validated for mono-energetic mono-directional beams against GEANT4 and data, using the gamma analysis and dosimetric quantities. A new development, oriented to provide a real MC-based treatment planning is presented in Ref. [226]. An example of results is given in **Figure 11**, for three patient cases (prostate, pancreas, and brain) treated with ^{12}C ions. The total time needed, including MC simulation, optimization, and final dose calculation, ranged from about 800 to 6,400 s, depending also on the adopted hardware.

Recently, a GPU simulation framework called FRoG (Fast Recalculation on GPU) was developed allowing to simulate protons, carbon, helium, and oxygen ions [236]. Although Frog is reported to have MC accuracy, the framework used an analytical dose calculator.

5.1.2 Usage of Phase-Space Files

Rather than fully modeling the beam line and treatment head, a fixed machine output for a given installation can be used for treatment simulations. In that case, "phase-space files" can be produced for a given treatment head, containing the physical properties (energy, direction) of the primary particles that exit a given treatment head. This technique is common in conventional radiotherapy. In particle therapy with passive scattering techniques, usage of phase space files is typically not possible because the treatment head varies. However, even for active scanning techniques applying this method is not straightforward, because of facility dependence of the characteristics of outgoing particles, for instance, due to differences in the beam line devices or differences in operational beam parameters like beam size. In that case, using "optimized" phase space files could be an option [237–239], in which the parameters are somehow tuned until the simulations match the measurements (typically longitudinal and lateral dose profiles) at a certain treatment site. This method was recently applied at the Shanghai Proton and Heavy Ion Center [239].

5.1.3 Track-Repeating Algorithms

The track-repeating approach, originally proposed by Li et al. [240] for protons, is based on the idea to use pre-generated events during simulation to accelerate dose simulations. First, a full MC simulation is performed to generate events of protons interacting in water, with various initial beam energies. These events, including particle trajectories with path length, scattering angles, energy losses, and deposits in water for each step, are stored in a large database. All the physics interactions (in water), including secondary particles, are thus calculated by a general purpose MC code. Then, during particle transport in a given medium, the particle track length in a given material is adjusted to that of water, using the local density. For materials such as bone, corrections can be included by considering the different stopping power. Angles are adjusted according to the direction of the incident particle. At each step, appropriate tracks are selected from this pre-generated database, which are tracked further. This so-called track-repeating approach is different from the normal MC simulation, where physics interactions are sampled on the fly at each step. The track-repeating approach was clinically validated [241] against data and GEANT4, using the gamma index analysis and dosimetric quantities (DVHs) and is in use at the Shanghai particle therapy facility [238]. **Figure 12** shows a comparison between the fast dose calculator (CDC) described by Yepes et al. [241].

A GPU implementation was also performed by the authors [242]. The usage of pre-generated tracks from a database was also adopted by [243], reusing ideas from available codes from conventional radiotherapy. The advantage of their approach is

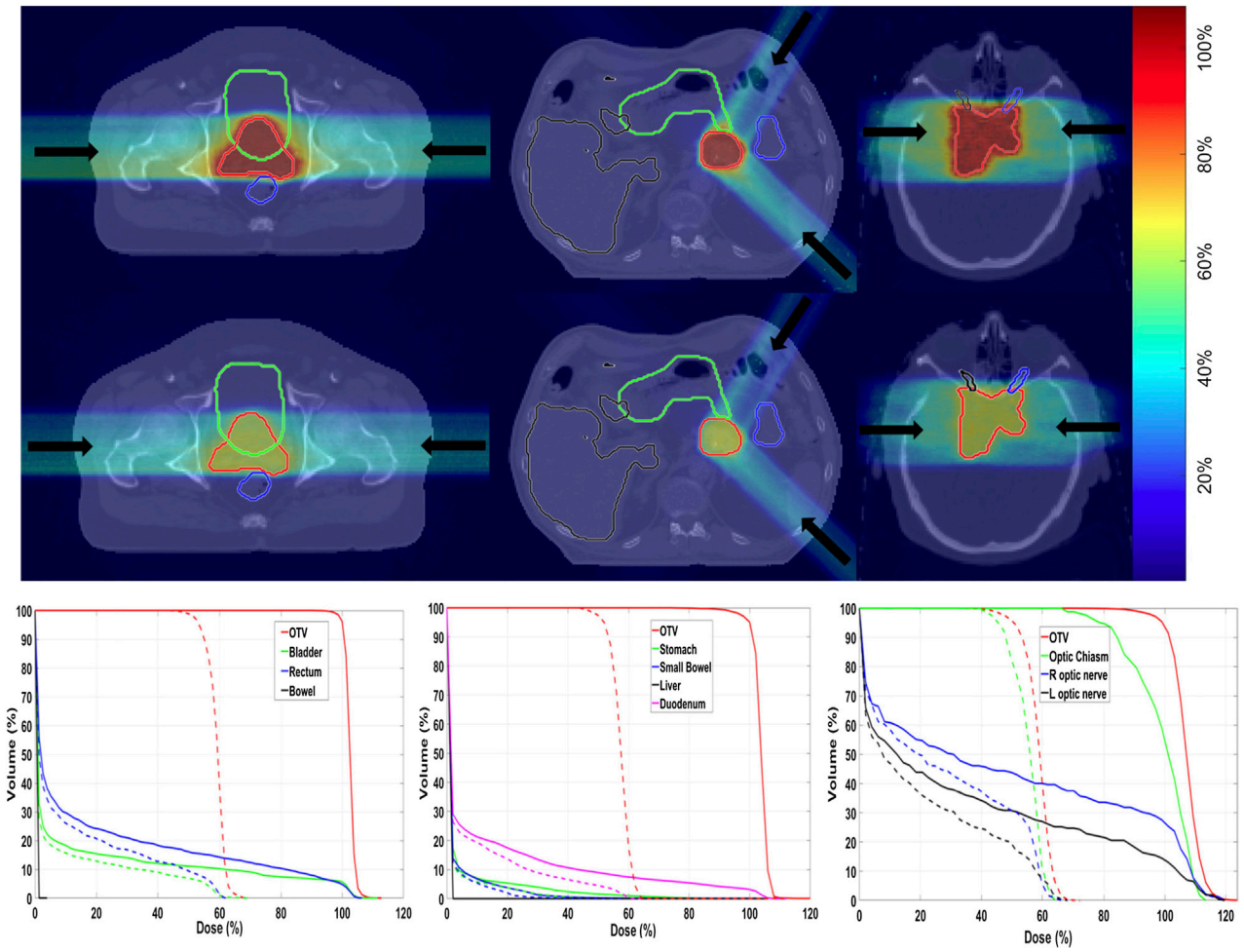

FIGURE 11 | Example of TPS calculation with the GPU framework described in Ref. 226. First and second rows are biological dose and physical dose, overlaid on CT images, in three patient cases. From left to right: prostate, pancreatic, and brain cancers. The color bar indicates the dose levels relative to the prescription dose. Arrows indicate beam directions. The bottom row is the corresponding dose–volume histograms (DVHs). Solid lines and dashed lines denote biological dose and physical dose, respectively. The OTV represents the optimization target volume, a similar concept to CTV.

that they use pre-generated events in many different materials, rather than only in water. They used MCNPX for the generation of the pre-calculated tracks, as well as for the validation of the code. The latter was based on depth–dose curves along the central axis and lateral dose distributions.

A possible shortcoming of the track repeating approach, in the context of particle therapy, concerns nuclear interactions. While there are assessed methods to perform scaling of stopping power for different materials and densities with respect to water, there may be a substantial dependence of nuclear cross sections on the actual elemental composition. It is therefore questionable whether using events based on the physics interactions in water is sufficiently accurate. Regarding the calculation of dose, which is dominated by electromagnetic interactions, the accuracy is probably sufficient. In those cases where an accurate description of nuclear interaction is desired, as those we have discussed in Sections 2.3 and 2.4, this could not be the case. This problem could probably be overcome by pre-generating full events also in other materials.

5.1.4 Voxel Monte Carlo Algorithms

Based on ideas from traditional radiotherapy algorithms, a Voxel MC code for proton (VMCpro) therapy was developed [234]. Here, protons are step-by-step traced through a voxelized volume (typically a CT scan). One step is equal to the distance between the voxel boundaries, unless a discrete interaction took place within the voxel. The geometrical step length is calculated from the geometrical step length in water according to the ratio of densities and the ratio of the stopping power in a given voxel density to that in water, using an empirical fit formula. A multiple scattering angle is sampled at the new position, and the proton is rotated accordingly. Nuclear interactions are modeled as corrections to electromagnetic processes, treating all soft tissues as water. In the quoted article, the authors claim that they succeeded to achieve, at that time, a computing speed higher

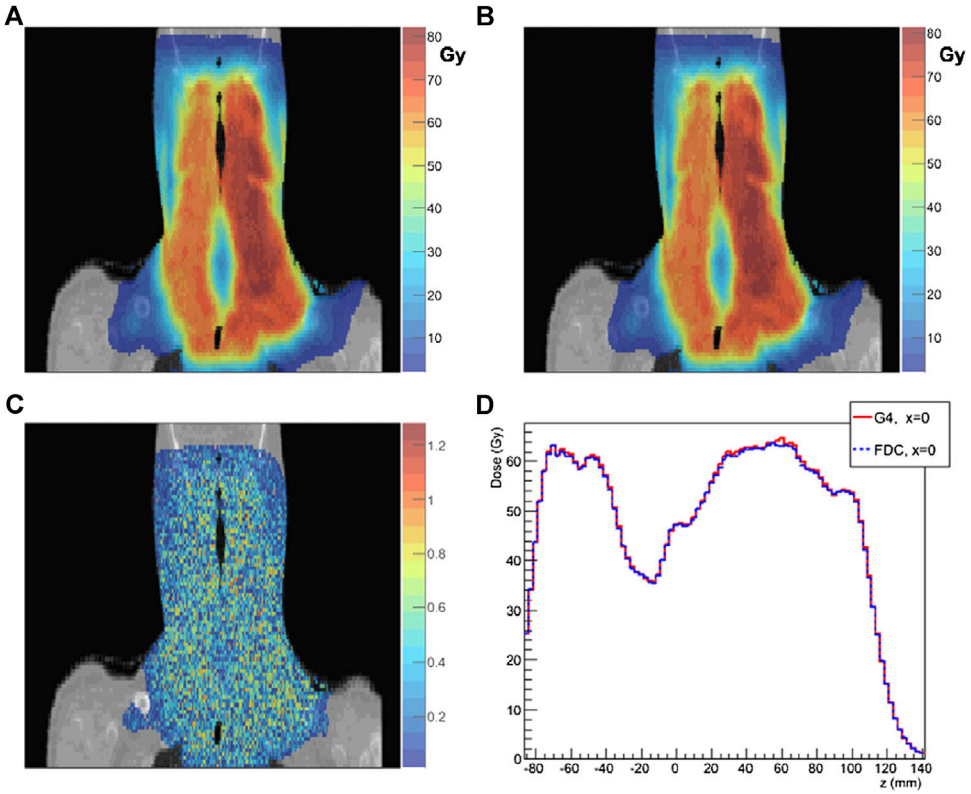

FIGURE 12 | Comparison of results from the FDC developed by Yepes et al. [241] and GEANT4. Dose distribution for a particular coronal section of a head-and-neck patient: as **(A)** GEANT4 and **(B)** FDC. **(C)** 2 mm/2% gamma-index for the voxels on that particular section of FDC relative to GEANT4. **(D)** For the same section, the dose along the *z*-axis (inferior-superior) for x = 0 calculated with GEANT4 and FDC for that section.

by a factor of 13 with respect to FLUKA and of 35 with respect to GEANT4.

5.1.5 Macro Monte Carlo Simulations

In the work of Fix e al. [244], a method inherited from electron dose calculations is adapted to proton therapy: Macro Monte Carlo simulations (MMC). In this method, full MC simulations (in this case with GEANT4) of protons in different spheres of different materials with many energies are performed, and exiting particles with all their characteristics are stored (macro-steps). The dose distribution in a voxelized grid can be obtained by a sequence of macro steps. The method was validated by comparing depth–dose curves and lateral dose curves with GEANT4.

5.1.6 Other Approaches

An example of a dedicated in-house proton MC code developed at PSI for assessing possible deficiencies of analytical dose calculations in inhomogeneous patient tissue is described in Ref. [245]. Here, a slab-by-slab approach is adopted for proton transport, calculating energy loss and taking into account multiple Coulomb scattering in the voxel. However, nuclear interactions are simulated analytically, with no tracking of secondary particles. The code was tested on a variety of patient plans.

Yet another approach of speeding up MC simulations for protons is with simplified Monte Carlo (SMC) simulations [246]. The approach is based on an effective model to take into account all physics processes relevant to dose calculations, using measured depth–dose curves in water. At each voxel, two effects are modeled. First, the residual range of protons is decreased according to the local material properties and corresponding energy loss. Second, MCS is modeled according to a Gaussian distribution. Thus, rather than sampling detailed interaction processes step by step, they capture all net effects (including nuclear interactions) in terms of dose deposition in each voxel. The code was also implemented on a GPU platform.

5.2 GPU-Based MC for Radiobiological Calculations

The use of GPU allowed to develop efficient MC applications specifically oriented to radiobiological purposes. As discussed in **Section 3**, the quantitative evaluation of radiation damage in biological cells, such as DNA strand breaks and base damage, in general take a considerably long execution time. This is particularly relevant for track structure computations. We report here three interesting examples.

In the work of Kalantzis et al. [247], the authors present an implementation of a MC code for microdosimetric calculations of low energy electrons and protons tracks on a GPU under the above quoted CUDA® platform developed by NVIDIA®. Performance and accuracy have been tested on a commercially available general purpose GPU. They also developed a hybrid implementation employing OpenMP (an application program interface (API) used to explicitly direct multi-threaded, shared memory parallelism among CPU cores) and CUDA® in order to demonstrate the potential of utilizing simultaneously a multi-core CPU and a GPU for further acceleration of the MC simulations.

Another interesting example is reported by Okada et al. [248], where a new MC simulator named MPEXS-DNA is described, allowing high computing performance by using a GPU. The code has been developed for track structure and radiolysis simulations at the subcellular scale. Physics and chemical processes are based on GEANT4-DNA processes available in GEANT4 version 10.02 p03. The validation was performed by comparison with existing experimental data and simulation results obtained by other simulation codes, including PARTRAC [169]. By using NVIDIA® GPU devices adopting the Volta architecture, MPEXS-DNA has achieved speedup factors up to 2,900 against GEANT4-DNA simulations performed with a single CPU core.

Finally, Tsai et al. [249] present a GPU-based fast microscopic MC simulation package, gMicroMC. They also built a human lymphocyte nucleus DNA model and implemented a DNA damage calculation method to compute single- and double-strand breaks of different complexities. The comparison of the simulation results with those generated by GEANT4-DNA gives good agreement. They achieved speedup factors of ~ 540 times for the entire simulation process, as compared to the computations by GEANT4-DNA executed on a CPU using a single thread.

5.3 Role of Full MC Frameworks

From the amount of literature written about fast simulation frameworks, it is evident that there is a large interest in speeding up calculation codes, as this brings us a step closer to application in a clinical environment. At the same time, we have seen that all fast codes have validated their calculations also by means of comparison with general purpose MC codes. Thus, we can conclude that codes like MCNPX, GEANT, or FLUKA remain important role also for the development of new calculation methods to be adopted in particle therapy. Summarizing, we can conclude that in the context of fast MC developing, there are two main tasks for full general purpose codes:

- To generate realistic pre-generated data bases for track-repeating approaches.
- To serve as validation for accelerated simulation codes.

In the case of phase space file and track-repeating algorithms, attention has to be paid to possible artifacts. The size of pre-calculated samples need to be carefully considered. In fact, when using standard sampling techniques, the very long period in the cycling of random number generation algorithms allows a totally safe margin against the possible repetition of the same events. Instead, when sampling from a file of pre-generated events, which is necessarily limited in size, more attention has to be paid if the same configuration has to be used more than once. In this case, there is the risk of generating fake structures and correlations in the distribution of scored variables.

In addition it has to be remarked that for specific applications going beyond dose calculations, like, for instance, the case of range monitoring, general purpose MC codes still remain the most appropriate tool.

6 DISCUSSION

In this review, we have discussed some of the ongoing research and challenges that remain to be faced in order to improve MC simulations for particle therapy so as to facilitate their use in clinics and in research. One of the challenges is the improvement of nuclear interaction models. In particular, there is still the need of more new experimental data sets of double differential cross section measurements for radiotherapeutic beams and tissue like targets, since this is essential for benchmarking and tuning nuclear interaction models. Although the calculation of physical dose has already reached in most cases a satisfactory level of accuracy, improved models can lead to more accurate biological dose calculations and improved range monitoring methods, not only for carbon and protons but also for new ions like helium and oxygen. New experimental activities designed for this purpose are at present in progress [110].

Another important challenge for MC development concerns the reliability of modeling radiobiological factors in simulations. The coupling with radiobiological models, or databases, may allow to evaluate the onset of initial DNA damages, but the task of treating all later processes governed by radiochemical processes is out of scope, at least in general purpose MC codes. The uncertainties in this context are particularly difficult to mitigate. The experimental radiobiological measurements, which provide results that are the most useful references for RBE evaluation, still exhibit important uncertainties, as demonstrated in the data base of the particle irradiation data ensemble (PIDE) project [250].

Regarding MC-based treatment planning, many interesting developments are ongoing, and MC-based biological dose calculations are entering more and more in the clinical workflow for all patients. Fast MC codes based on GPU-based calculations or special algorithms are very valuable to come a step closer toward MC-based biological treatment planning. However, such fast MC calculations should always be carefully validated with full MC codes, which then maintain their important role.

There are certainly other topics which are still relevant to the development of MC simulations in particle therapy that we have not considered in this review. For instance, we have not discussed the possible benefits related to improving the description of patient composition in MC simulations, through new imaging techniques. Currently, MC simulations of all processes in patients are based on CT scans. When hadronic interactions are relevant,

the actual nuclear composition of tissues has a relevance. Parameterization as a function of CT Hounsfield numbers, like the one by Schneider et al. [251], provides mean values. Improvements could derive by the adoption of imaging techniques with a higher resolving power in distinguishing material differences, like Dual Energy computed tomography (DECT) or multi-energy computed tomography (MECT). Research and development on new approaches like proton-CT can be also an alternative solution. Also, much research is ongoing to how to simulate time-dependent geometries (4D-MC simulations) to include motion effects in dose calculations, which was not treated in this review. There are also some arguments which are related to quality control, dosimetry, and microdosimetry which surely benefit from the use of MC. New developments in this direction are ongoing [252]. Last, but not least, we have not entered in the discussion about the importance of easy user interfaces for MC codes. Several interesting developments in this context are ongoing [21, 22, 253]. Examples on this subject, in view of clinical application of MC in proton therapy, have been recently published [254–256]. The spread of MC tools in clinical practice can be also facilitated providing nonexpert users with clear tutorials and easy installation procedures.

Despite the important progresses achieved so far in the application of MC simulations in particle therapy, we are still far away from efficient MC simulation codes that can model the physical interactions and biological response of tissue at multi-scale level, that is, from the level of DNA segments (nm) to large populations of cells (cm). Such MC codes should include simulation of physical, physicochemical, and chemical processes in human tissue, within short time scales and without the need of enormous computing resources. It is also clear that MC tools, for their nature, need to be continuously improved and maintained, also from the point of view of computing technology. Frequent code upgrades, close collaboration, and resources are also necessary to further improve the usage of MC calculations. Not only developers but also users of MC simulations in particle therapy can contribute by validating their simulation framework with measurements, whereby it is essential that the beam model and dose delivery system are accurately simulated. Finally, the diversity of the literature studied in this review highlights the need for a balanced multidisciplinary multi-scale approach to realize such codes, combining physics, biology, chemistry, medicine, and computing. Bridging the gaps between the various research fields is therefore of prime importance for the development of efficient MC tools in particle therapy.

7 CONCLUSION

Having access to accurate MC simulation codes is considered crucial in particle therapy, not only because such codes provide more accurate calculations of dose in patients but also in several research fields including range verification techniques, neutron dose calculations, modeling of biological effects, and research to new treatment techniques. In this review, we have discussed a few of the challenges that are to be faced before MC simulations can be widely and efficiently used by the particle therapy community. Improving nuclear interaction physics models, radiobiological modeling, MC-based treatment planning, and development in fast MC codes are the topics selected for this review, but many other topics remain to be addressed.

We have tried to emphasize how the successful development of these codes is a task that need a multidisciplinary approach, as in fact is true for the whole subject of particle therapy. Applied nuclear physicists can have an important role in bringing the particle physics community a step closer toward an efficient use of MC simulations. In particular, the expertise and data from nuclear physics experiments are very important to improve the radiobiological modeling of tissue response to particle treatments in MC simulations.

AUTHOR CONTRIBUTIONS

SM promoted this work; GB and AK performed editing and reviewing. AK coordinated the work.

ACKNOWLEDGMENTS

This work has been carried out in the context of MC-INFN experiment of INFN. The authors wish to thank A. Schiavi for the useful suggestions and help in reviewing the manuscript.

REFERENCES

1. Parodi K, Mairani A, Brons S, Hasch B, Sommerer F, Naumann J, et al. Monte Carlo simulations to support start-up and treatment planning of scanned proton and carbon ion therapy at a synchrotron-based facility. *Phys Med Biol.* (2012). 57:3759–84. doi:10.1088/0031-9155/57/12/3759
2. Grassberger C, Daartz J, Dowdell S, Ruggieri T, Sharp G, Paganetti H. Quantification of proton dose calculation accuracy in the lung. *Int J Radiat Oncol Biol Phys.* (2014). 89:424–30. doi:10.1016/j.ijrobp.2014.02.023
3. Schuemann J, Giantsoudi D, Grassberger C, Moteabbed M, Min CH, Paganetti H. Assessing the clinical impact of approximations in analytical dose calculations for proton therapy. *Int J Radiat Oncol Biol Phys.* (2015). 92: 1157–64. doi:10.1016/j.ijrobp.2015.04.006.
4. Seco J, Verhaegen F. *Monte Carlo techniques in radiation therapy.* Boca Raton, FL: CRC Press (2013). 334 p.
5. Paganetti H. *Proton therapy physics.* Boca Raton, FL: CRC Press (2012). 691 p.
6. Paganetti H. Range uncertainties in proton therapy and the role of Monte Carlo simulations. *Phys Med Biol.* (2012). 57:R99–117. 10.1088/0031-9155/57/11/R99
7. Dedes G, Parodi K. Monte Carlo simulations of particle interactions with tissue in carbon ion therapy. *Int J Part Ther.* (2015). 2:447–58. 10.14338/IJPT-15-00021
8. Kraan AC. Range verification methods in particle therapy: underlying physics and Monte Carlo modeling. *Front Oncol.* (2015). 5:150. doi:10.3389/fonc.2015.00150.
9. El Naqa I, Pater P, Seuntjens J. Monte Carlo role in radiobiological modelling of radiotherapy outcomes. *Phys Med Biol.* (2012). 57:R75–97. doi:10.1088/0031-9155/57/11/R75.

10. Jia1 X, Pawlicki T, Murphy K, Mundt A. Proton therapy dose calculations on GPU: advances and challenges. *Transl Canc Res.* (2012). 1:207–16. doi:10.3978/j.issn.2218-676X.2012.10.03
11. Zyla P, Barnett R, Beringer J, Dahl O, Dwyer DA, Groom DE, et al. The review of particle physics. *Prog Theor Exp Phys.* (2020). 2020:083C01. doi:10.1093/ptep/ptaa104
12. Durante M, Paganetti H. Nuclear physics in particle therapy: a review. *Rep Prog Phys.* (2016). 79:096702. doi:10.1088/0034-4885/79/9/096702.
13. Agostinelli S, Allison J, Amako K, Apostolakis J, Araujo H, Arce P, et al. GEANT4 - a simulation toolkit. *Nucl Instrum Methods.* (2003). 506:250–303. doi:10.1016/S0168-9002(03)01368-8
14. Allison J, Amako K, Apostolakis J, Araujo H, Arce P, Asai M, et al. GEANT4 developments and applications. *IEEE Trans Nucl Sci.* (2006). 53:270–8. doi:10.1109/TNS.2006.869826
15. Allison J, Amako K, Apostolakis J, Arce P, Asai M, Aso T, et al. Recent development in GEANT4. *Nucl Instrum Methods A.* (2016). 835:186–225. doi:10.1016/j.nima.2016.06.125
16. GEANT4. *GEANT4 physics list.* (2019). Available from: https://geant4.web.cern.ch/node/628.
17. Bleicher M, Zabrodin E, Spieles C, Bass S, Ernst C, Soff S, et al. Relativistic hadron-hadron collisions in the ultra-relativistic quantum molecular dynamics model. *J Phys G.* (1999). 25:1859. doi:10.1088/0954-3899/25/9/308
18. Niita K, Chiba S, Maruyama S, Maruyama T, Takada H, Fukahori T, et al. Analysis of the (N,xN) reactions by quantum molecular dynamics plus statistical decay model. *Phys Rev C.* (1995). 52:2620–35. doi:10.1103/physrevc.52.2620
19. Sorge H. Flavor production in Pb(160 AGeV) on Pb collisions: effect of color ropes and hadronic rescattering. *Phys Rev C.* (1995). 52:3291.
20. Mancini-Terracciano C, Asai M, Caccia B, Cirrone G, Dotti A, Faccini R, et al. Preliminary results coupling stochastic mean field and Boltzmann-Langevin One Body models with GEANT. *Phys Med.* (2019). 67:116–22. doi:10.1016/j.ejmp.2019.10.026
21. Perl J, Shin J, Schumann J, Faddegon B, Paganetti H. TOPAS: an innovative proton Monte Carlo platform for research and clinical applications. *Med Phys.* (2012). 39:6818–37. doi:10.1118/1.4758060.
22. Faddegon B, Ramos-Méndeza J, Schuemann J, McNamara A, Shin J, Perl J, et al. The TOPAS tool for particle simulation, a Monte Carlo simulation tool for physics, biology and clinical research. *Phys Med.* (2020). 72:114–21. doi:10.1016/j.ejmp.2020.03.019
23. Jan S, Santin G, Strul D, Staelens S, Assié K, Autret D, et al. Gate: a simulation toolkit for pet and spect. *Phys Med Biol.* (2004). 49:4543–61. doi:10.1088/0031-9155/49/19/007.
24. Grevillot L, Bertrand D, Dessy F, Freud N, Sarrut D. A Monte Carlo pencil beam scanning model for proton treatment plan simulation using GATE/GEANT4. *Phys Med Biol.* (2011). 56:5203–19. doi:10.1088/0031-9155/56/16/008.
25. Jan S, Frisson T, Sarrut D. Gate simulation of 12c hadrontherapy treatment combined with a pet imaging system for dose monitoring: a feasibility study. *IEEE Trans Nucl Sci.* (2013). 60:423–9. doi:10.1109/TNS.2012.2233496
26. Resch A, Elia A, Fuchs H, Carlino A, Palmans H, Stock M, et al. Evaluation of electromagnetic and nuclear scattering models in GATE/GEANT4 for proton therapy. *Med Phys.* (2019). 46:2444–56. doi:10.1002/mp.13472.
27. Arce P, Bolst D, Cutajar D, Guatelli S, Le A, Rosenfeld A, et al. Report on G4-Med, a GEANT4 benchmarking system for medical physics applications developed by the GEANT4 medical simulation benchmarking group. *Med Phys.* (2020). doi:10.1002/mp.14226.
28. Hall D, Makarova A, Paganetti H, Gottschalk B. Validation of nuclear models in GEANT4 using the dose distribution of a 177 MeV proton pencil beam. *Phys Med Biol.* (2016). 61:N1–10. doi:10.1088/0031-9155/61/1/N1
29. Böhlen T, Cerutti F, Chin M, Fassò A, Ferrari PAO, Mairani A, et al. The FLUKA code: developments and challenges for high energy and medical applications. *Nucl Data Sheets.* (2014). 120:211–4. doi:10.1016/j.nds.2014.07.049
30. Ferrari A, Sala P, Fassò A, Ranft J. FLUKA: a multi-particle transport code. CERN (2005). INFN/TC 05/11, SLAC-R-773.
31. Fassò A, Ferrari A, Ranft J, Sala P. FLUKA: status and prospective for hadronic applications. In: A Kling, F Barão, M Nakagawa, L Távora, P Vaz, editors. Proc. MonteCarlo 2000 conference; Berlin, Germany: Springer-Verlag (2001). p. 159–64.
32. Fassò A, Ferrari A, Ranft J, Sala P. FLUKA: performances and applications in the intermediate energy range. In: P Dragovitsch, S Linn, M Burbank, editors. Proc. 1 AEN/NEA specialists' meeting on shielding aspects of accelerators, targets and irradiation facilities (SATIF 1). Paris, France: OECD (1995). p. 287–304.
33. Ferrari A, Sala P. The physics of high energy reactions. In: A Gandini G Reffo, editors. Proc. workshop on nuclear reaction data and nuclear reactors physics, design and safety. Singapore: World Scientific (1998). 424 p.
34. Ferrari A, Ranft J, Roesler S, Sala P. Cascade particles, nuclear evaporation, and residual nuclei in high energy hadron-nucleus interactions. *Eur Phys J C (EPJ C), - Part Fields.* (1996). 70:413–26. doi:10.1007/s002880050119
35. Cavinato M, Fabrici E, Gadioli E, Erba E, Risi E. Boltzmann master equation theory of angular distributions in heavy-ion reactions. *Nucl Phys A.* (1998). 643:15–29. doi:10.1016/S0375-9474(98)00545-4
36. Sorge H, Stocker H, Greiner W. Relativistic quantum molecular dynamics approach to nuclear collisions at ultrarelativistic energies. *Nucl Phys A.* (1989). 498:567–76. doi:10.1016/0375-9474(89)90641-6
37. Sato T, Iwamoto Y, Hashimoto S, Ogawa T, Furuta T, Abe S, et al. Features of particle and heavy ion transport code system (PHITS) version 3.02. *J Nucl Sci Technol.* (2018). 55:684–90. doi:10.1080/00223131.2017.1419890
38. Sato T, Niita K, Matsuda N, Hashimoto S, Iwamoto Y, Noda S, et al. Particle and heavy ion transport code system PHITS, version 2.52. *Nucl Sci Technol.* (2013). 50:913–23. doi:10.1080/00223131.2013.814553
39. Nara Y, Otuka H, Ohnishi A, Niita K, Chiba S. Relativistic nuclear collisions at 10 AGev energies from p+Be to Au+Au with the hadronic cascade model. *Phys Rev C.* (2000). 61:024901. doi:10.1103/PhysRevC.61.024901
40. Furihata S. Statistical analysis of light fragment production from medium energy proton-induced reactions. *Nucl Instrum Methods B.* (2000). 171:251–8. doi:10.1016/S0168-583X(00)00332-3
41. Iwamoto Y, Sato T, Hashimoto S, Ogawa T, Furuta T, Abe S, et al. Benchmark study of the recent version of the PHITS code. *J Nucl Sci Technol.* (2017). 54:617–35. doi:10.1080/00223131.2017.1297742
42. Goorley T, James M, Booth T, Brown F, Bull J, Cox LJ, et al. Initial MCNP6 release overview MCNP6 version 0.1. *Nucl Technol.* (2012). 180:298–315. doi:10.13182/NT11-135.
43. Yariv Y, Frankel Z. Intranuclear cascade calculation of high- energy heavy-ion interactions. *Phys Rev C.* (1979). 20:2227–43. doi:10.1103/PhysRevC.20.2227
44. Prael R, Bozoian M. Adaption of the multistage preequilibrium model for the Monte Carlo method (1988). LANL. LA-UR-88-3238.
45. Dresner L. Evap - a fortran program for calculating the evaporation of various particles from excited compound nuclei (1962). ORNL. TM196. doi:10.2172/4638868.
46. Atchison F. Spallation and fission in heavy metal nuclei under medium energy proton bombardment. In: G Bauer, editor. Meeting on targets for neutron beam spallation sources; 1979 Jun 11–12; Jülich, Germany. Jülich, Germany: Forschungszentrum Jülich (1980). p. 17–46.
47. Barish J, Gabriel T, Alsmiller FS, Alsmiller RG. HETFIS high-energy nucleon meson transport code with fission (1981). Oak Ridge National Laboratory. ORNL/TM-7882.
48. Alsmiller FS, Alsmiller RG, Gabriel T, Lillie R, Barish J. A phenomenological model for particle production from the collisions of nucleons and pions with fissile elements at medium energies. *Nucl Sci Eng.* (1981). 79:147–61. doi:10.13182/NSE81-A27403
49. Mashnik S, Sierk A. CEM03.03 user manual (2012). Los Alamos National Laboratory. LA-UR-12-01364.
50. Gudima KK, Mashnik SG, Toneev VD. Cascade-exciton model of nuclear reactions. *JINR Commun.* (1980). 80:774–7.
51. Gudima KK, Mashnik SG, Toneev VD. Cascade-exciton model of nuclear reactions. *Nucl Phys A.* (1983). 401:329–61. doi:10.1016/0375-9474(83)90532-8
52. Boudard A, Cugnon J, Leray S, Volant C. Intranuclear cascade model for a comprehensive description of spallation reaction data. *Phys Rev C.* (2002). 66:044615. doi:10.1103/PhysRevC.66.044615
53. Gaimard J, Schmidt K. A reexamination of the abrasion-ablation model for the description of the nuclear fragmentation reactions. *Nucl Phys A.* (1991). 531:709–45. doi:10.1016/0375-9474(91)90748-U
54. Junghans A, de Jong M, Clerc H, Ignatyuk A, Kudyaev G, Schmidt K. Projectile-fragment yields as a probe for the collective enhancements in the

nuclear level density. *Nucl Phys A.* (1998). 629:635–55. doi:10.1016/S0375-9474(98)00658-7
55. Hansen DC, Lühr A, Sobolevsky N, Bassler N. Optimizing SHIELD-HIT for carbon ion treatment. *Phys Med Biol.* (2012). 57:2393–409. doi:10.1088/0031-9155/57/8/2393.
56. Bassler N, Hansen D, Lühr A, Thomsen B, Petersen J, Sobolevsky N. SHIELD-HIT12A - a Monte Carlo particle transport program for ion therapy research. *J Phys: Conf. Ser.* (2014). 489:012004. doi:10.1088/1742-6596/489/1/012004
57. Botvina AS, Dementyev AV, Smirnova ON, Sobolevsky NM, Toneev VD. International codes and model intercomparison for intermediate energy activation yields (1997). NEA/OECD. NSC/DOC (97)-1.
58. Toneev VD, Gudima KK. Particle emission in light and heavy ion reactions. *Nucl Phys A.* (1983). 400:173–89. doi:10.1016/0375-9474(83)90433-5
59. Amelin NS, Gudima KK, Toneev VD. Further development of the quark-gluon strings model for describing high-energy collisions with nuclear target. *Sov J Nucl Phys.* (1990). 52:172–8.
60. Amelin NS, Gudima KK, Toneev VD. Further development of the quark-gluon strings model for describing high-energy collisions with nuclear target. *Yad Fiz.* (1990). 52:272.
61. Gudima KK, Mashnik SG, Toneev VD. Cascade-exciton model of nuclear reactions (1976). Nuclear Physics and Radiation Physics. ZFK–324.
62. Botvina AS, Iljinov AS, Mishustin IN, Bondorf JP, Donangelo R, Sneppen K. Statistical simulation of the break-up of highly excited nuclei. *Nucl Phys.* (1987). 475:663–86. doi:10.1016/0375-9474(87)90232-6
63. Böhlen TT, Cerutti F, Dosanjh M, Ferrari A, Gudowska I, Mairani A, et al. Benchmarking nuclear models of FLUKA and GEANT4 for hadron therapy. *Phys Med Biol.* (2010). 55:5833–47. doi:10.1088/0031-9155/55/19/014
64. Mirandola A, Molinelli S, Vilches Freixas G, Mairani A, Gallio E, Panizza D, et al. Dosimetric commissioning and quality assurance of scanned ion beams at the Italian national center for oncological hadrontherapy. *Med Phys.* (2015). 42:5287. doi:10.1118/1.4928397.
65. Sommerer F, Parodi K, Ferrari A, Poljanc K, Enghardt W, Aiginger H. Investigating the accuracy of the FLUKA code for transport of therapeutic ion beams in matter. *Phys Med Biol.* (2006). 51:4385–98. doi:10.1088/0031-9155/51/17/017
66. Lechner A, Ivanchenko VN, Knobloch J. Validation of recent GEANT4 physics models for application in carbon ion therapy. *Nucl Instrum Methods B.* (2010). 268:2343–54. doi:10.1016/j.nimb.2010.04.008
67. Tessonnier T, Mairani A, Brons S, Sala P, Cerutti F, Ferrari A, et al. Helium at the Heidelberg ion beam facility center: comparisons between FLUKA MC code predictions and dosimetric measurements. *Phys Med Biol.* (2017). 62:6784–803. doi:10.1088/1361-6560/aa7b12
68. Tessonnier T, Mairani A, Brons S. Experimental dosimetric comparison of ^{1}H, ^{4}He, ^{12}C and ^{16}O scanned ion beams. *Phys Med Biol.* (2017). 62:3958–82. doi:10.1088/1361-6560/aa6516
69. Pfuhl U, Horst F, Weber U. Dose build-up effects induced by delta electrons and target fragments in proton Bragg curves - measurements and simulations. *Phys Med Biol.* (2018). 63:175002. doi:10.1088/1361-6560/aad8fc
70. Knopf A, Lomax A. *In vivo* proton range verification: a review. *Phys Med Biol.* (2013). 58:R131–160. doi:10.1088/0031-9155/58/15/R131
71. Parodi K, Polf JC. *In vivo* range verification in particle therapy. *Med Phys.* (2018). 45:e1036. doi:10.1002/mp.12960.
72. Zhu X, El Fahkri G. Proton therapy verification with PET imaging. *Theranostics.* (2013). 3:731–40. doi:10.7150/thno.5162
73. Krimmer J, Dauvergne D, Létang J, Testa E. Prompt-gamma monitoring in hadrontherapy: a review. *Nucl Instrum Methods Phys Res Sect A Accel Spectrom Detect Assoc Equip.* (2017). 10:1016. doi:10.1016/j.nima.2017.07.063
74. Capote R, Herman M, Oblozinsky P, Young P, Goriely S, Belgya T, et al. RIPL – reference input parameter library for calculation of nuclear reactions and nuclear data evaluations. *Nucl Data Sheets.* (2009). 110:3107–214. doi:10.1016/j.nds.2009.10.004
75. Amaldi U, Hajdas W, Iliescu S, Malakhov N, Samaratti J, Sauli F, et al. Advanced quality assurance for CNAO. *Nucl Instrum Methods A.* (2010). 617:248–9. doi:10.1016/j.nima.2009.06.087
76. Piersanti L, Bellini F, Bini F, Collamati F, De Lucia E, Durante M, et al. Measurement of charged particle yields from PMMA irradiated by a 220 MeV/u C beam. *Phys Med Biol.* (2012). 59:1857–72. doi:10.1088/0031-9155/59/7/1857
77. Dudouet J, Juliani D, Labalme M, Cussol D, Angélique J, Braunn B, et al. Double-differential fragmentation cross-section measurements of 95 MeV/nucleon C beams on thin targets for hadron therapy. *Phys Rev C.* (2013). 88:024606. doi:10.1103/PhysRevC.88.024606
78. Divay C, Colin J, Cussol D, Finck C, Karakaya Y, Labalme M, et al. Differential cross section measurements for hadron therapy: 50 MeV/nucleon C reactions on H, C, O, Al, and Ti targets. *Phys Rev C.* (2017). 95:044602. doi:10.1103/PhysRevC.95.044602
79. Chadwick M, Herman M, Oblozinsky P, Dunn ME, Danon Y, Kahler A, et al. ENDF/B-VII.1 nuclear data for science and technology: cross sections, covariances, fission product yields and decay data. *Nucl Data Sheets.* (2011). 112:2887–996. doi:10.1016/j.nds.2011.11.002
80. JENDL. JENDL (2011). Available from: http://wwwndc.jaea.go.jp/jendl/jendl.html.
81. Schneider U, Lomax A, Timmermann B. Second cancers in children treated with modern radiotherapy techniques. *Radiother Oncol.* (2008). 89:135–40. doi:10.1016/j.radonc.2008.07.017.
82. Newhauser WD, Fontenot JD, Mahajan A, Kornguth D, Stovall M, Zheng Y, et al. The risk of developing a second cancer after receiving craniospinal proton irradiation. *Phys Med Biol.* (2009). 54:2277–91. doi:10.1088/0031-9155/54/8/002.
83. Newhauser WD, Durante M. Assessing the risk of second malignancies after modern radiotherapy. *Nat Rev Canc.* (2011). 11:438–48. doi:10.1038/nrc3069.
84. Schneider U, Hälg R. The impact of neutrons in clinical proton therapy. *Front Oncol.* (2015). 5:235. doi:10.3389/fonc.2015.00235.
85. Hälg R, Schneider U. Neutron dose and its measurement in proton therapy-current state of knowledge. *Br J Radiol.* (2020). 93:20190412. doi:10.1259/bjr.20190412.
86. Barth RF, Soloway AH, Fairchild RG. Boron neutron capture therapy of cancer. *Canc Res.* (1990). 50:1061.
87. Barth R. A critical assessment of boron neutron capture therapy: an overview. *J Neuro Oncol.* (2003). 62:1–5. doi:10.1007/BF02699929
88. Team XMC. MCNP - a general Monte Carlo n-particle transport code, version 5,- volume I: overview and theory (2003). Los Alamos National Laboratory. Tech. Rep. LA-UR-03-1987.
89. Goorley J, Kiger W, III, Zamenhof RGR. Reference dosimetry calculations for neutron capture therapy with comparison of analytical and voxel models. *Med Phys.* (2002). 29:145–56. doi:10.1118/1.1428758
90. Kumada H, Yamamoto K, Matsumura A, Yamamoto T, Nakagawa Y. Development of JCDS, a computational dosimetry system at JAEA for boron neutron capture therapy. *J Phys Conf.* 74 (2007). 012010. doi:10.1088/1742-6596/74/1/021010
91. Chen Z, Yang P, Lei Q, Wen Y, He D, Wu Z, et al. Comparison of BNCT dosimetry calculations using different GEANT4 physics lists. *Radiat Protect Dosim.* (2019). 187:88–97. doi:10.1093/rpd/ncz144.
92. Herrera MS, González SJ, Minsky DM, Kreiner AJ. Evaluation of performance of an accelerator-based BNCT facility for the treatment of different tumor targets. *Phys Med.* (2013). 29:436. doi:10.1016/j.ejmp.2013.01.006.
93. Bortolussi S, Altieri S. Thermal neutron irradiation field design for boron neutron capture therapy of human explanted liver. *Med Phys.* (2007). 34:4700. doi:10.1118/1.2795831.
94. Norbury J, Miller J, Adamczyk A, Heilbronn L, Townsend L, Blattnig S, et al. Nuclear data for space radiation. *Radiat Meas.* (2012). 12:315–63. doi:10.1016/j.radmeas.2012.03.004
95. Sihver L, Lantz M, Takechi M, Kohama A, Ferrari A, Cerutti F, et al. A comparison of total reaction cross section models used in particle and heavy ion transport codes. *Adv Space Res.* (2012). 49:812–9. doi:10.1016/j.asr.2011.11.029
96. Bauhoff W. Tables of reaction and total cross sections for proton-nucleus scattering below 1 GeV. *Atomic Data Nucl Data Tables.* (1986). 35:429–47. doi:10.1016/0092-640X(86)90016-1
97. Nakamura T, Heilbronn L. *Handbook on secondary particle production and transport.* Singapore: World Scientific (2006). p. 236.
98. Horst F, Schuy C, Weber U. Measurements of He charge and mass changing cross sections for He+C collisions in the energy range 80-220 MeV/u for applications in ion beam therapy. *Phys Rev C.* (2017). 96:024624. doi:10.1103/PhysRevC.96.024624

99. Horst F, Arico G, Brinkman K, Brons S, Ferrari A, Haberer T, et al. Measurements of He charge and mass changing cross sections on H,C, O, and Si targets in the energy range 70-220 MeV/u for radiation transport calculations in ion-beam therapy. *Phys Rev C.* (2019). 99:014603. doi:10.1103/PhysRevC.99.014603
100. Kox S, Gamp A, Cherkaoui R, Cole AJ, Longequeue N, Menet J, et al. Direct measurements of heavy ion total reaction cross section at 30 and 83 MeV/nucleon. *Nucl Phys A.* (1984). 420:162–72. doi:10.1016/0375-9474(84)90663-8
101. Kox S, Gamp A, Perrin C, Arvieux J, Bertholet R, Bruandet JF, et al. Trends of total reaction cross sections for heavy ion collisions in the intermediate energy range. *Phys Rev C.* (1987). 35:1678–91. doi:10.1103/physrevc.35.1678
102. Takechi M, Fukuda M, Mihara M, Tanaka K, Chinda T, Matsumasa T, et al. Reaction cross sections at intermediate energies and Fermi-motion effects. *Phys Rev C.* (2009). 79:061601. doi:10.1103/PhysRevC.79.061601
103. Toshito T, Kodama K, Sihver L, Yusa K, Ozaki M, Amako K, et al. Measurements of total and partial change-changing cross sections for 200 and 400 MeV/nucleon C on water and polycarbonate. *Phys Rev C.* (2007). 75:054606. doi:10.1103/PhysRevC.75.054606
104. De Napoli M, Agodi C, Battistoni G, Blancato A, Cirrone G, Cuttone G, et al. Carbon fragmentation measurements and validation of the GEANT4 nuclear reaction models for hadron therapy. *Phys Med Biol.* (2012). 57:7651. doi:10.1088/0031-9155/57/22/7651
105. Mattei I, Alexandrov A, Alunni Solestizi L, Ambrosi G, Argirò S, Bartosik N, et al. Measurement of C fragmentation cross sections on C, O, and H in the energy range of interest for particle therapy applications. *IEEE Trans Radiat Plasma Med Sci.* (2020). 4:269. doi:10.1109/TRPMS.2020.2972197
106. Braunn B, Boudard A, Colin J, Cugnon J, Cussol D, David J, et al. Comparisons of hadrontherapy-relevant data to nuclear interaction codes in the GEANT4 toolkit. *J Phys Conf.* (2013). 420:1. doi:10.1088/1742-6596/420/1/012163
107. Dudouet J, Cussol D, Durand D, Labalme M. Benchmarking GEANT4 nuclear models for hadron therapy with 95 MeV/nucleon carbon ions. *Phys Rev C.* (2014). 89:054616. doi:10.1103/PhysRevC.89.054616
108. Tsai P, Lai B, Heilbronn L, Sheu R. Benchmark of neutron production cross sections with Monte Carlo codes. *Nucl Instrum Methods Phys Res B.* (2018). 416:16–29. doi:10.1016/j.nimb.2017.11.029
109. Braunn B, Boudard A, David J. Assessment of nuclear-reaction codes for proton induced reactions on light nuclei below 250 MeV. *Eur Phys J Plus.* (2015). 130:153. 10.1140/epjp/i2015-15153-x
110. Spighi R, Alexandrov A, Alpat B, Ambrosi G, Argirò S, Battistoni G, et al. Foot: fragmentation of target experiment. *Nuovo Cim C.* (2019). 42:134.
111. Schall I, Schardt D, Geissel H, Irnich H, Kankeleit E, Kraft G, et al. Charge-changing nuclear reactions of relativistic light-ion beams (5Z10) passing through thick absorbers. *Nucl Instrum Methods B.* (1996). 117:221–34. doi:10.1016/0168-583X(96)00325-4
112. Haettner E, Iwase H, Schardt D. Experimental fragmentation studies with C therapy beams. *Radiat Protect Dosim.* (2006). 122:485. doi:10.1093/rpd/ncl402
113. Haettner E, Iwase H, Krämer M, Kraft G, Schardt D. Experimental study of nuclear fragmentation of 200 and 400 Mev/u C ions in water for applications in particle therapy. *Phys Med Biol.* (2013). 58:8265–79. doi:10.1088/0031-9155/58/23/8265.
114. Golovchenko A, Skvarc J, Yasuda N, Giacomelli M, Tretyakova SP, Ilić R, et al. Total charge-changing and partial cross-section measurements in the reactions of 110-250 MeV/nucleon C in carbon, paraffin and water. *Phys Rev C.* (2002). 66:014609. doi:10.1103/PhysRevC.66.014609
115. Golovchenko A, Skvarc J, Yasuda N, Giacomelli M, Tretyakova SP, Ilić R, et al. Erratum: total charge-changing and partial cross-section measurements in the reactions of 110-250 MeV/nucleon C in carbon, paraffin and water. *Phys Rev C.* (2002). 66:039901. doi:10.1103/PhysRevC.66.039901
116. Puchalska M, Tessonnier T, Parodi K, Sihver L. Benchmarking of PHITS for carbon ion therapy. *Int J Part Ther.* (2018). 4:48. doi:10.14338/IJPT-17-00029.1
117. Gunzert-Marx K, Iwase H, Schardt D, Simon R. Secondary beam fragments produced by 200 MeV u C ions in water and their dose contributions in carbon ion radiotherapy. *New J Phys.* (2008). 10:075003. doi:10.1088/1367-2630/10/7/075003
118. Aricò G, Gehrke T, Jakubek J, Gallas R, Berke S, Jäkel O, et al. Investigation of mixed ion fields in the forward direction for 220.5 MeV/u helium ion beams: comparison between water and PMMA targets. *Phys Med Biol.* (2017). 62:8003–24. doi:10.1088/1361-6560/aa875e.
119. De Napoli M, Romano F, D'Urso D, Licciardello T, Agodi C, Candiano G, et al. Nuclear reaction measurements on tissue-equivalent materials and GEANT4 Monte Carlo simulations for hadrontherapy. *Phys Med Biol.* (2014). 59:7643. doi:10.1088/0031-9155/59/24/7643
120. Aricò G, Gehrke T, Gallas R, Mairani A, Jäkel O, Martišíková M. Investigation of single carbon ion fragmentation in water and PMMA for hadron therapy. *Phys Med Biol.* (2019). 64:055018. doi:10.1088/1361-6560/aafa46
121. Rinaldi I, Ferrari A, Mairani A, Paganetti H, Parodi K, Sala P. An integral test of FLUKA nuclear models with 160 MeV proton beams in multi-layer Faraday cups. *Phys Med Biol.* (2011). 56:4001–11. doi:10.1088/0031-9155/56/13/016
122. Henkner K, Sobolevsky N, Jäkel O, Paganetti H. Test of the nuclear interaction model in SHIELD-HIT and comparison to energy distributions from GEANT4. *Phys Med Biol.* (2009). 54:N509–N517. doi:10.1088/0031-9155/54/22/N01.
123. Mascia A, De Marco J, Chow P, Solberg T. Benchmarking of the MCNPX nuclear interaction models for use in the proton therapy energy range. Proc. 14th ICCR; Seoul, South Korea. Piscataway, NJ: IEEE Nuclear and Plasma Sciences Society (2004)). 478–81.
124. Zacharatou Jarlskog C, Paganetti H. Physics setting for using GEANT4 toolkit in proton therapy. *IEEE Trans Nucl Sci.* (2008). 55:1018–25. doi:10.1109/TNS.2008.922816
125. Rovituso M, Schuy C, Weber U, Brons S, Cortés-Giraldo M, La Tessa C, et al. Fragmentation of 120 and 200 MeV/u He ions in water and PMMA targets. *Phys Med Biol.* (2017). 62:1310–26. doi:10.1088/1361-6560/aa5302
126. Marafini M, Paramatti R, Pinci D, Battistoni G, Collamati F, De Lucia E, et al. Secondary radiation measurements for particle therapy applications: nuclear fragmentation produced by He ion beams in a PMMA target. *Phys Med Biol.* (2017). 62:1291–309. doi:10.1088/1361-6560/aa5307
127. Sihver L, Giacomelli M, Ota S, Skvarc J, Yasuda N, Ilic R, et al. Projectile fragment emission angles in fragmentation reactions of light ions in the energy region 200 MeV/nucleon: experimental study. *Radiat Meas.* (2013). 48:73–81. doi:10.1016/j.radmeas.2012.08.006
128. Matsufuji N, Fukumura A, Komori M, Kanai T, Kohno T. Influence of fragment reaction of relativistic heavy charged particles on heavy-ion radiotherapy. *Phys Med Biol.* (2003). 48:1605–23. doi:10.1088/0031-9155/48/11/309.
129. Gowsch K, Hartmann B, Jakubek J, Granja C, Soukup P, Jäkel O, et al. Non-invasive monotoring of therapeutic carbon ion beams in a homogeneous phantom by tracking of secondary ions. *Phys Med Biol.* (2013). 58:3755–73. doi:10.1088/0031-9155/58/11/3755
130. Matsufuji N, Komori M, Sasaki H, Akiu K, Ogawa M, Fukumura A, et al. Spatial fragment distribution from a therapeutic pencil-like carbon beam in water. *Phys Med Biol.* (2005). 50:3393–403. doi:10.1088/0031-9155/50/14/014.
131. Schardt D, Schall I, Geissel H, Irnich H, Kraft G, Magel A, et al. Nuclear fragmentation of high-energy heavy-ion beams in water. *Adv Space Res.* (1996). 17:87–94. doi:10.1016/0273-1177(95)00516-h.
132. España S, Zhu X, Daartz J, El Fakhri G, Bortfeld T, Paganetti H. The reliability of proton-nuclear interaction cross-section data to predict proton-induced pet images in proton therapy. *Phys Med Biol.* (2011). 56:2687–98. doi:10.1088/0031-9155/56/9/003
133. Matsushita K, Nishio T, Takana S, Tsuneda M, Sugiura A, Leki K. Measurement of proton induced target fragmentation cross sections in carbon. *Nucl Phys A.* (2016). 946:104–16. doi:10.1016/j.nuclphysa.2015.11.007
134. Sommerer F, Cerutti F, Parodi K, Ferrari A, Enghardt W, Aiginger H. In-beam PET monitoring of mono-energetic O and C beams: experiments and FLUKA simulations for homogeneous targets. *Phys Med Biol.* (2009). 54:3979–96. doi:10.1088/0031-9155/54/13/003
135. Battistoni G, Bauer J, Böhlen T, Cerutti F, Chin M, et al. The FLUKA code: an accurate simulation tool for particle therapy. *Fron Oncol.* (2016). 6:116. doi:10.3389/fonc.2016.00116
136. Horst F, Adi W, Aricò G, Brinkmann K, Durante M, Reidel M, et al. Measurement of PET isotope production cross sections for protons and carbon ions on carbon and oxygen targets for applications in particle therapy range verification. *Phys Med Biol.* (2019). 64:205012. doi:10.1088/1361-6560/ab4511
137. Ferrero V, Bisogni M, Camarlinghi N, Fiorina E, Giraudo G, Morrocchi M, et al. Double-field hadrontherapy treatment monitoring with the inside in-

beam PET scanner: proof of concept. *IEEE Trans Radiat Plasma Medical Sci.* (2018). 2:588–93. 10.1109/TRPMS.2018.2870478
138. Bongrand A, Busato E, Force P, Martin F, Montarou G. Use of short-lived positron emitters for in-beam and real-time β. *Phys Med.* (2020). 69:248–55. doi:10.1016/j.ejmp.2019.12.015.
139. Dendooven P, Buitenhuis H, Diblen F, Heeres PN, Biegun AK, Fiedler F, et al. Short-lived positron emitters in beam-on PET imaging during proton therapy. *Phys Med Biol.* (2015). 60:8923–47. doi:10.1088/0031-9155/60/23/8923.
140. Min C, Kim C. Prompt gamma measurements for locating the dose falloff region in the proton therapy. *Appl Phys Lett.* (2006). 89:183517. 10.1063/1.2378561
141. Le Foulher F, Bajard M, Chevallier M, Dauvergne D, Freud N, Henriquet P, et al. Monte Carlo simulations of prompt-gamma emission during carbon ion irradiation. *IEEE Trans Nucl Sci.* (2010). 57:2768–72. doi:10.1109/ANIMMA.2009.5503665
142. European NoVel Imaging Systems for ION therapy. *Envision project.* (2012). Available from: https://envision.web.cern.ch/.
143. Smeets J, Roellinghoff F, Prieels D, Stichelbaut F, Benilov A, Busca P, et al. Prompt gamma imaging with a slit camera for real time range control in proton therapy. *Phys Med Biol.* (2012). 57:3371–405. doi:10.1088/0031-9155/57/11/3371.
144. Pinto M, Bajard M, Brons S, Chevallier M, Dauvergne D, Dedes G, et al. Absolute prompt-gamma yield measurements for ion beam therapy monitoring. *Phys Med Biol.* (2015). 60:565–94. doi:10.1088/0031-9155/60/2/565
145. Dedes G, Pinto M, Dauvergne D, Freud N, Krimmer J, Létang JM, et al. Assessment and improvements of GEANT4 hadronic models in the context of prompt-gamma hadrontherapy monitoring. *Phys Med Biol.* (2014). 59:1747–72. doi:10.1088/0031-9155/59/7/1747.
146. Testa M, Min CH, Verburg JM, Schümann J, Lu H, Paganetti H. Range verification of passively scattered proton beams based on prompt gamma time patterns. *Phys Med Biol.* (2014). 59:4181–95. doi:10.1088/0031-9155/59/15/4181.
147. Pinto M, Dauvergne D, Freud N, Krimmer J, Létang JM, Testa E. Assessment of GEANT4 prompt-gamma emission yields in the context of proton therapy monitoring. *Front Oncol.* (2016). 28:10. 10.3389/fonc.2016.00010
148. Muraro S, Battistoni G, Collamati F, De Lucia E, Faccini R, Ferroni F, et al. Monitoring of hadrontherapy treatments by means of charged particle detection. *Front Oncol.* (2016). 6:177. doi:10.3389/fonc.2016.00177.
149. Traini G, Mattei I, Battistoni G, Bisogni MG, De Simoni M, Dong Y, et al. Review and performance of the dose profiler, a particle therapy treatments online monitor. *Phys Med.* (2019). 65:84–93. doi:10.1016/j.ejmp.2019.07.010.
150. Félix-Bautista R, Gehrke T, Ghesquière-Diérickx L, Reimold M, Amato C, Turecek D, et al. Experimental verification of a non-invasive method to monitor the lateral pencil beam position in an anthropomorphic phantom for carbon-ion radiotherapy. *Phys Med Biol.* (2019). 64:175019. doi:10.1088/1361-6560/ab2ca3
151. Verburg MJ, Riley K, Bortfeld T, Seco J. Energy and time resolved detection of prompt gamma rays for proton range verification. *Phys Med Biol.* (2013). 58:L37–49. doi:10.1088/0031-9155/58/20/L37
152. Verburg J, Seco J. Proton range verification through prompt gamma-ray spectroscopy. *Phys Med Biol.* (2014). 59:7089–106. doi:10.1088/0031-9155/59/23/7089.
153. Polf J, Panthi R, Mackin D, McCleskey M, Saastamoinen A, Roeder B, et al. Measurement of characteristic prompt gamma rays emitted from oxygen and carbon in tissue- equivalent samples during proton beam irradiation. *Phys Med Biol.* (2013). 58:5821–31. doi:10.1088/0031-9155/58/17/5821.
154. Testa E, Bajard M, Chevallier M, Dauvergne D, Le Foulher F, Poizat J, et al. Monitoring the Bragg peak location of 73 MeV/u carbon ion beams by means of prompt gamma-ray measurements. *Appl Phys Lett.* (2008). 93:093506. doi:10.1063/1.2975841
155. Testa E, Bajard M, Chevallier M, Dauvergne D, Le Foulher F, Freud N, et al. Dose profile monitoring with carbon ions by means of prompt-gamma measurements. *Nucl Instrum Methods B.* (2009). 267:993–6. doi:10.1016/j.nimb.2009.02.031
156. Testa M, Bajard M, Chevallier M, Dauvergne D, Freud N, Henriquet P, et al. Real-time monitoring of the Bragg peak position in ion therapy by means of single photon detection. *Radiat Environ Biophys.* (2010). 49:337–43. doi:10.1007/s00411-010-0276-2.
157. Vanstalle M, Mattei I, Sarti A, Bellini F, Bini F, Collamati F, et al. Benchmarking GEANT4 hadronic models for prompt-γ monitoring in carbon ion therapy. *Med Phys.* (2017). 44:4276–86. doi:10.1002/mp.12348
158. Agodi C, Bellini F, Cirrone G, Collamati F, Cuttone G, De Lucia E, et al. Precise measurement of prompt photon emission for carbon ion therapy. *J Instrum.* (2012). 7:P03001. doi:10.1088/1748-0221/7/03/P03001
159. Mattei I, Bini F, Collamati F, De Lucia E, Frallicciardi P, Iarocci E, et al. Secondary radiation measurements for particle therapy applications: prompt photons produced by He, C and O ion beams in a PMMA target. *Phys Med Biol.* (2017). 62:1438–55. doi:10.1088/1361-6560/62/4/1438
160. Agodi C, Battistoni G, Bellini F, Cirrone GAP, Collamati F, Cuttone G, et al. Charged particle's flux measurement from PMMA irradiated by 80 MeV/u carbon ion beam. *Phys Med Biol.* (2012). 57:5667–78. doi:10.1088/0031-9155/57/18/5667
161. Mattei I, Battistoni G, Collini F, De Lucia E, Durante M, Fiore S, et al. Addendum: measurement of charged particle yields from PMMA irradiated by a 220 MeV/u C beam. *Phys Med Biol.* (2017). 62:8483. doi:10.1088/1361-6560/aa8b35
162. Rucinski A, Battistoni G, Collamati F, De Lucia E, Faccini R, Frallicciardi PM, et al. Secondary radiation measurements for particle therapy applications: charged particles produced by ^{4}He and ^{12}C ion beams in a PMMA target at large angle. *Phys Med Biol.* (2018). 63:055018. doi:10.1088/1361-6560/aaa36a
163. Rucinski A, Traini G, Baratto Roldan A, Battistoni G, De Simoni M, Dong Y, et al. Secondary radiation measurements for particle therapy applications: charged secondaries produced by ^{16}O ion beams in a PMMA target at large angles. *Phys Med.* (2019). 64:45–53. doi:10.1016/j.ejmp.2019.06.001
164. Aleksandrov A, Consiglio L, De Lellis G, Di Crescenzo A, Lauria A, Montesi M, et al. Measurement of large angle fragments induced by 400 MeV/u carbon ion beams. *Meas Sci Technol.* (2015). 26:094001. 10.1088/0957-0233/26/9/094001
165. Alexandrov A, De Lellis G, Di Crescenzo A, Lauria A, Montesi M, Pastore A, et al. Measurements of ^{12}C ions beam fragmentation at large angle with an emulsion cloud chamber. *J Instrum.* (2017). 12:P08013. 10.1088/1748-0221/12/08/P08013
166. Pshenichnov I, Mishustin I, Greiner W. Distributions of positron-emitting nuclei in proton and carbon-ion therapy studied with GEANT4. *Phys Med Biol.* (2006). 51:6099–112. doi:10.1088/0031-9155/51/23/011.
167. Akagi T, Yagi M, Yamashita T, Murakami M, Yamakawa Y, Kitamura K, et al. Experimental study for the production cross section of positron emitters induced from C and O nuclei by low-energy proton beams. *Radiat Meas.* (2013). 59:262–9. doi:10.1016/j.radmeas.2013.07.005
168. Tommasino F, Scifoni E, Durante M. New ions for therapy. *Int J Par Therapy.* (2016). 2:428–38. doi:10.14338/IJPT-15-00027.1.
169. Dingfelder M, Hantke D, Inokuti M, Paretzke H. Electron inelastic-scattering cross sections in liquid water. *Radiat Phys Chem.* (1998). 53:1–18. doi:10.1016/S0969-806X(97)00317-4
170. Krämer M, Kraft G. Calculations of heavy-ion track structure. *Radiat Environ Biophys.* (1994). 33:91–109. doi:10.1016/0168-583X(95)00538-2
171. Wälzlein C, Krämer M, Scifoni E, Durante M. Advancing the modeling in particle therapy: from track structure to treatment planning. *Appl Radiat Isot.* (2014). 83:171–6. doi:10.1016/j.apradiso.2013.01.019
172. Incerti S, Baldacchino G, Bernal M, Capra R, Champion C, Francis Z, et al. The GEANT4-DNA project. *Int J Model Simul Sci Comput.* (2010). 1:157–78. doi:10.1142/S1793962310000122
173. Schuemann J, McNamara A, Ramos-Méndez J, Perl J, Held K, Paganetti H, et al. TOPAS-nBio: an extension to the TOPAS simulation toolkit for cellular and subcellular radiobiology. *Radiat Res.* (2019). 191:125–38. doi:10.1667/RR15226.1.
174. Kellerer A, Rossi H. A generalized formulation of dual radiation action. *Radiat Res.* (1978). 75:471–88. doi:10.2307/3574835
175. Scholz M, Kraft G. Track structure and the calculation of biological effects of heavy charged particles. *Adv Space Res.* (1996). 18:5–14. doi:10.1016/0273-1177(95)00784-C
176. Scholz M, Kellerer A, Kraft-Weyrather W, Kraft G. Computation of cell survival in heavy ion beams for therapy - the model and its approximation. *Radiat Environ Biophys.* (1997). 36:59–66. doi:10.1007/s004110050055.
177. Krämer M, Scholz M. Treatment planning for heavy-ion radiotherapy: calculation and optimization of biologically effective dose. *Phys Med Biol.* (2000). 45:3319–30.
178. Krämer M, Scholz M. Rapid calculation of biological effects in ion radiotherapy. *Phys Med Biol.* (2006). 51:1959–70. doi:10.1088/0031-9155/51/8/001.

179. Hawkins R. A statistical theory of cell killing by radiation of varying linear energy transfer. *Radiat Res.* (1994). 140:366–74.
180. Hawkins R. A microdosimetric-kinetic model of cell death from exposure to ionizing radiation of any let, with experimental and clinical application. *Int J Radiat Biol.* (1996). 69:739–55. doi:10.1080/095530096145481
181. Hawkins R. A microdosimetric-kinetic model for the effect of non-Poisson distribution of lethal lesions on the variation of RBE with LET. *Radiat Res.* (2003). 160:61–9. doi:10.1667/rr3010
182. Kase Y, Kanai T, Matsumoto Y, Furusawa Y, Okamoto H, Asaba T, et al. Microdosimetric measurements and estimation of human cell survival for heavy-ion beams. *Radiat Res.* (2006). 166:629–38. doi:10.1667/RR0536.1.
183. Kase Y, Kanai T, Matsufuji N, Furusawa Y, Elsässer T, Scholz M. Biophysical calculation of cell survival probabilities using amorphous track structure models for heavy-ion irradiation. *Phys Med Biol.* (2008). 53:37–59. doi:10.1088/0031-9155/53/1/003.
184. Inaniwa T, Furukawa T, Kase Y, Matsufuji N, Toshito T, Matsumoto Y, et al. Treatment planning for a scanned carbon beam with a modified microdosimetric kinetic model. *Phys Med Biol.* (2010). 55:6721–37.doi:10.1088/0031-9155/55/22/008.
185. Inaniwa T, Kanematsu N, Matsufuji N, Kanai T, Shirai T, Noda K, et al. Reformulation of a clinical-dose system for carbon-ion radiotherapy treatment planning at the national institute of radiological sciences Japan. *Phys Med Biol.* (2015). 60:3271–86.doi:10.1088/0031-9155/60/8/3271.
186. Kase Y, Kanematsu N, Kanai T, Matsufuji N. Biological dose calculation with Monte Carlo physics simulation for heavy-ion radiotherapy. *Phys Med Biol.* (2006). 51:N467–75. doi:10.1088/0031-9155/51/24/N03.
187. Carante M, Aimè C, Tello Cajiao J, Ballarini F. BIANCA, a biophysical model of cell survival and chromosome damage by protons, C-ions and He-ions at energies and doses used in hadrontherapy. *Phys Med Biol.* (2018). 63:075007. doi:10.1088/1361-6560/aab45f
188. Carante M, Aricò G, Ferrari A, Kozlowska W, Mairani A, Ballarini F. First benchmarking of the BIANCA model for cell survival prediction in a clinical hadron therapy scenario. *Phys Med Biol.* (2019). 64:215008. doi:10.1088/1361-6560/ab490f
189. Elsässer T, Weyrather W, Friedrich T, Durante M, Iancu G, Krämer M, et al. Quantification of the relative biological effectiveness for ion beam radiotherapy: direct experimental comparison of proton and carbon ion beams and a novel approach for treatment planning. *Int J Radiat Oncol Biol Phys.* (2010). 78:1177–83. doi:10.1016/j.ijrobp.2010.05.014
190. Fossati P, Molinelli S, Matsufuji N, Ciocca M, Mirandola A, Mairani A, et al. Dose prescription in carbon ion radiotherapy: a planning study to compare NIRS and LEM approaches with a clinically-oriented strategy. *Phys Med Biol.* (2012). 57:7543–54. doi:10.1088/0031-9155/57/22/7543.
191. Molinelli S, Magro G, Mairani A, Matsufuji N, Kanematsu N, Inaniwa T, et al. Dose prescription in carbon ion radiotherapy: how to compare two different RBE-weighted dose calculation systems. *Radiother Oncol.* (2016). 120:307–12. doi:10.1016/j.radonc.2016.05.031.
192. Magro G, Dahle T, Molinelli S, Ciocca M, Fossati P, Ferrari A, et al. The FLUKA Monte Carlo code coupled with the NIRS approach to clinical dose calculation in carbon ion therapy. *Phys Med Biol.* (2017). 62:3814–27. doi:10.1088/1361-6560/aa642b
193. Mein S, Dokic I, Klein C, Tessonnier T, Böhlen T, Magro G, et al. Biophysical modeling and experimental validation of relative biological effectiveness (RBE) for ^{4}He ion beam therapy. *Radiat Oncol.* (2019). 14:123. doi:10.1186/s13014-019-1295-z.
194. Wedemberg M, Lind B, Hardemark B. A model for the relative biological effectiveness of protons: the tissue specific parameter of photons is a predictor for the sensitivity to let changes. *Acta Oncol.* (2013). 52:580–8. doi:10.3109/0284186X.2012.705892
195. Wilkens J, Oelfke U. Analytical linear energy transfer calculations for proton therapy. *Med Phys.* (2003). 30:806–15. doi:10.1118/1.1567852.
196. McNamara A, Schuemann J, Paganetti H. A phenomenological relative biological effectiveness (RBE) model for proton therapy based on all published *in vitro* cell survival data. *Phys Med Biol.* (2015). 60:8399–416. doi:10.1088/0031-9155/60/21/8399.
197. Carabe A, Moteabbed M, Depauw N, Schuemann J, Paganetti H. Range uncertainty in proton therapy due to variable biological effectiveness. *Phys Med Biol.* (2012). 57:1159–72. doi:10.1088/0031-9155/57/5/1159.
198. Scifoni E, Tinganelli W, Kraft-Weyrather W, Durante M, Maier A, Krämer M. Including oxygen enhancement ratio in ion beam treatment planning: model implementation and experimental verification. *Phys Med Biol.* (2013). 58:3871–95. doi:10.1088/0031-9155/58/11/3871
199. Sokol O, Scifoni E, Tinganelli W, Kraft-Weyrather W, Wiedemann J, Maier A, et al. Oxygen beams for therapy: advanced biological treatment planning and experimental verification. *Phys Med Biol.* (2017). 62:7798–813. doi:10.1088/1361-6560/aa88a0.
200. Sokol O, Krämer M, Hild S, Durante M, Scifoni E. Kill painting of hypoxic tumors with multiple ion beams. *Phys Med Biol.* (2019). 64:045008. doi:10.1088/1361-6560/aafe40.
201. Tommasino F, Durante M. Proton radiobiology. *Cancers.* (2015). 7:353–81. doi:10.3390/cancers7010353
202. TIFPA. Modeling and verification for ion beam treatment planning (2020). Available from: http://www.tifpa.infn.it/projects/move-it/.
203. Petringa G, Romano F, Manti L, Pandola L, Attili A, Cammarata F, et al. Radiobiological quantities in proton-therapy: estimation and validation using GEANT4-based Monte Carlo simulations. *Phys Med.* (2019). 58:72–80. doi:10.1016/j.ejmp.2019.01.018.
204. Cirrone G, Manti L, Margarone D, Petringa G, Giuffrida L, Minopoli A, et al. First experimental proof of proton boron capture therapy (PBCT) to enhance protontherapy effectiveness. *Sci Rep.* (2018). 8:1141. doi:10.1038/s41598-018-19258-5.
205. Vozenin MC, Hendry J, Limoli C. Biological benefit of ultra-high dose rate flash radiotherapy: sleeping beauty awoken. *Clin Oncol.* (2019). 31:407–415. doi:10.1016/j.clon.2019.04.001
206. Colangelo NW, Azzam E. The importance and clinical implications of FLASH ultra-high dose-rate studies for proton and heavy ion radiotherapy. *Radiat Res.* (2020). 193:1–4. doi:10.1667/RR15537.1
207. Laboratories R. Raystation carbon ion planning (2020). Available from: http://www.raysearchlabs.com.
208. Saini J, Maes D, Egan A, Bowen S, St James S, Janson M, et al. Dosimetric evaluation of a commercial proton spot scanning Monte-Carlo dose algorithm: comparisons against measurements and simulations. *Phys Med Biol.* (2017). 62:7659–81. doi:10.1088/1361-6560/aa82a5.
209. Widesott L, Lorentini S, Fracchiolla F, Farace P, Schwarz M. Improvements in pencil beam scanning proton therapy dose calculation accuracy in brain tumor cases with a commercial Monte Carlo algorithm. *Phys Med Biol.* (2018). 63:145016. doi:10.1088/1361-6560/aac279.
210. Lin L, Huang S, Kang M, Hiltunen P, Vanderstraeten R, Lindberg J, et al. A benchmarking method to evaluate the accuracy of a commercial proton Monte Carlo pencil beam scanning treatment planning system. *J Appl Clin Med Phys.* (2017). 18:44–9. doi:10.1002/acm2.12043.
211. Krämer M, Jäkel O, Haberer T, Kraft G, Schardt D, Weber U. Treatment planning for heavy-ion radiotherapy: physical beam model and dose optimization. *Phys Med Biol.* (2000). 45:3299–317. doi:10.1088/0031-9155/45/11/313.
212. Krämer M, Durante M. Ion beam transport calculations and treatment plans in particle therapy. *Eur Phys J D.* (2010). 60:195–202. doi:10.1140/epjd/e2010-00077-8
213. Jäkel O, Krämer M, Karger C, Debus J. Treatment planning for heavy ion radiotherapy: clinical implementation and application. *Phys Med Biol.* (2001). 46:1101–16. doi:10.1088/0031-9155/46/4/314
214. Krämer M. Treatment planning for heavy-ion radiotherapy: biological optimization of multiple beam ports. *J Radiat Res.* (2001). 42:39–46. 10.1269/jrr.42.39.
215. Syngo TPS. Tech. Rep. Manheim, Germany: Siemens AG (2009).
216. Iancu G, Kraemer M, Zink K, Durante M. Implementation of an efficient Monte Carlo algorithm in TriP: physical dose calculation. *Int J Part Therapy.* (2015). 2:415–25. 10.14338/IJPT-14-00030.1
217. Kanematsu N, Inaniwa T. *Treatment planning of carbon-ion radiotherapy.* H Tsujii, T Kamada, T Shirai, K Noda, H Tsuji, K Karsawa, editors. Tokyo, Japan: Springer (2014).
218. Russo G, Attili A, Battistoni G, Bertrand D, Bourhaleb F, Cappucci F, et al. A novel algorithm for the calculation of physical and biological irradiation quantities in scanned ion beam therapy: the beamlet superposition approach. *Phys Med Biol.* (2016). 61:183–214. doi:10.1088/0031-9155/61/1/183.
219. Manganaro L, Russo G, Cirio R, Dalmasso F, Giordanengo S, Monaco V, et al. A Monte Carlo approach to the microdosimetric kinetic model to account for dose

rate time structure effects in ion beam therapy with application in treatment planning simulations. *Med Phys.* (2017). 44:1577–89. doi:10.1002/mp.12133.
220. Mairani A, Böhlen TT, Schiavi A, Tessonnier T, Molinelli S, Brons S, et al. A Monte Carlo-based treatment planning tool for proton therapy. *Phys Med Biol.* (2013). 58:2471–90. doi:10.1088/0031-9155/58/8/2471.
221. Böhlen T, Bauer S, Dosanjh M, Ferrari A, Haberer T, Parodi K, et al. A Monte Carlo-based treatment-planning tool for ion beam therapy. *J Radiat Res.* (2013). 54:i77–i81. 10.1093/jrr/rrt050
222. Böhlen T, Brons S, Dosanjh M, Ferrari A, Fossati P, Haberer T, et al. Investigating the robustness of ion beam therapy treatment plans to uncertainties in biological treatment parameters. *Phys Med Biol.* (2012). 57:7983–8004. doi:10.1088/0031-9155/57/23/7983.
223. Tessonnier T, Böhlen T, Ceruti F, Ferrari A, Sala P, Brons S, et al. Dosimetric verification in water of a Monte Carlo treatment planning tool for proton, helium, carbon and oxygen ion beams at the Heidelberg ion beam therapy center. *Phys Med Biol.* (2017). 62:6579–94. doi:10.1088/1361-6560/aa7be4.
224. Tinganelli W, Durante M, Hirayama R, Krämer M, Maier A, Kraft-Weyrather W, et al. Kill-painting of hypoxic tumours in charged particle therapy. *Sci Rep.* (2015). 5:17016. doi:10.1038/srep17016.
225. Schiavi A, Senzacqua M, Pioli S, Mairani A, Magro G, Molinelli S, et al. Fred: a GPU-accelerated fast-Monte Carlo code for rapid treatment plan recalculation in ion beam therapy. *Phys Med Biol.* (2017). 62:7482–504. doi:10.1088/1361-6560/aa8134.
226. Qin N, Shen C, Tsai M, Pinto M, Tian Z, Dedes G, et al. Full Monte Carlo-based biological treatment plan optimization system for intensity modulated carbon ion therapy on GPU. *Int J Radiat Biol Phys.* (2018). 100:235–43. 10.1016/j.ijrobp.2017.09.002
227. NVIDA Corporation. NVIDA corporation (2020). Available from: http://www.nvidia.com.
228. Rucinski A, Barana J, Battistoni G, Chrostowska A, Durante M, Gajewski J, et al. Investigations on physical and biological range uncertainties in Kraców proton beam therapy center. *Acta Phys Pol B.* (2020). 51:9–16. doi:10.5506/APhysPolB.51.9
229. Pepin M, Tryggestad E, Seum Wan Chan Tseung H, Johnson JE, Herman MG, Beltran C. A Monte-Carlo-based and GPU-accelerated 4D-dose calculator for a pencil beam scanning proton therapy system. *Med Phys.* (2018). 45:5293–304. doi:10.1002/mp.13182
230. Seum Wan Chan Tseung H, Ma J, Beltran C. A fast GPU-based Monte Carlo simulation of proton transport with detailed modeling of nonelastic interactions. *Med Phys.* (2015). 42:2967–78. doi:10.1118/1.4921046
231. Ma J, Beltran C, Seum Wan Chan Tseung H, Herman M. A GPU-accelerated and Monte Carlo-based intensity modulated proton therapy optimization system. *Med Phys.* (2014). 41:121707. doi:10.1118/1.4901522
232. Maneval D, Bouchard H, Ozell B, Després P. Efficiency improvement in proton dose calculations with an equivalent restricted stopping power formalism. *Phys Med Biol.* (2017). 63:015019. doi:10.1088/1361-6560/aa9166
233. Jia X, Schümann J, Paganetti H, Jiang SB. GPU-based fast Monte Carlo dose calculation for proton therapy. *Phys Med Biol.* (2012). 57:7783–97. doi:10.1088/0031-9155/57/23/7783.
234. Fippel M, Soukup M. A Monte Carlo dose calculation algorithm for proton therapy. *Med Phys.* (2004). 31:2263–73. doi:10.1118/1.1769631
235. Qin N, Pinto M, Tian Z, Dedes G, Pompos A, Jiang S, et al. Initial development of goCMC: a GPU-oriented fast cross-platform Monte Carlo engine for carbon ion therapy. *Phys Med Biol.* (2017). 62:3682–99. doi:10.1088/1361-6560/aa5d43.
236. Mein S, Choi K, Kopp B, Tessonnier T, Bauer J, Ferrari A, et al. Fast robust dose calculation on GPU for high-precision ^{1}H, ^{4}He, ^{12}C and ^{16}O ion therapy: the FRoG platform. *Sci Rep.* (2018). 8:14829. doi:10.1038/s41598-018-33194-4
237. Martins J, Saxena R, Neppl S, Alhazmi A, Reiner M, Veloza S, et al. Optimization of phase space files from clinical linear accelerators. *Phys Med.* (2019). 64:54–68. doi:10.1016/j.ejmp.2019.06.007.
238. Wang Q, Schlegel N, Moyers M, Lin J, Hong L, Chen H, et al. Validation of the fast dose calculator for Shanghai proton and heavy ion center. *Biomed Phys Eng Express.* (2018). 4:06500. 10.1088/2057-1976/aae039
239. Wang Q, Zhu C, Bai X, Deng Y, Schlegel N, Adair A, et al. Automatic phase space generation for Monte Carlo calculations of intensity modulated particle therapy. *Biomed Phys Eng Express.* (2020). 6:025001. doi:10.1088/2057-1976/ab7152.
240. Li JS, Shahine B, Fourkal E, Ma CM. A particle track-repeating algorithm for proton beam dose calculation. *Phys Med Biol.* (2005). 50:1001–10. doi:10.1088/0031-9155/50/5/022
241. Yepes PP, Eley JG, Liu A, Mirkovic D, Randeniya S, Titt U, et al. Validation of a track repeating algorithm for intensity modulated proton therapy: clinical cases study. *Phys Med Biol.* (2016). 61:2633–45. doi:10.1088/0031-9155/61/7/2633.
242. Yepes PP, Mirkovic D, Taddei PJ. A GPU implementation of a track-repeating algorithm for proton radiotherapy dose calculations. *Phys Med Biol.* (2010). 55:7107–20. doi:10.1088/0031-9155/55/23/S11.
243. Jabbari J, Seuntjens J. A fast Monte Carlo code for proton transport in radiation therapy based on MCNPX. *Med Phys.* (2014). 39:156–63. doi:10.4103/0971-6203.139004
244. Fix M, Frei D, Volken W, Born E. Macro Monte Carlo for dose calculation of proton beams. *Phys Med Biol.* (2013). 58:2027–44. doi:10.1088/0031-9155/58/7/2027.
245. Tourovsky A, Lomax AJ, Schneider U, Pedroni E. Monte Carlo dose calculations for spot scanned proton therapy. *Phys Med Biol.* (2005). 50:971–81. doi:10.1088/0031-9155/50/5/019.
246. Kohno R, Takada Y, Sakae T, Terunuma T, Matsumoto K, Nohtomi A, et al. Experimental evaluation of validity of simplified Monte Carlo method in proton dose calculations. *Phys Med Biol.* (2003). 48:1277–88. doi:10.1088/0031-9155/48/10/303.
247. Kalantzis G, Tachibana H. Accelerated event-by-event Monte Carlo microdosimetric calculations of electrons and protons tracks on a multi-core CPU and a CUDA-enabled GPU. *Comput Methods Progr Biomed.* (2014). 113:116–25. doi:10.1016/j.cmpb.2013.09.009
248. Okada S, Murakami K, Incerti S, Amako K, Sasaki T. MPEXS-DNA, a new gpu-based Monte Carlo simulator for track structures and radiation chemistry at subcellular scale. *Med Phys.* (2019). 1483–500. doi:10.1002/mp.13370.
249. Tsai M, Tian Z, Qin N, Yan C, Lai Y, Hung SH, et al. A new open-source GPU-based microscopic Monte Carlo simulation tool for the calculations of DNA damages caused by ionizing radiation – part I: core algorithm and validation. *Med Phys.* (2020). 47:1958–70. doi:10.1002/mp.14037
250. PIDE. Particle irradiation data ensable project (2019). Available from: https://www.gsi.de/work/forschung/biophysik/forschungsfelder/radiobiological_modelling/pide_project.htm.
251. Schneider W, Bortfled T, Schlegel W. Correlation between CT numbers and tissue parameters needed for Monte Carlo simulations of clinical dose distributions. *Phys Med Biol.* (2000). 45:459–78. 10.1088/0031-9155/45/2/314
252. Bolst D, Guatelli S, Tran L, Chartier L, Davis J, Biasi G, et al. Validation of GEANT4 for silicon microdosimetry in heavy ion therapy. *Phys Med Biol.* (2020). 65:045014. doi:10.1088/1361-6560/ab586a.
253. Jan S, Benoit D, Becheva E, Carlier T, Cassol F, Descourt P, et al. GATE V6: a major enhancement of the GATE simulation platform enabling modelling of CT and radiotherapy. *Phys Med Biol.* (2011). 56:881–901. doi:10.1088/0031-9155/56/4/001
254. Shin J, Kooy H, Paganetti H, Clasie B. DICOM-RT ion interface to utilize MC simulations in routine clinical workflow for proton pencil beam radiotherapy. *Phys Med.* (2020). 74:1. doi:10.1016/j.ejmp.2020.04.018.
255. Deng W, Younkin J, Souris K, Huang S, Augustine K, Fatyga M, et al. Technical note: integrating an open source Monte Carlo code "MCsquare" for clinical use in intensity-modulated proton therapy. *Med Phys.* (2020). 47:2558–574. doi:10.1002/mp.14125
256. Guterres Marmitt G, Pin A, Ng Wei Siang K, Janssens G, Souris K, Cohilis M, et al. Platform for automatic patient quality assurance via Monte Carlo simulations in proton therapy. *Phys Med.* (2020). 70:49–57. doi:10.1016/j.ejmp.2019.12.018.

Conflict of Interest: The authors declare that the research was conducted in the absence of any commercial or financial relationships that could be construed as a potential conflict of interest.

frontiers in Physics

REVIEW
published: 26 November 2020
doi: 10.3389/fphy.2020.568206

Preclinical Challenges in Proton Minibeam Radiotherapy: Physics and Biomedical Aspects

Gerd Datzmann[1,2]*, *Matthias Sammer*[1], *Stefanie Girst*[1], *Michael Mayerhofer*[1], *Günther Dollinger*[1] *and Judith Reindl*[1]

[1]*Institut für Angewandte Physik und Messtechnik (LRT2), Universität der Bundeswehr München, Neubiberg, Germany,*
[2]*Datzmann Interact & Innovate GmbH, Munich, Germany*

The concept of spatial fractionation in radiotherapy was developed for better sparing of normal tissue in the entrance channel of radiation. Spatial fractionation utilizing proton minibeam radiotherapy (pMBRT) promises to be advantageous compared to X-ray minibeams due to higher dose conformity at the tumor. Preclinical *in vivo* experiments conducted with pMBRT in mouse ear models or in rat brains support the prospects, but the research about the radiobiological mechanisms and the search for adequate application parameters delivering the most beneficial minibeam therapy is still in its infancy. Concerning preclinical research, we consider glioma, non-small cell lung cancer and hepatocellular carcinoma as the most promising targets and propose investigating the effects on healthy tissue, especially neuronal cells and abdominal organs. The experimental setups for preclinical pMBRT used so far follow different technological approaches, and experience technical limitations when addressing the current questions in the field. We review the crucial physics parameters necessary for proton minibeam production and link them to the technological challenges to be solved for providing an optimal research environment. We consider focusing of pencil or planar minibeams in a scanning approach superior compared to collimation due to less beam halos, higher peak-to-valley dose ratios and higher achievable dose rates. A possible solution to serve such a focusing system with a high-quality proton beam at all relevant energies is identified to be a 3 GHz radio-frequency linear accelerator. We propose using a 16 MeV proton beam from an existing tandem accelerator injected into a linear post-accelerator, boosted up to 70 MeV, and finally delivered to an imaging and positioning end-station suitable for small animal irradiation. Ion-optical simulations show that this combination can generate focused proton minibeams with sizes down to 0.1 mm at 18 nA mean proton current - sufficient for all relevant preclinical experiments. This technology is expected to offer powerful and versatile tools for unleashing structured and advanced preclinical pMBRT studies at the limits and also has the potential to enable a next step into precision tumor therapy.

Keywords: proton minibeam radio therapy, spatial fractionation, linear accelerator, preclinic, irradiation facility, pencil beam scanning, proton therapy

OPEN ACCESS

Edited by:
Yolanda Prezado, INSERM U1021 Signalisation Normale et Pathologique de l'Embryon aux Thérapies Innovantes des Cancers, France

Reviewed by:
Pawel Olko, Institute of Nuclear Physics, Poland
Avraham Dilmanian, Stony Brook University, United States

***Correspondence:**
Gerd Datzmann
gerd@datzmann.eu

Specialty section:
This article was submitted to Medical Physics and Imaging, a section of the journal Frontiers in Physics

Received: *31 May 2020*
Accepted: *22 September 2020*
Published: *26 November 2020*

Citation:
Datzmann G, Sammer M, Girst S, Mayerhofer M, Dollinger G and Reindl J (2020) Preclinical Challenges in Proton Minibeam Radiotherapy: Physics and Biomedical Aspects. Front. Phys. 8:568206. doi: 10.3389/fphy.2020.568206

1 INTRODUCTION

Radiotherapy treatment of tumors is used in approximately 50% of all cancer cases worldwide and is therefore besides chemotherapy, surgery and immunotherapy one of the four pillars of cancer treatment throughout the last decades [1–4]. External beam and especially intensity modulated radiotherapy using X-rays, where radiation is applied from the outside of the body, is the standard procedure for performing state-of-the-art radiotherapy [4]. The damaging effects of radiation originate from the ionization of biochemical molecules and lead to the destruction of DNA in cells. Therefore, it is not only limited to cancerous tissue, but also normal tissue is affected by radiation. The unwanted side effects occurring in the normal tissue located in the beam path in front and behind the tumor is one of the main limiting factors for the dose which can be applied to the tumor within one fraction of radiotherapy. Modern therapy concepts aim to overcome the limits of radiotherapy and try to widen the therapeutic window, by either reducing the risks of side effects or by enhancing tumor control. One of these approaches is the radiotherapy with protons instead of X-rays, which was already introduced in 1946 [5]. When protons traverse matter, the dose is distributed following the Bragg curve, where the maximum of dose is deposited at the end of the particle range [6]. Due to this unique dose distribution, there is near-zero radiation applied behind the tumor. Additionally, the integral dose in the normal tissue in front of the tumor is reduced substantially compared to X-rays although still non-negligible. Together, proton therapy clearly widens the therapeutic window decreasing the risks of side effects and enhancing the potential of tumor control.

Originally, patient treatments with high energy protons typically have been carried out at large-scale research facilities such as iThemba Labs (formerly NAC) [7], Paul Scherrer Institute (PSI) (starting at 1996) [8] in Switzerland or Harvard Cyclotron Lab (starting at 1973) in the USA [9] and various others, by installing an extra treatment room besides several experimental target stations used for fundamental research in nuclear physics [10]. In the 1990s, first stand-alone centers have been built dedicated to treat cancer patients with proton therapy. One of the first was the cancer center in Loma Linda (USA) [11, 12]. With an increasing number of companies offering turn-key solutions for proton therapy systems (PTS), the number of proton therapy centers has increased rapidly since the beginning of the 21st century. In the following, the term "standard proton therapy" is used for this type of treatment modality.

Apart from using a different type of radiation other methods to reduce side effects have been proposed. Temporal fractionation has been established as the common solution to keep side effects in external radiation therapy under control [13]. One further approach in proton therapy is the reduction of the lateral penumbra by reducing the size of the pencil-beams in spot scanning therapy systems, which provides advantages in the treatment of shallowly situated tumors e.g. in children. A group at the St. Jude Children's Research hospital (US) decreased the size of the beam at 221 MeV to 1.5 mm (σ) at a synchrotron-based facility compared to about 2.1 mm (σ) in the conventional mode of this system [14]. Another option is spatial fractionation that opens new possibilities. It was originally proposed in 1909 by Alban Köhler [15]. Here the use of metal grids in the beam path leads to high X-ray doses in the irradiated channels and low doses in the valleys shadowed by the grid. Thus, by sparing parts of normal tissue from radiation, side effects are reduced. Since then, several different approaches of spatial fractionation have been made. A meticulous overview is presented by Meyer et al. [16]. In the 1990s, the idea of spatial fractionation with X-rays was picked-up again and was coined microbeam radiotherapy (MRT) [17, 18]. Research in this field led to the development of dedicated beamlines at research facilities in Europe [17] and the USA [18], investigating the benefits and constraints of MRT for patient treatment in preclinical studies. Thereby, typically planar beams with beam sizes of 25–100 μm and an inter-beam distance of several hundred μm, with beam doses of several hundred Grays and valley doses of approx. 10–30 Gy are used [19–21]. Studies in rat and mouse brains lead to promising results, opening the possibility to push this method further to clinical trials [22–24]. Nevertheless, several problems remain. It is important to note that in MRT technique the tumor is irradiated with the same peak and valley pattern as the normal tissue. As the non-negligible doses in the valleys still damage normal cells this might limit the beneficial sparing effect, whereas the valley doses in the tumor might be too low to efficiently kill all cancer cells. In addition, going below the confidence interval of the prescribed tumor dose is not in accordance with the ICRU-requirements for dose homogeneity in tumor tissue [25]. The recommendations of the ICRU are well accepted in tumor therapy and act as a paradigm which has to be respected at all times during tumor therapy. But in some preclinical studies a better tumor control could be achieved using heterogeneous tumor doses in MRT [26, 27]. Additionally, simulation studies show better results when looking at the cell survival, when using heterogeneous tumor dose neglecting the upper bound of ICRU [28]. Therefore, using new therapy approaches fully exploiting the benefits of spatial fractionation could make it necessary to change the paradigm from the IRCU report 50 [25]. To do so precise and detailed preclinical research has to be performed. The major disadvantage of MRT is that this therapy approach uses X-rays, which still deposit a considerable amount of dose behind the tumor.

A method that combines both, the beneficial effects of proton radiotherapy and spatial fractionation, is proton minibeam radiotherapy (pMBRT), which was introduced in 2013 independently by two groups in France [29] and Germany [30]. In pMBRT the protons are applied like in MRT, but it can benefit from two big advantages. First, as explained above, the protons stop at the end of range and, therefore, no dose is deposited behind the tumor. Second, the angular straggling from multiple Coulomb scattering of the protons in the tissue causes a widening of the beams increasing with depth and a merging of distinct beams to a homogeneous dose distribution in the tumor, like in every conventional radiotherapy [31]. For achieving the same dose at any position in the tumor, as required in standard proton therapy, the total number of applied particles must be the same. The difference is that the

protons are applied in sub-millimeter sized planar beams or pencil beam spots with center-to-center (ctc) distances in the millimeter range at the skin of the patient. In consequence, no or a low dose of radiation is applied in-between the minibeams. The ctc distances of the beams must be chosen in a way that the small angle scattering together with initial beam divergence leads to an overlapping of the beams and a quasi-homogeneous dose distribution already at the beginning of the tumor when considering unidirectional irradiation schemes [32]. Interlaced minibeams from two or more directions and heterogeneous tumor dose distributions are an additional option to increase sparing of healthy tissue up to the close tumor vicinity. The dose profiles of minibeam arrays may be chosen as steep as possible resulting in a high ratio between peak and valley doses (peak-to-valley dose ratio, PVDR), i.e., high doses in the minibeams and lowest possible doses in the valleys. With a high PVDR, the cells in the beams are in general killed due to the high doses, but the cells in the valleys get low doses that most normal cells survive without severe damage. Healthy cells in large valleys probably offer repair options by their proliferation and migration capabilities when replacing eliminated cells within the minibeam irradiated healthy tissue [32]. Although the basic principles are not yet known it is assumed that the so-called "dose-volume effect" [33, 34] and the "microscopic prompt tissue repair effect" [35, 36] play a major role in the healing of healthy tissue in pMBRT.

Preclinical studies conducted at the ion microprobe SNAKE (Superconducting Nanoprobe for Applied nuclear (Kern-) physics Experiments) [37, 38] in a mouse ear model showed that acute side effects in normal tissue are reduced by using pMBRT with PVDR = 540 compared to quasi homogeneous irradiation (PVDR 1–1.2) when pencil spot beams are applied with sizes in the range of 0.1–1 mm, a ctc distance of 1.8 mm, and a mean dose of 60 Gy [31, 39]. Side effects are negligible when beam sizes are small compared to the ctc distance. They steadily increase but are still lower than for homogeneous irradiation when decreasing the PVDR down to PVDR = 2.7 due to larger, Gaussian shaped beam sizes. Irradiations by individual X-ray pencil minibeams showed, in addition, the importance of minibeam sizes that allow for their efficient repair. While beam diameters smaller 2 mm showed nearly no side effects, a strong but gradual increase of the side effects was obtained for larger beam diameters at 60 Gy plateau dose [40].

Preclinical studies from Prezado et al. with rats showed also substantial reduction of side effects after proton minibeam irradiation of the brain with planar beams at a minibeam width of 1.1 mm and ctc of 3.2 mm (PVDR of ~6.5) compared to homogeneous irradiation at 25 Gy mean dose [41]. Additional experiments exploiting the minibeam effect on tumor control showed that at least the same tumor control in high-grade gliomas in rats was achieved whereas survival after treatment was increased to 67% compared to 22% after homogeneous irradiation [22, 24]. The most recent study shows that cognitive function and also emotional and motor processes are mainly conserved after pMBRT [42]. Also, Dilmanian et al. have proven the technical feasibility of pMBRT at the MD Anderson Proton Therapy Center (Houston, Texas, US) [36]. Eley et al. recently used the same facility to perform a study of neurologic toxicity in a proton minibeam irradiation experiment with mice [43]. One specific approach is reported by a group from Krakow that performed first dosimetric characterization of mesh-formed collimators that are supposed to spare the eye lid during proton therapy treatment of uveal melanomas [44]. Overall, it can be concluded that pMBRT shows great potential in reducing side effects in front and behind the tumor while keeping tumor control.

Up to now although pMBRT is applicable to various kinds of tumors and therefore affects a lot of different tissues the preclinical testing at the moment is limited to studies either showing side effects in mouse ears and rat brains or only treating rat brain tumors. Effects of minibeams to various, more complex tissues such as lung, liver, heart, muscles or nervous tissue are not yet known. Furthermore, the effectiveness of pMBRT in various tumor types has also not been studied until now. Further research on these two topics is of urgent need to fully foresee the possible benefits and limits of this new type of therapy and to be able to bring it into clinics. The two main research facilities conducting pMBRT experiments in Germany and France are very specialized for the experiments on mouse ears (Germany) and rat brain (France) [32]. To be able to study various tumor types and the effects on different kinds of healthy tissue within a systematic roadmap to translate this method into clinical treatments, we believe it is necessary to build a dedicated preclinical pMBRT facility, which has also been suggested by Meyer et al. [16].

In this article, we will discuss the technical parameters which are of crucial importance for developing a preclinical small animal irradiation facility that is feasible to answer the most important questions in pMBRT. The minibeam sizes, the dose rate at the target and the energy range play an important role and are depending on the used technology related to each other. Based on existing standard proton therapy technology and methods, it will be evaluated which accelerator type and beam application method provides the best opportunities for a preclinical proton minibeam facility. The gained knowledge and the experience from the field of X-ray MRT and proton minibeam research will be reassessed for its applicability to the powerful and versatile preclinical testing facility. It will be discussed whether radio-frequency linear accelerators (RF-LINACs), which are currently being developed for standard proton therapy, can be a promising approach to fulfill the technical requirements. We will further present our idea of a research facility, capable of fully covering the preclinical experiments which are essential to prove the concept of pMBRT right and be able to bring it into clinic. This will be accompanied by our thoughts on which questions have to be answered and which kinds of tumors are best suited to be treated by pMBRT and should, therefore, be included in preclinical studies.

2 PHYSICS REQUIREMENTS FOR PROTON MINIBEAM RADIOTHERAPY

In the following, we will review and discuss the necessary parameters that are needed for designing a preclinical proton

minibeam facility. This is based on the experience gained from the research performed on pMBRT so far as well as on the technological progress made in standard PTS serving in today's clinical treatment centers.

2.1 Beam Application in Standard Proton Therapy

Concerning the acceleration of the protons to clinically relevant energies two types of accelerators have become established in the market of PTS: cyclotrons and synchrotrons. Synchrotrons are typically the first choice if a therapy center wants to use heavier ions such as carbon for therapeutic purposes in addition to protons. In almost all other cases where only protons are applied, cyclotrons are state-of-the-art. According to the PTCOG website [45], more than 95 particle therapy centers are reported to be in clinical operation at the beginning of 2020. In Europe, more than 80% of them are equipped with cyclotrons and less than 20% with synchrotrons [45].

Once accelerated, the particles are guided by magnetic fields and transported to the treatment rooms. Therein, a proton beam is shaped and measured by several devices in the nozzle, so that it can finally be applied to the target in the isocenter. Passive scattering for generating a homogeneous dose distribution in a field was the technology used in the early days of standard proton therapy [46]. For delivering a better conformal dose to the shape of the tumor, patient-specific apertures made from brass were used, while the energy was varied by range modulator wheels [47]. The PSI started to develop a new and more sophisticated beam application method called spot scanning or pencil beam scanning [8, 48, 49]. Thereby, the proton beam is magnetically focused to form a spot in the isocenter with a lateral Gaussian distribution and a size around 4–8 mm, which is increasing with decreasing beam energy [50, 51]. This pencil beam is deflected with fast dipole magnets in two perpendicular directions (x- and y-direction), producing a dose pattern that corresponds to the shape of the tumor in the beam's eye view [52]. Compared to the simpler method of passive scattering, the spot scanning approach is able to achieve a better three dimensional dose conformity to the shape of the tumor, sparing additional healthy tissue from undesired dose [8, 53–55]. Moreover, handling of heavy patient-specific apertures at the beam nozzle–in the case of the passive scattering technology–is eliminated, saving a lot of time and costs in the treatment routine. Furthermore, a potential source of failure by using the wrong aperture is eliminated. As a consequence, almost 100% of the new PTS installations nowadays rely on the pencil beam scanning technology [45].

2.2 Minibeam Irradiation Methods – Collimation Versus Focusing

Originally, in the GRID X-ray therapy, standard metal grids with a few millimeter thickness were used that have been directly attached to the skin of the patient to laterally shape the beam in millimeter dimensions [15]. For X-ray planar microbeams and submillimeter minibeams in the 20–500 keV regime, multi-slit collimators have been manufactured with beam widths in the order of 25–75 μm or up to 0.7 mm [17, 56, 57].

When moving from X-rays to protons in early 2010s it was clear that μm-sized beams would not be needed since protons spread in tissue quickly to several 100 μm. However, in order to obtain submillimeter proton beams, the continuation of using collimators to form the proton minibeams seemed to be the logic consequence. Although proton pencil beams were available in several PT-systems the minimum sizes of a Gaussian shaped proton beam were several millimeters (σ). This was approx. one order of magnitude too large for spatial fractionation as considered in pMBRT. Therefore, the research groups actively working in the field of MRT needed to reassess the topic of beam collimation completely. In the case of clinical proton therapy, several centimeters thick metal collimators are required to safely stop the protons with therapy relevant energies. Extensive simulations were performed to optimize several parameters like material and thickness for the collimator [36, 58]. Manufacturing slits or holes of a few hundred μm width or diameter in collimators with several centimeters thickness is very challenging [51]. In complex Monte Carlo-simulations the characteristic parameters – slit width and center-to-center distance – and its influence on the dose distribution in the target were investigated [51, 59, 60]. Peucelle et al. manufactured collimators for pMBRT applications and tested them at an existing proton therapy facility [60]. They used a proton beam of 100 MeV penetrating a multislit collimator with 400 μm wide slits and a thickness of 50 mm to generate a planar minibeam. In 1 cm depth of tissue they measured a beam width of 1.1 ± 0.05 mm (fwhm) and a PVDR value of about 6.5 [60]. While all above mentioned studies investigated planar collimator designs, the following works analyzed collimators generating mesh- or grid-like minibeam patterns [44, 61, 62].

In most of these studies maximizing of the PVDR in the tissue proximal to the tumor was the major goal. However, large PVDR ratios cannot be produced either in planar minibeam cases and even worse in pencil beam minibeam cases due to scattering of the protons at the walls of the channels and penetrating portions at the collimator edges. Although PVDRs are not much larger than 15 at the entrance to the patient and decrease quickly, Prezado et al. showed that it is possible to adapt a clinical proton therapy facility for successfully performing preclinical pMBRT experiments [22, 24, 42] via using collimators with a planar multislit design. In a recent work from Lansonneur et al. a 6.5 cm brass collimator is used for a first theoretical study on clinical relevant proton minibeam treatment plans [59].

On the other hand, protons being charged particles leave the option of being focused to beam spots or lines by electromagnetic lenses which is not easily done with X-rays. This method has the potential to form minibeams with PVDRs of 100–10,000 [31, 63, 64]. The SNAKE group began simultaneously but independently from the group of Prezado to perform preclinical experiments in pMBRT, but utilizing focused 20 MeV proton beams. Instead of using a clinical PTS they utilized a proton microbeam facility and applied focused submillimeter proton pencil beams in a scanning mode to mice ears. With this method a matrix of 4×4 spots spread to Gaussian-like spot sizes of 0.09 mm (σ) or larger have

been applied [31]. A recent work of Schneider et al. extends this idea to larger beam energies presenting extensive simulations of magnetically focused proton minibeams at a clinical proton center at the clinically relevant energies and proposes an adapted and optimized nozzle system [63]. Simulations result in PVDR values up to 1,000 at the entrance of the target.

In the following, several advantages and disadvantages of both methods for producing proton minibeams based on recent research in the field of pMBRT are presented:

(1) Collimation of the proton beam is a passive beam shaping method that unavoidably leads to a large decrease of the beam current at the target. This is independent whether the collimator is illuminated completely by a broad homogeneous dose profile or is scanned by a pencil beam scanning over the entire area of slits. When considering a ratio of irradiated to non-irradiated area of 1 : 100 as already performed in preclinical experiments using a magnetically focused pencil minibeam [31, 39, 65], the beam current at the target would be reduced at least by a factor of 100 when using a collimator. If the beam current upstream of the collimator cannot be increased, the application would take at least 100 times longer for delivering the same dose to the tumor compared to focused pencil minibeams. Even when considering planar minibeams, as shown in a recent study, the use of a multislit collimator results in a huge reduction in dose rate at the Bragg peak maximum of a 123 MeV proton beam from 2.6 Gy/s (broad beam without collimator) to 0.12 Gy/s (multislit) or even 0.09 Gy/s (SOBP condition) [51].
(2) The scattering of the proton beam at the edges of the slits (or holes) leads to enhanced lateral spreading of the proton beam adding to an unavoidable beam halo that enhances the valley dose [51, 66]. Thus, the PVDR is much lower in collimated minibeam systems compared to magnetically focused minibeams. The preclinical experiments from Sammer et al. revealed measured PVDR values larger than 540:1 for the smallest spot size used in mouse ear experiments [31]. Schneider et al. concluded that the dose simulations showed PVDR >50 in all investigated focused proton minibeam cases [63]. According to their work this is at least a factor of three more than feasible with mechanical collimators. Additionally, corresponding to the high aspect ratio, e.g., 0.4 mm (opening) to 65 mm (thickness), the slit geometry works as a divergence aperture. It cuts parts of the beam due to its intrinsic divergence. DeMarzi et al. [51] simulated this effect and showed that an 0.1° divergent collimator can theoretically mitigate this issue. However, the production and the alignment of divergent collimators to the beam would be a challenge in practical use.
(3) Preclinical simulations showed evidence that circular minibeam spots are superior to planar beams when irradiating from one side [67]. However, initial beam currents are even more reduced (quadratic reduction) when small bore holes in a grid pattern are considered compared to slits. Both geometries are acting as a collimation tool. Simulations using grids with submillimeter sized holes like $0.6 \times 0.6\ mm^2$ or even $0.05 \times 0.05\ mm^2$ indicate that not only the beam current is reduced but also the proton depth dose distribution along the beam axis is severely distorted. Martínez-Rovira et al. conclude a strong reduction in range of 105 MeV protons with these small grid sizes [62].
(4) The use of collimators for blocking high energy protons produces additional radiation due to nuclear reactions of the protons in the collimator. This leads to secondary radiation such as gamma-rays and neutrons [63] and lower energy protons, which unavoidably hit the patient. This will give an additional unwanted whole-body neutron dose to the patient [55, 68] and increase the risk of late side effects or secondary tumor induction. However, Guardiola et al. have calculated this unwanted additional biologic neutron dose in the patient to be less than 1% of the total absorbed dose [58]. On the other hand, due to the 4π characteristic of the neutron emission this dose is distributed to the whole patient. Further studies, e.g., using mesh-shaped pinhole instead of multislit collimators and performing measurements of the neutron doses would be helpful to assess the associated risks.
(5) There is a high effort for modeling the nozzle to simulate the correct depth dose distribution downstream of the interaction with the collimator. Especially the interaction at the edges of the slits has a considerable impact on the valley doses [51]. Moreover, experiments and simulations revealed that the lateral dose distribution downstream from the collimator is strongly dependent on the length of the air-gap between the collimator and the target [58]. All effects have to be modeled and implemented thoroughly in a treatment planning system for calculating the correct dose deposition in the target [69]. A recent study from Lansonneur et al. performed first theoretic investigations of therapy treatment plans with collimated minibeams and developed therefore a dedicated dose engine on the basis of TOPAS/Geant4 [59].

All of these mentioned issued do either not exist or have only minor implications if a magnetically focused beams are used as minibeam application method. Nevertheless, there are also advantages for using beam collimation:

(6) Placing a collimator in a fixed holder at the nozzle in front of the patient and illuminating it with a broad homogeneous beam is, from a technical point of view, easier to accomplish compared to focusing a hundred MeV proton beam to submillimeter spots or lines and scanning them.
(7) The collimator setup requires much less space than a magnetic focusing unit for pencil minibeams and can, therefore, be more easily integrated into rotating gantry setups at a standard PTS as demonstrated by DeMarzi et al. However, one suggestion to integrate a magnetically focused minibeam setup into a clinical proton gantry has been designed and presented by Schneider et al. [63]. They concluded that the current pencil beam scanning nozzle is not suitable for proton minibeam generation. Though, with a substantial nozzle redesign they proposed that beam spots

with 0.66–1.67 mm (fwhm) are feasible at energies of 100 and 200 MeV. Beam currents are not specified, which makes it difficult to compare the benefit in the achievable dose rates at the target with the case of the collimated beams. Another possible solution for a focusing unit described in **Section 3** has a length of 6 m [64]. This is too long to be integrated in a gantry nozzle, but an integration in a fixed beam nozzle of a standard PTS seems to be possible.

This study has the primary goal to evaluate the best suited technology for building a dedicated preclinical irradiation facility for proton minibeam application. To sum up the discussion so far, we conclude that for this purpose magnetically focused pencil minibeams are superior for the following reasons. This application method can provide the largest PVDR values and has therefore the highest potential for sparing healthy tissue. Especially in the testing and evaluation phase of preclinical experiments focused and scanned minibeams have a huge flexibility in producing different beam sizes, patterns and shapes as well as seamlessly variable ctc distances, and the resulting dose distributions can be modeled faster and easier. Furthermore, focusing and scanning minibeams is the only irradiation method feasible of providing intensity-modulated radiation therapy in all three dimensions [63]. Additionally, they ensure the lowest possible secondary radiation contribution. Last but not least, compared to collimation the focused minibeams offer the highest possible dose rates at the target. In particular the latter topic is an ongoing trend in the radiation oncology community for three reasons: the mitigation of moving targets [70–73], the exploration of hypofractionation [74–76] and the potential of reduced normal tissue toxicity due to the FLASH-effect at ultra-high dose rate [32, 77]. The topic of dose rate i.e. beam current will be elaborated in more detail in the next section. The preference for focused and scanned minibeams is supported also by other researchers in the field [16, 63]. Nevertheless, the technical layout of the nozzle in a preclinical facility should have the possibility to implement a collimator as well, for further evaluation of the individual advantages of both application methods.

In the process of the transition from preclinical experiments with tiny targets to clinical patient treatments with large tumors, the question of the best fitted beam application method probably has to be reassessed. Once the technical and bio-medical parameters are investigated more in-depth, it might be found out that the collimation method is a reasonable alternative for certain indications. On the other hand, the acceptance in the proton therapy community for going back to passive beam application technology with all its listed drawbacks might be very low. As nowadays proton pencil beam scanning is the state-of-the-art method in standard proton therapy the step forward to using submillimeter beams for spatial fractionation to spare healthy tissue seems feasible. The current requirements on scanning velocity, position accuracy and beam deflection are almost equal to those needed for pMBRT. Finally, the choice may also partly depend on the effort to integrate a minibeam focusing and scanning unit into a PTS nozzle, e.g., as suggested by Schneider and co-workers [63]. Another approach is based on a completely different accelerator technology [64], as used today for proton therapy, and will be discussed further in this work.

2.3 Beam Parameters for a Preclinical Facility

For the assessment of a suitable accelerator technology for producing proton minibeams within the scope of a preclinical irradiation facility, the relevant technical parameters have to be defined in a first step. These are the beam energy range, proton beam current (i.e., dose rate) at the target and beam spot size.

Considering beam energy, the existing proton therapy centers were reevaluated. The proton beam energy needed for patient treatment in clinics is typically defined to range between 70 and 230 MeV [46], sometimes up to 250 MeV [78], leading to projected ranges of protons in water between 4.1 and 33 cm [79] in water equivalent. However, for preclinical experiments with small animals such as mice or rats the energies have to be scaled down according to the animals' size. A maximum energy of 70 MeV protons would be acceptable in a first step, as the bodies of these animals can be penetrated using this energy. But it has to be considered that in the case of small animal irradiation it is crucial to decrease the energy down to approximately 35 MeV (corresponding to a range in water of 1.2 cm [79]) in best case without the use of a range shifter. Otherwise the propagation of the minibeam size in dependence of the depth in the tissue will be substantially influenced due to the additional lateral straggling in the range shifter material.

The required beam current at the isocenter was originally determined by the maximum time tolerated for irradiating a tumor with one fraction of the dose. In this case, a general accepted rule has been established in particle therapy, that the irradiation of a tumor with a dose of 2 Gy should not last longer than 1 min [46]. In the passive beam application mode with double scattering the beam current at the target is reduced by a factor of up to five [46]. In the case of pencil beam scanning typically nearly 100% of the beam that reaches the nozzle is transported to the target. The back-calculation from a required dose rate to the necessary beam current at the nozzle depends on different additional factors such as beam diameter, scanning velocity and the time required for switching the beam energy. Thus, the application time strongly depends on the tumor volume. In the proton therapy community, an average beam current of 1 nA or a few nA at the target has been established to fulfill the mentioned dose application requirement for normal tumor volumes as used in classical X-ray fractionation schemes [46, 53, 80]. Therefore, we conclude that 1 nA proton beam current at the target should be considered as a lower limit for a preclinical as well as clinical facility.

Of course, when performing preclinical experiments, one typically deals with small tumor sizes. On the other hand, most of the small animal experiments have been conducted in single dose fractionation schemes (hypofractionation) with doses in the range of 25–60 Gy. In addition, heavily discussed challenges in radiotherapy like moving targets as well as

modern therapy approaches in particular FLASH therapy require beam currents that are orders of magnitudes higher. For using the advantages of the FLASH effect, a dose rate of at least 40 Gy/s is necessary [77]. Looking at dose rates as specified by vendors for standard PTSs with pencil beam mode one finds values of 100 Gy/min (corresponding to 1.7 Gy/s) [81], which is still a factor of 23 below the lower limit set by Favaudon et al. [77]. It is certainly favorable for a preclinical facility to be able to vary the beam current over many orders of magnitude.

The specification of the required beam spot sizes for minibeam applications can for obvious reasons not be derived from standard proton therapy. The question of an optimal minibeam spot size of pencil minibeams has been addressed in two preclinical experiments [31, 40]. Besides experimental data, Sammer et al. also simulated the effects of pMBRT using dose profiles and corresponding cell survival using parameters α and β from LQ model provided by the PIDE platform [31]. Here beam spots and σ/ctc values are different to the measured ones. We think this is due to possible limitations regarding the choice of cell line and the corresponding α and β parameters. We therefore refer only to the measured beam sizes and σ/ctc here. The first experiment used single spot irradiation of mouse ears with beam sizes varying from 0.5 to 6 mm (fwhm) using X-rays at a small animal radiation research platform [40], which have comparable biological effects as proton irradiation, as shown before [39]. The smallest beam sizes of single pencil beam spots (0.5 and 1 mm diameter of pencil X-ray beams) showed no side effects, while for bigger beam sizes starting from 2 mm, side effects were increasing linearly with increasing beam sizes [40]. This result of the *in vivo* mouse ear study defines an upper limit of single spot irradiation with no side effects in the outermost tissues where the beams have not widened much. Another experiment was performed applying 20 MeV proton beam spots in a 4×4 matrix of 1.8 mm spacing at the ion microprobe SNAKE [31]. In this study the size of the Gaussian-shaped spots varied between 0.224 mm fwhm ($\sigma = 0.095$ mm) and 2.075 mm fwhm ($\sigma = 0.883$ mm). The experiment showed in both examined end points – maximum ear thickness and scoring of desquamation and erythema – the smaller the beam size the better the tissue has been spared, and the fewer side effects have shown up. The smallest spot size ($\sigma = 0.095$ mm) led to almost no side effects and therefore showed a considerable reduction compared to the second smallest ($\sigma = 0.2$ mm). Consequently, the experimental part of this study requests a beam size of $\sigma < 0.1$ mm for side effect free treatment in the superficial tissues of small animals. Slightly larger beam spot sizes might be acceptable when larger ctc's are applied in the clinics, which show no side effects. Whether these size limits will be the same in other organs or in human tissue is to be addressed in further experiments when considering pMBRT. But beam sizes in the range of σ~0.1 mm are requested in a preclinical facility to serve all necessary parameters for radiobiological studies in small animals.

In the case of clinical radiotherapy, the dose needed for tumor control cannot be applied in a single fraction in most of the cases. Therefore, fractionated therapy schemes are standard in conventional radio-oncology. Considering the topic in pMBRT, performing (temporal) fractionated therapy adds another complex parameter in the case of applying submillimeter beams on a day-to-day basis. This issue was already addressed in another preclinical study within the mouse ear model [65]. Here the authors wanted to investigate whether in each (temporal) fraction the very same beam spot locations have to be hit or if the exact spot position on the skin in each fraction is irrelevant. Again, the 4×4 beam geometry was applied using beams with a σ of 0.222 mm to the mouse ear model. The irradiation was performed in four fractions with 30 Gy each. The results revealed that the group where each spot was hit repeatedly at the same position within an accuracy of ~0.5 σ (in this case corresponding to ≈0.1 mm accuracy) showed substantially less acute side effects compared to the irradiation where in each fraction deliberately different regions were hit and also compared to the positive control irradiation. In total, in a future preclinical facility, similar studies on optimum beam sizes and on the combination of spatial and temporal fractionation requires beam sizes in the range of σ~0.1 mm and also an imaging and repositioning accuracy of 0.1 mm at proton energies of up to 70 MeV.

2.4 Achieving the Requirements

2.4.1 Review of Facilities in Operation

Up to now, the two European groups leading the field of preclinical pMBRT research used existing facilities and experimental setups with appropriate adaption to perform the first irradiation experiments by proton minibeams on small animals. However, both attempts are limited with respect to the important technical parameters discussed in the previous section. In the case of SNAKE, the beam sizes are well below the 0.1 mm limit and adjustable to wider beam spots by either beam scanning of a 1 μm focused beam or by passive beam spreading within a thin aluminum sheet. In addition, it has proven to deliver dose rates in a wide range from 0.01 Gy/s to about 1,000 Gy/s. But the proton energy is too low, as the tandem Van-de-Graaff accelerator, at which SNAKE is installed, delivers protons only up to an energy of about 25 MeV [82]. This corresponds to a water equivalent range of 0.64 cm [79] and thus is not sufficient for the treatment of tumors in deeper organs in mice or rats.

The French group has chosen another approach by using an existing clinical proton therapy facility based on a cyclotron accelerator at the Institute Curie-Centre de Protontherapie d'Orsay for first preclinical pMBRT experiments [22, 24, 41]. This strategy makes sense for two reasons: First, this solution allows direct access to an existing clinical system, with the opportunity to use the whole infrastructure of a clinical institute and a certified medical device. Second, it would certainly help gaining acceptance in the community if existing clinical treatment facilities can use their PTS with a possible technical upgrade also for pMBRT and thereby spread the new treatment modality widely. As mentioned above, about 80% of the PTS in Europe use cyclotrons.

Prezado et al. have already demonstrated that normal rat brains can be irradiated with planar proton minibeams produced through a collimator. A PVDR ~10 was obtained with all drawbacks of creating minibeams by collimation as discussed above [60]. However, they could show reduced side

effects in the brain compared to homogeneous irradiation. This study has been performed at 100 MeV leading to a shoot through the head of the rat, which is reasonable when only studying side effects in normal tissue. For delivering treatment doses to tumor tissue in small animals, proton energies at and below 70 MeV are needed. This ensures the maximum range of the protons is lower than the size of the animal and a tumor can be treated with full use of the Bragg peak. This can either be achieved by degrading the energy of protons coming from a clinical accelerator or by using an especially designed accelerator facility. Advantages and disadvantages of both methods are described below.

The lowest possible energy, without additional range shifters, at clinical cyclotron facilities is typically 70 MeV [46, 83]. This low energy limit of therapy cyclotrons originates from the process of energy variation and the requirement for a certain beam current at the isocenter. These cyclotrons extract the proton beam at a fixed maximum energy of about 230 MeV at maximum proton beam currents between 300 and 800 nA [78]. The emittance of the extracted beam is in the order of 5 π mm mrad [84] to 10 π mm mrad (root mean square, unnormalized) [85]. For achieving the clinically relevant energies the beam is decelerated by a degrader unit consisting of carbon wedges that are inserted in the beam path. This process completely destroys the phase space of the beam in the transverse and longitudinal dimension [86]. For transporting the beam further to the isocenter, it must be drastically cut by apertures to stay within the acceptance of the beam transport system (transverse phase space). Furthermore, an achromatic section has to be added to cut the broadened energy distribution, keeping the energy spread below a certain limit (dE/E ± 0.7%) [83] so that the Bragg peak is not smeared out too much compared to a monoenergetic beam. This is assuring a reasonable range accuracy of the proton beam within ±1 mm [85]. Both destructive beam-shaping methods lead to the fact that the transmission of the protons through the energy selection system (ESS) drops rapidly with decreasing energy. Already at about 200 MeV, the transmission is below 10%, at 70 MeV it is below 0.2% [80, 84]. Together with the maximum beam current at the extraction of the cyclotron this results in maximum beam currents of 1–2 nA at the isocenter for 70 MeV protons [78, 80]. Due to this effect, the lower limit of the proton beam current is already reached and there is no more space for further cutting the beam.

For translating the beam current into a dose rate the study of DeMarzi et al. is helpful [51]. Although they do not specify the beam current at the nozzle, it can be expected that it is in the order of a few nanoampere due to the transmission at a proton energy of 123 MeV. DeMarzi has measured a dose rate of 2.6 Gy/s at the target generated at the Bragg peak of a 123 MeV in the middle of proton pencil beam field of 5×5 cm^2. Using the multislit collimator for minibeam widths of 1.1 mm at the depth of a rat brain, the dose rate was reduced to 0.12 Gy/s (multislit) or even 0.09 Gy/s (for SOBP condition). In consequence, the dose rate using a multislit collimator is reduced by at least a factor of 23. For reaching the lowest dose rate where FLASH effects are expected (40 Gy/s) an enhancement factor of more than 300 is necessary. Going to energies of 70 MeV and below the situation worsens due to the rapid decline in transmission.

The question is whether focusing the beam to minibeams in this scenario is an option for keeping the dose rate at least at the level of a few Gy/s and to obtain large PVDR ratios. The smallest beam size achievable at standard cyclotron-based PTS at the isocenter at an energy of 100 MeV is approximately between 5 mm [87] and 7.5 mm (σ) [69]. A demagnification of the lateral beam size with a magnetically focusing unit for example from 6 to 0.1 mm (σ) in beam size in one direction requires a demagnification factor of 60. This would imply a ratio of object distance to image distance of 60 : 1. It is unrealistic to achieve this in particular in a gantry nozzle due to three reasons: The total length in a gantry nozzle for a focusing unit is limited to about 3 m. Concerning the high demagnification factor, this would results in a distance of about 5 cm between the last magnet and the focal plane. Neither a strong enough focusing lens exists for this short focal length nor is it possible for animal treatments to have so little room for positioning and other devices such as an exit window. Additionally, one would obtain an inherent increase of the beam divergence by a factor of 60 resulting in lower PVDRs already when entering the tissue.

For further considerations, the parametrization of the Orsay gantry universal pencil beam scanning nozzle as presented by DeMarzi et al. [69] has been used as a starting point for estimation of the beam current in a minibeam resulting from a theoretical magnetic focusing unit, being well aware that there is not enough space for such a setup in a gantry. A beam spot size of 11 mm (σ) at a mean proton energy of 100 MeV and a beam divergence of 3.3 mrad (σ) at the nozzle entrance derived from [69] was used. A 5 m drift distance followed by a triplet of quadrupole magnets was simulated, which creates the focus after 0.6 m drift. The particle tracking code TRAVEL [88] is used to determine the detailed particle distributions at the beam focus for 10^6 protons, Gaussian distributed in the given initial longitudinal and transverse phase space. The resulting particle distribution at the focus was cut in x-y-space with a virtual aperture (radius of 0.3 mm). The transmission of protons (from the 10^6 protons) into this circle is 3.3% for the 100 MeV beam. Thus, the beam has to be cut by apertures to form a proton minibeam of that size without halo. The maximum current obtainable is estimated as follows: A maximum beam current of 800 nA is assumed for common cyclotron types [78]. Due to the degrader it can be expected that the beam current is reduced to 1% for 100 MeV resulting in maximal 8 nA behind the degrader and subsequently 0.27 nA (3.3%) for a spot size 0.3 mm (radius). Beam current might be even less since a lens that accepts the large divergence may be not technically feasible. In addition, the focused minibeam would have a divergence of about 30 mrad that would result in a larger beam spreading behind the beam focus than from multiple scattering. In the case of 70 MeV protons, the beam current would further reduce by a factor of approximately five due to the reduced transmission at the degrader.

In summary, using therapy cyclotrons for achieving very small spot sizes together with a high beam current for achieving high dose rate seems not possible. The situation becomes even worse when going to lower energies as needed for preclinical animal

irradiation, because the lower the energy the lower the available beam current at the target due to the rapidly decreasing transmission trough the ESS. Therefore, we conclude that considering a preclinical irradiation facility for pMBRT research, proton therapy cyclotrons are not well suited because they do not provide the versatility to perform research exploring the entire parameter space for dose rate, minibeam size and energy.

To the authors' knowledge, there is not a single proton therapy facility in operation worldwide that achieves 0.1 mm sized proton pencil spots fulfilling the requirements for energy and beam current as derived in the last chapter.

Nevertheless, it could be possible to use other types of cyclotrons with energies suited for preclinical needs. For instance, cyclotrons that are feasible of producing proton currents up to 500 μA at an output energy of about 70 MeV [89] or sector cyclotrons, also delivering 70 MeV at high beam quality [90]. These cyclotrons could be adapted to meet the requirements. Focusing a minibeam from the high current cyclotron could lead to a radical cropping of the beam by apertures to generate the required emittance but keeping tens of nA in tiny beam spots. As a consequence, a collimation process is needed but could be performed with a radiation shielding positioned far away upstream of the target in order to avoid parasitic irradiation from the large amount of secondary radiation. In 2020, several low energy cyclotrons are in clinical operation for eye tumor treatment. Among these are the cyclotrons in Clatterbridge [91], Nice [92] and Berlin [90] providing maximum energies of 62–68 MeV. For assessing the applicability of using these low energy cyclotrons to provide protons for a preclinical proton minibeam facility, a detailed study has to be conducted, which was beyond of the scope of our consideration here.

2.4.2 Radio-Frequency LINAC Concepts

Instead, a completely different particle accelerator type for PTS came into focus in the past years, since this technology has some unique physical characteristics that are complementary to a cyclotron [93]. Already in 1991, Hamm et al. suggested a compact, low current, normal conducting proton linear accelerator (LINAC) based on 3 GHz side-coupled structures for standard proton therapy [94]. The same technological principle is used in every modern clinical LINAC for X-ray radiotherapy of cancer patients in hospitals around the world. The only fundamental difference is that in this case electrons are accelerated to generate high energy (6–18 MeV) X-rays, enabling these LINACs to be built compact and light-weighted for mounting them on a small rotating gantry [95]. However, for the purpose of proton therapy the LINAC systems are more complex and need different sub-types of linear accelerators in a sequence to bring the energy up to 250 MeV for clinical use.

The existing technology of high current proton LINACs for nuclear physics experiments have been redesigned for the needs of proton therapy, which does not need particle currents in the μA to mA region. Going to much higher radio-frequencies allowed to produce higher electric fields and led to a reduction of the system length [93]. Furthermore, this high frequency enables to design smaller structure sizes allowing drift tube apertures with radii as small as 2–3 mm. The side effect of using normal conducting resonator structures is that only pulses of about 5 μs length can be generated at a maximum repetition rate of approximately 200 Hz [95]. Thus, the mean current obtained is in the range of about 20 nA due to the low duty cycle.

Two groups are currently leading the challenge to build the first clinical PTS made from these RF-LINACs: The TOP-IMPLART project headed by Dr Picardi at ENEA Frascati, Italy [96] and the CERN spin-off company AVO-ADAM with its project LIGHT [97]. Both systems follow the all-LINAC approach. For the first acceleration of the proton beam behind the ion source, a Radio-Frequency Quadrupole unit (RFQ) is used up to energies of about 5 MeV followed by Drift Tube LINACs (DTL) [95]. The second stage of acceleration is performed by a so-called SCDTL (Side-Coupled Drift Tube LINAC) [98], which has been specially designed for standard PTSs. They close the gap between the RFQs for the low beta ($\beta = v/c$) protons ($\beta < 0.06$) and the Coupled Cavity LINACs (CCL) that are becoming efficient at energies around 70 MeV [93, 99]. With the CCL technology, the proton beam can be accelerated to 230 MeV or more for clinical systems. These systems require a length between 25 and 30 m [93].

This design promises to obtain any kind of proton energy at about the same beam current but better beam quality than degraded cyclotron beams. Thus, also protons with 35–70 MeV are expected with high beam quality and tens of nanoampere beam currents being sufficient for preclinical pMBRT therapy. The calculated transverse root mean square (rms) emittances for these systems are ≈0.5 π mm mrad (unnormalized) at 70 MeV (i.e., 0.2 π mm mrad normalized) [96] which is at 70 MeV at least a factor of 10 smaller than a beam extracted from a therapy cyclotron after the ESS unit with 16–36 π mm mrad [80]. The feature of having an exceedingly small transverse emittance makes the linear accelerators a promising candidate for producing proton minibeams with high brilliance and very high dose rates within single 5 μs pulses.

For analyzing the potential of a 3 GHz LINAC in detail, a 3D-simulation study has been performed in collaboration with AVO-ADAM to calculate the transport and focusing of the proton beam for generating a minibeam at the target [64]. In this collaboration, extensive Monte Carlo beam transport simulations were performed. As an alternative to the all-LINAC approach, a 16 MeV proton beam coming from a tandem accelerator was injected into the third section of the LINAC system as a post-accelerator to achieve a proton energy of 70 MeV. Details of this setup will be presented in section 3. Simulations showed focusing the beam after the LINAC via a magnetic quadrupole triplet is feasible of delivering a mean current of 18 nA to a target in a square of 0.1×0.1 mm at a repetition rate of 200 Hz [64].

It can be concluded that the energy, the beam currents and the spot size required for minibeam applications in a preclinical facility can be fulfilled with this technology. Besides these crucial parameters, the LINAC technology has the potential to provide additional features that are of interest for standard proton therapy but can be advantageous even for pMBRT. In contrast to cyclotron systems, a fast and continuous energy modulation

can be obtained by switching off the power of LINAC modules and tuning the power of the last LINAC module, without the use of degrading material. This feature together with high dose rates and spot scanning opens the possibility of fast dose repainting in all three dimensions. Additionally, this electronic energy variation enables to reduce remarkable amounts of radiation shielding and in consequence save costs [96].

While the beam originating from a therapy cyclotron is quasi-continuous, the LINAC structure accelerates the beam in bunches of a few μs due to its inherent duty-cycle with a mean beam current in the order of about 20 nA. Considering a bunch width of 5 μs and a maximum repetition rate of 200 Hz the beam current in one bunch is expected to be about 20 μA (1,000 times higher). In the case of small irradiation targets where only one or a few single minibeam spots are required, the effective dose rate can be orders of magnitude higher than the mean current indicates. An exploitation of this unique feature of LINACs can be used for combining pMBRT with FLASH therapy approaches. Furthermore, the omission of a beam degrading unit keeps the phase space conserved and simplifies the generation of proton minibeams. Finally, a further unique feature of LINACs is their modular structure allowing a sequenced expansion of maximum proton energy by simply adding additional structures in a later stage of the preclinical tests, e.g., for the irradiation of larger animals or even to convert the preclinical facility into a clinical one.

The two above-mentioned systems are following the roadmap on their way to manufacture a clinical standard PTS for a pencil beam scanning therapy using an all-LINAC approach. The prototype machine of TOP-IMPLART has successfully accelerated protons up to 35 MeV at the ENEA institute [100]. AVO-ADAM produced a proton beam of 52 MeV at their test site at CERN in autumn 2018 [101]. Especially the company AVO-ADAM is already very close to the energy of 70 MeV for the first phase of a preclinical irradiation facility. Nevertheless, the target energy of 70 MeV is not yet reached. Therefore, a full characterization and validation of the calculated beam parameters (emittance, beam current) is still missing. However, a measurement of the emittance at 7.5 MeV (after the first SCDTL module) showed a value $\approx 0.1\pi$ mm mrad (normalized; rms) and a peak beam pulse current of 39 μA [97].

3 DESIGN IDEA OF A RESEARCH FACILITY FOR PRECLINICAL EXPERIMENTS

Following the technology assessment described above, the RF-LINAC system seems to open the largest possibilities for conducting preclinical research with pMBRT. In early 2020, the LIGHT and the TOP-IMPLART system are not accessible for external users for performing preclinical experiments with small animals, since they are used for commissioning and validation.

However, we are convinced that it is the right time to enter the next step of preclinical pMBRT research. Concerning the technological aspects, we have the goal to minimize costs and time to operation of a preclinical facility. Therefore, we propose using an accelerator at an operating laboratory and implementing copies of a certain number of LINAC modules as a post-accelerator for reaching the desired preclinical energies. Moreover, there is another striking argument for this combined solution. Due to the complexity and the administrative effort of performing preclinical tests with living animals, it is very likely that the available beam time of dedicated stand-alone preclinical setup cannot be used for research at full capacity. We suggest the usage of an existing high energy tandem accelerator and installing a LINAC at one of its high-energy beam lines. The total beam time can be shared between the preclinical experiments and other multidisciplinary research activities, such as material analysis and modification, fundamental radiobiology research or high resolution accelerator mass spectroscopy [82]. This approach would also distribute the running costs of such a facility among several other research partners. In the following, we want to propose a setup for such a preclinical pMBRT irradiation facility. This will be discussed with respect to technological and biomedical aspects.

3.1 The Tandem-LINAC Setup

Regarding the arguments listed above, a tandem Van-de-Graaff machine was chosen as an injector for the LINAC-structures for performing an in-depth study of the beam transport for two reasons. First, the brilliance of a tandem beam when using a multi-cusp ion-source [102] is well-suited to the acceptance of a LINAC. Second, the sharp energy distribution of the tandem beam after the 90° analyzing magnet can be utilized for matching the direct current (DC) beam coming from the tandem to the longitudinal phase acceptance of a 3 GHz LINAC and gaining transmission. In the following, the results from a study performed by Mayerhofer et al. are summarized [64]: The injection energy of 16 MeV was set for two reasons. First, this spares additional costs, because two SCDTL modules compared to the all-LINAC solution can be skipped. Second, starting at 16 MeV instead of 5 MeV (all-LINAC solution) the power efficiency and the effective field gradient (i.e., gained energy per unit length) of the SCDTL is already enhanced [96]. The 6-dimensional phase space of the proton beam coming from the "pre"-accelerator have been measured at the Munich 14 MV tandem Van-de-Graaff accelerator. These data have been used as a realistic input for the beam transport simulations through the LINAC structures and the focusing unit to produce minibeams [64]. For the acceleration from 16 to 70 MeV in total two SCDTL and four CCL (Coupled Cavity LINAC) modules are foreseen. The total setup is shown in **Figure 1**.

For adapting the 6-dimensional phase space of the DC proton beam coming from the tandem to the acceptance of the LINAC, a buncher unit and a quadrupole quartet is needed matching the longitudinal phase space as well as the transverse phase space, respectively. Details about the optimization of this matching process can be taken from Mayerhofer et al. [64]. Simulations show that these two matching devices increase the total transmission of the proton beam coming from the tandem through the LINAC up to 49%. This means that every second proton from the tandem is accelerated to 70 MeV and can be used for experiments. Although it is difficult to compare, in the case of

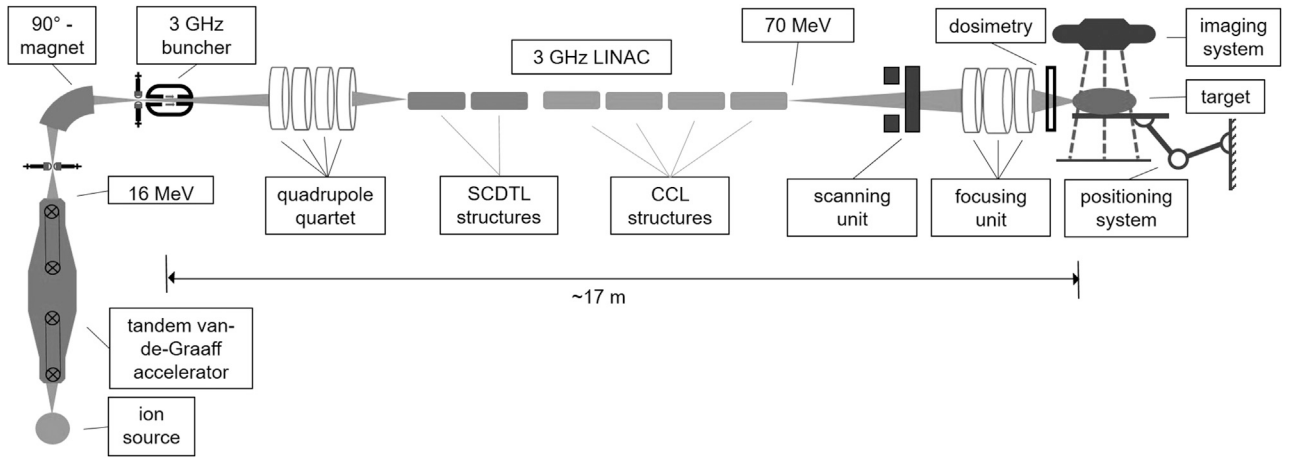

FIGURE 1 | Scheme of the proposed tandem-LINAC system including matching unit, focusing stage as well as an imaging and target positioning system.

a proton therapy cyclotron only one out of 500 accelerated protons reaches the target if an energy of 70 MeV is selected. All the others are stopped in the ESS producing secondary radiation that needs to be shielded with meter-thick walls.

As discussed in **Section 2**, we are convinced that the generation of the smallest possible proton minibeams with highest possible PVDR and at high dose rate can only be realized by focusing rather than by collimation. Thus, after extraction of the 70 MeV beam, a focusing unit has been foreseen. This ion-optical lens system demagnifies the beam to the desired minibeam spot size. Simulations showed that an electromagnetic quadrupole-triplet configuration is feasible of producing proton minibeams in a square of 0.1 mm by 0.1 mm with more than 90% of the LINAC beam, meaning an overall transmission of the tandem beam of 49% [64]. Based on measurements of the proton beam brilliance as delivered at the Munich tandem accelerator, the calculated beam current delivered in this area at the focal plane (under vacuum) is 18 nA at a repetition rate of 200 Hz. The total length of the focusing unit after the LINAC is about 6 m, therein the distance from the last quadrupole to the focal plane is designed to be about 0.6 m [64], leaving space for dose and position detection as well as an vacuum window. A two-dimensional scanning system is planned upstream of the focusing triplet. This system is still in the design phase, but a total deviation of 7 and 9 cm seems feasible in x- and y-direction, respectively. The last part of the nozzle directly before the target consists of a vacuum window and a detector measuring dose and beam position. In the case of minibeams with submillimeter sizes the propagation of the protons in air should be minimized as much as possible for keeping beam size as small as possible and PVDR values high. A detailed planning of the monitor detectors is the scope of an extra study.

We expect that similar beam parameters can be achieved when using other accelerator types as injectors for the 3 GHz LINAC proposed above. Besides using the high energy tandem accelerator, also other options exist for boosting the protons to preclinically relevant energies. As mentioned, the lowest possible proton energy for injecting into an SCDTL module is 5 MeV. This energy could even be delivered by a single ended or a smaller tandem Van-de-Graaff machine. Furthermore, in previous studies so-called "Cyclinac" solutions were already investigated for standard proton therapy. In these proposals a cyclotron was favored injecting the beam into a LINAC e.g., at energies of 24 or 62 MeV [103, 104]. Both options open additional possibilities for adapting RF-LINAC approaches for the use at existing facilities. It could be worth investigating some of these suggestions for their potential to produce proton minibeams for preclinical or even clinical applications.

3.2 End Station for Small Animal Irradiation

The configuration of the end station for the preclinical irradiation experiments has not been performed in detail, yet. However, basic considerations are described based on the experience of the small animal irradiations conducted so far. Although single fraction experiments are easier to accomplish in terms of positioning accuracy, a preclinical pMBRT system should be capable of conducting multi-fraction experiments. At the SNAKE setup a positioning system was installed for performing mouse ear irradiations. The day-to-day animal positioning during the experiment with a fractionated irradiation relied on the imaging of the blood vessels in the ear with a camera at ambient light. Using cross correlation of the reference image (day 1) and the actual image (day 2–4) the displacement vector was determined by calculation of the x- and y-displacement as well as the corresponding angular displacement (θ). A correction of the angular displacement in z-directions was excluded by animal holder design. The calculated displacement was corrected using a movable stage with motorized x- and y-axis and also a rotation axis in the plane perpendicular to the beam, where the animal holder was mounted. Using this positioning system, a day-to-day (relative) position accuracy of the ears of 0.1 mm was achieved [65].

For treatment of deeper tumors, the imaging of blood vessels via a camera will not be possible. For this kind of experiments, an image-guided system feasible of resolving deeper lying organs, bones, and tissue is necessary. We are in favor of using an existing system such as the SARRP (Xstrahl LTD., Surrey, United Kingdom) that is capable of performing a CT scan of the object to be irradiated. This stand-alone X-ray irradiation platform system already offers an imaging and positioning system for small animals with an accuracy of 0.24 mm [105]. First systems have already been added to particle irradiation facilities, where the SARRP system is adapted to be used also with a beam coming from an exterior accelerator [106, 107]. We are convinced that it is possible to further improve the positioning accuracy of such a system, e.g., by adding a more precise positioning system. However, we think that additional in-depth studies are inevitable to investigate this issue of absolute and relative positioning accuracy together with multi-fractionation treatment schemes, with a focus on the technical side as well as on the bio-medical side.

3.3 Biomedical Aspects

The final goal we are heading for is treating patients with proton minibeams in the near future. The motivation behind this large endeavor is the promising potential of reducing stress for the patient and side effects while keeping or even improving tumor control. Therefore, when thinking on building a dedicated pre-clinical research platform it is crucial to determine which tumor indication can profit most as this in consequence defines the animal models, which must be investigated during the pre-clinical phase.

Looking at particle therapy statistics it is clear that many different kinds of tumors are treated. In the search of suitable tumors which can be considered for pMBRT the following criteria were included. In general, tumors showing bad prognosis and tumors where patients suffer from severe side effects have to be tackled by new therapy options. In these cases, pMBRT might be able to add further benefit in curing the tumor as well as in sparing of normal tissue. Furthermore, one should also consider the economic aspects including possible sponsors and target market, as without financing the barrier for introducing a new therapy method is insurmountable. Therefore, the tumors which are investigated should not only be rare occasions. In the following, a selection of tumors is presented that meet one or more of the mentioned criteria for different reasons.

Pediatric cancer, which gives 10% of all treated tumors in 2014 [45] is quite promising for several reasons. First, the infant tissue is still highly proliferating and therefore prone to severe long-term side effects. As treatment gets more effective and more successful, cured patients have good prognosis and the number of long-term survivors is increasing [108]. With longer lifetime, the probability of developing late side effects or the chance for induction of a secondary cancer is increasing, especially for children as the lifespan is long in this case [109]. Last, geometrical factors also play a role in the side effects occurring in childhood cancer therapy. As the organs and therefore also the organs at risk are much smaller compared to adults, hitting these organs during treatment can have much more effect in infants compared to adults. Furthermore, children are more prone to secondary total body dose. Therefore, it is necessary to deliver effective treatment with less morbidity [110]. pMBRT is decreasing the damage to the healthy tissue as much as possible while keeping tumor control. The sparing effect in this case can be achieved in two ways; the number of healthy cells hit by radiation is decreased and these are mostly exposed to lethal doses and therefore cannot develop long term side effects. In particular, the genetic damage within cells after the first division after proton minibeam irradiation of high PVDR was much reduced as measured by induction of micronuclei [30].

Apart from childhood cancer in total and here in particular brain tumors and other malignancies of the nervous system, which are the second most diagnosed cancers in children [108] and also occur in adults, seem to be a promising target for pMBRT. The major problem in these kinds of cancers is that neurons cannot be reproduced, once dead the function is lost [111]. However, we think that neuronal cells are well suited to be spared using pMBRT. The reason lies in their structure. Neuronal cells can get up to 1 m long [112] with a cell nucleus of only several μm in diameter [113]. The cell nucleus is the sensitive target for radiation as damage to the DNA, which is stored in the nucleus, is the major reason for cell death and secondary malignancies. Therefore, when hitting a composite of neuronal cells with a pMBRT of small size the probability of hitting the nucleus of a single cell is $<<1$, which makes pMBRT advantageous compared to conventional therapy. Additionally, if this potential advantage can be verified using the preclinical setup, neuronal bundles such as the spinal cord are no longer a hyper-sensitive organ at risk. This opens the possibility for treatment of other tumors as also irradiation from the back might get possible.

Two types of tumors, where severe side effects occur in the affected organ itself, could be a promising target for pMBRT: lung cancers such as non-small cell lung cancer (NSCLC) and hepatocellular carcinoma (HCC) in the liver. In NSCLC, severe side effects like pulmonary fibrosis, esophagitis, pneumonitis and bronchial fistulae occur [114]. HCC have an even worse prognosis, as treatment of this kind of tumors can only be successfully performed with particle therapy not with X-rays [115]. But still the treatment is limited to small tumors as severe side effects can occur, since the liver is one of the most radiosensitive organs in the human body [116]. In these two presented examples new therapy schemes, including dose escalation and different angles of incidence, are discussed to increase patient survival, decrease side effects and open the possibility for treatment of bigger tumors and tumors of progressed state. pMBRT with its spatial fractionation scheme is an attractive option to bring radiotherapy to the next stage of controlling these tumors.

Furthermore, not only the radiosensitivity of the affected organ itself can serve as criterion for selection of a suitable tumor type for pMBRT. Also, the location in the body can serve as a deciding factor. We think that especially the treatment of tumors in the abdominal region can benefit from pMBRT. The abdominal organs are quite radiosensitive [116] and sparing those by using minibeams opens the possibility of new

dose and fractionation schemes using alternative angles of incidence.

The journey for pMBRT to a first patient treatment is still long. In our opinion, investigating the effectiveness of pMBRT in treatment of glioblastoma, NSCLC and HCC can be a first step in this direction. Possible studies on pMBRT urgently need to include the investigation of side effects in the affected organs as well as in adjacent organs. Focus should not only lie on acute but also on the late side effects such as cognitive and organ disfunction, fibrosis and secondary cancer. These studies will help to identify further types of cancers which could be treated such as the ones in the abdominal region. Preclinical studies should also fully exploit the feasibility of new therapy schemes using different angles of incidence, hypofractionation and dose escalation.

4 CONCLUSION AND OUTLOOK

In this article we proposed a setup for a preclinical irradiation facility to fully exploit the potential of proton minibeam radiotherapy. This method is an advancement of standard proton therapy, which has already proven in first experiments to spare healthy tissue in the entrance channel by spatial fractionation with proton minibeams at sizes in the range of 0.1 mm. We are convinced that the pMBRT research stands at a turning point, right now. In preclinical experiments performed since 2013, first evidence was found that pMBRT is a promising new approach in radio-oncology. It has the potential of further improving the quality of outcome in cancer treatment of solid tumors. However, the research on important physical parameters and methods as well as research on biomedical aspects is still in its infancy.

We have given an overview of the status and limitations of preclinical experiments performed in mice and rats so far. First, we are convinced that the production of minibeams using focusing is superior compared to collimation and opens a wider range of options for testing with different beam shapes and sizes. Furthermore, when using focusing the beam current can be sustained, whereas collimation is blocking the majority of particles and thus reducing beam current at the patient. At the same time collimation increases secondary radiation due to nuclear interaction of the protons with the collimator material. In addition, the production of collimators for beams of this small size is challenging and only possible when accepting disadvantages such as decreasing the PVDR and inflexibility in the treatment process.

Second, we have discussed the beam parameters, that have to be met by a preclinical irradiation facility, i.e., beam energy, dose rate and beam spot size. Due to the animals' size, the proton energy must allow experiments at and below 70 MeV. The required beam current at the isocenter is defined by the dose rate, which has to be applied to the tumor. We conclude that this should be at least 1-2 nA, as available in standard proton therapy. The available size of the minibeams should be as low as 0.1 mm as shown in preclinical studies to generate the least side effects. The mentioned values for beam current and beam size represent only a lower limit. A powerful preclinical setup should give the opportunity to vary both parameters in a wide range to be able to fully exploit the limitations of pMBRT and evaluating the sweet spots for these parameters for a most efficient treatment and highest possible benefit for the patient. We believe that it shall be feasible to tune the beam current into a domain where analyzing minibeams in combination with the FLASH effect can be studied as well as synergies with hypofractionation can be evaluated. These considerations led to the conclusion that existing therapy cyclotrons are not well suited for such a preclinical facility, since they only fulfill a fraction of these parameter setting and therefore do not offer the full versatility for preclinical research.

We discussed that 3 GHz RF-LINACs, currently developed for standard proton therapy facilities, are expected to meet all requirements for pMBRT and have the potential to serve as a unique and versatile tool for evaluating the benefits in all possible directions. We presented beam transport simulations of this modular acceleration concept that support its performance regarding possible beam currents and small emittances, which enable tiny pencil beams. However, the two currently existing LINAC systems are in the stage of the commissioning of their first prototype for standard proton therapy systems and therefore not open for preclinical research purposes. Nevertheless, the commissioning of these LINACs delivers first promising results and reported acceleration up to 52 MeV.

Therefore, we suggest using an existing Van-de-Graaff tandem accelerator as an injector for a 3 GHz RF-LINAC post-accelerator consisting of two SCDTL and 4 CCL structures providing a beam at 70 MeV. Beam transport simulations showed that focusing the proton beam to 0.1 mm spots is feasible at a proton current of 18 nA. This provides a comparatively cost-efficient solution, where infrastructure and beamtime can be shared with other research activities. The current status of knowledge and technology also allows to think out of the box. The pulsed time structure of the minibeams provided by RF-LINACs provides the opportunity to exploit the FLASH effect in combination with pMBRT. This has the potential to further enhance normal tissue protection and give space for thinking about the opportunity of hypofractionation.

Concerning an end station for small animal irradiation, we think the adaption of a commercially available SARRP beamline is the best option as CT-imaging and animal positioning is already implemented there. But adaptions have still to be done to achieve the required positioning accuracy of 0.1 mm to address all options for reirradiation the same beam spot in multi-fraction experiments.

In the last section we examined the biomedical aspects that have to be considered for a preclinical facility. When starting a project with a large financial investment and a long lead time until realization, it is mandatory to develop clear goals for the research focus. We think that defining tumor types that profit most from using pMBRT compared to standard proton therapy is one of the most important objectives. The definition has to rely on the occurrence of severe acute and late side effects in current radiation treatment, as well as if tumors are untreatable or difficult to treat with current radiotherapy approaches. Not to forget, the frequency of occurrence, as this could help to raise

funding for research and a latter implementation into clinics. Consequently, we conclude that primary attention in the biomedical research at the facility should lie on glioma, NSCLC and HCC. On the other hand, investigation of the potential reduction of side effects on healthy tissue, especially neuronal cells and abdominal organs is of similar importance.

As the final goal is to treat patients, also certification procedures have to be considered already at this early stage of research gaining more and more importance as the process is going on. For example, it is necessary to take into account how the technology can be transferred into clinics and how the implementation can be realized. Furthermore, it has to be checked if and in which parts of the process already existing certification can be adapted to pMBRT, making the process of approval faster and more cost-efficient.

From the technical point of view, the outcome of the preclinical phase will give answers to the definition of the optimal parameters for beam size, beam shape (pencil or planar), the application method (focusing or collimating) and the necessary beam current. Furthermore, new application schemes such as interlacing of beams from different irradiation angles with heterogeneous tumor dose can be investigated by a dedicated preclinical approach. These adaptations could further improve the sparing of the healthy tissue but add a whole new parameter space to the testing phase.

To conclude, in our opinion it is the right time for the implementation of a preclinical irradiation facility for performing further in-depth research programs with this new treatment modality and for understanding its radiobiological mechanisms in different tissues as well as in living animals. Consequently, this research on advantages and limitations will prepare the field of pMBRT for the treatment of the first patient. Taking all this together, proton minibeam radiotherapy is a fascinating area of investigation and a huge step into the future of precision tumor therapy.

AUTHOR CONTRIBUTIONS

GDA, JR, and GDO planned the study, GDA, JR did literature research, SG, MS, and MM contributed the chapters which are in their area of expertize, GDA and JR combined all parts and wrote the body of the paper, GDO, MS, MM, and SG did proofreading.

FUNDING

This study was funded by the DFG cluster of excellence, and the European transnational access program RADIATE.

REFERENCES

1. Baskar R, Lee KA, Yeo R, Yeoh K-W. Cancer and radiation therapy: current advances and future directions. *Int J Med Sci* (2012) **9**(3):193–9. doi:10.7150/ijms.3635.
2. Delaney G, Jacob S, Featherstone C, Barton M. The role of radiotherapy in cancer treatment: estimating optimal utilization from a review of evidence-based clinical guidelines. *Cancer* (2005) **104**(6):1129–37. doi:10.1002/cncr.21324.
3. Barton MB, Jacob S, Shafiq J, Wong K, Thompson SR, Hanna TP, et al. Estimating the demand for radiotherapy from the evidence: a review of changes from 2003 to 2012. *Radiother Oncol* (2014) **112**(1):140–4. doi:10.1016/j.radonc.2014.03.024.
4. Rosenblatt E. *Radiotherapy in cancer care: facing the global challenge* Vienna, Austria: International Atomic Energy Agency (IAEA) (2017) 578 p.
5. Wilson RR. Radiological use of fast protons. *Radiology* (1946) **47**(5):487–91. doi:10.1148/47.5.487.
6. Bortfeld T. An analytical approximation of the Bragg curve for therapeutic proton beams. *Med Phys* (1997) **24**(12):2024–33. doi:10.1118/1.598116.
7. Jones DT, Schreuder AN, Symons JE, de Kock EA, Vernimmen FJ, Stannard CE, et al. Status report of the NAC particle therapy programme. *Strahlenther Onkol* (1999) **175** (Suppl. 2):30–2. doi:10.1007/bf03038883.
8. Pedroni E, Bacher R, Blattmann H, Böhringer T, Coray A, Lomax A, et al. The 200-MeV proton therapy project at the Paul Scherrer Institute: conceptual design and practical realization. *Med Phys* (1995) **22**(1):37–53. doi:10.1118/1.597522.
9. Munzenrider JE, Austin-Seymour M, Blitzer PJ, Gentry R, Goitein M, Gragoudas ES, et al. Proton therapy at harvard. *Strahlentherapie* (1985) **161**(12):756–63.
10. Miller DW. A review of proton beam radiation therapy. *Med Phys* (1995) **22**(11):1943–54. doi:10.1118/1.597435.
11. Slater JM, Miller DW, Archambeau JO. Development of a hospital-based proton beam treatment center. *Int J Radiat Oncol Biol Phys* (1988) **14**(4):761–75. doi:10.1016/0360-3016(88)90099-5.
12. Slater JM, Archambeau JO, Miller DW, Notarus MI, Preston W, Slater JD. The proton treatment center at loma Linda university medical center: rationale for and description of its development. *Int J Radiat Oncol Biol Phys* (1992) **22**(2):383–9. doi:10.1016/0360-3016(92)90058-p.
13. Arcangeli G, Mauro F, Morelli D, Nervi C. Multiple daily fractionation in radiotherapy: biological rationale and preliminary clinical experiences. *Eur J Cancer* (1965) **15**(9):1077–83. doi:10.1016/0014-2964(79)90123-3.
14. Farr JB, Moskvin V, Lukose RC, Tuomanen S, Tsiamas P, Yao W. Development, commissioning, and evaluation of a new intensity modulated minibeam proton therapy system. *Med Phys* (2018) **45**.9: 4227–4237. doi:10.1002/mp.13093.
15. Köhler A. A method of deep roentgen irradiation without injury to the skin. *AJR Am J Roentgen* (1909) **14**(5):141–2. doi:10.1259/arr.1909.0062.
16. Meyer J, Eley J, Schmid TE, Combs SE, Dendale R, Prezado Y. Spatially fractionated proton minibeams. *Br J Radiol* (2019) **92**(1095):20180466. doi:10.1259/bjr.20180466.
17. Laissue JA, Geiser G, Spanne PO, Dilmanian FA, Gebbers J-O, Geiser M, et al. Neuropathology of ablation of rat gliosarcomas and contiguous brain tissues using a microplanar beam of synchrotron-wiggler-generated X rays. *Int J Cancer* (1998) **78**(5):654–60. doi:10.1002/(sici)1097-0215(19981123)78:5<654::aid-ijc21>3.0.co;2-l.
18. Slatkin DN, Dilmanian FA, Spanne PO. *Method for microbeam radiation therapy* Brookhaven Science Associates LLC. U.S. Patent No US5339347A (1992)
19. Anschel DJ, Bravin A, Romanelli P. Microbeam radiosurgery using synchrotron-generated submillimetric beams: a new tool for the treatment of brain disorders. *Neurosurg Rev* (2011) **34**(2):133–42. doi:10.1007/s10143-010-0292-3.
20. Grotzer MA, Schültke E, Bräuer-Krisch E, Laissue JA. Microbeam radiation therapy: clinical perspectives. *Phys Med* (2015) **31**(6):564–7. doi:10.1016/j.ejmp.2015.02.011.
21. Prezado Y, Deman P, Varlet P, Jouvion G, Gil S, Le Clec' H C, et al. Tolerance to dose escalation in minibeam radiation therapy applied to normal rat brain: long-term clinical, radiological and histopathological analysis. *Radiat Res* (2015) **184**(3):314–21. doi:10.1667/rr14018.1.

22. Prezado Y, Jouvion G, Guardiola C, Gonzalez W, Juchaux M, Bergs J, et al. Tumor control in RG2 glioma-bearing rats: a comparison between proton minibeam therapy and standard proton therapy. *Int J Radiat Oncol Biol Phys* (2019) **104**(2):266–71. doi:10.1016/j.ijrobp.2019.01.080.
23. Prezado Y, Sarun S, Gil S, Deman P, Bouchet A, Le Duc G. Increase of lifespan for glioma-bearing rats by using minibeam radiation therapy. *J Synchrotron Radiat* (2012) **19**(Pt 1):60–5. doi:10.1107/s0909049511047042.
24. Prezado Y, Jouvion G, Patriarca A, Nauraye C, Guardiola C, Juchaux M, et al. Proton minibeam radiation therapy widens the therapeutic index for high-grade gliomas. *Sci Rep* (2018) **8**(1):1–10. doi:10.1038/s41598-018-34796-8.
25. Landberg T, Chavaudra J, Dobbs J, Hanks G, Johansson K-A, Möller T, et al. Report 50. *J ICRU* (1993) **os26**(1):NP. doi:10.1093/jicru/os26.1.report50.
26. Bouchet A, Bräuer-Krisch E, Prezado Y, El Atifi M, Rogalev L, Le Clec' HC, et al. Better efficacy of synchrotron spatially microfractionated radiation therapy than uniform radiation therapy on glioma. *Int J Radiat Oncol Biol Phys* (2016) **95**(5):1485–94. doi:10.1016/j.ijrobp.2016.03.040.
27. Bräuer-Krisch E, Serduc R, Siegbahn EA, Le Duc G, Prezado Y, Bravin A, et al. Effects of pulsed, spatially fractionated, microscopic synchrotron X-ray beams on normal and tumoral brain tissue. *Mutat Res* (2010) **704**(1-3):160–6. doi:10.1016/j.mrrev.2009.12.003.
28. Sammer M, Girst S, Dollinger G. Optimizing proton minibeam radiotherapy by interlacing and heterogeneous tumor doLeerraum the basis of calculated clonogenic cell survival. *Sci Rep* (Forthcoming 2020)
29. Prezado Y, Fois GR. Proton-minibeam radiation therapy: a proof of concept. *Med Phys* (2013) **40**(3):031712. doi:10.1118/1.4791648.
30. Zlobinskaya O, Girst S, Greubel C, Hable V, Siebenwirth C, Walsh DWM, et al. Reduced side effects by proton microchannel radiotherapy: study in a human skin model. *Radiat Environ Biophys* (2013) **52**(1):123–33. doi:10.1007/s00411-012-0450-9.
31. Sammer M, Zahnbrecher E, Dobiasch S, Girst S, Greubel C, Ilicic K, et al. Proton pencil minibeam irradiation of an *in-vivo* mouse ear model spares healthy tissue dependent on beam size. *PloS One* (2019) **14**(11):e0224873. doi:10.1371/journal.pone.0224873.
32. Reindl J, Girst S. pMB FLASH - status and perspectives of combining proton minibeam with FLASH radiotherapy. *Cancer Immunol Res* (2019) **1**(1).
33. Withers HR, Thames HD. Dose fractionation and volume effects in normal tissues and tumors. *Am J Clin Oncol* (1988) **11**(3):313–29. doi:10.1097/00000421-198806000-00008.
34. Straile WE, Chase HB. The use of elongate microbeams of X-rays for simulating the effects of cosmic rays on tissues: a study of wound healing and hair follicle regeneration. *Radiat Res* (1963) **18**(1):65. doi:10.2307/3571426.
35. Dilmanian FA, Eley JG, Rusek A, Krishnan S. Charged particle therapy with mini-segmented beams. *Front Oncol* (2015) **5**:269. doi:10.3389/fonc.2015.00269.
36. Dilmanian FA, Eley JG, Krishnan S. Minibeam therapy with protons and light ions: physical feasibility and potential to reduce radiation side effects and to facilitate hypofractionation. *Int J Radiat Oncol Biol Phys* (2015) **92**(2):469–74. doi:10.1016/j.ijrobp.2015.01.018.
37. Datzmann G, Dollinger G, Goeden C, Hauptner A, Körner H-J, Reichart P, et al. The Munich microprobe SNAKE: first results using 20 MeV protons and 90 MeV sulfur ions. *Nucl Instrum Methods Phys Res* (2001) **181**(1-4):20–6. doi:10.1016/s0168-583x(01)00549-3.
38. Hauptner A, Dietzel S, Drexler GA, Reichart P, Krücken R, Cremer T, et al. Microirradiation of cells with energetic heavy ions. *Radiat Environ Biophys* (2004) **42**(4):237–45. doi:10.1007/s00411-003-0222-7.
39. Girst S, Greubel C, Reindl J, Siebenwirth C, Zlobinskaya O, Walsh DWM, et al. Proton minibeam radiation therapy reduces side effects in an in vivo mouse ear model. *Int J Radiat Oncol Biol Phys* (2016) **95**(1):234–41. doi:10.1016/j.ijrobp.2015.10.020.
40. Sammer M, Teiluf K, Girst S, Greubel C, Reindl J, Ilicic K, et al. Beam size limit for pencil minibeam radiotherapy determined from side effects in an *in-vivo* mouse ear model. *PloS One* (2019) **14**(9):e0221454. doi:10.1371/journal.pone.0221454.
41. Prezado Y, Jouvion G, Hardy D, Patriarca A, Nauraye C, Bergs J, et al. Proton minibeam radiation therapy spares normal rat brain: long-term clinical, radiological and histopathological analysis. *Sci Rep* (2017) **7**(1):1–7. doi:10.1038/s41598-017-14786-y.
42. Lamirault C, Doyère V, Juchaux M, Pouzoulet F, Labiod D, Dendale R, et al. Short and long-term evaluation of the impact of proton minibeam radiation therapy on motor, emotional and cognitive functions. *Sci Rep* (2020) **10**(1):13511. doi:10.1038/s41598-020-70371-w.
43. Eley JG, Chadha AS, Quini C, Vichaya EG, Zhang C, Davis J, et al. Pilot study of neurologic toxicity in mice after proton minibeam therapy. *Sci Rep* (2020) **10**(1):11368. doi:10.1038/s41598-020-68015-0.
44. Tobola-Galus A, Swakon J, Olko P. Dosimetric characterization of collimators for spatially fractionated proton therapy of the eye. *Radiat Protect Dosim* (2018) **180**(1-4):351–4. doi:10.1093/rpd/ncy015.
45. Particle Therapy Co-Operative Group. *Particle Therapy Co-operatvie Group* Available from: https://www.ptcog.ch/ (Accessed April 20, 2020).
46. Bortfeld T, Paganetti H, Kooy H. MO-A-T-6B-01: proton beam radiotherapy—the state of the art. *Med Phys* (2005) **32**(6Part13):2048–9. doi:10.1118/1.1999671.
47. Koehler AM, Schneider RJ, Sisterson JM. Range modulators for protons and heavy ions. *Nucl Instrum Methods* (1975) **131**(3):437–40. doi:10.1016/0029-554x(75)90430-9.
48. August Schubiger P. PSI life sciences newsletter 1988. Switzerland: Paul Scherrer Institut (1989) Available from: http://inis.iaea.org/search/search.aspx?orig_q=RN:21075176.
49. Blattmann H, Coray A. A horizontal proton beam line for the development of a scanning technique. *Radiother Oncol* (1990) **17**(1):17–20. doi:10.1016/0167-8140(90)90044-w.
50. Grevillot L, Bertrand D, Dessy F, Freud N, Sarrut D. A Monte Carlo pencil beam scanning model for proton treatment plan simulation using GATE/GEANT4. *Phys Med Biol* (2011) **56**(16):5203–19. doi:10.1088/0031-9155/56/16/008.
51. De Marzi L, Patriarca A, Nauraye C, Hierso E, Dendale R, Guardiola C, et al. Implementation of planar proton minibeam radiation therapy using a pencil beam scanning system: a proof of concept study. *Med Phys* (2018) **45**(11):5305–16. doi:10.1002/mp.13209.
52. Pedroni E, Meer D, Bula C, Safai S, Zenklusen S. Pencil beam characteristics of the next-generation proton scanning gantry of PSI: design issues and initial commissioning results. *Eur. Phys. J. Plus* (2011) **126**(7):1–27. doi:10.1140/epjp/i2011-11066-0.
53. Farr JB, Mascia AE, Hsi W-C, Allgower CE, Jesseph F, Schreuder AN, et al. Clinical characterization of a proton beam continuous uniform scanning system with dose layer stacking. *Med Phys* (2008) **35**(11):4945–54. doi:10.1118/1.2982248.
54. Karger CP, Jäkel O. Current status and new developments in ion therapy. *Strahlenther Onkol* (2007) **183**(6):295–300. doi:10.1007/s00066-007-1645-x.
55. Brenner DJ, Hall EJ. Secondary neutrons in clinical proton radiotherapy: a charged issue. *Radiother Oncol* (2008) **86**(2):165–70. doi:10.1016/j.radonc.2007.12.003.
56. Bräuer-Krisch E, Bravin A, Zhang L, Siegbahn E, Stepanek J, Blattmann H, et al. Characterization of a tungsten/gas multislit collimator for microbeam radiation therapy at the European synchrotron radiation facility. *Rev Sci Instrum* (2005) **76**(6):64303. doi:10.1063/1.1915270.
57. Bräuer-Krisch E, Requardt H, Brochard T, Berruyer G, Renier M, Laissue JA, et al. New technology enables high precision multislit collimators for microbeam radiation therapy. *Rev Sci Instrum* (2009) **80**(7):74301. doi:10.1063/1.3170035.
58. Guardiola C, Peucelle C, Prezado Y. Optimization of the mechanical collimation for minibeam generation in proton minibeam radiation therapy. *Med Phys* (2017) **44**(4):1470–8. doi:10.1002/mp.12131.
59. Lansonneur P, Mammar H, Nauraye C, Patriarca A, Hierso E, Dendale R, et al. First proton minibeam radiation therapy treatment plan evaluation. *Sci Rep* (2020) **10**(1):7025. doi:10.1038/s41598-020-63975-9.
60. Peucelle C, Nauraye C, Patriarca A, Hierso E, Fournier-Bidoz N, Martínez-Rovira I, et al. Proton minibeam radiation therapy: experimental dosimetry evaluation. *Med Phys* (2015) **42**(12):7108–13. doi:10.1118/1.4935868.
61. Charyyev S, Artz M, Szalkowski G, Chang C-W, Stanforth A, Lin L, et al. Optimization of hexagonal-pattern minibeams for spatially fractionated radiotherapy using proton beam scanning. *Med Phys* (2020) **47**(8):3485–95. doi:10.1002/mp.14192.

62. Martínez-Rovira I, Fois G, Prezado Y. Dosimetric evaluation of new approaches in GRID therapy using nonconventional radiation sources. *Med Phys* (2015) **42**(2):685–93. doi:10.1118/1.4905042.
63. Schneider T, De Marzi L, Patriarca A, Prezado Y. Advancing proton minibeam radiation therapy: magnetically focussed proton minibeams at a clinical centre. *Sci Rep* (2020) **10**(1):1384. doi:10.1038/s41598-020-58052-0.
64. Mayerhofer M, Datzmann G, Degiovanni A, Dimov V, Dollinger G. Magnetically focused 70 MeV proton minibeams for preclinical experiments combining a tandem accelerator and a 3 GHz linear post accelerator. *Med Phys* (Forthcoming 2020)
65. Sammer M, Dombrowsky AC, Schauer J, Oleksenko K, Bicher S, Schwarz B, et al. Normal tissue response of combined temporal and spatial fractionation in proton minibeam radiation therapy. *Int J Radiat Oncol Biol Phys* (2020). In Press, Available online 14 August 2020 doi:10.1016/j.ijrobp.2020.08.027.
66. Schmelmer O, Dollinger G, Datzmann G, Goeden C, Körner H-J. A novel high precision slit system. *Nucl Instrum Methods Phys Res* (1999) **158**(1-4):107–12. doi:10.1016/s0168-583x(99)00357-2.
67. Sammer M, Greubel C, Girst S, Dollinger G. Optimization of beam arrangements in proton minibeam radiotherapy by cell survival simulations. *Med Phys* (2017) **44**(11):6096–104. doi:10.1002/mp.12566.
68. Hälg RA, Besserer J, Boschung M, Mayer S, Lomax AJ, Schneider U. Measurements of the neutron dose equivalent for various radiation qualities, treatment machines and delivery techniques in radiation therapy. *Phys Med Biol* (2014) **59**(10):2457–68. doi:10.1088/0031-9155/59/10/2457.
69. De Marzi L, Da Fonseca A, Moignier C, Patriarca A, Goudjil F, Mazal A, et al. Experimental characterisation of a proton kernel model for pencil beam scanning techniques. *Phys Med* (2019) **64**:195–203. doi:10.1016/j.ejmp.2019.07.013.
70. Grassberger C, Dowdell S, Sharp G, Paganetti H. Motion mitigation for lung cancer patients treated with active scanning proton therapy. *Med Phys* (2015) **42**(5):2462–9. doi:10.1118/1.4916662.
71. Knopf A-C, Lomax AJ. In the context of radiosurgery—pros and cons of rescanning as a solution for treating moving targets with scanned particle beams. *Phys Med* (2014) **30**(5):551–4. doi:10.1016/j.ejmp.2014.03.010.
72. Zhang Y, Huth I, Weber DC, Lomax AJ. A statistical comparison of motion mitigation performances and robustness of various pencil beam scanned proton systems for liver tumour treatments. *Radiother Oncol* (2018) **128**(1):182–8. doi:10.1016/j.radonc.2018.01.019.
73. Rietzel E, Bert C. Respiratory motion management in particle therapy. *Med Phys* (2010) **37**(2):449–60. doi:10.1118/1.3250856.
74. Friedrich T. Proton RBE dependence on dose in the setting of hypofractionation. *Br J Radiol* (2020) **93**(1107):20190291. doi:10.1259/bjr.20190291.
75. Hong TS, Wo JY, Yeap BY, Ben-Josef E, McDonnell EI, Blaszkowsky LS, et al. Multi-Institutional phase II study of high-dose hypofractionated proton beam therapy in patients with localized, unresectable hepatocellular carcinoma and intrahepatic cholangiocarcinoma. *J Clin Oncol* (2016) **34**(5):460–8. doi:10.1200/jco.2015.64.2710.
76. Quinn TJ, Hamstra D. Hypofractionation in prostate cancer using proton beam. *Int J Radiat Oncol Biol Phys* (2019) **105**(4):723–6. doi:10.1016/j.ijrobp.2019.08.006.
77. Favaudon V, Caplier L, Monceau V, Pouzoulet F, Sayarath M, Fouillade C, et al. Ultrahigh dose-rate FLASH irradiation increases the differential response between normal and tumor tissue in mice. *Sci Transl Med* (2014) **6**(245):245ra93. doi:10.1126/scitranslmed.3008973.
78. M Schillo. Global industrial development of accelerators for charged particle therapy. in: The 5th International Particle Accelerator Conference (IPAC 2014); 2014 Jul; Dresden, Germany. Geneva, Switzerland: JACoW (2014) p. 5. Available from: https://inspirehep.net/literature/1313907 (Accessed September 20, 2020).
79. Berger MJ, Inokuti M, Andersen HH, Bichsel H, Powers D, Seltzer SM, et al. Report 49. *J ICRU* (1993) **os25**(2):NP. doi:10.1093/jicru/os25.2.report49.
80. Rizzoglio V, Adelmann A, Baumgarten C, Frey M, Gerbershagen A, Meer D, et al. Evolution of a beam dynamics model for the transport line in a proton therapy facility. *Phys Rev Accel Beams* (2017) **20**(12). doi:10.1103/physrevaccelbeams.20.124702.
81. Varian medical systems inc. *Flash forward TM - konsortium*. (2020) Available from: https://www.varian.com/de/about-varian/research/flashforward-consortium (Accessed September 20, 2020).
82. Dollinger G, Faestermann T. Physics at the Munich tandem accelerator laboratory. *Nucl Phys News* (2018) **28**(1):5–12. doi:10.1080/10619127.2018.1427405.
83. Schippers JM, Dölling R, Duppich J, Goitein G, Jermann M, Mezger A, et al. The SC cyclotron and beam lines of PSI's new protontherapy facility PROSCAN. *Nucl Instrum Methods Phys Res* (2007) **261**(1-2):773–6. doi:10.1016/j.nimb.2007.04.052.
84. Liang Z, Chen W, Qin B, Liu X, Liu K, Zha J. Design of the energy selection system for proton therapy based on GEANT4. In: Proceedings of Cyclotrons; September 11–16, 2016; Zurich, Switzerland. Geneva, Switzerland; JACoW (2016) Available from: https://accelconf.web.cern.ch/cyclotrons2016/papers/mod01.pdf (Accessed September 20, 2020).
85. Coutrakon G, Slater JM, Ghebremedhin A. Design considerations for medical proton accelerators. In: Proceedings of the 1999 particle accelerator conference (cat. No.99CH36366); March 27–April 2, 1999; New York, United States. New York, NY; IEEE (1999) p. 11–5.
86. Jongen Y, Laycock S, Abs M, Amelia J-C, Beeckman W, Kleeven W, et al. The proton therapy system for the NPTC: equipment description and progress report. *Nucl Instrum Methods Phys Res* (1996) **113**(1-4):522–5. doi:10.1016/0168-583x(95)01319-9.
87. Langner UW, Eley JG, Dong L, Langen K. Comparison of multi-institutional Varian ProBeam pencil beam scanning proton beam commissioning data. *J Appl Clin Med Phys* (2017) **18**(3):96–107. doi:10.1002/acm2.12078.
88. Perrin A. TRAVEL v4.07: user manual (2007) Available from: https://lombarda.web.cern.ch/DTL-linac4/Travel.pdf (Accessed April, 2007).
89. Sabaiduc C, Boiesan T, Carlson M, Du D, Piazza LAC, Ryikov V, et al. Best 70P cyclotron comissioning at INFN LN Legnaro. In: Proceedings of Cyclotrons; September 11–16, 2016; Zurich, Switzerland. Geneva, Switzerland: JACoW (2016) 241–3. Available from: http://accelconf.web.cern.ch/cyclotrons2016/papers/tud04.pdf.
90. Denker A, Bundesmann J, Daerow T, Fanselow T, Hildebrand D, Hiller U, et al. Status of HZB cyclotron. In: Proceedings of Cyclotrons; September 20, 2013; Vancouver, BC. Geneva, Switzerland: JACoW (2019) p. 254–6. Available from: https://accelconf.web.cern.ch/CYCLOTRONS2013/papers/moppt002.pdf (Accessed September 20, 2020).
91. Damato B, Kacperek A, Chopra M, Campbell IR, Errington RD. Proton beam radiotherapy of choroidal melanoma: the Liverpool-Clatterbridge experience. *Int J Radiat Oncol Biol Phys* (2005) **62**(5):1405–11. doi:10.1016/j.ijrobp.2005.01.016.
92. Bettega D, Calzolari P, Chauvel P, Courdi A, Herault J, Iborra N, et al. Radiobiological studies on the 65 MeV therapeutic proton beam at Nice using human tumour cells. *Int J Radiat Biol* (2000) **76**(10):1297–303. doi:10.1080/09553000050151565.
93. Amaldi U, Braccini S, Puggioni P. High frequency linacs for hadrontherapy. *Rev Accl Sci Tech* (2009) **02**(01):111–31. doi:10.1142/s179362680900020x.
94. Hamm RW, Crandall KR, Potter JM. Preliminary design of a dedicated proton therapy linac. In: Conference record of the 1991; 2019 May 19–24; Melbourne, Australia. IEEE Particle Accelerator Conference (1991) p. 2583–5:**4**.
95. Degiovanni A. Future trends in linacs. In: Proceedings of the CAS-CERN accelerator school on accelerators for medical applications/CERN yellow reports: school proceedings; 2015 May 26–June 5; Vösendorf, Austria. CERN Yellow Reports (2017) p. 151:**Vol. 1**.
96. Ronsivalle C, Picardi L, Ampollini A, Bazzano G, Marracino F, Nenzi P, et al. First acceleration of a proton beam in a side coupled drift tube linac. *Europhys Lett* (2015) **111**(1):14002. doi:10.1209/0295-5075/111/14002.
97. A Degiovanni, J Adam, D Aguilera Murciano, S Ballestrero, A Benot-Morell, R Bonomi, et al. Status of the commissioning of the LIGHT prototype. in: The 9th International Particle Accelerator Conference; 2018 Jun; Vancouver, BC. Geneva, Switzerland: JACoW Publishing (2018) p. 4. Available from: https://inspirehep.net/literature/1691387 (Accessed September 20, 2020).
98. Picardi L, Ronsivalle C, Vignati A. TOP LINAC design; Progetto del TOP LINAC (1997) Report No.: ENEA Technical Report RT/INN/97/17. Available from: https://www.osti.gov/etdeweb/biblio/610871 (Accessed September 20, 2020).
99. De Martinis C, Giove D, Amaldi U, Berra P, Crandall K, Mauri M, et al. Acceleration tests of a 3GHz proton linear accelerator (LIBO) for hadrontherapy. *Nucl Instrum Methods Phys Res* (2012) **681**:10–5. doi:10.1016/j.nima.2012.04.017.

100. Picardi L, Ampollini A, Bazzano G, Cisbani E, Ghio F, Montereali RM, et al. Beam commissioning of the 35 MeV section in an intensity modulated proton linear accelerator for proton therapy. *Phys Rev Accel Beams* (2020) **23**(2): 20102. doi:10.1103/physrevaccelbeams.23.020102.
101. Caldara M., Presentation a the OMA International Conference on Medical Accelerators and Particle Therapy. (2019). Available from: https://indico.cern.ch/event/803528/contributions/3378749/attachments/1902950/3141897/20190618_OMA_BD_Caldara.pdf (last access date: 17.10.2020)
102. Moser M, Greubel C, Carli W, Peeper K, Reichart P, Urban B, et al. Transport of a high brightness proton beam through the Munich tandem accelerator. *Nucl Instrum Methods Phys Res* (2015) **348**:34–42. doi:10.1016/j.nimb.2014.11.068.
103. Amaldi U, Berra P, Crandall K, Toet D, Weiss M, Zennaro R, et al. LIBO—a linac-booster for protontherapy: construction and tests of a prototype. *Nucl Instrum Methods Phys Res* (2004) **521**(2-3):512–29. doi:10.1016/j.nima.2003.07.062.
104. Degiovanni A, Amaldi U. Proton and carbon linacs for hadron therapy. (2014) p. 4, 2014 . Report No.: CERN-ACC-2014-362. Available from: https://cds.cern.ch/record/2062622 (Accessed September 20, 2020).
105. Matinfar M, Ford E, Iordachita I, Wong J, Kazanzides P. Image-guided small animal radiation research platform: calibration of treatment beam alignment. *Phys Med Biol* (2009) **54**(4):891–905. doi:10.1088/0031-9155/54/4/005.
106. Kim MM, Irmen P, Shoniyozov K, VerginadisII, Cengel KA, Koumenis C, et al. Design and commissioning of an image-guided small animal radiation platform and quality assurance protocol for integrated proton and X-ray radiobiology research. *Phys Med Biol* (2019) **64**(13):135013. doi:10.1088/1361-6560/ab20d9.
107. Ford E, Emery R, Huff D, Narayanan M, Schwartz J, Cao N, et al. An image-guided precision proton radiation platform for preclinical *in vivo* research. *Phys Med Biol* (2017) **62**(1):43–58. doi:10.1088/1361-6560/62/1/43.
108. Siegel R, DeSantis C, Virgo K, Stein K, Mariotto A, Smith T, et al. Cancer treatment and survivorship statistics, 2012. *CA A Cancer J Clin* (2012) **62**(4): 220–411. doi:10.3322/caac.21149.
109. Hall EJ. Intensity-modulated radiation therapy, protons, and the risk of second cancers. *Int J Radiat Oncol Biol Phys* (2006) **65**(1):1–7. doi:10.1016/j.ijrobp.2006.01.027.
110. Chapman TR, Ermoian RP. Proton therapy for pediatric cancer: are we ready for prime time?. *Future Oncol* (2017) **13**(1):5–8. doi:10.2217/fon-2016-0373.
111. Pettmann B, Henderson CE. Neuronal cell death. *Neuron* (1998) **20**(4): 633–47. doi:10.1016/s0896-6273(00)81004-1.
112. Fletcher DA, Theriot JA. An introduction to cell motility for the physical scientist. *Phys Biol* (2004) **1**(1-2):T1–10. doi:10.1088/1478-3967/1/1/t01.
113. McGovern Medical School at UTHealth Department of Neurobiology and Anatomy. *Neuroscience Online an electronic textbook from the neurosciences* (1997) Available from: https://nba.uth.tmc.edu/neuroscience/ (Accessed May 15, 2020).
114. Werner-Wasik M, Paulus R, Curran WJ, Byhardt R. Acute esophagitis and late lung toxicity in concurrent chemoradiotherapy trials in patients with locally advanced non-small-cell lung cancer: analysis of the radiation therapy oncology group (RTOG) database. *Clin Lung Canc* (2011) **12**(4):245–51. doi:10.1016/j.cllc.2011.03.026.
115. Greten TF, Malek NP, Schmidt S, Arends J, Bartenstein P, Bechstein W, et al. Diagnosis of and therapy for hepatocellular carcinoma. *Z Gastroenterol* (2013) **51**(11):1269–326 [in German, with English summary]. doi:10.1055/s-0033-1355841.
116. Diethelm L, Heuck F, Olsson O, Strnad F, Vieten H, Zuppinger A, et al. *Strahlengefährdung und strahlenschutz/radiation exposure and radiation protection*. In: Handbuch der medizinischen Radiologie/ encyclopedia of medical radiology. Berlin: Springer Verlag (2013). Vol. **20**.

Conflict of Interest: Author GD was employed by the company Datzmann interact and innovate GmbH.

The remaining authors declare that the research was conducted in the absence of any commercial or financial relationships that could be construed as a potential conflict of interest.

frontiers in Physics

ORIGINAL RESEARCH
published: 30 November 2020
doi: 10.3389/fphy.2020.566679

Delivery, Beam and Range Monitoring in Particle Therapy in a Highly Innovative Integrated Design

L. Bottura[1], *E. Felcini*[1,2], *V. Ferrero*[3], *E. Fiorina*[3], *V. Monaco*[4,3], *F. Pennazio*[3], *G. de Rijk*[1] *and P. Cerello*[3]*

[1]CERN, Geneva, Switzerland, [2]EPFL, Lausanne, Switzerland, [3]INFN, Sezione di Torino, Torino, Italy, [4]Department of Physics, University of Torino, Torino, Italy

The design of a particle therapy system that integrates an innovative beam delivery concept based on a static toroidal gantry and an imaging configuration suitable for beam and online range monitoring is proposed and discussed. Such approach would provide a compact and cost-effective layout, with a highly flexible and fast beam delivery, single particle counting capability for fast measurement of beam fluence and position and a precise real time verification of the compliance between the treatment delivery and its prescription. The gantry configuration is discussed, presenting an analysis of the residual magnetic field in the bore and of the feasibility of irradiating a realistic target volume. Moreover, the expected performance of the PET-based range monitor is assessed through Monte Carlo simulations, showing a precision in the reconstruction of the activity distribution from a clinical treatment plan better than the state-of-the-art devices. The feasibility of the proposed design is then discussed through an assessment of the technological improvements required to actually start the construction and commissioning of a system prototype.

Keywords: particle therapy, gantry, beam monitor, range monitor, treatment verification, PET, PGT

OPEN ACCESS

Edited by:
Yolanda Prezado, INSERM U1021 Signalisation normale et pathologique de l'embryon aux thérapies innovantes des cancers, France

Reviewed by:
Giacomo Cuttone, Laboratori Nazionali del Sud (INFN), Italy
Denis Dauvergne, Centre National de la Recherche Scientifique (CNRS), France

***Correspondence:**
P. Cerello
piergiorgio.cerello@to.infn.it

Specialty section:
This article was submitted to Medical Physics and Imaging, a section of the journal Frontiers in Physics

Received: *28 May 2020*
Accepted: *28 October 2020*
Published: *30 November 2020*

Citation:
Bottura L, Felcini E, Ferrero V, Fiorina E, Monaco V, Pennazio F, de Rijk G and Cerello P (2020) Delivery, Beam and Range Monitoring in Particle Therapy in a Highly Innovative Integrated Design. Front. Phys. 8:566679. doi: 10.3389/fphy.2020.566679

1 INTRODUCTION

Particle therapy exploits the energy deposition pattern of ion beams, with the *Bragg peak* at the end of range, to minimise the unwanted dose to healthy tissues. However, the cost, complexity, and large footprint of the installations have somehow limited its diffusion; the lack of well-established real-time verification tools to precisely verify the compliance between the planned and delivered treatment is an additional limitation to the full exploitation of its clinical potential.

Operating particle therapy facilities implement beam delivery through either a fixed beam line [1] or a mobile gantry [2], a rotating transfer line able to deliver the required dose from virtually any direction.

Fixed beam lines are relatively simple to implement with respect to gantries, but the beam incident angle on the patient in some conditions does not allow an optimal design of the dose distribution and the treatment field geometry; also, fixed lines require moving the patients, with both translations and rotations, in order to complete a full treatment session.

Rotating gantries overcome this limitation, at the cost of a more complex and technically challenging implementation. The gantry itself and the supporting mechanical structure are remarkably large and bulky, both for protons and, especially, for heavier ions. While in the

proton case commercial solutions are in the range of 4–5 m in radius and up to 200 tons in weight, existing carbon ion gantries can exceed the 14 m in diameter and 600 tons in weight [3]. Making use of superconducting magnets, it is possible to increase the magnetic field and reduce the footprint of the machine down to about 9 m and 300 tons [4].

Several new concepts of rotating gantries have been proposed recently, making use of combined function [5, 6] or large acceptance magnets [7, 8] to reduce their size.

In any case, the gantry rotation requires high mechanical precision and increases the treatment session duration; also the rotation of cryogenic parts and the ramping of the magnetic field create challenging operating conditions for the superconducting systems, particularly sensitive to unwanted transitions to normal-conducting state. As a consequence, most of the treatments are delivered from only a small subset of the possible incident angles [9], suggesting that a decrease in the gantry structure complexity might be achieved at the cost of decreasing the possible treatment angles.

As reported in [10] one of the driving factors of particle therapy facilities is the gantry footprint, as well as the size of the building required to contain it. The design and construction of more compact and lighter gantries is of utmost importance to facilitate the accessibility of particle therapy to the largest number of patients.

Regardless of the selected solution for beam delivery, beam monitoring functionality is essential and is usually integrated in the nozzle. A limitation in beam monitoring arises from the technology, based on gas detectors, currently employed to measure the number of delivered particles and the beam position [11]. The slow collection time of gas detectors, of the order of hundreds of μs, and their poor sensitivity, with a minimum threshold of the order of thousands of protons, prevent their use in fast delivery modality, which is required, for example, to improve the treatment of moving targets, for which shorter response times and higher sensitivity are needed [12].

New implementations based on solid state detectors, that could overcome these limitations, are being investigated: in particular the short pulse duration in thin sensors can be exploited to directly count the number of delivered particles, instead of measuring it indirectly from the charge produced in a gas. Silicon detectors with moderate internal gain (Low-Gain Avalanche Detectors, LGAD [13]) can be used to compensate for the reduction of signal in small thicknesses.

Segmented LGAD detectors optimized for timing measurements, also known as Ultra Fast Silicon Detectors (UFSD) [14], could concurrently provide position and time information for each beam particle with extremely high resolutions: nowadays the time resolution reached by 45 μm thick UFSD sensors for Minimum ionizing Particles is about 27 ps [15].

Online range monitoring is a crucial step to provide early treatment assessment in particle therapy. Intrinsic uncertainties in the beam range limit the exploitation of the advantages of particle therapy: for example, current treatment plans for protons implement a safety margin up to 3.5% + 3 mm [16]. In order to reduce this margin, a better control on range uncertainties is mandatory. Moreover, over the course of a treatment, often lasting several weeks, morphological changes can occur in the tissues and require a reassessment of the treatment plan: range monitoring tools can effectively identify if and when such reevaluation should take place.

The issue of online range monitoring can be addressed by taking advantage of passive signals originating from beam-induced effects: prompt photon production from nuclear de-excitation, back-to-back monochromatic photons from electron-positron annihilation following β^+ decay and, for treatment with ion beams, protons from beam fragmentation are strictly correlated to the beam path, and can therefore be exploited to indirectly monitor the delivered dose. In particular, β^+ emitting isotopes have been thoroughly investigated with Positron Emission Tomography (PET) techniques. Due to tissue composition mostly short-lived emitting isotopes are produced (e.g., ^{11}C and ^{15}O, with half-lives of about 20 and 2 min, respectively): therefore, PET measurements are best performed simultaneously to the beam irradiation (in-beam PET). This is also a key factor to minimise the biological washout, and therefore maximise the correlation between the delivered dose and the measured activity. The production yield of positron emitters is also low, resulting in a much smaller number of detected events with respect to nuclear medicine PET. These attributes imply that high sensitivity scanners are required for in-beam-PET measurements; moreover, the scanner geometry is constrained by the requirement of not interfering with the passage of the beam and the patient positioning and handling subsystems. Although geometries with full angular coverage have been proposed [17], past and present in-beam PET scanners feature open geometries and limited angular coverage: the BASTEI scanner [18], BOLPs-RGp [19], LAPD [20], the dual-ring OpenPET [21] and DOPET [22], as well as the state-of-the-art INSIDE scanner [23].

As of now, however, only few results were obtained in real time in a clinical environment with proton beams: tests on a small number of patients show that prompt gamma imaging [24] provides an accuracy in range verification that is better than the range uncertainty margin set in the treatment plans, while in-beam PET provides a range agreement within 1 mm between consecutive delivery sessions [25] and in the comparison of simulations to data [26].

We discuss in the following the concept design of an innovative system that would allow hybrid *in-vivo* real-time high-precision imaging thanks to the combination of a static toroidal gantry, a single particle beam counting device and a hybrid range monitoring system, providing a lightweight, cost effective and highly performant solution. We then focus on a specific implementation of a prototype to be used for proton treatment delivery and present the results of our first simulations of the response of a PET detector as online range monitor in the *GaToroid* layout when a treatment plan is delivered in a clinical setting.

2 MATERIALS AND METHODS

The heart of the proposed design is a radically new gantry concept [27], based on a superconducting toroidal magnet generating an axially symmetrical field, that allows focusing beams of different energies on the same point.

The static gantry will preserve the advantage of rotating gantries, allowing to deliver the beam from many directions, with a much simpler and lightweight circular layout, consisting of a toroidal magnet operated in steady state conditions. The magnet coils are arranged so as to form a large number of beam channels with windows, corresponding to the pre-selected subset of beam delivery directions. Hence, the gantry does not need to rotate, and can be conveniently built using superconductors, resulting in dimensions that are a factor two to four smaller than those of state-of-the-art facilities.

The inner part of the static gantry will host both the beam delivery monitor and the online treatment verification system.

The beam monitoring system, made of multiple LGAD silicon detectors, would be positioned either on each beam window or on an internal rotating nozzle.

PET rings, installed either on both sides of the beam delivery windows or, in case of a single rotating beam monitor, in a ring with a gap in which the beam monitor itself would be mounted, would cover a large fraction of the solid angle, increasing both the field of view and the precision on the 3D activity map reconstruction with respect to presently available systems. In both options, sufficient statistics for reconstructing the beam-induced activity distribution would be collected in a short time and geometrical artefacts related to the limited angular coverage would be minimised.

Gantry

GaToroid represents a novel gantry concept for particle therapy, based on the use of an axially symmetric magnetic field generated by toroidal coils to bend and focus the particle beam. Such a gantry allows the dose delivery from a discrete number of angles, depending on the magnetic design.

This machine is conceived to work in steady-state, with no rotation of major mechanical components and no variations of the magnetic field. These features properly suit the use of superconductive technology, simplifying cryogenics stability, as well as remarkably increasing the intensity of the generated magnetic field.

The coils can be designed to have a very large acceptance, able to cover the complete range of treatment energies [28], i.e. from 70 to 250 MeV for protons and from 120 to 430 MeV/u for carbon ions, without changing the current or field. The Vector Magnet, an upstream bending magnet, rotating or combined vertical/horizontal, is used to steer the particles into the gantry with a proper angle, depending on the beam rigidity and the required treatment directions.

In the present work, we will focus our attention on a *GaToroid* for proton beams, constituted by 16 coils and the corresponding beam windows between the coils. Such a toroidal magnet configuration, discussed in detail in Ref. [29], is characterized by an inner free bore diameter of 0.8 m and an outer diameter of 3.3 m, resulting in a total mass of about 12 tons, including the main mechanical supports. The torus resulting from the optimization is presented in **Figure 1**, together with a schematic representation of a human for size comparison.

The selected configuration is considered so far the most suitable to address the magnetic design challenges, allow the proper incorporation of the solid state beam monitoring devices and PET detectors and it would be suitable for building a first prototype. The use of superconductors operating in steady-state high fields (B > 3T) remarkably reduces the footprint and the weight of the gantry in comparison with the state of the art. The magnet was designed to allow the use of both Low (LTS) and High (HTS) Temperature Superconductors, limiting the peak field to about 8T. Considering the former option, Nb-Ti would be a simple and effective choice, given the maturity of the technology and the relatively low price of the material. As for the latter, the use of superconductors above liquid helium temperature is an intriguing, yet challenging proposal, and the possibility to use Rare-earth Barium Copper Oxide (ReBCO) conductors is being investigated.

At the proposed magnetic field intensity, HTS would allow to operate in simpler cryogenics conditions, i.e. helium gas at 20 K, reducing cooling cost and power consumption. On the other hand, the use of HTS in liquid helium, i.e., 4.2 K, would open the possibility for a further increase of magnetic field beyond 10 T, with a drastic reduction of the gantry footprint and weight, but also an increase of complexity in terms of mechanics and quench protection.

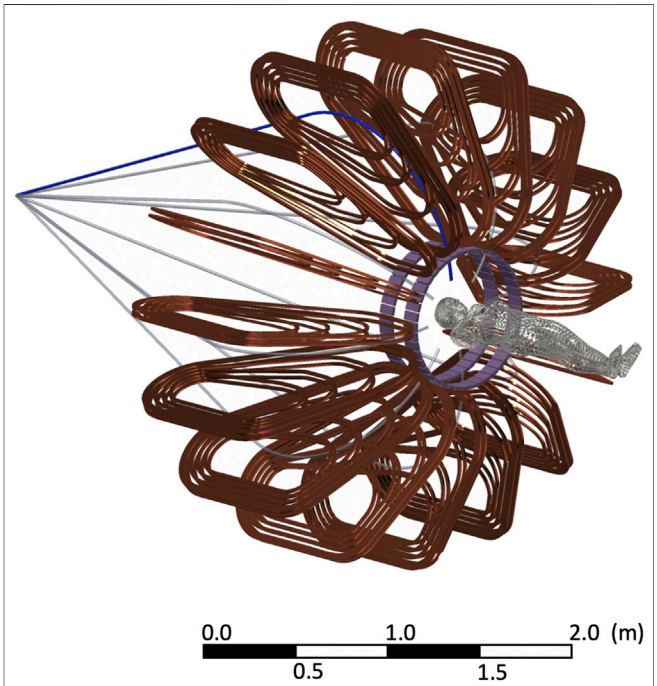

FIGURE 1 | Representation of the *GaToroid* coil configuration for the beam delivery together with two PET rings used for the range monitoring simulations (case 1 in the following). The shape of the patient is used for size comparison. The beam lines start diverging after the vector magnet, that directs them toward the *GaToroid* with the appropriate angles.

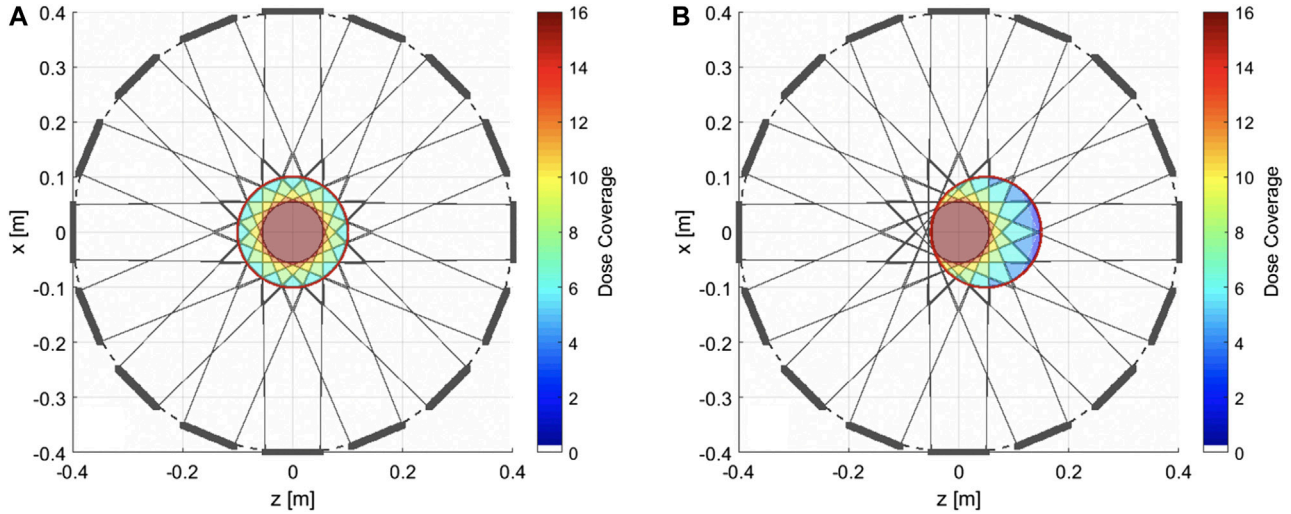

FIGURE 2 | Beam coverage map. Beam exit windows are represented by the gray thick lines, in a *Gatoroid* configuration with 16 coils and an 80 cm diameter bore. For each beam window, the beam coverage area is drawn (light gray lines). **(A)** A cylindrical target volume of 20 cm diameter is highlighted at the isocenter. The color map indicates the number of beam windows from which the target volume can be accessed. **(B)** For non-isocentric targets, the same volume can be reached, with the limitation of fewer beam windows available.

Figure 2 shows the number of beam entrance windows (i.e., directions) from which any given point in a 20 cm diameter cylinder is reachable with the proposed configuration. The beam windows, shown in gray thick lines, have a size of about 10·10 cm^2. Considering a SAD (Source-to-Axis Distance) of 4 m, necessary to limit the superficial dose increase [30], the maximum divergence of the beam during the scanning is 0.7°. With these geometric specifications the centered innermost disk of 11 cm diameter, highlighted in red, can be reached from 16 directions. The outermost disk, enclosed by a red line, shows a possible coverage of 20 cm diameter. The target volume can be reached at the isocenter from any of the beam windows (**Figure 2A**), while non-isocentric targets could be covered by using selected beam windows (**Figure 2B**).

Due to the axisymmetric configuration of the coils, the magnetic field at the isocentre, calculated with Field2017 [31] using a direct Biot-Savart method on the plane transversal to the toroidal axis around the isocenter location, is below the critical threshold for instrumentation and humans safety (order of μT). Similarly, the magnetic field rapidly decays with the radius inside the bore and at 30 cm radius is in the order of 10 mT.

In case of a loss of symmetry, for instance due to a short-circuit in a coil, the magnetic field strongly penetrates inside the bore exceeding hundreds of mT close to the patient region. For this reason, the quench protection system of the superconducting torus considers the simultaneous discharge of all the coils on external resistors [29].

Beam Monitoring

Segmented LGAD detectors with dedicated fast electronics are a promising option to overcome the limitation of gas detectors nowadays used for beam monitoring in charge particle therapy and would allow new delivery schemes with enhanced speed, sensitivity, spatial and time resolutions. Solid state detectors would be the natural choice for a monitoring device to be positioned in a region close to the *GaToroid* coils, where the performance of traditional gas detectors could be affected by the residual magnetic field, shown in **Figure 3**. The field residual values in the vicinity of the beam windows, where the beam and range monitor would be installed, drops quickly to zero.

Preliminary results from test of 50 μm thick LGAD silicon sensors segmented in strips show that the number of particles of a therapeutic beam can be measured with a maximum error of 1% up to a flux of more than 10^8 p/(cm^2s), limited by pile-up effects at higher fluxes, and that a fast online measurement of the beam energy for each spot can be obtained with the required clinical accuracy with time of flight techniques exploiting the high time resolution of the LGAD technology [32]. However, a measurement of the number of beam particles up to therapeutic fluxes of 10^{10} p/(cm^2s) or more can be achieved only with silicon sensors segmented in pixels.

The main difficulties in designing silicon detectors for beam monitoring in the clinical practice are related to the technology complexity, high cost, and radiation resistance of large area pixelated silicon sensors and of their readout electronics. For this reason, the technological choice for the beam monitoring devices is still open to several possibilities, including traditional ionization chambers in case the time schedule and the budget of the prototype construction did not fit the time and costs required for the development of LGAD detectors. However, it should be remarked that the technology selected for the beam monitoring will be an important feature in defining the speed and precision of the delivery schemes that could be adopted with the *GaToroid* system. In addition, the time resolution of LGAD design could be exploited to enhance the capabilities of the range monitoring

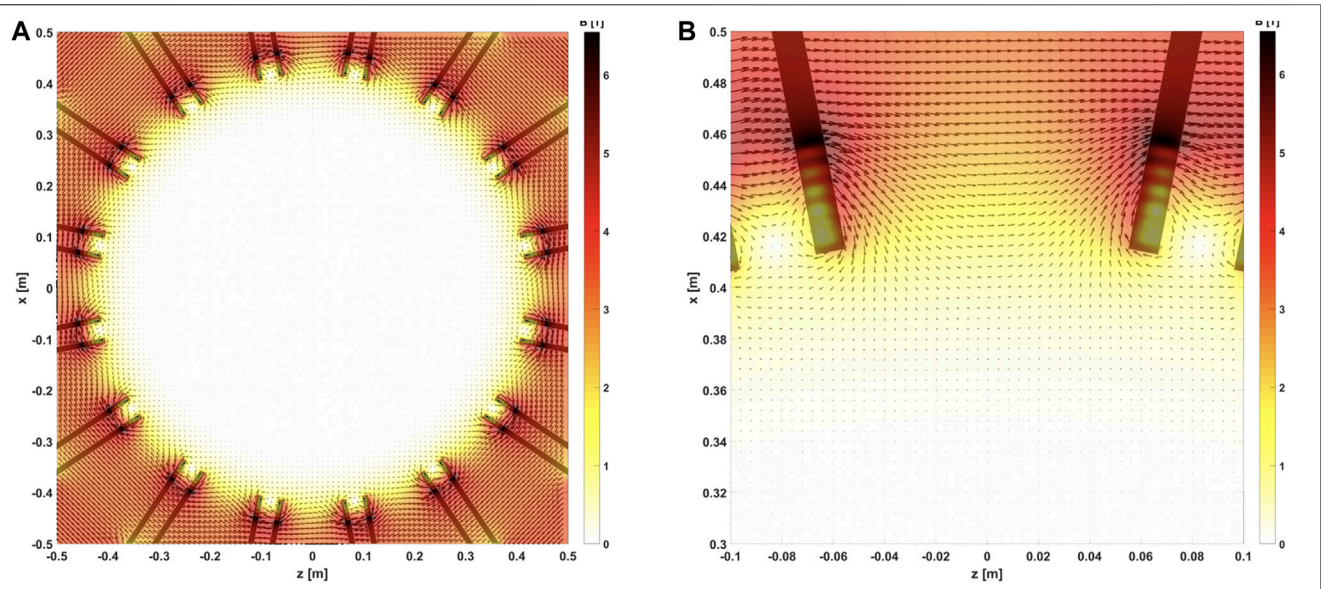

FIGURE 3 | (A) Map of the magnetic field inside the bore (80 cm diameter) volume. The field value, when exiting the coils, drops quickly to values in the order of μT. **(B)** Zoom on the transition volume between the coils and the bore. The magnetic field in the beam and range monitor volumes, at 40 cm radius, is about 0.7 T, and drops to 10 mT at about 30 cm.

devices integrated in the gantry, while ionization chambers do not provide useful timing information.

Independently of the technological choice, the beam monitoring detectors will match the beam delivery windows foreseen by the *GaToroid* prototype design and will have to meet all the requirements for their use in clinical practice.

Online Range Monitoring

The *GaToroid* design, thanks to its circular symmetry, allows for the simple integration of a PET-based range monitoring system. In this work, we investigate two different configurations. The first one (case 1) is an open geometry consisting of two individual rings, shifted in the axial direction and positioned on each side of the *GaToroid* beam delivery windows. A similar geometry was proposed in Ref. [33], where it was shown how an axially-shifted dual ring detector could be suitable for in-beam-PET monitoring, as the image quality is almost independent of the width of the gap between the two rings, with uniform spatial resolution in the *trans*-axial direction, but a decreasing resolution in the axial direction as the gap width increases.

The second geometry (case 2) features a single-ring design, to be installed on a rotating structure inside the gantry, comprising a gap for the integration of the beam monitor. An additional geometry comprising a single ring with no gaps (case 0), is simulated as the reference case. All geometries, shown in **Figure 4**, have a 0.8 m diameter that fits the gantry design.

The reconstruction performances corresponding to the proposed geometries were assessed with simulations based on the FLUKA Monte Carlo simulation tool [34, 35]. Lutetium-based state-of-the-art scintillating modules are considered as PET

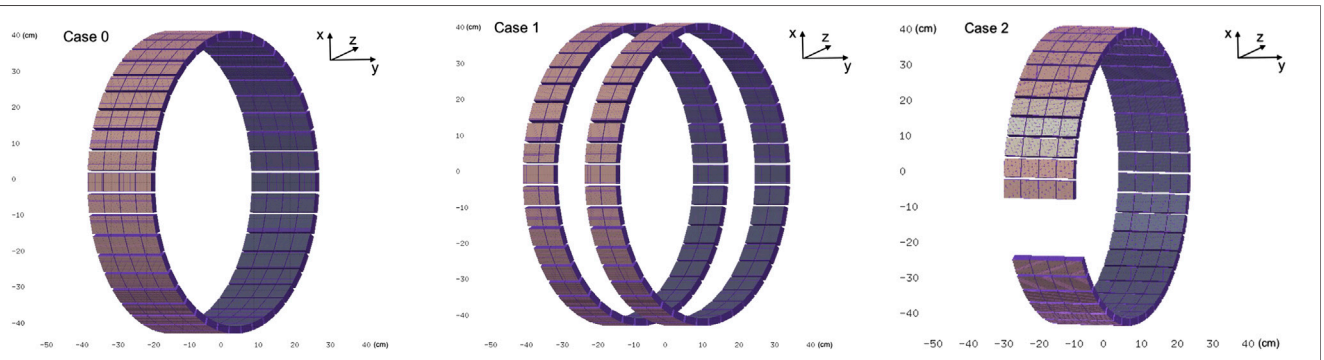

FIGURE 4 | Solid model of the proposed PET detector geometries to be integrated within the *GaToroid* system. Case 0: single ring geometry, reference. Case 1: static dual ring open geometry, with the PET detectors positioned on each side of the beam entrance windows. Case 2: dynamic single ring geometry, to be mounted on a rotating structure inside the gantry, with a gap for the beam path.

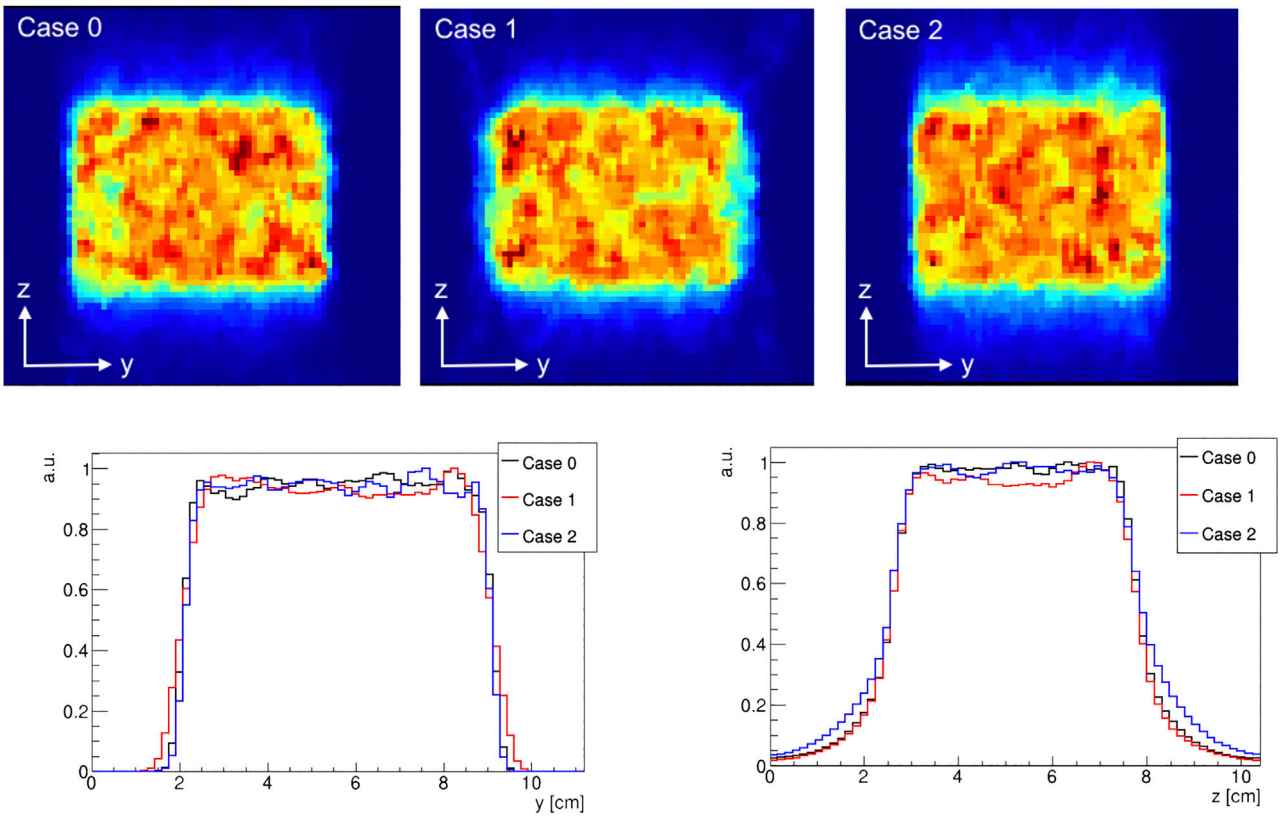

FIGURE 5 | central slice in the (y, z) plane of a reconstructed homogeneous activity distribution for case 0, case 1, and case 2 **(top)**. The corresponding activity profiles along the *y* and *z* directions, evaluated at the central slice **(bottom)**.

detectors elements, each of them made of 16·16 pixels (3.1·3.1·20 mm^3, with 3.2 mm pitch), coupled one-to-one to Silicon PhotoMultiplier tiles. Case 1 and case 2 configurations include 176 (44·2 module arrays per ring) and 164 (41·4 module arrays) PET detector modules, respectively. For the reference case 176 modules, organized in 44 · 4 arrays, are simulated. Each detector module has an overall dimension of 52.1 · 52.1 · 21 mm^3. Modules belonging to the same ring are distanced by 2 mm along the axial direction. The air gap between the two PET rings presented in case 1 is of 106.2 mm, corresponding to the overall dimension of each PET ring. As for case 2, the opening for the beam passage corresponds to about 16 cm length, which is compatible with the *GaToroid* beam window dimension.

Multiple scattering processes, electronic stopping power, energy loss fluctuations and nuclear reaction chains are modeled in the simulation [36], with positron and electron ranges traced down to 100 keV. The energy and interaction time of the detected events are smeared with a Gaussian distribution, considering a 15% dE/E and 300 ps FWHM timing resolution. A filtering algorithm is then used to search for events in a 2.7 ns coincidence window.

As benchmark, a homogeneous activity distribution corresponding to 10^6 annihilation events was simulated inside a 5 · 7 · 5 cm^3 water phantom to assess the imaging performances of the proposed geometries (**Figure 5**).

Moreover, a proton treatment plan was simulated to assess the quality and precision of the reconstructed activity distribution. A clinical proton beam, modeled after the CNAO synchrotron facility clinical beam, was used for this purpose. The injected clinical treatment plan corresponds to the first field of a double-field adenoid cystic carcinoma (ACC) treatment, with the delivery of a horizontal beam line with the beam entrance from the left side (see **Figures 6** and **7**). A total of 1.8 · 10^9 protons were simulated in the beam field, in the [62, 141] MeV energy range.

The simulation tool was successfully validated both in controlled conditions (phantom tests) and in a clinical environment, providing an agreement with the data comparable to the variability of data from consecutive treatment sessions [26].

The activity images were reconstructed using an MLEM algorithm computed with Siddon's single-ray-tracing system matrix which was validated on a previous work [37]. A 140 · 70 · 165 Field of View (FOV), with a pixel size of 1.6 mm, was used. Due to the missing projections in the case 1 and 2 geometries, the image quality is expected to worsen with respect to the reference condition (case 0).

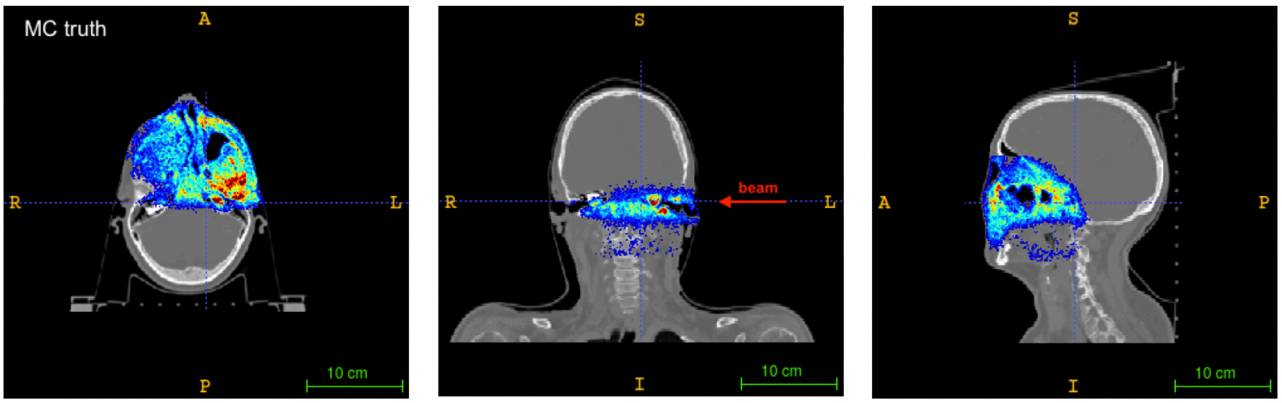

FIGURE 6 | Axial **(left)**, coronal **(center)** and sagittal **(right)** sections of the patient CT with the Monte Carlo activity distribution superimposed. The beam direction is shown for the coronal slice. A standard RAI coordinate system is considered.

3 RESULTS

The present work focuses on the expected performance of the real time imaging system, by analysing different PET configurations integrated in the gantry, whose delivery configuration has already been discussed in detail in Ref. [28]. The beam monitoring design parameters are somehow set by the size of the beam entrance windows in the gantry; the technology choice will be addressed later on, in view of the construction of a prototype, based on results of ongoing R&D studies.

PET Image Quality Assessment

An assessment of the imaging performance of each considered geometry was carried out considering the reconstructed activity distribution coming from the simulation of a homogeneously activated $5 \cdot 7 \cdot 5\,\mathrm{cm}^3$ water phantom. The number of coincidences detected for each case is reported in **Table 1**. As expected, case 1 has the smallest number of coincidences, due to the larger gap and therefore larger number of missing projections that lead to a decrease in the number of detected events, while the reference case reports the highest. Still, the detected number of coincidences is of the same order of magnitude, with a minimal difference due to the diverse geometry, that does not significantly change the reconstructed activity distribution among the considered cases.

The reconstructed activity distributions and their profiles are shown in **Figure 5**, normalized to their maximum value: case 1 and 2 show slight image artefacts with respect to the reference case, due to truncation effects in the axial direction for case 1 and in the azimuthal one for case 2.

A comparison was performed on the activity profiles along the axial axis y and *trans*-axial axis z. The profiles were calculated by considering a rectangular area of $3 \cdot 3\,\mathrm{cm}^2$ in the plane transverse to the preferred direction: for the z profile, a rectangular area at the center of the (x, y) plane is considered; similarly, for the y profile a rectangular area at the center of the (x, z) plane is considered. The rising and falling edges of the activity profile were fitted with a sigmoidal function as described in Ref. [23]. The inflection points of the sigmoidal fits were thus used to identify the beginning and the end of the distribution, calculating the activity range as the difference between the two. Results, reported in **Table 1**, show that the range values, both in the axial direction y and in the *trans*-axial direction z, are compatible, within the error, with the nominal values.

Clinical Treatment Plan Simulation

Figure 6 shows the axial (left), coronal (center) and sagittal (right) views of the patient CT superimposed with the activity distribution of the treatment plan under consideration, as obtained from the Monte Carlo simulation. The central slice of the corresponding reconstructed activity maps for each of the considered geometries are reported in **Figure 7**, with all the images shown in Right-to-Left, Anterior-to-Posterior, Inferior-to-Superior (RAI) coordinates.

A good visual comparison is found between the reconstructed activity distributions and the Monte Carlo truth, with the absence of strong image artefacts which are typically found in dual-head geometry detectors [37] that can hamper image quality and therefore the range assessment. A preliminary comparison between the reconstructed activity maps was done by considering the activity profiles along the beam direction (see for reference the coronal slice in **Figure 7**). The profiles, calculated considering a $7 \cdot 7$ voxels area (i.e., about $1\,\mathrm{cm}^2$) at the center of the (x, y) plane, are shown in **Figure 8**. The number of coincidences found for each case, and the rising and falling edges, calculated as the inflection points of a sigmoidal function, are reported in **Table 2** for each profile. Even though a small difference is appreciated between the number of events detected by each of the simulated PET configurations, results show an excellent agreement between both case 1 and case 2 with the reference case 0, confirming the feasibility of using either geometry to implement online treatment monitoring in the *GaToroid* static gantry.

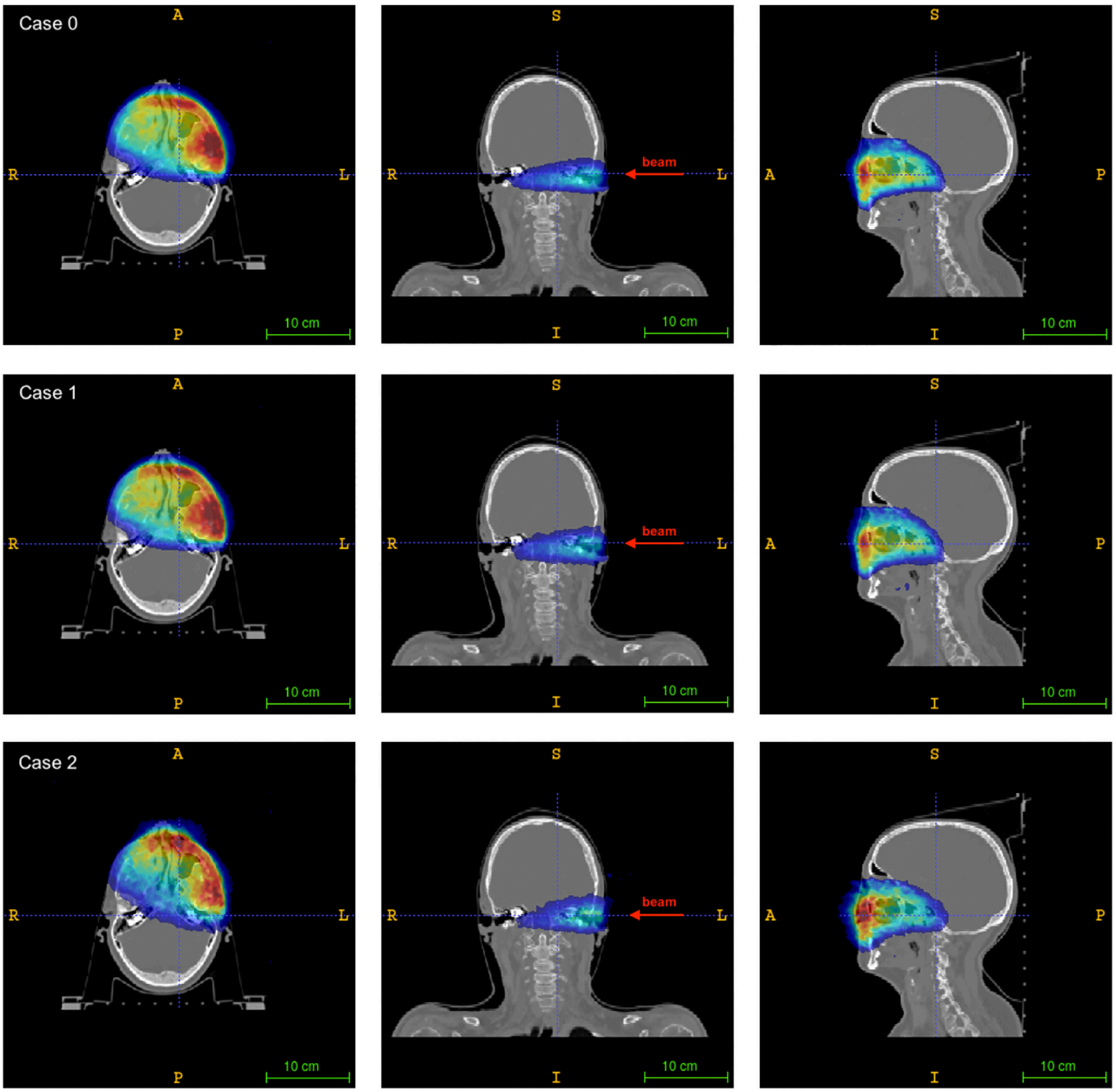

FIGURE 7 | Axial **(left)**, coronal **(center)** and sagittal **(right)** sections of the patient CT superimposed to the reconstructed activity distributions for the different geometries: case 0 **(upper row)**, case 1 **(central row)**, case 2 **(lower row)**. The activity maps are normalized to their maximum intensity. The beam direction is shown for the coronal slice. A standard RAI coordinate system is considered.

TABLE 1 | Number of coincidences and range parameters of the activity profile in the *y* and *z* direction for a simulated $5 \times 7 \times 5$ cm^3 homogeneous activity. The reconstructed range matches the expected value within the error, for both projections and for all the configurations.

	Number of coincidences	y_rising (cm)	y_falling (cm)	y_range (cm)	z_rising (cm)	z_falling (cm)	z_range (cm)
case 0	2.48×10^5	2.07 ± 0.08	9.12 ± 0.08	7.06 ± 0.11	2.59 ± 0.24	7.84 ± 0.23	5.25 ± 0.33
case 1	1.94×10^5	2.03 ± 0.14	9.15 ± 0.14	7.12 ± 0.19	2.56 ± 0.24	7.79 ± 0.23	5.23 ± 0.34
case 2	2.14×10^5	2.12 ± 0.10	9.00 ± 0.08	6.97 ± 0.13	2.55 ± 0.35	7.90 ± 0.58	5.35 ± 0.67

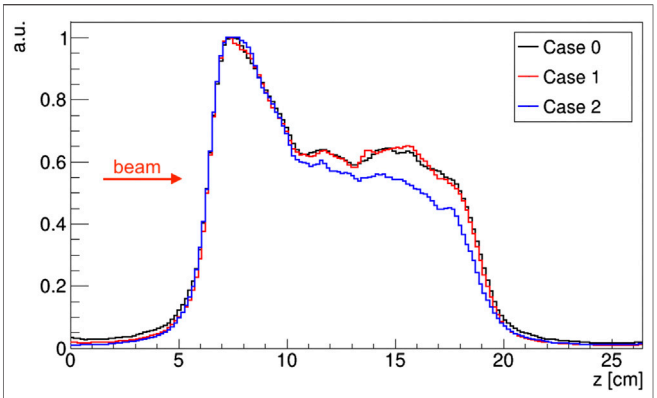

FIGURE 8 | Activity profiles of a proton treatment plan evaluated along the beam direction for the considered PET geometry configurations. Profiles are normalized to their maximum.

TABLE 2 | Rising and falling edge defining the activity profile distribution for each of the considered PET geometries.

	Number of coincidences	Rising edge (cm)	Falling edge (cm)
case 0	1.19×10^6	6.39 ± 0.17	18.89 ± 0.30
case 1	0.92×10^6	6.39 ± 0.16	18.89 ± 0.28
case 2	1.00×10^6	6.36 ± 0.35	18.68 ± 0.77

4 DISCUSSION

The proposed design addresses in an innovative and integrated way the three key components that are necessary to fulfill particle therapy's promise of high-precision cancer treatment coupled to minimum damage to healthy tissue: beam delivery, dose monitoring and treatment verification.

Although a final technical design of the proposed system is not ready yet, the focus of this manuscript is on the description of the concept and on the evaluation of the expected performance of the imaging system to be integrated in *GaToroid*.

GaToroid is a gantry design concept that completely changes the approach to the beam delivery: the recently patented [38] lightweight, static toroidal gantry will allow a very precise beam modulation coupled to a very fast delivery time. The delivery of typical treatment plans can thus be quicker and simpler, while retaining the flexibility of firing the beam from many directions.

Moreover, the static configuration also allows a much lighter footprint, with remarkably smaller size, lower weight and lower cost, compared to existing gantries.

These advantages come at the price of restricting the set of delivery angles, since the entrance windows only cover a fraction of the azimuthal angle, with the rest taken by the coils. However, the design optimisation, in terms of bore size, number of coils, beam windows size will focus on maximising the angular acceptance for the incoming beam.

Beam monitoring is currently based on ionization chambers, a solid technology but a limiting factor for more performing delivery schemes requiring higher speed, sensitivity, spatial and time resolution. The development of LGAD thin silicon sensors offers the possibility to design innovative monitoring detectors that would overcome many limitations of gas chambers, opening at the same time the possibility to exploit extremely accurate time information. *GaToroid* allows the implementation of both options, and at the present stage no decision has been made in view of the design and implementation of a prototype system yet.

High precision range monitoring by means of *in-vivo* real time imaging is crucial in order to achieve full control of the treatment delivery and implement adaptive strategies in particle therapy. The few tests performed in clinical conditions show promising - but not optimized - results: with a gamma camera only the 1D beam profile along its delivery direction is measured [24], with two flat in-beam PET heads, the 3D activity distribution is reconstructed with limited statistics and a modest precision on the vertical coordinate [25].

We propose a PET-based online range monitoring, which is easily integrated in the *GaToroid* static configuration, that allows a ring-like layout similar to standard commercial scanners and, by means of a (nearly) full azimuthal angular coverage, will both enhance the statistics and limit the effect of geometry-related artefacts in the reconstruction.

The simulations of the delivery of a clinical treatment plan for adenoid cystic carcinoma provide a high quality 3D activity map, with no significant artefact, for both the PET configurations considered in the study,confirming the suitability of the proposed design.

In view of the choice of the beam monitoring technology, LGADs present an interesting option, as they would provide time-of-flight information, which, as already proposed by a previous study [39], could be combined to PET-based photon detection to implement a prompt-gamma-timing analysis. By coupling 3D activity maps and prompt-gamma distributions, the combination of the LGAD beam monitor and the PET range monitor would be a hybrid imaging device.

Technology Readiness

Although the construction of a prototype implementing the proposed design could be started with presently existing technologies, some ongoing developments would allow important improvements in view of the design of a full size system.

HTS conductors represent one of the most challenging aspects of the *GaToroid* magnetic design. Rare-earth-based Barium Copper Oxide (ReBCO) conductors are nowadays deeply investigated for high field application, such as toroidal fusion magnets [40, 41], particle accelerator magnets [42] and even for traditional rotating gantries [43]. While already providing the possibility of working well above the liquid helium temperature in a magnetic field of about 10 T, HTS conductors still present technological limits and challenges, such as insufficient field quality, not established quench protection techniques and limited amount of industrial manufacturing, inadequate for series production and costs reduction.

The ongoing development of *GaToroid* HTS coils will tackle these technical problems, for example by further investigating insulated windings with stacked tapes and Non or Partially-Insulated [44, 45] configurations for such large magnets. Beyond the cable topology and the insulation, effective and robust solutions for joints between grades and pancake layers are crucial aspects for the magnet design. At the same time, simulation tools and experimental validation are challenging aspects of HTS quench protection and must be faced to propose a solid and reliable machine for particle therapy.

Furthermore, the use of this kind of conductors for medical applications can also contribute to drive the ReBCO market toward a price reduction and a much wider spread, as was for Nb-Ti in MRI in the last decades.

For beam monitoring, the choice of segmented silicon detectors based on the LGAD technology naturally matches the requirements of the *GaToroid* design. However, this technology still has to face many challenges, starting from the need of a segmentation in small pixels to cope with the fluxes of therapeutic beams when the detectors are operated in counting mode. A high number of channels is required for the electronics, that must be bump-bonded to the sensor pads, and at the same time the total material thickness must be kept low enough to avoid significant beam perturbations. Another issue to be addressed for the use of LGAD detectors for beam monitoring is their limited radiation resistance, which was recently improved [46], in particular in view of their applications in high energy physics experiments; further progress is expected in the near future. For all the above mentioned reasons, the technology choice for implementing the beam monitoring functionality is still open.

However, the use of LGAD detectors would allow to implement more sophisticated analysis tools, giving access to the imaging of fast-decaying isotopes [47, 48], i.e., isotopes whose half life is in the ns-ms time-scale. As shown in a previous work by some of the authors [39], if a background rejection method based on data acquired in the inter-bunch period is implemented so as to discriminate only fast-decaying isotopes data, the activity range shows a stronger and more linear correlation to the primary particle range than longer-decaying isotopes, therefore yielding an enhanced detector sensitivity and range detection precision. Indeed, the real-time information collected within a few tens of milliseconds at a single beam-spot scale minimizes the long-lived contributions accumulated from previous spots that often correspond to different ranges.

Also, the timing information provided by LGAD detectors can be used to provide a start signal that, combined with a stop given by PET detectors, would generate a Time-Of-Flight (TOF) spectrum that could be analyzed with the Prompt Gamma Timing (PGT) technique [39, 49]. The TOF depends on the particle beam path and the photon emission point, therefore correlating the measured spectrum to the range in the delivered treatment. Moreover, prompt-gammas are emitted on a ps-scale, yielding a stronger correlation to the beam path than any distribution obtained measuring very-short- (i.e., shorter than the spill) or short-lived (i.e., mostly ^{11}C and ^{15}O) in-beam PET isotopes.

State-of-the-art PET detectors and electronics [50] can measure photons with a time resolution of the order of 100 ps; on the other hand, a single PET detector has a smaller active volume and energy resolution worse than a system optimised for photons in the MeV range. As shown in a preliminary feasibility study [39], it is in principle possible to implement PGT measurements with a PET detector. With a large angular coverage, as for the proposed in-beam PET scanner configuration, the information obtained by prompt photons can be exploited, as long as it is integrated with the position-dependent measurements of each detector. An algorithm designed for this purpose is in an advanced development stage, and will be the object of a future publication. Preliminary simulation results [51] show that the proposed in-beam PET scanner geometry could measure the prompt photons range with about 5 mm precision. The experimental implementation of the proposed technique will be definitely challenging, with the bottleneck being the high proton rate crossing the LGAD detector; however, the requirements for prompt gamma timing are less strict than for beam monitoring, where pile-up effects must be kept well under control. Although a full efficiency cannot be achieved at therapeutic rates, due to DAQ bandwidth limitations and to the overlap of signals very close in time (the last effect also depending on the beam time structure), the detection of these fast signals, combined with PET information, should lead to an enhanced correlation between the delivered dose and the measured distribution.

5 CONCLUSIONS

Large acceptance, steady-state configuration and superconducting magnets offer interesting reduction of size, weight and cost of gantries and related infrastructures, creating an attractive alternative to the state of the art. Furthermore, such a structural integration with beam and range monitoring represent an additional step toward compact gantries and single room facilities.

The *GaToroid* concept was presented, and a configuration suitable for proton beam delivery was defined, with an 80 cm diameter bore. The feasibility of irradiating a realistic target volume was assessed for the proposed configuration, and the residual magnetic field inside the bore was evaluated, in view of the choice of the dose delivery system. Moreover, an accurate simulation study of the expected performance of a PET-based range monitor, integrated in the gantry with different configurations, showed that a reliable, high resolution 3D activity image can be reconstructed from the delivery of a clinical treatment plan.

Further work will focus on defining the specifications of a beam monitor based on solid-state detectors, in terms of required area, pixelization, readout speed, sensitivity, spatial and flux measurement precision, and in developing the tools to exploit its time resolution to improve the treatment monitoring quality with the Prompt Gamma Timing (PGT) technique, in view of the final design of a *GaToroid* prototype with hybrid imaging capabilities.

DATA AVAILABILITY STATEMENT

The raw data supporting the conclusions of this article will be made available by the authors, without undue reservation.

AUTHOR CONTRIBUTIONS

LB, EFe and GDR designed and simulated the GaToroid configuration; VF, EFi, FP and VM defined the imaging system configuration, assessed the potential of a UFSD-based beam monitor device and implemented the simulation of the PET detector response in case of delivery of a clinical treatment plan; PC coordinated the development, in the framework of the ATTRACT/H2I2 project (see next section on Funding), and edited the manuscript.

FUNDING

This work is part of the ATTRACT project funded by the EC under Grant Agreement 777222, with project name *Hybrid High-precision In-vivo Imaging in Particle Therapy (H2I2)*. The project is co-funded by the CERN Budget for Knowledge Transfer to Medical Applications.

REFERENCES

1. Rossi S. The national centre for oncological hadrontherapy (CNAO): status and perspectives. *Phys Med* (2015) 31:333–51. doi:10.1016/j.ejmp.2015.03.001.
2. Pedroni E, Bacher R, Blattmann H, Böhringer T, Coray A, Lomax A, et al. The 220-MeV proton therapy project at the Paul Scherrer Institute: conceptual design and practical realization. *Med Phys* (1995) 22(1):37–53.
3. Fuchs R, Weinrich U, Emde P. The heavy ion gantry of the HICAT facility (2004) Lucerne. EPAC-2004-THPLT033.
4. Iwata Y, Noda K, Shirai T, Murakami T, Furukawa T, Mori S, et al. Design of a superconducting rotating-gantry for heavy-ion therapy. *Phys Rev Spec Top Accel Beams* (2012) 15:044701. doi:10.1103/PhysRevSTAB.15.044701
5. Robin DS, Arbelaez D, Caspi S, Sun C, Sessler A, Wan W, et al. Superconducting Toroidal Combined-Function Magnet for a compact ion beam cancer therapy gantry. *Nucl Instrum Methods Phys Res* (2011) 659:484–93. doi:10.1016/j.nima.2011.08.049
6. Wan W. Alternating-gradient canted cosine theta superconducting magnets for future compact proton gantries. *Phys Rev Spec Top Accel Beams* (2015) 18:103501. doi:10.1103/PhysRevSTAB.18.103501
7. Trbojevic D. Carbon/proton therapy: a novel gantry design. *Phys Rev Accel Beams* (2007) 10:053503. doi:10.1103/PhysRevSTAB.10.053503
8. Gerbershagen A. A novel beam optics concept in a particle therapy gantry utilizing the advantages of superconducting magnets. *Z Med Phys* (2016) 26:224–37. doi:10.1016/j.zemedi.2016.03.006
9. Haberer T. The heidelberg ion beam therapy center, workshop: ideas and technologies for a next generation facility for medical research and therapy with ions (2018) Available at: https://indico.cern.ch/event/682210/contributions/2960999/attachments/1670825/2682144/Haberer_IONS2018_HITandMIT-Status_2018Jun19_public.pdf.
10. Yan S, Lu HM, Flanz J, Adams J, Trofimov A, Bortfeld T. Reassessment of the necessity of the proton gantry: analysis of beam orientations from 4332 treatments at the Massachusetts general hospital proton center over the past 10 years. *Int J Radiat Oncol* (2016) 95(1):224–33. doi:10.1016/j.ijrobp.2015.09.033
11. Giordanengo S, Donetti M, Garella MA, Marchetto F, Alampi G, Ansarinejad A, et al. Design and characterization of the beam monitor detectors of the Italian national center of oncological hadron-therapy (CNAO). *Nucl Instrum Meth A* (2013) 698:202–7. doi:10.1016/j.nima.2012.10.004
12. Farr JB, Flanz JB, Gerbershagen A, Moyers MF. New horizons in particle therapy systems. *Med Phys* (2018) 45(11): e953–83. doi:10.1002/mp.13193.
13. Sadrozinski HW, Ely S, Fadeyev V, Galloway Z, Ngo J, Parker C, et al. Ultra-fast silicon detectors. *NIMA* (2013) 730:226–231. doi:10.1016/j.nima.2013.06.033
14. Staiano A, Arcidiacono R, Boscardin M, Dalla Betta GF, Cartiglia N, Cenna F, et al. Development of ultra-fast silicon detectors for 4D tracking. *J Inst Met* (2017) 1017:C12012. doi:10.1088/1748-0221/12/12/C12012
15. Cartiglia N, Staiano A, Sola V, Arcidiacono R, Cirio R, Cenna F, et al. Beam test results of a 16 ps timing system based on ultra-fast silicon detectors. *NIMA* (2017) 850:83–88. doi:10.1016/j.nima.2017.01.021
16. Paganetti H. Range uncertainties in proton therapy and the role of Monte Carlo simulations. *Phys Med Biol* (2012) 57(11):R99–117. doi:10.1088/0031-9155/57/11/R99
17. Tashima H, Yoshida E, Inadama N, Nishikido F, Nakajima Y, Wakizaka H, et al. Development of a small single-ring OpenPET prototype with a novel transformable architecture, *Phys Med Biol* (2016) 61(4):1795–809. doi:10.1088/0031-9155/61/4/1795.
18. Enghardt W, Parodi K, Crespo P, Fiedler F, Pawelke J, Pönisch F. Dose quantification from in-beam positron emission tomography. *Radiother Oncol* (2004) 73(2):S96–98. doi:10.1016/S0167-8140(04)80024-0
19. Nishio T, Miyatake A, Ogino T, Nakagawa K, Saijo N, Esumi H. The development and clinical use of a beam on-line PET system mounted on a rotating gantry port in proton therapy. *Int J Radiat Oncol Biol Phys* (2010) 76(1):277–86. doi:10.1016/j.ijrobp.2009.05.065
20. Binet S, Bongrand A, Busato E, Force P, Guicheney C, Insa C, et al. Construction and first tests of an in-beam PET demonstrator dedicated to the ballistic control of hadrontherapy treatments with 65 MeV protons. *IEEE Trans Radiat Plasma Med Sci* (2018) 2(1):51–60. doi:10.1109/TRPMS.2017.2780447
21. Yoshida E, Tashima H, Shinaji T, Shimizu K, Wakizaka H, Mohammadi A, et al. Development of a whole-body dual ring OpenPET for in-beam PET. *IEEE Trans Radiat Plasma Med Sci* (2017) 4(1):293–300. doi:10.1109/TRPMS.2017.2703823
22. Topi A, Muraro S, Battistoni G, Belcari N, Bisogni MG, Camarlinghi N, et al. Monitoring proton therapy through in-beam PET: an experimental phantom study. *IEEE Trans Radiat Plasma Med Sci* (2020) 4(2):194–201. doi:10.1109/TRPMS.2019.2924036
23. Bisogni MG, Attili A, Battistoni G, Belcari N, Camarlinghi N, Cerello P, et al. INSIDE in-beam positron emission tomography system for particle range monitoring in hadrontherapy. *J Med Imag* (2017) 4(1):011005. doi:10.1117/1.JMI.4.1.011005
24. Xie Y, Bentefour EH, Janssens G, Smeets J, Vander Stappen F, Hotoiu L, et al. Prompt gamma Imaging for *in vivo* range verification of pencil beam scanning proton therapy. *Int J Radiat Oncol Biol Phys* (2017) 99(1):210–8. doi:10.1016/j.ijrobp.2017.04.027
25. Ferrero V, Fiorina E, Morrocchi M, Pennazio F, Baroni G, Battistoni G, et al. Online proton therapy monitoring: clinical test of a Silicon-photodetector-based in-beam PET. *Sci Rep* (2018) 8:4100. doi:10.1038/s41598-018-22325-6.
26. Belcari E, Ferrero V, Pennazio F, Baroni G, Battistoni G, Belcari N, et al. Monte Carlo simulation tool for online treatment monitoring in hadrontherapy with in-beam PET: a patient study. *Phys Med* (2018) 51:71–80. doi:10.1016/j.ejmp.2018.05.002.
27. Bottura L, Felcini E, De Rijk G, Dutoit B. GaToroid: a novel toroidal gantry for hadron therapy. *Nucl Instrum Methods Phys Res* (2020) 983:164588. doi:10.1016/j.nima.2020.164588
28. Felcini E, Bottura L, van Nugteren J, Gerbershagen A. Particle tracking and beam optics analysis on toroidal gantry for hadron therapy, submitted for publication to focus on early career researchers. *Phys Med Biol* (2020)

29. Felcini E, Bottura L, van Nugteren J, De Rijk G, Kirby G, Dutoit B. Magnetic design of a superconducting toroidal gantry for hadron therapy. *IEEE Trans Appl Supercond* 30(2020)
30. Pullia M, Lante V, Necchi M, Savazzi S, Moreno JO. Deliverable report JRA6.3 conceptual design of a carbon ion gantry. ULICE Union of Light Centres in Europe (2009)
31. Van Nugteren J Software development for the science and design behind superconducting magnet systems (2011) CERN Internship Report.
32. Vignati A, Donetti M, Fausti F, Ferrero M, Giordanengo S, Hammad Ali O, et al. Thin low gain avalanche detectors for particle therapy applications, proceedings of the mini-micro-nano dosimetry and innovative technologies in radiation oncology conference, 10-16 February 2020, north Wollongong, Australia. *J Phys Conf* 1662 (2020) 012035.
33. Yoshida E, Tashima H, Nishikido F, Yamaya T. Development of open-type PET scanners with single-ring and dual ring geometries. *J Nucl Med* (2016) 57:105.
34. Ferrari A, Sala P, Fassò A, Ranft J. FLUKA: a multi-particle transport code (program version 2005) (2005) Rep. SLAC-R-773. Available from: https://www.osti.gov/biblio/877507.
35. Böhlen TT, Cerutti F, Chin MPW, Fassò A, Ferrari A, Ortega PG, et al. The FLUKA code: developments and challenges for high energy and medical applications. *NuclData Sheets* (2014) 120:211–4. doi:10.1016/j.nds.2014.07.049
36. Battistoni G, Bauer J, Böhlen TT, Cerutti F, Chin MPW, Ortega PG, et al. The FLUKA code: an accurate simulation tool for particle therapy. *Front Oncol* (2016) 6:116. doi:10.3389/fonc.2016.00116
37. Ferrero V, Pennazio F, Cerello P, Fiorina E, Garbolino S, Monaco V, et al. Evaluation of in-beam PET treatment verification in proton therapy with different reconstruction methods. *IEEE TRPMS* (2020) 4(2):202–11. doi:10.1109/TRPMS.2019.2942713
38. Bottura L. A Gantry and apparatus for focussing beams of charged particles. WO2019/224215. (2019)
39. Ferrero V, Cerello P, Fiorina E, Monaco V, Rafecas M, Wheadon RJ, et al. Innovation in online hadrontherapy monitoring: an in-beam PET and prompt-gamma-timing combined device. *NIMA* (2019) 936:48–9. doi:10.1016/j.nima.2018.08.065
40. Sykes A, Costley AE, Windsor CG, Asunta O, Brittles G, Buxton P, et al. Compact fusion energy based on the spherical tokamak. *Nucl Fusion* (2018) 58(1):016039. doi:10.1088/1741-4326/aa8c8d
41. Whyte DG, Minervini J, LaBombard B, Marmar E, Bromberg L, Greenwald M. Smaller & sooner: exploiting high magnetic fields from new superconductors for a more attractive fusion energy development path. *J Fusion Energy* (2016) 35(1):41–53. doi:10.1007/s10894-015-0050-1
42. Kirby GA, van Nugteren J, Bajas H, Benda V, Ballarino A, Bajko M, et al. First cold powering test of REBCO roebel Wound coil for the EuCARD2 future magnet development project. *IEEE Trans Appl Supercond* (2017) 27(4):1–7. doi:10.1109/TASC.2017.2653204
43. Takayama S, Kiyanagi K, Yamaguchi A, Tasaki K, Kurusu T, Ishii Y, et al. Design of conduction-cooled HTS coils for a rotating gantry. *Phys Procedia* (2015) 67:879–84. doi:10.1016/j.phpro.2015.06.148
44. Hahn S, Park DK, Bascunan J, Iwasa Y. HTS pancake coils without turn-to-turn insulation. *IEEE Trans Appl Supercond* (2011) 21(3):1592–5. doi:10.1109/TASC.2010.2093492
45. Hahn S, Kim K, Kim K, Lee H, Iwasa Y. Current status of and challenges for no-insulation HTS winding technique. *J Cryog Supercond Soc Jpn* (2018) 53(1):2–9. doi:10.2221/jcsj.53.2
46. Cartiglia N, Sadrozinski H, Seiden A. Tracking particles at fluences 5-10·1E16 n_{eq}/cm^2. In: Proceedings, 27th international workshop on vertex detectors (VERTEX 2018); 2018 Oct 21–26; Chennai, India. Vertex (2018) 9 p.
47. Miyatake A, Nishio T, Ogino T, Sajio N, Esumi H, Uesaka M. Measurement and verification of positron emitter nuclei generated at each treatment site by target nuclear fragment reactions in proton therapy. *Med Phys*. (2010) 37(8):4445–55. doi:10.1118/1.3462559
48. Dendooven P, Buitenhuis HJT, Diblen F, Heeres PN, Biegun AK, Fiedler F, et al. Short-lived positron emitters in beam-on PET imaging during proton therapy. *Phys Med Biol* (2015) 60(23):8923–47. doi:10.1088/0031-9155/60/23/8923
49. Golnik C, Fernando Hueso-González F, Müller A, Dendooven P, Enghardt W, Fiedler F, et al. Range assessment in particle therapy based on prompt gamma-ray timing measurements. *Phys Med Biol* (2014) 59(18):5399–422. doi:10.1088/0031-9155/59/18/5399
50. Bugalho R, Di Francesco A, Ferramacho L, Leong C, Niknejad T, Oliveira L, et al. Experimental results with TOFPET2 ASIC for time-f-flight applications. *Nucl Instrum Methods Phys Res A* (2018) 912:195–8. doi:10.1016/j.nima.2017.11.034
51. Bottura L, Felcini E, Ferrero V, Fiorina E, Monaco V, Pennazio F, et al. Hybrid high-precision in-vivo imaging in particle therapy (H2I2). (2020) Available from: https://attract-eu.com/wp-content/uploads/2019/05/H2I2.pdf.

Conflict of Interest: The authors declare that the research was conducted in the absence of any commercial or financial relationships that could be construed as a potential conflict of interest.

frontiers in Physics

REVIEW
published: 30 November 2020
doi: 10.3389/fphy.2020.565954

Are Further Cross Section Measurements Necessary for Space Radiation Protection or Ion Therapy Applications? Helium Projectiles

John W. Norbury[1], Giuseppe Battistoni[2], Judith Besuglow[3,4], Luca Bocchini[5], Daria Boscolo[6], Alexander Botvina[7], Martha Clowdsley[1], Wouter de Wet[8], Marco Durante[6,9], Martina Giraudo[5], Thomas Haberer[10], Lawrence Heilbronn[11], Felix Horst[6], Michael Krämer[6], Chiara La Tessa[12,13], Francesca Luoni[6,9], Andrea Mairani[10], Silvia Muraro[2], Ryan B. Norman[1], Vincenzo Patera[14], Giovanni Santin[15,16], Christoph Schuy[6], Lembit Sihver[17,18], Tony C. Slaba[1], Nikolai Sobolevsky[7], Albana Topi[6], Uli Weber[6], Charles M. Werneth[1] and Cary Zeitlin[19]*

[1]NASA Langley Research Center, Hampton, VA, United States, [2]Istituto Nazionale di Fisica Nucleare (INFN), Sezione di Milano, Milan, Italy, [3]German Cancer Research Center (DKFZ), Heidelberg, Germany, [4]University of Heidelberg, Heidelberg, Germany, [5]Thales Alenia Space, Torino, Italy, [6]GSI Helmholtzzentrum für Schwerionenforschung, Darmstadt, Germany, [7]Institute for Nuclear Research of the Russian Academy of Sciences, Moscow, Russia, [8]University of New Hampshire, Durham, NH, United States, [9]Technische Universität Darmstadt, Darmstadt, Germany, [10]Heidelberg Ion Beam Therapy Center, Heidelberg, Germany, [11]University of Tennessee, Knoxville, TN, United States, [12]University of Trento, Trento, Italy, [13]Trento Institute for Fundamental Physics and Applications (INFN-TIFPA), Trento, Italy, [14]Universita' di Roma "Sapienza", Roma, Italy, [15]European Space Agency, Noordwijk, Netherlands, [16]RHEA System, Noordwijk, Netherlands, [17]Technische Universität Wien, Atominstitut, Vienna, Austria, [18]Chalmers University of Technology, Gothenburg, Sweden, [19]Leidos Innovations Corporation, Houston, TX, United States

The helium (^{4}He) component of the primary particles in the galactic cosmic ray spectrum makes significant contributions to the total astronaut radiation exposure. ^{4}He ions are also desirable for direct applications in ion therapy. They contribute smaller projectile fragmentation than carbon (^{12}C) ions and smaller lateral beam spreading than protons. Space radiation protection and ion therapy applications need reliable nuclear reaction models and transport codes for energetic particles in matter. Neutrons and light ions (^{1}H, ^{2}H, ^{3}H, ^{3}He, and ^{4}He) are the most important secondary particles produced in space radiation and ion therapy nuclear reactions; these particles penetrate deeply and make large contributions to dose equivalent. Since neutrons and light ions may scatter at large angles, double differential cross sections are required by transport codes that propagate radiation fields through radiation shielding and human tissue. This work will review the importance of ^{4}He projectiles to space radiation and ion therapy, and outline the present status of neutron and light ion production cross section measurements and modeling, with recommendations for future needs.

Keywords: helium projectile cross section measurements, space radiation cross sections, ion therapy cross sections, helium projectile ion therapy, helium projectile space radiation

OPEN ACCESS

Edited by:
Federico Giove, Centro Fermi - Museo storico della fisica e Centro studi e ricerche Enrico Fermi, Italy

Reviewed by:
Loredana G. Marcu, University of Oradea, Romania
Giacomo Cuttone, Laboratori Nazionali del Sud (INFN), Italy

****Correspondence:***
John W. Norbury
john.w.norbury@nasa.gov

Specialty section:
This article was submitted to Medical Physics and Imaging, a section of the journal Frontiers in Physics

Received: *26 May 2020*
Accepted: *21 August 2020*
Published: *30 November 2020*

Citation:
Norbury JW, Battistoni G, Besuglow J, Bocchini L, Boscolo D, Botvina A, Clowdsley M, de Wet W, Durante M, Giraudo M, Haberer T, Heilbronn L, Horst F, Krämer M, La Tessa C, Luoni F, Mairani A, Muraro S, Norman RB, Patera V, Santin G, Schuy C, Sihver L, Slaba TC, Sobolevsky N, Topi A, Weber U, Werneth CM and Zeitlin C (2020) Are Further Cross Section Measurements Necessary for Space Radiation Protection or Ion Therapy Applications? Helium Projectiles. Front. Phys. 8:565954. doi: 10.3389/fphy.2020.565954

1 INTRODUCTION AND REVIEW

The International Biophysics Collaboration[1] (IBC) was recently formed at the GSI Helmholtzzentrum für Schwerionenforschung, with the aim of utilizing the future Facility for Antiproton and Ion Research (FAIR) and other accelerators for biophysics studies relevant to space radiation protection, ion therapy, and other biophysics applications. Within the IBC, a cross section working group has been formed to study what cross section measurements and modeling need to be performed to support the broad aims of the IBC. Membership of the cross section working group is open, and other colleagues are encouraged to participate: An important objective for the cross section working group is to have broad support within the international scientific community.

Previous analyses of experimental data [1–4] focused on measurement gaps for space radiation. The highest priority measurement recommendations were double differential cross sections for the following ion[2] reactions,

$$\text{He, C, O, Si, Fe} + \text{H, C, O, Al, Fe} \rightarrow {}^{1,2,3}\text{H}, {}^{3,4}\text{He} + \text{X}, \qquad (1)$$

where X is anything, thereby denoting an inclusive reaction, where a particular nuclide, say ^{2}H, is measured[3] along with anything (X) else. The projectiles He, C, O, Si, and Fe were chosen[4] because of their prominence in the free space galactic cosmic ray (GCR) spectrum. The targets H, C, O, Al, and Fe were chosen as being representative elements in the human body and spacecraft. For applications in ion therapy, projectiles ranging from H to O interacting with targets composed of H, C, and O as main constituents of the human body are typically considered crucial. Therapy facilities employing H and ^{12}C in the energy range of a few hundred MeV/n have been in use for many years around the world, whereas ions such as ^{4}He and ^{16}O are considered important extensions of the currently offered treatments [6]. Consequently, the needs of space radiation protection can be seen as a superset encompassing the needs of therapy applications in most cases, due to the significantly larger range of projectile, energy, and target combinations of interest for the space radiation community [7].

The aim of the present study was therefore to consider whether further cross section measurements are necessary for space radiation protection or ion therapy applications, define overlaps in interest for both disciplines, and prioritize needed experiments and measurement quantities.

1.1 Importance of Light Ion Fragments

In the context of space radiation protection, light ion fragments ^{1,2,3}H and ^{3,4}He were emphasized [1–4] for future double differential cross section measurement recommendations in **Eq. 1** for the following reasons:

(1) Neutrons and light ion fragments dominate dose equivalent [8–10] for realistic spacecraft shield thicknesses ($\geq$ 20 g/cm^2). This can be seen in **Figure 1**, which shows the contribution to blood-forming organ dose equivalent for free space, simple geometries, and various spacecraft locations.

(2) Because they have small charge and mass, neutrons and light ion fragments are scattered at large angles, and therefore require full 3-dimensional transport [11] methods (as opposed to 1-dimensional straight-ahead scattering approximations). Full 3-dimensional transport methods, in turn, require nuclear physics double differential cross sections [12, 13] as input.

(3) Transport code (GEANT, FLUKA, MCNP, PHITS, HZETRN, and SHIELD) comparisons [14] show the largest differences for light ion fragment production. The disagreements are mainly due to inaccurate light ion nuclear physics models and lack of experimental data to be used to improve these models. As an illustration of this, **Figure 2** shows large disagreements for numerous transport code comparisons for the production of ^{3}H and ^{3}He.

(4) An experimental double differential cross section measurement program was recently completed at the NASA Space Radiation Laboratory (NSRL), located at Brookhaven National Laboratory (BNL), using oxygen and iron beams on several targets, with the production of light ion fragments [16]. Large differences were seen between measurements and the light ion cross-section models used in the PHITS [17] transport code.

(5) An experimental thick target program was also recently completed at the NSRL, using unique combinations of double thick targets where incident beam particles scattered from the first target and secondary fragments subsequently scattered from a back target. This simulated the scattering geometry in a spacecraft, where fragments are produced when GCRs interact with a spacecraft wall and more scattered products are produced from the far, back, and surrounding walls. These measurements show significant discrepancies [18] compared to transport codes (MCNP and PHITS) for light ions. Further cross section measurements of light ion fragments have been recommended to resolve these discrepancies.

(6) Mars Science Laboratory Radiation Assessment Detector (MSL-RAD) light ion flux measurements highlight the

[1]Spokesperson: Vincenzo Patera (Universita' di Roma "Sapienza", Roma, Italy).

[2]The very first ion collision experiments [5] were carried out more than 100 years ago by Ernest Rutherford, who scattered helium (He) projectiles (alpha particles) from gold (Au) targets. Of course, no accelerators were available, and the helium projectiles were produced from the radioactive decay of radium. The helium projectile kinetic energy was only 5 MeV (about 1 MeV/n) and the scattering was elastic (no fragments could be produced), but some of the helium projectiles suffered large deflections from the incident direction, which indicated scattering from a tiny atomic core. This was the discovery of the atomic nucleus, with a size of order 10 m. Helium projectiles are also the subject of the present work.

[3]An exclusive measurement would mean that ^{2}H is measured as well as all other possible reaction products. Note that an inclusive measurement is the sum of all exclusive measurements.

[4]He(Z = 2), C(Z = 6), O(Z = 8), Si(Z = 14), Fe(Z = 26).

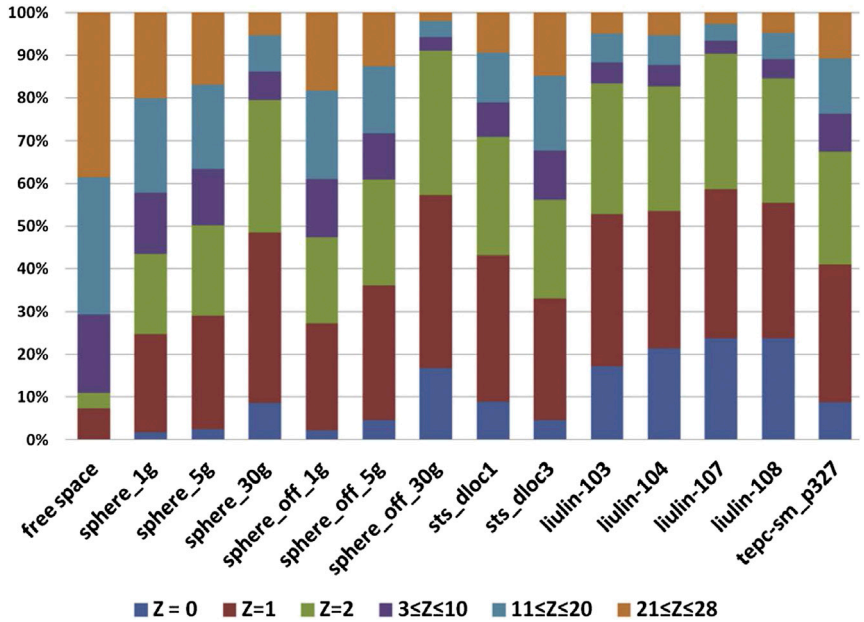

FIGURE 1 | Calculated percent contribution to blood-forming organ (BFO) dose equivalent for free space (far left), simple spherical geometries in free space, and detector locations inside the space shuttle (STS) and the International Space Station (ISS) in free space. The vehicles included three aluminum spheres with areal densities 1, 5, and 30 g/cm^2 where the body was placed at the center of the sphere (sphere_1g, sphere_5g, and sphere_30g) and three spheres of the same areal densities where the body was placed against the wall of the sphere (sphere_ off_1g, sphere_off_5g, and sphere_off_30g). For the latter cases, the spheres were constructed so that they would each have the same habitable volume as the Multi-Purpose Crew Vehicle (MPCV), 316 cubic feet (8.95 m^3). Thus, each sphere had an inner radius of 1.288 m. Also, six locations were studied in the STS (shuttle) where detectors have historically been placed (sts_dloc1-6). Five locations in the ISS 6A configuration were also used: two points in the Destiny (Lab) module laboratory area (Liulin_103, Liulin_107); two points in the Unity (Node1) module (Liulin_104, Liulin_108); and one point in the Zvezda (SM; service module) module on panel number 327 (TEPC-sm_p327). Reprinted from Walker et al. [8].

need for improved nuclear interaction models. Light ion model results show moderate to large discrepancies [19–21] over the MSL-RAD energy range,[5] with model errors mainly attributed to inaccurate light ion nuclear physics models.

(7) Calculations with the HZETRN transport code underpredict dose measurements from the International Space Station [22, 23], at high latitudes where GCRs contribute most. The cause of the discrepancy has yet to be fully clarified, but improvements to the underlying cross section models will help remove some measure of uncertainty.
(8) Light ion cross sections represent the largest physics uncertainty in space radiation.
(9) Light ion cross section measurements [1] are needed to improve inaccurate light ion nuclear physics models.
(10) Light ion cross section measurements represent the largest gap in the cross section database [1].

The importance of light fragments, and nuclear fragmentation in general, follows a similar rationale in ion therapy as for space radiation and was already discussed previously [24–26].

(1) Base data used for treatment planning are typically generated using either Monte Carlo [27, 28] or dedicated deterministic [29, 30] transport codes. Therefore, the physical models used in each transport code directly translate to the quality of a treatment, especially for "novel" ions [31–33].
(2) Inter-code comparisons of Monte Carlo transport codes show important differences for the spatial distributions of prompt gamma rays, light charged fragments, and neutrons [34].
(3) Heavier projectiles, like ^{12}C, undergo significant amounts of nuclear fragmentation along their beam path, and the lighter fragments produced deposit a significant dose behind the Bragg peak (fragment tail) [35].
(4) Light fragments are of special interest for online monitoring purposes in ion beam therapy [36].
(5) If the projectile fragmentation cross sections are not precisely modeled, then dose calculation algorithms become inaccurate, which can lead to inhomogeneous dose distributions and underdosage or overdosage of tumor sites [37].

[5]In this particular case, the observed discrepancies did not contribute significantly to dose-equivalent, but improvements would yield better agreement with MSL-RAD.

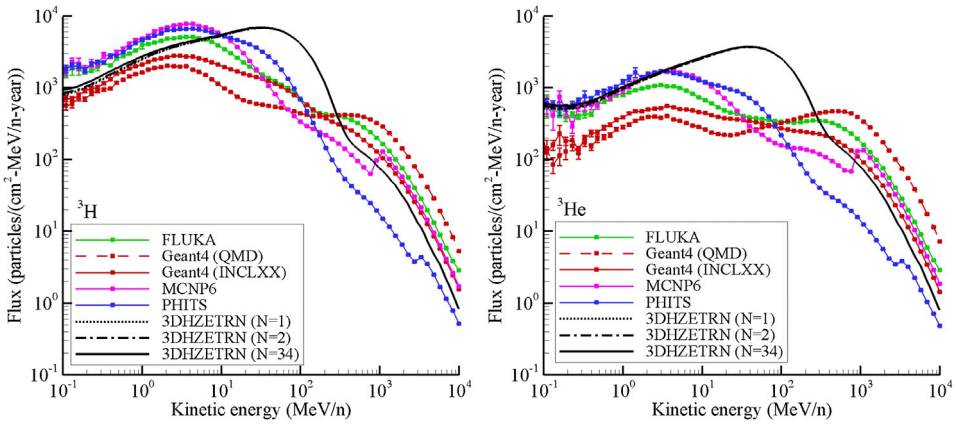

FIGURE 2 | ^{3}H and ^{3}He flux behind 60 g/cm^2 Al shield for GCR minimum spectrum. Reprinted from Slaba et al. [15].

(6) In addition to projectile fragmentation, fragmentation of the target is also highly relevant for precise dose calculations in ion therapy [38].

As emphasized above, light ions make large contributions to dose equivalent and are essential for treatment planning, but the physics of their production remains poorly understood. One would hope to compare theoretical nuclear physics models to cross section measurements to resolve these issues, but the largest gap in the cross section database occurs for light ions. This is why a further cross section measurement program is recommended for space radiation and ion therapy applications.

1.2 Importance of Double Differential Cross Sections

Neutrons and light ion fragments are scattered at large angles because they have small charge and mass. They therefore require full 3-dimensional transport methods, which need double differential cross sections [12, 13] as input. This is why double differential[6] cross sections are highlighted in the present work, with emphasis on isotopic production cross sections, $d^2\sigma/dEd\Omega$, where E is the total energy of a fragment given[7] by $E \equiv T + m$, where T is the kinetic energy and m is the rest mass.[8] The fragment solid angle is Ω.

Other reasons for emphasizing double differential isotopic cross sections are as follows. Single differential spectral, $d\sigma/dE$, and angular, $d\sigma/d\Omega$, cross sections can be obtained from $d^2\sigma/dEd\Omega$ by integrating over angle or energy as in $d\sigma/dE = \int d\Omega\,(d^2\sigma/dEd\Omega)$ and $d\sigma/d\Omega = \int dE\,(d^2\sigma/dEd\Omega)$. Total cross sections are obtained *via* $\sigma = \int dEd\Omega\,(d^2\sigma/dEd\Omega)$. Therefore, from a theoretical point of view, if one would measure a complete set of double differential cross sections, then one could generate all necessary single differential and total cross sections. In practice, this is typically not feasible. However, there are examples of systematic measurements of double differential fragmentation cross sections of light projectiles on different thin targets, for example, with 50 MeV/n (3°–39°) and 95 MeV/n (4°–39°) ^{12}C beams [39–41] performed at GANIL. As usual, this experimental setup does not cover the entire spectrum of fragment information (mass, charge, energy, and angle). Especially for heavier projectile, there are large gaps in the published data. Therefore, future experimental programs should focus on measuring double differential cross-section data sets as completely as possible (covering all angles, energies, and fragments including neutrons) to be able to cross-check them against measured total and single differential cross sections. The single differential data could be efficiently measured by accompanying experiments.

Similar reasoning applies to isotopic fragment cross sections vs. elemental or charge changing cross sections. Consider light ions: An isotopic measurement would provide double differential production cross sections for each ^{1}H, ^{2}H, ^{3}H, ^{3}He, and ^{4}He, whereas elemental measurements only provide cross sections for H and He. Yet, the elemental cross sections can all be obtained from the isotopic cross sections by adding the individual isotopic contributions. Isotopic cross sections cannot be obtained from elemental measurements. Again, some applications require only elemental or charge changing cross sections, and some require isotopic cross sections. It therefore makes sense to focus future measurements on attaining isotopic resolution so that the cross sections are useful for all possible future applications. Of course, isotopic double differential cross sections are more difficult to measure than, for example, charge changing total cross sections. However, given the very broad range of future applications of cross section measurements covering both space radiation and ion therapy, it is deemed worthwhile to focus future measurements on isotopic double differential cross sections.

[6]Other double differential cross sections, such as Lorentz-invariant double differential cross sections or double differential cross sections written in terms of momentum, transverse momentum, etc., are equivalent to $d^2\sigma/dEd\Omega$.

[7]Unless specified otherwise, standard particle physics units are used in the text, with the speed of light defined as unity, $c \equiv 1$. This is why the total energy is written as $E \equiv T + m$ and not $E \equiv T + mc^2$.

[8]Note that $dE = dT$. Most experiments measure differential cross sections as a function of T.

All of the above discussion in this subsection has centered on measurement issues, but the same is true for theoretical modeling. At the most fundamental level, a particle physics Feynman diagram gives the quantum mechanical amplitude for a given process which is inserted directly into a formula for the double differential cross section. Spectral, angular and total cross sections are obtained by integrating as described above. Even if one is not using Feynman diagrams directly, the quantum mechanical amplitude, obtained by some theoretical model, is the most fundamental quantity. In other words, double differential cross sections are most fundamental. Another matter concerns comparing theoretical model results to experimental measurements. Comparisons of double differential cross section models with double differential cross section measurements is the most precise sort of validation test of a theoretical model. Comparing theoretical models for single differential spectral or angular cross section measurements is less precise: The models might get these correct, even though the underlying double differential cross sections might be incorrect. Comparing total cross section models with experiment is the least precise. In summary, the most precise test of a theoretical model is comparison of double differential cross sections with experiment. If these are correct, then single differential spectral and angular cross sections, as well as total cross sections, will automatically be correct. The reverse situation does not hold; for example, comparing total theoretical model cross sections with experiment will not guarantee that the double differential cross sections are correct. The considerations are the same for isotopic vs. elemental cross sections. If all the theoretical model isotopic cross sections agree with experiment, then the elemental and charge changing cross sections will automatically be correct as well. The reverse situation does not hold.

However, it is important to note that in many modern Monte Carlo transport codes, the removal of primary ions and the fragment production are treated separately. The interaction probability is typically sampled according to parameterized total reaction cross sections for which semi-empirical models fine-tuned to experimental data are used, while the fragment production and their double differential distribution is obtained from nuclear event generators and coalescence/evaporation models. Therefore, to optimize such transport codes, experimental data on both the total reaction cross section and the double differential fragment distributions are required.

The conclusion of this subsection is that the most useful and precise types of cross sections are isotopic double differential cross sections. This is true for both experimental measurements and theoretical models. If these types of cross sections give good comparisons between models and experiment, then all other types of cross sections will automatically also give good comparisons. Also, all other types of cross sections (both theoretical and experimental) can be obtained from isotopic double differential cross sections. This behavior should be exploited to cross-check total and single differential datasets.

1.3 Measurements

Previous measurement studies [1–4] will now be summarized, for all types of projectiles, emphasizing double differential cross sections for light ion fragment production. **Figures 3–7** show where isotopic double differential cross section data have been measured for light ion production. The following conclusions can be stated:

- In the low energy region below the pion threshold (< 280 MeV/n), double differential cross sections for light ion production mainly exist for H, He, C, O, Ne, and Ar[9] projectiles.
- In the medium energy (280–3,000 MeV/n) region, double differential cross sections for light ion production mainly exist for H, He, C, Ne, and Ar projectiles.
- In the high energy (3–15 GeV/n) and very high energy (> 15 GeV/n) regions, there are no double differential cross-section data[10] for light ion production.
- Even though there are a moderate number of experimental measurement articles dealing with helium projectiles, further detailed analysis of He data below 3 GeV/n reveals significant problems and flaws with the data, leading to the conclusion that there is almost no high-quality double differential data for helium projectiles over the entire energy region.[11] This is discussed in more detail later in this article.
- No double differential cross section data exist for light ion fragment production from helium projectiles above 3 GeV/n.
- No double differential cross section data exist for light ion fragment production from oxygen projectiles[12] above the pion threshold (> 280 MeV/n).
- No double differential cross section data exist for light ion fragment production from silicon (Si) projectiles in any energy region.
- No double differential cross section data exist for light ion fragment production from iron (Fe) projectiles[13] in any energy region. This is particularly surprising, given the prominent role of Fe projectiles in space radiation biophysical studies [44].

1.3.1 Measurement Strategies and Experimental Setup

When planning and setting up measurements of double differential cross sections, there are a number of factors to be considered, ranging from detector system, detection efficiency,

[9]Ne(Z = 10), Ar(Z = 18).

[10]Except for proton + target → proton + X.

[11]A set of total cross sections for helium ions in the therapeutic energy range was recently measured within the scope of their application in ion therapy [42, 43].

[12]This situation is currently being partially addressed. An article describing a new set of measurements for O projectiles at 300 MeV/n is currently in preparation [16].

[13]This situation is currently being partially addressed. An article describing a new set of measurements for Fe projectiles at 600 MeV/n is currently in preparation [16].

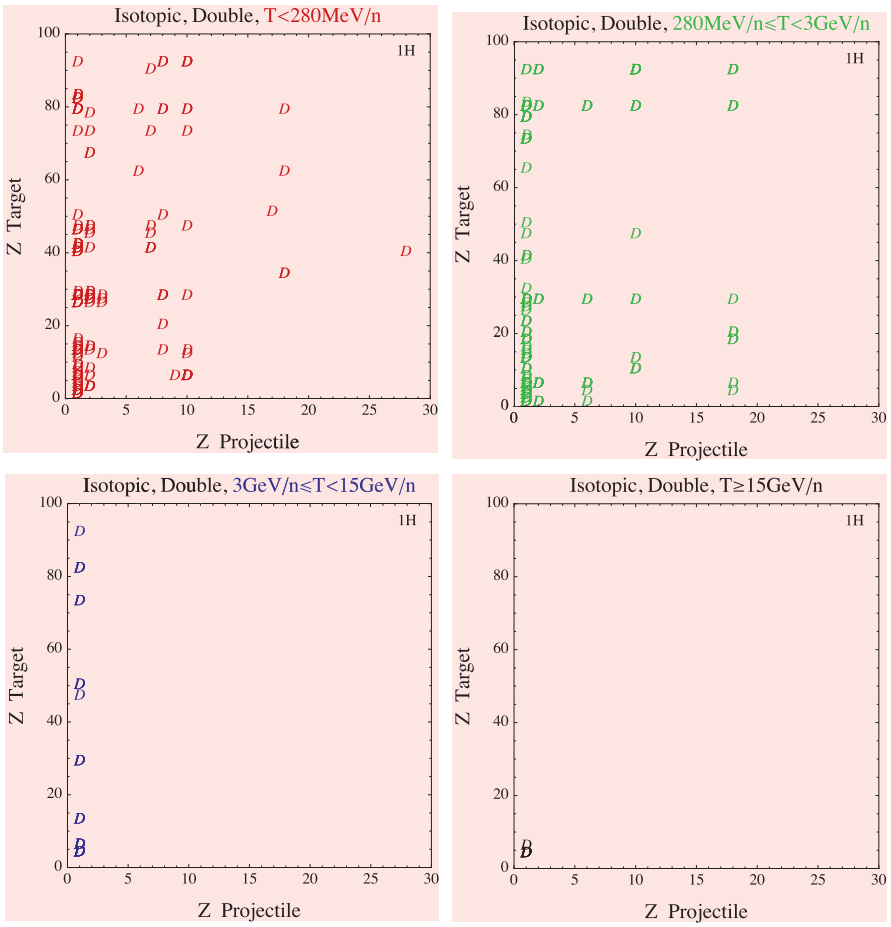

FIGURE 3 | Available isotopic double differential cross section measurements for ^{1}H fragment production. The symbol D represents where a measurement has occurred. Projectile kinetic energies, T, are listed at the top of each panel. Reprinted from Norbury et al. [1].

statistics, beam monitor, acceptance angles, data acquisition system, target thickness, and time resolution for TOF (time of flight) techniques.

In order to measure the angular distributions, several different configurations are possible. One standard option is a TOF setup with a fast counting detector (e.g., plastic scintillator, silicon detector, and diamond detector) that provides trigger information, that is, the start signal, before the target, and a plastic scintillator, for example, some distance downstream from the target, providing the stop of the TOF, and measurements of the energy loss. After this, a thick dense crystal calorimeter (e.g., BGO and NaI) can be located to provide the projectile fragment residual energies. Additional detector systems can be added to this general setup to improve its capabilities. Tracking detectors in front and after the target allow vertexing and different magnet configurations, and large-area drift chambers behind the target can be employed to increase particle identification performance. Silicon detectors in different configurations, for example, silicon micro-strips or silicon pixel detectors, or emulsion chambers, can also be used. Time resolution between the start detector and the stop detector and the angular acceptances are important. To obtain the double differential cross sections, in addition to the angular distributions, the energy distributions also need to be determined at each point of the angular distributions.

In principle, all cross sections should be measured in targets with infinitesimal thickness, which are, however, not optimal from the experimental point of view since targets which are too thin increase the beam time requirements and increase susceptibility to systematic errors. The target thicknesses are therefore a trade-off between thick enough to give acceptable statistics when exposed during a reasonable time, but not so thick to give rise to substantial corrections for secondary and higher-order interactions in the targets. Targets should also not be thick enough to cause a significant decrease of the projectile energies in the target, since the cross sections are energy dependent. Measured fragment yields need to be converted to cross sections and require correction for the finite depth target which is applied to the cross section values of each fragment. The corrections are typically of the order of half the fraction of an interaction length presented by the target to the primary. For example, for a target depth of 20% of an interaction length, about 20% of the incident primary particles undergo a charge-changing

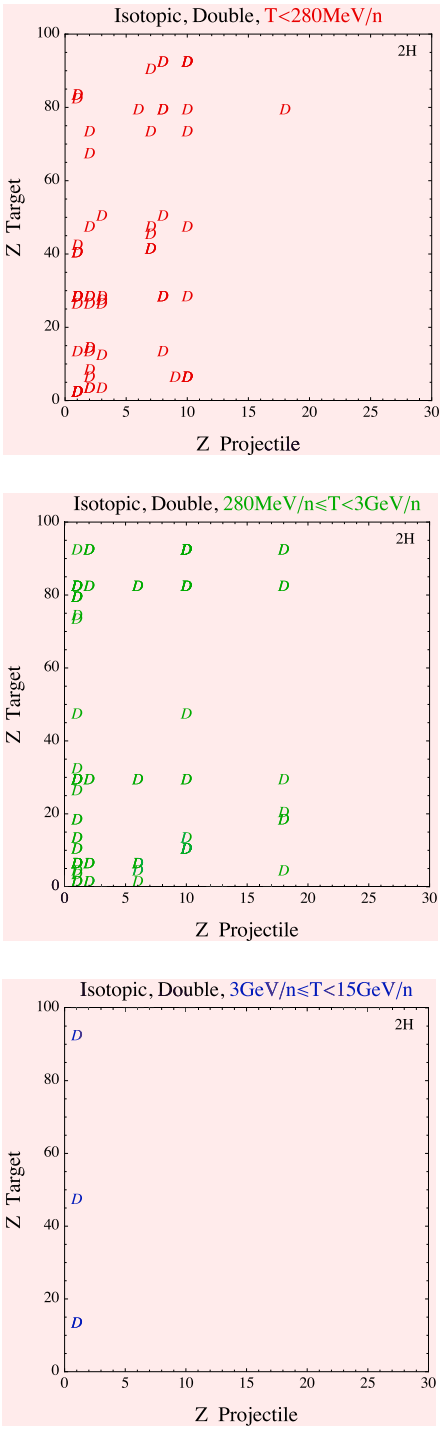

FIGURE 4 | Available isotopic double differential cross section measurements for ^{2}H fragment production. The symbol D represents where a measurement has occurred. Projectile kinetic energies, T, are listed at the top of each panel. No measurements are available above 15 GeV/n, which is why the bottom right panel is blank. Reprinted from Norbury et al. [1].

interaction in the target, and therefore about 10% of the fragments within a few charge units of the primary will undergo secondary charge-changing interactions. For experiments with a heavy projectile, the corrections for lighter fragments are more complicated, because they are both depleted by interactions in the target and are also produced as third- and higher-generation fragments by interactions of heavier fragments as they traverse the target.

It is always important to certify that particles created in other materials in the beam line are not measured. It is therefore essential that the beam never hits anything other than the target. When measuring neutron energy distributions, this is especially important since the neutron detectors are also picking up neutrons that scatter around the room before striking the detectors. Because their flight paths are unknown, those neutrons must be subtracted from the data. Measurements of the room-scattered neutrons should therefore be performed and subtracted from the total detected neutrons. Depending on the setup, this can be done by placing a shadow bar (a long, solid piece of iron, or other material, thick enough to stop the neutrons that enter it) directly between the target and the neutron detector, so that all neutrons originating from the target are blocked, and only room-scattered neutrons are detected. By subtracting the neutrons measured during the shadow bar run from the non-shadow bar run, the neutrons originating from the target can be determined. It is important to note that all of the previously mentioned experimental techniques do not scale well with increasing primary particle energy due to, for example, the inability to stop the light fragments in a crystal calorimeter or the increasing demands on TOF resolution and distance.

2 IMPORTANCE OF HELIUM PROJECTILES

2.1 Space Radiation

A discussion of the importance of helium projectiles in the galactic cosmic ray environment now follows.[14] Subsequent to the analyses of measurement gaps [1–4] discussed in **Section 1.3**, an important work was published by Slaba and Blattnig [46], which analyzed the contributions of each external boundary condition GCR ion to effective dose. Not only was the charge number (Z) contribution specified but also the energy range contributing to effective dose. Previous studies [1–4] emphasized measurement gaps, but the study of Slaba and Blattnig [46] enabled one to prioritize which measurement gaps were the most important ones to close for space radiation. **Figure 8** shows how helium projectiles dominate the effective dose contribution compared to heavier projectiles over the GCR energy region. For Al shield thickness of 20 g/cm^2, the study of Slaba and Blattnig [46] showed the following results at solar minimum:

- 86% of effective dose is contributed from GCR ions with kinetic energy > 500 MeV/n.
- 50% of effective dose is contributed from GCR ions with kinetic energy > 1.5 GeV/n.

[14]Helium projectiles are absent from the geomagnetically trapped radiation environment. They are present in solar particle events [45], but are of insufficient flux to make any significant contribution to the space radiation field.

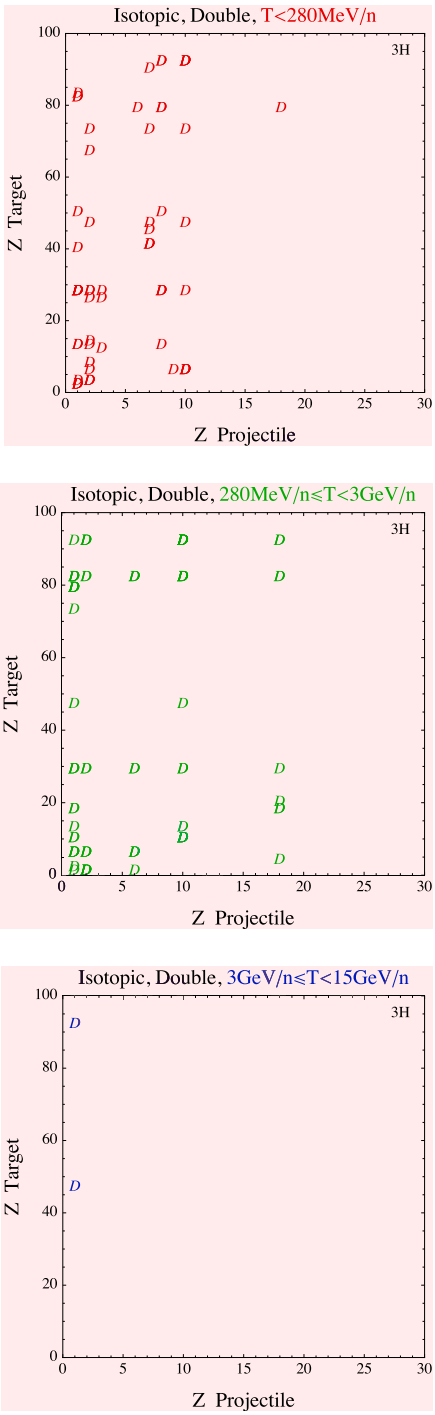

FIGURE 5 | Available isotopic double differential cross section measurements for ^{3}H fragment production. The symbol D represents where a measurement has occurred. Projectile kinetic energies, T, are listed at the top of each panel. No measurements are available above 15 GeV/n, which is why the bottom right panel is blank. Reprinted from Norbury et al. [1].

- 32% of effective dose is contributed from ions with Z > 1.
- He contribution to effective dose is 30% of the total ion (Z > 1) effective dose.

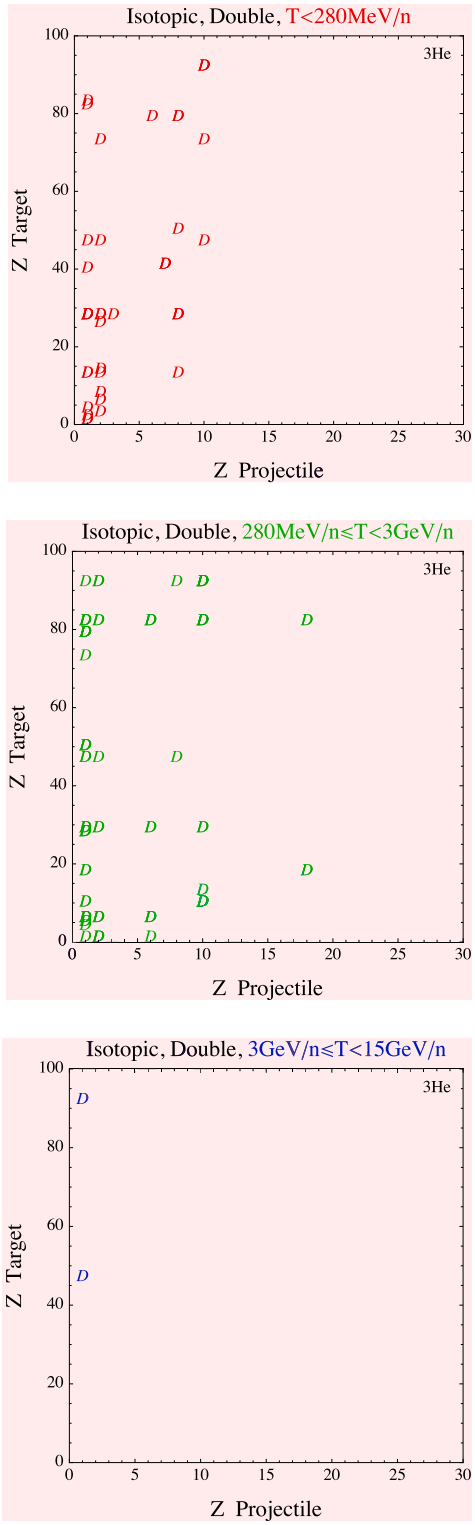

FIGURE 6 | Available isotopic double differential cross section measurements for ^{3}He fragment production. The symbol D represents where a measurement has occurred. Projectile kinetic energies, T, are listed at the top of each panel. No measurements are available above 15 GeV/n, which is why the bottom right panel is blank. Reprinted from Norbury et al. [1].

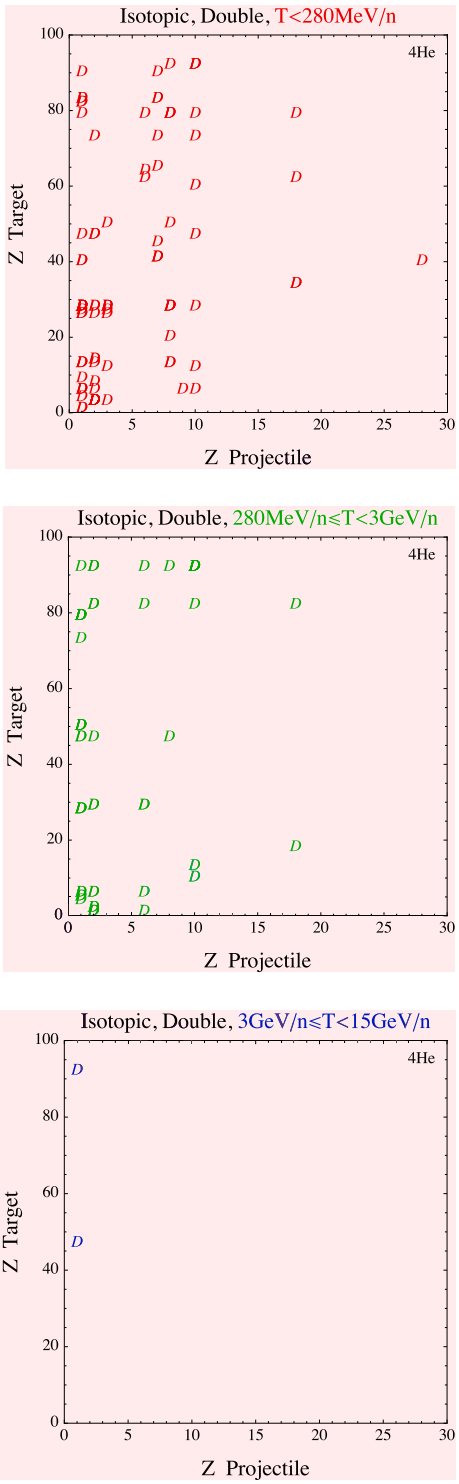

FIGURE 7 | Available isotopic double differential cross section measurements for ^{4}He fragment production. The symbol D represents where a measurement has occurred. Projectile kinetic energies, T, are listed at the top of each panel. No measurements are available above 15 GeV/n, which is why the bottom right panel is blank. Reprinted from Norbury et al. [1].

- He contribution to effective dose is 12% of the total effective dose (from all Z).

For Al shield thickness of 40 g/cm^2,

- 90% of effective dose is contributed from GCR ions with kinetic energy > 500 MeV/n.
- 60% of effective dose is contributed from GCR ions with kinetic energy > 1.5 GeV/n.
- He contribution to effective dose is 46% of the total ion (Z > 1) effective dose.
- He contribution to effective dose is 14% of the total effective dose (from all Z).

Using the calculations of reference [46], **Table 1** shows the percent contribution of each energy range to total He effective dose from the external GCR spectrum. For a shield thickness of 20 g/cm^2, all energy regions need to be covered, whereas for thicker 40 g/cm^2 shielding, only energies above 250 MeV/n are important. The following important conclusions can now be stated.

- More than half of the effective dose delivered by all GCR ions (including protons, i.e., Z ≥ 1) is in the high energy region > 1.5 GeV/n. Yet, this is the energy region with the largest measurement gaps.
- Of all external GCR ions heavier than protons (Z ≥ 2), helium contributes more than any other individual ion to effective dose, with almost half of the contribution in the high energy region > 1.5 GeV/n.

Also, similar results have been obtained by Bocchini et al. [47] obtained using Geant4. In particular, for Al thickness of 20 g/cm^2:

- 57% of male effective dose is contributed from GCR ions with kinetic energy higher than 1 GeV/n and about 24% of the dose is delivered by ions with E > 3 GeV/n.
- About 55% of the male effective dose due to GCR He particles is delivered by particle with energies greater than 1 GeV/n.
- GCR proton contribution to the male effective dose is about 57%, while the He contribution is about 19%, and all other ions (up to ^{56}Fe) contribute 24% of the total dose.
- He contribution to the male effective dose is 43% of the total ion Z > 1 effective dose.

However, at 40 g/cm^2 shielding thickness, the He particle with energies greater than 1 GeV/n represents 67% of the total male effective dose deposition due to GCR He particles, and most of the dose is deposited by particles in the energy range 1.5 GeV/n to 3 GeV/n. For thickness greater than 40 g/cm^2, the contribution of He particles with energies above 3 GeV/n also becomes significant. Differences in results can be due to the different simulations methods between the two works: HZTREN for [15, 23] and GRAS [48] in the latter case.

Extensive simulations have been performed by Bocchini et al. [47] to iteratively characterize the GCR contribution to the effective dose with Geant4, and here, results for He are reported. An aluminum spherical shell was modeled in GRAS [48], with varying thickness (i.e., from 10 up to 100 g/cm^2), and interplanetary GCR particles were isotropically generated, using the Badhwar-O'Neill 2010 model in 1977 solar minimum condition, with energies up to 100 GeV/n. Geant4 QGSP_BIC physics list was used, and a sensitivity study varying the physics list has been conducted. Effective dose has been calculated on a virtual scoring volume placed in the middle of the spherical shell, ICRP Publication 123 fluence to dose conversion factors [49] have been used, with NASA quality factors.

Figure 9 shows the male effective dose deposited by primary GCR He (including its secondary particles), while the percentage contribution of the different particle species to the dose is shown in **Figure 10**. The increase in the dose with thickness is in line with results reported in 50 for dose reduction of 1 GeV/n He particles against different spacecraft materials. At 30 g/cm^2, about 60% of the male effective dose is provided by secondary particles, mostly neutrons and protons, as shown in **Figure 10**. While in a low shielded scenario, representative for the first manned mission in the Lunar gateway, most of the He contribution to the dose is delivered by primary alpha particles, characterized by higher RBE values.

Geant4 simulations were also carried out to calculate the GCR He contribution to the dose in terms of energy range of the primary particle responsible for the dose deposition, to better prioritize testing activities. **Figure 11** shows the dose delivered by GCR helium particles in Sv/y per different thicknesses, considering both primary He and its generated secondary particles. For all thicknesses, the majority of the dose delivered by He is in the following energy ranges: 200–500 MeV (20–28% of total He dose) and 1.5–3 GeV/n (17–25% of total He dose), contributing overall to about 50% of the dose. Based on these results, availability of nuclear interaction cross section data for He in the 500 MeV/n–3 GeV/n energy range interacting with spacecraft materials should be a priority for space research, allowing transport code optimization.

2.2 Heavy Ion Therapy

After the treatment of more than 2000 patients with ^{4}He at the 184 inch synchrocyclotron and at the Bevalac in Berkeley [51], the interest of the therapy community shifted to the technically less demanding protons [52] and to the higher biological effectiveness offered by carbon ions [53, 54] instead. However, ^{4}He has physical and biological properties in between the protons and carbon ions currently in use. It is being considered as a clinical beam at the Heidelberg Ion Beam Therapy Center (HIT). Preclinical evaluation studies showed promising indications in the application of helium beam therapy, especially in pediatric patients [55] and tumors growing in close proximity to multiple organs at risk (OARs) [56]. From a radiobiological point of view, helium ions show a larger relative biological effectiveness (RBE) [57] and smaller oxygen enhancement ratio (OER) than protons for similar penetration depths in water. Additionally, helium ions undergo less multiple scattering than protons, leading to reduced distal and lateral beam straggling, and less projectile fragmentation than carbon ions, reducing the dose delivered in the distal part of the target volume. Several studies have been carried out investigating the possible advantages of treating cancer by combining helium ions with other particles, in order to exploit the radiobiological properties of different ions simultaneously [58, 59]. Additionally, helium ions have been identified as a good candidate for spatially fractionated therapy applications, such as mini-beam radiation therapy, due to their reduced multiple Coulomb scattering and reduced nuclear fragmentation with respect to protons and heavier ions [60]. Besides its direct application in therapy, helium is also very interesting for radiography applications, due to its favorable physical properties compared to protons [61]. Additionally, the possibility of directly mixing helium and carbon beams for direct online monitoring (helium) of the treatment (carbon) is currently being explored [62]. Based on the current interest in embracing helium as a viable alternative for proton and carbon beams, the following conclusion can be stated:

- The availability of high-quality ^{4}He cross section data for transport code optimization and validation in the energy region of interest for ion therapy (< 220 MeV/n) is crucial for reestablishing helium as a safe alternative for proton and carbon treatments and to enable novel medical use cases.

2.3 Required Cross Section Measurements

Having discussed the importance of He projectiles for space radiation and ion therapy, the question of which reactions are necessary to meet requirements is now addressed. A variety of low to medium mass targets are needed as well as a range of projectile energies.

- Inclusive, isotopic, double differential cross sections should be measured for the complete set of neutron and light ion fragments,

$$^4\mathrm{He} + \mathrm{H, C, O, Al, Fe} \rightarrow \mathrm{n}, {}^{1,2,3}\mathrm{H}, {}^{3,4}\mathrm{He} + \mathrm{X} \qquad (2)$$

for projectile kinetic energies ranging over 50 MeV/n–50 GeV/n and fragment angles ranging over 0°–180°.

3 PRESENT STATUS

3.1 Measurements

Section 1.3 discussed the availability of measurements for all types of projectiles. However, previous work [1–4] did not discuss the quality or usefulness of the measurements, and it will be seen below that when measurement quality is considered, there is an even more pressing need for a new set of cross section data. Another aspect that should be considered when the quality of a

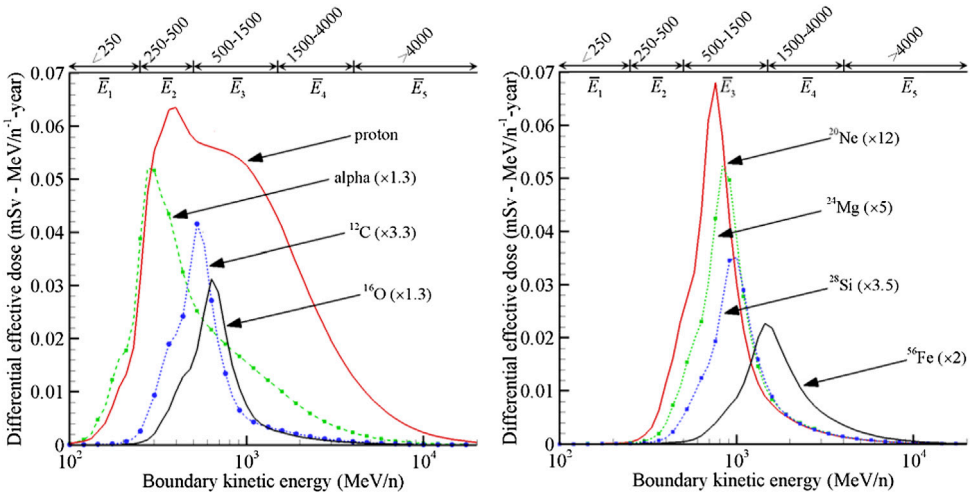

FIGURE 8 | Effective dose contributions as a function of external GCR energy behind 20 g/cm^2 of aluminum exposed to solar minimum GCR. Reprinted from Slaba and Blattnig [46].

TABLE 1 | Percent contribution of each energy range (MeV/n) to total He effective dose from external GCR spectrum for Al shield thicknesses of 20 g/cm^2 and 40 g/cm^2.

MeV/n	< 250 (%)	250 – 500 (%)	500 – 1,500 (%)	1,500 – 4,000 (%)	> 4000	
20 g/cm^2	10	18	34	24	14%	100%
40 g/cm^2	1	18	35	28	18%	100%

cross section dataset is evaluated is the target that was used for the measurement. Thinner targets give better data (better defined projectile kinetic energy, less elastic scattering, and less probability of multiple reactions) but increase the required beam time to collect data with appropriate statistical uncertainty. There is no universal definition what is a *thin* target. This should be judged based on the accuracy requirements for the measured cross sections as well as the ion species and energy used (see also **section 1.3.1**).

3.1.1 Total Cross Sections

Concerning total reaction cross sections for ^{4}He-induced reactions, there exists a quite comprehensive database, especially for light targets [42, 43, 63–80]. **Figure 12** shows an overview of this total cross section data set. Recently, measurements of charge- and mass-changing cross sections at therapeutic energies (70–220 MeV/n) were performed at HIT, Heidelberg, because for this energy range there were practically no data available in the literature [42, 43]. Accurate nuclear reaction models are required for precise dose calculations and treatment planning in ion therapy [53] and for transport code simulations of dose reduction in space shielding materials [81].

The energy range of the ^{4}He component in galactic cosmic radiation overlaps with the therapeutic energy range but also reaches up to very high energies. Therefore, ^{4}He nuclear interaction cross sections must be accurately modeled up to 50 GeV/n and above for radiation transport calculations related to space radiation. ^{4}He ions are also produced as secondaries through nuclear fragmentation of heavier ions of the GCR spectrum within the structural and shielding materials of a spacecraft. On the one hand, transport codes must consider the dose contribution from these secondary ^{4}He ions in human tissue (astronauts), and, on the other hand, their transport through shielding materials should also be calculated accurately. For these scenarios, ^{4}He reaction cross sections at lower energies become crucial.

The measurement of helium fragments produced from the fragmentation of heavier ions interacting with different target materials is important for nuclear models developed for space radiation transport models. NASA has specifically been interested in these data for validation of the nuclear fragmentation model NUCFRG. With this in mind, NASA collected experimental total cross sections, as NUCFRG only models the total cross section for production of isotopic fragments. This data gathering effort was restricted to projectiles with charge less than or equal to nickel. A total of 157 cross section values were found in the open literature at the time that work was performed [82–88]. The data are concentrated in the medium projectile energy range (280–3,000 MeV/n) with 135 cross sections. In the low projectile energy range (< 280 MeV/n), there were 18 cross sections measured by 82, 83, while in the high projectile energy region (3–15 GeV/n), there were only three cross section measurements by 84 (and none for energies larger than 15 GeV/n). Interestingly, the data found only spanned projectiles between carbon (Z = 6) to magnesium (Z = 12). For model development and model

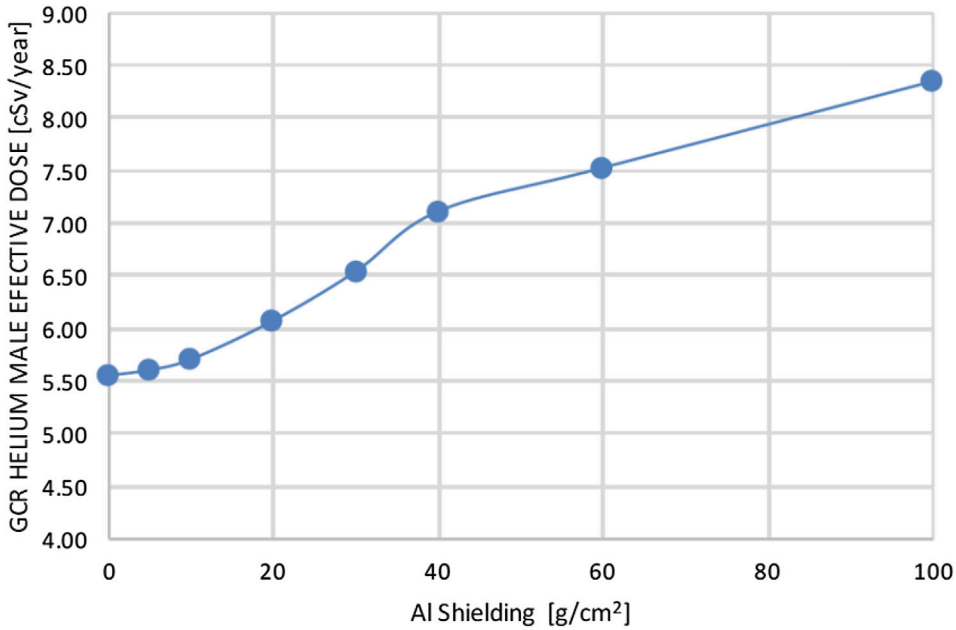

FIGURE 9 | Geant4 simulation of Male Effective dose due to GCR He (including its secondary particles), calculated using the ICRP Publication 123 fluence to dose conversion factors with NASA quality factors.

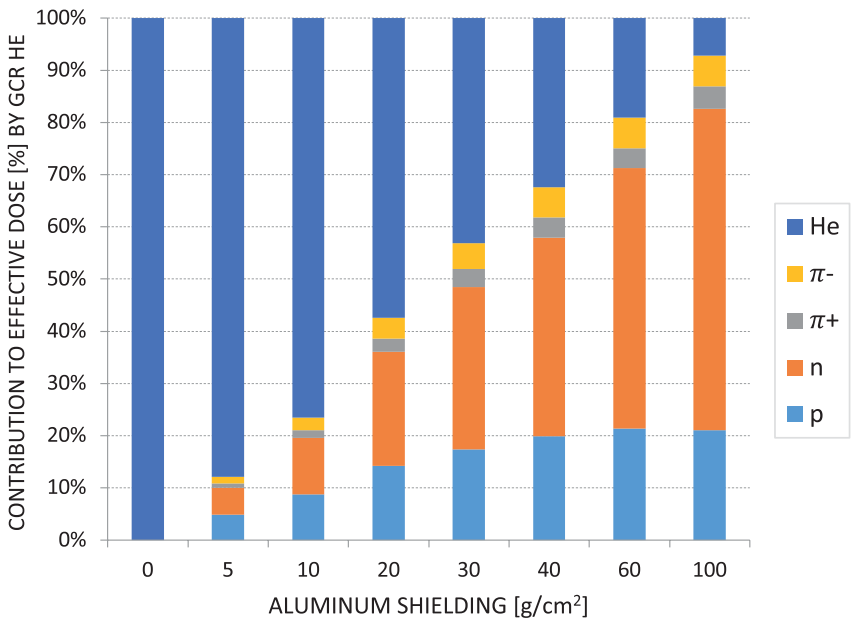

FIGURE 10 | Geant4 simulation of the percent contribution to the male effective dose of He GCR, showing in percentage the radiation component responsible for the GCR HE dose (either primary He or secondary particle generated by GCR He). Total male NASA effective dose has been calculated with ICRP Publication 123 fluence to dose conversion factors. 0 g/cm^2 refers to a free space scenario and applying the NASA quality factors.

validation purposes, this dataset is limited. Additional measurements at all projectile energies for projectiles with atomic number less than six and larger than 12 are desired. Also, more measurements are needed outside the medium energy range to better understand model development needs. For space research, He projectile measurements in the 0.2–3 GeV/n energy range should be prioritized, as indicated by the results in **Figure 11**.

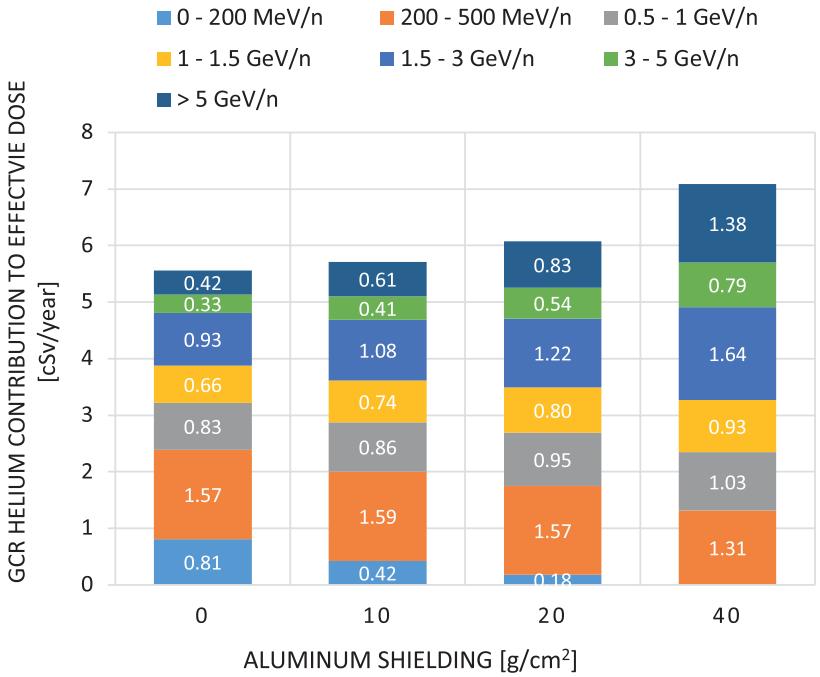

FIGURE 11 | GCR He energy ranges contributing to the 1 year NASA male effective dose for different thickness, using fluence to dose conversion factors from ICRP Publication 123.

3.1.2 Light Ion Fragment Production

Partial (Non-Differential) Cross Sections

Cross sections for ^{4}He fragmentation reactions on H, C, and O targets were recently collected for radiation transport modeling in ion therapy [31]. Within the framework of this data collection, only limited partial cross section data were found, some for ^{1}H targets [89] and some for ^{12}C targets [90]. In [91], the cross section for ^{1}H production by 27 MeV/n ^{4}He impinging on ^{165}Ho is reported.

Additional cross sections for ^{1}H, ^{2}H, ^{3}H, ^{3}He, and ^{4}He production by 400 MeV/n ^{4}He projectiles on U targets are presented in 92. Inclusive ^{3}He production cross sections can be obtained by subtracting ^{4}He charge- from mass-changing cross sections. This method has been used to calculate ^{3}He production cross section data for ^{4}He projectiles on ^{12}C, ^{16}O, and ^{28}Si targets [42, 43]. ^{3}He production cross sections for 630, 970, and 1,017 MeV/n ^{4}He projectiles impinging on H targets were reported by 70, 93, 94.

Differential cross sections

The available helium projectile double differential data are listed in **Table 2**. A high-quality data set is required, and therefore some data are not useful. For example, many data do not include error bars [92, 97], and other data have not been published in refereed journals. Also, many data are for proton fragments only [91, 96, 99]. In addition, many data sets measured only large angles or only very small angles. There are certainly no data sets covering all the requirements of the necessary reactions of **Eq. 2**. Given these problems, it is recommended that a new experimental program be initiated that covers all the reactions listed in **Eq. 2**. There might be a *small* amount of overlap with *some* of the reactions on **Table 2**, but that will serve as a very useful benchmark to check the accuracy of new measurements.

Some recent investigations in the scope of helium ion therapy [102, 103] provided experimental data about double differential fragment yields behind thick water and PMMA targets which can also be useful for nuclear model validation.

3.1.3 Neutron Production

From **Figure 10**, it is possible to see how the neutron contribution increases with spacecraft shielding thickness. From 104, discrepancies are found when comparing neutron ambient dose with PHITS and Geant4 simulations results. There is a need to have better models to simulate neutron production from space GCR.

Differential Cross Sections

There is a limited set of inclusive double differential cross-sectional data available on neutron production from medium and high energy ^{4}He ions, especially when compared to the amount of data available from He interactions in thick (stopping) targets. The last two rows of **Table 2** list the measurements taken and published to date. The quality of the data from the 135 MeV/n He systems [105] is very good due to the experimental setup at RIKEN that provides a low background environment for time-of-flight measurements, as well as the capability to measure neutrons at 0° relative to the beam axis. Neutrons below 10 MeV were not measured in those systems, however, in part to avoid contamination from background neutrons in the measurement. The measurements at 230 MeV/n [106] were taken at HIMAC and had a higher background

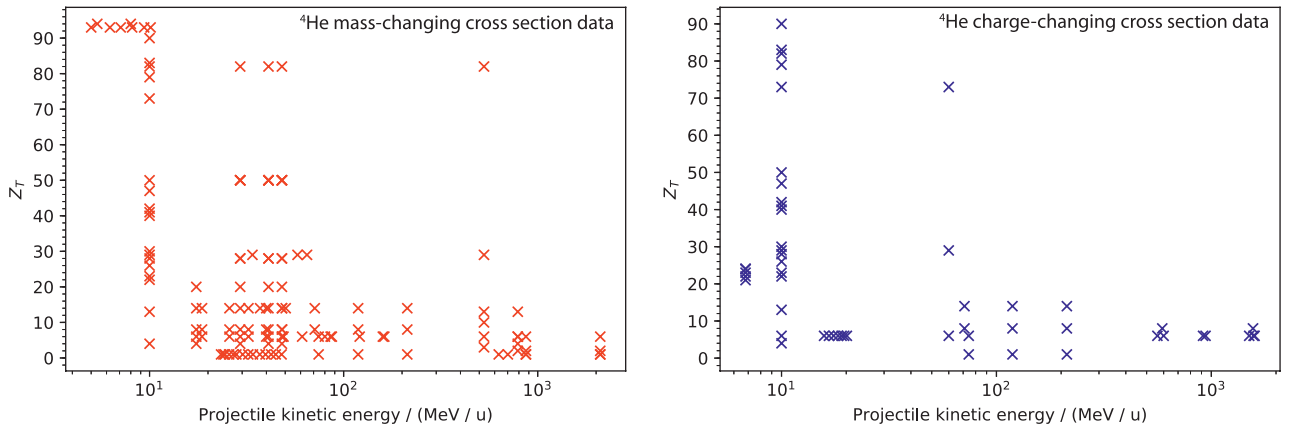

FIGURE 12 | Overview of ^{4}He experimental cross section data for different target atomic numbers Z_T as a function of kinetic energy for mass-changing **(left panel)** and charge-changing reactions **(right panel)**.

subtraction than the data taken at RIKEN. As a result, the 230 MeV/n double differential cross sections have fewer data points with larger error bars in each spectrum than the RIKEN data. The HIMAC data had lower neutron energy thresholds, however, extending the spectra down to three–5.5 MeV, depending on the angle of measurement. Measurements at 0° were not possible at HIMAC. In total, six systems were measured. The RIKEN measurements used C, Al, Cu, and Pb targets, and the HIMAC measurements used Al and Cu targets. All targets were composed of natural abundances of each element. There are good data from both systems at forward angles that characterize projectile fragmentation. For target fragmentation, measurements extend to 110°, yielding an incomplete picture of that process, especially given the relatively high neutron energy thresholds.

3.2 Modeling

While it is relatively easy to develop accurate models for total cross sections and more difficult to develop accurate single differential spectral or angular cross sections, it is most difficult to develop accurate double differential models. And again, charge changing or elemental production models are easiest, while isotopic models are the most difficult. Accurate isotopic double differential cross section models are the most difficult of all to develop, but once available, they automatically generate accurate total and single differential cross sections including charge-changing and elemental cross sections.

3.2.1 Applications in Ion Therapy and Space Radiation Research

Treatment planning systems (TPS) are standard applications in ion therapy. The first TPS for scanned ion beams was the GSI code TRiP98 [29, 107]. It has been used clinically in the carbon ion pilot project at GSI [53]. Special emphasis has not only been on dose calculation but also on dose optimization including radiobiological effects. It features a built-in deterministic transport model to create the base data necessary for treatment planning, that is, depth dose profiles and particle spectra which are necessary for radiobiological modeling. TRiP98 is now further developed as a research prototype for use with ion beams other than carbon, in particular oxygen [32] and helium [31]. TPS predictions have been validated in dosimetric and radiobiological experiments at HIT and KVI Groningen.

TRiP98 is a deterministic code based on a set of tables comprising single particle energy loss (dE/dx) for primary and secondary ions, nuclear reaction cross sections describing the loss of the primary ion beam, and fragmentation cross sections to compute the build up of the produced secondary ions. In this respect, it needs the same basic physics data as the various Monte Carlo codes. ^{4}He related cross sections are important in two ways. First, they are important for an accurate description of beam attenuation when ^{4}He is the primary beam. Second, they are also important to properly describe the "fragmentation tail" in case of heavier primary beams, since helium fragments are the second most abundant species after protons. ^{4}He cross sections are handled semi-empirically, as described in 31.

For space radiation research, TRiP98 is being extended to SpaceTRiP, in the framework of the ESA ROSSINI project. The latter is designed to calculate the dose reduction due to different space radiation shielding materials. The native TRiP98 transport model is extended to more types of ion projectiles than in ion therapy. This extension will allow the simulation of the multitude of HZE particles found in GCR spectra, of which ^{4}He is one of the most important ions.

Furthermore, the ^{4}He fragments are crucial for both ion therapy and space radiation due to the high penetration in various materials, compared to smaller penetration by heavier fragments. In ion therapy, He fragments can travel past the Bragg peak, which leads to undesirable dose to OARs, and in space radiation research, these fragments contribute significantly to dose buildup after the beam has traversed the shielding material.

TABLE 2 | He projectile double differential cross section measurement details. T_n is the kinetic energy of the outgoing neutron.

Projectile	Energy (MeV/n)	Target	Fragment	Author	Notes	Comments
^{3}He	33	Ho	^{1,2,3}H	Motobayashi [95]	17°–120°	**Figure 1**
^{3}He	67	Ag	^{1}H	Zhu [96]	> 33°	**Figure 1**
^{4}He	27	Ho	^{1}H	Shibata [91]	20°–140°	FIGURES 1 and **2**
^{4}He	180	Al,Ag,Ta	^{1,2,3}H,^{3,4}He	Doering [97]	> 60°	Often no error bars
^{4}He	383	C	^{1,2,3}H,^{3}He	Anderson [98]	0°	FIGURE 24, Unpublished
^{4}He	250	U	^{1,2,3}H,^{3,4}He	Gossett [92]	> 20°	**Figure 10**, No error bars
^{4}He	400	U	^{1}H	Westfall [99]	> 30°	**Figure 3**
^{4}He	400	U	^{1,2,3}H,^{3,4}He	Gossett [92]	> 20°	**Figure 10**, No error bars
^{4}He	400	U	^{1}H,Li, ^{7,9,10}Be,B	Gossett [92]	> 30°	**Figure 18**, No error bars Figure 26
^{4}He	400	C	^{1}H	Anderson [100]	0°	FIGURE 23 x_F axis
^{4}He	1,010	H	^{3}He	Bizard [93]	1°–10°	—
^{4}He	1,050	^{2}H,^{3,4}He	^{4}He	Banaigs [101]	< 15°	Elastic and inelastic
^{4}He	1,050	C	^{1}H	Anderson [100]	0°	**Figure 7**
^{4}He	1,050	C	^{4}He	Anderson [100]	$p^{\perp}$ axis	**Figure 10**
^{4}He	1,050	C	^{1,2,3}H,^{3}He	Anderson [100]	0°	**Figure 3**
^{4}He	1,050, 2,100	C	^{1}H	Anderson [100]	0°	FIGURE 23 x_F axis
^{4}He	1,050, 2,100	C	^{1,2,3}H,^{3}He	Anderson [98]	0°	FIGURES 25 and 26, Unpublished
^{4}He	1,050, 2,100	C	^{1}H	Anderson [100]	0°	FIGURE 21
^{4}He	2,100	C	^{1}H	Anderson [100]	$p^{\perp}$ axis	**Figure 8**
^{4}He	2,100	H,C,Cu,Pb	^{4}He	Anderson [100]	$p^{\perp}$ axis	**Figure 19**
^{4}He	2,100	C	^{1}H	Anderson [98]	$p^{\perp}$ axis	FIGURE 28, Unpublished
^{4}He	2,100	U	^{4}He	Gossett [92]	90°	**Figure 6**, No error bars
^{4}He	135	C,Al,Cu,Pb	n	Sato [105]	0°–110°	$T_n \geq$ 10 MeV
^{4}He	230	Al,Cu	n	Heilbronn [106]	5°–80°	$T_n \geq$ 3–5 MeV

3.2.2 Total Reaction Cross Sections

An important quantity for light and heavy ion transport codes is the total reaction cross section σ_R, which is typically obtained from a parameterization for the projectile–target combination and kinetic energy of interest. Most of these parameterizations are semi-empirical models that are fine-tuned to experimental cross sections.

Figure 13 shows a collection of total cross section data for ^{4}He-induced reactions [42, 43, 63–71] compared with two different parameterizations. It can be observed that the agreement of the models with the experimental data is better for light targets. Toward heavier targets, the deviations of the models from the experimental cross sections get larger, probably because the models have been optimized mostly for light target data. It is clear that for very light targets like H or He, the Tripathi parameterization for light systems [108], which was specifically optimized for those targets, is the one fitting the best for a broad range of energies, while the Shen parameterization fails in reproducing very low energy cross section data for H targets. For intermediate weight targets (from C to Si), the general parameterization by Tripathi et al. [109], with parameter optimizations described by Horst et al. [43], has been used for the left panel because it has been specifically optimized for targets in this atomic number range, while the Tripathi light system parameterization [108] is optimized for very light targets. For very heavy targets, on the other hand, the Shen parameterization [110, 111] seems to work better, especially at higher energies. Nevertheless, none of the parameterizations can accurately reproduce the cross section data for targets heavier than Si. More experimental data points at high energy for heavy targets could help to optimize the models.

The modified Hybrid Kurotama model [112] for proton + nucleus and nucleus + nucleus total reaction cross sections can handle complex targets containing different target nuclei with both natural and unnatural abundances, for projectile energies from below 5 MeV/n to well above 10 GeV/n, where limiting fragmentation occurs. The model is based on the Black Sphere (BS) cross section formula for proton + nucleus reactions and extended to nucleus + nucleus reactions. However, the BS model requires that the de Broglie wavelength of the proton is considerably smaller than the nuclear size, and the BS model therefore breaks down below around 100 MeV/n. In addition, the Coulomb repulsion causes resonance features and a sharp increase at energies below 100 MeV/n, at which an energy dependent transparency parameter and the influence of the Fermi motion and Coulomb effects should be included. To solve the limitations of the BS model at low energies and to create a general purpose total reaction cross section model which can also be used for reactions with projectile energies below around 100 MeV/n, the BS model has been connected to the parameterization developed by Tripathi et al. [108, 109, 113]. The Hybrid Kurotama model has been extensively benchmarked against experimental total reaction cross section data, and an overall better agreement has been found than for earlier published models. The model is used in the PHITS transport code [17].

3.2.3 Partial (Non-Differential) Cross Sections

In addition to total reaction cross sections, models for partial (elemental and isotopic) cross sections are also required for calculation of the production of different fragment species. ^{4}He fragmentation reactions occur *via* a remarkably small number of channels where the only products are ^{3}He, ^{3}H, ^{2}H, ^{1}H, and neutrons. This allows for individual modeling of all reaction channels. **Figure 14** shows model predictions for the

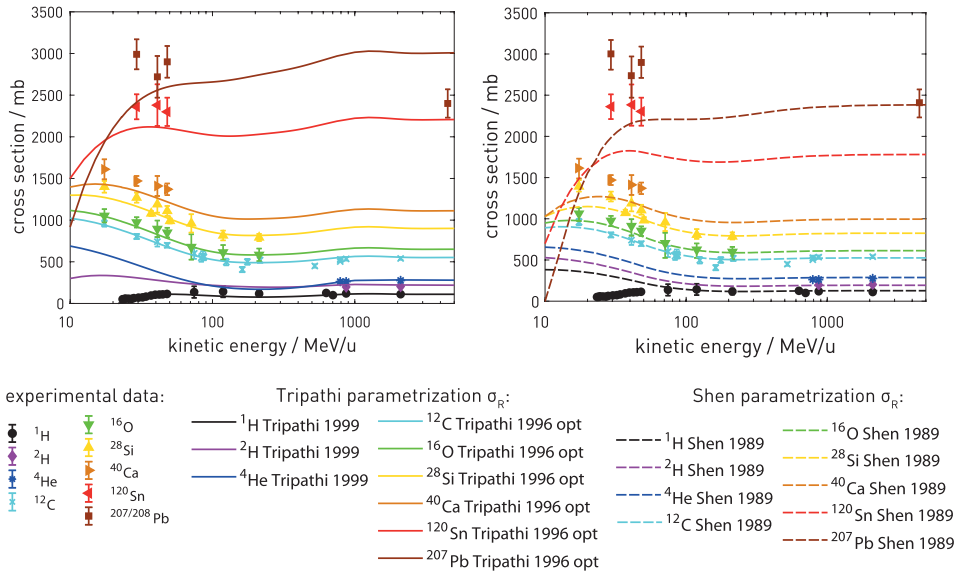

FIGURE 13 | Experimental data of total cross sections for ^{4}He-induced reactions on different targets, whose atomic numbers range from low (^{1}H) to high (^{207}Pb), compared with two different parameterizations. In the left panel the predictions by the Tripathi parameterization of the total reaction cross section are shown. The light system model by Tripathi et al. [108] is used for low atomic number targets (^{1}H, ^{2}H, and ^{4}He) and the general model by Tripathi et al. [109] with the modifications described by Horst et al. [43] is used for higher atomic number targets. In the right panel, the predictions by the model by Shen et al. [110] with the modifications proposed by Sihver et al. [111] are shown. The experimental data were taken from 42, 43, 63–71.

total reaction cross section and the inclusive ^{3}He production cross section compared with data.

The total reaction cross section model shown in **Figure 14** is the parameterization by Tripathi et al. [109], and modified by Horst et al. [42, 43], based on recent experimental cross sections. These modifications result in a significant improvement of the agreement between calculated and measured ^{4}He Bragg curves in water, which are important for ion therapy applications [33, 115].

^{3}He production is the only channel that can occur for ^{4}He projectiles which changes the mass but not the charge. Therefore, the ^{3}He production cross section can be obtained by subtracting experimental cross sections for charge-changing reactions from those for mass-changing reactions. This is how the red symbols in **Figure 14** were obtained. A semi-empirical model for inclusive ^{3}He production in ^{4}He-nucleus collisions was developed by Cucinotta et al. [114]. This model accounts for break-up of the ^{4}He projectile into ^{3}He and a neutron, as well as for the decay into ^{3}He and ^{2}H after proton pickup. A scaling with $A_T^{1/3}$, where A_T is the mass number of the target, which corresponds to the radius of the target nucleus, has been proposed in order to use the model for heavier targets, because neutron stripping was assumed to occur mostly in surface reactions. However, it was found empirically, by comparison of model predictions with the recent experimental data, that a $A_T^{2/3}$ scaling, corresponding to the geometrical cross section of the target nucleus, better describes the dependence of ^{3}He production on the target material. In addition to the replacement of the target mass number scaling, also a downscaling of the parameterization by a factor of 0.85 is proposed for an optimal fit of the model to the experimental data. As demonstrated in **Figure 14**, the agreement between the predictions of those two optimized models with the experimental cross section data for ^{12}C, ^{16}O, and ^{28}Si targets is reasonable.

3.2.4 Double Differential Cross Sections

Heavy ion production isotopic double differential cross sections can be modeled with relatively simple physical ideas because the ions are mostly produced from simple abrasion–ablation processes, and because the ions are heavy, they proceed mostly in the forward direction. The abrasion–ablation model [116] assumes that the dominant source of heavy ion production is from the incident projectile. On the other hand, neutron, proton, and composite light ions are scattered at large angles because they are relatively light. Also, composite light ions have a complicated production mechanism, often involving not only abrasion–ablation but also coalescence.

The general picture for high-energy heavy ion projectile collisions is the following: The projectile and target nuclei collide and form a central fireball overlap region, together with deformed and excited projectile and target pre-fragments, which decay into lighter fragments. The fireball is very hot and decays quickly with the emission of pions, other mesons, and baryons such as neutrons, protons, and other particles. The cooler excited projectile and target pre-fragments decay more slowly, generally by emitting nucleons, which may coalesce into light ions. There are therefore three different sources of particles, the projectile and target pre-fragments and the central fireball. Each of these three sources can produce the same type of particle that eventually reaches detectors in the lab frame (or an astronaut's body in a spacecraft). Because the fireball is very hot, light ion

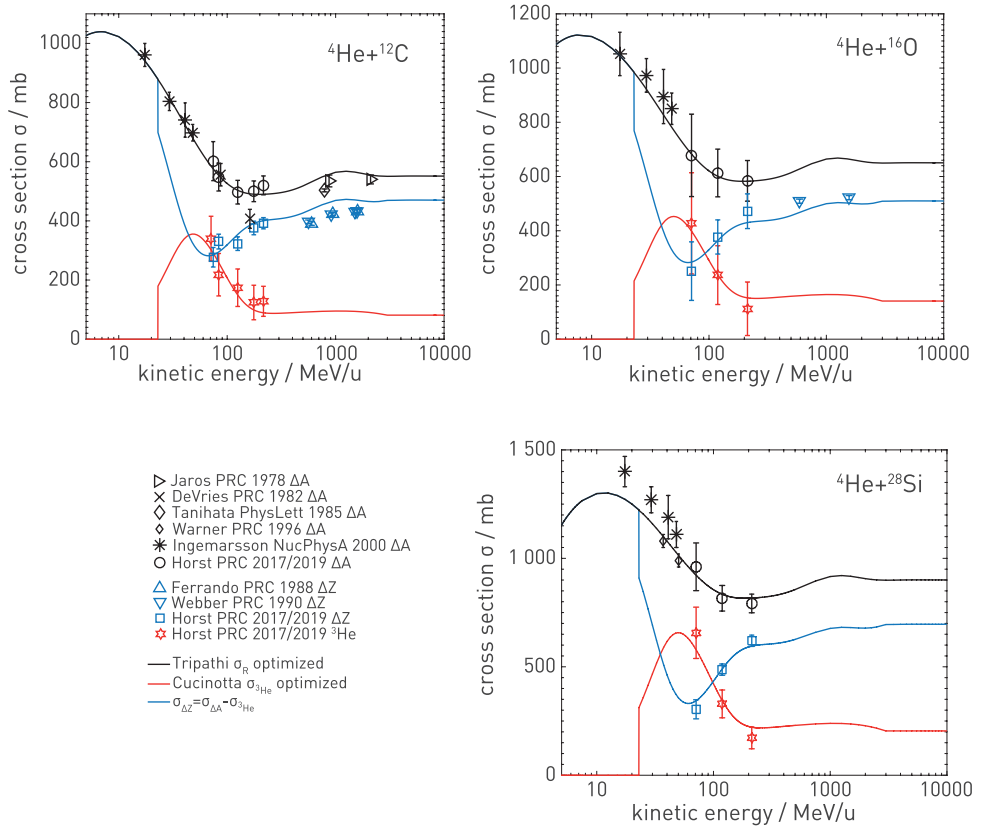

FIGURE 14 | ^{4}He nuclear fragmentation models compared with experimental cross sections. Black symbols: mass-changing ΔA, blue symbols: charge-changing ΔZ, red symbols: inclusive ^{3}He production. Cross sections are obtained by subtracting the charge- from the mass-changing experimental cross sections. The black line shows the Tripathi model of the total reaction cross section [109] with optimized parameters described in 43. The red line shows a model designed by Cucinotta et al. [114], optimized according to the description in the text. The blue line shows the charge-changing cross section calculated by subtracting red from black. The plotted experimental data are from 42, 43, 63–66, 68.

fragments cannot survive and will be broken up into baryons and mesons. However, what happens when the fireball cools? The answer is similar to what happened in the very early Universe. After a rapid period of inflation, the Universe started as a quark-gluon plasma, which then cooled and formed hadrons such as pions, kaons, other mesons, nucleons, deltas, and other baryons. After further cooling the baryons decayed to nucleons, which later *coalesced* into light ions: H, He, and some Li. Then, the density dropped too rapidly to form heavier ions, which were made much later in stellar interiors, supernovae [117], and binary neutron star mergers [118]. As the Universe cooled further, electrons and light ions coalesced into atoms. Aspects of the nuclear fireball cooling are similar to the early Universe scenario. As the fireball cools and decays and emits neutrons and protons, these are cool enough to coalesce into the light ion isotopes of H and He (and also some Li). As with the early Universe, the fireball density drops very rapidly, and nucleons are unable to coalesce to form heavier ions, which come from projectile and target pre-fragments. Of course, the projectile and target pre-fragments also emit nucleons (neutrons and protons), and these can also coalesce. Thus, light ions are produced from nucleon coalescence [12, 13, 119] of all three sources: projectile, fireball, and target. This is in contrast to the simpler mechanism of abrasion–ablation of heavy ions, where the dominant source is the incident projectile. Another complicating factor for neutron, proton, and composite light ion production is that there are two production mechanisms from each of the three sources, namely, direct production vs. thermal emission of nucleons with subsequent coalescence.

Despite all these complications, models for neutron, proton, and composite light ion production have been recently developed [12, 13, 119, 120] and compared to a variety of data. DDFRG is a double differential fragmentation model based on Lorentzian parameterizations of the projectile, fireball, and target sources including direct and thermal/coalescence production. Results for helium projectiles producing fragments at 0° are shown in **Figure 15**, and compared to the cross section models used in the SHIELD transport code, which incorporates nuclear models that include both the internuclear and intranuclear processes in matter. Inelastic nuclear reactions present the following sequential stages of the whole interaction: fast intranuclear cascade, coalescence of the cascade nucleons, possible pre-equilibrium decay of residual nuclei, and the equilibrium de-excitation of the residual nuclei. The last includes the advances evaporation,

fission, multifragmentation (for large residues), and Fermi-Break-up (for light residues) processes. All of these models have a good performance in description of experiment [121–128]. **Figure 15** shows that proton, triton (^{3}H), and helion (^{3}He) production is described well with both DDFRG and SHIELD models. Deuteron production data are not as well described by the SHIELD models, and presents somewhat of a puzzle. DDFRG describes the data quite well only because several parameters have been tuned to the data. The production of ^{3}H and ^{3}He is described in the SHIELD models due to stripping of a single nucleon, rather than coalescence production, which is why SHIELD results for deuteron (^{2}H) production give much smaller values than ^{3}H and ^{3}He production. There is therefore an urgent need for the following:

- Experimental double differential cross section results [100] for light ion production from He projectiles need to be confirmed, including angles 0°–180°.
- SHIELD double differential cross section results for light ion production from He projectiles need to be confirmed by comparing to other cross section models.

Other approaches to nuclear cross section modeling are under development. A deterministic Serber nuclear model was developed for use in the radiation transport code, HZETRN, with the aim of improving nucleon spectral and angular distributions. Various implementations of the Serber nuclear models have been employed successfully in Monte Carlo codes for internuclear cascade processes. The underlying theory describes the propagation of an incident nucleon through target media modeled with a characteristic density and potential well. The target nucleus is composed of nucleons that are bound within a Fermi sea. When a projectile nucleon strikes a target nucleon, the kinetic energy of the struck nucleon must exceed the Fermi energy to escape the target. Both the spectra of the projectile nucleon and the recoil nucleons are tracked. The primary nucleon is assumed to traverse in the straight-forward direction, whereas the recoil spectra are assumed to have an angular dependence [129]. This model is being extended to nucleus–nucleus reactions for the evaluation of nucleon double differential and spectral distributions. Primary nucleons and nucleons resulting from internuclear processes, including abrasion and de-excitation, are among the most consequential reactions for the projection of radiation risk. Additional nucleon and light ion fragmentation data for space radiation relevant reactions are needed to validate the nuclear models. The current process of validating models (when data are not available) is to compare transport code results in thin target simulations, which ultimately is a comparison of the different cross section models. Ideally, the nuclear cross section models would be compared directly to nuclear data, but additional experiments are needed to support these efforts and is the subject of the current work.

4 REVIEW OF ACCELERATORS

The aim of this section is to summarize the availability of accelerators for helium ion beams. The ideal accelerator facility for the intended cross section measurements would provide helium ions in an energy range from typically 50 MeV/n up to 50 GeV/n. These conditions can only be met by large-scale research facilities like GSI/FAIR, the Joint Institute for Nuclear Research (JINR, Dubna), and the NASA Space Radiation Laboratory (NSRL) at Brookhaven National Laboratory (BNL). However, since beam time at these accelerators is relatively expensive and has to be planned on a long time scale, it might be convenient to supplement the use of high-energy accelerators with medium-energy accelerators, which are more readily available. Especially, medical facilities often provide experimental beam during the night after finishing quality assurance. Thus, medium to high energies (100–800 MeV/n) could be delivered by some medical facilities for ion beam therapy like the HIMAC accelerator in Chiba or the HIT facility in Heidelberg. In some cases, low-energy facilities, such as the KVI in Groningen, could be a cost effective addition for the helium cross-section measurement program. However, in order to meet the requirements for space radiation research and ion beam therapy, a minimum energy of 50 MeV/n is specified that should be reached by the accelerator. This limit defines a subset of existing accelerators that will be presented for this study. **Table 3** comprises the eligible accelerators corresponding to the above mentioned requirements.

GSI/FAIR. GSI Helmholtzzentrum für Schwerionenforschung plays a special role among the facilities listed in **Table 3** because it fulfills all requirements for a comprehensive cross section measurement program. During FAIR-phase-0, the current project phase until completion of the SIS100 synchrotron cross section, experiments can be conducted at different irradiation sites with different profiles. Cave M and Cave A, which are used by the GSI biophysics group, can accommodate compact experiments such as the FOOT [130] experiment. Cave C provides space for experiments with larger detectors [131], while the fragment separator (FRS) [132] allows high precision charge-changing cross-section and double differential measurements at small angles ($< 1°$). The GSI control system allows very flexible settings for the beam intensity (100–10^9 ions/s), different extraction modalities, and spill extraction duration times (< 1 ms up to 10 s and more). After commissioning of the SIS100 synchrotron, helium cross sections can be measured additionally at very high energies ($E < 10$ GeV/n), relevant for space radiation research. A suitable irradiation site will be at the BIOMAT beamline in the APPA Cave [133].

NSRL/BNL. NSRL is a multidisciplinary center for space radiation research funded by NASA and located at the Brookhaven National Laboratory (BNL). Operational since 2003, the scope of NSRL is to provide ion beams in support of NASA programs in radiobiology, physics, and engineering [134]. Recently, it has also been recognized as the only facility in the United States currently capable of contributing to heavy ion therapy research. The facility provides a large room (10 m long from exit window to beam dump), well suited for time of flight (TOF) and double differential cross section measurements [135].

Nuclotron. The Dubna Nuclotron was the world's first superconducting synchrotron, built by the Joint Institute

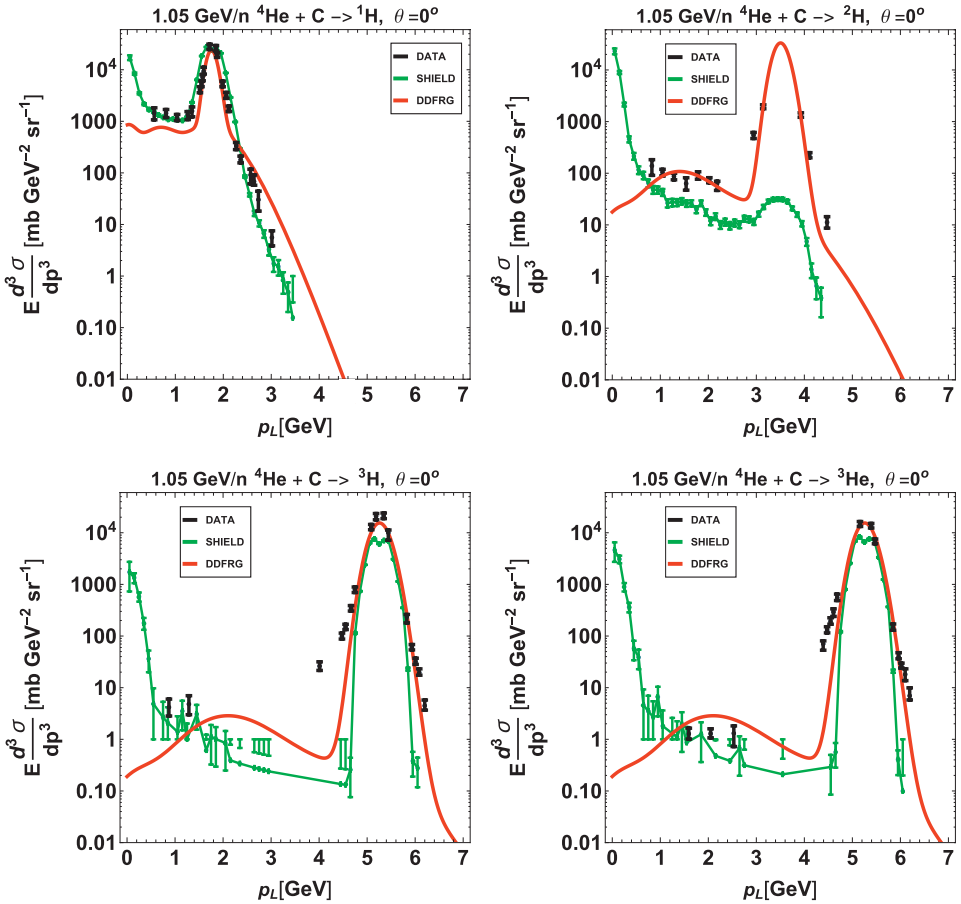

FIGURE 15 | Lorentz-invariant double differential cross section data [100] compared to DDFRG [119] and nuclear physics models from the SHIELD transport code [121–128].

for Nuclear Research (JINR), Russia. In the past, the accelerator was used to extract ion beams with Z = 1–36 up to energies of 2.2 GeV/n. As part of the upgrade for the NICA project [136], the beam energy can be increased up to 4.5 GeV/n in future. The nuclotron facility comprises various large experimental rooms and would enable the full spectrum of cross section measurements with helium beams.

Clinical facilities: HIT, HIMAC, MedAustron, and CNAO. Clinical facilities with medium to high energy can complement the measurements at the large-scale research facilities and can decrease the costs and effort for the whole cross section program. The Heavy Ion Medial Accelerator in Chiba (HIMAC) in Japan is part of the National Institute of Radiological Sciences (NIRS) and has been operational since 1993 as a medical facility for treating cancer patient with protons and carbon ions. The center has also served as a multi-user facility for medical, biological, and physics research. It can accelerate all ions between ^{4}He - ^{20}Ne up to 800 MeV/n. The HIMAC provides beam lines and experimental rooms to allow cross section measurements with helium beams [137]. The same applies for the Heidelberg Ion-Beam Therapy Center (HIT) facility. HIT intends to start the clinical treatment of cancer patients with helium ions at the end of 2020. This will be the first resumption of helium ion therapy worldwide after a long time. HIT provides a well-equipped experimental room, which has been used intensively in the past for helium cross section measurements [42, 43] and provides energies up to 430 MeV/n. The Centro Nazionale di Adroterapia Oncologica (CNAO) medical facility for ion beam therapy in Italy also accommodates an experimental room which meets the conditions for cross-section experiments [138]. The CNAO is updating their accelerator for a helium ECR source and intends to deliver ^{4}He beams up to 330 MeV/n from the beginning of 2021. The MedAustron ion-beam therapy facility in Wiener Neustadt (Austria) [139] also has the hardware available to accelerate helium ions up to 400 MeV/n. However, a commissioning for helium beam will not take place before 2023.

AGOR/KVI-CART and LNS. In case of difficulty obtaining helium beams at large-scale and medical facilities, the AGOR cyclotron facility (KVI-Centre, Groningen) could provide ^{4}He beams for energies $\leq$ 90 MeV/n ($\leq$ 120 MeV/n for ^{3}He). Similar ^{4}He beams, but at slightly lower energies (62 and 80 MeV/n), can

TABLE 3 | Suitable accelerator facilities for helium cross-section measurements.

Facility name Location/country	Ion	Energy range
Existing facilities		
GSI/FAIR		
Darmstadt/Germany	^{1}H	E = 70–4,500 MeV
SIS18 synchrotron	^{3}**He** - ^{20}N	**E = 70–2,000 MeV/u**
BNL/NSRL		
Brookhaven/United States	^{4}**He** - ^{56}Fe	**E ≤ 1,500 MeV/u**
AGS Booster, synchrotron		
JINR		
Dubna/Russia	^{4}**He** - ^{56}Fe	**E ≤ 2,200 MeV/u**
Nuclotron supercond. synchrotron		
NIRS/HIMAC		
Chiba/Japan	^{4}**He** - ^{20}Ne	**E = 50–800 MeV/u**
Synchrotron		
HIT		
Heidelberg/Germany	^{1}H	E = 50–480 MeV/u
compact synchrotron	^{4}**He** - ^{16}O	**E = 100–430 MeV/u**
AGOR/KVI-CART	^{1}H	E ≤ 190 MeV
Groningen/Netherlands	^{3}**He**	**E ≤ 120 MeV/u**
supercond. cyclotron	^{4}**He**, ^{12}C, ^{16}O	**E ≤ 90 MeV/u**
K800/LNS		
Catania/Italy	^{2}H, ^{4}**He**, ^{12}C, ^{16}O	**E = 62 and 80 MeV/u**
supercond. cyclotron		
Future facilities		
GSI/FAIR		
Darmstadt/Germany	^{1}H	E ≤ 29 GeV/u (not before 2025)
SIS100 supercond. synchrotron	^{4}**He** - ^{20}N	**E ≤ 14 GeV/u** (not before 2025)
JINR/NICA		
Dubna/Russia	^{4}**He** - ^{56}Fe	**E ≤ 4.5 GeV/u** (not before 2020)
Nuclotron (upgr.) supercond. synchrotron		
MedAustron	^{1}H	E ≤ 800 MeV (available)
Wiener Neustadt/Austria	^{12}C	E ≤ 400 MeV/u (available)
Synchrotron	^{4}**He**	**E ≤ 400 MeV/u** (not before 2023)
CNAO		
Pavia/Italy	^{1}H	E = 63–230 MeV (available)
compact synchrotron	^{12}C	E = 115–400 MeV/u (available)
to be upgraded for He	^{4}**He**, ^{7}Li, ^{16}O	**E = 115–330 MeV/u** (not before 2023)

be provided by the superconducting K800 cyclotron at the INFN Southern National Laboratory (LNS) in Catania.

5 FOOT PROGRAM

5.1 Description of Program

FOOT (FragmentatiOn Of Target) [140–142] is an experiment funded by the INFN (Istituto Nazionale di Fisica Nucleare, Italy), aiming at the measurement of double differential cross sections for the production of charged particles in nuclear fragmentation which are of interest for medicine (hadron therapy) and radioprotection in space missions. The experiment has been originally designed with the main goal of investigating target fragmentation in proton therapy by means of an inverse kinematic approach, using beams of ^{12}C, and ^{16}O on graphite and polyethylene targets, to extract cross sections for the production of charged fragments in p+C and p+O collisions. The inverse kinematic approach is needed because the target fragments produced by proton beams would have too short ranges in matter (tens of microns), preventing the possibility of a direct measurement. However, it is straightforward for the same apparatus to investigate the fragmentation cross section in the direct processes C+H, C+C, O+H, and O+C. Using different target materials, like PMMA, also the collisions with other nuclei of interest for biological effects, like oxygen, can be studied. One can also consider possible direct kinematics measurements, and primaries other than C and O. The case of ^{4}He has been recognized as one of the main priorities. The energy range of nuclear projectiles under consideration by FOOT spans from 100 to 200 MeV/n, useful for the applications to hadron therapy (and proton therapy in particular), up to 700–800 MeV/n for the investigation of direct kinematics reactions relevant for space radioprotection. A summary of the physics program of FOOT is reported in **Table 4**.

The accuracy goal of FOOT is to identify charge and mass of the produced fragments with an accuracy of 3% and 5%, respectively, and to measure their energy spectra with a

resolution of 2 MeV. Taking into account these goals, the idea is to realize a "portable" experimental setup in order to operate it in different facilities and to have some flexibility to optimize its configuration for different energy ranges. The detector design has been guided by Monte Carlo simulations, based on the FLUKA code [143, 144]. It shows that in the whole energy range under consideration, light ($Z \leq 3$) fragments have a wide emission angle, while the heavier fragments are forward peaked within a narrow cone: a semi-aperture of $\theta \sim 10^{\circ}$ ensures sufficient containment. In order to give an idea of energy and angle distribution of secondary fragments in ^{4}He interactions, the differential cross sections, in energy and angle have been considered for different fragments at the projectile energy of 700 MeV/n, as predicted by the FLUKA code. In **Figure 16**, $d\sigma/dE$ is shown for three different targets (H, C, and O) integrated in the forward hemisphere ($0^{\circ} \leq \theta < 90^{\circ}$), while $d\sigma/d\Omega$ is given in **Figure 17**.

On the basis of the experimental goals summarized above, the FOOT experiment has been conceived considering two complementary experimental configurations:

(1) An electronic configuration based on a magnetic spectrometer dedicated to the momentum reconstruction and an identification section made of a plastic scintillator and a calorimeter. This setup aims to measure fragments heavier than ^{4}He ($Z \geq 3$) and covering a polar angle of $\theta \pm 10^{\circ}$ with respect to the beam axis;
(2) A configuration based on an emulsion spectrometer supplying complementary measurements for light fragments emitted at an angle up to about 70°.

This approach of employing two complementary detection techniques is particularly useful in the measurement of ^{4}He interactions, with only $Z \leq 2$ fragments; the angular acceptance of the emulsion setup allows one to cover a large part of the necessary phase space, and a cross-check in the acceptance cone of the electronic detector allows a cross-check of results and a control of possible systematics. A sketch of the electronic detector is shown in **Figure 18**, and fragment momentum, kinetic energy, time of flight (TOF), and energy loss (dE/dx) are measured. The detector geometry consists of the following:

(1) Upstream/target region: A thin plastic scintillator counter provides the start signal of the TOF and the trigger system, and downstream, a drift chamber operates as a beam monitor, tracking the direction and the position of the beam. The target is positioned beyond the beam monitor.
(2) Magnetic region: It is composed of three stations of pixel and strip detectors allocated between and downstream of the magnets providing the vertex reconstruction and the initial tracking of the produced fragments; two permanent dipole magnets supply the magnetic field (up to 1.4 T).
(3) Identification region: It is the distal part of the detector, located at least 1 m away from the target (more for higher energies). It is composed of two orthogonal planes of plastic scintillator rods, providing the stop of the TOF and the measurement of the energy loss. A BGO calorimeter provides the fragment kinetic energy measurements.

TABLE 4 | FOOT research program.

Physics	Beam	Target	Energy	Kinematic
—	—	—	(MeV/n)	Approach
Target fragmentation in proton therapy	^{12}C	C, C_2H_4	200	Inverse
Target fragmentation in proton therapy	^{16}O	C, C_2H_4	200	Inverse
Beam fragmentation in proton therapy	^{4}He	C, C_2H_4, PMMA	250	Direct
Beam fragmentation in proton therapy	^{12}C	C, C_2H_4, PMMA	350	Direct
Beam fragmentation in proton therapy	^{16}O	C, C_2H_4, PMMA	400	Direct
Space radioprotection	^{4}He	C, C_2H_4, PMMA	700	Direct
Space radioprotection	^{12}C	C, $C_2H.$, PMMA	700	Direct
Space radioprotection	^{16}O	C, C_2H_4, PMMA	700	Direct

The TOF, measured by the start counter and the scintillator, has an estimated resolution at the level of 70–100 ps. The silicon detectors, in the magnetic region, are able to perform momentum measurements with an expected resolution of about 5%, while the resolution supplied by the scintillator and by the calorimeter is about 3 and 2%, respectively, in the measurement of the energy loss and kinetic energy. The emulsion spectrometer is built using Emulsion Cloud Chamber (ECC) technology, alternating nuclear emulsion films with passive material [145]. A sketch of the ECC is shown in **Figure 19**.

The ECC acts as a micrometric tracking device, ionization chamber, and a spectrometer for isotope separation. The nuclear emulsion films consist of two 50-μm thick sensitive emulsion layers deposited on both sides of a plastic base, 200 μm thick, resulting in a total thickness of 300 μm. AgBr crystals, dispersed in a gelatine matrix, are sensitive to ionizing particles and record their trajectory acting as latent image centers. A chemical process of development produces the latent image as silver grains recorded as dark pixels by an optical microscope. A dedicated software recognizes aligned clusters of dark pixels producing a track related to the path of the charged particle. The present design of the experiment does not allow for an efficient measurement of neutron production, which however is considered a relevant issue in radioprotection for space missions. Different ideas to extend the capability of FOOT to neutron detection are under study.

5.2 Present Status of the Experiment

Data have been taken using the ECC setup at GSI, in 2019 with O ions at 200 and 400 MeV/n on C and C_2H_4 targets, and in 2020 with ^{12}C ions at 700 MeV/n, on the same targets. Data analysis is still in progress. The electronic apparatus is under construction, and first data taking in this configuration are being scheduled at CNAO, using ^{12}C ions at 200 MeV/n. An application for beam

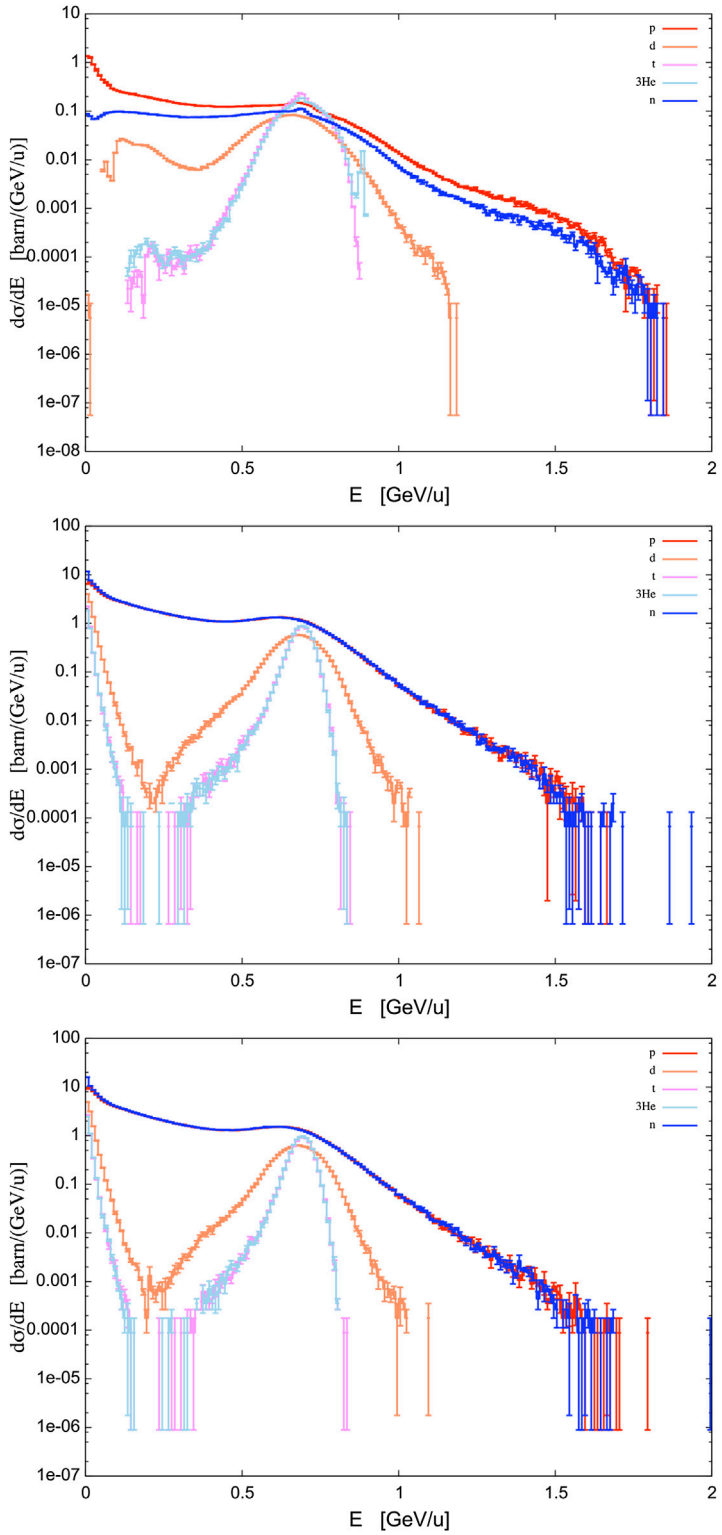

FIGURE 16 | Cross section differential in energy, integrated in the forward hemisphere, for inclusive production of secondaries of ^{4}He ions at 700 MeV/n impinging on different targets, as predicted by the FLUKA code. Three different targets have been considered: H **(top)**, C **(middle)**, and O **(bottom)**. Red: protons, blue: neutrons, orange: deuterons, violet: tritons, and sky blue: ^{3}He.

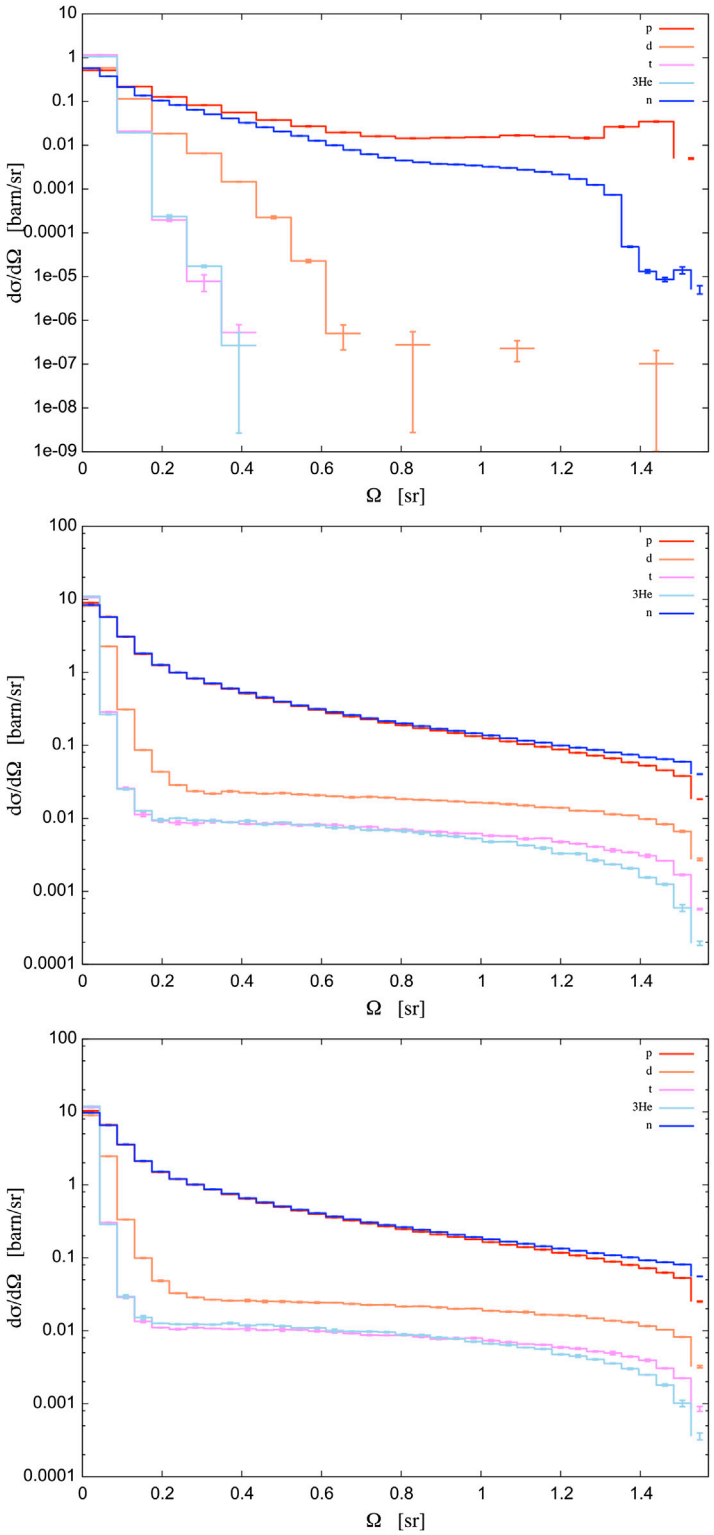

FIGURE 17 | Cross section differential in solid angle (forward hemisphere), integrated in energy, for inclusive production of secondaries of ^{4}He ions at 700 MeV/n impinging on different targets, as predicted by the FLUKA code. Three different targets have been considered: H **(top)**, C **(middle)**, and O **(bottom)**. Red: protons, blue: neutrons, orange: deuterons, violet: tritons, and sky blue: ^{3}He.

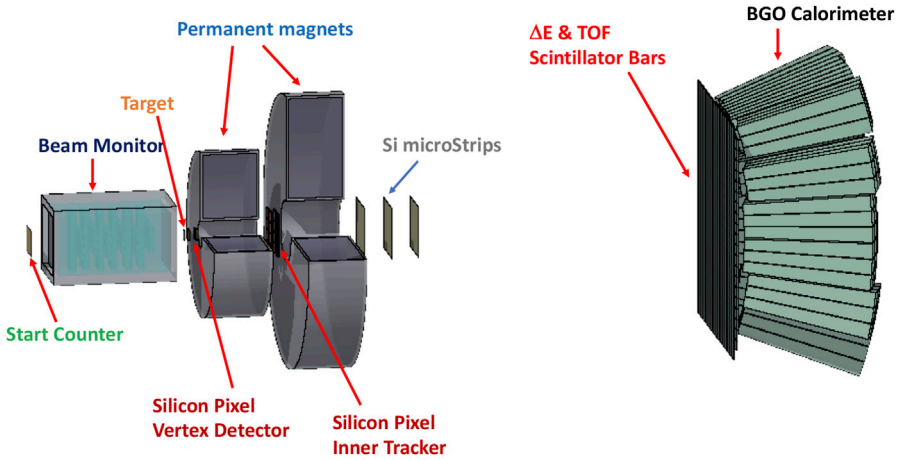

FIGURE 18 | Pictorial view of the FOOT electronic apparatus as obtained from the FLUKA graphical interface.

time in 2021/2022 at GSI is in preparation, having as one of the main priorities the request of a ^{4}He ion beam at 700 MeV/n.

6 FUTURE RECOMMENDATIONS

6.1 Measurements

6.1.1 Total Reaction Cross Sections

Total reaction cross section data for ^{4}He projectiles on heavy targets are missing, especially for elemental targets heavier than oxygen at high energies (see **Figures 12** and **13**). The semi-empirical models match the existing data only roughly and more experimental data points are required in order to improve the models. These types of data are particularly interesting in the framework of simulating the propagation of GCR through spacecraft structural and shielding materials, whose atomic number can be high. The human body is also rich in high atomic number atoms, for example, Ca in the bones, as well as in different implants, for example, amalgam in the teeth and titanium implants in hips and bones, which makes such experimental data interesting for ion therapy as well.

Very low energy data are missing. They are important for modeling the energy dependence of the cross sections below and at the Coulomb barrier, which seems to be shifted toward to high energies for very heavy targets in the currently used parameterizations (see **Figure 20**). An appropriate modeling of the Coulomb barrier is important to accurately predict nuclear reaction thresholds.

6.1.2 Light Ion Production

Given the sparseness of the present data set and the need for a uniform set of data covering all energies appropriate to ion therapy and space radiation, new set of inclusive, isotopic, double differential cross sections should be measured for a complete set of neutron and light ion fragments for the reactions ^{4}He + H, C, O, Al, Ca, Fe $\rightarrow$ n, ^{1,2,3}H, ^{3,4}He + X for projectile kinetic energies ranging over 50 MeV/n–50 GeV/n and fragment angles ranging over 0°–180°.

6.1.3 Neutron Production

Given the limited set of direct measurements taken to date, there are a number of recommendations for additional neutron production data. Data are needed for He energies above 230 MeV/n, at all angles, especially angles beyond the existing measurements at 110°, and for neutron energies down to 1 MeV. Data are needed for hydrogen, nitrogen, and oxygen targets (tissue constituents), in addition to a range of solid targets used in previous experiments. Investigations of neutron production from He targets may be able to produce useful data through the use of inverse kinematics. For example, translation of data from the ^{4}He (p,n)X system to the ^{1}H(^{4}He,n)X system can yield information on production from hydrogen targets, which are difficult to implement in the laboratory.

6.2 Modeling

The ultimate use of new cross section measurements is the development of accurate theoretical cross section models that can be used in modern transport codes. As mentioned previously in the text, isotopic production double differential cross section will give more detailed information about the nuclear reactions, so measurements of these cross sections are important to verify the theoretical models. Some models have been developed previously, but often they are compared to only a limited data set. Ion therapy and space radiation applications require models to be accurate for a wide range of projectiles, energies, and targets. Therefore, a cross section modeling program proceeding in parallel with the measurement program needs to be initiated. The cross section models should be compared to *all* available cross section data, including previously measured total and single differential cross sections.

A special emphasis will be given to modeling the high energy ^{4}He beams. This can be achieved when experimental cross section data for ^{4}He projectiles with high energy (~ 10 GeV/n) will be

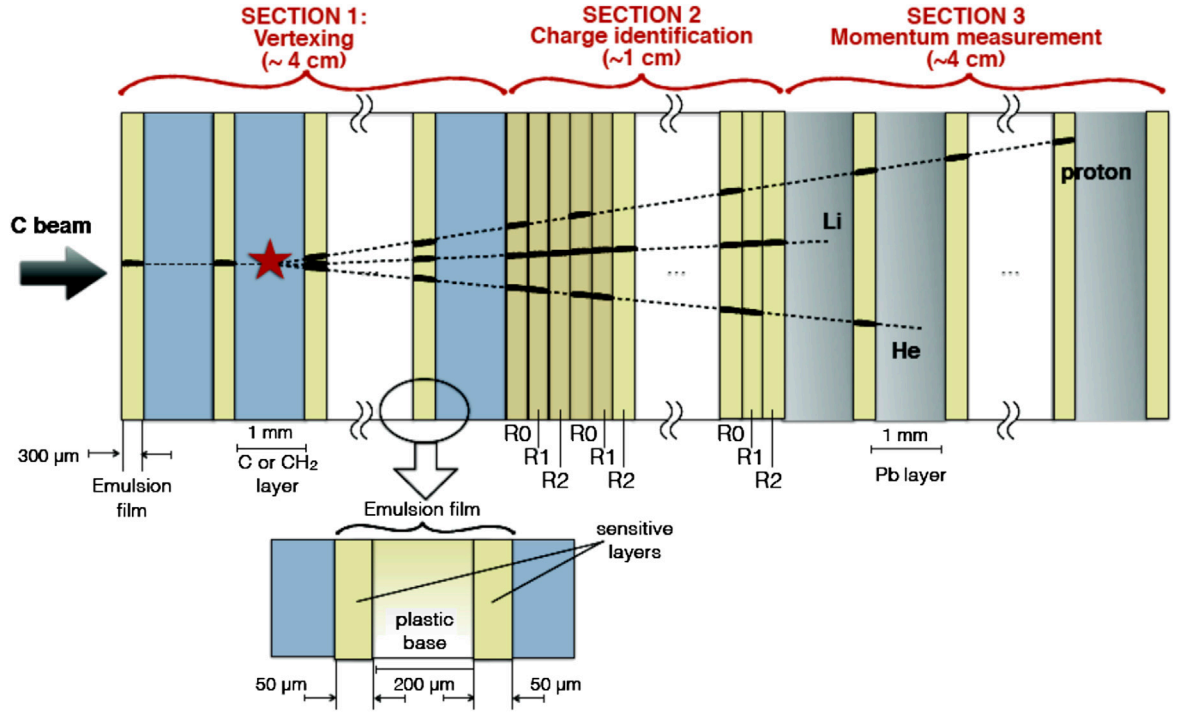

FIGURE 19 | Schematic overview of the ECC layout. Drawing is not to scale.

available at FAIR. These data will answer many questions raised so far and they will validate the models used in various simulation tools.

Some modeling approaches for ^{4}He total reaction and ^{3}He production cross sections were presented in **section 3.2.2**. More experimental data for the other reaction channels (production of ^{1}H, ^{2}H, ^{3}H, and neutrons) are required to improve the modeling.

Recent experiments pointed out problems with dose calculation in the beam halo of ^{4}He ions [33]. Those may be improved by optimization of ^{4}He nuclear models against double differential cross sections.

Although double differential cross section models are preferred for comparisons to experimental data, accurate total reaction and fragmentation cross sections are also needed by radiation transport codes for prediction of particle fluences. Moreover, total fragmentation cross section models can be used for normalizing and anchoring parametric models, such as DDFRG [12, 13, 119]. Werneth et al. [146–150] developed a relativistic (kinematics) multiple scattering theory (RMST) for the prediction of reaction, elastic, total, and elastic differential cross sections for space radiation–relevant reactions. The fundamental nuclear constituents of the MST are defined as the nucleons, and the quark structure of individual nucleons is not considered. Consequently, the interaction of nucleon–nucleus and nucleus–nucleus reaction is modeled as the sum of nucleon–nucleon interactions, which may be parameterized to free nucleon–nucleon transition amplitudes. Elastic differential, total, reaction, and elastic cross sections may be found by solving the Lippmann–Schwinger (LS) equation or with a high-

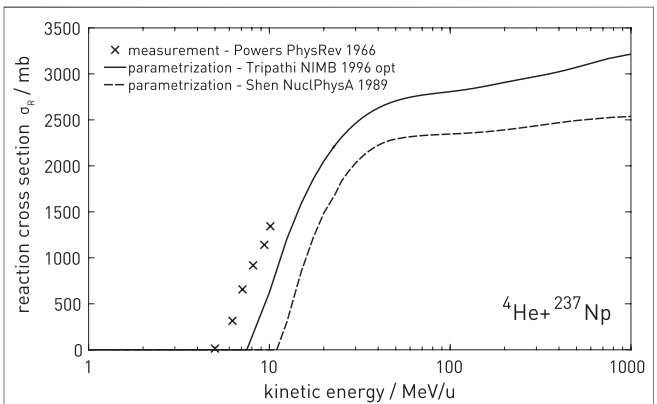

FIGURE 20 | Experimental data of total reaction cross sections for ^{4}He-induced reactions on ^{237}Np targets, compared with two different parameterizations. The parameterizations shown are by Tripathi et al. [109] with the modifications described by Horst et al. [43] and the parameterization by Shen et al. [110] with the modifications proposed by Sihver et al. [111]. The experimental data taken are from Powers et al. [73].

energy, small angle approximation known as the Eikonal approximation. Relativistic kinematics are easily incorporated into the momentum–space formulation of the LS equation [146, 147], and a large shift toward small angles and with larger magnitude is observed in the elastic differential cross sections. Another interesting result is that relativistic kinematic effects will depend on both energy and relative mass of the projectile and target [148]. A comprehensive validation effort [149] showed that the

relativistic three dimensional LS model (LS3D) agrees best with experimental data. Additional model improvements led to LS3D predictions of the reaction cross sections that were of the same fidelity to data as the Tripathi parameterizations [150]. In order to improve computational efficiency, a momentum–space formulation of the Eikonal approximation was developed.

The relativistic abrasion–ablation de-excitation fragmentation (RAADFRG) model has been formulated for fragments produced from nucleus–nucleus collisions by coupling the highly efficient Eikonal model for nuclear abrasion to a de-excitation model described by the Weisskopf–Ewing mechanism. Relativistic kinematics may be incorporated by renormalizing the sum of the Eikonal abrasion cross sections to the reaction cross section produced from the LS3D theory. As the projectile nucleus collides with a target nucleus, nucleons are sheared away from the projectile and target during a very short time scale, leaving the pre-fragment (remaining projectile nuclear constituents) in an excitation state. The pre-fragment is assigned an excitation energy, which may include multiple scattering and energy depositions from nucleon–nucleon collisions. After a much longer time scale, the excited pre-fragment will emit light ions and neutrons with probabilities described by the Weisskopf–Ewing formalism until all available excitation energy is exhausted. Nuclear structure is manifested in the fragmentation cross sections with proper choice of the nuclear partition function and excitation energy model. Furthermore, RAADFRG may be used to anchor parametric double differential cross section models such as DDFRG [12, 13, 119]. The dearth of experimental light ion fragmentation data makes it difficult to fully validate the RAADFRG model and other nuclear models that are needed for space radiation applications.

Finally, another modeling activity required in future is to confirm the SHIELD double differential cross section results for light ion production from He projectiles, shown in **Figure 15**. Comparisons need to be made with other cross section models.

7 SUMMARY AND CONCLUSION

Helium projectile double differential cross sections for the production of neutrons and light ions are of great importance to space radiation and ion therapy studies. However, transport codes and cross section models display significant problems when compared with limited data on both thick and thin targets. Also, there is a very significant lack of high-quality experimental data available that could resolve these problems. The following recommendations are made:

- A new set of inclusive, isotopic, double differential cross sections should be measured for a complete set of neutron and light ion fragments for the reactions

$$^{4}\mathrm{He} + \mathrm{H, C, O, Ca, Al, Fe} \rightarrow \mathrm{n}, ^{1,2,3}\mathrm{H}, ^{3,4}\mathrm{He} + \mathrm{X}$$

- for projectile kinetic energies ranging over 50 MeV/n–50 GeV/n and fragment angles ranging over 0°–180°.
- Those experiments should be accompanied by measurements of total reaction and single differential fragment production cross sections for ^{4}He projectiles, in particular for targets heavier than oxygen in the energy range between 50 MeV/n–50 GeV/n and at energies around the Coulomb barrier.
- A parallel program of cross section model development needs to be initiated in order to develop accurate models for these new measurements.
- A parallel program of transport code validation needs to be undertaken.

The present work has focused on helium projectiles because they represent the highest priority. Nevertheless, other projectiles, such as C, O, Si, and Fe are important for both ion therapy and space radiation, as discussed in **Section 1.3**. A program similar to that described above would be very worthwhile for these other projectiles, as summarized by **Eq. 1**.

AUTHOR CONTRIBUTIONS

All authors contributed to the planning, ideas, debating, writing, and editing of the manuscript.

ACKNOWLEDGMENTS

We wish to thank Laura Bagnale (Federico II University, Naples, Italy) for help with data analysis and collection, and Dr. Steve Smith (NASA Langley) for reviewing the manuscript. Bocchini, Giraudo, and Santin were partially supported by the European Space Agency under contract Number 4000125785 ("ROSSINI 3"). Experiments with He ions are performed in Cave A at GSI in the framework of FAIR Phase-0 supported by the GSI Helmholtzzentrum für Schwerionenforschung in Darmstadt (Germany).

REFERENCES

1. Norbury JW, Miller J, Adamczyk AM, Heilbronn LH, Townsend LW, Blattnig SR, et al. Nuclear data for space radiation. *Radiat Meas.* (2012) 47:315–63. doi:10.1016/j.radmeas.2012.03.004.
2. Norbury JW, Miller J, Adamczyk A, Heilbronn L, Townsend L, Blattnig S, et al. Review of nuclear physics experiments for space radiation. NASA Technical Paper, NASA/TP-2011-217179, National Aeronautics and Space Administration, Washington DC (2011)
3. Norbury JW. Nuclear physics and space radiation. *J Phys Conf Ser.* (2012) 381: 012117. doi:10.1088/1742-6596/381/1/012117.
4. Norbury JW, Miller J. Review of nuclear physics experimental data for space radiation. *Health Phys.* (2012) 103:640–2. doi:10.1097/hp.0b013e318261fb7f.
5. Rutherford E. The scattering of α and β particles by matter and the structure of the atom. *Phil Mag.* (1911) 21:669–688. doi:10.1080/14786440508637080.
6. Tommasino F, Scifoni E, Durante M. New ions for therapy. *Int J Particle Therapy.* (2015) 2:428–38. doi:10.14338/ijpt-15-00027.1.

7. Norbury JW, Slaba TC, Aghara S, Badavi FF, Blattnig SR, Clowdsley MS, et al. Advances in space radiation physics and transport at NASA. *Life Sci Space Res.* (2019) 22:98–124. doi:10.1016/j.lssr.2019.07.003.
8. Walker SA, Townsend LW, Norbury JW. Heavy ion contributions to organ dose equivalent for the 1977 galactic cosmic ray spectrum. *Adv Space Res.* (2013) 51: 1792–1799. doi:10.1016/j.asr.2012.12.011.
9. Norbury JW, Slaba TC. Space radiation accelerator experiments - the role of neutrons and light ions. *Life Sci Space Res.* (2014) 3:90–4. doi:10.1016/j.lssr.2014.09.006.
10. Slaba TC, Blattnig SR, Norbury JW, Rusek A, La Tessa C. Reference field specification and preliminary beam selection strategy for accelerator-based GCR simulation. *Life Sci Space Res.* (2016) 8:52–67. doi:10.1016/j.lssr.2016.01.001.
11. Wilson JW, Slaba TC, Badavi FF, Reddell BD, Bahadori AA. Advances in NASA radiation transport research: 3DHZETRN. *Life Sci Space Res.* (2014) 2: 6–22. doi:10.1016/j.lssr.2014.05.003.
12. Norbury JW, Latysheva L, Sobolevsky N. Light ion double-differential cross section parameterizations and results from the SHIELD transport code. *Nucl Instrum Methods Phys Res A.* (2019) 947:162576. doi:10.1016/j.nima.2019.162576.
13. Norbury JW. *Light ion double-differential cross sections for space radiation.* NASA Technical Publication, NASA/TP-2018-220077, National Aeronautics and Space Administration, Washington DC (2018)
14. Norbury JW, Slaba TC, Sobolevsky N, Reddell B. Comparing HZETRN, SHIELD, FLUKA and GEANT transport codes. *Life Sci Space Res.* (2017) 14:64–73. doi:10.1016/j.lssr.2017.04.001.
15. Slaba TC, Bahadori AA, Reddell BD, Singleterry RC, Clowdsley MS, Blattnig SR. Optimal shielding thickness for galactic cosmic ray environments. *Life Sci Space Res.* (2017) 12: 1–15. doi:10.1016/j.lssr.2016.12.003.
16. Beach M, Castellanos L, Clowdsley M, Heilbronn L, La Tessa C, McGirl N, et al. Double differential light ion production cross sections from 300 AMeV oxygen and 600 AMeV iron beams on aluminum, carbon and polyethylene targets. *Nucl Instrum Methods Phys Res B.* (submitted).
17. Sato T, Niita K, Matsuda N, Hashimotot S, Iwamoto Y, Noda S, et al. Particle and heavy ion transport code system PHITS, version 2.52. *J Nucl Sci Technol.* (2013) 50:913–23. doi:10.1080/00223131.2013.814553.
18. Heilbronn H, et al. to be published.
19. Matthiä D, Ehresmann B, Lohf H, Köhler J, Zeitlin C, Appel J, et al. The Martian surface radiation environment - a comparison of models and MSL/RAD measurements. *J. Space Weather Space Clim.* (2016) 6:A13. doi:10.1051/swsc/2016008.
20. Hassler DM, Norbury JW, Reitz G. Mars science laboratory radiation assessment detector (MSL/RAD) modeling workshop proceedings. *Life Sci Space Res.* (2017) 14:1–2. doi:10.1016/j.lssr.2017.06.004.
21. Matthiä D, Hassler DM, de Wet W, Ehresmann B, Firan A, Flores-McLaughlin J, et al. The radiation environment on the surface of Mars - summary of model calculations and comparison to RAD data. *Life Sci Space Res.* (2017) 14:18–28. doi:10.1016/j.lssr.2017.06.003.
22. Slaba TC, Blattnig SR, Badavi FF, Stoffle NN, Rutledge RD, Lee KT, et al. Statistical validation of HZETRN as a function of vertical cutoff rigidity using ISS measurements. *Adv Space Res.* (2011) 47:600–10. doi:10.1016/j.asr.2010.10.021.
23. Slaba TC, Blattnig SR, Reddell B, Bahadori A, Norman RB, Badavi FF. Pion and electromagnetic contribution to dose: comparisons of HZETRN to Monte Carlo results and ISS data. *Adv Space Res.* (2013) 52:62–78. doi:10.1016/j.asr.2013.02.015.
24. Battistoni G, Mattei I, Muraro S. Nuclear physics and particle therapy. *Adv Phys X.* (2016) 1:661–86. doi:10.1080/23746149.2016.1237310.
25. Durante M, Paganetti H. Nuclear physics in particle therapy: a review. *Rep Prog Phys.* (2016) 79:096702. doi:10.1088/0034-4885/79/9/096702.
26. Zeitlin C, La Tessa C. The role of nuclear fragmentation in particle therapy and space radiation protection. *Front. Oncol.* (2016) 6:1–13. doi:10.3389/fonc.2016.00065.
27. Parodi K, Mairani A, Brons S, Hasch BG, Sommerer F, Naumann J, et al. Monte Carlo simulations to support start-up and treatment planning of scanned proton and carbon ion therapy at a synchrotron-based facility. *Phys Med Biol.* (2012) 57:3759–84. doi:10.1088/0031-9155/57/12/3759.
28. Battistoni G, Bauer J, Boehlen TT, Cerutti F, Chin MPW, Dos Santos Augusto R, et al. The FLUKA code: an accurate simulation tool for particle therapy. *Front Oncol.* (2016) 6:1–24. doi:10.3389/fonc.2016.00116.
29. Krämer M, Jäkel O, Haberer T, Kraft G, Schardt D, Weber U. Treatment planning for heavy-ion radiotherapy: physical beam model and dose optimization. *Phys Med Biol 60th Anniversary Collection.* (2016) 37.
30. Haettner E, Iwase H, Krämer M, Kraft G, Schardt D. Experimental study of nuclear fragmentation of 200 and 400 MeV/u12C ions in water for applications in particle therapy. *Phys Med Biol.* (2013) 58(23):8265–8279. doi:10.1088/0031-9155/58/23/8265.
31. Krämer M, Scifoni E, Schuy C, Rovituso M, Tinganelli W, Maier A, et al. Helium ions for radiotherapy? Physical and biological verifications of a novel treatment modality. *Med Phys.* (2016) 43:1995–2004. doi:10.1118/1.4944593.
32. Sokol O, Scifoni E, Tinganelli W, Kraft-Weyrather W, Wiedemann J, Maier A, et al. Oxygen beams for therapy: advanced biological treatment planning and experimental verification. *Phys Med Biol.* (2017) 62:7798–813. doi:10.1088/1361-6560/aa88a0.
33. Tessonnier T, Mairani A, Brons S, Sala P, Cerutti F, Ferrari A, et al. Helium ions at the Heidelberg ion beam therapy center: comparisons between FLUKA Monte Carlo code predictions and dosimetric measurements. *Phys Med Biol.* (2017) 62:6784. doi:10.1088/1361-6560/aa7b12.
34. Robert C, Dedes G, Battistoni G, Böhlen TT, Buvat I, Cerutti F, et al. Distributions of secondary particles in proton and carbon-ion therapy: a comparison between GATE/Geant4 and FLUKA Monte Carlo codes. *Phys Med Biol.* (2013) 58:2879. doi:10.1088/0031-9155/58/9/2879.
35. Kase Y, Kanematsu N, Kanai T, Matsufuji N. Biological dose calculation with Monte Carlo physics simulation for heavy-ion radiotherapy. *Phys Med Biol.* (2006) 51:N467. doi:10.1088/0031-9155/51/24/n03.
36. Piersanti L, Bellini F, Bini F, Collamati F, De Lucia E, Durante M, et al. Measurement of charged particle yields from PMMA irradiated by a 220 MeV/u12Cbeam. *Phys Med Biol.* (2014) 59:1857. doi:10.1088/0031-9155/59/7/1857.
37. Lühr A, Hansen DC, Teiwes R, Sobolevsky N, Jäkel O, Bassler N. The impact of modeling nuclear fragmentation on delivered dose and radiobiology in ion therapy. *Phys Med Biol.* (2012) 57:5169–85. doi:10.1088/0031-9155/57/16/5169.
38. Kodaira S, Kitamura H, Kurano M, Kawashima H, Benton ER. Contribution to dose in healthy tissue from secondary target fragments in therapeutic proton, He and C beams measured with CR-39 plastic nuclear track detectors. *Sci Rep..* (2019) 9:3708. doi:10.1038/s41598-019-39598-0.
39. Dudouet J, Juliani D, Labalme M, Cussol D, Angélique JC, Braunn B, et al. Double-differential fragmentation cross-section measurements of 95 MeV/n ^{12}C beams on thin targets for hadron therapy. *Phys Rev C.* (2013) 88:24606. doi:10.1103/physrevc.88.024606.
40. Dudouet J, Juliani D, Labalme M, Cussol D, Angélique JC, Braunn B, et al. Erratum: double-differential fragmentation cross-section measurements of 95 MeV/n ^{12}C beams on thin targets for hadron therapy. *Phys Rev C.* (2014) 89: 069904. doi:10.1103/physrevc.89.069904.
41. Divay C, Colin J, Cussol D, Finck Ch, Karakaya Y, Labalme M, et al. Differential cross section measurements for hadron therapy: 50 MeV/n ^{12}C reactions on H, C, O, Al, and natTi targets. *Phys Rev C.* (2017) 95:044602. doi:10.1103/physrevc.95.044602.
42. Horst F, Schuy C, Weber U, Brinkmann KT, Zink K. Measurement of charge- and mass-changing cross sections for ^{4}He + ^{12}C collisions in the energy range 80 - 220 MeV/n for applications in ion beam therapy. *Phys Rev C.* (2017) 96: 024624. doi:10.1103/physrevc.96.024624.
43. Horst F, Aricó G, Brinkmann KT, Brons S, Ferrari A, Haberer T, et al. Measurement of ^{4}He charge- and mass-changing cross sections on H, C, O, and Si targets in the energy range 70 - 220 MeV/n for radiation transport calculations in ion-beam therapy. *Phys Rev C.* (2019) 99:014603. doi:10.1103/physrevc.99.014603.
44. Datta K, Suman S, Kallakury B, Fornace A. Exposure to heavy ion radiation induces persistent oxidative stress in mouse intestine. *PloS One.* (2012) 7: e42224. doi:10.1371/journal.pone.0042224.
45. Mewaldt RA, Cohen CMS, Labrador AW, Leske RA, Mason GM, Desai MI, et al. Proton, helium, and electron spectra during the large solar particle events of October-November 2003. *J Geophys Res.* (2005) 110:A09S18. doi:10.1029/2005ja011038.
46. Slaba TC, Blattnig SR. GCR environmental models I: sensitivity analysis for GCR environments. *Space Weather.* (2014) 12:217–24. doi:10.1002/2013sw001025.

47. Bocchini L, et al. To be published.
48. Santin G, Ivanchenko V, Evans H, Nieminen P, Daly E. GRAS: a general-purpose 3-D modular simulation tool for space environment effects analysis. *IEEE Trans Nucl Sci.* (2005) 52(6):2294–2299. doi:10.1109/tns.2005.860749.
49. Dietze G, Bartlett DT, Cool DA, Cucinotta FA, Jia X, McAulay IR, et al. ICRP publication 123: assessment of radiation exposure of astronauts in space. *Ann ICRP.* (2013) 42(4):1–339. doi:10.1016/j.icrp.2013.05.004.
50. Giraudo M, Schuy C, Weber U, Rovituso M, Santin G, Norbury JW, et al. Accelerator-based tests of shielding effectiveness of different materials and multilayers using high-energy light and heavy ions. *Radiat Res.* (2018) 190(5):526–37. doi:10.1667/rr15111.1.
51. Castro JR, Char DH, Petti PL, Daftari IK, Quivey JM, Singh RP, et al. 15 years experience with helium ion radiotherapy for uveal melanoma. *Int J Radiat Oncol Biol Phys.* (1997) 39:989–996. doi:10.1016/s0360-3016(97)00494-x.
52. Pedroni E, Böhringer T, Coray A, Egger E, Grossmann M, Lin S, et al. Initial experience of using an active beam delivery technique at PSI. *Strahlenther Onkol.* (1999) 175:18–20. doi:10.1007/bf03038879.
53. Schardt D, Elsässer T, Schulz-Ertner D. Heavy-ion tumor therapy: physical and radiobiological benefits. *Rev Mod Phys.* (2010) 82:383. doi:10.1103/revmodphys.82.383.
54. Kamada T, Tsujii H, Blakely EA, Debus J, De Neve W, Durante M, et al. Carbon ion radiotherapy in Japan: an assessment of 20 years of clinical experience. *Lancet Oncol.* (2015) 16:e93-e100. doi:10.1016/s1470-2045(14)70412-7.
55. Knäusl B, Fuchs H, Dieckmann K, Georg D. Can particle beam therapy be improved using helium ions? - a planning study focusing on pediatric patients. *Acta Oncologica..* (2016) 55:751–759. doi:10.3109/0284186x.2015.1125016.
56. Tessonnier T, Mairani A, Chen W, Sala P, Cerutti F, Ferrari A, et al. Proton and helium ion radiotherapy for meningioma tumors: a Monte Carlo-based treatment planning comparison. *Rad. Oncol.* (2018) 13:2. doi:10.1186/s13014-017-0944-3.
57. Grün R, Friedrich T, Krämer M, Zink K, Durante M, Engenhart-Cabillic R, et al. Assessment of potential advantages of relevant ions for particle therapy: a model based study. *Med Phys.* (2015) 42:1037–47. doi:10.1118/1.4905374.
58. Inaniwa T, Suzuki M, Hyun Lee S, Mizushima K, Iwata Y, Kanematsu N, et al. Experimental validation of stochastic microdosimetric kinetic model for multi-ion therapy treatment planning with helium-, carbon-, oxygen-, and neon-ion beams. *Phys Med Biol.* (2020) 65:045005. doi:10.1088/1361-6560/ab6eba.
59. Sokol O, Krämer M, Hild S, Durante M, Scifoni E. Kill painting of hypoxic tumors with multiple ion beams. *Phys Med Biol.* (2019) 64:045008. doi:10.1088/1361-6560/aafe40.
60. Schneider T, Patriarca A, Prezado Y. Improving the dose distributions in minibeam radiation therapy: helium ions vs protons. *Med Phys.* (2019) 46:3640–3648. doi:10.1002/mp.13646.
61. Gehrke T, Amato C, Berke S, Martisikova M. Theoretical and experimental comparison of proton and helium-beam radiography using silicon pixel detectors. *Phys Med Biol.* (2018) 63:035037. doi:10.1088/1361-6560/aaa60f. |
62. Volz L, Kelleter L, Brons S, Burigo LN, Graeff C, Niebuhr NI, et al. Experimental exploration of a mixed helium/carbon beam for online treatment monitoring in carbon ion beam therapy. *Phys Med Biol.* (2020) 65:055002. doi:10.1088/1361-6560/ab6e52.
63. Ingemarsson A, Nyberg J, Renberg PU, Sundberg O, Carlson RF, Cox AJ, et al. New results for reaction cross sections of intermediate energy α-particles on targets from Be to Pb. *Nucl Phys.* (2000) 676:3–31. doi:10.1016/s0375-9474(00)00200-1.
64. DeVries RM, DiGiacomo NJ, Kapustinsky JS, Peng JC, Sondheim WE, Sunier JW, et al. Dominance of nucleon-nucleon interactions inα+C12total reaction cross sections. *Phys Rev C.* (1982) 26:301. doi:10.1103/physrevc.26.301.
65. Tanihata I, Hamagaki H, Hashimoto O, Nagamiya S, Shida Y, Yoshikawa N, et al. Measurements of interaction cross sections and radii of He isotopes. *Phys Lett B.* (1985) 160:380–384. doi:10.1016/0370-2693(85)90005-x.
66. Jaros J, Wagner A, Anderson L, Chamberlain O, Fuzesy RZ, Gallup J, et al. Nucleus-nucleus total cross sections for light nuclei at 1.55 and 2.89 GeV/cper nucleon. *Phys Rev C.* (1978) 18:2273. doi:10.1103/physrevc.18.2273.
67. Aksinenko VD, Anikina MKh, Buttsev VS, Chkaidze LV, Glagoleva NS, Golokhvastov AI, et al. Streamer chamber study of the cross sections and multiplicities in nucleus-nucleus interactions at the incident momentum of 4.5 GeV/c per nucleon. *Nucl Phys.* (1980) 348:518–34. doi:10.1016/0375-9474(80)90269-9.
68. Warner RE, Patty RA, Voyles PM, Nadasen A, Becchetti FD, Brown JA, et al. Total reaction and 2n-removal cross sections of 20-60AMeVHe4,6,8,Li6-9,11, andBe10on Si. *Phys Rev C.* (1996) 54:1700. doi:10.1103/physrevc.54.1700.
69. Sourkes AM, Houdayer A, van Oers WTH, Carlson RF, Brown Ronald E Total reaction cross section for protons onHe3andHe4between 18 and 48 MeV. *Phys Rev C.* (1976) 13:451. doi:10.1103/physrevc.13.451.
70. Kozodaev MS, Kulyukin MM, Sulyaev RM, Filippov AI, Shcherbakov Yu.A Interactions between 630 MeV protons and ^{4}He nuclei. *Sov Phys JETP.* (1960) 38:511–516.
71. Neumaier SR, Alkhazov GD, Andronenko MN, Dobrovolsky AV, Egelhof P, Gavrilov GE, et al. Small-angle proton elastic scattering from the neutron-rich isotopes 6He and 8He, and from 4He, at 0.7 GeV in inverse kinematics. *Nucl Phys.* (2002) 712:247–268. doi:10.1016/s0375-9474(02)01274-5.
72. Saint-Laurent MG, Anne R, Bazin D, Guillemaud-Mueller D, Jahnke U, Gen MJ, et al. Total cross sections of reactions induced by neutron-rich light nuclei. *Z. Physik A - Atomic Nuclei.* (1989) 332:457–465. doi:10.1007/bf01292431.
73. Powers JA, Wogman NA, Cobble JW. Mass distribution in the fission ofNp237andPu239by intermediate-energy helium ions. *Phys Rev.* (1966) 152:1096. doi:10.1103/physrev.152.1096.
74. Webber WR, Kish JC, Schrier DA. Total charge and mass changing cross sections of relativistic nuclei in hydrogen, helium, and carbon targets. *Phys Rev C.* (1990) 41:520–532. doi:10.1103/physrevc.41.520.
75. Ferrando P, Webber WR, Goret P, Kish JC, Schrier DA, Soutoul A, et al. Measurement ofC12,O16, andFe56charge changing cross sections in helium at high energy, comparison with cross sections in hydrogen, and application to cosmic-ray propagation. *Phys Rev C.* (1988) 37:1490–1501. doi:10.1103/physrevc.37.1490.
76. Igo G, Wilkins BD. Alpha-particle reaction cross sections at 40 MeV. *Phys. Rev.* (1963) 131:1251. doi:10.1103/physrev.131.1251.
77. Labie E, Lega J, Leleux P, Macq PC. Total reaction cross section of α-particles on carbon between 15.8 and 20.1 MeV. *Nucl Phys.* (1973) 205:81–89. doi:10.1016/0375-9474(73)90121-8.
78. Millburn GP, Birnbaum W, Crandall WE, Schecter L. Nuclear radii from inelastic cross-section measurements. *Phys. Rev.* (1954) 95:1268. doi:10.1103/physrev.95.1268.
79. Bilaniuk OMP, Tokarevskii VV, Bulkin VS, Dubar LV, Nemets OF, Slyusarenko LI. Deuteron and alpha-particle total reaction cross sections for nuclei with A~50. *J Phys G Nucl Phys.* (1981) 7:1699. doi:10.1088/0305-4616/7/12/020.
80. Bilaniuk OMP, Tokarevskii VV, Bulkin VS, Dubar LV, Nemets OF, Slyusarenko LI. Fragment mass, energy, and angular distributions for the ^{12}C(^{4}He,heavy ion) reaction between 49 and 159 MeV. *Phys Rev C.* (1984) 29:1595.
81. Durante M, Cucinotta FA. Physical basis of radiation protection in space travel. *Rev Mod Phys.* (2011) 83:1245. doi:10.1103/revmodphys.83.1245.
82. Auble RL, Ball JB, Bertrand FE, Fulmer CB, Hensley DC, Lee IY, et al. Light ion emission from reactions induced by 0.8-2.4 GeVO16projectiles. *Phys Rev C.* (1983) 28:1552–1564. doi:10.1103/physrevc.28.1552.
83. Fukuda T, Ishihara M, Ogata H, Miura I, Shimoda T, Katori K, et al. Light-particle emission in the reaction of 93Nb + 14N at 132, 159 and 208 MeV. *Nucl Phys.* (1984) 425:548–572. doi:10.1016/0375-9474(84)90023-x.
84. Korejwo A, Giller M, Dzikowski T, Perelygin VV, Zarubin AV. Isotopic cross sections of 12C fragmentation on hydrogen measured at 1.87 and 2.69 GeV/nucleon. *J Phys G Nucl Part Phys.* (2002) 28:1199–208. doi:10.1088/0954-3899/28/6/304.
85. Lindstrom PJ, Greiner DE, Heckman HH, Cork B, Bieser FS. *Isotope production cross sections from the fragmentation of ^{16}O and ^{12}C at relativistic energies..* LBL-3650 (1975)
86. Nagamiya S, Lemaire MC, Moeller E, Schnetzer S, Shapiro G, Steiner H, et al. Production of pions and light fragments at large angles in high-energy nuclear collisions. *Phys Rev C.* (1981) 24:971–1009. doi:10.1103/physrevc.24.971.

87. Olson DL, Berman BL, Greiner DE, Heckman HH, Lindstrom PJ, Crawford HJ. Factorization of fragment-production cross sections in relativistic heavy-ion collisions. *Phys Rev C.* (1983) 28:1602–1613. doi:10.1103/physrevc.28.1602.
88. Zeitlin C, Miller J, Guetersloh S, Heilbronn L, Fukumura A, Iwata Y, et al. Fragmentation of ^{14}N, ^{16}O, ^{20}Ne, and $_{24}$mg nuclei at 290 to 1000 MeV/n. *Phys Rev C.* (2011) 83:034909. doi:10.1103/physrevc.83.034909.
89. Meyer J. Deuterons and He^3 formation and destruction in proton induced spallation of light nuclei ($Z < = 8$). *Astron AstroPhys Suppl.* (1972) 7:417–467.
90. Abdurakhimov AK, Anikina MK, Buttsev VS, Chikovani LD, Chkhaidze LV, Dementjev EA, et al. A study of pion production in 4.5 GeV/c)/nucleon 4He interactions with nuclear targets. *Nucl Phys.* (1981) 362:376–390. doi:10.1016/0375-9474(81)90500-5.
91. Shibata T, Maeda K, Okada K, Ejiri H, Sakai H, Shimizu A. The pre-equilibrium process of the 165Ho(α, xnyp) reaction at Eγ = 109 MeV studied by particle-gamma coincidence measurements. *Nucl Phys.* (1985) 441:445–460. doi:10.1016/0375-9474(85)90155-1.
92. Gosset J, Gutbrod HH, Meyer WG, Poskanzer AM, Sandoval A, Stock R, et al. Central collisions of relativistic heavy ions. *Phys Rev C.* (1977) 16:629–657. doi:10.1103/physrevc.16.629.
93. Bizard G, Le Brun C, Berger J, Duflo J, Goldzahl L, Plouin F, et al. ^{3}He production in 4He fragmentation on protons at 6.85 GeV/c. *Nucl Phys.* (1977) 285:461–468. doi:10.1016/0375-9474(77)90645-5.
94. Riddiford L, Williams AW. The interaction of 970 MeV protons with helium. *Proc. Roy. Soc. A.* (1960) 257:316–325.
95. Motobayashi T, Ejiri H, Shibata T, Okada K, Sasao M, Maeda K, et al. Breakup process for 100 MeV 3He interacting with 165Ho and 166, 167Er nuclei. *Nucl Phys.* (1984) 413:290–310. doi:10.1016/0375-9474(84)90376-2.
96. Zhu F, Lynch WG, Murakami T, Gelbke CK, Kim YD, Nayak TK, et al. Light particle correlations for theHe3+Ag reaction at 200 MeV. *Phys Rev C.* (1991) 44:R582–R585. doi:10.1103/physrevc.44.r582.
97. Doering RR, Schweizer TC, Thornton ST, Dennis LC, Cordell KR, Ziock KOH, et al. Correlated energy spectra of light fragments from 720-MeVα-induced reactions. *Phys Rev Lett.* (1978) 40:1433–1435. doi:10.1103/physrevlett.40.1433.
98. Anderson LMJ. Fragmentation of relativistic light nuclei: longitudinal and transverse momentum distributions. [0. 93 GeV/c/nucleon, 0. 5 to 11. 5, cross sections, limiting fragmentation, nuclear structure, production mechanism]. *LBL report.* 6769 (1977) doi:10.2172/5335548.
99. Westfall GD, Gosset J, Johansen PJ, Poskanzer AM, Meyer WG, Gutbrod HH, et al. Nuclear fireball model for proton inclusive spectra from relativistic heavy-ion collisions. *Phys Rev Lett.* (1976) 37:1202–1205. doi:10.1103/physrevlett.37.1202.
100. Anderson L, Brückner W, Moeller E, Nagamiya S, Nissen-Meyer S, Schroeder L, et al. Inclusive particle production at forward angles from collisions of light relativistic nuclei: nuclear fragments. *Phys Rev C.* (1983) 28:1224–1245. doi:10.1103/physrevc.28.1224.
101. Banaigs J, Berger J, Berthet P, Bizard G, Boivin M, De Sanctis M, et al. Inelastic scattering ofαparticles on light nuclei atPα=7.0 GeV/c. *Phys Rev C.* (1987) 35:1416–1424. doi:10.1103/physrevc.35.1416.
102. Rovituso M, Schuy C, Weber U, Brons S, Cortés-Giraldo MA, La Tessa C, et al. Fragmentation of 120 and 200 MeV u−14He ions in water and PMMA targets. *Phys Med Biol.* (2017) 62:1310. doi:10.1088/1361-6560/aa5302.
103. Marafini M, Paramatti R, Pinci D, Battistoni G, Collamati F, De Lucia E, et al. Secondary radiation measurements for particle therapy applications: nuclear fragmentation produced by4He ion beams in a PMMA target. *Phys Med Biol.* (2017) 62:1291. doi:10.1088/1361-6560/aa5307.
104. Schuy C, Tessa C, Horst F, Rovituso M, Dyrante M, Giraudo M, et al. Experimental assessment of lithium hydride's space radiation shielding performance and Monte Carlo benchmarking 2019. *Radiat Res.* (2019) 191(2):154–161.
105. Sato H, Kurosawa T, Iwase H, Nakamura T, Uwamino Y, Nakao N Measurements of double differential neutron production cross sections by 135 MeV/nucleon He, C, Ne and 95 MeV/nucleon Ar ions. *Phys Rev C.* (2001) 64:034607. doi:10.1103/physrevc.64.034607.
106. Heilbronn L, Zeitlin CJ, Iwata Y, Murakami T, Iwase H, Nakamura T, et al. Secondary neutron-production cross sections from heavy-ion interactions between 230 and 600 MeV/nucleon. *Nucl Sci Eng.* (2007) 157:142–158. doi:10.13182/nse07-a2719.
107. Krämer M, Scholz M. Treatment planning for heavy-ion radiotherapy: calculation and optimization of biologically effective dose. *Phys Med Biol.* (2000) 45:3319–3330. doi:10.1088/0031-9155/45/11/314. |
108. Tripathi RK, Cucinotta FA, Wilson JW. Accurate universal parameterization of absorption cross sections III - light systems. *Nucl Instrum Methods Phys Res Sect B Beam Interact Mater Atoms.* (1999) 155:349–356. doi:10.1016/s0168-583x(99)00479-6.
109. Tripathi RK, Cucinotta FA, Wilson JW. Accurate universal parameterization of absorption cross sections. *Nucl Instrum Methods Phys Res Sect B Beam Interact Mater Atoms.* (1996) 117:347–349. doi:10.1016/0168-583x(96)00331-x.
110. Shen W-q., Wang B, Feng J, Zhan W-l., Zhu Y-t., Feng E-p.. Total reaction cross section for heavy-ion collisions and its relation to the neutron excess degree of freedom. *Nucl Phys.* (1989) 491:130–146. doi:10.1016/0375-9474(89)90209-1.
111. Sihver L, Lantz M, Kohama A. Improved parameterization of the transparency parameter in Kox and Shen models of total reaction cross sections. *Phys Rev C.* (2014) 89:067602. doi:10.1103/physrevc.89.067602.
112. Sihver L, Kohama A, Ida K, Oyamatsu K, Iwase H, Hashimoto S, et al.. Current status of the Hybrid Kurotama mode for total reaction cross sections. *Nucl Instrum Methods B.* (2014) 334:34–39. doi:10.1016/j.nimb.2014.04.021.
113. Tripathi RK, Wilson JW, Cucinotta FA, Accurate universal parameterization of absorption cross sections II - neutron absorption cross sections. *Nucl Instrum Methods B.* (1997) 129:11–15.
114. Cucinotta FA. *Calculations of cosmic-ray helium transport in shielding materials..* NASA Technical Publication, NASA/TP-3354, National Aeronautics and Space Administration, Washington DC (1993)
115. Aricó G, Ferrari A, Horst F, Mairani A, Reidel CA, Schuy C, et al. Developments of the nuclear reaction and fragmentation models in FLUKA for ion collisions at therapeutic energies. *CERN proc. 1 - 15th international conference on nuclear reaction mechanisms.* (2019)
116. Hüfner J, Schäfer K, Schürmann B. Abrasion-ablation in reactions between relativistic heavy ions. *Phys Rev C.* (1975) 12:1888–98. doi:10.1103/physrevc.12.1888.
117. Tatischeff V, Gabici S. Particle acceleration by supernova shocks and spallogenic nucleosynthesis of light elements. *Annu Rev Nucl Part Sci.* (2018) 68:377–404. doi:10.1146/annurev-nucl-101917-021151.
118. Bartos I. A new cosmic messenger. *Phys World.* (2018) 31:23–26. doi:10.1088/2058-7058/31/1/29.
119. Norbury JW. *DDFRG - double-Differential FRaGmentation models for proton and light ion production in high energy nuclear collisions valid for both small and large angles..* . NASA Technical Publication (in preparation).
120. Nakamura T, Heilbronn L. *Handbook on secondary particle production and transport by high-energy heavy ions..* World Scientific, Singapore (2006)
121. Botvina AS, Dementyev AV, Smirnova ON, Sobolevsky NM, Toneev VD. MSDM - multi stage dynamical model. International codes and model intercomparison for intermediate energy activation yields. In: RR Michel PP Nagel, (Eds.), *NSC/DOC(97)-1.*, NEA/P & T No 14, OECD, Paris, (1997) p. 307.
122. Toneev VD, Gudima KK. Particle emission in light and heavy ion reactions. *Nucl Phys.* (1983) 400:173–189. doi:10.1016/0375-9474(83)90433-5.
123. Amelin NS, Gudima KK, Toneev VD. *Yad Fiz.* (1990) 51:1730, 1990 (in Russian). Preprint GSI-89-52 (in English).
124. Amelin NS, Gudima KK, Siviklokov SY, Toneev VD. *Yad Fiz.* (1990) 52:272, 1990 (in Russian).
125. Gudima KK, Mashnik SG, Toneev VD. Cascade-exciton model of nuclear reactions. *Nucl Phys.* (1983) 401:329–361. doi:10.1016/0375-9474(83)90532-8.
126. Botvina AS, Iljinov AS, Mishustin IN, Bondorf JP, Donangelo R, Sneppen K. Statistical simulation of the break-up of highly excited nuclei. *Nucl Phys.* (1987) 475:663–686. doi:10.1016/0375-9474(87)90232-6.
127. Eren N, Buyukcizmeci N, Ogul R, Botvina AS. Mass distribution in the disintegration of heavy nuclei. *Eur. Phys. J. A.* (2013) 49:48. doi:10.1140/epja/i2013-13048-1.
128. Bondorf JP, Botvina AS, Iljinov AS, Mishustin IN, Sneppen K. Statistical multifragmentation of nuclei. *Phys Rep.* (1995) 257:133–221. doi:10.1016/0370-1573(94)00097-m.

129. Wilson JW, Werneth CM, Slaba TC, Badavi FF, Reddell BD, Bahadori AA. *Effects of the serber first step in 3DHZETRN-v2.1.*. NASA Technical Publication, NASA/TP-2019-220401, National Aeronautics and Space Administration, Washington DC (2019)
130. Valle SM, et al. FOOT: a new experiment to measure nuclear fragmentation at intermediate energies. *Perspect. Sci.* (2019) 12:100415.
131. Pleskac R, Abou-Haidar Z, Agodi C, Alvarez MAG, Aumann T, Battistoni G, et al. The FIRST experiment at GSI. *Nucl Instrum Methods Phys Res Sect A Accel Spectrom Detect Assoc Equip.* (2012) 678:130–138. doi:10.1016/j.nima.2012.02.020.
132. Geissel H, Armbruster P, Behr KH, Brünle A, Burkard K, Chen M, et al. The GSI projectile fragment separator (FRS): a versatile magnetic system for relativistic heavy ions. *Nucl Instrum Methods Phys Res Sect B Beam Interact Mater Atoms.* (1992) 70:286–297. doi:10.1016/0168-583x(92)95944-m.
133. Stöhlker T, Bagnoud V, Blaum K, Blazevic A, Bräuning-Demian A, Durante M, et al. APPA at FAIR: from fundamental to applied research. *Nucl Instrum Methods Phys Res Sect B Beam Interact Mater Atoms.* (2015) 365:680–685. doi:10.1016/j.nimb.2015.07.077.
134. La Tessa C, Sivertz M, Chiang I-H, Lowenstein D, Rusek A. Overview of the NASA space radiation laboratory. *Life Sci Space Res.* (2016) 11:18–23. doi:10.1016/j.lssr.2016.10.002.
135. McGirl N, Castellanos L, Srikrishna A, Heilbronn L, La Tessa C, Rusek A, et al. Double differential neutron yields from thick targets used in space applications. *EPJ Web Conf.* (2017) 158:04002.
136. Kekelidze VD, Matveev VA, Meshkov IN, Sorin AS, Trubnikov GV. Project nuclotron-based ion collider fAcility at JINR. *Phys Part Nucl.* (2017) 48: 727–741. doi:10.1134/s1063779617050239.
137. Kurosawa T, Nakao N, Nakamura T, Uwamino Y, Shibata T, Nakanishi N, et al. Measurements of secondary neutrons produced from thick targets bombarded by high-energy helium and carbon ions. *Nucl Sci Eng.* (1999) 132: 30–57. doi:10.13182/nse98-53.
138. Mattei I, Giuseppina MB, Bruni G, Camarlinghi N, Carra P, Catanzani E, et al. Measurement of ^{12}C fragmentation cross sections on C, O and H in the energy range of interest for particle therapy applications. *IEEE Transactions.* (2020) 4:269–282.
139. Pivi M, de Franco A, Farinon F, Kronberger M, Kronberger M, Kulenkampff T. Overview and status of the MedAustron ion therapy center accelerator. *Proceedings of IPAC2017.* (2017)
140. *FOOT conceptual design report.*, https://pandora.infn.it/public/912bb8
141. Alexandrov A, Alpat B, Ambrosi G, Argirò S, Battistoni G, Bisogni MG, et al. The FOOT (fragmentation of target) experiment. *PoS.* (BORMIO2017) (2017) :023.
142. Argiro S, Barbosa D, Battistoni G, Belcari N, Bruni G, Giuseppina MB, et al. The FOOT (fragmentation of target) experiment. *PoS.* (2016) :128.
143. Ferrari A, Sala PR, Fassò A, Ranft J. *FLUKA: a multi-particle transport code.*. CERN-2005-10 (2005) INFN/TC_05/11, SLAC-R-773.
144. Böhlen TT, Cerutti F, Chin MPW, Fassò A, Ferrari PG, Ortega A, et al. The FLUKA code: developments and challenges for high energy and medical applications. *Nucl Data Sheets.* (2014) 120:211–214. doi:10.1016/j.nds.2014.07.049.
145. Alexandrov A, et al. The FOOT experiment: fragmentation measurements in particle therapy. *Rad. Applic.* (2018) 3(3):190–6.
146. Werneth CM, Maung KM, Ford WP, Norbury JW, Vera MD. Elastic differential cross sections for space radiation applications. *Phys Rev C.* (2014) 90:064905. doi:10.1103/physrevc.90.064905.
147. Werneth CM, Maung KM, Ford WP, Norbury JW, Vera MD. *Elastic differential cross sections.*. NASA Technical Publication, NASA/TP-2014-218529, National Aeronautics and Space Administration, Washington DC (2014)
148. Werneth CM, Maung KM, Ford WP. Relativistic elastic differential cross sections for equal mass nuclei. *Phys Lett B.* (2015) 749:331–336. doi:10.1016/j.physletb.2015.08.002.
149. Werneth CM, Xu X, Norman RB, Ford WP, Maung KM. Validation of elastic cross section models for space radiation applications. *Nucl Instrum Methods Phys Res B.* (2017) 392:79–93. doi:10.1016/j.nimb.2016.12.009.
150. Werneth CM, Xu X, Norman RB, Maung KM, Maung KM. Relativistic three-dimensional Lippmann-Schwinger cross sections for space radiation applications. *Nucl Instrum Methods Phys Res Sect B Beam Interact Mater Atoms.* (2017) 413:75–78. doi:10.1016/j.nimb.2017.10.016.

Conflict of Interest: Author CZ was employed by the company "Leidos Innovations Corporation". Authors MG and LB were employed by the company "Thales Alenia Space".

The remaining authors declare that the research was conducted in the absence of any commercial or financial relationships that could be construed as a potential conflict of interest.

frontiers in Physics

ORIGINAL RESEARCH
published: 23 December 2020
doi: 10.3389/fphy.2020.578605

Implementation of a Compact Spot-Scanning Proton Therapy System in a GPU Monte Carlo Code to Support Clinical Routine

Jan Gajewski[1], *Angelo Schiavi*[2,3], *Nils Krah*[4,5], *Gloria Vilches-Freixas*[6], *Antoni Rucinski*[1], *Vincenzo Patera*[2,3] *and Ilaria Rinaldi*[6]*

[1]Institute of Nuclear Physics Polish Academy of Sciences,Krakow, Poland, [2]INFN - Sezione di Roma, Rome, Italy, [3]Dipartimento di Scienze di Base e Applicate per l'Ingegneria, Sapienza Université Roma, Rome, Italy, [4]University of Lyon, CREATIS; CNRS UMR5220, Inserm U1044, INSA-Lyon, Université Lyon 1, Centre Léon Bérard, Lyon, France, [5]University of Lyon, Université Claude Bernard Lyon 1, CNRS/IN2P3, IP2I Lyon, Villeurbanne, France, [6]Department of Radiation Oncology (Maastro), GROW School for Oncology, Maastricht University Medical Centre+, Maastricht, Netherlands

The purpose of this work was to implement a fast Monte Carlo dose calculation tool, FRED, in the Maastro proton therapy center in Maastricht (Netherlands) to complement the clinical treatment planning system. FRED achieves high accuracy and computation speed by using physics models optimized for radiotherapy and extensive use of GPU technology for parallelization. We implemented the beam model of the Mevion S250i proton beam and validated it against data measured during commissioning and calculated with the clinical TPS. The beam exits the accelerator with a pristine energy of around 230 MeV and then travels through the dynamically extendable nozzle of the device. The nozzle contains the range modulation system and the multi-leaf collimator system named adaptive aperture. The latter trims the spots laterally over the 20×20 cm^2 area at the isocenter plane. We use a single model to parameterize the longitudinal (energy and energy spread) and transverse (beam shape) phase space of the non-degraded beam in the default nozzle position. The range modulation plates and the adaptive aperture are simulated explicitly and moved in and out of the simulation geometry dynamically by FRED. Patient dose distributions recalculated with FRED were comparable with the TPS and met the clinical criteria. Calculation time was on the order of 10–15 min for typical patient cases, and future optimization of the simulation statistics is likely to improve this further. Already now, FRED is fast enough to be used as a tool for plan verification based on machine log files and daily (on-the-fly) dose recalculations in our facility.

Keywords: proton therapy, Monte Carlo dose calculation, GPU-accelerated dose calculation, phase space modelling, pencil beam scanning, quality assurance

OPEN ACCESS

Edited by:
Anna Vignati,
University of Turin, Italy

Reviewed by:
Jacobo Cal-Gonzalez,
Ion Beam Applications (Spain), Spain
Lorenzo Manganaro,
aizoOn Technology Consulting, Italy

***Correspondence:**
Ilaria Rinaldi
ilaria.rinaldi@maastro.nl

Specialty section:
This article was submitted to Medical Physics and Imaging, a section of the journal Frontiers in Physics

Received: *30 June 2020*
Accepted: *04 November 2020*
Published: *23 December 2020*

Citation:
Gajewski J, Schiavi A, Krah N, Vilches-Freixas G, Rucinski A, Patera V and Rinaldi I (2020) Implementation of a Compact Spot-Scanning Proton Therapy System in a GPU Monte Carlo Code to Support Clinical Routine. Front. Phys. 8:578605. doi: 10.3389/fphy.2020.578605

1. INTRODUCTION

In radiation therapy, the treatment planning system (TPS) is a crucial part of the clinical workflow. Based on anatomical information about the patient, typically derived from X-ray computed tomography (CT) images, this software predicts the dose administered to a patient in a given irradiation scenario and inversely optimizes the treatment plan starting from a desired dose

distribution. The dose engine in a TPS needs a sufficiently precise model of the treatment machine to be able to make accurate dose estimates. This is particularly true for proton therapy because the protons' dose distribution includes sharp spatial gradients which can lead to severe under- or overdosage if incorrectly delivered. Dose recalculation based on an independent dose engine can be an important element of quality assurance (QA) [1, 2]. The expected benefit is to achieve better overall QA and to reduce machine time for QA measurements. This contribution describes the implementation of our proton treatment system in a fast MC software to eventually build such a QA tool.

Traditionally, dose engines in proton therapy have relied on numerical algorithms which use analytical models of the proton beam and its propagation through the patient. Often, these algorithms need to make some simplifying assumptions about the detailed interaction of protons with the complex tissue distribution inside the patient. More recently, Monte Carlo (MC) codes have become an alternative tool for dose calculation. Such codes transport particles one by one across objects of interest and evaluate physical interactions step-by-step along each particle's trajectory. MC simulations offer more accurate modeling of proton interactions with heterogeneous media and improved dose calculation accuracy in complex geometries with respect to analytical pencil beam algorithms [3, 4].

General purpose MC simulation toolkits originally developed in other fields of physics including accelerator and particle physics have been used in the context of proton therapy. These include FLUKA [5–7], Shield-HIT [8], and Geant4 [9], as well as Geant4-based applications specific to medical physics like GATE/GATE-RTion [10, 11] and TOPAS [12, 13]. However, a challenging factor when attempting to employ MC simulation in daily clinical routine is the long calculation time (on the order of hours on multiple CPUs) [3]. To address this, GPU-accelerated MC codes started to be investigated in the field of proton therapy, for example, gPMC, FRED, and a code developed at the Mayo Clinic [14–17]. GPU acceleration has also been exploited to speed up analytical dose engines [18], yet without the precise physics modeling of MC. We decided to use the GPU-accelerated MC code FRED [16] in our proton facility, the Maastro proton therapy center in Maastricht (Netherlands).

Before a MC code can be used for recalculating patient plans, the simulation needs to be implemented in such a way as to mimic the clinical proton beam irradiating the patient. This step is essential to guarantee accurate dose prediction. Previous authors have presented the MC implementations of their treatment machines, and approaches can be roughly sorted into two categories. On the one hand, the treatment machine is purely described by an effective phase space which is conveniently parameterized [19, 20]. In other words, the MC simulation has no explicit knowledge about the proton beam line, and particles are generated at the exit nozzle directly according to the phase space parameterization and tracked from that point on. On the other hand, a full geometrical description of the proton beam line or at least the exit nozzle can be implemented in the Monte Carlo simulation so that particles are explicitly transported through these parts of the beam line [21–23]. This latter approach is not optimal from the point of view of computation speed as protons need to be tracked over again through the same beam line for each new patient.

The peculiarities of the treatment system in our facility, a Mevion S250i Hyperscan system, were such that none of the existing methods in the literature were directly applicable. Rather, we needed to design a new hybrid method to implement our treatment machine in FRED. Specifically, the Mevion system uses one fixed pristine beam energy which is reduced by degrader plates in the nozzle. The nozzle is positioned in air downstream of the beam's vacuum pipe. Furthermore, the collimator leaves of an adaptive aperture continuously move into and out of the beam during a patient irradiation. Finally, the entire beam nozzle is extendable, and its distance to the isocenter may vary during treatment. Existing methods where the proton beam is described by an effective phase space model would not have been feasible because one parameterization of such a model would have been necessary for each possible configuration of the nozzle. We therefore chose an approach where the proton beam is described *via* a phase space model upstream of the nozzle and then tracked explicitly across the nozzle. A practical concern was that the nozzle can move so close to the patient that in the simulation it would overlap with the box containing the voxelized patient CT image. We implemented a dedicated new functionality in FRED to cope with this. Finally, the continuously changing nozzle geometry required optimized geometry handling in FRED to efficiently communicate with the GPU hardware.

In this work, we present the implementation of our treatment machine in FRED, the optimization of model parameters based on experimental data acquired during the commissioning of the facility [24], and validation based on additional data. Finally, we compare dose distributions recalculated with FRED and with the clinical TPS.

2. MATERIALS AND METHODS

2.1. The Mevion S250i

The Mevion S250i Hyperscan system (cf. **Figure 1**) is a small superconducting synchrocyclotron with only 15 tons and a diameter of 1.8 m. It consists of two coaxial gantries. The superconducting synchrocyclotron (10 T) with the ion source and the scanning magnets is mounted on the outer gantry. The inner gantry carries the beam monitor system, the range modulation system, and a multi-leaf collimator system referred to as "adaptive aperture". The components taken into account in FRED, that is, the range shifter, the adaptive aperture, and the nozzle window, are sketched in **Figure 2**. For more details, we also refer to [24].

The system accelerates a fixed energy beam of about 230 MeV, the so-called pristine energy, and extracts it toward the single treatment room. The treatment line is equipped with a dose delivery system and an extendable nozzle at the end of the beam line. The dose delivery system consists of three elements: a thin 80 quadrant foil position detector, the beam scanning magnet, and six transmission ionization chambers or beam monitors. The vacuum window is located immediately after the scanning

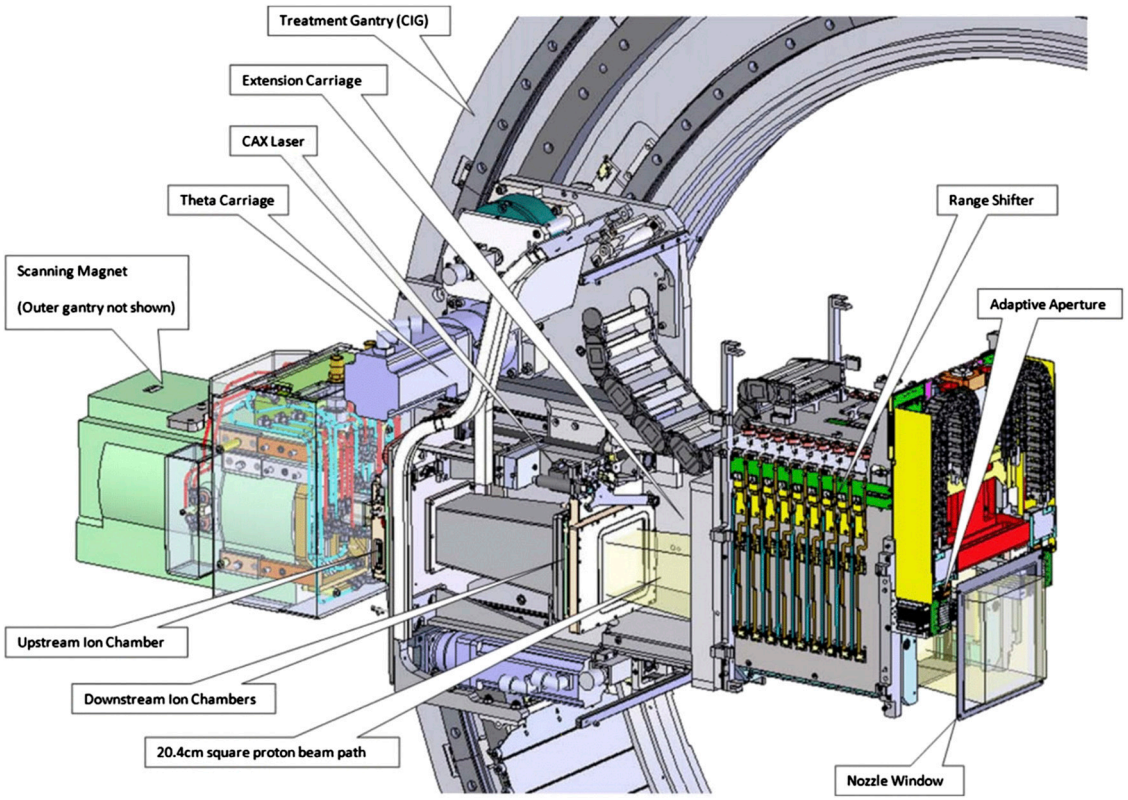

FIGURE 1 | Layout of the Mevion S250i. Courtesy of Mevion.

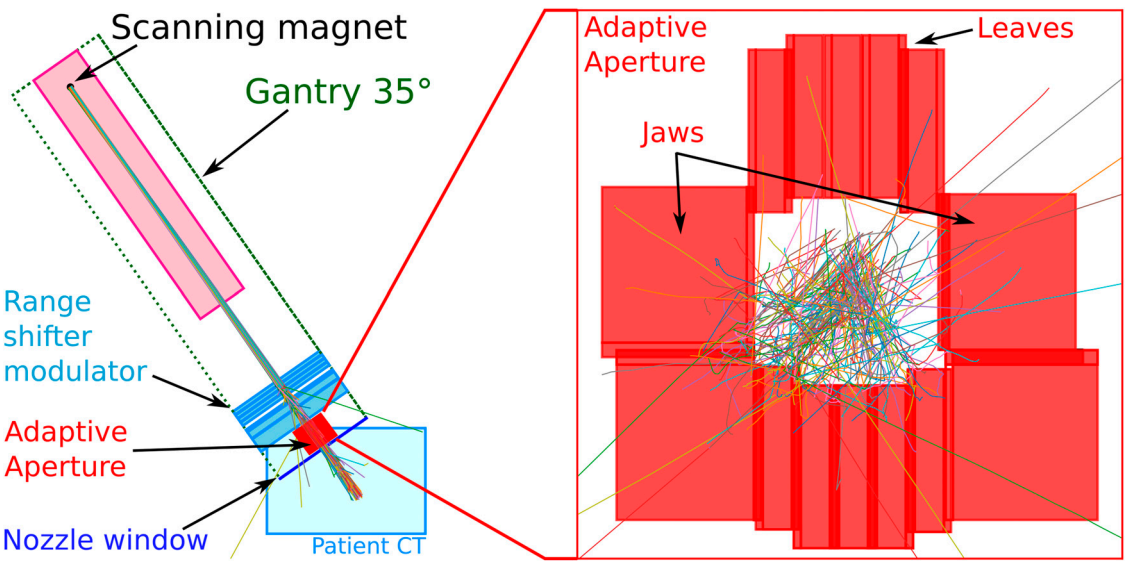

FIGURE 2 | Elements of the beam model.

magnets, at about 2 m from the room isocenter, and all components mounted on the inner gantry are in air. To obtain clinically relevant energies, which cover a range from 0 cm to 32.2 cm in water, the pristine energy is degraded by the range modulation system, mounted in the nozzle. It consists of 18 Lexan plates of different thicknesses whose combinations allow

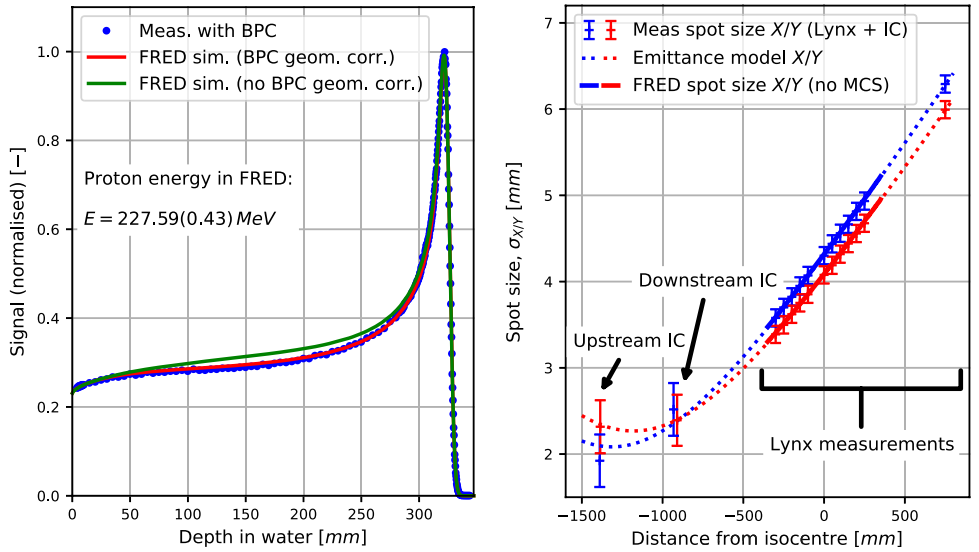

FIGURE 3 | (Left) Bragg peaks measured with the Bragg peak chamber (BPC) of diameter 81.6 mm and simulated for the optimal energy and energy spread in the BPC, mimicking the experimental setup, as well as in full 40 × 40 × 40 cm^3 water phantom for comparison. **(Right)** Emittance model fit to measured spot sizes (Lynx and IC) in the in-plane (*X*) and cross-plane (*Y*) directions along with the beam sizes simulated with FRED in air without multiple Coulomb scattering.

the generation of 161 energies with 2.1 mm range steps in water. The distance from the nozzle window to the isocenter is adjustable from 3.6 to 33.6 cm. The adaptive aperture is the most downstream functional element of the beam line, also mounted in the nozzle. The gantry system can rotate from 355° to 185° with an angular accuracy of ±0.25°. The 360° beam entrance coverage is achieved by rotating the six-degrees-of-freedom robotic couch.

The Maastro proton therapy center started clinical activity in February 2019, and 137 patients have been treated since then. The clinical TPS at the time of writing this study is RayStation version 9B (RaySearch Laboratories, Sweden) which uses a Monte Carlo dose engine (on CPU).

2.2. Implementation of Proton Beam Source in FRED

To implement the therapeutic proton beam source of the Mevion accelerator system in FRED, we used a phase space model to describe the pristine proton beam in a plane downstream of the scanning magnets and simulated explicitly in Fred the geometry of the components included in the extendable nozzle, that is, the range shifter, the adaptive aperture, and the nozzle window. We will use the term "beam model" to refer to a combination of both.

In particular, the phase space model was split into a longitudinal component (energy spectrum) and a transverse component (beam shape), both modeled empirically as Gaussian distributions. This kind of phase space description had already been used successfully by other authors [19]. The longitudinal phase space component is parameterized by the mean proton energy and the energy spread (variance) and the transverse component by the width of the transverse distribution (beam size, i.e., variance).

The beam size evolves along the beam axis as a function of distance z from the virtual source plane ($z = 0$). The propagation beam model used in this work is the so-called emittance model, that is, the beam evolution in phase space is characterized by a constant emittance, both in x and y directions. **Equation 1** describes the evolution of the envelope of the beam in one transverse direction along the propagation direction z. The model has three parameters per transverse direction [25] and describes what is called a drift in accelerator language, namely, a section of the beam line where no active elements (such as bending magnets or focusing quadrupoles) are present. We are considering the beam section after the focusing optics (quadrupole magnets) so that the waist of the beam, that is, the position where the beam width is minimal, is downstream of the source plane (as it can be seen in **Figure 3**). The emittance model is used when the virtual point source model is not accurate enough, namely, when the focal length of the last quadrupoles is relatively short. The Mevion machine is in fact a compact accelerator, with a Rayleigh length of about 1 m.

$$\sigma^2(z) = \epsilon \cdot \left(\beta - 2 \cdot \alpha \cdot z + \frac{1+\alpha^2}{\beta} \cdot z^2\right). \quad (1)$$

Clearly, the emittance model is only valid if $\sigma^2 > 0$ for all z. Furthermore, because the quadrupole magnets of the proton beam line focus the beam, one has $\partial\sigma^2/\partial z < 0$ from the magnets down to the beam waist. Regarding the model parameters, the emittance ϵ determines the area of the beam distribution in the phase space and must be positive, β is the characteristic length over which the beam size changes and must be positive, and α determines whether the beam is focusing ($\alpha > 0$) or defocusing ($\alpha < 0$).

It is important to underline that the source plane (where z = 0) only plays the role of a reference frame in which the protons are generated. The beam size is purely determined by the three parameters α, β, and ε. This is different from a virtual point source model where the point source position determines the beam divergence.

The clinical TPS uses the so-called monitoring units (MU) as a dosimetric scale based on an internal calibration. The Monte Carlo code, on the other hand, requires the number of primary protons to be specified. Therefore, a scaling factor is needed to parameterize the relationship between the two quantities (cf. **Section 2.4.3**).

The explicitly implemented nozzle components are the adaptive aperture, the range modulation system, and the nozzle window. Their size, placement, and composition were taken from the manufacturer's specifications of the proton accelerator. The aperture leaves have a step-like interleaving structure to reduce proton leakage when closed. This was constructed in FRED as a composition of 60 cuboid regions. The elemental composition of the energy degrader plates was fixed, but their mass density was optimized as a part of the beam model calibration (cf. **Section 2.4.4**).

2.3. New Functionality in FRED

Two new technical features needed to be implemented in FRED. The first one was due to the fact that the beam nozzle of the Mevion system is extendable. In some treatment configurations, this leads to an overlap in the simulation of the cuboid regions enclosing the beam nozzle and patient geometry. In which of the two regions, a proton needs to be tracked then becomes ambiguous. To cope with this specific problem, FRED now allows specifying the region where a proton was generated, that is, the nozzle region, propagates protons up to the boundaries of this region, and only then switches to the overlapping patient volume.

The second issue was the variability of the nozzle's geometrical configuration. More specifically, each beam spot delivered to the patient potentially has a different set of degrader plates moved into the beam path as well as a different positioning of the adaptive aperture. The initial approach to implement this was to iteratively communicate the current configuration of the simulated geometry to the GPU and track the protons belonging to the associated beam spot. This led to an interfering computational overhead which prevented the GPU from exploiting its potential. Most of the simulation was actually spent in handling the communication with GPU. A new scheme was therefore implemented in which all configurations of the geometry are communicated once to the GPU at the beginning. Each simulated pencil beam is internally associated to a specific configuration in which it needs to be tracked. In this way, all protons in a treatment plan can be tracked on the GPU without interruption.

2.4. Beam Model Calibration

The beam model was calibrated according to the following overall scheme: experimental data were acquired as a part of the facility commissioning or specifically for this work. Details about the commissioning can be found in [24]. The measurement conditions were mimicked in FRED, and the beam model parameters were determined by optimizing the match between measured and simulated data. The following sections describe the calibration in detail.

2.4.1. Transverse Phase Space Component—Emittance Model

The emittance model describes the beam spot size in air as a function of the position along the beam axis (cf. **Equation 1**). To calibrate the model parameters, transverse profiles of the pristine beam were measured at twelve distances from the isocenter using a scintillator detector (IBA Lynx, Louvain-la-Neuve, Belgium). The nozzle window was removed during the measurements because it would alter the pristine beam. To avoid confusion, we recall that the nozzle window is not the end of the vacuum beam line, but only a protective cover of the air-filled nozzle.

The spot size at each measured distance was determined as standard deviation, σ, of a Gaussian fit to the cross-plane and in-plane profiles through the spot mass center. Additionally, the spot sizes measured by the beam monitor system in the nozzle were used. The emittance model parameters were determined by fitting **Equation 1** to the set of spot sizes, as a function of depth. No constraints were imposed on the parameters in the fit routine, but the plausibility of the fit parameters was checked manually.

2.4.2. Longitudinal Phase Space Component—Pristine Energy

The laterally integrated depth dose distribution (IDD) of the pristine energy was measured with a large-area plane-parallel ionization chamber of 8.16 cm diameter (Bragg Peak IC TM34070, PTW, Freiburg, Germany) mounted on the mechanical arm of a water phantom (PTW MP3-PL). The nozzle window was removed during the measurements (cf. **Section 2.4.1**). The distance from the virtual source plane (scanning magnets position) to the isocenter was fixed to 182.14 cm for all gantry angles and the same for the cross-plane and in-plane scanning directions.

FRED simulations were performed in a $40 \times 40 \times 40$ cm^3 virtual phantom of $1 \times 1 \times 1$ mm^3 voxel size, mimicking the measurement setup. The ionization potential of water was set to 78 eV. The geometrical acceptance due to the limited size of the Bragg Peak IC was taken into account in FRED.

Simulated and measured IDDs were analyzed by fitting an analytical model [26], as well as by using a spline function. The beam model parameters, that is, beam energy and energy spread, were found by matching the measured and simulated IDDs, minimizing differences of full width at half maximum (FWHM) and the range, defined as 80% of the maximal value at the distal falloff.

2.4.3. Dosimetric Calibration Factor

The scaling factor was determined based on absolute dose measurements of a uniform 10×10 cm^2 monoenergetic field with 1,000 MU for the whole plan consisting of 1,681 spots. Dose was measured at a depth corresponding to 1/4 of the proton range in water, which was 79 mm, with a plane-parallel ionization

chamber (IBA PPC05) positioned in a water tank (PTW MP3-PL). The size of the active volume of the PPC05 detector (diameter of 9.9 mm and thickness of 0.6 mm) was considered in the analysis of the FRED simulations to estimate the mean dose in this volume. The scaling factor was determined by matching simulated and measured dose.

2.4.4. Range Modulation System

The thickness and position of the Lexan plates in the range modulator system were extracted from the manufacturer's technical drawings. The density of each modulation plate was optimized in FRED, following the procedure of the clinical TPS. In particular, for each range modulator plate, depth dose profiles in water were measured and simulated with and without the plate present. The range was determined as the depth in water at 80% of the maximum value at the distal Bragg peak falloff. Each plate's water equivalent thickness was determined as the difference in range with and without plate.

2.4.5. Adaptive Aperture

The adaptive aperture module consists of two carriages of five leaves, each 5 mm wide (in-plane direction, i.e., perpendicular to the leaves' movement), and one top and one bottom jaw, each 20 mm wide, made of nickel alloy (cf. **Figure 2**). The thickness of the leaves and jaws in the beam direction is 100 mm. The aperture can trim spots laterally over a 20×20 cm^2 area at the isocenter plane. The inner surface of the leaves has an interlocking tongue and groove shape to prevent leakage when the collimators are closed. This was implemented in FRED based on technical drawings using 60 cuboid regions, that is, the cuboid regions were combined in such a way as to approximately represent the shape of the aperture leaves.

Commissioning of the beam delivery system includes a procedure to adjust the alignment of the adaptive aperture in the in-plane and cross-plane directions with respect to the beam axis. This was reproduced in FRED as part of the beam model calibration. To this end, the snout position was set to 19.5 cm, and five range modulator plates were inserted to broaden the beam. The aperture was closed, except for the middle leaves which were opened ±2.5 cm, leaving a square-shaped opening of about 5×5 mm^2. A 3×3 cm^2 field was irradiated in a regular spot grid of 2.5 mm steps. The dose was scored in a water phantom positioned at the isocenter at 5 mm below the water surface.

Moving the adaptive aperture in in-plane and cross-plane directions, an offset with respect to its nominal position (from the technical drawings) was determined in FRED to obtain symmetrical transverse dose profiles.

2.5. Beam Model Validation

2.5.1. Pencil Beams in Water

The range shifter model was validated with measurements performed during commissioning of the facility. In particular, laterally integrated depth dose profiles were measured with an ionization chamber (Bragg Peak IC TM34070 from PTW) in a water phantom at selected clinically available energy settings. Transverse profiles of single spots were measured in water with a microdiamond detector (PTW TN60019). The nozzle window was present during the measurements.

It is important to point out the difference between the calibration and validation measurements. Both were performed with the same kind of equipment and following the same measurement principle. The difference lies in the combination of degrader plates in either case. For the calibration measurements, individual plates were inserted into the beam so that the retrieved calibration parameters corresponded to this plate specifically. The independent validation measurements used clinical energy settings which generally require combinations of multiple degrader plates to be inserted into the beam. In this sense, the validation measurements were used to assess the consistency of the calibration parameters.

2.5.2. Monoenergetic Layers in Water

Dose coverage in a proton therapy treatment is achieved by overlapping multiple pencil beams with different transverse positions. It is therefore important to verify that the total dose in such a scenario is correctly simulated in FRED. To this end, absolute point dose was measured in the water phantom for single energy layers at different field sizes. We used the PPC05 (IBA) for fields larger than 5×5 cm^2, a semi-flex 3D ionization chamber (PTW TN31021) for 5×5 cm^2 and 4×4 cm^2 fields, and a microdiamond detector (PTW TN60019) for the 3×3 cm^2 field. Absolute point dose was measured for 15 energies and nine field sizes (i.e., overall 135 measurements) at the depth of 1/4 of the BP position in water. The isocenter was located at 19.9 mm depth in water, and the snout position was 30.01 cm, that is, the air gap to the water surface was 10.11 cm. The nozzle window was present during the measurements. The dose layers were simulated in FRED, and absolute point dose measurements were compared. The size of the detector was taken into account when analyzing FRED dose simulations by calculating the mean dose in the detector volume. No adaptive aperture was used for the measurements.

2.5.3. Dose Cubes in Water

A 3D proton dose volume is achieved by combining multiple energy layers, that is, pencil beams of different energies which form a spread-out Bragg peak (SOBP). Their relative weights are optimized to best match the required dose distribution.

Following common protocols in proton therapy, we used cube-shaped dose distributions to validate the simulation accuracy of FRED. In particular, absolute point dose of spread-out Bragg peaks in water was measured with an ionization chamber along the central axis and off-axis, at three depths each, of a 125 cm^3 cube at 5 and 10 cm depth and of a 1,000 cm^3 cube at 10 cm depth. In sum, six measurement points per cube were measured. The prescribed dose level was 1.82 Gy (2 Gy (RBE)). The dose cubes were simulated in FRED and compared with the absolute point dose measurements. The size of the ionization chamber was taken into account when analyzing FRED dose simulations. All plans included the adaptive aperture.

2.5.4. Patient Quality Assurance

A useful application of FRED in clinical practice would be to reproduce patient QA measurements *via* simulation. This could

help to reduce the amount of manual QA tasks in clinical routine. In our proton facility, patient QA measurements are performed with an array of ionization chambers (OCTAVIUS 1500 XDR) in RW3 solid water measuring 2D dose distributions at a few selected depths. We implemented the experimental procedure also in FRED and compared the results against the experimental data. The depth in the RW3 solid water phantom used for the measurements was recalculated into water equivalent depth by rescaling with the RW3's relative stopping power by 1.045. We tested FRED for all clinical patient plans delivered in our proton facility since clinical operation began in 2019, that is, around 300 QA plans for different indications (i.e., head and neck (8%), brain (18%), breast (29%), lung (36%), lymphoma (3%), and esophagus (6%) tumors). The simulations were performed with 10^5 protons/spot in a 1 mm^3 dose grid in a virtual water phantom.

The gamma index analysis was applied to compare 2D dose slices extracted from simulated 3D dose distributions to 2D measured dose distributions. As criteria, we used a dose difference (DD) of 2% or 3% (local dose), distance to agreement (DTA) of 2 mm or 3 mm, and a dose cutoff (DCO) of 2%, in accordance with clinical protocols.

2.6. Full Simulations of Patient Plans

Another clinical application of FRED is to recalculate the full treatment plans in the patient geometry provided by CT images. The photon attenuation coefficients in a CT image must be converted into quantities required by FRED, that is, mass density, relative stopping power, elemental composition, and radiation length. We implemented the two-step conversion method presented in [27], which uses a conversion from photon attenuation to mass density and one from mass density to the other quantity. The former can be obtained from phantom-based CT calibration and was readily available in our facility. The latter is based on a set of tissue descriptions representative of the human body and piecewise linear interpolations of the quantities of interest. We used the same tissues as in [27] and extended the parameters provided therein with radiation length values for each tissue (http://pdg.lbl.gov/2020/AtomicNuclearProperties/). This calibration procedure is similar to the one in RayStation, although we had now access to the implementation details.

To test the beam model, we recalculated several patient plans including the brain, head and neck, breast, and lung cases (5 each). Simulations were run with 10^5 protons per spot.

3. RESULTS

3.1. Beam Model Calibration

3.1.1. Transverse Phase Space Component

The right panel of **Figure 3** reports the beam spot size in air as a function of distance from the isocenter. Data points were measured inside the nozzle by built-in beam monitors as well as outside of the nozzle as explained in **Section 2.4.1**. The dotted lines represent the emittance model fitted to the data, and the solid lines were obtained in the FRED simulation in air using the model, that is, reproducing the measurement. The simulated spot sizes in the treatment area, that is, ±35 cm around the isocenter, agree with the measurements better than 0.03 mm, showing that the fit results are consistent. According to the fitted emittance model, the beam waist (i.e., its narrowest point) lies between −1,000 mm and −1,300 mm. This is reasonable because the quadrupole magnets first focus the beam before it subsequently diverges toward the isocenter (cf. **Section 2.2**).

3.1.2. Longitudinal Phase Space Component

The left panel of **Figure 3** compares simulated and measured integrated depth dose profiles in water of a pristine proton beam, that is, without range modulator plates and the nozzle window. This configuration has no corresponding nominal energy as nominal energies are only defined with the nozzle window mounted. When accounting for the geometrical acceptance of the Bragg peak chamber (red curve), the simulated profile matches very well with the measurements, achieving BP range and FWHM differences below 0.05 mm.

The two parameters of the longitudinal phase space component of the proton source model, that is, the mean initial energy and the Gaussian energy spread, were determined by matching simulated and measured data (cf. **Section 2.4.2**). They were thus determined to be 227.59 MeV and 0.43 MeV, respectively.

3.1.3. Dosimetric Calibration Factor

The scaling factor from monitoring units to the number of primaries was calculated to be 7.417×10^7 protons/MU.

3.1.4. Range Modulation System

Figure 4 shows integrated depth dose profiles in water with a few selected individual range modulator plates or the nozzle window inserted into the beam path. The measured profiles (dots) match the simulated ones (solid) well. The legend reports the water equivalent thickness of the plates determined from measured and simulated data, respectively. Agreement for all the range modulator plates and the nozzle window was better than 0.1 mm. It is worth noting that a good match is obviously expected because the simulated degrader plate densities were calibrated to achieve this (cf. **Section 2.4.4**). In this sense, the residual mismatch of 0.1 mm is indicative of the goodness of the calibration procedure and not of the range accuracy in dose calculation which was instead verified by the calibration.

3.1.5. Adaptive Aperture

The adaptive aperture implemented in FRED was aligned with the beam axis as described in **Section 2.4.5**. The offset to be applied in FRED with respect to the nominal aperture position (from technical drawings) was found to be 0.995 mm in the in-plane direction, that is, perpendicular to the leaves, movement, and −0.005 mm in the cross-plane direction, that is, along the leaves' movement.

3.2. Beam Model Validation

3.2.1. Pencil Beams in Water

Figure 5 presents validation results for single pencil beams in water for selected beam energies (range shifter plate

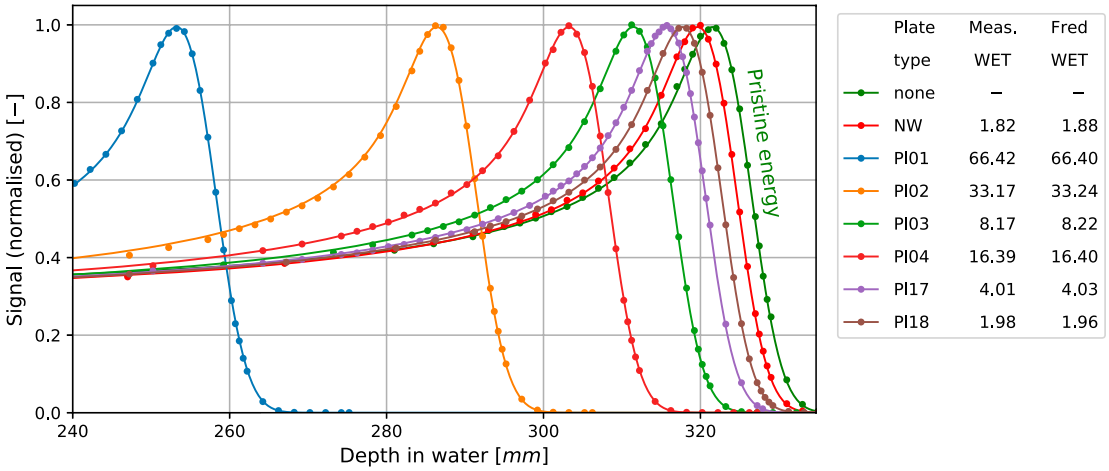

FIGURE 4 | Measured (dots) and simulated (solid lines) BPs for selected RS plates and the nozzle window (NW) WET compared to the BP of pristine energy. All the simulation results account for the geometrical acceptance correction for the BPC. The table presents calculated and measured WET in mm.

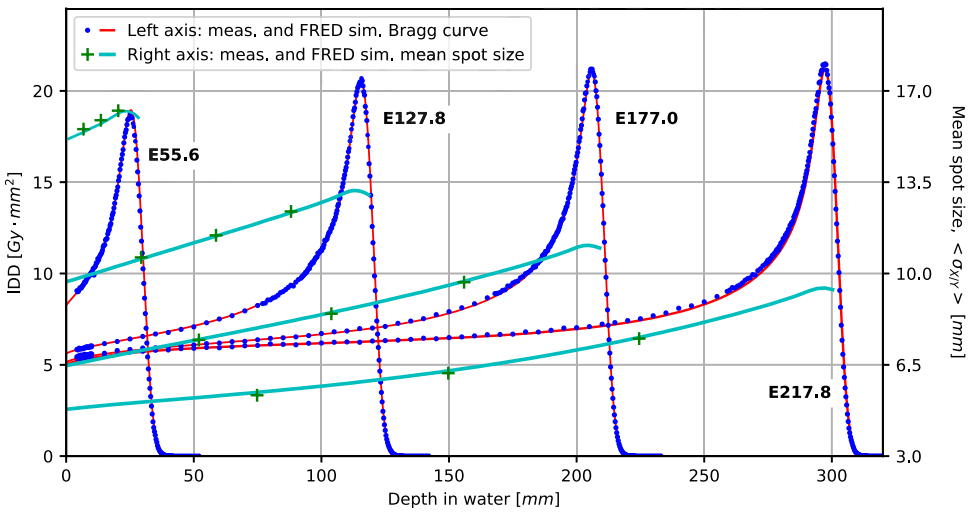

FIGURE 5 | Comparison of simulated (solid lines) and measured BPs (dots) and spot sizes (crosses) in water for four main nominal energies (in MeV): E55.6, E127.8, E177.0, and E217.8. All the simulated Bragg curves account for the geometrical acceptance of the Bragg peak chamber detector.

configurations) as explained in **Section 2.5.1**. Blue dots and red lines show measured and simulated integrated depth dose profiles, respectively. Measured and simulated data match very well in the plateau region and around the Bragg peak, indicating FRED accurately reproduces electromagnetic energy loss and pileup due to nuclear interactions. The agreement between measured and simulated range is better than 0.25 mm for all combinations of range modulator plates.

The green data points and light blue curves (referring to the right ordinate) show the measured and simulated beam spot size at different depths in water. Agreement is better than 0.5 mm for all data points and thus well within clinical acceptance criteria.

3.2.2. Monoenergetic Layers in Water

We used monoenergetic layers in water to validate the dosimetric accuracy of FRED when multiple pencil beams are superimposed, as explained in **Section 2.5.2**. The left and center panels of **Figure 6** show the relative difference of the measured and simulated dose, that is, in FRED and TPS. The average relative differences between measurement and FRED do not exceed ±2%, except for very small fields of 1×1 cm^2 and 2×2 cm^2. It should be noted that uncertainty in the detector position is particularly important in small fields and likely to be (partially) responsible for the these larger differences. In any case, FRED is at least as accurate as the clinical TPS. The right panel depicts the mean proton range difference between FRED and TPS determined from the distal falloff of the dose cube's central axis profiles. The slight

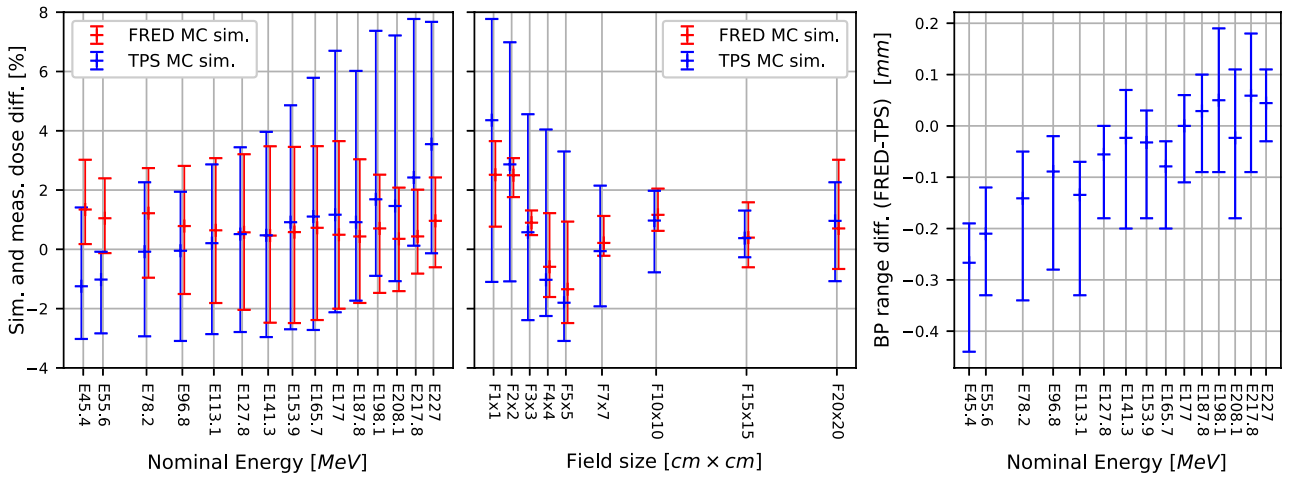

FIGURE 6 | Relative differences between measured doses calculated in FRED and the TPS as a function of nominal energy **(left panel)** and field size **(center panel)**, as well as absolute range differences between FRED and the TPS as a function of nominal energy **(right panel)**. Each data point represents the average over all field sizes in the left and right panels and over all energies in the center panel. The error bars indicate minimum and maximum values in a group.

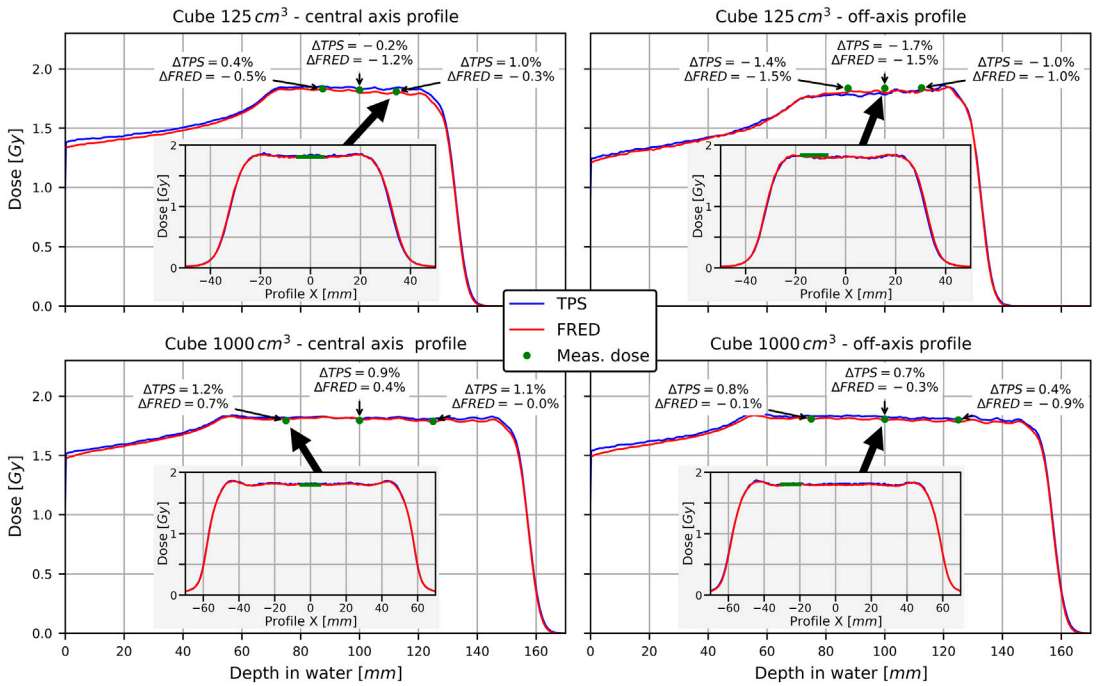

FIGURE 7 | Longitudinal profiles across dose cubes along the central axis **(left)** and off-axis **(right)**. The inlays show transverse profiles at the depth indicated by the arrow. Annotation boxes show relative difference between FRED/TPS and measurement at the indicated points.

systematic discrepancy remains within −0.3 mm and 0.1 mm and is clinically acceptable.

3.2.3. Dose Cubes in Water

Dosimetric validation based on dose cubes in water was performed to quantify the accuracy of FRED dose simulations when multiple pencil beams of various energies are superimposed in the transverse and longitudinal direction. Simulations were run with 10^6 protons per spot on a single GPU and took 2 min for the 125 cm^3 cube and 7 min for the 1,000 cm^3 cubes. **Figure 7** shows example profiles across two dose cubes simulated with the TPS and FRED and measured, as explained in **Section 2.5.3**. Relative

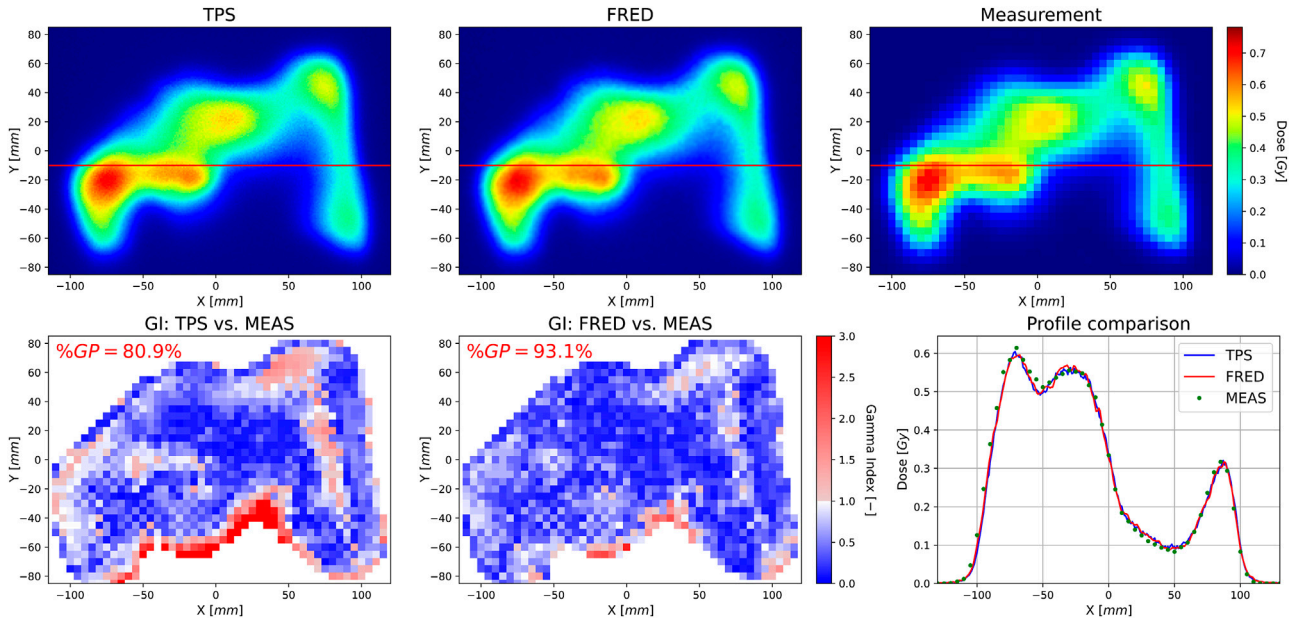

FIGURE 8 | Transverse 2D dose distribution layer calculated by the TPS **(upper left)** obtained from FRED MC simulations **(upper middle)** and measured with an array of ionization chambers in the water phantom **(upper right)**, as well as a GI map computed comparing the TPS **(lower left)** and FRED **(lower middle)** simulations to the measurement using the GI (2%/2 mm) method. The gamma passing rate (%GP) indicates the percent of pixels passing the GI test. The **lower right** panel shows dose profiles along the red line indicated on the upper panels.

dose differences with FRED and the TPS are of similar magnitude. The relative dose difference between simulation and measurement averaged over the six data points per cube were

- $+0.19^{+0.90}_{-0.17}\,(0.37)\%$ for the 125 cm^3 cube placed at 5 cm depth,
- $-1.00^{-0.27}_{-1.55}\,(0.51)\%$ for the 125 cm^3 cube placed at 10 cm depth,
- $-0.05^{-0.68}_{-0.93}\,(0.56)\%$ for the 1,000 cm^3 cube placed at 10 cm depth.

They do not exceed 2%, and thus meet the clinical criteria.

3.2.4. Patient Quality Assurance

Figure 8 shows an example of a patient QA measurement and simulation (see **Section 2.5.4**). Simulations were performed with 10^5 protons per spot on a single GPU card (Nvidia Titan Xp) and took a few minutes per QA plan. The resolution of the measured transverse dose map is limited by the 5×5 mm^2 pixel size of the detector. For TPS and FRED, a voxel size of 1 mm^3 was used. The lower row shows the gamma index maps for the TPS and FRED vs. measurement, respectively. Accepted gamma index values are blue, while unacceptable ones are red. The gamma index (GI) passing rate (%GP), that is, the percent of pixels passing the GI test, is better comparing the FRED results to the measurements than the clinical TPS calculations. The lower right panel shows an example profile along the red line of the dose maps in the upper panel. The mean %GP out of the 10 measured transverse dose maps of this example treatment plan was 88.1 (4.1%) (FRED) and 80.6 (8.4%) (TPS). The results shown here are representative of all 300 simulated cases, and agreement of FRED with the TPS and data was always well within the clinically acceptable level.

3.3. Patient Simulations

Figure 9 shows a representative example of a full patient simulation performed with FRED and with the clinical TPS. The color wash figures present dose distributions recalculated in the patient geometry. Note that the clinical TPS (lower panels) masks the dose outside the patient contour. The treatment plan in this case includes three fields of pencil beams delivered under different angles. The upper right panel shows a profile across the patient volume (along the red line in the dose maps). The slight difference between the TPS and FRED at −190 mm to −170 mm is created by the lateral edge of the field coming from the upper left. We attribute this to differences in the CT calibration of lung tissue in FRED and the TPS which are currently under investigation. The lower right panel shows a dose volume histogram, that is, a cumulative distribution quantifying how many voxels within a certain geometrical region received at least a certain dose level. The match between the TPS and FRED is largely acceptable from a clinical point of view.

Simulations were performed with 10^5 protons per spot on a single GPU card (Nvidia Titan Xp). Calculation times per treatment plan were about 25–30 min without and 10–15 min with the optimized geometry handling (cf. **Section 2.3**).

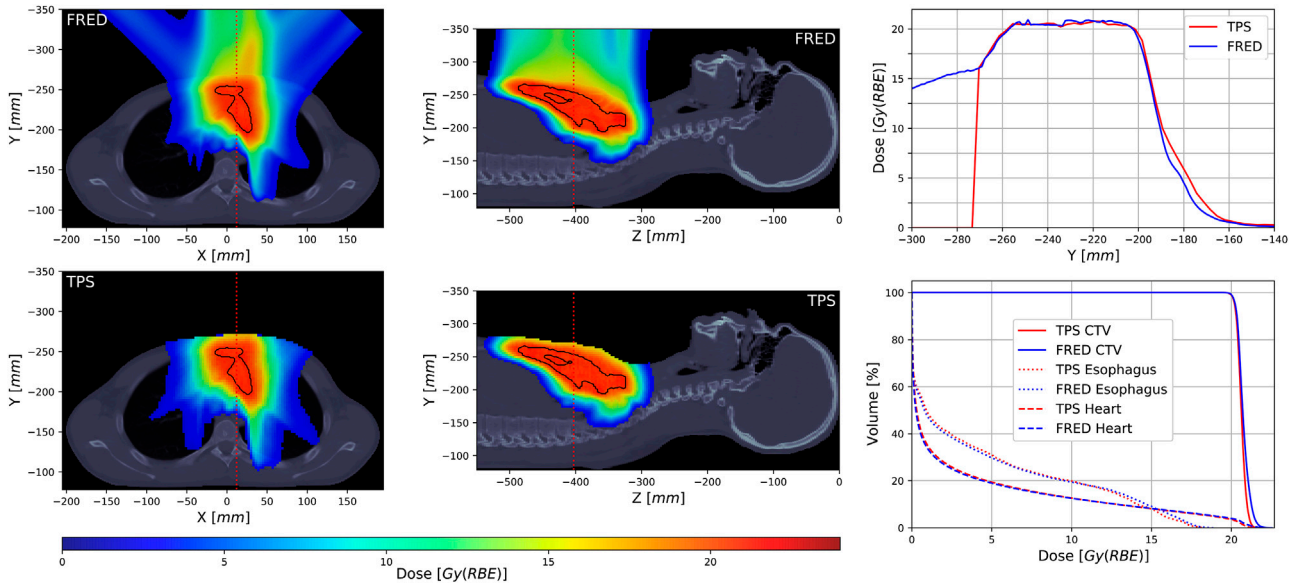

FIGURE 9 | Dose distribution example (left and middle columns) of a patient treatment plan calculated with FRED MC **(upper row)** and the TPS **(lower row)** with a clinical target volume (CTV) structure marked with the black line, dose profiles **(upper right)** along the red dotted line indicated on the dose distribution panels, and comparison of dose volume histograms calculated for CTV and two selected organs at risk **(lower right)**.

4. DISCUSSION

We implemented the proton beam source of the therapeutic Mevion S250i proton accelerator in the Monte Carlo code FRED. This delivery system is more complex to implement than others because of the many degrees of freedom of the range modulation system and the adaptive aperture in the beam path which need to be considered. We chose to describe the pristine proton beam by a phase space model in a plane located at the scanning magnet position and to implement the geometry of the range modulation system and the adaptive aperture explicitly in FRED. Instead, we could have devised a phase space model at the exit of the beam nozzle without explicitly implementing the components. This would, however, have resulted in a very large phase space library because of the many degrees of freedom of the adaptive aperture and range modulator system. An interesting alternative to potentially investigate in the future would be the use of generative neural networks as recently proposed for phase space modeling of therapeutic linear accelerators [28]. We underline that FRED is not specific to the Mevion accelerator but can handle any other currently available proton therapy system if the beam line is properly implemented. For example, the therapeutic cyclotron of the proton therapy facility in Krakow has previously been implemented in FRED [29].

We modeled both the longitudinal and transverse components of the phase space model as Gaussian distributions characterized by their mean (which is zero for the transverse component) and variance. The motivation was mainly empirical, that is, it simply works in practice, and had been used in the past by other authors. A more refined model based on a detailed description and simulation of the full beam line would possibly deviate from a pure Gaussian distribution. On the other hand, the practical relevance of this is limited because scattering in the range shifter plates largely dominates the transverse beam shape. A pristine beam is rarely used in clinical treatment plans.

We chose to use an emittance model to describe the evolution of the beam size along the beam path from the virtual source plane to the beam nozzle. Another choice would have been a virtual point source model where the protons are all generated in a single point upstream of the exit window. Such a model generates a linearly divergent beam, and the opening angle is determined by the depth of the point source. From the theoretical point of view, the emittance model is more correct because it accounts for the correlation for the proton's direction (momentum) and position in phase space. In fact, a proton beam can only have a waist (minimum of the emittance model), but not a point-like vertex, and a point source model thus gives an accurate representation of the beam only sufficiently far away from the waist. From the practical point of view, the transverse phase space model needs to be accurate only in the depth range where objects are present in the simulated geometry. According to **Figure 3**, the beam size evolves almost linearly in a range of about ±50 cm around the isocenter. In certain treatment configurations, however, the upstream surface of the nozzle region can be slightly more than 1 m away from the isocenter where the quadratic shape of the emittance model begins to be relevant. We therefore judge that the emittance model was a better choice in our case than a point source model.

Validation of the beam model was based on dose measurements and simulations because dose is the quantity of interest in a clinical application. Single pencil beams in water were used to assert the accuracy of the longitudinal phase space parameters and the parameterization of the range modulator plates. Validation based on dose layers and cubes showed that

FRED correctly reproduced the superposition of pencil beams, both laterally and in depth as needed in patient treatments. Dose differences were on the level of 1–2% and met all the dosimetric criteria. In recalculated patient QA plans, FRED's accuracy was at least as good as the clinical TPS when comparing simulation with measured data. Such a recalculation is an important use case for FRED, and we judge that our results justify its use as secondary dose engine for QA tasks. Full patient simulations, of which we showed a representative example here, also showed very good agreement between FRED and the clinical TPS.

FRED has initially been developed as a fast MC tool for dose calculation in particle therapy, and its functionality and physics models were implemented with this application in mind. Compared to general purpose MC codes, FRED has several limitations. First, only cuboid-shaped volumes can be defined. Other shapes, such as cylindrical detector devices, need to be approximated, for example, by a voxelized representation. Second, only voxel-based scorers are available, for example, to score dose, LET, or deposited energy on a grid. Scoring phase space properties (position and momentum) of individual particles, for example, is currently not available natively in FRED (but can be implemented by the user *via* plugins). Third, FRED tracks only those particles which are dosimetrically relevant on the scale of typical dose grids, that is, 1–2 mm. Specifically, FRED tracks secondary protons and deuterons, but lets heavier secondary particles deposit their energy locally because their range would anyhow be shorter than the voxel size. Neutrons and gamma rays are created, but not tracked, that is, they do not contribute to the deposited dose in the phantom. Some of this functionality is currently being developed and will probably be available in future versions of FRED.

A comparison of FRED with a general purpose of Monte Carlo software like Geant4 and FLUKA would have required a separate implementation of the Mevion system in these codes, which was clearly beyond the scope of this work. However, FRED's proton tracking engine was validated against other codes and experimental data during the initial development of FRED [16]. From experiences with other proton therapy systems (unpublished), we know that FRED's accuracy in clinical dose calculation is comparable to that of Geant4, while computation time is faster by orders of magnitude (minutes compared to tens of hours) at equal statistics.

A new functionality of FRED implemented as part of this work was the correct handling of situations where the beam nozzle overlaps with the volume containing the patient CT (cf. **Section 2.3**). It is worth noting that overlap of geometrical objects is a general difficulty encountered in most particle transport MC codes of our knowledge. In Geant4 (and derived applications) and FLUKA, for example, objects might be inserted into each other following a hierarchical child–parent structure, but partial overlap is not allowed, because the code would otherwise not be able to uniquely identify the object in which the particle needs to be traced. Geant4 provides a way to handle parallel geometries [30], which might be a starting point to handle overlapping volumes. Our implementation is not a general solution to the overlap problem. It works in this specific application because the beam nozzle is known to be the proton's origin. Another solution would have been to use the outer patient surface as a boundary of the patient volume because overlap occurs only among those parts of the patient box containing air and not those containing tissue-filled voxels. Technically, however, this would have been much more difficult to handle because many parameters would be required to define such an irregular volume as opposed to a simple air-filled box enclosing the patient.

We conclude with a short discussion on the calculation times reported in the Results section for the different kinds of simulation. In particular, they were on the order of 10–15 min for full patient simulations which is largely sufficient for our main purpose of daily dose recalculation. Another measure of computational speed is the tracking time per proton, which was on the order of $3–5\times10^6$ protons per second on the Nvidia Titan Xp card used in this work. This rate can only be reached if the card is optimally exploited, that is, if the number of primaries is large enough so that tracking is the dominant contribution compared to overhead due to data transfer to and from the GPU card. This was what prompted us to optimize the geometry handling in FRED in the first place (cf. **Section 2.3**), and indeed, calculation times improved by up to 70% for the full patient simulations. Furthermore, the number of protons per spot is currently set to a fixed number. A more elaborate scheme would set the number individually for each spot based on a requested noise level in the dose distributions, as it is implemented, for example, in the clinical TPS. Furthermore, no variance reduction techniques nor post-processing to de-noise the dose distributions are currently used in FRED (except for the fact that FRED is a condensed history code like all other general purpose Monte Carlo programs). All these methods are expected to improve calculation time even further.

5. CONCLUSION

We implemented a proton beam source for the Monte Carlo code FRED using a combination of the phase space model and explicit geometry of the beam nozzle components. The beam model was calibrated and validated by comparing measured and simulated data. The dosimetric accuracy was found to be sufficiently high to use FRED as the secondary dose calculator and at least as good as the clinical TPS.

DATA AVAILABILITY STATEMENT

The raw data supporting the conclusions of this article will be made available by the authors, without undue reservation.

ETHICS STATEMENT

Ethical review and approval was not required for the study on human participants in accordance with the local legislation

and institutional requirements. Written informed consent for participation was not required for this study in accordance with the national legislation and the institutional requirements.

AUTHOR CONTRIBUTIONS

JG and IR developed and validated the beam model, and designed the project. JG, IR, and NK drafted the manuscript. IR and GV-F provided the experimental data and the technical information required to implement the beam model. AS and VP updated the FRED source code with the needed changes to perform this work. NK implemented the HU conversion in FRED. IR, AR, and VP provided their expertize in medical physics and in beam modeling. All the authors reviewed and approved the manuscript.

FUNDING

AR and JG acknowledged the Reintegration programme of the Foundation for Polish Science cofinanced by the EU under the European Regional Development Fund–grant no. POIR.04.04.00-00-2475/16-00.

ACKNOWLEDGMENTS

We would like to thank the commissioning team of the MAASTRO proton facility, that is, GV-F, Mirko Unipan, Jonathan Martens, Erik Roijen, and Geert Bosmans, for proving the measured data and for the fruitful discussions. We thank also Bas Nijsten for supporting this project. We gratefully acknowledge the support of NVIDIA Corporation with the donation of the GPU cards used for this research.

REFERENCES

1. Beltran C, Tseung HWC, Augustine KE, Bues M, Mundy DW, Walsh TJ, et al. Clinical implementation of a proton dose verification system utilizing a GPU accelerated Monte Carlo engine. *Int J Part Ther* (2016) 3:312–9. doi:10.14338/IJPT-16-00011.1
2. Meijers A, Guterres Marmitt G, Ng Wei Siang K, van der Schaaf A, Knopf AC, Langendijk JA, et al. Feasibility of patient specific quality assurance for proton therapy based on independent dose calculation and predicted outcomes. *Radiother Oncol* (2020) 150:136–41. doi:10.1016/j.radonc.2020.06.027
3. Paganetti H, Jiang H, Parodi K, Slopsema R, Engelsman M. Clinical implementation of full Monte Carlo dose calculation in proton beam therapy. *Phys Med Biol* (2008) 53:4825–53. doi:10.1088/0031-9155/53/17/023.
4. Paganetti H Range uncertainties in proton therapy and the role of Monte Carlo simulations. *Phys Med Biol* (2012) 57:R99–117. doi:10.1088/0031-9155/57/11/R99
5. Battistoni G, Boccone V, Boehlen T, Broggi F, Brugger M, Brunetti G, et al. *FLUKA Monte Carlo calculations for hadrontherapy application*. 13th international conference on nuclear reaction mechanisms, 2012 January 11–15; Varenna, Italy. Geneva: CERN (2013). p. 461.
6. Böhlen TT, Cerutti F, Dosanjh M, Ferrari A, Gudowska I, Mairani A, et al. Benchmarking nuclear models of FLUKA and GEANT4 for carbon ion therapy. *Phys Med Biol* (2010) 55:5833–47. doi:10.1088/0031-9155/55/19014
7. Parodi K, Mairani A, Brons S, Hasch BG, Sommerer F, Naumann J, et al. Monte Carlo simulations to support start-up and treatment planning of scanned proton and carbon ion therapy at a synchrotron-based facility. *Phys Med Biol* 57 (2012) 3759–84. doi:10.1088/0031-9155/57/12/3759
8. Henkner K, Sobolevsky N, Jäkel O, Paganetti H. Test of the nuclear interaction model in SHIELD-HIT and comparison to energy distributions from GEANT4. *Phys Med Biol* 54 (2009) N509–17. doi:10.1088/0031-9155/54/22/n01
9. Agostinelli S, Allison J, Amako K, Apostolakis J, Araujo H, Arce P, et al. GEANT4– a simulation toolkit. *Nucl Instrum Methods Phys Res, Sect A* (2003) 506:250–303. doi:10.1016/S0168-9002(03)01368-8
10. Santin G, Staelens S, Taschereau R, Descourt P, Schmidtlein CR, Simon L, et al. Evolution of the GATE project: new results and developments. *Nucl Phys B Proc Suppl* (2007) 172:101–3. doi:10.1016/j.nuclphysbps.2007.07.008
11. Sarrut D, Bardiès M, Boussion N, Freud N, Jan S, Létang JM, et al. A review of the use and potential of the GATE Monte Carlo simulation code for radiation therapy and dosimetry applications. *Med Phys* (2014) 41:1–14. doi:10.1118/1.4871617
12. Perl J, Shin J, Schümann J, Faddegon B, Paganetti H. TOPAS: an innovative proton Monte Carlo platform for research and clinical applications. *Med Phys* (2012) 39:6818–38. doi:10.1118/1.4758060
13. Testa M, Schümann J, Lu HM, Shin J, Faddegon B, Perl J, et al. Experimental validation of the TOPAS Monte Carlo system for passive scattering proton therapy. *Med Phys* (2013) 40:121719. doi:10.1118/1.4828781
14. Jia X, Schümann J, Paganetti H, Jiang SB. GPU-based fast Monte Carlo dose calculation for proton therapy. *Phys Med Biol* (2012) 57:7783–97. doi:10.1088/0031-9155/57/23/7783
15. Qin N, Botas P, Giantsoudi D, Schuemann J, Tian Z, Jiang SB., et al. Recent developments and comprehensive evaluations of a GPU-based Monte Carlo package for proton therapy. *Phys Med Biol* (2016) 61:7347–62. doi:10.1088/0031-9155/61/20/7347
16. Schiavi A, Senzacqua M, Pioli S, Mairani A, Magro G, Molinelli S, et al. Fred: a GPU-accelerated fast-Monte Carlo code for rapid treatment plan recalculation in ion beam therapy. *Phys Med Biol* (2017) 62:7482–504. doi:10.1088/1361-6560/aa8134
17. Wan Chan Tseung H, Ma J, Beltran C. A fast GPU-based Monte Carlo simulation of proton transport with detailed modeling of nonelastic interactions. *Med Phys* (2015) 42:2967–78. doi:10.1118/1.4921046
18. Mein S, Choi K, Kopp B, Tessonnier T, Bauer J, Ferrari A, et al. Fast robust dose calculation on GPU for high-precision 1H, 4He, 12C and 16O ion therapy: the FRoG platform. *Sci Rep* (2018) 8:14829. doi:10.1038/s41598-018-33194-4
19. Grevillot L, Bertrand D, Dessy F, Freud N, Sarrut D. A Monte Carlo pencil beam scanning model for proton treatment plan simulation using GATE/GEANT4. *Phys Med Biol* (2011) 56:5203–19. doi:10.1088/0031-9155/56/16/008
20. Grevillot L, Bertrand D, Dessy F, Freud N, Sarrut D. GATE as a GEANT4-based Monte Carlo platform for the evaluation of proton pencil beam scanning treatment plans. *Phys Med Biol* (2012) 57:4223–44. doi:10.1088/0031-9155/57/13/4223
21. Paganetti H, Jiang H, Lee SY, Kooy HM. Accurate Monte Carlo simulations for nozzle design, commissioning and quality assurance for a proton radiation therapy facility. *Med Phys* (2004) 31:2107–18. doi:10.1118/1.1762792
22. Cirrone G, Cuttone G, Guatelli S, Lo Nigro S, Mascialino B, Pia M, et al. Implementation of a new Monte Carlo-GEANT4 Simulation tool for the development of a proton therapy beam line and verification of the related dose distributions. *IEEE Trans Nucl Sci* (2005) 52:262–5. doi:10.1109/TNS.2004.843140
23. Prusator M, Ahmad S, Chen Y. TOPAS Simulation of the Mevion S250 compact proton therapy unit. *J Appl Clin Med Phys* (2017) 18:88–95. doi:10.1002/acm2.12077
24. Vilches-Freixas G, Unipan M, Rinaldi I, Martens J, Roijen E, Almeida IP, et al. Beam commissioning of the first compact proton therapy system with spot scanning and dynamic field collimation. *Br J Radiol* (2020) 93:20190598. doi:10.1259/bjr.20190598
25. Twiss RQ, Frank NH. Orbital stability in a proton synchrotron. *Rev Sci Instrum* (1949) 20:1–17. doi:10.1063/1.1741343

26. Bortfeld T, Schlegel W. An analytical approximation of depth - dose distributions for therapeutic proton beams. *Phys Med Biol* (1996) 41: 1331–9. doi:10.1088/0031-9155/41/8/006.
27. Kanematsu N, Inaniwa T, Nakao M. Modeling of body tissues for Monte Carlo simulation of radiotherapy treatments planned with conventional x-ray CT systems. *Phys Med Biol* (2016) 61:5037–50. doi:10.1088/0031-9155/61/13/5037
28. Sarrut D, Krah N, Létang JM. Generative adversarial networks (GAN) for compact beam source modelling in Monte Carlo simulations. *Phys Med Biol* (2019) 64:215004. doi:10.1088/1361-6560/ab3fc1
29. Garbacz M, Battistoni G, Durante M, Gajewski J, Krah N, Patera V, et al. Proton therapy treatment plan verification in CCB Krakow using fred Monte Carlo TPS tool. In: L Lhotska, L Sukupova, I Lacković, GS Ibbott, editors *World congress on medical physics and biomedical engineering 2018*. Singapore: Springer Singapore (2019). p. 783–7.
30. Apostolakis J, Asai M, Cosmo G, Howard A, Ivanchenko V, Verderi M. Parallel geometries in Geant4: foundation and recent enhancements. 2008 IEEE nuclear science symposium conference record, 2008 October 19–25; Dresden, Germany. IEEE (2008). p. 883–6. doi:10.1109/NSSMIC.2008.4774535

Conflict of Interest: The authors declare that the research was conducted in the absence of any commercial or financial relationships that could be construed as a potential conflict of interest.

frontiers in Physics

MINI REVIEW
published: 14 January 2021
doi: 10.3389/fphy.2020.568296

Biological Pathways as Substantiation of the Use of Copper Radioisotopes in Cancer Theranostics

Dana Niculae[1], Ramona Dusman[1,2]*, Radu A. Leonte[1], Livia E. Chilug[1,2], Cristina M. Dragoi[3], Alina Nicolae[3], Radu M. Serban[1,4], Dragos A. Niculae[3], Ion B. Dumitrescu[3] and Doina Draganescu[1,3]*

[1]Radiopharmaceutical Research Centre, Horia Hulubei National Institute for Physics and Nuclear Engineering, Magurele, Romania, [2]Faculty of Applied Chemistry and Materials Science, Politehnica University of Bucharest, Bucharest, Romania, [3]Faculty of Pharmacy, Carol Davila University of Medicine and Pharmacy, Bucharest, Romania, [4]Faculty of Biology, University of Bucharest, Bucharest, Romania

OPEN ACCESS

Edited by:
Yolanda Prezado, INSERM U1021 Signalisation normale et pathologique de l'embryon aux thérapies innovantes des cancers, France

Reviewed by:
Rosa Maria Moresco, University of Milano-Bicocca, Italy
Shi-Ying Li, Guangzhou Medical University, China

***Correspondence:**
Ramona Dusman
ramona.dusman@nipne.ro
Dana Niculae
dana.niculae@nipne.ro

Specialty section:
This article was submitted to Medical Physics and Imaging, a section of the journal Frontiers in Physics

Received: *31 May 2020*
Accepted: *27 November 2020*
Published: *14 January 2021*

Citation:
Niculae D, Dusman R, Leonte RA, Chilug LE, Dragoi CM, Nicolae A, Serban RM, Niculae DA, Dumitrescu IB and Draganescu D (2021) Biological Pathways as Substantiation of the Use of Copper Radioisotopes in Cancer Theranostics. Front. Phys. 8:568296. doi: 10.3389/fphy.2020.568296

Copper, a cofactor for many enzymes, is a bioelement that is involved in many main biochemical processes; although high levels of copper promote the proliferation of cancer cells. Further development of radiopharmaceuticals based on copper radioisotopes depend on understanding and taking advantage of its biochemical pathways in oncogenesis. As with other radiometals used in molecular imaging and/or targeted therapy, biological vectors are employed to transport copper radioisotopes to a target, aiming for high specific uptake at tumor sites and precise delivery of ionizing radiation. Evidence of the clinical utility of copper radioisotopes in the ionic form $CuCl_2$ were also proven in an *in vivo* study of the copper metabolism, guiding personalized copper-chelating treatment in cancer patients and in imaging pathological sites associated with copper imbalance. Five of the copper radioisotopes have gained interest for nuclear medicine applications, based on their emissions, energies, and half-lives, as they can be produced with pharmaceutical-grade quality. The uptake mechanism, kinetics, and metabolic parameters are important findings in molecular imaging, which are decisive when designing individualized targeted radiotherapy for dose calculations of high linear energy transfer Auger electrons and β^- emissions of ^{64}Cu and ^{67}Cu. As radiation deposits a high amount of energy within the intra-cellular space, the biochemical involvement of copper determines targets in drug design and validation. The biochemical pathways depict copper metabolism in normal cells and highlight its increased activity in tumor progression and angiogenesis. The avid uptake of copper into inter- and intra-mitochondrial spaces, as constituents of cytochrome C oxidase, substantiate the selection of $^{64/67}CuCl_2$ as theranostic agents.

Keywords: molecular imaging, theranostics (combined therapeutic and diagnostic technology), copper, emergent radioisotopes, cancer, Cu-64/67

INTRODUCTION

The natural occurrence of copper (69.17% ^{63}Cu, 30.83% ^{65}Cu [1]), either in metallic form or as a mineral, confers a wide exposure to humans. Its inorganic salts are highly toxic but its varied coordination complexes have gained a lot of interest in drug design, as they are selective and also exhibit convenient pharmacokinetics and pharmacodynamics.

Copper is an essential microelement involved in important biochemical processes, such as: homeostasis, iron transport, respiration, and metabolism, as a result of its redox abilities in the biological environment: reversible translation between oxidized form (cupric ion, Cu^{2+}) and the reduced form (cuprous ion, Cu^{+}). It is a transition metal with 29 isotopes, out of which 27 are radioactive [2].

Along with the progress of nuclear medicine practices and technology, approaching molecular imaging and personalized treatment, five of the copper radioisotopes have gained interest for medical applications, considering their emissions, energies, production route, and availability, with half-lives ranging from 9.7 min (^{62}Cu) to 2.6 days (^{67}Cu) [2, 3]. Especially, ^{64}Cu and ^{67}Cu were intensively investigated as medically emergent radioisotopes for theranostic applications and therapy, respectively. Still, there is a need for more data regarding the production of ^{60}Cu, ^{62}Cu, and particularly ^{67}Cu in medical small cyclotrons.

Recent studies demonstrated the usefulness of $^{64/67}$Cu agents, containing biological vectors to carry radioisotopes to target, aiming for high specific uptake at tumor sites, and precise delivery of ionizing radiation, such as peptides, antibodies, or other biologically active small molecules [2, 3]. Besides using such carriers, the clinical utility of copper radioisotopes in their most simple chemical form, copper chloride, was also proven, either for an *in vivo* study into the copper metabolism, guiding personalized copper-chelating treatment in cancer patients, or to image pathological sites associated with copper imbalance in inflammation, tumor angiogenesis, and metastasis.

As many of these findings are evidence-based and sourced directly from clinical practice (e.g., the significantly higher copper levels measured in serum and tumor cells of patients with cancer compared to normal subjects [4]), there is a need for an in-depth biological evaluation of the involved mechanisms and quantification. Therefore, we reviewed the relevant literature regarding the biological and biochemical pathways of copper, to substantiate the use of copper radioisotopes in oncology and promoting its further development.

BIOLOGICAL PATHWAYS OF COPPER IN HUMANS

Copper Bioavailability and Dietary Interactions

Humans are exposed to environmental copper from water, food, and tools or household goods, therefore the World Health Organization (WHO) defined a safe range for copper intake and acknowledged its effects, either positive or negative, on human health [1]. In an adult organism there is approximately 1.5 copper mg/kg bw, still up to 2.2 mg/kg bw is considered acceptable in the physiological range. Foods most abundant in copper are seafood, dry nuts and seeds, dark chocolate, and mushrooms [5]. A high nutritional intake does not represent any risk considering copper toxicity, as the human organism has a dynamic mechanism of homeostasis.

Copper bioavailability is fairly affected by dietary factors, such as carbohydrate, iron, zinc, molybdenum, and ascorbic acid co-ingestion. Large quantities of dietary zinc can decrease copper absorption and induce the symptoms of systemic copper deficiency. Also, an increased molybdenum intake drives the organism toward secondary copper deficiency, which can be rapidly corrected by copper supplementation. On the other hand, iron-copper interactions in the intestines conduct the regulation of copper transport modulation by the iron levels. Reduced levels of copper lead to a series of physiological changes, inducing pathological conditions, while high intake of copper, found as chronic or acute exposure, can result in liver damage [1].

Copper Metabolism and Physiological Role

The intestines are the main absorption site, the process being conducted by the enterocytes, with the participation of copper permease and human copper transporter-1 (hCTR1) [1–7]. Dietary Cu^{2+} is reduced to Cu^{+} by reductases, prior to being transported through the brush border membrane of the enterocytes by hCTR1 [1, 5, 8], yet the mechanisms for selective permeation of Cu^{+} ions across cell membranes are unknown [9]. After absorption, copper, bound to metallochaperone proteins, is delivered to the mitochondrion [10, 11] by the SLC25A3 inner membrane transporter [11, 12], which is required for the metalation of enzymes within the mitochondrial inter-membrane space [13]. The exceeding amount of copper can be deposited in an inert form in metallothionein, the main intracellular copper storage protein. Subsequently, it is released under the influence of ATP7A. At the end of the process, Cu^{+} is effluxed from enterocytes, chemically reconverted to Cu^{2+}, and is thus able to bind to the transport proteins, albumin and alpha-2-macroglobulin. The carrier proteins deliver copper to the hepatic tissue, from where it is subsequently redirected to the target sites; therefore liver is the main organ that controls copper homeostasis mechanisms [1, 5]. Copper is distributed mostly in the bone and muscle tissues (up to 67%), but also in the liver, brain, and heart [1, 8].

Copper is further transferred to the cytoplasm, in inter-mitochondrial and intra-mitochondrial spaces, where it becomes a constituent of cytochrome c oxidase (CcO) and superoxide dismutase-1 (SOD1) [10–12]. Under normal circumstances, copper is transferred into the trans-Golgi network, where it is used for the synthesis of other cuproenzymes (ceruloplasmin, lysis oxidase, peptidylglycine alpha-amidating monooxygenase, and dopamine beta-hydroxylase) [1]. In the case of high intracellular copper influx, the same transporters will move to the cell surface, where they will mediate the efflux of excessed copper to the plasma (ATP7A) or bile (ATP7B) [1, 8]. Copper excretion is mainly achieved through bile, in the form of bile salts; the urinary excretion is rather insignificant [1, 8]. The ubiquitarian role of copper derives from its structural importance in a wide array of

functional and modulatory proteins that are deeply involved in physiological and pathological mechanisms [13–15] (**Supplementary Table S1**). Copper is an enzymatic cofactor, an essential component of Cu-dependent enzymes: ceruloplasmin, cytochrome C oxidase, metallothionein, Cu/Zn superoxide dismutase-1, amine oxidases, lysyl oxidase, tyrosinase, zyklopten, and mono-oxygenases, and also represents an up-regulating trigger for a series of redox status modulatory enzymes: catalase, glutathione peroxidase, hepaestin, cartilage matrix glycoprotein, and Protein-6-lysine oxidase [1, 13]. Reduced activity of these enzymatic proteins is found in copper deficiency states [13, 16].

Copper Deficiency and Pathological Implications

Reduced or minimal activity of copper-dependent enzymes results in symptoms that may include hypochromic anemia, neutropenia, thrombocytopenia, and hypopigmentation, bone, cardiovascular, and neurological abnormalities, as well as immune system depression [1, 8]. Copper-related genetic diseases include Menkes syndrome (a mutation of ATP7A gene) which is expressed by reduced intestinal copper absorption and Wilson's disease (a mutation of the ATP7B gene), when copper accumulates in excess in different organs (liver, brain, cornea) [1, 5, 8]. Wilson's disease is caused by the cerebral and hepatic tissue accumulation of copper, leading to neurologic and psychiatric symptoms, and liver impairment [16, 17].

Children can develop potentially fatal idiopathic copper toxicosis when drinking contaminated water or food [8, 18, 19]. Correlations with Alzheimer's disease have also been observed; elevated levels of free (unbound) copper in the blood were present, as well as high copper levels in amyloid senile plaque deposits [18, 20]. Diabetic patients exhibit elevated plasma copper levels [19, 21]. Copper deficiency is also associated with cardiovascular diseases [22].

The proliferation of cancer cells is promoted by high levels of copper [8, 23]. Elevated copper levels were found in different types of tumors while cancer growth was minimized when copper was chelated [5, 24]. Considering its redox properties, copper is a source for reactive oxygen species [1].

MEDICAL RADIOISOTOPES OF COPPER

Molecular Imaging, Targeted Therapy, and Theranostic Role of Radio-Copper

Molecular imaging allows for the quantification of functional parameters of an organ or process; moreover the interactions of a drug with its desired target can be analyzed, side effects can be determined, and the delivery, absorption, distribution, metabolism, and elimination in a living system can be precisely evaluated [25–27]. Among the molecular imaging techniques, positron emission tomography (PET) is most often used to tailor and deliver personalized treatment, as a result of receptor identification and mapping their density to a tissue or organ of interest, or by exploiting the imbalanced metabolism in different stages of pathological processes.

The positron-emitting radionuclide is customarily selected taking into account several factors, such as: the half-life of the radionuclide (this should match with the vector pharmacokinetics to allow optimal uptake), the energy of the positron emission (which determines the precision and image resolution), and the availability and cost of the production. Moreover, the specific/molar activity and carrier-free specifications, as quality parameters, become tremendously important when associated with molecular term (either imaging or therapy), together with radiobiological parameters, mainly the affinity, uptake, and retention profiles (radio)toxicity, blood clearance, and elimination route.

Five radioisotopes of copper (**Table 1**) can be produced at a cyclotron, with characteristics required for clinical use [28–31]. Based on their radioisotope emissions, ^{60}Cu, ^{61}Cu, ^{62}Cu, and ^{64}Cu are suitable for molecular imaging applications, while ^{64}Cu and ^{67}Cu are selected for targeted radionuclide therapy [30–32]. Due to their short half-lives, they are used in ionic form (as chlorides) or in combination with fast kinetic peptides. While the radiopharmaceuticals based on longer-lived radionuclides, such as ^{177}Lu, ^{89}Zr, or ^{90}Y enable the investigation of the biological processes over a number of hours, which is often demanded by the study or imposed by slow kinetics of the vector [33–35], copper-64 is a theranostic radionuclide of particular interest due to its simultaneous emission of both β^+ (17.52%) and β^- (38.48%) particles [36–44]. The positron emission allows for high resolution PET imaging, while low abundance gamma emissions do not affect the imaging process compared to other positron emitters [30, 45]. It decays also through electron capture (EC 43.53%), when high linear energy transfer Auger electrons are emitted. When this happens in the close vicinity of a cancerous cell nucleus, it may cause DNA damage, eventually triggering cell death and thus, achieving a therapeutic effect. Taking advantage of the positron emissions, real-time therapy follow-up can be performed by PET imaging, presumably at any time point during therapy.

Production of Medical Radioisotopes of Copper, with Particular Interest on ^{64}Cu

Researchers are investigating different routes to produce carrier-free and high specific activity copper radioisotopes [29]. Copper-64 can be produced in a reactor by (n,γ) and (n,p) reactions, on enriched targets [30], at thermal neutron fluxes ($6\text{-}7\cdot10^{12}$ $n^{\star}cm^{-2\star}s^{-1}$). The average specific activity of ^{64}Cu obtained was 2.4 TBq/g Cu, at the end of irradiation. Using this route, radionuclide impurities ^{65}Zn and ^{60}Co are co-produced and should be eliminated by radiochemical processing, using an anion exchange separator [31]. Higher specific activity can be achieved when fast neutron reactions are employed, but thermal neutron reactions also occur, leading to high amounts of long-lived radionuclide impurities, such as ^{65}Zn ($T_{1/2}$ = 245 days) [29].

The most common way to produce ^{64}Cu is by using a small/medium energy cyclotron [32, 36–49]. Several nuclear reactions can be triggered on nickel or zinc targets by proton beams: ^{64}Ni(p,n)^{64}Cu, ^{nat}Zn(p,xn)^{64}Cu or ^{68}Zn(p,αn) [49–57], but also deuterons induced reactions: ^{64}Ni(d,2n), ^{66}Zn(d,α), ^{64}Zn(d,2p)

TABLE 1 | Radioisotopes of copper produced in medium energy cyclotrons.

Radioisotope and half-life	Decay mode and energy	Most intense γ emissions	Nuclear reaction and cross-section data [74]
^{67}Cu 61.8 h	β$^-$ (100%) 121 keV (57%) 154 keV (22%) 189 keV (20%)	91.2 keV (7%) 93.3 keV (16.1%) 184.6 keV (48.7%)	
^{64}Cu 12.7 h	β$^-$ (38.5%) 191 keV (38.5%) EC and β$^+$ (61.5%) 278.2 keV (17.6%)	- 1,345.77 keV (0.475%)	
^{62}Cu 9.7 min	EC and β$^+$ (100%) 1,321 keV (98)	875.7 keV (0.15%) 1,173 keV (0.342%)	
^{61}Cu 3.32 h	EC and β$^+$ (100%) 524 keV (51%)	282.9 keV (12.2%) 656.0 keV (10.8%) 1,185.2 keV (3.7%)	
^{60}Cu 23.7 min	EC and β$^+$ (100%) 872 keV (49%)	1,332.4 keV (88%) 1791.6 keV (45.4%)	

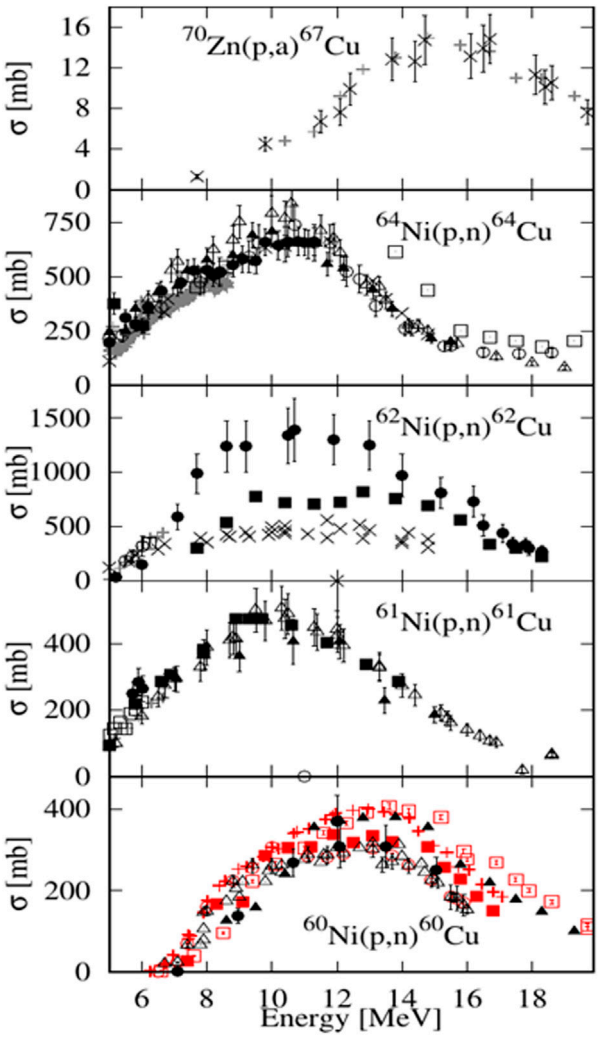

[52–54, 56]. Good yields of ^{64}Cu production, with low radionuclide impurities, were obtained using enriched ^{64}Ni or $^{64/66/68}$Zn targets [49]. The irradiation of ^{nat}Zn targets is a less expensive method to conveniently obtain lower activities of ^{64}Cu, while the use of deuteron beams on these targets requires energies above 20 MeV to obtain reasonable yields [56].

The ^{64}Ni(p,n)^{64}Cu reaction is used at large scale for the production of ^{64}Cu, although bearing the disadvantage of costly target material, this route is preferred for the high yields that can be achieved, even at small medical cyclotrons [54, 55, 58]. Using a 12 MeV cyclotron, specific activity of >87 × 10^4 GBq/g and an irradiation yield of >111 MBq/μAh were reported [42]. ^{64}Ni (99.5% enrichment) is electrodeposited from the ^{64}Ni(NO$_3$)$_2$ solution, resulting in a^{64}Ni solid target [46]. Alternatively, liquid targets consisting of solutions of ^{64}Ni(NO$_3$)$_2$ are conveniently used, with lower production yield [47]. The irradiation process parameters are tuned for best yields, according to the experimental set-up and needs of a site; optimal parameters: 2–4 h irradiation time, 40–50 mg ^{64}Ni on target, lead to 9.99–18.5 GBq of ^{64}Cu and high specific activity (11.47 × 10^6 GBq/g Cu). The production yield, on 15–55 mg of enriched ^{64}Ni targets, ranges from 82.9 to 185 MBq/μAh [48]. Separation of Cu from the Ni targets employs ion-exchange chromatography, using a cation exchanger column (AG1-X8). Enriched ^{64}Ni can be recovered up to 95% [42]. During proton irradiation of enriched ^{64}Ni, ^{61}Co is produced as a contaminant, which can be separated with 4M HCl as an eluent [49].

$^{64}CuCl_2$ as Radiopharmaceutical and/or Precursor

^{64}CuCl$_2$ is used either as a radiopharmaceutical or as a precursor for radiolabeling specific carriers, such as monoclonal antibodies,

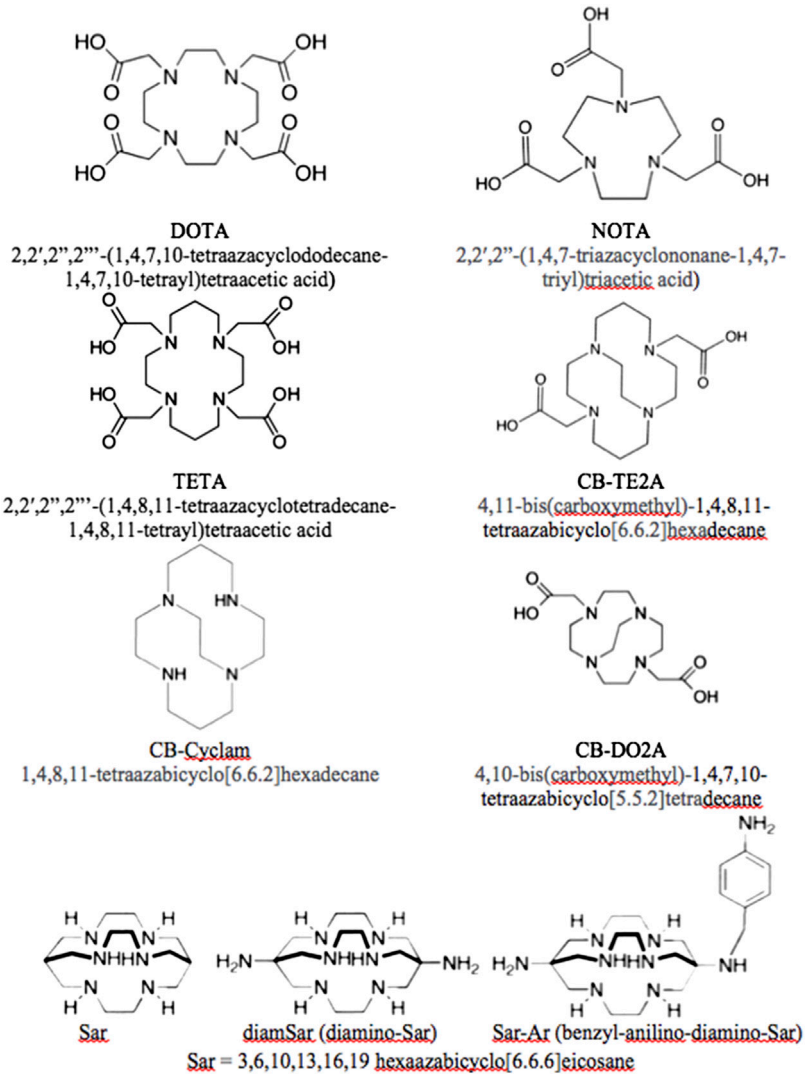

FIGURE 1 | Chelators used for binding radio-copper to biomolecules.

peptides, amino acids, hormones, nanoparticles, or small molecules, using chelating agents [58–60]. This is also the case for all the other copper radionuclides. Various cold copper complexes were studied and also used as anticancer agents [60].

After IV administration, $^{64}CuCl_2$ accumulates in the liver (uptake fraction 0.65), brain (uptake fraction 0.1), kidney (uptake fraction 0.01), and pancreas (uptake fraction 0.0002). Based on preclinical studies, the calculated effective dose (ED) is 70 mSv for the whole body of a 70 kg adult, after the intravenous injection of 925 MBq of $^{64}CuCl_2$ [61].

The chelators used for binding radio-copper to biomolecules (**Figure 1**) should have high thermodynamic stability; compact structures of macrocyclic or macro-bicyclic ligands with increased kinetic stability are preferred [62–71]. When dissociated from the complexes, Cu^{2+} is reduced to Cu^{+} and binds to SOD in high concentrations [63]. DOTA have been used for chelating ^{64}Cu, however, its ability to bind many different metal ions, *trans*-chelation to liver proteins, and its decreased stability compared to TETA/CB-TE2A make it less attractive [64, 65]. By comparison, NOTA and the hexaamino sarcophagine ligands demonstrate ease of conjugation, high radiolabeling yields, and *in vivo* stability [58, 66]. They also achieve better clearance from the blood, liver, and kidneys [65, 66]. The kinetic stability of copper (II) cross-bridged cyclam complexes is superior to those of the TETA and DOTA complexes [63], while ^{64}Cu-CB-TE2A proved to be the most stable, when compared to CB-cyclam, CB-DO2A, DOTA, and TETA, respectively [62].

Comparing the biodistribution, at 24 h p.i., of ^{64}Cu-CB-DO2A, ^{64}Cu-CB-TE2A, ^{64}Cu-DOTA, and ^{64}Cu-TETA, a larger amount of ^{64}Cu-labeled cross-bridged chelates was cleared form the blood, liver, and kidney than the non cross-bridged analogues; moreover, ^{64}Cu-CB-TE2A was the most resistant to *trans*-chelation in rat liver [65]. Hexaaza macrobicyclic

sarcophagines (Sar) are very compact structures, acting like a "cage" around Cu^{2+}, which increases the thermodynamic and kinetic stability, leading to low accumulation at non-targeted tissues. Evaluating the biodistribution data of ^{64}Cu-Sar, ^{64}Cu-diamSar, and ^{64}Cu-SarAr in balb/c mice, it was found that all three complexes had been cleared from the blood rapidly, while the uptake was low in bone, heart, stomach, spleen, muscle, lungs, and the gastrointestinal tract [66].

^{64}Cu as Radioisotope Contained in Theranostic Agents Intended for Different Tumors

$^{64}CuCl_2$ shows an increased and specific uptake in melanoma expressing high hCTR1: 12.7% ± 0.26 in B16F10 cells and 4.6% ± 0.04 in A375M cells, the tumor-to-muscle ratio was 4.11 ± 0.07 for B16F10 and 3.46 ± 1.25 for A375M. During $^{64}CuCl_2$ treatment, tumor growth in both melanoma models was slower than without treatment, suggesting that $^{64}CuCl_2$ radiotherapy is effective for hCTR1 high-expressing tumors [67].

In a xenograft model of glioblastoma multiforme (GBM) U87MG, the biodistribution of $^{64}CuCl_2$ indicated no brain uptake, while PET images showed an uptake in glioma cells; a decrease of the tumor volume with more than 68% was noticed, raising the survival rate of the treated mice [68]. SI113 inhibits SGK1, a protein with increased the expression of glioblastoma. The combination of SI113 and $^{64}CuCl_2$ has a synergistic effect and affects cell viability, triggering apoptosis, and necrosis. The inhibitory dose, tested in three cell lines in glioblastoma ((LI) PARI, ADF, and T98G) with different mutational status for p53, was 40 MBq [68].

In a study using the hypoxia-selective agent ^{64}Cu-ATSM on hamsters implanted with GW39 (human colorectal carcinoma), the inhibition of tumor growth was observed for a 220 MBq injected dose; the animals presented an increased rate of survival with no acute toxicity. After administration, PET scans revealed that ^{64}Cu-ATSM was localized in the GW39 tumor and PET imaging could be performed regularly [69].

Administration of 555 MBq of ^{64}Cu-TETA-Y3-TATE in a single dose to CA20948 rats, a model of somatostatin receptor-positive pancreatic cancer, decreased the tumor volume (29–73%) and inhibited its growth. The multiple dose radiotherapy study (3 × 370 MBq) decreased the tumor volume (36–81%) and provided a tolerable radiation exposure level over an extended period [70].

^{64}Cu-ATSM (^{64}Cu-diacetyl-bis(N-4-methylthiosemicarbazone) showed a high cytotoxic effect, decreasing the clonogenic survival of LL/2 cells (Mouse Lewis Lung carcinoma cells) in a dose dependent manner; the uptake of 1.50 Bq/cell of ^{64}Cu killed 99% of the cells. Under hypoxic conditions, ^{64}Cu was accumulated in the cells and produced DNA damage, detected by comet assay and Annexin V-FITC and propidium iodide staining methods [71].

DU-145 human prostate cancer xenografts were visualized by PET using $^{64}CuCl_2$, the cellular uptake was mediated by hCTR1, demonstrated by negative control PC-3 prostate cancer cells. Knockdown of hCTRl reflected the decreased cellular uptake and inhibition of tumor growth [72]. After $^{64}CuCl_2$ administration, a rapid uptake in the PCa lesions reached the maximum value in 1 h [73].

CONCLUSIONS

The biochemical pathways show copper metabolism in normal cells and highlight its increased activity in human cancer cells, at a higher metabolic rate. Its involvement in tumor progression and angiogenesis and its pivotal role in preserving the intracellular homeostasis are particular indicators used in functional imaging. Thus, specific processes are targeted by radio-copper chloride, but also specific vectors radiolabeled with copper radioisotopes are used. Moreover, the copper presence in intermitochondrial and intramitochondrial spaces, as constituents of cytochrome *c* oxidase, substantiates the selection of ^{64}Cu, a short range high LET emitter (Auger electrons), as a therapeutic agent, in a bioavailable chemical form, $^{64}CuCl_2$.

The uptake mechanism, kinetics, and metabolic parameters are very important findings for PET imaging using ^{60}Cu, ^{61}Cu, ^{62}Cu, or ^{64}Cu which are decisive when designing an individualized targeted therapy and, also, for dose calculations of high LET Auger electrons and β^- emissions of ^{64}Cu and ^{67}Cu. The concept of theranostic applications applies perfectly to copper radioisotopes, by matching pairs for diagnostics and therapy (e.g., ^{61}Cu and ^{67}Cu) or by taking advantage of the dual emissions of ^{64}Cu for both purposes. In this latter case, a real-time therapy follow-up brings important benefits for patients.

AUTHOR CONTRIBUTIONS

DN, RD, and RL reviewed the data regarding copper radioisotopes production and radiochemistry and edited the article. LC, RS, and DAN reviewed the data regarding biological assessment of ^{64}Cu-labelled biomolecules, CD, AN, ID, and DD reviewed pharmaceutical and pharmacological data.

FUNDING

The work has been funded by the UEFISCDI, Romanian Ministry of Education and Research, under contract 64PCCDI/2017. The work of Ramona Dusman, PhD student, has been funded by the Operational Program Human Capital of the Ministry of European Funds through the Financial Agreement 51668/09.07.2019, SMIS code 124705.

SUPPLEMENTARY MATERIAL

The Supplementary Material for this article can be found online at: https://www.frontiersin.org/articles/10.3389/fphy.2020.568296/full#supplementary-material.

REFERENCES

1. Bertinato J, Caballero B, Finglas PM, Toldrá F. *"Copper: physiology" in: reference module in food science, encyclopedia of food and health*: Waltham: Academic Press (2016) p. 321–6.
2. Ahmedova A, Todorov B, Burdzhiev N, Goze C. Copper radiopharmaceuticals for theranostic applications. *Eur J Med Chem* (2018) 157:1406–25. doi:10.1016/j.ejmech.2018.08.051
3. Wadas TJ, Wong EH, Weisman GR, Anderson CJ. Copper chelation chemistry and its role in copper radiopharmaceuticals. *Curr Pharmaceut Des* (2007) 13(1): 3–16. doi:10.2174/138161207779313768
4. Evangelista L, Mansi L, Cascini GL. New issues for copper-64: from precursor to innovative pet tracers in clinical oncology. *Curr. Rad* (2013) 6(3):117–23. doi:10.2174/18744710113069990020
5. Latorre M, Troncoso R, Uauy R. Biological aspects of copper. In *Clinical and translational perspectives on WILSON DISEASE*: Waltham: Academic Press (2019) p. 25–31.
6. Maryon EB, Molloy SA, Ivy K, Yu H, Kaplan JH. Rate and regulation of copper transport by human copper transporter 1 (hCTR1). *J. Biol. Chem* (2013) 288(25):18035–46. doi:10.1074/jbc.M112.442426
7. Spreckelmeyer S, van der Zee M, Bertrand B, Bodio E, Sturup S, Casini A. Relevance of copper and organic cation transporters in the activity and transport mechanisms of an anticancer cyclometallated gold (III) compound in comparison to cisplatin. *Front. Chem* (2018) 6:377. doi:10.3389/fchem.2018.00377
8. Hordyjewska A, Popiołek Ł, Kocot J. The many "faces" of copper in medicine and treatment. *Biometals* (2014) 27:611–21. doi:10.1007/s10534-014-9736-5
9. Ren F, Logeman BL, Zhang X, Liu Y, Thiele DJ, Yuan P. X-ray structures of the high-affinity copper transporter Ctr1. *Nat. Commun* (2019) 10:1086. doi:10.1038/s41467-019-09376-7
10. Baker ZN, Cobine PA, Leary SC. The mitochondrion: a central architect of copper homeostasis. *Metallomics* (2017) 9(11):1501–12. doi:10.1039/c7mt00221a
11. Winge DR. Filling the mitochondrial copper pool. *J. Biol. Chem* (2018) 293: 1897–8. doi:10.1074/jbc.H118.001457
12. Boulet A, Vest KE, Maynard MK, Gammon MG, Russell AC, Mathews AT, et al. Copper trafficking to the mitochondrion ansd assembly of copper metalloenzymes. *Biochim. Biophys. Acta* (2006) 1763(7):759–72. doi:10.1016/j.bbamcr.2006.03.002
13. Tapiero H, Townsend DM, Tew KD. Trace elements in human physiology and pathology. copper. *Biomed. Pharmacother* (2003) 57(9):386–98. doi:10.1016/S0753-3322(03)00012-X
14. Martínez-González J, Varona S, Cañes L, Galán M, Briones AM, Cachofeiro V, et al. Emerging roles of lysyl oxidases in the cardiovascular system: new concepts and therapeutic challenges. *Biomolecules* (2019) 9(10):610. doi:10.3390/biom9100610
15. Chen H, Attieh ZK, Syed BA, Kuo YM, Stevens Y, Fuqua BK, et al. Identification of zyklopen, a new member of the vertebrate multicopper ferroxidase family and characterization in rodents and human cells. *J. Nutr* (2010) 140(10):1728–35. doi:10.3945/jn.109.117531
16. Borchard S, Bork F, Rieder T, Eberhagen C, Popper B, Lichtmannegger J. The exceptional sensitivity of brain mitochondria to copper. *Toxicol. In Vitro* (2018) 51:11–22. doi:10.1016/j.tiv.2018.04.012
17. Drăgoi CM, Moroşan E, Dumitrescu IB, Nicolae AC, Arsene AL, Drăgănescu D, et al. Insights into chrononutrition: the innermost interplay amongst nutrition, metabolism and the circadian clock, in the context of epigenetic reprogramming. *Farmacia* (2019) 67(4):557–71. doi:10.31925/farmacia.2019.4.2
18. Banci L, Bertini I, Ciofi-Baffoni S, Kozyreva T, Zovo K, Palumaa P. Affinity gradients drive copper to cellular destinations. *Nature* (2010) 465(7298): 645–8. doi:10.1038/nature09018
19. Blockhuys S, Celauro E, Hildesjo C, Feizi A, Stal O, Fierro-Gonzalez JC. Defining the human copper proteome and analysis of its expression variation in cancers. *Metallomics* (2017) 9(2):112–23. doi:10.1039/c6mt00202a
20. Mursa J, Robien K, Hamack LJ, Park K, Jacobs DR. Dietary supplements and mortality rate in older women: the iowa women's health study. *Arch. Intern. Med* (2011) 171(18):1625–33. doi:10.1001/archinternmed.2011.445
21. Drăgoi CM, Nicolae AC, Dumitrescu IB, Popa DE, Ritivoiu M, Arsene AL. DNA targeting as a molecular mechanism underlying endogenous indoles biological effects. *Farmacia* (2019) 67(2):367–77. doi:10.31925/farmacia.2019.2.24
22. Klevay LM. Is the western diet adequate in copper?. *J. Trace Elem. Med. Biol* (2011) 25(4):204–12. doi:10.1016/j.jtemb.2011.08.146
23. Morris MC, Evans DA, Tangney CC, Bienias JL, Schneider JA, Wilson RS, et al. Dietary copper and high saturated and trans fat intakes associated with cognitive decline. *Arch. Neurol* (2006) 63(8):1085–8. doi:10.1001/archneur.63.8.1085
24. Barros MH, Johnson A, Tzagoloff A. COX23, a homologue of COX17, is required for cytochrome oxidase assembly. *J. Biol. Chem* (2004) 279:31943–7. doi:10.1074/jbc.M405014200
25. Wadas J, Wong EH, Weisman GR, Anderson CJ. Copper chelation chemistry and its role in copper radiopharmaceuticals. *Curr. Pharm. Des* (2007) 13(1): 3–16. doi:10.2174/138161207779313768
26. Rowland DJ, Lewis JS, Welch MJ. Molecular imaging: the application of small animal positron emission tomography. *J. Cell Biochem. Suppl* (2002) 39:110–5. doi:10.1002/jcb.10417
27. Knowles R, Friedrich F, Fischer C, Paech D, Ladd ME. Beyond T2 and 3T: new MRI techniques for clinicians. *Clin. Transl. Radiat. Oncol* (2019) 18:87–97. doi:10.1016/j.ctro.2019.04.009
28. Coenen HH, Gee AD, Adam M, Antoni G, Cutler CS, Fujibayashi Y, et al. Consensus nomenclature rules for radiopharmaceutical chemistry–setting the record straight. *Nucl. Med. Biol* (2017) 55:v–xi. doi:10.1016/j.nucmedbio.2017.09.004
29. Sun X, Anderson CJ. Production and applications of copper-64 radiopharmaceuticals. *Methods Enzymol* (2004) 386:237–61. doi:10.1016/S0076-6879(04)86011-7
30. *Manual for reactor produced radioisotopes*. Viena: IAEA – International Atomic Energy Agency (2003) 257 p.
31. Vimalnath KV, Rajeswari A, Chirayil V, Sharad PL, Jagadeesan KC, Joshi PV, et al. Studies on preparation of ^{64}Cu using (n,γ) route of reactor production using medium ux research reactor in india. *J. Radioanal. Nucl. Chem* (2011) 290:221–5. doi:10.1007/s10967-011-1301-x
32. Kastleiner S, Coenen HH, Qaim SM. Possibility of production of ^{67}Cu at a small-sized cyclotron via the (p,α)-Reaction on enriched ^{70}Zn. *Radiochim. Acta* (1999) 84:107–10. doi:10.1524/ract.1999.84.2.107
33. Niculae D, Lungu V, Anghel R, Gruia I, Iliescu M. Labelling of anti-epidermal growth factor monoclonal antibody with 177Lu: radiochemical and biological evaluation. *J. Labelled Cmpds. Radiopharmaceuticals* (2010) 53:355–9. doi:10.1002/jlcr.1771
34. Jauw YWS, Menke-van der Houven van Oordt CW, Hoekstra OS, Hendrikse NH, Vugts DJ, Zijlstra JM, et al. Immuno-positron emission tomography with zirconium-89-labeled monoclonal antibodies in oncology: what can we learn from initial clinical trials?. *Front. Pharmacol* (2016) 7:131. doi:10.3389/fphar.2016.00131
35. Sgouros G, Bodei L, McDevitt MR. Radiopharmaceutical therapy in cancer: clinical advances and challenges. *Nat. Rev. Drug Discov* (2020) 19:589–608. doi:10.1038/s41573-020-0073-9
36. Szelecsenyi F, Blessing G, Qaim SM. Excitation functions of proton induced nuclear reaction on enriched Ni-61 and Ni-64: possibility of production of no-carrier-added Cu-61 and Cu-64 at a small cyclotron. *Appl. Radiat. Isot* (1993) 44:575–80. doi:10.1016/0969-8043(93)90172-7
37. Adam Rebeles R, Van den Winkel P, Hermanne A, Tarkanyi F. New measurement and evaluation of the excitation function of 64Ni(p,n) reaction for the production of 64Cu. *Nucl. Instrum. Methods Phys. Res. B* (2009) 267:457–61. doi:10.1016/j.nimb.2008.11.038
38. Uddin M, Chakraborty A, Spellerberg S, Shariff M, Das S, Rashid M, et al. Experimental determination of proton induced reaction cross sections on natNi near threshold energy. *Radiochim. Acta* (2016) 104(5):305–14. doi:10.1515/ract-2015-2527
39. Piel H, Qaim SM, Stöcklin G. Excitation functions of (p,xn)-Reactions on natNi and highly enriched 62Ni: possibility of production of medically important radioisotope 62Cu at a small cyclotron. *Radiochim. Acta* (1992) 57(1):1–6. doi:10.1524/ract.1992.57.1.1
40. Singh BP, Sharma MK, Musthafa MM, Bhardwaj HD, Prasad R. A study of pre-equilibrium emission in some proton- and alpha-induced reactions. *Nucl.*

Instrum. Methods Phys Res A (2006) 562(2):717–20. doi:10.1016/j.nima.2006.02.030
41. Amjed N, Tárkányi F, Hermanne A, Ditrói F, Takács S, Hussain M. Activation cross-sections of proton induced reactions on natural Ni up to 65MeV. *Appl. Radiat. Isot* (2014) 92:73–84. doi:10.1016/j.apradiso.2014.06.008
42. Obata A, Kasamatsu S, McCarthy DW, Welch MJ, Saji H, Yonekura Y, et al. Production of therapeutic quantities of 64Cu using a 12 MeV cyclotron. *Nucl. Med. Biol* (2003) 30:535–9. doi:10.1016/S0969-8051(03)00024-6
43. Synowiecki MA, Perk LR, Nijsen JFW. Production of novel diagnostic radionuclides in small medical cyclotrons. *EJNMMI Radiopharm. Chem* (2018) 3(1):3. doi:10.1186/s41181-018-0038-z
44. Kozempel J, Abbas K, Simonelli F, Zampese M, Holzwarth U, Gibson N, et al. A novel method for n.c.a. 64Cu production by the 64Zn(d,2p)64Cu reaction and dual ion-exchange column chromatography. *Radiochim. Acta* (2007) 95:75–80. doi:10.1524/ract.2007.95.2.75
45. Asabella N, Cascini GL, Altini C, Paparella D, Notaristefano A, Rubin G. The copper radioisotopes: a systematic review with special interest to 64Cu. *BioMed Res. Int* (2014) 2014:786463. doi:10.1155/2014/786463
46. Niculae D, Ilie S, Leonte R, Chilug L, Craciun L. Automated production and purification of copper medical radioisotopes in a variable energy cyclotron using solid targetsThe 23rd International Symposium on Radiopharmaceutical Sciences (ISRS 2019). *J. Label Compd. Radiopharm* (2019) 62(S1):S301–S302. doi:10.1002/jlcr.3725
47. do Carmo SJC, Scott PJH, Alves F. Production of radiometals in liquid targets. *EJNMMI Radiopharm. Chem* (2020) 5:2. doi:10.1186/s41181-019-0088-x
48. McCarthy DW, Shefer RE, Klinkowstein RE, Bass LA, Margeneau WH, Cutler CS, et al. Efficient production of high specific activity 64Cu using A biomedical cyclotron. *Nucl. Med. Biol* (1997) 24:35–43. doi:10.1016/s0969-8051(96)00157-6
49. Avila-Rodriguez MA, Nyeb JA, Nickles RJ. Simultaneous production of high specific activity 64Cu and 61Co with 11.4MeV protons on enriched 64Ni nuclei. *Appl. Radiat. Isot* (2007) 65:1115–20. doi:10.1016/j.apradiso.2007.05.012
50. So LV, Pellegrini P, Katsifis A, Howse J, Greguric I. Radiochemical separation and quality assessment for the 68Zn target based 64Cu radioisotope production. *J. Radioanal. Nucl. Chem* (2008) 277(2):451–66. doi:10.1007/s10967-007-7143-x
51. Williams HA, Robinson S, Julyan P, Zweit J, Hastings D. A comparison of PET imaging characteristics of various copper radioisotopes. *Eur. J. Nucl. Med. Mol. Imag* (2005) 32(12):1473–80. doi:10.1007/s00259-005-1906-9
52. Smith SV, Waters DJ, Bartolo ND. Separation of Cu from ^{67}Ga waste products using anion exchange and low acid aqueous/organic mixtures. *Radiochim. Acta* (1996) 75:65–8. doi:10.1524/ract.1996.75.2.65
53. Mettler FA, Jr, Guiberteau MJ. Radioactivity, radionuclides and radiopharmaceuticals. In: FA MettlerMilton J. Guiberteau, editors *Esentials of nuclear medicine Imaging*. 6th ed:Philadelphia: W.B. Saunders (2012). p. 1–21.
54. Zweit J, Smith AM, Downey S, Sharma HL. Excitation functions for deuteron induced reactions in natural nickel: production of No-carrier-added 64Cu from enriched 64Ni targets for positron tomography emission. *Appl. Radiat* (1991) 42(2):193–7. doi:10.1016/0883-2889(91)90073-a
55. Alves F, Alves VHP, do Carmo SJC, Neves ACB, Silva M, Abrunhosa AJ. Production of copper-64 and gallium-68 with a medical cyclotron using liquid targets. *Mod. Phys. Lett* (2017) 32 (17). doi:10.1142/S0217732317400132
56. Abbas K, Kozempel J, Bonardi M, Groppi F, Alfarano A, Holzwarth U, et al. Cyclotron production of 64Cu by deuteron irradiation of 64Zn. *Appl. Radiat. Isot* (2006) 64:1001–5. doi:10.1016/j.apradiso.2005.12.021
57. Ferrari C, Asabella AN, Villano C, Giacobbi B, Coccetti D, Panichelli P, et al. Copper-64 dichloride as theranostic agent for glioblastoma multiforme: a preclinical study. *BioMed Res. Int* (2015). doi:10.1155/2015/129764
58. Jalilian AR, Osso J, Jr The current status and future of theranostic copper-64 radiopharmaceuticals. *Iran. J. Nucl. Med* (2017) 25(1):1–10.
59. Ma MT, Donnelly PS. Peptide targeted copper-64 radiopharmaceuticals. *Curr. Top. Med. Chem* (2011) 11:500–20. doi:10.2174/156802611794785172
60. Santini C, Pellei M, Gandin V, Porchia M, Tisato F, Marzano C. Advances in copper complexes as anticancer agents. *Chem. Rev* (2014) 114(1):815–62. doi:10.1021/cr400135x
61. Evangelista L, Mansi L, Cascini GL. New issues for copper-64: from precursor to innovative pet tracers in clinical oncology. *Curr. Rad* (2013) 6(3):117–23. doi:10.2174/18744710113069990020
62. Anderson CJ, Ferdani R. Copper-64 radiopharmaceuticals for PET imaging of cancer: advances in preclinical and clinical research. *Cancer Biother. Radiopharm* (2009) 24(4):379–93. doi:10.1089/cbr.2009.0674
63. Bass LA, Wang M, Welch MJ, Anderson CJ. In Vivo transchelation of copper-64 from TETA-octreotide to superoxide dismutase in rat liver. *Bioconjug. Chem* (2000) 11(4):527–32. doi:10.1021/bc990167l
64. Cai Z, Anderson CJ. Chelators for copper radionuclides in positron emission tomography radiopharmaceuticals. *J. Label Compd. Radiopharm* (2014) 57(4):224–30. doi:10.1002/jlcr.3165
65. Boswell CA, Sun X, Niu W, Weisman GR, Wong EH, Rheingold AL, et al. Comparative *in Vivo* stability of copper-64-labeled cross-bridged and conventional tetraazamacrocyclic complexes. *J. Med. Chem* (2004) 47(6):1465–74. doi:10.1021/jm030383m
66. Wei L, Yea Y, Wadas TJ, Lewis JS, Welch MJ, Achilefu S, et al. 64Cu-labeled CB-TE2A and diamsar-conjugated RGD peptide analogs for targeting angiogenesis: comparison of their biological activity. *Nucl. Med. Biol* (2009) 36:277–85. doi:10.1016/j.nucmedbio.2008.12.008
67. Qin C, Liu H, Chen K, Hu X, Ma X, Lan X, et al. Theranostics of malignant melanoma with $64CuCl_2$. *J. Nucl. Med* (2014) 55(5):812–7. doi:10.2967/jnumed.113.133850
68. Catalogna G, Talarico C, Dattilo V, Gangemi V, Calabria F, D'Antona L, et al. The SGK1 kinase inhibitor SI113 sensitizes theranostic effects of the 64CuCl2 in human glioblastoma multiforme cells. *Cell Physiol. Biochem* (2017) 43:108–19. doi:10.1159/000480328
69. Lewis JS, Laforest R, Buettner TL, Song SK, Fujibayashi Y, Connett JM, et al. Copper-64-diacetyl-bis(N^4-methylthiosemicarbazone): an agent for radiotherapy. *Proc. Natl. Acad. Sci. U.S.A* (2001) 98(3):1206–11. doi:10.1073/pnas.98.3.1206
70. Lewis JS, Lewis MR, Cutler PD, Srinivasan A, Schmidt MA, Schwarz SW, et al. Radiotherapy and dosimetry of 64Cu-TETA-Tyr3-Octreotate in a somatostatin receptor-positive, tumor-bearing rat model. *Clin. Cancer Res* (1999) 5(11):3608–16.
71. Obata A, Kasamatsu S, Lewis JS. Basic characterization of 64Cu-ATSM as a radiotherapy agent. *Nucl. Med. Biol* (2005) 32(1):21–8. doi:10.1016/j.nucmedbio.2004.08.012
72. Cai H, Wu JS, Muzik O, Hsieh JT, Lee RJ, Peng F. Reduced 64Cu uptake and tumor growth inhibition by knockdown of human copper transporter 1 in xenograft mouse model of prostate cancer. *J Nucl. Med* (2014) 55(4):622–8. doi:10.2967/jnumed.113.126979
73. Righi S, Ugolini M, Bottoni G. Biokinetic and dosimetric aspects of $64CuCl_2$ in human prostate cancer: possible theranostic implications. *EJNMMI Res* (2018) 8(1):18. doi:10.1186/s13550-018-0373-9
74. Experimental nuclear reaction data (EXFOR) database. IAEA – International Atomic Energy Agency. Available from: https://www-nds.iaea.org/exfor/ (Accessed May 30, 2020).

Conflict of Interest: The authors declare that the research was conducted in the absence of any commercial or financial relationships that could be construed as a potential conflict of interest.

frontiers in Physics

ORIGINAL RESEARCH
published: 18 January 2021
doi: 10.3389/fphy.2020.584326

Structural Changes in HPRT Gene of V79 Cells After Irradiation With Heavy Ions—Immediate and Delayed Effects

Pavel Bláha[1,2], Igor V. Koshlan[1,3], Nataliya A. Koshlan[1], Yulia V. Bogdanova[1], Daria V. Petrova[1], Raisa D. Govorun[1], Viliam Múčka[2] and Evgeny A. Krasavin[1,3]*

[1]Laboratory of Radiation Biology, Joint Institute for Nuclear Research, Dubna, Russia, [2]Faculty of Nuclear Sciences and Physical Engineering, Czech Technical University in Prague, Prague, Czech Republic, [3]Faculty of Natural and Engineering Science, Dubna State University, Dubna, Russia

The radiobiological effects of accelerated ions with high charge and high energy (HZE) on mammalian cells and their propagation in time are still not sufficiently explained and attract great deal of attention. This work aims to compare the immediate and delayed effects with emphasis on the latter. As shown by our group, the dependence of mutant fraction on expression time after irradiation may have interesting, non-monotonic, character depending on LET (linear energy transfer) of the used heavy ions. We speculate that this phenomenon may occur due to the induced genomic instability. Another area of our research is the study of the DNA structural changes in these mutants induced at different expression times. Chinese hamster V79 cells were irradiated with accelerated ions ^{11}B, ^{18}O, ^{20}Ne, and gamma radiation. The LET was ranging from 0.23 keV/μm of ^{60}Co gamma rays up to 136 keV/μm of ^{20}Ne ions. DNA of unique HPRT mutants was isolated, concentration measured, HPRT exons amplified, and analyzed at several different time points, up to about 40 days, after exposure. Over 1200 HPRT mutants were analyzed for deletions of exons and sorted into three main categories: partial deletion, PD—with deletion of one to eight exons; total deletions, TD—with all nine exons deleted; and no deletions—no change in the HPRT structure observed. In general, the number of samples with partial deletion was increasing with LET of the used radiation, suggesting that higher energy deposition to the cell nucleus is more likely to cause larger structural changes. In the case of total deletions, increase in their number with LET was observed up to LET ~115 keV/μm followed by a sharp decrease. The samples were also analyzed for the distribution of deletions, in particular exons at various expression times, the so-called mutational patterns. Hypothesis of the mechanisms behind observed phenomena is given, and possible implications for further research are discussed.

Keywords: accelerated heavy ions, V79 hamster cells, HPRT mutants, HPRT structural changes, delayed effects of radiation, genomic instability

OPEN ACCESS

Edited by:
Vincenzo Patera, Sapienza University of Rome, Italy

Reviewed by:
Marie Dutreix, Institut Curie, France
Charlot Vandevoorde, iThemba Laboratory, South Africa

****Correspondence:***
Pavel Bláha
pavel.blahax@gmail.com

Specialty section:
This article was submitted to Medical Physics and Imaging, a section of the journal Frontiers in Physics

Received: *16 July 2020*
Accepted: *16 November 2020*
Published: *18 January 2021*

Citation:
Bláha P, Koshlan IV, Koshlan NA, Bogdanova YV, Petrova DV, Govorun RD, Múčka V and Krasavin EA (2021) Structural Changes in HPRT Gene of V79 Cells After Irradiation With Heavy Ions—Immediate and Delayed Effects. Front. Phys. 8:584326. doi: 10.3389/fphy.2020.584326

INTRODUCTION

Accelerated heavy ions (HZE: high Z, high energy) are in the focus of biophysical and radiobiological research fields for some time now. It is mainly due to two reasons: biological effects of ions in galactic cosmic rays (GCR) that will impact (to a higher extent) astronauts during the flight missions beyond the magnetosphere of Earth [1], and their medical use in radiation therapy of cancer which grows continually [2, 3]. The knowledge of biological effects of HZE ions is limited compared to sparsely

ionizing radiation such as gamma rays or X-rays, particularly due to the limited availability of ion-capable accelerators usable for irradiation of biological samples.

Research focusing on the mutation induction, their type, and the radiation-induced genomic instability is significant for understanding of the long-term effects of radiation, probably more than the cell killing [4]. Only the surviving cells may form mutations that are considered as one of the triggers of carcinogenesis [4–8], which can be developed in later stages as a delayed effect of exposure [9]. The hypoxanthine–guanine phosphoribosyltransferase (HPRT) gene mutation assay is a well-known system for easy mutagenic studies, based on the 6-thioguanine (6-TG) mutant selection [10], which has been widely used to study the mutagenic effects of ionizing radiation (IR) of various qualities in mammalian cell cultures [11–16].

It has been shown that heavy ions with high LET (linear energy transfer) can cause biological damage fundamentally different from sparsely ionizing radiation—heavy ions are usually reported as being more effective in inducing various biological effects [12, 13, 17]. Their energy deposition within the track of their particles is more prone to create complex clustered lesions within DNA—containing single strand breaks as well as double strand breaks of DNA—that are extraordinarily difficult for the cells to repair and therefore susceptible to misrepair [18]. The literature data available for the quality of HPRT gene mutations induced by heavy accelerated ions are very scarce. A number of articles describe the mutational spectra induced by IR, which seems to be different in dependence on the type of radiation used: several about the effects of sparsely ionizing radiation (X-ray, gamma rays): [8, 11, 19–24]; a few using alpha particles (or He ions): [5, 11, 14, 20, 25, 26]; but only a couple exposing the cells to heavy charged ions: [8, 21, 27–29].

The published data seem to have a high degree of variety; nevertheless, some general conclusions can be drawn: radiation with higher LET (mainly alpha particles tested) usually caused more total deletions and lower number of partial deletions [19] or samples with no deletions [8, 20] in comparison to low LET radiation (gamma or X ray). However, studies showing the same or very similar levels of total deletions after irradiation with alpha particles or gamma radiation can be found as well [24, 26, 30]—a minority of authors even observed lower numbers of total deletions after irradiation with higher LET radiation [31]. Particularly for accelerated heavy ions, Baumstark-Khan et al. reported the number of total deletions of the HPRT gene increasing with LET of accelerated oxygen ions up to approximately 318 keV/μm followed by decrease, while the number of partial deletions was changing mildly in the same LET interval. It has been shown that even heavy ions can cause small alterations or point mutations [27], possibly due to the created secondary electrons. The results of HPRT gene molecular spectra induced by different ion species show high level of heterogeneity. It was reported that the deletion spectrum was nonspecific with regard to LET for mutants induced by neon ions, but LET specific for carbon-induced mutants [21]. It points to the fact that LET may not be the only parameter governing the biological effect, and that the mechanism behind it might be substantially more complex.

This work follows up our previous publication [32] that deals mainly with the effects of HZE ions on induction of HPRT mutants in prolonged expression times (ET). Surprisingly, it was found that the maximum of mutations was reached at different ET in dependence on LET of the used radiation. With increasing LET, the maximum was moving toward later ET. The current work focuses on structural analysis of these isolated mutants (on the level of exons of HPRT gene). This could give us answer about the type of mutations caused by different kinds of radiation and help to confirm our previous hypothesis that the delayed mutations are created *de novo* as a manifestation of genomic instability. This investigated topic, effects of prolonged expression times on the mutational spectra induced by radiation of various qualities, has been surprisingly little mentioned in the literature. The mutational patterns were usually studied in the first days after irradiation only and were not followed through in later ET. Usually, the mutants were chosen at a set ET [8, 28, 29], after particular number of population doublings [21], or similar. Therefore, the aim of this article was to bring some possible new insights into the development of HPRT mutation deletion spectra and to help to explain the connection between the late radiation effects and the quality of radiation.

MATERIALS AND METHODS

Cell Culture Cultivation

Detailed information about the cell culture and cultivation procedures have been described earlier [32]. Briefly, V79 Chinese hamster lung fibroblasts culture (ECACC 86041102) was provided by the Institute of Cytology of the Russian Academy of Sciences. During standard cultivation and recultivations, the culture was grown in Dulbecco's modified Eagle medium (DMEM; PanEco, C410p) supplemented with 10% of fetal bovine serum (FBS; PAA Laboratories, A15–011), 0.3 mg/ml L-glutamine (PanEco, F032), 100 units/ml penicillin, 100 μg/ml streptomycin, and 0.25 μg/ml amphotericin (Sigma-Aldrich, A5955) at 37°C, 95% humidity, and in 5% CO_2:95% air atmosphere.

Irradiation Conditions

During all experiments (both with sparsely and densely ionizing radiations), exponentially growing cells were irradiated in suspension in the standard nutrient medium, and the cell concentration was kept constant at 10^6 cells/ml. Detailed description of the irradiation setups, beam characteristics, and dosimetry was already provided [32]. In short, gamma irradiation (applied for comparison with heavy ions irradiation) was delivered *via* the ^{60}Co therapy unit "Rokus-M" of the Dzhelepov Laboratory of Nuclear Problems, Joint Institute for Nuclear Research (JINR), Dubna, Russia. Accelerated heavy ion irradiations were performed with the isochronous cyclotron U400M of the Flerov Laboratory of Nuclear Reactions, JINR. Cell samples were irradiated at the radiobiological facility

TABLE 1 | Irradiation parameters

Particle	Dose, Gy	Energy, MeV/n	Fluence[a], 1/cm^2	Dose rate, Gy/min	Avg. LET, keV/μm
γ (^{60}Co)	0.5–7	1.17 + 1.33[b]	$2.71{\cdot}10^9$	0.9	0.23[c]
^{11}B	0.5, 1, 2	32.4	$1.27{\cdot}10^7$	~1	49
^{18}O	0.5, 2	35.2	$5.43{\cdot}10^6$	~1	115
^{20}Ne	0.5, 2	51.8	$4.59{\cdot}10^6$	~1	136

[a]*Fluence per 1 Gy absorbed in water.*
[b]*Photon energy per decay.*
[c]*Estimated [38].*

Genome-M. The homogeneity of the beam (95% at the biological sample) and the scattered ions (less than 1%) were monitored by five ionization chambers [33]. Cell samples were kept at minimum thickness (iunder 2 mm) and irradiated in the plateau region of the Bragg curve to guarantee uniform irradiation. Ion energies when entering and leaving the cell suspension were calculated using LISE++ software [34], and LET within the sample was estimated using SRIM software [35] as the weighted average over the sample. Three different types of ions were used in this work: ^{11}B, ^{18}O, and ^{20}Ne irradiation parameter details in **Table 1**.

Mutation Assay and Mutant Subclone Isolation

Work procedures with cells after irradiation have been explained in detail previously [32]. The whole experimental procedure is summarized in **Figure 1**. Briefly, cells were detached from the irradiation cylinders within 30 min after irradiation, pooled by absorbed dose, and seeded at appropriate concentrations in a standard cultivation medium in order for the mutations to be expressed (to Recultivation 0 in **Figure 1**). After reaching confluence of about 80–90%, part of the cells was used for recultivation under the same conditions, prolonging the time after irradiation for expression of mutations (expression time, ET). Other part of the cells was used for the HPRT mutation assay using the 6-thioguanine (6-TG; Sigma-Aldrich, A4882) selection agent. After 10–12 days of growth, random mutant colony was isolated from each flask carefully not to be contaminated with other colonies. These isolated HPRT mutant subclones were cultured and later used for DNA extraction and following procedures. Mutant subclones were isolated approximately every third recultivation (with higher frequency at the beginning) for up to 40 days after exposure (usually 12 recultivations). Nonirradiated cells were treated in the same manner to determine the levels of spontaneous mutants (SM) during the whole investigated period.

Hypoxanthine–Guanine Phosphoribosyltransferase Gene Structural Analysis

The cultured HPRT mutant subclones had their DNA isolated (not less than 10^6 cells per sample) using the DNK-EXTRAN-1 (Syntol, EX-509-100) kit. The DNA concentration was measured utilizing fluorescent double-stranded DNA selective Qubit dsDNA BR Assay Kit (Thermo Fisher, Q32853) on Qubit 2.0 Fluorometer (Thermo Fisher, Q32866).

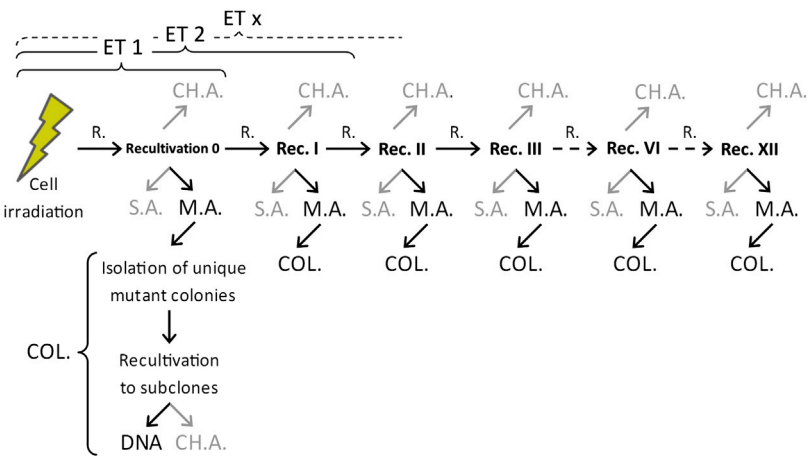

FIGURE 1 | Scheme of the general experimental procedure after irradiation. In gray–methods and assays not directly covered by this work. R, recultivation; ET, expression time; M.A., mutation assay (6-thioguanine); S.A., survival assay; COL, isolation of individual mutant colonies + cell multiplication for use in other assays; DNA, analysis of DNA (isolation, concentration measurements, PCR amplifications, gel electrophoresis analysis, and evaluation); CH.A, chromosome aberration assay.

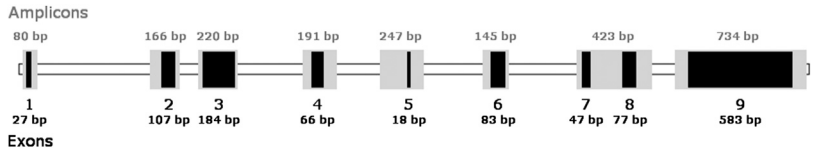

FIGURE 2 | Diagram of the HPRT gene in V79 Chinese hamster cells with its exons and amplicons used in this study.

Our structural analysis of the HPRT gene was based on the presence/absence of the exons. The HPRT gene consists of nine exons, and as a whole, it was sequenced by Rossiter et al. [36]. Each of the exons was amplified individually with the exception of exons 7 and 8 that are spatially close to each other and were amplified together as one amplicon. Schematic diagram of the exons, amplicons, and their sizes used in this work can be seen in **Figure 2**.

Used primers were based mainly on studies by Rossiter et al. [36] and Xu et al. [37] with the exception of the primers for exon 1 that were created *de novo* to comply with our PCR conditions. All the used primers for HPRT gene can be seen in **Table 2**, together with elongation factor two gene (EF) serving as control of the correctly performed PCR (all of the primers were assembled by the company Syntol). We used the approach where there is separate reaction for each exon (pair of primers). Each of the PCR tubes contained 40% of PCR mix (Syntol, M-439) with EVA Green intercalating fluorescent dye, each of the primers in concentration of 400 nM, DNA at 4 ng/μL of DNA, and deionized water up to the total volume of 25 μL.

PCR amplification was carried out in CFX96 Touch Real-Time PCR detection system (Bio-Rad, 1855195) with the usual five steps. Initial denaturation at 95°C for 180 s was followed by 35 cycles of annealing at 60°C for 45 s, elongation at 72°C for 30 s, and denaturation at 95°C for 20 s, with a final elongation at 72°C for 300 s. Afterward, a melting procedure was run; temperature was continually rising from 65 to 95°C in 0.4°C steps, with the "waiting time" of 5 s at each temperature point. Due to this approach, the fluorescent signal gives the information of presence/absence of the particular exon. Usually, this result was also confirmed on gel electrophoresis using 2% agarose gel (Helicon, AM-O710–0.5) dissolved in TAE buffer (Tris Acetate-EDTA buffer; 25x; PanEco, El040). Voltage was set to 5 V/cm of the distance between electrodes, and the power was turned on for 1 h at room temperature. The gel was stained with SYBR Safe (10,000x; Thermo Fisher, S33102) and documented on Gel Doc EZ (Bio-Rad, 170-8270).

Data Analysis

Our results, obtained by analyzing the samples for the presence or absence of the nine exons forming the HPRT gene, follow the Bernoulli distribution, where the variance can be calculated as

$$Var[X] = p \cdot q = p(1-p), \tag{1}$$

where p is the probability of samples having the deletion, and q is the probability of samples not having the deletion. Therefore, the standard error of the mean is

$$SE_X = \sqrt{\frac{p(1-p)}{n}}. \tag{2}$$

Important part of this article builds on our previous work [32]. Results from HPRT gene structural analysis are compared to the results of HPRT mutant induction with the same type of

TABLE 2 | Oligonucleotide primers for the HPRT gene exons used in this study.

Exon	Direction	Nucleotide sequence	Primer size, bp	Amplicon size, bp
1	+	GCC GAC CGA TTC CGT CAT	18	80
	–	CTG GCT GTC CGC TCT GC	17	
2	+	AGC TTA TGC TCT GAT TTG AAA TCA GCT G	28	166
	–	ATT AAG ATC TTA CTT ACC TGT CCA TAA TC	29	
3	+	CCG TGA TTT TAT TTT TGT AGG ACT GAA AG	29	220
	–	AAT GAA TTA TAC TTA CAC AGT AGC TCT TC	29	
4	+	GTG TAT TCA AGA ATA TGC ATG TAA ATG ATG	30	191
	–	CAA GTG AGT GAT TGA AAG CAC AGT TAC	27	
5	+	AAC ATA TGG GTC AAA TAT TCT TTC TAA TAG	30	247
	–	GGC TTA CCT ATA GTA TAC ACT AAG CTG	27	
6	+	TTA CCA CTT ACC ATT AAA TAC CTC TTT TC	29	145
	–	CTA CTT TAA AAT GGC ATA CAT ACC TTG C	28	
7 + 8	+	GTA ATA TTT TGT AAT TAA CAG CTT GCT GG	29	423
	–	TCA GTC TGG TCA AAT GAC GAG GTG C	25	
9	+	CAA TTC TCT AAT GTT GCT CTT ACC TCT C	28	734
	–	CAT GCA GAG TTC TAT AAG AGA CAG TCC	27	
EF	+	GAT CAT TCC CAC AGC TCG TC	20	321
	–	GAC ACT CAC CAA AGG ACT CG	20	

HPRT, hypoxanthine-guanine phosphoribosyltransferase.

radiation. Different levels of induced mutants are described by mutant fraction (MF) that can be calculated as

$$MF = \frac{\alpha_M}{\beta_M} \cdot S, \quad (3)$$

$$S = \frac{\alpha_S}{\beta_S}, \quad (4)$$

where α_M is the number of mutant colonies counted during mutation assay, β_M is the number of cells seeded for the mutation assay, S is the cloning efficiency, α_S is the number of colonies counted during survival assay, and β_S is the number of cells seeded for the survival assay.

Calculations, mathematical operations, and data plotting were performed on the data in Microsoft Office 365 Excel and in SigmaPlot (v. 12.5, Sysat Software, Inc.).

RESULTS

Induced Deletions in Dependence on Linear Energy Transfer of the Used Radiations

In the course of our experiments, DNA of over 1,200 unique HPRT mutants (irradiation induced and spontaneous) originating in a single cell was isolated and analyzed for HPRT gene exon deletions. Three main categories were distinguished (in accordance with the usual methodology): partial deletion, PD—with deletion of one to eight exons; total deletions, TD—with all nine exons deleted; and no deletions—no change in the HPRT structure observed.

Figure 3A shows a summarizing graph of all the samples analyzed with any deletion (partial or total) in relation to the ionizing radiation (IR) used for induction of mutations (error bars represent standard error of the mean of Bernoulli distribution). In order to see the general effect of used radiation, the doses and time points investigated, for a particular radiation, were averaged. The IR are ordered by increasing LET—from 0.23 keV/μm of gamma radiation [38] up to 136 keV/μm of Ne ions (details in **Table 1**). All of the radiation-induced mutants contained higher number of observable larger deletions than in the case of spontaneous mutants (SM; 10 ± 3.1%). It can be seen that, in general, the higher the LET, the higher the number of deletions (see also **Table 3**).

Figure 3B shows increase in the number of partial deletions with increasing LET of the incident radiation. Highest value, 36.3 ± 3.14%, was reached after irradiation with neon ions (LET ~136 keV/μm), which is about eight times higher than that at SM (4.4 ± 2.1%). Analysis of the total deletions, where the whole HPRT gene was missing, shows a surprising phenomenon: increase in the number of total deletions with LET was observed up to oxygen ions (LET ~115 keV/μm) followed by a sharp decrease at ^{20}Ne ions (**Figure 3C**). The number of total deletions after irradiation with neon was extraordinarily low—only 4 out of 234 samples (1.7 ± 0.85%) had all the exons missing, which is lower than that at spontaneous mutants with 5.5 ± 2.4% of total deletions.

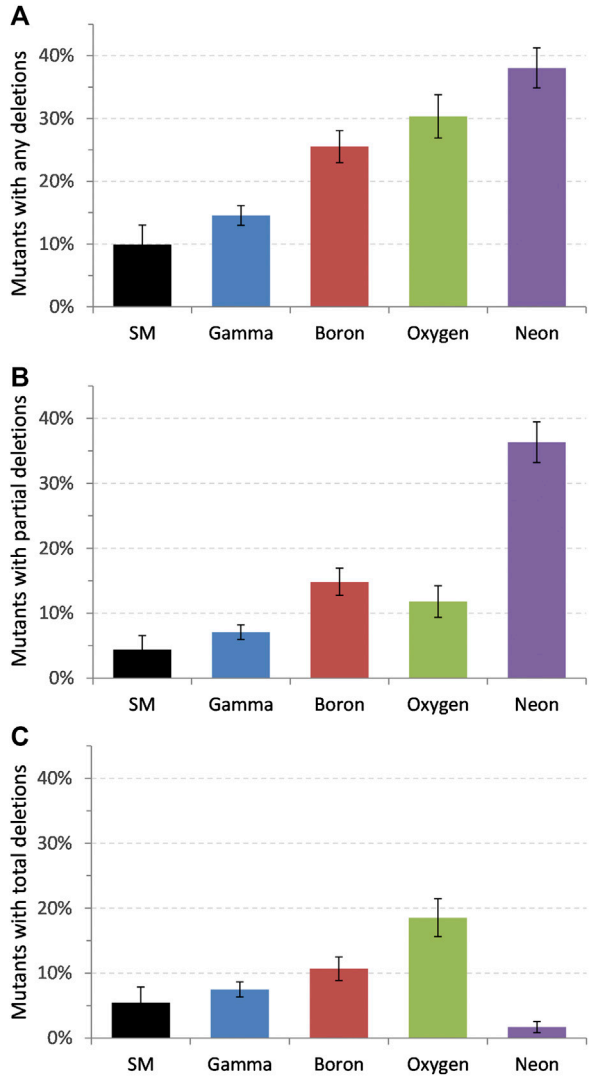

FIGURE 3 | Distribution of deletions in HPRT gene for all samples (average of all the doses and time points assayed). **(A)** All deletions scored, **(B)** partial deletions, and **(C)** total deletions; SM, spontaneous mutants. Error bars represent standard error of the mean.

Deletions in Dependence on Expression Time

The mutant subclones for structural analysis of HPRT gene were collected in various times after irradiation (up to about 40 days since exposure) to see how the composition of deletions is changing during normal recultivation. No clear dependence on dose was observed, and the data points in **Figure 4** represent the average of doses used with the specific type of radiation (details in **Table 1**). The gamma-irradiated samples (508 analyzed samples) for structural analysis were taken in the interval of expression times: 3–39 days. It can be seen in **Figure 4A** that the maximum of total deletions is reached soon after irradiation (about 6 days) followed by continuous decrease to the levels of spontaneous mutants. On the other hand, partial deletions are at their maximum cca 22 days after exposure

TABLE 3 | Results of the HPRT gene structural analysis.

Radiation type	Avg. LET, keV/μm	Number of samples	# Partial del	%	# Total del	%	# All del	%	# No del	%
SM	N/A	91	4	4,4	5	5,5	9	9,9	82	90,1
γ (^{60}Co)	0.23[a]	508	36	7,1	38	7,5	74	14,6	434	85,4
^{11}B	49	290	43	14,8	31	10,7	74	25,5	216	74,5
^{18}O	115	178	21	11,8	33	18,5	54	30,3	124	69,7
^{20}Ne	136	234	85	36,3	4	1,7	89	38,0	145	62,0

[a]*Estimated [38].*

SM, spontaneous mutants; N/A, not applicable; HPRT, hypoxanthine-guanine phosphoribosyltransferase.

and are only coming close to the background levels after around 40 days of cultivation. The data were also compared to our previous results focusing on the induction of mutations [32]. The mutant fraction (MF) is the ratio of the number of counted mutant colonies and the number of cells seeded, normalized to their cloning efficiency (details in Chapter: Data Analysis). **Figure 4A** shows this comparison of the averaged mutant fraction (MF) induced by gamma radiation at similar ET as in the case of the analysis of deletions. MF is monotonously declining from its maximum at the beginning, reaching SM levels around 20 days after. The survival of cells (their cloning efficiency) was measured at prolonged expression times as well (every time when the cells were assayed for mutations in HPRT gene) in order to correctly estimate the MF. In general, the spread in cloning efficiency was found to be about 20–30%, which is fairly typical for clonogenic measurements in V79 cell culture, without any obvious dependence on dose or time after irradiation.

Partial deletions induced by boron ions (LET ~49 keV/μm; 290 samples collected between 4 and 40 days after exposure), **Figure 4B**, are at their maximum in the first days after irradiation (4–7 days) with consequent decrease around 13 days, followed by second, local, maximum around 22 days after exposure before reaching the spontaneous mutants level at around 40 days. Initial rise in the number of TD is followed by decrease around 13–15 days after irradiation to the levels similar to SM. The MF is falling down continuously from its maximum shortly after irradiation, reaching background levels around 20–25 days postexposure and staying at this level.

In a tentative experiment with accelerated oxygen ions (178 samples), **Figure 4C**, around 72% of samples were isolated at the first time point after irradiation (5 days); therefore, the results from prolonged recultivation times have mainly informative character. The number of total deletions seems to be increasing toward 17 days since exposure, while PD stays at similar, slightly elevated, level. The estimated average of MF is peaking somewhere around 11 days after irradiation.

Extremely low levels of total deletions were observed during the whole observed period, between 4 and 38 days, after irradiation with neon ions, **Figure 4D**. Only 1.7% samples (4 out of 234) contained TD. On the other hand, partial deletions reached high levels (~50%) within 9 days and remained there for approximately 8 days before decreasing. The average of PD stayed above the SM background even 38 days after irradiation.

Mutational Patterns

Mutational spectra of spontaneous as well as ionizing radiation-induced mutants (doses and time points pooled together) are depicted in **Figure 5**. Results of all SM samples (from all the experiments) show similar percentage of the particular missing exons from all the samples analyzed (between 5 and 9% of all the samples). Similar, uniform, distribution is found also at gamma-induced mutants; however, the absolute levels are higher ~11–12%. Different character can be found after irradiation with boron and neon ions where particular exons exhibit significantly increased levels: exons 9 and 1 + 2 for ^{11}B and ^{20}Ne, respectively. Slightly elevated levels can be also seen after irradiation with oxygen ions at the first four exons.

Closer look at the specific mutant deletions induced by 2 Gy of boron and neon ions, **Figure 6**, reveals a general trend: after an initial increase in the number of mutants with the aforementioned distinctive deletions, their number decreases (with the exception in the case of boron irradiation at 24 days where the number of mutants increases before decreasing again; it will need to be investigated if it is an example of non-monotonic dependence or an outlying value). Around 40 days after irradiation, the mutants with missing exons 1 and 2, in the case of neon irradiation, are almost completely mitigated. In mutants induced by boron ions, the number of samples with missing exon 9 is still around 15% after about 40 days.

Non-contiguous Deletions

In the course of all the experiments, low number of noncontiguous deletions (NCD) was found—deletion of separate exons with a non-changed DNA between them [20, 28]. Their number is increasing with the LET of used radiation with the exception in irradiation with neon ions, **Table 4**; however, the number stays very low. Therefore, these results have so far been considered preliminary. No noncontiguous deletions were observed at spontaneous mutants.

DISCUSSION

The number of deletions (both partial and total deletions added together = larger structural deletions) was increasing with increasing LET of the incident ionizing radiation, **Figure 3A**. It suggests that higher density of energy depostion in the cell

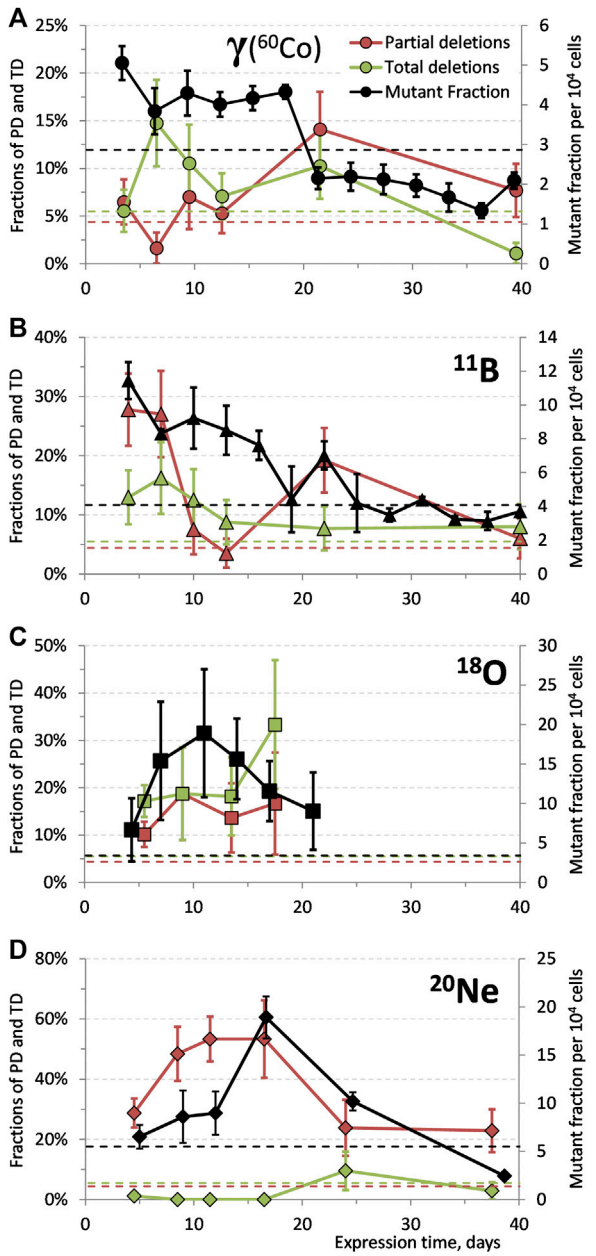

FIGURE 4 | Dependences of fractions of partial and total deletions (average of used doses), and mutant fraction on expression time for HPRT mutants induced by **(A)** gamma radiation (^{60}Co), **(B)** ^{11}B ions, **(C)** ^{18}O ions, and **(D)** ^{20}Ne ions. Dashed horizontal lines represent levels of spontaneous mutants: red line, partial deletions; green line, total deletions; black line, mutant fraction. The data points were connected to guide the eye. Data for mutant fraction were taken from our previous work [32]. Error bars represent standard error of the mean.

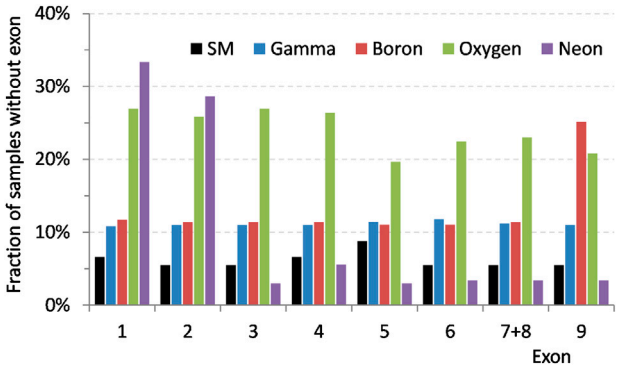

FIGURE 5 | Mutational spectra of HPRT spontaneous and ionizing radiation-induced mutants (doses and time points pooled together for each particular radiation) showing percentages of all the samples with particular missing exon.

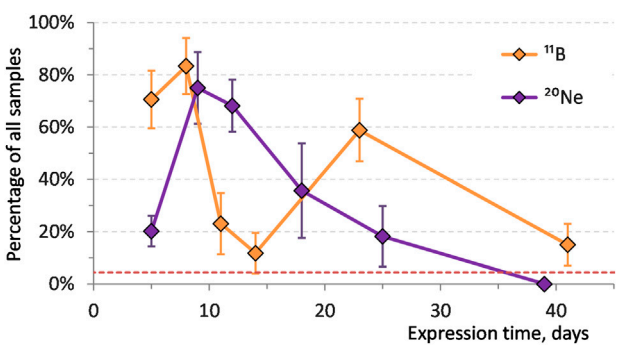

FIGURE 6 | Distributions of the characteristic exons missing in HPRT mutants on expression time after irradiation by 2 Gy of ^{11}B ions—exon 9 deletions and ^{20}Ne ions—exons 1 and 2 deletions. Red dashed line represents partial deletions level of spontaneous mutants. Error bars represent standard error of the mean.

nucleus is more likely to cause larger structural changes. The rest of the mutants (e.g., 90% for spontaneous mutants) contained mutations not detectable by our technique, likely point or very small deletions. Another explanation is the breakage within the intron region of HPRT gene and translocation of exon/s [20, 39], which would be also amplified correctly on PCR.

Similar growing trend can be seen also in the case of partial deletions, **Figure 3B**. It is worth mentioning that many different results are reported in the literature. For example, Suzuki et al. observed decrease in the number of partial deletions with increasing LET of C-ion beams (39–230 keV/μm) in the human embryonic fibroblast-like cells [29], but in the case of Ne-ion beams (63–335 keV/μm), the number of mutants with partial deletions stayed practically the same [21]. Our findings coincide with the observations of Jostes et al. (X-rays and alpha particles of ^{222}Rn and its decay products) [30], Bao et al. (same as Jostes et al.) [26], or Baumstark-Khan et al. [8] who, as one of the few, actually studied the effects of accelerated heavy ions instead of alpha particles. Baumstark-Khan et al. observed increase in the number of PD with LET up to 250–300 keV/μm of oxygen ions followed by decrease with even higher LET.

The distribution of total deletions reveals significantly different character of dependence: a non-monotonic progression with maximum at 115 keV/μm (^{18}O), **Figure 3C**. Radiation with the highest LET (^{20}Ne) causes the lowest number

TABLE 4 | Noncontiguous deletions.

	LET, keV/μm	Number of samples	Number of NCD	% NCD
Spontaneous mutants	0	91	0	0,0
Gamma (^{60}Co)	0.23[a]	508	1	0,2
Boron	49	290	2	0,7
Oxygen	115	178	5	2,8
Neon	136	234	1	0,4

[a]*Estimated [38].*
NCD, noncontiguous deletion.

of total deletions. Minimum (or in fact zero) total deletions were reported with a high LET radiation several times. Suzuki et al. observed the number of total deletions to decrease after irradiation with Ne-ion beams from 65% down to 30% at LET ~63 and 335 keV/μm, respectively [21], and also to fall to 0% after exposure to C-ion beams (LET ~230 keV/μm) [29]. Similar results were reached also in the case of Ni ions [5]. The most likely explanation of such phenomenon lies in the different energy deposition by different ion species due to the largely different track structure as suggested by other authors as well [8, 21, 25, 29]. Plausible hypothesis is that large clusters of energy from high LET radiations absorbed by DNA are causing large-scale deletions, making the cells more prone to cell death [12]. Only the created, secondary, lower LET electrons would be responsible for the induction of mutations [29], which could be a part of the explanation why we see high number of PD, but almost no TD after irradiation with high LET neon ions. Moreover, the high energetic high LET radiation may induce deletions not only in the HPRT gene but also in other vital genes necessary for survival [11]. As a result, the cell would be either dead or in serious proliferation disadvantage, not capable of reproduction and creation of mutant colony and therefore would not be observed, isolated, and analyzed. The effect of radiation of different LET on clonogenic survival immediately after irradiation was found as expected (e.g., refs. 13 and 40)—decreasing survival with increasing LET of radiation. Nevertheless, direct mechanism behind this is not known and needs to be studied further.

To the authors' knowledge, no studies have directly focused on the effects of **expression time** on the mutation spectra in HPRT mutants induced by different types of radiation. We have studied the structural alterations in the HPRT gene in prolonged times after exposure together with induction of mutations. The observations were made up to approximately 70–80 cell generations after irradiation. We did not observe a clear general dependence on dose in the applied dose intervals (see **Table 1**), with a few special cases which will be mentioned. Therefore, for comprehensible comparison and in accordance with other authors [8, 21, 29], results from all the doses used were averaged.

In the case of gamma radiation **Figure 4A**, one of the aforementioned special cases of dose effect was observed at samples irradiated with 7 Gy that lead to the highest addition to the number of total deletions. No clear correlation of TD to dose for the lower doses used and no obvious dose dependence in the case of partial deletions were observed. It indicates that after irradiation with sparsely ionizing radiation, there has to be multiple hits within the studied region in order to cause larger deletions, and with increasing dose, the chance for multiple hits increases. This is possibly due to the repair processes and DSB mis-rejoining. Similar to us, Park et al. observed increase in the number of TD (from 21 to 39%) with dose (1–4 Gy) after gamma irradiation (^{60}Co) in primary human skin fibroblasts [22], or Schwartz et al. (from 11 to 39%) who irradiated CHO-K1 cells with gamma rays of ^{137}Cs with doses 0.5–6 Gy [41]. Other authors saw only negligible difference in the number of TD or PD with increasing dose after low LET irradiation [8, 11, 14]. The total deletions reach their maximum in about 7 days after irradiation—there is some time needed for them to be "expressed." After 40 days since irradiation, the number of TD has fallen down under the level of deletions typical for spontaneous mutants. Mutant fraction follows similar trend with the main difference that the background level is reached already in about 20 days post-exposure. It seems that mutants with the gamma-induced TD are struggling during proliferation and are overgrown by healthy cells. The maximum of PD reached at about 20 days indicates the complexity of the mechanism of creation and genetic stability of deletions.

After irradiation with boron ions, we witnessed very surprising situation. The dose of 0.5 Gy did not induce any structural mutations at any of the times after irradiation. We tested a significant number of samples (101), analyzed in the same manner as all the rest of the radiation-induced mutant subclones, but we did not see a single deletion. In fact, this irradiation with the lowest tested dose of ^{11}B ions (LET ~49 keV/μm) caused disappearance of partial and total deletions that are normally present in the spontaneous mutants (around 10% of all deletions). At the moment, we have no explanation why this type of exposure should lead to lesser number of exon deletions than SM—this phenomenon needs to be investigated further. Some similarities can be found between the progression of TD and MF induced by boron ions (**Figure 4B**): maximum of both dependencies is close to the beginning of observations, followed by a decrease with time, and reaching plateau around 15 and 20 days for TD and MF, respectively. For the rest of the observed time period, both values stay in proximity of the SM level. A highly non-monotonic course of dependences obtained after irradiation with oxygen ions, and the lack of data in prolonged ET, did not allow an objective evaluation of these relations, **Figure 4C**. In the case of neon ions (**Figure 4D**), the PD levels, to certain degree, correlate with the MF levels—after the maximum at

17 days post-exposure, both values fall down to the vicinity of spontaneous mutants. In this case, PD significantly predominates over TD. These dependences, **Figures 4A–D**, show the importance of studying the structural changes in different times after irradiation. If only one time after irradiation is chosen, some potential information might be lost and incorrect results drawn.

It seems that the mutant fraction dependence on ET possibly approximately correlates with the total deletion dependence in case of gamma rays (^{60}Co; LET ~0.23 keV/μm) and with the partial deletion dependence of ^{20}Ne ions (LET ~136 keV/μm). This difference in trends suggests a presence of LET threshold (perhaps, there can be found a weak correlation between MF and both PD and TD after boron ions with "intermediate" LET of 49 keV/μm). This threshold would then relate to the different types of ion beams used for irradiation and the tracks created by them in the cell nuclei. There are differences in energies (possibly connected to the induction and range of delta electrons), track core and penumbra sizes [42], and differences in energy deposition in general that can lead to clustering of number of damaged sites in a small volume of DNA [12]. Signs of similar threshold were also seen in our previous work [32] when studying LET dependence of the mutant fraction maximum position. Significant increase in the expression time of the MF maximum was observed at cells irradiated with very high LET radiations (e.g., neon ions), not after exposure to sparsely ionizing radiation. This may point to another piece of evidence of the different mechanism of action of sparsely ionizing and densely ionizing radiations.

It is possible to theorize that the emergence of TD maximum could be a consequence of the increased number of mutations (higher MF), the TD maximum seems to appear after the MF maximum. One of the hypothetical explanations could be that the increased number of TD reflects the cell repair mechanisms and processes needed to cope with high number of mutations, and one of them could be the complete excision of the HPRT gene. The potential logic behind it would be that completely missing HPRT gene would not trigger the salvage pathway processes for purine synthesis. In this manner, the cell would not waste any energy and resources on non-working (or only half-working) gene, and constructed the purines *de novo* which would be, in this case, beneficial, as hypothesized also by Krasavin et al. [43]. Govorun et al. speculated that similar process could lead to a decrease in chromosomal instability with an increase of LET [44]. However, the total HPRT gene deletions can be parts of much larger deletions [11] affecting other, possibly vital, genes as well, so the mechanisms might, and probably will, be more complex.

Subclones with total deletions of HPRT gene are being removed with time after irradiation, with the exception at the very beginning, while the mutations are still being formed. This trend can probably be branded as general (found after irradiation with all of the radiations used); the fraction of mutants with total deletions is decreasing with increasing time since exposure and achieving levels typical for SM. It is plausible that a proliferating disadvantage of cells without HPRT exon plays an important role here, and the cells with total deletions are slowly overgrown by other cells.

Our results show the possible long-term effects of radiation. As mentioned in the paragraph above, total deletions have fallen to the SM levels within our observation period. This is mostly true also for partial deletions with the exception in the case of ^{20}Ne-induced mutants (radiation with the highest LET used ~136 keV/μm), where the levels of PD stayed elevated even 38 days after irradiation. This points to the radiobiological uncertainties of high LET radiations. Translation of *in vitro* results to higher organisms (or humans) is, of course, difficult, but it shows the necessity to continue in the research of radiobiological effects of HZE ions that can be meaningful for future space travel as well as heavy ion radiation therapy.

Several studies confirmed that ionizing radiation may induce point as well as deleterious mutations in radiation-induced HPRT mutants [11, 23, 45]. As it has been shown, the type and quantity of structural changes depends on the used radiation type and its parameters as well as on time after irradiation, **Figures 3**, **4**. Study of the particular exons deleted shows that in case of spontaneous mutants, deletion patterns were stable across all the experiments and times of cultivation tested. Similar spectra of spontaneous mutants—mostly no large deletions or distinctive patterns—were observed by other authors as well [8, 11, 22, 24, 46]. However, conflicting reports regarding the SM can be found-some studies observed higher levels of partial [25, 47] or total deletions [26]; for example, Kiefer et al. [39] show that in their case, the mutational spectra of spontaneous mutants were changing from experiment to experiment (total deletions ranging from 4 up to 52%).

The characteristic mutational spectra of boron and neon ions, in contrast to uniform spectra of SM or gamma radiation, indicate, once again, a varied interaction of ionizing radiation of different quality, **Figure 5**. It might be explained by the different mechanisms of action of sparsely ionizing radiation, where gamma radiation transfers energy in many rather low-energetic events, while heavy ions create a few highly ionized tracks through the cell nucleus. Therefore, the damage by gamma rays will likely be more homogeneous than that by the HZE ions—fluence of the used gamma radiation (^{60}Co) is two and three orders of magnitude higher than in the case of boron and neon ions, respectively (**Table 1**). This way, it might be possible for the heavy ions to cause heterogenous damage only in part of the genome. This effect seems to be dependent on the density of ionizations induced by the different types of ionizing radiation [11]. The typical deletion in the exon 9 after boron irradiation was produced almost solely by the dose of 2 Gy. In the case of neon ions, the distinctive spectrum (missing exons 1 and 2) was observed after both doses 0.5 and 2 Gy (to higher extent for the higher dose). As seen also for other endpoints (such as cell killing and induction of mutations), LET is not the sole parameter governing the final radiation effect [4, 13, 48] and the differences in track structure of high energetic particles may considerably affect the quality of mutations [8]. Except for our data supporting this hypothesis, the difference in mutation spectra based on the type of radiation used was documented by other authors as well: for carbon and neon ions of similar LET values [21, 28]. Radiations with high LET deposit large amount of energy in a

small volume of DNA creating clusters of locally highly damaged DNA [12]; combination of such cluster damage and spatial distribution of the observed genetic material can substantially influence the mutational patterns. Moreover, strand breaks may occur not only as a consequence of direct IR damage, but also due to repair processes that are started as a result of a base change or damage [39, 49]; therefore, the mutational spectra may vary depending on the prevailing repair mechanism as well. So far, oxygen irradiation remains an open question from this point of view, where the orientation spectrum is relatively constant. This will need to be verified by further experiments.

The elimination of specific structural deletions with time, **Figure 6**, and the fact that both doses of high LET radiation (^{20}Ne) caused the same type of deletion suggest that the mutants containing them are not duplicating at the same rate as healthy cells and also that the mutations are not clonally replicating. These results support the hypothesis in our previous article, stating that the delayed mutations are being created *de novo* due to sublethal damage caused by radiation and as manifestation of radiation-induced genomic instability. Even though we cannot reject the possibility of distribution of some of the mutations by cloning during normal cell replication, our results advocate that it should not be the reason for delayed maxima of mutant fraction as observed after high LET irradiation [32].

Noncontiguous deletions were found in all radiation-induced mutants. In general, their numbers were low—maximum of 2,8% in the case of irradiation with oxygen ions, **Table 4**. It has been mentioned that this type of deletions is also not induced by sparsely ionizing radiation (e.g., X-ray or gamma rays) [20, 21, 39]. We were able to detect one mutant with such a pattern after ^{60}Co irradiation; however, the sample size was 508 gamma samples, which represents approximately 0.2%. It is therefore possible to find this type of deletion even after gamma irradiation, but the chances are at the level of error in measurement. Some authors consider the noncontiguous deletions as signature of high LET radiations [20, 39]. Due to the extremely low occurrence (even after HZE ion irradiation), and due to the fact that some studies did not observe any NCDs (e.g., 11), we do not consider the noncontiguous deletions as an usable tool for recognizing exposure to densely ionizing radiations.

CONCLUSION

It was shown that the fraction of exon partial deletions in HPRT gene was increasing with LET of the used radiation in the tested range from 0.23 keV/μm of gamma radiation to 136 keV/μm of ^{20}Ne ions. Similarly, the total deletions were increasing with LET, with the exception at the highest LET radiation. It was suggested that total deletions are possibly the consequence of increased number of mutations and/or repair processes that are taking place at the same time. The number of mutants with TD is generally decreasing with expression time, reaching levels typical for SM maximally in about 30 days in all experiments—possibly due to their proliferative disadvantage. It has been shown how the proportions of deletions are changing in time after irradiation. This time dependence must be kept in mind if observed only in a single time point. Correlation between the MF dependence on ET and TD was found for sparsely ionizing radiation, while in the case of high LET neon ions, the MF correlated with PD. Distinctive mutational patterns were created by high LET radiations, contrary to sparsely ionizing radiation. We hypothesize that these LET effects are linked with differences in the tracks created by heavy ions and the spatial energy deposition within them. This could, as consequence, induce clustered DNA damage with various degrees of complexity. Lesions with different complexity may be repaired with different efficiency and also by different repair processes. Future research will be necessary to clarify the exact mechanisms behind the observed phenomena. It would be fruitful to test various heavy ions (in a wide interval of doses) and up to higher LET values.

DATA AVAILABILITY STATEMENT

The raw data supporting the conclusions of this article will be made available by the authors, without undue reservation.

AUTHOR CONTRIBUTIONS

IK, PB, NK, and RG designed the project. PB, IK, NK, YB, and DP were part of the team conducting experiments and preparing samples. IK and VM supervised the project. PB processed samples, analyzed data, and drafted the manuscript. PB, IK, NK, VM, and EK participated in the discussion and revision of the manuscript. All authors participated in the discussion of the data obtained. All authors read and approved the final manuscript.

FUNDING

This work has been carried out in the framework of financial topic 04-9-1077-2009/2023 JINR and supported by the grants of the Representative of the Czech Republic in the Committee of Plenipotentiaries of JINR and by the projects solved in cooperation between the Czech Republic and the JINR. This work has been cofunded by the project of Ministry of Education Youth and Sports, Czech Republic, project "Center for advanced applied science," no. CZ.02.1.01/0.0/0.0/16_019/0000778.

ACKNOWLEDGMENTS

The authors thank Yu. G. Teterev and A. A. Bezbakh of the Flerov Laboratory of Nuclear Reactions (JINR), and G. N. Timoshenko and V. A. Krylov of the Laboratory of Radiation Biology (JINR) for their help with irradiation of our samples with accelerated heavy ions using the U400M cyclotron and V. N. Gaevsky of the Dzhelepov Laboratory of Nuclear Problems (JINR) for gamma irradiation at the Rokus-M unit.

REFERENCES

1. Simpson JA. Elemental and isotopic composition of the galactic cosmic rays. *Annu Rev Nucl Part Sci* (1983) 33:323–82. doi:10.1146/annurev.ns.33.120183.001543
2. Ebner DK, Kamada T. The emerging role of carbon-ion radiotherapy. *Front Oncol* (2016) 6:6–11. doi:10.3389/fonc.2016.00140
3. Jermann M. Particle therapy statistics in 2014. *Int J Part Ther* (2015) 2:50–4. doi:10.14338/IJPT-15-00013
4. Stoll U, Barth B, Scheerer N, Schneider E, Kiefer J. HPRT mutations in V79 Chinese hamster cells induced by accelerated Ni, Au and Pb ions. *Int J Radiat Biol* (1996) 70:15–22. doi:10.1080/095530096145283
5. Kiefer J. Mutagenic effects of heavy charged particles. *J Radiat Res* (2002) 43:S21–S25. doi:10.1269/jrr.43.S21
6. Suzuki K, Ojima M, Kodama S, Watanabe M. Radiation-induced DNA damage and delayed induced genomic instability. *Oncogene* (2003) 22:6988–93. doi:10.1038/sj.onc.1206881
7. Smith LE, Nagar S, Kim GJ, Morgan WF. Radiation-induced genomic instability: radiation quality and dose response. *Health Phys* (2003) 85:23–9. doi:10.1097/00004032-200307000-00006
8. Baumstark-Khan C, Rosendahl IM, Rink H. On the quality of mutations in mammalian cells induced by high LET radiations. *Adv Space Res* (2007) 40:474–82. doi:10.1016/j.asr.2006.11.034
9. Allen CP, Hirakawa H, Nakajima NI, Moore S, Nie J, Sharma N, et al. Low- and high-LET ionizing radiation induces delayed homologous recombination that persists for two weeks before resolving. *Radiat Res* (2017) 188:82. doi:10.1667/RR14748.1
10. Thacker J, Stephens MA, Stretch A. Factors affecting the efficiency of purine analogues as selective agents for mutants of mammalian cells induced by ionising radiation. *Mutat Res* (1976) 35:465–78. doi:10.1016/0027-5107(76)90208-6
11. Rothkamm K, Gunasekara K, Warda SA, Krempler A, Löbrich M. Radiation-induced HPRT mutations resulting from misrejoined DNA double-strand breaks. *Radiat Res* (2008) 169:639–48. doi:10.1667/RR1185.1
12. Rosendahl IM, Baumstark-Khan C, Rink H. Mutation induction in mammalian cells by accelerated heavy ions. *Adv Space Res* (2005) 36:1701–9. doi:10.1016/j.asr.2005.03.067
13. Sørensen BS, Overgaard J, Bassler N. *In vitro* RBE-LET dependence for multiple particle types. *Acta Oncol* (2011) 50:757–62. doi:10.3109/0284186X.2011.582518
14. Little JB, Nagasawa H, Pfenning T, Vetrovs H. Radiation-induced genomic instability: delayed mutagenic and cytogenetic effects of X rays and alpha particles. *Radiat Res* (1997) 148:299–307. doi:10.2307/3579514
15. Stoll U, Schmidt A, Schneider E, Kiefer J. Killing and mutation of Chinese hamster V79 cells exposed to accelerated oxygen and neon ions. *Radiat Res* (1995) 142:288. doi:10.2307/3579138
16. Kumar PRV, Mohankumar MN, Hamza VZ, Jeevanram RK. Dose-rate effect on the induction of HPRT mutants in human G 0 lymphocytes exposed in vitro to gamma radiation. *Radiat Res* (2006) 165:43–50. doi:10.1667/RR-3467.1
17. Goodhead DT. Mechanisms for the biological effectiveness of high-LET radiations. *J Radiat Res* (1999) 40:1–13. doi:10.1269/jrr.40.S1
18. Nickoloff JA, Sharma N, Taylor L. Clustered DNA double-strand breaks: biological effects and relevance to cancer radiotherapy. *Genes* (2020) 11:99. doi:10.3390/genes11010099
19. Schwartz JL, Rotmensch J, Sun J, An J, Xu Z, Yu Y, et al. Multiplex polymerase chain reaction-based deletion analysis of spontaneous, gamma ray- and alpha-induced hprt mutants of CHO-K1 cells. *Mutagenesis* (1994) 9:537–40. doi:10.1093/mutage/9.6.537
20. Schmidt P, Kiefer J. Deletion-pattern analysis of α-particle and X-ray induced mutations at the HPRT locus of V79 Chinese hamster cells. *Mutat Res* (1998) 421:149–61. doi:10.1016/S0027-5107(98)00159-6
21. Suzuki M, Tsuruoka C, Kanai T, Kato T, Yatagai F, Watanabe M. Cellular and molecular effects for mutation induction in normal human cells irradiated with accelerated neon ions. *Mutat Res* (2006) 594:86–92. doi:10.1016/j.mrfmmm.2005.08.007
22. Park MS, Hanks T, Jaberaboansari A, Chen DJ. Molecular analysis of gamma-ray-induced mutations at the hprt locus in primary human skin fibroblasts by multiplex polymerase chain reaction. *Radiat Res* (1995) 141:11. doi:10.2307/3579084
23. Colussi N, van Leeuwen X, Lohman PH. Similar mutational spectra in the HPRT gene of human and hamster cell lines after exposure to either low dose rate or high dose rate X-rays. *Mutat Res* (1998) 401:89–97. doi:10.1016/S0027-5107(97)00318-7
24. Aghamohammadi SZ, Morris T, Stevens DL, Thacker J. Rapid screening for deletion mutations in the hprt gene using the polymerase chain reaction: X-ray and α-particle mutant spectra. *Mutat Res* (1992) 269:1–7. doi:10.1016/0027-5107(92)90155-U
25. Zhu LX, Waldren CA, Vannais D, Hei TK. Cellular and molecular analysis of mutagenesis induced by charged particles of defined linear energy transfer. *Radiat Res* (1996) 145:251. doi:10.2307/3578979
26. Bao C-Y, Ma A-H, Evans HH, Horng MF, Mencl J, Hui TE, et al. Molecular analysis of hypoxanthine phosphoribosyltransferase gene deletions induced by α- and X-radiation in human lymphoblastoid cells. *Mutat Res* (1995) 326:1–15. doi:10.1016/0027-5107(94)00152-U
27. Stoll U, Schneider E, Kranert T, Kiefer J. Induction of HPRT- mutants in Chinese hamster V79 cells after heavy ion exposure. *Radiat Environ Biophys* (1995) 34:91–4. doi:10.1007/BF01275212
28. Kagawa Y. Complex hprt deletion events are recovered after exposure of human lymphoblastoid cells to high-LET carbon and neon ion beams. *Mutagenesis* (1999) 14:199–205. doi:10.1093/mutage/14.2.199
29. Suzuki M, Watanabe M, Kanai T, Kase Y, Yatagai F, Kato T, et al. Let dependence of cell death, mutation induction and chromatin damage in human cells irradiated with accelerated carbon ions. *Adv Space Res* (1996) 18:127–36. doi:10.1016/0273-1177(95)00799-K
30. Jostes RF, Fleck EW, Morgan TL, Stiegler GL, Cross FT. Southern blot and polymerase chain reaction exon analyses of HPRT - mutations induced by radon and radon progeny. *Radiat Res* (1994) 137:371. doi:10.2307/3578712
31. Thacker J. The nature of mutants induced by ionising radiation in cultured hamster cells III. Molecular characterization of HPRT-deficient mutants induced by γ-rays or α-particles showing that the majority have deletions of all or part of the hprt gene. *Mutat Res* (1986) 160:267–75. doi:10.1016/0027-5107(86)90137-5
32. Bláha P, Koshlan NA, Koshlan IV, Petrova DV, Bogdanova YV, Govorun RD, et al. Delayed effects of accelerated heavy ions on the induction of HPRT mutations in V79 hamster cells. *Mutat Res* (2017) 803–805:35–41. doi:10.1016/j.mrfmmm.2017.08.004
33. Bezbakh AA, Zager VB, Kaminski G, Krylov AI, Krylov VA, Teterev YG, et al. Upgrading the genome facility for radiobiological experiments with heavy-ion beams. *Phys Part Nucl Lett* (2013) 10:175–8. doi:10.1134/S1547477113020039
34. Tarasov OB, Bazin D. LISE++: radioactive beam production with in-flight separators. *Nucl Instrum Methods Phys Res Sect B Beam Interact Mater Atoms* (2008) 266:4657–64. doi:10.1016/j.nimb.2008.05.110
35. Ziegler JF, Ziegler MD, Biersack JP. Srim–the stopping and range of ions in matter (2010). *Nucl Instrum Methods Phys Res Sect B Beam Interact Mater Atoms* (2010) 268:1818–23. doi:10.1016/j.nimb.2010.02.091
36. Rossiter BJF, Fuscoe JC, Muzny DM, Fox M, Caskey CT. The Chinese hamster HPRT gene: restriction map, sequence analysis, and multiplex PCR deletion screen. *Genomics* (1991) 9:247–56. doi:10.1016/0888-7543(91)90249-E
37. Xu Z, Yu Y, Gibbs RA, Thomas Caskey C, Hsie AW. Multiplex DNA amplification and solid-phase direct sequencing for mutation analysis at the hprt locus in Chinese hamster cells. *Mutat Res* (1993) 288:237–48. doi:10.1016/0027-5107(93)90090-3
38. Linear ICRU. Energy transfer journal of the international commission on radiation units and measurements (1970). Report 16. Available from: https://doi.org/10.1093/jicru/os9.1.Report16 (Accessed April 27, 2016).
39. Kiefer J, Schreiber A, Gutermuth F, Koch S, Schmidt P. Mutation induction by different types of radiation at the Hprt locus. *Mutat Res* (1999) 431:429–48. doi:10.1016/S0027-5107(99)00184-0
40. Barendsen GW. The relationships between RBE and LET for different types of lethal damage in mammalian cells: biophysical and molecular mechanisms. *Radiat Res* (1994) 139:257. doi:10.2307/3578823

41. Schwartz JL, Jordan R, Sun J, Ma H, Hsieb a W. Dose-dependent changes in the spectrum of mutations induced by ionizing radiation. *Radiat Res* (2000) 153: 312–7. doi:10.1667/0033-7587(2000)153[0312:DDCITS]2.0.CO;2
42. Chatterjee A, Schaefer HJ. Microdosimetric structure of heavy ion tracks in tissue. *Radiat Environ Biophys* (1976) 13:215–27. doi:10.1007/BF01330766
43. Krasavin EA, Govorun RD, Shmakova NL, Koshlan IV, Nasonova EA, Repin MV. Genetical action of radiation with different physical characteristics on human and mammalian cells. *Phys Part Nucl* (2004) 35:1483–515
44. Govorun RD, Koshlan IV, Koshlan NA, Krasavin EA, Shmakova NL. Chromosome instability of HPRT-mutant subclones induced by ionising radiation of various LET. *Adv Space Res* (2002) 30:885–90. doi:10.1016/S0273-1177(02)00407-6
45. Fuscoe JC, Zimmerman LJ, Fekete A, Setzer RW, Rossiter BJF. Analysis of X-ray-induced HPRT mutations in CHO cells: insertion and deletions. *Mutat Res* (1992) 269:171–83. doi:10.1016/0027-5107(92)90198-B
46. Yamada Y, Park MS, Okinaka RT, Chen DJ. Molecular analysis and comparison of radiation-induced large deletions of the HPRT locus in primary human skin fibroblasts. *Radiat Res* (1996) 145:481. doi:10.2307/3579070
47. Suzuki K, Ojima M, Kodama S, Watanabe M. Delayed activation of DNA damage checkpoint and radiation-induced genomic instability. *Mutat Res* (2006) 597:73–7. doi:10.1016/j.mrfmmm.2005.04.024
48. Cucinotta FA, Wilson JW, Shavers MR, Katz R. Effects of track structure and cell inactivation on the calculation of heavy ion mutation rates in mammalian cells. *Int J Radiat Biol* (1996) 69:593–600. doi:10.1080/095530096145607
49. Menichini P, Vrieling H, van Zeeland AA. Strand-specific mutation spectra in repair-proficient and repair-deficient hamster cells. *Mutat Res* (1991) 251: 143–55. doi:10.1016/0027-5107(91)90224-C

Conflict of Interest: The authors declare that the research was conducted in the absence of any commercial or financial relationships that could be construed as a potential conflict of interest.

frontiers in Physics

ORIGINAL RESEARCH
published: 21 January 2021
doi: 10.3389/fphy.2020.567300

Commissioning of GPU–Accelerated Monte Carlo Code FRED for Clinical Applications in Proton Therapy

*Jan Gajewski[1], Magdalena Garbacz[1], Chih-Wei Chang[2], Katarzyna Czerska[1], Marco Durante[3,4], Nils Krah[5], Katarzyna Krzempek[1], Renata Kopeć[1], Liyong Lin[2], Natalia Mojżeszek[1], Vincenzo Patera[6,7], Monika Pawlik-Niedzwiecka[1,8], Ilaria Rinaldi[9], Marzena Rydygier[1], Elzbieta Pluta[10], Emanuele Scifoni[11], Agata Skrzypek[1], Francesco Tommasino[11,12], Angelo Schiavi[6,7] and Antoni Rucinski[1]**

[1]Institute of Nuclear Physics Polish Academy of Sciences, Krakow, Poland, [2]Department of Radiation Oncology and Winship Cancer Institute, Emory University, Atlanta, GA, United States, [3]Biophysics Department, GSI Helmholtzzentrum fur Schwerionenforschung, Darmstadt, Germany, [4]Technische Universitat Darmstadt, Institut fur Festkorperphysik, Darmstadt, Germany, [5]CNRS/CREATIS, UMR 5220, Lyon, France, [6]INFN - Sezione di Roma, Roma, Italy, [7]Dipartimento di Scienze di Base e Applicate per l'Ingegneria, Sapienza Università di Roma, Roma, Italy, [8]Institute of Physics, Jagiellonian University, Krakow, Poland, [9]ZonPTC/Maastro Clinic, Maastricht, Netherlands, [10]Maria Sklodowska-Curie Institute – Oncology Center, Krakow, Poland, [11]Trento Institute for Fundamental Physics and Applications, Trento, Italy, [12]Maria Sklodowska-Curie Institute – Oncology Center, Krakow, Poland, [13]Department of Physics, University of Trento, Trento, Italy*

OPEN ACCESS

Edited by:
Kris Thielemans, University College London, United Kingdom

Reviewed by:
Julien Bert, INSERM U1101 Laboratoire de Traitement de l'information Médicale (LaTIM), France
Xiaoying Liang, University of Florida, United States

***Correspondence:**
Antoni Rucinski
antoni.rucinski@ifj.edu.pl;
antoni.rucinski@gmail.com

Specialty section:
This article was submitted to Medical Physics and Imaging, a section of the journal Frontiers in Physics

Received: *29 May 2020*
Accepted: *19 August 2020*
Published: *21 January 2021*

Citation:
Gajewski J, Garbacz M, Chang C-W, Czerska K, Durante M, Krah N, Krzempek K, Kopeć R, Lin L, Mojżeszek N, Patera V, Pawlik-Niedzwiecka M, Rinaldi I, Rydygier M, Pluta E, Scifoni E, Skrzypek A, Tommasino F, Schiavi A and Rucinski A (2021) Commissioning of GPU–Accelerated Monte Carlo Code FRED for Clinical Applications in Proton Therapy. Front. Phys. 8:567300. doi: 10.3389/fphy.2020.567300

We present commissioning and validation of FRED, a graphical processing unit (GPU)–accelerated Monte Carlo code, for two proton beam therapy facilities of different beam line design: CCB (Krakow, IBA) and EMORY (Atlanta, Varian). We followed clinical acceptance tests required to approve the certified treatment planning system for clinical use. We implemented an automated and efficient procedure to build a parameter library characterizing the clinical proton pencil beam. Beam energy, energy spread, lateral propagation model, and a dosimetric calibration factor were parametrized based on measurements performed during the facility start-up. The FRED beam model was validated against commissioning and supplementary measurements performed with and without range shifter. We obtained 1) submillimeter agreement of Bragg peak shapes in water and lateral beam profiles in air and slab phantoms, 2) $<2\%$ dose agreement for spread out Bragg peaks of different ranges, 3) average gamma index (2%/2 mm) passing rate of $>95\%$ for >1000 patient verification measurements using a two-dimensional array of ionization chambers, and 4) gamma index passing rate of $>99\%$ for three-dimensional dose distributions computed with FRED and measured with an array of ionization chambers behind an anthropomorphic phantom. The results of example treatment planning study on >100 patients demonstrated that FRED simulations in computed tomography enable an accurate prediction of dose distribution in patient and application of FRED as second patient quality assurance tool. Computation of a patient treatment in a CT using 10^4 protons per pencil beam took on average 2′30 min with a tracking rate of 2.9×10^5 p^+/s. FRED was successfully commissioned and validated against the clinical beam model, showing that it could potentially be used in clinical routine. Thanks to high computational performance due to GPU acceleration and an automated beam model implementation

method, the application of FRED is now possible for research or quality assurance purposes in most of the proton facilities.

Keywords: Monte Carlo, treatment planning, GPU, radiation therapy, proton theraphy, dosimetry, commissioning, beam modelling

1 INTRODUCTION

In proton radiation therapy, Monte Carlo (MC) methods offer more accurate modeling of proton interactions with heterogeneous media and improve dose calculation accuracy in complex geometries with respect to analytical pencil beam algorithms [1–4]. The application of MC algorithms in treatment planning can eventually lead to a reduction in the target volume safety margins by about 2% and more accurate prediction of the treatment outcomes [5]. The state-of-the-art commercial proton beam therapy (PBT) treatment planning systems (TPS) employ MC methods for treatment plan optimization and dose calculation [6, 7], but they are still not the standard treatment planning tools in all clinically operating PBT facilities. Many proton facilities still use analytical pencil beam algorithms of limited accuracy in heterogeneous media. Also, the time performance of the MC-based TPS remains to be an issue, especially when applying robust optimization algorithms that require computing several dose distributions for one computed tomography (CT) image or in treatments of moving targets where 4D-CT consisting of a series of CT images of several motion phases of one patient are employed in treatment plan optimization [8]. In addition, proton radiation therapy quality assurance (QA) procedures are time consuming and require manpower for experimental measurements of dose distributions in phantoms, typically performed at a few depths in water for each treatment field. In fact, time needed for patient QA could be dedicated for the actual patient treatment. Therefore, reduction in the number of measurements is widely discussed among medical physicists [9–14]. Supplementing or replacing patient QA measurements with dose distribution recalculation using a second, independent, dose-calculation engines can be beneficial for PBT facilities.

In several PBT facilities, general purpose MC simulation toolkits, such as: FLUKA [15], Geant4 [16, 17], or Shield-HIT [18] as well as more user-friendly environments built on Geant4 like GATE/GATE-RTion [19–21] and TOPAS [22, 23], are used to support research activities and/or simulations for patient QA. The clinical application of general purpose MC tools is limited, mainly due to the time required to recalculate a complete plan ranging from tens of minutes to even a few hours. For this reason, the parallelization of the particle tracking on several central processing units (CPU) or general purpose graphical processing units (GPU) is of interest for radiotherapy. The PBT-dedicated GPU-based MC code gPMC implemented by Jia et al. [24] was further developed [25] and validated using clinical patient data [26]. Following the gPMC development, Wan Chen Tseung and colleagues presented a high-performance GPU-accelerated MC code, which is used for routine clinical QA and as the dose calculation engine in a clinical MC-based Intensity Modulated Proton Therapy (IMPT) treatment planning system [27]. Recently, an analytical pencil beam algorithm, the FRoG platform, was implemented on GPU for clinical investigations with different ion types [28, 29].

The commissioning and validation of the independent, MC-based dose calculation engine for research or patient QA purposes is a time-consuming process that requires knowledgeable and experienced manpower. Only recently, standards for beam modeling and beam model commissioning for MC dose calculation–based radiation therapy treatment planning were proposed [30]. The experimental characterization of the proton beam properties (longitudinal and lateral profiles as well as dosimetric calibration) as a function of primary beam energy is facility dependent because different PBT centers use different accelerators, measurement methods, and TPS. The complete implementation of passive and active beam delivery nozzle geometry was described by Paganetti et al. [1] for cyclotron-based facilities and by Parodi et al. [31] for synchrotron-based facilities. However, it was suggested later that for MC dose calculation purposes, defining the beam model following the clinical commissioning procedure and avoiding detailed simulations of the beam nozzle geometry is possible with a precision that is sufficient for clinical application [10, 32, 33].

This article reports on commissioning of the GPU-accelerated MC code FRED [34] and its validation at two cyclotron-based proton beam therapy facilities of different beam line design: Varian ProBeam in Atlanta, GA (United States), and IBA Protheus C-235 in Krakow (Poland). The software toolkit FRED (Fast paRticle thErapy Dose evaluator) [34] was developed at the University of Rome for parallelized proton beam transport simulations in heterogeneous geometry defined by the patient CT. We describe in detail FRED commissioning steps, that is, automated characterization of the beam model that describes the proton beam used for patient treatment and follows the clinical QA procedures. Finally, we validated our commissioning procedure using the optimized beam models. We simulated dose distributions in FRED and compared the results with verification measurements performed in homogeneous and heterogeneous phantoms with and without range shifters as suggested by Winterhalter et al. [35]. Such extensive experimental validation of FRED accuracy and time performance has been never reported before. To increase the confidence of the reader about the accuracy of FRED simulations, selected results were also compared with clinical TPS simulations. Eventually, we evaluated clinical cases of patient treatment plans to demonstrate the clinical applicability of FRED.

2 MATERIALS AND METHODS

2.1 GPU–Accelerated Monte Carlo Code FRED

The great benefit of FRED with respect to general purpose MC codes is its computation performance achievable on a variety of different hardware without compromising the dose computation accuracy. The typical tracking rates range from 10–100 thousand protons per second using a single CPU to about million particles per second using GPU cards. FRED is equipped with an interface to convert phantom/patient geometries stored in DICOM CT images to a voxelized geometry of the patient containing the atomic tissue composition using a conversion table based on stoichiometric calibration [36]. In addition to patient geometry, user-defined geometries of specific material composition can be included enabling simulations of proton transport in passive elements like range shifter.

The physical interaction models implemented in FRED are trimmed down with respect to general purpose MC codes, such as Geant4/FLUKA within the regime that is relevant for particle therapy, in order to speed up the execution time without compromising the accuracy of dose-deposition calculations. In particular, the physics processes contributing to the dose deposited by protons in patient tissue, that is, mean energy loss, energy fluctuations, nuclear elastic and inelastic interactions with target nuclei as well as the trajectory deflection via a multiple Coulomb scattering, are implemented in FRED [34]. Moreover, FRED offers linear energy transfer (LET) and relative biological effectiveness (RBE)–weighted dose calculations by means of different RBE models, providing further information, which is not available in the state-of-the-art commercial TPS. The LET and RBE computations in FRED are out of the scope of this study.

2.2 Commissioning Measurements and FRED Simulations

FRED commissioning was performed for one gantry room of two PBT facilities of different beam line design equipped with scanned proton beams that are in clinical operation since 2016 and 2018, respectively. Krakow facility is an IBA design based on Proteus C-235 cyclotron equipped with two rotational gantries, an eye treatment room and an experimental hall. The TPS Eclipse from Varian, version 13.6, is used for treatment planning in CCB. It uses analytical proton convolution superposition (PCS) algorithm for the dose calculation and optimization [37]. EMORY PBT center in Atlanta is a ProBeam system designed by Varian and equipped with three rotational gantries and two horizontal beam lines. The TPS RayStation from RaySearch laboratories, version 8A, equipped with MC dose algorithm is used for treatment planning in EMORY [7]. The properties of proton beams and the measurement methods used for the acquisition of clinical beam model commissioning data at both facilities are listed in **Table 1**.

The commissioning measurements that include depth dose distribution measurements in water phantom, measurements of the lateral profiles (without range shifter) in air, and absolute dose measurements in a water phantom were used to build parameter libraries characterizing the FRED beam model for Krakow and Atlanta facilities. The water phantom and in-air setup used for commissioning measurements are schematically illustrated in **Figures 1 A and B** respectively. The figure indicates how the proton beam is transported from the nozzle toward the detector/phantom. During irradiation, the beam is deflected vertically and horizontally by scanning magnets and crosses a position sensitive ionization chamber (IC23), which is used for beam lateral position and size measurement. The procedure of the commissioning data acquisition is not described here in detail as it is out of the scope of this article.

The FRED simulation setup mimics the commissioning measurements setup shown in **Figures 1 A and B**. The virtual beam source is located at the position of the scanning magnet located closer to the isocenter because at this position, the deflection of the beam in both X and Y directions is defined. The different position of the X and Y scanning magnets is taken into account, while calculating the direction of a single pencil beam. The beam propagation in the IC23 is omitted in the simulations and is taken into account by adjusting beam source parameters, in such a way that the beam size fits the results of beam size measurements in air performed with scintillating screen (*Lynx*). The proton beam was propagated without and with range shifter. FRED simulations in water were performed in $40 \times 40 \times 40$ cm^3 virtual phantoms of $1 \times 1 \times 1$ mm^3 voxel size (**Figure 1A**). The ionization potential of water was set to 80 eV [38]. FRED simulations of the in-air setup used for beam model validation were performed in a virtual air phantom. The total time of FRED MC simulations includes tracking time, time needed for memory allocation, and the file writing. The tracking rate of simulation is given as the number of protons tracked per second (p^+/s).

2.3 Beam Model Parameters

The beam model parameters characterize longitudinal and lateral pencil beam profiles as well as dosimetric calibration. Two parameters, energy (E) and energy spread (E_o), characterize proton pencil beam depth dose distribution (longitudinal) profile. One further parameter, monitor units (MU) to the number of particles conversion factor (SF_{MU}), characterizes integral dose distribution (IDD) dosimetrically, by means of dose measurement at 2 cm depth, following TPS commissioning protocol and other references [37, 39, 40]. The lateral propagation of the proton pencil beam can be characterized by a quadratic model by means of modeling beam emittance or bilinear model by defining virtual point source. In fact, the bilinear model is an approximation of a quadratic model in a limited range. The virtual point source approach can be applied when the waist of the quadratic function of emittance model is far enough from the isocenter to approximate lateral beam propagation behind the nozzle exit by a bilinear function. FRED is capable of handling lateral beam propagation using both virtual point source or emittance approaches.

TABLE 1 | Selected properties of CCB and EMORY PBT centers and measurement methods used for the proton beam model commissioning.

Parameter	CCB	EMORY
Energy range [MeV]	70-226.1	70-242
Measurement step [MeV]	10	10
RS thicknesses [mm] (density [g/cm^3])	36.7 (1.168)	20, 30, 50 (1.202, 1.191, 1.191)
RS material	PMMA	Lexan
Snout position [cm]	Fixed: 36.9	Variable: 5.5-42
SM distance (*X*/*Y*) [cm]	221.5/184.6	200/256
Lateral profile meas. Method (air)	*Lynx* (IBA)	*Lynx* (IBA)
Detector position relative to isocenter [cm]	−20, −10, 0, +10, +20	−30, −20, −10, 0, +5
Water phantom	Blue phantom^2 (IBA)	Blue phantom^2 (IBA)
IDD meas. method (water)	Bragg peak chamber (PTW)	StingRay (IBA dosimetry)
—	ϕ = 81.6 mm	ϕ = 120 mm
IDD meas. acceptance correction	Yes (FLUKA)	No
Abs. dosimetry meas. method (water)	Markus (PTW) at 2 cm	PPC-40 (IBA) at 2 cm
Monoenergetic field size	10 × 10 cm^2	10 × 10 cm^2

RS : range shifter; SM : scanning magnet; meas.: measurement; IDD : integrated depth dose; Abs.: absolute.

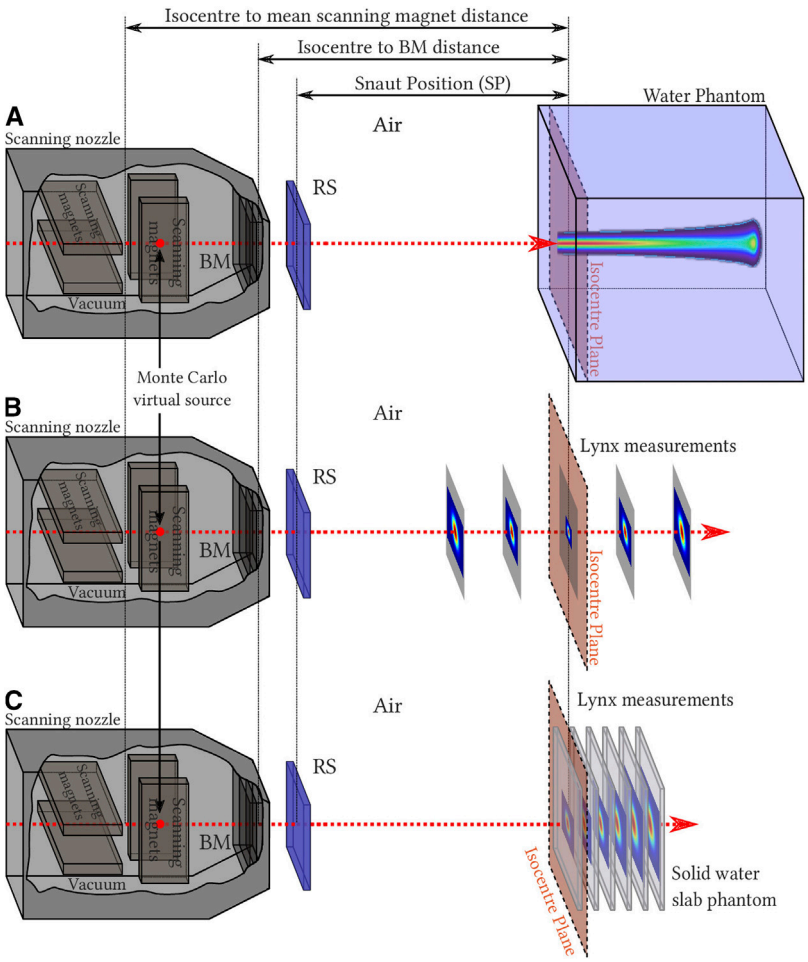

FIGURE 1 | Experimental and simulation setups for water phantom **(A)**, in-air scintillating screen measurements **(B)**, and measurements in a solid water slab phantom **(C)**. On the left, beam nozzle elements (scanning magnets and position sensitive beam monitor (BM) chambers), not taken into account in MC simulations, are shown (gray scale). In MC simulations, the primaries are generated in *Monte Carlo virtual source* and transported through range shifter (RS) to phantoms/detectors (blue). The figure is not to scale.

For characterizing the lateral propagation, the lateral beam profiles measured during facility commissioning in air at different Z positions (cf. **Figure 1B**) were fitted using the Gaussian fit, and its $\sigma(z)$ was calculated. Additionally, the $\sigma(z)$ measured with the beam monitor chambers in the nozzle can be used [41]. This improves the quality of the lateral beam propagation modeling, especially in cases where the waist of the beam is located between the nozzle and the first measured point in air. Fitting $\sigma(z)$ to commissioning data from both facilities at different distances from the isocenter using bilinear and quadratic functions indicated that the emittance model is appropriate for Krakow facility, whereas the virtual point source model can be used for EMORY.

For characterizing the beam lateral propagation in Krakow, six emittance model parameters (ϵ, α, β), three in X direction and three in Y direction, were used. The Twiss parameters ϵ, α, and β were obtained according to the following formula [42]:

$$\sigma^2(z) = \epsilon \cdot \left(\beta - 2 \cdot \alpha \cdot z + \frac{1+\alpha^2}{\beta} \cdot z^2 \right), \quad (1)$$

where the emittance ϵ corresponds to the area in the X/Y position–velocity phase space and is assumed to be constant over the beam propagation in air. The Twiss parameter α is related to the focusing/defocusing of the beam, whereas β characterizes the length over which the beam changes its transverse shape.

For characterizing the beam lateral propagation in Atlanta, four parameters, two in X direction and two in Y direction, specific for a bilinear approximation were used. The parameters were obtained according to the following formula:

$$\sigma(z) = S \cdot z - VSD, \quad (2)$$

where the S is the function slope and corresponds to the rate of the spot size variation and VSD stands for virtual source distance and corresponds to the distance from the virtual source to the isocenter. Note that for both approaches, virtual point source and emittance model of lateral beam propagation, particles are transported starting from the position of the scanning magnets regardless of the position the emittance waist and VSD.

For TPS exploiting analytical pencil beam algorithm, the emittance model is defined for configurations with and without range shifter, whereas in MC-based TPS and in FRED, only the configuration without range shifter is defined, and proton transport in range shifter is simulated according to its model parameters (material composition, density, physical thickness).

2.4 Generation of Beam Model Parameter Library

We implemented a set of software tools that calculate beam model parameters in three automated steps (see **Figure 2**). The beam model parameter libraries were generated in the entire proton beam energy range in 10 MeV steps (**Table 1**) for both facilities. **Figure 2** schematically illustrates how the FRED MC commissioning procedure uses the facility commissioning measurements as the input to obtain beam model parameters per nominal energy, that is, beam energy E, energy spread E_σ, MU scaling factor SF_{MU}, and six emittance or four virtual point source parameters. The procedure is automated and does not require any interaction with the user, except preparation of the measurement data. FRED simulations of single pencil beams were performed using 10^8 primary protons.

Step 1. In the first step (**Figure 2**: Step 1), the emittance or virtual point source model (**Eqs 1** and **2**) was fitted to the measured beam spot size ($\sigma_{x/y}$) as a function of the position along the beam (see **Section 2.3**). For Krakow beam model, in addition to the beam size measurements performed with *Lynx* (pixel size 0.5 × 0.5 mm^2), the beam size measurements performed during irradiation with IC23 (resolution 5 mm in X/Y directions) installed close to the nozzle exit were used to fit the emittance model (see **Section 2.3**). In this way, emittance model parameters (ϵ, α, β) or virtual point source parameters (S, VSD) were obtained for X and Y directions and each energy.

Step 2. In the second step (**Figure 2**: Step 2), beam energy (E) and energy spread (E_σ) were obtained. The measured and simulated IDD profiles were fitted using a formalism proposed by Bortfeld [43, 44]. Using the fit and semiempirical relations proposed by Bortfeld [43], the initial energy and energy spread of protons producing an IDD distribution were computed. The Bragg peak range ($R_{80\%}$) defined as 80% of the maximal value at the distal falloff and the Bragg peak full width at half maximum (FWHM) were numerically calculated from the fitted curve. The E, E_σ, $R_{80\%}$, and FWHM parameters were calculated for experimental data and each FRED simulation. An automated iterative optimization procedure was developed to find such E and E_σ values in FRED, which minimize the absolute difference of Bragg peak range ($|\Delta R_{80\%}|$) and FWHM ($|\Delta$FWHM$|$) between simulation and measurement. The dependence of $|\Delta R_{80\%}|$ and $|\Delta$FWHM$|$ on E and E_σ is a continuous function with a single global minimum. The optimization procedure was implemented in *Python* exploiting the Nelder–Mead simplex algorithm [45]. The initial guess of energy and energy spread was estimated from the Bortfeld curve fitted to measured data. Each consecutive step of the optimization algorithm included the following: 1) new simulation of a depth dose distribution in water with energy and energy spread computed by the optimization algorithm, 2) Bortfeld curve fit and estimation of $R_{80\%}$ and FWHM for the simulated curve, and 3) estimation of $|\Delta R_{80\%}|$ and $|\Delta$FWHM$|$ comparing measurement and new simulation. The FRED beam energy (E) and energy spread (E_σ) are considered optimal when $|\Delta R_{80\%}|$ and $|\Delta$FWHM$|$ are less than or equal to 0.05 mm.

Step 3. In the third step (**Figure 2**: Step 3), the dosimetric calibration from TPS MU to the number of particles ($SFSF_{MU}$) was obtained for each nominal energy, mimicking the measurement setup. For this purpose, a monoenergetic 10 × 10 cm^2 field in water was simulated with spot spacing 2.5 mm, 1 MU per spot and unitary MU scaling factor. The dose in the uniform field center at 2 cm depth in water, $D_{2\,cm}$, was derived from the simulation. The MU scaling factor (SF_{MU}) was obtained as the ratio between $D_{2\,cm}$ obtained from commissioning measurement and FRED MC simulation.

The output of the characterization procedure is a list of beam model parameters per nominal energy and is stored in a text file.

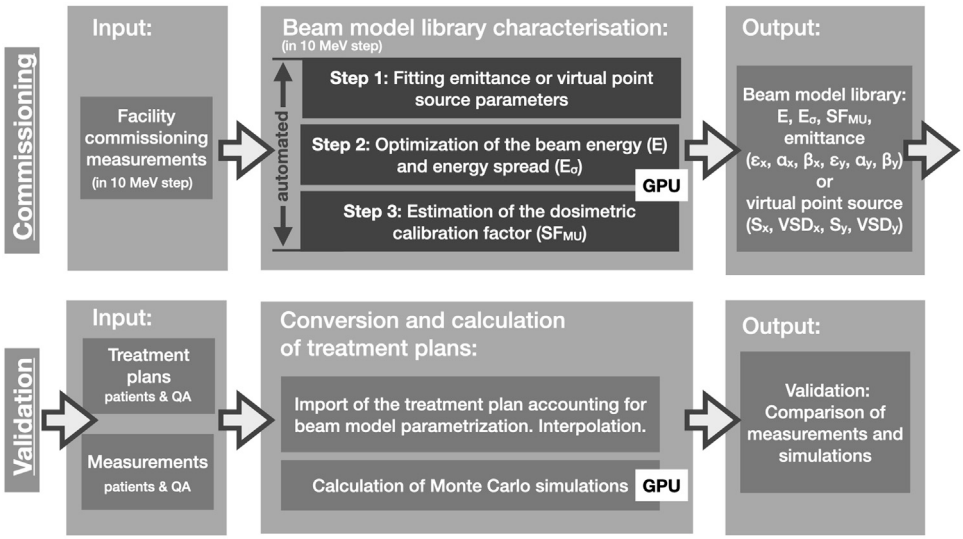

FIGURE 2 | A flow chart illustrating FRED commissioning and validation steps. Simulations steps benefiting from GPU-accelerated MC simulations are indicated (GPU).

We developed a software tool that converts clinical TPS treatment plan into FRED input files using the beam model library (cf. **Figure 2**: Conversion and calculation of treatment plans). The parameters in between nominal energies are linearly interpolated, mimicking the procedures applied by TPS and beam line control system.

2.5 Validation in Homogeneous Media

This section describes how the beam model library was validated by comparing FRED simulations with measurements performed at each facility. We compared 1) lateral propagation of proton pencil beams, 2) treatment plans of dose cubes, and 3) patient QA treatment plans. The beam model validation steps are schematically illustrated in **Figure 2** (lower row). The treatment plans were exported from TPS and converted from DICOM to FRED input file format. The QA treatment plans were simulated in FRED using 10^5 protons per pencil beam. After simulation, the dose from each spot was scaled to the actual number of particles optimized in the treatment plan using dosimetric calibration (SF_{MU}). This approach warranties the same statistical precision of calculation of dose delivered by each pencil beam, regardless of its weight in the treatment plan.

Lateral propagation of proton pencil beams. The measurements of lateral profiles of proton pencil beams at 100, 150, and 200 MeV were performed using the *Lynx* scintillating screen (IBA Dosimetry) in air for CCB and EMORY [46] at five positions behind the range shifter. The beam lateral profiles in solid phantoms were measured with *Lynx* in RW3 slab phantom for beam energies 100, 150, and 200 MeV at CCB and in PMMA slab phantom for beam energies 130, 180, and 240 MeV at EMORY.

FRED simulations for pencil beams were performed at the corresponding positions behind the range shifter in air and in solid phantoms. The transverse shape of the beam in *X* and *Y* directions was fitted with a single Gaussian fit, and the σ obtained from measurements and simulations were compared.

Spread Out Bragg Peak (SOBP). The longitudinal profiles of dose cubes (SOBPs) were measured 1) at CCB using a dosimetrically calibrated plane-parallel Markus chamber placed in a water phantom (sensitive volume 0.055 cm^3) with variable 0.1-1 cm step length and 2) at EMORY using the Zebra detector (IBA Dosimetry) without dosimetric calibration. The QA treatment plans of dose cubes were optimized in clinical TPS aiming at achieving homogeneous biological dose of 1 Gy (RBE) and 4 Gy (RBE) at CCB and EMORY, respectively. All cubes had a lateral size of $10 \times 10\,cm^2$. At CCB, dose cubes of 5 cm length (modulation) and variable range of 10, 15, 20, 25, and 30 cm without range shifter were optimized and evaluated. At EMORY, dose cubes of 10 cm length (modulation) and constant range of 15 cm without and with three range shifters of different thickness were investigated. For each measurement, the isocenter position in water was in the middle of SOBP, causing that the measurements were performed with air gaps ranging from 5 to 32 cm for EMORY and from 11.2 to 29.4 cm for CCB. Simulations of the SOBP plans were performed in a virtual water phantom. The measured SOBP dose profiles were compared with the profile extracted from three-dimensional (3D) dose calculation obtained from FRED MC simulations. Absolute dose comparison was performed for Markus chamber measurements conducted at CCB, whereas relative dose comparison was performed for Zebra measurements conducted at EMORY.

Patient QA. To evaluate the accuracy of FRED simulations, patient QA treatment plans were simulated in a virtual water phantom and compared with patient QA measurements routinely performed in the clinic. The comparison of TPS vs. measurement is also shown.

In CCB and EMORY, the MatriXX PT (IBA Dosimetry) is currently in use for patient QA [47]. MatriXX is a two-

dimensional (2D) array of 1020 plane-parallel ionization chambers of 4 mm diameter arranged in a 32 × 32 grid with the distance between chambers of 7.62 mm. In both facilities, the MatriXX detector was calibrated to dose in water according to protocol proposed by the manufacturer. Patient QA measurements are typically performed at 3-5 depths at CCB and at 1-3 depths at EMORY. The measurement depths are selected by a medical physicist during the QA preparation process for each patient individually, to cover the entire treatment field. For EMORY, the air gap ranges from 5 to 22 cm, whereas for CCB, it ranges from 21.7 to 27.7 cm. The patient QA treatment plans of 74 patients (1077 measured layers, 967 without and 110 with range shifter) treated in Krakow and 13 patients (56 measured layers) treated in EMORY were evaluated. The dose distributions obtained from TPS and FRED calculations were compared to measured data by means of dose profile and gamma index (GI) analysis [48]. GI calculation tools implemented in PyMedPhys Python package [49] were used for evaluation. The 3D GI test (2 mm distance-to-agreement and 2% of local dose difference criteria, with the dose cutoff at 2% of the maximum dose) was used to compare 2D slice of dose field measurement (reference) with 3D FRED dose distribution calculation (evaluation).

2.6 Validation in Heterogeneous Media

The end-to-end experimental validation of FRED physics models, beam model, and CT calibration using a heterogeneous CIRS head-and-neck phantom (model 731-HN) [50] was performed in Krakow. The experimental setup is shown in **Figure 3**. The CIRS phantom consists of five materials equivalent to the following tissues/organs: brain, bone, larynx, trachea, sinus, teeth, and nasal cavities. One half of the phantom consists of single piece, and the other is sliced into three segments as shown in **Figure 3A**. The CIRS phantom was positioned in the treatment room using orthogonal X-ray imaging system and the phantom CT scan, following the clinical patient positioning procedure applied in Krakow. The irradiation plans of 10 × 10 cm^2 monoenergetic fields at nominal energies 100, 150, and 200 MeV were prepared in clinical TPS with and without range shifter. The dose distribution downstream from the CIRS phantom was measured using the MatriXX detector placed in the DigiPhant water phantom (IBA Dosimetry, see **Section 2.5**). Data were acquired in 5 mm water-equivalent steps yielding 3D dose distribution with lateral resolution of 7.62 mm and longitudinal resolution of 5 mm. Dose distributions were measured behind half CIRS head in water for nominal energies 150 and 200 MeV (cf. **Figure 3B**). The dose distribution was measured behind 1/6 slice of CIRS head in water-equivalent RW3 slab phantom using 100 MeV proton beam (IBA Dosimetry; cf. **Figure 3C**) because 100 MeV protons have insufficient range to traverse the half-head phantom to acquire dose distribution in water using MatriXX (with and without range shifter).

The measurements were compared to FRED simulations of the experimental setup performed in the CT image of the CIRS and water phantoms. The CT image of CIRS phantom was acquired using the CT scanner (Siemens SOMATOM) calibrated for treatment planning in Krakow. The comparison of measured and simulated 3D dose distributions was performed using a 3D GI method.

2.7 Patient Data

A retrospective patient study was performed to investigate time performance of FRED as an independent, MC-based, proton dose computation tool and demonstrate its applicability for patient QA in the clinic. For this purpose, we referred our results to the TPS computations.

The 122 treatment plans (including boost plans) of 90 head and neck as well as brain patients treated at CCB from 2016 to 2018 and an example treatment plan of a patient treated in EMORY in 2019 [7] were simulated in FRED on CT geometries. The clinical CT images were sampled down to 1.5 × 1.5 × 1.5 mm^3 voxel size. The facility-specific clinical CT calibration curve obtained from stoichiometric calibration [36] was implemented in FRED. The CT calibration curve used in FRED contains information on the composition, relative stopping power (RSP) of protons, radiation length, and density of 93 materials. The density and RSP of CT numbers between 93 predefined points are linearly interpolated. The CT images of the patient anatomy and delineated contours were used for the optimization of plans in clinical TPS using an analytical intensity modulated proton therapy (IMPT) optimization algorithm. Depending on the target size and the number of fields, the number of pencil beams in a treatment plan varied from 1,378

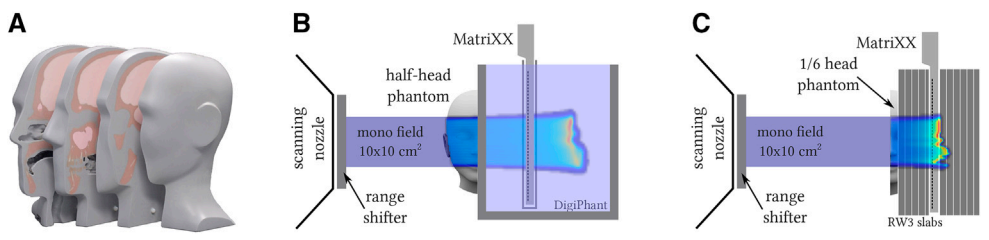

FIGURE 3 | Schematic illustration of CIRS phantom **(A)** and setup used for experiment and FRED MC simulations **(B, C)**. **(A)** CIRS head phantom sliced into one-piece half-head and the other half sliced further into three segments; **(B)** setup with half-head CIRS and MatriXX detector placed in water phantom; **(C)** setup with one slice of CIRS and MatriXX detector placed between water-equivalent RW3 solid phantom. Setup **(B)** was irradiated with monoenergetic field at nominal proton beam energy 150 and 200 MeV, whereas setup **(C)** at 100 MeV, all with and without range shifter.

to 32,290 with the median value of 10,989. 10^4 protons per pencil beam were simulated for each patient treatment plan recalculated in FRED, and the obtained dose was scaled to the actual number of particles optimized in the treatment plan. In order to investigate the impact of PTV volume on the FRED dose calculation accuracy, we divided treatment plans of patients treated in CCB into three subgroups distinguishing 12 plans with small PTV volume ($V_{PTV} < 50$ ml), 60 plans with medium PTV volume (50 ml $\leq V_{PTV} < 200$ ml), and 50 plans with large PTV volume ($V_{PTV} \geq 200$ ml). PTV volumes ranged from 28.5 ml to 1,010 ml

An example treatment planning study on 122 plans included a comparison of dose distributions obtained from FRED and from clinical TPS. We evaluated four parameters based on dose volume histogram (DVH) that characterize the quality of dose distribution. 1) The mean dose (D_{mean}) is related to the prescribed dose (D_p). 2) The homogeneity index (HI) characterizes the slope of the DVH; hence, the uniformity of the dose distribution in the PTV. The HI is defined as $HI = (D_{2\%} - D_{98\%})/D_p$, where $D_{2\%}$ and $D_{98\%}$ are the doses received by 2% and 98% of the PTV, respectively [51]. 3) The conformity index (CI) describes how much dose prescribed to the planning target volume (PTV) is delivered outside the PTV, possibly to organs at risk. The CI is defined as $CI = V_{95\%}^{body}/V_{95\%}^{PTV}$, where $V_{95\%}^{body}$ and $V_{95\%}^{PTV}$ are the volumes of the body and PTV, which receive at least 95% of the prescribed dose D_p [52]. 4) The relative mean square error (RMSE) characterizes the deviation of a DVH from the prescribed dose D_p. It was calculated at the slope of a DVH, in a range between $D_{5\%}$ and $D_{95\%}$, and it is defined as $RMSE = \sqrt{\sum_5^{95} (D_{x\%} - D_p)^2/90}$.

3 RESULTS

3.1 Generation of the Beam Model Parameter Library

The beam model parameter libraries characterizing the proton beam model for CCB and EMORY facilities were generated using an automated procedure (cf. **Section 2.3**) and are illustrated as a function of nominal proton beam energy in **Figure 4**. Using the beam model library, the nominal primary proton beam energy for each pencil beam from the treatment plan is used to define the initial parameters of the pencil beams used by FRED simulations. **Figure 4** (top-left panel) shows a linear relation between the nominal proton beam energy used by TPS and FRED. The energy spread values fluctuate within 1 MeV and are slightly smaller for Krakow than for Atlanta proton center. **Figure 4** (top-right panel) shows the dosimetric scaling factors used to convert MU to the number of primary particles per pencil beam spot. The bottom panels of **Figure 4** show the six parameters of emittance model used for Krakow (bottom-left panel) and the four parameters of VPS model used for Atlanta facility, characterizing the lateral beam propagation (bottom-right panel). The lateral asymmetry of the pencil beams in *X* (filled circles) and *Y* (empty circles) directions is taken into account in the beam model characterization.

The IDD profiles of single proton beams in water for three nominal energies: 100, 150, and 200 MeV are given in **Figures 5 A and B** for the Krakow and Atlanta facilities. The profiles are in agreement with the commissioning measurements: the range ($R_{80\%}$) of the pencil beams agrees within 0.02 mm, the relative dose difference along the pencil beam profile is below 4%, the FWHM of the Bragg peak agrees within 0.05 mm, the distal falloff width between 80% and 20% Bragg peak dose agrees within 0.04 mm, and the peak-to-plateau ratio agrees within 0.11.

The fitted single beam sizes in air obtained in commissioning measurements, described by $\sigma_{x/y}$ of lateral pencil beam profiles is shown in the **Figures 5 C and D** for three nominal energies: 100, 150, and 200 MeV for the Krakow and Atlanta facilities, respectively. The maximum absolute difference between fitted and measured beam sizes ranging from −20 to 20 cm (CCB) and −30 to 5 cm (EMORY) in *Z* direction with respect to the isocenter is smaller than 0.05 mm. We deem this sufficiently accurate to model lateral beam propagation in clinical applications. The quadratic and linear shape of the fit justifies the use of the emittance (**Figure 5C**) and VPS (**Figure 5D**) model for the Krakow and Atlanta facilities, respectively.

Dose computation time for a single pencil beam at 100, 150, and 200 MeV simulated with 10^8 primary protons was 36, 44, and 53 s, respectively. The corresponding tracking rate is 10.1×10^6, 5.7×10^6, and 3.6×10^6 p^+/s. The tracking rate decreases with the beam range as more interactions must be processed.

The total computation time needed to determine the beam model parameters for all reference energies following the automated procedure described in **Section 2.3** was approximately 12 h. Within this time, 1) the parameters characterizing beam lateral propagation were fitted (**Figure 2** step 1; total time: few seconds), 2) simulations required for E and E_σ optimization were performed and the optimization procedure itself was executed (**Figure 2** step 2; total time: approximately 10 h), and 3) simulations of monoenergetic $10 \times 10\,cm^2$ fields required for SF_{MU} calculation were performed (**Figure 2** step 3; total time: approx. 2 h). For CCB, full-beam model characterization required a total of 303 FRED MC simulations, including 286 simulations for E and E_σ optimization and 17 simulations for $SFSF_{MU}$ calculation (average time of single simulation was approximately 2 and 7 min, respectively).

3.2 Validation in Homogeneous Media

Lateral propagation of proton pencil beams. The lateral propagation of pencil beams in air behind range shifter of different thickness (**Figure 6**) and in slab phantoms (**Figure 7**) was simulated in FRED and compared with the beam size $\sigma_{x/y}$ of lateral pencil beam profiles obtained experimentally. Note that the comparison was performed at different positions/depths and for different primary proton beam energies at CCB and EMORY facilities.

The lateral propagation of the beam in range shifter and in slab phantom is accurately modeled in FRED. The values of $\sigma_{x/y}$

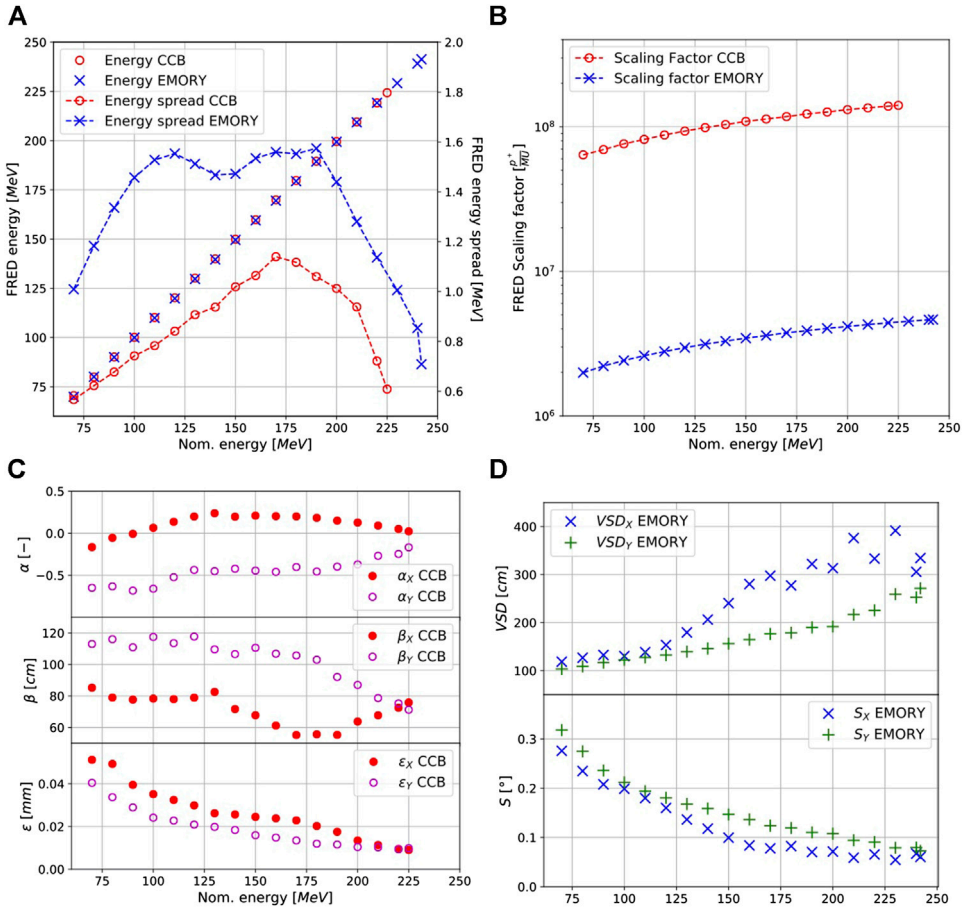

FIGURE 4 | The parameters characterizing proton beam model used in CCB and EMORY facilities at the entire primary proton beam energy range. Nominal energy corresponds to energy used by clinical TPS. **Top-left panel:** Beam energy and energy spread; **Top-right panel:** dosimetric calibration; **bottom-left panel:** emittance model parameters used in CCB; **bottom-right panel:** VPS model parameters used in EMORY.

obtained from measurements agree with simulated values mostly within 100 μm, as indicated by error bars in **Figures 6** and **7**. The results in air and in slab phantoms are within the spot size QA acceptance criterion of ± 0.6 mm used by CCB therapy center.

Spread Out Bragg Peak (SOBP). Depth dose distribution profiles of cubic volumes obtained from measurements and FRED simulations are shown in **Figure 8** for CCB in the top panels and for EMORY in the bottom panels. The results obtained for CCB are absolute dose, whereas they are relatively normalized to the dose value in the middle of the SOBP for EMORY. Because the treatment plans were optimized in clinical TPS, the obtained physical dose differs from the prescribed biological dose by the RBE factor of 10%.

Good agreement between FRED MC simulations and dose measurements along the SOBP profiles was obtained. The maximum relative dose difference is 2% for most of the measurement points. The largest relative dose differences are observed at the distal falloff, that is, a high-dose gradient region, and result from the detector positioning uncertainties, estimated to be about ± 0.3 mm. Small variations between the measurements and simulations are present at the beginning of the plateau and in the SOBP of cubes between the range of 25 and 30 cm. They are potentially related to the implementation of the nuclear interaction model in FRED for the highest beam energies. This accuracy is acceptable for the scope of the presented clinical application.

The tracking rate of the dose cube simulation ranged from 4.5×10^6 to 2.0×10^6 p^+/s and the complete dose computation time for a single dose cube was up to 10 min, with the statistics 10^5 primaries per pencil beam.

Patient QA. 2D transversal dose maps obtained from measurements performed with the MatriXX detector in water phantom were compared with FRED and TPS simulations of patient treatment plans using the GI analysis. Data from 1077 measurements performed at CCB and 52 measurements performed at EMORY were investigated, and the results of the comparison are summarized in **Figure 9**. The average GI passing rate obtained comparing all simulated and measured layers was 97.83% (4.94) (1σ) for CCB and 95.51% (3.88) (1σ) for EMORY. Of 1,077 layers evaluated for CCB, 1,022 fulfilled the requirement for the GI passing rate (%GP) to be greater than 90%. For EMORY, 47 of 52 investigated layers fulfilled this requirement.

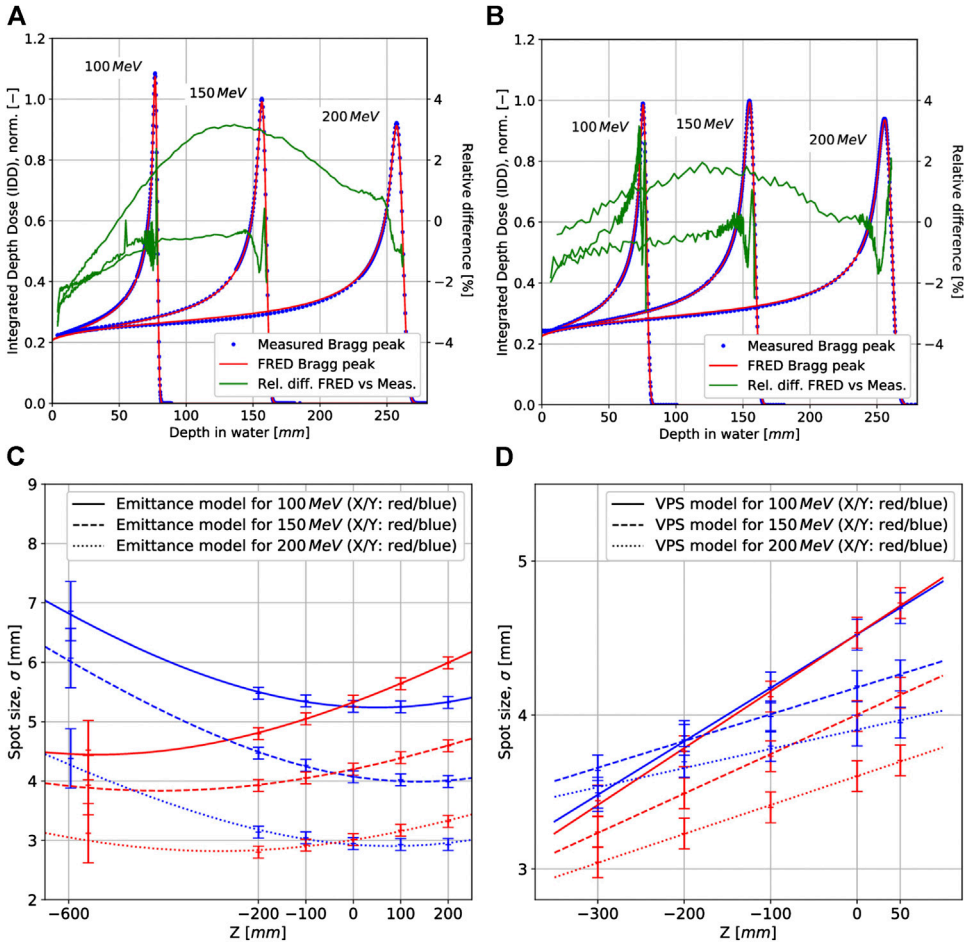

FIGURE 5 | Examples of longitudinal proton beam propagation in water **(top panels)** and lateral proton beam propagation (σ) in *X* and *Y* directions in air **(bottom panels)** for CCB **(left)** and EMORY **(right)** facilities at three proton beam energies: 100, 150, and 200 MeV. Depth dose distribution profiles of proton pencil beams simulated with beam model parameters in FRED (FRED Bragg peak) and obtained experimentally during the facility commissioning (measured Bragg peak) for CCB **(panel A)** and EMORY **(panel B)**. The transverse shape and velocity evolution of the proton beam represented by means of the emittance model for CCB **(panel C)** and VPS model for EMORY **(panel D)**.

Figure 10 shows an example of a transversal dose field layer extracted from FRED MC simulation and the corresponding dose distribution measured with MatriXX at the same depth in water, as well as in the GI map.

For a patient verification treatment plan, the average tracking rate and complete dose computation time were $3.4(0.4)\times10^6$ p^+/s (1σ) and 2'34 (1'38) min (1σ), respectively.

3.3 Validation in Heterogeneous Media

The experimental validation of FRED accuracy was performed by comparing 3D dose distributions behind the heterogeneous phantom obtained experimentally and from FRED simulations (cf. **Section 2.6**). An example of the comparison of FRED simulation against the experimentally acquired data is shown in **Figure 11**. Two 3D dose measurements, one with and other without range shifter, were performed for each of the investigated energies (100, 150, 200 MeV). An excellent agreement between FRED simulations and measurements was achieved. For all the investigated cases, the 3D GI (2%/2 mm) is greater than 99%. Comparing the clinical (analytical) TPS simulation and the measurements, the GI passing rate is $93.2^{98.0}_{76.3}$% (σ = 8.4%). See the **Supplementary Material** of the article for detailed results of other measurements performed at 100 and 200 MeV, with and without range shifter.

3.4 Example Clinical Application of FRED

As an example, dose distributions, dose profiles, and DVHs recalculated with FRED and clinical TPS, for one patient case from CCB and one from EMORY, are shown in **Figure 12**. For CCB patient case (**Figure 12** top panels), dose distributions computed with FRED are less uniform compared to the analytical TPS calculations. This is also observed analyzing the dose profiles and the DVH for PTV and results in the reduction of the mean dose in PTV and organ at risk. For EMORY patient case (**Figure 12** bottom panels), the differences in dose distributions are less visible as MC-based TPS was used for the dose

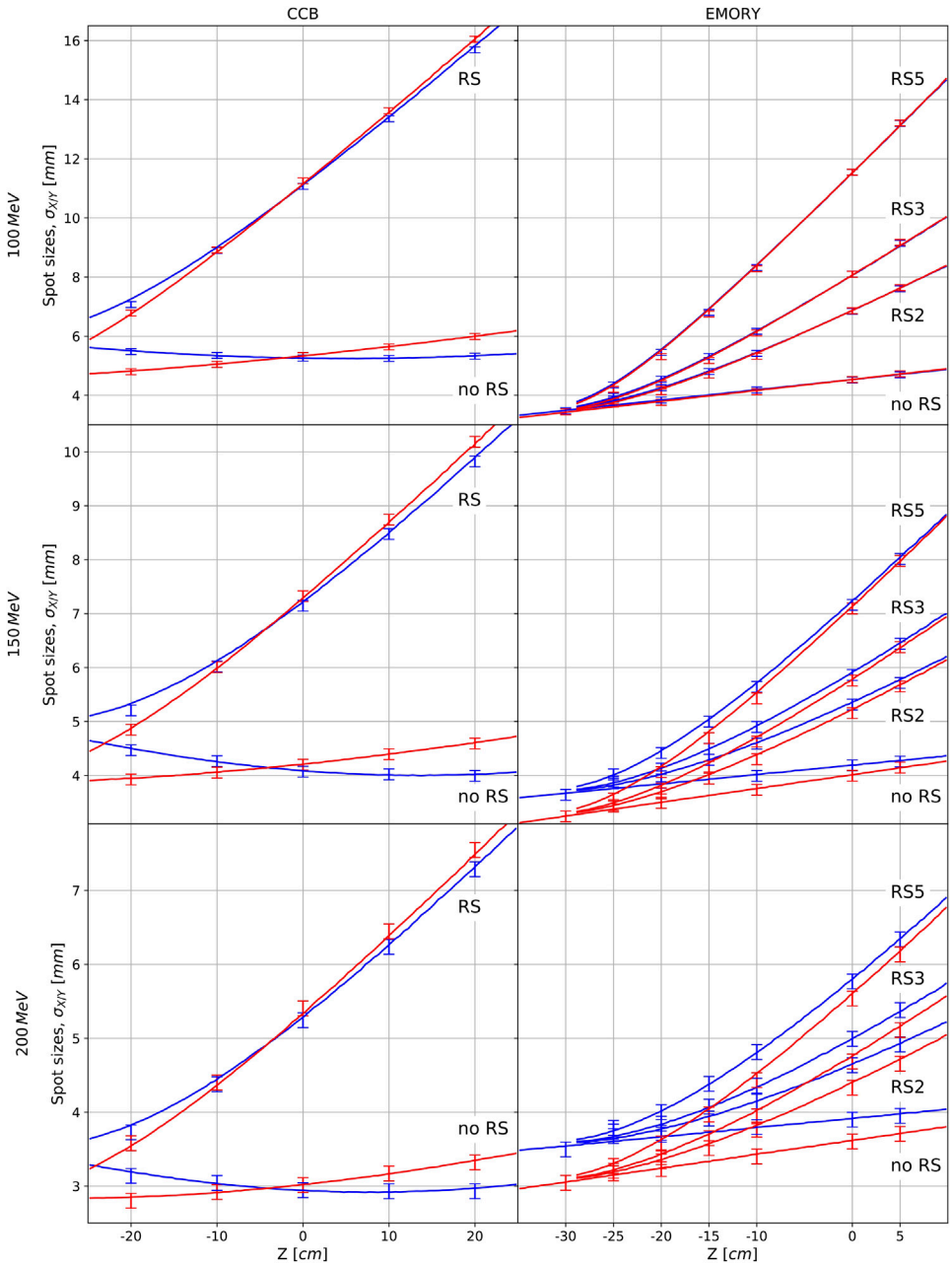

FIGURE 6 | Spot sizes in air in *X* (blue) and *Y* (red) directions for CCB and EMORY without range shifter and behind the range shifters used at facility (single range shifter (RS) of thickness 36.7 mm for CCB and RS2, RS3, and RS5 of thickness 20, 30, and 50 mm, respectively, for EMORY). The measured spot sizes are shown as points with error bars (± 0.1 mm), and the solid lines show the simulation results.

optimization and calculation. The observed differences between FRED and RayStation MC-based TPS are similar to the results obtained comparing RayStation with ECLIPSE MC algorithm reported by Chang et al. [7].

Analysis of 122 treatment plans of patients treated at CCB was performed to quantify the time performance and demonstrate the clinical applicability of FRED dose computations for patient QA. Comparing dose distributions in PTV, we observed that the ratio D_{mean}/D_p obtained with FRED is more dispersed than the one obtained with analytical TPS, while the effect is more pronounced for small targets. The average relative difference in median value ranges from 3% for small targets, through 1.5% for medium size target volumes, to 1% for large target volumes, as shown in **Figure 13** (left panel). The analysis of HI in PTV is shown in **Figure 13** (middle-left panel). On average, the median HI is 0.11 and 0.16 for clinical TPS and FRED, respectively. Independently on

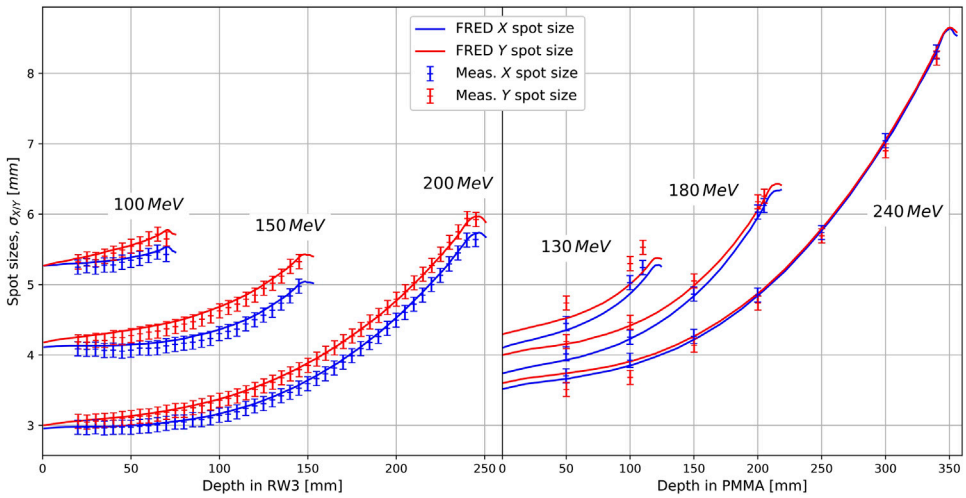

FIGURE 7 | The transverse shape evolution (σ) of proton pencil beam measured and simulated in water equivalent slab phantom.

the target volume, the HI in PTV calculated with FRED is higher, that is, dose distribution is less homogeneous than the HI calculated with analytical TPS. **Figure 13** (middle-right panel) shows the CI distributions, which present no substantial difference between both, FRED and TPS calculations (median CI is 1.26 and 1.23 for TPS and FRED, respectively). In general, for both, FRED and TPS calculations, dose distributions of small PTV are less conformal with respect to dose distributions for large PTV. The comparison of DVH in PTV by means of RMSE analysis confirms the conclusions from D_{mean}/D_p ratio and HI analysis. The histogram of RMSE for TPS distribution is narrower with smaller mean value, whereas for FRED, the RMSE distribution is wider with slightly greater mean value. This is because the dose distributions calculated with FRED are less uniform in PTV, as indicated by HI analysis, and the mean dose in PTV differs from the dose in PTV calculated with TPS, as indicated by D_{mean}/D_p ratio analysis.

For a treatment plan, the total simulation time varied depending on the complexity of the plan, that is, the total number of pencil beams and the presence of range shifter in the plan. For the simulations in CT geometry rescaled to $1.5 \times 1.5 \times 1.5\ mm^3$ voxels, the computation

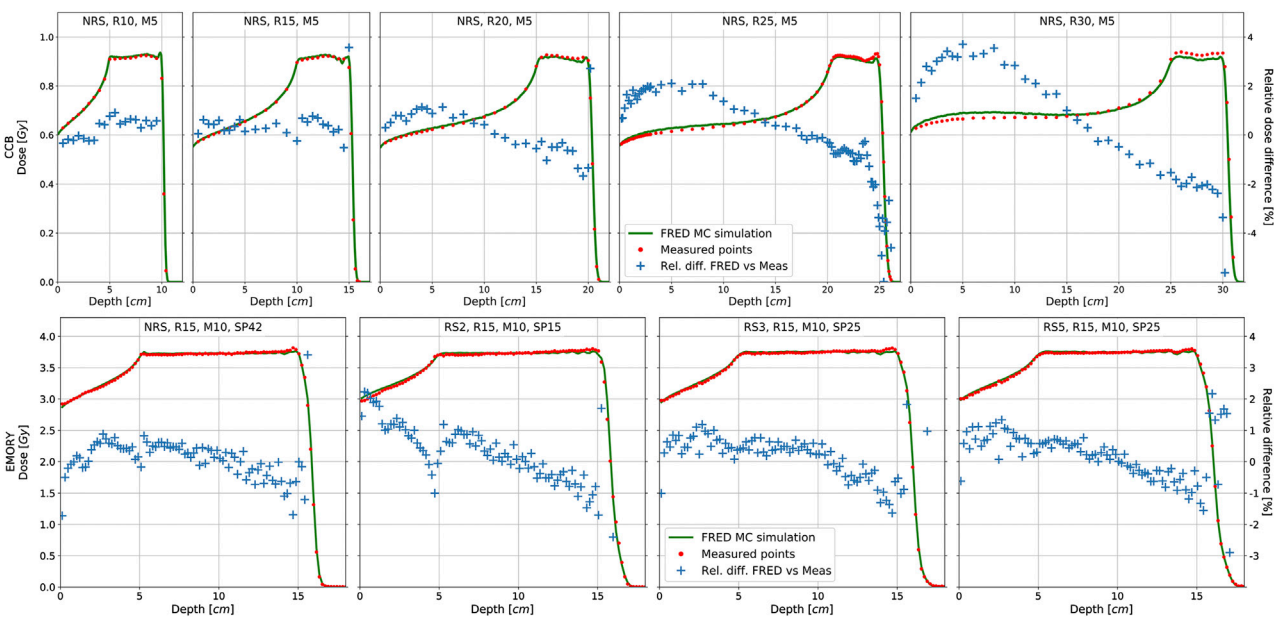

FIGURE 8 | Dose profiles of cubic volumes of SOBP obtained from FRED MC calculations (solid line) and measurements (dots) for CCB **(top panel)** and EMORY **(bottom panel)** facilities. The relative dose difference between the measurement and simulation is illustrated by crosses.

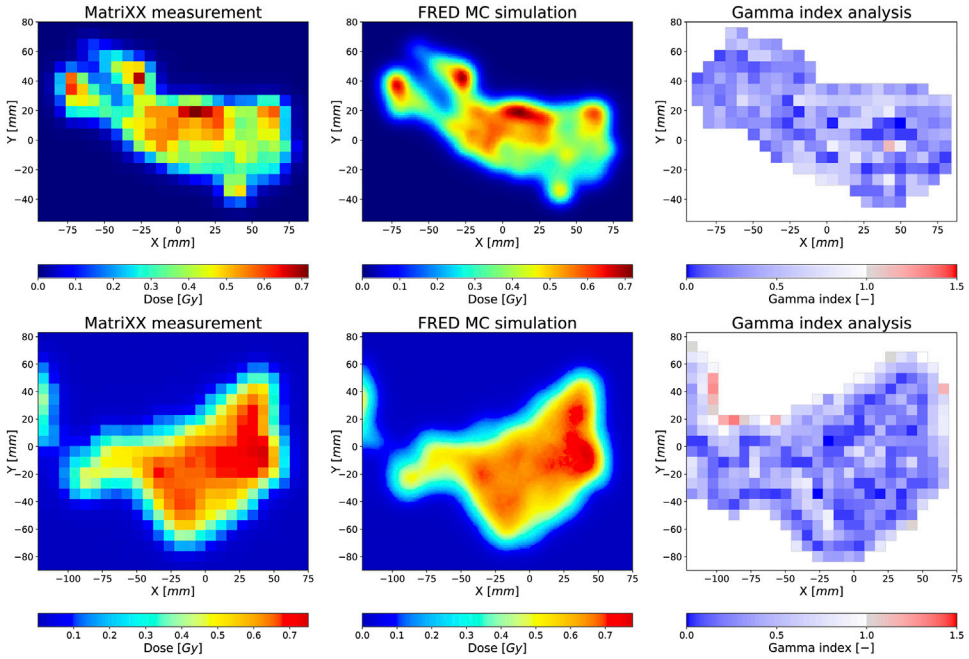

FIGURE 9 | A transversal 2D dose distribution layer measured with an array of ionization chambers in water phantom **(left panel)**, obtained from FRED MC simulations **(middle panel)** and a GI map computed comparing FRED simulation and measurement using GI (2%/2 mm) method **(right panel)**. GI passing rate is 99.53% for the CCB case shown in the top panels and 95.95% for EMORY case shown in bottom panel.

time ranged from 21 s to 6′26 min (average value 2′28 (1′25) min (1σ)) with the average tracking rate of 2.9 (1.1)×10^5 p^+/s (1σ).

4 DISCUSSION

We have built a proton beam model libraries for FRED MC code according to the QA protocols, and we accomplished acceptance tests required for beam model validation in a commercial TPS at proton therapy facilities. We performed MC commissioning avoiding the nozzle geometry modeling, similar to the work presented by other groups [10, 32, 33]. The beam model library parameters containing the information on initial proton energy and energy spread, lateral beam propagation, and dosimetric calibration were identified in 10 MeV energy steps in the therapeutic energy range to best fit the commissioning measurements of proton pencil

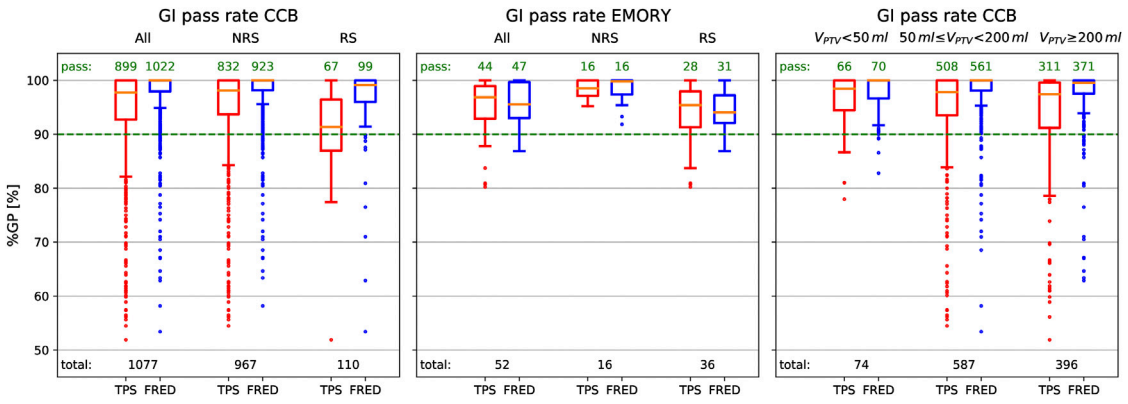

FIGURE 10 | Evaluation of gamma index passing rate (%GP) for 2D dose maps obtained from patient QA of 1,077 layers measured in CCB **(left and right panels)** and of 52 layers measured in EMORY **(middle panel)**. Red and blue box plots correspond to the distribution of %GP obtained from the comparison of measurements to TPS and FRED calculations, respectively. In the left and middle panels, we compared the layers planned with range shifter (RS) and without range shifter (NRS), whereas in the right panel, small (V_{PTV} < 50 ml), medium (50 ml ≤ V_{PTV} < 200 ml), and large (V_{PTV} ≥ 200 ml) PTV volumes. Green numbers labeled as "pass" stand for the number of cases passing %GP > 90% criterion, whereas "total" is the population of a given group.

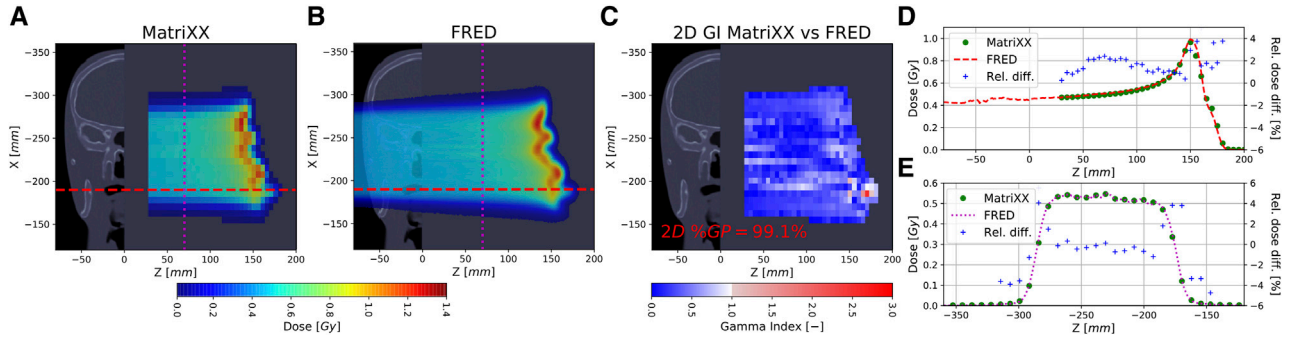

FIGURE 11 | The experimental validation of FRED simulations in heterogeneous CIRS phantom. Panel **(A)**: measurement of 3D dose distribution in water phantom performed using MatriXX. Panel **(B)**: FRED simulation of 3D dose distribution. Panel **(C)**: 2D GI map (2%/2 mm) obtained comparing experiment to FRED simulations. The color maps on panels **A–C** are overlaid on CT scan of CIRS and water phantom. Panels **(D)** and **(E)** show longitudinal and lateral profiles, respectively, obtained from measurements (dots) and simulations (solid line). See **Supplementary Material** for the complete report of the validation.

beams (cf. **Section 3.1**). A submillimeter agreement between simulated and measured Bragg peaks shape and range in water and lateral beam sizes in air and in solid phantoms was obtained with and without range shifter for beam model of two facilities of different beam line design.

In the study, we assumed the uncertainty of single pencil beam and SOBP depth dose profile measurements to be ± 3%. The uncertainty of positioning of the ionization chamber in the water phantom is about 0.3 mm. The uncertainty of the lateral pencil beam size measurement performed with scintillating screen (*Lynx* detector) in air and in the RW3/PMMA slab phantom is ± 0.1 mm, whereas the measurement with IC23 has 0.5 mm uncertainty [32]. We estimate the uncertainty of the slab phantom positioning at 1 mm, but it has negligible impact on the beam lateral profile measurements.

We performed beam model commissioning and validation using the proton per pencil beam statistics that it is required to assure no impact of the statistical uncertainty on these results. For single pencil beams, 10^8 protons per beam offer statistical uncertainty below 1% in 3σ distance from the beam core, when simulations are performed in $1 \times 1 \times 1$ mm^3 grid. Lower statistics can be used for recalculation of treatment plans in water in the same $1 \times 1 \times 1$ mm^3 grid because dose distribution is obtained from superposition of hundreds of pencil beams. We found that for treatment plan recalculation in water, the statistical uncertainty below 1% can be achieved using 10^5 protons per beam for small fields. For clinical application of FRED, the limiting factor is the time of simulations. We found that for resampling the patient geometry in CT to $1.5 \times 1.5 \times 1.5$ mm^3, 10^4 primaries per pencil beams can be used, achieving statistical uncertainty of about 2%. We consider this setting as a good compromise between simulation time and simulation accuracy, allowing treatment plan recalculation in CT scan within a few minutes. No statistical uncertainty of the dose calculated with analytical TPS used as CCB was considered, whereas the dose was calculated with the statistical uncertainty of 0.5% in MC-based RayStation TPS on $2 \times 2 \times 2$ mm^3 grid in water phantom and 3×3×3 mm^3 grid in patient CT.

The comparison of FRED simulations to QA measurements in water presented in **Section 3.2** indicates that, on average, FRED dose distributions agree better with measurements than the prediction made by TPS pencil beam algorithm used in CCB (**Figure 9**, left panel); however, FRED dose distributions are comparable to predictions of commercial MC-based TPS used in EMORY (**Figure 9**, middle panel). Analysis of CCB patient QA data shows that for small, medium, and large PTV volumes, on average, the dose distributions computed by FRED agree better with measurements when compared with dose distributions computed with pencil beam algorithm (**Figure 9**, right panel). We have not observed substantial differences in FRED dose calculation accuracy between different PTV volume categories. Note that small PTV volumes ranging from 28.5 to 50 ml were investigated for CCB. In **Section 3.3**, we presented the results of end-to-end FRED validation of FRED simulations. For various beam energies, large air gaps, and setups with and without range shifter, we compared FRED simulations with measurements of 3D dose distributions behind anthropomorphic CIRS head phantom containing high-density gradients on the boundary between head bones and nasal cavities. The high accuracy of the FRED dose calculations was confirmed in the results of GI tests better than 99% for all of the investigated cases.

Comparison of experimental results in homogeneous media and anthropomorphic phantom with FRED simulations (cf. **Sections 3.2 and 3.3** and **Supplementary Materials**) indicates that fast dose recalculations in patient CT performed with FRED (cf. **Section 3.4**) is a very accurate simulation of proton treatment. A retrospective treatment planning study and the statistical evaluation of DVH parameters are example of routine clinical application of FRED for patient QA. The dose nonuniformities in PTV shown in an example CCB patient case recalculated with FRED (**Figure 12**) are also observed in the analysis of D_{mean}/D_p and HI for 122 patient cases summarized in **Figure 13**. The differences of the mean dose delivered to PTV structures, calculated by FRED and predicted by TPS are more pronounced for small PTV volumes (**Figure 13**, left panel). FRED calculations predict dose nonuniformity for small, medium, and large PTV volumes, which cannot be calculated with analytical TPS used in Krakow. In general, dose distributions are less conformal in small targets than in large targets because it is predicted both by

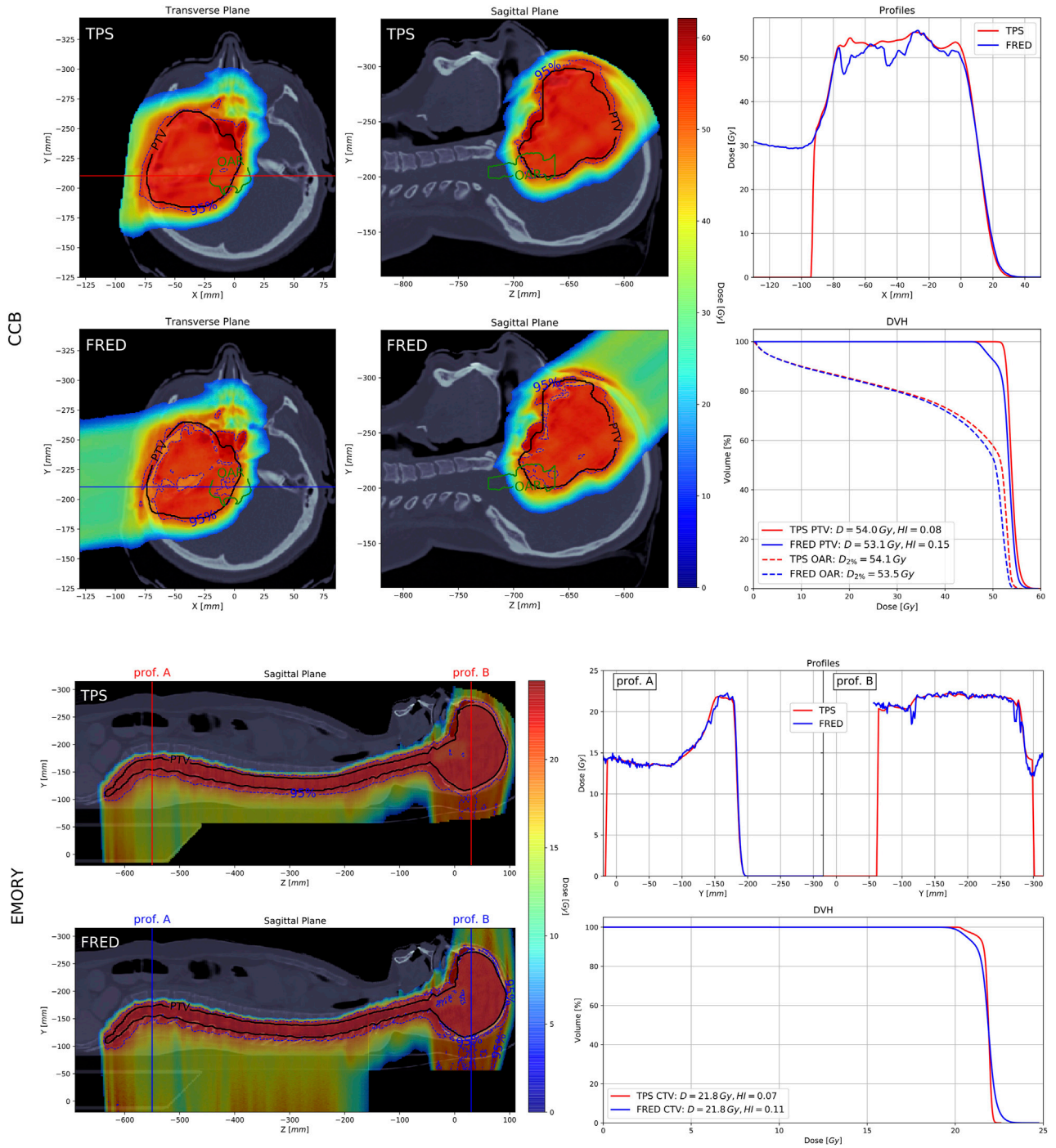

FIGURE 12 | The evaluation of the treatment plan of patient treated at CCB **(top panels)** and at EMORY **(bottom panels)**. On the left panels, dose distributions computed with clinical TPS and FRED are shown. PTV (black solid line) and 95% isodose (blue dashed line) are delineated. The corresponding dose profiles and DVHs are shown in top-right and bottom-right panels, respectively.

FRED simulations and by TPS pencil beam algorithm calculations (**Figure 13**, right panel). Note that these clinical results, both from TPS and FRED, include uncertainties related to acquisition of commissioning data, beam model implementation, CT calibration, and the like. On the other hand, the distribution of D_{mean}/D_p, HI, and CI indicate that overall, the dose distribution calculations performed with both clinical TPS and FRED are within the clinically relevant acceptance.

In clinical practice, additional information about dose, LET and RBE-weighted dose distributions calculated with FRED can be an

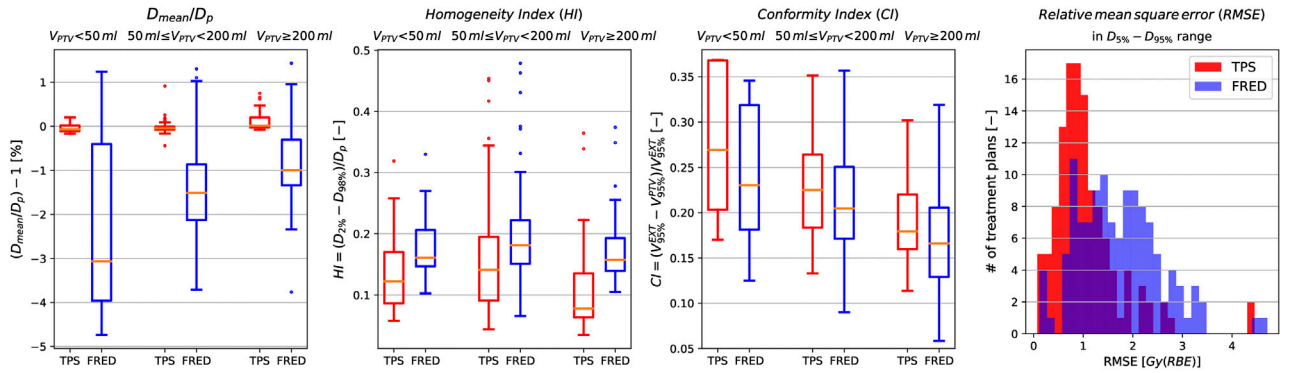

FIGURE 13 | The parameters characterizing the quality of 122 dose distribution obtained from patient treatment plans computed with clinical TPS (blue) and FRED (red) for small (V_{PTV} < 50 ml), medium (50 ml ≤ V_{PTV} < 200 ml), and large (V_{PTV} ≥ 200 ml) PTV. The left panel shows the ratio D_{mean}/D_p, the middle-left panel shows the homogeneity index (HI), the middle-right panel the conformity index (CI), and the right panel shows relative mean square error between a prescribed dose and DVH in PTV computed with FRED and clinical TPS (the dark blue area depicts overlapping of two histograms).

indication for medical physicists to revise the treatment plan optimization or to perform additional experimental validation, when the results deviate from the predictions of TPS exceeding acceptance criteria. The time performance of FRED enables to obtain this information within about 2.5 min. FRED is currently adapted to be executed as a stand-alone library, which will enable its easy integration with commercial TPS (eg, Eclipse or RayStation) and dedicated software tools for patient QA (eg, MyQAion).

Schiavi et al. [34] reported that simulation of dose deposition in a water phantom induced by 10^6 primary protons can be reduced from 22 min required by FLUKA MC code to 0.5 s when employing FRED running on two GPU modules [34]. Regarding dose distribution simulation in patients, Grassberger, Anthony Lomax, and Paganetti [33] reported that the patient simulation for the head and neck took 371 min (10^6 primaries simulated) on single CPU using TOPAS (Geant4), which corresponds to a tracking rate of 45 p^+/s, whereas the average tracking rate obtained with FRED is 2.9×10^5 p^+/s in patient CT rescaled to $1.5 \times 1.5 \times 1.5$ mm^3 using two GPUs. The time performance results presented in this article can be linearly scaled as a function of the number of GPU cards applied [34]. Note that the simulation time depends on the number of primaries simulated per pencil beam, tumor depth (i.e. the beam energy), and scoring resolution used for the simulation. The most accurate dose calculations in tissue heterogeneities can be obtained performing the simulation in original CT grid. In order to achieve the statistical uncertainty below 1% on CT grid used at CCB $0.7 \times 0.7 \times 1.2$ mm^3, 10^5 primaries per pencil beam should be simulated. The average simulation time for the patient group investigated in **Section 3.4** in original CT resolution is $31.8^{161.8}_{3.5}$ (σ = 23.8) min.

The clinical application of proton therapy and development of new treatment protocols, for example, studies on the reduction of safety margins accounting for treatment plan robustness, require treatment planning studies that can only be performed analyzing several treatment planning approaches. The total simulation time of all 122 patient cases shown in **Section 3.4** was about 5 h. An example study of 10 possible treatment planning approaches on our patient group could be performed using FRED within about two days of simulation. Another application is robust optimization of treatment plans, that is, particularly relevant for treatment planning of moving targets, when several dose distributions must be computed on 4D CT. Performing such studies without the time performance offered by FRED would not be possible with any general purpose MC code in reasonable time.

In addition to its clinical applications, the time performance of FRED enables preparation of the proton beam model faster with respect to a general purpose MC codes. This is particularly useful when a new beam model must be implemented in the clinical routine due to technical modifications or maintenance at accelerator. When the facility beam commissioning measurements are available, the GPU acceleration offered by FRED allows to parametrize the beam model within about 12 h, requiring minimal manual interventions. This potentially enables easy and quick use of FRED for research and patient QA purposes in most of the proton facilities with little experimental efforts.

5 CONCLUSION

In this article, we share our experience on commissioning and validation of GPU-accelerated MC code FRED based on commissioning measurements of two proton beam therapy facilities of different beam line design: CCB (Krakow) from IBA and EMORY (Atlanta) from Varian. FRED passed acceptance tests required to approve TPS for clinical use. The approach we used combines the application of a new GPU-accelerated MC code, implementation of two proton beam lateral beam propagation models, automated beam model optimization method, experimental validation of beam model parameters in an anthropomorphic phantom with and without range shifter, and comparison of patient treatment plans computed with FRED and clinical TPS in patient CT. Our commissioning and validation results demonstrate the universal and accurate implementation of the physics models in FRED, allowing its flexible applications for medical physics and research purposes. The application of FRED as a secondary MC engine for patient QA in clinical routine is

foreseen in Krakow proton facility. FRED is currently used for treatment planning studies evaluating radiobiologically effective dose using variable RBE.

DATA AVAILABILITY STATEMENT

The datasets generated during and/or analysed during the current study are available from the corresponding author on reasonable request.

AUTHOR CONTRIBUTIONS

JG, MG, AS, ASc, and AR developed the beam model for CCB. JG developed automated beam model library implementation method and performed data analysis to validate the beam model. JG, MG and ASc developed the emittance and virtual point source models for FRED. JG, NM and AR designed, while JG, MG, NM, AR, MR performed validation experiments with proton beams at CCB. JG performed data analysis of experiments. KC, NK and MPN supported data analysis. RK provided access to beam model commissioning and validation data from CCB. JG participated in commissioning measurements in CCB. CC and LL provided commissioning, validation, and patient data from EMORY. JG implemented beam model for EMORY and performed analysis of validation and patient data. RK and EP provided access to patient data from CCB. KK and MR exported the patient data from clinical TPS. MG and JG performed simulations and analysis of patient data. ASc and VP developed and made substantial improvements in FRED source code required to enable presented studies. MD, IR, ES, and FT provided expertise in beam modeling and medical physics. JG prepared all figures. JG and AR designed the project and drafted the manuscript. AR acquired funding. All the authors reviewed and approved the manuscript.

ACKNOWLEDGMENTS

This project is carried out within the Reintegration program of the Foundation for Polish Science cofinanced by the EU under the European Regional Development Fund—grant no. POIR.04.04.00-00-2475/16-00. MG acknowledge the support of InterDokMed project no. POWR.03.02.00-00-I013/16. This research was supported in part by computing resources of ACC Cyfronet AGH. We acknowledge the support of NVIDIA Corporation with the donation of the GPU used for this research. We acknowledge Aleksander Krempa from CCB Krakow proton therapy center for IT support during implementation of this project.

SUPPLEMENTARY MATERIAL

The Supplementary Material for this article can be found online at: https://www.frontiersin.org/articles/10.3389/fphy.2020.567300/full#supplementary-material.

REFERENCES

1. Paganetti H, Jiang H, Parodi K, Slopsema R, Engelsman M. Clinical implementation of full Monte Carlo dose calculation in proton beam therapy. *Phys Med Biol* **53** (2008) 4825.
2. Saini J, Maes D, Egan A, Bowen SR, James SS, Janson M, et al. Dosimetric evaluation of a commercial proton spot scanning Monte-Carlo dose algorithm: comparisons against measurements and simulations. *Phys Med Biol* **62** (2017) 7659.
3. Widesott L, Lorentini S, Fracchiolla F, Farace P, Schwarz M. Improvements in pencil beam scanning proton therapy dose calculation accuracy in brain tumor cases with a commercial Monte Carlo algorithm. *Phys Med Biol* **63** (2018) 145016. doi:10.1088/1361-6560/aac279
4. Tommasino F, Fellin F, Lorentini S, Farace P. Impact of dose engine algorithm in pencil beam scanning proton therapy for breast cancer. *Phys Med: Eur J Med Plants* **50** (2018) 7–12. doi:10.1016/j.ejmp.2018.05.018
5. Paganetti H. Range uncertainties in proton therapy and the role of Monte Carlo simulations. *Phys Med Biol* **57** (2012) 99–117. doi:10.1088/0031-9155/57/11/R99
6. Langner UW, Mundis M, Strauss D, Zhu M, Mossahebi S. A comparison of two pencil beam scanning treatment planning systems for proton therapy. *J Appl Clin Med Phys* **19** (2018) 156–63. doi:10.1002/acm2.12235
7. Chang CW, Huang S, Harms J, Zhou J, Zhang R, Dhabaan A, et al. A standardized commissioning framework of Monte Carlo dose calculation algorithms for proton pencil beam scanning treatment planning systems. *Med Phys* (2020) doi:10.1002/mp.14021
8. Trnková P, Knäusl B, Actis O, Bert C, Biegun AK, Boehlen TT, et al. Clinical implementations of 4D pencil beam scanned particle therapy: report on the 4D treatment planning workshop 2016 and 2017. *Phys Med* **54** (2018) 121–30. doi:10.1016/j.ejmp.2018.10.002
9. Guterres Marmitt G, Pin A, Ng Wei Siang K, Janssens G, Souris K, Cohilis M, et al. Platform for automatic patient quality assurance via Monte Carlo simulations in proton therapy. *Phys Med* **70** (2020) 49–57. doi:10.1016/j.ejmp.2019.12.018
10. Fracchiolla F, Lorentini S, Widesott L, Schwarz M. Characterization and validation of a Monte Carlo code for independent dose calculation in proton therapy treatments with pencil beam scanning. *Phys Med Biol* **60** (2015) 8601–19. doi:10.1088/0031-9155/60/21/8601
11. Winterhalter C, Fura E, Tian Y, Aitkenhead A, Bolsi A, Dieterle M, et al. Validating a Monte Carlo approach to absolute dose quality assurance for proton pencil beam scanning. *Phys Med Biol* **63** (2018) doi:10.1088/1361-6560/aad3ae
12. Johnson JE, Beltran C, Wan Chan Tseung H, Mundy DW, Kruse JJ, Whitaker TJ, et al. Highly efficient and sensitive patient-specific quality assurance for spot-scanned proton therapy. *PloS One* **14** (2019) doi:10.1371/journal.pone.0212412
13. Zhu XR, Li Y, Mackin D, Li H, Poenisch F, Lee AK, et al. Towards effective and efficient patient-specific quality assurance for spot scanning proton therapy. *Cancers* **7** (2015) 631–47. doi:10.3390/cancers7020631
14. Matter M, Nenoff L, Meier G, Weber DC, Lomax AJ, Albertini F. Alternatives to patient specific verification measurements in proton therapy: a comparative experimental study with intentional errors. *Phys Med Biol* **63** (2018) doi:10.1088/1361-6560/aae2f4
15. Battistoni G, Boehlen T, Cerutti F, Chin PW, Esposito LS, Fassò A, et al. Overview of the FLUKA code. *Ann Nucl Energy* **82** (2015) 10–8. doi:10.1016/j.anucene.2014.11.007
16. Allison J, Amako K, Apostolakis J, Araujo H, Dubois PA, Asai M, et al. Geant4 developments and applications. *Nuclear Science, IEEE Trans Nucl Sci* **53** (2006) 270–8. doi:10.1109/TNS.2006.869826
17. Jarlskog CZ, Paganetti H. Physics settings for using the Geant4 toolkit in proton therapy. *Nuclear Science, IEEE Transactions on Nuclear Science* **55** (2008) 1018–25.
18. Henkner K, Sobolevsky N, Jäkel O, Paganetti H. Test of the nuclear interaction model in SHIELD-HIT and comparison to energy distributions from GEANT4. *Phys Med Biol* **54** (2009) N509.

19. Jan S, Santin G, Strul D, Staelens S, Assié K, Autret D, et al. GATE: a simulation toolkit for PET and SPECT. *Phys Med Biol* **49** (2004) 4543.
20. Jan S, Benoit D, Becheva E, Carlier T, Cassol F, Descourt P, et al. Gate V6: a major enhancement of the GATE simulation platform enabling modelling of CT and radiotherapy. *Phys Med Biol* **56** (2011) 881.
21. Sarrut D, Bardiès M, Boussion N, Freud N, Jan S, Létang J, et al. A review of the use and potential of the GATE Monte Carlo simulation code for radiation therapy and dosimetry applications. *Med Phys* **41** (2014) 64301. doi:10.1118/1.4871617
22. Perl J, Shin J, Schumann J, Faddegon B, Paganetti H. TOPAS: an innovative proton Monte Carlo platform for research and clinical applications. *Med Phys* **39** (2012) 6818–37. doi:10.1118/1.4758060
23. Testa M, Schümann J, Lu HM, Shin J, Faddegon B, Perl J, et al. Experimental validation of the TOPAS Monte Carlo system for passive scattering proton therapy. *Med Phys* **40** (2013) 121719. doi:10.1118/1.4828781
24. Jia X, Schümann J, Paganetti H, Jiang SB. GPU-based fast Monte Carlo dose calculation for proton therapy. *Phys Med Biol* **57** (2012) 7783–97. doi:10.1088/0031-9155/57/23/7783
25. Qin N, Botas P, Giantsoudi D, Schuemann J, Tian Z, Jiang SB, et al. Recent developments and comprehensive evaluations of a GPU-based Monte Carlo package for proton therapy. *Phys Med Biol* **61** (2016) 7347.
26. Giantsoudi D, Schuemann J, Jia X, Dowdell S, Jiang S, Paganetti H. Validation of a GPU-based Monte Carlo code (gPMC) for proton radiation therapy: clinical cases study. *Phys Med Biol* **60** (2015) 2257.
27. Wan Chan Tseung H, Ma J, Beltran C. A fast GPU-based Monte Carlo simulation of proton transport with detailed modeling of nonelastic interactions. *Med Phys* **42** (2015) 2967–78. doi:10.1118/1.4921046
28. Mein S, Choi K, Kopp B, Tessonnier T, Bauer J, Ferrari A, et al. Fast robust dose calculation on GPU for high-precision 1H, 4He, 12C and 16O ion therapy: the FRoG platform. *Sci Rep* **8** (2018) 14829. doi:10.1038/s41598-018-33194-4
29. Choi K, Mein SB, Kopp B, Magro G, Molinelli S, Ciocca M, et al. FRoG - a new calculation engine for clinical investigations with proton and carbon ion beams at cnao. *Cancers* **10** (2018) doi:10.3390/cancers10110395
30. Ma CMC, Chetty IJ, Deng J, Faddegon B, Jiang SB, Li J, et al. Beam modeling and beam model commissioning for Monte Carlo dose calculation-based radiation therapy treatment planning: report of AAPM Task Group 157. *Med Phys* **47** (2020) e1–e18. doi:10.1002/mp.13898
31. Parodi K, Mairani A, Brons S, Hasch BG, Sommerer F, Naumann J, et al. Monte Carlo simulations to support start-up and treatment planning of scanned proton and carbon ion therapy at a synchrotron-based facility. *Phys Med Biol* **57** (2012) 3759.
32. Grevillot L, Bertrand D, Dessy F, Freud N, Sarrut D. A Monte Carlo pencil beam scanning model for proton treatment plan simulation using GATE/GEANT4. *Phys Med Biol* **56** (2011) 5203.
33. Grassberger C, Lomax A, Paganetti H. Characterizing a proton beam scanning system for Monte Carlo dose calculation in patients. *Phys Med Biol* **60** (2015) 633. doi:10.1088/0031-9155/60/2/633
34. Schiavi A, Senzacqua M, Pioli S, Mairani A, Magro G, Molinelli S, et al. Fred: a GPU-accelerated fast-Monte Carlo code for rapid treatment plan recalculation in ion beam therapy. *Phys Med Biol* **62** (2017) 7482–504. doi:10.1088/1361-6560/aa8134
35. Winterhalter C, Aitkenhead A, Oxley D, Richardson J, Weber DC, MacKay RI, et al. Pitfalls in the beam modelling process of Monte Carlo calculations for Proton pencil beam scanning. *Br J Radiol* (2020) 20190919. doi:10.1259/bjr.20190919
36. Schneider U, Pedroni E, Lomax A. The calibration of CT Hounsfield units for radiotherapy treatment planning. *Phys Med Biol* **41** (1996) 111.
37. Varian Medical System Inc. Proton algorithm reference guide (Eclipse). *Tech. Rep. August*, Varian Medical Systems, Inc., Palo Alto (2013)
38. ICRU. Report 90: Key data for ionizing-radiation dosimetry: measurement standards and applications. *J Int Comm Radiation Units Measure* **14** (2016) 1–118. doi:10.1093/jicru/ndw029
39. Zhu RX, Poenisch F, Lii M, Sawakuchi GO, Titt U, Bues M, et al. Commissioning dose computation models for spot scanning proton beams in water for a commercially available treatment planning system. *Med Phys* **40** (2013) 041723. doi:10.1118/1.4798229
40. Langner UW, Eley JG, Dong L, Langen K. Comparison of multi-institutional Varian ProBeam pencil beam scanning proton beam commissioning data. *J Appl Clin Med Phys* **18** (2017) 96–107. doi:10.1002/acm2.12078
41. Almhagen E, Boersma DJ, Nyström H, Ahnesjö A. A beam model for focused proton pencil beams. *Phys Med* **52** (2018) 27–32. doi:10.1016/j.ejmp.2018.06.007
42. Twiss RQ, Frank NH. Orbital stability in a proton synchrotron. *Rev Sci Instrum* **20** (1949) 1–17. doi:10.1063/1.1741343
43. Bortfeld T. An analytical approximation of the Bragg curve for therapeutic proton beams. *Med Phys* **24** (1997) 2024. doi:10.1118/1.598116
44. [Dataset]Gajewski J. *Bragg peak analysis* (2017)
45. Nelder JA, Mead R. A simplex method for function minimization. *Comput J* **7** (1965) 308–13. doi:10.1093/comjnl/7.4.308
46. Lin L, Ainsley CG, Mertens T, De Wilde O, Talla PT, McDonough JE. A novel technique for measuring the low-dose envelope of pencil-beam scanning spot profiles. *Phys Med Biol* **58** (2013) doi:10.1088/0031-9155/58/12/N171
47. Lin L, Huang S, Kang M, Solberg TD, McDonough JE, Ainsley CG. Technical Note: validation of halo modeling for proton pencil beam spot scanning using a quality assurance test pattern. *Med Phys* **42** (2015) 5138–43. doi:10.1118/1.4928157
48. Low DA, Harms WB, Mutic S, Purdy JA. A technique for the quantitative evaluation of dose distributions. *Med Phys* **25** (1998) 656–61. doi:10.1118/1.598248
49. Biggs S, Jennings M. *PyMedPhys python package* (2019)
50. Albertini F, Casiraghi M, Lorentini S, Rombi B, Lomax AJ. Experimental verification of IMPT treatment plans in an anthropomorphic phantom in the presence of delivery uncertainties. *Phys Med Biol* **56** (2011) 4415–31. doi:10.1088/0031-9155/56/14/012
51. ICRU. Report 83. Prescribing, recording, and reporting photon-beam intensity-modulated radiation therapy (IMRT). *J Int Commission Radiation Units Measure* **10** (2010) 112.
52. Pathak P, Vashisht S. A quantitative analysis of intensity-modulated radiation therapy plans and comparison of homogeneity indices for the treatment of gynecological cancers. *J Med Phys* **38** (2013) 67–73. doi:10.4103/0971-6203.111309

Conflict of Interest: The authors declare that the research was conducted in the absence of any commercial or financial relationships that could be construed as a potential conflict of interest.

frontiers in Physics

ORIGINAL RESEARCH
published: 27 January 2021
doi: 10.3389/fphy.2020.578388

Detection of Interfractional Morphological Changes in Proton Therapy: A Simulation and *In Vivo* Study With the INSIDE In-Beam PET

Elisa Fiorina[1,2], Veronica Ferrero[1], Guido Baroni[2,3], Giuseppe Battistoni[4], Nicola Belcari[5,6], Niccolo Camarlinghi[5,6], Piergiorgio Cerello[1], Mario Ciocca[2], Micol De Simoni[7,8], Marco Donetti[2], Yunsheng Dong[4,9], Alessia Embriaco[10], Marta Fischetti[8,11], Gaia Franciosini[7,8], Giuseppe Giraudo[1], Aafke Kraan[5], Francesco Laruina[5,6], Carmela Luongo[5,12], Davide Maestri[2], Marco Magi[11], Giuseppe Magro[2], Etesam Malekzadeh[13], Carlo Mancini Terracciano[7,8], Michela Marafini[8,14], Ilaria Mattei[4], Enrico Mazzoni[5], Paolo Mereu[1], Riccardo Mirabelli[7,8,14], Alfredo Mirandola[2], Matteo Morrocchi[5,6], Silvia Muraro[4], Alessandra Patera[1], Vincenzo Patera[8,11,14], Francesco Pennazio[1], Alessandra Retico[5,6], Angelo Rivetti[1], Manuel Dionisio Da Rocha Rolo[1], Valeria Rosso[5,6], Alessio Sarti[8,11,14], Angelo Schiavi[8,11], Adalberto Sciubba[11,14,15], Elena Solfaroli Camillocci[7,8,16], Giancarlo Sportelli[5,6], Sara Tampellini[2], Marco Toppi[11,15], Giacomo Traini[8,14], Serena Marta Valle[4], Francesca Valvo[2], Barbara Vischioni[2], Viviana Vitolo[2], Richard Wheadon[1] and Maria Giuseppina Bisogni[5,6]*

[1]Istituto Nazionale di Fisica Nucleare, Sezione di Torino, Torino, Italy, [2]Centro Nazionale di Adroterapia Oncologica, Pavia, Italy, [3]Politecnico di Milano, Milano, Italy, [4]Istituto Nazionale di Fisica Nucleare, Sezione di Milano, Milano, Italy, [5]Istituto Nazionale di Fisica Nucleare, Sezione di Pisa, Pisa, Italy, [6]Dipartimento di Fisica, Universitá di Pisa, Pisa, Italy, [7]Dipartimento di Fisica, Sapienza Universitá di Roma, Roma, Italy, [8]Istituto Nazionale di Fisica Nucleare, Sezione di Roma, Roma, Italy, [9]Dipartimento di Fisica, Universitá di Milano, Milano, Italy, [10]Istituto Nazionale di Fisica Nucleare, Sezione di Pavia, Pavia, Italy, [11]Dipartimento di Scienze di Base e Applicate per l'Ingegneria, Sapienza Universitá di Roma, Roma, Italy, [12]Dipartimento di Chimica, Universitá di Pisa, Pisa, Italy, [13]Medical Physics Department, Tarbiat Modares University, Tehran, Iran, [14]Museo Storico della Fisica e Centro Studi e Ricerche "E. Fermi", Roma, Italy, [15]Istituto Nazionale di Fisica Nucleare, Sezione dei Laboratori di Frascati, Roma, Italy, [16]Scuola di Specializzazione in Fisica Medica, Sapienza Università di Roma, Roma, Italy

OPEN ACCESS

Edited by:
Claudia Kuntner,
Austrian Institute of Technology (AIT), Austria

Reviewed by:
Gérard Montarou,
UMR6533 Laboratoire de Physique de Clermont (LPC), France
Denis Dauvergne,
Centre National de la Recherche Scientifique (CNRS), France

***Correspondence:**
Veronica Ferrero
veronica.ferrero@to.infn.it

Specialty section:
This article was submitted to Medical Physics and Imaging, a section of the journal Frontiers in Physics

Received: 30 June 2020
Accepted: 22 December 2020
Published: 27 January 2021

Citation:
Fiorina E, Ferrero V, Baroni G, Battistoni G, Belcari N, Camarlinghi N, Cerello P, Ciocca M, De Simoni M, Donetti M, Dong Y, Embriaco A, Fischetti M, Franciosini G, Giraudo G, Kraan A, Laruina F, Luongo C, Maestri D, Magi M, Magro G, Malekzadeh E, Mancini Terracciano C, Marafini M, Mattei I, Mazzoni E, Mereu P, Mirabelli R, Mirandola A, Morrocchi M, Muraro S, Patera A, Patera V, Pennazio F, Retico A, Rivetti A, Da Rocha Rolo MD, Rosso V, Sarti A, Schiavi A, Sciubba A, Solfaroli Camillocci E, Sportelli G, Tampellini S, Toppi M, Traini G, Valle SM, Valvo F, Vischioni B, Vitolo V, Wheadon R and Bisogni MG (2021) Detection of Interfractional Morphological Changes in Proton Therapy: A Simulation and In Vivo Study With the INSIDE In-Beam PET. Front. Phys. 8:578388. doi: 10.3389/fphy.2020.578388

In particle therapy, the uncertainty of the delivered particle range during the patient irradiation limits the optimization of the treatment planning. Therefore, an in vivo treatment verification device is required, not only to improve the plan robustness, but also to detect significant interfractional morphological changes during the treatment itself. In this article, an effective and robust analysis to detect regions with a significant range discrepancy is proposed. This study relies on an in vivo treatment verification by means of in-beam Positron Emission Tomography (PET) and was carried out with the INSIDE system installed at the National Center of Oncological Hadrontherapy (CNAO) in Pavia, which is under clinical testing since July 2019. Patients affected by head-and-neck tumors treated with protons have been considered. First, in order to tune the analysis parameters, a Monte Carlo (MC) simulation was carried out to reproduce a patient who required a replanning because of significant morphological changes found during the treatment. Then, the developed approach was validated on the experimental measurements of three patients recruited for the INSIDE clinical trial (ClinicalTrials.gov ID: NCT03662373), showing the capability to estimate the treatment compliance with the prescription both when no

morphological changes occurred and when a morphological change did occur, thus proving to be a promising tool for clinicians to detect variations in the patients treatments.

Keywords: proton therapy, *in vivo* treatment verification, in-beam pet, range monitoring, Monte Carlo simulation, adaptive therapy, clinical trial

1 INTRODUCTION

In vivo treatment verification is currently an open issue in particle therapy, driven by the clinical need to increase the treatment planning optimization [1], through the reduction of range uncertainties that might give dose distributions significantly different from the clinical prescription, thus requiring a plan adaptation.

On the one hand, the proton energy deposition distribution allows releasing the prescribed dose to the tumor volume with a lower dose to the healthy tissues in comparison with the most advanced techniques of conventional radiotherapy [2]. On the other hand, particle therapy is more sensitive than photon radiotherapy to differences in the particle range inside the patient body [3]. During treatment planning, the range uncertainty is taken into account in order to design the most robust irradiation plan. In clinics, the safety margin included in the treatment planning and calculated on the basis of the range uncertainty contributions is of about $(2.5 - 3.5)\% + 1 - 3$ mm [4]. This evaluation takes into account several sources of uncertainty, some of which are independent of the dose calculation (i.e., beam reproducibility, patient setup, and measurement in water for commissioning), while others depend on the dose calculation (CT calibration, tissue conversion, mean ionization energy estimation, and range degradation for complex inhomogeneities).

In addition, in some cases, the patient morphology changes during the treatment period and, even though this is recognized as a cause of suboptimal irradiation [5], these modifications are not so easy to model and quantify. They strongly depend on the type of tumor (e.g., early therapy response and fast growth of the tumor mass) and irradiation district (moving organs, presence of cavities, toxicity, and site inflammation). In [6], for example, a retrospective analysis was performed over 730 patients treated with proton therapy and affected by cranial and extracranial tumor. Patients underwent periodic CTs to estimate morphological or anatomic variations and in 5.5% of cases an adaptive replanning was required. Hence, in particle therapy, morphological and anatomic changes must be monitored to smoothly tailor the treatment plan to the Clinical Target Volume (CTV [7]) without any undesired increase of the dose in the surrounding healthy tissues. In literature, this issue is thoroughly explored for lung treatments because the problem is enhanced in case of moving organs and requires an intrafractional optimization [8].

In order to address this crucial treatment optimization, a system able to verify the compliance of the ongoing treatment with the prescribed therapy during the irradiation itself is fundamental.

Positron Emission Tomography (PET) is the most mature in vivo range monitoring technique used in clinics [9–13]. It relies on the production of positron emitters inside the patient due to the nuclear interactions between the primary particles and the tissues. In particular, about 1% of the primary protons undergo nuclear interaction in each cm of range in water [14], inducing a slight activation of the patient tissues that is spatially correlated with the Bragg Peak position of the primary beam [15]. Due to tissue composition, the produced positron emitters are mostly carbon and oxygen isotopes. In particular, ^{11}C, ^{10}C, and ^{15}O, whose half-lives are about 20 min, 19 s, and 2 min, respectively, are the most abundant ones. The former is fundamental to PET scanners acquiring data only after the treatment (i.e., in-room and off-room systems), whereas the others become more important for PET scanners acquiring data during the treatment (in-beam PET). The latter technique, in particular, allows for treatment verification during the irradiation, without slowing down the clinical workflow. In clinics, PET monitoring has already been tested for treatment verification and this approach proved to be able to identify differences in the patient morphology which are significant from the clinical point of view [16, 17]. However, an established and clinically validated analysis, presently still missing, has to be implemented to evaluate whether the detected range differences are actually related to interfractional morphological changes and not to statistical fluctuations.

The INSIDE collaboration built an innovative bimodal device able to perform in vivo verification of both proton and carbon ion treatments during the irradiation [18, 19]. It relies on a planar PET system with two heads [20] and a tracker for secondary charged particles, named Dose Profiler, that exploits the secondary protons emitted during ion treatments (e.g., carbon ion treatments) [21, 22]. The in-beam PET was first tested in vivo in 2016, proving its capability to provide an evaluation of the treatment compliance between two consecutive fractions by acquiring data only during the treatment and thus obtain reliable PET images before the end of the fraction irradiation [18]. This is a key factor to minimize the signal loss due to isotope decay and also to minimize the biological washout. In July 2019, a clinical trial with the INSIDE system (ClinicalTrials.gov ID: NCT03662373) started at the National Center of Oncological Hadrontherapy (CNAO) in Pavia, Italy [23]. Specific head-and-neck and brain pathologies are included in the trial: those in which no morphological changes are expected and, therefore, can be exploited to assess the reproducibility of a range analysis and those in which morphological changes may occur and, therefore, could be helpful to test the sensitivity of the system in terms of variation detection.

In this work, a robust and reliable procedure for detecting interfractional morphological changes by means of in-beam PET detection is proposed. The final aim is to give the physicians a reliable tool representative of the particle range differences

TABLE 1 | Treatment field parameters and irradiation duration times for each of the considered cases.

Patient	Patient position angle	Energy range [MeV]	Number of protons [10^{10}]	Irradiation duration [s]
MCP	B1-270°	66.3–167.7	2.13	231
MCP	B2-0°	67.3–136.5	2.62	141
MCP	B3-180°	66.3–144.4	2.14	165
002P	240°	96.8–144.4	1.64	88 [87, 91]
003P	235°	64.3–155.3	2.21	153 [150, 162]
006P	175°	64.3–151	5.64	239 [205, 274]

detected during in vivo monitoring, useful to evaluate the compliance of the delivered treatment with respect to the prescribed therapy and possibly define a patient-tailored control CTs scheduling.

2 MATERIALS AND METHODS

2.1 Patient Data

In this study, we consider four patients treated with proton therapy at the CNAO facility to test the effectiveness and reliability of the proposed analysis in presence of different degrees of morphological changes during the treatment. First, the analysis was tuned by considering the Monte Carlo (MC) simulation of a patient with a head-and-neck tumor, who required a treatment replanning due to a nasal cavity emptying. This patient (here named MCP) was not part of the INSIDE trial but was chosen because of the severe morphological changes detected during the treatment with the control CT. The analysis was then validated on the experimental measurements of three patients monitored in the framework of the INSIDE clinical trial, which involves a longitudinal monitoring, i.e., a monitoring of the patient treatment sessions, acquiring data on average twice a week. In two of the patients (trial ID: 002P, 003P) no morphological changes occurred, whereas a moderate degree of variation was detected in the third one (trial ID: 006P).

2.1.1 Monte Carlo Simulation Case Study: Replanned Patient

The Monte Carlo simulated patient (MCP) was chosen because of a replanning due to a severe morphological variation in the CTV during the treatment, revealed with a control CT. The patient was a 70-year-old male, affected by Squamous Cell Carcinoma (SCC) of the left sinonasal cavity. The CTV was irradiated with Intensity Modulated Proton Therapy (IMPT) in 33 fractions with 2.0*GyE*/fraction, five fractions/week, to deliver 66*GyE* on the high risk CTV and 60*GyE* on the low risk CTV. Each daily treatment comprised three orthogonal treatment fields, corresponding to the patient position angles 0, 180, and 270° IEC (International Electrotechnical Commission). The treatment characteristics are summarized in **Table 1**.

Because of possible morphological changes due to the inclusion of the sinonasal cavities into the CTV and the close proximity of the right maxillary and frontal sinuses to the target, a control CT was performed after 22 fractions from the beginning of the treatment. **Figure 1** shows the planning and control CTs, with the CTV margins overlaid, where it can be seen that a nasal cavity was almost completely emptied during the treatment course. By calculating with the Treatment Planning System (TPS) the effective dose distribution on the control CT, an overdosage in the surrounding healthy tissues and into the CTV was found; hence, the treatment was replanned.

2.1.2 Experimental Data: Patients Included in the INSIDE Clinical Trial

Three patients recruited in the INSIDE clinical trial (ID: 002P, 003P, 006P) were selected to test the reliability of the proposed analysis. The 002P patient was 80 years old, male, affected by an inoperable skull base meningioma. His IMPT irradiation comprised the delivery of 54*GyE* total dose divided in 30 fractions (1.8*GyE*/fraction). The treatment plan included two fields corresponding to the patient position angles of 240 and 165° IEC, but only the first field was monitored due to mechanical incompatibility of the INSIDE setup with the patient bed movements. The 003P patient was 25 years old, male, affected by recurrent meningioma of the right orbit region after previous surgery and Cyberknife. The CTV was irradiated with IMPT so as to deliver a total dose of 54*GyE* in 27 fractions. The treatment relied on two fields corresponding to the patient position angles of 235 and 180° IEC. Even if both treatment fields were acquired, only the first field was considered for this study. For these two patients, no control CTs were scheduled because patients affected by meningioma are not prone to morphological modifications related to the treatment or the tumor growing/shrinking.

The 006P patient was 39 years old, female, affected by Adenoid Cystic Carcinoma (ACC) of minor salivary glands arising by the rhinopharynx and involving the skull base, the right nasal cavity, and the homolateral maxillary sinus. The CTV was irradiated with IMPT in 35 fractions with conventional fractionation 2.0*GyE*/fraction, five fractions/week, to deliver 70*GyE*. Each daily treatment comprised two opposite beams, corresponding to 15 and 175° IEC angles. Due to mechanical incompatibility of the INSIDE system with the patient couch movements, only the field corresponding to 175° IEC was monitored. A control CT was scheduled after 20 fractions in order to check the correct dose coverage of the target and the prescribed sparing of organs at risk. The planning and control CTs of patient 006P are shown in **Figure 2**: a partial emptying of the cavities due to an early response of the tumor can be appreciated. The modification in the dose distribution due to the changed morphology produced an increase of the dose to the right chambers and the right lens. However, the dose distribution in these regions of interest still complied with the clinical prescription. Thanks to the robust field geometry with respect to interfractional morphological changes, the patient was allowed to continue the therapy with the same treatment plan without any additional treatment optimization.

The information about the considered treatment fields for all the in vivo monitored patients is summarized in **Table 1**. For the clinical measurements, the irradiation duration corresponds to the average treatment time of all the acquired fractions;

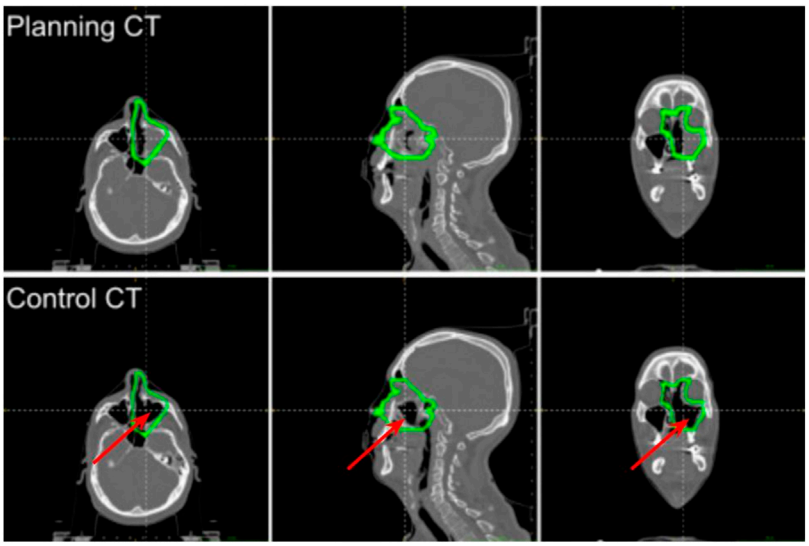

FIGURE 1 | Slices of the planning and control CTs of the MCP patient at the isocenter (from left to right: axial, sagittal, and coronal). The isocenter is at the crossing point of the dashed lines. The CTV margins are drawn in green. The emptied region is pointed out with the red arrow.

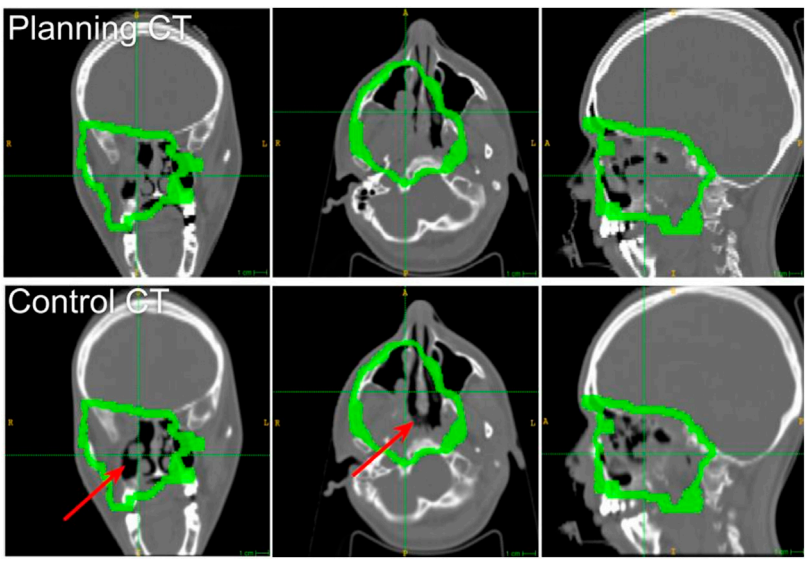

FIGURE 2 | Slices of the planning and control CTs of the 006P patient at the isocenter (from left to right: axial, sagittal, and coronal). The isocenter is at the crossing point of the dashed lines. The CTV margins are drawn in green. The emptied region is pointed out with the red arrow.

additionally, the maximum and minimum irradiation times are also reported.

2.2 The INSIDE In-Beam PET

The INSIDE in-beam PET features two planar heads (10×25 cm^2 active area) made of 2×5 array of detection modules based on Lutetium Fine Silicate (LFS) scintillating crystals (3.2 cm pixel pitch). The 511 keV coincidence photons are selected within a coincidence window of 2 ns; the detector energy and timing resolution are 13% *dE/E* and 450*psσ*, respectively.

Both simulated and experimental PET images are reconstructed by means of a Maximum Likelihood Expectation Maximization (MLEM) algorithm [24], featuring $140 \times 70 \times 165$ voxels with a pixel size of 1.6 mm that is half of the pitch of the PET module (Field Of View (FOV) = $22.4 \times 11.2 \times 26.4$ cm^3).

2.3 Monte Carlo Simulation

The MC simulation is very useful to compare an experimental PET image with the expectation because the induced activity distribution is not straightforwardly correlated to the dose and depends on the acquisition time [25–28]. An extensive review of the use of MC simulation in particle range monitoring is discussed in [29] and [30].

The MC simulation was developed in FLUKA, including all the characteristics and calibration of the INSIDE in-beam PET detector and all the features of the CNAO beam line and pencil beam scanning temporal structure [31, 32]. The MC simulation was previously validated on phantoms with both monoenergetic beams [33] and treatment plans, for either protons [34, 35] or carbon ions [36]. Furthermore, it was validated with the clinical measurement of the first patient ever monitored with the INSIDE in-beam PET scanner, where its agreement with the experimental measurements was found to have an uncertainty compatible with the agreement found when comparing two consecutive days measurements [37].

The beam delivery was simulated taking into account the average clinical intensity on the CNAO synchrotron (2×10^9 pps in the case of proton beams), the temporal structure of the beam extraction (1s of spill, named inspill, followed by 2s of pause between spills, named interspill) and the experimental beam size at the isocenter (whose modelization is described in [37]).

Using both the planning and control CTs, the MCP patient morphology has been modeled in FLUKA with the stoichiometric approach [38] adapted to the CNAO CT calibration curve [39]. The original treatment plan (i.e., calculated on the planning CT) was then irradiated using both CTs, exploiting the developed biased approach described in [37], so as to optimize the simulation run time while preserving the signal statistical significance.

2.4 PET Image Analysis and Compliance Map Definition

This study aims at developing a reliable analysis method for verifying the compliance of the ongoing and prescribed proton treatment and, eventually, at detecting interfractional morphological changes. Moreover, a graphical representation of the numerical results that can be easily overlaid with the patient CT and shared with the clinicians through the TPS is proposed. Such a graphical representation is designed to point out regions in which the treatment compliance with the prescription is poorly detected and it could boost the use of the in-beam PET feedback to adapt the patient schedule of control CT exams depending on the treatment progression.

To implement and test the proposed analysis, in-beam PET images comprising the data acquired during the treatment in the interspill pauses plus 10s of after treatment have been considered. This short acquisition time after the end of the irradiation does not slow down the clinical workflow, avoiding to add discomfort to the patient. At the same time, it also provides additional data that can be useful to increase the statistics of the last irradiated slices, which in the case of the CNAO synchrotron are the highest energies and therefore possibly the most significant in the detection of eventual range differences located at the distal part of the irradiated volume.

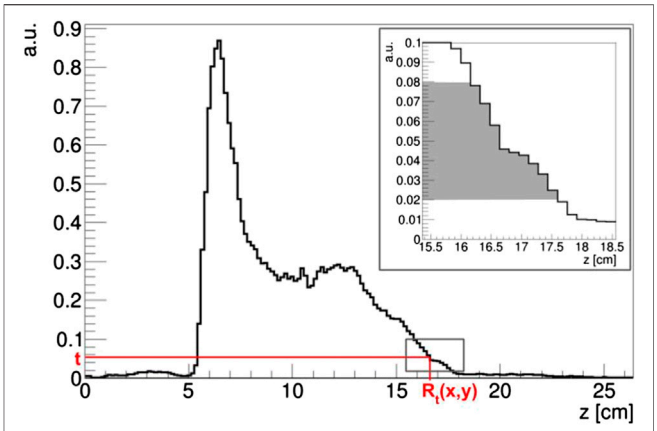

FIGURE 3 | Example of $R_t(x,y)$ calculation on an activity profile normalized at the maximum intensity in the PET image. In the box, the range of the t threshold used in the proposed analysis is highlighted in gray.

The proposed analysis comprises four steps: the image preprocessing, the extraction of a set of isoactivity surfaces, the calculation of the average activity range difference in the beam direction, and the construction of the final 3D compliance map. For the simulated patient, the analysis is carried out by comparing the two PET images obtained with the modelization of the patient anatomy with the planning and control CTs. For the clinical trial patients, where experimental data is available, the analysis is carried out by comparing the image corresponding to the first measured fraction with the subsequent acquisitions.

First, since the raw in-beam PET images suffer from hot spots due to poor statistics with respect to standard diagnostic PET images, the image contrast was modified by masking the highest and lowest intensity values. Additionally, a median filter with a radius of 5 mm was applied to reduce the salt-and-pepper noise in the images.

After that, a set of isoactivity surfaces was extracted with a multithreshold approach. We considered $N = 13$ activity threshold values t between 8 and 2% with respect to the maximum image intensity with a step of 0.5%, obtaining then 13 isoactivity surfaces $A_t(x,y,z)$ for each PET image, where x and y are the coordinates in the transverse plane and z is the coordinate in the beam direction. The activity threshold values used in the isoactivity surface extraction have been chosen in order to take into account at most the contribution given by the last irradiated energies that poorly contribute to the final PET image but that are strongly important in the detection of possible range deviations. A previous study reports the use of erosion and dilation filters to obtain the isoactivity surfaces [18]. This additional filtering can be avoided in this work, because the PET images, here considered at the end of the treatment, are less noisy than the images reported in [18], where the activity distribution was analyzed as a function of the treatment time.

From the isoactivity surfaces $A_t(x,y,z)$, we calculated the activity range distribution $R_t(x,y)$ by considering only the

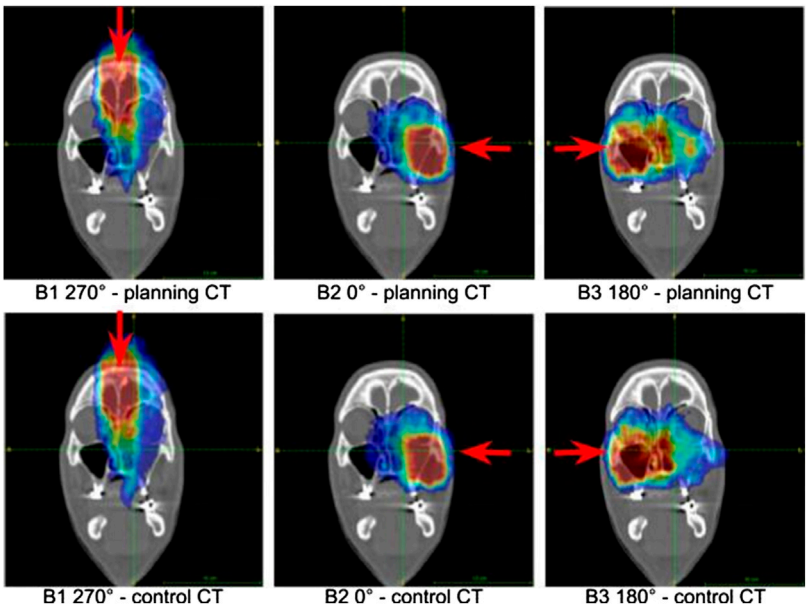

FIGURE 4 | Coronal sections of the activity images of the simulated patient at the isocenter. **Upper row:** images obtained by considering the planning CT in the MC simulation. **Bottom row:** images referring to the MC simulation in which the control CT was taken into account. The beam fields (B1, B2, B3) of the treatment are reported. The beam direction is identified by the red arrow.

activity depth differences along the beam direction z (Beam Eye's View - BEV). The activity range distribution $R_t(x,y)$ was defined as the maximum depth z belonging to the isoactivity surface $A_t(x,y,z)$ for each point (x,y) in the transverse plane (i.e., the most distal z above the given threshold for each point in the transverse area covered by the impinging pencil beams):

$$R_t(x,y) = z_{max} A_t(x,y,z). \tag{1}$$

A representation of the $R_t(x,y)$ calculation is shown in **Figure 3**, taking into account the activity profile along the z axis.

The set of threshold-dependent activity range distributions $R_t(x,y)$ in the transverse plane was used to compare two PET images i and j. For each couple of images, the corresponding activity range distributions for a given threshold t were $R_t^i(x,y)$ and $R_t^j(x,y)$, and the average activity range difference $\Delta R^{i,j}(x,y)$ was calculated as follows:

$$\Delta R^{i,j}(x,y) = \frac{1}{N}\sum_{t}^{N}\left[R_t^i(x,y) - R_t^j(x,y)\right]. \tag{2}$$

In principle, thanks to the multithreshold approach, this analysis, which is based on the evaluation of the average activity range difference $\Delta R^{i,j}(x,y)$, is rather insensitive to statistical fluctuations in the activity values and does not need any patient-related threshold optimization for assessing the compliance of the expected and actual particle range.

To give useful feedback to clinicians, the average activity range difference $\Delta R^{i,j}(x,y)$ was stored in a dedicated 3D compliance map $C^{i,j}(x,y,z)$ in order to graphically improve the understanding of the spatial location and transverse dimension of the regions where a critical activity range variation has been detected.

For each given voxel $(x',y',0)$, belonging to the beam entrance plane of the 3D compliance map, we filled $C^{i,j}(x,y,z)$ along the z coordinate with the obtained value $\Delta R^{i,j}(x,y)$, starting from $z = 0$ until the voxel $(x',y',z*)$ where $z* = R^i_{t*}(x,y)$ in which the threshold t^* is chosen equal to 8% to graphically identify the distal part of the activity distribution, in order to avoid an eventual noise contribution. In short, the compliance map $C^{i,j}(x,y,z)$ has been filled in agreement with the following equations:

$$\begin{cases} C^{i,j}(x,y,z) = \Delta R^{i,j}(x,y) & \text{if } z \le R^i_{8\%}(x,y) \\ C^{i,j}(x,y,z) = 0 & \text{if } z > R^i_{8\%}(x,y). \end{cases} \tag{3}$$

The compliance map $C^{i,j}(x,y,z)$ has the same size and voxel dimensions of the original PET images, covering the same FOV and can be uploaded in DICOM format into the TPS.

To better point out to the clinicians the regions in which the detected activity range difference is more critical and could therefore produce significant deformation into the delivered dose map, a dedicated Color Look-Up Table (CLUT) for the compliance map $C^{i,j}(x,y,z)$ has also been developed. By taking into account the 002P and 003P patients, not prone to morphological changes, it was possible to define an interval within which the detected average activity range difference can be considered not significant by considering the FWHM values of the $\Delta R^{i,j}(x,y)$ distributions. So, in the compliance map $C^{i,j}(x,y,z)$, values within $1.96 \times FWHM/2.35$ have been considered as differences only statistically related to a confidence level of 95%. With the

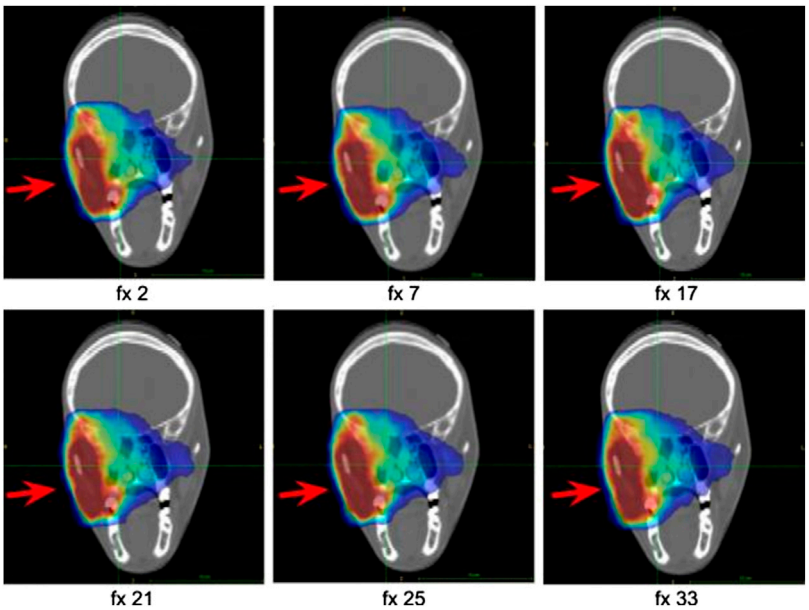

FIGURE 5 | Coronal sections at the isocenter of the activity images of patient 006P corresponding to six different fractions along the treatment course. The activity distribution is shown superimposed to the planning CT. The beam direction is identified by the red arrow.

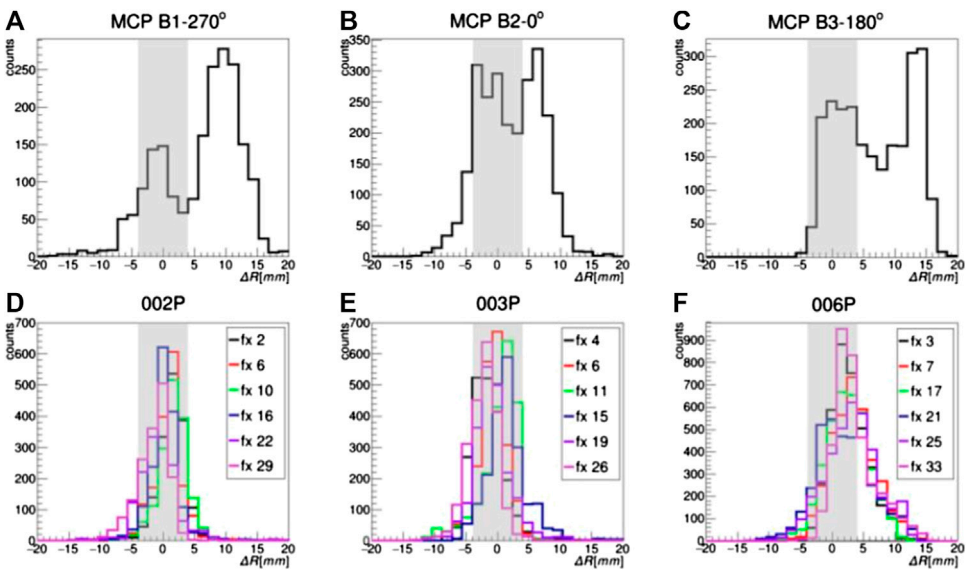

FIGURE 6 | Distributions of $\Delta R^{i,j}(x,y)$ values. The $\Delta R^{i,j}(x,y)$ values highlighted in gray are considered not statistically relevant with a confidence level of 95%. **Upper row:** comparison of the activity distribution of the planning and control CTs obtained for the replanned simulated patient: **(A)** *B*1–270° field; **(B)** *B*2–0° field; and **(C)** *B*3–180° field. **Bottom row:** comparison between the first monitored fraction (fx) and subset of fractions acquired in the following days: **(D)** patient 002P (first monitored fraction fx1); **(E)** patient 003P (first fraction fx1); and **(F)** patient 006P (first fraction fx2).

proposed CLUT, values included in this interval have been shown as transparent. Hence, values that are related to an increase of the particle range are drawn in yellow/red while values corresponding to a decrease are in light blue/blue. Due to experimental limitations and poor statistics in the activity images, even for the patients in which no morphological changes occur, there were still some outlier values for $\Delta R^{i,j}(x,y)$, but they were in practice not relevant because they were not spatially correlated to each other (hot/cold spots in the compliance map).

TABLE 2 | Results of patients 002P and 003P and definition of the compliance interval at 95% confidence level, used for the design of the CLUT for the compliance map. The percentages of outlier voxels when considering a level of confidence of 95 (±4 mm) or 99.7% (±6 mm) and the total number of produced compliance maps, corresponding to the analyzed fractions, are also reported.

Patient	Average range activity difference $\langle \Delta R \rangle$ [mm]	FWHM$_{\langle \Delta R \rangle}$ [mm]	Semiamplitude of the confidence interval 95% tailored for each patient [mm]	Percentage of voxels outside [–4, 4] mm (confidence level 95%)	Percentage of voxels outside [–6, 6] mm (confidence level 99.7%) (%)	Number of analyzed compliance maps
002P	0.4	4.1	3.5	12	4	11
003P	–0.5	5.2	4.4	16	6	8

3 RESULTS

The simulated activity images referring to the MCP patient are shown in **Figure 4** for the three irradiation fields. For both planning and control CT, the coronal slice is shown at the isocenter. In this patient, the almost complete emptying of the left nasal cavity, which is included into the CTV, produced in the PET images a significant and clearly visible elongation of the activity region in the beam direction. This effect is shown in all treatment fields even if they quantitatively contribute with different weights to the total dose deposition in the morphologically changing volume.

As for the MCP patient, a slight elongation of the activity distribution can be appreciated in correspondence to the partial emptying of the cavity of patient 006P, even though a replanning was not required in this case. The activity distributions referring to different acquired fractions are reported in **Figure 5**.

From a quantitative point of view, it is necessary to study the distributions of the average activity range difference $\Delta R^{i,j}(x, y)$ values stored into the 3D compliance map $C^{i,j}(x, y, z)$ for all the patients included in this study (**Figure 6**).

In the case of 002P and 003P, where no morphological changes are expected because of the pathology and the treatment region, the $\Delta R^{i,j}(x, y)$ distributions are peaked around 0 with a FWHM of 4.1 and 5.2 mm, respectively. The obtained results, reported in **Table 2**, were used to define the CLUT for the compliance map used in the following.

In the case of the P006 patient, in which a partial morphological variation was detected in the control CT, the $\Delta R^{i,j}(x, y)$ distribution is slightly asymmetrical with a pronounced tail in the positive branch meaning an increasing particle range. For this patient, the average $\langle \Delta R \rangle$ is equal to 2.8 mm and the FWHM increases with respect to the 002P and 003P patients to 6.8 mm, indicating that some morphological changes could have occurred and therefore the compliance map has to be checked. For 006P, the percentage of voxels for which the compliance of the ongoing and prescribed treatment was not guaranteed were 39 and 20% with a confidence level of 95 and 99.7%, respectively, showing an increase of more than a factor 2 with respect to the values obtained for the 002P and 003P patients taken as reference for no critical changes.

In **Figure 6**, the $\Delta R^{i,j}(x, y)$ distribution is also shown for the simulated treatment fields referring to the MCP patient. A double peaked structure can be appreciated: the peak centered around zero represents the pencil beams in which no significant difference in activity range was found in the proposed analysis; the peak centered at 5–15 mm corresponds to the nasal cavity whose emptying caused an increased average particle range. Hence, the percentages of voxels for which the compliance of the ongoing and prescribed treatment was not guaranteed with a confidence level of 95 and 99.7% were very high and equal to 73% (B1)-49% (B2)-62% (B3) and 64% (B1)-29% (B2)-53% (B3), respectively, depending on the irradiated beam.

The coronal sections of the compliance map referring to the simulated patient are reported in **Figure 7**. They clearly show that the pencil beams of each irradiation field that have to pass through the morphologically changed nasal cavity report a significant positive range difference (i.e., the particle beam penetrates more in the patient tissues).

Some of the compliance maps $C^{i,j}(x, y, z)$ obtained from the analysis of the 006P patient are reported in **Figure 8** as an example. Starting from the beginning of the treatment course, there are some regions in which values outside the compliance interval are detected (see comparison between fractions (fx) 2 and 3). During the treatment course, the regions in which a significant average activity range difference was found become wider and more spatially correlated in correspondence with the region where the partial cavity emptying happened.

4 DISCUSSION

In particle therapy, several quantitative methods for PET image analysis and range difference evaluations have been developed (e.g., [40–43]). Those methods mainly rely on PET monitoring systems that acquire data after the end of the treatment. On the one hand, the reduced acquisition time of the in-beam PET technique allows to do treatment verification in a straightforward way that does not slow down the clinical workflow. On the other hand, the poor statistics of in-beam PET acquisitions has to be dealt with. This can be addressed developing a robust analysis for the identification of critical regions with respect to particle range deviations. Moreover, there is no general consensus on the best way to quantify the compliance of the ongoing treatment to the prescribed one. This study aimed at developing and validating an analysis that takes into account as preferential direction the beam axis (BEV) to obtain a reliable

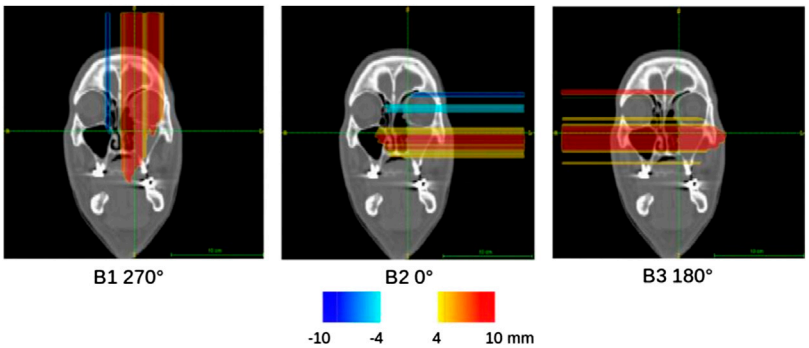

FIGURE 7 | Compliance maps referring to the activity image analysis for each beam field (B1, B2, B3) of the MCP patient, overlaid on the planning CT with the proposed CLUT.

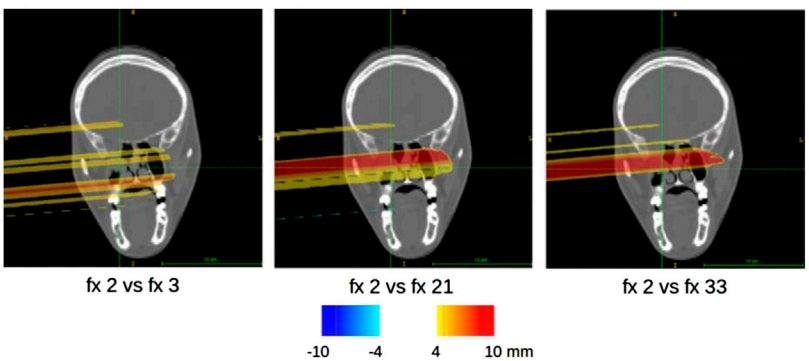

FIGURE 8 | Sample of compliance maps referring to the activity image analysis of different fractions (fx) of the 006P patient, overlaid on the planning CT with the proposed CLUT.

evaluation of possible detected particle range variations. A similar BEV approach has been applied both to prompt photons [44] and to PET [40]. Moreover, a 3D compliance map has been proposed to be used in vivo to give a feedback to the clinicians in order to tailor, for each patient, the schedule of eventual control CTs. In the compliance map, the average activity range difference calculated for each pencil beam is reported. It is important to remark that this quantity is not a direct measurement of the Bragg Peak shift in the beam direction. There is in fact a correlation between these two quantities, but the average activity range difference depends on other variables, such as acquisition duration, image elongation artifacts, and detector features, that have to be considered during the visual analysis on the patient CT. The proposed analysis was tested with simulated and real patients monitored with the INSIDE in-beam PET system, which is under clinical validation at the CNAO treatment center. Only interspill data were considered in the analysis because, even if the INSIDE system is able to acquire useful data during the spills, they have not yet been used for online range monitoring. In fact, inspill data are noisy and require filtering procedures to reduce the unwanted contribution of the prompt signals not correlated with the beam position. Some strategies to consider also inspill data acquired by the first two modules of the INSIDE in-beam PET were discussed in [45] and [46].

From the analysis of two measured patients in which no morphological changes were expected, it was possible to define a compliance interval within which a detected range difference is considered as a statistical fluctuation with a 95% confidence level. In other words, a range difference falling in the compliance interval has to be considered not critical with respect to a possible need for a patient morphology verification exam. We found a compliance interval of −4 mm; 4 mm. Based on these results, we have built a dedicated CLUT to show the compliance map overlaid with the patient CT. Only two patients were used to define the confidence interval used in the CLUT, because they were affected by pathologies showing no morphological changes. Nevertheless, the interval was calculated considering the whole volume, irradiated over the course of the monitored treatment fractions, yielding the comparison of 23 PET images.

For the simulated and monitored patients, in which morphological changes were certified by control CTs, the developed analysis identified some critical regions with respect to the particle range variation which were compatible with the morphological variations happened during the patients treatment. However, these patients did not have to be replanned. This means that the proposed analysis seems to be able to detect morphological changes before they become severe enough to require a plan adaptation to the new clinical scenario. Only patients treated with proton therapy were considered at this

stage. However, patients treated with carbon ions were also included in the INSIDE trial. For these patients, the PET performances are lower due to the lower statistics. Moreover, the short acquisition time impacts the detected isotopes signal (i.e., in carbon ion therapy, mainly ^{11}C is produced, but, having a half-life way longer than the treatment time, this signal is partially lost). Nevertheless, research strategies to analyze carbon ion PET data are being investigated in the framework of the INSIDE clinical trial.

5 CONCLUSION

A reliable approach for in vivo treatment verification by means of in-beam PET monitoring was developed and tested on simulated and measured patients. The selected patients, affected by head-and-neck tumors, were treated with proton therapy at the CNAO facility and represented different degrees of morphological modifications that can occur during the treatment course. The activity images acquired during irradiation were analyzed with a robust approach based on a multithreshold procedure in order to detect possible particle range deviations. The proposed compliance map was found to be an effective tool for clinical evaluation of the studied cases. The map can be overlaid on the patient CT to evaluate the spatial position of the critical region. Furthermore, the developed CLUT can help clinicians to foresee an eventual dose discrepancy in the treatment so as to better plan for a control CT and look for possible morphological changes with a patient-tailored schedule. The proposed analysis will be tested on the complete database of patients recruited during the ongoing INSIDE clinical trial in order to better assess its performance in a clinical environment, mainly in the case of patients affected by pathologies in which a morphological change may happen. These patients, in particular, will help clinicians to make an assessment about the patient schedule of control CT exams during the treatments.

DATA AVAILABILITY STATEMENT

The raw data supporting the conclusions of this article will be made available by the authors, without undue reservation.

ETHICS STATEMENT

The studies involving human participants were reviewed and approved by Comitato etico Fondazione CNAO-San Matteo, Pavia. The patients/participants provided their written informed consent to participate in this study.

AUTHOR CONTRIBUTIONS

EF and VF developed the proposed analysis and wrote the manuscript. MB, FP, ASa, GS, GT, EMal, and AK reviewed the manuscript. FV, BV, VV, ST, and DM recruited the analysed patients. FV, VV, ST, GBar, AM, and MC contributed in the clinical trial design. GBat, VF, EF, SV, GM, IM, SM, AK, and FP developed Monte Carlo simulations. PC, MS, YD, AE, VF, EF, MF, EMal, GT, ASa, ASci, FP, and MB acquired the data. GG, PM, AR, MR, RW, MM, FP, EF, VF, and MB constructed and commissioned the in-beam PET. VF, EF, MM, AP, and FP developed SW for the PET acquisition and analysis. FL, CL, EMaz, AR, and GS implemented the INSIDE database. NC developed the image reconstruction algorithm. MB, NB, and VR performed preliminary test with PET systems. MD, GF, MMag, CMT, MMar, RM, VP, ASch, EC, and MT participated in the development of the INSIDE bimodal system.

FUNDING

The INSIDE project (INnovative Solutions for In-beam Dosimetry in HadronthErapy) was funded by the Italian Ministry of Education under the national research program PRIN MIUR 2010P98A75 from 2013 to 2016, the Italian Institute of Nuclear Physics (INFN) (RDH and PETRA projects) from 2016, the Historical Museum of Physics and the Enrico Fermi Study and Research Center, the Tuscany Government (POR FSE 2014 -2020, through the PETRA-INFN-RT2 172800 Project) from 2018, and the CNAO Foundation from 2017.

REFERENCES

1. Parodi K, Polf JC *In vivo* range verification in particle therapy. *Med Phys* (2018) 45(11):e1036–50. doi:10.1002/mp.12960
2. Durante M, Orecchia R, Loeffler JS Charged-particle therapy in cancer: clinical uses and future perspectives. *Nat Rev Clin Oncol* (2017) 14(8):483–95. doi:10.1038/nrclinonc.2017.30
3. Paganetti H. *Proton therapy physics*. Boca Raton, FL: CRC Press (2016).
4. Paganetti H Range uncertainties in proton therapy and the role of Monte Carlo simulations. *Phys Med Biol* (2012) 57(11):R99–117. doi:10.1088/0031-9155/57/11/R99
5. Cubillos-Mesías M, Troost EGC, Lohaus F, Agolli L, Rehm M, Richter C, et al. Including anatomical variations in robust optimization for head and neck proton therapy can reduce the need of adaptation. *Radiother Oncol* (2019) 131:127–34. doi:10.1016/j.radonc.2018.12.008
6. Placidi L, Bolsi A, Antony J, Schneider RA, Malyapa R, Weber DC, et al. Effect of anatomic changes on pencil beam scanned proton dose distributions for cranial and extracranial tumors. *Int J Radiat Oncol Biol Phys* (2017) 97(3):616–23. doi:10.1016/j.ijrobp.2016.11.
7. Engelsman M, Schwarz M, Dong L Physics controversies in proton therapy. *Semin Radiat Oncol* (2013) 23:88–96. doi:10.1016/j.semradonc.2012.11.003
8. Hoffmann L, Alber M, Jensen MF, Holt MI, Møller DS Adaptation is mandatory for intensity modulated proton therapy of advanced lung cancer to ensure target coverage. *Radiother Oncol* (2017) 122(3):400–5. doi:10.1016/j.radonc.2016.12.018
9. Guerra AD, Belcari N, Bisogni M Positron emission tomography: its 65 years. *Riv Nuovo Cimento* (2016) 39(155):155–223. doi:10.1393/ncr/i2016-10122-6
10. Parodi K On- and off-line monitoring of ion beam treatment. *Nucl Instrum Methods Phys Res Sect A Accel Spectrom Detect Assoc Equip* (2016) 113–9. doi:10.1016/j.nima.2015.06.056
11. Brombal L, Barbosa D, Belcari N, Bisogni MG, Camarlinghi N, Cristoforetti L, et al. Proton therapy treatment monitoring with in-beam pet: investigating space and time activity distributions. *Nucl Instrum Methods Phys Res Sect A Accel Spectrom Detect Assoc Equip* (2017) 71–6. doi:10.1016/j.nima.2017.05.002

12. Pawelke J, Byars L, Enghardt W, Fromm WD, Geissel H, Hasch BG, et al. The investigation of different cameras for in-beam PET imaging. *Phys Med Biol* (1996) 41(2):279–96. doi:10.1088/0031-9155/41/2/006
13. Enghardt W, Crespo P, Fiedler F, Hinz R, Parodi K, Pawelke J, et al. Charged hadron tumour therapy monitoring by means of PET. *Nucl Instrum Methods Phys Res Sect A Accel Spectrom Detect Assoc Equip* (2004) 525(1):284–8. doi:10.1016/j.nima.2004.03.128
14. Tommasino F, Durante M Proton radiobiology. *Cancers* (2015) 7(1):353–81. doi:10.3390/cancers7010353-
15. Buitenhuis HJT, Diblen F, Brzezinski KW, Brandenburg S, Dendooven P Beam-on imaging of short-lived positron emitters during proton therapy. *Phys Med Biol* (2017) 62(12):4654–72. doi:10.1088/1361-6560/aa6b8c
16. E Combs S, Bauer J, Unholtz D, Kurz C, Welzel T, Habermehl D, et al. Monitoring of patients treated with particle therapy using positron-emission-tomography (PET): the miranda study. *BMC Cancer* (2012) 12(1):133. doi:10.1186/1471-2407-12-133
17. Nishio T, Miyatake A, Ogino T, Nakagawa K, Saijo N, Esumi H The development and clinical use of a beam on-line PET system mounted on a rotating gantry port in proton therapy. *Int J Radiat Oncol Biol Phys* (2010) 76(1):277–86. doi:10.1016/j.ijrobp.2009.05.065
18. Ferrero V, Fiorina E, Morrocchi M, Pennazio F, Baroni G, Battistoni G, et al. Online proton therapy monitoring: clinical test of a silicon-photodetector-based in-beam PET. *Sci Rep* (2018) 8(1):4100. doi:10.1038/s41598-018-22325-6
19. Fischetti M, Baroni G, Battistoni G, Bisogni MG, Cerello P, Ciocca M, et al. Interfractional monitoring of C ions treatments: results from a clinical trial at the cnao facility. *Sci Rep* (2020) 10(1):20735. doi:10.1038/s41598-020-77843-z
20. Bisogni MG, Attili A, Battistoni G, Nicola BelcariCerello P, Coli S, et al. Inside in-beam positron emission tomography system for particle range monitoring in hadrontherapy. *J Med Imaging* (2017) 4(1):011005. doi:10.1117/1.JMI.4.1.011005
21. Traini G, Battistoni G, Bollella A, Collamati F, De Lucia E, Faccini R, et al. Design of a new tracking device for on-line beam range monitor in carbon therapy. *Phys Med* (2017) 34:18–27. doi:10.1016/j.ejmp.2017.01.004
22. Mattei I, Battistoni G, De Simoni M, Dong Y, Embriaco A, Fischetti M, et al. Scintillating fiber devices for particle therapy applications. *IEEE Trans Nucl Sci* (2018). doi:10.1109/TNS.2018.2843179
23. Rossi S The status of CNAO. *Eur Phys J Plus* (2011) 126(8):1–39. doi:10.1140/epjp/i2011-11078-8
24. Camarlinghi N, Sportelli G, Battistoni G, Belcari N, Cecchetti M, Cirrone GAP, et al. An in-beam pet system for monitoring ion-beam therapy: test on phantoms using clinical 62 mev protons. *J Instrum* (2014) 9(04):C04005. doi:10.1088/1748-0221/9/04/c04005
25. Kraan AC, Muraro S, Battistoni G, Belcari N, Bisogni MG, Camarlinghi N, et al. Analysis of time-profiles with in-beam PET monitoring in charged particle therapy. *Med Phys* (2018) arXiv preprint arXiv:1809.11055. doi:10.1088/1748-0221/14/02/C02001
26. Muraro S, Camarlinghi N, Belcari N, Bisogni MG, Guerra AD, Kraan A, et al. Low statistics positron activity reconstruction methods for proton therapy. *Nucl Instrum Methods Phys Res Sect A Accel Spectrom Detect Assoc Equip* (2018) 936:52–3. doi:10.1016/j.nima.2018.10.015
27. Li Z, Fan Y, Dong M, Tong L, Zhao L, Yin Y, et al. In-beam pet imaging in carbon therapy for dose verification. *IEEE Trans Radiat Plasma Med Sci* (2018) 2(1):61–7. doi:10.1109/trpms.2017.2769109
28. Bongrand A, Busato E, Force P, Martin F, Montarou G Use of short-lived positron emitters for in-beam and real-time β+ range monitoring in proton therapy. *Phys Med* (2020) 69:248–55. doi:10.1016/j.ejmp.2019.12.015
29. Kraan AC Range verification methods in particle therapy: underlying physics and Monte Carlo modeling. *Front Oncol* (2015) 5:150. doi:10.3389/fonc.2015.00150
30. Seco J, Frank V. *Monte Carlo techniques in radiation therapy*. Boca Raton, FL: CRC Press (2013).
31. Ferrari A, Sala PR, Fasso A, Ranft J Fluka: a multi-particle transport code (program version 2005) (2005). Geneva, Switzerland: CERN. Technical report. Report No.: CERN-2005-010, SLAC-R-773, INFN-TC-05-11, CERN-2005-10.
32. Battistoni G, Bauer J, Boehlen TT, Cerutti F, Santos Augusto RD, Ferrari A, et al. The fluka code: an accurate simulation tool for particle therapy. *Front Oncol* (2016) 6:116. doi:10.3389/fonc.2016.00116
33. Ma P, Belcari N, Bisogni MG, Camarlinghi N, Cerello P, Coli S, et al. First results of the inside in-beam PET scanner for the on-line monitoring of particle therapy treatments. *J Instrum* (2016) 11(12):C12011. doi:10.1088/1748-0221/11/12/C12011
34. Ferrero V The inside project: in-beam PET scanner system features and characterization. *J Instrum* (2017) 12(03):C03051. doi:10.1088/1748-0221/12/03/c03051
35. Ferrero V, Bisogni MG, Camarlinghi N, Fiorina E, Giraudo G, Morrocchi M, et al. Double-field hadrontherapy treatment monitoring with the inside in-beam PET scanner: proof of concept. *IEEE Trans Radiat Plasma Med Sci* (2018) 2(6):588–93. doi:10.1109/trpms.2018.2870478
36. Pennazio F, Battistoni G, Bisogni MG, Camarlinghi N, Ferrari A, Ferrero V, et al. Carbon ions beam therapy monitoring with the inside in-beam PET. *Phys Med Biol* (2018) 63(14):145018. doi:10.1088/1361-6560/aacab8
37. Fiorina E, Ferrero V, Pennazio F, Baroni G, Battistoni G, Belcari N, et al. Monte Carlo simulation tool for online treatment monitoring in hadrontherapy with in-beam PET: a patient study. *Phys Med* (2018) 51:71–80. doi:10.1016/j.ejmp.2018.05.002
38. Schneider W, Bortfeld T, Schlegel W Correlation between CT numbers and tissue parameters needed for Monte Carlo simulations of clinical dose distributions. *Phys Med Biol* (2000) 45(2):459–78. doi:10.1088/0031-9155/45/2/314
39. Lima TV, Dosanjh M, Ferrari A, Molineli S, Ciocca M, Mairani A Monte Carlo calculations supporting patient plan verification in proton therapy. *Front Oncol* (2016) 6:62. doi:10.3389/fonc.2016.00062
40. Nischwitz SP, Bauer J, Welzel T, Rief H, Oliver J, Haberer T, et al. Clinical implementation and range evaluation of *in vivo* PET dosimetry for particle irradiation in patients with primary glioma. *Radiother Oncol* (2015) 115(2):179–85. doi:10.1016/j.radonc.2015.03.022
41. Hee Min C, Zhu X, Winey BA, Grogg K, Testa M, El Fakhri G, et al. Clinical application of in-room positron emission tomography for *in vivo* treatment monitoring in proton radiation therapy. *Int J Radiat Oncol Biol Phys* (2013) 86(1):183–9. doi:10.1016/j.ijrobp.2012.12.010
42. Bauer J, Unholtz D, Sommerer F, Kurz C, Haberer T, Herfarth K, et al. Implementation and initial clinical experience of offline PET/CT-based verification of scanned carbon ion treatment. *Radiother Oncol* (2013) 107(2):218–26. doi:10.1016/j.radonc.2013.02.018
43. Frey K, Unholtz D, Bauer J, Debus J, Min CH, Bortfeld T, et al. Automation and uncertainty analysis of a method for *in vivo* range verification in particle therapy. *Phys Med Biol* (2014) 59(19):5903–19. doi:10.1088/0031-9155/59/19/5903
44. Xie Y, Hassane EB, Janssens G, Smeets J, Vander Stappen F, Hotoiu L, et al. Prompt gamma imaging for *in vivo* range verification of pencil beam scanning proton therapy. *Int J Radiat Oncol Biol Phys* (2017) 99(1):210–8. doi:10.1016/j.ijrobp.2017.04.027
45. Piliero MA, Pennazio F, Bisogni MG, Camarlinghi N, Cerello PG, Guerra AD, et al. Full-beam performances of a PET detector with synchrotron therapeutic proton beams. *Phys Med Biol* (2016) 61(23):N650–66. doi:10.1088/0031-9155/61/23/N650
46. Kostara E, Sportelli G, Belcari N, Camarlinghi N, Cerello P, Guerra AD, et al. Particle beam microstructure reconstruction and coincidence discrimination in PET monitoring for hadron therapy. *Phys Med Biol* (2019) 64(3):035001. doi:10.1088/1361-6560/aafa28

Conflict of Interest: The authors declare that the research was conducted in the absence of any commercial or financial relationships that could be construed as a potential conflict of interest.

frontiers in Physics

REVIEW
published: 29 January 2021
doi: 10.3389/fphy.2020.567466

South East European International Institute for Sustainable Technologies (SEEIIST)

Ugo Amaldi[1], Elena Benedetto[1], Sanja Damjanovic[2], Manjit Dosanjh[3,4], Marco Durante[5,6], Petya Georgieva[1], Thomas Haberer[7], Mark Plesko[8], Mimoza Ristova[2,3,9], Sandro Rossi[10], Nicholas Sammut[11], Mariusz Sapinski[5], Herwig Schopper[3], Hans Specht[12], Rudiger Voss[3], Maurizio Vretenar[3] and Horst Wenninger[3†]*

[1]TERA Foundation, Novara, Italy, [2]SEEIIST Association, Geneva, Switzerland, [3]CERN, Geneva, Switzerland, [4]Department of Physics, University of Oxford, Oxford, United Kingdom, [5]GSI Helmholtzzentrum für Schwerionenforschung, Darmstadt, Germany, [6]Technische Universität Darmstadt, Darmstadt, Germany, [7]HIT, University of Heidelberg, Heidelberg, Germany, [8]Cosylab, Ljubljana, Slovenia, [9]Faculty of Natural Sciences and Mathematics, UKIM, Skopje, North Macedonia, [10]CNAO, Pavia, Italy, [11]Microelectronics & Nanoelectronics, Faculty of Information & Communication Technology, University of Malta, Msida, Malta, [12]Ruprecht-Karls-Universitaet Heidelberg, Heidelberg, Germany

OPEN ACCESS

Edited by:
Wouter van Elmpt, Maastricht University, Netherlands

Reviewed by:
Dimitris Emfietzoglou, University of Ioannina, Greece
Tom Depuydt, University Hospitals Leuven, Belgium

***Correspondence:**
Sanja Damjanovic
Sanja.Damjanovic@cern.ch

†Deceased

Specialty section:
This article was submitted to Medical Physics and Imaging, a section of the journal Frontiers in Physics

Received: *29 May 2020*
Accepted: *26 November 2020*
Published: *29 January 2021*

Citation:
Amaldi U, Benedetto E, Damjanovic S, Dosanjh M, Durante M, Georgieva P, Haberer T, Plesko M, Ristova M, Rossi S, Sammut N, Sapinski M, Schopper H, Specht H, Voss R, Vretenar M and Wenninger H (2021) South East European International Institute for Sustainable Technologies (SEEIIST). Front. Phys. 8:567466. doi: 10.3389/fphy.2020.567466

The South East European International Institute for Sustainable Technologies (SEEIIST) was proposed in 2016 at the World Academy of Art and Science, with the objective of building a facility for charged particle cancer therapy for the South Eastern European countries. SEEIIST will offer the world-class research needed to reduce or even revert the brain drain that is causing a shortage of talent and economic losses in South East Europe. There is no particle therapy in South-East Europe in spite of a growing number of cancers being diagnosed. The facility beam time will be shared 50:50 between treating patients and performing research with a wide spectrum of different light ions beyond the presently used protons and carbon ions, which will make the facility unique in the world. SEEIIST Project is presently in a Conceptual to a Design Phase, implemented with the support of the EU and the involvement of CERN and GSI. The next phase of the project realization will include a final technical design for the facility, a structure and a business plan for the organization and the definition of conditions for the site selection.

Keywords: SEEIIST, Research Infrastructure, Particle Therapy, Cancer Treatment, South East Europe

INTRODUCTION

The SEE region consists of the countries that are EU Member States (Bulgaria, Croatia, Greece and Slovenia), as well as of the countries that are aspiring for membership in the near future (Albania, Bosnia and Herzegovina, Kosovo, Montenegro, North Macedonia and Serbia). Due to recent turbulent times in South East Europe, all scientific and economic activities have slowed down. As a consequence, the region also suffered from an extensive brain drain of the young and prosperous scientists. In contrast, the region once featured intensive research and technological development and made significant scientific contributions on the European scale. A prime example of this is the first research nuclear reactor in the former Yugoslavia that was operational already in 1959, only two years after such a research reactor was commissioned in Germany. It is worth mentioning that this region (former Yugoslavia) played an important role as a cofounder of CERN in 1954[1] as well. The most efficient and effective way to

[1]https://en.wikipedia.org/wiki/CERN.

recover this tradition, i.e., to catch up with the EU current excellent research and to revert the brain drain, is to establish a large-scale internationally competitive research infrastructure in the SEE region. To meet this goal, the SEE countries have recently consolidated their forces to set up a large-scale competitive research infrastructure–the South East European International Institute for Sustainable Technologies (SEEIIST[2]).

ORIGIN OF SEEIIST

The idea of SEEIIST was conceived more than 2 years ago, when the Government of Montenegro, led by the Minister of Science, Dr Sanja Damjanovic, initiated the establishment of the SEEIIST Project, originally proposed by Prof. Herwig Schopper, a former Director General of CERN. The initiative was formalized as a regional project once a **Declaration of Intent** was signed, on October 25, 2017 at a Ministerial meeting at CERN. The signatory parties were Albania, Bosnia and Herzegovina, Bulgaria, Kosovo*[3], Montenegro, Serbia, Slovenia and Northern Macedonia. Croatia and Greece took an observer status. Most recently, a SEEIIST **Memorandum of Cooperation** was signed by six Prime Ministers of the countries of the region (Albania, Bosnia and Herzegovina, Bulgaria, Kosovo, Montenegro and North Macedonia) on July 5, 2019 during the Berlin Process Summit at Poznan, Poland.

In response to this initiative, the EC stated that in order to bring "*. . .our citizens and economies closer together* (. . .) *it is determined to strengthen and intensify its engagement at all levels to support the region's political, economic and social transformation, including through increased assistance*." The statement underlined the ongoing efforts by the EC to bring the SEE countries closer to the EU in terms of its shared values, social cohesion and economic prosperity. Outgoing EC President Juncker, in his 2018 State of the Union Address, and the incoming EC President Von der Leyen, have both stressed the need for intensive cooperation, and Von der Leyen has stated that this would be one of the priorities for the next 5 years.

The overarching objective of the SEEIIST project is to foster regional cooperation in the fields of science, health care, technology, innovation and industry in the spirit of the existing joint research infrastructures successfully implementing the model of 'Science for Peace,' such as CERN and SESAME. The project has three main socio-economic objectives: 1) making hadron cancer treatment available to the patients from the SEE region; 2) promoting transnational collaboration between science, technology and industry by bringing together the people from different countries of the region, not only scientists and medical doctors, but also engineers, industrial and administration personnel; 3) providing a common platform to educate talented young people and engineers on the basis of knowledge and technology transfer from European centers, such as CERN and others, and finally mitigating or even reverting the brain drain from the SEE region. This research infrastructure would greatly address the common challenges and needs in the SEE region, triggering, in particular, the sustainable development of economy and social cohesion.

The scope of the SEEIIST is to be an international research infrastructure not only for researchers but also for medical treatment. This implies that all medical infrastructure required will be available at this international center. The Business plan prepared for the SEEIIST@ESFRI application contains this concept as part of the investment. The site of SEEIIST will be sufficiently close to an existing hospital for supplementary medical treatment when necessary.

JOINT RESEARCH INFRASTRUCTURE – SEEIIST

The new RI - South East European International Institute for Sustainable Technologies (SEEIIST) will focus on hadron cancer therapy and biomedical research with protons and heavy ions. SEEIIST will thus enable scientists from different countries to work together in the fight against cancer. This particular initiative has been chosen partly because it binds people together against a "common enemy," but also as an example of cooperation among people in the region. In this regard, SEEIIST's mission is aligned with the basic concepts behind other large-scale RIs, such as CERN: Science for Peace, Science for Diplomacy and Science for Society. A second reason for placing a hadron facility in the SEE area is the fact that in contrast to Western Europe, no technical provision exists in SEE to treat patients with certain malignant types of tumors with this modality. The selection of a hadron facility over other types of Radiation Therapy (RT), like an X-ray treatment center, or other non-radiological treatment modalities (such as immunotherapy), is motivated by the fact that a particle therapy center is urgently needed to achieve major research advances in pre-clinical physics, pre-clinical radiobiology and medical physics related to cancer treatment, as well as a means to retain the young and talented research human potential in the region.

SEEIIST state-of-the-art RI has already moved from a conceptual to a design phase, thanks to the first financial support from the European Commission. The status of the project was presented to the public at a SEEIIST Kick-off meeting[4] 'Start of the SEEIIST Design Phase,' held on September 18, 2019 in Budva, Montenegro. The next steps are underway for preparing a defined technical design for the facility, to propose a user's structure and business plan for the organization and to define the conditions for the site selection. The SEEIIST site selection process is planned to be completed by early 2021, whereas the construction is expected to start in 2023. The first patient is expected to be treated in 2029.

SEEIIST will maintain strong collaboration links with all the relevant particle therapy cancer research groups in Europe,

[2]https://seeiist.eu/.

[3]*This designation is without prejudice to positions on status and is in line with UNSC 1244/1999 and the ICJ opinion on the Kosovo Declaration of Independence.

[4]https://seeiist.eu/start-of-the-seeiist-design-phase-september-2019-budva-montenegro/.

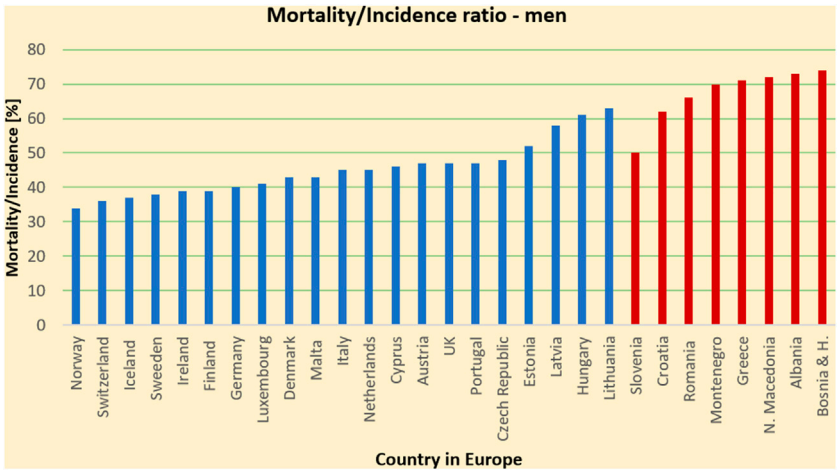

FIGURE 1 | Mortality-to-incidence ratio due to all cancers, all ages, man (2018) for SEE and several Western EU countries for comparison. The image highlights a higher outcome with fatality of the cancer patients in the SEE countries compared to some of the EU countries.

United States, and Japan, it should be noted that there are already links with PTCOG, ESTRO EPTN, and ENLIGHT. Dedicated and specific networking will be initiated with the groups who are currently involved in research in molecular targeting for radioresistant tumors, cancer molecular research, immunotherapy, and the groups that examine the effective antitumor immune response induced by PT. The next ambition for SEEIIST is to become part of the EIT Health Regional Innovation Scheme.

SCIENTIFIC CASE FOR SEEIIST FACILITY

Cancer is a critical societal issue. Worldwide, in 2018 alone, 18.1 million cases were diagnosed, 9.6 million people died and 43.8 million people were living with cancer [1, 2]. Currently, it is the second leading cause of death [3], after cardiovascular diseases but recent extrapolations show that it could take over and become the leading cause of death [4]. Demographic drivers of increasing population[5], size, life expectancy and aging populations (particularly in higher-income countries), along with progress against many other causes of deaths, imply that the total number of cancer deaths continues to increase. Current projections anticipate an increase with approximately 24.6 million newly diagnosed patients, and 13 million related deaths by 2030[5], **Figure 1** shows the mortality-to-incidence ratio in most of the countries in Europe in 2015. As shown in the figure, in this common fight, some countries struggle more than the others partly because of the lack of advanced diagnostics and treatment equipment. In particular, in the heart of Europe, in its South Eastern (SEE) region, the mortality rates from tumors are up to 40% higher compared to the rest of Europe [4]. Cancer not only has a negative impact on an individual's health but also comes at a very high cost to the economy. Cancer costs the EU circa €126 billion with health care accounting for €51 billion, productivity losses due to early death estimated at €43 billion, lost working days estimated at €9 billion and informal care estimated at €23 billion [5]. It is for this reason that the European Commission invested €1.6 billion in FP7 and, so far, €1.2 billion in H2020 on cancer research. H2020 policy prioritizes health and wellbeing to be a societal challenge under which cancer research is categorized[6]. In Horizon Europe, the commission gives the fight against cancer even more priority by considering it to be one of the greatest world challenges and specifically placing the mission against cancer as a top priority in its mission-oriented policy[7].

Currently over half of the patients diagnosed with cancer undergo radiation therapy (RT), and about 50% of all cured cancer patients have RT as part of their treatment [1, 5]. In this scenario, any significant improvements in RT could have a dramatic impact on patient survival, quality of life and economic costs.

Research and innovation efforts have been currently carried out worldwide to improve the effectiveness of RT. The main goal of advanced radiotherapy treatment is to maximize the damage of ionizing radiation to the tumor cells while minimizing exposure of the surrounding normal tissue and critical organs, to enhance the likelihood of patient cure while the side effects of the treatment are minimized. To achieve this goal, RT has considerably progressed with the development of new technologies and methodologies able to increase the conformity of the dose delivered to deep-seated tumors. While the most frequently used modern RT modalities still rely on high energy (MeV) X-rays, there is a rapidly growing interest in the curative effects of accelerated charged particles, i.e., protons and heavier ions, such as carbon. This so-called particle therapy (PT)

[5]https://www.who.int/en/news-room/fact-sheets/detail/cancer.

[6]https://ec.europa.eu/research/.

[7]"Commission Announces Top Experts to Shape Horizon Europe's Missions" https://ec.europa.eu/info/news/commission-announces-top-experts-shape-horizon-europe-missions-2019-jul-30_en.

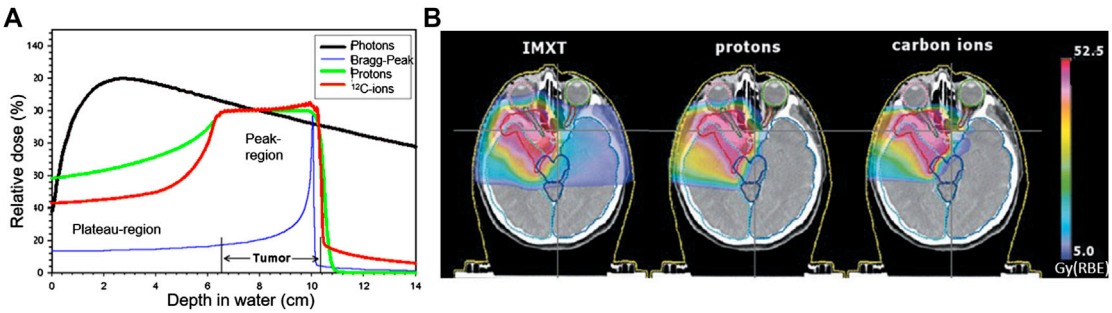

FIGURE 2 | Depth dose profiles in water **(A)** and treatment plans **(B)** [6] comparing photons, delivered with the most advanced intensity modulated X-ray RT (IMXT), and state-of-the-art scanned protons and C-12 ions, showing the increased tumor-dose conformity of ion therapy due to the characteristic Bragg peak **(A)**.

FIGURE 3 | PT centers in Europe, none in SEE region with around 40 million inhabitants.

can offer superior tumor-dose conformality with a reduced number of treatment fields, compared to conventional X-ray radiation, mainly due to the favourable depth-dose deposition of ions in tissue, presented in **Figure 2**. However, despite the considerable recent progress of PT, numerous challenges and new opportunities are yet to be addressed to maximize clinical outcome and cost-effectiveness of this advanced RT modality for improved and uniformly accessible healthcare.

An important aspect that needs to be addressed is the geographical inhomogeneous distribution of the PT centers in Europe. **Figure 3** shows that the majority of Western Europe has access to PT whereas 26 centers[8] provide proton therapy for the citizens of Germany (six centers), United Kingdom (5), France (3), Italy (3), The Netherlands (3), Austria (1), Spain (1), Sweden (1), Switzerland (1), Poland (1), and Denmark (1), while South-East Europe with a population of about 40 million inhabitants has not a single PT facility yet. The SEEIIST project is currently in a technical design phase, thanks to the first financial support of the EC (Directorate for Research and Innovation DG RTD). The hosts of this phase are the renowned institutions, such as CERN in Geneva and GSI[9] in Darmstadt. The task of the SEEIIST facility is twofold: cancer treatment and associated research program, which should ultimately become an integral part of the PT field.

In order to ensure the future operation of the facility, it is necessary to develop highly qualified trained personnel and the

[8]https://www.ptcog.ch/index.php/facilities-in-operation.

[9]https://www.gsi.de/.

technical capacity in parallel to the design and construction of the SEEIIST facility. This effort will be supported by collaborating with the European Network for Light Ion Hadron Therapy (ENLIGHT)[10], established nearly 20 years ago to strengthen EU-PT in clinical research, in R&D for technology and in education and training, based on the principle of open collaboration.

European epidemiological studies preliminary to the Italian, Austrian and French carbon therapy projects made it possible to establish a consensus of priority cases for this type of therapy. From these studies, it was found that the cases eligible for hadron therapy account for about 10% of all radiotherapy patients, which are about 25,000 patients per 10 million inhabitants. About 1% out of this 10% are considered in the very first level of priority. The entire SEE region is covering about 40 million inhabitants and at present there is no medical treatment facility using either proton or heavy-ions in that region yet. Therefore around 1,000 patients will the very first level of priority [6]. As a whole, it can be emphasized that for most of the cases it is a question of rare tumors, the recruitment of which, in order to obtain a particle therapy decision, requires at the first place a healthcare system that is efficient and able to handle all types of cancers and to cover the entire population in an equitable manner. Recruiting them will be one of the main challenges of this initiative. SEEIIST's projected ability is to treat around 400 patients/year, and after 3 years of activity about one third of the theoretical needs of the Region populations regarding medical cases of highest priority for ion therapy. Those numbers can be gradually increased to 1000 patients over time, mainly by allocated longer beam-time for treatments and/or by upgrading the SEEIIST facility with up to three more treatment rooms.

SEEIIST THERAPY FACILITY DESIGN

The SEEIIST design will significantly move beyond the current state-of-the-art technology used at the operational facilities in the EU. The envisaged technological improvement will allow Europe to compete with Japan, a current leader in Carbon medical facilities, and will further increase its lead over developments in the United States. The following will be the innovative and beyond state-of -the-art aspects in the SEEIIST facility design:

- **Outstanding Beam Intensity,** higher than the current European centers (HIT [7], CNAO [8], MedAustron [9]) and the present record intensity realized in Japan [10].
- **Flexible Dose Delivery system,** to deliver the standard slow-extracted beam for active painting of the tumor in a time efficient way, and to achieve dose rates >50 Gy/s, for research purposes and eventually for so called FLASH treatment (irradiation with short impulses and higher intensity beams)
- **Flexibility of using different ion species**, to support a wide experimental program covering all of the new treatment modalities and providing different ion species from protons to argon, focusing in particular on helium, carbon and oxygen.
- **Compact design, Lower Construction and Operation Costs**, to achieve a smaller footprint and about 30% lower construction and operation costs for the accelerator with respect to existing facilities, thanks to an extended use of superconductivity and other modern accelerator technologies.
- **Effective Beam-time sharing solutions.** There will be a highly detailed program developed for the sharing of the beam-time. The treatment rooms (HL, HL + VL, and Superconducting Gantry) are independent of experimental rooms for research (served by two separate beamlines). The patient treatment and animal studies will be space- and function-wize completely independent.
- **Green Infrastructure.** In addition, SEEIIST will be the first High Energy Physics green infrastructure in Europe. It will be powered by a solar panel photovoltaic farm or a wind farm, hence keeping the facility 100% carbon neutral. A detailed sustainability plan will be drawn up for the SEEIIST RI. It is expected that the patient treatment will ensure full financial sustainability of the facility. The production of isotopes with the injector linac, in particular for PET imaging which can be delivered to hospitals in the region, will also contribute to this financial sustainability. With a specific time-planning and beam management, SEEIIST will dedicate 50% of the beam time for patient treatment and 50% for research and training purposes. The machine will be designed in a manner that can be expanded from the initial configuration. At the exit of the injector linac, a space will be reserved for the medical radioisotope production facility.

SEEIIST Facility – Accelerator Technical Choices

While the proton therapy is well commercialized and production of proton beams is based on compact and relatively cheap machines, the Carbon therapy requires much higher beam energies and therefore larger and more complex accelerator systems.

The production of proton beams for therapy is done by cyclotrons[11] or small synchrotrons[12] whose footprint is less than 10 m × 10 m. Carbon ions, due to higher stopping power and smaller charge-to-mass ratio, require three times larger synchrotrons or three times stronger magnets. As a positive aspect, accelerators capable of producing therapy carbon ions can also serve for acceleration of protons and other light ion species to the energies required by therapy. All of the 13 currently operational carbon therapy centers in the world are based on

[10]https://enlight.web.cern.ch/enlight.

[11]E.g., IBA: https://iba-worldwide.com/proton-therapy/proton-therapy-solutions.

[12]E.g., HITACHI: https://www.hitachi.com/businesses/healthcare/products-support/pbt/index.html.

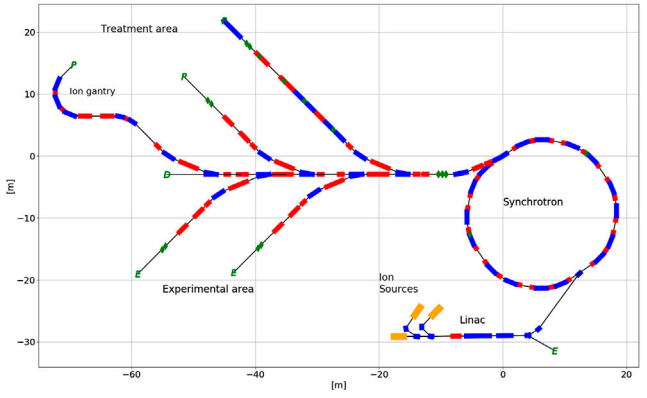

FIGURE 4 | A preliminary layout of the SEEIIST facility. The upper beamlines are dedicated to patient treatment while the lower ones are dedicated to radiobiology and materials research.

synchrotrons [11]. The alternative, on-going developments are cyclotrons [12], linacs [13], rapid-cycling synchrotron [14] and FFA [15].

Cyclotron producing carbon beam is a very large and heavy machine which produces lots of beam losses and has a fixed-energy output, meaning that degraders have to be used for energy reduction. Linacs, currently under development, are expected to provide energy variation at a 100 Hz rate, which is very promising for therapy applications. However, since one of the major features of SEEIIST, as a research laboratory, is the capability to switch to various ion species, linacs are not very flexible in this respect. Also, the linac solution is still in an intensive R&D phase. Rapid-cycling synchrotrons and FFA have also been discarded as alternatives for SEEIIST as the technology is not mature yet and they do not provide significant advantage in terms of cost or reducing footprint and saving space. Therefore, it was concluded that a traditional synchrotron technology should be used for SEEIIST and, as a long-term development option, a synchrotron with super-conducting magnets will be studied to reduce the footprint and complexity and make it comparable to proton synchrotrons.

The main technical elements of the SEEIIST carbon therapy center are depicted in **Figure 4**: two to four ion sources allowing for a fast change of the accelerated ion species, injector linac, which accelerates the beam to energies of about 4–10 MeV/u, a synchrotron with about 60–80 m of circumference (in case of normal conducting magnets) which brings the beam energy up to the required maximum 430 MeV/u and high energy beam transfer lines which bring the extracted beams to the patients or to the experimentalists and researchers.

The main parameters of ion sources critical for carbon therapy applications are: intensity, emittance, and reliability. Currently all centers use Electron Cyclotron Resonance (ECR) ion sources, which provide very stable beams and have very high reliability. The technical developments focus on increase of the ECR source currents and on development of Electron Beam Ion Source (EBIS). EBIS sources offer significantly smaller emittance, that can potentially lead to better transmission in the following injector linac and to significant increase of beam intensity in the synchrotron due to higher efficiency of multi-turn injection. Reliability, though still remains to be proven. The injector linac accelerates the ions from initial energy from the ion source (10–30 keV/u) to injection energy of the synchrotron, which is in the range of 4–10 MeV/u, with optimum around 7 MeV/u. The transmission and final beam energy are the main physical parameters of the linac. It is also a rather expensive system; therefore, the accelerator team is developing a cost-competitive solution for SEEIIST, e.g., by using higher RF frequency which would allow to power up the whole system with a single klystron.

The function of the synchrotron is to accelerate the beams to final energies and extract them in what is called a slow extraction process to the transfer lines and to the patient. The synchrotrons are made of normal conducting magnets which is limiting their circumference to a minimum of about 60 m. The option to use superconducting magnets could cut down the circumference to about 30 m, which is comparable with proton therapy machines.

Several lattice options have been developed for normal-conducting medical synchrotrons. In Europe two distinct approaches have been followed, one proposed by GSI and the other one by CERN/PIMMS [16]. The focus of GSI design was set on compactness and reduced complexity of the machine, while PIMMS was focused on flexibility. As a result of these efforts, the Heidelberg Ion Therapy (HIT)[13] synchrotron is about 10 m shorter than the PIMMS one, and the number of components is also significantly reduced. HIT design was taken over by industry, optimized, and two other facilities based on this design were built: in Marburg and in Shanghai, before Siemens withdrawal from ion cancer therapy market. The PIMMS design went through cycles of improvements and its two implementations: CNAO[14] and MedAustron, are very mature.

Both European designs, even if the lattices are different, share similar characteristics and in particular they all provide only up to maximum of 10^9 Carbon ions per cycle, have a similar circumference size, the same linac and source design. Combining the experience of the two major research laboratories behind their designs, our goal is to make SEEIIST accelerator facility compact, flexible and less complex.

Currently, in order to prove feasibility with regard to the major project challenges, it has been assumed that an upgraded design based on PIMMS study [17] and CNAO implementation will serve as a baseline for SEEIIST, with other lattice options explored in parallel. A second long-term development foresees the use of superconducting magnets [18]. **Figure 5** shows the SEEIIST (HITRI-design) footprint of the facility if superconducting synchrotron and gantry are used, in comparison to the footprints of the existing ion therapy infrastructures in Europe (CNAO and MedAustron).

The main challenge for the SEEIIST (HITRI) design is the increase of the beam intensity. This will be achieved by the increase of ion source intensity, transmission through the linac and optimization of the multi-turn injection process. The slow

[13]HIT cited before.

[14]CNAO and MedA cited before.

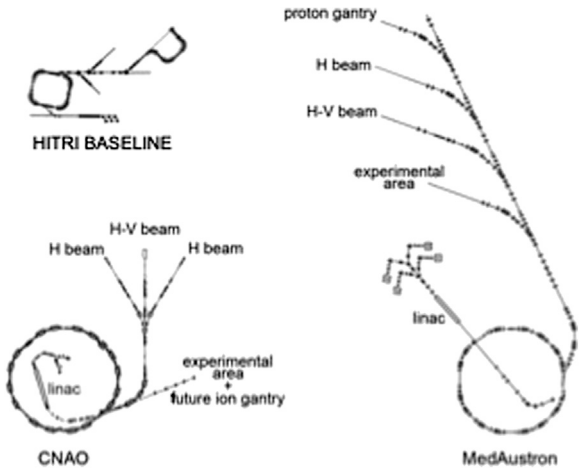

FIGURE 5 | Overall size of the SEEIIST (HITRI) footprint compared to CNAO and MedAustron ion treatment facilities (cfr. **Figure 4** in [Ref. UA 19).

extraction process from a synchrotron is a complex set of procedures and the quality of the extracted beam depends on machine parameters. Optimization of this process and development of new techniques is a subject of active ongoing research. In SEEIIST, we propose to use RK-KO technique, which is successfully used in HIT and in Japan. Moreover, extraction from multi-energy flat-top is also proposed as a baseline, to reduce the treatment time.

The final parts of the facility are the beam transfer lines to the patient and to the experimental hall. The transfer lines should transport stable beams of various sizes to the patient. This task is complicated by the particular shape of the beam produced by the slow extraction process (bar of charge). Furthermore, there are also two main approaches to transfer line design present in current facilities: minimalistic one, facilitated by HIT and the one with a maximum flexibility - the PIMMS design, where various functions of the beam line are spread among various magnet groups. SEEIIST approach is a compromise between the two approaches, that allows a lot of flexibility and, at the same time, does not take too much space. The state-of-art dose delivery systems relies on 3D beam scanning and the last part of the beam lines contain fast scanning magnets which allow for application of this 3D technique. In the second construction stage, a superconducting compact and innovative gantry will be installed in the facility [18, 19].

RESEARCH IN PARTICLE THERAPY

The number of particle therapy centers is rapidly growing, especially in Europe [20, 21]. In the European landscape, unlike in the United States, these centers are often built with public funds, and it is therefore common that scientific research has a prominent role in the activities of these clinical centers [22]. The biological effects of protons are similar to X-rays [23], and therefore most of the research in proton therapy centers focuses on medical physics [24]. Range uncertainty is typically tackled with different technologies based on range prediction [25, 26] or verification [27, 28]. However, for heavy ion centers research in radiobiology is prominent, because of the different biological properties of densely ionizing radiation compared to X-rays [29]. Research is essential to justify the higher costs of the heavy ion centers compared to conventional radiotherapy (**Figure 6**).

For many years, radiobiological research was focusing on RBE. The topic has been widely and systematically studied in a large number of human and rodent cell lines in Berkeley [30], GSI [31] and NIRS [32]. The results are well known, and summarized in **Figure 7** [33]. The RBE increases with LET until reaching a maximum around 100–200 keV/μm, before declining for the overkilling effect. The high variance in **Figure 7** reflects the dependence of the RBE, some of them being physical (e.g., the dependence on charge and velocity, rather than LET alone, and on the dose rate) others biological (e.g., the cell-cycle stage or the survival level). One of the main uncertainties is related to the intrinsic radiosensitivity of the cells (or tumor), the so-called 5th R of radiotherapy [34]. However, this is the same uncertainty encountered in clinical practice for establishing the biological effective dose (BED), which is indeed directly dependent on the α/β ratio [35]. Thinking that RBE uncertainty is a showstopper for heavy ion therapy would be similar to state that no fractionation can be done because we do not know the α/β ratio precisely enough.

Being well understood the RBE dependence on LET, modern radiobiological research is shifting toward topics that are also mainstream in conventional radiotherapy, especially with the current emphasis on precision medicine [36]. A few examples are given below, while more comprehensive reviews could be found in Refs. 37 and 38.

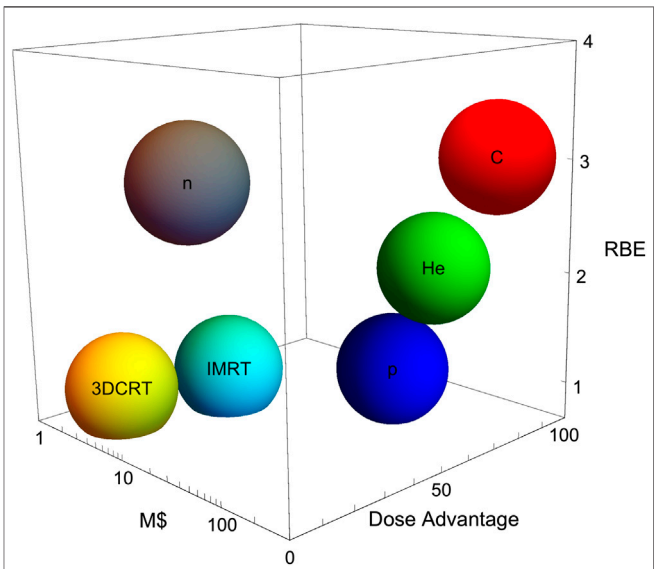

FIGURE 6 | The cost-effectiveness of particle therapy. The plot shows physical advantages (dose, in an arbitrary scale), biological advantages (RBE, in a realistic clinic scale), and cost in millions $ for 3D conformal radiotherapy (3DCRT), intensity modulated radiotherapy (IMRT), neutrons and three charged particles (protons, helium, and carbon).

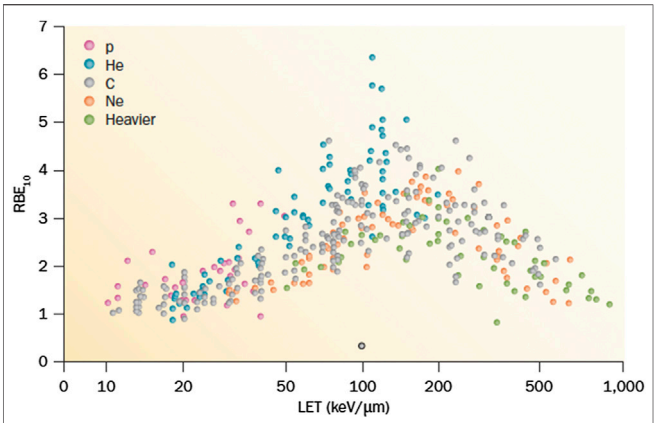

FIGURE 7 | A collection of different RBE values for different cell lines as a function of LET. Data from the PIDE database, available online at www.gsi.de/bio-pide.

Hypoxia

Tumor hypoxia remains one of the worst prognostic factors in cancer therapy [39]. Overcoming hypoxia was one of the main rationales for using heavy ions in the Lawrence Berkeley Laboratory pilot trial in the 70s [40]. Carbon ions, now used in a dozen of centers in Asia and Europe, can only partly solve the problem, because their LET is relatively low and OER goes to one only at LET > 100 keV/μm [41] (**Figure 8**). While drugs overcoming hypoxia are entering in the clinics [42, 43], strategies based on the physics can certainly contribute in decreasing hypoxia-mediated radio resistance. Kill-painting with carbon ions [44] provides intensity modulation to boost the hypoxic regions, thus overcoming resistance provided that the hypoxic volumes can be visualized by PET before the treatment [45]. Oxygen ions, slightly heavier than carbon, can be more effective against hypoxic tumors maintaining acceptable toxicity [46], and for this very reason they will be used in the Heidelberg Ion Therapy (HIT) clinical center in the coming years for radioresistant cancers [47]. Another approach is to use multi-ions, that can provide high-LET in the target and low-LET in the normal tissue, thus sterilizing the hypoxic tumor with minimal toxicity [48, 49].

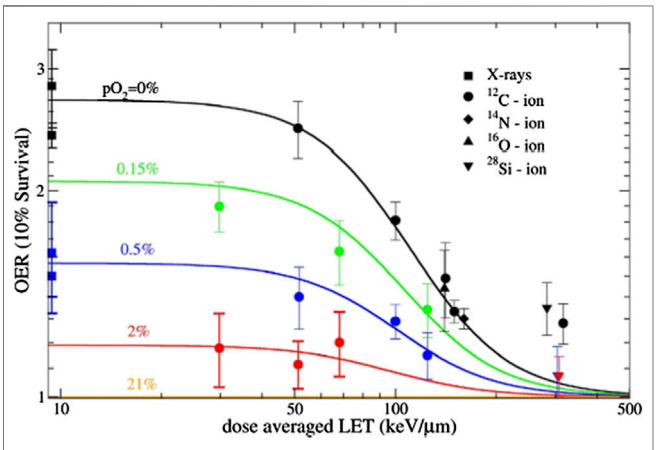

FIGURE 8 | Dependence of oxygen effective ratio from LET in CHO cells. Plot from Ref. 44, reproduced under CC BY license from NPG publisher.

Combined Treatments

Immunotherapy of cancer is considered the most promising strategy to reduce mortality, which is largely due to metastatic tumors [50]. However, local treatments remain necessary to tackle the primary tumor and, beyond surgery, radiotherapy has the advantage of eliciting an immune response that can boost immunotherapy [51–53]. Re-activation of immune response is indeed now called the 6th R of radiotherapy [54]. While the recent trials in lung cancer patients have demonstrated the significant survival, advantages expected by combining radio- and immune-therapy [55, 56], the question is whether heavy ion therapy can be more beneficial than X-rays in these combined treatments [57].

This is arguably the most important question for the future of particle therapy, because should radioimmunotherapy by X-rays maintain the promise of largely improving the survival of stage-IV patients, the higher cost of particle therapy (**Figure 6**) could not be justified. Particle therapy has, however, both physical and biological advantages compared to X-rays in combination with immunotherapy [58]. The main physical advantages are the sparing of the lymphocytes, essential cells to set off an immune response against the metastatic cancer cells. In fact, sparing lymph nodes is now being proposed as a standard practice also for conventional radiotherapy [59]. In addition, cell-death pathways induced by heavy ions seem to be more immunogenic than for X-rays, resulting in enhanced biological effectiveness [60, 61].

SEEIIST and FLASH

Very high-dose radiotherapy (>40 Gy/s) is generally acknowledged as a promising, and potentially evolutionary, pathway for radiotherapy [62, 63]. Pre-clinical data in animal models have indeed shown that at high-dose rate normal tissue toxicity is significantly reduced, while tumor control is not modified [64–66]. The potential advantages in terms of widening the therapeutic windows are enormous. However, reaching these high-dose rates is difficult with X-rays, due to the conversion of electrons in Bremsstrahlung radiation [67]. A first patient has been treated with electrons under FLASH conditions [68], and several proton therapy centers are increasing the cyclotron intensity to reach the FLASH regime [69–71]. For having heavy ion FLASH, high intensity has to be achieved in synchrotrons [72]. This is one of the goals of the new SEEIIST accelerator, as well as of many new accelerators under development worldwide for nuclear research [73]. It is therefore likely that FLASH radiotherapy will be an important topic at SEEIIST, both for clinical and pre-clinical research.

SOCIOECONOMICAL BENEFITS OF SEEIIST

Before the wars and the crisis in former Yugoslavia, the region had a long history of excellence in science. Before CERN was

established in Geneva in 1954, and the International Center for Theoretical Physics in Trieste and the European Molecular Biology Organization in Heidelberg in 1964, former Yugoslavia already had three older research institutes. The Vinča Institute of Nuclear Science in Belgrade was founded in 1948, the Jožef Stefan Institute in Ljubljana in 1949 and the Ruđer Bošković Institute in Zagreb in 1950. Yugoslavia was also one of the founding countries of CERN. However, the scientific progress began to crumble in 1991, along with Yugoslavia's dissolution and the 1991–2001 wars in former Yugoslavia diminished the economies and science capacity of all countries in the area. An entire generation of young scientists migrated to the Western countries, continuing to do so even in the period after the crisis. This is what gave rise to the political will of the countries of the region and of the EU, "To bring back the tradition in science and technology that the region had in the past." Furthermore, SEEIIST will revive the scientific and technological potential of the Balkans, whilst helping its economy and bringing people together around a shared endeavor, a vision of a world-leading research institute, built under the same collaborative model as CERN. A €200 million investment in an international research facility in the Balkans could heal the wounds left by the years of ethnic/religious conflicts, help to stop the brain drain and enable the region to regain its former scientific glory. The countries involved in the SEEIIST project hope it will help the region overcome economic difficulties and bring them closer to EU membership.

Inclusion of SEEIIST on the next EU's roadmap for research infrastructures being drawn up by the European Strategy Forum on Research Infrastructures (ESFRI) in 2021 will be of crucial importance to place the project on the "scientific and political map".

The average cost of the treatment of a normal patient with heavy ions (not only protons) is estimated to be 25 kEUR in the presently accessible European facilities (HIT, CNAO, MedAustron, and MIT). With the estimated ~400 patients foreseen to be treated per year in the early phase, SEEIIST will be able to cover 50% of the annual running costs (~10 MEUR). The remaining cost will be covered by other sources such as membership fees of users (including industry), country contributions (memberships), and research projects from the Horizon Europe programmes.

AUTHOR CONTRIBUTIONS

All authors listed have made a substantial, direct, and intellectual contribution to the work and approved it for publication.

FUNDING

A large part of this work has been supported by funding from the EU DG-RTD via a special instrument 'Service Facility in Support of the Strategic Development of International Cooperation in Research and Innovation N°30-CE-0838742/00-87'.

REFERENCES

1. Bray F, Ferlay J, Soerjomataram I, Siegel R-L, Torre L-A, Jemal A. Global cancer statistics 2018: GLOBOCAN estimates of incidence and mortality worldwide for 36 cancers in 185 countries. *CA Cancer J Clin* (2018) 68(6):394–424. doi:10.3322/caac.21492
2. Fitzmaurice C, Abate D, Abbasi N, Abbastabar H, Abd-Allah F, Abdel-Rahman O, et al. Global, regional, and national cancer incidence, mortality, years of life lost, years lived with disability, and disability-adjusted life-years for 29 cancer groupsA systematic analysis for the global burden of disease study, global burden of disease cancer collaboration. *JAMA Oncol* (1990) 5(12):1749–68. doi:10.1001/jamaoncol.2019.2996
3. Dagenais G-R, Leong D-P, Rangarajan S, Lanas F, Lopez-Jaramillo P, Gupta R, et al. Variations in common diseases, hospital admissions, and deaths in middle-aged adults in 21 countries from five continents (PURE): a prospective cohort study. *Lancet* (2020) 395:785–94. doi:10.1016/S0140-6736(19)32092-6
4. Rosenblatt E, Izewska J, Anacak Y, Pynda Y, Scalliet P, Boniol M, et al. Radiotherapy capacity in European countries: an analysis of the directory of radiotherapy centres (DIRAC) database. *Lancet Oncol* (2013) 14(2):e79–86. doi:10.1016/S1470-2045(12)70556-9
5. Luengo-Fernandez R, Leal J, Gray A, Sullivan R. Economic burden of cancer across the European Union: a population-based cost analysis. *Lancet Oncol* (2013) 14(12):1165–74. doi:10.1016/S1470-2045(13)70442-X
6. U Amaldi eds. A facility for tumour therapy and biomedical research in South-eastern Europe. CERN-2019-002. doi:10.23731/CYRM-2019-002
7. NuPECC. F Azaiez, A Bracco, J Dobeš, A Jokinen, G-E Körner, A Maj, et al. editors *Nuclear physics for medicine. Printing: Ireg Strasbourg* (2014).
8. Haberer T, Debus J, Eickhoff H, Jäkel O, Schulz-Ertner D, Weber U. The Heidelberg ion therapy center. *Radiat Oncol* (2004) 73(2):186–90. doi:10.1016/s0167-8140(04)80046-x
9. Rossi S. The status of CNAO. *Eur Phys J Plus* (2011) 126:8. doi:10.1140/epjp/i2011-11078-8
10. Benedikt M, Gutleber J, Palm M, Pirkl W, Dorda U, Fabich A. "Overview of the MedAustron design and technology choices," in Proceedings, 1st international particle accelerator conference. Kyoto, Japan (2010): 186–90.
11. Iwata Y, Kadowaki T, Uchiyama H, Fujimoto T, Takada E, Shirai T, et al. Multiple-energy operation with extended flattops at HIMAC. *Nucl Phys Meth A* (2010) 624:33–8. doi:10.1016/j.nima.2010.09.016
12. Jongen Y, Abs M, Blondin A, Kleeven W, Zaremba S, Vandeplassche D, et al. "Current status of the iba C400 cyclotron project for hadron therapy," in Proceedings of IPAC2008. Genova, Italy: CERN (2008) p. TUPP120.
13. Verdú-Andrés S, Amaldi U, Faus-Golfe A. CABOTO, a high-gradient linac for hadrontherapy. *J Radiat Res* (2013) 54(1):i155–61. doi:10.1093/jrr/rrt053
14. Trbojevic D, Alessi J, Blaskiewicz M, Cullen C, Hahn H, Lowenstein D, et al. "Lattice design of A rapid cycling medical synchrotron for carbon/proton therapy," in Proceedings of IPAC2011. San Sebastian, Spain: CERN (2011) p. WEPS028.
15. Peach K-J, Aslaninejad M, Barlow R, Beard C-D, Bliss N, Cobb J-H, et al. Conceptual design of a nonscaling fixed field alternating gradient accelerator for protons and carbon ions for charged particle therapy. *Phys Rev ST-AB* (2013) 16:030101. doi:10.1103/PhysRevSTAB.16.030101
16. Benedikt LM, Bryant P, Crescenti P, Holy P, Knaus P, Maier A, et al. Proton-ion medical machine study (PIMMS)—Part I (1999) p. 232. CERN/PS 99-010 DI Geneva, Switzerland.
17. Bryant PJ, Badano L, Benedikt M, Crescenti M, Holy P, Maier AT, et al. Proton-ion medical machine study (PIMMS) Part 2 (2000) p. 340. CERN-PS-2000-007-DR Switzerland, Geneva.
18. Al Harbi N, Amaldi U, Bergesio D, Garonna A, Ljubicic V, Riboni P, et al. Carbon ion superconducting gantry and synchrotron based on canted cosine-theta magnets. *Phys Med Biol* (2021).

19. Amaldi U. Oblique raster scanning: an ion dose delivery procedure with variable energy layers. *Phys Med Biol* (2019) 64:115003. doi:10.1088/1361-6560/ab0920
20. Dosanjh MK, Amaldi U, Mayer R, Poetter R. Enlight. European Network for light ion hadron therapy. *Radiother Oncol* 128:76–82. doi:10.1016/j.radonc.2018.03.014
21. Grau C, Durante M, Georg D, Langendijk JA, Weber DC. Particle therapy in Europe. *Mol Oncol* (2020) 14:1492–99. doi:10.1002/1878-0261.12677
22. Durante M. Proton beam therapy in Europe: more centres need more research. *Br J Canc* (2019) 120:777–8. doi:10.1038/s41416-018-0329-x
23. Tommasino F, Durante M. Proton radiobiology. *Cancers* (2015) 7:353–81. doi:10.3390/cancers7010353
24. Lomax AJ. Myths and realities of range uncertainty. *Br J Radiol* (2020) 93: 20190582. doi:10.1259/bjr.20190582
25. Bär E, Lalonde A, Royle G, Lu H-M, Bouchard H. The potential of dual-energy CT to reduce proton beam range uncertainties. *Med Phys* (2017) 44:2332–44. doi:10.1002/mp.12215
26. Johnson RP. Review of medical radiography and tomography with proton beams. *Rep Prog Phys* (2018) 81:016701. doi:10.1088/1361-6633/aa8b1d
27. Krimmer J, Dauvergne D, Létang JM, Testa É. Prompt-gamma monitoring in hadrontherapy: a review. *Nucl Instrum Methods Phys Res Sect A Accel Spectrometers Detect Assoc Equip* (2018) 878:58–73. doi:10.1016/j.nima.2017.07.063
28. Parodi K. Vision 20/20: positron emission tomography in radiation therapy planning, delivery, and monitoring. *Med Phys* (2015) 42:7153–68. doi:10.1118/1.4935869
29. Durante M. New challenges in high-energy particle radiobiology. *Br J Radiol* (2014) 87:20130626. doi:10.1259/bjr.20130626
30. Blakely EA, Ngo F, Curtis S, Tobias CA. Heavy-ion radiobiology: cellular studies. *Adv Radiat Biol* (1984) 11:295–389. doi:10.1016/B978-0-12-035411-5.50013-7
31. Kraft G. Radiobiological effects of very heavy ions : inactivation, induction of chromosome aberrations and strand breaks. *Nucl Sci Appl* (1987) 3:1.
32. Furusawa Y, Fukutsu K, Aoki M, Itsukaichi H, Eguchi-Kasai K, Ohara H, et al. Inactivation of aerobic and hypoxic cells from three different cell lines by accelerated (3)He–, (12)C– and (20)Ne-ion beams. *Radiat Res* (2000) 154: 485–96. doi:10.1667/0033-7587(2000)154[0485:IOAAHC]2.0.CO;2
33. Friedrich T, Scholz U, Elsässer T, Durante M, Scholz M. Systematic analysis of RBE and related quantities using a database of cell survival experiments with ion beam irradiation. *J Radiat Res* (2013) 54:494–514. doi:10.1093/jrr/rrs114
34. Brown JM, Carlson DJ, Brenner DJ. The tumor radiobiology of SRS and SBRT: are more than the 5 Rs involved?. *Int J Radiat Oncol* (2014) 88:254–62. doi:10.1016/j.ijrobp.2013.07.022
35. Fowler JF. 21 Years of biologically effective dose. *Br J Radiol* (2010) 83:554–68. doi:10.1259/bjr/31372149
36. Baumann M, Krause M, Overgaard J, Debus J, Bentzen SM, Daartz J, et al. Radiation oncology in the era of precision medicine. *Nat Rev Canc* (2016) 16: 234–49. doi:10.1038/nrc.2016.18
37. Durante M, Orecchia R, Loeffler JS. Charged-particle therapy in cancer: clinical uses and future perspectives. *Nat Rev Clin Oncol* (2017) 14:483–95. doi:10.1038/nrclinonc.2017.30
38. Durante M, Flanz J. Charged particle beams to cure cancer: strengths and challenges. *Semin Oncol* (2019) 46:219–25. doi:10.1053/j.seminoncol.2019.07.007
39. Bertout JA, Patel SA, Simon MC. The impact of O2 availability on human cancer. *Nat Rev Canc* (2008) 8:967–75. doi:10.1038/nrc2540
40. Tobias CA. Failla memorial lecture. The future of heavy-ion science in biology and medicine. *Radiat Res* (1985) 103:1–33. doi:10.2307/3576668
41. Scifoni E, Tinganelli W, Weyrather WK, Durante M, Maier A, Krämer M. Including oxygen enhancement ratio in ion beam treatment planning: model implementation and experimental verification. *Phys Med Biol* (2013) 58: 3871–95. doi:10.1088/0031-9155/58/11/3871
42. Ashton TM, Fokas E, Kunz-Schughart LA, Folkes LK, Anbalagan S, Huether M, et al. The anti-malarial atovaquone increases radiosensitivity by alleviating tumour hypoxia. *Nat Commun* (2016) 7:12308. doi:10.1038/ncomms12308
43. McGowan DR, Skwarski M, Bradley KM, Campo L, Fenwick JD, Gleeson FV, et al. Buparlisib with thoracic radiotherapy and its effect on tumour hypoxia: A phase I study in patients with advanced non-small cell lung carcinoma. *Eur J Canc* (2019) 113:87–95. doi:10.1016/j.ejca.2019.03.015
44. Tinganelli W, Durante M, Hirayama R, Krämer M, Maier A, Kraft-Weyrather W, et al. Kill-painting of hypoxic tumours in charged particle therapy. *Sci Rep* (2015) 5:17016. doi:10.1038/srep17016
45. Horsman MR, Mortensen LS, Busk M, Overgaard J, Horsman MR, Mortensen LS, et al. Imaging hypoxia to improve radiotherapy outcome. *Nat Rev Clin Oncol* (2012) 9:674–87. doi:10.1038/nrclinonc.2012.171
46. Sokol O, Scifoni E, Tinganelli W, Kraft-Weyrather W, Wiedemann J, Maier A, et al. Oxygen beams for therapy: advanced biological treatment planning and experimental verification. *Phys Med Biol* (2017) 62:7798–813. doi:10.1088/1361-6560/aa88a0
47. Kurz C, Mairani A, Parodi K. First experimental-based characterization of oxygen ion beam depth dose distributions at the Heidelberg Ion-Beam Therapy Center. *Phys Med Biol* (2012) 57:5017–34. doi:10.1088/0031-9155/57/15/5017
48. Kopp B, Mein S, Dokic I, Harrabi S, Böhlen TT, Haberer T, et al. Development and validation of single field multi-ion particle therapy treatments. *Int J Radiat Oncol Biol Phys* (2020) 106:194–205. doi:10.1016/j.ijrobp.2019.10.008
49. Sokol O, Krämer M, Hild S, Durante M, Scifoni E. Kill painting of hypoxic tumors with multiple ion beams. *Phys Med Biol* (2019) 64:045008. doi:10.1088/1361-6560/aafe40
50. Tran E, Robbins PF, Rosenberg SA. "Final common pathway" of human cancer immunotherapy: targeting random somatic mutations. *Nat Immunol* (2017) 18:255–62. doi:10.1038/ni.3682
51. Formenti SC, Demaria S. Combining radiotherapy and cancer immunotherapy: a paradigm shift. *J Natl Cancer Inst* (2013) 105:256–65. doi:10.1093/jnci/djs629
52. Weichselbaum RR, Liang H, Deng L, Fu Y-X. Radiotherapy and immunotherapy: a beneficial liaison?. *Nat Rev Clin Oncol* (2017) 14:365–79. doi:10.1038/nrclinonc.2016.211
53. Ngwa W, Irabor OC, Schoenfeld JD, Hesser J, Demaria S, Formenti SC. Using immunotherapy to boost the abscopal effect. *Nat Rev Canc* (2018) 18:313–22. doi:10.1038/nrc.2018.6
54. Boustani G, Grapin M, Laurent P-A, Apetoh L, Mirjolet C. The 6th R of radiobiology: reactivation of anti-tumor immune response. *Cancers* (2019) 11: 860. doi:10.3390/cancers11060860
55. Antonia SJ, Villegas A, Daniel D, Vicente D, Murakami S, Hui R, et al. Overall survival with durvalumab after chemoradiotherapy in stage III NSCLC. *N Engl J Med* (2018) 379:2342–50. doi:10.1056/NEJMoa1809697
56. Formenti SC, Rudqvist N-P, Golden E, Cooper B, Wennerberg E, Lhuillier C, et al. Radiotherapy induces responses of lung cancer to CTLA-4 blockade. *Nat Med* (2018) 24:1845–51. doi:10.1038/s41591-018-0232-2
57. Durante M, Brenner DJ, Formenti SC. Does heavy ion therapy work through the immune system ? *Int J Radiat Oncol Biol Phys* (2016) 96:934–6. doi:10.1016/j.ijrobp.2016.08.037
58. Durante M, Formenti S. Harnessing radiation to improve immunotherapy: better with particles?. *Br J Radiol* (2020) 93:20190224. doi:10.1259/bjr.20190224
59. Lambin P, Lieverse RIY, Eckert F, Marcus D, Oberije C, van der Wiel AMA, et al. Lymphocyte-sparing radiotherapy: the rationale for protecting lymphocyte-rich organs when combining radiotherapy with immunotherapy. *Semin Radiat Oncol* (2020) 30:187–93. doi:10.1016/j.semradonc.2019.12.003
60. Takahashi Y, Yasui T, Minami K, Tamari K, Hayashi K, Otani K, et al. Carbon ion irradiation enhances the antitumor efficacy of dual immune checkpoint blockade therapy both for local and distant sites in murine osteosarcoma. *Oncotarget* (2019) 10:633–46. doi:10.18632/oncotarget.26551
61. Ebner DK, Tinganelli W, Helm A, Bisio A, Yamada S, Kamada T, et al. The immunoregulatory potential of particle radiation in cancer therapy. *Front Immunol* (2017) 8:99. doi:10.3389/fimmu.2017.00099
62. Harrington KJ. Ultrahigh dose-rate radiotherapy: next steps for FLASH-RT. *Clin Canc Res* (2019) 25:3–5. doi:10.1158/1078-0432.CCR-18-1796
63. Durante M, Brauer-Krisch E, Hill M. Faster and safer? FLASH ultra-high dose rate in radiotherapy. *Br J Radiol* (2017) 91:20170628. doi:10.1259/bjr.20170628
64. Favaudon V, Caplier L, Monceau V, Pouzoulet F, Sayarath M, Fouillade C, et al. Ultrahigh dose-rate FLASH irradiation increases the differential response between normal and tumor tissue in mice. *Sci Transl Med* (2014) 6:245ra93. doi:10.1126/scitranslmed.3008973

65. Vozenin MC, De Fornel P, Petersson K, Favaudon V, Jaccard M, Germond JF, et al. The advantage of FLASH radiotherapy confirmed in mini-pig and cat-cancer patients. *Clin Canc Res* (2019) 25:35–42. doi:10.1158/1078-0432.CCR-17-3375
66. Montay-Gruel P, Acharya MM, Petersson K, Alikhani L, Yakkala C, Allen BD, et al. Long-term neurocognitive benefits of FLASH radiotherapy driven by reduced reactive oxygen species. *Proc Natl Acad Sci USA* (2019) 116:10943–51. doi:10.1073/pnas.1901777116
67. Bazalova-Carter M, Esplen N. On the capabilities of conventional x-ray tubes to deliver ultra-high (FLASH) dose rates. *Med Phys* (2019) 46:5690–5. doi:10.1002/mp.13858
68. Bourhis J, Sozzi WJ, Jorge PG, Gaide O, Bailat C, Duclos F, et al. Treatment of a first patient with FLASH-radiotherapy. *Radiother Oncol* (2019) 139:18–22. doi:10.1016/j.radonc.2019.06.019
69. van Marlen P, Dahele M, Folkerts M, Abel E, Slotman BJ, Verbakel WFAR. Bringing FLASH to the clinic: treatment planning considerations for ultrahigh dose-rate proton beams. *Int J Radiat Oncol* (2020) 106:621–9. doi:10.1016/j.ijrobp.2019.11.011
70. Diffenderfer ES, VerginadisII, Kim MM, Shoniyozov K, Velalopoulou A, Goia D, et al. Design, implementation, and *in vivo* validation of a novel proton FLASH radiation therapy system. *Int J Radiat Oncol* (2020) 106:440–8. doi:10.1016/j.ijrobp.2019.10.049
71. Patriarca A, Fouillade C, Auger M, Martin F, Pouzoulet F, Nauraye C, et al. Experimental set-up for FLASH proton irradiation of small animals using a clinical system. *Int J Radiat Oncol* (2018) 102:619–26. doi:10.1016/j.ijrobp.2018.06.403
72. Colangelo NW, Azzam EI. The importance and clinical implications of FLASH ultra-high dose-rate studies for proton and heavy ion radiotherapy. *Radiat Res* (2019) 193:1–4. doi:10.1667/RR15537.1
73. Durante M, Golubev A, Park W-Y, Trautmann C. Applied nuclear physics at the new high-energy particle accelerator facilities. *Phys Rep* (2019) 800:1–37. doi:10.1016/j.physrep.2019.01.004

Conflict of Interest: Author MP was employed by the company COSYLAB.

The remaining authors declare that the research was conducted in the absence of any commercial or financial relationships that could be construed as a potential conflict of interest.

frontiers in Physics

ORIGINAL RESEARCH
published: 08 February 2021
doi: 10.3389/fphy.2020.568242

Measuring the Impact of Nuclear Interaction in Particle Therapy and in Radio Protection in Space: the FOOT Experiment

Giuseppe Battistoni[1], *Marco Toppi*[2,3]*, *Vincenzo Patera*[3,4] *and The FOOT Collaboration*

[1]INFN Section of Milano, Milano, Italy, [2]INFN Laboratori Nazionali di Frascati, Frascati, Italy, [3]Department of Scienze di Base e Applicate per l'Ingegneria (SBAI), University of Rome La Sapienza, Rome, Italy, [4]INFN Section of Roma 1, Rome, Italy

In Charged Particle Therapy (PT) proton or ^{12}C beams are used to treat deep-seated solid tumors exploiting the advantageous characteristics of charged particles energy deposition in matter. For such projectiles, the maximum of the dose is released at the end of the beam range, in the Bragg peak region, where the tumour is located. However, the nuclear interactions of the beam nuclei with the patient tissues can induce the fragmentation of projectiles and/or target nuclei and needs to be carefully taken into account when planning the treatment. In proton treatments, the target fragmentation produces low energy, short range fragments along all the beam path, that deposit a non-negligible dose especially in the first crossed tissues. On the other hand, in treatments performed using ^{12}C, or other (^{4}He or ^{16}O) ions of interest, the main concern is related to the production of long range fragments that can release their dose in the healthy tissues beyond the Bragg peak. Understanding nuclear fragmentation processes is of interest also for radiation protection in human space flight applications, in view of deep space missions. In particular ^{4}He and high-energy charged particles, mainly ^{12}C, ^{16}O, ^{28}Si and ^{56}Fe, provide the main source of absorbed dose in astronauts outside the atmosphere. The nuclear fragmentation properties of the materials used to build the spacecrafts need to be known with high accuracy in order to optimise the shielding against the space radiation. The study of the impact of these processes, which is of interest both for PT and space radioprotection applications, suffers at present from the limited experimental precision achieved on the relevant nuclear cross sections that compromise the reliability of the available computational models. The FOOT (FragmentatiOn Of Target) collaboration, composed of researchers from France, Germany, Italy and Japan, designed an experiment to study these nuclear processes and measure the corresponding fragmentation cross sections. In this work we discuss the physics motivations of FOOT, describing in detail the present detector design and the expected performances, coming from the optimization studies based on accurate FLUKA MC simulations and preliminary beam test results. The measurements planned will be also presented.

Keywords: particle therapy, space radioprotection, fragmentation, cross section, nuclear interactions, protons RBE

OPEN ACCESS

Edited by:
Paul Sellin,
University of Surrey, United Kingdom

Reviewed by:
Miguel Antonio Cortés-Giraldo,
Sevilla University, Spain
Sally Seidel,
University of New Mexico,
United States

***Correspondence:**
Marco Toppi
marco.toppi@uniroma1.it

Specialty section:
This article was submitted to Radiation Detectors and Imaging, a section of the journal Frontiers in Physics

Received: *01 July 2020*
Accepted: *02 November 2020*
Published: *08 February 2021*

Citation:
Battistoni G, Toppi M, Patera V and The FOOT Collaboration (2021) Measuring the Impact of Nuclear Interaction in Particle Therapy and in Radio Protection in Space: the FOOT Experiment. Front. Phys. 8:568242. doi: 10.3389/fphy.2020.568242

INTRODUCTION

In the last decade a continuous increase in the number of cancer patients treated with charged Particle Therapy (PT) [1] has been registered, as a consequence of its effectiveness in the treatment of deep-seated solid tumors [2]. While protons and carbon ions are, nowadays, used in PT clinical routines, an interest also in helium and oxygen ions as therapeutic beams is growing [3, 4].

The use of light ion beams to treat tumors in PT is mainly motivated by the depth-dose profile of charged particles. This is characterized by an entrance channel where a low amount of dose is released, followed by a narrow region, the Bragg Peak (BP), where the maximum of the dose is deposited that is used to cover the cancer region, allowing to spare the surrounding healthy tissues. Furthermore the increase in the radiation Linear Energy Transfer (LET) in the BP region enhances its Relative Biological Effectiveness (RBE) in cell killing when comparing with conventional radio therapy using photons. Even though the track structure also plays a role, as a general approximation, high LET corresponds to high RBE, so the effect is particularly important for ions like ^{12}C or ^{16}O, where the LET increases significantly near the BP region. The RBE increase as a function of LET stops around 100–200 keV/μm, where the RBE peaks, depending on the ion specie, and than drops down for further LET increases [5, 6].

The increase in the RBE of ^{12}C or ^{16}O beams comes at the price of an increased difficulty in planning the treatment to properly account for the beam fragmentation. In the interaction with the atomic nuclei inside the patient body, the beam particles can fragment producing secondary particles with lower atomic number Z. Such fragments have a longer range that results in an energy loss tail beyond the BP region. Moreover the lightest fragments, especially protons and neutrons, can be emitted with large angle with respect to the beam direction. Fragmentation processes modify the delivered dose map with respect to the one that can be computed only accounting for the primary ions contribution [7]. This effect strongly depends on the mass and the energy of the ion beam and on the target involved in the interaction. Treatment plans, generally based on deterministic codes [8], and benchmarked against MC simulations [9–12], are not yet able to include the fragmentation contribution with the accuracy (3%) required for radiotherapy applications [13, 14]. This is due to the lack of experimental data, and in particular of double differential cross section measurements with respect to the angle and the kinetic energy of the fragment. In recent years some experiments have been dedicated to the measurement of the ^{12}C ions fragmentation cross sections, however this program was carried out only for a few, energies-target combinations [15–17] and the completion of the experimental data inputs collected using thin targets is still eagerly needed. The targets of main interest for the study of fragmentation cross sections for PT applications are the ^{16}O, ^{12}C and ^{1}H nuclei, being the most abundant elements in the human tissues, while, as for the beams, together to ^{12}C and ^{16}O, ^{4}He is of great interest due to the low fragmentation yield and to the good compromise between LET and RBE [18, 19].

The landscape is quite different for proton treatments: no beam fragmentation is expected and due to the low and slowly varying LET a constant RBE value equal to 1.1 is currently adopted in clinical practice. However, recent radiobiological measurements provided indications of a significant increase in the RBE above 1.1 [20]. In particular the such increase could lead to a biological range extension after the BP or to an enhancement of the biological damage in the entrance channel (plateau region in the Bragg curve before the BP), i.e. in the region where the beam crosses the healthy tissues [21, 22]. The increase could be connected to the nuclear interactions occurring between the beam and the patient tissues. In the case of proton beams, only target fragmentation occurs, generating a spectrum of low energy fragments whose recoil depends on the beam energy and target materials. These secondary charged particles have an extremely short range (e.g. order of 10-100 μm), and are characterized by very high LET and, hence, high RBE. Particles produced in target fragmentation interactions [21] could be one of the causes of the proton RBE increase [23]. In proton therapy this process can have an impact in particular in the entrance channel, where the contribution to the dose deposition from the primary beam ionization processes is smaller with respect to the one occurring in the Bragg Peak region.

Unfortunately at present this effect is difficult to explore due to the missing cross sections measurements related to the production of heavy fragments induced by the proton irradiation with energies in the range of interest for PT (≤200 MeV). The process of target fragmentation so far has been almost completely neglected. The only available measurements cover the light fragment ($Z < 3$) production, with a total lack of data for the heavier fragments. In order to improve the modeling of the RBE, including the contribution from target fragmentation, the study of protons interactions with O and C targets are of fundamental importance.

The fragmentation of light ions on light targets is of interest also in the field of radioprotection in space. ESA, NASA and other space agencies have started, since several years, the astronauts risk assessment studies in view of long duration space missions (E.g. the travel to Mars). An efficient spacecraft shielding system from space radiation is mandatory to ensure the astronauts safety [24, 25]. There are three main sources of energetic particles in space: Solar Particle Events (SPEs), Galactic Cosmic Rays (GCR) and the geomagnetically trapped particles. SPEs are mainly composed of protons emitted from the sun during coronal mass ejections and solar flares. Their energy spectrum can reach the GeV region and, being unpredictable, they can fluctuate and become so intense as to inflict a lethal dose to the astronauts. GCRs are originated from supernovae within the Milky Way Galaxy and consist mainly of high energy protons ($\simeq$86%), helium ($\simeq$12%) and heavier nuclei ($\simeq$1%) up to ^{56}Fe, called HZE - high (H) energetic (E) charged (Z) nuclei. GCRs energy spectrum ranges from MeV to TeV, peaking around 100–800 MeV/nucleon. The geomagnetically trapped particles consist of protons and electrons confined by the Earth magnetic field in two regions named Van Allen belts. Protons reach energies up to a few hundreds MeV in the inner belt and electrons up to 100 keV in the outer belt.

When the incident radiation, and in particular ^{4}He and HZE ions from GCRs, interacts with the spacecraft hull and internal

materials, the nuclear fragmentation modifies the space radiation spectra, producing of secondary fragments that contribute to the dose release. This process has to be taken into account when designing the proper shield to reduce the dose delivered to astronauts and to prevent damages to the electronic systems and instrumentations [24]. Dose estimates can be obtained, with a limited precision, through direct measurements, but the main tools available for the planning task are calculations with deterministic and Monte Carlo transport codes [26]. An essential ingredient for validating and benchmarking the simulation results is the comparison with the measured nuclear fragmentation cross sections for the interaction of the space primary ion components on different types of shielding [27]. Light materials, rich in hydrogen, are now considered as best shielding candidates and are preferred to aluminium, the material currently used to build most spacecraft structures. While the mass stopping power (depending on Z/A) is maximized for light elements, the nuclear interaction cross section (proportional to σ/A) is minimized, reducing to a minimum the yield of neutrons produced in the interaction with the shield [24, 25]. Low Z, and especially liquid hydrogen, are hence among the most effective materials to be used to build shielding structures for space applications [28]. While liquid hydrogen is not a suitable practical choice, being a low temperature liquid, shielding structures can be built using hydrogen stored in graphite nanofibers or lithium hydride compounds (^{6}LiH). So far, polyethylene has been extensively studied and is regarded as a good compromise between the achieved performance and easiness of practical integration with the spacecraft structure.

Summarizing, there is a common ground between protecting the astronauts from the harmful effects of space radiation and improving the tumor therapy planning of patients treated with protons and ions. The particle species currently available in PT (protons and ^{12}C) or considered as promising alternative candidates (^{4}He, ^{16}O) are among the most abundant in space. The overlap is also in terms of targets (H and C) and energy, especially in the region of interest for tumor therapy applications that is the same of solar flare protons and Van Allen trapped protons and is placed near the peak of the GCR spectrum.

In this landscape the FOOT (FragmentatiOn Of Target) collaboration has the purpose of performing precise measurements of differential fragmentation cross sections, with respect to the emitted fragment kinetic energy and production angle [29, 30]. The FOOT measurements campaign foresees an extensive program focused on the nuclear fragmentation of ^{4}He, ^{12}C and ^{16}O beams impinging on thin C and H rich targets, like polyethylene C_2H_4, in the energy range 100-800 MeV/nucleon, of interest for PT and radioprotection in space (RPS) applications.

THE FOOT EXPERIMENT

The FOOT experiment, funded by INFN (Istituto Nazionale di Fisica Nucleare, Italy), has been designed to detect, track and identify all the charged fragments produced in ion collisions with different targets, with the aim of measuring both projectile and target fragmentation. The latter, which is of interest for applications in the proton-Nucleus (p-N) collisions field, is an exceptionally challenging task because of the very short range of the produced fragments that results in a very low probability of escaping the target. Their range is limited to tens of microns and even a very thin solid target would stop them or badly spoil their energy measurement.

Target fragmentation cross sections will be hence measured using an *inverse kinematic approach*, studying the interactions of different ion beams (like ^{12}C and ^{16}O) impinging on hydrogen enriched targets, such as C_2H_4, with an energy in the 50-200 MeV/nucleon range. The p-N cross sections will be therefore computed using the data collected using C_2H_4 and C targets by means of a subtraction method whose feasibility has been already shown by the authors of refs. [31, 32].

When the projectile nucleus (^{12}C or ^{16}O) collides with a H nucleus of the target, the projectile fragments in the laboratory frame can be seen (applying a suitable Lorentz boost) as the products of a process where a p collides onto a C or O target nucleus, but can be more easily measured. While the process of boosting the fragments in the reference frame in which the patient is at rest is a procedure that implies some additional uncertainties (related to the limited precision achievable on the physical quantities used to perform the Lorentz boost), the proposed method allows to perform the differential cross section measurements that would have been impossible otherwise.

A detector capable of performing the target fragmentation measurement using the inverse kinematic approach can as well perform the direct measurement of projectile fragmentation cross sections induced by C, He and O beams. The targets are the same (graphite and polyethylene) both for PT applications and to explore the higher incoming beam energy range for RPS in deep space applications. Using additional target materials, like polymethyl methacrylate (PMMA, $C_5O_2H_8$), also other nuclei of interest for biological effects, like oxygen, can be studied. A summary of the physics program of FOOT is reported in **Table 1**.

The most stringent requirements on the precision that FOOT has to reach are driven by the study of the target fragmentation process.

The final goal of the FOOT experiment is to measure differential cross sections with respect to the kinetic energy ($d\sigma/dE_{kin}$) for the target fragmentation process with an accuracy better than 10% and double differential cross sections ($d^2\sigma/d\Omega \cdot dE_{kin}$) for the projectile fragmentation process with an accuracy better than 5% on the determination of the fragment yields in angle and in kinetic energy.

To achieve these performances the charge and isotopic identification capability of the fragments should reach the level of 2–3% and 5% precision respectively, in order to have a clear separation of all the isotopes under study. Such requirements become particularly difficult to match in the inverse kinematic approach, translating in a needed resolution on reconstructed momentum and kinetic energy of the order of few percent and a resolution on the emission angle with respect to the beam direction of the order of few mrad. To minimize the multiple scattering impact and the probability of secondary fragmentation inside the target, its overall density weighted thickness has to be of the order of 2-4 g/cm^2, limiting the fragmentation probability to ~10^{-2}.

TABLE 1 | FOOT physics program: in the last column the interaction processes to be studied for a given combination of beam, target, energy and kinematic approach are shown.

Physics	Application field	Beam	Target	Upper Energy (MeV/nucleon)	Kinematic approach	Interaction process
Target fragmentation	PT	^{12}C	C,C_2H_4	200	inverse	p+C
Target fragmentation	PT	^{16}O	C,C_2H_4	200	inverse	p+C
Beam fragmentation	PT	^{4}He	C, C_2H_4, PMMA	250	direct	α+C, α+H, α+O
Beam fragmentation	PT	^{12}C	C, C_2H_4, PMMA	400	direct	C+C, C+H, C+O
Beam fragmentation	PT	^{16}O	C, C_2H_4, PMMA	500	direct	O+C, O+H, O+O
Beam fragmentation	Space	^{4}He	C, C_2H_4, PMMA	800	direct	α+C, α+H, α+O
Beam fragmentation	Space	^{12}C	C, C_2H_4, PMMA	800	direct	C+C, C+H, C+O
Beam fragmentation	Space	^{16}O	C, C_2H_4, PMMA	800	direct	O+C, O+H, O+O

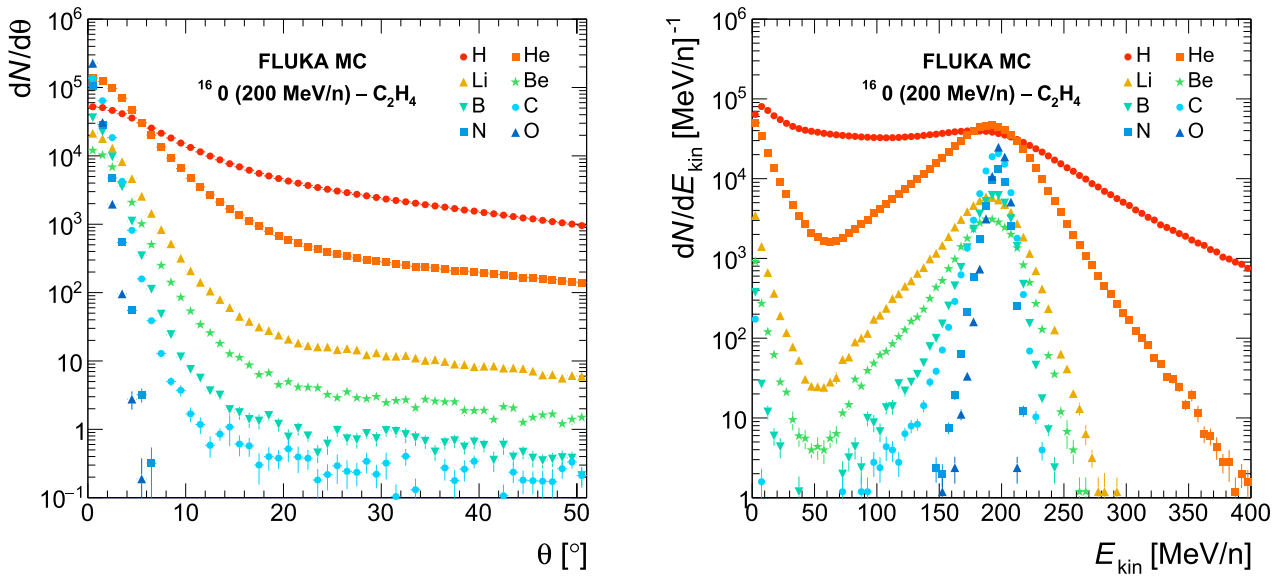

FIGURE 1 | MC calculation [33, 34] of the angular **(Left)** and kinetic energy **(Right)** distributions of different fragments produced by a 200 MeV/nucleon ^{16}O beam impinging on a C_2H_4 target.

A MC simulation of a ^{16}O beam of 200 MeV/nucleon kinetic energy impinging on a C_2H_4 target has been implemented using the FLUKA code [33, 34] to design and optimize the detector. The results of such simulation in terms of fragments yields in angle (**Figure 1** (Left)) and in kinetic energy (**Figure 1** (Right)) show that heavier fragments ($Z > 2$) are forward peaked within a polar angle of $\simeq 10^{\circ}$ and with a kinetic energy per nucleon peaked around the corresponding primary beam value. The light fragments, instead, have wider angular and kinetic energy distributions. Such distribution have been considered when designing the experimental setup, as they have a strong impact on the detector geometrical acceptance.

Another constraint for the FOOT experiment comes from the request to have a "movable" detector capable of fitting the space limitations set by the different experimental rooms where ion beams of therapeutic energies are available. The standard choice, for a fixed target experiment like FOOT, would be a magnetic spectrometer composed by a dipolar magnet and high precision tracking detectors, together with some detector for particle identification.

However as seen in **Figure 1** low mass fragments ($Z < 3$) are emitted with a wide angular aperture and the necessary cost, size, and weight of a magnetic apparatus capable of tracking them with the required precision would become impracticable in view of a "table top" setup design.

The FOOT experiment will implement an "upstream region" composed by the pre-target detectors, that will be used to monitor the impinging beam, and a region, including the target, for the tracking and the identification of the fragments that foresee two alternative and complementary setups:

1. a setup that implements a **magnetic spectrometer**, coupled with detectors for tracking and detectors optimized for the identification of fragments heavier than ^{4}He. Such setup covers an angular acceptance up to a polar angle of about 10° with respect to the beam axis;

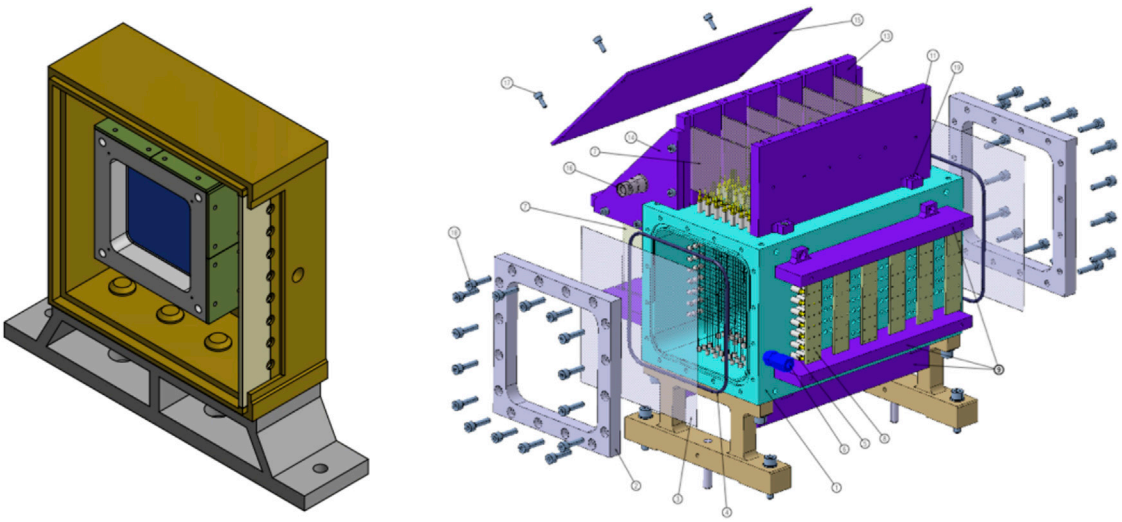

FIGURE 2 | Left: Start Counter detector inside the plastic box. The aluminum mechanical structure holds the EJ-228 plastic scintillator foil (in dark blue). **Right:** Technical drawing of the Beam Monitor drift chamber. The two orthogonal views *x*–*y* of the wires are clearly visible. Two enclosing mylar windows held by aluminum frames are shown as well.

2. a setup based on an **emulsion spectrometer**, optimized for low *Z* fragments identification emitted at large polar angles that will extend the angular acceptance of FOOT up to about 70°.

The construction of the FOOT detector has started in 2018 and will be completed by the end of 2020, allowing to take data in the following years. Most of the upstream region and of the magnetic spectrometer detectors have already been built and tested in different calibration campaigns at CNAO (Pavia, Italy), TIFPA (Trento, Italy) and GSI (Darmstadt, Germany), with different ion beams of different energies. In the following sections a general description of these detectors will be provided. A detailed review of the technologies employed by the detectors and their measured performances will be reported in dedicated papers, whereas some of them have been already published [35].

Fragmentation cross section measurements using carbon beams impinging on different thin targets in the energy range 115–353 MeV/nucleon have been performed studying fragments emitted at large angles. Such preliminary studies [36] have been performed with an experimental setup very far from the final, optimised, one.

Tests carried out at LNS of the FOOT emulsion chambers have already proved their capability in achieving the required FOOT performances in charge separation [37]. Measurements with the full emulsion chamber setup have been already performed at GSI in 2019 and 2020 using ^{16}O beams of 200 and 400 MeV/nucleon kinetic energy and a ^{12}C beam of 700 MeV/nucleon kinetic energy impinging on C and C_2H_4 thin targets. The ongoing analysis will be the subject of a dedicated paper.

The Upstream Region

The upstream region is composed of pre-target detectors that will be used to monitor the beam, providing its direction and the interaction point on the target, and to count the number of impinging ions. The overall material budget, crossed by the beam, has to be minimised to reduce the out-of-target fragmentation, as well as the multiple scattering of the beam. The chosen configuration foresees two detectors: the Start Counter, a thin plastic scintillator read out by SiPMs, followed by the Beam Monitor, a drift chamber, placed upstream of the target.

The Start Counter

The Start Counter (SC) consists of a thin squared foil of EJ-228 plastic scintillator 250 μm thick. The foil has an active surface with a 5 cm side that is sufficient to cover the typical beam transverse size (see **Figure 2** (Left)) and is held by means of an aluminum frame enclosed in a black 3D printed box to provide the light tightness needed for the detector operation. In the black box, two squared windows are placed in correspondence of the scintillator field of view and closed with a thin layer of 4 μm aluminized mylar.

The light produced in the scintillator is collected laterally by 48 (AdvanSiD ASD-NUV3S[1]) 3 × 3 mm^2 SiPMs, 12 per side, bundled in eight electronic channels, each reading a chain of 6 SiPMs. The readout and powering of the SiPMs is handled by the WaveDAQ system [38], capable of sampling signals at rates up to 5 Gsamples/s in a dynamic range of 1 V. A gain between 0.5 and 100 can be applied to the incoming signal before digitization allowing to optimise the detector response in case of different beam types or energies. In this way it is possible to maximise the detector efficiency compensating for the low light signal released due to the scintillator thinness.

The acquired waveforms are analyzed offline with a constant fraction discriminator technique to extract the event time t_0.

[1]http://advansid.com/products/product-detail/asd-rgb-nuv-3s-p.

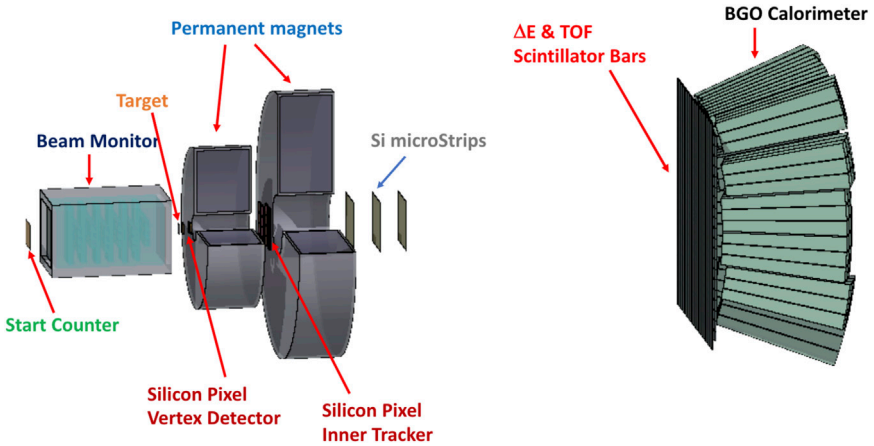

FIGURE 3 | Schematic view of the upstream region and the Magnetic Spectrometer setup.

The SC, placed upstream of the BM and of the target, fulfills four main tasks: it provides the Minimum Bias trigger of the experiment, measures the incoming ion flux (with an efficiency >99%), provides the reference time for all the other detectors and it is used to perform the Time-Of-Flight (TOF) measurement in combination with the TOF-detector (called Tof Wall, TW, see *Tof Wall Detector*). A time resolution of the order of $\sigma_t \simeq 60$ ps has been measured using a ^{12}C beam of 700 MeV/nucleon kinetic energy at GSI. Different thicknesses (ranging from 250 μm to 1 mm) can be used to monitor different beam projectiles and energy range combinations, in order to preserve the SC high performances in terms of efficiency and time resolution. A different Start Counter, developed within the FIRST experiment [17, 39], made with the same plastic scintillator, 250 μm thick, but read by PMT, has been used for the Emulsion chamber setup characterization so far as time performances were not requested (see Section *The Emulsion Spectrometer*, **Figure 10** (Left)) and the detector was only used to count the incoming ions.

The Beam Monitor

The Beam Monitor (BM), already used in the FIRST experiment [17], is a drift chamber consisting of twelve wire layers, with three drift cells per layer (see **Figure 2** (Right)). Planes with wires oriented along the x and y axes are alternated allowing the beam profile reconstruction in both views. The cell shape is rectangular (16 mm × 10 mm). In each view, two consecutive layers are staggered by half a cell to solve left-right ambiguities in track reconstruction [39]. New studies of BM working operations and achievable performances have been done in the context of the FOOT experiment. The BM operates at $\simeq$0.9 bar with a 80/20% gas mixture of Ar/CO_2, at a working point ranging between 1850 and 2200 V, depending on the primary beam. A BM efficiency of $\simeq$90% has been measured, at the working point, for different combinations of ion beam and energies. A lower limit on the spatial resolution of 100 μm, in the central part of the BM cell, has been achieved [40]. The BM detector will be placed between the SC and the target and will be used to measure the direction and impinging point of the beam ions on the target, a crucial information needed to address the pile-up ambiguity in the tracking devices downstream the target and to discard events in which the beam has fragmented in the SC producing one or more deviated tracks. In order to reject pile-up vertices, an high precision alignment is required between the BM and the devices downstream the target. The BM high spatial resolution is fundamental to measure the direction of the fragments with respect to the beam with an accuracy of few mrad, needed to measure the kinetic energy of the fragments in inverse kinematic with the required resolution. Finally, the BM information about the beam spot size is essential, particularly in the case of the emulsion spectrometer, to monitor the very low intensity beams used for the FOOT acquisitions (see Section *Trigger and Data Acquisition System*), whereas the monitoring performed with the standard facilities devices, especially in centers for patients treatment, usually cannot provide the required accuracy and resolution at such low rates.

The Magnetic Spectrometer

The driving criterion of the FOOT detector design is the need for an accurate charge and isotopic identification of the produced fragments. To achieve the experimental goals a redundancy in measuring the different kinematic variables is needed, exploiting different particle identification (PID) techniques. For this reason the FOOT setup includes a Time-Of-Flight (TOF) system and a calorimeter for the fragments energy measurement, that, combined with the measurement of the energy released in thin detectors and with the information provided by the magnetic spectrometer, allows the isotope mass identification. The charge Z of fragments reaching the TW can be identified from the energy loss ΔE and the TOF information, exploiting the Bethe-Bloch formula. The tracking through the magnetic field provides the fragment rigidity (p/Z) and its path L that coupled with the measurement of TOF and Z provides the momentum p and the velocity $\beta \cdot c = L/\mathrm{TOF}$ of the particle. Finally the fragment mass

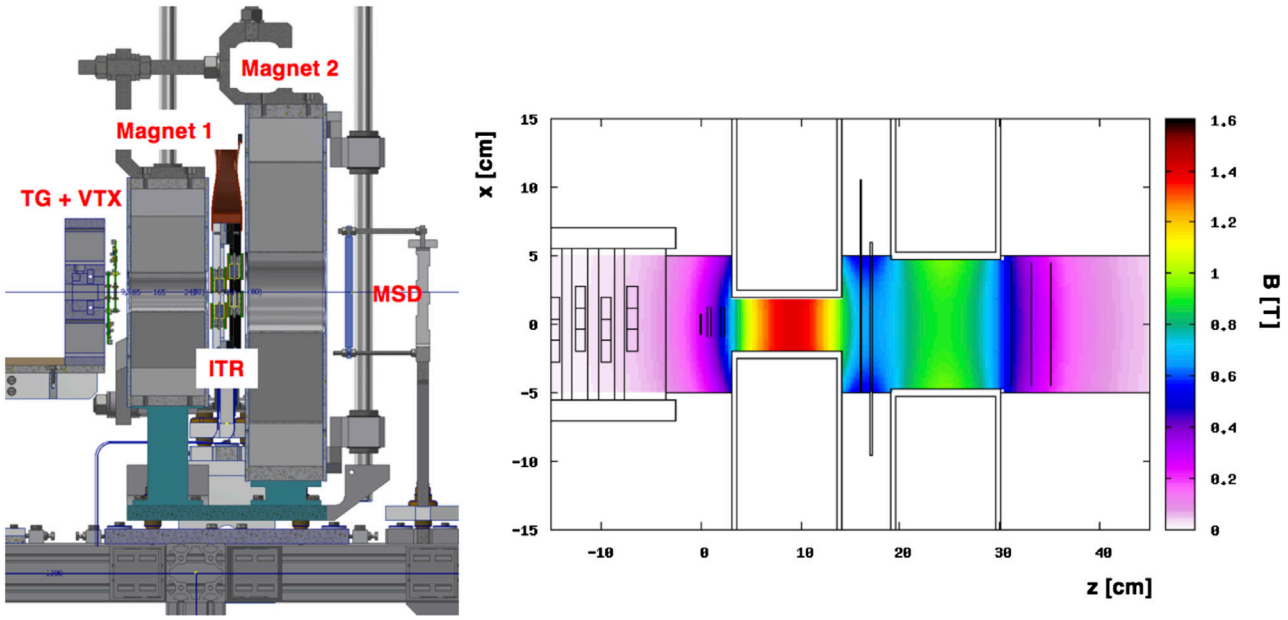

FIGURE 4 | (Left) Technical design of the interaction and tracking regions: the vertical axis is the *y* axis, while the horizontal axis is the *z* axis. The beam coming from the left, along the *z*-axis, cross sequentially the target (TG), the vertex detector (VTX), moves into the magnets region and crosses the Inner Tracker (ITR) and, immediately after the second magnet, passes through the Micro Strip Detetor (MSD). **(Right)** Computed magnetic field map produced by the FOOT magnets in Halbach configuration. The magnetic field intensity *B*, shown in the palette, is referred to its *y*-axis component.

identification can be achieved by momentum p, velocity β and kinetic energy E_{kin} measurements using the following relationships:

$$p = mc\beta\gamma, E_{\text{kin}} = mc^2(\gamma - 1), E_{\text{kin}} = \sqrt{p^2c^2 + m^2c^4} - mc^2 \quad (1)$$

where γ is the Lorentz factor. Once the mass and the charge Z are measured the fragment is uniquely identified.

In order to match the precision requirements stated before on the final cross section measurements, it will be necessary to achieve the following experimental resolutions:

$\sigma(p)/p$ at level of 4-5%;
$\sigma(TOF)$ at level of 100 ps;
$\sigma(E_{\text{kin}})/E_{\text{kin}}$ at level of 1-2%;
$\sigma(\Delta E)/\Delta E$ at level of 5%.

The detector design has to keep the fragmentation contribution due to the detector material as low as possible and should result in a full apparatus sufficiently compact to be transported and installed in the different facilities where ^{4}He, ^{12}C and ^{16}O beams are available. The overall detector size should lie within the 2–3 m range. The actual length of the setup will change according with the β of the beam to allow an almost constant resolution on the fragment TOF. Extensive FLUKA simulations (**Figure 1**) have been used to optimise the transverse dimension of the detectors in order to fit the required angular acceptance, and their granularity studying the minimum separation angle between the emitted fragments.

A schematic view of the final choice for the Magnetic Spectrometer setup, together with the upstream region, is shown in **Figure 3**. Three main regions can be identified in the experimental setup:

1. The upstream region, composed of the Start Counter and the Beam Monitor (see Section *The Upstream Region*).

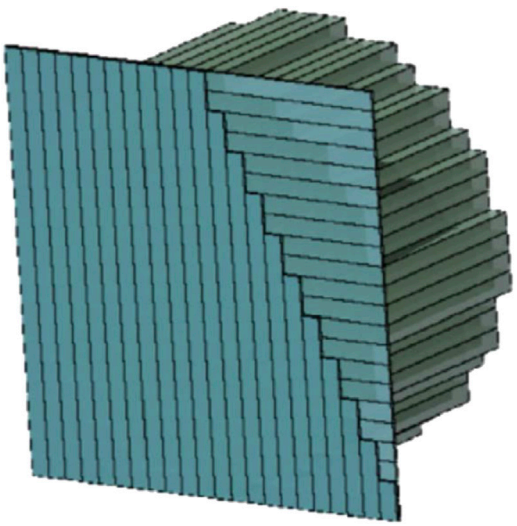

FIGURE 5 | Schematic view of the fragment identification region. The two orthogonal layers of 20 plastic scintillator bars are shown in front of the matrix of BGO crystals used to build the calorimeter.

2. The interaction and tracking region, composed of the target followed by three stations of pixel and strip detectors placed upstream, between and downstream of two permanent magnets providing the fragments production vertex and momentum measurement through the tracking in the magnetic field.
3. The PID region, in the distal part of the detector located at least 1 m away from the target. It is composed of two orthogonal planes of thin plastic scintillator bars, providing the stop of the TOF and the measurement of the energy loss ΔE. A BGO calorimeter, placed immediately after the TW, provides the fragment kinetic energy measurement.

Interaction and Tracking Region

The overall tracking system of the FOOT experiment is conceived as three measuring stations allocated upstream, between and downstream of two permanent magnets, as shown in **Figure 4** (Left). The first tracking station is coupled to the target acting as vertex detector (VTX) of the experiment. The needs in terms of momentum resolution and global acceptance together with the minimization of multiple scattering and re-fragmentation in both the sensors and the mechanical structures themselves suggest the use of monolithic pixel sensors in the two upstream stations, the VTX and the inner tracker (ITR), while a telescope of silicon microstrip detectors (MSD) is envisaged for the downstream station. In between the three stations two permanent magnets, in Halbach configuration, provide the required magnetic field.

Target and Vertex Detector

The target and the Vertex detector (VTX) are hosted in a mechanical structure designed to hold up to five different targets in a sliding tray that can eventually be moved by a remote controlled actuator [17, 41]. The Vertex detector is organized in 4 different pixel sensor layers of $2 \times 2\text{cm}^2$ transverse dimension, placed along the z axis, respectively at 0.6-0.9-2.1–2.4 cm from the target center guaranteeing a geometrical acceptance of about 40° for the emitted fragments. In order to fulfill the requirements of low material budget and high precision and efficiency, the technology of the MIMOSA-28 (M28) Monolithic Active Pixel Sensors (MAPS) has been adopted for each layer of the VTX. The M28 sensor, developed by the Strasbourg CNRS PICSEL group [42] for the upgrade of the vertex detector inner layer of the STAR experiment at RHIC [43, 44], consists of a matrix with 928 (rows) × 960 (columns) pixels of 20.7 μm pitch. The chip total size is 20.22 mm × 22.71 mm. The M28 sensor is implemented in the AMS-C35B4/OPTO design process that uses 4 metal- and 2 poly-layers. The thickness of the epitaxial layer is 15 μm on a high resistivity substrate of the order of 400 Ω·cm. All four M28 sensors are thinned to 50 μm, resulting in an overall material budget for the entire Vertex tracker of 200 μm. The architecture of the M28 integrates a binary readout and a zero suppression in-chip logic to reduce the amount of data transferred. Each pixel includes an amplification and a Correlated Double Sampling (CDS) circuitry. The sensor employs a rolling shutter readout technique with a 185.6 μs frame readout time: all the pixels CDS output of one row are read out in parallel row by row at the end of the column where 960 discriminators are placed, one per column, each with a configurable threshold level. The VTX readout has been implemented by means of a DE10 board system housing an Intel System-on-Chip (SoC) FPGA (Cyclon V) with a dual-core Cortex-A9 CPU. The FPGA is interfaced with the sensors and with the DAQ control (trigger, time-stamping and busy signals) and the CPU is used to send data to the central DAQ via a 1 GbE connection. The kinematic inverse approach requires the beam particles direction before the target and the fragment emission angle after the target to be tracked with an angular accuracy at the mrad level. The high spatial resolution of 5 μm achieved [45] with the VTX, matched with the information from the BM, can provide such angular resolution while minimizing the multiple scattering thanks to the reduced material budget of both BM and VTX.

The magnetic System

A key element for the FOOT spectrometer is the magnetic system used to bend the fragments produced in the target. The portability of the system, when matched with the needed momentum resolution, forces the choice in the direction of having permanent magnets generating the needed $(B \times L)$ in a limited sizes and weight, where $B = B(z)$ is the magnetic field intensity, strongly dependent on the fragment z-position, while L is the length along the z-axis of the magnetic field region where the particles experience the magnetic field effect and that can be roughly assumed to be placed between the VTX and the MSD trackers. A magnetic dipole in vacuum with two tracking stations placed upstream and downstream would ensure as well that the needed momentum resolution is achieved, but is not a viable solution to be implemented in a 'portable' table top experiment. The final choice is hence to have a magnetic system kept in air composed of two magnets, in Halbach configuration, which allow an additional tracking station in between the two needed to match the required momentum resolution. In the Halbach configuration an approximately dipolar magnetic field is obtained in the internal hole of a cylindrical permanent magnet. The magnetic field increases with the external cylinder radius while decreases with the gap radius. So in order to match the final momentum resolution producing the needed $(B \times L)$ and at the same time have an angular acceptance of 10° for the emitted fragments, two different magnet dimensions have been chosen. The first magnet has a gap diameter of 5 cm while the second one of 10.6 cm. They can provide respectively a maximum intensity of 1.4 T and 0.9 T along the y axis in the internal cylindrical hole. The magnetic field intensity along the cylinder z axis exhibits a gaussian shape for each magnet, according to the computed magnetic map shown in **Figure 4** (Right): the inner tracker, sitting in-between the two magnets, will experience a field with an intensity of ~0.6 T. Each magnet will be made of twelve single units of Samarium-Cobalt, which maintains its magnetic properties also in a high radiation environments. The two magnets will be assembled in a single mechanical structure sufficiently robust to withstand the magnetic forces produced and to provide a high precision in the alignment with the tracking stations. Thanks to a detailed field map, it will be possible to reach the intrinsic achievable accuracy of about 10 μm. The capability of vertically displacing, of about 40 cm, the magnets with respect to the beam line, will give the

opportunity to inter-align the tracking stations in specific runs without the magnets, to adapt the setup to different experimental rooms and will ease the tracking detectors access and cabling once the setup will be finally assembled.

Inner Tracker

The FOOT Inner Tracking (ITR) station foresees two planes of pixel sensors to track the fragments in the magnetic region. In order to fit the required acceptance, granularity and tracking performances each plane will cover a sensitive area of about 8 × 8 cm^2, with 16 M28 sensors per layer. The main reasons for such choice are again the quest for the material budget reduction together with the need of high tracking performances. Furthermore the tracking performances of M28 sensors are not expected to be significantly affected by the foreseen residual magnetic field in between the permanent magnets [46]. In addition, by using the same technology implemented by the VTX the architecture of the DAQ system will be simplified. Differently with respect to the VTX, the large detector area implies the use of a mechanical support, that results in an increase of the overall material budget.

The ITR will be built using ladders similar to the ones implemented in the PLUME project [47]. The ITR ladder will implement a double-sided layout, which consist of two modules of M28-sensor layers glued on the opposite sides of a support structure, 2 mm thick, made of low density silicon carbide (SiC) foam. Each module is composed of 4 M28 sensors glued and bonded on a kapton-metal flex cable. The flex cables provide all the communications and services of the sensors from and to the outside world. The overall material budget of an ITR ladder is $x/X_0 \simeq 0.3\%$, where x and X_0 are respectively the overall thickness and radiation length of the ITR ladder. The ITR will be composed of four ladders, two for each plane, supported by a metallic frame to hold the entire tracker. While the described design is the final one, the detector still has to be fully assembled and tested.

Micro Strip Detector

The fragments tracking downstream the magnetic region is essential for the measurement of momentum and for the matching of the reconstructed tracks with the hits in the TW and in the calorimeter. This task is entrusted to a microstrip silicon detector (MSD), that, operating with an analogue readout, can also provide a redundant measurement of dE/dx [48–50], for fragments charge Z identification, complementary to the one performed by the TW. A tracking station of three MSD x-y planes with an active area of 9.6 × 9.3 cm^2, separated by a 2 cm gap along the beam direction and positioned right after the second magnet, ensure the needed angular acceptance to measure ions with $Z > 2$, as expected from the FLUKA simulation. In order to reduce the amount of material and to provide the x-y coordinate readout, a solution exploiting two perpendicular Single-Sided Silicon Detector (SSSD) sensors thinned down to 150 μm has been adopted for each MSD x-y plane. Each sensor is glued on a hybrid Printed Circuit Board (PCB) that provides the needed mechanical support and the interface with the MSD readout. Light tightness of each plane is ensured using the metallized sensors backplane. A strip pitch size of 50 μm has been chosen in order to minimize the fragment pile-up in the same strip. Each SSSD is readout by 10 VA1140 chips, with a readout pitch of 150 μm, bonded and glued on the PCB, for a total of 640 channels. The front-end hybrids, hosting the readout chips, is glued at one side of each silicon module minimizing the dead space in the beam region. A digital readout of the strips with pitch of 150 μm would provide a spatial resolution of $\simeq 40$ μm, while with the selected analog readout a further factor 3 can be gained, as shown in [51, 52], with the additional advantage to measure also the dE/dx, for each x-y view of each layer independently. The analog signals provided by the VA1140 readout chips are digitized by 1 MHz 12-bits ADC and their data are sent to a TERASIC DE10 nano board for data collection and event shipping to the general FOOT DAQ.

Fragment Identification Region

The fragment identification region is the distal part of the detector, located at least 1 m away from the target. It is composed of two orthogonal planes of plastic scintillator bars (Tof-Wall detector), providing the stop of the TOF and the measurement of the energy loss, followed by a BGO calorimeter used to measure the fragment kinetic energy (see **Figure 5**).

Tof Wall Detector

The Tof-Wall detector (TW) is composed of two layers of 20 plastic scintillator bars (EJ-200 by Eljen Technology), arranged orthogonally and wrapped with reflective aluminum and darkening black tape [35, 53]. Each bar is 0.3 cm thick, 2 cm wide and 44 cm long. The two orthogonal x-y layers form a 40 × 40 cm^2 active area detector that provides the measurements of the energy deposited ΔE, the needed information to compute the TOF (using as input the t_0 from SC), and the hit position. The simultaneous measurement of ΔE and TOF allows to identify the charge Z of the impinging ions [54, 55]. The Z-identification plays a fundamental role in determining the fragment mass and is used, together with the x-y hit position, as a seed for the fragments tracking through the magnetic field. The TW transverse dimensions have been chosen to match the angular aperture of the heavy fragments at the distance of the detector from the target (1–2 m) set by the experimental room conditions. The chosen granularity keeps the pile-up of multiple fragments in the same bar below $\simeq 1\%$. The thickness of the bar has been chosen as a trade-off between a higher scintillation signal (reflecting in better timing and energy resolution) and a lower secondary fragmentation probability in the bars, that would spoil the particle identification and tracking.

Each of the two edges of the TW bars is coupled to 4 SiPM (MPPC S13360-3025PE[2]) with a 3 × 3 mm^2 active area and 25 μm microcell pitch. The signals of each channel (two channels per bar) are digitized at rates of 3–4 Gsamples/s depending on the trigger scheme adopted (see Section *Trigger and Data Acquisition System*) by the WaveDAQ system [38] as described in Section *The Start Counter*. A total of 1024 samples are collected for each signal

[2]https://www.hamamatsu.com/resources/pdf/ssd/s13360_series_kapd1052e.pdf.

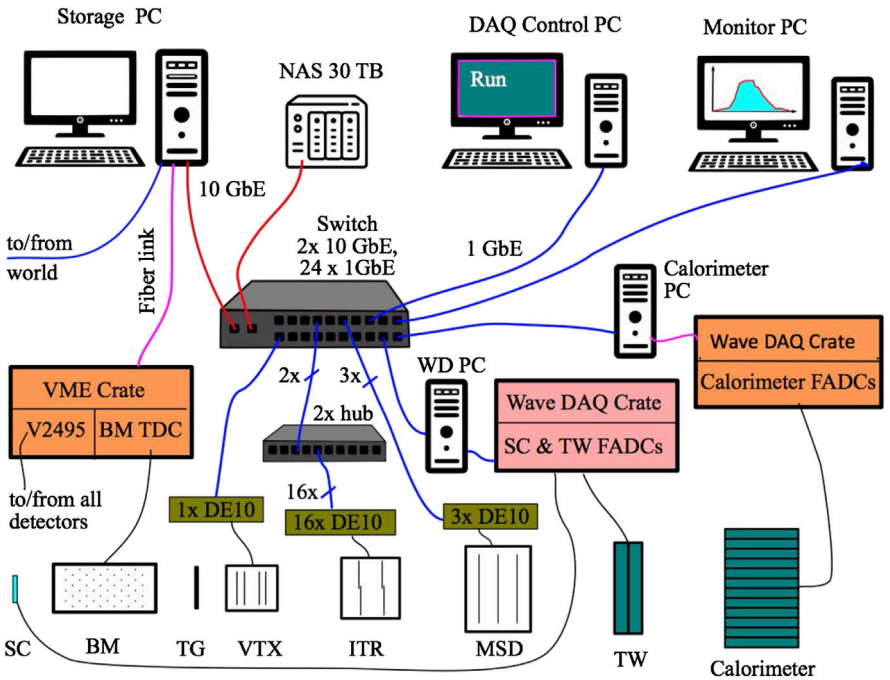

FIGURE 6 | DAQ logical scheme.

allowing to record the whole waveform, and to extract offline the time and the charge information. The thickness of the bars and the selected readout chain, have been chosen to meet the FOOT requirements of a TOF resolution better than 100 ps and an energy loss resolution $\sigma(\Delta E)/\Delta E \simeq 5\%$, for the heavier fragments [35]. Thanks to the high number (4×14400) of pixels per channel of the SiPM, this setup is able to guarantee a dynamic range spanning over two orders of magnitude and allow the identification of fragments with significantly different energy release (from proton to oxygen with different kinetic energies). Finally, the high precision time measurement can be used to reconstruct the hit position along the bar [35] with a precision $\sigma_{pos} <$ 8 mm, better than the one achievable only exploiting the information about the bars crossing, an important information used to reduce the combinatorial association of multiple fragments in the front and rear side of the TW in the offline reconstruction.

Calorimeter

The FOOT calorimeter is the most downstream detector and it is designed to measure the fragments kinetic energy needed to compute their mass A. Depending on the energy of the incoming fragment, different phenomena can take place in the calorimeter in the energy range of interest for the FOOT experiment. At the highest energies, $\simeq$700–800 MeV/nucleon, that will be explored in the context of space radiation protection studies, the pion production threshold is exceeded and hadronic showering takes place. In these conditions a full containment cannot be achieved with affordable calorimeter dimensions, and this results in a worsening of the achievable resolution at these energies. On the other hand, the highest resolution is needed for the case of target fragmentation studies, that involves ^{12}C and ^{16}O up to 200 MeV/nucleon. In this energy range, the main mechanism of energy loss is by far through electromagnetic interaction with the target electrons and nuclei. In that case a proper containment of the fragments can be achieved allowing to maximise the energy resolution. In all cases, however, it shuold be noted that for a fraction of the events neutron production takes place and part of the fragment energy escapes the detector, causing a systematic error that spoils the energy resolution. The impact of such effect can be minimised exploiting the redundant information coming from the other detectors. Since FOOT will work at a relatively low beam intensity, the ideal material for a calorimeter is a dense crystal, with high light yield, without strict requirements on the response speed: BGO was identified as the best candidate providing the needed performance, on one side, while easing the matching with the mechanical constraints and the overall cost on the other. The high density of this material (ρ = 7.13 g/cm^3) guarantees a high stopping power, that, coupled to a light yield of $\simeq$10 photon/keV, meets the requirements on the energy resolution. The FOOT calorimeter will be composed of 320 $Bi_4Ge_3O_{12}$ (BGO) crystals positioned with an approximately disk-like arrangement ($\simeq$20 cm radius) and mechanically divided in modules of 3×3 crystals, in order to best handle their weight and positioning. The crystals have a truncated pyramid shape with a front (back) face of about 2×2 cm^2 (3×3 cm^2) and a length of 24 cm. The BGO crystal transverse size is similar to the TW granularity. The probability of pile-up in the same crystal due to multi-fragmentation events is kept below $\simeq$1–2%, depending on the beam energy/experimental room setup configuration. The crystal depth has been chosen in order to minimize the energy leakage

mainly due to neutrons escaping the calorimeter. Each BGO crystal is coupled to a 25 SiPMs matrix with an active surface of $2 \times 2\ cm^2$, where each microcell has a pitch of 15 μm, small enough to have a linear response in the energy range up to about 10 GeV. Each SiPM matrix is coupled to a readout board specifically designed to match the dimensions of the SiPMs, ensuring a very compact design of the overall detector. The Front-end board will be interfaced with the WaveDAQ system, the same readout system used for SC and TW detectors [38], that will sample the signal at 1 Gsample/s, allowing a measurement based on both the signal amplitude and its integral, as well as a shape analysis. The same board is used to readout the SiPM temperature sensor, useful to compensate the variation of the system response caused by temperature variations and to equalize the calorimeter response offline. Several beam tests have been performed in a wide energy range (from 70 MeV protons to 400 MeV/nucleon ^{12}C), in order to choose the optimal combination of SiPM array, readout configuration and BGO wrappings. A very good linearity response is achieved in the whole investigated energy range and the measured energy resolution $\sigma(E_{kin})/E_{kin}$ below 2% meets the experiment requirements for the heavier fragments [56, 57].

Trigger and Data Acquisition System

The FOOT detector will be equipped with a DAQ system designed to acquire the data with high accuracy in a controlled and online-monitored environment.

The main experiment trigger (Minimum Bias) will be based on signals provided by the SC and will be fired whenever the multiplicity of the channels above thresholds exceeds a programmable value (majority trigger). This choice minimise the source of systematic uncertainties on the cross section measurements due to the events trigger selection. A fragmentation trigger asking for activity outside the central bars of the TW in a logical OR can also be used, in addition to a prescaled Minimum Bias trigger, to enhance the fraction of recorded fragmentation events. The technology that will be used to implement the trigger is provided by a CAEN V2495 board[3], whose FPGA and internal logic is fully programmable. The maximum acquisition rate affordable when operating with a Minimum Bias trigger would depend on the slowest detectors in the experiment. These are the MIMOSA 28 chips used in the pixel trackers (VTX and ITR), which have a frame readout time of 185.6 μs, needed to read about 10^6 pixels per chip. The overall maximum readout rate would be hence of about R_{max} = 5 kHz. The system will be designed to handle a maximum DAQ rate of $R_{daq} = R_{max}$, but in order to reduce pile-up effects in the MIMOSA chips the actual trigger rate will be of the order of $R_{trigger}$ = 1 kHz. With this rate, considering a duty cycle of f_{dc} = 30%, during stable running conditions, up to $N_{day} \simeq 86400 \cdot 1k \cdot 0.3 = 26$ M events per day can be collected with a Minimum Bias trigger.

The DAQ system that will be implemented for the whole apparatus is a flexible hierarchical distributed system based on linux PCs, VME crates and boards, detector integrated readout systems and standard communication links like ethernet, USB and optical fibers, schematized in **Figure 6**.

The system control will be hosted on a controller PC used to run the DAQ GUI interface to start/stop a single run, to control and to configure other nodes in the system. Another PC (Storage PC) will be used to collect the information coming from the different detectors, to perform an event building and to store on disk the acquired data. On the same PC, a MYSQL DataBase (DB) will have the role to store the configuration data (structured DB tables or in form of retrievable text files) and to store the DAQ process information (start/stop DAQ time, events collected, other global DAQ information). An electronic logbook interfaced with the DAQ system will be installed on the same machine.

The steering of the acquisition process and the reading of the other nodes will be managed through an ethernet switch connected via a 10 GbE cable and a CAEN V2718[4] VME to PCI Optical Link Bridge. The switch is used to collect all the data from the detectors via 1Gbps ethernet connections: the whole tracking system (VTX, ITR and MSD), based on 20 DE10-nano or DE10 Terasic boards, the time of flight system (SC and TW) and the calorimeter based on the WaveDAQ system. The DE10-nano boards have an FPGA for detector reading and a dual core ARM cortex 9 processor for event formatting, zero suppression and data shipping via ethernet. The WaveDAQ boards for the TOF system and for the calorimeter send its data to intermediate PCs providing data calibration, compression and data shipping. The VME to PCI Optical Link Bridge in the storage PC is connected to a VME crate holding the trigger board V2495 and the Beam Monitor discriminators and TDC board CAEN V1190B. The expected typical event size is of the order of 30 kB, but can be increased if needed up to 100 kB. The availability of RAM memories along the data collection paths (in the FPGAs, in the DE10, in the PCs, in the switch and in the CAEN boards) allows an almost complete decoupling of the trigger signal time from the event building time in the storage PC that can happen several seconds apart, while still keeping an average DAQ rate of 1 kHz (with rate peaks of 5 kHz). The whole system is designed to store data on a SSD disk (max rate 400 MB/s) during data taking and to transfer the data to a dedicated (>20 TB) NAS system during idle times. The DAQ system will be equipped with a set of online monitoring tools. The DAQ running related information can be easily collected from each VME board or data provider at a rate ~Hz, depending on the specific sub-detector system, and provided to a network of PCs connected to the experiment. Typical online monitoring histograms based either on local or distributed data will show detector occupancy, particle arrival times, particle energies, collected charges and so on. The online monitoring foresee also a fast online event reconstruction performed, on the fly, on a fraction of the events. Performing a complete event reconstruction it will be possible to monitor the fragments momentum spectra, TOF, reconstructed charges and masses.

MC Simulation and Fragment Identification Performances

Detailed MC simulations with the FLUKA software [33, 34] have been developed for different combinations of ion beams, beam kinetic energy and targets, in order to optimize the detector

[3]https://www.caen.it/products/v2495/

[4]https://www.caen.it/products/v2718/

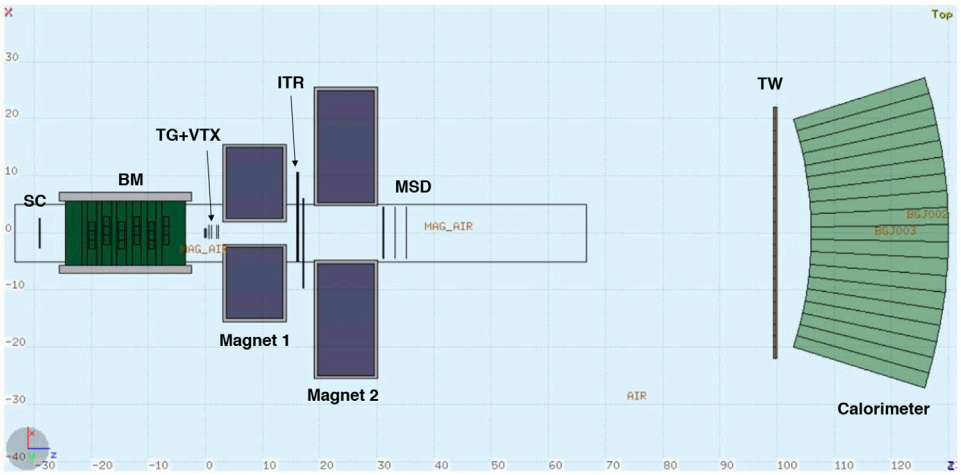

FIGURE 7 | 2-D top view of the full FOOT setup geometry implemented in the FLUKA MC simulation.

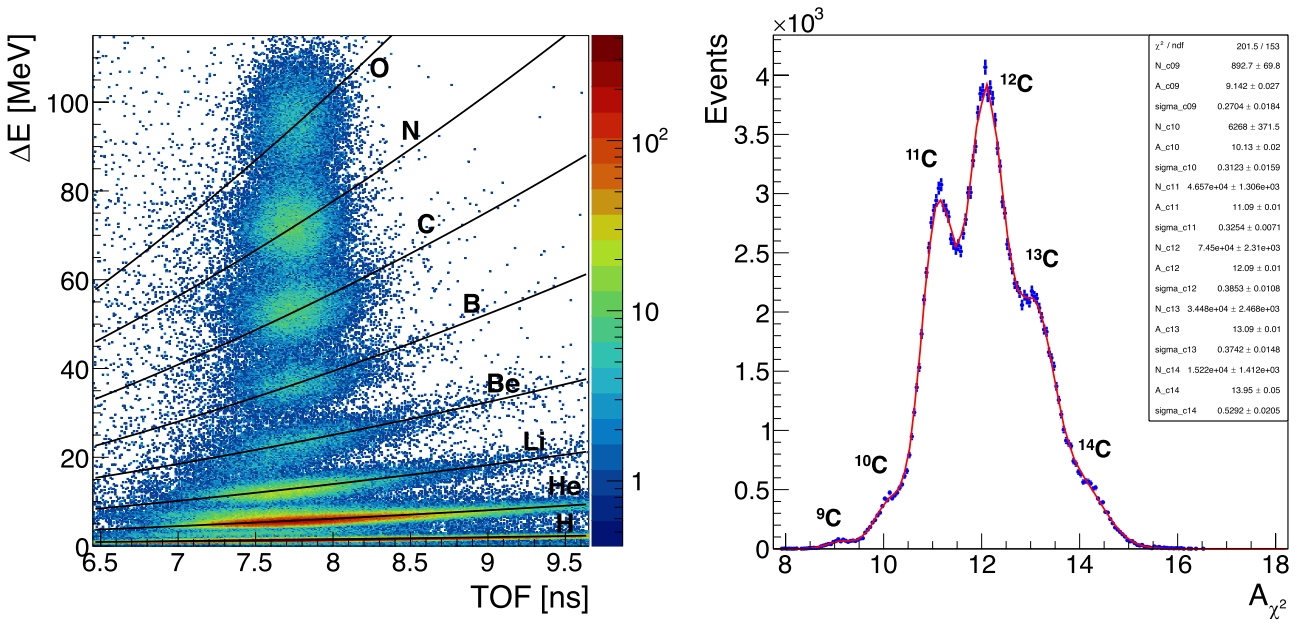

FIGURE 8 | (Left) Fragments charge identification in TW using the energy release in the scintillators ΔE and the TOF calculation performed together to the SC. For each region a Bethe-Bloch curve (shown as a different black curve), parametrized as a function of TOF, has been used to fit the MC simulation results to describe the average energy loss of fragments of the same charge Z impinging on TW with different angles, kinetic energies, TOF and path lenghts L. **(Right)** An example of mass number determination obtained with the χ^2 fit for the carbon fragments for the case of $\sigma(\text{TOF}) \simeq 70$ ps, $\sigma(p)/p \simeq 3.7\%$ and $\sigma(E_{\text{kin}})/E_{\text{kin}} \simeq 1.5\%$. The ^{11}C, ^{12}C and ^{13}C isotopes are clearly visible.

design and evaluate its expected performances taking into account the constraints set by the different experimental rooms where FOOT will acquire data. The full detector geometry and materials, already described in Section *The Magnetic Spectrometer*, have been implemented in the MC simulation to properly evaluate the interactions in all the active detectors and the production of secondary particles in out-of-target fragmentation processes. Care has been taken in detailing at the highest possible degree the different detector subsystems to evaluate with high accuracy the acceptances, efficiencies and resolutions needed for the cross-section measurement.

In the following, the results of a FLUKA simulation of a ^{16}O beam of 200 MeV/nucleon kinetic energy impinging on a 2 mm

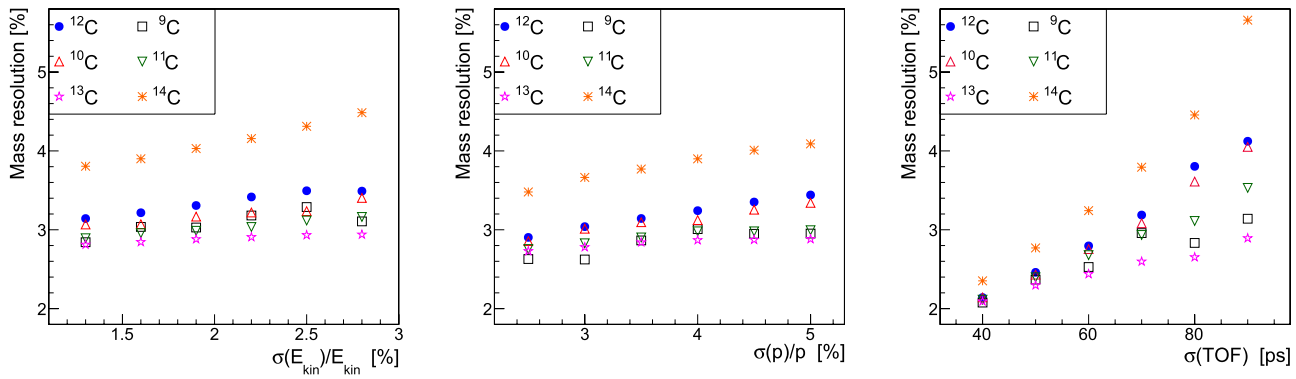

FIGURE 9 | Mass resolution of the identified isotopes of carbon ions (^{9}C, ^{10}C, ^{11}C, ^{12}C , ^{13}C, ^{14}C) as a function of: A) kinetic energy resolution (σ(TOF) = 70 ps and $\sigma(p)/p$ = 3.7%) B) momentum resolution (σ(TOF) = 70 ps and $\sigma(E_{kin})/E_{kin}$ = 1.5%) C) carbon ions TOF ($\sigma(p)/p$ = 3.7% and $\sigma(E_{kin})/E_{kin}$ = 1.5%).

thick C_2H_4 target are shown to document the expected performances of the magnetic spectrometer setup in terms of fragment identification [58, 59].

The 2-D top view of the full FOOT detector setup is shown in **Figure 7**, in a geometrical configuration in which the distance between TG and TW is 1 m, compatible with most of the experimental rooms where FOOT experiment is expected to collect data.

The MC scoring provides the fundamental quantities related to each FOOT detector sub-system: times in SC, fired cells in BM, fired pixels in VTX and ITR detectors, energy released in MSD strips, and time and energy released in TW bars and calorimeter crystals. The reconstruction of the quantities of interest, like clusters, tracks, TOF, fragment charge Z and kinetic energy, is performed locally for each detector. To estimate the detector capability in identifying the fragments in terms of charge and mass, the experimental resolutions of the fundamental quantities necessary for particle identification, when available, have been included in the MC simulation, by means of a Gaussian smearing. No signal digitization has been performed.

The Time Of Flight (TOF), energy loss (ΔE) and kinetic energy (E_{kin}) resolutions implemented in the simulation have been extracted from the results obtained during specific test beams for SC (Section *The Start Counter*), TW (Section *Tof Wall Detector*) and for calorimeter (Section *Calorimeter*). The momentum (p) resolution, not yet measurable due to the absence of the magnets and downstream tracking stations, has been evaluated by means of dedicated MC simulations using a standard Kalman tracking algorithm. The resolutions of the quantities of interest included in the simulation are ranging in the following intervals:

$\sigma(p)/p \simeq$ 3–5%;
$\sigma(TOF) \simeq$ 70–250 ps;
$\sigma(E_{kin})/E_{kin} \simeq$ 1.5–2.5%;
$\sigma(\Delta E)/\Delta E \simeq$ 3–10%

where the best performances are always referred to the ones expected for the highest fragment charges.

A nuclear fragment is uniquely identified when its charge and mass number are correctly measured. The charge Z of the fragment is measured by means of the TW detector. As shown in **Figure 8** (Left) the TW resolution allows the discrimination of eight regions in the ΔE-TOF plane, related to different fragment charges. For each region a Bethe-Bloch curve, parametrized as a function of TOF, has been used to fit the MC simulation results to describe the average energy loss of fragments of the same charge Z impinging on TW with different angles, kinetic energies, TOF and path lenghts L. For each fragment the charge corresponding to the closest Bethe-Bloch curve in the ΔE-TOF plane is assigned. The identification capability depends mainly on the ΔE resolution, that, with the aforementioned values, implies a fragment charge mis-identification <4%. The fragments pile-up in the same TW bar can partially spoil this value. The MSD information can be exploited to improve the charge identification capabilities partially reducing this latter background source.

The fragments charge measurement, when coupled to the rigidity (p/Z) one provided by the fragment tracking inside the magnetic field, allows to compute the momentum p. As discussed in Section *The FOOT Experiment*, by using the measurement of p, TOF and E_{kin} and inverting the set of **Eq. 1**, it is possible to have three different, correlated, measurements of the fragment mass. The mass identification resolution is directly related to the precision achieved on p, TOF and E_{kin}. These have to be maximised to match the final cross section precision requirements. In order to get the best mass estimation, taking advantage of the measurement redundancy, a standard χ^2 minimization approach or an Augmented Lagrangian Method (ALM) [60] approach can be pursued, performing a fit to the mass values. The two fit procedures lead to compatible results, centering the mass of the selected fragments always around the expected values. The final mass resolution ranges between 3% for ^{12}C to 6% for protons. Additionally, the χ^2 of the selected fit procedure can be used to exclude the events with a worse mass determination. Once the mass and Z of each fragment are determined the isotopic identification of each fragment is completed. In addition, the fit provides as output better evaluations of the TOF, p and E_{kin} observables.

An example of mass number determination obtained with the χ^2 minimization fit after applying a $\chi^2 < 5$ cut in the case of carbon ions fragmentation studies is shown in **Figure 8** (Right).

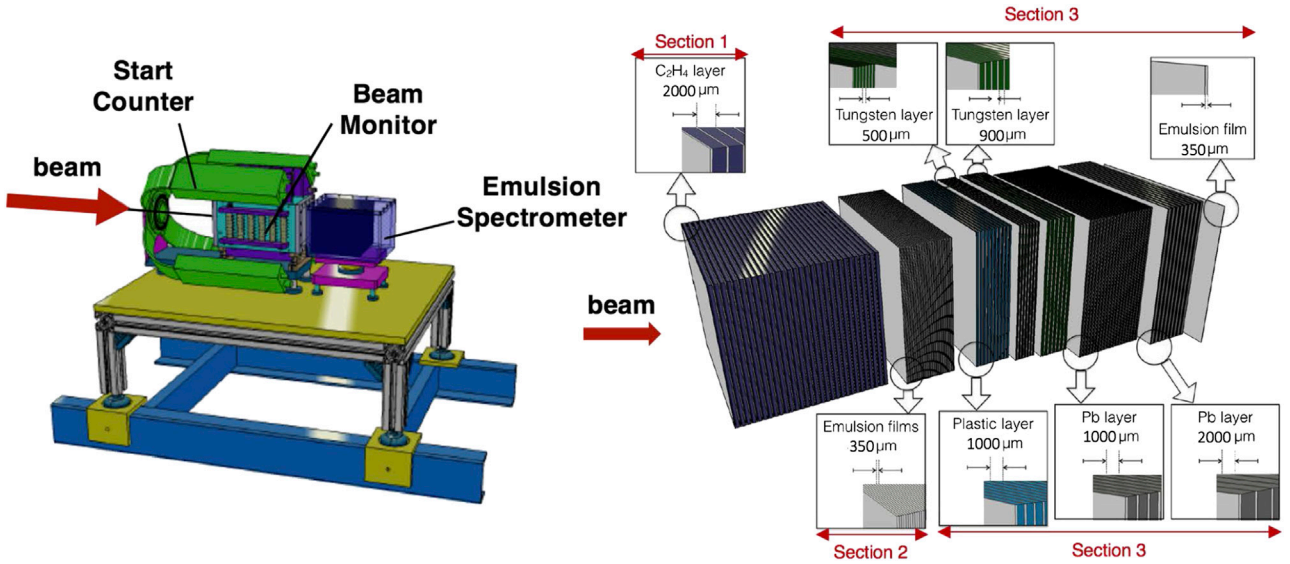

FIGURE 10 | (Left) Emulsion spectrometer setup placed downstream the SC and the BM. **(Right)** Scheme of the emulsion spectrometer composition with the C2H4 target.

These results have been obtained with the following parameters: $\sigma(\mathrm{TOF}) \simeq 70$ ps, $\sigma(p)/p \simeq 3.7\%$ and $\sigma(E_{\mathrm{kin}})/E_{\mathrm{kin}} \simeq 1.5\%$.

To understand which detectors mostly affect the precision achievable on the mass determination, a systematic study varying the TOF, p and E_{kin} resolutions has been performed. The carbon isotopes mass resolution dependence on each of the three parameters (TOF, p, E_{kin}) is shown in **Figure 9**. A major influence of the TOF resolution value is evident as shown in **Figure 9**.

The Emulsion Spectrometer

To characterize the production of low Z fragments, an emulsion spectrometer (ES) has been included in the FOOT setup as described in Section *The FOOT Experiment*. In **Figure 10** (Left) the arrangement of the emulsion chambers inside the FOOT detector is shown: the ES is placed after the SC and the BM, with the beam incoming from the left. The SC and BM are used only for beam monitoring purposes and their DAQ (see Section *Trigger and Data Acquisition System*) is completely decoupled from the ES that acts as a complete, self standing, experiment. The SC and BM have been used to perform an on-line control of the beam flux on the active ES surface, to avoid spatial pile-up of events in the ES.

Among all tracking devices used in particle physics, nuclear emulsion detectors achieve the highest spatial resolution (sub-micrometric) for tracking ionizing particles. Emulsion chambers integrate target and detector in a very compact setup and provide a very accurate reconstruction of the interactions occurring inside the target. Moreover, no power supply or any readout electronics is required and this helps to keep the emulsion setup compact maximising its active area. The use of emulsions is coupled to the continuous development in the field of automated scanning system techniques: last generation microscopes [61–64] allow very fast scanning with wide angular acceptances of huge data sets. Furthermore, it was demonstrated that a controlled fading of the emulsions in terms of different thermal treatments extends their dynamical range when crossed by different ions, providing charge identification capabilities [37, 65, 66]. The possibility to measure particles emitted with an angular acceptance above 70° with respect to the incident angle, coupled to the very high spatial resolution and charge identification capability, made the nuclear emulsion technology an ideal choice for new generation of measurements of differential fragmentation cross sections. For this reason, emulsion detectors have been already adopted in different measurements campaigns to study fragments produced at large angles by ^{12}C ions impinging on thin targets in the energy range of interest for PT [67, 68], showing their capability in the charge identification of the produced fragments [65, 66]. The nuclear emulsion films, used for the FOOT experiment, consist of two 70 μm thick sensitive layers deposited on both sides of a 210 μm plastic base, resulting in a total thickness of 350 μm. The sensitive regions are made of AgBr crystals of 0.2 μm diameter scattered in a gelatine binder, able to detect charged particles. The charged particle trajectory is recorded by a series of sensitised AgBr crystals along its path acting as latent image centres. A chemical process, known as development, enhances latent images, inducing the growth of silver clusters (grains) with a diameter of 0.6 μm which can be seen with an optical microscope. The density of grains is proportional to the charge particle ionization within the detector dynamical range. After the development, the emulsions are scanned by an automated system. The acquired image is then analyzed by a dedicated software to recognize clusters of dark pixels aligned, which represent the track produced by the penetrating particle. A straight sequence of pixels in one emulsion layer defines a "*micro-track*". Two aligned micro-tracks belonging to the top and bottom layers of an emulsion film form a "*base-track*". The

reconstructed base-track has a micrometer accuracy of 1.0 μm in position and 3 mrad in angle [64]. Base-tracks belonging to a straight line along different films, are connected to form "*volume-tracks*". The sum of the pixels of the grains belonging to the volume-track is a variable sensitive to the specific ionization, hence to the particle charge. This variable is called track volume (see Section *Charge Identification Region*).

The Emulsion Spectrometer for the FOOT experiment has been designed with passive materials alternated to nuclear emulsions films acting both as high-resolution tracking devices and ionization detectors. It is composed of three sections with different purposes, as shown in **Figure 10** (Right):

1. Interaction and vertexing region (ES Section 1)
2. Charge identification region (ES Section 2)
3. Momentum measurement region (ES Section 3)

The imprinting process due to the passage of a particle in the emulsion film and the following development process makes the emulsion spectrometer a one-shot detector: for each data taking with a fixed combination of ion beam, energy and target, a different emulsion spectrometer has to be assembled, exposed and lately scanned and analyzed.

Interaction and Vertexing Region

The ES Section 1 is made of several elementary cells composed of layers of target element, Carbon or C_2H_4, alternated with emulsion films, as shown in **Figure 10** (Right). Whenever the ion beam interacts within the cells of this section, secondary fragments will be emitted and detected by the following regions of the spectrometer. The detector emulsion structure will track the fragments and reconstruct the interaction vertex position. The length of this section will be optimized for each different data taking, to achieve a statistically significant number of reactions accordingly to the combination of ion beam, energy and target. In the GSI 2019 data taking, four emulsion spectrometer setups have been used: for each of the two ^{16}O beam configurations, at 200 and 400 MeV/nucleon, two different stacks of 30 cells have been used. Each cell was composed of an emulsion film and a target layer of 1 mm of Carbon in one case and of 2 mm of C_2H_4 in the other case. According to MC simulation, based on FLUKA code, about 32% and 30% of ^{16}O ions at 200 MeV/n are expected to interact within 60 mm of C_2H_4 and within 30 mm of Carbon, respectively.

Charge Identification Region

The particles at the minimum of their ionizing power (MIPs) generate in nuclear emulsion thin tracks whose grain density ranges from 30 to 50 grains/100 μm, according to the emulsions sensitivity. Highly ionizing particles cause a saturation effect suppressing the charge identification. Nevertheless, by keeping the emulsions for an appropriate time (about 24 h) at a relatively high temperature (above 28°C) and a high relative humidity (around 95%), a fading is induced which partially or totally erases the particles tracks. Thus, for instance, films may be made insensitive to MIPs and suited for highly ionizing particles. The combination of several films, having undergone different thermal treatments after exposure, allows overcoming saturation effects for particles with largely different ionizations. This technique has already been used in previous works [37, 65, 66] to enlarge the dynamical range of emulsions. The ES Section 2 aimed to the charge identification for low Z fragments (H, He, Li), is made by elementary cells composed of four emulsion films. After the exposure and before the chemical development, four different thermal treatments were applied to the emulsions, hereafter denoted as R0 (not thermally treated), R1 (28°C), R2 (34°C) and R3 (36°C). For each thermal condition, each track is characterized by four track volume variables, VR0, VR1, VR2 and VR3, respectively, that are proportional to the silver grain density along the trajectory. In the not thermally treated emulsions (R0), all the tracks are visible and the saturation effect makes not possible the charge separation. The R1 thermal process produces the complete erasing of all tracks due to MIPs. The fragments charge separation is obtained by looking at correlations between appropriate pairs of track volume variables, or by a linear combination of them. In the GSI 2019 data taking, a set of nine quadruplets of emulsion films refreshed as explained before has been used.

TABLE 2 | ES Section 3 composition in the GSI 2019 data taking.

Stack	passive material	N. passive layers	thickness (mm)	N. emulsion films
S1	Lexan	10	1.0	10
S2	W	7	0.5	7
S3	W	7	0.9	7
S4	Pb	20	1.0	20
S5	Pb	9	2.0	9

Momentum Measurement Region

The ES Section 3, dedicated to the momentum measurement, is made of emulsion films interleaved with layers of passive material, as shown in **Figure 10** (Right). The section length, the number of passive layers and their thicknesses are set according to the incident beam energy. The materials used as passive layers are Lexan, W and Pb. As an example, the composition of the ES Section 3 used in the GSI 2019 data taking is shown in **Table 2**, where five different stacks of different combination of passive layer material/thickness have been used. The momentum will be evaluated with the range technique. Measuring the length of the whole particle track, its momentum will be estimated on the basis of the correlation between range and kinetic energy, using data supplied by NIST [69]. The accuracy of this method strongly depends on the segmentation of the ES Section 3 in passive layers and on their thickness and material, chosen in order to stop the crossing fragments, as in a calorimeter. As shown in **Table 2**, the lower Z passive layers are placed at the beginning of the stack, while the higher Z layers at the end, in order to increase the dynamical range of the momentum measurement. The particle trajectory measurements provide also an estimate of the charged particles momentum through the Multiple Coulomb Scattering (MCS) method [70, 71]. For each particle track, the x-y spatial coordinates and the slope (θ_x, θ_y) are estimated with high accuracy. Thanks to the measurements along a track of the particle direction, provided by the high segmentation of the

ES, the particle momentum can be estimated by the MCS method according to the formula:

$$p\,(\mathrm{MeV/c}) = \frac{13.6}{\beta \cdot \delta\theta\,(\mathrm{mrad})} \cdot Z \cdot \sqrt{\frac{x}{X_0}} \qquad (2)$$

where p is the fragment momentum, β its velocity, Z its charge, x the traversed distance, X_0 the radiation length in the material and $\delta\theta$ the deviation of the track slope along its path. By using two independent methods for the energy and momentum estimation (i.e the range and multiple Coulomb scattering), combined to the charge measurement performed by the ES Section 2, the fragments mass for the isotopic identification can be assessed. According to FLUKA MC simulation, 77% and 72% of the fragments produced by the interaction of the ^{16}O (400 MeV/nucleon) beam on C and C_2H_4 targets, respectively, is contained inside the ES.

CONCLUSION

The FOOT (FragmentatiOn Of Target) experiment, funded by INFN (Istituto Nazionale di Fisica Nucleare, Italy), has been designed to perform measurements of differential cross sections for the production of charged fragments in the nuclear interaction between ion beams (p, ^{4}He, ^{12}C, ^{16}O) and targets (H, C, O) of interest for charged Particle Therapy and space radioprotection applications. The experiment has been designed with the main goal of investigating target fragmentation in proton therapy by means of an inverse kinematic approach, using beams of ^{12}C, ^{16}O impinging on graphite and polyethylene targets, to extract cross sections for the production of charged fragments in p+C and p+O collisions in the energy range of 50–200 MeV/nucleon. The same apparatus will be used to investigate the double differential cross sections of the projectile fragmentation process for beams of ^{4}He, ^{12}C and ^{16}O impinging on graphite, polyethylene and PMMA targets up to 500 MeV/nucleon for charged PT and up to 800 Mev/nucleon for space radioprotection. The FOOT detector exploits two alternative complementary setups, a magnetic spectrometer and an emulsion spectrometer, for the tracking and the identification of the fragments in order to provide high acceptance, efficiency and identification capability in a wide dynamical range that spreads from protons to heavier ions up to ^{16}O. The construction of the detector is being finalized and several beam tests have already been performed for calibration purposes. The experiment started its scientific program using the Emulsion setup at GSI, in 2019 with ^{16}O ions of 200 and 400 MeV/nucleon kinetic energy on C and C_2H_4 targets, and in 2020 with ^{12}C ions of 700 MeV/nucleon kinetic energy, on the same targets. Data analysis is still in progress. The magnetic spectrometer setup is under construction and a first data taking in this configuration is being scheduled at CNAO, using ^{12}C ions of 200 MeV/nucleon kinetic energy. An application for beam time in 2021/2022 at GSI is in preparation, having as one of the main priorities the request of a ^{4}He ion beam of 700 MeV/nucleon kinetic energy. In future, an upgrade of the FOOT detector is being considered: the evaluation of the neutron production together with the charged fragments can constrain even more strongly MC nuclear production models that are relevant both for PT and RPS. Different strategies for providing neutron detection capability to the FOOT experiment are currently under study.

DATA AVAILABILITY STATEMENT

The original contributions presented in the study are included in the article/Supplementary Material, further inquiries can be directed to the corresponding author.

THE FOOT COLLABORATION

A. Alexandrov, INFN Section of Napoli, Napoli, Italy, Department of Physics "E. Pancini", University of Napoli, Napoli, Italy, National University of Science and Technology, MISIS, RUS-119049 Moscow, Russia, and Lebedev Physical Institute of the Russian Academy of Sciences, RUS-119991 Moscow, Russia; **B. Alpat**, INFN section of Perugia, Perugia, Italy; **G. Ambrosi**, INFN section of Perugia, Perugia, Italy; **S. Argirò**, INFN Section of Torino, Torino, Italy and Department of Physics, University of Torino, Torino, Italy; **R. Arteche Diaz**, Ceaden, Centro de Aplicaciones Tecnologicas y Desarrollo Nuclear, Havana, Cuba; **N. Bartosik**, INFN Section of Torino, Torino, Italy; **G. Battistoni**, INFN Section of Milano, Milano, Italy; **N. Belcari**, INFN section of Pisa, Pisa, Italy and Department of Physics, University of Pisa, Pisa, Italy; **E. Bellinzona**, Trento Institute for Fundamental physics and applications, Istituto Nazionale di Fisica Nucleare (TIFPA-INFN), Trento, Italy; **S. Biondi**, INFN section of Bologna, Bologna, Italy and Department of Physics and Astronomy, University of Bologna, Bologna, Italy; **M. G. Bisogni**, INFN section of Pisa, Pisa, Italy and Department of Physics, University of Pisa, Pisa, Italy; **G. Bruni**, INFN section of Bologna, Bologna, Italy; **P. Carra**, INFN section of Pisa, Pisa, Italy and Department of Physics, University of Pisa, Pisa, Italy; **P. Cerello**, INFN Section of Torino, Torino, Italy; **E. Ciarrocchi**, INFN section of Pisa, Pisa, Italy and Department of Physics, University of Pisa, Pisa, Italy; **A. Clozza**, INFN Laboratori Nazionali di Frascati, Frascati, Italy; **S. Colombi**, Trento Institute for Fundamental physics and applications, Istituto Nazionale di Fisica Nucleare (TIFPA-INFN), Trento, Italy and Department of Physics, University of Trento, Trento, Italy; **G. De Lellis**, INFN Section of Napoli, Napoli, Italy and Department of Physics "E. Pancini", University of Napoli, Napoli, Italy; **A. Del Guerra**, INFN section of Pisa, Pisa, Italy and Department of Physics, University of Pisa, Pisa, Italy; **M. De Simoni**, INFN section of Roma 1, Rome, Italy and Department of Physics, University of Rome La Sapienza, Rome, Italy; **A. Di Crescenzo**, INFN Section of Napoli, Napoli, Italy and Department of Physics "E. Pancini", University of Napoli, Napoli, Italy; **B. Di Ruzza**, Trento Institute for Fundamental physics and applications, Istituto Nazionale di Fisica Nucleare (TIFPA-INFN), Trento, Italy; **M. Donetti**,

Centro Nazionale di Adroterapia Oncologica (CNAO), Pavia, Italy amd INFN Section of Torino, Torino, Italy; **Y. Dong**, INFN Section of Milano, Milano, Italy and Department of Physics, University of Milano, Milano, Italy; **M. Durante**, Biophysics Department, GSI Helmholtzzentrum für Schwerionenforschung, Darmstadt, Germany and Technische Universität Darmstadt Institut für Festkörperphysik, Darmstadt, Germany; **R. Faccini**, INFN section of Roma 1, Rome, Italy and Department of Physics, Rome, University of Rome La Sapienza, Italy; **V. Ferrero**, INFN Section of Torino, Torino, Italy; **E. Fiandrini**, INFN section of Perugia, Perugia, Italy and Department of Physics and Geology, University of Perugia, Perugia, Italy; **Ch. Finck**, CNRS, IPHC UMR 7871, F-67000, Université de Strasbourg, Strasbourg, France; **E. Fiorina**, INFN Section of Torino, Torino, Italy; **M. Fischetti**, INFN section of Roma 1, Rome, Italy and Department of Scienze di Base e Applicate per l'Ingegneria (SBAI), University of Rome La Sapienza, Rome, Italy; **M. Francesconi**, INFN section of Pisa, Pisa, Italy and Department of Physics, University of Pisa, Pisa, Italy; **M. Franchini**, INFN section of Bologna, Bologna, Italy and Department of Physics and Astronomy, University of Bologna, Bologna, Italy; **G. Franciosini**, INFN section of Roma 1, Rome, Italy and Department of Physics, University of Rome La Sapienza, Rome, Italy; **G. Galati**, INFN Section of Napoli, Napoli, Italy; **L. Galli**, INFN section of Pisa, Pisa, Italy; **V. Gentile**, INFN Section of Napoli, Napoli, Italy and National University of Science and Technology, MISIS, RUS-119049 Moscow, Russia; **G. Giraudo**, INFN Section of Torino, Torino, Italy; **R. Hetzel**, RWTH Aachen University, Physics Institute III B, Aachen, Germany; **E. Iarocci**, INFN Laboratori Nazionali di Frascati, Frascati, Italy; **M. Ionica**, INFN section of Perugia, Perugia, Italy; **A. Iuliano**, INFN Section of Napoli, Napoli, Italy and Department of Physics "E. Pancini", University of Napoli, Napoli, Italy; **K. Kanxheri**, INFN section of Perugia, Perugia, Italy; **A. C. Kraan**, INFN section of Pisa, Pisa, Italy; **V. Lante**, Centro Nazionale di Adroterapia Oncologica (CNAO), Pavia, Italy; **C. La Tessa**, Trento Institute for Fundamental physics and applications, Istituto Nazionale di Fisica Nucleare (TIFPA-INFN), Trento, Italy and Department of Physics, University of Trento, Trento, Italy; **M. Laurenza**, INFN Laboratori Nazionali di Frascati, Frascati, Italy; **A. Lauria**; INFN Section of Napoli, Napoli, Italy and Department of Physics "E. Pancini", University of Napoli, Napoli, Italy; **E. Lopez Torres**, INFN Section of Torino, Torino, Italy; Ceaden, Centro de Aplicaciones Tecnologicas y Desarrollo Nuclear, Havana, Cuba; **M. Marafini**, INFN section of Roma 1, Rome, Italy; Museo Storico della Fisica e Centro Studi e Ricerche Enrico Fermi, Rome, Italy; **C. Massimi**, Department of Physics and Astronomy, University of Bologna, Bologna, Italy; **I. Mattei**, INFN Section of Milano, Milano, Italy; **A. Mengarelli**, INFN section of Bologna, Bologna, Italy; **A. Moggi**, INFN section of Pisa, Pisa, Italy; **M. C. Montesi**, INFN Section of Napoli, Napoli, Italy; Department of Chemistry, University of Napoli, Napoli, Italy; **M. C. Morone**, Department of Physics, University of Rome Tor Vergata, Rome, Italy; INFN section of Roma tor Vergata, Rome, Italy; **M. Morrocchi**, INFN section of Pisa, Pisa, Italy and Department of Physics, University of Pisa, Pisa, Italy; **S. Muraro**, INFN Section of Milano, Milano, Italy; **F. Murtas**, Department of Physics, University of Rome La Sapienza, Rome, Italy; **L. Narici**, Department of Physics, University of Rome Tor Vergata, Rome, Italy and INFN section of Roma tor Vergata, Rome, Italy; **A. Pastore**, INFN section of Bari, Bari, Italy; **N. Pastrone**, INFN Section of Torino, Torino, Italy; **V. Patera**, INFN section of Roma 1, Rome, Italy and Department of Scienze di Base e Applicate per l'Ingegneria (SBAI), University of Rome La Sapienza, Rome, Italy; **F. Pennazio**, INFN Section of Torino, Torino, Italy; **P. Placidi**, INFN section of Perugia, Perugia, Italy and Department of Engineering, University of Perugia, Perugia, Italy; **M. Pullia**, Centro Nazionale di Adroterapia Oncologica (CNAO), Pavia, Italy; **F. Raffaelli**, INFN section of Pisa, Pisa, Italy; **L. Ramello**, INFN Section of Torino, Torino, Italy and Department of Science and Technological Innovation, University of Piemonte Orientale, Alessandria, Italy; **R. Ridolfi**, Department of Physics and Astronomy, University of Bologna, Bologna, Italy; **V. Rosso**, INFN section of Pisa, Pisa, Italy and Department of Physics, University of Pisa, Pisa, Italy; **C. Sanelli**, INFN Laboratori Nazionali di Frascati, Frascati, Italy; **A. Sarti**, INFN section of Roma 1, Rome, Italy and Department of Scienze di Base e Applicate per l'Ingegneria (SBAI), University of Rome La Sapienza, Rome, Italy; **G. Sartorelli**, INFN section of Bologna, Bologna, Italy and Department of Physics and Astronomy, University of Bologna, Bologna, Italy; **O. Sato**, Department of Physics, Nagoya University, Nagoya, Japan; **S. Savazzi**, Centro Nazionale di Adroterapia Oncologica (CNAO), Pavia, Italy; **L. Scavarda**, INFN Section of Torino, Torino, Italy and Department of Physics, University of Torino, Torino, Italy; **A. Schiavi**, INFN section of Roma 1, Rome, Italy and Department of Scienze di Base e Applicate per l'Ingegneria (SBAI), University of Rome La Sapienza, Rome, Italy; **C. Schuy**, Biophysics Department, GSI Helmholtzzentrum für Schwerionenforschung, Darmstadt, Germany, **E. Scifoni**, Trento Institute for Fundamental physics and applications, Istituto Nazionale di Fisica Nucleare (TIFPA-INFN), Trento, Italy; **A. Sciubba**, INFN Laboratori Nazionali di Frascati, Frascati, Italy and Department of Scienze di Base e Applicate per l'Ingegneria (SBAI), University of Rome La Sapienza, Rome, Italy; **A. Sécher**, Université de Strasbourg, CNRS, IPHC UMR 7871, F-67000 Strasbourg, France; **M. Selvi**, INFN section of Bologna, Bologna, Italy; **L. Servoli**, INFN section of Perugia, Perugia, Italy; **G. Silvestre**, INFN section of Perugia, Perugia, Italy and Department of Physics and Geology, University of Perugia, Perugia, Italy; **M. Sitta**, INFN Section of Torino, Torino, Italy; Department of Science and Technological Innovation, University of Piemonte Orientale, Alessandria, Italy; **R. Spighi**, INFN section of Bologna, Bologna, Italy; **E. Spiriti**, INFN Laboratori Nazionali di Frascati, Frascati, Italy; **G. Sportelli**, INFN section of Pisa, Pisa, Italy and Department of Physics, University of Pisa, Pisa, Italy; **A. Stahl**, RWTH Aachen University, Physics Institute III B, Aachen, Germany; **V. Tioukov**, INFN Section of Napoli, Napoli, Italy; **S. Tomassini**, INFN Laboratori Nazionali di Frascati, Frascati, Italy; **F. Tommasino**, Trento Institute for Fundamental physics

and applications, Istituto Nazionale di Fisica Nucleare (TIFPA-INFN), Trento, Italy and Department of Physics, University of Trento, Trento, Italy; **M. Toppi**, INFN Laboratori Nazionali di Frascati, Frascati, Italy; University of Rome La Sapienza, Department of Scienze di Base e Applicate per l'Ingegneria (SBAI), Rome, Italy; **G. Traini**, INFN section of Roma 1, Rome, Italy and Department of Physics, University of Rome La Sapienza, Rome, Italy; **S. M. Valle**, INFN Section of Milano, Milano, Italy; **M. Vanstalle**, Université de Strasbourg, CNRS, IPHC UMR 7871, F-67000 Strasbourg, France; **M. Villa**, INFN section of Bologna, Bologna, Italy and Department of Physics and Astronomy, University of Bologna, Bologna, Italy; **U. Weber**, Biophysics Department, GSI Helmholtzzentrum für Schwerionenforschung, Darmstadt, Germany; **R. Zarrella**, INFN section of Pisa, Pisa, Italy and Department of Physics, University of Pisa, Pisa, Italy; **A. Zoccoli**, INFN section of Bologna, Bologna, Italy and Department of Physics and Astronomy, University of Bologna, Bologna, Italy.

AUTHOR CONTRIBUTIONS

All authors of the FOOT collaboration have made a substantial, direct, and intellectual contribution to the work and approved it for publication.

ACKNOWLEDGMENTS

The FOOT Collaboration acknowledges the INFN for its support in building and running the detector. We would like to acknowledge all the personnel of the CNAO and APSS-Trento centres that provided us support during the operational tests performed using carbon and proton beams at their facilities. The GSI data were taken in the IBER_006 experiment, supported by European Space Agency (ESA) -IBER17 project, in the frame of FAIR Phase-0.

REFERENCES

1. Jermann M. Particle therapy statistics in 2014. *International Journal of Particle Therapy* (2015) 2(1):50–4. doi:10.14338/IJPT-15-00013
2. Durante M, Loeffler JS. Charged particles in radiation oncology. *Nat Rev Clin Oncol* (2010) 7(1):37–43. doi:10.1038/nrclinonc.2009.183
3. Tommasino F, Scifoni E, Durante M. New Ions for therapy. *Int J Part Therapy* (2016) 2(3):428–38. doi:10.14338/IJPT-15-00027.1
4. Krämer M, Scifoni E, Schuy C, Rovituso M, Tinganelli W, Maier A, et al. Helium ions for radiotherapy? Physical and biological verifications of a novel treatment modality. *Med Phys* (2016) 43(4):1995. doi:10.1118/1.4944593
5. Durante M, Paganetti H. *Nuclear physics in particle therapy: a review, Reports on Progress in Physics* (2016) 79: 096702. doi:10.1088/0034-4885/79/9/096702
6. Schardt D, Elsasser T, Schulz-Ertner D. Heavy-ion tumor therapy: physical and radiobiological benefits. *Rev Mod Phys* (2010) 82(1):383–425. doi:10.1103/RevModPhys.82.383
7. Schardt D, Schall I, Geissel H, Irnich H, Kraft G, Magel A, et al. Nuclear fragmentation of high-energy heavy-ion beams in water. *Adv Space Res* (1996) 17(2):87–94. doi:10.1016/0273-1177(95)00516-H
8. Krämer M, Durante M. Ion beam transport calculations and treatment plans in particle therapy. *Eur Phys J D* (2010) 60:195–202. doi:10.1140/epjd/e2010-00077-8
9. Sommerer F, Parodi K, Ferrari A, Poljanc K, Enghardt W, Aiginger H. Investigating the accuracy of the FLUKA code for transport of therapeutic ion beams in matter. *Phys Med Biol* (2006) 51:4385. doi:10.1088/0031-9155/51/17/017
10. Sato T, Kase Y, Watanabe R, Niita K, Sihver L. Biological dose estimation for charged-particle therapy using an improved PHITS code coupled with a microdosimetric kinetic model. *Radiat Res* (2009) 171(1):107–17. doi:10.1667/RR1510.1
11. Böhlen TT, Cerutti F, Dosanjh M, Ferrari A, Gudowska I, Mairani A, et al. Benchmarking nuclear models of FLUKA and GEANT4 for carbon ion therapy. *Phys Med Biol* (2010) 55(19):5833–47. doi:10.1088/0031-9155/55/19/014
12. Bolst D, Cirrone G, Cuttone G, Folger G, Incerti S, Ivanchenko V, et al. Validation of Geant4 fragmentation for heavy ion therapy. *Nucl Instrum Meth A* (2017) 869:68–75. doi:10.1016/j.nima.2017.06.046
13. Pleskac R, Abou-Haidar Z, Agodi C, Alvarez MAG, Aumann T, Battistoni G, et al. The FIRST experiment at GSI. *Nucl Instrum Meth A* (2012) 678:130–8. doi:10.1016/j.nima.2012.02.020
14. Thwaites D. Accuracy required and achievable in radiotherapy dosimetry: have modern technology and techniques changed our views? *J Phys Conf* (2013) 444: 012006. doi:10.1088/1742-6596/444/1/012006
15. De Napoli M, Agodi C, Battistoni G, Blancato AA, Cirrone GA, Cuttone G, et al. Carbon fragmentation measurements and validation of the GEANT4 nuclear reaction models for hadrontherapy. *Phys Med Biol* (2012) 57:7651–71. doi:10.1088/0031-9155/57/22/7651
16. Dudouet J, Labalme M, Cussol D, Finck C, Rescigno R, Rousseau M, et al. Zero-degree measurements of ^{12}C fragmentation at 95 MeV/nucleon on thin targets. *Phys Rev C* (2014) 89:064615. doi:10.1103/PhysRevC.89.064615
17. Toppi M, Abou-Haidar Z, Agodi C, Alvarez MAG, Aumann T, Balestra F, et al. Measurement of fragmentation cross sections of ^{12}C ions on a thin gold target with the FIRST apparatus. *Phys Rev C* (2016) 93:064601. doi:10.1103/PhysRevC.93.064601
18. Marafini M, Paramatti R, Pinci D, Battistoni G, Collamati F, De Lucia E, et al. Secondary radiation measurements for particle therapy applications: nuclear fragmentation produced by ^{4}He ion beams in a PMMA target. *Phys Med Biol* (2017) 62:1291–309. doi:10.1088/1361-6560/aa5307
19. Rovituso M, Schuy C, Weber U, Brons S, Cortés-Giraldo MA, La Tessa C, et al. Fragmentation of 120 and 200 MeV/u ^{4}He ions in water and PMMA targets. *Phys Med Biol* (2017) 62:1310–26. doi:10.1088/1361-6560/aa5302
20. Tang JT, Inoue T, Inoue T, Yamazaki H, Fukushima S, Fournier-Bidoz N, et al. Comparison of radiobiological effective depths in 65-MeV modulated proton beams. *Br J Cancer* (1997) 76:220–5. doi:10.1038/bjc.1997.365
21. Tommasino F, Durante M. Proton radiobiology. *Cancers (Basel)* (2015) 7(1): 353–81. doi:10.3390/cancers7010353
22. Carabe A, Moteabbed M, Depauw N, Schuemann J, Paganetti H. Range uncertainty in proton therapy due to variable biological effectiveness. *Phys Med Biol* (2012) 57(5):1159–72. doi:10.1088/0031-9155/57/5/1159
23. Mairani A, Dokic I, Magro G, Tessonnier T, Bauer J, Böhlen TT, et al. A phenomenological relative biological effectiveness approach for proton therapy based on an improved description of the mixed radiation field. *Phys Med Biol* (2017) 62:1378–95. doi:10.1088/1361-6560/aa51f7
24. Durante M, Cucinotta FA. Physical basis of radiation protection in space travel. *Rev Mod Phys* (2011) 83:1245. doi:10.1103/RevModPhys.83.1245
25. Durante M. Space radiation protection: destination mars. *Life Sci Space Res (Amst)* (2014) 1:2–9. doi:10.1016/j.lssr.2014.01.002
26. Durante JH, Slaba TC, Blattnig SR, Tripathi RK, Townsend LW, Handler T, et al. Comparison of the transport codes HZETRN, HETC and FLUKA for a solar particle event. *Adv Space Res* (2011) 47:1079–88. doi:10.1016/j.asr.2010.11.012
27. Norbury JW, Miller J, Adamczyk AM, Heilbronn LH, Townsend LW, Blattnig SR, et al. Review of nuclear physics experimental data for space radiation. *Health Phys* (2012) 103(5):640–2. doi:10.1016/j.radmeas.2012.03.00410.1097/HP.0b013e318261fb7f
28. Wilson JW, Miller J, Konradi A, Cucinotta FA. Shielding strategies for human space exploration. NASA Conference Publication 3370 (1997)
29. Patera V, Argiró S, Barbosa D, Battistoni G, Belcari N, Bruni G, et al. The foot (fragmentation of target) experiment, PoS INPC (2016) 128.
30. Battistoni G, Alexandrov A, Argiró S, Barbosa D, Belcari N, Bisognic MG, et al. The foot (fragmentation of target) experiment, PoS BORMIO (2017) 23.

31. Webber WR, Kish JC, Schrier DA. Total charge and mass changing cross sections of relativistic nuclei in hydrogen, helium, and carbon targets. *Phys Rev C Nucl Phys* (1990) 41(2):520. doi:10.1103/PhysRevC.41.52.0
32. Dudouet J, Juliani D, Labalme M, Cussol D, Angelíque JC, Braunn B, et al. Double-differential fragmentation cross-section measurements of 95 MeV/nucleon ^{12}C beams on thin targets for hadron therapy. *Phys Rev C* (2013) 88(2):064615. doi:10.1103/PhysRevC.88.024606
33. Ferrari A, Sala P, Fassó A, Ranft J. *FLUKA: a multi-particle transport code*. (2005). Technical Report No.: CERN-2005-10, INFN/TC-05/11, SLAC-R-773, CERN, INFN, SLAC.
34. Böhlen TT, Cerutti F, Chin M, Fassó A, Ferrari A, Ortega P, et al. FLUKA code: developments and challenges for high energy and medical applications. *Nucl Data Sheets* (2014) 120:211–4. doi:10.1016/j.nds.2014.07.049
35. Morrocchi M, Ciarrocchi E, Alexandrov A, Alpat B, Ambrosi G, Argiró S, et al. Development and characterization of a Δ*E*-TOF detector prototype for the FOOT experiment. *Nucl Instrum Meth A* (2019) 916:116–24. doi:10.1016/j.nima.2018.09.086
36. Mattei I, Alexandrov A, Solestizi LA, Ambrosi G, Argiró S, Bartosik N, et al. Measurement of ^{12}C Fragmentation cross sections on C, O and H in the energy range of interest for particle therapy applications. *IEEE TRANSACTIONS ON RADIATION AND PLASMA MEDICAL SCIENCES* (2020) 4:269–82. doi:10.1109/TRPMS.2020.2972197
37. Montesi MC, Lauria A, Alexandrov A, Solestizi LA, Ambrosi G, Argiró S, et al. Ion charge separation with new generation of nuclear emulsion films. *Open Phys* (2019) 17:233–40. doi:10.1515/phys-2019-0024
38. Galli L, Baldini AM, Cei A, Chiappini M, Francesconi M, Grassi M, et al. WaveDAQ: an highly integrated trigger and data acquisition system. *Nucl Instrum Meth A* (2019) 936:399–400. doi:10.1016/j.nima.2018.07.067
39. Abou-Haidar Z, Agodi C, Alvarez MAG, Anelli A, Aumann T, Battistoni G, et al. Performance of upstream interaction region detectors for the FIRST experiment at GSI. *J Inst Met* (2012) 7:P02006. doi:10.1088/1748-0221/7/02/P02006
40. Dong Y, Gianluigi S, Sofia C, Andrey A, Behcet A, Giovanni A, et al. The Drift Chamber detector of the FOOT experiment: performance analysis and external calibration. *Nucl Instrum Meth A* (2021) 986:164756. doi:10.1016/j.nima.2020.164756
41. Rescigno R, Finck C, Juliani D, Spiriti E, Baudot J, Abou-Haidar Z, et al. Performance of the reconstruction algorithms of the FIRST experiment pixel sensors vertex detector. *Nucl Instrum Meth A* (2014) 767:34–40. doi:10.1016/j.nima.2014.08.024
42. Strasbourg In2p3 PICSEL group. Available at: www.iphc.cnrs.fr/PICSEL.html
43. Greiner L, Anderssen E, Matis HW, Ritter HG, Schambach J, Silber J, et al. A MAPS based vertex detector for the STAR experiment at RHIC. *Nucl Instrum Meth A* (2011) 650:68–72. doi:10.1016/j.nima.2010.12.006
44. Valin I, Hu-Guo C, Baudot J, Bertolone G, Besson A, Colledani C, et al. A reticle size CMOS pixel sensor dedicated to the STAR HFT. *J Inst Met* (2012) 7:C01102. doi:10.1088/1748-0221/7/01/C01102
45. Spiriti E, Finck C, Baudot J, Divay C, Juliani D, Labalme M, et al. CMOS active pixel sensors response to low energy light ions. *Nucl Instrum Meth A* (2017) 875:35–40. doi:10.1016/j.nima.2017.08.058
46. de Boer W, Bartsch V, Bol J, Dierlamm A, Grigoriev E, Hauler F, et al. Measurements with a CMOS pixel sensor in magnetic fields. *Nucl Instrum Meth A* (2002) 487:163–9. doi:10.1016/S0168-9002(02)00960-9
47. PLUME web site. Available at: www.iphc.cnrs.fr/PLUME.html
48. Meroli S, Passeri D, Servoli L. Energy loss measurement for charged particles in very thin silicon layers. *J Inst Met* (2011) 6:P06013. doi:10.1088/1748-0221/6/06/P06013
49. Alpat B, Ambrosi G, Balboni C, Battiston R, Biland A, Bourquin M, et al. High-precision tracking and charge selection with silicon strip detectors for relativistic ions. *Nucl Instrum Meth A* (2000) 446:522–35. doi:10.1016/S0168-9002(99)01184-5
50. Zuccon P. On behalf of the AMS Tracker collaboration. The AMS silicon tracker: construction and performance. *Nucl Instrum Meth A*(2008) 596:74–8. doi:10.1016/j.nima.2008.07.116
51. Adriani O, Babucci E, Bacchetta N, Bagliesi G, Bartalini P, Basti A, et al. Beam test results for single- and double-sided silicon detector prototypes of the CMS central detector. *Nucl Instrum Meth A* (1997) 396:76–92. doi:10.1016/S0168-9002(97)00750-X
52. Alpat B, Ambrosi G, Azzarello P, Battiston R, Bertucci B, Bourquin M, et al. The internal alignment and position resolution of the AMS-02 silicon tracker determined with cosmic-ray muons. *Nucl Instrum Meth A* (2010) 613:207–17. doi:10.1016/j.nima.2009.11.065
53. Ciarrocchi E, Belcari N, Camarlinghi N, Carra P, Del Guerra A, Francesconi M, et al. The ΔE-TOF detector of the FOOT experiment: experimental tests and Monte Carlo simulations. *Nucl Instrum Meth A* (2019) 936:78–9. doi:10.1016/j.nima.2018.08.117
54. Kraan AC, Battistoni G, Belcari N, Camarlinghi N, Carra P, Ciarrocchi E, et al. Charge identification performance of a ΔE-TOF detector prototype for the FOOT experiment. *Nucl Instrum Meth A* (2020) 958:162422. doi:10.1016/j.nima.2019.162422
55. Galli L, Kraan AC, Ciarrocchi E, Battistoni G, Belcari N, Camarlinghi N, et al. Fragment charge identification technique with a plastic scintillator detector using clinical carbon beams. *Nucl Intrum Meth A* (2020) 953:163146. doi:10.1016/j.nima.2019.163146
56. Scavarda L. On behalf of the FOOT collaboration. Design and performance of the Calorimeter for the FOOT experiment. Il Nuovo Cimento 43 C (2020)123:1–7. doi:10.1393/ncc/i2020-20123-3
57. Scavarda L. On behalf of the FOOT collaboration. The foot experiment: measuring proton and light nuclei fragmentation cross sections up to 700 MeV/A. *Bull Russ Acad Sci Phys* (2020) 84:480–484. doi:10.3103/S1062873820040267
58. Spighi R, Alexandrov A, Alpat B, Ambrosi G, Argiró S, Battistoni G, et al. FOOT: FragmentatiOn of target experiment. *Il Nuovo Cimento C* (2019) 42:134. doi:10.1393/ncc/i2019-19134-6
59. Valle SM, Alexandrov A, Alpat B, Ambrosi G, Argiró S, Battistoni G, et al. FOOT: a new experiment to measure nuclear fragmentation at intermediate energies. *Perspectives in Science* (2019) 12:100415. doi:10.1016/j.pisc.2019.100415
60. Cho WS, Gainer JS, Kim D, Lim SH, Matchev KT, Moortgat F, et al. OPTIMASS: a package for the minimization of kinematic mass functions with constraints. *JHEP* (2016) 01:26. doi:10.1007/JHEP01(2016)026
61. Alexandrov A, Tioukov V, Vladymyrov M. Further progress for a fast scanning of nuclear emulsions with large angle scanning system. *J Inst Met* (2014) 9:C02034. doi:10.1088/1748-0221/9/02/C02034
62. Alexandrov A, Buonaura A, Consiglio L, D'Ambrosio N, De Lellis G, Di Crescenzo A, et al. A new fast scanning system for the measurement of large angle tracks in nuclear emulsions. *J Inst Met* (2015) 11:P11006. doi:10.1088/1748-0221/10/11/P11006
63. Alexandrov A, Buonaura A, Consiglio L, D'Ambrosio N, De Lellis G, Di Crescenzo A, et al. A new generation scanning system for the high-speed analysis of nuclear emulsions. *J Inst Met* (2016) 11:P06002. doi:10.1088/1748-0221/11/06/P06002
64. Alexandrov A, Buonaura A, Consiglio L, D'Ambrosio N, Lellis G, Crescenzo AD, et al. The continuous motion technique for a new generation of scanning systems. *Sci Rep* (2017) 7:7310. doi:10.1038/s41598-017-07869-3
65. De Lellis G, Buontempo S, Di Capua F, Marotta F, Migliozzi P, Petukhov Y, et al. Emulsion Cloud Chamber technique to measure the fragmentation of high-energy carbon beam. *J Inst Met* (2007) 2:P06004. doi:10.1088/1748-0221/2/06/P06004
66. De Lellis G, Buontempo S, Di Capua F, Di Crescenzo A, Migliozzi P, Petukhov Y, et al. Measurements of the fragmentation of Carbon nuclei used in hadron therapy. *Nucl Phys* (2015) 853(1):124–34. doi:10.1016/j.nuclphysa.2011.01.019
67. Alexandrov A, Consiglio L, De Lellis G, Di Crescenzo A, Lauria A, Montesi MC, et al. Measurement of large angle fragments induced by 400 MeV/n carbon ion beams. *Meas Sci Technol* (2015) 26:094001. doi:10.1088/0957-0233/26/9/094001
68. Alexandrov A, De Lellis G, Di Crescenzo A, Lauria A, Montesi MC, Pastore A, et al. Measurements of ^{12}C ions beam fragmentation at large angle with an Emulsion cloud chamber. *J Inst Met* (2017) 12:P08013. doi:10.1088/1748-0221/12/08/P08013

69. National Institute of Standards and Technology, Gaithersburg, MD. Available at: https://www.nist.gov.
70. Agafonova N, Aleksandrov A, Altinok O, Anokhina A, Aoki S, Ariga A, et al. Momentum measuremets by the multiple coulomb scattering method in the OPERA lead-emulsion target. *New J Phys* (2012) 14:013026. doi:10.1088/1367-2630/14/1/013026
71. De Serio M, Ieva M, Simone S, Giorgini M, Sioli M, Sirri G, et al. Momentum measurement by the angular method in the emulsion cloud chamber. *Nucl Instrum Meth A* (2003) 512(3):539–45. doi:10.1016/S0168-9002(03)02016-3

Conflict of Interest: The authors declare that the research was conducted in the absence of any commercial or financial relationships that could be construed as a potential conflict of interest.

frontiers in Physics

REVIEW
published: 10 February 2021
doi: 10.3389/fphy.2020.578492

Linking Microdosimetric Measurements to Biological Effectiveness in Ion Beam Therapy: A Review of Theoretical Aspects of MKM and Other Models

V. E. Bellinzona[1,2], *F. Cordoni*[2,3], *M. Missiaggia*[1,2], *F. Tommasino*[1,2], *E. Scifoni*[2], *C. La Tessa*[1,2] *and A. Attili*[4]*

[1]Department of Physics, University of Trento, Trento, Italy, [2]Department of Physics, TIFPA-INFN, Trento, Italy, [3]Department of Computer Science, University of Verona, Verona, Italy, [4]INFN Sezione di Roma Tre, Roma, Italy

OPEN ACCESS

Edited by:
Yolanda Prezado, INSERM U1021 Signalisation normale et pathologique de l'embryon aux thérapies innovantes des cancers, France

Reviewed by:
Dimitris Emfietzoglou, University of Ioannina, Greece
Anatoly Rosenfeld, University of Wollongong, Australia
Lucas Norberto Burigo, German Cancer Research Center (DKFZ), Germany

***Correspondence:**
A. Attili
andrea.attili@roma3.infn.it

Specialty section:
This article was submitted to Medical Physics and Imaging, a section of the journal Frontiers in Physics

Received: *30 June 2020*
Accepted: *30 November 2020*
Published: *10 February 2021*

Citation:
Bellinzona VE, Cordoni F, Missiaggia M, Tommasino F, Scifoni E, La Tessa C and Attili A (2021) Linking Microdosimetric Measurements to Biological Effectiveness in Ion Beam Therapy: A Review of Theoretical Aspects of MKM and Other Models. Front. Phys. 8:578492. doi: 10.3389/fphy.2020.578492

Different qualities of radiation are known to cause different biological effects at the same absorbed dose. Enhancements of the biological effectiveness are a direct consequence of the energy deposition clustering at the scales of DNA molecule and cell nucleus whilst absorbed dose is a macroscopic averaged quantity which does not take into account heterogeneities at the nanometer and micrometer scales. Microdosimetry aims to measure radiation quality at cellular or sub-cellular levels trying to increase the understanding of radiation damage mechanisms and effects. Existing microdosimeters rely on the well-established gas-based detectors or the more recent solid-state devices. They provide specific energy z spectra and other derived quantities as lineal energy (y) spectra assessed at the micrometer level. The interpretation of the radio-biological experimental data in the framework of different models has raised interest and various investigations have been performed to link *in vitro* and *in vivo* radiobiological outcomes with the observed microdosimetric data. A review of the major models based on experimental microdosimetry, with a particular focus on ion beam therapy applications and an emphasis on the microdosimetric kinetic model (MKM), will be presented in this work, enlightening the advantages of each one in terms of accuracy, initial assumptions, and agreement with experimental data. The MKM has been used to predict different kinds of radiobiological quantities such as the relative biological effects for cell inactivation or the oxygen enhancement ratio. Recent developments of the MKM will be also presented, including new non-Poissonian correction approaches for high linear energy transfer radiation, the inclusion of partial repair effects for fractionation studies, and the extension of the model to account for non-targeted effects. We will also explore developments for improving the models by including track structure and the spatial damage correlation information, by using the full fluence spectrum and by better accounting for the energy-deposition fluctuations at the intra- and inter-cellular level.

Keywords: microdosimetry, microdosimetric kinetic model, relative biological effectiveness, oxygen enhancement ratio, biophysical modeling, ion beam therapy

1 INTRODUCTION

Ion beam therapy is becoming a well-established clinical option for tumor treatment, particularly advantageous for the highly localized dose deposition and for the radiobiological properties [1]. While the first feature is obvious, for the macroscopic energy deposition profile, characterized by the Bragg peak in depth, and also often by a sharper lateral penumbra, due to the small multiple Coulomb scattering of fast and heavy particles, the second one is related to microscopic features of the ionization pattern induced by particle radiation, for different charge and energy, down to the molecular scale of the biological target (DNA). The accurate prediction of relative biological effectiveness (RBE) in different positions of an irradiating field is a fundamental requirement, in order to correctly estimate treatment responses [2]. Moreover, RBE depends on several factors, of different nature, biological, patient, and treatment-specific, because of the complexity of the mechanisms of action underlying tumor and normal tissue responses in radiation therapy. A numbers of models have been presented, historically, to predict RBE, attempting to account for such effects. Among these models, the following four main categories can be identified:

(1) Purely phenomenological models: NIRS[1] mixed beam approach [3–6], mainly used for carbon ion beams.
(2) Dose-averaged LET (LET_D)-based models that exploit a linear relationship between the RBE and the LET_D [7–10], used exclusively for proton beams.
(3) Local effect model (LEM)-based models [11–17], mainly used for heavier ions, such as carbon ions;
(4) More general models based on microdosimetry concepts:

   a. Models based on the microdosimetric kinetic model (MKM), proposed initially by Hawkins in 1994 [18] and then explored and extended till nowadays [19–23];
   b. Other models, such as the repair–misrepair–fixation RMF model [24–26] and phenomenological models based on RBE-weighting functions [27–33].

All the different models present different advantages and limitations. While RBE is not measurable with physical methods, the fourth category allows a strong link with physics measurements through different types of microdosimeters. The present paper is focused on reviewing the modeling of biological effect of protons and other ions used in ion beam therapy based on the microdosimetry concepts with particular emphasis to the MKM, a widely used model to predict the cell survival and the RBE by using microdosimetric data. This topical review is organized as follows: the fundamental microdosimetric quantities [34, 35], required for addressing the problem, are defined in **Section 2** together with a focus on relevant experimental quantities. Then, the original formulation of MKM is presented in **Section 3** with its theoretical bases (**Section 3.1**) and followed by the main extensions such as non-Poisson and saturation corrections [19, 20] (**Section 3.5**), the incorporation of a track model [21], a variable β parameter deriving from the effects of the lesion yield fluctuations in the cell nucleus and domains, [22, 23] in **Section 3.8**, and the generalization of the model in case of a time structured irradiation introduced in **Section 3.7**. The available experimental *in vitro* and *in vivo* validations are also reported for each extensions. **Figure 1** represents a conceptual scheme of the main MKM formulations and extensions presented in this paper. Further, an example of treatment planning systems (TPS) implementation of the MKM [36] will be given in **Section 3.6**. Other applications of the MKM, such as the oxygen enhancement ratio (OER) modeling [37, 38] and the incorporation of non-targeted effects [39] will be described in **Section 3.9**. Finally, other models based on microdosimetry as well, i.e., the distribution function by Loncol et al. [40] and the RMF model [24, 25], will be presented in **Section 4**.

[1]National Institute of Radiological Sciences (NIRS, Chiba, Japan).

2 MICRODOSIMETRIC DISTRIBUTIONS AND THEIR MOMENTS

The main microdosimetric quantities of interest are the *specific energy z* and *lineal energy y* [34, 41–43]. The *specific energy z* is the ratio between energy imparted by ionizing radiation ε and the mass *m* of the matter that has received the radiation, that is,

$$z = \frac{\varepsilon}{m}. \tag{1}$$

The energy imparted ε may be due to one or more energy deposition events, i.e., due to one or more statistically independent particle tracks. The *lineal energy y* is the ratio between energy imparted to the matter in a volume of interest by a single energy-deposition event, ε_1, and the mean chord length in that volume, $\bar{l}$, that is,

$$y = \frac{\varepsilon_1}{\bar{l}}. \tag{2}$$

The stochastic nature of ε and ε_1 implies that also *z* and *y* are stochastic quantities. In the following, given a probability density distribution $f(z)$, we will assume that the probability that a specific energy *z* is produced in the interval $[z_a, z_b]$ is given by

$$\int_{z_a}^{z_b} f(z)dz. \tag{3}$$

When dealing with *specific energy spectra*, it is important to distinguish between the *single-event distribution* and the *multi-event distribution*. It is worth stressing that, although experimental microdosimetry determines single event quantities such as the ε_1 or the *lineal energy y*, the starting point for models are multi-event quantities such as the *specific energy z* and its distribution.

The *single-event distribution*, denoted by $f_1(z)$, is the probability distribution of *z* conditioned to the fact that precisely a single-event happened. The single-event distribution is the building block to define the more-general *n*-event distribution $f_n(z)$ and the *multi-event distribution* $f(z)$.

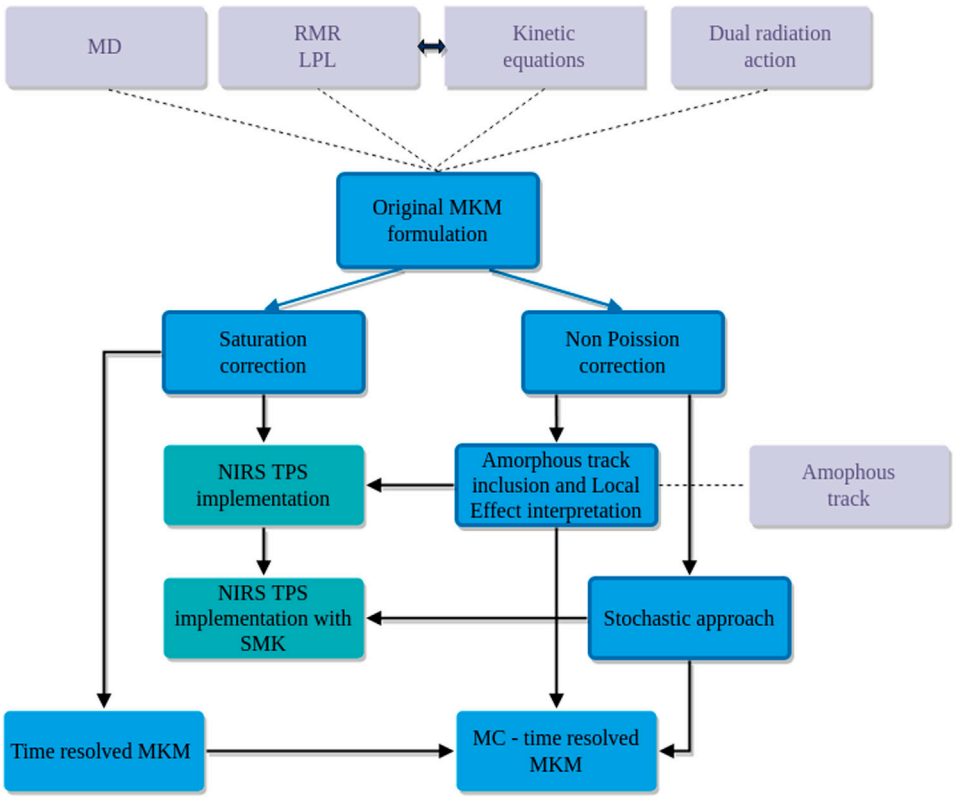

FIGURE 1 | Conceptual map of the evolution of some of the microdosimetric kinetic models (blue) considered in this review. Some of these models are currently used for RBE and RBE-weighted dose evaluations in TPS applications (dark cyan). Solid lines refer to the consequentialism of the corrections and extensions while the dotted lines mark the theoretical bases of the considered formulation (light gray color).

The n-event distribution $f_n(z)$, that is, the probability distribution conditioned to the fact that precisely n events occurred, can be computed as the n-fold convolution of the single-event distribution $f_1(d)$, as follows:

$$\begin{aligned} f_2(z) &:= \int_0^\infty f_1(z')f_1(z-z')dz', \\ &\cdots, \\ f_n(z) &:= \int_0^\infty f_1(z')f_{n-1}(z-z')dz', \end{aligned} \tag{4}$$

see [42] for details.

Using the n-event distributions defined above, we can define the general *multi-event distribution* as

$$f(z;\lambda_n) := \sum_{n=0}^{\infty} p(n;\lambda_n) f_n(z), \tag{5}$$

with $p(n;\lambda_n)$ an integer valued probability distribution with average λ_n, meaning that

$$\lambda_n := \sum_{n=0}^{\infty} np(n;\lambda_n).$$

The *multi–event distribution* $f(z;\lambda_n)$ plays a crucial role in the development of microdosimetric-based radiobiological models. It is worth noticing that $f(z;\lambda_n)$ depends on the number of events n only through $p(n;\lambda_n)$, which is independent of specific energy z. Also, given $p(n;\lambda_n)$, the single-event distribution f_1 completely determines the multi-event distribution $f(z;\lambda_n)$.

Typically, since events are statistically independent, $p(n;\lambda_n)$ is assumed to be a Poisson distribution with mean value λ_n, so that **Eq. (5)** becomes

$$f(z;\lambda_n) := \sum_{n=0}^{\infty} e^{-\lambda_n} \frac{\lambda_n^n}{n!} f_n(z). \tag{6}$$

Denoting by $\langle z \rangle$ the first moment of the distribution $f(z;\lambda_n)$, formally

$$\langle z \rangle := \int_0^\infty z f(z;\lambda_n) dz, \tag{7}$$

it follows that the following relation holds true,

$$\langle z \rangle = \lambda_n z_F, \tag{8}$$

being z_F the *frequency-average* of the single-event specific energy defined as

$$z_F := \int_0^\infty z f_1(z) dz, \tag{9}$$

see [42], Chapter II. In microdosimetry, $\langle z \rangle$ is often identified with the absorbed dose D; we shall use this identification in the following of the paper.

Above argument, with particular reference to **Eq. (8)**, yields the form for the average value λ_n of the *multi–event distribution* to be

$$\lambda_n = \frac{D}{z_F}, \tag{10}$$

see [34, 42]. Again, in the following, if not differently specified, we will consider λ_n to be defined as in **Eq. (10)**.

Further computations, see [34, 42], shows that regarding the second moment it holds

$$\int_0^\infty z^2 f(z;\lambda_n) dz = D^2 + z_D D, \tag{11}$$

with z_D the *dose-average* of the single-event specific energy

$$z_D := \frac{1}{z_F}\int_0^\infty z^2 f_1(z) dz = \frac{\int_0^\infty z^2 f_1(z) dz}{\int_0^\infty z f_1(z) dz}. \tag{12}$$

Notation and computations performed in the current section will be extensively used through the work to formally derive analytical solution for some relevant biological endpoints, typically the cell–survival probability, starting from a mathematical model for DNA damage.

In the following, we assume that a cell nucleus is divided into N_d domains, so that the above microdosimetric distributions will be used both on single-domain and on the whole cell nucleus. In particular, the superscript (c, d) will denote that the corresponding quantity, such as a microdosimetric distribution or a corresponding average value, is considered on the domain d of the cell c. Further, the subscript n denotes that microdosimetric distributions are on the cell-nucleus, whereas if no subindex is specified, it is assumed that the corresponding distribution is on the domain.

In order to make computations less heavy as possible, whenever we will say that we average a function $g(z)$ over all domains of a cell nucleus, denoted for short by $\langle g \rangle_d^{(c)}$, it formally means

$$\langle g \rangle_d^{(c)} := \frac{1}{N_d}\sum_{d=1}^{N_d}\int_0^\infty g(z) f^{(c,d)}(z;z_n)\,\mathrm{d}z, \tag{13}$$

where $f^{(c,d)}(z;z_n)$ denotes the probability density of z in a domain for cell with nucleus specific energy z_n. Similarly, by averaging over all cell population function $g_n(z)$ defined over a nucleus, denoted by $\langle g_n \rangle_c$, we mean

$$\langle g_n \rangle_c := \frac{1}{N_c}\sum_{c=1}^{N_c}\int_0^\infty g_n(z) f_n^{(c)}(z;D)), \tag{14}$$

where N_c is the total number of the considered cells and $f_n^{(c)}(z;D)$ denotes the probability density of z in a nucleus for a population of cells irradiated with macroscopic dose D. Notice that in practical computations of an irradiated population of cells, such as those described in the immediate next sections, the probability densities are reasonably considered equals among different cells and domains. In this case, we will drop the indexes c and d and the sums in **Eqs (13)** and **(14)** can be carried out implicitly:

$$\langle g \rangle_d = \int_0^\infty g(z) f(z;z_n)\,\mathrm{d}z, \tag{15}$$

$$\langle g_n \rangle_c = \int_0^\infty g_n(z) f_n(z;D))\mathrm{d}z. \tag{16}$$

2.1 Experimental Quantities

In order to account for the different densities and sizes of the sites of radiobiological interests. (e.g., the cell nucleus and the domain), the specific energy z used in the models as described in the following sections can be obtained experimentally through the *lineal energy* y defined in Eq. (2).

The lineal energy can be measured through a microdosimeter detector, where the most frequently used are the tissue-equivalent proportional counters (TEPC) [44–47]; analogous information can be achieved also by solid-state detectors [48, 49] and gas electron multiplier (GEM) detectors [50, 51], recently investigated for their use in microdosimetric measurements [52, 53]. The relationship between $\bar{l}$ of the tissue-equivalent volume of the microdosimeter, from which the lineal energy is calculated, and the physical mean chord of the detector, $\bar{l}_{\mathrm{det}}$, is given approximately by

$$\bar{l} = \bar{l}_{\mathrm{det}}\frac{\rho_{\mathrm{det}}}{\rho}, \tag{17}$$

where ρ and ρ_{det} are the densities of the tissue and the detector material, respectively. For more general conversion methods of microdosimetric spectra between different materials and shapes see, for example, [54, 55], for an MC-based method.

The theoretical single-event imparted energy, z_1, can be estimated from the lineal energy y as

$$z_1 = y\bar{l}_t / m_t, \tag{18}$$

where $\bar{l}_t$, m_t are the mean chord length and the mass of the biological site of interest, respectively. The subscript t is used in this context to indicate the tissue in terms of material, mass, and geometry of the biological site. The single-event dose-averaged specific energy z_D can be obtained from the mean-dose lineal energy y_D as

$$z_D = \frac{\bar{l}_t}{m_t y_F}\int_0^\infty y^2 f(y)\,\mathrm{d}y = \frac{\bar{l}_t}{m_t} y_D, \tag{19}$$

where y_F is the frequency-average lineal energy.

In the case of a spherical volume with density $\rho_t = 1$ g/cm^3, the specific energy z_1 is linked to the lineal energy y [56] as

$$z_1\,(\mathrm{Gy}) = 0.204 \times \frac{y\,(\mathrm{keV}/\mu\mathrm{m})}{[2r_{\mathrm{det}}\,(\mu\mathrm{m})]^2}, \tag{20}$$

where the constant factor is due to the Gy-keV conversion (1 Gy= 1.6×10^{-16} keV) and to the consideration that the mean chord length in the case of a sphere is $\bar{l} = 4/3 r_{det}$.

3 MICRODOSIMETRIC KINETIC MODEL

The microdosimetric kinetic (KM) model has been developed by Roland B. Hawkins [18] by taking inspiration from the theory of dual radiation action (TDRA) [57, 58], the repair-misrepair model [59, 60], and the lethal-potentially lethal (LPL) model [61, 62]. In the following sections, after a brief description of the historical bases of the model and the details of its original formulation, we compare and contrast the more recent developments of the model.

3.1 Historical Bases

This section presents a brief explanation of the theoretical formulations on which the considered models are based on. In the theory of dual radiation action (TDRA), the concept of *dual radiation action* is introduced as a process in which cellular lesions are produced as a result of the interaction of pairs of sublesions that are molecular alterations produced by ionizing radiation that in turn results in an observable cellular effect such as a chromosome aberration or cell reproductive death. The TDRA in its original formulation developed for neutron irradiation and then further generalized [57] assumes that, after the cell irradiation, the number of lethal lesions ϵ in a small volume of the cell nucleus, defined *site*, is proportional to the square of the specific energy z in that site.

$$\epsilon(z) = kz^2. \tag{21}$$

By evaluating the expectation value of z^2 (**Eq. 11**), it is possible to derive a linear-quadratic relation between ϵ and the dose:

$$\epsilon(D) = k\langle z^2\rangle = k\left(z_D D + D^2\right) = k(z_D + D)D. \tag{22}$$

The interpretation of **Eq. (22)** is that the number of sublesions is proportional to D and the mean energy concentration around the individual sublesions is proportional to $(z_D + D)$. Within the bracket, z_D represents the energy concentration produced by the same particle track (*intratrack action*), and D represents the contribution from other particle tracks (*intertrack action*). A problem in **Eq. (22)** arise when one has to account the possibility of a non-vanishing linear term in the dose (observable for low doses) even for sparsely ionizing radiation, such as photons, since the term z_D is expected to be negligible for such radiation. This is obtained by generalizing **Eq. (21)** by including an additional linear term:

$$\epsilon(z) = k\left(\lambda_0 z + z^2\right), \tag{23}$$

from which one obtains the dose dependence:

$$\epsilon(D) = k\left((z_D + \lambda_0)D + D^2\right). \tag{24}$$

An important additional assumption that drives the dual action process is that sublesions can be produced throughout the nucleus of the cell but can combine with appreciable probability only over distances smaller than the dimension of the nucleus. This effect of sublesion proximity on the formation of lethal lesions was incorporated in the TDRA by the concept of the *sites* within which such sublesions can combine. In a generalization of the TDRA [58], the interaction probability of sublesions has been also further refined using an explicit function of their separation.

MKM inherits the concept of damage time evolution for the repair or conversion into a lethal irreparable lesion (chromosome aberration) [18, 63, 64] of the primary potentially lethal radiation induced lesions in DNA from the *repair–misrepair (RMR) model*, developed by Tobias *et al.* to interpret radiobiological experiments with heavy ions [59, 60]. The RMR model considers that the amount of DSBs in the DNA, $U(t)$, is linearly proportional to the radiation dose-rate $\dot{D}(t) = \mathrm{d}D(t)/\mathrm{dt}$; a number of DSBs evolve in lethal lesions, $L(t)$, while most breaks are successfully repaired with a first-order process. The model includes also the possibility of a misrepair as a second-order process since it involves two broken DNA strands to form a chromosomal aberration. The idea of misrepair was initially applied by Lea and Catcheside [65] to describe the formation of chromosome aberrations in *Tradescantia*.

These assumptions yield the following kinetic equations:

$$\begin{aligned}\frac{\mathrm{d}U}{\mathrm{d}t} &= \underbrace{\delta\dot{D}}_{\text{damage}} - \underbrace{\lambda U}_{\text{repair}} - \underbrace{\kappa U^2}_{\text{misrepair}},\\ \frac{\mathrm{d}L}{\mathrm{d}t} &= \underbrace{(1-\phi)\lambda U}_{\text{unsuccessful repair}} + \underbrace{\sigma\kappa U^2}_{\text{lethal misrepair}},\end{aligned} \tag{25}$$

where δ is the number of DSBs induced per Gy of radiation, λ is the rate at which DSBs are repaired, κ is the rate constant for second-order DSB interaction, and ϕ is the fraction of simple repairs that are successful. The fraction of misrepairs that result in a lethal lesion is σ.

Like the RMR model, the *lethal-potentially lethal (LPL)* model [61, 62] accounts that the damages caused by ionizing radiation at the molecular level and contributing to cell death can be separated into two broad classes (i) that which has the potential of being lethal, $P(t)$ (by fixing or binary misrepair) but also can be repaired correctly and (ii) that which is lethal *ab initio* and cannot be repaired correctly, $L(t)$. Both lesions are linearly proportional to the radiation dose-rate [66], and after a prescribed time, the remaining potentially lethal lesions become lethal as described in the following equations:

$$\begin{aligned}\frac{\mathrm{d}P}{\mathrm{d}t} &= \underbrace{\delta\eta\dot{D}}_{\text{reparable damage}} - \underbrace{\lambda P}_{\text{repair}} - \underbrace{\kappa P^2}_{\text{misrepair}},\\ \frac{\mathrm{d}L}{\mathrm{d}t} &= \underbrace{\delta(1-\eta)\dot{D}}_{\text{irreparable damage}} + \underbrace{\kappa P^2}_{\text{lethal misrepair}},\end{aligned} \tag{26}$$

where η is the amount of radiation induced DSBs that are reparable, while all the other parameters correspond in meaning to the ones in **Eq. (25)**.

The solutions of the RMR and the LPL models are similar. However, in contrast to the RMR, the LPL predicts that the probability of the interaction between potentially lethal lesions is strongly dependent to the dose-rate and becomes negligible for low dose-rates, where only the channel of the direct creation of lethal events through δ dominate.

3.2 Original Formulation and General Considerations

The MKM computes the cell survival in a way that emphasizes subcellular microdosimetry while abstracting the specific description and modeling of the radiation-induced damage to the cell by using the general categories of lethal and potentially lethal lesions as defined in [61]. More specifically, the MKM is based on the following assumptions [18, 67, 68]:

(1) The cell nucleus is the sensitive target and it is divided into N_d sub-units, called domains, similar to the sites of TDRA. In general, domains have a variety of shapes that fit together to fill the nucleus. In the case of mammalian cells, the domain diameter is usually considered to be in the range $0.5 \le d_d \le 1.0\,\mu$m and the number of domains per nucleus is in the order of few hundreds.
(2) Radiation can create two different types of DNA damages, called of type I and II.
(3) Type I lesions represent damage that cannot be repaired, for this reason will be also called lethal lesion. On the contrary, type II lesions, also called sub-lethal or potentially-lethal lesions, can be repaired or converted into a lethal lesion either by spontaneous conversion or by binary combination with another sub-lethal lesion.
(4) Type I and II lesions are confined to the domain in which they are created. This assumption defines a sub-nuclear correlation length among lesions in a way that the interaction of two lesions can happen only if they are in close spatial proximity. Specifically, a pair of type II lesions can combine to form a type I lesion only if they are created in the same domain; a remark on this assumption is needed. The idea behind the division of a cell into subvolumes arises because couples of type II lesions are all likely to happen in a short time period, even for lesions that are far away in the cell-nucleus. In order to overcome such a problem, a possible approach is to divide the nucleus into smaller subdomains so that interactions might happen solely inside a single volume, as it is assumed in the MKM. It is important to stress the key role that the choice of such domains plays. In fact, if too big domains imply that far away lesions can interact, on the contrary, too small domains yield that the overall number of lesions inside a single domain is so small that couple interactions are less likely to happen. Therefore, the choice of the best possible division of the cell nucleus into smaller domain is a key aspect of the model and different choices of domains can in principle lead to different results. A possible solution to reduce the sensitivity of the model from the arbitrary choice of the domains is to assume that interactions are possible also within different domains, allowing therefore lesions to move from one domain to another or pairs of lesions to interact if in adjacent domains.
(5) The initial number of type I and II lesions in a single domain d is proportional to the specific energy z in the domain.

If above assumptions hold, then the following further assumption is made regarding the reproductive survival of the cell:

(6) If at least one domain contains a lethal lesion, then the whole cell is "dead."

It has to be noted that, while the MKM assumptions reported in this section are general, in many studies [69, 70], the lethal lesions are intended to represent a specific complex DNA damage (e.g., lethal chromosome aberrations) that cannot be repaired, whereas the creation of sub-lethal lesions are explicitly associated to the induction of double-strand breaks (DSB) that can be repaired.

Following the MKM notation, we denote by $x_I^{(c,d,z)}(t)$ and $x_{II}^{(c,d,z)}(t)$ the time-dependent average number of type I and type II lesions for a cell-domain (c,d) caused by an acute dose $z^{(c,d)}$ at $t = 0$ deposited in the cell c and domain d. Starting from the concept, introduced in the TDRA, that a cell experiences a randomly varying dose in a microscopic volume [34, 41], the microscopic specific energy $z^{(c,d)}$ is considered as a random variable with $\langle\langle z^{(c,d)}\rangle_d\rangle_c = D$, the macroscopic dose experienced by the cell population.

Type II lesions are assumed that can be repaired with a constant repairing rate r or can be converted to irreparable lesions through a first order process with constant rate a, or at the second order, representing pairwise combinations, with constant rate b. The average number of type I and II lesions at time 0 is proportional to the amount of specific energy $z^{(c,d)}$ with factors λ and κ. These assumptions formally define the following set of coupled ODE similar in concept to **Eq. (25)**:

$$\begin{cases} \dot{x}_I^{(c,d,z)} = a x_{II}^{(c,d,z)} + b\left(x_{II}^{(c,d,z)}\right)^2, \\ \dot{x}_{II}^{(c,d,z)} = -(a+r) x_{II}^{(c,d,z)} - 2b\left(x_{II}^{(c,d,z)}\right)^2, \end{cases} \tag{27}$$

subject to the initial average number of lesions

$$x_I^{(c,d,z)}(0) = \lambda z^{(c,d)}, \quad x_{II}^{(c,d,z)}(0) = \kappa z^{(c,d)}. \tag{28}$$

In the case of ion radiation, typically the rate of pairwise combination between type II lesions is negligible with respect to the first order evaluation of x_{II} for low dose [67], that is,

$$2b\left(x_{II}^{(c,d,z)}\right)^2 \ll (a+r) x_{II}^{(c,d,z)}, \tag{29}$$

so that the time-evolution of the average number of type II lesion can be rewritten as

$$\dot{x}_{II}^{(c,d,z)} = -(a+r) x_{II}^{(c,d,z)}. \tag{30}$$

The solution to **Eq. (30)** can be seen to be

$$x_{II}^{(c,d,z)}(t) = \kappa z^{(c,d)} e^{-(a+r)t}. \tag{31}$$

Substituting **Eq. (31)** into the kinetic **Eq. (27)** and integrating $x_{II}^{(c,d,z)}$ with respect to time, it follows that

$$x_I^{(c,d,z)}(t) = \lambda z^{(c,d)} + a\kappa z^{(c,d)}\left(\frac{1 - e^{-(a+r)t}}{a+r}\right) + b\kappa^2\left(z^{(c,d)}\right)^2\left(\frac{1 - e^{-2(a+r)t}}{2(a+r)}\right). \tag{32}$$

An example of the temporal evolution of lesions in a cell is depicted in **Figure 2**.

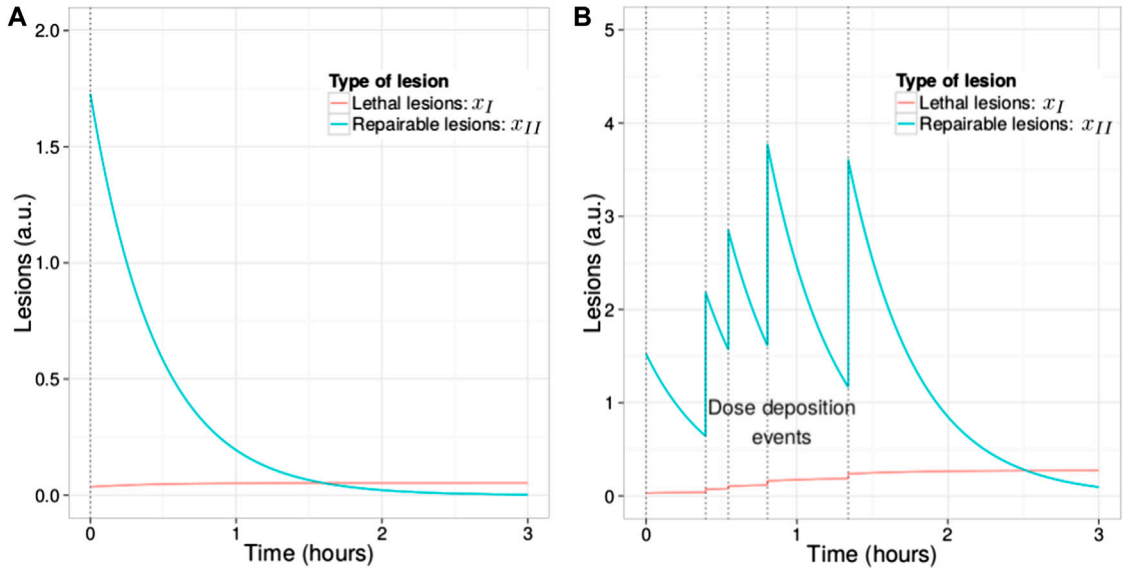

FIGURE 2 | Time evolution of x_I and x_{II} damages for a single instantaneous irradiation as described by **Eqs (31)** and **(32)**, respectively **(A)**. Generalization of the temporal evolution for any time structured irradiation as describe in **Sections 3.7 and 3.8.1**. The dotted vertical lines represent the energy deposition events in the cell nucleus due to the passage of ionizing particles **(B)**. Figure from [71].

It is important to remark that the exponential decay in **Eq. (32)** derives from the assumption of first order repair kinetics and that it could likely represents an approximation of more complex repair kinetics present in the real cell [72–75]. Postulating that the total number of lesions $x_I(t) + x_{II}(t) \sim N_{\mathrm{DSB}}(t)$ describes specifically the number of double strand breaks (DSBs) in the DNA, the repair kinetics represented in **Eq. (32)** can be verified through H2AX phosphorylation mapping experiments (γ-H2AX) [76, 77]. In the case of high-LET particle irradiation, such as carbon ions, the presence of a plateau (offset) in the observed $N_{\mathrm{DSB}}(t)$ [75, 78, 79] suggests the presence of irreparable complex clustered damage that can be related directly to the parameter λ of the kinetic equations and hence to the linear parameter α_0 of the macroscopic cell survival LQ formulation that will be introduced in the following (see **Eqs 35** and **39**).

In order to connect the above explicit solution of **Eqs (31)** and **(32)**, i.e., the average number of type I and II lesions given a certain energy deposition $z^{(c,d)}$, to the survival probability, one more fundamental assumption must be made:

(7) The lethal lesion distribution given a specific energy z follows a Poisson distribution.

Under the Poisson distribution assumptions stated above, the probability that the domain d does not contain a lethal lesion at time $t \to \infty$ when exposed to the specific energy $z^{(c,d)}$, denoted by $s^{(c,d)}(z^{(c,d)})$, can be computed as the probability that the random outcome of a Poisson random variable is null. Therefore, $s^{(c,d)}$ is given by

$$s^{(c,d)}\left(z^{(c,d)}\right) = e^{-\lim_{t\to\infty} x_I^{(c,d,z)}(t)}. \tag{33}$$

Using **Eq. (32)**, it can be seen that the average number of lethal lesion given $z^{(c,d)}$ as $t \to \infty$ can be computed as

$$\lim_{t\to\infty} x_I^{(c,d,z)}(t) = \left(\lambda + \frac{a\kappa}{a+r}\right) z^{(c,d)} + \frac{b\kappa^2}{2(a+r)}\left(z^{(c,d)}\right)^2, \tag{34}$$

so that the log-survival for the domain d is given by

$$\log s^{(c,d)}\left(z^{(c,d)}\right) = -Az^{(c,d)} - B\left(z^{(c,d)}\right)^2, \tag{35}$$

with A and B defined as

$$A = \left(\lambda + \frac{a\kappa}{a+r}\right), \quad B = \frac{b\kappa^2}{2(a+r)}. \tag{36}$$

We remark that these constants are independent of the domain d and specific energy $z^{(c,d)}$ in the domain d.

Indicating with $S_n^{(c)}(z_n^{(c)})$ the probability of the reproductive survival of the cell c that has received exactly a specific energy $z_n^{(c)}$ in the nucleus, the log-survival of this quantity, $-\log S_n^{(c)}(z_n) = x_{I,n}^{(c)}(z_n)$, represents the expected number of lethal lesions in the whole cell nucleus and can be therefore evaluated by summing of the single-domain log-survival $-\log s^{(c,d)}(z) = x_I^{(c,d)}(z)$ over all the domains of the cell or, equivalently, by formally using the average of this quantity over the domains. Assuming that the probability density function of specific energy is the same over all domains and cell, we can drop the index c and d and use **Eq. (15)** to write

$$\begin{aligned}\log S_n(z_n) &:= -x_{I,n}(z_n)\\ &= -N_d\langle x_I(z)\rangle_d = -N_d\langle \log s(z)\rangle_d\\ &= -N_d\left(A\langle z\rangle_d + B\langle z^2\rangle_d\right)\\ &= -N_d A\int_0^\infty z f(z;z_n)\,\mathrm{d}z - N_d B\int_0^\infty z^2 f(z;z_n)\,\mathrm{d}z,\end{aligned} \tag{37}$$

where $f(z;z_n)$ denotes the probability density of z in a domain for a cell with a mean specific energy in the nucleus z_n. In particular, as shown in **Section 2**, the following holds:

$$z_n = \langle z \rangle_d = \int_0^\infty z f(z; z_n) dz. \tag{38}$$

Using **Eqs (11)** and **(12)** derived in **Section 2**, the log survival in **Eq. (37)** can be written as

$$\log S_n(z_n) = -(\alpha_0 + z_D \beta_0) z_n - \beta_0 (z_n)^2, \tag{39}$$

with $\alpha_0 := N_d A$ and $\beta_0 := N_d B$. Also, z_D is the dose-averaged z per event in a domain, obtained from **Eq. (12)** applied to the domain (compare for reference **Eq. 24** of the TDRA).

Notice that in **Eq. (37)**, we have used the notation $f(z; z_n)$ to denote the *multi-event distribution*, rather than $f(z; \lambda_n)$, as done in **Section 2**. This is due to the fact that, since the following relation holds true,

$$\lambda_n = \frac{z_n}{z_F}, \tag{40}$$

we have preferred to specify the dependence upon the *multi-event distribution* average.

In order to obtain the cell survival $S(D)$ for a population of cells irradiated with macroscopic dose D, the quantity $S_n(z_n)$ defined in **Eq. (37)** should be averaged accounting for the distribution of the specific energy z_n over the cell population. In terms of the logarithm of the cell population survival, log$S$, under again the assumption that all the cells have the same probability distribution of specific energy z_n, this can be written as

$$\begin{aligned} \log S(D) &:= \log \langle S_n(z_n) \rangle_c \\ &= \log \left(\int_0^\infty S_n(z_n) f_n(z_n; D)\, \mathrm{d}z_n \right), \end{aligned} \tag{41}$$

where similar to above, we have denoted by $f_n(z_n; D)$ the probability density of z_n for a macroscopic absorbed dose D over the cell population, i.e.,

$$D = \langle z_n \rangle_c = \int_0^\infty z_n f_n(z_n; D)\, \mathrm{d}z_n. \tag{42}$$

We remark that **Eq. (41)** is fundamentally different from **Eq. (37)** since it considers the average of the argument of the logarithm, whereas in **Eq. (37)**, the average of the logarithm has been taken. This basically indicates that, due to the stochastic nature of z_n, the distribution of lethal lesions $\log S_n(z_n)$ over the cell population is in general non-Poisson and hence that the log of the survival cannot be directly related to the average number of lethal lesions per cell, $\log S(D) \neq -\langle x_{I,n}(z_n) \rangle_c$. However, provided that the variance of z_n is small, a Poisson approximation is assumed and the same procedure used to obtain **Eq. (37)** can be used. In this approximation, **Eq. (41)** can be written as follows:

$$\begin{aligned} \log S(D) &= \log \langle S_n(z_n) \rangle_c \\ &\approx -\langle x_{I,n}(z_n) \rangle_c = \langle \log S_n(z_n) \rangle_c \\ &= \int_0^\infty \log(S_n(z_n)) f_n(z_n; D)\, \mathrm{d}z_n \\ &= -(\alpha_0 + (z_D + z_{n,D}) \beta_0) D - \beta_0 D^2, \end{aligned} \tag{43}$$

with $z_{n,D}$ the dose-averaged z_n in the nucleus per event. All the quantities $z_{n,D}$, z_D, and $z_n \approx \langle z_n \rangle_c = D$ are assumed to be the same for each cell or domain. All other notations are used as previously introduced. Since the size of the domain is usually much smaller than the size of the nucleus, it holds that $z_{n,D} \ll z_D$ (see [67]) so that we eventually obtain

$$\log S = -\alpha_P D - \beta D^2, \tag{44}$$

with

$$\alpha_P := \alpha_0 + z_D \beta_0, \quad \beta := \beta_0. \tag{45}$$

where the subscript P indicates that the relationships hold when the assumption of Poisson distribution of lethal lesions among the irradiated cell population is reasonable, i.e., for low-LET irradiation, as it is discussed in the following section.

A further refinement of the MKM kinetic equations involves a fourth type of possible interaction that happens at time t_r. The following is assumed:

(8) After a time $t_r > 0$, all the remaining sub-lethal lesions are automatically transformed into lethal lesions.

The mathematical formulation of the main kinetic equations remain the same as in **Eqs (27)–(32)** in the time interval $t \in [0, t_r)$. As soon as t_r passes, all type II lesions that have not been either repaired or converted into type I lesion, will immediately be converted into type I lesions, meaning

$$x_{II}(t) = 0, \quad t > t_r. \tag{46}$$

The solution for the average number of type I lesions can be now explicitly found for $t > t_r$, adding all type II lesions that persisted after t_r passes, that is,

$$x_I^{(c,d,z)}(t) = x_I^{(c,d,z)}(t) + x_{II}^{(c,d,z)}(t_r), \tag{47}$$

so that we obtain

$$\begin{aligned} \lim_{t \to \infty} x_I^{(c,d,z)}(t) &= \lim_{t \to \infty} x_I^{(c,d,z)}(t) + x_{II}^{(c,d,z)}(t_r) \\ &= \left(\lambda + \frac{a\kappa}{(a+r)} + \frac{\kappa r}{(a+r)} e^{-(a+r)t_t} \right) z^{(c,d)} \\ &\quad + \frac{b\kappa^2}{2(a+r)} \left(1 - e^{-2(a+r)t_r}\right) \left(z^{(c,d)}\right)^2. \end{aligned} \tag{48}$$

Proceeding as above, taking therefore the average over all cell domains and cell population, we obtain the generalization of **Eq. (44)** to be

$$\log S = -\alpha D - \beta D^2, \tag{49}$$

with

$$\begin{cases} \alpha := \overline{\alpha}_0 + z_D^{(c,d)} \overline{\beta}_0, \quad \beta := \overline{\beta}_0 \\ \overline{\alpha}_0 := N_d \left(\lambda + \frac{a\kappa}{(a+r)} + \frac{\kappa r}{(a+r)} e^{-(a+r)t_t} \right), \\ \overline{\beta}_0 := N_d \frac{b\kappa^2}{2(a+r)} \left(1 - e^{-2(a+r)t_r}\right). \end{cases} \tag{50}$$

3.3 Link to the Radiobiological Observables

From **Eqs (44)** and **(45)**, it is possible to obtain the direct link of the model to the phenomenological LQ formulation of the cell

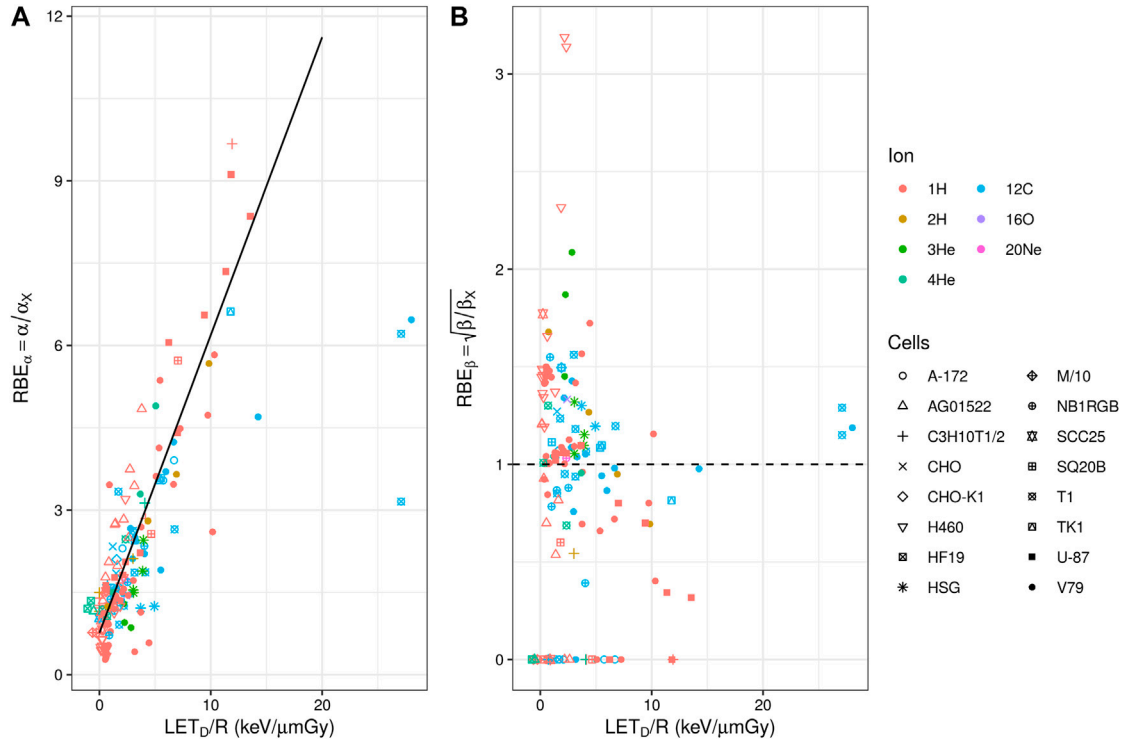

FIGURE 3 | (A) Experimental *in vitro* RBE$_\alpha$ (panel a) and RBE$_\beta$ (panel b) vs. LET$_D$/*R*. The data have been taken from the Particle Irradiation Data Ensemble (PIDE v3.2) database [82]. The continuous line in **(A)** is the fit of the linear Poisson solution of the MKM (**Eq. 53**) carried out in the low-LET region (LET$_D$ < 20 keV/µm) for ion irradiation with charge $Z \leq 11$. The dashed line in **(B)** corresponds to the constant RBE$_\beta$ = 1.

survival. The α coefficient is therefore explicitly dependent on the radiation quality through a single term, the dose-averaged specific energy per event z_D, that can be related to microdosimetric measurements (**Eq. 19**). It has to be noted that, in this formulation of the MKM, there is no explicit dependence to the radiation quality in the quadratic coefficient β_0 that is considered constant analogously to the result of the TDRA [57]. The latter is an approximation of the model that is in contrast with experimental observations [80–82] although in many cases, considering in particular the experimental uncertainties associated to the β_0 determination (see for example **Figure 3**), and it is assumed to be reasonable. In an evolution of the model which accounts for the stochastic aspects of the irradiation, as described in **Section 3.8**, this approximation will be relaxed and the β coefficient will be considered dependent on the quality of the radiation.

From the knowledge of the LQ parameters, it is possible to derive the dose (D) and radiation quality (z_D) dependent RBE [83, 84]:

$$\mathrm{RBE}(D, z_D) = \frac{R}{2D}\left(-1+\sqrt{1+\frac{4}{R}\left(\mathrm{RBE}_\alpha(z_D)D+\frac{\left(\mathrm{RBE}_\beta D\right)^2}{R}\right)}\right), \quad (51)$$

where $R = \alpha_X/\beta_X$, $\mathrm{RBE}_\alpha(z_D) = \alpha(z_D)/\alpha_X$, and $\mathrm{RBE}_\beta = \sqrt{\beta/\beta_X}$, and α_X and β_X are the phenomenological LQ coefficient for the photon reference radiation.

Since the parameters α_0 and β_0 are assumed to be independent on the radiation quality and $\beta = \beta_0$, it is possible to identify $\alpha_0 = \alpha(\mathrm{LET} \to 0)$ and $\beta_0 \simeq \beta_X$ ($\mathrm{RBE}_\beta \simeq 1$).

In the case of LET low enough that lethal lesions are Poisson distributed, it is possible to write

$$\mathrm{RBE}_\alpha = \frac{\alpha_P}{\alpha_X} = \frac{\alpha_0}{\alpha_X} + \frac{\beta_0}{\alpha_X} z_D^{(c,d)} \approx \frac{\alpha_0}{\alpha_X} + \frac{1}{R} z_D, \quad (52)$$

where the ratio R can be derived from a nonlinear regression analysis of measured cell survival data for a low-LET reference radiation. **Equation (52)** can be generalized as

$$\mathrm{RBE}_\alpha = k_1 + \frac{k_2}{R} y_D, \quad (53)$$

where k_1 and k_2 are phenomenological parameters. Since z_D is proportional to the dose-averaged lineal energy y_D (**Eq. 19**), **Eq. (53)** is analogous to the linear RBE models based on the dose-averaged LET (LET$_D$) used for protons [7–10]. Following the MKM model premises, **Eq. (53)** could also be generally used for other ions to describe the linear growth of the RBE as a function of the y_D (or LET$_D$) in the low-LET region (see **Figure 3**). However, the linear dependence on the LET fails to be adequate in the region of mid- and high-LET as found in experimental studies [82]. In these regions, further corrections to the MKM are used to reproduce the experimental observations. Different corrective approaches

for high-LET irradiation are described in the following sections.

3.4 Non-Poisson Correction

In the approximation introduced in **Eq. (43)**, it is assumed that the variance of the specific energy z_n among cells is sufficiently small. In this assumption, the number of lethal events follows the same Poisson distribution in each cells, with average $x_{n,I}$.

However, in general, the specific energy observed in the cell is a stochastic quantity that varies from cell to cell, bringing also a deviation from the Poisson distribution when considering the whole population of irradiated cells. We remark that this deviation is present even if the radiation is perfectly mono-energetic. In this case, the variance of the specific energy z_n arises from the fluctuation of the number of particles that are hitting the cells. The fluctuations are particularly relevant when the LET of the particle is relatively high since, given a macroscopic dose D, the average number of high-LET particles interacting with the cell is lower than the number of low-LET particles. To account for the non-Poisson distribution of the lethal events, a correction to the MKM has been introduced by Hawkins in 2003 [19], bringing a deviation from the linear behavior of the RBE vs. LET, described in **Eq. (52)**, in the high-LET region.

The effect of the non-Poisson distribution of lethal lesions is considered by explicitly evaluating the fraction of hit and non-hit cell nuclei. Considering a high-LET irradiation in the limit of very low dose, $D \to 0$, the probability for a cell to interact with more than one particle is negligible. In this case, the population of cells can be subdivided in a fraction Φ of cells that suffer a single particle interaction and a fraction $1-\Phi$ of cells with zero interactions.

A further approximation is assumed in order to match the request of still having a Poisson distribution in the population of hit cells: only a single well defined value of $z_n = z_{n,D}$ is observed when the particle hits the cell. Generally, this is not the case and the specific energy can also vary due to energy straggling and the random impact parameter of the particle with respect to cell nucleus. This assumption can be reasonable when low energy particles with high LET (see also **Section 3.6**) are considered.

We denote with $x_{I,n}(z_{n,D})$ the average number of type I lethal lesions in the fraction Φ of cells whose sensitive nucleus has been hit by a single particle imparting exactly a specific energy $z_{n,D}$ in the nucleus. Then, recalling **Eq. (39)**, we obtain

$$x_{I,n}(z_{n,D}) = -\log S(z_{n,D}) = (\alpha_0 + z_D\beta_0)z_{n,D} + \beta_0 z_{n,D}^2. \tag{54}$$

It is possible to explicitly write the global surviving fraction of cells (including both hit and non-hit nuclei) as

$$S(D) = (1-\Phi) + \Phi e^{-x_{I,n}(z_{n,D})}. \tag{55}$$

This corresponds to consider a probability density function $f_n(z_n; D) = (1-\Phi)\delta(z_n) + \Phi\delta(z_n - z_{n,D})$ in **Eq. (41)**. Since the number of lethal lesions per cell averaged over the whole cell population (including both hit and non-hit nuclei) exposed to the macroscopic dose D can be directly evaluated as

$$\langle x_{I,n}(z_n)\rangle_c = \Phi x_{I,n}(z_{n,D}), \tag{56}$$

Equation (55) can be rewritten as

$$\begin{aligned} S(D) &= 1 + \frac{\langle x_{I,n}(z_n)\rangle_c}{x_{I,n}(z_{n,D})}\left(e^{-x_{I,n}(z_{n,D})} - 1\right) \\ &= 1 + \left[\frac{e^{-(\alpha_0 + z_D\beta_0)z_{n,D} - \beta_0 z_{n,D}^2} - 1}{(\alpha_0 + z_D\beta_0)z_{n,D} + \beta_0 z_{n,D}^2}\right]\left((\alpha_0 + \beta_0 z_D)D + \beta_0 D^2\right). \end{aligned} \tag{57}$$

Notice that, in the last passage, we exploited **Eq. (43)** in order to evaluate the average $\langle x_{I,n}(z_n)\rangle_c$ as an explicit function of the dose. Taking the log of S, expanding around $D = 0$ and dropping terms in D^2 or higher powers, the linear term of $\log S(D)$ can be written as

$$-\log S(D)\big|_{D\to 0} \approx (\alpha_0 + z_D\beta_0)\left(\frac{1 - e^{-(\alpha_0 + z_D\beta_0)z_{n,D} - \beta_0 z_{n,D}^2}}{(\alpha_0 + z_D\beta_0)z_{n,D} + \beta_0 z_{n,D}^2}\right)D. \tag{58}$$

The explicit non-Poisson α coefficient is then derived from **Eq. (58)** and can be formulated as a correction to α_P (defined in **Eq. 45**) as

$$\begin{aligned} \alpha_{NP} &= \alpha_P\left(\frac{1 - e^{-\alpha_P z_{n,D} - \beta_0 z_{n,D}^2}}{\alpha_P z_{n,D} + \beta_0 z_{n,D}^2}\right) \\ &\simeq \left(1 - \exp(-\alpha_P z_{n,D})\right)\left(\frac{1}{z_{n,D}}\right), \end{aligned} \tag{59}$$

where following also the original formulation of Hawkins [19], in the last passage, the quadratic terms $z_{n,D}^2 \ll z_{n,D}$ were also neglected. According to Hawkins, one can also approximate $z_{n,D} \propto \mathrm{LET}_\infty/A$, where LET_∞ is the unrestricted linear energy transfer in keVμm^{-1} of the incident particle and A is the area of the cell nucleus in μm^2, assuming $\rho = 1$ g cm^{-3} for the density of water. By assuming $A = \pi R_n^2$, **Eq. (59)** becomes

$$\alpha_{NP} \simeq \left(1 - \exp\left(-\alpha_P \frac{\mathrm{LET}_\infty}{\rho\pi R_n^2}\right)\right)\left(\frac{\rho\pi R_n^2}{\mathrm{LET}_\infty}\right). \tag{60}$$

No correction is considered for the β coefficient and it is still assumed to be independent on the energy and particle type.

The non-Poisson correction to the RBE in the limit of zero dose (RBE_α) is given by

$$\mathrm{RBE}_{\alpha,NP} = \frac{\alpha_{NP}}{\alpha_X} = \left(\frac{1 - e^{-\alpha_P z_{n,D}}}{\alpha_P z_{n,D}}\right)\mathrm{RBE}_{\alpha,P}, \tag{61}$$

with $\mathrm{RBE}_{\alpha,P}$ given by **Eq. (52)**. No corrections are applied to the RBE_β, that is still assumed constant ($\mathrm{RBE}_\beta \sim 1$) and independent on the quality of the radiation.

The correction causes the RBE_α to be less than indicated by the extrapolation of the linear relationship (**Eq. 53**) to higher LET and to pass through a maximum in the range of LET of 50–150 keV/μm. This behavior is compatible with several experimental studies from the literature [82] and it shows also a sensitivity of the maximum of the RBE to the response of the cell

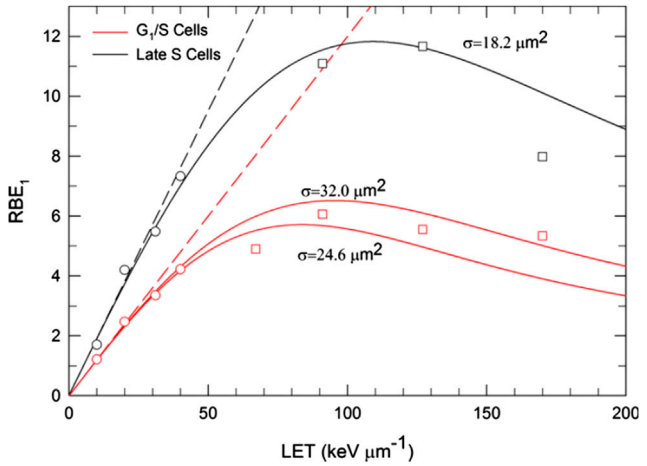

FIGURE 4 | Comparison of MKM estimates of particle RBE_α to experimental values for V79 cells. Red curves show RBE_α for cells synchronized at G1-S transition for cross sections of σ = 32.0 and 24.6 μm^2 (reference radiation: 250 kVp X-rays, α_R = 0.234 Gy^{-1}, and β_R = 0.042 Gy^{-2}). Black curve shows RBE_α for cells synchronized in late S phase for cross sections of σ = 18.2 μm^2 (reference radiation: 250 kVp X-rays, α_R = 0.064 Gy^{-1}, and β_R = 0.0165 Gy^{-2}). Dashed lines represent RBE_α = 0.02 + 0.19 × LET in the Poisson regime. Experimental data are from [86, 87], plot taken from [26].

at low-LET, related to the parameter $R = \alpha_X/\beta_X$ [85]. An exemplification of the RBE behavior and the prediction of the model is reported in **Figure 4**.

We remark that, while the non-Poisson correction factor associated to the linear parameter α is derived in the limit $D \to 0$ (and, by definition, it is independent on the dose), the non-Poisson concept of Hawkins's correction is in general inapplicability to a high dose irradiation, since all nuclei and domains will be hit in such irradiation. The quantity RBE_α defined in **Eq. (61)** is hence expected to represent the relevant behavior for low doses, where the linear term is dominant and the RBE is maxed out [83, 84], whereas the correct stochastic evaluation of β could be critical in the study of clinical applications with high doses per fraction (see **Section 3.8**). In **Figure 5**, some qualitative implications of the non-Poisson regime in high-LET and low dose per fraction ion beam therapy are depicted.

3.5 The Saturation Correction

Kase et al. [20] introduced a correction factor in the MKM to account for the decrease in RBE due to the overkill effect observed in high-LET radiations (see, for example, **Figure 6**). The correction factor was applied to the dose-averaged specific energy per event, z_D, for mixed radiation field with wide-ranging spectra.

In terms of lineal energy, the corrected value of y_D (and hence z_D) was obtained by applying a correction for each lineal energy component of the lineal energy spectrum. The correction of the components was obtained by using an empirical *saturation parameter* y_0 based on the saturation correction method introduced by [89] and then used in the TDRA [58]

$$y_D^* = \frac{y_0^2 \int [1 - \exp(-y^2/y_0^2)] f(y)\, dy}{\int y f(y)\, dy}. \tag{62}$$

The saturation parameter indicates the lineal energy above which the correction due to the overkill effects became important.

The correction to cell survival is then obtained by evaluating the saturation-corrected dose-averaged specific energy per event z_D^* in the domain, which can be obtained from the saturation-corrected dose-averaged lineal energy **(62)** using the relationships reported in **Eqs (12)** and **(19)**:

$$z_D^* = \frac{\bar{l}_d}{m_d} y_D^* = \frac{y_D^*}{\rho \pi r_d^2}, \tag{63}$$

where ρ, r_d, $\bar{l}_d$, and m_d are the density, radius, mean cord length, and mass of the domain, respectively. The equation for the cell survival (**Eq. 44**) is then modified as follows:

$$-\ln(S) = (\alpha_0 + \beta_0 z_D^*) D + \beta_0 D^2. \tag{64}$$

Considering the linear term in the macroscopic dose D, the corrected α^* coefficient is hence

$$\alpha^* = (\alpha_0 + \beta_0 z_D^*). \tag{65}$$

No correction is considered for the β coefficient and it is still assumed to be independent on the energy spectrum.

An example of the prediction by MKM modified with the saturation correction compared with experimental data is reported in **Figure 6**, where the α vs. y_D for HSG cells irradiated with carbon ions is shown. It is interesting to note, by comparing **Eqs (59)** and **(65)**, that the saturation correction can be considered an alternative way to describe the non-Poisson correction defined in **Section 3.4**, since both factors modulate the behavior of RBE_α in similar ways (see also **Figure 4**). In particular, it was shown in [20] that in the case of mono-energetic spectra, **Eqs (58)** and **(65)** are functionally equivalent for $y < 500$ keV/μm. Thus, by matching these equations in the limit of low LET ($y_D \to 0$), and defining $z_{n,D} = y_D/\rho\pi R_n$, with R_n the radius of the nucleus, analogously to **Eq. (63)** for the domain, it is possible to link the saturation correction parameter y_0 with the other parameters of the model

$$y_0 = \frac{\rho \pi r_d R_n^2}{\sqrt{\beta_0 (r_d^2 + R_n^2)}}. \tag{66}$$

A typical used value of the saturation parameter was y_0 = 150 keV/μm [20, 36].

Other quantities that one needs to determine for the RBE evaluations are the lineal energy spectra, obtainable with a microdosimeter detector such as TEPC [43] and the values of α_0, r_d, and R_N from which the correction to the y_D^* is calculated. The α_0 and r_d coefficients can be extrapolated experimentally from the initial slope of the survival curves (**Eq. 65**) for low-LET irradiation (in the limit of $y_D \to 0$ and $D \to 0$)

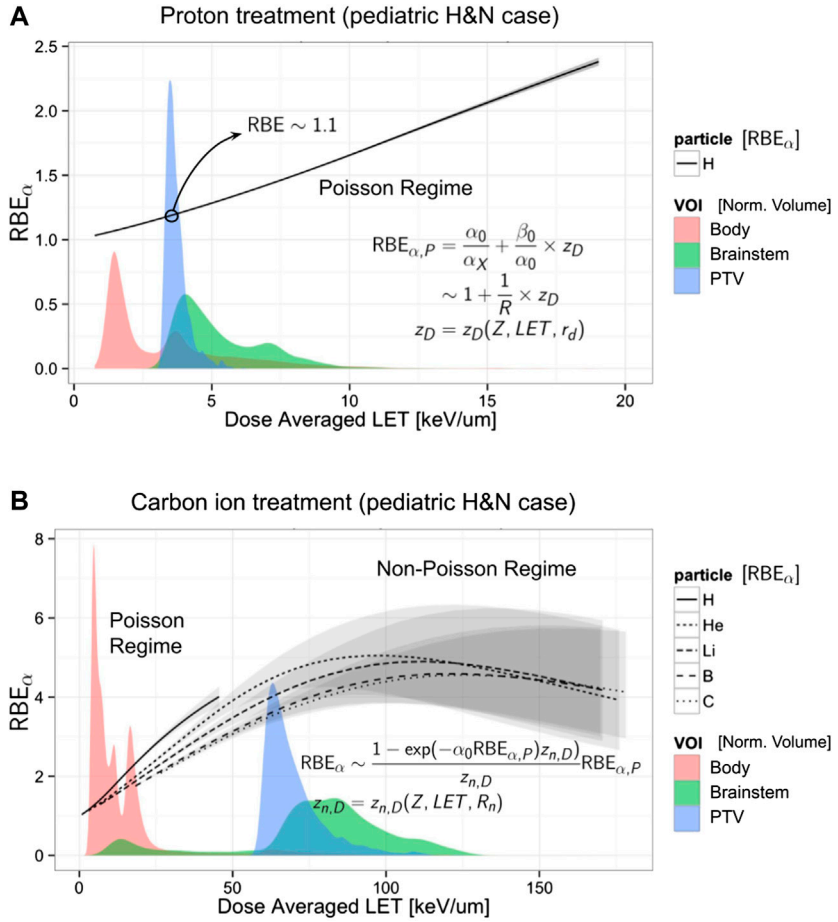

FIGURE 5 | Evaluation of the RBEα *vs.* LET$_D$ evaluated via **Eq. (61)** in combination with an amorphous track model (see **Section 3.6**) for proton **(A)** and for carbon and other ions **(B)**. Using the same *x* axis of the plot is reported for comparison of the LET$_D$ volumetric distribution (filled areas) found in a patient (a pediatric brain tumor case) irradiated with a primary beam of protons **(A)** and carbon ions **(B)**. The LET$_D$ distribution is normalized and evaluated in 3 volumes: total body (red), brainstem (green), and the planning target volume, PTV (blue). Annotated in the plot are the low-LET range for the Poisson regime, applicable mainly for the proton treatment, and the Non-Poisson regime, in the case of high-LET carbon ion treatment (for both the primary carbon ions and the fragments). The gray bands represent the 95% confidence band obtained with a bootstrap procedure to the fit of the input parameters $(\alpha_0, \beta_0, R_n, r_d)$ of the model to the *in vitro* experimental data taken for cells with $R \simeq 10$ Gy from the PIDE database [82]. The evaluations have been carried out with a research TPS [88].

$$r_d = \sqrt{\frac{\beta\left(y_D - (y_D)_X\right)}{\rho\pi(\alpha - \alpha_X)}}, \qquad \lim_{y_D \to 0} \alpha \equiv \alpha_0 = \alpha_x - \left(\frac{\alpha - \alpha_x}{y_D - (y_D)_X}\right)(y_D)_X, \tag{67}$$

where $\rho = 1.0\,\mathrm{g/cm^3}$, α_X is the LQ parameter of the X-Ray, and $(y_D)_X$ is the dose-averaged lineal energy for X-ray irradiation.

The saturation-corrected formulation of the MKM is one of the most widely used approaches to estimate the RBE from microdosimetric measurements. Many studies have been published where the computed RBE is compared with the RBE measured along single Bragg peaks or more complex mixed field irradiations [49, 90–92]. In **Figure 7**, the RBE vs. depth for a proton spread-out Bragg peak is reported as an example of these assessments [92].

3.6 Track Structure Model Incorporation

In 2008, Kase et al. [21] introduced the usage of amorphous track structure models as an alternative numerical approach to evaluate theoretically the dose-averaged per event in the nucleus $z_{n,D}$ and in the domain z_D for the MKM calculations. This approach has the advantage of bypassing the necessity to acquire experimental lineal energy spectra to evaluate the RBE; this approach is particularly useful when experimental spectra are not available, such as in TPS calculations. Another interesting aspect is the possibility to evince the dependence of LET-RBE curves on the ion type.

The amorphous track model adopted for the MKM calculation is based on a combination of the Kiefer model for the penumbra region [93] and the Chatterjee model for the core radius [94], introduced for explaining the responses of the diamond detector to heavy-ion beams [95]. Here, the core radius R_c (μm), the penumbra radius R_p (μm), and the dose z_{KC} as function of track radius r (μm) are evaluated as follows:

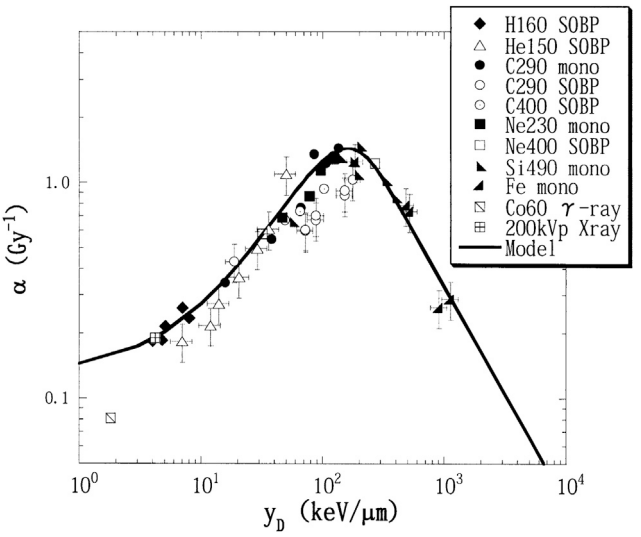

FIGURE 6 | Experimental α values, fitted by the linear-quadratic model from the survival curves of HSG cells value with $\beta_0 = 0.05\,\mathrm{Gy}^{-2}$, as a function of the dose-averaged lineal energy, y_D. The y_D were measured by the TEPC with a simulated diameter of 1.0 μm. The solid line indicates the curve calculated using **Eq. (65)** with the following model parameters: $r_d = 0.42$ μm, $R_n = 4.1$ μm, $\alpha_0 = 0.13\ \mathrm{Gy}^{-1}$, and $\beta_0 = 0.05\ \mathrm{Gy}^{-2}$. Plot taken from [20].

$$R_c = 0.0116 \times \beta_{\mathrm{ion}}, \tag{68}$$

$$R_p = 0.0616 \times (E_s)^{1.7}, \tag{69}$$

$$z_{\mathrm{KC}}(r \le R_c) = \frac{1}{R_c^2}\left(\frac{\mathrm{LET}_\infty}{r\rho} - 2\pi K_p \ln\left(R_p / R_c\right)\right), \tag{70}$$

$$z_{\mathrm{KC}}(r > R_c) = 1.25 \times 10^{-4}\left(Z^*/\beta_{\mathrm{ion}}\right)^2 r^{-2}, \tag{71}$$

where E_s is the specific kinetic energy in MeV/u, Z^* is the effective charge given by the Barkas expression, β_{ion} is the velocity relative to the speed of light, LET_∞ is the unrestricted LET, and ρ is the density of water ; K_p is a parameter that depends only on the effective charge given with the Barkas expression and the β ion is the velocity relative to the light velocity [21]. In order to evaluate the dose-averaged specific energy, the domain and nucleus are assumed to have a cylindrical symmetry with the direction of the incident ion parallel to the cylinder axis. Using this geometry, it is possible to write explicitly the single-track dose-averaged specific energy (**Eq. 12**) for both domain and nucleus as

$$z_D = \int_0^{b_{\max}} z_{\mathrm{KC}}(b)^2 b\,\mathrm{d}b \Big/ \int_0^{b_{\max}} z_{\mathrm{KC}}(b) b\,\mathrm{d}b, \tag{72}$$

$$z_{n,D} = \int_0^{b_{\max}^{(n)}} z_{\mathrm{KC}}(b)^2 b\,\mathrm{d}b \Big/ \int_0^{b_{\max}^{(n)}} z_{\mathrm{KC}}(b) b\,\mathrm{d}b, \tag{73}$$

where $b_{\max}$ and $b_{\max}^{(n)}$ are the maximum impact parameters to have a non-negligible energy deposition in the domain and in the nucleus, respectively. These parameters, or equivalently the radius of the domain r_d and of the nucleus R_n, represent two parameters of the model. Examples of these evaluations are shown in **Figure 8**. In principle, R_n can be related to direct observations while r_d does not represent a measurable quantity, since it cannot be uniquely identified with any structure in the cell or cell nucleus. r_d can be used as a free parameter to be fixed by fitting the model to the experimental survival and RBE data.

As seen in **Section 3.4**, in the case of high LET irradiation, the z_D value is comparably very large with respect to the $(z_D)_X$ evaluated for photon; consequently, from **Eq. (36)**. α_0 and β_0 can be approximated with the experimental α_X and β_X. An example of the model evaluations compared to the experimental data is reported in **Figure 9**.

Interestingly, the explicit usage of a track model shows how some aspects of the MKM are conceptually similar to that of the LEM [11–17]. In both MKM and LEM, the principal target is the cell nucleus for any radiation quality, the nucleus is divided into small independent sub-volumes (infinitesimal volumes in the case of LEM and domains in the case of MKM), and a cell survival curve for X-rays is adopted as the local dose-effect curve of each sub-volume. Finally, the summation of the local effect in all sub-volumes over the whole nucleus determines the cell survival probability.

The inclusion of the amorphous track model allows to evaluate directly z_D and $z_{n,D}$ without the necessity to obtain these values by extrapolating them from microdosimetric measurements via scaling relationships such as **Eq. (19)**. This aspect can be particularly advantageous for some applications where these spectra are generally not easily or partially available such as in the simulation and optimization of treatments in TPS applications, where the biological effect should be evaluated in the whole irradiated 3-D patient volume.

At present, the MKM is implemented in the proton and carbon ion TPS used clinically at the National Institute of Radiological Sciences (NIRS) in Japan to evaluate the RBE and the RBE-weighted dose optimized for the individual patients. The computation method, developed by Inaniwa et al. [36, 96], takes advantage of the incorporation of the amorphous track model in combination with the saturation-corrected dose-averaged approach developed by Kase et al. [20] described in **Section 3.5**, for evaluations in case of mixed field irradiation. In the TPS implementation, a set of pre-calculated look-up tables of the saturation corrected specific energies for mono-energetic beams are created using a generalization of **Eqs (72), (73)** where the saturation effect is explicitly included for the dose-averaged specific energy for the domain

$$z_D^* = \int_0^{b_{\max}} z_{\mathrm{sat}}(b) z_{\mathrm{KC}}(b) b\,\mathrm{d}b \Big/ \int_0^{b_{\max}} z_{\mathrm{KC}}(b) b\,\mathrm{d}b \tag{74}$$

and equivalently for the nucleus, where z_{sat} is the saturation-corrected specific energy

$$z_{\mathrm{sat}}(b) = \frac{z_0^2}{z_{\mathrm{KC}}(b)}\left(1 - \exp\left(-\frac{z_{\mathrm{KC}}(b)^2}{z_0^2}\right)\right), \tag{75}$$

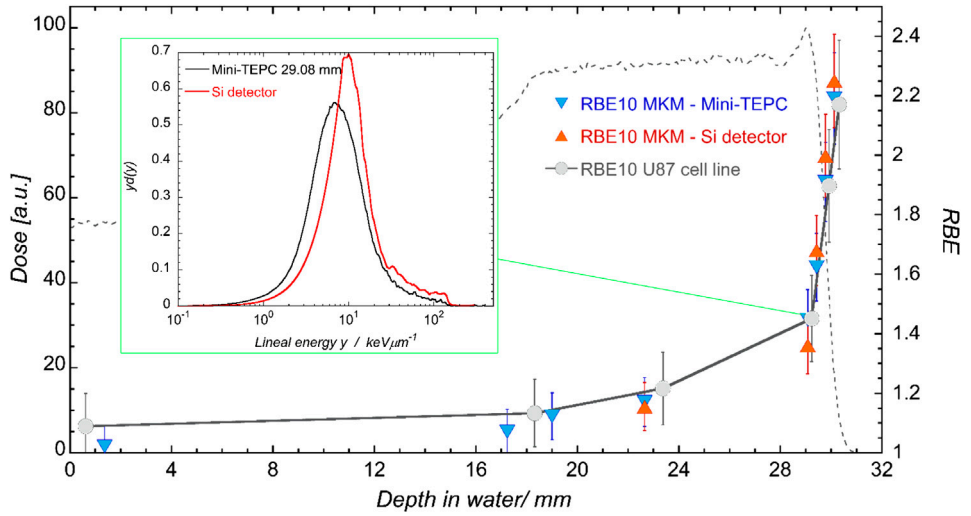

FIGURE 7 | Clinical SOBP of CATANA. Dose profile measured with the Markus chamber in black, total LET-dose from Geant4 MC simulation in blue. Crosses indicate positions at which both detectors are measured. The box reports the normalized spectra obtained with the mini-TEPC (black) and the silicon telescope (red) at a depth of 29.08 mm. Plots taken from [92].

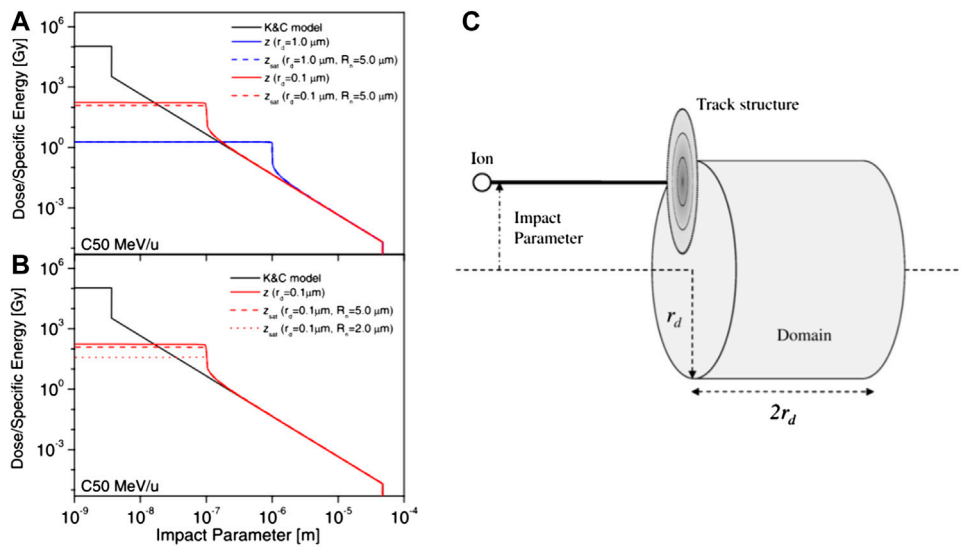

FIGURE 8 | (A) and **(B)** track structures for a carbon-ion beam with a specific kinetic energy of 50 MeV/u calculated with the Kiefer–Chatterjee model and the corresponding dose-averaged specific energy z and saturation-corrected dose-averaged specific energy z_{sat} as functions of the impact parameter for domain and nucleus with different sizes. **(C)** Schematic of an incident ion with respect to a cylindrical sensitive volume. Plots taken from [36].

with saturation coefficient $z_0 = y_0(\bar{l}_d/m_d)$ (see **Eq. 66**) evaluated in the cylindrical geometry (see also panel (c) of **Figure 8**). The effect of the mixed-field of the treatment at a position is hence evaluated through a dose-weighted linear combination

$$\left(z^*_{D,\mathrm{mix}}\right)_i = \frac{\sum_{j=1}^{N_b} D_{ij}\left(z^*_D\right)_{ij}}{\sum_{j=1}^{N_b} D_{ij}}, \tag{76}$$

where N_b is the number of beams of the treatments, $D_{i,j}$ is the dose released at position i by the beam j, and

$$\left(z^*_D\right)_{ij} = \frac{\sum_{k=1}^{N_{ij}} e_k \left(z^*_D\right)_k}{\sum_{k=1}^{N_{ij}} e_k} \tag{77}$$

is the saturation-corrected dose-averaged specific energy of the domain of cells at position i delivered by the j-th beam, obtained through the sum of mono-energetic evaluations, $(z^*_D)_k$, described in **Eq. (74)**, where k is an index of the deposition events and the sum is performed from 1 to N_{ij}, the observed number of the deposition events in cell i delivered by the j-th beam.

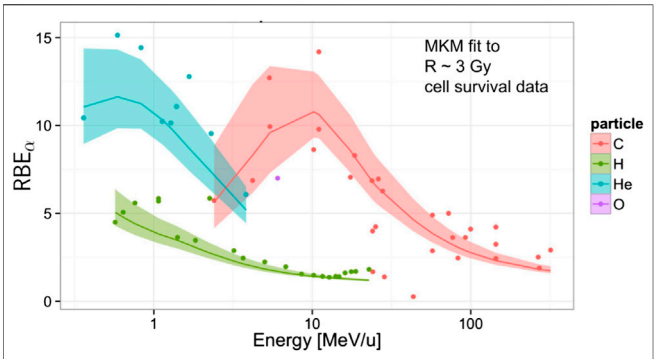

FIGURE 9 | Global fitting of the MKM to experimental RBE$_\alpha$ data for different ion irradiation subsetted from the PIDE database [82] with $R = \alpha_X/\beta_X \in [2.8, 3.2]$ Gy. The plotted points indicate the experimental results and the lines represent the MKM results calculated with the Kiefer–Chatterjee track structure model. The bands represent the 90% confidence band obtained from the MKM parameters $\{\alpha_0, \beta_0, R_n, r_d\}$ probability distribution, evaluated through a bootstrap procedure.

To obtain the energy imparted e_k and the number N_{ij}, Monte Carlo (MC) simulations are used, taking advantage of available codes such as, for example, those derived from the Geant4 libraries [97–99] and Fluka [100].

3.7 The Dependence of the Biological Effect on the Dose-Rate Time Structure

One of the interesting features of the MKM, in contrast to other radiobiological models used in ion beam radiotherapy such as the LEM, is the possibility to account inherently for arbitrary time dependent dose-rates, such as protracted irradiations and fractionations. This feature derives from the explicit description of the time depending response of the cell to the irradiation through the kinetic equations (**Eq. 32**).

Different approaches to investigate and to model the dose-rate time effects have been carried out using the MKM as a theoretical base. Some examples of these approaches can be found in [23, 39, 67, 101–104]. In these studies, the kinetic **Eq. (27)** is slightly generalized to account for an arbitrary time dependent specific energy deposition rate $\dot{z}^{(c,d)}$ in the domains:

$$\begin{cases} \dot{x}_I^{(c,d)} = \lambda \dot{z}^{(c,d)} + a x_{II}^{(c,d)} + b\left(x_{II}^{(c,d)}\right)^2, \\ \dot{x}_{II}^{(c,d)} = \kappa \dot{z}^{(c,d)} - (a+r) x_{II}^{(c,d)} - 2b\left(x_{II}^{(c,d)}\right)^2 \simeq \kappa \dot{z}^{(c,d)} - (a+r) x_{II}^{(c,d)}, \end{cases} \tag{78}$$

where in the second equation, as described in **Section 3.2**, the second order process describing the pairwise combination between type II lesions has been removed since it is considered negligible if compared to the first-order process.

In [101, 104], the effects of dose-delivery time structure on the RBE in a mixed radiation field of therapeutic carbon ion beams are investigated using the modified microdosimetric kinetic model introduced by Kase et al. [20, 21, 36]. These studies evaluate the biological effect of the irradiation in two different dose-rate conditions: a split-dose irradiation and a protracted continuous irradiation.

In the case of a *split-dose irradiation*, a population of cells is considered exposed to a macroscopic dose D_1 at time $t = 0$ and a dose D_2 at time $t = \Delta T$, where a domain absorbs z_1 and z_2 from the two separate irradiations, respectively. Evaluating x_I in the limit $t \to \infty$ by integrating **Eq. (27)** and using the saturation-corrected dose-averaged specific energy as given in **Eq. (64)**, we obtain for the cell survival

$$\ln S(D, \Delta T) = -\left(\alpha_0 + \beta\left(z_D^*\right)_1\right) D_1 - \beta D_1^2 - \left(\alpha_0 + \beta\left(z_D^*\right)_2\right) D_2 - \beta D_1^2 - 2\beta D_1 D_2 e^{-(a+c)\Delta T} \frac{1 - e^{-2(a+c)(t_r - \Delta T)}}{1 - e^{-2(a+c)t_r}}, \tag{79}$$

where $(z_D^*)_1$ and $(z_D^*)_2$ are the saturation-corrected dose-averaged specific energy of the first and second irradiation and the total dose $D = D_1 + D_2$. The time parameters t_r indicate the time after which all sub-lethal lesions that are still unrepaired are fixed in lethal lesions, according to assumption (9) introduced in **Section 3.2**. If the quality of the radiation does not change between the two irradiations, then $(z_D^*)_1 = (z_D^*)_2 = z_D^*$ and **Eq. (79)** can be simplified as

$$\ln S(D, \Delta T) = -\alpha_0 (D_1 + D_2) - z_D^* \beta (D_1 + D_2) - \beta (D_1 + D_2)^2 + 2\beta D_1 D_2 \left[1 - e^{-(a+c)\tau} \frac{\left(1 - e^{-2(a+c)(t_r - \tau)}\right)}{\left(1 - e^{-2(a+c)t_r}\right)}\right]. \tag{80}$$

The values of $(a + c)$ and t_r can be determined by using the following approximations (see Eqs 35, 40 in [101]):

$$(a + c) \cong \frac{1}{2\beta D_1 D_2} \left[\frac{1}{S} \frac{dS}{d\tau}\right]_{\tau=0}, \tag{81}$$

$$t_r = -\frac{\ln(\alpha/\kappa)}{(a + c)}. \tag{82}$$

In the case of a *continuous protracted irradiation*, a population of cells receive a constant macroscopic dose-rate of $\dot{D}$ starting at time $t = 0$ and ending at $t = T$. In order to carry out the evaluation, the irradiation is assumed microscopically equivalent to a number N of instantaneous irradiations with random doses to a domain delivering every infinitesimal interval. The time interval between these irradiations is $\delta t = T/(N - 1)$, with $\delta t \ll 1/(a + c)$, and each domain absorbs $z_1, z_2, \ldots, z_N$. The number of lethal lesions per domain x_I is therefore obtained by integrating and summing the solution of **Eq. (27)** for each time segment. The final cell survival probability is then obtained by introducing the corresponding saturation-corrected dose-averaged specific energy in a way analogous to the split dose evaluation. In the case in which the quality of the radiation does not change with time, the final log survival is given as

$$\ln S = -\left(\alpha_0 + \beta_0 z_{d,D}^*\right) D - \beta' D^2, \tag{83}$$

where

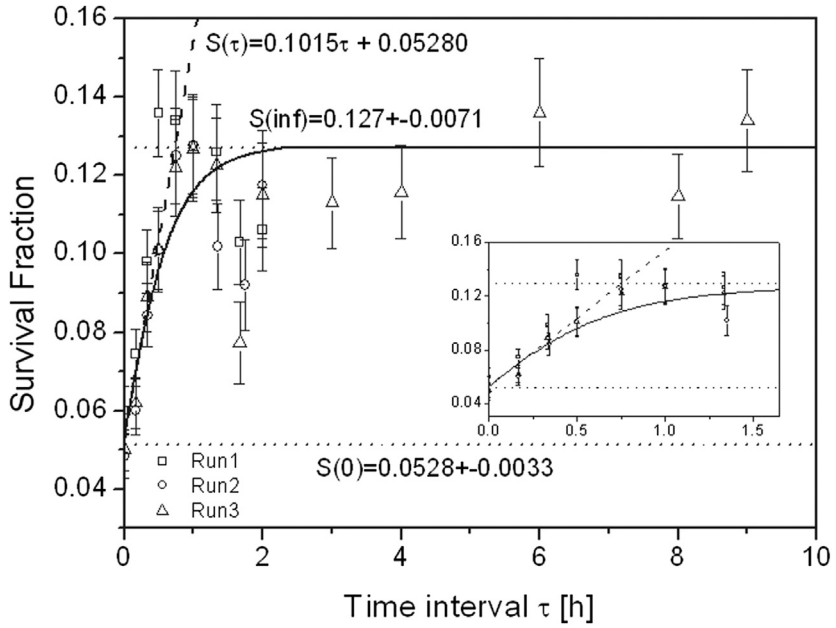

FIGURE 10 | Survival fraction of HSG tumor cells after exposure to two equal doses of carbon-ion beams with $D_1 = D_2 = 2.5$ Gy separated by time interval τ (ΔT in the text) from 0 to 9 h. Three different series of experiments (runs) are shown. The estimated tangent at $\tau = 0$ h is reported in dashed line, while the solid curve is the predicted survival by **Eq. (80)** with $\beta = 0.0703$ Gy^{-2}, $\beta = 0.237$ Gy^{-2}, $(a + c) = 2.187$ h^{-1}, and $t_r = 2.284$. Plot taken from [101].

$$\beta' \equiv \beta_0 \left[1 - \frac{2}{N^2} \sum_{n=1}^{N-1} \left\{ (N-n) \left(1 - e^{-(a+r)\frac{n}{N-1}T} \times \frac{\left(1 - e^{-2(a+r)\left(t_r - \frac{n}{N-1}T\right)}\right)}{\left(1 - e^{-2(a+r)t_r}\right)} \right) \right\} \right]. \tag{84}$$

The notation used in **Eqs (83)** and **(84)** highlights the importance of the quadratic term β, which modulates the impact of the dose-rate time structure, according to the LQ interpretation of the biological effects [105–108].

It is worth remarking that these MKM-based temporal formulations of the cell survival derived from the kinetic **Eq. (78)** do not account for re-population and cell cycle redistribution. **Figure 10** reports the evaluation via **Eq. (80)** of the survival fraction of HSG cell line for various time intervals compared to experimental data. An initial rise in cell survival due to repair is visible until time interval $\Delta T = 0.75$ h followed by a decrease in survival due to cell cycle redistribution and a rise due to re-population ($1.4 < \Delta T < 4$ h) and by the saturation region for $\Delta T > 4$ h. The predicted cell survival reasonably agrees with data in the first and last regions, while it does not account for re-population and redistribution. The temporal formulations described in this section have been also incorporated in the TPS used at NIRS [36] (see also **Section 3.6**) and successfully used to estimate the impact of the beam interruption in single-fractionated treatments with carbon ions for patients with prostate tumor [104].

3.8 Stochastic Approaches and Variable β

As discussed in the previous sections, the MKM accounts for the stochastic aspects of the induction of damage in the cell by exploiting probability theory to develop simple formulas for the LQ coefficients of the cell survival (**Eqs 44**, **45**, **58**, **64**, and **83**). These formulations of the model are obtained introducing approximations [19] or ad-hoc corrections [20] that shows some discrepancies with experiments for high-LET irradiation, in particular in the determination of the β coefficient, since the measured β tends to decrease at very high LET [82, 109–111], while the β derived from the MKM is considered constant.

The disagreements in the β coefficient are ultimately acknowledged to be induced by the partial accounting of the stochastic nature of the specific energies in the MKM calculations that play an important role for high-LET irradiation [22]. Following these considerations, attempts to improve the model, introducing more refined approaches to account a variable β, have been made [22, 23, 70, 112]. In the rest of this section, some of these developments, based on improved stochastic modelings of the specific energy depositions, are described in detail.

3.8.1 Monte Carlo-Based Evaluations

A method to account in a natural and straightforward way the inherent stochastic nature of the irradiation is to implement a Monte Carlo algorithm in the MKM, as recently shown by Manganaro et al. [23, 113] in their formulation of the model named MCt-MKM (Monte Carlo temporal microdosimetric kinetic model). The implemented model accounts also for the stochastic temporal correlations characteristic of the irradiation process and the cellular repair kinetics by solving explicitly in the MC evaluations the kinetic **Eq. (78)** where the time dependent specific energy rate $\dot{z}^{(c,d)}$ appears explicitly [101, 114].

In the MC approach, the irradiation of a complete population of N_c cells is simulated, where N_c is supposed to be large enough in order to achieve statistical convergence. The irradiation is modeled as an ordered temporal sequence of particles (primaries and secondaries) that interact with the cell nucleus at random spatial coordinates and random times $t_0^{(c)} \le t_1^{(c)} \le t_2^{(c)} \le \cdots$, compatible with the chosen irradiation setting and the definition of the time-dependent macroscopic dose-rate $\dot{D}(t)$. The irradiation is hence modeled as a sequence of spikes in $\dot{z}^{(c,d)}(t)$, each one of them corresponding to the passage of a particle through or nearby the nucleus, delivering a sequence of random specific energies in the domains

$$z_0^{(c,d)}(t_0), z_1^{(c,d)}(t_1), z_2^{(c,d)}(t_2), \ldots \tag{85}$$

depending on the particle spectra and track impact positions with respect to the cell. A depiction of the temporal evolution of the lesions (x_I and x_{II}) due to the effects of the irradiation as described in **Eq. (85)** is reported in panel (b) of **Figure 2**. For a macroscopic dose D and a component e, indicating a specific particle and bin of the kinetic energy histogram sampled from the particles interacting with the cell nucleus, the total number of particles N_e interacting with the nucleus follow a Poisson distribution with mean

$$\overline{N}_e = \frac{\rho \sigma D w_e}{\mathrm{LET}_F}, \tag{86}$$

where LET_F is the frequency-average LET of the radiation computed on the total energy spectrum, considering all the contributing particles, σ is the cross section of the nucleus, ρ is the density of the tissue, and w_e is the normalized weight of the e-th bin of the energy and particle histogram.

In principle, the tracks can be directly sampled from the full measured microdosimetric spectra (i.e., not only the first and second moment) from which the experimental w_e can be obtained. From a practical point of view, the specific energies deposited randomly in each domain of each nucleus are evaluated by coupling general purpose MC tools (such as Geant4 [97, 115] or Fluka [116]) in combination with an amorphous track structure model as described in [21, 36]. The MC code is used to identify the ions that can interact with a cell located in a certain point of the irradiated macroscopic volume at a certain time. The domains are arranged according to a close packing hexagonal structure inside the nucleus.

Once the time sequence of specific energies in the domains **(85)** are obtained, the kinetic **Eq. (78)** can be formally solved for $t \to \infty$ to obtain the average number of lethal lesions for each cell-domain (c, d):

$$-\log s^{(c,d)} = x_I^{(c,d)}\big|_{t\to\infty} = \frac{\alpha_0}{N_d}\sum_{i=0}^{n_c-1} z_i^{(c,d)} + G_{c,d}\frac{\beta_0}{N_d}\left(\sum_{i=0}^{n_c-1} z_i^{(c,d)}\right)^2, \tag{87}$$

where n_c is a Poisson random variable indicating the number of particles that interacted with the cell c, $\tau = 1/(a+r)$ is the time constant that defines the first order repair kinetics, and G is the generalized Lea-Catcheside time factor [57, 65] defined at the nanodosimetric level of the domain:

$$G^{(c,d)} = 1 - \frac{2}{\left(\sum_{i=0}^{n_c-1} z_i^{(c,d)}\right)^2}\sum_{i=0}^{n_c-2}\sum_{j=i+1}^{n_c-1}\left(1 - e^{-\frac{1}{\tau}\left(t_j^{(c)} - t_i^{(c)}\right)}\right) z_i^{(c,d)} z_j^{(c,d)}. \tag{88}$$

The survival fraction S is obtained by averaging over the entire cell population the survival probability evaluated for each single cell $S_n(c)$ (see for comparison **Eqs 37, 41**)

$$\begin{aligned} S(D) &= \langle S_n^{(c)}; D\rangle_c = \left\langle \exp\left(-\sum_{d=1}^{N_d} x_I^{(c,d)} \right)\right\rangle_c \\ &= \left\langle \exp\left(-N_d \left\langle x_I^{(c,d)}\right\rangle_d \right)\right\rangle_c . \end{aligned} \tag{89}$$

Notice that the Monte Carlo approach does not compute directly the LQ coefficients α and β, in contrast to the analytical approaches described in the previous sections. However, it is possible to derive the LQ coefficients by simulating a complete survival curve, i.e., by evaluating (89) using different macroscopic doses $D_1 < D_2 < D_3 < \ldots$, and then fitting the curve with the LQ formula. An example of a complete simulated survival curve is reported in **Figure 11**. We remark also that, as done in **Section 3.7**, the cell population generated by the solutions of the kinetic **Eq. (78)** neglects re-population and cell cycle re-distributions.

One of the benefits of the MCt-MKM approach is that both α and β coefficients, obtained through the survival fitting, show the expected saturation behavior for high-LET irradiation without adding any corrective factors, like the non-Poisson (**Section 3.4**) or (**Section 3.5**) saturation. The disadvantage of the approach, other than the inherent approximations specific to the used MC transport code and the adoption of an amorphous track model, is that it can be particularly computing intensive, although this is mitigated by exploiting the multi-core parallelism of modern CPUs [113].

The MCt-MKM has been validated on *in-vitro* experiments considering acute and *split-dose* irradiation on HSG, T1, and V79 cell lines in aerobic conditions of H, He, C, and Ne ion beams [23]. An example of the behavior of the LQ α and β coefficients is reported in **Figure 12**, where also a comparison with the prediction of other models, a non-stochastic MKM evaluation, the LEM, and the repair–misrepair–fixation (RMF) model (see **Section 4.2**), is shown. The main difference with respect to the original MKM is that the MCt-MKM predicts a non-constant and vanishing β with high LET values. This behavior is ultimately due to the non-Poisson statistics inherently implemented in the model. However, we remark that, although, as previously noted, there is a general consensus for a vanishing β for high LET irradiation, there are still contradictory experimental results and significant uncertainties for β vs. LET behavior (see, for example, also [118]). In particular, in Figure 12, the data show a beta significantly larger than zero for a large number of experimental points for He and C ions also for relatively high LET.

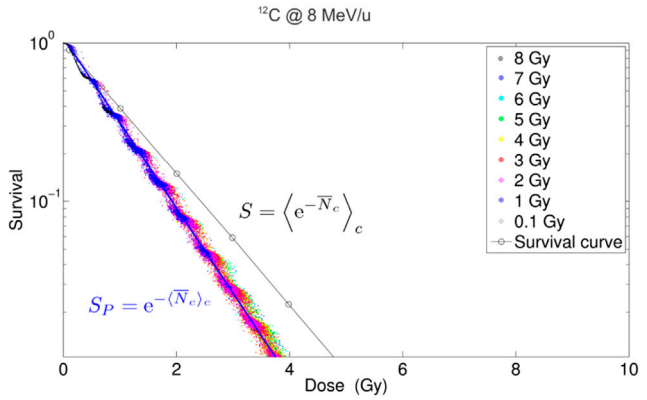

FIGURE 11 | Simulated survival curves obtained for acute irradiation, ($t_0 = t_1 = t_2 = \cdots$), of mono-energetic carbon ion (8 MeV/u) with imposed macroscopic doses ranging from 0.1 to 8 Gy represented in different colors. The dots represent the values of cell survival $S_n^{(c)}(z_n^{(c)})$ with specific energy $z_n^{(c)} = N_d \sum_{d=1}^{N_d} \sum_{i=0}^{(n_c-1)} z_i^{(c,d)}$ delivered in the cell c (a small dot for each simulated cell); the variability of the delivered dose with respect to the imposed dose derives by the fluctuation determined by the MC simulation. The two curves were fitted using the LQ model (solid and dashed lines, respectively) in order to get the LQ parameters. The blue curve is fitted directly to the $S_n^{(c)}(z_n)$ data and corresponds to the Poisson approximation described in **Eq. (43)**. The black line corresponds to the fit to the population averages $\langle S_n^{(c)}; D \rangle_c$ defined in **Eq. (89)** for each imposed dose D (open dots) and corresponds to the non-Poisson formulation of **Eq. (59)**. Plot taken from [117].

The model was also implemented in a TPS [88] to evaluate the effect of the temporal protraction of treatments with different ion beams. The effect of the protraction, described microscopically by **Eq. (88)**, was shown to be compatible with a macroscopic first order effect with temporal constant τ [23]. We remark that, in the framework of the LQ formalism, in the studies of high dose irradiation and the dose-rate effect, such as those reported in [23, 101–104], the specific way β is modeled which plays a fundamental role [119, 120]. In particular, the behavior of a vanishing β for high LET is compatible with the experimental observation of a reduction of the sensitivity to the dose-rate (including the fractionation) in healthy tissues for treatments with high-LET ions and, hence, the potential advantage of hypofractionated treatments with these particles.

3.8.2 The Stochastic Microdosimetic Kinetic Model

The analytical computation method proposed by Sato and Furusawa [22] introduces a correction to the original formulation of MKM, taking into account the stochastic nature of specific energy in both the domain z and the cell nucleus z_n, to improve the adherence of the model to the measured survival fractions for high-LET and high-dose irradiation. The new model is named double-stochastic microdosimetric kinetic (DSMK) model. In the same study [22], a second model, termed stochastic microdosimetric kinetic (SMK) model, is derived to represent the stochastic nature of domain specific energy z by its approximated mean value and variance in order to reduce the computational time.

Based on radiobiological evidences that state that DNA damage saturates at high-LET regions [121, 122], the original assumption of the MKM, that the initial numbers of lethal and sub-lethal lesions produced in a domain to be proportional to the specific energy in the site, is changed in the DSMKM, assuming that the initial numbers of lethal and sub-lethal lesions produced in a domain are proportional to the *saturation-corrected specific energy*, z^* in the domain, calculated as

$$z^* = z_0 \sqrt{1 - \exp\left[-(z/z_0)^2\right]}, \tag{90}$$

where z_0 can be obtained from $z_0 = y_0 (\bar{l}_d / m_d)$ with the saturation correction parameter y_0 defined in **Eq. (66)**.

By applying this new parameter, the natural logarithm of survival for a domain and the nucleus, **Eqs (35)** and **(37)**, can be rewritten, respectively, as

$$\begin{aligned} \log(s(z)) &= -Az^* - Bz^{*2}, \\ \log(S_n(z_n)) &= -\alpha_0 \int_0^\infty z^* f(z; z_n)\, dz - \beta_0 \int_0^\infty z^{*2} f(z; z_n)\, dz, \end{aligned} \tag{91}$$

with the natural log of the survival fraction of cell irradiated with dose D, $\log S(D) = \langle S_n \rangle_c$, given by substituting **Eq. (91)** in **Eq. (41)**.

The evaluation of the multi-event probability density $f(z; z_n)$ is obtained numerically by applying a general n-fold convolution method such as the one presented in **Section 2** (**Eqs 4** and **6**) to the single event probability density $f_1(z)$. The evaluation of $f_1(z)$ is performed exploiting a microdosimetric function implemented in the PHITS Monte Carlo code [123, 124]. The sum in **Eq. (6)** can be truncated for practical purposes, with 100 events being enough to evaluate the density probability function of cells with $z_n = 100$ Gy.

The same approach is used to calculate the multi-event probability density of the cell nucleus specific energy, for an absorbed macroscopic dose D, $f_n(z_n, D)$, from the single event function $f_{n,1}(z_n)$. However, since the nucleus radius is over the available range of the microdosimetric function implemented in PHITS, $f_{n,1}(z_n)$ is determined from the frequency distribution of the LET L, $F_L(L)$:

$$f_{n,1}(z_n) = \int_0^\infty F_L(L) f_{n,1}(z_n, L)\, dL, \tag{92}$$

where $f_{n,1}(z_n, L)$ represents the probability density of z_n from a particle with LET = L. Following the formalism carried out in [125], the expression for $f_{n,1}(z_n, L)$ is written as a Fermi function:

$$f_{n,1}(z_n, L) = \frac{2C}{(L\eta)^2} \frac{z_n}{\exp\left[(z_n - L\eta)/\gamma\right] + 1}, \tag{93}$$

where C is a normalization constant and η is a units conversion coefficient. The parameter γ tunes the slope of the Fermi function or, equivalently, the magnitude of the fluctuation of z_n due to the energy straggling.

Once $f_{n,1}(z_n)$ is determined, the multi-event function $f_n(z_n; D)$ for the nucleus is obtained with the same n-fold convolution procedure used in the case of $f(z; z_n)$. In this case, however, due to the higher average number of events that can happen in the nucleus

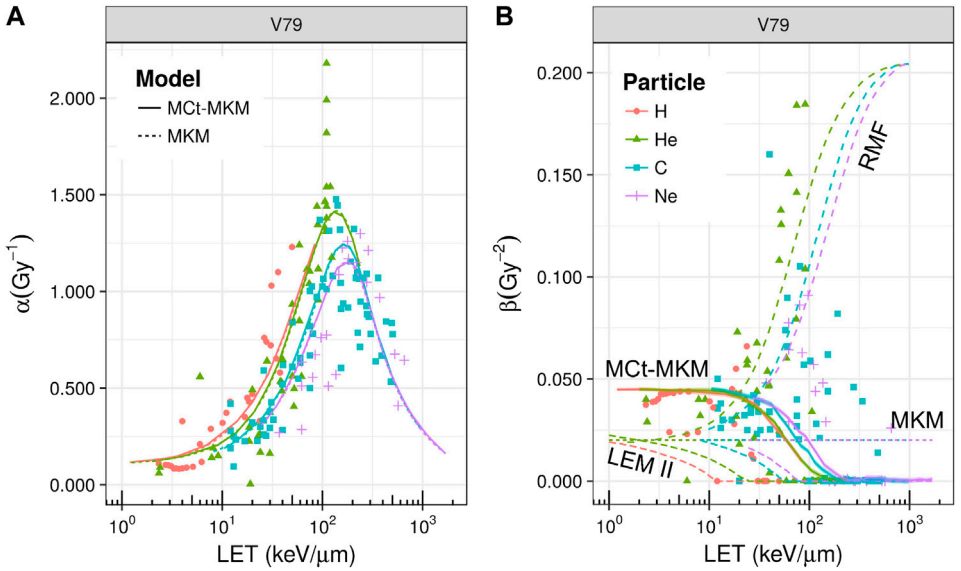

FIGURE 12 | Linear quadratic α **(panel A)** and β **(panel B)** parameters as a function of LET for the irradiation of V79 cells with different ions. Points represent experimental data taken from PIDE [82], different colors/gray levels and shapes refer to H, He, C, and Ne ions, respectively (the color/gray level and shape legend refers both to **panels A and B**). In panel A, solid and dashed lines represent, respectively, the extrapolation with the MCt-MKM and the original MKM, while in panel B, a comparison between different models is reported (namely, MKM, MCt-MKM, LEM-II, and RMF). In the case of the MCt-MKM, overlapped to the α and β curves, the MC statistical confidence bands (68%) are reported. These bands are small due to the high statistics and they blend with the curves' thickness. A saturation effect is observed for both α and β parameters. Plot taken from [23].

compared to the domain, $\lambda_n(D) \gg \lambda(z_n)$, the computation is significantly more demanding and cannot be practically used for applications inherently complex such as TPS evaluations for ion beam treatments. To overcome this problem, in the case of high-dose irradiations, a pre-evaluated database of probability densities derived from mono-energetic irradiations is used and combined in a central limit approximation.

To overcome the long computational time of the DSMK model in a TPS workflow, a further optimization is performed for the computation of the survival in **(91)** that bypasses the necessity to compute the n-fold convolution integral (**Eq. 6**). In this formulation of the model (SMK), it is assumed that a saturation effect triggered by multiple hits of radiations to a domain is negligibly small so that the magnitude of the effect for the n-event energy deposition can be derived from the estimate with the single event density probabilities (see also **Eqs 9** and **12**):

$$\frac{\int_0^\infty z^* f(z,\lambda_n)\,\mathrm{d}z}{\int_0^\infty z f(z,\lambda_n)\,\mathrm{d}z} \approx \frac{\int_0^\infty z^* f_1(z)\,\mathrm{d}z}{\int_0^\infty z f_1(z)\,\mathrm{d}z} = \frac{z_F^*}{z_F} \tag{94}$$

and

$$\frac{\int_0^\infty z^{*2} f(z,\lambda_n)\,\mathrm{d}z}{\int_0^\infty z^2 f(z,\lambda_n)\,\mathrm{d}z} \approx \frac{\int_0^\infty z^{*2} f_1(z)\,\mathrm{d}z}{\int_0^\infty z^2 f_1(z)\,\mathrm{d}z} = \frac{z_D^*}{z_D}. \tag{95}$$

Following these approximations, the natural log of the survival fraction of a cell can be calculated by substituting **Eqs (94)** and **(95)** in **Eq. (91)**, 0btaining

$$\log(S_n(z_n)) = -\alpha_0 z_n \frac{\overline{z}F^*}{z_F} - \beta_0 (z_D z_n + z_n^2)\frac{z_D{}^*}{z_D}. \tag{96}$$

In order to reduce further the computational effort for TPS applications, assuming that in standard condition of ion beam radiotherapy the events inducing the saturation of complex DNA damages are rare, and hence $z_F^*/z_F \approx 1$, the following approximation of **Eq. (41)** was derived [112]:

$$\log S(D) = \log\left\{1 + D\left[-\beta_{\mathrm{SMK}} + \frac{1}{2}(\alpha_{\mathrm{SMK}} + 2\beta_{\mathrm{SMK}} D)^2\right] z_{n,D}\right\} - \alpha_{\mathrm{SMK}} D - \beta_{\mathrm{SMK}} D^2, \tag{97}$$

with

$$\alpha_{\mathrm{SMK}} := (\alpha_0 + z_D^* \beta_0), \tag{98}$$

$$\beta_{\mathrm{SMK}} := \beta_0 (z_D^*/z_D). \tag{99}$$

Both DSMK and SMK models can reproduce the measured survival fractions, even for high-LET and high-dose irradiations, whereas the simple saturation-based MKM [20] predicts lower values for these irradiations due to the intrinsic ignorance of the stochastic nature of the cell nucleus specific energies (see **Figure 13**). In particular, the DSMK model can account for the decrease in the β parameter observed in high-dose irradiations over 10 Gy due to the saturation effect triggered by multiple hits of radiations to a domain.

3.9 Extensions and Further Improvements

In recent years, a number of studies have been published reporting further refinements and extensions of the MKM. Among these are further improvement accounting of the non-Poissonian statistics [112, 126], the inclusion of an explicit DNA modeling [69, 70], the effect of a heterogeneous cell population

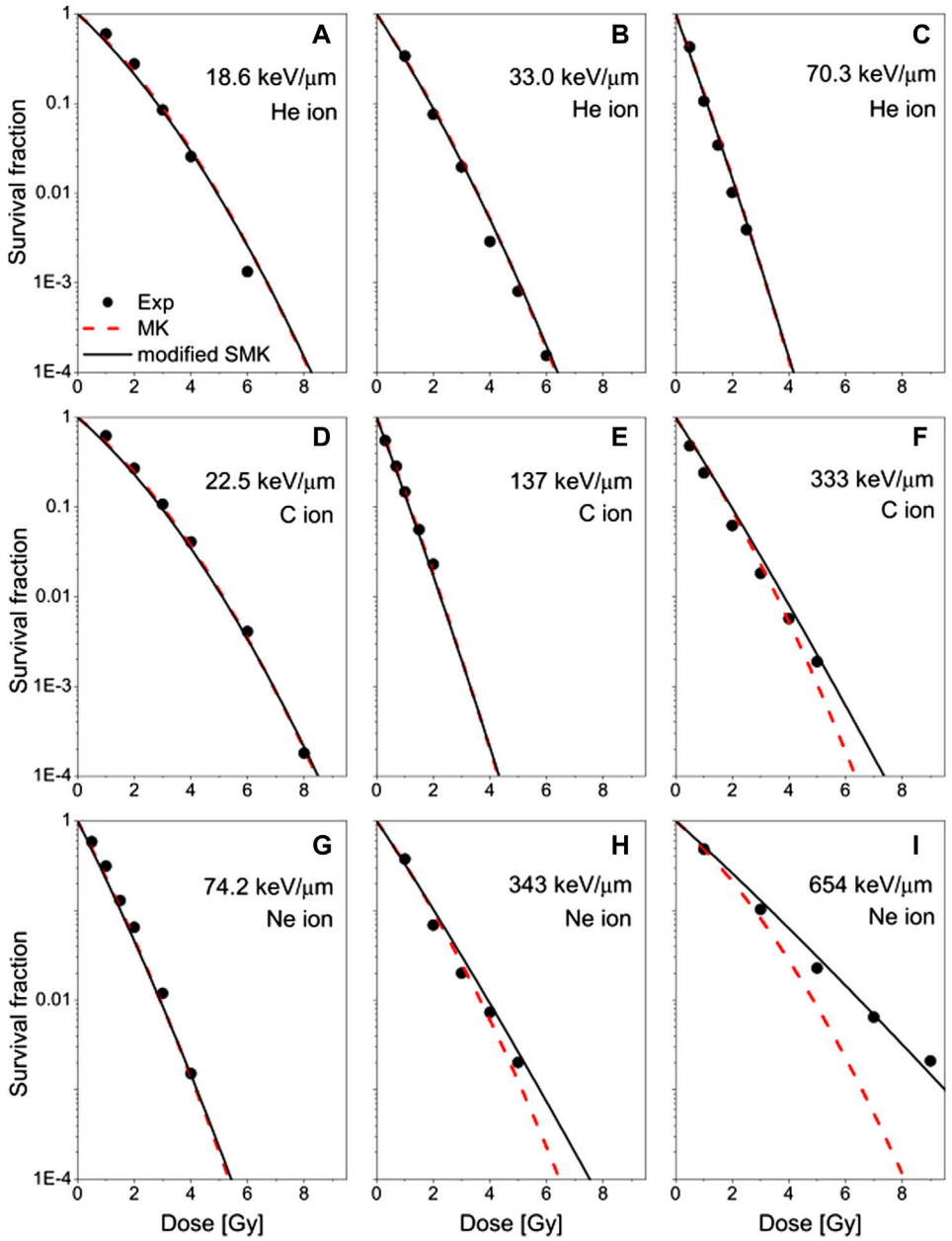

FIGURE 13 | The measured survival fractions of the HSG cell exposed to 3He, **(A)–(C)**; 12C, **(D)–(F);** and 20Ne-ion beams, **(G)–(I)** at different LETs reported by Furusawa et al. [109] (dots), compared with the estimations based on the modified SMK (solid curves) and the MKM (dashed curves). Experimental data taken from [109]. Plot taken from [112].

including the cell-cycle variance [39, 114, 127], and the inclusion of non-target effects [128]. Extension of the model has been also proposed to compute quantities beyond the RBE, such as the oxygen enhancement ratio (OER) [37, 38]. In the following of this section, some details about a selection of these developments are described.

3.9.1 Oxygen Enhancement Ratio (OER) Modeling

Several experiments show that cellular oxygenation condition strongly affects their response to ionizing radiation. In particular, a significantly lower cell death rate is observed after exposure to ionizing radiation in the presence of a reduced concentration of oxygen in the cells, i.e., in hypoxic conditions. As clinically observed, solid tumors can contain oxygen-deficient regions, thus increasing their radioresistance and potentially leading to treatment failure [129, 130]. An understanding of why high-LET radiations are so effective at overcoming tumor hypoxia [131, 132] is also particularly relevant for the individualization and optimization of ion beam radiotherapy. For this purpose, attempts to extend the MKM to describe the dependence of

the radiation effects on the oxygen concentration in cells and to model the oxygen enhancement ratio (OER) have been made [37, 38].

It is interesting to note that these MKM-based approaches, although different, do not focus on OER modeling, a relative value, but directly on the prediction of hypoxic cell survival data, being the OER a derived quantity.

In [37], the reduction of lethal (x_I) and potentially lethal (x_{II}) damage due to the absence of oxygen is linked in the low-LET region to the phenomenological photon OER. This linking is realized through the application of an Alper and Flanders functional formalism [133] to add an explicit dependence to the oxygen concentration to the parameters λ and κ (**Eq. 28**) and the sizes of the domain and nucleus. In particular, the parameters λ and κ and the domain size are assumed to vary with the inverse of the photon OER while the nucleus size is assumed to be proportional to the photon OER as a function of oxygen concentration.

In [38], the general approach proposed by Wenzl and Wilkens [134] has been adapted to the amorphous track approach to the MKM [21] (the latter described in **Section 3.6**). The inclusion of track model ultimately brings to the OER an explicit dependence on ion type while the Wenzl and Wilkens formalism brings an explicit dose and oxygen concentration dependence in the α and β parameters. These characteristics have been exploited, by integrating the model in a TPS, to evaluate the tumor control probability (TCP), to facilitate the identification of the optimal treatment conditions in terms of ion choice and dose fractionation in the presence of hypoxia.

The MKM-based OER models were verified against *in vitro* data from HSG, V79, and CHO cells in aerobic and hypoxic conditions, irradiated with different ion beams [109]. Examples of the model prediction vs. the experimental data are reported in **Figure 14**.

3.9.2. Non-Targeted Effects

In the majority of cell survival modeling approaches, it is assumed that biological effects of radiation are exclusively due to direct DNA damage resulting from the ionization caused by the incident radiation. In recent years, this assumption has been extensively challenged by considering a variety of indirect processes, also referred to as bystander or non-targeted effects (NTE) that significantly impact on the cellular response to the radiation [137]. NTEs have been interpreted as a result of intercellular communication with cell-killing signals between hit and non-hit cells [138, 139], resulting in induced DNA damage in non-hit cells [140].

Attempts to derive kinetic equations to model the intercellular signaling which incorporates signal production and response kinetics have been made [141–143]. In recent studies, such as by Matsuya et al. [128], an integration of these signaling kinetic equations in the MKM has been proposed.

In this formulation, denoted integrated microdosimetric kinetic (IMK) model, the number of signaling activation events, N_{NT}, in the domain is assumed to be a linear-quadratic function of the specific energy z. Thus, following the same procedure and the assumption of a Poisson statistics used to derive **Eqs (44), (45)**, the dose dependent fraction of receiving cells that are activated is written as

$$f_{\mathrm{NT}}(D) = 1 - e^{-\langle N_{\mathrm{NT}}\rangle_c} = 1 - e^{-\left(\alpha_{\mathrm{NT}} + z_D\beta_{\mathrm{NT}}\right)D + \beta_{\mathrm{NT}}D^2}, \tag{100}$$

where α_{NT} and β_{NT} are the LQ coefficients of the signal activation process. The propagation of the cell-killing signal is modeled as a diffusion process with diffusion constant θ and a simple exponential decay with a rate constant λ. The signal concentration $\rho_s(\underline{r}, t)$, where $\underline{r}$ is a spatial position and t is time, can hence be obtained by solving the continuity equation:

$$\frac{\partial \rho_s(\underline{r}, t)}{\partial t} = \theta \nabla^2 \rho_s(\underline{r}, t) - \lambda \rho(\underline{r}, t). \tag{101}$$

In non-hit cells, the NTE sub-lethal lesions $[x_{II}]_{\mathrm{NT}}$ are assumed to be induced in proportion to the signal concentration $\rho_s(\underline{r}, t)$ and then converted to lethal lesions x_I with the same constant rate a of **Eq. (27)** so that the number of sub-lethal lesions is written as

$$\begin{aligned}\left[\dot{x}_{II}(\underline{r}, t)\right]_{\mathrm{NT}} = {} & \left(1 - f_{\mathrm{NT}}(D)\right)\left[x_{II}(\underline{r}, t)\right]_{\mathrm{NT}} \kappa_{\mathrm{NT}} R_{\mathrm{NT}} \rho_s(\underline{r}, t) \\ & - (a + r_{\mathrm{NT}})\left[x_{II}(\underline{r}, t)\right]_{\mathrm{NT}},\end{aligned} \tag{102}$$

where R_{NT} is the constant rate for cell-killing signals reacting with the nucleus of non-hit cells, κ_{NT} is the number of sub-lethal lesions per domain caused by the signals, and r_{NT} is a constant rate for repair in non-hit cells (in general, $r_{\mathrm{NT}} \neq r$, i.e., the repair rates in target and non-target cells are different). In [128], the following functional form for the cell survival fraction by the NTE (S_{NT}) has been proposed as an approximate solution of the previous equations

$$\log S_{\mathrm{NT}} = -\left\langle \left[x_{I,n}\right]_{\mathrm{NTE}} \right\rangle_c = -\delta\left(1 - e^{-\left(\alpha_{\mathrm{NT}} + z_D\beta_{\mathrm{NT}}\right)D + \beta_{\mathrm{NT}}D^2}\right) e^{-\left(\alpha_{\mathrm{NT}} + z_D\beta_{\mathrm{NT}}\right)D + \beta_{\mathrm{NT}}D^2}, \tag{103}$$

where δ is a function of the other parameters introduced in the former equations that characterize the intercellular signaling process.

In order to compute the cell survival probability S with the inclusion of both NTEs and targeted effects, an approximation is made in which it is assumed that the probability of interactions between sub-lethal lesions x_{II} and $[x_{II}]_{\mathrm{NT}}$ in the domain is negligible. This assumption factorizes the two systems of **Eqs (27)** and **(102)** and hence considers the total cell survival as the product of $S = S_{\mathrm{T}} \times S_{\mathrm{NT}}$, where the survival for targeted cells, S_{T}, is given by **Eq. (43)**. **Figure 15** shows an example of the fitting of the IMK model with experimental clonogenic data. It is interesting to note the possibility of the IMK model to account for deviations from the LQ formalism, reproducing the low-dose hypersensitivity behavior of cell response and evincing its relation with DNA repair mechanisms.

4 OTHER MODELS

This section presents alternative models to determine RBE based on microdosimeric approaches.

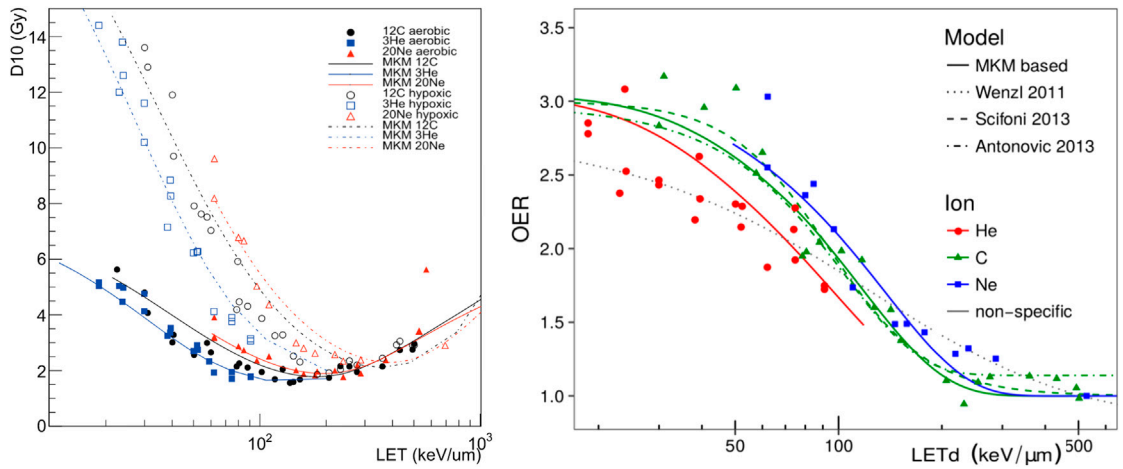

FIGURE 14 | (Left) D_{10}% values for oxic (closed symbols) and extremely hypoxic (open symbols) V79 cells as a function of dose-averaged LET [109]. The lines represent the MKM calculations (solid lines) and the hypoxia-adapted MKM calculations with parameters optimised for the V79 cell line (dashed lines). Plot from [37]. **(Right)** The OER as a function of the dose-averaged LET for the irradiation of HSG cells with different ions. The points represent the experimental data taken from Furusawa et al. [109]. The continuous lines represent the OER simultaneously evaluated by means of the MKM-based model for He, C, and Ne. In the same plot, the OER calculated by other models is reported for comparison (non-continuous lines). The model by Scifoni et al. [135] is associated with carbon ions only, while the model by Wenzl and Wilkens [134] is not associated with any specific ion. An evaluation with the model proposed in Antonovic [136] is also shown. Plot taken from [38].

4.1 RBE Weighting Functions

The microdosimetric RBE weighting function approach has been proposed initially by Menzel, Pihet, and Wambersie et al. [27, 33] to compare the beam quality of different neutron [27] and proton [144, 145] therapeutic installations using measured microdosimetric distributions of lineal energy. Based on previous studies on proton beams [146, 147], this approach uses measured microdosimetric distributions of lineal energy, y, combined with an experimentally derived *biological weighting function*, for specific cell line and endpoints, $r(y)$, to evaluate the RBE.

Let $P(y)$ be the cellular response function for a population suffering the fraction of dose $d(y)\mathrm{d}y$ corresponding to the lineal energy y. $d(y)$ is the dose probability density of y and can be evaluated as $d(y) = \frac{y}{\bar{y}_F} f(y)$ [34]. The linear α parameter, interpreted as the biological effect E per unit dose, is expressed as

$$\alpha = E/D = \int \frac{P(y)}{y} d(y)\,\mathrm{d}y \equiv \int r(y) d(y)\,\mathrm{d}y, \tag{104}$$

where $r(y)$ is defined as the response function. Therefore, the model is rigorously valid under the assumption of a low dose approximation where the cellular response function is linear.

$P(y)$ or directly $r(y)$ is experimentally derived. A formulation for $r(y)$ is given in the following [148, 149]:

$$r(y) = \sigma_E \left[1 - \exp\left(-a_1 y - a_2 y^2 - a_3 y^3\right)\right]/y, \tag{105}$$

where the σ_E, a_1, a_2, and a_3 are parameters specific to the radiobiological end points and are independent on the quality of the radiation. These parameters are determined experimentally by fitting a set of different measurements of α_i or $\mathrm{RBE}_{\alpha,i} = \alpha_i/\alpha_X$ using different irradiation modalities with different radiation qualities $i = 1, 2, 3, \ldots, N$.

The set of relations that have to be fitted is hence

$$\mathrm{RBE}_{\alpha,i} = \int r(y) d_i(y)\,\mathrm{d}y;\ i = 1, \ldots, N. \tag{106}$$

The solution of the system of **Eq. (106)** can be obtained with different methods, such as non-parametric multi-objective optimization methods [150] or iterative procedures [40] through which an initial guess function $r(y)$ is iteratively updated to best fit **Eq. (106)**.

4.2 The Repair–Misrepair–Fixation (RMF) Model

The repair–misrepair–fixation (RMF) model combines the RMR and LPL models, adding the consideration of intra- and inter-track[2] binary misrepair to predict the biological effect of LET [24–26]. The RMF model considers the entire cell nucleus as the volume for pairwise DSB interactions. In the RMF model, a coupled system of nonlinear ordinary differential equations is used to model the time-dependent kinetics of DSB induction, rejoining, and pairwise DSB interaction to form lethal (and nonlethal) chromosome damage. The model treats initial DSB formation as a compound Poisson process and postulates a first-order repair term that gives rise to exponential rejoining kinetics for most DSB (> 98%) and a second-order (quadratic) term to

[2]Intratrack binary misrepair occurs when an energy deposition along the track forms two or more DSBs that interact in pairwise mode to form an exchange. Intertrack, instead, is a binary misrepair arising from the pairwise interaction of break ends associated with DSBs that were formed by two separate radiation tracks through a cell.

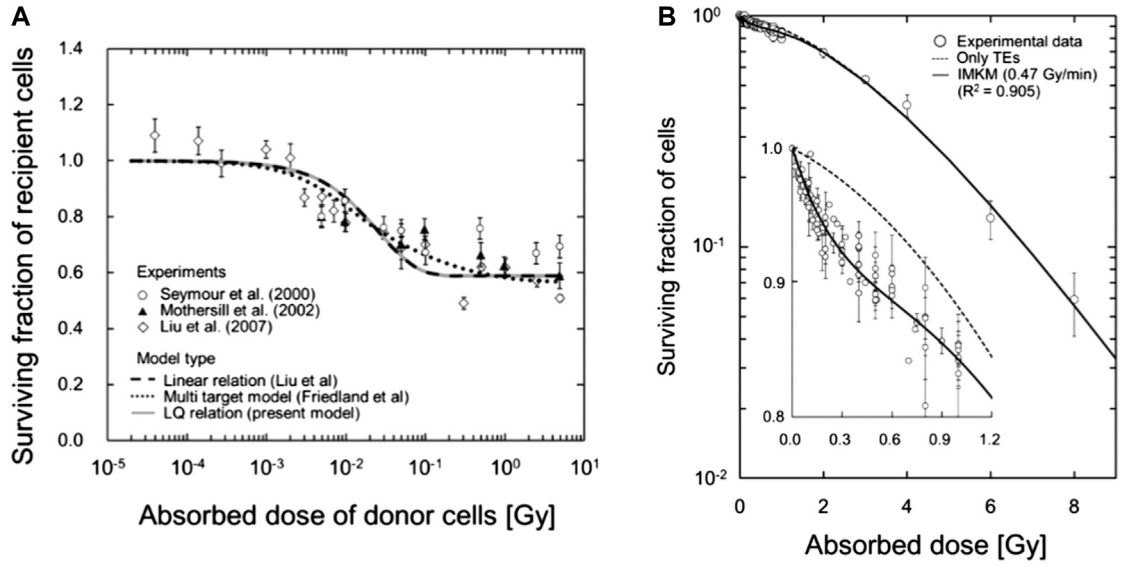

FIGURE 15 | (A) Comparison between the IMK model (**Eq. 103**), continuous gray line in the plot, and experimental medium transfer bystander effect (MTBE) cell survival data. **(B)** Fitting of the IMK model to experimental cell survival data for V79-379A. Plot taken from [128] (http://creativecommons.org/licenses/by/4.0/).

account for the small subset of the initial DSB (< 2%) that undergo pairwise DSB interactions to form an exchange.

An LQ approximation of the solution of the RMF system of differential equations can be expressed as follows [24, 25]:

$$\mathrm{RBE}_{\alpha} = \frac{\Sigma}{\Sigma_X}\left(1 + \frac{2}{R\Sigma_X}\left(\Sigma z_{n,F} - \Sigma_X\left(z_{n,F}\right)_X\right)\right), \tag{107}$$

$$\mathrm{RBE}_{\beta} = \frac{\Sigma}{\Sigma_X}, \tag{108}$$

where Σ is the initial number of DBS per gray per giga base pair (Gy^{-1} Gbp^{-1}) and $z_{n,F}$ is the frequency-average specific energy evaluated in the nucleus (see **Eq. 9**), for the particle radiation. The suffix X indicates the same quantities for the reference photon radiation. RBE_{α}, RBE_{β}, and R are defined in **Eq. (51)**, while the ratio $\Sigma/\Sigma_X = \mathrm{RBE}_{\mathrm{DSB}}$ can be interpreted as the RBE for DSB induction.

From **Eq. (107)**, it follows that the radiation response of a cell exposed to a low- or high-LET radiation is uniquely determined by one microdosimetric parameter ($z_{n,F}$) and two biological parameters ($\mathrm{RBE}_{\mathrm{DSB}}$) and R. $z_{n,F}$ can be derived from microdosimetric measurements or computed via Monte Carlo simulations. Implicit in the determination of $z_{n,F}$ is the knowledge of the size of the nucleus. For a spherical water target of diameter d, the frequency-average specific energy can be approximated by **Eq. (20)**. A complication arises from the fact that, in general, $\mathrm{RBE}_{\mathrm{DSB}}$ also strongly depends on particle type and kinetic energy (and thus LET or lineal energy) although it is considered to be the same among all eukaryotes. Consequently, R is basically left as the main parameter of the RMF is needed to discriminate the radiation response among different cell lines (compare also the MKM formulation, **Eq. 53**).

From a practical point of view, $\mathrm{RBE}_{\mathrm{DSB}}$ is obtained and stored in a look-up table as a function of particle type and kinetic energy by means of Monte Carlo computations. The MCDS Monte Carlo code [151, 152], which is able to simulate also the dependence on the oxygen concentration, is typically used in these computations, so that the RMF has been also used to predict the OER [153] along with the clonogenic data [25] and DSB induction estimates [24] for ion irradiations.

In panel (b) of **Figure 12**, the RMF prediction of the RBE_{β} compared with experimental data and the evaluations of other models is reported. It is worth noting that the RMF model predicts an increasing β for increasing LET (see **Eq. 107**). This is in contrast with other models, such as the LEM, which predict a decreasing β, or the MKM, which, depending on the specific formulation, predicts both a constant and a decreasing β.

The RMF has been also implemented in a TPS to evaluate the 3D RBE distribution in irradiated patients [154]. It is interesting to note that one of the appealing aspects of the RMF for TPS studies is that the specific response of the tissue, both healthy and tumoral, is explicitly determined by a single parameter, R. This is a simplification, but allows to study the effect of the specificity of the tissue response in a direct way, also allowing for a distribution of R values and hence easily accounting for the variability and the uncertainty associated to this clinical parameter.

5 SUMMARY

In clinical treatment planning, the RBE has to be calculated by radiobiological mathematical models, which, in spite of all validation efforts, still involve significant sources of uncertainty.

The aim of this review was to present the theoretical aspects of a selection of radiobiological models that emphasize the link of *in vitro* and *in vivo* radiobiological outcomes, such as the RBE, to microdosimetric experimental data. We approached these models through a conceptual sketch of their assumptions, highlighting the continuity and leaps of their mathematical formulations. For each model, we addressed the limit of applicability and eventual improvements and the link of their input parameters to experimental observables.

A particular emphasis to the microdosimetric kinetic (MKM)-based models has been given. Starting from its first seminal formulation by Hawkins [18], the MKM has represented an effective approach to link the microdosimetric quantities, which describe the quality of the radiation, to the radiobiological effects and, at present, it is one of the most widely used models to evaluate the RBE in both research and clinical applications. The MKM approach for RBE evaluations has gained a particular interest in recent years, with the appearance of different studies aimed to improve the accuracy of the model and to extend its range of applicability in different biological contexts, such as the OER prediction and non-target effects.

Although sharing similar theoretical bases, the MKM-based models make different assumptions and approximations in their implementation. Based on these differences, the models considered in this review (including also the RMF model) make, in particular, different predictions in the dependence of β on particle LET and the RBE for cell survival in the overkill regime, for particles with a LET$\gtrsim$150 keV/μm.

Two main aspects of the considered models, where recent efforts have brought interesting insight, and where further future studies could bring potential improvements, could be identified. One aspect is the ascertainment of a more accurate link of the theoretical descriptions to specific cellular mechanisms of DNA damage induction and its evolution, exploiting also information from nanodosimetric data. Another aspect is to improve the theoretical statistical description of the involved processes, be them either the stochastic nature of the energy deposition or the stochastic nature of the cell response to the irradiation.

Future comparisons of model predictions with experimental data are hence needed to fully discriminate among competing mechanisms to be incorporated for the improvement of these models to evaluate the RBE.

AUTHOR CONTRIBUTIONS

VB and AA have provided a critical interpretation of the theoretical aspects of each model and its applications, deciding structure and principal contents of this review. They have cured the links with experimental data underlining limitations and strengths of each approach. The experience and accuracy of AA have leaded the entire work. FG has principally handled the mathematical aspects of the work, his help has been precious in revising notation and clarifying model formulation. ES has helped particularly in the general parts and introduction and has given also his valuable opinion on the structure and contents. MM and FT have given a contribution to experimental links, CT has supervised.

FUNDING

This work has been partially funded by MoVeIT, NEPTUNE INFN CSN5 projects, and Fondazione CARITRO Cassa di Risparmio di Trento e Rovereto.

REFERENCES

1. Durante M, Orecchia R, Loeffler JS. Charged-particle therapy in cancer: clinical uses and future perspectives. *Nat Rev Clin Oncol* (2017) 14:483. doi:10.1038/nrclinonc.2017.30
2. Durante M, Loeffler JS. Charged particles in radiation oncology. *Nat Rev Clin Oncol* (2010) 7:37. doi:10.1038/nrclinonc.2009.183
3. Kanai T, Furusawa Y, Fukutsu K, Itsukaichi H, Eguchi-Kasai K, Ohara H. Irradiation of mixed beam and design of spread-out Bragg peak for heavy-ion radiotherapy. *Radiat Res* (1997) 147:78–85.
4. Kanai T, Endo M, Minohara S, Miyahara N, Koyama-Ito H, Tomura H, et al. Biophysical characteristics of HIMAC clinical irradiation system for heavy-ion radiation therapy. *Int J Radiat Oncol Biol Phys* (1999) 44:201–10.
5. KawachiMatsufuji H, Mizoe J, Kamada T, Baba M, Kato S, Kato H, et al. Overview of clinical experiences on carbon ion radiotherapy at NIRS. *Radiother Oncol* (2004) 73(Suppl 2) S41–9. doi:10.1016/s0167-8140(04)80012-4
6. MiyamotoTsuji J, Wambersie A, Octave-Prignot M, De Coster B, Grégoire V. Radiobiological characterisation of clinical beams: importance for the quality assurance (QA) programme in ion beam therapy. *Int J Radiat Oncol Biol Phys* (2006) 9:173–178. doi:10.1080/713844023
7. Carabe A, Moteabbed M, Depauw N, Schuemann J, Paganetti H. Range uncertainty in proton therapy due to variable biological effectiveness. *Phys Med Biol* (2012) 57:1159–72. doi:10.1088/0031-9155/57/5/1159
8. Wedenberg M, Toma-Dasu I. Disregarding RBE variation in treatment plan comparison may lead to bias in favor of proton plans. *Med Phys* (2014) 41:091706. doi:10.1118/1.4892930
9. Jones B. Towards achieving the full clinical potential of proton therapy by inclusion of LET and RBE models. *Cancers* (2015) 7:460–80. doi:10.3390/cancers7010460
10. McNamara AL, Schuemann J, Paganetti H. A phenomenological relative biological effectiveness (RBE) model for proton therapy based on all published *in vitro* cell survival data. *Phys Med Biol* (2015) 60:8399–416. doi:10.1088/0031-9155/60/21/8399
11. Scholz M, Kraft G. A parameter-free track structure model for heavy ion action cross sectionsBiophysical modelling of radiation effects. *Radiat Res* (1997) 147:78–85 (1992).
12. Scholz M, Kraft G. Track structure and the calculation of biological effects of heavy charged particles. *Adv Space Res* (1996) 18:5–14. doi:10.1016/0273-1177(95)00784-c
13. Scholz M, Kellerer AM, Kraft-Weyrather W, Kraft G. Computation of cell survival in heavy ion beams for therapy. The model and its approximation. *Radiat Environ Biophys* (1997) 36:59–66. doi:10.1007/s004110050055
14. Elsässer T, Scholz M. Cluster effects within the local effect model. *Radiat Res* (2007) 167:319–29. doi:10.1667/RR0467.1

15. Elsässer T, Krämer M, Scholz M. Accuracy of the local effect model for the prediction of biologic effects of carbon ion beams *in vitro* and *in vivo*. *Int J Radiat Oncol Biol Phys* (2008) 71:866–72. doi:10.1016/j.ijrobp.2008.02.037
16. Elsässer T, Weyrather WK, Friedrich T, Durante M, Iancu G, Krämer M, et al. Quantification of the relative biological effectiveness for ion beam radiotherapy: direct experimental comparison of proton and carbon ion beams and a novel approach for treatment planning. *Int J Radiat Oncol Biol Phys* (2010) 78:1177–83. doi:10.1016/j.ijrobp.2010.05.014
17. ScholzKragl T, Scholz U, Elsässer T, Durante M, Scholz M. Calculation of the biological effects of ion beams based on the microscopic spatial damage distribution pattern. *Int J Radiat Biol* (2012) 88:103–7. doi:10.3109/09553002.2011.611213
18. Hawkins RB. A statistical theory of cell killing by radiation of varying linear energy transfer. *Radiat Res* (1994) 140:366–74.
19. Hawkins RB. A microdosimetric-kinetic model for the effect of non-Poisson distribution of lethal lesions on the variation of RBE with LET. *Radiat Res* (2003) 160:61–9. doi:10.1667/rr3010
20. Kase Y, Kanai T, Matsumoto Y, Furusawa Y, Okamoto H, Asaba T, et al. Microdosimetric measurements and estimation of human cell survival for heavy-ion beams. *Radiat Res* 166 (2006) 629–38. doi:10.1667/RR0536.1
21. ShinodaSakama Y, Kanai T, Matsufuji N, Furusawa Y, Elsässer T, Scholz M. Biophysical calculation of cell survival probabilities using amorphous track structure models for heavy-ion irradiation. *Phys Med Biol* (2007) 53:37. doi:10.1088/0031-9155/53/1/003
22. Sato T, Furusawa Y. Cell survival fraction estimation based on the probability densities of domain and cell nucleus specific energies using improved microdosimetric kinetic models. *Radiat Res* (2012) 178:341–56. doi:10.1667/rr2842.1
23. Manganaro L, Russo G, Cirio R, Dalmasso F, Giordanengo S, Monaco V, et al. A Monte Carlo approach to the microdosimetric kinetic model to account for dose rate time structure effects in ion beam therapy with application in treatment planning simulations. *Med Phys* (2017) 44:1577–89. doi:10.1002/mp.12133
24. AttiliMuraro DJ, Stewart RD, Semenenko VA, Sandison GA. Combined use of Monte Carlo DNA damage simulations and deterministic repair models to examine putative mechanisms of cell killing. *Radiat Res* (2008) 169:447–59. doi:10.1667/RR1046.1
25. Frese MC, Yu VK, Stewart RD, Carlson DJ. A mechanism-based approach to predict the relative biological effectiveness of protons and carbon ions in radiation therapy. *Int J Radiat Oncol Biol Phys* (2012) 83:442–50. doi:10.1016/j.ijrobp.2011.06.1983
26. Stewart RD, Carlson DJ, Butkus MP, Hawkins R, Friedrich T, Scholz M. A comparison of mechanism-inspired models for particle relative biological effectiveness (RBE). *Med Phys* (2018) 45:e925–2. doi:10.1002/mp.13207
27. Pihet P, Menzel H, Schmidt R, Beauduin M, Wambersie A. Biological weighting function for RBE specification of neutron therapy beams. Intercomparison of 9 European centres. *Radiat Protect Dosim* (1990) 31:437–42.
28. Menzel HG, Pihet P, Wambersie A. Microdosimetric specification of radiation quality in neutron radiation therapy. *Int J Radiat Biol* (1990) 57:865–83. doi:10.1080/09553009014550991
29. Wambersie A, Pihet P, Menzel H. The role of microdosimetry in radiotherapy. *Radiat Protect Dosim* (1990) 31:421–32.
30. Wambersie A. Contribution of microdosimetry to the specification of neutron beam quality for the choice of the clinical RBE'in fast neutron therapy. *Radiat Protect Dosim* (1994) 52:453–60.
31. Gerlach R, Roos H, Kellerer AM. Heavy ion RBE and microdosimetric spectra. *Radiat Protect Dosim* (2002) 99:413–8. doi:10.1093/oxfordjournals.rpd.a006821A
32. Wambersie A, Hendry JH, Andreo P, DeLuca PM, Gahbauer R, Menzel H, et al. The RBE issues in ion-beam therapy: conclusions of a joint IAEA/ICRU working group regarding quantities and units. *Radiat Protect Dosim* 122 (2006) 463–70. doi:10.1093/rpd/ncl447
33. Whitmore A, Sato T, Matsuya Y, Kase Y, Magrin G, Verona C, et al. Development of a new microdosimetric biological weighting function for the RBE10 assessment in case of the V79 cell line exposed to ions from 1H to 238U. *Phys Med Biol* (2020) 27:87–123. doi:10.1088/1361-6560/abbf96
34. Booz J, Braby L, Coyne J, Kliauga P, Lindborg L, Menzel H, et al. *Journal of the International Commission on radiation Units and measurements. NP–NP* (1983). Report 36.
35. Kellerer AM, et al. Fundamentals of microdosimetry. *Dosim Ion Radiat* (1985) 1:77–162.
36. Inaniwa T, Furukawa T, Kase Y, Matsufuji N, Toshito T, Matsumoto Y, et al. Treatment planning for a scanned carbon beam with a modified microdosimetric kinetic model. *Phys Med Biol* (2010) 55:6721. doi:10.1088/0031-9155/55/22/008
37. NodaFurusawa C, Hirayama R, Inaniwa T, Kitagawa A, Matsufuji N, Noda K. Adaptation of the microdosimetric kinetic model to hypoxia. *Phys Med Biol* (2016) 61:7586. doi:10.1088/0031-9155/61/21/7586
38. Strigari L, Torriani F, Manganaro L, Inaniwa T, Dalmasso F, Cirio R, et al. Tumour control in ion beam radiotherapy with different ions in the presence of hypoxia: an oxygen enhancement ratio model based on the microdosimetric kinetic model. *Phys Med Biol* (2018) 63:065012. doi:10.1575/1912/bco-dmo.712761.1
39. Matsuya Y, McMahon SJ, Tsutsumi K, Sasaki K, Okuyama G, Yoshii Y, et al. Investigation of dose-rate effects and cell-cycle distribution under protracted exposure to ionizing radiation for various dose-rates. *Sci Rep* (2018a) 8:8287–14. doi:10.1038/s41598-018-26556-5
40. DateMori T, Cosgrove V, Denis J, Gueulette J, Mazal A, Menzel H, et al. Radiobiological effectiveness of radiation beams with broad LET spectra: microdosimetric analysis using biological weighting functions. *Radiat Protect Dosim* (1994) 52:347–52.
41. Rossi HH, Zaider M. Elements of microdosimetry. *Med Phys* (1991) 18:1085–92. doi:10.1118/1.596616
42. Zaider M, Rossi BHH, Zaider M. *Microdosimetry and its applications*. Berlin: Springer (1996).
43. Lindborg L, Waker A. *Microdosimetry: experimental methods and applications*. Boca Raton: CRC Press (2017).
44. Wilson KS, Field SB. Measurement of LET spectra using a spherical tissue-equivalent proportional counter. *Phys Med Biol* (1970) 15:657.
45. Lindborg L, Kyllönen JE, Beck P, Bottollier-Depois JF, Gerdung S, Grillmaier RE, et al. The use of TEPC for reference dosimetry. *Radiat Protect Dosim* (1999) 86 285–8. doi:10.1093/oxfordjournals.rpd.a032959
46. Schrewe H, Khvostunov IK, Cucinotta FA. The response of tissue-equivalent proportional counters to heavy ions. *Radiat Res* (2002) 157:435–45. doi:10.1667/0033-7587(2002)157[0435:trotep]2.0.co;2
47. Conte V, Moro D, Grosswendt B, Colautti P. Lineal energy calibration of mini tissue-equivalent gas-proportional counters (TEPC). *AIP Conf Proc Am Inst Phys* (2013) 1530:171–8. doi:10.3403/30106322u
48. Bradley PD, Rosenfeld AB, Zaider M. Solid state microdosimetry. *Nucl Instrum Methods Phys Res B* (2001) 184:135–57. doi:10.3403/30106322
49. Rosenfeld AB. Novel detectors for silicon based microdosimetry, their concepts and applications. *Nucl Instrum Methods Phys Res Sect A Accel Spectrom Detect Assoc Equip* (2016) 809:156–70. doi:10.1016/j.nima.2015.08.059
50. Byun SH, Spirou GM, Hanu A, Prestwich WV, Waker AJ. Simulation and first test of a microdosimetric detector based on a thick gas electron multiplier. *IEEE Trans Nucl Sci* (2009) 56:1108–13. doi:10.1109/tns.2008.2009214
51. Orchard G, Chin K, Prestwich W, Waker A, Byun S. Development of a thick gas electron multiplier for microdosimetry. *Nucl Instrum Methods Phys Res Sect A Accel Spectrom Detect Assoc Equip* (2011) 638:122–6. doi:10.1016/j.nima.2011.01.179
52. Schuhmacher H, Dangendorf V. Experimental tools for track structure investigations: new approaches for dosimetry and microdosimetry. *Radiat Protect Dosim* (2002) 99:317–23. doi:10.1093/oxfordjournals.rpd.a006793
53. Braby L. Experimental microdosimetry: history, applications and recent technical advances. *Radiat Protect Dosim* (2015) 166:3–9. doi:10.1093/rpd/ncv137
54. Magrin G. A method to convert spectra from slab microdosimeters in therapeutic ion-beams to the spectra referring to microdosimeters of different shapes and material. *Phys Med Biol* (2018) 63:215021. doi:10.1088/1361-6560/aae655

55. Bolst D, Guatelli S, Tran LT, Chartier L, Lerch ML, Matsufuji N, et al. Correction factors to convert microdosimetry measurements in silicon to tissue in 12C ion therapy. *Phys Med Biol* (2017) 62:2055. doi:10.1088/1361-6560/aa5de5
56. Kase K. *The dosimetry of ionizing radiation*. Elsevier (2012).
57. Kellerer AM, Rossi HH. The theory of dual radiation action. *Curr Top Radiat Res* (1972) 8:85–158. doi:10.1667/RRAV17.1
58. Kellerer AM, Rossi HH. A generalized formulation of dual radiation action. *Radiat Res* (1978) 75:471–88.
59. Tobias CA. *The repair–misrepair model of cell survival*. Berlin: Springer. (1980).
60. Tobias CA. The repair-misrepair model in radiobiology: comparison to other models. *Radiat Res Suppl* (1985) 8:S77–95.
61. Curtis SB. Lethal and potentially lethal lesions induced by radiation--a unified repair model. *Radiat Res* (1986) 106:252–70.
62. Curtis SB. *Quantitative mathematical models in radiation biology. The lethal and potentially lethal model—a review and recent development*. Berlin: Springer. (1988). p. 137–46.
63. Schürmann R, Vogel S, Ebel K, Bald I. The physico-chemical basis of DNA radiosensitization: implications for cancer radiation therapy. *Chem A Eur J* (2018) 24:10271–9. doi:10.1002/chem.201884161
64. Van Houten B, Santa-Gonzalez GA, Camargo M. DNA repair after oxidative stress: current challenges. *Curr Opin Toxicol* (2018) 7:9–16. doi:10.1016/j.cotox.2017.10.009
65. Lea DE, Catcheside DG. The mechanism of the induction by radiation of chromosome aberrations in Tradescantia. *J Genet* (1942) 12:60–9. doi:10.1007/BF02982830
66. Kuang Y, Nagy JD, Eikenberry SE. *Introduction to mathematical oncology*. Boca Raton: CRC Press (2016).
67. Hawkins R. A microdosimetric-kinetic model of cell death from exposure to ionizing radiation of any LET, with experimental and clinical applications. *Int J Radiat Biol* (1996) 69:739–55. doi:10.1080/095530096145481
68. Hawkins RB. A microdosimetric-kinetic theory of the dependence of the RBE for cell death on LET. *Med Phys* (1998) 25:1157–70. doi:10.1118/1.598307
69. Matsuya Y, Ohtsubo Y, Tsutsumi K, Sasaki K, Yamazaki R, Date H. Quantitative estimation of DNA damage by photon irradiation based on the microdosimetric-kinetic model. *J Radiat Res* (2014) 55:484–93. doi:10.1093/jrr/rrt222
70. Chen Y, Li J, Li C, Qiu R, Wu Z. A modified microdosimetric kinetic model for relative biological effectiveness calculation. *Phys Med Biol* (2017) 63:015008. doi:10.1118/1.4958000
71. Manganaro L. *Dose delivery time structure effects in particle therapy: development of a time-resolved microdosimetric-kinetic model and implementation of spatiotemporal treatment plan optimization*. [Ph.D. thesis]. Italy: University of Turin (2018).
72. Dikomey E, Franzke J. DNA repair kinetics after exposure to X-irradiation and to internal beta-rays in CHO cells. *Radiat Environ Biophys* (1986) 25:189–94. doi:10.1007/BF01221225
73. Fowler JF. Is repair of DNA strand break damage from ionizing radiation second-order rather than first-order? A simpler explanation of apparently multiexponential repair. *Radiat Res* (1999) 152:124–36.
74. Dale RG, Fowler JF, Jones B. A new incomplete-repair model based on a 'reciprocal-time' pattern of sublethal damage repair. *Acta Oncol* (1999) 38:919–29. doi:10.1080/028418699432608
75. Carabe-Fernandez A, Dale RG, Paganetti H. Repair kinetic considerations in particle beam radiotherapy. *Br J Radiol* (2011) 84:546–55. doi:10.1259/bjr/19934996
76. Schettino G, Ghita M, Richard DJ, Prise KM. Spatiotemporal investigations of DNA damage repair using microbeams. *Radiat Protect Dosim* (2011) 143:340–3. doi:10.1093/rpd/ncq485
77. Mariotti LG, Pirovano G, Savage KI, Ghita M, Ottolenghi A, Prise KM, et al. Use of the γ-H2AX assay to investigate DNA repair dynamics following multiple radiation exposures. *PloS One* 8 (2013) e79541–12. doi:10.1371/journal.pone.0079541
78. Schettino A, Uematsu N, Chatterjee A, Story MD, Burma S, Chen DJ. Repair of HZE-particle-induced DNA double-strand breaks in normal human fibroblasts. *Radiat Res* (2008) 169:437–46. doi:10.1667/rr1165.1
79. Asaithamby A, Hu B, Chen DJ. Unrepaired clustered DNA lesions induce chromosome breakage in human cells. *Proc Natl Acad Sci USA* (2011) 108:8293–8. doi:10.1073/pnas.1016045108
80. Prise KM. A review of DSB induction data for varying quality radiations. *Int J Radiat Biol* (1998) 74:173–84. doi:10.1080/095530098141564
81. StenerlöwAhnström JA, Harper JV, Cucinotta FA, O'Neill P. Participation of DNA-PKcs in DSB repair after exposure to high- and low-LET radiation. *Radiat Res* (2010) 174:195–205. doi:10.1667/RR2071.1
82. Friedrich T, Scholz U, Elsässer T, Durante M, Scholz M. Systematic analysis of RBE and related quantities using a database of cell survival experiments with ion beam irradiation. *J Radiat Res* (2013) 54:494–514. doi:10.1093/jrr/rrs114
83. Dale RG, Jones B. The assessment of RBE effects using the concept of biologically effective dose. *Int J Radiat Oncol Biol Phys* (1999) 43:639–45.
84. Carabe-Fernandez A, Dale RG, Jones B. The incorporation of the concept of minimum RBE (RbEmin) into the linear-quadratic model and the potential for improved radiobiological analysis of high-LET treatments. *Int J Radiat Biol* (2007) 83:27–39. doi:10.1080/09553000601087176
85. Weyrather WK, Debus J. Particle beams for cancer therapy. *Clin Oncol* (2003) 15:S23. doi:10.1053/clon.2002.0185
86. Bird RP. Cysteamine as a protective agent with high-LET radiations. *Radiat Res* (1980) 82:290. doi:10.2307/3575380
87. Bird RP, Zaider M, Rossi HH, Hall EJ, Marino SA, Rohrig N. The sequential irradiation of mammalian cells with X rays and charged particles of high LET. *Radiat Res* (1983) 93:444. doi:10.2307/3576024
88. Russo G, Attili A, Battistoni G, Bertrand D, Bourhaleb F, Cappucci F, et al. A novel algorithm for the calculation of physical and biological irradiation quantities in scanned ion beam therapy: the beamlet superposition approach. *Phys Med Biol* (2015) 61:183. doi:10.1088/0031-9155/61/1/183
89. MarchettoCiocca EL, Lyman JT, Tobias CA. Some effects of accelerated charged particles on bacterial spores. *Int J Radiat Biol Relat Stud Phys Chem Med* (1968) 14:313–30. doi:10.1080/09553006814551171
90. Kase Y, Kanai T, Sakama M, Tameshige Y, Himukai T, Nose H, et al. Microdosimetric approach to NIRS-defined biological dose measurement for carbon-ion treatment beam. *J Radiat Res* (2011) 52:59–68.doi:10.1269/jrr.10062
91. Matsufuji C, Fleta C, Rodríguez J, Lozano M, Gómez F. Preliminary microdosimetric measurements with ultra-thin 3D silicon detectors of a 62 MeV proton beam. *J Instrum* (2015) 10:P01008. doi:10.1088/1748-0221/10/01/p01008
92. Bianchi A, Selva A, Colautti P, Bortot D, Mazzucconi D, Pola A, et al. Microdosimetry with a sealed mini-TEPC and a silicon telescope at a clinical proton SOBP of CATANA. *Radiat Phys Chem* (2020) 171:108730. doi:10.1088/1742-6596/444/1/012058
93. Kiefer J, Straaten H. A model of ion track structure based on classical collision dynamics. *Phys Med Biol* (1986) 31:1201.
94. Chatterjee A, Schaefer HJ. Microdosimetric structure of heavy ion tracks in tissue. *Radiat Environ Biophys* (1976) 13:215–27. doi:10.1007/BF01330766
95. Sakama M, Kanai T, Kase Y, Komori M, Fukumura A, Kohno T. Responses of a diamond detector to high-LET charged particles. *Phys Med Biol* (2005) 50:2275. doi:10.1088/0031-9155/50/10/007
96. Inaniwa T, Kanematsu N, Matsufuji N, Kanai T, Shirai T, Noda K, et al. Reformulation of a clinical-dose system for carbon-ion radiotherapy treatment planning at the National Institute of Radiological Sciences, Japan. *Phys Med Biol* 60 (2015a) 3271–86. doi:10.1088/0031-9155/60/8/3271
97. TsujiiTsuji S, Allison J, Amako K, Apostolakis J, Araujo H, Arce P, et al. GEANT4 - a simulation toolkit. *Nucl Instrum Methods Phys Res Sect A Accel Spectrom Detect Assoc Equip* (2003) 444:63. doi:10.1016/S0168-9002(03)01368-8
98. Aso T, Kimura A, Kameoka S, Murakami K, Sasaki T, Yamashita T. GEANT4 based simulation framework for particle therapy system. *IEEE Nucl Sci Symp Conf Rec* (2007) 33:278–9. doi:10.1109/NSSMIC.2007.4436673
99. Zhu H, Chen Y, Sung W, McNamara AL, Tran LT, Burigo LN, et al. The microdosimetric extension in TOPAS : development and comparison with published data. *Phys Med Biol* (2019) 64:145004. doi:10.1088/1361-6560/ab23a3
100. Magro G, Dahle TJ, Molinelli S, Ciocca M, Fossati P, Ferrari A, et al. The FLUKA Monte Carlo code coupled with the NIRS approach for clinical dose calculations in carbon ion therapy. *Phys Med Biol* (2017) 62:3814. doi:10.1088/1361-6560/aa642b

101. MairaniInaniwa T, Suzuki M, Furukawa T, Kase Y, Kanematsu N, Shirai T, et al. Effects of dose-delivery time structure on biological effectiveness for therapeutic carbon-ion beams evaluated with microdosimetric kinetic model. *Radiat Res* 180 (2013) 44–59. doi:10.1667/RR3178.1
102. Hawkins RB, Inaniwa T. A microdosimetric-kinetic model for cell killing by protracted continuous irradiation including dependence on LET i: repair in cultured mammalian cells. *Radiat Res* (2013) 180:584–94. doi:10.1667/RR13257.1
103. Hawkins RB, Inaniwa T. A microdosimetric-kinetic model for cell killing by protracted continuous irradiation II: brachytherapy and biologic effective dose. *Radiat Res* (2014) 182:72–82. doi:10.1667/rr13558.1
104. Inaniwa T, Kanematsu N, Suzuki M, Hawkins RB. Effects of beam interruption time on tumor control probability in single-fractionated carbon-ion radiotherapy for non-small cell lung cancer. *Phys Med Biol* (2015b) 60:4105. doi:10.1088/0031-9155/60/10/4105
105. Deehan C, O'Donoghue JA. Biological equivalence between fractionated radiotherapy treatments using the linear-quadratic model. *Br J Radiol* (1988) 61:1187–8. doi:10.1259/0007-1285-61-732-1187
106. Fowler JF. The linear-quadratic formula and progress in fractionated radiotherapy. *Br J Radiol* (1989) 62:679–94. doi:10.1259/0007-1285-62-740-679
107. Yaes RJ, Patel P, Maruyama Y. On using the linear-quadratic model in daily clinical practice. *Int J Radiat Oncol Biol Phys* (1991) 20:1353–62. doi:10.1016/0360-3016(91)90249-4
108. McMahon SJ. The linear quadratic model: usage, interpretation and challenges. *Phys Med Biol* (2018) 64:01TR01. doi:10.1088/1361-6560/aaf26a
109. Furusawa Y, Fukutsu K, Aoki M, Itsukaichi H, Eguchi-Kasai K, Ohara H, et al. Inactivation of aerobic and hypoxic cells from three different cell lines by accelerated (3)He-, (12)C- and (20)Ne-ion beams. *Radiat Res* (2000) 154 485–96. doi:10.1667/0033-7587(2000)154[0485:ioaahc]2.0.co;2
110. AndoYatagai C, Suzuki M, Kanai T, Fujitaka K. LET and ion species dependence for cell killing in normal human skin fibroblasts. *Radiat Res* (2005) 163:494. doi:10.1667/rr3360
111. Czub J, Banaś D, Błaszczyk A, Braziewicz J, Buraczewska I, Choinski J, et al. Biological effectiveness of (12)C and (20)Ne ions with very high LET. *Int J Radiat Biol*, 84, 821 (2008). doi:10.1080/09553000802389652
112. WojcikGorak T, Kanematsu N. Adaptation of stochastic microdosimetric kinetic model for charged-particle therapy treatment planning. *Phys Med Biol* (2018) 63:095011. doi:10.1088/1361-6560/aabede
113. Manganaro L, Russo G, Bourhaleb F, Fausti F, Giordanengo S, Monaco V, et al. "Survival": a simulation toolkit introducing a modular approach for radiobiological evaluations in ion beam therapy. *Phys Med Biol* (2018) 63: 08NT01. doi:10.1088/1361-6560/ab6eba
114. Hawkins RB. Effect of heterogeneous radio sensitivity on the survival, alpha beta ratio and biologic effective dose calculation of irradiated mammalian cell populations. *Clin Transl Radiat Oncol* (2017) 4:32–8. doi:10.1016/j.ctro.2017.03.001
115. Incerti S, Kyriakou I, Bernal M, Bordage M, Francis Z, Guatelli S, et al. Geant4-DNA example applications for track structure simulations in liquid water: a report from the Geant4-DNA Project. *Med Phys* (2018) 45: e722–e739. doi:10.1007/s10898-020-00902-2
116. Ferrari AS, Fasso PR, Ranft A. *FLUKA: a multi-particle transport code (Program version 2005)*. Berlin: Springer. (2005). doi:10.5170/cern-2005-010
117. Russo G. *Development of a radiobiological database for carbon ion Treatment Planning Systems*. [Ph.D. thesis]. Italy: University of Turin (2011).
118. Guan F, Bronk L, Titt U, Lin SH, Mirkovic D, Kerr MD, et al. Spatial mapping of the biologic effectiveness of scanned particle beams: towards biologically optimized particle therapy. *Sci Rep* (2015) 5:9850. doi:10.1038/srep09850
119. GrosshansZhu JF, Welsh JS, Howard SP. Loss of biological effect in prolonged fraction delivery. *Int J Radiat Oncol Biol Phys* (2004) 59:242–9. doi:10.1016/j.ijrobp.2004.01.004
120. Carabe-Fernandez A, Dale RG, Hopewell JW, Jones B, Paganetti H. Fractionation effects in particle radiotherapy: implications for hypo-fractionation regimes. *Phys Med Biol* (2010) 55:5685. doi:10.1088/0031-9155/55/19/005
121. Friedland W, Jacob P, Paretzke HG, Ottolenghi A, Ballarini F, Liotta M. Simulation of light ion induced DNA damage patterns. *Radiat Protect Dosim* (2006) 122:116–20. doi:10.1093/rpd/ncl451
122. Hada M, Georgakilas AG. Formation of clustered DNA damage after high-LET irradiation: a review. *J Radiat Res* (2008) 49:203. doi:10.1016/j.dnarep.2015.01.007
123. Iwamoto Y, Sato T, Hashimoto S, Ogawa T, Furuta T, Abe S, et al. Benchmark study of the recent version of the PHITS code. *J Nucl Sci Technol* (2017) 54: 617–35. doi:10.1269/jrr.40.s60
124. Sato T, Iwamoto Y, Hashimoto S, Ogawa T, Furuta T, Abe S, et al. Features of particle and heavy ion transport code system (PHITS) version 3.02. *J Nucl Sci Technol* (2018) 55:684–90. doi:10.1007/s00411-006-0070-3
125. Olko P, Booz J. Energy deposition by protons and alpha particles in spherical sites of nanometer to micrometer diameter. *Radiat Environ Biophys* (1990) 29:1. doi:10.1007/BF01211231
126. Abolfath R, Peeler CR, Newpower M, Bronk L, Grosshans D, Mohan R. A model for relative biological effectiveness of therapeutic proton beams based on a global fit of cell survival data. *Sci Rep* (2017) 7:8340–12. doi:10.1038/s41598-017-08622-6
127. Hawkins RB. Survival of a mixture of cells of variable linear-quadratic sensitivity to radiation. *Radiat Res* (2000) 153:840–3. doi:10.1667/0033-7587(2000)153[084010.1667/0033-7587(2000)153[0840:soamoc]2.0.co;2
128. Matsuya Y, Sasaki K, Yoshii Y, Okuyama G, Date H. Integrated modelling of cell responses after irradiation for DNA-targeted effects and non-targeted effects. *Sci Rep* (2018b) 8:1–14. doi:10.1038/s41598-018-23202-y
129. Höckel M, Knoop C, Schlenger K, Vorndran B, Baussmann E, Mitze M, et al. Intratumoral pO2 predicts survival in advanced cancer of the uterine cervix. *Radiother Oncol* 26 (1993) 45–50. doi:10.1016/0167-8140(93)90025-4
130. VaupelKnapstein RH, Gray LH. The histological structure of some human lung cancers and the possible implications for radiotherapy. *Br J Canc* (1955) 9:539–49. doi:10.1038/bjc.1955.55
131. Ito A, Nakano H, Kusano Y, Hirayama R, Furusawa Y, Murayama C, et al. Contribution of indirect action to radiation-induced mammalian cell inactivation: dependence on photon energy and heavy-ion LET. *Radiat Res* (2006) 165, 703. doi:10.1667/rr3557.1
132. ShinoharaMori T, Suzuki Y, Ohno T, Kato S, Suzuki M, Morita S, et al. Carbon beam therapy overcomes the radiation resistance of uterine cervical cancer originating from hypoxia. *Clin Canc Res* (2006) 12:2185–90. doi:10.1158/1078-0432.CCR-05-1907
133. TsujiiSato T, Howard-Flanders P. Role of oxygen in modifying the radiosensitivity of *E. coli* B. *Nature* (1956) 178:978–9. doi:10.1038/178978a0
134. Wenzl T, Wilkens JJ. Modelling of the oxygen enhancement ratio for ion beam radiation therapy. *Phys Med Biol* (2011) 56:3251–68. doi:10.1088/0031-9155/56/11/006
135 Scifoni E, Tinganelli W, Weyrather WK, Durante M, Maier a, Krämer M. Including oxygen enhancement ratio in ion beam treatment planning: model implementation and experimental verification. *Phys Med Biol* (2013) 58: 3871–95. doi:10.1088/0031-9155/58/11/3871
136. Antonovic L, Brahme A, Furusawa Y, Toma-Dasu I. Radiobiological description of the LET dependence of the cell survival of oxic and anoxic cells irradiated by carbon ions. *J Radiat Res* (2013) 54:18–26. doi:10.1093/jrr/rrs070
137. Mothersill C, Seymour C. Radiation-induced bystander effects: past history and future directions. *Radiat Res* (2001) 155:759. doi:10.1667/0033-7587(2001)155
138. Hamada N, Matsumoto H, Hara T, Kobayashi Y. Intercellular and intracellular signaling pathways mediating ionizing radiation-induced bystander effects. *J Radiat Res* (2007) 48:87. doi:10.1269/jrr.06084
139. Hamada N, Maeda M, Otsuka K, Tomita M. Signaling pathways underpinning the manifestations of ionizing radiation-induced bystander effects. *Curr Mol Pharmacol* (2012) 27:66. doi:10.2174/1874467211104020079
140. Hu B, Wu L, Han W, Zhang L, Chen S, Xu A, et al. The time and spatial effects of bystander response in mammalian cells induced by low dose radiation. *Carcinogenesis* (2006) 27:245. doi:10.1093/carcin/bgi224
141. YuHei SJ, Butterworth KT, Trainor C, McGarry CK, O'Sullivan JM, Schettino G, et al. A kinetic-based model of radiation-induced intercellular signalling. *PloS One* (2013) 8:e54526. doi:10.1371/journal.pone.0054526
142. PriseHounsell P, Friedland W. Mechanistic modelling of radiation-induced bystander effects. *Radiat Protect Dosim* (2015) 166:148–51. doi:10.1093/rpd/ncv170
143. Mcmahon SJ, Schuemann J, Paganetti H, Prise KM. Mechanistic modelling of DNA repair and cellular survival following radiation-induced DNA damage. *Sci Rep* (2016) 6:33290. doi:10.1038/srep33290

144. Robertson JB, Eaddy JM, Archambeau JO, Coutrakon GB, Miller DW, Moyers MF, et al. Relative biological effectiveness and microdosimetry of a mixed energy field of protons up to 200 MeV. *Adv Space Res* 14 (1994) 271–5. doi:10.1016/0273-1177(94)90477-4
145. DicelloSiebers G, Cortese J, Ghebremedhin A, Hubbard J, Johanning J, Koss P, et al. Microdosimetry spectra of the Loma Linda proton beam and relative biological effectiveness comparisons. *Med Phys* (1997) 24:1499–506. doi:10.1118/1.598038
146. ZuccarelliMaudsley PJ, Colvett RD, Lam YM, Rossi HH. The relative biological effectiveness of 160 MeV protons. I. Microdosimetry. *Int J Radiat Oncol Biol Phys* (1978) 4:1001–8.
147. Hall EJ, Kellerer AM, Rossi HH, Lam YM. The relative biological effectiveness of 160 MeV protons--II. Biological data and their interpretation in terms of microdosimetry. *Int J Radiat Oncol Biol Phys* (1978) 4:1009–13.
148. Morstin K, Bond VP, Baum JW. Probabilistic approach to obtain hit-size effectiveness functions which relate microdosimetry and radiobiology. *Radiat Res* (1989) 120:383–402.
149. Paganetti H, Olko P, Kobus H, Becker R, Schmitz T, Waligorski MP, et al. Calculation of relative biological effectiveness for proton beams using biological weighting functions. *Int J Radiat Oncol Biol Phys* (1997) 37:719–29.
150. Müller-GärtnerFilges P. Fluctuations of energy deposited in biological targets by ionising radiation. [Ph.D. thesis]. Jülich: Institute of Medicine KFA (1989).
151. Semenenko VA, Stewart RD. A fast Monte Carlo algorithm to simulate the spectrum of DNA damages formed by ionizing radiation. *Radiat Res* (2004) 161:451–7. doi:10.1667/rr3140
152. Wang CC, Hsiao Y, Lee CC, Chao TC, Wang CC, Tung CJ. Monte Carlo simulations of therapeutic proton beams for relative biological effectiveness of double-strand break. *Int J Radiat Biol* (2012) 88:158–63. doi:10.3109/09553002.2011.611214
153. Stewart RD, Yu VK, Georgakilas AG, Koumenis C, Park JH, Carlson DJ. Effects of radiation quality and oxygen on clustered DNA lesions and cell death. *Radiat Res* (2011) 176:587–602. doi:10.1667/rr2663.1
154. Kamp F, Cabal G, Mairani A, Parodi K, Wilkens JJ, Carlson DJ. Fast biological modeling for voxel-based heavy ion treatment planning using the mechanistic repair–misrepair–fixation model and nuclear fragment spectra. *Int J Radiat Oncol Biol Phys* (2015) 93:557–68. doi:10.1016/j.ijrobp.2015.07.2264

Conflict of Interest: The authors declare that the research was conducted in the absence of any commercial or financial relationships that could be construed as a potential conflict of interest.

frontiers in Physics

ORIGINAL RESEARCH
published: 11 February 2021
doi: 10.3389/fphy.2020.578444

A Novel Hybrid Microdosimeter for Radiation Field Characterization Based on the Tissue Equivalent Proportional Counter Detector and Low Gain Avalanche Detectors Tracker: A Feasibility Study

*M. Missiaggia[1,2,3], E. Pierobon[1], M. Castelluzzo[1], A. Perinelli[1], F. Cordoni[2,5], M. Centis Vignali[3], G. Borghi[2,3], E. V. Bellinzona[1,2], E. Scifoni[2], F. Tommasino[1,2], V. Monaco[4], L. Ricci[1,2], M. Boscardin[2,3] and C. La Tessa[1,2]**

[1] Department of Physics, University of Trento, Trento, Italy, [2] TIFPA, INFN, Trento, Italy, [3] FBK, Trento, Italy, [4] Department of Physics, University of Torino, Torino, Italy, [5] Department of Computer Science, University of Verona, Verona, Italy

OPEN ACCESS

Edited by:
Yolanda Prezado,
INSERM U1021 Signalisation Normale Et Pathologique De L'embryon Aux Thérapies Innovantes Des Cancers, France

Reviewed by:
Anatoly Rosenfeld,
University of Wollongong, Australia
Yadong Xu,
Northwestern Polytechnical University, China

***Correspondence:**
C. La Tessa
chiara.latessa@unitn.it

Specialty section:
This article was submitted to Radiation Detectors and Imaging, a section of the journal Frontiers in Physics

Received: 30 June 2020
Accepted: 22 September 2020
Published: 11 February 2021

Citation:
Missiaggia M, Pierobon E, Castelluzzo M, Perinelli A, Cordoni F, Centis Vignali M, Borghi G, Bellinzona EV, Scifoni E, Tommasino F, Monaco V, Ricci L, Boscardin M and La Tessa C (2021) A Novel Hybrid Microdosimeter for Radiation Field Characterization Based on the Tissue Equivalent Proportional Counter Detector and Low Gain Avalanche Detectors Tracker: A Feasibility Study. Front. Phys. 8:578444. doi: 10.3389/fphy.2020.578444

In microdosimetry, *lineal energies y* are calculated from energy depositions ϵ inside the microdosimeter divided by the *mean chord length*, whose value is based on geometrical assumptions on both the detector and the radiation field. This work presents an innovative two-stages hybrid detector (HDM: hybrid detector for microdosimetry) composed by a tissue equivalent proportional counter and a silicon tracker made of 4 low gain avalanche diode. This design provides a direct measurement of energy deposition in tissue as well as particles tracking with a submillimeter lateral spatial resolution. The data collected by the detector allow to obtain the real track length traversed by each particle in the tissue equivalent proportional counter and thus estimates microdosimetry spectra without the mean chord length approximation. Using Geant4 toolkit, we investigated HDM performances in terms of detection and tracking efficiencies when placed in water and exposed to protons and carbon ions in the therapeutic energy range. The results indicate that the mean chord length approximation underestimate particles with short track, which often are characterized by a high energy deposition and thus can be biologically relevant. Tracking efficiency depends on the low gain avalanche diode configurations: 34 strips sensors have a higher detection efficiency but lower spatial resolution than 71 strips sensors. Further studies will be performed both with Geant4 and experimentally to optimize the detector design on the bases of the radiation field of interest.The main purpose of HDM is to improve the assessment of the radiation biological effectiveness via microdosimetric measurements, exploiting a new definition of the *lineal energy* (y_T), defined as the energy deposition ϵ inside the microdosimeter divided by the real track length of the particle.

Keywords: particle tracking, ion therapy, low gain avalanche diode, tissue equivalent proportional counter, microdosimetry

INTRODUCTION

Microdosimetry was developed to study the effect of radiation on cells. At a scale comparable to the structures of interest, the energy deposition is affected by stochastic fluctuations and cannot be accurately described with macroscopic mean values, such as the dose or the Linear Energy Transfer (LET) [1].

Measuring the energy loss in a microscopic volume called for the development of new detection techniques. Currently, there are two types of microdosimeters: tissue equivalent proportional counters (TEPCs) and semiconductor-based detectors. The latter category includes silicon detectors based on different technologies (telescope detectors, silicon on insulator detectors, arrays of cylindrical p-n junctions with internal amplification [2, 3]) and diamond microdosimeters which are under study for their radiation hardness and tissue equivalence [4].

The TEPC was invented by Harald H. Rossi and co-workers, who were the first to explore the field of experimental microdosimetry [5], and is considered the reference microdosimeter [6]. TEPCs have been used in numerous works, see, e.g., refs. 7–11. The TEPC detection system is based on the fact that the detection gas parameters (e.g., composition and density) are adjusted to match the stopping power of the desired tissue equivalent volume.

The basic microdosimetric quantity provided by all detectors is the energy ϵ imparted to the matter in the volume of interest, from which the lineal energy y, defined as the ratio between ϵ and the *mean chord length* $\bar{l}$ [12], is calculated. The $yf(y)$ and $yd(y)$ spectra are the standard microdosimetric distributions, where $f(y)$ is the frequency distribution of y and $d(y)$ is equal to $yf(y)$, hence representing the dose distribution.

A limitation shared by all microdosimeters is that while ϵ is directly measured, the value of $\bar{l}$ has to be theoretically estimated as the mean path traveled by a particle inside the detector, and thus it depends on the detector geometry. In addition, $\bar{l}$ values calculated for standard geometries can be used only if the microdosimeter is exposed to a homogeneous and isotropic field (also called uniform isotropic randomness) [13] and a different $\bar{l}$ value will be obtained under different irradiation conditions, i.e., for other types of randomness. Some attempts have been made to overcome the limited accuracy of the mean chord length concept, e.g., in unidirectional particle field when the isotropicity assumption drops. An example are silicon on insulator microdosimeters [14], which are composed of 3D sensitive volumes arrays with a well defined thickness, and thus path lenght. Furthermore, few theoretical studies focused on finding a formula of the mean path length for both uniform [15] and non uniform [16] radiation fields. So far, only the calculation for a uniform isotropic randomness could be successfully applied to experimental methodologies. Estimating the path length l is a critical parameter in microdosimetry that will influence the accuracy of the radiation field quality characterization [17]. In fact, for a given energy ϵ deposited in the detector, the resulting y value can assume a wide range of values depending on the l. For example, if ϵ = 10 keV in a 2 μm diameter sphere made of tissue, y can varies from 5 keV/μm to 1,000 keV/μm just considering l values ranging from the sphere diameter to 0.01 μm.

For this reason, since the quantity y is traditionally intended as the ϵ over the mean chord length value $\bar{l}$, we introduce a new quantity y_T, defined as ϵ divided by the particle real track length l.

In this work, we present a novel two-stage hybrid microdosimeter (HDM: hybrid detector for microdosimetry) designed to measure the y_T. This detector have been specifically intended for particle therapy application, where a knowledge of the y_T yields a more direct link to the biological damage. Microdosimetry is a well establish tool to assess Relative Biological Effectiveness (RBE) [18, 19]. This work focuses on the feasibility of HDM, however future investigation will be carried out in order to directly link microdosimetric spectra using the real track length to a radibiological damage assessment. Together with providing a direct measurement of the track length l, this design also improve the lateral spatial resolution of existing TEPCs. HDM is composed of a spherical TEPC followed by four layers of Low Gain Avalanche Detectors (LGADs) [20]. LGAD is a recent technology in silicon systems featuring detection of particles in a wide energy range with improved accuracy for timing and tracking measurements [20]. The LGAD application in particle therapy has been also recently investigated [21]. In the proposed setup, the TEPC will provide the energy deposition ϵ directly in a tissue-equivalent medium while the LGADs will offer information about particle spatial distribution with a precision of about 200 or 300 μm, depending on the chosen configuration.

Details of the detector components, geometrical configurations as well as read-out solutions are illustrated here. Using GEANT4 toolkit, we investigated HDM performances when exposed to protons and carbon ions in the therapeutic energy range. The influence on all microdosimetric quantities when the real l is used instead of the mean track length approximation is discussed. Detection efficiency and tracking precision are also reported.

MATERIAL AND METHODS

A detailed description of the proposed hybrid detector is given here. The components as well as the whole setup, including the read-out electronics, are presented. Additionally, the geometry of all Monte Carlo simulations performed to study the HDM performances when exposed to a mixed radiation beam is illustrated. As TEPC efficiency studies can be found in literature, we focused on the tracking efficiency of the proposed setup, being the novel aspect to the existing microdosimeter.

Hybrid Detector for Microdosimetry Components

Tissue Equivalent Proportional Counter

TEPCs have two main advantages compared to other microdosimeters: 1) the sensitive volume is confined in a macroscopic region of a well defined size and 2) the energy deposition is directly measured in tissue and thus does not require a conversion. It is worth mention that advantage 1) is also shared with silicon microdosimeter based on 3-D MEMS fabrication technology (e.g., ref. 22). Furthermore, the gas-

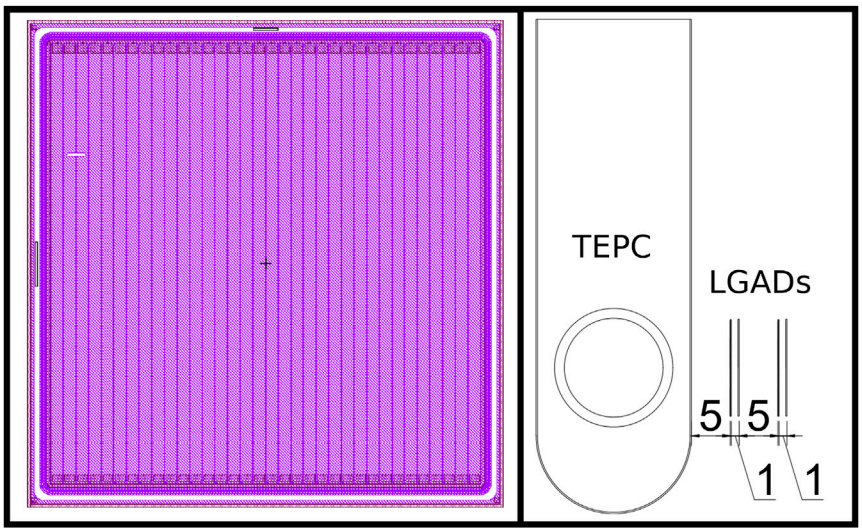

FIGURE 1 | Left panel: design of one low gain avalanche diode (LGAD) sensor with 34 active strips. **Right panel:** Scheme of the hybrid detector for microdosimetry (HDM) setup, showing the tissue equivalent proportional counter (TEPC) followed by four LGAD layers. Distances between detectors are reported in millimeters.

based detection offers a large dynamic range of energy depositions down to 0.1 keV/μm. The main disadvantages are: 1) large physical size (above 0.5 mm), which limits the lateral spatial resolution and 2) wall effects. The latter stems from the interaction of the incoming radiation with the gas container and leads to the production of secondary particles, which can deposit additional energy in the detector. This effect does not occur in biological cells with micron size as modeled by TEPC and causes an overestimate of energy deposition [23].

The TEPC included in the detector design is the commercial model type LET-1/2 from Far West Technology, Inc. The detector sensitive volume is a sphere made of A-150 tissue-equivalent plastic and filled with a pure propane gas whose pressure is adjusted to reach a density of 1.08 10^{-4} g/cm [24]. Under these conditions, the detector simulates a tissue-equivalent sphere of 2 μm diameter. For this TEPC, the mean chord length is 2/3·12.7 mm = 8.47 mm.

Low Gain Avalanche Detectors

LGAD is a recent technology in silicon detection system. It was first fabricated at CNM-IMB [25] clean room facilities by diffusing a p-type layer just below the n+ electrode [20]. From then it has been used for particle timing and tracking and, more recently, its application in radiotherapy has been explored [21]. LGADs, using n-in-p silicon diodes, differ from standard Avalanche Photodiodes due to their low and controlled internal multiplication mechanism for detecting charged particles. This technique allows also to produce thinner sensors with the same output signal of standard thick substrates.

The main features of the LGADs used for the HDM prototype can be found in [26]. In particular, the active region is 50 μm thick while the substrate is 300 μm and can be thinned down to 100 μm postproduction.

An additional LGAD production for HDM is under development at FBK and will include sensors with alternative geometries and active layer doping in order to obtain different spatial resolutions and gains.

A constraint on the detector geometry is that the optimal active area of one strip is ~ 2 mm^2, which correspond to 5 pF of capacitance; in fact, the read-out chip have been designed for this value. For what concerns the 71-strips configuration, the area is already optimized, while the 34-strips configuration has a larger area. However, previous experiments with similar area have shown the feasibility of this capacitance also.

Furthermore, the dead area between two strips must be 66 μm wide independently of the strip width. Thus, narrower strips result into a higher spatial resolution but also a decreased detection efficiency due to a larger dead area and a resulting lower fill factor. In addition, to cover the same area more strips are needed, which translates into a larger number of channels to be read-out.

To find the optimal detector geometry for our application, we simulated three configurations: 1) 34 strips, each 294 μm wide and 12.5 mm high (sensor height 13.8 mm and width 13.4 mm); 2) 71 strips, each 114 μm wide and 12.5 mm high (sensor width 14 mm and height 13.8 mm) and 3) 288 strips, each 114 μm wide and 50.22 mm high (sensor height 51.52 mm and width 51.84 mm). An image of the design project of this configuration of the complete sensor is given in **Figure 1** (left panel). While the first two configurations are now being produced, configuration 3) is not currently feasible and was tested to investigate the tracking efficiency for a larger detector with the same spatial resolution of the 71 strips detector 2).

HDM Geometry

The LGAD position with respect to the TEPC determine the detector performances and the optimal configuration depends on

the goal of the specific measurement. In this paper, we investigated the configuration with the TEPC upstream of the 4 LGAD layers. This setup has been chosen because we wanted to characterize the radiation field with standard microdosimetric measurements, without possible artifacts due to the LGADs in front. The distances between the detectors can be found in **Figure 1** (right panel). In particular, the first LGAD have been placed as close as possible to the TEPC to minimize lateral scattering and energy loss of particles exiting the microdosimeter.

Read-Out System

LGAD sensors are read out through the ABACUS chip [27] designed and produced at the University and Italian National Institute for Nuclear Physics of Turin (Italy). Each chip reads 24 channels. By default, the output driver provides data via a Current Mode Logic differential stage, which, for HDM purposes and practical reasons, is converted into a Low-Voltage Differential Signaling (LVDS) logic.

After the conversion, the read-out signals are fed to a board hosting an Field Programmable Gate Arrays (FPGA) and an Advanced RISC Machine (ARM) processor running Linux. A suitable FPGA program identifies events according to the time of occurrence with a 1 μs resolution, along with the channel number corresponding to the detector strip hit by a particle. The data are then saved in the on-board Random-access memory (RAM) memory. The board processor allows to program the FPGA and to read out the data out of the RAM. The board can be remotely accessed via Ethernet, and data transferred as simple text files.

Geant4 Simulations of the Hybrid Detector for Microdosimetry Detector

To investigate the detector performances, we run Monte Carlo calculations using Geant4 toolkit [28]. As the HDM design is optimized for applications in particle therapy, we focused the study on the response to protons and carbon ions at therapeutic energies. Several physics lists are available in Geant4 for different energy ranges. For electromagnetic interactions, the high accuracy list *G4EmLivermorePhysics* based on Livermore physics model has been used while hadronic interactions were managed by *QGSP BIC*. All calculations were run to acquired a minimum of 10^6 events on the TEPC, which is considered an adequate statistics for experimental measurements [19].

In addition, since microdosimetry deals with patterns of single energy deposition in tissue at the micrometer scale, we computed the energy deposition ϵ of a particle traversing the TEPC as the sum of the energy deposited by the primary event and all the related secondary particles that entered the detector.

The simulation geometry consisted of a water phantom with PMMA walls (1.74 cm water equivalent thickness) where the hybrid system was placed. To reproduce a realistic setup, HDM was contained in an additional air box 2.8 × 20 × 2.8 cm thick. A 3D view of the setup is shown in **Figure 2**.

The water phantom was irradiated with 290 MeV/u carbon ions and 150 MeV protons, which have the same range in water (~ 160 mm). The beam spots were circular with a 3 cm radius to ensure that the detectors were fully immersed in a homogeneous and isotropic radiation field. The detector box was placed at 10.74 cm in water along the beam direction. This depth represented a good compromise to assess HDM performances in a relatively mixed field in terms of particle species and energies, but upstream of the Bragg peak, where most particles have a low energy and thus might stop inside the TEPC.

Tracking

Tracking Algorithm

To measure a particle track, the LGADs were positioned to have the strips in different directions, two horizontals (x plane) and two verticals (y plane). By coupling two sensors with different orientations, a spatial position for a particle can be measured. Thus, two pairs of sensors are the minimum requirement for reconstructing a particle track. To reproduce a realistic experimental scenario, in the simulation we scored only the position of the strip hit by the particle. Then, we used a lineal interpolation to reconstruct the particle path inside the TEPC, from which we could estimate the real track length.

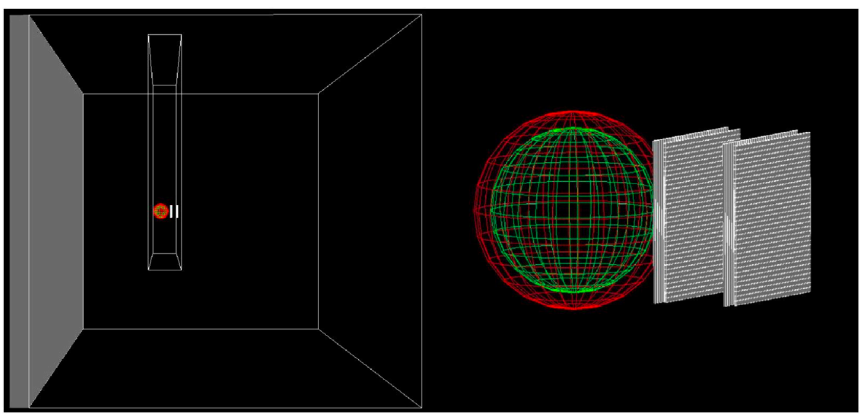

FIGURE 2 | 3D scheme of the geometry used for all Geant4 simulations. Both the TEPC and the four 24-strips LGADs are contained in PMMA box filled with air. The box is placed inside a water phantom, whose walls are made of PMMA. A broader view is show in left panel, while a zoom on HDM is illustrated in right panel.

Tracking Efficiency

Using Geant4 simulations, we studied the HDM tracking efficiency. As a first step, we focused on identifying the lost events and divided them into three categories:

(1) particles that reach all the detectors, but traverse an inter-strip dead zone in at least one of the LGADs;
(2) particles that range out before reaching the fourth LGAD;
(3) particles that undergo lateral scattering and are deflected outside the solid angle covered by all detectors.

Category 1 is related to the probability to hit a dead region and thus depends on the LGAD geometry. Assuming a uniform radiation field, the probability to reach an active strip is given by A_{act}/A_{tot}, where A_{act} is the total area covered by active strips and A_{tot} the total area of the sensor, including both active strips and dead inter-strips. As the probabilities of hitting the active region of two sensors are independent, the overall probability of the joint event is the product of the single probabilities. To test the validity of these assumptions, in the simulation we also scored the particles traversing the inter-strip regions.

For category 2, we investigated the minimum detectable kinetic energy for each ion type, i.e., the minimum energy that a particle must have to pass through all detectors. The values for all particle species of interest have been estimated with LISE++ toolkit version 10.0.6a [29]. These kinetic energy cutoffs depends only electromagnetic interactions in the detector layers and do not take into account additional losses due to multiple Coulomb scattering (MCS). To estimate a realistic kinetic energy detection threshold, we performed simulations of HDM exposed to a given particle species and decreases the initial energy until we found the minimum value required to traverse all detectors. We then repeated the test for the ion types of most interest.

The percentage of particles deflected outside the solid angle covered by all detectors (category 3) dependent on the LGADs size. To assess this value and its dependence on the LAGDs geometry, we performed simulations for every configuration described in **Section 2.1**.

For the events seen by the TEPC and by an active zone of each of the 4 silicon layers (i.e., the trackable particles), we investigated the tracking accuracy using the algorithm described in **Section 2.4**. From the simulations, we could extract the real particle track and compare it to that reconstructed with the tracking algorithm, estimating a mean discrepancy between the predicted and actual values. The tests were repeated for all LGADs configurations taken into consideration.

RESULTS

Radiation Field Characterization in the Tissue Equivalent Proportional Counter

The composition of the radiation field entering the TEPC was investigated at a depth of 10.74 cm in beam. The results include kinetic energy spectra of all particle species, track length distributions and microdosimetric spectra $yd(y)$ obtained with both the real track length and the mean chord length. The results are shown in **Figures 3** and **4** for protons and carbon ions, respectively. In detail: panels **A, B** of **Figure 3** and panels **A, B, C, D** of **Figure 4** illustrate the kinetic energy distributions of all particles entering the TEPC, with and without the contribution from the primary ions (in both cases the energy distributions of the single components are normalized to one); the track distributions of all the particles are plotted in panel **C** for protons and in panel **E** for carbons, with the mean chord length of 8.47 mm marked with a dashed red line; panels **D** for protons and **F** for carbons contain a comparison between the microdosimetric spectra calculated with the mean chord length approximation ($yd(y)$) or the real track length ($y_T d(y_T)$). Furthermore, the mean values and standard deviations of the track length distributions are also reported in **Table 1** for both ions of interest.

Secondaries produced by protons, are mostly low-energy (below 10 MeV) and the distribution does not have a peak. For carbon ions, the energy of all fragments species peaks around 170 MeV/u, which is the residual primary beam energy (**Figure 3A**). Protons can only generate fragments from the target nuclei, and thus their energy will be relatively low [30]. Carbon ions, instead, can produce both projectile and target fragments, whose kinetic energies have a much wider range, peaking at the same value as the primary ions [31, 32].

The track length distributions of both protons and carbon ions are very broad and do not present a peak. Furthermore, the mean track length calculated for both protons and carbon ions is higher than the mean chord length, indicating that the latter does not provide an accurate description of the system. The limitation of the mean chord length approximation can be further investigated by comparing the standard microdosimetric $yd(y)$ spectra with those obtained with the real track length [$y_T d(y_T)$]. The latter distributions show a non negligible contribution in the high y_T region. Those contributions are due to events that deposit energy along a small chord length and they are underestimated in the $yd(y)$ spectra where the mean chord length value is used. These events have a very high y_T and thus can be relevant for radiobiological effects, especially for y up to 150 keV/μm (overkill effect).

Particles Tracked by Hybrid Detector for Microdosimetry

We investigated HDM tracking efficiency as well as the characteristics of the tracked events. **Table 2** illustrates for carbon ions and protons the percentage of particles tracked by HDM, their mean track length values, their standard deviations and the average discrepancy between the reconstructed and the real track length. The latter values are reported for the three sensor geometries (34, 71, and 288 strips) described in **Section 2.1**.

The results show that, as expected, the 71 strips configuration collects the least amount of events because of the reduced fill factor. Increasing the sensor dimension while keeping the same fill factor increases the number of collected events (288 strips configuration). The mean track length and standard deviation obtained with the tracking algorithm are in good agreement with the real values obtained directly from the simulation. This is

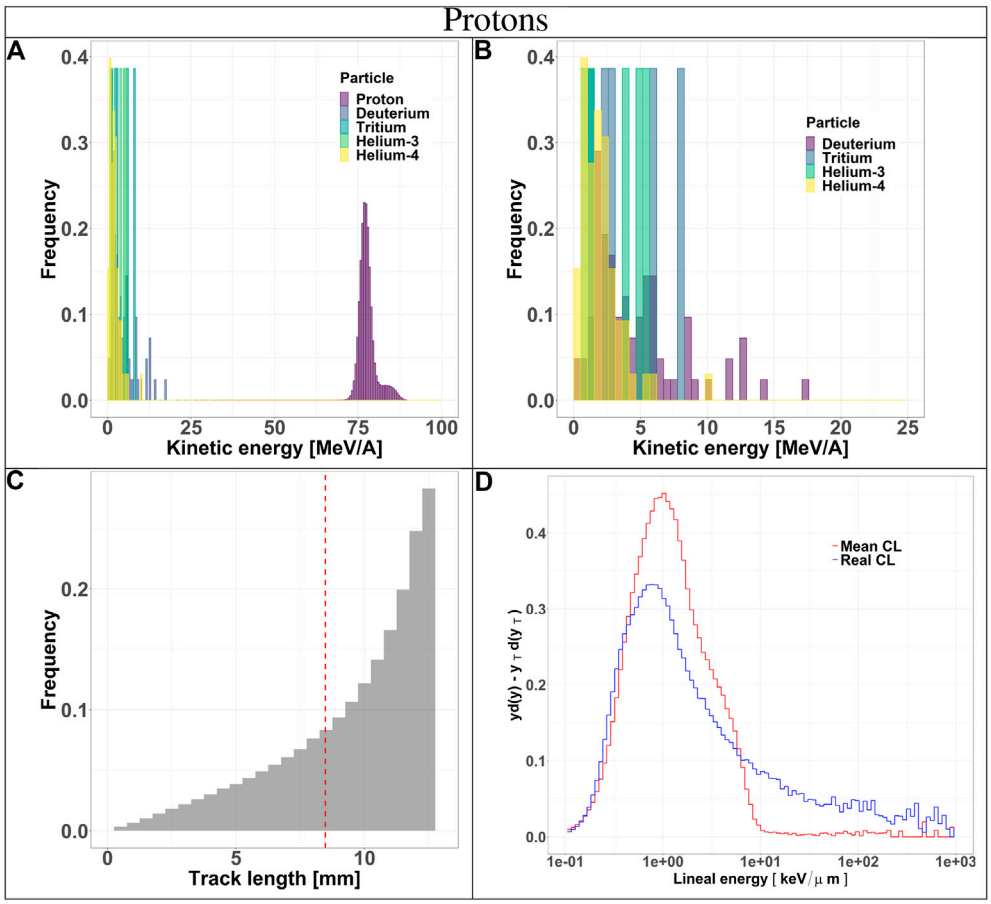

FIGURE 3 | Characterization of the radiation field generated by 150 MeV protons after traversing 10.74 cm of water and seen by the TEPC. Panels **(A)** and **(B)**: kinetic energy spectra of the most abundant components of the radiation field including and excluding the primary ions. Panel **(C)**: track length distribution of all the particles detected by the TEPC. The mean chord length at 8.47 mm is marked with a red dotted line. Panel **(D)**: microdosimetric yd(y) spectra obtained with the mean chord length approximation (red line) and microdosimetric $yd_T(y_T)$ spectra obtained using the real chord length values (blue line).

confirmed also by the small values of the mean absolute error, defined as the average absolute value of the difference between the real track length and the reconstructed one.

The accuracy of the reconstructed tracks in the three sensor configurations (34, 71, and 288 strips) was further studied in **Figures 5** and **6** for protons and carbon ions, respectively. We compared the track length distribution obtained directly from Geant4 with that reconstructed with the algorithm. The data are presented as density color plots in panels **A, C** and **E**; the green dotted line marks a perfect prediction of the algorithm, the red and blue colors represent regions of high and low events density, respectively. The distributions have a cone-like shape, implying a better accuracy of the reconstructed tracks of large lengths. This result is further supported by the presence of high density regions around the green line in the large track lengths zones.

To further assess the accuracy of the tracking algorithm, in panels **B, D** and **F** we compared the track distributions of all particles traversing the TEPC with those detected by HDM and either obtained directly from the simulation or estimated with the tracking algorithm. Independently of the primary ion type, the 34 and 71 strips configurations systematically underestimate the distributions for small tracks. On the contrary, the 288 strips configurations provide a more accurate estimation of the whole track distributions, especially for protons.

The track distributions obtained with the three configurations were used to calculate microdosimetric $yd(y)$ and $y_T d(y_T)$ spectra for all particles tracked by HDM. The results are shown in **Figures 7** and **8** for protons and carbon ions respectively. Results show that the $yd(y)$ spectra differ from the $y_T d(y_T)$ ones, with a peak value shifted to the right in all cases. On the contrar $y_T d(y_T)$, the $y_T d(y_T)$ distributions obtained with the real track length and with the reconstructed track length are similar mostly in the bell shape regions. It can be nonetheless seen that they differ in the tails due to the higher discrepancy between the real track length and the reconstructed ones for small track lengths. The accuracy between the two increases from the first sensor configuration (panels **A**) to the last one (panels **C**) under both radiation fields.

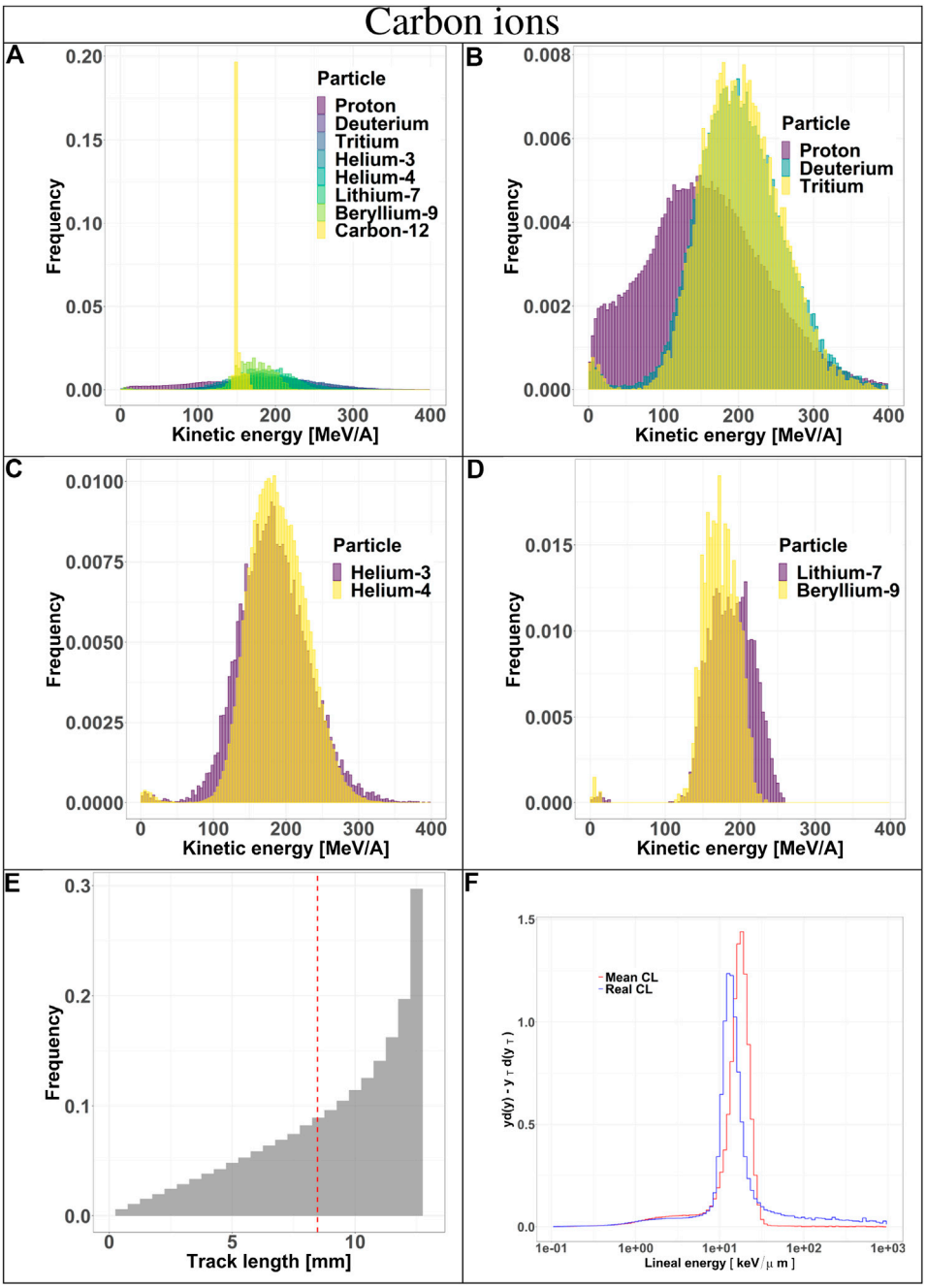

FIGURE 4 | Characterization of the radiation field generated by 290 MeV/u carbon ions after traversing 10.74 cm of water and seen by the TEPC. Panels **(A–D)**: kinetic energy spectra of the most abundant components of the radiation field including and excluding the primary ions. Panel **(E)**: track length distribution of all the particles detected by the TEPC. The mean chord length at 8.47 mm is marked with a red dotted line. Panel **(F)**: microdosimetric yd(y) spectra obtained with the mean chord length approximation (red line) and microdosimetric $y_T d(y_T)$ spectra obtained using the real chord length values (blue line).

Particles Lost by Hybrid Detector for Microdosimetry

As discussed in **Section 2.4**, we can group lost particles into three categories: 1) particles with a kinetic energy under the minimum required to traverse all the detectors, 2) particles lost due to MCS and 3) particles that reach all detectors, but cross an inter-strip in at least one LGAD.

The minimum kinetic energies necessary to pass all detectors have been studied and are reported in **Table 3** for all particles of interest. The values calculated with LISE++ are indicated for all particles while those obtained with Geant4 only for selected ions representative of the radiation field. The results obtained with the two methodologies agree very well for protons but have a higher discrepancy for carbon ions.

TABLE 1 | Percentage of particles tracked by HDM, including their mean track length, standard deviations and the absolute values of the mean tracking error of the algorithm with respect to the actual value. The results are reported for both protons and carbon ions and for three LGAD configurations (34, 71 and 288 strips).

Ion	Configuration	Tracked particles [%]	Mean track length of tracked particles [mm]		Standard deviation [mm]		Mean absolute tracking error [mm]
			Real	Reconstructed	Real	Reconstructed	
Carbon	*34 strips*	31.4	10.10	10.09	2.42	2.43	0.38
—	*71 strips*	12.1	9.99	10.00	2.53	2.52	0.20
—	*288 strips*	14.6	9.53	9.55	2.81	2.79	0.25
Proton	*34 strips*	45.8	10.06	9.89	2.37	2.50	0.91
—	*71 strips*	15.3	9.91	9.91	2.46	2.47	0.24
—	*288 strips*	16.6	9.63	9.64	2.68	2.67	0.28

TABLE 2 | Minimum kinetic energies for several isotope types necessary to traverse all the detectors. The values have been calculated with LISE++ toolkit and, for the most representative of the radiation field, also with Geant4.

	Proton [MeV/A]	Deuterium [MeV/A]	Tritium [MeV/A]	Helium-3 [MeV/A]	Helium-4 [MeV/A]	Lithium-7 [MeV/A]	Beryllium-9 [MeV/A]	Boron-11 [MeV/A]	Carbon-12 [MeV/A]
LISE++	17	11	8	20	17	20	24	28	34
GEANT4	17	12	9	-	17	-	-	-	37

Using Geant4 outputs, we characterized the particles lost in terms of kinetic energy when entering the TEPC and track length traversed inside the detector. The results are reported in **Figures 9** and **10** for protons and carbon ions, respectively. In panels **A** and **B** of **Figure 9** and **A**, **B, C** and **D** of **Figure 10** the kinetic energy spectra of all particle types are plotted with and without the contribution from the primaries. Independently of the fragment type, the energy spectra have the same shape of those reported in **Figures 3** and **4**, where all events are considered. These result indicate that the probability for a particle to be lost is independent of the charge and energy (for energies above the minimum threshold reported in **Table 3**). Panels **C** of 9 and **E** of 10 illustrate the track distributions of lost particles, together with the mean chord length (red dotted line). The left side of the distribution appears to be more populated compared to the distribution of all events (**Figures 3** and **4**), suggesting that there is a higher chance of loosing a particle if it has a small track length. Such events, in fact, traverse the TEPC edges and geometrically have a larger probability of missing the sensors, considering also MCS effects. In panels **D** for protons and **F** for carbons, the microdosimetric $y_T d(y_T)$ and $y_T d(y_T)$ spectra of particles that are not tracked by HDM are shown. Similarly to panels **D** of **Figure 3** and **F** of **Figure 4**, where all particles are taken into account, the $y_T d(y_T)$ distribution peaks are shifted to the left for both protons and carbon ions radiation fields. Further, the high-y regions are significantly lower than the high-y_T regions; again, this is due to the real track lengths overestimation caused by using the mean chord length value.

Furthermore, the number of particles that reach at least one of the inter-strip passive regions with respect to the total number of events reaching the detectors (i.e., traversing either an active strip or an inter-strip region) has been estimated to be 63% for the 34 strips configuration and 81.5% for the 71 strips configuration. Increasing the number of strips in each sensor results in a significant improvement of the detection efficiency.

Finally, to asses the HDM capability to provide an accurate microdosimetric characterization of the radiation field, the following quantities have been calculated: standard y_D values considering all events traversing the TEPC; $y_{D_T,\,TEPC}$ values calculated from the $y_T d(y_T)$ spectra for all particles traversing the TEPC; $y_{D_T,\,TRACKED}$ values calculated from the $y_T d(y_T)$ spectra for all particles tracked by HDM. The results for both ions of interested are reported in **Table 4**.

The large discrepancy between y_D and $y_{D_T,\,TEPC}$ confirm the results shown in **Figures 3, 4, 7,** and **8**) and proves that the mean chord length approximation applied to the TEPC spectra does not provide an accurate description of the radiation field quality. The $y_{D_T,\,TRACKED}$, instead, is very close to $y_{D_T,\,TEPC}$, suggesting that the population of events tracked by HDM is representative of the actual field.

Discussion

An innovative design for a hybrid microdosimeter (HDM: hybrid detector for microdosimetry) is presented in this paper. HDM is a two-stage detector composed by a TEPC and four layers of LGAD sensors. The combination of two different types of sensors (gas- and silicon-based) results in detection performances not offered by any existing microdosimeter. In fact, the TEPC gives a direct measurement of energy deposition in tissue while the LGADs provides particle tracking. The latter information has two main advantages: it improves the TEPC lateral spatial resolution to submillimetric precision and offer the real track length traverse by each

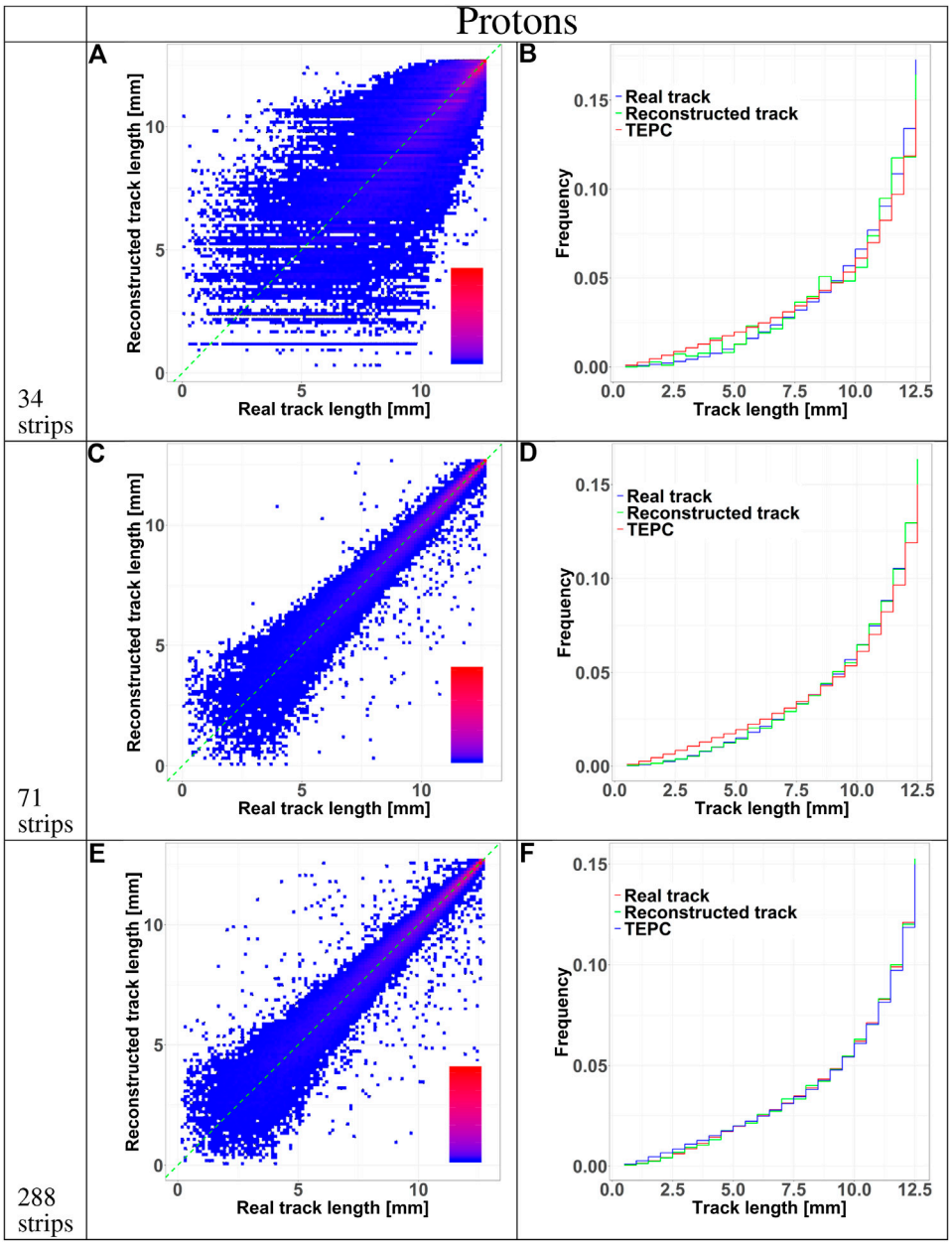

FIGURE 5 | HDM performances when exposed to 150 MeV protons at 10.74 cm depth in water. The results are shown for 34, 71, and 288 strips LGAD configurations. Panels **(A)**, **(C)**, and **(E)** shows 2D color plots of track length obtained with HDM vs. real track length calculated directly with Geant4. The green dashed line at 45 degrees indicates the perfect agreement between the two datasets. The colors represent regions with a high (red) or low (blue) density of events. Panels **(B)**, **(D)**, and **(F)** illustrate the comparison between the track length distributions of particles tracked by HDM considering the real track lengths calculated with Geant4 (blue line) or that reconstructed with the tracking algorithm (green line). The distributions of the real track lengths obtained directly from the simulation is also shown (red line).

particle in the TEPC. An improved lateral spatial resolution is helpful especially in a non homogeneous field, as he beam edges (both lateral and near the end-of-range). In these regions, the TEPC is only partially traversed by primary particles, whose path length might substantially deviate from the mean chord, depending on the detector position.

To assess the detector capability, we performed Monte Carlo simulations using Geant4 toolkit. As the primary application of HDM is particle therapy, we investigated its performances exposed to protons and carbon ions at a certain water depth.

The limitations of the mean chord length for our geometry are evident by looking at the track length distributions of all particles traversing the TEPC (**Figures 3** and **4** and **Table 1**). This approximation is based on the specific assumption that the TEPC is exposed to a uniform isotropic radiation field. In the cases considered here, although the beam generates such type of

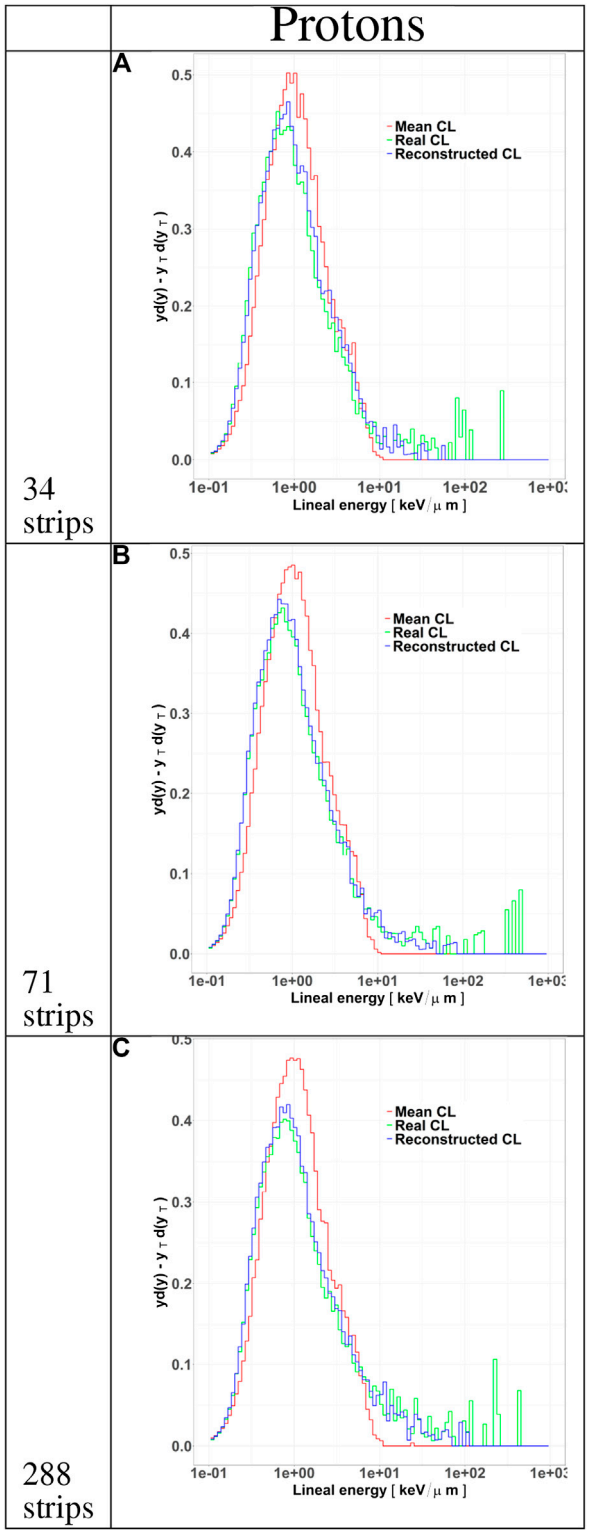

FIGURE 6 | Microdosimetric spectra of all particles tracked by HDM when irradiated with 150 MeV protons at a depth of 10.74 cm in water. The distributions include the standard yd(y) spectra calculated with the mean chord length (red line) and the $Y_Td(y_T)$ spectra obtained either with the real track length (green line) or with the value estimated with the tracking

(*Continued*)

randomness, the water surrounding the TEPC causes the isotropy assumption to drop, with a direct consequence on the resulting mean track length. To further validate this, simulations without the water phantom has been performed and a mean track length value of 8.56 has been obtained for protons and 8.45 for carbon ions, both in accordance to the nominal mean chord length value.

However, even if a mean value of chord length based on more appropriate kind of randomness is used, the data reveal that a mean value is non representative of the whole track length distribution, since the standard deviations are rather large. This behavior is noticeable by the broadness of the track distributions in panels **C** of **Figure 3** and **E** of **Figure 4**.

Discrepancies between the mean chord and the real track length translate into difference between the standard $yd(y)$ and the alternative $y_Td(y_T)$ microdosimetry spectra (**Figures 3** and **4**), the more evident being in the high y_T regions. The majority of particles populating these areas have a track length substantially smaller than the mean chord, and thus their actual lineal energy is systematically underestimated if using the mean chord approximation.

The detector efficiency is defined by the number of particles that traverse the LGADs active regions, i.e., those that are tracked. This number depends on the LAGD configuration, i.e., the number of detection strips contained in a sensor. As the dead interstrip area is the same independently of the configuration, for a given total area of the sensor, by lowering the number of strips the detection efficiency increases. However, a larger number of strips results in a superior spatial resolution. To optimize the detector design for our application, we investigated HDM performances using three different LGAD configurations: 34, 71, and 288 strips per sensor.

Detection and tracking efficiencies were assessed by studying the composition of the radiation field detected by HDM vs. the radiation field incoming on the TEPC. We identified three categories of events: 1) particles detected by the entire system (i.e., tracked events); 2) particles lost (i.e., only traversing the active volume of some detectors); 3) particles non-trackable (i.e., those with not enough energy to reach the fourth LGAD).

For each category, we studied the kinetic energy spectra, track length distribution, real track vs. track reconstructed with the tracking algorithm and microdosimetric spectra.

Independently of the primary ion and LGAD configuration, the mean track length of the tracked events is always higher that the value of all incoming particles. Events traversing the TEPC with a small track have a higher probability to miss the LGAD detectors. In fact, LGADs with 34 and 71 strips configurations have a total height and width comparable to the TEPC diameter, so if a particle reaches the TEPC with a given angle with respect to the primary beam direction, it is probable that its path will not cross all the LGADs. This hypothesis is confirmed by the fact that the 288 strips

FIGURE 6 | algorithm (blue line). The distributions are shown for LGAD configurations with 34 (panel **A**), 71 (panel **B**) and 288 (panel **C**) strips.

configuration collects a significantly higher portion of small-track particles (**Figures 5** and **6**). Furthermore, for this configuration the mean track length of the tracked events is closer to the value of all particles (see **Table 2**). The mean tracks obtained when HDM is exposed to protons and carbon ions are similar for the 34 and 71 strips configurations. For the 288 strips configuration, HDM provides a more accurate track distribution for protons than for carbon ions. In fact, secondary fragments produced by protons reach, on average, smaller scattering angles compared to those generated by carbon ions [33].

However, those are the chords that suffer most from a high error on the tracking, as panels **A**, **C** and **E** of **Figures 5** and **6** show for all the configurations. Furthermore, panels **A**, **D** and **G**, besides confirming the above mentioned fact that the bigger sensor takes better into account lower track lengths, they demonstrate also that the spatial resolution of the sensors, namely the widths of their strips, has a clear effect on the

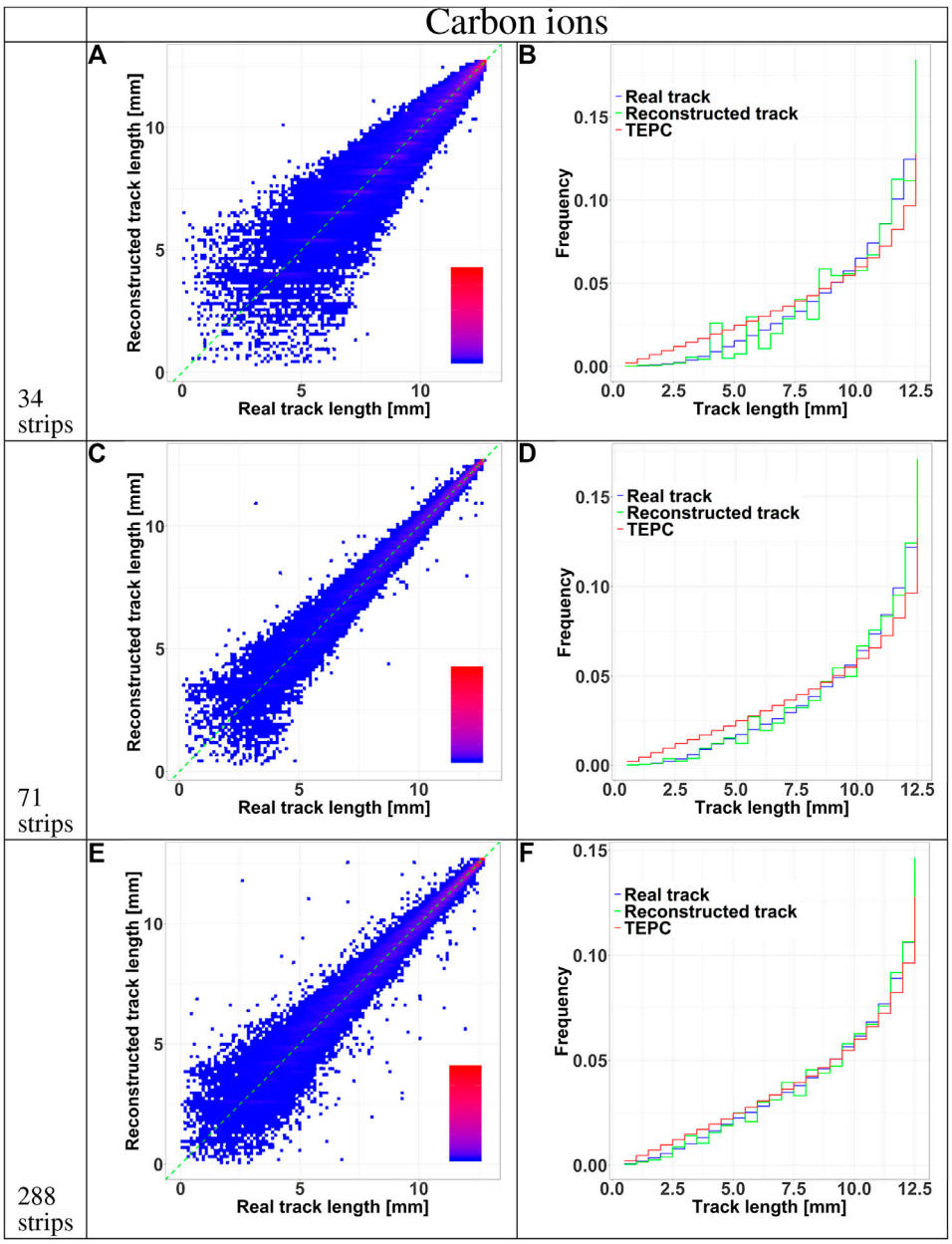

FIGURE 7 | HDM performances when exposed to 290 MeV/u carbon ions at 10.74 cm depth in water. The results are shown for 34, 71 and 288 strips LGAD configurations. Panels **A, C, E** shows 2D color plots of track length obtained with HDM versus real track length calculated directly with Geant4. The green dashed line at 45 degrees indicates the perfect agreement between the two datasets. The colors represent regions with a high (red) or low (blue) density of events. Panels **B, D, F** illustrate the comparison between the track length distributions of particles tracked by HDM considering the real track lengths calculated with Geant4 (blue line) or that reconstructed with the tracking algorithm (green line). The distributions of the real track lengths obtained directly from the simulation is also shown (red line).

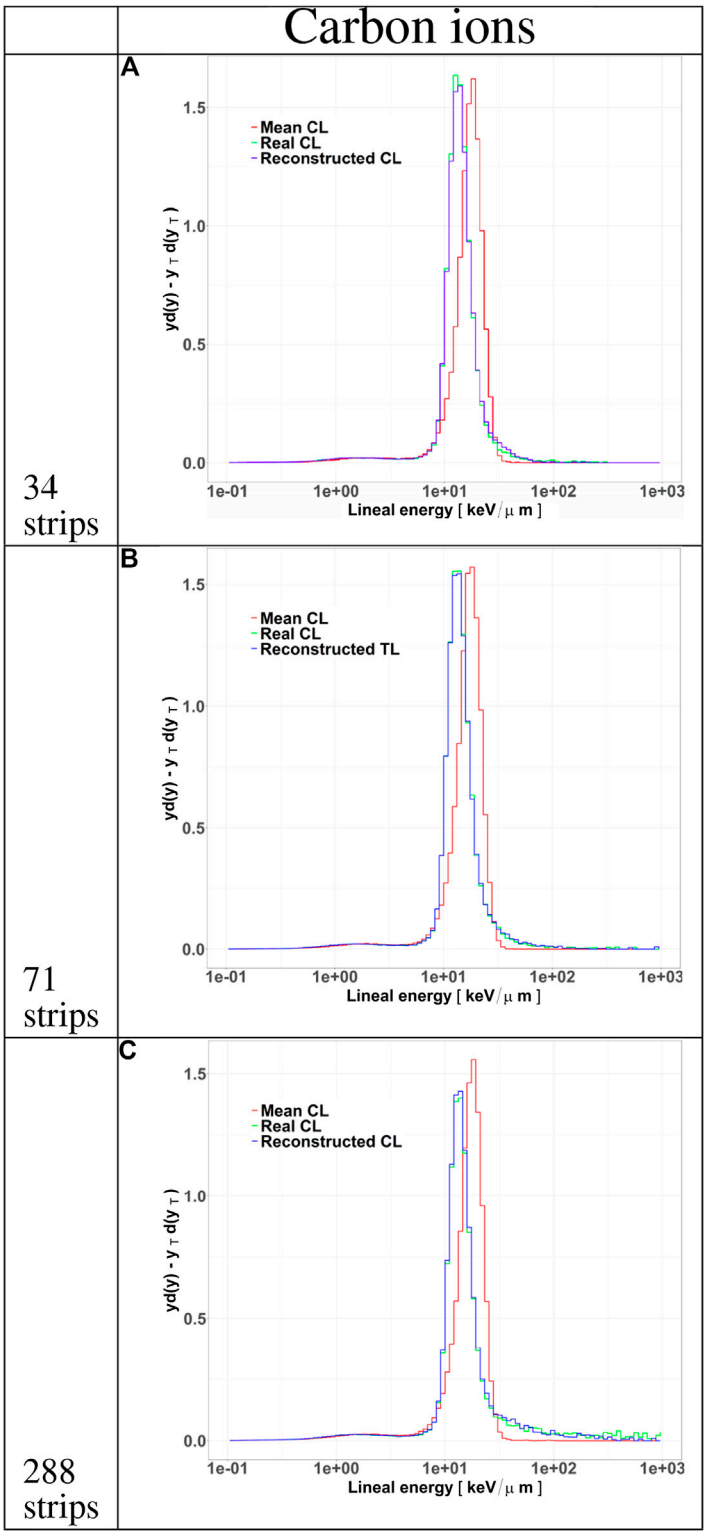

FIGURE 8 | Microdosimetric spectra of all particles tracked by HDM when irradiated with 290 MeV/u carbon ions at a depth of 10.74 cm in water. The distributions include the standard *yd* (*y*) spectra calculated with the mean chord length (red line) and the $Y_T d(Y_T)$ spectra obtained either with the real track length (green line) or with the value estimated with the tracking algorithm (blue line). The distributions are shown for LGAD configurations with 34 **(A)**, 71 **(B)**, and 288 **(C)** strips.

TABLE 3 | y_D and y_{D_T} values evaluated for both carbon and proton ions. y_{D_T} values have been calculated for all the particles that traverse the TEPC ($y_{D_T, \text{TEPC}}$) and for particles that HDM is able to track $y_{D_T, \text{TRACKED}}$ with the 288 strips configuration.

	y_D	$y_{D_T, \text{TEPC}}$	$y_{D_T, \text{TRACKED}}$
Carbon	16.53	40.49	40.79
Proton	3.75	23.73	21.08

homogeneity of the track distribution. In fact, it can be noticed that the lower the spatial resolution is, the more the reconstructed tracks will have some preferential track lengths.

Finally, a comparison between panels **F** of **Figures 5** and **6** supports the hypothesis that, for protons, the 288 strips configuration is able to collect a track distribution which is very similar to the real one, while for carbon ions the distribution is still slightly underestimated for the small tracks.

Differences in the track length distributions for the LGAD configurations translate into different microdosimetric $y_T d(y_T)$ spectra (**Figures 7** and **8**). A bigger sensor, like the 288 strips configuration, is able to collect more events with smaller TEPC tracks, which are the main contributors of the high y_T region.

The characterization of lost events indicates that the majority is caused to the LGADs fill-factor (interstrip regions). Thus, this issue can be resolved by increasing the measurement time to collect enough statistics.

For events that suffer MCS in the detectors, if the deviation angle is large enough they will be lost. In fact, even trying to enlarge LGADs or place them at a given angle with respect to the beam direction, the reconstructed track would be affected by errors too large to make the data of any value. The probability of loosing a particle because of MCS strongly depends on the HDM position in the radiation field. Depths in the Bragg peak regions as well as distal positions represent the worst cases because of the low kinetic energy

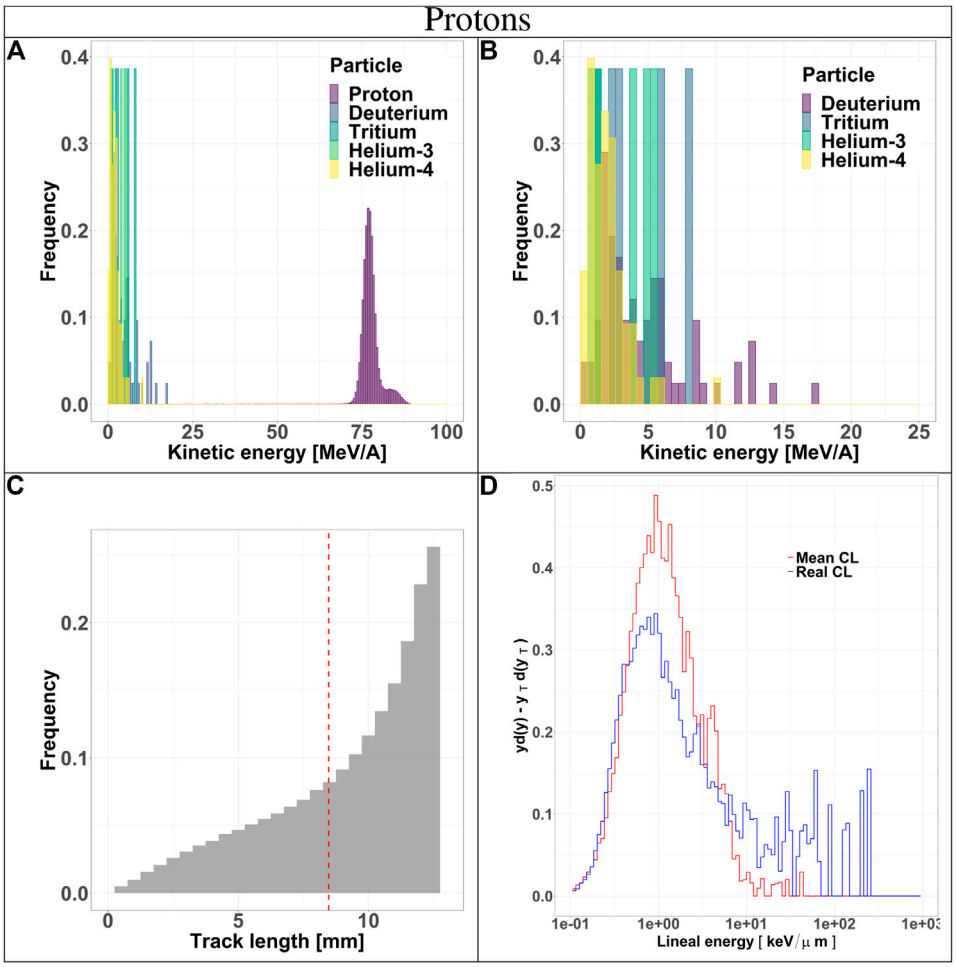

FIGURE 9 | Characterization of the particles lost by HDM when irradiated with 150 MeV protons at a depth of 10.74 cm in water. Panels **(A)** and **(B)**: kinetic energy spectra of the most abundant components of the radiation field including and excluding the primary ions. Panel **(C)**: track length distribution of all the particles detected by the TEPC. The mean chord length at 8.47 mm is marked with a red dotted line. Panel **(D)**: microdosimetric yd(y) spectra obtained with the mean chord length approximation (red line) and microdosimetric $Y_T d(y_T)$ spectra obtained using the real chord length values (blue line).

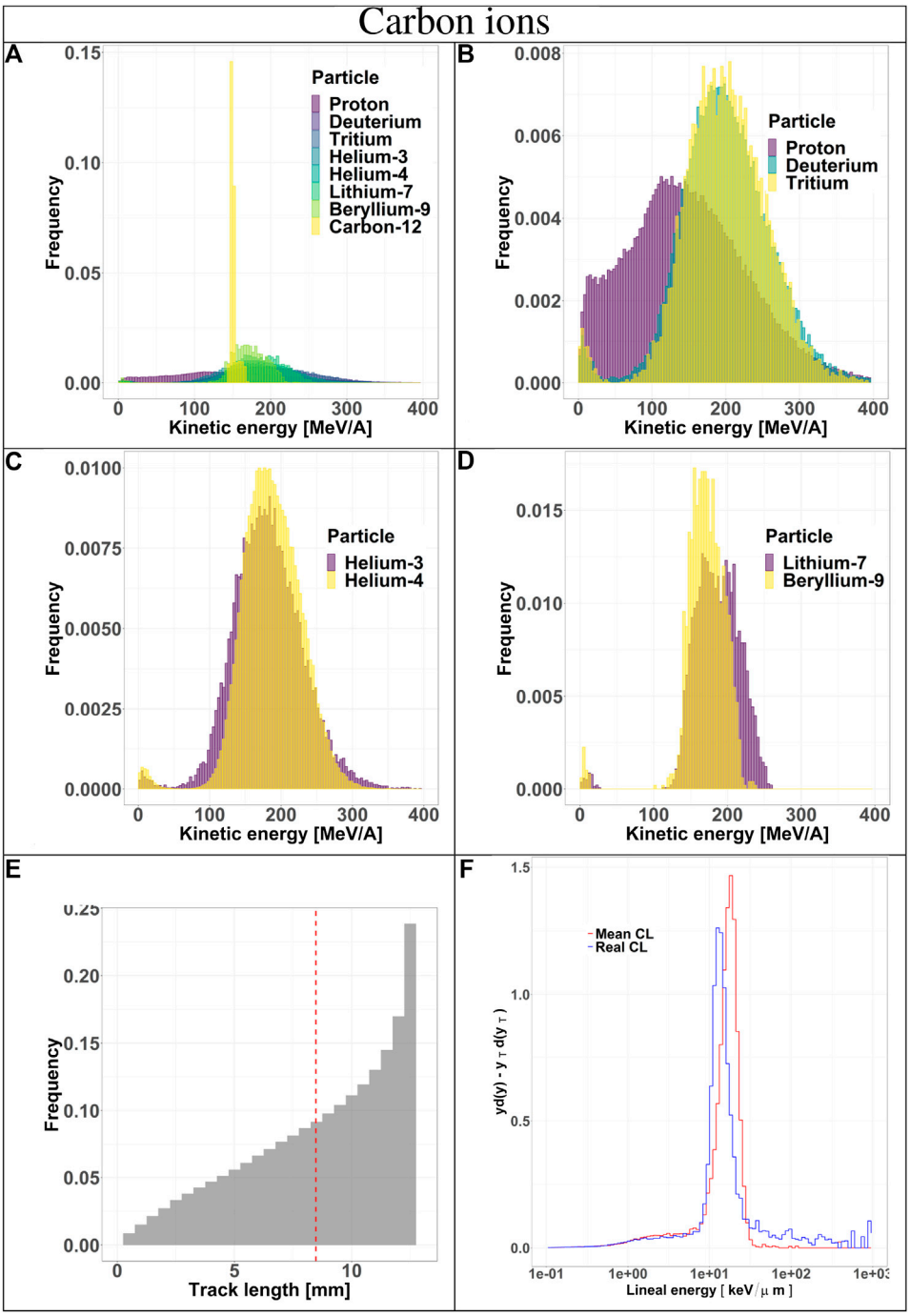

FIGURE 10 | Characterization of the particles lost by HDM when irradiated with 290 MeV/u carbon ions at a depth of 10.74 cm in water. Panels **(A–D)**: kinetic energy spectra of the most abundant components of the radiation field including and excluding the primary ions. Panel **(E)**: track length distribution of all the particles detected by the TEPC. The mean chord length at 8.47 mm is marked with a red dotted line. Panel **(F)**: microdosimetric yd(y) spectra obtained with the mean chord length approximation (red line) and microdosimetric $y_T d(y_T)$ spectra obtained using the real chord length values (blue line).

of the particles populating these regions. This reflects on the fact that the proposed HDM configuration has limitations in those regions since it cannot operate close to and at distal part of the SOBP.

Finally, particles that do not have enough kinetic energy to reach all detectors are also a limit of HDM detection efficiency. Nonetheless, this issue can be partly solved by exploring the possibility of producing LGADs with thinner active layers or decreasing the substrate width. For instance, reducing the total LGAD thickness down to 100 μm is considered achievable in the near future.

TABLE 4 | Mean track length values and standard deviations of protons and carbon ions traversing a spherical TEPC of 12.6 mm diameter. The mean chord length of this detector exposed to a uniform and isotropic radiation field is 8.47 mm.

Ion	Mean track length [mm]	Standard deviation [mm]
Carbon	9.17	3.03
Proton	9.53	2.8

CONCLUSION

The design of a new hybrid detector for microdosimetry (HDM: hybrid detector for microdosimetry) is presented in this work. HDM is composed by a TEPC followed by four LGADs, and provides energy deposition in tissue as well as tracking of single particles with a submillimeter spatial precision. HDM unique feature is that it can provide the real track length that a particle travel inside the TEPC, from which the microdosimetric spectra can be calculated without using the mean chord approximation. To investigate the detector efficiency, we performed Monte Carlo simulations with Geant4 toolkit and exposed HDM to both protons and carbon ions at therapeutic energies.

Results show evidence on both the feasibility of the proposed hybrid system and on the advances that this detector will contribute to in particle therapy. The possibility of exploiting a tracker instead of geometrical assumptions are of great help in several situations, especially in a mixed and non isotropic radiation field. In addition, a precise *a priori* knowledge of the beam characteristics is not always easy to achieve.

The LGAD technology chosen for this scope is constantly evolving and improving. The possibility of using more advanced versions of LGADs will be considered in future, for example, to drastically increase the fill factor by reducing the interstrip layers, while keeping the same spatial resolution. Moreover, as the spatial resolution can be improved by using narrower strips, we will test these configurations, which can also increase the tracking efficiency. Additionally, the advantage of being able to select the gain of LGADs according to specific experimental needs is of great help in view of a wide-ranging use of HDM in different irradiation scenarios.

Further, additional efforts will be put on studying more advanced tracking algorithms to better take into account significant deviations from a linear track, with specific reference to scattering events.

Finally, to improve the field characterization, we will explore the possibility to use the LGADs for acquiring information on the particle charge.

DATA AVAILABILITY STATEMENT

The raw data supporting the conclusions of this article will be made available by the authors, without undue reservation.

AUTHOR CONTRIBUTIONS

MM has contributed to the methodology development of the algorithms, the investigation and formal analysis of data and results presented in the paper. CLT has participated in the conceptualization, supervision and project administration. EP has contributed to the implementation of the simulations and to the formal analysis of the obtained results. FC has contributed to the investigation and formal analysis to data and results presented in the paper. MC, AP and LR has contributed to the electronic read-out system of the detector. MB, MCV, GB and VM were involved in the design and production of LGAD sensors. All authors contributed to the manuscript preparation, review and editing.

ACKNOWLEDGMENTS

This work was supported by CARITRO foundation. The authors thank Valeria Conte for the many precious suggestions and useful discussions that helped improve the quality of this work.

REFERENCES

1. Andreo P, Burns DT, Nahum AE, Seuntjens J, Attix FH. *Fundamentals of ionizing radiation dosimetry*. Hoboken, NJ: John Wiley & Sons (2017)
2. Agosteo S, Pola A. Silicon microdosimetry. *Radiat Protect Dosim* (2011) **143**: 409–15. doi:10.1093/rpd/ncq408
3. Rosenfeld AB. Novel detectors for silicon based microdosimetry, their concepts and applications. *Nucl Instrum Methods Phys Res Sect A Accel Spectrom Detect Assoc Equip* (2016) **809**:156–70. doi:10.1016/j.nima.2015.08.059
4. Davis JA, Petasecca M, Guatelli S, Lerch ML, Rosenfeld AB. Evolution of diamond based microdosimetry. In: Journal of physics: conference series. Bristol, UK: IOP Publishing (2019). **vol. 1154**, p. 012007.
5. Rossi HH, Rosenzweig W. A device for the measurement of dose as a function of specific ionization. *Radiology* (1955) **64**:404–11. doi:10.1148/64.3.404
6. Lindborg L, Waker A. *Microdosimetry: experimental methods and applications*. Boca Raton, FL: CRC Press (2017).
7. Conte V, Bianchi A, Selva A, Petringa G, Cirrone G, Parisi A, et al. Microdosimetry at the CATANA 62 MeV proton beam with a sealed miniaturized TEPC. *Phys Med* (2019) **64**:114–22. doi:10.1016/j.ejmp.2019.06.011
8. De Nardo L, Colautti P, Hérault J, Conte V, Moro D. Microdosimetric characterisation of a therapeutic proton beam used for conjunctival melanoma treatments. *Radiat Meas* (2010) **45**:1387–90. doi:10.1016/j.radmeas.2010.05.034
9. De Nardo L, Dal Corso F, Pegoraro M. Microdosimetric Measurements in Gamma and neutron Fields with a Tissue Equivalent Proportional Counter Based on a Gas Electron Multiplier. *Radiat Prot Dosimetry* (2017) **175**(2): 260–266.
10. Martino G, Durante M, Schardt D. Microdosimetry measurements characterizing the radiation fields of 300 MeV/u 12C and 185 MeV/u 7Li pencil beams stopping in water. *Phys Med Biol* (2010) **55**:3441–9. doi:10.1088/0031-9155/55/12/011
11. Zhou D, Semones E, Weyland M, Johnson S. Radiation measured with TEPC and CR-39 PNTDs in low earth orbit. *Adv Space Res* (2007) **40**:1571–4. doi:10.1016/j.asr.2006.12.006

12. Zaider M, Rossi BHH, Zaider M. *Microdosimetry and its applications*. New York, NY: Springer (1996)
13. Kellerer AM. Fundamentals of microdosimetry. In: *The Dosimetry of Ionizing Radiation*, **Vol. 1**, London, UK: Academic Press (1985), p. 77–162.
14. Bolst D, Guatelli S, Tran LT, Chartier L, Lerch ML, Matsufuji N, et al. Correction factors to convert microdosimetry measurements in silicon to tissue in 12C ion therapy. *Phys Med Biol* (2017) **62**:2055–69. doi:10.1088/1361-6560/aa5de5
15. Cruz GS, Palmer M, Matatagui E, Zamenhof R. A theoretical model for event statistics in microdosimetry. i: uniform distribution of heavy ion tracks. *Med Phys* (2001) **28**:988–96. doi:10.1118/1.1376439
16. Santa Cruz G, Palmer M, Matatagui E, Zamenhof R. A theoretical model for event statistics in microdosimetry. ii: nonuniform distribution of heavy ion tracks. *Med Phy* (2001) **28**:997–1005. doi:10.1118/1.1376440
17. Abolfath R, Helo Y, Carlson DJ, Stewart R, Grosshans D, Mohan R. A new approach to modeling the microdosimetry of proton therapy beams. *Med phys* (2020) **47**:3184–90. doi:10.1002/mp.14165
18. Kase Y, Kanai T, Sakama M, Tameshige Y, Himukai T, Nose H, et al. Microdosimetric approach to NIRS-defined biological dose measurement for carbon-ion treatment beam. *J Radiat Res* (2011) **52**:59–68. doi:10.1269/jrr.10062
19. Missiaggia M, Cartechini G, Scifoni E, Rovituso M, Tommasino F, Verroi E, et al. Microdosimetric measurements as a tool to assess potential in-and out-of-field toxicity regions in proton therapy. *Phys Med Biol* (2020) [Epub ahead of print] doi:10.1088/1361-6560/ab9e56
20. Pellegrini G, Fernández-Martínez P, Baselga M, Fleta C, Flores D, Greco V, et al. Technology developments and first measurements of Low Gain Avalanche Detectors (LGAD) for high energy physics applications. *Nucl Instrum Methods Phys Res Sect A Accel Spectrom Detect Assoc Equip* (2014) **765**:12–6. doi:10.1016/j.nima.2014.06.008
21. Vignati A, Monaco V, Attili A, Cartiglia N, Donetti M, Mazinani MF, et al. Innovative thin silicon detectors for monitoring of therapeutic proton beams: preliminary beam tests. *J Instrum* (2017) **12**:C12056. doi:10.1088/1748-0221/12/12/c12056
22. Tran LT, Chartier L, Prokopovich DA, Bolst D, Povoli M, Summanwar A, et al. Thin silicon microdosimeter utilizing 3-D MEMS fabrication technology: charge collection study and its application in mixed radiation fields. *IEEE Trans Nucl Sci* (2018) **65**:467–72. doi:10.1109/tns.2017.2768062
23. Farahmand M. A novel tissue-equivalent proportional counter based on a gas electron multiplier (2004).
24. Mazza G, Cirio R, Olave J, Fausti F, Sacchi R, Monaco V. ABACUS: two fast amplifiers for the readout of LGAD detectors. In: Proceedings of topical workshop on electronics for particle physics-PoS (TWEPP2018) (2019) **Vol. 343**, PoS, 071; 2018 Sept 17–21; Antwerpen, Belgium: SISSA.
25. CNM-IMB (2020). Cnm-imb website [Dataset]. http://www.imb-cnm.csic.es
26. Sola V, Arcidiacono R, Boscardin M, Cartiglia N, Dalla Betta G-F, Ficorella F, et al. First FBK production of 50 μm ultra-fast silicon detectors. *Nucl Instrum Methods Phys Res Sect A Accel Spectrom Detect Assoc Equip* (2019) **924**:360–8. doi:10.1016/j.nima.2018.07.060
27. Chiriotti S, Moro D, Colautti P, Conte V, Grosswendt B. Equivalence of pure propane and propane TE gases for microdosimetric measurements. *Radiat Protect Dosim* (2015) **166**:242–6. doi:10.1093/rpd/ncv293
28. Agostinelli S, Allison J, Amako K, Apostolakis J, Araujo H, Arce P, et al. GEANT4—a simulation toolkit. *Nucl Instrum Methods Phys Res Sect A Accel Spectrom Detect Assoc Equip* (2003) **506**:250–303. doi:10.1016/S0168-9002(03)01368-8
29. Tarasov O, Bazin D. LISE++: radioactive beam production with in-flight separators. *Nucl Instrum Methods Phys Res Sect B Beam Interact Mater Atoms* (2008) **266**:4657–64. doi:10.1016/j.nimb.2008.05.110
30. Tommasino F, Durante M. Proton radiobiology. *Cancers* (2015) **7**:353–81. doi:10.3390/cancers7010353
31. Mohamad O, Yamada S, Durante M. Clinical indications for carbon ion radiotherapy. *Clin Oncol* (2018) **30**:317–29. doi:10.1016/j.clon.2018.01.006
32. Tommasino F, Scifoni E, Durante M. New ions for therapy. *Int J Part Ther* (2015) **2**:428–38. doi:10.14338/IJPT-15-00027.1
33. Rovituso M, La Tessa C. Nuclear interactions of new ions in cancer therapy: impact on dosimetry. *Transl Cancer Res* (2017) **6**:S914–33. doi:10.21037/tcr.2017.06.46

Conflict of Interest: The authors declare that the research was conducted in the absence of any commercial or financial relationships that could be construed as a potential conflict of interest.

frontiers in Physics

MINI REVIEW
published: 25 February 2021
doi: 10.3389/fphy.2020.598257

Secondary Radiation in Ion Therapy and Theranostics: A Review

*Maitreyee Nandy**

Saha Institute of Nuclear Physics, Kolkata, India

Ion therapy has emerged as one of the preferred treatment procedures in some selective indication of cancer. The actual dose delivered to the target volume may differ from the planned dose due to wrong positioning of the patient and organ movement during beam delivery. On the other hand, some healthy tissues outside the planned volume may be exposed to radiation dose. It is necessary to determine the primary particle range and the actual exposed volume during irradiation. Many proposed techniques use secondary radiation for the purpose. The secondary radiation consists mainly of neutrons, charged fragments, annihilation photons, among others, and prompt gammas. These are produced through nuclear interaction of the primary beam with the beam line and the patient's body tissue. Besides its usefulness in characterizing the primary beam, the secondary radiation contributes to the risk of exposure of different tissues. Secondary radiation has significant contribution in theranostics, a comparatively new branch of medicine, which combines diagnosis and therapy. Many authors have made detailed study of the dose delivered to the patient by the secondary radiation and its effects. They have also studied the correlation of secondary charged particles with the beam range and the delivered dose. While these studies have been carried out in great detail in the case of proton and carbon therapy, there are fewer analyses for theranostics. In the present review, a brief account of the studies carried out so far on secondary radiation in ion therapy, its effect, and the role of nuclear reactions is given.

Keywords: theranostics, neutrons, prompt gamma, charged particle, ion therapy, secondary radiation

OPEN ACCESS

Edited by:
Marco Durante,
GSI Helmholtz Center for Heavy Ion Research, Germany

Reviewed by:
Alessio Sarti,
Sapienza University of Rome, Italy
Satoshi Kodaira,
National Institutes for Quantum and Radiological Science and Technology, Japan
Ilaria Mattei,
INFN-Sezione di Milano, Italy

***Correspondence:**
Maitreyee Nandy
maitreyee.nandy@saha.ac.in

Specialty section:
This article was submitted to Medical Physics and Imaging, a section of the journal Frontiers in Physics.

Received: *24 August 2020*
Accepted: *31 December 2020*
Published: *25 February 2021*

Citation:
Nandy M (2021) Secondary Radiation in Ion Therapy and Theranostics: A Review. Front. Phys. 8:598257. doi: 10.3389/fphy.2020.598257

INTRODUCTION

In the growing incidence of malignant diseases, ion therapy has emerged as a preferred choice of treatment in the case of some selective indications [1–4]. During the passage of charged particles through the patient's body, electronic interactions contribute to the major part of energy deposition, while nuclear reactions lead to the production of neutrons, gamma rays, and secondary charged particles (SCPs). The energy deposition characteristics and the depth dose profile of the charged particle beams help to have high-dose conformity in the target volume in a static patient in an ideal situation. But variation in patient positioning and organ movement during treatment cause a fraction of the dose to be delivered outside the planned target volume [5, 6]. The problem can be circumvented if the actual volume of dose distribution can be dynamically imaged. This is achieved to some extent in image-guided radiotherapy (IGRT) [7] whence the target volume is imaged during treatment. Proposed techniques also use the SCPs to determine the primary particle range and the delivered dose during patient irradiation. Theranostics is an improved version of therapy [8] which combines treatment with simultaneous imaging of the region of interest. This is gradually emerging as a targeted and efficient mode of treatment.

Secondary particle dose is clinically important because neutrons can result in radiation dose to a distant organ, while heavy fragments can locally deposit a high dose. Both neutrons and SCPs have high radiobiological effectiveness (RBE). So measurement of yield, flux, and dose of the secondary particles is crucial for assessing the probability of radiogenic cancer [9] at a later stage. As the prospect of new beams is being studied, benefits as well as risks from secondary radiation need to be investigated thoroughly.

This is a review work of the studies carried out by different authors on secondary radiation in ion therapy and in theranostics, its effect, and the role of nuclear reaction. Yield and dose distribution of charged particles and neutrons from ion-induced reaction in tissue, their correlation with the primary ion range, and contribution to the total dose will be discussed.

SECONDARY RADIATION IN ION BEAM THERAPY

In radiotherapy, exposure to the healthy tissues is lesser in the case of charged particle therapy (CPT) compared to that in the case of photon therapy due to the characteristic of interaction and energy deposition of charged particles in matter. In charged particle therapy, the energy of the carbon beam is in the range of ~80–430 MeV/u, while the proton energy is in a lower range. For these moderately relativistic particles, the energy loss takes place through Coulomb and nuclear interaction. Nuclear interaction results in the loss of beam intensity contributing to both longitudinal and lateral dose profile [10, 11]. Multiple elastic scattering on the target nuclei contributes to the lateral profile and results in a broadening of the beam. Inelastic scattering with the atomic electrons contributes to the longitudinal profile. In CPT, nuclear reaction of the primary beam takes place both with the beam line components and within the patient's body. This leads to the production of neutrons, protons, heavier nuclear fragments, and deexcitation gamma rays. The nuclear fragments may consist of positron emitters and other radioactive isotopes. The former will give rise to annihilation gamma rays. Annihilation gammas, prompt gamma rays, neutrons, and the SCPs may help in dynamic imaging of the dose distribution. In proton therapy, nuclear fragmentation results in target fragments which consist mainly of secondary protons and neutrons. In heavy ion therapy, both target and projectile fragments are produced. Both the projectile and the target fragments contribute to the increase in the RBE. The projectile fragments enhance the lateral spread of the beam and add to the dose in the tail region of the Bragg peak. The dose distribution due to SCPs, neutrons, and gammas needs to be determined accurately to assess the biological effect.

Proton and carbon beams are most widely investigated for ion beam therapy. New beams like ^{4}He, ^{16}O are being studied to assess their possible advantages in ion beam therapy. ^{4}He ions might turn out to be a good choice, as projectile fragmentation and neutron production are expected to be lower than in the case of ^{12}C beams while having good localization of the energy deposition [12, 13]. For ^{16}O, fragmentation is higher and *in vitro* studies had also provided a slightly larger RBE value [14, 15] compared to ^{12}C, but carbon beam has a higher impact on cell survival. However, in all the cases, actual volume which is exposed to primary and secondary radiation strongly depends on patient positioning and on anatomical variation of the target organ during treatment [5, 6]. This necessitates determination of the actual volume where the dose is released. The SCPs produced in the nuclear reaction, particularly the secondary protons, can be well used as a tool for imaging in CPT [16, 17].

Secondary Charged Particles

Experimental Studies

Cross-section, total yield, fluence distribution of SCPs, and their contribution to the total dose had been investigated by several authors [12–39]. Target fragmentation for proton induced reactions in tissue equivalent targets like water, PMMA, C, and CH_2 was studied in the energy range of 40–250 MeV [19–21]. A study on 250 MeV proton on water showed that around 40% of the primary particles were lost in inelastic collision on their way up to the Bragg peak. The LET value and the range of the target fragments produced in these interactions were between 983 keV/μm down to 14 keV/μm and 2.3–68.9 μm, respectively. This resulted in the alteration of the fixed RBE of 1.1 used for proton therapy beam and contributed to the dose beyond the planned target volume [21]. For an unmodulated 160 MeV proton beam and a target volume of $3 \times 3 \times 3\ cm^3$, the dose from secondary protons to the proximal part of the Bragg peak was ~10% [19]. The dose contribution from d, t, α, and ^{3}He was less than 0.1% of the total dose proximal to the Bragg peak.

Nuclear fragmentation in carbon-induced reaction in tissue equivalent targets at 80–430 MeV/u was measured in many works [22–39] to determine the actual dose and range. The total [22–26] and partial (ΔZ = 1, 2, 3 for the formation of B, Be, and Li, respectively) [22, 23] charge-changing cross-sections in the interaction of ^{12}C in water were determined between 110 and 600 MeV/u. The total SCP production cross-section was found to decrease as the beam energy increased in the work of Golovchenko et al. [22], while no such trend was observed in [23]. Production of B was measured to be ~2.3–3 times that for Be [22, 23]. Charge-changing cross-sections for ^{16}O beam incident on thick targets of water and carbon were also measured [24].

Kinetic energy of the secondary protons emitted in the interaction of therapeutic ^{12}C beams extended beyond the primary beam energy per nucleon [27, 28]. At 80 MeV/u beam energy, yield of protons with E_p = 83 MeV was found to be $\sim 2.7 \times 10^{-4}\ sr^{-1}$ [27]. At 200 MeV/u, energy of emitted protons extended beyond twice the beam energy per nucleon [28] and the yield of protons with E_p = 350 MeV was $\sim 5 \times 10^{-5}\ ion^{-1}\ sr^{-1}\ MeV^{-1}$.

Production of secondary fragments for carbon-induced reactions at 95 MeV/u [25, 29] and for 200–400 MeV/u was measured and discussed in several works [28, 30–39]. Among all the fragments, yield of H and He was highest [28, 30, 31] and was similar or higher than the primary ions near the end of range. The yield fell off rapidly as the fragment charge increased [28]. Beyond the Bragg peak, light fragments H, He, Li, Be, and B had significant contribution. At 400 MeV/u beam energy, the

fragments penetrated few centimeters after the Bragg peak [30, 33]. These fragments would thus contribute to the delocalization of dose.

The angular distribution of the fragments was forward peaked for all fragments, was broad for light fragments, and became narrower as nuclear charge increased [30, 33]. At 219 and 280 MeV/u beam energy, protons had a broad angular range (up to 10°), but the primaries were confined within a narrow cone [34]. At 200 MeV/u, fragments heavier than He were confined in a cone of about 5° width. This suggested that the angular distribution was governed by the fragmentation process and not affected much by Coulomb scattering. The yield of secondary fragments integrated between 0 and 10° was highest for protons and lowest for Be [28]. At 400 MeV/u beam energy, the FWHM for H, He, and B was 10, 5.3, and 3°, respectively [30]. Higher FWHM was measured in the works of G. D. Lellis et al. [32] and K. Gunzert-Marx et al. [28].

The contribution of the secondary fragments to the dose equivalent within the Bragg peak was ~20%, 13%, and less than ~8% of the total dose for 157 MeV proton, 145 MeV/u ^{4}He, and 219–383 MeV/u 12C beams, respectively [12, 13, 34]. Beyond the Bragg peak, the total dose was contributed by the secondary fragments only. This dose in the tail region might affect the healthy tissue [30, 33].

At therapeutic energies, the target fragmentation rate was ~3.62 times higher for carbon ion compared to that for proton beam [12]. But the absorbed dose and dose equivalent due to the secondary target fragments (STFs) were 0.22% and 4%, respectively, of the primary ion dose for ^{12}C, compared to 1.2% and 20%, respectively, for proton beam. This was explained from the fact that though the yield of STFs increased with Z/β (β = velocity of primary ion), the number of primary ions required to produce a given dose decreased as Z^2 [40]. These results excluded the dose contribution due to secondary neutrons produced in the reaction. Among the secondary fragments, the highest dose was contributed by the light fragments H and He [30, 31] in the tail region behind the Bragg peak. They caused delocalization of the dose, followed by Li.

Besides proton and carbon, performance of ions like ^{4}He, ^{16}O, and ^{20}Ne in heavy ion therapy was investigated in several works [14, 15, 41–49]. The total number of secondary protons produced by 220 MeV ^{12}C beam in PMMA target at 90° was (4.49 ± 0.13±0.59)x10^{-3} sr^{-1} which was ~4.5 times that produced by 125 MeV ^{4}He (having the same range as 220 MeV ^{12}C in PMMA) [41, 42]. Production of ^{2}H and ^{3}H was ~5%–10% and ~1%–2%, respectively, of the total production of ^{1}H+^{2}H+^{3}H. For 125 MeV/u ^{4}He projectile, the energy of the emitted ^{1}H extended beyond 240 MeV at 5° [42]. Significant production of β^{+} was also reported for ^{4}He ion on PMMA target [43]. Secondary proton fluence from 300 MeV/u ^{16}O induced reaction on PMMA target was measured to be (74.18 ± 0.40±13.02)x10^{-3} sr^{-1} at 60° and was ~6.5 times lower at 90° [14]. At 210 MeV/u ^{16}O beam energy, these values were ~3.3–3.6 times lower. For the interaction of 670 MeV/u Ne beam in water, oxygen, and fluorine had the highest yield among the target fragments with Z ≥ 3, while at 400 MeV/u in PMMA target, oxygen had the highest yield followed by carbon and nitrogen [31]. Boron was found to have significant contribution at both the energies [31, 46]. In studying the efficacy of intensity modulated composite particle therapy (IMPACT), influence of the secondary particles on LET distribution was assessed [47, 48].

In CPT, annihilation gammas from positron emitters produced in nuclear fragmentation can be used for imaging during therapy. In measuring the mean range of different stable beams in water, polyethylene, and PMMA, from activity distribution using annihilation gammas, highest amount of information was obtained in the case of ^{16}O beam to determine the mean range of the beam accurately. Thus, ^{16}O turned out to be the optimum among stable beams for monitoring the range from annihilation gammas [50]. In proton therapy, annihilation gammas could be used to achieve a dose-volume guided radiotherapy system with a 2 mm spatial resolution [51, 52]. The profile of the prompt gamma rays produced in the interaction of the ion beam was also used to establish a relation between the gamma ray profile and the primary ion range [53–58]. Time-of-flight (TOF) technique was used to discriminate between prompt gammas, neutrons, and neutron-induced gamma rays. With less background and higher contrast, the peak and the dose fall off position could be measured with millimetric precision for proton beams [58].

The tracks of SCPs, their flux, velocity, and spatial distribution were analyzed and reviewed for monitoring in hadron therapy [16, 17, 19, 59, 60]. The Bragg peak position could be determined from the emission profile of the SCPs with high accuracy. A linear correlation was observed between the position of the distal edge of the secondary particle tracks and the Bragg peak position [19]. Accuracy of the method depended on several factors like multiple scattering of the SCPs, inherent fluctuation in the number of emitted charged particles, and overall statistics of the measured data. Feasibility study of range monitoring of carbon ions with secondary protons was carried out using interaction vertex imaging [17, 59] which showed that single proton detection in coincidence with the incoming beam was more promising.

Simulation Studies

Simulation studies of ^{12}C interaction in water, with the Monte Carlo Geometry and Tracking 4 (GEANT4) [61] code, showed that, at a beam energy of 155 MeV/u, more than 6% of the total dose was deposited by the SCPs and gamma rays from the phantom surface to 90% of the distal edge of the Bragg peak [62]. At beam energies of 262 and 369 MeV/u, these contributions were, respectively, ~14% and 23%. As the primary dose sharply fell off beyond the Bragg peak, the secondary radiation played a much more important role. From 90% of the distal edge to 5 cm after the Bragg peak, the SCPs along with the gamma radiation contributed ~71%, 82%, and 87% to the total dose, at beam energies of 155, 262, and 369 MeV/u, respectively [62]. The major contributor to the secondary dose was ^{11}B along with H and He near and beyond the Bragg peak [63]. At 290 MeV/u, contribution from H and He ions extended more than 160 mm beyond the Bragg peak. This could affect healthy tissues outside the target volume. In the initial part of the

primary beam path, LET of the primary ^{12}C beam was ~33.6 keV/μm while those for ^{14}N, ^{15}N, and ^{16}O were almost 30 times more. However, this pattern drastically changed near and beyond the distal end of the Bragg peak. Here, ^{11,12}C, ^{16}O, and ^{13,14,15}N had almost comparable LET [62]. Experimentally measured LET distribution of SCPs, for 380 MeV/u ^{12}C beam, was compared with the GEANT simulation [64, 65]. The measured values were well reproduced by the simulation [65]. In a benchmark analysis of the reaction models available in GEANT4 simulation kit for fragmentation studies [66, 67], it was observed that the measured fragment yields were reproduced by the models within 5–35%. The QMD model with Frag option gave the best agreement. The kinetic energy and the angular distributions were best reproduced by the QMD and INCL++ models, respectively [67]. GEANT4 simulation was used to compare the mixed radiation field produced by 162, 290 MeV/u ^{12}C beam and 192, 245 MeV/u ^{16}O beam in water [68]. At these energies, the ranges of the C and O beams were the same in the target. Production of nuclear fragments was higher for ^{16}O compared to that for ^{12}C. As a result, energy deposition beyond the Bragg peak and out of the field would be more for ^{16}O.

The PHITS code [69] was used to investigate the role of nuclear fragmentation and secondary radiation in carbon therapy [70, 71]. In the PHITS simulation, the Bragg curve peaked at a depth slightly lower than that given by the measured data. This was attributed to PHITS underestimating the probability of fragment production [70]. Using the Monte Carlo particle transport code FLUKA [72], the energy distribution, range distribution, and fragment fluence were studied for H, He, Li, B, Be, C, N, and O in proton-induced reaction on water between 40 and 200 MeV [73]. The energy distribution was highly asymmetric. For Li and heavier fragments, the energy distribution extended only well below 20 MeV. Proton energy spectrum had a broad shoulder and extended above 20 MeV.

Dedes and Parodi had reviewed the status of Monte Carlo simulation of particle interaction in tissue in carbon ion therapy [74].

Neutrons

Experimental and simulation studies were carried out by several authors [28, 75–91] to investigate the fluence and dose of secondary neutrons in proton and carbon ion therapy. Production of secondary neutrons and their dose profile were found to strongly depend on the irradiation facility [75–79]. Epidemiological studies were also undertaken to analyze the significance of the neutron dose in proton therapy [92].

The incident beam energy in ion therapy is high but gradually decreases in tissue. For carbon beam from therapeutic energy down to ~12 MeV/u, the reaction cross-section is highest at the latter point [80]. At these energies, the neutron field consists of both thermal and high-energy neutrons. Thermal neutrons have isotropic distribution while the fast neutrons produced have a strong energy dependence and forward peaked angular distribution. Neutrons with energy above 20 MeV were observed only close to the beam axis [81]. The high-energy neutrons, above 20 MeV, could contribute as high as 53% of the total dose at the position of highest neutron dose. The scattered neutron distribution was highly complex and depended on the spatial characteristics of the treatment facility. This necessitated a detailed Monte Carlo simulation of the secondary neutron field [82].

In proton radiotherapy at ~172 MeV, the largest neutron dose was obtained at a distance of 115 cm from the isocenter. The finding conformed to the fact that neutrons could significantly contribute to the dose outside the target volume [83].

From a comparison of the secondary neutron ambient dose equivalent (H^*_n (10)) in passive particle radiotherapy, it was confirmed that, for passively scanned beams, H^*_n (10) was less in carbon therapy than in proton therapy [84]. This dose depended on the operational beam setting but not on the method for making a laterally uniform field. H^*_n (10) for active scanned beam was similar for carbon and proton beams. For an active scanned carbon beam, this dose was at the most 15% of passive beam [85]. The observation could be attributed to the fact that the contribution to the total neutron dose from external neutrons was much reduced by an active scanned beam compared to a passive one. For a 250 MeV passively scanned proton beam, ~35% of the total neutron dose was due to neutrons with $E_n \geq 20$ MeV [86]. The neutron dose in passive particle radiotherapy was either similar to or less than that in photon therapy [84]. Comparison of the neutron yield in CPT and in high-energy photon therapy showed that, at therapeutic energies, the yield of most effective neutrons (~1MeV with w_R of 20) was much lower in ion therapy [87]. This was one of the main advantages of ion therapy over photon therapy.

A FLUKA Monte Carlo simulation was used to model a neutron tracker developed to track secondary neutrons produced in proton therapy [93]. This would help in better modeling of secondary neutrons.

THERANOSTICS USING RADIOACTIVE ISOTOPES

Feasibility of radioactive ion beams ^{10,11}C, ^{13}N, ^{14,15}O, ^{17,18}F and ^{18,19}Ne was investigated [50, 94–96] and reviewed [97] for in-beam positron emission tomography imaging in ion therapy. In the case of ^{11}C and ^{15}O, the difference in the Bragg peak position and the position of the maximum positron emitting fragments was negligible for ideal monoenergetic beams, but this difference increased with and was strongly influenced by the energy spread of the primary beams [94]. The difference also increased with energy of the primary beam. For 250 MeV/u ^{15}O and 350 MeV/u ^{11}C beams, the measured differences of 2.0 and 4.4 mm, respectively, were well reproduced by the PHITS simulations. Of the radioactive ion beams mentioned above, ^{15}O turned out to have the best feasibility for in-beam imaging and range monitoring [50].

Another set of isotopes emerging as potential diagnostic and therapeutic nuclides are the two radioisotopes of Cu–^{62,64}Cu [95, 96, 98–107]. Cu is one of the most abundant trace transition elements in human body and plays a key role in various physiological processes. Among the five radioisotopes of Cu,

namely, ^{60,61,62,64,67}Cu, ^{62}Cu (half-life 9.67 min) decays by β+ emission and is used for diagnosis. ^{64}Cu with a half-life of 12.7 h decays by electron capture β+ and β-emission. Electron capture results in the emission of Auger electrons which can be used for therapy [100]. So ^{64}Cu is increasingly investigated for use in diagnosis as well as in therapy. In normal cells, Cu remains in the cytoplasm, but in tumor cells it migrates to the nucleus [98]. Thus, ^{64}Cu can be used for theranostics without causing toxicity to the normal cell. The effect of $^{64}CuCl_2$ on human glioblastoma multiforme cell lines was studied by Catalogna et al. [101]. This study supported the theranostic potential of $^{64}CuCl_2$ in this tumor. $^{64}CuCl_2$ could be efficiently used for PET imaging in glioblastoma multiforme [102] which supported the prospect of ^{64}Cu as a diagnostic isotope for tumors of central nervous system. $^{64}CuCl_2$ as a PET probe with PET-CT imaging could be efficiently used for determining the stage of prostate cancer in the works of Capasso et al. [103]. ^{64}Cu-ATSM radiopharmaceutical was studied for imaging of hypoxic tumor tissue. A difference between normal and hypoxic cells was revealed around 10–15 min after administration of the compound [104]. Efficacy of ^{64}Cu-labelled-DOTATATE was investigated for imaging of neuroendocrine tumors. High spatial resolution, very good image quality, and significantly improved lesion detection capability were observed compared to ^{111}In-DTPA-octreotide [105] and ^{68}Ga-DOTATOC [106], respectively. ^{64}Cu was also used to study the uptake of specific antibody in patients with metastatic or advanced primary colorectal cancer. It showed higher specificity than ^{18}F-FDG for detection of colorectal tumors [107]. Feasibility of ^{64}Cu-labelled receptor antibody was studied for early detection and image-guided surgery of pancreatic cancers and gastrointestinal cancer using PET imaging [94, 95]. It was observed that pancreatic tumors larger than 3 mm could be detected and well resected [94]. Biodistribution and radiation dosimetry studies of $^{64}CuCl_2$ showed that liver has the highest uptake of ^{64}Cu in this form [108]. This was followed by intestine and pancreas. It was suggested that therapeutic activity with ^{64}Cu (in chloride form) up to several GBq would be safely feasible for these organs.

Several nuclides mentioned above are prospective candidates for theranostic applications–there are a few bottlenecks though. For radionuclides, the specific characteristics required for good imaging are different from those required for treatment. So only a few isotopes, for instance, ^{64}Cu, offer a combination of diagnostic and therapeutic capability. Secondly, phenotype-specific radiopharmaceutical is required for theranostic applications [109]. There are difficulties also related to dosimetry and delivery of the radionuclides to the target tissue. The drug compound may not be distributed uniformly in the target volume, and dose assessment is a complex task [110]. Moreover, theranostic application requires cost-effective supply of radioisotopes, clinical and regulatory approval of radiopharmaceuticals, and trained, competent manpower.

CONCLUSION

Ion therapy has emerged as one of the preferred methods of treatment in certain indications of malignancy. Detailed studies by different authors showed that the secondary radiation produced by the beam interaction in the patient's body can be used for range correlation and fine tuning of the primary beam. ^{16}O was detected to be the optimum among stable beams for range monitoring using annihilation gammas from positron emitting fragments. Prompt gammas and SCPs could be employed for monitoring the range of the primary beam with millimetric precision. This will help to determine the actual volume where the dose is deposited. On the other hand, the secondary radiation also causes dose deposition outside the target volume. This secondary radiation includes SCPs (from projectile and target fragmentation and particle emission), neutrons, and prompt gamma radiation. Neutrons produced in the patient's body may cause exposure to some healthy tissue well outside the target volume, though the dose would be small, whereas in photon therapy a large volume of healthy tissue is exposed to significant amount of radiation dose from the primary beam itself. Thus, the probability of secondary radiogenic cancer is decreased in ion therapy compared to that in the case of photon therapy. The neutron ambient dose equivalent H^*_n (10) in passive scanning method is substantially higher than that for active scanned beam. Among all the SCPs produced, light charged particles have the highest yield and show a broad angular distribution. Heavier fragments have lower yield and are confined to a narrow cone. In theranostics using radioactive beam, new isotopes are being investigated in detail by several authors. Of these, ^{15}O has appeared as a good candidate for in-beam PET imaging and range monitoring. ^{64}Cu in its ionic form as $^{64}CuCl_2$ has good prospect as a diagnostic agent for tumors of central nervous system, hypoxic tumors, and prostate cancer. ^{64}Cu-labelled radiopharmaceuticals are effective in imaging of neuroendocrinal tumors and colorectal cancer. Annihilation gammas from the positron emitting isotope ^{64}Cu could be efficiently used for image-guided surgery in pancreatic and gastrointestinal cancer. Prospective isotopes for theranostics need to be studied in great detail in order to come up with the most effective choices.

Review Criteria

Data for this review are compiled searching the published literature including archived works with no limitation on date. Searched phrases include "ion therapy", "particle therapy", "secondary radiation", "neutrons", "theranostics", among others. References have been quoted for all the works mentioned.

AUTHOR CONTRIBUTIONS

The author confirms being the sole contributor of this work and has approved it for publication.

FUNDING

The work has been carried out under the XII plan project "Biomolecular Architecture Recognition and Dynamics (BARD)" of Saha Institute of Nuclear Physics, Department of Atomic Energy, Kolkata, Govt. of India.

REFERENCES

1. Durante M, Cucinotta FA, Loeffler JS Editorial: Charged particles in oncology. *Front Oncol* (2017) 7:301. doi:10.3389/fonc.2017.00301
2. Malouff TD, Mahajan A, Krishnan S, Beltran C, Seneviratne DS, Trifiletti DM Carbon ion therapy: A modern review of an emerging technology. *Front Oncol* (2020) 10:82. doi:10.3389/fonc.2020.00082
3. Durante M, Debus J Heavy charged particles: does improved precision and higher biological effectiveness translate to better outcome in patients? *Semin Radiat Oncol* (2018) 28(2):160–67. doi:10.1016/j.semradonc.2017.11.004
4. Durante M, Formenti S Harnessing radiation to improve immunotherapy: better with particles? *Br J Radiol* (2020) 93(1107):20190224. doi:10.1259/bjr.20190224
5. van der Horst A, Houweling AC, van Tienhoven G, Visser J, Bel A Dosimetric effects of anatomical changes during fractionated photon radiation therapy in pancreatic cancer patients. *J Appl Clin Med Phys* (2017) 18(6):142–51. doi:10.1002/acm2.12199
6. Yokoyama A, Kubota Y, Kawamura H, Miyasaka Y, Kubo N, Sato H, et al. Impact of inter-fractional anatomical changes on dose distributions in passive carbon-ion radiotherapy for prostate cancer: comparison of vertical and horizontal fields. *Front Oncol* (2020) 10:1264. doi:10.3389/fonc.2020.01264
7. Sterzing F, Engenhart-Cabillic R, Flentje M, Debus J Image-guided radiotherapy: a new dimension in radiation oncology. *Dtsch Arztebl Int* (2011) 108(16):274–80. doi:10.3238/arztebl.2011.0274
8. Jeelani S, Jagat Reddy RC, Maheswaran T, Asokan GS, Dany A, Anand B Theranostics: A treasured tailor for tomorrow. *J Pharm BioAllied Sci* (2014) 6(Suppl. 1):S6–S8. doi:10.4103/0975-7406.137249
9. Eley JG, Friedrich T, Homann KL, Howell RM, Scholz M, Durante M, et al. Comparative risk predictions of second cancers after carbon-ion therapy versus proton therapy. *Int J Radiat Oncol Biol Phys* (2016) 95(1):279–86. doi:10.1016/j.ijrobp.2016.02.032
10. Durante M, Paganetti H Nuclear physics in particle therapy: a review. *Rep Prog Phys* (2016) 79:096702. doi:10.1088/0034-4885/79/9/096702
11. Battistoni G, Mattei I, Muraro S Nuclear physics and particle therapy. *Adv Phys X* (2016) 1(4):661. doi:10.1080/23746149.2016.1237310
12. Kodaria S, Kitamura H, Kurano M, Kawashima H, Benton ER Contribution to dose in healthy tissue from secondary target fragments in therapeutic proton, He and C beams measured with CR-39 plastic nuclear track detectors. *Sci Rep* (2019) 9(1):3708. doi:10.1038/s41598-019-39598-0
13. Kodaira S, Konishi T, Kitamura H, Kurano M, Kawashima H, Uchihori Y, et al. On the use of CR-39 PNTD with AFM analysis in measuring proton-induced target fragmentation particles. *Nucl Instrum Methods Phys Res Sect B Beam Interact Mater Atoms* (2015) 349:163. doi:10.1016/j.nimb.2015.02.052
14. Rucinski A, Traini G, Roldan AB, Battistoni G, De Simoni M, Dong Y, et al. Secondary radiation measurements for particle therapy applications: charged secondaries produced by ^{16}O ion beams in a PMMA target at large angles. *Phys Med* (2019) 64:45–53. doi:10.1016/j.ejmp.2019.06.001
15. Tinganelli W, Durante M, Hirayama R, Krämer M, Maier A, Kraft-Weyrather W, et al. Kill-painting of hypoxic tumours in charged particle therapy. *Sci Rep* (2015) 5:17016. doi:10.1038/srep17016
16. Piersanti L, Bellini F, Bini F, Collamati F, De Lucia E, Durante M, et al. Measurement of charged particle yields from PMMA irradiated by a 220 MeV/u (12)C beam. *Phys Med Biol* (2014) 59(7):1857–72. doi:10.1088/0031-9155/59/7/1857
17. Gwosch K, Hartmann B, Jakubek J, Granja C, Soukup P, Jäkel O, et al. Non-invasive monitoring of therapeutic carbon ion beams in a homogeneous phantom by tracking of secondary ions. *Phys Med Biol* (2013) 58(11):3755–73. doi:10.1088/0031-9155/58/11/3755
18. Granja C, Martisikova M, Jakubek J, Opalka L, Gwosch K Imaging and characterization of primary and secondary radiation in ion beam therapy. *AIP Conf Proc* (2016) 1753:080007. doi:10.1063/1.4955377
19. Paganetti H Nuclear interactions in proton therapy: dose and relative biological effect distributions originating from primary and secondary particles. *Phys Med Biol* (2002) 47:747. doi:10.1088/0031-9155/47/5/305
20. Cucinotta FA, Katz R, Wilson JW, Townsend LW, Shinn J, Hajnal F Biological effectiveness of high-energy protons: target fragmentation. *Radiat Res* (1991) 127(2):130–7. doi:10.2307/3577956
21. Tommasino F, Durante M Proton radiobiology. *Cancers* (2015) 7:353. doi:10.3390/cancers7010353
22. Golovchenko AN, Skvarč J, Yasuda N, Giacomelli M, Tretyakova SP, Ilic R, et al. Erratum: total charge-changing and partial cross-section measurements in the reactions of 110–250 MeV/nucleon 12 C in carbon, paraffin, and water. *Phys Rev C* (2002) 66(1):014609. doi:10.1103/physrevc.66.014609
23. Toshito T, Kodama K, Sihver L, Yusa K, Ozaki M, Kameoka AS, et al. Measurements of total and partial charge-changing cross sections for 200- to 400-MeV/nucleaon 12C on water and polycarbonate. *Phys Rev C* (2007) 75(5):054606. doi:10.1103/PhysRevC.75.054606
24. Schall I, Schardt D, Geissel H, Irnich H, Kankeleit E, Kraft G, et al. Charge-changing nuclear reactions of relativistic light-ion beams ($5 \leq Z \leq 10$) passing through thick absorbers. *Nucl Instrum Methods Phys Res Sect B Beam Interact Mater Atoms* (1996) 117(3):221–34. doi:10.1016/0168-583x(96)00325-4
25. Dudouet J, Juliani D, Labalme M, Cussol D, Angelique JC, Braunn B, et al. Double-differential fragmentation cross-section measurements of 95 MeV/nucleon 12C beams on thin targets for hadron therapy. *Phys Rev C* (2013) 88:024606. doi:10.1103/PhysRevC.88.024606
26. Mattei I, Alexandrov A, Alunni Solestizi L, Ambrosi G, Argiro S, Bartosik N, et al. Measurement of 12C fragmentation cross sections on C, O, and H in the energy range of interest for particle therapy applications. *IEE Trans Radiat Plasma Med Sci* (2020) 4(2):269–82. doi:10.1109/TRPMS.2020.2972197
27. Agodi C, Battistoni G, Bellini F, Cirrone GAP, Collamati F, Cuttone G, et al. Charged particle's flux measurement from PMMA irradiated by 80 MeV/u carbon ion beam. *Phys Med Biol* (2012) 57(18):5667–78. doi:10.1088/0031-9155/57/18/5667
28. Gunzert-Marx K, Iwase H, Schardt D, Simon RS Secondary beam fragments produced by 200 MeV u^{-1} ^{12}C ions in water and their dose contributions in carbon ion radiotherapy. *New J Phys* (2008) 10(7):075003. doi:10.1088/1367-2630/10/7/075003
29. Braunn B, Labalme M, Ban G, Chevallier M, Colin J, Cussol D, et al. Nuclear reaction measurements of 95 MeV/u ^{12}C interactions on PMMA for hadrontherapy. *Nucl Instrum Methods Phys Res Sect B Beam Interact Mater Atoms* (2011) 269(22):2676–84. doi:10.1016/j.nimb.2011.08.010
30. Haettner E, Iwase H, Krämer M, Kraft G, Schardt D Experimental study of nuclear fragmentation of 200 and 400 MeV/u12C ions in water for applications in particle therapy. *Phys Med Biol* (2013) 58(23):8265–79. doi:10.1088/0031-9155/58/23/8265
31. Matsufuji N, Fukumura A, Komori M, Kanai T, Kohno T Influence of fragment reaction of relativistic heavy charged particles on heavy-ion radiotherapy. *Phys Med Biol* (2003) 48(11):1605–23. doi:10.1088/0031-9155/48/11/309
32. De Lellis G, Buontempo S, Di Capua F, Di Crescenzo A, Migliozzi P, Petukhov Y, et al. Measurement of the fragmentation of Carbon nuclei used in hadrontherapy. *Nucl Phys A* (2011) 853(1):124–34. doi:10.1016/j.nuclphysa.2011.01.019
33. Haettner E, Iwase H, Schardt D Experimental fragmentation studies with ^{12}C therapy beams. *Radiat Prot Dosimetry* (2006) 122:485–7. doi:10.1093/rpd/ncl402
34. Greilich S, Ulrich L, Kouwenberg JJM, Rahmanian S Measurement of fluence, LET, and dose in a carbon ion spread-out Bragg-peak using fluorescent nuclear track detectors and an automated reader. *arXiv:1610.05054v3* (Forthcoming 2017).
35. Matsufuji N, Komori M, Sasaki H, Akiu K, Ogawa M, Fukumura A, et al. Spatial fragment distribution from a therapeutic pencil-like carbon beam in water. *Phys Med Biol* (2005) 50(14):3393–403. doi:10.1088/0031-9155/50/14/014
36. Golosio B, Gadow K, Goettlich M, Silenzi A, Xu C Single channel optimization for an endoscopic time-of-flight positron emission tomography detector. In: NSS/MIC'11: IEEE nuclear science symposym conference record, 2011 Oct 23–29, Valencia, Spain. IEEE (2011). p. 2277.
37. Golovkov M, Aleksandrov D, Chulkov L, Kraus G, Schardt D, et al. Advances in Hadrontherapy. In: U Amaldi, B Larsson, Y Lemoigne, editors *Excerpta medica international congress series*, Vol 1144, Amsterdam, Netherland: Elsevier (1997). p. 316.

38. Aleksandrov A, Consiglio L, De Lellis G, Di Crescenzo A, Lauria A, Montesi MC, et al. Measurement of large angle fragments induced by 400 MeV n−1carbon ion beams. *Meas Sci Technol* (2015) 26(9):094001. doi:10.1088/0957-0233/26/9/094001
39. Schardt D, Schall I, Geissel H, Irnich H, Kraft G, Magel A, et al. Nuclear fragmentation of high-energy heavy-ion beams in water. *Adv Space Res* (1996) 17(2):87–94. doi:10.1016/0273-1177(95)00516-H
40. Bethe H Zur theorie des durchgangs schneller korpuskularstrahlen durch materie. *Ann Phys* (1930) 397(3) 325–400. doi:10.1002/andp.19303970303
41. Rucinski A, De Lucia E, Battistoni G, Collamati F, Faccini R, et al. Secondary radiation measurements for particle therapy applications: Charged secondaries produced by 4He and 12C ion beams in a PMMA target at large angle (2016). Available from: arXiv:1608.04624v1 (Accessed August 16, 2016).
42. Rucinski A, Battistoni G, Collamati F, De Lucia E, Faccini R, Fralliccardi PM, et al. Secondary radiation measurements for particle therapy applications: charged particles produced by ^{4}He and ^{12}C ion beams in a PMMA target at large angle. *Phys Med Biol* (2018) 63(5):055018. doi:10.1088/1361-6560/aaa36a
43. Marafini M, Paramatti R, Pinci D, Battistoni G, Collamati F, De Lucia E, et al. Secondary radiation measurements for particle therapy applications: nuclear fragmentation produced by ^{4}He ion beams in a PMMA target. *Phys Med Biol* (2017) 62(4):1291–1309. doi:10.1088/1361-6560/aa5307
44. Toppi M, Battistoni G, Bellini F, Collamati F, De Lucia E, Durante M, et al. Measurement of secondary particle production induced by particle therapy ion beams impinging on a PMMA target. *EPJ Web Conf* (2016) 117:05007. doi:10.1051/epjconf/201611705007
45. Maccabee HD, Ritter MA Fragmentation of high-energy oxygen-ion beams in water. *Radiat Res* (1974) 60:409–21. doi:10.2307/3574021
46. Schimmerling W, Miller J, Wong M, Rapkin M, Howard J, Spieler HG, et al. The fragmentation of 670A MeV neon-20 as a function of depth in water: I. Experiment. *Radiat Res* (1989) 120(1):36–71. doi:10.2307/3577634
47. Inaniwa T, Kanematsu N, Noda K, Kamada T Treatment planning of intensity modulated composite particle therapy with dose and linear energy transfer optimization. *Phys Med Biol* (2017) 62(12):5180–197. doi:10.1088/1361-6560/aa68d7
48. Noda K Progress of radiotherapy technology with HIMAC. *J Phys Conf Ser* (2019) 1154:012019. doi:10.1088/1742-6596/1154/1/012019
49. Rovituso M, Schuy C, Weber U, Brons S, Cortés-Giraldo MA, La Tessa C, et al. Fragmentation of 120 and 200 MeV u^{-14} He ions in water and PMMA targets. *Phys Med Biol* (2017) 62(4):1310–26. doi:10.1088/1361-6560/aa5302
50. Inaniwa T, Tomitani T, Kohno T, Kanai T Quantitative comparison of suitability of various beams for range monitoring with induced β+activity in hadron therapy. *Phys Med Biol* (2005) 50(6):1131–45. doi:10.1088/0031-9155/50/6/007
51. Nishio T, Ogino T, Nomura K, Uchida H Dose-volume delivery guided proton therapy using beam on-line PET system. *Med Phys* (2006) 33(11):4190–7. doi:10.1118/1.2361079
52. Nishio T, Miyatake A, Ogino T, Nakagawa K, Saijo N, Esumi H The development and clinical use of a beam ON-LINE PET system mounted on a rotating gantry port in proton therapy. *Int J Radiat Oncol Biol Phys* (2010) 76(1):277–86. doi:10.1016/j.ijrobp.2009.05.065
53. Min C-H, Kim CH, Youn M-Y, Kim J-W Prompt gamma measurements for locating the dose falloff region in the proton therapy. *Appl Phys Lett* (2006) 89(18):183517. doi:10.1063/1.2378561
54. Pinto M, Bajard M, Brons S, Chevallier M, Dauvergne D, Dedes G, et al. Absolute prompt-gamma yield measurements for ion beam therapy monitoring. *Phys Med Biol* (2015) 60(2):565–94. doi:10.1088/0031-9155/60/2/565
55. Testa E, Bajard M, Chevallier M, Dauvergne D, Le Foulher F, Freud N, et al. Dose profile monitoring with carbon ions by means of prompt-gamma measurements. *Nucl Instrum Meth B* (2009) 267(6):993–6. doi:10.1016/j.nimb.2009.02.031
56. Roellinghoff F, Benilov A, Dauvergne D, Dedes G, Freud N, Janssens G, et al. Real-time proton beam range monitoring by means of prompt-gamma detection with a collimated camera. *Phys Med Biol* (2014) 59(5):1327–38. doi:10.1088/0031-9155/59/5/1327
57. Kelleter L, Wrońska A, Besuglow J, Konefał A, Laihem K, Leidner J, et al. Spectroscopic study of prompt-gamma emission for range verification in proton therapy. *Phys Med* (2017) 34:7–17. doi:10.1016/j.ejmp.2017.01.003
58. Krimmer J, Dauvergne D, Létang JM, Testa É Prompt-gamma monitoring in hadronthreapy: a review. *Nucl Inst Meth Phys Res A* (2017) 878:58–73. doi:10.1016/j.nima.2017.07.063
59. Henriquet P, Testa E, Chevallier M, Dauvergne D, Dedes G, Freud N, et al. Interaction vertex imaging (IVI) for carbon ion therapy monitoring: a feasibility study. *Phys Med Biol* (2012) 57(14):4655–69. doi:10.1088/0031-9155/57/14/4655
60. Muraro S, Battistoni G, Collamati F, De Lucia E, Faccini R, Ferroni F, et al. Monitoring of hadrontherapy treatments by means of charged particle detection. *Front Oncol* (2016) 6:177. doi:10.3389/fonc.2016.00177
61. Agostinelli S, Allison J, Amako K, Apostolakis J, Araujo H, Arce P, et al. GEANT4—a simulation toolkit. *Nucl Instr Meth Phys Res A* (2003) 506(3):250–303. doi:10.1016/S0168-9002(03)01368-8
62. Johnson D, Chen Y, Ahmad S Dose and linear energy transfer distributions of primary and secondary particles in carbon ion radiation therapy: a monte carlo simulation study in water. *J Med Phys* (2015) 40(4):214–9. doi:10.4103/0971-6203.170785
63. Ying C, Bolst D, Rosenfeld A, Guatelli S Characterization of the mixed radiation field produced by carbon and oxygen ion beams of therapeutic energy: a Monte Carlo simulation study. *J Med Phys* (2019) 44(4):263–69. doi:10.4103/jmp.jmp_40_19
64. Hirano Y, Kodaira S, Souda H, Osaki K, Torikoshi M Estimations of relative biological effectiveness of secondary fragments in carbon ion irradiation of water using CR-39 plastic detector and microdosimetric kinetic model. *Med Phys* (2020) 47(2):781–9. doi:10.1002/mp.13916
65. Hirano Y, Kodaira S, Souda H, Matsumura A, Torikoshi M Linear energy transfer (LET) spectra and survival fraction distribution based on the CR-39 plastic charged-particle detector in a spread-out Bragg peak irradiation by a ^{12}C beam. *Phys Med Biol* (2018) 63(18):185006. doi:10.1088/1361-6560/aadaa6
66. Mancini-Terracciano C, Caccia B, Colonna M, De Napoli M, Dotti A, Faccini R, et al. Validation of Geant4 nuclear reaction models for hadron therapy and preliminary results with BLOB. In: World congress on medical physics and biomedical engineering. IFMBE proceedings; 2018 Jun 3–8; Prague, Czech Republic, Vol 68, Singapore: Springer Singapore (2019). p. 675–85.
67. Bolst D, Cirrone GAP, Cuttone G, Folger G, Incerti S, Ivanchenko V, et al. Validation of Geant4 fragmentation for heavy ion therapy. *Nucl Instum Meth Phys Res A* (2017) 869:68–75. doi:10.1016/j.nima.2017.06.046
68. Ying CK, Bolst D, Tran LT, Guatelli S, Rosenfeld AB, Kamil WA, et al. Contributions of secondary fragmentation by carbon ion beams in water phantom: Monte Carlo simulation. *J Phys: Conf Ser* (2017) 851:012033. doi:10.1088/1742-6596/851/1/012033
69. Niita K, Sato T, Iwase H, Nose H, Nakashima H, Sihver L PHITS-a particle and heavy ion transport code system. *Radiat Meas* (2006) 41(9–10):1080–90. doi:10.1016/j.radmeas.2006.07.013
70. Zeitlin C, La Tessa C The role of nuclear fragmentation in particle therapy and space radiation protection. *Front Oncol* (2016) 6:65. doi:10.3389/fonc.2016.00065
71. Puchalska M, Tessonnier T, Parodi K, Sihver L Benchmarkin of PHITS for carbon ion therapy. *Int J Part Ther* (2018) 4(3):48–55. doi:10.14338/IJPT-17-00029.1
72. Battistoni G, Boehlen T, Cerutti F, Chin PW, Esposito LS, et al. Overview of the FLUKA code. *Ann Nucl Energy* (2015) 82:10–8. doi:10.1016/j.anucene.2014.11.007, T. T. Bohlen, F. Cerutti, M. P. W. Chin, A. Fassò, A. Ferrari, et al. Nucl. Data Sheets 120 (2014) 211.
73. Embriaco A, Dong Y, Mattei I, Muraro S, Valle SM, Battistoni G Target fragmentation in proton therapy. *Il Nuovo Cimento C* (2018) 41(6):207. doi:10.1393/ncc/i2018-18207-4
74. Dedes G, Parodi K Monte carlo simulations of particle interactions with tissue in carbon ion therapy. *Int J Part Ther* (2015) 2(3):447–58. doi:10.14338/IJPT-15-00021
75. Howell RM, Kry SF, Burgett E, Hertel NE, Followill DS Secondary neutron spectra from modern Varian, Siemens, and Elekta linacs with multileaf collimators. *Med Phys* (2009) 36(9):4027–38. doi:10.1118/1.3159300
76. Prez-Andujar A, Newhauser WD, DeLuca PM. *Nucl Technol* (2010) 55:7009.

77. Schardt D, Elsässer T, Schulz-Ertner D Heavy-ion tumor therapy: physical and radiobiological benefits. *Rev Mod Phys* (2010) 82:383. doi:10.1103/RevModPhys.82.383
78. Xu G, Bednarz B, Paganetti H A review of dosimetry studies on external-beam radiation treatment with respect to second cancer induction. *Phys Med Biol* (2008) 53(13):R193. doi:10.1088/0031-9155/53/13/R01
79. Pérez-Andújar A, Newhauser WD, DeLuca PM Neutron production from beam-modifying devices in a modern double scattering proton therapy beam delivery system. *Phys Med Biol* (2009) 54(4):993–1008. doi:10.1088/0031-9155/54/4/012
80. Nandy M, Sarkar PK, Sanami T, Takada M, Shibata T Neutron emission and dose distribution from natural carbon irradiated with a 12 MeV amu^{-1} $^{12}C^{5+}$ ion beam. *J Radiol Prot* (2016) 36(3):456. doi:10.1088/0952-4746/36/3/456
81. Mares V, Romero-Expósito M, Farah J, Trinkl S, Domingo C, Dommert M, et al. A comprehensive spectrometry study of a stray neutron radiation field in scanning proton therapy. *Phys Med Biol* (2016) 61(11):4127–40. doi:10.1088/0031-9155/61/11/4127
82. Trinkl S, Mares V, Englbrecht FS, Wilkens JJ, Wielunski M, Parodi K, et al. Systematic out-of-field secondary neutron spectrometry and dosimetry in pencil beam scanning proton therapy. *Med Phys* (2017) 44(5):1912–20. doi:10.1002/mp.12206
83. Farah J, Mares V, Romero-Expósito M, Trinkl S, Domingo C, Dufek V, et al. Measurement of stray radiation within a scanning proton therapy facility: EURADOS WG9 intercomparison exercise of active dosimetry systems. *Med Phys* (2015) 42(5):2572. doi:10.1118/1.4916667
84. Yonai S, Matsufuji N, Kanai T, Matsui Y, Matsushita K, Yamashita H, et al. Measurement of neutron ambient dose equivalent in passive carbon-ion and proton radiotherapies. *Med Phys* (2008) 35(11):4782–92. doi:10.1118/1.2989019
85. Yonai S, Furukawa T, Inaniwa T Measurement of neutron ambient dose equivalent in carbon-ion radiotherapy with an active scanned delivery system. *Radiat Prot Dosimetry* (2014) 161(1–4):433–6. doi:10.1093/rpd/nct251
86. Howell RM, Burgett EA Secondary neutron spectrum from 250-MeV passively scattered proton therapy: measurement with an extended-range Bonner sphere system. *Med Phys* (2014) 41(9):092104. doi:10.1118/1.4892929
87. La Tessa C, Berger T, Kaderka R, Schardt D, Burmeister S, Labrenz J, et al. Characterization of the secondary neutron field produced during treatment of an anthropomorphic phantom with x-rays, protons and carbon ions. *Phys Med Biol* (2014) 59(8):2111–25. doi:10.1088/0031-9155/59/8/2111
88. Takam R, Bezak E, Marcu LG, Yeoh E Out-of-field neutron and leakage photon exposures and the associated risk of second cancers in high-energy photon radiotherapy: current status. *Radiat Res* (2011) 176(4):508–20. doi:10.1667/RR2606.1
89. Kaderka R, Schardt D, Durante M, Berger T, Ramm U, Licher J, et al. Out-of-field dose measurements in a water phantom using different radiotherapy modalities. *Phys Med Biol* (2012) 57(16):5059–74. doi:10.1088/0031-9155/57/16/5059
90. La Tessa C, Berger T, Kaderka R, Schardt D, Körner C, Ramm U, et al. Out-of-field dose studies with an anthropomorphic phantom: comparison of X-rays and particle therapy treatments. *Radiother Oncol* (2012) 105(1):133–8. doi:10.1016/j.radonc.2012.04.004
91. Douglass M, Bezak E Physical modelling of proton and heavy ion radiation using Geant4. *EPJ Web Conf* (2012) 35:04001. doi:10.1051/epjconf/20123504001
92. Schneider U, Hälg R The impact of neutrons in clinical proton therapy. *Front Oncol* (2015) 5:235. doi:10.3389/fonc.2015.00235
93. Gioscio E, Battistoni G, Bochetti A, De Simoni M, Dong Y, Fischetti M, et al. Development of a novel neutron tracker for the characterisation of secondary neutrons emitted in particle therapy. *Nucl Inst Meth Phys Res A* (2019) 958:162862. doi:10.1016/j.nima.2019.162862
94. Mohammadi A, Tashima H, Iwao Y, Takyu S, Akamatsu G, Nishikido F, et al. Range verification of radioactive ion beams of ^{11}C and ^{15}O using in-beam PET imaging. *Phys Med Biol* (2019) 64(14):145014. doi:10.1088/1361-6560/ab25ce
95. Yoshii Y, Tashima H, Iwao Y, Yoshida E, Wakizaka H, Akamatsu G, et al. Immuno-OpenPET: a novel approach for early diagnosis and image-guided surgery for small resectable pancreatic cancer. *Sci Rep* (2020) 10(1):4143. doi:10.1038/s41598-020-61056-5
96. Yoshii Y, Yoshimoto M, Matsumoto H, Tashima H, Iwao Y, Takuwa H, et al. Integrated treatment using intraperitoneal radioimmunotherapy and positron emission tomography-guided surgery with ^{64}Cu-labeled cetuximab to treat early- and late-phase peritoneal dissemination in human gastrointestinal cancer xenografts. *Oncotarget* (2018) 9(48):28935–50. doi:10.18632/oncotarget.25649
97. Durante M, Parodi K Radioactive beams in particle therapy: past, present, and future. *Front Phys* (2020) 8:00326. doi:10.3389/fphy.2020.00326
98. Gutfilen B, Souza S, Valentini G Copper-64: a real theranostic agent. *Drug Des Dvel Ther* (2018) 12:3235–45. doi:10.2147/DDDT.S170879
99. Boschi A, Martini P, Janevik-Ivanovska E, Duatti A The emerging role of copper-64 radiopharmaceuticals as cancer theranostics. *Drug Discov Today* (2018) 23(8):1489–1501. doi:10.1016/j.drudis.2018.04.002
100. Righi S, Ugolini M, Bottoni G, Puntoni M, Lacozzi M, Paparo F, et al. Biokinetic and dosimetric aspects of $^{64}CuCl_2$ in human prostate cancer: possible theranostic implications. *EJNMMI Res* (2018) 8(1):18. doi:10.1186/s13550-018-0373-9
101. Catalogna G, Talarico C, Dattilo V, Gangemi V, Calabria F, D'Antona L, et al. The SGK1 kinase inhibitor SI113 sensitizes theranostic effects of the 64CuCl2 in human glioblastoma multiforme cells. *Cell Physiol Biochem* (2017) 43(1):108–19. doi:10.1159/000480328
102. Panichelli P, Villano C, Cistaro A, Bruno A, Barbato F, Piccardo A, et al. Imaging of brain tumors with copper-64 chloride: early experience and results. *Canc Biother Rad* (2016) 31(5):159–67. doi:10.1089/cbr.2016.2028
103. Capasso E, Durzu S, Piras S, Zandieh S, Knoll P, Haug A, et al. Role of (64)CuCl2 PET/CT in staging of prostate cancer. *Ann Nucl Med* (2015) 29(6)482–8. doi:10.1007/s12149-015-0968-4
104. Bourgeois M, Rajerison H, Guerard F, Mougin-Degraef M, Barbet J, Michel N, et al. Contribution of [64Cu]-ATSM PET in molecular imaging of tumour hypoxia compared to classical [18F]-MISO - a selected review. *Nucl Med Rev Cent East Eur* (2011) 14(2):90–5. doi:10.5603/nmr.2011.00022
105. Pfeifer A, Knigge U, Mortensen J, Oturai P, Berthelsen AK, Loft A, et al. Clinical PET of neuroendocrine tumors using 64Cu-DOTATATE: first-in-humans study. *J Nucl Med* (2012) 53(8):1207–15. doi:10.2967/jnumed.111.101469
106. Johnbeck CB, Knigge UA, Loft A, Berthelsen AK, Mortensen J, Oturai P, et al. Head-to-Head comparison of ^{64}Cu-DOTATATE and ^{68}Ga-DOTATAC PET/CT: a prospective study of 59 patients with neuroendocrine tumors. *J Nucl Med* (2017) 58(3):451–57. doi:10.2967/jnumed.116.180430
107. Philpott GW, Schwarz SW, Anderson CJ, Dehdashti F, Connett JM, Zinn KR, et al. RadioimmunoPET: detection of colorectal carcinoma with positron-emitting copper-64-labeled monoclonal antibody. *J Nucl Med* (1995) 36(10):1818–24.
108. Avila-Rodriguez MA, Rios C, Carrasco-Hernandez J, Manrique-Arias JC, Martinez-Hernandez R, Garciá-Pérez FO, et al. Biodistribution and radiation dosimetry of [^{64}Cu]copper dichloride: first-in-human study in healthy volunteers. *EJNMMI Res* (2017) 7(1):98. doi:10.1186/s13550-017-0346-4
109. Kraeber-Bodéré F, Barbet J Challenges in nuclear medicine: innovative theranostic tools for personalized medicine. *Front Med* (2014) 1:16. doi:10.3389/fmed.2014.00016
110. Buscombe J Therapeutic nuclear medicine in the United Kingdom. In: R McCready, G Gnanasegaran, J Bomanji, editors *A history of radionuclide studies in the United Kingdom: 50th anniversary of the british nuclear medicine society*. Chap. 16, Cham, Switzerland: Springer (2016). p. 121–8. doi:10.1007/978-3-319-28624-2_16

Conflict of Interest: The author declares that the research was conducted in the absence of any commercial or financial relationships that could be construed as a potential conflict of interest.

frontiers in Physics

ORIGINAL RESEARCH
published: 16 March 2021
doi: 10.3389/fphy.2021.568139

PAPRICA: The Pair Production Imaging Chamber—Proof of Principle

M. Toppi[1,2], I. Avanzolini[3,4], L. Balconi[5], G. Battistoni[6], G. Calvi[6], M. De Simoni[3,4], Y. Dong[5,6], A. Fantoni[2], G. Franciosini[3,4], M. Marafini[2,7], M. Fischetti[1,4], V. Muccifora[2], S. Muraro[6], V. Patera[1,4,7], F. Ronchetti[2], A. Sarti[1,4,7], A. Sciubba[1,4,7], G. Traini[4], S. M. Valle[6] and I. Mattei[6]*

[1]Dipartimento Di Scienze Di Base E Applicate Per l'Ingegneria, Sapienza Università Di Roma, Rome, Italy, [2]INFN Laboratori Nazionali Di Frascati, Frascati, Italy, [3]Dipartimento Di Fisica, Sapienza Università Di Roma, Rome, Italy, [4]INFN Section of Rome, Rome, Italy, [5]Dipartimento Di Fisica, Università Degli Studi Di Milano, Milan, Italy, [6]INFN Section of Milan, Milan, Italy, [7]Museo Storico Della Fisica E Centro Studi E Ricerche E. Fermi, Rome Italy

In Particle Therapy, safety margins are applied around the tumor to account for the beam range uncertainties and ensure an adequate dose coverage of the tumor volume during the therapy. The reduction of safety margins is in great demand in order to diminish the Particle Therapy side effects especially in the case of treatment of tumors close to Organs at Risk (OAR) and of pediatric patients. To this aim, beam range monitoring techniques are being developed by the scientific community, most of all based on the detection of secondary particles produced by the nuclear interactions of the beam with the patient's tissue nuclei. In this contribution, a novel beam range monitoring technique is proposed, based on the detection of prompt photons exploiting the pair production mechanism. The proof of principle of the PAir PRoduction Imaging ChAmber (PAPRICA) is studied through the development of a Monte Carlo simulation and the detector performances toward a more realistic scenario are determined.

Keywords: reconstruction, pair production, particle therapy, range monitoring, prompt photons

OPEN ACCESS

Edited by:
Federico Giove, Centro Fermi–Museo Storico Della Fisica E Centro Studi E Ricerche Enrico Fermi, Italy

Reviewed by:
Etienne Testa, Université Lyon 1, France
Jean Michel Létang, Institut National Des Sciences Appliquées De Lyon (INSA Lyon), France

****Correspondence:***
G. Traini
giacomo.traini@roma1.infn.it

Specialty section:
This article was submitted to Medical Physics and Imaging, a section of the journal Frontiers in Physics

Received: *31 May 2020*
Accepted: *19 January 2021*
Published: *16 March 2021*

Citation:
Toppi M, Avanzolini I, Balconi L, Battistoni G, Calvi G, De Simoni M, Dong Y, Fantoni A, Franciosini G, Marafini M, Fischetti M, Muccifora V, Muraro S, Patera V, Ronchetti F, Sarti A, Sciubba A, Traini G, Valle SM and Mattei I (2021) PAPRICA: The Pair Production Imaging Chamber—Proof of Principle. Front. Phys. 9:568139. doi: 10.3389/fphy.2021.568139

1 INTRODUCTION

Particle Therapy (PT) is a type of external radiotherapy exploiting charged ion beams (mainly protons and carbon ions) to treat solid tumors. The typical charged particle dose-depth profile in tissues, characterized by a low dose release in the entrance channel followed by a narrow high-dose region called Bragg peak, elects the PT as the favorable treatment of unresectable deep-seated tumors close to Organs at Risk (OAR) [1]. Carbon ions can also profit from their high Relative Biological Effectiveness (RBE), which could be exploited to treat radioresistant tumors [2]. On the other hand, the intrinsic high-dose conformity to the target volume that could be achieved in PT is limited by the several sources of beam range uncertainties arising during the treatment (*e.g.*, patient positioning and anatomical changes) and/or in the treatment plan itself (*e.g.*, Hounsfield units, dE/dx conversion) [3]. To ensure a complete dose coverage of the tumor volume, safety margins are foreseen by the treatment planning, with a consequent unnecessary dose delivery to healthy tissues that can be potentially dangerous. The minimization of safety margins would be of large importance especially when tumors are seated in the proximity of OARs or in the treatment of long-life expectation patients as the pediatric ones [4], in which the occurrence of long-term side effects has a stronger impact. For such reasons, a large effort is being made by the scientific community in order to develop a beam range verification technique [5, 6] capable of operating on-line, *i.e.*, during the PT treatment, to provide prompt feedback on the actual administered dose spatial distribution. Different techniques have been proposed in the last decade, based on the detection of sound waves [7] or secondary

particles produced in the nuclear interactions of the beam projectiles with the patient's tissue nuclei, as annihilation photons produced in the decay of beam-induced β^+ emitters [8, 9], prompt gammas (PG) [10, 11], and charged secondary particles [12, 13].

Prompt gamma detection is a promising and deeply investigated solution [14] since different PG physics properties could be correlated to the beam range as the Time of Flight (TOF) [15] with Prompt Gamma Timing (PGT) technique, the energy spectrum [16] with Prompt Gamma Spectroscopy (PGS) technique, and the emission spatial distribution (PG imaging). In particular, the PGT technique is facility dependent, while the PGS was shown to be a very promising technique, reaching an accuracy of the order of few millimeters [16]. In the case of PGI, mechanical collimators [17] or Compton Cameras [18, 19] are used to reconstruct the PG production points. At present, one of the latest researches exploiting the prompt gamma imaging with a mechanical collimator has been published by Xie *et al.* [20] using a knife-edge slit camera. Data acquisition during a proton treatment on a patient has been reported and a 2 mm shift on the Bragg peak position has been observed by aggregating beam spots for a 7 mm kernel on the same tumor layer. One of the updated works regarding the prompt gamma electronic collimation with a Compton Camera is related to Draeger *et al.* [21], where a resolution of 3 mm has been obtained with a pencil beam of 10^8 protons, performing three measurements in three different detector positions as if the detector is made by six modules of the presented prototype. The obtained results by these two studies are very promising too, even though in the case of Compton Cameras limitations mainly due to the complex reconstruction algorithms have not yet been overcome [22].

In this contribution, a novel 3D PG imaging technique is proposed, exploiting the pair production (PP) interactions to reconstruct the incoming photon emission direction. The proof of principle of such a technique will be studied by means of the PAir PRoduction Imaging ChAmber (PAPRICA), a novel detector under development within the PAPRICA project[1].

The prompt photon imaging based on the pair production mechanism has been already investigated by Rohling *et al.* in 2015 [23]. The authors performed a Monte Carlo (MC) study with a simple detector geometry using photon point-like sources of different energies. Their study showed that such technique is mainly limited by the multiple scattering suffered by the produced lepton pair within their CZT converter, leading to a large angular resolution on the reconstructed photons and observing a bias on the photon emission point which is dependent on the detector geometry. The authors finally state that a pair production camera cannot match the precision requested in range monitoring applications in PT. The work presented in this manuscript aims to further explore the method proposed by the Rohling *et al.*, evaluating its feasibility using a detector designed to work in a clinical environment, with an optimized geometry in order to improve the detection efficiency while reducing the multiple scattering of e^+-e^- pairs within the converter plane. Moreover, the developed reconstruction algorithm would improve the imaging ability of a PP chamber by correcting the bias observed by the cited authors.

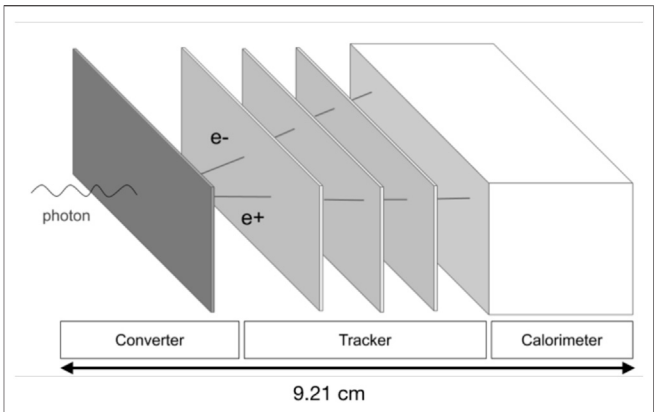

FIGURE 1 | Sketch of the PAPRICA design: the converter, the tracker, and the calorimeter blocks are shown. The total detector length is reported.

The PAPRICA design and its expected performances, evaluated by means of Monte Carlo simulations performed with the FLUKA software [24, 25], will be shown hereafter.

2 THE PAPRICA DEVICE

The pair telescope is a technology adopted in astrophysics research to image cosmic photons having energies higher than 30 MeV, recently explored also in the range ~5–200 MeV [26]. Telescopes are typically formed by layers of converter material, where photons undergo PP producing a e^+-e^- couple, interleaved with tracking material used to reconstruct the leptons' direction. The leptons' momentum could be assessed from either the analysis of the scattering or measuring the particles' kinetic energy by means of a scintillator. As highly inflammable and toxic gas mixtures such as Ar/CS and Ne/C_2H_8 are commonly employed as tracking material, the use of such technology cannot be easily extended in medical applications. The aim of the PAPRICA project is to investigate the feasibility of a novel 3D prompt gamma imaging technique based on the PP interaction of photons with energy below 10 MeV typically emitted in PT. The detector is designed in order to set the fundamental characteristics of a pair production-based prompt photon imaging device that could operate in a clinical environment and capable of a photon backtracking resolution compatible with the requirements set by the PT monitoring applications.

PAPRICA will intrinsically exploit the PG with energy greater than 4 MeV, above which the PP cross section becomes significant and PP is the most likely process to occur in several materials. Moreover, such photons are best correlated with the Bragg peak position [27], with a consequent background reduction due to the uncorrelated neutron-induced photons ($^1H(n,\gamma)^2H$). The topological signature of the PP allows for neutrons' discrimination, opening the possibility of exploiting such a range monitoring technique also in the carbon ion PT. To

[1]INFN (National Institute of Nuclear Physics, Italy) young researcher grant.

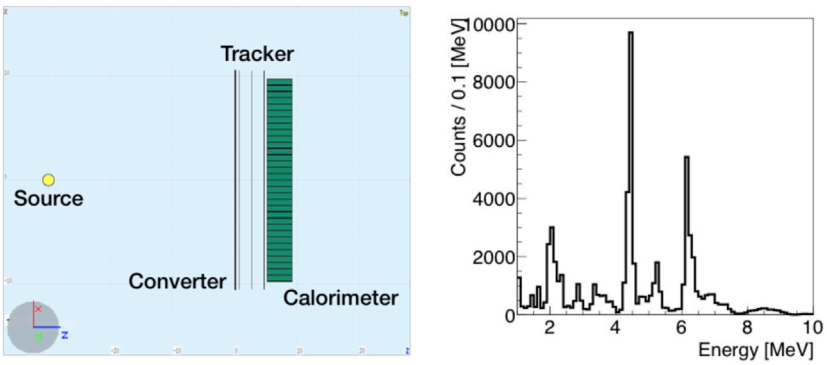

FIGURE 2 | Left: visualization of the FLUKA simulated geometry (top view). The photon point source is represented by the yellow dot. **Right:** PG energy spectrum at production obtained from the simulation of a 160 MeV proton beam impinging on a PMMA target.

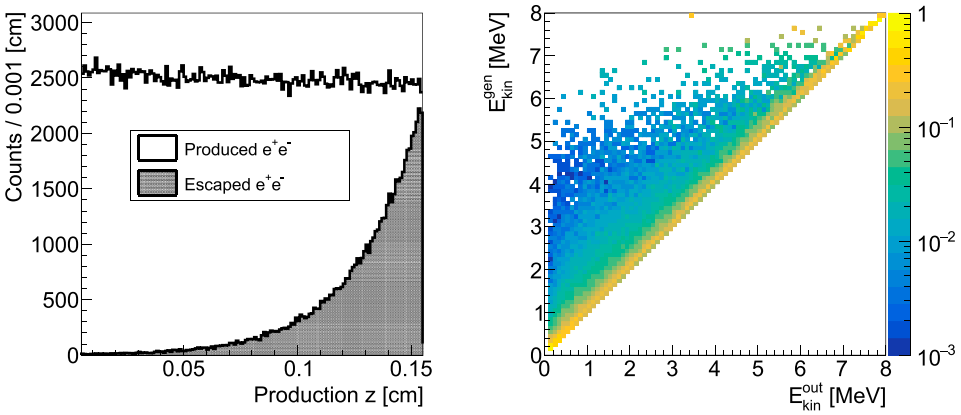

FIGURE 3 | Left: production coordinate of the pairs on the longitudinal axis z of the converter layer (white area) superimposed to the same distribution for the pairs able to exit the converter (black area). The observed exponential behavior represents the pair absorption toward the converter exit face. **Right:** probability distribution that an electron with a given kinetic energy at the converter exit (E_{kin}^{out}) is produced with a given kinetic energy at generation (E_{kin}^{gen}). The same distribution is observed for positrons.

image the incoming PG, no collimation technique, neither mechanical nor electronic, as well as no TOF information are needed. Moreover, a fast 3D reconstruction of the PG emission position could be performed thanks to the simplicity of the reconstruction algorithm, allowing for an on-line application of the technique. In the following section, the criteria adopted for the detector design are described.

2.1 Detector Design

The PAPRICA design oversees three detector blocks, as shown in **Figure 1**. A converter layer, made of a high Z material to maximize the PP cross section ($\sigma_{PP} \propto Z^2$), is used as a target for the photon conversion. A tracking system consisting of a set of three tracking stations based on silicon pixel detectors provides the e^+-e^- direction to reconstruct the interaction vertex. The needs in terms of momentum resolution, translating into the minimization of the multiple scattering and of the energy loss suffered by the leptons inside the tracker itself, have suggested the use of monolithic active pixel sensors (MAPS) for the three tracker stations. Finally, a matrix of pixelated plastic scintillator acts as a calorimeter, measuring the pair kinetic energy left. The incoming PG momentum is obtained using **Eq. 1**

$$\vec{p}_{\gamma} = \vec{p}_{e^+} + \vec{p}_{e^-}, \tag{1}$$

in which the unaccessible momentum of the recoiled nucleus has been neglected. As will be discussed in Section 2.1.1, such assumption represents the major intrinsic limit of PP-based imaging at the energy range of interest in PT. At the photon energy of interest, the PG 4-momentum resolution is also significantly affected by the multiple scattering (MS) suffered by the lepton pair to exit from the converter layer and cross the silicon-based tracking stations. To optimize the PAPRICA performance, the converter material and size as well as the full detector geometry have been finely tuned by means of an MC simulation developed with the FLUKA software. A point-like photon source, emitting in a cone with an angular aperture of ~0.7 rad and pointing toward the converter, has been placed at

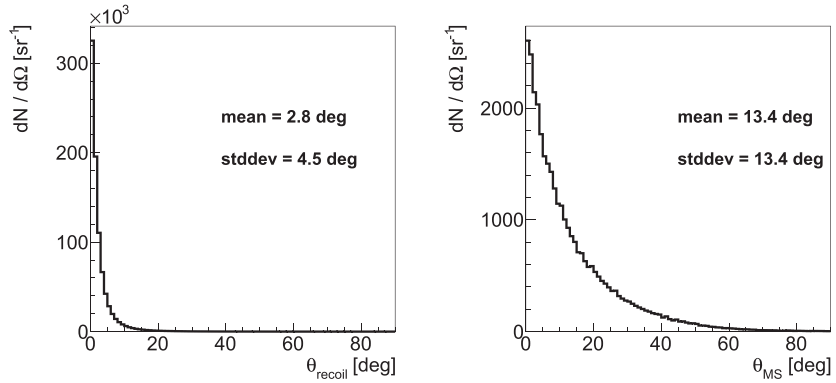

FIGURE 4 | Left: θ_{recoil} distribution due to the nuclear recoil of the converter. **Right:** θ_{MS} distribution due to the multiple scattering effect suffered by leptons within the converter. The distributions have been weighted with the solid angle $2\pi\sin(\theta)d\theta$, with $d\theta = 1^\circ \cdot \pi/180^\circ$.

30 cm distance from the converter surface (see **Figure 2** (left)), an attainable distance of the detector from a patient in a treatment room. The photon energy has been sampled from the emission spectrum (predicted by FLUKA) resulting from the interaction of a 160 MeV proton beam impinging on a PMMA (polymethilmethacrylate) target (see **Figure 2** (right)). The energy peaks due to the deexcitation of the $^{12}C^*$ (4.44 MeV) and $^{16}O^*$ (6.13 MeV) are clearly visible.

2.1.1 Converter

The converter layer has been optimized in terms of material (atomic number Z and density ρ) and thickness in order to balance the pair production efficiency, maximizing the number of PP interactions, while minimizing the converter MS. Using an optimized thickness, the LYSO (Z^{eff} = 66; ρ = 7.1 g/cm^3) scintillating crystal material has been chosen over tungsten (Z = 74; ρ = 19.3 g/cm^3) and lead (Z = 82; ρ = 11.3 g/cm^3). The advantage of using an active medium with respect to a passive one has been pursued: it will allow us to develop a trigger for the acquisition exploiting the time coincidence of the converter and calorimeter signals. The converter layer will be composed of ~130 LYSO fibers placed side by side, 1.5 × 1.5 × 50 mm^3 each, for a total surface of ~ 5 × 20 cm^2 and 1.5 mm thickness. The fibers are read out by two 64-channel Multianode Photomultipliers (MAPMs) (Hamamatsu H8500). Each LYSO fiber, painted with a white reflector (EJ-510) to prevent from optical cross-talk, will be coupled to a MAPM anode using optical fibers. The MAPM power supply and read-out will be provided by a system of ASIC and FPGA inherited by the Dose Profiler, a detector developed for range monitoring purposes in PT, whose full description can be found in ref. 28.

Despite the PP interactions are almost uniformly distributed along the converter thickness, 85% of the exiting leptons are produced in the last 500 μm as shown in **Figure 3** (left): the white solid area represents the production coordinate distribution along the longitudinal axis of the converter (z), while the black area shows the production coordinate of the pairs capable of exiting the converter. Nevertheless, the use of thinner LYSO fibers has been excluded due to their high mechanical fragility. The average

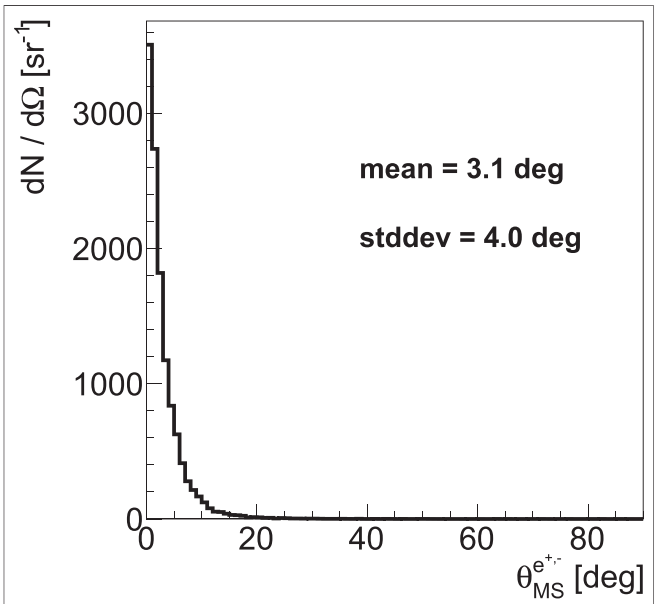

FIGURE 5 | Distribution of the angle $\theta_{MS}^{e^{+,-}}$ between the leptons' momentum directions at the entrance and at the exit of the first tracker plane, due to the multiple scattering within the first tracker plane, for the lepton pairs reaching the calorimeter. The distribution has been weighted with the solid angle $2\pi\sin(\theta)d\theta$, with $d\theta = 1^\circ \cdot \pi/180^\circ$.

energy of the exiting pair is ~2 MeV. **Figure 3** (right) shows the probability distribution that an electron with a given kinetic energy at the converter exit (E_{kin}^{out}) is produced with a given kinetic energy at generation (E_{kin}^{gen}). The displacement of the 2D plot diagonal elements from the bisector represents the effect of the electrons energy deposition within the LYSO fibers, resulting in an average energy shift of 0.5 MeV of E_{kin}^{out} with respect to E_{kin}^{gen}.

The contribution on the photon reconstruction of the converter nuclear recoil in the LYSO material has been evaluated accessing to the Monte Carlo scored information, calculating the angle θ_{recoil} between the photon direction

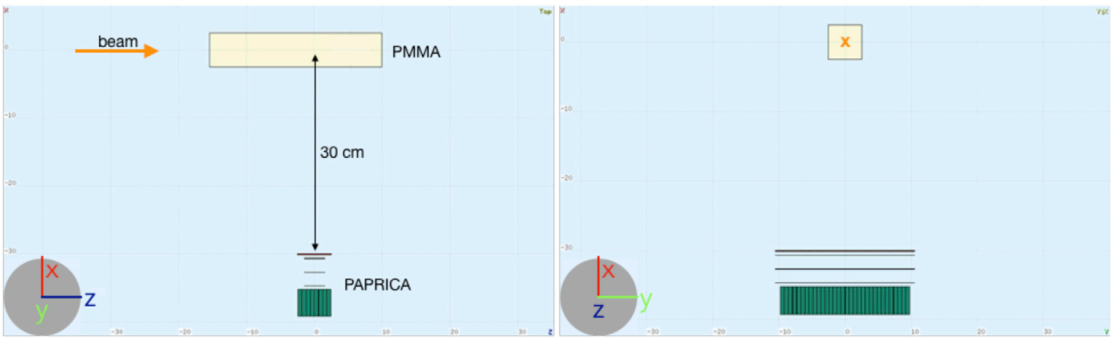

FIGURE 6 | Visualization of the FLUKA simulated geometry. The beam direction (in orange) is along the positive *z*-axis. **Left:** side view (*xz* plane). **Right:** front view (*xy* plane).

derived summing up the leptons momentum at their production and the true photon direction. **Figure 4** (left) shows the θ_{recoil} distribution due to the converter nuclear recoil with an average value of 2.8°. **Figure 4** (right) shows the effect of the multiple scattering suffered by leptons within the converter on the reconstructed photon direction: θ_{MS} has been computed as the angle of the leptons momentum sum at the converter exit and the true photon direction. The average value of the distribution, taking into account also the effect of the nuclear recoil on the degradation of the incident photon direction, is 13.4°.

2.1.2 Tracker

The tracking stations of the PAPRICA chamber are based on the ALPIDE (ALice PIxel DEtector) [29, 30] sensor, developed for the Outer Barrel (OB) of the new Inner Tracking System (ITS) of the ALICE detector [31, 32], in view of the LHC Run 3. Tests of ALPIDE telescopes, performed within the ALICE collaboration using minimum ionization particles, have shown a tracking efficiency > 99% and a fake hits rate $<10^{-6}$/pixel×event, exceeding the PAPRICA required performances in terms of achievable spatial resolution ($\simeq$ 5 μm).

The ALPIDE chip is a 15 mm × 30 mm MAPS, implemented in a 180 nm CMOS imaging sensor process. The sensor is segmented in 512 × 1024 pixels of 29 μm × 27 μm each. A periphery circuit region of 1.2 mm × 30 mm implements control and read-out functionalities and constitutes a dead area for crossing particles. Each pixel contains an n-well sensing diode (~2 μm diameter), an amplifying and shaping stage, a discriminator, and a digital section with three-hit storage register (Multievent Buffer). The digital read-out is managed by an in-matrix zero suppression circuit ("priority encoder"), providing to the periphery the addresses of pixels over the threshold. The circuits are fabricated on a high resistivity (> 1 kΩ·cm) P-type epitaxial layer (25 μm thick) on a P-type substrate (75 μm thick) for a total sensor thickness of 100 μm. A configurable discrimination time of 5–10 μs constitutes the pixel dead time. However, the high detector granularity (> 5 Mpixels/sensor) matches with the low multiplicity per event foreseen for PAPRICA, ensuring a higher rate capability than 100–200 kHz set by the time over discrimination threshold. Each layer of the PAPRICA tracker is

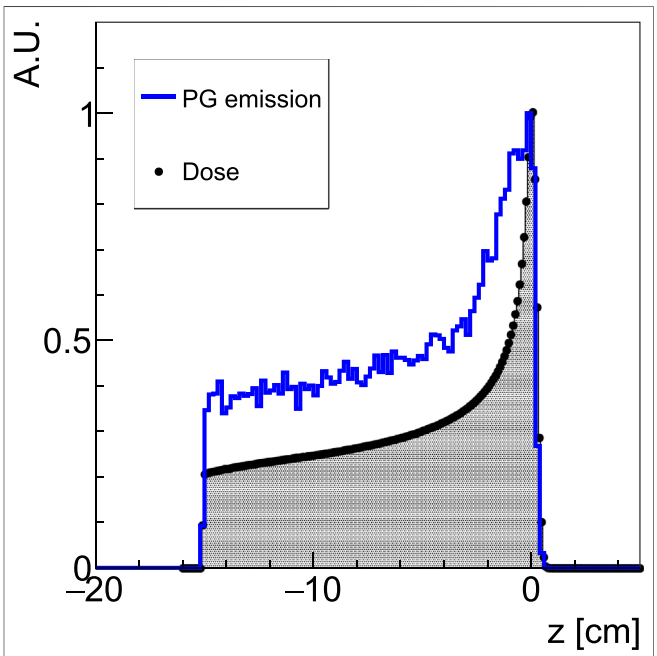

FIGURE 7 | 160 MeV proton beam dose deposition (full dots; black area) within the PMMA target, superimposed to the prompt photons (selected requiring production energy larger than 4 MeV) spatial emission distribution along the beam axis (solid blue line; white area). Each distribution is normalized to its maximum value. The PMMA entrance face is at z = −15.05 cm.

based on an OB-HIC (Hybrid Integrated Circuit) of the OB of the new ALICE ITS [33]. The OB-HIC consists of an assembly of two rows of 7 ALPIDE chips, for a total of 14 ALPIDEs with an overall surface $\simeq$ 21 × 3 cm^2, soldered and glued on an FPC (Flexible Printed Circuit). The FPC provides the connection for the powering, the bias voltage of the sensors, and the lines for signal propagation. For each row, a master chip manages the intercommunication with the other 6 slaves, through dedicated ports and lines. Differential pairs (100 μm width and pitch), from the master chip to the off-detector electronic, are used to distribute control and clock signals and to read out the pixel data. The OB-HIC FPC uses Cu-clad Pyralux, with a 75 μm

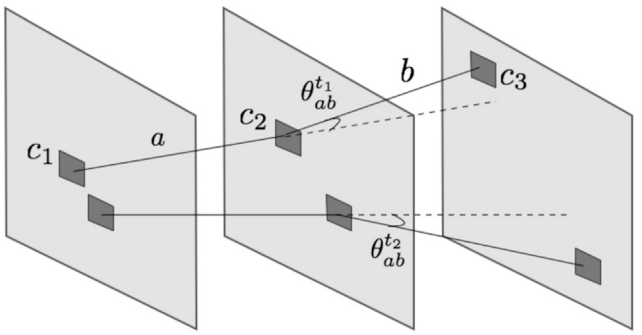

FIGURE 8 | Sketch of the cluster assignment to a track in the reconstruction algorithm (not to scale). The MAPS planes are represented in light gray, while the clusters are highlighted in dark gray. c_1, c_2, and c_3 belong to track t_1. *a* and *b* are the segments between c_1-c_2 and c_2-c_3, respectively. The angle $\theta_{ab}^{t_1}$ is reported, as well as for the second track t_2.

thick substrate of Kapton polyimide film and copper foils 18 μm thick on both sides. Two layers of 20 μm overlay enclose the FPC.

The front-end read-out logic is fully integrated into the ALPIDE sensor, which is able to drive signals directly over 2 m copper cables by integrated high-speed transmitters toward the off-detector electronics with rates up to 400 Mb/s. The off-detector read-out is managed by a MOSAIC board [34], FPGA-based board, that connects to control, clock, and data lines on the detector side, and interfaces with the DAQ PC via an Ethernet link. 3 MOSAIC units are employed, each connected to one of the tracker layers through the copper cables. High-speed receivers are connected to a 1 GB DDR3 memory that stores data waiting to be sent to the DAQ PC through a gigabit Ethernet interface. An external trigger can be provided to the MOSAIC board and then distributed to the sensors. The powering of the tracker layers is managed by a Power Board, interfaced and controlled by the MOSAIC, providing the possibility to power and monitor the voltages and currents for each layer, independently.

The three layers of the tracker are hosted in a mechanical structure designed to have the possibility to change the interlayers distance. Each layer is held by a rectangular frame provided of two windows in correspondence with the layer active region. The final mechanical structure has still to be finalized and the HIC assembly on the frames tested. The interplane distance has been optimized in order to meet the converter constraints and the minimum distance of ~2 cm allowed by the mechanics and electronics has been chosen: it maximizes the collectable pair statistics, geometrically selecting pairs from PG with energy > 4 MeV. Indeed, enlarging the interplane distance would cause a larger loss of the pairs due to the smaller angular acceptance, reducing the events generated by the 4.44 MeV prompt gammas, which are the most correlated to the beam range [27], of a factor ~2 when doubling the interplane distance.

To evaluate the impact of the multiple scattering suffered by the lepton pair crossing the tracker planes, all the detector details have been implemented in the simulation. An overall material budget of $x/X_0 \sim 0.22\%$ per layer has been estimated. **Figure 5** shows the angle $\theta_{MS}^{e^+,e^-}$ between the direction of the lepton momentum at the entrance in the first tracker plane and the momentum direction at the exit of the first tracker plane, computed for the lepton pairs reaching the calorimeter: the effect on $\theta_{MS}^{e^+,e^-}$ is due to the leptons multiple scattering within one tracker plane, and the obtained average value is 3.1°.

2.1.3 Calorimeter

In order to measure the kinetic energy of the pair, a calorimeter made of a plastic scintillator has been chosen. The material choice has been driven by the need of minimizing the lepton backscattering on the entrance surface, which can occur with a non-negligible probability for the < 10 MeV e^+-e^- [35]. As an outcome of the Monte Carlo simulation, the plastic low atomic number ($Z^{eff} = 4$) allows keeping the backscattering fraction at the 10% level, avoiding degradation in the photon momentum reconstruction and in the event selection where the calorimeter energy information will be exploited.

The scintillator (EJ-200) will be segmented in 256 rods $6 \times 6 \times 50$ mm^3, arranged in an 8×32 matrix, forming a surface of $\sim 5 \times 20$ cm^2, allowing for intercepting > 98 % of the pair traversing the three HIC planes. As foreseen for the converter fibers, each rod will be painted with white reflector (EJ-510) to prevent from optical cross-talk. The rod side has been determined from the average distance between the e^+-e^- tracks crossing the calorimeter surface, while the length is the one needed to absorb the maximum energy pair. Two MAPMs Hamamatsu H8500, whose anode size match with the rod size, will be coupled to the scintillator matrix to detect the scintillation light. The calorimeter shares the full read-out chain of the converter previously described in **Section 2.1.1**.

3 EXPECTED PERFORMANCES TOWARD A REALISTIC CASE

The PAPRICA expected performances toward a realistic case have been evaluated by means of a FLUKA Monte Carlo simulation of 160 MeV proton beam, 10^{11} primary particles, impinging on a PMMA thick target with a volume of $5 \times 5 \times 25$ cm^3. The beam has a Gaussian profile with $\sigma_{x,y} = 0.5$ cm [36], and the beam range is ~15 cm in PMMA. The simulation setup is shown in **Figure 6**. The PMMA has been positioned along z (beam direction) in order to have the Bragg peak at the origin of the coordinate reference system. The detector is positioned at 90° with respect to the beam direction, in order not to affect the reconstruction with the beam lateral spread and to preferentially select the prompt photons emitted from the distal part of their spatial emission distribution. The distance of the chamber converter from the coordinate system origin is 30 cm. The distance and angle chosen for the detector refer to a possible detector positioning in a treatment room. **Figure 7** shows the dose deposition of the simulated beam superimposed to the prompt photons emission distribution along the beam axis as simulated by FLUKA. The prompt photons selected are the ones produced with an energy

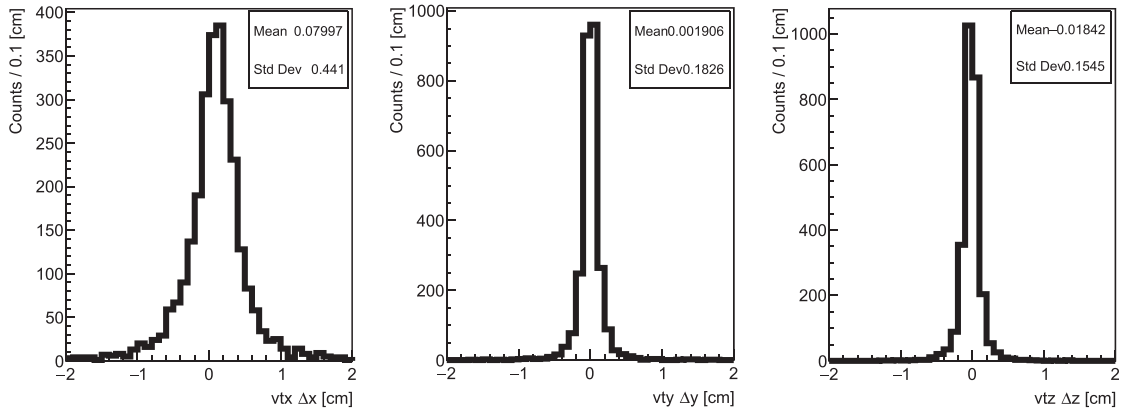

FIGURE 9 | Resolution on the reconstructed vertex position along the *x* **(left)**, *y* **(middle)**, and *z* **(right)** axes. The resolution has been computed for the tracks where an e^+-e^- leptons' pair has been correctly reconstructed and the leptons have been generated by a photon undergoing pair production within the converter plane.

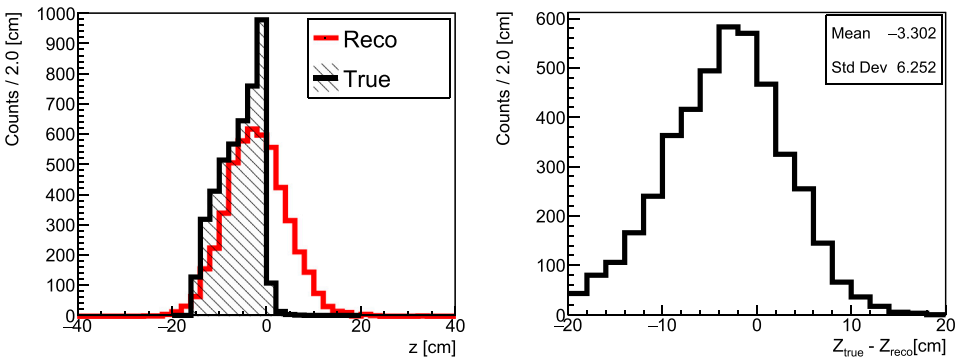

FIGURE 10 | Left: reconstructed prompt photons emission distribution along the beam axis (z coordinate) (red line; white area) obtained from 10^{11} 160 MeV protons impinging on a PMMA target. The distribution of the actual points at production is superimposed (black line; black area). **Right:** the difference between the z coordinate of the photon at generation (Z_{true}) and of the reconstructed photon (Z_{reco}), obtained from 10^{11} 160 MeV protons impinging on a PMMA target. A ~ –3 cm bias on the mean value of the distribution is visible.

greater than 4 MeV. The distributions are normalized to their maximum value. The well-known correlation between the Bragg peak position and the distal fall-off of the PG emission spatial distribution can be observed.

3.1 Prompt Gamma Emission Profile

In order to image the PG emission distribution, the incoming direction of the PG impinging on the converter and creating the electron-positron pair has been reconstructed in three steps: reconstruction of the leptons production vertex, photon momentum measurement (using **Eq. 1**), and photon emission coordinate reconstruction. To this aim, an ad hoc simulation output has been built by means of dedicated FLUKA user routines. The simulation output is given on an event-by-event basis. In order to develop a data-like MC output, the concept of a detector *hit* has to be introduced: a *hit* is defined as the energy release of one or more particles within an active detector (LYSO fiber, MAPS Si pixel, and plastic scintillator rod), which is above the detector energy threshold (E_{th}). No energy threshold has been set for the LYSO fibers and MAPS in the reported event reconstruction, while E_{th} = 500 keV has been chosen for the calorimeter rods, as a result of a dedicated analysis performed to optimize the trigger efficiency while minimizing the selection of background events. The Events of Interest (EoI), defined as the events where a photon produces in the converter an e^+-e^- pair intercepting the calorimeter, have been selected applying a two-level trigger strategy. First, a hardware-like trigger has been implemented at the simulation analysis level, asking for the presence of at least 1 converter hit and at least 2 calorimeter rods over the threshold. Then, a further selection has been applied asking for the presence of at least 2 hits in each tracker plane. The resulting trigger efficiency, defined as the ratio between the triggered EoI with respect to the whole EoI sample, is of the order of ~93%. The fraction of background events in the triggered sample of events is of the order of 20%.

3.2 Lepton Track Reconstruction

A combinatorial reconstruction algorithm has been developed in order to identify the leptons tracks, evaluate their direction, and

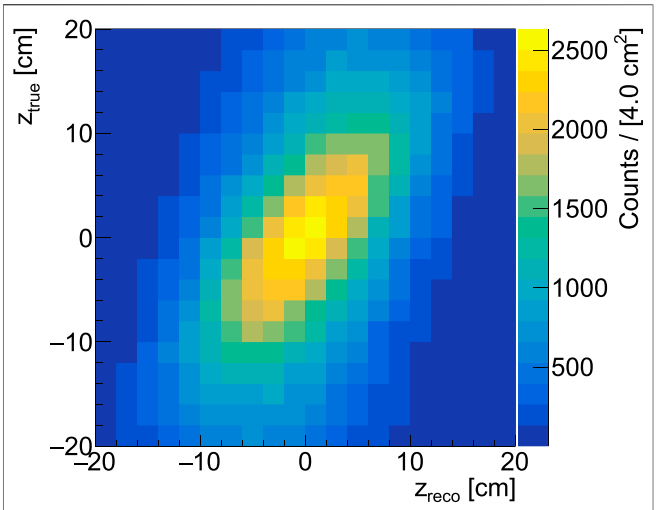

FIGURE 11 | Unfolding matrix computed from a *FLAT*sim (extended photon source within a PMMA target). Z_{reco} is the photon coordinate reconstructed by the PAPRICA detector having the same geometry of the *FULL*sim, while Z_{true} is its generation coordinate.

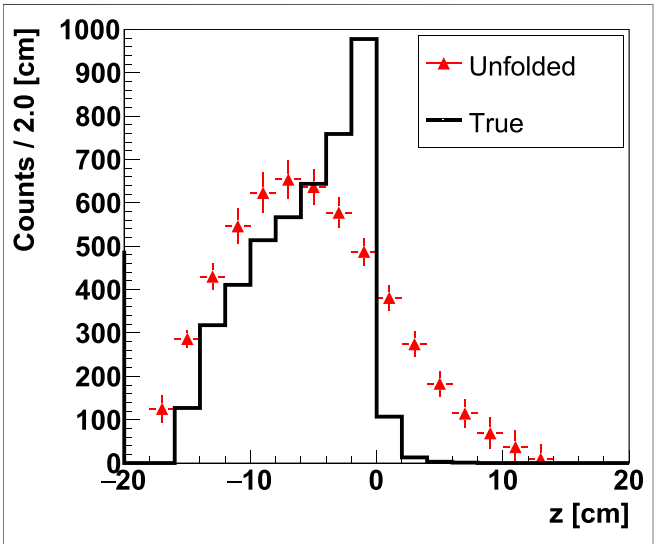

FIGURE 12 | Unfolded distribution of the reconstructed prompt photons emission along the beam axis (z coordinate) (red triangles) obtained from 10^{11} 160 MeV protons impinging on a PMMA target. The distribution of the actual points at production is superimposed (black line). The errors on the unfolded spectrum are only statistical, mainly due to the unfolding procedure.

finally reconstruct the production vertex position within the converter as the Point of Closest Approach (POCA) between the tracks direction. Adjacent hits in the tracker planes have been grouped in *clusters*, to whom the arithmetic average of the single hit positions is assigned.

For each event selected with the strategy described above, the algorithm looks for a couple of tracks pointing to the converter. All the possible combinations of three clusters c_1, c_2, and c_3 (one per plane, see **Figure 8**) are considered as track candidates. Firstly, as shown in **Figure 8**, the angle θ_{ab} between the first segment *a* (from c_1 to c_2) and the second segment *b* (from c_2 to c_3) is computed for each track candidate. Then, for each candidate, the direction defined by the segment connecting c_1 and c_2 is assigned. The c_3 point is not used in order not to include the contribution of multiple scattering suffered by particles in the second MAPS plane. Finally, the vertex candidate position and its distance d_{conv} from the converter plane are computed. The best track pair is selected from the candidates as a couple of tracks (t_1 and t_2), not having clusters in common, which minimizes the sum between their θ_{ab} $(\theta_{ab}^{t_1} + \theta_{ab}^{t_2})$ and d_{conv}. The reconstruction algorithm efficiency is ~90%, computed as the ratio between the number of tracks where an e^+-e^- leptons' pair has been identified, over the number of reconstructed tracks.

TABLE 1 | Proton beam parameters of the MC simulations used to build the calibration: beam energy, full width at half maximum, and theoretical Bragg peak position. The error on the BP is 0.03 cm, from the finite binning of the obtained dose distributions.

Energy [MeV]	FWHM [cm]	BP [cm]
110.96	1.19	−7.15
130.57	1.04	−4.55
150.99	0.93	−1.45
170.64	0.85	1.75
190.28	0.79	5.25

Indeed, the reconstruction algorithm reconstructs an e^+-e^- leptons' pair in 90% of the reconstructed tracks and in 74% of pairs the track belongs to the same particle. The background events are mainly represented by uncorrelated e^+-e^- leptons (7% of reconstructed tracks) and by the presence of an e^+ or e^- with a secondary proton within the chamber (2% of reconstructed tracks). 0.5% of background events are represented by (p, 2p) reactions within the converter plane.

The spatial resolution on the reconstructed vertex position has been assessed in the case of the EoI (see **Section 3.1**) computing the difference between the true and the reconstructed production vertexes, shown in **Figure 9**. A $\sigma^v \sim 2$ mm has been obtained for the vertex reconstruction on the yz transversal plane. On the *x*-axis, which corresponds to the PAPRICA longitudinal axis, the vertex distribution is not symmetrical, having a slight bias of +1 mm, with a standard deviation of ~4 mm.

3.3 Photon Emission Point Reconstruction

In order to reconstruct the prompt photon emission position, the photon momentum has been computed according to **Eq. 1**. The leptons' momentum is assessed exploiting the energy released in the calorimeter. Kinetic energy is assigned to each chosen track extrapolating the direction identified by the segment connecting c_2 and c_3 (see **Section 3.2**) on the calorimeter entrance surface. The closest rods to the track projection, within a 2.5 cm radius, are assigned to a track and the corresponding deposited energy in each rod is added, applying a 5% calorimeter resolution.

Once the particle incoming direction on the converter plane has been calculated, the gamma emission position is assessed as the POCA between the beam axis (the *z*-axis in the simulated setup geometry) and the reconstructed particle direction. In **Figure 10** (left), the reconstructed PG emission profile along

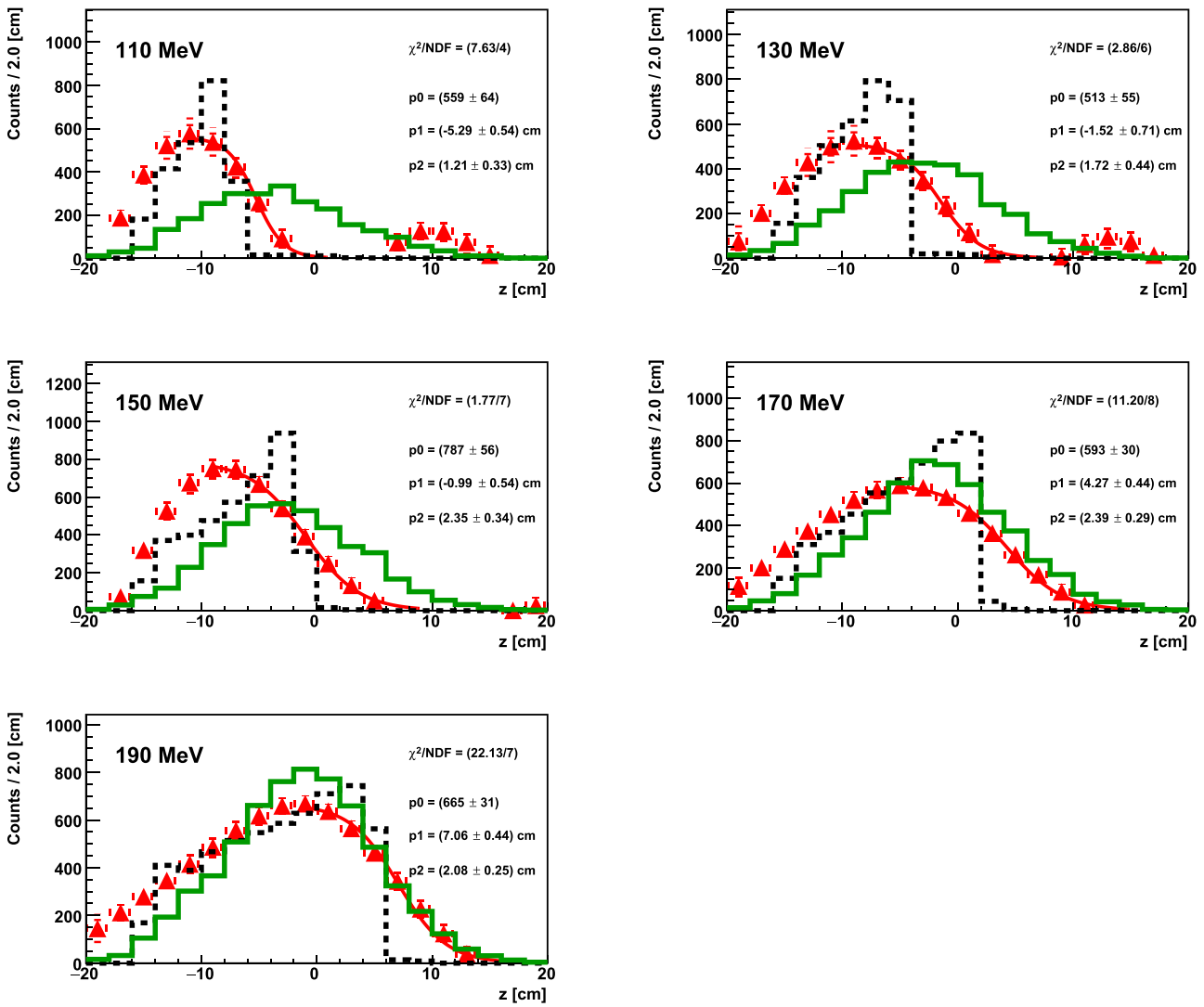

FIGURE 13 | True photon emission distribution (dotted black line) superimposed to the raw reconstructed prompt photons emission spectrum (solid green line) and to the unfolded distributions (red triangles) for the *FULL* simulations of protons (10^{11} primaries) at different energies impinging on a PMMA target. The geometrical setup of the simulations is the one shown in **Figure 6**. The fit on the unfolded distributions is performed with the function in **Eq. 2** and the fit parameters are reported on each canvas.

the beam direction is shown (white area) and compared with the actual emission profile of the reconstructed sample (black area). A systematic error in the reconstructed position can be noticed, as shown in **Figure 10** (right), due to a geometrical effect arising as the angle of the incident photon on the converter plane increases.

The bias observed affects mainly the tracks with a large incidence angle on the converter plane and is due to geometrical reasons: it arises when backprojecting the reconstructed tracks toward the beam direction, as a consequence of the poor track angular resolution. This unavoidable reconstruction artifact significantly degrades the correlation between the fall-off of the reconstructed prompt gamma distribution and the Bragg peak position, and it has been corrected by applying an unfolding procedure.

3.3.1 Unfolding

The unfolding technique has been implemented and encoded using the ROOT TUnfold software tool [37, 38]. The unfolding matrix or migration matrix is built in order to retrieve the emission profile at the production of the reconstructed events. The matrix has been computed simulating an extended photon source with 10^{12} primaries, located inside an 80 cm long PMMA target (*FLAT*sim). The PMMA target sides have the same dimensions as the target used in the 160 MeV proton beam simulation (*FULL*sim). The gamma source is uniformly distributed in z = [−40, 40] cm, while having a Gaussian shape in x and y (μ = 0 cm, $\sigma_{x,y}$ = 0.4 cm, computed from the *FULL*sim). The energy spectrum is the same as shown in **Figure 2**. The photon direction is isotropic. The PAPRICA detector is placed as in the *FULL*sim geometry (see

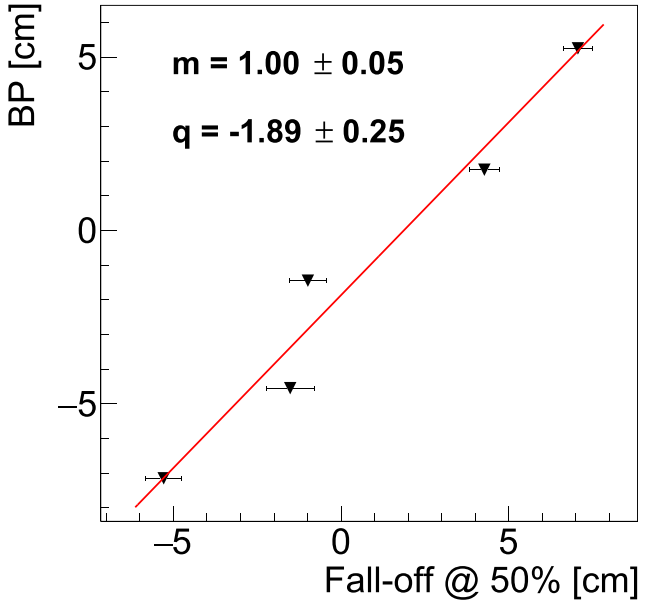

FIGURE 14 | Calibration curve of the theoretical Bragg peak positions for each simulated proton beam energy as a function of the fall-off at 50% of the unfolded distributions of the reconstructed prompt photon profiles. The point related to the 160 MeV proton beam has been removed from the calibration since it is used to assess the PAPRICA performances toward a realistic case.

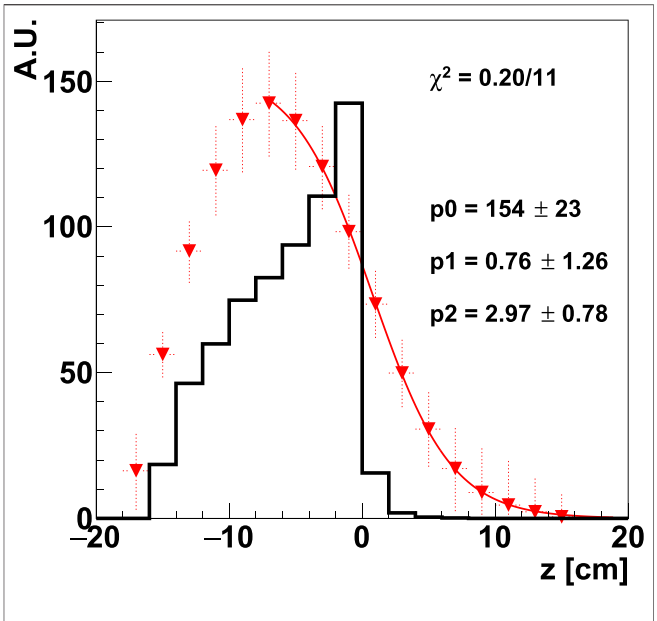

FIGURE 15 | True (black solid line) and unfolded (red triangles) distributions for a number of 1000 photons reconstructed exploiting the 160 MeV proton simulation. The true spectrum has been normalized to the maximum of the unfolded one. The errors on the unfolded distribution are statistical errors, due to the unfolding procedure. The solid line is the Fermi-Dirac fit function reported in **Eq. 2**.

Figure 6). The unfolding matrix is shown in **Figure 11**: it has on the *x*-axis Z_{reco}, the z coordinate of the photon reconstructed following the same procedure described for the *FULL*sim, while on the *y*-axis, there is the true z coordinate of that reconstructed photon, Z_{true}. The matrix is filled event by event.

The choice of using an extended photon source is based on the assumption that the MC is well able to reproduce the photons transport and interaction, and therefore, it is not dependent on the FLUKA MC nuclear cross sections of the prompt photon production. The photon source extension is of 80 cm, which is well beyond the PMMA extension in the *FULL*sim, in order to consider the whole phase-space of the generation and reconstructed photon directions. The configuration of the TUnfold algorithm has been optimized in order to minimize the differences of the unfolded spectrum with respect to the true one and the following parameters have been chosen: the regularization scheme is the *kRegModeCurvature*, 20 bins for the unfolded final output starting from 20 measured bins, a regularization strength $\tau \sim 0.01–0.02$, with variations related to the different samples. In **Figure 12**, the measured spectrum obtained from the *FULL*sim (red white area distribution of **Figure 10** (left)) has been unfolded with the presented matrix. The unfolded spectrum (red triangles) is superimposed to the true z distribution (black line). The fall-off of the unfolded distribution is clearly better related to the fall-off of the true emission spectrum in comparison to the raw distribution shown in **Figure 10** (left).

3.3.2 Calibration

The capability of monitoring the Bragg peak position using the PAPRICA chamber has been evaluated by performing an MC-based calibration with the aim of parameterizing the Bragg peak position vs. fall-off trend. *FULL* simulations of different proton beam energies impinging on the PMMA target have been run. The beam parameters of the simulations are reported in **Table 1** and are extracted from the therapeutic beams of the CNAO center (Pavia, Italy). The statistics of primary particles simulated is 10^{11} protons.

Figure 13 shows the raw reconstructed photon spectra (solid green line) that have been unfolded with the afore-mentioned procedure, and the resulting emission profiles (red triangles) superimposed together to the true emission profile (dotted black line). The bias in the reconstruction that mainly affects the tracks with a large incidence angle on the converter plane (as explained in **Section 3.3**) is more noticeable for lower beam energies, since for larger energies more detected photons have smaller incident angles. The distributions obtained with protons at 110 MeV and 130 MeV present an unfolding artifact whose origin is still under investigation. The fall-off of each distribution has been parameterized using a Fermi-Dirac function:

$$f(z) = p0 \cdot \frac{1}{1 + e^{\frac{z-p1}{p2}}}, \tag{2}$$

where $p0$ represents the normalization parameter, $p1$ is the z coordinate of the fall-off of the distribution at 50% of its maximum, and $p2$ is the slope of the falling edge of the curve. The theoretical Bragg peak positions, listed in **Table 1**, as a function of the $p1$ parameters of the unfolded spectra, in **Figure 13**, are shown in **Figure 14**. A linear fit (red line) is superimposed.

3.4 Absolute Proton Beam Range Verification

When evaluating the precision of the PAPRICA detector in monitoring the beam range in a realistic scenario, the proper reconstructed statistics have to be considered. We have used as a reference the prompt photon yield produced by a 160 MeV proton beam impinging on a PMMA target, measured by Pinto *et al.* in 2015 [39]: $\Phi_\gamma \sim 2 \times 10^{-5}$ PG/p/mm/sr. Identifying as a monitoring volume the distal part of a tumor $1 \times 1 \times 0.2$ cm^3, 25 pencil beams are needed to target it (~10^8 protons each, interspaced by 2–3 mm [40]), for a total number of primaries of ~3×10^9. The range of a 160 MeV proton beam is ~150 mm. In such application, envisaging a detector covering 1 sr (*i.e.,* a factor ~10 larger than the acceptance of PAPRICA in the described setup), a number of ~1000 reconstructed tracks would be expected. The statistics of the 160 MeV proton beam simulation have been therefore sampled in order to have a spectrum containing 1000 reconstructed photons and such subsampled distribution has been unfolded and fitted with the Fermi-Dirac function in **Eq. 2**, as shown in **Figure 15**. The unfolded distribution is superimposed to the true emission spectrum of the reconstructed photons from the 160 MeV proton simulation with full statistics, which has been normalized to the maximum of the unfolded distribution to guide the eye in the comparison. The parameter $p1$ representing the 50% distal fall-off is $p1 = (0.8 \pm 1.3)$ cm. Applying the calibration obtained in **Figure 14**, the retrieved Bragg peak position is $BP_{160_{1000}} = (-1.13 \pm 1.28)$ cm. In this analysis, the systematic errors on the unfolded distributions have not been treated, but they have to be computed by varying the matrix binning and simulation code to compute the matrix (for example, by using Geant4).

The ~1 cm accuracy obtained on the absolute verification proton beam range does not match the clinical requests. However, it can be improved by performing a further optimization of the unfolding procedure and by using an unfolding matrix with higher statistics, as well as a higher statistics in the *FULL* simulation used to build the calibration function. Moreover, a study on other geometrical configurations of the PAPRICA setup with respect to the beam field has to be investigated.

4 CONCLUSION

The aim of the PAPRICA project is the proof of principle of a novel beam range monitoring technique based on prompt gamma imaging exploiting the pair production mechanism. A prompt gamma-based range monitoring exploiting the pair production mechanism has several advantages with respect to other proposed techniques: a 3D imaging that could be in principle possible, the simple reconstruction algorithm, the intrinsically E > 4 MeV targeted prompt photons which are the ones with the stronger correlation to the beam range, the topological event signature allowing good background discrimination enhancing the possibility of exploiting the prompt photon imaging also in the case of carbon ion therapy, and the no need of mechanical collimation nor time or energy analyses of the detected signal. A FLUKA Monte Carlo simulation of a prompt photon source impinging on the chamber has been performed in order to optimize the PAPRICA detector geometry, with a focus on each PAPRICA subdetector: the converter, the tracker, and the calorimeter. The intrinsic limit on the prompt photon reconstruction considering the low prompt gamma energy range (1–10 MeV) is the recoil of the nuclei participating in the e^+-e^- pair production, giving a degradation on the angular resolution of ~3°. Due to the low pair production cross section at the prompt gamma energies, a high atomic number material for the converter has been chosen: the thickness of the converter assures to have a sufficient e^+-e^- pair statistics to reconstruct the impinging photon direction. On the other hand, the converter thickness contributes to the angular resolution degradation due to the multiple scattering suffered by the leptons' pair while exiting the converter surface. The optimized PAPRICA converter thickness is a trade-off between the resolution on the single reconstructed prompt photon, the produced statistics, and the high mechanical fragility of thin LYSO fibers.

The expected PAPRICA performances in retrieving the Bragg peak position for absolute verification of the proton beam range have been computed in a more realistic case scenario, with ~3×10^9 160 MeV protons impinging on a PMMA target and considering a 1 sr PAPRICA detector to increase the collectable prompt gamma statistics. By applying a developed MC calibration to a low statistics simulation in order to consider the expected number of reconstructed prompt photons in the outlined scenario, a resolution on the retrieved Bragg peak of ~1 cm has been obtained, demonstrating that the PAPRICA detector, with larger solid angle, would not be able to perform an absolute range verification with the clinically required resolution of ~2 mm on the computed beam range. Nevertheless, there is room for optimization of the proposed pair production imaging technique and further investigations to perform 3D imaging and to improve the PAPRICA resolution on the imaged photons are foreseen and will be the subject of future studies.

DATA AVAILABILITY STATEMENT

The original contributions presented in the study are included in the article/Supplementary Material; further inquiries can be directed to the corresponding author.

AUTHOR CONTRIBUTIONS

MT: leader of the INFN LNF unit, development of the ALPIDE tracker detector, and Monte Carlo simulation of the PAPRICA tracker. IA: Monte Carlo simulation of the PAPRICA calorimeter and work on the trigger logic optimization. LB: Monte Carlo simulation, data analysis, and development of the calibration method. GB: Monte Carlo simulation and development of the FLUKA user routines. GC: Monte Carlo simulation, PAPRICA detector optimization, development of the reconstruction algorithm, and data analysis. MD: development of the tracks

reconstruction code. YD: development of the tracks reconstruction code. AF: work on the ALPIDE tracker optimization. GF: data analysis. MM: Monte Carlo simulation and data analysis. MF: optimization of the reconstruction algorithm. VM: optimization of the ALPIDE tracker geometry. SM: Monte Carlo simulation. VP: Monte Carlo simulation and converter optimization. FR: optimization of the ALPIDE tracker geometry. ASa: data analysis. ASc: full detector design optimization. GT: unit leader of the INFN Roma1 unit, work on the trigger logic optimization, development of the reconstruction algorithm, and data analysis. SV: Monte Carlo simulation. IM: PI of the PAPRICA project, Monte Carlo simulation, and data analysis.

FUNDING

The project is supported by INFN Gruppo V with a Young Researchers Grant (2019–2021).

ACKNOWLEDGMENTS

We would like to thank Marco Magi from "Sapienza", Università di Roma, SBAI Department, for his valuable work in the design of the detector mechanical structure. We also thank the LNF electronic service for the technical support in the design and test of the read-out electronics and DAQ system.

REFERENCES

1. Durante M, Orecchia R, Loeffler J. Charged-particle therapy in cancer: clinical uses and future perspectives. *Nat Rev Clin Oncol* (2017) 14(8):483–95. doi:10.1038/nrclinonc.2017.30
2. Malouff TD, Mahajan A, Krishnan S, Beltran C, Seneviratne DS, Trifiletti DM. Carbon ion therapy: a modern review of an emerging technology. *Front Oncol* (2020) 10:82. doi:10.3389/fonc.2020.00082
3. Paganetti H. Range uncertainties in proton therapy and the role of Monte Carlo simulations. *Phys Med Biol* (2012) 57(11):R99–R117. doi:10.1088/0031-9155/57/11/r99
4. Thomas H, Timmermann B. Paediatric proton therapy. *Br J Radiol* (2020) 93(1107):20190601. doi:10.1259/bjr.20190601.PMID:31529979
5. Knopf AC, Lomax A. *In vivo* proton range verification: a review. *Phys Med Biol* (2013) 58(15):R131–60. doi:10.1088/0031-9155/58/15/r131
6. Parodi K, Polf JC. *In vivo* range verification in particle therapy. *Med Phys* (2018) 45(11):e1036–50. doi:10.1002/mp.12960
7. Parodi K, Assmann W. Ionoacoustics: a new direct method for range verification. *Mod Phys Lett* (2015) 30(17):1540025. doi:10.1142/S0217732315400258
8. Parodi K. On- and off-line monitoring of ion beam treatment. *Nucl Instrum Methods Phys Res Sect A Accel Spectrom Detect Assoc Equip* (2016) 809:113–9. doi:10.1016/j.nima.2015.06.056. Advances in detectors and applications for medicine.
9. Ferrero V, Fiorina E, Morrocchi M, Pennazio F, Baroni G, Battistoni G, et al. Online proton therapy monitoring: clinical test of a Silicon-photodetector-based in-beam PET. *Sci Rep* (2018) 8(1):4100. doi:10.1038/s41598-018-22325-6
10. Krimmer J, Dauvergne D, Létang J, Testa E. Prompt-gamma monitoring in hydrotherapy: a review. *Nucl Instrum Methods Phys Res Sect A Accel Spectrom Detect Assoc Equip* (2018) 878:58–73. doi:10.1016/j.nima.2017.07.063
11. Mattei I, Bini F, Collamati F, Lucia ED, Frallicciardi PM, Iarocci E, et al. Secondary radiation measurements for particle therapy applications: prompt photons produced by 4He, 12C and 16O ion beams in a PMMA target. *Phys Med Biol* (2017) 62(4):1438–55. doi:10.1088/1361-6560/62/4/1438
12. Piersanti L, Bellini F, Bini F, Collamati F, Lucia ED, Durante M, et al. Measurement of charged particle yields from PMMA irradiated by a 220 MeV/u 12C beam. *Phys Med Biol* (2014) 59(7):1857–72. doi:10.1088/0031-9155/59/7/1857
13. Traini G, Mattei I, Battistoni G, Bisogni M, Simoni MD, Dong Y, et al. Review and performance of the Dose Profiler, a particle therapy treatments online monitor. *Phys Med* (2019) 65:84–93. doi:10.1016/j.ejmp.2019.07.010
14. Pausch G, Berthold J, Enghardt W, Römer K, Straessner A, Wagner A, et al. Detection systems for range monitoring in proton therapy: needs and challenges. *Nucl Instrum Methods Phys Res Sect A Accel Spectrom Detect Assoc Equip* (2020) 954:161227. doi:10.1016/j.nima.2018.09.062
15. Werner T, Berthold J, Hueso-González F, Koegler T, Petzoldt J, Roemer K, et al. Processing of prompt gamma-ray timing data for proton range measurements at a clinical beam delivery. *Phys Med Biol* (2019) 64(10):105023. doi:10.1088/1361-6560/ab176d
16. Hueso-González F, Rabe M, Ruggieri TA, Bortfeld T, Verburg JM. A full-scale clinical prototype for proton range verification using prompt gamma-ray spectroscopy. *Phys Med Biol* (2018) 63(18):185019. doi:10.1088/1361-6560/aad513
17. Richter C, Pausch G, Barczyk S, Priegnitz M, Keitz I, Thiele J, et al. First clinical application of a prompt gamma based *in vivo* proton range verification system. *Radiother Oncol* (2016) 118(2):232–7. doi:10.1016/j.radonc.2016.01.004
18. Aldawood S, Thirolf P, Miani A, Bömer M, Dedes G, Gernhäuser R, et al. Development of a Compton camera for prompt-gamma medical imaging. radiat. phys. chem. In: 2nd International Conference on Dosimetry and its Applications (ICDA-2), July 3-8, 2016. Guildford, United Kingdom: University of Surrey (2017). p. 190–7.
19. Llosá G, Trovato M, Barrio J, Etxebeste A, MuÃ±oz E, Lacasta C, et al. First images of a three-layer Compton telescope prototype for treatment monitoring in hadron therapy. *Front Oncol* (2016) 6:14. doi:10.3389/fonc.2016.00014
20. Xie Y, Bentefour EH, Janssens G, Smeets J, Stappen FV, Hotoiu L, et al. Prompt gamma imaging for *in vivo* range verification of pencil beam scanning proton therapy. *Int J Radiat Oncol Biol Phys* (2017) 210–8. doi:10.1016/j.ijrobp.2017.04.027
21. Draeger E, Mackin D, Peterson S, Chen H, Avery S, Beddar S, et al. 3D prompt gamma imaging for proton beam range verification. *Phys Med Biol* (2018) 63(3):035019. doi:10.1088/1361-6560/aaa203
22. Rohling H, Priegnitz M, Schoene S, Schumann A, Enghardt W, Hueso-González F, et al. Requirements for a Compton camera for *in-vivo* range verification of proton therapy. *Phys Med Biol* (2017) 62(7):2795–811. doi:10.1088/1361-6560/aa6068
23. Rohling H, Golnik C, Enghardt W, Hueso-Gonzàlez F, Kormoll T, Pausch G, et al. Simulation study of a combined pair production - Compton camera for *in-vivo* dosimetry during therapeutic proton irradiation. *IEEE Trans Nucl Sci* (2015) 62(5):2023–30. doi:10.1109/TNS.2015.2448235
24. Ferrari A, Sala PR, Fasso A, Ranft J. FLUKA: a multi-particle transport code (Program version 2005). p. 405. *CERN-2005-010, SLAC-R-773, INFN-TC-05-11* (2005). doi:10.5170/CERN-2005-010
25. Böhlen T, Cerutti F, Chin M, Fassó A, Ferrari A, Ortega P, et al. The FLUKA code: developments and challenges for high energy and medical applications. *Nucl Data Sheets* (2014) 120:211–4. doi:10.1016/j.nds.2014.07.049
26. Hunter SD, Bloser PF, Depaola GO, Dion MP, DeNolfo GA, Hanu A, et al. A pair production telescope for medium-energy gamma-ray polarimetry. *Astropart Phys* (2014) 59:18–28. doi:10.1016/j.astropartphys.2014.04.002
27. Verburg JM, Riley K, Bortfeld T, Seco J. Energy- and time-resolved detection of prompt gamma-rays for proton range verification. *Phys Med Biol* (2013) 58(20):L37–49. doi:10.1088/0031-9155/58/20/l37
28. Traini G, Battistoni G, Bollella A, Collamati F, Lucia ED, Faccini R, et al. Design of a new tracking device for on-line beam range monitor in carbon therapy. *Phys Med* (2017) 34:18–27. doi:10.1016/j.ejmp.2017.01.004
29. Aglieri Rinella G. The ALPIDE pixel sensor chip for the upgrade of the ALICE Inner Tracking System. *Nucl Instrum Methods A Accel Spectrom Detect Assoc Equip* (2017) 845:583–7. doi:10.1016/j.nima.2016.05.016

30. Kushpil S, Krizek F, Isakov A. Recent results from beam tests of the ALPIDE pixel chip for the upgrade of the ALICE inner tracker. *IEEE Trans Nucl Sci* (2019) 66(11):2319–23. doi:10.1109/tns.2019.2945234
31. Abelev B(ALICE collaboration). Upgrade of the ALICE experiment: letter of intent. *J Phys G Nucl Part Phys* (2014a) 41(8):087001. doi:10.1088/0954-3899/41/8/087001
32. Abelev B(ALICE collaboration). Technical design report for the upgrade of the ALICE inner tracking system. *J Phys G* (2014b) 41(8):087002. doi:10.1088/0954-3899/41/8/087002
33. Di Mauro AOn behalf of the ALICE collaboration. The new inner tracking system for the ALICE upgrade at the LHC. *Nucl Instrum Methods A Accel Spectrom Detect Assoc Equip* (2019) 936:625–9. doi:10.1016/j.nima.2018.10.047
34. De Robertis G, Fanizzi G, Loddo F, Manzari V, Rizzi M. A MOdular System for Acquisition, Interface and Control (MOSAIC) of detectors and their related electronics for high energy physics experiment. *EPJ Web Conf* (2018) 174:070024. doi:10.1051/epjconf/201817407002
35. Tabata T. Backscattering of electrons from 3.2 to 14 MeV. *Phys Rev* (1967) 162(2):336–47. doi:10.1103/PhysRev.162.336
36. Grevillot L, Bertrand D, Dessy F, Freud N, Sarrut D. A Monte Carlo pencil beam scanning model for proton treatment plan simulation using GATE/GEANT4. *Phys Med Biol* (2011) 56(16):5203–19. doi:10.1088/0031-9155/56/16/008
37. Schmitt S. TUnfold, an algorithm for correcting migration effects in high energy physics. *J Instrum* (2012) 7(10):T10003. doi:10.1088/1748-0221/7/10/t10003
38. Cern. *ROOT data analysis framework*. Available from: https://root.cern.ch/.
39. Pinto M, Bajard M, Brons S, Chevallier M, Dauvergne D, Dedes G, et al. Absolute prompt-gamma yield measurements for ion beam therapy monitoring. *Phys Med Biol* (2015) 60(2):565–94. doi:10.1088/0031-9155/60/2/565
40. Verburg JM, Seco J. Proton range verification through prompt gamma-ray spectroscopy. *Phys Med Biol* (2014) 59(23):7089–106. doi:10.1088/0031-9155/59/23/7089

Conflict of Interest: The authors declare that the research was conducted in the absence of any commercial or financial relationships that could be construed as a potential conflict of interest.

The handling editor declared a shared affiliation with the authors MM, VP, AS, and AS at the time of review.

frontiers in Physics

ORIGINAL RESEARCH
published: 26 March 2021
doi: 10.3389/fphy.2021.595721

Monte Carlo Comparison of Proton and Helium-ion Minibeam Generation Techniques

Tim Schneider[1,2]*, *Ludovic De Marzi*[3,4], *Annalisa Patriarca*[5] *and Yolanda Prezado*[6]

[1]*Université Paris-Saclay, CNRS/IN2P3, IJCLab, Orsay, France,* [2]*Université de Paris, IJCLab, Orsay, France,* [3]*Institut Curie, PSL Research University, University Paris Saclay, LITO, Orsay, France,* [4]*Institut Curie, PSL Research University, Radiation Oncology Department, Proton Therapy Centre, Centre Universitaire, Orsay, France,* [5]*Institut Curie, PSL Research University, Proton Therapy Centre, Centre Universitaire, Orsay, France,* [6]*Institut Curie, Université PSL, CNRS UMR3347, Inserm U1021, Signalisation Radiobiologie et Cancer, Orsay, France*

Proton minibeam radiation therapy (pMBRT) is a novel therapeutic strategy that combines the normal tissue sparing of submillimetric, spatially fractionated beams with the improved dose deposition of protons. In contrast to conventional approaches which work with comparatively large beam diameters (5 mm to several centimetres) producing laterally homogeneous fields, pMBRT uses submillimetric minibeams to create a distinct spatial modulation of the dose featuring alternating regions of high dose (peaks) and low dose (valleys). This spatial fractionation can increase the tolerance of normal tissue and may allow a safe dose escalation in the tumour. Important quantities in this context are the valley dose as well as the peak-to-valley dose ratio (PVDR). Creating submillimetric proton beams for clinical applications is a challenging task that until now has been realized with mechanical collimators (metal blocks with thin slits or holes). However, this method is inherently inefficient, inflexible and creates undesirable secondary neutrons. We therefore recently proposed a method for obtaining clinical minibeams using only magnetic focusing. In this study, we performed Monte Carlo simulations in order to compare minibeams generated using the new method of magnetic focusing with two techniques involving mechanical collimators (collimator and broad beam irradiation, collimator and pencil beam scanning). The dose deposition in water was simulated and dosimetric aspects [beam broadening, depth-dose profiles, PVDR and Bragg-peak-to-entrance dose ratio (BEDR)] as well as irradiation efficiencies were evaluated. Apart from protons, we also considered helium ions which, due to their reduced lateral scattering and sharper Bragg peak, may present a promising alternative for minibeam radiation therapy. Magnetically focused minibeams exhibited a 20–60 times higher PVDR than mechanically collimated minibeams and yielded an increase in irradiation efficiency of up to two orders of magnitude. Compared to proton minibeams, helium ion minibeams were found to broaden at a slower rate and yield an even higher PVDR (at the same minibeam spacing) as well as a more favourable BEDR. Moreover, the simulations showed that methods developed for proton minibeams are suitable for the generation of helium ion minibeams.

Keywords: proton minibeam radiation therapy, collimator, magnetic focusing, Monte Carlo simulations, spatial fractionation of the dose, helium ions

OPEN ACCESS

Edited by:
Anatoly Rosenfeld,
University of Wollongong, Australia

Reviewed by:
Susanna Guatelli,
University of Wollongong, Australia
Liyong Lin,
University of Pennsylvania, United States

****Correspondence:***
Tim Schneider
tim.schneider@curie.fr

Specialty section:
This article was submitted to Medical Physics and Imaging, a section of the journal Frontiers in Physics

Received: *17 August 2020*
Accepted: *15 January 2021*
Published: *26 March 2021*

Citation:
Schneider T, De Marzi L, Patriarca A and Prezado Y (2021) Monte Carlo Comparison of Proton and Helium-ion Minibeam Generation Techniques. Front. Phys. 9:595721. doi: 10.3389/fphy.2021.595721

1 INTRODUCTION

Technological advances in radiation therapy have led to a notable improvement of dose conformity in the tumour as well as a reduction of the dose given to organs-at-risk [1]. Nonetheless, the tolerance dose of normal tissue continues to be an important limitation for the treatment of some radioresistant tumours, such as brain tumours, or certain paediatric cancers.

Spatial modification of the dose distribution, as in spatially fractionated radiation therapy (SFRT), has shown great potential in this context [2–7]. In SFRT, the dose profiles are a succession of areas of high dose (peaks) and areas of low dose (valleys). The ratio between the peak and valley doses (peak-to-valley dose ratio, PVDR) is believed to be a biologically relevant parameter: high PVDR with low valleys favours normal tissue sparing [8]. While the exact radiobiological effects underlying SFRT are not yet completely known, possible actors promoting normal tissue sparing might include dose-volume effects [9, 10], cell signalling effects [11] and the so called microscopic prompt tissue-repair effect [7].

While SFRT has been mainly explored with X-rays [12], the use of protons can offer several advantages [13, 14]. Proton beams can stop in the patient and exhibit a depth-dose distribution characterized by a localized maximum (Bragg peak) beyond which only a negligible dose is deposited. This helps to improve the dose conformity and increase tissue sparing in particular in healthy tissue behind the tumour which can further reduce secondary effects. In addition, the gradual beam broadening caused by multiple Coulomb scattering of protons allows to obtain a homogeneous dose distribution in the tumour with only one array of proton minibeams [13, 14]. In contrast to this, SFRT with X-rays requires a superposition of several arrays to yield a (quasi-)homogeneous dose distribution in the target which leads to a more complex and error-prone irradiation geometry. Along these lines, proton minibeam radiation therapy (pMBRT) has already shown a remarkable reduction of neurotoxicity [15] as well as an important widening of the therapeutic window for the treatment of high-grade gliomas in small animal experiments [16, 17].

Next to protons, helium ions might also present a good candidate for MBRT [18]. Compared to protons, they experience reduced multiple Coulomb scattering which could lead to further improvements of the dose distributions and a higher PVDR. Moreover, the cross-section for nuclear fragmentation of helium ions is lower than that of heavier ions such that issues related to fragmentation tails beyond the Bragg peak can be avoided [19–22].

Recently, pMBRT was implemented at the Orsay Proton Therapy Centre (ICPO) using a multislit collimator attached at the end of the nozzle. This method has been evaluated both in passive scattering [23, 24] and pencil beam scanning mode [25]. While such a mechanical collimation presents a straightforward way to implement pMBRT at an existing facility, it may come at the cost of a reduced dose rate and overall efficiency. Furthermore, the collimator becomes an additional source of secondary neutrons which, although contributing less than 1% to the patient dose [24], are generally undesirable. Lastly, this technique is rather inflexible as it may be necessary to fabricate a new collimator for different patients or patient groups.

As an approach to overcome these limitations, we have recently considered pMBRT with magnetically focused and scanned minibeams [26]. While this method is conceptually very similar to established pencil beam scanning (PBS) techniques, a crucial difference lies in the beam sizes used in the two cases: Beams used for PBS typically have a diameter of 1–2 cm (full width at half maximum at the isocentre) [27, 28] whereas minibeams are preferably no wider than about 1 mm to optimally exploit tissue sparing effects. We recently proposed a new nozzle design capable of generating such minibeams through magnetic focusing only [26].

The goal of this study was to perform a thorough comparison of the three minibeam generation techniques (collimator and broad beam, collimator and PBS, magnetic focusing) and to assess the possible advantages and shortcomings of each method in terms of dose distributions, PVDR and efficiency. The study was realized as Monte Carlo simulations using the toolkit TOPAS and proton as well as helium ion minibeams were considered.

2 MATERIALS AND METHODS

Monte Carlo simulations were conducted to evaluate three different techniques for generating planar minibeams:

- Collimator and broad beam (C+BB),
- Collimator and magnetically scanned pencil beam (C+PBS),
- Magnetically focused and scanned minibeam (MF).

The three techniques were compared with respect to the dose distribution in a water phantom and the irradiation efficiency (average dose deposited per primary particle). Each technique was evaluated both with protons and ^{4}He ions and for different, clinically relevant ranges. The considered ranges were approximately 7.7 cm (protons 100 MeV, helium ions 400 MeV), 11.1 cm (protons 123 MeV, helium ions 492 MeV) and 15.8 cm (protons 150 MeV, helium ions 600 MeV).

2.1 Monte Carlo Simulation Details

The simulations were performed with the Geant4-based toolkit TOPAS[1] version 3.2. p2 [29]. The physics list was built using the Geant4_Modular option with the recommended modules for proton therapy (g4em-standard_opt3, g4h-phy_QGSP_BIC_HP, g4decay, g4ion-binarycascade, g4h-elastic_HP, g4stopping and g4radioactivedecay) [30–33] and the range cut was 10 µm in all volumes and for all particles. While the simulated beam-shaping components were different for each minibeam generation technique (see below), the irradiation target was always a $4 \times 4 \times 20$ cm^3 water phantom.

[1]http://www.topasmc.org

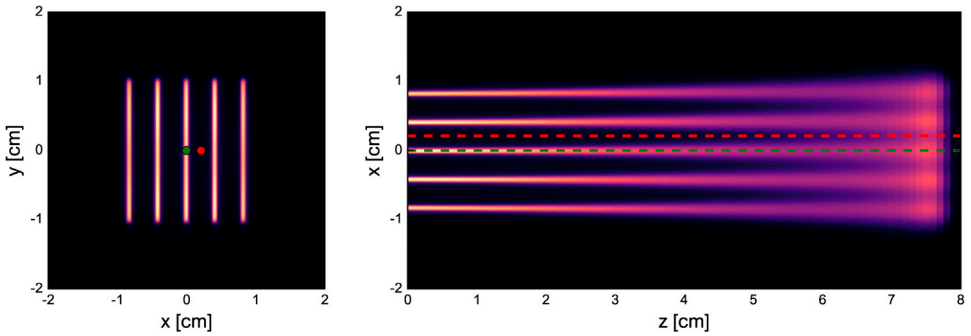

FIGURE 1 | Dose distribution in the water phantom for 100-MeV minibeams obtained with collimator and PBS (C+PBS). Left: lateral cross section at the phantom entrance. Right: longitudinal cross section at y = 0 cm. The green and red dots/dashed lines indicate considered peak and valley regions, respectively.

TABLE 1 | FWHM and PVDR at phantom entrance and Bragg peak depth and BEDR of all considered cases.

	Beam energy (MeV)	FWHM (mm)		PVDR		BEDR
		Entrance	Bragg peak	Entrance	Bragg peak	
Protons						
C + BB	100	0.57 ± 0.01	3.78 ± 0.01	34.6 ± 0.1	1.18 ± 0.01	0.65 ± 0.01
	123	0.53 ± 0.01	5.43 ± 0.01	35.7 ± 0.1	1.06 ± 0.01	0.52 ± 0.01
	150	0.50 ± 0.01	7.48 ± 0.01	32.2 ± 0.1	1.00 ± 0.01	0.45 ± 0.01
C + PBS	100	0.67 ± 0.01	3.83 ± 0.01	20.5 ± 0.1	1.26 ± 0.01	0.65 ± 0.01
	123	0.65 ± 0.01	5.50 ± 0.01	18.0 ± 0.1	0.99 ± 0.01	0.54 ± 0.01
	150	0.61 ± 0.01	7.53 ± 0.01	16.6 ± 0.1	0.98 ± 0.01	0.48 ± 0.01
MF	100	0.62 ± 0.01	3.88 ± 0.01	722 ± 2	1.34 ± 0.01	0.70 ± 0.01
	123	0.66 ± 0.01	5.44 ± 0.01	701 ± 2	1.06 ± 0.01	0.54 ± 0.01
	150	0.71 ± 0.01	7.34 ± 0.01	608 ± 2	1.00 ± 0.01	0.48 ± 0.01
Helium ions						
C + BB	400	0.41 ± 0.01	1.91 ± 0.01	90.5 ± 0.1	7.49 ± 0.01	0.89 ± 0.01
	492	0.39 ± 0.01	2.69 ± 0.02	79.2 ± 0.1	2.24 ± 0.01	0.54 ± 0.01
	600	0.39 ± 0.01	3.73 ± 0.03	40.1 ± 0.1	1.16 ± 0.01	0.45 ± 0.01
C + PBS	400	0.60 ± 0.01	2.02 ± 0.01	23.8 ± 0.1	6.78 ± 0.01	1.02 ± 0.01
	492	0.60 ± 0.01	2.81 ± 0.01	22.6 ± 0.1	2.42 ± 0.01	0.68 ± 0.01
	600	0.55 ± 0.01	3.84 ± 0.01	19.2 ± 0.1	1.43 ± 0.01	0.50 ± 0.01
MF	400	0.68 ± 0.01	2.24 ± 0.01	1315 ± 7	6.26 ± 0.01	1.10 ± 0.01
	492	0.67 ± 0.01	3.05 ± 0.01	1179 ± 4	2.47 ± 0.01	0.69 ± 0.01
	600	0.65 ± 0.01	4.06 ± 0.02	973 ± 5	1.31 ± 0.01	0.48 ± 0.01

An identical minibeam pattern was simulated in all cases, consisting of five vertical planar minibeams spaced out horizontally at a centre-to-centre distance of 4 mm. This corresponds to an irradiation configuration that was frequently used in our previous preclinical experiments [15, 16, 25, 34]. **Figure 1** shows an example of a dose distribution produced with this pattern. The horizontal full width at half maximum (FWHM) of the minibeams at the phantom entrance was between 0.39 and 0.71 mm (see **Table 1**) and the total area covered by the minibeams was roughly 2×2 cm^2. The minibeam geometry and pattern were therefore similar to those used in previous pMBRT studies [13, 15, 16, 18, 25, 34].

Details of the different minibeam generation techniques are given in the following subsections. Schematics of the simulated geometries are shown in **Figure 2** and the beam source parameters are compiled in **Table 2**.

2.1.1 Collimator and Broad Beam

The first evaluated technique represents the most straightforward approach of minibeam generation where a collimator is uniformly irradiated with a broad beam. A cylindrical brass collimator (radius 4.5 cm, thickness 6.5 cm) with five parallel slits (400 μm × 2 cm) was used. The centre-to-centre distance between the slits was 4 mm and there was a 5 cm air gap between the collimator exit and the phantom entrance.

A theoretical beam source was considered with parameters corresponding to a best case scenario, i.e. the beam particles propagate parallel to each other and the collimator is covered uniformly. For this, an instance of TOPAS' *beam* type source was used with a flat spatial distribution and a Gaussian angular distribution with a very small standard deviation of 0.5 mrad. The field size was 10×10 cm^2 and covered the entire collimator

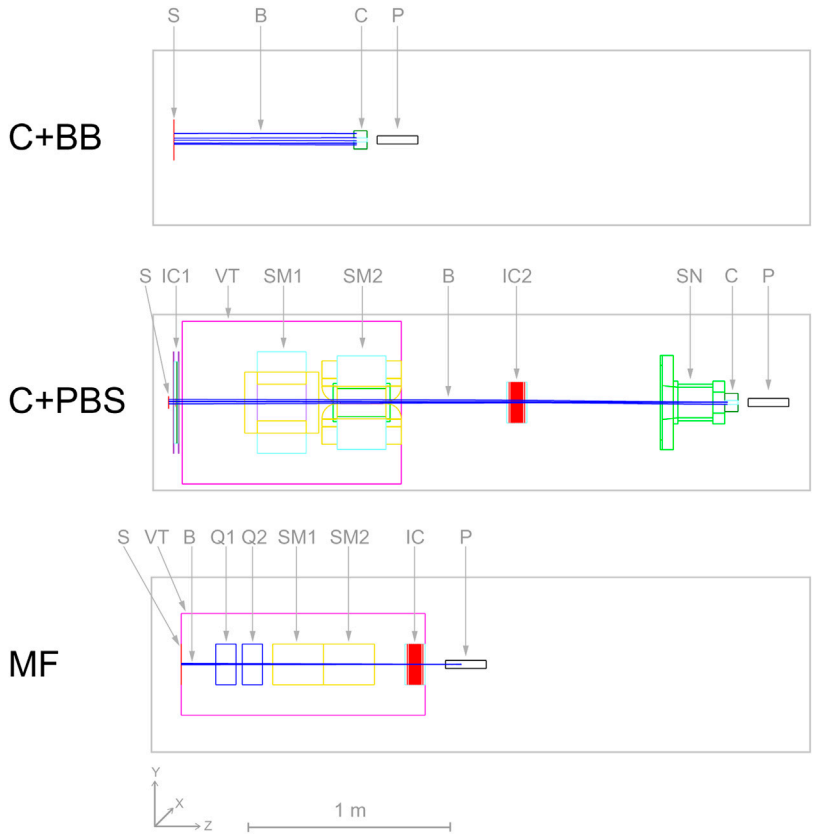

FIGURE 2 | Simulated geometries of the three different minibeam generation techniques. Abbreviations stand for: S - source, B - beam, C - collimator, P - phantom, IC - ionization chamber, VT - vacuum tank, SM - scanning dipole magnet, SN - snout, Q - focusing quadrupole magnet.

TABLE 2 | Beam source parameters used for protons and helium ions. The energy of the helium ion beams (values in parantheses) was four times that of the proton beams.

	Energy of proton (He ion) beams (MeV)	Energy spread (%)	Beam size σ_x/σ_y (mm)	Beam divergence $\sigma_{x'}/\sigma_{y'}$ (mrad)	Correlation factor $r_{xx'}/r_{yy'}$
C + BB	100 (400)	1.00	–	0.50	–
	123 (492)	1.00	–	0.50	–
	150 (600)	1.00	–	0.50	–
C + PBS	100 (400)	0.65	10.99	3.05	–0.95
	123 (492)	0.61	9.23	3.02	–0.93
	150 (600)	0.57	7.26	2.17	–0.90
MF	100 (400)	1.00	4.00	3.00	–1.00
	123 (492)	1.00	4.00	2.95[a]	–1.00
	150 (600)	1.00	4.00	2.80[a]	–1.00

[a]*For helium ions, the divergence was 3.00 mrad in these cases.*

(diameter of 9 cm). The beam source was placed 100 cm upstream of the phantom entrance (88.5 cm upstream of the collimator) and an energy spread of 1% was assumed.

2.1.2 Collimator and Pencil Beam Scanning

The second minibeam generation technique was based on the method of De Marzi et al. [25], where a pencil beam is magnetically scanned across the collimator. Compared to the broad beam approach, this is expected to reduce the proportion of the beam getting blocked by the collimator which in turn should improve the delivery efficiency, increase the dose rate and decrease the neutron production.

For this case, the complete universal nozzle of the Orsay Proton Therapy Centre in PBS mode was simulated. The individual nozzle components and the collimator had the same geometry as in the work of De Marzi et al. [25, 28] and

the air gap between collimator exit and phantom entrance was again 5 cm. The beam source was placed at the nozzle entrance (vacuum window) and the source parameters are listed in **Table 2**.

The pencil beam was laterally moved across the entrance face of the collimator by simulating magnetic dipole fields in the scanning magnets SM1 and SM2 (see **Figure 2**) using TOPAS' *DipoleMagnet* feature. It should be emphasized that, in contrast to the parallel slits of the collimator irradiated with broad beams, the collimator used in this case had slightly divergent slits (angle of 0.125 degrees between adjacent slits) to account for the inclination angle of the scanned pencil beams. The scanning pattern for the uncollimated beam consisted of five columns corresponding to the five slits in the collimator: the beam was scanned vertically along each slit such that the centres of the slit and beam spot coincided. It should be noted that a beam spot always covered multiple slits due to the comparatively large size of the pencil beams. Therefore, the relative weights of the columns had to be adjusted to yield a laterally more homogenous dose distribution in the phantom.

2.1.3 Magnetic Focusing

We have previously proposed a new nozzle design suitable for the delivery of magnetically focused and scanned minibeams which forms the basis of the third technique considered in this study. This new design features a more compact nozzle comprised of a pair of focusing quadrupole magnets, a pair of scanning dipole magnets and an ionization chamber for beam monitoring, all contained in an evacuated environment (see Schneider et al., 2020 [26] for more details). The configuration considered in this study assumed an air gap of 10 cm between the nozzle exit and phantom entrance.

The beam source was placed at the nozzle entrance and parametrized according to the aforementioned article. **Table 2** summarizes the used beam source parameters. The setting of the focusing quadrupole magnets was adjusted such that the beam size at the phantom entrance was approximately constant (0.6–0.7 mm FWHM) for all considered beam energies. Note that the magnetic focusing produced symmetric pencil-shaped minibeams, i.e. the horizontal and vertical beam sizes were equal. Thus, in order to obtain the same planar minibeams generated with the collimators, the pencil-shaped minibeams were magnetically scanned across the phantom to create five vertical columns with a height of 2 cm and a centre-to-centre distance of 4 mm. A number of 50 and 100 spot positions per column were used for proton and helium ion beams, respectively, in order to obtain a homogeneous vertical profile. The scanning was again simulated by attaching dipole fields to the according volumes (SM1 and SM2), using TOPAS' *DipoleMagnet* feature.

2.2 Dosimetric Evaluation

The dose distributions in the phantom were recorded using TOPAS' *DoseToWater* scorer. The voxel size was $0.1 \times 0.1 \times 1\ \text{mm}^3$. For each voxel, the dose uncertainty was calculated by considering the standard deviation of multiple repetitions of the simulations (between 20 and 120, depending on the number of primary particles arriving at the phantom in each case). Subsequently, the global relative uncertainty was then computed as the root mean square of the voxel uncertainties over all voxels with at least half the maximum dose. It was ≤1.28% in all cases.

The analysis of the dose distributions included the consideration of depth-dose profiles along the central peak and an adjacent valley region and the calculation of the Bragg-peak-to-entrance dose ratio (BEDR) for the central minibeam. Moreover, the peak-to-valley dose ratio (PVDR) and the size of the central minibeam were assessed as functions of the depth. For the latter, additional simulations were performed considering only the central minibeam (using a special single-slit collimator in the cases C+BB and C+PBS). The beam size of this central beam is stated as the FWHM of the lateral dose profile in the phantom and was determined *via* a Gaussian fit.

The uncertainties of the PVDR and BEDR values were calculated by propagating the uncertainties of the corresponding dose voxels while the beam size uncertainties were provided by the fitting algorithm.

2.3 Irradiation Efficiency

The efficiency was determined as the laterally integrated dose at the Bragg peak depth divided by the number of primary particles. In the case C+BB, the number of primaries included a correction factor to account for the fact that the beam was larger than the collimator: As the size of the beam was $10 \times 10\ \text{cm}^2 = 100\ \text{cm}^2$ whereas the cross-sectional area of the collimator was only $\pi \times 4.5^2\ \text{cm}^2 \approx 63.6\ \text{cm}^2$, the number of primaries was first reduced by a factor of 0.636 to obtain the effective number of primaries incident on the collimator.

As before, stated uncertainties correspond to the standard deviation of multiple repetitions of the simulations.

3 RESULTS

3.1 Dosimetric Evaluation

The dosimetric evaluation was separated into multiple parts. The evolution of the beam size as a function of the depth is shown in **Figure 3** while lateral dose profiles at the phantom entrance are displayed in **Figure 4**. **Figure 5** presents the peak and valley depth-dose profiles as well as the associated PVDR as a function of the depth. Finally, **Table 1** compiles the beam sizes (FWHM) and PVDR at the phantom entrance and Bragg peak depth and lists the BEDR for all cases.

3.1.1 Beam size

The beam broadening is virtually identical for the three minibeam techniques and only depends on the beam energy. Beams with a higher energy grow at a slower rate because they have a greater forward momentum and are therefore less affected by lateral deflections due to multiple Coulomb scattering [35, 36]. The same principle explains why the size of the mechanically collimated beams at the phantom entrance decreases slightly with increasing beam energy (see **Table 1**). For the case of magnetic focusing, it should be noted that the quadrupole settings and beam source parameters were manually adapted as to always yield a beam size between 0.6 and 0.7 mm FWHM at the phantom entrance.

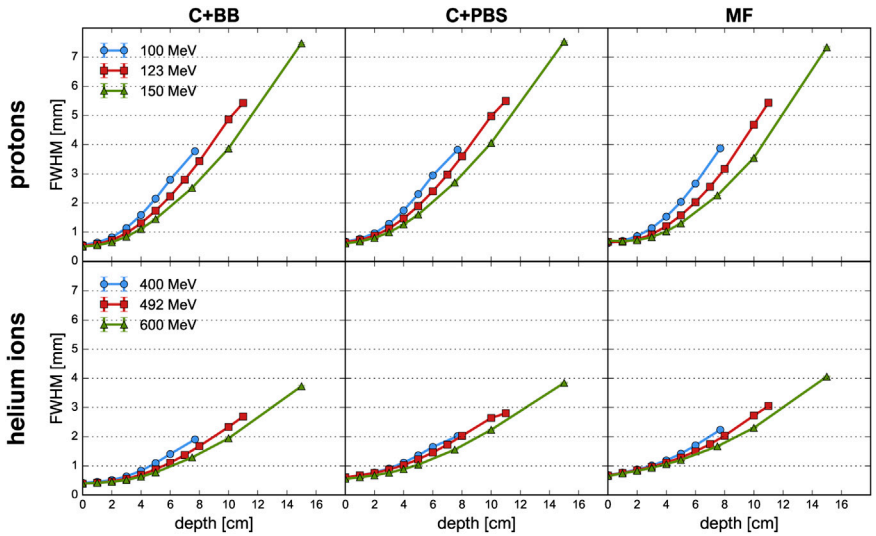

FIGURE 3 | Evolution of the FWHM as a function of depth for proton beams **(top row)** and helium ion beams **(bottom row)** and for the different minibeam techniques (columns). The uncertainty bars are smaller than the markers.

Therefore, the effect of a decreasing beam size with increasing beam energy is not observed for this technique.

Compared to protons, helium ions experience much less lateral scattering which results in a much slower growth of the beam width. At Bragg peak depth, the FWHM is only about half as large as for the corresponding proton minibeams.

Lastly, small differences in beam broadening are observed between the collimator techniques: For PBS, the minibeams were observed to broaden slightly quicker than for the case of broad beam irradiation. This can be seen in particular for the higher energies where the FWHM at the phantom entrance and at the Bragg peak is consistently at least 0.1 mm larger for C+PBS than for C+BB. The reason for this lies in the different divergences that were used for the beam sources (2–3 mrad for the pencil beams vs. 0.5 mrad for the broad beam). It should be reiterated that the small divergence of the broad beam was chosen deliberately to represent a best case scenario.

3.1.2 Lateral Dose Profiles

Figure 4 shows the horizontal and vertical dose profiles at the phantom entrance. As explained in the work by De Marzi et al. [25], the orientation of the collimator slits must be tailored to the irradiation setup in order to account for the internal divergence of the uncollimated beam. For the case of C+PBS, variations are observed between the intensities of the five minibeams and the vertical dose profiles exhibit inhomogeneities. It was attempted to mitigate these effects by adjusting the weights of the individual pencil beam spots and a continued optimization of the spot weights may be expected to further improve the profiles.

At any rate, the need for these adjustments shows that the use of collimators for minibeam generation complicates treatment planning and underlines the inflexibility of collimated minibeams. In comparison to this, much smoother dose profiles could be obtained with the magnetically focused minibeams.

3.1.3 Depth-Dose Profiles and Peak-to-Valley Dose Ratio

Figure 5 shows the peak and valley depth-dose profiles as well as the PVDR as a function of depth. The sampling locations of the depth-dose profiles are indicated in **Figure 1**. The depth-dose profiles obtained with the different minibeam techniques are generally very similar except for one important difference: compared to magnetic focusing, mechanical collimation yields higher valley doses at low depths which can be attributed to intra-slit leakage and scattered primary particles as well as an increased number of secondaries produced in the collimator.

For the case of magnetic focusing, the peak profiles exhibit a small shoulder at a depth of 1–2 cm, in particular for proton beams of 123 and 150 MeV. This can be interpreted as a consequence of the focal point of the beam being located inside the phantom so that the beam broadening due to lateral scattering is compensated by a converging motion of the focused beam particles. Indeed, considering again the beam broadening (**Figure 3**), one observes that in these two cases the width of the minibeams stays almost constant over the first 2 cm whereas the curve corresponding to the 100 MeV beam exhibits notable broadening.

Helium ions yield a much sharper and higher Bragg peak than protons. As a result, the BEDR is about 30–40% higher for the lowest energies (100 MeV proton beams, 400 MeV He beams), however this difference becomes less pronounced as the beam energy increases. Moreover, the Bragg peak becomes more smeared out and the BEDR decreases for higher energies. This is because range straggling becomes more important as the range increases and more primary particles are lost in nuclear interactions, leading to a reduction of the Bragg peak height

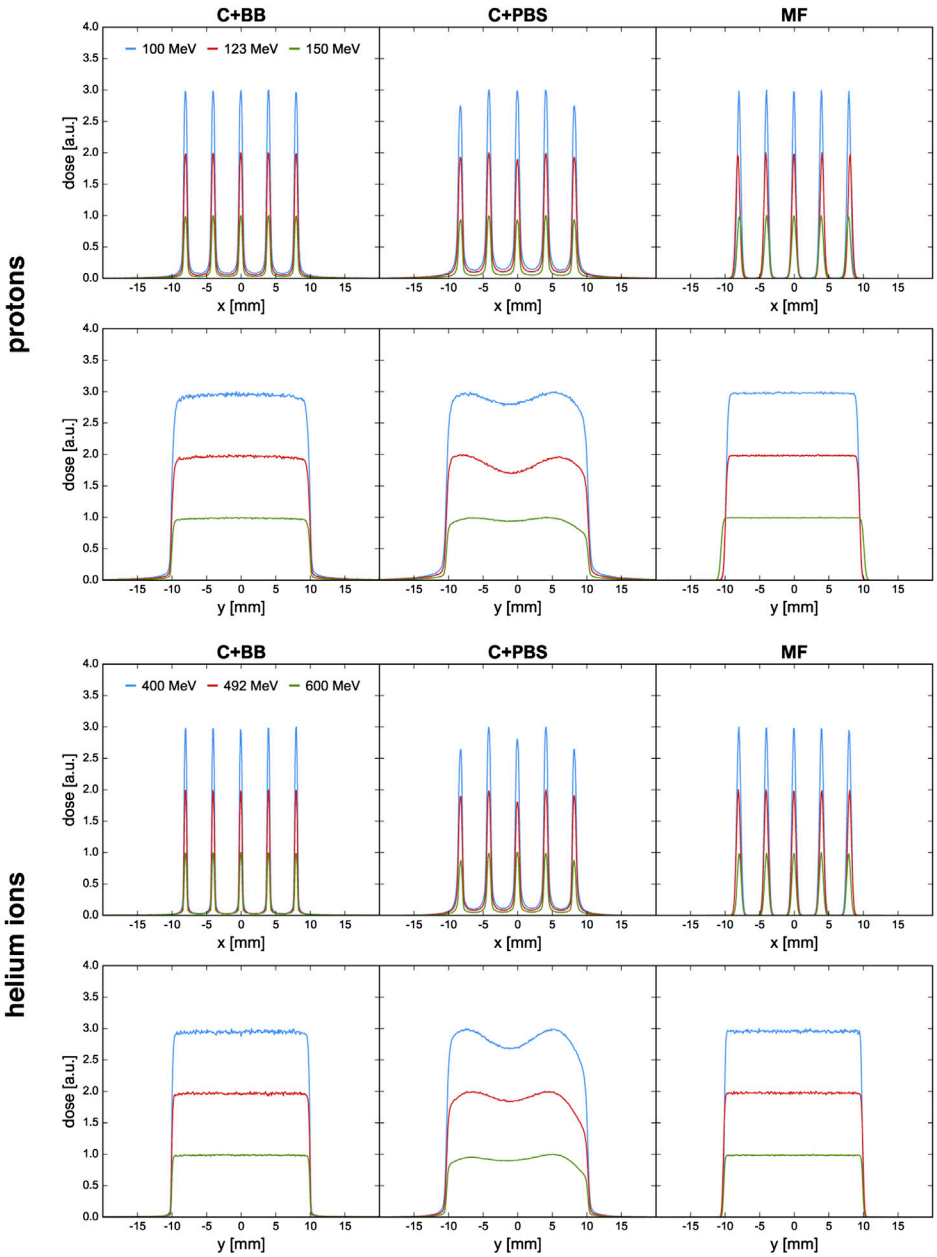

FIGURE 4 | Lateral dose profiles at the phantom entrance for proton and helium ion beams and for the different minibeam techniques (columns). The blue and red curves are artificially scaled by a factor of 3 and 2, respectively, to provide better visual distinction. The first and third row show the horizontal profiles at $y = 0$ cm; the second and fourth row show the vertical profiles at $x = 0$ cm.

[37]. In almost all cases, the BEDR of the peak dose profiles is <1 which represents an important difference compared to the standard Bragg curve observed for conventional hadron therapy with supermillimetric beams. A BEDR smaller than one implies an increased dose deposition in shallow tissue or at the skin level and must be considered disadvantageous for healthy tissue sparing. However, the high entrance dose is restricted to the peak regions and may be compensated for by the tissue sparing effects of the spatial fractionation.

A high PVDR >10 is observed in all cases, at least at shallow depths. By far the highest PVDR is observed for magnetic focusing (about 20–60 times higher than those for C+BB and C+PBS, respectively). This is a direct consequence of the much lower valley doses. Analogously, the helium ion beams yield a higher PVDR than the proton beams.

The PVDR decreases more slowly when the beam energy is higher. This can be understood as a consequence of the reduced multiple Coulomb scattering at higher energies: higher-energetic beams broaden more slowly which means that the valleys fill up

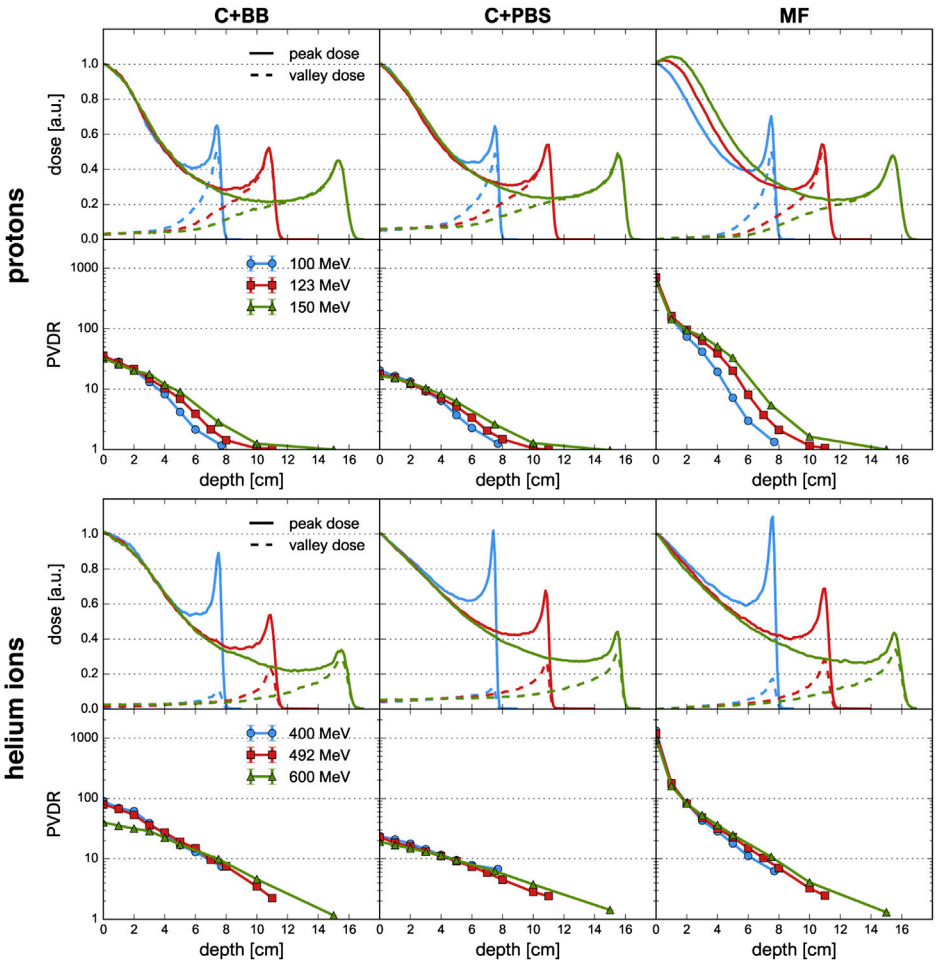

FIGURE 5 | Depth-dose profiles and PVDR evolution for proton and helium ion beams and for the different minibeam techniques (columns). First and third row: depth-dose profiles along peak (solid lines) and valley (dashed lines) regions. Second and fourth row: Evolution of PVDR as a function of depth, the uncertainty bars are smaller than the markers.

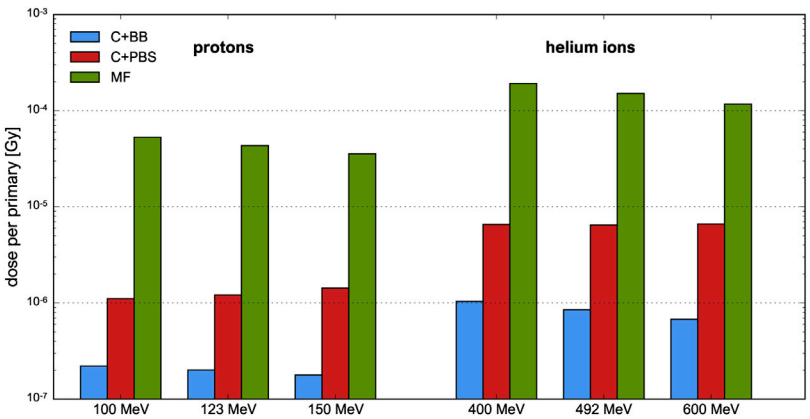

FIGURE 6 | Efficiency of proton and helium ion beams at different beam energies and for different minibeam techniques. The uncertainty bars are very small and barely visible.

more slowly. At the phantom entrance, however, beams with a higher energy were observed to yield a lower PVDR (**Table 1**).

Lastly, it should be noted that lateral homogenization of the dose (i.e. PVDR ≈ 1) at the Bragg peak depth is only observed for the proton beams at an energy of 123 and 150 MeV. This is because the spacing of the collimator slits was optimized for these cases but the same minibeam pattern with identical centre-to-centre distances was also considered for all other cases. More details on this are given in **Section 4**.

3.2 Efficiency

Figure 6 shows the dose efficiencies (mean dose deposited at Bragg peak depth per primary particle). Magnetic focusing is found to be the most efficient minibeam delivery method, both for protons and helium ions, yielding an increase in efficiency of one to two orders of magnitude compared to the collimator techniques. Moreover, the efficiency of helium ions is 3–4 times higher than that of protons. This is in agreement with the fact that helium ions yield sharper and higher Bragg peaks, as mentioned before.

For the cases C+BB and MF, the efficiency tends to decrease slightly as the beam energy increases. This is a consequence to the Bragg peak becoming flatter and more smeared out due to enhanced range straggling, as argued in **Section 3.1.3**. An opposite effect is observed for the case C+PBS with proton beams (and to a much smaller degree also with helium ion beams) which may be explained with the widths of the uncollimated pencil beams. The widths become smaller as the energy increases, so a larger proportion of the initial beam passes the collimator.

Between the two methods involving a collimator, irradiation with a scanned pencil beam was found to be about 5–10 times more efficient than broad beam irradiation. It should be noted, however, that the efficiency of the C+BB case strongly depends on the ratio between the sizes of the initial uncollimated beam and the collimator but also on the size and number of the collimator slits. This point is further discussed in the next section.

4 DISCUSSION

Proton minibeam radiation therapy is a novel therapeutic approach which, in preclinical experiments, has shown significant increases in the preservation of normal tissue [38, 39] while providing equivalent or superior tumour control [16, 17]. The generation of very narrow proton beams, intense enough to deliver the required dose in a reasonable amount of time (a few minutes) at existing clinical facilities, is a challenging task. The current implementation at clinical centres uses mechanical collimation which, despite representing a straightforward and readily applicable method, is suboptimal due to flux reduction, limited flexibility and neutron production (although evaluations have shown only a modest increase of <1% for the biological neutron dose in the patient [24]). In a previous work, we have thus proposed a new nozzle design capable of generating magnetically focused proton minibeams at a clinical centre [26].

In this study, we evaluated the differences between minibeam techniques using mechanical collimation and magnetic focusing. The aim of this comparison was twofold, considering gains in terms of efficiency but also whether there exists any advantage concerning the dose distributions. The simulations were performed with protons as well as helium ions which experience less multiple Coulomb scattering and which could therefore further improve the dose distributions.

As expected, magnetic focusing was shown to be much more efficient than mechanical collimation due to the fact that the entire beam can be used for dose deposition in the target. Compared to the collimator techniques, the mean dose per primary particle deposited at Bragg peak depth was at least 20 times higher with magnetic focusing in all cases. Such a gain is interesting in particular regarding a potential combination of pMBRT and FLASH therapy [40, 41] which requires very high dose rates. Moreover, helium ions were observed to be more efficient than protons which, in the context of the used metric, can be explained by the sharper Bragg peaks.

Between the two collimator techniques, irradiation with scanned pencil beams (C+PBS) has shown an improved efficiency compared to broad beam irradiation (C+BB). As stated above, the efficiency in the latter case depends strongly on the field size and the collimator geometry. The considered collimator was already used in previous studies [25, 42] (with the exception that parallel slits were used for the case C+BB) and a uniform irradiation of the entire cross-section of the collimator was assumed, approximating the conditions of a passively scattering beamline. It should be noted, however, that a reduction of the size of the uncollimated beam could drastically improve the efficiency. For instance, a four-fold increase of the efficiency would be expected from geometrical considerations for a field size of $5 \times 5\ \mathrm{cm}^2$.

Concerning the dosimetric evaluation, a substantially enhanced PVDR at shallow depths was observed for magnetically focused minibeams compared to mechanically collimated ones. Similarly, helium ions were found to yield a higher PVDR than protons. This is desirable as it has been shown that a high PVDR favours normal tissue sparing [8]. In terms of BEDR, magnetic focusing does not offer any improvements over mechanical collimation. Instead, protons could be replaced by helium ions to obtain a more favourable ratio between the entrance and Bragg peak doses.

It should be emphasized again that the PVDR is very dependent on the spacing between the minibeams and that the value considered in this study was optimized for proton beams of 123–150 MeV (cf. De Marzi et al. [25]). The idea here was to use the model of an existing collimator for proton beams and to evaluate whether it could also be used with helium ions. Our results show that collimators designed for proton beams could also be used to produce helium ion minibeams.

In order to attain lateral homogenization at the Bragg peak depth with helium ions, a narrower centre-to-centre distance would be required, in particular at lower beam energies. This

would result in a significantly lower PVDR which generally implies a reduction of tissue sparing effects. However, recent experiments indicate that homogenous dose coverage of the target may not be needed to achieve tumour control [16, 17]. A more detailed discussion of these aspects can be found in one of our previous works [18].

While the focus of this study lay on the comparison of the dose distributions and neutron production, another important factor is the linear energy transfer (LET) as it can influence the biological effectiveness of the irradiation. Previous works on pMBRT by our group found a slightly higher LET in the valley regions than in the peak regions [18, 42]. From these studies, it appears that collimator-generated minibeams [42] yield a less favourable ratio (i.e. higher valley LET) than magnetically focused minibeams [18]. In this light, future studies should therefore also evaluate the *peak-to-valley LET ratio* (see e.g. González and Prezado [43]).

Following previous works [25, 42], this study evaluated beam energies between 100 and 150 MeV/u which would be adequate e.g. for the treatment of brain tumours [15, 16, 42]. Nonetheless, proton minibeams of ≥200 MeV have also been considered, using both collimation techniques [28] and magnetic focusing [26]. Due to the reduced importance of lateral scattering, the generation of magnetically focused minibeams becomes easier at higher energies whereas the production of unwanted secondary particles in the collimator increases. The advantages of magnetic focusing over mechanical collimation demonstrated in this study can therefore be expected to apply also at higher energies. It should be noted, however, that the results presented here are based on Monte Carlo simulations. We are currently working toward a physical implementation of magnetically focused minibeams and hope to soon be able to perform experimental validations.

Lastly, it should be mentioned that, at least for now, mechanical collimation represents the technically easier approach for minibeam generation. Indeed, all existing implementations of pMBRT at clinically relevant energies use collimators [17, 23, 25] and this technique can in principle be readily applied at any proton therapy centre [26, 44]. In contrast to this, the generation of magnetically focused minibeams will likely not be achievable with current clinical nozzles [26]. However, our simulations indicate the compatibility of the new nozzle design considered in this study with existing proton therapy technology such as synchrotron-based facilities (see Schneider et al. [26] for more details).

The new minibeam nozzle design uses standard components (electromagnets, ionization chambers) so that no additional costs are expected compared to conventional PBS nozzles. On the contrary, the improved flexibility and efficiency of magnetic focusing would likely allow a much more economic implementation of pMBRT than mechanical collimators. Moreover, also standard PBS techniques could benefit from the new nozzle design and its ability to deliver smaller beams with sharper penumbrae.

5 CONCLUSION

The results of our study show that magnetic focusing represents a better approach for minibeam generation than mechanical collimation, exhibiting substantial improvements in terms of irradiation efficiency and PVDR. Moreover, they indicate that helium ion minibeams can be generated using the same techniques that were developed for pMBRT. Despite the technical challenges related to a practical implementation of magnetically focused minibeams, our results support and further motivate the work toward the physical realization of such a system at a clinical centre.

DATA AVAILABILITY STATEMENT

The datasets generated for this study are available on request to the corresponding author.

AUTHOR CONTRIBUTIONS

TS designed and carried out the studies (Monte Carlo simulations and data analysis) and wrote the manuscript. YP conceived the project. YP and AP supervised the studies. LD provided data and template files for the Monte Carlo simulations of the C+PBS case. All authors participated in scientific discussions, read and approved the manuscript.

FUNDING

This project has received funding from the European Research Council (ERC) under the European Union's Horizon 2020 research and innovation programme (Grant Agreement No 817908) and this project has also been partially funded by SIRIC 2018–2022: INCa-DGOS-Inserm_12,554. Calculation time was granted at the supercomputer Joliot Curie SKL Très grand centre de calcul (TGCC) of Commisariat Energie Atomique (CEA), from the Partnership for Advanced Computing in Europe (PRACE Project Access Call 19th, proposal number 2019204903).

ACKNOWLEDGMENTS

TS thanks Consuelo Guardiola for her help in initial discussions regarding the simulations of the C+BB case.

REFERENCES

1. Garibaldi C, Jereczek-Fossa BA, Marvaso G, Dicuonzo S, Rojas DP, Cattani F, et al. Recent advances in radiation oncology. *Ecancermedicalscience* (2017) 11: 785. doi:10.3332/ecancer.2017.785
2. Köhler A. Theorie einer methode, bisher unmöglich unanwendbar hohe dosen röntgenstrahlen in der tiefe des gewebes zur therapeutischen wirksamkeit zu bringen ohne schwere schäden des patienten, zugleich eine methode des schutzes gegen röntgenverbrennungen überhaupt. *Fortschr Geb Roentgenstr* (1909) 14:27–9.
3. Mohiuddin M, Fujita M, Regine WF, Megooni AS, Ibbott GS, Ahmed MM. High-dose spatially-fractionated radiation (grid): a new paradigm in the management of advanced cancers. *Int J Radiat Oncol Biol Phys* (1999) 45: 721–7. doi:10.1016/s0360-3016(99)00170-4
4. Slatkin DN, Spanne P, Dilmanian FA, Gebbers JO, Laissue JA. Subacute neuropathological effects of microplanar beams of x-rays from a synchrotron wiggler. *Proc Natl Acad Sci USA* (1995) 92:8783–7. doi:10.1073/pnas.92.19.8783
5. Dilmanian FA, Zhong Z, Bacarian T, Benveniste H, Romanelli P, Wang R, et al. Interlaced x-ray microplanar beams: a radiosurgery approach with clinical potential. *Proc Natl Acad Sci USA* (2006) 103:9709–14. doi:10.1073/pnas.0603567103
6. Prezado Y, Deman P, Varlet P, Jouvion G, Gil S, Le Clec'H C, et al. Tolerance to dose escalation in minibeam radiation therapy applied to normal rat brain: long-term clinical, radiological and histopathological analysis. *Radiat Res* (2015) 184:314–21. doi:10.1667/RR14018.1
7. BouchetSerduc R, Laissue JA, Djonov V. Effects of microbeam radiation therapy on normal and tumoral blood vessels. *Phys Med* (2015) 31:634–41. doi:10.1016/j.ejmp.2015.04.014
8. Dilmanian FA, Button TM, Le Duc G, Zhong N, Peña LA, Smith JAL, et al. Response of rat intracranial 9L gliosarcoma to microbeam radiation therapy. *Neuro Oncol* (2002) 4:26–38. doi:10.1093/neuonc/4.1.2610.1215/15228517-4-1-26
9. Curtis HJ. The use of deuteron microbeam for simulating the biological effects of heavy cosmic-ray particles. *Radiat Res Suppl* (1967) 7:250–7. doi:10.2307/3583718
10. Hopewell JW, Trott KR. Volume effects in radiobiology as applied to radiotherapy. *Radiother Oncol* (2000) 56:283–8. doi:10.1016/s0167-8140(00)00236-x
11. Crosbie JC, Anderson RL, Rothkamm K, Restall CM, Cann L, Ruwanpura SS, et al. Tumor cell response to synchrotron microbeam radiation therapy differs markedly from cells in normal tissues. *Int J Radiat Oncol Biol Phys* (2010) 77: 886–94. doi:10.1016/j.ijrobp.2010.01.035
12. Yan W, Khan MK, Wu X, Simone CB, Fan J, Gressen E, et al. Spatially fractionated radiation therapy: history, present and the future. *Clin Transl Radiat Oncol* (2020) 20:30–8. doi:10.1016/j.ctro.2019.10.004
13. Prezado Y, Fois GR. Proton-minibeam radiation therapy: a proof of concept. *Med Phys* (2013) 40:031712. doi:10.1118/1.4791648
14. Zlobinskaya O, Girst S, Greubel C, Hable V, Siebenwirth C, Walsh DWM, et al. Reduced side effects by proton microchannel radiotherapy: study in a human skin model. *Radiat Environ Biophys* (2013) 52:123–33. doi:10.1007/s00411-012-0450-9
15. Prezado Y, Jouvion G, Hardy D, Patriarca A, Nauraye C, Bergs JJ, et al. Proton minibeam radiation therapy spares normal rat brain: long-term clinical, radiological and histopathological analysis. *Sci Rep* (2017) 7:14403. doi:10.1038/s41598-017-14786-y
16. Prezado Y, Jouvion G, Patriarca A, Nauraye C, Guardiola C, Juchaux M, et al. Proton minibeam radiation therapy widens the therapeutic index for high-grade gliomas. *Sci Rep* (2018) 8:16479. doi:10.1038/s41598-018-34796-8
17. Prezado Y, Jouvion G, Guardiola C, Gonzalez W, Juchaux M, Bergs J, et al. Tumor control in RG2 glioma-bearing rats: a comparison between proton minibeam therapy and standard proton therapy. *Int J Radiat Oncol Biol Phys* (2019) 104:266–71. doi:10.1016/j.ijrobp.2019.01.080
18. Schneider T, Patriarca A, Prezado Y. Improving the dose distributions in minibeam radiation therapy: helium ions vs protons. *Med Phys* (2019) 46: 3640–8. doi:10.1002/mp.13646
19. González W, Peucelle C, Prezado Y. Theoretical dosimetric evaluation of carbon and oxygen minibeam radiation therapy. *Med Phys* (2017) 44:1921–9. doi:10.1002/mp.12175
20. Ströbele J, Schreiner T, Fuchs H, Georg D. Comparison of basic features of proton and helium ion pencil beams in water using gate. *Z Med Phys* (2012) 22: 170–8. doi:10.1016/j.zemedi.2011.12.001
21. Grün R, Friedrich T, Krämer M, Zink K, Durante M, Engenhart-Cabillic R, et al. Assessment of potential advantages of relevant ions for particle therapy: a model based study. *Med Phys* (2015) 42:1037–47. doi:10.1118/1.4905374
22. Tessonnier T, Mairani A, Chen W, Sala P, Cerutti F, Ferrari A, et al. Proton and helium ion radiotherapy for meningioma tumors: a Monte Carlo-based treatment planning comparison. *Radiat Oncol* (2018) 13:2. doi:10.1186/s13014-017-0944-3
23. Peucelle C, Nauraye C, Patriarca A, Hierso E, Fournier-Bidoz N, Martínez-Rovira I, et al. Proton minibeam radiation therapy: experimental dosimetry evaluation. *Med Phys* (2015) 42:7108–13. doi:10.1118/1.4935868
24. Guardiola C, Peucelle C, Prezado Y. Optimization of the mechanical collimation for minibeam generation in proton minibeam radiation therapy. *Med Phys* (2017) 44:1470–8. doi:10.1002/mp.12131
25. De Marzi L, Patriarca A, Nauraye C, Hierso E, Dendale R, Guardiola C, et al. Implementation of planar proton minibeam radiation therapy using a pencil beam scanning system: a proof of concept study. *Med Phys* (2018) 45:5305–16. doi:10.1002/mp.13209
26. Schneider T, De Marzi L, Patriarca A, Prezado Y. Advancing proton minibeam radiation therapy: magnetically focussed proton minibeams at a clinical centre. *Sci Rep* (2020) 10:1384. doi:10.1038/s41598-020-58052-0
27. Pedroni E, Meer D, Bula C, Safai S, Zenklusen S. Pencil beam characteristics of the next-generation proton scanning gantry of psi: design issues and initial commissioning results. *Eur Phys J Plus* (2011) 126:66. doi:10.1140/epjp/i2011-11066-0
28. De Marzi L, Da Fonseca A, Moignier C, Patriarca A, Goudjil F, Mazal A, et al. Experimental characterisation of a proton kernel model for pencil beam scanning techniques. *Phys Med* (2019) 64:195–203. doi:10.1016/j.ejmp.2019.07.013
29. Perl J, Shin J, Schumann J, Faddegon B, Paganetti H. Topas: an innovative proton Monte Carlo platform for research and clinical applications. *Med Phys* (2012) 39:6818–37. doi:10.1118/1.4758060
30. Arce P, Bolst D, Bordage MC, Brown JMC, Cirrone P, Cortés-Giraldo MA, et al. Report on G4-med, a geant4 benchmarking system for medical physics applications developed by the geant4 medical simulation benchmarking group. *Med Phys* (2020) 48:19–56. doi:10.1002/mp.14226
31. Testa M, Schümann J, Lu HM, Shin J, Faddegon B, Perl J, et al. Experimental validation of the topas Monte Carlo system for passive scattering proton therapy. *Med Phys* (2013) 40:121719. doi:10.1118/1.4828781
32. Zacharatou Jarlskog C, Paganetti H. Physics settings for using the geant4 physics settings for using the geant4 toolkit in proton therapy. *IEEE Trans Nucl Sci* (2008) 55:1018–25. doi:10.1109/tns.2008.922816
33. Grevillot L, Frisson T, Zahra N, Bertrand D, Stichelbaut F, Freud N, et al. Optimization of geant4 settings for proton pencil beam scanning simulations using gate. *Nucl Instr Methods Phys Res Sec B: Beam Interaction Mater Atoms* (2010) 268:3295–305. doi:10.1016/j.nimb.2010.07.011
34. Peucelle C, Martínez-Rovira I, Prezado Y. Spatial fractionation of the dose using neon and heavier ions: a Monte Carlo study. *Med Phys* (2015) 42: 5928–36. doi:10.1118/1.4930960
35. Gottschalk B. Chapter 2 - Physics of Proton Interactions in Matter. In: Paganetti H, editor. Proton Therapy Physics. 2nd ed. Taylor & Francis (2018).
36. Highland VL. Some practical remarks on multiple scattering. *Nucl Instr Methods* (1975) 129:497–9. doi:10.1016/0029-554X(75)90743-0
37. Newhauser WD, Zhang R. The physics of proton therapy. *Phys Med Biol* (2015) 60:R155–209. doi:10.1088/0031-9155/60/8/R155
38. Prezado Y, Dos Santos M, Gonzalez W, Jouvion G, Guardiola C, Heinrich S, et al. Transfer of minibeam radiation therapy into a cost-effective equipment for radiobiological studies: a proof of concept. *Sci Rep* (2017) 7:17295. doi:10.1038/s41598-017-17543-3
39. Girst S, Greubel C, Reindl J, Siebenwirth C, Zlobinskaya O, Walsh DWM, et al. Proton minibeam radiation therapy reduces side effects in an *in vivo* mouse ear model. *Int J Radiat Oncol Biol Phys* (2016) 95:234–41. doi:10.1016/j.ijrobp.2015.10.020

40. Favaudon V, Caplier L, Monceau V, Pouzoulet F, Sayarath M, Fouillade C, et al. Ultrahigh dose-rate flash irradiation increases the differential response between normal and tumor tissue in mice. *Sci Transl Med* (2014) 6:245ra93. doi:10.1126/scitranslmed.3008973
41. Reindl J, Girst S. Pmb flash-status and perspectives of combining proton minibeam with flash radiotherapy. *J Cancer Immunol* (2019) 1:14–23. doi:10.33696/cancerimmunol.1.003
42. Lansonneur P, Mammar H, Nauraye C, Patriarca A, Hierso E, Dendale R, et al. First proton minibeam radiation therapy treatment plan evaluation. *Sci Rep* (2020) 10:7025. doi:10.1038/s41598-020-63975-9
43. González W, Prezado Y. Spatial fractionation of the dose in heavy ions therapy: an optimization study. *Med Phys* (2018) 45:2620–7. doi:10.1002/mp.12902
44. McAuley GA, Teran AV, McGee PQ, Nguyen TT, Slater JM, Slater JD, et al. Experimental validation of magnetically focused proton beams for radiosurgery. *Phys Med Biol* (2019) 64:115024. doi:10.1088/1361-6560/ab0db1

Conflict of Interest: The authors declare that the research was conducted in the absence of any commercial or financial relationships that could be construed as a potential conflict of interest.

frontiers in Physics

REVIEW
published: 08 April 2021
doi: 10.3389/fphy.2021.624963

Radiobiology Experiments With Ultra-high Dose Rate Laser-Driven Protons: Methodology and State-of-the-Art

Pankaj Chaudhary[1], Giuliana Milluzzo[2], Hamad Ahmed[2,3], Boris Odlozilik[2,4], Aaron McMurray[2], Kevin M. Prise[1]* and Marco Borghesi[2]**

[1]The Patrick G. Johnston Centre for Cancer Research, Queens University Belfast, Belfast, Northern Ireland, [2]Centre for Plasma Physics, School of Mathematics and Physics, Queen's University Belfast, Belfast, Northern Ireland, [3]Central Laser Facility, Rutherford Appleton Laboratory, Science and Technology Facilities Council, Didcot, Oxford, United Kingdom, [4]Institute of Physics ASCR, v.v.i. (FZU), ELI-Beamlines Project, Prague, Czech Republic

OPEN ACCESS

Edited by:
Marco Durante,
GSI Helmholtz Center for Heavy Ion Research, Germany

Reviewed by:
Elke Beyreuther,
Helmholtz-Gemeinschaft Deutscher Forschungszentren, Germany
Lorenzo Manti,
University of Naples Federico II, Italy

***Correspondence:**
Pankaj Chaudhary
p.chaudhary@qub.ac.uk
Kevin M. Prise
k.prise@qub.ac.uk
Marco Borghesi
M.borghesi@qub.ac.uk

Specialty section:
This article was submitted to Medical Physics and Imaging, a section of the journal Frontiers in Physics

Received: 01 November 2020
Accepted: 29 January 2021
Published: 08 April 2021

Citation:
Chaudhary P, Milluzzo G, Ahmed H, Odlozilik B, McMurray A, Prise KM and Borghesi M (2021) Radiobiology Experiments With Ultra-high Dose Rate Laser-Driven Protons: Methodology and State-of-the-Art. Front. Phys. 9:624963. doi: 10.3389/fphy.2021.624963

The use of particle accelerators in radiotherapy has significantly changed the therapeutic outcomes for many types of solid tumours. In particular, protons are well known for sparing normal tissues and increasing the overall therapeutic index. Recent studies show that normal tissue sparing can be further enhanced through proton delivery at 100 Gy/s and above, in the so-called FLASH regime. This has generated very significant interest in assessing the biological effects of proton pulses delivered at very high dose rates. Laser-accelerated proton beams have unique temporal emission properties, which can be exploited to deliver Gy level doses in single or multiple pulses at dose rates exceeding by many orders of magnitude those currently used in FLASH approaches. An extensive investigation of the radiobiology of laser-driven protons is therefore not only necessary for future clinical application, but also offers the opportunity of accessing yet untested regimes of radiobiology. This paper provides an updated review of the recent progress achieved in ultra-high dose rate radiobiology experiments employing laser-driven protons, including a brief discussion of the relevant methodology and dosimetry approaches.

Keywords: protontherapy, cancer, radiobiology, laser-driven ions, particle accelerator, ultra-high dose rate

INTRODUCTION

Radiotherapy is delivered to over 50% of cancer patients with curative intent for solid localized tumours [1]. Most radiotherapy facilities across the world still rely on high energy photon or electron sources [1]. With recent technological advances, modalities such as Intensity Modulated Radiotherapy (IMRT), Stereotactic Body Radiotherapy (SBRT) or Volumetric Modulated Arc Therapy (VMAT) can conform doses to tumours more precisely than possible a few decades ago sparing the normal tissue to a larger extent. However, the risk of exposure of the surrounding normal tissues remains a concern for patient outcomes [2], with the potential for late tissue damage and escalating the risk of initiating secondary cancers in a patient's lifetime, especially for paediatric patients [3]. Proton therapy has been proposed as the most effective treatment of solid tumours in critical locations including the brain, medulloblastoma and other central nervous system tumours [4, 5]. The dose deposition profile of protons in the form of a "Bragg peak" imparts a unique normal tissue sparing ability [6] while depositing maximal dose within tumours [4, 7]. Due to this higher

normal tissue sparing effect relative to any of the photon based modalities, proton therapy has drawn an increasing interest with globally over 150 proton therapy centres being operational and under construction or at the planning stage [8]. Several clinical trials have confirmed the benefit of proton therapy in patients with localized solid tumours giving enhanced quality of life and better tumour control [9–11].

While proton therapy is clearly envisaged to significantly benefit patients, the underlying operational and construction costs pose a significant obstacle for widespread access to this form of treatment [12–14]. Alternative strategies for ion acceleration to clinically relevant energies with a smaller footprint technology and at reduced costs have been pursued for a long time and in this direction high power lasers have been suggested as a potentially transformative technology (see [15–17] and references within). Thanks to the Chirped Pulse Amplification (CPA) technique, it is now possible to amplify ultra-short laser pulses to the Petawatt level, an approach which led to the award of 2018 Physics Nobel Prize to Strickland and Mourou [18]. Based on the application of CPA, several investigators have demonstrated the generation of high-energy laser-accelerated ions and developed an understanding of their physical properties as well as their upscaling through different approaches potentially enabling radiological and radiobiological application [15, 17, 19, 20]. The unique properties of laser-driven protons [15, 17] include ultra-high field acceleration gradient, high brightness with $\sim 10^{12}$ ions in picosecond-scale bunches, high laminarity, ultra-low emittance and scalable energy cut-off, ultra-short pulse duration, energy-dependent collimation which increases with proton energy. Furthermore, laser acceleration potentially allows controlling the accelerated ion species by changing the target material, as well as producing multispecies ion beams, a capability that could be valuable for mixed field irradiations, currently not possible even with the more advanced RF accelerators.

The vision of laser-driven ion acceleration for hadrontherapy was first proposed by Bulanov et al. [21] and further supported by Fourkal et al. and Malka et al. [22, 23]. This stimulated significant interest in the biomedical application of laser-accelerated ions, and has led to the demonstration of methods for handling and irradiating cell culture models in order to develop a radiobiological understanding of ion irradiations at the ultra-high dose rates deliverable with this acceleration technique (up to $\sim 10^9$ Gray per second (Gy/s)).

The impact of dose rate on the biological effects and clinical response of radiation exposure has been studied for many years and several clinical modalities such as hypo- and hyper-fractionation have emerged based on the dose rate concept [24, 25]. Hall and Brenner reviewed the clinical importance of dose rate effects about 30 years ago, where a dose rate of 10^{11}–10^{13} cGy/min was specifically defined as ultra-high dose rate [26] and a dose rate of 0.1–0.2 Gy/s was considered as a radiotherapy relevant dose rate or, in other words, a "conventional" dose rate. Since then, these conventional dose rates have been widely used in various modalities of external beam radiotherapy (reviewed by Ling et al. in Ref. 25).

Recently, numerous investigators have used dose rates significantly higher than the conventional ones, often in the context of FLASH radiotherapy where the dose rate usually ranges between 40 and 1000 Gy/s [27–30]. The term "ultra-high dose rate" is often used to indicate these "FLASH" dose rates, which is confusing and can lead to a misinterpretation of ultra-high dose-rate radiobiology. It is important to understand the differences between these various regimes, as the biological effects at each dose rate may involve a different mechanism of action. Recently, Vozenin et al. [31] have emphasized the importance of properly reporting beam parameters for the characterization of the biological effects of FLASH irradiations. They also point out that not all irradiations at ultra-high dose rate may lead to FLASH effects and thus to understand the differences between the two regimes is important. FLASH dose rate effects have been shown to involve the differential response of normal and cancer cells, in the removal and decay of hydroperoxide and other free radicals [32] and oxygen saturation during the irradiation mainly observed *in-vivo* [33]. This results in significant sparing of the normal cells and thus provides a larger therapeutic window compared to conventional dose rate irradiation [34]. Durante et al. [35] introduced a Dose Rate Effectiveness Factor (DREF), and defined the radiobiological effectiveness of exposures ranging from low to Flash dose rates. However the behaviour of DREF at ultra-high dose rates of 10^9–10^{10} Gy/s has not yet been clearly defined, as indicated in **Figure 1**. In order to capitalize on any future radiobiological applications of laser-driven protons it is imperative to properly understand the effects arising at such dose rates. This manuscript aims to present an update on recent radiobiological research in this area with an overview of the methodology, mechanisms, dosimetry approaches and radiobiological assays employed to study the radiobiology of laser-accelerated protons.

LASER-DRIVEN PROTON ACCELERATION

Research on the acceleration of ions by ultra-intense laser pulses has been pursued over the last 2 decades, and has driven continual progress in delivering higher laser intensities on target, creating new target types and improving diagnostic systems underpinning new scientific results.

Research on the acceleration of ions by ultra-intense laser pulses is mostly based on interactions with solid targets. In a typical experimental setting, as shown in **Figure 2**, an intense laser pulse, typically at intensities above 10^{19} W/cm^2, interacts with a thin foil with thickness in the order of μms to 10s of μm and, during this interaction, a significant amount of laser energy is transferred to a population of relativistic electrons. These energetic electrons propagate through the target and create a strong sheath electric field at its rear surface, leading to the acceleration of protons originally present as impurities on the target surfaces. This Target Normal Sheath Acceleration (TNSA) process [36], is currently the most explored and robust mechanism of laser-driven proton acceleration [15, 17, 20, 37, 38]. Nevertheless, further improvements in cut-off energy, spectral and angular properties and repetition rate are

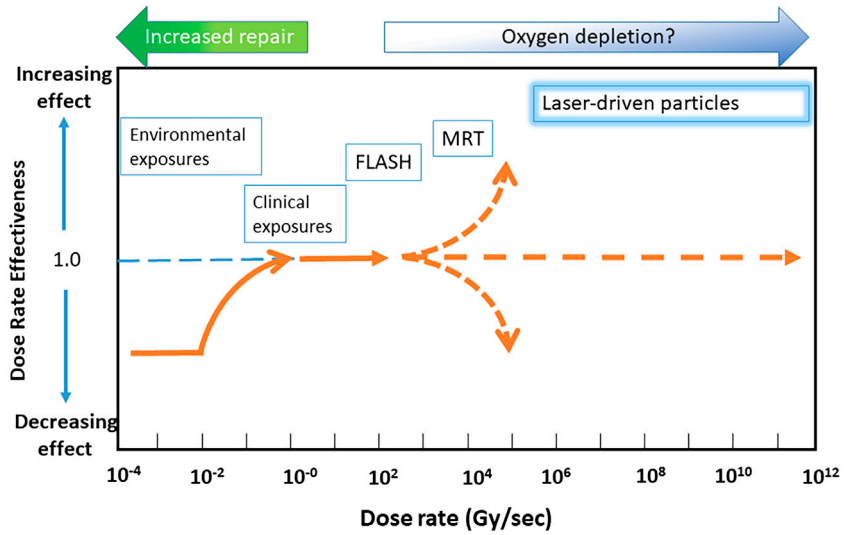

FIGURE 1 | Representation of dose rate effectiveness as a function of dose rate. *Y*-axis shows the dose rate effectiveness and *X*–axis shows the dose rate. Various radiotherapy modalities are displayed according to their approximate DREF values and dose rates. Abbreviations: MRT, Microbeam Radiotherapy.

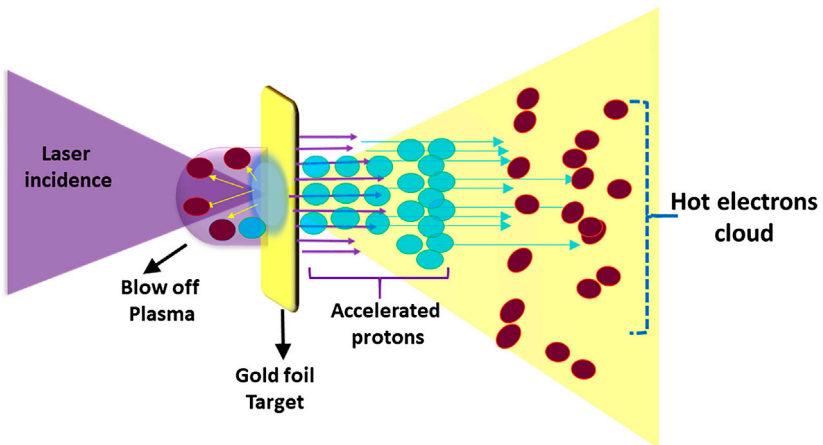

FIGURE 2 | Target Normal Sheath Acceleration mechanism of laser driven ions acceleration. The laser is focused onto in (5–10 μm) foil targets (e.g., gold as in the example shown) generating a beam of hot electrons which propagate through the target, and set-up a large sheath field at its rear. This field can reach up to a few Tera Volts per metre (TV/m) ionizing the atoms present at the target surface (inlcuding contaminants). The ions are then accelerated in the sheath field along the target normal direction.

required for effective application of laser-accelerated beams. For instance, applications in cancer therapy would require the delivery of high-energy protons (60–250 MeV) with a narrow energy spread and sufficient particle flux at appropriate distances from the interaction targets, so that any extraneous radiation produced during the intense laser interaction can be shielded adequately.

While control of TNSA beams has been a topic of active research over the last decade, significant attention has also been devoted to the exploration of a number of new acceleration mechanisms, including, for example, radiation pressure acceleration (RPA), which can in principle, produce beams with smaller divergence and narrow energy spread, particularly in the Light-Sail (LS) regime [15, 39]. RPA approaches are particularly suited to the acceleration of bulk ions in the irradiated target (e.g., carbon ions as opposed to contaminant protons [40]). There has recently been significant progress in increasing the maximum proton energies delivered through laser-driven processes, with reports of the acceleration of near 100 MeV protons by hybrid acceleration schemes [41] where acceleration is initiated by the TNSA mechanism followed by RPA until the target becomes transparent, with a

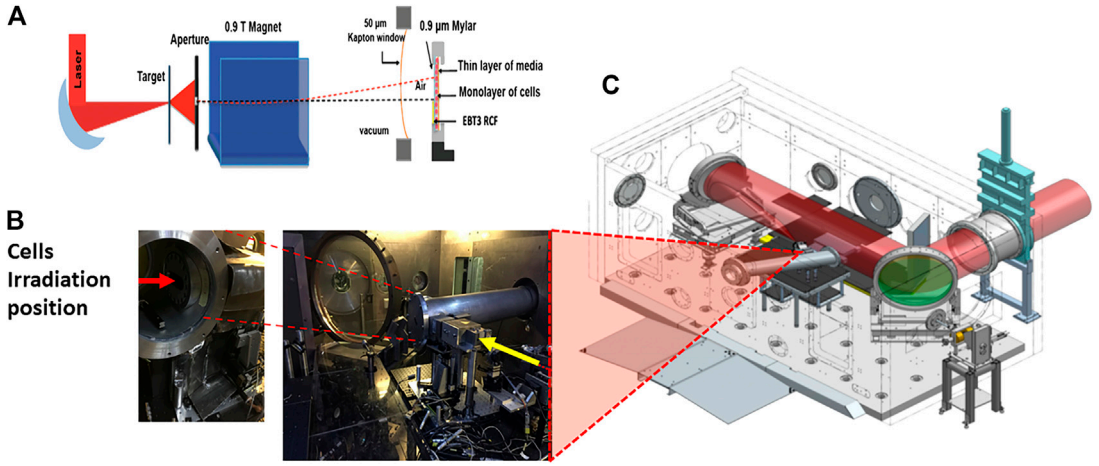

FIGURE 3 | Experimental set up demonstrating laser driven proton acceleration. **(A)** Schematic of the arrangement of the target, aperture, magnet, beam exit and cells. **(B)** Actual image showing the laser target interaction point setup along with the beam exit and sample irradiation position. **(C)** Overview of the Laser Interaction chamber of the Vulcan Target Area Pettawatt Laser of the Central Laser Facility at the Rutherford Appleton laboratory, Didcot, Oxford, England.

further energy boost provided in a relativistic transparency regime.

Main Centres Involved in the Radiobiology Study of Laser-Driven Proton

Motivated by its potential applications in research, technology and medicine, laser-driven proton acceleration research has gained significant support from funding agencies and academia in many countries. A number of laboratories across Europe have a specific interest and focus on the radiobiological and clinical applications of laser-driven proton. In Germany, Ludwig Maximilian University (LMU) Munich (currently starting activities at the new Centre for Advanced Laser Applications, CALA) and Helmholtz-Zentrum Dresden-Rossendorf (HZDR) have been very actively involved in radiobiological applications of laser-driven protons and several publications have resulted from the work performed at these facilities (discussed later). Investigators in France, are also actively engaged in radiobiology research with laser-driven beams, particularly at Laboratoire d'Optique (LOA), Palaiseau [42, 43]. A focus for future activities in this area across Europe will be at the facilities of the Extreme Light Infrastructure (ELI), particularly at ELI Beamlines (Czech Republic), where the Extreme Light Infrastructure Multidisciplinary Applications of Laser-Ion Acceleration (ELIMAIA) beam lines in Prague are being commissioned [44]. ELI Nuclear Physics (ELI NP) Romania, is also planning an involvement in laser-driven ion radiobiology research [45]. In the United Kingdom, the main facilities used for this research are located at the Central Laser Facility of the Rutherford Appleton Laboratory (RAL) (GEMINI and VULCAN lasers), the University of Strathclyde (SCAPA) and Queen's University Belfast (TARANIS), with activities in this area carried out so far within the EPSRC-funded A-SAIL consortium. In Asia, pioneering activities in this area were carried out in Japan at APRC-JAEA (now QST) [46, 47], while a proton beamline for radiobiology applications (CLAPA) has recently been developed at Peking University [48].

Typical Set Up for Laser-Driven Proton Irradiation

An example of an arrangement for radiobiology experiments employing laser-driven protons is shown in **Figures 3A–C** (based on the set-up employed for several experiments on the VULCAN and ASTRA GEMINI laser systems [49, 50]). Amplified laser light enters the evacuated interaction chamber and, after reflection from a plasma mirror (used for contrast enhancement), the laser is focused within a spot of a few microns onto a thin target, as shown in **Figure 3A**. The ions accelerated from the target are spatially selected by a narrow slit (of a few hundred µm) mounted in front of a ~1 T magnet (**Figure 3B**), which deflects the positively charged protons and other ions at an angle from the target normal separating them from other emitted radiation (electrons, X-rays). The deflected ions finally pass through a 50-200 µm-thick Kapton exit window (**Figure 3C**) and irradiate the cell sample positioned immediately after the window inside a sample holder. The sample holder is often a stainless steel dish covered with a thin Mylar foil (0.9–4 µm) which allows the ions to pass through with minimal beam attenuation, even at moderate energies.

DIAGNOSTICS AND DOSIMETRY

The monitoring of laser-accelerated ion parameters, such as beam composition, energy spectrum and dose distribution at the irradiation point is fundamental to achieving a controlled and accurate cell irradiation. Bolton et al. have provided an extensive

update on the instrumentation for diagnosis and control of laser-accelerated proton beams in Ref. 51. The beam characteristics are typically diagnosed using a range of techniques and detectors such as Thomson Parabola Spectrometers (TPS), Radiochromic Films (RCF) and Time of Flight (TOF) detectors [51]. The TPS and the RCF are usually placed along the target-normal direction to measure the higher-energy component and used for the full beam characterization in advance of the cell irradiations. In contrast, TOF detectors (typically diamond and silicon carbide) [52, 53] can be placed at various angles both in the forward and backward directions to monitor the particle flux and energy on-line during the irradiation, and detect any shot-to-shot variations [54]. A crucial task in view of meaningful radiobiological investigations is a precise measurement of the dose delivered to the cells. For conventional clinical beams, since the 2000s, a protocol for proton/ion dose measurement has been established where ionization chambers and calorimeters are defined as the absolute reference dosimeters [55]. In contrast, novel features of laser-driven protons such as ultra-high dose-rate, short pulse duration, as well as the presence of large electromagnetic pulses [56] generated by the laser-target interaction, require the development of new approaches and protocols for dose measurements [57].

The use of ionization chambers with pulsed beams at high dose rates is complicated due to an increase in ion recombination. Several authors have measured correction factors for Markus or Roos chambers developing new calibration procedures and models for both electrons and protons under different conditions relevant to FLASH radiotherapy [58–60]. They mainly used radiofrequency cavity (RF) accelerated protons up to 26 Gy/min and electrons up to 10^7 Gy/s. Extending the use of ionization chambers as absolute dosimeters for laser-driven protons at dose-rates near 10^9 Gy/s and at therapeutic doses (1–10 Gy) delivered per pulse, as typical in single-shot radiobiology experiments, is however a significant challenge, as it requires a large correction factor for the ion collection efficiency, which may affect the reliability of the dose measurement, as pointed out by McManus et al. [59].

The use of Faraday cups as suitable online dosimeters for laser-driven protons has also been proposed, e.g., by Richter et al. [61], who developed an integrated dosimetry and cell irradiation system (IDOCIS) that had about 13% dose uncertainty based on the quadratic summation of various contributing factors. An absolute dosimetry approach based on the use of Faraday cups is also being pursued on the ELIMED beamline at ELI Beamlines [62, 63].

In the attempt to further reduce dose uncertainties with laser-driven protons, an alternative approach employing graphite calorimeters as absolute dosimeters for laser-driven protons is under investigation at the National Physical Laboratory (NPL) in the framework of the European- Joint Research Project "UHDPulse" [57], aimed at establishing protocols and procedures for the dosimetry of ultra-high-pulse electron and proton beams [57, 64]. The measurement of the temperature increase in the calorimeter core upon irradiation is a direct measurement of the energy and dose deposited [65]. A first proof-of-principle experiment employing the high-energy laser-driven protons accelerated with the Vulcan PW laser at Rutherford Appleton Laboratory (RAL) has been reported in Ref. 66.

The use of passive detectors such as radiochromic films (Gafchromic EBT2 or EBT3), previously calibrated with beams generated by RF accelerators is a simple and widespread technique for dose measurements in laser-based radiobiology experiments [67, 68]. A single layer of the film can be used for 2D (transverse) monitoring of the proton dose, while stacks of multiple layers can be used for 3D dose mapping and reconstruction of the local proton spectrum by using deconvolution procedures. In a set-up as shown in **Figure 3A**, depending on the energy of the protons and cell dish arrangement, the RCF films can be placed either behind or in front of the cell dish. On a single-shot radiobiology experiment, this provides shot-to-shot monitoring of the dose, although this is available only after scanning of the film, using a suitably calibrated scanner. Recently RCF dosimetry (employing customized, unlaminated EBT3 films) has also been demonstrated with laser-accelerated carbon ions [50].

Real time dose monitoring during an irradiation is also crucial for an accurate characterization of the radiobiological effects of ultra-high dose rate irradiations. In radiobiology experiments at conventional accelerators, large area transmission ionization chambers are typically calibrated against the absolute dosimeter and then used as current monitors during the irradiation. In a laser-driven context, this is particularly important in multi-shot radiobiological experiments (as well as in future *in-vivo* experiments) to control the dose delivered in every single laser shot. Commercially available standard transmission ionization chambers have been used to monitor dose stability and reproducibility, e.g., on experiments on the Draco laser facility at HZDR, where standard transmission chambers cross-calibrated against radiochromic film at the cell irradiation position have been employed effectively (as described in Refs. 69 and 70). Modified transmission ionization chambers based on a double-gap structure [63] have been developed for dose monitoring along the ELIMED beam line, where the second gap is used to quantify, on each shot, the ion recombination occurring in the first gap at high dose-rates and to correct the collection efficiency.

Other approaches based on modified ionization chambers, such as the DOSION beam monitoring equipment [71], have been applied successfully in FLASH regimes [57], and may have scope for application with laser-driven sources. Several real-time approaches employing volumetric scintillation detectors [72], fibre optic dosimeters [73, 74], radioluminescence and Cherenkov emission based dosimeters have also been used for conventional dose rate proton beams as well as FLASH protons. In a laser-driven context, the use of scintillator blocks for approximated online monitoring of the lateral and depth dose distribution of the proton beam has been reported in Ref. 70, while approaches based on optical fibre arrays have not yet been applied to laser-driven protons. Finally, an approach for depth dose reconstruction employing acoustic traces generated by laser-driven protons stopping in a water phantom has been demonstrated and reported in Ref. 75.

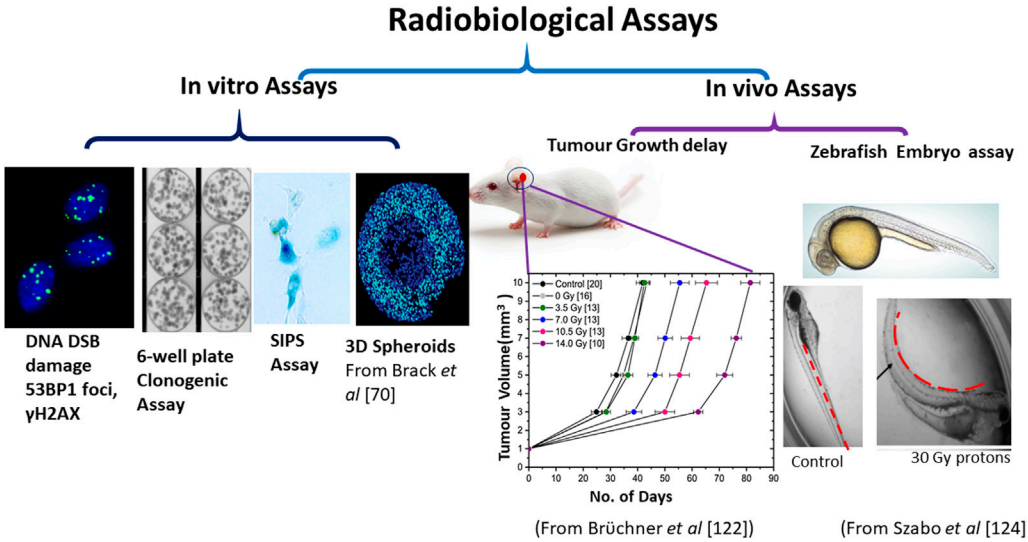

FIGURE 4 | Main radiobiological models used with laser-driven ions. The models are classified as *in-vitro* or cellular models and *in vivo* or animal models. The *in-vitro* models mainly used the DNA DSB damage assay using γ-H2AX or 53BP1 foci formation (in both 2D monolayers and 3D spheroids), stress induced pre-mature senescence (SIPS) and clonogenic assay. The *in-vivo* or animal model studies mainly used the tumour growth delay assay (mice ear tumour) as shown by Brüchner et al. [122] or organ deformation assays in zebrafish model as shown by Szabó et al. [124].

RADIOBIOLOGICAL APPROACHES

Radiation effects were first observed as a function of dose rate in the 1950s by Brasch et al. [76]. In 1969, Prempree et al. [77] studied the effects on the repair time of chromosome breaks induced by X-rays delivered at a dose rate of 4.5×10^8 Gy/s. Later, Berry in 1972–73 compared the effects of radiation dose rate from protracted, continuous irradiation to ultra-high dose rates of 10^9 Gy/s from pulsed accelerators [78, 79], noticed some non-predictable effects and discussed the impact of these dose rates on responses under hypoxia. Weiss et al. [80] demonstrated the depletion of oxygen in mammalian cells after ultra-high dose rate exposure. In all these studies, pulsed electron beams were mainly used and the pulse duration was of the order of a microsecond to a nanosecond. It was another two to 3 decades before studies were possible with laser-driven protons at comparable dose rates. During the early years of laser-driven proton radiobiology research, most experiments relied on multi-shot dose delivery, where several shots were required to deliver Gy level doses, and detect biological changes [81, 82]. Yogo et al. [81] delivered 200 shots to deposit a dose of 20 Gy in A549 lung adenocarcinoma cells that translates to an effective dose rate of 0.1 Gy/s with a single bunch dose rate of 1×10^7 Gy/s. Similarly, Kraft et al. [82] irradiated SKX squamous carcinoma cells using 12, 20, and 29 pulses, respectively, for low (1.5 Gy), medium (2.7 Gy) and high (4.1 Gy) doses of laser driven protons, demonstrating the feasibility of irradiating human cells with laser driven ions. These studies all employed femtosecond Titanium: Sapphire systems with limited energy per pulse, but were able to operate at sufficiently high repetition rates to make these multiple shot irradiations feasible.

A different approach, used by other groups, has been that of delivering Gy level doses in a single short burst of ~ns duration, therefore reaching dose rates of $\sim 10^9$ Gy/s. This has been possible on higher energy systems, typically delivering 10s–100s J per pulse [49, 83] or by focusing tightly the protons into a small spot [84]. Arguably, the approach employing single-shot irradiation, where the dose is not averaged over time, could in principle be better suited to test any biological effect related to the ultra-high dose rate.

The radiobiological assays that were applied in the above studies and also used more recently in laser-driven proton radiobiology research are briefly summarised in **Figure 4**, which includes endpoints for both the lethal and sub-lethal effects of radiation described in the following sub-sections.

Cell Based *In-Vitro* Studies

DNA Double Strand Break (DSB) Damage

The first experiments aimed at understanding the radiobiological effects of laser-driven protons quantified the yields of DNA damage in the form of DNA DSB using the foci formation assay. This assay uses immunofluorescent detection of the phosphorylated form (γ-H2AX) of the histone variant H2AX. The phosphorylation of the serine 139 amino acid residue on the H2AX protein is an early cellular response to DNA double strand break damage. The role of γ-H2AX in the formation of DNA DSB was first proposed by Rogakou et al. [85]. Sedelnikova et al. [86] found a direct correlation between the number of γ-H2AX foci and the number of radioiodine decay induced DNA DSBs providing a quantitative relationship for DNA DSB damage in human cell lines. Since then the γ-H2AX assay has been widely used in radiobiology and for over a decade has been an important biomarker of radiation induced DNA DSB damage from various

type of radiations including low linear energy transfer (LET) X-rays [87], protons and high LET ions such as silicon, iron [88] and carbon ions [89, 90]. Subsequently, additional biomarkers related to γ-H2AX were also identified which phosphorylate in the close proximity of DNA DSB. Among these, the-p53 binding protein-1(53BP1) protein which recruits to the nuclear structures at the site of DNA damage and forms readily visualized ionizing radiation induced foci [91, 92] showed a good correlation with γ-H2AX [93, 94]. This has been used by numerous investigators, including in our own work quantifying proton induced DNA DSB damage in human cells [95].

Laser-driven proton-induced DNA DSB damage in mammalian cells were first detected by using the γ-H2AX foci formation assay by Yogo et al. [81] in A549 lung adenocarcinoma cells monolayers irradiated with 2.4 MeV protons delivered in multiple 15 nanosecond pulses. Using a similar set up for cell handling Kraft et al. [82] also used a multi-shot approach to study DNA DSB damage induced by variable doses. In their study, Kraft et al. reached a dose rate of 4×10^7 Gy/s and irradiated cells with doses ranging from 1.4–4.5 Gy in about 12–29 pulses. Bin et al. [84] used a single shot approach and showed the induction of γ-H2AX foci in cervical cancer cells (Hela cells) exposed to 1 Gy dose of 4.45 MeV protons. In this study, the proton beam was generated using nanometre-thin, diamond-like carbon targets and delivered at dose rates in the range of 10^9–10^{10} Gy/s, reporting 7 Gy as the highest dose [84]. Overall, in these studies, laser-driven protons induced more DNA DSB damage than conventional X-rays but no comparison with cyclotron-accelerated protons, delivered at conventional dose-rates, was made.

Such a comparison was first made by Zeil et al. [96] who compared the yields of γ-H2AX foci induced by laser-driven protons to conventionally accelerated protons and found no significant differences. A few years later Raschke et al. [97] also found that laser-accelerated protons induce similar DSB damage to that induced by cyclotron-accelerated protons measured by γ-H2AX foci formation. In both of these studies, multi-shot irradiation methodology was used to deliver the desired doses.

Our group at QUB also performed single shot irradiation of human skin fibroblast cells (AG01522B) with 10 MeV laser-accelerated protons at a dose rate of 10^9 Gy/s. We compared the 53BP1 foci per cell per track induced by the laser driven ions to results obtained with cyclotron-accelerated protons at the same energy but at a dose rate of 0.06 Gy/s and also, in this case, did not observe any significant differences between the two dose-rates [49].

Clonogenic Cell Survival

The clonogenic assay has been used since the 1950s to study the radiation survival dose-response relationship for mammalian cell lines. Markus and Puck were the first to develop this assay [98] and since then it is considered a gold standard in radiation biology. Using this assay, the relative biological effectiveness (RBE), which is defined as the ratio of the doses required to cause the same biological effect using protons or other ions [99, 100] compared to reference X-ray radiation, can be calculated. RBE has contributed to a better understanding of radiotherapy dose treatment plans by providing the modeling parameters for various cell lines derived from tumour and normal tissues. Yogo et al. [46] for the first time used the clonogenic assay to determine the RBE of laser-driven protons using human salivary gland tumour cells and reported it as 1.2 ± 0.11 with reference to X-rays. In this study, the cells were irradiated with 2.25 MeV protons with a single bunch dose rate of 10^7 Gy/s. The cumulative doses were deposited using a multi-shot approach reducing the effective dose rate to 0.2 Gy/s on the cells. Later Doria et al. [83] also reported the cell killing effects of laser driven protons at a dose rate exceeding 10^9 Gy/s in V79 cells. This was the first study that employed the single shot delivery of 1–5 MeV protons at Gy level doses. Doses as high as 5 Gy were delivered in single pulses of picosecond duration. In this study an RBE of 1.4 ± 0.2 at a surviving fraction of 10% was reported.

Zeil et al. [96] compared the cell killing ability of pulsed laser-driven protons to a continuous proton beam when the squamous cell carcinoma cell line (SKX) was irradiated with energies above 6.5 MeV at a peak dose rate of 4×10^7 Gy/s. The authors did not explicitly quantify the RBE value in this paper, although the cell killing effects of the laser driven protons were reported to be similar to those delivered continuously from a Tandem accelerator at conventional dose-rates. Overall, based on the results from these papers, the RBE values for laser-driven protons ranged between 1.2 and 1.4, similar to those reported for RF-accelerated protons in the same energy range.

In summary, none of the studies discussed above highlighted significant deviations in biological response associated with the use of ultra-high dose rates provided by a laser-driven approach. Only recently, Bayart et al. [43] from the LOA group in France have reported that temporal delivery of laser-driven protons at an ultra-high dose rate of 1.5×10^8 Gy/s, may change the biological response of the human cells to synthetic lethality or cell killing induced by inhibiting the DNA damage response protein, PARP-1.

Several investigators have suggested that ultra-high dose rate exposure with electrons leads to oxygen depletion, inducing radioresistance in cells by reducing the reactive oxygen species-mediated indirect DNA DSB damage [33, 80]. When normoxic cells were irradiated with ultra-high dose rate electrons an increase in cell survival was noticed. However, there is limited information available on the response of hypoxic cells irradiated at ultra-high dose rates with protons, e.g., whether any additional DNA DSB induced are additive or synergistic in nature. We have tested this hypothesis experimentally by irradiating normal human skin fibroblast cells under hypoxic as well as normoxic conditions and we detected a significant increase in residual DNA DSB damage in hypoxic cells at 24 h post irradiation compared to the normoxic cells [101].

Sub-lethal Effects

Although a key advantage of hadrontherapy is that healthy tissues can be spared much more effectively than in X-ray radiotherapy, the sub-lethal effects induced by low dose deposition in the healthy cells surrounding a solid tumour may eventually result in the initiation of secondary cancers or other complications and

are arguably as important as lethal effects for an effective radiotherapy treatment outcome. Sub-lethal effects have been demonstrated in the promotion of migration and invasion in brain tumours and liver cancer [102, 103]. Among various sub-lethal effects, cell senescence has been studied for a long time [104] and has been associated with an onset of inflammation [105], secondary tumours and cancer relapse [106] in patients undergoing radiotherapy [107–109]. Stress induced pre-mature senescence (SIPS), a process in which a sub-lethally damaged cell enters a permanent state of inactivity, has attracted interest for its possible long-term health implications after radiation exposures [110, 111]. It is different from the phenomenon of *in-vitro* replicative senescence, where a cell loses its ability to proliferate after a finite number of cell divisions. Normal tissue sparing and differential sub-lethal effects induction have been reported in several FLASH radiotherapy studies, and highlighted as the main advantage of this approach (e.g. in Ref. 30). Investigating whether these advantages extend to the ultra-high dose regime delivered by laser-driven ions is one of the current research objectives of laser-driven radiobiology. Manti et al. [112] irradiated human vein endothelial cells with laser-driven protons and found that laser-driven proton beams, at a dose rate of 10^9 Gy/s, yielded a higher number of senescent cells at quasi therapeutic doses, while causing a lower percentage of cells to enter pre-mature senescence at doses typical of healthy tissues. This work therefore provided indication of sparing effects at ultra-high dose rate. Raschke et al. [97] have shown that, while laser-driven protons induce similar levels of DNA DSB damage to cyclotron–accelerated protons, the levels of protein nitroxidation (a marker of non-targeted effects) as studied through 3- nitrotyrosine generation was lower with laser-driven proton as compared to cyclotron-accelerated protons or X-rays.

3D Cell Culture Models

3D spherical or organoid model systems have been suggested as a link between cellular *in-vitro* models and *in vivo* animal tumours [113] as they recapitulate cancer drug effects more closely to the effects observed in animal models [114, 115] and especially in Glioblastoma tumours [116, 117]. These 3D neurosphere models are highly relevant for laser-driven ion studies as the current energies achieved with laser driven ions may not be suitable for the uniform irradiation of mouse *in-vivo* tumours which have dimensions of a few millimetres to a centimetre. In contrast, these 3D spheres are about 500–700 μm (1 week after seeding) in diameter which enables complete irradiation of these neurospheres using laser driven ions beams with energies above 20 MeV. Recently, Brack et al. [70] have demonstrated the uniform irradiation of 3D spheroids of human tongue cancer cells with a solenoid focused laser-driven proton beam. They evaluated the impact of laser-driven protons on DNA DSB damage in 3D spheroids after a total deposited dose of 15.3 Gy delivered in multiple shots.

Animal Based *In-Vivo* Studies

Mice have been used in many biological studies ranging from pharmacology, drug development, and as disease models [118]. Radiation oncology has also benefitted from pre-clinical studies using the large variety of genetically modified mouse models [119, 120]. Using conventionally accelerated protons or external beam radiotherapy for *in vivo* experiments is however much easier than doing similar experiments with laser-driven proton beams since, as mentioned earlier, the beam energy attained with laser-driven protons is generally not yet sufficient to fully irradiate deep-seated tumours with the required doses.

Due to this limitation, one has to carefully choose the type of tumour suitable for studies with laser driven ions. A mouse ear tumor model has been recently proposed, which has been proven suitable for experiments with ~20 MeV protons [121]. Laser-driven electrons have been used to irradiate the mouse ear tumour model and the tumour growth delay after irradiation was found comparable to X-ray induced growth delay [122]. To date no mouse based *in-vivo* irradiation has been reported with laser-driven protons, although they can be readily used with the above-mentioned models. The only published evidence of *in-vivo* research comes from a recent study published by Rösch et al. [123]. Due to a good match of the beam spot dimensions of laser-driven protons and the body size of zebrafish embryos, they can be potentially used as suitable *in vivo* models. 24 h after fertilization, these embryos can be easily handled, irradiated, and monitored for various radiobiological endpoints. One of the most accessible endpoints is the shape of the embryo's spine; whereas the un-irradiated controls are lengthy and have a straight spine, their irradiated counterparts are shorter in length and show a curved spine along with pericardial swelling and inhibition of yolk sac resorption (as described by Szabó et al. [124]).

CONCLUSION

While hadrontherapy was highlighted as a key application for laser-driven protons at an early stage of the development of laser acceleration, it is clear that direct application of laser-driven beams remains challenging, and significant progress is still needed to match the parameters required for clinical particle therapy. Efforts to upscale the energies, control the dose and improve the reliability of beam production are continuing, and there has been significant recent progress especially in developing advanced acceleration mechanisms, new techniques for beam transport and delivery, as well as novel beam diagnostics and dosimetry approaches. While further progress is being pursued, alternative applications of laser-driven protons can be exploited [125]. The answer to whether laser-driven protons at ultra-high dose rate can elicit a different biological response than conventional dose rate protons is still uncertain, but emerging indications do warrant continuation of this research, coupled to improvements in the dose delivery, dosimetry and energy range investigated. Although the maximum observed energy of laser-driven protons have recently approached 100 MeV, significant doses allowing radiobiology investigations have only been demonstrated up to ~30 MeV. RF-accelerated proton beams at such energies may not have robust dosimetry, as the primary beam is typically degraded, which introduces uncertainties in the beam composition and range, and makes accurate comparisons challenging. For a better understanding of the radiobiological mechanisms at ultra-high dose rates there is therefore an urgent

need to enhance the energy output of laser-driven proton beams, as well as to advance techniques for the uniform irradiation of large surface areas of cells in adherent monolayers or tissues within larger volumes (3D). Ultra-high dose rate radiobiology is a relatively new field and still evolving but certainly has great potential, as suggested by the recent advances of FLASH radiotherapy which has shown unique normal tissue sparing effects [30, 126, 127] that can lead to a higher therapeutic index in cancer radiotherapy [128–131]. There is no doubt that a close collaboration between the cyclotron accelerator, high power laser and FLASH radiotherapy communities will be beneficial for advancing the prospects of ultra-high dose rate proton radiobiology.

AUTHOR CONTRIBUTIONS

PC, MB and KMP conceptualized the article. PC, GM, HA, BO and AM collected the literature, wrote various subsections. PC, KMP and MB finalized the manuscript. All authors listed have made a substantial, direct, and intellectual contribution to the work and approved it for publication.

FUNDING

We acknowledge funding from the Engineering and Physical Sciences Research Council (EPSRC), through Grants EP/K022415/1 and EP/P010059/1. This project 18HLT04 UHDpulse has received funding from the EMPIR programme co-financed by the Participating States and from the European Union's Horizon 2020 research and innovation programme. Additionally, BO acknowledges funding from the European Union's Horizon 2020 research and innovation program under the Marie Sklowdowska-Curie grant agreement no 754507. AM acknowledges funding support provided by Department for the Economy, Northern Ireland.

ACKNOWLEDGMENTS

We would like to thank Kerstin Brüchner Elke Beyreuther and Florian-Emanuel Brack, HZDR, Dresden Germany and Emilia Rita Szabo at ELI- ALPS Hungary for allowing us to reuse material from their earlier published articles.

REFERENCES

1. Citrin DE Recent developments in radiotherapy. *N Engl J Med* (2017) 377(11): 1065–75. doi:10.1056/NEJMra1608986
2. Kinsara A, El Gizawy AS, Banoqitah E, Ma X Review of leakage from a linear accelerator and its side effects on cancer patients. *J Nucl Med Radiat Ther* (2016) 7(3):288. doi:10.4172/2155-9619.1000288
3. Yoon M, Ahn SH, Kim J, Shin DH, Park SY, Lee SB, et al. Radiation-induced cancers from modern radiotherapy techniques: intensity-modulated radiotherapy versus proton therapy. *Int J Radiat Oncol Biol Phys* (2010) 77(5):1477–85. doi:10.1016/j.ijrobp.2009.07.011
4. Durante M, Cucinotta FA, Loeffler JS Charged particles in oncology. *Front Res Top* (2018) 7:301. doi:10.3389/978-2-88945-391-7
5. Durante M Proton beam therapy in Europe: more centres need more research. *Br J Cancer* (2018) 120(8):777–8. doi:10.1038/s41416-018-0329-x
6. Bragg WH, Kleeman R XXXIX. On the α particles of radium, and their loss of range in passing through various atoms and molecules. *Philos Mag J Sci* (1905) 10(57):318–40. doi:10.1080/14786440509463378
7. Newhauser WD, Zhang R The physics of proton therapy. *Phys Med Biol* (2015) 60(8):R155–209. doi:10.1088/0031-9155/60/8/R155
8. Flanz J, Kamada T, Durante M, Jermann M, Mahajan A, et al. Proceedings to the 58th Annual Conference of the Particle Therapy Cooperative Group (PTCOG58) 10–15 June 2019. (2020). *Int J Part Ther* (2017) 6 (4):45–491. doi:10.14338/IJPT.19-PTCOG-6.4
9. Hu M, Jiang L, Cui X, Zhang J, Yu J Proton beam therapy for cancer in the era of precision medicine. *J Hematol Oncol* (2018) 11(1):1–16. doi:10.1186/s13045-018-0683-4
10. Ng J, Shuryak I Minimizing second cancer risk following radiotherapy: current perspectives. *Cancer Manag Res* (2014) 7:1–11. doi:10.2147/CMAR.S47220
11. Newhauser WD, Durante M Assessing the risk of second malignancies after modern radiotherapy. *Nat Rev Cancer* (2011) 11(6):438–48. doi:10.1038/nrc3069
12. Peeters A, Grutters JP, Pijls-Johannesma M, Reimoser S, De Ruysscher D, Severens JL, et al. How costly is particle therapy? cost analysis of external beam radiotherapy with carbon-ions, protons and photons. *Radiother Oncol* (2010) 95(1):45–53. doi:10.1016/j.radonc.2009.12.002
13. Newhauser WD, Zhang R, Jones TG, Giebeler A, Taddei PJ, Stewart RD, et al. Reducing the cost of proton radiation therapy: the feasibility of a streamlined treatment technique for prostate cancer. *Cancers* (2015) 7(2):688–705. doi:10.3390/cancers7020688
14. Schippers JM, Lomax A, Garonna A, Parodi K Can technological improvements reduce the cost of proton radiation therapy? *Semin Radiat Oncol* (2018) 28(2):150–9. doi:10.1016/j.semradonc.2017.11.007
15. Macchi A, Borghesi M, Passoni M. Ion acceleration by superintense laser interaction. *Rev Mod Phys* (2013) 85:751–793. doi:10.1103/RevModPhys.85.751
16. Ledingham K W, Bolton P R, Shikazono N, Ma CM Towards laser driven hadron cancer radiotherapy: a review of progress. *Appl Sci* (2014) 4:402-443. doi:10.3390/app4030402
17. Schreiber J, Bolton PR, Parodi K "Hands-on" laser-driven ion acceleration: A primer for laser-driven source development and potential applications. *Rev Sci Inst* (2016) 87:071101. doi:10.1063/1.4959198
18. Strickland D, Mourou G Compression of amplified chirped optical pulses. *Opt Commun* (1985) 56(3):219–21. doi:10.1016/0030-4018(85)90120-8
19. Kar S, Ahmed H, Prasad R, Cerchez M, Brauckmann S, Aurand B, et al. Guided post-acceleration of laser-driven ions by a miniature modular structure. *Nat Commun* (2016) 7:10792. doi:10.1038/ncomms10792
20. Robson L, Simpson P T, Clarke RJ, Ledingham KWD, Lindau F, Lundh O, et al. Scaling of proton acceleration driven by petawatt-laser-plasma interactions. *Nat Phys* (2007) 3:58–62. doi:10.1038/nphys476
21. Bulanov SV, Khoroshkov VS Feasibility of using laser ion accelerators in proton therapy. *Plasma Phys Rep* (2001) 28(5):453–6. doi:10.1134/1.1478534
22. Fourkal E, Li JS, Xiong W, Nahum A, Ma CM Intensity modulated radiation therapy using laser-accelerated protons: a Monte Carlo dosimetric study. *Phys Med Biol* (2003) 48(24):3977–4000. doi:10.1088/0031-9155/48/24/001
23. Malka V, Fritzler S, Lefebvre E, d'Humières E, Ferrand R, Grillon G, et al. Practicability of protontherapy using compact laser systems. *Med Phys* (2004) 31(6):1587–92. doi:10.1118/1.1747751
24. Dale RG Dose-rate effects in targeted radiotherapy. *Phys Med Biol* (1996) 41(10):1871–84. doi:10.1088/0031-9155/41/10/001
25. Ling CC, Gerweck LE, Zaider M, Yorke E Dose-rate effects in external beam radiotherapy redux. *Radiother Oncol* (2010) 95(3):261–8. doi:10.1016/j.radonc.2010.03.014

26. Hall EJ, Brenner DJ The dose-rate effect revisited: radiobiological considerations of importance in radiotherapy. *Int J Radiat Oncol Biol Phys* (1991) 21(6):1403–14. doi:10.1016/0360-3016(91)90314-T
27. Fouillade C, Curras-Alonso S, Giuranno L, Quelennec E, Heinrich S, Bonnet-Boissinot S, et al. FLASH irradiation spares lung progenitor cells and limits the incidence of radio-induced senescence. *Clin Cancer Res* (2019) 26(6): 1497–506. doi:10.1158/1078-0432.ccr-19-1440
28. Venkatesulu BP, Sharma A, Pollard-Larkin JM, Sadagopan R, Symons J, Neri S, et al. Ultra high dose rate (35 Gy/sec) radiation does not spare the normal tissue in cardiac and splenic models of lymphopenia and gastrointestinal syndrome. *Sci Rep* (2019) 9(1):17180. doi:10.1038/s41598-019-53562-y
29. Wilson JD, Hammond EM, Higgins GS, Petersson K Ultra-high dose rate (FLASH) radiotherapy: silver bullet or fool's gold?. *Front Oncol* (2020) 9:1563. doi:10.3389/fonc.2019.01563
30. Montay-Gruel P, Petersson K, Jaccard M, Boivin G, Germond JF, Petit B, et al. Irradiation in a flash: unique sparing of memory in mice after whole brain irradiation with dose rates above 100Gy/s. *Radiother Oncol* (2017) 124(3): 365–9. doi:10.1016/j.radonc.2017.05.003
31. Vozenin M-C, Montay-Gruel P, Limoli C, Germond JF All irradiations that are ultra-high dose rate may not be FLASH: the critical importance of beam parameter characterization and in vivo validation of the FLASH effect. *Radiat Res* (2020) 194(6) 571–2. doi:10.1667/RADE-20-00141.1
32. Spitz DR, Buettner GR, Petronek MS, St-Aubin JJ, Flynn RT, Waldron TJ, et al. An integrated physico-chemical approach for explaining the differential impact of FLASH versus conventional dose rate irradiation on cancer and normal tissue responses. *Radiother Oncol* (2019) 139:23–7. doi:10.1016/j.radonc.2019.03.028
33. Adrian G, Konradsson E, Lempart M, Bäck S, Ceberg C, Petersson K The FLASH effect depends on oxygen concentration. *Br J Radiol* (2020) 93(1106): 20190702. doi:10.1259/bjr.20190702
34. Martin S, Prise KM, Hill MA Pushing the frontiers of radiobiology: a special feature in memory of sir oliver scott and Professor Jack fowler. *Br J Radiol* (2019) 92(1093):20189005. doi:10.1259/bjr.20189005
35. Durante M, Bräuer-Krisch E, Hill M Faster and safer? FLASH ultra-high dose rate in radiotherapy. *Br J Radiol* (2018) 91:20170628. doi:10.1259/bjr.20170628
36. Wilks SC, Langdon AB, Cowan TE, Roth M, Singh M, Hatchett S, et al. Energetic proton generation in ultra-intense laser–solid interactions. *Phys Plasmas* (2000), 8:542. doi:10.1063/1.1333697
37. Fuchs J, Antici P, d'Humieres E, Lefevbre E, Borghesi M, Brambrink E, et al. Laser-driven proton scaling laws and new paths towards energy increase. *Nature Phys* (2006), 2:48–54. doi:10.1038/nphys199
38. Wagner F, Deppert O, Brabetz C, Fiala P, Kleinschmidt A, Poth P, et al. Maximum Proton Energy above 85 MeV from the Relativistic Interaction of Laser Pulses with Micrometer Thick CH2 Targets. *Phys. Rev.Lett* (2016) 116: 20500. doi:10.1103/PhysRevLett.116.205002
39. Macchi A Theory of light sail acceleration by intense lasers: an overview. *High Power Laser Science and Engineering* 2, (2014) e10. doi:10.1017/hpl.2014.13
40. Scullion C, Doria D, Romagnani L, Sgattoni A, Naughton K, et al. Polarization dependence of bulk Ion acceleration from Ultrathin foils irradiated by high-intensity ultrashort laser pulses. *Phys Rev Lett* (2017) 119, 054801. doi:10.1103/PhysRevLett.119.054801
41. Higginson A, Gray RJ, King M, Dance RJ, Williamson SDR Butler NMH et al. Near 100 MeV protons via a laser driven transparency enhanced hybrid acceleration scheme. *Nat Commun*. (2018) 9:724. doi:10.1038/s41467-018-03063-9
42. Pommarel L, Vauzour B, Megnin-Chanet F, Bayart E, Delmas O, Goudjil F, et al. Spectral and spatial shaping of a laser-produced ion beam for radiation-biology experiments. *Phys Rev Acc Beams* (2017) 20:082301. doi:10.1103/PhysRevAccelBeams.20.03280143
43. Bayart E, Flacco A, Delmas O, Pommarel L, Levy D, Cavallone M, et al. Fast dose fractionation using ultra-short laser accelerated proton pulses can increase cancer cell mortality, which relies on functional PARP1 protein. *Sci Rep* (2019) 9:10132. doi:10.1038/s41598-019-46512-1
44. Margarone D, Cirrone G, Cuttone G, Amico A, Andò L, Borghesi M, et al. ELIMAIA: a laser-driven ion accelerator for multidisciplinary applications. *Quantum Beam Sci* (2018) 2(2):8. doi:10.3390/qubs2020008
45. Asavei T, Bobeica M, Nastasa V, Manda G, Naftanaila F, Bratu O, et al. Laser-driven radiation: biomarkers for molecular imaging of high dose-rate effects. *Med Phys* (2019) 46(10):e726–34. doi:10.1002/mp.13741
46. Yogo A, Maeda T, Hori T, Sakaki H, Ogura K, Nishiuchi M, et al. Measurement of relative biological effectiveness of protons in human cancer cells using a laser-driven quasimonoenergetic proton beamline. *Appl Phys Lett* (2011) 98(5):053701. doi:10.1063/1.3551623
47. Yogo A, Sato K, Nishikino M, Maeda T, Sakaki H, Hori T, et al. Measurement of DNA double-strand break yield in human cancer cells by high-current, short-duration bunches of laser-accelerated protons. *Jpn J Appl Phys* (2011) 50(10R):106401. doi:10.1143/JJAP.50.106401
48. Zhu JG, Wu MJ, Liao Q, Geng YX, Zhu K, Li CC, et al. Experimental demonstration of a laser proton accelerator with accurate beam control through image-relaying transport. *Phys Rev Accel Beams* (2019) 22(6): 061302. doi:10.1103/PhysRevAccelBeams.22.061302
49. Hanton F, Chaudhary P, Doria D, Gwynne D, Maiorino C, Scullion C, et al. DNA DSB repair dynamics following irradiation with laser-driven protons at ultra-high dose rates. *Sci Rep* (2019) 9(1):4471. doi:10.1038/s41598-019-40339-6
50. Milluzzo G, Ahmed H, Romagnani L, Doria D, Chaudhary P, Maiorino C, et al. Dosimetry of laser-accelerated carbon ions for cell irradiation at ultra-high dose rate. *J Phys Conf Ser* (2020) 1596:012038. doi:10.1088/1742-6596/1596/1/012038
51. Bolton PR, Borghesi M, Brenner C, Carroll DC, De Martinis C, Fiorini F, et al. Instrumentation for diagnostics and control of laser accelerated proton (ion) beams. *Phys Med* (2014) 30 (3):255–70. doi:10.1016/j.ejmp.2013.09.00252
52. Margarone D, Krása J, Giuffrida L, Picciotto A, Torrisi L, Nowak T, et al. Full characterization of laser-accelerated ion beams using Faraday cup, silicon carbide, and single-crystal diamond detectors. *J Appl Phys* (2011) 109(10): 103302. doi:10.1063/1.3585871
53. Milluzzo G, Scuderi V, Amico AG, Borghesi M, Cirrone GAP, Cuttone G, et al. Laser-accelerated ion beam diagnostics with TOF detectors for the ELIMED beam line. *J Instrum* (2017) 12(02):C02025. doi:10.1088/1748-0221/12/02/C02025
54. Scuderi V, Milluzzo G, Doria D, Alejo A, Amico AG, Booth N, et al. TOF diagnosis of laser accelerated, high-energy protons. *Nucl Instrum Methods Phys Res Sect A Accel Spectrom Detect Assoc Equip* (2020) 978:164364. doi:10.1016/j.nima.2020.164364
55. Mather SJ, Mansi L IAEA technical report series. *Eur J Nucl Med Mol Imaging* (2008) 35(5):1030–1. doi:10.1007/s00259-008-0767-4
56. Consoli F, Tikhonchuk VT, Bardon M, Bradford P, Carroll DC, Cikhardt J, et al. Laser produced electromagnetic pulses: generation, detection and mitigation. *High Power Laser Sci Eng* (2020) 8:e22. doi:10.1017/hpl.2020.13
57. Schüller A, Heinrich S, Fouillade C, Subiel A, De Marzi L, Romano F, et al. The European Joint Research Project UHDpulse–metrology for advanced radiotherapy using particle beams with ultra-high pulse dose rates. *Phys Medica* (2020) 80:134–50. doi:10.1016/j.ejmp.2020.09.020
58. Petersson K, Jaccard M, Germond JF, Buchillier T, Bochud F, Bourhis J, et al. High dose-per-pulse electron beam dosimetry–a model to correct for the ion recombination in the Advanced Markus ionization chamber. *Med Phys* (2017) 44(3):1157–67. doi:10.1002/mp.12111
59. McManus M, Romano F, Lee ND, Farabolini W, Gilardi A, Royle G, et al. The challenge of ionisation chamber dosimetry in ultra-short pulsed high dose-rate Very High Energy Electron beams. *Sci Rep* (2020) 10(1):9089. doi:10.1038/s41598-020-65819-y
60. Palmans H, Thomas R, Kacperek A Ion recombination correction in the Clatterbridge Centre of Oncology clinical proton beam. *Phys Med Biol* (2006) 51(4):903–17. doi:10.1088/0031-9155/51/4/010
61. Richter C, Kaluza M, Karsch L, Schlenvoigt HP, Schürer M, Sobiella M, et al. Dosimetry of laser-accelerated electron beams used for *in vitro* cell irradiation experiments. *Radiat Meas* (2011) 46(12):2006–9. doi:10.1016/j.radmeas.2011.04.019
62. Leanza R, Romano F, Scuderi V, Amico AG, Cuttone G, Larosa G, et al. Faraday cup: absolute dosimetry for ELIMED beam line. *J Instrum* (2017) 12(03):C03046. doi:10.1088/1748-0221/12/03/C03046
63. Scuderi V, Amato A, Amico AG, Borghesi M, Cirrone GAP, Cuttone G, et al. Diagnostics and dosimetry solutions for multidisciplinary

applications at the ELIMAIA beamline. *Appl Sci* (2018) 8(9):1415. doi:10.3390/app8091415
64. Bourgouin A, Schüller A, Hackel T, Kranzer R, Poppinga D, Kapsch RP, et al. Calorimeter for real-time dosimetry of pulsed ultra-high dose rate electron beams. *Front Phys* (2020) 8:567340. doi:10.3389/fphy.2020.567340
65. Rossomme S, Palmans H, Thomas R, Lee N, Bailey M, Shipley D, et al. SU-E-T-146: reference dosimetry for protons and light-ion beams based on graphite calorimetry. *Med Phys* (2012) 39(6):3736–7. doi:10.1118/1.4735204
66. Romano F, Subiel A, McManus M, Lee ND, Palmans H, Thomas R, et al. Challenges in dosimetry of particle beams with ultra-high pulse dose rates. *J Phys Conf Ser* (2020) 1662:012028. doi:10.1088/1742-6596/1662/1/012028
67. Fiorini F, Kirby D, Borghesi M, Doria D, Jeynes JC, Kakolee KF, et al. Dosimetry and spectral analysis of a radiobiological experiment using laser-driven proton beams. *Phys Med Biol* (2011) 56(21):6969–82. doi:10.1088/0031-9155/56/21/013
68. Polin K, Doria D, Romagnani L, Chaudhary P, Cirrone GAP, Maiorino C, et al. Irradiation and dosimetry arrangement for a radiobiological experiment employing laser-accelerated protons. *J Instrum* (2019) 14(10):C10015. doi:10.1088/1748-0221/14/10/c10015
69. Richter C, Karsch L, Dammene Y, Kraft SD, Metzkes J, Schramm U, et al. A dosimetric system for quantitative cell irradiation experiments with laser-accelerated protons. *Phys Med Biol* (2011) 56(6):1529–43. doi:10.1088/0031-9155/56/6/002
70. Brack FE, Kroll F, Gaus L, Bernert C, Beyreuther E, Cowan TE, et al. Spectral and spatial shaping of laser-driven proton beams using a pulsed high-field magnet beamline. *Sci Rep* (2020) 10:9118. doi:10.1038/s41598-020-65775-7
71. Boissonnat G, Fontbonne JM, Balanzat E, Boumard F, Carniol B, Cassimi A. Characterization and performances of DOSION, a dosimetry equipment dedicated to radiobiology experiments taking place at GANIL. *Nuclear Inst Meth A(2017)* (2017) 856:1–6.doi:10.1016/j.nima.2016.12.04072
72. Beddar S Real-time volumetric scintillation dosimetry. *J Phys Conf Ser* (2015) 573:012005. doi:10.1088/1742-6596/573/1/012005
73. O'Keeffe S, Fitzpatrick C, Lewis E, Al-Shamma AI A review of optical fibre radiation dosimeters. *Sens Rev* (2008) 28(2):136–42. doi:10.1108/02602280810856705
74. Hoehr C, Morana A, Duhamel O, Capoen B, Trinczek M, Paillet P, et al. Novel Gd3+-doped silica-based optical fiber material for dosimetry in proton therapy. *Sci Rep* (2019) 9(1):16376. doi:10.1038/s41598-019-52608-5
75. Haffa D, Yang R, Bin J, Lehrack S, Brack FE, Ding H, et al. I-BEAT: ultrasonic method for online measurement of the energy distribution of a single ion bunch. *Sci Rep* (2019) 9(1):6714. doi:10.1038/s41598-019-42920-5
76. Brasch A, Huber W, Waly A Radiation effects as a function of dose rate. *Arch Biochem Biophys* (1952) 39:245–7. doi:10.1016/0003-9861(52)90287-7
77. Prempree T, Michelsen A, Merz T The repair time of chromosome breaks induced by pulsed x-rays on ultra-high dose-rate. *Int J Radiat Biol Relat Stud Phys Chem Med* (1969) 15(6):571–4. doi:10.1080/09553006914550871
78. Berry RJ Effects of radiation dose-rate from protracted, continuous irradiation to ultra-high dose-rates from pulsed accelerators. *Br Med Bull* (1973) 29(1):44–7. doi:10.1093/oxfordjournals.bmb.a070955
79. Berry RJ, Stedeford JB Reproductive survival of mammalian cells after irradiation at ultra-high dose-rates: further observations and their importance for radiotherapy. *Br J Radiol* (1972) 45(531):171–7. doi:10.1259/0007-1285-45-531-171
80. Weiss H, Epp ER, Heslin JM, Ling CC, Santomasso A Oxygen depletion in cells irradiated at ultra-high dose-rates and at conventional dose-rates. *Int J Radiat Biol Relat Stud Phys Chem Med* (1974) 26(1):17–29. doi:10.1080/09553007414550901
81. Yogo A, Sato K, Nishikino M, Mori M, Teshima T, Numasaki H, et al. Application of laser-accelerated protons to the demonstration of DNA double-strand breaks in human cancer cells. *Appl Phys Lett* (2009) 94(18):181502. doi:10.1063/1.3126452
82. Kraft SD, Richter C, Zeil K, Baumann M, Beyreuther E, Bock S, et al. Dose-dependent biological damage of tumour cells by laser-accelerated proton beams. *New J Phys* (2010) 12(8):085003. doi:10.1088/1367-2630/12/8/085003
83. Doria D, Kakolee KF, Kar S, Litt SK, Fiorini F, Ahmed H, et al. Biological effectiveness on live cells of laser driven protons at dose rates exceeding 10^9 Gy/s. *AIP Adv* (2012) 2(1):011209. doi:10.1063/1.3699063
84. Bin J, Allinger K, Assmann W, Dollinger G, Drexler GA, Friedl AA, et al. A laser-driven nanosecond proton source for radiobiological studies. *Appl Phys Lett* (2012) 101(24):243701. doi:10.1063/1.4769372
85. Rogakou EP, Pilch DR, Orr AH, Ivanova VS, Bonner WM DNA double-stranded breaks induce histone H2AX phosphorylation on serine 139. *J Biol Chem* (1998) 273(10):5858–68. doi:10.1074/jbc.273.10.5858
86. Sedelnikova OA, Rogakou EP, Panyutin IG, Bonner WM. Quantitative detection of 125IdU-induced DNA double-strand breaks with γ-H2AX antibody. *Radiat Res* (2002), 158(4): 468–492. doi:10.1667/0033-7587(2002)158[0486:QDOIID]2.0.CO;287
87. Ugenskiene R, Prise K, Folkard M, Lekki J, Stachura Z, Zazula M, et al. Dose response and kinetics of foci disappearance following exposure to high- and low-LET ionizing radiation. *Int J Radiat Biol* (2009) 85(10):872–82. doi:10.1080/09553000903072462
88. Desai N, Davis E, O'Neill P, Durante M, Cucinotta FA, Wu H Immunofluorescence detection of clustered gamma-H2AX foci induced by HZE-particle radiation. *Radiat Res* (2005) 164(4):518–22. doi:10.1667/rr3431.1
89. Ghosh S, Narang H, Sarma A, Kaur H, Krishna M Activation of DNA damage response signaling in lung adenocarcinoma A549 cells following oxygen beam irradiation. *Mutat Res* (2011) 723(2):190–8. doi:10.1016/j.mrgentox.2011.05.002
90. Schmid TE, Zlobinskaya O, Multhoff G Differences in phosphorylated histone H2AX foci formation and removal of cells exposed to low and high linear energy transfer radiation. *Curr Genomics* (2012) 13(6):418–25. doi:10.2174/138920212802510501
91. Schultz LB, Chehab NH, Malikzay A, Halazonetis TD P53 binding protein 1 (53BP1) is an early participant in the cellular response to DNA double-strand breaks. *J Cell Biol* (2000) 151(7):1381–90. doi:10.1083/jcb.151.7.1381
92. Gupta A, Hunt CR, Chakraborty S, Pandita RK, Yordy J, Ramnarain DB, et al. Role of 53BP1 in the regulation of DNA double-strand break repair pathway choice. *Radiat Res* (2014) 181(1):1–8. doi:10.1667/RR13572.1
93. Neumaier T, Swenson J, Pham C, Polyzos A, Lo AT, Yang P, et al. Evidence for formation of DNA repair centers and dose-response nonlinearity in human cells. *Proc Natl Acad Sci USA* (2012) 109(2):443–8. doi:10.1073/pnas.1117849108
94. Asaithamby A, Uematsu N, Chatterjee A, Story MD, Burma S, Chen DJ Repair of HZE-particle-induced DNA double-strand breaks in normal human fibroblasts. *Radiat Res* (2008) 169(4):437–46. doi:10.1667/RR1165.1
95. Chaudhary P, Marshall TI, Currell FJ, Kacperek A, Schettino G, Prise KM Variations in the processing of DNA double-strand breaks along 60-MeV therapeutic proton beams. *Int J Radiat Oncol Biol Phys* (2016) 95(1):86–94. doi:10.1016/j.ijrobp.2015.07.2279
96. Zeil K, Baumann M, Beyreuther E, Burris-Mog T, Cowan TE, Enghardt W, et al. Dose-controlled irradiation of cancer cells with laser-accelerated proton pulses. *Appl Phys B* (2013) 110(4):437–44. doi:10.1007/s00340-012-5275-3
97. Raschke S, Spickermann S, Toncian T, Swantusch M, Boeker J, Giesen U, et al. Ultra-short laser-accelerated proton pulses have similar DNA-damaging effectiveness but produce less immediate nitroxidative stress than conventional proton beams. *Sci Rep* (2016) 6(1):32441. doi:10.1038/srep32441
98. Puck TT, Marcus PI Action of x-rays on mammalian cells. *J Exp Med* (1956) 103(5):653–66. doi:10.1084/jem.103.5.653
99. Blomquist E, Russell KR, Stenerlöw B, Montelius A, Grusell E, Carlsson J Relative biological effectiveness of intermediate energy protons. Comparisons with 60Co gamma-radiation using two cell lines. *Radiother Oncol* (1993) 28(1):44–51. doi:10.1016/0167-8140(93)90184-A
100. Wouters BG, Lam GK, Oelfke U, Gardey K, Durand RE, Skarsgard LD Measurements of relative biological effectiveness of the 70 MeV proton beam at TRIUMF using Chinese hamster V79 cells and the high-precision cell sorter assay. *Radiat Res* (1996) 146(2):159–70. doi:10.2307/3579588
101. Chaudhary P, Gwynne D, Doria D, Romagnani L, Maiorino C, Padda H, et al. Laser accelerated ultra high dose rate protons induced DNA damage under hypoxic conditions. *Radiother Oncol* (2016) 118 (Suppl. 1):S24–5. doi:10.1016/S0167-8140(16)30049-4
102. Wild-Bode C, Weller M, Rimner A, Dichgans J, Wick W Sublethal irradiation promotes migration and invasiveness of glioma cells: implications for radiotherapy of human glioblastoma. *Cancer Res* (2001) 61(6):2744–50.

103. Chung YL, Jian JJ, Cheng SH, Tsai SY, Chuang VP, Soong T, et al. Sublethal irradiation induces vascular endothelial growth factor and promotes growth of hepatoma cells: implications for radiotherapy of hepatocellular carcinoma. *Clin Cancer Res* (2006) 12(9):2706–15. doi:10.1158/1078-0432.CCR-05-2721
104. Hayflick L, Moorhead PS The serial cultivation of human diploid cell strains. *Exp Cell Res* (1961) 25(3):585–621. doi:10.1016/0014-4827(61)90192-6
105. Pribluda A, Elyada E, Wiener Z, Hamza H, Goldstein RE, Biton M, et al. A Senescence-inflammatory switch from cancer-inhibitory to cancer-promoting mechanism. *Cancer Cell* (2013) 24(2):242–56. doi:10.1016/j.ccr.2013.06.005
106. Demaria M, O'Leary MN, Chang J, Shao L, Liu S, Alimirah F, et al. Cellular senescence promotes adverse effects of chemotherapy and cancer relapse. *Cancer Discov* (2017) 7(2):165–76. doi:10.1158/2159-8290.CD-16-0241
107. Nguyen HQ, To NH, Zadigue P, Kerbrat S, De La Taille A, Le Gouvello S, et al. Ionizing radiation-induced cellular senescence promotes tissue fibrosis after radiotherapy. a review. *Crit Rev Oncol Hematol* (2018) 129:13–26. doi:10.1016/j.critrevonc.2018.06.012
108. Tabasso AFS, Jones DJL, Jones GDD, Macip S Radiotherapy-induced senescence and its effects on responses to treatment. *Clin Oncol (R Coll Radiol)* (2019) 31(5):283–9. doi:10.1016/j.clon.2019.02.003
109. Jeon HY, Kim JK, Ham SW, Oh SY, Kim J, Park JB, et al. Irradiation induces glioblastoma cell senescence and senescence-associated secretory phenotype. *Tumour Biol* (2016) 37(5):5857–67. doi:10.1007/s13277-015-4439-2
110. Suzuki M, Boothman DA Stress-induced premature senescence (SIPS)–influence of SIPS on radiotherapy. *J Radiat Res* (2008) 49(2): 105–12. doi:10.1269/jrr.07081
111. Goligorsky MS, Chen J, Patschan S Stress-induced premature senescence of endothelial cells: a perilous state between recovery and point of no return. *Curr Opin Hematol* (2009) 16(3):215–9. doi:10.1097/MOH.0b013e32832a07bd
112. Manti L, Perozziello FM, Borghesi M, Candiano G, Chaudhary P, Cirrone GAP, et al. The radiobiology of laser-driven particle beams: focus on sub-lethal responses of normal human cells. *J Instrum* (2017) 12 (03):C03084. doi:10.1088/1748-0221/12/03/C03084
113. Weiswald LB, Bellet D, Dangles-Marie V Spherical cancer models in tumor biology. *Neoplasia* (2015) 17(1):1–15. doi:10.1016/j.neo.2014.12.004
114. Estrada MF, Rebelo SP, Davies EJ, Pinto MT, Pereira H, Santo VE, et al. Modelling the tumour microenvironment in long-term microencapsulated 3D co-cultures recapitulates phenotypic features of disease progression. *Biomaterials* (2016) 78:50–61. doi:10.1016/j.biomaterials.2015.11.030
115. Azzarelli R Organoid models of glioblastoma to study brain tumor stem cells. *Front Cell Dev Biol* (2020) 8:220. doi:10.3389/fcell.2020.00220
116. Caragher S, Chalmers AJ, Gomez-Roman N Glioblastoma's next top model: novel culture systems for brain cancer radiotherapy research. *Cancers* (2019) 11(1):44. doi:10.3390/cancers11010044
117. Gomez-Roman N, Stevenson K, Gilmour L, Hamilton G, Chalmers AJ A novel 3D human glioblastoma cell culture system for modeling drug and radiation responses. *Neuro Oncol* (2017) 19(2):229–41. doi:10.1093/neuonc/now164
118. Rosenthal N, Brown S The mouse ascending: perspectives for human-disease models. *Nat Cell Biol* (2007) 9(9):993–9. doi:10.1038/ncb437
119. Kahn J, Tofilon PJ, Camphausen K Preclinical models in radiation oncology. *Radiat Oncol* (2012) 7(1):223. doi:10.1186/1748-717X-7-223
120. Butterworth KT Evolution of the supermodel: progress in modelling radiotherapy response in mice. *Clin Oncol (R Coll Radiol)* (2019) 31(5): 272–82. doi:10.1016/j.clon.2019.02.008
121. Beyreuther E, Brüchner K, Krause M, Schmidt M, Szabo R, Pawelke J An optimized small animal tumour model for experimentation with low energy protons. *PLoS One* (2017) 12(5):e0177428. doi:10.1371/journal.pone.0177428
122. Brüchner K, Beyreuther E, Baumann M, Krause M, Oppelt M, Pawelke J Establishment of a small animal tumour model for *in vivo* studies with low energy laser accelerated particles. *Radiat Oncol* (2014) 9:57. doi:10.1186/1748-717X-9-57
123. Rösch TF, Szabó Z, Haffa D, Bin J, Brunner S, Englbrecht FS, et al. A feasibility study of zebrafish embryo irradiation with laser-accelerated protons. *Rev Sci Instrum* (2020) 91(6):063303. doi:10.1063/5.0008512
124. Szabó ER, Brand M, Hans S, Hideghéty K, Karsch L, Lessmann E, et al. Radiobiological effects and proton RBE determined by wildtype zebrafish embryos. *PLoS One* (2018) 13(11):e0206879. doi:10.1371/journal.pone.0206879
125. Bolton PR, Parodi K, Schreiber J. *Applications of laser-driven particle acceleration*. Boca Raton, FL; London, United Kingdom; New York, NY: CRC Press Taylor and Francis Group (2018).
126. de Kruijff RM FLASH radiotherapy: ultra-high dose rates to spare healthy tissue. *Int J Radiat Biol* (2019) 96(4):419–23. doi:10.1080/09553002.2020.1704912
127. Zhou G Mechanisms underlying FLASH radiotherapy, a novel way to enlarge the differential responses to ionizing radiation between normal and tumor tissues. *Radiat Med Prot* (2020) 1(1):35–40. doi:10.1016/j.radmp.2020.02.002
128. Al-Hallaq H, Cao M, Kruse J, Klein E Cured in a FLASH: reducing normal tissue toxicities using ultra-high-dose rates. *Int J Radiat Oncol Biol Phys* (2019) 104(2):257–60. doi:10.1016/j.ijrobp.2019.01.093
129. Symonds P, Jones GDD FLASH radiotherapy: the next technological advance in radiation therapy?. *Clin Oncol (R Coll Radiol)* (2019) 31(7):405–6. doi:10.1016/j.clon.2019.05.011
130. Yilmaz MT, Hurmuz P, Yazici G FLASH-radiotherapy: a new perspective in immunotherapy era?. *Radiother Oncol* (2020) 145:137. doi:10.1016/j.radonc.2019.12.015
131. Favaudon V, Caplier L, Monceau V, Pouzoulet F, Sayarath M, Fouillade C, et al. Ultrahigh dose-rate FLASH irradiation increases the differential response between normal and tumor tissue in mice. *Sci Transl Med* (2014) 6(245):245ra93. doi:10.1126/scitranslmed.3008973

Conflict of Interest: The authors declare that the research was conducted in the absence of any commercial or financial relationships that could be construed as a potential conflict of interest.

frontiers in Physics

MINI REVIEW
published: 27 April 2021
doi: 10.3389/fphy.2021.639290

Continuing Nuclear Data Research for Production of Accelerator-Based Novel Radionuclides for Medical Use: A Mini-Review

Syed M. Qaim[1]*, *Mazhar Hussain*[2†], *Ingo Spahn*[1†] and *Bernd Neumaier*[1†]

[1]Institut für Neurowissenschaften und Medizin, INM-5: Nuklearchemie, Forschungszentrum Jülich, Jülich, Germany, [2]Department of Physics, Government College University Lahore, Lahore, Pakistan

Nuclear data are important for production and medical application of a radionuclide. This brief review concentrates on nuclear reaction cross-section data. The availability of standardized nuclear data for accelerator-based production of medical radionuclides is outlined. Some new directions in radionuclide applications, for example, theranostic approach, bimodal imaging, and radionuclide targeted therapy, are considered and the status of relevant nuclear data is discussed. The current trends in nuclear data research using accelerators are elaborated. The increasing significance of intermediate energy accelerators in production of therapeutic radionuclides is emphasized.

Keywords: accelerator-produced radionuclides, decay properties, reaction cross sections, positron emitters, therapeutic radionuclides, theranostic approach, radionuclide targeted therapy

OPEN ACCESS

Edited by:
Zhen Cheng,
Stanford University, United States

Reviewed by:
Ferid Haddad,
Université de Nantes, France
Gaia Pupillo,
Legnaro National Laboratories (INFN), Italy

***Correspondence:**
Syed M. Qaim
s.m.qaim@fz-juelich.de

[†]These authors have contributed equally to this work

Specialty section:
This article was submitted to Medical Physics and Imaging, a section of the journal Frontiers in Physics

Received: *08 December 2020*
Accepted: *08 January 2021*
Published: *27 April 2021*

Citation:
Qaim SM, Hussain M, Spahn I and Neumaier B (2021) Continuing Nuclear Data Research for Production of Accelerator-Based Novel Radionuclides for Medical Use: A Mini-Review. Front. Phys. 9:639290. doi: 10.3389/fphy.2021.639290

INTRODUCTION

Radionuclides find application in medicine, both in diagnosis and internal radiotherapy. Diagnostic investigations are carried out using short-lived radionuclides which emit either a single or major γ-ray of energy between 100 and 250 keV or a positron, the former in single photon emission computed tomography (SPECT) and latter in positron emission tomography (PET). In internal radionuclide therapy, on the other hand, radionuclides emitting low-range highly ionizing radiation, that is, α- or β^--particles, conversion, and/or Auger electrons are used. A detailed knowledge of decay properties of a radionuclide is, therefore, essential to decide about its application. Furthermore, the radionuclidic purity and specific activity (defined as the radioactivity per unit mass of the material) play an important role in its medical application. Radionuclidic purity reduces the radiation dose due to impurities and higher specific activity ensures that the biological equilibrium is not disturbed and imaging is carried out at real molecular level. Those two parameters are controlled by knowledge of nuclear reaction cross sections, especially in production of radionuclides *via* charged particle-induced reactions [1, 2]. The level and type of radionuclidic impurity varies with the chosen reaction route and the projectile energy range effective in the target.

The positron emitters are generally produced at small-sized cyclotrons, the number of which worldwide is now increasing to about 1200 [3]. Attempts are presently also underway to produce several therapeutic radionuclides at cyclotrons/accelerators, using either the charged particle beam or secondary radiation, that is, neutrons and photons, generated at accelerators (for recent reviews, cf [4, 5]). Nuclear data play a continuing role in the development of radionuclides for applications. In this brief review, the availability of standardized data for production of medical radionuclides using

accelerators is outlined, some new directions in radionuclide applications are discussed, and the current trends in nuclear data research are described.

AVAILABILITY AND STATUS OF STANDARDIZED DATA

Experimental data are compiled in the international file EXFOR, managed by the IAEA. Radionuclides to be used for a suitable modality of the medical procedure demand well-established data. The decay data of medical radionuclides are compiled and constantly updated in the MIRD file of the Society of Nuclear Medicine (SNM) of United States. Decay data of all radionuclides are available in the Evaluated Nuclear Structure and Decay Data File (ENSDF) and neutron-induced reaction cross-section data in the Evaluated Nuclear Data File (ENDF/B-VIII.0). In contrast, the evaluation methodology for charged particle-induced reaction cross sections started developing only about 2 decades ago [2] under the umbrella of IAEA in the form of coordinated research projects (CRPs), with major contributions from Jülich, Debrecen, Brussels, and Obninsk. To date three CRPs have been completed. The first two were related to radionuclides commonly used in diagnosis (IAEA-TECDOC-1211, 2001) and internal therapy (IAEA-Technical Report-473, 2011). In the third CRP, some updates were done but also the production data of some novel radionuclides were standardized [6–8]. The initial work was rather empirical. Later, however, strong application of nuclear models was built in. All modern calculation codes are based on the statistical model, taking into account angular momentum, nuclear structure, and level density effects, and also incorporate pre-compound emission contributions. Each code reproduces the experimental data to a certain degree of success. The nuclear model calculations performed using the codes EMPIRE 3.2 and TALYS 1.95 are generally very successful in reproducing the experimental data up to about 50 MeV, if only a few nucleons are emitted. Deviations are observed when emission of many nucleons and complex particles is involved. The adjustable parameters of the nuclear model codes are fitted within their prescribed limits to reproduce the experimental data in the process of validation and evaluation. All evaluated data are available on the website of the IAEA [9]. Using theory-aided evaluation, some work has been also carried out outside the abovementioned CRPs (see for example [10–14]). The evaluation efforts have provided reliable standardized data for accelerator-based radionuclides routinely used in patient care (PET/SPECT imaging and internal radiotherapy), produced either directly or obtained through positron-emitting generator systems ^{68}Ge/^{68}Ga and ^{82}Sr/^{82}Rb. Furthermore, data for a few novel and less commonly used radionuclides, for example, ^{64}Cu, ^{89}Zr, ^{124}I, ^{103}Pd, and ^{211}At, have also been standardized. Standardized data are also available for the ^{100}Mo(p,2n)^{99m}Tc reaction [10]. This is a very promising route for accelerator-based production of the most commonly used SPECT radionuclide ^{99m}Tc, which is generally available *via* the fission-produced ^{99}Mo/^{99m}Tc generator system. However, further extensive work is needed to settle the question of impurities in cyclotron production of this radionuclide. Similarly, for emerging radionuclides more experimental and evaluation work is necessary (see below).

NEW DIRECTIONS IN RADIONUCLIDE APPLICATIONS AND RELEVANT NUCLEAR DATA

For investigating slow metabolic processes, about 25 longer lived metallic positron emitters, termed as "nonstandard" positron emitters, have been developed [15]. Similarly, several metallic radionuclides emitting low-energy corpuscular radiation are in development for internal therapy (cf [1, 16]). In parallel, considerable chemical research has led to enhanced possibilities of labeling monoclonal antibodies (mAbs) and other versatile organo-metallic chemical complexes with radionuclides for targeted therapy (for reviews cf [17, 18]). Based on those advances, applications of radionuclides are enhancing today in the following directions:

i) Radiolabeled monoclonal antibodies
ii) Peptide receptor radiotherapy
iii) Small molecules
iv) Theranostic approach
v) Bimodal imaging
vi) Radioactive nanoparticles

Radiolabeled monoclonal antibodies: Monoclonal antibodies (mAbs) labeled with radionuclides are used in diagnosis and therapy of tumors. The application of mAbs labeled with positron emitters is called immunoPET (cf. [19]). To date, the most widely used radionuclide for this purpose is ^{89}Zr, but also ^{64}Cu has found application in preclinical studies. For immunotherapy, ^{90}Y, ^{111}In, and ^{225}Ac are potential candidates, for example, [^{90}Y]ibritumomab tiuxetan (Zevalin).

Peptide receptor radiotherapy (PRRT) makes use of peptide-based radiopharmaceuticals which can target different receptor systems like somatostatin receptors (SSTR), integrins, chemokine receptors, or the prostate-specific membrane antigen (PSMA). The most common approach uses octreotide derivatives labeled with ^{90}Y or ^{177}Lu to treat neuroendocrine tumors effectively, that is, [^{90}Y]Y-DOTATOC and [^{177}Lu]Lu-DOTATATE. Also [^{225}Ac]Ac-DOTATATE is under study. A further important molecular target is the chemokine receptor-4 CXCR-4. This can be targeted with Pentixafor and studies with ^{177}Lu-labeled Pentixafor in cancer patients are underway.

Small molecules: Besides radioiodinated pharmaceuticals, different radiometal-labeled small molecules have been developed to treat oncological diseases, for example, PSMA-617, a urea-based derivative with excellent affinity to PSMA overexpressing prostate cancer tumor cells. After binding to the target, the molecule is internalized and facilitates eradication of the tumor cells. Therefore [^{225}Ac]Ac-PSMA-617 and [^{177}Lu]Lu-PSMA-617 are under different clinical trials.

Theranostic approach entails a combination of diagnosis (molecular imaging) and internal radionuclide therapy (molecular targeted treatment). It makes use of two

radionuclides of the same element in the same chemical form, a positron emitter which allows quantitative diagnosis *via* PET and a therapeutic nuclide. Originally, the pair ^{86}Y/^{90}Y was developed (cf. [20]), but today several other theranostic pairs are also known, for example, ^{44g}Sc/^{47}Sc, ^{64}Cu/^{67}Cu, ^{124}I/^{131}I, and ^{152}Tb/^{161}Tb (for review cf [4]). Two other concepts also exist: 1) use of an analog pair of trivalent metallic radionuclides, that is, a positron emitter (^{44g}Sc or ^{68}Ga) and a β^-- (^{177}Lu) or an α-emitter (^{225}Ac). 2) use of a single radionuclide, emitting a β^-- or α-particle as well as a low-energy γ-ray, which could be utilized for SPECT measurement to deliver data for dosimetry. Examples are ^{47}Sc, ^{67}Cu, ^{177}Lu, and ^{186}Re for β^--therapy and ^{211}At, ^{223}Ra, ^{225}Ac, ^{213}Bi, ^{212}Pb/^{212}Bi generator, and ^{149}Tb for targeted alpha therapy (TAT). Several other alpha-particle emitters are also under consideration (cf [21]).

Bimodal imaging involves a combination of two organ-imaging techniques, for example, PET and magnetic resonance imaging (MRI) (for review cf [22]). From the viewpoint of PET, the major focus is on the elements Mn and Gd which are important contrast agents in MRI. The positron-emitting radionuclide ^{52g}Mn is of great current interest (cf [23, 24]). For Gd, no positron-emitting radionuclide is available and the use of ^{68}Ga-labeled Gd(III) complexes has been proposed.

Radioactive nanoparticles in medicine constitute a long-term perspective, provided the stability and toxicity problems are overcome. In animal and preclinical studies, considerable success has been reported (for review cf [25, 26]) but application in humans has yet to be demonstrated. The radionuclides ^{64}Cu and ^{68}Ga are widely used positron emitters for surface labeling of nanoparticles. The longer lived ^{52g}Mn and ^{89}Zr are also of great interest. For therapy, ^{186}Re and ^{225}Ac are considered to be very useful.

In the abovementioned new applications seven positron emitters, namely ^{44g}Sc ($T_{1/2}$ = 3.9 h), ^{52g}Mn ($T_{1/2}$ = 5.6 d), ^{64}Cu ($T_{1/2}$ = 12.7 h), ^{68}Ga ($T_{1/2}$ = 1.13 h), ^{86}Y ($T_{1/2}$ = 14.7 h), ^{89}Zr ($T_{1/2}$ = 78.4 h), and ^{124}I ($T_{1/2}$ = 4.18 d) are in great demand. Similarly, eight therapeutic radionuclides, namely ^{47}Sc ($T_{1/2}$ = 3.35 d), ^{67}Cu ($T_{1/2}$ = 2.58 d), ^{90}Y ($T_{1/2}$ = 2.7 d), ^{117m}Sn ($T_{1/2}$ = 13.6 d), ^{177}Lu ($T_{1/2}$ = 6.65 d), ^{186}Re ($T_{1/2}$ = 3.78 d), ^{223}Ra ($T_{1/2}$ = 11.4 d), and ^{225}Ac ($T_{1/2}$ = 10.0 d) are of great interest. For each radionuclide, the stringent criteria of purity and specific activity must be met.

The production of the listed positron emitters is generally carried out *via* the low-energy (p,n) reaction on a highly enriched solid target isotope. In the case of ^{68}Ga, the generator route is more commonly used. The status of the available cross-section data of the abovementioned positron emitters was reviewed and found to be generally good (cf. [1, 15]), except for ^{86}Y where considerable discrepancy existed.

In contrast to positron emitters, the therapeutic radionuclides ^{90}Y and ^{177}Lu are routinely produced using nuclear reactors. For the six other therapeutic radionuclides, it was shown (cf. [8, 16]) that the reactor production methods are not sufficient. For ^{47}Sc and ^{67}Cu, the required radionuclidic and chemical purity is not achieved and for ^{186}Re and ^{117m}Sn, the specific activity is too low. The supply of ^{225}Ac and ^{223}Ra *via* reactor route is limited. Efforts are therefore underway to produce those radionuclides at accelerators, ^{186}Re at a small cyclotron and others at intermediate energy accelerators.

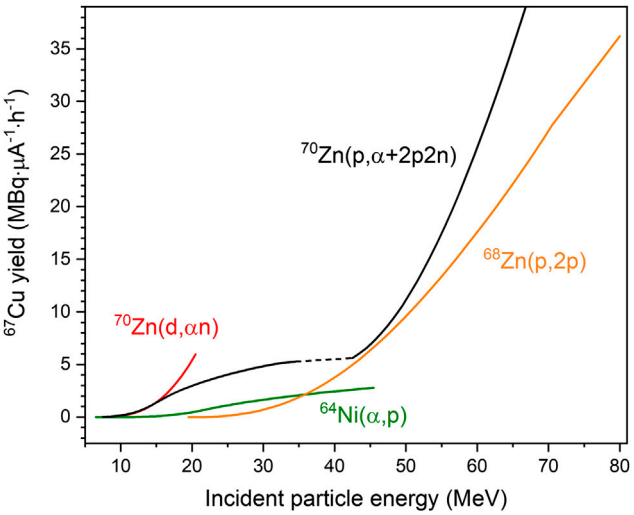

FIGURE 1 | Integral yield of ^{67}Cu, calculated from the excitation function of each reaction for an irradiation time of 1 h, shown as a function of incident particle energy. The dashed part of the curve for the ^{70}Zn(p,x)^{67}Cu process is an extrapolation because no data exist.

CURRENT NUCLEAR DATA ACTIVITIES

Nuclear modeling and theory-aided evaluations are continuing. The emphasis is, however, on new experimental studies; some of the most recent examples are given below.

Low-energy charged particle beam: Low-energy medical cyclotrons ($E_P \leq 18$ MeV; $E_d \leq 9$ MeV) are mainly utilized for the production of the standard positron emitters (^{11}C, ^{13}N, ^{15}O, and ^{18}F) using gas and liquid targets. Since solid targetry is not available, a new methodology for the production of some nonstandard positron emitters *via* the (p,n) reaction at those cyclotrons has emerged. It makes use of "solution targets", especially for ^{44g}Sc, ^{64}Cu, ^{68}Ga, ^{86}Y, ^{89}Zr, and ^{94m}Tc (for review cf. [27]). The product yield is low but sufficient for local use. This approach has, however, put an extra demand on chemical purification of the product as well as on the accuracy of the cross-section data near the threshold of the reaction (cf. [28, 29]). To improve the cross-section data of the ^{86}Sr(p,n)^{86}Y reaction, an accurate measurement was very recently completed [30]. The new results agree with the TALYS calculation and the discrepancy has been solved.

Intermediate energy charged particle beam: In the energy range up to 30 MeV, several routinely used radionuclides are conveniently produced, especially the SPECT radionuclides ^{67}Ga, ^{111}In, ^{123}I, and ^{201}Tl. At a higher proton energy up to 100 MeV, several radionuclides could be produced *via* (p,x) reactions, where x stands for multiparticle emission. Such accelerator facilities are now available at several places, for example Nantes (France), Legnaro (Italy), Moscow (Russia), Cape

Town (South Africa), Brookhaven (United States), and Los Alamos (United States). A recent example is the measurement of the excitation function of the ^{75}As (p,4n)^{72}Se reaction [31] for the production of ^{72}Se which is useful for preparing the β^+-emitting generator system ^{72}Se/^{72}As.

The intermediate energy range, however, is now being utilized more extensively for the production of therapeutic radionuclides. A recent cross-section measurement on the reaction ^{70}Zn(p,α+2p2n)^{67}Cu [32] is very interesting. Although the experimental data are not reproduced by the model calculation (due to complexity of reaction and energy range), they are of great technical value. In **Figure 1** the yields of ^{67}Cu are shown. They were calculated from the excitation functions of relevant charged-particle–induced reactions using the standard activation equation [1]. It is an updated version of the diagram given earlier [16]. In order to minimize the impurities of ^{64}Cu (radioactive) and ^{65}Cu (stable, decreasing the specific activity of ^{67}Cu), the energy range E_p = 80 → 30 MeV was found to be very suitable for the production of ^{67}Cu *via* the ^{68}Zn(p,2p) process. From the new results, it is concluded that protons of energy up to about 80 MeV are very suitable for the production of ^{67}Cu not only when isotopically enriched ^{68}Zn is used as target material [16, 33] but also if enriched ^{70}Zn would be the target, provided good radionuclidic purity is achieved. For production of the β^--emitter ^{47}Sc (for review see [4]), neither the intermediate energy reaction ^{48}Ti(p,2p)^{47}Sc investigated earlier nor the ^{51}V(p,αp)^{47}Sc process studied recently [34] appears to be successful because of the high level of the radionuclidic impurity ^{46}Sc. With regard to the conversion electron emitter ^{117m}Sn, the production route ^{116}Cd(α,3n)^{117m}Sn was established [11]. Yet, a new measurement suggests that the nuclear process ^{nat}Sb(p,xn)^{117m}Sn over the proton energy range of 30–90 MeV could also be potentially useful [35]. Regarding the α-particle emitters ^{225}Ac and ^{223}Ra, the present emphasis is on their production through proton-induced reactions on ^{232}Th, either directly or *via* the indirect routes $^{232}\mathrm{Th}\,(p,x)^{225}\mathrm{Ra}\xrightarrow{\beta^-}{}^{225}\mathrm{Ac}$ and $^{232}\mathrm{Th}\,(p,x)^{227}\mathrm{Th}\xrightarrow{\alpha^-}{}^{225}\mathrm{Ac}$, respectively, over the energy range up to 200 MeV. Several cross-section measurements exist (for review cf [8]) and studies on radionuclidic impurities, for example, about 0.3% ^{227}Ac in ^{225}Ac, as well as technical development are in progress. Besides its direct use, the radionuclide ^{225}Ac also serves as the parent of the α-emitter ^{213}Bi.

It should be mentioned that besides protons, intermediate energy deuterons and alpha-particles are also potentially useful for production of a few special radionuclides, for example, ^{103}Pd and ^{186}Re using deuterons and ^{211}At using alpha-particles. Furthermore, in recent years it has been demonstrated that the high-spin isomers of a few radionuclides, for example, ^{117m}Sn and ^{193m}Pt, can be advantageously produced using alpha-particles [36]. They are useful in therapy because they emit low-energy conversion and Auger electrons. In general, however, the use of protons is preferred due to their easier availability and the resulting higher yields of the products.

High-energy charged-particle beam: The spallation process with high-energy protons (E_p > 500 MeV) combined with on-line mass separation was utilized at CERN in cooperation with the Paul Scherrer Institute (PSI) to produce some exotic radionuclides in the region of rare earths, especially ^{149}Tb ($T_{1/2}$ = 4.1 h) and ^{152}Tb ($T_{1/2}$ = 17.5 h). The former is a unique low-energy α-particle emitter suited for TAT. The latter is a theranostic PET partner. A new measurement gives cross sections for the formation of several terbium radioisotopes in the spallation of tantalum as a function of proton energy [37]. For more general use of the two radionuclides, however, development of alternative production methods, preferably using intermediate energy protons, are called for. Preliminary cross-section measurements on the reactions ^{155}Gd(p,4n)^{152}Tb and ^{152}Gd(p,4n)^{149}Tb are promising [38].

Use of photons and fast neutrons: The use of electron linear accelerator (LINAC) to deliver high-energy photons for the production of the therapeutic radionuclides ^{47}Sc and ^{67}Cu *via* the ^{48}Ti (γ,p)^{47}Sc and ^{68}Zn (γ,p)^{67}Cu reactions, respectively, is presently under investigation. The excitation functions are known (cf. IAEA-TECDOC-1178, 2000) but further improvement in the data is needed. The production for preclinical tests has been reported [39, 40]. In practice, however, GBq amounts of ^{67}Cu have been produced whereas the methodology for ^{47}Sc production is still developing. Some on-going nuclear data work deals with determination of spectrum-averaged cross sections and production yields [41, 42]. The production of ^{225}Ac *via* the $^{226}\mathrm{Ra}\,(\gamma,n)^{225}\mathrm{Ra}\xrightarrow{\beta^-}{}^{225}\mathrm{Ac}$ process is also being investigated. The estimated cross section is relatively high but the use of the radioactive target is a deterrent.

The use of accelerator-generated fast neutrons is also under investigation. In particular, a 30 or 40 MeVd(Be) or d(C) breakup neutron source is considered to be suitable for the production of a few radionuclides *via* the (n,p) or (n,np) reaction [43]. The estimated integral cross sections amount to a few mb [5]. The spallation neutrons also appear to be interesting for the formation of a few radionuclides [44]. However, extensive further nuclear data work is called for.

CONCLUDING REMARKS

Nuclear data play an important role in the production and medical application of accelerator-based radionuclides. The data for routine production of radionuclides for patient care have been standardized. For development of novel radionuclides, however, continuing data research is needed. The present thrust in medical application of radionuclides is directed toward PET studies using metallic positron emitters as well as toward targeted radionuclide therapy, preferably applying the theranostic approach. With tremendous developments in antibody labeling and organo-metallic complex formation chemistry, a big impetus has come to the field of theranostics. This is leading to an enhanced interest in accelerator-based production of radionuclides. The nonstandard positron emitters are produced at small-sized cyclotrons and now development of

production methodologies of many therapeutic radionuclides is shifting from nuclear reactors to intermediate energy accelerators. Another strategy is to utilize hard photons from powerful LINACs or fast neutrons from intermediate energy accelerators. With enhancing interest in versatile accelerators to produce novel medical radionuclides, the need of relevant nuclear data research is continuing.

AUTHOR CONTRIBUTIONS

SQ developed the concept. MH elaborated the section on standardization of data. IS reviewed experimental data and calculated radionuclide yields. BN advised on new directions in medical applications. All authors contributed to the writing of the article and approved the submitted version.

REFERENCES

1. Qaim SM Nuclear data for production and medical application of radionuclides: present status and future needs. *Nucl Med Biol* (2017) 44: 31–49. doi:10.1016/j.nucmedbio.2016.08.016
2. Qaim SM *Medical radionuclide production: science and technology*. Berlin/ Boston: Walter de Gruyter (2019) 978-3-11-060156-5..
3. Synowiecki MA, Perk LR, and Nijsen JFW Production of novel diagnostic radionuclides in small medical cyclotrons. *EJNMMI Radiopharmacy Chem* (2018) 3(3):1–25. doi:10.1186/s41181-018-0038-z
4. Qaim SM, Scholten B, and Neumaier B New developments in the production of theranostic pairs of radionuclides. *J Radioanal Nucl Chem* (2018) 318: 1493–509. doi:10.1007/s10967-018-6238-x
5. Qaim SM Theranostic radionuclides: recent advances in production methodologies. *J Radioanal Nucl Chem* (2019) 322:1257–66. doi:10.1007/ s10967-019-06797-y
6. Tárkányi FT, Ignatyuk AV, Hermanne A, Capote R, Carlson BV, Engle JW, et al. Recommended nuclear data for medical radioisotope production: diagnostic gamma emitters. *J Radioanal Nucl Chem* (2019) 319:487–531. doi:10.1007/s10967-018-6142-4
7. Tárkányi FT, Ignatyuk AV, Hermanne A, Capote R, Carlson BV, Engle JW, et al. Recommended nuclear data for medical radioisotope production: diagnostic positron emitters. *J Radioanal Nucl Chem* (2019) 319:533–666. doi:10.1007/s10967-018-6380-5
8. Engle JW, Ignatyuk AV, Capote R, Carlson BV, Hermanne A, Kellett MA, et al. Recommended nuclear data for the production of selected therapeutic radionuclides. *Nucl Data Sheets* (2019) 155:56–74. doi:10.1016/j.nds.2019.01.003
9. IAEA. *Nuclear data section* (2020) Available from: https://www-nds.iaea.org/relnsd/vcharthtml/MEDVChart.html (Accessed December 1, 2020).
10. Qaim SM, Sudár S, Scholten B, Koning AJ, and Coenen HH Evaluation of excitation functions of ^{100}Mo(p,d+pn)^{99}Mo and ^{100}Mo (p,2n)^{99m}Tc reactions: estimation of long-lived Tc-impurity and its implication on the specific activity of cyclotron-produced 99mTc. *Appl Radiat Isot* (2014) 85:101–13. doi:10.1016/j.apradiso.2013.10.004
11. Aslam MN, Zubia K, and Qaim SM Nuclear model analysis of excitation functions of α-particle induced reactions on in and Cd up to 60 MeV with relevance to the production of high specific activity ^{117m} Sn. *Appl Radiat Isot* (2018) 132:181–8. doi:10.1016/j.apradiso.2017.12.002
12. Ali SKI, Khandaker MU, and Kassim HA Evaluation of production cross-sections for ^{186} Re theranostic radionuclide via charged-particle induced reactions on tungsten. *Appl Radiat Isot* (2018) 135:239–50. doi:10.1016/j.apradiso.2018.01.035
13. Ali W, Tashfeen M, and Hussain M Evaluation of nuclear reaction cross sections via proton induced reactions on ^{55}Mn for the production of ^{52}Fe: a potential candidate for theranostic applications. *Appl Radiat Isot* (2019) 144: 124–9. doi:10.1016/j.apradiso.2018.11.016
14. Amjed N, Wajid AM, Ahmad N, Ishaq M, Aslam MN, Hussain M, et al. Evaluation of nuclear reaction cross sections for optimization of production of the important non-standard positron emitting radionuclide ^{89}Zr using proton and deuteron induced reactions on ^{89}Y target. *Appl Radiat Isot* (2020) 165: 109338. doi:10.1016/j.apradiso.2020.109338
15. Qaim SM, Scholten B, Spahn I, and Neumaier B Positron-emitting radionuclides for applications, with special emphasis on their production methodologies for medical use. *Radiochim Acta* (2019) 107:1011–26. doi:10.1515/ract-2019-3154
16. Qaim SM, and Spahn I Development of novel radionuclides for medical applications. *J Label Compd Radiopharm* (2018) 61:126–40. doi:10.1002/jlcr.3578
17. Aluicio-Sarduy E, Ellison PA, Barnhart TE, Cai W, Nickles RJ, and Engle JW PET radiometals for antibody labeling. *J Label Compd Radiopharm* (2018) 61: 636–51. doi:10.1002/jlcr.3607
18. Kostelnik TI, and Orvig C Radioactive main group and rare earth metals for imaging and therapy. *Chem Rev* (2019) 119:902–56. doi:10.1021/acs.chemrev.8b00294
19. Wei W, Rosenkrans ZT, Liu J, Huang G, Luo Q-Y, and Cai W ImmunoPET: concept, design, and applications. *Chem Rev* (2020) 120(8):3787–851. doi:10.1021/acs.chemrev.9b00738
20. Rösch F, Herzog H, and Qaim S The beginning and development of the theranostic approach in nuclear medicine, as exemplified by the radionuclide pair ^{86}Y and ^{90}Y. *Pharmaceuticals* (2017) 10:56. doi:10.3390/ph10020056
21. Ferrier MG, Radchenko V, and Wilbur DS Radiochemical aspects of alpha emitting radionuclides for medical application. *Radiochim Acta* (2019) 107: 1065–85. doi:10.1515/ract-2019-0005
22. Picchio M, and Pampaloni MH Current status and future perspectives of PET/MRI hybrid imaging. *Clin Transl Imaging* (2017) 5:79–81. doi:10.1007/s40336-016-0215-6
23. Lewis CM, Graves SA, Hernandez R, Valdovinos HF, BarnhartCai TEWB, Cai W, et al. ^{52}Mn production for PET/MRI tracking of human stem cells expressing divalent metal transporter 1 (DMT1). *Theranostics* (2015) 5: 227–39. doi:10.7150/thno.10185
24. Brandt MR, Vanasschen C, Ermert J, Coenen HH, and Neumaier B $^{52g/55}$Mn-Labelled CDTA-based trimeric complexes as novel bimodal PET/MR probes with high relaxivity. *Dalton Trans* (2019) 48:3003–8. doi:10.1039/c8dt04996c
25. Farzin L, Sheibani S, Moassesi ME, and Shamsipur M An overview of nanoscale radionuclides and radiolabeled nanomaterials commonly used for nuclear molecular imaging and therapeutic functions. *J Biomed Mater Res* (2019) 107:251–85. doi:10.1002/jbm.a.36550
26. Ge J, Zhang Q, Zeng J, Gu Z, and Gao M Radiolabeling nanomaterials for multimodality imaging: new insights into nuclear medicine and cancer diagnosis. *Biomaterials* (2020) 228:119553. doi:10.1016/j.biomaterials.2019.119553
27. Pandey MK, and DeGrado TR Cyclotron production of PET radiometals in liquid targets: aspects and prospects. *Curr Radiopharm* (2020) 13:1–15. doi:10.2174/1874471013999200820165734
28. Uddin MS, Chakraborty AK, Spellerberg S, Shariff MA, Das S, Rashid MA, et al. Experimental determination of proton induced reaction cross sections on ^{nat}Ni near threshold energy. *Radiochim Acta* (2016) 104:305–14. doi:10.1515/ract-2015-2527
29. Carzaniga TS, Auger M, Braccini S, Bunka M, Ereditato A, Nesteruk KP, et al. Measurement of ^{43}Sc and ^{44}Sc production cross-section with an 18 MeV medical PET cyclotron. *Appl Radiat Isot* (2017) 129:96–102. doi:10.1016/j.apradiso.2017.08.013
30. Uddin MS, Scholten B, Basunia MS, Sudár S, Spellerberg S, Voyles AS, et al. Accurate determination of production data of the non-standard positron emitter ^{86}Y via the ^{86}Sr(p,n)-reaction. *Radiochim Acta* (2020) 108:747–56.
31. DeGraffenreid AJ, Medvedev DG, Phelps TE, Gott MD, Smith SV, Jurisson SS, et al. Cross-section measurements and production of ^{72}Se with medium to high energy protons using arsenic containing targets. *Radiochim Acta* (2019) 107: 279–87. doi:10.1515/ract-2018-2931
32. Pupillo G, Mou L, Martini P, Pasquali M, Boschi A, Cicoria G, et al. Production of ^{67}Cu by enriched ^{70}Zn targets: first measurements of formation cross sections of ^{67}Cu, ^{64}Cu, ^{67}Ga, ^{66}Ga, ^{69}mZn and ^{65}Zn in interactions of ^{70}Zn

with protons above 45 MeV. *Radiochim Acta* (2020) 108:593–602. doi:10.1515/ract-2019-3199

33. Pupillo G, Sounalet T, Michel N, Mou L, Esposito J, and Haddad F New production cross sections for the theranostic radionuclide ^{67}Cu. *Nucl Instr Methods Phys Res Section B: Beam Interactions Mater Atoms* (2018) 415:41–7. doi:10.1016/j.nimb.2017.10.022
34. Pupillo G, Mou L, Boschi A, Calzaferri S, Canton L, Cisternino S, et al. Production of ^{47}Sc with natural vanadium targets: results of the PASTA project. *J Radioanal Nucl Chem* (2019) 322:1711–8. doi:10.1007/s10967-019-06844-8
35. Ermolaev SV, Zhuikov BL, Kokhanyuk VM, Matushko VL, and Srivastava SC Cross sections and production yields of ^{117m}Sn and other radionuclides generated in natural and enriched antimony with protons up to 145 MeV. *Radiochim Acta* (2020) 108:327–51. doi:10.1515/ract-2019-3158
36. Qaim SM, Spahn I, Scholten B, and Neumaier B Uses of alpha particles, especially in nuclear reaction studies and medical radionuclide production. *Radiochim Acta* (2016) 104:601–24. doi:10.1515/ract-2015-2566
37. Verhoeven H, Cocolios TE, Dockx K, Farooq-Smith GJ, Felden O, Formento-Cavaier R, et al. Measurement of spallation cross sections for the production of terbium radioisotopes for medical applications from tantalum targets. *Nucl Instr Methods Phys Res Section B: Beam Interactions Mater Atoms* (2020) 463: 327–9. doi:10.1016/j.nimb.2019.04.071
38. Steyn GF, Vermeulen C, Szelecsényi F, Kovács Z, Hohn A, van der Meulen NP, et al. Cross sections of proton-induced reactions on 152Gd, 155Gd and 159Tb with emphasis on the production of selected Tb radionuclides. *Nucl Instr Methods Phys Res Section B: Beam Interactions Mater Atoms* (2014) 319: 128–40. doi:10.1016/j.nimb.2013.11.013
39. Starovoitova VN, ColeCole PLPL, and Grimm TL Accelerator-based photoproduction of promising beta-emitters ^{67}Cu and ^{47}Sc. *J Radioanal Nucl Chem* (2015) 305:127–32. doi:10.1007/s10967-015-4039-z
40. Rotsch DA, Brown MA, Nolen JA, Brossard T, Henning WF, Chemerisov SD, et al. Electron linear accelerator production and purification of scandium-47 from titanium dioxide targets. *Appl Radiat Isot* (2018) 131:77–82. doi:10.1016/j.apradiso.2017.11.007
41. Aliev RA, Belyshev SS, Kuznetsov AA, Dzhilavyan LZ, Khankin VV, Aleshin GY, et al. Photonuclear production and radiochemical separation of medically relevant radionuclides: ^{67}Cu. *J Radioanal Nucl Chem* (2019) 321:125–32. doi:10.1007/s10967-019-06576-9
42. Inagaki M, Sekimoto S, Tanaka W, Tadokoro T, Ueno Y, Kani Y, et al. Production of ^{47}Sc, ^{67}Cu, ^{68}Ga, ^{105}Rh, ^{177}Lu, and ^{188}Re using electron linear accelerator. *J Radioanal Nucl Chem* (2019) 322:1703–9. doi:10.1007/s10967-019-06904-z
43. Sugo Y, Hashimoto K, Kawabata M, Saeki H, Sato S, Tsukada K, et al. Application of ^{67}Cu produced by ^{68}Zn(n,n′p+d)^{67}Cu to biodistribution study in tumor-bearing mice. *J Phys Soc Jpn* (2017) 86:023201. doi:10.7566/jpsj.86.023201
44. DeLorme K, Engle JW, Kowash B, Nortier FM, Birnbaum E, McHale S, et al. Production potential of ^{47}Sc using spallation neutrons at the Los Alamos isotope production facility. *J Nucl Med* (2014) 55(Suppl. 1):1468.

Conflict of Interest: The authors declare that the research was conducted in the absence of any commercial or financial relationships that could be construed as a potential conflict of interest.

Advantages of publishing in Frontiers

OPEN ACCESS
Articles are free to read for greatest visibility and readership

FAST PUBLICATION
Around 90 days from submission to decision

HIGH QUALITY PEER-REVIEW
Rigorous, collaborative, and constructive peer-review

TRANSPARENT PEER-REVIEW
Editors and reviewers acknowledged by name on published articles

Frontiers
Avenue du Tribunal-Fédéral 34
1005 Lausanne | Switzerland

Visit us: www.frontiersin.org
Contact us: frontiersin.org/about/contact

REPRODUCIBILITY OF RESEARCH
Support open data and methods to enhance research reproducibility

DIGITAL PUBLISHING
Articles designed for optimal readership across devices

FOLLOW US
@frontiersin

IMPACT METRICS
Advanced article metrics track visibility across digital media

EXTENSIVE PROMOTION
Marketing and promotion of impactful research

LOOP RESEARCH NETWORK
Our network increases your article's readership